2017 3rd International Conference on Electrical Information and Communication Technology (EICT), 7-9 December 2017, Khulna, Bangladesh

# Convolutional Recurrent Neural Network for Question Answering

M.M. Arefin Zaman
Department of Computer Science & Engineering
Rajshahi University of Engineering & Technology
Rajshahi-6204, Bangladesh
Email: arefinzamansifat@gmail.com

Sadia Zaman Mishu
Department of Computer Science & Engineering
Rajshahi University of Engineering & Technology
Rajshahi-6204, Bangladesh
Email: sadia.cse09@gmail.com

***Abstract*—Question answering has become a very important task for natural language understanding as most natural language processing problems can be posed as a question answering problem. Recurrent neural network (RNN) is a standard baseline model for various sequence prediction tasks including question answering. Recurrent networks can represent global information for a long period of time but they do not preserve local information very well. To address this problem we propose a model which is a combination of recurrent and convolutional network that can be trained end to end using backpropagation. Our experiments on bAbI dataset demonstrate that this model can achieve significant improvement over RNN model for question answering task.**

***Keywords*—Deep learning, convolutional neural network, recurrent neural network, natural language processing, question answering**

## I. Introduction

Question Answering (QA) is a complex and difficult natural language processing task as it requires understanding context and reasoning through a long sequence of sentences. A QA system is given a story and a question. It is supposed to find the correct answer by going through the relevant facts from the story. Various tasks in Natural Language Processing (NLP) can be presented as a question answering problem [1]. Moreover, QA can be used to develop dialogue systems and chatbots [2]. Therefore, improving QA will enable the ubiquitous personal assistants (e.g. siri,cortana) to become more robust and helpful.

QA has been studied in the field of information retrieval for a long period of time. But the datasets used to evaluate QA systems were very small. Traditional approaches typically involved rule-based algorithms or linear classifiers over hand-engineered features. With the advent of more expressive models like deep neural networks, larger datasets were required. Hermann et al. proposed a large scale dataset for QA [3]. Since then more attempts have been taken to create a large dataset to test critical reasoning ability of computer [4] [5]. Weston et al. proposed a set of artificial tasks called bAbI tasks which is used for evaluating the model in this paper [6].

Recurrent Neural Network (RNN) is a class of neural network which contains recurrent connection between hidden layers in consecutive timesteps. This type of architecture is very suitable for predicting temporal or sequential data (e.g. speech, text). RNN and its variants have become a standard architecture for various natural language processing tasks [7] [8]. In principle, it is possible to select an answer from all possible words of the vocabulary from the joint representation of the story and question by using a Recurrent Neural Network Language Model [9].

Convolutional Neural Network (CNN) is one kind of feed-forward neural network primarily inspired by human visual cortex which contains consecutive convolutional and subsampling layer. Although CNN has helped revolutionize the computer vision field [10], it has also started impacting natural language processing domain in recent years. Dos Santos and Gatti have achieved state of the art result in sentiment analysis of single sentence using CNN [11]. CNN has also been used for sentence classification [12] and sentence modeling [13].

Since RNN can contain long term dependency well, it can be augmented with more localized feature detector like CNN to improve its performance. This idea where convolutional and recurrent networks are used together have already been implemented for machine translation [14] and music classification [15]. We propose similar kind of model for question answering which obtains better result than single RNN model.

We discuss the relevant background study in Section II. Then we discuss the dataset with examples in Section III and then present our proposed model for the task of question answering in Section IV. We describe the experimental result in Section V and finally conclude in Section VI.

## II. Background Study

### A. Word Embedding

Word embedding creates a distributed representation of words where semantically similar words are mapped to nearby points in the vector space. Vector space models like

978-1-5386-2307-7/17/$31.00 ©2017 IEEE

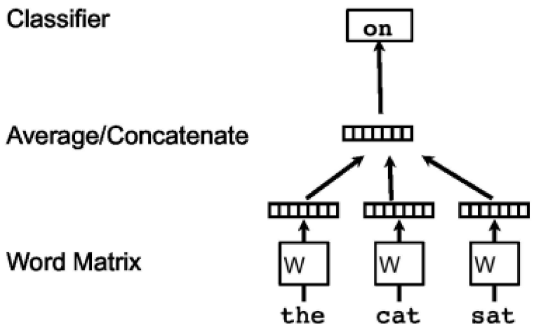


Fig. 1. A general approach for learning word embedding [21]

tf-idf or n-gram are traditionally used to create fixed length vector representation of words. Recently, embedding models like word2vec [16] or Glove [17] is popular for embedding words into low dimensional vectors.

The idea of distributed representation of concept is inspired from human cognition. This idea was proposed during the connectionist resurgence in 1980's [18] [19]. Bengio et al. showed neural network along with distributional representation can surpass standard n-gram model in language modeling task [20]. Mikolov et al. proposed a Continuous Bag-of-Words model (CBOW) and a Skip-Gram model for learning word embedding from raw text [16].

In Fig. 1, a very well known framework for word embedding is shown. Here, every word is represented by a column in matrix W. The $i$th column of the W indicates the $i$th word in the vocabulary. Here the whole task was to predict the next word given the context. Sum or concatenation of the matrices corresponding to words in the context is used for prediction. After training the model, words with similar meaning usually have similar values in many dimensions of the vector.

For example, word vectors can learn about semantic similarity [22].

| **Tiger** |
|---|
| Leopard |
| Dhole |
| Warthog |
| Rhinoceros |
| Lion |

Difference in word vectors also represents different relation between words like gender, number, degree etc. [23]

$\theta_{king} - \theta_{man} \approx \theta_{queen} - \theta_{woman}$ (Gender)
$\theta_{france} - \theta_{french} \approx \theta_{mexico} - \theta_{spanish}$(Language)
$\theta_{car} - \theta_{cars} \approx \theta_{apple} - \theta_{apples}$(Number)

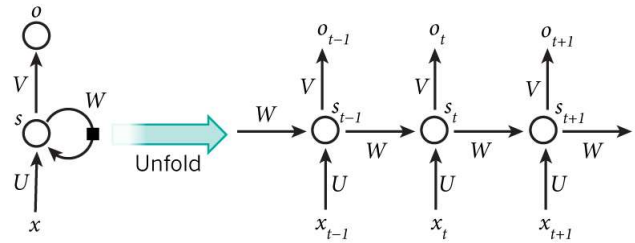


Fig. 2. A recurrent neural network unfolded through time [24]

These properties led to a wide range of use of word vectors in language modeling and understanding tasks.

### B. Recurrent Neural Network

A neural network is called recurrent if it has one or more cycles, if it is possible to follow a path from a unit back to itself, then the network is referred to as recurrent network [25]. Generally, the recurrent architecture used in modern recurrent networks is the one shown in Fig. 1 called elman network [26]. This kind of network allows the hidden layer information from previous step to propagate through different timesteps in future hidden nodes.

The hidden state at timestep $t$ is a function of the previous hidden state and the input in current timestep.

$$s_t = f(Ux_t + Ws_{t-1}) \tag{1}$$

The output($y$) at time step $t$ is then calculated as

$$o_t = f(Vs_t) \tag{2}$$

Here,
$x_t$ = Input at t timestep
$s_t$ = Hidden state at t timestep
$o_t$ = Output at t timestep
$f$ = an activation function like $\sigma$ or $\tanh$
$U$ = Weight between input and hidden state
$W$ = Recurrent weight between hidden states
$V$ = Weight between hidden state and output

In equation (1), the hidden state is a function of previous context and current input. Due to this property, RNN is theoretically capable of learning long term dependency among timesteps. But in practice, the gradient becomes very small after certain amount of timesteps [27]. This problem has been solved by Hochreiter and Schmidhuber [28] who invented a new way to calculate recurrent unit called long short term memory (LSTM).

*1)* ***RNN language model:*** Language modeling is an important problem of Artificial Intelligence (AI). Statistical language model captures the hidden statistical characteristics of the distribution of word sequences in a document. Language models have very important applications in speech

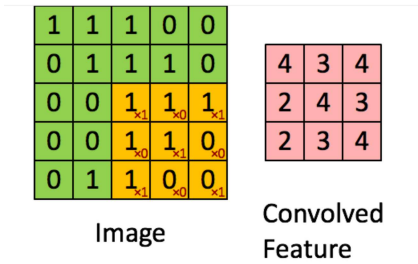


Fig. 3. Convolution operation using 3x3 kernel [31]

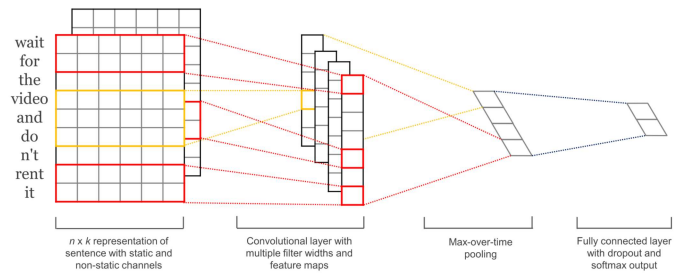


Fig. 4. Convolutional Neural Networks for sentence classification [12]

recognition, machine translation, natural language processing etc. The goal of a word level language model is to give the probability of the next word given all the previous words. Concretely, $P(w_n|w_{n-1}, ....., w_2, w_1)$.

For example, $P($ red | The color of roses is$)$ =?

Neural network based language model was proposed in a seminal paper by Bengio et al. which used a feedforward neural network [20]. Later, Mikolov et al. proposed Recurrent Neural Network based Language Model [9]. This model and its variants are now used in many sequence prediction problems including various natural language tasks like translation or text classification.

### C. Convolutional Neural Network

Convolutional networks are a family of neural networks that are primarily inspired by the human vision system. These networks are especially suitable for processing data that have n-dimensional grid like structure(e.g. image). The inspiration behind CNN goes back to the experiment of Hubel and Wiesel where they showed that visual cortex has a special kind of hierarchical architecture which creates a special representation from raw image signal [29]. CNN with end to end training has been used for document recognition [30] which showed its usefulness in the 1990s. In recent years, it has become a standard in the field of computer vision.

The working procedure of CNN is first shown using an image example as it feels more intuitive this way. Then CNN for language processing is illustrated. Usually, convolutional networks have 2 major kinds of layers. They are explained below:

*1) Convolution layer:* Convolution layer generally takes an input and convolve the input with different kernels or filters and creates a new activation map (i.e. feature map). The values in different positions of the kernel act as the weights of the network which are trainable. The convolution operation can be expressed as summation after doing elementwise multiplication of the kernel and small portion of the input(same size as the kernel) for all different positions in the input. The operation is illustrated in Fig. 3. Then the convolved features go through a non-linearity (e.g. ReLU) to the next layer.

There are 4 hyperparameters to choose in case of convolution. They are:

K = Number of filters
F = Spatial extent of the filters
S = Stride number
P = The amount of zero padding

*2) Pooling layer:* It is also called subsampling layer because the job of a pooling layer is to reduce the spatial size of its input so that number of parameters is also decreased. It keeps the computational complexity low and also helps prevent overfitting by reducing parameters required to train. There are 2 hyperparameters in this layer which are not trainable.

F = Spatial extent of filters
S = Stride number

Generally, max or average pooling is used in this layer which means taking the maximum or average value within a certain window.

In case of language processing, a document or sequence of sentences is generally represented as a matrix where each row corresponds to a token (e.g. words). Each row is a word vector typically obtained using word embedding technique mentioned earlier. The number of columns is the dimension of the word vector. The width of the filter is same as the number of columns of the input matrix. The length of the filter can be a small odd number. How CNN works for NLP is shown in Fig. 4.

## III. The Dataset

We have performed experiments on the synthetic question answering tasks collectively known as facebook bAbI dataset [6]. This dataset tests a model's ability to retrieve relevant facts and reason over them. It consists of 20 different tasks where each task tests a specific ability like counting, time reasoning or basic induction/deduction.

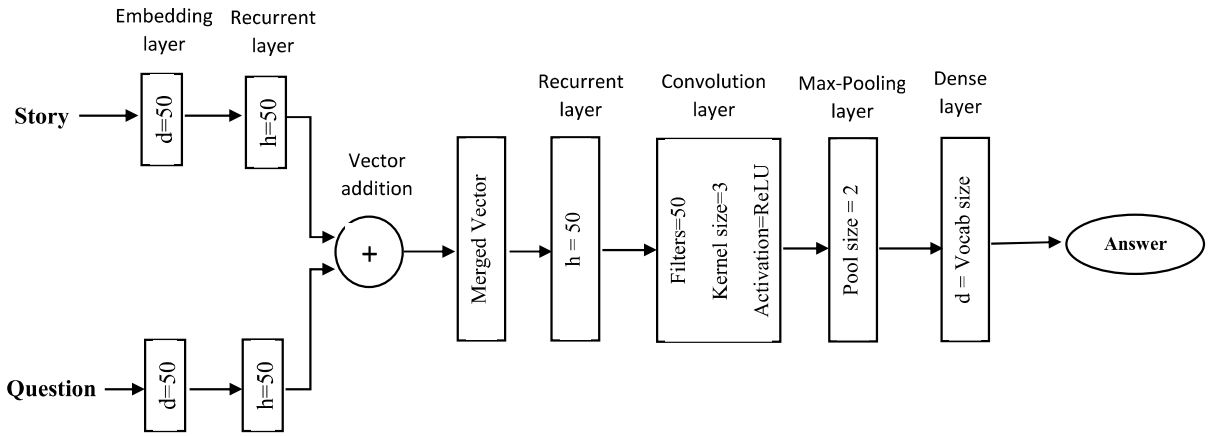


Fig. 5. Proposed model for question answering.

Every task consists of a set of statements (story), a question and an answer (typically a single word). The answer is available at training time, but must be predicted at test time. Only a subset of the statements is necessary facts while others are just noise. The model has to be able to ignore them to reach to an answer. There are two versions of the training data. The first one has 1000 training samples per task and the second one is larger with 10,000 samples per task. Our model is trained on the second version. Some examples of the dataset are given below:

| **Task 7: Counting** | **Task 14: Time Reasoning** | **Task 16: Basic Induction** |
|---|---|---|
| 1.Daniel picked up the football.<br>2.Daniel dropped the football.<br>3.Daniel got the milk.<br>4.Daniel took the apple.<br><br>How many objects is Daniel holding?<br>**A: two** | 1.In the afternoon Julie went to the park.<br>2.Yesterday Julie was at school.<br>3.Julie went to the cinema this evening.<br><br>Where was Julie before the park?<br>**A:school** | 1.Lily is a swan.<br>2.Lily is white.<br>3.Bernhard is green.<br>4.Greg is a swan.<br><br>What color is Greg?<br>**A:white** |

Although performing well on this synthetic dataset does not guarantee that the model would do the same in real world datasets, it is necessary for a question answering model to ace these tasks in order to perform well in more challenging tasks.

## IV. The Model

Since CNN model contains local connections to a fixed number of words, it represents local information within its context by creating higher level features from them. Moreover, semantic representation created by CNN are rotation and translation invariant. A kernel $k \in R^{cd}$ considers $c$ words as context and generate a more abstract feature from that. This can often act as an n-gram feature detector [32]. Multiple kernels of different size are applied to the input matrix and only the most important features are selected by using max-pooling. But CNN cannot learn long term dependency and its context size is also fixed. On the other hand, RNN updates its state with current input and previous state at each timestep thus preserving the global information. So it can model interdependence between words for an arbitrary amount of timesteps. For this reason, recurrent networks having LSTM or GRU cells are most commonly used for processing text data.

To take the advantage of both worlds we propose a new model. Our proposed model is illustrated in Fig. 5. Here, the story and the question are converted into word vector first using an embedding layer. Then both the embeddings are used as input to an RNN with 50 LSTM units and the outputs of these layers are merged into a single vector. Another RNN takes this merged vector as input and produces a fixed length vector. This vector goes through a convolutional layer composed of 50 filters of size 3 and a max-pooling layer. Finally, a fully connected softmax layer is applied over the whole vocabulary to get the index of the answer. Dropout [33] has been applied to the embedding and convolutional layers to prevent overfitting which is not shown in the figure.

## V. Experiments

The model is evaluated on bAbI question answering dataset. For training purpose, 10000 samples (story, question and answer tuple) are used and the model is evaluated on 1000 test samples per task. All experiments are done using only CPU (intel corei5, 2.5GHz), no GPU is used. The model is created and run using Keras deep learning library (with Tensorflow backend) on jupyter notebook. The model is trained using backpropagation and Adam [34].

TABLE I
TEST SET ACCURACY(%) OF LSTM BASELINE AND OUR PROPOSED MODEL

| Task | LSTM | C-RNN |
|---|---|---|
| 1: Single Supporting Fact | 50 | 88.9 |
| 2: Two Supporting Facts | 20 | 45.0 |
| 3: Three Supporting Facts | 20 | 36.9 |
| 4: Two Argument Relations | 61 | 77.1 |
| 5: Three Argument Relations | 70 | 99.2 |
| 6: Yes/No Questions | 48 | 83.0 |
| 7: Counting | 49 | 93.8 |
| 8: Lists/Sets | 45 | 78.2 |
| 9: Simple Negation | 64 | 88.5 |
| 10: Indefinite Knowledge | 44 | 71.1 |
| 11: Basic Coreference | 72 | 95.1 |
| 12: Conjunction | 74 | 95.0 |
| 13: Compound Coreference | 94 | 95.2 |
| 14: Time Reasoning | 27 | 41.5 |
| 15: Basic Deduction | 21 | 54.2 |
| 16: Basic Induction | 23 | 48.6 |
| 17: Positional Reasoning | 51 | 95.0 |
| 18: Size Reasoning | 52 | 96.4 |
| 19: Path Finding | 8 | 17.8 |
| 20: Agents Motivations | 91 | 98.4 |
| Mean Accuracy | 49 | 74.95 |

### A. Quantitative Result

The experimental result is presented in table 1. From table 1, we can see that our proposed Convolutional Recurrent Neural Network (C-RNN) has outperformed the LSTM baseline proposed in [6] on every task. The mean accuracy of the LSTM model is 49%. On the other hand, the mean accuracy of C-RNN is 74.95% which is 25.95% better than the LSTM model. A task is said to be solved if an accuracy of equal or greater than 95% is achieved [6]. By this standard, our model solves 7 out of 20 tasks.

The result on 20 tasks is also shown in Fig. 6 by plotting the corresponding accuracy scores. On task 13, task 19 and task 20 both model performs very closely. But on multiple tasks (task 1, task 6, task 7, task 17 and task 18) our model exceeds the LSTM baseline by a big margin.

## VI. CONCLUSION

In this paper, we proposed a convolutional recurrent neural network model for question answering task. The model involves feeding outputs of the LSTM to a convolutional layer for detecting short term dependency between words better. Our experiments on bAbI question-answering dataset demonstrate that the proposed model improves accuracy as compared to an LSTM model. An improvement of 25.95% in average accuracy is observed on the test set.

However, there is still much to do. Our model performs better for large training set. But it takes more time to train. Use of external memory and attention along with this model can be very effective for answering questions from long stories. It can also help decrease the training data size. We want to further explore different memory augmented architectures like [35] [1].

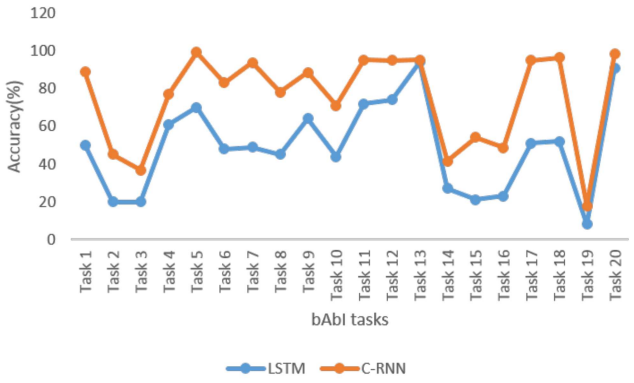


Fig. 6. The plot shows the accuracy(%) comparison of the LSTM baseline and our proposed model for every task in the bAbI dataset

## REFERENCES


[1] A. Kumar, O. Irsoy, P. Ondruska, M. Iyyer, J. Bradbury, I. Gulrajani, V. Zhong, R. Paulus, and R. Socher, "Ask me anything: Dynamic memory networks for natural language processing," in *International Conference on Machine Learning*, pp. 1378–1387, 2016.

[2] S. Quarteroni and S. Manandhar, "A chatbot-based interactive question answering system," *Decalog 2007*, p. 83, 2007.

[3] K. M. Hermann, T. Kocisky, E. Grefenstette, L. Espeholt, W. Kay, M. Suleyman, and P. Blunsom, "Teaching machines to read and comprehend," in *Advances in Neural Information Processing Systems*, pp. 1693–1701, 2015.

[4] M. Richardson, C. J. Burges, and E. Renshaw, "Mctest: A challenge dataset for the open-domain machine comprehension of text.," in *EMNLP*, vol. 3, p. 4, 2013.

[5] P. Rajpurkar, J. Zhang, K. Lopyrev, and P. Liang, "Squad: 100,000+ questions for machine comprehension of text," *arXiv preprint arXiv:1606.05250*, 2016.

[6] J. Weston, A. Bordes, S. Chopra, A. M. Rush, B. van Merriënboer, A. Joulin, and T. Mikolov, "Towards ai-complete question answering: A set of prerequisite toy tasks," *arXiv preprint arXiv:1502.05698*, 2015.

[7] I. Sutskever, O. Vinyals, and Q. V. Le, "Sequence to sequence learning with neural networks," in *Advances in neural information processing systems*, pp. 3104–3112, 2014.

[8] D. Tang, B. Qin, and T. Liu, "Document modeling with gated recurrent neural network for sentiment classification.," in *EMNLP*, pp. 1422–1432, 2015.

[9] T. Mikolov, M. Karafiát, L. Burget, J. Cernockỳ, and S. Khudanpur, "Recurrent neural network based language model.," in *Interspeech*, vol. 2, p. 3, 2010.

[10] A. Krizhevsky, I. Sutskever, and G. E. Hinton, "Imagenet classification with deep convolutional neural networks," in *Advances in neural information processing systems*, pp. 1097–1105, 2012.

[11] C. N. Dos Santos and M. Gatti, "Deep convolutional neural networks for sentiment analysis of short texts.," in *COLING*, pp. 69–78, 2014.

[12] Y. Kim, "Convolutional neural networks for sentence classification," *arXiv preprint arXiv:1408.5882*, 2014.

[13] N. Kalchbrenner, E. Grefenstette, and P. Blunsom, "A convolutional neural network for modelling sentences," *arXiv preprint arXiv:1404.2188*, 2014.

[14] P. Dakwale and C. Monz, "Convolutional over recurrent encoder for neural machine translation," *The Prague Bulletin of Mathematical Linguistics*, vol. 108, no. 1, pp. 37–48, 2017.

[15] K. Choi, G. Fazekas, M. Sandler, and K. Cho, "Convolutional recurrent neural networks for music classification," in *Acoustics, Speech and Signal Processing (ICASSP), 2017 IEEE International Conference on*, pp. 2392–2396, IEEE, 2017.

[16] T. Mikolov, I. Sutskever, K. Chen, G. S. Corrado, and J. Dean, "Distributed representations of words and phrases and their compositionality," in *Advances in neural information processing systems*, pp. 3111–3119, 2013.

[17] J. Pennington, R. Socher, and C. Manning, "Glove: Global vectors for word representation," in *Proceedings of the 2014 conference on empirical methods in natural language processing (EMNLP)*, pp. 1532–1543, 2014.

[18] G. E. Hinton, "Learning distributed representations of concepts," in *Proceedings of the eighth annual conference of the cognitive science society*, vol. 1, p. 12, Amherst, MA, 1986.

[19] D. E. Rumelhart, J. L. McClelland, P. R. Group, *et al.*, *Parallel distributed processing*, vol. 1. MIT press Cambridge, MA, USA:, 1987.

[20] Y. Bengio, R. Ducharme, P. Vincent, and C. Jauvin, "A neural probabilistic language model," *Journal of machine learning research*, vol. 3, no. Feb, pp. 1137–1155, 2003.

[21] Q. Le and T. Mikolov, "Distributed representations of sentences and documents," in *Proceedings of the 31st International Conference on Machine Learning (ICML-14)*, pp. 1188–1196, 2014.

[22] P. Liang, "Natural language understanding: Foundations and state-of-the-art." http://icml.cc/2015/tutorials/icml2015-nlu-tutorial.pdf.

[23] T. Mikolov, W.-t. Yih, and G. Zweig, "Linguistic regularities in continuous space word representations.," in *hlt-Naacl*, vol. 13, pp. 746–751, 2013.

[24] Y. LeCun, Y. Bengio, and G. Hinton, "Deep learning," *Nature*, vol. 521, no. 7553, pp. 436–444, 2015.

[25] M. I. Jordan, "Serial order: A parallel distributed processing approach," *Advances in psychology*, vol. 121, pp. 471–495, 1997.

[26] J. L. Elman, "Finding structure in time," *Cognitive science*, vol. 14, no. 2, pp. 179–211, 1990.

[27] Y. Bengio, P. Simard, and P. Frasconi, "Learning long-term dependencies with gradient descent is difficult," *IEEE transactions on neural networks*, vol. 5, no. 2, pp. 157–166, 1994.

[28] S. Hochreiter and J. Schmidhuber, "Long short-term memory," *Neural computation*, vol. 9, no. 8, pp. 1735–1780, 1997.

[29] D. H. Hubel and T. N. Wiesel, "Receptive fields of single neurones in the cat's striate cortex," *The Journal of physiology*, vol. 148, no. 3, pp. 574–591, 1959.

[30] Y. LeCun, L. Bottou, Y. Bengio, and P. Haffner, "Gradient-based learning applied to document recognition," *Proceedings of the IEEE*, vol. 86, no. 11, pp. 2278–2324, 1998.

[31] D. Britz, "Understanding convolutional neural networks for nlp." http://www.wildml.com/2015/11/understanding-convolutional-neural-networks-for-nlp/.

[32] R. Collobert and J. Weston, "A unified architecture for natural language processing: Deep neural networks with multitask learning," in *Proceedings of the 25th International Conference on Machine Learning*, ICML '08, (New York, NY, USA), pp. 160–167, ACM, 2008.

[33] N. Srivastava, G. E. Hinton, A. Krizhevsky, I. Sutskever, and R. Salakhutdinov, "Dropout: a simple way to prevent neural networks from overfitting.," *Journal of machine learning research*, vol. 15, no. 1, pp. 1929–1958, 2014.

[34] D. Kingma and J. Ba, "Adam: A method for stochastic optimization," *arXiv preprint arXiv:1412.6980*, 2014.

[35] J. Weston, S. Chopra, and A. Bordes, "Memory networks," *arXiv preprint arXiv:1410.3916*, 2014.

# A Feature Fusion Based Optical Character Recognition of Bangla Characters Using Support Vector Machine

Mst. Tasnim Pervin[1], Shyla Afroge[2], Aminul Huq[3]
[1, 2, 3]Dept. of Computer Science and Engineering (Rajshahi University of Engineering and Technology, Bangladesh)
Email: tasnimpervin@gmail.com[1], shyla.ruet@gmail.com[2], aminul.huq11@gmail.com[3].

*Abstract*— **This paper introduces a feature fusion based optical Bangla character recognition approach using Support Vector Machine (SVM) including the feature extraction method named Zoning and Gabor Filter. Optical character recognition (OCR) is mostly dependent on the features extracted from characters which highly influences the classification and recognition accuracy. This paper emphasizes on the feature fusion of two different feature vectors obtained by Zoning and Gabor filter of suitable frequencies and orientations along with finding the recognition rate by passing the features into a well-developed classifier, Support Vector Machine (SVM) for classification. Here, a comparison has also been made among the recognition accuracy by individual features and by feature fusion which reveals that feature fusion based method performs better (92.99%) than a single feature extraction method (68.15% for Zoning, 89.73% for Gabor filter) during classification.**

***Keywords—Feature extraction, Zoning, Gabor filter, Feature fusion, SVM classifier..***

## I. INTRODUCTION

Optical character recognition (OCR) plays a vital role in document image analysis which has become a challenging research since recent years [1]. Advance automation process for human-machine interaction is mostly dependent on OCR. Bangla is the 4th most widely spoken language with approximately 200 million speakers of Bangladesh and West Bengal of Indian state [2]. But, Bangla OCR is slightly lagging behind for having multifold, modifiers, and complexity of the script. Besides, most researches were done using classifier designs which are hugely based on simple feed-forward and back-propagation neural networks and as a result, there is a lack of high performance OCR engine for Bangla [3], [4], [5], [6]. The first step of the system is pre-processing of the image before applying feature extraction methods such as projection, zoning, histograms, gabor filter, chain code, contour profiles, zernike moments etc. [7]. In this paper, Zoning method and Gabor filters have been used to extract relevant features from the images. Zoning method works with statistical distribution of pixel of several overlapping or non-overlapping regions [8]. Features generated by Gabor filters are used for their invariance to illumination, rotation, scale and translation and can be used as input to a classification or segmentation operator [9], [10]. In the final step of classification, extracted features are fed to a classifier like Artificial Neural Networks (ANN), Support Vector Machines (SVM), Back-Propagation Neural Network (BPNN), Kohonen network etc.

## II. RELATED WORKS

The Bangla OCR systems started emerging in mid of 1980 and various efforts to establish a working Bangla OCR have been continued since then. Some of these efforts have emphasized on only printed but not handwritten characters. Md. Mahbub Alam and Dr. M. Abul Kashem used Freeman chain code for feature extraction and Multilayered feed forward neural network for classification [14]. Shamim Ahmed, Mohammod Abul Kashem tried to improve the accuracy of character segmentation of Bangla characters using Back Propagation Neural Network (BPNN) [15]. Md. Mojahidul Islam, Md. Imran Hossain & Md. Kislu Noman worked on Automatic Feature Extraction using XOR Operation where XOR operation was performed between the scaled image and the database image and the percentage of accuracy was calculated which showed 80% average recognition accuracy [16]. Several works have been done using digital curvelet transform and K-nearest neighbour (KNN) classifier for recognition using curvelet coefficients and the trained model values were fused later by a simple majority voting scheme to obtain the final result.

## III. METHODOLOGY

The proposed system, overall works are divided into three major parts: Pre-processing, Feature Extraction, Classification of the characters which is shown below in Fig.1 diagram.

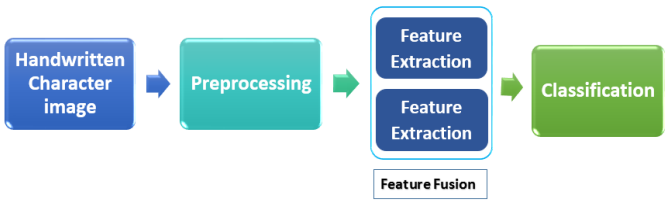


Fig. 1 Overview of the proposed system of Bangla Optical Character Recognition

978-1-5386-2307-7/17/$31.00 ©2017 IEEE

### A. Preprocessing

The initial stage to process the scanned image before feature extraction is preprocessing which includes binarization, noise reduction, skew detection, segmentation and normalization. These steps are discussed below.

*1) Binarization:* Input Character images are binarized using Otsu's method [13]. After converting the image into gray level, it is converted to binary image by turning all the pixels to zero below the threshold and one exceeding the threshold.

*2) Noise Reduction:* Depending on the resolution on the scanner and the success of the applied technique for thresholding, the characters may be noisy or broken. These noise causes poor recognition rates, can be eliminated by using a preprocessor or filters to smooth the digitized characters.

*3) Skew Detection:* During scanning document manually or mechanically, a few degrees of skew is unavoidable. Skew angle is the angle deviation between text lines and the horizontal direction. Hough transform are commonly used for skew correction. It can be done by (i) estimating the skew angle, $\theta$ and (ii) rotating the image by the $\theta$ in the opposite direction. These steps make the digital image look-alike to original image.

*4)* Segmentation: Segmentation process includes line segmentation, word segmentation and character segmentation. Segmentation is done by observing the histogram of horizontal or vertical scanning of image and counting foreground pixel frequency. Segmentation occurs at that point where count is zero.

*5) Normalization:* The size normalization or scaling is applied to obtain characters of uniform size and same dimension of feature vectors. In this paper, each character is scaled into 40x48 before proceeding to feature extraction.

### B. Feature Extraction

The Feature extraction is considered as the most difficult phase of recognition. The main objective of feature extraction is to identify special characteristics of any character symbol that characterizes that individual character uniquely and eliminates unnecessary attributes from total feature space.

In this paper, two methods are used named Zoning and Gabor filter to obtain feature vectors. Following sections describe these methods theoretically.

*1) Zoning:* Zoning is statistical feature extraction method that extracts features from character symbol on the basis of distribution of pixels. In this method, the scaled binary images are divided into 8x8 zones of predefined sizes of 6x5 dimension to obtain 64 blocks or zones. The features are extracted by counting the number of black pixels and white pixels of each blocks to calculate pixel density where black pixels are represented by 0s and white pixels are represented by 1s. For average pixel density, $d_{avg}$ of a zone, the total number of foreground black pixels are divided by the total number of pixels (foreground and background) of each zone [17]. Each zone contribute to the value of the overall feature vector. The average pixel density calculated by following equation for each consicutive zone helps to form the feature vectors for each character image. Equation (1) is the formula to compute $d_{avg}$.

$$d_{avg} = \frac{\text{Number of foreground pixels in a zone}}{\text{Total number of pixels in that zone}} \quad (1)$$

*2) Gabor filters:* Gabor filters are a powerful tool for feature extraction. The most advantageous properties of Gabor filters are their invariance properties to rotation, scale, and translation, robustness against photometric disturbances such as illumination of noise. The Gabor filters provide the optimal resolution in both the spatial domain and transform domain to extract local features of an image. Relations between activations for a specific spatial location are very distinctive between objects in an input character image. Unit variance and zero mean are used for normalization [18]. Gabor filters can be used as a directional feature extractor where features can be captured in various directions, which is quite similar to Human Visual System (HVS) [11],[12]. The two-dimensional Gabor filter represents a convolutional band pass linear filter whose impulse response is defined by a complex sinusoid harmonic function multiplied by a Gaussian kernel function. Equation (2) shows this expression below.

$$G_{(x,y)} = g_{(x,y)} s_{(x,y)} \quad (2)$$

Where, $g_{(x,y)}$ is a Gaussian function known as envelope and $s_{(x,y)}$ is a complex sinusoid harmonic function. Equation (3) represents the mathematical representation of the complex sinusoid, $s_{(x,y)}$.

$$s_{(x,y)} = e^{-j(2\pi(u_0 x + v_0 y) + \varphi)} \quad (3)$$

Where, $(u_0, v_0)$ is the spatial frequency and $-$ represents the negative phase of the sinusoid. Equation (4) and (5) shows that complex sinusoid consists of real and imaginary part.

$$R(s_{(x,y)}) = \cos(2\pi(u_0 x + v_0 y) + \varphi) \quad (4)$$

$$I(s_{(x,y)}) = \sin(2\pi(u_0 x + v_0 y) + \varphi) \quad (5)$$

Equation (6) represents the 2-D Gaussian function.

$$g_{(x,y)} = \frac{1}{\sqrt{2\pi}\sigma} e^{-\frac{1}{2}\left(\frac{x^2}{\sigma_x^2} + \frac{y^2}{\sigma_y^2}\right)} \quad (6)$$

Finally, Equation (7) shows the 2-D Gabor filter below.

$$G_{x,y,\theta,f,\sigma_x,\sigma_y} = e^{-\frac{1}{2}\left(\frac{x'^2}{\sigma_x^2} + \frac{y'^2}{\sigma_y^2}\right)} X\left(\cos 2\pi f x' + j \sin 2\pi f x'\right) \quad (7)$$

Where, $\sigma_x$ and $\sigma_y$ are the standard deviations of the Gaussian envelop along x and y direction respectively, f is the frequency and $\theta$ is the orientation. Again $x^{'}$ and $y^{'}$ can be represented by-

$$x^{'} = x\cos\theta + y\sin\theta$$
$$y^{'} = -x\sin\theta + y\cos\theta$$

### C. Classification

Support Vector Machine (SVM) is a well-developed supervised machine learning algorithm which can be used for both classification and regression challenges. The standard SVM is a binary classifier which takes the set of input data, classifies them in one of the two distinct classes and plot each data item in n dimensional space (where n is number of features) where the value of each feature represents the value of a particular coordinate. It was determined by Cortes and Vapnik [12] in about 1946. The ability to transform data to a high dimensional space using a hyperplane to separate the data items by maximizing distance margin is considered to be basic power of SVM [12]. However, the optimization process for learning SVM with different parameters of hyperplane has great influence over recognition accuracy rate. For classification, SVM is trained by training dataset to obtain a hyperplane based on the features to predict an output over testing dataset using previous knowledge of training phase. Equation (8) can be used to represent the hyperplane.

$$w^0 x + b = 0 \tag{8}$$

Where, $w^0$ is the normal to the hyperplane and b is the bias from the origin to the hyperplane. The points that lie on the hyperplane must satisfy the above equation. For a given training set that contains pairs of $(X_i, Y_i)$, where, feature vectors can be depicted as i = 1,.....,n and the class label are y = ±1 must satisfy the following conditions.

$$w^0 x + b > 0 \qquad \text{if} \quad Y_i = 1$$

$$w^0 x + b < 0 \qquad \text{if} \quad Y_i = -1$$

The margin is maximized by the optimization process to increase the distance. Equation (9) that represents the decision boundary function for input pattern x with binary classifier is as follows:

$$f(x) = \sin(w^0 x + b) \tag{9}$$

The distance between the hyperplane margin $w^0 x + b = 1$ and $w^0 x + b = -1$ can be represented by $2/\|\mathrm{w}\|$. Therefore, the optimization process that generates support vectors can be presented by the equation below:

$$\frac{1}{2}\|w\|^2 - (w^0 x + b) \tag{10}$$

In machine learning, kernel methods are a class of algorithms for pattern analysis that takes two inputs and spits out the similarity between them. Three kernels are used for support vector machines. Although, in this paper, linear kernel has been used only.

TABLE I
KERNELS OF SUPPORT VECTOR MACHINE

| | |
|---|---|
| Linear Kernel | $K(x,y) = X^T Y_i$ |
| Polynomial Kernel | $K(x,y) = (X^T Y_i + 1)^d$ |
| RBF Kernel | $K(x,x_i) = \exp^{-y\|x-y\|^2}$ |

## IV. EXPERIMENTAL RESULTS

### A. Dataset Description:

Because of the lack of the standardization of any Bangla dataset, existing dataset has been used [19]. For total experimental purpose, including training and testing about 35000 character images have been used for 50 Bangla characters. Among these, for each character 500 data, a total of 25000 data has been used for training and for each character 200 data, a total of 10000 data has been used for testing using conventional validation of 70-30 ratio to evaluate the recognition accuracy.

### B. Results of Feature Extraction Methods:

After applying two different feature extraction methods (Zoning and Gabor filters) described above, two different feature vectors can be obtained. Zoning gives a feature vector of dimension 1x64. Sample result for a basic bangla character 'ক' has been given here applying zoning method. Fig.2 (b) shows the pixel value for zone-8 of dimension 6x5. Table II shows the matrix format of corresponding feature vector for the used character.

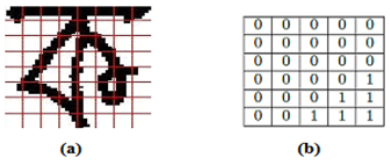


Fig. 2. (a)8x8 zoning of BW image , (b)binary value of pixels of zone-8.

TABLE II
FEATURE MATRIX BY ZONING OF CHARACTER 'ক'

| | | | | | | | |
|---|---|---|---|---|---|---|---|
| 0.266 | 0.333 | 0.333 | 0.266 | 0.266 | 0.333 | 0.233 | 0.200 |
| 0.866 | 1 | 0.966 | 0.266 | 0.400 | 1 | 0.833 | 1 |
| 1 | 1 | 0.433 | 0.600 | 0.233 | 0.433 | 1 | 1 |
| 1 | 0.700 | 0.500 | 0.666 | 0.866 | 0.400 | 0.833 | 1 |
| 0.933 | 0.300 | 0.966 | 0.566 | 0.933 | 0.300 | 0.200 | 0.900 |
| 0.800 | 0.366 | 0.366 | 0.466 | 0.866 | 0.300 | 0.433 | 1 |
| 1 | 1 | 0.900 | 0.166 | 0.800 | 0.7667 | 0.900 | 1 |
| 1 | 1 | 1 | 0.733 | 0.700 | 1 | 1 | 1 |

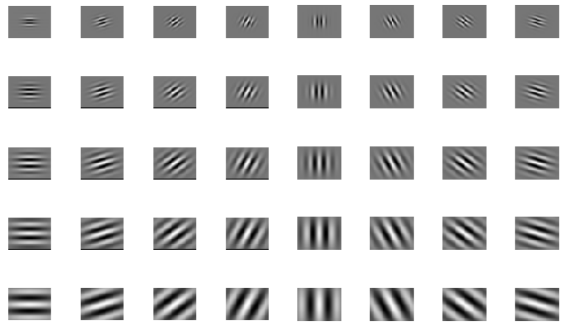

Fig.3: Real part of the Gabor filter

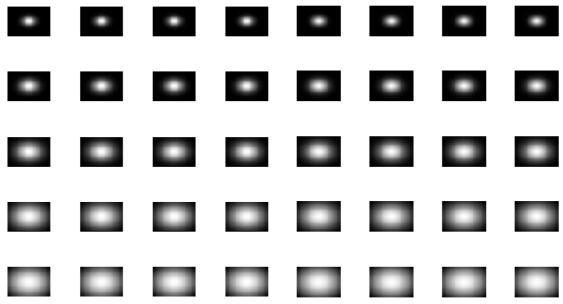

Fig.4: Magnitude of Gabor filter

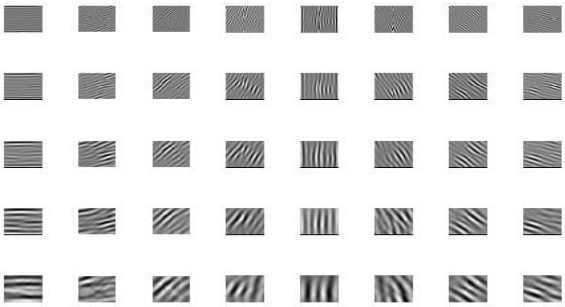

Fig. 5: Real part of the filtered character image

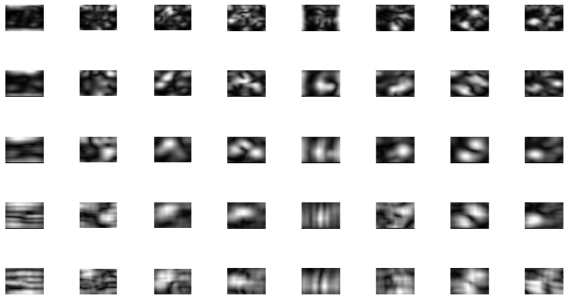

Fig. 6: Magnitude of filtered character image

Gabor produces a feature vector of dimension 1x2560 for each character image. Forty Gabor filters with a set of 5 radial frequencies and 8 successive orientations has been used here as shown in figures. Fig.3 and Fig.4 show those filters which are convolved with the sample input image resulting in a Gabor space. Fig.5 and Fig.6 are the resulting response for convolving filters with character image 'ক'. These filtered real part and magnitude provide the feature vector. Later, these two feature vectors are concatenated to form a fusion that produces a larger feature vector of dimension 1x2624 for each character image which is then passed to further steps for classification.

### *C. Recognition Accuracy*

As the title depicts, Both Zoning and Gabor feature vectors are fed to SVM classifier using linear kernel and OneVsAll (OVA) coding scheme to check individual class recognition accuracy rate. Then these two feature vectors are fused together as described in previous section by concatenation producing another stronger set of feature vector which gives higher recognition accuracy as expected. This method is followed for both training and testing data. Table III shows the number of correctly recognized data and Table IV shows the recognition accuracy of different characters using following formula.

$$\text{Recognition accuracy} = \frac{\text{total no. of character image - no. of misclassified caharacter image}}{\text{total no. of character image}} * 100\%$$

Here,
Number of misclassified characters =
False Acceptance + False Rejection.
CR = Correctly Recognized
FR = False Rejection
FA = False Acceptance
ACC = Accuracy Percentage.

TABLE III
NUMBER OF RECOGNIZED CHARACTERS BY DISCUSSED FEATURE EXTRACTION METHODS.

| Input Character | Number of Recognized Data by different approach (500 Training image & 200 Testing image per character) | | | | | | | | |
|---|---|---|---|---|---|---|---|---|---|
| | Zoning | | | Gabor | | | Fusion of both | | |
| | CR | FA | FR | CR | FA | FR | CR | FA | FR |
| অ | 106 | 60 | 94 | 162 | 18 | 38 | 168 | 12 | 32 |
| ঈ | 134 | 28 | 66 | 174 | 14 | 26 | 180 | 8 | 20 |
| ক | 152 | 38 | 48 | 178 | 13 | 28 | 184 | 6 | 16 |
| ঙ | 134 | 28 | 66 | 176 | 23 | 26 | 186 | 13 | 14 |
| ঞ | 158 | 25 | 42 | 154 | 10 | 46 | 162 | 2 | 38 |
| ঠ | 170 | 103 | 30 | 190 | 39 | 10 | 198 | 31 | 2 |
| ণ | 168 | 67 | 32 | 192 | 14 | 8 | 192 | 11 | 8 |
| র | 154 | 80 | 46 | 188 | 19 | 12 | 194 | 13 | 6 |
| স | 104 | 126 | 43 | 190 | 48 | 10 | 194 | 40 | 6 |
| ঢ় | 174 | 134 | 26 | 192 | 5 | 8 | 194 | 3 | 6 |
| ং | 194 | 25 | 6 | 190 | 12 | 10 | 196 | 7 | 4 |

The accuracy rate of a character recognition is affected by misclassification by false acceptance and false rejection. For example, ‘ত’ is falsely accepted as ‘ভ’, again ‘স’ is falsely rejected by its own class and falsely accepted as ‘ম’. ‘অ’ and ‘আ’ are also victim of this problem. ‘ব’ and ‘র’ also lead to misclassification because of slight difference of single dot between them. This problem is mainly severe in case of handwritten characters because of pattern variation of handwriting among people. Table IV shows the percentage of accuracy for above table.

TABLE IV
RECOGNITION ACCURACY BY DISCUSSED FEATURE EXTRACTION METHODS.

| Input charac-ters | Trai ning data | Testi -ng data | Zoning | | Gabor | | Fusion of both | |
|---|---|---|---|---|---|---|---|---|
| | | | CR | ACC (%) | CR | ACC (%) | CR | ACC (%) |
| অ | 500 | 200 | 106 | 23 | 162 | 72 | 168 | 78 |
| ঈ | 500 | 200 | 134 | 53 | 174 | 80 | 180 | 86 |
| ক | 500 | 200 | 152 | 57 | 178 | 79.5 | 184 | 89 |
| ঙ | 500 | 200 | 134 | 53 | 176 | 75.5 | 186 | 86.5 |
| ঞ | 500 | 200 | 158 | 66.5 | 154 | 72 | 162 | 80 |
| ঠ | 500 | 200 | 170 | 33.5 | 190 | 75.5 | 198 | 83.5 |
| ণ | 500 | 200 | 168 | 50.5 | 192 | 89 | 192 | 90.5 |
| র | 500 | 200 | 154 | 37 | 188 | 84.5 | 194 | 90.5 |
| স | 500 | 200 | 104 | 15.5 | 190 | 71 | 194 | 77 |
| ড় | 500 | 200 | 174 | 20 | 192 | 93.5 | 194 | 95.5 |
| ং | 500 | 200 | 194 | 84.5 | 190 | 89 | 196 | 94.5 |

The following graphical representation in Fig. 7 shows the overall accuracy for 50 characters using 10000 testing data. These accuracy vary slightly for multiple runs and averaging them gives an approximation of final accuracy.

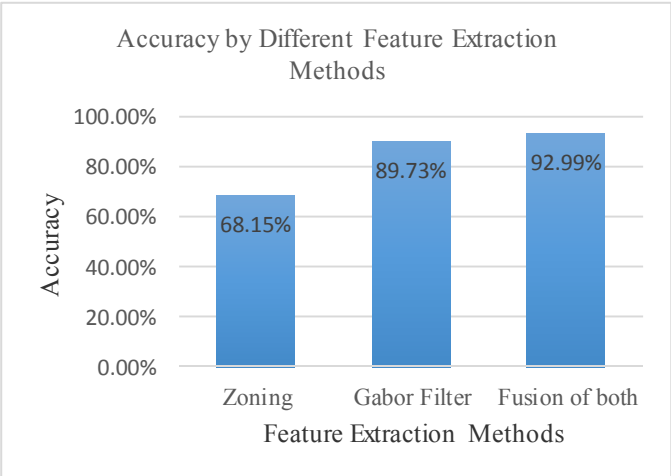


Fig. 7. Recognition accuracy by different feature extraction methods.

## V. CONCLUSION

In this paper, the problem of Bangla optical character recognition has been addressed. Feature fusion technique has been addressed using Zoning and Gabor filter. Support Vector Machines are utilized for classification and recognition. From above works, it can be assumed that feature fusion based technique gives higher accuracy (92.99%) during recognition than individual ones (68.15% for Zoning, 89.73% for Gabor filter). Accuracy mostly depends on the preprocessing stage and feature extraction methods. By increasing efficiency of these phases, it might offer greater accuracy. However, some important directions for the future work may be to extend this work by incorporating modifiers along with handwritten Bangla characters, fusion of some more significant features using different fusion algorithms and try to implement other classification approaches on used dataset to evaluate comparative performance with proposed system.

## REFERENCES


[1] Mori, Shunji, Ching Y. Suen and Kazuhiko Yamamoto. "Historical review of OCR research and development." Proceedings of the IEEE 80.7 (1992): 1029-1058.80.7 (1992): 1029-1058.

[2] Comrie, Bernard, ed. The world's major languages. Routledge, 2009.

[3] M.A. Hasan, P.P. Paul, M.W. Islam, S. Biswas, S. Ahmed, “Bangla digit recognition using Eigen digits”.

[4] Chowdhury, Ahmed Asif, et al. "Optical Character Recognition of Bangla Characters using neural network: A better approach." 2nd ICEE. 2002.

[5] Hasan, Md Rafiul, Mohammad Azizul Haque, and Syeda Umme Farhana Malik. "Bangla optical character recognition system." Proc. 2nd International Conference on Computer and Information Technology, ICCIT. 1999.

[6] Shatil, Adnan Md. Bangla optical character recognition using Kohonen network. Diss. BRAC University, 2006.

[7] Pradeep, J., E. Srinivasan, and S. Himavathi. "Diagonal based feature extraction for handwritten character recognition system using neural network." Electronics Computer Technology (ICECT), 2011 3rd International Conference on. Vol. 4. IEEE, 2011.

[8] LineEikvil, “Optical Character Recognition”, citeseer.ist.psu.edu/142042.html (1993).

[9] Kamarainen, J-K., Ville Kyrki, and Heikki Kalviainen. "Invariance properties of Gabor filter-based features-overview and applications." IEEE Transactions on image processing 15.5 (2006): 1088-1099.

[10] Grigorescu, Simona E., Nicolai Petkov, and Peter Kruizinga. "Comparison of texture features based on Gabor filters." IEEE Transactions on Image processing 11.10 (2002): 1160-1167.

[11] Al-Jamimi, Hamdi A., and Sabri A. Mahmoud. "Arabic character recognition using gabor filters." Innovations and advances in computer sciences and engineering (2010): 113-118.

[12] Chaudhari, Shailesh, and Ravi M. Gulati. "Script Identification Using Gabor Feature and SVM Classifier." Procedia Computer Science 79 (2016): 85-92.

[13] Otsu N (1979) A threshold selection method from grey-level histograms. IEEE Trans Syst Man Cybern 9:377–393.

[14] Alam, Md Mahbub, and Dr M. Abul Kashem. "A complete Bangla OCR system for printed characters." JCIT 1.01 (2010): 30-35.

[15] Ahmed, Shamim, and Mohammod Abul Kashem. "Enhancing the Character Segmentation Accuracy of Bangla OCR using BPNN." International Journal of Science and Research (IJSR) ISSN (Online): 2319-7064.

[16] Islam, Md Mojahidul, Md Imran Hossain, and Md Kislu Noman. "Bangla character recognition system is developed by using automatic feature extraction and XOR operation." Global Journal of Computer Science and Technology (2013).

[17] Siddharth, Kartar Singh, et al. "Handwritten Gurmukhi Character Recognition Using Statistical and Background Directional Distribution." International Journal on Computer Science and Engineering (IJCSE) 3.06 (2011): 2332-2345.

[18] Haghighat, Mohammad, Saman Zonouz, and Mohamed Abdel-Mottaleb. "CloudID: Trustworthy cloud-based and cross-enterprise biometric identification." Expert Systems with Applications 42.21 (2015): 7905-7916.

[19] Mohammed, Nabeel; Momen, Sifat; Abedin, Anowarul; Biswas, Mithun; Islam, Rafiqul; Shom, Gautam; Shopon, Md. (2017), “BanglaLekha-Isolated”, Mendeley Data, v2.

2017 3rd International Conference on Electrical Information and Communication Technology (EICT), 7-9 December 2017, Khulna, Bangladesh

# Customer Segmentation using Centroid Based and Density Based Clustering Algorithms

A. S. M. Shahadat Hossain
Department of Computer Science & Engineering
Rajshahi University of Engineering & Technology
Rajshahi - 6204, Bangladesh
shahadat.ruet.cse@gmail.com

***Abstract*—In recent years, customer segmentation has become one of the most significant and useful tools for e-commerce. It plays a vital role in online product recommendation system and also helps to understand local and global wholesale or retail market. Customer segmentation refers to grouping customers into different categories based on shared characteristics such as age, location, spending habit and so on. Similarly, clustering means putting things together in such a way that similar type of things remain in the same group. Due to having similarities between these two terms, it is possible to apply clustering algorithms for ensuring satisfactory and automatic customer segmentation. Among different types of clustering algorithms, centroid based and density based are the most popular. This paper illustrates the idea of applying density based algorithms for customer segmentation beside using centroid based algorithms like $k$-means. Applying DBSCAN (Density-Based Spatial Clustering of Applications with Noise) algorithm as one of the density based algorithms results in a meaningful customer segmentation.**

***Keywords*—Customer segmentation, Market segmentation, Clustering algorithms, Centroid based clustering, Density based clustering.**

## I. Introduction

The concept of 'Customer Segmentation' which is also alternatively known as 'Market Segmentation' was introduced by Smith in 1956. It was stated as "Market segmentation involves viewing a heterogeneous market as a number of smaller homogeneous markets in response to differing preferences, attributable to the desires of consumers for more precise satisfaction of their varying wants" [1]. To ensure customer satisfaction and optimal profit, customer segmentation helps to study and understand behaviors of customers. Actually, it is done by analyzing different types of information about customers.

Customer segmentation can be done focusing on different aspects such as demographic, geographic, behavioral and so on. Among them, this paper concentrates mostly on behavioral perspective as it is the most effective and practical one. Spending habit can be considered as one of the behavioral instances of customers which varies from one to another.

Clustering means partitioning a set of data in a set of groups of similar data. Clustering algorithms refer to those machine learning algorithms which are associated with unlabeled data. Among all other types of clustering algorithms, centroid based and density based algorithms are the most popular two types. In 'Centroid Based' clustering, clustering is done based on some randomly initialized points and minimum distance from a point to others. On the other hand, in 'Density Based' clustering, points are clustered based on their densities in a particular region.

In spite of the existence of a few works related to cluster based customer segmentation, no one of them has considered applying any density based clustering algorithm. Therefore, this paper implements DBSCAN algorithm as one of the density based algorithms while applying $k$-means with different distance metrics as a centroid based clustering algorithm.

The rest of the paper is organized as follows: section II discusses related work, section III gives a brief overview of the theoretical terms used in this paper and section IV presents the implementation. Besides, section V discusses on the experimental results. Finally, section VI concludes focusing on future work.

## II. Related Work

Namvar et al. [2] introduced a new customer segmentation method consisting of two phase clustering. They showed that combining demographic data with two phase clustering results in a relatively better clustering. Hruschka and Natter [3] compared performances of feedforward Neural Network and $k$-means algorithms for cluster based market segmentation and found that cluster analysis done by Neural Network is better than of $k$-means clustering. Besides, Wu and Lin [4] studied cluster based customer segmentation model, Lee and Park [5] surveyed customer satisfaction for satisfactory customer segmentation and Teichert et al. [6] studied a specific case of customer segmentation in airline industry while customer segmentation in case of banking selection was presented by Anderson et al. [7]. How data driven customer segmentation is done in case of tourism was shown by Dolnicar [8].

## III. Background Study

The theoretical terms behind this work such as customer segmentation, clustering, centroid based algorithms, density based algorithms etc. are briefly discussed here:

978-1-5386-2307-7/17/$31.00 ©2017 IEEE

Fig. 1: Customer Segmentation (Source: Adapted from [9])

### A. Customer Segmentation

Customer Segmentation is a process to divide customers of a consumer or business market in groups based on some shared characteristics. There are various aspects on which customer segmentation can be done such as demographic, behavioral, geographic and so on; however, among them, customer segmentation based on user behavior is the most effective one as it considers attitudes, opinions, interests and some related criteria of the customers. Focusing on spending habits of the customers and few other behavioral aspects is expected to provide a relatively better customer segmentation. Figure 1 illustrates the concept of customer segmentation.

### B. Clustering

Cluster analysis or clustering is a general task to group a set of objects in such a way that same type of objects remain in same group. It is one of the main aspects of data mining and a common technique for statistical data analysis used in different fields including machine learning, pattern recognition, image analysis, bioinformatics, data compression and so on. There are mainly four types of clustering algorithms- centroid based, density based, hierarchy based and distribution based clustering algorithms. Among them, centroid based algorithms work using some randomly initialized points called 'centroid' while density based algorithms consider the density of points in a region, hierarchy based algorithms work assuming that the nearby objects are more similar and distribution based algorithms work based on statistical distribution models.

*1) Centroid Based Clustering:* In centroid based algorithms, a predefined number of points are selected randomly which are called 'Centroid' where that predefined number denotes the number of expected clusters. After that, each point is assigned into a cluster based on the closest centroid. Then, position of centroids are changed to the mean position of their respective clusters. Finally, this process goes on iteratively until it finds expected number of meaningful clusters. A number of centroid based algorithms have been proposed to date. $K$-means, $k$-medoids, fuzzy $c$-means are some of them; however, $k$-means is the most popular among them.

*a) K-means:* $K$-means is a popular way to do vector quantization. Target of this algorithm is to group $n$ objects into $k$ clusters. Let $X = \{x_i\}, i = 1, 2, 3, ..., n$ be the set of $d$-dimensional points and $C = \{C_k, k = 1, 2, 3, ..., k\}$ where $C$ is set of clusters. Let $\mu_k$ be the centroid of cluster $c_k$. The squared error between $\mu_k$ and the points in cluster $C_k$ is to be minimized according to Equation 1 as follows:

$$J(C_k) = \sum_{X_i \epsilon C_k} ||X_i - \mu_k||^2 \tag{1}$$

According to Equation 2, actual objective of $k$-means is to minimize the sum of the squared error over all $k$ clusters.

$$J(C_k) = \sum_{k=1}^{K} \sum_{X_i \epsilon C_k} ||X_i - \mu_k||^2 \tag{2}$$

$k$-means works as follows:

1) Initializes $k$ number of centroids randomly within the data domain.
2) Clusters the data into $k$ groups by assigning each data point to its closest centroid based on the distance between them.
3) Calculates the mean of all objects in each cluster and moves the centroid to that position.
4) Repeats steps 2 and 3 until the same points are assigned to each cluster in consecutive iteration.

Any of the several distance metrics [10] can be used to calculate the minimum distance between any two points such as: Euclidean distance, Manhattan distance, Chebyshev distance, Minkowski distance etc.

Distance between two $n$-dimensional vectors $X$ and $Y$ can be calculated using Euclidean distance according to Equation 3 and Manhattan distance according to Equation 4.

$$D(X, Y) = \sqrt{\sum_{i=1}^{n} (X_i - Y_i)^2} \tag{3}$$

$$D(X, Y) = \sum_{i=1}^{n} |X_i - Y_i| \tag{4}$$

Figure 2 illustrates an example of initial and final positions of centroids for $k$-means.

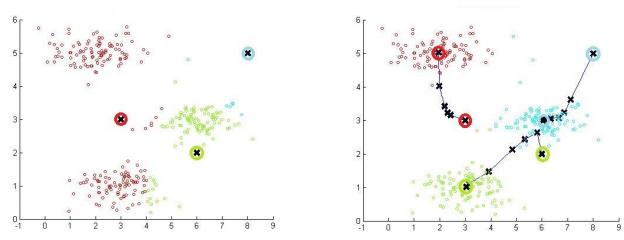

(a) Initial position (b) Final position

Fig. 2: Initial and final position of centroids during $k$-means

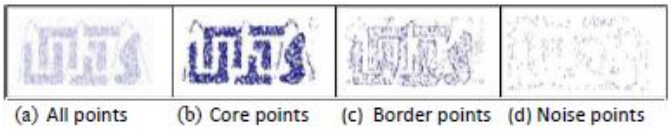


Fig. 3: Points identified by density based clustering algorithms (Source: Adapted from [11])

*2) Density Based Clustering:* Density-based clustering means creating clusters having different densities. Density refers to the number of data points within a specific region around a point $P$. This region is generally a $N$-sphere with radius $\epsilon$ which represents the maximum distance between any data point and $P$. Usually, these algorithms consider data points with lower density as noise or border points as shown in Figure 3. DBSCAN and OPTICS are two most commonly used density based clustering algorithms. There is a key drawback of this type of algorithms that they expect some kind of density drop to detect cluster borders.

*a) DBSCAN:* Density-Based Spatial Clustering of Applications with Noise (DBSCAN) discovers clusters with arbitrary shape based on the $\epsilon$ neighborhood principle which means that points within $\epsilon$ radius are neighbors. It was first proposed by Ester et al. in 1996 [12]. Size of a cluster can be controlled by a parameter called 'MinPts'(number of minimum points to be considered as a cluster) . DBSCAN outperforms many other centroid based clustering algorithms in case of noisy datasets.

DBSCAN algorithm works as follows:

1) Categorizes each point as either core point, border point or noise point.
2) Eliminates noise.
3) Makes new clusters with unclustered core points by assigning each point into a cluster based on neighborhood.

Time complexity of this algorithm is $O(n\log n)$ where, $n$ denotes the number of total points in dataset to cluster.

*b) OPTICS:* Ordering Points To Identify the Clustering Structure (OPTICS) is an algorithm presented by Ankerst et al. in 1999 [13]. Working principle of this algorithm is similar to DBSCAN algorithm. But it outperforms DBSCAN in case of data with varying density. It finds intrinsic clustering structure by producing a special order of the database with respect to its density based clustering structure. Unlike DBSCAN, it puts more importance on choosing number of minimum points to form a cluster instead of fixing the radius. It makes a priority heap of data points to keep nearest points in neighbor list while number of minimum points roughly controls the size of cluster. Thus, this algorithm ensures better clustering. Besides, this algorithm provides flexibility of controlling the cluster size.

## IV. Implementation

As it is described earlier that this paper implements customer segmentation using two types of clustering algorithms, implementation is done following the given steps:

### A. Experimental Setup

Implementation is done on Intel Core i5 CPU which has a processor speed of 3.2 GHz with a 4 GB RAM. WEKA (Waikato Environment for Knowledge Analysis) [14] and scikit-learn [15] are used. WEKA is developed by University of Waikato, New Zealand as a suite of machine learning software written in Java while scikit-learn is a machine learning library for Python programming language.

### B. Dataset

This paper uses Wholesale customers dataset [16] from University of California Irvine machine learning repository for customer segmentation. That dataset refers to clients of a wholesale distributor and contains data regarding consumption of different items by customers showing their annual spending. There are 440 instances and 8 attributes in total. Each instance in the dataset represents a customer while the attributes show each customer's annual spending on different commodities. To ease the implementation, two attributes from the dataset named as 'Channel' and 'Region' are excluded since they are not that much related to the spending habits of customers. Moreover, interest of this paper lies in considering the spending habits of customers rather than anything else for segmentation. Hence, this paper will be using the other 6 attributes on which the spending of customers are recorded. According to the University of California Irvine machine learning repository, this dataset is originated from another larger dataset referred in a paper [17]. Table 1 shows few samples of the dataset used.

### C. Customer Segmentation using Centroid Based Algorithm

In this paper, $k$-means has been chosen among all centroid based algorithms for implementation as it is considered as the most popular one of its type. Before applying on dataset, $K$-means needs to decide the value of $k$ and the distance metric to use. The appropriate number of total clusters, $k$ can be estimated using a few methods [18]. This paper considers 2 to 5 clusters of customers. Euclidean distance and Manhattan distance are used here as distance metrics for $k$-means though finally they do not show that much differences.

To scale all the values within a range between -1 and 1, 'Feature Normalization' process is applied.

Table I: Few samples of the dataset used

| Fresh | Milk | Grocery | Frozen | Detergents_Paper | Delicassen |
|---|---|---|---|---|---|
| 3157 | 4888 | 2500 | 4477 | 273 | 2165 |
| 12356 | 6036 | 8887 | 402 | 1382 | 2794 |
| 112151 | 29627 | 18148 | 16745 | 4948 | 8550 |
| 694 | 8533 | 10518 | 443 | 6907 | 156 |
| 36847 | 43950 | 20170 | 36534 | 239 | 47943 |

Table II: Results on applying $k$-means with different distance metrics and different values of $k$

| Distance Metrics | | Number of clusters (k) | | | |
|---|---|---|---|---|---|
| | | 2 | 3 | 4 | 5 |
| Euclidean Distance | No. of iteration | 14 | 14 | 13 | 13 |
| | Sum of squared error | 17.24 | 13.87 | 10.76 | 9.98 |
| | Time elapsed (sec) | 0.00 | 0.01 | 0.01 | 0.00 |
| Manhattan Distance | No. of iteration | 6 | 11 | 16 | 14 |
| | Sum of within cluster distances | 109.46 | 99.91 | 89.59 | 85.96 |
| | Time elapsed (sec) | 0.00 | 0.00 | 0.01 | 0.01 |

Table III: Results on applying DBSCAN with different radius of neighborhoods ($\epsilon$) and MinPts

| | $\epsilon$ = 0.06 MinPts = 3 | $\epsilon$ = 0.06 MinPts = 4 | $\epsilon$ = 0.06 MinPts = 6 | $\epsilon$ = 0.14 MinPts = 4 | $\epsilon$ = 0.15 MinPts = 4 |
|---|---|---|---|---|---|
| No. of clusters | 4 | 2 | 2 | 2 | 2 |
| No. of unclustered instances | 91 | 102 | 124 | 22 | 20 |
| Time elapsed (sec) | 0.02 | 0.02 | 0.02 | 0.02 | 0.02 |

Feature Normalization is done according to the following Equation 5:

$$x' = \frac{x - \bar{x}}{x_{max} - x_{min}} \tag{5}$$

where, $x$ is the original value, $\bar{x}$ is the mean, $x_{max}$ is the maximum value, $x_{min}$ is the minimum value and $x'$ is the normalized value.

Finally, $k$-means is applied on the dataset varying the value of $k$ roughly and the experimental results found for two different distance metrics are shown in Table II.

### D. Customer Segmentation using Density Based Algorithm

Due to the vast popularity of DBSCAN over other density based clustering algorithms, this paper implements that algorithm on the dataset. Applying DBSCAN algorithm does not need to define the total number of cluster to make from the user. It is itself able to determine the number of meaningful clusters using its two parameters: radius of neighborhoods $\epsilon$ within which points are considered neighbor to each other and MinPts which refers to the number of minimum points needed to be considered as a cluster. Table III shows the experimental results on applying DBSCAN algorithm on the dataset varying $\epsilon$ and MinPts. For each combination of these two parameters, number of clusters determined by the algorithm, number of unclustered instances and time elapsed are recorded and shown.

## V. Discussion

Table II shows that the sum of squared error for Euclidean distance is decreasing with the increasing of total number of clusters. Because, the more clusters are created, the more compact and dense the points become in a cluster. Similarly, about Manhattan distance, the sum of the distances within cluster is also decreasing as the points become closer when the number of clusters increases. Besides, Table III shows that DBSCAN can find the total number of clusters itself without being defined explicitly. If the number of points needed to get recognition as a cluster is increased, then more number of unclustered instances are found as they can not form cluster.

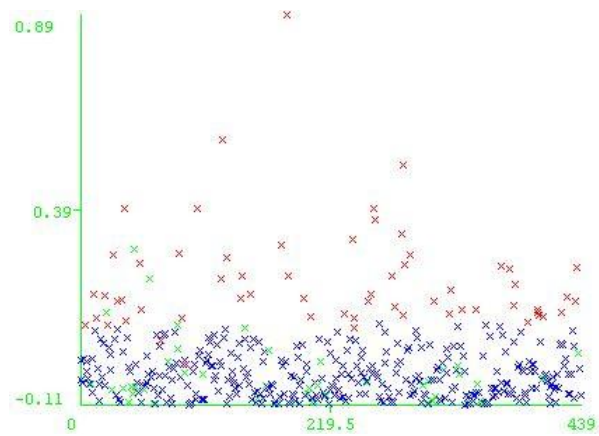


Fig. 4: Clusters found by $k$-means for 440 customers (red, green and blue colors represent instances of different clusters)

From the visualization of the experimental results found from implementation, customer segmentation observed for the dataset considered is shown in Figure 4. It is found by applying $k$-means algorithm where value of $k$ is 3 and Euclidean distance is considered as distance metric. From this figure, it seems that there are two prominent clusters of customers marked by red and blue colors and one other cluster marked by green color which does not seem that meaningful. Customers of this green cluster can be considered as noise or anomalous from density based perspective.

To observe the effectiveness of these two algorithms, performances shown by both of the algorithms can be compared based on the time elapsed and also the number of unclustered instances.

Table IV: Comparison between performances of $k$-means and DBSCAN for customer segmentation

| Subject(s) of comparison | K-means | DBSCAN |
|---|---|---|
| Maximum time elapsed (sec) | 0.01 | 0.02 |
| Min. number of unclustered instances | 0 | 20 |
| Max. number of unclustered instances | 0 | 124 |

Table IV shows a comparison between the performances of $k$-means and DBSCAN for customer segmentation. According to the data of this table, Figure 5 shows that DBSCAN takes relatively longer time than $k$-means; however, in spite of consuming more time, it provides a meaningful customer segmentation as well as detects some anomalous customers whose spending habits are different.

If the data of the table other than only time elapsed are considered, then concentration should also be put on the total number of unclustered instances. It can be seen that for using any type of distance metric, $k$-means algorithm clusters all the points of the dataset. Hence, both the minimum and the maximum number of unclustered instances found from this algorithm are zero. On the other hand, minimum and maximum number of the unclustered instances found using DBSCAN algorithm are 20 and 124 respectively.

In case of customer segmentation, these unclustered instances can play an important role. Because, this unclustered instances which are also alternatively known as noise from density based algorithm perspective can be used to identify customers having different behaviors. For example, customers having unusual spending habits can be detected considering their respective data points as noise by applying DBSCAN algorithm.

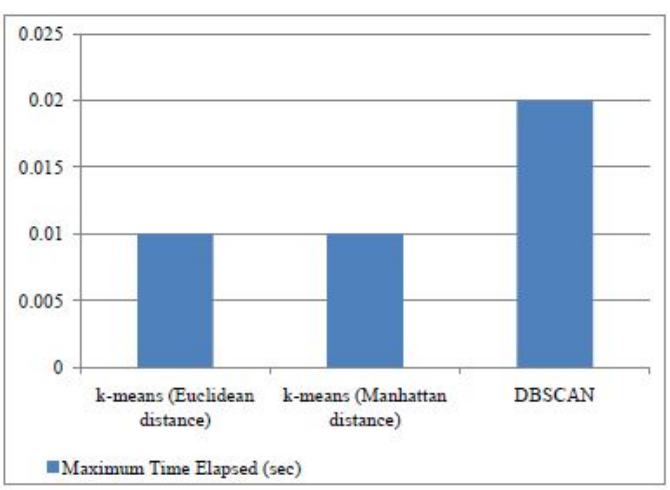


Fig. 5: Maximum time elapsed (sec) by $k$-means and DBSCAN for customer segmentation

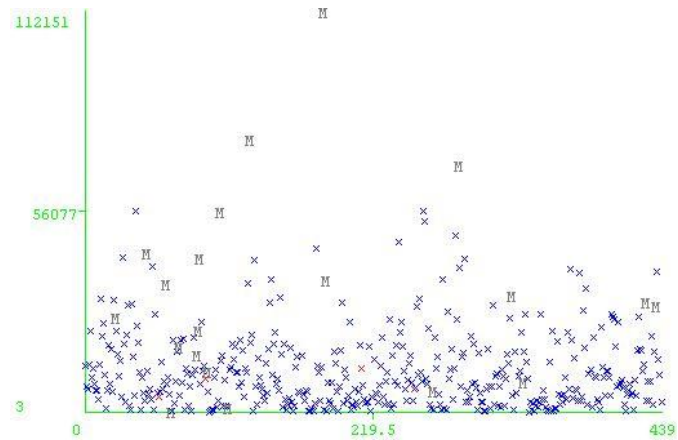


Fig. 6: Identifying customers having unusual spending habits with the help of DBSCAN algorithm

For real life applications and industrial use, performance often gets more priority than time taken. Hence, in order to get satisfactory customer segmentation, customers showing different behaviors also need to be identified beside just grouping them based on shared characteristics. For that reason, time consumed by the DBSCAN algorithm can be ignored. Because, unlike $k$-means clustering, DBSCAN algorithm does not only categorize customers into groups based on shared characteristics but also is able to spot customers having unusual behavior like relatively more spending habits. Figure 6 shows how DBSCAN algorithm is able to identify customers (denoted by 'M') having aberrant type of spending habits with the help of its unclustered instances. In this figure, vertical axis shows annual spending of customers where it clearly shows that DBSCAN identifies customers who spend relatively more than others. This identification is very useful to detect potential customers. That is why this paper claims that using density based clustering algorithm can result in relatively more meaningful clustering or customer segmentation.

## VI. Conclusion & Future Work

In this paper, $k$-means and DBSCAN algorithms are chosen to represent centroid based and density based algorithms for data clustering respectively. Results obtained from the implementation of these two algorithms show that any of them can be used for customer segmentation; however, in contrast to $k$-means, DBSCAN provides an extra option to find unusual customers having different spending habits which is very effective to ensure customer satisfaction and optimal profit. Besides, the results found from the implementation of density based clustering algorithm seem meaningful for the dataset considered. Hence, it can be said that density based clustering algorithms are also worth considering to apply in order to get satisfactory customer segmentation. Hopefully, to get more satisfactory customer segmentation in future, while using Neural Network for cluster analysis, other types of clustering algorithms will also be applied on different datasets and their performances will be evaluated as well.

## REFERENCES


[1] W. R. Smith, "Product differentiation and market segmentation as alternative marketing strategies," *Journal of marketing,* Vol. 21, No. 1, pp. 3-8, July 1956.

[2] M. Namvar, M. R. Gholamian, S. KhakAbi, "A Two Phase Clustering Method for Intelligent Customer Segmentation," *International Conference on Intelligent Systems, Modelling and Simulation,* 2010.

[3] H. Hruschka, and M. Natter, "Comparing performance of feedforward neural nets and K-means for cluster-based market segmentation," *European Journal of Operational Research,* Vol. 114, No. 2, pp. 346-353, July 1999.

[4] J. Wu, and Z. Lin, "Research on customer segmentation model by clustering," *Proceedings of the 7th international conference on Electronic commerce,* 2005.

[5] J. H. Lee, Jang Hee, and S. C. Park, "Intelligent profitable customers segmentation system based on business intelligence tools," *Expert systems with applications,* Vol. 29, No. 1, pp 145-152, 2005.

[6] T. Teichert, E. Shehu, and I. V. Wartburg, "Customer segmentation revisited: The case of the airline industry," *Transportation Research Part A: Policy and Practice,* Vol. 42, No. 1, pp. 227-242, 2008.

[7] W. T. Anderson, E. P. Cox, and D. G. Fulcher, "Bank selection decisions and market segmentation," *Journal of Marketing,* Vol. 40, No. 1, pp 40-45, January 1976.

[8] S. Dolnicar, "A review of data-driven market segmentation in tourism," *Journal of Travel & Tourism Marketing* Vol. 12, No. 1, pp 1-22, July 2002.

[9] ReachForce.com, "4 Ways to Segment Your Big Data and Super-Boost Your Lead Generation Efforts," [Online] Available: https://www.reachforce.com/blog/4-ways-to-segment-your-big-data-and-super-boost-your-lead-generation-efforts [Accessed: August 18, 2017].

[10] A. Singh, A. Yadav, and A. Rana, "K-means with Three different Distance Metrics," *International Journal of Computer Applications,* Vol. 67, No. 10, 2013.

[11] L. Ertöz, M. Steinbach, and V. Kumar, "Finding clusters of different sizes, shapes, and densities in noisy, high dimensional data," *Proceedings of the 2003 SIAM International Conference on Data Mining,* 2003.

[12] M. Ester, H.P. Kriegel, J. Sander, and X. Xu, "A Density-Based Algorithm for Discovering Clusters in Large Spatial Databases with Noise," *Kdd ,* Vol. 96, No. 34, pp. 226-231, 1996.

[13] M. Ankerst, M. M. Breunig, H. P. Kriegel, and J. Sander, "OPTICS: Ordering Points To Identify the Clustering Structure," *ACM Sigmod record,* Vol. 28, No. 2, pp. 49-60, 1999.

[14] M. Hall, E. Frank, G. Holmes, B. Pfahringer, P. Reutemann, and I. H. Witten, "The WEKA Data Mining Software: an Update," ACM SIGKDD explorations newsletter, Vol. 11, No. 1, pp. 10-18, 2009.

[15] F. Pedregosa, G. Varoquaux, A. Gramfort, V. Michel, B. Thirion, O. Grisel, M. Blondel, P. Prettenhofer, R. Weiss, V. Dubourg, J. Vanderplas, A. Passos, D. Cournapeau, M. Brucher, M. Perrot, and E. Duchesnay, "Scikit-learn: Machine Learning in Python," *Journal of Machine Learning Research,* Vol. 12, pp. 2825-2830, October 2011.

[16] "Wholesale Customers Data Set," [Online] Available: https://archive.ics.uci.edu/ml/datasets/wholesale+customers [Accessed: September 11, 2017].

[17] N. Abreu, "Analise do perfil do cliente Recheio e desenvolvimento de um sistema promocional," *Mestrado em Marketing,* ISCTE-University Institute of Lisbon, 2011.

[18] T. M. Kodinariya, and P. R. Makwana, "Review on determining number of Cluster in K-Means Clustering," *International Journal of Advance Research in Computer Science and Management Studies,* Vol. 1, No. 6, pp. 90-95, 2013.

# Combined Zernike Moments, Binary Pixel and Histogram of Oriented Gradients Feature Extraction Technique for Recognizing Hand Written Bangla Characters

Aminul Huq[1], Shyla Afroge[2], Mst. Tasnim Pervin[3]
[1] Dept. of Computer Science Engineering (Rajshahi University of Engineering and Technology, Bangladesh)
[2] Dept. of Computer Science Engineering (Rajshahi University of Engineering and Technology, Bangladesh)
[3] Dept. of Computer Science Engineering (Rajshahi University of Engineering and Technology, Bangladesh)
aminul.huq11@gmail.com, shyla.ruet@gmail.com, tasnimpervin@gmail.com

*Abstract*— **Feature selection is an essential step of optical character recognition. Accurate and distinguishable feature plays an important role to improve the performance of a classifier. There are several methods for feature extraction techniques for recognizing Bangla hand written characters; however the constraints of high recognition rate should be taken into consideration. The target of this paper is to provide an improvement in recognizing hand written Bangla Characters using combined Histogram of Oriented Gradients, Zernike Moments and Binary Pixel for feature extraction technique than each individual feature extraction techniques. A total of 30000 characters have been used, 24,000 for training dataset and 6,000 for testing dataset for this proposed system and this system shows 46.98% for Zernike Moments, 66.60% for Binary Pixels and 87.62% for Histogram of Oriented Gradients where overall combined features achieve an accuracy of 94.88% in recognizing characters.**

***Keywords— Histogram of oriented gradients;Zernike moments; Binary Pixel;support vector machine;Bangla OCR***

## I. INTRODUCTION

In the field of pattern recognition an important section is detection of characters such as automatic data extraction, institutional repository, captcha recognition, optical music character recognition and many more. Bangla is currently the world's seventh most used language in regard to population and second in the Indian sub-continent [1]. So the need for digitizing Bangla characters is increasing day by day. As the world progresses, Bangla language are used in many systems for this huge population that uses Bangla as their mother tongue. In the past many research works have been implemented on recognizing Bangla characters however this system faced many challenges like accuracy of recognition characters, extensive calculations which slowed the operations. Most of these problems can be solved by improving the feature extraction techniques. In the past many feature extraction techniques have been used as well as different classifiers for Bangla OCR. In this paper an improved feature extraction technique is proposed which is followed by justification of the improvement.

There are many types of feature extraction methods which can be classified in to three major groups [2]: Zoning, Characteristic loci, Crossing and Distances etc. fall in the category of statistical features. Fourier Transforms, Gabor Transforms, Wavelets, Moments these are members of Global Transformation and Series Expansion Features. Chain codes, Stroke Direction and Bays, Stroke are Geometric and Topological features.

The proposed system is divided into three major parts such as image preprocessing, feature extraction and classification of characters. The organization of this correspondence is as follows. Section II describes Methodologies which contains the image preprocessing steps. Section III describes feature extraction techniques. Section IV discusses the classification algorithm. In section V performance comparisons of these features are described both individually and combined way and the conclusion of this study are given in section VI.

## II. METHODOLOGY

To improve the recognition of Bangla characters the following system is hereby proposed. In our proposed system we have used three different feature extraction techniques they are Histogram of Oriented Gradients (HOG) features, Zernike moments and binary pixel of the image. These three techniques are used to capture the features of an image and hence used for classifying an image accordingly. The reason for using these three techniques is that they each possess different strong points based upon which they extract features from an image and collectively they provide a much better feature than each of them individually. For classification of the data we have used Support Vector Machine which provides a very good performance for multiclass classification [3].

### *A. PreProcessing*

Before performing feature extraction of image the steps that are performed are part of preprocessing. The steps can be shown in figure 1. These steps include image acquisition, binarization of the image, noise removal, skew detection, segmentation and scaling.

978-1-5386-2307-7/17/$31.00 ©2017 IEEE

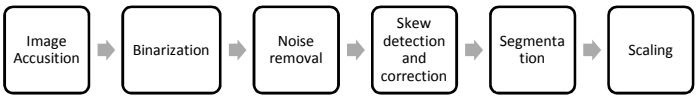


Figure 1. Preprocessing steps of images.

*1) Image Acquisition*

Images can be acquired through any device that has a camera. Then those pictures need to be fed into the system. The images can be of a single character or a text paragraph.

*2) Binarization*

After acquiring an image the first step is to make it a grayscale image from the RGB image. Then binarization process is performed on the image based on a particular threshold value. Here Otsu's method [5] is used for binarizing the image.

Figure 2. Binarization of an image.

*3) Noise Removal*

Noise removal is an important section of preprocessing an image. By doing so the image provides better visibility and features. Here median Filter is used upon the images which smoothens the image surface but at the same time blurs the edges as well.

*4) Skew Detection and Correction*

Skew is an angle to which the image displaces when an image is acquired. If theta is the angle that is displaced when acquiring the image if we rotate it in the opposite direction with same value then the skew will be removed.

*5) Segmentaition*

Segmentation is the process of creating many sub images from a particular image. Three types of segmentation such as line segmentation, word segmentation and character segmentation are performed. [6]. In line segmentation the image is scanned horizontally and is the checked for a particular number of rows for which there is no interference with characters which can be further processed. Word segmentation can be performed in the similar manner but in this case the image is scanned vertically rather than horizontally. Next step is character segmentation. In Bangla language each character of a word is connected with a line called Matra. Detection and removal of Matra is similar to line segmentation [6].

*6) Scaling*

After all the previous steps have been done the final step in preprocessing an image is scaling. Scaling refers to the size of the image upon which feature extraction techniques will occur. As the size of the image increases more features can be extracted accurately but the cost of computation will increase as well so the images are scaled to 32 x 32 matrixes.

## III. FEATURE EXTRACTION

Feature Extraction technique is the main focus of this correspondence. Here we have used three techniques for Feature Extraction those are Histogram of Oriented Gradients, Zernike Moments, and Binary Pixels.

### *A. Zernike Moments*

Moments or functions of moments are very popular feature extraction technique in pattern recognition. These are used in many applications [7][8][9]. Regular Moments can be defined as

$$m = \int_{-\infty}^{\infty}\int_{-\infty}^{\infty} x^p y^q f(x,y)\, dxdy$$

Where $m_{(p+q)}$ is the $(p+q)^{th}$ order moment of the image defined by f(x,y). For digital images the integrals are replaced by summations and thus $m_{(p+q)}$ becomes

$$m = \sum_x \sum_y x^p y^q f(x,y)$$

In [10], Zernike proposed a set of complex polynomials which created a complete orthogonal set over the interior of the unit circle, i.e., $x^2 + y^2 = 1$ [7]. Zernike Moment provides the advantage of being translation, rotation and scale invariant for recognizing an image. This complex polynomial is defined as $V_{nm}(x,y)$. It can be denoted as

$$V_{nm}(x,y) = V_{nm}(\rho,\theta) = R_{nm}(\rho)\exp(jm\theta)$$

Where

- n Positive integer or zero
- m Positive and negative integers , | m | <= n and n - | m | = even
- $\rho$ Length of the vector from origin to (x, y)
- $\theta$ Angle between the vector $\rho$ and x axis in counterclockwise direction

$R_{nm}(\rho)$, is the Radial Polynomial. It is denoted by,

$$R_{nm}(\rho) = \sum_{s=0}^{(n-|m|)/2} (-1)^s \frac{(n-s)!}{s!\left(\frac{n+|m|}{2}-s\right)!\left(\frac{n-|m|}{2}-s\right)!}\rho^{n-2s}$$

and

$$R_{n,-m}(\rho) = R_{nm}(\rho).$$

Zernike moments are projection of the image function onto these orthogonal basis functions [7]. The Zernike moment of order n with repetition m for a continuous image function $f(x,y)$ is

$$A_{nm} = \frac{n+1}{\pi}\iint_{x^2+y^2\le 1} f(x,y)\; V_{nm}^*(\rho,\theta)dxdy$$

Where * is the complex conjugate operator. For a digital image the integrals are replaced with summations

$$A_{nm} = \frac{n+1}{\pi}\sum_x\sum_y f(x,y)\; V_{nm}^*(\rho,\theta), \quad x^2 + y^2 \le 1$$

The following Table lists the first 36 moments of up to order 10.

Table 1: List of no. of moments up to order 10

| Order(n) | Zernike Moment of order n with repetition m($A_{nm}$) | No. of Moments |
|---|---|---|
| 0 | $A_{00}$ | 1 |
| 1 | $A_{11}$ | 1 |
| 2 | $A_{20}, A_{22}$ | 2 |
| 3 | $A_{31}, A_{33}$ | 2 |
| 4 | $A_{40}, A_{42}, A_{44}$ | 3 |
| 5 | $A_{51}, A_{53}, A_{55}$ | 3 |
| 6 | $A_{60}, A_{62}, A_{64}, A_{66}$ | 4 |
| 7 | $A_{71}, A_{73}, A_{75}, A_{77}$ | 4 |
| 8 | $A_{80}, A_{82}, A_{84}, A_{86}, A_{88}$ | 5 |
| 9 | $A_{91}, A_{93}, A_{95}, A_{97}, A_{99}$ | 5 |
| 10 | $A_{10,0}, A_{10,2}, A_{10,4}, A_{10,6}, A_{10,8}, A_{10,10}$ | 6 |

### *B. Binary Pixels*

After the binarization process an image becomes a 2D matrix with values of 1 and 0 only. A feature vector can be created from those pixel values by taking all the values of the image and making it a row vector. Now this row vector is capable of being a feature extraction technique where each column corresponds to a feature of that image.

### *C. Histogram of Oriented Gradients*

Histogram of Oriented Gradients (HOG) features has become very popular in object detection in recent years specifically in human detection [13]. The process of extracting features is shown in figure 3.

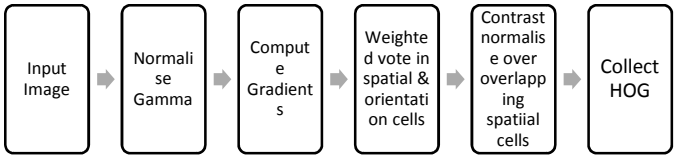


Figure 3. Feature Extraction using Histogram of Oriented Gradients.

The image is at first divided into small spatial regions called cells. Votes are accumulated in the cells. These cells can be either rectangular or radial. Each cell has a 1-D Histogram of gradient directions. The gradient orientation is quantized into 9 bins spaced from $0\,°\,to\,180°$ . The votes are gradient magnitude. To reduce aliasing votes are interpolated bi-linearly between neighboring bin center. In order to get good performance contrast normalization is very important. The final descriptor is then the vector of all components of normalized cells of all blocks. Generally the blocks are overlapped which seems redundant but in order to get good normalization it is important and this also provides better performance [13].

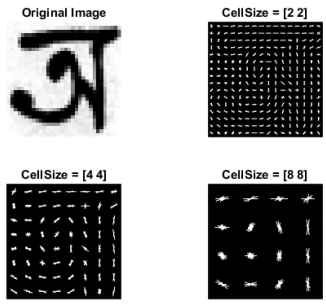


Figure 4. HOG features of a Bangla character for different cell size.

## IV. CLASSIFICATION

In this section we will review about Support Vector Machine (SVM) for classification problems [11]. Support Vector Machine was mainly designed for binary classification for determining the optimal hyper-plane to maximize the margin of separation between positive and negative data set [12]. Although this can be extended to multiclass classification by using the one versus all technique. The goal of SVM is to predict the output y on the testing set based on the features provided by the testing set after being trained using the training data set in supervised manner. For a given a training data set $\{(x_i, y_i),\ 1 \le i \le n\}$ where n is the total no. of data points, $x_i \in R^n$ is the $i^{th}$ input pattern and $y_i \in R^n$ is the $i^{th}$ output pattern. The SVM maximizes the cost function $\frac{1}{2} W^T W$ which is subject to constraints

$$x_i.w + b \ge 1 \text{ for } y_i = 1 \text{ and}$$

$$x_i.w + b \le -1 \text{ for } y_i = -1$$

Where $w$ the weight factor and b is the bias term. In case a separating hyper plane in this higher dimensional space does not exist, variables ξ are introduced such that

$$y_i[w^T \varphi(x_i) + b] \ge 1 - \xi_i \text{ , i = 1... n,}$$

$$\xi_i \ge 0 \text{ , i = 1, ..., n}$$

Where φ is a nonlinear function which maps the input space into a higher dimensional space. SVM now tries to determine w which minimizes

$$\frac{1}{2} W^T W + C \sum_{i=1}^{n} \xi_i$$

A kernel is similarity function. It takes two inputs and returns how similar they are. Some popular used kernels are: Polynomial of degree d:$K(x, x_i) = (xx_i + 1)^d$. Radial Basis Function (RBF) or commonly known as Gaussian kernel: $K(x, x_i) = \exp(-\frac{\|x - x_i\|^2}{2\sigma^2})$. Both of these two kernels are used for non-linear SVM.

## V. EXPERIMENTAL RESULTS & ANALYSIS

As there is no standard dataset for Bangla OCR for the experimental purpose we have used the dataset which is collected from [4].For each character 500 data has been used as a total of 30,000 characters for training and testing Bangla characters and numerals. 24,000 characters have been used for training and 6,000 characters have been used for testing. Before collecting features and passing it to the classifiers all the preprocessing steps mentioned above have been performed for both the training data set and testing dataset. For feature extraction in Histogram of Oriented Gradients we have used cell size of [8X8] which makes the calculation computationally faster. In Zernike Moment the moments of an
Image are collected till the order of 17. Support Vector Machine was implemented here using linear kernel and one vs. all coding scheme. All three feature extraction technique Zernike moments, Histogram of Oriented Gradients and Binary Pixel were combined by means of a simple concatenation operation. So that the whole string length is now the sum of all three individual string length.
The following Table shows the accuracy of identifying characters using these three feature extraction technique individually and in a combined manner which has been proposed here.

Table 2. Accuracy rate corresponding to different feature extraction techniques for different characters.

| Input | No. of Testing data | No. of Correctly Identified Data | | | |
|---|---|---|---|---|---|
| | | Zernike Moments | Binary Pixels | Histogram of Oriented Gradients | Combined |
| ১ | 100 | 42 | 88 | 87 | **91** |
| ৩ | 100 | 46 | 91 | 93 | **98** |
| অ | 100 | 68 | 96 | 99 | **99** |
| আ | 100 | 78 | 73 | 91 | **99** |
| ক | 100 | 24 | 65 | 83 | **99** |
| গ | 100 | 33 | 77 | 88 | **95** |
| ঞ | 100 | 67 | 38 | 91 | **92** |
| য | 100 | 28 | 42 | 75 | **90** |
| স | 100 | 33 | 79 | 77 | **95** |
| ঝ | 100 | 50 | 52 | 85 | **97** |
| ঢ় | 100 | 57 | 46 | 92 | **92** |

Here Figure 5 shows a comparative accuracy rate for different feature extraction techniques based on correct recognition of characters.

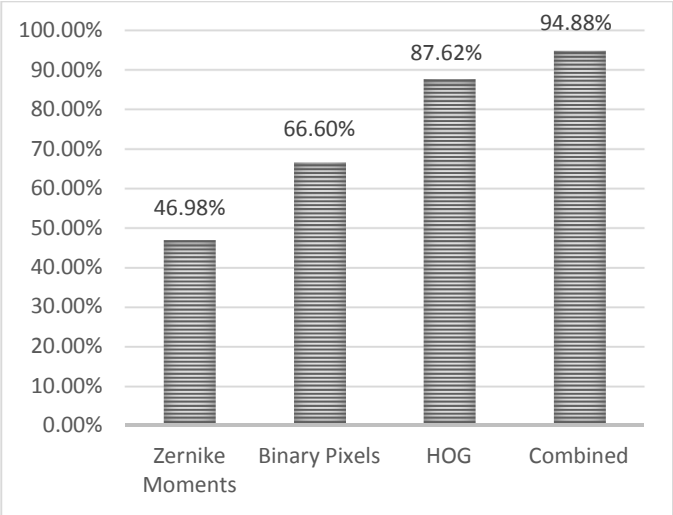


Figure 5. Accuracy rates of different feature extraction techniques.

A detailed Table 3.is shown to acknowledge the number of correctly identified data.

Table 3. No. of correctly identified characters when using different feature extraction techniques.

| | Total Testing Data | Correctly Identified Data | Accuracy |
|---|---|---|---|
| Zernike Moments | 6000 | 2819 | 46.98% |
| Binary Pixels | 6000 | 3996 | 66.60% |
| Histogram of Oriented Gradients | 6000 | 5257 | 87.62% |
| Combined | 6000 | **5693** | **94.88%** |

## VI. CONCLUSION

In this correspondence main focus is emphasized on a feature extraction technique which combines three individual feature extraction techniques. Using this combined technique it has been shown that it can be more reliable and it correctly recognize characters to 94.88% accuracy. However, this accuracy depends largely on skew correction, line segmentation, word segmentation, removal of matra. As these are performed more efficiently the recognition rate will improve as well. In the near future these issues will be taken care of and a comparison with other ensemble algorithms will be done as well.

## VII. REFERENCE

[1] Wikipedia contributors. "Bengali language." *Wikipedia, The Free Encyclopedia*. Wikipedia, The Free Encyclopedia, 5 Jul. 2017. Web.7 Jul. 2017.

[2] Gaurav Kumar, Pradeep Kumar Bhatia, "A Detailed Review of Feature Extraction in Image Processing System," International Conference on Advanced Computing & Communication Technologies,2014 .

[3] Burges, Christopher JC. "A tutorial on support vector machines for pattern recognition." *Data mining and knowledge discovery* 2.2 (1998): 121-167.

[4] Mohammed, Nabeel; Momen, Sifat; Abedin, Anowarul; Biswas, Mithun; Islam, Rafiqul; Shom, Gautam; Shopon, Md. (2017), "BanglaLekha-Isolated", Mendeley Data, v2.

[5] Otsu, Nobuyuki. "A threshold selection method from gray-level histograms." *IEEE transactions on systems, man, and cybernetics* 9.1 (1979): 62-66.

[6] Rownak, Ahnaf Farhan, et al. "An efficient way for segmentation of Bangla characters in printed document using curved scanning." *Informatics, Electronics and Vision (ICIEV), 2016 5th International Conference on*. IEEE, 2016.

[7] Khotanzad, Alireza, and Yaw Hua Hong. "Invariant image recognition by Zernike moments." *IEEE Transactions on pattern analysis and machine intelligence* 12.5 (1990): 489-497.

[8] Abu-Mostafa, Yaser S., and Demetri Psaltis. "Image normalization by complex moments." *IEEE Transactions on Pattern Analysis and Machine Intelligence* 1 (1985): 46-55.

[9] Hu, Ming-Kuei. "Visual pattern recognition by moment invariants." *IRE transactions on information theory* 8.2 (1962): 179-187.

[10] F. Zernike, Physica, vol. 1, p. 689, 1934

[11] Cortes, Corinna, and Vladimir Vapnik. "Support-vector networks." *Machine learning* 20.3 (1995): 273-297.

[12] Das, Nibaran, et al. "Handwritten Bangla basic and compound character recognition using MLP and SVM classifier." *arXiv preprint arXiv:1002.4040* (2010).

[13] Dalal, Navneet, and Bill Triggs. "Histograms of oriented gradients for human detection." *Computer Vision and Pattern Recognition, 2005. CVPR 2005. IEEE Computer Society Conference on*. Vol. 1. IEEE, 2005.

2017 3rd International Conference on Electrical Information and Communication Technology (EICT)
7-9 December 2017, Khulna, Bangladesh

# Developing a Pixel Value Ordering based Reversible Data Hiding Scheme

Sultan Abdul Hasib* Hussain Nyeem†
Department of Electrical, Electronic and Communication Engineering
Military Institute of Science and Technology (MIST), Mirpur Cantonment, Dhaka-1216
*hasib_3635@hotmail.com †h.nyeem@eece.mist.ac.bd

***Abstract*—Pixel Value Ordering (PVO)-based Reversible Data Hiding (RDH) schemes are promising for the applications requiring high fidelity embedded images. This paper presents modeling and analysis of an improved PVO-based RDH scheme. For computing non-overlapping blocks in PVO-embedding, neighborhood pixels are important for better embedding rate-distortion performance. However, only horizontal neighborhood pixels with a block of size $1 \times 3$ have so far been considered. In this paper, we investigate PVO-embedding with block-sizes $3 \times 1$, $2 \times 3$ and $3 \times 2$ for better utilization of redundancy and correlation of image pixels. Particularly, with mixed neighborhood (*i.e.*, horizontal, vertical and diagonal) pixels, an image block of size $3 \times 2$ (or $2 \times 3$) that creates a pair of pixels-trios of triangular shape possesses a greater possible correlation among the pixels. We therefore adopt these modifications in modeling a PVO-based RDH scheme for computing image blocks, and experimental results have demonstrated the improvement in embedding rate-distortion performance of the proposed modified scheme.**

***Index Terms*—pixel-value ordering; reversible embedding; data hiding; digital watermarking; prediction; sorting**

## I. Introduction

Reversible Data Hiding (RDH) is an evolving forensic and covert-communication technology that embeds data into a *cover* image (or other media like video and audio). The embedded data later can be extracted for different applications like the cover-image's authentication, copy-right protection, integrity establishment or annotation. A RDH scheme thus has two main processes: *generation* and *embedding* [1], [2]. In *generation*, embeddable data are generated and processed for an intended application. The *embedding* on the other hand deals with how and where the data are to be embedded in the cover image. In data hiding research, development of the *embedding* techniques has attracted much attention for digital image applications. [3]–[24].

Different types of reversible embedding techniques have underpinned the development of RDH schemes; for example, Difference Expansion (DE) schemes [3], [4], Histogram Shifting (HS) schemes [5], [6]; Reversible Contrast Matching (RCM) schemes [7], [8], Prediction Error Expansion (PEE) schemes [14]–[23]. Amongst them, PEE-has received much attention for better rate-distortion performance (*i.e.*, higher embedding rate with lower distortion) as it combines the potential of HS and DE techniques to better utilize the image redundancy. Embedding distortion in PEE highly depends on the prediction-error histogram as such a sharp distribution of the histogram offers lower embedding distortion. A better *predictor* is thus always desirable in PEE that helps obtain a sharper histogram [15].

Additionally, sorting of prediction errors has been another consideration for improving embedding performance of PEE [6]. With the sorted prediction errors, lower values of errors are used for embedding to ensure lower distortion in an embedded image. Li *et al*. [16] reported that higher embedding rate with lower distortion is obtainable by embedding in the prediction-errors with lower complexities. Coatrieux *et al*. [18] proposed an adaptive embedding technique that determines the most suitable carrier class according to its local specificity for data embedding. For better embedding rate-distortion performance, a PEE-based RDH scheme therefore aims to utilize correlations of the embeddable-pixels.

Pixel Value Ordering (PVO) technique has lately demonstrated better utilization of image correlations for PEE-based RDH. Unlike the earlier PEE-based schemes, PVO-based schemes predict a pixel in its non-overlapping block of nearest neighborhood pixels. Li *et al*. [17] introduced the PVO-based RDH scheme that either increases (or decreases) or keeps unchanged the maximum (or minimum) pixel in a block for embedding one bit of data. That scheme is later improved with the consideration of dual maximum (or minimum) pixels for prediction errors [19], adaptive prediction of maximum (or minimum) valued pixel [20], pixel-wise PVO [21] and 2D-PVO with pairs of prediction errors [22].

Recently, Jung [23] proposed a scheme that considers three pixels block with sorting and prediction. The blocks are non overlapping and the pixels are sorted in ascending order. The maximum and minimum prediction errors are then computed to determine whether the data is embedded in the maximum or minimum pixels. That scheme offers better embedded image quality with reasonably higher embedding capacity. However, like other aforementioned PVO-based RDH schemes, computation of image blocks with higher pixels correlation has not been considered. This means that, better utilization of pixels correlation may lead to further improvement of the scheme for better rate-distortion performance.

978-1-5386-2307-7/17/$31.00 ©2017 IEEE

In this paper, we report modeling of an improved PVO-based RDH scheme with the consideration of better utilization of pixels' correlation in computing image blocks. We have analyzed the embedding rate-distortion performance of Jung's scheme [23] for different block sizes. Particularly, with mixed neighborhood (*i.e.*, horizontal, vertical and diagonal) pixels, an image block of size $3 \times 2$ (or $2 \times 3$) that creates a pair of pixels-trios of triangular shape possesses a greater possible correlation among the pixels. We therefore adopt these modifications in modeling a PVO-based RDH scheme for computing image blocks, Thereby, a greater possible correlation among the pixels can be obtained and utilized in embedding with better rate-distortion performance.

In what follows, we develop and present a general computational model of the improved PVO-based RDH scheme in Sec. II and analyze the experimental results of rate-distortion performance for different block sizes in Sec. III. Conclusions are given in Sec. IV.

## II. Improved PVO-based RDH Scheme

In this section, modeling of a PVO-based RDH scheme is presented that generally captures the principle of both Jung's scheme [23] and proposed modifications. The models of embedding and extraction processes are presented below followed by the proposed modifications for possible rate-distortion improvement.

### A. PVO-based Embedding

Let an image, $I$ of size $M \times N$ is an input (or *cover*) image and is used for embedding of secret-data, $D$. The embedding process follows the following steps to output the embedded image, $I'$.

Step 1: $B \leftarrow block\,(I, block_size)$

▷ Input image, $I$ is divided into a set of non-overlapping blocks, $B$ by the function, $block\,(\cdot)$ with $block_size$ of $1 \times 3$ such that $B = \{B_n\}$, where $B_n$ is a set of three pixels of $n^{th}$ block. That is, $B_n = \{b_i, b_{i+1}, b_{i+2}\}$ with $i = 1, 2, \cdots, M \times N$ for $n = 1, 2, \cdots, \frac{M \times N}{3}$.

Step 2: $P_n \leftarrow sort\,(B_n)$ for all $n$

▷ A set of three sorted pixels of $n^{th}$ block is obtained by the block-wise sorting function, $sort\,(\cdot)$ for each $B_n$. That is, $P_n = \{p_i, p_{i+1}, p_{i+2}\}$, where $p_i \leq p_{i+1} \leq p_{i+2}$.

Step 3: $E_n \leftarrow predict\,(P_n)$ for all $n$

▷ For all sorted block-pixels $\{P_n\}$, the function, $predict\,(\cdot)$ outputs a set of predicted errors $\{E_n\}$. That is, for each $P_n$, a pair of predicted errors $E_n = \{e^n_{max}, e^n_{min}\}$ is obtained as per Eq. (1).

$$e_{max} = p_{i+2} - p_{i+1} \tag{1a}$$

$$e_{min} = p_i - p_{i+1} \tag{1b}$$

Step 4: $P'_n \leftarrow embed\,(P_n, E_n, d)$ for all $n$

▷ A pair of predicted errors, $e_{max}$ and $e_{min}$ of $E_n$ gets embedded by the secret bits, $d \in D$ or expanded by unit value as in Eq. (2) and Eq. (3) to obtain the modified errors, $\hat{e}_{max}$ and $\hat{e}_{min}$ for each block. These modified errors are then used as per Eq. (4) to compute the set of estimated pixels, $P'_n = \{p'_i, p_{i+1}, p'_{i+2}\}$.

$$\hat{e}_{max} = \begin{cases} e_{max}, & \text{for } e_{max} = 0 \\ e_{max} + d, & \text{for } e_{max} = 1 \\ e_{max} + 1, & \text{for } e_{max} > 1 \end{cases} \tag{2}$$

$$\hat{e}_{min} = \begin{cases} e_{min}, & \text{for } e_{min} = \ \ 0 \\ e_{min} - d, & \text{for } e_{min} = -1 \\ e_{min} - 1, & \text{for } e_{min} < -1 \end{cases} \tag{3}$$

$$p'_{i+2} = p_{i+1} + \hat{e}_{max} \tag{4a}$$

$$p'_i = p_{i+1} + \hat{e}_{min} \tag{4b}$$

Step 5: $B'_n \leftarrow inverse_sort\,(P'_n)$ for all $n$

▷ Relocate the sorted embedded pixels of each block to their original locations.

Step 6: $I' \leftarrow de_block\,(B'_n, block_size)$ for all $n$

▷ Rearrange each of the embedded blocks to return the embedded image.

### B. PVO-based Extraction

The PVO-based extraction process follows similar steps with inverse computation of embedding as mentioned below. The embedded image, $I'$ and $block_size$ are given as inputs to obtain the original image, $I$ and extracted data, $D$.

Step 1: $B' \leftarrow block\,(I', block_size)$

▷ The embedded image, $I'$ is divided into a set of non-overlapping blocks, $B'$ by the function, $block\,(\cdot)$ with block size of $1 \times 3$ such that $B' = \{B'_n\}$, where $B'_n$ is a set three pixels of $n^{th}$ block. That is, $B'_n = \{b'_i, b'_{i+1}, b'_{i+2}\}$ with $i = 1, 2, \cdots, M \times N$ for $n = 1, 2, \cdots, \frac{M \times N}{3}$.

Step 2: $P'_n \leftarrow sort\,(B'_n)$ for all $n$

▷ A set of three sorted pixels of $n^{th}$ block is obtained by the block-wise sorting function, $sort\,(\cdot)$ for each $B'_n$. That is, $P'_n = \{p'_i, p'_{i+1}, p'_{i+2}\}$, where $p'_i \leq p'_{i+1} \leq p'_{i+2}$.

Step 3: $E'_n \leftarrow predict\,(P'_n)$ for all $n$

▷ For all sorted block-pixels $\{P'_n\}$, the function, $predict\,(\cdot)$ outputs a set of predicted errors $\{E'_n\}$. That is, for each $P'_n$, a pair of predicted errors $E'_n = \{\hat{e}^n_{max}, \hat{e}^n_{min}\}$ is obtained as per Eq. (5).

$$\hat{e}_{max} = p'_{i+2} - p'_{i+1} \tag{5a}$$

$$\hat{e}_{min} = p'_i - p'_{i+1} \tag{5b}$$

Step 4: $(P_n, D) \leftarrow extract\,(P'_n, E'_n)$ for all $n$

▷ An embedded secret bit, $d \in D$ is extracted from the embedded blocks, $P'_n$ and the pair of embedded/expanded predicted errors, $\hat{e}_{max}$ and $\hat{e}_{min}$ of $E'_n$ as in Eq. (6) for each block. These modified errors are also used to compute the set of original sorted pixels, $P_n = \{p_i, p_{i+1}, p_{i+2}\}$ as per Eq. (7).

$$d = \begin{cases} \hat{e}_{max} - 1, & \text{for } 1 \le \hat{e}_{max} \le 2 \\ -\hat{e}_{min} - 1, & \text{for } -2 \le \hat{e}_{min} \le -1 \end{cases} \tag{6}$$

$$p_{i+2} = \begin{cases} p'_{i+2}, & \text{for } \hat{e}_{max} = 0 \\ p'_{i+2} - d, & \text{for } 1 \le \hat{e}_{max} \le 2 \\ p'_{i+2} - 1, & \text{for } \hat{e}_{max} > 2 \end{cases} \tag{7a}$$

$$p_{i+1} = p'_{i+1} \tag{7b}$$

$$p_i = \begin{cases} p'_i, & \text{for } \hat{e}_{min} = 0 \\ p'_i + d, & \text{for } -2 \le \hat{e}_{min} \le -1 \\ p'_i + 1, & \text{for } \hat{e}_{min} < -2 \end{cases} \tag{7c}$$

Step 5: $B_n \leftarrow inverse_sort\,(P_n)$ for all $n$

▷ Relocate the sorted embedded pixels of each block to their original locations.

Step 6: $I \leftarrow de_block\,(B_n,\ block_size)$ for all $n$

▷ Rearrange each restored image-blocks to return the original image. Finally, return $I$ and the extracted data, $D$.

### C. Proposed Improvement

The main aim of a PVO-based embedding is to better utilize the image correlations for minimum embedding distortion with higher possible embedding capacity, as mentioned in Sec. I. Particularly, in the PVO-based embedding process presented in Sec. II-A, embedding is carried out only for the unit prediction error in a block with horizontal neighborhood pixels. This consideration restricts the embedding distortion controlled by the inter-pixel correlations of a block. Thus, consideration of defining non-overlapping blocks with better inter-correlated pixels may demonstrate better embedding rate-distortion performance.

To this end, we have investigated the embedding performance of the PVO-based RDH scheme for different orientations of non-overlapping image blocks. Only horizontal neighborhood pixels of size $1 \times 3$ is considered to constitute image blocks in the existing scheme [23]. We have considered image blocks of size $3 \times 1$ for vertical neighborhood pixels' correlation and the blocks of size $2 \times 3$ and $3 \times 2$ for mixed (*e.g.*, horizontal, vertical and diagonal) neighborhood pixels' correlations. The image blocks of size $3 \times 2$ and $2 \times 3$ give a pair of pixel-trios (*i.e.*, two image blocks, each of them with three pixels forms a triangular shape).

The above consideration of better possible utilization of block-pixels' correlation essentially modifies respective image blocking and de-blocking functions, $block\,(\cdot)$ and $de_block\,(\cdot)$ of the presented model with the input argument *block_size*. That is, for Jung's scheme, *block_size* is defined by $1 \times 3$, which is proposed to be modified with either $3 \times 1$, $3 \times 2$ or $2 \times 3$ as such a suitable *block_size* can be investigated for the presented models of PVO-based embedding and extraction.

## III. Experimental Results and Analysis

We now present here the performance of the proposed PVO embedding and compare it with the that of the Jung's PVO-based scheme [23]. We use the USC-SIPI test-images [25] of size $256 \times 256 \times 8$ for this performance evaluation. We determine both the embedding-capacity and embedding-rate in terms of total embedded bits and bit per pixels (bpp), respectively. For embedding, a set of pseudo-random bits is generated as *data*. The proposed model of PVO-embedding is implemented using MATLAB R2016b with a 1.3 GHz Intel core i5 CPU, 4 GB memory.

Additionally, for evaluating the embedded image quality, we consider two popular metrics, peak signal to noise ratio (PSNR) defined in Eq. (8) and structural similarity (SSIM) [26] defined in Eq. (9). Here, $M \times N$ is the image size, and $I(i,j)$ and $I'(i,j)$ are the pixel values of position $(i,j)$ in an original image and its embedded version, respectively. In Eq. (9), $\mu_x$ and $\mu'_x$ are the average values of $x$ and $x'$, where $x \in I$ and $x' \in I'$ are the pixels of original and embedded images, respectively. Similarly, $\sigma_x^2$ and $\sigma_{x'}^2$ are the variance of $x$ and $x'$, respectively; $\sigma_{xx'}$ is the covariance of $x$ and $x'$; $c_1$ and $c_2$ are two regularization constants, and $L$ is the dynamic range of the pixel values.

$$\text{MSE} = \frac{\sum_{j=1}^{N}\sum_{i=1}^{M}\left(I'(i,j) - I(i,j)\right)^2}{MN} \tag{8a}$$

$$\text{PSNR} = 10\log\frac{L^2}{\text{MSE}} \tag{8b}$$

$$\text{SSIM} = \frac{(2\mu_x\mu_{x'} + c_1)(2\sigma_{x,x'} + c_2)}{(\mu_x^2 + \mu_{x'}^2 + c_1)(\sigma_x^2 + \sigma_{x'}^2 + c_2)} \tag{9}$$

Our experimental results have demonstrated a better embedding rate-distortion performance for PVO embedding with mixed neighborhood pixels. This means that inter-pixel correlations can be better utilized in PVO embedding with blocks of size $2 \times 3$ or $3 \times 2$ resulting in better embedding rate-distortion performance as illustrated in Table I. For example, the total embedding capacity of Jung's Scheme is 44992 bits (or 0.1716 bpp) for Airplane image, which is increased to 46547 bits, 46612 bits and 46762 bits (or 0.1776 bpp, 0.1778 bpp and 0.1784 bpp) for $3 \times 1$, $2 \times 3$ and $3 \times 2$ size of image blocks, respectively for our proposed embedding.

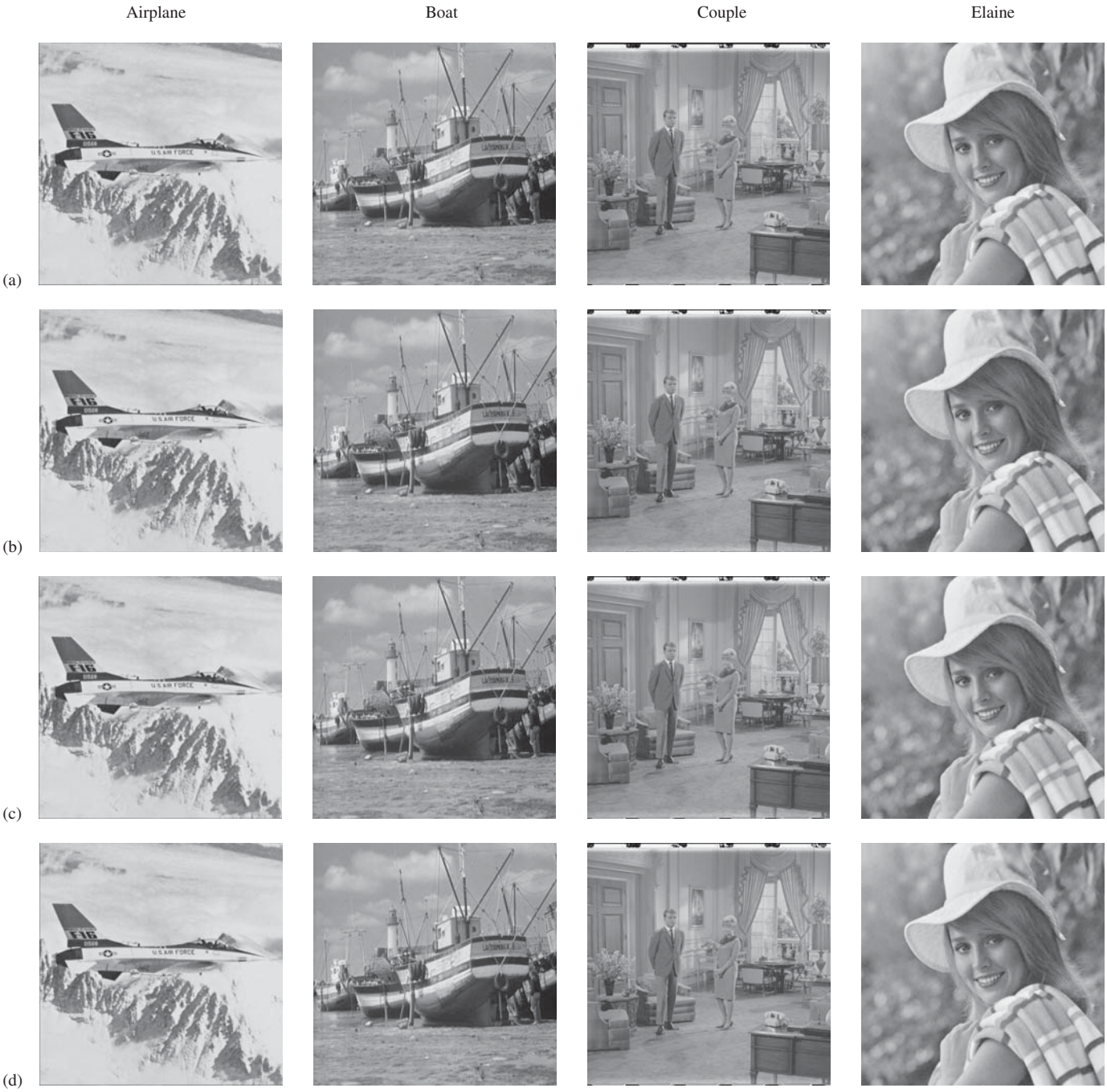


Fig. 1. Example of embedded images for blocks with different neighborhood pixels: (a) $1 \times 3$, (b) $3 \times 1$, (c) $2 \times 3$ and (d) $3 \times 2$.

Besides, visual quality of the embedded images is also reasonably improved as evident in Table I and also illustrated in Fig. 1 and Fig. 2. For example, PSNR and SSIM values of Airplane embedded image are 51.576 dB and 0.9759, respectively. In contrast, for our proposed embedding with $3 \times 1$, $2 \times 3$ and $3 \times 2$, respective PSNR and SSIM values are 51.617 dB and 0.9756, 51.639 dB and 0.9760, and 51.629 dB and 0.9759. We have particularly observed that, while performance of the proposed scheme with $3 \times 1$ block-size slightly improves over the Jung's scheme, this improvement becomes more noticeable for the other proposed block-sizes (*i.e.*, $2 \times 3$ and $3 \times 2$). This is because, with these block sizes, all three neighborhood (*i.e.*, horizontal, vertical and diagonal) pixels are present and more correlated than the other blocks (*i.e.*, proposed $3 \times 1$ and Jung's $1 \times 3$).

Our above argument is also supported by the average performance of the PVO embedding for all the test images and block sizes. In particular, the average embedding capacity

TABLE I
EMBEDDING RATE-DISTORTION PERFORMANCE OF PVO-EMBEDDING WITH DIFFERENT BLOCK SIZES

| Block Size | Metric | Airplane | Baboon | Elaine | Peppers | Tiffany | Average |
|---|---|---|---|---|---|---|---|
| Jung [23] ($1 \times 3$) | Capacity (bits) | 44992 | 13226 | 23306 | 33483 | 41750 | 31351 |
| | bpp | 0.1716 | 0.0505 | 0.0889 | 0.1277 | 0.1593 | 0.120 |
| | PSNR (dB) | 51.576 | 50.263 | 50.595 | 50.923 | 51.316 | 50.935 |
| | SSIM | 0.9759 | 0.9977 | 0.9929 | 0.9887 | 0.9829 | 0.988 |
| Proposed ($3 \times 1$) | Capacity (bits) | 46547 | 14046 | 23997 | 31933 | 38807 | 31066 |
| | bpp | 0.1776 | 0.0536 | 0.0915 | 0.1218 | 0.1480 | 0.119 |
| | PSNR (dB) | 51.617 | 50.283 | 50.612 | 50.869 | 51.183 | 50.913 |
| | SSIM | 0.9756 | 0.9977 | 0.9926 | 0.9885 | 0.9826 | 0.987 |
| Proposed ($2 \times 3$) | Capacity (bits) | 46612 | 14090 | 24392 | 33423 | 41864 | 32076 |
| | bpp | 0.1778 | 0.0537 | 0.0930 | 0.1275 | 0.1597 | 0.122 |
| | PSNR (dB) | 51.639 | 50.282 | 50.633 | 50.914 | 51.305 | 50.955 |
| | SSIM | 0.9760 | 0.9977 | 0.9928 | 0.9886 | 0.9829 | 0.988 |
| Proposed ($3 \times 2$) | Capacity (bits) | 46762 | 14087 | 24304 | 33802 | 41680 | 32127 |
| | bpp | 0.1784 | 0.0537 | 0.0927 | 0.1289 | 0.1590 | 0.123 |
| | PSNR (dB) | 51.629 | 50.286 | 50.629 | 50.916 | 51.303 | 50.953 |
| | SSIM | 0.9759 | 0.9977 | 0.9928 | 0.9886 | 0.9829 | 0.988 |

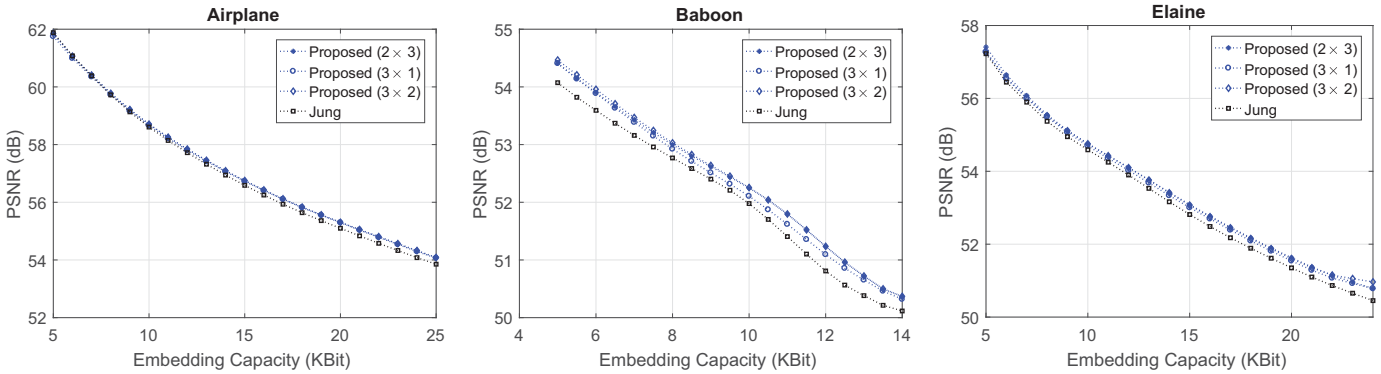


Fig. 2. Embedding rate-distortion performance comparison of the proposed embedding scheme with Jung's scheme [23].

achieved with $3 \times 2$ size block is 32127 bits and that with a block of size $2 \times 3$ is 32076 bits, whereas the capacity is 31351 bits and 31066 bits for the blocks of size $1 \times 3$ and $3 \times 1$, respectively. This improved embedding capacity also comes with improved average PSNR and SSIM values in case of $2 \times 3$ block size.

We note that the trend of improvements in rate-distortion performance of the proposed PVO embedding discussed above and illustrated for a few test images in Fig. 1, Fig. 2 and Table I also holds true for the other test images we experimented with.

## IV. CONCLUSIONS

In this paper, we have presented computational modeling of a PVO-based RDH scheme and analyzed its embedding rate-distortion performance for better utilization of block-pixels correlation. Non-overlapping blocks with different neighborhood pixels are computed and used in PVO-based embedding. We have observed better rate-distortion performance for the embedding with an image block with mixed (*i.e.*, horizontal, vertical and diagonal) neighborhood pixels. In other words, PVO-based embedding with $2 \times 3$ and $3 \times 2$ image-blocks demonstrated the highest improvement in rate-distortion performance compared to the other block-sizes (*i.e.*, $3 \times 1$ and block-size of Jung's scheme). This consideration may also be applied to other PVO-based RDH schemes for further improving their rate-distortion performance.

We continue our research to investigate other PVO-based

RDH schemes to adopt the proposed improvement for better utilization of image pixels' correlation in an extended experimental setup.

## References


[1] H. Nyeem, W. Boles, and C. Boyd, "Digital image watermarking: its formal model, fundamental properties and possible attacks," *EURASIP Journal on Advances in Signal Processing*, vol. 2014, no. 1, pp. 1–22, 2014.

[2] ——, "Developing a digital image watermarking model," in *Proc. DICTA*. IEEE, 2011, pp. 468–473.

[3] J. Tian, "Reversible data embedding using a difference expansion," *IEEE Trans. CSVT*, vol. 13, pp. 890–896, 2003.

[4] A. M. Alattar, "Reversible watermark using the difference expansion of a generalized integer transform," *IEEE Trans. Image Processing*, vol. 13, pp. 1147–1156, 2004.

[5] Z. Ni, Y.-Q. Shi, N. Ansari, and W. Su, "Reversible data hiding," *IEEE Trans. CSVT*, vol. 16, pp. 354–362, 2006.

[6] V. Sachnev, H. J. Kim, J. Nam, S. Suresh, and Y. Q. Shi, "Reversible watermarking algorithm using sorting and prediction," *IEEE Trans. CSVT*, vol. 19, pp. 989–999, 2009.

[7] D. Coltuc and J.-M. Chassery, "Very fast watermarking by reversible contrast mapping," *IEEE Sig. Proc. Let.*, vol. 14, no. 4, pp. 255–258, 2007.

[8] X. Chen, X. Li, B. Yang, and Y. Tang, "Reversible image watermarking based on a generalized integer transform," in *Proc. ICASSP*. IEEE, 2010, pp. 2382–2385.

[9] H. Nyeem, W. Boles, and C. Boyd, "Utilizing least significant bit-planes of roni pixels for medical image watermarking," in *Proc. DICTA'13*. IEEE, 2013, pp. 1–8.

[10] M. A. Wahed and H. Nyeem, "Developing a block-wise interpolation based adaptive data embedding scheme," in *Proc. ICEEICT'16*. IEEE, 2016, pp. 1–6.

[11] H. Nyeem, W. Boles, and C. Boyd, "Watermarking capacity control for dynamic payload embedding," in *Recent Advances in Information and Communication Technology 2015*. Springer, 2015, pp. 143–152.

[12] H. Nyeem, "A digital watermarking framework with application to medical image security," Ph.D. dissertation, Queensland University of Technology, 2014. [Online]. Available: https://eprints.qut.edu.au/74749/

[13] H. Nyeem, W. Boles, and C. Boyd, "Counterfeiting attacks on block-wise dependent fragile watermarking schemes," in *Proceedings of the 6th International Conference on Security of Information and Networks*. ACM, 2013, pp. 86–93.

[14] D. M. Thodi and J. Rodríguez, "Expansion embedding techniques for reversible watermarking," *IEEE Trans. Image Processing*, vol. 16, pp. 721–730, 2007.

[15] D. Coltuc, "Improved embedding for prediction-based reversible watermarking," *IEEE Transactions on Information Forensics and Security*, vol. 6, no. 3, pp. 873–882, 2011.

[16] X. Li, B. Yang, and T. Zeng, "Efficient reversible watermarking based on adaptive prediction-error expansion and pixel selection," *IEEE Trans. Image Processing*, vol. 20, pp. 3524–3533, 2011.

[17] X. Li, J. Li, B. Li, and B. Yang, "High-fidelity reversible data hiding scheme based on pixel-value-ordering and prediction-error expansion," *Signal processing*, vol. 93, no. 1, pp. 198–205, 2013.

[18] G. Coatrieux, W. P., B. N. Cuppens, F. Cuppens, and C. Roux, "Reversible watermarking based on invariant image classification and dynamic histogram shifting," *IEEE Trans. IFS*, vol. 8, pp. 111–120, 2013.

[19] F. Peng, X. Li, and B. Yang, "Improved pvo-based reversible data hiding," *Digital Signal Processing*, vol. 25, pp. 255–265, 2014.

[20] B. Ou, X. Li, Y. Zhao, and R. Ni, "Reversible data hiding using invariant pixel-value-ordering and prediction-error expansion," *Signal processing: image communication*, vol. 29, no. 7, pp. 760–772, 2014.

[21] X. Qu and H. J. Kim, "Pixel-based pixel value ordering predictor for high-fidelity reversible data hiding," *Signal Processing*, vol. 111, pp. 249–260, 2015.

[22] B. Ou, X. Li, and J. Wang, "High-fidelity reversible data hiding based on pixel-value-ordering and pairwise prediction-error expansion," *Journal of Visual Communication and Image Representation*, vol. 39, pp. 12–23, 2016.

[23] K.-H. Jung, "A high-capacity reversible data hiding scheme based on sorting and prediction in digital images," *Multimedia Tools and Applications*, vol. 76, no. 11, pp. 13 127–13 137, 2017.

[24] H. Nyeem, W. Boles, and C. Boyd, "Content-independent embedding scheme for multi-modal medical image watermarking," *BioMedical Engineering OnLine*, vol. 14, no. 1, p. 7, Feb 2015.

[25] "SIPI image database," http://sipi.usc.edu/database/, [Online; last accessed 23-Nov-2013].

[26] Z. Wang, A. C. Bovik, H. R. Sheikh, and E. P. Simoncelli, "Image quality assessment: From error visibility to structural similarity," *IEEE Trans. Image Processing*, vol. 13, no. 4, pp. 600–612, 2004.

# Digital Electric Meter Reading Recognition Based on Horizontal and Vertical Binary Pattern

Atif Anis[1], Md. Khaliluzzaman[1,2], Mohammad Yakub[1], Niloy Chakraborty[1], and Kaushik Deb[2*]

[1]Dept. of Computer Science and Engineering, International Islamic University Chittagong, Chittagong-4318, Bangladesh
[2]Dept. of Computer Science and Engineering, Chittagong University of Engineering & Technology, Chittagong-4349, Bangladesh
atifanis61@gmail.com, khalil_021@yahoo.co.in, mdyakub3028@gmail.com, niloycse36@gmail.com, *debkaushik99@cuet.ac.bd

***Abstract*— Digital meter reading recognition from a digital electric meter image is the key step in the field of digital image processing to evaluate the meter readings from different environmental conditions automatically. This work has gain important for the purpose of automatic generation of electric bill from digital electric meter image. In this regard, a digital electric meter reading recognition framework is proposed in this paper. For that initially, the input image is normalized and converted to YCbCr image. As the digital electric meter reading region is resolute with color light, especially green, the reading region is extracted from YCbCr image based on the value of the Cb and Cr. After that, Canny edge operator is employed on the extracted region to find the edge image. In this edge image, the individual digit's edge gaps are filled up through the morphological operation to find individually connected digit edge image. These individual digits are segmented from an edge image through the vertical projection. Furthermore, the individually segmented digits are filled and thinned to detect the shapes of the digits. From these segmented digit shapes the Horizontal and Vertical Binary (HVB) pattern features are extracted. This is the key contribution of this paper. Finally, based on the HVB patterns the digital meter reading sequence is recognized. The experimental result reveals that the proposed framework is practical and effective.**

***Keywords*— *YCbCr; Canny operator; morphological operation; image processing, digital electric meter; Horizontal and Vertical Binary (HVB) pattern***

## I. INTRODUCTION

In past few decades, to track the electricity consumption, electric meters are used in homes, industries, and offices. At present, it plays an important role in our daily life. In our country, the electric consumption reading is recorded by a person from door to door manually. The traditional practice creates the problem of wrong and unpunctual reading. This is because of, the digital number value and its relative positional value is measured by manipulator vision. So, the efficiency of reading accuracy is influenced by person's judgement. Furthermore, there is no proper procedure to show the evidence of the meter reading to the consumer.

For that, a framework is proposed in this paper to keep the evidence of the digital electric meter reading image as well as automatically recognize the digital meter reading.

To improve the limitations of the digital meter reading collection and recognition, many researchers and scientist have developed many efficient and effective methods. As the meter reading region detection and meter reading recognition is the main concern, many sophisticated methods have been demonstrated by the researchers in the last few decade. Such as, in [1], the author proposed a method to recognize the digits where a camera is composed to capture an image with an interval of time. Here, SVM classifier is used to classify the digits. Finally, the output is transmitted to the remote server with other necessary information, i.e., user name, user number, time and date etc. to generate the bill automatically. Image processing and digital signal processing based automatic meter reading recognition system device is introduced in [2]. Here, a neural network is used to train and recognize the meter reading. Where, NAT technology is used with ZigBee communication to create a connection to remote server.

A computer vision based automatic meter reading recognition method is proposed in [3]. Here, a fixed camera is used to capture the meter image. Individual meter reading is segmented by utilizing vertical as well as horizontal scanning. Finally, pattern match algorithm is used to recognize the meter reading. The proposed system is implemented using android studio software with OpenCV library. GSM energy meter and web interface based automatic billing system is proposed in [4]. Here, GSM wireless communication module is integrated with a digital electric meter. By this module, reading of the meter is estimated and sends to the server to generate the bill automatically. Later, Ad hoc based wireless meter reading system in introduced in [10]. Here, the authors integrate an Ad hoc network with the wireless meter reading system.

In [5], introduced a method where web camera is utilized to capture the meter image from where the digital meter reading is recognized. Here, the vertical edge detection algorithm is used to segment the individual digits and template matching is used to recognize the digits. Where, later proposed a system that uses the back camera of the mobile phone to acquire the image of the electricity meter is introduced in [9]. The meter reading sequence is segmented using a vertical edge detection algorithm. Finally, reading sequence is recognized through template matching. In [6], a robust recognition engine is proposed with commendable accuracy of recognition. Here authors mainly focus on the handwriting and printed data. To recognize the data directional, statistics, as well as geometric features are used on the segmented data. The ANN and SVM are used to classify the data.

In [7], a meter reading system is proposed which is consisting of three tiers. Where, the first tier is designed to capture images. The second tier is designed for preprocessing the image and recognized using digital recognition algorithm. The last tier is the server work which is responsible for storing the reading of the electric meter. In [8], a real time system is proposed to detect and recognize LCD or LED characters. In this work, the connected component analysis is used on binary video frame to estimate the "blobs". Finally, based on these blobs the candidate digits are detected.

In this paper, a new approach based digital electric meter reading recognition framework is proposed. The approach is

Horizontal and Vertical Binary (HVB) pattern. The pattern is estimated from individual digits. To extract the individual digits from reading region, initially the input image is normalized. The normalized image is converted to the YCbCr color image. And detect the reading region by utilizing Cb and Cr values. After that, Canny edge operator is employed on the detected reading region to find the digits edge image. Furthermore, vertical projection and morphological operations are used to segment and find the shapes of the individual digits. Finally, by utilizing HVB patter the individual segmented digits, i.e., meter reading sequence is recognized.

The paper is organized into the following Sections. In Section II, the proposed framework is explained with the processing examples. In the next Section the experimental results are demonstrated. Finally, Section IV encloses the conclusions of the paper.

## II. Proposed Framework

The proposed digital electric meter reading recognition framework has major two portions, i.e., individual digits segmentation and digit recognition by HVB pattern. The framework has eight main steps, i.e., 1) pre-processing, 2) RGB to YCbCr color conversion, 3) extracting meter reading region, 4) detecting digit edge image, 5) labeling and segmenting digits, 6) image filling and thinning, 7) Horizontal and Vertical Binary (HVB) pattern, and 8) digit recognition with HVB pattern. The proposed framework is shown in Fig. 1.

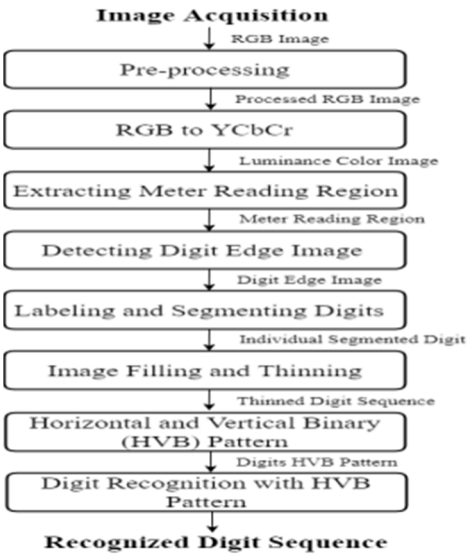


Fig. 1. The proposed digital electric meter reading recognition framework.

### A. Pre-processing

This section explains the process of normalizing and resizing the input digital electric meter image. As digital electric meter is located in different environmental conditions with different distances, hence the size of the captured meter image is varied. To process the all the captured meter image on the same procedure, the captured input digital electric meter image needs to be resized. For that, the input image is resized into 512x512.

### B. RGB to YCbCr Color Conversiton

Since RGB is more sensitive to illumination variations, the RGB images are converted into YCbCr. YCbCr color space is a linear luminance color space. In YCbCr, Y stands for luminance, Cb and Cr are the chromaticities of blue and red colors respectively. By this procedure, the RGB information is encoded. The information ranges from 16 to 235 for Y and 16 to 240 for Cb and Cr. The RGB image is converted into YCbCr color space by utilizing the Eq. (1), (2), and (3). The YCbCr image is shown in Fig. 2(b).

$$Y = 16 + (65.481 * R + 128.553 * G + 24.966 * B) \quad (1)$$

$$Cb = 128 + (-37.797 * R - 74.203 * G + 112 * B) \quad (2)$$

$$Cr = 128 + (112 * R + 93.786 * G + 18.214 * B) \quad (3)$$

(a) (b)

Fig. 2. Color conversion of digital meter reading region: a) input RGB image, and b) conversion to YCbCr image.

### C. Extracting Meter Reading Region

After conversion to the YCbCr color space, the threshold value of Cb and Cr are needed to represent the digital meter reading region. The color specially used in the digital electric meter is green. However, the resolution of this green color is not same all time. It could be varied in different environmental conditions, such as, at night time, day time, low illumination conditions, dark environment, and so on is shown in Fig. 3. According to the digital meter shown in Fig. 3, it is seen that the green light resolution at day time and at night time is not same. And, it is also seen that at the dark environment the lighting area is more speared than the other environments.

By analyzing digital electric meter reading region from different environments, it is observed that the following range of the Cb and Cr values can effectively identify the digital meter reading region. The range of the values are, Cb >= 0 & Cb <= 120 and Cr >= 0 & Cr <= 120. The threshold histogram value for the meter reading region based on Cb and Cr is shown in Fig. 4(a). The meter reading color region that is estimated by utilizing the above Cb and Cr values is shown in Fig. 4(b). The estimated reading region is converted to binary image to represent boundary region shown in Fig. 4(c). The detected meter reading region with bounding box is shown in Fig. 5(a). The extracted digital meter reading region from original meter image is presented in Fig. 5(b).

(a) (b) (c) (d)

Fig. 3. Different environmental digital electric meter: a) day time, b) night time, c) low illumination condition, and d) dark environment.

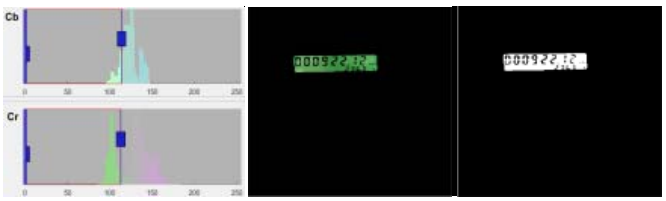


(a) (b) (c)

Fig. 4. Processing example of meter reading region color conversion: a) threshold value of meter reading region based on Cb and Cr, b) meter reading region with color conversion image, c) binary image.

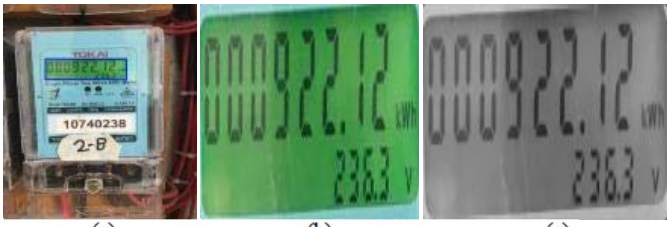


(a) (b) (c) Fig. 5. Extracting digital meter reading region: a) reading region with bounding box in meter image, b) extracted digital meter reading region, and c) reading region with smoothing.

### D. Detecting Digit Edge Image

As the digital electric meter is located in different illumination conditions, it is required to smooth the extracted reading region to eliminate noise and shadow effect from the image. For that, median filter is used to remove unnecessary information from the extracted reading region of the digital meter image. It preserves edge information while removing noise and is particularly effective on impulse noise. The effect of the median filter is shown in Fig. 5(c).

To detect the individual digits from the extracted digital meter reading region, the edge of the individual digits needs to be estimated. As digital digits, i.e., 0 to 9 specially contain the horizontal and vertical edges. For this reason, the Canny edge operator is applied on the extracted reading region. The output of the Canny digit edge image is shown in Fig. 6 (a).

### E. Labeling and Segmenting Digits

This section explains the process of segmenting individual digits from the canny digit edge image. As the meter reading reason is extracted with different orientation, the edge image may contain the border line. To process the digit edges properly, the borderline should be eliminated. The result of borderline elimination is shown in Fig. 6(b). In the edge image there exist some small edges that are not potential to represent the digit edge. These small edges are removed as noise edge from edge image is shown in Fig. 7(a).

In Fig. 7(a), it is also seen that, all the edges in a digital digital image are not connected. There exist some gaps or breaks in the individual digitized edges. This breaks or gaps should be filled up to extract the individual digit perfectly. As these gaps or breaks are not big enough, the morphological operation is used to fill these gaps and finds the individual digit label. These digit labels are individual connected components. The processing example of the edge image with edge break or gap is shown in Fig. 7(a). The result after applying the morphological operation is shown in Fig. 7(b).

In Fig. 7(b), it is observed that there exist additional connected components in the bottom left side of the connected edge image. These small connected components are located in a place which is bellowing the half height of the original meter reading digits. These connected components are not required to estimate the meter reading. So, these connected components are marked as unexpected connected components.

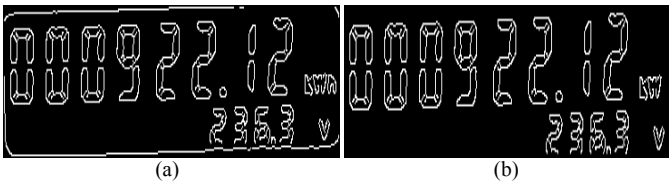

(a) (b)

Fig. 6. Processing example of edge image: a) digit edge image, and b) eliminating border of the digit edge image.

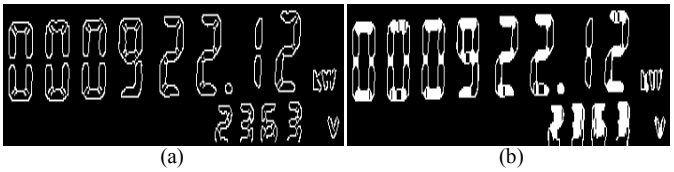

(a) (b)

Fig. 7. Processing example of removing small edges and labeling connected components: a) removing the small edges, and b) connected components.

These unexpected connected components in Fig. 7(b) are eliminated from connected edge image according to the procedure 1. The result of elimination unexpected connected components is shown in Fig. 8. From Fig. 8 it is seen that, the precision point is also eliminated. However, in all digital electric meters the precision point is placed after six digits.

**Procedure 1** Eliminating Unexpected Connected Components

| | | |
|---|---|---|
| **I** | : | Connected component image |
| **N** | : | Number of connected components in image I |
| **H(i)** | : | Height of the ith connected component located in upper half of the image I |
| $\mathbf{H_{Max}}$ | : | Maximum height in H |
| $\mathbf{Y_C(i)}$ | : | y coordinate value of the centre point of ith connected component located in upper half of the image I |
| $\mathbf{Y_{Max}}$ | : | Highest value of $Y_C$ |

For i = 1 to N

  Estimate the vertical height i.e., H(i) and y coordinate value of the centre point i.e., $Y_C(i)$ of ith connected component of upper half of the image I

End

$H_{max}$ = maximum value of H

$Y_{Max}$ = Highest value of $Y_C$

For i =1 to N

  If $(H(i) < H_{max})$ && $(Y_C(i) < Y_{Max})$

    Eliminate the ith connected component from image I

  End

End

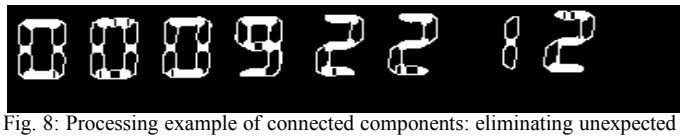

Fig. 8: Processing example of connected components: eliminating unexpected connected components.

After eliminating unexpected connected components from the connected edge image, the edge image mainly contains the candidate connected digit components. As the digits areas in the edge image are in the rectangular shape and contain the white value, i.e., pixel value is one, the remaining frame of the digit area is black i.e., pixel value is zero. The candidate digits are segmented from the connected digit edge image through the vertical projection is shown in Fig. 9.

(a) (b)

Fig. 9. Processing example of digit segmentation from connected components: a) segmented digit of meter reading, and b) digits with bounding box of meter reading.

### F. Image Filling and Thinning

For extracting the Horizontal and Vertical Binary (HVB) patterns from the digit edge image, the digit edge shape's horizontal and vertical edges are required. To extract the horizontal and vertical edges from the segmented digits, the

digits shapes are required to be thinned. For that morphological operations are used in this work. Initially, the holes on the individual digits are filled up. After that, filled digits are thinned to find the appropriate shape of the digits with horizontal and vertical edges. The filled and thinned digits edge image is shown in Fig. 10(a) and Fig. 10(b) respectively.

(a) (b)

Fig. 10. Processing example of morphological operations: a) filled binary digit image, and b) thinned digit image.

From the thinned digit edge images the Horizontal and Vertical Binary (HVB) pattern are extracted to recognize the digit sequence. The procedure of HVB pattern extraction is explained in the next section.

### G. *Horizontal and Vertical Binary (HVB) Pattern*

This section demonstrates the process of digit recognition for estimating electric meter reading sequence. For that, the segmented thinned digits edge images are utilized. In this paper, the digits are recognized by a new approach that is Horizontal and Vertical Binary (HVB) patterns.

To extract the Horizontal and Vertical Binary (HVB) pattern from the digit edge image, the edge image is resized into 64x64. After resize, the image is divided into three by two blocks. The processing example of dividing the digit's area into three by two blocks for digit nine is shown in Fig. 11.

For extracting HVB pattern from digit area, at first the individual digit's horizontal edges are searched in each of the blocks. If any block contains the horizontal edge, then place a one in that block. Otherwise, place a zero value in the respective block. After completing the horizontal edge search each block contains a binary value, i.e., either one or zero. Fig. 12(a) shows the processing example of Fig. 11(b) for horizontal edge searching.

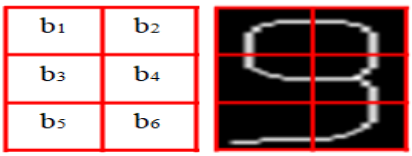


(a) (b)

Fig. 11. Processing example of dividing the digit region: a) format of three by two blocks, and b) divide the digit region into three by two blocks.

Accordingly to the horizontal edge searching procedure, the digit's vertical edges are searched in each of the blocks. If the blocks contain the vertical edges then binary one value is placed in the respective blocks. Otherwise, zero is placed in that blocks. The processing example of Fig. 11(b) for vertical edge searching is shown in Fig. 12(b). It is seen from Fig. 12(b) that all the blocks contain vertical edge except block $b_5$. So why, a binary value zero is placed in this block i.e., $b_5$.

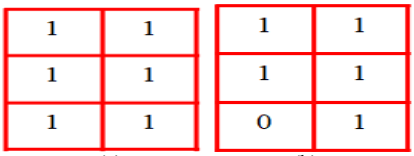


(a) (b)

Fig. 12. Processing example of searching horizontal and vertical edges in digit nine edge blocks: a) searching horizontal edges and respective binary values in each block, and b) searching vertical edges and respective binary values in each block.

From these two manners shown in Fig. 12, two binary patterns $HVB_H$ for horizontal edges and $HVB_V$ for vertical edges are estimated according to the procedure shown in Fig. 13(a). The binary pattern of $HVB_H$ and $HVB_V$ are shown in Fig. 13(b) and Fig. 13(c).

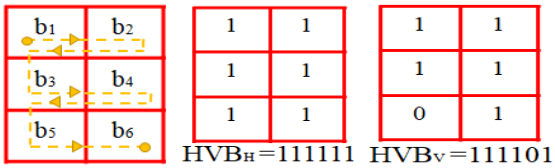


(a) (b) (c)

Fig. 13. Generation of HVB pattern: a) HVB binary pattern format, b) generates $HVB_H$ binary code, and c) generate $HVB_V$ binary code.

From these binary patterns, i.e., $HVB_H$ and $HVB_V$ two decimal codes $HVB_{HD}$ and $HVB_{VD}$ are evaluated by (4) and (5).

$$HVB_{HD} = \sum_{i=0}^{5} s(b^i)x2^i \;; s(x) = \begin{cases} 1 & if\ x = 1 \\ 0 & otherwise \end{cases} \quad (4)$$

$$HVB_{VD} = \sum_{i=0}^{5} s(b^i)x2^i \;; s(x) = \begin{cases} 1 & if\ x = 1 \\ 0 & otherwise \end{cases} \quad (5)$$

According to (4) and (5), the $HVB_{HD}$ and $HVB_{VD}$ code for Fig. 13(b) and Fig. 13(c) are $63_d$ and $61_d$ respectively. These two decimal codes i.e., $HVB_{HD}$ and $HVB_{VD}$ are summed up to generate final code $HVB_{FD}$ for each digit. The final decimal code of HVB pattern i.e., $HVB_{FD}$ for digit nine is $63+61=124_d$, which is the unique code for nine among 0 to 9 ten digits.

From the experimental result of digital digit 0 to 9, it is seen that the final decimal code of HVB pattern i.e., $HVB_{FD}$ is unique for every individual digit. The processing example of final decimal code for individual digits is shown in Fig. 14.

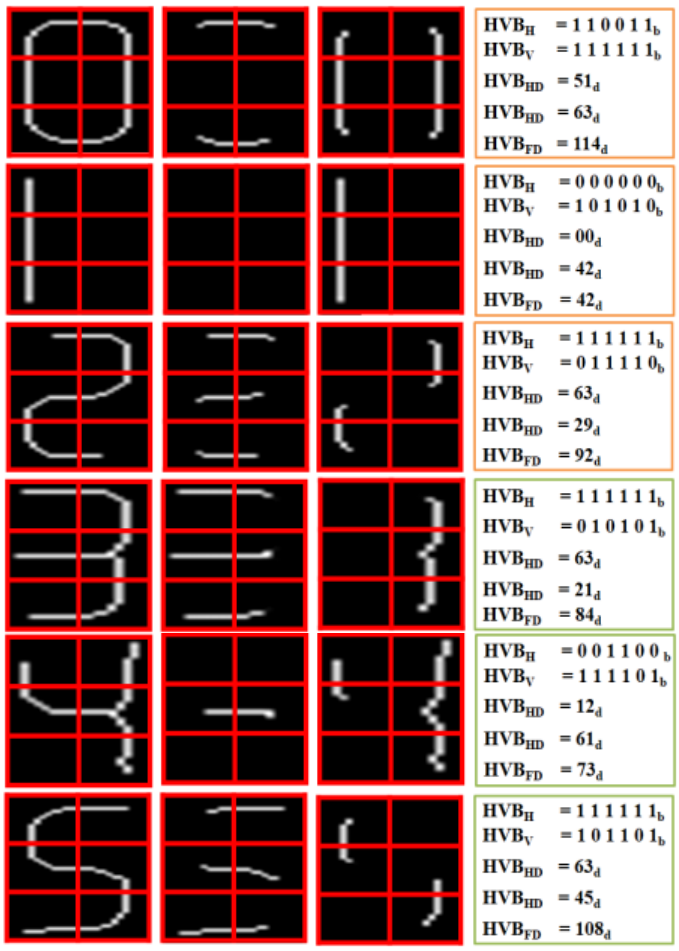

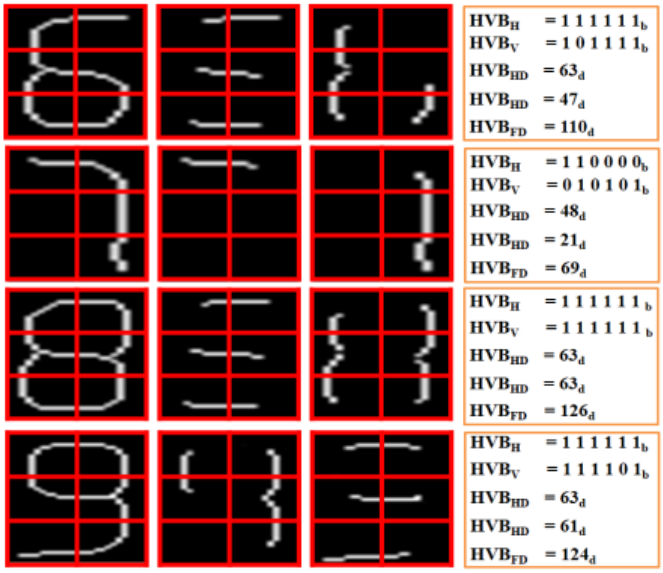


(a) (b) (c) (d)

Fig. 14. Proecessing example of extracting decimal code of HVB pattern for individual 0 to 9 digits: a) digit's area divided by three by two blocks, b) horizontal edges in different blocks, c) vertical edges in different blocks, d) binary sequence for $HVB_H$ and $HVB_V$ , and final decimal code of HVB pattern $HVB_{FD}$ with addition of $HVB_{HD}$ and $HVB_{VD}$ .

The summary of unique decimal code of HVB pattern i.e., $HVB_{FD}$ for 0 to 9 digital digits is shown in Table I.

TABLE I. THE UNIQUE DECIMAL CODE OF HVB PATTERN FOR 0 TO 9 DIGITAL DIGIT

| Digital Digit | Horizontal and Vertical binary patter $HVB_H$ and $HVB_V$ | Horizontal and Vertical decimal patter $HVB_{HD}$ and $HVB_{VD}$ | Final decimal code of HVB pattern i.e., $HVB_{FD}$ |
|---|---|---|---|
| 0 | $HVB_H$ =1 1 0 0 1 1 | $HVB_{HD}$ = 51 | 114 |
| | $HVB_V$ =1 1 1 1 1 1 | $HVB_{VD}$ = 63 | |
| 1 | $HVB_H$ =0 0 0 0 0 0 | $HVB_{HD}$ = 00 | 42 |
| | $HVB_V$ =1 0 1 0 1 0 | $HVB_{VD}$ = 42 | |
| 2 | $HVB_H$ =1 1 1 1 1 1 | $HVB_{HD}$ =63 | 92 |
| | $HVB_V$ =0 1 1 1 1 0 | $HVB_{VD}$ =29 | |
| 3 | $HVB_H$ =1 1 1 1 1 1 | $HVB_{HD}$ =63 | 84 |
| | $HVB_V$ =0 1 0 1 0 1 | $HVB_{VD}$ =21 | |
| 4 | $HVB_H$ =0 0 1 1 0 0 | $HVB_{HD}$ =12 | 73 |
| | $HVB_V$ =1 1 1 1 0 1 | $HVB_{VD}$ =61 | |
| 5 | $HVB_H$ =1 1 1 1 1 1 | $HVB_{HD}$ =63 | 108 |
| | $HVB_V$ =1 0 1 1 0 1 | $HVB_{VD}$ =45 | |
| 6 | $HVB_H$ =1 1 1 1 1 1 | $HVB_{HD}$ =63 | 110 |
| | $HVB_V$ =1 0 1 1 1 1 | $HVB_{VD}$ =47 | |
| 7 | $HVB_H$ =1 1 0 0 0 0 | $HVB_{HD}$ =48 | 69 |
| | $HVB_V$ =0 1 0 1 0 1 | $HVB_{VD}$ =21 | |
| 8 | $HVB_H$ =1 1 1 1 1 1 | $HVB_{HD}$ =63 | 126 |
| | $HVB_V$ =1 1 1 1 1 1 | $HVB_{VD}$ =63 | |
| 9 | $HVB_H$ =1 1 1 1 1 1 | $HVB_{HD}$ =63 | 124 |
| | $HVB_V$ =1 1 1 1 0 1 | $HVB_{VD}$ =61 | |

### *H. Digit Recognition with HVB Pattern*

From Fig. 14, it is seen that, the individual digits are represented by a unique HVB pattern's decimal value. Hence, the individual segmented digits are recognized by the HVB pattern.

Now, the segmented thinned meter reading sequence is recognized by the Horizontal and Vertical Binary (HVB) pattern. Applying the HVB procedure on the segmented thinned images shown in Fig. 10, the unique HVB pattern for each digit is estimated as like shown in Fig. 14.

The processing example of the segmented thinned digit image zero, one, two, and nine is shown in Fig. 15.

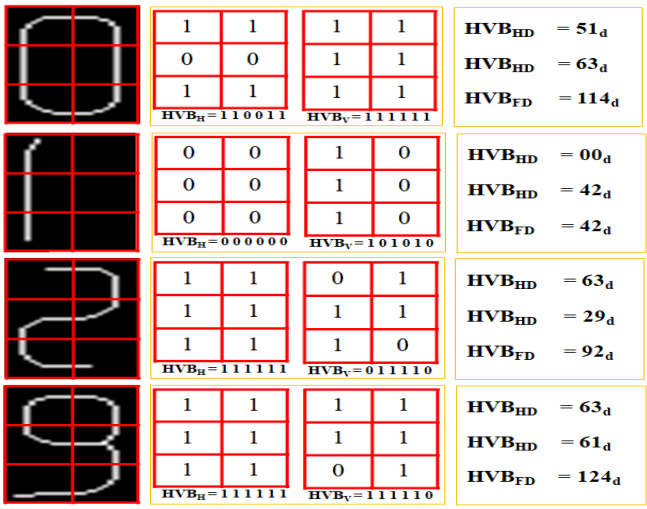


(a) (b) (c)

Fig. 15. Processing example of digit recognition: a) segmented digit, b) binary pattern for horizontal and vertical edge pattern of HVB, and c) decimal code for horizontal, vertical and final decimal HVB pattern code.

In Fig. 15, it is seen that the $HVB_{FD}$ value for zero, one, two, and nine digits are $114_d$, $42_d$, $92_d$, and $124_d$ respectively. These values are same as the values mentioned in Table I for zero, one, two, and nine digits. As the meter reading sequence contains only these four digits and these digits are recognized by the HVB pattern procedure. Hence, the sequence of the meter reading digits is recognized perfectly by HVB pattern. Now, this sequence of digits is used to generate the bill. For that, a precision point is placed after six decimal points such as 000922.12. This is the final meter reading of the given digital meter image.

## III. EXPERIMENTAL RESULTS

The experimental results of digital meter reading recognition are explained in this section. All experiments were performed on Intel(R) Core(TM) i3-3120M@2.5GHZ processor with 8GB RAM in the MATLAB environment. Here, used 135 images to measure the effectiveness of the proposed framework. These images are captured from different environments, orientations, and illumination conditions shown in Fig. 16. All the images are 512x512 sizes.

Fig. 17 shows the experimental result of the digital meter images for meter reading recognition. The readings are recognized by a new approach HVB pattern. The images are captured from the front side with different environmental conditions such as, noisy, low illumination condition, uneven illumination condition and so on.

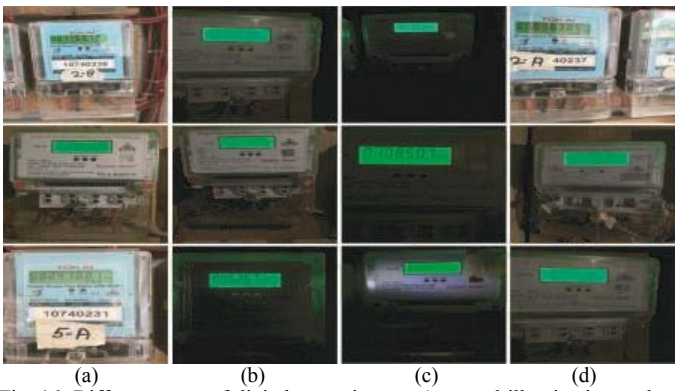

(a) (b) (c) (d)

Fig. 16. Different types of digital meter image: a) normal illumination at day and night, b) digital meter with noisy environment, c) meter at uneven illumination condition, d) meter at different orientation.

The input digital electric meter, electric meter with Cb and Cr value, detected meter reading area with the bounding box, segmented connected component digits, and thinned digit image with $HVB_{FD}$ decimal code is shown in Fig. 17(a), Fig. 17(b), Fig. 17(c), Fig. 17(d), and Fig. 17(e) respectively. The electric meter sample 1 is captured from noisy environment. Sample 2 and sample 3 are captured from low and uneven illumination conditions. Where, sample 4 is captured from normal condition with an angle. In these samples, some electric meters' reading region contain seven digits, others are contained eight digits. However, all types of electric meter precision point is placed after six decimal place, i.e., after six digits.

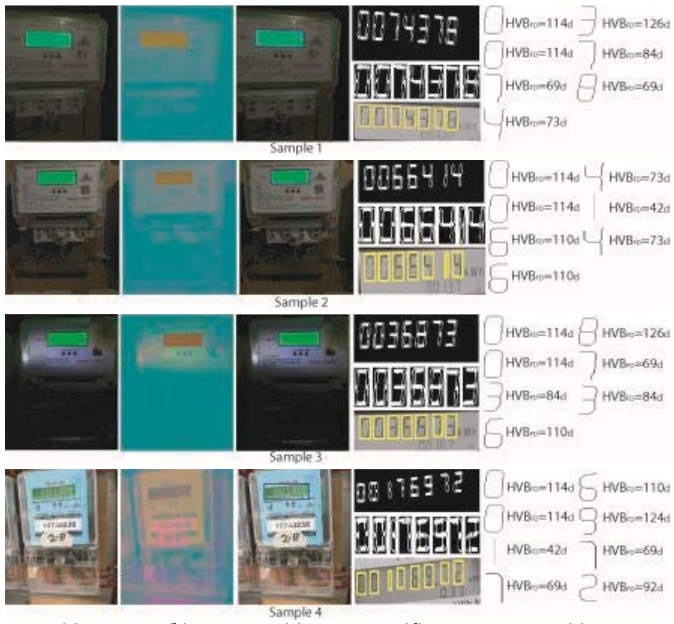


(a) (b) (c) (d) (e)

Fig. 17. Experimental example of digital electric meter reading recognition: a) input image, b) YCbCr color image, c) detected meter reading region, d) segmented individual digits, and e) meter reading sequence recognition.

In the experiment, the entire sample image meters' reading regions are detected efficiently with Cb and Cr value's, i.e., 0 to 120. By utilizing connected component concept the digits are segmented effectively shown in Fig. 17(d). All the digits in the samples are recognized appropriately through the HVB pattern decimal value. The performance of the proposed method is shown in Table II. In Table II, it is revealed that correctly detected meter reading region from electric meter with different environmental conditions is 96.30%.

TABLE II. PERFORMANCE OF THE PROPOSED FRAMEWORK

| Environmental condition | Number of Electric Meter | Correctly detected reading region | Correctly segmented individual digits | Correctly meter reading recognition |
|---|---|---|---|---|
| Normal | 48 | 48 (100.0%) | 48 (100.0%) | 48 (100.0%) |
| Noisy | 39 | 38 (97.44%) | 37 (94.87%) | 37 (94.87%) |
| Uneven Illumination | 26 | 24 (92.31%) | 23 (88.46%) | 23 (88.46%) |
| Different angular | 22 | 20 (90.91%) | 19 (86.36%) | 19 (86.36%) |
| **Total** | **135** | **130 (96.30%)** | **127 (94.10%)** | **127 (94.10%)** |

It is also revealed that, the percentage of correctly segmented individual digits and correctly meter reading recognition rate is 94.10% with respect to the input image. However, it is 97.69% with respect to the correctly detected reading region. The proposed framework is compared with [3] shown in Table III. From Table III, it is seen that the proposed framework shows better performance over [3].

TABLE III. COMPARISON OF PROPOSED FRAMEWORK WITH [3]

| Method | Number of images | Correctly detected reading region | Correctly segmented individual digits | Correctly meter reading recognition |
|---|---|---|---|---|
| **Proposed** | **135** | **96.30%** | **94.10%** | **94.10%** |
| [3] | 21 | 90.47% | 90.47% | 85.71% |

## IV. CONCLUSIONS

In this paper, a framework is proposed to recognize the digital electric meter reading automatically. This paper gives a clear concept about digital meter reading region extraction from YCbCr color meter image based on the Cb and Cr threshold value. It also gives the vertical projection based idea to segment the individual digits from the extracted meter reading region. After that, the morphological operation is performed to find the individual digit shapes. From these individual digit shapes the Horizontal and Vertical Binary (HVB) pattern's decimal values are estimated. This is the key idea of this proposed framework to recognize the digits, i.e., meter reading sequence. In this proposed framework different conditional digital meter images have been tested and most of them are achieved the goal successfully. The proposed system is attained 94.10% recognition rate.

## REFERENCES


[1] V. C. P. Edward, "Support Vector Machine based automatic electric meter reading system," IEEE International Conference on Computational Intelligence and Computing Research, pp. 1-5, IEEE, 2013.

[2] Y. Zhang, S. Yang, X. Su, E. Shi, H. Zhang, "Automatic reading of domestic electric meter: an intelligent device based on image processing and ZigBee/Ethernet communication," Journal of Real-Time Image Processing, Vol. 12, No. 1, pp 133–143, Springer, 2013.

[3] L. A. Elrefaei, A. Bajaber, S. Natheir, N. AbuSanab and M. Bazi, "Automatic electricity meter reading based on image processing," IEEE Jordan Conference on Applied Electrical Engineering and Computing Technologies (AEECT), pp. 1-5, IEEE, 2015.

[4] K. Ashna and S. N. George, "GSM based automatic energy meter reading system with instant billing," International Mutli-Conference on Automation, Computing, Communication, Control and Compressed Sensing (iMac4s), pp. 65-72, IEEE, 2013.

[5] Z. Shutao, L. Baoshu, Y. Jinsha and C. Guiyan , "Research on Remote Meter Automatic Reading Based on Computer Vision," IEEE/PES Transmission & Distribution Conference & Exposition: Asia and Pacific, pp. 1-4, IEEE, 2005.

[6] N. Sharma, B. Kumar and V. Singh, "Recognition of off-line hand printed English Characters, Numerals and Special Symbols," 5th International Conference - Confluence The Next Generation Information Technology Summit (Confluence), pp. 640-645, IEEE, 2014.

[7] D. Shu, S. Ma and C. Jing, "Study of the Automatic Reading of Watt Meter Based on Image Processing Technology," 2nd IEEE Conference on Industrial Electronics and Applications, pp. 2214-2217, IEEE, 2007.

[8] E. Tekin, J. M. Coughlan and H. Shen, "Real-time detection and reading of LED/LCD displays for visually impaired persons," IEEE Workshop on Applications of Computer Vision (WACV), pp. 491-496, IEEE, 2011.

[9] K. Parthiban and A. M. Palanisamy, "Reading values in electrical meter using image processing techniques," 2013 International Conference on Intelligent Interactive Systems and Assistive Technologies, pp. 1-7, IEEE, 2013,.

[10] G. Wang, N. QiuKaijin, and G. Xiao, "The design and implementation of an ad hoc-based wireless meter reading system," IEEE 4th International Conference on Software Engineering and Service Science, pp. 565-569, IEEE, 2013.

# A New Approach to Color Image Watermarking Based On Joint DWT-SVD Domain In YIQ Color Space

Emon Dey [1,*], Sharmin Majumder [2], Arnab Neelim Mazumder [3]
[1,2,3]Department of Electrical and Electronic Engineering
[1,2,3]Chittagong University of Engineering and Technology, Chittagong, Bangladesh
[1,*]emondey53@gmail.com, [2]sharminjouty48@gmail.com, [3]arnab007878@gmail.com

*Abstract*— **The rapid acceleration in the growth of digitized media has made authentication and protection of digital data through watermarking vitally important. In this paper, we proposed a semi blind watermarking scheme utilizing both Discrete Wavelength Transform (DWT) and Singular Value Decomposition (SVD). To embed the watermark, we transformed the host image into wavelet domain and generated a secondary host image using directive contrast. By remodeling the SVD coefficients of the watermark with the SVD coefficients of secondary image we inserted the watermark into the secondary image. A genuine extraction scheme has also been developed to recover the watermark from the cover image. The scheme has been employed using horizontal sub band. In addition to, evaluations have been added in terms of vertical and diagonal sub bands to compare the performance of the algorithm on the basis of specific sub bands. Experimental evaluations in terms of Normalized Correlation (NC) and Peak Signal to Noise Ratio (PSNR) give proof that our procedure is durable and imperceptible under variety of attacks.**

***Keywords—discrete wavelet transform, human visual system, singular value decomposition, watermarking, directive contrast.***

## I. INTRODUCTION

Security of digital information is of prime importance in this competitive world due to the rise in illegal copying, copyright violation, tampering of digital data etc. In this regard, digital watermarking paves the way towards a resolution. Digital watermarking is the process of encoding or hiding a digital data i.e. an image, a logo, an audio or video clip or any form of text into another digital media of identical class and type. The data to be encrypted will be invisible to the mundane eye and is called watermark signal and the signal or digital information in which the watermark is inserted is called cover or host signal.

The watermarking technique should be robust in the sense that it must not be vulnerable to common signal distortions as well as malicious signal processing attacks. The steps of watermarking include an embedding and an extraction algorithm. There are two approaches to image watermarking based on the domain that is used. Accordingly they are spatial domain and transform domain. In spatial domain or image space, the performance of the watermark scheme depends on the fidelity of the pixel concentrations. Watermarking in the spatial domain is less complex and has better frequency of operation but is not robust enough against different image processing operations. Conversely, the transform domain approach is more resilient against attacks compared to spatial domain. When the image is transformed, there is an uneven distribution of the watermark throughout the cover image. As a result, it becomes increasingly difficult for an attacker to extract information from the transformed domains. Different transforms are Discrete Wavelet Transform (DWT), Discrete Cosine Transform (DCT), Singular Value Decomposition (SVD), Slant Transform (ST), Contour let Transform (CT) etc. Among these transforms, wavelet based methods are more popular as localization in both the spatial and frequency domains results in better security. Besides, SVD converts the matrix of an image into singular values which makes it easier to manipulate the details while it ensures a certain degree of robustness. In many cases, joint domain approaches are favored.

A combined domain scheme of DWT-SVD provides better tradeoff between invisibility and durability. In this paper, our substantial goal is to encrypt the watermark with less complexity and to ensure that it stays resolute under different kinds of attacks and noisy conditions. For this purpose, a new process of 'secondary image' generation from the DWT sub-bands using directive contrast is introduced here. So, it can be used in secure data transmission system without the requirement of complex transmitter and receiver.

## II. BRIEF LITERARY

The need of digital surveillance and protection facilitates the use of digital watermarking. Some popular transforms like DWT [1-3], DCT [4], SVD [5-6], CT [7] and their combinations DWT-DCT [8], DWT-SVD [9-13], DCT-SVD [14] have been explored

978-1-5386-2307-7/17/$31.00 ©2017 IEEE

extensively in recent years. In this paper, only DWT-SVD based schemes have been explored. In [9] the watermark is decomposed using SVD and then the singular values are inserted in all four sub bands of DWT. A DWT-SVD technique for gray scale image was employed in [10], where, 2 level DWT was performed and the watermark was encrypted into the horizontal sub band. Moreover, the watermark is inserted into the RGB components of the $LH_3$ DWT sub band in [11]. Besides, the singular values of the host image are modified by the singular values of the watermark obtained by shuffled SVD in [12]. Furthermore, a chaotic watermarking procedure was introduced in [13] where LL sub band was used for watermark insertion. In most of the cases watermark is embedded only one or two sub-bands of the host image without inspecting the intensity values of the pixels where the watermark is embedded. So, in this cases most of the higher intensity valued pixels of the host image which are suitable for encryption are left alone.

The novelty in our method is that, the host image is used to generate a secondary host image and the watermark is embedded into the main image through the secondary image. Here, host image denotes the main image which is used to embed the watermark and the term 'secondary image' stands for the secondary image which is generated from selected pixels of the host image. The procedure that we have suggested, involves the decomposition of the host image into four DWT sub bands, then the pixels in the respective sub bands with high frequency or high content of intensity value than the threshold set for specific sub bands is extracted. The threshold value for LL, LH, HL and HH is determined from the directive contrast measurement of those sub bands. The extracted pixels are used to create the secondary image. The secondary image is then put through 2-level DWT on the HL sub band and the SVD contents of the secondary are updated with the SVD contents of the watermark. Then inverse DWT of the modified secondary image results in the final watermarked image. Our technique is capable of enduring a variety of signal processing attacks without any significant distortion in the hidden data.

## III. BACKGROUND OVERVIEW

### A. Discrete Wavelet Transform

The wavelet transform signifies a process of expansion which is used to decompose a given signal on the basis of orthogonal functions. The ability of DWT to provide both frequency and location information of the analyzed signal, makes it efficient to treat more and more advanced problems. Four non overlapping multi-resolution sub-bands are generated through DWT decomposition. They are: LL (Approximate sub-band), HL (Horizontal sub-band), LH (Vertical sub-band) and HH (Diagonal sub-band). The co-efficient sets are given below:

$$W_{Ll}^{J} = \sum_{x=0}^{N-1}\sum_{y=0}^{N-1} g(x)g(y)W_{LL}^{J-1}(2u-x)(2v-y) \quad (1)$$

$$W_{LH}^{J} = \sum_{x=0}^{N-1}\sum_{y=0}^{N-1} g(x)h(y)W_{LL}^{J-1}(2u-x)(2v-y) \quad (2)$$

$$W_{HL}^{J} = \sum_{x=0}^{N-1}\sum_{y=0}^{N-1} h(x)g(y)W_{LL}^{J-1}(2u-x)(2v-y) \quad (3)$$

$$W_{HH}^{J} = \sum_{x=0}^{N-1}\sum_{y=0}^{N-1} h(x)h(y)W_{LL}^{J-1}(2u-x)(2v-y) \quad (4)$$

Where, $W_{LL}$ represents approximation coefficient, $W_{LH}$ represents horizontal details coefficient, $W_{LH}$ represents vertical details coefficient and $W_{HH}$ represents diagonal detail coefficient. Here J indicates the maximum level of decomposition done on the image.

### B. Singular Value Decomposition

Singular value decomposition is a process of matrix factorization. For instance, any m × n real matrix can be factored after using SVD as, $A = UDV^{T_c}$ where columns of $U$ and $V$ are orthonormal and matrix $D$ is diagonal with positive real values. The diagonal elements of $D$ are called singular values. The $m$ rows of $U$ are called left-singular vectors and $n$ rows of $V$ are called right-singular vectors. The diagonal matrix D can be termed as following form:

$$D = \begin{Bmatrix} a_1 & 0 & 0 \\ 0 & a_2 & 0 \\ 0 & 0 & \ddots\, a_r \end{Bmatrix} \quad (5)$$

In the above equation, $a_1 \geq a_2 \geq \cdots \geq a_r > 0$ and $r$ = rank ($A$). The square roots of the Eigen values of $A^TA$ are $a_1, a_2$ and $a_r$. They are also known as the singular values of $A$. SVD features the representation of any image data within fewer coefficients which reduces the computational complexity of the whole process.

### C. Directive Contrast

The brightness and luminance of an object in equal field of view are differed by the term contrast. In the same manner, inequality of the intensity value of a pixel from its adjacent pixels gives rise to the term contrast which is equal to difference in intensity value of the pixels. So, development of local contrast of an image cam be defined as,

$$C_k = \frac{L - L_b}{L_b} = \frac{L_h}{L_b} \quad (6)$$

In the above, L is local luminance and $L_b$ is the luminance of the local background. Generally, $L_b$ is termed as local low frequency

and so $L_h$ is defined as local high frequency. In that case, directive contrast can be regarded as,

Vertical band contrast:

$$C_k^V = \frac{LH_k}{LL_k} \tag{7}$$

Horizontal band contrast:

$$C_k^H = \frac{HL_k}{LL_k} \tag{8}$$

Diagonal band contrast:

$$C_k^D = \frac{HH_k}{LL_k} \tag{9}$$

Where $LH_k$, $HL_k$, $HH_k$ and $LL_k$ are vertical, horizontal, diagonal (High frequency) and approximate (low frequency) sub-bands. Directive contrast can be used to depict the high frequency information of an image. Moreover, extracted detail information can be gained by the following formula,

Vertical band contrast:

$$LH_k = C_k^V \times LL_k \tag{10}$$

Horizontal band contrast:

$$HL_k = C_k^H \times LL_k \tag{11}$$

Diagonal band contrast:

$$HH_k = C_k^D \times LL_k \tag{12}$$

This extracted information can be used in reconstruction process of the image data with watermark information incorporated into it.

## IV. PROPOSED WATERMARKING TECHNIQUE

### A. *Algorithm for Embedding Process*

- Firstly, the cover image is converted from RGB color space to YIQ color space. The Q component is selected.
- 2 Level DWT on the $HL_1$ sub band to obtain $LL_2$, $LH_2$, $HL_2$ and $HH_2$ sub bands is applied.
- The directive contrast for the $LH_2$, $HL_2$ and $HH_2$ sub bands is derived.
- All wavelet coefficients that have directive contrast less than the threshold are made zero. The threshold is obtained by,

$$T_{CH} = sort(p * CH) \tag{13}$$

$$T_{CV} = sort(p * CV) \tag{14}$$

$$T_{CD} = sort(p * CD) \tag{15}$$

  Where, CH, CV and CD are directive contrasts of the Horizontal, vertical and Diagonal sub-band respectively; p is the percentage of coefficients we want to conserve.

- After that 1 level inverse DWT is performed on the extracted pixels from the sub bands to acquire the secondary or modified image.
- Then 1 level DWT on the modified image is carried out to generate the $LL_1$, $LH_1$, $HL_1$ and $HH_1$ sub bands.
- The watermark image is read. Conversion from RGB color space to YIQ color space is done. The Q component is selected.
- 1 level DWT is applied on the Q component of the watermark image to obtain $LL_w$, $LH_w$, $HL_w$, $HH_w$ sub bands. SVD operation is done on $HL_2$ sub band of the modified image and $HL_w$ sub band as follows,

$$HL_2 = US_C V^T \tag{16}$$

$$HL_W = US_W V^T \tag{17}$$

- The singular values of the secondary image are modified with singular values of the watermark image in the following way,

$$S_{CW} = S_C + \alpha * S_W \tag{18}$$

  Where, α is the watermark strength.
- Inverse SVD and 1 level inverse DWT are performed to obtain modified watermarked image.
- The modified watermarked image is used to backtrack to the host image. 2 level inverse DWT is performed to get the watermarked image on the Q channel.
- Finally, the new Q channel is combined with the previous Y and I components of the host image. The YIQ color space is then converted to RGB to get the final watermarked image.

### B. *Algorithm for Extraction Process*

- At first, the modified image is decomposed using 1 level DWT to get the $LL_1$, $LH_1$, $HL_1$, $HH_1$ sub bands. SVD is applied to $HL_1$ sub band to generate the SVD coefficients.
- The watermark image is read. The image is converted from RGB color space to YIQ color space. The Q component is selected.
- 1 level DWT is performed on it to get the $LL_w$, $LH_w$, $HL_w$, $HH_w$ sub bands. Also SVD is applied to the $HL_w$ sub band to obtain SVD coefficients of the watermark image.
- The watermarked image is acquired. It is converted to YIQ from RGB and the Q component is selected.
- 2 level DWT is performed on the HL sub band of the watermarked image to acquire the $LL_{2cw}$, $LH_{2cw}$, $HL_{2cw}$,

$HH_{2cw}$ sub band. SVD is applied on the $HL_{2cw}$ sub band to generate the SVD coefficients of the watermarked image.

- Now, the coefficients of the watermark are extracted as follow,

$$S_w^* = (S_{cw}^* - S_c)/\alpha \quad (19)$$

Where, $S_w^*$, $S_{cw}^*$, $S_c$ are the S components of the extracted watermark, watermarked image and cover image respectively.

- Inverse SVD and 2 level inverse DWT are applied to get the Q component of the extracted watermark.
- At last, the Q component is merged with previous Y and I component of the watermark and then the YIQ color space is converted to RGB to get the extracted watermark image.

## V. EXPERIMENTAL RESULTS

We used the 512 × 512 "Tape" image as our main host image and 256 × 256 "Colored Chips" image as our watermark image. The corresponding host, watermark, watermarked image and extracted watermark are shown in the Fig. 1(a), (b), (c) and (d) respectively. And NC values and retrieved watermark images corresponding to various attacks are shown in Table I and Fig. 3. Besides, more images like "Pears", "Peppers", "Concord Aerial" and "Greens" are used as Host image and the extracted watermarks are shown in Fig. 4. Peak Signal to Noise Ratio (PSNR) is enrolled to test the imperceptibility of the Host image and watermarked image. In addition, Normalized Correlation (NC) is used to check the resemblance between the original watermark and the extracted watermarks.

### A. Peak Signal to Noise Ratio

One prime objective of a digital image is improvement of visual quality of the image. So, measurement of image enhancement to ensure image quality is a necessary one. Peak-signal-to-noise ratio can act as a standard tool in this kind of investigation. The term Peak signal-to-noise ratio, often abbreviated PSNR, is a basic engineering term described as the ratio between the maximum possible signal power and the unwanted noise power that hampers the integrity of its expression. The mathematical representation of the PSNR is as follows:

$$PSNR = 20log_{10}\left(\frac{M_f}{\sqrt{MSE}}\right) \quad (20)$$

Where the MSE (Mean Squared Error) is:

$$MSE = \frac{1}{pq}\sum_0^{p-1}\sum_0^{q-1}||f(m,n) - g(m,n)||^2 \quad (21)$$

where, f stands for our original image's matrix data, g represents our degraded image's matrix data, p means the numbers of rows of pixels of the images and m is the index of that row, q is the number of columns of pixels of the image and n is the index of that column, $M_f$ is the maximum signal value existing in our original Host image.

### B. Normalized Correlation

The correlation between two signals (normalized correlation) is recognized as a standard approach to feature detection as well as a component of more sophisticated techniques. The Normalized form of correlation (correlation coefficient) preferred in template matching does not have a correspondingly simple and efficient frequency domain expression. The mathematical representation of it is as follows:

$$NC = \frac{\sum_{m=0}^{m-1}\sum_{n=0}^{n-1}W_1(m,n)W_2(m,n)}{\sum_{m=0}^{m-1}\sum_{n=0}^{n-1}(m,n)^2} \quad (22)$$

Where, $W_1$ (m, n) is the secondary mark and $W_2$ (m, n) is the extracted watermark image.

TABLE I. ROBUSTNESS (NC) CHECK FOR VARIOUS ATTACKS USING HL SUBBAND WATERMARK EMBEDD

| **Attacks** | **NC** | | | | | | | |
|---|---|---|---|---|---|---|---|---|
| | *α=0.1* | *α=0.2* | *α=0.3* | *α=0.4* | *α=0.5* | *α=0.6* | *α=0.7* | *α=0.8* |
| **No Attack** | 1.0000 | 1.0000 | 1.0000 | 1.0000 | 1.0000 | 1.0000 | 1.0000 | 1.0000 |
| **Gaussian Noise** | 0.9941 | 0.9982 | 0.9992 | 0.9996 | 0.9998 | 0.9999 | 0.9999 | 1.0000 |
| **Salt & Pepper** | 0.9968 | 0.9992 | 0.9997 | 0.9999 | 1.0000 | 1.0000 | 1.0000 | 1.0000 |
| **Gaussian Low Pass** | 0.9999 | 1.0000 | 1.0000 | 1.0000 | 1.0000 | 1.0000 | 1.0000 | 1.0000 |
| **Median Filter** | 1.0000 | 1.0000 | 1.0000 | 1.0000 | 1.0000 | 1.0000 | 1.0000 | 1.0000 |
| **JPEG Compression** | 1.0000 | 1.0000 | 1.0000 | 1.0000 | 1.0000 | 1.0000 | 1.0000 | 1.0000 |
| **Motion Blur** | 1.0000 | 1.0000 | 1.0000 | 1.0000 | 1.0000 | 1.0000 | 1.0000 | 1.0000 |
| **Rotate 5** | 0.9998 | 1.0000 | 1.0000 | 1.0000 | 1.0000 | 1.0000 | 1.0000 | 1.0000 |
| **Sharpening** | 0.9979 | 0.9996 | 0.9999 | 1.0000 | 1.0000 | 1.0000 | 1.0000 | 1.0000 |
| **Cropping** | 0.9097 | 0.9291 | 0.9455 | 0.9603 | 0.9743 | 0.9888 | 0.9999 | 1.0000 |
| **Histogram Eq.** | 0.9999 | 1.0000 | 1.0000 | 1.0000 | 1.0000 | 1.0000 | 1.0000 | 1.0000 |
| **Mean Filter** | 1.0000 | 1.0000 | 1.0000 | 1.0000 | 1.0000 | 1.0000 | 1.0000 | 1.0000 |

(a) (b) (c) (d)

Figure 1. (a) Host image, (b) Watermark image, (c) Watermarked image (HL) (PSNR=57.4275) and (d) Extracted watermark (HL) (NC=1.0000)

(a) (b) (c) (d)

Figure 2. (a) Watermarked image (LH) (PSNR= 56.6289), (b) Extracted watermark (LH) (NC= 0.9999), (c) Watermarked image (LL) (PSNR= 53.9254) and (d) Extracted watermark (LL) (NC= 0.9997)

TABLE II. IMPERCEPTIBILITY (PSNR) CHECK OF OUR PROPOSED METHOD FOR DIFFERENT TYPES OF IMAGES

| **Image name** | **PSNR in dB** | | | | |
|---|---|---|---|---|---|
| | α=*0.1* | α=*0.2* | α=*0.3* | α=*0.4* | α=*0.5* |
| **Tape** | 57.4275 | 57.0122 | 56.3946 | 55.6592 | 54.8985 |
| **Pears** | 57.1434 | 56.7525 | 56.1745 | 55.4721 | 54.7104 |
| **Peppers** | 50.6383 | 50.5397 | 50.4104 | 50.1932 | 49.9601 |
| **Concord Aerial** | 52.2176 | 52.1048 | 51.9524 | 51.7250 | 51.4590 |
| **Greens** | 53.2152 | 53.1052 | 52.8488 | 52.5160 | 52.1634 |

GN SP GLPF MDF MB SH CR HE MF JC R5

Figure 3. Extracted Watermarks for Various Attacks.

Pears
PSNR= 57.1434
NC= 1.0000

Peppers
PSNR= 50.6383
NC= 1.0000

Concord Aerial
PSNR= 52.2176
NC= 1.0000

Greens
PSNR=53.2152
NC= 1.0000

Figure 4. Extracted Watermarks with Different Host Image

The effectiveness of our scheme lies in achieving significant results in terms of robustness and imperceptibility against noisy states such as; Gaussian Noise (GN), Salt & Pepper Noise (SP), Gaussian Low Pass Filter (GLPF), Median Filter (MDF), JPEG Compression (JC), Motion Blur (MB), Rotation 5 (R5), Sharpening (SH), Cropping (CR), Histogram equalization (HE), Mean Filter (MF). Besides, the watermarks obtained against various attacks are depicted in Fig. 3 to ensure proper visualization of the procedure. It has also been tested against different cover images to exhibit the dynamism of our algorithm. Again, PSNR and NC values for the other two sub-bands are also derived and the corresponding watermarked image and the Images of extracted watermarks along with their respective PSNR and NC values are attached through Fig. 2(a), (b), (c) and (d).

From the experimental results it is evolved that HL sub-band shows better results than the other two on the basis of PSNR and NC. It corroborates the theoretical preference of HL sub-band due to its less sensitivity to human eye against any inspection of data in it and also its rigidity against image processing attacks. Comparative study of our acquired experimental values with previous works is enlisted on the basis of PSNR and NC. The PSNR values are compared with the methods [10] & [12].

TABLE III. COMPARATIVE STUDY ON THE BASIS OF PSNR

| α | Method [10] | Method [12] | Proposed method |
|---|---|---|---|
| 0.1 | 53.0433 | 39.8819 | 57.4275 |
| 0.2 | 47.1656 | 37.7588 | 57.0122 |
| 0.3 | 43.9450 | 37.2369 | 56.3946 |
| 0.4 | 41.8534 | 32.0000 | 55.6592 |
| 0.5 | 40.3698 | 30.0000 | 54.8985 |

In [10] 'Lena' image and in [12] 'Peppers' image are used as cover image respectively. Achievement of improved values varying watermark strength α dictates the validity of our process. The experimental values are available at Table III.

TABLE IV. COMPARATIVE STUDY ON THE BASIS OF NC

| Attacks | Method [10] | Method [13] | Method [14] | Proposed Method |
|---|---|---|---|---|
| **Gaussian noise** | 0.9797 | 0.9985 | 0.8775 | 0.9941 |
| **Median filtering** | 0.9878 | 0.9873 | 0.8075 | 1.0000 |
| **Gaussian low pass filter** | --- | --- | 1.0000 | 0.9999 |
| **Cropping (middle part)** | 0.9998 | 0.9755 | 0.9233 | 0.9097 |
| **JPEG compression** | 0.9998 | 0.9289 | 0.9566 | 1.0000 |
| **Motion blurring** | 0.9377 | --- | --- | 1.0000 |
| **Rotation** | 0.9943 | 0.9214 | --- | 0.9998 |
| **Sharpening** | 0.9943 | 0.9995 | --- | 0.9979 |

Performance of our method is also evaluated through comparison of the NC values against various attacks with methods [10], [13] & [14]. Derived data in this case are shown in Table IV. A close look at the values reveals that our proposed method shows superiority in most of the cases.

## VI. CONCLUSION

In this paper, a distinct method of DWT-SVD based watermarking featuring secondary image has been introduced. From the comparison of results obtained after applying our proposed process on HL, LH and LL bands, it can be concluded that the HL band shows better tradeoff between imperceptibility and robustness than the others. Hence the selection of HL band for embedding in our proposed method is justified. The LL band is kept unaltered in order to keep the detail information of the image intact. Again, the uniqueness of our method lies in the derivation of secondary image through directive contrast from the DWT sub-bands of the Host image. Moreover, PSNR and NC values over 50 dB and 0.99 respectively against a number of different Host images and also better resiliency against various image processing attacks establish our method as an operant one. In future, we look forward to modify our algorithm to make it effective for real time images and videos.

## REFERENCES


[1] M. Hsieh , D. Tseng , and Y. Huang , "Hiding digital watermarks using multi resolution wavelet transform," IEEE Trans. on Industrial Electronics, vol. 48,2001, pp.875-882.

[2] P. Tay, and J. Havlicek, "Image watermarking using wavelets, "IEEE Midwest Symposium on Circuits and Systems, USA, p: 258-261, 2002.

[3] S.H. Wang, and Y.P. Lin, "Wavelet tree quantization for copyright protection",IEEE Transactions on Image Processing, vol.13, 2004, pp.154–165.

[4] Wai C. Chu, "DCT-Based Image Watermarking Using Sub sampling", IEEE Transactions on Multimedia, vol.5, issue I, pp.34-38, 2003.

[5] R. Rykaczewski, "Comments on An SVD-Based Watermarking Scheme for Protecting Rightful Ownership", Journal of IEEE Trans. Multimedia, vol.9, no. 2, pp. 421-423, 2007.

[6] L. Chia-Chen, C. Chin-Chen and C. Yi-Hui, "A novel SVD-based watermarking scheme for protecting rightful ownership of digital images", Journal of Information Hiding and Multimedia Signal Processing, vol.5, no.2, pp-124-143, 2014.

[7] G. Duan, A.T.S. Ho and X. Zhao, "A novel non-redundant contour let transform for robust image watermarking against non-geometrical and geometrical attacks", 5th International Conference on Visual Information Engineering (VIE '08), China, p. 124–129, 2008.

[8] S. Emek, M. Pazarci, "A Cascade DWT-DCT Based Watermarking Scheme," 13th European Signal Processing Conference 2005 (EUSIPCO'05), Antalya Turkey, Sept, 2005.

[9] Nagaraj V. Dharwadkar ,B.B. Amberker & Avijeet Gorai ,"Non-blind Watermarking scheme for color images in RGB space using DWT-SVD",2011 International Conference on Communications and Signal Processing.

[10] Anuva Chowdhury ,Md. Shahjamal ,Kalyan Biswas ," A New DWT-SVD Based Image Watermarking Technique By Utilizing The Features Of Human Visual System", International Journal of Research in Computer Engineering and Electronics,vol:3,issue:6,2014.

[11] Rashedul Islam, Jong-Myon Kim, "Reliable RGB Color Image Watermarking using DWT and SVD", 3rd International Conference on Informatics, Electronics & Vision 2014.

[12] Tulika Bhuyan, Vinay Kumar Srivastava, Falgun Thakkar,"Shuffled SVD based Robust and Secure Digital Image Watermarking", International Conference on Electrical, Electronics, and Optimization Techniques,2016.

[13] Md. Moniruzzaman, Md. Abul Kayum Hawlader and Md .Foisal Hossain, "Robust RGB Color Image Watermarking Scheme Based on DWT-SVD and Chaotic System", The 8th International Conference on Software, Knowledge, Information Management and Applications, 2014.

[14] Morteza Heidari, Nader Karimi and Shadrokh Samavi, "A Hybrid DCT-SVD Based Image Watermarking Algorithm", 24th Iranian Conference on Electrical Engineering, 2016.

2017 3rd International Conference on Electrical Information and Communication Technology (EICT)
7-9 December 2017, Khulna, Bangladesh

# Modeling and Analysis of Interpolation based Adaptive Reversible Data Hiding

Md. Abdul Wahed* Hussain Nyeem†
Department of Electrical, Electronic and Communication Engineering
Military Institute of Science and Technology (MIST), Mirpur Cantonment, Dhaka-1216
*wahedruet@gmail.com †h.nyeem@eece.mist.ac.bd

***Abstract*—In this paper, an improved interpolation-based Reversible Data Hiding (IRDH) scheme is modeled and analyzed. All possible embeddable bits are sought to be effectively utilized to minimize embedding distortion with higher embedding capacity. Particularly, we propose to utilize the correlation between the embeddable pixel and estimated versions of embedded pixel. This proposed modification would help avoid the use of any flag bit for distinguishing the original payload bits from their complement as such an extra payload bit can be embedded therein. Experimental results have demonstrated that our improved scheme can embed varying size payload with higher embedding rate and better image quality compared to the recent IRDH schemes. A better embedded image quality can be ensured for a given capacity requirement with a deterministically selected capacity control parameter for adaptive embedding.**

***Index Terms*—quadratic interpolation; reversible embedding; data hiding; data extraction, image recovery**

## I. Introduction

Reversible data hiding (RDH) schemes have been widely investigated for different multimedia and digital image applications [1]–[17]. These schemes generally embed *payload* (*i.e.*, secret data with any side information) in an input (or cover) image such that the embedded payload can completely be extracted followed by the exact recovery of the input image [1]–[3]. An RDH scheme is usually evaluated by its embedding rate-distortion performance, *i.e.*, with higher embedding capacity (or rate) with lower embedding distortion yielding better quality embedded image. Development of such a scheme is therefore being investigated for better rate-distortion performance and different applications.

Interpolation based RDH (IRDH) schemes have recently reported for better embedding rate-distortion performance [11], [13]–[16]. Development of such schemes focuses on two main processes: (*i*) computation of interpolated pixels and (*ii*) embedding of payload. For computing interpolated pixels, quadratic interpolation offers better image quality so far [15], [16], [18]. For embedding, interpolated pixels of an input image are generally used, keeping the original pixels untouched that are desirable in military and medical image applications.

Additionally, existing IRDH schemes although offer relatively better visual quality of the embedded image, none of them seem to consider a varying embedding capacity requirement (*i.e.*, varying size payloads). It is generally assumed that embedding of payload will continue for the last bit of payload within the capacity limit that results in non-uniform distortion in the embedded image. Thereby, the best possible image quality for embedding varying size payloads is not always ensured. This embedding problem of varying size payload can be addressed using adaptive embedding which again poses three main challenges: (*i*) defining a universal capacity control parameter that ensures embedding of varying size payloads, (*ii*) keeping dynamic range of the capacity limit possibly 'higher' commensurate with an application requirement, and (*iii*) a uniform distribution of minimum possible distortion resulting in better rate-distortion performance.

As a first step to tackle the above challenges, we formulated a capacity control parameter in [16], [18] that deterministically selects a number of bit-planes for embedding original or complement form of payload bits. A flag bit was introduced to track whether the embedded payload is original or its complement. Interpolation technique of Zhang *et al*. [15] was simplified for computing interpolated image with better (or similar) image quality in [16]. While a high dynamic range of embedding capacity was obtained with the earlier schemes [16], [18], the capacity can be further increased if the flag bits are managed to be replaced with additional payload bits.

To this end, in this paper, we report a computational model of an improved IRDH scheme that can embed one more payload-bit per pixel without using a flag bit. We use the simplified quadratic interpolation technique [16] for up-sampling an input image. An adaptive embedding with a capacity control parameter is used for embedding of varying size payloads in the overlapping image-blocks. Unlike our previously reported scheme [16], the proposed scheme utilizes the correlation between the embeddable pixel and estimated versions of embedded pixel instead of using any flag bit. This helps increase the embedding rate by embedding one more payload bit in place of the flag bit resulting in better embedding rate-distortion performance.

The rest of this paper is structured as follows. Modeling our proposed IRDH scheme is presented in Sec. II. Preliminary results and performance analysis are presented in Sec. III and conclusions are given in Sec. IV.

978-1-5386-2307-7/17/$31.00 ©2017 IEEE

## II. Modeling Our Proposed IRDH Scheme

Three main processes of our proposed IRDH scheme (*i.e.*, image up-sampling, payload embedding, and payload extraction) are modeled and discussed in this section below.

### A. Image Up-Sampling

An input cover image is up-sampled to a higher spatial resolution image using interpolation. As mentioned in the previous section, quadratic interpolation offers better up-sampled image quality. Unlike our previous work [16], in this paper, we apply quadratic interpolation to an input image considering its overlapping blocks instead of non-overlapping blocks. It helps reduce the effect of inter-block visual artifacts. Modeling of the proposed image up-sampling process using quadratic interpolation is presented in Algorithm 1 as a function, $\texttt{interp}(\cdot)$. Particularly, this function takes the original image, $I$ and the factor, $F$ as input to generate an interpolated image, $C$. Individual steps of the function are indicated in comments of Algorithm 1.

An up-sampled image is initialized with $\texttt{upsample}(\cdot)$ by inserting interleaving zero columns and zero rows in the original image (*i.e.*, an $FM-1 \times FN-1$ sized image, $I_{up}$ is initialized with the $M \times N$ sized input image, $I$). $I_{up}$ is then divided into a set of overlapping blocks (either in horizontal, vertical or diagonal direction). Each block contains five consecutive pixels, where the original pixels remain at $1st$, $3rd$ and $5th$ location, and newly inserted pixels of zero (0) values are at the $2nd$ and $4th$ location. Here, $\{I_{Hblock}\}$, $\{I_{Vblock}\}$ and $\{I_{Dblock}\}$ are the sets of horizontal, vertical and diagonal blocks obtained from the functions, $\texttt{hblock}(\cdot)$, $\texttt{vblock}(\cdot)$ and $\texttt{dblock}(\cdot)$, respectively.

We then apply quadratic interpolation to compute newly inserted pixel values of $\{I_{Hblock}\}$, $\{I_{Vblock}\}$ and $\{I_{Dblock}\}$ using $\texttt{quadratic}(\cdot)$ to obtain respective interpolated blocks, $\{I'_{Hblock}\}$, $\{I'_{Vblock}\}$ and $\{I'_{Dblock}\}$. Combining these blocks with the interpolated pixels we obtain $I'_{up}$ using the function, $\texttt{construct}(\cdot)$. The last row and last column of $I'_{up}$ is replicated as padded pixels to make the image size $FM \times FN$ using $\texttt{pad}(\cdot)$. The output of $\texttt{pad}(\cdot)$, $I_{pad}$ is returned as the interpolated image, $C$. Usually, with the factor, $F=2$, a given input image, $I$ of size $M \times N$ is finally up-sampled to $C$ of size $2M \times 2N$. For more details of our simplified interpolation technique and its computational efficiency, see our earlier work [18].

### B. Proposed Payload Embedding

Our proposed payload embedding is modeled to embed the payload bits into the Least Significant Bit(s) (LSBs) of the interpolated pixels only either in original or in complement form. In this modeling, the correlation between interpolated pixels and the estimated versions of LSB substituted pixels is used to increase the embedding capacity and avoiding the use of flag bit unlike [16], [18]. A selective threshold, $T$ is defined to attain any varying embedding capacity requirement.

In general, $T$ is a predefined number of unchanged MSBs. So, the lesser the value of $T$, greater the number of embeddable LSBs and so is the embedding capacity. However, with a higher capacity requirement, embedding distortion is usually higher. So, a trade-off is required between the threshold, $T$ and the capacity requirement to obtain the best possible image quality within a given capacity limit. The proposed embedding is modeled in Algorithm 2 with necessary functions and their purposes in respective comments.

**Algorithm 1** $\texttt{interp}(I,F)$

$(M,N) \leftarrow \texttt{size}(I)$ ▷ number of rows and columns of $I$
$I_{up} \leftarrow \texttt{upsample}(I,M,N,F)$ ▷ up-sampling $I$ to $I_{up}$ by factor $F$ to a size $FM-1 \times FN-1$
$\{I_{Hblock}\} \leftarrow \texttt{hbolck}(I_{up})$ ▷ divides $I_{up}$ into overlapping horizontal 5 pixel blocks
$\{I_{Vblock}\} \leftarrow \texttt{vbolck}(I_{up})$ ▷ divides $I_{up}$ into overlapping vertical 5 pixel blocks
$\{I_{Dblock}\} \leftarrow \texttt{dbolck}(I_{up})$ ▷ divides $I_{up}$ into overlapping diagonal 5 pixel blocks
**for all** $I_{Hblock}, I_{Vblock}, I_{Dblock} \in I_{up}$ **do**
  $I'_{Hblock} \leftarrow \texttt{quadratic}(I_{Hblock},2,4)$ ▷ computes interpolated value of $2nd$ and $4th$ pixel in $I_{Hblock}$
  $I'_{Vblock} \leftarrow \texttt{quadratic}(I_{Vblock},2,4)$ ▷ computes interpolated value of $2nd$ and $4th$ pixel in $I_{Vblock}$
  $I'_{Dblock} \leftarrow \texttt{quadratic}(I_{Dblock},2,4)$ ▷ computes interpolated value of $2nd$ and $4th$ pixel in $I_{Dblock}$
**end for**
$I'_{up} \leftarrow \texttt{construct}(\{I'_{Hblock}\},\{I'_{Vblock}\},\{I'_{Dblock}\})$ ▷ updates $I_{up}$ with $I'_{Hblock}$, $I'_{Vblock}$ and $I'_{Dblock}$
$I_{pad} \leftarrow \texttt{pad}(I'_{up})$ ▷ padding in last row and last column of $I'_{up}$ to make its size $FM \times FN$
$C \leftarrow I_{pad}$ ▷ returns $C$ as interpolated image
Return $C$

The algorithm takes the interpolated image, $C$ , *data* and the threshold, $T$ as input and returns the desired embedded image $I_{em}$. For example, with a given interpolated pixel $y \in C$ the bit length, $n$ is calculated by the function $\texttt{bitlength}(\cdot)$ using Eq. (1). The the number of embeddable LSBs, $n_{em}$ is computed according to the condition given in Eq. (2) by the function $\texttt{getnem}(\cdot)$. Now, $n_{em}$ number of LSBs of $y$ is compared using bit-wise XOR operation with the $n_{em}$ bit of payload, $d$ and its complement $\bar{d}$ and are returned as $X_d$ and $X_{\bar{d}}$, respectively. Two versions of embedded pixel, $y_d$ and $y_{\bar{d}}$ are computed using the function $\texttt{substituteLSB}(\cdot)$, in which the payload bits and their complement are respectively substituted for the LSBs of $y$. At the end, the bit-wise XOR correlations, *i.e.*, $X_d$ and $X_{\bar{d}}$ are compared according to the condition given in Eq. (3), the final embedded pixel, $y'$ is chosen from $y_d$ and $y_{\bar{d}}$.

$$n = \begin{cases} \lceil \log_2(y) \rceil & \text{if } y > 1 \\ 1 & \text{otherwise} \end{cases} \tag{1}$$

$$n_{em} = \begin{cases} 2 & \text{if } n \leq 1+T \\ n-T & \text{otherwise} \end{cases} \tag{2}$$

**Algorithm 2** `embedding`$(C, data, T)$

**Initialize:**
$startbit \leftarrow 1$
**for all** $y \in C$ **do** ▷ $\{y\}$ are the interpolated pixels in $C$
$n \leftarrow$ `bitlength`$(y)$ ▷ returns bit-length of $y$ using Eq. (1)
$n_{em} \leftarrow$ `getnem`$(n, T)$ ▷ returns number of embeddable bits, $n_{em}$ as per Eq. 2
$P \leftarrow$ `getLSB`$(y, n_{em})$ ▷ returns $n_{em}$-LSBs of $y$
$d \leftarrow$ `getbit`$(data, n_{em}, startbit)$ ▷ returns $n_{em}$-bits of $data$ from starting bit-position, $startbit$
$\bar{d} \leftarrow$ `complement`$(d)$ ▷ returns 2's complement of $d$
$X_d \leftarrow$ `bitXOR`$(P, d)$ ▷ bit-wise XOR of $P$ and $d$
$X_{\bar{d}} \leftarrow$ `bitXOR`$(P, \bar{d})$ ▷ bit-wise XOR of $P$ and $\bar{d}$
$y_d \leftarrow$ `substituteLSB`$(y, d)$ ▷ returns a version of embedded pixel substituting $d$ for $n_{em}$-LSBs of $y$
$y_{\bar{d}} \leftarrow$ `substituteLSB`$(y, \bar{d})$ ▷ returns another version of embedded pixel substituting $\bar{d}$ for $n_{em}$-LSBs of $y$
$startbit \leftarrow startbit + n_{em}$
$y' \leftarrow$ `finalize`$(y_d, y_{\bar{d}}, X_d, X_{\bar{d}})$ ▷ choose the final embedded pixel, $y'$ as per conditions in Eq. 3
$y \leftarrow y'$ ▷ updating $y$ with $y'$
**end for**
Return $I_{em}$ ▷ updated version of $C$

$$y' = \begin{cases} y_d & \text{if } |X_d| \leq |X_{\bar{d}}| \\ y_{\bar{d}} & \text{otherwise} \end{cases} \tag{3}$$

### C. Proposed Payload Extraction with Image Recovery

Modeling of the payload extraction with image recovery of our IRDH scheme is presented in Algorithm 3. The model can blindly extract the embedded payload from the embedded image, $I_{em}$ and restore the original image, $I$ instantly by down-sampling $I_{em}$, *i.e.*, discarding the embedded pixels. With $I$, the interpolated image, $C$ is then reconstructed using `interp`$(\cdot)$. Now, for all embedded pixels $y' \in I_{em}$, the bit length, $n$ of $y'$and the number of embedded bits, $n_{em}$ in $y'$ are calculated using `bitlength`$(\cdot)$ and `getnem`$(\cdot)$ respectively as per Eq. (4) and (2). Now, $n_{em}$ number of LSBs of $y'$ and $y$ are extracted as $b$ and $P$, respectively using `getLSB`$(\cdot)$. Then $b$ and $P$ are compared using bit-wise XOR operation to determine if the set of embedded bits is equal to $b$ or its complement as per Eq. (5). Therefore, all the extracted payload-bits, $d$ are concatenated by `append`$(\cdot)$ to reconstruct the embedded payload.

$$n = \begin{cases} \lceil \log_2(y') \rceil & \text{if } y' > 1 \\ 1 & \text{otherwise} \end{cases} \tag{4}$$

$$d = \begin{cases} b & \text{if } |X_b| \leq |X_{\bar{b}}| \\ \bar{b} & \text{otherwise} \end{cases} \tag{5}$$

**Algorithm 3** `extraction`$(I_{em}, F)$

**Initialize:**
$D \leftarrow Null$ ▷ $D$ is an empty array to store $data$
$I \leftarrow$ `downsample`$(I_{em}, F)$ ▷ down-sample $I_{em}$ by $F$
$C \leftarrow$ `interp`$(I, F)$ ▷ up-sampling $I$ to $C$ by factor $F$
**for all** $y' \in I_{em}$ and all $y \in C$ **do** ▷ $\{y'\}$ are the embedded pixels in $I_{em}$ and $\{y\}$ are the interpolated pixels in $C$
$n \leftarrow$ `bitlength`$(y')$ ▷ returns bit-length of $y'$ using Eq.(4)
$n_{em} \leftarrow$ `getnem`$(n, T)$ ▷ returns number of embeddable bits, $n_{em}$ as per Eq.2
$P \leftarrow$ `getLSB`$(y, n_{em})$ ▷ returns $n_{em}$-LSBs of $y$
$b \leftarrow$ `getLSB`$(y', n_{em})$ ▷ returns $n_{em}$-LSBs of $y'$
$\bar{b} \leftarrow$ `complement`$(b)$ ▷ returns 2's complement of $b$
$X_b \leftarrow$ `bitXOR`$(P, b)$ ▷ bit-wise XOR of $P$ and $b$
$X_{\bar{b}} \leftarrow$ `bitXOR`$(P, \bar{b})$ ▷ bit-wise XOR of $P$ and $\bar{b}$
**if** $|X_b| \leq |X_{\bar{b}}|$ **then**
$d \leftarrow b$ ▷ payload bits-are embedded in original
**else**
$d \leftarrow \bar{b}$ ▷ payload bits-are embedded in complement
**end if**
$D \leftarrow$ `append`$(D, b)$ ▷ append selected payload bits, b with extracted payload, D
**end for**
Return $I$, $D$

## III. Experimental Results

Experimental results of our proposed IRDH scheme is presented in this section, where embedding rate-distortion performance of the scheme is evaluated and compared with Zhang *et al.*'s scheme [15] and our previous scheme [18]. Experiment is carried out for a set of standard USC-SIPI gray scale test-images [19] of size $256 \times 256$. As mentioned in Sec. II-A, we have used a factor, $F = 2$, for up-sampling the original test images to a size of $512 \times 512$. MATLAB R2016b with a 1.3 GHz Intel core i5 CPU of 4 GB memory is used for all necessary implementations.

Visual quality of interpolated and embedded versions of Bridge, Lena and Couple image for different values of the capacity controlling parameter, $T$ is illustrated in Fig. 1. A quantitative illustration of the rate-distortion performance is presented in Table I. Three main performance evaluation parameters along with $T$ are considered here: embedding rate, capacity and the embedded image quality. Embedding rate and capacity are expressed in terms of bpp (bit per pixel) and the total number of embedded bits. Visual quality of the embedded images is investigated in terms of PSNR (peak signal to noise ratio) and SSIM (structural similarity). The PSNR and SSIM are determined with respect to the interpolated images and embedded images.

A trade-off between the image quality and embedding rate is made with a suitable value of $T$ to obtain the best possible image quality for a given capacity requirement. This is be-

TABLE I
PERFORMANCE COMPARISON OF THE PROPOSED SCHEME

| Test Images | Performance Metric | Zhang *et al.* [15] | Our previous scheme [18] | | | | Proposed scheme | | | |
|---|---|---|---|---|---|---|---|---|---|---|
| | | | T=3 | T=4 | T=5 | T=6 | T=3 | T=4 | T=5 | T=6 |
| Airfield | Total bits | 698902 | 763301 | 567824 | 378693 | 215178 | 959807 | 763816 | 571255 | 393217 |
| | bpp | 2.666 | 2.912 | 2.166 | 1.445 | 0.821 | 3.661 | 2.914 | 2.179 | 1.500 |
| | PSNR (dB) | 22.53 | 27.61 | 33.50 | 39.55 | 45.42 | 33.46 | 39.53 | 45.67 | 50.92 |
| | SSIM | 0.8530 | 0.6494 | 0.8124 | 0.9140 | 0.9707 | 0.8120 | 0.9131 | 0.9691 | 0.9920 |
| Boats | Total bits | 440769 | 687627 | 509241 | 356615 | 260458 | 881426 | 695334 | 525975 | 393217 |
| | bpp | 1.681 | 2.623 | 1.943 | 1.360 | 0.994 | 3.362 | 2.652 | 2.006 | 1.500 |
| | PSNR (dB) | 29.15 | 28.68 | 34.59 | 40.46 | 45.43 | 34.53 | 40.52 | 45.96 | 48.05 |
| | SSIM | 0.9493 | 0.5738 | 0.7674 | 0.8976 | 0.9604 | 0.7696 | 0.9009 | 0.9615 | 0.9793 |
| Bridge | Total bits | 733636 | 618802 | 435031 | 301438 | 323632 | 813294 | 624163 | 462801 | 393217 |
| | bpp | 2.799 | 2.361 | 1.660 | 1.150 | 1.235 | 3.102 | 2.381 | 1.765 | 1.500 |
| | PSNR (dB) | 22.23 | 30.31 | 36.40 | 42.14 | 45.39 | 36.35 | 42.39 | 47.42 | 46.43 |
| | SSIM | 0.8479 | 0.8362 | 0.9345 | 0.9755 | 0.9873 | 0.9361 | 0.9787 | 0.9924 | 0.9938 |
| Couple | Total bits | 586075 | 667161 | 473734 | 305315 | 299875 | 861865 | 667800 | 486558 | 393217 |
| | bpp | 2.236 | 2.545 | 1.807 | 1.165 | 1.144 | 3.288 | 2.547 | 1.856 | 1.500 |
| | PSNR (dB) | 27.43 | 29.58 | 35.59 | 41.52 | 45.44 | 35.51 | 41.53 | 47.45 | 47.56 |
| | SSIM | 0.9230 | 0.5986 | 0.7858 | 0.9081 | 0.9536 | 0.7838 | 0.9069 | 0.9690 | 0.9788 |
| Lena | Total bits | 470653 | 656093 | 460611 | 326825 | 294693 | 852696 | 656654 | 491740 | 393217 |
| | bpp | 1.795 | 2.503 | 1.757 | 1.247 | 1.124 | 3.253 | 2.505 | 1.876 | 1.500 |
| | PSNR (dB) | 31.52 | 29.43 | 35.38 | 41.36 | 45.44 | 35.31 | 41.52 | 46.88 | 47.13 |
| | SSIM | 0.9546 | 0.5064 | 0.6818 | 0.8314 | 0.9207 | 0.6799 | 0.8327 | 0.9352 | 0.9678 |
| Average | Total bits | 585595 | 666055 | 475719 | 321748 | 291160 | 861874 | 668797 | 495273 | 393217 |
| | bpp | 2.234 | 2.541 | 1.815 | 1.227 | 1.111 | 3.288 | 2.551 | 1.889 | 1.500 |
| | PSNR (dB) | 26.55 | 29.40 | 35.43 | 41.32 | 45.43 | 35.37 | 41.42 | 46.97 | 47.61 |
| | SSIM | 0.8981 | 0.6507 | 0.8115 | 0.9140 | 0.9605 | 0.8114 | 0.9158 | 0.9682 | 0.9821 |

cause, as mentioned in Sec. II-B, number of embeddable bits decreases (and respective embedded image quality improves), while $T$ decreases. As illustrated in Table. I, our proposed scheme offers relatively better embedded image quality (*i.e.*, PSNR and SSIM) that gradually increases with the lower embedding rates and higher values of $T$. Moreover, for similar embedding rates managed by a suitable of value of $T$, our proposed scheme also generates a better quality embedded image compared to that obtained by the schemes in [15] and [18].

Particularly, we have modeled our scheme in Sec. II to avoid the use of flag bit unlike the schemes in [16] and [18]. Thus, a flag-bit in an embeddable pixel is replaced with one more payload bit. This improvement of embedding rate and capacity with better or almost similar embedded image quality becomes evident, while it is compared to [18] for the same values of $T$ as in Fig. 2 and Fig. 3. For example, with $T = 4$, our previous scheme [18] can embed up to 460611 bit payload with 1.76 bbp in Lena image, while the PSNR is 35.38 dB and SSIM is 0.6818; whereas, 656654 bit payload (2.51 bpp) with better image quality (*i.e.*, PSNR of 41.52 dB and SSIM of 0.8327) are embedded in our proposed scheme for the same value of $T$. This means that for a given value of $T$, our scheme achieves higher embedding rate with improved image quality compared to the scheme in [18].

Additionally, embedding capacity of our proposed scheme remains even higher with similar image quality for lesser number of embeddable bits than that used in [18]. For instance, for $T = 5$ and Lena image, our proposed scheme embeds total 491740 bits with 1.88 bpp, PSNR of 46.88 dB and SSIM of 0.9352. On the other hand, for $T = 4$ and Lena image, the scheme in [18] can embed total 460611 bits of payload with 1.78 bpp, PSNR of 35.38 dB and SSIM of 0.6818,which are lower than the proposed scheme. This trend of improvement is also evident for the other test images.

Our proposed scheme also performs better than the Zhang *et al.*'s scheme [15]. For example, the maximum capacity of Zhang *et al.*'s scheme [15] is 470Kb with 1.795 bpp, PSNR

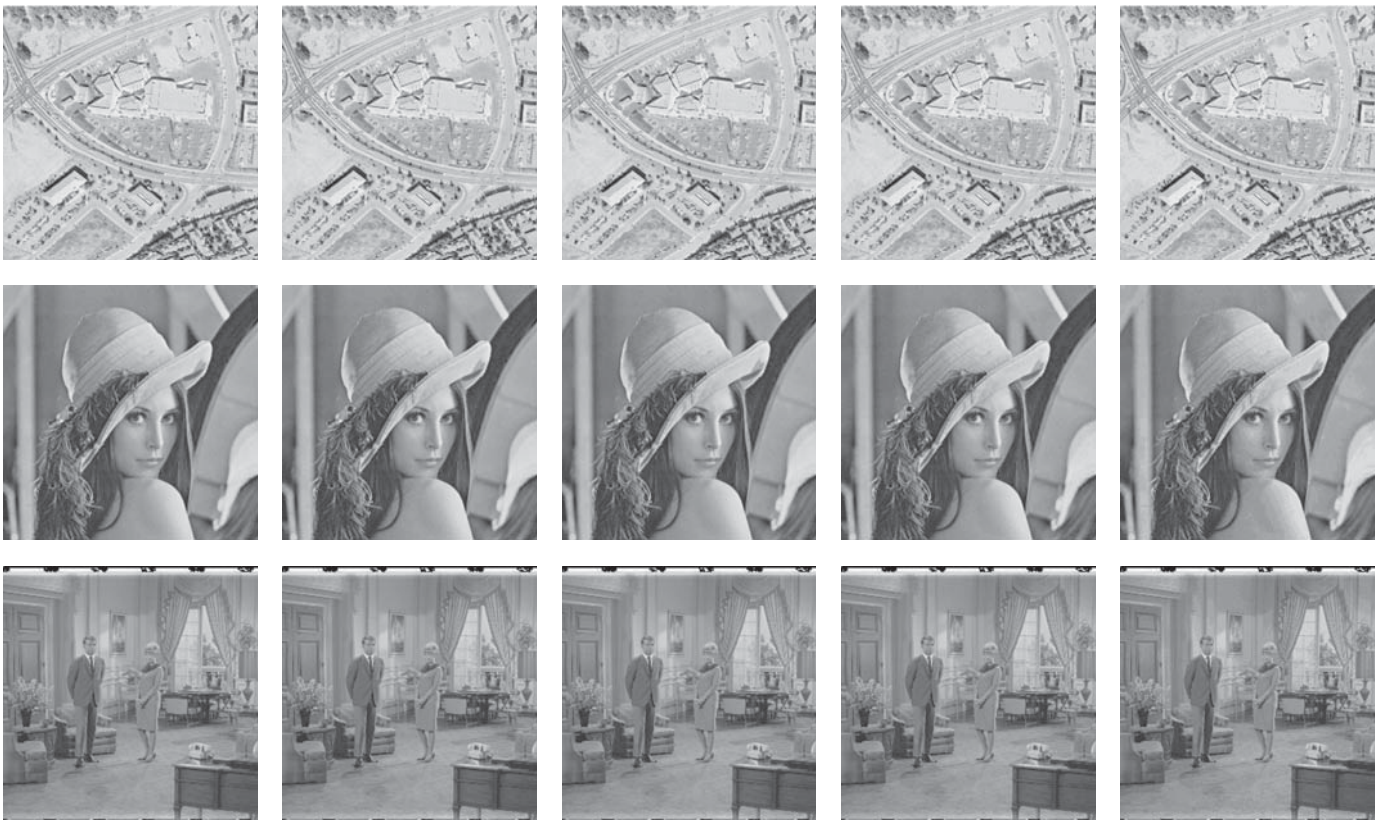

(a) (b) (c) (d) (e)

Fig. 1. Example of output images: (a) interpolated images, (b) embedded images for $T = 6$, (c) embedded images for $T = 5$, (d) embedded images for $T = 4$ and (e) embedded images for $T = 3$. (Images in rows from top: Airfield, Lena and Couple)

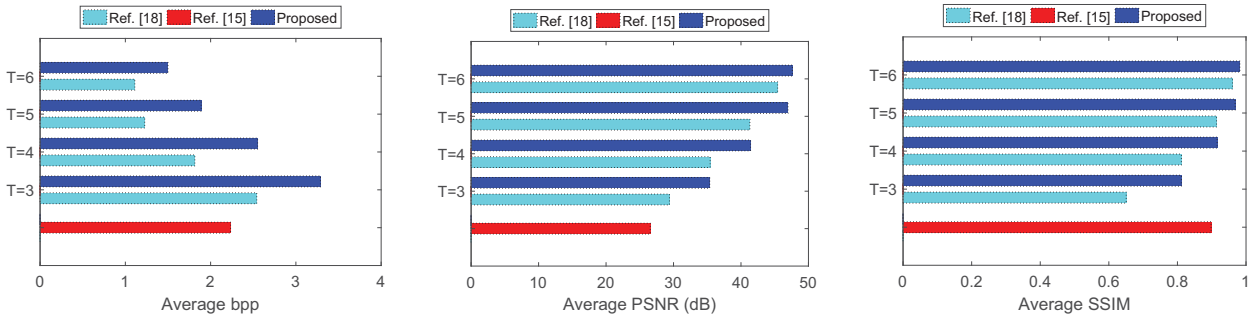


(a) (b) (c)

Fig. 2. Average performance comparison of the proposed scheme with other schemes for different values of $T$ in terms of: (a) bpp, (b) PSNR, and (c) SSIM.

of 31.52 dB and SSIM of 0.95. In contrast, the maximum embedding capacity of the Lena images varies in the range from 393 Kb to 852 Kb payload (*i.e.*, 1.50 bpp to 3.25 bpp) for $T = [3,6]$ with PSNR and SSIM ranged from 35.31 dB to 47.13 dB and 0.67 to 0.97, respectively. This improvement is also valid, while the performance of our scheme is compared to our previous scheme [18], where the maximum capacity ranges from 294 Kb to 656 Kb, PSNR from 31.52 dB to 45.44 dB and SSIM from 0.50 to 0.92 for the same range of $T$. This suggests that our proposed scheme also has higher dynamic range of embedding capacity with better embedded image quality.

In summary, the trend of improvement discussed above is also evident in the average embedding-rate distortion performance of our scheme compared to the schemes [15], [18] as illustrated in Table I, Fig. 2 and Fig. 3. For example, compared to our earlier scheme [18] (which was better than [15]), the embedding capacity of our proposed scheme increases 29%, 40%, 53% and 35% in bpp with increment of 20%, 16.9%, 13.6% and 4.8% in PSNR and 24.7%, 12.9%, 5.9% and 2.24% in SSIM for $T = 3,4,5\,\&\,6$, respectively. Thereby, the proposed scheme has demonstrated that it can effectively embed varying size payloads with higher embedding rate and better image

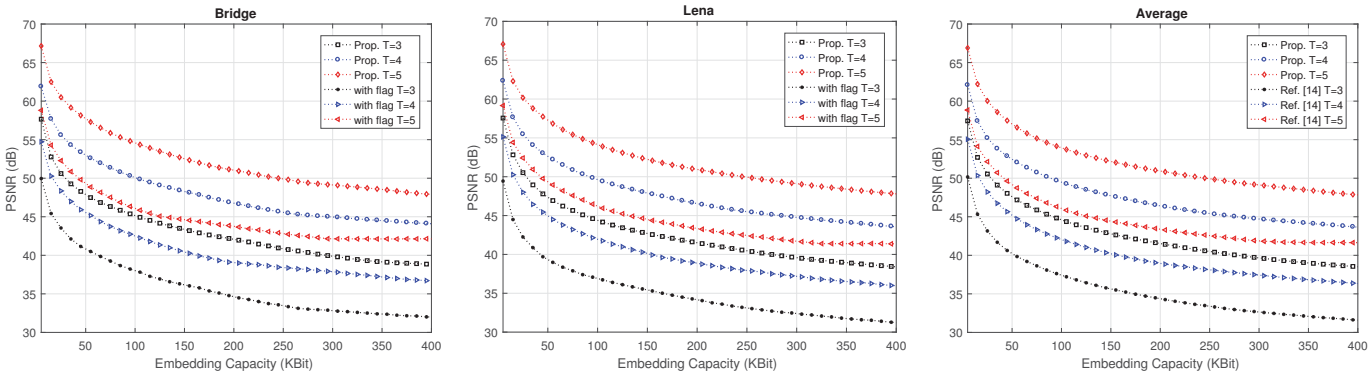


(a) (b) (c)

Fig. 3. Embedding rate-distortion performance comparison of the proposed scheme with our previous scheme [18] for different values of $T$: (a) Bridge, (b) Lena and (c) average of all test-images.

quality using a suitable capacity control parameter.

## IV. Conclusion

In this paper, we have modeled and analysed an improved IRDH scheme for better rate-distortion performance with varying size of payloads. We have used a simplified quadratic interpolation for computing interpolated pixels, and defined a capacity control parameter to attain embedding capacity requirements with minimum possible distortion. Embedding process is modeled to utilize the correlation between the embeddable pixel and estimated versions of embedded pixel to incorporate one more payload-bit per pixel replacing the flag bit. Experimental results have demonstrated that our improved scheme can effectively embed varying size payload with higher embedding rate and better image quality compared to some recent IRDH schemes. Embedding is carried out only in the interpolated pixels that would also minimize any possible concern of erratically modifying the input image and thus the proposed scheme could be useful in military and medical image applications.

In our future work, we will continue evaluation of the performance of our proposed scheme in an extended experimental setup and comparison with the other prominent IRDH schemes.

## References


[1] I. J. Cox, M. L. Miller, J. A. Bloom, J. Fridrich, and T. Kalker, "Models of watermarking," in *Digital Watermarking and Steganography (Second Edition)*. Burlington: Morgan Kaufmann, 2008, pp. 61–103.

[2] H. Nyeem, W. Boles, and C. Boyd, "Digital image watermarking: its formal model, fundamental properties and possible attacks," *EURASIP Journal on Advances in Signal Processing*, vol. 2014, no. 1, pp. 1–22, 2014.

[3] ——, "Developing a digital image watermarking model," in *Proc. DICTA*. IEEE, 2011, pp. 468–473.

[4] J. M. Barton, "Method and apparatus for embedding authentication information within digital data," Jul. 8 1997, US Patent 5,646,997.

[5] W. Bender, W. Butera, D. Gruhl, R. Hwang, F. J. Paiz, and S. Pogreb, "Applications for data hiding," *IBM systems journal*, vol. 39, no. 3.4, pp. 547–568, 2000.

[6] Y. Lee, H. Kim, and Y. Park, "A new data hiding scheme for binary image authentication with small image distortion," *Information Sciences*, vol. 179, no. 22, pp. 3866–3884, 2009.

[7] M. Wu and B. Liu, "Data hiding in binary image for authentication and annotation," *IEEE transactions on multimedia*, vol. 6, no. 4, pp. 528–538, 2004.

[8] J. Tian, "Reversible data embedding using a difference expansion," *IEEE Transactions on Circuits and Systems for Video Technology*, vol. 13, pp. 890–896, 2003.

[9] D. M. Thodi and J. Rodríguez, "Expansion embedding techniques for reversible watermarking," *IEEE Transactions on Image Processing*, vol. 16, pp. 721–730, 2007.

[10] Y. Hu, H.-K. Lee, and J. Li, "DE-based reversible data hiding with improved overflow location map," *IEEE Trans. CSVT*, vol. 19, pp. 250–260, 2009.

[11] K.-H. Jung and K.-Y. Yoo, "Data hiding method using image interpolation," *Computer Standards & Interfaces*, vol. 31, no. 2, pp. 465–470, 2009.

[12] H. Nyeem, W. Boles, and C. Boyd, "Content-independent embedding scheme for multi-modal medical image watermarking," *Biomedical engineering online*, vol. 14, no. 1, p. 7, 2015.

[13] C.-F. Lee and Y.-L. Huang, "An efficient image interpolation increasing payload in reversible data hiding," *Expert Systems with Applications*, vol. 39, no. 8, pp. 6712–6719, 2012.

[14] W.-J. Wang, Y.-H. Zhang, C.-T. Huang, and S.-J. Wang, "Steganography of data embedding in multimedia images using interpolation and histogram shifting," in *Proc of IIHMSP'13*. IEEE, 2013, pp. 387–390.

[15] X. Zhang, Z. Sun, Z. Tang, C. Yu, and X. Wang, "High capacity data hiding based on interpolated image," *Multimedia Tools and Applications*, pp. 1–24, 2016.

[16] M. A. Wahed and H. Nyeem, "Developing a block-wise interpolation based adaptive data embedding scheme," in *Proc. of ICEEICT 2016*. IEEE, 2016, pp. 1–6.

[17] H. Nyeem, W. Boles, and C. Boyd, "Utilizing least significant bit-planes of roni pixels for medical image watermarking," in *Proc. DICTA*. IEEE, 2013, accepted.

[18] M. A. Wahed and H. Nyeem, "A simplified parabolic interpolation based reversible data hiding scheme," in *Proc. of ICAEE 2017*, IEEE. (accepted), 2017.

[19] USC, "SIPI image database," http://sipi.usc.edu/database/, SIPI, [Online; last accessed 23-Mar-2017].

# Simulations of Threshold Logic Unit Problems Using Memristor Based Synapses and CMOS Neuron

Anik Chowdhury*, Afiya Ayman, Shovon Dey
School of Science, Engineering and Technology
East Delta University
Chittagong, Bangladesh
*anik.chy.113@gmail.com

Mrinmoy Sarker, Aqeeb Iqbal Arka
Department of Electrical and Electronic Engineering
Bangldesh University of Engineering and Technology
Dhaka-1205, Bangladesh

***Abstract*—This paper presents an implementation of Threshold Logic Units (TLU), the special case of an Artificial Neural Network (ANN), using discrete circuit elements like memristors as synapses and CMOS circuits as a neuron. Simple threshold logic gates have been developed using a single layer network to establish a base upon which more complex problems can be implemented. The XOR problem, benchmark for a simple multilayer neural network circuit, has also been simulated in this paper as an example of multiple layer networks. Once the circuit is developed, the memristors are trained to their weights. The logical output of the neuron is checked whether the circuits are working or not. Successful demonstrations and simulation of the basic logic gates have been shown which can contribute to the development of using the memristor-based neural network.**

***Index Terms*—Artificial neural network, CMOS neuron, memristor, linear and non linear separability, threshold logic unit, weighted synapse.**

## I. Introduction

As a model of biological computational networks, an artificial neural network consists of information processing units which can perform parallel computation by transmitting and receiving electric signals and pulses [1], [2]. Neural networks are formed by neural units where every neuron are connected through adaptive weights which are activated and trained during training. Comparing to the biological neural networks synapses which are the main memory zone and also the connection among the neurons; a passive device that behaves like a synapse called memristor (memory + resistor), has been invented and successfully used as a synapse [3], [4]. Like the biological network, the artificial neural network can be used for solving complex mathematical and logical functions. Generally, in the neural network, individual neurons accumulate the weighted synapses and produce an output through a linear or non-linear activation function with a threshold. A neural network may have multi-layered configurations like input layer, hidden layer and one output layer [5], [6].

The motivation of this work is to solve the threshold logic unit problems which can be used as a test bench to measure the performance of the ANN built with memristors. Circuits developed in [7], [8] has been reestablished using a new method of learning and programming of the memristor which is further used for higher level work like pattern recognition [9]. At first, weights of the network are calculated and then they are converted into the resistance values. Then the corresponding memristors are trained to certain resistance values. And then the output of the basic gates are checked whether they work or not. Synapses of the network are replaced with memristors and the neuron is replaced with CMOS circuits.

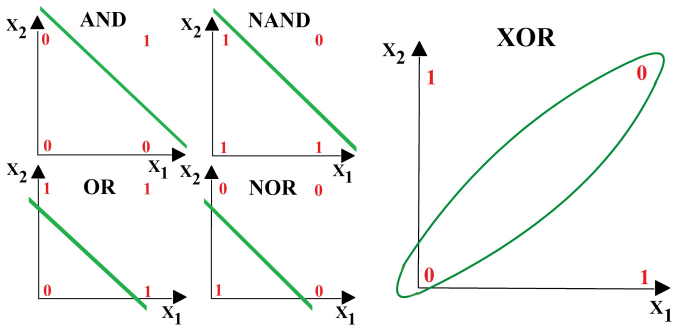


(a) Linearly separable problems: AND, NAND, OR, NOR operators (b) Non-linearly separable problems: XOR operators

Fig. 1. Linearly and non linearly separable TLUs

The rest of the paper is organized as follows. Important circuit elements of the proposed network are explained elaborately in Section II. Overall system operation and the programming learning rule are described in Section III. Experimental results are shown in Section IV and conclusions are made in Section V.

## II. Proposed System

Mainly two functional blocks build up the overall system. The first block is weighted synapses which are mainly memristors and the second block is the output neurons which is mainly op-amp. In the following subsections, ANN circuit realization, the memristor and the output neuron will be discussed in detail.

### A. ANN Circuit Realization

Threshold logic unit problems can imitate basic gates function like AND, NAND, OR, NOR, XOR, XNOR. Linearly separable problems like AND, NAND, OR, NOR as shown in Fig. 1a can be solved by using a single layer network where the input sets can be easily separated by a single straight boundary decision line. On the other hand, non-linearly separable problems like XOR, XNOR as shown in

978-1-5386-2307-7/17/$31.00 ©2017 IEEE

TABLE I
WEIGHT COMBINATION FOR LINEARLY SEPARABLE PROBLEMS

| | $W_1$ | $W_2$ | $W_3$ |
|---|---|---|---|
| AND | 5.75 | 5.25 | -7.00 |
| OR | 5.25 | 8.25 | 4.5 |
| NOR | -5.25 | -8.25 | -4.5 |
| NAND | -6.75 | -5.75 | 6.5 |

TABLE II
WEIGHT COMBINATION FOR NON LINEARLY SEPARABLE PROBLEMS

| | $W_1$ | $W_2$ | $W_3$ |
|---|---|---|---|
| Hidden weights | -8.5 | 6.5 | -3.0 |
| | 6.0 | -4.5 | -4.5 |
| Output weights | 5.25 | 8.25 | 4.5 |

Fig. 1b cannot be solved using a single layer network because the set cannot be separated by a single straight line which requires at least two layer networks. The basic layout of a network is shown in Fig. 2. For the linearly separable problems a single node with two inputs, one bias input, one output and three weights $W_1$, $W_2$, $W_3$ as shown in Fig.2 can be used. The output of the network is calculated for a specific weight combination which produces correct logic outputs for all four input pairs $(-1,-1),(-1,1),(1,-1)$, and $(1,1)$ is noted in Table I. For non-linearly separable problems, it requires a second layer with a total of 9 weights; 6 more than the previous one layer ANN structure. Table II shows a sample weight combination that works for the XOR operator.

### B. Memristor As A Synapse

Memristors can change its resistance value according to the voltage pulses [10]. A synaptic weight can be modeled with the memristor's resistance. Circuit level implementation of the basic network is shown in Fig 3. Three input weights are replaced with three memristors $R_{M1}$, $R_{M2}$, $R_{M0}$ and the weighted summation is replaced by op-amp to sum all the inputs. However, this circuit cannot calculate negative weights. As a result, a modified version of the circuit is developed in [7], [8] for a single synapse shown in Fig. 4. The same resistance value is used for $R_0$ and $R_1$ so that they invert the positive input voltage coming out of the op-amp which in this case is 1KΩ. According to the equations developed in [7], [8]; values of $R_M$, $R_N$ and $R_F$ can be calculated from (1), (2) and (3). Here $G$ is the weights of the memrsitors which is shown in Table I and Table II.

$$R_M = \frac{R_F R_N}{R_F - G \times R_N} \tag{1}$$

$$R_N = R_{MHigh} - \frac{R_{MHigh} G_{High}(R_{MHigh} - R_{MLow})}{R_{MHigh} G_{High} - R_{MLow} G_{Low}} \tag{2}$$

$$R_F = \frac{R_N(R_{MHigh} G_{High} - R_{MLow} G_{Low})}{R_{MHigh} - R_{MLow}} \tag{3}$$

$G_{High}$ and $G_{Low}$ are the maximum and minimum weight of the ANN which are 10 and $-10$ in this case, while $R_{MHigh}$ and $R_{MLow}$ are the highest and lowest optimal range of the memristors. The two resistors $R_N$ and $R_F$ set the gain of the circuit to be within the desired weight limit while adjusting the resistance of the memristor $R_M$ between 10 KΩ and 100 KΩ. Following (2) and (3), $R_N$ and $R_F$ were calculated to be 18.182 KΩ and 222.22 KΩ, respectively. Table III shows a summary of the conversion of the weights and logic levels between the theoretical ANNs and the circuit ANNs.

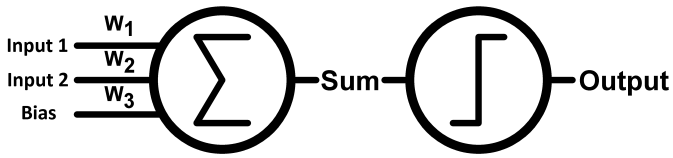


Fig. 2. Basic layout of a neuron

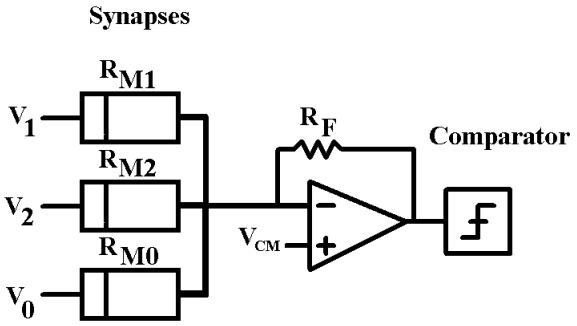


Fig. 3. Neuron with two input synapse and a bias synapse

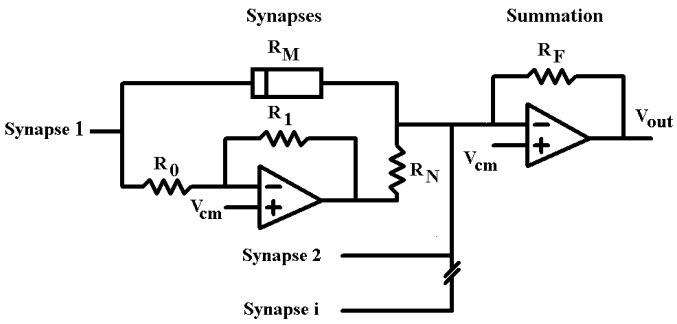


Fig. 4. Full circuit of the network supporting negative weights feeding into the summation circuit of the neuron

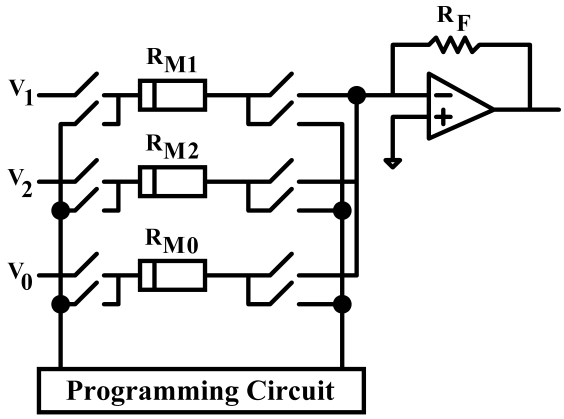


Fig. 5. Complete circuit of the ANN including the programming circuit and the main network

TABLE III
CONVERSION BETWEEN THEORETICAL ANNS AND CIRCUIT ANNS

| | Theoretical ANNs | Circuit ANNs |
|---|---|---|
| Weights | -10 | 10kΩ |
| | 10 | 100kΩ |
| Logic level | -1 | -100mV |
| | 1 | 100mV |

### C. Cmos Neuron

To replace the CMOS neuron, an op-amp is used which is an integral part of the circuit [11]. For the stable operation of the op-amp, proper biasing circuitry and effective compensation technique are necessary. There is also a comparator circuit after the summer block which is also implemented with the op-amp.

## III. SYSTEM OPERATION

This section describes the programming technique, proposed learning rule and the overall system operation of the circuit.

### A. Programming Technique

Generalized memristor model is used in this paper for simulation of memristor [12]. Writing and Reading are the two important parts of programming memristors. Writing changes the current state of the memristors and programs it to the desired resistance value. To reduce the voltage stress of the memristors, $1us$ pulse with amplitude beyond or above the threshold value is used for programming the memristors. To read the memristor pulse of 100mV which is less than the threshold value is used so that it cannot change the current state of the memristor.

### B. Proposed Learning Rule

For programming a memristor, a MATLAB script has been written. This script generates voltage pulses according to the differences of current resistance and desired resistance of the memristors. The amplitude of the pulses will increase if the difference is larger and vice-versa. If the difference is no more than 15Ω, then the programming will be finished. However, the amplitude value is limited to a maximum value to ensure the safety of the device.

### C. Overall System Operation

After proper programming of the memristors, they should be attached to the main network. A switching block as shown in Fig. 5 is necessary to switch the memristors between the programming circuit and the main circuit. Switches are mainly made using transmission gate topology which can easily switch the memristors between this blocks [13].

## IV. EXPERIMENTAL RESULTS

At first, single layer circuits are simulated which are linearly separable. And then, two layer non-linearly separable circuits are simulated.

TABLE IV
RESISTANCE VALUES FOR DIFFERENT GATES

| | $R_{M1}$ | $R_{M2}$ | $R_{M0}$ |
|---|---|---|---|
| AND | 34.333kΩ | 31.873kΩ | 11.561kΩ |
| OR | 31.873kΩ | 55.947kΩ | 28.778kΩ |
| NOR | 12.719kΩ | 10.855kΩ | 13.289kΩ |
| NAND | 11.713kΩ | 12.365kΩ | 38.386kΩ |

TABLE V
RESISTANCE VALUES FOR XOR GATE

| | $R_{M1}$ | $R_{M2}$ | $R_{M0}$ |
|---|---|---|---|
| Hidden layer | 20.726kΩ | 15.905kΩ | 16.495kΩ |
| Hidden layer | 15.905kΩ | 20.726kΩ | 16.495kΩ |
| Output layer | 31.873kΩ | 55.947kΩ | 28.778kΩ |

### A. Single Layer Circuits

Single layer circuits are built to realize four basic threshold logic gates: AND, NAND, OR and NOR which are linearly separable problems. The weight values as listed in Table I are converted into actual resistor values shown in Table IV based on the equations in Section II-B. At first, memristors are connected to the programming network and programmed to their desired resistance value. Then, the input signal is given to check whether the network is working or not. The output of the neuron is compared with the threshold value which is 0V in this case. Anything below this threshold voltage will be considered as negative which is identified as “0” and anything above this threshold voltage will be considered as positive which is identified as “1” in Fig. 6. The simulation result including inputs, summer output and the threshold function output is shown in Fig.6a-6d for AND, NAND, OR, and NOR gates using the same single layer ANN structure and the resistances listed in Table IV. From the figure, it can be concluded that the whole network is working properly.

### B. Multiple Layer Circuits

Further expansion of the simulation is to develop a two-layer neural network for XOR by expanding the single layer structure. The outputs of the first layer is used as the inputs of the second layer whose logic level is the same. The single layer circuit is duplicated three times to construct the multiple layer circuit. At first, the memristors are trained to the desired resistance value shown in Table V. Then the input is given to check whether the circuit is working or not. Input, summer and the output voltages are shown in Fig. 7. The output of the multiple layer networks is matched with the output of the original gate.

## V. CONCLUSION

The process of building an ANN circuit with memristors has been presented. The conversion between the theoretical weights and the resistance values is analyzed. The circuits are designed and confirmed to work correctly through simulations. These circuits include the single layer ANN, multilayer ANN, negative weight circuit and the interface between the first and

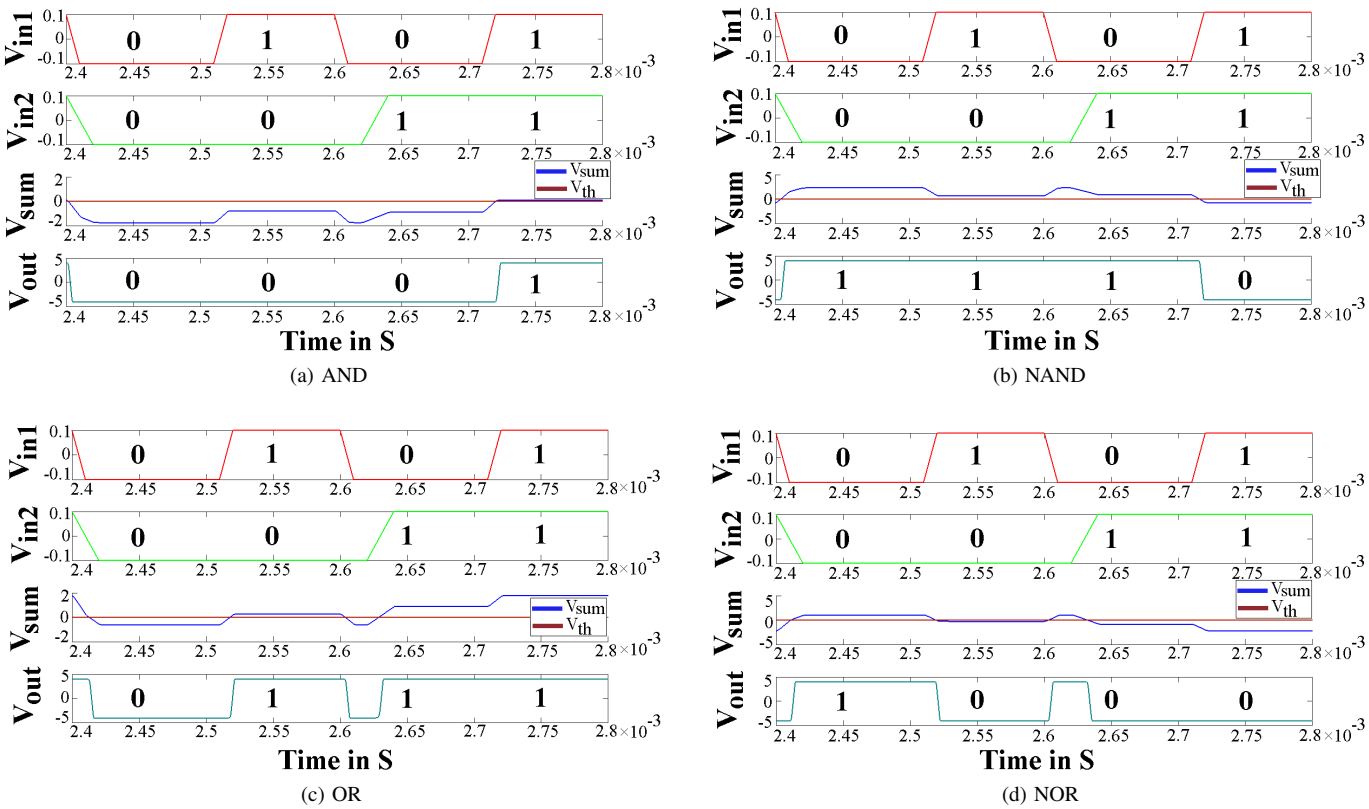


(a) AND (b) NAND

(c) OR (d) NOR

Fig. 6. Output from different gates including input, output and summer voltage

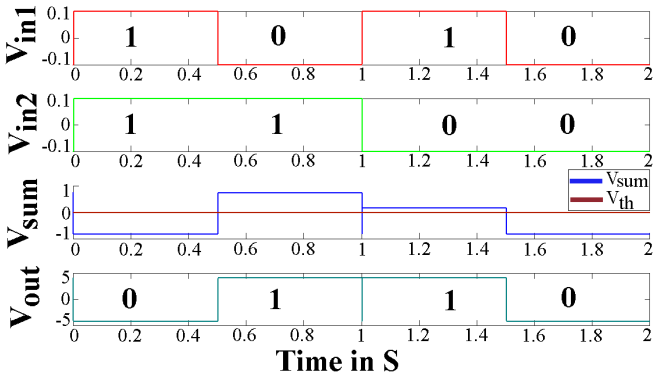


Fig. 7. Output of XOR gate

second layer of a multilayer ANN. The learning ability of the hardware ANN designed with memristors by solving linearly and non-linearly separable problems is also illustrated. This simpler form of ANN can be used for solving more complex problems like pattern recognition [14].

## References


[1] H. Khodabandehlou and M. S. Fadali, "A quotient gradient method to train artificial neural networks," *International Joint Conference on Neural Networks (IJCNN)*, pp. 2576–2581, 2017.

[2] R. Ruiz-Lombera, A. Piccolo, L. Rodriguez-Cobo, J. M. Lopez-Higuera, and J. Mirapeix, "Feasibility study of strain and temperature discrimination in a botda system via artificial neural networks," *25th Optical Fiber Sensors Conference (OFS)*, pp. 1–4, 2017.

[3] M. R. Azghadi, B. Linares-Barranco, D. Abbott, and P. H. W. Leong, "A hybrid cmos-memristor neuromorphic synapse," *IEEE Transactions on Biomedical Circuits and Systems*, vol. 11, pp. 434–445, 2017.

[4] A. Slavova and G. Bobeva, "Determination of edge of chaos in hysteresis cnn model with memristor synapses," *2017 European Conference on Circuit Theory and Design (ECCTD)*, pp. 1–4, 2017.

[5] R. Kamimura, "Potential layer-wise supervised learning for training multi-layered neural networks," *International Joint Conference on Neural Networks (IJCNN)*, pp. 518–525, 2017.

[6] G. Garcia-Molina, K. B. B. Steele, T. Tsoneva, S. Pfundtner, B. Riedner, D. P. White, and G. Tononi, "Automatic characterization of sleep need dissipation using a single hidden layer neural network," *2017 25th European Signal Processing Conference (EUSIPCO)*, pp. 1305–1308, 2017.

[7] A. Rothenbuhler, "A memristor-based neuromorphic computing application," Master's thesis, Boise State University, 2013.

[8] T. T. T. Tran, "Simulations of artificial neural network with memristive devices," Master's thesis, Boise State University, 2012.

[9] A. Chowdhury, M. Sarkar, A. I. Arka, and A. B. M. H. ur Rashid, "Associative memory algorithm for visual pattern recognition with memristor array and cmos neuron," *9th International Conference on Electrical and Computer Engineering (ICECE)*, pp. 42–45, 2016.

[10] L. Chua and S. M. Kang, "Memristive devices and systems," *Proceedings of the IEEE*, vol. 64, pp. 209–223, 1976.

[11] X. Wu and V. Saxena, "Enabling bio-plausible multi-level stdp using cmos neurons with dendrites and bistable rrams," *International Joint Conference on Neural Networks (IJCNN)*, pp. 3522–3526, 2017.

[12] C. Yakopcic, T. M. Taha, and R. E. P. Guru Subramanyam, *Advances in Neuromorphic Memristor Science and Applications*. Springer, 2015.

[13] S. Sayil, A. H. Shah, M. A. Zaman, and M. A. Islam, "Soft error mitigation using transmission gate with varying gate and body bias," *IEEE Design and Test*, vol. 34, pp. 47–56, 2017.

[14] Y. Zhang, Y. Li, X. Wang, and E. G. Friedman, "Synaptic characteristics of ag/aginsbte/ta-based memristor for pattern recognition applications," *IEEE Transactions on Electron Devices*, vol. 64, pp. 1806–1811, 2017.

# High Voltage Conversion DC-DC Step up Converter for Fuel Cell Applications

M. Al Mamun, Md. Ali Hasan, Eaqub Khan
Department of Electrical and Electronic Engineering, Southeast University, Dhaka-1208, Bangladesh
mamuneee@iut-dhaka.edu
mdalihasan9848@gmail.com
eaqubkhan420@gmail.com

*Abstract*— **Fuel cells are becoming one of the most prominent sources of renewable energy. The voltage level of these sources are not that much high, necessitating step up converters with large gain of voltage. Step up converters with large voltage gain are needed to interface the fuel cell system with power transmission and distribution networks. Conventional boost converter usually operates at maximal duty cycle to acquire large voltage conversion. Reverse recovery problems of power diodes, high conduction loss at power switches, electromagnetic interference, and increased ripple inductor current and output voltage arise due to the use of very large duty cycle of the switching signal. This paper demonstrates a dc-dc step up converter capable of providing very large voltage conversion operating at a very low duty cycle (i.e. duty cycle < 0.5). What is more, this converter works on same control signal for all the switches which lessens the complicacies during operation. The steady-state theoretical analysis has been described in this paper and finally the potency has been verified by simulation results.**

***Keywords— dc-dc converter, duty cycle, high voltage gain, fuel cell, voltage ripple, renewable energy.***

## I. INTRODUCTION

Day by day the fossil fuel reserve is decreasing, increasing the price beyond the affordable limit. Moreover, the vehicles using fossil fuels are polluting the environment, rising new regulations to lessen the emission of $CO_2$. Because of this, world researchers are heading towards the renewable energy systems. Fuel cells and photovoltaic systems, for example, have become the prominent sources of renewable energy. Fuel Cell, in particular, has been as an emerging technology in today's world, making it possible to achieve a green and clean environment.

However, the output voltage obtained from this source is very low. As this system is normally integrated with the gird or fed to ac loads shown in Fig. 1 via a high dc input inverter, large voltage gain dc-dc step up converters are required to lift the small output voltage of the fuel cell [1]. Also, high gain dc-dc converters are used in various applications, for instance, automobile, LED lighting, switch mode power supply, telecommunications etc. Hypothetically, a conventional dc–dc boot converter can secure a large output voltage by using large duty cycle [2]-[4], resulting in different major problems, for instance, reverse recovery, electromagnetic interference, conduction loss at the switches, increased ripple inductor current and ripple output voltage etc.

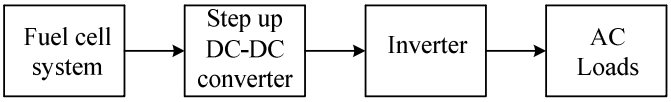


Figure 1. Typical fuel cell systems

To obtain high gain dc-dc conversion several dc-dc converters are employed which are basically divided into two categories- non-isolated and isolated converters. The conventional boost converter, cascaded converter, switched inductor and capacitor converters are the examples of the non-isolated converters. These converters can give a high output to input voltage ratio, but they need high duty cycle which causes ripple current of inductor and reverse recovery problem [5]-[6]. Thus, the power loss grows, declining the overall efficiency [7]-[8]. Cascaded step up converters can acquire large voltage gain easily. But they involve more devices which increases the size and cost of the converter. Thus, the efficiency goes down [9]. Very large voltage at the output is achievable by the switched capacitor converters. However, the supply current is fluctuating in nature and the load regulation is not good enough [10].

Therefore, it is evident that a highly efficient step up dc-dc converter is needed which can overcome the above mentioned issues and fulfill the demand. This paper presents a very high gain dc-dc step up converter which works at a very low duty ratio (i.e, duty ratio < 0.5). A single control signal is used to control the switches, cutting the operation complexity short and increasing the efficiency. Moreover, the discrepancies found during the operation are within the tolerable limit [11]-[12]. Finally, the rigorous steady-state analysis is justified by the simulation results obtained from the software PSIM.

Rest of the paper is presented as following. Theoretical operation is demonstrated in Section II. Section III illustrates the analysis and comparison between the proposed converter and the conventional boost converter. Simulation results are illustrated in section IV and section V ends the paper with a conclusion.

## II. PROPOSED CONVERTER AND ITS WORKING PRINCIPLE

The proposed converter is depicted in Fig. 2 and it involves four inductors ($L_1$, $L_2$, $L_3$ and $L_4$), four capacitors ($C_1$, $C_2$, $C_3$ and $C_4$), five diodes ($D_1$, $D_2$, $D_3$, $D_4$, and $D_5$) and five high frequency controlled switches ($S_1$, $S_2$, $S_3$, $S_4$ and $S_5$). The switches work simultaneously depending on an identical pulse

978-1-5386-2307-7/17/$31.00 ©2017 IEEE

width modulated signal. $V_i$ is the low dc input voltage from the fuel cell and the load is connected across the capacitor $C_4$.

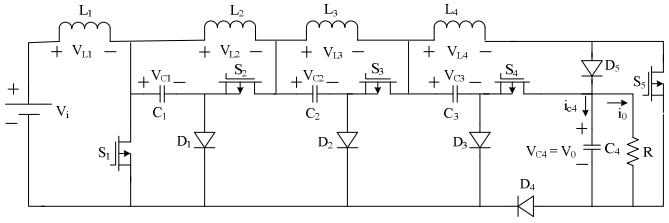


Figure 2. Proposed high dc-dc step up converter

For the steady-state analysis in continuous mode of operation it is assumed that, $V_i$ = low input voltage; $V_{L1}$ = voltage across $L_1$, $V_{L2}$ = voltage across $L_2$; $V_{L3}$ = voltage across $L_3$; $V_{L4}$ = voltage across $L_4$; $V_{C1}$ = voltage across $C_1$; $V_{C2}$ = voltage across $C_2$; $V_{C3}$ = voltage across $C_3$; $V_{C4}$ = voltage across $C_4$; $V_o = V_{C4}$= output voltage across $R$; $T_s$= switching period of controlled switches; $T_{on}$= on time of controlled switches; $D$ = duty cycle of controlled switches (ratio of $T_{on}$ to $T_s$ ). The analysis is performed as following,

**Mode 1:** During this time all the switches are OFF. Consequently, all the diodes are forward biased and this is shown in Fig. 3. Capacitors $C_1$, $C_2$, $C_3$, $C_4$ and the load are energized by $V_i$, $L_1$, $L_2$, $L_3$ and $L_4$. If KVL is applied in the loops of Fig. 3, then the voltages across $L_1$, $L_2$, $L_3$, and $L_4$ are derived as follows,

$$V_{L1} = V_i - V_{C1} \quad (1)$$
$$V_{L2} = V_{C1} - V_{C2} \quad (2)$$
$$V_{L3} = V_{C2} - V_{C3} \quad (3)$$
$$V_{L4} = V_{C3} - V_{C4} \quad (4)$$

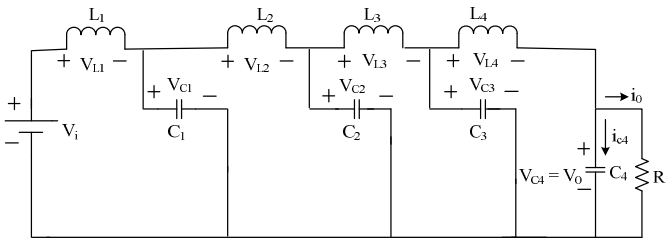


Figure 3. Equivalent circuit when all the switches are OFF

**Mode 2:** All the switches are turned ON during this time. Thus, all the diodes are reversed biased and this is presented in Fig. 4. Now, $L_1$, $L_2$, $L_3$ and $L_4$ are energized by the source voltage $V_i$ and the capacitors $C_1$, $C_2$, $C_3$ and $C_4$. The load is supplied by the capacitor $C_4$. Voltage across $L_1$, $L_2$, $L_3$, and $L_4$ are obtained as follows,

$$V_{L1} = V_i \quad (5)$$
$$V_{L2} = V_{C1} \quad (6)$$
$$V_{L3} = V_{C2} \quad (7)$$
$$V_{L4} = V_{C3} + V_{C4} \quad (8)$$

Now, by using equation (1) and (5), the volt-second balance of $L_1$ is given by

$$V_i D T_s = -(V_i - V_{C1})(1 - D)T_s$$

Or,

$$V_{C1} = \frac{V_i}{1 - D}$$

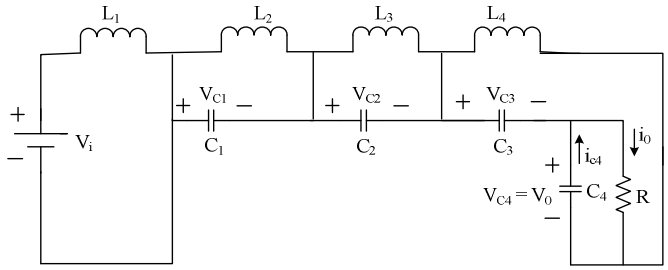


Figure 4. Equivalent circuit when all the switches are ON

Similarly, by using equation (2) and (6), the volt-second balance of $L_2$ is given by

$$V_{C1} D T_s = -(V_{C1} - V_{C2})(1 - D)T_s$$

Or,

$$V_{C2} = \frac{V_{C1}}{1 - D} = \frac{V_i}{(1 - D)^2}$$

Likewise, by using equation (3) and (7), the volt-second balance of $L_3$ is given by

$$V_{C2} D T_s = -(V_{C2} - V_{C3})(1 - D)T_s$$

Or,

$$V_{C3} = \frac{V_{C2}}{1 - D} = \frac{V_i}{(1 - D)^3}$$

In the similar way, by using equation (4) and (8), the volt-second balance of $L_4$ is given by

$$(V_{C3} + V_{C4}) D T_s = -(V_{C3} - V_{C4})(1 - D)T_s$$

Or,

$$V_{C4} - 2V_{C4}\, D = V_{C3}$$

Thus, the output voltage of the proposed converter is given by,

$$V_{C4} = V_o = \frac{V_{C3}}{1-2D} = \frac{V_i}{(1-D)^3(1-2D)} \quad (9)$$

Therefore, voltage gain, $G = \frac{V_o}{V_i} = \frac{1}{(1-D)^3(1-2D)}$ (10)

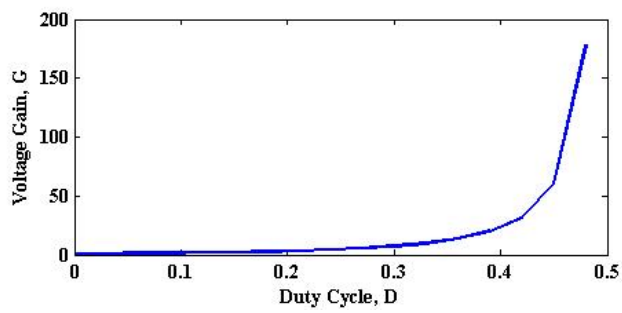


Figure 5. Voltage Gain versus Duty Cycle

The voltage gain versus the duty cycle curve is drawn in Fig. 5. It is observed that an extreme voltage gain can be achievable in continuous conduction mode by applying very low duty ratio. However, if the duty ratio $D > 0.5$, the voltage gain will be negative, and if $D = 0.5$, then the voltage gain will infinite at the output. That's why the duty ratio is limited to 0.5.

Voltage stresses across the switches are given as follows:

$$\begin{cases} V_{S1} = V_{C1} \\ V_{S2} = V_{C2} \\ V_{S3} = V_{C3} \\ V_{S4} = V_{S5} = V_{C4} \end{cases} \tag{11}$$

Voltage stresses across the diodes are given as follows:

$$\begin{cases} V_{D1} = V_{C1} \\ V_{D2} = V_{C1} + V_{C2} \\ V_{D3} = V_{C1} + V_{C2} + V_{C3} \\ V_{D4} = V_{C1} + V_{C2} + V_{C3} + V_{C4} \\ V_{D5} = V_{C4} \end{cases} \tag{12}$$

TABLE I. COMPARISON BETWEEN CONVENTIONAL BOOST CONVERTER AND PROPOSED CONVERTER

| | **Conventional boost Converter** | **Proposed Converter** |
|---|---|---|
| Voltage gain | $\frac{1}{1-D}$ | $\frac{1}{(1-D)^3(1-2D)}$ |
| Duty cycle, D | 0 < D < 1 | 0 < D < 0.5 |
| Output voltage ripple | 0.2939% of average output voltage | 0.138% of average output voltage |
| Input inductor current ripple | 16.73% of average inductor current | 2% of average inductor current |
| Highest voltage stress across the switch (es) | $\frac{Vi}{1-D}$ | $\frac{Vi}{(1-D)^3(1-2D)}$ across $S_5$ and $S_4$ |
| Highest voltage stress across the diode | $\frac{Vi}{1-D}$ | $\frac{Vi}{(1-D)^3} + \frac{Vi}{(1-D)^3(1-2D)}$ across $D_4$ |
| Conduction loss at the switches (proportional to D) | Higher due to extreme duty cycle | Lower due to small duty cycle |

## III. PERFORMANCE ANALYSIS

A detailed comparison between the proposed converter and the conventional boost converter is carried out and demonstrated in TABLE I. It is observed that the voltage gain in the proposed converter is extremely larger than that of the conventional one. The proposed converter operates at a duty cycle lower than 0.5, providing large voltage conversion. In contrast, the conventional converter must work at a duty ratio close to unity to obtain high gain. Moreover, the simulation shows lower percentage of ripple inductor current and the ripple output voltage. What is more, the proposed converter has lower switching conduction loss. Although, the voltage strain across the diodes and switches are higher than the conventional one, the proposed converter is very much suitable for the applications where very high voltage conversion is needed.

## IV. SIMULATION RESULTS

The theoretical analysis performed above has been justified by the PSIM 9.0 software. TABLE II demonstrates the values of different components and parameters used. Theoretical values of the output voltage, voltage strain across the switches and voltage strain across the diodes measured from equations (9), (11) and (12) respectively are approximately equal to the values achieved from the simulation results. Although the output voltage depicted in Fig. 6 contains some ripple, that can be controlled by controlling the capacitance of $C_4$.

TABLE II. VALUES OF DIFFERENT COMPONENTS AND PARAMETERS

| **Parameters with symbol** | **Value** |
|---|---|
| Input voltage ($V_i$) | 20 V |
| Switching frequency ($F_s$) | 10 kHz |
| Inductor ($L_1$) | 1 mH |
| Inductor ($L_2$) | 3 mH |
| Inductor ($L_3$) | 3 mH |
| Inductor ($L_4$) | 5 mH |
| Capacitor ($C_1$) | 1000 μF |
| Capacitor ($C_2$) | 1000 μF |
| Capacitor ($C_3$) | 1000 μF |
| Capacitor ($C_4$) | 1000 μF |
| Load resistance, $R$ | 120 Ω |
| Duty Cycle ($D$) | 0.369 |

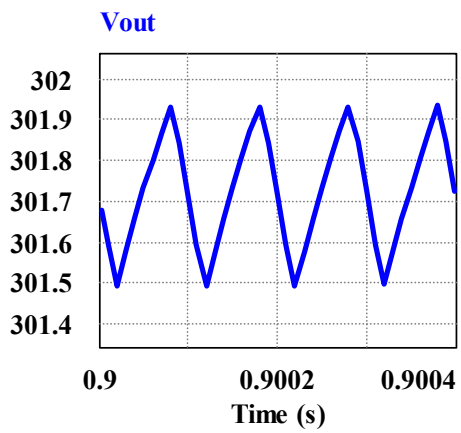


Figure 6. Output voltage

In case of diodes maximum voltage stress occurs across $D_4$ and maximum voltage stress occurs across $S_4$ and $S_5$ in case of switches. Therefore, these devices must be of higher voltage rating. The wave-shapes of $V_{D4}$ and $V_{S5}$ are illustrated in Fig. 7.

The volt-second balance of inductors are very important in designing an efficient converter. Volt-second balances of the inductors $L_3$ and $L_4$ are shown in Fig. 8. The simulated wave-shapes are nearly identical to the theoretical wave-shapes.

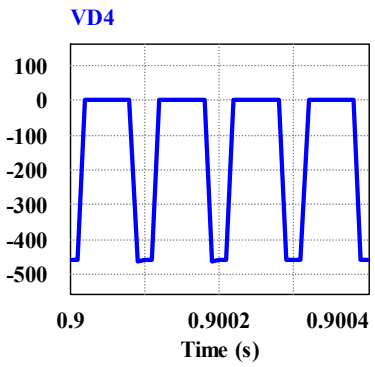


(a)

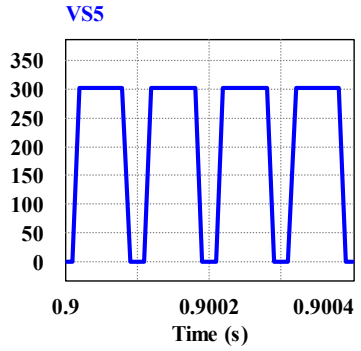


(b)

Figure 7. (a) Voltage stress across $D_4$ (b) Voltage stress across $S_5$

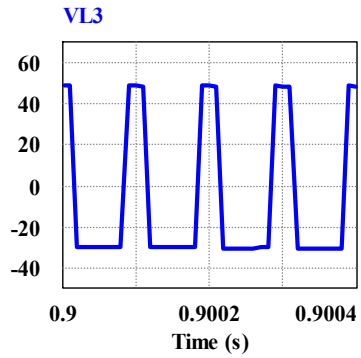


(a)

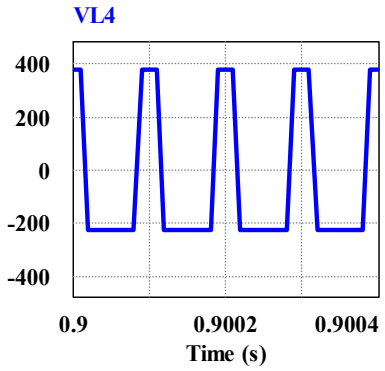


(b)

Figure 8. (a) Voltage across $L_3$ (b) Voltage across $L_4$

## V. Conclusion

A dc-dc step up converter with a large gain is illustrated in this paper. It has several advantages over the conventional boost converter. It requires a low duty ratio (i.e, duty ratio <0.5) for high voltage conversion which is almost impossible in case of conventional boost converter. Conduction loss at the switches, electromagnetic interference and reverse recovery problems are reduced at a great extent because of this low duty ratio. In addition, the switches are operated by a single control signal which decreases the operational complications. What is more the proposed converter offers low peak to peak ripple output voltage and peak to peak ripple input inductor current, making it possible to use small size of capacitors and inductors. Therefore, it is obvious that the proposed converter is appropriate to the applications where extremely high voltage gain is required.

## References


[1] Huber and M. M. Jovanovic, "A design approach for server power supplies for networking," in *Conf. Rec. IEEE Appl. Power Electron. Conf.*, 2000, pp. 1163–1169.

[2] B. Bryant and M. K. Kazimierczuk, "Voltage-loop power-stage transfer functions with MOSFET delay for boost PWM converter operating in CCM," *IEEE Trans. Ind. Electron.*, vol. 54, no. 1, pp. 347–353, Feb. 2007.

[3] X. Wu, J. Zhang, X. Ye, and Z. Qian, "Analysis and derivations for a family ZVS converter based on a new active clamp ZVS cell," *IEEE Trans. Ind. Electron.*, vol. 55, no. 2, pp. 773–781, Feb. 2008.

[4] D. C. Lu, K. W. Cheng, and Y. S. Lee, "A single-switch continuous conduction-mode boost converter with reduced reverse-recovery and switching losses," *IEEE Trans. Ind. Electron.*, vol. 50, no. 4, pp. 767–776, Aug. 2003.

[5] B. Axelrod, Y. Berkovich, and A. Ioinovici, "Transformer less DC-DC converters with a very high DC line-to-load voltage ratio," in *Porc. IEEE Int. Symp. Circuit Syst.*, 2003, pp. III-435-III-438.

[6] R. J. Wai and R. Y. Duan, "High-efficiency DC/DC converter with high voltage gain," *IEE Proc. Electric Power Applications*, vol. 152, no. 4, pp. 793-802, Jul. 2005.

[7] M. Prudente, L. L. Pfitscher, G. Emmendoerfer, E. F. Romaneli, and R. Gules, "Voltage multiplier cells applied to non-isolated dc–dcconverters," *IEEE Trans. Power Electron.*, vol. 23, no. 2, pp. 871–887, Mar. 2008.

[8] Y. Hsieh, J. Chen, T. Liang , and L. Yang, "Novel high step-up dc–dc converter for distributed generation system," *IEEE Trans. Ind. Electron.*, vol. 60, no. 4, pp. 1473–1482, Apr. 2013.

[9] K. Park, G. Moon, and M. Youn, "Nonisolated high step-up stacked converter based on boost-integrated isolated converter," *IEEE Trans. Power Electron.*, vol. 26, no. 2, pp. 577-587, Feb. 2011.

[10] E. H. Ismail, M. A. Al-Saffar, A. J. Sabzali, and A. A. Fardoun, "A family of single-switch PWM converters with high step-up conversion ratio," *IEEE Trans. Circuits and Systems I: Regular Papers*, vol. 55, no. 4, pp. 1159–1171, May 2008.

[11] Ned Mohan, " Power Electronics: A First Course," John Wiley & Sons, Inc. Wiley, 2012.

[12] H. Rashid, "Power Electronics Handbook: Devices, Circuits And Applications," 3rd Edition, Elsevier, 2011.

2017 3rd International Conference on Electrical Information and Communication Technology (EICT), 7-9 December 2017, Khulna, Bangladesh

# Speed Control of DC Motor with FZ-D Controller

Abu Shakil Ahmed[1], Ahmed Imteaz Kabir[2], Md. Shahjahan[3]
Khulna University of Engineering & Technology, Khulna-9203, Bangladesh
shakil.ahmed.bd71@gmail.com[1], kabir.imteaz@gmail.com[2], jahan@eee.kuet.ac.bd[3]

*Abstract*—**Effective control of speed for a DC motor using fuzzy derivative (FZ-D) controller by reducing the preshoot, overshoot, undershoot, peak to peak ripple, and steady-state error is the primary endeavor of this paper. We have worked out the mathematical modeling of a DC motor and designed an FZ-D controller to carry out the approach. For performance assessment of different controllers, the speed control action has been simulated individually with integral (I), proportional (P), proportional-integral (PI), proportional-derivative (PD), proportional-integral-derivative (PID), and the FZ-D controller. The effectiveness of the controllers has been evaluated based on the performance parameters mentioned above. According to the results, the FZ-D controller can regulate the speed of a DC motor most efficiently as the preshoot, overshoot, undershoot, peak to peak ripple, and steady-state error are the lowest.**

***Keywords—Speed control, DC motor, FZ-D controller, I controller, P controller, PI controller, PD controller, PID controller.***

## I. INTRODUCTION

DC motors are used for various purposes of research, industry, and housing appliances because it is reliable, easy to use, and less expensive. It takes DC electrical supply as input and produces mechanical output in the form of speed. Controlling a DC motor essentially means to control its speed, which is the primary concentration of this paper. The speed can be controlled in many ways, such as controlling voltage, armature resistance, and field flux. Different controllers are used such as I, P, PI, PD, and PID controller to apply these methods. The PID controller is widely used because of its simple structure as well as it has a combination of proportional, integral, and derivative controllers in parallel connection. Moreover, its control algorithm is comprehensible which can be regulated at ease. The novelty of the PID controller is that its proportional term reduces the present error, the integral term remembers the previous errors, and the derivative term assumes the future error. However, It takes a little longer time to respond, and the tuning process is relatively laborious. Besides, the preshoot, overshoot, undershoot, peak to peak ripple, and steady-state error it offers are incurious. The nature of system oscillation has to be scrutinized to tune the PID controller accurately for which the modeling of the system is a requirement. If the system is complex, it becomes challenging to model it which can be carried out at ease using fuzzy logic. Therefore, the fuzzy logic controller is being used as a complimentary for the current PID controller or as its alternative.

According to the literature, it is evident that FZ-PI and FZ-PID controllers offer better performance than the traditional P, I, PI, PD, and PID controller. The FZ-D controller is also worthy of drawing attention for comparison with the traditional ones. An FZ-D controller has been proposed in this paper, which limits the value of preshoot, overshoot, undershoot, peak to peak ripple, and steady-state error for a DC motor speed at much lower value than the PID controller does. As the proposed controller is that it is fuzzy assisted, speed can be controlled and kept constant more precisely by courtesy of the fuzzy logic. In contrast, speed control with an overdamped response by tuning the gains of the PI or PID controllers offers performance inferior to the fuzzy assisted ones. The tradition of using the fuzzy logic controllers in combination with I, P, PI, PD, or PID controller is not recent but trendy. Some significant approaches to enhance the speed control mechanism of the motor and the provisions have been stated in TABLE I.

TABLE I. LITERATURE REVIEW ON MOTOR SPEED CONTROL AND APPLICATION OF FUZZY LOGIC

| *Author/s* | *Methodology* | *Contribution* |
|---|---|---|
| Zadeh, L. [1] | The author has proposed fuzzy sets, an idea of using membership functions those may be appropriate for each possible value. Moreover, he has offered fuzzy numbers for fuzzy sets, and additionally the related rules for fuzzy arithmetic. | The proposed fuzzy set theory allows the continuous evaluation of the membership of components in a set with the guidance of a membership function esteemed in the interim [0, 1]. Fuzzy set theory can be utilized as a part of an extensive variety of areas in which data is inadequate or uncertain. |
| Mamdani, E. et al. [2] | An analysis of the linguistic synthesis related to steam generator controller has been depicted in the paper where fuzzy logic has been employed to achieve automatic control technique by changing heuristic control rules expressed by a human administrator. | The core purpose of this paper is to investigate the perception of collaboration between human and a learning controller. The linguistic control strategy proposed in the document has been ended up being better than anticipated. Moreover, the critical test of the synthesis strategy has been accounted for a non-learning controller. |
| Zhen-Yu Zhao et al. [3] | Fuzzy gain tuning method of PID controllers has been depicted in the paper. Fuzzy rules and reasoning have been used on-line for error signal and its first distinction. | The aftermath of the experiment outlines that better control execution has been accomplished with Ziegler-Nichols controllers and Kitamori's PID controllers. |

978-1-5386-2307-7/17/$31.00 ©2017 IEEE

| *Author/s* | *Methodology* | *Contribution* |
|---|---|---|
| Li, H. et al. [4] | An FZ-PID controller has been designed for auto-tuning through mathematical analysis in this paper. Additionally, a less coupled gain structure has been offered to improve the system performance. | More damping has been observed for FZ-PID controller than the conventional PID controller. Therefore, the oscillation has been reduced more quickly. However, the FZ-PID controller has delayed the rise time somewhat. |
| Guoshing Huang et al. [5] | This paper has proposed a PC based PID controller using LabVIEW software to observe the speed of a DC motor. This setup has been simulated using VisSim, and the system performance has been analyzed later. | The simulation result complies with the typical characteristics of PID controller, and the experimental result verifies the theoretical assumptions. The user is also able to monitor the performance of the motor. |
| Kickert, W. et al. [6] | The utilization of a fuzzy controller in a warm water plant has been outlined. Fuzzy algorithms have been employed to control the plant. A few sorts of such algorithms have been executed and analyzed. | A correlation has been made that suggests Fuzzy controllers have been faster than the Direct Digital Controllers (DDC) controllers. Though the results are promising, the preciseness and stability issue should be explored more profoundly. |
| Li, H. et al. [7] | This paper has highlighted the tradeoff between the robustness and simplicity in designing an industrial controller using fuzzy reasoning methods and provided an optimization for design avoiding inconsistent inference, maintaining sufficient robustness, and keeping the fuzzy reasoning method as simple as possible. | Both the theoretical and experimental analysis suggest that the optimization process has provided the desired characteristics of the industrial controller for the control system. It has also made the system more flexible and robust. Moreover, the nonlinear gains have been tuned precisely, and the system performance has been enhanced. The cost for the optimization is also reasonable. |
| Baogang Hu et al. [8] | The methodology has depicted a procedure for the construction of FZ-PID controller via theoretical calculation and genetic-based improvement along with utilizing another fuzzy single input interface with six tuning parameters including three rules. | The controller can deliver a reasonable estimation of a linear function for understanding a Guaranteed PID Performance (GPP) system and results obtained shows that it is capable of more prevalent regulation in comparison with typical PID-controllers, especially for taking care of nonlinearities. |
| Cheong, F. et al. [9] | This paper has attempted to design more human conceivable fuzzy logic controller by means of limiting the optimization level. A genetic algorithm has been utilized with some genetic operators to achieve this objective. | The result suggests that the proposed fuzzy logic controller is more flexible and human conceivable than the controllers designed without limiting the optimization. It yields a more efficient result when controlling becomes tougher. |
| Arulmozhiyal, R. et al. [10] | The performance of traditional PID controller and the FZ-PID controller has been reviewed in this paper. Moreover, a comparative analysis has been presented based on effectiveness. | The simulation result confirms that between the traditional PID controller and the FZ-PID controller, the later one is preferable concerning the controlling capability of brushless DC (BLDC) motor. |

We have organized the paper as follows. In section II, the methodology has been explained with emphasis on the system architecture and signal flow. In section III, we have substantiated underlying mathematical model for the plant and designed the PID and the fuzzy logic controller. In section IV, the proposed methodology has been simulated, and performance of each controller has been evaluated. In section V, the result has been accumulated, and the outcomes have been specified. To conclude the paper we have summarized the entire work in section VI.

## II. METHODOLOGY

In this paper, we have made use of the existing I, P, PI, PD, and PID controller for speed control of a DC motor and performance of each controller has been evaluated by the rise time, preshoot, overshoot, undershoot, peak to peak ripple, and steady-state error. According to the assessment, an enhanced controller has been designed using fuzzy logic to reduce preshoot, overshoot, undershoot, peak to peak ripple, and steady-state error. The performance of the controller has been compared with the conventional ones. For carrying out the performance test, a pulse generator has been used as the reference input, and feedback has been taken from the output while actuating signal has been generated using a summing junction. The control input, an input signal for the plant, has been generated as the output of the different controllers those takes the actuating signal as their input. The controlled variable is the motor speed which is intended to keep constant. The actuating signal has been multiplexed with its derivative to provide input to the fuzzy logic controller, and a constant gain has been used to obtain control input. The whole mechanism has been presented in Fig. 1.

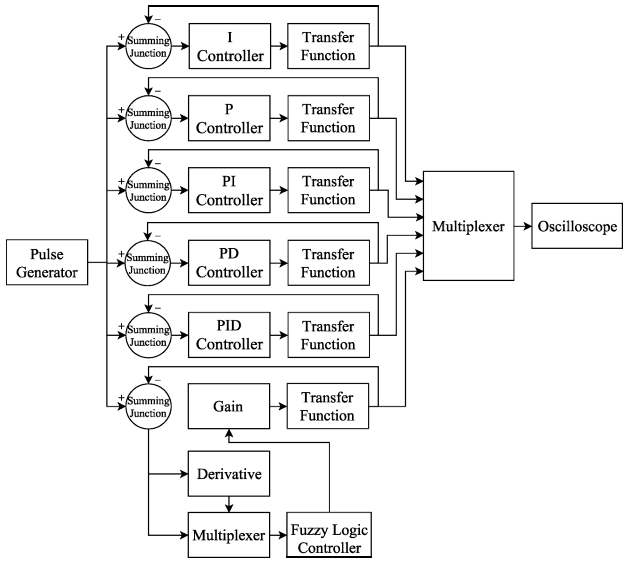


Figure 1. A block diagram employing different types of speed controller.

## III. MATHEMATICAL MODELING

### A. Plant Model

DC motor is a standard actuator in control system engineering as it delivers rotational displacement in the

direction defined by Fleming's left-hand rule as well as the translational action being combined with objects like the wheel. It offers speed as a mechanical output by receiving DC electrical input. The equivalent circuit representation of a DC motor has been shown in Fig. 2.

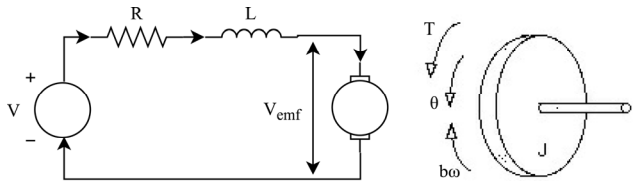


Figure 2. The equivalent circuit of a DC motor.

Here, V is source voltage (V), R is electrical resistance of armature circuit (Ω), L is electrical inductance of armature circuit (H), J is moment of inertia of the rotor ($kgm^2/s^2$), b is damping ratio of the mechanical system (Nms), T is motor torque (Nm), θ is angular displacement (rad), ω is output rotating speed (rad/s), i is armature current (A), and $V_{emf}$ is back emf (V). The mathematical formulation of back emf and torque have been expressed in (1) and (2) respectively.

$$V_{emf} = K_e\,\omega \tag{1}$$

$$T = K_t\, i \tag{2}$$

Here, $K_e$ is motor constant, and $K_t$ is armature constant both of which are equal in SI unit. Equation (1) suggests that the back emf varies proportionally with the output rotating speed and (2) indicates that the motor torque is proportional to the armature current. Using Newton's law and Kirchhoff's law (3) and (4) have been derived.

$$J\frac{d^2\theta}{dt^2} + b\frac{d\theta}{dt} = KI \tag{3}$$

$$L\frac{di}{dt} + Ri = V - K\frac{d\theta}{dt} \tag{4}$$

Here, $K$ is electromotive force constant (Nm/A). Applying Laplace transform on (3) and (4), (5) and (6) have been attained, and the transfer function of the DC motor expressed in (7) has been calculated from (5) and (6). Finally, we have used the value of system parameters of a DC motor to obtain its particular transfer function.

$$Js^2\theta(s) + bs\theta(s) = KI(s) \tag{5}$$

$$LsI(s) + RI(s) = V(s) - Ks\theta(s) \tag{6}$$

$$G(s) = \frac{\theta(s)}{V(s)} = \frac{K}{(Ls+R)(Js+b)+K^2} = \frac{0.036}{36.942\,s^2+12.1568\,s+0.451} \tag{7}$$

Feedback has been taken from the output continually for proper adjustment of the controlled variable. For the sake of simplicity, voltage mode unity feedback control loop has been preferred.

### B. PID Controller Design

The specification of PID controller includes three different parameters; the proportional, the integral, and the derivative connected in parallel. The proportional parameter is utilized to improve the corrective measure to the contemporary error of a stable system. However, it cannot control an unstable system, and steady-state error occurs as the gain remains the same for different frequencies. The integral parameter diminishes the steady state error to zero by accumulating the previous errors. However, it is unfavorable for loop stability as it generates a pole at the origin. The derivative parameter predicts the future error and reacts correspondingly to lessen it. However, it cannot deal with constant errors as the derivative of a constant value becomes zero. A weighting mechanism is convenient to adjust the response of the parameters for a PID controller. Equation (8) provides the mathematical formula to design a PID controller.

$$U(s) = [k_p + sk_d + \frac{k_i}{s}]\,E(s) \tag{8}$$

Here, U(S) is controlled variable, $K_p$ is proportional gain, $K_d$ is derivative gain, $K_i$ is integral gain, and E(S) is error value. The error value denotes the difference between the desired input and the actual output. The system performance has been evaluated based on rise time, preshoot, overshoot, undershoot, peak to peak ripple, and steady-state error. P and I controllers consist of only proportional and integral controller respectively while PI controller comprises both of them and PD controller includes the proportional and the derivative parameters. If the number of parameters in a controller is more than one, they are connected in parallel.

### C. Fuzzy Logic Controller Design

Fuzzy logic exceeds the limitation of binary logic and resembles the human philosophy. It considers every possible value including and in between "yes" and "no". The fuzzy system has four main components; fuzzification module, knowledge base, inference engine, and defuzzification module. Input data is inserted into the fuzzification module, and fuzzy sets are created. Required rules are put in the knowledge base section applying "If-Then" rules in general. Based on how the rules are defined, inference engine processes data from fuzzification module. Finally, defuzzification module converts the fuzzy sets to traditional or crisp set.

We have utilized "Fuzzy Logic Controller" block from MATLAB/Simulink in order to design the proposed FZ-D controller. Two input variables "SpeedError" and "ErrorChange", as well as one output variable "Voltage", have been defined with three suitable membership functions each. The design procedure of the fuzzy logic controller, the definition of input and output variables, as well as the setup of the fuzzy operator, fuzzification module, inference engine, and defuzzification module have been carried out using Fuzzy Inference System (FIS) editor in MATLAB/Simulink. The default Mamdani inference and aggregation method have been applied. A graphic view of the FIS editor has been presented in Fig. 3.

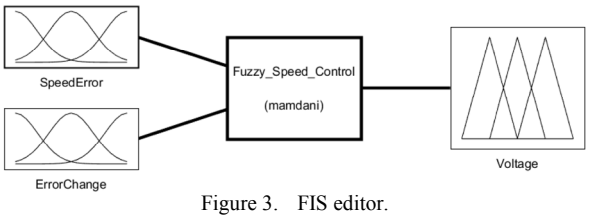


Figure 3. FIS editor.

For each input and output variable, we have defined three membership functions; “Small”, “Medium”, and “Large”. The proper range of the variables and suitable parameters for the membership functions have been chosen. Corresponding values of the range and the parameters have been denoted by Fig. 4, Fig. 5, and Fig. 6.

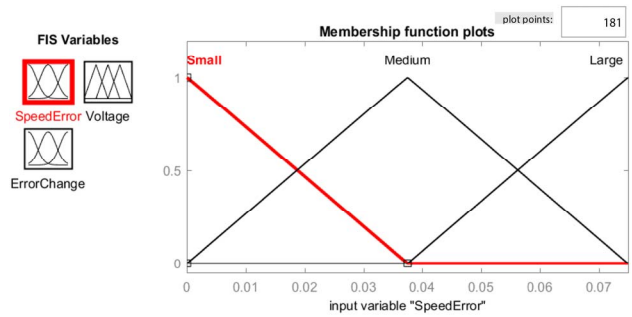


Figure 4. Membership functions for SpeedError.

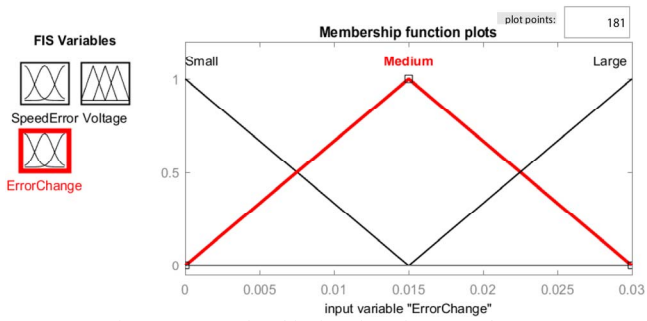


Figure 5. Membership functions for ErrorChange.

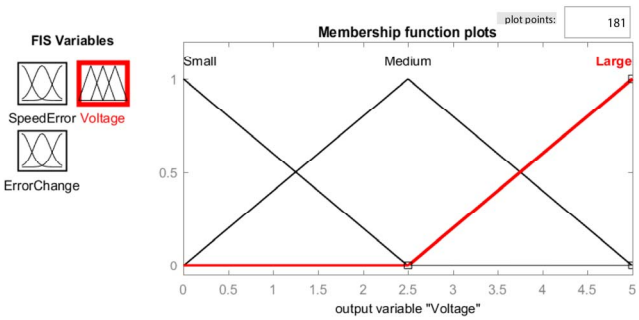


Figure 6. Membership functions for Voltage.

We have defined nine rules using If-Then format to design the fuzzy logic controller those have been specified in TABLE II. The input variables and the entire fuzzy set are respectively the input and output of the rule. Rule viewer has been used to display a road map of the fuzzy inference process. In Fig 7, the rows symbolize the rules, and the three columns characterize the variables. In Fig. 8, a mapping of the designed fuzzy logic controller has been plotted in three dimensions.

TABLE II. FUZZY LOGIC CONTROLLER RULES

| Sequence | Rule |
|---|---|
| 1 | If (SpeedError is Large) and (ErrorChange is Medium) then (Voltage is Large) (1) |
| 2 | If (SpeedError is Medium) and (ErrorChange is Large) then (Voltage is Large) (1) |
| 3 | If (SpeedError is Small) and (ErrorChange is Large) then (Voltage is Medium) (1) |
| 4 | If (SpeedError is Large) and (ErrorChange is Medium) then (Voltage is Medium) (1) |
| 5 | If (SpeedError is Medium) and (ErrorChange is Medium) then (Voltage is Medium) (1) |
| 6 | If (SpeedError is Small) and (ErrorChange is Medium) then (Voltage is Small) (1) |
| 7 | If (SpeedError is Large) and (ErrorChange is Small) then (Voltage is Large) (1) |
| 8 | If (SpeedError is Medium) and (ErrorChange is small) then (Voltage is medium) (1) |
| 9 | If (SpeedError is Small) and (ErrorChange is Small) then (Voltage is Small) (1) |

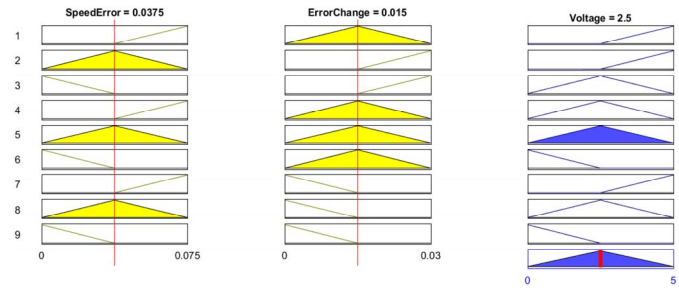


Figure 7. Fuzzy logic controller rule viewer.

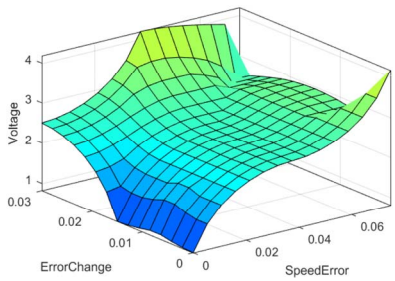


Figure 8. Fuzzy logic controller surface viewer.

## IV. SIMULATION

In this section, we have simulated and evaluated the performance of different controllers based on rise time, preshoot, overshoot, undershoot, peak to peak ripple, and steady-state error. In accordance with the circuit diagram shown in Fig. 9, speed control of a DC motor with the I controller has been simulated. The system input has been taken from a pulse generator and fed to the controller after comparing it with a feedback signal received from the output. The motor speed has been controlled accordingly. Finally, the speed response of the motor with respect to time has been observed on an oscilloscope and shown in Fig. 10.

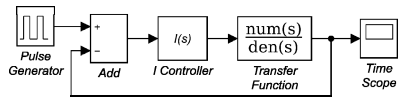


Figure 9. Block diagram of speed control with an I controller.

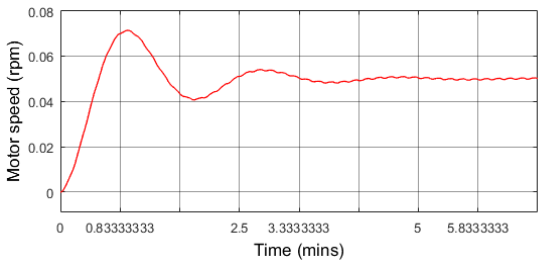


Figure 10. Speed response of DC motor with I control.

We have calculated the performance characteristics of speed control for I controller and according to the data rise time, preshoot, overshoot, undershoot, peak to peak ripple, and steady-state error is 22.61s, 0.71%, 42.14%, 11.49%, 1.18%, and 0.66% respectively. Similarly, the performance characteristics of the P, PI, PD, and PID controllers have also been calculated. Fig 11, Fig. 13, Fig. 15, and Fig. 17 represents the block diagrams for speed control of DC motor using these controllers, and the corresponding output waveforms have been presented in Fig. 12, Fig. 14, Fig. 16, and Fig. 18 respectively.

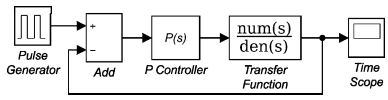


Figure 11. Block diagram of speed control with a P controller.

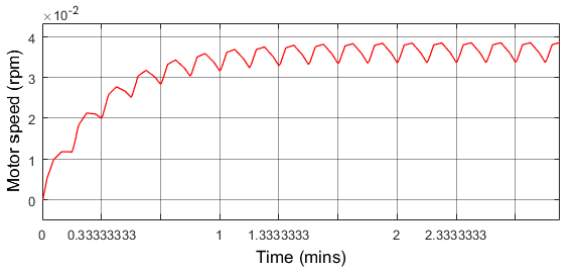


Figure 12. Speed response of DC motor with P control.

For P control of DC motor speed, the circuit diagram is almost similar to that of I controller, except for the P controller that has been used instead of I controller. The value of rise time, preshoot, overshoot, undershoot, peak to peak ripple, and steady-state error is 31.39s, 0.58%, 14.10%, 10.29%, 9.72%, and 27.22% respectively for P controller.

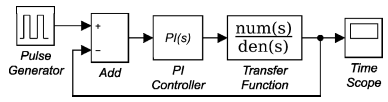


Figure 13. Block diagram of speed control with a PI controller.

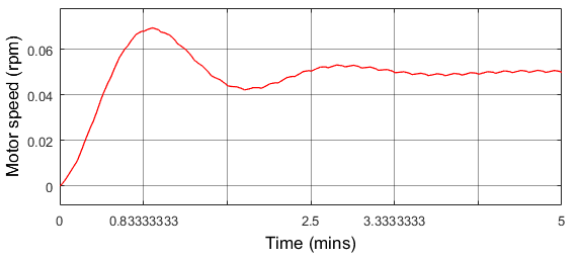


Figure 14. Speed response of DC motor with PI control.

In the case of PI control of DC motor speed, the P controller has been replaced by PI controller and rest of the circuit of Fig. 11 has been kept unchanged. The value of rise time, preshoot, overshoot, undershoot, peak to peak ripple, and steady-state error is 22.87s, 0.70%, 40.14%, 9.65%, 1.76%, and 0.34% correspondingly for PI controller.

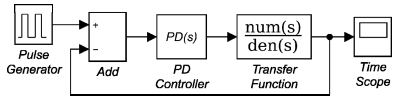


Figure 15. Block diagram of speed control with a PD controller.

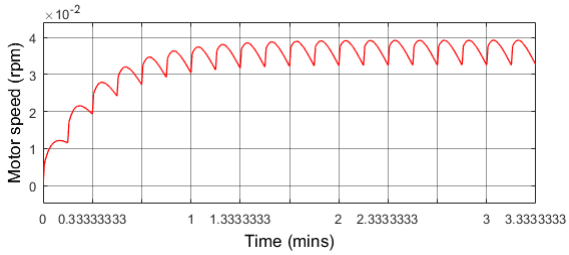


Figure 16. Speed response of DC motor with PD control.

The PI controller has been replaced by PD controller to design the PD controller circuit and rest of the components have been kept the same. The value of rise time, preshoot, overshoot, undershoot, peak to peak ripple, and steady-state error is 41.06s, 0.53%, 4.73%, 16.77%, 13.44%, and 28.60% respectively for PD controller.

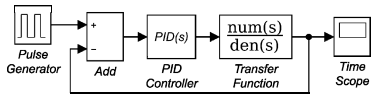


Figure 17. Block diagram of speed control with a PID controller.

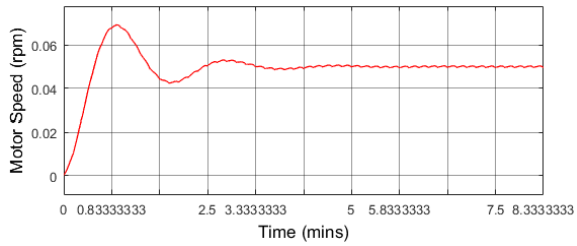


Figure 18. Speed response of DC motor with PID control.

The same practice has been continued for PID likewise the PD control circuit, where the PD controller has been replaced with a PID controller. The value of rise time, preshoot, overshoot, undershoot, peak to peak ripple, and steady-state error is 22.96s, 0.70%, 40.14%, 8.90%, 1.62%, and 0.62% in sequence for PID controller.

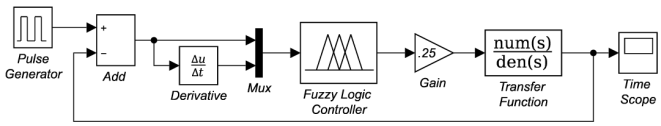


Figure 19. Block diagram of speed control with the proposed FZ-D controller.

Circuit controlled by fuzzy logic is a bit different from other control circuits. In case of FZ-D controller design, the

actuating signal and its derivative have been multiplexed to generate the input of the fuzzy logic controller. Therefore, the output of the proposed FZ-D controller causes the speed to increase four-fold. Hence, we have selected value of the gain constant to be 0.25. This signal has been provided as the input to the plant for speed control. The speed response has been observed concerning time on an oscilloscope that has been presented in Fig. 20.

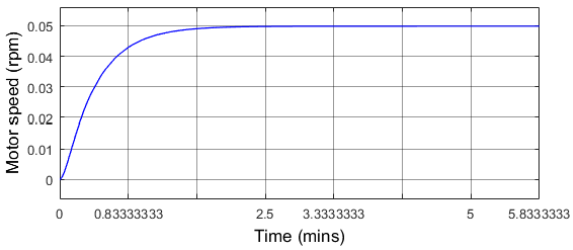


Figure 20. Speed responses of DC motor with the proposed FZ-D control.

For FZ-D controller, the value of rise time, preshoot, overshoot, undershoot, peak to peak ripple, and steady-state error is 51.77s, 0.51%, 0.50%, 1.75%, 0.00%, and 0.22% in a sequence. In case of load disturbance, the proposed prototype of the speed controller is capable of adjusting its input to motor by courtesy of the feedback system.

## V. OUTCOMES

The result of the simulation procedure has been summarized in TABLE III to clarify the contribution of FZ-D controller in controlling the speed for a DC motor comparing with other controllers based on the value of rise time, preshoot, overshoot, undershoot, peak to peak ripple, and steady-state error. From relative evaluation, we can maintain that the I controller has the lowest rise time, though the rise time of PI and PID controllers are relatively close to the I controller. The value of preshoot, overshoot, undershoot, peak to peak ripple, and steady-state error is the lowest for the FZ-D controller. Thus, in return for increasing the rise time, the fuzzy logic controller is capable of reducing the values of preshoot, overshoot, undershoot, peak to peak ripple, and steady-state error more than other controllers.

TABLE III. SPEED CONTROLLING PERFORMANCES OF DIFFERENT CONTROLLERS

| **Controllers** | **I** | **P** | **PI** | **PD** | **PID** | **FZ-D** |
|---|---|---|---|---|---|---|
| Rise Time | **22.61s** | 31.39s | 22.87s | 41.06s | 22.96s | 51.77s |
| Preshoot | 0.71% | 0.58% | 0.70% | 0.53% | 0.70% | **0.51%** |
| Overshoot | 42.14% | 14.10% | 40.14% | 4.73% | 40.14% | **0.50%** |
| Undershoot | 11.49% | 10.29% | 9.65% | 16.77% | 8.90% | **1.75%** |
| Ripple (Peak to Peak) | 1.18% | 9.72% | 1.76% | 13.44% | 1.62% | **0.00%** |
| Steady State Error | 0.66% | 27.22% | 0.34% | 28.60% | 0.62% | **0.22%** |

## VI. CONCLUSION

This paper aims to control DC motor speed efficiently. One of the toughest challenges of speed control from starting to any moment at running condition is to keep the speed constant. Practically, the speed of the motor cannot be maintained uniform continuously due to the preshoot, overshoot, undershoot, and peak to peak ripple those introduces steady-state error. However, it is practically impossible to eliminate these unwanted effects completely. Hence, to keep the value of these parameters as low as possible, we have designed an FZ-D controller and compared the performances with other well-known ones. For evaluation, we have chosen six parameters; rise time, preshoot, overshoot, undershoot, peak to peak ripple, and steady-state error and the performance of I, P, PI, PD, PID, and FZ-D have been compared based on the parameters. The data shown in TABLE III indicates that in consideration of rise time, the FZ-D controller is slower. Despite this inconvenience, it effectively controls the speed of a DC motor by significantly reducing the values of other performance parameters; preshoot, overshoot, undershoot, peak to peak ripple, and steady-state error. Therefore, the proposed fuzzy logic controller is capable of controlling DC motor speed more precisely than the conventional I, P, PI, PD, and PID controllers, which serves the purpose of this paper.

## REFERENCES


[1] L. Zadeh, "Fuzzy sets", *Information and Control*, vol. 8, no. 3, pp. 338-353, 1965.

[2] E. Mamdani and S. Assilian, "An experiment in linguistic synthesis with a fuzzy logic controller", *International Journal of Man-Machine Studies*, vol. 7, no. 1, pp. 1-13, 1975.

[3] Zhen-Yu Zhao, M. Tomizuka and S. Isaka, "Fuzzy gain scheduling of PID controllers", *IEEE Transactions on Systems, Man, and Cybernetics*, vol. 23, no. 5, pp. 1392-1398, 1993.

[4] H. Li and S. Tso, "Quantitative design and analysis of fuzzy proportional-integralderivative control a step towards autotuning", *International Journal of Systems Science*, vol. 31, no. 5, pp. 545-553, 2000.

[5] Guoshing Huang and Shuocheng Lee, "PC-based PID speed control in DC motor", *2008 International Conference on Audio, Language and Image Processing*, 2008.

[6] W. Kickert and H. Van Nauta Lemke, "Application of a fuzzy controller in a warm water plant", *Automatica*, vol. 12, no. 4, pp. 301-308, 1976.

[7] H. Li, L. Zhang, K. Cai and G. Chen, "An improved robust fuzzy-PID controller with optimal fuzzy reasoning", *IEEE Transactions on Systems, Man and Cybernetics, Part B (Cybernetics)*, vol. 35, no. 6, pp. 1283-1294, 2005.

[8] Baogang Hu, G. Mann and R. Gosine, "New methodology for analytical and optimal design of fuzzy PID controllers", *IEEE Transactions on Fuzzy Systems*, vol. 7, no. 5, pp. 521-539, 1999.

[9] F. Cheong and R. Lai, "Constraining the optimization of a fuzzy logic controller using an enhanced genetic algorithm", *IEEE Transactions on Systems, Man and Cybernetics, Part B (Cybernetics)*, vol. 30, no. 1, pp. 31-46, 2000.

[10] R. Arulmozhiyal and R. Kandiban, "Design of fuzzy PID controller for Brushless DC motor", *2012 International Conference on Computer Communication and Informatics*, 2012.

# Design of an FPGA Based System for High Speed Data Compression and Secured Transmission

Mohammad Rakib[1] and Md. Liakot Ali[2]
Institute of Information and Communication Technology,
Bangladesh University of Engineering and Technology,
Dhaka-1000, Bangladesh
[1]rakibsr@gmail.com
[2]liakot@iict.buet.ac.bd

*Abstract*— **In this era of big data, high speed data compression and its secured transmission are burning issues. Data compression and its reliable transmission are necessary especially for the storage and transmission related applications. This research presents a solution of this problem using the design and simulation of a field programmable gate array (FPGA) based system which offers advantages over software solution in terms of less area, higher speed, lower power, real-time performance, higher reliability, shorter time to market, re-configurability and also ease of integration with the existing consumer electronic devices. The proposed system is a blend of bit stuffing, Huffman and Hamming coding. It has been simulated in the MATLAB environment to ensure the accuracy of the system and then it is designed using Verilog hardware description language (HDL) and implemented into FPGA hardware environment. The results show high level reliability, security and reduction of memory which reduces bandwidth and transmission time.**

***Keywords— FPGA, HDL, Verilog, Compression, Encryption, Decryption, Huffman Algorithm, Hamming Coding, Bit-stuffing.***

## I. INTRODUCTION

This is an era of big data where big data refers to voluminous amounts of structured or unstructured complex data sets that can be potentially mined and analyzed for understanding the real world. Many emerging applications have come out based on big data such as spy satellites, remote sensing, medical imaging, customer relationship management, corporate surveillance etc. Again applications and simulations related to seismography, oceanography, bioinformatics, cosmology etc. are coming out where billions of terabyte data known as hyper spectral data are required to store and transmit securely which can easily overwhelm limited bandwidth [1-2]. A survey report stated companies are spending 12% of their IT budget on storage and this cost is doubling every two years [2]. In this context, data compression and its secured transmission has become a demanding issue of this day [3].

Our proposed technique is blend of bit stuffing, Huffman and Hamming algorithm. Software implementation for the proposed system cannot fulfill the performance and real-time requirements since it is inherently slow and the software designer does not have any direct control over the way with which random access memory (RAM) and processors interact. This imposes a limit on operating speed while a hardware designer has full control over timing operations into the RAM and direct control over the usage of expensive hardware resources. For hardware implementation, FPGA technology has brought revolution in the electronic system design and development. It is now being widely used in various applications such as telecommunications, networking, consumer, automotive and industrial applications, etc. [4]. Over the few decades, FPGA device market has been emerged as multi-billion dollar market due to its lower cost than ASIC, reusability, massive parallelism, higher speed than conventional computing, lower power, shorter time to market etc. [5]. The following sections of this paper describe the prior work, fundamentals of the related algorithms, design and implementation of the proposed system, results and discussion and then conclusion of the research.

## II. RELATED WORKS

A lot of researches has been conducted and also are ongoing to develop new techniques for data compression. Huffman algorithm is considered as one of the most popular algorithm for lossless compression. Though it was invented seven decades ago, a lot of researches [6-9] have been conducted in recent times based on this algorithm. Since software solution for data compression is essentially not fast and energy efficient a number of FPGA based lossless data compression solutions have been proposed focusing on high throughput, low cost and energy efficiency [10-12]. FPGA based researches on data compression have added a new dimension to invent robust methodology. Among the latest FPGA based researches, Dias et al. [13] proposed a new method of code compression for embedded systems which applies two compression techniques. They have presented a Huffman de-compressor using VHDL for FPGA and claimed that their proposed method reduces code size up to 30.6%. Rigler et. al. [14] presented a hardware implementation for the LZ77and Huffman encoders that form the base of a GZIP encoder. Their designs have been implemented as state machines using VHDL in such a way that they are suitable for both FPGA and ASIC technologies. However among all these software and FPGA based researches security and reliability issues have not much considered or lightly considered. So there is scope of conducting research which can provide low power, high speed, and real-time data compression and at the same time can ensure data security and reliability for transmission.

978-1-5386-2307-7/17/$31.00 ©2017 IEEE

## III. FUNDAMENTALS OF THE ALGORITHMS

In this section a basic introduction of Huffman algorithm and Hamming coding will be given which is used to develop proposed methodology for two level compressions of ASCII text data with error correction mechanism for secured transmission.

### *A. Huffman Coding*

Huffman algorithm [15] uses the frequency distribution of the alphabets of the source to develop the code-word for each symbol. According to the frequency, the code words are assigned. Shorter code-words for higher probabilities and longer code-words for smaller probabilities are assigned.

### *B. Hamming Code*

Around 1947 Richard W. Hamming [16] developed a technique for detecting and correcting single bit errors in transmitted data. In the Hamming code, k parity bits are added to n-bit data word, forming a new word of n + k bits. The bit positions are numbered in sequence from 1 to n+ k. The positions numbered with powers of two are used for the parity bits. The remaining bits are the data bits.

## IV. PROPOSED METHOD

The proposed method uses bit stuffing and Huffman algorithm to do a two level compression to achieve higher compression ratio and then uses Hamming (7, 4) coding for encrypting and securing data for transmission. Hamming (7, 4) code can detect and correct single bit error when data is sent via noisy channel. Fig. 1 shows the flowcharts of the proposed model.

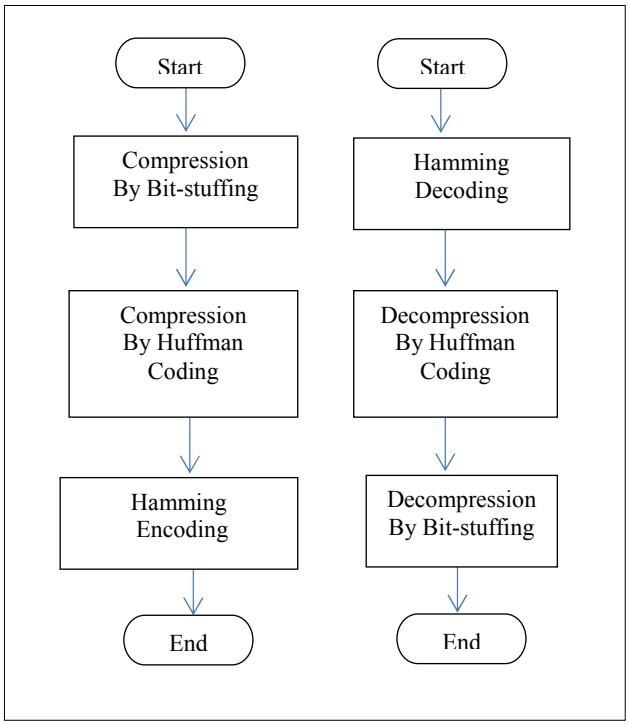


Fig. 1. Flowchart of the proposed method.

### *A. Sender Side Modules*

The process begins with two level compressions of input text data. First compression is done by bit stuffing and second level compression is done by Huffman coding. After completing two level compressions, generated output will be encoded by Hamming (7, 4) code to achieve further security.

#### *1) Level 1 Compression by Bit Stuffing*

Input: Original text data.

Output: First level compressed data.

1. Load the text data into memory and initialize counter, c = 0.
2. Read each bit into bit compression module and increment the counter.
3. If c = 7, write the bits back into memory and reset the counter. Thus we are discarding MSB of each character in the input text.

#### *2) Level 2 Compression by Huffman Coding*

Input: First level compressed data.

Output: Second level compressed data.

1. Count the frequencies of the symbols from the input and save the frequency information along with the symbols
2. Build a Huffman tree based on the frequency information. Used Huffman algorithm is described here-

*Huffman (C)*

i. n ←|C|
ii. Q ← C
iii. for i ← 1 to n-1
iv. do allocate a new node z
v. left[z] ← x ← EXTRACT-MIN(Q)
vi. right[z] ← y ← EXTRACTMIN(Q)
vii. f[z] ← f[x] + f[y]
viii. INSERT(Q,x)
ix. return EXTRACT-MIN(Q)

Where,

- C is a set of n symbols.
- f[c] denotes the frequency of c.
- Q is a min-priority queue which is used to identify the two least frequent symbols to merge together. A new symbol will be created after merging whose frequency is the sum of the frequencies of the two symbols that were merged.
- EXTRACT-MIN(x) is the function which returns minimum value from the queue.

- INSERT (Q, x) adds value 'x' in the min-priority queue 'Q'.

*3) Hamming (7,4) Encoding*

Input: Compressed text data.

Output: Hamming (7, 4) encoded output data

1. Read 4 bits from compressed data and calculate 3 parity bits namely $P_1$, $P_2$ and $P_4$.
2. Insert $P_1$, $P_2$ and $P_4$ into bit position 1, 2 and 4. Remaining positions (3, 5, 6 and 7) will be filled up by data bits read in step 1.
3. Write resulting Hamming (7, 4) code into memory.
4. Repeat steps 1-3 until the end of input compressed data.

*B. Receiver Side Modules*

Processing of receiver side begins with Hamming (7, 4) decoding. It will calculate check-bits to detect if any error occurs in transmission. If any single bit error is found then Hamming (7, 4) decoding will correct it. After decoding, output data will be decompressed by Huffman decompression using frequency distribution. A second level decompression of Huffman decompressed output will be required using bit-stuffing decompression technique.

*1) Hamming (7,4) Decoding*

Input: Received encoded compressed data

Output: Hamming (7, 4) decoded compressed data

1. Read 7 bits from encoded received data. This is a Hamming (7, 4) code-word.
2. Calculate check bits and create a 3 bit binary number with check bits to detect single bit error during transmission. Correct the error bit if found by flipping it.
3. Extract data bits from the position 3, 5, 6 and 7. Save the data bits into memory.
4. Repeat steps 1-3 until end of input encoded data.

*2) Level 1 Decompression by Huffman Algorithm*

Input: Hamming (7, 4) decoded compressed data.

Output: First level decompressed data.

1. Read frequency information and build Huffman tree.
2. Decode the input bits by traversing Huffman tree.
3. Write the decoded symbols into memory.

*3) Level 2 Decompression by Bit Stuffing*

Input: First level decompressed data.

Output: Original text data.

1. Initialize counter c = 0.
2. Read a bit into bit decompression module and increment the counter.
3. If c =7, add a 0 as MSB and write back into memory.
4. Repeat steps 1-3 until end of the input.

## V. FPGA DESIGN

A basic block diagram of the proposed design is shown on Fig. 2. Proposed design is divided into several logic modules. Synchronization among the processes in different modules plays a vital role in the design.

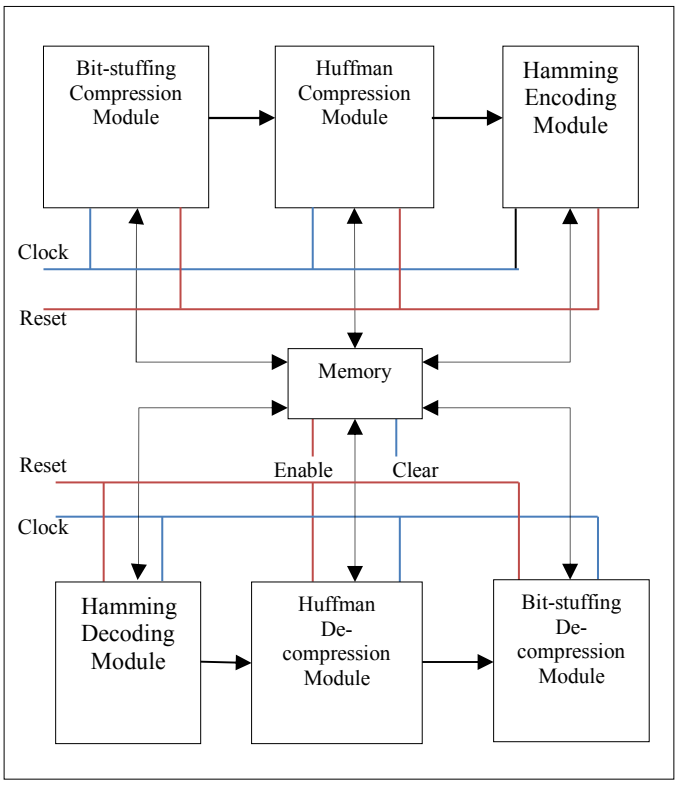


Fig. 2. Basic hardware block diagram

Huffman compression and decompression module is relatively complex than the others. It comprises of LUT (memory), adder, counter, sorter, Huffman tree builder, code generator and controller. The controller unit is responsible for overall operation of the Huffman module. Fig. 3 shows Huffman compression module.

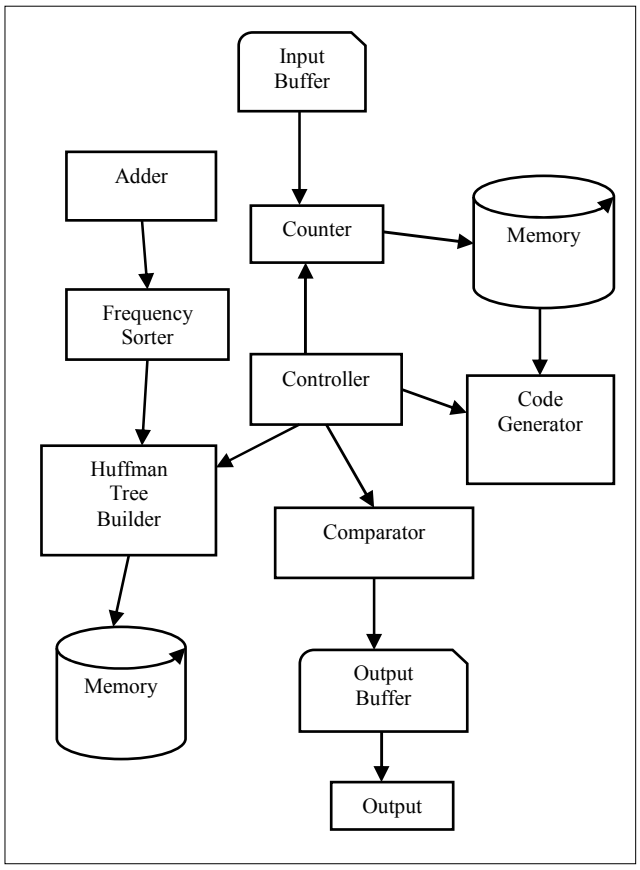


Fig. 3. Huffman compression module

## VI. MATLAB SIMULATION

The proposed method has been implemented and simulated in MATLAB software. Fig. 4 shows the simulation result.

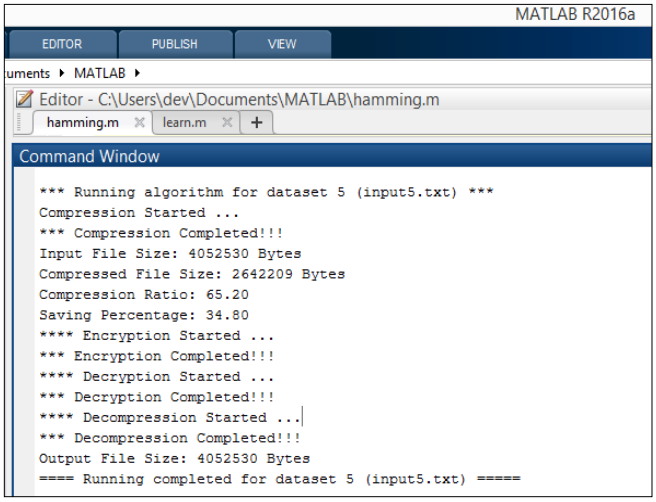


Fig. 4. Result of MATLAB simulation

## VII. FPGA SIMULATION

Proposed design has been implemented in Verilog HDL and simulated on ModelSim SE-64 10.5. The project is also compiled on Quartus II 32-bit Version 12.0 Build 263 08/02/2012 SP 2 SJ Web Edition with Cyclone II, Device EP2C20F484C7. To show simulation result let us consider the string "**hip hop happy**" as input. This string has total 13 symbols. Frequency of the symbols with corresponding ASCII [17] values are shown in TABLE I.

TABLE I FREQUENCY DISTRIBUTION AND ASCII VALUES OF A TEST STRING

| Char | Frequency | ASCII |
|---|---|---|
| h | 3 | 01101000 |
| a | 1 | 01100001 |
| p | 4 | 01110000 |
| y | 1 | 01101001 |
| i | 1 | 01010011 |
| o | 1 | 01100111 |
| space | 2 | 00100000 |

If we send the ASCII values of the test string then we have to send 104 bits. But two level compressions of proposed method reduce total bits of the test string to 34 bits. Fig. 5 shows two level compression results on the test string.

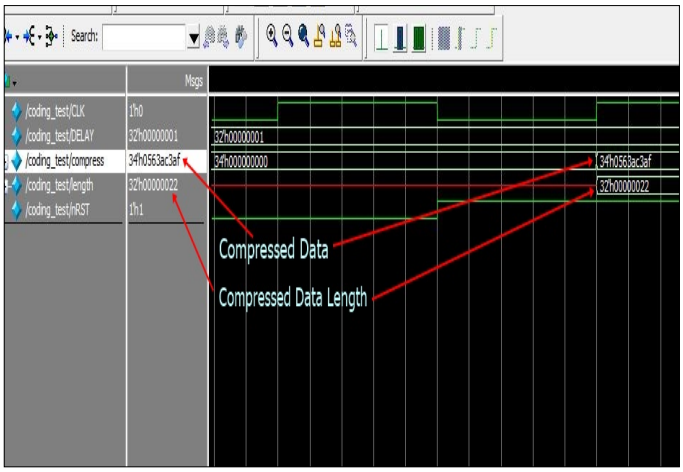


Fig. 5. Simulation result of Huffman and Bit-stuffing compression.

Hamming (7, 4) encoding can correct single bit error. So by applying this coding we can achieve higher error correction rate. For example, let us consider input data bits are "1101". By using Hamming (7, 4), generating code-word will be "1100110". If error occurs in transmission and receiver receives the data as 1100111, still receiver can get correct data. Fig. 6 shows the simulation result.

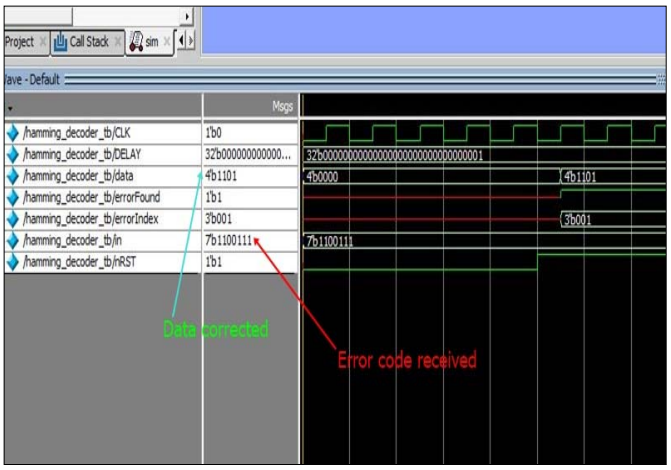


Fig. 6. Simulation result of the error correction of Hamming (7, 4) encoding.

## VIII. RESULTS AND DISCUSSION

The method has been evaluated by considering text data of varying size. The model is effective by correcting single bit errors during transmission and providing higher saving percentage. The method therefore provides multistage security as well as it achieves total reduction or shrinkage of 67.30% memory. As a result it will require less bandwidth and transmission time.

To find the error correction rate of the implemented system, some random bits have been changed intentionally in received encoded file. The proposed mechanism corrects error almost 100% efficiently. Technically each input character is encoded into two (7, 4) Hamming code-word. Each code-word can correct a single bit error. So if 25% of receiving data get corrupted during transmission, implemented system can correct 100% of them. TABLE II shows result of error corrections of proposed method for an 800 bit text file.

TABLE II ERROR CORRECTION RATE OF RECEIVED DATA FILE (800 BITS FILE)

| Number of Corrupted Bits | Number of Corrected Bits | Error Rate | Error Correction Rate (%) |
|---|---|---|---|
| 49 | 49 | 6.125 % | 100 % |
| 53 | 53 | 6.625 % | 100 % |
| 126 | 125 | 15.75 % | 99.20 % |
| 165 | 161 | 20.63 % | 97.58 % |
| 193 | 191 | 24.13 % | 98.86 % |

Depending on the nature of the application there are various criteria to measure the performance of a compression algorithm. When measuring the performance the main concern would be the space efficiency. Following are some measurements used to evaluate the performances of lossless algorithms.

*Compression Ratio(CR):* The ratio between the size of the compressed file and the size of the source file.

$$CR = (C_2/C_1) * 100\% \quad (1)$$

- $C_1$= Size before compression
- $C_2$= Size after compression

*Compression Factor(CF):* The inverse of the compression ratio. That is the ratio between the size of the source file.

$$CF = 1/CR \quad (2)$$

*Saving Percentage(SP):* Calculates the shrinkage of the source file as a percentage.

$$SP = = (C_1-C_2/C_1) * 100\% \quad (3)$$

Fig. 7 shows the result of two level compressions for different sample file sizes.

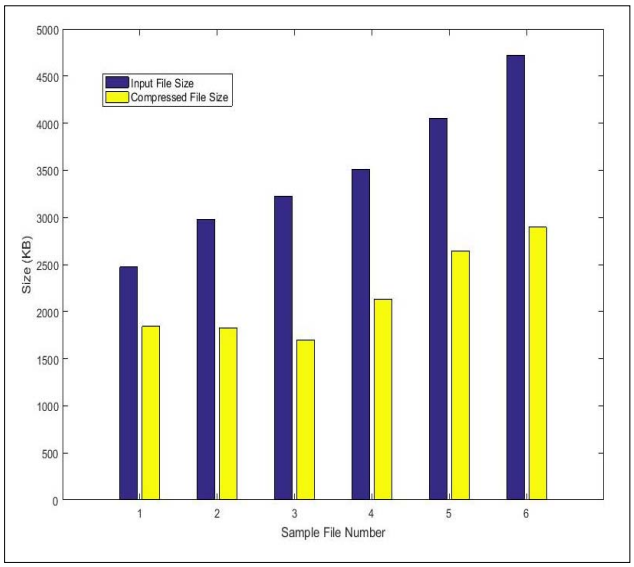


Fig. 7. Result of proposed 2 level compression

TABLE III shows the result of proposed comression mechanism for different file size. Comparison of saving percentage(3) obtained by proposed methodology and related works are shown in TABLE IV. Values obtained by all the related works listed in TABLE IV imply that the proposed methodology furnishes encouraging saving percentage. It shows lower compression ratio and better saving percentage to the most of the compression techniques which have been compared.

TABLE III RESULT OF PROPOSSED TWO LEVEL COMPRESSION METHOD

| File Index | 1 | 2 | 3 | 4 | 5 |
|---|---|---|---|---|---|
| **Input File Size (in bytes)** | 2977331 | 3221272 | 3506366 | 4052530 | 4722220 |
| **Compressed File Size (in bytes)** | 1825956 | 1700640 | 2127821 | 2642209 | 2895598 |
| **Compression Ratio (CR)** | 61.33 | 52.79 | 60.68 | 65.20 | 61.32 |
| **Saving Percentage (SP)** | 38.67 | 47.21 | 39.32 | 34.80 | 38.68 |

TABLE IV COMPARISON OF SAVING PERCENTAGE WITH RELATED WORKS

| Huff-man [18] | Adaptive Huffman [19] | LZW [20] | Shannon Fano [21] | LZOP [22] | This work |
|---|---|---|---|---|---|
| 45.41 | 42.11 | 69.03 | 40.83 | 61.58 | **67.30** |

## IX. CONCLUSION

The proposed system is a blend of bit stuffing, Huffman and Hamming algorithm for high speed data compression and secured transmission. FPGA implementation further improves the system performance in terms of security, reliability, speed, cost etc. The functionality of the design has been tested by simulating the design using FPGA environment. The simulation results show very impressive results in terms of storage savings and error correction capability. It has been compared with other related works and proved its superiority over other researchers. This method can be further secured by adding symmetric or asymmetric cryptographic module which can be considered as its future expansion. The method can also be extended to other types of data such as images, audios, videos, etc.

## REFERENCES


[1] Hofstee P. "The Big Deal about Big Data." In Proceedings of the 8th *IEEE International Conference on Networking, Architecture, and Storage*, July 2013.

[2] Carlos A. J., Carlos F. A., Oscar M. R.and Javier C., "FPGA implementation of a Huffman decoderfor high speed seismic data decompression", *Data Compression Conference*, 2014

[3] S. V. Smith. "Big Data creates big industry for storing data." *http://www.marketplace.org/topics/business/big-data-creates-big-industry-storing-data*, 2013, accessed on September, 2017.

[4] R. S. Chakraborty and S. Bhunia, "HARPOON: An obfuscation based SoC design methodology for hardware protection". *IEEE Transactions on Computer-Aided Design of Integrated Circuits and Systems*, vol. 28, no. 10, pp. 1493-1502, 2009.

[5] Maity, S.P., Kundu, M.K., 2013. "Distortion free image-in-image communication withimplementation in FPGA". *Int. J. Electron. Commun.* 67 (May (5)), 438–447.

[6] Wang W. and Zhang W., "Adaptive Spatial Modulation Using Huffman Coding". *IEEE Global Communications Conference (GLOBECOM)*, 2016.

[7] Sorokin A. and Makushenko E., "Identification of JPEG files fragments on digital media using binary patterns based on Huffman code table". *IEEE 3rd International Conference on Digital Information Processing, Data Mining and Wireless Communications (DIPDMWC),* 2016.

[8] Djusdek D., Studiawan H. and Ahmad T., "Adaptive image compression using Adaptive Huffman and LZW". *IEEE International Conference on Information & Communication Technology and Systems (ICTS),* 2016.

[9] Potthuri S., Shankar T. and Rajesh A., "Cluster head selection using Huffman coding algorithm for Wireless Sensor Networks". *IEEE International Conference on Innovations in Information, Embedded and Communication Systems (ICIIECS),* 2015.

[10] Marti D., Jamsed K., and Agarwal K., "FPGA-Based Application Acceleration: Case Study with GZIP Compression/Decompression Streaming Engine". *International Conference on Computer-Aided Design (ICCAD),* Nov 2013.

[11] Dandalis N., Prasanna V., "Configuration compression for FPGA-based embedded systems", *ACM/SIGDA International Symposium on Field-Programmable Gate Arrays,* 2001.

[12] Jamro M.W.E., Wiatr K., "FPGA implementation of the dynamic Huffman encoder", *Proceedings of IFAC Workshop on Programmable Devices and Embedded Systems,* 2006

[13] Dias W., David Moreno E. and Palmeira I., "A new code compression algorithm and its decompressor in FPGA-based hardware". *IEEE 26th Symposium on Integrated Circuits and Systems Design (SBCCI),* 2013.

[14] Rigler, S., Bishop, W. and Kennings, A., "FPGA-Based Lossless Data Compression using Huffman and LZ77 Algorithms". *Canadian Conference on Electrical and Computer Engineering,* 2007.

[15] D.Huffman, "A method for the construction of minimum redundancycodes", *Proceedings of the Institute of Radio Engineers,* vol. 40, no. 9, pp. 1098–1101, September 1952.

[16] Hamming, R. W., "Error Detecting and Error Correcting Codes", *Bell SystemTech. Jour.,* no.29, pp. 147–160, 1950.

[17] http://en.wikipedia.org/wiki/ASCII , accessed on Nov 2016.

[18] Kodabagi M.M., Jerabandi M.V, and Gadagin N., "Multilevel Security and Compression of Text Datausing Bit Stuffing and Huffman Coding". *International Conference on Applied and Theoretical Computing and Communication Technology (iCATccT),* 2015

[19] Kodituwakku S. R., Amarasinghe U. S., "Comparison of Lossless Data Compression Algorithms for Text Data", *Indian Journal of Computer Science and Engineering,* vol 1 No 4 416-425, ISSN : 0976-5166, 2015.

[20] Terry W., "A Technique for High-Performance Data Compression". Computer. 17 (6): 8–19. DOI:10.1109/MC.1984.1659158,

[21] Fano, R. M., "The transmission of information". Technical Report No. 65. Cambridge (Mass.), USA: Research Laboratory of Electronics at MIT, 1949.

[22] Comparison of compression,[Online]. Available: https://binfalse.de/2011/04/04/comparison-of-compression/, accessed on September, 2017.

# A Compact Planar Multiple-Input Multiple-Output (MIMO) Antenna for Ultra-wideband Applications

Foez Ahmed[1], Nisab Hasan[2] and Aurangzib Md Abdur Rahman[3]
[1,2,3]Department of Information and Communication Engineering
Faculty of Engineering, University of Rajshahi, Rajshahi-6205, Bangladesh
Email: [1]foez.kku@gmail.com

*Abstract*—**This paper presents a planar multiple-input multiple-output (MIMO) antenna for Ultra-wideband wireless applications. The antenna system consists of a radiating patch with stair steps, microstrip feed line and T- and L-like shape slots at the ground plane with low profile structure (54×30×0.8mm$^3$).**

**The proposed antenna can cover the wide frequency range from 3.04 GHz to 11.2 GHz. It shows nearly omnidirectional radiation pattern and high gain. To improve the isolation, a stub and two L-like shape slots are introduced into the ground plane and hence, the achieved isolation is higher than 15 dB over the entire frequency band.**

***Keywords—MIMO Antenna, UWB Antenna, Planar, Lowprofile, Monopole, Compact, Mutual Coupling.***

## I. INTRODUCTION

After the declaration of license free spectrum from 3.1 GHz to 10.6 GHz for ultra-wideband (UWB) applications [1], Ultra-wideband (UWB) technology is a rapidly developed potential candidate for wireless communication. UWB technique requires low transmitted power which confines UWB systems to short range communication only. However, the multiple input multiple-output (MIMO) technology could be the best solution to mitigate the multipath fading problem and hence, to improve the required date rate for UWB communication. But, one of the major challenges in the designing of UWB MIMO antenna systems is the planar and compact size with low mutual coupling between the antenna elements.

Over the last couple of years, different types of MIMO antennas have been investigated to achieve UWB applications. In [2], the proposed antenna system covers the bandwidth of 4.4 GHz to 10.7 GHz with the system size of 35×40×1.65mm$^3$. In [3], the designed antenna has the system size of 29×50×1.6mm$^3$ and covered frequency range of 7.5 GHz to 17.5 GHz. It is incapable of covering the lower frequency band of UWB operations. The antenna system presented in [4] has large system size of 40×68×1.5mm$^3$ showing the coverage bandwidth of 3.2 GHz to 10.6 GHz. Besides these, recently some of other UWB MIMO antennas have been studied. Such as, in [5] a compact microstrip antenna (38×91×1.5748mm$^3$) is designed for ultra-wideband applications. Another compact and planar antenna has been presented in [6] with the dimension of 55×50×0.8mm$^3$. A compact ultra-wideband MIMO antenna has also been designed [7] for breast cancer detection with system size of 70×35×1mm$^3$. However, none of the above mentioned antenna system is fit for all the aspects; either having high-profile and longer dimensions or fail to cover the entire bandwidth of UWB (3.1–10.6 GHz) operations.

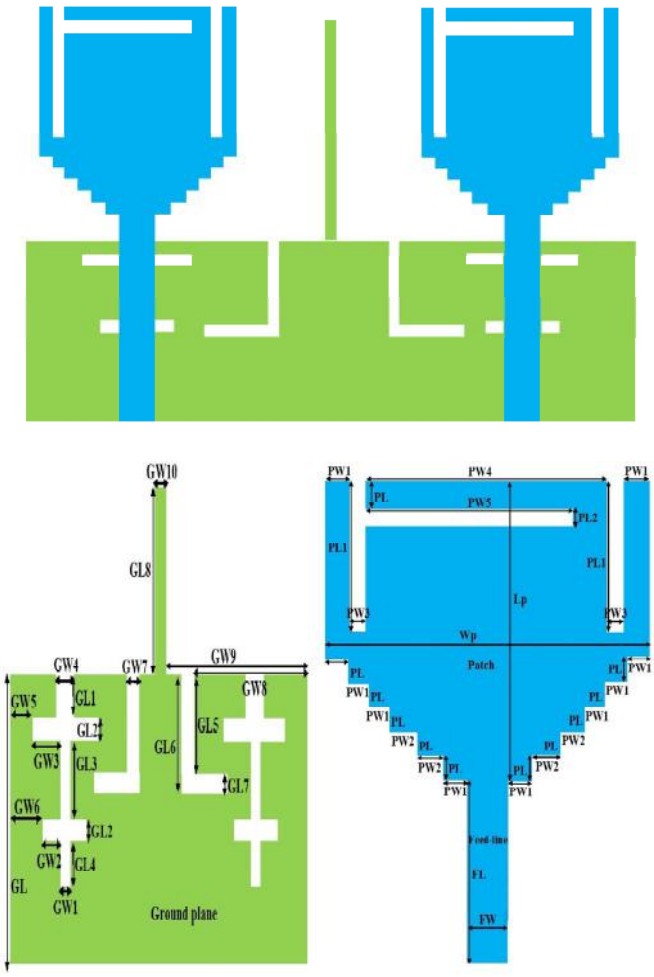


Figure 1. Details of Optimized UWB MIMO Antenna Geometry.

978-1-5386-2307-7/17/$31.00 ©2017 IEEE

In this paper, a compact planar UWB MIMO antenna system has been developed for UWB applications that can cover the entire UWB band (3.1–10.6 GHz). The applied decoupling techniques can also improve the antenna ports' isolation significantly. In our case, it is greater than 15 dB over the entire UWB frequency range which is good enough for UWB applications.

## II. MIMO Antenna Design And Parameter Study

### A. Antenna Structure

Fig.1 shows the proposed UWB MIMO antenna consist of two planar monopole elements placed parallel to each other with same ground plane fed by 50Ω microstrip line through port 1 and port 2 respectively. The antenna system is printed on the FR4 Epoxy substrate with a size of 54×30 $mm^2$, thickness of 0.8mm and relative dielectric constant of 4.4. The rectangular patch having the size of Wp × Lp, is printed on top surface of the substrate. It acts as a principal radiator and excites through the microstrip feed line with the dimension of FW×FL. On the other hand, a partial ground plane is printed on the bottom side of the substrate. Its length is GL having the same width as the substrate. However, the Ansoft HFSS v15 [8] was used to optimize our proposed antenna system. Table I shows the optimized numerical values in millimeters of the proposed geometry. However, the simulated reflection coefficient (S11) of the optimized proposed MIMO antenna is shown in Fig. 2.

TABLE I. NUMERICAL VALUES FOR THE OPTIMIZED ANTENNA GEOMETRY. (U NIT: MILLIMETERS)

| *Parameter* | *Value* | *Parameter* | *Value* | *Parameter* | *Value* |
|---|---|---|---|---|---|
| SubW | 54 | FL | 12 | Wp | 16 |
| GL2 | 0.5 | GW1 | 0.5 | GW4 | 1.4 |
| PL | 1 | PL1 | 11 | PW5 | 11.5 |
| SubL | 30 | FW | 2 | GL | 11 |
| GL3 | 3 | GW2 | 1.75 | GW5 | 5.5 |
| PW1 | 1 | PW3 | 0.5 | SubH | 0.8 |
| Lp | 17 | GL1 | 1 | GL4 | 1.5 |
| GW3 | 3.25 | GW6 | 7 | PW2 | 1.5 |
| PW4 | 13 | GW7 | 1 | GW8 | 20 |
| GW9 | 26.5 | GW10 | 1 | GL5 | 5 |
| GL6 | 6 | GL7 | 1 | GL8 | 17 |

### B. Explanation of Antenna Working Principle

In the proposed structure, to create impedance matching that results in bandwidth enhancement, a T-like shape slot has been introduced at the ground plane (just below the patch). Furthermore, the multiple stair steps are placed at the lower side of the patch. These stair steps slots enhance impedance bandwidth enormously. Another three slots are embedded in the patch that can also have a significant effect on the performance of our antenna. The details working principle for the single antenna element has been explained in author's another paper [9]. A stub and two L shaped slots are used on the ground plane to minimize the coupling effects between two antenna elements. This proposed isolation techniques also improve the impedance bandwidth to cover the complete UWB frequency range from 3.1 GHz to 10.6 GHz. However, in terms of simulated S parameters Fig. 4 shows the effects of various antenna structures such as Fig. 3(a) antenna without having stubs and L shaped slots, Fig. 3(b) antenna with stub, Fig. 3(c) antenna with stub and only left L slot and Fig. 3(d) the proposed antenna. In Fig. 4, it is seen that the proposed antenna has impedance bandwidth of 8.16GHz (3.04GHz to 11.2GHz) at bandwidth criterion of S11<-10 dB.

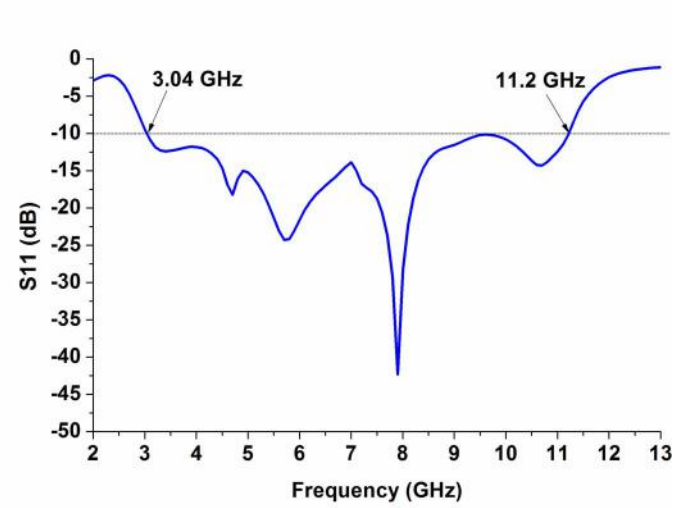


Figure 2. Simulated Reflection Coefficient (S11) Curve.

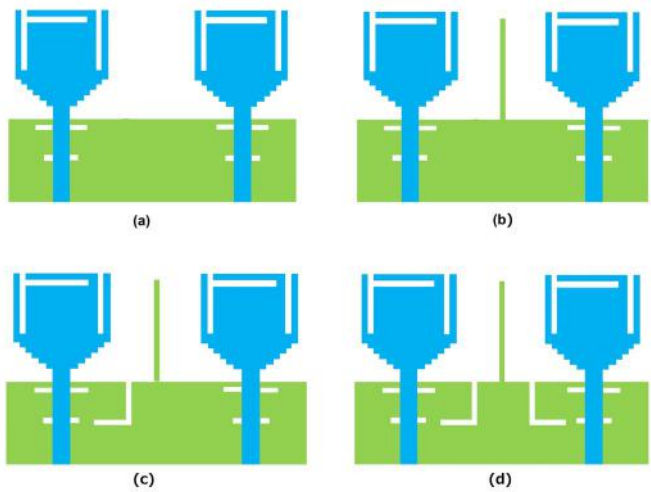


Figure 3. (a) Antenna without stub and 2L slots, (b) Antenna with stub and without 2L slots, (c) Antenna with stub and left L slot, (d) the proposed UWB MIMO antenna.

### C. *Explanation of Port-to-Port Decoupling Process*

In order to minimize mutual coupling effect, a stub and two L slots are used in the ground plane. The stub is treated as a reflector that separates the radiation patterns of the antenna unit to decrease the unwanted mutual coupling caused by near-field radiation and thus improves the isolation at the lower frequency. In addition, the two L slots have significant effects to reduce the mutual coupling of the antenna elements especially at the middle and higher bands. The mechanism for decoupling using L slots is that it acts as like a filter and hence blocks the current flowing from the excited port 1 to the couple port 2 as demonstrated in 5.

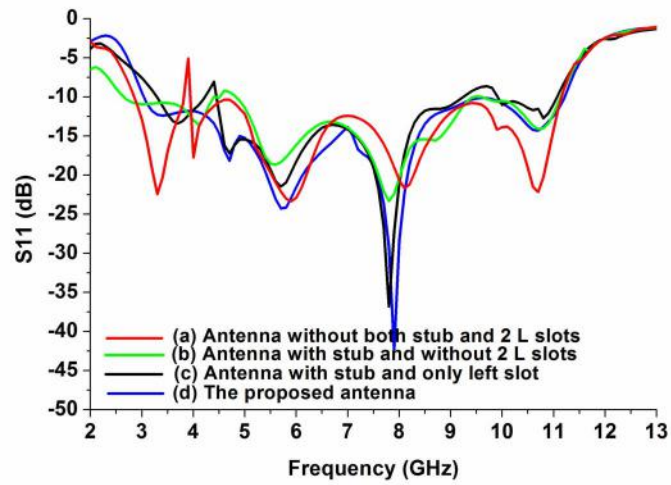


Figure 4. Simulated S-parameter (S11) for the various antenna geometry as shown in Fig.3.

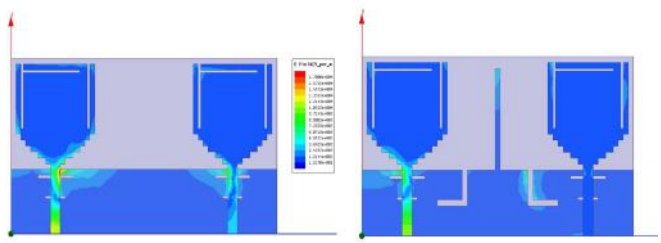

Figure 5. Surface current distribution at 5GHz – without (Left) and with (Right) decoupling techniques.

Fig. 6 shows the isolation curve over the UWB frequency range. From Fig. 6, it is clearly noted that the port-to-port isolation is well below the -15 dB over the entire operating band. However, the s-parameter (S12) less than -15 dB is considered to be enough for good isolation.

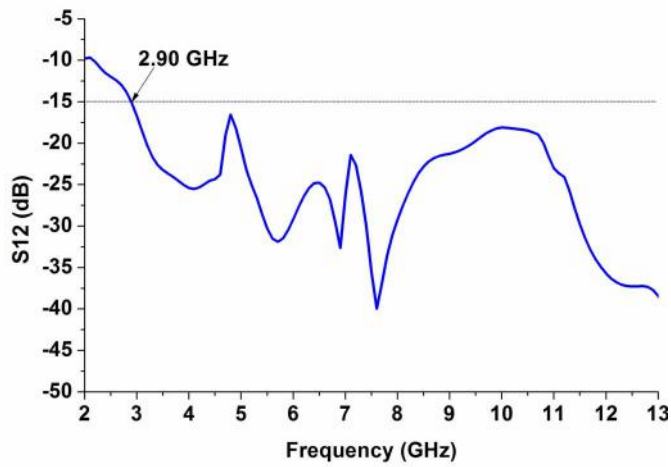


Figure 6. Simulated S-parameter (S12) curve showing port-to-port Isolation.

## III. ESULTS AND DISCUSSION

### A. *Peak Gain (dBi)*

The simulated peak Gain of proposed UWB MIMO antenna has been studied and shown in Fig. 7. The graph indicates high gain over the entire ultra-wideband communication range from 3.1 GHz to 10.6 GHz with moderate fluctuations.

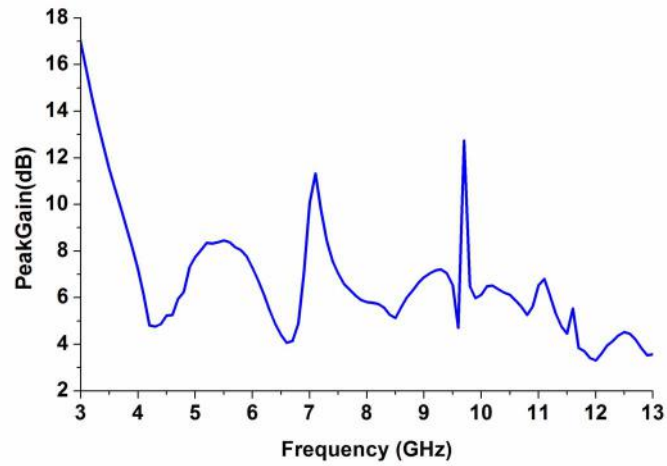


Figure 7. Simulated Reflection Coefficient (S11) Curve.

### B. *Radiation Pattern*

Fig. 8 and Fig. 9 show the simulated 3D and 2D radiation pattern when port 1 is excited and port 2 is terminated by 50Ω load (Left side) and when port 2 is excited and port 1 is terminated by 50Ω load (right side) respectively. It is noted that the radiation pattern is almost as like as a dipole antenna. The

radiation pattern is nearly omnidirectional with complementary directive a pattern which has a great advantage in ultra-wideband communication systems.

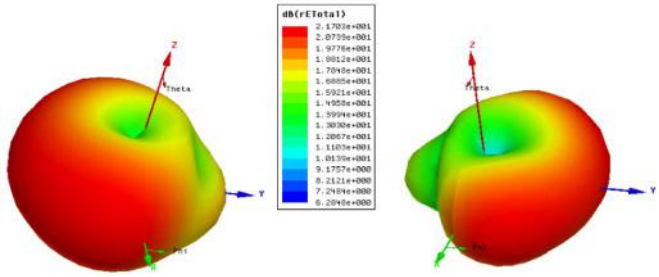


Figure 8. Simulated 3D Radiation Pattern of the proposed UWB MIMO antenna at 5 GHz.

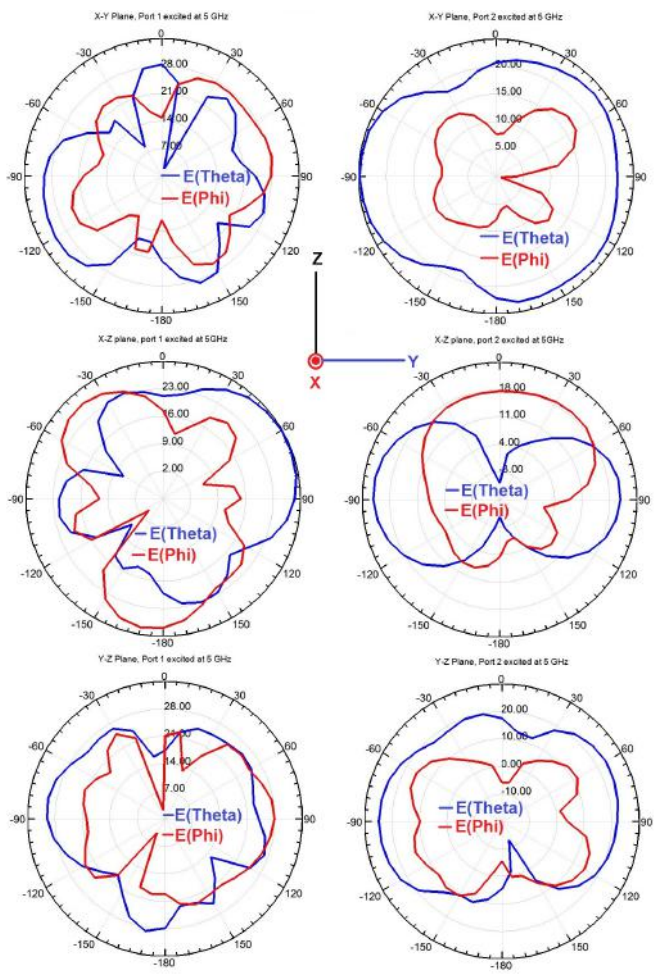


Figure 9. Simulated 2D Radiation Pattern of the proposed UWB MIMO antenna at 5 GHz.

### C. *Envelope Correlation Coefficient ($\rho_e$)*

Under the consideration of isotropic or uniform signal propagation environment, an analytical equation (1) provided by [10], is used to compute the correlation coefficient of a MIMO antenna system.

$$\rho_{ij}^{ee} = \left| \frac{\left| S_{ii}^{*} S_{ij} + S_{ij}^{*} S_{jj} \right|}{\left| \left(1 - |S_{ii}|^2 - |S_{ji}|^2\right)\left(1 - |S_{jj}|^2 - |S_{ij}|^2\right) \right|^{1/2}} \right|^2 \qquad (1)$$

However, Fig. 10 shows the analytical result of correlation coefficient computed form S-parameters for the proposed UWB MIMO antenna. It indicates that the correlation coefficients are well below 0.01 throughout the frequency range of UWB applications. This satisfies the conditions $\rho_e < 0.5$ [11], which confirms better functioning in terms of diversity.

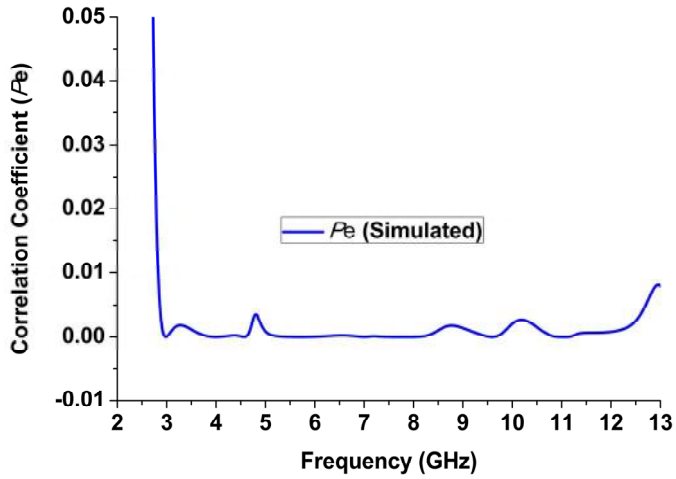


Figure 10. Computed correlation coefficient (ρe) curve.

## IV. CONCLUSIONS

The proposed UWB MIMO antenna can operate over the complete frequency range from 3.1 GHz to 10.6 GHz of ultra-wideband applications. The antenna has negligible coupling effect which is well below the -15 dB considered to be enough for good isolation. However, the achieved high gain, good isolation, bandwidth characteristics and very low correlation coefficient prove that the proposed MIMO antenna can outperform for UWB wireless applications.

## ACKNOWLEDGMENT

The authors would like to thank anonymous reviewers for their insightful comments and suggestions. We are also thankful to the Key Laboratory of Antenna for Wireless Communications, Department of Information and Communication Engineering, University of Rajshahi, for supporting all types of technical as well as simulation facilities.

## REFERENCES


[1] Federal Communications Commission (FCC), Revision of part 15 of the Commissions Rules Regarding Ultra-Wideband Transmission Systems, First Report and Order, FCC 02-48, 2002.

[2] V. Kumar, A. Pawaria, A Compact Two Element UWB MIMO Antenna, IJIREEICE, vol.3, issue 5, may 2015.

[3] N. Saha, S. Dey, Md. S. Mahmud, Design of Compact UWB MIMO Antenna for Two Different Stub structures, 7th European Conference on Antennas and Propagation (EUCAP), 2013.

[4] A. Najam, Y. Duroc, and S. Tedjni, UWB-MIMO Antenna with Novel Stub Structure, Progress In Electromagnetics Research C, vol. 19, pp. 245-257, 2011.

[5] M. Jusoh, M. F. Jamlos, M. R. Kamarudin, and F. Malek, A MIMO Antenna Design Challenges for UWB application, Progress in Electromagnetics Research B, vol.36, pp. 357-371, 2012.

[6] X. X. Xia, Q. X. Chu, and J. F. Li, Design of a Compact Wideband MIMO Antenna for Mobile Terminals, Progress in Electromagnetics Research C, vol. 41, pp. 163-174, 2013.

[7] L. Wang and B. Huang, Design of Ultra-Wideband MIMO Antenna for Breast Tumor Detection, International Journal of Antennas and Propagation, Article ID 180158, pp. 7, 2012.

[8] HFSS v.15, Ansoft Corporation, Pittsburgh, PA, USA.

[9] F. Ahmed, N. Hasan and H. M. Chowdhury, A Compact Low-profile Ultra Wideband Antenna for Biomedical Applications, IEEE International Conference on Electrical, Computer and Communication Engineering (ECCE), pp. 87–90, 2017.

[10] P. Hallbjorner, The Significance of Radiation Efficiencies when using S-parameters to Calculate the Received Signal Correlation from Two Antennas, IEEE Antenna and wireless propagation letters, vol. 4, 2005.

[11] R. G. Vaughan and J. B. Anderson, Antenna Diversity in Mobile Communications, IEEE Trans. Veh. Technol., vol. 4, no. 1, pp. 97-99, 2005.

# Design and Analysis of Four Elements E, H and Combined E-H Shaped Microstrip Patch Array Antenna for Wireless Applications

L. C. Paul[1*], M. S. Akhter[1], M. A. Haque[2], M. R. Islam[1], M. F. Islam[3], M. M. Rahman[2]
[1]Dept. of Electronic & Telecommunication Engineering
[1]Pabna University of Science & Technology, Pabna-6600, Bangladesh
[2, 3] Dept. of Electrical and Electronic Engineering
[2]Daffodil International University, Dhaka, Bangladesh
[3]Islamic University of Technology, Gazipur, Bangladesh
[*]litonpaulete@gmail.com

***Abstract*— In this paper, different shaped patch antenna and their array configurations have been designed and simulated by using advanced designed system (ADS) in order to improve the overall performance of microstrip patch antenna (MPA). FR4 dielectric material is used as substrate which has a dielectric constant of 4.4 and height of the dielectric substrste is 1 *mm* and loss tangent, tan δ is 0. Antennas are fed thruogh 50 Ω microstrip feed line. Each array consists of corresponding four single elements. Different antenna performance parameters like return loss, bandwidth, directivity, gain & radiation efficiency were analyzed for all the proposed antennas.**

***Keywords— Multiband; MPA; Array; ADS;***

## I. INTRODUCTION

The microstrip patch antenna creates a great attention among the researchers because of attractive advantages like low profile, ease of integrating with active devices, mechanically robust when mounted on a rigid surface, capability of dual and triple frequency operations and there are many wireless communication devices are widely using on various frequency bands [1]. The microstrip antenna is also referred to as patch antenna .The concept of microstrip patch antenna was first demonstrated in 1886 by Heinrich hertz and its practical application by Guglielmo Marconi in 1901 and it was newly proposed by Deschamps in 1953. Howell and Munson developed the first practical antenna in the early 1970's. In case of antenna design considerations, its physical size reduction and bandwidth improvement are the most crucial issues for practical applications [2]. This antenna has a very good quality factor and which leads to narrow bandwidth and low efficiency. In this case, with increasing the thickness of substrate material, the quality factor of the antenna can be reduced [3]. The goal of this work is to improve the antenna performance like bandwidth, gain, efficiency etc. of patch antenna. This is done by designing E and H shaped microstrip patch antenna and designing E shaped array (four E shaped elements), H shaped array (four H shaped elements) and E-H array (two E shaped elements and two H shaped elements).

The rest of the paper is arranged as following pattern. Some literature review and the necessary antenna design formulas are discussed in section II and section III respectively. Design and analysis of all the proposed antennas are represented in section IV. All the simulated antenna parameters are discussed in section V. The section VI shows a summary of the performance parameters of all the proposed antennas. At the end, conclusion and recommendation for the future scopes are drawn in section VII.

## II. LITERATURE REVIEW

In [4], author explained E shape microstrip patch antenna at resonant frequency 1.2 GHz for GSM and 3G applications. In this design FR4 was used as substrate of dielectric constant $\varepsilon_r$ = 4.4 and thickness h = 1 mm with loss tangent (*tan δ*) of 0. This antenna was designed and simulated by using ADS and got gain of 5.68 dB, directivity of 6.74 dB and return loss of -23.62 dB. By changing feeding points, center operating frequency of 1.5 GHz & return loss of -29 dB were achieved for GSM band and another center operating frequency of 1.9 GHz & return loss of -32 dB for 3G band after fabrication.

In [5], the corresponding author presented the H shape rectangular microstrip antenna with enhanced dual frequency bandwidth. This antenna was designed at 2.1 GHz and used glass epoxy substrate of dielectric constant 4.2 and thickness of 1.6 mm. The designed antenna was analyzed by using IE3D and Gain of 3.82 dB, Directivity of 3.87dB & efficiency of 98.1% were obtained.

In [6], author used ADS material as substrate with $\varepsilon_r$ = 2.8 to design E shape microstrip antenna at 1.17 GHz resonant frequency for GPS application. In this design ADS software was also used for simulation and return loss of -17.99 dB, gain of 2.27 dB and directivity of 6.90 dB were obtained.

In [7] author designed an H shape microstrip patch antenna using FR4 substrate material with dielectric constant of 4.3 at 2.3 GHz operating frequency for the antenna miniaturization and bandwidth improvement of the antenna. The simulation result was carried out by using ADS. In that design the return loss of –17.27 dB and bandwidth of 39 MHz and the voltage standing wave ratio 1.07 were obtained.

978-1-5386-2307-7/17/$31.00 ©2017 IEEE

## III. Design Formulas

The microstrip patch antenna commonly has a ground plane, substrate and conducting patch. The antenna radiates in the concept of fringing fields between the ends of the patch. The dielectric constant of the antenna must be small to get the higher bandwidth and impedance matching. To increase the bandwidth, comparatively thick dielectric substrate is used. FR4 substrate is the flame retardant which has low cost and good fabrication characteristics and has a good water absorption characteristics and it can be used in fabrication of glass, tube etc. Increasing the dielectric constant decreases the size but lowers the bandwidth and efficiency of the antenna while decreasing the dielectric constant increases the bandwidth with an increase in size. Effective antenna dimension virtually increases because of fringing effect that is why an effective dielectric constant, denoted by $\varepsilon_{reff}$, is appeared [8]. The expression effective dielectric constant $\varepsilon_{reff}$ is given by [9-10],

$$\varepsilon_{reff} = \frac{\varepsilon_r + 1}{2} + \frac{\varepsilon_r - 1}{2}\left[1 + 12\frac{h}{w}\right]^{-\frac{1}{2}} \quad (1)$$

Where $\varepsilon_r$ = Dielectric constant of substrate, $h$ = Height of the dielectric substrate and $w$ = width of the patch.

Now, the extended length of patch, $\Delta L$ is given by,

$$\Delta L = 0.412h\left[\frac{(\varepsilon_{reff} + 0.3)(\frac{w}{h} + 0.264)}{(\varepsilon_{reff} - 0.258)(\frac{w}{h} + 0.8}\right. \quad (2)$$

The effective length of the patch $L_{eff}$ now bacome

$$L_{eff} = \frac{c}{2f_0\sqrt{\varepsilon_{reff}}} \quad (3)$$

The effective patch length $L_{eff}$ is given as,

$$L_{eff} = L + 2\Delta L \quad (4)$$

The actual length of the patch can now be determined from

$$L = \frac{1}{2f_{fr}\sqrt{\varepsilon_{reff}}\sqrt{\mu_0\varepsilon_0}} - 2\Delta L \quad (5)$$

For a rectangular microstrip patch antenna, the resonant frequency is given as,

$$f_0 = \frac{c}{2\sqrt{\varepsilon_{reff}}}\left[\left(\frac{m}{L}\right)^2 + \left(\frac{n}{w}\right)^2\right]^{\frac{1}{2}} \quad (6)$$

where $m$ and $n$ are the modes along $L$ and $W$ respectively.

For efficient radiation, the width $W$ is given as,

$$W = \frac{c}{2f_0}\sqrt{\frac{2}{\varepsilon_r + 1}} \quad (7)$$

Resonant frequency $f_r$ is given by,

$$f_r = \frac{1}{2L\sqrt{\mu\varepsilon}} \quad (8)$$

Percentage bandwidth is given by

$$\%\text{Bandwidth} = (f_H - f_L) / f_C \quad (9)$$

where $f_c$ is the cut-off frequency or centre frequency.

## IV. Design and Analysis

This section represents all the proposed antennas and discusses the simulated results of the proposed antennas. The proposed antennas are designed and simulated by using ADS. FR4 material is used as substrate which has a dielectric constant of 4.4 and center frequency of the proposed antenna is 1.2 GHz. Height of the dielectric substrste is 1 *mm* and loss tangent, tan $\delta$ is 0. Antennas are fed thruogh 50 Ω microstrip feed line. The design parameters of the proposed antennas are listed in the table I.

Table I Antenna Design Parameters

| Antenna parameter | Specification |
|---|---|
| Dielectric constant ($\varepsilon_r$) | 4.4 |
| Oparating frequency ($f_r$) | 1.2 GHz |
| Height of substrate ($h$) | 1.6 *mm* |
| Loss tangent (tan δ) | 0 |

### A. Proposed Antennas

All the proposed and designed antennas, which are presented in this paper, are consisting of four single elements either E shaped patch or H shaped patch. The first step of the designed antenna array is to specify the dimensions of a single element microstrip patch antenna. Fig. 1(a) and (b) show the E-shape and H-shape microstrip patch antenna configurations with the necessary dimensions of the patch.

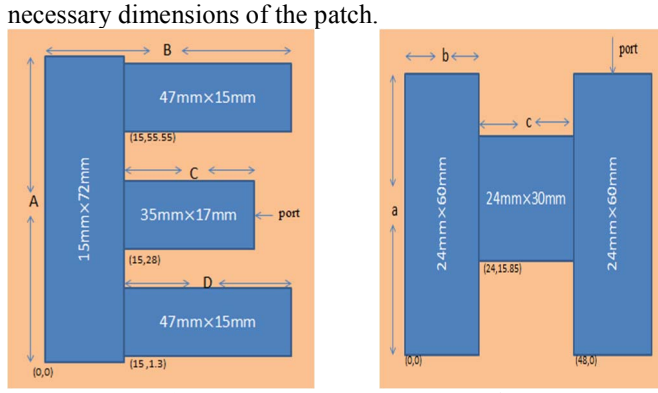


(a) (b)

Fig. 1(a). E shaped and (b) H shaped microstrip patch antenna.

The dimension of the patch antenna is 60 mm × 72 mm obtained by using the formulas mentioned in Section III. The E-shaped and H-shaped patch antennas are designed in the same dimensions. The geometry of microstrip array antennas with four radiating patches are shown in Fig. 2(a), (b) and (c) with proper leveling of dimensions. The four patches are having the same size. The radiating patches are energized using 50 Ω microstrip line feed. The ADS is used to simulate and calculate all the antenna performance parameters like return loss ($S_{11}$ curve), directivity, gain, bandwidth, power curve, efficiency, linear & circular axial ratio, current distribution and 3D radiation pattern.

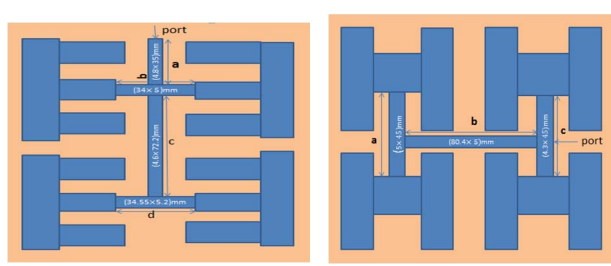


(a) (b)

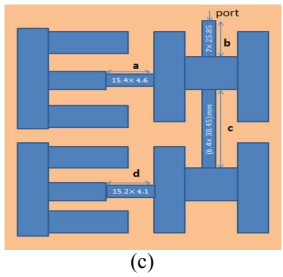


(c)

Fig. 2(a) Four elements E shaped, (b) Four elements H-shaped and (c) Four elements E-H shaped MPA array.

## V. Simulated Results and Discussion

### A. E-shaped Four Elements Array Antenna

Fig. 3(a) and (b) show the layout structure view of single E shaped MPA and four elements MPA array. The designed E shaped MPA shows multiband radiation characteristics as shown in Fig. 4(a) and (b). From the Simulated result of return loss curve of the antenna as shown in Fig. 4(a), the antenna shows four center operating frequencies viz $f_{r1}$, $f_{r2}$, $f_{r3}$ and $f_{r4}$. For the E shaped single element proposed antenna, the first resonant frequency $f_{r1}$ is 1.195 GHz, and the corresponding return loss & -10 dB bandwidth are -22.114 dB & 54 MHz respectively. For the second resonating frequency $f_{r2}$ is 774.7 MHz, the return loss and -10 dB bandwidth are -29.8 dB and 54 MHz respectively. Similarly for the third and fourth resonating frequency $f_{r3}$ and $f_{r4}$ are 2.953 GHz and 4.337 GHz, the obtained return loss and -10 dB bandwidth are -32.26 dB, 97 MHz and -22.79 dB, 88 MHz respectively.

On the otherhand four element E shaped array has three operating frequencies namely $f_{r1}$, $f_{r2}$ and $f_{r3}$. For the first resonant frequency $f_{r1}$ is 1.229 GHz and the corresponding return loss -10 dB bandwidth are -33.284 dB and 139 MHz. The return loss and -10 dB bandwidth of second and third resonating frequencies are -21.76 dB, -22.48 dB and 51 MHz, 281 MHz respectively.

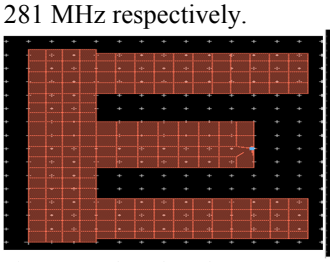

Fig. 3(a). E shaped patch antenna

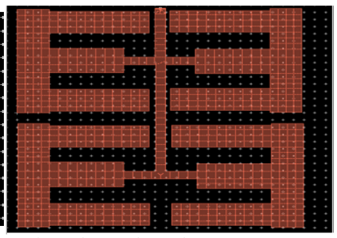

Fig. 3(b). E shaped array antenna

The gain and directivity of proposed E-shape single element patch antenna at first resonant frequency ($f_{r1}$ =1.192 GHz) is obtained as 6.098 dB and 6.277 dB respectively. For the other resonant frequencies including second, third and fourth frequency, the simulated gain and directivity are 6.012 dB, 4.7 dB, 7.64 dB and 6.0 dB, 5.45 dB, 8.18 dB respectively. On the other hand, for proposed E shaped MPA array, the gain and directivity at 1.229 GHz are determined by ADS as 7.72 dB and 8.248 dB respectively. Similarly, for $f_{r2}$ and $f_{r3}$, the observed gain and directivity are 10.96 dB, 6.997 dB and 11.02 dB, 7.97 dB respectively.

The simulated gain, directivity, efficiency, radiated power and effective area of E shape antenna and MPA array are presented in Fig. 5(a) and (b) where the efficiency levels are nearly 97% for single element patch and 88% for four elements array demonstrated within the band of interest. Fig. 6 represents electrical configuration and radiation patterns for the four elements MPA array.

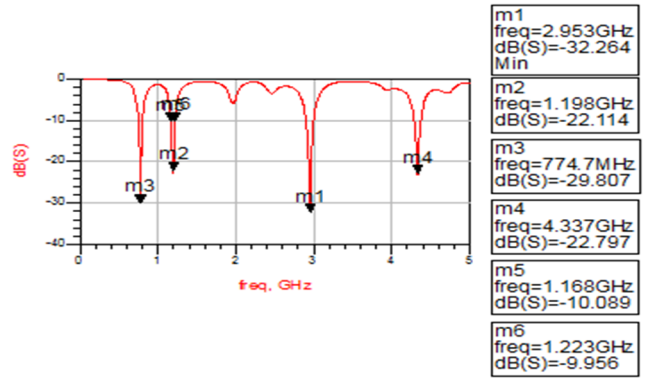


Fig. 4(a) Return loss curve for E-shaped patch antenna

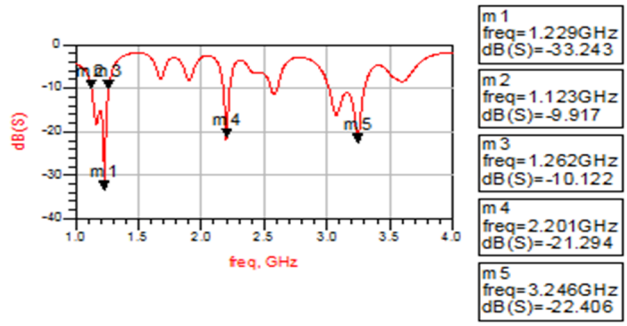


Fig. 4(b) Return loss curve for the array of E- shaped patch antenna

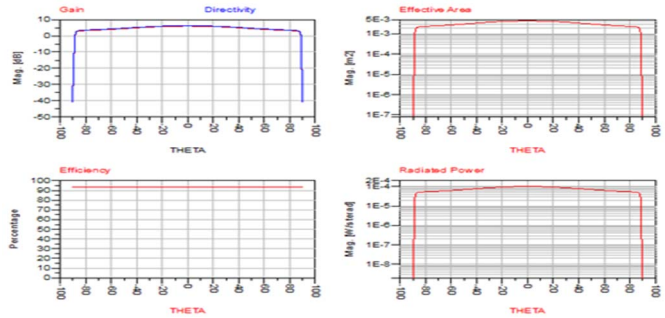


Fig. 5(a) Power curves of E-shaped patch antenna

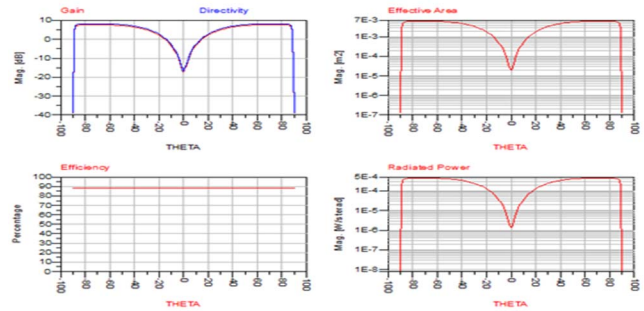


Fig. 5(b) Power curves for the array of E-shaped patch antenna

The electrical configuration shows the current distribution over the proposed E-shaped array antenna. The deep blue color indicates maximum current density. The patterns shown in Fig. 6 are the 3-D plots of radiation properties of the proposed E shaped array representing how well it radiates. The tri-band E shaped MPA array, which provides high gain and improved bandwidth, can be applicable for GPS, air traffic control radar, LTE-700, satellite, mobile phones, weather radar etc.

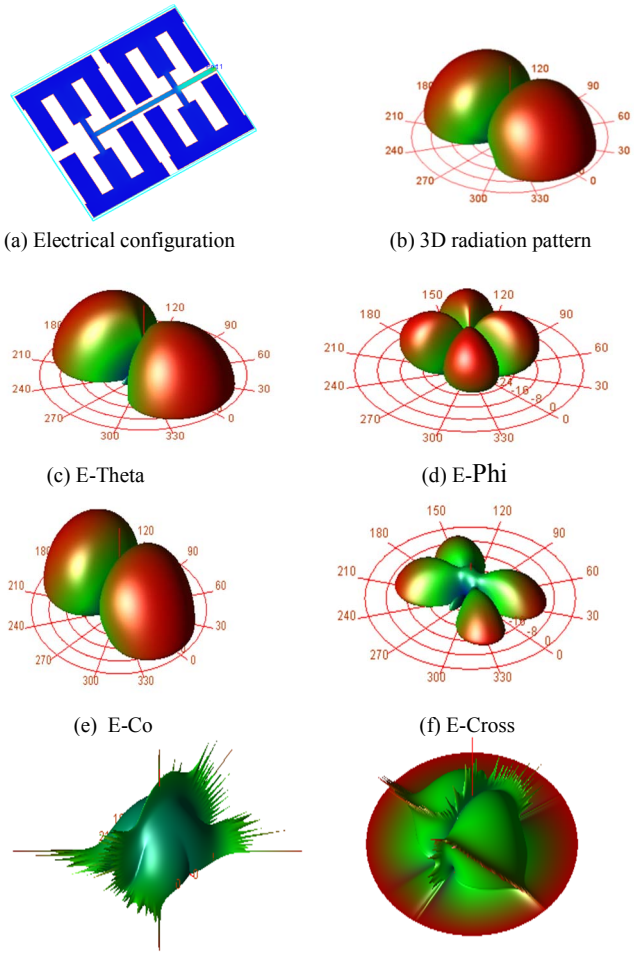

(a) Electrical configuration (b) 3D radiation pattern

(c) E-Theta (d) E-Phi

(e) E-Co (f) E-Cross

(g) Linear axial ratio (h) Circular axial ratio

Fig. 6. Electrical configuration and radiation properties of the array of E-shape patch antenna

### *B. H shaped Four Elements Antenna Array*

The proposed single element H shaped patch antenna and four elements array of it are presented in Fig. 7(a) and (b) respectively. Return loss is a measurement of how much power is delivered from the source to a load and measured by $S_{11}$ parameters. Bandwidth is the range of frequencies over which the antenna can operate effectively. In this paper bandwidth is calculated at - 10 dB point of return loss curve. Simulated return loss curves of single element H shaped patch antenna and four elements array are shown in Fig. 8(a) and (b). For the proposed H shaped single element antenna, the resonant frequency is 1.28 GHz and the corresponding return loss and -10 dB bandwidth are -24.029 dB and 74 MHz. From the Fig 8(b), it is seen that The H shaped MPA array supports dual operating frequency bands. For the proposed array antenna at resonant frequency $f_{r1}$ = 1.217 GHz, the corresponding return loss is -18.8 dB and -10 dB bandwidth is 131 MHz. At the second resonating frequency $f_{r2}$ = 1.629 GHz, the corresponding return loss is -14.58 dB and -10 dB Bandwidth is 44 MHz.

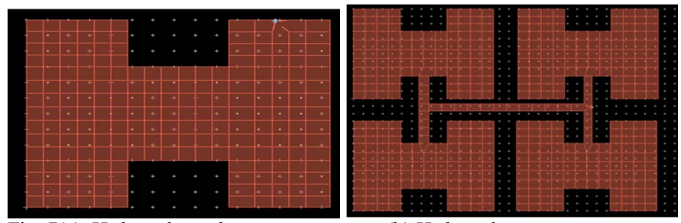

Fig. 7(a). H shaped patch antenna (b) H shaped array antenna

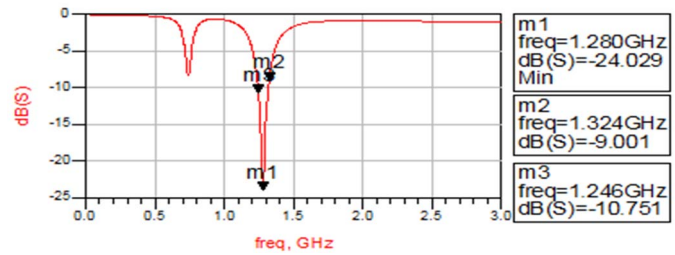


Fig. 8(a). Return loss curve for H-shaped patch antenna

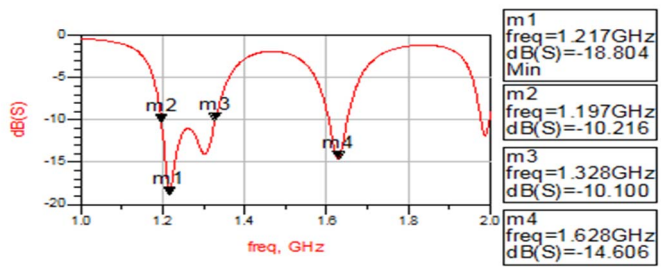


Fig. 8(b). Return loss curve for the array of H-shaped patch antenna

The obtained peak gain and directivity of single H shaped MPA are 6.17 dB and 6.41 dB at 1.28 GHz. On the other hand, for the proposed four elements H shaped MPA array, the gain and directivity are 8.43 dB and 8.78 dB respectively at first center operating frequency 1.212 GHz. At second resonating frequency $f_{r2}$ = 1.628 GHz, the gain and directivity are 2.678 dB and 6.044 dB respectively. The simulated gain, directivity, efficiency, radiated power and effective area of single element H shaped antenna and four elements MPA array are depicted in Fig. 9(a) and (b) where the efficiency level are 96.25% and 96% respectively. Current distribution, 3D radiation patterns and axial ratios of the designed four elements H shaped MPA array are shown in Fig. 10.

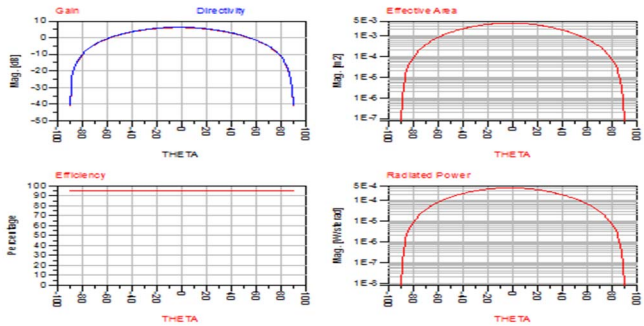


Fig. 9(a). Power curves of H-shaped patch antenna

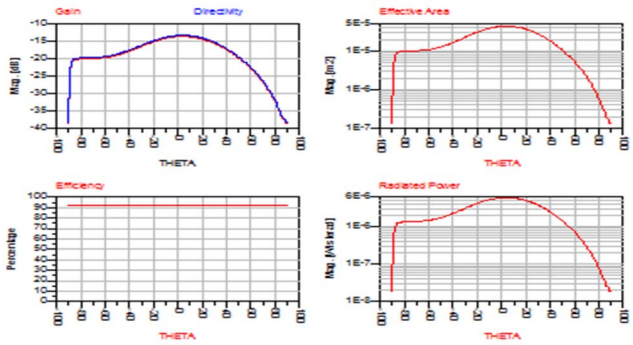


Fig. 9(b) Power curves for the array of H shaped patch antenna.

(a) Electrical configuration

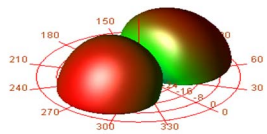

(b) 3D radiation pattern

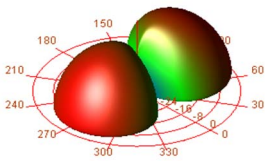

(c) E-Theta

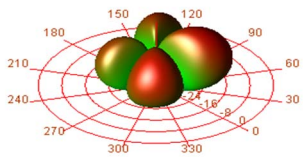

(d) E-Phi

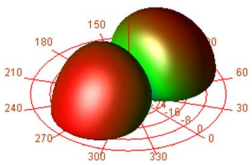

(e) E-Co

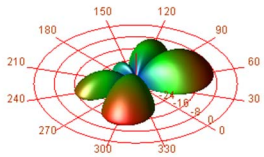

(f) E-Cross

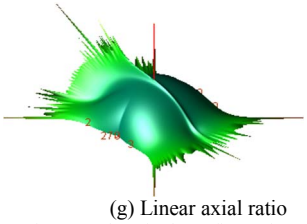

(g) Linear axial ratio

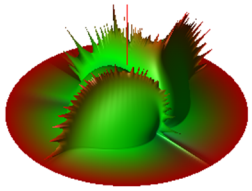

(h) Circular axial ratio

Fig. 10. Electrical configuration and radiation properties of the array of C-shape patch antenna

### C. *Combined E-H shaped patch antenna array*

The layout structure and simulated $S_{11}$ parameters curve of combined two elements E shaped and two elements H shaped MPA array are shown in Fig. 11(a) and (b). The antenna shows dual band operation at 1.28GHz and 2.802 GHz. For the first resonating frequency, the return loss is -33.017 dB and -10 dB bandwidth is 134 MHz. And at the second resonating frequency, the return loss and -10 dB bandwidth are -35.95 dB and 31 MHz respectively. The measured gain, directivity, efficiency, radiated power and effective area of combined E-H MPA array are presented in Fig. 12 where efficiency level of nearly 96.5% is demonstrated within the band of interest. The current distribution and simulated 3-D radiation pattern of the proposed antenna is shown in Fig. 13. In the isometric view as in Fig. 13(a), the blue color indicates the current distribution all over the patch. The gain and directivity of proposed antenna array at 1.28 GHz is measured as 7.5 dB and 7.77 dB respectively. At 2.082 GHz, the gain and directivity are 6.58 dB and 6.89 dB respectively.

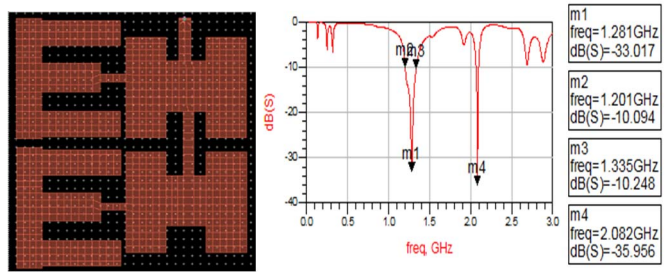


(a) (b)

Fig. 11(a) Combined two-elements E-shaped and two elements H-shaped antenna array, (b) Return loss curve for the array of combined two-elements E-shaped and two elements H-shaped patch.

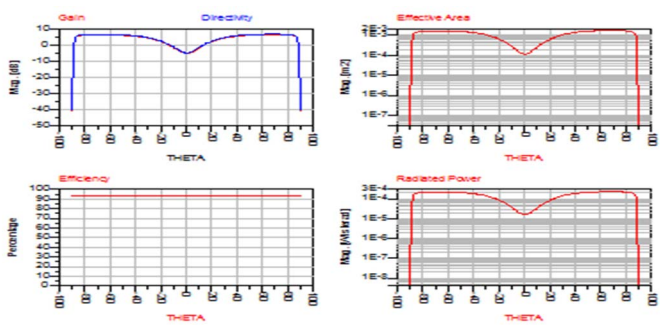


Fig. 12. Power curves for the array of combined two-elements E-shaped and two elements H-shaped patch.

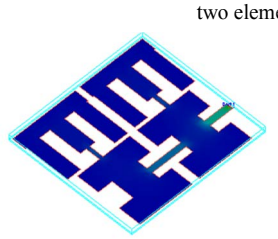

(a) Electrical configuration

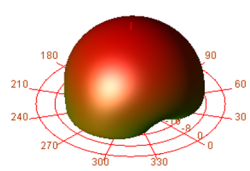

(b) 3D radiation pattern

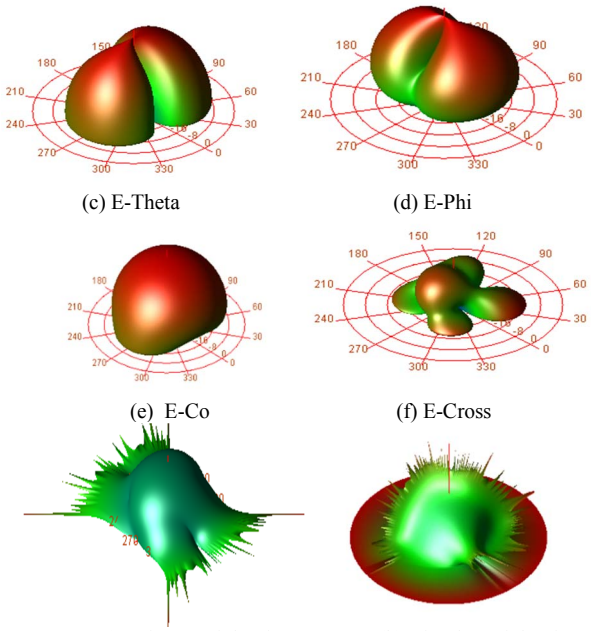

(c) E-Theta (d) E-Phi

(e) E-Co (f) E-Cross

(g) Linear axial ratio (h) Circular axial ratio

Fig. 13. Electrical configuration and radiation properties of the array of combined S-E-C-shape patch antenna

## VI. Summary of Proposed Antennas Performance Parameters

For enhancing the antenna bandwidth, gain and efficiency, antenna arrays including E, H and combined E-H shaped antenna are designed and simulated by using ADS. At first, single E shaped and single H shaped microstrip patch antennas have been designed. The proposed antennas are capable of providing good bandwidth to cover wireless applications at the resonant frequency of 1.2 GHz. Then antenna arrays which are consist of E and H shaped radiating patches are designed for providing high gain and wider bandwidth than the single radiating patch. It is clearly recognized from design summary table II that the proposed microstrip patch antennas and arrays provide better efficiency, gain, directivity and improved bandwidth than the reference [4].

Table-II: Observation of Antenna Parameters for the Proposed MPAs

| Antenna shape | Center frequency (GHz) | Return loss (dB) | Gain (dB) | Directivity (dB) | -10dB Bandwidth (MHz) | Efficiency (%) |
|---|---|---|---|---|---|---|
| E shaped | 1.92 | -22.114 | 6.098 | 6.28 | 54 | 97 |
| | 0.775 | -29.807 | 6.012 | 6.00 | 54 | 99.9 |
| | 2.953 | -32.26 | 4.7 | 5.45 | 97 | 86 |
| | 4.337 | -22.79 | 7.64 | 8.18 | 88 | 93 |
| H shaped | 1.28 | -24 | 6.17 | 6.41 | 76 | 96.25 |
| E shaped array | 1.229 | -33.28 | 7.72 | 8.248 | 139 | 88 |
| | 2.2 | -21.76 | 10.96 | 11.02 | 51 | 99.0 |
| | 3.25 | -22.48 | 6.997 | 7.98 | 281 | 87.5 |
| H shaped array | 1.21 | -18.8 | 8.43 | 8.78 | 131 | 96 |
| | 1.628 | -14.6 | 2.678 | 6.044 | 44 | 44 |
| E-H shaped array | 1.28 | -33.017 | 7.5 | 7.77 | 134 | 96.5 |
| | 2.08 | -35.95 | 6.58 | 6.89 | 31 | 95.5 |

## VII. Conclusion

The primary objective this work is to design and analysis the simulation of different shaped (E, H and Combined E-H) compact and planar MPA array for multiband wireless applications. The ADS is used as the simulation tool for all the proposed antennas. Different antenna performance parameters like return loss, bandwidth, directivity, gain, radiation efficiency and axial ratios were analyzed for the proposed antennas. In future work, different types of feeding techniques can be used to analyze the overall performance of the antenna. Therefore, antennas can be fabricated practically and compared with the experimental results and simulated results.

## References


[1] R S. Kushwaha, D.K.Srivastava and J.P. Saini,"A multi-slotted wide micro strip patch antenna for dual frequency," *International Journal of Computer Science and Information Technologies (IJCSIT)*, vol. 3, no. 2, pp. 3523-3525, 2012.

[2] S.I. Joy and R. Rekha,"Design and analysis of a slotted E shaped micro strip patch antenna for indoor wireless applications," *Journal of Multidisciplinary Engineering Science and Technology (JMEST)*, vol. 1, no. 5, pp. 396-399, Dec. 2014.

[3] M.Vinoth and M.S. Bashyam,"Modified H-shaped micro strip array antenna for WiMAX application," *IOSR Journal of Electronics and Communication Engineering ( IOSR-JECE)*, vol. 9, no. 2, pp. 14-18, March-April 2014.

[4] R.T. Prabu, K. Ramu, M.G. Reddy and K.K. Reddy,"Design and implementation of E-shaped antenna for GSM/3G applications," *International Journal of Innovative Science, Engineering and Technology*, vol. 2, no. 4, April 2015.

[5] S. Kumar, A.K. Saurabh and N.S. Beniwal, "Dual band H shape rectangular micro strip patch antenna for WLAN/Wi-MAX/Bluetooth applications," *International Journal of Advanced Research in electrical, Electronics and Instrumentation Engineering*, vol.3, no. 3, March 2014.

[6] B.P. Narendra, "Micro strip patch antenna design for GPS application using ADS software," *Journal of Information, knowledge and Research in Electronic and Communication Engineering*, vol. 2, no. 2, pp. 475-478, Oct. 2013.

[7] M.Priya, B.Senthil and R.Priya, "Design and development of slotted H-shape micro strip patch antenna for Wi-Fi applications," *International Journal of Innovative Research and Studies*, vol. 4, no. 1, Jan. 2015.

[8] P. Jothilakshmi, R.K. Vigneshwaran, R.Narasimman and B.Praveen, "Design and development of quad band H shape micro strip patch antenna for Wi-Fi and LTE application," *WSEAS Transactions on Communications*, vol. 13, pp. 234-241, 2014.

[9] L.C. Paul, M.S. Hossain, S. Sarker, M.H. Prio, M. Morshed and A.K. Sarkar, "The effect of changing substrate material and thickness on the performance of inset feed micro strip patch antenna," *American Journal of Networks and Communications*, vol. 4, no. 3, pp. 54-58, June 2015.

[10] C.A. Balanis,"Antenna theory: analysis design," ISBN 0-471-66782-X, Third Edition, pp. 811, 2005.

# Design and Performance Analysis of GaInNAsSb/GaAs MQW VCSEL Operating at 1550 nm

Md. Rabiul Karim, Md. Asifur Rahman, Jobaida Akhtar, and Mohammad Istiaque Reja*
Department of Electrical and Electronic Engineering,
Chittagong University of Engineering and Technology, Chittagong-4349, Bangladesh.
*istiaque@cuet.ac.bd

*Abstract*—**In this paper, GaAs-based 1550 nm multiple quantum well (MQW) Vertical-Cavity Surface-Emitting Laser (VCSEL) is designed using GaInNAsSb as active material and GaNAs as potential barrier. Variation of active material composition and design of AlAs/GaAs Distributed Bragg Reflector (DBR) mirror have been performed to obtain high material gain. A maximum output power of 85 mW has been obtained at 16 mA injection current. Peak material gain coefficient has been found to be as high as 4400 cm$^{-1}$ at 1550 nm. Better photoluminescence (PL) spectra has been achieved at 1550 nm. The designed 1550 nm VCSEL can be constructed using widely used chemical-vapor deposition (CVD) and Molecular Beam Epitaxy (MBE) processes.**

***Keywords—Vertical-cavity surface-emitting laser (VCSEL), multiple quantum well (MQW), material gain, photoluminescence spectra.***

## I. INTRODUCTION

The ever increasing demand for high speed optical communication necessitates new technological approaches. Vertical cavity surface emitting lasers (VCSELs) of long wavelength (LW) has proven to have the capability to meet these demands [1]. Semiconductor lasers in the LW range around 1300 nm and 1550 nm are much needed devices in the optical fiber communication systems to get the advantage of lower transmission loss. The Edge Emitting Lasers (EEL) are now being replaced by VCSELs because of their significant advantages over EEL [2].

Due to problems of forming full epitaxial structures, VCSEL technology has been stuck to shorter wavelengths for a long period of time. After successful fabrication of LW VCSELs, most of the VCSELs were designed with InGaAsP as active material and InP as substrate. This InGaAsP/InP structure exhibits poor temperature properties [3].

There are some advantages of GaInNAsSb as active material. Nitrogen (N) helps to reduce the band gap for reaching longer wavelength and compensating for the compressive strain of the GaInAs [4]. The higher electronegativity of N and its smaller covalent radius cause an extraordinary behavior in the energy band properties when N is added to GaAs or GaInAs [5]. In this design GaAs is used as substrate because previously used InP-based materials exhibit poor temperature properties. They show band gap discontinuity at high temperature, need costly cooling mechanism. On the other hand, GaAs has high refractive index contrast, low lattice mismatch and high thermal conductance [6]. Previously used InGaAsP/InP structure has several critical limitations to be used for VCSELs in the LW range, which include poor combination of alloys that have much lattice mismatch and cannot provide a large difference in refractive index for the Distributed Bragg Reflectors (DBRs) required for VCSELs with reasonable thermal conductivity [5].

Use of Antimony (Sb) in the active material improves optical quality of the quantum wells (QWs). Because of the lack of suitable materials monolithic GaAs-based VCSEL operating at 1550nm is demonstrated for the first time recently with external cavity structure [4]. The addition of Sb to GaInNAs was a very important step to reaching wavelengths greater than 1500 nm. Before introduction of Sb, the quality of GaInNAs showed rapid degradation for the wavelength beyond 1300 nm when more Indium (In) and N were added to increase the wavelength. Sb was found to act as a surface surfactant to maintain the layer-by-layer growth at higher In and N compositions that could not be achieved without Sb. Addition of Sb helps to achieve significantly higher luminescence efficiency at longer lasing wavelengths [5].

GaInNAsSb/GaAs materials have been used in a few works before. M. A. Wistey et al. demonstrated long-wavelength (>1.5 $\mu$m) VCSEL [7], S. R. Bank et al. used it for edge-emitting laser [8] and Korpijärvi et al. used it for semiconductor based optical amplifiers [9]. VCSELs based on GaInNAs/GaAs have been previously demonstrated but at shorter wavelengths because of the absence of Sb [10]. S. R. Bank et al. and M. Guina et al. demonstrated VCSEL of 1.18 $\mu$m [8], [11], Korpijärvi et al. demonstrated VCSEL of 1.22 $\mu$m [12] and J. M. Hopkins et al. demonstrated VCSEL of 1.32 $\mu$m [13]. Korpijärvi et al. showed the effect of varying nitrogen composition of GaNAs barriers on the photoluminescence spectra [4]. The peak output power of LW VCSELs has increased to a good considerable margin. Alias et al. obtained 0.73mW in 2008 [6], P. S. Menon et al. obtained 9.51 mW in 2010 [14] and Korpijärvi et al. obtained 78mW at the end of 2015 [4]. Output power increased due to the addition of Sb. A. Islam obtained the material gain coefficient as 4200 cm$^{-1}$ [3].

In this paper, a GaInNAsSb/GaAs MQW VCSEL opeating at 1550 nm is designed which has higher material gain coefficient, better PL spectra in active region and greater output power. Material composition and thickness of GaInNAsSb QWs are optimized in this design.

978-1-5386-2307-7/17/$31.00 ©2017 IEEE

## II. DEVICE STRUCTURE OF VCSEL

Vertical cavity laser structure is almost same as that of the typical semiconductor laser. The only difference is that the VCSEL output beam is perpendicular and it emits from the top surface. It has active region consisting of QWs and these QWs are separated by the potential barrier layers. These barrier layers confine photons. At top and bottom of the active region there are two cladding layers for improving optical confinement. For resonator two DBR mirrors are used that are placed parallel to the active region. Current is injected through the upper p-type contact of the device and the lower n-type contact is connected to substrate.

For the VCSEL design highly reflective mirrors is needed for obtaining the required very small cavity length. In this regard, DBR mirror is used which is made up of several quarter wavelength thick layers of semiconductors of alternating high and low refractive index. The thickness of each layer of DBR is calculated by Eqn.1 [15].

$$T = \frac{\lambda}{4n} \tag{1}$$

Where

$\lambda$ = Light Wavelength
n = Refractive index of each layer
T = Thickness of the Layer

High reflectivity of the DBR mirrors is required and optimum number of layers are calculated so that the desired high reflectivity can be achieved. It is calculated by Eqn.2.

$$R = \left[\frac{(1-\frac{n_L}{n_H})^{2N}}{(1+\frac{n_L}{n_H})^{2N}}\right]^2 \tag{2}$$

Where

R = Reflectivity
$n_L$ = Refractive index of lower refractive index material
$n_H$ = Refractive index of higher refractive index material
N = Number of the layer.

For fabrication of VCSEL structures Chemical-Vapor Deposition (CVD) and Molecular Beam Epitaxy (MBE) processes are used in general.

## III. DESIGN OF VCSEL STRUCTURE

### A. Design of the active region

The structure of the designed VCSEL in this work is shown in Fig. 1. In this design, the active region comprises of 4 QWs of GaInNAsSb each separated by GaNAs potential barrier layer. In this structure, $Ga_{0.591}In_{0.409}N_{0.028}As_{0.89}Sb_{0.08}$ QWs of 8 nm thickness are surrounded by $GaN_{0.047}As$ barrier layers of 24 nm thickness on both side. After studying and analyzing performance of 1550 nm VCSEL for different concentrations, these concentrations of QW and barrier layer material composition have been chosen which shows optimum performance. The active region is surrounded by 2 cladding layers of GaAs at top and bottom that are used for

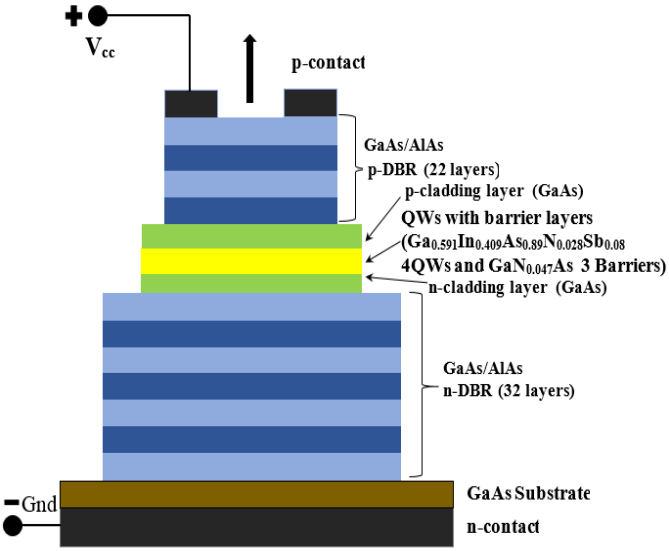


Figure 1. Structure of the designed VCSEL.

compensating the compressive strain [4]. Top cladding layer is p-doped and the bottom cladding layer is n-doped and energy bandgap of these 2 layers is 1.42 eV.

This active region is designed for 1550 nm wavelength VCSEL. The bandgap of the QW material is 0.8041 eV which almost corresponds to the 1550nm wavelength output. For this wavelength the barrier material is chosen $GaN_{0.047}As$ which has an energy bandgap 1.08 eV. The energy band diagram of the designed VCSEL structure is shown in Fig. 2.

The refractive index of QW material is 3.6893. The lattice constant of the barrier layer material $GaN_{0.047}As$ is 5.65325 and the refractive index is 3.5436. The barrier and the cladding layer are all fully lattice matched with the GaAs substrate [5].

### B. Design of DBR mirror

This active region is placed between a p-doped top and a n-doped bottom DBR mirror. GaAs/AlAs has been used as the DBR material as they are lattice matched and GaAs and AlAs

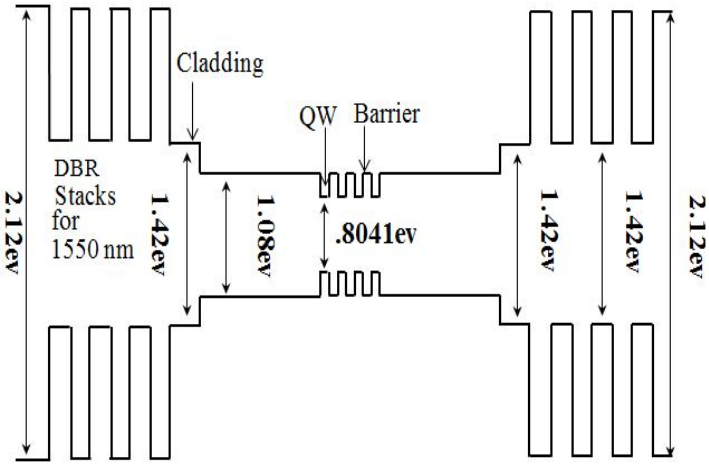


Figure 2. Energy band diagram of the designed VCSEL structure.

has low and high refractive index respectively. Due to the high refractive index contrast between these layers high reflectivity is obtained from the mirror. For the desired output beam of 1550 nm the thickness of the DBR mirror layers are calculated from Eqn.1. The refractive index of GaAs and AlAs at 1550 nm is 2.92 and 3.43 respectively. From calculation, thickness of GaAs and AlAs layers are obtained as 113 nm and 132 nm respectively. The number of layers of p-DBR and n-DBR required for attaining higher reflectivity is calculated from Eqn.2 and kept minimum. Total 32 layers are used for n-DBR and for p-DBR 22 layers are used. Doping concentration of both the p-DBR and n-DBR material is $3 \times 10^{24}$ $cm^{-3}$. Bandgap of GaAs and AlAs is 1.42eV and 2.12eV respectively.

## IV. Simulation Results and Discussions

The performance of the designed VCSEL is simulated using photonic integrated circuit simulator [16]. The photoluminescence (PL) spectra for the GaInNAsSb active region is shown in Fig. 3. From the PL spectra the peak spontaneous emission rate is obtained as $7.5 \times 10^{26}$ $cm^{-3}$/sec/eV at desired 1550 nm.

The material gain for the active region is depicted in Fig. 4. From this figure the peak material gain of the active region is obtained as 4400 $cm^{-1}$ at desired wavelength of 1550 nm.

The plot of reflectivity vs. wavelength for the top and bottom DBR mirror stack is shown in Fig. 5. From this figure it is shown that the reflectivity of the n-doped bottom DBR is 99.999% and the reflectivity of the p-doped top DBR is 98.5% at the desired lasing wavelength of 1550 nm. The thickness and number of layers of top and bottom DBR mirror and the thickness of the active region has been designed to attain this high reflectivity at 1550 nm.

The standing wave across the GaInNAsSb 1550nm VCSEL is illustrated in Fig. 6. For efficient operation of the laser it is required to design the antinode of the standing wave to overlap the QW position. From the figure it can be seen that the

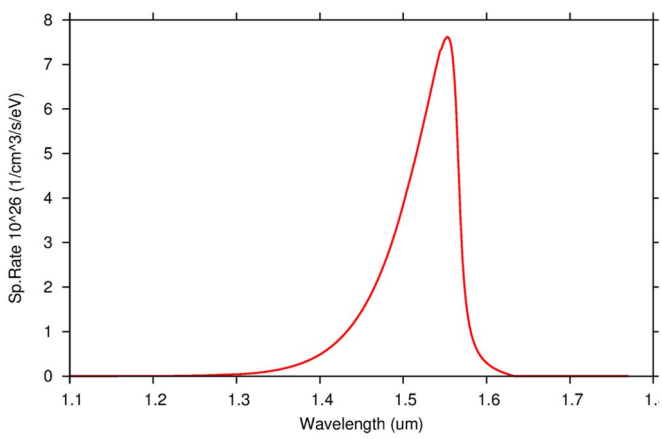


Figure 3. Photoluminescence spectra of the active region.

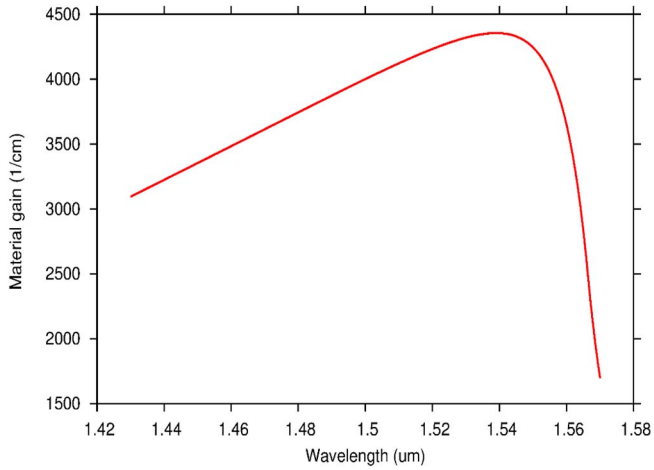


Figure 4. Material gain vs. wavelength for the active material.

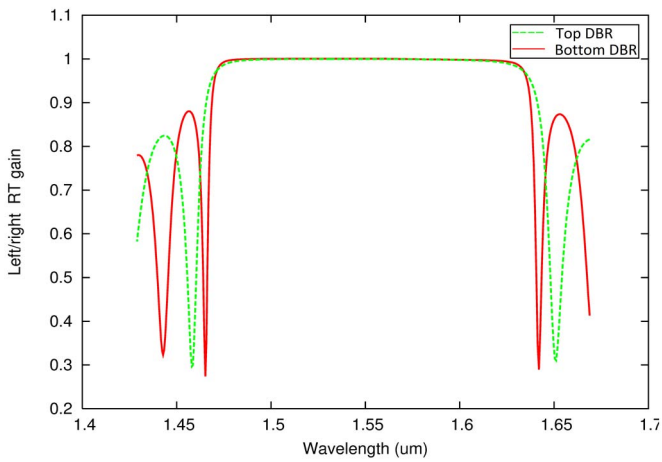


Figure 5. Plot of reflectivity vs. wavelength for top and bottom DBR.

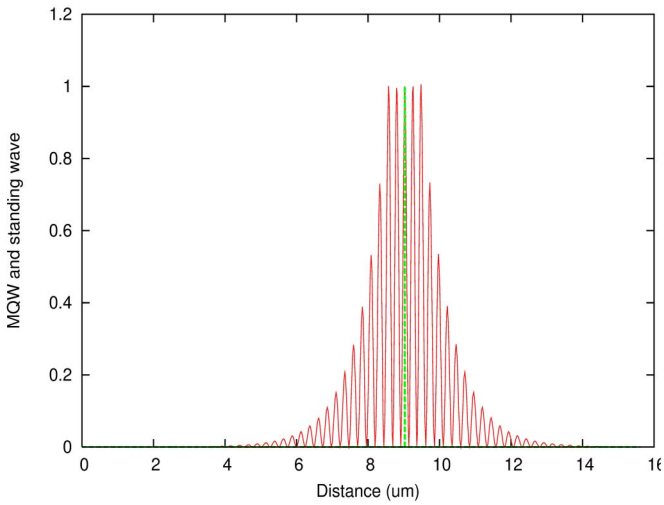


Figure 6. Standing wave profile across the VCSEL.

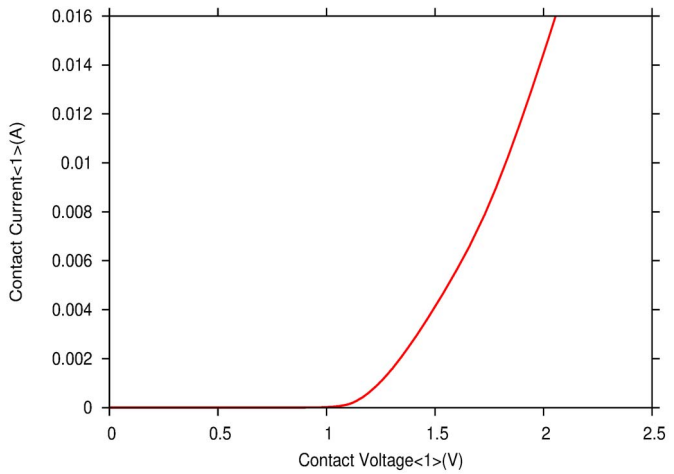


Figure 7. I-V characteristics for the GaInNAsSb VCSEL.

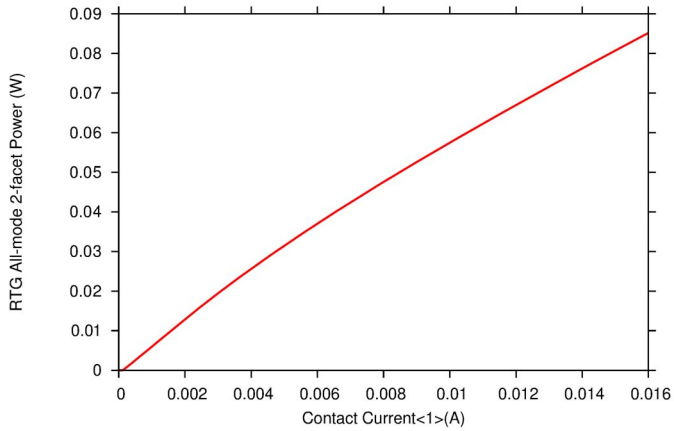


Figure 8. Output power vs. contact current for the designed VCSEL.

antinode of the standing wave is offset to the middle QW region. The highest standing wave is positioned in the middle of the structure approximately where the GaInNAsSb QW is located in the VCSEL structure.

The current-voltage (I-V) characteristic for this VCSEL is depicted in Fig. 7. From this figure the threshold voltage is seen to be 1.2 V and the threshold current for this VCSEL is 0.45 mA. After reaching threshold voltage, the contact current rises sharply with the increase of contact voltage.

The output lasing power vs. contact current curve is depicted in Fig. 8. Peak output lasing power for this VCSEL is 85 mW for injected current of 16 mA.

The output power spectra of the 1550 nm VCSEL designed in this work is depicted in Fig. 9. From this figure, it can be seen that the designed GaInNAsSb VCSEL emits laser beam output at 1550 nm with a higher single-mode output suppressing side modes. The side mode suppression ratio (SMSR) is approximately 100 dB which indicates good power relation between peak longitudinal mode and the side modes.

The comparison of obtained parameters of this work with previous works is shown in Table 1. from where notable improvements of different parameters are observed.

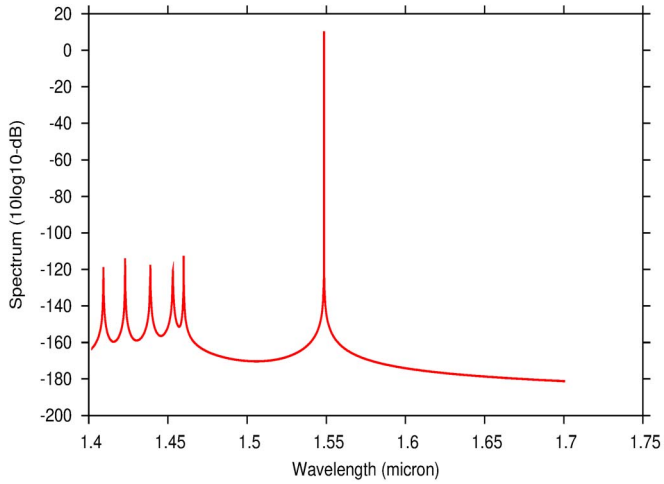


Figure 9. Output power spectra of the designed 1550 nm VCSEL.

TABLE I COMPARISON OF PARAMETERS WITH PREVIOUS WORKS

| **Works** | **Wavelength (nm)** | **QW Material** | **Material Gain Coefficient ($cm^{-1}$)** | **PL Spectra ($cm^{-3}$/sec/eV)** | **Peak Output Power (mW)** | **Side Mode Suppression Ratio (dB)** |
|---|---|---|---|---|---|---|
| [3] | 1550 | GaInAsN | 4200 | - | 7 | - |
| [4] | 1550 | GaInNAsSb | - | Arbitrary | 78 | - |
| [6] | 1310 | GaInNAs | 3600 | $1.6x10^{26}$ | 0.73 | 45 |
| [14] | 1550 | InGaAsP | - | - | 11.62 | - |
| Our Work | 1550 | GaInNAsSb | 4400 | $7.5x10^{26}$ | 85 | 100 |

## V. CONCLUSION

In this paper, the concentration of atoms in the quinary material of the active region is optimized and the structure of the VCSEL has been designed in such a way so that higher material gain and better photoluminescence spectra and higher output power can be achieved. Also, the number of layers in DBR mirror was kept minimum to obtain 99.999% reflectivity in bottom DBR and 98.5% reflectivity in top DBR. The characteristic curves show improved performance in terms of material gain, PL spectra and peak output power. Besides, standing wave profile, I-V characteristics and output power spectra are also analyzed. Material gain coefficient has been obtained as 4400 $cm^{-1}$ which is improved from [3]. Better PL spectra have been obtained at 1550 nm. The peak output power has been obtained as 85 mW for injected current of 16 mA which is improved from [4].

## REFERENCES


[1] Kenichi Iga, Fellow, IEEE, "Surface-Emitting Laser – Its Birth and Generation of New Optoelectronics Field", IEEE Journal of selected topics in Quantum Electronics, Vol. 6, No. 6, November/December 2000.

[2] David F. Welch, Senior Member, IEEE, "A Brief History of High-Power Semiconductor Lasers" , IEEE Journal of selected topics in Quantum Electronics, Vol. 6, No. 6, November/December 2000.

[3] A. Islam, S.I. Islam, S. Islam, "Designing an all epitaxial 1,550 nm intra-cavity VCSEL using GaInAsN/AlGaInAs in the active region and AlGaAsSb/AlAsSb in top and bottom DBRs". *Optical and Quantum Electronics,* vol. *45* no. 11, pp 1199-1212, 2013.

[4] V. M. Korpijärvi, E. L. Kantola, T. Leinonen, R. Isoaho & M. Guina, "Monolithic GaInNAsSb/GaAs VECSEL Operating at 1550 nm". *IEEE Journal of Selected Topics in Quantum Electronics,* vol. *21* , no.6, pp. 480-484, December 2015.

[5] J.S. Harris, H. Bae, T. Sarmiento, "GaInNAs(Sb) Long-Wavelength VCSELs". *Springer Series in Optical Sciences,* vol. *166* chapter 11, pp. 353-377, 2013.

[6] M. S. Alias, M. F. Maulud, S. Mitani, S. Shaari, & N. A. A. Manaf, "Design optimization of GaInNAs quantum wells for long wavelength VCSEL", *in Proc. of IEEE International Conference on Semiconductor Electronics*, Malaysia, 2008.

[7] M. A. Wistey *et al.*, "GaInNAsSb/GaAs vertical cavity surface emitting lasers at 1534 nm," *Electronics Letters*, vol. 42, pp. 282–283, 2006.

[8] S. R. Bank *et al.*, "11 W single gain-chip dilute nitride disk laser emitting around 1180 nm", *IEEE Journal of Quantum Electronics vol.* 43, no. 9 ,pp. 773–785,Sep. 2007.

[9] V. M. Korpijärvi *et al*., "1.55µm GaInNAsSb/GaAs ridge waveguide lasers and semiconductor optical ampilfiers for photonic integrated circuits." *in Proc. of* International Semiconductor Laser Conference 2014, pp. 151-152.

[10] V. M. Korpijärvi *et al.*, "Recent progress on 1.55-µm dilute nitride lasers", *Optical Express,* vol. 18, pp. 25633–25641, Sep. 2010.

[11] M. Guina *et al.*, "High-Power Disk Lasers based on dilute nitride heterostructures,"*New Journal of Physics, vol.* 11, pp. 125019, 2009.

[12] V. M. Korpijärvi *et al.*, "MBE grown GaInNAs-based multi-Watt disk lasers,"*Journal of Crystal Growth", vol.* 311, pp. 1868-1871, Mar. 2009.

[13] J.M. Hopkins *et al*., "0.6W CW GaIn NAs vertical external-cavity surface emitting laser operating at 1.32 $\mu$m", *Electronics Letters*., vol.40, pp. 30-31, 2004.

[14] P.S. Menon *et al*., "Peak power and wavelength optimization of a double-fused LW-VCSEL" *in Proc. of IEEE International Conference on Semiconductor Electronics*, Malaysia, 2010.

[15] Priyanka Goyal *et al*., "Design and analysis of VCSEL LASER for third window of optical communication system", *in Proc. of IEEE International Conference on Electrical, Electronic and Optimization Techniques*, India, 2016.

[16] PICS3D by Crosslight Software, 2017.

2017 3rd International Conference on Electrical Information and Communication Technology (EICT), 7-9 December 2017, Khulna, Bangladesh

# Millimeter-Wave Hexagonal Grid Microstrip Array Antenna for 5G Communication

Liton Chandra Paul, Md. Murshid Alam
Dept. of Electronic & Telecommunication Engineering
Pabna University of Science & Technology, Pabna-6600
litonpaulete@gmail.com, murshidpust@gmail.com

***Abstract*— In this paper, a new hexagonal grid microstrip array antennas (HGMAAs) has been proposed for upcoming 5G wireless communication systems. The grid microstrip array antenna (GMAA) is a good choice for 5G communication owing to the capability of acting in millimeter-wave range with having high gain, wide bandwidth and easy feeding. The performance and characteristics of HGMAAs are investigated and presented in this paper. All the performance characteristics of the proposed HGMAAs are analyzed by using commercially available CST version 2011 which is widely used by antenna researchers. It uses FDTD method for the simulation and analysis. The dielectric material Teflon ($\varepsilon_r$ = 2.1) was chosen as the substrate with the thickness of 0.8 mm and copper with the thickness of 0.02 mm as the patch and the ground plane. The total size of the both proposed antennas is 35×36 mm$^2$. To enhance the performance of the GMAA, hexagonal shaped cells are adopted. Both proposed HGMAAs radiate at around 28 GHz and show very good VSWR which are much closed to 1 as well as reduced return loss and better gain.**

***Keywords—HGMAA; 5G; mm-wave; CST.***

## I. INTRODUCTION

Wireless communication technology is already at the mature stage of fourth generation (4G) technology and now the wireless communication researchers are paying attention to the fifth generation (5G) technology. The wireless experts are expecting that the 5G wireless communication will be commercially available throughout the world within the next 2020 [1]. Millimeter wave (mm wave) means the range of 30 - 300 GHz having wave length in millimeter unit [2]. Millimeter wave technology is one of the most important aspect of the 5G wireless communication systems. It generally promises communication with very high speed and capacity [3-4] besides being applied in automotive radar systems [5]. Planar microstrip antenna is one of the best choices of the researcher for such mm wave applications because of having low profile and more economical property [6].

A microstrip grid array antenna (MGAA) is one sort of planar array antenna consisting of multiple cells or grids [7]. The length of the long side of each cell is usually one guided wavelength, while the short side is half as long. The long side of each loop works as a transmission line, while the short side works both as a transmission line and as a radiating element. The GAA was invented by J. Kraus in 1964 as a linearly polarized traveling wave (non-resonant) antenna with the main lobe of radiation in a backward fire direction [8]. The grid-array antenna was implemented in microstrip technology by Conti et al. in 1981 as a linearly polarized standing-wave (resonant) antenna, with the main beam of radiation in the broadside direction [9]. In 1990s, the GAAs became more popular due to its low profile, ease of fabrication, high gain, having high impedance bandwidth and simple feeding structure [10-11]. The grid array antennas are also suitable for higher mm wave applications. It was observed that the substrate choice influences the performance of the MGAAs [12-13]. Therefore, Teflon substrate is selected in this work. Based on these criteria, it's a good candidate for future use.

In [14], the author proposed a 9×12.66×1.5 mm$^3$ bent line MGAA at 28 GHz for 5G communication. The antenna was made on FR4 substrate having dielectric constant ($\varepsilon_r$) of 4.3 and loss tangent ($tan\ \delta$) of 0.01. The thickness of substrate and copper layer were 1.5 mm and 1.6 mm respectively. The obtained bandwidth of the antenna was of 3.65 GHz as well as the antenna grid area reduction factor was of 66.91% due to the use of bent line in the grid.

M. R. Ramli et al. analyzed a MGAA having 12 grids on three different substrates namely Rogers RT5880LZ, Taconic RF43 and FR4 at 15 GHz for 5G applications. The -10dB bandwidth for the aforementioned three substrates are of 2.76 GHz (14.06-16.82), 1.64 GHz (14.39-16.03) and 1.26 GHz (14.24-15.49) respectively [1].

In [11] the authors proposed a new MGAA with elliptical cells having overall antenna size of 126mm×100 mm. The antenna uses PCB as dielectric substrate with relative permittivity ($\varepsilon_r$) of 2.65 and thickness (h) of 1mm. The 4 mm thick aluminum board was used as ground plane. The maximum gain of the antenna is 15.1 dBi at 5.8 GHz and it has the bandwidth for $S_{11}$ < -10 dB and 3 dB gain-drop of 25% and 16.3% respectively. The corresponding authors of [12] widely described MGAAs considering different meshes on different substrate materials at mm wave frequencies. They claimed that the MGAA exhibits better performance at the parallel resonance instead of at the series resonance.

Z. Chen et al. designed an MGAA using FR4 substrate material at 29.2 GHz. The size of the antenna is 15×15×0.5 mm$^3$ and it showed bandwidth (at -10dB) of 7.16 GHz ranging from 23.86 GHz to 31.02 GHz [15].

978-1-5386-2307-7/17/$31.00 ©2017 IEEE

Rapid growth in the wireless technology with huge number of users as well as increasing the number day by day and limited bandwidth demands for an antenna which can operate at mm wave frequency. MGAA is one of suitable choices that can fulfill the requirement of the new era of 5G communication technology. One major disadvantage of the microstrip antenna is low gain but one of the characteristics of the GAA is high gain. By increasing the thickness of the grid array antenna, it can overcome the narrow bandwidth problem [16]. By choosing the appropriate cell shape, right numbers of cells, the performance of the MGAA can be enhanced. In this work, we designed, simulated and proposed new MGAA consisting of hexagonal cells.

However, the following sections of the paper are presented as follows: the section II represents the proposed hexagonal GMAAs geometry and the simulated results analysis. The brief design summary is clearly visualized in the section III. Finally, some effective conclusions are drawn and future scopes are pointed out in the section IV.

## II. Hexagonal Grid Microsrip Array Antennas

In this section, the antenna design steps will be discussed from the design of basic hexagonal block or cell until the optimization of dimension of hexagonal cell and antenna geometry in order to get the best result. The geometry of the mesh plays an important role in the performance of hexagonal grid array Antenna.

### *A. Antenna Geometry*

Antenna design process is started by designing a hexagonal block or cell of the antenna. Each single hexagonal block or cell is designed by using the equation of guided wavelength which depends on some parameters such as desired operating frequency and permittivity of substrate. Then, the single hexagonal block or cell is arranged in grid array form which composes of radiating element and transmission element. There are a few factors that need to be considered during design a grid array antenna in CST which are substrate parameters, mesh geometry and feeding type. Table I shows the dimension of substrate with some others design parameters of the proposed grid array antenna.

TABLE I DESIGN PARAMETERS OF GRID ARRAY ANTENNA

| Name of the parameter | Value |
|---|---|
| Substrate length (L) | 35 mm |
| Substrate width (W) | 36 mm |
| Substrate thickness (h) | 0.8 mm |
| Ground plane thickness ($h_g$) | 0.02 mm |
| Dielectric constant ($\varepsilon_r$) | 2.1 |
| Loss tangent (tan δ) | 0.0002 |

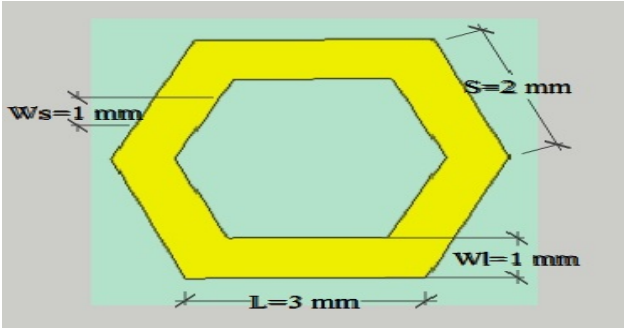


Fig.1. Hexagonal grid element

A single hexagonal grid or block having four short (s) sides and two long (l) sides is shown in Fig. 1. The length and width of the long side of each hexagonal grid are $L$ = 3 mm and $Wl$ = 1 mm respectively. For the short side of hexagonal grid, the length and width are $S$ = 2 mm and $Ws$ = 1mm respectively. All those dimensions of the grid are indicated in the Fig.1. Here short sides (s) work as the radiating elements as well as transmission lines. On the other hand, long sides (l) perform only as the transmission lines.

Fig.1 and Fig. 2 show front view of our two proposed hexagonal grid microstrip array antennas (HGMAAs). One is composed of 12 hexagonal cells with 40 radiating elements on the substrate as shown in Fig.2 and another is composed of 10 hexagonal cells with 36 radiating elements on the substrate as shown in Fig.3. The proposed both HGMAAs are designed on Teflon material considering as substrate ($\varepsilon_r$ = 2.1, tan $\delta$ = 0.0002) and simulated by using professional CST microwave studio 2011. And finally the gain, VSWR, reflection coefficient ($S_{11}$) and radiation patterns are optimized of the designed both HGMAAs. The dimension of the substrate of the antennas is 35×36 mm and for both antennas copper metal is used in the ground plane which is shown in Fig. 4.

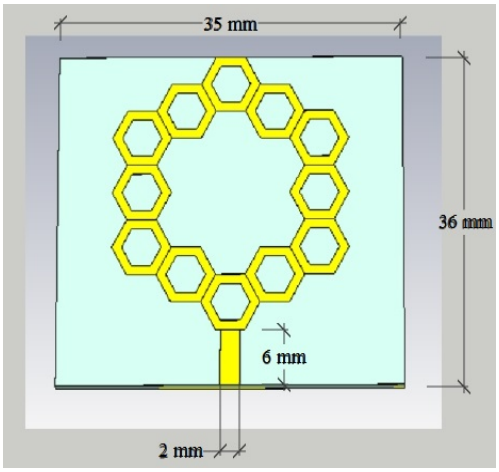


Fig. 2. Front view of 12 hexagonal GMAA

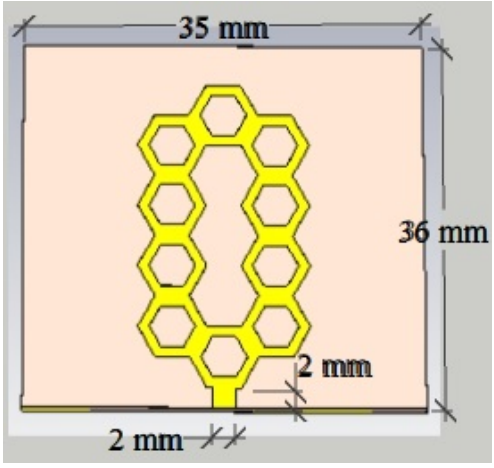


Fig. 3. Front view of 10 hexagonal GMAA

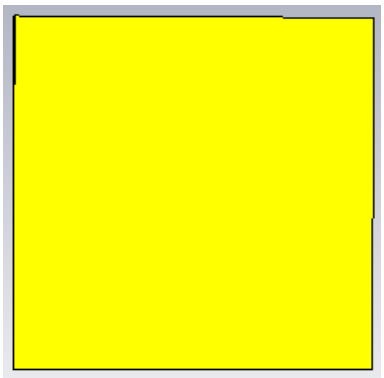

Fig. 4. Back view for both HGMAAs

## B. *Simulation Results and Analysis*

CST microwave studio software, version 2011, was used as the simulation tool to estimate the performance for the both proposed antennas having 12 hexagon and 10 hexagon blocks. Different performance parameters of the proposed HGMAAs such as return loss, both IEEE and realized gain, directivity, bandwidth, VSWR, axial ratio, power patter and radiation pattern are simulated and estimated using the aforementioned software. Fig. 5 and Fig. 6 show the return loss curves for the proposed 12 cells and 10 cells antennas.

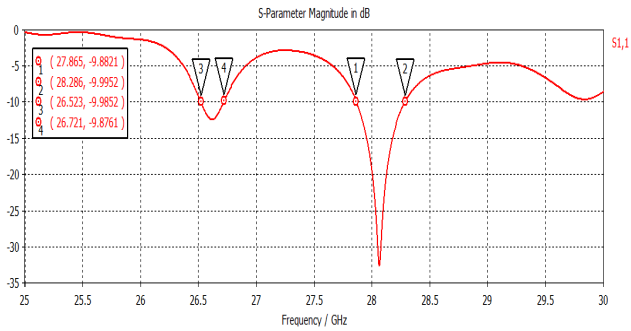


Fig. 5. Return loss curve for 12 cells HGMAA

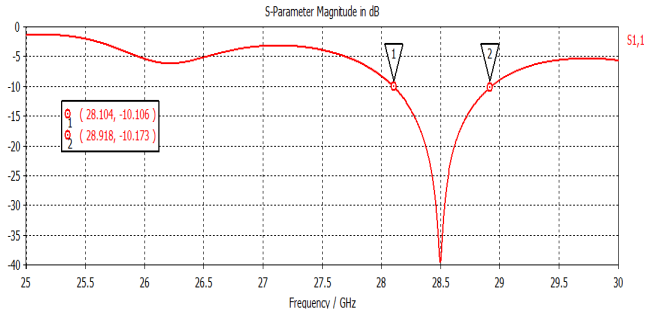


Fig. 6. Return loss curve for 10 cells HGMAA

From the curves, it is seen that the 12 grids antenna operates on dual bands of 26.614 GHz and 28.065 GHz center frequency as well as the antenna possesses return loss of -12.416 dB and -32.597 dB at the center operating frequency of the respective bands. It covers bandwidths of 198 MHz and 921 MHz bandwidth for the dual operating frequency bands respectively. On the other hand, proposed 10 grids antenna operates on single bands of 28.5 GHz center frequency and it shows returns loss of -39.5589 dB and bandwidth of 814 MHz. The real and imaginary values of *S* parameter ($S_{11}$) for 12 cells and 10 cells HGMAAs are presented in Fig. 7 and Fig. 8 respectively.

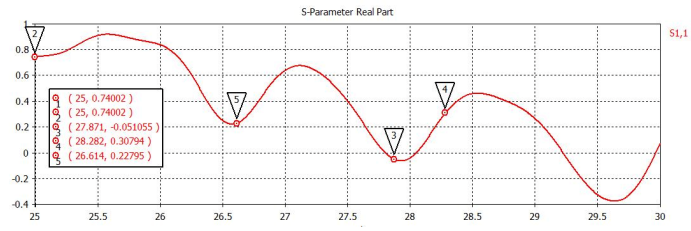


(a) Real part

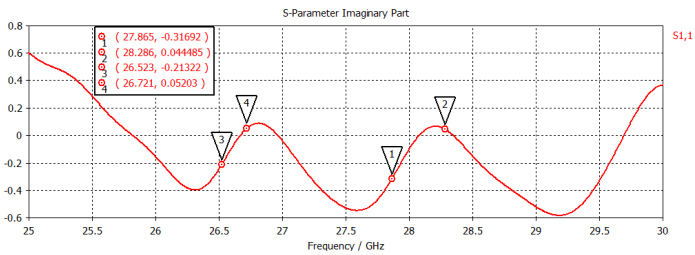


(b) Imaginary part

Fig. 7. Real and imaginary part of *S* parameter for 12 cells HGMAA.

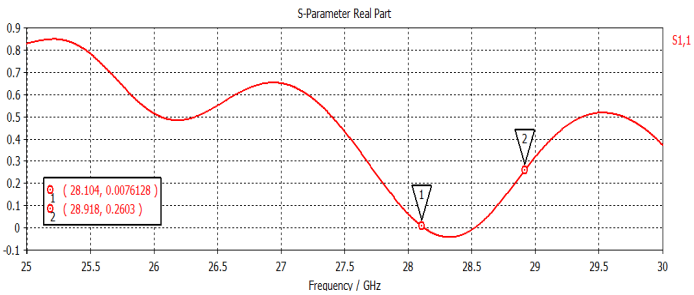


(a) Real part

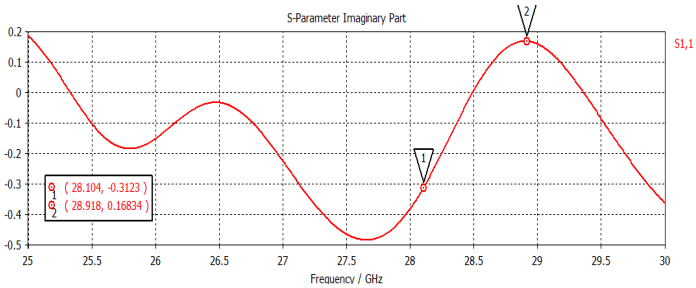


(b) Imaginary part

Fig. 8. Real and imaginary part of *S* parameter for 10 cells HGMAA.

We obtained realized gain of 5.536 dB and IEEE gain of 8.046 dB for 12 grids HGMAA as shown in Fig. 9 as well as realized gain of 6.595 dB and IEEE gain of 8.841 dB for 10 HGMAA as shown in Fig. 10 which are describing how much power from the antenna is radiated along the direction of major lobe to that of an isotropic antenna.

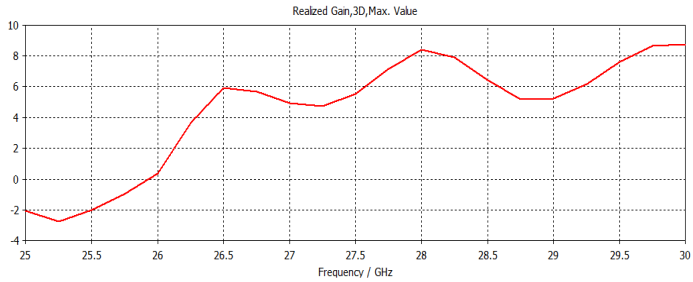


(a) Realized gain

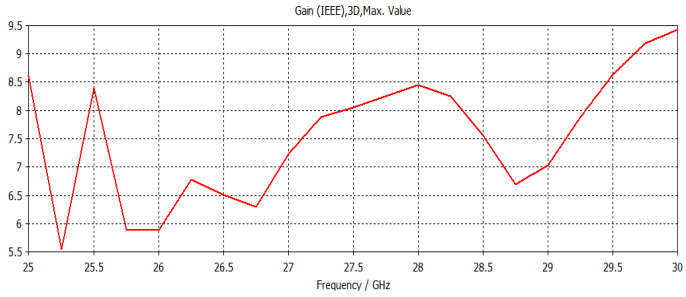


(b) IEEE gain

Fig.9. Realized and IEEE gain for 12 cells HGMAA

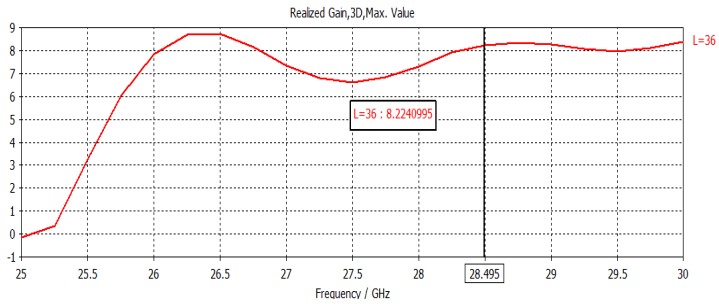


(a) Realized gain

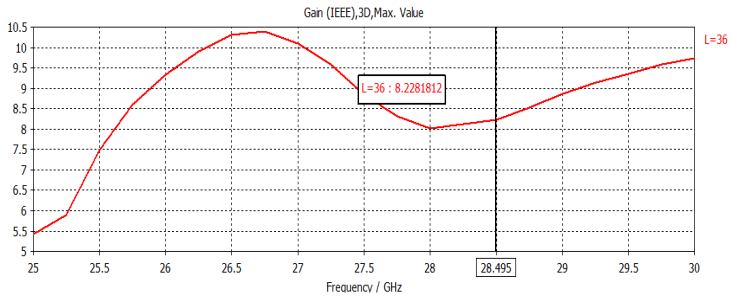


(b) IEEE gain

Fig.10. Realized and IEEE gain for 10 cells HGMAA

Directivity is a yardstick of the measurement of how directional an antenna is. An antenna having zero directionality radiates uniformly along all axes it means that it has 1 directivity i.e. 0 dB. Our proposed 12 cells HGMAA has directivity of 8.449 dB as shown in Fig. 11 whereas the 10 cells HGMAA has of 9.228 dB as shown in Fig. 12. Antenna having lower directivity is more suitable for such devices or applications where it is necessary to receive and transmit in various directions such as wifi, mobile phone etc.

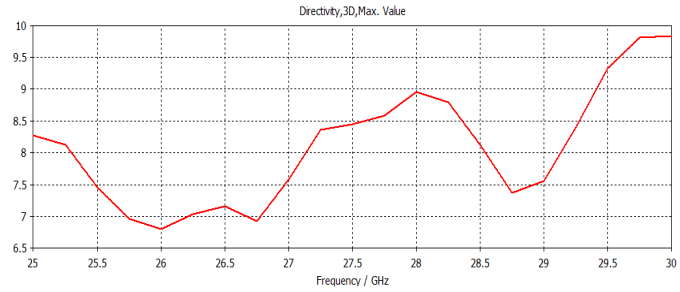


Fig. 11. Directivity of 12 cells HGMAA

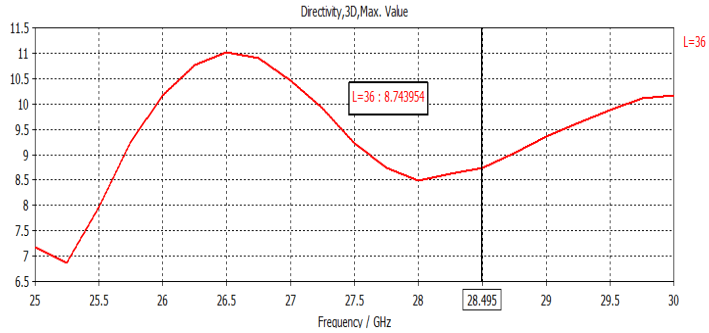


Fig. 12. Directivity of 10 cells HGMAA

Voltage standing wave ratio (VSWR) of 12 blocks proposed HGMAA (shown in Fig. 13) is of 1.048 and 1.63 at operating frequency 28.06 GHz and 26.614 GHz respectively whereas VSWR is of 1.021 at operating frequency 28.495 GHz for 10 blocks proposed HGMAA (shown in Fig. 14) which is the indication of perfection level of impedance matching. The polar and 3D plot of radiation patter of the both proposed antennas are presented in Fig. 15 and Fig. 16.

Fig. 17 and Fig. 18 show the smith chart and phase versus frequency curve of the designed 12 cells and 10 cells hexagonal grid microstrip array antennas. $S_{11}$ parameter for the proposed 10 cells HGMAA configuration indicates

comparatively more impedance matching condition than for the proposed 12 cell HGMAA.

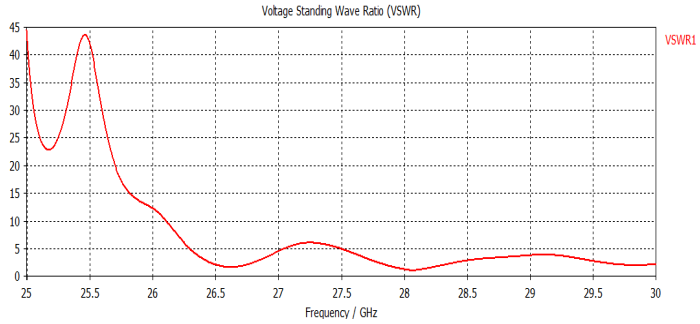


Fig. 13. VSWR of 12 cells proposed HGMAA

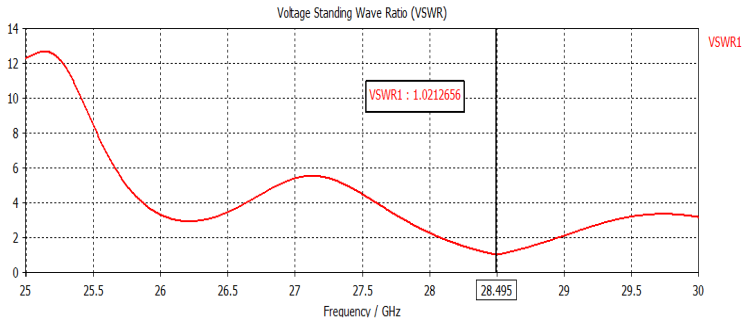


Fig. 14. VSWR of 10 cells proposed HGMAA

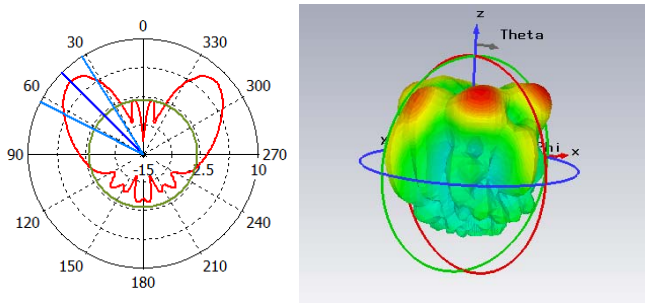


(a) Polar (b) 3D

Fig. 15. Radiation pattern of 12 cells HGMAA

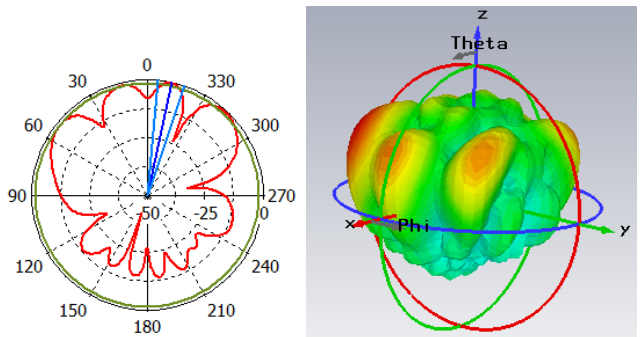


(a) Polar (b) 3D

Fig. 16. Radiation pattern of 10 cells HGMAA

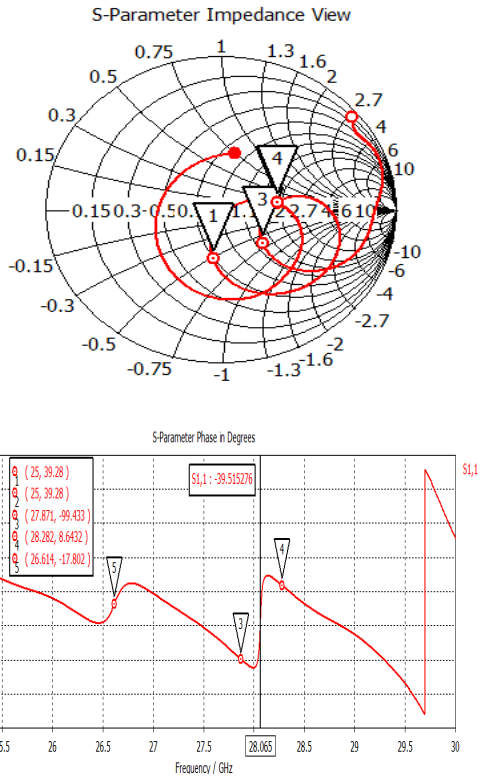


Fig. 17. Smith chart and phase curve of 12 cells proposed grid array antenna

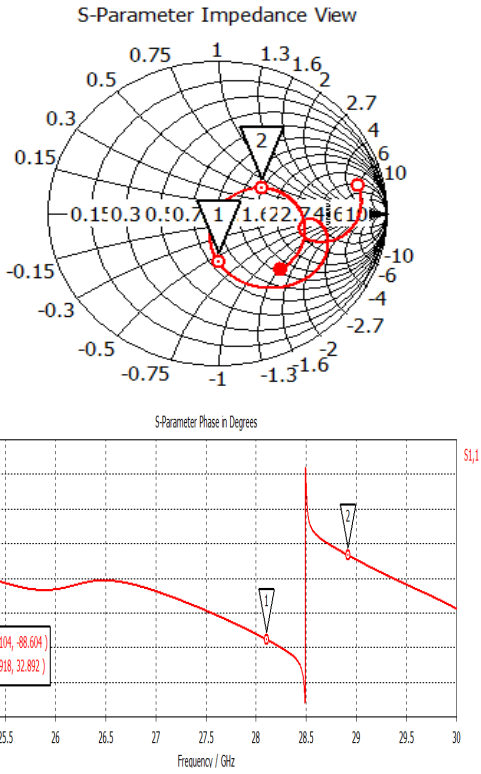


Fig. 18. Smith chart and phase curve of 10 cells proposed grid array antenna.

## III. DESIGN SUMMARY AND COMPARISON

This section represents the summary of the proposed 12 cells HGMAA and 10 cells HGMAA as well as a clear comparison between them. All the performance characteristics of both 12 cells and 10 cells Hexagonal GMAAs are listed in table II. The cell geometry of MGAA depends on the designer [17] which plays a great role on the radiation characteristics of the antenna this is because of the dimension of each grid array antenna may cause the antenna be resonant or non-resonant. In this work, hexagonal shaped grid is used instead of conventionally used rectangular grid. Finally, our proposed Hexagonal GMAAs provide better gain, directivity, reduced return loss, improved bandwidth and excellent VSWR which are much closed to unity (1).

TABLE II PERFORMANCE PARAMETERS OF THE PROPOSED HGMAAs

| Parameters | 12 Cells HGMAA | | 10 cells HGMAA |
|---|---|---|---|
| Center frequency (GHz) | 26.614 | 28.065 | 28.495 |
| -10dB BW (MHz) | 198 | 921 | 814 |
| Return loss (dB) | -12.416 | -32.597 | -39.558 |
| Realized Gain (dB) | 5.536 | | 6.595 |
| IEEE Gain (dB) | 8.046 | | 8.841 |
| Directivity (dB) | 8.449 | | 9.228 |
| VSWR | 1.63 | 1.048 | 1.021 |

## IV. CONCLUSION AND FUTURE WORKS

The operating frequency, bandwidth, gain, VSWR and radiation pattern depend not only on the geometry of the HGMAA but also on the number of cells used in the grid array. In order to optimize the efficiency and the performance of the designed antennas, the length and width of short side as well as long sides of the hexagonal cells are studied by trial and error method. Mainly, two hexagonal MGAA having excellent VSWR and reduced return loss has been designed and analyzed using CST 2011. The proposed both HGMAAs have around 28 GHz center operating frequency which is in mm-wave frequency for 5G communication. The proposed 10 cells hexagonal MGAA comparatively shows overall better performance than the proposed 12 cells HGMAA. Furthermore, in future, we are highly interested to fabricate the HGMAA in our laboratory and want to buttress our simulated analysis of the antennas.

## REFERENCES


[1] M.R. Ramli, S. Kamal, A. Rahim, M. Idzam and M.L. Samingan, "Performance analysis of microstrip grid array antenna on different substrates for 5G mobile communication," *Journal of Telecommunication, Electronic and Computer Engineering*, vol. 8, no. 6, pp. 1-4, 2016.

[2] W. Hong,"Millimeter wave antennas and arrays," *A Handbook of Antenna Technologies*, Springer Singapore, Online ISBN: 978-981-4560-75-7, pp. 1-53, 26 Feb. 2015.

[3] M. Nedil, L. Talbi and T.A. Denidni,"Design of broadband printed slot antennas for wireless millimeter-wave applications," *IEEE Topical Conference on Wireless Communication Technology*, pp. 23-24, 15-17 Oct. 2003.

[4] K. Sakakibara, N. Kikuma and H. Hirayama, "Travelling-wave planar array antennas for beamscanning systems in millimeter-wave band," *IEEE Asia-Pacific Conference on Applied Electromag-netics (APACE)*, pp.1-3, 8-10 Dec. 2014.

[5] Y. Niu, Y. Li, D. Jin, L. Su and A.V. Vasilakos, "A survey of mil-limeter wave (mmWave) communications for 5G: opportunities and challenges," *Journal Wireless Networks*, Springer-Verlag New York, vol. 21, no. 8, pp. 2657–2676, 9 April 2015.

[6] Y. Hayashi, K. Sakakibara, M. Nanjo, S. Sugawa, N. Kikuma and H. Hirayama,"Millimeter-wave microstrip comb-line antenna using reflection canceling slit structure," *IEEE Trans. Antennas Propag*., vol. 59, no. 2, pp.398–406, 2011.

[7] M. Sun and Y.P. Zhang, "*Grid Antenna Arrays*," Handbook of Antenna Technologies, Springer Singapore, Online ISBN 978-981-4560-75-7, pp. 1-23, March 2015.

[8] J. Kraus,"*A Backward Angle-Fire Array Antenna*," *IEEE Transactions on Antennas and Propagation,* vol. 12, no. 1, pp. 48–50, Jan. 1964.

[9] R. Conti, J. Toth, T. Dowling and J. Weiss, "The Wire-Grid Microstrip Antenna", *IEEE Transactions on Antennas and Propagation*, vol. AP-29, pp. 157-166, Jan. 1981.

[10] H. Nakano, I. Oshima, H. Mimaki, K. Hirosea and J. Yamauchi, "Center-fed grid array antennas," *IEEE International Symposium on Antennas and Propagation*, vol. 4, pp. 2010–2013, July 1995.

[11] X. Chen, G. Wang and K. Huang,"A novel wideband and compact microstrip grid array antenna," *IEEE Trans. Antennas Propag.*, Vol.58, no. 2, pp. 596–599, 2010.

[12] B. Zhang and Y.P. Zhang, "Analysis and synthesis of millimeter-wave microstrip grid-array antennas," *IEEE Antennas Propag. Mag.*, vol. 53, no. 6, Dec. 2011.

[13] L.C. Paul, M.S. Hosain, S. Sarker, M.H. Prio, M. Morshed and A. K. Sarkar,"The Effect of Changing Substrate Material and Thickness on the Performance of Inset Feed Microstrip Patch Antenna," *American Journal of Networks and Communications,* vol. 4, no. 3, pp. 54-58, 2015.

[14] S. Hakimi and S.K.A. Rahim,"Millimeter-wave microstrip Bent line Grid Array antenna for 5G mobile communication networks," *Asia-Pacific Microwave Conference (APMC)*, pp. 4-7 Nov. 2014.

[15] Z. Chen and Y.P. Zhang,"FR4 PCB grid array antenna for millimeter-wave 5G mobile communications," *IEEE MTT-S International Microwave Workshop Series on RF and Wireless Technologies for Biomedical and Healthcare Applications (IMWS-BIO)*, 9-11 Dec. 2013.

[16] D.M. Pozar,"A Review of Aperture Coupled microstrip Antennas: History, operation, Development and Applications," *IEEE Letters*, May, 1996.

[17] B. Zhang, L. Zhang and Y.P. Zhang, "Design of Low Cost Linearly-Polarized Microstrip Grid Array Antenna for 24 GHz Doppler Sensors," *International Topical Meeting on & Microwave Photonics Conference*, *Asia-Pacific MWP/APMP Microwave Photonics*, 18-21 Oct. 2011.

# Electron Beam Ni-layer Deposited $LaTiO_2N$ Photoanodes for the Enhanced Photoelectrochemical Performance of Water Oxidation

Md. Abdulla-Al-Mamun[1,2,3], and Kazunari Domen[3]
[1]Institute of Leather Engineering and Technology, University of Dhaka, Dhaka-1209, Bangladesh
[2]Deparment of Leather Engineering, Khulna University of Engineering & Technology, Khulna-9203, Bangladesh
[3]Deparment of Chemical System Engineering, School of Engineering, The University of Tokyo, Tokyo-113-8656, Japan
almamunchem@gmail.com

*Abstract*— **Improving the photoconversion efficiency of $LaTiO_2N$ photoanodes is crucial in the strong oxidizing conditions and in high overpotential of four-electron water oxidation system. It is essential for electrode to improve simultaneously reduce the recombination, photo/chemical corrosion resistivity and optical losses. In our present study, the photoelectrode has been fabricated by homogeneous CoOx co-catalyst aided by impregnation annealing method and coated with an ultrathin Ni layer by electron beam evaporation method (EB). The fabricated electrode was transferred to a three-electrode photoelectrochemical (PEC) cell system and electrodeposited of cobalt-phosphate (Co-Pi) loading as an oxygen evolution (OER) co-catalyst. The CoPi deposition was fixed and variable the Ni-coating and CoOx co-catalysts for optimization the best results of electrode. The optimal 2 nm Ni coating with 3wt% CoOx-co-catalyst loading on electrode, resulted in significantly enhanced the photocurrent and PEC water oxidation performance. The Ni and CoOx-modified $LaTiO_2N$ electrode serve as a highly active $O^{2-}$ evolving photoanode achieving 3.7 mA $cm^{-2}$ of the photocurrent density at 1.23V versus reversible hydrogen electrode ($V_{RHE}$) in 0.2 M $K_2HPO_4$ solution (adjusted pH 13 by addition of NaOH) under solar simulator irradiation Airmass 1.5 Global (AM 1.5G). The current-voltage was optimized off all modified electrode and found the maximum solar to energy conversion efficiency is 0.61% with IPCE 35% at 480 nm wavelength at 1 $V_{RHE}$. The maximum amounts of evolved $O_2$ and $H_2$ were found 16 and 32 µmol for two hours at 1 $V_{RHE}$ of optimal technique CoPi-Ni-modified CoOx-$LaTiO_2N$ electrode (CoPi/Ni/CoOx/$LaTiO_2N$/Ta/Ti) respectively. The optical transparency of the ultrathin Ni coating establishing as a particularly advantageous treatment for efficient and stable water oxidation photoanodes.**

***Keywords—$LaTiO_2N$; Ni-furnish; Photocatalysis; Water splitting; Oxynitrides; Oxygen Evolution; Cocatalyst; Ammonolysis.***

## I. INTRODUCTION

Photoelectrochemical (PEC) water splitting is an important technology as a means of solar-to-fuel conversion. Scarcity and increasing demand of energy sources such as oil and gas and awareness of severe environmental harm due to their combustion are accelerating the search for renewable, environmental-friendly energies. One attractive alternative concept is the direct energy transfer from solar radiation into chemical energy by using a semiconductor that absorbs photons and releases the energy gain *via* photocatalytic or photoelectrochemical water splitting into $H_2$ and $O_2$ [1-4]. Oxynitrides with a bandgap < 3 eV are an appealing class of materials since they absorb visible light that accounts for the major part of solar energy [5-10]. Much research effort has been spent on oxynitrides absorbing wavelengths up to 600 nm, establishing a number of active compounds for water oxidation/reduction half reactions such as $LaTiO_2N$ [11].

$LaTiO_2N$, which shows photocatalytic $O_2$ evolution from water using photons approaching 600 nm which allowing to the harvest the visible-sunlight more efficiently. The appropriate band gap, reasonable photocatalytic activity, and earth-abundant compositional elements implies promising application of $LaTiO_2N$ in the fields of photocatalysis and optoelectronics [11].

Most $LaTiO_2N$ semiconductor electrodes extensively studied to date are not stable in strong oxidizing conditions, which are relatively difficult to simultaneously improved the current-efficiency and longtime stability in high overpotential of four-electron water oxidation system. Therefore, there is a tremendous interest to identifying and preparing the cost-effective, highly efficient $LaTiO_2N$ photoanodes with a stable in high oxidizing conditions, good charge transport properties, and efficient for water splitting.

With the goal to achieve overall water splitting, activity for the individual half reactions must be improved first. With respect to the quality of photocatalytic materials, it is generally considered that high crystallinity, low defect densities, high dispersion, and large surface areas improve photocatalytic activity. Since the manifold requirements on a semiconductor (efficient light absorption, charge separation and transport, and surface redox reactions) are difficult to meet by a single-component material, heterostructures of photocatalysts and cocatalysts emerge indispensable and further work on both aspects is on-going [12]. Cocatalysts loaded on photocatalysts can enhance photocatalytic activity by providing active centers for the oxidation/reduction reactions and by improving charge carrier separation and lifetime.

978-1-5386-2307-7/17/$31.00 ©2017 IEEE

We have reported that the surface modification using thin Ni layers by EB-deposition was enhanced the anodic photocurrent from CoOx-$LaTiO_2N$ photoanodes as well increases the stability. The Ni metal-layer acted as a surface protection layer against corrosion and as a nonprecious metal electrocatalyst for oxygen evolution and electron tunneling with reduce the overpotential [13]. The Ni-dispersion modification on the surface of $LaTiO_2N$ also be protect the $Ti^{3+}$cations-defects from being reduced during the nitridation synthesis and light irradiation by forming of Ti–O–Ni bonds [14].

In this study, we demonstrate that the efficiency and photostability of CoOx/$LaTiO_2N$ photoanode is greatly improved by the Ni-layer surface modification. The EB deposited Ni-layer is effective for oxygen evolution and stability. The Ni and CoPi modified CoOx/$LaTiO_2N$ photoanode yielded high photocurrent density and durability rather than bare CoOx/$LaTiO_2N$/Ta/Ti electrode.

## II. EXPERIMENTAL SECTION

### *A. Powder $LaTiO_2N$ sample preparation*

Powder samples were prepared by the flux method. The preparation of the precursor and the experimental setup was described elsewhere [15, 16]. Typically, appropriate amounts of the raw powders of $La_2O_3$ (Kanto Chemical, 99.99%) and $TiO_2$ (Kanto Chemicals Co., 99.99%) were thoroughly mixed with flux agents of NaCl (Wako Pure Chemicals Co., 99.5%) with the molar ratio of La : Ti : Na = 1 : 1 : 10 in an ethanol media. After 1 h of mixing, the dried mass was placed in an alumina crucible to be heated at 1150 °C for 5 h at the heating rate of 10 °C min¯1. Subsequently, the sample was cooled to 800 °C at the cooling rate of 10 °Cmin¯1, and finally naturally cooled to room temperature. The product mass was washed more than 3 times and filtered with addition of sufficient amount of distilled water to dissolve any unreacted raw material and to completely remove the flux agents. The $La_2Ti_2O_7$ powders were obtained dried at 70 °C in an oven at overnight. Finally, $LaTiO_2N$ particles were obtained by thermal ammonalysis of the $La_2Ti_2O_7$ precursor at 950 °C for 5 h under an ammonia flow (Sumitomo, 99.9995%) of 250 mL min-1 in held by a quartz wool with a vertical-tube reactor.

### *B. CoOx loading onto powder $LaTiO_2N$*

0.1 g of $LaTiO_2N$ were taken in a glass tube, then the calculated amount of $Co(NO_3)_2$ was added with a 1 mL of water. Then the tube was attached with an evaporator (Eyela EVP-1000, Tokyo Rikakikai Co.) and setting the 10 hPa pressure and 50 ºC temperature. After attain the temperature and pressure, the shaking was start and continue until one hour. After that, collecting the impregnated powder and was transferred into a sealed alumina tube and heated at 550 °C for 1 h with 50 mL·min$^{-1}$ of $NH_3$ flow.

### *C. Electrod Fabrication by particles transfer (PT) method*

III. The required particles dispersed onto a glass substrate to file up the powder was carried out using the suspension of powder in isopropanol with a concentration of 25 gL¯ followed by drying as described elsewhere [17]. The contact layer Ta and conductor layer Ti were deposited by radio-frequency (RF) magnetron sputtering at a RF power of 200 W, an Ar-pressure ~0.3Pa, target to substrate length 70 mm and substrate temperature of 300 °C. Deposition time for the contact layer was 5 min with the rate of 2 Å/s and for conductor layer ~9 h with the rate of 1.33 Å/s. The thicknesses of the contact and conductor layers were estimated to be ~60 nm and 5~6 µm, respectively. After finished the sputtering, the thin layer were transferred to a glass-supported plastic sheet (thickness ca. 120 µm) by a hot plate assisted temperature (150~200 ºC). The melting conditions of plastic as for particles transfer gave the advantage to uniformly and homogeneously monolayer transfer, which is better than conventional carbon tape particles casting. After finishing the particles transfer, the assembly was sonicated in distilled water to remove excess particles of the particle layer. Finally, this assembly was connected with a soldered lead wire and molded with epoxy resin over the surface except an area where $LaTiO_2N$ particles were exposed for photoelectrochemical measurements.

### *D. Electron beam evaporation assisted Ni thin layer surface modification onto CoOx/LaTiO2N electrode*

Thin layer of a Ni were deposited on electrode surface by an electron beam evaporation (ULVAC, CV-S) method at a deposition rate of ~2.0Å/s from metallic Ni target (Kojundo Chemical Laboratory Co., Ltd. Japan). The deposition chamber was evacuated at the pressure ~$10^{-5}$ Pa and the temperature was set as 150 °C. The Ni were deposited onto the electrode by layer coatings with thicknesses varying from 2 to 5 nm.

### *E. Electrodeposition of Co-Pi loading*

IV. The electrode was transferred to a three-electrode PEC cell for electrodeposition of the Co-Pi loading. The electrode was used as a working electrode, Ag/AgCl as a reference electrode and a Pt wire as the counter electrode. The Co-Pi loading was carried out by the deposition of electrode in a stirred solution of 0.10M $Co(NO_3)_2$ in a 0.1M of $KH_2PO_4$ and $K_2HPO_4$ buffer at pH 7 at a constant potential of 1.10 Vs Ag/AgCl. All CoPi loading done by 100s scanning time. After complete the deposition, the electrode was rinsed with pure water and dried with $N_2$.

### *F. Photoelectrochemical measurement*

The PEC performance was measured in a typical air-tight three-electrode configuration cell, consisting of the working photoelectrode prepared above, a counter electrode (Pt coil), and the reference electrode (Ag/AgCl electrode in saturated KCl). The electrolyte used was aqueous 0.2 M $K_2HPO_4$ at pH 13, adjusted by NaOH. The potential of the working electrode was controlled using a potentiostat (Hokuto Denko, HSV-100) swept at 10 mVs$^{-1}$. The solution was purged with Ar for over 30 min prior to the measurement with vigorous stirring. The electrode current-potential was measured under intermittent and continues illumination from a solar simulator (SAN-EI electronic, XES40S1, AM 1.5G, 100 mW cm$^{-2}$). All measured potential versus Ag/AgCl were converted to the reversible hydrogen electrode potential ($V_{RHE}$) scale as calculated using the Nernst equation $V_{RHE} = V_{Ag/AgCl} + 0.199 + 0.0591 \times pH$ ($V°_{Ag/AgCl} = 0.199V$ at 25°C).

*G. IPCE measurement*

Incident photon-to-current conversion efficiency (IPCE) measurements were performed under the monochromatic irradiation from a Xe lamp (MAX-302, Asahi Spectra Co. Ltd., Japan) equipped with the bandpass filters (central wavelength: 420, 440, 480, 520, 570, 600 and 640 nm; full width at half maximum: 10 nm) and a variable neutral density filter. The irradiance spectra of the light incident on the electrode surface were measured with a spectroradiometer (Nova II, Ophir) in room dark condition. The IPCE at each wavelength (λ) were calculated via the following equation [18]:

$$\mathbf{IPCE} = \frac{(J_{light} - J_{dark})(mA \times cm^{-2}) \times 1240\ (nm)}{P_{mono}(mW \times cm^{-2}) \times \lambda\ (nm)} \times 100\%$$

*H. Gas evolution analysis*

An air-tight three-electrode system PEC cell with an Ag/AgCl reference electrode, a Pt-coil counter electrode and a micro gas chromatography (Micro GC) was used for a gas evolution measurement of electrode. Counter electrode of Pt-coil was coated with the $Cr_2O_3$ to prevent the back reaction. The PEC cell connected to a vacuum pump and a gas chromatograph with the circulation of cooling water (20 °C). Before the measurement, the PEC cell was pumped to low vacuum and then purged with Ar flow with sufficient times until no nitrogen and oxygen gases can be detected in micro GC. A solar simulator (AM 1.5G, 100 mW $cm^{-2}$) was used for a light sources and the amount of oxygen and hydrogen evolved from the photoelectrode and the Pt counter electrode were measured with the gas chromatograph (Inficon, GC-3000). Simultaneously current was also measured by a potentiostat (Versa STA3, Princeton Applied Research). The optimal photoelectrode was biased at 1.0V versus RHE in a stirred aqueous solution of 0.2M $K_2HPO_4$ with adjusted the pH to 13 by NaOH under AM 1.5G simulated sunlight.

*I. Structural Characterization*

The powder-samples and electrode were characterized by UV-visible diffuse reflectance spectroscopy (DRS; V-670, JASCO), and scanning electron microscopy (SEM; S-4700, Hitachi). The quantitative chemical composition of the photoanode surface was also measured using an energy dispersive X-ray spectroscopy (EDX; EMAX-7000, Horiba, microscope working at 10 kV) attached to the cold field SEM.

## III. RESULTS AND DISCUSSION

*A. Characterizations properties of Ni-modified electrode*

Fig. 1 (A) shows the absorption spectrum (Kubelka-Munk function) converted from the diffuse-reflectance spectrum (DRS) of the (a) $La_2Ti_2O_7$ precursor (b) as-nitrided $LaTiO_2N$, (c) annealed CoOx loading $LaTiO_2N$. As-nitrided $LaTiO_2N$ or CoOx-modified $LaTiO_2N$ exhibited strong background light absorption at wavelengths longer than the absorption edge wavelength (~ 600 nm). CoOx-loading on $LaTiO_2N$ by impregnated-nitridation annealed method, the absorption background is increases, which indicates reduced the cationic species ($Ti^{3+}$) and/or anion vacancies, which may act as a recombination centers [19].

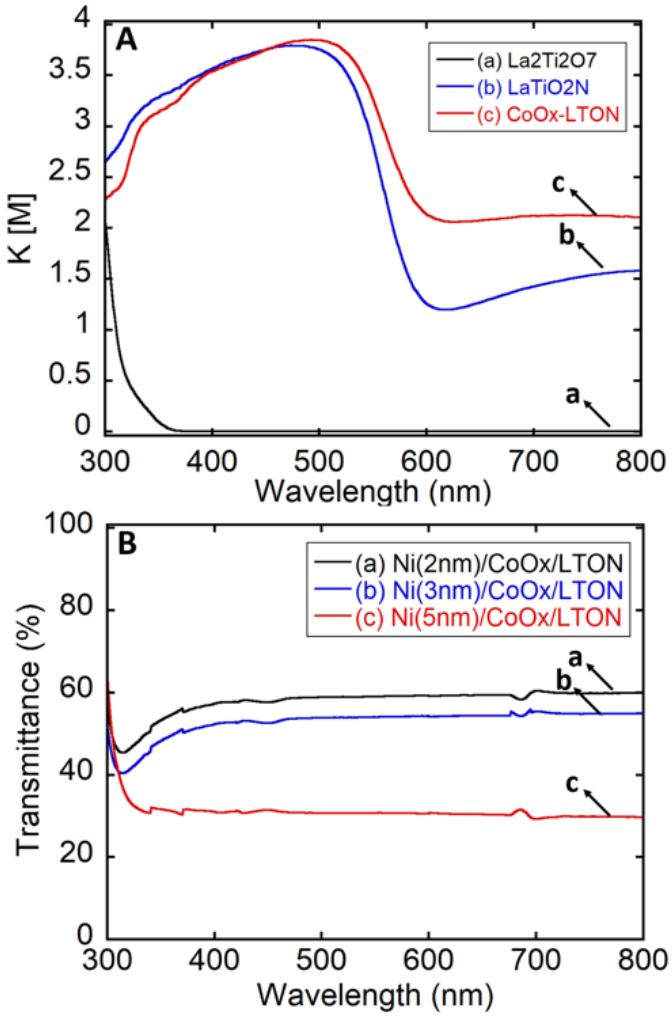


Figure 1. (A) Quasi-absorption spectra (Kubelka-Munk function) converted from diffuse-reflectance spectra of (a) $La_2Ti_2O_7$ (b) as-nitrided $LaTiO_2N$, (c) annealed CoOx loading $LaTiO_2N$, and (B) Light transmittance of electron beam deposited Ni layer on CoOx/$LaTiO_2N$ electrode for (a) 2 nm (b) 3nm, and (c) 5 nm

With an increase in Ni film thickness from 2 to 5 nm (Fig. 1 B), reduce the light transmittance through the Ni-film of PEC electrode. Thicker Ni films (3 nm and 5 nm) might afforded smaller saturation current densities shows in Fig. 3 B.

As seen in Fig. 2 (a), the tabular structure of LaTiO2N microcrystals and Fig. 2 (b) uniformly islanded by the CoOx co-catalysts. The average diameter of co-catalysts is about 20-40 nm with almost round morphology. It is also clearly seen that the LaTi2ON surface is a porous structure. The presence of the porous structure in the photoelectrodes provides an increased the interfacial area between electrolyte and particles monolayer [20]. Fig. 1 (c) clearly revels that the fuzzy effects of metallic ultra-thin Ni layer (2nm) was formatted on the surface of CoOx/LaTi2ON electrode after EB-deposition. The Ni-layer may act as a protective layer of photoanode and greatly alleviated in the aqueous electrolyte of better protection

under anodization and oxygen evaluation sites (OER) conditions.

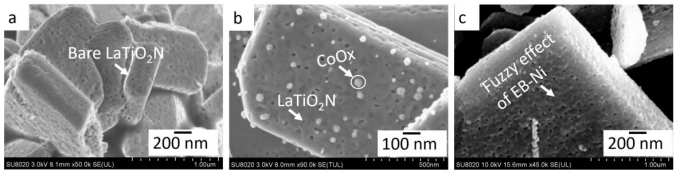


Figure 2. SEM images of (a) Bare-$LaTiO_2N$, (b) $CoOx/LaTiO_2N$, (c) EB-Ni/$CoOx/LaTiO_2N$ morphology.

### *B. Effect of Ni-modification on PEC performance*

Ni-layer modification techniques were done on $CoOx/LaTiO_2N$ surface by electron beam (EB) deposition. All layered electrode was optimized by PEC analyses and Ni-modified electrode showed the better durability rather than bare $CoOx/LaTiO_2N/Ta/Ti$ electrode. Initial investigated the use of ultra-thin Ni 2 nm and CoPi/Ni deposited on bare-$LaTiO_2N$ electrode and found little photocurrent response as shows in Fig. 3A. Primarily 2wt% CoOx co-catalyst loading on $LaTiO_2N$ and surface modified by 2, 3, and 5nm Ni-layer for optimization of Ni-thin layer at shows in Fig. 3B. The deposition of Ni-layer the photocurrent declining with increase the Ni-layer. Compared with unmodified Ni-sample, the Ni-modified samples showed lower PEC activity, whereas the Ni 2 nm-modified sample showed only slightly enhanced activity as compare to all other Ni modified sample. The layer might be insulating the electron tunneling on OER surface or obstacle the light irradiation. We found optimum loading of Ni-layer is 2 nm shows in Fig. 3B (b). For better performance, Co-Pi fixed at 100s electrodepositing-time and variable the CoOx-loading on $LaTiO_2N$ for optimized the photocurrent density by 1, 2, 3, and 4 wt%. The current is increasing with loading of CoOx co-catalysts until the 3wt% and then decline in 4wt%. The optimum current was found 3.7 mA at the water oxidation potential 1.23 $V_{RHE}$ for 3wt% CoOx co-catalysts loading. The 3wt% loading is better than other loading amount of CoOx catalyst at shows in Fig. 3B (c).

The PEC current of CoPi/CoOx deposited electrode was increased in all of the samples, and treated with CoPi as a co-catalysts is an essential for improvement the PEC activity rather than untreated one. CoPi/Ni/CoOx(3wt%)/$LaTi_2ON$ photoanode is optimal for PEC current and the advantageous for the stability in four-electron water oxidation system as shows in Fig. 4A. The forward and reverse scanning is confirmed there is no decay during light irradiation. It can be conclude that, the 2-nm Ni layer is protect to both the surface of n-type CoOx/$LaTi_2ON$ photoanode and serve as an OER catalyst in alkaline aqueous conditions.

Fig. 4B shows the solar-to-current-conversion efficiency (η) of optimum Ni-modified electrode. The efficiency was calculated from the current-potential curves measured in the dark and under AM 1.5G using the following equation [18]:

$$\eta = \frac{(J_{light} - J_{dark})(mA.cm^{-2}) \times (1.23 - V_{app})(V)}{P_{light}(mW.cm^{-2})} \times 100\%$$

Where Vapp is the applied potential versus RHE, $J_{dark}$ and $J_{light}$ are the respective current densities in the dark and in under AM 1.5 G, $P_{light}$ is the power density of AM 1.5G ($100mWcm^{-2}$). We found the maximum efficiency of CoPi/Ni/CoOx/LaTiO2N/Ta/Ti photoanode at 0.60% as shows in Fig. B.

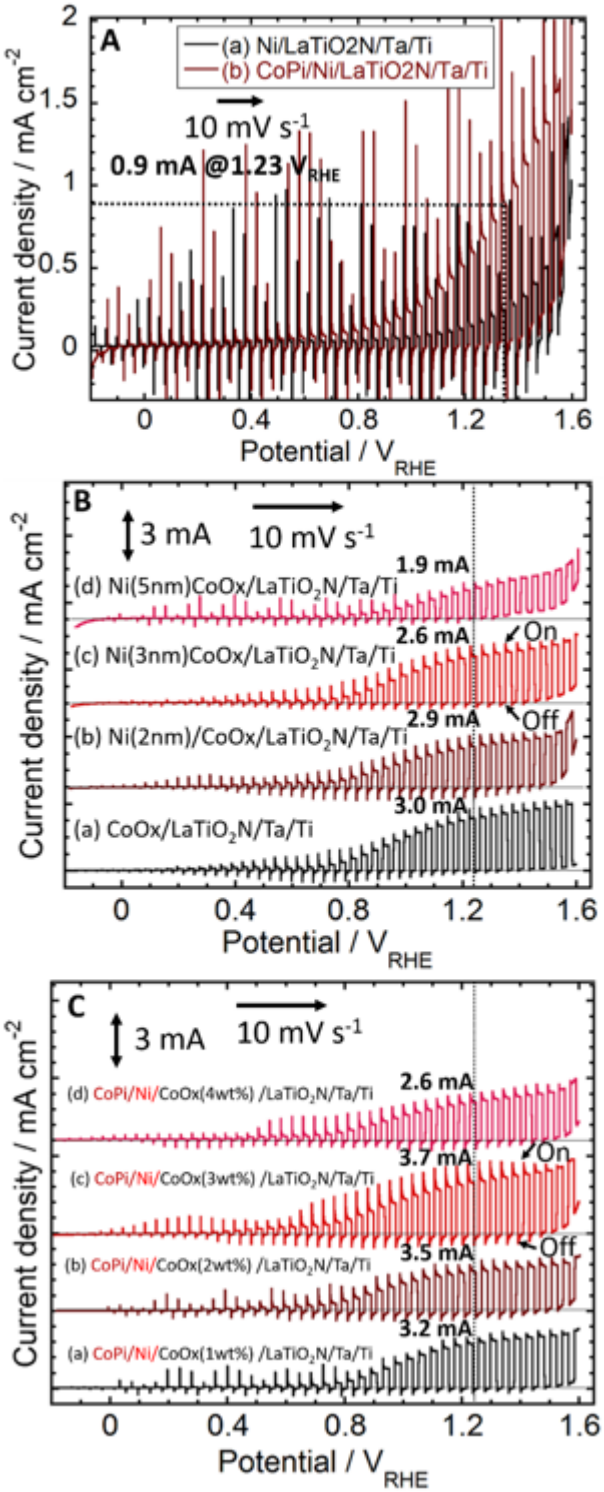


Figure 3. Linear swept voltammetry current-potential (I-E) forward chopped curves of (A) Bare LaTiO2N electrode surface modified by (a) Ni and (b)

CoPi-Ni; (B) CoOx/LaTiO2N electrode surface modified by (b) Ni 2 nm, (c) Ni 3 nm, and (d) Ni 5 nm; (C) Ni fixed at 2nm and variable CoOx-loading (a) 1 wt.% (b) 2wt.% (c) 3 wt.% and (d) 4wt.%. Ohmic contact Ta and Ti was used as a contact and conductor layer of electrode. The Electrolyte was a 0.2 M K2HPO4 solution and adjusted pH 13 by addition of NaOH. The solar simulator Air-mass1.5G with intensity 100 mWcm-2 was used for intermittent light radiation.PEC.

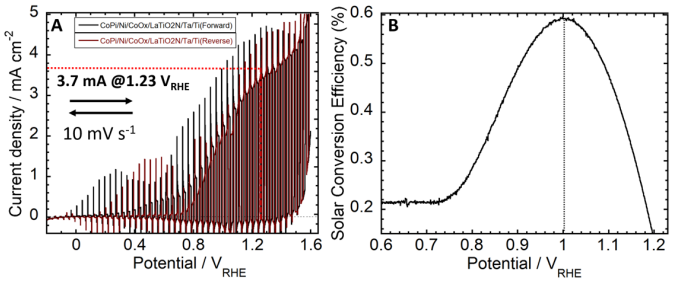


Figure 4. Ni modified optimal electrode PEC performance of LSV forward-reverse current potential curves. Forward-reverse scanning of electrode clearly shows no-corrosion at all. (B) Corresponding solar energy conversion efficiency (%) of the optimum Ni-modified photoanodes, calculated from the Fig. 4A I-E curves.

## C. *IPCE action spectra analysis*

Fig. 5 shows the wavelength dependence of the incident photon-to-current conversion efficiency (IPCE) for the Ni-modified CoOx/ $LaTi_2ON$ photoanode measured at different applied voltage versus RHE.

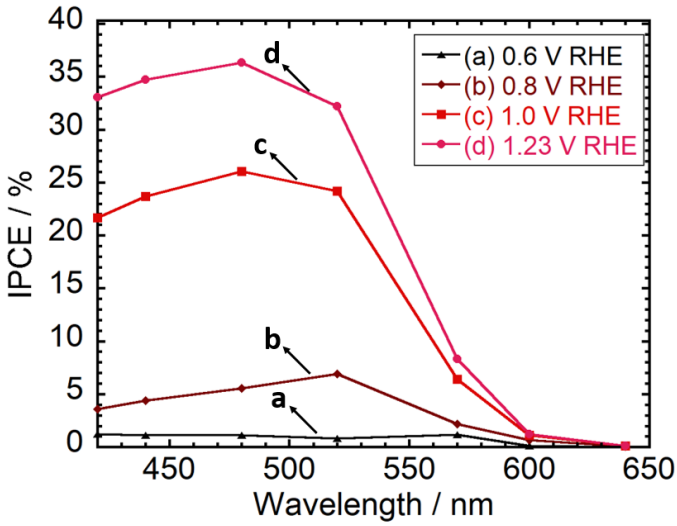


Figure 5. Wavelength dependence of IPCE for Ni-modified CoPi/Ni/CoOx/$LaTiO_2N$/Ta/Ti electrode photoanode at different applied potentials. The Electrolyte solution is 0.2 M $K_2HPO_4$ and pH 13 adjusted by the NaOH, Light source monochromatic irradiation from a Xe lamp.

The CoPi/Ni/CoOx/$LaTiO_2N$/Ta/Ti photoanodes highest IPCEs was found ~35% at 480 nm with applied potentials at 1.23 V versus RHE shows in Fig. 5. The individual IPCEs spectra at 0.6. 0.8, and 1.0 V versus RHE applied potential and wavelength also shows in Fig. 5. It is seen that, at the water oxidation potential (1.23V versus RHE, where the IPCEs of different photoanodes are usually compared), the IPCEs is quite higher in the 420–530nm range than the lower 1.0 V versus RHE applied potential. Below 1.0 V versus RHE the IPCEs are quite too lower. The relatively low IPCEs above 530nm indicated the possibility of further improving the overall efficiency of the photoanode by enhancing the efficiencies in this region of spectrum.

## D. *Evolved gas measurement analysis*

To confirm that the solar-driven water-splitting reactions taking place on the photoanode and the Pt counter electrode are the oxygen evolution reaction (OER) and hydrogen evolution reaction (HER) respectively, the gases evolved from the both electrodes were quantified by a gas chromatography. The Pt counter electrode were coated with $Cr_2O_3$ to prevent the back reaction. The photoanode was held at 1.0V versus RHE under AM 1.5G for 120 min.

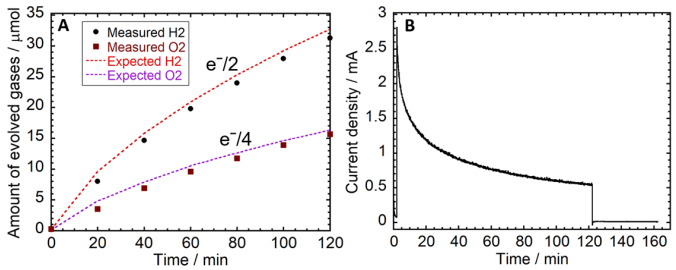


Figure 6. The Gas chromatography of the oxygen and hydrogen evolved (A) gas evolution plots and (B) chronoamperometric curves of CoPi/Ni/CoOx/$LaTiO_2N$/Ta/Ti electrode at 1.0 VRHE under simulated AM 1.5G light, in 0.2 M $K_2HPO_4$ at pH 13 adjusted by the NaOH in the air-tight closed vessel, with a CrOx-coated Pt counter electrode.

Fig. 6A shows the amounts of evolved O2 and H2 gases from photoanode and the Pt counter electrode 16 and 32 µmol cm-2 respectively. The 6.3 coulombs passing through the outer circuit of electrons during the 120 min measurement, which corresponding to 65.3 µmol cm-2 of electrons. This are converted into the theoretical amounts of hydrogen and oxygen (dashed lines, e−/2 and e−/4) as a function of time. The ratio of evolved $O_2$ and $H_2$ is close to stoichiometry, and the Faraday efficiencies of OER and HER are 98.30% and 94.50%, respectively for the whole period of test (120 min). Fig 6 B shows the photocurrent of electrodes simultaneously measured constantly at 1.0 V versus RHE under solar simulator AM 1.5G light in 0.2 M $K_2HPO_4$ at pH 13 adjusted by the NaOH. After 120 min irradiation (Fig. 6B), the photocurrent of optimal photoanode decreases to be ~0.5 mA, with a sharp decrease in the initial period followed by a gradual decay, which supported the PEC chronoampeometry stability test. The results also demonstrate that the photoanode has good stability for the OER. This is the suitable agreement with PEC chronoampeometry current and the gas evolved photocurrent at same potential of 1 $V_{RHE}$.

## E. *EDX analysis of optimal electrode*

The EDX spectra was demonstrates for the measure of crystals consists wt% and at% of La, Ti, N, O, Co, and Ni elements of optimal electrode shows in Fig. 7 and elemental analysis contain shows in Table 1. It is seen in Fig. 7 that the Co and Ni signal are very low due to small amount and small size of materials consistent. We expected Ni-content might be

one of the factor for improvement the photocurrent and stability, as seen in the table 1, Ni-elements is very low in CoPi/Ni/CoOx/$LaTiO_2N$/Ta/Ti electrode, which might be protected the electrode with proper transparency. The analyses were done in the three different regions and average was obtained consistently an atomic ratio. We also expected lower amount of Ni means the created a bond with cationic surface like as a link Ti-O-Ni and improve the electrode stability.

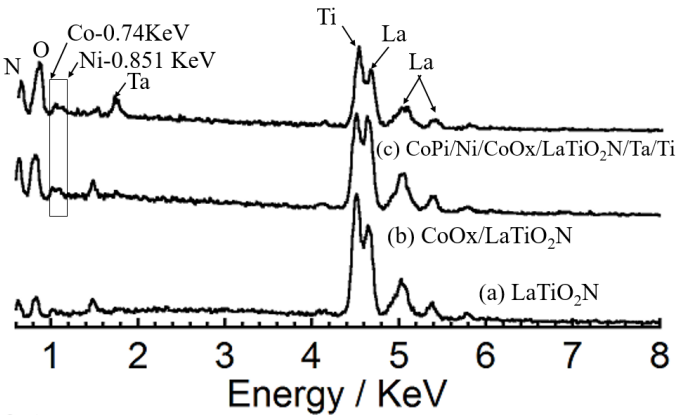


Figure 7. EDX spectra of the optimal CoPi/Ni/CoOx/LaTiO2N/Ta/Ti electrode.

The strong La, Ti, N and O signals in the EDX spectrum indicate the consist of mixed oxides, Ni and Co signal is very low due to the small amount consist of elements. Ta signal originate from electrode contact layer.

TABLE I. ELEMENTAL ANALYSIS OF OPTIMAL MODIFIED ELECTRODE

| Sample Name | Elements | Weight % | Atomic % |
|---|---|---|---|
| CoPi/Ni/CoOx/LaTi O2N/Ta/Ti | La | 58.22 | 15.42 |
| | Ta | 17.92 | 19.92 |
| | O | 11.18 | 37.21 |
| | N | 5.98 | 22.74 |
| | Co | 3.06 | 1.87 |
| | Ni | 3.64 | 2.84 |

We assumed that the EB-deposited Ni-layer modification only covered the surface of outer layer of electrode, but still exposed the inner side especially in pores totally exposed to electrolyte, which might be suffer from the photodegradation by hole, resultant photocurrent efficiency are decreased. But, the Ni/NiO (that is Ni converted NiO by hole and direct NiO-deposition its-self stoichiometric as act as a high conduction band barrier layer on electrode surface) is effectible for a built in potential on surface as provides the junction photovoltage, resultant suppresses the overpotential as well as onset was cathodic shifting shown reported elsewhere [21].

## IV. CONCLUSIONS

A layer types techniques of ultrathin Ni modification on oxynitrides based $LaTiO_2N$ semiconductors have been studied. The techniques is efficient, stable, and effective for photoanode as well water splitting with OER co-catalyst (that is, CoOx and/or Co-Pi). The photoanodic water splitting and its current-potential are dominated by the Ni modification techniques and depend on the surface properties of electrode. The Ni-modified with an OER co-catalyst (CoPi/Ni/CoOx/$LaTiO_2N$/Ta/Ti electrode) photoanode yielded a maximum solar energy conversion efficiency of 0.60% with a stable photocurrent. Further, stoichiometric $O_2$ and $H_2$ were stably produced on the photoanode and the Pt counter electrode with Faraday of almost unity. Our results for water splitting clearly indicated that the Ni-layer modification play a major role in the water oxidation enhancement of oxynitrides $LaTiO_2N$, which opens a new way for simultaneous improvement of the photoanode efficiency and stability.

## ACKNOWLEDGMENT


The author would like to thanks Artificial Photosynthesis Project of Japan (ARPChem), The University of Tokyo for successfully done the present work.


## REFERENCES


[1] A. Kudo, and Y. Miseki, "Heterogeneous Photocatalyst Materials for Water Splitting," *Chem.Soc. Rev.*, vol. 38, no. 1, pp. 253–278, Jan. 2009.

[2] F. E. Osterloh, "Inorganic Materials as Catalysts for Photochemical Splitting of Water," *Chem. Mater.*, vol. 20, no. 1, pp. 35–54, Dec. 2007.

[3] M. Gratzel, "Photoelectrochemical Cells," *Nature*, vol. 414, no. 6861, pp. 338–344, Nov. 2001.

[4] A. Fujishima, and K. Honda, "Electrochemical Photolysis of Water at a Semiconductor Electrode," *Nature*, vol. 238, no. 5358, pp. 37–38, Jul. 1972.

[5] S. G. Ebbinghaus, H.P. Abicht, R. Dronskowski, T. Muller, A. Reller, A.Weidenkaff, "Perovskite-Related Oxynitrides-Recent Developments in Synthesis, Characterisation and Investigations of Physical Properties", *Prog. Solid State Chem.*,vol. 37, no.2-3, pp. 173–205, Dec. 2009.

[6] A. Fuertes, "Chemistry and Applications of Oxynitride Perovskites", *J. Mater. Chem.*, vol. 22, no. 8, pp. 3293–3299, Feb. 2012.

[7] A. Fuertes, "Synthesis and Properties of Functional Oxynitrides - from Photocatalysts to CMR Materials", *Dalton Trans.*, vol. 39, no. 26, pp. 5942–5948, Jul. 2010.

[8] K.. Maeda, "(Oxy)nitrides with d0-electronic Configuration as Photocatalysts and Photoanodes that Operate under a Wide Range of Visible Light for Overall Water Splitting," *Phys. Chem. Chem. Phys.*, vol. 15, no. 26, pp. 10537–10548, Jul. 2013.

[9] R. Marchand, Y. Laurent, J. Guyader, P. L'Haridon, and P. Verdier, "Nitrides and Oxynitrides: Preparation, Crystal Chemistry and Properties," *J. Eur. Ceram. Soc.*, vol. 8, no. 4, pp. 197– 213, Jul. 1991.

[10] M. Jansen, and H. P. Letschert, "Inorganic Yellow-Red Pigments Without Toxic Metals," *Nature*, vol. 404, no. 6781, pp. 980–982, April 2000.

[11] A. Kasahara, K. Nukumizu, G. Hitoki, T. Takata, J. N. Kondo, M. Hara, H. Kobayashi, and K. Domen, "Photoreactions on $LaTiO_2N$ Under Visible Light Irradiation," *J. Phys. Chem. A*, vol. 106, no. 29, pp. 6750–6753, June 2002.

[12] Y. Qu, and X. Duan, "Progress, Challenge and Perspective of Heterogeneous Photocatalysts," *Chem. Soc. Rev.*,vol. 42, no. 7, pp. 2568–2580, April 2013.

[13] M. J. Kenney, M. Gong, Y. Li, J. Z. Wu, J. Feng, M. Lanza, and H. Dai, "High-performance silicon photoanodes passivated with ultrathin nickel films for water oxidation," *Science*, vol. 342, no.6160, pp. 836-840, Nov. 2013.

[14] K. Maeda, H. Terashima, K. Kase, M. Higashi, M. Tabata, K. Domen, "Surface Modification of TaON with Monoclinic $ZrO_2$ to Produce a Composite Photocatalyst with Enhanced Hydrogen Evolution Activity

under Visible Light," *Bull. Chem. Soc. Jpn.*, vol. 81, no. 8, pp. 927-937, Aug. 2008.

[15] F. Zhang, A.Yamakata, K. Maeda, Y. Moriya, T. Takata, J. Kubota, K. Teshima, S. Oishi, and K. Domen, "Cobalt-modified porous single-crystalline $LaTiO_2N$ for highly efficient water oxidation under visible light," *J. Am. Chem. Soc.*, vol. 134, no. 20, pp. 8348–8351, May 2012.

[16] A. E. Maegli, S. Pokrant, T. Hisatomi, M.Trottmann, K. Domen, and A. Weidenkaff, "Enhancement of Photocatalytic Water Oxidation by the Morphological Control of $LaTiO_2N$ and Cobalt Oxide Catalysts," *J. Phys. Chem. C*, vol. 118, no. 30, pp. 16344–16351, October 2014.

[17] T. Minegishi, N. Nishimura, J. Kubota, and K. Domen, "Photoelectrochemical properties of $LaTiO_2N$ electrodes prepared by particle transfer for sunlight-driven water splitting," *Chem. Sci.*, vol. 4, no. 3, pp. 1120–1124, March 2013.

[18] Z. Chen, F. T. Jaramillo, A. Kleiman-Shwarsctein, A. J. Forman *et al.*," Accelerating materials development for photoelectrochemical hydr ogen production: Standards for methods, definitions, and reporting protocols," *J. Mater. Res.*, vol. 25, no. 1, pp. 3-16, Jan. 2010.

[19] M. Matsukawa, R. Ishikawa, T. Hisatomi, Y. Moriya, N. Shibata, J. Kubota, Y. Ikuhara, and K. Domen, "Enhancing Photocatalytic Activity of $LaTiO_2N$ by Removal of Surface Reconstruction Layer," *Nano Lett.*, vol. 14, no. 2, pp. 1038−1041, Jan. 2014.

[20] S. K. Pilli, T. E. Furtak, L. D. Brown, T. G. Deutsch, J. A. Turner, and A. M. Herring, "Cobalt-phosphate (Co-Pi) catalyst modified Mo-doped $BiVO_4$ photoelectrodes for solar water oxidation," *Energy Environ. Sci.*, vol. 4, no. 12, pp. 5028–5034, Dec. 2011.

[21] K. Sun, N. Park, Z. Sun, J. Zhou, J. Wang, X. Pang, S. Shen, S. Y. Noh, Y. Jing, S. Jin, , P. K. L Yu, and D. Wang, "Nickel oxide functionalized silicon for efficient photo-oxidation of water," *Energy Environ. Sci.*, vol. 5, no. 7, pp. 7872-7877, July 2012.

# Substrate Effects on Channel Temperature Distribution of AlGaN/GaN HEMT

Amit Kumer Podder[1], A. S. M. Jannatul Islam[2], SM Hasanuzzaman[3], Md. Sherajul Islam[4] and A.G. Bhuiyan[5]
Dept. of Electrical and Electronic Engineering, Khulna University of Engineering & Technology, Khulna-9203, Bangladesh.
amitpodder09@yahoo.com[1], syed.113.kuet@gmail.com[2], sm_hasanuzzaman@hotmail.com[3], sheraj_ruet@yahoo.com[4], ashraf90344@yahoo.com[5]

***Abstract*— The channel temperature distribution of AlGaN/GaN HEMT on various substrates including Sapphire, Si, SiC, and Diamond is presented. A 2D electro-thermal model is used here. Joule heating is calculated and incorporated into the thermal model to find the temperature distribution which gives an idea of the maximum temperature in the channel. A comparative study is made on different substrates at different power density. The simulated results will be helpful for better temperature managing of AlGaN/GaN HEMT.**

***Keywords*—HEMT, Self-heating, Substrate, Channel temperature, 2DEG, Thermal modelling.**

## I. Introduction

AlGaN/GaN high electron mobility transistors (HEMTs) have developed as an alluring contender for immense power execution at microwave frequency and furthermore for immense voltage appliance. The thermal conductivity of GaN is around three times higher than GaAs and has a vast warmth limit which makes it reasonable for immense power enhancers. Besides, the wide-bandgap of GaN device gives a tough and solid technology able to do immense-voltage and immense-temperature operation which steps up a few industrial, car and airship applications like power and high voltage rectifiers and converters and significantly more [1].

Although the GaN-based device is promising, the high current flow in the material generates a lot of heat under high power operation which is concentrated in a little volume at the gate-drain edge of the device. So, the channel temperature rises up to several hundred degrees above ambient temperature and the device becomes heated. This self-heating degrades the mobility and other basic material properties which result in a reduction in the output power, transconductance, cut-off and maximum oscillation frequencies and the reliability. Therefore, self-heating and managing of the temperature of immense-power AlGaN/GaN HEMT are presently one of the prime worries of device fabricators [2].

Different management of temperature has been done, for example, the determination of the best possible substrate material for heat sinking [3], [4], [5], near junction thermal management [6], the coupling of temperature at the GaN/Au or substrate/GaN interfaces with non-linear thermal conductivity and noncontinuous thermal transport [7], [8], [9], modification of the device topology [10], the flip-chip bonding [11] and microfluidic cooling [12]. Among all the methods changing the substrate is relatively simplest, non-destructive and easier to apply to the extant technologies. In this work, the impacts of various substrates, for example, Si, Sapphire, SiC, and Diamond on channel temperature distribution are analyzed. Physics-based simulations are used here for the basic modeling of the AlGaN/GaN HEMT. Here the proposed model incorporates the impact of self-heating and temperature distribution in a wide range [3]. To ascertain temperature appropriation alongside the channel of AlGaN/GaN (x=0.15) HEMT COMSOL Multiphysics 5.0 was used together with the commercial MATLAB software [13].

## II. Structure Of The Device

The schematic cross-section of AlGaN/GaN HEMT layout is shown in Fig. 1. The physical structure of the device is symmetric along the x-axis, the growth of two-dimensional electron gas (2DEG) is along the z-axis and the transportation of electron occurs along XY plane. Diamond, SiC, Si, and Sapphire are used here as substrates. The sample consists of 20 nm high band-gap $Al_xGa_{1-x}N$ layer with a bulk concentration of $1.5\times10^{-19}$ $cm^{-3}$, followed by 3µm thick unintentionally doped (UIN) GaN layer, 10µm a low-temperature AlN buffer layer and a substrate layer (Sapphire, Si, SiC, Diamond) with a thickness of 100 µm. The gate length is considered as 0.4 µm and the gate width is 100 µm. The spacing between the gate and drain channel region is considered as the heat source for the thermal modeling of the device as shown in Fig. 1.

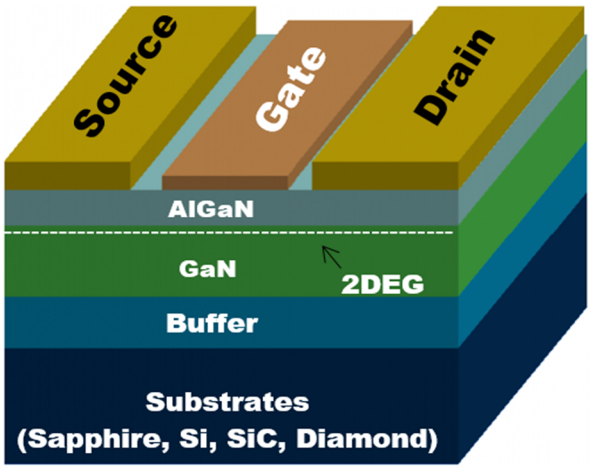


Fig.1 The basic structure of AlGaN/GaN HEMT .

978-1-5386-2307-7/17/$31.00 ©2017 IEEE

## III. Thermal Modelling

In this work, a 2D electro-thermal model of AlGaN/GaN HEMT is considered. The model depends on the drift-diffusion conditions utilizing isothermal or non-isothermal transport models. The drain current $I_d$ versus drain to source voltage $V_{ds}$ for different temperature and substrates are shown in our previous work in [5]. In this work, instead of settling the Poisson's condition to deliver the thermal dispersal inward the device, an outer thermal source was considered over the channel region to make the requisite thermal spread. The density of the current (Jn,p) including temperature inclination, electron, and hole quasi-Fermi potential can be conveyed as [2]:

$$Jn,p = nq\mu n,p(\nabla\Phi n,p + Pn,p\nabla T). \quad (1)$$

Where, μn,p narrates the mobilities of electron and hole, Φn,p presents the electrons and holes quasi-Fermi potential individually and Pn,p presents indisputably the thermoelectric power. The additional terminology appears up because of the non-uniform flow of the temperature inward the device. The thermal appropriation because of the self-heating might be figured by resolving the accompanying lattice heat flow equation [5]:

$$C_L \frac{\partial T}{\partial t} - \nabla.\kappa\nabla T = -\nabla\left[(P_n T + \phi_n)J_n + \left(P_p T + \phi_p\right)J_p\right] \quad (2)$$

Where $C_L$ states the lattice heat capacity of the material. The term T indicates the body temperature. Here only the thermal phenomenon inward the device structure was considered. In addition, it was assumed that the body of the device complies the equation of the heat and it makes its endemic heat (H) at the specific region called "heat source". In this manner, the temperature T satisfies the accompanying equation.[2].

$$C_L \frac{\partial T}{\partial t} - \nabla.\kappa\nabla T = H \quad (3)$$

Where $\kappa$ is the thermal conductivity having a unit of W/(cm·K)). The thermal conductivity can be anisotropic in a solid i.e. it has distinct esteem in various directions. Then $\kappa$ turns into a tensor

$$\kappa = \begin{bmatrix} \kappa_{xx} & \kappa_{xy} & \kappa_{xz} \\ \kappa_{yx} & \kappa_{yy} & \kappa_{yz} \\ \kappa_{zx} & \kappa_{zy} & \kappa_{zz} \end{bmatrix} \quad (4)$$

The single scalar means effective thermal conductivity is the mean value of the diagonal elements $\kappa_{xx}$, $\kappa_{yy}$, and $\kappa_{zz}$ [13].The heat generated per mm is calculated using the following equation,

$$H = JEW_g h_c \quad (5)$$

Where, $J$=current density,E =applied electric field,$W_g$=channel width, $h_c$=height of the channel and $J = nve$; n= carrier concentration, v= carrier velocity and e= electron charge. The value of channel width $W_g$ is considered as 100 µm and channel height is considered as 0.01 µm.

The boundary conditions considered in the simulation are (i) the outer surface is assumed to be adiabatic i.e. no heat outflows to the external atmosphere from the device, (ii) the transportation of heat in the external atmosphere from metallization is not taken into account for the simplification of the simulation, (iii) the posterior of the wafer is an isothermal surface and kept at ambient temperature (300K).

## IV. Simulation Result

At the point when the current begins to course through the devices, the heat is produced because of power dissemination beneath the gate. The dynamic areas become sources of heat and the chip's backward (i.e., base plane and assortment) turns into the sink of heat. The exchange of heat happens because of the temperature inclination between the source and sink of heat. Greater dispersal zones of heat and more slender substrate thicknesses prompt a lower end in temperature of the channel. The heat produced under the gate of AlGaN/GaN HEMT at the drain side appears in Fig. 2. It is discovered that the most extreme temperature happens on the gate-drain side of the device. The parameters used in the simulation are given in Table I. The temperature conveyance along the channel of AlGaN/GaN HEMT considering diverse substrates is portrayed underneath.

TABLE I. Table For The Parameters Used in Simulation

| Parameters | Value | Parameters | Value |
|---|---|---|---|
| AlGaN layer | | GaN layer | |
| Bandgap, $E_g$ | 3.9495 eV | Bandgap, $E_g$ | 3.42 eV |
| Electron affinity, $\chi$ | 3.14 eV | Electron affinity, $\chi$ | 3.5 eV |
| Relative permittivity, $\epsilon_r$ | 10.2845 | Relative permittivity, $\epsilon_r$ | 10.4 |
| Electron mobility,$\mu_n 0$ | 10 $cm^2/(V*s)$ | Electron mobility,$\mu_n 0$ | 425 $cm^2/(V*s)$ |
| Hole mobility,$\mu_p 0$ | 5 $cm^2/(V*s)$ | Hole mobility,$\mu_p 0$ | 5 $cm^2/(V*s)$ |
| Thermal conductivity, $\kappa_0$ | 0.3 W/(cm*K) | Thermal conductivity, $\kappa_0$ | 1.3 W/(cm*K) |
| Density, $\rho_0$ | 6.5 $g/cm^3$ | Density, $\rho_0$ | 6.15 $g/cm^3$ |
| Heat capacity, $C_L$ | 0.49 J/(g*°C) | Heat capacity, $C_L$ | 38.1+8.96e-3*T J/(g*°C) |
| Other parameters | | | |
| $\kappa_{300}$ (diamond) | 20 W/cm-K | $\kappa_{300}$ (SiC) | 4.0 W/cm-K |
| $\kappa_{300}$ (Si) | 1.5W/cm-K | $\kappa_{300}$ (Sapphire) | 0.35 W/cm-K |

### A. Sapphire Substrate

Sapphire is one of the widely used substrates for III-Nitride device fabrication with a thermal conductivity of 0.35 W/cm-K [6]. The temperature distribution of AlGaN/GaN HEMT on the sapphire substrate for 6W/mm power dissipation is shown in Fig. 3. The temperature peak occurs at the gate-drain edge and its value is about 330℃ for 6 W/mm. The channel temperature varies linearly from 105 to 555℃ if the input power density changes from 1 to 10 W/mm.

### B. Silicon Substrate

Si is one of the most suitable substrates for device fabrication because of its availability and low cost. It has almost 3 times higher thermal conductivity (1.5 W/cm-K) than sapphire [6]. The temperature distribution of AlGaN/GaN HEMT on Si substrate is shown in Fig. 4. The peak temperature is predicted at the gate-drain edge and its value is about 275℃ for 6 W/mm. The channel temperature varies from 75 to 475℃ if the input power density changes from 1 to 10 W/mm.

### C. SiC Substrate

SiC is one of the expensive substrates available but it is the highly promising substrate for HEMT fabrication since it has almost ten times higher thermal conductivity (4.0 W/cm-K) than

sapphire [6]. This is why it has been widely used in industries. The temperature distribution of AlGaN/GaN HEMT on SiC substrate is shown in Fig. 5. The peak temperature is calculated and its value is about 160℃ for 6 W/mm. The channel temperature varies from 55 to 285℃ if we change power density from 1 to 10 W/mm which shows that SiC is better than Sapphire and Si for better thermal management of the device.

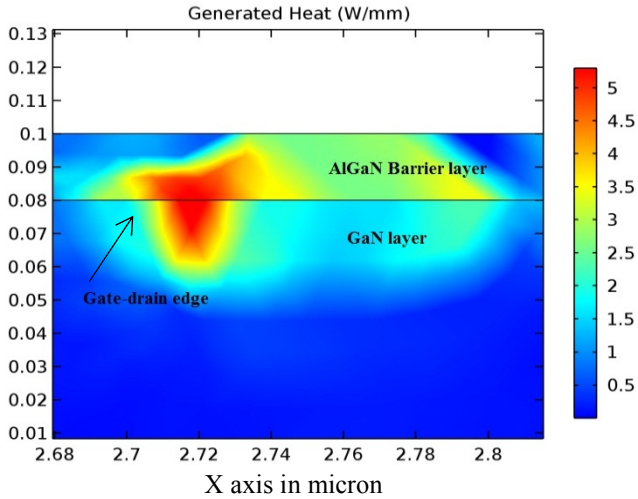


Fig. 2 Generated heat in the channel under the gate drain edge at $V_{ds}$ = 10V and $V_{gs}$ = 0V .

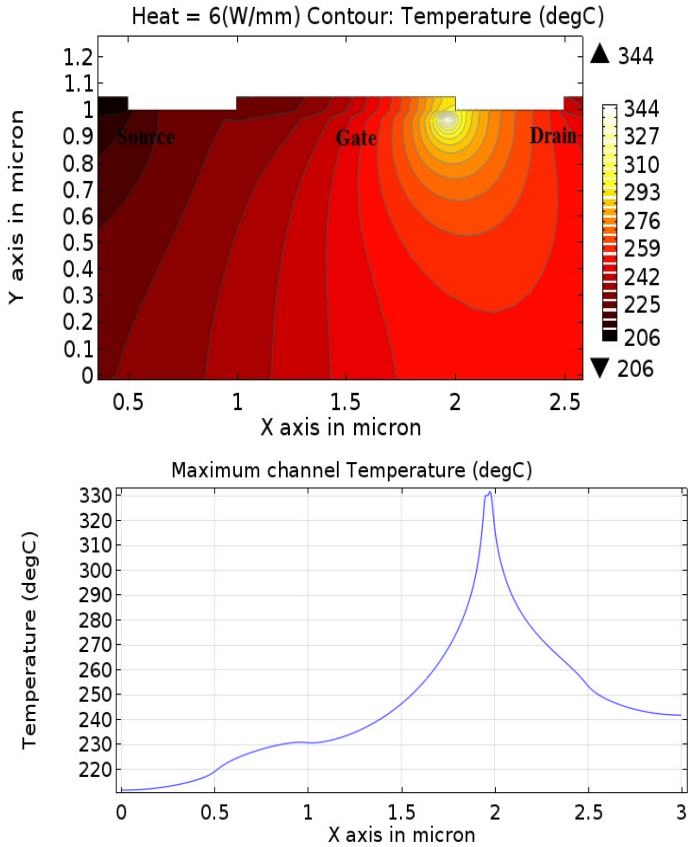


Fig. 3 Channel temperature distribution of AlGaN/GaN HEMT on sapphire substrate for 6W/mm power dissipation.

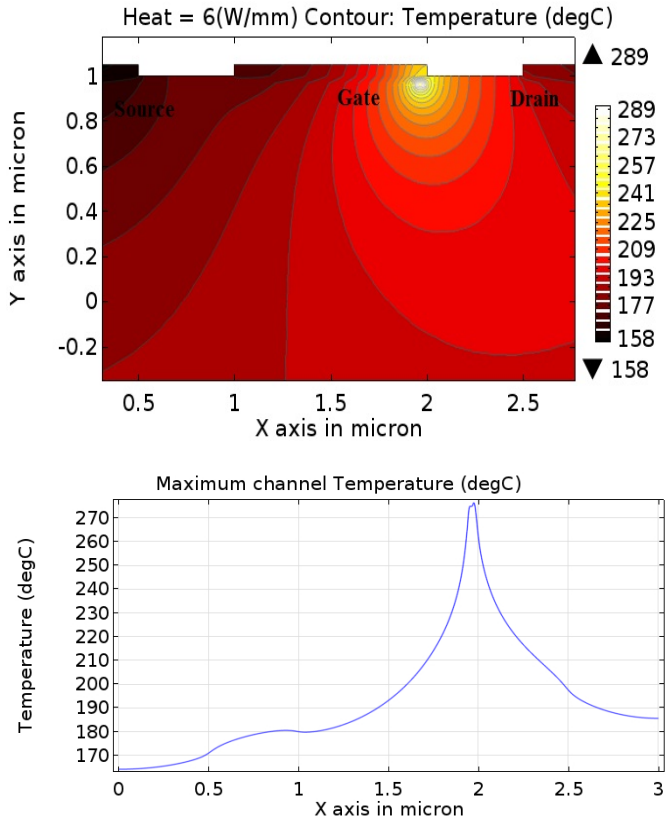


Fig. 4 Channel temperature distribution of AlGaN/GaN HEMT on silicon substrate for 6 W/mm power dissipation.

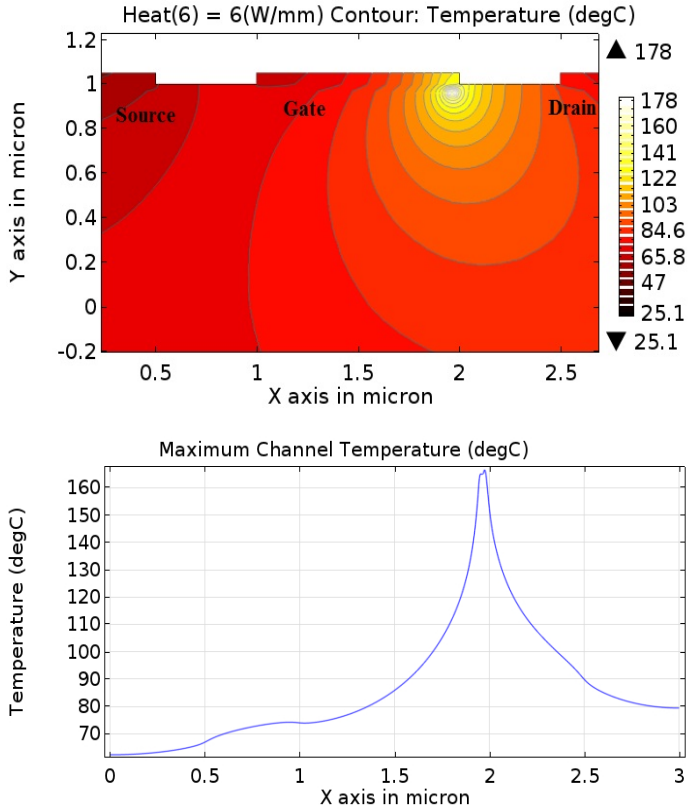


Fig. 5 Channel temperature distribution of AlGaN/GaN HEMT on SiC substrate for 6 W/mm power dissipation.

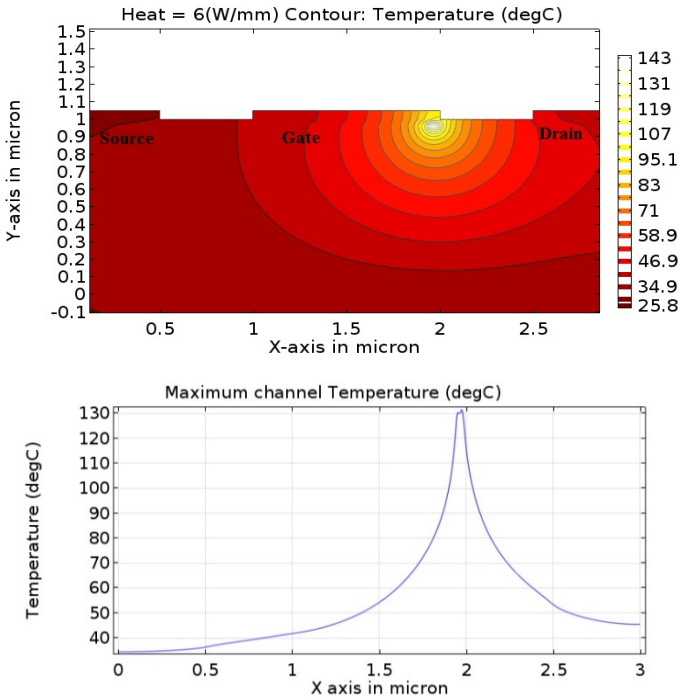


Fig.6 Channel temperature distribution of AlGaN/GaN HEMT on diamond substrate for 6 W/mm power dissipation.

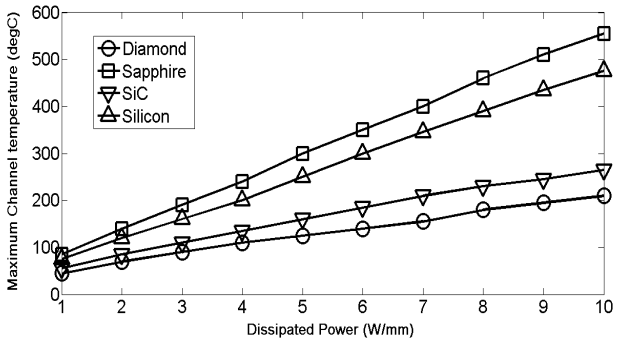


Fig.7 Maximum Channel Temperature vs. Dissipated Power for different Substrates

### *D. Diamond Substrate*

Recently diamond is being considered as a substrate for growing GaN layer since it has a thermal conductivity (20 W/cm-K) even superior to SiC [14]. Though the technology is still immature and the fabrication process on this substrate is still flawed, diamond shows great potentiality as a substrate. The thermal appropriation of AlGaN/GaN HEMT on the diamond substrate is shown in Fig. 6. From the figure, it is found that the peak temperature under the gate-drain edge is about 130℃ for the same amount of power. The device temperature varies from 45 to 225℃ if the input power density changes from 1 to 10 W/mm which indicates that diamond is better than other substrates for better thermal management of the device.

### *E. Comparison among Substrates*

The maximum channel temperature is recorded each time for Sapphire, Si, SiC, and Diamond substrates by varying the power density from 1 to 10 W/mm. Due to this variation of power density on Sapphire, Si, SiC, and Diamond substrate the maximum channel temperature variation occurring in the device are shown in Fig. 7. The channel temperature increases linearly as the power density increases for all the substrates (Sapphire, Si, SiC, and Diamond). For the same amount of power dissipation, the diamond substrate shows the lowest channel temperature than other substrates. The reason for this is that with the application of field introduces very high phonon scattering at the drain side which produces a massive amount of heat at the drain side under the gate and also reduces the mobility to a great deal making the velocity almost constant. The result that is found in the simulation matches with the experimental result in [4] which indicates the validity of the simulation.

## V. Conclusion

The channel temperature distribution of the AlGaN/GaN HEMT on different substrates such as Si, Sapphire, Diamond, and SiC are numerically solved and presented here. The amount of dissipated heat is incremented in step, and for each step the maximum channel temperature is calculated. In all cases, it is seen that the channel temperature raises almost linearly with the amount of dissipated heat. It is also seen the maximum temperature occurs under the gate region of the channel at the drain side. The peak temperature of 6 W/mm power dissipation is predicted to be 330, 275, 160 and 130℃ for sapphire, Si, SiC and diamond substrates, respectively.

## References


[1] S.N.Mohammad and H.Morkoç "Progress and Prospects of Group III-V Nitride Semiconductors", *Progress in Quantum Electronics,* vol.20, Issue 5-6, pp.361-525, 1996.

[2] A. K. Sahoo, N. K. Subramani, J.C. Nallatamby, N. Rolland, and F. Medjdoub, "Thermal analysis of AlN/GaN/AlGaN HEMTs grown on Si and SiC substrate through TCAD simulations and measurements", in *Proc. the 11th European Microwave Integrated Circuits Conference*, London, UK ,3 – 4 Oct,2016, pp. 145-148.

[3] J. Kuzmik, P. Javorka, A. Alam , M. Marso, M. Heuken, and P. Kordos, "Determination of channel temperature in AlGaN/GaN HEMTs grown on sapphire and silicon substrates using DC characterization method", *IEEE Transactions on Electron Devices* , vol. 49, no. 8, pp. 1496 – 1498, Aug. 2002.

[4] J. Pomeroy, M. Bernardoni, A. Sarua, A. Manoi, D.C. Dumka, D.M. Fanning, and M. Kuball,"Achieving the best thermal performance for GaN-on-diamond", *in Proc. IEEE CSICS,* 2013, pp. 1-4.

[5] A. Syed Md. J. Islam, SM Hasanuzzaman, AK Podder, MS Islam, and AG Bhuiyan, "Theoretical analysis of substrate effects on the DC performance of AlGaN/GaN high electron mobility transistor", in *Proc. IEEE 5th ICIEV,* DU, Dhaka, Bangladesh, 13-14 May, 2016, pp. 961-966.

[6] A. Bar-Cohen, J. D. Albrecht, and J.J. Maurer, "Near-junction thermal management for wide bandgap devices", *in proc. IEEE CSICS,* Waikoloa, HI, USA, 2011, pp. 1-5.

[7] M. P. Gupta, A. Vallabhaneni, and S. Kumar, "A self -consistent reduced order model for current and temperature in GaN HEMTs ", *in Proc. 16th IEEE ITHERM conference,*2017,pp. 930-935.

[8] A. Darwish, A. J. Bayba, and H. A. Hung, "Channel temperature analysis of GaN HEMTs with nonlinear thermal conductivity", *IEEE Transaction on Electron Device*, vol.62, no.3, March 2015.

[9] N. Donmezer and S. Graham,"The impact of noncontinuum thermal transport on the temperature of AlGaN/GaN HFETs", *IEEE Transaction on Electron Device,*vol.61, no. 6, June 2014.

[10] M. Kuball, S.Rajasingam,A Sarua,MJ Uren, T. Martin, BT Hughes et al., "Measurement of temperature distribution in multifinger AlGaN/GaN heterostructure field-effect transistors using microRaman spectroscopy ", *Applied Physics Letters* vol. 82,issue 1, 124–6,2003.

[11] J Das,H.Oprins, H.Ji, A.Sarua, W.Ruythooren, J. Derluyn et al. "Improved thermal performance of AlGaN/GaN HEMTs by an optimized flip-chip design", *IEEE Transactions on Electron Devices,* vol. 53, no.11, Nov. 2006.

[12] G. Agarwal, T. Kazior, T. Kenny, and D. Weinstein, "Modeling and analysis for thermal management in GaN HEMTs using microfluidic cooling", *ASME Journal of Electronic Packaging*, vol. 139 issue 1, 2016.

[13] Heat Transfer Module User's Guide, COMSOL Multiphysics v.3.5a, 2008.

[14] Y. Won, J. Cho, D. Agonafer, M. Asheghi, K. E. Goodson, "Cooling limit for GaN HEMT technology", *in Proc. of IEEE CSICS*, Monterey, CA, USA, Oct. 2013.

# Binding Energy of CNT-GNR Interface due to Different Orientation and Equilibrium Distance

Nabil Ahmed[1], G.R. Ahmed Jamal[1], Roman Ahmed[1]
[1]Department of Electrical & Electronic Engineering, University of Asia Pacific
Dhaka-1215, Bangladesh
nabilahmed1519@gmail.com, ahmed.eee@uap-bd.edu, romanahmed35@gmail.com

*Abstract*— **Carbon Nanotube (CNT) and Graphene Nanoribbon (GNR) are two most important nanomaterial of recent times. Besides their individual potential in nanoelectronic interface between CNT and GNR has also attracted significant attention of the researchers. In depth investigation of electrical and chemical properties of CNT-GNR interface is required to explore their potential application. The present work reports the interface property of CNT-GNR junction. Interface of GNR with two different SWCNT (armchair and zigzag) for two different orientation (lateral and vertical) have been analyzed through DFT based simulation. Based on different orientation, this work demonstrates the effect of equilibrium distance on binding energy. Observed behavior of binding energy is represented graphically with respect to chirality. Linear and non-linear equation have been devised to represent the relation of binding energy with chirality. The possible reason behind different nature of this relation due to orientation changes is discussed. The overall finding will help to understand the nature of CNT-GNR interface.**

***Keywords—CNT, GNR, Equilibrium distance, Binding energy, Interface state, Chiral Index.***

## I. INTRODUCTION

Carbon nanotube (CNT) and graphene are promising candidates for next generation nanoelectronic devices due to their extraordinary electronic property [1-4], outstanding mechanical strength [5-7], thermal conductivity [8,9], and optical properties [10-12].These interesting properties are not limited to the individual CNT and graphene but their hybrid junctions also exhibit novel properties. Recent advancement on CNT-Graphene hybrid shows that their novel properties are extended into three dimensions [13-15].One of the fabrication complication of graphene-metal junction is that, depositing metal on graphene sheet introduces some additional contact resistance resulting overall reduced conductance of the device. In the search for reducing the contact resistance in carbon devices, recent works suggest that graphitic materials could be an alternative to connect CNT and graphene [16–20].Usually, hybrid junctions made upon graphene rely on their physical environment as well as their interconnectivity with other material. In order to meet the demand of CNT-Graphene 2D, 3D devices studying their interface from different geometric orientation is very important.

Single walled carbon nanotube SWCNTs can be explained by the chiral index $n$ and $m$. Three types of SWCNT's are available according to their physical structures, i.e., armchair CNT (ACNT where $m = n$), zigzag CNT (ZCNT where $m= 0$) and chiral CNT (where $m \neq n$ and $n \neq 0$). On the other hand 2D graphene nanoribbon (GNR) which is a strip of graphene can be derived by cutting edge of three dimensional carbon nanotubes and two dimensional graphene. GNR with finite width (less than 50nm) can be divided into zigzag GNR (ZGNR) and armchair GNR (AGNR) according to the atomic arrangement pattern on their edges.

In this work we studied CNT-GNR interface from two different geometrical orientations. We took interfaces of zigzag carbon nanotube (ZCNT) with armchair graphene nanoribbons (AGNR) and armchair carbon nanotube (ZCNT) with armchair graphene nanoribbons (AGNR). We have used equilibrium distance and binding energy to describe the interfaces. Equilibrium distance is the minimum distance between two particle for which binding energy between these two reaches its minimum. A correlation between binding energy and chirality has been introduced, keeping CNT and GNR in equilibrium distance.

## II. PROPOSED MODELS

We used two different orientations for CNT-GNR interface as shown in fig. 1. We took CNT ranges from chiral index (5,0) & (5,5) to (30,0) & (30,30). Similarly GNR has been taken ranges from (5,5) to (30,30).

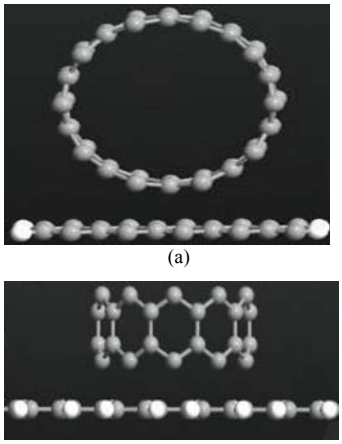


Figure 1: CNT-GNR interface (a) lateral (b) vertical.

978-1-5386-2307-7/17/$31.00 ©2017 IEEE

In lateral interface CNT is laid in AGNR and translational vector *T* of CNT coincides with GNR's length axis. In vertical interface CNT is mounted on AGNR and CNT's tube axis is perpendicular to GNR plane. Their equilibrium distance and binding energy has been computed using Quantumwise-Virtual Nanolab 2016.3 as a simulation software [21-23].The equilibrium distance between CNT and GNR was obtained by varying distance between these two at a point where the inter-wall binding energy is minimum. Any further compactness from equilibrium distance induces additional binding energy. Chemical bond between CNT & GNR can only be formed after crossing equilibrium distance.

## III. Results & Discussion

### *A. Lateral Interface*

As mentioned earlier zigzag and armchair nanotubes are specified by chiral index (*n,0*) and (*n=m*) respectively, knowing that the first chiral index *n* is enough to describe the CNT and GNR. Either way the binding energy of these interfaces are related to their corresponding value of first chiral index *n*.

Fig. 2(a) shows the variation of binding energy. It is observed that binding energy curve for ZCNT-AGNR interface is separated for even and odd values of chiral index *n*. Though binding energy decays in both cases as the chirality of CNT increases, the energy difference is quite high for lower dimension of CNT and quite low for higher dimension of CNT.

Combining these observations over this wide range of data with the insights, we have employed numerical method to predict data accurately. We have formed polynomial relation that best fits the observed energy curve. We made two separate polynomial expression for ZCNT-AGNR interface, as the energy curve splits into two different way and their difference in magnitude is quite high. The binding energy for ZCNT-AGNR interface for even value of chiral index n can be given by the following quadratic polynomial expression,

$$E = -0.07n^3 + 4.16n^2 - 87.36n + 111.55 \quad (1)$$

Here, $E$ = binding energy of the system and $n$ = first chiral index of CNT & GNR. Similarly, binding energy of ZCNT-AGNR interface for odd value of chiral index $n$ can be given by the following linear expression,

$$E = -12n - 196 \quad (2)$$

Fig. 2 (b) and (c) compares simulated data point with polynomial fitted curves. Fig. 3 shows the binding energy variation for ACNT-AGNR interface. Similar to the ZCNT-AGNR interface this curve shows the decay nature, but here binding energy decays quite sharp & linearly.

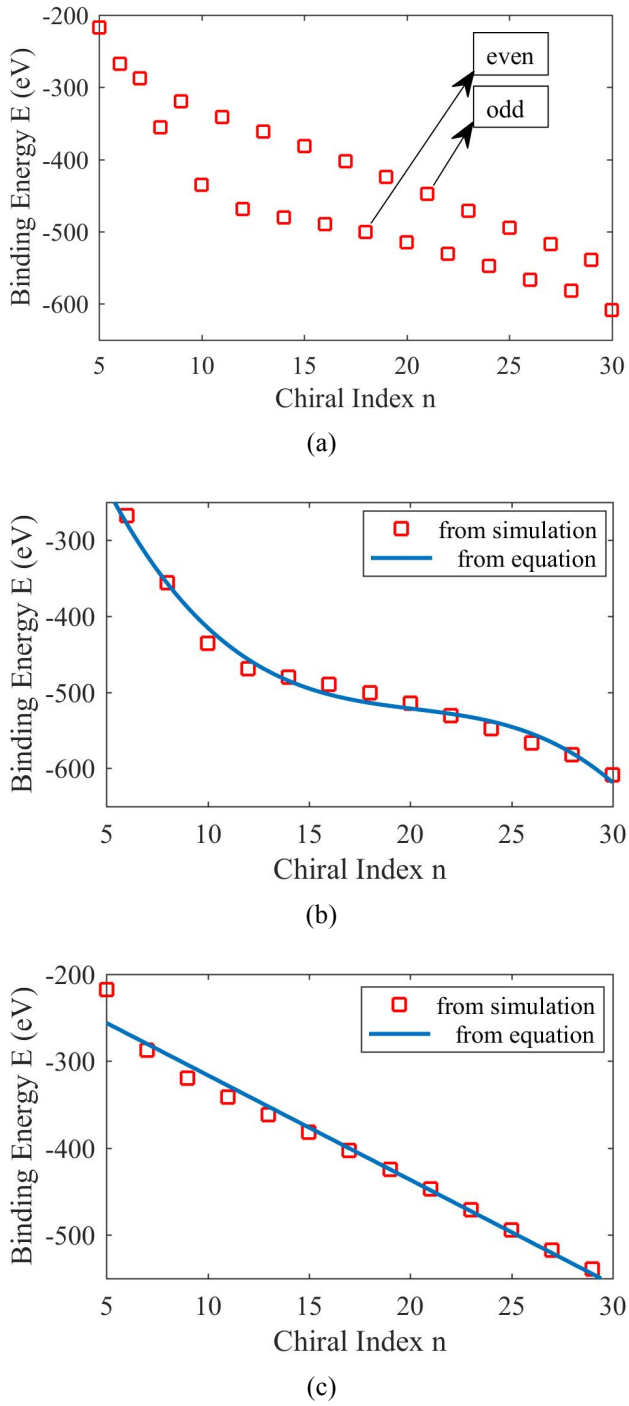


Figure 2: Binding energy as a function of chiral index *n* (a) even & odd chirality combined (b) even value of chirality (c) odd value of chirality.

The binding energy expressions for ACNT-AGNR interface relating first chiral index *n* as a function can be expressed by the following linear expression,

$$E = -41n - 6 \quad (3)$$

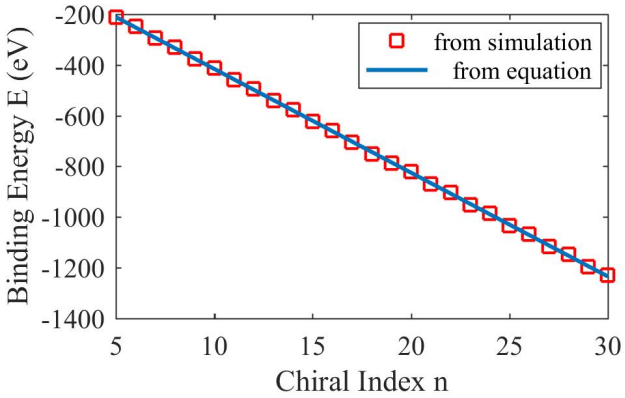


Figure 3: Binding energy $E$ vs chiral index $n$ curve for ACNT-AGNR interface.

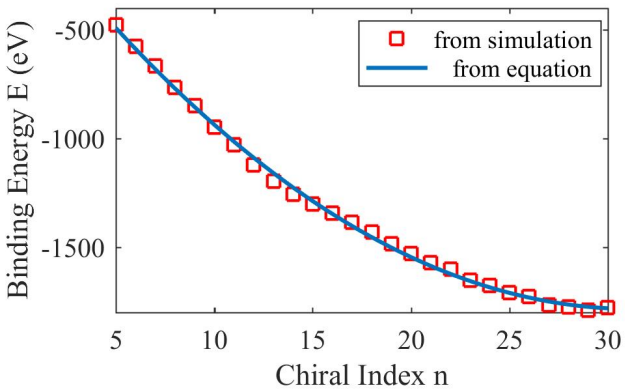


(a)

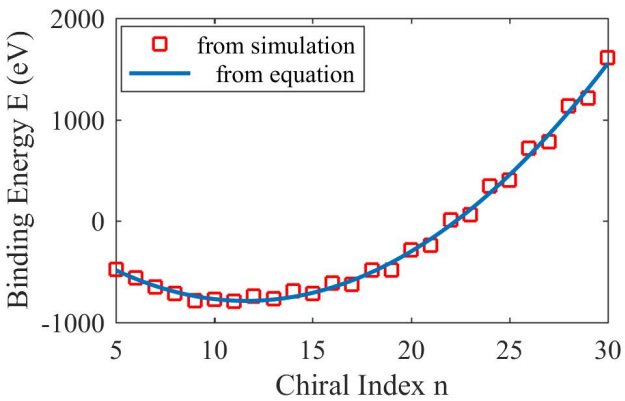


(b)

Figure 4: Binding energy as a function of chiral index $n$ (a) ZCNT-AGNR interface (b) ACNT-AGNR interface.

### B. *Vertical Interface*

As developed earlier in our orientation model, vertical interface incorporates CNT vertically mounted on GNR plane (shown in fig. 1-b), resulting that number of interacting atoms between CNT & GNR are higher than lateral interface. Hence, this arrangement shows higher energy transition than lateral interface Fig. 4-(a) demonstrates binding energy variation for ZCNT-AGNR interface, showing decay nature like lateral interface. But ACNT-AGNR interface shows completely opposite nature. Fig. 4-(b) shows that binding energy increases from negative to positive peak as the chirality increases from lower dimension to higher dimension, due to the armchair similarity of both CNT and GNR. It is observed that for ACNT-AGNR interface energy value of even chirality and odd chirality also maintains some equidistance from each other as occurred in lateral ZCNT-AGNR interface. The binding energy expressions for ZCNT-AGNR interface relating chiral index $n$ as a function of $E$ can be expressed by the following expression,

$$E=1.87n^2 - 117n + 48.2 \tag{4}$$

Similarly, for ACNT-AGNR interface the energy expression yields as,

$$E=6.93n^2 - 161n + 145 \tag{5}$$

Equation (1), (2), (3), (4) & (5) can be simultaneously used to find the value of binding energy for a particular given value of chiral index, for a particular CNT-GNR interface orientation.

## IV. Difference Between Lateral and Vertical Interface

Both of our orientation model shows some linear and non-linear relationship between binding energy and chiral index as shown in (1) to (5). However, these relationships are not consistent to each orientation. The lateral interface shows decaying nature of binding energy while one of the vertical interface shows rising nature. Equilibrium distance for two orientations have also showed some differences. It is observed that vertical interface shows higher energy transition than lateral interface. Unlike lateral interface, binding energy maintains non-linearity with chiral index in vertical interface. Table-I shows the variation of equilibrium distance and binding energy due to orientation of different CNT-GNR interfaces.

TABLE I.
VARIATION OF PROPERTIES OF DIFFERENT CNT-GNR INTERFACE ORIENTATION

| *Orientation of Interface* | *Interface* | *Binding Energy [eV]* | | *Equilibrium Distance [Å]* | |
|---|---|---|---|---|---|
| | | *max* | *min* | *max* | *min* |
| *Lateral Interface* | *ZCNT-AGNR* | *-201.21* | *-608.06* | *1.4* | *1.2* |
| | *ACNT-AGNR* | *-211.46* | *-608.96* | *1.4* | *1.2* |
| *Vertical Interface* | *ZCNT-AGNR* | *-477* | *-1778.86* | *2.2* | *2.1* |
| | *ACNT-AGNR* | *1608.81* | *-478.54* | *2.2* | *2.1* |

## V. CONCLUSION

In this work we have investigated two different orientation model for CNT-GNR interface. From the simulation we observed a wide range of variation in binding energy of CNT-GNR interface at their equilibrium distance. It is found that their binding energy maintains some mathematical linearity and non-linearity with first chiral index *n*. Depending on the data computed from a first principle based simulation software we have graphically plotted the effect of chirality on binding energy. We have found that binding energy for lateral interface are comparatively more linear than the vertical interface. Polynomial equations have been formed to express these linearity and non-linearity which can predict binding energy for any fixed chiral index for any orientation, which will help researcher in many ways.

## REFERENCES


[1] Geim, Andre K., and Konstantin S. Novoselov. "The rise of graphene." *Nature materials*,Vol 6, No. 3, pp. 183-191, 2007.

[2] Baughman, Ray H., Anvar A. Zakhidov, and Walt A. De Heer. "Carbon nanotubes--the route toward applications." *science* 297.5582, pp.787-792, 2002.

[3] Novoselov, K. S., Geim, A. K., Morozov, S. V., Jiang, D., Zhang, Y., Dubonos, S. V, & Firsov, A. A.. "Electric field effect in atomically thin carbon films". *science*, *306* (5696), 666-669, 2004.

[4] Bachtold, A., Hadley, P., Nakanishi, T., & Dekker, C. Logic circuits with carbon nanotube transistors. *Science*, *294*(5545), 1317-1320, 2001.

[5] Salvetat, J. P., Bonard, J. M., Thomson, N. H., Kulik, A. J., Forro, L., Benoit, W., & Zuppiroli, L. Mechanical properties of carbon nanotubes. *Applied Physics A*, *69*(3), 255-260, 1999.

[6] Yu, M. F., Files, B. S., Arepalli, S., &Ruoff, R. S. Tensile loading of ropes of single wall carbon nanotubes and their mechanical properties. *Physical review letters*, *84*(24), 5552, 2000.

[7] Lee, C., Wei, X., Kysar, J. W., & Hone, J. Measurement of the elastic properties and intrinsic strength of monolayer graphene. *science*, *321*(5887), 385-388, 2008.

[8] Berber, Savas, Young-Kyun Kwon, and David Tománek. "Unusually high thermal conductivity of carbon nanotubes." *Physical review letters* 84.20 4613, 2000.

[9] Balandin, A. A., Ghosh, S., Bao, W., Calizo, I., Teweldebrhan, D., Miao, F., & Lau, C. N. "Superior thermal conductivity of single-layer graphene". *Nano letters*, *8*(3), 902-907, 2008.

[10] Kataura, H., Kumazawa, Y., Maniwa, Y., Umezu, I., Suzuki, S., Ohtsuka, Y., &Achiba, Y. "Optical properties of single-wall carbon nanotubes". *Synthetic metals*, *103*(1-3), 2555-2558, 1999.

[11] Guo, G. Y., Chu, K. C., Wang, D. S., &Duan, C. G. "Linear and nonlinear optical properties of carbon nanotubes from first-principles calculations" *Physical Review B*, *69*(20), 205416, 2004.

[12] Prezzi, D., Varsano, D., Ruini, A., Marini, A., & Molinari, E. "Optical properties of graphene nanoribbons: The role of many-body effects." *Physical Review B*, *77*(4), 041404, 2008.

[13] Varshney, V., Patnaik, S. S., Roy, A. K., Froudakis, G., & Farmer, B. L. "Modeling of thermal transport in pillared-graphene architectures". *ACS nano*, *4*(2), 1153-1161, 2010.

[14] Novaes, Frederico D., Riccardo Rurali, and Pablo Ordejón. "Electronic transport between graphene layers covalently connected by carbon nanotubes." *ACS nano* 4.12 (2010), 7596-7602.

[15] Dimitrakakis, Georgios K., Emmanuel Tylianakis, and George E. Froudakis. "Pillared graphene: a new 3-D network nanostructure for enhanced hydrogen storage." *Nano letters* 8.10 3166-3170, 2008.

[16] Kane, A. A., Sheps, T., Branigan, E. T., Apkarian, V. A., Cheng, M. H., Hemminger, J. C,& Collins, P. G. "Graphitic electrical contacts to metallic single-walled carbon nanotubes using Pt electrodes:. *Nano letters*, *9*(10), 3586-3591, 2009.

[17] Robert, P. T., and R. Danneau. "Charge distribution of metallic single walled carbon nanotube–graphene junctions." *New Journal of Physics* 16.1 013019, 2014.

[18] Hong, T. K., Lee, D. W., Choi, H. J., Shin, H. S., & Kim, B. S. Transparent, flexible conducting hybrid multilayer thin films of multiwalled carbon nanotubes with graphene nanosheets. *Acs Nano*, *4*(7), 3861-3868, 2010.

[19] Wilhite, P., Vyas, A. A., Tan, J., Tan, J., Yamada, T., Wang, P,& Yang, C. Y. Metal–nanocarbon contacts. *Semiconductor Science and Technology*, *29*(5), 054006, 2014.

[20] Tamaoki, M., Kishimoto, S., Ohno, Y., & Mizutani, T. Electrical properties of the graphitic carbon contacts on carbon nanotube field effect transistors. *Applied Physics Letters*, *101*(3), 033101, 2012.

[21] Virtual NanoLab version 2016.3, QuantumWise A/S (www.quantumwise.com).

[22] Brandbyge, M., Mozos, J. L., Ordejón, P., Taylor, J., & Stokbro, K. Density-functional method for nonequilibrium electron transport. *Physical Review B*, *65*(16), 165401, 2002.

[23] Soler, J. M., Artacho, E., Gale, J. D., García, A., Junquera, J., Ordejón, P., & Sánchez-Portal, D. The SIESTA method for ab initio order-N materials simulation. *Journal of Physics: Condensed Matter*, *14*(11), 2745, 2002.

# Silicon on metal technology merged with cylindrical gate all around FET for enhanced performance

Abu Bakar Siddik[1], N. M. Mahmud Hossain[2], Sakib Quader[3], and Md. Iqbal Bahar Chowdhury[4]
Department of Electrical and Electronic Engineering
United International University, Dhaka, Bangladesh
Email: [1]a.siddik.bd@ieee.org, [2]n.m.hossain@ieee.org, [3]quader.sakib@hotmail.com, [4]ibchy@uiu.ac.bd

*Abstract*— **Buried oxide layer in SOI devices creates a few problems such as self-heating, which eventually flops the possibility of this device for future circuit analysis. A modification over a fully depleted SOI MOSFET merged with cylindrical gate all around (CGAA) structure is proposed in this work to incorporate improved performance along with a possibility to dissipate the heat generated in the device. The buried oxide layer is replaced with thin $P^+$ region and the substrate layer is replaced by a metallic nanowire which is located at the center of the GAA core. The metallic nanowire is shorted with the gate metal to give in strong govern over the flow of the current and helps the device to release its heat easily. This modified structure is termed as silicon on metal (SOM) CGAA FET and was simulated using SILVACO TCAD ATLAS for short technology nodes. To exhibit the superiority of the device the simulation results were compared with CGAA FET. The device shows an improved electrical characteristics and scaling possibility below 10nm technology node over CGAA FET which makes this modified device potentially suitable for future CMOS technology.**

***Keywords— silicon on metal, silicon on insulator, cylindrical gate all around, scaling, drain induced barrier lowering***

## I. INTRODUCTION

A MOSFET can be treated as the basic building block of VLSI circuits and so is for all the smart devices we are using now [1]. The transfer characteristics of a MOSFET is the main focus for its capability in VLSI circuit use. The parameters to determine the performance of a MOSFET is the off-state current ($I_{off}$), on state current ($I_{on}$), On-Off current ratio ($I_{on}/I_{off}$), drain induced barrier lowering (DIBL), subthreshold swing (SS) and threshold voltage ($V_{TH}$). DIBL can be addressed as the lowering of $V_{TH}$ for an increase in drain voltage. This is more prominent in short channel MOSFETs [2]. $V_{TH}$ is the minimum gate-to-source voltage difference that is responsible for creating a conducting channel between source and drain terminals. The gate voltage required to change the drain current by one decade is defined as Subthreshold Swing (SS). Apart from these the size of the MOSFET is required to reduce as much as possible in order to achieve high integration density [3]. Among the parameters the lower the $I_{off}$, SS, DIBL and $V_{TH}$ the better the performance. With minimized $I_{off}$ the leakage current is reduced and so is the static power loss [4]. With abased SS, the FET shows more ideal like characteristics in the transition period that downgrades the dynamic power loss [5]. A reduced DIBL allows a FET to offer similar output for different drain voltages. Lower $V_{TH}$ means that the FET can now work under much lower bias voltage, thus power can be saved as required bias voltage can be lowered, moreover it supports the scaling of a FET since in smaller FET a higher bias voltage may cause the FET to breakdown. Other than these parameters only $I_{on}$ and $I_{on}/I_{off}$ is needed to be increased. A maximized $I_{on}$ will boost the speed of the device. Since a maximized $I_{on}$ and a minimized $I_{off}$ is required for better performance, thus it is quite obvious that a higher $I_{on}/I_{off}$ is desirable. In accordance with all these performance parameters and the aid of downscaling a FET as much as possible, FET industries has seen many new structures and advancements throughout the decades. The major advancements from single gate MOSFET were multi gate MOSFETs, silicon on insulator (SOI) structures and cylindrical gate all around FET (CGAA FET) [6]- [9]. Although the advancements in this sector have not yet reached the end of its roadmap thus keeping ample amount of space for further research in this field.

A SOI FET faces some disadvantages out of which the extreme heating effect and huge width of the structure are major issues [10]- [11]. The buried oxide in a SOI structure need to be larger in width in order to restrict the flow of leakage current through the layer [12]. Since the insulator layer has a voltage difference in both ends thus power loss through extreme heating is visible in SOI FET. Moreover, the huge insulator layer results in an increase in its size and requires more oxide material.

In this work, we proposed a modification to fix the disadvantages of SOI FET by replacing the insulator and substrate layer by $P^+$ substrate and metallic nanowire respectively to reduce the size and extreme heating problem. This structure is then given a flavor of multi gate structure by merging it with a cylindrical gate all around structure as it is one of the most promising structure of GAA family [13]- [14]. By means of this merging with CGAA, the modified structure boosts the performance as enhancing gate control improves the performance of a FET by allowing strong control over the flow of current. The replacement of buried oxide layer in SOI-FET by extended $P^+$ substrate and core metal bring in the parasitic BJT effect, but since the core metal in the SOM-CGAA FET is shorted with the gate metal thus much better current control is achieved to allow the current to rise above the parasitic loss.

## II. DEVICE STRUCTURE AND SIMULATION

The 2D view of FDSOI and proposed SOM-CGAA FET are demonstrated in fig.1 (a) and (b) respectively. The marked part in fig. 1(a) is replaced with $p^+$ substrate and a metallic

978-1-5386-2307-7/17/$31.00 ©2017 IEEE

nanowire. Furthermore, the nanowire is shorted with the gate metal. The 3D device structure is presented through fig.2 (a), (b); that shows how the modified structure is merged with cylindrical gate all around structure.

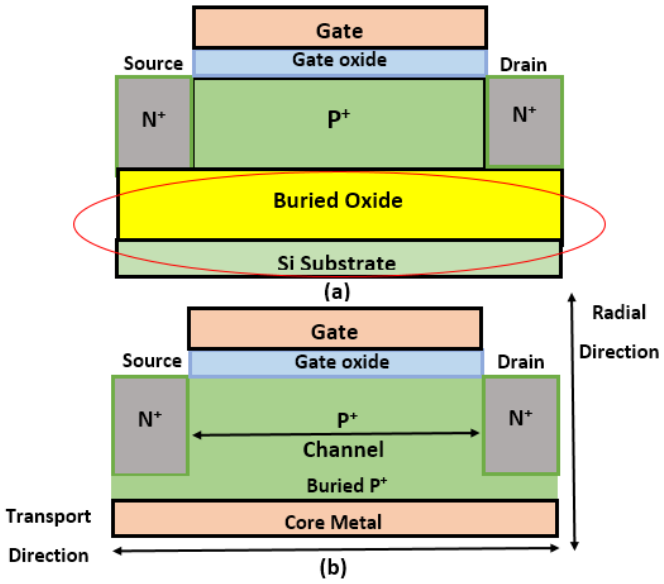


Figure 1. (a) 2D view of FDSOI (b) 2D view of proposed SOM-CGAA structure

The source and drain are doped by N-type dopant of concentration $10^{20}$ $cm^{-3}$, and the channel and rest silicon part are doped using P-type dopant of concentration $10^{18}$ $cm^{-3}$.

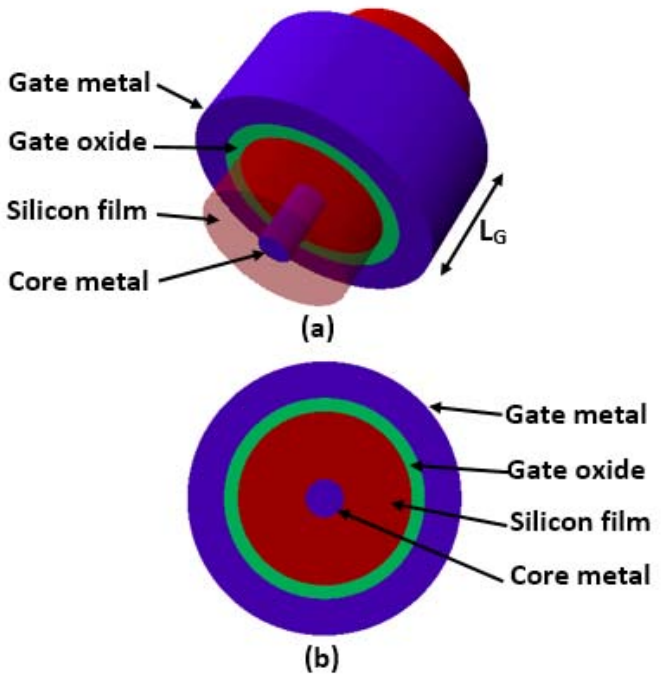


Figure 2. (a) 3D view of SOM-CGAA FET (b) cut plane view of the device

Since the source-channel-drain regions are silicon, so the gate oxide layer used was $SiO_2$, as Si and $SiO_2$ has negligible lattice mismatch [15]. The effective oxide thickness (EOT) for $SiO_2$ oxide layer is 2nm, calculated from the equation of EOT shown in equation 11 in the work by M. Charmi et.al [16]. Metal having work-function of 4.7eV is used for both gate and core metal. A minimum of 2nm thick gate oxide layer was used to avoid tunneling through gate metal to channel region [17]. The detailed view of device configuration is also shown in fig 2. ATLAS tool of Silvaco TCAD software was used to conduct all the simulations, by taking an ultra-thin 2D slice from the 3D structure. Initially Schrödinger–Poisson model was used to solve the eigenvalues and eigenfunctions at each slice in the Si and $SiO_2$ region. This model self-consistently solves the Poisson equation for potential and the Schrödinger equation for bound state energies in both valence and conduction bands. We will assume confinement to take place in one dimension, which we choose to be the x-direction. Therefore, the calculation of the quantum electron density relies upon a solution of a 1D Schrödinger equation at each slice perpendicular to the y-axis [18]. Later non-equilibrium Greens function (NEGF) was solved using mode-space approach to determine the quantum transport of the device. Von Neumann boundary condition was used due to the ballistic nature of transport which causes no voltage drop near the source and drain contacts [19]. Two different node sizes of 10nm and 14nm was studied to analyze the performance of the FET.

## III. SIMULATION RESULTS AND DISCUSSION

Initially a CGAA FET having node size of 14nm was studied, simulated and the major performance parameters were extracted.

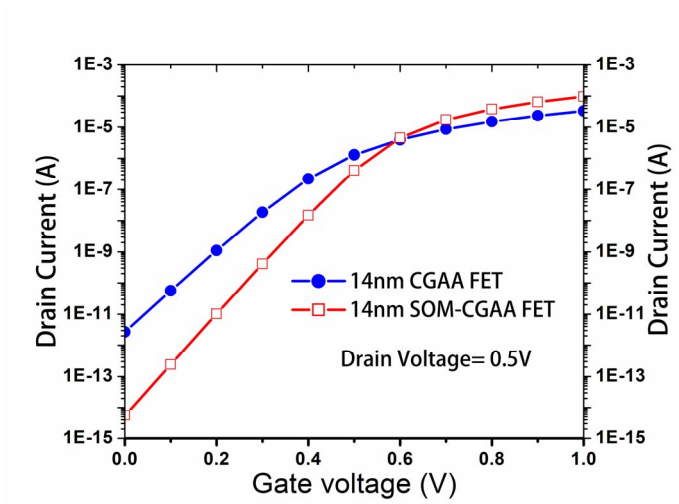


Figure 3. Transfer characteristics of 14nm CGAA and SOM-CGAA FET

The $I_{on}$ and $I_{off}$ were found to be $3.23\times10^{-5}$ A and $2.68\times10^{-12}$ A respectively along with a DIBL of 157.5 mV/V, SS of 77.18 mV/dec and $V_{TH}$ of 0.34 V. The work by Hosseini R et.al shows the simulated data for a 15nm CGAA FET and a close match between these simulated data proves the validity of our simulation [20]. Afterwards the SOM-CGAA FET was simulated and all the performance parameters were extracted. Fig. 3 and Table I are presented to compare between the 14nm SOM-CGAA FET and CGAA FET. Fig. 3 shows the

comparison between these two structures through transfer characteristic curves while table I compares between the performance parameter data. The SOM-CGAA FET gives an $I_{on}$ and $I_{off}$ of $9.59\times10^{-5}$ and $5.57\times10^{-15}$ A respectively along with a DIBL of 35 mV/V, SS of 61 mV/dec and $V_{TH}$ of 0.42 V.

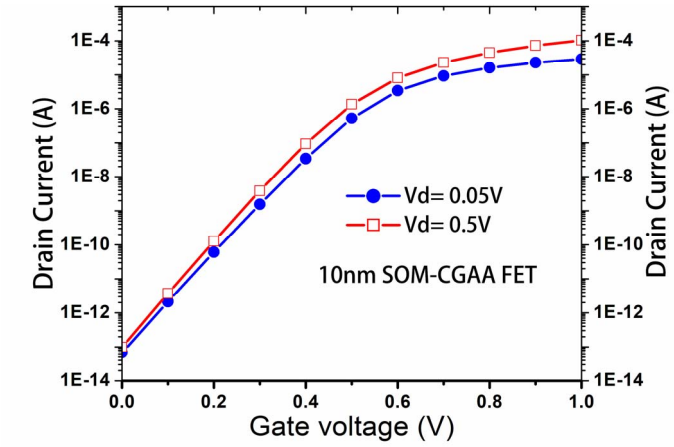


Figure 4. Transfer characteristic of 10nm SOM-CGAA FET for different drain voltages

A scrutinized comparison reveals that the SOM-CGAA FET is superior to CGAA FET in terms of $I_{on}$, $I_{off}$, DIBL, SS and $I_{on}/I_{off}$ on the other hand only the $V_{TH}$ lacks behind the CGAA structure by a minimal amount. Since a 14nm SOM-CGAA FET gives a promising outcome, so a 10nm SOM-CGAA FET was also simulated and the performance parameters were extracted as well.

The transfer characteristic curves of 10nm SOM-CGAA FET are advertised through fig. 4 and the extracted data representing the performance parameters are displayed in table II. It is evident from table II that even a 10nm SOM-CGAA FET offers an outstanding performance which proves that it is also a candidate to fabricate next generation ICs with sub-10nm technology node.

A comparison between 14nm CGAA FET and 10nm SOM-CGAA FET shows that SOM-CGAA FET offers a much reduced $I_{off}$ than 14nm CGAA FET. Similarly, a SOM-CGAA FET offers a boosted $I_{on}$ and improved DIBL, SS and $I_{on}/I_{off}$. Thus, marking the place of much scaled SOM-CGAA FET in place of CGAA FET. On the contrary the $V_{TH}$ for 10nm SOM-CGAA FET faces a trivial increment than 14nm CGAA FET. Moreover, it is also evident that as the drain voltage is increased for both CGAA FET and SOM-CGAA FET, the change in $V_{TH}$ for CGAA FET is much significant than SOM-CGAA FET which in turn causes the DIBL of CGAA FET to rise.

In order to support the rise of DIBL in CGAA structure than SOM-CGAA structure, the band diagrams as a function of coordinate in transport direction for both these structures at on state are displayed in fig. 5 and fig. 6. As the drain voltage is increased, a noticeable barrier lowering from drain to channel region for CGAA FET is observed as displayed in fig. 5 whereas, proposed SOM-CGAA FET shows a negligible barrier lowering at the same condition as shown in fig. 6. These band diagrams prove how SOM-CGAA FET offers a diminished DIBL.

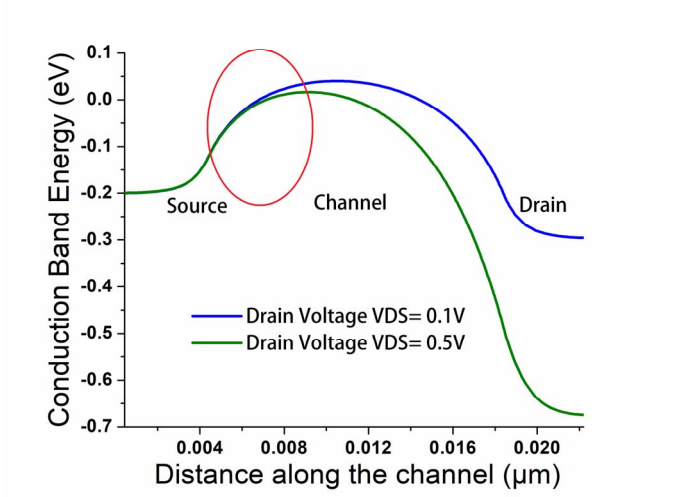


Figure 5. Conduction band energy as a function of position along channel for CGAA FET

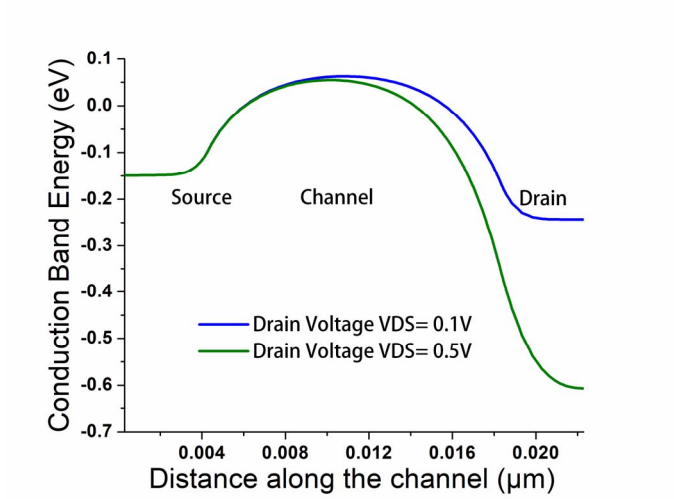


Figure 6. Conduction band energy as a function of position along channel for SOM-CGAA FET

In addition to all these advancements, a SOM-CGAA FET is also capable of reducing the heating problem caused in SOI devices, as in SOI devices the buried oxide has a poor thermal conductivity so the heat generated in channel cannot be removed leading to thermal runway. However, in SOM-CGAA FET the core metal allows the heat to be released which is how the heating problem is solved. Thus, for the modified structure the main advantages lie in SS, DIBL and reduced heat. This structure leads the SS nearly to the BOLTZMANN limit and minimizes the DIBL to the slightest.

TABLE I. PERFORMANCE PARAMETERS FOR THE CGAA AND PROPOSED SOM-CGAA FET FOR 14NM NODE SIZE

| Process | 14nm | |
|---|---|---|
| ***Drain Bias*** | ***0.5V*** | |
| Device | ***CGAA FET*** | ***SOM-CGAA FET*** |
| $I_{off}$ (A) | 2.68E-12 | 5.57E-15 |
| $I_{on}$ (A) | 3.32E-05 | 9.59E-05 |
| $I_{on}/I_{off}$ | 1.24E+07 | 1.72E+10 |
| SS (mV/dec) | 77.1859 | 61.0799 |
| DIBL (mV/V) | 157.584 | 35.0156 |
| $V_{TH}$ (V) | 0.340135 | 0.421551 |

TABLE II. PERFORMANCE PARAMETERS FOR PROPOSED 10NM SOM-CGAA FET FOR DRAIN VOLTAGE 0.05V AND 0.5V

| Process | 10nm | |
|---|---|---|
| ***Device*** | ***SOM-CGAA FET*** | |
| Drain Bias | ***0.05V*** | ***0.5V*** |
| $I_{off}$ (A) | 6.74E-14 | 9.80E-14 |
| $I_{on}$ (A) | 2.90E-05 | 1.04E-04 |
| $I_{on}/I_{off}$ | 4.30E+08 | 1.06E+09 |
| SS (mV/dec) | 66.7168 | 63.5408 |
| $V_{TH}$ (V) | 0.429947 | 0.401005 |
| DIBL (mV/V) | 64.31 | |

## IV. CONCLUSION

In this work, fully depleted SOI FET was modified and merged with cylindrical gate all around structure in order to eliminate the self-heating problem and decrease the SOI device's huge thickness. Proposed modification does not require huge buried oxide layer which can effectively reduce the excessive use of oxide material. The SOM-CGAA FET was simulated using SILVACO TCAD ATLAS for short channel length of 10 and 14nm. However, the results of SOM-CGAA FET were compared to that of CGAA FET. It was evident from the results that in terms of $I_{off}$, $I_{on}$, $I_{on}/I_{off}$, SS and DIBL this SOM-CGAA FET is dominant over silicon nanowire transistors. Moreover, it is also evident that the performance achieved from a CGAA FET can also be achieved from a more scaled SOM-CGAA FET, thus size of devices can be shrunk. All these advantages in performance makes this structure much more applicable for low power applications and its much-scaled size makes it a potential candidate in VLSI and nanoscale biomedical applications.

## ACKNOWLEDGMENT

The authors would like to thank Dr. Mohammad Mojammel Al Hakim, Dept. of EEE, East West University, Dhaka, Bangladesh for letting the support in using their licensed Silvaco TCAD software.

## REFERENCES

[1] N. Ali, D. Dheer, S. Paliwal and C. Periasamy, "TCAD analysis of variation in channel doping concentration on 45nm Double-Gate MOSFET parameters," *2015 Annual IEEE India Conference (INDICON)*, New Delhi, 2015, pp. 1-6.

[2] J. Qu, H. Zhang, X. Xu and S. Qin, "Study of Drain Induced Barrier Lowering(DIBL) Effect for Strained Si nMOSFET", *Procedia Engineering*, vol. 16, pp. 298-305, Jan. 2011.

[3] Ranka Deepesh, K. Rana Ashwani, Yadav Rakesh Kumar, Yadav Kamalesh, Giri Devendra, "Performance Evaluation of FD-SOI MOSFETs for Different Meetal Gate Work Function", *International Journal of VLSI design & Communication Systems (VLSICS)*, vol. 2, no. 1, March 2011.

[4] Nam Sung Kim, T. Austin, D. Blaauw, T. Mudge, K. Flautner, Jie S. Hu, M. Irwin, M. Kandemir and V. Narayanan, "Leakage current: Moore's law meets static power", *Computer*, vol. 36, no. 12, pp. 68-75, Dec. 2003.

[5] F. FALLAH, "Standby and Active Leakage Current Control and Minimization in CMOS VLSI Circuits", *IEICE Transactions on Electronics*, vol. 88-, no. 4, pp. 509-519, Apr. 2005.

[6] B. Khamaisi, O. Vaknin, O. Shaya and N. Ashkenasy, "Electrical Performance of Silicon-on-Insulator Field-Effect Transistors with Multiple Top-Gate Organic Layers in Electrolyte Solution", *ACS Nano*, vol. 4, no. 8, pp. 4601-4608, Jul. 2010.

[7] J. Colinge, "Multi-gate SOI MOSFETs", *Microelectronic Engineering*, vol. 84, no. 9-10, pp. 2071-2076, Sep. 2007.

[8] Suhas N. Yadav, M.S. Jadhv, "Multiple gate field-effect transistors for future mos technologies", *International Journal of Research in Engineering and Technology*, vol. 03, pp. 542-547, Feb. 2014.

[9] A. Sharma and S. Akashe, "Performance Analysis of Gate-All-Around Field Effect Transistor for CMOS Nanoscale Devices", *International Journal of Computer Applications*, vol. 84, no. 10, pp. 44-48, Jan. 2013.

[10] B. M. Tenbroek, M. S. L. Lee, W. Redman-White, J. T. Bunyan and M. J. Uren, "Self-heating effects in SOI MOSFETs and their measurement by small signal conductance techniques," in *IEEE Transactions on Electron Devices*, vol. 43, no. 12, pp. 2240-2248, Dec. 1996.

[11] Yi-chuen, J. t. Lin, K. d. Huang, T. y. Lee and K. c. Lin, "An investigation of the effects of Si thickness-induced variation of the electrical characteristics in FDSOI with block oxide," *2006 8th International Conference on Solid-State and Integrated Circuit Technology Proceedings*, Shanghai, 2006, pp. 61-64.

[12] J. Wana, C. Le Royer, A. Zaslavsky, S. Cristoloveanu, "Gate-induced drain leakage in FD-SOI devices: What the TFET teaches us about the MOSFET", *Microelectronic Engineering*, vol. 88, pp. 1301-1304, Jul. 2011.

[13] T. Fashtami and S. Seyed Ali, "Performance Investigation of Gate-All-Around Nanowire Fets for Logic Applications", *Indian Journal of Science and Technology*, vol. 8, no. 3, p. 231, Feb. 2015.

[14] G. Liang, "Structure Effects in the gate-all-around Silicon Nanowire MOSFETs," *2007 IEEE Conference on Electron Devices and Solid-State Circuits*, Tainan, 2007, pp. 129-132.

[15] Virginia Semiconductor, "The General Properties of Si, Ge, SiGe, SiO2 and Si3N4", June 2002.

[16] M. Charmi, "Novel attributes and design considerations of effective oxide thickness in nano DG MOSFETs", *Chinese Physics B*, vol. 24, no. 4, p. 047302, Apr. 2015.

[17] G. Timp et al., "The relentless march of the MOSFET gate oxide thickness to zero", *Microelectronics Reliability*, vol. 40, no. 4, pp. 557-562, Apr. 2000.

[18] J. L. Padilla, F. Gamiz and A. Godoy, "A Simple Approach to Quantum Confinement in Tunneling Field-Effect Transistors," in *IEEE Electron Device Letters*, vol. 33, no. 10, pp. 1342-1344, Oct. 2012.

[19] *ATLAS User's Manual*, Section 14.8.1, Silvaco Inc (2016).

[20] R. Hosseini, M. Fathipour and R. Faez, "Quantum simulation study of gate-all-around (GAA) silicon nanowire transistor and double gate metal oxide semiconductor field effect transistor (DG MOSFET)", *International Journal of the Physical Sciences*, vol. 7, no. 28, pp. 5054-5061, Jul. 2012.

# Performance Improvement of Superconducting Magnetic Energy Storage Based ACO Controlled Hybrid Micro-Grid System

Md. Asif-Ur Rahman Sarker, Md. Rafiqul Islam
Department of Electrical and Electronic Engineering
Khulna University of Engineering & Technology
Khulna, Bangladesh
au.rahman102@gmail.com, rafiq043@yahoo.com

***Abstract*— Replacement of traditional energy sources with renewable energy is the present trend. This has increased the existence of microgrid, which can be used as an islanded or grid connected system. This paper discusses about the design and control of hybrid microgrid. Here a hybrid energy source combination of PV and wind energy source is introduced in the micro-grid with a Super Conducting Magnetic Energy Storage (SMES) system. The usage of SMES is more efficient than a battery system with less distortions. To reduce more distortions in the AC power connected to the grid, ant colony optimization is used to control the inverter gating signal which converts DC power from the renewable energy to AC power. This creates the system more stable compared to other storage techniques. The results are discussed with the help of THD analysis. MATLAB R2013 is used for modelling of the system.**

***Keywords*— *Photovoltaic generation, Wind generation, Superconducting Magnetic Energy Storage, Ant Colony Optimization, Total Harmonic Distortion.***

## I INTRODUCTION

Renewable Power sources are now used for micro grids due to the pollution of surroundings created by coal and gas burned generators. The most attractive renewable energy systems are photovoltaic (PV) and wind turbine generators (WTG) because of their high energy production without any pollution.

A micro grid is specified as a system with a group of loads and micro sources which supplies electrical power to a local area. The change in the concept of power system and economy scale has made it possible to set up smaller and distributed power plants. Energy storage reduces the necessity of rotating reserves that ameliorates the efficiency and reliability of supply system. It makes possible to satisfy the power requirements, assures better utilization of effective base load propagation and provides larger use of random renewable energy technologies.

Permanent magnet synchronous generator (PMSG) is more favored option for WTG because of elimination of the excitation losses of a Field Excited synchronous generator (FESG) and system reliability. A PMSG can be brought together with a wind turbine having many poles in absence of a gearbox that importantly decreases the structure, process and maintenance expenditures of the WTG system [1].

Neither PV cell or a wind energy system can supply a uninterrupted energy supply for the irradiance of sun light and seasonal variation of the wind [2]. A hybrid system of wind turbine and PV cell can prevent the problem. As the power of the solar cell isn't stable, it can't meet the demand power always. Sometimes it generates excessive power than load demand too and it isn't good to flow different voltage and frequency to the grid. An energy storage system has a big influence to meet the demand and brand the system more stable [3].

Among the vast variety of energy storage system available, one of the newest and finest is the Superconducting Magnetic Energy Storage (SMES). This system is an electrical storage system, which stores electrical power as electrical power itself [4]. The SMES is way more efficient than the usual battery storage. Using SMES, a system with more power stability can be produced. [5]. The SMES has a capability to absorb and re-inject the active and reactive power, when it is connected to a power system. Two identical converters with a capacitor link combines to form a SMES, which is unified with power conversion system [6].

Optimized system for better performance and stability is another criterion of a stable system. Any system can be easily optimized using an Ant Colony Optimization (ACO) technique [7]. ACO is a swarm based system which is inspired by the food searching technique of an ant colony, that searches for a best and shortest path solution find, with the help of the ant pheromones [8]. The control of the advanced power system confronts primarily optimization tasks. Several individual and multiple optimization methods are: Decision making; Modification of the program of renewable sources for maximum efficiency; Problems with the energy storages; Optimization of the system module; Specification of the perfect power combination in individual and also multiple case; Territorial energy exchange [9].

978-1-5386-2307-7/17/$31.00 ©2017 IEEE

In this paper, the hybrid micro-grid system is designed based on ACO technique to reduce the harmonic distortion of the system. Yet, the SMES was applied to find a stable system with a charge controller. The proposed system is installed on the existing system with a better modification and with better outputs. The simulation process is presented with or without ACO technique implementation for all three categories in section III.

## II SYSTEM DESIGN

The block diagram of proposed ACO controlled SMES based hybrid micro grid system is depicted in the Fig.1. Solar and Wind are renewable energy sources which are adequate in nature, but they vary according to the environmental changes. Hence the production of constant power is not possible in these systems and the need of Maximum Power Point Tracking (MPPT).

The Solar or Photo voltaic (PV) system acquires isolation as input, when the light falls on a PV panel, the PV cells produce current and the cells are connected in series to form an array, the array are paralleled to form the PV module or panel. Using the open circuit voltage and short circuit current, the maximum voltage and current is derived.

The Wind Turbine works on the principle of kinetic energy, it depends on the pitch angle of the wind blades and wind speed. The wind energy is converted into kinetic energy with the wind turbine. The kinetic energy converted into mechanical energy at the shaft end, which is connected to the Permanent Magnet Synchronous Generator(PMSG). The PMSG produces three phase AC power, for obtaining maximum power and energy storage purpose, the AC power is converted into DC power.

The maximum PV and Wind power are given to the DC to DC Cuk Converter, which is a combination of buck boost converter. The switches of the Cuk Converter are triggered from the pulses produced by PV and wind MPPT. The modified DC power is used to energize superconducting magnetic energy storage device (SMES) and to the inverter.

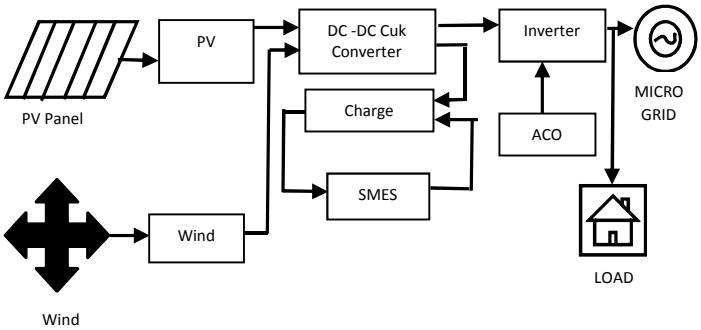


Fig.1. Block Diagram of Proposed System

The modified DC voltage is given to the Charge Controller which play the main role in controlling the SMES charge during run time and discharge during off time. In SMES energy is stored in superconducting coil (SCC) with the help of chopper. The current and state of charge of SCC are compared with modified DC voltage in Charge Controller to produce triggering pulses for the chopper in SMES connected to SCC.

The DC power from the Cuk Converter is given to the inverter, the inverter produces three phase AC power, the produced AC power given to local loads and the remaining power is given to microgrid. To trigger inverter switches, the reactive power of local load and grid terminal is analyzed and controlled using PI controller to produce gating pulses. To make the system more stable the PI controllers of the inverter is tuned with the help of ant colony optimization, which produces power with less harmonics.

### *A. Energy Source*

A hybrid PV and Wind energy sources are used to generate power. The PV system is a combination of parallel connected series array of PV cells. The equivalent circuit of a PV cell can be characterized using a PN junction diode [15] as shown in Fig.2. When the light falls on the PV cell, it works on the forward bias mode of PN junction diode with characterization of short circuit current (1) and open source voltage (2) which is given as follows:

$$I_{sc} = I_0\left[\exp\left(\frac{qV}{nKT}\right)-1\right]-I_L \tag{1}$$

and when $I_{sc} = 0$

$$V_{oc} = \frac{nkT}{q}\ln\left(\frac{I_L}{I_0}+1\right) \tag{2}$$

The PV cell can be characterized by its maximum power point, when the product of peak voltage (3) and current at its maximum as shown in Fig.3.

$$V_{mp} = V_{oc} - \frac{nkT}{q}\ln\left(\frac{V_{mp}}{(nkT/q)}+1\right) \tag{3}$$

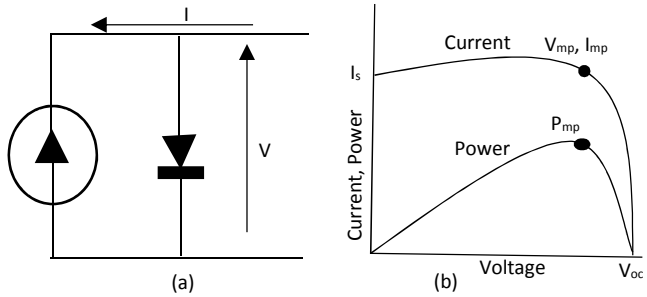


Fig. 2. (a) Equivalent circuit of PV cell and (b) Maximum power point curve of a PV cell

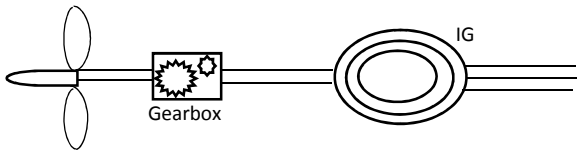


Fig.3. Wind Turbine

The maximum dc power of a PV panel is given as

$$P_m = V_{oc} I_{sc} FF \tag{4}$$

where fill factor, $FF = \dfrac{V_{mp} I_{mp}}{V_{oc} I_{sc}}$ (5)

A wind energy generation system consists of a wind turbine and induction generator [10] as shown in Fig.3. The kinetic energy, wind is converted into mechanical energy using wind turbine and using the mechanical torque (6) the induction generator produces ac power at rotor (7)

$$T_m = J\frac{d\omega_r}{dt} + D\omega_r + T_e \tag{6}$$

when $T_m = T_e$

$$P_r = -sT_m\omega_s \tag{7}$$

*B. Energy storage and conversion*

The SMES contains two primary sections, the transition module and the superconductor coil showed in Fig. 4, First, the transition module consists of two power converters, which are assigned to convert the alternative current to direct current. The second component of the SMES is a superconducting coil which resistivity is very low. When the direct current flows through the superconducting coil a magnetic energy will be produced close to the coil [11]. This energy keeps for a desired time without any losses in the superconducting coil [12,13].

A power conditioning system (PCS) having a three-phase voltage source converter as well as a dc-dc chopper is involved to move energy into the system. [14].

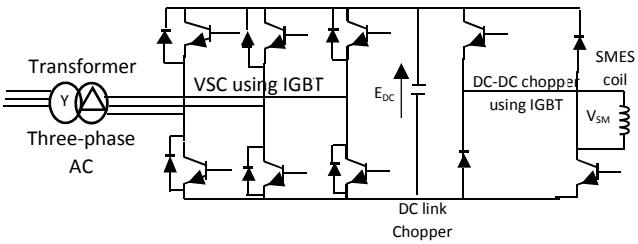


Fig.4. System design of a voltage source converter (VSC) based SMES system

Because of the capability to recover the active and reactive power quickly, SMES can be designed for low frequency oscillations maintenance [15], load power fluctuating level [16] and for the transient stability improvement. The active and reactive power of the system has been controlled by the firing angle of an AC/DC six-pulse bridge converter.

The dc output voltage of the converter is:

$$V_{sm} = V_{sm_0}\cos(\alpha) - R_c I_{sm} \tag{8}$$

The relation of voltage and current in the superconducting inductor can be expressed as:

$$I_{sm} = \frac{1}{L_{sm}}\int_{t_0}^{t} V_{sm}dt + I_{sm_0} \tag{9}$$

The active power ($P_{sm}$), received or returned by the SMES neglecting the switching loss of the converter is shown as:

$$P_{sm} = V_{sm} I_{sm} = V_{sm_0} I_{sm_0}\cos(\alpha) \tag{10}$$

Here, $P_{sm}$ is simply a function of α, dependent on the voltage of the superconducting coil ($V_{sm}$). The energy stored in the superconducting inductor is:

$$W_{sm} = W_{sm_0} + \int_{t_0}^{t} P_{sm}dt \tag{11}$$

$$W_{sm_0} = \frac{1}{2}L_{sm}I_{sm_0}^2 \tag{12}$$

where: $W_{sm0}$ is expressed as the initial energy

Consequently, the SMES has the ability to store a prominent amount of energy based on the current which passes through the superconducting coil.

*C. Microgrid*

A microgrid incorporated with power electronic interface creates an independent system, with likely self-reliant control, communication and protection.

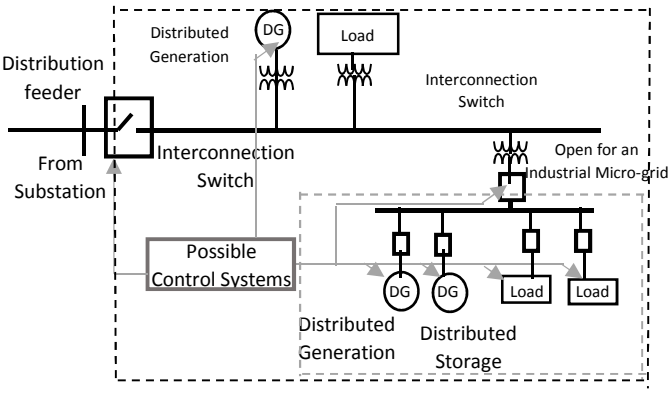


Fig.5. Schematic diagram of a micro-grid

It provides useful back-up to the transmission grid during grid-connected mode and when the capacity can't match the coincident peak load. Indeed, the Micro grids contains low voltage LV distribution systems with combination of various Energy Resources like PV cell, wind energy, bio-mass and fuel cell along with energy storage system like batteries, flywheels, super capacitors and Controllable Loads which works as an interconnected network with improved power electronic converters and controllers. A microgrid is covered with different types of distributed generators (DG), storages (DS) and different loads as indicated in Fig.5. Basically, it is a division of distribution system settled far away from the distribution substation. Thus, the point-of-common-coupling (PCC) of the microgrid places at the circumference of the LV side of the substation transformer [17].

*D. Ant Colony Optimization*

Ant Colony Optimization (ACO), is a probabilistic operational research technique, proposed by Marco Doringo in 1992, used in solving best path in graph plotting. It is one of the swarm intelligence based metaheuristic optimization that

works on the food searching behavior of ants [18]. The pheromones have the tendency to get evaporated with length and time, which would reduce the attraction of ants towards the driven path. The shortest path is compared frequently to avoid such situations.

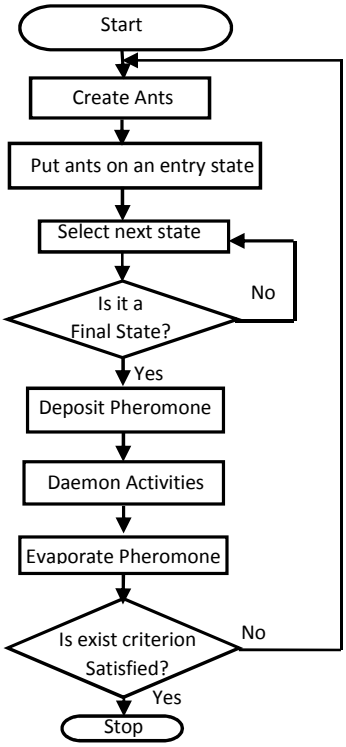


Fig 6. Flowchart of ACO

The goal of ACO is to obtain the shortest path between the source and destination like a round-trip to set up a link between a series of nodes. The basic algorithm is comparatively elementary. This algorithm is settled on the nature of a set of ants. Each of them makes a possible round-trip. In every stage, the ant selects a move from one node to the other one corresponding to the rules and the flowchart is given in the fig 6.

Step 1: The ant must go to each node exactly one time;
Step 2: A distant node doesn't have enough chance to be chosen;
Step 3: The more intense the pheromone tag put down on an edge between two nodes, the larger the chance of that edge will be elected;
Step 4: After finishing its trip, the ant sediments more pheromones on all edges it tracked, if the trip is short;
Step 5: Completing each loop, trails of pheromones disappear.

*E. Total Harmonic Distortion (THD)*

The total harmonic distortion is a measurement of a signal which is distorted because of the presence of harmonics. A voltage or current signal has no harmonic if it is pure sine wave but when there will be a periodic wave the harmonics make the signal distortion. THD analysis mainly calculates the accuracy of the signal comparing the pure signal.

$$THD = (\sqrt{\sum_{n=2}^{\propto} Vn_rms^2})/Vfun_rms^2 \quad (10)$$

## III SIMULATION AND RESULTS

The model of SMES based hybrid microgrid system is shown in Fig.7, the PV and Wind system are connected in parallel to the DC-DC Cuk Converter, which produces modified DC outputs to the charge controller and PWM inverter. The charge controller, controls the energy stored in SMES, the stored power is released back to the system by paralleling the outputs with the DC outputs from Cuk Converter. The PWM inverter converts the DC to AC power and gives it to the local loads, the remaining power obtained after the power abortion of local loads is given to the microgrid. The design parameter of the model is given in the Table.1.

TABLE.1: PARAMETERS FOR THE SYSTEM

| Elements | Item | Parameters |
|---|---|---|
| PV | Power rating<br>Voltage rating<br>$R_{sh}$ | 10kVA<br>66V<br>550ohms |
| Grid Connected Converter | Power Rating<br>Switching Frequency<br>Filter inductor | 30kVA<br>5kHz<br>2mH |
| SMES | Power Rating<br>Current through Inductor<br>Stored energy<br>Inductor | 25kVA<br>70A<br>14.49kJ<br>5H |
| Wind Generator | Power Rating<br>Switching Frequency<br>DC link Capacitor | 15kVA<br>10kHz<br>1000e-6 |

The DC output is connected to the PWM inverter to produce three phase AC power output supplies local loads and microgrid. It is triggered by the gating signal which is produced from control of its output power and the microgrid power. At the terminal of microgrid we obtain 3 phase voltages and current with less harmonics shown in Fig.8.

The performance of a signal can be analyzed using Total Harmonic Distortion. For the SMES based hybrid microgrid the 3-phase voltage as obtained as shown in Fig. 9 and the THD produced is 11.45%.

To make the system harmonics free, the PWM inverter is controlled using ACO. The error signal from the PI controller is taken as reference signal to the ACO.

A comparison of the energy source was carried out to find which alignment could be better. In addition to the proposed system, wind source without energy storage and only PV based system are designed and compared.

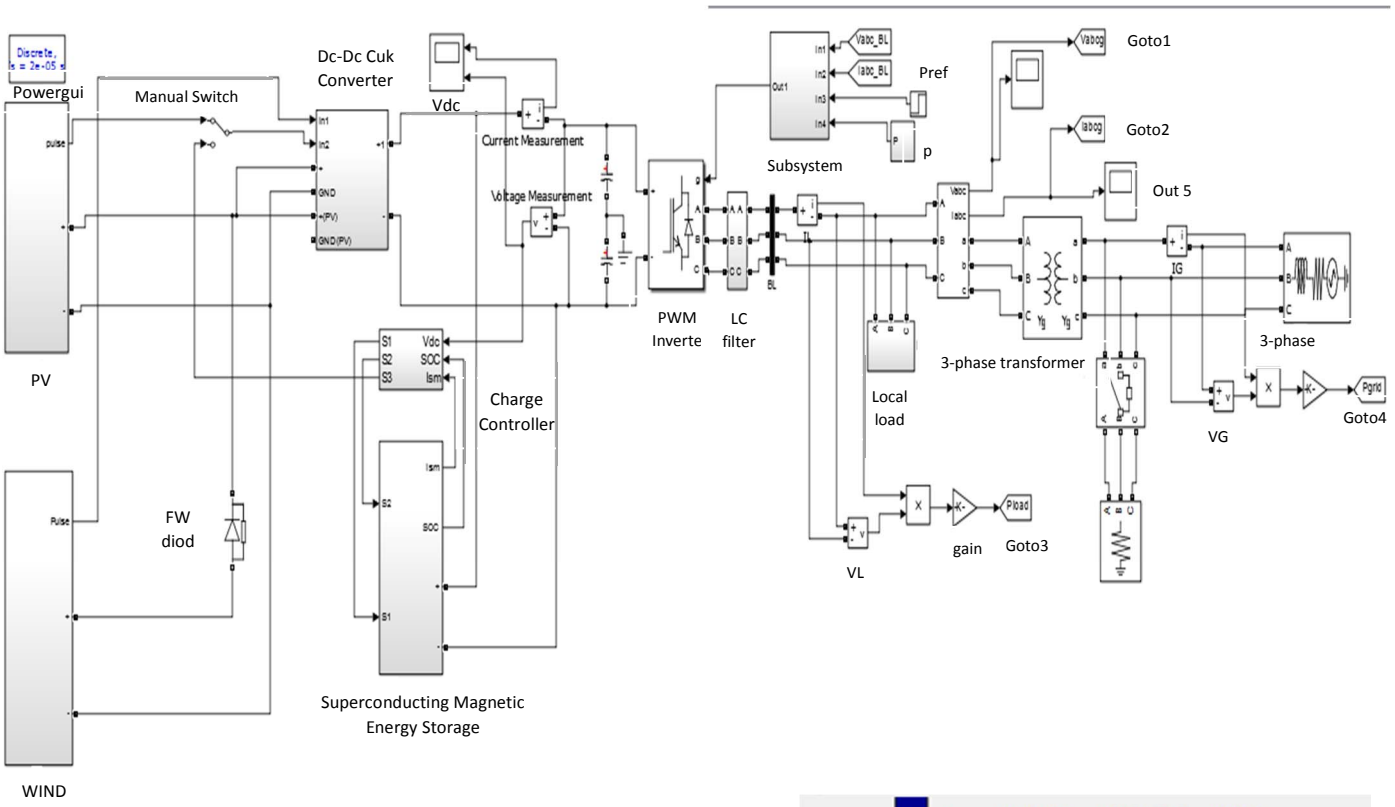


Fig.7. The Model of SMES based Hybrid Micro-Grid System

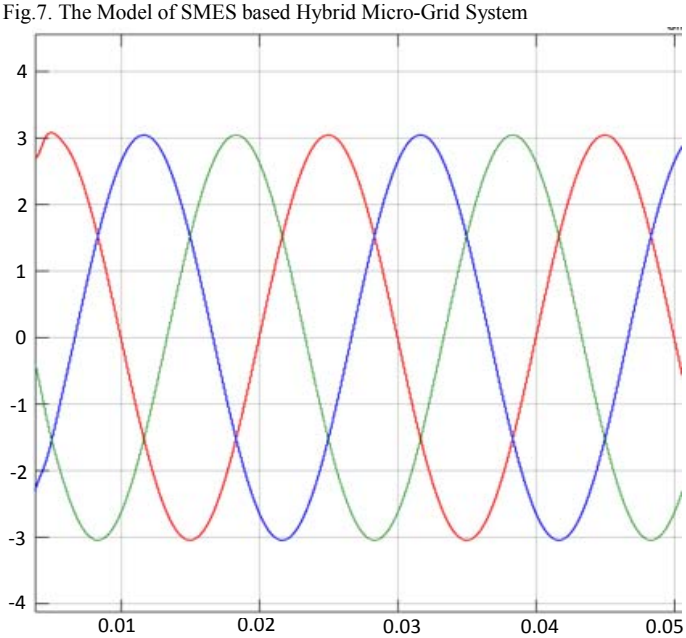

Fig.8. Three Phase Grid Output Voltage

The other two systems also been optimized with ACO. Among which the proposed system is proved to be the best with the help of THD analysis. The comparison is tabulated below in Table.2.

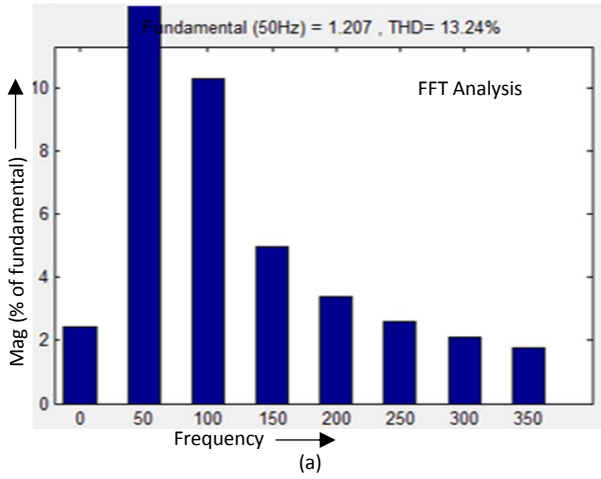


(a)

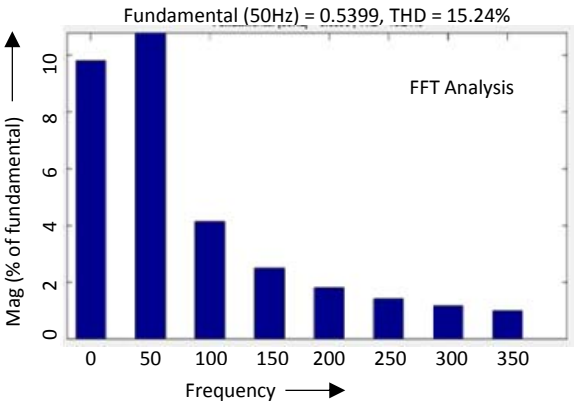


(b)

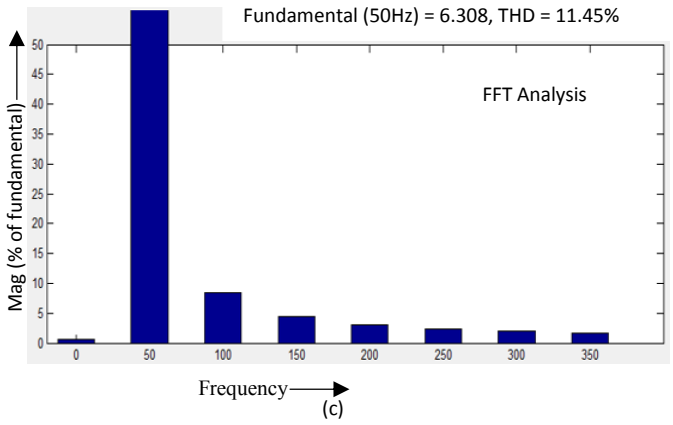


(c)

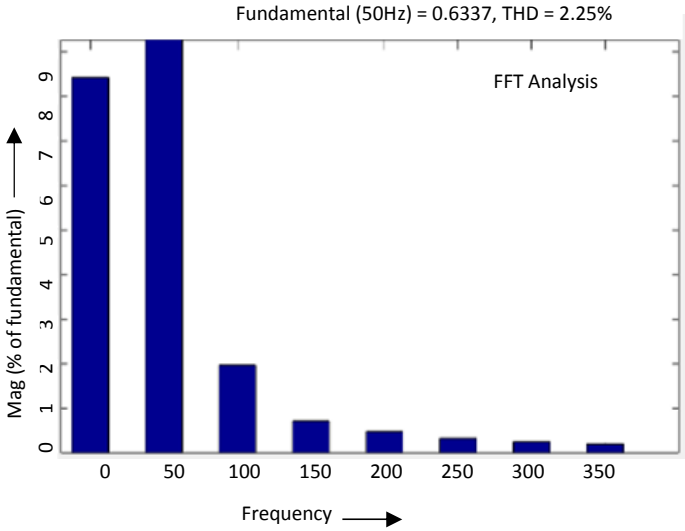


(d)

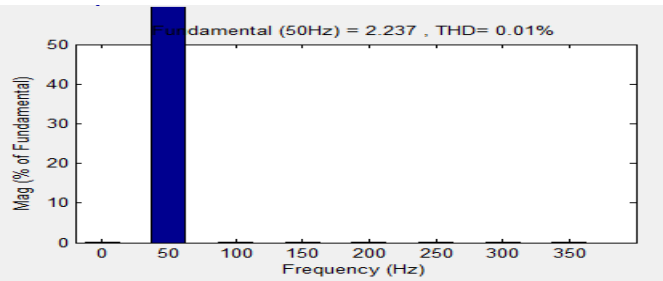


(e)

Fig.9. THD analysis of un-optimized (a) SMES based PV (b) Wind with SMES based PV (c) SMES based Hybrid and THD analysis of (d) SMES based PV (e) SMES based Hybrid

TABLE 2. THD ANANALYSIS OF VARIOUS SYSTEMS

| Types | Without ACO Optimized (%) | Ant Colony Optimized (%) |
|---|---|---|
| SMES based PV | 13.24 | 2.25 |
| Wind with SMES based PV | 15.24 | 3.90 |
| SMES based Wind and PV hybrid | 11.45 | 0.01 |

## IV CONCLUSION

A hybrid PV and wind system is designed to power up microgrid. From the simulation and results, it is proved that the SMES designed to work with energy sources makes the stable by producing output with less harmonics. It is about 11.45% in hybrid of PV and wind turbine system which further nullified with the help of Ant Colony Optimization. A better system is launched with a THD of only 0.01% which is desirable. If there is an inadequacy of enough wind power the PV array can be used only as energy source too and in all cases the ACO will minimize the distortion in an effective way.

## REFERENCE


[1] W. Qiao, X. Yang, and X. Gong, “Wind speed and rotor position sensorless control for direct-drive PMG wind turbines,” IEEE Trans. Ind. Appl.,vol. 48, no. 1, pp. 3–11, Jan./Feb. 2012

[2] Ekren, Orhan, and Banu Y. Ekren. "Size optimization of a PV/wind hybrid energy conversion system with battery storage using simulated annealing." Applied Energy 87.2 (2010): 592-598.

[3] Xie, Yang, et al. "Simulation on a micro-grid system based on superconducting magnetic energy storage." Power Electronics and Application Conference and Exposition (PEAC), 2014 International. IEEE, 2014.

[4] K.Y.C. Cheung, S.T.H. Cheung, R.G. Navin De Silvia, M.P.T. Juvonen, R Singh, J.J. Woo, "Large-Scale Energy Storage Systems", Imperial College London: ISE2, 2002/2003.

[5] W.V. Hassenzahl, " Applied Superconductivity, Superconductivity, an enabling technology for 21st century power systems", IEEE Transactions on Magnetics, pp. 1447-1453, vol.11, no. 1, Mar 2001.

[6] S. Embaiya, L. Stefan, B. Octavian, H. Daryoush, "Application of a superconducting magnetic energy storage unit for power systems stability improvement", Edith Cowan University, Research Online, 2014.

[7] Marzband, Mousa, et al. "Real time experimental implementation of optimum energy management system in standalone microgrid by using multi-layer ant colony optimization." International Journal of Electrical Power & Energy Systems 75 (2016): 265-274.

[8] M. Dorigo et L.M. Gambardella, Ant Colony System : A Cooperative Learning Approach to the Traveling Salesman Problem, IEEE Transactions on Evolutionary Computation, volume 1, numéro 1, pages 53-66, 1997.

[9] K. Peter, "Application of Optimization Techniques in the Power System Control", Acta Polytechnica Hungarica, pp:221 - 236, vol. 10, no. 5, 2013.

[10] S. Ashwanth, M. Manikandan, Dr. A. Mahabub Basha, "Superconducting Magnetic Energy Storage System based Improvement of Power Quality on Wind/PV Systems", International Journal of Emerging Technology and Advanced Engineering, pp. 676 - 682, vol 4, no 4, Apr 2014.

[11] R. Strzelecki and G. Benysek. (2008). Power Electronics in Smart Electrical Energy Networks. Available:

[12] J. Ekanayake, N. Jenkins, K. Liyanage, J. Wu, and A. Yokoyama. (2012). Smart Grid: Technology and Applications (2 ed.).

[13] J. Wen, X. J. Jian, G. J. Guo, and J. G. Zhu, "Theory and Application of Superconducting Magnetic Energy Storage," presented at the Australasian Universities Power Engineering (AUPEC'06), Australia 2006.

[14] D. S. Padimiti and B. H. Chowdhury, "Superconducting Magnetic Energy Storage System (SMES) for Improved Dynamic System Performance," in Power Engineering Society General Meeting, 2007. IEEE, 2007, pp. 1-6.

[15] C. T. Hsu, "Enhancement of Transient Stability of An Industrial Cogeneration System with Superconducting Magnetic Energy Storage Unit," IEEE Transactions on Energy Conversion,, vol. 17, pp. 445-452, 2002.

[16] S. Funabiki and T. Fujii, "Fuzzy Control of SMES for Levelling Load Power Fluctuation Based on Lukasiewicz Logic," Generation, Transmission and Distribution, IEE Proceedings C, vol. 140, pp. 91-95, 1993.

[17] Lidula, N.W.A., and A.D. Rajapakse. "Microgrids research: A review of experimental microgrids and test systems." Renewable and Sustainable Energy Reviews 15.1 (2011): 186-202.

[18] M. Dorigo et L.M. Gambardella, Ant Colony System : A Cooperative Learning Approach to the Traveling Salesman Problem, IEEE Transactions on Evolutionary Computation, vol 1, no 1, pages 53-66, 1997.

# Investigation on Parameters performance of Zn/Cu Electrodes of PKL, AVL, Tomato and Lemon juice based Electrochemical Cells: A Comparative Study

Md. Kamrul Alam Khan[1], Md. Siddikur Rahman[2], Tanmoy Das[2], Muhammad Najebul Ahmed[2], Kaushik Nandan Saha[2] and Shuva Paul[3]

[1]Jagannath University, Bangladesh
[2]American International University-Bangladesh, Bangladesh
[3]South Dakota State University, United States of America
kakhan01@yahoo.com, siddikur.sagor@gmail.com, shuva.paul@sdstate.edu

***Abstract*—This paper presents an experimental study on Electrode Power Density (EPD), Electrode Energy Density (EED), Specific Power Density (SPD) and Specific Energy Density (SED) of 1:1 Zn/Cu Electrodes of Pathor Kuchi Leaf (PKL), Aloe Vera Leaf (AVL), Tomato and Lemon juice based Electrochemical Cells. As a basic human needs now-a-days, Electricity plays a vital role for social as well as economic development and like all other third world countries rural people of Bangladesh doesn't have proper access to it. Generally rural people need electricity to light LED bulb, operate a radio or to charge a cell phone and these types of mundane work can be done using the ongoing relative study on PKL, AVL, Tomato and Lemon juice based Electrochemical Cells which uses biomass resources. The key aim of this paper is to find out which fruit or leaf juice based electrochemical cell produce enough amount of energy in terms of electricity to overcome the energy calamity of rural people of Bangladesh and to discuss important parameters of 1:1 Zn/Cu Electrodes of PKL, AVL, Tomato and Lemon juice based Electrochemical cells.**

***Keywords—PKL; Electrochemical Cell; Biomass Energy; Bioelectricity; Bioenergy***

## I. INTRODUCTION

The electrical form of energy has become virtually essential for human bustles [1]. Energy is a critical input for socio-economic development of developing countries like Bangladesh [2]. This development is shifting attention toward smart grid and cyber physical system which is rising demand for more electricity [15] [16]. The energy depletion of the world reached 12,730.4 million tons oil equivalent in 2013, which is almost double from the year 1980 and this is causing global warming which is a major concern regarding sustainability [3-6]. In Bangladesh, aboriginal trading energy e.g., natural gas, oil and coal are the major contributing sources in primary energy consumption [3]. Different existing studies shows that depleting these types of energy source is damaging the environment and to remedy this situation current scenario will be shifting towards green energy [17]-[20]. The bio electrochemical cell offers a potential solution to mitigate the problems. It uses the available substrates from renewable sources with a modified electrode and converts them into harmless by-products with simultaneous production of electricity [7]. Bioelectricity is a new term in the field of bioenergy.

The poor rural people of Bangladesh don't have proper access to electricity and alternating source is in need to provide energy for them. In Bangladesh, generation of electricity from biomass is very much available, environment friendly and the cost is bearable [8]. A new form of biomass energy is invented in Bangladesh named, "Electricity generation from Pathor Kuchi Leaf (PKL)" [9]. Several studies have been conducted to investigate different parameters of PKL electricity [21]-[23]. M.K.A. Khan and S. Paul had conducted research work on *Bryphyllum pinnatum* leaf (BPL) or PKL like electrochemistry of PKL, chemistry of PKL electricity, design of PKL Quasi Voltaic Cell and Conversion efficiency of PKL Cell [10]. M.K.A. Khan et al. had worked on *Bryophyllum pinnatum* leaf's unit cell, process of Electricity production, public desire of BPL, Voltage regulation, capacity of PKL, Energy efficiency of PKL system, discharge rates, capacity & discharge time, pulse performance, cycle life and deep discharge [11]-[13].

In this research, we have found some leaves and fruits e.g., PKL, AVL, Tomato and Lemon contain substances such as ascorbic acid, citric acid, iso-citric acid, malic acid and unknown organic acids (chemical that generates electrochemical energy). Under certain circumstances these chemicals act as electrolytes and then undergo electrolysis. Electrolysis means a chemical change produced by electric current passing through an electrolyte. The electrons flow from the cathode (negative electrode-copper wire) through the electrolytes to the anode (positive electrode-zinc wire). This process generates 'Electricity' just the same way as a voltaic cell. Investigation and experiment of this work is held at Solar Energy Research Center (SERC), Jagannath University, Bangladesh. This paper is organized as follows: Organic Electrochemical cell's reaction mechanism and Bio-electrochemical cell's design mechanism are described in section II. An overview of PKL, AVL, Lemon and Tomato are briefly discussed in section III. In section IV, specifications and experimental set-up of Electrochemical cells are discussed. Investigated parameters of 1:1 Zn/Cu electrodes of Electrochemical cells are analyzed in section V. Findings summary of this investigation are discussed in section VI and

This work is supported and funded by Ministry of Science and Technology, Bangladesh.

978-1-5386-2307-7/17/$31.00 ©2017 IEEE

section VII represents the conclusion and prospective study of this work.

## II. Reaction Mechanism of Organic Elecrochemical Cell and Design Mechanism Bio-Electrochemical Cell

Usage of fuel Cell, (i.e. PEMFC) in the modern smart grid and investigation on their characteristics brought to authors' consideration that, PKL cell can also be used as fuel cell [24]-[26]. The principle of electricity generation using bio-electrolyte is the same as a simple electrochemical cell which converts chemical energy into electrical energy. The basic difference in the present study with electric cell theory is only the utilization of organic acid such as citric acid, iso-citric acid, ascorbic acid, oxalic acid including other weak organic acid etc., which is found in acid-rich fruits and leaves as electrolyte. This is a renewable source for producing energy. In the case of citric acid, the organic sap contains about (90–95) % water. Dissociation of organic acid in this aqueous solution, according to equation no. 1, consequently increases the $H^+$ ions. In the meantime, the ***Zn*** plate dissolves in the organic electrolyte as $Zn^{2+}$ ion, sacrificing two electrons. Electrons pass through the external circuit and salts of ***Zn*** are produced. On the other hand, $H^+$ ions are adsorbed on the surface of the ***Cu*** plate and receive electrons & evolve as $H_2$ gas [13]. Approx. 9 L of the bio-electrolyte is used for the baffle agitation system during 100 hour operation. Electrolyte solution is prepared in such a way that contained raw sap and water with a proportion of 1:8. After pouring the mixture into a cell, zinc (***Zn***) and copper (***Cu***) plates are merged into the electrolyte with a proportion of 1:1 and 2:1. Immediately, chemical reaction took place, which in turn created positive and negative potentialities.

$$\begin{aligned} &HOOC\text{–}CH_2-C(OH)(COOH)-CH_2-COOH_{(aq)} \rightarrow \\ &HOOC\text{–}CH_2-C(OH)(COOH)-CH_2-COO^- + H^+ \end{aligned} \tag{1}$$

$$\begin{aligned} &2\left[HOOC\text{–}CH_2-C(OH)(COOH)-CH_2-COO^-\right]+Zn^{2+} \\ &\rightarrow\left[HOOC\text{–}CH_2-C(OH)(COOH)-CH_2-COO^-\right]_2 Zn \end{aligned} \tag{2}$$

In this way, the ***Zn*** plate became negatively charged and $H^+$ contacted the ***Cu*** plate becomes positively charged. As these two plates are connected by wire, current flowed from ***Cu*** to ***Zn*** through the outer circuit and from ***Zn*** to ***Cu*** through the bio-electrolyte. Therefore, the circular path of the cell generated DC. By applying the inverter, DC is converted into alternating current. At the anode, two electrons are then released from each zinc atom and giving the $Zn^{2+}$ ion, which is shown as follows:

$$Zn_{(S)} \rightarrow Zn^{2+}(aq) + 2e^- \tag{3}$$

At the cathode, the other reaction is called reduction, when positively charged hydrogen ions accept electrons and evolve as hydrogen gas, equation 4.

$$2H^+(aq) + 2e^- \rightarrow H_{2(g)} \tag{4}$$

And at the cathode, the other reaction is called reduction, when positively charged Copper ions accept electrons and stays on the surface of the ***Cu*** atom as neutral ***Cu*** atom, which is shown as follows:

$$Cu^{2+}(aq) + 2e^- \rightarrow Cu_{(solid)} \tag{5}$$

To prepare the cost-effective Cell, empty battery boxes are collected from local market. After washing the boxes, electrodes of copper and zinc having dimensions of height = 10.8 cm, length = 5.4 cm and weight = 12 g are inserted with sap of star fruits into the boxes. A multi-meter is connected for measuring the current and voltage. A box of four compartments is shown in figure 1, where each compartment has the following dimensions – width: 4 cm, length: 8.4 cm, height: 10.5 cm and effective height of the electrolyte: 9.5 cm. For achieving high voltage and high current yield, several types of cell connections had been observed. Among these observations, the combination of series and parallel connections had been found capable of producing maximum electricity (shown in figure 1).

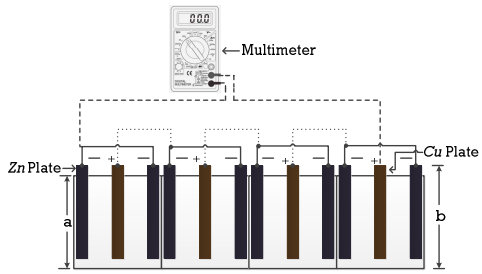


Fig. 1. Arrangement for a Bio-Electrochemical Cell (Anode & Cathode ratio is 2:1; Where dotted & plane lines are indicates series & parallel connections respectively; Symbol 'a' & 'b' denote Effective height of the electrolyte & Cell height, respectively).

The generation of electricity needs to be continued until the anode plate gets totally corroded [14]. A meaningful arrangement of the electrode (2:1 anode–cathode ratio) is added to generate the maximum yield by increasing the anodic surface area. The polymeric separator that had been used in between anode and cathode is chemically stable to the electrolyte.

## III. PKL, AVL, Lemon & Tomato : An Overview

Since this is a relative study among PKL, AVL, Tomato and Lemon, a brief discussion about them is given below:

Pathor Kuchi Leaf's (PKL) (*Bryophyllum pinnatum*) juice or malt is used to engender electricity with a process of chemical reaction [9]. It's been collected from the farmers and sometimes from the tub of the roof of the building. The cultivation of the PKL is very easy. It can be harnessed from anywhere of Bangladesh. It grows everywhere even in the cement and water. PKL cultivation doesn't need any cultivable or crop lands. It can be cultivated in the unused forests, islands and hilly areas of Bangladesh. Generally, PKL is collected in the morning but some interesting facts occurs when PKL is collected at night such as: 1. Increment of Malic Acid 2. Increment of Reactant ion ($H^+$), 3. Increment of Cell Voltage ($E_{cell}$), 4. Decrease of pH of PKL juice/sap, 5. Better

performance of PKL. Aloe Vera Leaf (AVL) (*Aloe Barbadensis Miller*), Lemon (*Citrus limon*), Tomato (*Solanum lycopersicum*) can be collected from the market. These leaf and fruits are also grown anywhere in Bangladesh. Covered & uncovered Aloe Vera, lemon and tomato are used for juice making. Green and ripe, both types of tomatoes are used for determination the performances of electricity generation.

## IV. Specifications and Experimental Set-up of Electrochemical Cells

Electrode strips are cleaned with extra fine steel wool to remove any corrosion on the surface thus, improve the conductivity. Fresh samples are used in each experiment. The amount of each sample used in the experiment at a time is obtained by considering the cubic space of the modified voltaic cell is tabulated below in Table I.

TABLE I. Specifications of Examined Electrochemical Cell

| Specifications | Leaves and Fruits | | | |
|---|---|---|---|---|
| | *PKL* | *AVL* | *Tomato* | *Lemon* |
| Amount (g) | 800 | 800 | 800 | 800 |
| Amount of water (g) | 200 | 200 | 200 | 200 |
| No. of anode | 1 | 1 | 1 | 1 |
| No. of cathode | 1 | 1 | 1 | 1 |
| Area of anode & cathode immersed in juice ($A_i$) ($cm^2$) | 95 | 120 | 90 | 110 |
| Distance between anode & cathode (cm) | 8 | 7 | 6.5 | 6 |
| Volume of electrolyte (ml) | 900 | 1000 | 750 | 850 |

The following equation is used to measure the concentration of juice in each case.

$$Concentration\ of\ Juice = \frac{x-y}{z}\frac{g}{ml} \qquad (6)$$

Here, weight of Fresh Leaves/fruits before blending (g), x; weight of Leaves after filtration (g), y; volume of Water after filtration (ml), z.

Using the specifications mentioned in Table I Electrochemical Cells were constructed which is represented in Figure 2. The Electrochemical Cells were used to light a 3 or 6 watt LED bulb which is also represented in Figure 2.

(a)

(b)

(c)

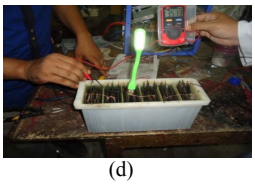

(d)

Fig. 2. (a) and (b) – Preparation for the Concentrations of PKL, AVL, Tomato & Lemon Juice for making an Electrochemical Cell; (c) and (d) – Representation of producing electricity from PKL, AVL, Tomato & Lemon juice based Electrochemical Cell and produced electricity used to enlight a led bulb.

In next section, some significant parameters of **1:1** Zn/Cu based electrodes of PKL, AVL, Tomato and Lemon juice based Electrochemical Cells are analyzed.

## V. Parameters to be Analyzed of 1:1 Zinc/Copper Based Electrodes

In this section, some key parameters are analyzed for PKL, AVL, Tomato and Lemon juice based Electrochemical Cells. Parameters are as follows:

- Electrode Power Density (EPD)
- Electrode Energy Density (EED)
- Specific Power Density (SPD)
- Specific Energy Density (SED)

For better understanding each parameter performance, experimental data has been recorded in three different days and this is mentioned in each and every figure.

### *A. Discussions on Experimental Analyzation of Electrode Power Density (EPD)*

Power Density is defined how much power a battery/cell can deliver/provide on demand. Basically, Power Density is measured in W/Kg but in this research Power Density is measured in $mWH/cm^2$. Batteries/cells with high Power Density are used for power tools, medical devices and transporting systems.

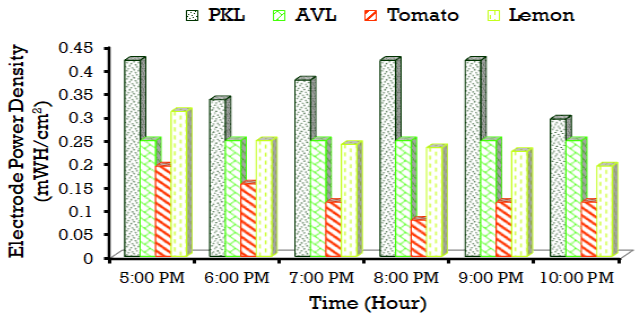


Fig. 3. Variation of Electrode Power Density (EPD) With Time (1st Day Data).

Figure 3, 4 & 5 are representing the variation of **EPD** over time of 1st, 2nd and 3rd day, resepectively. Experimental data are recorded at 5-10 pm, 3-8 pm and 4-9 pm of 1st, 2nd and 3rd day resepectively. If we have a close look at figure 3, 4 & 5 then each and in every figure PKL has better value of **EPD**

than AVL, Tomato and Lemon whereas Tomato has the worst value.

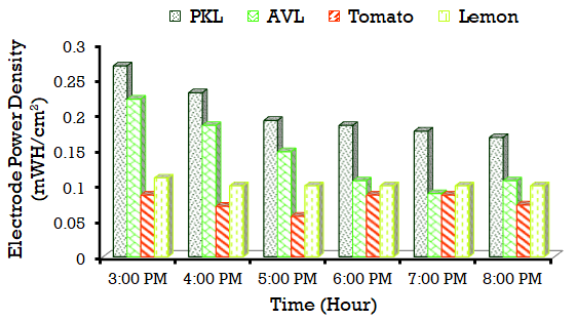


Fig. 4. Variation of Electrode Power Density With Time (2nd Day Data).

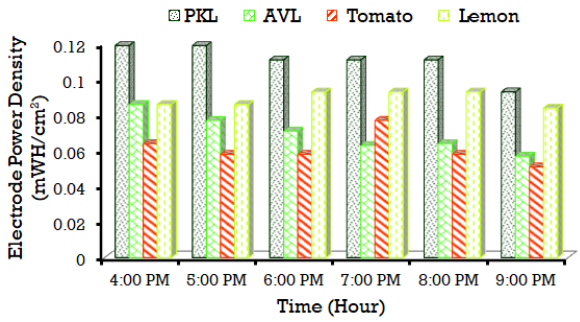


Fig. 5. Variation of Electrode Power Density (EPD) With Time (3rd Day Data).

## B. *Discussions on Experimental Analyzation of Electrode Energy Density (EED)*

Energy Density is a measurement of how much energy a battery/cell can hold. Basically, Energy Density is measured in Wh/Kg but in here Energy Density is measured in mWH/cm$^2$. Batteries/cells worth higher Energy Density will have longer runtime.

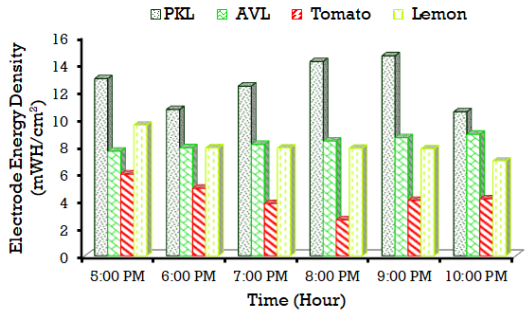


Fig. 6. Variation of Electrode Energy Density With Time (1st Day Data).

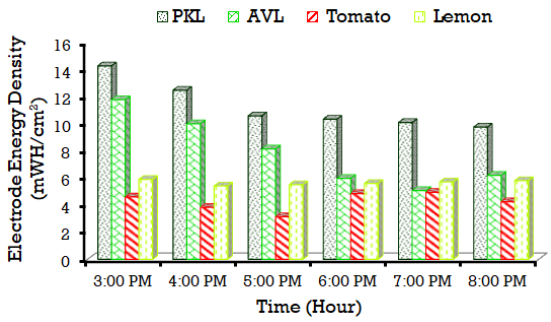


Fig. 7. Variation of Electrode Energy Density With Time (2nd Day Data).

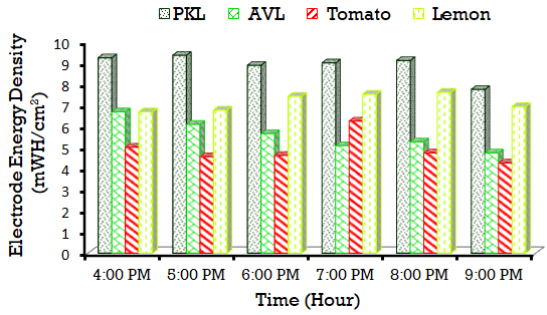


Fig. 8. Variation of Electrode Energy Density With Time (3rd Day Data).

Figure 6, 7 & 8 are representing the variation of **EED** over time of 1st, 2nd and 3rd day, resepectively. Experimental data are recorded at 5-10 pm, 3-8 pm and 4-9 pm of 1st, 2nd and 3rd day resepectively. If we gaze closely at figure 6, 7 & 8 then in each and every figure PKL has better value of Density' **EED** than AVL, Tomato and Lemon whereas Tomato has the worst value. These scenario are same as previous parameter.

## C. *Discussions on Experimental Analyzation of Specific Power Density (SSD)*

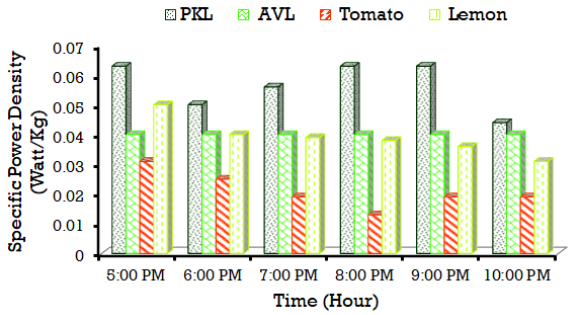


Fig. 9. Variation of Specific Power Density With Time (1st Day Data).

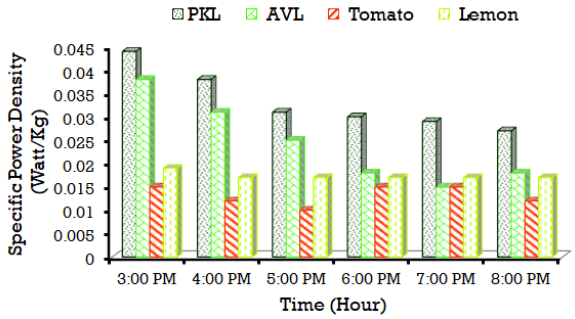


Fig. 10. Variation of Specific Power Density With Time (2nd Day Data).

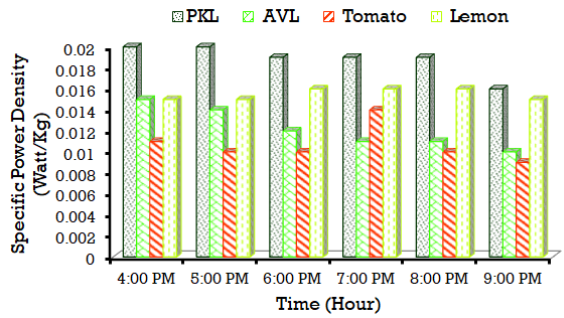


Fig. 11. Variation of Specific Power Density With Time (3rd Day Data).

Figure 9, 10 & 11 are representing the variation of **SSD** over time of 1st, 2nd and 3rd day, resepectively. In here, specific power density is measuerd in Watt/Kg. Experimental data are recorded at 5-10 pm, 3-8 pm and 4-9 pm of 1st, 2nd and 3rd day resepectively. If we have a close look at figure 9, 10 & 11 then in each and every figure PKL has better value of **SSD** than AVL, Tomato and Lemon whereas Tomato has the worst value.

### *D. Discussions on Experimental Analyzation of Specific Energy Density (SED)*

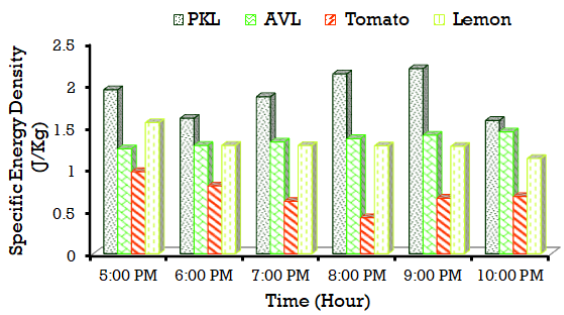


Fig. 12. Variation of Specific Energy Density With Time (1st Day Data).

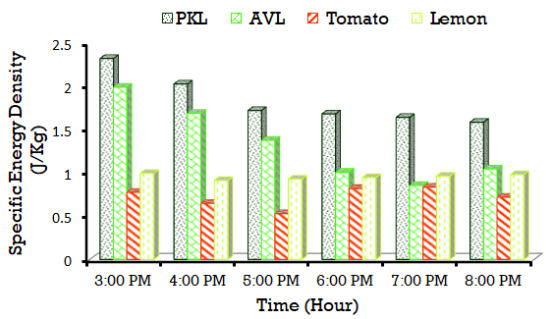


Fig. 13. Variation of Specific Energy Density With Time (2nd Day Data).

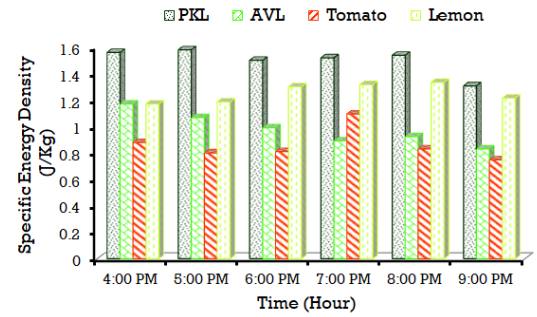


Fig. 14. Variation of Specific Energy Density With Time (3rd Day Data).

Figure 12, 13 & 14 are representing the variation of **SED**time of 1st, 2nd and 3rd day, resepectively. Specific Energy Density is meaasured as J/Kg in this work. Experimental data are recorded at 5-10 pm, 3-8 pm and 4-9 pm of 1st, 2nd and 3rd day, resepectively. If we have a close look at figure 12, 13 & 14 then in each and every figure PKL has better value of **SED** than others whereas Tomato has the worst value. These scenario are same as previous parameter.

## VI. Findings Summary

Experimental result summary based on Power & Energy Density and Specific Power & Energy Density of the Electrochemical cells are tabulated below in Table II.

TABLE II. Overall Experimental Results Summary

| No. | Analyzed Parameters | Performance of examined Electrochemical Cells | | | |
|---|---|---|---|---|---|
| | | ***PKL*** | ***AVL*** | ***Tomato*** | ***Lemon*** |
| 1. | Electrode Power Density | Good | Less than PKL | Bad | Less than PKL |
| 2. | Electrode Energy Density | Good | Less than PKL | Bad | Less than PKL |
| 3. | Specific Power Density | Good | Less than PKL | Bad | Less than PKL |
| 4. | Specific Energy Density | Good | Less than PKL | Bad | Less than PKL |

From experimental analysis, it is clear PKL Electrochemical cell's performance is better than others.

## VII. Conclusion and Prospective Study

Demand for energy is growing fast through worldwide and finding of new renewable sources are an absolute necessity. In this regard, this paper presents an innovative invention which is an Electrochemical Cell fueled with Pathor Kuchi Leaf (PKL), Aloe Vera Leaf (AVL), Tomato and Lemon sap (biomass). Electricity produced by this cell can be a primary source of electricity in future. Investigation and experiment are conducted on comparative studies of the Electrode Power & Energy Density, Specific Power & Energy Density of PKL, AVL, Tomato and Lemon juice based Electrochemical Cells for **1:1** Zn/Cu based electrodes. Observation clearly concluded that PKL Electrochemical cell is steady, stable, feasible, and has so much better performance and longevity than others. These cells needs more investigation and further study such as: Open circuit voltage, short circuit current, power and internal resistance. Also, inclusion of PKL electricity as hybrid energy source to grid (i.e. wind energy, tidal energy) can be a potential future study along this direction [27][28].

## References


[1] S. R. Rahman, N. A. Mahmud, M. rahman, M. Y. Hussain, M. S. Ali, "Overview of biomass energy," *International Journal of Engineering Research and Technology*, vol. 2, no. 11, pp. 379–385, 2013.

[2] N.F. Nasir, W. R. W. Daud, S. K. Kamarudin, Z. Yaakob, "Process system engineering in biodiesel production: a review," *Renewable and Sustainable Energy Reviews*, vol. 22, pp. 631-639, 2013.

[3] British Petroleum (BP). BP Statistical Review of World Energy, British: BP Plc. [Online]. Avaialable at : http://www.bp.com/content/dam/bp/pdf/Energy-economics/statistical-review-2014/BP-statistical-review-of-world-energy-2014-full-report.pdf [Last accessed on August 2016]

[4] Z. A. Chiari L, "Constraints of fossil fuels depletion on global warming projections," *Energy Policy*, vol. 39, no.9, pp. 5026–5034, 2011.

[5] M. Hoel and S. Kverndokk, "Depletion of fossil fuels and the impacts of global warming," *Resource and Energy Economics*, vol. 18, no. 2, pp. 115–136, 1996.

[6] C. CJ. Nel WP, "Implications of fossil fuel constraints on economic growth and global warming," *Energy Policy*, 2009; vol. 37, no. 1, pp. 166–180, 2009.

[7] V. K. Gupta, Bina Gupta, Arshi Rastogi, Shilpi Agarwal, and Arunima Nayak, "Pesticides removal from waste water by activated carbon prepared from waste rubber tire," *Water research*, vol. 45, no. 13, pp. 4047-4055, 2011.

[8] M. Hasan and K. Alam, "Bryophyllum pinnatum leaf fueled cell: An alternate way of supplying electricity at the off-grid areas in Bangladesh," In *Development in the in Renewable Energy Technology (ICDRET), 2016 4th International Conference on the*, pp. 1-5. IEEE, 2016.

[9] M. K. A. Khan, "Electricity Generation from Pathor Kuchi Leaf (PKL)," BD Patent 1 004 907, December 31, 2008.

[10] M. K. A. Khan and S. Paul, "A analytical study on Electrochemistry for PKL (Pathor Kuchi Leaf) electricity generation system," *Energytech, 2013 IEEE*, Cleveland, OH, 2013, pp. 1-6.

[11] M. K. A. Khan, M. H. Bakshi and A. A. Mahmud, "Bryophyllum Pinnatum Leaf (BPL) is an Eternal Source of Renewable Electrical Energy for Future World," *American Journal of Physical Chemistry*, vol. 3, no. 5, pp. 77-83, 2014.

[12] M. K. A. Khan, S. Paul, M. S. Rahman, R.K. Kundu, M. M. Hasan, M. Moniruzzaman and M.A. Mamun,"A Study of Performance Analysis of PKL electricity genration Parameters (An experimental analysis on voltage regulation, capacity and energy efficiency of pathor kuchi leaf (PKL) electricity cell)," In *7th Power India International Conference (PIICON), 2016 IEEE*, pp. 1-6. IEEE, 2016.

[13] K. A. Khan, A. Rahman, M. S. Rahman, A. Tahsin, K. M. Jubyer, and S. Paul, "Performance analysis of electrical parameters of PKL electricity (An experimental analysis on discharge rates, capacity & discharge time, pulse performance and cycle life & deep discharge of Pathor Kuchi Leaf (PKL) electricity cell)," In *Innovative Smart Grid Technologies-Asia (ISGT-Asia), 2016 IEEE*, pp. 540-544. IEEE, 2016.

[14] M. G. Fontana, and N. D. Greene, "Corrosion engineering, materials science & engineering series," vol. 51, 1978.

[15] S. Paul, M. S. Rabbani, R. K. Kundu and S. M. R. Zaman, "A review of smart technology (Smart Grid) and its features," *2014 1st International Conference on Non Conventional Energy (ICONCE 2014)*, Kalyani, 2014, pp. 200-203.

[16] S. Paul, A. Parajuli, M. R. Barzegaran and A. Rahman, "Cyber physical renewable energy microgrid: A novel approach to make the power system reliable, resilient and secure," *2016 IEEE Innovative Smart Grid Technologies - Asia (ISGT-Asia), 2016 IEEE*, pp. 659-664. IEEE, 2016.

[17] S. R. Zishan, S. Paul, M. Adibullah, S. Mahmud and M. R. Yousufe, "A study of Canada's Energy Situation and Probable Future in the Energy Sector," *International Journal of Scientific & Engineering Research*, vol. 3, no. 12, pp. 1-4, 2012.

[18] S. A. Yusuf, S. D. Gupta, S. Paul, M. S. Islam and S. Majumder, "A Study on Hubbert Peak for Natural Gas of Bangladesh: A System Dynamics Approach," *International Journal of Scientific & Engineering Research*, vol. 3, no. 10, pp. 1-8, 2012.

[19] M. K. A. Khan, S. Paul, M. R. Azad and M. A. Rahman, "Review of renewable energy Prospect in Bangladesh," *International Journal of Scientific & Engineering Research*, vol. 4, no. 5, pp. 2022-2026, 2013.

[20] S. Paul, M. R. Azad, S. S. Hossain and A. Rahman, "A brief study on the energy condition of Germany and their future prospect in the energy sector," *International Journal of Scientific & Engineering Research*, vol. 4, no. 5, pp. 1343-1346, 2013.

[21] M. K. A. Khan, S. Paul, M. Adibullah, M. F. Alam, S. M. Sifat and M. R. Yousufe, "Performance Analysis of BPL/ PKL Electricity module," *International Journal of Scientific & Engineering Research*, vol. 4, no. 3, pp. 1-4, 2013.

[22] M. K. A. Khan, S. Paul, S. R. Zishan, M. Adibullah and S. Mahmud, "Design of a Hybrid Model of BPL electricity Module and Solar Photovoltaic Cell," *International Journal of Scientific & Engineering Research*, vol. 3, no. 12, pp. 1-4, 2012.

[23] S. Paul, M. K. A. Khan, K. A. Islam, B. Islam and M. A. Reza, "Modeling of A Biomass Energy Based (BPL) Generating Power Plant and its Features in Comparison With Other Generating Plants," *2012 2nd International Conference of Environment and BioScience, IPCBEE*, Singapore, vol. 44, no. 3, pp. 12-16, 2012.

[24] M. S. Rahman, R. R. Riadh and S. Paul, "Investigate the Output Behavior of Alkaline Fuel Cell's (AFC's) parameters: Flow Rate & Supply Pressure," *Electrical & Electrical Engineering: An International Journal (ELELIJ)*, vol. 4, no. 4, pp. 99-119, 2015.

[25] S. Paul, M. S. Muhit, M. S. Rahman, "Analysis of Output Behavior of PEMFC by Varying Flow Rates (Air Flow Rate & Fuel Flow Rate)," *Trends in Electrical Engineering*, vol. 5, no. 2, pp. 1-8, 2015.

[26] M. S. Rahman, S. Paul and R. R. Riadh, "Study of 1.26 Kw- 24 Vdc Proton Exchange Membrane Fuel Cell's (PEMFC's) Parameters Output Behavior: Composition & Temperature," *Electrical & Computer Engineering: An International Journal (ECIJ)*, vol. 4, no. 3, pp. 43-59, 2015.

[27] S. Paul, M. S. Rahman, A. Rahman and M. H. Shahed, "Wind Energy Integration in Smart Grid," *International Journal of Scientific & Engineering Research*, vol. 5, no. 11, pp. 220-223, 2014.

[28] M. K. A. Khan, M. A. Shatter, S. Paul, S. R. Zishan and M. R. Yousufe, "A Study on Tidal Power Conversion for use in Bangladesh," *International Journal of Scientific & Engineering Research*, vol. 3, no. 12, pp. 1-9, 2012.

# Application of Energy Capacitor System with Minimum Energy Storage Capacity for Smoother Frequency and Output Power of a Grid Connected Wind Farm

S. M. Shaikh[1], M. S. A. Hossain[1], T. B. Zaman[2],U. B. Tayab[3], and M. A. Humayun[4]
[1]Bangladesh Power Development Board, Dhaka, Bangladesh
[2]University of information Technology and Sciences, Dhaka, Bangladesh
[3]Griffith School of Engineering, Griffith University, Queensland, Australia
[4]Department of Electrical and Electronic Engineering, Green University of Bangladesh, Dhaka, Bangladesh

shaikh_ruet@yahoo.com, sadeedbpdb@gmail.com, tbzaman@yahoo.com, usmanbashir.tayab@griffithuni.edu.au, humayun0403063@gmail.com

*Abstract*—**Stability enhancement of output power and frequency in grid connected wind farms are major challenges nowadays. A model of a grid connected wind farm consisting of a fixed speed wind turbine based induction generator (IG) connected to the transmission line with an energy capacitor system (ECS) in parallel has been considered in this research work to analyze the output characteristics. ECS consists of converters, inverters along with electric double layer capacitor (EDLC). Choice of line power reference is one of the major factors for stable output power and frequency of the wind farm. In this paper simple low pass filter (LPF) method has been applied to generate line power reference for ECS. It has been revealed from the outcome of the research that line power reference and frequency of the output power obtained is more stable using LPF method. Furthermore, LPF method requires a shorter charging-discharging time and smaller storage capacity. Moreover, a control system is proposed which employs a lead lag compensator for smoothing the output power much more even during fault conditions. PSCAD/EMTDC software is used for simulation purposes.**

***Keywords—Electric Double-Layer Capacitor (EDLC), Energy Capacitor System (ECS), Exponential Moving Average (EMA), Fixed Speed Wind Generator, Induction Generator (IG), PWM inverter, Lead Lag Compensator, Low Pass Filter (LPF), Simple Moving Average (SMA).***

## I. INTRODUCTION

We are dependent of different kinds of natural sources like: coal, gas, biomass and so on, which are sinking day by day due to the huge consumption of energy across the world. In addition to that these sources are polluting our environment at an alarming rate. In addition to that power crisis has become a burning question in the era of modern industrialization. Therefore, researchers are looking for alternative sources of energy to cope up the ever-increasing demand of power in an environment friendly manner [1]. Researchers have found that wind is a natural energetic process that can produce energy with very little pollution. Considering these facts, a large number of wind farms have already been connected to the existing power system. In 2015, global wind power capacity expanded 17% to 432,419 MW [2]. Wind turbine is widely used to convert the wind energy to electrical energy. Wind turbine output is proportional to the cube of the wind speed. Consequently a huge output power fluctuation occurs when there is a little variation in wind speed. Due to stochastic nature of wind speed and subsequent output power fluctuations, integrating wind power into the existing power system has became a matter of concern [3-5]. For controlling such power and frequency fluctuations, several methods have been proposed. Some group of researchers have proposed pitch angle control of windmill blades [6-7], but this method has several drawbacks such as it works for a rated wind speed region, reduces wind energy utilization efficiency and so on. On the other hand, energy storage devices are free from such weaknesses. Some other researchers have proposed Superconducting Magnetic Energy Storage System (SMES) devices for reducing wind power fluctuations [8]. Again, few research groups have proposed Battery Energy Storage System (BESS) [9] and Flywheel Energy Storage System (FESS) [10] to control fluctuations. However these methods have several shortcomings such as: BESS is expensive, causes environmental pollution and requires longer charging and discharging time and FESS is a complex system and can only smooth short-term fluctuations. To overcome these shortcomings, another technology known as Energy Capacitor System (ECS) combined with Electric Double-Layer Capacitor (EDLC) and electronic circuits are being used [11].

EDLCs have several advantages such as: shorter charging and discharging time, lesser weight, longer lifetime, lower resistance, higher safety and environment friendliness. Due to its shorter charging and discharging time, it is suitable for irregular power sources like wind farms. Simple Moving Average (SMA) method has also been used by different researchers for generating line power reference in variable

978-1-5386-2307-7/17/$31.00 ©2017 IEEE

speed wind turbines [12] while others have used Exponential Moving Average (EMA) in fixed speedwind turbines [13]. Both these methods are practically complex and bulky due to the presence of a lot of complex circuits. ECS has been used to compensate fluctuation of power in a wind and diesel hybrid power system [14]. The researcher proposed a networking based load following control supervisor, which may fail anytime. With the advancements in power electronics devices, STATCOM is being used for stabilizing voltage fluctuations in wind generators [15], but conventional STATCOM has the abilityto supply reactive power only [16]. Therefore, we have used ECS and LPF in our system. We have shown that LPF method is better than SMA and EMA methods in generating line power reference. Moreover, lead-lag compensator based controller is employed in this system to stable output power during fault conditions.

## II. PROPOSED SYSTEM MODEL

The proposed system is a composite system of 50 MVA and consists of a fixed speed IG based wind farm, which is delivering power to an infinite bus through transmission line Figure 1 presents a schematic view of the proposed model. The main parts of the system model are: wind turbine, IG, capacitor bank (c), ECS block, power transformer and transmission line. The capacitor bank is connected with IG to compensate reactive power and the ECS block is connected in parallel with the transmission line. The ECS consists of an EDLC bank, a buck/boost converter and a PWM-Voltage source converter (PWM-VSC). The PWM-VSC is used to control output frequency. The DC link circuit voltage is fixed at 3.6 KV. By changing the voltage of the buck-boost converter, the EDLC can be charged or discharged.

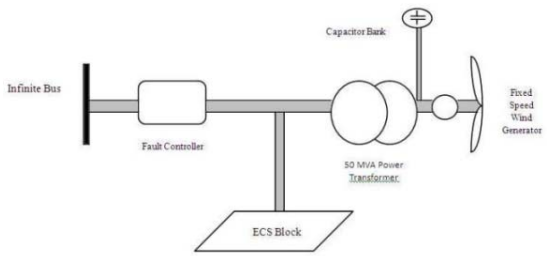


Figure 1. Proposed System Model

TABLE I. PARAMETERS OF THEFIXEED SPEED INDUCTION GENERATOR

| SL. No. | Parameter | Value |
|---|---|---|
| 1 | Rated Capacity | 50 MVA |
| 2 | Rated RMS Phase Voltage | 0.398 KV |
| 3 | Rated RMS Phase Current | 41.83 KA |
| 4 | Armature resistance | 0.01 p.u. |
| 5 | Armature leakage Reactance | 0.1 p.u. |
| 6 | Magnetizing Reactance | 3.5 p.u. |
| 7 | Rotor Mutual Reactance | 0.12 p.u. |
| 8 | Rated frequency | 50 Hz |
| 9 | DC link voltage | 3 kV |
| 10 | DC link capacitance | 50,000 µF |
| 11 | Air gap factor | 1 |

## III. PROPOSED ECS MODEL

As discussed in Section II, the ECS block consists of an EDLC bank, a buck/boost converter and a PWM-VSC. In this section, detailed description is provided. Figure 2 shows a schematic representation of ECS.

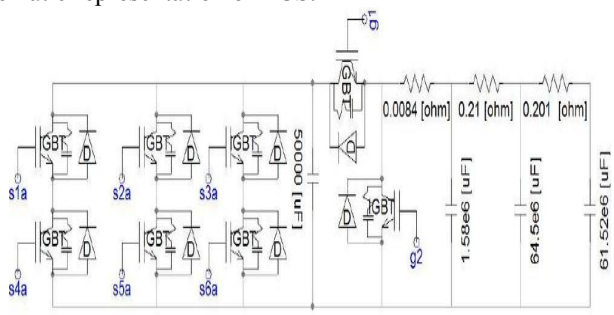


Figure 2.Schematic Representation of ECS

### A. Proposed EDLC Model

EDLC achieves low equivalent series resistance (ESR) and high capacitance in a small package with lower voltage ratings. Due to low ESR, it has higher charging and discharging efficiency. Distributed model of the EDLC cell is shown in Figure 3.

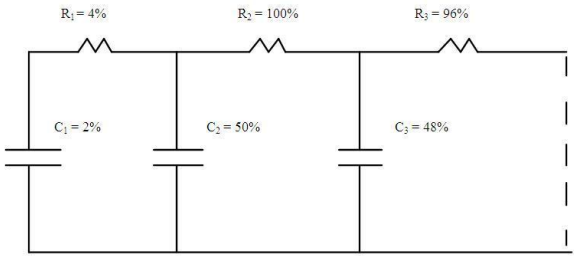


Figure 3. EDLC Cell Model

Capacitance of EDLC is given by the following equation:

$$C_{EDLC} = \frac{n_p}{n_s} \times C_{Rated} \quad (1)$$

where, $n_s$ = Number of series capacitors in a string, $n_p$ = Number of parallel capacitors in a string, $C_{Rated}$= Capacitance of one cell.

Energy of EDLC is given by the following equation;

$$E_{EDLC} = \frac{1}{2} C V^2 \quad (2)$$

Total Voltage,

$$V_{Total} = V_{Cell} \times n_s \quad (3)$$

In this system, $n_S$= 1000, $n_P$= 86, $C_{Rated}$= 1500F, $C_{EDLC}$= 129F, $V_{Cell}$= 3V, $V_{Total}$ = 3kV

### B. Line Power Reference Selection

The purpose of the proposed ECS topology is to supply both active and reactive powers, which can significantly reduce the voltage and power fluctuations of grid connected fixed-speed wind generators. However setting of the reference output power is one of the vital issues in wind generator

output power smoothing. The generator's output line power reference, $P_{ref}$ can be generated by using the following ways:

*1) Simple Moving Average (SMA) Method*

The n period SMA for period d is computed by the following equation:

$$SMA_d = \frac{\sum_{i=1}^{n} M_{(d-i)+1}}{n}; (n \leq d) \quad (4)$$

If ten measurements, $M_1$ through $M_{10}$ are available, the successive 4 period SMA, are as follows:

$SMA_4 = \frac{M_4+M_3+M_2+M_1}{4}$, $SMA_5 = \frac{M_5+M_4+M_3+M_2}{4}$ and so on.

From the above equations it is seen that, to compute a 4-period moving average until 4 period's data are available.

*2) Exponential Moving Average (EMA)Method*

In this method, N periods EMA is calculated using the formula given below

$$EMA_C = [(C - P) \times K] + P \quad (5)$$

Where, C = Current Value, P = Previous EMA and K = Weighing Factor; for a period-based EMA, K= $\frac{2}{1+N}$, where N is the specified number of periods.

***Proposed Method for Line power reference: LPF Method***

Reference value of the transmission line power, $P_{ref}$, is determined by using a LPF as shown in Figure 4, where $P_G$ is the generated power. The LPF suggests an increase or a decrease in the level of wind power output, which corresponds to charging or discharging of the stored energy.

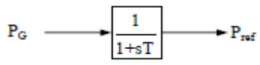


Figure 4. Determination of $P_{ref}$ using a low pass filter

The first-order passive LPF is mathematically described as

$$P_{IG} = P_{Lref} + T \times P'_{Lref} \quad (6)$$

Where, $T$ is the filtering time constant corresponding to energy storage capacity, $P_{Lref}$ is the filter output function corresponding to the wind turbine output together with the storage unit, $P'_{Lref}$ is the first derivative of $P_{Lref}$ and $P_{IG}$ is the filter input function that corresponds to the wind turbine output without energy storage.

Equation 6 can be rearranged in the following form

$$P_{Lref,k} = \beta P_{Lref,k-1} + (1 - \beta) P_{IG,k} \quad (7)$$

Where k is the step, $\beta = \frac{T}{T+\Delta t}$ and $\Delta t$ is the time step.

The power absorbed by the storage unit is given by

$$P_{sk,t} = P_{IG,k} - P_{Lref,k} \quad (8)$$

The stored energy is given by

$$E_k = \sum_{m=1}^{k} P_{st,m} \Delta t \quad (9)$$

$$E_{Storage} = E_{kmax} - E_{kmin}, \text{ for k = 1,2,3,…. n} \quad (10)$$

Where, n= No. of sample points

*C. DC-DC Buck-Boost Converter*

Figure 5 shows the dc-dc buck boost controller which is used to control the charging and discharging of EDLC. The gate signals $g_1$ and $g_2$ are used to control this process as shown in Figure 2. The difference between the grid power, $P_G$ and the generated reference power $P_{ref}$ is modified by the PI controller. The gate signals $g_1$ and $g_2$ are generated when the PI controller's output is compared with a 1 kHz triangular wave signal.

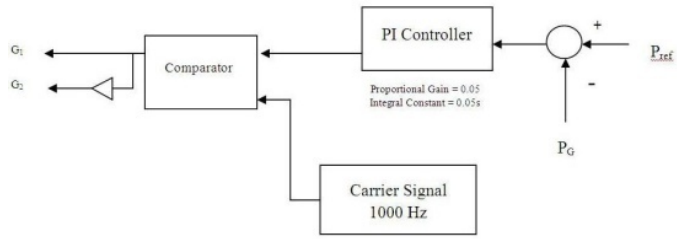


Figure 5. Buck-Boost Converter Controller

TABLE II. CHEARGING AND DISCHARGING STATE OF EDLC

| $g_1$ | $g_2$ | Charging-DischargingState of EDLC |
|---|---|---|
| On | Off | Charging |
| Off | On | No charging/discharging |
| Off | Off | Discharging |

*D. PWM-VSC Model*

The PWM-VSC model is required for proper interfacing between the EDLC and grid power. The dc link voltage is kept fixed at 1.47 kV by the VSC. Using PWM, sine waves are generated by IGBT. This is achieved by comparing the 1 kHz triangular carrier signal with the reference signal.

*E. Proposed Controller*

Figure 6 shows the block diagram of the proposed fault controller. Lead-lag compensator is used and the comparator carrier signal of controlling circuit is adjusted in such a way that the carrier signal frequency will vary based on the fault level. This reference signal is compared in a comparator to generate gate signals $g_1$ and $g_2$.

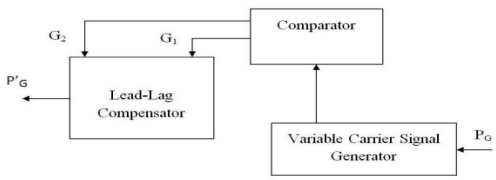


Figure 6. Fault Controller

## IV. RESULT AND DISCUSSUION

*A. Simulation Using Moderate Wind Speed Data*

PSCAD/EMTDC software has been used to simulate wind farm response at various conditions. Figure 7 shows moderate wind speed data obtained from Hokkaido, Japan. The simulation time was chosen to be 600S with a step of 50µS.

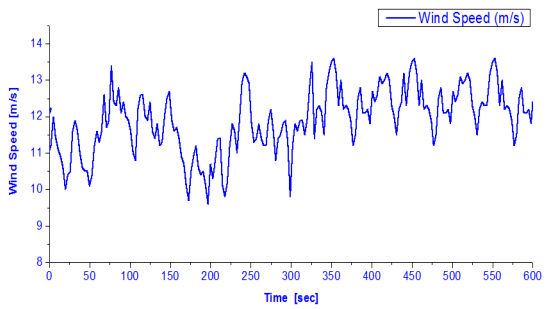


Figure 7. Moderate Wind Speed for 600s

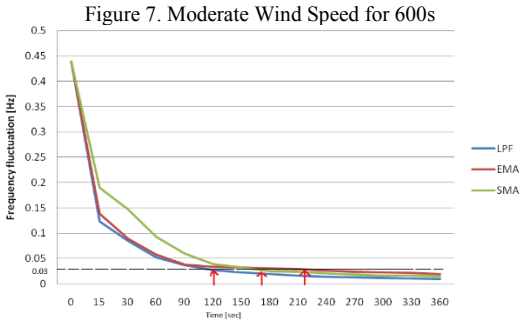


Figure 8. Frequency Fluctuation Comparison for SMA, EMA & LPF

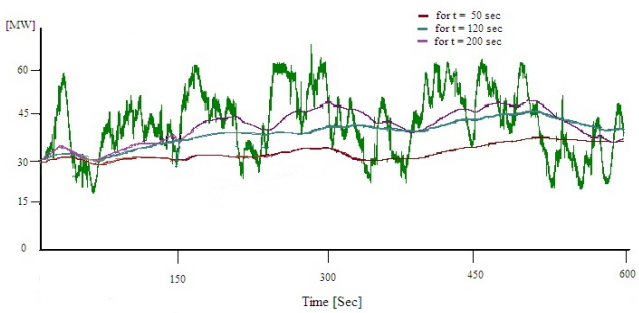


Figure 9. Reference Power with LPF for Different Time Constants

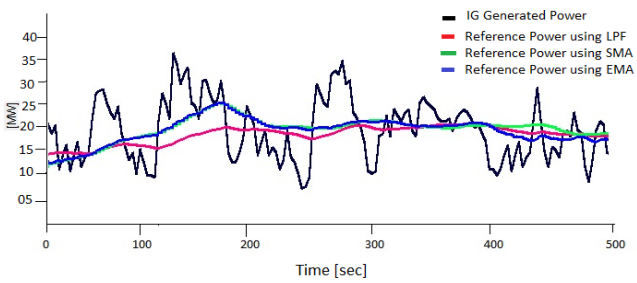


Figure 10. Reference Power with Different Methods

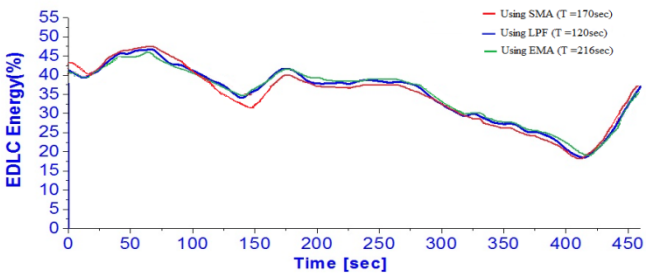


Figure 11. EDLC Energy Storage Comparison for SMA, EMA & LPF

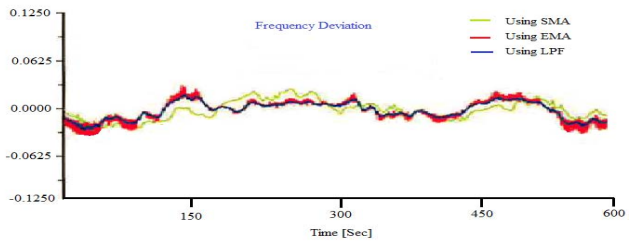


Figure 12. Frequency Deviation Comparison for SMA, EMA & LPF

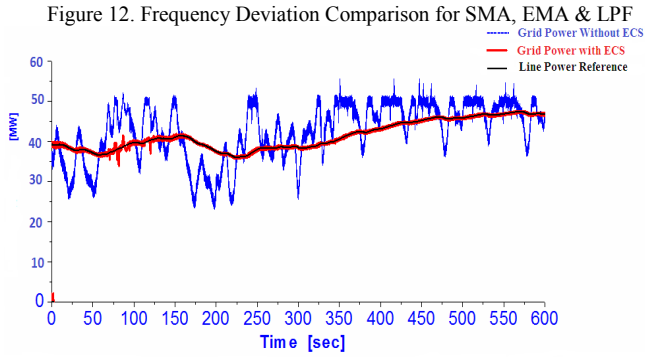


Figure 13. Response of Grid Power with ECS and without ECS

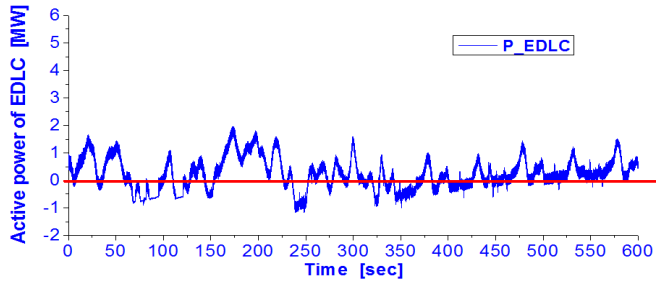


Figure 14. Active Power of the EDLC

Figure 8 shows the maximum frequency fluctuation with respect to time constant. Frequency fluctuation decreases as filtering time constant increases. Therefore, if the transmission line power is compensated according to $P_{ref}$, it is possible to decrease the system frequency fluctuations due to the wind generator output fluctuations. It is clear from Figure 8 and Figure 9 that if 120 [sec] LPF time constant is adopted then suitable reference value with enough smoothing effect can be obtained. For this maximum frequency fluctuation with 120 [sec] LPF time constant is seemed to be better for smoothing control of output fluctuations. However, same smoothing effect can be obtained by using SMA and EMA with a time constant 170 [sec] and 216 [sec] respectively as shown in Figure 8.

It is revealed from Figure 10 and 12 that reference power with enough smoothing effect can be obtained and frequency fluctuations are also very small in this method. When LPF method is used, the time constant is small and so smaller ECS energy storage capacity is needed (Figure11). Although from Figure 11 it is ascertained that the energy storage capacity required is almost same for LPF and EMA methods, it is found that frequency fluctuations are smaller in LPF than EMA (Figure 12). Moreover, EMA and SMA methods need many delay and adder circuits which make their control system more complicated than LPF. Therefore, the size of the

energy storage system and frequency fluctuation can be reduced significantly using LPF method and it seems to be a better reference generation technique. Thus, LPF method is finally considered for the next simulation.

Figure 13 shows the response of grid power (active) with the ECS being active and inactive and it is evident from the figure that the power response is much better with ECS.

Figure 14 shows the active power of EDLC. When the power is positive, the EDLC gets charged or consumes energy from the system. When it is below the zero line, the EDLC gets discharged or supplies energy to the system.

Figure 15 shows the energy of EDLC with respect to time. When the EDLC is charged, the percentage of energy increases. Percentage of energy decreases when EDLC is discharged.

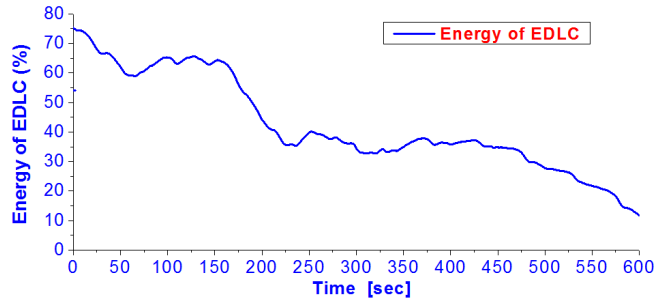


Figure 15. Energy of EDLC

Figures 16 and 17 show the grid voltage and frequency response with and without ECS respectively. There is an obvious improvement has been reported in grid voltage and frequency fluctuations after using ECS.

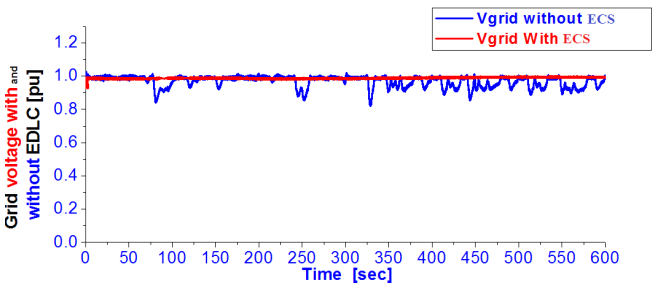


Figure 16. Grid Voltage With and Without ECS

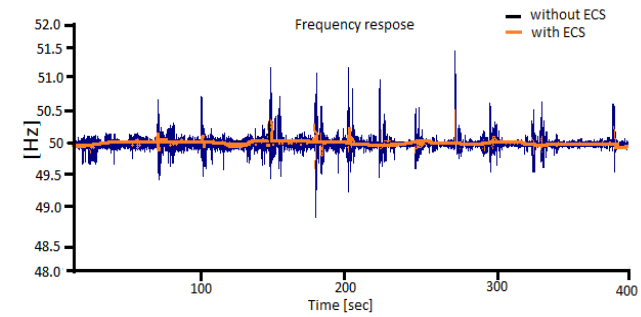


Figure 17. Frequency Response With and Without ECS

*B. Simulation Using Variable Wind Speed Data*

This section presents the simulation results for variable wind speed.

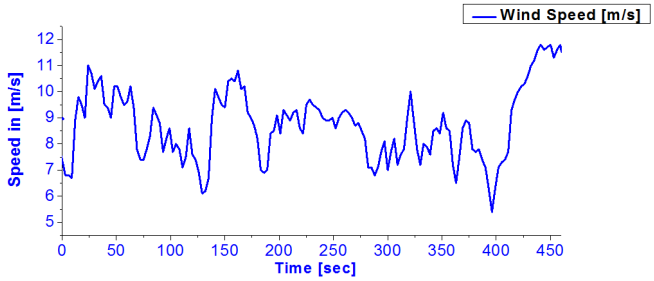


Figure 18. Fluctuating Wind Speed for 450s

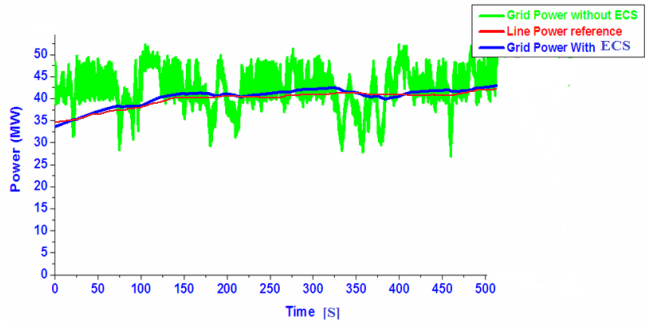


Figure 19. Active Power With and Without ECS

Figure 18 shows fluctuating wind speed data obtained from Hokkaido Island, Japan. The simulation time was chosen to be 450 seconds with a time step of 50 µS.

Figure 19 and 20 show the response of grid active power active and grid voltage with and without ECS. Again a certain improvement has been reported in grid power fluctuation using ECS.

We know that wind power is proportional to cube of the wind velocity and so highly varying wind gives rough output. It can be seen from Figure 20 that the proposed system can smoothen the voltage and power when the wind speed is widely varying.

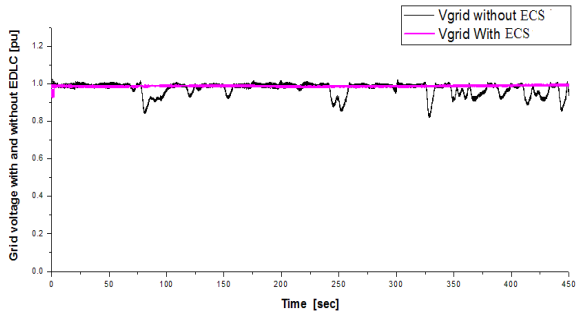


Figure 20. Grid Voltage With and Without ECS

Figure 21 shows the response of the induction generator during a three-phase fault condition with a lead-lag based variable carrier signal controller. Figure 22 shows the output power response when a fixed carrier signal based controller is used. It can be seen that the power fluctuations are much less

when a lead-lag based variable carrier signal controller is used instead of a fixed carrier signal controller.

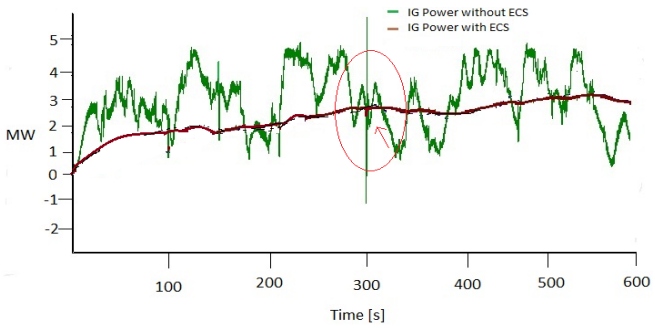


Figure 21. Power Response for a Variable Carrier Signal Controller

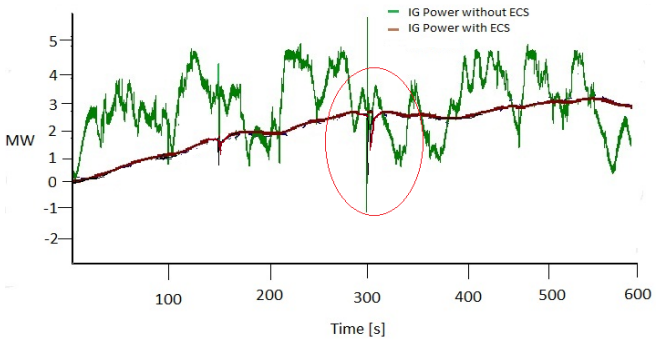


Figure 22. Power Response for a Fixed Carrier Signal Controller

## V. CONCLUSION

In this paper, a system has been proposed for smoothing the output power fluctuations of wind farms having a fixed speed induction generator. Several methods for generating line power reference have been analyzed and the LPF method has been found to be better choices than SMA and EMA methods. Moreover, the LPF method is simpler and cost effective. In addition to that the newly designed controller can significantly smooth the output power fluctuations during normal and fault conditions. The overall system can be effectively applied for harnessing wind power. It would be more useful to investigate the response with DFIG wind turbine or PMSG-based wind turbine in future.

## REFERENCES


[1] M. A. Humayun, M. A. Rashid, F. Malek,b S. Hasan, ”Analysis of temperature dependence on solar energy radiation pattern at different wavelengths.”, *ARPN Journal of Engineering and Applied Sciences,* vol. 9, no. 9, pp.1436-1441, 2014.

[2] “Global Wind Statistics 2015,” Global Wind Energy Council, Brussels, Belgium, Rep., 10, Feb. 2016.

[3] H. Bindner and P. Lundsager. “Integration of wind power in the power system,” in *Proc. 28th IEEE Annual Conference of the Industrial Electronics Society.*, Nov. 2002, vol. 4, pp. 3309-3316.

[4] F. Koch, I. Erlich, F. Shewarega, and U. Bachmann, "The effect of large offshore and onshore wind farms on the frequency of a national power supply system; simulation modelled on Germany." *Wind Engineering,* vol. 27, no. 5, pp. 393-404, Sep. 2003.

[5] Y. Z. Sun, J. Wu and G. J. Li, “Influence research of wind power generation on power systems.”*Power System Technology,* vol. 31, no. 20, pp: 55-62, Nov. 2007.

[6] T. Senjyu, R. Sakamoto, N. Urasaki, T. Funabashi, H. Fujita and H. Sekine, “Output power leveling of wind turbine generator for all operating regions by pitch angle control.”, *IEEE Transactions on Energy Conversion,* vol. 21, no. 2, pp 467-475, Jun. 2006.

[7] Y. Liao, J .B. He and J. Yao, Liao, Yong, Jin-bo He, Jun Yao, and Kai Zhuang. "Power smoothing control strategy of direct-driven permanent magnet synchronous generator for wind turbine with pitch angle control and torque dynamic control," in*Proceedings of the CSEE*29, 2009, no. 18, pp. 71-77.

[8] M. R. I. Sheikh, N. Mondol. and F. Eva,“Stabilization of wind generator by PWM-VSC controlled SMES.”InDevelopments in*Proc. of 2nd IEEE International Conference on Renewable Energy Technology (ICDRET),* pp. 1-5, Jan.5 2012.

[9] A. Sattar, A. Al Durra, C. Caruanaand J. Tamura, “Real-Time Implementation of BESS to Smooth the Output Power Fluctuation of Variable Speed Wind Turbine Generator,” *IEEJ Journal of Industry Applications*, vol. 3, no. 3, pp.198-205, 2014.

[10] S. L. Liu, Y. Liu J. and Y. Wen. Optimized controller design of a FESS for power fluctuation smoothing of a wind farm. In *Proc. of Presented at International Conference on Sustainable Power Generation and Supply (SUPERGEN 2012),* p.85, 8-9 Sep. 2012.

[11] T. Kinjyo, T. Senjyu, K. Uezato, H. Fujita and T. Funabashi,“Output power leveling of wind energy conversion system by current source ECS”, Presented at IEEE Power Engineering Society General Meeting, ( 6-10 June 2004).

[12] S. M. Muyeen, R. Takahashi, T. Murata and J. Tamura,“Integration of an energy capacitor system with a variable speed wing generator,”*IEEE Transaction on Energy Conversions*, vol. 24, no. 3, pp 740-749, Sep. 2009.

[13] T. Kinjo, T. Senjyu, N. Urasaki and H. Fujita,“Output power leveling of renewable energy by EDLC applied for energy storage system”, *IEEE Transaction on Energy Conversions,* vol. 21, no. 1, pp 221-227, Mar.2006.

[14] A. A. Elbaset, “Smoothing of grid connected wind-diesel power output using Energy Capacitor System”,*Journal of Engineering Science and Technology Review,* vol. 7, no. 2, pp. 47-52, Jun.2014.

[15] Z. S. Saoud, M. L. Lisboa, J. B. Ekanayake, N. Jenkins and G. Strbac. Application of STATCOMs to wind farms. IEE Proceedings – Generation, Transmission and Distribution. 145(5). pp 511-516, Aug. 2002.

[16] A. N.Hussain, F. A. Malek, M. A. Humayun, and M. A. Rashid, "Power system oscillations damping by optimal coordinated design between multiple damping stabilizers based on STATCOM device." In *2012 IEEE Conference on Sustainable Utilization and Development in Engineering and Technology (STUDENT)*, pp. 18-23, 2012.

# Performance Comparison of Various Wavelets in Compression of PMU Generated data in Smart Grid

Baizeed Ahmed Bhuiyan[1], Md. Wasif Absar[2], Ayon Roy[3]
Department of Electrical and Electronic Engineering
Ahsanullah University of Science and Technology, Dhaka, Bangladesh
baizeedahmed@gmail.com[1], wasifabsar@gmail.com[2], ayonroy699@gmail.com[3]

***Abstract*— With the advent of smart grid concept, a large number of smart meters and monitors will be deployed for broad observability and real-time monitoring of the behavior of power system. An important factor for the implementation of smart grid is the introduction of Phasor Measurement Unit (PMU) or Synchrophasor in power system. The current Supervisory Control and Data Acquisition (SCADA) technique measures 1 sample in every 2-4 seconds whereas PMU measures 10-60 samples per second. Huge storage space and large channel bandwidth will be needed for exchanging information. Hence, power system data compression becomes very much essential. In this paper, Wavelet Transform has been used for PMU generated data compression. Two discrete wavelets, namely Daubechies 2 (db2) and Coiflet 1 (coif1) have been used for the compression purpose. Results show that db2 is comparatively better than coif1 for compression of PMU generated signal.**

***Keywords—Smart Grid, Phasor Measurement Unit (PMU), Wavelet Transform, Discrete Wavelet Transform (DWT), Signal Compression.***

## I. INTRODUCTION

To confront the striding technological development, the prevailing power generation system felt the need of a grid system to handle the groundswell of digital and computerized equipment and to manage electricity demand in a sustainable, reliable and economic manner by providing the utility companies with maximum visibility over their assets and services, and empowering consumers to interact with the providers for energy usage adjustments and cost reduction. Ameliorating data management and introducing two-way communication between supplier and consumer ends enable the utilities to provide a layer of intelligence over their infrastructure thus allowing introduction of new processes in their businesses. Infrastructural change to the conventional grid system necessitates the inception of smart meters, meter data management system, distribution automation, substation automation, etc. [1].

For allowing broad observability and real-time monitoring, deployment of a large number of automation and measuring devices is imperative for the generation and transmission networks. The situation gives rise to requirements concerning the communication interface, computational intelligence and the ability to process data or signals and information sharing, hence increasing the amount of data exchange and storage considerably [2]. Supervisory Control and Data Acquisition (SCADA) system has been gathering system data from Remote Terminal Units (RTUs), Relays and Transducers to provide system information to the system operator which plays a crucial role in system operation and properly mediating system anomalies. Due to the asynchronous and slow nature of data acquisition of SCADA, at a sub-second time frame the dynamic nature of the system state cannot be enclosed and thus accuracy of the state information is reduced [3]. Alternatively, phasor measurement units are time stamped to an extremely precise and accurate time reference and take voltage and current samples many times a second. Phasor measurement data can be used to supplement existing control center functions as well as provide new functionalities and with a GPS signal can provide synchronized voltage and current phasor measurements across a wide region.

SCADA system takes 1 sample in every 2-3 seconds whereas PMU takes 10-60 samples per second which entails huge storage space and large channel bandwidth for information exchange thereby constrains data compression for faster data exchange. The recommended schemes for power system data compression include Fast Fourier Transform, Adaptive Differential Pulse Code Modulation, Discrete Wavelet Transform, Wavelet Packet Transform, and Embedded Zero-Tree Wavelet [2], [4]. In this paper, Discrete Wavelet Transform (DWT) has been used for compressing PMU generated data in smart grid. The goal of this paper is to analyze the results obtained through compressions by using Daubechies and Coiflet wavelets of the wavelet family and to find out which wavelet performs better. In this paper the primary focus was to compress sample PMU generated data in the distribution system of a power system.

Section II describes the basics of PMU and its importance in smart grid. Section III presents the basic theory of wavelet based compression and the parameter used in the work for comparing compression performance. Section IV shows simulation results obtained in MATLAB and analyze them. Section V concludes the paper highlighting its findings and future scope.

## II. PHASOR MEASUREMENT UNIT (PMU) AND ITS IMPORTANCE IN SMART GRID

A sinusoidal signal can be represented by means of a phasor. Phasor measurement unit measures an electrical signal in terms of its voltage and phase with respect to a time reference and frequency. The measurement can be conducted over a wide area using multiple PMU units where the time synchronization can be done with help of Global Positioning System (GPS) and Phasor Data Concentrator (PDC).

978-1-5386-2307-7/17/$31.00 ©2017 IEEE

Synchronized measurements from multiple sites in the grid network can increase the probability of accurate identification of the instability [5]. Fig. 1 shows the basic components of PMU in blocks [6].

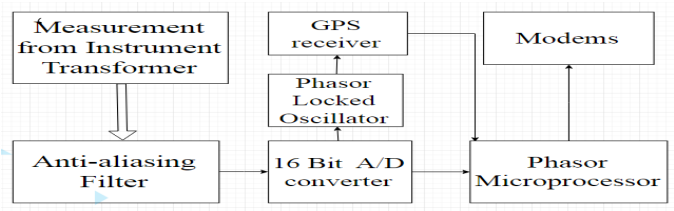


Fig.1. Block Diagram of PMU [6].

Synchrophasor data measurements are regarded as the significant facilitator for real-time power grid situational awareness and control. PMU shows a very promising application during restoration and emergency restoration procedures. PMUs take 10-60 samples per second and thus require huge amount of storage space and bandwidth for propagation. Due to scarcity of communication resources, the data is not sent normally but rather it is compressed to a point where it's almost accurate reconstruction is possible and thus save us the trouble of consuming too much of our resources. Several algorithms have been proposed for PMU data compression over the past few decades. Reference [7] proposed a combined algorithm of Exception Compression (EC) with Swing Door Trending (SDT) compression. Two stage compression algorithm proposing Principle Component Analysis and Discrete Cosine Transform has been mentioned in [8]. A modified Delta encoding technique has been put forward where PMU data can be compressed by a more generic, statistical compression technique [9]. Discrete wavelet transform has been used as a compression technique in various aspects of smart grid including the PMU data compression [10]-[11]. In this paper, we have used DWT as the PMU generated data compressor in the distribution level of the power system. The advantage of using DWT is not only the compression of PMU generated data but also the reduction of sinusoidal and white noise contained in the signal. Detailed discussion on wavelet transform as a compression technique has been presented in the next section of the paper.

## III. Wavelet Transform Based Compression and Performance Parameters

Compressing data using wavelet transform is based on a hierarchical decomposition technique known as Multi-Resolution Analysis (MRA) where a signal is dilated to get Scaling coefficients and Wavelet coefficients and further transforms are applied on the already decomposed signal. Scaling coefficients contain the lower frequency components and Wavelet coefficients possess the higher components. WT based MRA has been discussed in detail in [10] with a brief mention of the technique's properties. While using DWT for data compression, selection of the wavelet plays a crucial role as the energy content at different decomposition level of different wavelets reflects the quantity of preserved information. Common wavelets chiefly include the Haar Wavelet, Daubechies Wavelet (belongs to the orthogonal wavelet family and db2-db20 are commonly used), Symlet Wavelet, Coiflet Wavelet [12]-[15]. For better performance in analyzing dynamic signals Daubechies and Symlet Wavelet have been used in [10] for compressing data of disturbance signals during generation loss, load drop and load surge. Coiflets, Symlet and Daubechies wavelets have been used in PMU data compression using Wavelet Packet Decomposition based technique in [16] for having highest number of vanishing moments for a given support width. Haar, Daubechies, Coiflet, and Bi-orthogonal wavelets have been studied in [17] for image compression on account of their dominance in symmetry, orthogonality, regularity, and degree of smoothness. References [18]-[19] also reflect the usage of Daubechies and Coiflet wavelets in other compression techniques. Considering the superiority of the above mentioned wavelets, db2 and coif1 have been analyzed in this paper for compressing data in the distribution level of a power system.

In order to compare compression performance of various wavelets, different parameters such as Energy Recovery Parameter (ERP)/Energy Retained [20], Data Compression Ratio (DCR)/No. of Zeros [21], Percentage of Error [20] have been used.

$$\text{ERP} = \frac{\text{sum of squares of data in reconstructed signal}}{\text{sum of squares of data in original signal}} \quad (1)$$

$$\text{DCR} = \frac{\text{number of zeroes at current decomposition level}}{\text{number of coefficients}} \quad (2)$$

But many of the coefficients generated are zeroes even before thresholding for the signals used in this paper, so the modified formulae used is-

$$\text{DCR} = \{(\text{Number of zeroes after thresholding - Number of zeroes before thresholding}) \text{ at a given decomposition level}\} \div \text{Number of coefficients} \quad (3)$$

$$\%\ \text{Error} = \frac{\text{root mean square (rms) of error signal}}{\text{root mean square (rms) of original signal}} \times 100\% \quad (4)$$

Threshold, thr(n)= $u_n \times \max(|v_n|)$ [20]

Where n is wavelet series; thr(n) is the setting threshold of the n-th high-frequency; $u_n$ is threshold parameter of the n-th high-frequency, be able to adjust itself with error limit, $0 \leq u_n \leq 1$; $v_n$ is the n-th high-frequency decomposition coefficient. Data compression using wavelet is to eliminate decomposition coefficients less than threshold parameter. Original signal is compressed greatly if coefficients $\overline{v_n}$ meet:

$$\overline{v_n} = \begin{cases} v_n, |v_n| \geq \text{thr(n)} \\ 0, |v_n| < \text{thr(n)} \end{cases}$$

## IV. Simulation Results

In this part, different types of input signals are compressed at different levels and then reconstructed. DIgSILENT PowerFactory R14 software has been used for the generation of all the PMU signal waveforms from a 43 bus grid

connected system. The system has been shown in fig. 2. The microgrid system has 21.76 MW and 9 MVAR of real and reactive power load [22]. Two synchronous machines are connected to bus 4 and bus 50. A solar PV plant is connected to bus 41. MATLAB R2014a (8.3.0.532) has been used to carry out all the Wavelet Transform related simulation.

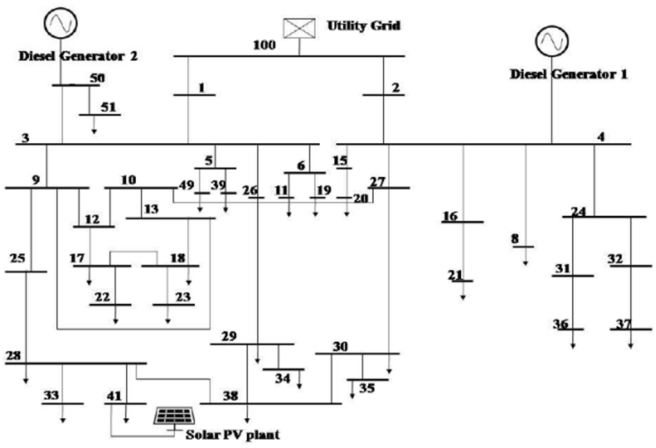


Fig. 2. A 43 bus micro grid system [22].

In fig. 3, voltage disturbance for 3-Φ fault at a bus near generator bus 4 has been shown.

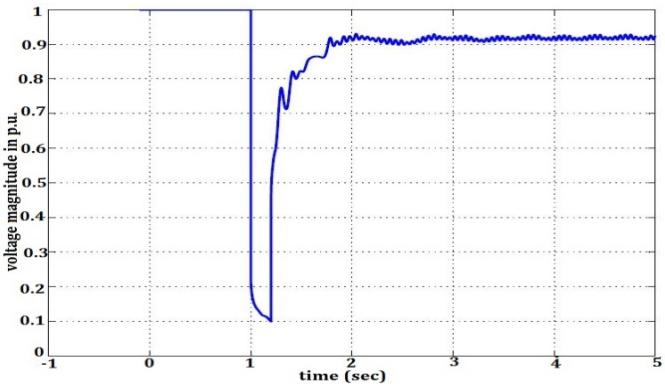


Fig. 3. Voltage Disturbance signal.

Table I shows results obtained from compression of Voltage Disturbance signal by db2 wavelet using MATLAB Editor.

TABLE I. Compression Results using db2 wavelet

| Level of Decomposition | ERP/ Energy Retained | DCR/ No. of Zeroes | %Error | Threshold |
|---|---|---|---|---|
| 3 | 100.002% | 87.16% | 0.0495% | 0.0283 |
| 4 | 99.9993% | 93.32% | 0.1822% | 0.0426 |
| 5 | 100.003% | 96.33% | 0.4482% | 0.0584 |
| 6 | 99.9997% | 97.77% | 0.5620% | 0.0800 |
| 7 | 99.9926% | 98.66% | 0.8067% | 0.1209 |

From analysis it has been observed that when the signal is compressed at level 7 decomposition using db2, the voltage variations violate the tolerable range of ±5% at a certain instant in pre-fault condition [23]. In the following figure 4, the best case plot and the worst case plot for both db2 and coif1 from the Table I have been shown to depict compression performances of these wavelets for the Voltage Disturbance signal.

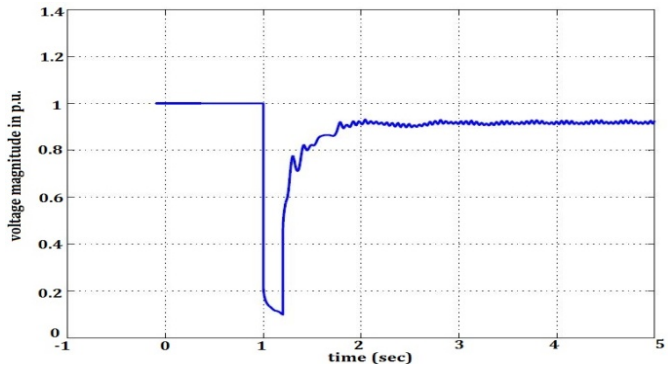


(a)

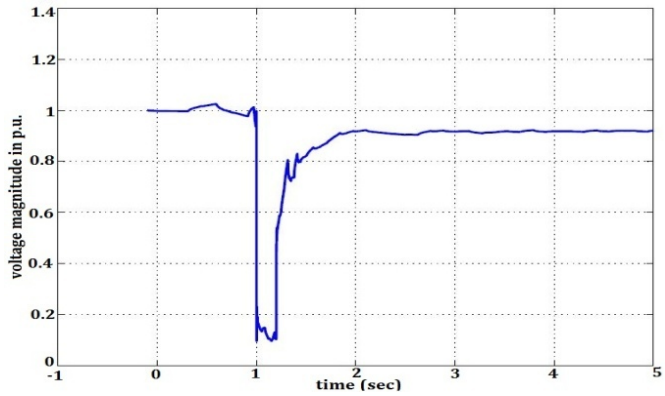


(b)

Fig. 4. Compressed Voltage Disturbance signal for decomposition at level (a) 3 (b) 7 by db2 wavelet.

Table II shows results obtained from compression of Voltage Disturbance signal by coif1 wavelet using Wavelet Design and Analysis Toolbox.

TABLE II. Compression Results using coif1 wavelet

| Level of Decomposition | ERP/ Energy Retained | DCR/ No. of Zeroes | %Error | Threshold |
|---|---|---|---|---|
| 3 | 99.93% | 87.45% | 1.8929% | 0.9153 |
| 4 | 99.90% | 93.67% | 2.1452% | 0.9153 |
| 5 | 99.85% | 96.79% | 3.1797% | 1.139 |

Distortion of the signal was observed for compression at level 3 decomposition of the Voltage Disturbance signal while using coif1 wavelet. In pre-fault condition, the voltage variations violate the tolerable range of ±5% at several instants [23]. Also, percentage of error was greater than desired level

of 2% [20]. The problem persisted as we increased the decomposition level further. In the following figure 5, the best case plot and the worst case plot from the Table II have been shown. However, for Voltage Disturbance signal, compression performance of coif1 wavelet is not that good since the Grid Code for voltage variation limit in normal operating condition is violated at any level of decomposition [23].

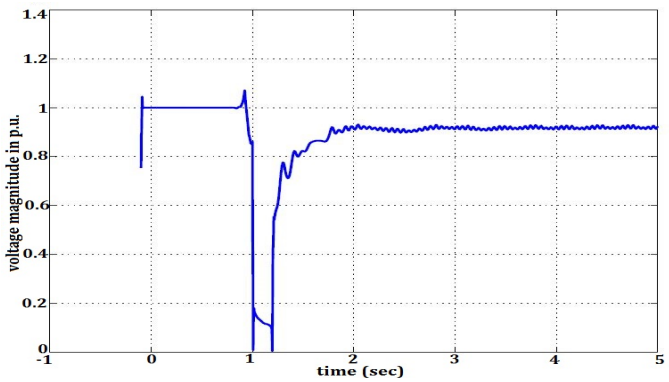


(a)

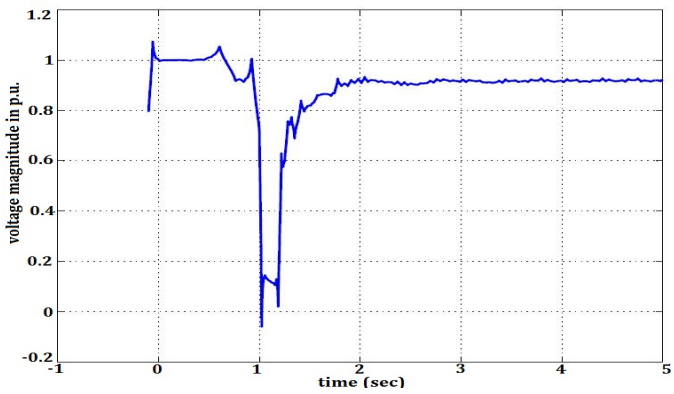


(b)

Fig. 5. Compressed Voltage Disturbance signal for decomposition at level (a) 3 (b) 5 by coif1 wavelet.

Frequency disturbance for 3-Φ fault near generator bus 4 has been shown in fig. 6.

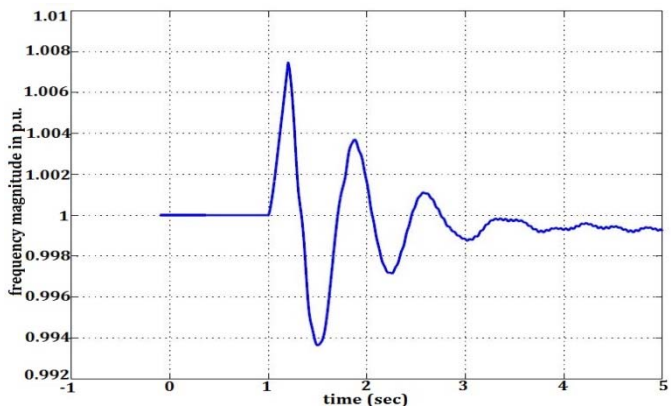


Fig. 6. Frequency Disturbance signal.

Table III shows results obtained from compression of Frequency Disturbance signal by coif1 wavelet using MATLAB Editor.

TABLE III. Compression Results using db2 wavelet

| Level of Decomposition | ERP/ Energy Retained | DCR/ No. of Zeroes | %Error | Threshold |
|---|---|---|---|---|
| 3 | 100% | 86.20% | $4.55\times10^{-4}$ % | 0.0285 |
| 4 | 100% | 92.43% | 0.0014% | 0.0403 |
| 5 | 100% | 95.56% | 0.0048% | 0.0570 |
| 6 | 100% | 97.12% | 0.013% | 0.0805 |
| 7 | 100% | 97.89% | 0.0423% | 0.1138 |

In case of the Frequency Disturbance signal, it has been observed that for compression at level 7 decomposition by db2 wavelet, the reconstructed signal distorts significantly, which is evident from fig. 7(b). In the following figure 7, the best case plot and the worst case plot from the Table III have been shown to depict compression performance of db2 wavelet for the Frequency Disturbance signal.

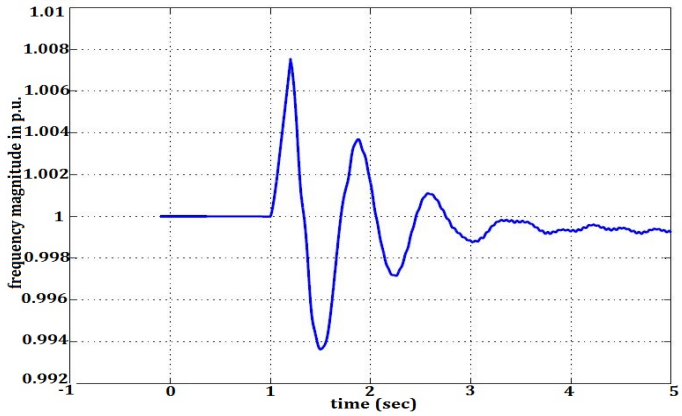


(a)

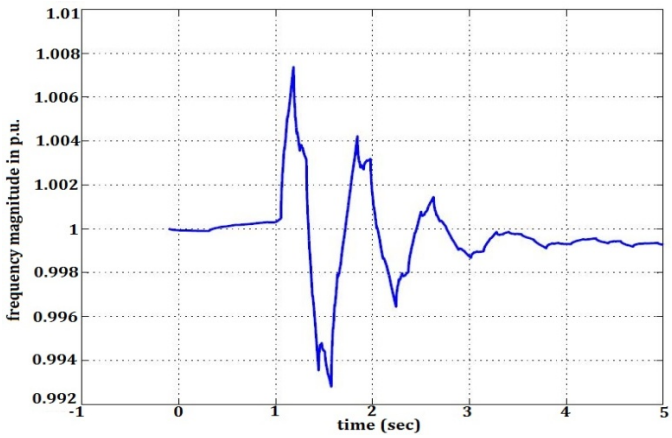


(b)

Fig. 7. Compressed Frequency Disturbance signal for decomposition at level (a) 3 (b) 7 by db2 wavelet.

Table IV shows results obtained from compression of Frequency Disturbance signal by coif1 wavelet using Wavelet Design and Analysis Toolbox.

TABLE IV. Compression Results using coif1 wavelet

| Level of Decomposition | ERP/ Energy Retained | DCR/ No. of Zeroes | %Error | Threshold |
|---|---|---|---|---|
| 3 | 100% | 87.45% | $5.03\times10^{-4}$% | 0.0001994 |
| 4 | 100% | 93.67% | 0.0015% | 0.0004103 |
| 5 | 100% | 96.79% | 0.0048% | 0.002003 |
| 6 | 100% | 98.35% | 0.0137% | 0.005697 |
| 7 | 100% | 99.12% | 0.0311% | 0.01129 |

For compression of Frequency Disturbance signal by coif1 wavelet at levels of decomposition 4 and 5, there were distortions in the first positive peak of the reconstructed signal. At decomposition level 6, the reconstructed signal showed distortions in the positive and negative peak. For decomposition at level 7, the reconstructed signal distorted significantly which is evident from fig. 8(b). In the following figure 8, the best case plot and the worst case plot from the Table IV have been shown to depict compression performance of coif1 wavelet for the Frequency Disturbance signal.

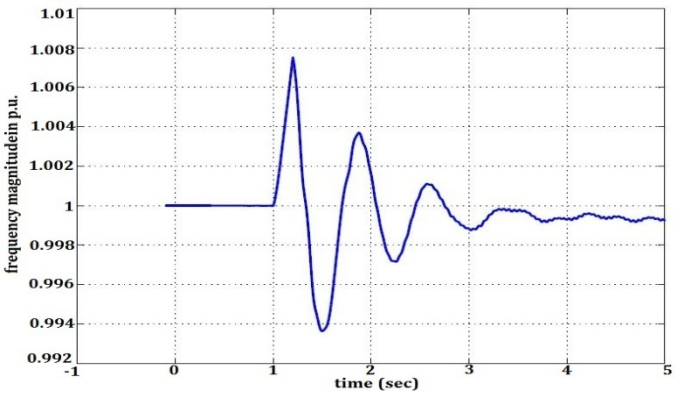


(a)

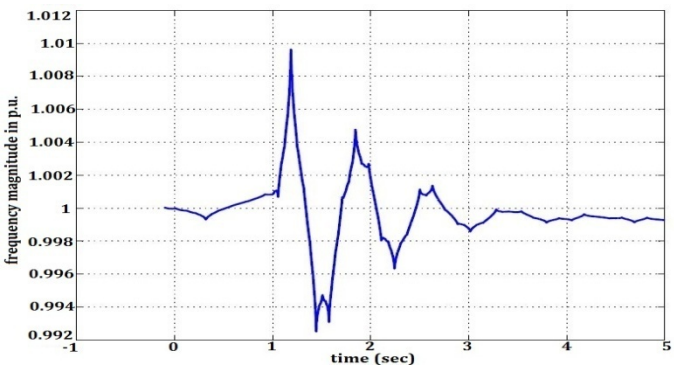


(b)

Fig. 8. Compressed Frequency Disturbance signal for decomposition at level (a) 3 (b) 7 by coif1 wavelet.

In this work, findings from the analysis can be listed as follows:

i) For voltage disturbances, db2 appears to be a better choice over coif1 in terms of compression.
ii) Decomposition at level 3 seems to be suitable for compressing voltage and frequency signals. It keeps the % Error limited within 2%.
iii) For voltage and frequency disturbances, significant distortion in compressed signals can be seen when coif1 is used.
iv) For frequency disturbance- both db2 and coif1 perform almost in similar way in terms of ERP/Energy Retained and Percentage of Error.

The highest priority in selecting the wavelet type and decomposition level has been given to two parameters- % Error and DCR [18]-[20].

## V. Conclusions

In this paper, a comparative study of the compression performances of two discrete wavelets, namely db2 and coif1, in compressing PMU generated signals has been done. The sample signals used in this work have been constructed taking 100 samples per second, which is close approximation to PMU signals that take 10-60 samples per second. Voltage and Frequency disturbance signals generated due to 3-Φ fault near a generator bus of the test system have been compressed at various decomposition levels by the mentioned wavelets and several parameters were determined. The study comes to the conclusion that for both types of disturbances, the compression performance of db2 seems to be better than coif1 and decomposition at level 3 can be a suitable choice for this purpose. Coif1 produces significant distortions in both types of reconstructed signals which are undesired. In future, we wish to explore more discrete wavelet families for further comparative study of compression performances of these wavelets in compressing PMU signals.

## References


[1] Hassan Farhangi, “The path of the Smart Grid”, *IEEE Power and Energy Magazine*, January/February 2010.

[2] Michel P. Theo, Lasiandra Lovisolo, Moises V. Ribeiro, Eduardo A. B. da Silva, Marco A. M. Rodrigues, João M. T. Romano, and Paulo S. R. Diniz, “The Compression of Electric Signal Waveforms for Smart Grids: State of the Art and Future Trends”, *IEEE Trans. On Smart Grid*, vol. 5, no. 1, Jan. 2014.

[3] Mangapathirao V. Mynam, Ala Harikrishna, and Vivek Singh, “Synchrophasors redefining SCADA systems”, *13th Annual Western Power Delivery Automation Conference*, Mar. 2011.

[4] K. Mehta, and B. D. Russell, “Data Compression for Digital Data From Power Systems Disturbances: Requirements and Technique Evaluation”, *IEEE Trans. On Power Delivery*, vol. 4, no. 3, pp. 1683–1688, Jul. 1989.

[5] Mudathir Funsho Akorede, and Hashim Hizam, “Wavelet Transforms: Practical Applications in Power Systems”, *Journal of Electrical Engineering & Technology*, vol. 4, No. 2, pp. 168~174, 2009.

[6] Saikat Chakrabarti, Elias Kyriakides, and Mihaela Albu, "Uncertainty in Power System State Variables Obtained Through Synchronized Measurements", *IEEE Trans. on Instrumentation and Measurement*, vol. 58, No. 8, pp. 2452-2458, Aug. 2009.

[7] F. Zhang *et al.*, "Application of a real-time data compression and adapted protocol technique for WAMS," *IEEE Trans. Power Syst.*, vol. 30, no. 2, pp. 653–662, Mar. 2015.

[8] Phani Harsha Gadde, Milan Biswal, Sukumar Brahma and Huiping Cao, "Efficient Compression of PMU Data in WAMS", *IEEE Trans. on Smart Grid,* vol. 7, no. 5, pp. 2406-2413, Sep. 2016.

[9] R. Klump, P. Argawal, J. E. Tate, and H. Khurana, "Lossless Compression of Synchronized Phasor Measurements," in *Proc. IEEE Power Energy Soc. Gen. Meeting*, Jul. 2010, pp. 1–7.

[10] J. Ning, J. Wang, W. Gao, and C. Liu, "A Wavelet-Based Data Compression Technique for Smart Grid," *IEEE Trans. on Smart Grid*, vol. 2, no. 1, pp. 212–218, Mar. 2011.

[11] J. Khan, S. Bhuiyan, G. Murphy, and M. Arline, "Embedded Zerotree Wavelet Based Data Compression for Smart Grid," in *Proc. IEEE Ind. Appl. Soc. Annu. Meeting*, Lake Buena Vista, Oct. 2013, pp. 1–8.

[12] Piotr Porwik, and Agnieszka Lisowska, "The Haar–Wavelet Transform in Digital Image Processing: Its Status and Achievements", *Machine Graphics and Vision*, vol. 13, no. 1/2, pp. 79-98., Nov. 2004.

[13] Colm Mulcahy, "Image Compression Using the Haar Wavelet Transforms", *Spelman Science and Mathematics Journal*, vol.1, No. 1, pp. 22-31, 1997.

[14] Fang Ding, and Tianjie Cao "Application of Daubechies Wavelet Transform in the Estimation of Standard Deviation of White Noise", *2nd International Conference on Digital Manufacturing and Automation (ICDMA),* Aug. 2011, pp. 212-215.

[15] A.V. Ovanesova, and L.E. Suárez, *Applications of Wavelet Transforms to Damage Detection in Frame Structures*, Engineering Structures, Elsevier, vol. 26, issue 1, pp. 39-49, 2004.

[16] Jesmin Khan, Sharif Bhuiyan, Gregory Murphy, and Johnathan Williams, "PMU Data Analysis in Smart Grid using WPD", *Industrial Electronics Society (IECON 2014) - 40th Annual Conference of the IEEE,* Oct.-Nov. 2014, pp. 2438-2444.

[17] Sonja Grgic, Mislav Grgic and Branka Zovko-Cihlar, "Performance Analysis of Image Compression Using Wavelets", *IEEE Trans. on Industrial Electronics*, vol. 48, no. 3, Jun. 2001.

[18] S. Santoso, E. J Powers and W. M Grady, "Power Quality Disturbance Data Compression using Wavelet Transform Methods", *IEEE Trans. on Power Delivery*, vol. 12, no. 3, Jul. 1997.

[19] Effrina Yanti Hamid, and Zen-Ichiro Kawasaki, "Wavelet-Based Data Compression of Power System Disturbances Using the Minimum Description Length Criterion", *IEEE Trans. on Power Delivery*, vol. 17, no. 2, Apr. 2002.

[20] Yue Yuan, Xiaoming Yu, and Hongji Du, "Power System Fault Data Compression Using the Wavelet Transform and Vector Quantification", *2006 International Conference on Power System Technology,* Oct. 2006, pp. 1-6.

[21] P.V. Kranthi Kumar, and M.S.R Naidu, "An Automated Threshold Selection using Wavelet Based PSO for Image Compression", *IOSR Journal of Electronics and Communication Engineering (IOSR-JECE) e-ISSN: 2278-2834,p- ISSN: 2278-8735*, vol. 9, issue 5, ver. III, pp. 26-31 , Sep. - Oct. 2014.

[22] *IEEE Recommended Practice for Industrial and Commercial Power Systems Analysis*, IEEE Std. 399-1997, 1998.

[23] Pradeep Kumar, and Asheesh K. Singh, *Grid Codes: Goals and Challenges*, Renewable Energy Integration, Singapore: Springer, 2014, pp. 17-39.

# GA-Based Adaptive Fuzzy Logic Controller for a Robotic Arm in the Presence of Moving Obstacle

Soniya Yeasmin and Pintu Chandra Shill
Department of Computer Science and Engineering (CSE)
Khulna University of Engineering and Technology
Khulna-9203, Bangladesh
soniya.cse08@gmail.com, lpintucskuet@yahoo.com

*Abstract*— **The design and implementation of a fuzzy logic controller (FLCs) for intelligent control of robotics is very complicated and time consuming process due to articulated robot platforms. In order to automate the controlling and design process, the machine learning techniques are used. In this paper, FLCs and GAs are integrated to control the robot arm in existence of an obstacle. Here, genetic algorithms are employed to optimize the fuzzy knowledge base in three different ways concurrently: select the optimal number of linguistic levels, optimize the parameters of membership functions and optimize the rule base. In this way, evolutionary strategy can be used to minimize the number of mandatory rules and maximize the performance of the fuzzy logic controller by searching for a subset of rule, number of linguistic levels, parameters of membership functions from a given knowledge base. The simulated results depict the validity of the fuzzy logic control system and better performance is obtained.**

***Keywords— Fuzzy control, Evolutionary Algorithms, Robotic Arm,Obstacle avoidance, Fuzzy knowledge base.***

## I. INTRODUCTION

Fuzzy control has a vital influence in the area of robotics [1]-[2], involving the environment with the high uncertainty in the fuzzy knowledge base (KB). The fuzzy logic controller (FLCs) mainly worked according to the KB developed with the help of the heuristic knowledge of the expert operators. A FLCs has a large number of functional applications in control [3]-[4], prediction [5] and inference [6] and has been used to construct rigid controller that are capable to produce quite suitable performance in examination problems with uncertainty and imprecision. For this reason, an automated method of knowledge acquisition is necessary for FLCs that has given satisfactory performance similar to the human operators.

Numerous approaches have been suggested in past few years for learning and tuning of fuzzy controller using evolutionary algorithms (EAs) [7]-[12]. Some of the methods use EAs for learning the membership functions [13]-[14]. Most of the methods use predefined database while learning the rule base (RB) only [7], [9]-[11]. But our proposed method learns both the rule base (RB) and data base (DB) i.e. complete fuzzy knowledge base to achieve the interpretability and efficiency of the FLCs.

In this study, An Integrated architecture of fuzzy logic controller (FLCs) and genetic algorithms (GAs) have been developed for perceptive and rational control of an arm of a robot in the existence of an obstacle. Here, GAs is employed in two different ways: definition and selection of fuzzy control rules, selection of membership function parameters and number of optimal linguistic levels for linguistic variable. It is demonstrated that by using a self learning adaptive approach, the suggested innovative unified FLCs and GA architecture can develop an apprehensible and feasible fuzzy rules for nonlinear and dynamic systems especially for the path planning in collision-avoidance problems. In our method, no restrictions for the selection of number of linguistic levels and optimal parameters to define the membership functions.

Bearing these concepts, the remaining parts of the study are arranged as shown below: Section II introduces genetic algorithms and explains the process to use it for developing a suitable fuzzy KB in building FLCs. This section describes the knowledge base acquisition technique, encoding technique of chromosome also. Section III presents the detail description of robotic arm that can be used to validate the proposed control algorithm. Based on this conception Section IV presents the simulation results and analyzed results on the basis of obstacle and constraints. Finally, section V sketches the key points of our proposed method referred to as conclusions.

## II. KNOWLEDGE BASES LEARNING THROUGH GA

This section describes our new technique which uses the genetic learning approach and generates the KBs automatically. Here, the knowledge bases consist of the following parts: the number of linguistic levels, the parameters defining the membership functions and the rule base. Fig. 1 shows how the genetic algorithm (GAs) decides which parts of the KB are to be considered to optimize and learning process through GAs. In this case, three components of knowledge base are learned through GAs. The GAs in the integrated KBs learning architecture operates as following steps:

**Step 1: Initialization:** A set of chromosomes (possible solutions) is encoded by the parameters of set of KBs of a FLCs and solution of the problem is assessed. In this case, each possible solution can be represented as a string of typical both the integer and real numbers. Each possible solution has two sections where the first section employs a number of linguistic levels and the second part is used to define the parameters of membership function as well as fuzzy rules.

978-1-5386-2307-7/17/$31.00 ©2017 IEEE

**Step 2: Evaluation:** Evaluate each chromosome by the objective function and assign a fitness value according to the solving performance of the problem. Finally reorder the chromosomes based on their fitness value.

**Step 3: Recombination:** Form new chromosome along with new generation by using crossover and mutation operator to chromosomes. In this study, a highly disruptive mutation, HUX [13] and BLX-$\alpha$ crossover [14] is used respectively.

**Step 4:** Evaluate the chromosomes how they perform to solve the problem and check the possible solutions to reach the termination criteria.

**Step 5:** Stop the process when termination criterion is achieved and receive the most accurate chromosome (fuzzy rules set, parameters defining the membership functions and number of linguistic levels) otherwise go to step 3.

It is mentioned that the arguments number such as the population size and the probability of applying crossover and mutation operators influence GAs.

### *A. GA encoding scheme and population initialization*

The main step for designing the control algorithm is to encode a knowledge base of fuzzy logic controller to represent the chromosome of genetic algorithm. In this study, the parameters to specify the membership function and rule base is encoded by the real values and the number of linguistic levels is encoded by the integer number. The parameters for defining the knowledge base are shown in Fig. 2. The chromosome has two parts as follows:

$$C \equiv \{C_M, C_N\}$$

where $C_M$ and $C_N$ are the genotypes of the parameters for defining membership function as well as fuzzy rules and number of linguistic levels respectively. $FS_i$ represents fuzzy sets in fuzzy rules and all variables are classified by two parameters center $a_{ji}$ and width $b_{ji}$ .KB's parameters represent all the information and are encoded in the structure called string or chromosome. Every chromosome can be partitioned into two parts (Fig. 2):

$C_M$: The $(C_M)$ part is the real gene sequence which is used to define the membership function as well as fuzzy rules.

$C_N$: The $(C_N)$ part is a sequence of integer numbers which is used to specify the number of linguistic levels.

The new developed genetic algorithms are used for adjusting two internally related elements of KBs and seeking optimum FLCs to present the least objective error.

### *B. Evolution Criteria*

The overall process of this strategy from the initial population of FLCs to the optimal FLCs is described as following manner:

**Selection:** The GAs starts generating new FLCs after evaluating initially randomized generated population. The selection of the FLC-chromosomes is obtained from the parent population and is used to generate new offspring FLC-chromosomes. For reproducing the next FLC-chromosome generation, a combination of N parents along with their offspring is used for selecting the finest N FLC- chromosomes.

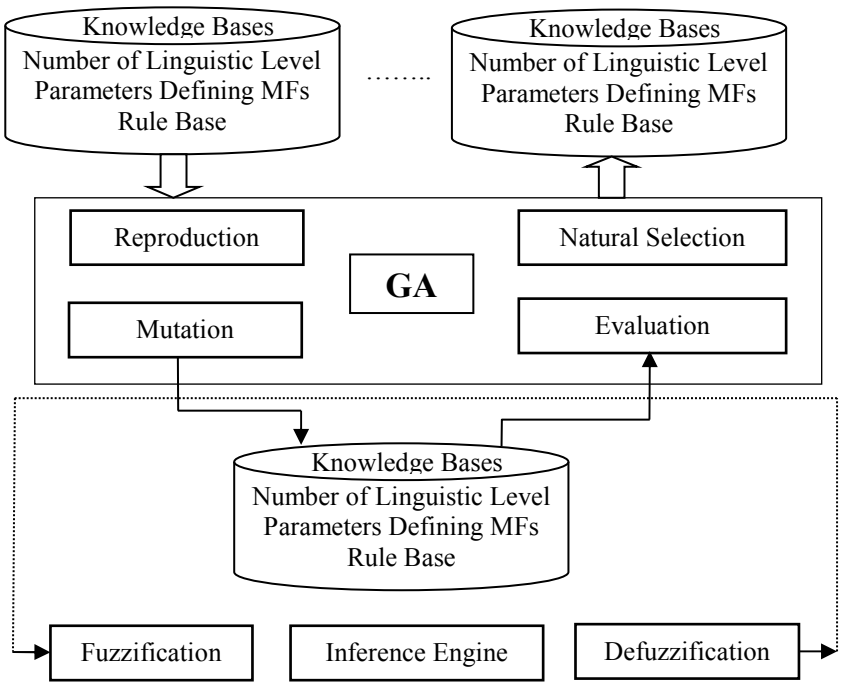


Figure 1. Fuzzy Knowledge base Learning through Genetic Algorithm

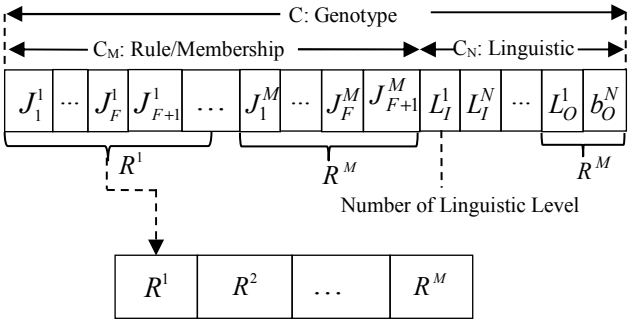


Figure 2. Chromosome Encoding by the Parameters of Knowledge base

**Crossover:** According to the selection mechanism, two best chromosomes are selected from population. After the selection, their vectors are joined for producing a pair of new FLC using genetic operators. The two major genetic operators are mutation and crossover that are used with differing probabilities. When the probability experiment is satisfied, crossover happens otherwise the formed offspring stay the same as their parents.

A uniform crossover operator has been used in case of binary GA and the max-min-arithmetical (MMA) operator was used as a crossover operator in case of real GA. Four new individuals (I) may be produced in case of crossing $C_u^t$ and $C_v^t$.

$$\begin{aligned} I_1^{t+1} &= \alpha I_v^t + (1-\alpha) I_u^t \\ I_2^{t+1} &= (1-\alpha) I_v^t + \alpha I_u^t \\ I_3^{t+1} &\text{ with } I_{3k}^{t+1} = \min\{c_k, c_k^{'}\} \\ I_4^{t+1} &\text{ with } I_{4k}^{t+1} = \min\{c_k, c_k^{'}\} \end{aligned} \tag{1}$$

The value of constant parameter $\alpha$ was selected equal to 0.5 for our experiments. According to their higher fitness value, best two individuals are placed in the new population by substituting the parents with newly generated offspring.

**Mutation:** In case of binary encoding, each argument of the offspring chromosomes goes through a probability test. The Michalewicz's nonuniform mutation operator is used to alert the parameter by the mutation operator whenever the offspring gets passed the probability test. The details on the operators are as follows:

If $C_u^t = \{P_1, .....P_k .....P_L\}$ represents FLCs- chromosome vector with length L and $P_k$ represents FLC parameter that is chosen for a mutation, then after mutation the new output $P_k^{mut}$ will be:

$$P_k^{mut} = \begin{cases} P_k + \Delta(t, P_{kr} - P_k) & if\ r = 0 \\ P_k - \Delta(t, P_k - P_{kl}) & if\ r = 1 \end{cases} \tag{2}$$

Here, $r$ denotes the random parameter, $(P_{kr}, P_{kl})$ denotes the range of parameter where $P_k\,(k \in 1,2,.....L)$ and also $\Delta(t,x)$ stands for the function with the returning value between 0 to x in the range which increases with $t$.

$$\Delta(t,x) = x.(1-\eta^{(1-t/T)^c}) \tag{3}$$

Where $\eta$ denotes the random floating point number in the range [0,1]; t and T denote the current generation and maximum number of generation respectively. The parameter c calculates the degree of dependence on the number of generations. The value of c parameter was set equal to 5 for our experiment. Using this selection method and crossover operators will incline to cause the algorithms to converge.

In this scheme, at the time of generation, mutation probability changes in between the values from 0.04% to 0.24% per bit and 1% to 10% per real parameter dynamically. The introduced adaptive parameter control for crossover rate has the values range from 40% to 90% per chromosomes.

An instance of how the MF's parameters, fuzzy rule sets and number of linguistic levels in linguistic variable are integrated all together in a chromosome is shown in Fig. 2. Then the fuzzy rules decode and represent this chromosome with their respective MFs parameters, rule base and number of linguistic levels. After that, build the fuzzy logic controller using the generated knowledge base.

## III. Robotic Arm Problem

Now days, in various applications, robots are being used efficiently, they have to acquire the knowledge working in uncertain and changing environments. For this reason, to verify our proposed approach, we used three link robot arms. This paper presents the trajectory planning problem of a three-link robotic arm in an environment with an obstacle it faces. Fig. 3 shows the sample diagram of robotic Arm with an obstacle and goal position.

The arm should move in two dimensional environments containing a randomly placed obstacle. The initial position and

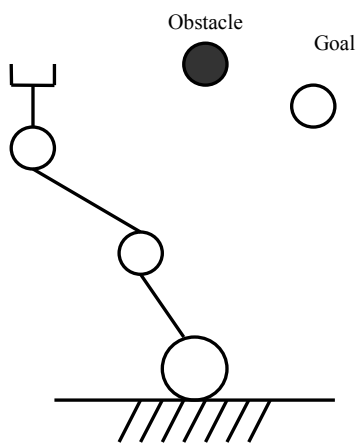


Figure 3. Robotic Arm with obstacle and Goal Position

final position of the arm are random too; the arm will be modelled as a three-link planar manipulator. To form a fuzzy logic controller that will resolve a list of joint angles. $\Theta(t)$, that moves the end-effector from a given starting position $(x_s, y_s)$ to the ending position $(x_g, y_g)$ without hitting the obstacle situated at $(x_o, y_o)$.

The dynamic equations given below describe the robot arm kinematics model:

$$\begin{aligned} X_e &= l_1 Cos\theta_1 + l_2 Cos(\theta_1+\theta_2) + l_3 Cos(\theta_1+\theta_2+\theta_3) \\ Y_e &= l_1 Sin\theta_1 + l_2 Sin(\theta_1+\theta_2) + l_3 Sin(\theta_1+\theta_2+\theta_3) \end{aligned} \quad (4)$$

Where ($X_e, Y_e$) is the cartesian coordinate of the robotic arm's end-effector whose calculation is directly depend on its link lengths and joint angles as shown in Fig. 4.Table I presents the link lengths and physical constraints of the joints of robot arm is given below:

TABLE I. THE PHYSICAL CHARACTERISTICS OF A REMOTEC ROBOTIC ARM AND CONSTRAINTS

| Physical Characteristic | Minimum Angle | Normalized Length | Maximum Angle |
|---|---|---|---|
| Link length, $l_1$ | - | 1 | - |
| Link length, $l_2$ | - | 0.824 | - |
| Link length, $l_3$ | - | 0.737 | - |
| Joint Constraints, $\theta_1$ | $0^0$ | - | $180^0$ |
| Joint Contraints, $\theta_2$ | $-90$ | - | $+90$ |
| JointConstraints, $\theta_3$ | $+25$ | - | $-25$ |

It is to be considered that the potential reach of the end-effector and the obstacle must exist within and outside the passage of link respectively.

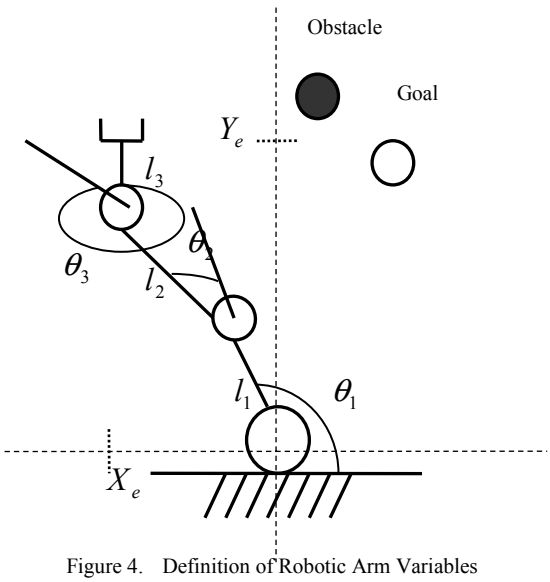


Figure 4. Definition of Robotic Arm Variables

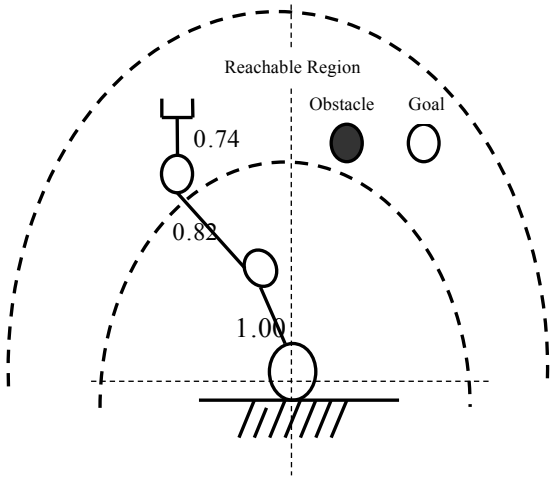


Figure 5. Normalized Dimensions for Robotic Arm and attainable area

The direct kinematics equations helps determining all potential locations for the end-effector with the constraints given in the table I and the one final constraint, $Y \geq 0$ .Fig. 5 explains the whole scenario of robotic arm with obstacle. We therefore summarize the problem given underneath:

Given a robotic arm with:

- $\Theta(t)$ denotes the current joint angles
- $(x_o, y_o)$ holds a known position where an obstacle is located,
- $(x_g, y_g)$ holds the desired position,

Determine a trajectory, $\Theta(t)$ , such that

- The end-effector reaches the goal
- The obstacle stays free from any contact with the arm,
- The current hardware can perform the evaluation in real-time.

## IV. SIMULATION RESULTS

The proposed architecture is implemented using visual C++ programming language and the source code is successfully compiled using visual C++ compilers. After 100 generations and from the best chromosomes of GA, we have attained the fuzzy rules in case of robot arm problem.

The fuzzy controller discover the angle change $d\theta_i$ (i= 1 ,2,3) which helps to move the end effector from the starting to ending position. For the three link robot arm, the cartesian position change both $x$ ($dx'$) and $y$ ($dy'$) coordinates while changing the joint angles as the relationship exists between the change of joint angle and Cartesian position for small joint angle deviation (dq<<l). Here, the linguistic variables $dx'$ , $dy'$ and $d\theta_i$ can be divided into the following linguistic value.

$$dx', dy', d\theta_1 = \{NB, NS, ZE, PS, PB\}$$

TABLE II. SAMPLE FUZZY CONTROL RULE SET FOR ROBOT ARM CONTROL

| | $d\theta_1$ | $dx'$ | | | | |
|---|---|---|---|---|---|---|
| | | NB | NS | ZE | PS | PB |
| $dy'$ | NB | 1 NS | 2 PS | 3 ZE | 4 PB | 5 NS |
| | NS | 6 PB | 7 NB | 8 NS | 9 ZE | 10 PS |
| | ZE | 11 PS | 12 NB | 13 PB | 14 ZE | 15 PB |
| | PS | 16 NS | 17 NM | 18 ZE | 19 PS | 20 NS |
| | PB | 21 PB | 22 NB | 23 NS | 24 PS | 25 PB |

Here NB, NS, ZE, PS, PB represents Negative Below, Negative Small, Zero, Positive Small, Positive Below respectively. At the initial stage of the simulation, the successive part of every rule i.e. FAM (Fuzzy Associative Memories) cell is blank. After the simulation of developed double coded genetic algorithm discovers the rule base given in table II.

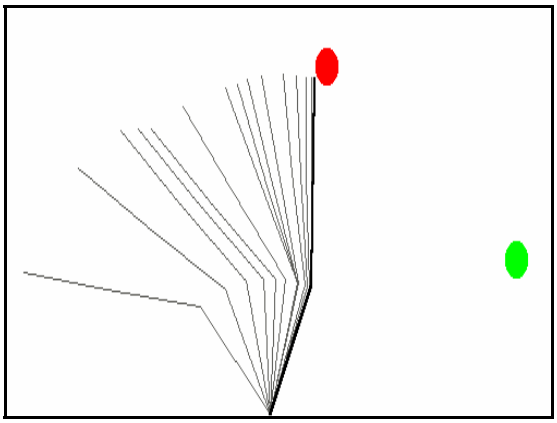

(a)

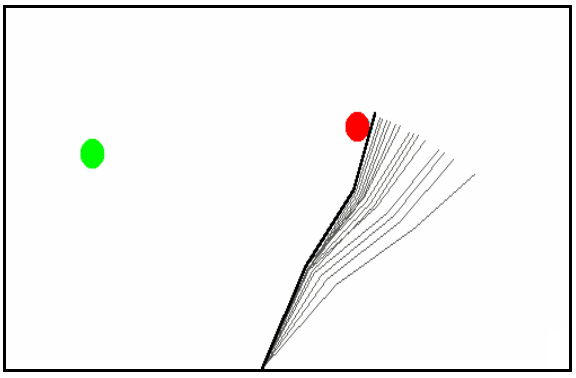

(b)

Figure 6. Samples of collisions while under genetic-fuzzy control

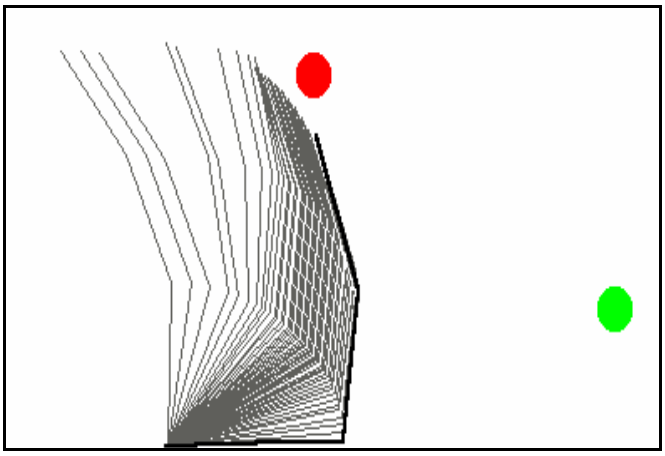

(a)

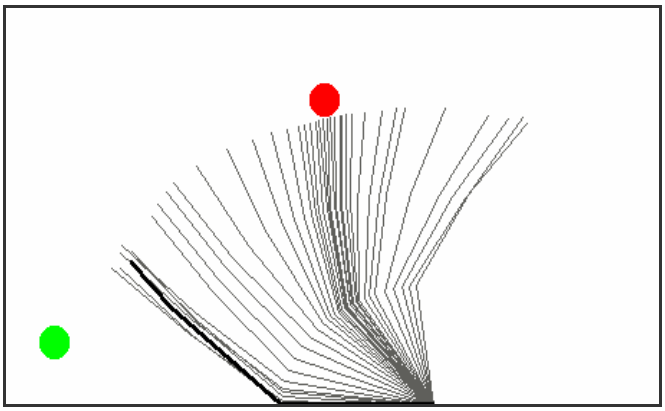

(b)

Figure 7. genetic-fuzzy control samples that have exceeded the constraint limits

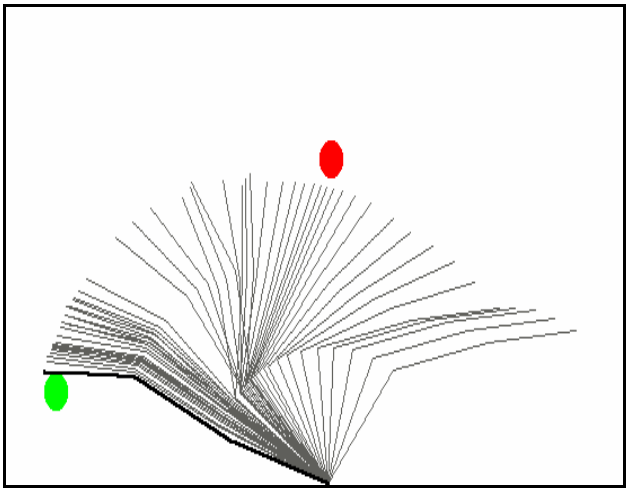

(a)

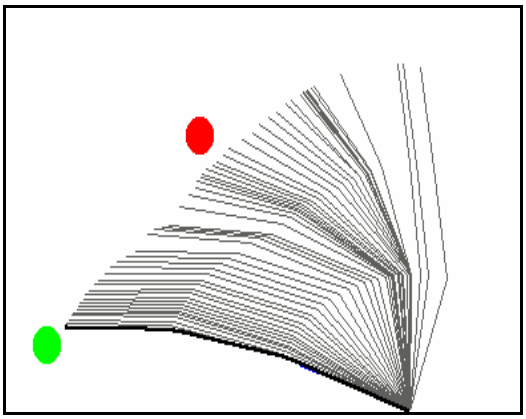

(b)

Figure 8. Samples of successful control by the genetic-fuzzy controllers

When the robotic arm touches the obstacle then a collision occurred. Fig. 6 shows the samples of collisions while under genetic-fuzzy control. Fig. 7 shows the genetic-fuzzy control samples that have exceeded the constraint limits. On the other hand, our designed controller gives the successful results in most of the cases and it was successful when the controller generates the optimal fuzzy rules and using these rules the robotic arm reaches the goal position and does not touch the obstacle. Fig. 8 shows the successful control given by our proposed controller.

## V. CONCLUSIONS

Here, we have discovered that the innovative unified FLC and GA architecture is capable for setting up an apprehensible and feasible fuzzy If-Then rule by a self-learning complied technique for nonlinear and dynamic systems especially for the path planning in collision-avoidance problems. We applied GAs to learn the parameters of membership function, number of linguistic level and rule base for fuzzy logic controllers.

The integrated FLC and GA architecture is an automated knowledge acquiring system and is capable of learning the rules of fuzzy control without any previous knowledge. The architecture has a self-acquired learning ability for establishing FLCs for robotic arm with moving obstacle avoidance.

## REFERENCES


[1] HamitErdem, "Application of Neuro-Fuzzy Controller for Sumo Robot control," *Expert Systems with Applications*, Vol. 38, Issue 8, pp. 9752-9760, 2011.

[2] AndreaBonarini, MatteoMatteucci, and MarcelloRestelli, "Concepts and fuzzy models for behavior-based robotics," *International Journal of Approximate Reasoning*, Vol.41, Issue 2, pp. 110-127, 2006.

[3] A. Daftaribesheli, M. Ataei, and F. Sereshki, "Assessment of rock slope stability using the fuzzy slope mass rating (FSMR) system," *Applied Soft Computing*, vol. 11, no. 8, pp. 4465–4473, Dec. 2011.

[4] S. E. Oltean, "Swing-up and Stabilization of the Rotational Inverted Pendulum Using PD and Fuzzy-PD Controllers," *in Proce. 7th Int. Conference Inter disciplinarity in Engineering*, INTER-ENG, 2013, pp. 57-64.

[5] A.I. Azmi, "Design of Fuzzy Logic Model for the Prediction of Tool Performance During Machining of Composite Materials," *Procedia Engineering*, vol. 38, pp. 208–217, 2012.

[6] C. S. Chen, Y. D. Jhong, T. Y. Wu, and S.-T. Chen, "Typhoon event-based evolutionary fuzzy inference model for flood stage forecasting," *Journal of Hydrology*, vol. 490, pp. 134-143, 2013.

[7] D.K. Pratihar, K. Deb and A. Ghosh, "Optimal path and gait generations simultaneously of a six-legged robot using a GA-fuzzy approach," *IEEE Robot. Auton. Syst.*, vol. 41, pp. 1–20, 2002.

[8] C. Zhou, "Robot learning with GA-based fuzzy reinforcement learning agents," *Inf. Sci.*, vol. 145, no. 1, pp. 45–68, 2002.

[9] D. Gu, H. Hu and L. Spacek, "Learning fuzzy logic controller for reactive robot behaviours," *in Proceedings of the 2003 IEEE/ASME International Conference on Advanced Intelligent Mechatronics (AIM 2003)*, 2003, pp. 46-51.

[10] D. Gu, H. Hu, J. Reynolds and E. Tsang, "GA-based learning in behavior based robotics," *in Proceedings of the 2003 IEEE International Symposium on Computational Intelligence in Robotics and Automation.*, Kobe, Japan, 2003 , pp. 1521–1526.

[11] H. Hagras, V. Callaghan and M. Collin, "Learning and adaptation of an intelligent mobile robot navigator operating in unstructured environment based on a novel online fuzzy-genetic system," *Fuzzy Sets Syst.*, vol. 141, pp. 107–160, 2004.

[12] M. Mucientes, D.L. Moreno, C.V. Regueiro, A. Bugarin and S. Barro, "Design of a fuzzy controller for the wall-following behavior in mobile robotics with evolutionary algorithms," *in Proceedings of the International Conference of Information Processing and Management of Uncertainty in Knowledge-based Systems (IPMU'2004)*, Perugia, Italy, 2004 , pp. 175-182

[13] S. Oha, W. Pedryczb, and K. Parka,"Identification of Fuzzy Systems by Means of Genetic Optimization and Data Granulation," *Journal of Intelligent & Fuzzy Syst.*, vol. 18, pp. 31–41, 2007.

[14] Z. Michalewicz, *Genetic Algorithms+Data Structures = Evolution Programs*, Springer-Verlag, New York, 1996.

# Design and Construction of an Automatic Electric Wheelchair: An Economic Approach for Bangladesh

Amit Sutradhar, Md. Samiul Haque Sunny, Manash Mandal, Rubel Ahmed
Khulna University of Engineering & Technology (KUET), Khulna-9203, Bangladesh
amitndc12@gmail.com, mdshs31@gmail.com, manashmndl@gmail.com, rubel9ahmed@gmail.com

*Abstract*—**This paper focuses on the minimization of cost for the construction of an automatic electric wheelchair with well-structured design and control system for the disabled people. In a developing country like Bangladesh, most of the physically disabled people of middle class and lower middle-class families can't afford to buy electric wheel chair as the cost is pretty high. Moreover, the existing features of the wheel chair available in market are not sufficient enough to meet all the requirements for all types of physically disabled people. That's why a design of electric wheel chair is proposed in this paper which contains more features and a developed control system along with the minimization of manufacturing cost about four-five times of recent market price. Multi means of controlling operation can be executed here either by keypad, joystick, and accelerometer or by voice. In the design, modularity of various parts is taken into consideration for the ease of repair work in any instant which adds a new dimension in the uniqueness of the designed structure. Also, the drawbacks of the controlling system of the modern existing chairs are eliminated with the implementation of automatic horn system along with the automatic and manually controlled headlight which assists in the communication at night time. Effective implementation of this design can pave the way of movement for all types of physically disabled people to a great extent within their affordability.**

***Keywords—Electric wheelchair, voice control, keypad control, joystick control, accelerometer, sensors.***

## I. INTRODUCTION

In worldwide context, an estimated 100-130 million people with disabilities need wheelchairs. Experts predict that the number of people who need wheelchairs will increase by 22 percent over the next ten years [1]. Wheel-chair is still the best transportation means for them since its invention in 1595for Phillip II of Spain by an unknown inventor; and this is the reason why this particular chair with wheels is developing in newer shapes with additional latest enhancements following its conversion into an electric one. In USA, almost 200,000 physically challenged people use electric wheel-chair for their daily life needs. On the other hand, in Bangladesh handicap people still depend on the old formatted normal wheel-chair as major portion of this poor country cannot afford the huge cost of a basic electric wheelchair. One research report shows that the amount of physically challenged people in Bangladesh is around 5.6% (8.4 million) of total population [2]. Large portion of physically disabled people of developing countries either depend on crutches or manual wheelchairs for their maneuvering. Because of physical weakness, many users cannot access manual wheelchair by using hand rim as shown in Fig.1. A lot of research works have been performed all over the world since the last two decades. In 1994, MITRE Corporation presented their research works on low cost automated wheelchair which was a theoretical alteration of manual wheelchair and their practical implementation was established in 1995 [3]. Barea et al. described an eye-control method to control automatic wheelchair in 2002, based on electrooculography (EOG) [4]. In 2002, Felzer introduced muscle control of automatic wheelchair based on EMG (electromyogram) signal. But this complicated proposal cannot be implemented for the well-being of lowered people [5]. In 2004 Simpson presented an EPW which was assembled with laptop and different sensors with joystick. High sensitivity of this EPW is still confined in experimental study rather than welfare of common people [6]. GRASP laboratory presented their EPW in 2005 with special control frame work including different sensors, video interfacing system and others which is not commercially implementable for common users because of its sensitivity and large dimensions [7]. Horn et al. showed perception mode of smart wheelchair and used ultrasound, and vision sensors during 2009 for better control [8]. In 2009 Jin Sun Ju showed a system in which EPW is propelled through face-inclination and mouth-shape information [9]. Ren proposed a navigation based wheelchair system in 2009 where GPS based trajectory was generated [10]. Rofer presented a joystick or head joy stick based control system in 2009 which is not only sensitive in controlling but also expensive for general people of developing countries [11]. In 2013 Kalantri proposed a model of gesture recognition based control system which is basically a head movement system. It is not still implemented practically [12]. Kokate showed a theoretical representation of voice controlling operated controlling system which is not implementable in technological and economical perspective of common people [13]. The design and implementation of wheelchair by Humaira salmin [14] is as same as "Tin man" by MITRE Corporation [3]. Anderson et al. examined the EEG of a subject by classifying brain-wave patterns belonging to consecutive time windows with the help of a back-propagation neural network. Their idea was to identify recurring patterns associated with certain mental states, and to enable subjects to communicate e.g. with an electrical wheelchair by composing sequences of those states. Unfortunately, the resulting classification accuracy hardly exceeded 70% which is much too low for the projected application [15]. Simpson et al. showed in how to combine discrete driving commands coming from voice control, with navigation assistance provided by reactive navigation approaches [16-17].

But it can be mentioned that the need of common people was always out of focus in the above stated researches. That's why,

978-1-5386-2307-7/17/$31.00 ©2017 IEEE

Figure. 1. Manual wheelchair users in developing or under developed countries.

a new design of automatic wheelchair is proposed in this research work concerning this limitations and economic perspective of developing countries like Bangladesh. On the other hand, electric powered wheelchairs are not available everywhere in developing countries and the price is also high with respect to the financial range of the general individuals. So, this paper details the project about an electric wheel-chair (EWC) which is much more comfortable and flexible for movement compared to a normal wheel-chair and also costs 65-70% less compared to the available or regular EWCs. Here for the implementation of the above stated features, a prototype is constructed where all the features are included. Also cost analysis is shown for this technology if it is used for practical purpose.

## II. CALCULATIONS BEFORE CONSTRUCTION

While selecting drive wheel motors for mobile vehicles, a number of factors must be taken into account to determine the maximum torque required. The following calculation represents the method of computing this torque [18]. The design criteria include:

- Gross vehicle weight (*GVW*):

$$90\ Kg * 9.81\ ms^{-2} = 883\ N$$

- Weight on each drive wheel (*WW*):

$$23\ Kg * 9.81\ ms^{-2} = 225.63\ N$$

- Radius of wheel/tire ($R_w$): 0.102 $m$
- Desired top speed ($V_{max}$): 0.3 $ms^{-1}$
- Desired acceleration time (*TA*): 1 $sec$
- Maximum incline angle (α): $15^o$
- Worst working surface: $Good\ concrete$

To choose motors capable of producing enough torque to propel the example vehicle, it is necessary to determine the total tractive effort (TTE) requirement for the vehicle:

$$TTE\ [N] = RR\ [N] + GR\ [N] + FA\ [N] \quad (1)$$

Where:

*TTE* = Total tractive effort [*N*]

*RR* = Force necessary to overcome rolling resistance [*N*]

*GR* = Force required to climb a grade [*N*]

*FA* = Force required to accelerate to final velocity [*N*]

The components of this equation will be determined in the following steps.

### A. Rolling Resistance

Rolling Resistance (*RR*) is the force necessary to propel a vehicle over a particular surface. The worst possible surface type to be encountered by the vehicle should be factored into the equation.

$$RR\ [N] = GVW\ [N] * C_{rr}\ [N] \quad (2)$$

$$RR = 90 * 9.81 * 0.01 = 8.83\ N$$

Where:

*RR* = Rolling resistance [N]

*GVW* = Gross vehicle weight [N]

$C_{rr}$= Surface friction (For good concrete $C_{rr} = 0.01$)

### B. Grade Resistance

Grade Resistance (*GR*) is the amount of force necessary to move a vehicle up a slope or "grade". This calculation must be made using the maximum angle or grade the vehicle will be expected to climb in normal operation. To convert incline angle, α, to grade resistance:

$$GR\ [N] = GVW\ [N] * Sin(\alpha) \quad (3)$$

$$GR = 883\ [N] * Sin(15^o) = 228.54\ N$$

Where:

*GR* = Grade resistance [*N*]

*GVW* = gross vehicle weight [*N*]

*α* = maximum incline angle [*degrees*]

### C. Acceleration Force

Acceleration Force (*FA*) is the force necessary to accelerate from a stop to maximum speed in a desired time.

$$FA\ [N] = \frac{GVW\ [N] * V_{max}\ [ms^{-1}]}{9.81\ [ms^{-2}] * TA\ [sec]} \quad (4)$$

$$FA = \frac{883\ N * 0.30 ms^{-1}}{9.81\ ms^{-2} * 1\ sec} = 27\ N$$

Where:

$FA$ = Acceleration force [$N$]

$GVW$ = Gross vehicle weight [$N$]

$V_{max}$ = Maximum speed [$ms^{-1}$]

$TA$ = Time required to achieve maximum speed [$sec$]

### D. Total Tractive Effort

The Total Tractive Effort (TTE) is the sum of the forces calculated in previous steps. On higher speed vehicles friction in drive components may warrant the addition of $10\% - 15\%$ to the total tractive effort to ensure the acceptable vehicle performance.

$$TTE\ [N] = RR\ [N] + GR\ [N] + FA\ [N] \quad (5)$$

$$TTE = 8.83 + 228.54 + 27 = 264.37\ N$$

### E. Wheel Motor Torque

To verify the fact that the vehicle will perform according to the designed tractive effort and acceleration, it is necessary to calculate the required wheel torque ($T_w$) based on the tractive effort.

$$T_w[Nm] = TTE\ [N] * R_w * RF \quad (6)$$

Where:

$T_w$ = Wheel torque [$Nm$]

TTE = Total tractive effort [$N$]

$R_w$ = Radius of the wheel/tire [$m$]

RF = Resistance factor

The resistance factor accounts for the frictional losses between the caster wheels and their axles and the drag on the motor bearings. Typical values range between 1.1 and 1.15 (10 to 15%).

$$T_w = 264.37 * 0.102\ m * 1.1 = 29.66\ Nm$$

## III. CONSTRUCTION OF THE PROTOTYPE

The structure of the wheelchair is made of wood and galvanized irons. These are low cost materials with enough load carrying capacity of a human body. Different cutting, joining and shaping operations are performed through welding machine, lathe machine, shaper machine and drilling machine. The length and width of the frame are 50cm and 45cm respectively. The radius of the wheel is 25.4 cm whereas the height of the chair from frame base is 90 cm. The weight of wheelchair along with motors and battery is 40 kg. The constructed prototype is shown in Fig. 2. Fig. 3 shows the motor, motor controller and battery arrangement of the wheelchair. To control the wheelchair through push button, joystick and relay module are used as the external input command. Bluetooth module is attached in the arrangement in order to facilitate the connection with android platform to operate the wheelchair using voice and acceleration. LED, buzzer and headlight are connected with ATmega2560 controller along with sensors which help to distinguish between day and night and detect obstacle in its way. Overall circuit connection in terms of logic level and voltage is shown in Fig. 4. High current motors are operated through a motor driver.

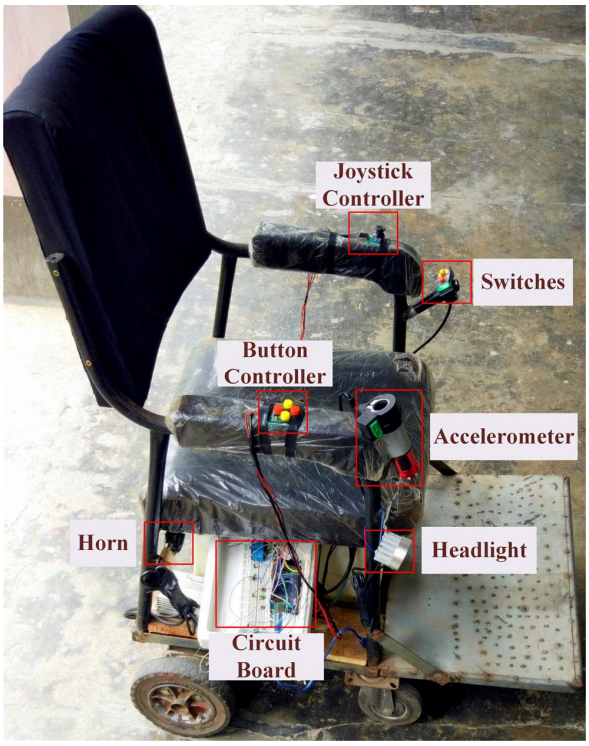


Figure. 2. Side view of the constructed prototype.

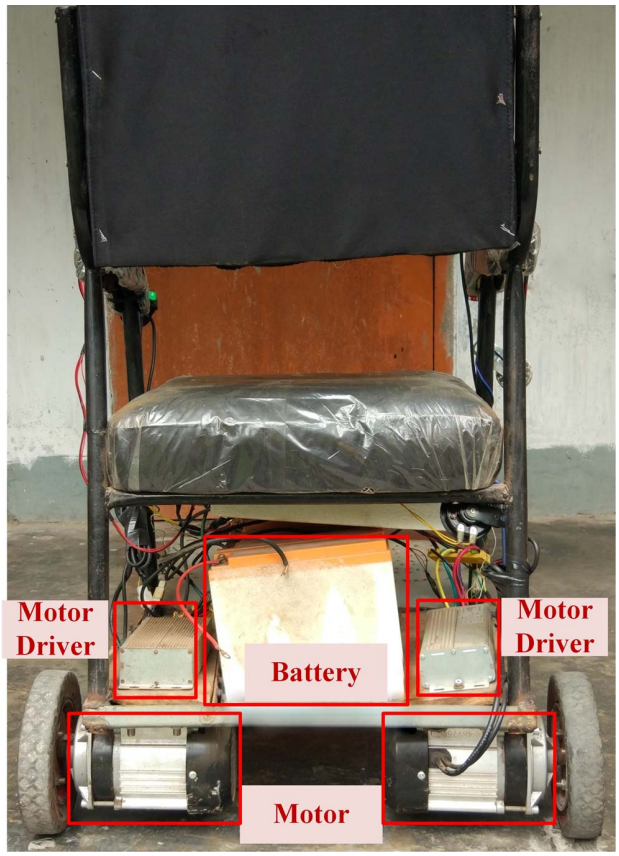


Figure. 3. Back view of the structure.

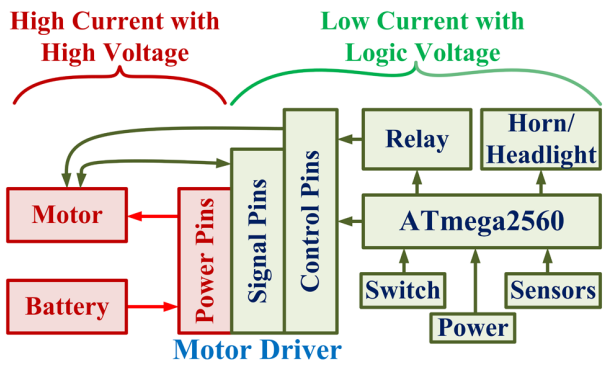


Figure. 4. Overall connection of electrical wheelchair structure.

## IV. Control Strategy of EWC

The direction and movement of wheelchair are controlled through the four controlling systems as stated before i.e. joystick, button, and accelerometer of android phone and voice commands. Fig. 5 depicts that after getting the reading from press button or the Bluetooth serial, it is mapped in accordance to the control logic and the relay action takes place which causes the motor to run accordingly. The axis interpretation of the joystick is delineated in terms of desired speed and direction in Fig 6. The control algorithm calculates the appropriate commands for the right and the left wheel motors in order to drive the wheelchair in the desired speed and direction. In Fig. 6, 1 denotes maximum speed and 2 denotes maximum rotation. For conducting the voice test, at first several keywords are tried to find out which words the android app can recognize easily. Avoiding the inconvenience, listed voice commands in Table I are selected and used which can easily be recognized by android app and it can perform smoothly without creating any trouble.

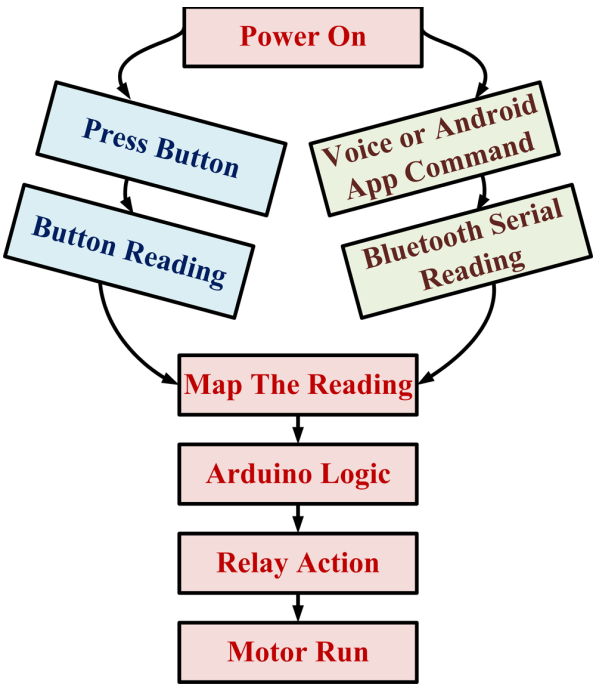


Figure. 5. Block diagram of the control algorithm of electric wheel chair.

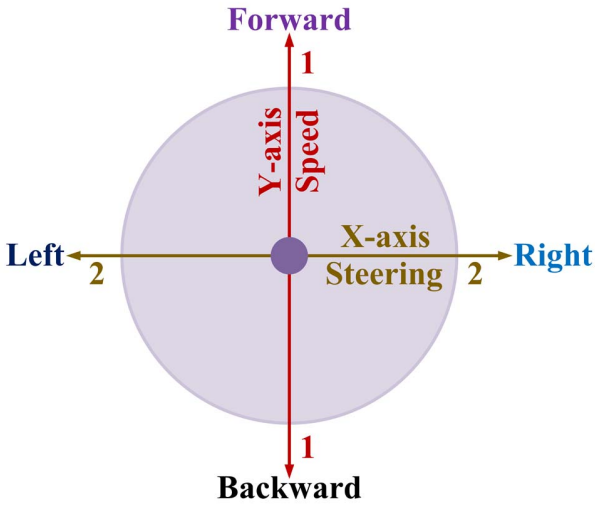


Figure. 6. Axis interpretation of the joystick.

TABLE I. List of Voice Commands

| Voice Command | Description |
|---|---|
| Go | The chair starts moving at a distance that the chair is facing |
| No | The Chair starts moving in the direction opposite to that which the chair is facing. |
| Right | The chair turns right |
| Left | The chair turns left |

## V. Discussion

The main difference between the automatic wheelchairs available in the market and the constructed wheelchair is that market chairs use the motor drivers which cost pretty high. But here controller is customized in such a way that is capable of eliminating the need for that expensive motor controller and results in cost minimization. All the equipment used in the prototype are plenty in the local electronic shops in Bangladesh. From Table III it's obvious that this construction costs only around 21,000 BDT whereas the electric wheel chairs available in the Bangladeshi market which are imported from foreign countries cost about 1.5-2 lac BDT with the less features than the proposed design in this paper. Table II shows the scenario clearly.

TABLE II. Cost Estimation of the Proposed Automatic Wheelchair

| Name of the Equipment | Price of Equipment (BDT) |
|---|---|
| DC Motors | 6,000 |
| Electronic Components | 2,000 |
| Construction of Mechanical Structure | 2,000 |
| Battery | 11,000 |
| **Total** | **21,000** |

TABLE III. PRICE OF WHEELCHAIRS AVAILABLE IN MARKET

| Name of the EPW/ Company | Price (BDT) |
|---|---|
| Shop Rider Jimmie Power Chair | 1,06,250 |
| Pride Go-Chair Travel Power chair | 1,13,370 |
| EZ Lite Cruiser Power chair | 1,85,825 |
| EZ Lite Cruiser Heavy Duty Power chair | 2,24,945 |
| Invacare Nutron R51 Motorized Wheelchair | 2,18,997 |
| Heavy Duty Smart Chair (KD Healthcare) | 2,18,685 |
| Invacare P9000 XDT Motorized Wheelchair | 1,95,525 |

Several extra features can be added to this design to facilitate more controlling system i.e. Artificial Intelligence system can be used to operate the wheelchair through brain signal. Also, GPS system can play a significant role for ensuring the proper positioning of the wheelchair user in this context.

## VI. CONCLUSION

In a developing country like Bangladesh, this technology is very much effective to pave the way of communication of the physically disabled general people. Though some low-cost wheelchair projects were accomplished, no effective electric powered wheelchair was proposed with low production cost. Thus, the facility for physically disabled people of lower class were overlooked. This research work shows a new automatic wheelchair which will lessen the inaccessibility of automated wheelchair for the common people of developing or undeveloped countries. The project develops an easy control system of wheelchair which can be accessible to each suffered individual. If this type of chair is used in Bangladesh, general people would be greatly benefitted as it reduces the cost to a great amount. After all, it can be concluded that this design of automatic wheel chair is quite feasible enough to implement in this country.

## REFERENCES


[1] Y. K. Tan and S. Sasidhar, "Engineering better electric- powered wheelchairs to enhance rehabilitative and assistive needs of disabled and aged populations, Rehabilitation Engineering," Tan Yen Kheng (Ed.), ISBN: 978-953-307-023-0, INTECH, Singapore, 2009. (79-108).

[2] P. Norek, M. Ahmed, et al, "Livelihood challenges for extremely poor disabled people in the southwest costal region of Bangladesh," Shiree working paper 12, January 2013.

[3] P. Miller and M. G. Slack, "Increasing access with a low-cost robotic wheelchair," *IEEE Int. conf.,* vol. 3, pp. 1663-1667, Sept. 1994.

[4] R. Barea, L. Boquete, M. Mazo and E. López, "Wheelchair guidance strategies using EOG," *Journal of Intelligent and Robotic Systems* 34: 279–299, 2002, Kluwer Academic Publishers.

[5] T. Felzer and B. Freisleben, HaWCoS: "The "hands-free" wheelchair control system," published in "Assets-2002"

[6] R. Simpson, E. LoPresti, et. al., "The smart wheelchair component system," Volume 41, Number 3B, Pages 429–442, *Journal of Rehabilitation Research & Development,* May/June 2004.

[7] S.P. Parikh , V. Grassi Jr., V. Kumar, J.Okamoto Jr., "Usability study of a control framework for an intelligent wheelchair," Proceedings of the 2005 *IEEE International Conference on Robotics and Automation Barcelona*, Spain, April 2005.

[8] O. Horn and M. Kreutner, "Smart wheelchair perception using odometry, ultrasound sensors, and camera," Robotica (2009) volume 27, pp. 303–310, 2008 Cambridge University Press doi:10.1017/S0263574708004773, Printed in the United Kingdom.

[9] Jin Sun Ju , Y. Shin and Eun Yi Kim, "Intelligent wheelchair (IW) interface using face and mouth recognition," IUI'09, February 8–11, 2009, Sanibel Island, Florida, USA. Copyright 2009 ACM 978-1-60558-331-0/09/02.

[10] M. Ren, H. A. Karimi, "A hidden markov model-based map-matching algorithm for wheelchair navigation," *The Journal of Navigation* (2009), 62, 383–395 The Royal Institute of Navigation doi:10.1017/S0373463309005347 , Printed in the United Kingdom.

[11] T. Rofer, C.Mandel, T. Laue, "Controlling an automated wheelchair via joystick/head-joystick supported by smart driving assistance," *IEEE 11th International Conference on Rehabilitation Robotics Kyoto International Conference Center, Japan*, June 23-26, 2009.

[12] R. A. Kalantri, D.K. Chitre, "Automatic wheelchair using gesture recognition," *International Journal of Engineering and Advanced Technology (IJEAT*), ISSN: 2249 –8958, Volume-2, Issue-6, August 2013.

[13] J. K. Kokate, A. M. Agarkar, "Voice operated wheel chair," *International Journal of Research in Engineering and Technology.*

[14] Salmin, H. Rakibul, et al, "Design and implementation of an electric wheel-chair to economize it with respect to bangladesh," *International Journal of multidisciplinary Science and Engineering,* vol. 5, NO. 2, FEB. 2014.

[15] C. W. Anderson, S. V. Devulapalli, and E. A. Stolz. "EEG as a means of communication: preliminary experiments in EEG analysis using neural networks," In *ASSETS '94 – Proceedings of the First Annual ACM Conference on Assistive Technologies*, pages 141–147,1994.

[16] R. Simpson and S. Levine, "Voice control of a powered wheelchair," *IEEE Transactions on Neural Systems and Rehabilitation Engineering*, vol. 10, no. 2, pp. 122–125, June 2002.

[17] S. Levine, D. Bell, L. Jaros, Y. Koren, and J. Borenstein, *Assistive Technology and Artificial Intelligence*: *An Assistive Wheelchair Navigation System with Automatic Adaption*, Lecture Notes in Computer Science, Springer Berling/Heidelberg, ch. NavChair:, pp. 235–255.

[18] Drive wheel motor torque calculations ,EML2322L – MAE design and manufacturing laboratory, Reference Citation: White hydraulics drive products.

2017 3rd International Conference on Electrical Information and Communication Technology (EICT), 7-9 December 2017, Khulna, Bangladesh

# Multi-label Sentence Classification Using Bengali Word Embedding Model

**Md. Nowshad Hasan**
Department of CSE, SUST
Sylhet, Bangladesh.
nowshadapu@gmail.com

**Sourav Bhowmik**
Department of CSE, SUST
Sylhet, Bangladesh.
sourav.bhowmik52@gmail.com

**Md. Mahfuzur Rahaman**
Department of CSE, SUST
Sylhet, Bangladesh.
mahfuzsustbd@gmail.com

***Abstract*—Multi-label sentence classification is a very popular technique to categorize text into several classes now-a-days. TThe classification process may vary based on the type of text used such as crime data, weather forecast data, accident data etc. We worked with only crime type news data from several famous newspapers. We made sub-categories such as victim, suspect, crime-type, crime-time, crime-place, police station, hospital and neutral for every sentences. We used two libraries LibSVM and Scikit-Learn to implement different kinds of algorithms like- SVM, Logistic Regression, Neural Network, Decision Tree, Linear Regression etc. We showed accuracy comparison using two libraries between different algorithms removing or having stop words in every sentence with 5000, 7500 and 10000 sentence corpus individually. We also showed the accuracy, F-score, recall and so on for every class we discussed before to observe how precisely our system can detect those classes. Our classifier can easily handle two or three classes for every sentence but most of the time it is not predictive for all of the classes of a sentence. We also discussed about how LibSVM and Scikit Learn work with multi-label classes in this paper.**

***Index Terms*—Sentence Classification, Multi-label, Word Embedding Model, Bengali Sentence, Word Cluster, Crime News.**

## I. Introduction

Sentence Classification is a system of classifying a sentence into some classes. Traditionally, classes for sentence classification are – sports, entertainment, politics, education, crime etc. In popular definition, sentence classification is always a mono-label classification that means, at most one class for one sentence with the highest probability. The system will try to classify the given sentence for every class. The class having the highest probability for a sentence, will be the output class for that sentence. But in terms of multi-label sentence classification, if system predicts that in a single sentence, there is higher probability for more than one class, all of them will be the output classes. That means, one or two or more classes may be the answer for one sentence. If no class falls in given sentence that is also called multi-label.

Single-label sentence classification is very important to predict its actual category. Such as, if we know that a sentence is very likely to be of politics or sports category then, we can pull out the information of that type from the sentence easily. It will help us to get precise information from the sentence. Because, in a sentence, there is little information about any category we described here. So, information will be precise with this little information. But if we talk with the multi-label sentence classification, we think that pulled out information will be more precise when we know multiple classes (multiple information) for a sentence are present here. That means, when a sentence falls in sports and politics both categories, then the information we will get from them are likely to be more useful and more precise. And, this is one of the strengths of multi-label sentence classification.

There are many works in sentence classification with single-label and multi-label both in different languages. Some of them are binary classification, emotion detection in Bengali language, classification of research paper's abstract, a series of experiment with Convolutional Neural Network etc.

In this paper, we did not work with actual classes like- crime or sports or politics etc. rather than we selected 'Crime' type class. After that, we selected some sub-categories under 'Crime' class like- Victim, Suspect, CrimePlace, CrimeTime etc. so that we can know useful information about crime news like- its type, its place, its time and lots of information. We used cluster information as a feature which was generated with 'Word Embedding Model' [4].Here we got the good result under the 'Crime' class. But we believe that working with another class and making a sub category will also give satisfying result.

## II. Background Study

The most inspiring paper for us was written by Adnan et al. [4]. We followed the same procedure they used to classify their document classification but we worked here with multi-label sentence classification. We used their word embedding model for our features. As they achieved 90 % accuracy using the model, so we tried this model for our sentence classification problem.

We got some ideas about binary classification of any text with sentiment mining. In a work of Das et al., a text either subjective or objective is classified using Conditional Random Field (CRF) based technique [1] with English and Bengali languages both.

6 types of emotion detection is carried out by Dipankar Das et al. in Bengali from different web blogs [2]. Here they worked with happiness, sadness, anger, fear, surprise, disgust, neutral tag and a CRF (Conditional Random Field) based model.

A work from Harikrishna et al. is very interesting where they worked with children fables and short stories [5]. They classified each sentence into 5 emotional levels- happy, sad, anger, fear and neutral. In this paper they worked with two kind of processes - POS (Parts of Speech) & ESF (Emotion Specific Features). They got highest accuracy for POS+ESF features with SVM implementation.

Michael et al.'s work is very similar to our work [3]. Here, they described a method for automatically classifying person instances into eight subcategories like athlete, politician/government, clergy, businessperson, entertainer/artist, lawyer, doctor/scientist, and police. They actually worked with supervised learning method where they considered context of an entity and global semantic information.

Carmen Dayrell et al. also made a classifier for multi-label sentence classification [6] to classify science research paper's abstract. They made a corpus consisting of 645 abstracts from physical science and engineering, 690 from life and health science.

Yunong Wu et al. made an excellent work of multi-label sentence classification from three different perspectives [8]. The labels they used are like- Joy, Love, Surprise, Anxiety, Sorrow, Anger, Hate, Expect .

Yoon Kim made a series of experiment with CNN in sentence classification which is one of the advanced models now-a-days [9]. Here, they discussed sentiment analysis and question classification. They used different kinds of experimental setup.

## III. Data Set Preparation

### A. Data

We collected almost 10000 sentences of Crime news category. These include all kinds of crimes like accident , political, family problem, land problem, revenge etc. We got 5 files of cluster information like- 25, 50, 200, 400 and 600 clusters where same types of words are in the same cluster made with 'Word Embedding Model' by Adnan et. al. [4]. We also collected a nice list of Stop Word which includes less important words like - ও, এ, থেকে, করে, হয়, এবং, করা, হয়েছে, না, জন্য.

### B. Data Source

Our Data sentences are collected from different famous daily newspapers like- Prothom Alo, Jugantor, Manabzamin, Kaler kantho etc. We got these sentences nicely organized. We got almost 5-10 crime news folders under a date containing crime newses on this date where a date is sequential. And under every news, we got 10-20 crime related sentences. So, we can say that we have almost 4 months of crime informations. Word Embedding Model [4] actually made different kinds of clusters from 20,000 different kinds of newspaper documents that we discussed before.

### C. Pre-processing

We selected sub-categories under crime class type and their corresponding numbering. Those are- Neutral-0, Victim-1, Suspect-2, Crime Place-3, Crime Type-4, Crime Time-5, Police Station -6, Hospital-7

Here we manually tagged every sentence with these sub-classes. When we get a name of a victim, suspect, crime place, crime type, hospital, police station, we tagged them as these classes. If we get crime time like any specifically defined time in a day like- সকাল, দুপুর, বিকাল, রাত, মধ্য রাত, ভোর, সন্ধ্যা or any day of a week from Saturday to Friday or any month from January to December, we tagged them as crime time. If none of this classes falls in any sentence, we tagged those as 'neutral' class. Here are some examples in the figure 1.

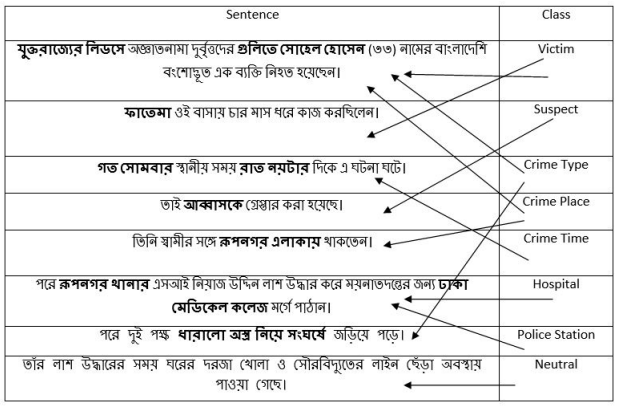


Fig. 1. Example of manual tagging of different classes

We had two training files for every kind of cluster like- for 25, 50, 200, 400 & 600 clusters. The two kinds are- with stop word (not removing stop word from sentence words) & without stop word (removing stop word from sentence words). At the first time, we worked with 5000 sentences and after that, for better performance, we also

tagged more 2500 sentences. After that we also tagged more 2500 sentences. So, at first, we experimented with 5000 sentences, then with 7500 sentences and finally with 10,000 sentences. So, finally we got 30 different kinds of files to experiment. For every file, we took 70% data for training and 30% for testing. Figure 2 illustrates this idea.

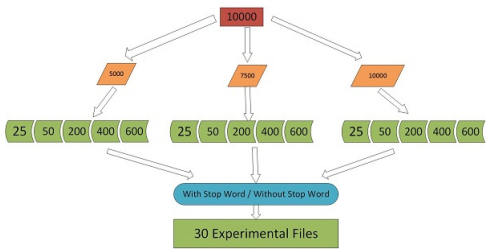


Fig. 2. Different kinds of Experimental Setup

Here is an example of dataset:
1,2,3 1:1 2:1 4:1 10:2
0 2:1 3:2
The first portion of a row means the label which is converted numerically from 0-7. Here, multiple labels are separated with the comma (,). Then, every segment containing ';', means feature information. The first part of the colon (:) represents the feature number. The feature numbers which are not present in a row means that no word are mutual with the corresponding cluster and those values are zero. When we worked with 25 clusters we have 25 features, 50 features for 50 clusters and so on.

## IV. Methodology

We trained our system with two libraries. At first one was with LibSVM and another was with Scikit Learn. With LibSVM, only Support Vector Machine (SVM), is supported. But with Scikit Learn, many more algorithm can be implemented. But these two libraries work same for the same algorithm but map multiple labels in different ways which are discussed below.

### A. LibSVM

At first, training and testing files are given in this system. And, all the combinations of multiple labels it get from this two files, map in a new file like in this figure 3. There may be one or more labels for a single label. Here is an example of mapping file in this figure 3.

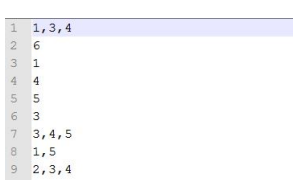

```
1,3,4
6
1
4
5
3
3,4,5
1,5
2,3,4
```

Fig. 3. Mapping File in LibSVM

That means, now LibSVM makes all the multi-labels in a single label representation.

After that, it creates two separate files for training and testing file correspondingly where it transforms actual multi-label into a single label set.

So, when it guesses any label for any sentence it always guesses a single label for testing file defined in mapping file which may correspond to multi-label or single-label.

### B. Scikit Learn

It's internal SVM algorithm may be same with LibSVM library but its mapping system of multiple labels is different. At first, multi-label should be transformed with a library of Scikit-Learn named 'MultiLabel Binarizer '. It creates a simple combination of 0 & 1 of any multi-label. Here is an example of 4 sentences of output list of training file.
[[1,2],[1,3,4],[0],[]]
It actually goes to system like this-
[[0,1,1],[0,1,0,1,1],[1],[]]
Here, [] means that no label is defined for the input file which is an important attribute of multi-label classification. After training, when testing file is given for testing, system also give output as a list of 0,1 combination. Then output are reversed with 'MultiLabel Binarizer' to actual output.
Here is a figure 4 for better visualization of this whole process.

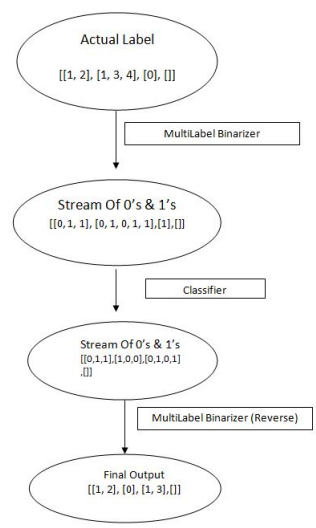


Fig. 4. Conversion of Multi-label with MultiLabel Binarizer

## V. Experiment and Result Analysis

### A. Implementation With LibSVM

Here is our accuracy measurement of 5000 sentences with stop word and without stop word.

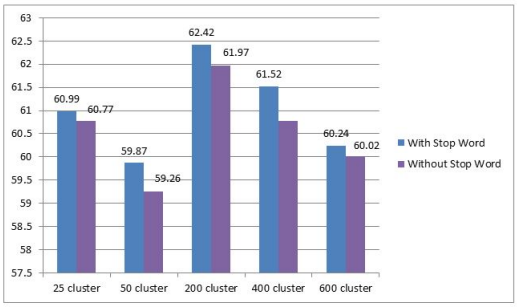


Fig. 5. Accuracy with 5000 Sentences Using LibSVM

LibSVM measured accuracy with label. Here is an example in the figures6 and 7

```
Victim >> crimeType >> crimePlace True
 Victim True
```

Fig. 6. True Sentence with True Label

```
crimePlace >> crimeTime False  crimeTime
 crimePlace crimeTime False  crimeType  crimePlace  crimeTime
```

Fig. 7. False Sentence with True Label

In the figures 6 and 7, left side of the true/false represents the actual label and right part represents the labels which are detected by our system.
LibSVM calls a true sentence it can detect all the labels as given. But if any of the those labels are wrongly predicted, then it takes the sentence as false. It takes all the labels from the 'true sentence' and classifies them as 'right label'. But it doesn't take any labels from 'false sentence' though there may one or two labels are correct. In figure 6, LibSVM will take all the labels as that is true sentence. But in figure 7, no labels will be counted as right label.

From the figure 5 and analysis from 7500 and 10,000 sentences, it is shown that having stop words in a sentence gives better result than not having stop words. Because, there are very few words in a sentence and all of these are important. If we remove one or two words saying that these are stop words then, useful informations are also removed . So, accuracy decreases then. Now, we show comparison of different corpus having stop words. Here is the accuracy, micro-average F-score and macro-average F-score comparison of different kinds of corpus with cluster information used as a feature value.

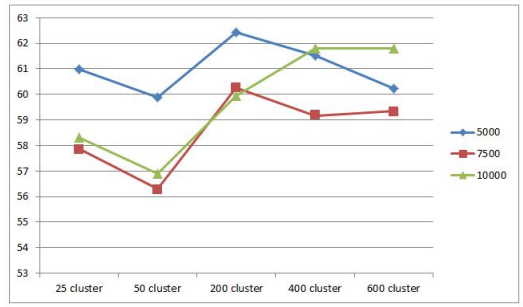


Fig. 8. Accuracy Comparison Between Different Corpus Using LibSVM

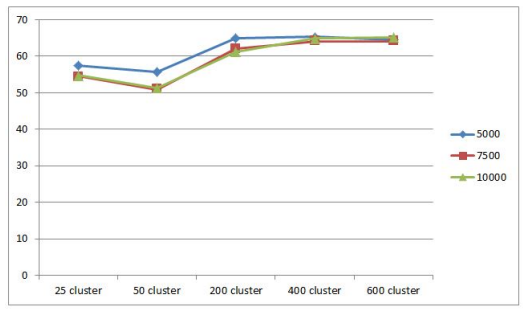


Fig. 9. Micro Average Comparison Between Different Corpus Using LibSVM

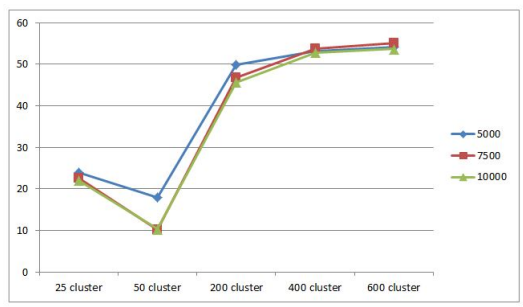


Fig. 10. Macro Average Comparison Between Different Corpus Using LibSVM

Here we observed that larger corpus (10000 sentences) with 600 cluster information gives better result. Because, 600 cluster makes our feature value more accurate to detect the classes individually. But there are not many mentionable differences between them. Now, we present label based difference between different corpus with only 600 cluster information.

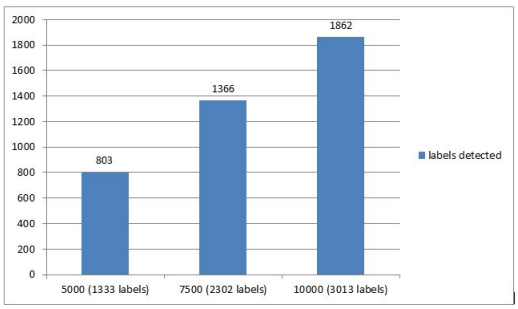


Fig. 11. Label Based Difference

Actually LibSVM divides the detected labels from total labels to get the accuracy.

$$Accuracy[LibSVM] = \frac{\text{Detected labels}}{\text{All labels}}$$

We tagged our corpus with only 8 classes. But LibSVM transforms the multi-labels into single label in another file. So, The figure shows the actual single labels it works when to classify our sentences between different corpus like - 56 for 5000, 63 for 7500 and 71 for 10000 sentences. Again, we've some problems as LibSVM only guesses the combination from training and testing set. It doesn't guess any new combination. And it measures label based accuracy. So, we're now moving into new library named Scikit Learn.

### B. Implementation With Scikit Learn

The main benefit of using Scikit Learn is, it can generate new combination for testing data.
In this section, we only worked with 10000 sentences with 600 cluster information used a feature value as it gives better result in the previous section. This time we measured our accuracy as full sentence based. From figure 6 and 7, we got the idea of measuring accuracy.

$$Accuracy[ScikitLearn] = \frac{\text{True Sentence}}{\text{True Sentence + False Sentence}}$$

Measuring accuracy like this, we've implemented different algorithms. Here is the comparison below.

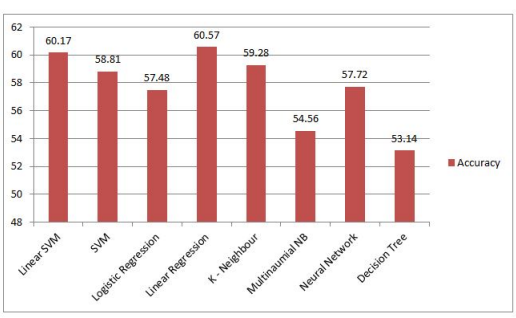


Fig. 12. Comparison between different algorithms

Some of the algorithms give better result. But all are not good. Like- K - Neighbour gives a good result but it is very slow. Again, we worked with Gaussian NB but gives very bad result of 5.54% accuracy where its False Negative for every class is very high.
But as we're taking true sentence when full multi-label is true and false sentence when at least one label is false, we think it is a strict idea. Because, there may be one label faulty, but others are successfully detected but we take the sentence as false. Again we don't know which classes are most faulty that are hard to predict by our system. So, now we want to show confusion matrix for Linear Regression (as it gives the best result) for every class we're working in this thesis.

| | True Positive | False Positive | False Negative | True Negative |
|---|---|---|---|---|
| Victim | 347 | 291 | 269 | 2106 |
| Suspect | 65 | 151 | 161 | 2636 |
| Crime Type | 177 | 164 | 190 | 2482 |
| Crime Place | 222 | 119 | 211 | 2461 |
| Crime Time | 119 | 91 | 165 | 2638 |
| Hospital | 102 | 9 | 62 | 2840 |
| Police Station | 92 | 21 | 71 | 2829 |
| Neutral | 1325 | 389 | 414 | 885 |

TABLE I
CONFUSION MATRIX FOR DIFFERENT CLASSES

For better visualization, we want to show now precision comparison for every classes.

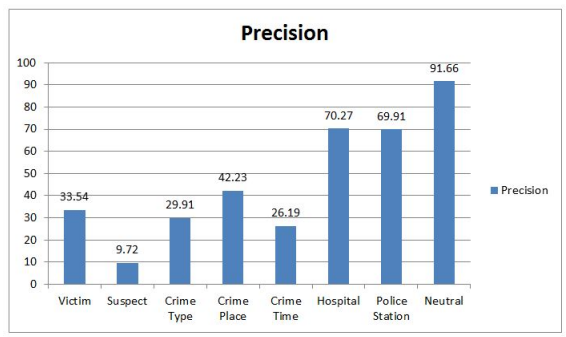


Fig. 13. Precision Comparison between different classes

Here we're seeing that Suspect precision is very low. Let's see an example.
করিম সিলেটে এসে খুন করে গেল।
করিম সিলেটে এসে খুন হয়ে গেল।
In the first sentence it is 'Suspect' type and in the second sentence it is 'Victim' type. But both sentences have very low difference. So, maximum time our system classifies Suspect which is actually a victim. Because, Victim class is many more times in our data set rather than suspect. So, it can not detect suspect name very precisely.
Precision of crime time is also very low. Because, we tagged a sentence as crime time when we got any time like -ভর দুপুর, মধ্য রাত, বিকাল, ভর সন্ধ্যা, বেলা ১ টায়, রাতে, সোমবার, জানুয়ারিতে, বেলা ১০ টা, ভোরে . There are more difference in a single tag. So it gets confused.
Again, if we see other classes like - crime place, hospital,

police station all of these are name of some places. That means most of the police stations and hospitals are named with the name of the area these belong. So, if place name or hospital name or police station name are not present in our cluster that we used for features our system can not classify those. Again, we tagged a sentence for crime place just seeing the place name. But the place may be very unpopular among news to focus. So, the place will not be present in our cluster and can't be detected. This same theory also falls in for hospital and police station name. But still, hospital or police station are not situated in a remote place. So, these names are published in different newspapers repeatedly. So, these are easy to detect. But on the other hand, crime can be held in any rural area and remote place but unpopular. So, our classifier is not smart enough to detect a crime place easily because of lacking enough information that build our features.

Another reason for bad precision for every class is the length of a sentence. That means, number of words present in a sentence. When more words in a sentence and less class to detect, our system can easily know the labels. But in reverse, if less words and more labels to detect, then our system can not identify all the labels but one or two. We will see this scenery comparing classes for Recall also. Let's see.

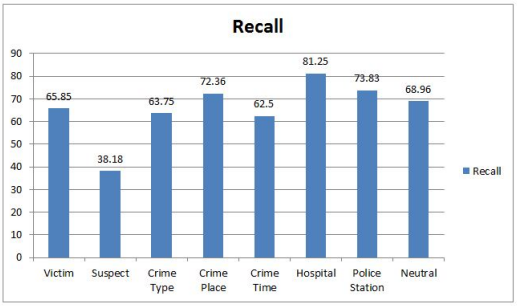


Fig. 14. Recall Comparison Between Different Classes

Again, we want to show F-score difference between classes.

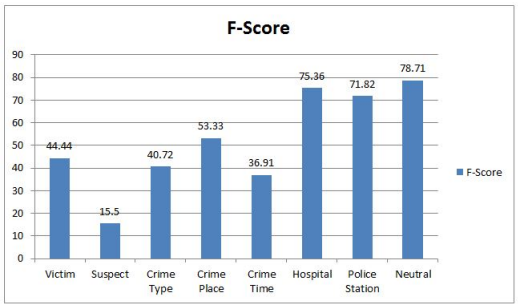


Fig. 15. F-Score Comparison Between Different Classes

When we present accuracy measurement for different classes, we got 85% up accuracy for every class.

Here we observed an interesting thing. That is, problematic 'Suspect' class has very nice accuracy. Actually, most of the time our system doesn't guess 'Suspect' class and on the other hand our corpus has also very less information of 'Suspect' tag. So, in maximum sentences, 'Suspect' becomes True Negative which has an huge impact on accuracy measurement. So, in term of comparison, we can say that Precision, Recall and F-Score have excellent measurement to give.

## VI. Conclusion

We tried to categorize any sentence into multiple labels but we are stuck at an unvarying accuracy now. Increasing dataset was not very helpful on this time. May be we should use another method with our system to improve the accuracy. Next time, we'll dig into deep with this work.

## References


[1] A. Das and S. Bandyopadhyay "Subjectivity detection in english and bengali: A crf-based approach," Proceeding of ICON, 2009.

[2] D. Das and S. Bandyopadhyay, "Word to sentence level emotion tagging for bengali blogs," in Proceedings of the ACL-IJCNLP 2009 Conference Short Papers. Association for Computational Linguistics, 2009, pp. 149–152.

[3] M. Fleischman and E. Hovy, "Fine grained classification of named entities," in Proceedings of the 19th international conference on Computational linguistics-Volume 1. Association for Computational Linguistics, 2002, pp. 1–7.

[4] A. Ahmad and M. R. Amin, "Bengali word embeddings and it's application in solving document classification problem," in Computer and Information Technology (ICCIT), 2016 19th International Conference on. IEEE, 2016, pp. 425–430.

[5] D. Harikrishna and K. S. Rao, "Emotion-specific features for classifying emotions in story text," in Communication (NCC), 2016 Twenty Second National Conference on. IEEE, 2016, pp. 1–4.

[6] C. Dayrell, A. Candido Jr, G. Lima, D. Machado Jr, A. A. Copestake, V. D. Feltrim, S. E. Tagnin, and S. M. Aluísio, "Rhetorical move detection in english abstracts: Multi-label sentence classifiers and their annotated corpora." in LREC, 2012, pp. 1604–1609.

[7] Z. Ren, M.-H. Peetz, S. Liang, W. Van Dolen, and M. De Rijke, "Hierarchical multi-label classification of social text streams," in Proceedings of the 37th international ACM SIGIR conference on Research & development in information retrieval. ACM, 2014, pp. 213–222.

[8] Y. Wu, K. Kita, and K. Matsumoto, "Three predictions are better than one: Sentence multiemotion analysis from different perspectives," IEEJ Transactions on Electrical and Electronic Engineering, vol. 9, no. 6, pp. 642–649, 2014.

[9] Y. Kim, "Convolutional neural networks for sentence classification," arXiv preprint arXiv:1408.5882, 2014.

# Nose Tracking Cursor Control for the People with Disabilities: An Improved HCI

Shadman Sakib Khan[1], Md. Samiul Haque Sunny[2], M. Shifat Hossain[2], Eklas Hossain[3], and Mohiuddin Ahmad[2]
[1]Northern University Bangladesh (NUB), Dhaka, Bangladesh
[2]Khulna University of Engineering & Technology (KUET), Khulna, Bangladesh
[3]Oregon Tech, Department of Electrical and Renewable Energy, OR-97601, USA
[1]sskhanniloy@gmail.com

***Abstract*—People with tetraplegia, suffering from traumatic brain injury, cerebral palsy, neurological injury or stroke, face a lot of difficulties to use standard input interface of personal computers, such as the keyboard and the mouse, during their rehabilitation and everyday life activities. Therefore, it is highly desired to develop Assistive Technologies (ATs) for people with tetraplegia. In this paper, Human Computer Interface (HCI) is implemented with digital image processing and a new approach to control personal computers with high efficiency. The main three features of this interface are nose tracking cursor control, auto brightness control and display control based on the presence and detection of valid human face. The proposed system is low cost and exhibits inherent security and power saving capabilities. MATLAB environment is used to perform the experiments and performance is analyzed by comparing the results with recent works.**

***Keywords—Human Computer Interface, Viola Jones algorithm, Disabled people, Assistive Technologies, Nose Tracking.***

## I. INTRODUCTION

As Human-Computer Interface (HCI) systems allows more natural communication with machines, the research interest has increased on this topic in recent years. The point of communication between human user and computer is defined as HCI. Keyboard, mouse, touchpad and touchscreen are the main interfacing devices for which hand is necessary. But the people who cannot move their hands cannot use computers. For these disabled people, some Assistive Technologies (ATs) are developed.

A comprehensive solution of HCI with Assistive Technologies is presented in [1] with nose movement and voice interaction. To achieve this, speech Application Program Interface (API) is used and passed to the system using system API call. In [2] a yawn detector along with face and nose detector is described for driver fatigue monitoring system. Convolutional neural network, a deep learning algorithm, is used to detect the driver's face area and nose location. Facial feature based HCI for handicapped people is depicted in [3]. Patients who are capable of voluntary blinking, a system is developed which uses the blink durations and sequence to perform HCI functions. Using face recognition and extraction of user eyes' location as a new method is proposed in [4] to implement 'camera mouse' for the individuals with disability. To prevent the false detections outside the area of head tracker, a method employing combined face and nose detector is presented in [5], which is based on geometric features. In [6] a low cost HCI is implemented with eye tracking and the technique of video-oculography assisted by corneal reflections. For improving pointing device usability and performance, a non-intrusive facial tracking based HCI along with an embedded system based on PID controller is presented in [7]. To provide computer access to people with severe disabilities, a camera mouse system is developed and the body features are examined for robust tracking in [8]. A two-stage model for interfacing target identity and cursor control from natural gaze trajectories based on hidden Markov model is described in [9]. A novel wearable Electrooculography (EOG) based HCI is proposed in [10]. Here double eye blinks are used for generating EOG signal. So, Electroencephalogram (EEG), Electromyography (EMG), EOG are the signal based ATs where signal to noise ratio is very low. Voice command based ATs are unreliable in noisy environment. Mechanical motion based ATs such as sip-and-puff are unhygienic. Motion tracking based ATs such as eye, tongue, face tracker need calibration and constant head position.

The primary contribution of this paper is proposing and implementing a low-cost human computer interface using webcam – which provides an easy way for disabled people to seamlessly operate personal computers. Main features of the proposed system are nose tracking cursor control, auto brightness control, and display control based on presence and detection of valid human face. The nose tracking system allows anyone to control the mouse cursor by moving nose and changing mouth status – enabling user to click or drag any element on the screen. The click function is activated on the detection of teeth. Its performance is better than camera mouse and any other similar system. Auto brightness control system changes the display brightness automatically to make the display more comfortable to eyes. Face presence based display control turns off the display when no one is using it, which lowers the consumption of power. This display controlling system can also be used to plug in an extra personal security layer to activate the display whenever an authenticated person is present in front of the computer. All these features make using a computer easier, more convenient and more efficient for disabled people.

In this paper, section II discusses mathematical background of Viola-Jones, which is adopted in this work for face detection and recognition techniques. Section III presents the proposed methodology. Simulation results are discussed in section IV with comparisons of the proposed method with similar

978-1-5386-2307-7/17/$31.00 ©2017 IEEE

techniques. Section V shows real-world performance of the proposed system, which demonstrates its utility to people with and without disability. The conclusion is drawn in section VI.

## II. Mathmatical background

Many algorithms are available to detect and recognize face structure and facial features from images. Viola Jones algorithm is the one of the most notable algorithms used for research purposes [11]. This algorithm can detect objects (i.e. facial features) in real-time. It can also be trained to detect different types of objects. To detect faces using Viola-Jones algorithm, the face must have a fully observable frontal-upright view. But these limits are acceptable in practice [12]. The Viola-Jones algorithm has four stages of processing. The Haar features selection, integral image generation, Adaboost training and cascading classifiers [13]. The Haar features are very similar to convolution kernels. But in this case the sum of pixel values under the white rectangle is subtracted from the sum of pixel values under the black rectangle.

*value = ∑ (pixel values in black area) - ∑ (pixel values in white area)*

A standard 24x24 pixels sub-window can generate a total of 162336 possible features [14]. These features are then checked to generate the integral image. The third stage of Viola-Jones algorithm is called the Adaboost training stage. The Adaboost is a form of machine learning algorithm [15]. The features (160000+) previously calculated is evaluated in this stage to identify the relevant and irrelevant features. This algorithm constructs "strong" classifiers as a linear combination of "weak" classifiers.

$$h(x) = sign(\sum_{j=1}^{M} a_j h_j(x)) \quad (1)$$

$$h_j(x) = \begin{cases} -s_j & \text{if } f_j < \theta_j \\ s_j & \text{otherwise} \end{cases} \quad (2)$$

The threshold value $\theta_j$, polarity $s_j$ and the coefficients $\alpha_j$ are determined in the training. The last stage is the cascading classifiers. The basic principle of face detection by this algorithm is to scan the detector many times. Each time same image is used but with a new size [16]. In Fig. 1, these four stages are shown in a flowchart depicting a face detection operation. If a face is detected, this process returns the boundary of the detected feature. On the other hand, if nothing significant is found by this algorithm, it will continue to find and detect features by restarting itself from the beginning.

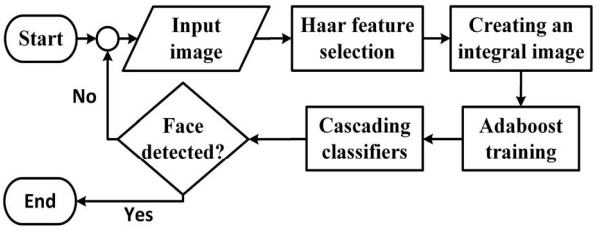


Figure. 1. Steps of Voila-Jones for face detection.

## III. Proposed methodology

Proposed interaction and additional features are described in this section with separate subsections.

### A. Nose Tracking Cursor Control

In this process, initially the input image is cropped down to a smaller size where the probability of finding face is maximum which saves time. After RGB to gray conversion, Viola-Jones algorithm is used to detect nose. Then from four corner points of the detected nose bounding box, its middle point is calculated. Some parameters depending on screen size and desired cursor speed are used to convert this middle point of nose to cursor position. To remove jittering, weighted average values are calculated. In Fig. 2, the reduction of jittering block describes its process where P(1)-P(5) creates an array and previous five values are held there to calculate average cursor position. The following stage is the detection of mouth which can be easily done by changing four corner point position of detected nose bounding box. Mouse left click is performed when teeth are detected and this is performed until mouth is closed which helps to drag. Teeth are detected by calculating the mean value of the detected mouth. Z(1, 1)-Z(5, 1) array helps to store these mean values which help to apply conditions for clicking and dragging as described in Fig. 2.

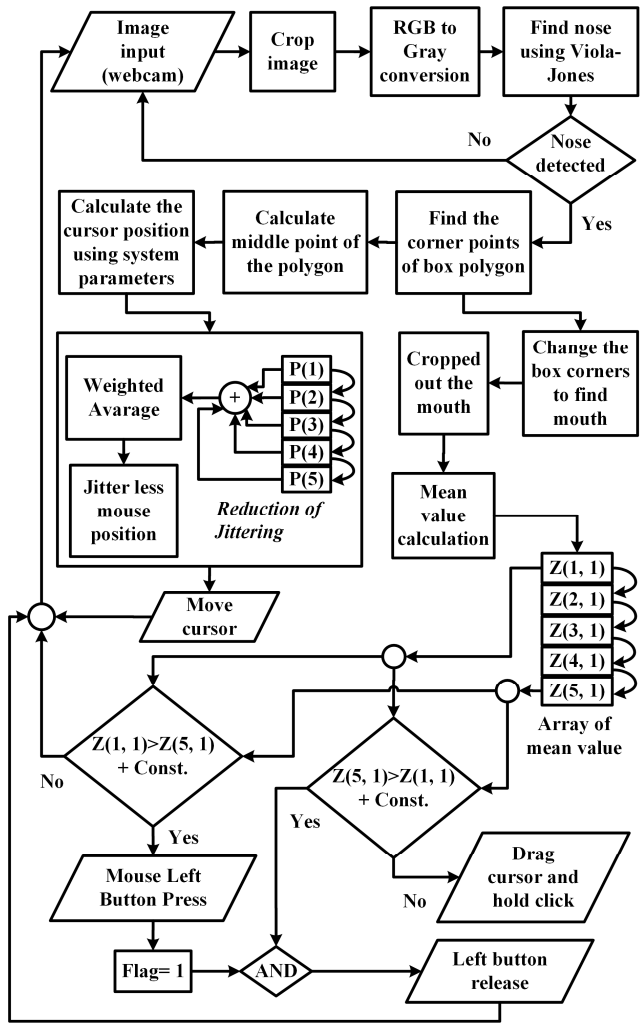


Figure. 2. Flowchart of nose tracking cursor control.

### B. *Auto brightness Control*

Input images are taken by the webcam at a specified interval. RGB to grayscale conversion helps to estimate the mean value. Then the mean value is compared with the threshold value. If the mean value is in the threshold range, the brightness of the display panel remains unchanged. And if it is larger than the threshold, brightness will increase. Otherwise, the brightness will diminish. Here, the threshold values are determined based on the screen brightness based illuminance, apart from the environment light. A flowchart in Fig. 3 describes this auto brightness control mechanism. When Esc button is pressed, this process will terminate.

### C. *Face Controlled Display Off*

Using webcam, input is taken and Viola-Jones algorithm is employed to find faces in this image. If a face is detected and if it is greater than the threshold face size, that means someone is sitting in front of the display and using it, then the display panel will remain on. On the other hand, when no face is detected or the detected face is smaller than the threshold face size, the display panel will turn off. That implies no one is present or someone is present in the room but not using the display panel. In Fig. 4 this process is explained in a flowchart. Here, the threshold face size is evaluated by averaging human face sizes at a certain distance from the camera.

## IV. RESULT AND DISCUSSION

Small image consumes less time in this algorithm, which saves time. So, firstly the input image is cropped and then using Viola-Jones algorithm, face is detected which is demonstrated in Fig. 5(a). In Fig. 5(b) nose is detected using the same algorithm. Without detecting the mouth by Viola-Jones, it is detected by

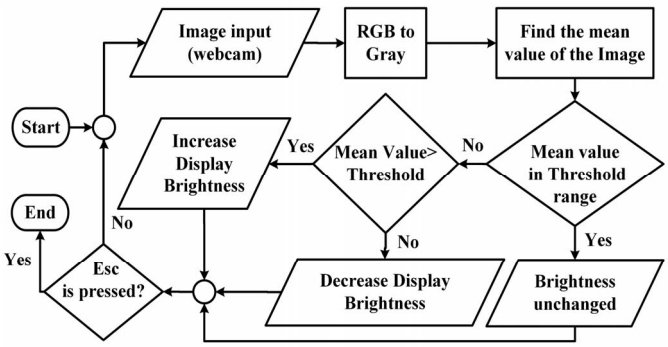


Figure. 3. Flowchart of auto brightness control.

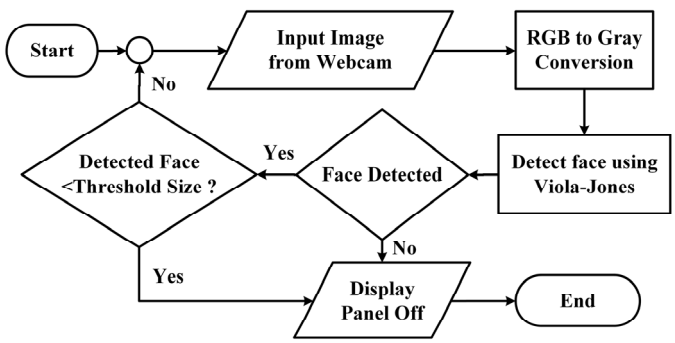


Figure. 4. Flowchart of face controlled display off.

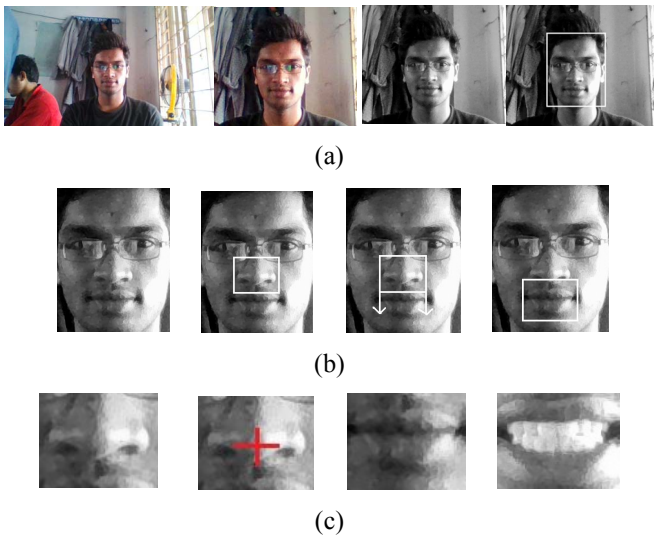


Figure. 5. (a) Face detection, (b) Nose and mouth detection, (c) Cursor position set and clicking condition.

changing corner points of detected nose bounding-box, which also reduces computational cost. In Fig. 5(c), nose middle point detection for cursor control and detected mouth in various conditions for clicking are shown. Nose middle point is also the facial middle point. So, it is more convenient to use this point than any other features of the face. Our proposed method for controlling cursor using nose tracking system is very low cost and high precision system. No additional hardware is needed for implementation. Disabled people can practice it with foremost comfort. This paper's result shows that, in every lighting condition, it is robust. The accuracy of the projected scheme is sound and the CPU usage is lower than other comparative systems. Users who tested this system, expressed positive reviews in most cases. As the performance of the system can be observed by the cursor translational error, so the primary target is to decrease the mean error of pixels' distance.

For a trial experiment, "Camera mouse 2017" is used with very high sensitivity to match with the sensitivity of our proposed system. In Fig. 6, red points represent our proposed method and blue points represent "Camera mouse 2017". The task was to click every intersection point. And for an accurate calculation of the system, total 50 trials were performed by six different users who were physically sound. All trials were done on an Intel core i7, 2.50 GHz PC with 15.6 inch LCD display panel with a resolution of *1366x768*. The camera resolution was *1280x720*.

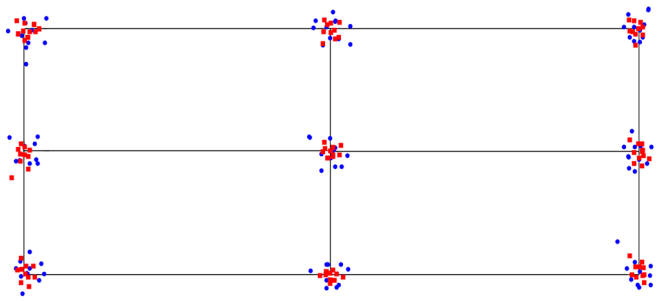

Figure. 6. Comparision between camera mouse and nose tracking system using typical trial.

In Table I, three technique's error pixels are given which were practiced in several environments. In daylight, pixels translational error in eye tracking system [6] is maximum. On the other hand, Camera mouse and nose tracking errors are quite close. But at night, without light, nose tracking performs better than camera mouse. From Table II it can be observed that though the clicking speed of nose tracking is slow, its precision is higher than Camera Mouse.

This nose tracking system was also extended to have a dragging capability, which helps to trace cursor in a definite path and like the original algorithm no calibration is required here; no need to fix the head for clicking, and the cursor can be stopped easily. It is comfortable than eye tracker, because of the absence of eye blinking problem. The performance of the proposed method is better than camera mouse and its cost is lower as no additional hardware is necessary.

The intensity levels of light change from time to time and it is also dependent on the environment. Therefore, the captured image's mean value also changes, according to which display panel brightness change. This method makes usage of computer more comfortable for the eyes. The step change algorithm is used in auto brightness method, which is represented in red in Fig. 7. If this step size is reduced, brightness change will be smooth, as shown in blue in the figure. The step sizes are determined by the screen based illuminance value ignoring other environmental light sources. This method of calculating step sizes reduce the probability of shuffling in between two steps at a very high rate. It also reduces the possibility of occurring an avalanche effect in both direction (i.e. drastic reduction or increment of screen brightness without getting stabilizing in a certain stage). A computer without auto brightness sensor can use a webcam to control brightness automatically with the suggested method.

Normally a display panel consumes around 20W of power and our proposed face controlled display off method saves this power by turning off display when no one is using it. Though the CPU power consumption remains constant, as depicted in Fig. 8. This can increase battery lifetime.

## V. IMPLIMENTATION RESULTS

The proposed system has been put up for trial with 34 able and 6 disabled people. They have been provided a brief introduction on the working principle of the system, and allowed to practice it for some time. Then they were asked to sign and draw some shapes.

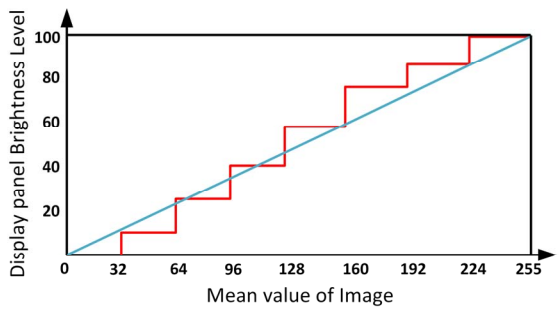


Figure. 7. Change of brightness level with the mean value of input image.

TABLE I. ERROR PIXELS COMPARISON AMONG TECHNIQUES

| Lighting conditions | | Techniques with their error pixels | | |
|---|---|---|---|---|
| | | *Eye tracking* | *Camera mouse* | *Nose tracking* |
| **Day** | | 53.97 | 16.3 | 14.53 |
| **Night** | **With room light** | 55.23 | 17.08 | 14.86 |
| | **Only with pc screen** | 59.15 | 20.09 | 15.97 |

TABLE II. COMPARISON BETWEEN CAMERA MOUSE AND NOSE TRACKING WITH DIFFERENT FACTORS

| Techniques | Factors to be compared | | | |
|---|---|---|---|---|
| | *Precision* | *Recall* | *Accuracy* | *Avg. Time for 1 click* |
| **Camera mouse** | 98.41% | 98.41% | 96.87% | 3.33s |
| **Nose tracking** | 100% | 95.1% | 95.1% | 4.12s |

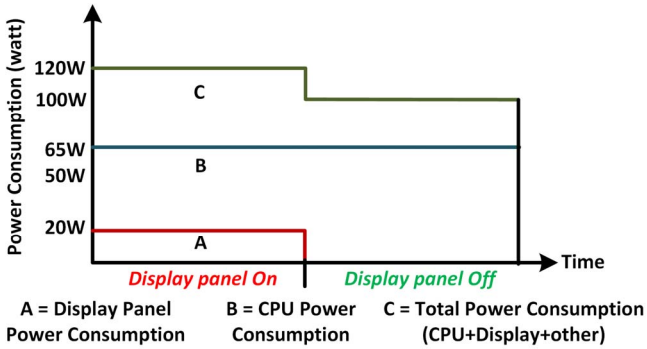


Figure. 8. Power consumption of display panels for proposed method

### A. *People without disabilities*

A software sketchpad for the Windows platform is used to compare the drawing capabilities between the touchpad and the nose tracker which are presented in Fig. 9. From this figure, it can be discovered that drawing capability of the proposed nose tracking system is similar to the touchpad apart from the beginning and ending displacements. From above demonstration, a conclusion can be drawn that the proposed method is better than camera mouse and some other similar assistive technologies.

### B. *People with disabilities*

To check the robustness and user-friendliness of the interface, it has been tested in Dhaka Medical College and Hospital with people having disabilities and diseases that limit their speaking capabilities and allow very limited voluntary muscle control. The results are summarized in Table III and their feedbacks were noted along with the time they needed to get adapted with the system. It can be noted from the table that the comparatively younger people (aged 21, 29, 35) found the system easy to use, and took less time (7-8 minutes) to get adapted to it. But that does not necessarily indicate a drawback of this system. Older generation of Bangladeshis have little computer knowledge and face difficulties to operate even if they are totally healthy and fit. That explains the feedback of people aged 39 and above in this case. The difficulties they have faced can be a result of a lack of familiarization with computers, and not related with the proposed interface itself. Fig. 10 depicts some of the patients using the system.

*(a)*

*(b)*

Figure. 9. Comparison between Touchpad and Nose Tracking drawing using Sketchpad, (a)Touchpad; (b) Nose tracking

Figure. 10. Nose tracking control by the patients.

TABLE III. IMPLEMENTATION OF THE SYSTEM WITH ILL AND HANDICAPPED PEOPLE

| Age | Gender | Disease | Time to adapt (min) | Feedback |
|---|---|---|---|---|
| 21 | M | Muscular dystrophy | 7 | Easy |
| 29 | M | Cerebral palsy | 7 | Easy |
| 35 | M | Spinal cord injury | 8 | Easy |
| 39 | M | Parkinson's disease | 15 | Hard |
| 40 | M | Multiple sclerosis | 10 | Medium |
| 45 | M | Lost or damage of limbs | 13 | Hard |

## VI. CONCLUSION

A novel low-cost Human Computer Interface (HCI) employing Viola-Jones algorithm has been proposed and implemented in this paper. The aspects of the proposed system were described in detail alongside with the mathematical backgrounds of some important feature blocks of this system. Simulation results were given to validate the system that has been presented and compared with similar systems, which proved the proposed system's supremacy over other methods. The proposed system has also been implemented in real world situations and tested with both able-bodied and disabled people. And these tests also produced very satisfactory results.


## ACKNOWLEDGMENT

The authors thank the Director of the Dhaka Medical College and Hospital for their support and collaboration.


## REFERENCES


[1] S. K. Chathuranga, K. C. Samarawickrama¤, H. M. L. Chandima, K. G. T. D. Chathuranga and A. M. H. S. Abeykoon, "Hands free interface for Human Computer Interaction," 2010 Fifth International Conference on Information and Automation for Sustainability, Colombo, 2010, pp. 359-364. doi: 10.1109/ICIAFS.2010.5715687.

[2] Weiwei Zhang, Y. L. Murphey, Tianyu Wang and Qijie Xu, "Driver yawning detection based on deep convolutional neural learning and robust nose tracking," 2015 International Joint Conference on Neural Networks (IJCNN), Killarney, 2015, pp. 1-8. doi: 10.1109/IJCNN.2015.7280566.

[3] K. Parmar, B. Mehta and R. Sawant, "Facial-feature based Human-Computer Interface for disabled people," 2012 International Conference on Communication, Information & Computing Technology (ICCICT), Mumbai, 2012, pp. 1-5. doi: 10.1109/ICCICT.2012.6398171.

[4] P. Gyawal, A. Alsadoon, P. W. C. Prasad, L. S. Hoe and A. Elchouemi, "A novel robust camera mouse for disabled people (RCMDP)," 2016 7th International Conference on Information and Communication Systems (ICICS), Irbid, 2016, pp. 217-220. doi: 10.1109/IACS.2016.7476114.

[5] M. Bohme, M. Haker, T. Martinetz and E. Barth, "Head tracking with combined face and nose detection," 2009 International Symposium on Signals, Circuits and Systems, Iasi, 2009, pp. 1-4. doi: 10.1109/ISSCS.2009.5206211.

[6] J. B. Hiley, A. H. Redekopp and R. Fazel-Rezai, "A Low Cost Human Computer Interface based on Eye Tracking," 2006 International Conference of the IEEE Engineering in Medicine and Biology Society, New York, NY, 2006, pp. 3226-3229. doi: 10.1109/IEMBS.2006.260774.

[7] R. A. Antunes, L. B. Palma, F. V. Coito, H. Duarteramos and P. Gil, "Intelligent human-computer interface for improving pointing device usability and performance," 2016 12th IEEE International Conference on Control and Automation (ICCA), Kathmandu, 2016, pp. 714-719. doi: 10.1109/ICCA.2016.7505363.

[8] M. Betke, J. Gips and P. Fleming, "The Camera Mouse: visual tracking of body features to provide computer access for people with severe disabilities," in IEEE Transactions on Neural Systems and Rehabilitation Engineering, vol. 10, no. 1, pp. 1-10, March 2002. doi: 10.1109/TNSRE.2002.1021581.

[9] Z. Chen and B. E. Shi, "A Two-stage model for inference of target identity during 2D cursor control from natural gaze trajectories," 2015 37th Annual International Conference of the IEEE Engineering in Medicine and Biology Society (EMBC), Milan, 2015, pp. 474-477. doi: 10.1109/EMBC.2015.7318402.

[10] A. M. S. Ang, Z. G. Zhang, Y. S. Hung and J. N. F. Mak, "A user-friendly wearable single-channel EOG-based human-computer interface for cursor control," 2015 7th International IEEE/EMBS Conference on Neural Engineering (NER), Montpellier, 2015, pp. 565-568. doi: 10.1109/NER.2015.7146685.

[11] Y. Wang, "An Analysis of the Viola-Jones Face Detection Algorithm", Image Processing On Line, vol. 4, pp. 128-148, 2014.

[12] P. Viola and M. Jones, "Robust Real-Time Face Detection", International Journal of Computer Vision, vol. 57, no. 2, pp. 137-154, 2004.

[13] P. Viola and M. Jones, "Rapid object detection using a boosted cascade of simple features," in IEEE Comp. Soc. Conf. on Computer Vision and Pattern Recognition. CVPR 2001, vol. 1. IEEE, 2001, pp. 1-511.

[14] P. Lammertsma, "Viola-Jones' face detection claims 180k features," Stack Overflow, 10 11 2009. [Online].

[15] R. Schapire, "Explaining adaboost.," in Empirical Inference: Festschrift in Honor of Vladimir N. Vapnik, Verlag Berlin Heidelberg, Springer, 2013, pp. 37-52.

[16] O. H. Jensen, Implementing the Viola-Jones Face Detection Algorithm, Kongens Lyngby, Denmark: IMM·DTU, 2008

# Determination of EM Parameters in Human Head Phantom by Transcranial Magnetic Stimulation

Laila Khairunnahar[1], Md. Kamal Hosain[2], Md. Rabiul Islam[3]
Rajshahi University of Engineering & Technology
Rajshahi-6204, Bangladesh
laila.ete11ruet@gmail.com[1], kamaleteruet@gmail.com[2], rabiul_cse@yahoo.com[3]

*Abstract*— **Transcranial magnetic stimulation (TMS) has recently founded itself as an endeavoring therapeutic tool as well as a very feasible diagnostic and researching technique of several neurological and psychiatric disorders. The deep transcranial magnetic stimulation may play a vital role in the motivation mechanism. It has become popular because of its noninvasive operation method. In this paper, the numerical simulation for deep transcranial magnetic stimulation (dTMS) has been performed by considering a conventional figure of eight (Fo8) coil operating with the Halo coil [Halo-Fo8 assembly coil (HFA coil)]. The 3D distributions of the electric field, magnetic flux density as well as the current density were numerically calculated by the impedance method. Instead of a realistic head model, a human head phantom was used for the simulation purpose. It was observed for this simulation setup, the HFA coil provides more concentrated magnetic flux density and improved penetration depth in the deep bran regions which is better than that can be achieved from the Fo8 coil operating alone.**

**Keywords—*deep transcranial magnetic stimulation (dTMS), impedance method, magnetic coil, transcranial magnetic stimulation (TMS).***

## I. INTRODUCTION

Transcranial magnetic stimulation (TMS) is a noninvasive procedure that uses magnetic fields to stimulate nerve cells in the brain to improve symptoms of depression. It is used to stimulate small region of the brain. The technique of generating the stimulation is done by passing a brief and transient electric current through a magnetic coil placed upon the scalp and underlying cortex which produces localized axonal depolarization [1-3]. To stimulate in the deep brain neuronal region, leads to induce higher stimulation intensities as the electric field decreases as a function of tissue depth [4]. As far, there are several coil configurations potentially suitable for dTMS: double cone [5], H- coil [6] and Halo coils [7] [8]. The TMS stimulation is achieved using electromagnetic field pulses that induce electromagnetic field in the brain from the outside of the head. Through a current carrying coil the intense magnetic field pulses are applied to the underlying neuronal tissues. This field can be sufficient enough in magnitude to depolarize neurons [9].

As far the main problem associated with TMS system includes when stimulating particular areas of the brain, magnetic field generated by the coil affects the outside area as well and TMS stimulates area much more than the desired or located areas for brain stimulation. Moreover, when stimulating particular areas of the brain, magnetic field generated by the coil affects the outside area as well i.e., the field is not concentrated.

Hereby, the most important considerations are the type of material used to construct the core of the coil, the geometry of the coil configuration for more concentrated field distribution, analyzing the coil performance placing and simulating with human head phantom model designed with tissue properties appropriate with brain tissues, optimum distance between coil and the head model during simulation and, the biophysical characteristics of the pulse produced by the coil. The proposed methodology of this research work is to design and optimize the coil parameters to make it suitable for deep brain stimulation. By calculating the induced field and the penetration depth of the field, there will be a comparative summarization of the coil. In this paper, we will discuss the field characteristics of the Fo8 coil, round coil and the halo coil working with a conventional Fo8 coil, i.e., HFA coil.

## II.DESIGN OF PHANTOM AND COIL FOR TMS

HFSS is a high performance full wave electromagnetic (EM) field simulator. HFSS is basically used for arbitrary 3D volumetric passive device modelling. Ansoft HFSS employs the Finite Element Method (FEM), adaptive meshing, and brilliant graphics to give incomparable performance and perception to all of 3D EM problems. Ansoft HFSS can be used to calculate parameters such as s-parameters, resonant frequency, and fields.

Three types of coil for transcranial magnetic stimulation have been proposed and numerically designed as shown in Fig. 1, where Fig. 1(a)-(c) show the figure-of-eight (Fo8) coil, circular coil, halo-Fo8 assembly coil (HFA coil) respectively. These proposed coils are placed upon a six-layered human head phantom which is also represented in Fig. 1. The coordinate system employed in this paper was Cartesian coordinate system.

The pulse current of 5000A with the same operating frequency of 3.7 kHz was fed into each of the coil. The boundary condition such as near E field was applied during the simulation process. The surrounding region of the model was considered as air. The material used for designing the coil is “copper”. Copper is a conducting material, it’s permittivity of 1, permeability of 0.99991 and zero dielectric loss. The coil specifications are summarized in Table I. It should be noted, although both the halo and Fo8 coils are operating at the same frequency as mentioned in Table I, the direction of the current flowing in the

978-1-5386-2307-7/17/$31.00 ©2017 IEEE

halo coil is the same as that one of the Fo8 coil wing, but it is in the opposite direction of another wing. The designed coil is placed upon the skin layer of a six layer of a spherical head model. The modeled head with the coils placed upon it are presented in Fig. 1(a)-(c).

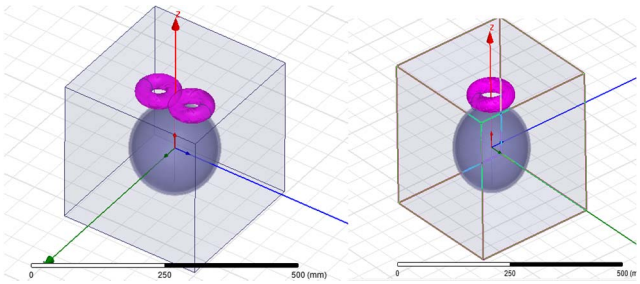

(a) (b)

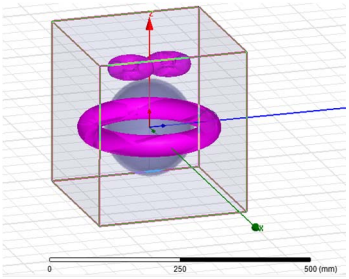

(c)

Fig. 1: Six-layer head model with TMS coil placed upon it, with (a) figure-of-eight (Fo8) coil, (b) circular coil, and (c) halo-Fo8 assembly coil (HFA coil).

TABLE I: COIL PARAMETERS

| Coil | Major radius(mm) | Minor radius(mm) | Current(A) |
|---|---|---|---|
| Fo8 | 30 | 15 | 5000 |
| Halo | 120 | 20 | 5000 |
| Circular | 40 | 15 | 5000 |

Now, Fig. 2 (a)-(b) shows a close view of the part of the human head phantom where the coil is placed. The structure of the six layer head model can be seen in Fig. 2.

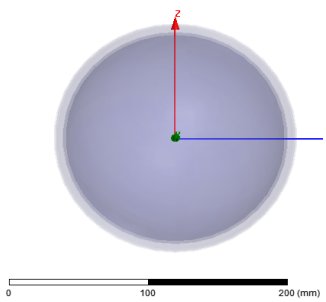


(a)

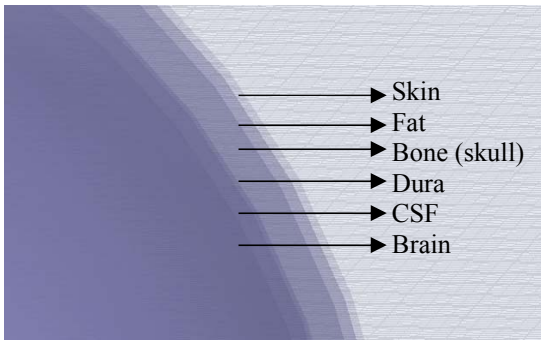


(b)

Fig. 2: (a) Six layer human head model designed in HFSS software and (b) side view of the six-layered head model.

Although the human head is more complex in structure, here a simple six-layer spherical model was considered to simplify the simulation. To design the six-layer spherical human head model, six spheres of different radiuses consisting entirely of materials with dielectric property of the human head tissues were used. The model contains six layers of skin, fat, bone (e.g. skull), dura, cerebrospinal fluid (CSF) and brain. A sphere of radius 80 mm as the human brain tissue was used. The modeled thickness of the skin, fat, skull, dura, CSF are assumed to be 1 mm, 1.5 mm, 4 mm, 0.5 mm, and 2 mm respectively. The dielectric properties of the materials used in head model at 3.7 kHz are shown in Table II.

TABLE II: DIELECTRIC PROPERTIES OF THE SIX LAYER HEAD MODEL [10]-[12]

| Layer name | Permittivity (F/m) | Conductivity (s/m) |
|---|---|---|
| Skin (dry) | 1130 | 0.000201 |
| Fat | 3820 | 0.0426 |
| Bone (skull) | 1080 | 0.0203 |
| Dura | 2030 | 0.501 |
| CSF | 109 | 2 |
| Brain (Grey matter) | 57200 | 0.127 |

## III. SIMULATION RESULTS AND PERFORMANCE ANALYSIS

Fig. 3(a)-(c) shows the electric field distribution due to the excitation of the coil across the different tissues of the head model. In order to determine the electromagnetic power absorbed by the tissues beneath the coil, a numerical analysis of SAR was performed at the frequency of 3.7 kHz. Fig.4 shows the graphical representation of magnitude of electric fields due to Fo8, circular and HFA coil respectively.

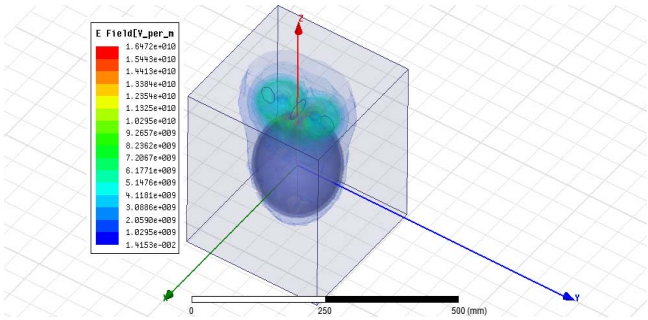


(a)

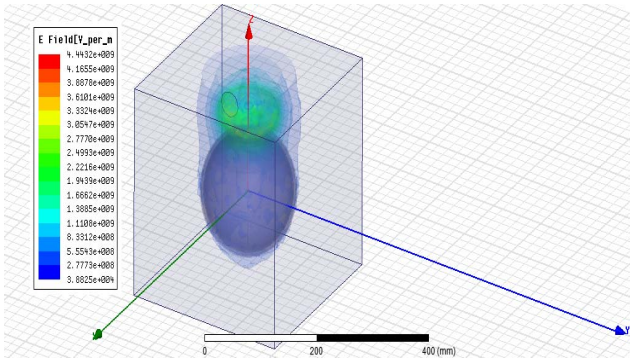


(b)

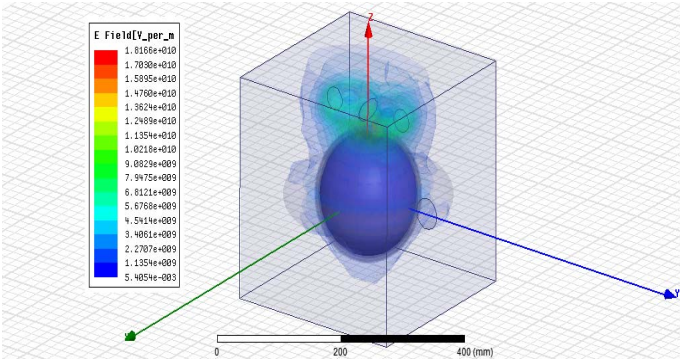


(c)

Fig.3: E-field distribution for (a) Fo8 coil (b) Circular coil and (c) HFA coil.

Fig.4 (a)-(c) presents the graphical representation of the magnitude of the electric field as a function of distance field. These graphical representations show that the magnitude of the E field for the Fo8 coil is maximum and for circular coil and HFA coil the values are almost equal. These figures also indicates that the E-field decreases with the distance from the coil and the maximum E-field distribution is obtained at the center of the distance line.

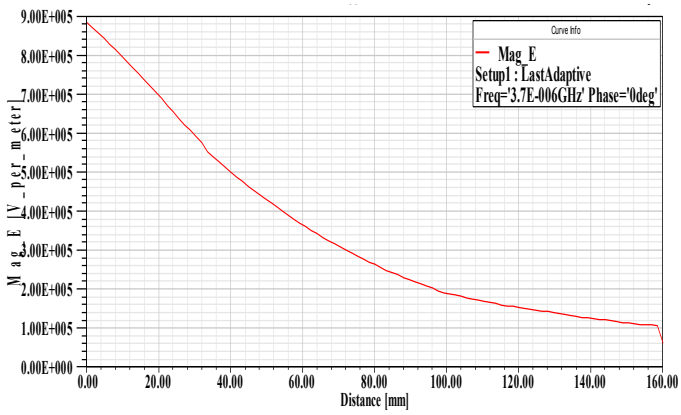


(a)

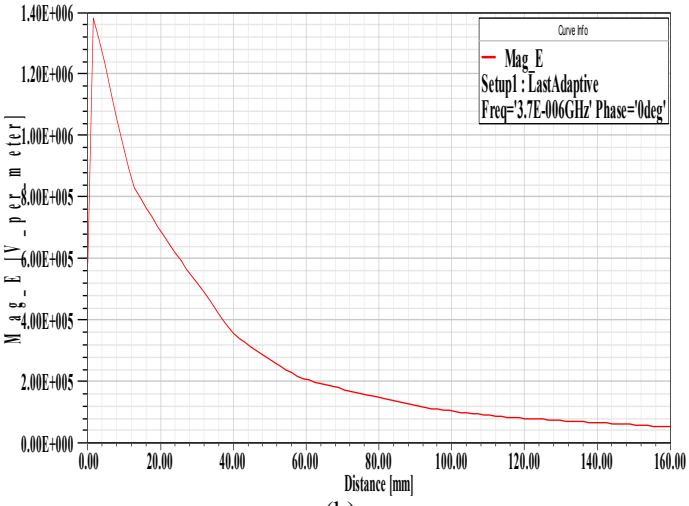


(b)

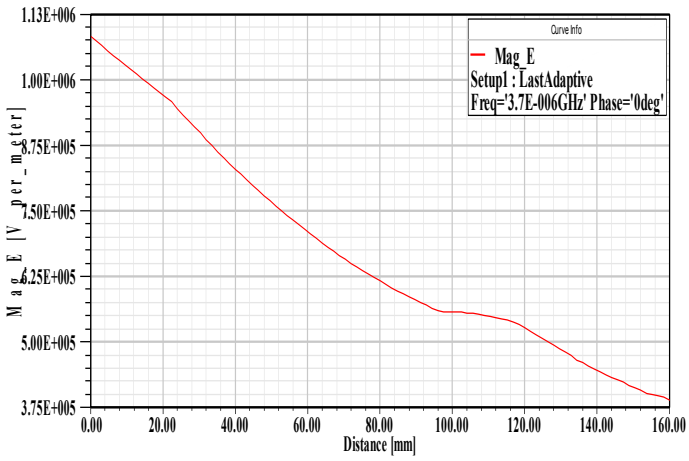


(c)

Fig.4: Magnitude of E-field distribution with respect to distance for (a) Fo8 coil (b) Circular coil and (c) HFA coil.

Fig. 5(a)-(c) presents a magnetic field of the three coils as a function of distance. For Fo8 coil the field amplitude decreases from a peak value of 7.00 kA/m. As from the circular coil the peak magnitude of the field is almost half in magnitude than that of the Fo8 coil (3.7kA/m). In the case of HFA coil, the magnitude is about 8.75kA/m. It can also be found from these

graphs that, the magnetic field in more concentrated in the HFA coil as compared to the other two coils.

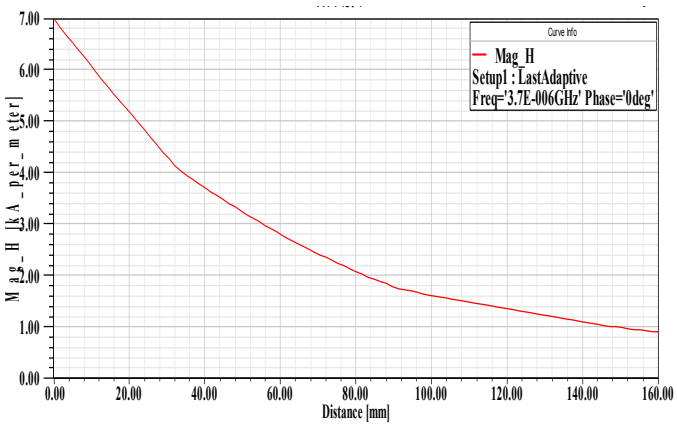


(a)

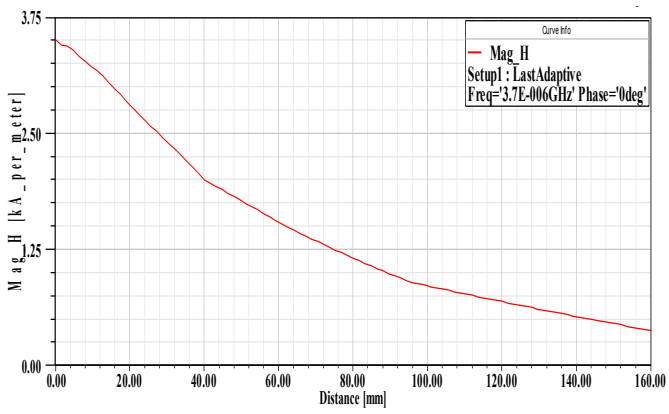


(b)

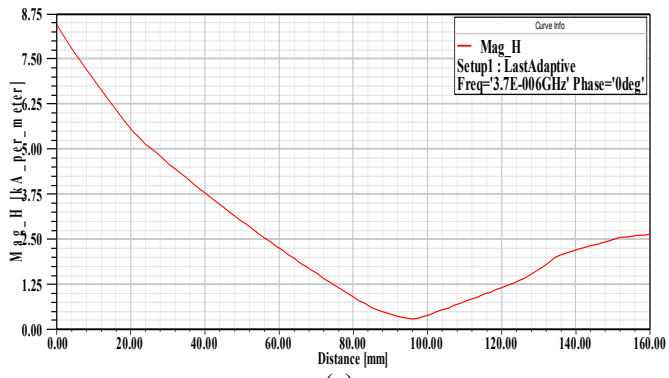


(c)

Fig.5: Magnitude of H-field distribution with respect to distance for (a) Fo8 coil (b) Circular coil and (c) HFA coil.

However, in Fig. 6(a)-(c) the current density of the three proposed coils have shown. It is observed from Fig. 6(a)-(c) that, the current density of HFA coil is 1.40e+005A/m$^2$ and decreases slowly and smoothly covering large distance. Whereas for both Fo8 coil and circular coil the peak value of the current densities are almost equal (approximately 1.20e A/m$^2$). But the difference is, for Fo8 coil the peak value has a slow decay as found form the graph as well, which is transient as for circular coil.

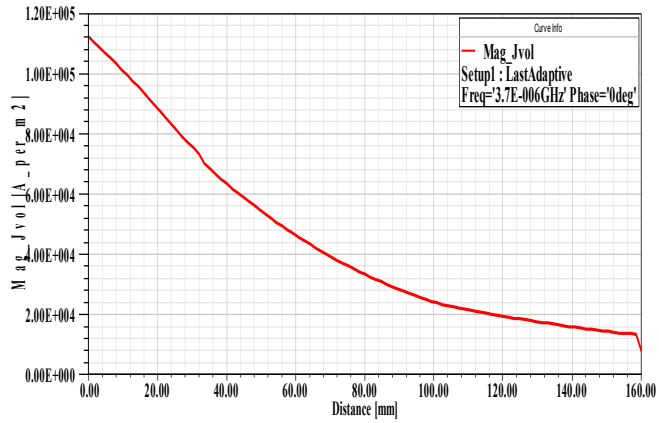


(a)

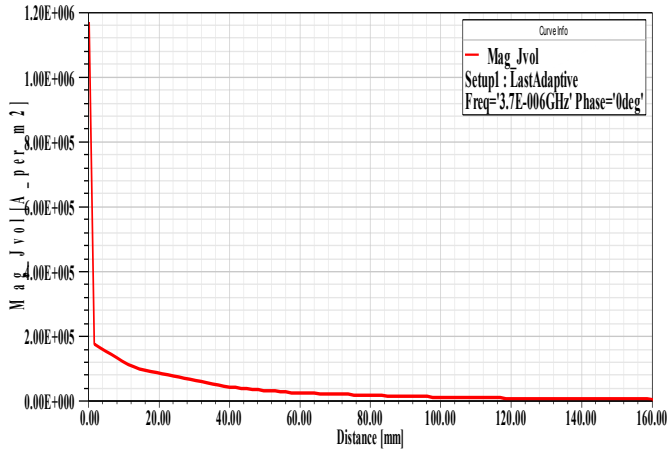


(b)

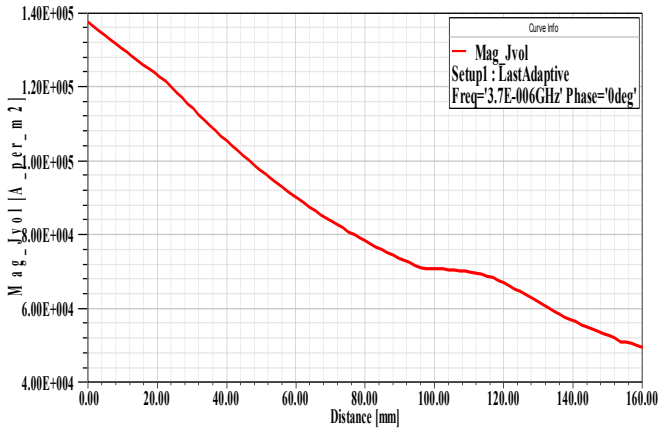


(c)

Fig.6: Magnitude of current density with respect to distance for (a) Fo8 coil (b) Circular coil and (c) HFA coil.

Fig. 7(a)-(c) shows the 3D near E field plot of the three proposed coils. The peak value of near E Total obtained is 3.6669e+005V, 2.3774e+005V and 9.3466e+005V for Fo8, circular and HFA coil respectively. Here, from the 3D near E field plot it can be observed that the value of the near ETotal for HFA coil is maximum as compared to Fo8 and circular coil.

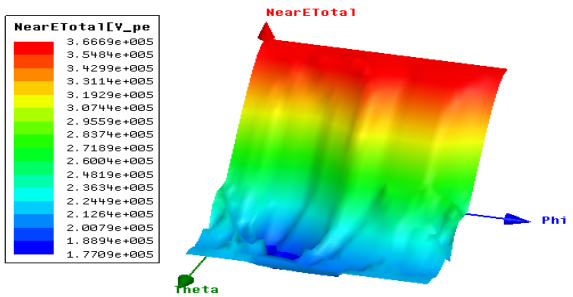


(a)

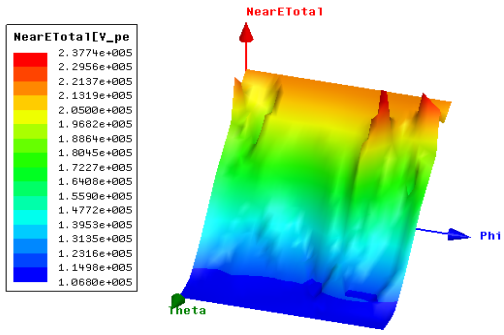


(b)

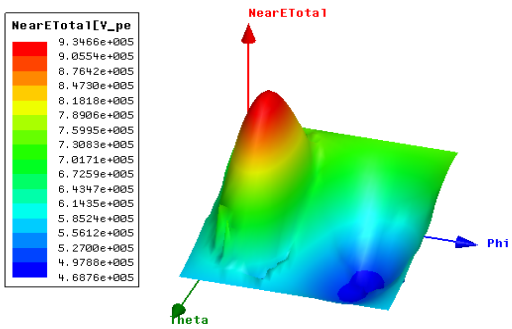


(c)

Fig.7: 3D rectangular near E field for (a) Fo8 coil (b) Circular coil and (c) HFA coil.

SAR is a measure of the amount of the EM energy absorbed by the biological tissue. The SAR is calculated by [13]:

$$SAR = \frac{\sigma}{\rho}|E| = \frac{J^2}{\sigma\rho}[W/kg] \qquad (1)$$

where $\sigma$ is the conductivity of the body tissue [S/m], $\rho$ is the density of body tissues [kg/m3], $E$ is the rms value of the electric field strength in the tissue [V/m], and $J$ is the current density [A/m]. It is observed from Equation (1) that the SAR is directly related to the electric field magnitude. Moreover, the value of SAR depends on the operating frequency, the coil type, and the distance between the coil and the body tissue.

However, as presented in Fig.8 (a)-(c) the local and average SAR plot as a function of distance from the coil is shown. The calculation of the local and average SAR is based on the electric field distribution. It is obvious that SAR is higher near the coil and then rapidly goes to zero after a short distance. It is also found that the highest peak value for the local and average SAR was obtained for HFA coil. The performance analysis shows that the HFA coil is more suitable for stimulating brain in deep cortical region. The HFA coil produces larger field penetration in deep brain regions. As for circular coil, the field strength decreases less rapidly as compared with conventional Fo8 and HFA coil. Most importantly it was observed that the E-field penetration depth formed by Fo8 coils can be further increased with the help of the Halo coil (HFA coil), although the stimulation focality of the E-field becomes poor.

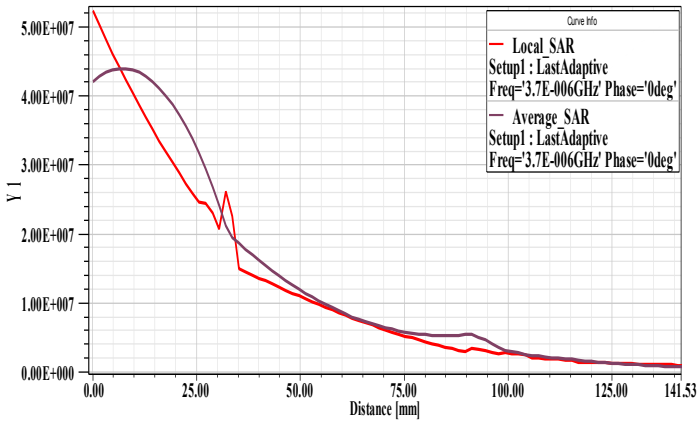


(a)

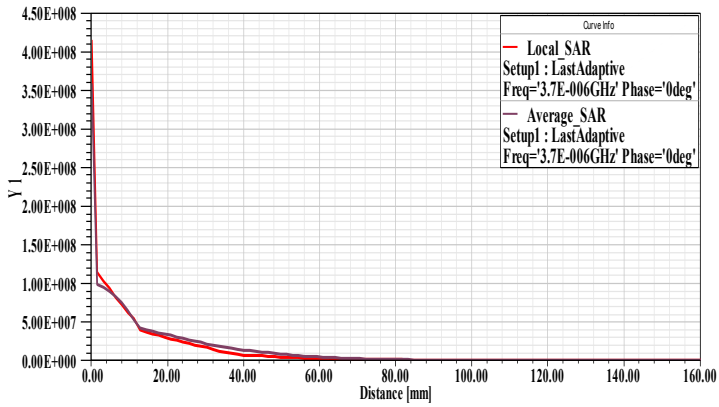


(b)

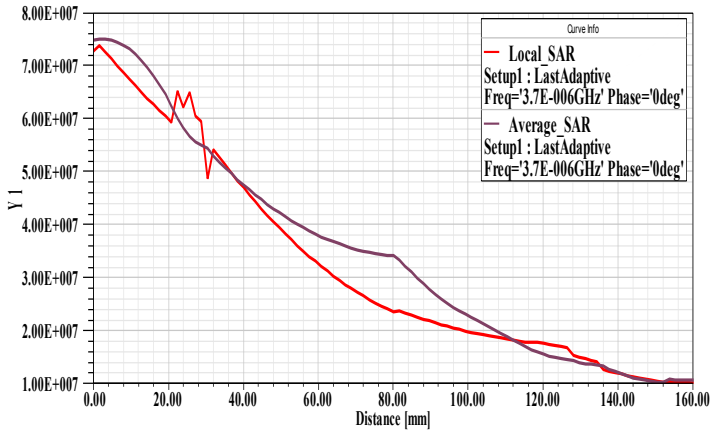


(c)

Fig.8: Local and average SAR variations at different coil-head distance in head model for (a) Fo8 coil, (b) Circular coil and (c) HFA coil.

## IV. CONCLUSION AND OBSERVATIONS

For the purpose of the beep brain stimulation (dTMS), the conventional Fo8 coil working with halo coil has been designed and numerically analyzed. The 3-D distribution of the electric and magnetic field intensity along with the current density in the human head phantom model due to Fo8, circular and HFA coil was obtained by impedance method. By changing the parameter of coil and frequency of phantom of human head model better penetration depth is obtained along with better and wider spreading electric field. Use of higher source value and then simulation gives better SAR than the work done before [14]-[15]. The improved field distribution and penetration depth was achieved by the HFA coil which provides stimulation of the brain in the deeper region than is achievable with the conventional Fo8 coil. As the human head phantom used for the simulation is homogenous rather than the inhomogeneous realistic human head model, the performance analysis may not be that much authenticated. The future work will intend to investigate the dependence of penetration depth and focality on different assembly of Fo8 coils with more precise evaluation of induced electric field to realize the focused stimulation in deep brain regions using realistic human head model.

## REFERENCES


[1] A.T. Barker, R. Jalinous and I.L. Freeston, "Non-invasive magnetic stimulation of human motor cortex," Lancet, vol.1, pp. 1106-1107, 1985.

[2] S. Ueno, T. Tashiro, and K. Harada, "Localized stimulation of neural tissues in the brain by means of a paired configuration of time-varying magnetic fields," J. Appl. Phys., vol. 64, no. 10, pp. 5862-5864, 1988.

[3] S. Ueno, T. Matsuda, and M. Fujiki, "Functional mapping of the human motor cortex obtained by focal and vectorial magnetic stimulation of the brain," IEEE Trans. Magn., vol. 26, No. 5, pp. 1539-1544, 1990.

[4] Groppa, S, et al.,"A practical guide to diagnostic transcranial magnetic stimulation: Report of an IFCN committee," J. Clin. Neurophysiology. 123 (5): 858–882.

[5] E. R. Lontis, M. Voigt, and J. J. Struijk, "Focality assessment in transcranial magnetic stimulation with double and cone coils," J. Clin. Neurophysiol., vol. 23, no. 5, pp. 462–471, 2006.

[6] Y. Roth, A. Zangen, and M. Hallett, "A coil design for Transcranial magnetic stimulation of deep brain regions," J. Clin. Neurophysiol., vol. 19, no. 4, pp. 361–370, 2002.

[7] L. J. Crowther, P. Marketos, P. I. Williams, Y. Melikhov, D. C. Jiles, and J. H. Starzewski, "Transcranial magnetic stimulation: Improved coil design for deep brain investigation," J. Appl. Phys., vol. 109, no. 7, p. 07B314, 2011.

[8] Y. Meng, R. L. Hadimani, L. J. Crowther, Z. Xu, J. Qu, and D. C. Jiles, "Deep brain transcranial magnetic stimulation using variable 'Halo coil' system," J. Appl. Phys., vol. 117, no. 17, p. 17B305, 2015.

[9] T. A. Wagner, M. Zahn, A. J. Grodzinsky and A. Pascual-Leone, "Three-Dimensional Head Model Simulation of Transcranial Magnetic Stimulation," IEEE Trans. Biomedical Engineering, vol. 51, pp. 1586-1598, Sep. 2004.

[10] C. Gabriel, S. Gabriel, and E. Corthout, "The dielectric properties of biological tissues: I. Literature survey," Physics in medicine and biology, vol. 41, p. 2231, 1999.

[11] S. Gabriel, R. Lau, and C. Gabriel, "The dielectric properties of biological tissues: II. Measurements in the frequency range 10 Hz to 20 GHz," Physics in medicine and biology, vol. 41, p. 2251, 1999.

[12] S. Gabriel, R. Lau, and C. Gabriel, "The dielectric properties of biological tissues: III. Parametric models for the dielectric spectrum of tissues," Physics in medicine and biology, vol. 41, p. 2271, 1999.

[13] N. A. Saidatul, A. A. H. Azremi, R. B. Ahmad, P. J. Soh, and F. Malek, "Multiband fractal planar inverted F antenna (F-PIFA) for mobile phone application," PIER B, vol. 14, pp. 127-148, 2009.

[14] M.Lu and S.Ueno, "Deep Transcranial Magnetic Stimulation Using Figure-of-Eight and Halo Coils," IEEE Trans. on Magn.,vol. 51, no. 11, Nov 2015.

[15] M.Lu, and S.Ueno, "Dependence of Electromagnetic Fields in Human Brain on Coil Bending Angle in Transcranial Magnetic Stimulation," XXXIth URSI General Assembly and Scientific Symposium (URSI GASS) IEEE, 2014.

2017 3rd International Conference on Electrical Information and Communication Technology (EICT), 7-9 December 2017, Khulna, Bangladesh

# SAR Reduction of Bio-tissue in Cellular Communication

Siddhartha Dey[1], Sourin Dey[2], Abu Shakil Ahmed[3], Md. Nurunnabi Mollah[4]
Khulna University of Engineering & Technology, Khulna-9203, Bangladesh
siddharthakuetece11@gmail.com[1], sourin21@gmail.com[2], shakil.ahmed.bd71@gmail.com[3], nurunnabim12@gmail.com[4]

*Abstract*—**Mobile phones are being used extensively for wireless communication, and its usage is proliferating day after day. Different radio frequencies are used in cellular communication between the mobile and the base stations. The electromagnetic radiation at Radio Frequency (RF) can have an adverse effect on bio-tissue. This paper has estimated the Specific Absorption Rate (SAR) of bio-tissue at 900 MHz and 1800 MHz as well as analyzed its variation for different distances. Moreover, an electromagnetic absorber has been placed between the cell phone and the bio-tissue in order to reduce the value of SAR for mitigating the harmful effect when the bio-tissue is exposed to electromagnetic radiation. The simulation result indicates the objective has been achieved since the observer has been able to decrease the value of SAR up to 96.06 percent and 77.39 percent at RF 900 MHz and 1800 MHz correspondingly.**

***Keywords—SAR, RF, Electromagnetic radiation, Microstrip patch antenna, Bio-tissue.***

## I. INTRODUCTION

The electromagnetic radiation is the formation of electric and magnetic energy that propagates through space at the speed of light. Transmission of radio waves from antenna produces the electromagnetic radiation which is detrimental to the human body as the bio-tissue is prone to absorb the electromagnetic radiation. The quantity of radiation absorption can be expressed by Specific Absorption Rate (SAR). Analyzing the value of SAR provides us information about the maximum permissible exposure of bio-tissue to electromagnetic radiation as per Federal Communications Commission (FCC). SAR testing is the measurement of electric field exists in various parts of our body due to exposure to the RF. The value of SAR is affected by the distance of its source from the living organisms. Therefore, SAR can be determined by measuring the strength of the electromagnetic field in different parts of our body with a variation in the distance while the source, i.e., a cell phone, in this case, radiates with its highest power level at the operating frequency. Researchers have proposed different techniques to determine SAR and undertaken various approaches in order to restrict its value within the permissible limit of FCC. P. Dutta et al. have used different kinds of Shields to restrict the SAR below an acceptable limit and determined its distribution in various layers of the head. They have concluded that proper choice of material can improve shielding performance and observed that materials having conductivity range between 0.1 to 3 $Sm^{-1}$ are suitable for this purpose [1]. N. Karmakar et al. and S. Hassan et al. have shown many designs of electromagnetic bandgap structures (EBGSs) that are capable of producing wider and deeper stop band as well as shown different applications of EBGSs. [2-4]. S. Kwak et al. have employed electromagnetic bandgap structure (EBGS) and inserted it in the cellphone with a view to reducing the exposure to the electromagnetic fields as well as decreasing the value of SAR [5]. L. Ungureanu et al. have investigated the effects of heat produced by the electromagnetic radiation of cell phone for lengthy conversation and attempted to reduce the harmful effect of it by placing an absorber inside the cell phone [6]. O. Jonah et al. have conducted an experiment in order to determine the effect of electromagnetic radiation on different kinds of human tissue for variable distances between the source of the radiation and the tissues [7]. A. Pradier et al. have accessed the rate of SAR for various tissues of the body under five different frequencies such as 300 MHz, 450 MHz, 900 MHz, 1800 MHz, and 2100 MHz by using integral equations [8]. Mai Lu et al. have applied Finite Difference Time Domain (FDTD) method for the assessment of SAR and evaluated the adverse effects of electromagnetic radiation for RF. After evaluation of the SAR values, they have concluded that endocrine glands are most severely affected by the radiation [9]. T. Wu et al. have been evaluated Tissue Specified Specific Absorption Rate (TSSAR) of two different sets of tissues such as tissues from 12 months old infant and 22 years old Chinese female as samples. They have fit the models using principal component regression method and applied Principal Component Analysis (PCA) to simplify the procedure. The study suggests that connectivity of tissues contribute saliently for the evaluation of TSSAR [10]. N. Kumaran et al. have focused on reducing SAR by incorporating a wideband and miniaturized Frequency Selective Surface (FSS) having a high insertion loss that ranges from 0.5 GHz to 6 GHz. The proclaimed reduction of SAR is stated to be 52 percent at 1800 MHz frequency [11]. S. Kwak et al. have used a Planner Inverted-F Antenna (PIFA) in order to reduce SAR and advised to wear a wireless device with a view to lessening the exposure to electromagnetic radiation [12]. In this paper, SAR of bio-tissue has been estimated, its variation has been analyzed with distances, and an absorber has been utilized to reduce it.

The paper is organized in five sections. In Section II, the methodology has been elaborated with a key concentration of reducing SAR. In section III, the simulation works have been presented. In Section IV, a comparative analysis has been presented to justify the contribution of the absorber, and the

978-1-5386-2307-7/17/$31.00 ©2017 IEEE

outcomes have been clarified. Section V contains the conclusion of the paper.

## II. METHODOLOGY

The primary concentration of this paper is to reduce the value of SAR. Two different frequencies are used for cellular communication such as 900 MHz and 1800 MHz. Therefore, a microstrip patch antenna has been designed with a dimension of 46*36mm$^2$ for both of the frequencies to estimate the impact of emitted electromagnetic radiation on bio-tissue. The bio-tissue has been designed with a radius of 74.75 mm, the density of 1100 kgm$^{-3}$, the thermal conductivity of 0.293 Wm$^{-1}$K$^{-1}$, the specific heat of 3.5 kJkg$^{-1}$K$^{-1}$, the diffusivity of 7.61039*10$^{-8}$ m$^2$s$^{-1}$, blood flow of 9100 WK$^{-1}$ m$^{-3}$, and metabolic rate of 1620 Wm$^{-3}$. When people talk over the cell phone, they usually keep it as close as possible to the ear. However, the distance differs from person to person. Hence, varying the distance between the bio-tissue and the patch antenna starting from 0 mm up to 16 mm with a view to analyzing the variation in SAR with the change in distance. This procedure has been conducted at both 900 MHz and 1800 MHz frequency. An electromagnetic absorber is placed between the microstrip patch antenna and bio-tissue to reduce the value of SAR. The measurement process of SAR for both of the frequencies has been repeated after placing the absorber to evaluate its effectiveness for mitigation of the adverse effect caused by electromagnetic radiation. The procedure of the research work has been shown in the form of a flowchart in Fig. 1.

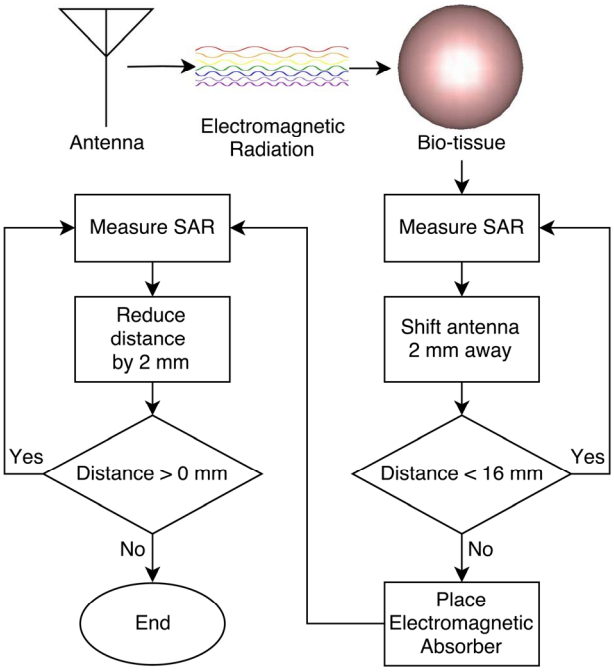


Figure 1. Algorithm of operation.

SAR depends on the internal electric field, electric conductivity, and the density of the medium. The value of SAR can be calculated from (1) [13].

$$\mathrm{SAR} = \frac{\sigma\,|E|^2}{\rho} \tag{1}$$

Here E denotes the internal electric field, σ denotes the electric conductivity (Sm$^{-1}$), and ρ denotes the density of the medium (kgm$^{-3}$).

## III. SIMULATION

In this section, microstrip patch antenna and a bio-tissue is designed as well as analyzed the impact of electromagnetic radiation originated at two different radio frequencies such as 900 MHz and 1800 MHz by measuring the value of SAR. Moreover, an absorber is placed between the antenna and bio-tissue after configuring it properly to reduce the adverse effect of electromagnetic radiation. CST STUDIO SUITE is used for the design and simulation. Initially, the antenna is placed as close as possible to the bio-tissue, and in practice, the distance has been maintained as 0 mm. The antenna has been shifted gradually away from the bio-tissue up to 16 mm to measure the effect of distance on SAR. In CST, parameter sweep method has been applied to displace the antenna from the initial position (0 mm) to the farthest distance (16 mm) from the bio-tissue with a step width of 2 mm. Fig. 2 represents the design of microstrip patch antenna with the dimension of 46*36 mm$^2$ where the x-axis indicates v, and the y-axis indicates u i.e., the antenna has been designed on the v-u plane.

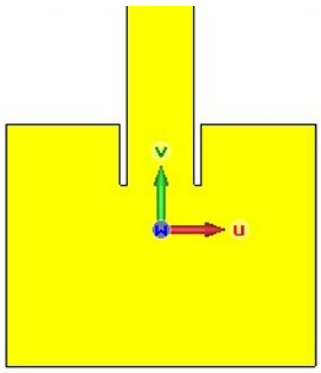


Figure 2. Microstrip patch antenna.

Fig. 3 displays the initial placement of the antenna when it is adjacent to the bio-tissue. The bio-tissue has been designed on the v-w plane as the x-axis represents w, and the y-axis represents v.

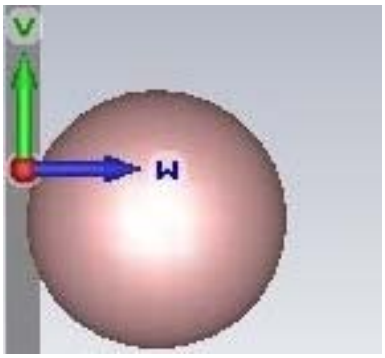


Figure 3. Placement of the antenna at 0 mm distance from the bio-tissue.

Fig. 4 presents a pictorial view of the sweep parameters. Here, linear sweep method is applied where the starting and

ending values are 0 and 16 respectively. The incremental value or the step width has been set 2.

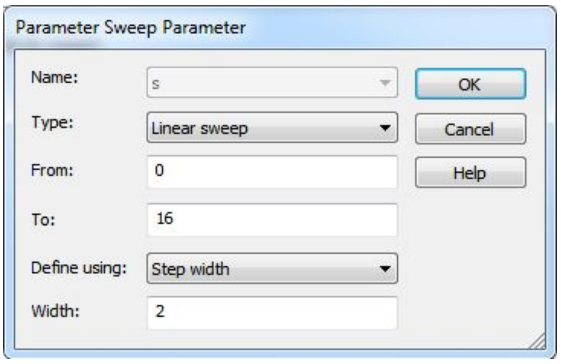


Figure 4. Sweep parameters.

Fig. 5 shows the final position of the microstrip antenna after shifting it 16 mm away from the bio-tissue.

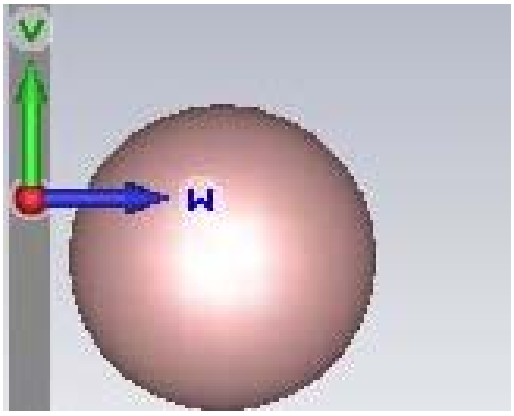

Figure 5. Final position of the antenna at 16 mm away from the bio-tissue.

While applying the sweep method for both 900 MHz and 1800 MHz frequencies, the value of SAR is determined for every 2 mm and plotted the curve shown in Fig. 6 and Fig. 7. The distance between the microstrip patch antenna and the bio-tissue has been represented by the horizontal axis as well as the vertical axis represents the corresponding values of SAR. It is observed that in Fig. 6 the value of SAR is the maximum for the distance 0 mm, and it decreases sharply until the antenna is shifted 2 mm apart from the bio-tissue. After 2 mm, the value of SAR decreases at a very negligible rate.

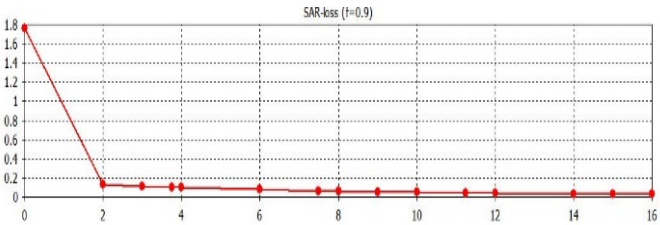


Figure 6. Variation in SAR with distance at RF 900 MHz.

The value of SAR has been observed to be higher at 1800 MHz frequency than 900 MHz as per Fig. 7. Therefore, it is evident that the value of SAR increases with the increase in frequency. In Fig. 7, SAR decreases sharply between 0 and 2 mm distance as well as the rate of decline gradually becomes less steep beyond 2 mm.

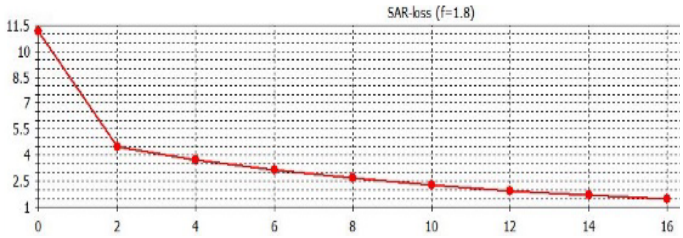


Figure 7. Variation of SAR with distance at RF 1800 MHz.

After determination of SAR for both 900 MHz and 1800 MHz frequencies, we have attempted to reduce SAR by placing an absorber between the microstrip antenna and the bio-tissue in order to mitigate the harmful effects of electromagnetic radiation. An electromagnetic observer of ECCOSORB MCS model is used from the material library of CST STUDIO SUITE 2011. Fig. 8 shows the placement of the electromagnetic absorber between the microstrip antenna and the bio-tissue.

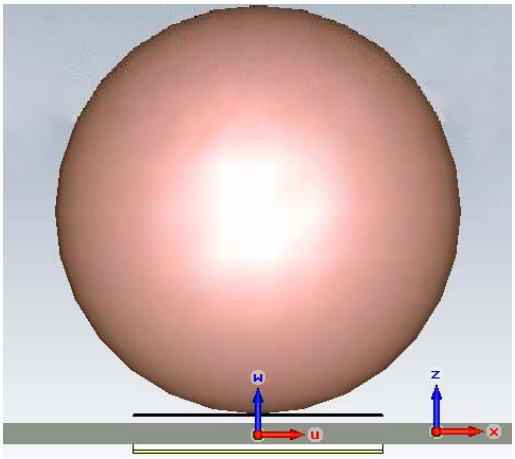

Figure 8. Placement of an electromagnetic absorber between the microstrip antenna and the bio-tissue.

Fig. 9 exhibits the variation in SAR with altering distances from 0 mm to 16 mm at 900 MHz frequency after the placement of an electromagnetic absorber. The placement of the absorber in between the microstrip antenna and the bio-tissue offers significant reduction of SAR. Without using the absorber, the value of SAR has been observed to have sharp decrease until the antenna is shifted to 2 mm apart from the bio-tissue and beyond 2 mm, the value of SAR decreases at a very negligible rate. Therefore, the bio-tissue is pretty vulnerable for the proximity of cell phone in the absence of an absorber. The harmful effect has been reduced significantly using the absorber since it keeps the value of SAR considerably low. However, the absorber cannot reduce the SAR further with the increase in distance unlike the scenario when it is absent instead it keeps the SAR constant for a distance of extended range. Our observation validates this phenomenon as the value of SAR remains constant throughout the simulation for the distance from 0 mm to 16 mm.

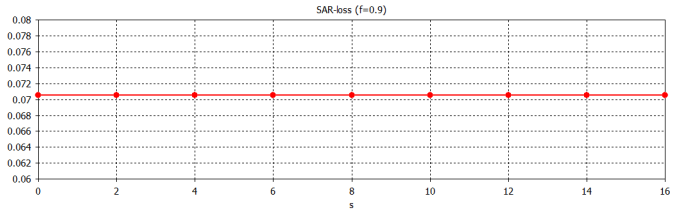


Figure 9. Variation of SAR with distance at RF 900 MHz using absorber.

Fig. 10 exhibits the variation in SAR with variable distances in between 0 mm and 16 mm at 1800 MHz frequency after the placement of an electromagnetic absorber.

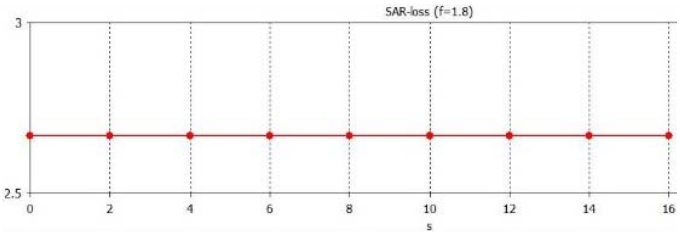


Figure 10. Variation of SAR with distance at RF 1800 MHz using absorber.

Without using the absorber, the value of SAR has been detected to be higher at 1800 MHz frequency than 900 MHz, and it decreases sharply between 0 and 2 mm distance as well as the rate of decrease gradually becomes less steep beyond 2 mm. The harmful effect on the higher value of SAR has been reduced substantially using the absorber at both of the RF frequencies. The absorber maintains a constant value of SAR throughout the simulation despite the variation in distance.

## IV. Outcomes

The work has simulated the designed scenario using the parameter sweep method and obtained a downward slope of SAR for the increment of distance for both 900MHz and 1800MHz frequency. The maximum value of SAR has been observed 1.8 $Wkg^{-1}$ and 11.5 $Wkg^{-1}$ at 900 MHz and 1800 MHz frequency respectively at 0 mm distance where the antenna has been placed initially. A sharp decrease in SAR has been recorded up to 2 mm from the origin, and the slope of curve is negative i.e. the value of SAR decreases with the increase in distance between the antenna and the bio-tissue. In the second step, the value of SAR is determined after placing the electromagnetic absorber between the microstrip patch antenna and the bio-tissue. SAR has been observed to be constant throughout the range of distance, and it has been determined 0.071 $Wkg^{-1}$ and 2.6 $Wkg^{-1}$ respectively at 900 MHz and 1800 MHz. Therefore, the placement of an electromagnetic absorber is capable of reducing the value of SAR significantly though its efficiency decreases with the increase in distance. The maximum efficiency has been noted 96.06% and 77.39% correspondingly for 900 MHz and 1800 MHz at a distance 0 mm. Thus, it is evident that the electromagnetic absorber is more efficient for reducing the value of SAR at low frequency and its efficiency decreases when the frequency increases. The data recorded during simulation has been presented in TABLE I and TABLE II for both of the microstrip antennas.

TABLE I. SAR for 900 MHz Microstrip Patch Antenna

| Distance (mm) | SAR (without Absorber) ($Wkg^{-1}$) | SAR (with absorber) ($Wkg^{-1}$) | %Decrement in SAR |
|---|---|---|---|
| 0 | 1.8 | 0.071 | **96.06%** |
| 2 | 0.2 | 0.071 | 64.50% |
| 4 | 0.19 | 0.071 | 62.63% |
| 6 | 0.18 | 0.071 | 60.55% |

TABLE II. SAR for 1800 MHz Microstrip Patch Antenna

| Distance (mm) | SAR (without Absorber) ($Wkg^{-1}$) | SAR (with absorber) ($Wkg^{-1}$) | %Decrement in SAR |
|---|---|---|---|
| 0 | 11.5 | 2.6 | **77.39%** |
| 2 | 4.3 | 2.6 | 39.53% |
| 4 | 4 | 2.6 | 35% |
| 6 | 2.8 | 2.6 | 7.14% |

## V. Conclusion

The key concentration of this paper is to reduce the harmful effect of electromagnetic radiation upon bio-tissue. SAR indicates the rate of energy absorption by the bio-tissue for its exposure to an electromagnetic field created by Radio Frequency (RF). Hence, the reduction of SAR in practice decreases the adverse effect of electromagnetic radiation upon bio-tissue. In this research work, an electromagnetic absorber has been employed to serve this purpose. The simulation result indicates the objective has been achieved since we have been able to decrease the value of SAR up to 96.06 percent and 77.39 percent at RF 900 MHz and 1800 MHz respectively. Therefore, it is evident that the electromagnetic absorber is useful to protect the bio-tissue up to a certain extent.

## References

[1] P. Dutta, P. Jayasree and V. Baba, "SAR reduction in the modelled human head for the mobile phone using different material shields", Human-centric Computing and Information Sciences, vol. 6, no. 1, 2016.

[2] N. Karmakar and M. Mollah, "Investigations into nonuniform photonic-bandgap microstripline low-pass filters", IEEE Transactions on Microwave Theory and Techniques, vol. 51, no. 2, pp. 564-572, 2003.

[3] S. Hassan, S. Anayetullah and M. Mollah, "Sinusoidal appearance of nonuniform dumbbell shape EBGSs in microstrip transmission line", 2013 International Conference on Electrical Information and Communication Technology (EICT), 2014.

[4] N. Karmakar, M. Mollah and S. Padhi, "Photonic bandgap assisted aperture coupled patch antennas", IEEE Antennas and Propagation Society International Symposium (IEEE Cat. No.02CH37313).

[5] S. Kwak, D. Sim, J. Kwon and H. Choi, "Experimental tests of SAR reduction on mobile phone using EBG structures", Electronics Letters, vol. 44, no. 9, p. 568, 2008.

[6] L. Ungureanu, L. Cristea, M. Baritz and D. Cazangiu, "The heating level analysis of facial tissue during the exposure of electromagnetic radiations provided from a mobile phone", 2013 E-Health and Bioengineering Conference (EHB), 2013.

[7] O. Jonah and S. Georgakopoulos, "Specific Absorption Rate (SAR) distribution in human tissue with magnetic resonance", Proceedings of

the 2012 IEEE International Symposium on Antennas and Propagation, 2012.

[8] A. Pradier, D. Lautru, M. Wong, V. Hanna and J. Wiart, "Rigorous Evaluation of Specific Absorption Rate (SAR) Induced in a Multilayer Biological Structure", The European Conference on Wireless Technology, 2005.

[9] Mai Lu and Xiao-Yan Wu, "Study of specific absorption rate (SAR) induced in human endocrine glands for using mobile phones", 2016 Asia-Pacific International Symposium on Electromagnetic Compatibility (APEMC), 2016.

[10] T. Wu and C. Li, "Statistical evaluation of the tissue specified specific absorption rate using principal component regression", 2017 11th European Conference on Antennas and Propagation (EUCAP), 2017.

[11] N. Kumaran and K. Arunachalam, "A wideband non-resonant FSS with finite number of unit cells for mobile phone SAR reduction", 2016 International Conference on Electromagnetics in Advanced Applications (ICEAA), 2016.

[12] S. Kwak, D. Sim, J. Kwon and Y. Yoon, "Design of PIFA With Metamaterials for Body-SAR Reduction in Wearable Applications", IEEE Transactions on Electromagnetic Compatibility, vol. 59, no. 1, pp. 297-300, 2017.

[13] D. Le, L. Hamada, S. Watanabe and T. Onishi, "A Fast Estimation Technique for Evaluating the Specific Absorption Rate of Multiple-Antenna Transmitting Devices", IEEE Transactions on Antennas and Propagation, vol. 65, no. 4, pp. 1947-1957, 2017.

# Performance Analysis of a Modified Implantable PIFA Operates at MICS Band For Human Head Phantom Model

Sadia Sultana[1], M Mohiuddin Miran [2], Sk Md Asif Uddin[3], Md. Mahmudun Naby [4], Mahmudul Haque [5]
Department of EEE, American International University – Bangladesh.
Dhaka, Bangladesh.
E-mail: sadiakhl02@gmail.com, miran.dhk@gmail.com, smasifp3@gmail.com,mahmudunnabyemon0@gmail.com, ankonhaque@gmail.com,

*Abstract*— **A modified design and implantable planar inverted F-antenna is examined in this paper. This design structure can be applied to improve antennas for various implantation scenarios and biomedical applications. The proposed antenna is designed for human head (scalp) phantom and analyzed the performance in bio-environment. This flexible PIFA is operated at Medical Implant Communication Service (MICS) Band (402-405 MHz). MICS band has been chosen because of its tractability towards higher bandwidth with the reducing size of the antenna. By introducing a miniature expansion, the proposed antenna gives a better resonant performance for the head phantom model. The antenna is chosen a meandered strategy for design methodology. The ultimate design has the actual dimension of 20 x 24.4mm$^2$. This paper has monitored the results of the radiation pattern, return loss, gain at operation frequency by stabilizing all the electrical properties human tissue. All the calculations and performance measurement of this antenna have been evaluated by using CST Microwave Studio. Finally, the specific absorption rate is tested to satisfy with the antenna safety concern.**

***Keywords— PIFA, implantable, MICS band, human head phantom, specific absorption rate (SAR).***

## I. INTRODUCTION

Antennas are recently used to execute an increasing variety of diagnostic and medicinal functions in biomedical applications. To communicate wirelessly with exterior equipment, an antenna has been shortened the labor of human nursing struggle. So with the help of intra-body communication system, implantable antenna preserves patient comfort [1]. Nowadays, the implantable antenna has drawn much interest to perform various type of tumor detection due to its accuracy and resolution. To establish the proper depth that signals can penetrate into human tissues and resolution of the image, the bandwidth of antenna should be wide enough to fulfill the requirement. Modern investigations on antenna based tumor detection have been growing advanced. This paper represents such a type of antenna which analysis the radiation performance of human head phantom and propose for brain wave sensing for the paralyzed, brain tumor and brain edema evolution monitoring purpose [2].

PIFA is widely used for the medical application due to its broad bandwidth, low backward radiation and polarization properties. This antennas are attractive for their well-known efficient features such as compatibility with multiband and wideband operation, light weight, less fragile, low profile etc. So, planar inverted F-antennas are highly preferable for biomedical applications as a wearable on body device. Because of its less electromagnetic wave absorption aspect and easy fabrication PIFA can be suggested over the current methods.

MICS band is used for diagnostic and medical purposes for its Reasonable signal propagation characteristics in the human body. This bands include short-range which link to connect low-power implanted therapeutic equipment with monitoring and control instruments. Implanted Medical Devices (IMD) such as cardiac pacemakers, implantable cardioverter/ defibrillator (ICD), neurostimulators that help restore sensation, mobility, and other functions to limbs and organs [5]. In 1999 FCC established of Medical Implant Communication Service band or MICS at 402-405MHz spectrum for IMD. In 2009, FCC added additional spectrum at 401-406 MHz [7] and created the Medical Device Radio communications Service (MedRadio) frequency distribution.

On the other hand wireless local area networks (WLAN) system, as well as emerging applications such as mobile technology, satellite links (GPS), radio technology, tablet computers (such as Bluetooth, GSM & Wifi) often require antennas with low cost, compactness, thus requiring planar technology [4]. Due to reduced size and easy to integrate, the covenance of PIFA antennas in mobile communication is increasing.

In this paper, the parameters have been measured of the antenna such as return loss, resonant frequency, Far field region, radiation efficiency, Voltage standing wave ratio for a human head (scalp) phantom model. Finally, SAR has analyzed whether the antenna is safe to be implanted human head as wearable on body device.

## II. Antenna Model And Design Specification

A compact PIFA is proposed here for head phantom implementation. A flexible rectangular shaped quarter wave

978-1-5386-2307-7/17/$31.00 ©2017 IEEE

length patch antenna is designed by CST Microwave Studio. The geometry of proposed antenna is calculated using the equation is given below [8],

$$W=c/2f_0\sqrt{((\varepsilon_r+1)/2)} \quad (1)$$

$$\varepsilon_{reff} =( \varepsilon_r +1)/2 +( \varepsilon_r -1)/2[1+12h/W]^{-1/2} \quad (2)$$

$$L_{reff} =c/(2f_0\sqrt{\varepsilon_{reff}}) \quad (3)$$

$$\Delta L=0.412h(\varepsilon_{reff} +0.3)((W/h)+0.264)(\varepsilon_{reff} -0.258) *(W/h +0.8) \quad (4)$$

$$L= L_{eff}-2 \Delta L \quad (5)$$

$$Lg= 6h + L \quad (6)$$

$$Wg= 6h + W \quad (7)$$

Here, fo= Resonant frequency, c= speed of light=3x10^8m/s, Ɛr = Relative permittivity = 10.2, W= width of patch, L= length of patch. h= height of substrate, Ɛreff= effective dielectric constant, Leff=effective length of the patch, ΔL= length extension, Wg= width of ground plane, Lg= length of ground plane.

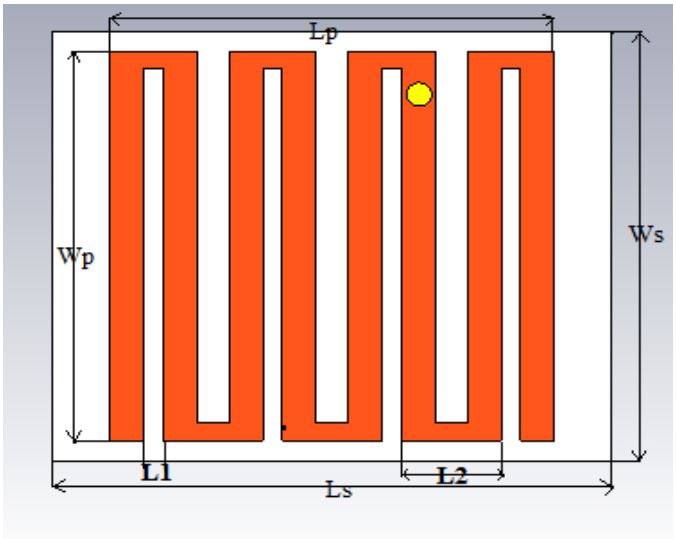


(a)

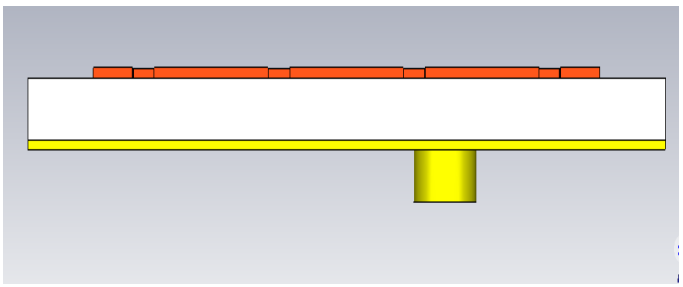

(b)

Figure 1. Model of the Antenna : (a) Front veiw ; (b) Side veiw

In figure 1 the antenna is designed on CST Microwave studio where MICS (402-405 MHz) band is used as the operating frequency. RO3210 is used as the substrate material where substrate length, Ls= 24.4mm and substrate width, Ws=20mm, respectively. Copper is used as the patch and ground plane. Patch length and width are Lp=19.4mm and Wp=18.10mm respectively. To improve desired resonant frequency, other parameters have been changed from the reference model [8]. In order to accomplish excellent performance of the antenna, eight strips planar inverted F-antenna is designed and three-layer structure is employed. The thickness of the substrate is, Tsub =1.25mm and relative permittivity is 10.2. A shorting pin with radius 0.07mm and a feed point radius 0.55mm are attached to the antenna structure. The size of the antenna is miniaturized and its directivity is enhanced using a proper meandered technique.

TABLE I. ANTENNA SIZE PARAMETER

| Parameters | Size (mm) |
|---|---|
| Ws | 20mm |
| Ls | 24.4 |
| Wp | 18.10 |
| Lp | 19.4 |
| L1 | 0.8 |
| L2 | 4.39 |
| Tsub(substrate thickness) | 1.25 |
| Rs(shorting pin radius) | 0.07 |
| Rf (feed point radius) | 0.55 |

## III. SIMULATION AND RESULT ANALYSIS

At first the antenna is simulated in free space of CST Microwave studio and then it is tested on head phantom model for examining the analysis onwards. 50 ohms is set as input impedance to calculate the study.

### *A. Simulated Result in free space*

In figure 2, the S11 parameter of the antenna is -13.19 dB at resonance frequency 404MHz. S11 parameter is also known as return loss or reflection coefficient. The reflection coefficient or return loss is a parameter that specifies how much of an electromagnetic wave is reflected by an impedance discontinuity in the transmission channel. So it is used to calculate the amount of power is reflected by an antenna.

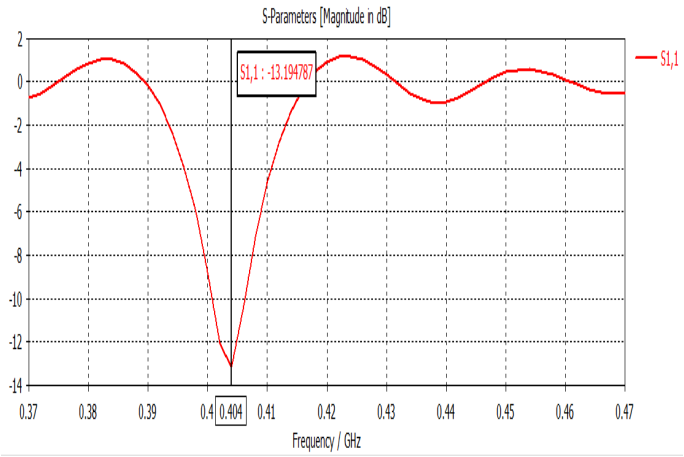


Figure 2. S11 parameter of the antenna in free space.

In figure 3, the 2D view of far field region of the antenna in free space. The main lob magnitude of the antenna is -0.998 dBi. It is centered with 88 degree and angular width is 160.6 degree. And figure 4 illustrates the directivity of the antenna in free space is -0.1909 dBi and radiation efficiency is -37.48 dB at operating frequency 404 MHz.

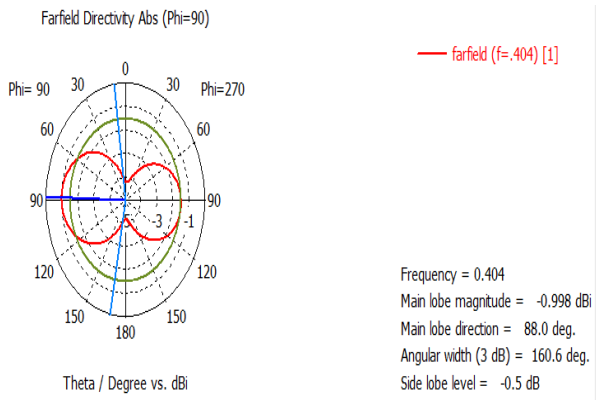


Figure 3. 2D veiw of far field region of the antenna in free space

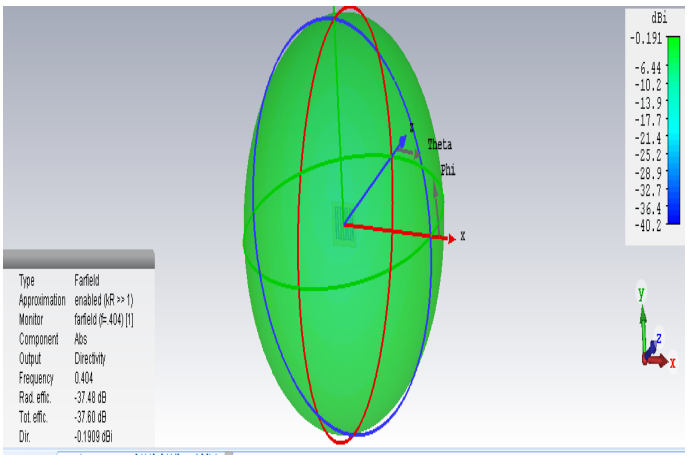


Figure 4. 3D veiw of far field region of the antenna in free space

## B. *Simulated Result on human head phantom*

This PIFA is constructed as wearable antenna with a low profile, simple structure and easy to wear on human head. From figure 5, it shows that antenna is placed on the human head (scalp) phantom model.

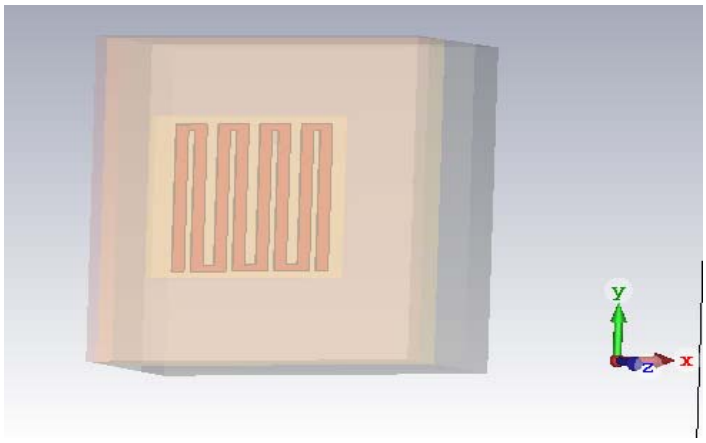

Figure 5. Transparent view of Implanted Antenna of human Head phantom model

The human head phantom model is constructed by using CST software which is anatomically representative. The four layers homogenous head phantom model is consisted with Skin, Fat, Skull (bone), and brain. Table II describes the eletrical properties of tissue at operating frequency 404MHz [6].

TABLE II. TISSUE PROPERTIES AND THICKNESS OF FOUR LAYER GEOMETRIC HUMAN HEAD PHANTOM MODEL

| Tissue | Permittivity | Conductivity (S/m) | Density (Kg/m$^3$) | Thickness (mm) |
|---|---|---|---|---|
| Skin | 46.75 | 0.68 | 1090 | 3 |
| Fat | 5.58 | 0.041 | 910 | 4 |
| Bone (skull) | 12.15 | 0.091 | 1850 | 8 |
| Brain | 49.68 | 0.59 | 1030 | 5 |

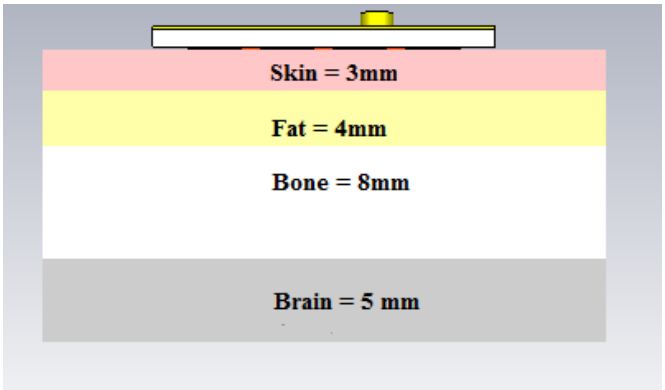


Figure 6. Antenna is tested on four layer geometric human head phantom model

From figure 7, S11 parameter of the antenna is estimated. The antenna has a return loss -17.29 dB which is operated at resonance frequency at 404MHz. The return loss or reflection coefficient should be kept less than -10dB, otherwise almost 90% of the energy is radiated. Return loss or S11 parameter of an antenna indicates the amount of power radiated and reflected from the antenna [10]. The bandwidth is found around 57dB of the antenna using RO3210 substrate material of human phantom model.

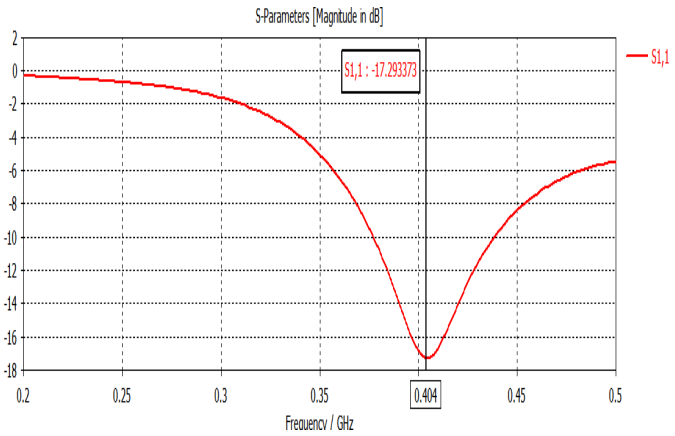


Figure 7. S11 parameter of the antenna of human head phantom model

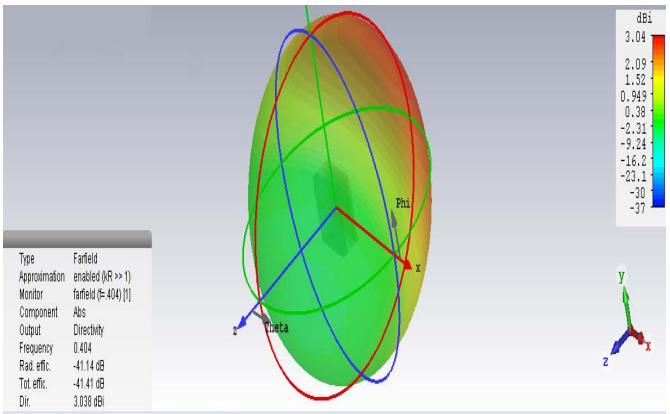


Figure 8. 3D veiw of far field region of the antenna for human head model

From figure 8 shows the 3D view of far field region of the antenna for human head phantom model. This figure shows the directivity is 3.038 dBi and radiation efficiency is -41.14 dB at operating frequency 404 MHz. On the other hand figure 9 demonstrates the 2D view or polar view of the antenna where the main lob magnitude is 2.61 dB. It is centered with 111 degree and angular width is 252.7 degree. The maximum gain of this antenna is -38.09 dBi.

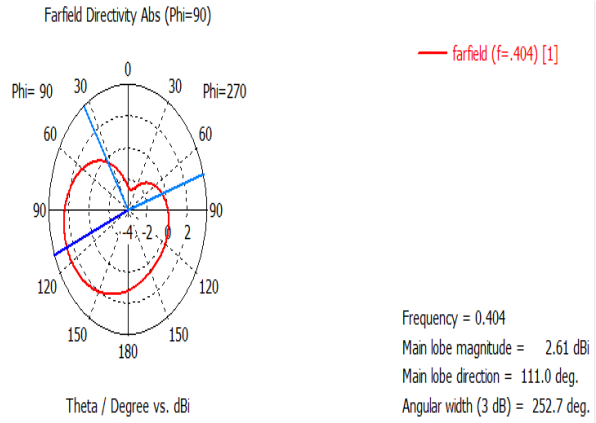


Figure 9. 2D veiw of far field region of the antenna for human head model

From figure 10 shows the voltage standing wave ratio (VSWR) which is found 1.34 at resonance frequency 404 MHz. So it gives a satisfactory output and impedance is matched properly.

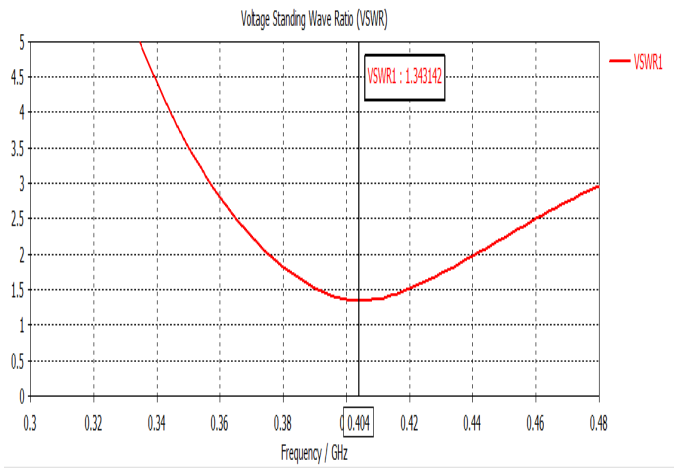


Figure 10. VSWR value of the antenna for human head model

The specific absorption rate (SAR) is the size associated with the absorption of electromagnetic radiation by biological tissues and based on which safe exposure limits for electromagnetic radiation frequencies. SAR is the largest size to quantify the effects of electromagnetic radiation on the human body and can be determined theoretically or measured in simulated biological tissue by exposure to electromagnetic radiation. It can be calculated from the electric field within the tissue. The unit of measurement of specific absorption rate (SAR) in the international system is W/kg. In 1999 and 2005 adopted by the IEEE the limits IEEE C95.1-1999.According to 1g average SAR is less than 1.6 W/kg to fulfill ICNIRP and

FCC guidelines [11]. From figure 8 shows that maximum SAR is found 0.55 W/kg for human head phantom model and fulfill the requirement of ICNIRP and FCC guidelines regarding SAR.

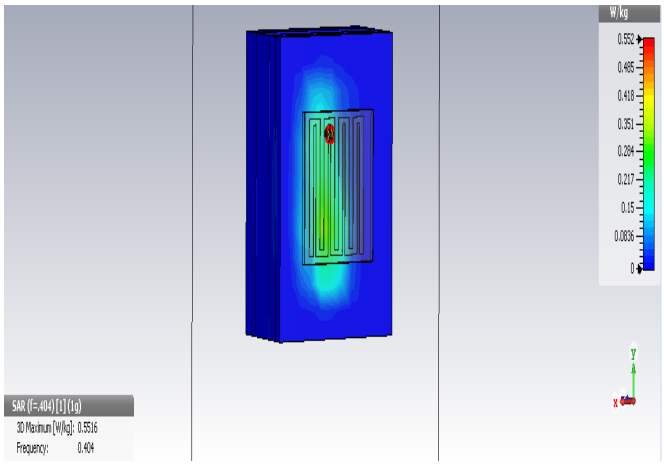


Figure 11. SAR value of the antenna for human head model

## IV. CONCLUTION

A miniaturized planar inverted F-antenna with meandered strategy has been presented. The performance of the antenna has been analyzed for the head phantom model. By verifying all the results, the proposed antenna is safe to be tested on the human phantom model. SAR results show that, this antenna will provide a large prospect in future for brain tumor, paralyzed and brain cancer detection research.

## REFERENCES


[1] Kim, Jaehoon, and Yahya Rahmat-Samii. "Planar inverted-F antennas on implantable medical devices: Meandered type versus spiral type." *Microwave and Optical Technology Letters* 48, no. 3 (2006): 567-572.

[2] A. Kiourti, K. A. Psathas, and K. S. Nikita, "Implantable and ingestible medical devices with wireless telemetry functionalities: A review of current status and challenges," *Wiley Bioelectromagn.*, vol. 35, no. 1, pp. 1–15, Jan. 201473.

[3] Lee, C-M., T-C. Yo, F-J. Huang, and C-H. Luo. "Dual-resonant π-shape with double L-strips PIFA for implantable biotelemetry." *Electronics Letters* 44, no. 14 (2008): 837-839.

[4] Wong, Kin-Lu. "Planar antennas for wireless communications." *Microwave Journal* 46, no. 10 (2003): 144-145.

[5] https://www.fcc.gov/medical-device-radiocommunications-service-medradio [accessed 5 october,2017]

[6] Khodabakhshi, H., & Cheldavi, A. (2010). Irradiation of a six-layered spherical model of human head in the near field of a half-wave dipole antenna. *IEEE Transactions on Microwave Theory and Techniques*, *58*(3), 680-690.

[7] http://stf.ucsd.edu/presentations/2007/2007-08%20STF%20-%20Zarlink%20ULP%20transceivers.pdf [accessed 5 october,2017]

[8] *Wasiq, Sumaiya, Shubhi Gupta, Varun Kumar Chandra, and Vivek Varshney. "DESIGN AND SIMULATION OF RHOMBUS SHAPED MICROSTRIP PATCH ANTENNA USING HFSS."*

[9] Khabiri, Mehrnoosh. "Design and Simulation of Implantable PIFA in Presence of ANSYS Human Body Model for Biomedical Telemetry Using ANSYS HFSS."

[10] Kang, Joseph, and David Wedge. "Method and apparatus for determining at least an indication of return loss of an antenna." U.S. Patent Application 10/779,667, filed February 18, 2004.

[11] Hwang, Jiunn-Nan, and Fu-Chiarng Chen. "Reduction of the peak SAR in the human head with metamaterials." *IEEE Transactions on Antennas and Propagation* 54, no. 12 (2006): 3763-3770.

2017 3rd International Conference on Electrical Information and Communication Technology (EICT), 7-9 December 2017, Khulna, Bangladesh

# *Real Time Activity Recognition Framework for Health Monitoring Support in Home Environments*

Shaikh Farhad Hossain[1], Al-Mahmud*[2], Ali Reza[3], Alvi Ataur Khalil[2] and Asif Ahmed[2]
[1] Institute of Information and Communication Technology
[1] Bangladesh University of Engineering and Technology (BUET)
[2] Department of Computer Science and Engineering
[2] Khulna University of Engineering & Technology (KUET)
[3] Computer Science & Engineering Discipline
[3] Khulna University (KU)
*{farhadcse05, rocky_cse_05, ali_cse05}@yahoo.com, {alvivvv, ahmedasif767}@gmail.com*

***Abstract*— Technology advances accelerate the quality and type of services provided for health care and especially for monitoring health conditions. Sensors have turned out to be more effective to detect diverse physiological signs and can be worn on the human body utilizing remote correspondence modules. An assortment of programming devices have been created to help in preparing a difference rundown of essential signs by examining and envisioning information produced by different sensors. In this proposition, we presented a Health signs and Activity acknowledgment monitoring system. Utilizing off-the-rack sensors, we executed a movement location system for identifying five sorts of action: falling, lying down, sitting, standing, and walking. The framework collects and analyzes sensory data in real-time, and provides different feedback to the users. In addition, it can generate alerts based on the detected events and store the data collected to a medical server.**

***Keywords—ADL, Accelerometer, SVM, TRIL, MEMS.***

## I. INTRODUCTION

With the rising number of elderly individuals in numerous nations around the globe, the hope of getting better social insurance administrations builds the weight on human services suppliers. Accordingly, unique rundown of innovative arrangements happen to enthusiasm for the two analysts and researchers to push the headway in Information Technology (IT) toward enhancing the nature of medicinal services. One of the arrangements towards such upgrades is thinking about a long haul checking of the patient's wellbeing circumstance by building a wellbeing observing framework. Wearable sensors are viewed as one of the essential answers for such observing necessities. Utilizing wearable sensors, we can identify any crisis that shows up in the patients wellbeing status as right on time as could be allowed. Such sensors can help in constant checking of patients with various ceaseless illnesses. For example, patients who experience the ill effects of intellectual cognitive heart failure, hypertension, atrial fibrillation, Parkinson's Disease, or Alzheimer's Disease can profit by many existing wearable frameworks [1] [2] [3]. To beat our requirements, we built up a system that can be connected for various wellbeing checking applications serving an assortment of requirements which incorporate identification, hazard anticipation, and a helpful technique for observing physical restoration. We used single sensor including an accelerometer, all of which are wireless and wearable so patients can wear and roam freely in their home environment.

## II. RELATED WORK

Accelerometers are broadly utilized as a part of various checking situations. They have been utilized as a part of checking and regarding distinctive ailments, for example, hand tremors in Parkinson Disease and in stroke and cardiovascular restoration. Particularly, they are useful in catching diverse appraisal examples of hand developments and the level of engine incapacities, for example, the gradualness of executing development [4], [5]. Continuous observing frameworks likewise consider accelerometers for measuring the level of useful capacity. Estimation of utilitarian capacities is accomplished by breaking down various physical exercises, for example, strolling, cycling, rising or plummeting stairs. Moreover, fall identification, and vitality spent in executing every action is likewise investigated utilizing pre-set example acknowledgment and settled edge.

T. Tamura et al. [6], constructed an instrument for demonstrating the hue between movement increasing speeds and the heart rate. The investigation concentrates on catching the movement designs alongside the heart rate while subjects are performing every day exercises. It additionally demonstrates the kind of exercises where heart rate was higher than amid different exercises.

Marie-Laure Wetzler et al. [7], examined the two-hub speeding up flag while observing the subjects pulse and heart ECG flag. The objective of their work is to assess the precision and dependability of checking the subject's exercises in view of a double pivot accelerometer joined to the thigh. The examination of the speeding up signals gathered utilizing their framework depended on the wavelet change.

Oliver and Flores-Mangas [8], proposed a remote ongoing framework for observing diverse physiological signs. They utilized a wearable sensor associated by means of Bluetooth to a mobile phone. The PDA stores, transmits, and investigates the physiological information. The fundamental reason for their framework is to naturally distinguish rest apnea. Mercury

978-1-5386-2307-7/17/$31.00 ©2017 IEEE

[20], is another wearable sensor arrange utilized for high-loyalty movement examination. It was intended to help applications that are information escalated.

Gleam sensors [9] have been utilized as a part of the Mercury framework for ensuring neuro-motor clutters, which is a similar sort of sensor we utilized as a part of our proposed system. The targets of the Mercury system are not quite the same as what we are endeavoring to accomplish here since Mercury concentrates more on the equipment and hub computational load including assets utilization and execution.

Lombriser et al. [10] utilized TinyOS 2.0 to program a portion of the accelerometer sensors to gather body movement increasing speeds so as to distinguish a few sorts of exercises. The exercises incorporate moving a PC mouse, composing on a white board, opening a drawer,opening a cabinet, writing on a console, and composing utilizing a pen. The example rate utilized is 32 Hz with 2.5 seconds as a window measure with 70 for each penny covering. The gathered information is investigated disconnected utilizing WEKA apparatus [11]. WEKA has been utilized to prepare the K-NN classifier with Manhattan separate contrasted with the execution of J48/C4.5 technique. The K-NN classifier was fruitful in scoring 91 for each penny for the acknowledgment rate where the k=5.

Parody [12] is another body arranges that characterizes day by day living exercises by dissecting the increasing speeds came about because of body development. The action grouping utilized as a part of SATIRE depends on Hidden Markov Model connected on the flag control.

Nisham Ravi et al. [13], endeavored to utilize a solitary triaxial accelerometer to recognize eight arrangement of exercises: standing, sitting, strolling, running, ascending stairs, moving down stairs, vacuuming, and brushing teeth. Amid their examinations an accelerometer sensor was joined to the pelvic district of the patients and designed to test at 50 Hz. A HP iPAQ was utilized to gather the information from the sensor utilizing Bluetooth. The elements separated from the accelerometer signals included mean, standard deviation, vitality, and connection. Five classifiers were executed utilizing WEKA toolbox to recognize the distinctive exercises. Subsequently, the paper demonstrates an execution assessment of utilizing choice tables, choice trees (C4.5), K-closest neighbors, SVM, and Naôve Bayes. The fundamental objective of thework displayed was to answer an issue of in the case of consolidating diverse classifiers would expand the acknowledgment rate.

CodeBlue [14], is another remote sensor system to help medicinal services. Unill the season of composing this postulation, CodeBlue is still being worked on. Its framework source code,according to their site, is purchased out soon. The fundamental target of their work is to incorporate distinctive medicinal sensors with a low-control remote choice. CodeBlue utilizes TinyOS programming alongside Graphical User Interface (GUI) application to question and show essential signs.

Karantonis et al. [15] constructed an ongoing observing framework to screen human development classifier utilizing a triaxial accelerometer. This work is not a structure, yet rather a usage of constant grouping framework.

Wood et al. [16], proposed a setting mindful remote sensor organize for helping elderly individuals. The framework empowers an entrance to information continuously procuring distinctive tactile data. It gives setting mindfulness by incorporating condition and physiological information by actualizing a two-path convention of information stream.

Rajasekaran et al. [17] proposed a framework made out of wearable sensors for observing elderly individuals under medication treatment. The calculation of ready recognition is carried on the sensor sheets while conveying to therapeutic informatics administrations with the information gathered.

Lombriser et al. [18] proposed an online movement acknowledgment framework in view of Sensor Button engineering for perceiving body movement. The Sensor Button used to gather setting data for characterization. The stage introduced on the sensor hub is TinyOS 2.0 to bit an accelerometer sensor.

## III. System Design

The framework comprises of two principle parts: Body sensor organize (BSN) and the checking application (Fig 1).

Fig. 1: Real time ADL detection system

The BSN contains wearable sensor that accumulates accelerometer data. Sensor has a remote Bluetooth to talk with the customer's server side. The watching application is presented in the customer's server side (patient's home or prosperity foundation). The server should have the Internet system to send alert to the therapeutic administrations provider or adaptable message to relative and send/recuperate data from the remedial server. In case a patient's fall happens, at that point customer server handle the alert by actuating caution locally and furthermore sending notification to human administrations provider by methods for web and message to mobile phone. Tolerant fall related information will be recorded in the remedial server for facilitate essential. The patient's counselor has specific interface for study and controlling the material data and an association board is executed to manage the striking data.

## IV. METHODOLOGY

**Hardware setup:** To get the expanding speed data of the subject, one SHIMMER [19] sensor center point is used for data acquirement and transmission from subjects to a remote PC. Sensor center point involves a 3D accelerometer, a

Bluetooth contraption and a MSP430F1611 microcontroller device. The SHIMMER sensor center point is showed up in Fig. 2.

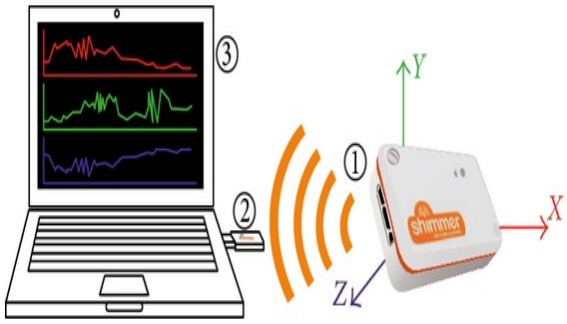


Fig. 2: Data streaming sensor device to server

The three-dimensional (3D) accelerometer (MMA7260Q) from free scale Semiconductor has a range up to ±6g. The Bluetooth contraption (Rovering Network RN-42) has a range outperforming 10 m, a default transmission rate of 115k baud, and is a class 2 Bluetooth module.

**Placement of sensors:** The single 3D accelerometer is associated with body section: Chest (Fig 3). The game plan of the sensor and course of the three tomahawks are kept up the same for each one of the subjects shared in the trials.

Fig. 3: Placement of SHIMMER sensor nodes on subjects

**Feature selection:** Finding the perfect component subset is as basic as picking a fitting count. Feature extraction is generally called dimensionality diminishing. Basically, we select the most renowned parts, which are known as a wrapper methodology. The calculation and extraction of critical

elements from the movement signals (Fig 4) begin from figuring the Mean, Standard deviation, Median, MAX, MIN, Range, Sum, PCA and FFT for every axis (gx, gy and gz) and their resultant $g = (gx2+gy2+gz2)^{½}$.

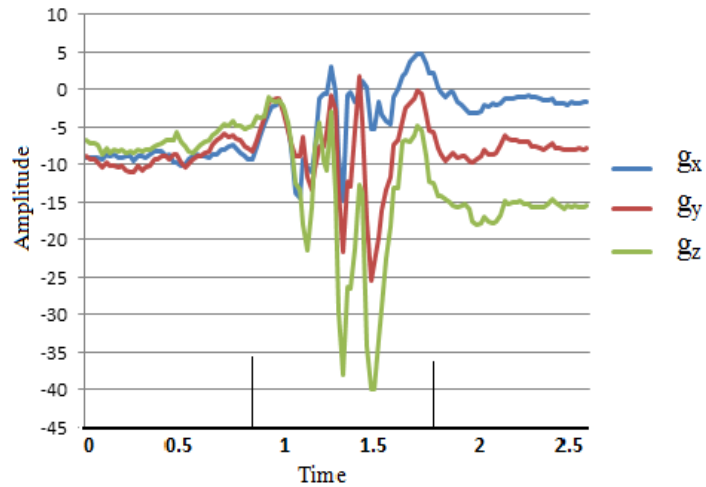


Fig. 4: A segment of acceleration signal

Inconsequential information features provoke more conspicuous computational cost. Mean and Standard deviation components are the fundamental 2 most basic segments in the dataset.

**Classifier selection:** We require an algorithm to compute to have the ability to arrange detection with course by seeing the banner plans with pre-learned ones. Table I exhibits the perplexity cross section obviously tricky fall, using SVM classifier. Classifier was successful in scoring 97.2 for the learning rate. In this work, SVM learning classifier was used to learn to distinguish among ADL. A total of 1200 ADL have been performed by the 13 subjects. Whole data are divided in two parts .One for training (75%) and another for testing (25%). Result of test data of SVM classifier is shown below.

Table I. Confusion matrix (SVM)

| | **Task** | | | | | |
|---|---|---|---|---|---|---|
| True Class | Falling | 53 | 5 | 2 | | |
| | Lying down | 7 | 52 | 1 | | |
| | Sitting | 2 | 6 | 50 | 2 | |
| | Standing | | | 1 | 57 | 2 |
| | Walking | | | | 2 | 58 |
| | | Falling | Lying down | Sitting | Standing | Walking |
| | Predicted Class | | | | | |

Table II shows the summary results of direction-sensitive fall, using SVM classifier.

Table II. Summary results of SVM

| Task | Total | Accuracy (%) | Precision (%) | Recall (%) |
|---|---|---|---|---|
| Falling | 60 | 92.29 | 88.33 | 95.92 |
| Lying down | 60 | 91.04 | 86.66 | 94.97 |
| Sitting | 60 | 91.04 | 83.33 | 98.52 |
| Standing | 60 | 96.66 | 95.00 | 98.27 |
| Walking | 60 | 97.91 | 96.66 | 96.66 |

Summary of the methodology is provided in Table III.

Table III. Accelerometer, features and algorithm

| Sensor | Accelerometer |
|---|---|
| Segmentation | Sample frequency 50 Hz |
| Window Size | 2.56 seconds |
| Window Overlap | 50 % |
| Features | Mean, standard deviation, PCA |
| Classification | SVM |

## V. Real time implementation

As SVM classifier is providing better results based on tuning parameters. We implement the SVM algorithm in real time. Real time fall detection is developed in MATLAB language to be executed on the SHIMMER MSPP430 microprocessor. Third party software Realterm version 2.0.0.70 is used for PC port scanning (recommended by SHIMMER [9]. Port is scanned every .256s. SVM algorithm is implemented using "classificationLearner" of MATLAB R2016a toolkit. We develop a GUI to show the real time directive fall detection result using SVM algorithm. A 3D accelerometer is attached to chest of human subjects. 3D accelerometer data is captured by MATLAB and calculate the value. After calculating the functional value (Mean, Std_dev, and PCA), features vector is fed to SVM classifier. SVM apply its classification logic to find out the class of inputted vector. A total of five classes are classified. If a fall occurs , then the classifier show "fall detect" and create alarm with red background (Fig 5).

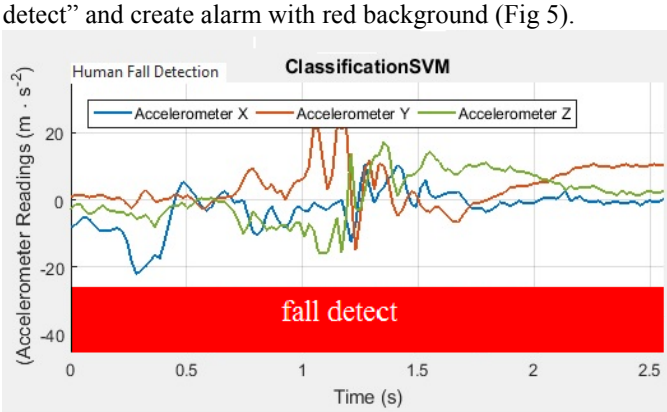


Fig. 5: Trained model SVM to predict fall

In other activities , it shows the real activity with blue background color and no alarm (Fig 6) or or stay idle.

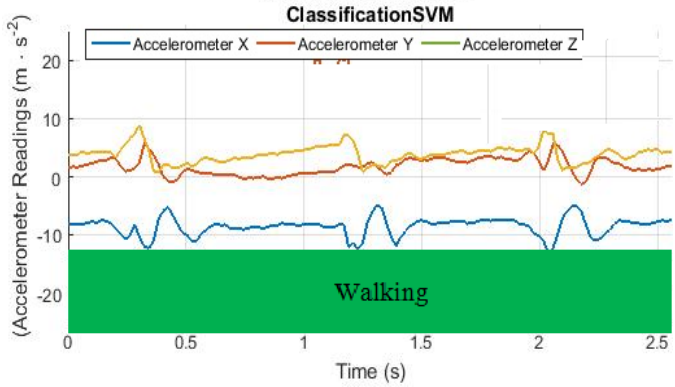


Fig. 6: Trained model to predict ADL

## VI. Results

After developing the real time system, again thirteen human subjects who are recruited for this testing work. A total of 150 144 ADL have been performed and we get the result (table IV and table V).

Table IV. Confusion matrix (SVM)

| | Task | Falling | Lying down | Sitting | Standing | Walking |
|---|---|---|---|---|---|---|
| True Class | Falling | 26 | 3 | 1 | | |
| | Lying down | 3 | 26 | 1 | | |
| | Sitting | 2 | 2 | 24 | 2 | |
| | Standing | | | 1 | 28 | 1 |
| | Walking | | | 1 | 1 | 28 |
| | Predicted Class | | | | | |

Table V. Summary results of SVM

| Task | Total | Accuracy (%) | Precision (%) | Recall (%) |
|---|---|---|---|---|
| Falling | 30 | 91.25 | 86.66 | 95.41 |
| Lying down | 30 | 91.25 | 86.66 | 95.41 |
| Sitting | 30 | 88.33 | 80.00 | 96.00 |
| Standing | 30 | 95.41 | 93.33 | 97.39 |
| Walking | 30 | 96.25 | 93.33 | 99.11 |

From the table, we think about the reenactment result and ongoing outcome table II versus V. We bring up the execution of the continuous is fundamentally the same as the reproduction result. Indeed, the comparable exactness (Fig. 7), accuracy (Fig. 8), review (Fig. 9) were acquired. These outcomes affirm the nature of the ongoing framework to precisely characterize fall and ADL occasions. Grown constant fall discovery framework is giving comparative outcome like reenactment result with less specialized blunder rate and high order precision.

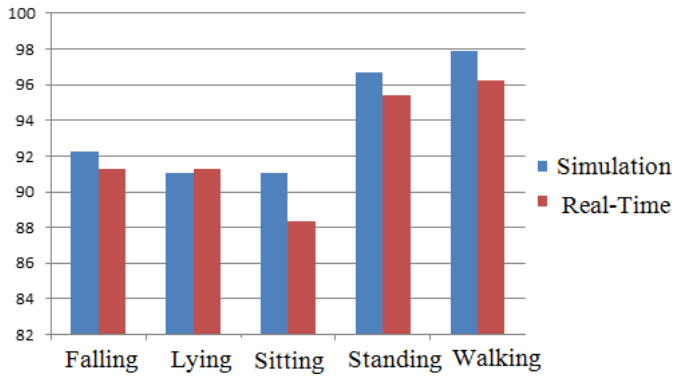


Fig. 7: Accuracy of simulation & real time ADL

Fig. 8: Precision of simulation & real time ADL

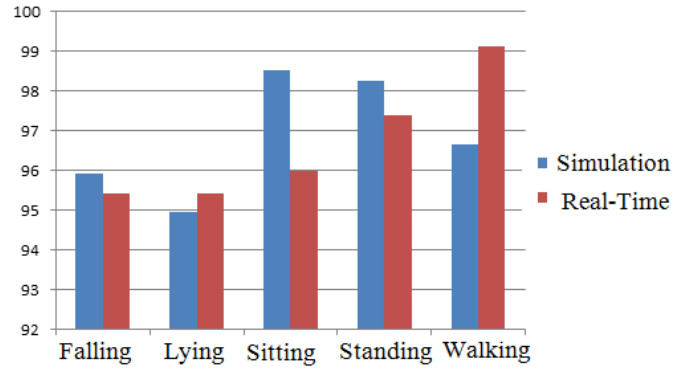


Fig. 9: Recall of simulation & real time ADL

## VII. CONCLUSIONS

We execute the estimation in bona fide condition and found the execution of the progressing is essentially the same as the reenactment that constructs the affirmation of the fall revelation system. This work not simply shows a machine learning figuring that gives accuracy past at introduce open counts furthermore demonstrates course tricky, fiscally canny and continuous fall revelation structure using single 3D accelerometer.

**Limitations:** The elderly and weak individuals are the essential end-clients of fall identification arrangements. Be that as it may, because of moral concerns, the framework created in this work is just assessed utilizing information from youthful and solid subjects. Consequently, it is important that the proposed ongoing is assessed on information accumulated from the elderly and impaired subjects.

**Future Work:** There are a few zones of future work that can serve to enhance the framework usefulness and give extra assessment of its execution. 1. Chest is the best body area for fall recognition exactness however midsection is the best agreeable body areas for position of sensor as indicated by subjects. In future, fall location studies might be improved the situation a sensor set in the midriff while keeping the precision on a similar level. 2. Additionally work may concentrate on: web based observing and informing framework to cell phone.

## REFERENCES

[1] W. Dafoe, and P. Huston ìCurrents trends in cardiac rehabilitation,î Canadian Medical Association Journal, vol. 156, pp. 527-532, 1997.

[2] P. Bonato, ìApplications of wearable technology in rehabilitation,î pHealth, 2008.

[3] T.G. Russell, ìPhysical rehabilitation using telemedicine,î Journal of Telemedicine and Telecare, vol. 13(5), pp. 217-220, 2007.

[4] T. Hester, R. Hughes, D.M. Sherril, B. Knorr, M. Akay, J. Stein, and P. Bonato,"Using wearable sensors to measure motor abilities following stroke," Proceeding of the International Workshop on Wearable and Implantable Body Sensor Network, 2006.

[5] R.J.W. Dunnewold, C.E. Jacobi, and J.J. van Hilten, ìQuantitative assessment of bradykinesia in patients with Parkinsonís disease,î J. of Neuroscience Method, vol. 74, pp. 107-112, 1997.

[6] T. Tamura, T. Fujimoto, H. Sakaki, Y. Higashi, T. Yoshida, and T. Togawa, "A solid-state ambulatory physical activity monitoring and its application to measuring daily activity of the elderly," Journal of Medical Engineering & Technology, vol. 21, pp. 96-105, 1997.

[7] M. Wetzler, J.R. Borderies, O. Bigaignon, P. Guillo, and P. Gosse, "Validation of a two-axis accelerometer for monitoring patient activity during blood pressure or ECG hotler monitoring," Clinical and Pathological Studies, 2003.

[8] N. Oliver and F. Flores-Mangas, ìHealthGear: A real-time wearable system for monitoring and analyzing physiological signals,î Micorsoft Corporation, Redmond, Wass, USA, 2005.

[9] http://www.shimmersensing.com/menu/products/matlab-id [accessed last on 11 June, 2017]

[10] C. Lombriser, N.B. Bharatula, and D. Roggen, "On-body recognition in Dynamic sensor network," Proceedings of the ICST 2nd international conference on Body area networks, 2007.

[11] Weka: a Data Mining Software in Java, http://www.cs.waikato.ac.nz/ml/weka. Accessed May 2017

[12] R.K. Ganti, P. Jayachandran, T.F. Abdelzaher, and J.A. Stankovic, ìSATIRE: a software architecture for smart AtTIRE,î MobiSys, Sweden, 2006.

[13] N. Ravi, N. Dandekar, P. Mysore, and M.L. Littman, "Activity Recognition from accelerometer data," Proceedings of the Seventeenth Innovative Applications of Artificial Intelligence Conference, pp. 11-18, 2005.

[14] CodeBlue, http://fiji.eecs.harvard.edu/CodeBlue . Accessed January 2017.

[15] D.M. karantonis, M.R. Narayanan, M.Mathie, N.H. Lovell, and B.G. Celler, "Implementation of a real-time human movement classifier using a triaxial accelerometer for ambulatory monitoring," IEEE Transaction on Information Technology in Biomedicine, vol. 10(1), 2006.

[16] A. Wood, J. Stankovic, G. Virone, L. Selavo, Z. He, Q. Cao, T. Doan, Y. Wu, L. Fang, R. Stoleru,ìContext-aware wireless sensor network for assisted living and residential monitoring,î IEEE Network, 2008.

[17] M.P. Rajasekaran, S. Radhakrishnan, and P. Subbaraj, "Elderly patient monitoring system using a wireless sensor network," Telemedicine and e-Health, vol. 15, pp. 73-79, 2009.

[18] C. Lombriser, N.B. Bharatula, and D. Roggen, "On-body recognition in Dynamic sensor network," Proceedings of the ICST 2nd international conference on Body area networks, 2007.

[19] Vallejo, M., Isaza, C. V., and Lopez, J. D., " Artificial Neural Networks as an Alternative to Traditional Fall Detection Methods," in 35th Annual International Conference of the IEEE EMBS, Jul. 2013, pp. 1648-1651 (2013).

[20] K. Lorincz, B. Chen, G.W. Challen, A.R. Chowhury, S. Patel, P. Bonato, and M. Welsh, ìMercury: a wearable sensor network platform for high-fidelity motion analysis,î SenSys, 2009

# Detection and Recognition of Bangladeshi Road Sign Based on Maximally Stable Extremal Region

Mohammed Shahed[1], MD. Ahsan Ullah Khan[1], Shayhan Ameen Chowdhury[1*]
[1]Dept. of Computer Science and Engineering, International Islamic University Chittagong (IIUC), Chittagong-4318, Bangladesh
Email: shahedcseiiuc@gmail.com, rafi.adr009@yahoo.com, [1*]shayhan@yahoo.com

***Abstract*—Road sign detection and recognition systems (RSDRS) offers an autonomous driver support system, which mainly concerns of safety for drivers, road users as well as passengers as a portion of Advanced Driver Assistance System (ADAS). RSDRS are mainly used to help the drivers (especially those who have a disability to drive) by warning them about the existence of road signs to lessen the risks in a situation of driving disruption, tiredness and in rough weather. Though many RSDRS has been proposed in the literature as well as many research areas. But detecting and recognizing of road sign is still challenging matter because of uneven illumination, complex background, different shape, various distance and different angle. This research aims to detect and recognize road signs of Bangladesh. A system has been proposed in this paper for automatic detection and recognition of Bangladeshi road sign which generates a chromatic normalized image that has two channels and detects the candidate regions as maximally stable extremal regions (MSERs), which offers physique in a variation of illumination conditions of Bangladeshi road sign. The recognition process is done by a cascade of support vector machine (SVM) classifiers in which the images are trained by using histogram of oriented gradient (HOG) features.**

***Keywords—road sign detection and recognition, chromatic normalized image, maximally stable extremal regions (MSERs), histogram of oriented gradiants (HOG).***

## I. INTRODUCTION

In past few years, many new technologies have been introduced by many researchers that could make our life easier and safer. Transportation system also developed to make sure that people are safe while they are being transported. Keeping in mind of the safety of peoples many advanced systems have been built in many advanced vehicles. Road sign detection and recognition system is one of them. RSDRS is more challenging in today's perspective because people started to pay attention to more advanced, efficient, accurate and intelligent transportation system that could make sure that driver and passengers are safe while they are being transported. RSDRS process is being divided into two groups by its literature namely those that concentrate on 1: Road Sign Detection (RSD) and 2: Road Sign Recognition (RSR). Firstly, the detection process finds the region of interests (ROIs) and is typically done by using various types of color separation process, followed by some method of road signs shape recognition. Detected regions by some sort of shape recognition method are being passed into classification to classify the types, for example, pattern matching or some sorts of classifiers namely as SVMs or Artificial Neural Networks(ANN).

The detection performance of color-based road signs habitually be reduced in images having low illumination, poor lighting condition, or in confrontational weather conditions. To improve the detection rate various color model is used such as hue-saturation-value (HSV), YUV and CIECAM97 were being used in an effort to overawed these problems. In [2], YCbCr color model was applied for color separation and pattern matching was applied to classify shapes. In [3], RGB color model was used with chromatic and achromatic colors for color separation. And then, ROI extracted by geometric mean to classify the candidates. In [5], a method created by two new standards to examine various shapes with basic geometric characteristics has been proposed. The first one is, image segmentation is used to integrate the shape of candidate regions. And the second one is filtering process is used by Gabor Wavelet filter. One vs. others SVM is used in this framework to recognize and classify the road signs. SVM is also used in [4] to classify the road sign classes. The candidate connected components of road signs can also be found as maximally stable extremal regions (MSERs) which was recognized in [7]. If some objects remain their shape after a number of thresholds than they are taken as the maximally stable region. This process is used because of its strengthens which can also work if the lighting and illumination condition is varied. In preference detecting the objects as road signs by the edge color, MSER detects the objects by the background color of signs, since these background colors can be persisted by using the MSER [1] [6] method. Two shape measurements were used in [8] to recognize the circular and triangular shape of signs. In [9], DtBs vectors are acquired from the partitioned road sign from four different viewing point and then the shapes are passed into a linear SVM for classification. In [11] for shape extraction, Hough Transform process is applied and in [12] a median filter is used to detect the triangular, circular and quadrangular road sign shapes.

This paper introduces a framework to detect and recognize Bangladeshi road signs. At first, an image which is in RGB is converted into a normalized gray scale image by using chromatic equation. And then the normalized image is sent to MSERs feature to get the MSER objects. After getting the MSER object some filtering parameters are used to get the desired ROI. The chromatic equation was first used to eliminate shadow region in [10]. The chromaticity of an image can be

978-1-5386-2307-7/17/$31.00 ©2017 IEEE

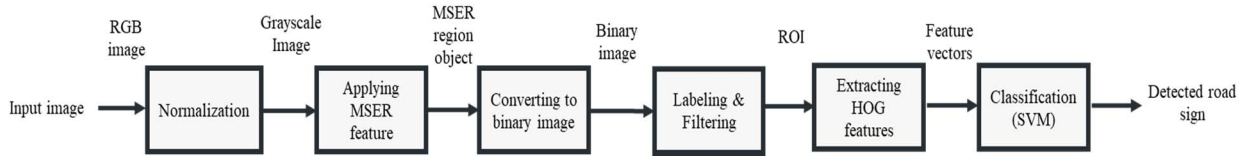


Figure 1. The proposed framework for detection and recognition of Bangladeshi road sign.

defined as "an image without intensity". In [10], they have used all three channels of RGB image to get the chromatic image. But in this paper, a normalized gray scale image was generated by the chromatic equation which has two channels that is RED and BLUE. Because RED and BLUE signs are generally used in Bangladesh. So, for the proposed framework a channel is deducted to generate a normalized image by using the chromatic equation which could help in two ways firstly, it saves some execution time and secondly, for the framework the RED and BLUE channels which help the system to get the color information of road sign from the image. Later on, that image renovated into a gray scale image to extract the ROIs using Maximally Stable Extremal Regions (MSERs).

## II. Proposed Framework for Detection and Recognition of Road Sign

In this portion of the paper, the proposed framework will be described in details. The proposed framework contains six main phases: (1) Converting RGB to normalized gray scale image, (2) Applying MSERs feature, (3) Converting MSER object to binary, (4) Labeling and filtering, (5) HOG features extraction and (6) Classification phase. Fig.1 shows the phases of the proposed framework for detection and recognition of Bangladeshi road sign.

### *A. Converting RGB to normalized gray scale image*

At first, it is needed to highlight the red and blue portions of the road sign to detect the signs. There is also a challenge while detecting the road signs if it has shadows around the sign or uneven illumination. So, to detect the road sign in such condition that is stated above, the RGB image needs to be converted into a normalized grayscale image. To generate the normalized grayscale image, it shall be followed a typical definition of chromaticity, i.e., an image color content having no intensity can be defined as: I = [r, g, b] ≡ [R, G, B]/ (R + G + B). In this formula it is seen that, there are three channels are situated those channels are Red, Green, Blue. For the framework, it is needed to use only two channel which are Red and Blue. So, the Green channel should be removed. To generate the normalized image all color channels should be added at the begainning. equation (1) is used in [10] for adding all three channels.

$$S_m = \sqrt[3]{(R.G.B)} \tag{1}$$

Where $S_m$ = Sum of channels; R = Red channel; G = Green channel; B = Blue channel of the image.

Then input image is normalized in particular Red and Blue channel. And chromaticity is amended as follows:

$$C_i = S_{r,b}/S_m \tag{2}$$

(a) (b) (c)

Figure 2. Processing example of getting MSERs object: (a) original image, (b) normalized image and (c) MSERs objects.

Where, $S_{r,b}$ = Red and Blue channel that are divided separately by $S_m$; $S_m$ = Sum of channels, $C_i$ = Normalized color channel. And log version for two channel is:

$$k_i = \log(C_i) = \log(S_{r,b}/S_m) \tag{3}$$

And for the moment it is being carried all two (thus no independent) components of chromaticity. But a 2-dimensional representation will be appropriate for this log chromaticity space p. It should be noted that, in log space, p will be orthogonal to $u = 1/\sqrt[3]{S_m}$. That is, p lives on a plane that is orthogonal to u, as in [10] p ·u should be zero.

After all, two plane is drawn the plane by following formula:

$$X_1 = k_{i,1} * 1/\sqrt{2} - k_{i,2} * 1/\sqrt{2} \tag{4}$$

$$X_2 = k_{i,1} * 1/\sqrt{2} + k_{i,2} * 1/\sqrt{2} - k_{i,3} * 1/\sqrt{6} \tag{5}$$

In the $X_1, X_2$ plane, it must be found the precise direction of θ in which direction it must be projected. In the plane, such that the peripheral distribution along a 2D projection line is orthogonal to the lighting direction. By using (6) the final chromatic grayscale normalized image I is generated.

$$I = X_1 \cos\theta * \pi/180 + X_2 \sin\theta * \pi/180 \tag{6}$$

Where θ is the projection direction and θ = 90°. For generating the normalized grayscale image, projection direction θ = 90° is used for the framework. But the range of θ can be used, θ = 0° … … … 180°. Fig.2 (b) shows an example of normalized gray scale image.

### *B. Applying Maximally Stable Extremal Regions*

In the proposed framework Maximally Stable Extremal regions (MSERs) [7] feature is applied to detect the object which are highlighted after normalized from the input RGB image. In computer vision, MSER as maximum stable extremal regions are used as a framework of blob detection in image. Actually, MSERs [7] are regions that maintain any image's objects regions when the image is thresholded at different levels. For the proposed framework this method is selected due to its robustness to variation contrast and lighting conditions.

In Fig. 3 how MSERs [7] work is being highlighted by thresholding several times in different value. After increasing the threshold value on the normalized grayscale image, it is seen that some pixels are not changed or lost. There are some pixels that remain stable which is shown in the Fig. 3. And MSER takes these pixels as stable. Even though MSER gives a strong form of road signs detection in different illumination scenes, it can be computationally expensive. So, to overcome this problem, the threshold values are selected between 80 and 190, because MSER objects that contains road signs generally appear within this range. From Fig.3 it is seen that in the MSER objects the road sign is situated. According to [7] MSER function takes these stable regions and represents with the plot by giving every maximally stable region with some sort of different colors Fig.2 (c) shows the MSER object result.

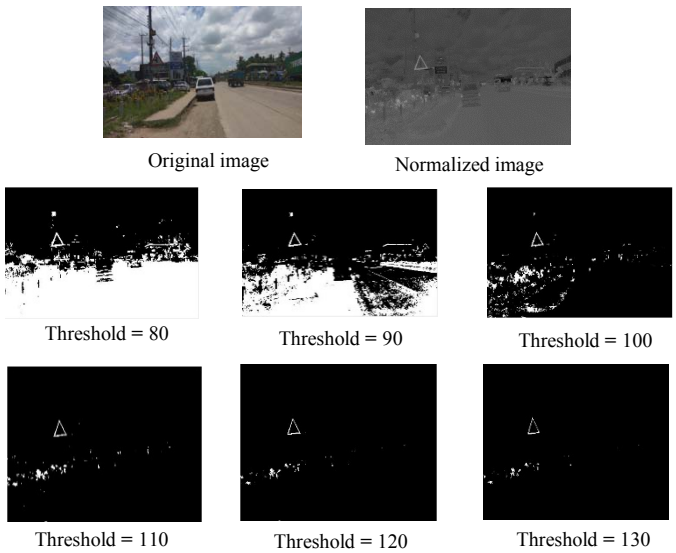


Figure 3. Sample example of Thresholding process as MSERs works.

### C. MSER region object to Binary image conversion

Binary image actually refers, which has only two possible values for each pixel. To differentiate this pixel values generally two different colors are used in a binary image these are 'black' and 'white'. However, any two colors can be used to represent a binary image. The color used for the objects pixel in a binary image is foreground color that is (white) and the remaining portion of the image is the background color (black). Binary image can be called as a two-level image which means that each pixel has only two possible values that is 0 and 1.

In the MSER image, there is situated some other objects with the candidate sign object which can be seen in Fig. 4. To remove other objects, the MSER image is changed into a binary image which has a single bit 0 or 1 for every pixel. After converting to MSER image some objects remains stable that can be said as MSER region objects which have no pixel values. To convert the MSER region objects into binary the bit of every pixel of the objects is changed to 1 in Fig.4 (d) the example is shown.

### D. Labeling and Filtering

To get the region of interest (ROI) it is mandatory to fill the holes of the object that contain background color. To fill the small background holes, the morphological closing operation is applied. After that, two different features are used to sort the detected connected component regions ad to minimize the number of candidates. The features are aspect ratio and solidity.

Figure 4. Regions of HOG feature.

TABLE I. PROPERTIES USED TO SORT CONNECTED COMPONENT

| Filtering Parameter | Minimum | Maximum |
|---|---|---|
| Aspect Ratio | 1 | 1.32 |
| Solidity | 0.8 | 1 |

Aspect ratio is referred that the width to height ratio of a rectangle. It is often used to ensure that image is displayed in the correct ratio irrespective of the size.

Another sorting feature is solidity which can also be called as the convexity. Solidity is the ratio of the pixels in a convex hull and the pixel in the object. It can be computed as Area of the object/Convex Area (bounding box area). Solidity is a slightly more difficult process than aspect ratio, but potentially returns a better discrimination of cells with protuberances or irregular shape versus commonly round cells. The container shape is called convex hull or bounding box.

### E. Histogram of Oriented Gradient (HOG)

To classify the candidate regions after filtering, a feature named Histogram of Oriented Gradients (HOG) which was introduced in [13] is beang used. The features are generated from the image, which presents the incidence of the gradient alignments in the image. HOG feature vectors are generated for each candidate objects. The items of the HOG feature vectors are the values from the histogram of each normalized cell which is shown in Fig.4. The image is divided into cells and HOG block that produces the features vectors. The framework is taken a 32×32 candidates from the image. By considering the size of the candidate *RF* feature vectors (8) can be computed as,

$$RF = BL \times BX \times BY \times H \tag{8}$$

Where BL is the cells per block, BX is the Blocks along X-Axis, BY is the Blocks along Y-Axis and H is the histograms in a cell. The value used were BL = 4, BX = 7 (With 50% overlap), BY = 7 (With 50% overlap), H = 9. According to (8), the feature vector is 1764.

### F. Classification

The idea of SVM is to obtain an optimal hyperplane for linearly separable patterns and in case of the training data are not

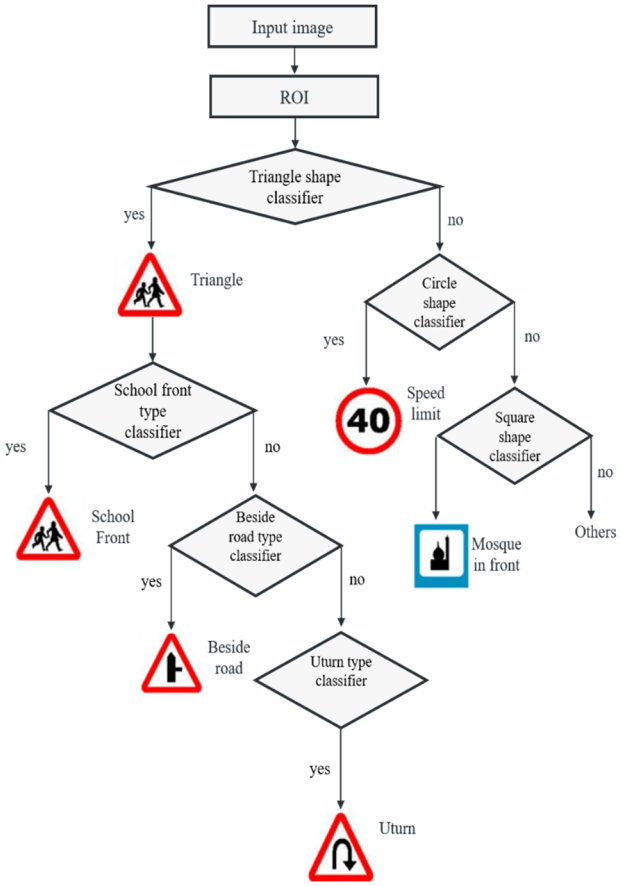


Figure 5. Flow diagram of SVM classifier.

linearly separable, SVM transforms the data by replacing of original data to map into new space by using kernel function.

Each region in the framework is classified using SVM classifier, the framework has multiple classes. The classifier of the framework classified multiple (five) road sign classes but the approach is chosen is linear classification for recognition of Bangladeshi road sign which is illustrated in Fig.5. At first, HOG feature vectors are applied to classify the shape of the regions as triangle, circle and square. After classifying shape, the type of the triangle road sign is classified as school in front, beside road and u-turn sign as the dataset contains this three types of triangle road sign.

But if a region is not found in shape classifier, then it will be taken as other object. According to type classifier if the region is found as triangle shape, then it will be passed to triangle type classifier to find triangle types those are school front, beside road and u-turn road sign. Otherwise there is no alternative is given the image will be considered as a negative image and it will be rejected by the SVM classifier.

## III. Experimental Result

This section represents the experimental results of the proposed framework for detection and recognition of Bangladeshi road signs. Experiments are accomplished on intel Core i3 3.20 GHz CPU and 12 GB RAM memory using MATLAB software. However, the system retains a latency

Figure 6. Some example of input images for the proposed method.

TABLE II. Detection Rate of Proposed Framework

| Sign color | Number of sign | Detected sign | Accuracy (%) |
|---|---|---|---|
| **Red** | 156 | 148 | 94.87 |
| **Blue** | 34 | 31 | 91.17 |
| **Total** | 190 | 179 | 94.21 |

TABLE III. Confusion Matrix of Proposed Framework

| | | | | | | Others |
|---|---|---|---|---|---|---|
| | 100% | 0 | 0 | 0 | 0 | 0 |
| | 0 | 100% | 0 | 0 | 0 | 0 |
| | 0 | 0 | 100% | 0 | 0 | 0 |
| | 0 | 0 | 0 | 97% | 0 | 3% |
| | 0 | 0 | 0 | 0 | 89% | 11% |
| Others | 0 | 3% | 0 | 3% | 0 | 94% |

TABLE IV. Precision, Recall and Accuracy value of Proposed Framework

| | | | | | | **Others** |
|---|---|---|---|---|---|---|
| **True Positive** | 10 | 10 | 10 | 29 | 16 | 28 |
| **True Negative** | 93 | 93 | 93 | 74 | 87 | 75 |
| **False Positive** | 0 | 1 | 0 | 1 | 0 | 3 |
| **False Negative** | 0 | 0 | 0 | 1 | 2 | 2 |
| **Precision (%)** | 100 | 90.9 | 100 | 96.66 | 100 | 90.32 |
| **Recall (%)** | 100 | 100 | 100 | 96.66 | 88.88 | 93.33 |
| **Accuracy (%)** | 100 | 99.03 | 100 | 98.09 | 98.09 | 95.37 |
| **Avg. Accuracy (%)** | 98.43 | | | | | |

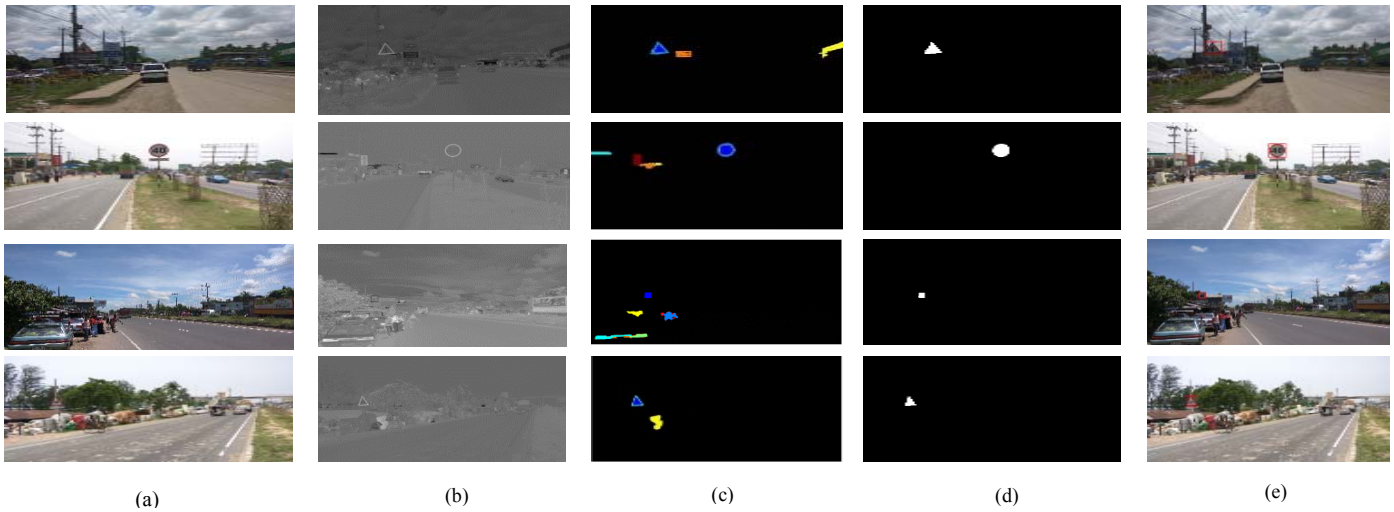


Figure 7. Processing example of detection and recognition of Bangladeshi road sign: (a) original image, (b) normalized image, (c) MSERs objects, (d) binary image after filtering and (e) detected road sign.

TABLE V. COMPARISON TABLE WITH PROPOSED FRAMEWORK OF [4]

| Framework | True Positive | False Positive | True Negative | False Negative | Accuracy (%) |
|---|---|---|---|---|---|
| **Proposed Framework** | 103 | 5 | 515 | 5 | 98.43 |
| **Greenhalgh [4]** | 72 | 34 | 360 | 34 | 86.4 |

around 0.59s. The dataset contains 190 images where the images are taken in uneven illumination, from various distances, from different angle and with a complex background that has the same color property as sign. For the proposed framework 175 images are trained and 108 images are tested.

Fig.7 shows some detection example of various types of road sign. The first row shows a detection process of a triangle road sign that is road beside sign. But to detect this sign was challenge for the proposed framework because the illumination of that sign is uneven. The second row has a sign that is speed limit and the third row is a mosque in front sign that has a very long distance from view point and the sign is hardly seen. And in the last row a triangle school in front sign which has a big angle from the view point. All the images are taken from Bangladeshi highways in outdoor illumination.

Considering the above condition, the detection rate of the proposed system is 94.21%. Table II shows the result of detection rate of various road sign. In the proposed system 190 images is used as input for detection and 179 images have been detected. Fig. 6 shows some input images that are used for detection and recognition of Bangladeshi road sign.

To recognize the road signs according to Section II (F) for the proposed framework a linear SVM classifier is used. Table III shows the confusion matrix of proposed method of all classes. Table IV shows the result of recognition. The precision, recall and accuracy rates are computed for different types of road signs that have different distances, various angle, situated in uneven illumination and some have a complex background. In Table IV True Positive, False Positive, True Negative and False Negative values are shown along with precision, recall and accuracy rate for each class. True Positive and True Negative refers the positive events and negative events respectively that are correctly labeled to the belonging class. In table IV the values are shown in True Positive for each class that are road sign images correctly recognized by the classifier to its belonging class. And the other five classes data are taken as True Negative for each class. False Positive refers events incorrectly labeled as belonging to the class. In Table IV False Positive values are images that are incorrectly labeled to a class. False Negative refers the events which were not labeled as belonging to the positive class.

Results extracted from the proposed framework is compared with [4] Table V represents the comparison result. The comparison is performed with the accuracy rate of recognition. According the result shows in Table IV the proposed framework expressively beats [4]. Table IV illustrates that the framework that proposed in this paper, is robust enough on detecting and recognizing Bangladeshi road sign than the framework proposed in [4] in uneven illumination, from different distances and from various distances.

## IV. CONCLUSION

The goal of this paper was to detect and recognize Bangladeshi road sign with coping with existing challenges. This paper proposed a framework that can cope with the challenges by generating chromaticity image and then passed into in MSER and after applying the labeling and filtering framework the proposed framework gets the ROI. Then the ROIs is sent to HOG to generate the feature vector and then it passed to SVM to classify and recognize the road sign. The proposed framework can effectively work on the different Bangladeshi road sign and can also fulfill the challenges and the system capable of increasing its performance. However the proposed framework still not capable on detection the occulated road sign and detect road sign that are very old that it is hardly recognizable. So, in future our work could be extented detection of occulated road sign and old road sign that are roten by color.

## REFERENCES


[1] Yang, Yi, and Fuchao Wu. "Real-time traffic sign detection via color probability model and integral channel features." In *Chinese Conference on Pattern Recognition*, pp. 545-554. Springer, Berlin, Heidelberg, 2014.

[2] Kale, Amol Jayant, and R. C. Mahajan. "A road sign detection and the recognition for Driver Assistance Systems." In *Energy Systems and Applications, 2015 International Conference on*, pp. 69-74. IEEE, 2015.

[3] Houben, Sebastian, Johannes Stallkamp, Jan Salmen, Marc Schlipsing, and Christian Igel. "Detection of traffic signs in real-world images: The German Traffic Sign Detection Benchmark." In *Neural Networks (IJCNN), The 2013 International Joint Conference on*, pp. 1-8. IEEE, 2013.

[4] Greenhalgh, Jack, and Majid Mirmehdi. "Real-time detection and recognition of road traffic signs." *IEEE Transactions on Intelligent Transportation Systems* 13, no. 4 (2012): 1498-1506.

[5] Zaklouta, Fatin, and Bogdan Stanciulescu. "Real-time traffic-sign recognition using tree classifiers." *IEEE Transactions on Intelligent Transportation Systems* 13, no. 4 (2012): 1507-1514.

[6] Simon, Ludovic, Jean-Philippe Tarel, and Roland Brémond. "Alerting the drivers about road signs with poor visual saliency." In *Intelligent Vehicles Symposium, 2009 IEEE*, pp. 48-53. IEEE, 2009.

[7] Matas, Jiri, Ondrej Chum, Martin Urban, and Tomás Pajdla. "Robust wide-baseline stereo from maximally stable extremal regions." *Image and vision computing* 22, no. 10 (2004): 761-767.

[8] Malik, Rabia, Javaid Khurshid, and Sana Nazir Ahmad. "Road sign detection and recognition using colour segmentation, shape analysis and template matching." In *Machine Learning and Cybernetics, 2007 International Conference on*, vol. 6, pp. 3556-3560. IEEE, 2007.

[9] Gudigar, Anjan, B. N. Jagadale, and Raghavendra U. "Kernel based automatic traffic sign detection and recognition using svm." *Eco-friendly computing and communication systems*(2012): 153-161.

[10] Finlayson, Graham D., and Mark S. Drew. "4-sensor camera calibration for image representation invariant to shading, shadows, lighting, and specularities." In *Computer Vision, 2001. ICCV 2001. Proceedings. Eighth IEEE International Conference on*, vol. 2, pp. 473-480. IEEE, 2001.

[11] Huang, Hua, Chao Chen, Yulan Jia, and Shuming Tang. "Automatic detection and recognition of circular road sign." In *Mechtronic and Embedded Systems and Applications, 2008. MESA 2008. IEEE/ASME International Conference on*, pp. 626-630. IEEE, 2008.

[12] Kuo, Wen-Jia, and Chien-Chung Lin. "Two-stage road sign detection and recognition." In *Multimedia and Expo, 2007 IEEE International Conference on*, pp. 1427-1430. IEEE, 2007.

[13] Dalal, Navneet, and Bill Triggs. "Histograms of oriented gradients for human detection." In *Computer Vision and Pattern Recognition, 2005. CVPR 2005. IEEE Computer Society Conference on*, vol. 1, pp. 886-893. IEEE, 2005.

# Training Denoising Autoencoder Using Printed Text Image for Classification of Handwritten Numeral from Noisy Images

Sudipta Singha Roy[1], Sk. Imran Hossain[1], Tajul Islam[2], Shaikh Akib Shahriyar[1], Md. Aminul Haque Akhand[1], Kazuyuki Murase[3]
[1]Khulna University of Engineering & Technology, Bangladesh
[2]North Western University, Bangladesh
[3]University of Fukui, Japan
roysudipta1990@gmail.com, imran@cse.kuet.ac.bd, tajulkuet09@gmail.com. akibsawon@gmail.com, akhand@cse.kuet.ac.bd, murase@u-fukui.ac.jp

*Abstract*— **Accurate classification of handwritten numeral is mandatory for the successful implementation of various applications like postal system automation, number plate identification etc. While identifying the inherent pattern in a handwritten numeral most of the classification models work with preprocessed data collected from lab ignoring the fact that in practical situations image of a handwritten numeral gets corrupted with noise during acquisition and transmission process. To solve this issue various deep learning based models specially variants of Auto Encoders (AE) are used prior to classification tasks. In our proposed model we have considered Denoising Auto Encoder (DAE) for noise removal task. Rather than training the DAE in a conventional way we have incorporated printed text images in the training process with an intention of forcing the DAE to encode the handwritten numeral image to a printed form. This process simplifies the classification task for the following classifier Convolutional Neural Network (CNN). Our proposed model DAEPT-CNN is a feed forward network which consists of a DAE to map noisy image towards its scaled down printed form and a CNN. Proposed model's weights are tuned to the corresponding parameters of the pre-trained DAE and CNN. To test the classification accuracy of our proposed model it has been tested over two benchmark datasets: one for Bengali and another for English handwritten numerals. The classification accuracy shows the superiority of the proposed model in case of handwritten numeral recognition from noisy images.**

***Keywords—Handwritten numeral, image denoising, denoising auto encoder, printed text, convolutional neural network.***

## I. INTRODUCTION

Recognition of handwritten numeral is considered as an important research topic dur to its numerous application potentials such as automatic processing of bank cheque, postal system automation, number plate identification, analyzing passports and documents, solving puzzles etc. [1]. Because of the inconsistency of writing style of individuals handwritten numeral recognition is tougher than printed numeral recognition. Still, facing these challenges, a notable number of researches have been conducted in recent years and showed satisfactory classification accuracy while working over Roman, English, Chinese, Arabian and Bengali scripts [1,2,3,4]. While training an artificial neural network (ANN) Khan et al. [5] deployed evolutionary technique. Dempster-Shafer (DS) model was used by Basu et al. [3]. They incorporated the output from two different classifiers for final classification of handwritten numerals. Bhattacharya and Chaudhuri [6] proposed a MLP classifier based multistage cascaded architecture using majority voting method for recognition purpose. Pal et al. [2] extracted features from the handwritten numerals using water overflow technique from the reservoir prior to binary tree classifier to serve the same purpose of digit recognition. In recent times, deep neural network based models are being used most frequently for pattern recognition task because of their ability to imitate the inherent features from the image data throughout their deep layer-wise structure. Oval et al. [7] demonstrated a recurrent neural network (RNN) based classifier model to classify Devanagari words. Prior to using the RNN, they utilized Stentiford thinning technique for feature reduction.

Though DNNs performs better in pattern recognition and image classification tasks than the traditional methods their performance degrades when handling real life data due to the addition of noise during acquisition and transmission process. So, a denoiser is necessary prior to the classifier. Currently a lot of researches are being conducted on removing noise from images. Partial differential equation based model [8], scant coding approach [9] as well as wavelet transformation method [10] were initially applied for noise removal task. Later DNN based models outperformed previous techniques. Buurger et al. [11] used multi-layer perceptron (MLP) for denoising image. Jain et al.[12] utilized Convolutional Neural Nettwork (CNN) for noise removal that performed well even with fewer training samples. Recently conventional denoising methods has been convincingly outperformed by many autoencoder based models [13-15]. Vincent et al. [14] invented denoising autoencoder (DAE) which pollutes input image with random noise during learning period and learns to reconstruct original image from noisy input image in that process. DAEs can also be stacked to

978-1-5386-2307-7/17/$31.00 ©2017 IEEE

create deep unsupervised learning architecture named as stacked denoising autoencoder (SDAE) [15]. Stacked convolutional autoencoder proposed by Masci et al.[16] retains more innate structure of image data which is not the case for SDAE.

The main objective of our work is to build a system to better classify noisy handwritten numeral characters. If a traditional DAE is used for noise removal part then it tries to reconstruct the input by removing noise from it and the reconstructed image is used as the input for the classifier. The problem with this approach is that reconstructed image is of same dimension as the noisy input image so, a huge amount of time is wasted for updating weights. Moreover, image of a single handwritten numeral tends to vary from person to person. This numerous variation of a single handwritten numeral makes it tough for DAE to learn the weights and it also becomes harder for the classifier to map varying reconstructed images to appropriate class labels. Both of these problems can be solved by mapping input noisy images to a lower dimensional printed format as it reduces the number of weights to be learned, forces the DAE to converge faster and also boosts the performance of the classifier as it's easy to map printed data to appropriate class label if the reconstruction from handwritten to printed for performs well [17]. To address these issues, we propose an architecture named DAEPT-CNN which incorporates DAE, printed text and CNN. To test the classification accuracy of our proposed model it has been tested over two benchmark datasets: one for Bengali and another for English handwritten numerals. The classification accuracy shows the superiority of the proposed model over existing methods in case of handwritten numeral recognition from noisy images.

The rest of the paper is organized as follows. Section II describes the proposed DAEPT-CNN architecture, dataset description along with some prerequisites for better understanding. Section III shows experimental results of the proposed method as well as performance comparison with other existing related works. Finally, a brief conclusion of the work is given in Section IV.

## II. Training DAE Using Printed Text Image for Classification of Handwritten Numeral from Noisy Images

Real world handwritten numeral recognition suffers from noise and other imperfections. Our goal of the study is to provide a robust system for solving the problem of noisy handwritten numeral by incorporating DAE, printed text and CNN. This section describes our proposed method DAEPT-CNN along with required prerequisites and also contains the description of used datasets.

### *A. Dataset Description*

To test the effectiveness of our proposed model it has been tested over two benchmark datasets: one for Bengali and another for English handwritten numerals.

For English handwritten numerals we considered a well-established dataset named MNIST dataset [18] which contains 70000 images of English handwritten numerals provided by individuals practicing different writing styles.

And Bengali handwritten numerals are collected from benchmark dataset of ISI[19] which contains 22000 sample images.

Images of both the datasets are divided into training and test sets. Test set for English language contains 10000 images (1000 samples per digit) and Bangla language contains 4000 images (400 samples per digit) whereas training set consists of 60000(6000 samples per digit) samples for English and 18000(1800 samples per digit) samples for Bengali Language.

For both datasets, the image data are corrupted with 25% random noise in a multiplicative manner in order to check the performance of our proposed model while classifying noisy images.

### *B. Convolutional Neural Network*

CNN [18] is a variation of multi-layered neural networks which performs great when working with two-dimensional data. Image classification tasks saw the beginning of a new era with the rise of CNN as it utilizes moderately little pre-processing contrasted with other image classification algorithms. This implies that CNN learns filters that in customary algorithms were hand-built.

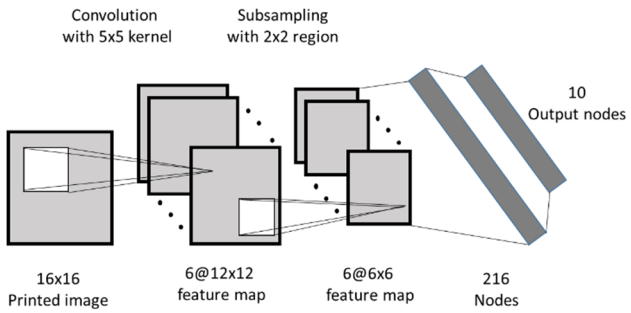


Fig. 1. CNN architecture considered in this study.

for our experiment is shown in Fig. 1. It comprises of a convolutional layer and a subsampling layer just after the single convolutional layer. Kernel size used for the convolutional layer is 5x5 whereas size of the pooling area is 2x2 for subsampling layer. A dense layer containing a linear representation of the terminal subsampled feature map units follows the subsampling layer. These units, at last, are connected to the 10 neurons in the output layer for image classification into 10 classes. Each neuron of the output layer corresponds to a specific digit. For each input a particular neuron's value of output layer becomes 1 and other 9 neurons' value stays 0. Hidden-output weights and also the kernels get updated during the continuation of training procedure for a specified number of epochs until picking up the preferred accuracy. As we can see from Fig. 1. training input images for our CNN are 16x16 printed numeral character images.

### *C. Denoising Autoencoder*

Auto-encoder is a three-layered variation of traditional neural network which uses unsupervised learning algorithm and

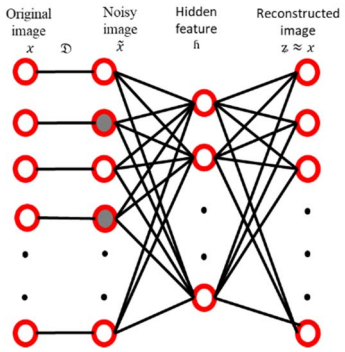


Fig. 2. Architecture of DAE.

mandates the output to be indistinguishable to the input with an aim of reducing dimensions or features. DAE is a stochastic version of auto-encoder as it extends conventional autoencoder by incorporating stochastic extensions so that input can be recreated from its noisy version[cp17]. DAE tries to undo the effect of a corruption process stochastically applied to the input of the auto-encoder. Architecture of a DAE is shown in Fig. 2. Noisy image $\tilde{x}$ is generated by adding noise to input image $x$ using deterministic distribution. DAE then maps $\tilde{x}$ (using encoder) to a hidden representation $\mathfrak{h}$ through a deterministic mapping:

$$\mathfrak{h} = s(\mathrm{W}\tilde{x} + b) \tag{1}$$

Where s is the activation function, $\mathfrak{W}$ is the weight connecting noisy input-hidden units and b is the bias. y is then mapped back (using decoder) to a reconstruction $\mathfrak{z}$ of same shape as input using Eq. (2),

$$\mathfrak{z} = s(\mathrm{W}'\mathfrak{h} + b') \tag{2}$$

Where, $\mathrm{W}' = \mathrm{W}^T$ (tied weights) and same goes for bias $b'$. $\mathfrak{z}$ can be considered as a prediction of $x$ thus reconstruction error need to be minimized as shown in Eq. (3)

$$L(x, \mathfrak{z}) \propto logp(x|\mathfrak{z}) \tag{3}$$

*D. Classification using DAE-AE-CNN*

Fig. 3 presents our proposed DAE-AE-CNN architecture where a DAE having 784 input units, 500 hidden units, 784 output units and a AE of 500 input units, 256 hidden units, 500 output units are used. Handwritten numeral image of size 28x28 is given as input the DAE. DAE encodes the input image to 500 hidden unit features which are again encoded to 256 hidden units by the AE. Next, we consider a NN of 784 input units, hidden layer of 500 units and 256 output units. Input-hidden weights of this NN are initialized by DAE whereas hidden-hidden weights are initialized by the AE. These 256 output units of the NN are then reshaped to 16x16 sized image which serves as input for the CNN.

*E. Classification using DAEPT-CNN*

Fig. 4. illustrates the proposed DAEPT-CNN architecture in which Fig. 4(a) shows the DAE used for mapping noisy handwritten numeral into printed form and Fig. 4(b) is the CNN used for printed form to output class mapping. The DAE is constructed using 784 input units, 500 hidden units and 256 output units so that, input noisy handwritten image gets mapped to a particular 16x16 printed image. This is done to reconstruct a noisy input handwritten image to a corresponding printed form. The CNN shown in Fig. 4 Is trained using 16x16 printed numeral image with corresponding label at the output layer. Then DAE of Fig. 4(a) and CNN of Fig. 4(b) are merged together by reshaping 256 output units and feeding it to the input of CNN which results in the combined architecture DAEPT-CNN as shown in Fig. 4(c). ReLU is used as the activation function for all the networks and conventional Backpropagation evaluates derivative of gradient for both DAE and CNN during backward pass. Network parameters are updated using this gradient. The final network DAEPT-CNN doesn't need any fine tuning as it retains the pre-trained weights and kernels from DAE and CNN of Fig. 3(a) and Fig. 3(b) respectively

## III. Experimental Setup and Ressult Analysis

This section describes the experimental outcome of the proposed DAEPT-CNN architecture while classifying noisy images over two benchmark datasets (described in section II(A)). For both datasets, samples are evenly distributed over 10

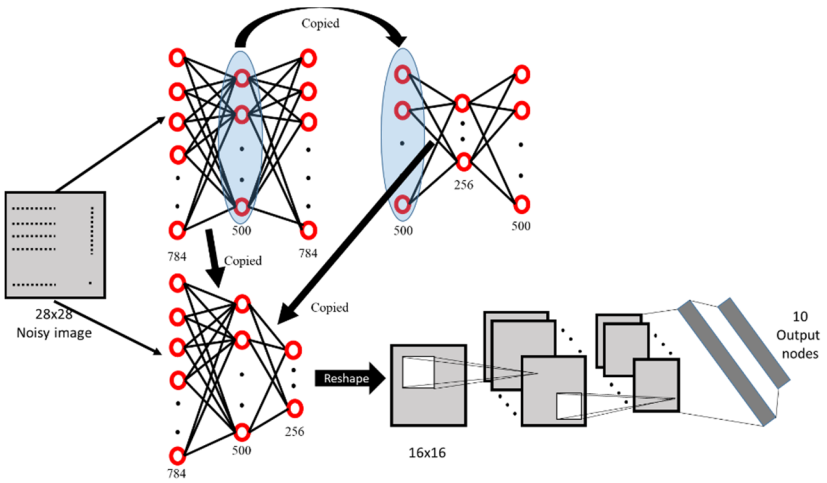


Fig. 3. Architecture of DAE-AE-CNN.

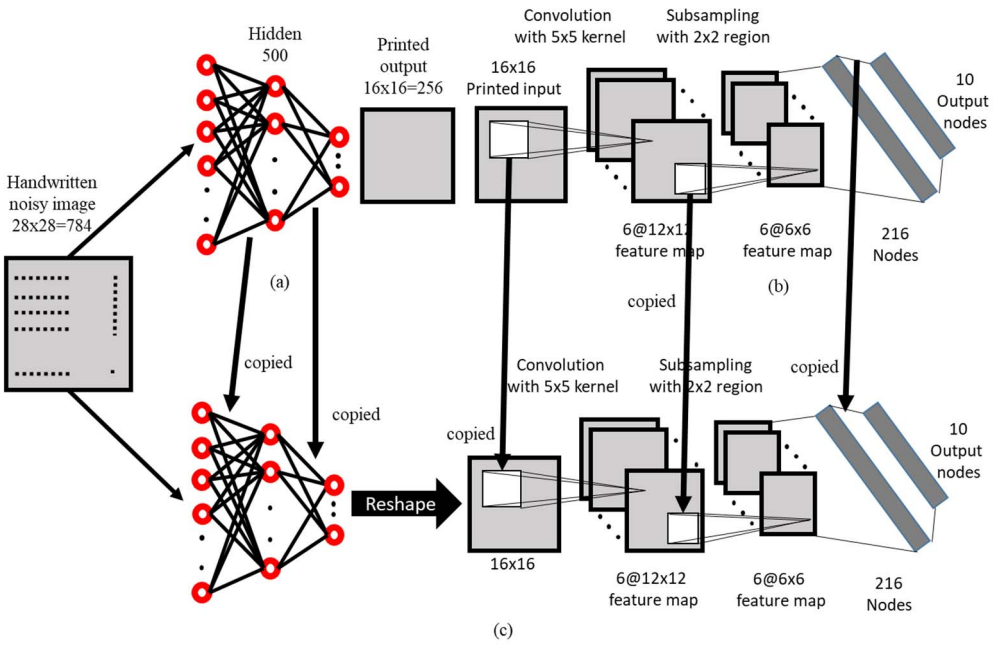


Fig. 4. Architecture of DAEPT-CNN.

fundamental classes where each class represents a particular numeral of corresponding language. The classification accuracy stated in this paper is only for test set. The model is implemented in Matlab R2015a. The experimental analysis has been conducted on MacBook Pro portable PC machine (CPU: Intel Core i5 @ 2.70 GHz and RAM: 8.00 GB) in OS X Yosemite environment.

Fig. 5 displays the test set recognition performance of proposed network architecture along with DAE-AE-CNN as well as CNN are considered in this study with 25% noise. Up to 400 iteration values are recorded and it can be clearly seen from Fig. 5(a) that the DAEPT-CNNN outperforms the other two classifiers achieving the classification accuracy of 98.52% while working with MNIST dataset. The recognition accuracy of DAE-AE-CNN is 96.33% whereas the single CNN trained with 0% noise accurately classifies 9531 image samples from 10000 test data samples. Fig. 5(b) displays the classification accuracies of these three classifiers while working over test sets of Bengali handwritten numerals collected from ISI database. This time the classification accuracy of all these models is reduced by a little percentage. The classification accuracy of DAEPT-CNN, DAE-AE-CNN and conventional two layered CNN are 94.23%, 93.98% and 92.11% respectively. The main reason behind this drop of classification accuracy while working over Bengali handwritten numerals is that this dataset contains significantly less image samples for both training and testing. For both cases, the CNN with the printed image of the numeral are run for 200 iterations. More iterations lead the CNN towards overfitting.

Table I replicates the confusion matrices of the DAEPT-CNN of test set image samples for both datasets after fixed 400 iterations. From Table I(a) it is clearly observable that, for English handwritten images from MNIST dataset, the classifier performs best for numeral “0”. Even with 25% noise present in the images, the DAEPT-CNN classifier accurately classifies this digit 994 times out of 1000 samples. For numeral “1”, “2” and “8” it shows a good classification accuracy. The DAEPT-CNNN classifier classifies both “1” and “2” 990 times correctly and 992 times for numeral “8”. It performs worst for numeral “9”. The proposed classifier misclassifies it 11 times as numeral “7”. In total, numeral “9” is misclassified as other digits 28 times.

Table I(b) represents the confusion matrix of the classifier

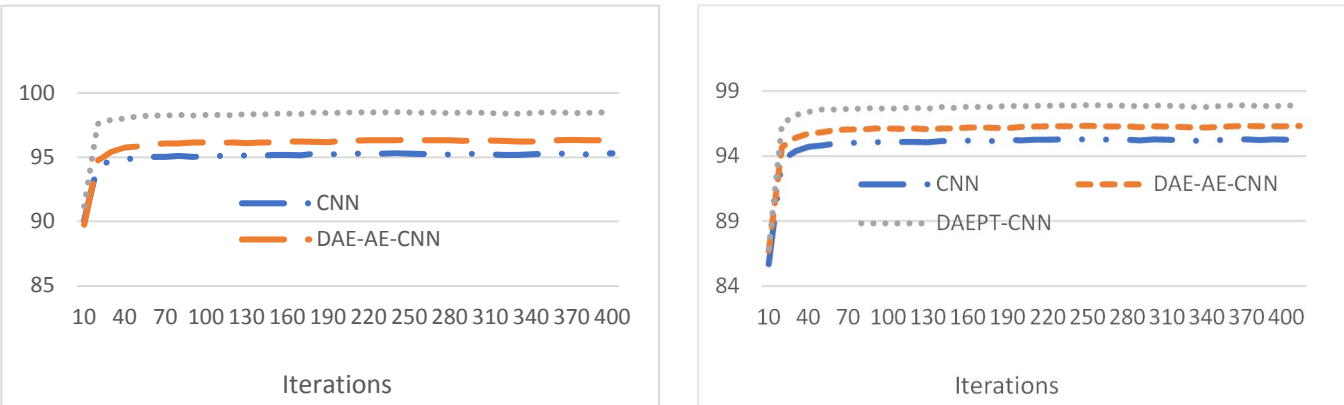


(a) Accuracy over English Handwritten numeral with 25% noise

(b) Accuracy over Bengali Handwritten numeral with 25% noise

Fig. 5. Test Set Recognition Accuracy with batch size 50 and learning rate 1.0 for different networks for both English and Bengali handwritten numerals.

TABLE I. TABLE I. CONFUSION MATRIX OF DAEPT-CNN NETWORK FOR TEST SAMPLES FROM MNIST AND ISI DATASET WITH 25% NOISE

(a) English Handwritten Numeral

| English Numeral | 0 | 1 | 2 | 3 | 4 | 5 | 6 | 7 | 8 | 9 |
|---|---|---|---|---|---|---|---|---|---|---|
| 0 | 994 | 0 | 0 | 0 | 0 | 0 | 1 | 1 | 4 | 0 |
| 1 | 0 | 990 | 2 | 1 | 2 | 0 | 1 | 2 | 1 | 1 |
| 2 | 3 | 2 | 990 | 0 | 3 | 0 | 0 | 6 | 2 | 0 |
| 3 | 0 | 0 | 4 | 981 | 0 | 10 | 0 | 1 | 2 | 2 |
| 4 | 1 | 5 | 0 | 1 | 982 | 0 | 1 | 2 | 1 | 4 |
| 5 | 1 | 0 | 0 | 11 | 0 | 978 | 1 | 1 | 7 | 1 |
| 6 | 2 | 6 | 0 | 0 | 0 | 1 | 986 | 0 | 5 | 0 |
| 7 | 0 | 4 | 8 | 2 | 0 | 0 | 0 | 983 | 1 | 5 |
| 8 | 3 | 0 | 1 | 3 | 0 | 1 | 0 | 0 | 992 | 0 |
| 9 | 1 | 2 | 0 | 0 | 5 | 0 | 0 | 11 | 9 | 972 |

(b) Bengali Handwritten Numeral

| Bengali Numeral | ০ | ১ | ২ | ৩ | ৪ | ৫ | ৬ | ৭ | ৮ | ৯ |
|---|---|---|---|---|---|---|---|---|---|---|
| ০ | 380 | 0 | 3 | 8 | 0 | 0 | 6 | 3 | 0 | 0 |
| ১ | 0 | 352 | 9 | 0 | 4 | 0 | 4 | 0 | 0 | 31 |
| ২ | 0 | 2 | 391 | 0 | 0 | 0 | 0 | 0 | 0 | 7 |
| ৩ | 6 | 0 | 0 | 384 | 0 | 3 | 6 | 0 | 0 | 1 |
| ৪ | 7 | 0 | 0 | 0 | 387 | 4 | 0 | 0 | 2 | 0 |
| ৫ | 0 | 0 | 0 | 2 | 5 | 384 | 9 | 0 | 0 | 0 |
| ৬ | 1 | 0 | 0 | 20 | 0 | 12 | 366 | 0 | 0 | 1 |
| ৭ | 3 | 0 | 4 | 0 | 0 | 9 | 0 | 384 | 0 | 0 |
| ৮ | 2 | 0 | 0 | 0 | 0 | 11 | 0 | 0 | 387 | 0 |
| ৯ | 15 | 18 | 3 | 5 | 2 | 0 | 3 | 0 | 0 | 354 |

for Bengali handwritten numeral image data. While working with this dataset, our proposed model performs best for numeral "২". It correctly classifies 391 samples out of total 400 test samples. Numeral "২" is misclassified only 7 times as numeral "৯". The worst performance of the classifier is found for numeral "১". It was correctly classified for 352 times. Most of the cases (31 times) it is misclassified as numeral "৯". The reason behind this is the similarity in the shape of these two numerals. Moreover, the shape of the actual numeral varies in shape when it is collected from various humans' handwriting documents. Additional noise distorts the shape furthermore and makes it quite difficult even for humans to correctly identify these images.

Table II shows the comparative result analysis of our proposed DAEPT-CNN noisy image classifier for MNIST dataset. Additionally, particular feature selection processes deployed by the other prominent methods are also reported in the table. One significant up hand of our proposed model is that it doesn't need any additional feature extraction model like other models. Each of the other models requires at least one and in most of the cases more than one feature extraction methods prior classification. Moreover, with 97.92% accuracy, DAEPT-CNN outperforms most of the existing models and proves the

TABLE II. A COMPARATIVE DESCRIPTION OF PROPOSED DAE-CNN, CDAE-CNN AND DAE-CDAE-CNN WITH SOME CONTEMPORARY METHODS.

| The work reference | Classification | Noise | Recog. Acc. |
|---|---|---|---|
| Bengio et al. [18] | DBN | 0% | 98.50% |
| | Deep net | 0% | 98.4% |
| | Shallow net | 0% | 95% |
| Vincent et al. [14] | Sda-3 | 10% | 97.20% % |
| Vincent et al. [15] | SVM | 25% | 98.37% |
| | SDAE-3 | 25% | 98.5% |
| Proposed DAEPT-CNN | CNN | **25%** | **98.52%** |

superiority of itself. Furthermore, it reduces the computational cost for the classifier ass the prior DAEPT encodes the handwritten numeral images towards a fixed printed form of significantly lower dimension. As the CNN has to classify 16X16 sized image rather than 28X28 sized image it requires less parameter values to be updated. Additionally, only a fixed single shape for each numeral in printed text images makes the CNN enable to learn the inherent structure of the images in comparably less iterations and with less image samples. But, unfortunately no such noticeable work is found that works over noisy Bengali handwritten numeral data. Still, with only 18000 train and 4000 test samples our proposed DAEPT-CNN model achieves 94.23% accuracy. From this accuracy value it can be said that our proposed model works good with Bengali handwritten numerals also.

## IV. CONCLUSION

While working in a real-life scenario, classifying handwritten numerals from any document is more complex task than to do with preprocessed images data obtained from lab. The main reason behind the drastically fall of the performance of the DNN based classifiers is the presence of noise in the handwritten numeral images. For a practical case, working with handwritten numerals containing zero noise is kind of impossible incident. To deal with this abnormality, image denoising prior to classification is a must. With the intension to solve this problem we have proposed a noble noisy image classifier where the image denoiser (DAE) is trained incorporating printed text image data forcing the autoencoder to eliminate the noise as well as encode the image towards a fix-shaped low-dimensioned printed form. It not only reduces the complexity of the classifier model but also improves the classification accuracy of the handwritten numerals significantly even if the images contain a noticeable amount of noise in them. Still, the model has some scope of upgradation. It is tested for only one type of noise. It can be reformed to an ensemble model to classify handwritten numerals subject to any type of noise. In future, we would try to implement the ensemble model that can classify handwritten numerals corrupted with any kind of noise.

## REFERENCES


[1] Plamondon, Réjean, and Sargur N. Srihari. "Online and off-line handwriting recognition: a comprehensive survey", *IEEE Transactions on pattern analysis and machine intelligence*, vol. 22, pp. 63-84, 2000.

[2] Umapada Pal, B. B. Chaudhuri, and A. Belaid. "A complete system for Bangla handwritten numeral recognition.", *IETE journal of research,* vol. 52 pp. 27-34, 2006.

[3] S. Basu, R. Sarkar, N. Das, M. Kundu, M. Nasipuri and D. K. Basu, "Handwritten BanglaDigit Recognition Using Classifier Combination Through DS Technique," *LNCS,* vol. 3776, pp. 236–241, 2005.

[4] M. A. H. Akhand, Mahtab Ahmed and Md. Hafizur Rahman, "Convolutional Neural Network based Handwritten Bengali and Bengali-English Mixed Numeral Recognition.", *International Journal of Image, Graphics and Signal Processing, vol.* 8.9, pp. 40-50, 2016.

[5] M. M. R. Khan, Md Arifur Rahman Shah, and M. M. Alam, "Bangla handwritten digits recognition using evolutionary artificial neural networks.", *In Proc. of the 7th International Conference on Computer and Information Technology (ICCIT 2004)*, pp. 26-28, 2004.

[6] U. Bhattacharya, and B. B. Chaudhuri, "Handwritten numeral databases of Indian scripts and multistage recognition of mixed numerals.", *IEEE transactions on pattern analysis and machine intelligence*, vol. *31*, pp. 444-457, 2009.

[7] S.G. Oval, and S. Shirawale, "Recognizing handwritten devanagari words using recurrent neural network", In *Proceedings of the 3rd International Conference on Frontiers of Intelligent Computing: Theory and Applications (FICTA),* pp. 413-421, 2015.

[8] Perona Pietro, and Jitendra Malik. "Scale-space and edge detection using anisotropic diffusion." *IEEE Transactions on pattern analysis and machine intelligence* , vol. 12, pp 629-639, 1990.

[9] Elad, Michael, and Michal Aharon. "Image denoising via sparse and redundant representations over learned dictionaries." *IEEE Transactions on Image processing* , vol. 15, pp. 3736-3745, 2006.

[10] Coifman, Ronald R., and David L. Donoho. Translation-invariant denoising. *Springer New York,* vol. 103, pp. 125-150*,* 1995.

[11] Burger, Harold C., Christian J. Schuler, and Stefan Harmeling. "Image denoising: Can plain neural networks compete with BM3D?." *In Proc of Computer Vision and Pattern Recognition (CVPR)*, 2012 IEEE Conference on. IEEE, June 2012.

[12] Jain, Viren, and Sebastian Seung. "Natural image denoising with convolutional networks." , *In Proc of Advances in Neural Information Processing Systems 21*. pp. 769-776*,* 2008.

[13] Cho, Kyunghyun. "Boltzmann machines and denoising autoencoders for image denoising." *arXiv preprint* arXiv:1301.3468 ,Jan 2013.

[14] Vincent, Pascal, et al. "Extracting and composing robust features with denoising autoencoders.", *In Proc. of the 25th international conference on Machine learning.* ACM, pp. 1096-1103, July 2008.

[15] Vincent, Pascal, et al. "Stacked denoising autoencoders: Learning useful representations in a deep network with a local denoising criterion."*Journal of Machine Learning Research* , vol. 11. pp. 3371-3408, 2010.

[16] Masci, Jonathan, et al. "Stacked convolutional auto-encoders for hierarchical feature extraction." , *In Proc. International Conference on Artificial Neural Networks*. Springer Berlin Heidelberg, pp. 52-59, 2011.

[17] Mahtab Ahmed, Animesh Kumar Paul, M. A. H. Akhand, "Stacked Auto Encoder Training incorporating Printed Text Data for Handwritten Bangla Numeral Recognition", *In proc. Of 19th International Conference on Computer and Information Technology (ICCIT)*, 2016.

[18] Y. LeCun, L. Bottou, Y. Bengio, and P. Haffner, "Gradient-based learning applied to document recognition," *Proc. IEEE*, vol. 86, no. 11, pp. 2278–2324, Nov. 1998.

[19] Off-Line Handwritten Bangla Numeral Database, http://www.isical.ac.in/~ujjwal/download/database.html

# Development of a Self-Navigating Algorithm for Library Book Finder Robot

Md. Rezaur Rashid[1], Nahid Uzzaman[2], Sanzida Hossain[3] and Neel Kanto Das Shuvra[4]
[1,4]Department of Computer science and Engineering, BRAC University (BRACU), Bangladesh
[2,3]Department of Mechanical Engineering, Military Institute of Science and Technology (MIST), Bangladesh
[1]aadrick045@gmail.com, [2]nahiduzzaman.eefat@gmail.com, [3]sanzidahossain92@gmail.com, [4]neelkando.d@gmail.com

***Abstract*—In this paper a self-navigating library robot is presented that goes to the required book shelf as a human would do and does not need to follow any line or fixed path. To achieve this performance a self-navigating algorithm is developed. The library is considered as a 2D array of book shelves. The robot uses 5 ultrasonic sensors to measure the distances of its surrounding objects. These measured distances are prerequisite of achieving all the necessary performances, such as calculating the current row-column positon of the robot, help the robot to move in a straight path, making an accurate turn etc. The robot works perfectly using the developed algorithm and shows satisfactory outcome which indicates the validity of the developed algorithm.**

***Keywords—library robot; book finder; self-navigating algorithm; self-navigating object locator.***

## I. Introduction

Finding books in the Library can sometimes be a challenging task. In some cases, the librarians pick and give books by themselves which causes chaos and hassle if the floor is too large and there isn't enough librarian. In other scenarios, readers find their own books by traversing through every shelves and index which is tough task and for new comers mostly. In today's world, robots are highly used to find objects industrially or socially because robots are time saving, accurate and adjustable to dynamic environment [1-3]. Robotic automation system can be very useful in any library management system because an object finder robot can be used as a book finder to overcome this problem [4-5]. In many existing system, line follower robots are used as book finder where they have to follow a fixed line or path as their navigation track [4]. Required book is pointed from a position in some systems [6-7]. Book handling robotic arm is developed too [8]. But this isn't convenient as the track is fixed and there may come new shelf and may happen a rearrangement of the interior.

In our system, we have built a self-navigating book finder robot which can take book indexes as input and find the desired book shelf. We have developed an algorithm for this self-navigation. When human try to go anywhere or find anything, first, they observe the environment for next step and analyze which way is clear or which is not. They never follow a fixed path for their movements. Our aim was to develop an algorithm based on which our robot will drive itself to the destination without any external navigation. Analyzing the sensor data, the robot also chooses the simplest track to reach the destination and return to the initial starting position after accomplishing intended task. The advantage of our algorithm is that it won't follow any fixed track like line following robots [4]. Therefore, if the arrangement of the library is changed, our algorithm will not have any problem to work in the new arrangement, whereas other methods of book finding may need to be modified.

## II. Construction of the Robot

The prototype robot is developed on a plastic wood chassis board. It contains 2 DC motors that are positioned at the front of the robot and drive two wheels. A movable wheel is attached to support the load of the rear side, while allowing flexible turning for the front wheels. Five distance measuring ultrasonic sensors are used to take input from the working environment and to navigate the movement. A laser pointer is attached with a Servo motor in the middle front side of the robot to point out the required book's position upon reaching to the necessary location Fig. 1.

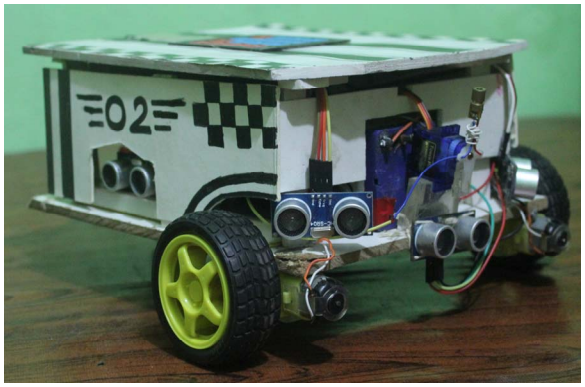

Figure 1. Structural build up of the Robot.

All those motors, sensors and laser pointer are connected with a controller. An input taking keyboard is also connected with the controller for taking the input value of searching book. The controller first takes date from the input keyboard (row-column and shelf-position of the book) and saves them as destination location. Then the controller takes data from the sensor and decides necessary actuations to control the motors and laser pointer accordingly until it reaches the destination. The whole system is powered from a 12V DC battery.

## III. Sensor arrangement

The sensors are named $S_L$, $S_R$, $S_{Lc}$, $S_{Rc}$, $S_F$ and the distance measured by those sensors are $d_L$, $d_R$, $d_{Lc}$, $d_{Rc}$, $d_F$ respectively.

978-1-5386-2307-7/17/$31.00 ©2017 IEEE

Arrangement of the sensor is shown in Fig. 2. Working principle and algorithm depends on this arrangement. These sensors measure the distance of any physical entity from the robot. Depending on which sensor is giving the concerning data, the robot can realize its position in different condition.

## IV. Working Principle and Algorithm

Our robot finds the book in a library after an input is given to it. This input can be come from library management system and database. The robot considers the library shelves as a 2D array. It takes the value of array row, column and shelf as input. Also for a particular row-column position the robot has to decide whether to point the laser towards right side or left side. This should be also come as an input parameter. The arrangement of library we used to develop the algorithm is shown in Fig. 3. The columns are the vertical roads in the Fig. 3. And the book shelves are considered as rows. The width of the roads is predefined.

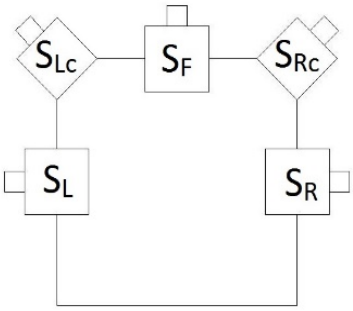


Figure 2. Arrangement of sensors.

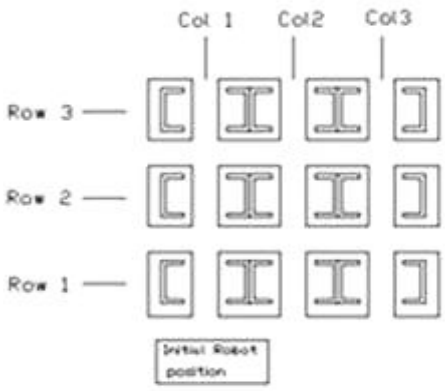


Figure 3. Library bookshelf arrangement.

### A. Row column counting

The whole system of our robot works according to the distance of the surrounding objects measured by the sensors. For understanding its own current position in the array, it uses these data from sensor. The robot has a defined starting position. It starts moving from this position after any input command is found. While moving the column wise direction, if $d_L + d_R$ <= road width, the current row position value is incremented. Again, if $d_L + d_R$ > road width and $d_F$ > a certain range, 4 ways junction is detected. After crossing the 4 ways junction, if $d_L + d_R$ <= road width, the row position will be again incremented Fig. 4.

For column counting, if $d_L + d_R$ > road width and $d_F$ > a certain range, 4 ways junction is detected and the current column position value is incremented. Again, if $d_L + d_R$ <= road width, it detects itself between two shelves. After passing the shelves, if $d_L + d_R$ <= road width, the column position will be again incremented Fig. 5.

Thus, the library or array can be of any size and with our row-column measuring algorithm the robot can go and find out the book for the user.

### B. Route selection

When the column number of the required position is 1 the robot goes straight from its starting position and stops in the input row number which essentially located between shelves Fig. 6.

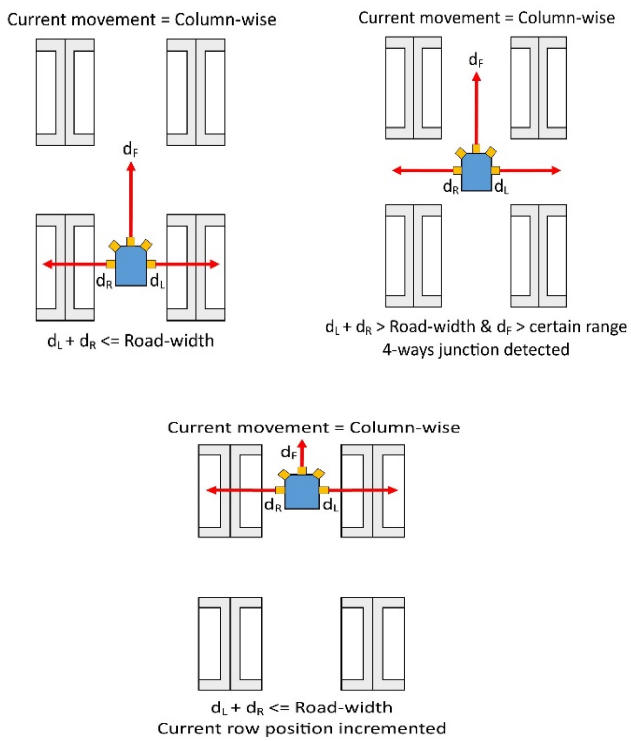


Figure 4. Row counting.

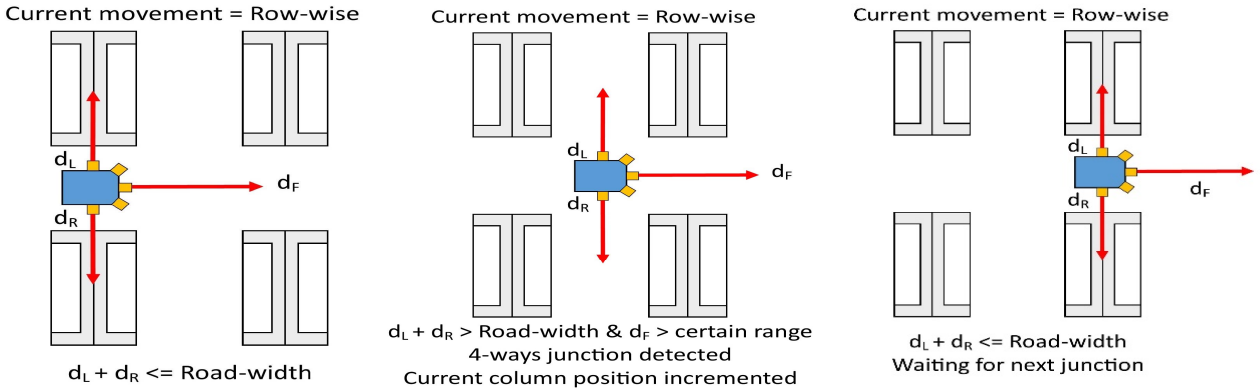


Figure 5. Column counting.

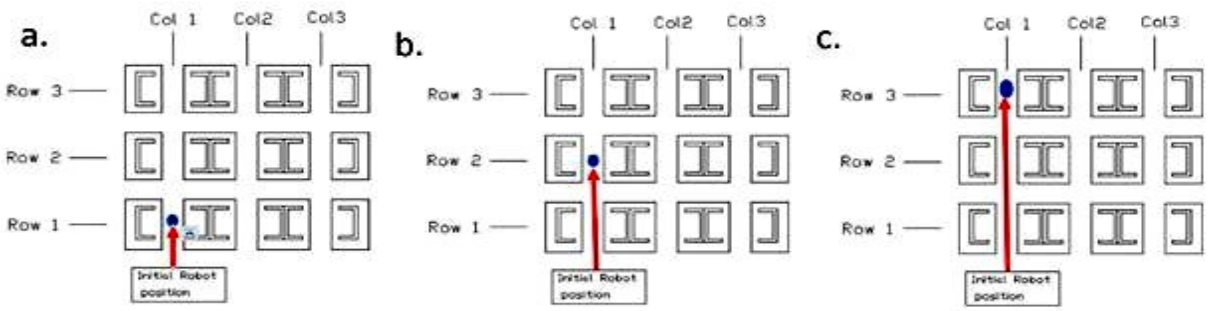


Figure 6. Route selection for column=1 (a) Col-1, Row-1, (b) Col-1, Row-2 and (c) Col-1, Row-3.

If the column number of the required position is greater than 1 robot goes in right direction after crossing row 1. This is an always maintained routine to achieve simplicity in the route selection. The robots continue to go in the right direction until the current column number is matched with the input column number. Afterwards, if the required row number is 1 the robots goes right direction again from the current position Fig. 7. If the required row number is greater than 1 it goes to left direction and continues until the current row number is equal to required row number Fig. 8.

### *C. Straightening process*

As the robots starts moving it has to move forward in a straight manner and sometimes may need to take turns. But in its way to the destination it can be deflected from the straight path and proceed towards the book shelf wall and collide. To avoid these situations a self-straightening process is included in the algorithm. The controller always checks the distance value measured by the side ($S_L$, $S_R$) and corner ($S_{Lc}$ and $S_{Rc}$) sensors. If one of the value is reducing in a significant manner it means the robot is stepping towards one side. One property of the ultrasonic sensor is it only detects the distance of an object that is normal to the sensor thrown sound waves. So, if the one of the corner sensors is detecting distance reduction, it means the robot is going in a tilted way from the straight path. The controller then turns the robot to come to the straight path by handling the wheel motors. If the side sensors $S_L$ and $S_R$ start-

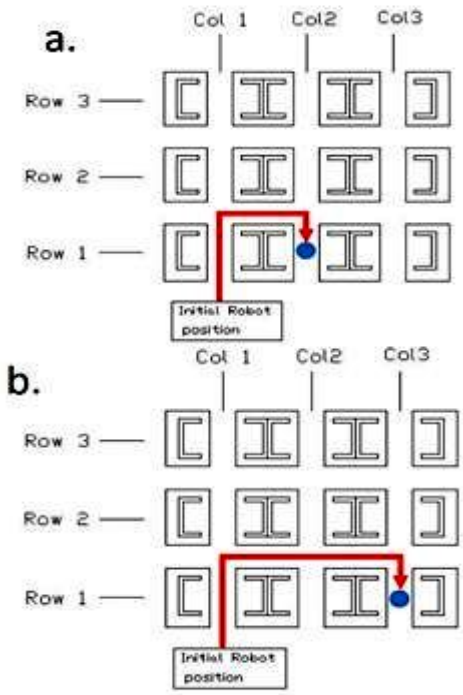


Figure 7. Route selection for Column>1 and Row=1 (a) Col-2, Row-1 and (b) Col-3, Row-1.

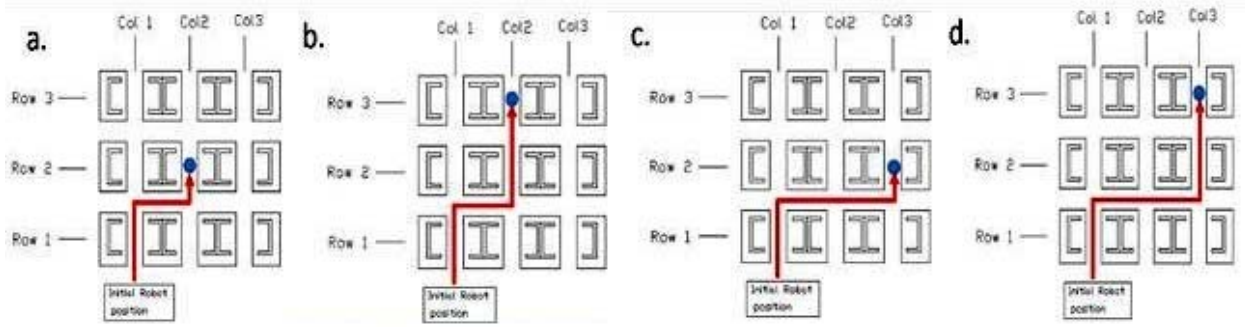


Figure 8. Route selection for Column>1 and Row>1 (a) Col-2, Row-2 and (b) Col-2, Row-3 (c) Col-3, Row-2 and (d) Col-3, Row-3.

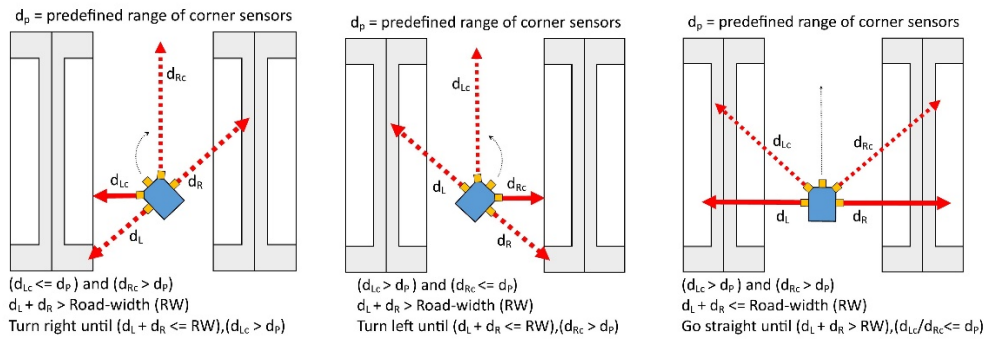


Figure 9. Straightening process.

-measuring distances, it means the robot is now moving in a straight path which has been shown in Fig. 9.

### *D. Turning*

To accomplish an accurate turn, all the sensors work simultaneously. When, the robot starts to turn, the controller checks $d_L$, $d_R$, and $d_F$ values. When the $d_F$ value starts increasing it means the robot is becoming straight. However, for turning in a particular direction the distance of the opposite side will be increasing gradually until entering in the path between two shelves. When robot enters in the path both the side sensors will have some values, by which the controller will be aware of the situation. If any overturning or less turning is occurred, the side sensors will be used to determine that condition. Then using the straightening algorithm, the robot will start to move in straight path again Fig. 10.

### *E. Laser pointing*

When the robot reaches the required row-column position it has one more task to do. There are two book shelves in the left and right side of the robot for a particular row-column position. For this reason, a laser pointer is added with our robot. Upon reaching to the required destination the laser pointer points the required book in the correct shelf. The pointer is attached with a servo motor with the help of which the controller aims the pointer at the required direction. For the laser pointer angle less than 90 degrees, left side shelf is pointed and for angle greater than 90 degrees, right side shelf is pointed. If the shelf is very large in length it can be divided into multiple segment to better performance of pointing out mechanism.

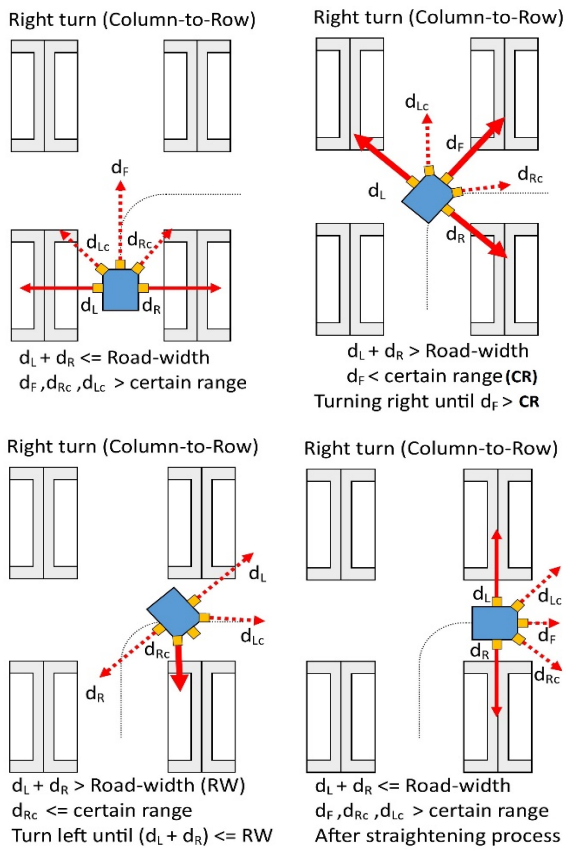


Figure 10. Turning of the robot to right.

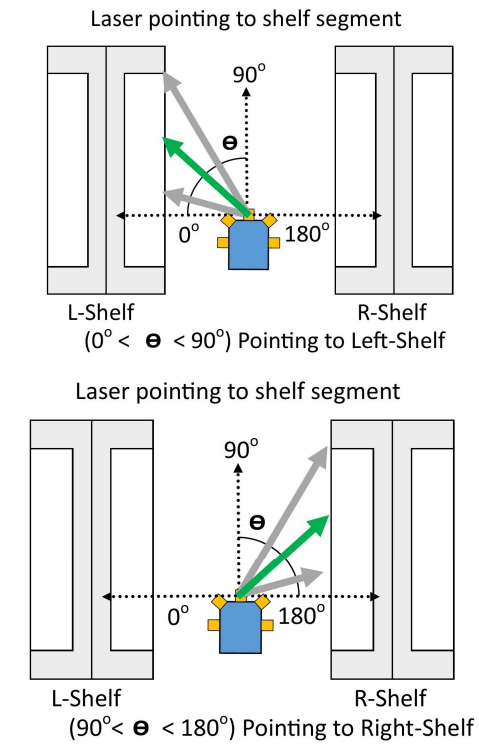


Figure 11. Laser's pointing to required shelf.

## V. EXPERIMENTAL PERFORMANCE ANALYSIS

Our robot was tested in a model array library. When the input parameters are given, the robot starts for the destination immediately and points the required book containing shelf. With this arrangement and developed algorithm our robot works perfectly. Initially, we only used $d_F$, $d_L$ and $d_R$ sensors for our robot.

In a random study, we made our robot to travel in varying destinations of the array. For the case, column =1, row = 2 (Fig. 5-b) we used the robot 30 times to simulate the algorithm. We observed that the robot reached its destination successfully in every occasion which is shown in Table 1.

For the case, column =2, row = 1 (Fig. 6-a) we again used the robot 30 times to simulate the algorithm. We observed that 17 out of 30 times it reached the destination successfully and 13 out of 30 times it was unsuccessful which is shown in Table 2.

We then analyzed both the cases and found that, the robot could go perfectly in straight path however, in junction turning it faced difficulties. Because, the sensors $d_R$ and $d_L$ was attached on the middle of robot's right and left sides respectfully. Therefore, when the robot reads data from these sensors, the driving half of the robot body has already passed-

| **Mean Sensor values, $d_L$, $d_R$, $d_F$ (inch)** | **Current position. (Through Row or Colum)** | **$d_L + d_R$ <= Road Width (25 inch)** | **$d_F$ < Range (40 inch)** | **Is this Position a Junction?** | **Current Column (C) and Row (R) Position** | **Desired Column (C) and Row (R)** | **Current Position = Desired Position** | **Next Action** |
|---|---|---|---|---|---|---|---|---|
| 21.32, 28.63, 67.18 | Column | No | No | - | C=1, R=0 | C=1, R=2 | No | Go forward |
| 10.58, 11.46, 68.72 | Column | Yes | No | No | C=1, R=1 | C=1, R=2 | No | Go forward |
| 22.28, 28.12, 63.27 | Column | No | No | Yes | C=1, R=1 | C=1, R=2 | No | Go forward |
| 9.97, 12.87, 65.43 | Column | Yes | No | No | C=1, R=2 | C=1, R=2 | Yes | Stop, Point Laser |

Table 1. Simulated mean data for the position column = 1, row = 1. This table shows all the sensor values and the route position in the library shelves' array.

| **Mean Sensor values, $d_L$, $d_R$, $d_F$ (inch)** | **Current position (Through Row or Colum)** | **$d_L + d_R$ <= Road Width (25 inch)** | **$d_F$ < Range (40 inch)** | **Is this Position a Junction?** | **Current Column (C) and Row (R) Position** | **Desired Column (C) and Row (R)** | **Current Position = Desired Position** | **Next Action** |
|---|---|---|---|---|---|---|---|---|
| 22.93, 29.32, 68.24 | Column | No | No | - | C=1, R=0 | C=2, R=1 | No | Go forward |
| 11.67, 11.19, 67.96 | Column | Yes | No | No | C=1, R=1 | C=2, R=1 | No | Go forward |
| 21.73, 27.31, 65.82 | Column | No | No | Yes | C=1, R=1 | C=2, R=1 | No | Turn Right |
| 9.97, 12.87, 65.43 | Row | Yes | No | No | C=1, R=1 | C=2, R=1 | No | Go forward |
| 23.56, 22.31, 68.72 | Row | No | No | Yes | C=2, R=1 | C=2, R=1 | Yes | Turn Right, Stop, P.L. |

Table 2. Simulated mean data for the position column = 2, row = 1. This table shows all the sensor values and the route position in the library shelves' array. First column from left shows the sensors readings while the 2nd column shows the position of the robot. The last column shows in certain position after getting such values what decision the robot takes to reach to its destination.

| Mean Sensor values, $d_L$, $d_R$, $d_F$, $d_{Lc}$ (integer), $d_{Rc}$ (integer) (inch) | Current position (Through Row or Colum) | $d_L + d_R$ <= Road Width (25 inch) | $d_F$ < Range (40 inch) | Is this Position a Junction? | Current Column (C) and Row (R) Position | Desired Column (C) and Row (R) | Current Position = Desired Position | Next Action |
|---|---|---|---|---|---|---|---|---|
| 23.08, 27.89, 67.37, 41, 43 | Column | No | No | - | C=1, R=0 | C=2, R=2 | No | Go forward |
| 10.57, 12.31, 68.01, 41, 42 | Column | Yes | No | No | C=1, R=1 | C=2, R=2 | No | Go forward |
| 22.43, 27.97, 66.91, 42, 41 | Column | No | No | Yes | C=1, R=1 | C=2, R=2 | No | Turn Right |
| 12.27, 11.73, 68.77, 43, 42 | Row | Yes | No | No | C=1, R=1 | C=2, R=2 | No | Go forward |
| 23.53, 28.17, 67.79, 43, 43 | Row | No | No | Yes | C=2, R=1 | C=2, R=2 | No | Turn Left, |
| 11.37, 11.83, 67.61, 42, 41 | Column | Yes | No | No | C=2. R=2 | C=2. R=2 | Yes | Stop, Point Laser |

Table 3. Simulated mean data for the position column = 2, row = 2. This table shows all the sensor values and the route position in the library shelves' array. First column from left shows the sensors readings while the 2nd column shows the position of the robot. The last column shows in certain position after getting such values what decision the robot takes to reach to its destination.

-the junction-point. As a result, sometimes the robot faces difficulties such as colliding with bookshelves, getting misplaced from its desired route or reading incorrect row and column counting.

Then, we attached two additional sensors named $d_{Lc}$ and $d_{Rc}$ in the corner edges of the robot's driving front (Fig. 1) to overcome the turning difficulties and better straitening. Then we simulated our robot 50 times for the case, column=2, row=2 and we observed that the robot ran more efficiently and reached the destination successfully 48 out of 50 times with the success rate of 96% which is shown in Table 3. This means our developed algorithm is feasible and for varying positions in the array it has a smooth travel without any hassle and collision. The 2 unsuccessful observations can be due to malfunction of the system which can be overcome by using more efficient sensors and controller.

## VI. Conclusion

The aim of our study was to develop a library book finder robot that does not need to follow any line or fixed path. The robot will go to the required book shelf as a human would do. It will navigate itself to the destination in a simple route. For this purpose, an algorithm was developed. Five distance measuring sensors are used to do all the required duties, such as row-column counting, ensuring a straight forward movement, accurate turning etc. Performance of the robot was satisfactory which makes the algorithm acceptable.

## References


[1] Yunting Pang, Qiang Huang, Xiaolei Quan, Juan Zheng and Xiaobing Wu, "Fast object location and tracing using two CCD cameras and laser range finder," 2005 IEEE International Conference on Information Acquisition, 2005, pp. 5

[2] A. R. F. Quiros, A. C. Abad and E. P. Dadios, "Object locator and collector robotic arm using artificial neural networks," Humanoid, Nanotechnology, Information Technology,Communication and Control, Environment and Management (HNICEM), 2015 International Conference on, Cebu City, 2015, pp. 1-6.

[3] H. Y. Chung, C. C. Hou, Y. S. Chen and C. L. Chao, "An intelligent service robot for transporting object," Industrial Electronics (ISIE), 2013 IEEE International Symposium on, Taipei, Taiwan, 2013, pp. 1-6.

[4] J. Thirumurugan, M. Vinoth, G. Kartheeswaran and M. Vishwanathan, "Line following robot for library inventory management system," Emerging Trends in Robotics and Communication Technologies (INTERACT), 2010 International Conference on, Chennai, 2010, pp. 1-3.

[5] A. C. Polycarpou, T. Samaras and J. N. Sahalos, "An RFID-based library management system using smart cabinets: A pilot project," The 8th European Conference on Antennas and Propagation (EuCAP 2014), The Hague, 2014, pp. 2954-2955.

[6] M. Mikawa, Y. Morimoto and K. Tanaka, "Guidance method using laser pointer and gestures for librarian robot," 19th International Symposium in Robot and Human Interactive Communication, Viareggio, 2010, pp. 373-378.

[7] Masahiko Mikawa, Masahiro Yoshikawa, Takeshi Tsujimura and Kazuyo Tanaka, "Librarian robot controlled by mathematical AIM model," ICCAS-SICE, 2009, Fukuoka, 2009, pp. 1200-1205.

[8] Corina Monica Pop, Gheorghe Leonte Mogan, "Robotic grippers for handling books in libraries," International Conference of Scientific Paper Afases, Brasov, 2015.

2017 3rd International Conference on Electrical Information and Communication Technology (EICT), 7-9 December 2017, Khulna, Bangladesh

# Enhancing Secure Cloud Computing Environment by Detecting DDoS Attack Using Fuzzy Logic

Himadri Shekhar Mondal*, Md. Tariq Hasan, Md. Bellal Hossain, Md. Ekhlasur Rahaman and Rabita Hasan
Electronics and Communication Engineering Discipline, Khulna University, Khulna, Bangladesh.
*bdhimadri@gmail.com

***Abstract*—Cloud computing has become a part and parcel of our daily life. It just made our life easier with its amazing features. To support increasing number of users as well as smart devices, it is needed to keep the cloud environment more and more secure and reliable. Cloud computing security has become a major challenging field now a days. In this paper we presented a Fuzzy based mechanism, which may be helpful for the detection of Distributed Denial of Service (DDoS) attack in cloud computing environment. As DDoS attack becomes powerful with the passing of time, if it is detected at first, then the attack may be minimized. So we focused on attack detection mechanism to secure the cloud environment using Fuzzy logic.**

***Index Terms*—Cloud computing environment, Fuzzy logic, DDoS attack.**

## I. Introduction

Present world is blessed with computing technology. Cloud computing technology has added a new dimension in the internet based system with its adaptive and reliable features. Without the rise of cloud computing, it may not possible to enjoy high speed internet for the increasing number of users. Now a days increasing security has become a major challenging factor for service providers. The anomalous attack is going on which damages both the money and valuable time. If it is possible to mitigate the attacks in the cloud system, then, the end users will enjoy the beauty of secure cloud environment more perfectly.

There are many types of attack, which may destroy the cloud environment within a second if there is no preventing mechanism. The most common attack in cloud environment is Distributed Denial of Service (DDoS) attack. This attack targets the machine running in a networking system and generates large number of traffics. These traffics attacks the server system in the cloud environment. The cloud servers suddenly get pressurized as it has to process huge number of traffic. If there is no prevention mechanism in the cloud system, then, the packet arrival rate becomes high with the increasing of time. As a result, at one stage, the cloud system fails to serve its users.

We proposed a Fuzzy based mechanism to detect the attack in the cloud system. We know Fuzzy system is used to reduce the human brain pressure, as it can perform logical operation like human brain can do. So it is possible to detect the anomalous behavior of packets if we implement the Fuzzy logic in the cloud system. All the incoming data will be filtered through the Fuzzy system before arriving in the cloud environment. A Fuzzy logic based IF-THEN rule is implemented in the Fuzzy inference engine system which will analyze the incoming data packet behavior and send the report to the cloud system. If there is huge number of data, which load seems to heavy for the cloud environment, the defense mechanism may active or the data may be discarded by the cloud system automatically. Thus, the cloud system can provides secure, friendly and reliable service to its users.

In this paper we mainly focused on DDoS attack detection mechanism using Fuzzy logic. The outline is designed as, related works are discussed in section II, the methodology of the proposed system is presented in section III. The results are discussed in section IV, where we have presented results by changing the parameters. Section V is based on conclusion and future works.

## II. Related works

Plenty of research works are going on to ensure the secure cloud environment. The history of developing this attack mechanism was observed on 1980s, a network research group discovered that internet control message protocol (ICMP) packets making the network complex for the users, which is marked as the concept of DDoS attack. The DDoS attack first traced in June, 1998 by a group of network researchers [1]. Lo *et al* [2] presented a method which is based on Intrusion Detection System framework. Bakshi *et al* [3] presented a secure cloud computing model which can prevent the DDoS attack. N. Jeyanthi [4] proposed a model using Packet Resonance Strategy (PRS) which can be helpful for preventing the DDoS from spoofed address. Chen *et al* [5] proposed a filtering technique to prevent the DDoS attack. S. Chavan [6] presented a Intrusion Detection System (IDS) which is based on neuro-fuzzy system.

The Fuzzy system was first invented by L.A. Zadeh [7] at 1965. The proposed system was not good enough then and didn't gain much popularity. He then started research again to improve the system. As a result his landmark paper [8] was published on 1973. The reason of popularity was much more effective when Mamdani [9] applied his inference engine rule on the Fuzzy system.

Lee *et al* [10] presented the security techniques in cloud system. Zhu *et al* [11] presented a Fuzzy based authorization system in cloud computing architecture. A. Visconti *et al* [12] presented a Fuzzy based algorithm, which collects data from various networking elements and detects the misbehaving nodes by comparing the collected data. Watkins et al [13]

978-1-5386-2307-7/17/$31.00 ©2017 IEEE

also presented a comparison based attack techniques in cloud computing environment using Fuzzy system. Lou *et al* [14] discussed the piracy prevention techniques in Content Delivery network. Research challenges in cloud system were presented by Boutaba *et al* [15].

## III. Methodology

In this section we've discussed our proposed methodology for detection of DDoS attack in cloud environment.We've mainly proposed a system which needs to implement in the cloud environment for a quick detection of attacks and ensure the safe working environment. In the system we've taken three inputs and calculated one output. In the input section, entropy of source IP, port address and packet arrival rate are considered. Using these parameters we have shown attack status based on Fuzzy IF-THEN rules. The entropy is calculated mainly based on Shannon's theorem [16], which indicates that, If a source is independent and the source carries *n* variables having the probability of $P_i$, then the entropy *E* will be calculated through this equation,

$$E = -\sum_{i=1}^{n} P_i log_2 P_i \tag{1}$$

DDoS attack targets the remote servers and attacks the machines with a huge number of packets. If the attack can gain the access of central server by bypassing the vulnerable security system, then it creates a huge number of fake traffic which is impossible to handle for the central server system of cloud. As a result, new arrival packets can't be processed by the machine and have to face the anomalous environment for the user. With the passing of time the attack becomes higher, so it is possible to minimize the attack if it is identified at the beginning. If we use Fuzzy system in the cloud environment then it can detect the anomalous behavior of the incoming packets. As we know, Fuzzy system is helpful for decision making criteria, it can help to reduce the human thinking, we can easily implement it. We considered the different protocols [17] like Internet Control Message Protocol (ICMP), Transmission Control Protocol (TCP) User Datagram Protocol (UDP) etc.

The Fuzzy system has three stages in its working principle. They are,

1) Fuzzification
2) Inference mechanism
3) Defuzzification

In the Fuzzy system the crisp values are needed to be converted for the calculation, and this work is done by the fuzzification steps. The fuzzified values are then used by inference engine, which actually maps the data systems using the logistic operations. Finally the defuzzification system converts the fuzzified values to the crisp values. For our better realization, consider a Fuzzy set F which has Z elements, these values are mapped pair domains and remains between the value of 0 and 1. Mathematically we can written as,

$$F = \{(z_1, 0.6), (z_2, 0.4), (z_3, 0.2), (z_4, 1)\} \tag{2}$$

Using Zadeh's [8] notation we can write this equation as,

$$F = \{\frac{0.6}{z_1} + \frac{0.4}{z_2} + \frac{0.2}{z_3} + \frac{1}{z_4}\} \tag{3}$$

The membership function is used to mapped the data according to their values in the rule base inference engine. Let us consider a membership function $\mu_F$ , which will map the elements of Z in between 0 and 1. Mathematically this can be written as,

$$F = \{(z, \mu_F(z)) \,|\, z \in Z\} \tag{4}$$

The basic block diagram of Fuzzy system in presented in Fig. 1.

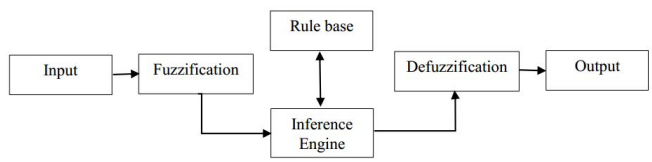


Fig. 1. Fuzzy basic block diagram

***1. Fuzzification***

The fuzzification is the first step in the fuzzy system in which the inputted values are converted to the fuzzified values. This system may work in the two ways.

Let consider $F_{ui}$ is the Fuzzy singleton, so we can express it as,

$$F_{ui}(u) = \begin{cases} 1 & if\ u = u_i \\ 0 & otherwise \end{cases} \tag{5}$$

Also, if $F_{ui}$ is Fuzzy set, then,

$$\mu_{F_{ui}} = \begin{cases} 1 & if\ u = u_i \\ decrease\ from\ 1 & when\ moving\ from\ u_i \end{cases} \tag{6}$$

***2. Inference Engine***

Fuzzy inference engine is the heart of the Fuzzy system as the logic based operation is performed here. We choose Mamdani [9] type inference which is a popular and widely used inference engine. The basic rule for inference engine is,

***IF x is A and y is B THEN z is C***

Here we have more than two input. In this type of case, the output will be the minimum membership degree of the input parameters. We have implemented Fuzzy based IF-THEN rule in the inference system which can be presented as,

***IF*** *Entropy of Source IP is* {*Low, Medium, High*} ***AND*** *Port Address is* {*Low, Medium, High*} ***AND*** *Packet Arrival Rate is* {*Low, Medium, High*} ***THEN*** *the attack type is* {*Low, Medium, High*}

According to IF-THEN rule we designed a rule based lock which is presented in the table 1.

Table 1: Fuzzy based implemented IF-THEN rule

| EoSIP (i) | PA (i) | PAR (i) | AS (o) |
|---|---|---|---|
| Low | Low | High (ICMP) | High |
| Low | (none) | High | High |
| High | High | Low | Medium |
| Low | Low | High (UDP) | High |
| Low | High | High | High |
| Medium | Medium | High | High |
| High | High | High | High |
| Low | Medium | Low | Low |
| Low | High | Medium | Medium |
| High | Medium | Medium | Low |
| High | Medium | High | Medium |
| Low | Medium | High | High |
| High | Low | Medium | Low |
| Low | Low | Medium | Medium |
| Medium | Low | Low | Low |
| Medium | Low | High | High |
| Medium | Medium | Low | Low |
| High | Medium | Low | Low |

Here in this Table 1, EoSIP refers to Entropy of Source IP, PA indicates Port Address, PAR refers to Packet Arrival Rate, AS indicates Attack Status, i indicates the inputs and o indicates the output.

***3. Defuzzification***

The defuzzification is needed for converting the fuzzified rule based values to the crisp values. This reverse process of fuzzification system helps to determine the values to the readable values for the calculation.

The Fuzzy system described here is used to determine the attack status in the cloud environment. As heavy packets generates by the DDoS attacker, the main target is to detect the attack at its earlier stage. If earlier detection is possible then it is possible to mitigate the attack for ensuring secure cloud environment. The Fuzzy system including cloud environment is presented in the Fig. 2.

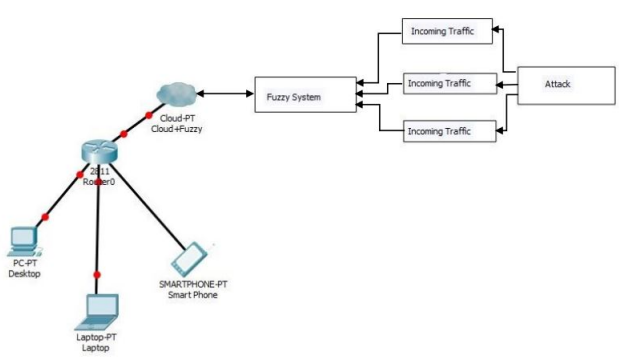


Fig. 2. Implemetation of attack detection model

.

## IV. Result

The Fuzzy IF-THEN rule is implemented using Matlab software and the result is shown here. The figure 3 is based on normal value which shows the surface base view.

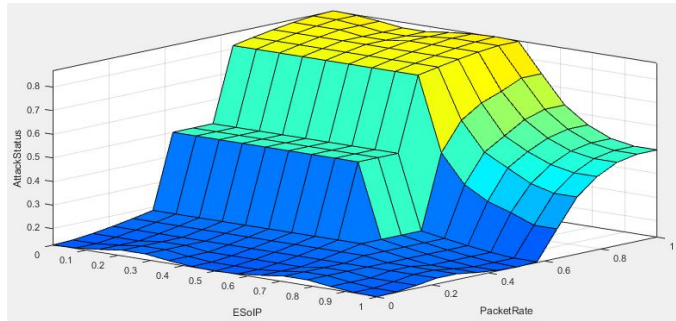


Fig. 3. Attack status at normal stage

Figure 4 is just the representation of figure 3 as rule base view,

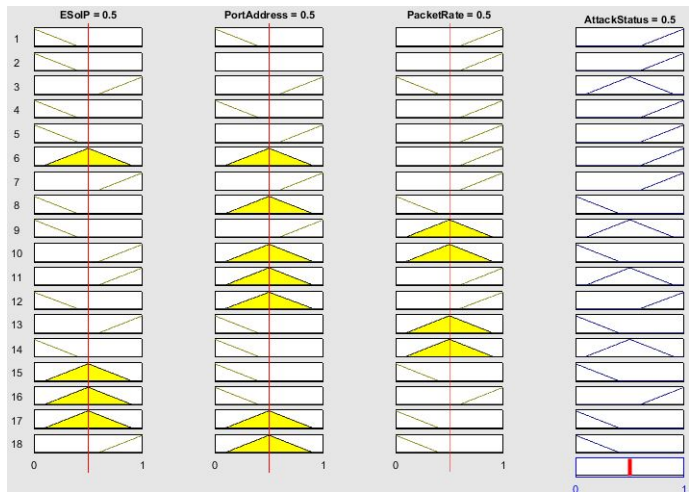


Fig. 4. Rule base relationship status

Here all the value remains between 0 and 1, we considered 0 as the minimum value and 1 as the maximum value also, 0.5 is considered as the normal value. Now let increase the packet arrival rate, the result is shown in figure 5.

From the figure 5, we can see that, due to increase of the packet arrival rate, the attack status becomes high. Now lets increase the entropy of source IP. the result is shown in the figure 6.

From the figure 6, we can see as soon as we increase the entropy of source IP, the attack status decrease from its previous increased stage. So we can easily determine the attack status in cloud computing environment by implementing Fuzzy logic.

There are so many DDoS attack detecting mechanisms but, the Fuzzy logic implemented mechanism is cost effective, reliable and easy method for the cloud system. The cloud environment has to deal with a huge number of process for providing better service to its users, so if we implement a heavy method for attack detection, then the user may not get desired service from the cloud. As this Fuzzy logic is easy and

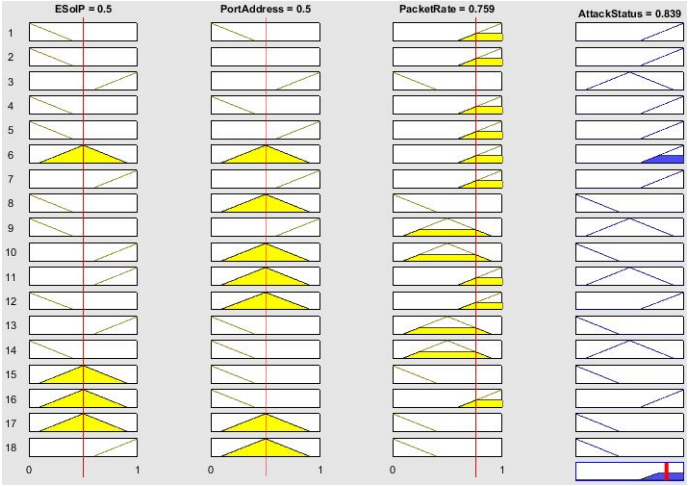


Fig. 5. Packet arrival rate increased

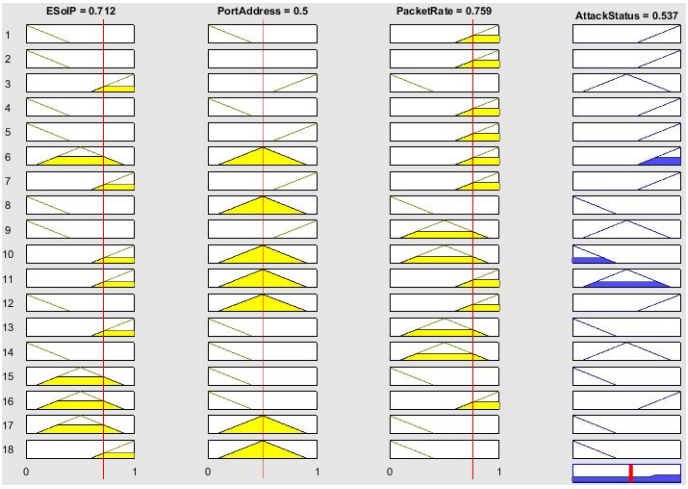


Fig. 6. Attack status due to changing of parameters

reliable, then it can be easily implemented in cloud computing environment to ensure secure cloud environment for its users.

## V. Conclusion

Attack in cloud computing may be minimized but early detection is needed, which is presented in this paper. The attackers always try to discover a way to bypass the security system to make the system vulnerable. So the security system may need more research to prevent the new discovered attacks. It is possible to acquire more fruitful result in the future by adding more variable using the Fuzzy system, which will be more reliable, dynamic and provide better secure performance for the users.

## References

[1] S.-C. Lin and S.-S. Tseng, "Constructing detection knowledge for ddos intrusion tolerance," *Expert Systems with applications*, vol. 27, no. 3, pp. 379–390, 2004.

[2] C.-C. Lo, C.-C. Huang, and J. Ku, "A cooperative intrusion detection system framework for cloud computing networks," in *Parallel processing workshops (ICPPW), 2010 39th international conference on*, pp. 280–284, IEEE, 2010.

[3] A. Bakshi and Y. B. Dujodwala, "Securing cloud from ddos attacks using intrusion detection system in virtual machine," in *Communication Software and Networks, 2010. ICCSN'10. Second International Conference on*, pp. 260–264, IEEE, 2010.

[4] N. Jeyanthi and N. C. S. Iyengar, "Packet resonance strategy: a spoof attack detection and prevention mechanism in cloud computing environment," *International Journal of Communication Networks and Information Security*, vol. 4, no. 3, p. 163, 2012.

[5] Q. Chen, W. Lin, W. Dou, and S. Yu, "Cbf: a packet filtering method for ddos attack defense in cloud environment," in *Dependable, Autonomic and Secure Computing (DASC), 2011 IEEE Ninth International Conference on*, pp. 427–434, IEEE, 2011.

[6] S. Chavan, K. Shah, N. Dave, S. Mukherjee, A. Abraham, and S. Sanyal, "Adaptive neuro-fuzzy intrusion detection systems," in *Information Technology: Coding and Computing, 2004. Proceedings. ITCC 2004. International Conference on*, vol. 1, pp. 70–74, IEEE, 2004.

[7] L. A. Zadeh, "Fuzzy sets," *Information and control*, vol. 8, no. 3, pp. 338–353, 1965.

[8] L. A. Zadeh, "Outline of a new approach to the analysis of complex systems and decision processes," *IEEE Transactions on systems, Man, and Cybernetics*, no. 1, pp. 28–44, 1973.

[9] E. H. Mamdani and S. Assilian, "An experiment in linguistic synthesis with a fuzzy logic controller," *International journal of man-machine studies*, vol. 7, no. 1, pp. 1–13, 1975.

[10] R. K. Ko, M. Kirchberg, and B. S. Lee, "From system-centric to data-centric logging-accountability, trust & security in cloud computing," in *Defense Science Research Conference and Expo (DSR), 2011*, pp. 1–4, IEEE, 2011.

[11] S. Zhu and G. Gong, "Fuzzy authorization for cloud storage," *IEEE Transactions on Cloud Computing*, vol. 2, no. 4, pp. 422–435, 2014.

[12] A. Visconti and H. Tahayori, "A biologically-inspired type-2 fuzzy set based algorithm for detecting misbehaving nodes in ad-hoc wireless networks," *INTERNATIONAL JOURNAL FOR INFONOMICS*, vol. 3, no. 2, pp. 373–382, 2010.

[13] D. Watkins, "Tactical manet attack detection based on fuzzy sets using agent communication," tech. rep., MORGAN STATE UNIV BALTIMORE MD, 2004.

[14] X. Lou and K. Hwang, "Collusive piracy prevention in p2p content delivery networks," *IEEE Transactions on Computers*, vol. 58, no. 7, pp. 970–983, 2009.

[15] R. Boutaba, L. Cheng, and Q. Zhang, "On cloud computational models and the heterogeneity challenge," *Journal of Internet Services and Applications*, vol. 3, no. 1, pp. 77–86, 2012.

[16] C. E. Shannon, "A mathematical theory of communication," *ACM SIGMOBILE Mobile Computing and Communications Review*, vol. 5, no. 1, pp. 3–55, 2001.

[17] B. A. Forouzan, *TCP/IP protocol suite*. McGraw-Hill, Inc., 2002.

# Frequency Component Grouping Based Sound Source Extraction from Mixed Audio Signals Using Spectral Analysis

Shifat Hossain[1,3], Shadman Sakib Khan[2], Md Samiul Haque Sunny[1], and Mohiuddin Ahmad[1]
[1]Khulna University of Engineering & Technology (KUET), Khulna, Bangladesh
[2]Northern University Bangladesh (NUB), Dhaka, Bangladesh
[3]shifathosn@gmail.com

*Abstract*— **The extraction of the polyphonic sounds from mix of different sources is natural, even to normal human listeners. For this reason, human auditory recognition system is very robust compared to the algorithms used to analyze audio in different computing systems. This work is a frequency domain based approach for sound source extraction from any mixed audio signal to improve the efficiency of audio recognition algorithms. In this work, we propose a new approach to estimate, analyze and extract different melodies from different physical sources without modeling the signal or sources. This process uses one or two microphone(s) based systems to analyze sound signal to be compatible to human hearing. Our work is specifically aiming the extraction of sound sources by matching frequency patterns and calculation of delay times, providing the spatial and temporal data of the signal sources and their outputs.**

***Keywords—Signal extraction, BSS, spectrogram, spectral analysis, sound signal, physical sound sources.***

## I. INTRODUCTION

The extraction of sound sources by polyphonic sound approximation is a new concept in audio processing technologies. A polyphonic sound source emits different notes at the same time as sound energy. Transforming the sound waves in the frequency domain the "main frequency" and "harmonics" can be analyzed.

From the frequency spectrum of the sound waves it becomes evident that different sound sources have different number of harmonics, harmonic components, velocity patterns in each note. Different notes also have distinctive velocity and harmonics pattern but they can be classified with some similarities [1].

Extraction of signals from different sources is very important due to its wide applicability in audio processing systems. Extraction of data can efficiently remove noise or separate "Unfocused" sources from the raw signal. Focusing sources containing voice data can give a clean and semantically rich output which can be used in vocal analysis, voice recognition etc. Analysis of music data can be used in several Music Information Retrieval (MIR) applications or simply remove any musical component in post-processing of the music. It can also be used in humming or singing search systems [2], music search engines [3], detection or analysis of the structure of music [4] and in many applications.

On the other hand, the human hearing system works in a very complex way. Though it is not known exactly how the human brain is able to separate different sound sources. Different algorithms are implemented to mimic this brain function. In one approximation, it is stated that human perception can work without the help of previously known audio sources or any predefined instrument signature. Because the brain can process any unknown sound and evaluate the properties of it. In another approximation, human perception can only work when major training is undergone on the sound parameters or instrument signatures. This effect is similar to the speech perception of the infants [5].

A number of methods have been proposed previously to solve the sound separation problem in audio processing. And they can be roughly separated into two categories –

a) Modeled sound source based signal separation algorithm

b) Blind signal separation based algorithm

But both of them have their own limits. In the modeled source based algorithms, the separation is efficient but the result contains a noticeable amount of glitch. On the other hand, the blind source separation algorithms do not depend on the modeled source signature database. But these algorithms cannot determine the sound sources effectively with fixed two sound observers.

Some notable works can be considered in the scope of this study.

Poliner and Ellis proposed a classification based system for music transcription. Here SVM was trained by labeled audio feature vectors where each note was distinguished by the system [6]. Goto proposed a probabilistic modeling of the spectrogram for detection of melody and bass lines in CD recordings in [7]. Ryynänen and Klapuri proposed a method of separation of signals by classical signal processing algorithms in [8].

Here, a proposed algorithm is discussed that

a) does not depend on the predefined modeling of the physical sources.

b) does not require more than two sound observers to identify physical sources.

978-1-5386-2307-7/17/$31.00 ©2017 IEEE

The contribution of this method lies in the use of dynamic grouping of spectral harmonic components obtained from the spectral analysis of the channel(s). Furthermore, the evaluation of performance of this proposed algorithm is also presented.

## II. METHODOLOGY

This proposed method is based on some assumptions that is required to be considered for polyphonic source separation from a mixed audio signal. These are –

1. The physical sources are independent.

2. The physical sources do not mimic other physical source timings.

3. The physical sources should not mimic other sources' notes or frequency levels.

4. Maximum number of sound observers (sound inputs to this system) are two.

5. The specimen system might have any number of physical sources.

Here the term "instruments" is not limited to musical instruments only. Each and every object that can produce sound (including human voice) is considered as a physical source or instrument in this scope. The main concept of this proposed method is that each and every real-world instrument creates overtones when sound is being created by them. These overtones generated varies with the pitch change and timing of the fundamental frequency of the tone. This work recognizes the close approximated tones and groups those and recognize these as a virtual source. Then the signatures of the virtual sources are evaluated. This signature is added to its dictionary and is used to search other groups of the same audio signal and they are grouped as an instrumental super-group. Then all the different instrumental super-groups are reconstructed and given output for further processing outside the scope of this work. So, this proposed method of source separation uses the geometry, pattern and timing of the sound components to recognize and separate physical sound sources. The proposed algorithm is illustrated in Figure 1.

### A. Audio acquisition

The sound data is either collected from recording or it may be computer synthesized data. The sound data can be of single or dual channel.

For N number of independent physical sources (S), the input to the two channels of this system shown in (1) and (2).

$$x_R[n] = \sum_{k=0}^{N-1} S_R(k)[n] \tag{1}$$

$$x_L[n] = \sum_{k=0}^{N-1} S_L(k)[n] \tag{2}$$

The subscripts R and L indicate the right and left channel of the input audio (x) respectively. $S_R(k)$ and $S_L(k)$ sources indicate sound generated from the same source S(k), but these two quantities are modified based on spatial parameters of the source (i.e. location in space).

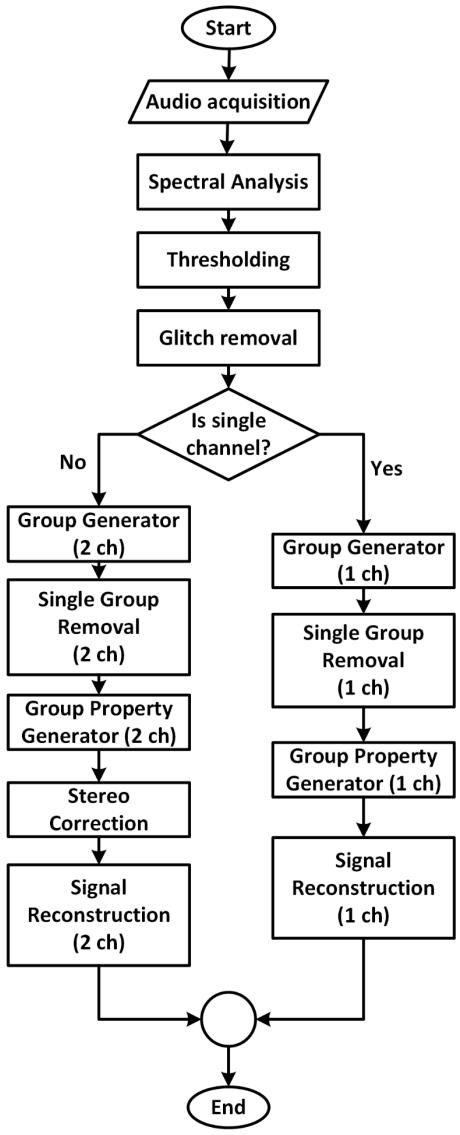


Figure 1. System flow overview of spectrogram based sound source separation algorithm.

### B. Spectral analysis

For the spectral analysis, fixed frame STFT algorithm was chosen with frame size fixed to a value different for different files and same for a single audio data and with a 0 sample overlapping. The equation used for counting DFT points can be represented as (3). And the general STFT is shown mathematically in (4).

$$N = \lceil 0.07 * F_S \rceil \tag{3}$$

$$STFT\{x[n]\}(k,n) = \sum_{m=0}^{N-1} x[n-m] * w[m] * e^{-j2\pi km/N} \tag{4}$$

In our case the sampling frequency (Fs) is 44100 Hz and so the number of DFT points (N) become 3088 (i.e. 71ms). This frame size can give around 1500 frequency resolution

(frequency bins), which is mostly the same as the human ear pitch resolution. And it has (N-Fs/100 =) 2847 point overlap for a 10ms grid. Which limits the maximum detectable pitch change in this algorithm to 1.4 Hz s^-1 (df = 14 Hz, dt = 10ms).

### *C. Thresholding and mask image generation*

For the thresholding of the spectrogram generated in the previous stage, the gradient thresholding technique is used. Gradient thresholding is the process where the amplitude of each frequency is subtracted from the previous frequency amplitude. If the subtracted value is larger than a fixed predefined value, the pixel's value of the output mask image is set as 1 but if the value is smaller than the threshold limit, the output value is set to 0.

### *D. Glitch removal*

At the glitch removal stage, the mask image from the thresholding stage is taken into account. But the mask image might have three major glitches detected in a threshold mask. These are –

a) Single pixel

b) Two head glitch

c) Side frequency

Single pixel glitch is having a single pixel in the threshold mask image having no pixels attached to it. If one of the harmonic lines has two single pixel heads or tails, then these glitches are categorized as two head glitch. And if any harmonic line in the mask image or threshold image has another harmonic line attached to it then this is called the side frequency glitch.

Convolution is used to detect these glitches and remove it from the spectroscopic image. Different kernels were constructed for each distinctive glitch removal. Fig. 2 illustrates the typical glitch examples of mask image snippets and the convolution kernels used to remove these glitches are illustrated in Figure 3.

### *E. Group generator*

The harmonic frequencies detected in the mask image are now taken into account individually and grouped according to an algorithm. The grouping algorithm is illustrated in Figure 4.

Each harmonic line is given an identifier. The value of the identifier is the same as the first position of the harmonic frequency mask in the image co-ordinates. So, the line identifier (ID) is a paired value as depicted mathematically in (5).

$$ID = (x, y) \tag{5}$$

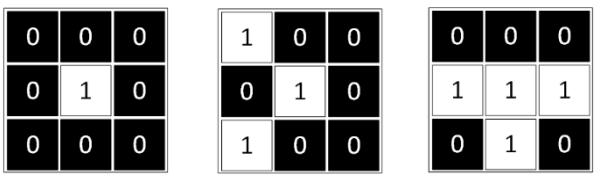


Figure 2. Typical arrangements of single pixel, two head and side frequency glitches (from left to right).

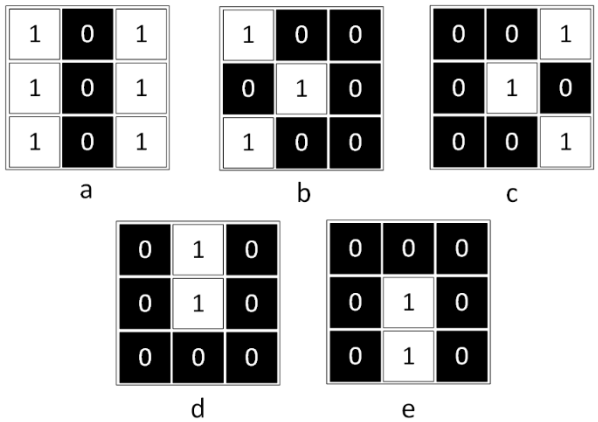


Figure 3. Convolution kernels for removal of single pixel (a), two head (b, c) and side frequency (d, e) glitches.

The group generating algorithm will search every pixel of an image for a line. If a line is detected, then it will execute the grouping algorithm showed in Figure 4. In the grouping algorithm, for every line it will first identify itself and check itself if it is previously added to any group. If it is a new line, then it will be added to a new group and a group id will be assigned.

In the grouping algorithm, for every line it will first identify itself and check itself if it is previously added to any group. If it is a new line, then it will be added to a new group and a group id will be assigned.

Then the grouping algorithm will advance one pixel through frequency axis and search for any line pixel (1 valued pixel). If any line is detected, then it is checked whether it is added to any group. If not, then it is checked if the current line length is equal length to the length of the derived line. If the length differs by 2 time units then it is added to the current group id. If already added, then the line is skipped. This is continued for the full frequency span.

This same procedure is done for the next time pixel (column). As it supports the maximum delay for the harmonics is 1-time unit.

After this step, all the lines will be in their respective groups. Then the group list is checked and those groups are removed which have only one harmonic member.

### *F. Group properties*

In this stage, the generated groups are considered for calculating properties of that group.

Each group is taken into consideration one by one. The members of each group are sorted in ascending order according to the frequency level. The lower eight frequencies are kept and others are not taken into calculation. Then the ratio of each consecutive frequency is calculated and stored in a database. The result is a 1x7 matrix. This matrix is called the instrument signature or group signature. Instrument signatures of different instruments are illustrated in the results section.

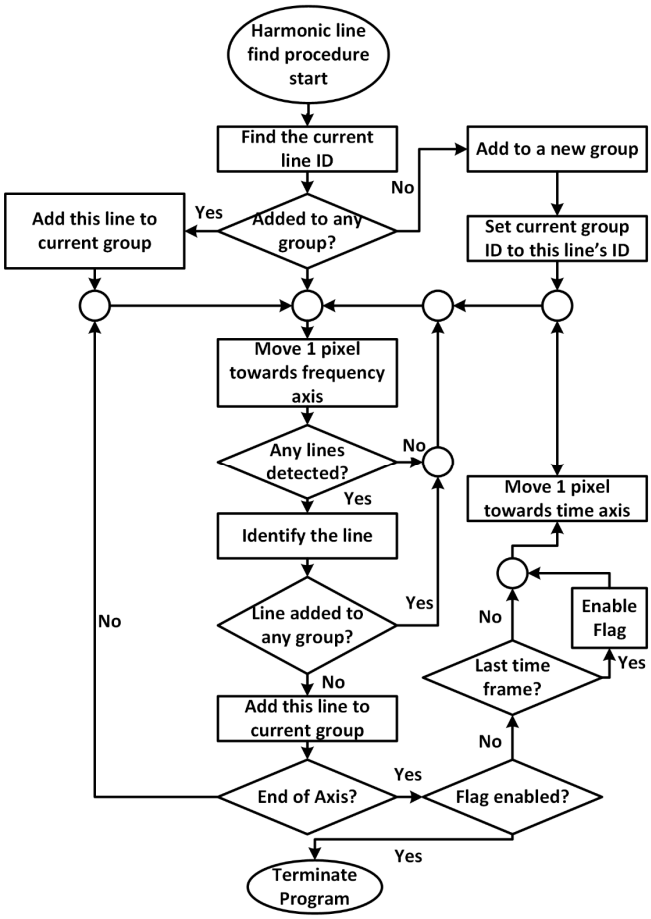


Figure 4. Frequency component group generation algorithm.

### G. Signature Recognition

The signatures generated for each group is now being matched with all groups' signatures and the closely matched groups are brought into a super-group. The group of the sound signifies an instrument playing in a time frame. A super-group signifies the same instrument playing in different time frames.

To match the signatures of each group, the signatures are first differentiated and these differentiated values of the instrument signatures are cross-correlated. For a good match, it is stated that the normalized cross-correlation value must be greater than or equal 0.8 in this case of evaluation.

### H. Stereo correction

The recognized super-groups are further validated if a stereo track is available. This is an optional step for further purification of the reconstruction. The groups of each super-group are checked for the amplitude in both channels. If a super-group only contains one instrument, then the amplitude difference of one group between both the channels will be similar for all groups in that super-group. If the difference value is outside the tolerance limit then the group is discarded from the super-group.

### I. Reconstruction

The super-groups are reconstructed by adding the group masks and by inverse STFT.

## III. Results and Analysis

The sound source separation in the spectrogram component geometry approach is evaluated and compared with original audio sources. 16 audio specimens were taken for the evaluation of this algorithm. Among them 13 specimens were recorded using standard microphones and others were synthesized using computer programs. Table I shows the detail information of the specimens.

In Table I the keywords 'f', 'g', 'h', 'fl', 'p' and 'v' indicate the sound sources' names as 'flute', 'steel guitar', 'harmonica', 'flamenco guitar', 'piano' and 'violin' respectively. And the keyword 'sy' indicates that the instrument is synthesized.

The mixed audio signals were generated by mixing these specimens. For experimental purposes three audio samples were generated "sy_p1+sy_fl1", "f2+g1" and "g4+h1". The mixing was unbiased and had equal individual volume. These audio signals were analyzed and source separated using our algorithm. During the analysis, instrument signatures were generated for each group. The groups with similar signatures are stored in a runtime dictionary. These signatures for each group are compared with each other and for those groups having similar signatures are regrouped in a super-group. Fig 5 depicts the generated instrument signatures. The generated super-groups are reconstructed as separated audio signals. These separated audio signals were cross-correlated with the source specimen signals. And this correlation value is used as a parameter for measuring how much correlated the reconstructed signal was with the source signal.

For each audio sample ("sy_p1+sy_fl1", "f2+g1" and "g4+h1") the reconstructed signals were labeled as "A" and "B" for two significant super-groups. Then "A" and "B" both were cross-correlated with the source signals in combination. The reconstructed signal of higher correlation with a source signal is taken as the separated signal from the mixed audio sample consisting same origin. For instance, in "f2+g1", if "A" has a highest correlation with the original signal of "f2", then "A" is considered as the separated "f2" signal from the mixed audio sample. Table II, III and IV consist the separated correlation results from these three mixed audio samples.

TABLE I. Table of Specimen Information

| Specimen code | Sound acquisition method | Instrument |
|---|---|---|
| f1 | Recorded | Flute |
| f2 | Recorded | Flute |
| f3 | Recorded | Flute |
| f4 | Recorded | Flute |
| f5 | Recorded | Flute |
| g1 | Recorded | Guitar (Steel String) |
| g2 | Recorded | Guitar (Steel String) |
| g3 | Recorded | Guitar (Steel String) |
| g4 | Recorded | Guitar (Steel String) |
| g5 | Recorded | Guitar (Steel String) |
| g6 | Recorded | Guitar (Steel String) |
| g7 | Recorded | Guitar (Steel String) |
| h1 | Recorded | Harmonica |
| sy_fl1 | Synthesized | Flamenco guitar |
| sy_p1 | Synthesized | Piano |
| sy_v1 | Synthesized | Violin |

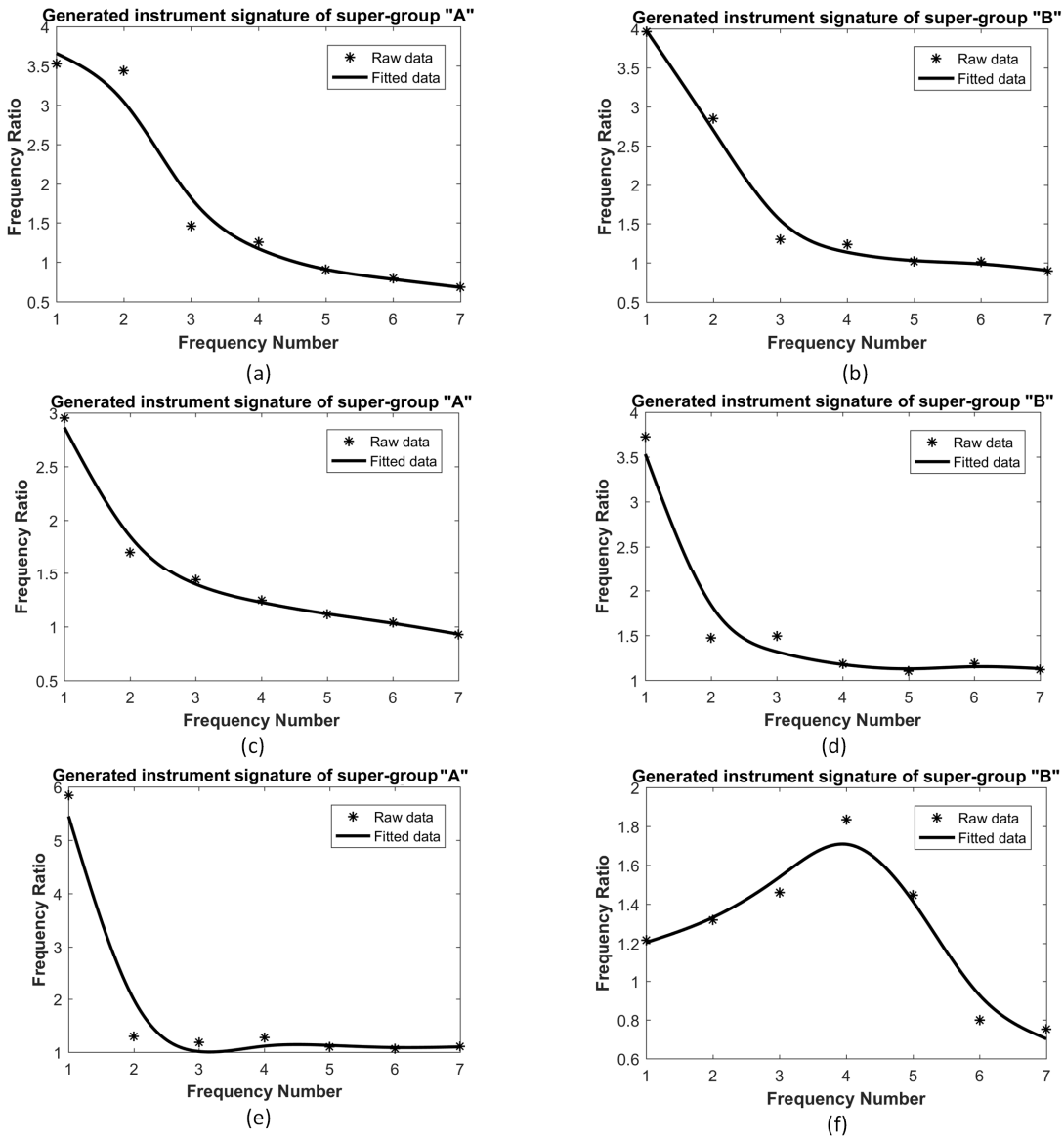


Figure 5. Generated instrument signatures from analyzing the audio samples. (a), (b) from audio sample "sy_p1+sy_fl1", (c), (d) from "f2+g1" and (e), (f) from audio sample "g4+h1".

For mixed audio samples "sy_p1+sy_fl1", the "sy_p1" specimen has a higher cross-correlation factor for the super-group "A". And "sy_fl1" has a higher correlation factor for super-group "B". A point to note here is the significant super group "A" has a higher correlation factor for "sy_fl1" (0.6334) compared to "sy_p1" (0.6127) but the cross-correlation of "B" and "sy_fl1" has the highest cross-correlation factor among all these values. So, it can be concluded that "B" is more correlated to "sy_fl1" specimen than correlating "A" with the same specimen. And so, the result can be written as (A, sy_p1), (B, sy_fl1) for convenience.

For mixed audio samples "f2+g1" and "g4+h1" the results after sound separation are (A, f2), (B, g1) and (A, g4), (B, h1) respectively.

TABLE II. CORRELATION COEFFICIENT OF SIGNIFICANT OUTPUTS A AND B AND THE SY_P1 AND SY_FL1 SIGNALS.

| sy_p1+sy_fl1 | Super-groups | sy_p1 | sy_fl1 |
|---|---|---|---|
| | **A** | 0.6127 | 0.6334 |
| | **B** | 0.5486 | 0.7530 |

TABLE III. CORRELATION COEFFICIENT OF SIGNIFICANT OUTPUTS A AND B AND THE F2 AND G1 SIGNALS.

| f2+g1 | Super-groups | f2 | g1 |
|---|---|---|---|
| | **A** | 0.6386 | 0.5171 |
| | **B** | 0.4604 | 0.4658 |

TABLE IV. CORRELATION COEFFICIENT OF SIGNIFICANT OUTPUTS A AND B AND THE G4 AND H1 SIGNALS.

| g4+h1 | Super-groups | g4 | h1 |
|---|---|---|---|
| | **A** | 0.6775 | 0.6188 |
| | **B** | 0.5910 | 0.5505 |

In Table IV the decision is also dependent on the maximum value of the cross-correlation factor. “A” and “g4” samples are having the highest correlation factor. So, “A” is taken more correlated to “g4”. So, “B” is decided to be correlated to specimen “h1”, though the correlation is lower.

## IV. Conclusion

This work is based on sound source separation by spectral analysis. The proposed algorithm separates sound sources by estimating the pattern, time availability of the geometry of sound pattern in the spectrogram. Then potential physical sound sources are separated detecting the instrument signature of those sources without any pre-training phase. Though there are many algorithms to separate sound sources from mixed audio signal, none of them can work with single or double microphone system to detect undefined number of sources. This work tries to mimic the process of the human ear and sound processing systems.

Though there are some drawbacks in this system. The current algorithm does not support percussion instruments. Again, any instrument pitch changing more than 1.4Hz/s is not detectable by this system. And the thresholding process loses a lot of potential data. Lastly the number of instruments mixed, is inversely proportional to the efficiency of the system.

To improve these drawbacks, the spectrogram generation, thresholding system, group generation and super-group generation system can be improved. And being a new approach, this work requires more research with this algorithm in future.

## References


[1] D. K. T. Panagopoulos, "Automated Classification of Piano–Guitar Notes," IEEE Transactions on Audio, Speech and Language Processing, vol. 14, no. 3, pp. 1040-1050, 2006.

[2] M. Ryynänen and A. Klapuri, "Query by humming of midi and audio using locality sensitive hashing," in *Proc. IEEE Int. Conf. Acoust.*, Speech, Signal Process., 2008.

[3] J. Serra, E. Gomez, P. Herrera and X. Serra, "Chroma binary similarity and local alignment applied to cover song identification," IEEE Trans. Audio, Speech, Lang. Process., vol. 16, no. 6, pp. 1138-1151, 2008.

[4] G. Peeters, "Sequence representation of music structure using higherorder similarity matrix and maximum-likelihood approach," in *Proc. Int. Conf. Music Inf. Retrieval*, 2007.

[5] Y. Minagawa-Kawai, K. Mori, N. Naoi and S. Kojima, "Neural Attunement Processes in Infants during the Acquisition of a Language-Specific Phonemic Contrast," The Journal of Neuroscience, vol. 27, no. 2, pp. 315-321, 2006.

[6] G. Poliner and D. Ellis, "A classification approach to melody transcription," in *Proc. Int. Conf. Music Inf.*, 2005.

[7] M. Goto, "Robust predominant-F 0 estimation method for real-time detection of melody and bass lines in CD recordings," in *Proc. IEEE Int. Conf. Acoust.*, Speech, Signal Process., 2000.

[8] M. P. Ryynänen and A. P. Klapuri, "Transcription of the singing melody in polyphonic music," in *Proc. Int. Conf. Music Inf. Retrieval*, 2006.

# A Saliency Based Approach for Foreground Extraction from a Video

Sk. Md. Masudul Ahsan, Abu Naser Md. Nafew, Rifat Haque Amit
Department of Computer Science and Engineering
Khulna University of Engineering & Technology (KUET)
Khulna, Bangladesh
smahsan@cse.kuet.ac.bd, wayfarernafew@gmail.com, rifathaqueamit@gmail.com

***Abstract*— In the field of Computer Vision, success of the most research works like detecting or recognizing some object partially or sometimes completely depends on the success of a decent segregation of foreground from background. In this paper, we describe a novel approach of foreground extraction from video based on saliences that handles the motion in foreground, background or in camera considerably well. We assume that foreground objects are less likely to be positioned in the border. We use the color contrast information to identify the foreground by using visual saliency. Using our assumption, we construct a border based saliency which improves our overall visual saliency information. We also use the optical flow information from video frames to find motion of regions. Again, using the same assumption, we construct a background model using the flow magnitude and angle information of the border pixels to suppress unwanted background movement or camera motion. We then mix up the both information of visual and motion saliency values to get a grayscale saliency map of foreground. We then apply Otsu's thresholding to extract binary foreground mask from saliency map. We remove some noises from the frames using contour detection and comparison of regions to get the final foreground mask. Both qualitative and quantitative experiments are performed on a benchmark dataset which show that the proposed approach performs quite well for practical use.**

***Keywords—foreground extraction, visual saliency, motion saliency, border motion.***

## I. INTRODUCTION

It is a human perceptive ability that they can easily determine the object of interest or foreground object from any image or video whatever the scene is. This complex cognitive capability manifested in human brain is also known as segregation of background and foreground from a source. However, this task is still very challenging in the field of computer vision without any prior knowledge about the foreground object or training data. There are many challenges in this task like camouflage, changes in illumination, moving object, oscillating background etc. So, for a successful extraction of foreground an algorithm needs to handle all these challenges.

The matter of fact is, it is quite impracticable to manipulate all possible foreground object for supervised extraction. That's why one need to extract information from foreground and background in order to extract foreground object in unsupervised way.

A common technique is to perform foreground segmentation by background subtraction in case of a stationary camera. This works by subtracting concurrent frames from each other, the regions where the images do not match are classified as foreground. As background subtraction is a far from perfect art, there are several problems one needs to take into account when developing background subtraction algorithms.

In this paper, we propose a new, robust and efficient implementation scheme of foreground extraction problem with the help of visual saliency and motion saliency. We are mainly focusing on handling the problem of moving background or the foreground or when the camera is in motion. We are using the motion velocity and direction of border region to establish our background model. After simple addition of the visual and motion saliency, we extract the foreground object mask. We fine tune our result by contour detection and removal of unwanted regions. Fig. 1 illustrates the overview of our proposed framework for foreground extraction.

The later part of this paper is organized as follows. Section II reviews our study on recent works on foreground extraction and focuses on the contributions of our method. Details of our proposed methodology are presented in Sections III and IV. Section V shows our qualitative and quantitative results on a standard dataset to support the effectiveness and robustness of our method. Finally, we conclude our paper on Section VI.

## II. RELATED WORKS

The foreground extraction problem can be categorized in two separate approaches: Supervised and Unsupervised. For example, Wu and Nevatia [1] and Lin and Davis [2] both train object part detectors and these detectors describe foreground objects every possible situation. Image segmentation algorithms proposed in [3], [4] that focused on an interactive scheme and required users to manually provide the ground truth label information. So that needs user interaction.

Jhong and Sclaroff [5] proposed a method that uses Autoregressive Moving Average Model (ARMA) to model dynamic textures in background cloud moving, crowd, waving trees etc. However, even though this method can segment foreground objects from a Dynamic textured background, it doesn't give pleasant result in presence of noise or high motion in background. Wu-Chih hu [6] proposed a method using motion and gradient variation to extract foreground object rather than

978-1-5386-2307-7/17/$31.00 ©2017 IEEE

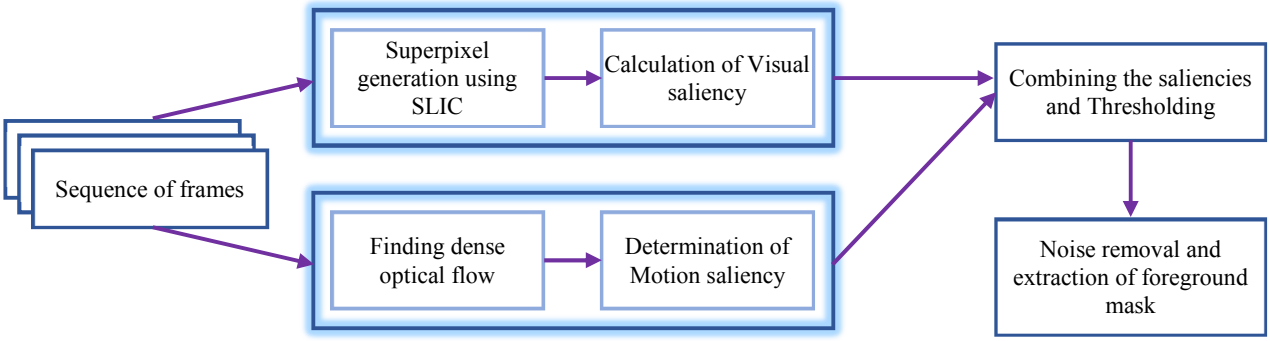


Figure 1. Overview of our proposed Model

constructing the background model. But, their method works well only when the background is static and the foreground object is on the move with small variation in motion. With the help of Kinect sensor, Kedar A. Bhartiya *et al.* [7] proposed a saliency based approach to extract object from video. Their method exploits visual and motion saliency information extracted from the input video frames. But, their method is not always feasible as they needed Kinect sensor for their method.

Wei-Te Li *et al.* [8] combines both visual and motion saliency in each frame for automatic video object extraction. In each of the video frame, they have calculated the optical flow map. From the flow map, they calculated the motion saliency values for each pixel. From that motion saliency, they created the shape likelihood. Then, by applying color GMM, they framed out the motion induced cues. At the same time, they calculated visual saliency values in each frame. Then they integrated the motion induced cues with the visual saliency via conditional random field (CRF). Even though they have got impressive results, their method misses the foreground object completely in some videos. Federico Perazzi *et al.* [9] proposed a method for salient Foreground Detection for Images and Video using Fiedler Vectors with the combination of SVM based classifier. The good side of this method is straight forward to implement and parameter-free. But their method performs poor in presence of background motion or in camouflage. Some researchers [10], [11], [12] used graph-based methods, which identify the foreground object regions by minimizing the cost between adjacent hidden nodes/pixels in terms of color, motion, etc. information. More specifically, one can segment the foreground object by dividing a graph into disjoint parts whose total energy is minimized without using any training data. But the problem is, for general model for static scenes to create feature maps at multiple spatial scales and propose a Graph-Based Visual Saliency model (GBVS). There are again three main steps but during the feature extraction step, motion and flicker channels can be added to compute the saliency maps of some video sequences. The algorithm then builds a fully connected graph over all grid locations of each feature map (intensity, orientation, color such as RGB, motion and flicker). Itti *et al.* [13] used center surround differences on a single image to get conspicuity maps. Ying Li *et al.* [14] presented a method by obtaining orientation map using oriented Gabor filtering and Color maps and image regions using K-means clustering. Even though, their proposed system is fast as they have only calculated the salient region in one frame and then track it, this system is not robust in situations like where background motion is dominant or foreground objects move in a high velocity.

In this paper, we represent our aim at automatically detecting and extracting the foreground object without any prior knowledge or user interaction. Here, we do not assume the camera is static or the background motion is dominant or the foreground motion is different from that of background like many other approaches as discussed in Section II. Instead we relax this assumption and allow the foreground object to be presented in freely moving scenes. Our assumption is that, it is less likely for a foreground object to be places at border regions of any frame. Inspired from this method [15], we calculate visual saliency information using color contrast and information from the border pixels. As for the motion, we use optical flow. Here, also using our assumption, we learn the motion velocity and direction and construct our background model to learn about the foreground. We verify our methods performance with the qualitative and quantitative results.

## III. Calculating Saliencies

The first step of our workflow is to calculate the visual and motion saliencies for the input frames as seen in our proposed foreground extraction. We now detail each step in the following subsections and Section IV.

### A. *Calculation of Visual Saliency*

The measurement of visual saliency is calculated for each frame of the input video. For calculating visual saliency, in the first step we perform image segmentation on each video frame. For image segmentation, we use Simple Linear Iterative Clustering (SLIC) [16] method which segments the frame which are called superpixels. For using SLIC, we convert the input frame into Lab Color Space. Fig. 2 shows a superpixelized frame of an original frame generated by using SLIC. After segmentation, we calculate the mean color of each superpixel using (1).

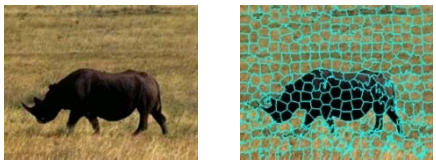

(a) (b)

Figure 2. Frame segmentation using SLIC: (a) Original frame, (b) superpixelized frame.

$$\overline{clr}(r_i) = \frac{1}{n} \sum_{x,y \in r_i} f(x,y) \quad (1)$$

Where $r_i$ is a region or superpixel, $n$ is the number of pixels in that particular superpixel. We consider this mean color as the color of all pixels available to the particular superpixel. This process reduces the number of overall computations required to calculate the visual saliency for a certain frame. For each region or superpixel $r_i$, we calculate global saliency ($S_{gbl}$) using (2). Eq. (3) determines the Euclidean distance of the mean color of the region $r_i$ and $r_j$ in Lab color space.

$$S_{gbl}(r_i) = \frac{1}{N} \sum_{j=1}^{N} \left( 1 - \exp\left\{ -\frac{dif_{\overline{clr}}(r_i, r_j)^2}{\delta^2} \right\} \right) \quad (2)$$

$$dif_{\overline{clr}}(r_i, r_j) = \sqrt{(\overline{L}_i - \overline{L}_j)^2 + (\overline{a}_i - \overline{a}_j)^2 + (\overline{b}_i - \overline{b}_j)^2} \quad (3)$$

In (2), the $\delta$ is a constant and $N$ is the number of superpixels. The more a region is different from all other regions in a frame, the higher global saliency value is for that region. We call this saliency as global because it is measured by considering all the regions of a particular frame at a single time. An example of global saliency calculation is shown in Fig. 3(a).

From Fig. 3(a), we notice that global saliency alone does not suppress the background effectively. In this stage, we recalculate the saliency measure of a region considering the idea presented in [15]. The method assumes that the regions that are touched with border mostly belongs to the background. Using this assumption, an internal region with similar color attribute to the border regions will be suppressed and a dissimilar region will be highlighted. To achieve this phenomenon, we first determine the border contrast for each region $r_i$ using (4), where $r_i$ is any region and $r_j$ is a region that is touched with the border of the frame. For $K$ number of border regions, we get $K$ border contrast values for $r_i$ and store them in a vector $brdCntrst_i$.

$$brdCntrst_i[j] = 1 - \exp\left\{ -\frac{dif_{\overline{clr}}(r_i, r_j)^2}{\delta^2} \right\} \quad (4)$$

$$brdCntrst_i = sort(brdCntrst_i) \quad (5)$$

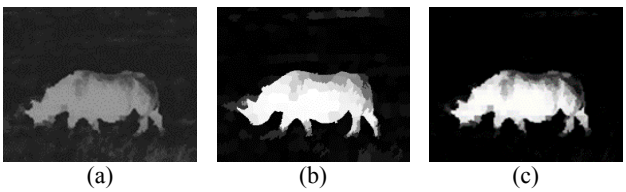

(a) (b) (c)

Figure 3. Calculation of visual saliency: (a) Global saliency, (b) Border saliency, (c) Final saliency.

$$S_{brd}(r_i) = \frac{1}{k} \sum_{j=1}^{k} brdCntrst_i[j] \quad (6)$$

The stored border contrast values are sorted increasingly (eq. (5)). Then we take only first $k$ items from this vector, take an average of those items using (6) and termed it as border saliency ($S_{brd}$). The value $k$ here we considered is the 30% of the total number of regions that are touched with the border.

The global saliency and border saliency values are mixed up to get the final saliency value or the visual saliency using (7).

$$S_{fnl}(r_i) = S_{brd}(r_i)\left[1 + S_{gbl}(r_i)\right] \quad (7)$$

Here the value of border saliency is kept as is it and it is again multiplied with global saliency instead of taking it as it is so that the border saliency value always be dominant over global saliency. Example of border saliency and final saliency is shown in Fig. 3(b), 3(c) respectively.

### *B. Calculation of Motion Saliency*

What we have seen so far is that we are calculating visual saliency for each frame in video. Visual saliency allows us to find visually conspicuous region in a single frame and thereby helps to detect a static foreground region, but it may fail to detect if the foreground is cluttered or have very similar color attribute with background. Since foreground extraction a preliminary computation of many computer vision application where most of the time the subjects are in motion, we use this information to detect the foreground region.

We use a very common and widely used method of motion detection called optical flow. Optical flow is the pattern of apparent motion of objects in a frame caused by the relative motion between two or more successive frames. Farneback[17] has given solution is to estimate the motion, or displacement, field from only two frames and try to compensate for the background motion. It is related to the orientation tensor methods in which the first processing step, a signal transform called polynomial expansion. Then, use the model of polynomial to approximate the motion for each pixel. Using this method of dense optical flow, we calculate each pixel's optical flow information. This method converts color information of each frame and converts it to grayscale for using intensity value. After retrieving that information, We propose to derive the Motion Saliency scores $M(i, t)$ for each pixels $i$ at frame $t$, in terms of the associated optical flow information.

But the resultant motion saliency values may detect false foreground object if a dominant motion is present at the background. Fig. 4 shows an example of such problems where optical flow (Fig. 4(c)) is computed from two successive frames (Fig. 4(a), 4(b)). Even though the camera was almost static, there was a strong oscillating motion in the background compared to the foreground object (the rhinoceros). Fig. 4(c) shows that the optical flow detects the motion but in this case the background motion. Similar situation can happen if the camera is zooming in / out or panning left / right.

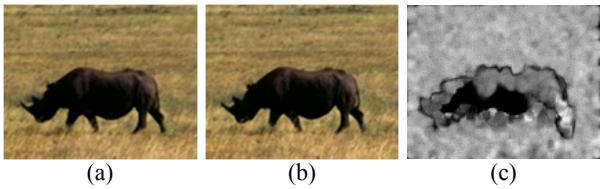

(a) (b) (c)

Figure 4. Computation of optical flow: (a)-(b) Two consecutive frames, (c) The dense optical flow as motion saliency.

To solve these types of problems, we again assume that the foreground object generally locates in the center of the image or or frames. Using this assumption, we can say that, if motion is present in the border pixels, those motion values can be considered as the background motion. The pixels that contains same or nearly same motion values are also background.

In simple terms, we are trying to construct a model of background using the assumption of foreground object is less likely to stay to in the border region. So, to remove these noises, we have considered movement near the border of frame as the movement of background. We calculated the average motion for these areas and considered this value as background motion.

Now to calculate the average motion, we take a certain number of rows and columns of pixels from each of the four side (named boundary pixels, *bndPxls*) and measured their average motion specifically direction and magnitude of the motion using (8), (9).

$$\overline{brdFl}_{dir} = \frac{1}{|bndPxls|} \sum_{x,y \in bndPxls} optFl_{dir}(x,y) \tag{8}$$

$$\overline{brdFl}_{mag} = \frac{1}{|bndPxls|} \sum_{x,y \in bndPxls} optFl_{mag}(x,y) \tag{9}$$

Now for each pixel in the frame, we calculate two differences with this average background motion. One is angular difference and another one is difference in magnitude using (10) and (11). These two differences give us an estimation of how much a pixel's flow differs from that of the boundary motion which are more likely to be background or to be the foreground. We have calculated the dissimilarity by (12).

$$difFl_{dir}(x,y) = \left| optFl_{dir}(x,y) - \overline{brdFl}_{dir} \right| \tag{10}$$

$$difFl_{mag}(x,y) = \left| optFl_{mag}(x,y) - \overline{brdFl}_{mag} \right| \tag{11}$$

$$dismlrty(x,y) = difFl_{mag}(x,y) * difFl_{dir}(x,y) \tag{12}$$

The more the difference, the more we can say a pixel is not belonging to the background. Fig. 6 (c) illustrates the improved result after applying (12) on the motion saliency calculated before.

### C. Combining Visual and Motion Saliency

In the process of combining the obtained saliencies, we simply added the visual saliency and motion saliency using

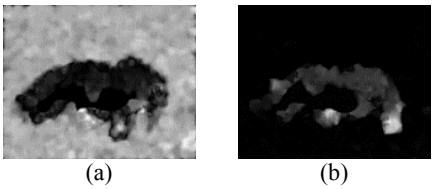

(a) (b)

Figure 5. Improvement of motion saliency: (a) Previous motion saliency, (b) motion saliency after improvement

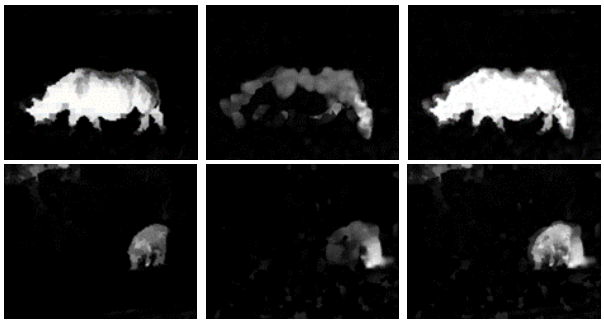

Visual saliency Motion saliency Combined saliency

Figure 6. Combined saliency after addition of both saliencies

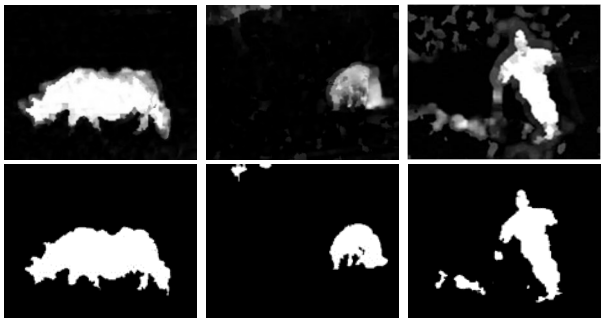

Figure 7. Before (top) and after thresholding (bottom) foreground mask.

pixel-wise intensity summation. We have used 70% of Visual Saliency value and 30% of Motion Saliency value in the process of addition, where these percentages are empirically chosen. Fig. 6 illustrates some results for two sample video sequences.

## IV. Foreground Extraction and Noise Removal

The mixing of visual saliency and motion saliency gives a saliency map which is in fact a grayscale image where the regions with higher saliency value tends to be the foreground and rest of the part should be the background. But the problem here is that a region can be either background or foreground, but cannot be both. So, it is required to know which part of the frame is actually in foreground, and which part needs to be considered as background. That's why after addition of both of these saliencies the final image needs a binary thresholding. In our approach, we use Otsu's [18] thresholding. Fig. 7 illustrates the output.

The thresholding process leaves some unwanted pixels or noises which leads some non-foreground pixels on the output as foreground. To remove these portions, we find contours of all the separated regions and their convex hull. Then we remove the regions on which convex hulls are having an area less than 15% of the largest convex hull and also have distance more than

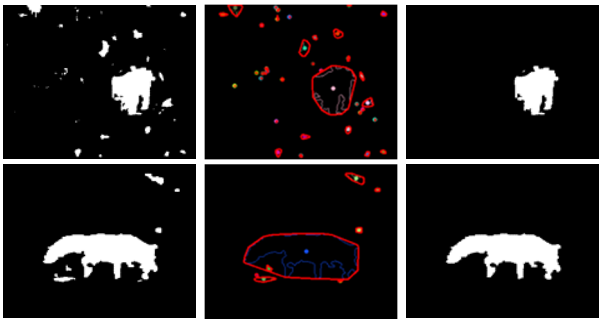

Figure 8. Removal of unwanted regions.

a threshold from the largest convex hull's centroid. Fig. 8 illustrates the final foreground mask. From this mask, we extract our final foreground object.

## V. Experimental Results

We evaluate our proposed method on a benchmark dataset [19]. The dataset contains 8 videos with an average of 72 frames in each video and in total 579 frames. In most of the videos, the backgrounds are dynamic i.e. there exist an oscillating motion in the background or the camera is panning in some direction. We measure the performance of our system using three metrics namely recall, precision and accuracy. Recall tells how much foreground pixels are correctly predicted as foreground by the system. Precision measures how much foreground pixels are correctly classified out of all prediction of foreground pixels. Accuracy is the overall measure of correctly classifying foreground pixels as foreground and background pixels as background, i.e. it measures overall foreground-background segregation correctness. Equations (13), (14), and (15) defines how those metrics are calculated for each video, where $v$ means a video, $i$ means a frame in a video. Here, TP and FP are the pixels that are correctly and wrongly classified as foreground pixels respectively. Similarly, TN and FN are correctly and wrongly classified background pixels.

$$recall_v = \frac{\sum TP_i}{\sum TP_i + \sum FN_i} \tag{13}$$

$$precision_v = \frac{\sum TP_i}{\sum TP_i + \sum FP_i} \tag{14}$$

$$accuracy_v = \frac{\sum TP_i + \sum TN_i}{\sum TP_i + \sum FP_i + \sum TN_i + \sum FN_i} \tag{15}$$

Fig. 9 shows the quantitative results of different metrics for various videos. For almost all the cases the accuracy of segregating foreground from background is above 80%. For the video named BRT130T, the precision is a little bit low due to very cluttered background. The last bars in Fig. 9 presents the average performance of the proposed method for all the videos. We find that in overall, the system accuracy is 92.81% with a recall and precision of 77.47% and 71.77% respectively. A system with more than 50% recall and more than 50% precision means that it covers the desired subject and practically usable.

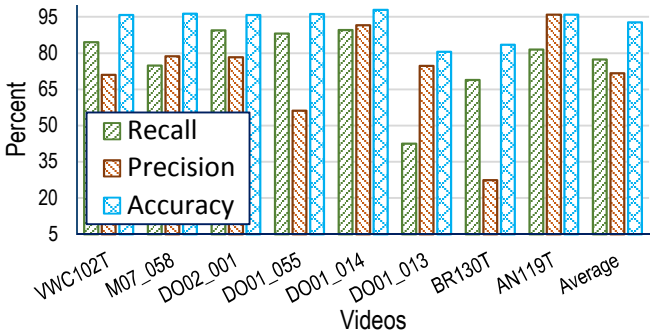


Figure 9. Experimental results for different videos.

TABLE I. Comparative Results of the Proposed Method for Videos BR103T and DO01_014.

| Method | [10] | [20] | [21] | [22] | Ours |
|---|---|---|---|---|---|
| **Avg. Accuracy (%)** | 67.89 | 98.05 | 98.15 | 49.9 | 90.74 |

Fukuchi *et al.* [19] did not report their experimental results in quantitative form. In [20], quantitative results for only two videos of this dataset (BR103T and DO01_014) are reported for different methods [10], [21], [22]. Table I presents the segmentation accuracies of the proposed method along with other methods for those videos.

We also compare the proposed method using the full dataset with the existing OpenCV implementation of the background subtraction method named Mixture of Gaussians (MoG) [23]. For MoG we get an overall score of 85.05% of accuracy, 63.54% precision and 20.87% of recall which is far worse than proposed method. Moreover, MoG needs an initial time to learn the background model which makes it unusable when the background is very dynamic or quickly changing. The qualitative or a visual comparison of the proposed method with MoG is shown in Fig. 10 on the randomly taken 50$^{th}$ frame of each of the videos. We see that for all cases the proposed method extracts the foreground better. The proposed method can detect foreground objects, even if the foreground or background or both is static as it uses Visual Saliency. Moreover, the method is robust against the oscillating motion in the background. The limiting factor of the method is SLIC superpixeling which may be improved by parallelization.

## VI. Conclusion

The main idea of this proposed model is to extract foreground object by visual saliency in an efficient way and then if it fails due to motion in the background, foreground or in the camera, we are detecting optical flow in the frame and then detect the foreground based on the motion information. For visual saliency, we have first applied a SLIC method for superpixeling to get the contour mask in the frame. Then we have calculated the color means of the region and the calculated visual saliency values for each pixel. We, further improve this values by post-processing based on border pixel's information. And for motion, we have calculated the optical flow and then with that we get the motion saliency values for each pixel. Here we also detect whether the foreground object is in motion or the background. Using border pixels information, we detected and improved the result which is the main novelty of the method.

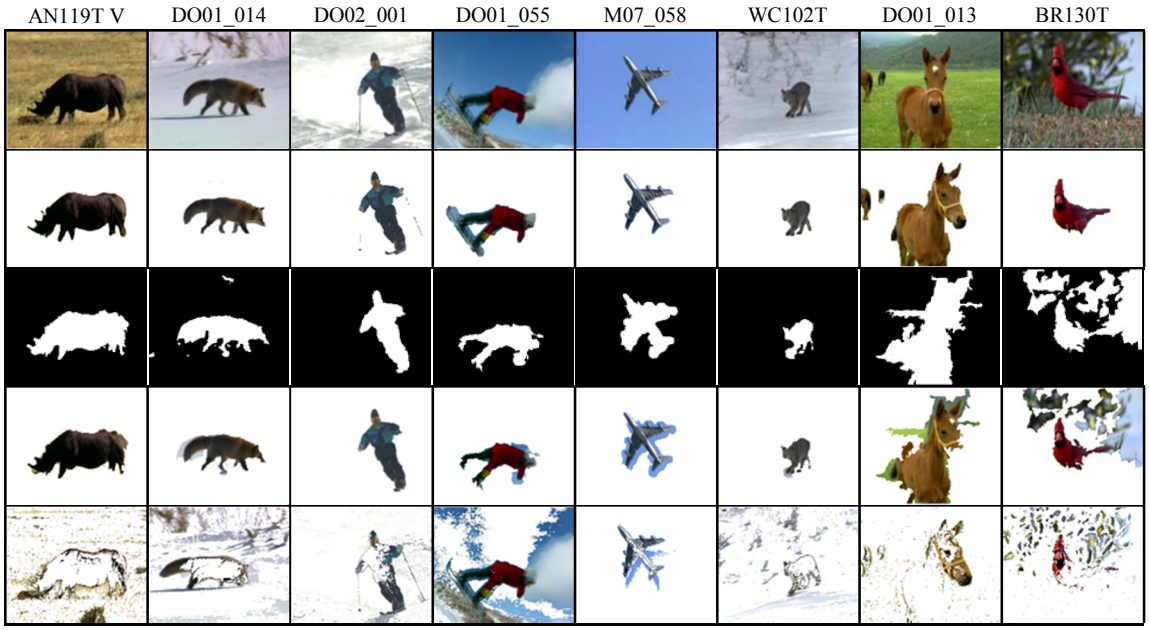


Figure 10. Sample visual output on 50th frame. From top to bottom: original frame, ground truth, foreground mask by proposed method, extracted foreground using proposed method, extracted foreground using MoG.

The experimental results justify the applicability of the proposed method. We compared the proposed scheme with other foreground background segregation schemes and found that it performs quite well. As for future recommendation, high level extraction like extracting hairs, feathers and other soft objects of foreground can be extracted in precise way. If necessary, implementation of this proposed method and it's algorithms can be done in parallel platform and using GPU with OpenCL for real time applications. This can be used as a preprocessing step of many problems like video surveillance, action recognition and other Computer Vision related works.

## REFERENCES


[1] B. Wu and R. Nevatia, "Detection and segmentation of multiple, partially occluded objects by grouping, merging, assigning part detection responses," *Intl. J. of Computer Vision*, vol. 82, no. 2, pp. 185-204, 2009.

[2] Z. Lin and L. S. Davis, "Shape based human detection and segmentation via hierarchical part-template matching," *IEEE Trans. PAMI*, vol. 32, no. 4, pp. 604-618, 2010.

[3] Y. Y. Boykov, O. Veksler, and R. Zabih, "Fast approximate energy minimization via graph cuts," *IEEE Trans. PAMI.*, vol. 23, no. 11, pp. 1222-1239, 2001.

[4] C. Rother, V. Kolmogorov, and A. Blake, "GrabCut: Interactive foreground extraction using iterated graph cuts, " *ACM Trans. Graph.*, vol. 23, no. 3, pp. 309-314, 2004.

[5] J. Zhong and S. Sclaroff, "Segmenting foreground objects from a dynamic textured background via a robust Kalman filter," in *Proc. 9th IEEE Int. Conf. Computer Vision*, Oct. 2003, pp. 44-50.

[6] Wu-Chih hu, "Real-time on-line video object segmentation based on motion detection without background construction," *Int. J. of Innovative Computing, Information and Control*, vol. 7, no. 4, pp. 1845-1860, 2011.

[7] K. A. Bhartiya, S. Pathak, M. P. Shah, and S. M. Rokade, "Saliency approach to extract object from video via kinect sensor," *Int. J. of Emerging Technology and Innovative Engineering*, vol. 1, no. 3, pp. 195-200, 2015.

[8] W. T. Li, H. T. Chang, H. S. Lyu and Y. C. F. Wang, "Automatic saliency inspired foreground object extraction from videos," *IEEE Trans. Image Processing*, vol. 22, no. 7, pp. 1089-1092, 2012.

[9] F. Perazzi, O. Sorkine-Hornung, and A. Sorkine-Hornung, "Efficient salient foreground detection for images and video using fiedler vectors," in *Eurographics Workshop on Intelligent Cinematography and Editing*, 2015, pp. 21-29.

[10] F. Liu and M. Gleicher, "Learning color and locality cues for moving object detection and segmentation," in *Proc. IEEE Conf. Computer Vision and Pattern Recognition*, Jun. 2009, pp. 320-327.

[11] K.-C. Lien and Y.-C. F. Wang, "Automatic object extraction in single concept videos," in *Proc. IEEE Int. Conf. Multimedia Expo*, 2011, pp. 1-6.

[12] J. Harel, C. Koch, and P. Perona, "Graph-based visual saliency," *Advances in Neural Information Processing Systems*, pp. 545-552, 2007.

[13] L. Itti, C. Koch and E. Niebur, "A model of saliency-based visual attention for rapid scene analysis," *IEEE Trans. PAMI*, vol. 20, no. 11, pp. 1254-1259, 1998.

[14] Ying Li, Yu-Fei Ma, and H. M. Zhang, "Salient region detection and tracking in video," in *Proc. Int. Conf. on Multimedia and Expo*, 2003, pp. II-269-72 vol. 2.

[15] S. M. M. Ahsan, J. K. Tan, H. Kim, and S. Ishikawa, "Boundary aware regional contrast based visual saliency detection," in *Proc. of ISAROB*, Mar. 2016, pp. 258-262.

[16] R. Achanta, A. Shaji, K. Smith, A. Lucchi, P. Fua and S. Süsstrunk, "SLIC Superpixels Compared to State-of-the-Art Superpixel Methods," in *IEEE Trans. PAMI*, vol. 34, no. 11, pp. 2274-2282, 2012.

[17] G. Farneback, "Two-frame motion estimation based on polynomial expansion," in *SICA: Image analysis*, 2003 pp. 363-370.

[18] N. Otsu, "A threshold selection method from gray-level histograms," *IEEE Trans. Sys., Man., Cyber.*, vol. 9, pp. 62-66, 1979.

[19] K. Fukuchi, K. Miyazato, A. Kimura, S. Takagi, and J. Yamato, "Saliency based video segmentation with graph cuts and sequentially updated priors," in *Proc. of ICME*, 2009, pp. 638-641.

[20] W. T. Li, H. S. Chang, K. C. Lien, H. T. Chang, and Y. C. F. Wang, "Exploring visual and motion saliency for automatic video object extraction" *IEEE Trans. on Image Processing*, vol. 22, no. 7, pp. 2600-2610, 2013.

[21] Y. J. Lee, J. Kim, and K. Grauman, "Key-segments for video object segmentation," in *Proc. IEEE Int. Conf. Comput. Vis.*, Nov. 2011, pp. 1995–2002.

[22] M.-M. Cheng, G.-X. Zhang, N. J. Mitra, X. Huang, and S.-M. Hu, "Global contrast based salient region detection," in *Proc. IEEE Conf. Comput. Vis. Pattern Recognit.*, Jun. 2011, pp. 409–416.

[23] P. KaewTraKulPong and R. Bowden, "An improved adaptive background mixture model for real-time tracking with shadow detection," in *Proc. 2nd European Workshop on Advanced Video-based surveillance systems*, 1, pp.135-144, 2002.

# Density Based Smart Traffic Control System Using Canny Edge Detection Algorithm for Congregating Traffic Information

Taqi Tahmid[1], Eklas Hossain[2], Kazi Mohammad Abidur Rahman[1]

[1]Khulna University of Engineering & Technology, Dept. of EEE, Khulna 9203, Bangladesh

[2]Oregon Tech, Department of Electrical Engineering & Renewable Energy, OR-97601, USA

taqitahmid@gmail.com; eklas.hossain@oit.edu; abidurrahman.425@gmail.com;

***Abstract*— As the problem of urban traffic congestion intensifies, there is a pressing need for the introduction of advanced technology and equipment to improve the state-of-the-art of traffic control. The current methods used such as timers or human control are proved to be inferior to alleviate this crisis. In this paper, a system to control the traffic by measuring the real-time vehicle density using canny edge detection with digital image processing is proposed. This imposing traffic control system offers significant improvement in response time, vehicle management, automation, reliability and overall efficiency over the existing systems. Besides that, the complete technique from image acquisition to edge detection and finally green signal allotment using four sample images of different traffic conditions is illustrated with proper schematics and the final results are verified by hardware implementation.**

***Keywords—Smart Traffic Control; Density based Traffic Control; Edge Detection; Image Processing in Traffic Control.***

## I. INTRODUCTION

Traffic congestion is one of the major modern-day crisis in every big city in the world. Recent study of World Bank has shown that average vehicle speed has been reduced from 21 km to 7 km per hour in the last 10 years in Dhaka [1]. Intermetropolitan area studies suggest that traffic congestion reduces regional competitiveness and redistributes economic activity by slowing growth in county gross output or slowing metropolitan area employment growth [2]. As more and more vehicles are commissioning in an already congested traffic system, there is an urgent need for a whole new traffic control system using advanced technologies to utilize the already existent infrastructures to its full extent. Since building new roads, flyovers, elevated expressway etc. needs extensive planning, huge capital and lots of time; focus should be directed upon availing existing infrastructures more efficiently and diligently.

Previously different techniques had been proposed, such as infra-red light sensor, induction loop etc. to acquire traffic date which had their fair share of demerits. In recent years, image processing has shown promising outcomes in acquiring real time traffic information using CCTV footage installed along the traffic light. Different approaches have been proposed to glean traffic data. Some of them count total number of pixels [3], some of the work calculate number of vehicles [4-6]. These methods have shown promising results in collecting traffic data. However, calculating the number of vehicles may give false results if the intravehicular spacing is very small (two vehicles close to each other may be counted as one) and it may not count rickshaw or auto-rickshaw as vehicles which are the quotidian means of traffic especially in South-Asian countries. And counting number of pixels has disadvantage of counting insubstantial materials as vehicles such as footpath or pedestrians. Some of the work have proposed to allocate time based solely on the density of traffic. But this may be disadvantageous for those who are in lanes that have less frequency of traffic.

Edge detection technique is imperative to extract the required traffic information from the CCTV footage. It can be used to isolate the required information from rest of the image. There are several edge detection techniques available. They have distinct characteristics in terms of noise reduction, detection sensitivity, accuracy etc. Among them, Prewitt [7], canny [8], Sobel [9], Roberts and LOG are most accredited operators. It has been observed that the Canny edge detector depicts higher accuracy in detection of object with higher entropy, PSNR (Peak Signal to Noise Ratio), MSE (Mean Square Error) and execution time compared with Sobel, Roberts, Prewitt, Zero crossing and LOG [10-12]. Here is a comparison between distinct edge detection techniques [13].

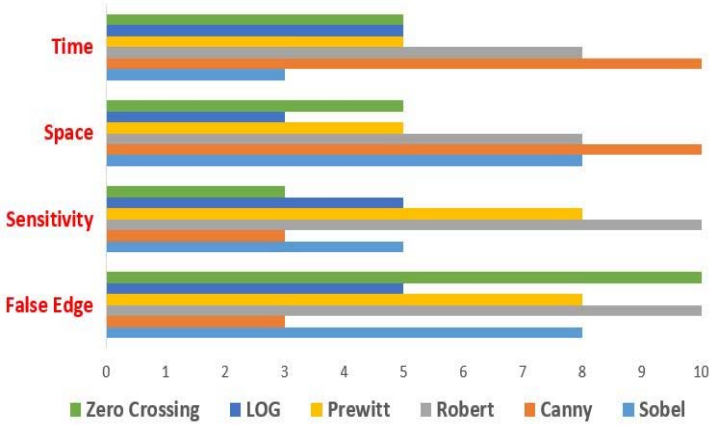


Fig 1: Comparative analysis of distinct edge detection techniques

In this paper, a system in which density of traffic is measured by comparing captured image with real time traffic information against the image of the empty road as reference image is proposed. Here, in figure 1, the block diagram for proposed traffic control technique is illustrated.

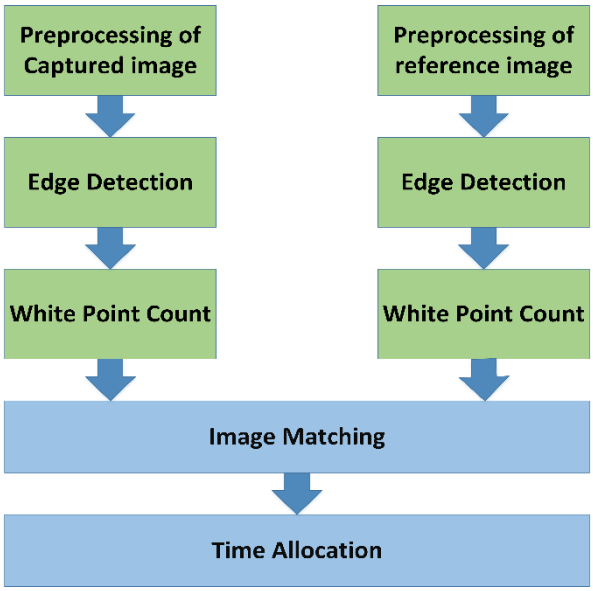


Fig 2: Block diagram of proposed density based smart traffic control system.

Each lane will have a minimum amount of green signal duration allocated. According to the percentage of matching allocated traffic light duration can be controlled. The matching is achieved by comparing the number of white points between two images. The entire image processing before edge detection i.e. image acquisition, image resizing, RGB to gray conversion and noise reduction is explained in section II. At section III, canny edge detection operation and white point count are depicted. Canny edge detector operator is selected because of its greater overall performance. Percentage matching for different sample images and traffic time allocation for them are demonstrated in section IV. The content of this paper completely serves the purpose of demonstrating the limitations of current traffic control techniques and the solution of this limitations with detailed explanation. Image matching by comparing detected edges is a novel approach to identify the vehicular density with propitious accuracy. As far as we know, matching images by comparing detected edges has not been used before for smart traffic control application.

## II. IMAGE PREPROCESSING

In this section, image preprocessing is performed to convert the raw images into more accessible form for edge detection purpose. At first, four images of different traffic scenario are selected and image of the empty road is chosen as reference image. All the images are then resized into 400*400 pixel using the following formula for constant spatial resolution and greater computational efficiency.

Original height/original width*new width = new height (1)

Original width/original height*new height = new width (2)

As grayscale image has superior signal to noise ration compared to RGB image, it is advantageous to convert RGB images into grayscale for further processing. When converting an RGB image to grayscale, it is pertinent to consider the RGB values for each pixel and make as output a single value reflecting the brightness of that pixel. One of the approaches is to take the average of the contribution from each channel: (R+B+C)/3. However, since the perceived brightness is often dominated by the green component, a different, more "human-oriented", method is to consider a weighted average:

$$I=0.3R + 0.59G + 0.11B \quad (3)$$

Since Gaussian noise is the preeminent source of noise in digital image, the cardinal purpose of applying Gaussian filter is to eliminate these noises. This step is crucial to impede noises associated with the digital images detected as false edge. The equation for a Gaussian filter kernel of size (2k+1)*(2k+1) is given by,

$$H_{ij} = \frac{1}{2\pi\sigma^2} e^{\left(-\frac{(i-(k+1))^2+(j-(k+1))^2}{2\sigma^2}\right)} \quad (4)$$

It is important to understand that the selection of the size of the Gaussian kernel will affect the performance of the detector. The larger the size is, the lower the detector's sensitivity to noise. Additionally, the localization error to detect the edge will slightly increase with the increase of the Gaussian filter kernel size. A 5×5 is an appropriate size for most cases, but this will also vary depending on specific situations. A 5×5 Gaussian filter with sigma=1.4 is used in this paper. Once a suitable kernel has been selected, then the Gaussian smoothing can be performed using standard convolution methods. After image preprocessing the resultant outputs are depicted in Fig 3.

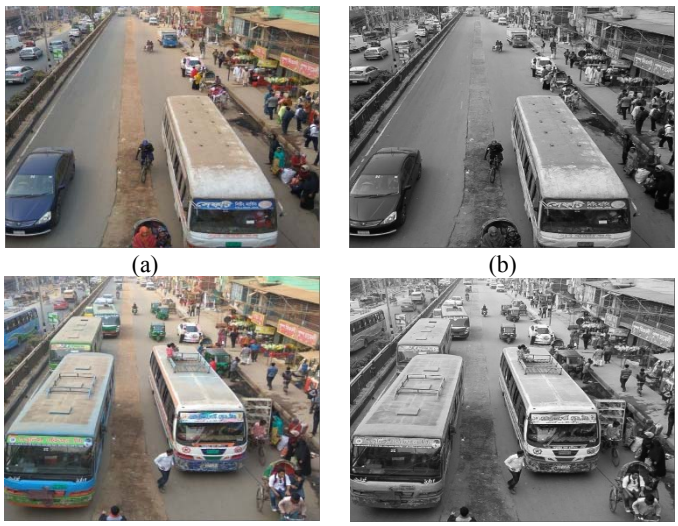

(a) (b) (c) (d)

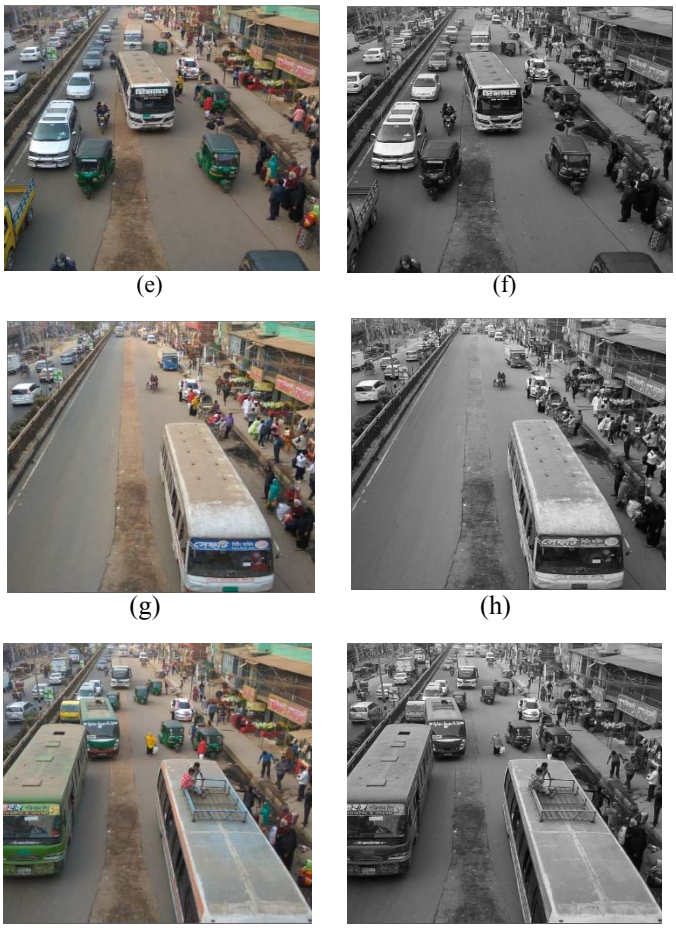

(e) (f) (g) (h) (i) (j)

Fig 3: (a) First sample image (image A) with fairly congested traffic (b) Preprocessed output of first image (c) Second sample image (image B) with minor traffic (d) Preprocessed output of second image (e) Third sample image (image C) with moderate traffic (f) Preprocessed output of third image (g) Fourth sample image (image D) with moderate traffic (h) Preprocessed output of fourth image (i) Reference image (j) Preprocessed output of reference image

## III. EDGE DETECTION AND WHITE POINT COUNT

Edge detection is used to identify distinct types of shapes. In this paper, it is used for isolating different shapes of vehicles from rest of the image. After comparing different edge detectors, canny edge detector is found suitable for this experiment. At first, images are smoothed by applying Gaussian filter to reduce unwanted texture and details,

$$g(x,y) = G\sigma(x,y) * I(x,y) \tag{5}$$

where,

$$G_\sigma(x,y) = \frac{1}{\sqrt{2\pi\sigma^2}} e^{\left(-\frac{m^2+n^2}{2\sigma^2}\right)} \tag{6}$$

Then the intensity gradient is computed using Sobel gradient operator,

$$M(x,y) = \sqrt{g_m^2(x,y) + g_n^2(x,y)} \tag{7}$$

and,

$$\theta(x,y) = \tan^{-1} g_n(x,y) \big/ g_m(x,y) \tag{8}$$

Threshold M

$$M_T(x,y) = \begin{cases} M(x,y) & if\ M(x,y) > T \\ 0 & otherwise \end{cases} \tag{9}$$

Where T is so chosen that all edge elements are kept while most of the noise is suppressed. After that, non-maxima suppression is applied by checking whether each non-zero $M_T(x,y)$ is greater than its two neighbors along the gradient direction θ(x,y). If so, $M_T(x,y)$ is kept unchanged, otherwise, set to 0. The resultant output examples after edge detection are delineated in Fig 4.

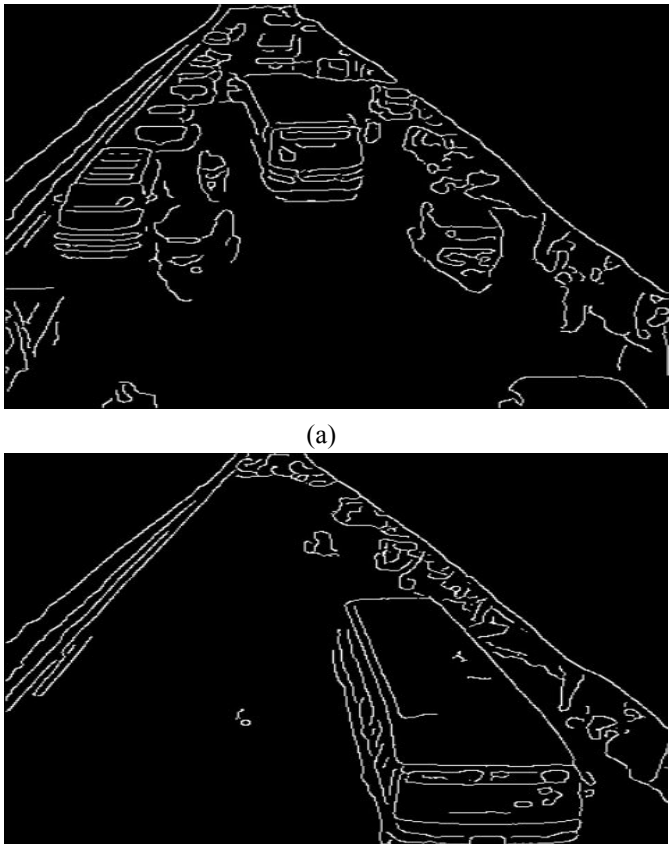

(a)

(b)

Fig 4: Edge detected output of (a) image A and (b) reference image

Other images also share the same resemblance. After edge detection, the resultant images are binary image with only black and white pixels. Binary image is originally a two-dimensional matrix of values 0 and 1. The value '0' denotes black color while value '1' denotes white color. The white pixels essentially represent the detected edges. So, images with different traffic conditions will have different white point counts. Since the reference image has least number of vehicles, it would have the least number of white pixels among these five images. Therefore, this image is used as a unit image to measure the traffic density. Total number of white pixels are calculated for each individual image intended for matching purpose.

## IV. PERCENTAGE MATCHING AND TIME ALLOCATION

Since reference image is basically an image of the empty road, the less the similarity between sample image and reference image, the more vehicles are present on the road. As irrelevant edges detected in sample images such as edges of footpaths, islands etc. are also existent in reference image, their effects are nullified when comparing them with reference image. The percentage of matching is calculated using the following formula,

$$\%match = \frac{Total\ number\ of\ white\ points\ in\ reference\ image}{Total\ number\ of\ white\ points\ in\ sample\ image} * 100 \quad (9)$$

Time allocated to green signal is governed by the percentage of matching of consecutive lanes. The proposed time allocation is based on assumption. Contemporary time allocation may depend on miscellaneous factors; for instance, number of vehicles, traffic condition on neighboring intersections etc. For example, if the vehicle queue is larger than average, it would require longer time to clear. Additionally, it would be pernicious if other vehicles from neighboring intersections exacerbate the traffic congestion of adjacent intersections.

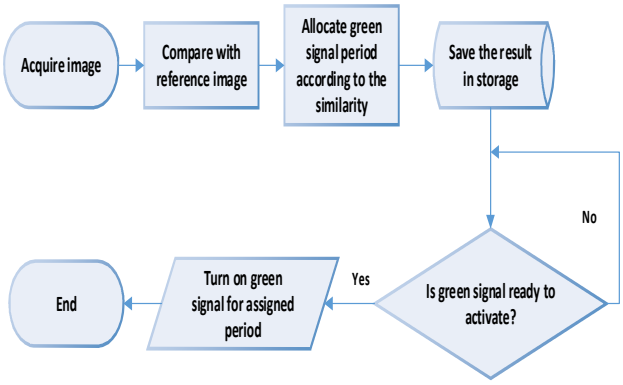


Fig 5: Proposed time allocation algorithm for autonomous traffic control system

Table 1: Green signal allocation table.

| Similarity in Percentage | Allocated Green Signal Time |
|---|---|
| 0%-50% | 60 seconds |
| 51%-60% | 50 seconds |
| 61%-70% | 40 seconds |
| 71%-80% | 30 seconds |
| 81%-100% | 20 seconds |

Now implementing the proposed algorithm, four different similarity in percentage and consequently different allotted green signal time are found for four sample images. The similarity in percentage and allocated green signal time are calculated using python programming language. These outcomes are illustrated in Fig 6.

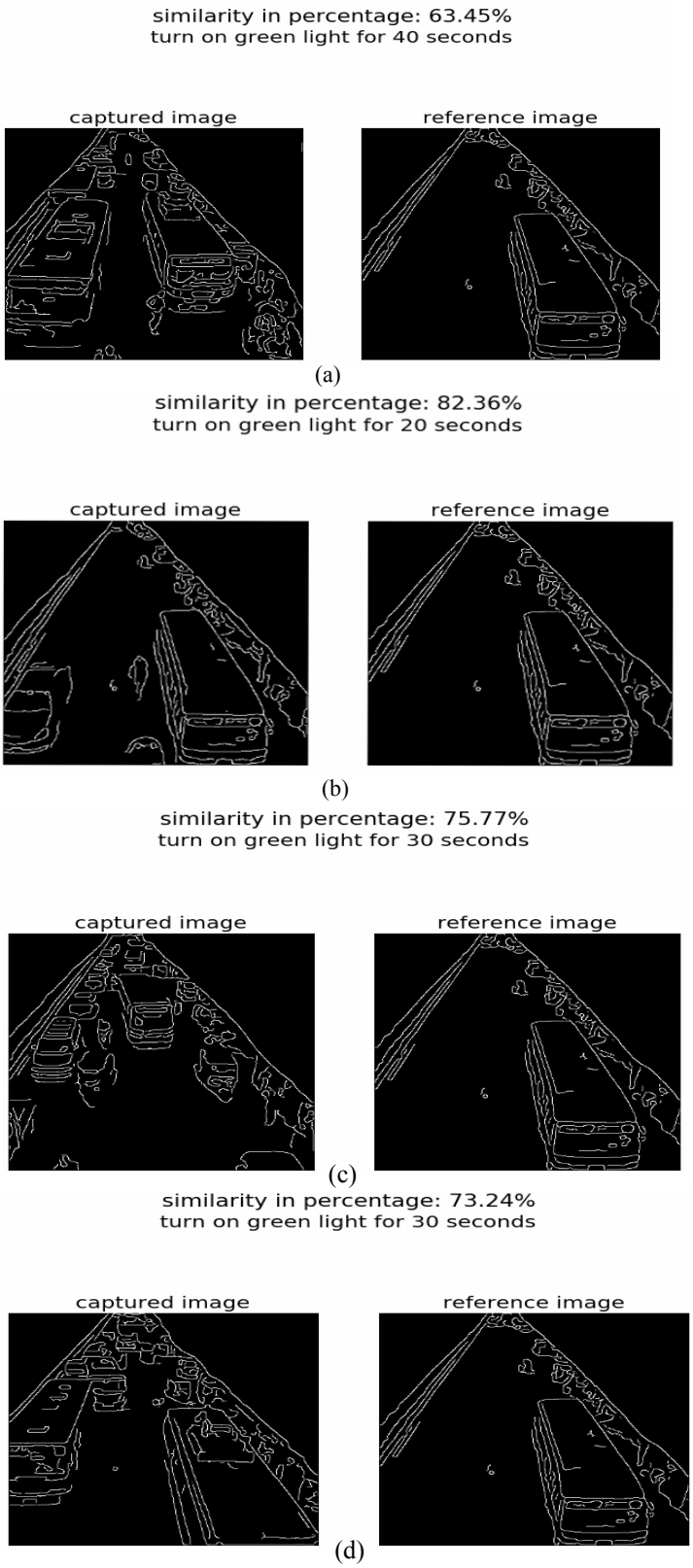


Fig 6: (a) Similarity between first sample image and reference image is found 63.45% (b) Similarity between second sample image and reference image is found 82.36% (c) Similarity between third sample image and reference image is found 75.77% (d) Similarity between fourth sample image and reference image is found 73.24%

All this collected information are composed in the following table.

Table 2: Allocated time derived from percentage matching

| Designation | Similarity in Percentage | Allocated Green Signal Period |
|---|---|---|
| Image A | 63.45% | 40 seconds |
| Image B | 82.36% | 20 seconds |
| Image C | 75.77% | 30 seconds |
| Image D | 73.24% | 30 seconds |

## V. HARDWARE IMPLEMENTATION

To verify the above autonomous traffic control technique, a four-way traffic intersection is modeled. Each sample image is used to represent the density of each traffic lane. This four-way intersection is rendered by four arrays of LEDs with each array encompassing a red and a green LED. Python programming language is used for image processing and Arduino development board is used to control the LEDs.

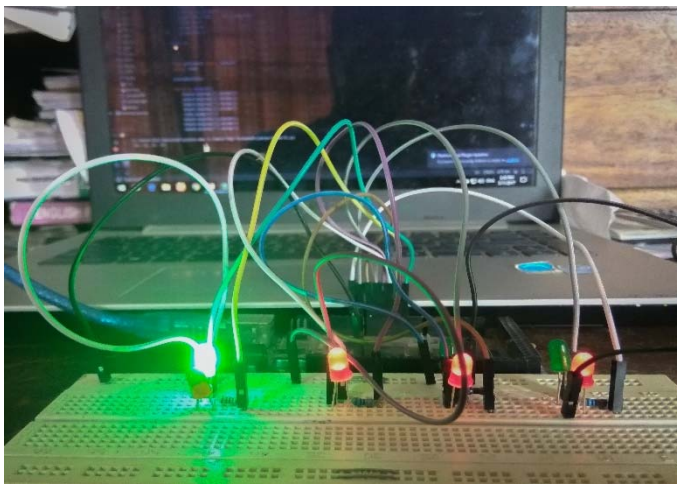

Fig 7: Hardware implementation of a four way traffic intersection

The inputs of these LEDs are connected to the digital I/O pins of the Arduino. All of the pins have common ground connected to the ground of Arduino. The first array of red and green LEDs is considered as lane A. Second, third and fourth arrays of LEDs are considered as lane B, lane C and lane D respectively. These LEDs are controlled by the output pins of the Arduino, which are controlled by the time, allocated to each consecutive lane. At first, the green signal for lane A is activated for 40 seconds. Throughout this time, red signals of other lanes are turned on concurrently. Similarly, after lane A, green signals of second, third and fourth lanes are sequentially activated for 20 seconds, 30 seconds and 30 seconds respectively. Whenever the green signal of one lane is activated, red signals of other lanes are also activated simultaneously.

## VI. CONCLUSION

In this paper, a smart traffic control system availing image processing as an instrument for measuring the density has been proposed. Besides explaining the limitations of current near obsolete traffic control system, the advantages of proposed traffic control system have been demonstrated. For this purpose, four sample images of different traffic scenario have been attained. Upon completion of edge detection, the similarity between sample images with the reference image has been calculated. Using this similarity, time allocation has been carried out for each individual image in accordance with the time allocation algorithm. In addition, similarity in percentage and time allocation have been illustrated for each of the four sample images using Python programming language. Besides presenting the schematics for the proposed smart traffic control system, all the necessary results have been verified by hardware implementation.

## REFERENCES


[1] Siddique, A. (2017). *WB: Dhaka's average traffic speed 7kmph*. [online] Dhaka Tribune. Available at: http://www.dhakatribune.com/bangladesh/dhaka/2017/07/19/dhaka-average-traffic-speed-7-kmph/ [Accessed 25 Jul. 2017].

[2] M. Sweet, "Traffic Congestion's Economic Impacts: Evidence from US Metropolitan Regions," *Urban Studies*, vol. 51, no. 10, pp. 2088–2110, Oct. 2013.

[3] Md. Munir Hasan, Gobinda Saha, Aminul Hoque and Md. Badruddoja Majumder, "Smart Traffic Control System with Application of Image Processing Techniques," in *3rd International Conference on Informatics, Electronics & Vision*, Dhaka, May 2014.

[4] Vismay Pandit, Jinesh Doshi, Dhruv Mehta, Ashay Mhatre and Abhilash Janardhan, "Smart Traffic Control System Using Image Processing," *International Journal of Emerging Trends & Technology in Computer Science (IJETTCS)*, Volume 3, Issue 1, January – February 2014.

[5] Pallavi Choudekar, Sayanti Banerjee and M. K. Muju, "Implementation of image processing in real time traffic light control," in *3rd International Conference on Electronics Computer Technology*, April, 2011.

[6] T. Semertzidis, K. Dimitropoulos, A. Koutsia and N. Grammalidis, "Video sensor network for real-time traffic monitoring and surveillance," *The Institution of Engineering and Technology*, Volume 4, Issue 2, June 2010, pp. 103 – 112.

[7] Lei Yang, Dewei Zhao and Xiaoyu Wu, "An improved Prewitt algorithm for edge detection based on noised image," in *4th International Congress on Image and Signal Processing*, Shanghai, China, October 2011.

[8] Weibin Rong, Zhanjing Li and Wei Zhang, "An improved canny edge detection algorithm," in *IEEE International Conference on Mechatronics and Automation*, August 2014.

[9] Wenshuo Gao, Xiaoguang Zhang and Lei Yang, "An improved Sobel edge detection," in *3rd International Conference on Computer Science and Information Technology*, July 2010.

[10] G.T. Shrivakshan and Dr.C. Chandrasekar, "A Comparison of various Edge Detection Techniques used in Image Processing," *International Journal of Computer Science Issues*, Vol. 9, Issue 5, No 1, September 2012.

[11] Pinaki Pratim Acharjya, Ritaban Das and Dibyendu Ghoshal, "Study and Comparison of Different Edge Detectors for Image Segmentation," *Global Journal of Computer Science and Technology Graphics & Vision*, Volume 12 Issue 13 Version 1.0 Year 2012.

[12] Jiaqiao He, Liya Hou and Weiyi Zhang, "A Kind of Fast Image Edge Detection Algorithm Based on Dynamic Threshold Value," *Sensors & Transducers*, Vol. 24, Special Issue, August 2013, pp. 179-183.

[13] S.K. Katiyar and P.V. Arun, "Comparative analysis of common edge detection techniques in context of object extraction," *IEEE Transactions on Geoscience and Remote Sensing,* Vol.50 no.11b.

# Bengali Sign Language to Text Conversion using Artificial Neural Network and Support Vector Machine

Anika Raisa Chowdhury, Akash Biswas, SM Farzana Hasan, Tanjina Mehnaz Rahman and Jia Uddin
Department of Computer Science and Engineering, BRAC University, 66 Mohakhali, Dhaka 1212, Bangladesh
{anikaraisa.cse, biswasakashh, farzana.hp33, tanjinamehnaz, engrjiauddin}@gmail.com

*Abstract*— **This paper presents a novel system that converts Bengali Sign language to text using an optimum system comprising of artificial neural networks and support vector machine (SVM). Microsoft Kinect is used to take the input, which is the hand sign performed in front of the camera. The captured hand sign is eventually recognized, after joint and wrist detection and by assessing the contours. Contour feature is extracted and is run through a SVM for classification of the sign. The contour finding algorithm utilizes the convex hull method, and the features extracted after detection is passed through the support vector model for recognition. To validate the performance of the proposed model, a dataset that consists of both male and female hand gesture images is utilized. Experimental results demonstrate 84.11% classification accuracy for our tested dataset.**

***Keywords— Kinect, Hand Gesture, Neural Network, Bengali Sign, Classification Accuracy.***

## I. INTRODUCTION

Sign language is a form of communication that people with speech and/or hearing impairment utilize. This form of language combines symbols made from hand gestures to form letters, phrases, or sentences. It uses manual communication to convey meaning, as opposed to spoken language. This can also involve orientation and movements of the hands, arms or body and even facial expression to express a speaker's thoughts with simultaneously combining hand shapes. The importance of interpreting sign language resides, while communicating with other people. Bengali language consists of 51 alphabets which are represented using 38 isolated hand signs [10]. Bengali language is the fifth widely spoken languages in the world, so we cannot disdain any adversity related to this language.

Innumerable researches have been done on sign language converter to accelerate the facility for the hearing impaired in different languages to ease the complexity of their communication but there are inadequate researches made for Bengali sign language, which were conducted very recently. M. Jarman *et al.* have presented an automated Bengali sign recognition system that utilizes the fingertip finder algorithm and a feed-forward neural network [1]. They take into consideration of the protruding fingertips, location of wrist on the binary threshold image to determine the sign that is being made. However, in the Bengali Sign Language there are many similar hand signs namely the hand signs for ক and খ. Our paper tackles this issue by taking into account the structure of the hand along with the wrist location. In addition, authors in [8] compare various methods that have been utilized for the recognition of signs. This paper aided in finalizing the utilization of Kinect technology due to the several features present in the Kinect. In [9,10], authors describe alternate methods utilized in association with the Kinect sensor. Neural networks have been utilized in many sign recognition systems [1,11]. Garcia *et al.* have created such a system for ASL (American Sign Language). They had utilized a three-layer neural network with one input layer, one hidden layer and one output layer. In [12], several recognitions methods have been described and compared the results. This provided a straight-forward assumption into which methods we deemed most suitable for our task. Whereas, the previous paper provided insight into the algorithms suitable for our task, [13] provided combinations of hardware and software that went along with our desired systems. Grzejszczak *et al.* have described a very unique way to detect and recognize different hand-signs [14]. They focused on finding landmarks in the hand and localization. There is a similar method to this paper utilized as both concentrate on pointing out marking features of the hand structure. The papers described above have not taken response time to consideration.

To overcome the limitation of existing system, our work focuses on creating a faster recognition mechanism and incorporates five layer of neural network, to serve the purpose. Moreover, the use of the Kinect camera as an input device, provides clearer image and faster image processing capability to the system.

The remaining part of the paper is presented as follows. Chapter II focuses on describing the proposed model and experimental setup and results analysis is in Chapter III and finally chapter IV concludes the paper.

## II. PROPOSED MODEL

Figure 1 presents a block diagram corresponding to our proposed model. Initially, the program is trained using test and training images which consist of 38 different male and female hand gestures. One such set of dataset image is shown in Figure 2.

While execution of the system, a Red-Green-Blue (RGB) image is captured by Kinect. The image is converted to

978-1-5386-2307-7/17/$31.00 ©2017 IEEE

grayscale and then to a binary threshold image, where size of images are 300x300 pixels.

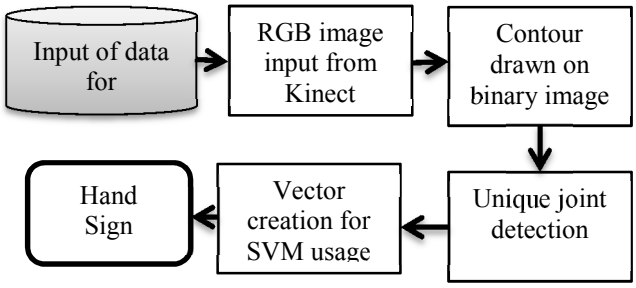


Figure 1. Block diagram of the Proposed Model

Figure 2. Sample Dataset of Bengali Sign Language

The system then identifies the joints and bends and angles in the input hand shape and by implementing convex algorithm draws a polygon around the total shape, upon the threshold image. Figure 3 shows the shape drawn over the input image.

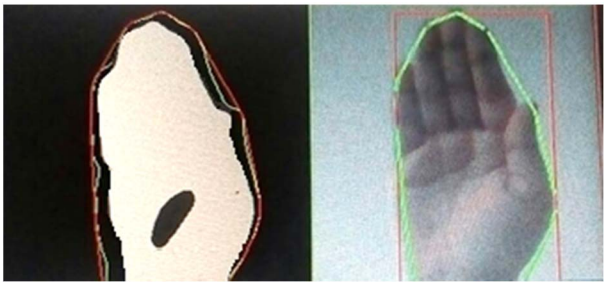

Figure 3. Contour determination over threshold image (left) and RGB image (right)

The joint detection algorithm has been newly devised for this paper. It attempts to estimate the bone and joint layout in the hand. This is theoretically more accurate than blob and skin detection as those are dependent on vague structure and light. However, as we are already using a Kinect that works independent of light availability both these issues are eradicate.

Upon detection of joints, Support Vector Machine (SVM) is used primarily for classification. The SVM divides data into two different classes and then hyper-plane is drawn between the two classes that achieves maximum marginal distance [3,4]. Using the data from the testing sets the algorithm has to be able to recognize the targeted value, or in this case, hand sign. The following equations and values have been used following the steps shown in [5], in creating the SVM for this paper is utilized to aid in proper building of the recognition algorithm.

Training set of instance label pairs are denoted by $(x_i, y_i), x_i \epsilon R^n, y_i \epsilon \{1, -1\}, i = 1 \dots, l.$

The following equation is then solved by SVM.

$$min_{w,b} = \frac{1}{2} w^T w + \sum_{i=1}^{l} \xi(w, b; x_i, y_i) \qquad \text{(i)}$$

Contingent to

$$y_i(w^T \varphi(x_i) + b) \geq 1 - \xi_i$$
$$\xi_i \geq 0 \qquad \text{(ii)}$$

The previously discussed hyper-plane is drawn using the following formula:

$$f(x) = \omega \cdot \varphi(x) + b = \sum_i a_i^0 \, y_i K(x_i, x) + b \qquad \text{(iii)}$$

After classification, the image is parsed through directories and maps the input to the dataset template to figure out a match. Upon matching the corresponding letter is displayed in the interface.

In this paper, a five layer model, illustrated in Figure 4 has been used. The first layer is basically the input layer, which takes in the input. In our case, the input is the scenario that is seen by the camera. The second layer figures out hand in the scenario and converts the image to grayscale. The third layer finds the convexity defect and draws a polygon, after figuring out the largest difference between the nodes. The fourth layer converts the image within the convex hull into a threshold image, which is used for mapping and matching with the stored datasets for finding similarity. If similarity has been found then the appropriate text output is displayed else an error message notifying failure is displayed as output. The output displaying layer is the fifth and final layer of our model.

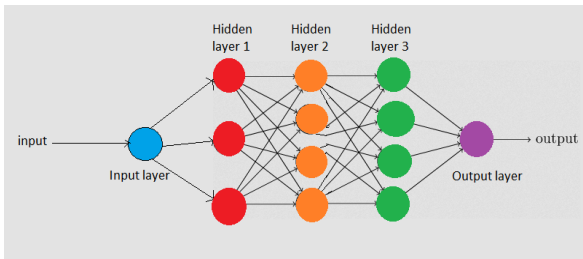


Figure 4. Neural Network Model used

## III. Experimental Setup and Result Analysis

In order to carry out the experiment, a dataset was used. In the tested dataset, there is a total of 38 hand signs in the Bengali Sign language which includes 9 স্বরবর্ণ (Shoroborno) or vowels 27 ব্যঞ্জনবর্ণ (Benjonborno) or the consonants. The

actual Bengali alphabet has a total of 51 letters and due to same phonetics, few of the letters share common sign. For example, letter খ(Kho) and ক্ষ (Khio). We created 4 variations of each letter to provide ourselves a large enough data set for the system to utilize. We have created another recognition algorithm, which uses normal webcams for input, to compare with our system and both were run 22 times. The time taken to get a result, as well as, the accuracy of the result has been calculated and tested.

TABLE 1. ACCURACY RESULT OF THE PROPOSED MODEL

| | Number of run | | | | | | | | | | | | | | | | | | | | | |
|---|---|---|---|---|---|---|---|---|---|---|---|---|---|---|---|---|---|---|---|---|---|---|
| বর্ণমালা (Boramala) | 1 | 2 | 3 | 4 | 5 | 6 | 7 | 8 | 9 | 10 | 11 | 12 | 13 | 14 | 15 | 16 | 17 | 18 | 19 | 20 | 21 | 22 | Accuracy % |
| অ (Shorey-O) | √ | √ | √ | √ | √ | √ | √ | √ | √ | √ | √ | X | √ | √ | √ | X | √ | √ | √ | √ | √ | √ | 90.901 |
| ক (Ko) | √ | X | √ | √ | √ | √ | √ | √ | √ | √ | √ | X | √ | X | √ | √ | √ | √ | √ | √ | √ | √ | 86.374 |
| গ (Ga) | √ | X | √ | √ | √ | √ | √ | X | √ | √ | √ | X | √ | √ | √ | X | √ | √ | √ | √ | √ | √ | 81.861 |
| খ (Kho) | X | √ | √ | √ | √ | X | √ | √ | X | X | √ | √ | √ | √ | √ | √ | √ | √ | √ | X | √ | √ | 77.274 |

| | |
|---|---|
| √ | Matched |
| × | Not Matched |

**Accuracy = (No. of times matched / total times tested )*100%**

The total accuracy after the 22 test on four hand signs was 84.11%. Table 1 illustrates the result we had found for the 4 hand signs when conducting 22 tests. Figure 5 shows the response time for the system.

For the first run, a simple gesture was tested to be identified, namely ক(Ko). As can be seen from Figure 3, the hand sign is very prominent and thus, our proposed model was able to easily form its contour. Also, as the finger has several discrete angles the unique joint algorithm is able to detect the angle changes and thus locate the joints. Due to the hand sign being a favorable composition, it took less time for the system to run it.

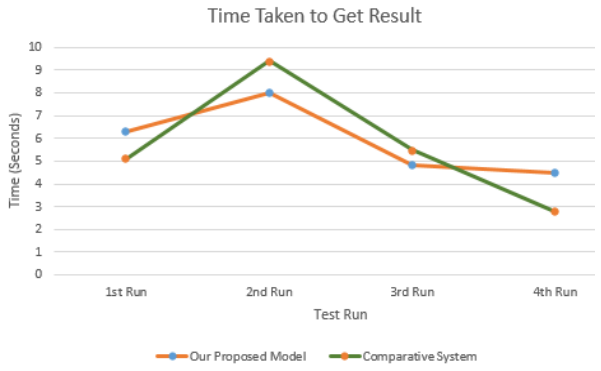


Figure 5. Time taken to get output

In the second run, the letter খ(Kho) was used. As depicted in Figure 5, খ bares resemblance to অ(Shorey-O) which exhibits greater response time compare to other tested letters.

গ(Ga), was the sample utilized for the third run. This hand sign is completely unique in its form and thus, it takes less time for the primary hand locations, i.e. the fingertips, wrist and joints are easily located.

In the fourth run, the স্বরবর্ণ (Shoroborno) - অ(Shore-O), is used. During this test, the fingertip detection algorithm had completed its task the fastest, allowing the other tasks a head start in comparison to the other hand signs.

The time taken to achieve the right output using a stop watch was measured; the cumulative accuracy from 22 recorded tests was 84.11 percent. However, the datasets collected and the tests carried involved normal untrained people, but it can be assured that if the tests were conducted on trained individuals the accuracy would be almost 100. Moreover, many of the hand signs for the different letter are very similar, which leads to confusion and thus wrong recognition results, sometimes. Figure 6 presents the detail graphical user interface of our system where the proposed model successfully detects the letter from signs.

Figure 6. User Interface and output

## IV. CONCLUSION

In this paper, isolated sign which refers to static gesture have been trained and tested using neural network which made the work more reliable, since neural network provides an adaptive learning technique with problem solving capability to complex real world problem. The three basic features that have been extracted from the image were contour using convex hull method, fingertip and our self-developed joint location for fair and better result. Choosing these three as features was the best decision which made our work comparatively better because of the accuracy rate of the result analysis. SVM algorithm was run to process the end result based on these the supporting features. Experimental results show that the proposed model exhibited average 84.11% detection accuracy for our tested letters.

## REFERENCES

[1] A. M. Jarman, S. Arshad, N. Alam, J. Islam, "An Automated Bengali Sign Language Recognition System Based on Fingertip Finder Algorithm", *Int. Journal of Electronics and Informatics,* vol. 4, no.1, pp. 1-10, July2015.

[2] (1996) Stergiou, C. (n.d.). "What is a Neural Network?" [Online] https://www.doc.ic.ac.uk/~nd/surprise_96/journal/vol1/cs11/article1.html.

[3] A. R. Patil, and S. S. Subbaraman, "A Review on Vision Based Hand Gesture Recognition Approach Using Support Vector Machines," *IOSR Journal of Electronics and Communication Engineering, pp. 7-12*

[4] C. R. DeSouza, and E. B. Pizzolato, "Sign Language Recognition with Support Vector Machines and Hidden Condtional Random Fields: Going from Fingerspelling to Natural Articulated Words," in *Proc. of the 9th International Conference on Machine Learning and Data Mining in Pattern Recognition*, pp. 84-98, Berlin, 2013.

[5] C.-W. Hsu, C.-C. Chang, and C.-J. Lin, "A Practical Guide to Support Vector Classification", Taipei: National Taiwan University, 2013.

[6] J. Weston, S. Mukherjee, O. Chapelle, M. Pontil, T. Poggio, and V. Vapnik, "Feature Selection for SVMs", 2001.

[7] Y. W. Chang, and C. J. Lin, "Feature Ranking Using Linear SVM. JMLR," in *Proc. Workshop and Conference Proceedings 3*, pp. 63-64, Taiwan 2008.

[8] P. K. Vijay, N. N. Suhas, C. S. Chandrashekhar, and D. K Dhananjay, "Recent Development in Sign Language," *A Review* (2nd ed.), vol. 1, 2013.

[9] S. Lang, "Sign language recognition with Kinect," Bachelor, InstitutfürInformatik, Freie Universitä t Berlin, 2011

[10] Z. Ren, J. Yuan and J. Meng, "Robust part-based hand gesture recognition using Kinect sensor," in *IEEE Transactions on Multimedia*, vol. 15, no. 5, 2013.

[11] B. Garcia, S. A. Viesca, "Real-time American Sign Language Recognition with Convolutional Neural Networks," in *Proc. of Machine Learning Research,* pp. 225-232.

[12] S. S. Rautaray, and A. Agrawal, "Vision based hand gesture recognition for human computer interaction: a survey," *Artificial Intelligence Review*, vol. 43, no. 1, pp. 1-54, 2015.

[13] S. Corera and N. Krishnarajah, "Capturing Hand Gesture Movement: A Survey on Tools, Techniques, and Logical Considerations," *Chi Sparks 2011 HCI Research, Innovation and Implementation, Arnhem, Netherlands,* June 2013.

[14] T. Grzejszczak, M. Kawulok and A. Galuszka, "Hand landmarks detection and localization in color images," *Multimedia Tools and Applications, vol.* 75, no. 23, pp 16363–16387, December 2016

[15] S. Yinying, J. Yunzhe, G. Ting, "An Integrated Approach of Real-time Hand Gesture Recognition Based on Feature Points," *International Journal of Multimedia and Ubiquitous Engineering,* vol. 10, no.4, 2015.

[16] N. S. Juthy, B. G. Shaha, S. A. Shojol, "IsharaBhashayJogajog (Communicating through Sign Language)," Dhaka: Center for Disability in Development, 2005.

*[17]* B. Wang, A. Quattoni, L. P. Morency, D. Demirdjian, T. Darrell, "Hidden Conditional Random Field for Gesture Recognition," in *Proc. IEEE Computer Society Conference on Computer Vision and Pattern Recognition,* pp. 1-7, 2006.

[18] M. Alauddin and A.H. Joarder, "Deafness in Bangladesh," in Suzuki JI., Kobayashi T., Koga K. (eds) Hearing Impairment. Springer, Tokyo, 2004.

2017 3rd International Conference on Electrical Information and Communication Technology (EICT), 7-9 December 2017, Khulna, Bangladesh

# Discrete Time Model Predictive Controller Design for Voltage Control of an Islanded Microgrid

Subroto K. Sarkar*, Faisal R. Badal* Sajal K. Das* and Yuan Miao†
*Department of Mechatronics Engineering, Rajshahi University of Engineering & Technology, Bangladesh.
†Department of Information Technology, College of Engineering and Science, Victoria University, Australia.
Email: skshuvo138008@gmail.com; faisalrahman1312@gmail.com; das.k.sajal@gmail.com; yuan.miao@vu.edu.au

***Abstract*—This paper presents the design of a robust model predictive controller for grid voltage control of an islanded microgrid. Several distributed generation units are connected in parallel for making a microgrid. The uncertain and unknown nature of the load produces un-modeled dynamics. This un-modeled dynamic introduces the measurable effect of the performance of the microgrid. The objective of the design of the controller is to control the grid voltage against different type loads. The design of this controller is done by using the discrete valued function that provides the extensive tracking performance of microgrid. The effectiveness of the proposed controller is validated by using MATLAB/Simulink SimPowerSystems. The simulation results show that the proposed controller provides the high tracking performance for voltage control of the microgrid system.**

***Keywords:*** **MPC controller, islanded Microgrid, voltage control.**

## 1. Introduction

Natural assets such as fossil fuel, natural gas, oil, coal named nonrenewable energy sources are used to generate electricity. The generation of electricity in present world is accordingly raised up due to its large amount of demand near to supplier. Due to lack of nonrenewable energy sources, researchers are interested to develop a new research area to produce electricity. Microgrid (MG) is one process to produce electricity from renewable energy sources. It is a small network of power having the ability to produce uninterrupted power when it is disconnected from the main grid.

Microgrid consists of a number of distributed generation (DG) namely wind turbines, photovoltaic panels, fuel cells, bio-gases, hydroelectric energy sources, point of common coupling (PCC), energy storage element, low voltage distribution systems, loads etc. The power of microgrid is come from renewable energy sources. Higher reliability, lower capital investment, proper utilization of renewable energy source makes the microgrid acceptable throughout the world [1]. Microgrid can operate in two mode such as grid-connected mode and islanded mode. In grid-connected mood, the voltage and frequency of microgrid is controlled directly by the main grid and enables to take power from the main grid. Microgrid is separated from the main grid when it is subjected to large disturbance such as faults, voltage collapse and make it to operate in islanded mode [2], [3].

Islanded microgrid is preferable when the transmission losses and investment increase in a remote place where no main grid is available. This contour provides a proper control of active and reactive power as well as makes the voltage and frequency stable for a wide range of operation. According to the consortium for electric reliability technology solutions (CERTS), microgrid is able to provide both power and heat that ensures the difference between islanded and grid-connected mode [4], [5].

Wind speed, sun-light, solar capacity and strength etc. are the factors of generating electricity from renewable energy sources that deviate the performance of microgrid due to number of reason. Unpredictable uncertainties and unknown load dynamics may also hampers the performance of islanded microgrid and make the voltage unstable [6]. Hence, controlling of voltage of microgrid becomes a challenging nature for the operators.

H-infinity controller has been already developed to achieve robust performance of microgrid against un-modeled load and uncertainties [1], [7]. It provides robust stability with the variation of load dynamics. The design of H-infinity depends on the norms minimization and order of the system. High order system needs high order controller which may required advanced digital signal processing system to control the performance of microgrid [8].

Proportional-Integral-Derivative (PID) and Combined Proportional-Integral (PI) controller have been proposed to improve the limitation of H-infinity controller [9], [10]. It is easy to design and implementation and able to maintain the power balance in both steady-state and transient condition. Low bandwidth and poor robustness are the limitations of these controller [11].

Fast and accurate dynamic response of microgrid is achieved by using Linear quadratic regulator (LQR) [12]. This method depends of stationary frame regulator and does not need the requirement of communication link. A set of linear equation is used to model this controller that eliminates the error in the system. Mean-value theorem is used to linearize the system model. The system may unstable with the variation of plant dynamics that constrains the

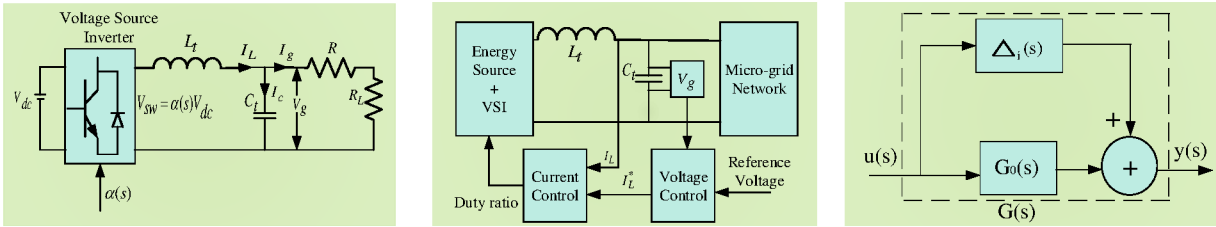


(a) (b) (c)

**Figure 1:** (a) Single phase single energy source microgrid system, (b) Closed-loop control strategy in single phase microgrid with VSI, (c) Control structure of islanded microgrid.

**TABLE 1:** Parameter values for single phase microrid

| Description | Value |
|---|---|
| DC bus voltage ($V_{dc}$) | $300V$ |
| Capacitor filter ($C_t$) | $15\mu F$ |
| Inductor filter ($L_t$) | $2mH$ |
| Line resistance ($R_{line}$) | 0.45 Ω |
| Consumer load ($R$) | 40 Ω |

application of LQR controller in microgrid.

This paper presents a robust model predictive controller (MPC) [13] to control the voltage of islanded microgrid. The advantage of proposed controller is its ability to predict the future behavior of the system. The proposed technique is able to deal with constraints that are often encountered in practice. MPC uses the current plant measurement, current dynamic state of the plant, the process variable target and calculates the future events that are rarely well addressed by other control techniques. This controller uses predefined cost function which ensure the high tracking performance of microgrid system.

The rest of the paper is organized as follows. Section 2 presents the modeling of islanded microgrid. Controller design for the proposed system is carried out in Section 3. Performance evaluation of the proposed controller for single phase microgrid system under various operational scenarios is presented in Section 4. The paper is concluded in Section 5.

## 2. Modeling of Islanded Microgrid

### 2.1. Microgrid Configuration

Fig. 1(a) represents a single phase microgrid with a DC voltage source, voltage source inverter (VSI), power electronics interface, LC filter, energy storage systems (ESS). ESS units provide a bridge to meet the power and energy requirements of the microgrid. The VSI units interface the DG units and the microgrid to convert the DC voltage and provides AC voltage for supplying to loads. MOSFET, IGBT are typically used as VSI unit whose switching action is represented by $V_{sw} = \alpha(s)V_{dc}$ where $V_{dc}$ represents the DC source voltage and $\alpha(s) \in$ {-1, 1}. The harmonics of the high frequency switching is attenuated by the $LC$ filter at the ac side.

The voltage control strategy of islanded microgrid with VSI units is shown in Fig. 1(b). The function of current controller is to controls the duty ratio $\alpha(s)$ of VSI units that signifies the pulse width modulation (PWM) principle. The outer control loop is voltage controller that controls the desired grid voltage $v_g$. The comparison between the grid voltage and reference voltage of the microgrid produces an error and gose through the voltage controller that produces reference inductor current ($I_L^*$). The inductor current ($I_L$) is injected to the current controller in which it is compared with the reference inductor current and produce duty ratio $\alpha$.

### 2.2. Single Phase MG Modeling

Let $V_L$ be considered the inductor voltage. Then the current across the inductor in Fig. 1(a) can be written as

$$V_L = L\frac{dI_L}{dt} \tag{1}$$

$$\frac{dI_L}{dt} = \frac{V_L}{L} = \frac{V_{sw} - V_g}{L} \tag{2}$$

where $I_L$ is the inductor current. The laplace transform of (1) is

$$V_L(s) = sLI_L(s)$$

$$sI_L(s) = \frac{V_L(s)}{L} = \frac{V_{sw}(s) - V_g(s)}{L} = -\frac{V_g(s)}{L} + \frac{V_{sw}(s)}{L} \tag{3}$$

with $V_{sw}$ is the source or switching voltage which is the product of duty ratio of VSI and the supply dc voltage.

$$V_{sw} = \alpha(s)V_{dc}(s)$$

From Fig. 2 (a), the capacitor voltage which is known as grid voltage can be obtained as

$$C\frac{dV_g}{dt} = I_c$$

$$\frac{dV_g}{dt} = \frac{1}{C}I_c = \frac{1}{C}[I_L - I_g] = \frac{1}{C}I_L - \frac{1}{C}I_g \tag{4}$$

where $I_c$ represent the capacitor current. The laplace transform of (4) is

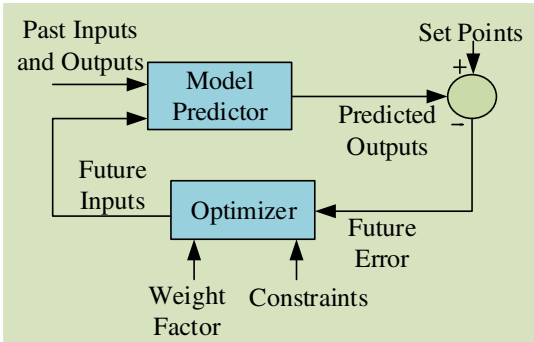


**Figure 2:** Control structure of Model Predictive Controller.

$$sV_g(s) = \frac{1}{C}I_L(s) - \frac{1}{C}I_g(s) \tag{5}$$

The above (3) and (5) can be represented as follows:

$$\frac{d}{dt}\begin{bmatrix} I_L \\ V_g \end{bmatrix} = \begin{bmatrix} 0 & -\frac{1}{L} \\ \frac{1}{C} & 0 \end{bmatrix}\begin{bmatrix} I_L \\ V_g \end{bmatrix} + \begin{bmatrix} \frac{1}{C} \\ 0 \end{bmatrix}\begin{bmatrix} V_{sw} \end{bmatrix} + \begin{bmatrix} 0 \\ -\frac{1}{C} \end{bmatrix}\begin{bmatrix} I_g \end{bmatrix} \tag{6}$$

$$y = \begin{bmatrix} V_g \end{bmatrix} = \begin{bmatrix} 0 & 1 \end{bmatrix}\begin{bmatrix} I_L \\ V_g \end{bmatrix}$$

which can be transformed into Fig. 1(c) such that $G(s) = G_0(s) + \Delta(s)$, where the nominal plant $G_0(s) = C(sI - A_m)^{-1}B_m + D_m$, state matrix $A_m = \begin{bmatrix} 0 & -\frac{1}{L} \\ \frac{1}{C} & 0 \end{bmatrix}$, input matrix $B_m = \begin{bmatrix} \frac{1}{C} \\ 0 \end{bmatrix}$, output matrix $C_m = \begin{bmatrix} 0 & 1 \end{bmatrix}$, transition matrix $D_m = 0$, uncertainty to output from input $\Delta(s) = \begin{bmatrix} 0 \\ -\frac{1}{C} \end{bmatrix} I_g(s)$. The different parameters of single phase microgrid system is presented in Table 1.

## 3. Controller Design

This section presents a brief discussion of the design of model predictive controller (MPC). The control structure of model predictive controller is reported in Fig. 2. It is an advanced method of process control used in control industries. It enables to reduce the tracking error by balancing and sampling the system model. The sampling of system model plays an important role for designing MPC. The sampling means the average number of samples obtained in one second. In this parer, for designing of this controller the sampling frequency is used as $10KHz$. The design objective of MPC is to predict the future events. It also enables to take the control action for optimizing the future behaviour of the plant output accordingly. The design of MPC systems are based on the dynamic models of the nominal plant.

The plant state-space models to design the controller is represented as follows:

$$x_p(k+1) = A_p x_p(k) + B_p u(k) \tag{7}$$

$$y(k) = C_p x_p(k) + D_p u(k) \tag{8}$$

where $A_p$, $B_p$, $C_p$ and $D_p$ represents the discrete state-space plant model, $u$ is the manipulated or input variable, $y$ is the plant output and $x_p$ is the state variable vector of nominal plant. we have implicitly assumed that the input $u(k)$ cannot affect the output y(k) at the same time. Thus, $D_p$ = 0 in the plant model. The increments of the variable $x_p(k)$ and $u(k)$ is represented as follows:

$$\Delta x_p(k+1) = A_p \Delta x_p(k) + B_p \Delta u(k) \tag{9}$$

and

$$y(k+1) = C_p x_p(k+1) \tag{10}$$

where

$$\Delta u(k) = u(k) - u(k-1)$$
$$\Delta x_p(k+1) = x_p(k+1) - x_p(k)$$
$$\Delta x_p(k) = x_p(k) - x_p(k-1)$$

The increment of the plant is incorporated to disturbance rejection and tracking a reference signal in the MPC algorithm. The state-space models of augmented plant can be represented in the following way

$$\begin{bmatrix} \Delta x_p(k+1) \\ y(k+1) \end{bmatrix} = \begin{bmatrix} A_p & 0 \\ C_p A_p & I \end{bmatrix}\begin{bmatrix} \Delta x_p(k) \\ y(k) \end{bmatrix} + \begin{bmatrix} B_p \\ C_p B_p \end{bmatrix}\Delta u(k) \tag{11}$$

$$y(k) = \begin{bmatrix} 0 & I \end{bmatrix}\begin{bmatrix} \Delta x_p(k) \\ y(k) \end{bmatrix} \tag{12}$$

Here $A = \begin{bmatrix} A_p & 0 \\ C_p A_p & I \end{bmatrix}, B = \begin{bmatrix} B_p \\ C_p B_p \end{bmatrix}, C = \begin{bmatrix} 0 & I \end{bmatrix}$ that are used

to design of predictive controller. The future state variables and output sequence can be denoted by

$$x(k+H_y|k) = A^{H_y}x(k) + A^{H_y-1}B\Delta u(k) + .... + A^{H_y-H_c}B\Delta u(k+H_c-1)$$

and

$$y(k+H_y|k) = CA^{H_y}x(k) + CA^{H_y-1}B\Delta u(k) + .... + CA^{H_y-H_c}B\Delta u(k+H_c-1).$$

where $H_y$ is prediction horizon and $H_c$ is control horizon that chosen to less than or equal to $H_y$. The function of $H_c$ parameter is to measure the future control action of MPC.

From (10) and (11), the future state variables are sequentially calculated as follows:

$$x(k_j+1|k_j) = Ax(k_j) + B\Delta u(k_j)$$
$$x(k_j+2|k_j) = Ax(k_j+1|k_j) + B\Delta u(k_j+1)$$
$$= A^2x(k_j) + AB\Delta u(k_j) + B\Delta u(k_j+1)$$
$$\vdots$$

$$x(k_j + H_y|k_j) = A^{H_y}x(k_j) + A^{H_y-1}B\Delta u(k_j) + A^{H_y-2} B\Delta u(k_j+1) + ..... + A^{H_y-H_c}B\Delta u(k_j + H_c - 1)$$

Hence, the periodic output variables can be written as

$$y(k_j+1|k_j) = CAx(k_j) + CB\Delta u(k_j)$$

$$y(k_j+2|k_j) = CA^2x(k_j) + CAB\Delta u(k_j) + CB\Delta u(k_j+1)$$

$$\vdots$$

$$y(k_j + H_y|k_j) = CA^{H_y}x(k_j) + CA^{H_y-1}B\Delta u(k_j) + C A^{H_y-2}B\Delta u(k_j+1) + ..... + CA^{H_y-H_c}B\Delta u(k_j + H_c - 1)$$

The dimension of $H_y$ is $Y$ and $H_c$ is $\Delta u$ for the single input and single output case, then

$$Y = [y(k_j+1|k_j)y(k_j+2|k_j)...y(k_j + H_y + |k_j)]^T$$

$$\Delta U = [\Delta u(k_j)\Delta u(k_j+1)...\Delta u(k_j + H_c - 1)]^T$$

The prediction horizon can be arranged in a compact matrix form

$$Y = \alpha x(k_j) + \beta\Delta U$$

Here, the $\alpha$ matrix having dimension $(H_y, n)$ and the $\beta$ matrix having dimension $(H_y, H_c)$ as follows:

$$\alpha = \begin{bmatrix} CA \\ CA^2 \\ CA^3 \\ \vdots \\ CA^{H_y} \end{bmatrix}$$

$$\beta = \begin{bmatrix} CB & 0 & \dots & 0 \\ CAB & CB & \dots & 0 \\ CA^2B & CAB & \dots & 0 \\ \vdots & & & \\ CA^{H_Y-1}B & CA^{H_Y-2}B & \dots & CA^{H_Y-H_C}B \end{bmatrix}$$

The cost function C that reflects the control objective as

$$C = \sum Q(y(k_j + p|k_j) - R_p(k_j + p))^2 \sum R(\Delta u(k_j + p - 1))^2 \quad (13)$$

where $Q$ is the state weighting matrix, $R_p$ is the reference signal and R is the control weighting matrix.

The first and last term of (13) are used to predict and control the horizon of MPC system respectively. The problem of MPC system is related to the translation of system input into the set of linear equation that is parameterized using vector $\Delta U$. Predictive control problem is solved in the framework of receding horizon control by allowing to vary the constraints at the beginning of each optimization window. It also gives the means to tackle the constrained control problem numerically. The constraints at sample time $k_j$ are expressed as

$$\Delta u^{min} \leq \Delta u(k_j) \leq \Delta u^{max}$$

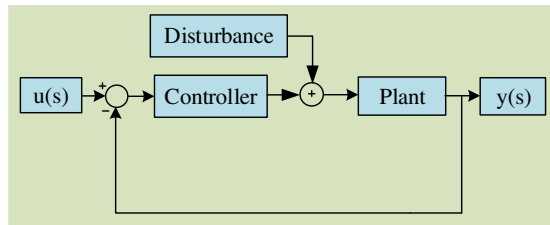


**Figure 3:** Block diagram of closed-loop system.

where $u^{min}$ and $u^{max}$ are the low and high levels of the control action respectively.

The next constraints at future sample can be written as

$$\Delta u^{min} \leq \Delta u(k_j+1) \leq \Delta u^{max}$$

However, the inequality linear constraints for the parameter vector $\Delta U$ that minimizes the cost function is

$$\begin{bmatrix} M_1 \\ M_2 \\ M_3 \end{bmatrix} \Delta U = \begin{bmatrix} N_1 \\ N_2 \\ N_3 \end{bmatrix} \quad (14)$$

Where $N$ is the element of $\Delta u^{min}$ and $\Delta u^{min}$ and $M$ is a matrix reflecting the constraints having the rows equal to the number of constraints and columns equal to the dimension of $\Delta U$. However, an optimal solution of (14) is,

$$M\Delta U \leq \gamma \; ; \gamma \in \mathbb{R}^{N*1}$$

## 4. Performance Evaluation

The performance of the proposed controller is investigated in this section with different scenarios. The tracking performance of the microgrid system against the unknown load dynamics, highly nonlinear and dynamics as well as harmonics loads are verified. The inclusion of proposed controller with the nominal plant is shown in Fig. 3. The results are obtained by implementing the MATLAB Simulation environment. The details of simulation results for both single and three phase microgrid in the presence of loads and fault conditions are given below:

### 4.1. Performance against constant loads

The performance of microgrid may be affected by the constant loads such as induction motor. It reduces the stability and produces variable performance of microgrid. To investigate the performance of microgrid in the presence of constant load, a single phase dynamic load block is modeled as a current source with active power of 50 MW and reactive power of 25 MW at initial voltage. The simulation results in the presence of constant load is presented in Figs 4(b), 4(e), 5(b) and 5(e) that ensure the tracking and reliable performance of the proposed controller.

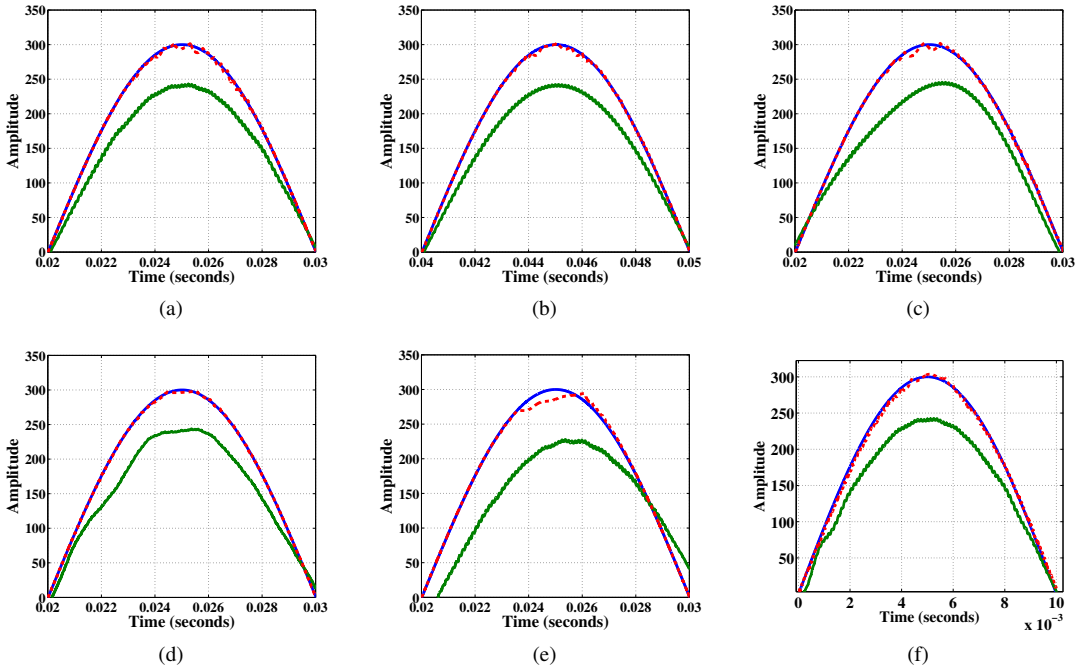


**Figure 4:** Grid Voltage tracking using model predictive controller for (a) Consumer Load, (b) Dynamic Load, (c) Harmonics Load, (d) Unknown Load, (e) Asynchronous machine Load, (f) Nonlinear load. The blue (-) and green (-) solid line represents the reference and open-loop voltage respectively and red (- -) dashed line represents the closed-loop grid voltage.

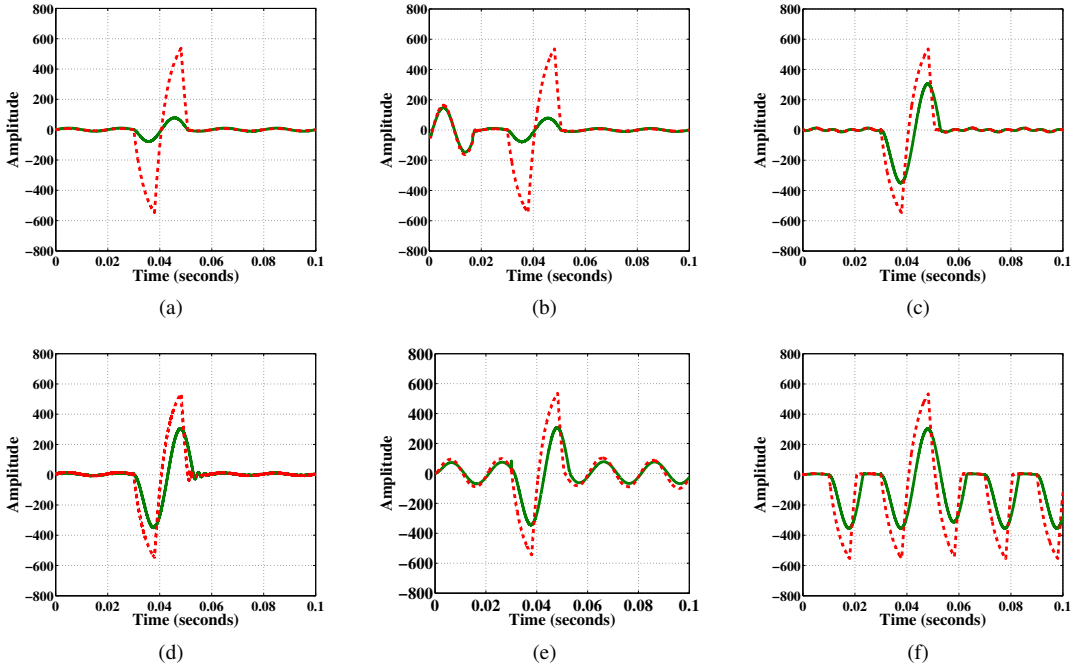


**Figure 5:** Fault Current tracking using model predictive controller for (a) Consumer Load, (b) Dynamic Load, (c) Harmonics Load, (d) Unknown Load and (e) Asynchronous machine Load, (f) Nonlinear load. The green (-) solid line represents the closed-loop fault current and red (- -) dashed line represents the open-loop fault current.

### 4.2. Performance against harmonic loads

Television, computer, printers, Fluorescent lighting, battery chargers, rectifiers and variable-speed drives are the example of harmonic load. The harmonic loads produce considerable voltage and current harmonic in the power system which unbalanced the performance of microgrid. The current waveform becomes quite complex due to the presence of harmonic load which increases excessive amount of current in the system. To investigate the performance of the microgrid, a $3^{rd}$ order harmonic current source is designed of amplitude 7A and frequency 150Hz with a $30\Omega$ resistance which is connected in series with the current source. The obtained results using the proposed controller are shown in Figs 4(c) and 5(c) that verify the high performance of controller.

### 4.3. Performance against unknown loads

Any un-modeled loads can be introduced in the power system which vary the voltage and power. The un-modeled load is connected with the microgrid at $t$= 0.3 second when the switch is pressed. The parameters of microgrid system introduce a new steady-state that may vary the performance of microgrid. The peak amplitude of grid voltage and the fault current is investigated in Figs 4(d) and 5(d) which indicate the robustness and tracking performance of the proposed controller.

### 4.4. Performance against asynchronous machine loads

Asynchronous machine loads such as induction motor distort the performance of microgrid and reduce the stability of the system. To investigated the influence of the asynchronous load on microgrid, an induction motor is modeled in the dq stator reference frame, having a zero steady-state condition is paralleled with the microgrid. Due to the presence of asynchronous machine load the grid voltage may fluctuate which vary the active and reactive power of microgrid. The proposed controller reduce the fluctuation of voltage and current and provide most reliable performance of the microgrid system shown in figs 4(e) and 5(e).

### 4.5. Performance against non-linear loads

The operation of microgrid is influenced by the highly non-linear load namely television, computer. A non-linear load is modeled in this section by two-phase four-pulse diode bridge rectifier connected to the PCC. The output terminal is connected with a RC load having $R = 80\Omega$ and $C = 5\mu$F. The input current of the rectifier may be distorted but the proposed controller provides stable, reliable and high quality voltages investigated in Figs 4(f) and 5(f).

## 5. Conclusion

The design of robust discrete-valued model predictive controller is presented in this paper for voltage oscillation control in islanded microgrid. The controller is designed for single phase islanded microgrid. The performance of this controller is investigated against different scenarios. This controller provides the reliable performance of microgrid against different load dynamics and shows the high tracking performance.

## References


[1] M. Mahmoud, S. A. Hussain, and M. Abido, "Modeling and Control of Microgrid: An Overview," *Journal of the Franklin Institute*, vol. 351, no. 5, pp. 2822–2859, 2014.

[2] A. Llaria, O. Curea, J. Jiménez, and H. Camblong, "Survey on Microgrids: Unplanned Islanding and Related Inverter Control Techniques," *Renewable energy*, vol. 36, no. 8, pp. 2052–2061, 2011.

[3] G. Carpinelli, F. Mottola, D. Proto, and P. Varilone, "Minimizing Unbalances in Low-Voltage Microgrids: Optimal Scheduling of Distributed Resources," *Applied Energy*, vol. 191, pp. 170–182, 2017.

[4] A. M. Bouzid, J. M. Guerrero, A. Cheriti, M. Bouhamida, P. Sicard, and M. Benghanem, "A survey on Control of Electric Power Distributed Generation Systems for Microgrid Applications," *Renewable and Sustainable Energy Reviews*, vol. 44, pp. 751–766, 2015.

[5] D. E. Olivares, C. A. Cañizares, and M. Kazerani, "A Centralized Energy Management System for Isolated Microgrids," *IEEE Transactions on smart grid*, vol. 5, no. 4, pp. 1864–1875, 2014.

[6] M. Hamzeh, M. Ghafouri, H. Karimi, K. Sheshyekani, and J. M. Guerrero, "Power Oscillations Damping in DC Microgrids," *IEEE Transactions on Energy Conversion*, vol. 31, no. 3, pp. 970–980, Sept 2016.

[7] J. Mongkoltanatas, D. Riu, and X. LePivert, "H Infinity Controller Design For Primary Frequency Control of Energy Storage in Islanding MicroGrid," in *Power Electronics and Applications (EPE), 2013 15th European Conference on*. IEEE, 2013, pp. 1–11.

[8] S. K. Sarkar and S. K. Das, "Nonlinear modeling and control of dc machines: A partial feedback linearization approach," in *Electrical, Computer & Telecommunication Engineering (ICECTE), International Conference on*. IEEE, 2016, pp. 1–4.

[9] S. K. Sarkar, F. R. Badal, and S. K. Das, "A comparative study of high performance robust pid controller for grid voltage control of islanded microgrid," *International Journal of Dynamics and Control*, pp. 1–11, 2017.

[10] M. Armin, P. N. Roy, S. K. Sarkar, and S. K. Das, "LMI Based Robust PID Controller Design for Voltage Control of Islanded Microgrid," *Asian Journal of Control*, Sept 2017.

[11] S. K. Sarkar and S. K. Das, "High performance nonlinear controller design for ac and dc machines: partial feedback linearization approach," *International Journal of Dynamics and Control*, pp. 1–15, 2017.

[12] T. L. Vandoorn, B. Renders, L. Degroote, B. Meersman, and L. Vandevelde, "Voltage Control in Islanded Microgrids by Means of a Linear-Quadratic Regulator," in *Proc. IEEE Benelux Young Researchers Symposium in Electrical Power Engineering (YRS10), Leuven, Belgium*, 2010.

[13] L. Wang, *Model predictive control system design and implementation using MATLAB®*. Springer Science & Business Media, 2009.

# Design and Construction of Product Separating Conveyor based on Color

Md. Mostafizur Rahman Komol[1], Amit Kumer Podder[2]
Khulna University of Engineering & Technology, Khulna-9203, Bangladesh.
amit_eee_kuet@yahoo.com[1], amitpodder09@yahoo.com[2],

***Abstract*— This research paper is a work on control engineering or production technology. This paper aims at the problem we are attempting to solve to create an automation system of product passing & separating through color difference. The products will be placed on moving conveyor belt through different colored packaging system. A color detecting device will be situated in a position of conveyor belt that will detect two different color of the packaged product and a divider will separate different colored package product to different destination. This product passing and separating to the intended destination is done by a color difference in an automatic way. In many packaging industries color object sorting and separating is a major task that needs to be done at final dispatch system. Manual sorting is a traditional approach that is preferred by industries. This approach is performed by human operators which is tedious, time-consuming, slow and non-consistent. Therefore, the efforts are made to design and implement an automatic technique of product passing & separating through color difference.**

***Keywords*—Conveyor, Color Sorting, Control, Automation.**

## I. INTRODUCTION

Presently a Conveyor belt system as item separators is broadly utilized as a part of power generation plant, cement industries, sustenance ventures, production enterprises and so on [1]. The adjustment and most recent advancements or approaches utilized as a part of various applications to diminish disappointments, support cost and hardware related a deadly mishap happens amid operation. A conveyor belt is an extreme and broadly utilized choice in the vast majority of the assembling mechanical applications where there is a requirement for finish sequential construction system computerization like synthetic enterprises, packaging plant, food preparing and bundling industrial facilities [2], [3], [4]. The whole procedure from creation to sort items for bundling is carried on a solitary conveyor belt and the procedures are done in the middle of, while they are moving [5], [6]. Deciding constant and very exact qualities of little objects in a quick-flowing stream would open new headings for industrial arranging processes [7].

Item separator based on color is where two items can be isolated by two diverse line as per their colors. Conveyor belt system with a color indicator can be utilized for such reason. The conveyor belt is a nonstop moving band produced using texture, metal or elastic utilized for transporting objects starting with one place then onto the next principally inside the industry. A conveyor system comprises a transport line, at least two pulleys that turn around in an unending circle of the conveyor belt. Either of the pulleys is controlled which causes the belt and the material on the belt forward. The driving pulley is the fueled pulley while the idler pulley is unpowered pulley [8].

By ordering the colored objects by its colors, which is going ahead of the conveyor by arranging the items in its particular pre-modified place which definitely diminishes the dull work done by the human, expanding precision and speed in the work. In that, the microcontroller sends a flag to a circuit which drives the different servo engines joined at a particular area on the conveyor. In view of the identified protest, the servo engine pivots and pushes the objects its predetermined area, and comes back to the first position [5].

In this paper, efforts have been made to use a single assembly line for the classifying and sorting purpose of different objects using electronic systems, advanced sensors on the basis of color characterization of each object. The project involves color identification of an object which is done by Light dependent resistors arrangement acting as a color sensor which identifies the object's color and sends the signal to the ATMEGA microcontroller in Arduino [9]-[13]. The microcontroller in response to the received signal generates an appropriate control signal which is sent to the circuit which drives the servo-motor and it also synchronizes the direction of movement of the servo-motor propeller with the color of the product. Based upon the color detected, the propeller of servo-motor act as divider pushes the object to the specified location. It points to grouping and arranging the colored items which are going ahead a conveyor belt by setting them in their particular pre-customized put. Because of this, just a single conveyor is adequate rather than many, thereby accomplishing high exactness and speed in the work; while wiping out the dreary work done by the human.

## II. DESIGN OF THE SYSTEM

### *A. Design Consideration*

Various types of the conveyor belt are used worldwide. But these types are used in industries and high production services. Among all of them, a simple Horizontal Wood-based conveyor belt system was designed in this work. Belt was made of cloth and a support was given beneath the cloth by wood so that the cloth doesn't get loose or curvy. For Color detection a Color detecting sensor TCS3200 was used and the system was made for the detection and separation of only two

978-1-5386-2307-7/17/$31.00 ©2017 IEEE

colors —red and green. According to design consideration, the CAD design of conveyor system with measurement of parts is given in following Fig. 1.

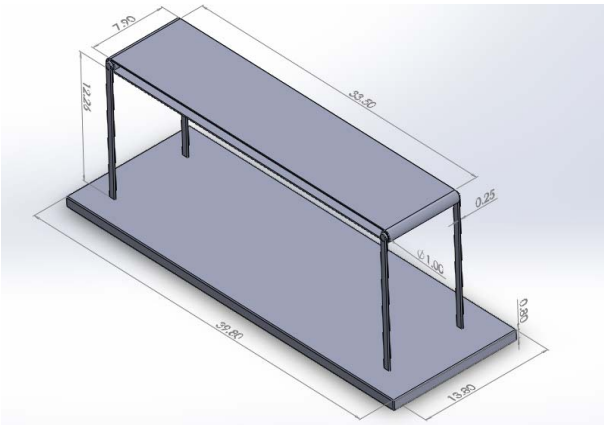


Fig. 1 Design of conveyor belt system

For separating the colored products, the propeller of the servo-motor act as separator divider was used. For the separating system, slide force mechanism of divider was used instead of other thrust force or another mechanism system for some improve modification and application purposes.

## B. Conveyor Belt Rotating System

For the rotating system of the conveyor belt, DC motor was used. For the control of the speed of the motor a control circuit was used as the rotating speed of conveyor belt directly depends on the speed of the motor. A potentiometer in that control circuit controls the voltage in motor and by this way it controls both motor and conveyor belt rotating speed. For fixed or constant speed application, AC motor or gear motor is well suited. For the application of speed control or higher speed or maximum torque in a small area is needed, the AC and brushless motor speed control system can be used. For precise positioning oriental motor's stepper or servo, the motor package is ideal. The CAD design of rotating part of the conveyor belt is given in following Fig. 2.

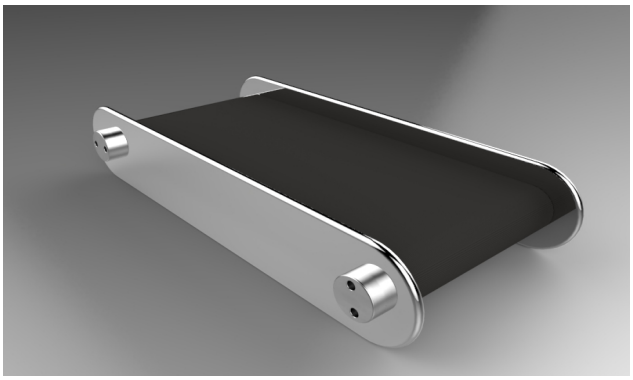

Fig. 2 Design of the rotating part of Conveyor belt system

## C. Color Detecting System

At first, the whole system was connected according to Fig. 3. But at this stage, it was not known what are the values from analogRead() function for the two LDRs. So the different value of red and green color was detected first. This programming was done on Arduino programming language. A power LED in the color sensor TCS3200 is used to illuminate the sensor area. The circuit diagram of the color detection and separation system is given in following Fig. 3 and the schematic view of the circuit connection part of the system are given in following Fig. 4.

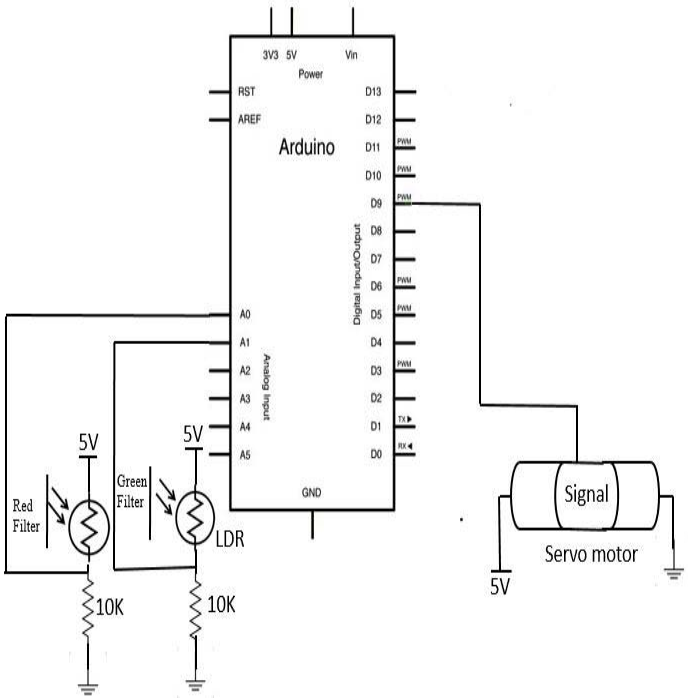


Fig. 3 Circuit diagram of the system

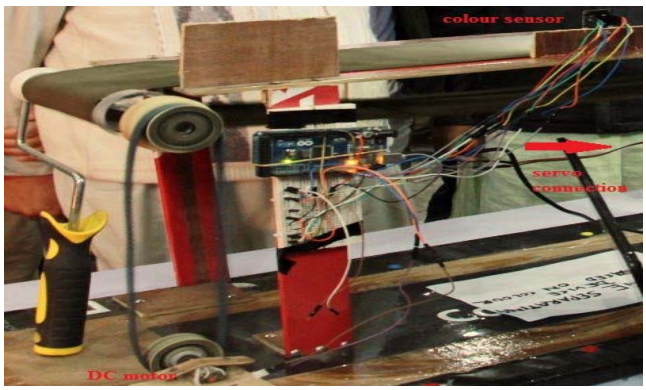


Fig. 4 Schematic view of circuit connection of the system

DC 6V power supply was provided to the system and LM298 motor driver was used for regulating the voltage for fixed slow speed dc motor rotation, safe product passing, sorting and separating the product accurately.

The Final Program for the Color detector device and direct separator servo motor was done based on the reading of the analog value of colors. Delay times were also set based on the position of the product how near it is to the divider on the conveyor to be separated and it was done by practicing it many times practically for precise control.

### *D. Separating System*

For the separation of product, a divider was used that was directly attached to a servo motor. The divider of movement of the product was run by a servo motor. The divider is like linear actuator. Servo motor can rotate 180 degrees. So it was kept on 90 degrees position and the program was written as it moves anticlockwise for red-colored products and clockwise for green colored ones. Every time it divides the movement of products, it returns to its 90 degrees position after a 2-second delay. The schematic view of the arrangement of the separating system with a servo motor and a divider attached to it are shown in following Fig. 5.

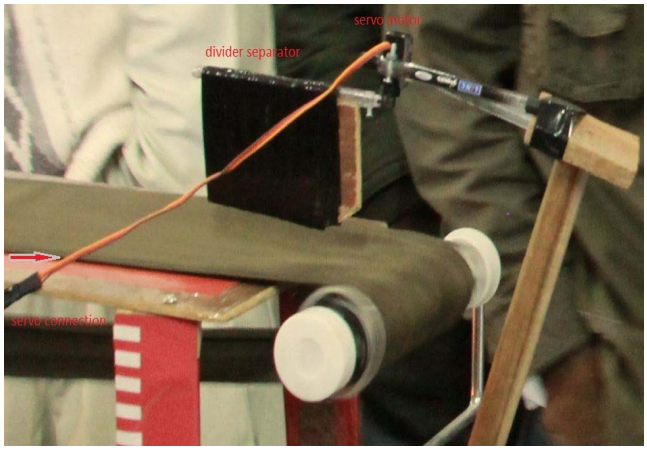


Fig. 5 Schematic view of arrangement of separating system

### *E. Package Storage System*

After the movement of the product being divided, two different colored product will be stored serially in two different bins. The red colored product is separated from the red bin and green product on the green bin. Both different colored products are collected from their specific bins. Also, the accepted and rejected products can be separated in this system, packaging them respectively in the green box and red box and collecting the rejected from the red bin and accepted products in the green bin.

## III. CONSTRUCTION OF THE SYSTEM

For the construction of a total system of the line separating device based on color, it was needed to combine three systems of conveyor belt for product passing, a color detector for the detection of the color of packaged products and the servo motor controlling system for the separation of products to their intended destination. The conveyor belt system was made of wood and fabrics. The DC motor was included with the driving pulley with a chain and it was voltage controlled with a circuit attached to a microcontroller. The rotating part of the conveyor belt was fixed with driving pulley and Fabrics was used as a belt for rotation for product passing. Construction parts of the system are shown with a systematic sequence in following Fig. 6 and the schematic view of the final construction of product separating device is shown in Fig. 7.

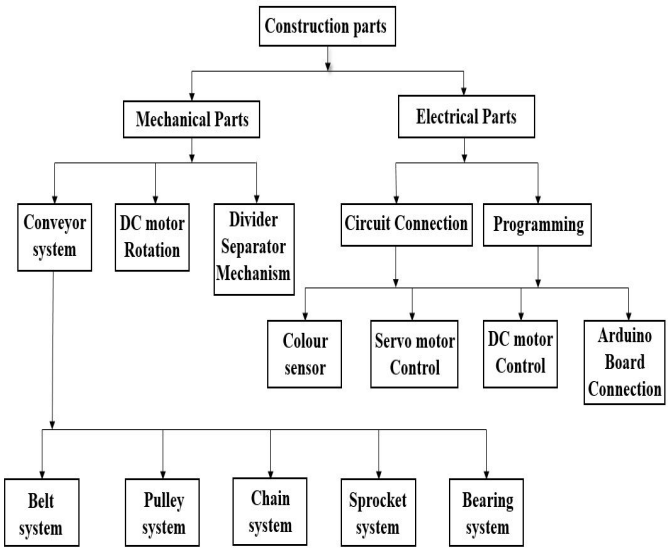


Fig 6 Flow chart of Construction parts

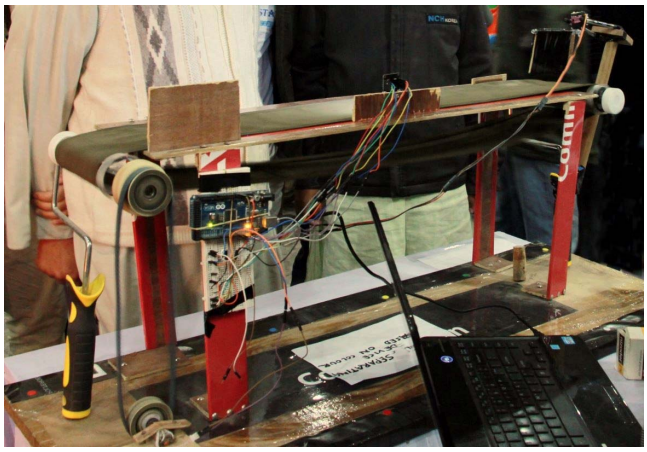

Fig. 7 Construction of Product separating device based on colors

A color sensor module TCS3200 was attached to a position of the conveyor belt which was intended to sense the color of the product that passes through the conveyor belt. The sensor was covered with paper for avoiding error and miscalculation problems for incident light fall. At the end of the conveyor belt, a servo motor was placed with an external standard to separate the product according to their color that passing through the conveyor belt. The green products bin and the red product bin is placed respectively on the left side and

right side of the divider separator. This is how product separating device based on the color system was constructed.

## IV. METHODOLOGY & PERFORMANCE TEST

The DC motor was run at the 6Volt power supply and the belt in the conveyor started rotating. The program was set to regulate the speed of belt rotation and the speed was regulated to keep moving it slow at 70-80 rpm so that the product in the belt pass slowly and sensed in the color sensor accurately. The green products bin and the red product bin is placed respectively on the left side and right side of the divider separator. The flow chart of working procedure of the system is shown in following Fig. 8.

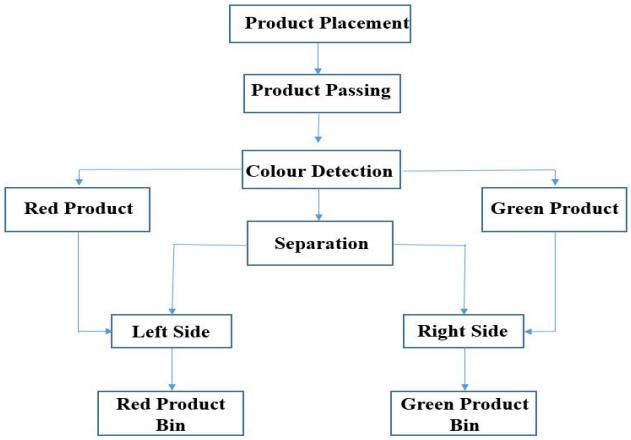


Fig. 8 Flow chart of methodology process

When the Green colored product is placed on the conveyor, the belt drags it with its rotating movement to the Color sensor. The green Color of the product is sensed by the sensor and according to the program, the divider with servo motor make an alignment way to pass the product to the desired green products bin. Normally the servo divider separator is kept 90 degrees at neutral position whereas that servo motor can rotate 180 degrees. So there remains a chance of rotating the divider 90 degrees on both left and right side. When the product is detected green on the color sensor, the divider automatically rotates 60 degrees right from the neutral position. At the time when the green product leaves the color sensor and come close in the range of divider, the divider automatically rotates 35 degrees to the left which drive the green product to the Green product bin with a little slide force. On the verge of red product passing, the divider makes alignment way to pass the product to the desired red product bin. When the product is detected red on the color sensor, the divider automatically rotates 60 degrees left from the neutral position. At the time when the red product leaves the color sensor and come close in the range of divider, the divider automatically rotates 35 degrees to the right which drive the red product to the red product bin with a little slide force. Every time after the divider separator rotates 35 degrees to drive the product with slide force to the pre-determined bin, it returns to its neutral position so that it prepares for the next product to separate. In this system of product separating, there is an advantage of safely and efficiently passing of soft and fragile product and separating them without any rejectable trace or spot. Here, the mechanism of the separating system to drive the product with small slide force is very much efficient to separate product safely rather than a thrust force mechanism system. In thrust force mechanism system, products are separated with thrust force to the destined places and this force of this system may cause harm of creating reject able trace or spot on the soft and fragile products like cakes, sweets, butter foods etc. But in this system of slide force mechanism, the failure of soft and fragile product separating is drastically reduced and safely separation is ensured.

For testing the performance of the system, 10 sample of red and green colored box were taken and they were used on the running system to be tested to be separated. The test result is given in following Table I.

TABLE I. PERFORMANCE TEST RESULTS

| Red Box Samples | Separation | Mention | Green Box Samples | Separation | Mention |
|---|---|---|---|---|---|
| 01 | Succeed | As usual | 01 | Succeed | |
| 02 | Succeed | | 02 | Succeed | |
| 03 | Succeed | | 03 | Succeed | |
| 04 | Fail | Sensor miscalcul-ated as intensity of both color were same | 04 | Succeed | |
| 05 | Succeed | | 05 | Succeed | |
| 06 | Succeed | | 06 | Succeed | |
| 07 | Succeed | | 07 | Fail | Sensor mis-calculale d as intensity of both color were same |
| 08 | Succeed | | 08 | Succeed | |
| 09 | Fail | Sample got hindered by sensor module | 09 | Succeed | |
| 10 | Succeed | | 10 | Fail | Sample went through out of range of sensor |

From the result, the failure chance and probable miscalculations of the color sensor were detected. The reasons for miscalculations were mentioned. For proper and accurate detection of the color of the product, there must be maintained a dark environment around the color detector sensor to maintain a constant intensity of light and also for avoiding the

incident light on the color sensor from outside. Here, the sensor is needed to cover with black paper to avoid these problems of miscalculation. Also, a better color sensor than TCS3200 is preferable.The accuracy of the system is compared with [9] and found satisfctory results.

## V. CONCLUSION

As the world is getting modern and digitalized, human labor is being replaced by technologies and intelligence for bringing higher comfort in human life and also for saving time and precise operation and mass production. In small and large scale industries to sort the products based on the various parameters or in food industries to identify the rotten or damaged fruits, this system of product separation based on color is essential for quick, accurate operation and mass production than using traditional human labor. Not only for bringing comfort but also for improving product quality and reducing cost these type of technological system using is a step of a digital life. The system is more improved and modified and very much essential in Practical life and Industrial activities.

## REFERENCE


[1] M. Young, *The Technical Writer's Handbook*, Mill Valley, CA: University Science, 1989.

[2] J. Chen, S. K. Lau, L. Chen, S. Wang, and J. Subbiah, "Modeling radio frequency heating of food moving on a conveyor belt", *Food and Bioproducts Processing*, vol. 102, pp. 3017-319, March 2017.

[3] A. Karnik, "Performance of TCP congestion control with rate feedback: TCP/ABR and rate adaptive TCP/IP," M. Eng. thesis, Indian Institute of Science, Bangalore, India, Jan. 1999.

[4] J. Padhye, V. Firoiu, and D. Towsley, "A stochastic model of TCP Reno congestion avoidance and control," Univ. of Massachusetts, Amherst, MA, CMPSCI Tech. Rep. 99-02, 1999.

[5] W. Xu, C. Zhao, P. Zhou, and Y. Yang, "Efficient adaptive resource allocation for multiuser OFDM systems with minimum rate constraints," in *Proc. IEEE Int. Conf. Commun.*, Jun. 2007, pp. 5126–5131.

[6] F. M. Pedrero and P. Tierno, "Magnetic propulsion of self-Assembled colloidal carpets: efficient cargo transport via a conveyor-belt effect", Phys. Rev. Applied, vol. 3 issue 5 , May 2015.

[7] Y. J. Zhang and K. B. Letaief, "Multiuser adaptive subcarrier-and-bit allocation with adaptive cell selection for OFDM systems," *IEEE Trans. Wireless Commun.*, vol. 3, no. 5, pp. 1566–1575, Sep. 2004.

[8] H. Mosadegh, S.M.T. F. Ghomi, and G.A. Süer, "A control theoretical modelling for velocity tuning of the conveyor belt in a dynamic mixed-model assembly line", *International Journal of Production Research* DOI: 10.1080/00207543.2017.1370150, pp. 1-23, 2017.

[9] A. Semenchenko, M. Stadnik, P. Belitsky, D. Semenchenko, and O. Stepanenko, " The impact of an uneven loading of a belt conveyor on the loading of drive motors and energy consumption in transportation", *Eastern-European Journal of Enterprise Technologies,* vol. 4, no. 1 (82), 2016.

[10] *FLEXChip Signal Processor (MC68175/D)*, Motorola, 1996.

[11] "PDCA12-70 data sheet," Opto Speed SA, Mezzovico, Switzerland.

[12] A. Kondhare, G. Singh, N. Hiralkar, and M. S. Vanjale, "Colour and shape based object sorting", *IJSAE Journal*, vol. 2, Issue 3, pp. 553 – 562, 2014.

[13] M. S. Telgote and G. S. Sable, "Object sorting system in MATLAB using robotic arm", *IJSEI Journal*, ISSN: 2251-8843, vol. 2, Issue 22, November 2013.

# Quantized Input Field Oriented Control of Sensorless Homopolar Synchronous Motor Drives

Shantanu Bose, A. S. M. Zadid Shifat, and Md Abdur Rafiq
Department of Electrical and Electronic Engineering (EEE)
Khulna University of Engineering and Technology (KUET), Khulna -9203, Bangladesh
Email: shantanu67eee@gmail.com; zadid_shifat@outlook.com;

*Abstract*— *Abstract*—**This paper represents a new method of controlling homopolar synchronous motor based on defining a Control Lyapunov function by creating quantized realizable inputs. Other control methods such as vector control, direct torque control etc. rely on heuristically chosen hysteresis band in order to choose switching instants which can create unwanted switching events. Conventional methods of switching like space vector modulation (SVM) rely on high frequency state space averaging that yields unnecessary switching. Here, we present the use of energy related Lyapunov function owing to selecting input based on the stabilizing effect it has on the system and thus minimizing switching events. A theoretical design of mechanical and electrical system has been presented here. Efficacy of the system performance is verified through computer simulation.**

Keywords—***Control Lyapunov Function, Field Oriented Control, Direct Torque Control, Homopolar Synchronous Motor, Quantized Input.***

## I. INTRODUCTION

Synchronous homopolar machines are being researched in various fields of applications. These machines can be a good choice for flywheel energy storage and drive system because have some advantageous features than induction motors such as don't have field winding on rotor which reduces rotor inertia and weight, and brushes, slip rings which reduces loss [1]. There is another one, homo-heteropolar machines [2]–[4], that is also capable to remove the limitations of classic synchronous machines. They are sometimes referred to as homopolar inductor generators and motors [5], [6] or simply homopolar generators and motors [7], [8]. The feature that defines this machine is the homo or homo-heteropolar d-axis magnetic field created by the field winding on stator [5], [6], [8] - [10] and permanent magnets and winding [7].

Synchronous homopolar machines have their field winding fixed to stator that encircles the rotor rather than being placed on it. There are advantages of having field winding on stator. The first of them is the elimination of slip rings that simplifies the rotor construction, making it practical to construct the rotor with a single piece of high-strength steel. The other rotor designs are to increase strength and reduce windage losses [6], [7], [8]. Other advantages include ease of cooling and increased available volume [2], [11], [12] and higher power factor even at low speed than induction motors. They have losses much less than induction motors and cheaper than Permanent Magnet Synchronous Motors (PMSMs) as the maintenance required is less and less vulnerable to environment. They are also effective where torque response and efficiency are critical. But problem can arise when phase current is large as in low speed applications of high power, the maximum attainable switching frequency shrivels as a result of thermal limitations of switching devices. So, the design engineer is faced with the problem of maximizing closed loop performance using highly forced actuators. This paper represents a simple sensor-less field oriented control (FOC) algorithm which is capable of minimizing switching events while providing fast dynamic response, robustness to parameter uncertainty, and stability guarantees.

Perchance the first remarkable proposed technique to improve performance and efficiency of electrical machines is based on FOC proposed first in [13] and again thorough in [14]. This method uses a rotating reference frame which when posed the trigonometric non-linearities are cut off that results in a bilinear system allowing independent regulation of torque producing and flux producing currents. FOC controllers rely on standard pulse width modulation (PWM) such as sine triangle PWM, space vector modulation (SVM) to track the desired signal using high switching frequency which leads to decrease efficiency and thermal problems of switching devices. We propose a FOC technique in this paper that is capable of minimizing unwanted switching events. A popular approach alternative to FOC is direct torque control (DTC). As in [15], DTC doesn't compute reference vectors in dq reference frame but uses hysteresis bands and look up table to track the command input and keep it in bounds. DTC has fast dynamic response and faster flux control ability than FOC [16], [17], though it suffers from enlarged torque ripple and high switching losses depending on the width of the hysteresis band [18], [19].

This paper represents a model in dq frame and propose a control strategy using a combination of Lyapunov and back-stepping approaches based on quantized realizable input system providing stability and accuracy. Here a quantized set of realizable inputs is used and a control Lyapunov function (CLF) is evaluated for every realizable input to decide the switching state of a two-level inverter and minimize unwanted switching. The main proposal is a sensor less technique taking into account the variable torque response demand of load for homopolar synchronous motor (HSM) drives.

978-1-5386-2307-7/17/$31.00 ©2017 IEEE

## II. MODEL OF HSM IN $d_q$ REFERENCE FRAME

Applying Kirchoff's voltage law and Newton's second in rotational form, HSM can be modelled and transformed into the direct and quadrature field oriented rotating reference frame [1], [2]. The model can be as follows

$$\frac{di_d}{dt} = \frac{v_d}{L_d} - \frac{R}{L_d} i_d + p\omega_r \frac{L_q}{L_d} i_q - p\omega_r \frac{\phi_f}{L_d} \tag{1}$$

$$\frac{di_q}{dt} = \frac{v_q}{L_q} - \frac{R}{L_q} i_q - p\omega_r \frac{L_d}{L_q} i_d \tag{2}$$

$$\frac{d\omega_r}{dt} = -\frac{3p\phi_f}{2J} i_q - \frac{3p}{2J}(L_d - L_q) i_d i_q - \frac{\beta}{J}\omega_r + \frac{\tau_l}{J} \tag{3}$$

where d-axis and q-axis currents are $i_d$ and $i_q$ , rotational velocity is $\omega_r$ , d and q axis inductances are $L_d$ and $L_q$ , stator resistance is $R$ , number of magnetic poles is $p$, magnetic flux is $\phi_f$ which is constant throughout the whole process, damping coefficient is $\beta$ , load torque is $\tau_l$ and rotor moment of inertia is $J$ .Here $v_d$ and $v_q$ are two inputs and output can be defined as rotor velocity or torque. In order to design the closed loop system to the origin, state errors can be defined as follows-

$$\Delta\tau_l = \tau_l - \tau_l^* \tag{4}$$

$$\Delta i_d = i_d - i_d^* \tag{5}$$

$$\Delta i_q = i_q - i_q^* \tag{6}$$

where, the asterisk signs signify the targeted values of the respective signals and delta signs signify the errors. We will also use a speed error integral defined by-

$$\Delta\omega_r = \frac{d\Delta\theta_r}{dt} \tag{7}$$

which will provide zero steady state error in spite of unknown load torque and damping coefficient. The complete dynamic system can be expanded using Eq. (4) - (6) when needed.

## III. CONTINUOUS TIME-SPACE CONTROLLER USING INTEGRATOR BACKSTEPPING

### A. *Stabilization of Mechanical Subsystem*

We will proceed our controller design by introducing a Control Lyapunov Function (CLF) that entirely depends on the output of the mechanical system (3), (7) defined as [20],

$$V_1 = \frac{1}{2}\Delta\tau_l^2 + \frac{1}{2}K_{\theta r}\Delta\theta_r^2 \tag{8}$$

where, $K_{\theta r}$ is a positive design gain factor.

Evaluation of the function mentioned above along with the trajectories of state using the chain rule yields-

$$\dot{V}_1 = \Delta\tau_l \frac{d\Delta\tau_l}{dt} + K_{\theta r}\Delta\theta_r \frac{d\Delta\theta_r}{dt}. \tag{9}$$

As the inputs are not available at output, we treat the quadrature axis current as a virtual input and back-step category through an integrator into the electrical dynamics that governs torque producing current. Designing an additional gain $K_\tau \geq 0$ and choosing the stabilization function as follows -

$$i_q^* = \frac{-K_\tau\Delta\tau_l + \frac{\beta}{J}(\Delta\tau_l + \tau_l^*) + \frac{\tau_l}{J} - K_{\theta r}\Delta\theta_r}{\frac{3}{2}\frac{p}{J}\phi_f} \tag{10}$$

This condition will stabilize the mechanical subsystem about the origin.

### B. *Stabilization of the Electrical Subsystem*

The back-stepping procedure is used to ensure that the quantized inputs will drive the state errors to zero. We can now extend CLF including states $\Delta i_d$ and $\Delta i_q$ as follows-

$$V_2 = V_1 + \frac{1}{2}K_q\Delta i_q^2 + \frac{1}{2}K_d\Delta i_d^2 \tag{11}$$

$$\dot{V}_2 = \dot{V}_1 + K_q\Delta i_q \frac{d\Delta i_q}{dt} + K_d\Delta i_d \frac{d\Delta i_d}{dt} \tag{12}$$

We can express the derivative of quadrature current error by differentiating (5) as-

$$\frac{d\Delta i_q}{dt} = \frac{di_q}{dt} - \frac{di_q^*}{dt} \tag{13}$$

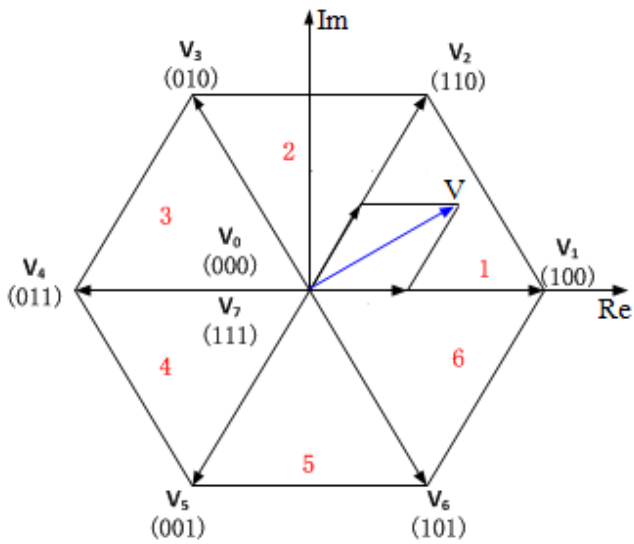


Fig. 1: Quantized input space of the inverter

The derivative of direct current error can be calculated as following-

$$i_d^* = \frac{di_d^*}{dt} = 0 \tag{14}$$

and thus we can say, $\Delta i_d = i_d$. (15)

These aforementioned derivations lead to the fact that, at $V_2 = 0$, evaluation of (11) yields the following.

$$-K_\tau \Delta\tau_l = 0. \tag{16}$$

So, there is no solution for the dynamic system rather than trivial solution and the closed loop error system is nonlinear which gives the origin is exponentially stable. A two-level power inverter has been used here in this case whose quantized input space is shown in Fig. 1.

## IV. THE CONTROL ALGORITHM

The block diagram of the control technique is presented here in Fig. 2. With the condition derived in [21], we may impose numerous input selection to optimize performance and assure stability. We have derived the time derivative of the Lyapunov stability function in (12). We have computed it for every possible input that results from the switching state table of the inverter. The step by step procedure of the minimum switching control law is as follows-

- Compute the state of the motor and express in synchronous frame the rotor angular position, $\theta_e=(p/2)\theta_r$, torque, direct axis current and quadrature axis current.
- Following the procedure in Section III, compute torque error, rotor position error, reference quadrature current and its derivative.
- Use the measured electrical speed and angle including (12) to define the seven unique voltage inputs in synchronous reference frame.
- Using dynamics of the system given by (1)-(3), evaluate all the seven values of the derivative given in Eq. (12).
- Select input k which satisfies $\min_k \dot{V}_k \le 0$.

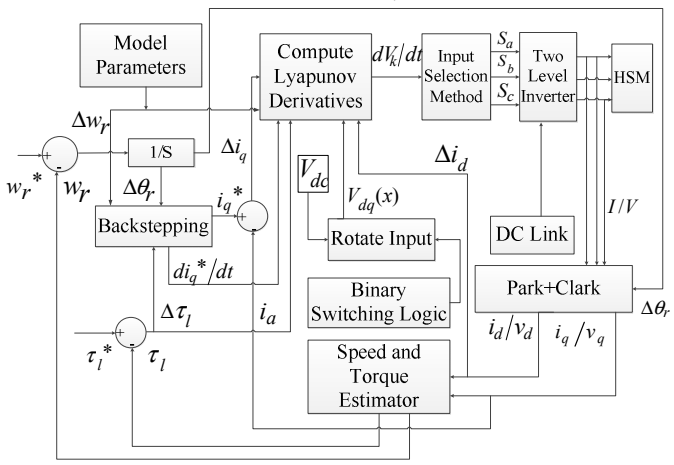


Fig. 2: Block diagram of the proposed model

where $k$ = 0, 1, . . ., 7, as we know that at any instant at least one of the input states will give a negative stability function.

- Without switching, continue state measurement and update (12) until stability would be lost if switching is not performed.
- Re-evaluate (12) and again select minimizing input. The point worth sharing is that the motor drive is without any position encoder and reduces unwanted switching as we have proposed earlier.

## V. SIMULATION RESULTS

### A. Investigation of System Response

The motor drive system is simulated using C++ programming language with the system dynamics computed using classical fourth order Runge-Kutta (RK4) integrator taking step time equal to 10 times the control frequency. Other simulation parameters used in this proposed modelling are listed here in Table I.

TABLE I
MODEL PARAMETERS USED IN SIMULATION

| Symbol | Value | Description |
|---|---|---|
| $p$ | 10 | Number of poles |
| $L_d$ | 24 mH | Direct axis inductance |
| $L_q$ | 18 mH | Quadrature axis inductance |
| $R$ | 22 mΩ | Stator resistance per phase |
| $J$ | 0.7 kgm$^2$ | Rotor moment of inertia |
| $\beta$ | 0.2 Nm.s/rad | Viscous damping coefficient |
| $\Phi_f$ | 0.45 W | Magnetic flux |
| $K_\tau$ | 2 | Torque error gain |
| $K_{\theta r}$ | 11 | Speed error integrator gain |
| $K_q$ | 1.5 | Quadrature axis current error gain |
| $K_d$ | 1 | Direct axis current error gain |
| $f_s$ | 10 | Maximum switching frequency |
| $V_{dc}$ | 600 | DC link voltage |

In order to perform more insightful investigation on the proposed system, we have used a varying command that varies from -200 to 200 rpm where, torque being -15 to 15 N-m for a viscous load. The load is unknown and as well as asymmetric as it exerts force in opposite direction. All of these have been illustrated in Fig. 3. The proposed method shows its ability to track slowly varying load which is both unknown and asymmetric. The average switching frequency remains much lower in this case which reduces as the rotation of rotor reverses and is also much less than conventional FOC as in Fig. 3 (c). We have preferred a variable speed and torque command owing to showing the adaptivity of the system to load variations. As the speed increases, faster switching is a requirement. Although, switching frequency in this case increases with speed whereas, the average switching frequency remains much lower than classical FOC. When data shows a slight overshoot at command transitions, the controller achieves rapid regulation despite low switching frequency. This scenario is illustrated in Fig. 4.

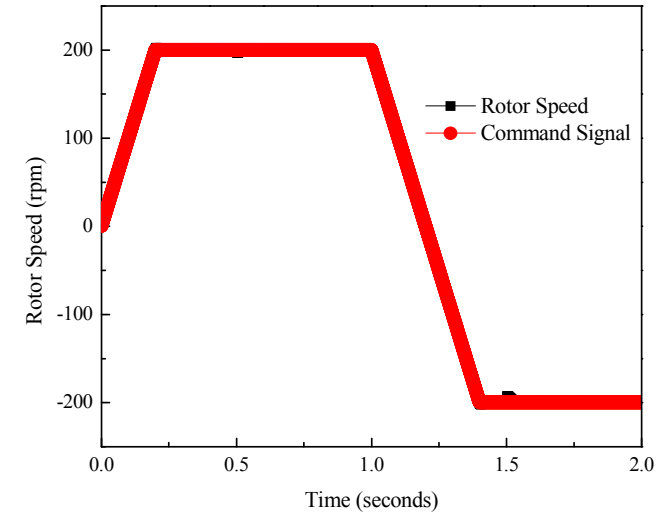


(a)

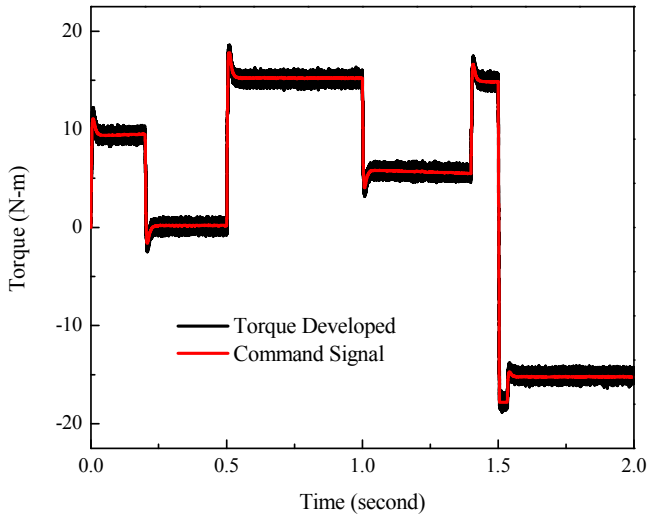


(b)

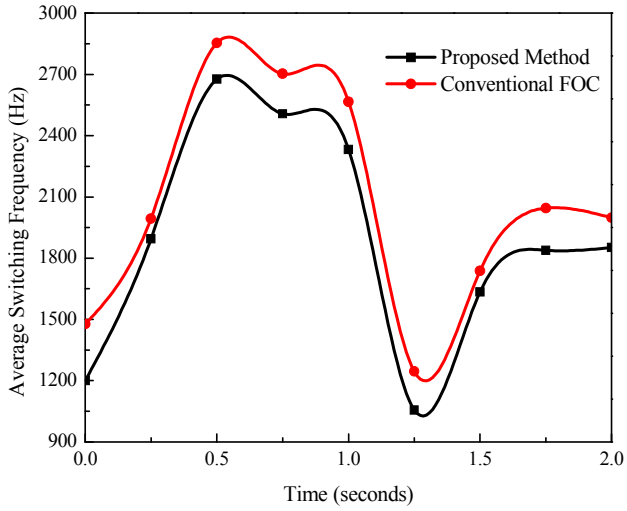


(c)

Fig. 3: Simulation result of (a) rotor speed, (b) torque, (c) comparison of switching frequency

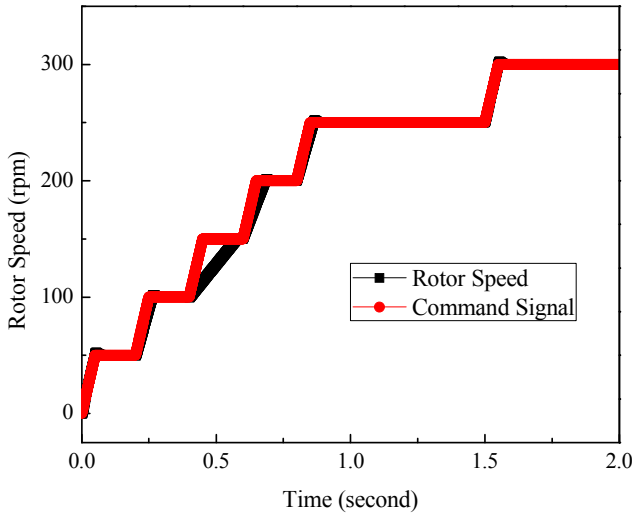


(a)

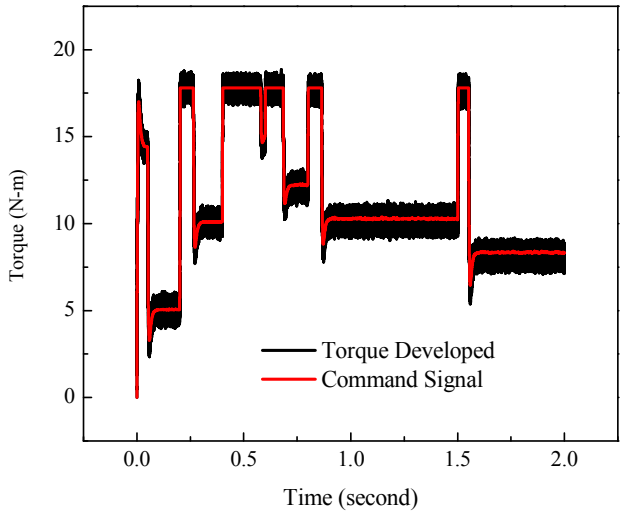


(b)

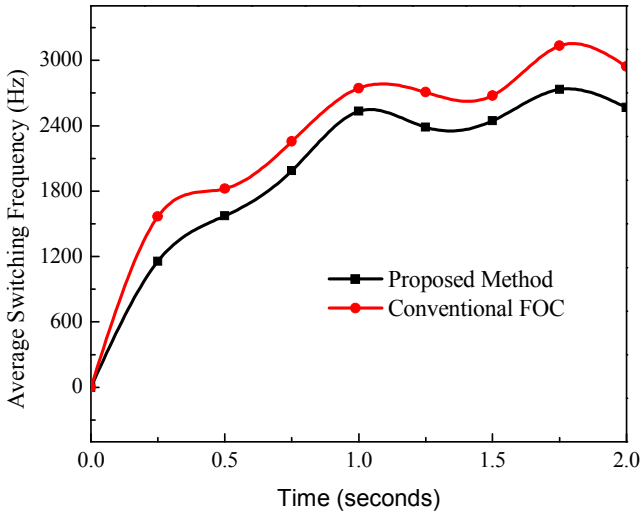


(c)

Fig. 4: Simulation result of (a) rotor speed, (b) torque, (c) comparison of switching frequency

## B. *Robustness to Parametric Uncertainty*

A desirable quality of any control system, as we mentioned earlier, is robustness to parametric uncertainty. When exposed to various application environments, parametric uncertainty may occur as a regular event and can disturb desired response. We here present the robustness of our proposed system revealed by a series of plots in Fig. 5. Although a detail analysis of robustness is beyond the scope of this paper, we varied rotor moment of inertia, inductances of the machine, damping coefficient and dc link voltage to examine this characteristic of the control system. The system has smooth response under those uncertainties as we proposed to be expected. A dynamic system is simulated here that produces a huge amount of data. These data are close enough and as a result, the curves are visible in such a way that they are a single one.

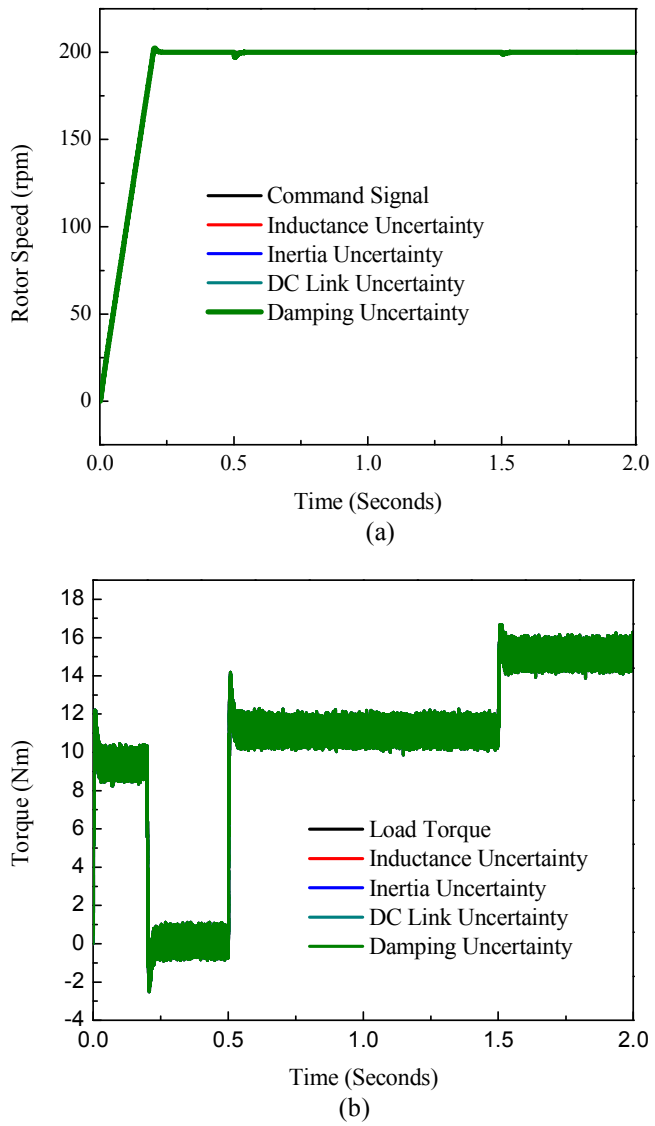


Fig. 5: Robustness to parametric uncertainty: (a) rotor speed, (b) torque

## VI. CONCLUSION

We have presented a method here using the space phasor model of HSM which takes the advantage of field orientation without position sensor that has energy related commutation strategy built in the control act. It uses model based stability actions to choose a quantized input that conserves stability. The system produces low switching frequency and smooth torque response even under slowly or quickly varying load. This helps to reduce unwanted switching, increases efficiency, minimizes torque ripple and has robustness to parametric uncertainty. It is expected that, with the addition of some modifications, this model may possess the capability of producing sinusoidal phase currents while controlling torque and flux independently.

## REFERENCES


[1]. S.I. Deaconu, L.N. Tutelea, G.N. Popa, T. Latinovici, "Mathematical models and the control of homopolar and homo-heteropolar reactive synchronous machines with stator excitation," in proceedings of *European conference of circuits technology and devices*, 2010, pp. 78-83.

[2]. S.I. Deaconu, L.N. Tutelea, G.N. Popa, I. Popa and C. Abrudean, "Optimizing the Designing of a Reactive Homopolar Synchronous Machine with Stator Excitation," in proceedings of *34th Annual Conference of the IEEE Industrial Electronics Society*, November 2008, pp. 1311-1318.

[3]. S.I. Deaconu, M. Topor, L.N. Tutelea, G.N. Popa and C. Abrudean, "Mathematical Model of a Reactive Homopolar Synchronous Machine with Stator Excitation," in proceedings of *13th European Conference on Power Electronics and Applications*, September 2009, pp. 2269-2277.

[4]. S.I. Deaconu, M. Topor, L.N. Tutelea, G.N. Popa and C. Abrudean, "Modeling and Experimental Investigations of a Reactive HomoHeteropolar Brushless Synchronous Machine," in proceedings of *35th Annual Conference of the IEEE Industrial Electronics Society*, November 2009, pp. 1209-1216.

[5]. J. He and F. Lin, "A high frequency high power IGBT inverter drive for 45 HP/16.000 RPM brushless homopolar inductor motor," in proceedings of *IEEE Industrial Application Conference*, Jul. 1995 pp. 9-15.

[6]. M. Siegl and V. Kotrba, "Losses and cooling of a high-output power homopolar alternator," in proceedings of *EEE International Conference on Electrical Machine and Drives*, September 1991, pp. 295-299.

[7]. G. P. Rao, J. L. Kirtby, D. C. Meeker Jr. and K. J. Donegan, "Hybrid permanent magnet/homopolar generator and motor", U. S. Patent 6097124 A, August 2000.

[8]. O. Ichikawa, A. Chiba and T. Fukao, "Development of Homo-Polar Type of Bearingless Motors," in proceedings of *IEEE IAS Annual Meeting*, 1999, pp. 1223-1228.

[9]. M. Hippner and R. G. Harley, "High speed synchronous homopolar and permanent magnet machines comparative study," in proceedings of *IEEE IAS Annual Meeting*, 1992, pp. 74-78.

[10]. H. Hofman and S. R. Sanders, "High speed synchronous machine with minimized rotor losses," *IEEE Transactions on Industrial Applications*, vol. 36, no. 2, pp. 531-539, March 2000.

[11]. P. Tsao, M. Senesky and S. Sanders, "A Synchronous Homopolar Machine for High-Speed Applications," in proceedings of *IEEE IAS Annual Meeting*, 2002, pp. 406-416.

[12]. L. Vido, M. Gabsi, M. Lecrivain, Y. Amara and F. Chabot, "Homopolar and Bipolar Hybrid Excitation Synchronous Machine," *IEEE Transactions on Energy Conversion*, vol. 21, no. 3, pp 1212-1218. September 2006.

[13]. F. Blaschke, “The principle of field orientation as applied to the new transvector closed loop control for rotating field machines,” *Siemens Review*, vol. 39, pp. 217–220, May 1972.

[14]. P. C. Krause, O. Wasynczuk, and S. D. Sudhoff, “Analysis of Electric Machinery and Drive Systems*”*, 3rd Edition, *Willey-IEEE Press*, 2013.

[15]. I. Takahashi and T. Noguchi, “A new quick-response and high-efficiency control strategy of an induction motor,” *IEEE Transactions on Industrial Applications*, vol. 22, no. 5, pp. 820–827, Sep. 1986.

[16]. N. Farid, B. Sebti, K. Mebarka, and B. Tayeb, “Performance analysis of field-oriented control and direct torque control for sensorless induction motor drives,” in *Proceedings of Meditarian Conference on Control and Automation*, Jun 2007, pp. 1–6.

[17]. H. Le-Huy, “Comparison of field-oriented control and direct torque control for induction motor drives,” in *Proceedings of 34th IAS Annual Meeting*, 1999, vol. 2, pp. 1245–1252.

[18]. K. Basu, J. S. S. Prasad, G. Narayanan, H. K. Krishnamurthy, and R. Ayyanar, “Reduction of torque ripple in induction motor drives using an advanced hybrid PWM technique,” *IEEE Transactions on Industrial Electronics*, vol. 57, no. 6, pp. 2085–2091, Jun 2010.

[19]. J. Beerten, J. Verveckken, and J. Driesen, “Predictive direct torque control for flux and torque ripple reduction,” *IEEE Transactions on Industrial Electronics*, vol. 57, no. 1, pp. 404–412, Jan. 2010.

[20]. G. Prior, M. Krstic, “Quantized-Input Control Lyapunov Approach for Permanent Magnet Synchronous Motor Drives,” *IEEE Transactions on Control System Technology*, vol. 21, no. 5, pp. 1784-1794, Sept. 2013.

[21]. D. Liberzon, “Switching in Systems and Control”, *Birkhäuser Boston*, Basel, Switzerland, 2003.

# High Performance Parameter Observation of Induction Motor With Sensorless Vector Control Using Extended Kalman Filter

Md. Samiul Haque Sunny[1], Manash Mandal[1], Eklas Hossain[2], Md. Adbur Rafiq[1]
[1]Khulna University of Engineering & Technology (KUET), Khulna-9203, Bangladesh
[2]Oregon Tech, Department of Electrical and Renewable Energy, OR-97601, USA
mdshs31@gmail.com, manashmndl@gmail.com, eklas.hossain@oit.edu, dmar@eee.kuet.ac.bd

*Abstract*— **Speed sensor less vector control of induction motor drive faces two major problems: speed estimation, and rotor flux observation. Because of the multiplication terms of state variables, the induction motor model is consisted of nonlinear state equations. To estimate the state variables of the motor model and gain the rotor flux and speed signals, a method is proposed in this paper using extended Kalman filter. Software programs are used to carry out extended Kalman filter (EKF) algorithm to estimate the rotor speed and fluxes. The obtained results prove that extended Kalman filter algorithm can estimate rotor speed and flux very accurately, and based on that, the speed sensor less drive system can have good static and dynamic performance.**

***Keywords—Induction Motor, Sensorless Vector Control, Speed Estimation, Flux observer, Extended Kalman Filter.***

## I. INTRODUCTION

For a large spectrum of industrial applications, to make the induction motor suitable, the speed is needed to be controlled; and the most common way of doing this is by vector control. But it requires a speed sensor on the shaft of the machine - which is quite tough. Moreover, being costly, the speed sensor reduces reliability and robustness of the induction motor. Thus, it has introduced a new area of research recently, and among the variety of solutions, sensorless vector control has become very popular as the industrial standard. As the examples of this new technology, artificial intelligence and neural networks come first. But they need offline calculations and under speed changes, they show weak performance. Also, the nonlinear model of the induction motor is in fifth order, containing unknown state variables and external inputs – which have made this sensorless control a challenging theoretical problem.

Several approaches have been proposed in recent years to enhance the reliability of the system and lessen the cost by reducing or eliminating the speed and flux sensors from industrial induction motor drives. An auxiliary system is introduced as alternatives to transducers and encoders to estimate the state of the system, which is called an observer. An adaptive observer with one phase current sensor is shown in [1]. On-line trained multilayer feed forward neural networks with a fuzzy nonlinear observer is presented in [2]. Model reference adaptive system MRAS is shown in [3]. Sliding mode observers [4], Luerberger observer [5] are also proposed. These are the systems to reduce the number of the sensors. Based on the model of induction motor in the stationary reference frame, an adaptive observer is presented in [6]. Linear feedback is used to estimate the fluxes and the adaptive law estimates the speed here; the gains are designed using Lyapunov's nonlinear stability method. Torque model reference adaptive schemes (TMRAS) are proposed in [7] to enhance the performance under low and zero speed conditions.

Being able to take into account the model uncertainties and inherent non-linearities in last few years, the Extended Kalman Filter (EKF) is the most used observer for stochastic nonlinear systems such as induction motor drives. An extended Kalman filter is used in [8] to simultaneously estimate stator stationary axis parameters for direct torque controlled induction motor. A tuned EKF is proposed for estimation in [9] where particle swarm optimization is used to optimize the covariance matrices. Fig. 1 shows the list of categorized approaches for estimation. Spectral analysis is required for rotor slot harmonics methods which is a time-consuming task. It also provides a narrow band of speed control. And in case of frequency signal injection, the probing signals produces high frequency torque pulses and as a result, speed ripple occurs. On the other hand, model based methods are popular among researchers due to better performance at high speed, and simplicity. Multiple model extended Kalman filter is presented in [12] which obeys the Markov chain. The estimation is done here by mixing different model outputs with different weights. A robust reduced order extended Kalman filter is proposed in [13] for better estimation performance during speed and flux estimation of induction motor where the gross error on estimation accuracy is analyzed. An approach for rotor flux estimation is shown in [14]. Avoiding sixth order complexity is represented by a forth order descriptor type robust Kalman filter which improves the degree of robustness of the estimates. A fifth-order extended Kalman filter is used in [15] in order to reduce the sampling time as well as the process of the estimation when the system is running at a very low speed. To linearize the process of the extended Kalman filter, fast execution time is considered and no change has been made of conventional look up table of the direct torque control.

In this paper, the rotor speed and the flux of the induction motor are estimated by a novel extended Kalman filter using the mathematical model of induction motor. Section II discusses about the nonlinear model of the induction motor. Section III presents the mathematical strategy of the extended Kalman filter. Estimation of Speed and flux of the induction motor using extended Kalman filter is proposed in section IV. Section V shows the estimation results with respect to actual values and the

978-1-5386-2307-7/17/$31.00 ©2017 IEEE

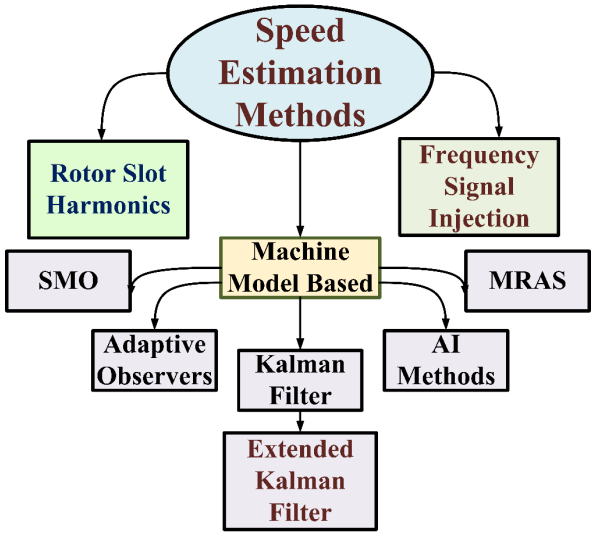


Figure. 1. Speed estimation methods of sensorless systems. The Extended Kalman Filter approach falls under the 'Machine Model Based Methods' category.

performance of the extended Kalman filter. The conclusion is drawn in section VI.

## II. Nonlinear Model of Induction Motor

To transform nonlinear system for certain cases, reference frames are used in most controllers as a fundamental tool for development of equivalent circuits. In case of induction motor modelling, three reference frames are available. They are stationary or stator reference frame, rotor reference frame, and synchronously rotating reference frame. The state and mechanical motion equations [10] in $\alpha - \beta$ frame are:

$$\dot{i}_{s\alpha} = -\left(\frac{R_s}{\sigma L_s} + \frac{1-\sigma}{\sigma\tau_r}\right) i_{s\alpha} + \frac{L_m}{\sigma L_s L_r \tau_r}\lambda_{r\alpha} + \frac{L_m}{\sigma L_s L_r}\omega_r \lambda_{r\beta} - \frac{1}{\sigma L_s} u_{s\alpha} \quad (1)$$

$$\dot{i}_{s\beta} = -\left(\frac{R_s}{\sigma L_s} + \frac{1-\sigma}{\sigma\tau_r}\right) i_{s\beta} + \frac{L_m}{\sigma L_s L_r}\lambda_{r\alpha} + \frac{L_m}{\sigma L_s L_r \tau_r}\omega_r \lambda_{r\beta} - \frac{1}{\sigma L_s} u_{s\beta} \quad (2)$$

$$\dot{\lambda}_{s\alpha} = \frac{L_m}{\tau_r} i_{s\alpha} + \frac{1}{\tau_r}\lambda_{r\alpha} - \omega_r \lambda_{r\beta} \quad (3)$$

$$\dot{\lambda}_{s\beta} = \frac{L_m}{\tau_r} i_{s\beta} + \frac{1}{\tau_r}\lambda_{r\beta} - \omega_r \lambda_{r\alpha} \quad (4)$$

$$\dot{\omega}_r = \frac{P_n^2 L_m}{J L_r}\left(i_{s\beta}\lambda_{r\alpha} - i_{s\alpha}\lambda_{r\beta}\right) - \frac{P_n}{J} M_l \quad (5)$$

Where $i_s$ is the current component in $\alpha$ and $\beta$ frame, $\lambda_s$ is the rotor flux component, $\omega_r$ is the rotor speed, $R_s$ is the stator resistance, $R_r$ is the rotor resistance, $L_s$ and $L_r$ are the self-inductances of stator and rotor accordingly, and $L_m$ is the mutual inductance between stator and rotor. $\frac{L_r}{R_r} = \tau_r$ is rotor time constant. The leakage coefficient is denoted by $\sigma$, here $\sigma = \frac{L_s L_r - L_m^2}{L_r L_s}$. $u_{s\alpha}$ and $\omega_{s\beta}$ are $\alpha$ and $\beta$ axis component of stator voltage. $M_l$ is the motor load torque, $J$ is the inertia and $P_n$ is the number of motor pole pairs. Rotor electrical angular velocity is represented by $\omega_r$.

## III. Extended Kalman Filter

Linear quadratic estimation, also known as Kalman filter, is an algorithm that produces estimation of unknown variables using series of measurements over time, containing statistical noise and other inaccuracies. This basic Kalman filter is limited to a linear assumption. For more complex systems which are nonlinear in nature such as induction motor, the nonlinearity may occur from the process model or the observation model or for both. So, to handle the nonlinear functions of the systems, extended Kalman filter is introduced. And for extended Kalman filter the functions are of differentiable type. Two equations of Kalman filter are:

$$x_t = Ax_{t-1} + Bu_t + w_{t-1} \quad (6)$$

$$z_t = Hx_t + v_t \quad (7)$$

The system must fit in these two equations. Here, $z_t$ is the measurement value. $A$, $B$, $H$ are the matrices in general form. $u_t$ is the control signal and $w_t$ is the process noise and $v_t$ is the measurement noise. Next step is to determine initial values and necessary parameters. In the iteration process there are time update equations and measurement update equations. Time update equations are used to predict; on the other hand, measurement update equations are used for correction at each $t^{th}$ state. Equation for projecting the state ahead is,

$$\hat{x}_{\bar{t}} = A\hat{x}_{t-1} + Bu_t \quad (8)$$

Here, $\hat{x}_t$ is the estimation of the original signal $x$. Equation for projecting the error covariance ahead from initial estimates at t=0 is,

$$P_{\bar{t}} = AP_{t-1}A^T + Q \quad (9)$$

For correction, the Kalman gain is computed by:

$$K_t = P_{\bar{t}}H^T(HP_{\bar{t}}H^T + R)^{-1} \quad (10)$$

Equation (1) is used to update the estimation by:

$$\hat{x}_t = \hat{x}_{\bar{t}} + K_t(z_t - H\hat{x}_{\bar{t}}) \quad (11)$$

The error covariance is updated and the outputs at $t$ will be the input for $t+1$.

$$P_t = (1 - K_t H)P_{\bar{t}} \quad (13)$$

## IV. Speed and Flux Estimation Using Extended Kalman Filter

In sensorless vector control, speed is considered as an unknown state variable. From the motor mechanical equation and the original state equation, a new state equation is produced where the system input and output remain invariable. To estimate the states of the induction motor, the equations must be in discrete form because EKF is a recursive state estimation algorithm. So, according to the discrete formula, the discrete forms of the machine equations are:

$$i_{s\alpha}(t+1) = \left(1 - \left(\frac{R_s}{\sigma L_s} + \frac{L_m^2}{\sigma L_s L_r \tau_r}\right)T\right) i_{s\alpha}(t) + \frac{L_m}{\sigma L_s L_r \tau_r} T\lambda_{r\alpha}(t) + \frac{L_m}{\sigma L_s L_r} T\lambda_{r\beta}(t)\omega_r(t) + \frac{1}{\sigma L_s} T u_{s\alpha}(t) \quad (14)$$

$$i_{s\beta}(t+1) = \left(1 - \left(\frac{R_s}{\sigma L_s} + \frac{L_m^2}{\sigma L_s L_r \tau_r}\right)T\right) i_{s\beta}(t) + \frac{L_m}{\sigma L_s L_r \tau_r} T\lambda_{r\beta}(t) + \frac{L_m}{\sigma L_s L_r} T\lambda_{r\alpha}(t)\omega_r(t) + \frac{1}{\sigma L_s} T u_{s\beta}(t) \quad (15)$$

$$\lambda_{r\alpha}(t+1) = -\frac{L_m}{\tau_r} T i_{s\alpha}(t) + \left(1 - \frac{T}{\tau_r}\right)\lambda_{r\alpha}(t) - T\lambda_{r\beta}(t)\omega_r(t) \quad (16)$$

$$\lambda_{r\beta}(t+1) = -\frac{L_m}{\tau_r} T i_{s\beta}(t) + \left(1 - \frac{T}{\tau_r}\right)\lambda_{r\beta}(t) + T\lambda_{r\alpha}(t)\omega_r(t) \quad (17)$$

Where:

$$\omega_r(t+1) = \omega_r(t) \quad (18)$$

As the noise vector cannot be determined in advance, the values of the states are predicted by the deterministic equations.

The calculation of covariance matrix of predictive error is:

$$P(t+1|t) = A(t) * P(t|t) * A^T(t) + Q \quad (19)$$

$$A(t) = \begin{bmatrix} 1 - \left(\frac{R_s}{\sigma L_s} + \frac{L_m^2}{\sigma L_s L_r \tau_r}\right)T & 0 & \frac{L_m}{\sigma L_s L_r \tau_r} T & \frac{L_m}{\sigma L_s L_r} T\omega_r(t) & \frac{L_m}{\sigma L_s L_r} T\lambda_{r\beta}(t) \\ 0 & 1 - \left(\frac{R_s}{\sigma L_s} + \frac{L_m^2}{\sigma L_s L_r \tau_r}\right)T & -\frac{L_m}{\sigma L_s L_r} T\omega_r(t) & \frac{L_m}{\sigma L_s L_r \tau_r} T & -\frac{L_m}{\sigma L_s L_r} T\lambda_{r\beta}(t) \\ -\frac{L_m}{\tau_r} T & 0 & 1 - \frac{T}{\tau_r} & -\frac{L_m}{\sigma L_s L_r} T\omega_r(t) & -T\lambda_{r\beta}(t) \\ 0 & -\frac{L_m}{\tau_r} T & T\omega_r(t) & -\frac{1}{\tau_r} T & T\lambda_{r\alpha}(t) \\ 0 & 0 & 0 & 0 & 1 \end{bmatrix} \quad (20)$$

Kalman gain K and the covariance matrix P of the predictive error is calculated then at the moment *t+1*.

$$K(t+1) = P(t+1|t) * C^T * \{C * P(t+1|t) * C^T + R\}^{-1} \quad (21)$$

$$P(t+1|t+1) = \{1 - K(t+1) * C\} * P(t+1|t) \quad (22)$$

And then the state estimation *x(t+1)* at moment *t+1* is calculated.

TABLE I shows the parameters of the induction motor model used in the simulation to get actual flux and speed.

TABLE I. PARAMETERS FOR INDUCTION MOTOR MODELLING

| Parameter name | Value | Unit |
|---|---|---|
| Phase | 3 | - |
| Supply voltage | 220 | Volt |
| Number of poles | 3 | - |
| Inductance of stator ($L_s$) | 0.1004 | Henry |
| Inductance of rotor ($L_r$) | 0.0969 | Henry |
| Mutual inductance ($L_m$) | 0.0915 | Henry |
| Rotor resistance ($R_r$) | 1.294 | Ohm |
| Stator resistance ($R_s$) | 1.54 | Ohm |
| Inertia ($J$) | 0.095 | $\mathrm{Nmsec}^{-1}$ |
| Maximum speed ($\omega_{max}$) | 80 | $\mathrm{radsec}^{-1}$ |
| Rated torque ($\tau$) | 13 | Nm |
| Magnetic field ($B$) | 0.005 | $\mathrm{Nmsecrad}^{-1}$ |

## V. RESULT AND DISCUSSION

With the defined parameters and the model equations, a Simulink model of induction motor is built; and with proper external inputs, the simulation is done. The actual speed is calculated from the simulation, and calculation of the current component gave the rotor flux amount. After discretizing the machine equations, a system is built to fit the extended Kalman filter equations. By time update and measurement update, the projections of state parameters are done. The covariance matrix and the Kalman gain is calculated for the iteration of the extended Kalman filter. The estimation performance depends on the system parameters, covariance matrices, state and measurement noises. As the covariance matrices are not known for containing the weight factors, they were first tuned to get maximum performance from the extended Kalman filter during the estimation.

Estimation of the constant speed of the induction motor is shown in Fig. 2. By changing the load torque, the speed can be varied during the simulation. To check the performance of the EKF estimation of speed at varying speed, load torque of the model is changed and the speed estimation is presented in Fig. 3.

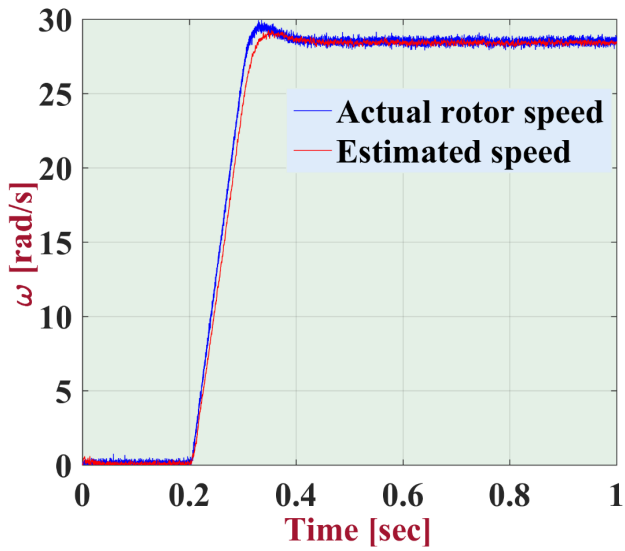


Figure. 2. Estimated constant speed of induction motor. The estimated speed appeared very close to the actual speed.

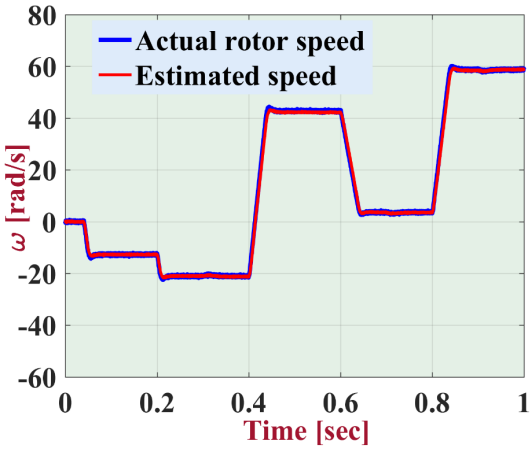


Figure. 3. Estimated speed changing the load torque of the model. It appeared to accurate in predicting the actual speed with respect to varying load torques.

Estimated rotor flux at both alpha and beta axis along with the actual rotor flux are calculated from the current component of the simulated induction motor model by extended Kalman filter. Results and parameters are shown in Fig. 4 and Fig. 5 accordingly.

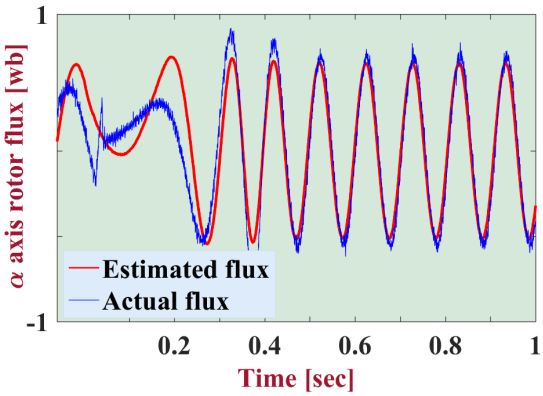


Figure. 4. Actual and estimated α axis rotor flux. Though the estimation showed some in predicting the initial flux, it became accurate as steady state approached.

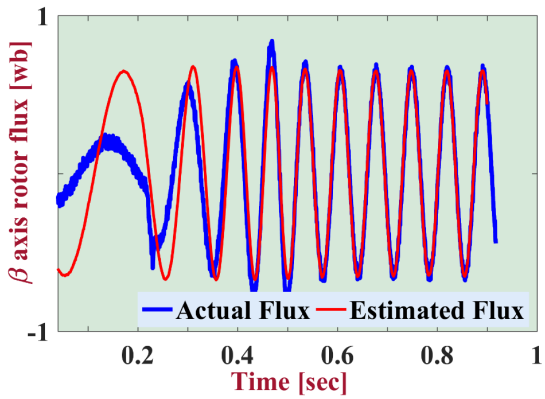


Figure. 5. Actual and estimated β axis rotro flux. The estimation was accurate for steady state flux prediction, though it exhibited error at the beginning.

To measure the performance of the EKF estimation, statistical analysis is done with calculating the cross correlation between the actual and the estimated values of speed and flux. High degree of symmetry in Fig. 6 and Fig. 7 shows the high correlation of speed and flux with negligible noise respectively. The mean square error of the EKF estimation is compared with the result of [11]. Back propagation (BP), uncorrelated real time recurrent learning (URTRL), and correlated real time recurrent learning (CRTRL) conducted to verify the performance of the method are shown in Fig. 8. And with minimum mean square error, EKF shows the highest performance.

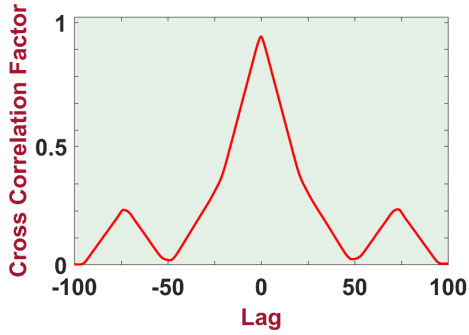


Figure. 6. Normalized cross correlation between actual and estimited speed. High degree of symmetry indicates the noise is negligible.

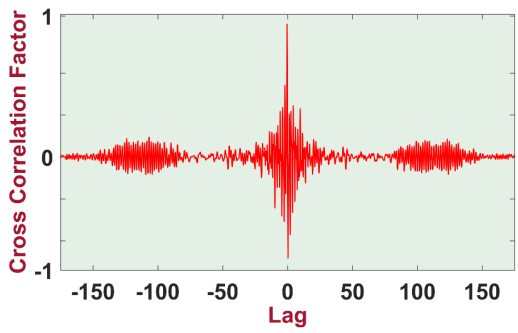


Figure. 7. Normlized Cross correlation plot between estimated and actual flux. High correlation factor is observed.

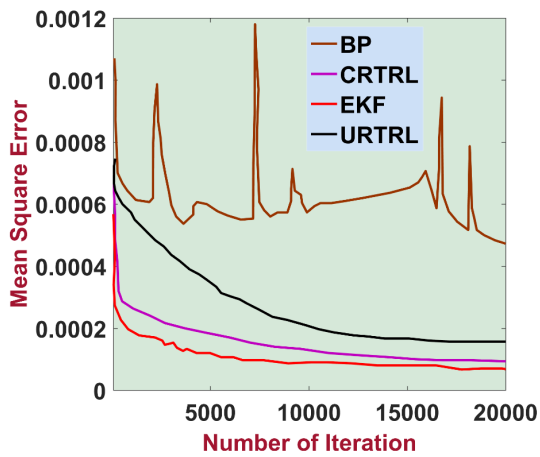


Figure. 8. Mean square error comparison. Extended Kalman Filter (EKF) demonstrated the least amount of mean square error, and therefore, it is the superior performer.

## VI. CONCLUSION

Rotor speed and flux of an induction motor have been estimated in this paper using extended Kalman filter. A mathematical model of induction motor has been modeled with nonlinear equations. With suitable machine parameters, a Simulink model of the induction motor has been designed. Applying Field orientation control to the induction motor model, the stator current and voltage has been observed. These results have been used in the software program of the extended Kalman filter to estimate the motor parameters. For this, the induction motor's nonlinear equations are converted into state variable equations at the alpha beta frame. After discretizing the motor state equations, the deterministic equations have been predicted to calculate the covariance matrix of prediction error. Kalman gain has been calculated from above results and the rotor speed and flux of the induction motor have been estimated. Results have been compared with the actual value of the speed and flux and quality has been analyzed with statistical analysis.

## REFERENCES


[1] F. R. Salmasi and T. A. Najafabadi, "An Adaptive Observer With Online Rotor and Stator Resistance Estimation for Induction Motors With One Phase Current Sensor," IEEE Transactions on Energy Conversion, vol. 26, no. 3, pp. 959–966, Sep. 2011.

[2] B. Karanayil, M. F. Rahman, and C. Grantham, "Stator and rotor resistance observers for induction motor drive using fuzzy logic and artificial neural networks," IEEE Transactions on Energy Conversion, vol. 20, no. 4, pp. 771–780, Dec. 2005.

[3] P. Rao, J. Nakka and R. Shekar, "Sensorless vector control of Induction machine using MRAS techniques", International Conference on Circuits, Power and Computing Technologies (ICCPCT), 2013.

[4] A. Ammar, A. Bourek and A. Benakcha, "Modified load angle Direct Torque Control for sensorless induction motor using sliding mode flux observer",4th International Conference on Electrical Engineering (ICEE), 2015.

[5] H. Talhaoui, A. Menacer, A. Kessal and R. Kechida, "Fast Fourier and discrete wavelet transforms applied to sensorless vector control induction motor for rotor bar faults diagnosis", ISA Transactions, 53(5), 2014, pp.1639-1649.

[6] M. Comanescu, "A hybrid adaptive observer for the speed and flux estimation of induction motors," 2016 IEEE Applied Power Electronics Conference and Exposition (APEC), Long Beach, CA, 2016, pp. 2855-2860. doi: 10.1109/APEC.2016.7468269

[7] A. N. Smith, S. M. Gadoue and J. W. Finch, "Improved Rotor Flux Estimation at Low Speeds for Torque MRAS-Based Sensorless Induction Motor Drives," in IEEE Transactions on Energy Conversion, vol. 31, no. 1, pp. 270-282, March 2016. doi: 10.1109/TEC.2015.2480961

[8] R. Demir, M. Barut, R. Yildiz, R. Inan and E. Zerdali, "EKF based rotor and stator resistance estimations for direct torque control of Induction Motors," 2017 International Conference on Optimization of Electrical and Electronic Equipment (OPTIM) & 2017 Intl Aegean Conference on Electrical Machines and Power Electronics (ACEMP), Brasov, 2017, pp. 376-381. doi: 10.1109/OPTIM.2017.7974999

[9] S. Allaoui, K. Chafaa, Y. Laamari and B. Athamena, "Induction motor state estimation using tuned Extended Kalman Filter," 2015 4th International Conference on Electrical Engineering (ICEE), Boumerdes, 2015, pp. 1-5. doi: 10.1109/INTEE.2015.7416676

[10] Zhang Wei and J. J. Luo, "Speed and rotor flux estimation of induction motors based on extended kalman filter," The 6th International Conference on Networked Computing and Advanced Information Management, Seoul, 2010, pp. 157-160.

[11] M. A. Rafiq, N. K. Roy and B. C. Ghosh, "Three algorithms for learning artificial neural network: A comparison for induction motor flux estimation," 2009 12th International Conference on Computers and Information Technology, Dhaka, 2009, pp. 355-360.

[12] Z. Yin, G. Li, Y. Zhang, J. Liu, X. Sun and Y. Zhong, "A Speed and Flux Observer of Induction Motor Based on Extended Kalman Filter and Markov Chain," in IEEE Transactions on Power Electronics, vol. 32, no. 9, pp. 7096-7117, Sept. 2017. doi: 10.1109/TPEL.2016.2623806.

[13] Z. Yin, C. Zhao, J. Liu and Y. Zhong, "Research on Anti-Error Performance of Speed and Flux Estimator for Induction Motor Using Robust Reduced-Order EKF," in IEEE Transactions on Industrial Informatics, vol. 9, no. 2, pp. 1037-1046, May 2013. doi: 10.1109/TII.2012.2222422.

[14] F. Alonge, F. D'Ippolito and A. Sferlazza, "Sensorless Control of Induction-Motor Drive Based on Robust Kalman Filter and Adaptive Speed Estimation," in IEEE Transactions on Industrial Electronics, vol. 61, no. 3, pp. 1444-1453, March 2014. doi: 10.1109/TIE.2013.2257142.

[15] I. M. Alsofyani and N. R. N. Idris, "Lookup-Table-Based DTC of Induction Machines With Improved Flux Regulation and Extended Kalman Filter State Estimator at Low-Speed Operation," in IEEE Transactions on Industrial Informatics, vol. 12, no. 4, pp. 1412-1425, Aug. 2016. doi: 10.1109/TII.2016.2571682.

2017 3rd International Conference on Electrical Information and Communication Technology (EICT), 7-9 December 2017, Khulna, Bangladesh

# Design and Performance Analysis of a Novel Electromagnetic Bandgap Structure Assisted Phased Array Antenna

Elora Nahid[1], Amit Kumer Podder[2], Md. Nurunnabi Mollah[3]
Khulna University of Engineering & Technology, Khulna-9203, Bangladesh
eloranahid@gmail.com[1], amitpodder09@yahoo.com[2], nurunnabim12@gmail.com[3]

**Abstract— With the development of novel wireless technologies, the requests for bigger data transfer capacity, high efficiency and high capacity Radio Frequency (RF) and microwave gadgets have been developing massively. Electromagnetic bandgap structures (EBGSs) are such new materials which have been rising as potential methods for enhancing the execution of existing RF dynamic and passive devices. EBGSs are periodic or aperiodic in nature. The profundity and width of the stopband rely upon few variables like Filling Factor (FF), number of components, periods and substrate properties. Here, an examination of uniform square designed EBGSs, dumbbell shape square designed with one narrow slot and dumbbell shape square designed with two narrow slots have been done. The stopband - passband properties are accounted for by S-parameter exhibitions. It is additionally observed that the dumbbell shape EBGS with two narrow slots gives more beam steering capacity than the dumbbell shape EBGS with one narrow slot. Therefore, a novel EBGS assisted 4×1 phased array antenna is realized.**

***Keywords— EBGS, S Parameter, Passband and Stopband Characteristics, FF, Dumbbell shape EBGS, Phased array.***

## I. INTRODUCTION

Electromagnetic bandgap structures (EBGSs) are electromagnetic gems. Electromagnetic (EM) waves act in photonic substrates as electrons carry on in semiconductors. Because of these qualities, EBGSs are known as photonic bandgap structures (PBGSs). The fundamental distinction amongst PBGS and EBGS is that the PBGS is periodic or may be aperiodic. EBGSs show wide band pass and band dismissal properties at microwave and millimeter wave frequencies and have offered valuable applications in dynamic and passive devices [1]-[4]. Presenting periodic perturbation, for example, dielectric rods, holes, and patterns in waveguides and microstrip substrates shape PBG materials. While different designs have been proposed in the writing, just the planar etched EBG setups have pulled in much enthusiasm because of their solid creation and mix with different circuits with photolithographic forms. The passband of EBGSs is utilized as a moderate wave medium that is utilized for the conservative design. Then again, the stopband is utilized to stifle the surface wave, leakage and spurious transmission [5]-[7]. Because of these remarkable properties of EBG structures, they find different applications in filters, antennas, waveguides phased arrays and numerous other microwave devices and components.

The stopband characteristic causes the dramatic change in the execution by smothering surface waves, leakage, and spurious transmission. FF is one of the essential controlling variables to yield more extensive and unmistakable stop band that ought to be enhanced to keep up a smoother transmission in the passband. In this work for a uniform round designed EBGSs, the optimized FF of 0.25 is considered. This sort of configuration is considered as a traditional EBGS design. After completing the review of gainful impacts of EBGS, the phased array antennas are displayed.

The objective is to outline a novel EBGS assisted phased array antenna. In the present outline, the customary square designed EBGS will be intended to observe the S-parameter exhibitions. At that point the dumbbell shape designed EBGS with one narrow slot in the centre and dumbbell shape designed EBGS with two narrow slots at two extremes will be examined under the 50 ohm transmission line. The EBGS feed network will be acknowledged by various states of EBGSs. For each situation, the phase properties are key issues. The beam will be guided by differing the state of the EBG components that are situated under the feed lines of the arrays. The design of the correct structure is an indispensable issue to accomplish the better S-parameter execution of the designed components for all the EBGS assisted phased array antenna outlines. The investigations will be confined mainly to square designed EBGS, dumbbell shape designed EBG with one narrow slot, and dumbbell shape designed EBGS with two narrow slots under the feed network.

## II. DESIGN STRUCTURE OF EBGS

Uniform EBG structures have limitations of filling factor (FF). FF is characterized to be the volumetric proportion of one EBG component to one cell. FF controls the width and profundity of the stopband. The general idea of expanding the stopband is the upgrade of FF. It is observed that if the quantity of EBG components is increased, the phase angles are increased too. Again if the state of the EBGS is changed from uniform square to dumbbell shape square with one slot and with two slots respectively then the relative phase shift will be

978-1-5386-2307-7/17/$31.00 ©2017 IEEE

expanded individually. However, after some estimation of FF the S-parameter execution apparently is most exceedingly terrible in traditional uniform EBGS. The optimized value of FF = 0.25 is proposed; but for uniform square patterned EBGS FF is considered as 0.5. In all cases 1-D EBGS is considered, as 2-D and 1-D EBGS provide identical performances. The related designs are shown below. We have simulated two transmission lines assisted by dumbbell shape EBGSs. In Figure 1(a), dumbbell shape EBGSs consisting of two bigger slots connected with one narrower slot. Whereas in Fig. 1(b) the dumbbell shape EBGSs has two narrower slots. It is reported in the literature that dumbbell shape EBGSs provide wider stopband than uniform square patterned EBGSs [8]. This has motivated us to implement these EBGSs structures to realize phased array antennas. Actually the phase properties of different structures are key issues instead of stopband. It is also reported in the literature that EBGS has beam steering properties [9].

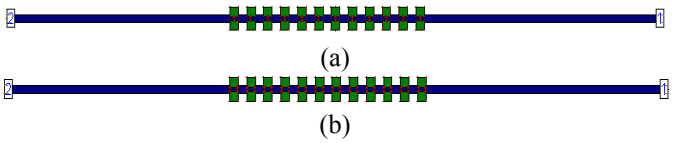


Fig. 1 Geometry of dumbellshape EBGSs consisting of 2 bigger slots connected with (a) one narrow (b) two narrow slots generated by MGRID of EM Software Zeland IE3D.

Two phased array microstrip antennas assisted by 0-4-8-16 dumbellshape EBGS are shown in Fig. 2. It is seen that in Fig. 2(a), dumbell shape EBGs consist of two bigger slot connected with one narrow slot. On the other hand, in Fig. 2(b) there are two narrower slots in dumbellshape EBGSs. We have already reported in [9] the technique of EBGS distribution under the feed line of a simple array to realize a phased array antenna. The concept of reconfiguration with the various distribution of EBGSs under the feedline of an array can be seen in [9]. In this paper we have highlighted that EBGSs having two narrower slot provides better stopband performances than one narrower slot connected dumbellshape EBGSs. Having motivated on this issue we have implemented these two types of structures for developing phased arrays with a view to achieving improved performance.

EBG structure is normally used to generate stopband. The stopband varies with the variation of shape and size of EBG elements. Here, this idea was imparted to implement in phase properties of EBG structure. It is expected that with the change of shape and size of EBG structure, the phase properties will also be changed. This idea can be used to squint the beam of array. Thus the idea of developing a phased array antenna was developed. Finally the development of EBGS assisted phased array antenna will be realized by utilizing the performances of the above EBGS assisted transmission lines.

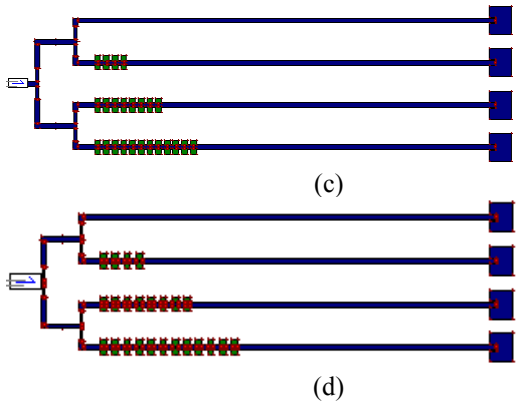


Fig. 2 Geometry of 4×1 microstrip patch antenna array generated by MGRID of Zeland IE 3D EM software (a) dumbbell shape square patterned EBGS assisted 4 ×1 array with one narrow slot (b) dumbbell shape square patterned EBGS assisted 4 ×1 array with two narrow slots

## III. SIMULATION RESULTS

The S-parameter performances of dumbbell shape square patterned EBG assisted transmission line with one narrow slot is shown in Fig. 3.

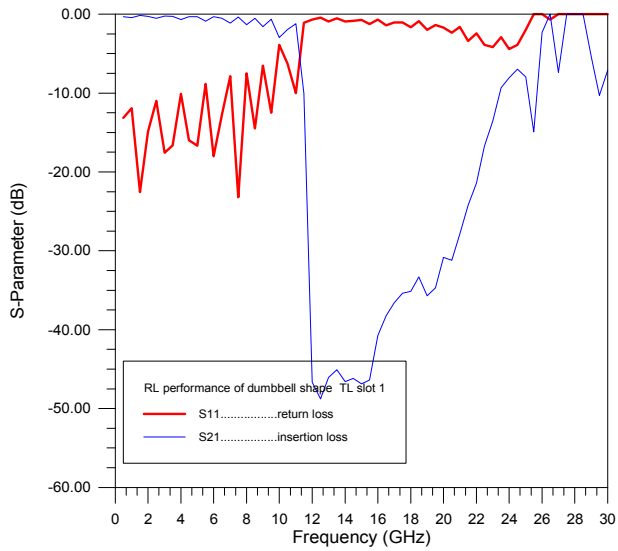


Fig. 3 S-parameter performance of dumbbell shape square patterned EBG assisted transmission line with one narrow slot.

Here, it is seen that the average 10 dB passband RL bandwidth is 12 GHz. The antenna frequency is 8.65 GHz. Therefore, it is seen that antenna frequency resides within the passband. The S- parameter performances of dumbbell shape square patterned EBG assisted transmission line with two narrow slots is shown in Fig. 4. From the figure it is seen that the average 10 dB passband RL bandwidth is 14 GHz. The antenna frequency is 8.65 GHz. Therefore, it is seen that antenna frequency resides within the passband.

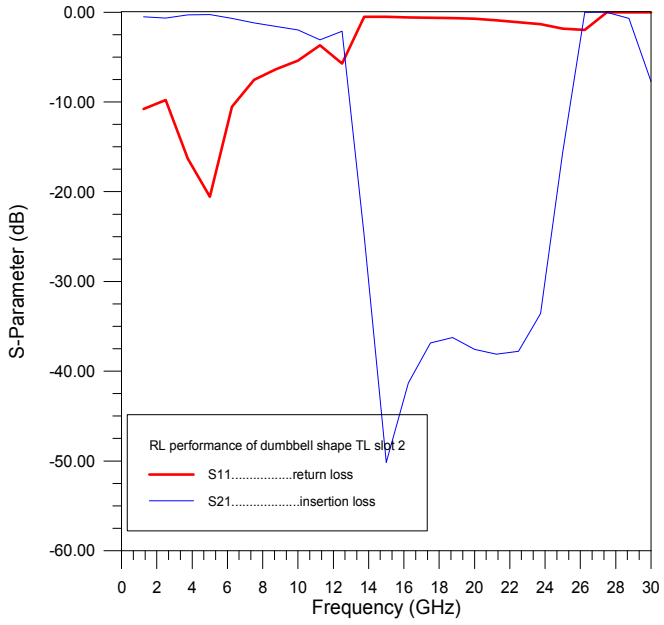


Fig. 4 S - parameter performances of Dumbbell shape square patterned EBGS assisted transmission line with two narrow slots.

The radiation pattern of a reference 4×1 array antenna is shown in Fig. 5. In the radiation pattern of the reference 4×1 array the peak gain is also is in the direction of 0 degree. The peak gain is 9.52806dB and the average gain is 1.70508dB. Here it is seen that the peak gain and the average gain are increased. Because, there are four antennas here to form an array. There is no backlobe here too.

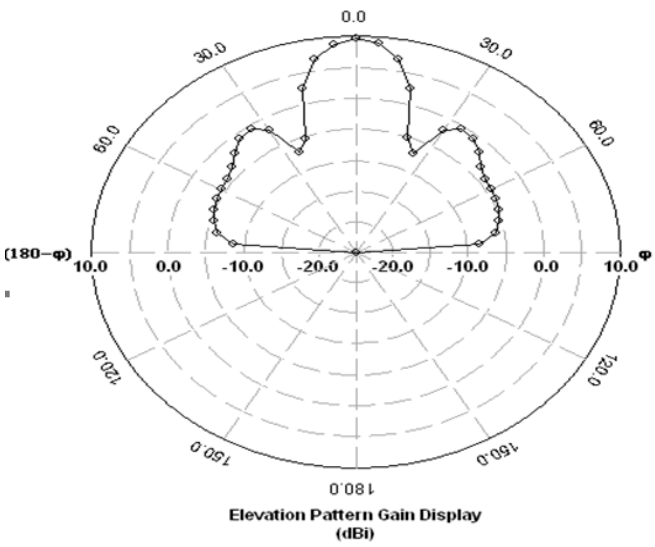


Fig. 5 Radiation pattern of a reference 4×1 array antenna.

The radiation pattern of 1-D uniform square patterned EBGS assisted 4×1 antenna array is shown in Fig. 6.

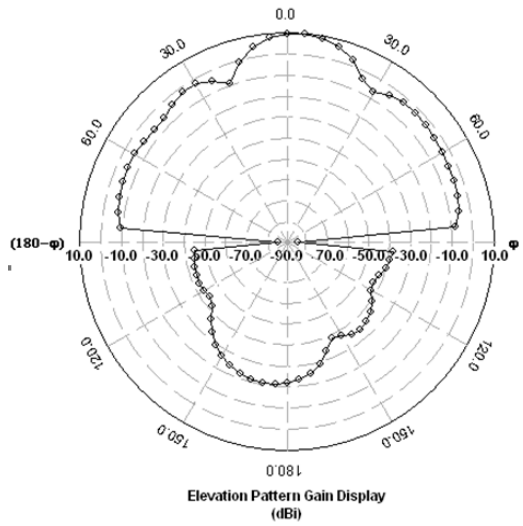


Fig. 6 Radiation pattern of uniform square patterned EBGS assisted 4×1 antenna array.

Here from the Fig. 6, it is seen that the beam steering angle is 10 degree. The peak gain is 9.78105dB and the average gain is 1.51028dB.There is some back lobe here. Due to the inclusion of EBG elements under the feed network of the array, the beam has been squinted by the amount of 10 degree. The back lobe is an unattenuated issue. Further attempt may be taken to reduce this back lobe.

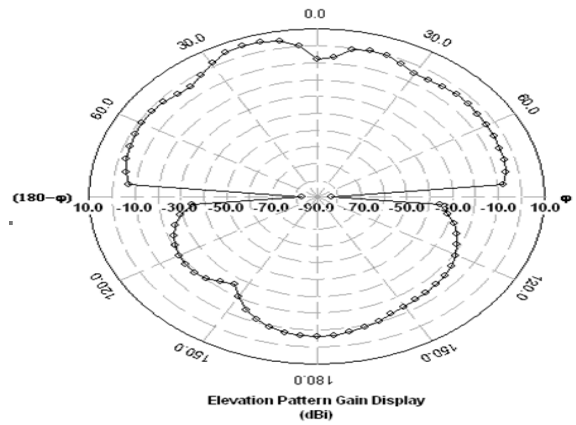


Fig. 7 Radiation pattern of dumbbell shape square patterned EBGS assisted array antenna with one narrow slot.

The radiation pattern of dumbbell shape square patterned EBGS assisted 4×1 array antenna with one narrow slot is shown in Fig.7. From Fig.7, it is seen that the maximum beam steering angle is 20 degree. The peak gain is 5.71654 dB and the average gain is 3.78671dB.There also some back lobe here. The inclusion of dumbbell shape EBGS with one narrow slot under the feed network has squinted the beam by the amount of 20 degree. The beam steering angle is 10 degree more than the previous one. The radiation pattern of dumbbell shape

square patterned EBG assisted 4×1 array antenna with two narrow slots is shown in Fig. 8.

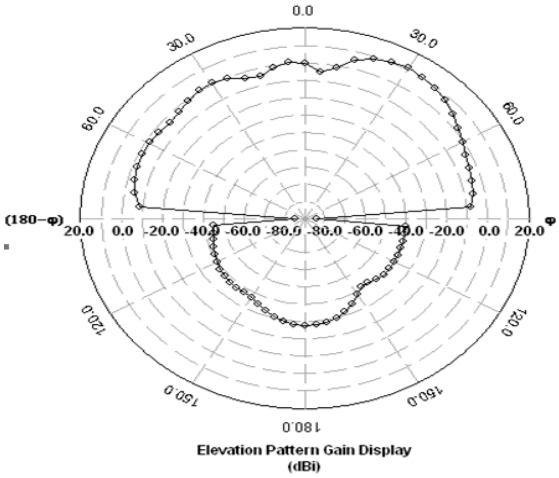


Fig. 8 Radiation pattern of dumbbell shape square patterned EBGS assisted 4×1 array antenna with two narrow slots

From the Fig. 8, it is seen that the maximum beam steering angle is 30 degree. The peak gain is 10.146 dB and the average gain is 0.259856 dB. Back lobe is also present here. From all the aforementioned radiation pattern of square EBGS assisted 4×1 array, dumbbell shape square patterned EBG assisted 4×1 array with one narrow slot and dumbbell shape square patterned EBG assisted 4×1 array with two narrow slots it is seen that the beam steering angle is 10 degree, 20 degree and 30 degree respectively .That is the beam steering angle is increased gradually and it is obviously seen that the EBGSs with dumbbell shape square patterned with two narrow slots provides the largest beam steering angle.

## IV. CONCLUSION

Here, EBG assisted phased array antenna is presented. In this work different types of EBGS such as conventional square patterned EBGS, dumbbell shape EBGS with one narrow slot and dumbbell shape EBGS with two narrow slots have been investigated. The S-parameter performances of dumbbell shape EBGSs consisting of one and two narrower slots are reported respectively. From the background knowledge of wider stopband generated by dumbbell shape EBGS, we have implemented dumbbell shape EBGSs consisting of two bigger slots connected with one and two narrower slots respectively. It is also necessary that the antenna frequency should reside within the passband. It is seen that in every case the antenna frequency 8.65 GHz resides within the passband of EBGS assisted transmission line. Achieving this requirement has led to design EBGS assisted phased array antenna. It is found that dumbbell shape structures provide more beam squinting properties than conventional square patterned EBGS. From the theoretical investigations of all 4×1 microstrip array it is seen that conventional square patterned EBGS designed at 14 GHz located under the feed network provides beam steering angle of 10 degree. On the other hand, the dumbbell shape EBGS with one and two narrow slots have resulted in 20 and 30 degrees beam steering angle respectively for same distribution of EBG elements. It is also seen that the dumbbell shape EBGS with two narrow slots provides more beam steering capacity than the dumbbell shape EBGS with one narrow slot. Thus a novel EBGS assisted 4×1 phased array antenna is achieved.

## REFERENCES


[1] D. Sievenpiper, L. Zhang, R.F. Broas, N. G. Alexopolous, and E. Yablonovitch, “High – impedance electromagnetic surfaces with a forbidden frequency band,” IEEE Trans. Microwave Therory Tech., vol. 47, no. 11, pp. 2059 – 2074, Nov. 1999.

[2] Y.Qian, R. Coccioli, D. Sievenpiper, V. Radisic, E. Yablnovitch and T. Itoh, “ Microstrip patch antenna using novel photonic band gap structures, ” Microwave J., vol . 42, no.1, pp. 66 – 76, Jan 1999.

[3] A. Byers, I. Rumsy, Z. popovic, and M –P May, “Surface – wave guiding using periodic structures.” APS – International symposium, 2000, IEEE, vol. 1, pp. 342- 345. (13), 2000.

[4] S. K. Sharma and L. Shafai, “Enhanced performance of an aperture – coupled rectangular microstrip antenna on a simplified unipolar compact photonic bandgap (UC – PBG) structure,” IEEE – APS Digest 2001, pp.498 – 501.

[5] P. de Maagt, R. Gonzalo, C. Vardaxoglou, and J. M. Baracco, “Electromagnetic bandgap antennas and components for microwave and (sub) millimeter wave applications”, *IEEE Trans. Antennas Propag.*, vol. 51, no. 10, pp. 2667-2677, Oct. 2003.

[6] A. R. Weily, L. Horvath, K. P. Esselle, B. C. Sanders, and T. S. Bird, "A planar resonator antenna based on a woodpile EBG material", *IEEE Trans. Antennas Propag.*, vol. 53, no. 1, pp. 216-223, Jan. 2005.

[7] A. R. Weily, K. P. Esselle, B. C. Sanders, and T. S. Bird, "High-gain 1D EBG resonator antenna", *Microw. Opt. Technol. Lett.*, vol. 47, no. 2, pp. 107-114, Oct. 2005.

[8] S. Parvez, N. Sakib and N. Mollah, "Dumbbell annular ring with circular patterned microstrip low-pass filter with higher selectivity, wider stopband and lower insertion loss", 2015 2nd International Conference on Electrical Information and Communication Technologies (EICT), Khulna, 2015.

[9] M. Mollah, N. Karmakar and J. Fu, "Development of phased array antenna by controlling the filling factor of periodic structure", *International Journal of RF and Microwave Computer-Aided Engineering*, vol. 17, no. 3, pp. 353-359, 2007.

2017 3rd International Conference on Electrical Information and Communication Technology (EICT), 7-9 December 2017, Khulna, Bangladesh

# A Miniaturized On-Body Matched Antenna Design and Its Performance Evaluation at ISM Band

Akash Biswas[1]*, Akib Jayed Islam[2], Khandoker Tanjim Ahammad[3], Bithi Barua[4]
[1,2]Department of EEE American International University-Bangladesh (AIUB), Dhaka, Bangladesh
[3]Department of Microelectronics and Microsystems, Technische Universität Hamburg
[4]Dept. of Electronics and Communication Engineering (ECE), Khulna University of Engineering & Technology
*E-mail: akshbiswas101@gmail.com

*Abstract*—**In the field of biomedical research, continuous communication with a living body and data processing to take immediate actions on necessary points is the key concern. The advancing miniaturization of electronic devices combined with the latest evolution in on-body matched antenna is experiencing scrutiny in the biomedical telemetry. A miniaturized design of an on-body matched antenna along with its simulation-based parameter analysis is proposed in this paper. Industrial, Scientific, and Medical (ISM) band (2.4-2.5 GHz) allows a wider bandwidth with a considerably tiny size of the antenna and that is why the operating frequency of this designed antenna is tuned within this band. The proposed antenna is smaller in size and permits reasonable bend ability that improves its suitability for biomedical telemetry applications. The designed antenna's dimension is 12.150mm×10.474mm×1.488mm. The Microwave Studio of Computer Simulation Technology (CST) software is used to design the antenna with human phantom model and calculate various performance results, such as the return loss, radiation pattern, operating frequency, directivity, gain, total efficiency, power analysis and also sensitivity of the antenna in bending condition without changing the dielectric properties of human phantom model. Finally, the Specific Absorption Rate (SAR) is evaluated to check the biocompatibility of the antenna.**

***Keywords—Biomedical Telemetry, Miniaturized Antenna, ISM band, Human Phantom Model, SAR.***

## I. INTRODUCTION

Research on biomedical telemetry devices has been getting attention because of the progression in microelectronics and medical technologies. A biomedical telemetric system is a mechanism which allows the transmission of necessary bio-signals from a human body towards a designated receiver system. These bio-signals are retrieved from transducers and after processing of the signals, they are forwarded to external monitoring devices. The attention in biomedical telemetry has incredibly extended because of its advantages and the applications such as medical care, post-surgery inspections, real-time tracking and diagnosis of fatal diseases [1]. A physician can supervise the patients by observing the signals from implantable or wearable devices. Patients who need to visit hospital more often, can take advantage of such kind of devices. Cardioverter-defibrillators and pacemakers [2], temperature monitors [3], blood-glucose sensors [4], functional electrical simulators [5], cochlear and retina implants [6-7] are some notable executions in the field of biomedical telemetric system.

Regarding implanted or wearable telemetry applications, the antenna plays one of the most vital roles in achieving vigorous transmission and a notable miniaturization of the whole device. Miniaturization, being congruent with human tissue, standard dissemination with the medical device and patient's safety are the primary challenges for designing the antennas in biomedical telemetry applications. Human tissue models used in the simulation tools are pivotal to precise the characteristics of the antennas [8-9]. The tissue model is intricate and the divergence behavior of human tissue model varies from one patient to another. Industrial, Scientific and Medical (ISM), Ultra-Wideband (UWB), Medical Implant Communication Service (MICS) and Wireless Medical Telemetry Service (WMTS) are the most common frequency bands used for designing biocompatible antennas. According to the FCC regulation, 401 MHz to 406 MHz are allocated for Medical Device Radio communications Service (Med-Radio) and 2.4 GHz to 2.5 GHz is chosen for medical application in ISM band [10]. Researchers prefer ISM band to design a smaller sized antenna with higher frequency.

The recent research on ISM band antennas exhibits tremendous possibility in the domain of biomedical engineering. Designing of an implantable, as well as flexible antenna performing in the ISM band, is established in the paper [11]. The antenna was analyzed with several simulation tests to check the versatility of different parameters. The dimensions are not satisfactory in terms of biomedical applications. The tuning problem resulted in a high return loss in the ISM band; however, the antenna's simulation results of the other parameters were satisfactory. The model introduced in [11], later developed with a fifty percent size reduction has been presented in the literature [12] and [13]. The tuning problem has been overcome in these works. Considering the other parameters, the improved performances with a miniaturized dimension introduced in these papers are satisfactory. Another novel model of a strip line-fed antenna has been presented in the paper [14]. Though the antenna has a tiny dimension with a low return loss, no SAR calculation has been performed. An on-body matched flexible UWB band antenna has been introduced in the literature [15]. The return loss in both the planar and bend condition is low but the dimensions (40mm×40mm×1.44mm) of the antenna are high considering the biomedical applications. A unique design of miniaturized, simulation-based antenna with implantable

978-1-5386-2307-7/17/$31.00 ©2017 IEEE

configuration is introduced in the literature [16] operating in ISM band. Having a miniaturized dimension along with good return loss, this antenna perfectly fits for various biomedical applications.

Considering the in-body to an on-body scenario, the implantable antenna is located in the physical body whereas the on-body antenna is placed over the human body surface. With reference to the on-body matched antenna, a firm structure to be embedded in the patient's body is necessary. Besides, the antenna coupling should be established within the whole operating frequency band. Designing on-body matched antennas integrated with the human phantom model is a strenuous task as different characteristics like size restriction, wider frequency requirement, SAR evaluation, radiation efficiency, and biocompatibility needs be considered. The on-body antenna should be tiny in dimension for physiological acceptability. The on-body antenna should have a wide frequency range to avoid being coupled far away from the operating bandwidth as the dielectric properties of human phantom model vary tremendously and are convoluted. The characteristics mentioned above have been followed to overcome the limitations of the literatures [11-15]. To check the versatility and precise workability with biomedical telemetry applications, simulation tests are performed over a different types of human phantom model as well as various substrate materials.

Designing an on-body matched antenna and performance scrutiny in ISM band are concentrated in this paper. The following parts of the paper are organized as follows. The design procedure of the proposed antenna embedded with human phantom model and variations of dielectric properties in different frequencies are briefly narrated in section II. Section III deals with the simulations and the results of the performance parameters to verify the adaptability of the proposed model. The biocompatibility test is evaluated to check its performance while bending and its comparison with the planar state is discussed in section IV. This section also includes the SAR calculation to recheck its implementation with human tissue model. Section V summarizes the overall implementation and presents conclusions.

## II. Design Procedure of the Antenna

In order to design and simulation result analysis of the antenna, CST Microwave Studio is used here. At first, free space design of the antenna is done and then a human phantom model is built to calculate its performance results. Antenna size is an important point that should be kept in mind as the miniaturized antennas overcome the difficulties of practical implementation. Though having an on-body application, keeping the antenna dimension as low as possible without having a discrepancy in performance, was the key concern of this design. ISM band is chosen as the antenna operating frequency band because of its higher bit rate performance after implementation with a high bandwidth which makes it an optimum fit for applications like, biomedical telemetry [17-18]. Necessary antenna parameter calculations and modifications are done to tune the operating frequency within ISM band. A list of antenna parameters is used in the simulation is given in TABLE I. As the radiating patch, as well as the ground plane material, Copper is used with a thickness of 0.210mm. With a dielectric constant of 4.3, FR4 is used as a substrate material that has a thickness of 1.068mm.This whole free space design of the antenna then put upon a human body phantom model to perform the simulation procedure. A human body phantom model consisting skin, fat, and muscle is designed using the material library of CST Microwave Studio. Through iteration technique, the lowest possible dimension is determined without compromising the antenna performance. The overall dimension of the proposed antenna is calculated as 12.150mm × 10.474mm × 1.488 mm, which represents an optimum and miniaturized design that can be performed neatly in on-body matched biomedical telemetry applications.

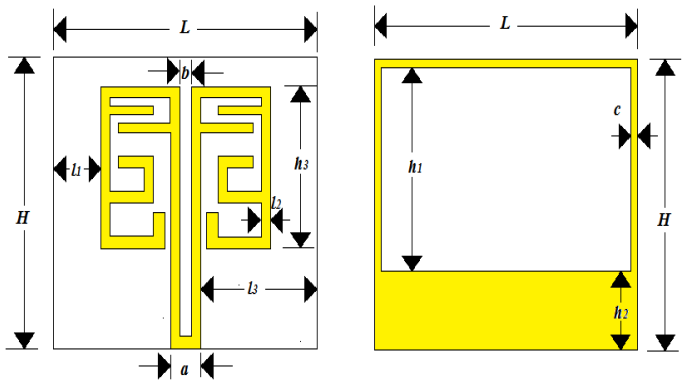


(a) (b)

Fig.1. Antenna Geometric Model (a) Radiating Patch (b) Ground Plane

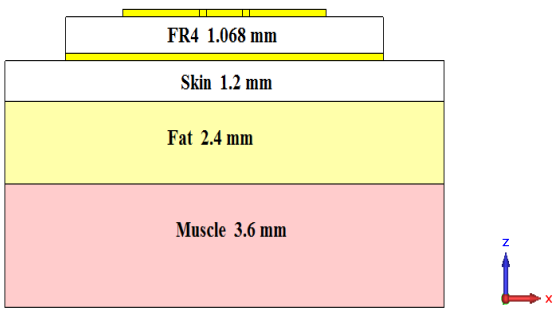


Fig.2. Proposed antenna structure along with human phantom model

In Fig.1, the geometric model of the antenna is shown where (a) represents the radiating patch which is the top layer and (b) is the bottom layer denoting the ground plane. Frontal view of the proposed antenna on human phantom model along with their thicknesses (in mm) is shown in Fig.2.

TABLE I. ANTENNA SIZE PARAMETERS

| Parameter | Value(mm) | | Parameter | Value(mm) |
|---|---|---|---|---|
| ***L*** | 12.150 | | $h_1$ | 7.348 |
| ***H*** | 10.474 | | $h_2$ | 3.126 |
| $l_1$ | 2.178 | | $h_3$ | 5.837 |
| $l_2$ | 0.419 | | ***a*** | 1.382 |
| $l_3$ | 11.459 | | ***b*** | 0.454 |
| ***c*** | 0.315 | | | |

The human phantom model is introduced here in order to maintain the realistic scenario of a human body to perform simulation procedure more accurately. Since the proposed antenna is an on-body matched antenna, a simple human phantom model is designed using the material library provided in CST Microwave studio. Here, the model has a Skin layer with the thickness of 1.2mm, a Fat layer of 2.4mm and Muscle layer of 3.6mm, upon which the antenna is placed alike Fig.2. While designing a phantom model, it is important to keep in mind that the dielectric properties (Permittivity & Conductivity) of human muscle have some significant effects on antenna performance. TABLE II represents the dielectric values (conductivity and permittivity) of human muscle tissue used with variety of frequencies [19].

TABLE II. DIELECTRIC VALUES OF HUMAN MUSCLE TISSUE IN DIFFERENT FREQUENCIES

| **Frequency (GHz)** | **Permittivity** $\varepsilon_r$ | **Conductivity** $\sigma$ **S/m** |
|---|---|---|
| 2.1 | 53.2 | 1.51 |
| 2.3 | 52.9 | 1.64 |
| **2.48** | **52.7** | **1.76** |
| 2.6 | 52.5 | 1.84 |
| 2.8 | 52.3 | 1.99 |

## III. SIMULATION & RESULTS

Simulation procedure and performance result analysis of the designed antenna are done to check its work ability and various features. In Fig.3, the whole antenna structure along with human phantom model is illustrated. Complete simulation procedure is done with this structure. In order to measure the amount of reflected and received power, the return loss which is also known as S11 parameter in the case of single port input, is measured and shown in Fig.4. Here, it is found that the operating frequency 2.48 GHz, which lies within the ISM band (2.4 GHz-2.5 GHz) and the value of return loss on that point is -29.856dB. This result indicates a promising value to be performed well. In order to calculate the antenna bandwidth, a horizontal line is to be drawn at -10dB point and here the value of the bandwidth is 491.2 MHz (2.2055 GHz -2.6967 GHz).

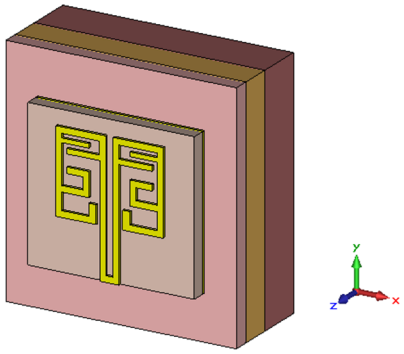

Fig.3. Antenna on Human Phantom Model

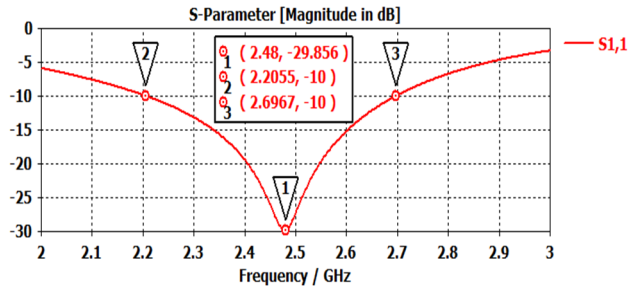


Fig.4. S11 parameter calculation result of the antenna

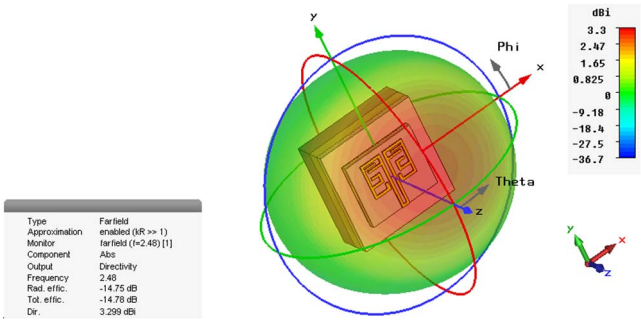


Fig.5. Far-Field region view (3D) with the antenna model inside

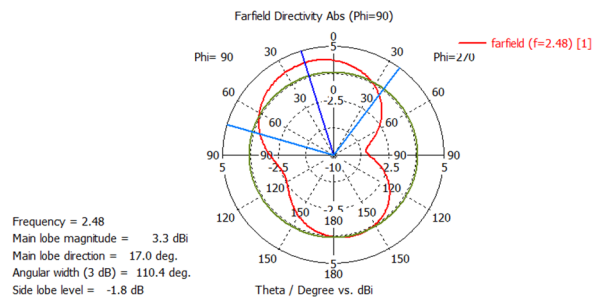


Fig.6. Far-Field region view (polar)

The directivity of the designed antenna is simulated by analyzing Far-field region that represents how much directional and focused the antenna is. The 3D view of the Far-Field region is represented in Fig.5, along with the antenna model inside. The polar view of the same Far-Field region is shown in Fig.6. Here, it is found that the directivity is

3.3dBi which is shown as the main lobe magnitude. Additionally, 17.0 degree is the main lobe direction, where the Angular width is of 110.4 degree.

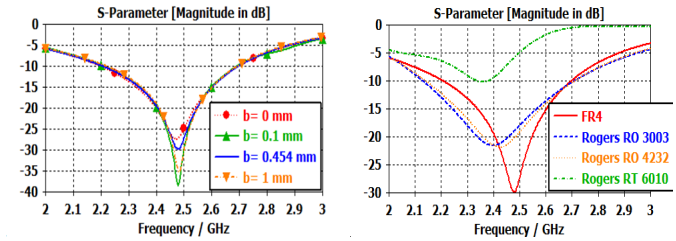


(a) (b)

Fig.7. S11 parameter comparisons (a) variety of '*b*' (b) different substrate materials.

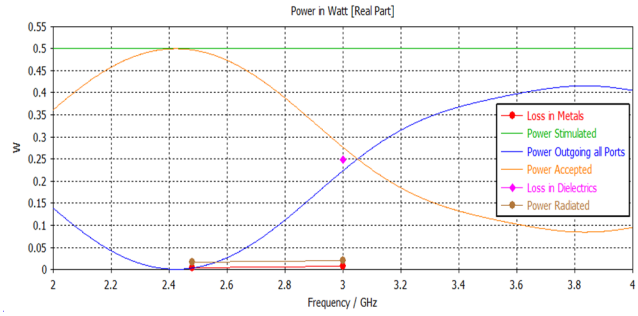


Fig.8. Power analysis of simulation process

In Fig.7, the two graphs are showing the comparison of S11 parameter analysis result of different scenarios of the designed antenna. While undergoing the simulation procedure, it is noticed that the front side of the radiation patch has a parameter named "b", which value has significance on the return loss value at the operating frequency of the antenna. The graph of Fig.7 (a) is showing the return loss value comparison of this antenna by changing different width value of "b". Though the value of 0.1mm is showing the best result here, for the final design, 0.454mm is chosen because it gives the best output in the case of other parameter analysis like Far-Field result, SAR calculation and gain without compromising the performance. The another graph, Fig.7 (b), is on the basis of using different substrate materials for the antenna which clearly indicates the best performance is of FR4 and that is why it is chosen for the final design. For the power supply and distribution analysis through the antenna, Fig.8 is provided here that shows the results like accepted, radiated, simulated power, loss in dielectrics and metals in watt.

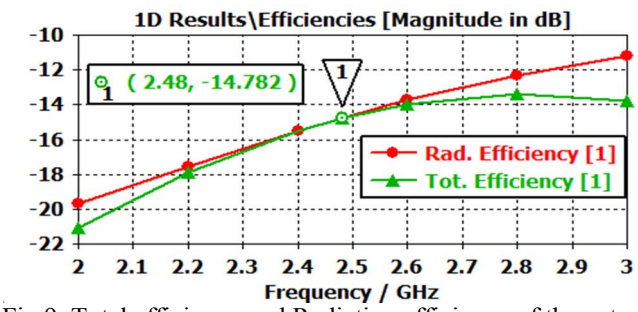


Fig.9. Total efficiency and Radiation efficiency of the antenna

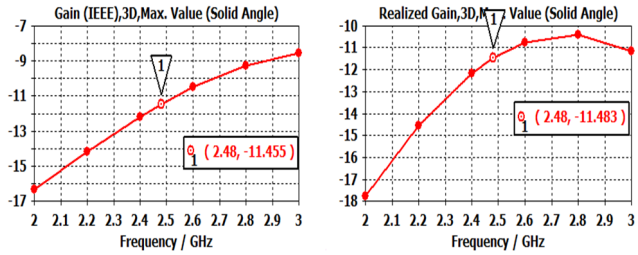


(a) (b)

Fig.10. (a) Total gain and (b) Realized gain graphs

The antenna efficiency is another important measurement that is shown in Fig.9 that indicates the radiation and total efficiency at 2.48 GHz point which is -14.782dB. Two more performance graph of Gain (IEEE) and realized gain of the antenna is presented in Fig.10 (a) and (b) that represent the values of -11.455dB and -11.483dB respectively.

## IV. Biocompatibility analysis

Biocompatibility analysis is also done by taking the values of Specific Absorption Rate (SAR) and bend ability of the proposed antenna along with the curvature of human body. To avoid unwanted difficulties or damage of human tissue by antenna radiation, SAR calculation is performed. FCC and ICNIRP guidelines determined the maximum acceptable value of SAR that is 0.467 W/kg (1g tissue) [20]. The SAR calculation of the antenna is presented in Fig.11 from four different perspectives. The maximum value of the SAR here is found 0.328 W/kg (1g tissue) while 1mW power is used as input which lies under the maximum accepted value. So, it can be said that the antenna will work precisely without making any kind of damage to human tissue.

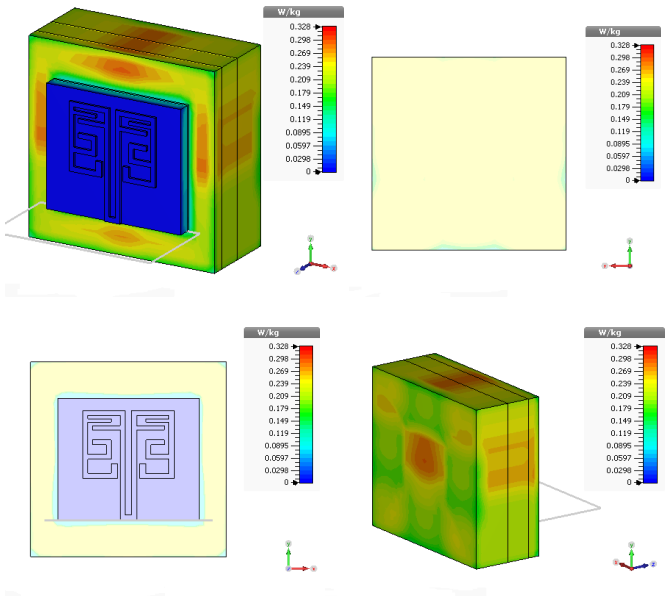

Fig.11. SAR distribution result from four different perspectives

Since the designed antenna application is of on-body matched and human body surface is not planner, the antenna must be supposed to bend up to some extent without compromising its performance. For the bend ability test, a 31 mm cylinder is used to bend the antenna around x-axis, along its curvature. The geometric representation of the antenna under bend test is shown in Fig.12.

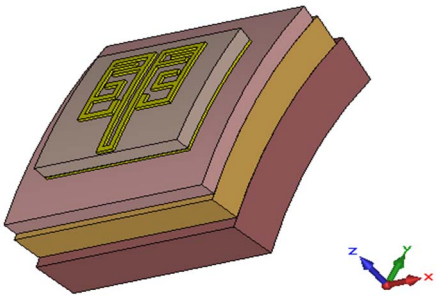


Fig.12. Antenna undergoing bend test

To determine and compare the bend test of the antenna with the planner result, S11 parameter is chosen and simulated. Fig.13 shows the comparison between planner and bend structure simulation result which are almost identical to each other except slight shift in return loss value.

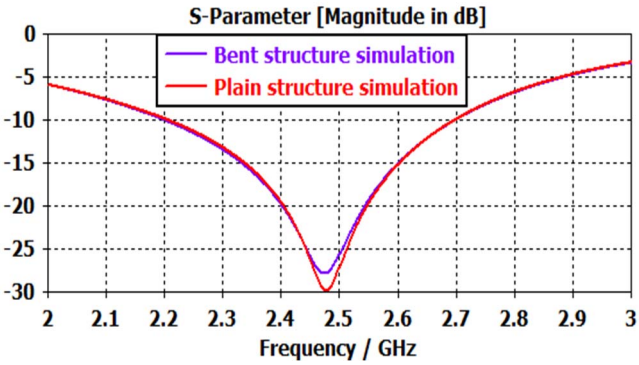


Fig.13. Comparison result of S11 parameter between plain and bent structure of the antenna

## V. Conclusion

An on-body matched antenna design and its performance evaluation with operating frequency in ISM band is presented in this paper with its application in biomedical telemetry. Here, completing the free space design, a human phantom model is built in order to measure the antenna parameters maintaining almost the exact scenario of real life implementation. By analyzing different materials for radiating patch and substrate, Copper and FR4 are chosen here for simulation procedure. Since miniaturization with subtle dimension is the key concern of this design; the antenna overcomes practical implantation problems of its similar kind. Good return loss value with a wide range of bandwidth also indicates its promising performance. Additionally, Realized and total gain data, power analysis and Far-Field result analysis also strengthened the claim. Importantly, for biomedical telemetry applications, SAR value calculation with bend ability test result fulfilled the biocompatibility of this antenna. Considering the dimension, design pattern and simulation data, it can be said that this antenna is a perfect match for biomedical telemetry applications. Antenna fabrication and collaboration with biomedical telemetry devices should be the future work to be performed for further development.

## References


[1] Kiourti, Asimina, and Konstantina S. Nikita. "A review of implantable patch antennas for biomedical telemetry: Challenges and solutions [wireless corner]." *IEEE Antennas and Propagation Magazine* 54.3 (2012): 210-228.

[2] Wessels, Dick. "Implantable pacemakers and defibrillators: device overview & EMI considerations." *Electromagnetic Compatibility, 2002. EMC 200P2. IEEE International Symposium on*. Vol. 2. IEEE, 2002.

[3] Scanlon, William G., Noel E. Evans, and Zita M. McCreesh. "RF performance of a 418-MHz radio telemeter packaged for human vaginal placement." *IEEE transactions on biomedical engineering* 44.5 (1997): 427-430.

[4] Shults, Marc C., et al. "A telemetry-instrumentation system for monitoring multiple subcutaneously implanted glucose sensors." *IEEE Transactions on Biomedical Engineering* 41.10 (1994): 937-942.

[5] Guillory, K. S., and R. A. Normann. "A 100-channel system for real time detection and storage of extracellular spike waveforms." *Journal of neuroscience methods* 91.1 (1999): 21-29.

[6] Buchegger, Thomas, et al. "Ultra-wideband transceivers for cochlear implants." *EURASIP Journal on Applied Signal Processing* 2005 (2005): 3069-3075.

[7] Gosalia, Keyoor, Gianluca Lazzi, and Mark Humayun. "Investigation of a microwave data telemetry link for a retinal prosthesis." *IEEE Transactions on Microwave Theory and Techniques* 52.8 (2004): 1925-1933.

[8] Gemio, J., Parron, J. and Soler, J., 2010. Human body effects on implantable antennas for ISM bands applications: Models comparison and propagation losses study. *Progress In Electromagnetics Research*, *110*, pp.437-452.

[9] Kim, J. and Rahmat-Samii, Y., 2004. Implanted antennas inside a human body: Simulations, designs, and characterizations. *IEEE Transactions on microwave theory and techniques*, *52*(8), pp.1934-1943.

[10] "FCC rules: CFR-47, part-15, ISM" FCC, Washington, DC, Oct. 2005. [Online]. Available: http://wireless.fcc.gov/services/index.htm.

[11] Maria Lucia Scarpello, Divya Kurup, Hendrik Rogier, Dries Vande Ginste, Fabrice Axisa, Jan Vanfleteren, Wout Joseph, Luc Martens, Gunter Vermeeren ''Design of an Implantable Slot Dipole Conformal Flexible Antenna for Biomedical Applications,'' *IEEE Transactions on Antennas and Propagation (Volume:59 , Issue: 10 )*, pp. 3556--3564, Oct. 2011.

[12] N. A. Islam, T. A. Aleef, U. Arafat and A. J. Islam, "Design improvement and performance comparison of an existing slot dipole bendable antenna for biomedical applications," *2016 5th International Conference on Informatics, Electronics and Vision (ICIEV)*, Dhaka, 2016, pp. 508-512.

[13] N. Al Islam, A. T. Abrar, U. Arafat, A. J. Islam and R. Hoque, "Design and performance measurement of an in-body implantable miniaturized Slot Dipole rectangular patch antenna for biomedical applications," *2015 International Conference on Advances in Electrical Engineering (ICAEE)*, Dhaka, 2015, pp. 59-63.

[14] T. A. Aleef and A. Biswas, "Design and measurement of a flexible implantable stripline-fed slot antenna for biomedical applications," *2016*

*3rd International Conference on Electrical Engineering and Information Communication Technology (ICEEICT)*, Dhaka, 2016, pp. 1-5.

[15] A. Biswas, A. J. Islam, A. Al-Faruk and S. S. Alam, "Design and performance analysis of a microstrip line-fed on-body matched flexible UWB antenna for biomedical applications," *2017 International Conference on Electrical, Computer and Communication Engineering (ECCE)*, Cox's Bazar, 2017, pp. 181-185.

[16] Aleef, Tajwar Abrar, Yeman Brhane Hagos, Vu Hoang Minh, Saed Khawaldeh, and Usama Pervaiz. "Design and simulation-based performance evaluation of a miniaturised implantable antenna for biomedical applications." *Micro & Nano Letters* (2017).

[17] Usui, Hiroki, Masaharu Takahashi, and Koichi Ito. "Radiation characteristics of an implanted cavity slot antenna into the human body." *Antennas and Propagation Society International Symposium* 2006, IEEE, pp. 1095-1098. IEEE, 2006.

[18] Xia, Wei, Kazuyuki Saito, Masaharu Takahashi, and Koichi Ito. "Performances of an implanted cavity slot antenna embedded in the human arm." *IEEE Transactions on Antennas and Propagation* 57, no. 4 (2009): 894-899.

[19] [Online]. Available: https://www.itis.ethz.ch/virtual-population/tissue-properties/database/tissue-frequency-chart

[20] ICNIRP, “Guidelines for limiting exposure to time-varying electric, magnetic, and electromagnetic fields,” *Health Phys.*, vol. 74, pp.494–5229, Oct. 2009.

# Designing of a High Birefringent Octagonal Photonic Crystal Fiber for Sensing Applications

Biplob Kumar Kundu, Selim Sheikh, and Ashraful Hossain Howlader
Bangabandhu Sheikh Mujibur Rahman Science and Technology University, Bangladesh
biplob.bsmrstu@gmail.com, ahhowlader.eee@gmail.com

*Abstract*— **This paper offers a novel design of an octagonal photonic crystal fiber (O-PCF) with high birefringence (0.04397 at 1550 nm) which is more compatible for sensing applications based on fiber optics. The proposed design exhibits a large negative chromatic dispersion of -360.98 to -556.97 ps/(nm-km) over S+C communication bands (1460-1565 nm). Besides, it proposes a large non-linear coefficient of 59.17 $W^{-1}km^{-1}$ at the wavelength of 1550 nm.**

***Keywords— Birefringence, dispersion compensating, non-linear coefficient, octagonal.***

## I. INTRODUCTION

Photonic crystal fiber (PCF) is one of the most popular techniques in advanced optics technology. It utilizes the phenomena of total internal reflection (TIR) of light wave. PCF contains microscopic air-holes in a silica background and forms the silica-air microstructure to manipulate refractive index of the waveguide [1]. By changing the geometrical and structural arrangements of the air-holes, high birefringence and nonlinearity with dispersion compensating ability can be obtained.

The engineering of birefringence is an attractive property of PCFs. Light converts into two orthogonal polarized parts with different refractive indices ensuing birefringence [2]. Effect of polarization maintaining dispersion can be mitigated by large birefringence [3]. High birefringence also has a major application of sensors like pressure sensing [4], curvature sensing [5], temperature-insensitive torsion sensing [6], and temperature-independent strain sensing [7].

Recently, dispersion compensating fibers (DCFs) are providing exciting possibilities to improve the quality of the transmitted signal through the conventional fiber without the necessity of using electronic renewal of signals [8]. Due to opposite in nature between material dispersion and waveguide dispersion, the compensation can be done by proper modeling and designing.

Moreover, high non-linear PCF is proved to be used as gas sensor [9]-[10].

Generally, the micro structured air holes are embedded with the shape of an equilateral triangle having six air holes in the initial ring surrounding the core and this kind of PCF is called the hexagonal-lattice PCF, which are more common. Besides the hexagonal structures, other design structures such as octagonal structure, decagonal structure have been designed. Circular PCFs are very available, whereas some unconventional designs such as spiral and elliptical-spiral PCFs are also proposed. In this paper, an O-PCF has been proposed and designed with circular air holes of different diameters and two elliptical shaped air holes adjacent to the silica core. The design offers a very high birefringence with a large negative chromatic dispersion and attractive nonlinear co-efficient with simple and uncomplicated structure for practical implementation.

## II. STRUCTURE OF PROPOSED O-PCF

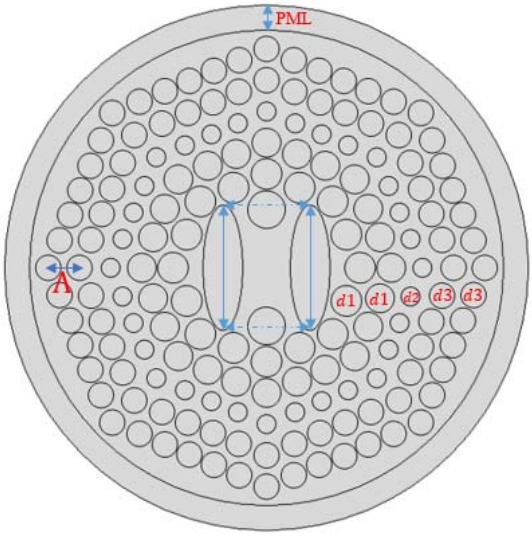


Figure 1. Transverse cross-section of the O-PCF.

Fig. 1 illustrates the designed structure of the proposed O-PCF. The core of the proposed O-PCF is configured as rectangular shaped, where the two ellipses and the two circles are equidistant from the center of the O-PCF. It is designed with five octagonal air hole rings of circles around the core to construct the cladding. The 1st, 2nd, 3rd, 4th and 5th rings contain 16, 24, 32, 40, 48 circles, respectively. The value of pitch is taken as $\Lambda$ = 0.5 µm and the perfectly matched layer (PML) is considered as 1 µm. The 1st ring radius of the air holes is 1.5 µm and the remaining is related as (1.5 + n$\Lambda$ ) µm, where n = 1, 2, 3, 4. The air hole diameters of 1st and 2nd ring is $d_1$ = 0.92

978-1-5386-2307-7/17/$31.00 ©2017 IEEE

μm, 4th and 5th ring is $d_3$ = 0.81 μm and 3rd ring is designed as of $d_2$ = 0.6 μm.

## III. Numerical Analysis

In this proposed design finite element method (FEM) with perfectly matched layer is used to describe its characteristics of the O-PCF. The simulation software COMSOL Multiphyscis is employed for the study of the simulated values. The wavelength dependent refractive index of the silica has included in the simulation from Sellmeier's equation. The birefringence can be obtained from the differences between the effective refractive indices of x and y polarized direction as follows:

$$B(\mu) = |\nu_\xi - \nu_\psi| \quad (1)$$

where $\nu_\xi$ and $\nu_\psi$ stand for the real parts of ξ (horizontal) and ψ (vertical)-axis refractive indices, respectively and μ represents the wavelength.

Chromatic dispersion (Δ), effective area (A), nonlinear coefficient (Γ) and confinement loss ($\Lambda_\chi$) can be determined by the following equations:

$$(\Delta) = -(\mu/\chi)\{\delta^2/\delta\mu^2(P\varepsilon[\nu_{\varepsilon\phi\phi}])\} \quad (2)$$

$$A = (\int_{-\infty \text{ to } \infty}\int_{-\infty \text{ to } \infty}|E|^2\delta\xi\delta\psi)^2/(\int_{-\infty \text{ to } \infty}\int_{-\infty \text{ to } \infty}|E|^4\delta\xi\delta\psi) \quad (3)$$

$$\Gamma = 6.2832/\mu)(\nu/\nu_{\varepsilon\phi\phi}), \quad (4)$$

$$\Lambda_\chi = (20000000/2.30)K_0 I\mu(\nu_{\varepsilon\phi\phi}) \quad (5)$$

where χ is the light velocity, $P\varepsilon[\nu_{\varepsilon\phi\phi}]$ and $I\mu(\nu_{\varepsilon\phi\phi})$ is the real part and imaginary part of effective refractive index ($\nu_{\varepsilon\phi\phi}$) and ν refers to the non-linear refractive index.

## IV. Simulation Result and Discussion

The asymmetric core of the proposed design gives the ultimate value of high birefringence. This is the most attractive value of our O-PCF. Fig. 2 shows the birefringence of 0.04397 at 1550 nm wavelength. This very high birefringence makes the O-PCF a suitable candidate for sensor based applications.

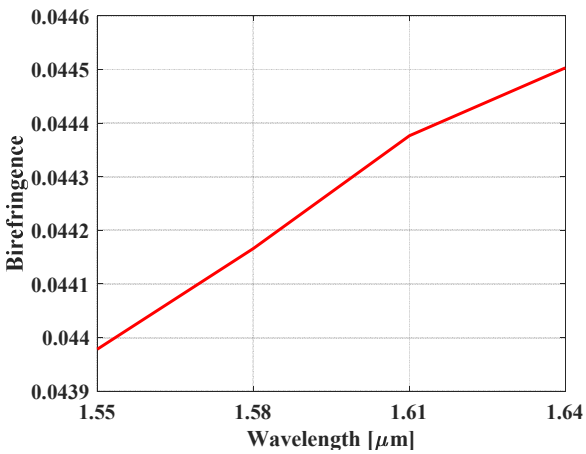


Figure 2. Exceptionally high birefringence assessment of 0.04397 for operating wavelength of 1.55 μm.

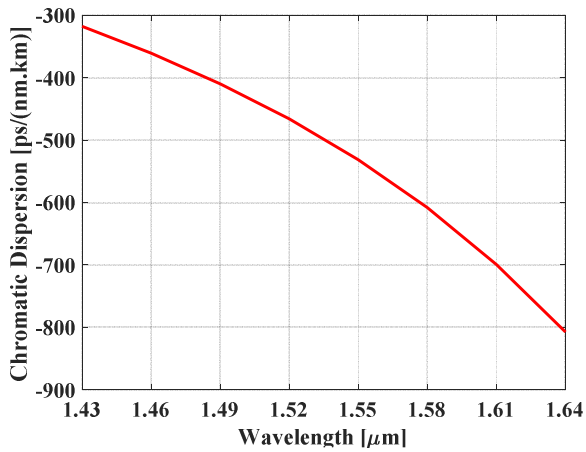


Figure 3. Chromatic dispersion curve with relation to wavelength from 1.43 to 1.64 μm.

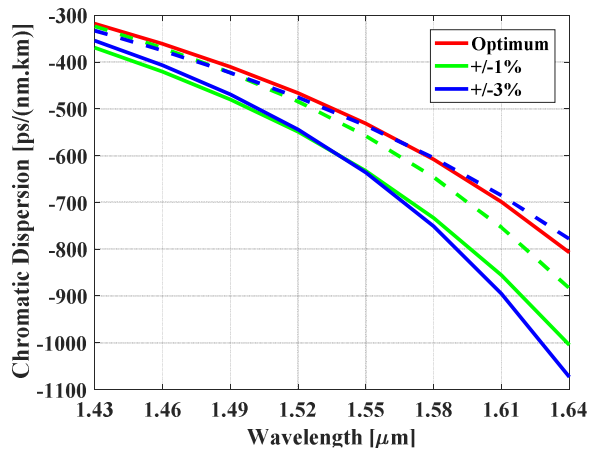


Figure 4. Chromatic dispersion variations with respect to wavelength with changing of 3rd ring air-hole diameter.

Another goal of designing this O-PCF is to maintain large negative dispersion at the desired wavelength of 1550 nm. The dispersion compensating curve in Fig. 3 shows simulated result of -531.39 ps/(nm.km) at the wavelength of 1550 nm. This large negative chromatic dispersion value is useful to balance the dispersion at all the frequencies of dense wavelength division multiplexing (DWDM) efficiently. It is also simulated the chromatic dispersions with the variation of 3rd ring air-hole diameter (see Fig. 4). The figure depicts that during manufacturing this O-PCF, a slight deformation of structural and physical values, will not create large fluctuations from optimized value. Thus the changes in chromatic dispersion as shown in Fig. 4 can help the study of fabrication processes for practical application. Further with the dispersion compensating property, the relative dispersion slope (RDS) should be matched with conventional single mode fiber at the same time. Our O-PCF shows about 0.004 $nm^{-1}$ RDS value, which is very close match to conventional optical fiber.

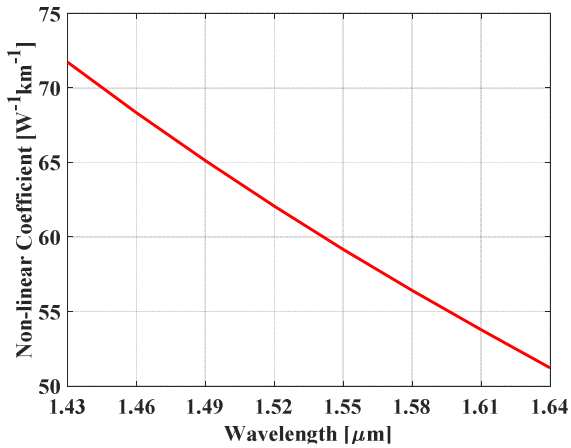


Figure 5. Non-linear coefficient of the proposed O-PCF as variation of wavelength.

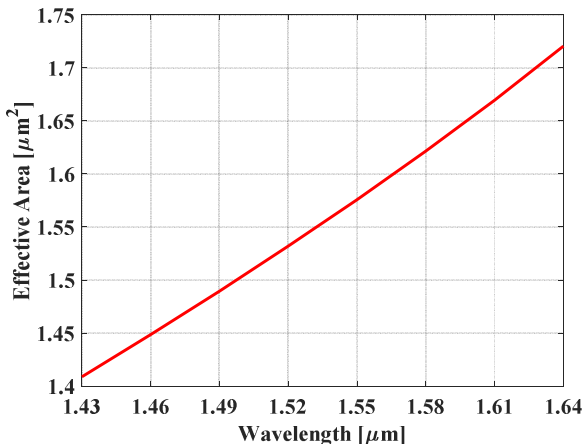


Figure 6. Effective area with respect to wavelength, which shows the designed O-PCF is single mode fiber.

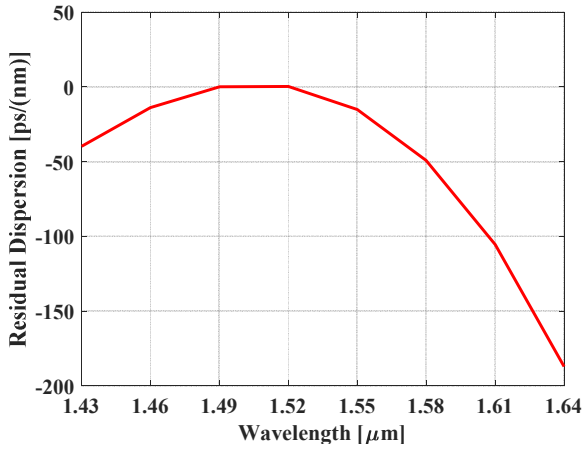


Figure 7. Residual dispersion vs. wavelength for proposed O-PCF. It confirms the ability of designed O-PCF for the operation over S+C band.

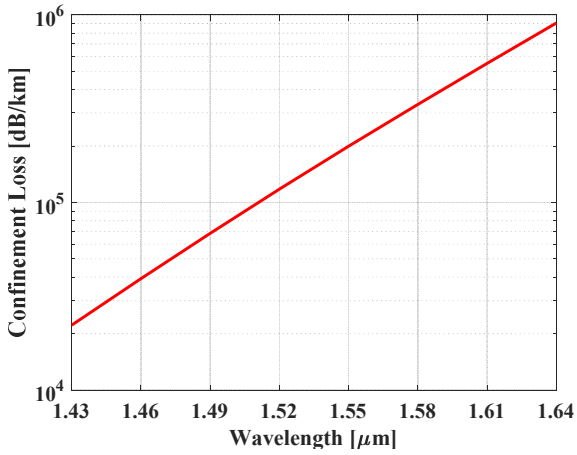


Figure 8. Confinement loss curve with respect to wavelength.

Fig. 5 and Fig. 6 represent the non-linear coefficient and effective area with the variation of wavelength, respectively. The simulated value of non-linear coefficient is found 59.17 $W^{-1}km^{-1}$ and effective area is 1.576 $\mu m^2$ at 1550 nm wavelength. These characteristics of low effective area with high nonlinearity will reduce the bending loss [11]. Hence the high nonlinearity is also preferable in optical parametric amplification, super continuum operation [12] and soliton generation. These findings also reveal that the suggested O-PCF is a single mode fiber. Thus no modal dispersion will occur. Fig. 7 depicts the residual dispersion as the function of wavelength from 1460 to 1565 nm, which enables the suggested O-PCF to be a better candidate for high-bit-rate communication systems over S+C band. Confinement loss of the proposed PCF is prescribed with the Fig. 8. It shows a moderate confinement loss at the operating wavelength of 1550 nm.

TABLE I. COMPARISION AMONG THE OPTIMIZED O-PCF WITH THE OTHER PAPERS AT 1550 NM WAVELENGTH

| **Designed PCF** | **Characteristics of the Proposed PCF** | | |
|---|---|---|---|
| | ***Birefringence*** | ***Chromatic Dispersion*** (ps/nm.km) | ***Non-linear Coefficient*** ($W^{-1}km^{-1}$) |
| Reference [2] | 0.02040 | - - - | 33.000 |
| Reference [3] | 0.02200 | -544.70 | 52.700 |
| Reference [13] | 0.03100 | -529.18 | 47.801 |
| Reference [14] | 0.02050 | -396.90 | 39.020 |
| Reference [15] | 0.01750 | -354.31 | 39.933 |
| Reference [16] | 0.02750 | -331.00 | - - - |
| Proposed Design | 0.04397 | -531.39 | 59.170 |

## V. CONCLUSION

The simulated design proposes an O-PCF with high birefringence of 0.04397. The chromatic dispersion of -531.39 ps/(nm-km) and large nonlinearity of 59.17 $W^{-1}km^{-1}$ is obtained at the operating wavelength of 1550 nm. The proposed design will be most useful in various sensor based applications, dispersion compensation for broadband transmission and non-linear optics applications over S+C band. The working waveband can be extended as a future work for the proposed design. We believe that the geometry of the presented O-PCF is simple enough to manufacture with less complexity.

## REFERENCES


[1] P. St. J. Russell, "Photonic crystal fibers," *Science*, vol. 299, no. 5605, pp. 358-362, Jan. 2003.

[2] M. M. Rashid, M. S. Anower, M. I. Hasan and M. R. Hasan, "Highly birefringent octagonal shaped photonic crystal fiber with two zero dispersion wavelengths in Ti:Sapphire oscillator range," in *Proc. 3rd Int.l Conf. on Electrical Engineering and Information Communication Technology*, Sept. 2016, pp. 1-6.

[3] M. I. Hasan, M. S. Habib and S. M. A. Razzak, "An elliptical-shaped core residual dispersion compensating octagonal photonic crystal fiber," *IEEE Photonics Technology Letters*, vol. 26, no. 20, pp. 2047-2050, Oct. 2014.

[4] D. Li and J. Hu, "Design on a novel birefringent photonic crystal fiber with polycarbonate-ellipse core for pressure sensing," in *Proc. OES China Ocean Acoustics*, Jan. 2016, pp. 1-4.

[5] O. Frazão *et al*. "Curvature sensor using a highly birefringent photonic crystal fiber with two asymmetric hole regions in a Sagnac interferometer." *Applied Optics*, vol. 47, no. 13, pp. 2520-2523, Apr. 2008.

[6] H. Kim *et al*. "Temperature-insensitive torsion sensor with enhanced sensitivity by use of a highly birefringent photonic crystal fiber." *IEEE Photonics Technology Letters*, vol. 22, no. 20, pp.1539-1541, Oct. 2010.

[7] O. Frazão, J. M. Baptista, and J. L. Santos. "Temperature-independent strain sensor based on a Hi-Bi photonic crystal fiber loop mirror." *IEEE Sensors Journal*, vol. 7, no. 10, pp.1453-1455, Oct. 2007.

[8] M. I. Hasan, S. M. A. Razzak and M. S. Habib, "Design and characterization of highly birefringent residual dispersion compensating photonic crystal fiber," *Journal of Lightwave Technology*, vol. 32, no. 23, pp. 4578-4584, Dec. 2014.

[9] Y. Hoo, W. Jin, C. Shi, H. Ho, D. Wang and S. Ruan, "Design and modeling of a photonic crystal fiber gas sensor," *Applied Optics*, vol. 42, no. 18. pp. 3509-3515, Jun. 2003.

[10] S. S. Mishra, V. K. Singh, "Study of non-linear properties of hollow core photonic crystal fiber," *Optik*, vol. 122, no. 8, pp. 687-690, Apr. 2011.

[11] N. A. Mortensen and J. R. Folkenberg, "Low-loss criterion and effective area considerations for photonic crystal fibers," *Journal of Optics A: Pure And Applied Optics*, vol. 5, no. 3, pp. 163–16, Mar. 2003.

[12] L. Fan, L. Xu, H. Cai, X. Sun, F. Zhao, Z. Li, and Z. Qi, "Study on dispersion of photonic crystal fiber". In *Proc. IEEE Int. Conf. on Manipulation, Manufacturing and Measurement on the Nanoscale*, Oct. 2015 , pp. 210-213.

[13] S. Chowdhury and J. Mondal, "Ultra-high birefringent and high non-linear PCF for S+C+L+U wavebands," in *Proc. Int. Conf. on Electrical, Computer and Communication Engineering*, Feb. 2017, pp. 60-62.

[14] M. M. Rashid, M. S. Anower, M. R. Hasan and N. Tabassum, "Hexagonal shaped core dodecagonal PCF with high birefringence and nonlinear coefficient," in *Proc. Int. Conf. on Electrical, Computer and Communication Engineering*, Feb. 2017, pp. 447-450.

[15] J. Mondal and M. S. Rahman, "Design of highly birefringent dispersion compensating spiral photonic crystal fiber," in *Proc. Int. Conf. on Electrical Engineering and Information Communication Technology*, May. 2015, pp. 1-4.

[16] M. S. Ali, K. M. Nasim, R. Ahmad, M. A. G. Khan and M. S. Habib, "A defected core highly birefringent dispersion compensating photonic crystal fiber," in *Proc. 2nd Int. Conf. on Advances in Electrical* Engineering, Feb. 2013, pp. 100-105.

# A Compact Modified Antipodal Vivaldi Antenna for Imaging Application

M.A.A. Syeed[1,a], M . Samsuzzaman[1,b], M. Z. Mahmud[2,c] and M. T. Islam[2,d]
[1] Patuakhali Science and Technology University, Patuakhali, Bangladesh
[2]Universiti Kebangsaan Malaysia, Malaysia
[a]shovon11@cse.pstu.ac.bd, [b]sobuz@pstu.ac.bd, [c]zulfikerm@siswa.ukm.edu.my, [d]tariqul@ukm.edu.my

*Abstract*—**In this paper, a modified compact and directive antipodal Vivaldi antenna is presented for the microwave imaging purposes. The modification is done on the radiating fins of the antipodal Vivaldi antenna by etching three slots on both planes. The increase of gain and efficiency with stronger radiation pattern are achieved by this modification. Simulation for this modified antenna is done on both simulation software named HFSS and CST. The overall electrical dimension of this antenna is 0.401λ×0.401λ×0.016λ at the lowest frequency 3.01 GHz. Simulated results show that this modified antenna operates at the frequency of 3.01 to 6.80 GHz which is suitable for microwave imaging techniques. Because of the antenna radiating fins, it shows the average efficiency of 94% with a peak gain of 5.90 dBi. Characteristics of this modified proposed antipodal Vivaldi antenna fulfill the requirements needed for microwave imaging techniques.**

***Keywords—Antipodal Vivaldi antenna; microwave imaging; modified plane.***

## I. INTRODUCTION

Nowadays for biomedical application one of the most promised methods for scanning the human body in search of malignant tissues is the microwave imaging technique. In recent years a huge interest is increasing the design of microwave imaging system. The advantages of microwave imaging system are low complexity, low cost, and high data rate. During these recent years' remarkable developments is going on the microwave imaging technology. A challenge is still there for developing this kind of imaging technology. For microwave imaging purposes different types of antennas are widely used. For the purpose of accurate microwave imaging system with dynamic range and high resolution, the antenna used for transmitting and receiving should be compact, directive planar with the efficiency of high radiation. In this case, a valuable tool used for microwave imaging system is the antipodal Vivaldi antenna because of its high directive patterns, low cost, compact size and end-fire radiation.

Recently microwave imaging is being used for breast cancer detection which has become a major issue for unwanted death all over the world for women. Presence of malignant call is the main due which remains inside the breast tissue[1]. Early detection and treatment of breast cancer can enrich the survival rate up to 97% for which a highly reliable requirement is needed having efficient methods for early detection of breast cancer [2]. For that microwave, imaging is the complementary tool to x-ray mammography which is being used currently for breast cancer detection [3]. Detecting malignant cells in the human body, microwave imaging is the most promising method [2]. Low spectral power density, high data rate, low cost, low complexity are the advantages of microwave imaging system. For impinging microwave signals on the human body antenna is being used as a transceiver in an imaging system [4]. On the various electrical properties of human body tissues, the principle of microwave imaging is based on the dielectric constant property. The unwanted tumor cells of the human body can be identified from the reflected scattered signal from antenna[5] which shows higher dielectric constant than normal breast tissue [6]. Recently different techniques have been proposed by several researchers to enhance the radiation properties at higher frequencies [4]. The several techniques which are being used like the use of lenses [7], zero index material[8] , high permittivity material [9] to guide the energy in the aperture flare in the end-fire direction. There are several types of antennas for microwave imaging, among them, the advantageous antenna is tapered slot Vivaldi [10] because of its end-fire radiation, low cost, ease of feeding technique, directional radiation pattern [1, 11]. The Vivaldi antenna challenging issues is the directivity, radiation pattern stability over frequency. At low frequencies, the antenna operates like a resonant antenna and at high frequencies. On each arm, the traveling wave current phases should be 180$^o$ apart from each other for having maximum radiation which is the direction of end-fire [12]. The radiation performance and the bandwidth are affected by some different factors when the frequency increases. A very compact antipodal Vivaldi antenna is presented in [13] which has the wide operating bandwidth and good fractional bandwidth but the efficiency and gain are respectively 70% and less than 5 dBi. In [12] a method is used for improving the performance of an antipodal Vivaldi antenna by adding a parasitic ellipse but the antenna overall size is (140mm×60mm) which is large and also lower frequencies can't be obtained. Also with planar directors, an antipodal Vivaldi antenna is presented in [14] which size (110mm×260mm) is also too large and voltage standing wave ratio is also non-contiguous. Another tapered slot Vivaldi antenna is presented in [15] which has an overall size is (75mm×75mm). It has directional radiation pattern but at higher frequency resonance is not obtained.

In this paper, a 40mm×40mm×1.6mm modified antipodal Vivaldi antenna is presented operating at the bandwidth of 3.01 to 6.80 GHz. FR4 substrate is used in both HFSS and CST simulation software. Both patch and ground of this antipodal antenna are etched by six side slots which make this antenna directive and suitable for microwave imaging application.

978-1-5386-2307-7/17/$31.00 ©2017 IEEE

## II. ANTENNA DESIGN STRUCTURE

The proposed modified antipodal Vivaldi antenna structure and configuration is represented in Fig. 1. Step by step the total design is presented in this figure with annotation of different position size of this proposed antenna. The proposed antipodal Vivaldi antenna consists of patch and ground facing 180° to each other. The substrate used for simulation is an FR4 substrate having a thickness of 1.6 mm with a relative permittivity of 4.6 and loss tangent 0.02. In the ground plane, there is also a rectangle shaped plane attached to the ground which length and width are sequentially denoted by $R_L$ and $R_W$. The proposed antenna has a dimension of 40 × 40 mm$^2$. The modified proposed antenna patch and ground is slotted three times in both denoted by $S_W$. By changing this fins width and used times, the results can be changed. The optimized proposed antenna dimension is given in this following Table I.

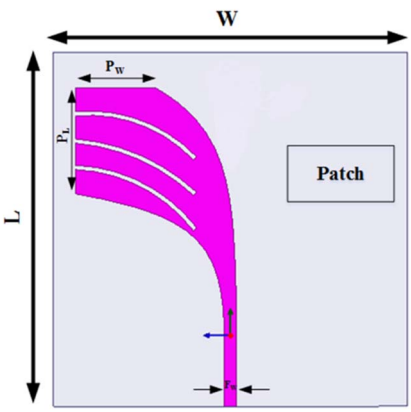


(a)

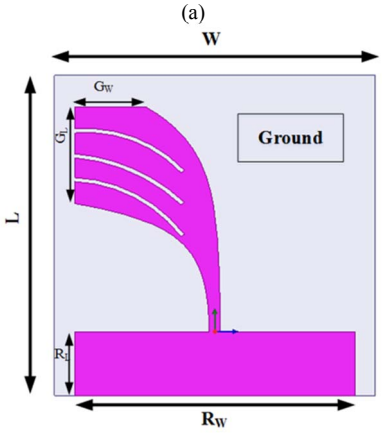


(b)

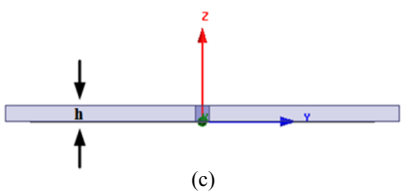


(c)

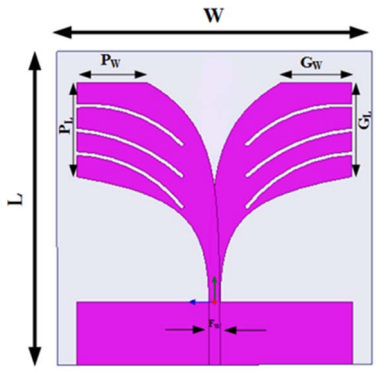


(d)

Figure 1. (a) Front view; (b) Back view; (c) Side view and (d) Total view

TABLE I: PROPOSED ANTENNA PARAMETERS

| Parameters | mm | Description |
|---|---|---|
| L | 40 | Length |
| W | 40 | Width |
| FW | 1.4 | Feed line width |
| PW | 9 | Patch width |
| PL | 12 | Patch length |
| GW | 9 | Ground width |
| GL | 12 | Ground length |
| SW | 0.5 | Slot width |
| RW | 35 | Rectangle width |
| RL | 8 | Rectangle length |
| h | 1.6 | Height |

## III. RESULT AND DISCUSSION

The proposed antenna performance is being optimized and analyzed using both HFSS and CST simulation software. HFSS is based on finite element method (FEM) and CST is based on finite integration technique (FIT). Because of their different calculation techniques, the proposed antenna results show some distortions. All the results are being plotted by using the scientific data analysis and graphing software Origin pro. Fig 2. Represents different modifications on patch and ground of the basic antipodal Vivaldi antenna. First of all three slots are etched from the patch and then three times same size slots are also etched from the ground. Afterwards, the antenna results are being studied. At the last both patch and ground both are etched and the obtained results are the fulfillment of the characteristics of the microwave imaging technique.

TABLE II. COMPARISON OF RESULTS ON DIFFERENT MODIFICATIONS

| Different structure | Operating bandwidth (GHz) | Peak Gain (dBi) |
|---|---|---|
| Normal | 3.01-5.31 | 2.15 |
| Patch cropped | 2.90-5.12 | 3.20 |
| Ground cropped | 3.01-5.36 | 3.36 |
| Proposed | 3.01-6.80 | 5.90 |

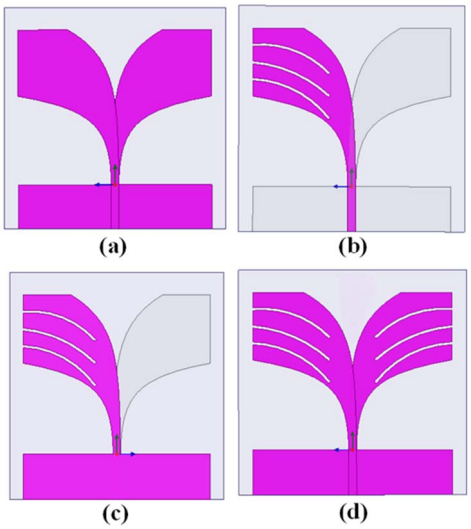


Figure 2. Different modifications on patch and ground (a) Basic (b) Patch cropped (c) Ground cropped (d) Proposed.

Because of different modifications on the antenna, it shows different reflection coefficients. Parametric study on different reflection coefficient is done and is represented in Fig 3. From the figure, it can be observed that the proposed antenna reflection coefficient is better than the other modifications. In Fig 4. Different antenna gain is represented by different modifications. From this figure, it can be easily observed that the proposed antenna has the highest gain than any other modifications. Different modifications show different results in both reflection coefficient and gain. The parametric study on this modifications shows that the proposed antenna operates at the required bandwidth with high gain than any other modifications. The results are represented in this following Table I. From this parametric study on the differently shaped antenna, it is observed that the proposed antenna shows the best result fulfilling the microwave imaging characteristics.

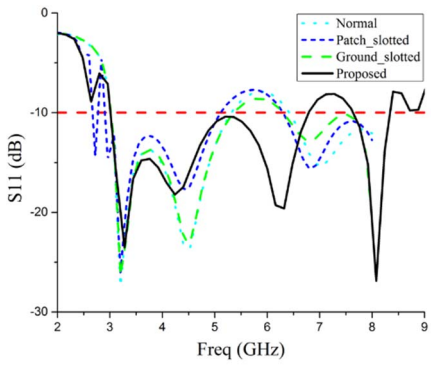


Figure 3. Different reflection coefficient results

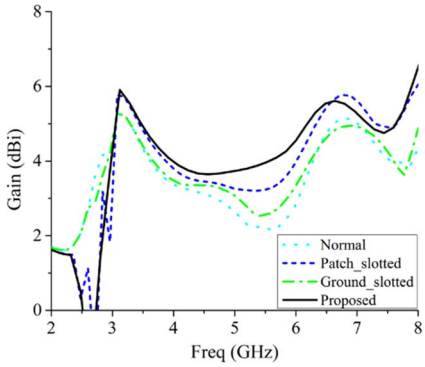


Figure 4. Different gain results

The modified antipodal Vivaldi antenna has three slots in both patch and ground. This modification makes the antenna radiation pattern stable and directional. Fig 5 represents the reflection coefficient ($S_{11}$) which is obtained from both HFSS and CST simulation software. Because of their different calculation technologies, their results show some difference. But in both, the result shows return loss from 3.01 GHz to 6.80 GHz. In CST there is a little bit distortion. The operating bandwidth between 3 to 6 GHz is suitable for microwave imaging for detection of breast cancer.

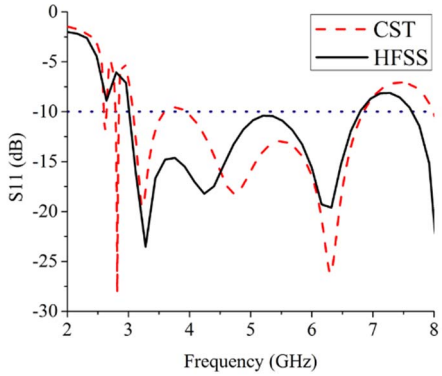


Figure 5. Reflection coefficient in HFSS and CST.

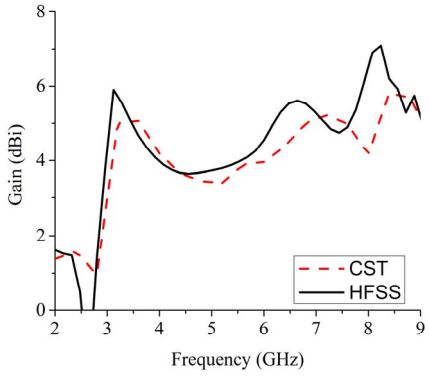


Figure 6. Simulated gain in HFSS and CST Software

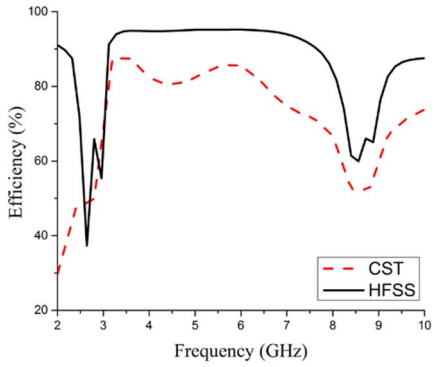


Figure 7. Simulated efficiency in HFSS and CST software

The proposed antenna has the highest gain of 5.90 dBi with an average gain of 3.66 dBi which is between 3 to 6 GHz frequency bandwidth. This gain of the proposed modified antipodal Vivaldi antenna is suitable for microwave imaging application. The gain result of both HFSS and CST simulator is represented in Fig 6. The Fig. 7 shows the efficiency result of the proposed antenna simulated in both HFSS and CST simulator software. In HFSS it represents the efficiency of average 94% and maximum efficiency of 95%. In between the operating bandwidth, it is observed that the efficiency is stable in the operating frequency range. By observing the current distribution of the proposed antenna, the electromagnetic behavior can be easily understood. The current distribution of the antipodal fin-shaped patch is shown in Fig 8. Fig (a) represents current distribution at 3.28 GHz. Fig (b) shows the current distribution at 4.24 GHz. At the last resonance frequency of 6.16 GHz, the current distribution is shown in figure (c). From the current distribution it can be observed that current supply through the feed line is being distributed over the antipodal fins and at higher current supply through the circle shaped edge is increasing and so the proposed antenna fulfills the required characteristics. At these frequencies, the patch and ground plane is observed. Fig 9 represents the two major planes simulated radiation pattern specifically the –XZ and –YZ plane for resonant frequencies of 3.29, 4.24 and 6.16 GHz. The red and black color is denoted the co-pol and cross-pol, respectively. Actually, cross pol radiation is comparatively low as co-pol radiation. From the radiation pattern for the low frequency of 3.28 GHz, it can be observed that the radiation pattern is directional. At the medium frequency of 4.24 GHz, the radiation pattern still shows directional radiation. At last at a higher frequency of 6.16 GHz, the radiation pattern shows directionality but some side lobes are created. This proposed antenna shows directionality to the 90° axis of this antenna.

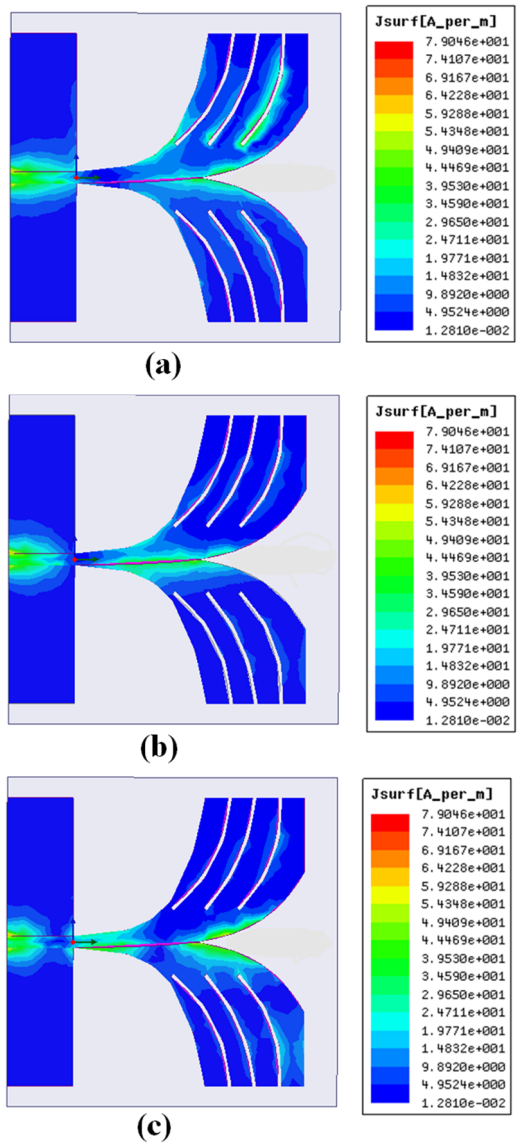


Figure 8. Simulated Surface Current Distribution Results at (a) 3.28 GHz, (b) 4.24 GHz, and (c) 6.16 GHz

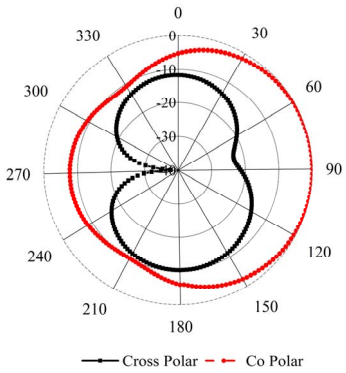


(a)

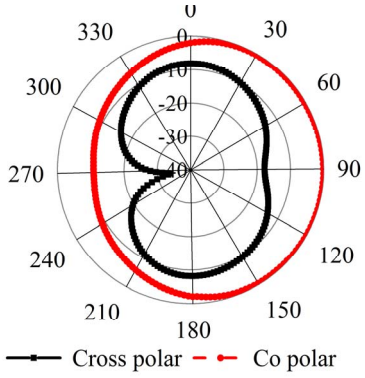


(b)

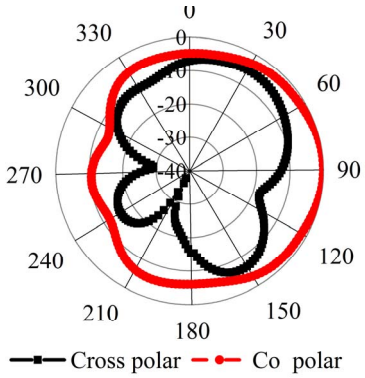


(c)

Figure 9. Simulated radiation patterns at different frequencies. (a) 3.28 GHz (b) 4.24 GHz (c) 6.16 GHz.

The comparison between the proposed modified antipodal Vivaldi antennas with the previous antennas from the literature is presented in Table III. It upholds the proposed antipodal Vivaldi antenna acceptance as a microwave imaging application with directional properties. The reference [13] shows compact size but the gain is low, reference [12] shows a good gain but the size is not compact overall the gain increases in higher frequency which are not needed in breast cancer microwave imaging. All these comparisons make the proposed modified antipodal Vivaldi antenna suitable for microwave imaging application.

TABLE III. COMPARISON BETWEEN DIFFERENT ANTENNAS WITH THE PROPOSED MODIFIED ANTENNA

| Ref. No. | Dimension $mm^2$ | Operating Bandwidth (GHz) | Average Gain (dBi) |
|---|---|---|---|
| [13] | 40×50 | 2-12 | 5.2 |
| [12] | 140×66 | 2-32 | 10 |
| [15] | 75×75 | 0.5-4.5 | 7 |
| Proposed | 40×40 | 3.01-6.80 | 5.90 |

## IV. CONCLUSION

In this paper, a modified, comprehensive and compact antipodal Vivaldi antenna is proposed for microwave imaging application which overall size is 40 mm×40 mm×1.6 mm. Simulation results of this proposed antenna show operating bandwidth of 3.01 to 6.80 GHz with return loss < 10dB and a peak gain of 5.90 dBi. It also shows the average efficiency of 94%. Because of the modification on the patch and ground plane, this proposed antenna shows a stable directional radiation pattern which is the main requirement for directional for directional microwave imaging. The observed performance of this proposed modified antipodal Vivaldi antenna is suitable for microwave imaging system application for detecting unwanted malignant tissues in human body.

## REFERENCES


[1] M. Z. Mahmud, M. T. Islam, M. N. Rahman, T. Alam, and M. Samsuzzaman, "A miniaturized directional antenna for microwave breast imaging applications," *International Journal of Microwave and Wireless Technologies,* pp. 1-6, 2017.

[2] H. Zhang, "Microwave imaging for ultra-wideband antenna based cancer detection," 2015.

[3] H. Bahrami, E. Porter, A. Santorelli, B. Gosselin, M. Popovic, and L. Rusch, "Flexible sixteen monopole antenna array for microwave breast cancer detection," in *Engineering in Medicine and Biology Society (EMBC), 2014 36th Annual International Conference of the IEEE*, 2014, pp. 3775-3778.

[4] M. Mahmud, M. T. Islam, M. Samsuzzaman, S. Kibria, and N. Misran, "Design and parametric investigation of directional antenna for microwave imaging application," *IET Microwaves, Antennas & Propagation,* vol. 11, pp. 770-778, 2016.

[5] M. Rokunuzzaman, M. Samsuzzaman, and M. T. Islam, "Unidirectional Wideband 3-D Antenna for Human Head-Imaging Application," *IEEE Antennas and Wireless Propagation Letters,* vol. PP, pp. 1-1, 2016.

[6] M. Abbak, M. Çayören, and I. Akduman, "Microwave breast phantom measurements with a cavity-backed Vivaldi antenna," *IET Microwaves, Antennas & Propagation,* vol. 8, pp. 1127-1133, 2014.

[7] G. Teni, N. Zhang, J. Qiu, and P. Zhang, "Research on a novel miniaturized antipodal Vivaldi antenna with improved radiation," *IEEE Antennas and Wireless Propagation Letters,* vol. 12, pp. 417-420, 2013.

[8] M. M. Islam, M. T. Islam, M. Samsuzzaman, M. R. I. Faruque, N. Misran, and M. F. Mansor, "A miniaturized antenna with negative index metamaterial based on modified SRR and CLS unit cell for UWB microwave imaging applications," *Materials,* vol. 8, pp. 392-407, 2015.

[9] M. T. Islam and M. S. Alam, "Compact EBG structure for alleviating mutual coupling between patch antenna array elements," *Progress In Electromagnetics Research,* vol. 137, pp. 425-438, 2013.

[10] P. Gibson, "The vivaldi aerial," in *Microwave Conference, 1979. 9th European*, 1979, pp. 101-105.

[11] M. A. Alzabidi, M. A. Aldhaeebi, and I. Elshafiey, "Development of UWB Vivaldi antenna for microwave imaging," in *Electronics, Communications and Photonics Conference (SIECPC), 2013 Saudi International*, 2013, pp. 1-4.

[12] I. T. Nassar and T. M. Weller, "A novel method for improving antipodal Vivaldi antenna performance," *IEEE Transactions on Antennas and Propagation,* vol. 63, pp. 3321-3324, 2015.

[13] G. Pandey, H. Verma, and M. Meshram, "Compact antipodal Vivaldi antenna for UWB applications," *Electronics Letters,* vol. 51, pp. 308-310, 2015.

[14] S. H. He, W. Shan, C. Fan, Z. C. Mo, F. H. Yang, and J. H. Chen, "An improved Vivaldi antenna for vehicular wireless communication systems," *IEEE Antennas and Wireless Propagation Letters,* vol. 13, pp. 1505-1508, 2014.

[15] B. Wu, Y. Ji, and G. Fang, "Design and measurement of compact tapered slot antenna for UWB microwave imaging radar," in *Electronic Measurement & Instruments, 2009. ICEMI'09. 9th International Conference on*, 2009, pp. 2-226-2-229.

2017 3rd International Conference on Electrical Information and Communication Technology (EICT), 7-9 December 2017, Khulna, Bangladesh

# Performance Appraisal of Wireless Energy Harvesting in IoT

Shishir Mallick[1], Al-Zadid Sultan Bin Habib[2], Abu Shakil Ahmed[3], Sk. Shariful Alam[4]
Khulna University of Engineering & Technology, Khulna-9203, Bangladesh
shishir9250@gmail.com[1], al.zadid.habib@gmail.com[2], shakil.ahmed.bd71@gmail.com[3], ssa1996@gmail.com[4]

*Abstract*—**Energy efficiency is a vital issue for the Internet of Things (IoT) to carry out its complex network activities. The energy-aware IoT devices can appease part of their energy demand by Wireless Energy Harvesting (WEH). In this paper, we have presented the lifetime curves of the sensor nodes in an IoT environment along with its dependency on EH Fraction value. Moreover, we have assessed the throughput gain and battery life for three different conditions and presented a comparison among them to determine the optimum one. Result verifies the proper implementation and operation of WEH method which is capable of improving energy efficiency, sensor lifetime, and application throughput of the designed IoT topology.**

***Keywords—WEH, IoT, IEEE 802.15.4, ZigBee, Performance metrics, Sensor lifetime, Application throughput.***

## I. INTRODUCTION

In recent years, the application area of Internet of Things (IoT) has been rapidly expanded as it offers potential internet connectivity for everything. The incorporation of Radio Frequency Identification (RFID) technique, cellular devices, and wireless sensors are propelling its advancement further. Each IoT device is connected to the internet without any human interaction, and they can exchange data via the internetworking feature offered by IoT. Moreover, IoT enables communication over a wide range using different protocols, domains, and applications. Automation in various sectors and some trending concepts like the smart city and the smart grid can be realized by IoT using the interconnectivity among the devices and internet access. The introduction of IPv6 has brought a revolution for the web framework worldwide as the number of IP address is practically far beyond the current necessity. Therefore, every smart device can be provided with an IP address those are accessible at any time from anywhere. Usually, an IP address is assigned to an intelligent device that can transmit and receive data over the Internet. Hence the concept of IoT can be implemented in different sectors such as healthcare, education, and transport while the domain of its application is widening fast [1].

The energy consumption of IoT infrastructures is enormous to provide the exciting features. Therefore, energy efficiency and longevity of battery are considered as two vital parameters for proper functionality and Quality of Service (QoS) in IoT. Energy harvesting method can enhance the energy efficiency of IoT devices as it offers a practical procedure to collect energy from the ambient environment of the device. Different kinds of energy harvesting mechanism such as vibration, light, energy extraction, and wireless energy harvesting (WEH) are available to serve this purpose. According to the literature, WEH is the most efficient and cost-effective energy harvesting method [1]. If any relevant energy source is present in the environment, wireless energy harvesting can be performed. For example, in wireless communication such as telecasting, broadcasting, and telecommunication, the transmission of radio frequency (RF) signal needs an enormous amount of energy that is available for harvesting. WEH enabled IoT device is not costly to manufacture as it consists of an antenna, a transceiver, a WEH unit, a power management unit (PMU), a sensor, and an onboard battery. The WEH unit is responsible for controlling energy harvesting, and PMU regulates the functionalities along with managing the energy consumption [2-3]. We have designed the topologies necessary to evaluate the performance of WEH using NetSim which is pretty cozy for both network simulation and emulation using various protocols [4].

We have organized the paper as follows. In Section II, we have elaborated the methodology of WEH and its mathematical formulation. In section III, the standard and the protocols used to conduct the research work have been stated. The IoT topology designed for the assessment of WEH has been presented along with its technical specification in Section IV. We have determined the performance metrics of WEH and addressed the network metrics to evaluate the statistical data and debug the source code in Section V. In Section VI, we have set up three conditions to determine the IoT metrics and presented a comparison among them to identify the excellent one. In conclusion, the entire work has been summarized in Section VII.

## II. WEH

Energy harvesting, alternatively known as power harvesting or energy scavenging, is a process of collecting energy from surroundings such as solar power, thermal energy, wind energy, kinetic energy, and particularly RF energy. The WEH unit receives the transmitted RF signal from an antenna and converts the energy into stable direct current sufficient to power up the sensors of an IoT device. Wireless energy sources can be classified into two broad categories according to the source, i.e., dedicated source and ambient source. A dedicated RF source like sink node is a predictable energy supply for the IoT device. The ambient sources can be further classified into two categories such as static and dynamic ambient source. The static or anticipated ambient sources are not optimized to

978-1-5386-2307-7/17/$31.00 ©2017 IEEE

supply the sensors since they produce stable power over time while the dynamic ambient sources periodically produce power. An intelligent WEH unit is set up for monitoring harvesting opportunities [10].

Both geometric requirements and sophisticated power converter are essential components for WEH method. The total harvested power ($P_r$) can be estimated from the Friis equation [9] presented in (1) and its value is proportional to the transmitter power ($P_t$), antenna gain of the transmitter ($G_t$), antenna gain of the receiver ($G_r$), power conversion efficiency of the converter (PCEH, depicted by $\dot{\eta}$), and the square of the wavelength ($\lambda$) as well as inversely proportional to the square of the communication distance (r) which is the distance between the source and the device. On the other hand, the communication energy has several components such as listening energy (ELs), transmitter energy (ETx), receiver energy (ERx), computation energy formed by the combination of processing energy (EPr) and sensing energy (ESn). The distributed energy is collected from the energy consumers where several weighting coefficients are assigned such as aLs, aTx, aRx, aPr, and aSn. The coefficients can be arranged in a decremental order of significance like this aLs, aTx, aRx, aPr, and aSn. The detected energy (ED) can be calculated using (3).

$$P_r = G_t G_r P_t \left(\frac{\lambda}{4\pi r}\right)^2 \quad (1)$$

The received RF power is converted to DC by the rectifier. All the losses associated with rectification and power conditioning can be modeled as a single multiplicative efficiency constant $\dot{\eta}$ whose value is between 0 to 1. Therefore, in case of power conversion efficiency of the converter (PCEH) is denoted by (2).

$$P_{DC} = \dot{\eta}\, P_r \quad (2)$$

$$ED = aLsELs + aTxETx + aRxERx + aPrEPr + aSnESn \quad (3)$$

The energy consumption for receiver, processor, and sensor has been assumed to be constant. Equation (3) states that aLs > aTx > aRx > aPr > aSn. The distributed energy is collected from energy consumers, and weighting coefficients are assigned in this form. However, for ring topology architecture, transmitter energy consumption (ETx) varies proportionally with $r_{ij}^2$ where $r_{ij}$ is the distance assumed between the source node j and the sink node i (ring topology) or the sensor device (multihop topology). The amount of energy available per active duty cycle for harvesting (EH) is inversely proportional to $r_{ij}^2$ where j is the sink node, and both $r_{ij}$ and $r_{ji}$ are equal [1] [5].

## III. Standard and Protocols

The IoT topology has been designed as per the IEEE 802.15.4 standard as it systematizes different issues related to network, data transfer, and security. In fact, it is a standard for wireless networking for the physical layer and access control layer as well as it focuses on the low-cost and low-power transmission of different devices which makes the framework easier to implement the concept of IoT. The IPv6 over Low-Power Wireless Personal Area Network (6LowPAN) gateway performs as a sink node for interconnection between the ZigBee and the Wide Area Network (WAN) interfaces as well as it offers short-range operation, low-cost and reliable data transfer along with extended battery life [7].

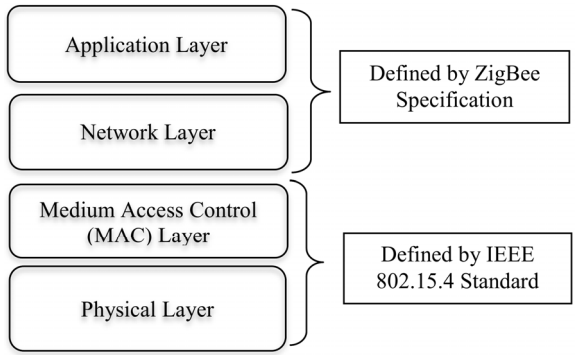


Figure 1. Architecture of IEEE 802.15.4 standard and ZigBee protocol.

Fig. 1 shows the architecture of IEEE 802.15.4 standard and ZigBee protocol [8]. It contains four layers such as physical layer, Medium Access Control (MAC) layer, network layer, and application layer. Physical layer and MAC layer are defined by IEEE 802.15.4 standard as well as network layer and application layer are defined by Zigbee specification. The IEEE 802.15.4 standardizes Low-Rate Wireless Personal Area Network (LR-WPAN) which has application in home automation, healthcare monitoring, military operation, smart city, and smart grid. MAC layer is significant particularly for wireless communication systems where the higher data rate is not an obligation. Moreover, it regulates the access to the wireless physical medium, ensures frame validation, manages node association, and addresses security issues of the wireless network. The standard authorizes Low Rate Personal Area Network (LR-PAN) to control the centralized and decentralized networks so that the wireless devices can communicate with one another within the range of RF transmission [8].

## IV. IoT Topology

We have designed an IoT topology shown in Fig. 2 in NetSim to assess the performance of WEH where ZigBee interface has been used for wireless connectivity, and a WAN interface with 6LowPAN gateway has been incorporated for a wired connection. In total three routers and a wired node (PC) have been connected to the WAN via cable. We have placed 16 sensors keeping the distance uniform between two consecutive sensors to simulate WEH. The wireless network consists of 16 uniformly set ZigBee devices whose properties can be configured and mobility model can be selected manually. The scenario we have created in the IoT topology uses User Datagram Protocol (UDP) for the transport layer and Ad Hoc On-Demand Distance Vector (AODV) routing protocol for the network layer. EH has been set on, and the battery has been incorporated to deliver power to the devices. Offset quadrature phase-shift keying (OQPSK) modulation technique has been applied for data transmission in the wireless network. The devices have been configured with unique IP addresses as per IPv6 and protocol of IEEE 802.15.4 standard has been implemented.

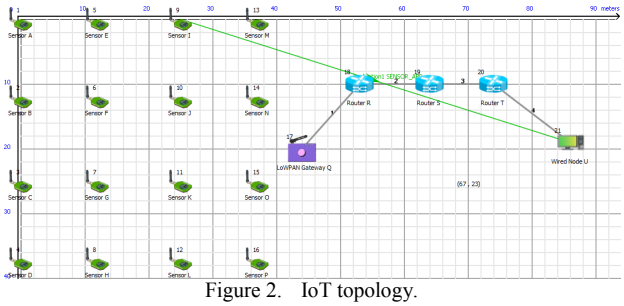


Figure 2. IoT topology.

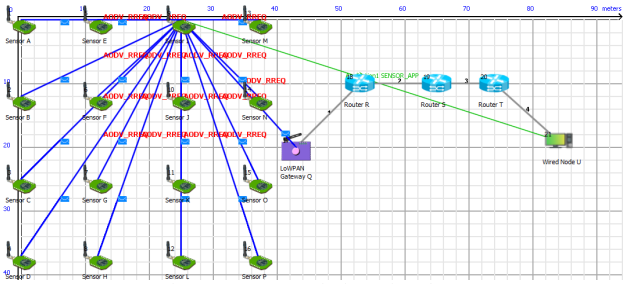


Figure 3. Transmission of packets.

The wired network uses a 6LowPAN gateway as the sink node and incorporates WAN to provide the routers and the destination node with wired connections. The routers and the gateway have been configured with Open Shortest Path First (OSPF) routing protocol at the application layer. Both Transmission Control Protocol (TCP) and UDP have been used at the transport layer for data transmission. Moreover, Virtual Private Network (VPN) and firewall have been activated as security measures. UDP and AODV have been applied to the application layer and network layer respectively. Unlike the wireless network, the devices of the wired network have been configured with IP as per IPv4 [6]. The transmission of packets after performing the simulation has been shown graphically in Fig. 3.

## V. Performance Metrics

In this section, the performance metrics of WEH has been determined, and the network metrics have been addressed those are applied to evaluate the statistical data and debug the source code. The values of different network metrics such as simulation time, number of the transmitted packets, number of error packets, number of collided packets, transmitted bytes, transmitted payload, and transmitted overheads have been presented in TABLE I after performing the simulation.

TABLE I. Network Metrics Analysis

| Metric | Value |
|---|---|
| Simulation Time (ms) | 10000.00 |
| Packets Transmitted | 1692 |
| Packets Errored | 1 |
| Packets Collided | 488 |
| Bytes Transmitted (Bytes) | 110702.00 |
| Payload Transmitted (Bytes) | 5846.00 |
| Overhead Transmitted (Bytes) | 104856.00 |

TABLE II. Queue Metrics Analysis

| Device ID | Port ID | Queued Packet | Dequeued Packet | Dropped Packet |
|---|---|---|---|---|
| 18 | 1 | 12 | 12 | 0 |
| 18 | 2 | 21 | 21 | 0 |
| 19 | 1 | 13 | 13 | 0 |
| 19 | 2 | 20 | 20 | 0 |
| 20 | 1 | 12 | 12 | 0 |
| 20 | 2 | 11 | 11 | 0 |

## VI. Comparative Analysis

For the measurement of the sensor lifetime, we have kept the EH at on state and assumed an arbitrary value for EH fraction. The EH fraction determines the quantity of harvested energy from the signal energy received by the sensors. Therefore, it controls sensor lifetime and EH in practice.

TABLE III. IoT Metrics when EH is on and EH Fraction is 0.5

| Node Name | Status | Time |
|---|---|---|
| SENSOR A | OFF | 211001312.000000 |
| SENSOR B | OFF | 271001312.000000 |
| SENSOR C | OFF | 271001312.000000 |
| SENSOR D | OFF | 271001312.000000 |
| SENSOR E | OFF | 271001312.000000 |
| SENSOR F | OFF | 271001312.000000 |
| SENSOR G | OFF | 271001313.000000 |
| SENSOR H | OFF | 271001313.000000 |
| SENSOR I | OFF | 271001312.000000 |
| SENSOR J | OFF | 271001313.000000 |
| SENSOR K | OFF | 271001313.000000 |
| SENSOR L | OFF | 271001312.000000 |
| SENSOR M | OFF | 271001312.000000 |
| SENSOR N | OFF | 271001312.000000 |
| SENSOR O | OFF | 271001312.000000 |
| SENSOR P | OFF | 271001312.000000 |

The IoT topology has been simulated for 300 seconds after proper configuration. We have set up three conditions to determine the IoT metrics and presented a comparison among them. The conditions are EH is on and EH fraction is 0.5, EH is on and EH fraction is 0.1, and EH is off. The IoT metrics obtained for the first condition has been presented in TABLE III. The lifetime of a single sensor node has been determined to be approximately 270 seconds. The value of EH fraction has been set to 0.1 for the second condition, and the IoT metrics obtained for the condition have been presented in TABLE IV keeping the runtime of the simulation unchanged.

TABLE IV. IoT METRICS WHEN EH IS ON AND EH FRACTION IS 0.1

| Node Name | Status | Time |
|---|---|---|
| SENSOR A | OFF | 94001312.000000 |
| SENSOR B | OFF | 94001312.000000 |
| SENSOR C | OFF | 97001312.000000 |
| SENSOR D | OFF | 97001312.000000 |
| SENSOR E | OFF | 97001312.000000 |
| SENSOR F | OFF | 97001312.000000 |
| SENSOR G | OFF | 97001312.000000 |
| SENSOR H | OFF | 97001312.000000 |
| SENSOR I | OFF | 97001312.000000 |
| SENSOR J | OFF | 97001312.000000 |
| SENSOR K | OFF | 97001313.000000 |
| SENSOR L | OFF | 97001312.000000 |
| SENSOR M | OFF | 97001312.000000 |
| SENSOR N | OFF | 97001312.000000 |
| SENSOR O | OFF | 97001312.000000 |
| SENSOR P | OFF | 97001312.000000 |

TABLE V. IoT METRICS WHEN EH IS OFF

| Node Name | Status | Time |
|---|---|---|
| SENSOR A | OFF | 82003169.000000 |
| SENSOR B | OFF | 83001312.000000 |
| SENSOR C | OFF | 83001312.000000 |
| SENSOR D | OFF | 83001312.000000 |
| SENSOR E | OFF | 83001312.000000 |
| SENSOR F | OFF | 83001312.000000 |
| SENSOR G | OFF | 83001312.000000 |
| SENSOR H | OFF | 83001312.000000 |
| SENSOR I | OFF | 83001313.000000 |
| SENSOR J | OFF | 83001312.000000 |
| SENSOR K | OFF | 83001312.000000 |
| SENSOR L | OFF | 83001312.000000 |
| SENSOR M | OFF | 83001312.000000 |
| SENSOR N | OFF | 83001312.000000 |
| SENSOR O | OFF | 83001312.000000 |
| SENSOR P | OFF | 83001312.000000 |

The energy harvesting method has not been utilized according to the third condition, and the IoT metrics obtained for the condition have been presented in TABLE V after performing the simulation for the same runtime as the previous conditions. From TABLE III, IV, and V, it is evident that EH affects the sensor lifetime and the sensor lifetime decreases with the reduction of the value of EH fraction as the lower value of EH fraction indicates the quantity of harvested energy from the signal energy received by the sensors is lesser. The values of sensor lifetime for each sensor node obtained by applying the three different conditions have been plotted in Fig. 4.

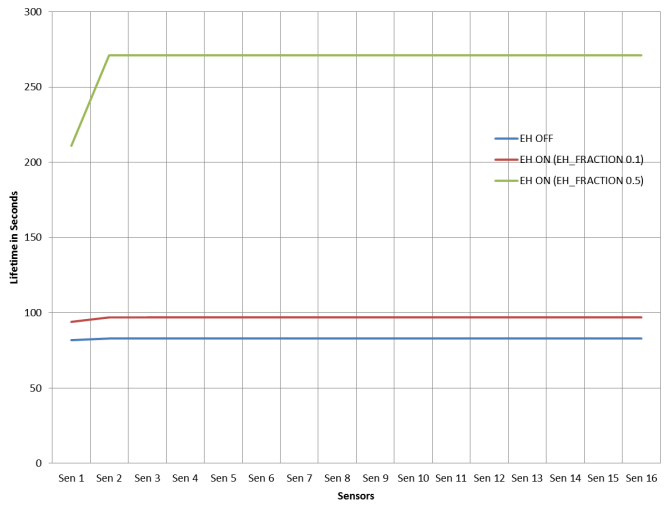


Figure 4. Lifetime of different sensor nodes.

We have plotted the sensor lifetime once again as shown in Fig. 5 by varying the value of EH fraction from 0 up to 1 considering a single sensor node for simplification while keeping the EH ON. The sensor lifetime is related to EH and EH fraction value, and initially, its value increases with the increase in the value of EH fraction exponentially. After a period when the value of EH fraction tends to 1, the lifetime increases linearly with EH fraction. Therefore, for a higher value of EH fraction value, a sensor obtains higher lifetime. Moreover, EH fraction value controls the quantity of harvested energy as collected energy increases with the increase in EH fraction. From Table III and IV, we can observe that sensor A has lower lifetime and it has been placed to the furthermost distance from the sink node which is shown in Fig. 2. Fig. 4 also represents the same statement. Hence it verifies (1) and shows that with the increase of distance, generated power decreases.

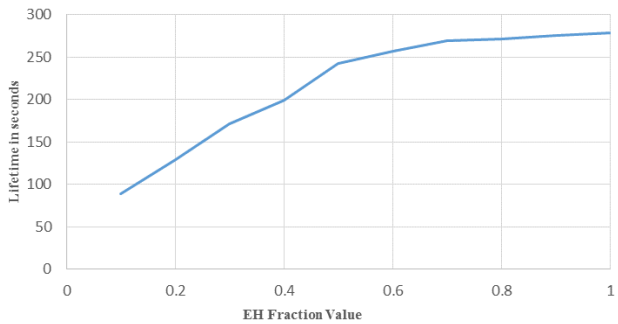


Figure 5. The lifetime of a single sensor node.

WEH can be considered scalable as its performance can be improved by increasing the value of EH fraction. The variation of application throughput with time for the IoT topology we have designed in section III has been shown in Fig. 6 with the maximum throughput of 0.000355 Mbps, the minimum throughput of 0.000000 Mbps, mean throughput of 0.000274 Mbps, and standard deviation (SD) of 0.000107.

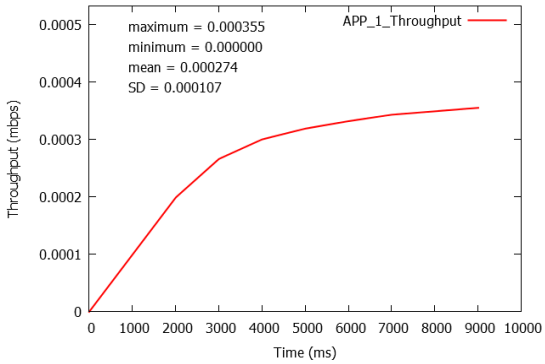


Figure 6. Application throughput of the designed IoT topology.

The variation of throughput for link 1 in the designed IoT topology when EH is set on and the value of EH fraction is 0.4 has been shown in Fig. 7 with the maximum throughput of 107.523740 Mbps, the minimum throughput of 0.000000 Mbps, the mean throughput of 72.207700 Mbps, and SD of 45.389800.

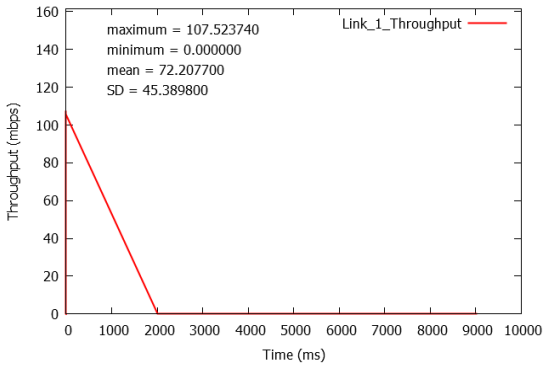


Figure 7. The throughput of link 1 when EH is on and EH fraction is 0.4.

The variation of throughput for link 2 in the designed IoT topology when EH is set on and the value of EH fraction is 0.5 has been shown in Fig. 8 with the maximum throughput of 108.616944 Mbps, the minimum throughput of 0.000000 Mbps, mean throughput of 74.854397 Mbps, and SD of 45.257586. The variation of throughput for link 3 in the designed IoT topology when EH is set on and the value of EH fraction is 0.6 has been shown in Fig. 9 with the maximum throughput of 107.612712 Mbps, the minimum throughput of 0.000000 Mbps, mean throughput of 71.866567 Mbps, and SD of 45.165006.

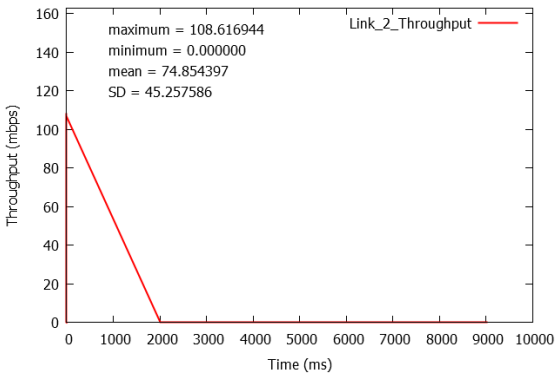


Figure 8. The throughput of link 2 when EH is on and EH fraction is 0.5.

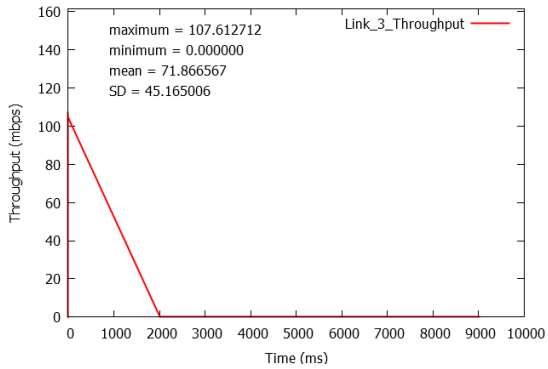


Figure 9. The throughput of link 3 when EH is on and EH fraction is 0.6.

The variation of throughput for link 4 in the designed IoT topology when EH is set off has been shown in Fig. 10 with the maximum throughput of 0.001123 Mbps, minimum throughput of 0.000000 Mbps, mean throughput of 0.000821 Mbps, and SD of 0.000298. Though a continuous throughput has been obtained, its value is negligible in comparison with others.

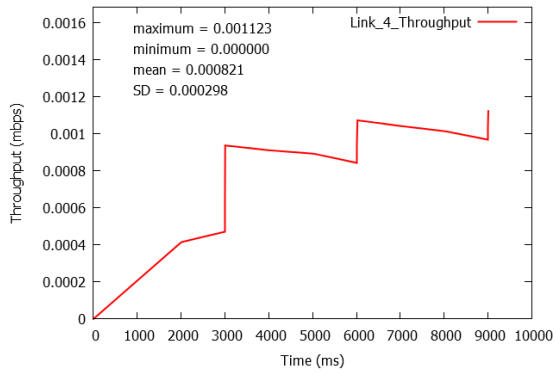


Figure 10. The throughput of link 4 when EH is off.

The variation of throughput for link 5 in the designed IoT topology when EH is set on and the value of EH fraction is 0.1 has been shown in Fig. 11 with the maximum throughput of 0.174260 Mbps, minimum throughput of 0.000000 Mbps, mean throughput of 0.105462 Mbps, and SD of 0.030576. The throughput gain is better than the throughput obtained for the off state of EH though it is significantly lesser than the throughputs obtained for other values of EH fraction. Therefore, it is evident that the throughput gain increases for the higher value of EH fraction.

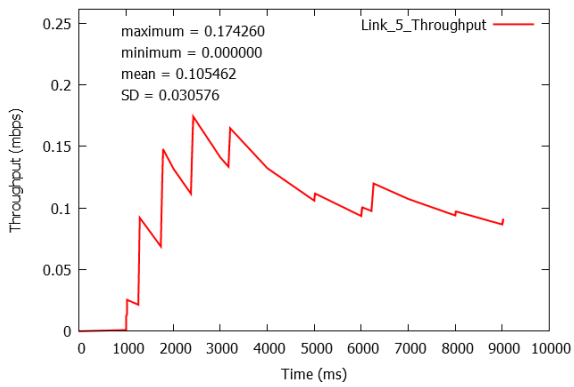


Figure 11. The throughput of link 5 when EH is on and EH fraction is 0.1.

Using comparison among the custom IoT metrics, it has been observed that the sensor nodes run out of energy at around 83 seconds without energy harvesting from RF signal. However, sensor nodes enabled with RF energy harvesting run out of energy at around 97 seconds if the value of EH fraction is set 0.1. The sensor lifetime has been increased up to 270 seconds by setting the value of EH fraction 0.5. Moreover, similar characteristics have been observed for a single node. Therefore, the simulation result verifies the proper implementation and operation of WEH method which is capable of improving energy efficiency, battery lifetime, and throughput gain of the designed IoT topology.

## VII. Conclusion

In this research work, we have designed an IoT topology for performance appraisal of wireless energy harvesting. The lifetime of different sensors has been evaluated for the topology, and its dependency on EH fraction value has been assessed. We have set up three distinct conditions to evaluate the sensor lifetime and determined the optimum one. Moreover, we have estimated the throughput gain and battery lifetime for various values of EH fraction. It has been observed that the sensor nodes run out of energy at around 83 seconds unless energy harvesting method is applied and the sensor lifetime can be extended up to 97 seconds if the value of EH fraction is set 0.1 as well as up to 270 seconds for EH fraction 0.5. Therefore, for a higher value of EH fraction value, a sensor obtains higher lifetime. The result indicates that we can extend sensor lifetime, improve application throughput, and make IoT more energy efficient by adjusting the EH fraction value as close as unity.

## References


[1] P. Kamalinejad, C. Mahapatra, Z. Sheng, S. Mirabbasi, V. M. Leung and Y. Guan, "Wireless energy harvesting for the Internet of Things", IEEE Communications Magazine, vol. 53, no. 6, pp. 102-108, 2015.

[2] Z. Sheng, S. Yang, Y. Yu, A. Vasilakos, J. Mccann and K. Leung, "A survey on the ietf protocol suite for the internet of things: standards, challenges, and opportunities", IEEE Wireless Communications, vol. 20, no. 6, pp. 91-98, 2013.

[3] Z. Sheng, C. Zhu and V. Leung, "Surfing the Internet-of-Things: Lightweight Access and Control ofWireless Sensor Networks Using Industrial Low Power Protocols", 2017.

[4] M. Lord and D. Memmi, "NetSim: a Simulation and Visualization Software for Information Network Modeling", 2008 International MCETECH Conference on e-Technologies (mcetech 2008), 2008.

[5] D. Niyato, D. Kim, P. Wang and L. Song, "A novel caching mechanism for Internet of Things (IoT) sensing service with energy harvesting", 2016 IEEE International Conference on Communications (ICC), 2016.

[6] P. Nayak and P. Sinha, "Analysis of Random Way Point and Random Walk Mobility Model for Reactive Routing Protocols for MANET Using NetSim Simulator", 2015 3rd International Conference on Artificial Intelligence, Modelling and Simulation (AIMS), 2015.

[7] K. Ting, G. Ee, C. Ng, N. Noordin and B. Ali, "The performance evaluation of IEEE 802.11 against IEEE 802.15.4 with low transmission power", The 17th Asia Pacific Conference on Communications, 2011.

[8] IEEE standard for Local and Metropolitan Area Networks, Part 15.4: Low-Rate Wireless Personal Area Network, IEEE Std. 802.15e, Apr. 2003.

[9] S. Belamgi, S. Ray and P. Das, "Suspended planar patch antenna for wireless energy transfer at 2.45GHz", International Conference on Electronics, Communication and Instrumentation (ICECI), 2014.

[10] C. Zhai, L. Zheng, P. Lan, H. Chen and Hongji Xu, "Decode-and-forward two-path successive relaying with wireless energy harvesting", 2017 IEEE International Conference on Communications Workshops (ICC Workshops), 2017.

# Performance Evaluation of Seven Machine Learning Classification Techniques for Movie Box Office Success Prediction

Nahid Quader[1], Md. Osman Gani[2] and Dipankar Chaki[3]
Department of Computer Science and Engineering
School of Engineering and Computer Science
BRAC University, Dhaka, Bangladesh
Email: [1]whereisnahidquader@gmail.com, [2]usmansujoy33@gmail.com, [3]joy.dcj@gmail.com

*Abstract*— **Movie industry is a multi-billion-dollar industry and now there is a huge amount of data available on the internet related to movie industry. Researchers have developed different machine learning methods which can make good classification models. In this paper, various machine learning classification methods are implemented on our own movie dataset for multi class classification. The main goal of this paper is to conduct performance comparison between various machine learning methods. We choose seven machine learning techniques for this comparison such as Support Vector Machine (SVM), Logistic Regression, Multilayer Perceptron Neural Network, Gaussian Naive Bayes, Random Forest, AdaBoost and Stochastic Gradient Descent (SGD). All of these methods predict an approximate net profit value of a movie by analyzing historical data from different sources like IMDb, Rotten Tomatoes, Box Office Mojo and Meta Critic. For all these seven methods, the system predicts a movie box office profit based on some pre-released features and post-released features. This paper analyzes the performance assessment of all these seven machine learning techniques based on our own dataset which contains 755 movies. Among these seven algorithms, Multilayer perceptron Neural Network gives better result.**

***Keywords— Movie industry, box office success, machine learning, classification techniques, performance evaluation.***

## I. INTRODUCTION

Movie industry is a very big industry. For big business sectors, it is hard to take a decision where to invest. Predicting a movie's box office success is a very complex task and for that, at first we need to clarify the definition of success. The definition of success for a movie is relative, some movies are called successful based on its worldwide gross income, where some may not shine in business part but can be called successful for good critics' review, good rating and popularity. In this paper, we consider a movie's box office success based on its profit only. Researches show that almost 25% of movie revenue comes within the first or second week of its release [1]. Predicting a movie's profit is hard before its release. In this research, two types of features called pre-released features and post-released features are considered. Pre-released features are responsible for upcoming movies' box office success prediction while both pre-released and post-released features will take place to predict further more after its release. Instead of binary classification like only flop or blockbuster movies [2], we rather choose to classify a movie based on its box office profit in one of five categories ranging from flop to blockbuster. In this research, we have calculated two types of prediction, one is exact match which refers correct classification and the other is, one away which means taking consideration of one class up or one class down from a particular class along with the exact match [3]. The reason behind considering one away is, sometimes percentage of accuracy becomes low because of the marginal value of target classes. For prediction, seven machine learning methods Support Vector Machine (SVM), Logistic Regression, Multilayer Perceptron Neural Network, Gaussian Naive Bayes, Random Forest, AdaBoost and SGD are implemented. These classifiers are good enough for binary classification and some of them can be used for multi class classification. In our dataset, most of the data point are overlapping for different classes. That is why, our dataset has a very complex pattern. However, when data pattern is very complex, Neural Network consistently produces better result. We have applied all these methods on our dataset for prediction. With all features in consideration, from 755 movies, neural network correctly classifies 442 movies. If we consider one away prediction the number of correctly classified movies becomes 677. One away prediction means difference between predicted class and target class is 1. Among all these methods MLP Neural Net (58.5%) and SVM (55.3%) work better than others.

In the next section, we mention about different research works related to movie box office success prediction. In section 3, we briefly explain our dataset. Seven machine learning classification techniques have been discussed in section 4. We discuss about experimental results in section 5. At the end of our paper, in section 6, conclusion along with future works are written. Finally, we conclude our paper by mentioning some references.

978-1-5386-2307-7/17/$31.00 ©2017 IEEE

## II. LITERATURE REVIEW

Previously many research works made prediction of a movie's box office gross based on data available at IMDb [4] - [6]. Few of them prioritized gross box office revenue [7] - [9]. Most of the cases, they used binary classification for prediction of a movie's success and classified as either flop or success. Success of a movie depends on many relevant issues like casting members, story of the movie, number of screens the movie will be shown etc. In some previous researches, prediction of a movie success was made based on available pre released data [3]. On the other side, few researches adopted different application of Nature Language Processing for sentiment analysis on reviews of audiences and movie's critics for forecasting the success of a movie [10], [11].

M. T. Lash and K. Zhao's [2] categorized their analysis into audience based, released based and movie based while developing their model using machine learning techniques. Their data source was Box Office Mojo and IMDb. They made the model by focusing on the movies released in USA and excluded all foreign movies. In [12], a neural network was implemented for movie box office gross prediction. They categorized the net profit in 9 classes and converted it into a classification problem. But a small number of features were considered in this research. On the other side Sivasantoshreddy et al. [13] focused on hype of twitter for the prediction [13]. Their hypothesis was the success of a movie mainly depended on its opening weekend income and hype it got from the audiences. Hype factor, number of screens where the movie was to be released and the price of tickets were taken in consideration in this research. In this work, they did not apply any application of NLP for analyzing the positivity and negativity of tweets. Furthermore, their model was based on very simple calculations.

M.H Latif and H. Afzal also used IMDb data in their model and they mentioned their data was not clean and inconsistent [14]. As a result, they applied central tendency to fill the missing data of different features. Jonas et al. [15] calculated intensity and positivity by analyzing sentiment of social network IMDb's sub forum Oscar Buzz. Their model failed to get a sentiment result when some words were used for negative meaning. In their work, they considered different awards for directors and casting of a movie but no category was taking in consideration. In the research [16], a model was made by analyzing news from different sources where data were generated by Lydia (high-speed text processing system for collecting and analyzing news data). They took high budget movies in consideration and applied regression and *k*-nearest neighbor. The significant problem was it could not identify the movie name from the news when common words were used as a movie name and it was unable to predict the success of a movie if there were no news about that movie.

In some early researches, neural networks were used for the prediction of a movie box office gross [3], [17]. While some other research models were based on social media, social networks and hype analysis [18] - [21]. In that cases, they figured out the sentiment of the audience reviews, the number of reviews and most of the cases their sources were IMDb sub forum Oscar Buzz, Twitter and YouTube. Audience reviews can be biased for a particular actor/actress and most of the previous works excluded movie critics' reviews. Furthermore, a large number of people did not consider the number of the screens in their analysis. For those reasons, the prediction accuracy will be doubtful and it is not possible to generate an appropriate result. For a movie, two types of data are available on the internet, one pre-released data including director, budget, cast members, the number of screens etc. The other one is post-released data which are available on IMDb, Box Office Mojo etc. In some cases, few researchers considered both types of data but very few of them were used in the prediction model.

## III. DATA DESCRIPTION

Our dataset contains 755 movies released in between 2012 to 2015. We exclude recent movies as movies' information are changing every day. Our data sources are IMDb, Rotten Tomatoes, Metacritic and Box Office Mojo. Initially our dataset contains 3183 movies. Most of the features are missing for most of the movies. In many cases, movies budgets are unavailable. After removing those movies, we have data for 800 movies. Among these, budget of some movies were available but other features were not found. After excluding those movies, finally we have a dataset containing all the information of 755 movies. Table I shows the description of all features in our dataset. We use both pre-released and post-released features in our model. Total 15 features are used in our proposed model. Among these 15 features MPAA, cast star power, director star power, no of screen, release month and budget are pre-released features, rest of the features are post released.

TABLE I. DATASET DISCRIPTION OF ALL FEATURES

| Features | Type | Description/Range of possible values |
|---|---|---|
| IMDb Rating | Float | 0 to 10 |
| Tomato Meter | Integer | 0 to 100 |
| Tomato Rating | Float | 0 to 10 |
| Audience Meter | Integer | 0 to 100 |
| Audience Rating | Float | 0 to 5 |
| Meta Score | Integer | 0 to 100 |
| MPAA | Integer | Value between 1 to 6 indicating G, PG, PG-13, R, NC-17, NR respectively. |
| Cast Star Power | Integer | Addition of all casts' lifetime gross income |
| User Review | Float | Sentiment value multiplied by no of reviews |
| Critics Review | Float | Sentiment value multiplied by no of reviews |
| IMDb Votes | Integer | Number of IMDb votes |
| Release Month | Integer | Between 1 to 12 |
| Budget | Integer | Budget of a movie |
| No of Screen | Integer | Number of screens a movie released |
| Director Star Power | Integer | Addition of directors' lifetime gross income |

We take in consideration of Motion Picture Association of America (MPAA) Rating, tomato critics' meter, tomato critics' rating, tomato audience score and tomato audience rating from Rotten Tomatoes, Meta score of Metacritic, IMDb rating from IMDb for a particular movie. We also count the number of viewers who rated the movies which is IMDB votes. Sentiment value of reviews and no of reviews are multiplied together and used as a single feature for both audience reviews from IMDb and Rotten Tomatoes along with critic reviews from Rotten Tomatoes. We calculate star power of actors, actresses and directors. Star power of a single artist is calculated by summing up the gross income of all movies done by that specific artist during his/her career. And Star power of a movie is the addition of those total gross value for all the casts involved in that movie. We also calculate directors' star power in the same manner.

In addition, we also consider the month of release, budget and the number of screens. This paper includes budget with inflation rate adjustment. Inflation rate is very important because value of money is changing over time, value of $100M five years ago is not same as now.

Instead of binary classification like "Flop" or "Blockbuster" movie, we rather choose to classify our target class into five classes. Table II describes our target class classification where lower class means lower profit, class 1 means flop movies and class 5 means blockbuster movies.

TABLE II. DATASET DISCRIPTION OF ALL FEATURES

| Target Class | Range (USD) |
|---|---|
| 1 | Profit <= 0.5M (Flop) |
| 2 | 0.5M < Profit <= 1M |
| 3 | 1M < Profit <= 40M |
| 4 | 40M < Profit <= 150M |
| 5 | Profit > 150M (Blockbuster) |

## IV. METHODS

We have used seven machine learning methods for performance assessment of our dataset. All these methods are briefly described in this section. We implement most of the algorithms using python library Scikit Learn [22].

### A. Logistic Regression

Logistic Regression is a kind of regression model where attributes are categorical and that is the reason to go for it. In our dataset we categorized most of the attributes [3]. Logistic regression is good for classification but for a small amount of data. In this case we have a very small dataset so we choose logistic regression as one of our methods for comparison. Furthermore, logistic regression works well with noisy data. Again it has low variance and so is less prone to over-fitting.

### B. Support Vector Machine

Support Vector Machine is a very popular machine learning algorithm for pattern recognition and classification. SVM is best for binary classification but it also can produce a good result for multiclass classification [2]. SVM works very efficiently when there is a higher number of dimensions. We decide to use SVM on our dataset because of its power of detecting different classes by making vectors using hyperplanes. We use different kernel functions like Gaussian radial basis function (RBF), linear kernel and polynomial kernel of SVM to have better accuracy.

### C. Random Forest

Random Forest is another famous machine learning algorithm; it is one kind of decision tree. Random forest is a very powerful predictive modelling method [2]. It can discover very complex dependences using more time in fitting but some time it is not very good at handling noisy data as well. Again it is able to make better accuracy when other may not make such result. The reason to add this algorithm is to see how it behaves on our dataset.

### D. Gaussian Naive Bayes

Gaussian Naive Bayes is a very simple algorithm for classification and one of the biggest advantages is training and prediction speed [2]. It is very fast and works better for small dataset. Moreover, it is very easy to train and understand the results. This algorithm assumes every feature is independent, however, each feature of our dataset is not independent. Hence, this algorithm doesn't perform well in our dataset.

### E. AdaBoost

Adaptive Boosting or AdaBoost is another popular machine learning method. AdaBoost is adaptive in a sense that it finds out some points on training data which are not well predicted. Those points have a significant error, by finding those points it can find out the weakest classifiers to make better classification. It is some time sensitive to label noise as it fits classification model to an exponential loss function. We choose this algorithm to see how it performs on our dataset.

### F. Stochastic Gradient Descent

Stochastic Gradient Descent is also a well-known machine learning algorithm. It is basically a first order iterative optimization algorithm but it can be used in classification problem and for minimizing error. The problem of Gradient Descent is when we have a big and complex dataset it takes too much time to predict but with SGD it takes smaller steps for training set and its faster and better. We include it to know is it possible to have a better performance.

### G. Multilayer Perceptron Neural Network

Multilayer Perceptron Neural Network is the most powerful machine learning method among all of these. MLP can handle very complex data pattern where other models are unable to detect any pattern and very good for a prediction model [12]. In this research, we use Scikit learn and Keras with tensorflow respectively to build and implement our MLP model [22], [23]. Our MLP model has three hidden layers with 15 features as input. For small datasets, the performance of multilayer perceptron neural network is not thriving.

## V. EXPERIMENTAL RESULT AND DISCUSSION

All these machine learning methods are good as classifiers. Some methods are good for small dataset like ours for example Naive Bayes or Logistic Regression but they are not good for recognizing complex pattern, where Neural Network and other methods like SVM works better. Among these seven methods, MLP Neural Network gives the best result. From 755 movies, our MLP model is able to predict 442 movies correctly and 677 movies if we consider one away prediction.

One away prediction means the difference between predicted and target class is 1. For example, suppose a movie is classified as class 5, means it is a blockbuster hit. But the prediction result is class 4. That means our classifier predicted one class less than the true value. For Exact match prediction it will be considered as classification error but if we take one away prediction in consideration, it will be accepted as correct result. We have used two types of features, pre-released features for upcoming movies' prediction and all features which includes both pre-released and post-released features for prediction after opening weekend. In Fig. 1 and Fig. 2 we can see different performance from all these algorithms considering both exact and one away prediction. Fig 1 shows performance comparison for all features where Fig. 2 is for only pre-released features.

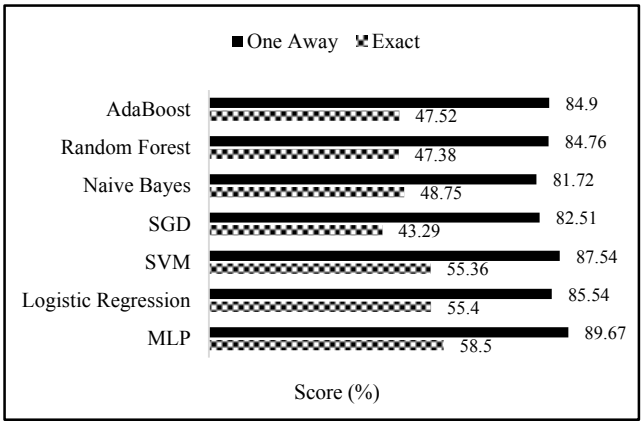


Figure 1. Performance comparision of different methods for all features.

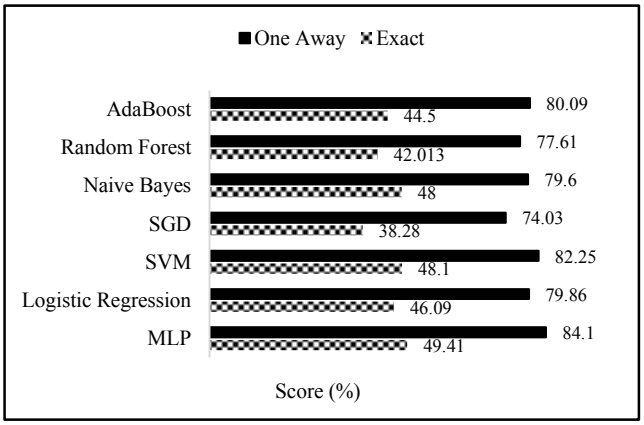


Figure 2. Performance comparision of different machine learning methods for pre-released features.

Among all these features, MLP gives better result. The reason is MLP is good for complex data pattern recognition. One of the major problem in our dataset is there are many data point which are overlapping, which is shown in Fig. 3. For this problem it is hard for algorithms to learn the pattern effectively. However, 58.53% exact accuracy and 89.67% one

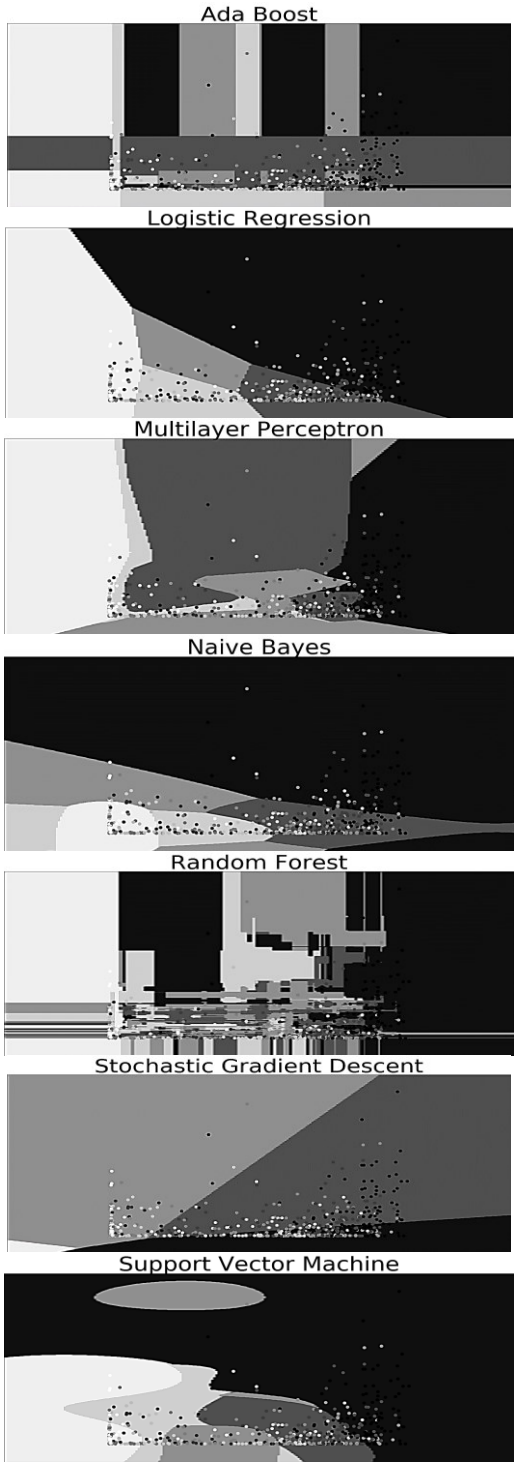


Figure 3. Data overlapping in different methods.

TABLE III. ACCURACY (IN PERCENTAGE) OF EACH FOLD FOR ALL SEVEN ALGORITHMS (ALL FEATURES)

| Algorithms | Fold 1 | Fold 2 | Fold 3 | Fold 4 | Fold 5 | Fold 6 | Fold 7 | Fold 8 | Fold 9 | Fold 10 | Final |
|---|---|---|---|---|---|---|---|---|---|---|---|
| MLP | 58.45 | 63.93 | 62.33 | 55.94 | 67.17 | 54.67 | 51.86 | 57.81 | 63.52 | 49.62 | **58.53** |
| SVM | 53.24 | 46.75 | 62.34 | 59.74 | 50 | 57.34 | 53.34 | 54.67 | 54.05 | 61.12 | **55.26** |
| SGD | 48.05 | 44.15 | 40.25 | 46.75 | 42.10 | 42.67 | 36 | 44 | 50 | 38.89 | **43.29** |
| Logistic Regression | 54.54 | 50.64 | 53.24 | 62.34 | 55.26 | 54.67 | 50.67 | 52 | 59.45 | 61.12 | **55.4** |
| Random Forest | 46.75 | 42.85 | 58.45 | 55.84 | 38.15 | 45.34 | 44.0 | 50.67 | 47.29 | 44.45 | **47.38** |
| Ada Boost | 50.64 | 38.96 | 55.84 | 50.64 | 50 | 42.67 | 41.34 | 53.34 | 45.94 | 45.34 | **47.47** |
| Naive Bayes | 37.67 | 51.94 | 51.04 | 52.84 | 55.26 | 49.34 | 40 | 48 | 50 | 51.38 | **48.75** |

away accuracy is a very good score for our MLP model comparing to other researches [3], [12]. Other methods do well, like SVM and Logistic Regression. SVM is a very powerful classifier but the main problem is separating data regions. While our data points are overlapping with each other, often it becomes hard for SVM to separate the region perfectly where logistic regression also does a very good job. Logistic Regression is good for categorical data and small dataset, both fits on our dataset. We can see performance of SGD, Ada Boost, Random Forest and Naive Bayes are poor related to MLP, SVM and Logistic Regression.

We implement all these methods using 10-fold cross validation which is the best way to test. Here, in Table III, we include all ten folds' accuracy along with the final accuracy for all seven algorithms. Data overlapping is the main reason for such performance of those algorithms shown in Fig. 3, it shows budget in X axes and number of screens in Y axes relations with the classification areas of different algorithms. In Fig. 3, different level of darkness represents specific class and their belonging data points. Here we can see lots of specific colored points in other colored regions which indicates the classification errors and it is occurring because of data overlapping. Points are overlapping on each other that is why we cannot see all the data points. Different data points of different classes are overlapping and classifiers become confused in determining their actual classes. We show this problem in 2D graph as it is a good way to understand the problem. We select budget and number of screens as those are the most important features and available before the release of movies, although other features can be used. In Fig. 3 different shades of dark regions are different from each other for different algorithms as classification calculations are different. Each color represents a class in Fig. 3 and the colors of data points are same as their belonging class. For instances, if white color area represents class 1 then all white data points belong to class 1. Again if you find some white points in other colored areas, that means they are incorrectly classified by the classifier.

Here in Fig. 4 and Fig. 5 visualize the precision, recall and f1 scores of all seven methods. Fig. 4 is for all features and Fig. 5 shows these scores for only pre-released features. These scores give a good comparison of performance assessment between different methods. Precision, recall and f1 scores are calculated differently. Before the explanation we need to know some important terms, they are true positive,

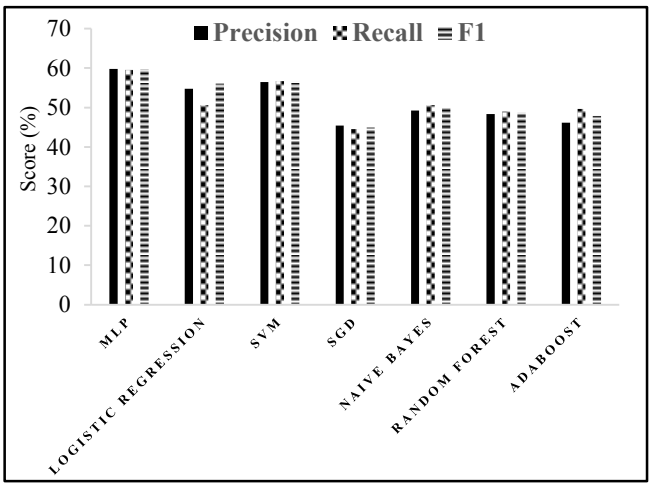


Figure 4. Precision, recall and F1 score for all features.

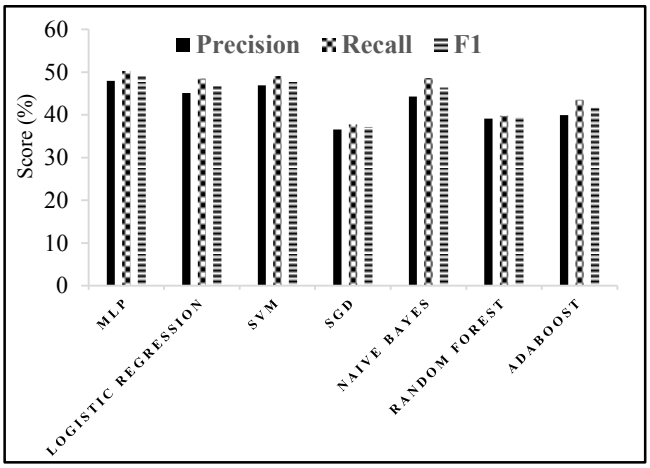


Figure 5. Precision, recall and F1 score for pre-released features.

true negative, false positive and false negative. True positive means where test class and predicted class both are true, true negative means both test class and predicted class are false, false positive means test class is false but predicted class is true and false negative means test class is true where predicted class is false. So precision formula is, TP/TP+FP. Which gives us how many selected classes are relevant where recall tells us how many relevant classes are selected. Formula of recall is TP/TP+FN. F1 score is the harmonic mean of precision and recall, it can be write as 2*(precision x recall)/precision + recall. Among all these algorithms MLP and SVM gives the best result. These scores are calculated based on exact prediction accuracy rather than one away prediction accuracy.

## VI. Conclusion and Future Works

A movie's box-office success depends on many parameters not only on some features related to movies. It also depends on other factors like number of audience. Also their appearance in theaters depends on the political and economic stability of a country. If economic and political condition of a country is not stable, then it does not matter how well the movie is made, there will be no one to watch that movie. So including a country GDP as an attribute is a good option for further analysis. We also suggest to analyze and include the number of audience for analysis. We can get number of annual audience by using total ticket sold in a particular year. Including these attributes will make the prediction more accurate.

In our research we exclude genre and sequel of movies. Forecasting the success of a sequel movie is hard, as some movies become successful just because of the fame from previous movie sequel. Previously other research works also excluded sequel movies [3]. In early days, most of the researches either considered only pre-released features [3], [16] or post-released features [5], [6] for their prediction, but we take both types of features in consideration for both upcoming movies' prediction and prediction after opening weekend. Our main goal for this research is to show how most popular machine learning algorithms act on movie related data for box office success prediction.

## References


[1] J. Valenti (1978). Motion Pictures and Their Impact on Society in the Year 2000, speech given at the Midwest Research Institute, Kansas City, April 25, p. 7.

[2] M. T. Lash and K. Zhao, "Early Predictions of Movie Success: The Who, What, and When of Profitability," *Journal of Management Information Systems*, vol. 33, no. 3, pp. 874–903, Feb. 2016.

[3] R. Sharda and E. Meany, "Forecasting gate receipts using neural network and rough sets," in *Proceedings of the International DSI Conference*, 2000, pp. 1–5.

[4] J. S. Simonoff and I. R. Sparrow, "Predicting Movie Grosses: Winners and Losers, Blockbusters and Sleepers," *Chance*, vol. 13, no. 3, pp. 15–24, 2000.

[5] A. Chen, "Forecasting gross revenues at the movie box office," *Working paper, University of Washington, Seattle, WA*, June 2002.

[6] M. S. Sawhney and J. Eliashberg, "A Parsimonious Model for Forecasting Gross Box-Office Revenues of Motion Pictures," *Marketing Science*, vol. 15, no. 2, pp. 113–131, 1996.

[7] D. Gregorio, "Prediction of movies box office performance using social media," *Proceedings of the 2013 IEEE/ACM International Conference on Advances in Social Networks Analysis and Mining - ASONAM '13*, 2013.

[8] S. Gopinath, P. K. Chintagunta, and S. Venkataraman, "Blogs, Advertising, and Local-Market Movie Box Office Performance," *Management Science*, vol. 59, no. 12, pp. 2635–2654, 2013.

[9] M. C. A. Mestyán, T. Yasseri, and J. Kertész, "Early Prediction of Movie Box Office Success Based on Wikipedia Activity Big Data," *PLoS ONE*, vol. 8, no. 8, 2013.

[10] B. Pang and L. Lee, "Thumbs up? Sentiment classification using machine learning techniques," in *Proceedings of the Conference on Empirical Methods in Natural Language Processing (EMNLP)*, Philadelphia, July 2002, pp. 79–86.

[11] P. Chaovalit and L. Zhou, "Movie review mining: a comparison between supervised and unsupervised classification approaches," in *Proceedings of the Hawaii International Conference on System Sciences (HICSS)*, 2005.

[12] R. Sharda and D. Delen, "Predicting box-office success of motion pictures with neural networks," *Expert Systems with Applications*, vol. 30, no. 2, pp. 243–254, 2006.

[13] A. Sivasantoshreddy, P. Kasat, and A. Jain, "Box-Office Opening Prediction of Movies based on Hype Analysis through Data Mining," *International Journal of Computer Applications*, vol. 56, no. 1, pp. 1–5, 2012.

[14] M.H Latif, H. Afzal "Prediction of Movies Popularity Using Machine Learning Techniques", National University of Sceinces and technology, H-12, ISB, Pakistan.

[15] K. Jonas, N. Stefan, S. Daniel, F. Kai "Predicting Movie Success and Academi Awards through Sentiment and Social Network Analysis" University of Cologne, Pohligstrasse 1, Cologne, Germany.

[16] W. Zhang and S. Skiena, "Improving Movie Gross Prediction through News Analysis," *2009 IEEE/WIC/ACM International Joint Conference on Web Intelligence and Intelligent Agent Technology*, 2009.

[17] T. G. Rhee and F. Zulkernine, "Predicting Movie Box Office Profitability: A Neural Network Approach," *2016 15th IEEE International Conference on Machine Learning and Applications (ICMLA)*, 2016.

[18] J. Duan, X. Ding, and T. Liu, "A Gaussian Copula Regression Model for Movie Box-office Revenue Prediction with Social Media," *Communications in Computer and Information Science Social Media Processing*, pp. 28–37, 2015.

[19] L. Doshi, J. Krauss, S. Nann, and P. Gloor, "Predicting Movie Prices Through Dynamic Social Network Analysis," *Procedia - Social and Behavioral Sciences*, vol. 2, no. 4, pp. 6423–6433, 2010.

[20] T. Liu, X. Ding, Y. Chen, H. Chen, and M. Guo, "Predicting movie Box-office revenues by exploiting large-scale social media content," *Multimedia Tools and Applications*, vol. 75, no. 3, pp. 1509–1528, Feb. 2014.

[21] Z. Zhang, B. Li, Z. Deng, J. Chai, Y. Wang, and M. An, "Research on Movie Box Office Forecasting Based on Internet Data," *2015 8th International Symposium on Computational Intelligence and Design (ISCID)*, 2015.

[22] Scikit-learn: Machine Learning in Python, Pedregosa *et al.*, JMLR 12, pp. 2825-2830, 2011.

[23] F. Chollet, Keras, 2015, GitHub repository, https://github.com/fchollet/keras. [Accessed: March-2016]

# National Digital Forensics Framework for Bangladesh

Mohammad Mahfuzul Haque[1], Syed Akther Hossain[2]
[1]Bangladesh University of Professionals, Bangladesh
[2]Daffodil International University, Bangladesh
[1]mahfuz.haque@outlook.com, [2]aktarhossain@daffodilvarsity.edu.bd

*Abstract*—**At recent time, cybercrime has increased significantly in the world and also in Bangladesh due to consequence of massive digitalization efforts in every sector. These types of offense require systematic probing in order to be revealed properly at the court of law. This research work proposed a comprehensive digital forensics framework to facilitate forensically ready common standard digital forensics to the investigators. The framework recommended proactive and reactive forensics to enable live and post forensics issues. The purpose of the proposed framework is to allow systematic postmortem of digital forensics. Moreover, it allows further investigations suggested during examination or analysis phase. An expert system is introduced into the framework to improve efficiency through inference engine. This assistive system included digital forensics case database as a history keeper to store all documentations and results of the accomplished forensics examination. The inference engine is expected to generate a priority list from the historical data by a proposed algorithm. In addition, the expert system is expected to guide examiners during forensics. Furthermore, dissemination of forensics outcomes anticipated automatically to the authorized investigators by this system. However, the proposed framework is based on theoretical approach which is expected to be evaluated and implemented using assistive expert system in the future.**

***Keywords—Digital forensics framework, assistive expert system, forensics readiness, proactive forensics, reactive forensics.***

## I. Introduction

Digital forensics (DF) is a subdivision of forensic science. It covers the retrieval and examination of evidences found in digital media often conducted as a response to computer crime [1]. According to Palmer, DF is defined as "The use of scientifically derived and proven methods towards the preservation, collation, validation, identification, analysis, interpretation, documentation and presentation of digital evidence derived from digital sources for the purpose of facilitating or furthering the reconstruction of events found to be criminal, or helping to anticipate unauthorized actions shown to be disruptive to planned operations." [2]. Kohn defines it in a broader way "Digital forensics is a specific, predefined and accepted process applied to digitally stored data or digital media using scientific proven and derived methods, based on a solid legal foundation, to extract after-the-fact digital evidence with the goal of deriving the set of events or actions indicating a possible root cause, where reconstruction of possible events can be used to validate the scientifically derived conclusions." [3]. Many researches were undertaken in this area to develop a better DF framework. However, rapid changes of information technologies need to incorporate into the DF framework by which all types of present and upcoming forensics are possible. In addition, to do efficient DF, an access to previous forensics cases in an assistive way is essential but it is not addressed properly by the researchers. Furthermore, investigations outcome dissemination is very poor among the examiners. As a result, expertise in this area is not growing equally within investigators.

Existing development in the field of DF is concentrating on real time network and cloud forensics. Researchers are highlighting on forensics readiness, new techniques of evidence acquisition, automated anomalies detection, history kipping, proactive and reactive forensics. Researches also have done approaching new process of Internet of Things (IoT) Forensics.

Though several researches are undertaken on DF framework but none of those researches covers all categories of DF in a complete manner. To overcome this and enabling guided DF a comprehensive DF framework including assistive expert system is proposed for the Bangladesh. The main contribution of this paper is the proposed Assistive Expert System which contains a historical database and an inference engine. This inference engine is expected to produce a priority list from this database. Secondly, mentionable value adding feature is the forensically readiness, which will supports proactive and reactive forensics. This paper is organized in these following sections. For example, in section II, relevant literatures are reviewed. In section III, problem formulation and solution procedures are discussed. In section IV, we discuss about the completed survey. Proposed digital forensics framework is described in section V. Results of the survey and analysis are presented in section VI. In section VII, future development scopes are mentioned. Finally, a conclusion is drawn in section VIII.

## II. Related Work: Literature Review

A number of researches have contributed to developed DF framework. At present, researchers are more focusing on specific type of DF framework or part of that framework. To add value in this area of research, all previous researches are meticulously studied and some of these researches are discussed below:

Alenezi *et al.* proposed the cloud computing readiness framework for an organization. The factors considered in this framework were: technical, legal and organizational factors [4]. Readiness ensured efficiency but only cloud forensics was considered and planning aspect was not included.

978-1-5386-2307-7/17/$31.00 ©2017 IEEE

In multidisciplinary DF investigation process model, covered computer, network, mobile and cloud forensics. This mobile forensic focused model was evaluated and proved its efficiency and effectiveness; however Internet of Things (IoT) forensics was not included and documentation was not addressed in it [5]. In IoT forensics digital evidence acquisition model, a zone wise evidence acquisition algorithm was developed for IoT forensics framework and a management platform also proposed. IoT forensics is a new area of research and this theoretical model will significantly contribute to further research but completeness needs to be ensured [6]. Kao proposed a cybercrime investigation framework which profiled crime evidences to address complex vulnerabilities and hacking specially for financial sector but he did not include presentation phase in his framework [7]. The network forensics framework IDFIF has four primary processes: preparation, proactive, reactive and presentation. This was a comprehensive model for network forensics but in preparation phase planning, legal and organizational factors were not included [8]. The Case history based digital forensics framework included case registration module and evidence loader & history keeper module. DF processes were arranged by six sequential comprehensive phases but DF examination was not there [9]. DF business model proposed by Prayudi *et al.* focused on human, digital evidence and process. Here human and digital evidences were given importance but readiness feature was not covered [10].

Accordingly, Alharabi *et al.* proposed proactive and reactive DF investigation process where examination and dissemination were not introduced [11]. Similar approach with more details was also found in [8]. Moreover, a Cloud DF for automated anomalies detection architecture was proposed to do layer based (management and virtualization layer) DF. This was also a proactive DF [12]. Furthermore, in distributed network forensics framework proposed agent and proxy-based server for proactive forensics [13]. The study of network forensics: today and tomorrow also discussed proactive and reactive forensics [14]. To enhance the accuracy of DF in the absence of sufficient evidences, a trace back phase was introduced [15]. All of the above frameworks need improvement by adding phases of readiness, dissemination or supportive system.

On the other hand, Bangladesh is developing in each sector significantly and its internet subscribers were 67.245 million at the end of Feb. 2017 whereas it was 31.141 million at the end of Feb. 2012 [16]. Accordingly, in Bangladesh 58 ministries and its divisions, 353 directorates, 8 divisional offices, 64 districts, 491 upazilas and 4554 unions have their own websites where they have more than one information systems available up to directorate level offices [17]. To know about DF status in Bangladesh, government policies, reports and manuals are studied. In Information Security Policy Guidelines, the Ministry of Posts, Telecommunications and Information Technology suggested a risk management process but no digital forensics guideline was provided [18]. In addition, in Government of Bangladesh Information Security Manual, mandatory and recommended controls were suggested for proactive incident response and forensics but no specific forensics process or framework was provided [19]. Therefore, now it is the most essential mandate to develop a comprehensive digital forensics framework for Bangladesh.

## III. Problem Formulation and Methodology

From the beginning to now, DF research area is not completely matured to address all the emerging technology forensics like IoT, big data and cloud forensics and so on. Moreover, no single DF framework addressed above mentioned forensics in a comprehensive way. Furthermore, DF learning outcomes of the examiners were not disseminated in an efficient way for the benefit of future investigations. Digital forensics is not a new area of research. The first DF Research Workshop (DFRWS) introduced their first technical report which is recurrently referred as base framework for DF research [2]. After that many researchers developed partial or distinct type of DF framework but a comprehensive digital forensic is now a real demand for the investigation.

According to the present growth of ICT in Bangladesh discussed in section II, digital incidents and crimes are also increasing proportionately. As observed from the surveys done in the three government organizations, there were no common and comprehensive DF frameworks. Therefore, it is now essential to develop a comprehensive DF framework.

To develop a comprehensive DF framework the following methodology is used. Firstly, to understand the present development and future scope, we have collected literatures on digital forensics framework, methods, process. We also considered related laws and standards. Secondly, a survey format was developed and surveys were done in three related Bangladeshi government organizations to understand the real scenario and practices in this area. Thirdly, by analyzing the collected research contents and findings from the survey, gaps of literatures were traced out and existing challenges were also identified. Fourthly, a draft digital forensics framework was developed by addressing the essential processes, sub-processes, functionalities from the literatures as well as observations from the survey. In addition, to make the framework more efficient, researchers proposed an assistive expert system within it. Finally, we reconstructed the framework and proposed it for Bangladesh.

## IV. Survey in Government Organization

To gather facts and know how digital forensics cases handled by the Bangladesh government, a form was developed covering three major areas. These are: digital forensics statistics, digital forensics framework/hardware/software tools used by the investigators, and guidelines/laws followed by them.

In digital forensics statistics, year wise types of forensic case (like: Network, Computer, Mobile/Smart Devices, Cloud/Virtual Service forensics, etc.) numbers were captured to analyze the trend and forensics types covered. To know the DF framework practices, discussion done on standard, steps, devices and tools. For the last part of the survey was to collect information about guidelines and laws practiced by the DF expert. The facts and findings discovered by the survey are discussed in section VI.

## V. PROPOSED DIGITAL FORENSICS FRAMEWORK

As it has been studied in the section II, most of the DF frameworks cover a specific area of digital forensics and these need improvements from readiness to storing forensics cases in a database system to use it for further DF investigations. The proposed DF framework addressed the areas needed to be enhanced are discussed in this section and the framework is illustrated in Fig. 1. Moreover, in this section, a DF Assistive Expert System (AES) is also proposed which is a unique contribution to ensure efficiency in DF process as shown in Fig. 2.

### *A. Framework Development*

The proposed digital forensics framework has two parts. In first part, a comprehensive DF framework is developed by analyzing recently developed digital forensics frameworks and findings from the surveys in three Bangladeshi government organizations. In second part, an algorithm is developed for AES to support the digital forensics experts.

### *B. The proposed Bangladesh Digital Forensics Framework (BDFF)*

The proposed framework is prepared for Bangladesh government and named as Bangladesh Digital Forensics Framework (BDFF). The framework has five modules as illustrated in Fig. 1. Each of these modules has several processes to accomplish digital forensics.

#### *1) Digital Forensics Types*

According to literature reviewed there are mainly five types of digital forensics. These are Computer Forensics, Network Forensics, Mobile Forensics, Cloud Forensics and IoT Forensics.

#### *2) Readiness*

After determining the type of digital forensics needed, the proposed framework suggests to starting it from the planning of readiness module. The readiness also includes three other essential processes: technical, legal and organizational factors [4].

a) *Plan:* Planning is the initial process to begin the readiness module. Before detection or identification of an incident a plan needs to be prepared. It will guide process wise execution of the investigation.

b) *Technical Factors:* The technical factors cover technological features which need to be considered during forensics. It includes infrastructure, architecture, forensics technologies, and security issues of the forensics environment.

c) *Legal Factors:* Legal factors cover regulatory issues of law and enforcement agencies for acceptability of digital evidences in court and chain of custody. Moreover, it includes deed between user and service provider to do forensics investigation. Furthermore, jurisdictions related matters need to be measured weather crime area is within the country or abroad.

d) *Organizational Factors:* Top management of the organization is ready to authorize, agreed and support to perform digital forensics are ensured here.

#### *3) Proactive/Physical Forensics*

Proactive forensics module refers to an immediate action that is taken to protect the evidences in case of live investigation to detect incident/crime. It also denotes to secure the evidences of identified crime. On the other hand, to support digital forensics and legal prosecution, physical forensics can be defined as to collect and preserve physical evidences, for example: DNA, fingerprint etc. This module has three processes: Securing the Scene, Preservation of Physical Scene, Detect Incident or Crime.

*a) Securing the Scene:* Securing the crime scene ensures the crime scene integrity by protecting unauthorized contamination of crime scene and potential evidences [8]. First responders of crime scene will follow the organizational policy and secure the crime scene as well as digital evidences then prevent unauthorized access or modification [20].

*b) Preservation of Physical Scene:* Proactive preservation refers to preserve integrity of the evidences. For this purpose digital evidence need plugin portable power supply first, to keep it alive then take measures for data protection and backup.

c) *Detect Incident/Crime:* Detection of incident or crime is essential part to start the digital forensics by informing the appropriate authority.

#### *4) Reactive Forensics*

This is the main module of the DF. After detection of digital crime, reactive DF is done to support the legal prosecution. This reactive digital forensic is divided in to five phases. Conditional iteration facility also included here to do further DF. The phases are: Identification, Acquisition, Preservation, Examination and Analysis.

a) *Identification:* By this phase an investigator identifies evidences and decides whether it is in internal network or in cloud environment. In addition, investigator also recognizes required tools and techniques for further processes.

b) *Acquisition:* DF evidence acquisition or imaging process is done to ensure usability and admissibility in the court of law. Moreover, it ensures the integrity of the original evidence.

c) *Preservation:* Preservation is done by the first responder to isolate and preserve the original evidences in a secured manner to avoid contamination.

d) *Examination:* Examination is the core process to discover facts through the support of forensics tools and techniques by a systematic approach.

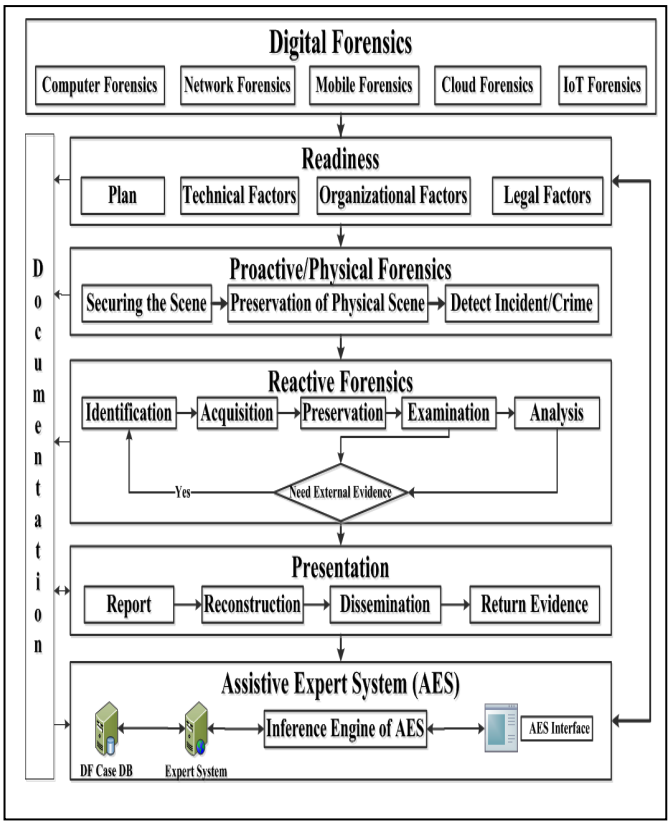


Figure 1. Bangladesh Digital Forensics Framework (BDFF)

e) *Analysis:* In this process, results of the examination are scrutinized, assessed, categorized and concluded to assist in digital forensics report preparation and presentation.

5) *Presentation*

This module is the final output to present end-result, facts and findings of the DF processes. Court of law or management of the organization takes the decision against a crime based on the disseminated facts and findings by the investigator. Phases of the presentation module are: Report, Reconstruction, Dissemination and Return of Evidences.

a) *Report:* A detailed descriptions of forensics case initiation, readiness to examination as well as investigator's identity are included in the report.

b) *Reconstruction:* Reconstruction is the entire procedure to do analysis and perform evaluation on the DF examination results [8]. This is generally required to verify how a certain result is accomplished for various purposes [3].

c) *Dissemination:* Spread learning outcomes of the completed DF to other investigators carried out to do future investigation of similar type.

d) *Return evidence:* Returning evidences to its owner are the last task done by the investigator.

6) *Assistive Expert System (AES)*

In the proposed BDFF a new expert system AES has been introduced to preserve case wise story in a systematic and structured way. This system will help and guide the investigators to do interactive digital forensics by the support from Digital Forensic Case Database (DF Case DB) and Inference Engine.

7) *Documentation*

After initiation of a forensics case, documentation from readiness to presentation module is the essential part of the proposed framework. This will be used to produce forensics report and the report helps the organization or court of law for taking decision against the occurred crime. Moreover, in the AES module, all the documentations are stored for further investigation assistance.

## C. *Inference Engine of AES*

Main part of AES is the interactive inference engine which will start by initial inputs then process those in a sequence of steps to guide an investigator during digital forensics and it is shown in Fig. 2. Algorithm of the inference engine is given bellow:

- *Step 1:* Take initial inputs of forensic type, and also collect probable evidence type with preferable examination tools from the investigator for the current case.
- *Step 2:* Based on the inputs a Case List will be created automatically from the DF Case DB.
- *Step 3:* If created list item number is greater than zero then generate a priority list of those by the priority matrix. Else, display a mismatch message to the examiner and stop further processing.

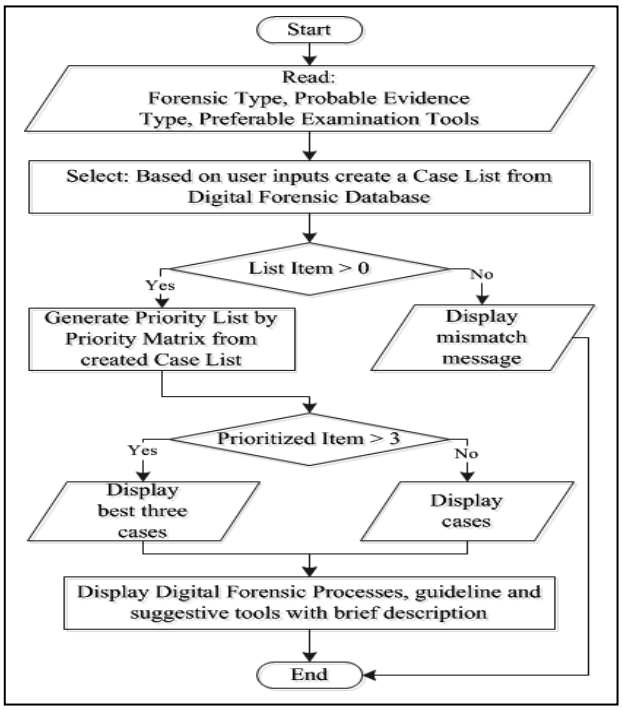


Figure 2. Process Flow of Assistive Expert System

- *Step 4:* If the prioritized item number is more than 3 then suggest best three forensic cases from the priority list else display the case or cases to the examiner.
- *Step 5:* Assist the investigator by providing sequential forensics processes with suggestive forensics tools align with each process with brief description. Finally, end the process.

The inference engine of the AES will help to reduce the planning time of readiness module. This engine will assist them by providing related forensic process with suggestive tools which will be aligned with the examiner choice. However, this engine will enable sharing of existing similar cases only but we are working on it for further development and it will be share in future after successful evaluation.

## VI. Result and Discussion

From the incident statistics of BGD e-Gov CIRT, recorded incident number was 379 from Feb. to Dec. 2016, whereas from Jan. to Aug. 6, 2017 it was 333. This indicates significant increase of incidents. The rate of vulnerability was 73%, whereas the second most one was due to malicious code and it was 15% [21], [22]. During the survey in this organization it was revealed that most of these incidents were detected from live networks. On the other hand, survey in organization X, it was found that about 60% of digital forensics was done on mobile or smart devices forensics and it was approximately 40% on computer and other devices forensics. The forensics steps followed by this organization were: Secure the Crime Scene, Identification, Collection, Analysis and Presentation. They are following international standard to do the forensics. They also use software and tools like: FTK, Encase, Tableau Imager, Magnet IEF, Cellbrite, XRY, FRED Workstation, etc. to perform digital forensics. Another Survey was done in organization Y where proactive network forensics was the most concern and that was about 50% of the total executed digital forensics by that organization. They have developed their own forensics framework. This framework has four phases: Direction, Collection, Processing and Dissemination. They use open sourced DF tools and some payment based tools. On an average they do one forensics case every day.

Apart from that, recent literatures were reviewed to identify gaps and new improvements in the digital forensics area. Next, a detailed analysis was done to propose a comprehensive digital forensics framework. Summary of the analysis is given below in Table 1.

The proposed framework is developed based on the facts from the survey and 12 digital forensics frameworks illustrated in Table 1. Module wise phases were considered in this study and redundant or unnecessary phased were discarded. New and effective phases were incorporated from the existing frameworks to make it comprehensive. An Assistive Expert System also introduced to increased efficiency. Finally, the proposed common standard framework will fulfill needs to do digital forensics in a comprehensive manner not only for the Bangladesh government but also for other practitioners.

TABLE I. Table 1. Mapping Phases of the Studied Framework/Model/Process to Proposed Framework [3]-[13], [15]

| Framework/ Model/Process, Author | Digital Forensics Module | | | | | | | | | | | | | | | | | | | | | | | |
|---|---|---|---|---|---|---|---|---|---|---|---|---|---|---|---|---|---|---|---|---|---|---|---|---|
| | *Readiness* | | | | | *Proactive Forensics* | | | | *Reactive Forensics* | | | | | | *Presentation* | | | | | *Systems* | | |
| | *Plan* | *Technical* | *Organizational* | *Legal* | *Discarded Phase* | *Securing Scene* | *Preservation* | *Detection* | *Discarded Phase* | *Identification* | *Acquisition* | *Preservation* | *Examination* | *Analysis* | *Discarded Phase* | *Report* | *Reconstruction* | *Dissemination* | *Return Evidence* | *Discarded Phase* | *DF Case DB* | *Auto System* | *Discarded Phase* |
| IDFPM, Kohn [3] | | √ | √ | √ | | √ | | √ | Confirm, Deploy | √ | √ | √ | √ | √ | | √ | √ | √ | | | | | |
| CLFR, Alenezi [4] | | √ | √ | √ | | | | | Assessment, First Response | | | | | | | | | | | | | | |
| MDFIPM, Lutui [5] | | | | | | √ | √ | √ | | √ | √ | √ | √ | √ | | √ | | | √ | | | | |
| Harbawi [6] | | √ | √ | √ | | √ | √ | √ | | √ | √ | √ | √ | √ | | √ | √ | | | | √ | √ | |
| CIF, Kao [7] | √ | | √ | √ | Stategy | √ | √ | √ | | √ | √ | √ | √ | √ | | √ | √ | | | | √ | | |
| IDFIF, Hikmatyar [8] | | | √ | √ | | √ | √ | √ | Protection, Monitoring | √ | √ | √ | √ | √ | | √ | √ | √ | | | | | |
| DFFFCHK, Jain [9] | √ | | √ | √ | Stategy | √ | | √ | | √ | √ | | | √ | Extract, Harvest, Destroy | √ | √ | | | Recover, Destroy | √ | √ | |
| DFBM, Prayudi [10] | | | √ | √ | | √ | √ | √ | Capture/Select | √ | √ | √ | √ | √ | Survey | √ | √ | | | | √ | | |
| PRDFIS, Alharbi [11] | | | | | | | √ | √ | Analysis, Report | √ | √ | √ | | √ | | √ | | | | | | | |
| FCA, Patrascu [12] | | √ | | | | √ | √ | √ | | | | | | | | √ | | | | | √ | √ | |
| NFDF, Chhabra [13] | | | | | | | | √ | | √ | √ | | √ | √ | | √ | | | | | √ | √ | |
| MEADF, Alanazi [15] | | √ | √ | √ | | √ | √ | √ | | | √ | √ | √ | √ | | √ | | | √ | | | | |
| BDDF | √ | √ | √ | √ | | √ | √ | √ | | √ | √ | √ | √ | √ | | √ | √ | √ | √ | | √ | √ | |

√ Symbol refers to phase that found in the framework

## VII. Future Work

For the implementation of the proposed framework a standard policy and guideline will be the next scope of work. Consequently, a secure expert system will be designed and developed where digital forensics cases data will be stored to guide the investigator with enhanced dissemination facility. For the inference engine of the AES, a priority generator matrix will also be developed. Though, the framework is proposed based on the analysis of reviewed literatures, this needs to be evaluated by implementing the proposed AES in digital forensics investigation practicing organization.

## VIII. Conclusion

In Bangladesh, frequency of crimes and incidents which take place using information and communication technology are increasing extremely. In response to this, standardize comprehensive digital forensics framework is not introduced yet. To meet this scarcity, this paper has proposed a common standard framework, named Bangladesh Digital Forensics Framework (BDFF). In comparison to existing available digital forensics frameworks, the proposed framework is more structured by its modularized approach. All types of digital forensics can be accomplished by its five modules: Readiness, Proactive/Physical Forensics, Reactive Forensics, Presentation and Assistive Expert System. Moreover, all the vital phases are included and redundant or unnecessary phases are rejected from the existing frameworks by extensive literature review, survey findings and analysis. Furthermore, the proposed framework is comprehensive in nature to guide the investigators from readiness to dissemination. Though, the proposed interactive Assistive Expert System (AES) of the framework will increase the digital forensics efficiency but it needs to be developed and evaluated by the experts. Last but not the least, the proposed framework is developed to target for Bangladesh government but it is also appropriate enough to any relevant investigators.

## Acknowledgment

This research is supported by the Information and Communication Division of Ministry of Posts, Telecommunication and Information Technology under the Masters Research Fellowship. Special thanks go to Md. Shameem Ahsan Jaglul who helped to get official approval for digital forensics lab survey.

## References

[1] A. Pichan, M. Lazarescu and S. T. Soh, "Cloud Forensics: Technical challenges, solutions and comparative analysis," *Digital Investigation*, vol. 13, pp. 38-57, Jun. 2015.

[2] G. Palmer, "A Road Map for Digital Forensics Research," DFRWS., Utica, NY, Tech. Rep. DTR-T-001-01 Final, Aug. 2001.

[3] M. D. Kohn, "Integrated Digital Forensic Process Model," M.S. thesis, Dept. Comput. Sci., Univ. Pretoria, Pretoria, South Afria, 2012.

[4] A. Alenezi, R. K. Hussein, R. J. Walters and G. B. Wills, "A Framework for Cloud Forensic Readiness in Organizations," presented at the 2017 5th IEEE Int. Conf. Mobile Cloud Computing, Services and Engineering, San Francisco, CA, USA, Apr. 6-8, 2017.

[5] R. Lutui, "A Multidisciplinary Digital Forensic Investigation Process Model," *Business Horizons,* vol. 59, no. 6, pp. 593-604, Nov.-Dec. 2016.

[6] M. Harbawi, A. Varol, "An Improved Digital Evidence Acquisition Model for the Internet of Things Forensics I: A Theoretical Framework," presented at the 2017 5th Int. Symp. Digital Forensic Security, Tirgu Mures, Romania, Apr. 26-28, 2017.

[7] D. Y. Kao, "Exploring the Cybercrime Investigation Framework of ATM Height from ISO/IEC 27043:2015," presented at the 2017 19th Int. Conf. Advanced Communications Technology, Bongpyeong, South Korea, Feb. 19-22, 2017.

[8] M. Hikmatyar, Y. Prayudi and I. Riadi, "Network Forensics Framework Development using Interactive Planning Approach*," Int. J. Computer Applications,* vol. 161, no. 10, pp. 41-48, Mar. 2017.

[9] N. Jain, D. D. R. Kalbande, "Digital Forensic Framework using Feedback and Case History Keeper," presented at the 2015 Int. Conf. Communication, Information & Computing Technology, Mumbai, India, Jan. 16-17, 2015.

[10] Y. Prayudi, A. Ashari and T. K. Priyambodo, "A Proposed Digital Forensics Business Model to Support Cybercrime Investigation in Indonesia," *Int. J. Computer Network and Information Security,* vol. 7, no. 11, Oct. 2015. [Online]. Available: http://www.mecs-press.org/ijcnis/ijcnis-v7-n11/IJCNIS-V7-N11-1.pdf

[11] S. Alharbi, J. Weber-Jahnke and I. Traori, "The Proactive and Reactive Digital Forensics Investigation Process: A Systematic Literature Revoew," *Int. J. Security and Its Applications,* vol. 5, no. 4, pp. 59-72, Oct 2011.

[12] A. Patrascu, M. Velciu and V. V. Patriciu, "Cloud Computing Digital Forensics Framework for Automated Anomalies Detection," presented at the 2015 10th Int. Symp. Applied Computational Intelligence and Informatics, Timisoara, Romania, May 2015.

[13] G. S. Chhabra, P. Singh, "Distributed Network Forensics Framework: A Systemetic Review," *Int. J. Computer Application,* vol. 119, no. 19, pp. 31-35, Jun. 2015.

[14] G. Shrivastava, K. Sharma and R. Kumari, "Network Forensics: Today and Tomorrow," presented at the 2016 3rd Int. Conf. Computing for Sustainable Global Development, New Delhi, India, Mar. 16-18, 2016.

[15] F. Alanazi, A. Jones, "A Method of Enhance the Accuracy of Digital forensics in the Absence of Sufficient Evidence in Saudi Arabia," Int. J. Social, Behavioral, Educational, Economic, Business and Industrial Engineering, vol. 11, no. 3, 2017.

[16] Bangladesh Telecommunication Regulatory Commission, "Internet Subscribers," The BTRC website. [Online]. Available: http://www.btrc.gov.bd/telco/internet?field_for_the_month_of_value[value]=. [Accessed: Aug. 3, 2017].

[17] Bangladesh National Portal, "Home Page," The NPF. [Online]. Available: http://bangladesh.gov.bd/. [Accessed: Aug. 3, 2017].

[18] Bangladesh, Ministry of Posts, Telecommunications and Information Technology, "Information Security Policy Guidelines," The ICT Division website., Apr. 6, 2014, [Online]. Available: http://ictd.gov.bd/main/policy. [Accessed: Aug. 4, 2017].

[19] Bangladesh, BGD e-Gov CIRT, "Government of Bangladesh Information Security Manual," The BGD e-Gov CIRT website., Feb. 29, 2016, [Online]. Available: https://www.cirt.gov.bd/wp-content/uploads/2017/06/GOBISM2.pdf. [Accessed: Aug. 4, 2017].

[20] M. B. Mukashe, J. L. Sedgwick and D. W. Hagy, "Electronic Crime Scene Investigation: A Guide for First Responders," NIJ., Washington, USA, Rep. NCJ 219941, 2001.

[21] Bangladesh, BGD e-Gov CIRT, "Incident Statistics," The BGD e-Gov CIRT website., 2017, [Online]. Available: https://www.cirt.gov.bd/incident-reporting/statistics/. [Accessed: Aug. 6, 2017].

[22] Bangladesh, BGD e-Gov CIRT, "Annual Report 2016," The BGD e-Gov CIRT website., Feb. 29, 2016, [Online]. Available: https://www.cirt.gov.bd/wp-content/uploads/2017/05/ANNUAL-REPORT-2016-BGD-e-Gov-CIRT.pdf. [Accessed: Aug. 4, 2017].

2017 3rd International Conference on Electrical Information and Communication Technology (EICT), 7-9 December 2017, Khulna, Bangladesh

# An Approach to Automate the Scorecard in Cricket with Computer Vision and Machine Learning

Md. Asif Shahjalal[1], Zubaer Ahmad[2], Rushrukh Rayan[3], Lamia Alam[4]
Department of Electrical and Electronic Engineering[1]
Department of Computer Science and Engineering [2 3 4]
Chittagong University of Engineering and Technology
Chittagong-4349, Bangladesh
asif.cuet93@gmail.com[1], mail2zubaer@gmail.com[2], rushrukhryan@gmail.com[3], lamiacse09@gmail.com[4]

***Abstract*—Cricket is beyond the shadow of a doubt one of the most popular forms of sports in the southern region of Asia. This form of sports is widely played in more than 125 countries recognized by the International Cricket Council. With the flourishing of cricket, various aspects of the game are being automated with the advent of technology. Use of computer vision in assisting third umpire decision is indubitably the well-liked one. One of the most challenging issues that first initiates the discussion on its prosperity is the duration of the game. The on-field umpire has to authorize decisions almost after each delivery following which modifications are carried out in the scorecard which is a very tedious process. The traditional approaches that have been considered so far involve wearing a specialized hand glove, which collides with the beauty of the originality in the field. In this paper, an approach is proposed and a prototype is implemented to automate the umpires decision by interpreting his hand gesture. The region of interest is selected using a Haar-cascade-classifier and then the particular gesture is recognized using logistic regression. This process would eliminate the manual updating of scorecards and thereby reduce the game duration notably. In addition, it excludes the prerequisite of wearing special gloves involving sensors. The efficiency of the algorithm is then cross-checked with the training and test data. This proved to be a very simple but efficient algorithm for umpires gesture detection.**

***Keywords*—Machine learning, scorecard automation, haar-cascade-classifier, computer vision, gesture detection, logistic regression.**

## I. Introduction

Gestures are known as expressive, meaningful body movement which involves physical motion of the fingers, hands, arms, head, face, or body with the intent of: 1) assigning meaningful information or 2) interacting with the environment. In recent years gestures are widely used by humans to interact with computers and machines. Many common everyday equipment like TV, Smartphone, Car dashboard etc. can now be controlled by simple hand gestures. Gestures are also applied in many fields [1] like developing aids for the hearing impaired, enabling very young children to interact with computers, recognizing sign language, medically monitoring patients emotional states or stress levels, lie detection, monitoring automobile drivers alertness/ drowsiness levels, etc.

Involvement of gesture recognition technology in sports will make the gameplay fairer and proficient. The gestures performed by the sports officials which indicate to what is going on in the game. Which also can provide something meaningful about a player, a team, or the entire game. If the gestures of these officials are able to be recognized, meaningful information can be derived. We refer to a gesture as an intentional action by a person whereby part of the body is moved in a predefined way to indicate a specific event. Detecting these events enables automatic generation of highlights, contextual labeling of video and more importantly helps in decision making and automatic score update.

Cricket is the most popular sport in Bangladesh. It is the 2nd most famous sports in Asia, 4th in Europe and also 2nd most famous sport in the whole world [2]. But from the 19th century the same old manual method is being use to update the scoreboard, which is a great burden for the scorekeeper. The way of viewing the score has changed a lot in time, but the basic score updating process is still the same and performed by a person. So in the 21st century an automatic system is very much needed at this sector. Automatic systems are taking places of many boring manual task which was performed by humans 5 or 10 years ago. So developing a fully operational automated system like this is in dire need. Using modern equipments and machine learning algorithms we can increase the accuracy of the decision and provide flawless result what the naked eye misses. This motivates us to design a system which will recognize gesture of cricket umpire in real time. Besides the reason for choosing cricket is because it is the most popular sports in Bangladesh and unlike other popular sports it doesnt have enough technological application to make it more fair and accurate.

Gesture recognition has been explored in both vision and sensor based. In vision based system some image processing or computer vision based method is used to recognize the gesture. On the other hand, in sensor based system the person

978-1-5386-2307-7/17/$31.00 ©2017 IEEE

who perform the gesture wears sensor/sensors, and when the gesture is performed the sensor data taken and used to identify the gesture. In the area of sports and other sector, several attempts have been made for gesture recognition using both sensor-based and vision based technique.

Sensor-based hand gesture recognition started with the invention of glove-based system, which was further divided into two distinct categories- active data glove and passive data glove over the years [3]. The first glove-based systems were designed as a part of a camera-based LED system to track body and limb position for real-time computer graphics animation in the 1970s, and since then, a number of different designs have been proposed [4]. A low-cost version named the Power Glove [5], was commercialized by Mattel Intellivision as a control device for the Nintendo video game console in 1989 and became well known among video games players. Chambers et. al proposed a probabilistic hierarchical framework to extract gestures and significant events of Kung Fu martial art movements acted out by an instructor in a simulated training video using accelerometers and the Hidden Markov Model [6]. In another work, Chambers et. al proposed the use of the Hierarchical Hidden Markov Model (HHMM) in conjunction with a filler model for segmenting and classifying gestures at differing levels of detail. In this work, sports video was augmented with accelerometer data from wrist band worn by umpires in the game. The gestures they recognized are: Dead Ball, Four, Last Hour, Leg-Bye, No Ball, One Short, Out, Penalty Runs, TV Replay and Wide [7], [8]. Another popular waay to recognize hand gesture is to use kineect [9].

Gesture detection was successfully recognized using a feature vector and a real-time histogram based algorithm by Gomez et. al.[10]. Wang et. al recently developed a simple and inexpensive for 3D articulated user-input using the hands [11]. Their approach uses a single camera to track a hand, wearing an ordinary cloth glove that is imprinted with a custom pattern. Bhansali et. al proposed a method of Gesture recognition to Make Umpire Decisions by using subtraction method and gradient method [12]. They tested the subsequent six gestures particularly OUT, SIX, NEWBALL, NO-BALL, DEADBALL and FOUR. Google is recently developing a system called project soli [13] where they use special radar sensor to detect the fingers movement. Soli sensor technology works by emitting electromagnetic waves in a broad beam. Objects within the beam scatter this energy, reflecting some portion back towards the radar antenna. Properties of the reflected signal, such as energy, time delay, and frequency shift capture rich information about the objects characteristics and dynamics, including size, shape, orientation, material, distance, and velocity. In project soli there are some sensors are used but those are not attached with the gesture performers hand or body. So these can be called as a hybrid system where sensor and radar vision both are used simultaneously.

Sensor-based systems had limited accuracy and were tethered to computers using cumbersome wiring [4-8]. They were meant for very specific applications and were never commercialized. Sensor-based techniques, however, have advantage that they can be used in much less constrained domains and are not reliant on lighting conditions or camera calibration. But vision based gesture recognition has to concentrate on recognition of individual gestures in constrained environments. Most of the vision based works stated above are designed only for detecting static hand gesture [9, 10]. They were unable to detect the dynamic hand gesture in constrained environment.

In contrast to these, we intended to design a vision-based system using logistic regression machine learning technique which can detect both static and dynamic hand gestures of a cricket umpire. Our goal is trying to recognize the gestures an umpire performs in a match and update the scoreboard for the corresponding gesture accurately. We trained a haar-cascade-classifier to detect human wrists from the video stream from a static camera. Then the selected region of interest is continuously checked through the multiclass logistic regression model if a gesture is matched. Then accordingly the score is updated.

## II. Proposed Methodology

Our proposed method for recognizing cricket umpire gesture from real time video using logistic regression algorithm has basic two parts. These are: 1) Learning Phase, 2) Recognition phase. In the learning phase we have to give a lot of gesture images as training data for input. Each of the training image is resized to 20x20 pixel. This is done for fast and efficient computation. Then the resized images are converted to grayscale which is also for efficiency. Then all the images put into a matrix where each row of the matrix refers the pixel intensity of an image. The last column of the matrix represents the output (which gesture picture is in the corresponding image) of that image. Then using the matrix cost function is calculated and minimized by using gradient descent algorithm. For the lowest value of the cost function the corresponding parameter values are consider as weight .

Now on the recognition phase we capture video from a static camera or any other source, then we separate the frames of the video. After separating to select the region of interest from the input images we use Haar-Cascade-Classifier. After selecting the region of interest we convert it to a 20x20 pixel image , vectorize it and send the image feature value X and previously obtain weight  to logistic regression hypothesis. The hypothesis gives the probability of a gesture to be true or false. The recognition step works in real time environment and it can provide output at a very decent amount of time.

### A. Learning Phase

*1) Input Training Image:* In first phase of learning the we have to collect a lot of sample data. We use cricket umpires gesture RGB image as input data. It is better to collect a large amount and accurate data because the performance of our system is directly proportional to the input data. Usually all the decisions in a cricket match involve some kind of gesture by hand from the umpire. So we particularly crop the wrist portion of the image which fairly defines a decision. After

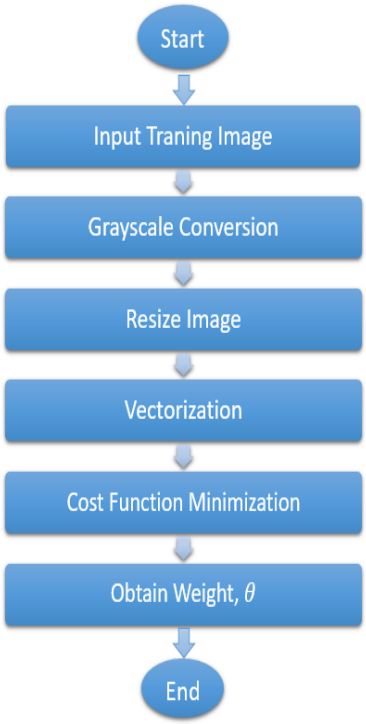


Fig. 1: Proposed Framework for Learning

collecting data for each gesture we have to give them as an input of the system.

*2) Grayscale Conversion:* Now we convert all the given RGB training images to grayscale. A grayscale digital image is an image in which the value of each pixel is a single sample, that is, it carries only intensity information. Images of this sort, also known as black-and-white, are composed exclusively of shades of gray, varying from black at the weakest intensity to white at the strongest. Grayscale images are often the result of measuring the intensity of light at each pixel in a single band of the electromagnetic spectrum (e.g. infrared, visible light, ultraviolet, etc.), and in such cases they are monochromatic proper when only a given frequency is captured. But also they can be synthesized from a full color image.

*3) Resize Image:* After giving all the training images we have to resize them to a very smaller version. This is because the image we give input are very high resolution which need much power and time to compute. So to increase efficiency we convert all the sample image into a smaller size. We resize the image into 20x20 pixel, which is very small in size, but sufficient for calculation.

*4) Vectorization:* In logistic regression we need to find out the feature value of each training image. So we take the pixel intensity of each pixel and create a two dimensional matrix. In our case we iterate through the previously resized 20x20 pixel images and save each image pixel values in each row of the matrix. Each column in the matrix represents a pixel value and each row represents a single image. Each row of the matrix contains 401 values where first 400 values are the pixel intensity of the image and the last value is the output of that image. All images from different gesture are stored in the same matrix.

*5) Cost Function Minimization:* We know the hypothesis of logistic regression is:

$$P(y=1|x) = h_\theta(x) = \frac{1}{1+\exp(-\theta^T x)} \equiv \sigma(\theta^T x) \quad (1)$$

$$P(y=0|x) = 1 - P(y=1|x) = 1 - h_\theta(x) \quad (2)$$

And the cost function is:

$$J(\theta) = -\sum_i \Big( y^i \log(h_\theta x^i) + (1-y^i)\ \log(1-h_\theta x^i)\ \Big) \quad (3)$$

We now have a cost function that measures how well a given hypothesis $h_\theta$ fits our training data. We have to minimize the cost function to find out the optimal value of the weight $\theta$. So we have our hypothesis function and we have a way of measuring how well it fits into the data. Now we need to estimate the parameters in the hypothesis function. That's where gradient descent is used.

Suppose that we graph our hypothesis function based on its fields $\theta_0$ and $\theta_1$.We put $\theta_0$ and $\theta_1$ on the x and y axis and the cost function on the vertical z axis respectively. The points on the graph will be the result of the cost function using the hypothesis with those specific $\theta$ parameters. We will have succeeded when our cost function is at the very bottom of the pits in our graph, i.e. when its value is the minimum.

*6) Obtain Weight($\theta$):* After we get the minimum value of J($\theta$) we take the corresponding values of $\theta$ which is our desired weight. We save the values of $\theta$ in a matrix and our learning phase is complete.

### *B. Recognition Phase*

*1) Video Input:* The first step of recognition phase is gesture video input. User have to open the program and perform an umpire gesture in front of the camera. This video is taken as input to the system and send for further analysis.

*2) Frame Separation:* When we have the input video, we have to separate the frame to analyze them. We will use each frame as an image. We use vectorization as before to keep the image as a matrix. Frame separation is applied because it is quiet hard to analyze the whole video rather than analyze a frame. So in video processing it is common use to separate the frames and then analyze those as an individual image.

*3) Region of Interest Selection:* Our goal is to recognize the gesture from an image, therefore we use only gesture images to train our system. But the image we got as an input there can be other things too. So we have to find the gesture part from the image which is our region of interest. In order to do that we use Haar-Cascade classifier algorithm. Haar-Cascade classifier can be used to classify a specific type of object. In our case we design the classifier to recognize human hand because most of the gesture of cricket umpire is performed by

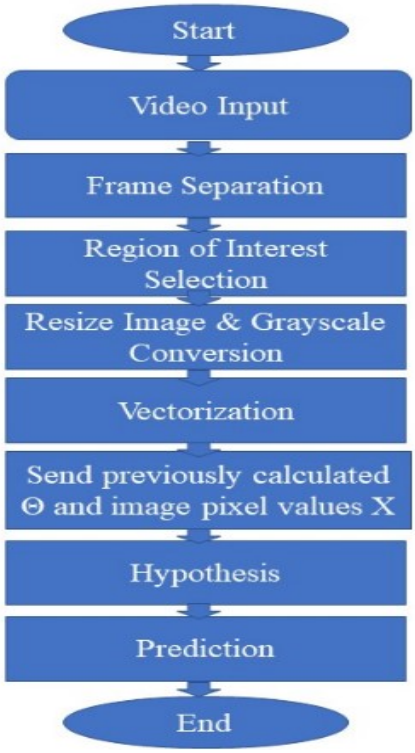


Fig. 2: Proposed Framework for Recognition

hand. After recognizing the hand area from the input image it crops that specific part of the image and we do our further calculation for that part only.

*4) Resize Image and Grayscale Conversion:* After selecting the region of interest, they are converted to grayscale format and resized into 20x20 pixel. This is because a high resolution image will take much longer time and computational power to compute, which is not preferable for real time operation.

*5) Prediction from Hypothesis:* In logistic regression it output a binary result "yes" or "no" which is derived as 1 or 0. So we use a hypothesis class to try to predict the probability that a given example belongs to the "1" class versus the "0" class. Specifically, we will try to learn a function of the form:

$$P(y=1|x) = h_\theta(x) = \frac{1}{1+\exp(-\theta^T x)} \equiv \sigma(\theta^T x) \quad (4)$$

$$P(y=0|x) = 1 - P(y=1|x) = 1 - h_\theta(x) \quad (5)$$

To get a prediction from the hypothesis function we need to calculate feature value X from the input image and weight $\theta$ from the training image. The form for our hypotheses $h_\theta(x)$ to satisfy $0 \leq h_\theta(x) \leq 1$. This is accomplished by plugging $\theta^T x$ into the Logistic Function.

$$h_\theta(x) = g(\theta^T x) \quad (6)$$

$$z = \theta^T x \quad (7)$$

$$g(z) = \frac{1}{1+e^{-z}} \quad (8)$$

The function g(z), shown here, maps any real number to the (0, 1) interval, making it useful for transforming an arbitrary-valued function into a function better suited for classification. $h_\theta(x)$ will give us the probability that our output is 1. For example, $h_\theta(x)$=0.7 gives us a probability of 70% that our output is 1. Our probability that our prediction is 0 is just the complement of our probability that it is 1 (e.g. if probability that it is 1 is 70%, then the probability that it is 0 is 30%). We used a multiclass one-vs-all classifier where each gesture is trained individually by choosing all other gestures to be not true.

## III. Result

For the experiment 5 different gestures were taken. 1000 samples were taken for each gesture. The samples were preprocessed. The images were converted to greyscale and resized into 20/20 pixel images. The pixel values were saved in a matrix. The last column of each row defined which gesture does it represent. This way a one-vs-all logistic regression model was used to build logistic regression classifier.

A few sample images are shown in Fig. 3.

Fig. 3: Sample input gestures for four (on top), six (on left), wide-ball (on middle) , no-ball (on bottom right), out (bottom middle)

The sample images are then converted to greyscale as in Fig. 4.

The region of interest is selected by the haar-cascade-classifier and then the logistic regression model predicts from the resized region of interest which gesture matches most with it. According to the matching the score is updated. A few output from the experiment are shared in Fig. 5.

A statistics of the performance is given below :

(a) Original Image

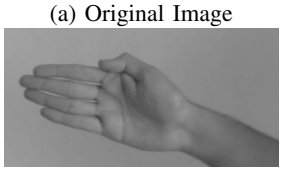

(b) Greyscale Image

Fig. 4: Greyscale conversion

We trained our system to recognize five different gestures. These gestures are delivered by 10 different users. Each of them deliver these 5 gesture multiple times and the success rate are calculated depending on accurately detection of those gestures by the system. We take those data and measure the accuracy of our system in two different ways 1) Accuracy rate based on different people and 2) Accuracy rate based on Different Gesture Accuracy rate based on different people: In this section the sample gesture along with its successful rate for each different person are discussed. For each different person the successful rate can be mentioned as following theory: SR= GR/GD*100Here, SR=Success rate for each different person GR=Total number of gesture successfully recognized by the system GD= Total number of gesture delivered by the user. Following the above theory, the chart with successful rate is found given in following.

TABLE I: Success rate of different people

| Person | GD | GR | SR |
|---|---|---|---|
| 1 | 75 | 68 | 90.66 |
| 2 | 75 | 69 | 92.00 |
| 3 | 75 | 66 | 88.00 |
| 4 | 75 | 70 | 93.33 |
| 5 | 75 | 67 | 89.33 |
| 6 | 75 | 65 | 86.66 |
| 7 | 75 | 71 | 94.66 |
| 8 | 75 | 69 | 92.00 |
| 9 | 75 | 68 | 90.66 |
| 10 | 75 | 70 | 93.33 |

Now if the average successful rate is considered over this chart than mean value will be 91.06%.

Accuracy Rate of Different Gesture: Previously result for different person are given. Now in cricket gesture for different event are different. Some are simple and some are complex. Some required the use of two hands and some required use of only one hand. Time is also variant for different gesture. Though much complex gesture is neglected. Here the accuracy rate for each gestures are given.

Now if the average successful rate is considered over this chart than mean value will be (88.00+90.00+86.00+83.33+93.33)/5 = 88.13 A total of 10 people participated to test our system, each of different body structure. We trained our system to recognize five cricket umpires gesture. Depending on these two criteria success rate is found which already being mentioned. If the results are shown in graph chart than we get the following charts.

(a) No Ball Detection

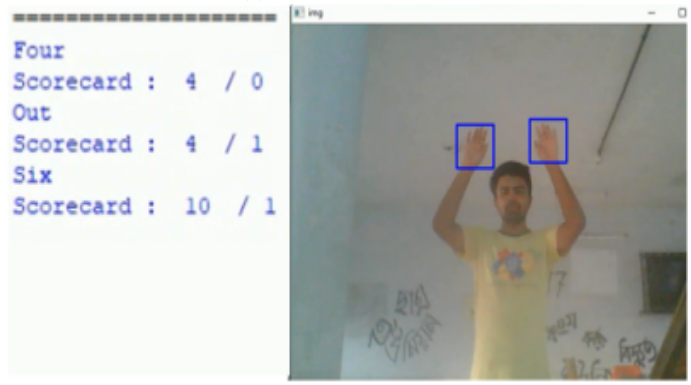


(b) Six Detection

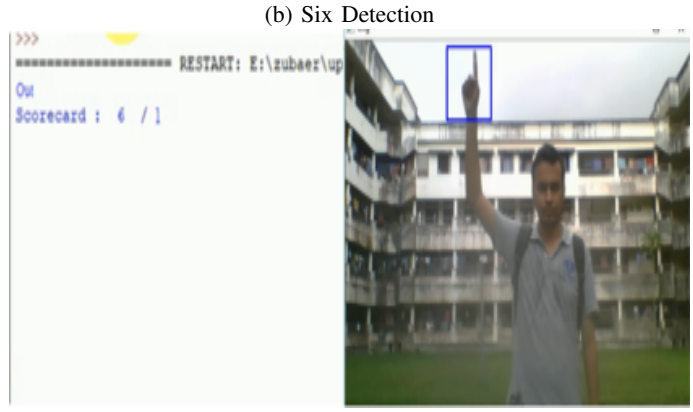


(c) Out Detection

Fig. 5: Scoreboard Update

TABLE II: Accuracy rate for different gesture

| Gesture | GD | GR | SR |
|---|---|---|---|
| Out | 150 | 132 | 88.00 |
| No-Ball | 150 | 135 | 90.00 |
| Wide-Ball | 150 | 129 | 86.00 |
| Four | 150 | 125 | 83.33 |
| Six | 150 | 140 | 93.33 |

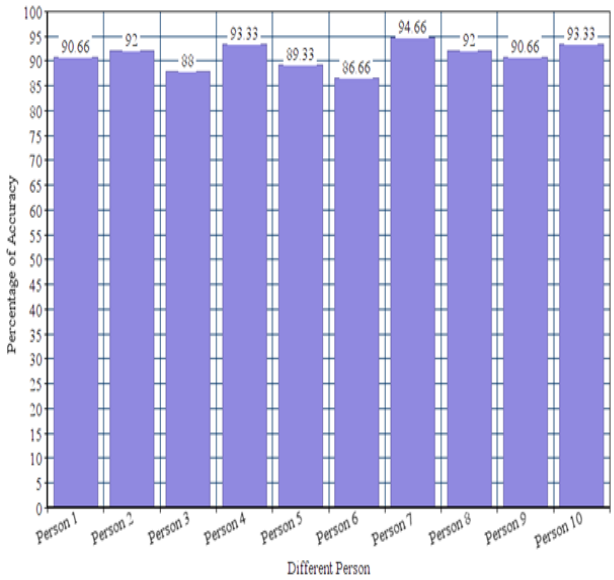


Fig. 6: Success rate depending on person

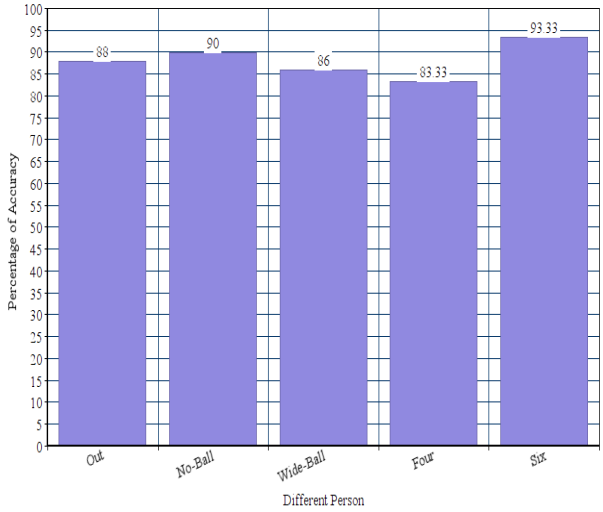


Fig. 7: Success rate depending on gesture

## IV. Conclusion

The novelty of our work is that it successfully detects the appropriate gestures in the game of cricket without the help of any specialized sensor or gloves. Only a static camera is needed on the umpire. As the background is mostly fixed the background subtraction is very easily done. However this approach worked better for static gestures like out, no, six, wide etc. However in case of dynamic gesture like four the efficiency was found to be poor. There is a room of improvement in this case.

Multiple classifiers were need to be trained in order to make it work. However, a much easier and simple solution to find out the region of interest can be found out which will decrease the complexity of the program as well as increase the efficiency with respect to time.

## References


[1] S. Mitra and T. Acharya, "Gesture recognition: A survey," *IEEE Transactions on Systems, Man, and Cybernetics, Part C (Applications and Reviews)*, vol. 37, no. 3, pp. 311–324, 2007.

[2] "Top 10 list of the internet world's most popular sports," http://www.topendsports.com/world/lists/popular-sport/fans.htm.

[3] P. Premaratne, "Historical development of hand gesture recognition," in *Human Computer Interaction Using Hand Gestures*. Springer, 2014, pp. 5–29.

[4] D. J. Sturman and D. Zeltzer, "A survey of glove-based input," *IEEE Computer graphics and Applications*, vol. 14, no. 1, pp. 30–39, 1994.

[5] D. L. Gardner, "The power glove," *Des. News*, vol. 45, pp. 63–68, 1989.

[6] G. S. Chambers, S. Venkatesh, G. A. West, and H. H. Bui, "Hierarchical recognition of intentional human gestures for sports video annotation," in *Pattern Recognition, 2002. Proceedings. 16th International Conference on*, vol. 2. IEEE, 2002, pp. 1082–1085.

[7] G. S. Chambers, S. Venkatesh, and G. A. West, "Automatic labeling of sports video using umpire gesture recognition," in *Joint IAPR International Workshops on Statistical Techniques in Pattern Recognition (SPR) and Structural and Syntactic Pattern Recognition (SSPR)*. Springer, 2004, pp. 859–867.

[8] G. S. Chambers, S. Venkatesh, G. A. West, and H. H. Bui, "Segmentation of intentional human gestures for sports video annotation," in *Multimedia Modelling Conference, 2004. Proceedings. 10th International*. IEEE, 2004, pp. 124–129.

[9] Y. Li, "Hand gesture recognition using kinect," in *Software Engineering and Service Science (ICSESS), 2012 IEEE 3rd International Conference on*. IEEE, 2012, pp. 196–199.

[10] I. Gómez-Conde, D. Olivieri, X. A. Vila, and S. Orozco-Ochoa, "Simple human gesture detection and recognition using a feature vector and a real-time histogram based algorithm," *Journal of Signal and Information Processing*, vol. 2, no. 04, p. 279, 2011.

[11] R. Y. Wang and J. Popović, "Real-time hand-tracking with a color glove," in *ACM transactions on graphics (TOG)*, vol. 28, no. 3. ACM, 2009, p. 63.

[12] L. Bhansali and M. Narvekar, "Gesture recognition to make umpire decisions," *International Journal of Computer Applications*, vol. 148, no. 14, 2016.

[13] "Your hands are the only interface you'll need," https://atap.google.com /soli/.

# Bangla Handwritten Digit Classification and Recognition Using SVM Algorithm with HOG Features

Hasin Rehana
Department of Computer Science & Engineering (Rajshahi University of Engineering & Technology, Bangladesh)
hasin.ruet13@gmail.com

*Abstract*— **This paper presents the basic approach of multiclass classification for handwritten digit recognition using Support Vector Machine and a comparative accuracy analysis for three well known kernel functions (linear, RBF and polynomial) and feature vectors corresponding to different cell sizes. However, the process of digit recognition includes several basic steps such as preprocessing, feature extraction and classification. Among them, feature extraction is the fundamental step for digit classification and recognition as accurate and distinguishable feature plays an important role to enhance the performance of a classifier. Histogram of Oriented Gradient (HOG) feature extraction technique has been used here. Therefore, for various cell sizes, the experimental results show around 98-100% accuracy for trained data and 91-97% accuracy for test set data according to various kernel functions. The target of this paper is to select a kernel function best suited for a particular resolution of image.**

***Keywords— Supervised Learning, HOG, Feature Extraction, Classification, Support Vector Machine, Kernel Function.***

## I. INTRODUCTION

Digit recognition is a subset of Optical Character Recognition (OCR). Digit recognition can be divided into two types, handwritten and fixed font printed digit recognition [1]. However, the main challenge of handwritten digit recognition is to deal with wide variety of writing styles. The objective of handwritten digit recognition is to read digits from scanned images such as envelope, license plate, bank cheque etc. and digitalize them for storing and further using [2]. Handwritten digit recognition is more difficult comparing to printed digits as the size, shape and style of digits vary from man to man. The accuracy of classification and recognition largely depends on the feature extraction method. In this paper Histogram of Oriented Gradient feature extraction technique is used to obtain features.

The rest of the paper is organized as follows: section II mentions the necessary steps of digit recognition and briefly describes the methodology of preprocessing, feature extraction and classification steps respectively. The main focus of this paper is section III that includes a comparative performance analysis among three major SVM kernels (linear, RBF and polynomial). Experimental results are reported in section IV to compare the accuracy level of digit recognition for different kernel functions and cell sizes. Finally, section V concludes the experimental analysis.

## II. METHODOLOGY

The digit recognition process is mainly divided into 3 major parts: preprocessing, feature extraction and classification. The steps are shown in figure 1.

### A. Preprocessing

The steps performed before feature extraction is called preprocessing. The aim of preprocessing is the improvement of the image data that suppresses unwanted distortions or enhances some image features important for further processing. Pre-processing steps include image acquisition, binarization, noise removal, skew detection, segmentation and scaling [3].

*1) Image Acqusition:* Images can be captured using any device that has a camera or scanner [4]. Images from PDF file can also be fed into the system. The images can be a single digit or a set of digits collected from number plate, bank cheque, postal code etc.

*2) Binarization of image:* RGB image is converted to gray scale before binarizing it. The binarization is performed based on a fixed threshold value using Otsu's threshold method [5].

*3) Noise Removal:* Noise removal is performed to reduce the probability of misclassification because of low quality of image. Here median filter is used for noise removal [6]. It is a highly used smoothing technique.

*4) Skew Detection:* Usually skew is occurred due to angular placement of image while acquisition. Skew is usually removed by rotating the image to opposite angle of the estimated skew value [2].

Figure 1. Fundamental steps of digit classification.

*5) Segmentation:* Digit segmentation is the operation that decomposes an image into sub images of individual digits. It includes line segmentation and character segmentation [7]. Line segmentation is performed by scanning the image horizontally for a particular number of frequency of white pixels in each raw. Then digit segmentation is done by scanning each line vertically to find gap between digits and store the sub images.

*6) Scaling:* To compare the feature vectors each digits have to be scaled to a particular size. With the increased size of

978-1-5386-2307-7/17/$31.00 ©2017 IEEE

image, more features can be extracted leading to higher accuracy. But the memory requirement and time complexity also increases as well. On the contrary, smaller images provide less features leading to lower accuracy. To balance between feature size and processing time, all the images are scaled to 32x32 matrices.

### *B. Feature Extraction:*

Feature extraction plays an important role in the area of image processing and machine learning. Feature extraction techniques are applied to get feature vector that will play an effective role in classifying and recognition of image or a class. A feature vector is a vector that contains information that can describe an object's important characteristics. A well-defined feature vector consists of discriminating information, which has the ability to distinguish one class from another. In image processing, features can take many forms. It may be the row intensity value of each pixels, color components, length, area, gradient magnitude, gray-level intensity value etc. However, feature extraction means generating a new set of features from a huge amount of original features. There are various types of feature extraction techniques such as zoning, Fourier transform, Gabor filter etc. [8]. In this paper, Histogram of Oriented Gradient (HOG) features are used. HOG feature extraction steps mainly include gradient calculation, histogram generation and block normalization [9], [10]. Firstly, the image is divided into predefined equal sized smaller regions called cells. Each cell has a one dimensional histogram of oriented gradient direction. The gradient orientation is quantized into 9 bins spaced from 0° to 180°. The cells are grouped into bigger units called blocks. These blocks are overlapped and the cells are shared among the neighboring blocks like figure 2. This overlapping may seem redundant but it is helpful for better performance. The number of elements for each block is n*n*9 for block size [n n]. Block normalization is done for contrast stretching.

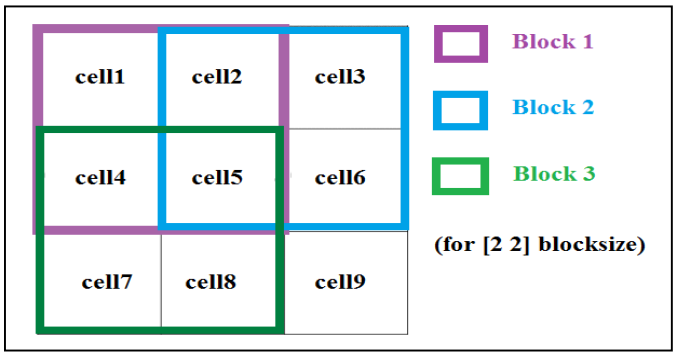


Figure 2. Overlapping of cells in neighboring blocks.

Figure 3. HOG feature extraction steps.

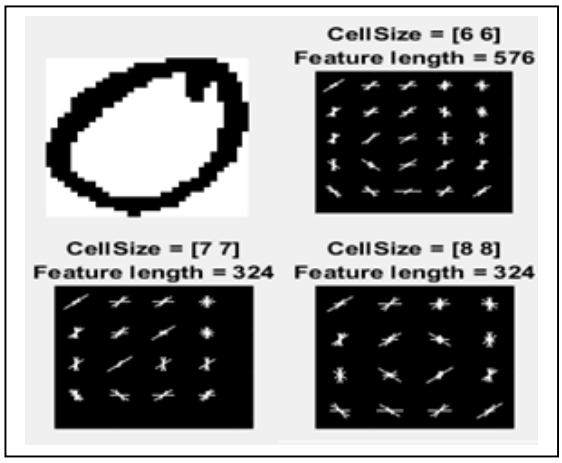


Figure 4. Extracted HOG features of "0"for different cell sizes

A simplified version of HOG feature extraction steps are shown in figure 3. However, histogram of oriented features of a sample digit is shown in figure 4 for three different cell sizes to understand the effect of cell size ie. resolution in HOG feature. The cell size must be small enough to capture the digits but large enough so that the analysis is efficient.

### *C. Classification:*

Classification is the method of identifying the category a test data, on the basis of features extracted from the training data set. If a training set of correctly identified observation is available for training classification algorithms, then it is called supervised learning. Well known classification algorithm includes Support vector machine, Decision trees, neural network, Naïve Bayes classifier etc. There are two types of classifications. Binary classification indicates that there must be two classes. On the contrary, multi class classification is the problem of classifying instances into more than two classes.

- *Multi class SVM classification*

Support vector machine are supervised learning based upon the idea of maximizing the margin i.e. maximizing the minimum distance from the separating hyper plane to the nearest example [11]. A supervised learning algorithm analyzes the training data and produces an inferred function, which can be used for mapping new examples. The basic SVM supports only binary classification, but extensions have been proposed to handle the multi class classification problems. In these extensions, additional parameters and constraints are added to the optimization problem to handle the separation of the different classes. K*(K-1)/2 binary SVM models using one-vs.-one coding design has been used here [12].

- *Kernel Function:*

Kernel methods are a class of algorithms for pattern analysis, whose best known member is the support vector machine. This approach is called kernel trick. Kernel functions are used to classify sequence of texts, images, data, graphs as well as vectors. It takes two inputs and split out how similar they are. In case of SVM, there are a few well-known kernel functions such

as linear kernel, RBF kernel, polynomial kernel etc. Linear kernel means no kernel, which is the simplest method. The Gaussian, i.e. redial basis function (RBF) kernel is a popular kernel function used in various kernelled learning algorithms. In particular, it is commonly used in SVM classification. The polynomial kernel is a kernel function also commonly used with SVM and other kernelled models, that present the similarity vectors in a feature space over polynomials of the original variables, allowing learning of non-linear models. These three kernels are mentioned in Table 1. C and Gamma are parameters for a non-linear SVM with RBF kernel. However, a standard SVM tries to find a margin that separates all positive and negative examples, which result in a poorly fit model if any of the examples are mislabeled. C is the parameter for soft margin cost function which minimizes this over-fitting problem.

TABLE I. KERNEL FUNCTIONS

| **Kernel** | ***Formula*** |
|---|---|
| Lineal | X1*X2 |
| Gaussian(RBF) | $\frac{\exp(-\|\|X1-X2\|\|^2)}{2\sigma^2}$ |
| Polynomial | $(1+X1*X2)^p$ |

Gamma plays an important role in Gaussian function. If the gamma is large, then variance is small implying the support vector does not have wide-spread influence. Actually, large gamma leads to high bias and low variance models and vice versa. However, the scale is selected heuristically based on the variance/covariance structure in the data. The value of $\sigma$ used here is 1. So the resulting equation of Gaussian kernel is,

$$f(X1,X2) = 0.5 * \exp(-||X1-X2||^2) \quad .(1)$$

On the other hand, the order of polynomial kernel used here is p=3 i.e. the function for polynomial kernel becomes,

$$f(X1,X2) = (1+X1*X2)^3 \quad .(2)$$

From equation (2) and (3) it is quite clear that the polynomial kernel has higher dimensionality than the Gaussian kernel which is a clear indication that the polynomial kernel should provide higher accuracy than the Gaussian kernel.

## III. COMPARATIVE ACCURACY ANALYSIS AMONG DIFFERENT KERNELS

6000 handwritten Bangla digit images from Mendeley Data were divided into training set (80%) and test set (20%) [13].

Number of training elements = 4800

Number of testing elements = 1200

Sample data set are shown in figure 5. Linear SVM is very fast. On the other hand RBF and polynomial kernels are comparatively slower. Despite these disadvantage, RBF and polynomial kernel is very much useful for the situation where the data analyst doesn't have large amount of features. Efficiency of SVM depends greatly on the size of feature vector used. With the increasing size of feature vector, both time complexity and space complexity is increased. The comparative relation among kernel functions, feature size and resulting accuracy is shown in figure 6 and 7. When feature vector is much bigger (such as 4 times bigger) than number of observation, RBF kernel becomes very much sensitive to outliers. Because of high variance of classifier margin, overfitting occurs and the accuracy of SVM degrades because of misclassification. In this case linear kernel suits good.

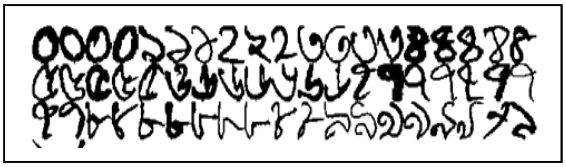

Figure 5. Sample Data set for training system.

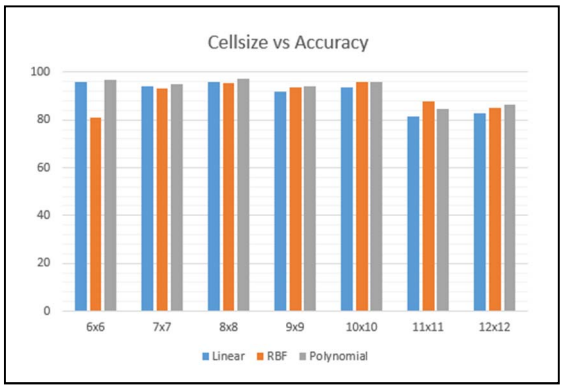


Figure 6. Cell size vs. accuracy(%) for three different kernels of SVM (linear, RBF, Polynomial).

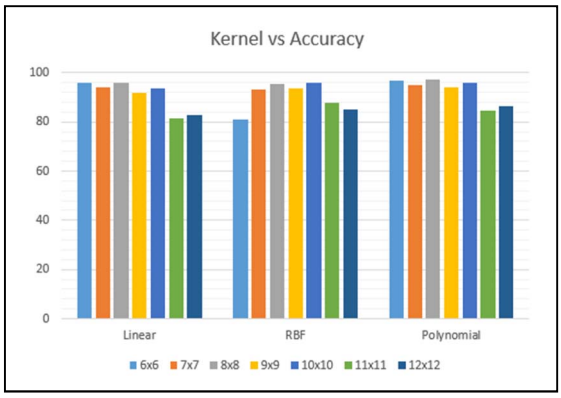


Figure 7. Kernels vs. accuracy(%) with respect to 7 different cell sizes.

On the other hand, when there is a large number of data set available but available feature is limited, RBF and polynomial kernel fits properly with the data set resulting better accuracy. Linear kernel doesn't work good in this case. But if the extracted feature vector is very much smaller than number of observation then using RBF or polynomial kernel results in under-fitting and performance degrades due to miss-classification. For such a situation linear kernel performed

better. Table 2 describes the performance of polynomial SVM classifier for 324 features.

TABLE II. ACCURACY RATE FOR POLYNOMIAL KERNEL USING 324 FEATURES.

| Digits | No. of test data | Correctly identified data | Misclassified with | Error (%) |
|---|---|---|---|---|
| ০ | 120 | 118 | ১ | 1 |
| ১ | 120 | 116 | ৭,৯ | 3 |
| ২ | 120 | 118 | ১ | 1 |
| ৩ | 120 | 115 | ৫,৬ | 4 |
| ৪ | 120 | 117 | ৫,৮ | 2 |
| ৫ | 120 | 112 | ৩,৬ | 6 |
| ৬ | 120 | 111 | ৩ | 7 |
| ৭ | 120 | 117 | ৪ | 2 |
| ৮ | 120 | 120 | - | 0 |
| ৯ | 120 | 114 | ১,৭ | 5 |

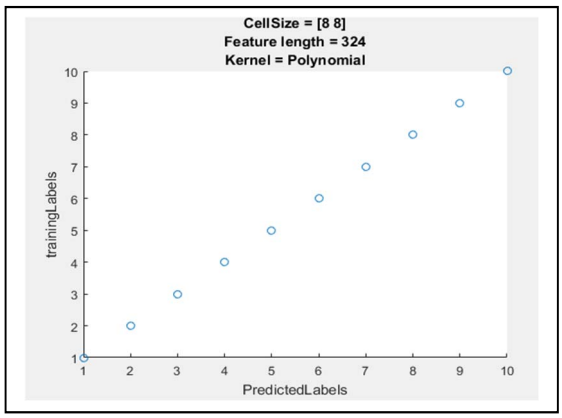


Figure 8. Scatterplot of training labels vs. predicted labels for polynomial kernel with cell size [8 8].

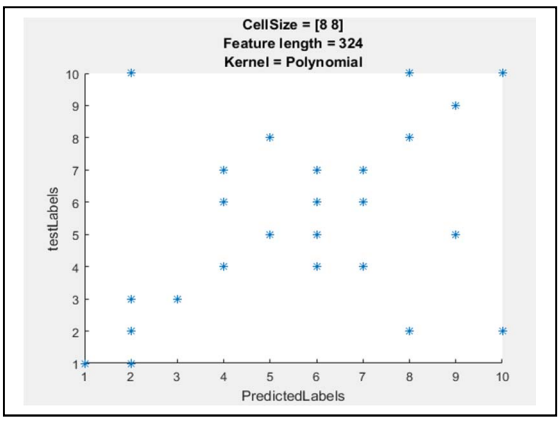


Figure 9. Scatterplot of test labels vs. predicted labels for polynomial kernel with cell size [8 8].

A scatter plot of training label vs. predicted label is shown in fig. 8 for polynomial kernel with 324 feature length. The plot is linear indicating very high accuracy. On the contrary the scatter plot of test label vs. predicted label is shown in fig. 9 which is quite scattered indicating some misclassified data.

## IV. RESULT

The result is summarized in Table 3 Shows that for a very large number of training features linear SVM works very much efficiently. But if the feature size is smaller than the number of observation then RBF or polynomial kernel is preferred because they fit this kind of data set properly, resulting in higher accuracy than linear SVM. A graphical comparison of table III is presented in figure 6 and 7 and the reasons behind such accuracy behavior is briefly described in section III.

TABLE III. COMPARATIVE ACCURACY FOR DIFFERENT KERNEL FUNCTIONS

| Case no. | Training set | | Linear Kernel | | RBF Kernel | | Polynomial Kernel | |
|---|---|---|---|---|---|---|---|---|
| | *Cell size* | *Feature Length* | *Training Accuracy (%)* | *Test Accuracy (%)* | *Training Accuracy (%)* | *Test Accuracy (%)* | *Training Accuracy (%)* | *Test Accuracy (%)* |
| I | 6x6 | 576 | 99.67 | 95.75 | 100 | 80.75 | 100 | 96.67 |
| II | 7x7 | 324 | 98.33 | 93.91 | 99.97 | 93.33 | 100 | 95 |
| III | 8x8 | 324 | 99.27 | 95.75 | 100 | 95.58 | 100 | 97.08 |
| IV | 9x9 | 144 | 95.81 | 91.92 | 98.67 | 93.67 | 99.97 | 93.83 |
| V | 10x10 | 144 | 97.31 | 93.42 | 99.23 | 95.67 | 99.98 | 95.67 |

## V. CONCLUSION

In this paper, comparative performance of three well-known kernels of SVM classification algorithm has been investigated to find out the appropriate kernel function for used sample dataset of Bangla handwritten digits. Experimental result shows that using HOG features, handwritten digit recognition shows at most 97.08% accuracy for polynomial kernel function. This performance mostly depends on the preprocessing and feature extraction techniques. However, the recognition rate can be improved using the combination of more than one feature extraction techniques.

## ACKNOWLEDGMENT

Thanks to my project supervisor Dr. Md. Ali Hossain (Assistant Professor, RUET) for his guidance, patience, suggestions and encouragement. Thanks to the anonymous reviewers of EICT-2017 for their insightful suggestions and comments that allowed me to improve this paper. However, any errors are my own and should not tarnish the reputation of these esteemed persons.

## REFERENCES

[1] J. Mantas, "An overview of character recognition methodologies." *Pattern recognition* 19.6 (1986): 425-430.

[2] B. B. Chaudhuri, and U. Pal. "A complete printed Bangla OCR system." *Pattern recognition* 31.5 (1998): 531-549.

[3] Md. Mahbub Alam, and Dr. M. Abul Kashem. "A complete Bangla OCR system for printed characters." *JCIT* 1.01 (2010): 30-35.

[4] Md. Mojahidul Islam, Md. Imran Hossain, and Md. Kislu Noman. "Bangla character recognition system is developed by using automatic feature extraction and XOR operation." *Global Journal of Computer Science and Technology* (2013).

[5] N. Otsu, "A threshold selection method from gray-level histograms." *IEEE transactions on systems, man, and cybernetics* 9.1 (1979): 62-66.

[6] Sumana Barman, Amit Kumar Samanta, and Tai-hoon Kim. "Design of a view based approach for Bengali Character recognition." *Int. J. Advanced Science and Technology*. 2010.

[7] Nallapareddy Priyanka, Srikanta Pal, and Ranju Mandal. "Line and word segmentation approach for printed documents." *IJCA Special Issue on Recent Trends in Image Processing and Pattern Recognition-RTIPPR* (2010): 30-36.

[8] Gaurav Kumar, and Pradeep Kumar Bhatia. "A detailed review of feature extraction in image processing systems." *Advanced Computing & Communication Technologies (ACCT), 2014 Fourth International Conference on*. IEEE, 2014.

[9] Yuqian Li, and Guangda Su. "Simplified histograms of oriented gradient features extraction algorithm for the hardware implementation." *Computers, Communications, and Systems (ICCCS), International Conference on*. IEEE, 2015.

[10] Navneet Dalal, and Bill Triggs. "Histograms of oriented gradients for human detection." *Computer Vision and Pattern Recognition, 2005. CVPR 2005. IEEE Computer Society Conference on*. Vol. 1. IEEE, 2005.

[11] Nibaran Das, et al. "Handwritten Bangla basic and compound character recognition using MLP and SVM classifier." *arXiv preprint arXiv:1002.4040* (2010).

[12] Christopher M. Bishop, *Pattern recognition and machine learning*. springer, 2006.

[13] Nabeel Mohammed, Sifat Momen, Anowarul Abedin, Mithun Biswas, Rafiqul Islam, Gautam Shom and Md Shopon, "BanglaLekha-Isolated", *Mendeley Data*, v2, 2017.

# A New Approach to Image Classification by Convolutional Neural Network

Shamim Ibne Shahid[1], Md. Shahjahan[2]
[1]Khulna University of Engineering & Technology, Bangladesh
[2]Khulna University of Engineering & Technology, Bangladesh
titu2297@yahoo.com, jahanATeee.kuet.ac.bd

*Abstract*— The backpropagation gradient through a convolutional neural network to train the weights of the filters(kernel) is the same as a regular deep network which is to calculate the partial derivative of the error function at the output of fully connected layer with respect to these weights. In this paper we introduce the Fixed Kernel Convolutional Neural Network that skips the training process of the filters between the convolutional layers and exploits the idea of a predefined kernel remaining fixed throughout the training process and a simple feedforward layer that can help acquiring invariances among images having similar kind of patterns at different locations. We compare the performance of the proposed architecture with few other classifying techniques which it outperforms using the Caltech-256 database.

***Keywords—Averagepooling,Maxpooling,Feedforward network, Target vector.***

## I. INTRODUCTION

Convolution neural networks(CNN) are designed in a way so it can perform classification/processing of data that are in the form of a matrix such as a colored image for example which consists of three 2D arrays of identical size. The basic idea behind a CNN which is known as convolution is to use a kernel consisting of an array of weights that is slided across a matrix data outputting another matrix whose elements are the summations of dot products of these weights with the corresponding elements of superimposed part of the first matrix. This step is always followed by subsampling and might be repeated several times until the fully connected layer. For a while now it has been believed that the use of neural network is most likely to transcend human capability for doing things like pattern recognition, image classification, self-driving etc. Although that sounds tangible, there is still a lot of improvements to be done. Until now, we have seen a few theories that has shown success in recognizing visual image. The first concept of Convolutional Neural Network was presented by Yann LeCun et al. in [1] in the 1980s. which was composed of two kinds of layers, respectively called convolutional layers and subsampling layers. However, many years after that, there was still not a major breakthrough of CNN. One of the main reason was that it was not possible to get ideal result for large size images.

In 2006, Geoffery Hinton and Salakhutdinov published an article in "Science" [2], which opened a new the door to a deep learning era. Hinton suggested that the neural network with multiple hidden layer it is possible to improve the accuracy of classification and prediction by improving different degrees of abstract representation of the original data. Since then artificial neural network has got huge attention. The network we present in this paper possesses a structure that uses the benefits of multilayered feedforward network [3] along with the convolution of image matrix and unlike the conventional CNN structure where several filters have to be learned by the network, we used only one fixed filter. In section 2, we discuss the related works, in section 3, we describe the overall structure of the network structure, in section 4 and 5 the training and testing procedures are described respectively. In section 6, we compare the result obtained by this network with some other classifying methodologies. Finally, we discuss about the lackings and future possibilities of the presented network.

## II. RELATED WORK

There are many classification systems based on multiple modules including feature extraction, segmentation and other image processing techniques. They are used for commercial purposes. The main objective of image processing is to reduce the size of data. Combined with CNN structure such works include the article of Hubel and Wiesel [4] on the structure of the visual cortex in a cat's brain. Even though it has inspired numerous architectures of artificial neural networks designed specifically for visual data processing, it was quite complicated to mimic the process on image recognition. Convolutional neural networks proposed by Yann LeCun [5] represents an structure embracing the idea of various types of neurons organized within one network, each one of them having its specific function in image processing. In [6],[7], [8], utilizing multi-level features in CNNs through skip-connections has been found to be effective for various vision tasks. But however, it is not appropriate in dealing with microscopic images. Convolutional networks are capable of processing the image data with minimum or no preprocessing. There are other notable network architecture innovations which have yielded competitive results. The Network in Network (NIN) [9] structure includes micro multi-layer perceptrons into the filters of convolutional layers to extract more complicated features. In Deeply Supervised Network (DSN) [10], internal layers are directly supervised by auxiliary classifiers, which can strengthen the gradients received by earlier layers. In [11],

978-1-5386-2307-7/17/$31.00 ©2017 IEEE

Deeply-Fused Nets (DFNs) were proposed to improve information flow by combining intermediate layers of different base networks. The augmentation of networks with pathways that minimize reconstruction losses was also shown to improve image classification models [12]. Highway Networks [13] were amongst the first architectures that provided a means to effectively train end-to-end networks with more than 100 layers using bypassing paths along with gating units. Highway Networks with hundreds of layers can be optimized without difficulty. Recent variations of ResNets [14] show that many layers contribute very little and can in fact be randomly dropped during training. This makes the state of ResNets similar to recurrent neural network. FractalNets [15] repeatedly combine several parallel layer sequences with different number of convolutional blocks to obtain a large nominal depth, while maintaining many short paths in the network .

## III. BRIEF DESCRIPTION OF THE PROPOSED ARCHITECTURE

The overall system flow is shown in Fig. 1.It begins with taking a RGB image from the training sample as input which are all resized equally(200×200).

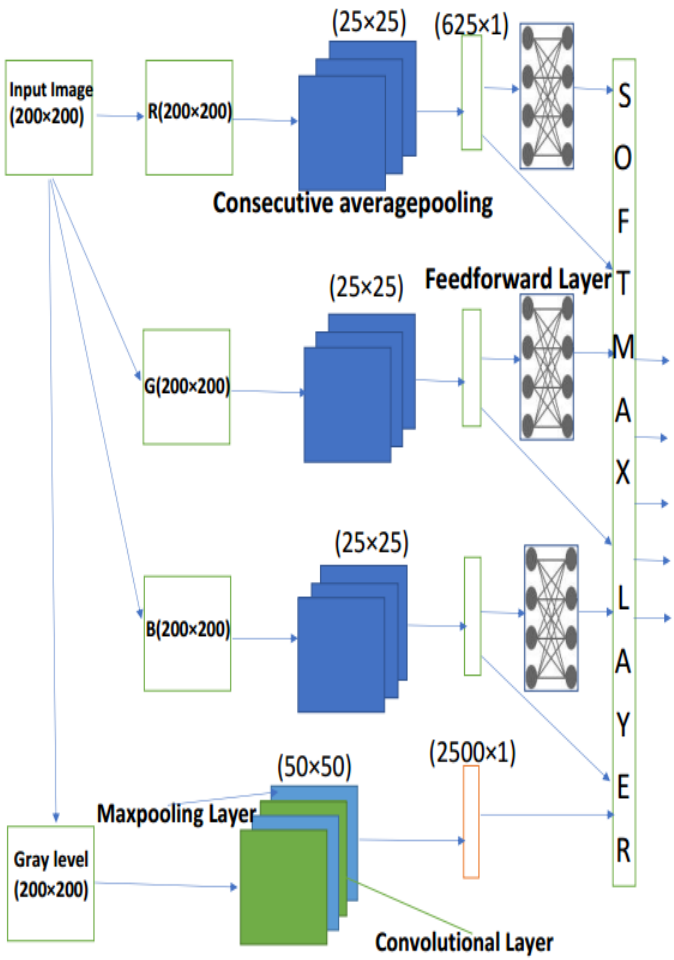


**Fig. 1. Proposed Fixed Kernel CNN Structure**

Each color component matrix of the RGB image is separated while at the same time it is converted into a gray level image. The component matrices are made to separately go through an average pooling layer. Here we average every 2×2 submatrices of the image component which reduces the matrix size into half of its previous value. For example, if we subsample a 200×200 matrix this way, the output layer will yield a matrix of the size 100×100. This process is repeated two more times until the size of the image component reduces to 25×25.The same procedure is followed for all the three-color components of the image. Meanwhile, we apply convolutional layer on the gray level image. For this process the convolution kernel applied here is well suited for extracting the shape of the image. In order to reduce the size of the image here we use a maxpooling layer after each convolution which outputs the maximum value for every 2×2 element of the gray level image. A consecutive convolution and maxpooling operation is applied two times on this network and as a result a 50×50 matrix yields for every input image. Now each 25×25 matrix derived from the three component images and the 50×50 from the gray level image are resized into vertical matrices of the size 625×1 and 2500×1 respectively. The reason why we have to form these vertical matrices is that a fully connected layer can not accept 2D input. The final three vertical matrices from the RGB component are used as input in the in the feedforward network as shown Fig. 1. We fix a target vector of 25 elements for each of the feedforward network whose values are dependent on the output of the last average pooling layer (it will be discussed in the next section). The outputs of every feedforward network are piled up followed by their inputs one after another as shown in the following Fig. 1 to form a vertical matrix which is further integrated with the 2500×1 matrix yielded from the gray level image and fed into the SoftMax layer.

Here in the network structure, we used only one predefined kernel for convoluting on the gray scale image. The filter is so designed that it prioritizes the edge of the object and ignores the background. In a conventional CNN, different kernels are trained for convoluting in different convolutional layers. In the Fixed Kernel CNN, there are two convolutional layers each of which uses the same fixed kernel for convolution. In this way when a gray scale image is repeatedly convoluted and pooled, the effects of different kind of shapes present in the image more or less tend to shift towards the center which is convenient to acquiring invariances. On the other hand, we also take the patterns color components into consideration after reducing its size by repeated average pooling and training a feedforward layer with it. Thus, the network can detect similar attributes of a particular class which helps the network to classify correctly.

## IV. TRAINING

The network keeps taking input data from the sample folder and after being resized equally the color component matrices are sent to a consecutive average pooling layers. The outputs of the last pooling layers are resized into a vertical matrix for all the color component matrices of the input sample which

then acts as input for both the feedforward and SoftMax layer. Each of the feedforward layer consists of 10 hidden neurons. We use tansig function for the hidden layer and pureline function for the output Layer. The target values for the output layer feedforward networks are fixed as a 25×1 vector formed by taking the maximum value of each 5×5 submatrix of the final output from the average pooling layer. The feedforward network uses the following error function for learning: -

$$E=(1/2)\sum_{j=1}^{25} (d_i - y_i)^2$$

where, $y_i$ =Output signal of j-th neuron ;
$d_i$=j-th element of the target vector;

Now once the feedforward networks are trained ,their input values are again forwarded through the network which contributes to the input matrix of the SoftMax layer.

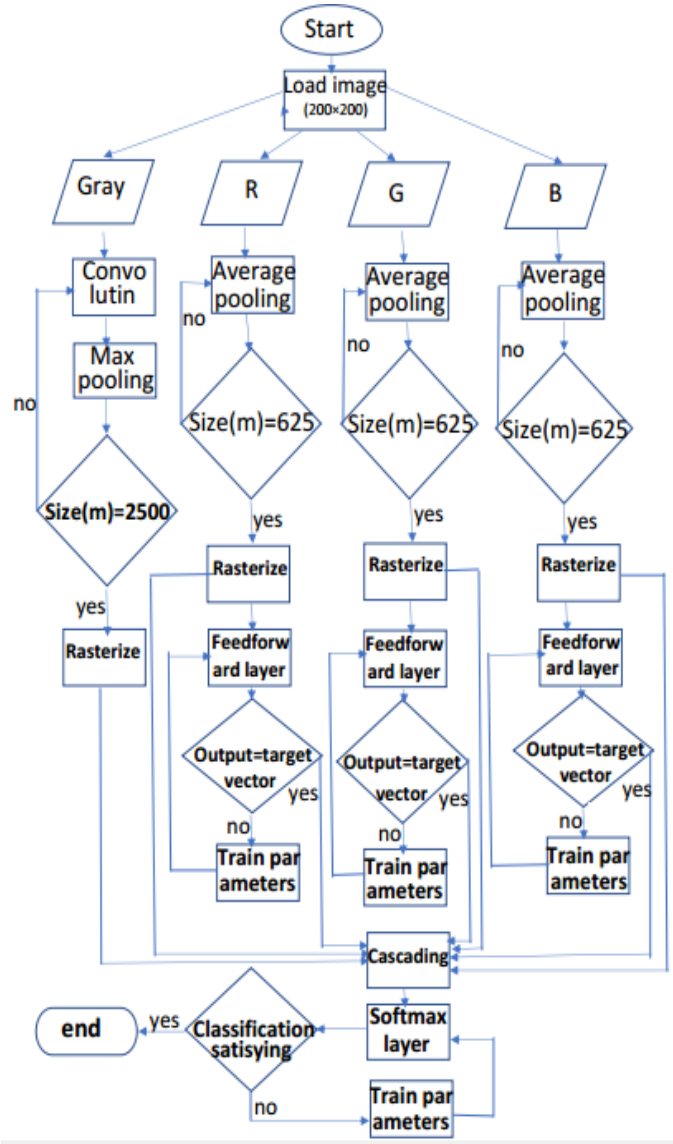


**Fig. 2. Training Flow Chart**

For convoluting the gray level image, the following predefined kernel is used.

$$K=\begin{bmatrix} -1 & -1 & -1 \\ -1 & 8 & -1 \\ -1 & -1 & -1 \end{bmatrix}$$

**Fig. 3(a).**

**Fig. 3(b).**

The filter is shown as image on the right side after its size was changed into 100×100.Each convolution is followed by a maxpooling layer whose function is the same as the average pooling layer except that here we have to take the maximum value for each 2×2 submatrix of the previous layer. The input matrix for the SoftMax layer is thereby set by cascading vertically the output of the feedforward layers followed by their inputs and also the result which is obtained from repeated convolution and maxpooling operation on the gray level image. The target vector for this layer is set as a vertical probability matrix by keeping the element at the position which specifies the type of the input image as 1 and all other elements as 0. The training process of the network finishes once the SoftMax layer is trained against these target values that leads to satisfactory classification of the training image.

## V. TESTING

For testing purpose, an image is processed in the same way as it was used to train the network. The color components after being separately made to pass through the consecutive average pooling layers are given as input to the feedforward layers whose output values help constituting the final input of the SoftMax layer. At the same time the gray level values of the image is also passed through the convolution and maxpooling layer in order. Now, we simply pile up all these values as shown in Fig. 1 and pass it through the trained SoftMax network. If we train the network with five classes, the output of the SoftMax layer would be a vertical matrix of five elements each of which representing the probability of the image to fall under the class specified by the row number of that element. In this network, we classified the image according to the class for which the image shows maximum probability.

## VI. EXPERIMENT & RESULT

For experimenting the performance of the network, we used the Caltech-256 Database[16].Here ,out of the 256 type images ,we selected 5 folders that had comparatively more number of items. After removing the black and white images, the first half portion of each folder was used for training while

the second half portion for testing purposes. The data characteristics so evolved are shown below:

Table 1. Data Characteristics

| | Type | Training | Testing |
|---|---|---|---|
| Class 1 | Motorbike | 394 | 393 |
| Class 2 | Leopard | 95 | 95 |
| Class 3 | Airplane | 400 | 400 |
| Class 4 | Human face | 218 | 217 |
| Class 5 | Watch | 101 | 100 |
| Total | | 1208 | 1205 |

Table 2. Sample images of the classes

| | Training image | Testing image |
|---|---|---|
| Class 1 | | |
| Class 2 | | |
| Class 3 | | |
| Class 4 | 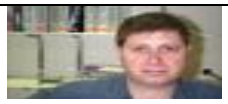 | |
| Class 5 | | |

After the network was trained by images of the following 5 classes, we let it classify a mixed folder containing a total of 1205 images. The %Precision (true positive/total image identified in a class) and %Recall (true positive/total image of that class in test data) shown by the fixed kernel CNN structure and a conventional convolutional neural network [17] with three input channels after having it trained with the same data mentioned in Table 1, is given below:

Table 3. Network Performance

| | Fixed kernel CNN | | Conventional CNN | |
|---|---|---|---|---|
| | %Precision | %Recall | %Precision | %Recall |
| Class 1 | 99.22 | 97.45 | 97.20 | 97.20 |
| Class 2 | 98.95 | 100 | 96.84 | 96.84 |
| Class 3 | 98.26 | 99.25 | 97.70 | 95.75 |
| Class 4 | 99.52 | 97.23 | 97.19 | 93.58 |
| Class 5 | 87.85 | 94 | 69.82 | 81 |
| %Avg. | 96.76 | 97.58 | 91.75 | 92.87 |

It is worth mentioning that the network performance is generally superior with increasing number of training samples. It also depends on what kind of images are used for training the network. If the training samples of a particular class contain variety then the network will be able to recognize different looking images of that class but at the same time it can also contribute to more misclassification owing to the fact that the various training samples of that class might share common attributes with other classes. For example, let us consider few misclassifications made by the network:

(a) (b) (c)

**Fig. 5. Few misclassified images**

Here the first image (a) was classified as motorbike since both type of images contain round figures and white background. In case of the second image (b), it was classified as watch as in the training folder, a lot of watches had color that resembles exactly as the background of this image. The third

image (b) was classified as airplane because of the similarity of the shirt color with a number of airplane images used for training that had the background of the sky in it.

We also calculated overall %accuracy (fraction of the total image on test data set that are rightly classified) of this network, the mentioned conventional CNN structure, support vector machine classifier [18] using bags of key points features[19], k-nearest neighbor classifier[20] and patternet[21] for the given data set in Table 1 and found them to be as:

| Methodology | %Accuracy |
|---|---|
| Proposed Fixed kernel CNN | 98 |
| Conventional CNN | 94.68 |
| SVM classifier | 92 |
| KNN classifier | 83.15 |
| Patternet | 82.65 |

## VII. CONCLUSION

The network structure we present here accounts only the color component and shape which is why it is more suitable to classify images of simple visual objects. Unlike many deep CNN structures which can take into account multiple features by training various filters at each convolutional layer, the Fixed Kernel CNN method is not apparently favorable to classify images which requires lots of complex feature to be grasped by the network until it is efficiently integrated with large number of parameters which can be derived from different image processing/segmentation techniques. However, the network is particularly useful for programming a relatively much faster classifier that involves less mathematics throughout the process.

## REFERENCES


[1] Lecun, Y. "Generalization and Network Design Strategies." Connectionism in perspective, 1989.

[2] Hinton G E; Salakhutdinov R R. "Reducing the dimensionality of data with neural networks".Science, 2006.

[3] Simon Haykin,Neural Network A Comprehensive Foundation,Ontario,Canada,CA:Mcmaster University.

[4] D.H Hubel and T.N Wiesel,"Receptive fields,binocular interaction and functional architecture in the cat's visual cortex."J.Physiology,vol.160,no. 1,pp 160-154,1962.

[5] Y. LeCun, L. Bottou, Y. Bengio, and P. Haffner, "Gradient-based learning applied to document recongnition",in Proc. of the IEEE,vol.86,no.11,pp.2278-2324,nov1998.

[6] B. Hariharan, P. Arbeláez, R. Girshick, and J. Malik. Hypercolumns for object segmentation and fine-grained localization. In CVPR, 2015.

[7] J. Long, E. Shelhamer, and T. Darrell. Fully convolutional networks for semantic segmentation.In CVPR, 2015.

[8] P. Sermanet, K. Kavukcuoglu, S. Chintala, and Y. LeCun.Pedestrian detection with unsupervised multi-stage feature learning.In CVPR,2013.

[9] C.-Y.Lee,S,Xie,p.Gallagher,Z.Zhang and Z. Tu, " Deeply-supervised nets".In AISTATS,2015.

[10] M. Lin, Q. Chen, and S. Yan, "Nenwork In Network". In ICLR,2014.

[11] J. Wang, Z. Wei,T.Zhang, " Deeply-fused nets". In ICML,2016.

[12] Y. Zhang, K. Lee, "Augmentation supervised neural networks with unsupervised obectives for large scale classification".In ICML,2016.

[13] R. K. Srivastava, K. Greff, and J. Schmidhuber. Training very deep networks.In NIPS,2015.

[14] G. Huang, Y. Sun, Z. Liu, D. Sedra, and K. Q. Weinberger.Deep networks with stochastic depth.In ECCV,2016.

[15] G. Larsson, M. Maire, and G. Shakhnarovich. Fractalnet: Ultra-deep neural networks without residuals.arXiv perprint arXiv:1605.07648.

[16] Caltecth-256 wesite,[online].Available: http://www.vision.caltech.edu/Image_Datasets/Caltech256/

[17] Conventional Convoulutional neural network,website,[online],available: https://www.mathworks.com/help/nnet/ref/trainnetwork.html

[18] Train an image category classifier-MATLAB,website,[online],available: https://www.mathworks.com/help/vision/ref/trainimagecategoryclassifier.html

[19] Csurka, G., C. R. Dance, L. Fan, J. Willamowski, and C. Bray Visual Categorigation with Bag of Keypoints, Workshop on Statistical Learning in Computer Vision, ECCV 1 (1-22), 1-2.

[20] K-nearest neighbor classification – MATLAB,website,[online],available: https://www.mathworks.com/help/stats/classificationknn-class.html

[21] Pattern recognition network – MATLAB,wesite,[online],available: https://www.mathworks.com/help/nnet/ref/patternnet.html

# Real-time Air Quality Monitoring System for Bangladesh's perspective based on Internet of things

Md. Mohiuddin Ahmed [1], Suraiya Banu[2], Bijan Paul[3]
[1]Student, Department of Computer Science and Engineering (East West University, Bangladesh)
[2]Student, Department of Computer Science and Engineering (East West University, Bangladesh)
[3]Senior Lecturer, Department of Computer Science and Engineering (East West University, Bangladesh)
sumon13mp@gmail.com, suraiya.lata@gmail.com, bijancse@gmail.com

*Abstract*— **Monitoring of air quality is becoming more and more important day by day due to significant impacts of air pollution on public health, global atmosphere, and worldwide economy. With the continuous development of the Internet of Things (IoT) is becoming progressively more important for air monitoring, traffic monitoring, smart home control, smart parking management and other industrial and home applications. A real-time air monitoring system is essential for Bangladesh because of gas leak-related incidents and other types of phenomena especially for Dhaka city. In this paper, we propose a smart real time Air Monitoring System with emergency alert based on Internet of Things (IoT), which allows users to track the surrounding air quality of their home or office or industries from anywhere. An alarm goes to user of the system in case of any emergency life threatening situation.**

***Keywords—Iot, Intel® Edison Board Microcontroller, Air Monitoring, Safety, Sensor***

## I. INTRODUCTION

A fundamental element to our well-being is decent air quality. Air is invisible gaseous substance. If the percentage of any gas cross its normal limit then it could be dangerous for human being. On average, a person breathes in about approximately 14,000 liters of air on average [1]. People's health can be adversely affected by the presence of contaminated elements in the air. Air pollution can cause both short term and long term effects on health and many people are concerned about pollution in the air that they breathe. According to recent studies, fewer people die every year from car accidents rather than from pollution related illnesses [2]. Due to air pollution, it affects our health, mostly in children, older people and those with heart or respiratory diseases such as asthma. Human activities as well as natural phenomenon cause air quality to be deteriorated. Because of expansion of industrialization diverse types of industries is established in and around the periphery of Dhaka such as garments, tanneries, fertilizer, cement, chemicals pesticides, pharmaceuticals etc. Titas gas transmission authority recently conducted a survey [3] that shows that at least 3,819 gas leak-related accidents occurred in 2013-14, which increased to 5,123 in 2014-15.

The air of Dhaka city is hazardous for human body as the volume of poisonous particles in air has reached far beyond the safe level. An additional severe form of air pollution is "Household Air Pollution (HAP)". It is caused from cooking with concrete fuels and it has become a primary cause of death and disability in many developing countries including Bangladesh [4]. According to statistics, gas leakage is common phenomena in Bangladesh. Gas leakage turns into pit of death. According to the experts of Air Quality Management Project (AQMP) under the Department of Environment (DoE) reveals that the poisonous carbon monoxide, sulphur-di-oxide, nitrogen dioxide, suspended particulate matter exist in Dhaka's air beyond permissible level for human body [5]. Recently, a woman was burnt in a fire at an apartment in Dhaka's Uttara area, died with her husband and two sons [6]. Most of the time people are unaware of the gas leakage. By the time they notice it is already too late and unavoidable loss of life and property occurred. So, proper air quality monitoring is gaining importance day by day.

In this paper, we are proposing a smart air monitoring System based on Internet of Things (IoT). The remainder of the paper is organized as follows: System Model and Methods is presented in Section II, Experiment and Result is presented in Section III. Related work is described in Section IV and conclusion and Future works in Section V and at the end references are added.

## II. SYSTEM MODEL AND METHODS

### *A. HARDWARE COMPONENTS USED IN PROPOSED SYSTEM MODEL*

To monitor the air quality we use Microcontroller board, three types of MQ sensors for environmental air sensing and Ethernet connectivity device. In addition, for sending notification to the user, we need Buzzer, Led and Android device.

978-1-5386-2307-7/17/$31.00 ©2017 IEEE

TABLE I. HARDWARE COMPONENTS AND ITS FUNCTIONALITIES

| Hardware components | Functionality |
|---|---|
| **Microcontroller Intel® Edison Board** | Gas sensor's data storage in built in server |
| **MQ-2 gas sensor** | For detecting H2, LPG, CH4, CO, Alcohol, Smoke or Propane |
| **MQ-3 gas sensor** | Detecting Alcohol, Benzine, Hexane, CO. |
| **MQ-7 gas sensor** | Carbon Monoxide (CO) sensor, appropriate for sensing CO concentrations in the air |
| **Buzzer** | For generating alarm sound to notify about unhealthy air |
| **LED** | For generating blinking light effect to notify user about unhealthy air |

### *B. Case Study*

We are calculating values from PPM (parts per million) unit system. For example, 120 PPM CO means that for every 999,880 molecules of air, there are 120 molecules of CO. From the table 2 we can see that a calculating system scheme for allowed CO level can be : (100/12800)*9 = 0.703%. So if our system get a PPM value of 9 or lower for CO it will show green freash air to the user's dashboard.

TABLE II. LEVEL OF CO AND IT'S HEALTH EFFECT

| CO Level | Health Effects, and Other Information |
|---|---|
| **0 PPM** | Normal, fresh air. |
| **9 PPM** | Maximum recommended indoor CO level (ASHRAE). |
| **10-24PPM** | Possible health effects with long-term exposure. |
| **25 PPM** | Max TWA Exposure for 8-hour work-day (ACGIH). |
| **50 PPM** | Maximum permissible exposure in workplace (OSHA). |
| **100 PPM** | Slight headache after 1-2 hours. |
| **200 PPM** | Dizziness, naseau, fagitue, headache after 2-3 hours of exposure. |
| **400 PPM** | Headache and nausea after 1-2 hours of exposure. Life threatening in 3 hours. |
| **1600 PPM** | Headache, nausea, and dizziness after 20 minutes of exposure. Death within 1-2 hours. |
| **6400 PPM** | Death within 30 minutes. |
| **12,800 PPM** | Immediate physiological effects, unconsciousness. Death within 1-3 minutes of exposure. |

### *C. Implementation of system*

At the beginning we set up our device by connecting sensors with Microcontroller and then generalizing ground and voltage input pin with a breadboard. Then microcontroller is connected to the internet over WIFI and user will get its ip address. By using SSH protocol [7] we can operate our device remotely. For this we used an open source SSH and telnet client called PuTTY [8]. After connecting with the device we can run our code. Then we implement a micro framework of python called flask [9] into our device.Pseudo code of our python script for gas sensor is given below:

```
START

IMPORT mraa,time,os,from flask import
Flask,request,redirect,render_template,flash,jsonify,math,sensorV
alues,from upm import pyupm_gas

    SET app = Flask(__name__)

    DEFINE gasCheck:

            GET mraa pin read value

            COMPUTE value
        IF value >= Xgas min value&& value <= Xgas max
value

             PRINT Xgas Found

    DEFINE gasUpm:

    SETsensor = upmGAS.MQX(Y) #X is sensor name, Y in pin
number

    SET threshContext= upmGAS.thresholdContext()

            SET threshContext.averageReading = 0

            SET  threshContext.runningAverage = 0

            SET threshContext.averagedOver = 2

    SET  mybuffer = upmGAS.uint16Array(128)

    SET result = 0

      FOR  i in xrange(1,10):

          SET  samplelen = sensor.getSampledWindow(2, 128,
          mybuffer)

              IF samplelen:

 SET thresh = sensor.findThreshold(threshContext, 30,mybuffer,
samplelen)

 SET result = threshContext.runningAverage

                ENDIF

       ENDFOR

       RETURN result

    SET @app.route('/getco/')

    DEFINE getCO():

    SET upmResult = gasUpm()

    SET mraaResult = gasDensity()


    RETURN jsonify({'CO' : '{}'.format(upmResult),'CO2' :
'{}'.format(mraaResult),'GAS3' : '{}'.format(upmResult),'GAS4' :
'{}'.format(upmResult)})

IF__name__ == "__main__":

    app.run(host=devices's ip', port=any free port ,debug = True)

    ENDIF

END
```

For a quick explanation of how it works, 1st of all we are importing some library from python [10], flask [11] and upm gas library [12]. Then we use mraa library [13]. gasCheck function determines which gas it is using mraa library fucntions. The generalized gasUpm [14] function work for mq sensors, we have to give X value equal sensor number and Y value equal pin number of microcontroller. After calculation this function returns a numerical value representing gas density. In getco part of our pseudo code we are making json object by taking values of different gas. Finally when the script run with microcontroller's ip and a free port number we can get that json object by sending http request to that routed address. An example request can be in this form http://192.168.0.105:800/getco where ip is microcontroller's ip, 800 is port and /getco is out defined path. Any http request sender can now get our data in json [15] format and processed for further application.

Data parsing from different device:

- Android Data parsing flowchart and process:

  When user runs the app for the first time it will establish connection with server. If user connects with the server, app will send request to server after every specified time. We are using volley [16] for our data parsing and json decoding. We are extending android's service [17] class for our alert service. After decoding json data app will check for inconvenience in data and if any data crosses predefined limit app will generate notification and send it to the user. The process will continue in background as long as user wants. Flow chart of the process is given in Fig. 1.

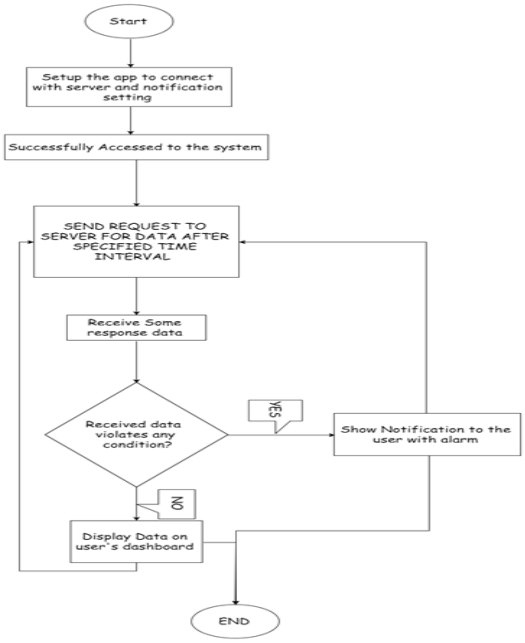


Figure 1. Flow Chart of android app System Flow Diagram

- Web data parsing flowchart and process:

  After successful login into the system user will have option to see their data. When user click on the view data an http request is sent to the server. Server will give a response and for a successful request system will get a json object in return. Using json_decode [18] system can easily get the data of specific sensor. Then system will run a check in these data to find out if any data reached dangerous level. If this event occurs an alarm notification added to user's account. If no triggering data arrives then user will see their air quality at the dashboard of the system. Flow chart of the process is given in Fig. 2.

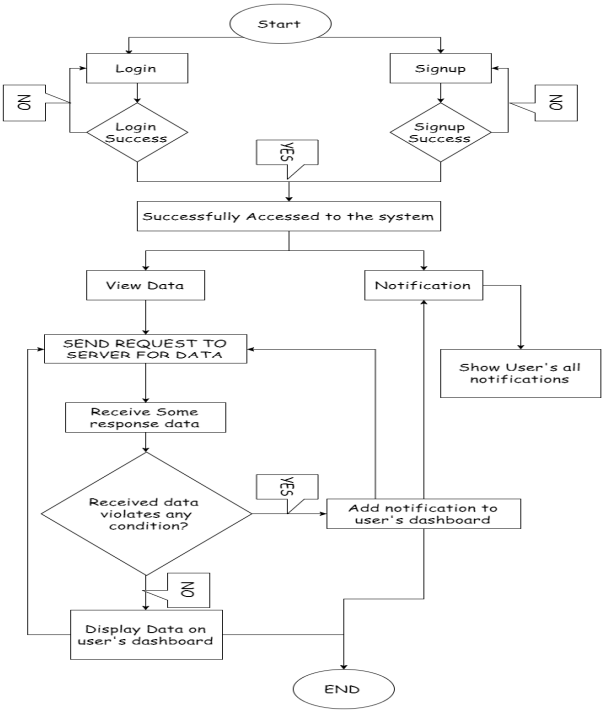


Figure 2. Flow Chart of Web Data Parsing

## III. EXPERIMENTS AND RESULTS

We have developed a prototype of the system shown in Fig. 3. Sensors will send data to our microcontroller and after processing our processed data will be sent to the cloud platform of our system.

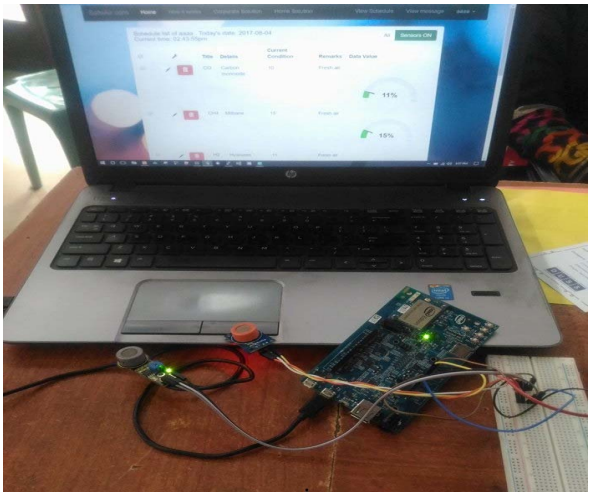

Figure 3. Proposed System

For Experimental purpose, we collect gases from our kitchen stove to a gas jar with a funnel and pipe and set our sensors to the jar. Normally in Bangladesh we use natural gas for cooking and the primary component of natural gas is methane. Now methane is a colourless, odourless gas and is extremely flammable. When mixed with air it can be dangerous explosive. It is also known as methyl hydride. **$CH_4$** is the chemical formula for methane. According to National Institute for Occupational Safety and Health's (NIOSH), 1,000 ppm of methane is the maximum recommended safe concentration for workers during an 8-hour period. Methane can cause asphyxiation at extremely high concentrations and can displace oxygen in the blood and this can result in unconsciousness or death [19]. In the Fig. 4 below some exposure level is given for methane gas.

| Exposure level (ppm) | Effect or symptom |
|---|---|
| 1000 | NIOSH 8-hours TLV* |
| 50,000 to 150,000 | Potentially explosive |
| 500,000 | Asphyxiation |

* TLV = Threshold Limit Value

Figure 4. Methane exposure level and sympton

Now in a normal fresh conditioning room user's dashboard might seem like Fig. 5.

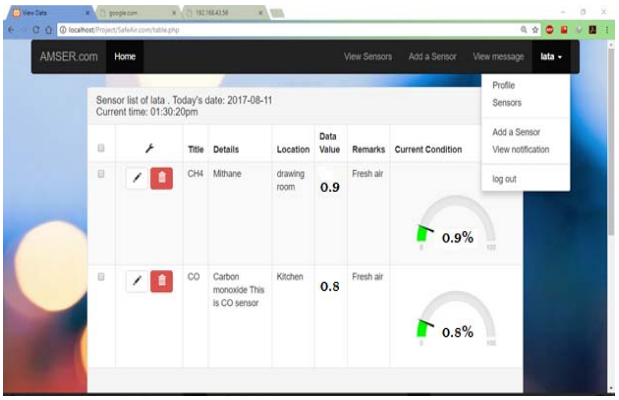


Figure 5. Sensor Data Parse

Here the number 0.8% and 0.9% denotes the RISK FACTOR for that gas. We first get the value of that gas element in ppm unit from json object, and then we are converting them as a percentage. An example of danger zone can be the following image.

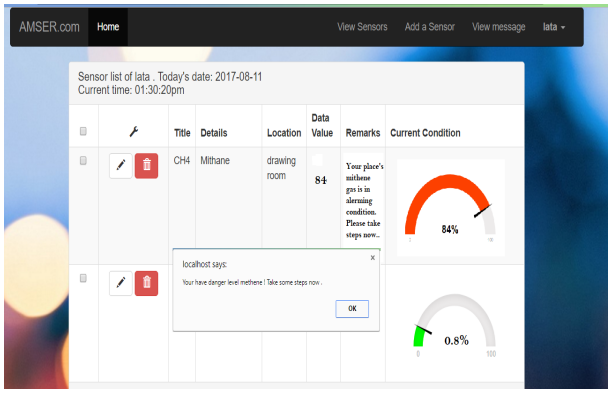


Figure 6. Risk Scenario generate alarm

It means the level of methane is now harmful for user and they should take some procedure to minimize it. When this system finds any danger level data it also triggers the led and buzzer. If we consider about an industry there are at least one main control or monitor room from where the whole security of the project is being checked. An alarm system of LED and Buzzer can be set on this security room. Then our system will automatically triggers these alarm systems for any type of risky condition arise in environment. Consequently, the monitoring system can ensure safety to the institutions as well as life threatening accidents can be avoided.

## IV. Related Work

1) Sniffer: Sniffer is a gas leak detector built by a Bangladeshi company named jolpi. Its main purpose is to ensure home safety. It can sense different kitchen gas and produce alarm sound. But this system is does not provide user any data about the air quality [20].
2) Aeroqual air quality monitoring system: Aeroqual makes different air quality monitoring system but all of them is hardware based and none of them is using iot thus user cannot monitor remotely. Also they do not provide any web based facility let alone iot based support [21].

## V. CONCLUSION AND FUTURE WORK

With the proper implementation of our proposed system we can be reduce dangerous accidents that occurs throughout the country. This is an excellent solution that can be installed in house for house safety as well as any industry or crowed workplace can use our system to maintain the air quality safe and boost their work speed. With proper business guideline this system can be industrialized and help people of all sectors of our country. Future plan of our project is to make it more user friendly and more usable in various

sector. Recently in our garments industry boilers are bursting frequently. One of the main reason of this is extreme air pressure. So in future we want to extend this system to detect air pressure of boiler so that it can prevent accidents and save many lives as well as industrial loss.

## REFERENCES


[1] http://www.mfe.govt.nz/more/environmental-reporting/air/air-domain-report-2014/why-good-air-quality-important

[2] https://www.brisbane.qld.gov.au/environment-waste/natural-environment/air-quality/why-air-quality-important

[3] http://www.dhakatribune.com/feature/tech/2017/06/09/sniffer-made-dhaka-reduce-household-gas-accidents/

[4] https://ehjournal.biomedcentral.com/articles/10.1186/s12940-017-0272-y

[5] http://www.bangladeshenvironment.com/index.php/polution-s/air-polution/291-air-pollution-in-dhaka-city

[6] http://m.bdnews24.com/en/detail/bangladesh/1115398

[7] https://www.ssh.com/ssh/protocol/

[8] http://www.putty.org/

[9] http://flask.pocoo.org/docs/0.12/installation/

[10] https://docs.python.org/3/library/index.html

[11] http://flask.pocoo.org/

[12] https://iotdk.intel.com/docs/master/upm/group__gaseous.html

[13] https://github.com/intel-iot-devkit/mraa

[14] https://iotdk.intel.com/docs/master/upm/group__gas.html

[15] http://www.json.org

[16] https://developer.android.com/training/volley/request.html

[17] https://developer.android.com/reference/android/app/Service.html

[18] http://php.net/manual/en/function.json-decode.php

[19] https://www.cdc.gov/niosh/ipcsneng/neng0291.html

[20] http://jolpi.io/

[21] https://www.aeroqual.com/outdoor-air-quality

# Exciton-phonon scattering effects on photoluminescence of hybrid lead halide perovskite

Md. Masud Rana[1], Md. Sherajul Islam[1], Takayuki Makino[2]
[1]Department of Electrical and Electronic Engineering, Khulna University of Engineering &Technology, Khulna-9203, Bangladesh
[2]Department of Electrical and Electronics Engineering, University of Fukui, Fukui-910-8507, Japan
sheraj_ruet@yahoo.com

*Abstract*—**Organometal halide perovskite materials have gained tremendous attention in the field of photovoltaic, light emitting and lasing devices. Perovskite materials offer some promising optical properties like tunable direct band gap, large light absorption coefficient, high quantum efficiency and long-range balanced electron-hole transport length. The mobility and the photoluminescence line width broadening in hybrid lead halide perovskite are affected by phonon scattering. For the development of efficient perovskite devices it is thus crucially important to establish how excitons interact with phonons in this material. Here we investigate the temperature dependence of the photoluminescence full width at half maximum (FWHM) for $CH_3NH_3PbI_3$ perovskite in the temperature regime of 10-300 K. We developed a quantitative model to calculate the photoluminescence (PL) peak energy variation as well as FWHM broadening adoptiong the Monte-Carlo simulation. Miller-Abrahams expression is used to incorporate the exciton hopping between the localized states assuming the Gaussian distribution of the excitons. Our computation elucidates that the FWHM broadens with increasing temperature due to scattering with exciton-optical phonons.**

***Keywords—Perovskite material, exciton, photoluminescence, monte-carlo simulation, full width at half maximum.***

## I. INTRODUCTION

Organic-inorganic halide perovskites are being used at present in the field of photovoltaics and light emitting devices [1]. The power conversion efficiencieny (PCE) of perovskite solar cell has remarkably increased and now attains in excess of 20% [2]. Organao-halide perovskites (OHP) are represented by the generic formula $ABX_3$, where A is an organic cation for example $CH_3NH_3^+$ (methylammonium) or $HC(NH_2)_2^+$ (formamidinium), B is the metal cation such as $Pb^{2+}$ (lead) or $Sn^{2+}$ (tin) and X is the halogen anion for instance $I^-$, $Br^-$ or $Cl^-$. Researchers also have found satisfactory performance in hybrid halide perovskite material based field effect transistors, light emitting diodes [3], and photodetectors [4]. Hybrid halide perovskite materials combine the features of both the organic materials such as flexibility and low temperature processing capability [5] and high charge carrier mobilities, charge carrier lifetime [6] like inorganic semiconductors. The perovskite materials also possess long charge carrier diffusion length [7] which is vitally needed for high efficieny photovoltaic cell. The band gap of perovskite material can be engineered if mixed halogen anion such as $I^-$ and $Cl^-$ are used instead of single halogen anion and this property is expedient for fabricating tandem solar cell. Along with the above mentioned intriguing properties, methyl ammonium lead iodide ($CH_3NH_3PbI_3$) perovskite offer high absorption coefficient in the visible and ultraviolet spectrum [8].

Although methyl ammonium lead iodide ($MAPbI_3$) is a promising material in the perovskite family, most of its research work focuses on photovoltaic issues. The interactions of exciton with phonon play a vigorous role in the development of efficient optoelectronic devices. Exciton-phonon scattering hinders the charge carrier mobility in a material. The photoluminescence parameter such as full width at half maximum is also affected by the phonon scattering. However, little attention has been paid to understand the exciton-phonon scattering effect. Hence, it is enormously important to figure out the scattering phenomena in organic-inorganic lead halide perovskites.

Realizing the significance of exciton-phonon scattering effects to the perovskite materials based optoelectronics, we have formulated a numerical model to investigate the photoluminescence (PL) properties of $CH_3NH_3PbI_3$ ($MAPbI_3$) perovskite. The numerical model is developed with the Monte Carlo Simulation approach of exciton hopping and recombination phenomena. We consider in our simulation that the localized excitons in $CH_3NH_3PbI_3$ have Gaussian density of states (DOS). For exciton hopping through the localized states, Miller-Abrahams rate expression is incorporated in the simulation model. Temperature induced phonon affected charge carrier lifetime is included in the simulation. We explore the temperature dependendent photoluminescence FWHM broadening in the temperature regime of 10-300 K in conjunction with the photoluminescence peak energy variation. Our results decisively reveal that exciton–phonon interaction in methyl ammonium lead iodide perovskite is dominated by scattering between excitons and optical phonons in the high-temperature regime.

## II. COMPUTATIONAL DETAILS

### A. Numerical Algorithm

We use here the same computational approach as recommended by Silver et al. [9] to investigate the hopping and recombination phenomena of excitons in methyl ammonium lead iodide perovskite. We consider a two

978-1-5386-2307-7/17/$31.00 ©2017 IEEE

dimensional rectangular space with the size of 100 × 100. Periodic boundary conditions are used in the simulation. Each site among the 10,000 sites of the rectangle is considered as the localized state for the exciton. For applying Monte Carlo Simulation in the hopping process of excitons [10], it is assumed that these localizes states are selected randomly. We distribute energy for the localized states in such a way that a Gaussian density of states (DOS) is achieved. For the each iteration of the simulation process, a particular number of localized states (25%) is considered from the 10,000 states. After getting thermal energy, the excitons either hop to neighboring state or recombine depending on the magnitude of the thermal energy. The rate of exciton hopping from a localized state *i* to another localized state *j* with a distance of $r_{ij}$ is given by Miller-Abrahams expression [11]

$$\nu_{ij} = \nu_0 \exp\left( -\frac{2r_{ij}}{\alpha} - \frac{E_j - E_i + \left|E_j - E_i\right|}{2k_B T} \right), \qquad (1)$$

where $E_i$ and $E_j$ represent the energies of the localized states $i$ and $j$ respectively, $\nu_0$ is the attempt-to-escape frequency, $\alpha$ denotes the decay length of the exciton wave function.

Firstly an exciton from the localized states located at site *i* is taken into account for the simulation. Then the exciton declining rate $\nu_i$ with lifetime $\tau_0$ is determined as

$$\nu_i = \tau_0^{-1} + \sum_j \nu_{ij} \,. \qquad (2)$$

The second term in the declining rate equation is summed for a number of 32 which does not affect the simulation result if increased upto 64.The time $t_i$ required for the next progression of the selected exciton is defined as

$$t_i^{-1} = -\nu_i \ln \xi_1 , \qquad (3)$$

where $\xi_1$ being a random number ranges from 0 to 1. If the exciton is hopped, then $t_i$ is incremented and the simulation procedure repeats. If the exciton recombines, the energy of the respective exciton is put into storage. Then another exciton is simulated and the same task repeats until all the excitons are simulated. Finally, the recombination energies produce the photoluminescence spectrum.

### *B. Simulation Details*

In disordered or alloy system, generally the excitons DOS is of either Gaussian or exponential type. However, for optically active excitons, a Gaussian DOS is more relevant than exponential one [12]. Therefore, we have chosen a Gaussian function for the exciton DOS in our simulation. The Gaussian density of states for the localized excitons is expressed as

$$g(E) = \left( \frac{N^2}{2\pi\sigma^2} \right)^{1/2} \exp\left[ -\frac{(E - E_0)^2}{2\sigma^2} \right], \qquad (4)$$

Table I. Parameters used in the simulation

| Parameters | Orthorhombic | Tetragonal |
|---|---|---|
| Temperature, T (K) | 10-163 | 164-300 |
| Temperature independent broadening parameter, σ (meV) | 12 [13] | 15 [13] |
| Concentration of localized states, N | 25% | 25% |
| Exciton lifetime, $\tau_0$ (ns) | 10-100 ns [14] | 100-300 ns [15] |
| Attempt to escape frequency, $\nu_0$ | $2\times10^{11}$/s [16] | $2\times10^{11}$/s [16] |
| Spatial fitting parameter, $\tau_0\,\nu_0$ | $(2\times10^{11})\times\ \tau_0$ | $(2\times10^{11})\times\ \tau_0$ |
| Temporal fitting parameter, $N\alpha^2$ | 0.01-0.3 | 0.01-0.3 |

where *N* represents the percentage of localized states that are taken into consideration for simulation and σ is the temperature-independent dispersion parameter of the distribution. The reference energy $E_0$ is considered to be zero, which is the mean of the Gaussian distribution. We consider only those energies lying in the negative portion of the distribution in our simulation. If an additional broadening parameter Γ is incorporated then the DOS of the localized excitons becomes

$$g(E) \propto \exp\left[ -\frac{(E - E_0)^2}{2(\sigma^2 + \Gamma^2)} \right]. \qquad (5)$$

We applied moment analysis methods to measure the photoluminescence peak energy and full-width at half maximum (FWHM) or PL line-width quantities for any photoluminescence spectrum. The first moment of the energy spectrum of the simulation can be considered the PL maximum energy value in the experiment. The FWHM value is obtained by multiplying 2.35 with the square root of the second moment of the spectrum. The parameters used to simulate the exciton hopping or recombination are detailed in table I.

## III. Results and Discussion

To investigate the exciton-phonon scattering in hybrid lead halide perovskite, we calculated the PL spectra of methyl ammonium lead iodide ($MAPbI_3$) over temperatures from 10 to 300 K as shown in Fig. 1. The full width at half maximum (FWHM) and the peak energy position of each PL spectrum are calculated and explained in the subsequent sections. The peak energy of a spectrum at a particular temperature denotes the exciton binding energy of that temperature. Exciton binding energy is that amount of energy by which the energy of emitted

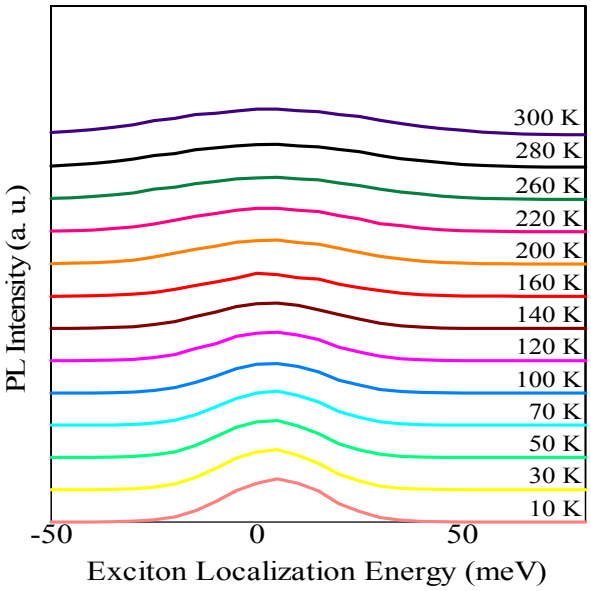


Figure 1. Temperature-dependent PL spectra of $MAPbI_3$

photon is smaller than the band gap energy of a material. The exciton binding energy, $E_b$ is expressed as

$$E_b = E - E_0, \tag{6}$$

where, $E$ is the band gap energy and $E_0$ is the energy of the emitted photon during photoluminescence. From PL spectra we observe that with the increasing temperature, the photoluminescence intensity decreases. This behavior can be described by the following well-known equation [17].

$$I(T) = \frac{I_0}{1 + A\exp\left(-\frac{E_b}{k_B T}\right)}, \tag{7}$$

where $I_0$ is the PL intensity at 0 K, $A$ is the fitting constant, $k_B$ is the Boltzmann constant, $E_b$ is the exciton binding energy and $T$ represents the measurement temperature. In our analysis, we obtained the exciton binding energy to be 3.414 meV at 300 K. This lower value of exciton binding energy in $MAPbI_3$ highlights the strong potentiality of this material for photovoltaic applications.

The temperature dependent PL peak energy is depicted in Fig. 2 in the temperature regime of 10-300 K. When the temperature is incremented from 10 K to 160 K, the peak energy position of the corresponding PL spectrum exhibits a blue-shift. This phenomena has the trend opposite to that of conventional semiconductors such as Si, Ge and InGaN. In these semiconductors, the band gap decreases with increasing temperature as a result of lattice expansion [18]. If the temperature is further increased upto 180 K then there occurs a red-shift of the PL peak energy. From 180 to 300 K the peak energy position of the photoluminescence follows again a blue-shift. Such an unusual and interesting behavior is observed in hybrid halide perovskite material and is due to the structural phase transition from the low-temperature orthorhombic to the high-temperature tetragonal phase at ~ 163 K [19]. For temperatures T < 163 K it is in the orthorhombic phase and for temperatures 163 K < T < 327.3 K the perovskite is in tetragonal phase. The $CH_3NH_3PbI_3$ perovskite material contains both organic material and inorganic material. The organic part and inorganic part are bonded by hydrogen bonds. The temperature variation changes the nature of the hydrogen bond. As a result, the crystal structure changes with the temperature. The respective positive temperature coefficient of the bandgap ($dE_g/dT$) is larger in the orthorhombic phase than the tetragonal phase and the temperature dependent band gap $E_g$ of a material can usually be expressed as [18], [20].

$$\left(\frac{dE_g}{dT}\right)_P = \left(\frac{dE_g}{dT}\right)_V + \left(\frac{dE_g}{d\ln(V)}\right)_T \times \left(\frac{d\ln(V)}{dT}\right)_P. \tag{8}$$

The first term denotes the electron-phonon coupling through the deformation potential which results in a decrease of the band gap with temperature. The second term represents the lattice dilatation term which causes the band gap to increase with temperature. The electron-phonon interaction term for most inorganic semiconductors is larger than the lattice dilatation term. As a result, the band gap decreases with temperature for many inorganic semiconductors. However, it is different in organometal halide perovskite such as $MAPbI_3$, where the second term i.e. the lattice dilatation term dominates over the electron-phonon interaction term for the hybrid lead halide perovskite described here and thus the band gap increases with temperature.

The investigation of temperature assisted PL full width at half maximum spreading is extensively used to explain the

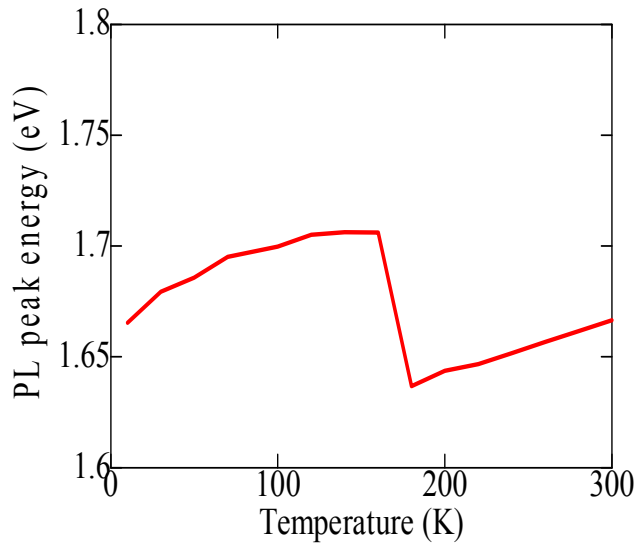


Figure 2. PL peak energy variation with the temperature in $MAPbI_3$

mechanism of exciton-phonon interactions in semiconductor materials [21]. The PL line width is an indication of the disorder present in the semiconductor. The disorder can be of structural and/or thermal nature – both will broaden the photoluminescence line width [22]. The FWHM variation of $CH_3NH_3PbI_3$ ($MAPbI_3$) with the temperature is shown in Fig. 3. The temperature-dependent PL line-width broadening is fitted using the following Bose- Einstein type expression [23], [24].

$$\Gamma(T) = \Gamma_0 + \frac{\Gamma_{op}}{\exp\left(\frac{E_{op}}{k_B T}\right) - 1}, \qquad (9)$$

where $\Gamma_0$ is the temperature-independent inhomogeneous broadening contribution, that is caused by the structural disorder and imperfections inherently present in the materials. The latter term is homogeneous broadening term that results from exciton-longitudinal optical phonon scattering with coupling constant $\Gamma_{op}$ and longitudinal optical phonon energy $E_{op}$. The PL line-width is broadened due to the scattering of excitons with acoustic and optical phonons. However, the line-width broadening due to acoustic phonon is negligible compared to longitudinal optical (LO) phonon [25]. Therefore, only LO phonon has been considered in the present calculation.

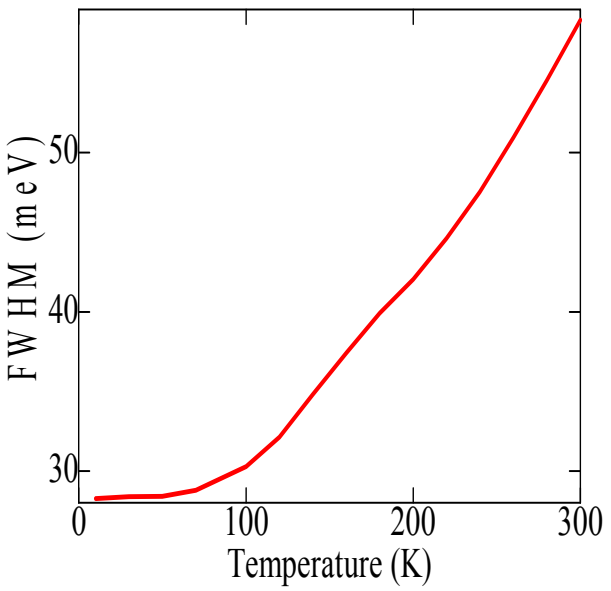


Figure 3. FWHM of $MAPbI_3$ as a function of temperature

Table II. Fitting parameters of $MAPbI_3$ in orthorhombic and tetragonal phase

| $MAPbI_3$ | Orthorhombic [13] | Tetragonal [13] |
|---|---|---|
| $\Gamma_0$ (meV) | 12 | 15 |
| $\Gamma_{op}$ (meV) | 26 | 36 |
| $E_{op}$ (meV) | 17 | 27 |

We observe here from table II that $\Gamma_0$ = 12 meV (orthorhombic) and $\Gamma_0$ = 15 meV (tetragonal) is small for both phases, which represents the high crystal quality of $MAPbI_3$. Again $\Gamma_0$ is smaller for the orthorhombic phase than the tetragonal phase, which suggests that the orthorhombic phase is relatively more ordered than the tetragonal in agreement with literature [26]. At low temperatures (upto 80 K), the smaller number of optical phonon makes the FWHM variation almost due to inhomogeneous broadening. But at high temperatures, the number of optical phonon increases and it scatters with the excitons frequently which results in an almost linear increment of FWHM with increased temperature.

## IV. Conclusion

In summary, we have analyzed exciton-phonon interactions in hybrid lead halide perovskite considering $MAPbI_3$ by temperature-dependent photoluminescence study. Both the orthorhombic and tetragonal phase shows blue-shift of the PL peak energy except a red-shift in the vicinity of the transition temperature of ~163 K. At room temperature, the temperature-dependent PL line width of $MAPbI_3$ interprets that the scattering of excitons with optical phonons is principally responsible for the FWHM broadening compared to that caused by structural disorder. Moreover, the lower exciton binding energy makes $CH_3NH_3PbI_3$ as a promising candidate for the photovoltaic applications.

## References


[1] H. He, Q. Yu et al, "Exciton localization in solution-processed organolead trihalide perovskites," *Nature Communications*, vol. 7, pp. 10896, March 2016.

[2] D. Bi et al., "Efficient luminescent solar cells based on tailored mixed-cation perovskites," *Science Advances*, vol. 2, no. 1, pp. e1501170-e1501170, January 2016.

[3] Z. Tan, R. Moghaddam et al., "Bright light-emitting diodes based on organometal halide perovskite," *Nature Nanotechnology*, vol. 9, no. 9, pp. 687-692 , August 2014.

[4] X. Hu, X. Zhang, L. Liang, J. Bao, S. Li, W. Yang and Y. Xie, "High-Performance Flexible Broadband Photodetector Based on Organolead Halide Perovskite," *Adv. Funct. Mater.,* vol. 24, no. 46, pp.7373–7380, September 2014.

[5] J. You, Z. Hong et al, "Low-Temperature Solution-Processed Perovskite Solar Cells with High Efficiency and Flexibility," *ACS Nano*, vol. 8, no. 2, pp. 1674–1680, January 2014.

[6] C. Wehrenfennig, G. Eperon, M. Johnston, H. Snaith, and L. Herz, "High Charge Carrier Mobilities and Lifetimes in Organolead Trihalide Perovskites," *Advanced. Materials*, vol. 26, no. 10, pp. 1584–1589, December 2013.

[7] S. Stranks, G. Eperon et al., "Electron-Hole Diffusion Lengths Exceeding 1 Micrometer in an Organometal Trihalide Perovskite Absorber," *Science* , Vol. 342, No. 6156, pp. 341-344, October 2013.

[8] M. Lee, J. Teuscher, T. Miyasaka, T. Murakami and H. Snaith, "Efficient Hybrid Solar Cells Based on Meso-Superstructured Organometal Halide Perovskites," *Science*, vol. 338, no. 6107, pp. 643-647, Novemver 2012.

[9] M. Silver, G. Schönherr, and H. Bässler, "Dispersive Hopping Transport from an Exponential Energy Distribution of Sites," *Phys. Rev. Lett*. Vol. 48, no. 5, pp. 352-355, February 1982.

[10] S. Baranovskii, R. Eichmann and P. Thomas, "Temperature-dependent exciton luminescence in quantum wells by computer simulation," *Phys. Rev. B,* vol. 58, no. 19, pp. 13081-13087, November 1998.

[11] K. Kazlauskas et al., "Double-scaled potential profile in a group-III nitride alloy revealed by Monte Carlo simulation of exciton hopping," *Appl. Phys. Lett.,* Vol. 83, no. 18, pp. 3722-3724, September 2003.

[12] R. Schnabel, R. Zimmermann et al, "Influence of exciton localization on recombination line shapes: $In_xGa_{1-x}As/GaAs$ quantum wells as a model," *Phys. Rev. B,*vol. 46, no. 15, pp. 9873-9876, October 1992.

[13] S. Sing, C. Li et al, "Effect of thermal and Structural Disorder on the Electronic Structure of Hybrid Perovskite Semiconductor $CH_3NH_3PbI_3$," *J. Phys. Chem. Lett*., vol. 7, no. 15, pp. 3014-3021, July 2016.

[14] C. Wehrenfenning, M. Liu et al, "Charge carrier recombination channels in the low-temperature phase of organic-inorganic lead halide perovskite thin films," *APL Mater.* vol. 2, no. 081513, pp. 1-10, August 2014.

[15] Y. Li, W. Yan et al, "Direct Observation of Long Electron-Hole Diffusion Distance in $CH_3NH_3PbI_3$ Perovskite Thin Film," *Sci. Rep.* vol. 5, no. 14485, pp. 1-7, September 2015

[16] M. Samiee, S. Konduri et al, "Defect density and dielectric constant in perovskite solar cells," *Appl. Phys. Lett,* vol. 105, no. 153502, pp. 1-4, October 2014.

[17] D. Jiang, H. Jung and K. Ploog, "Temperature dependence of photoluminescence from GaAs single and multiple quantum-well heterostructures grown by molecular-beam epitaxy," *J. Appl. Phys*., vol. 64, no. 3, pp. 1371-1377, March 1988.

[18] Y. Varshni, "Temperature dependence of the energy gap in semiconductors," *Physica,* vol. 34, no. 1, pp. 149–154 , 1967.

[19] A. Miyata, A. Mitioglu et al., "Direct measurement of the exciton binding energy and effective masses for charge carriers in organic–inorganic tri-halide perovskites," *Nature Physics,* vol. 11, no. 7, pp. 582–587, January 2015.

[20] H. Wantanabe, N. Yamada, and M. Okaji, "Linear Thermal Coefficient of Silicon from 293K to 1000K, " *Int. J. Thermo Phys.,* vol. 25, no. 1, pp. 221-236, January 2004.

[21] S. Rudin, T. Reinecke, and B. Segall, "Temperature-dependent exciton linewidths in semiconductors," *Phys. Rev. B,* vol. 42, no. 17, pp. 11218–11231, December 1990.

[22] S. Wasim, G. Marín et al, "Urbach–Martienssen's Tail in the Absorption Spectra of the Ordered Vacancy Compound $CuIn_3Se_5$," *J. Appl. Phys.,* vol. 84, no. 10, pp. 5823-5825, November 1998.

[23] Y. Chen, G. Kothiyal, J. Singh and P. Bhattacharya, "Absorption and Photoluminescence Studies of the Temperature Dependence of Exciton Life Time in Lattice-matched and Strained Quantum Well Systems," *Superlattice. Microst*, vol. 3, no. 6, pp. 657-664, August 1987.

[24] H. Qiang, F. Pollaka et al., "Size Dependence of the Thermal Broadening of the Exciton Linewidth in GaAs/Ga0.7Al0.3As Single Quantum Wells." *Appl. Phys. Lett.,* vol. 61, no. 12, pp. 1411-1413, July 1992.

[25] A. Wright, C. Verdi et al, "Electron-phonon coupling in hybrid lead halide perovskites," *Nature Communications*, vol. 7, May 2016.

[26] F. Brivio, J. Frost et al., "Lattice Dynamics and Vibrational Spectra of Orthorhombic, Tetragonal and Cubic Phases of Methylammonium Lead Iodide," *Phys. Rev. B*, vol. 92, no. 14, pp. 144308, October 2015.

# A Non-Invasive Technique of Early Heart Diseases Prediction from Photoplethysmography Signal

Monira Islam[1], Md.Ashikuzzaman[2], Tahmida Tabassum[3] and Md. Salah Uddin Yusuf[4]
[1234]Department of Electrical and Electronic Engineering
Khulna University of Engineering &Technology
Khulna-9203, Bangladesh
monira_kuet08@yahoo.com, ymdsalahu2@gmail.com

*Abstract*— **Now a day heart diseases are the major cause of death throughout the world. So, early prediction of heart diseases is essential to reduce premature death. In this paper a non- invasive technique is proposed to detect the heart rate from photoplethysmography (PPG) signal. Non-invasive measurement of heart rate plays a vital role in medical diagnosis due to less discomfort to patients because tissues can be damaged due to traditional sensors during the extraction of cardiac signal. Photoplethysmogram is the blood volume measurement technique which is based on optic principle. The blood volume changes in accordance with heart rate. In this work, a convenient heart diseases estimation technique is proposed from PPG which is extracted from human facial video. It will overcome the high cost of conventional expensive ECG machine for cardiac diseases prediction. The heart rate is identified from FFT analysis and verified with the conventional heart rate measurement system using ECG. The percentage error is 2.3%, 3.2% and 5.8% for green, red and blue channels respectively. From heart rate the cardiac diseases have been predicted which has great potential for cardiac heart rate monitoring for computing the heart rate variability (HRV) without any contact of traditional sensors.**

***Keywords— PPG, facial video, non- invasive technique,heart rate, FFT analysis.***

## I. INTRODUCTION

Cardiac arrhythmias are the major causes of premature death at present world. At a particular time a patient's current condition can be estimated using the pulse Rate or heart Rate. This is often regarded as the vital physiological parameter [1]. Heart rate can be non-invasively estimated by PPG signal analysis. Photoplethysmography or PPG is a non-invasive technique to measure the heartbeat that uses the ability of light to reflect and penetrate in human tissue. With every pulse the blood vessels increase in thickness and the body will therefore absorb more light as the light will have to travel through more tissue. PPG detects volumetric changes in arterial vessels that cause a change in the light absorption, reflection and therefore the light intensity detected by the photodetector [2].The non-contact measuring of the heart rate is a comfortable method in comparison with conventional contact methods. An electrocardiograph (ECG) is a traditional device for measuring heart rate. The ECG is an expensive device which requires connecting several electrodes to the body. However they require more preparations before the measuring compared to a contactless solution. These constraints prevent contact methods from their comfortable everyday use comparing the contactless methods which are unobstructive and cheap to estimate the heart rate (HR).

There are two main video based methods for the invasive measurement of heart rate and blood pressure and respiratory rate. The first one is based on monitoring small movements of the body caused by reaction to the waves of blood pushed from the heart according to the third Newton's law. The second one is based on small changes in skin color caused by the blood flow in tissues. The reflection capability of a skin with capillaries supplied with blood differs from the reflection capability of a skin containing less blood. The blood volume is changing in correspondence with the HR. The observing and analyzing of such signal is called a photoplethysmography (PPG) [2]. The PPG waveforms could be obtained in a regular red-green-blue (RGB) color spectrum using the ambient daylight as an illumination.

Recent work has demonstrated the viability of video based HR measurement [3]. In a real environment, many factors could make extraction of HR difficult. Rigid and non-rigid motion changes in illumination that would greatly affect the appearance of skin over time. In recent work Li et al. [4] achieved strong performance on a large collection of challenging videos from the MAHNOB-HCI Database [5]. The approach by Li et al. essentially works by using tracking to overcome rigid motion, using illumination changes in the background to rectify illumination changes on the face, and cropping out "noisy segments" from their estimated plethysmograph (PG) signals that were caused by non-rigid motion. In 2010, Gault, Blumenthal, Farag and Starr proposed a method to estimate the waveforms and rates of the arterial pulse from thermal imaging [6]. In 2013, Gault and Farag introduced a technique where vascular mapping, blood perfusion modeling and wavelet analysis are used to calculate heart rate [7]. While highly effective in some settings, their method has some drawbacks. The background's appearance changes over time cannot always be used to cancel out the effects of illumination change on skin. This is because the spectral reflectance of the background and skin are likely to be different. In addition, complex backgrounds (e.g. outdoors) would make such illumination rectification unreliable. Cutting out time segments that exhibit changes in emotion is also less than ideal as portions of the final estimated PG signal would be missing.

Most of the current work with diseases detection is covering problems of removing noise, detecting heartbeats and

978-1-5386-2307-7/17/$31.00 ©2017 IEEE

rhythm-based analysis. In this work a new method for the HR estimation is proposed based on measuring the PPG signal in the video of face without the requirement of background effect. In this research the whole work is subdivided in to three categories. They are: i) extraction of raw signal from video frame; ii) extraction of PPG signal and heart rate estimation; iii) diseases prediction and comparing with traditional technique with ECG signal.

In this paper section II describes heart diseases prediction concept with heart rate. Section III shows the methodology of the proposed approach. Section IV focuses the result and discussion and finally section V concludes the results.

## II. HEART DISEASES PREDICTION CONCEPT WITH HEART RATE

Heart rate is a vital physiological parameter for heart diseases detection. Different heart diseases like as cardiac arrhythmias depends on the abnormality of heart rate. Cardiac arrhythmias are any abnormality or perturbation in the normal activation sequence of the myocardium. The signs and symptoms of cardiac arrhythmias can range from none at all to loss of consciousness or sudden cardiac death. In general, more-severe symptoms are more likely to occur in the presence of structural heart disease [8]. Depending upon heart rate there are two types of arrhythmia and they are broadly classified as:

i) Bradycardia: The heart rate is less than 60 beats per minute
ii) Tachycardia: The heart rate is greater than 100 beats per minute

Furthermore heart diseases can be classified as hypertrophy (ventricular and atrial), atrial fibrillation, atrial flutter, ventricular tachycardia, heart block, bradycardia, myocardial infarction.

### A. Concept of Heart Diseases

Tachycardia occurs due to the presence of an ectopic focus in the atrium which beats regularly at a rapid rate. Myocardial infarction (MI), commonly known as heart attack, is due to the occlusion of one of the coronary arteries or one of its smaller branches. The pathogenesis for most of the MI cases is due to the progressive atherosclerotic plaques in coronary arteries [9].Atrial fibrillation is an arrhythmia where atria beat rapidly, chaotically and ineffectively, while the ventricles respond at irregular intervals, producing irregularly irregular pulse. Any conditions causing raised atrial pressure, increased atrial muscle mass, atrial fibrosis, inflammation and infiltration of the atrium can cause atrial fibrillation. The atria usually fire impulse at the rate of 350 to 600 BPM, ventricles respond at irregular intervals usually at the rate of 100 to 140 BPM. According to the heart rate, atrial fibrillation may be of two types:

i) Fast atrial fibrillation: $Heart\ rate > 100$ beats per minute
ii) Slow atrial fibrillation: $Heart\ rate < 100$ beats per minute

Apnea is a term for suspension of external breathing. During apnea, there is no movement of the muscles of inhalation and the volume of the lungs initially remains unchanged.

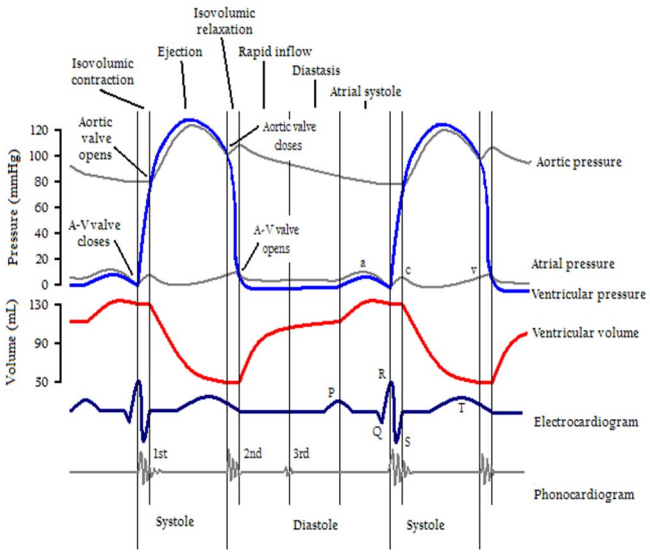


Figure 1. Interaction of Heart Beat with ECG signal.

TABLE I. VARIATION IN DIFFERENT FEATURES OF ECG SIGNAL FOR DIFFERENT CARDIAC ARRHYTHMIA

| Heart condition | Rhythm | Heart beat (BPM) |
|---|---|---|
| **Normal sinus rhythm** | Regular | 60-100 |
| **Atrial fibrillation** | Irregular | 400-600 |
| **Sinus tachycardia** | Regular | >100 |
| **Myocardial infarction** | Regular | - |
| **Apnea** | Regular | 60-67 |

### B. ECG Signal and Heart Rate Estimation

Electrocardiography (ECG) is the conventional technique of recording the electrical activity of the heart over a period of time using electrodes placed on the skin. These electrodes detect the tiny electrical changes on the skin that arise from the heart muscles during each heartbeat. The different waves and intervals in the ECG graph are divided into different parts and divided into the P wave, the QRS complex and the T wave. The different intervals depict different activities performed by the heart. In each phase waves goes from systole to diastole. The intervals between the segments and their changes in each phase detect the heart rate. Fig. 1 shows the different phases of the ECG influences the blood pressure rhythm.

Feature extraction from ECG signal is required to describe a large set of data. Extracted features reflect the heart condition of the subject. From the heart rate it can be determined that what kind of heart disease the subject possesses. The changes in heart rate for different cardiac disorder are shown in Table I. Observing the changes in heart beat and the rhythmic response, type of cardiac disorder is determined.

### C. Non Contact PPG Signal for Heart Rate Estimation

Plethysmography comes from Greek word plethysmos which means to increase the blood volume when light falls upon the blood vessels. Plethysmography measures volume changes in tissue related to the blood passing through it. Photoplethysmography (PPG) means that one uses light to find information related to the Plethysmography. Non-contact

refers to that there is no physical contact between the recording equipment used and the skin. There are two modes, transmission- and reflectance-mode PPG. Transmission mode measures how light is obstructed and absorbed by the tissue and uses a dedicated light source for this. It detects the variability in absorption through the extremity due to Plethysmography. Reflectance mode observes how the light is reflected from a light source, of the skin surface [10]. Human blood consists of 45 % red blood cells and 54.3 % plasma. The remaining percentage is other types of blood cells and proteins such as white blood cells and platelet [11]. The plasma is in itself mostly transparent, so the bulk of the reflectance and absorption we use to measure PPG signals are caused by the red blood cells. In this analysis human face is used extraction of PPG signal because it remains the uncovered region with continuous blood flow.

## III. METHODOLOGY

The process of estimating the HR from facial video can be split into two main phases. In the first phase, a video of a face is transformed into a low dimensional signal which contains the PPG information and suppresses the other irrelevant information. In the second phase the low dimensional signal is used to find the best estimation of the HR of the tested person. The proposed work is subdivided in to the following blocks as shown in Fig. 2.

### *A. Selection of ROI and Extraction of PPG*

This work processes the video with human face. The tested person on the video should be looking in the direction of the camera. The movement of the observed subject can cause failures of the tracker of the face and also remarkable changes in the illumination conditions thus making the heart rate estimation less precise. The first frame is used to detect face using Viola Jones face detection algorithm. Then 60% of facial region is selected as ROI. From every fame ROI is tracked by using Kanade-Lucas-Tomasi (KLT) Feature Tracker algorithm [13]. Using mask only ROI area's RGB component are separated and mean value of those component are taken for analysis.

### *B. Image Decomposition and ICA*

The ROI's were decomposed into three RGB channels. Analyses will be performed for a different channels combination: RGB, RG, GB, RB or separately using the channels. In this stage firstly the RGB signal is filtered using a bandpass filter in range of 0.83Hz to 4Hz. Then independent component analysis (ICA) is done in the filtered RGB signal and the signal is smoothed the signal x(t) using a Savitzky-Golay (polynomial) smoothing filter. Eq. (1) shows the ICA model assumes that the observed signals y(t) are linear mixtures of the unknown sources x(t):

$$y(t) = Ax(t) \tag{1}$$

Where, the mixing matrix A is also unknown. To estimate both A and x(t) we assume that the components of vector x are statistically independent and non-gaussian. After estimating A matrix it's inverse W (demixing matrix) is computed. Then independent components can be obtained from Eq. (2) [12].

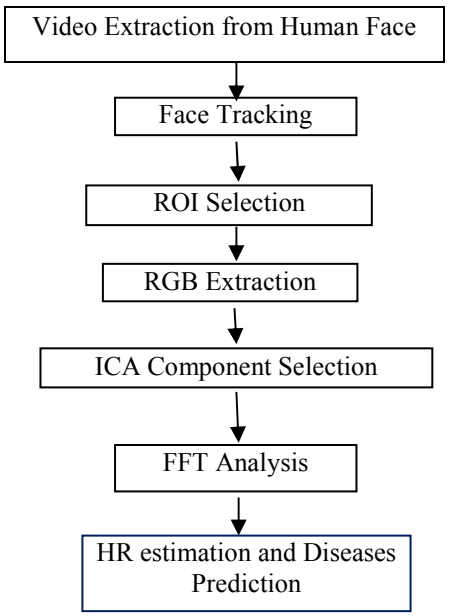


Figure 2. Block diagram of the proposed approach.

$$x(t) = Wy(t) \tag{2}$$

### *C. Heart Rate Estimation*

Frequency based features are most useful to diagnose diseases from signals which is not possible in time domain. To find the frequency spectrum a one dimensional Fourier transform is performed on each color channel. To find HR the maximum frequency is found from the transformed signal. Eq. (3) and Eq. (4) are used to estimate heart rate from PPG signal. If r is the PPG signal then the equations can be represented as:

$$R = FFT(r) \tag{3}$$

$$HR = \max(abs(R)) \tag{4}$$

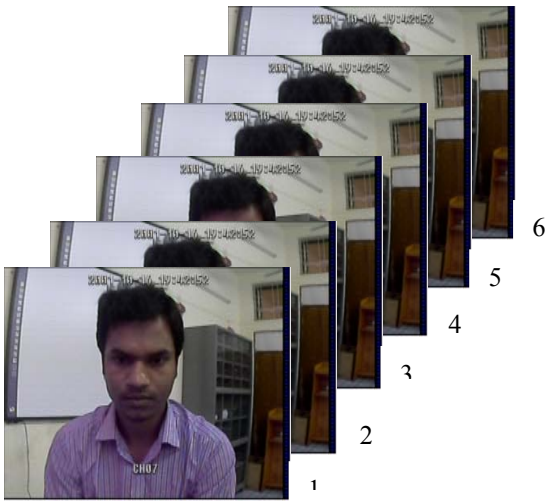


Figure 3. Extracted frames from video.

## IV. Result and Discussion

In this analysis eight different subjects are selected for collecting video samples. No age limit was allowed for data collection. Four subjects were lying in the ranges between 23-25 years. Rest of the subject was above 45 years old. The subjects were sitting in a chair with a resting pulse and less movement while data collection. The room was calm and less noisy. While video capturing ECG signals were collected at the same time for comparing the results. The captured video then converted in to frames as shown in Fig. 3. In this analysis first frame is used to selection of ROI and extraction of PPG signal.

### *A. Image Decomposition and Face Tracking*

Using Viola-Jones face detection algorithm face was detected from the first frame [14]. Then 60% of the face is selected as region of interest. The enclose area by blue line is region of interest (ROI), shown in Fig. 4. Using mask only ROI area's RGB component are separated and mean value of those component are taken. RGB component are shown in Fig.5. As

the high frequency component and low frequency than desired frequency are present in the signal, a FIR band pass filter is used for removing unwanted frequency component. For the experiment cut off frequency are chosen $f1 = 0.83$ Hz and $f2 = 4$ Hz.

Fig. 6 show the RGB extracted signal from the pixel values if red, green and blue color channels. And independent component analysis is applied with filtering to remove the high and low range component and final PPG signal is extracted as shown in Fig. 7. The FFT of the RGB signal is done to estimate the HR as shown in Fig. 8.

### *B. Heart Rate Estimation and Diseases Prediction*

In this work heart rates are estimated as the extracted frequency domain features. From Fig. 8 the peak is in 1.4 Hz. So the heart rate is $1.4 \times 60 = 84$ bpm. Here some high frequency components are present but they are negligible.

Red, Blue and Green the three channels are used to estimate the heart rate as shown in Table II. Comparing with the result with ECG signal it is found that the average error rate is less for green channel rather than red or blue channels. The percentage error is zero for green channel for subject 2 and subject 4 with a little exception for subject 6 and subject 8.

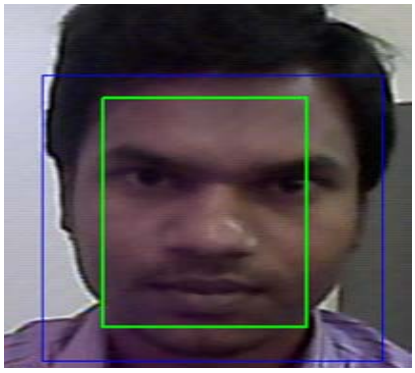

Figure 4. Detection of face and selected ROI from frame.

Figure 5. Extraction of ROI and decomposition of image into red, green and blue channels.

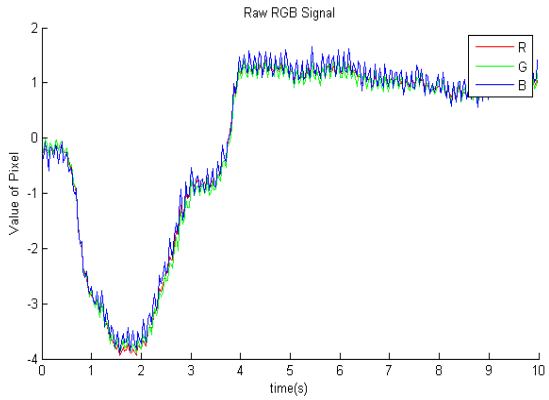


Figure 6.

Figure 7. Raw RGB signal extracted from facial image.

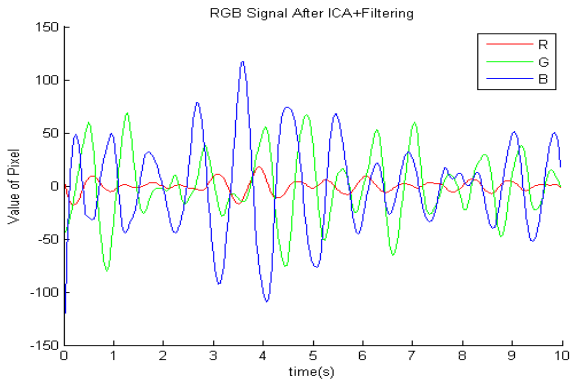


Figure 8. Extracted PPG signal after filtering.

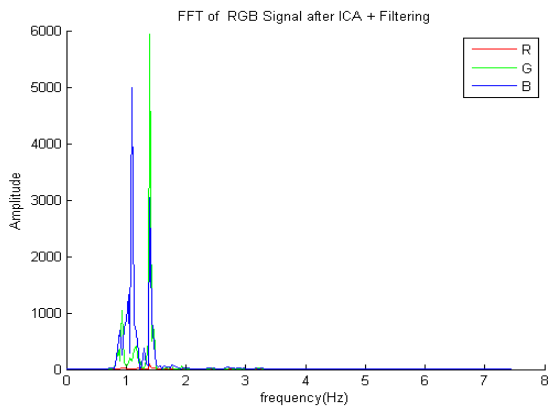


Figure 9. FFT of the PPG signal for HR estimation.

TABLE II. RESULTS OF ESTIMATED HEART RATE FROM PPG SIGNAL

| Subject | Video duration (Sec) | Heart Rate (bpm) | | | | Error in Red (%) | Error in Green (%) | Error in Blue (%) |
|---|---|---|---|---|---|---|---|---|
| | | Red | Green | Blue | ECG | | | |
| 1 | 30 | 84 | 84 | 66 | 86 | 2.3 | 2.3 | 23.2 |
| 2 | 30 | 222 | 220 | 214 | 220 | 0.09 | 0 | 2.7 |
| 3 | 30 | 81 | 86 | 84 | 85 | 4.7 | 1.2 | 1.2 |
| 4 | 30 | 80 | 80 | 82 | 78 | 2.5 | 2.5 | 5.1 |
| 5 | 30 | 79 | 75 | 76 | 75 | 5.3 | 0 | 1.3 |
| 6 | 30 | 75 | 73 | 74 | 78 | 3.8 | 6.4 | 5.1 |
| 7 | 30 | 185 | 182 | 188 | 180 | 2.7 | 1.11 | 4.4 |
| 8 | 30 | 62 | 63 | 62 | 60 | 3.33 | 5 | 3.3 |

TABLE III. HEART DISEASES PREDICTION FROM ESTIMATED HR USING PPG ANALYSIS

| Subject | Cardiac Condition | Disease |
|---|---|---|
| 2 | Abnormal Signal | Sinus Tachycardia |
| 7 | Abnormal Signal | Sinus Tachycardia |
| 8 | Abnormal Signal | Apnea |

From Table III it is found that for subject 2, 7 and 8 the heart rates are beyond the safe limit. So there cardiac condition is critical. Analyzing the heart rate it can be determined that subject 2 and 7 belong to the Sinus Tachycardia and subject 8 are affected with heart diseases termed as Apnea.

## V. CONCLUSION

This paper proposes a non-invasive technique of cardiac diseases prediction. The patients may not be able to take the stress of traditional sensors or heavy machine. A contactless technique can give a solution and detect the cardiac diseases at an early stage at that condition while the doctors are not available. It may give assurance to provide safety at an early stage for the patients. In this paper PPG is extracted from human face and the selected region is decomposed into red, blue and green channels. From the analysis it is found that green channels give more accurate heart rate than the other ones. We have found 97.7% accuracy for green channel. The subjects who possess heart rate within the normal limit are lying in the safe condition. But the subjects whose heart rates are 220, 180 and 60 bpm belongs to critical heart condition and their diseases are found as Sinus Tachycardia and apnea. So this paper represents an innovative idea to determine human health condition predicting the cardiac abnormalities.

## REFERENCES


[1] R. G. Haahr, "Reflectance Pulse Oximetry Sensor for the Electronic Patch," M.Sc. Thesis, MIC - Department of Micro and Nanotechnology Technical University of Denmark, Nov. 2006.

[2] J. Allen, "Photoplethysmography and its application in clinical physiological measurement," Journal of Physiological Measurement, vol. 28, no. 3, Feb. 2007.

[3] C. Antink, H. Gao, and C. Bruser, "Beat to beat heart rate estimation fusing multimodal video and sensor data," Biomedical Optics,vol. 6, no.8, Jul. 2015.

[4] Q. Li, R. G. Mark, and G.D. Clifford, "Robust heart rate estimation from multiple asynchronous noisy sources using signal quality indices and a Kalman filter," Physiological measures, vol. 29, no.1, pp15-32, Feb. 2008.

[5] S. Bilakhia, Stavros Petridis, Anton Nijholt, and MajaPantic, "The MAHNOB Mimicry Database: A database of naturaltic human interactions", Pattern recognition letters, vol. 66, pp.52-61, 2015.

[6] T. Gault, N. Blumenthal, A. Farag, and T. Starr, "Extraction of the superficial facial vasculature vital signs waveforms and rates using thermal imaging," In Computer Vision and PatternRecognition Workshops (CVPRW), 2010 IEEE Computer Society Conf., pp. 1-8, June 2010,

[7] T. Gault and A. Farag, "A fully automatic method to extract the heart rate from thermal Video", In Computer Vision and Pattern Recognition Workshops (CVPRW), 2013 IEEE Conf., pp. 336-341, June 2013.

[8] Er. J.S Dhir, Er. N.K. Panag, "ECG Analysis and R Peak Detection Using Filters and Wavelet Transform", Vol. 2, Issue 2, Feb. 2014.

[9] L. N. Sharma, R. K. Tripathy and S. Dandapat, "Multiscale Energy and Eigenspace approach to Detection and Localization of Myocardial Infarction", IEEE Trans. J. Magn, vol. 62, no. 7, pp. 1827-1837, June 2015.

[10] Asmund Rustand. Ambient-light photoplethysmography. Master's thesis, NTNU, 2012.

[11] VanPutte, Reagen, and Russo. Seeley's Essentials of Anatomy & Physiology. McGraw-Hill, (7 edition) edition, 2010.

[12] Ming-Zher Poh, Daniel J. McDuff, and Rosalind W. Picard, "Advancements in Noncontact, Multiparameter Physiological Measurements Using a Webcam", IEEE Trans. on Biomedical Enngineering, vol. 58, no. 1, pp. 7-11, Jan. 2011.

[13] J. K. Suhr, "Kanade-Lucas-Tomasi (KLT) Feature Tracker," Lecture on Computer Vision, 2009, Yonsei Univ.

[14] Y. Q. Wang, "An Analysis of the Viola-Jones Face Detection Algorithm, " Image Processing On Line, vol. 4, 2014, pp. 128–148.

# Epileptic seizure detection based on selected features of different complexities using ANN

Dipayan Biswas[1], Prof. Dr. Md. Foisal Hossain[2],
Department of Electronics and Communication Engineering,
Khulna University of Engineering & Technology, Khulna, Bangladesh.
dipayan1109033@gmail.com[1], foisalkuet@yahoo.com[2]

***Abstract*— Epilepsy indicates a short time of abnormalities in the function of brain that can cause serious brain damage. A common technique when analyzing with Epilepsy is based on EEG signals processing, taken from the surface area of human scalp. In this paper, mainly focused on the selection of how much less processing and complexity can be used for features extraction with the ability to provide high accuracy of classification. For this, features are extracted in three steps on the basis of how much computation are required in the processing. These three steps includes features directly from raw EEG, preprocessing EEG and wavelet decomposing. Time domain, frequency domain and time-frequency domain features are extracted for the classification purpose. After that, in each steps three experiments are performed to classify into two particular classes in each experiment. These classification are done by using Feed Forward Neural Network (FFNN). In the 3rd experiment where classification is done between seizure subjects vs. non-seizure subjects, FFNN gives accuracy as high as 99.2%.**

***Keywords—seizure; epilepsy; DWT; EEG signal; FFNN***

## I. Introduction

EEG (Electroencephalogram) is a method of acquiring the brain electro-chemical signal in the form of cumulative potential from a large number of brain cells mainly named as neurons. EEG is used as a common diagnostic tool for the treatment purpose of epilepsy, brain damage and sleep disorders and commonly used in a variety of research contexts. Seizure is a change in behaviour of a person after an abnormal electrical activity occurs in the human brain. Approximately, there are almost 1% of world population suffers from epilepsy [1], and in which 85% of the peoples are living in the developing countries [2]. Patients may experience Seizure in one or two times per week but that may be even more in numbers. Generally, Epilepsy is characterized by recurring Seizures but it's not the true case. Those patients having Seizures due to the brain disorder rather than another reason such as due to fever, drug addiction, poisons, a lot of alcohol and so on are called Epilepsy.

In human body different bio-signals exist to conduct different functions in the whole body. Where, EEG signal generated from brain that takes major part of the activity of these functions. So, the use of EEG signal in the detection process of Epilepsy is commonly used as Epilepsy describes the abnormalities in a group of brain cells. So far the identification of that disease are done by the visual observation of EEG signals in the monitor by some expert doctors but that process are not only huge time consuming but also limited as expertise are limited. So, we need an automatic detection method to serve that kind of patients.

In some recent years many detection methods are implemented for the detection of Epilepsy. Sliding window segmentation are performed to extract features in time domain are done in [3]. Then, using FFNN got 93.37% accuracy in detecting normal EEG and 95.508% accuracy in detecting Seizure subjects. Tzallas et al. in [4] uses Time-frequency features and Artificial Neural Network (ANN) to classify the Seizure and Non-seizure with accuracy of 97.73%. Authors in [5] extract features using Wavelet (WT) and approximate entropy, then uses ANN in classification. Guo et al. in [6] uses ANN after extracting features using Wavelet Transform-Line Length (WT-LL) Features and Accuracy was 97.75%. In [7] same types of features as in [5] but uses SVM to classify and got accuracy of 98.51%. Most of the researchers mainly have taken features in time-frequency domain after decomposing the signals by DWT and extracted features from its various sub-bands. This gives satisfactory results in some case but it is all known that a large number of computation should be performed in getting these sub-bands by DWT.

In this proposed work, very close looks on the signals are given on the selection of features. Some innovative features are extracted after close analysis on the nature of EEG signals in the Time-domain, Frequency-domain and Time-frequency-domain with some conventional features. Then, three groups of features are grouped together by choosing best combination of these extracted features that are intend to input the FFNN classifier. The FFNN are optimized by tuning the training parameters of Scaled Conjugate Gradient training function. At last all the results are compared on the selection of features vectors as well as with the previous works. All computation are performed in MATLAB toolbox environment.

## II. Materials and Methods

### *A. Description of the EEG Database*

The datasets used in this research are collected from the Epilepsy center in Bonn University, Germany by Ralph Andrzejak et al. in [8]. The data consists of five groups titled from set A until set E, each groups contains 100 single channel EEG segments of 23.6-sec having sampling rate of fs = 173.61 Hz. The first two groups set A & set B are recorded from five healthy subjects with their eyes open (A) and eyes close (B). The third and fourth groups are recorded when subjects are not experiencing Seizure, where set C data are recorded from opposite hemisphere (healthy region) of the brain and set D are recorded from the part of the brain with the epilepsy syndrome. The last set E are recorded at the time when patients are experiencing Seizure that is Seizure at ictal period where set C & set D are in inter-ictal period. In this work classification is divided in three experiments. For first two experiments 300 segments of data and for last experiment 500 segments are used to classify in that particular experiment.

978-1-5386-2307-7/17/$31.00 ©2017 IEEE

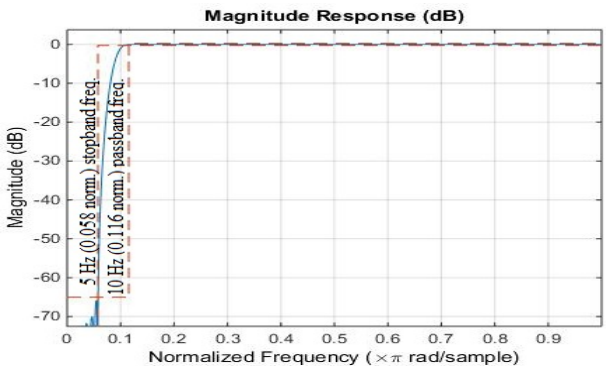


Fig. 1. Kaiser window basis FIR High-pass filter for pre-processing of EEG signals.

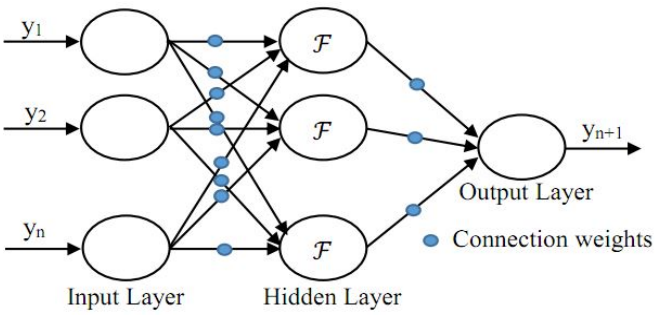


Fig. 2. General structure of FFNN

### *B. Pre-processing of EEG*

Generally, EEG signals contains very low frequencies from 0.1Hz to 50Hz and so experience different types of random noise. EEG signals also have its randomness due to its verse area of controlling all functions in the human body. But when detection of Seizure is the interest, we can neglect some of these very low frequency because in Seizure period a little higher frequency components are observed in EEG signals. So, High-pass filter is the basic need in pre-processing EEG to exclude these very low frequencies. In our work Finite Impulse Response (FIR) filter of Kaiser window with stopband frequency 5Hz and passband frequency 10Hz is used. The filter is shown in the Fig. 1.

### *C. Discrete Wavelet Transform (DWT)*

DWT plays an important task when signal are to be analyzed in the Time-frequency domain. It is a model of mathematical and computational to decompose a signal into its sub-bands with respect to different range of frequencies. After EEG decomposition (Daubechies WT with 4-level decomposition), delta, theta, alpha, beta and gamma sub-bands are extracted. They have their own range of frequencies characterized by different condition of brain functionalities. Details in [9].

### *D. Feed forward Neural Network (FFNN)*

A feed forward neural network is an artificial neural network where one layer's outputs are fed to the next layer functional elements that is artificial neurons. Input layer is formed by the number of features used to train the network. Each inputs are weighed by the weighted vectors and with an additional bias are summed together in each neurons at the next layer called hidden layer. Then outputs are obtained on that layer by transforming the summation by suitable transform function such as tan-sigmoid, log-sigmoid, pure-line transform function to the subsequent layers. In\ this network, the information moves in only one direction that is forward direction from the input layer, through the hidden layers (one or many) and to the output layer. There are no cycles or loops in the network [10] [11]. In the Fig. 2 shows a general structure of FFNN with "n" number of features marked by $y_1$, $y_2$,…. , $y_n$ and one hidden layer.

## III. Proposed Methodology

The proposed methodology is shown in Fig.3 that gives a brief summary of this research. In the proposed method, the main concentration was on the selection of suitable features that are extracted upon close analyzing the EEG signals. Features are categorized on how much computation are required for extraction. Features are extracted in three steps:

A) Directly from raw EEG signals
B) After pre-processing the EEG signals
C) After DWT decomposing the EEG signals

With the features of that three steps, three groups of features vectors are chosen upon the analysis of extracted features named, a) Group-1, b) Group-2 and c) Group-3 features. Group-1 features includes only the features from raw EEG, Group-2 includes features from both raw EEG and preprocessed EEG and Group-3 includes the all three steps of features extracted. These three groups of features are applied to FFNN separately. This is done mainly to compare how much accuracy we can obtain with both lower and higher complexity features vector.

After, extracted all the features vectors, next steps is to choose suitable classifier where FFNN is used. In FFNN, mainly three phase of procedures are involved a) initialize and configure the network, b) training and c) validation to satisfy performance goals. Among different training functions the proposed methodology use the custom version of "Scaled Conjugate Gradient" training functions. It uses Back Propagation Algorithm to train the Network. In which after the end of each epoch the gradient is calculated to determine in which way to propagate to modify the networks weight and bias values so that it can be more generalized to the inputs. Different training parameters are modified to adapt the network with this particular classification such as performance goal is set to 0.001 where default value is zero, minimum gradient is set to 1e-8, maximum training epochs up to 1000 and maximum validation fail up to 200. These parameters are selected to behave well for signals of this application.

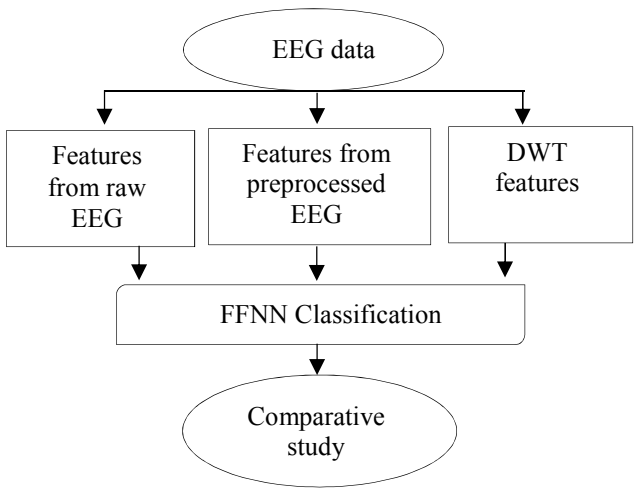


Fig. 3. Flowchart of proposed method

## IV. Feature Extraction and Selection

Previously mentioned that features are extracted in three steps in the proposed methodology.

### *A. Directly from raw EEG signals*

Features in this steps requires less computation to extract.

These features includes Min, Min-20p, Max, Max-20p, Standard deviation, Moment-2, Mean_abs-1st_diffentiation, Zero level crossing, Cross correlation, Energy spectral density (ESD) using FFT and Power spectral density (PSD) using Welch's method.

"Min-20" features has more impact on true classification than simple "Min" features. "Min" is a single minimum point where "Min-20p" is the 20 percent minimum points rather than single minimum point through the duration of signal that is if the signal is comprised of 100 sample points, then the mean value of 20 low-amplitude sample-points are taken respectively. This consequence can be understand in the Fig. 4. Normal distribution of 100 ictal EEGs(red color) signals and 100 inter-ictal EEGs(blue color) are plotted for each feature space such as in Fig. 4.(a), the left side for "Min" feature and on the right side for "Min-20p". These are the density plot for signal attribute for two different classes (Seizure and Non-seizure). On the left side plot, there is a large area of overlap portion of the two classes that indicates a huge number of subjects attributes fall in the same range of value creates more possibility of miss-classification between Seizure and Non-seizure. And for the right side the situation is just opposite with Min-20p.

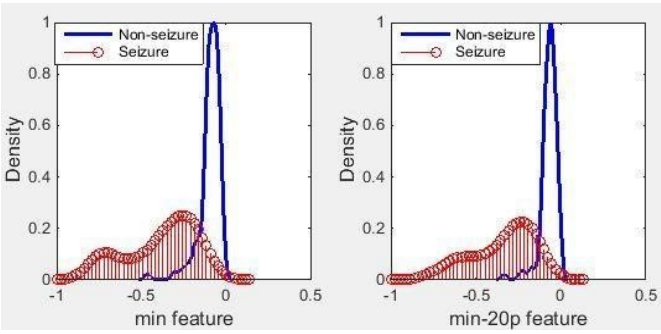


(a)

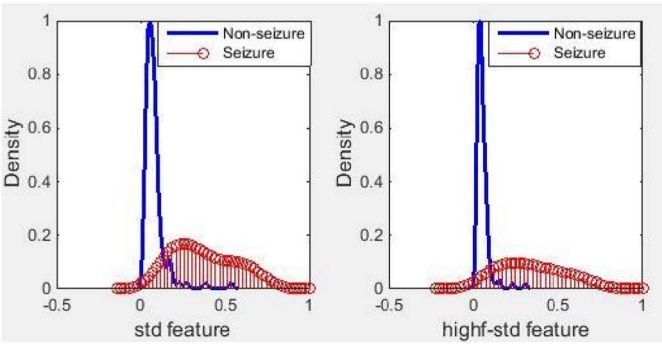


(b)

Fig. 4. Extracted feature's density plot of 200 subjects of two classes (100 ictal and 100 inter-ictal period Seizure patients) for (a) "min" & "min-20p" features and for (b) "standard deviation features" & "highf_standard deviation features".

### *B. After pre-processing the EEG signals*

In this steps also same features are extracted as in the previous steps but before that pre-processing is performed. So, some complexity and processing are increased in the process of this features extraction. Features in this steps is renamed by the prefix "highf" to the previous mentioned features of 1st step such as "highf_max-20p".

### *C. After DWT decomposing the EEG signals*

In this steps, at first DWT are performed to decompose the all frequency components of EEG into five sub-bands named delta, theta, alpha, beta and gamma. Then in each band Energy, covariance, moment-2 are computed.

Up to we extract a large number of features and by the density plot we can see how a particular feature is responsible for false/true classification by observing the overlapping area. After analyzing all features, optimum combination are taken for the inputs of FFNN. These are

**Three groups of selected features for classification:**

1. Group-1 (4 features)
   - *Min_20p, max_20p, momt2, ESD*
2. Group-2 (5 features)
   - *Min_20p, highf_max_20p, momt2, highf_momt2, ESD*
3. Group-3 (6 features)
   - *Min_20p,highf_max_20p, highf_momt2, ESD, Wav_momt2_alpha, Wav_eng_alpha*

## V. Result Analysis

Three experiments are designed in each groups of features to test the ability of the FFNN classifier to separate two classes in each particular experiment. These are

Exp.1) Normal EEG (sets A & B) and inter-ictal EEG (sets C & D)
Exp.2) Inter-ictal EEG (sets C & D) and ictal EEG (set E)
Exp.3) Non-seizure EEG (sets A, B, C, D) and Seizure EEG (set E)

Fig. 5 shows the error performance plot of FFNN while training the network. The errors are calculated by measuring mean square error after each epoch. Training stop when validation error reach at minimum value set by required performance goal. The validation error are marked by "green line". Close validation error with test error is desired for better network generalization. Training and testing errors are also shown by "blue" and "red" lines. From Fig. 5 it is clearly seen that these two curve are almost close means that network are well generalized to inputs.

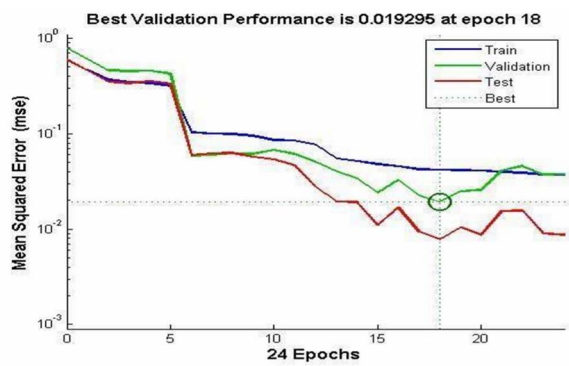


Fig. 5. Error performance plot while training Network

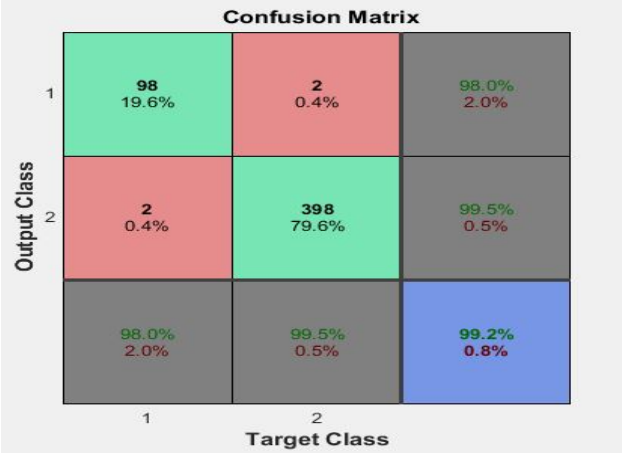


Fig. 6. ANN Confusion Plot after trained

In Fig. 6 confusion plot shows both the total number and the percentage of true classification and false classification for "experiment-3". Diagonal "green" cells indicates the output classes are matched with the target classes where off-diagonal cells are the indication of false-classification. Results shows that only 4 miss-classification among total 500 subjects and produces accuracy of 99.2%.

**Table-1:** OVERALL ACCURACY OF ALL GROUPS FEATURES AND ALL EXPERIMENTS IN PROPOSED METHOD.

| | Group-1 features | Group-2 features | Group-3 features |
|---|---|---|---|
| "Exp.1" accuracy (%) | 99 | 99.7 | 100 |
| "Exp.2" accuracy (%) | 97.3 | 97.7 | 99 |
| "Exp.3" accuracy (%) | 97.66 | 98 | 99.2 |

**Table-2:** COMPARISON BETWEEN PROPOSED METHODS TO OTHER METHODS

| Authors | Methods | Datasets | Accuracy |
|---|---|---|---|
| Vairavan et al. 2007 [10] | Approximate entropy & EN ,PNN | A vs. E | As high as 100% |
| Mushfiq et al. 2010 [11] | Sample entropy, variance based & ANN | A vs. E | 99.18% |
| Forrest et al. 2008 [12] | PSD, Fractal dimensions, hjorth parameters & PNN | AB vs. E<br>CD vs. E | 96.67%<br>97% |
| Guo et al. 2010b [6] | WT-LL Features & ANN | ABCD vs. E | 97.75% |
| Rivero et al. [13] | Tme-frequency analysis & ANN And RANN | ABCD vs. E | 97.73%<br>98.6% |
| Bizopoulos et al. [14] | EEMD & K-means clustering | ABCD vs. E | 98% |
| Proposed Method | Statistical, DWT based features & FFNN | AB vs. E<br>CD vs. E<br>ABCD vs. E | 100%<br>99.4%<br>99.2% |

## VI. Conclusion

In this work, the ultimate target of detecting Epilepsy has performed by using classifier FFNN. At first step, some innovative features have extracted from raw EEG segments with a great deal of close analyzing the signals. Some of them are generally statistical features but able to get better result than other commonly used features in statistical domain. Then preprocessing has performed to remove unwanted signals and all these same features of previous step have been extracted from that preprocessed signals. When these features have used, accuracy increase than before. For Time-frequency analysis DWT have used to find each sub-bands of EEG and features have extracted in each sub-bands. Then, three different groups of feature vectors have made in proposed method. Statistical density have plotted for some features to show how they can distribute the signal attributes of two classes of subjects into separate feature space. By these plots, it was easier to select the features group to suitable to true classification.

Table-1 shows accuracy of proposed method in all three experiments in the process of analysis. From Table-1, it can be noticed that using Group-1 features that have extracted directly only from raw EEG signals, much satisfactory accuracy can be obtained. Also, preprocessing of raw EEG increases the classification accuracy. At last, when DWT has used to extract features, accuracy reach much higher and found accuracy in "Exp.3" as high as 99.2%. Other experiments results are also shown in Table-1. In Table-2 a comparison is shown with other papers using their particular dataset. So, we can conclude that proposed methods give quite satisfactory classification compare to others. It also gives option to choose method based on how much processing in the detection process to be performed.

## References

[1] K. Lehnertz, F. Mormann, T. Kreuz, R. Andrzejak, C. Rieke, P. David, and C. Elger, "Seizure prediction by nonlinear eeg analysis," *IEEE Engineering in Medicine and Biology Magazine*, 2003.

[2] *Atlas: Epilepsy Care in the World*. World Health Organization, 2005.

[3] Anusha K S, Mathew T Mathews, Subha D.Puthankattil, "Classification of Normal and Epileptic EEG Signal using Time & Frequency Domain Features through Artificial Neural Network" International Conference on Advances in Computing and Communications, pp. 98 – 101, Aug. 2012.

[4] R. G. Andrzejak, K. Lehnertz, C. Rieke, F. Mormann, P. David, C. E. Elger, "Indications of nonlinear deterministic and finite dimensional structures in time series of brain electrical activity: Dependence on recording region and brain state", *Phys. Rev.* E, 64, 061907, 2001.

[5] A.T. Tzallas, M.G. Tsipouras and D.I. Fotiadis, "Automatic seizure detection based on time-frequency analysis and artificial neural networks," Computational Intelligence and Neuroscience Volume 2007, Article ID 80510, October 2007.

[6] L.Guo, D. Rivero and A. Pazos. "Epileptic seizure detection using multiwavelet transform based approximate entropy and artificial neural networks," J Neurosci Methods, Vol. 193, Issue -1, pp. 156-163, October 2010.

[7] L. Guo, D. Rivero, J. Dorado, J.R. Rabunal., and A. Pazos (2010). "Automatic epileptic seizure detection in EEGs based on line length feature and artificial neural networks," J Neurosci Methods, Vol 191, Issue-1, pp. 101-109, August 2010.

[8] S.F. Liang, H.C. Wang, and W.L. Chang. "Combination of EEG Complexity and Spectral Analysis for Epilepsy Diagnosis and Seizure Detection," EURASIP Journal on Advances in Signal Processing, 853434, 2010.

[9] U. Orhan, M. Hekim, and M. Ozer. "EEG signals classification using the K-means clustering and a multilayer perceptron neural network model," Expert Systems with Applications, Vol. 38, pp. 13475– 13481, 2011.

[10] Vairavan Srinivasan, Chikkannan Eswaranmand, Natarajan Sriraam, "Approximate Entropy-Based Epileptic EEG Detection Using Artificial Neural Networks," IEEE Transactions on information technology in Bio-medicine, vol. 11, no. 3, may 2007,

[11] Mushfiq U. Saleheen, Homa Alemzadeh, Ajay M. Cheriyan, Zbigniew Kalbarczyk, Ravishankar K. Iyer, "An Efficient Embedded Hardware for High Accuracy Detection of Epileptic Seizures," 3rd International Conference on Biomedical Engineering and Informatics (BMEI ), vol. 5, pp. 1889 – 1896, Oct. 2010.

[12] Forrest Sheng Bao, Donald Yu-Chun Lie, and Yuanlin Zhang," A New Approach to Automated Epileptic Diagnosis Using EEG and Probabilistic Neural Network," 20th IEEE International Conference on Tools with Artificial Intelligence, vol. 2, pp. 482 – 486, Nov. 2008.

[13] Daniel Rivero, Enrique Fernandez-Blanco, Julian Dorado, Alejandro Pazos, "Using Recurrent ANNs for the Detection of Epileptic Seizures in EEG Signals," IEEE Congress of Evolutionary Computation (CEC), pp. 587 – 592, June 2011.

[14] Paschalis A. Bizopoulos, Dimitrios G. Tsalikakis, Alexandros T. Tzallas, Dimitrios D. Koutsouris and Dimitrios I. Fotiadis, "EEG Epileptic Seizure Detection using k-Means Clustering and Marginal Spectrum based on Ensemble Empirical Mode Decomposition," IEEE 13th International Conference on Bioinformatics and Bioengineering (BIBE), pp. 1 – 4, Nov. 2013.

[15] Osman Salem, Amal Naseem and Ahmed Mehaoua, "Epileptic Seizure Detection From EEG Signal Using Discrete Wavelet Transform and Ant Colony Classifier" IEEE International Conference on Communications (ICC), pp. 3529 – 3534, June 2014.

# Segmented FPCA for Hyperspectral Image Classification

M. P. Uddin[1], M. A. Mamun[2] and M. A. Hossain[3]
Department of Computer Science and Engineering, Rajshahi University of Engineering & Technology (RUET), Rajshahi, Bangladesh
[1]palash_cse@hstu.ac.bd, [2]a.mamun@ruet.ac.bd, [3]ali.hossain@ruet.ac.bd

***Abstract*—Remote sensing hyperspectral image (HSI) contains significant information of ground surface which is actually acquired as a set of immense narrow and contiguous spectral bands. Proper classification approach can only give us the required knowledge from the hundreds of bands of HSI. Though it is quite difficult to extract features from these bands, dimensionality reduction techniques through feature extraction and feature selection are used to improve the classification performance of the HSI. Principal Component Analysis (PCA) is usually adopted as unsupervised linear feature extraction method for feature reduction. However, PCA can be failure to extract local characteristics of the HSI due to considering global variance. Thus, segmented-PCA (SPCA) and folded-PCA (FPCA) are used to efficiently extract the local structures in different ways. In this paper, feature extraction using FPCA, termed as segmented FPCA (SFPCA), has been improved through applying it on the highly correlated bands' segments of the real HSI rather than not applying on the whole dataset directly. The effectiveness of SFPCA is additionally compared with the unsupervised nonlinear feature extraction methods kernel-PCA (KPCA) and Kernel Entropy Component Analysis (KECA). The experimental result shows that the classification accuracy of SFPCA (95.6262%) outperforms conventional FPCA (95.1292%), SPCA (93.837%) and PCA (93.7376%) providing the least space complexity. Moreover, it attempts to fix the nonlinearity like very similar to KPCA (95.9245%) and KECA (95.6262%).**

***Keywords*—Feature extraction, hyperspectral image classification, PCA, SPCA, FPCA, Segmented FPCA, SFPCA, KPCA, KECA***

## I. INTRODUCTION

Remote sensing hyperspectral images (HSIs) are acquired at a huge number of narrow and contiguous spectral wavelength bands. The wavelength bands typically range from 0.4 $\mu m$ to 2.5 $\mu m$ that cover from visible light to infrared (near) region of electromagnetic-wave spectrum to capture the earth surface very well. This allows HSIs to use in a wide range of applications including mining, agriculture, geology, and military surveillance. Furthermore, HSI does not only promote in analysis of food quality, pharmaceutical, security and skin but also verifies counterfeit goods and documents [1], [2]. With the spectral resolution in *nm*, HSI offers high discrimination ability in data analysis [2] for various humanitarian services such as discrimination among vegetation categories, identification the presence or absence of specific elements in a soil or rock, eutrophication of lakes and so on [3]. Usually, HSI data forms a hypercube that contains 2D spatial information and a third dimension provides the spectral information about the earth objects. Thus, the entire data contained is $X*Y*F$, where $F$ is the number of image bands in the HSI, $X$ denotes the number of rows (height) and $Y$ denotes the number of columns (width) of each image band. Since the images are frequently captured by aircraft or satellite sensors some preprocessing such as atmospheric correction, radiometric or geometric correction should be performed [1], [3].

However, all the bands of the HSIs may not comprise same proportion of information and few bands may contain less discriminatory information though the neighboring bands are highly correlated [4]. Consequently, feature reduction techniques can be applied to select the relevant bands and to extract the inherent features through transforming the features with a view to fixing the curse of dimensionality problem or Hughes phenomenon [5]. The dimensionality should be reduced because if the ratio between the number of spectral bands and the number of training sample pixels is not balanced, then the classification accuracy is decreased. Consequently, feature extraction and feature selection are highly required to mitigate these issues for efficient classification [2], [5].

Both supervised and unsupervised feature extraction methods consist of linear and nonlinear transformation for extracting the appropriate features. Supervised methods need a priori knowledge for extracting the effective features. For example, Discriminant Analysis Feature Extraction (DAFE) plans to enhance the class separability and Decision Boundary Feature Extraction (DBFE) extracts discriminant features to form the decision boundary between classes. These methods could computationally be severe and the performance is highly dependent on the training pixels. Alternatively, unsupervised methods are used to extract effective features without using any a priori information [6].

On the other hand, the feature selection preserves the original data and selects the meaningful bands based on some searching standards [7], [8]. However, these search-based methods are sometimes challenging because of combinatorial explosion from high computational cost and local minima problem [9]. Therefore, information-based methods which have the ability to measure both linear and nonlinear relationships between the input image bands and the target classes [10] are often suitable.

However, FPCA has been theoretically proved as efficient over PCA and SPCA depending on the measure of PSNR, structural similarity index (SSIM), memory requirement and execution time [11]. Moreover, it can also offer better classification accuracy than PCA and SPCA [2]. In this paper,

the unsupervised linear feature extraction methods PCA, SPCA and FPCA are investigated with a view to improving the feature extraction through FPCA and SPCA for obtaining better classification result. Therefore, a segmented-FPCA (SFPCA) has been proposed for extracting both global and local characteristics of the whole dataset as well as the highly correlated bands' segments more finely than FPCA and SPCA. At last, the performance of SFPCA has been compared with its unsupervised linear predecessor feature extraction methods PCA, SPCA and FPCA together with unsupervised nonlinear feature extraction methods KPCA and KECA using various performance measure indexes for real hyperspectral image. The feature selection over the new transformed features was carried out using cumulative-variance accumulation based approach except for KECA that employs Renyi quadratic entropy based selection.

## II. Feature Extraction

### A. PCA for HSI

As an unsupervised linear statistical transformation PCA finds the correlation among the spectral wavelength bands of HSI for extracting the intrinsic bands information. To work fruitfully, it is based on the assumption that the neighboring bands of the HSI are highly correlated and they often represent almost same information about the ground objects. In its implementation for HSI [12]-[14], the HSI hypercube is first converted into a data matrix, denoted as **D**, of size $F\times S$, where $S=X*Y$. The spectral vector of a pixel, denoted as $\mathbf{x}_n$, in the hypercube or data matrix is defined as $\mathbf{x}_n= [x_{n1}\ x_{n2}\ \ldots\ldots\ x_{nF}]^T$, where, $n \in [1, S]$. Then, the zero-mean image, denoted as **I**, is produced from $\mathbf{I}_n$ as $\mathbf{I} = [\mathbf{I}_1\ \mathbf{I}_2\ \ldots..\ \mathbf{I}_n]$, where the mean image vector, $\mathbf{M} = \frac{1}{S}\sum_{n=1}^{S}\mathbf{x}_n$ and the mean-adjusted spectral vectors, $\mathbf{I}_n = \mathbf{x}_n - \mathbf{M}=[I_{n1}\ I_{n2}\ \ldots\ldots\ I_{nF}]^T$. After that, the covariance matrix, $\mathbf{C} = \frac{1}{S}\mathbf{I}\,\mathbf{I}^T$, is computed for Eigendecomposition in which eigenvectors ($\mathbf{V_1}\ \mathbf{V_2}...\mathbf{V_F}$), also known as principal components (PCs), and corresponding eigenvalues ($E_1E_2...\ E_F$) represent the core of PCA. The eigenvectors determine the directions of the new feature space and the eigenvalues determine their magnitude. In addition, the eigenvalues explain the variance of the data along the new feature axes. If $\mathbf{E}=diagonal(E_1E_2...\ E_F)$ is a diagonal matrix composed by the corresponding eigenvalues $E_1, E_2,..., E_F$ of **C** and **V** denotes the matrix of all respective eigenvectors, then **V** is calculated by solving the following equation:

$$\mathbf{C}=\mathbf{V}\mathbf{E}\mathbf{V}^T \tag{1}$$

Then, $k$ eigenvectors are chosen to form a $F\times k$ dimensional matrix, **w**, where $k$ is the number of dimensions of the new feature subspace with $k\leq F$ and often $k<<F$. In order to do so, the usual approach is to rank the eigenvalues from highest to lowest order to choose the top $k$ principal components. Additional approaches include discriminant analysis, divergence analysis e.g., Bhattacharyya distance, mutual information based selection crieteria etc. Finally, the projection matrix, **Y** can be obtained as $\mathbf{Y}=\mathbf{w}^T*\mathbf{I}$. Furthermore, the original data matrix with a very few loss, denoted as **d**, can be obtained as $\mathbf{d}=(\mathbf{w}*\mathbf{Y})+\mathbf{M}$.

### B. SPCA for HSI

It has been observed that PCA extracts more effective features if the entire original bands are highly correlated having a big covariance matrix of size $F\times F$ which requires a higher computational cost [15]. Moreover, it is also observed that the correlations between neighboring bands of HSI are usually higher than for the bands further apart, with high correlations appearing in blocks. Thus, SPCA is presented to modify the conventional PCA by avoiding the low correlations between the highly correlated blocks for better performance [15]. In the implementation of SPCA [15], first the whole zero–mean dataset is divided into $L$ subgroups based on correlation among the bands. Let $\mathbf{D}_i$ denote the subgroup datasets, where $i \in [1, L]$ and $n_i$ be the number of consecutive bands for each subgroup dataset. Then, $\mathbf{D_1}= [\mathbf{I}_1'\ \mathbf{I}_2'....\mathbf{I}_n']$, where $\mathbf{I}_j'$ contains first $n_1$ rows of the respective $\mathbf{I}_j$, $\mathbf{D_2}= [\mathbf{I}_1''\ \mathbf{I}_2''....\mathbf{I}_n'']$, where $\mathbf{I}_j''$ contains $n_2$ rows skipping first $n_1$ rows of the respective $\mathbf{I}_j$ with $j,\ n \in [1, S]$ and so on. Similarly, $\mathbf{M}_i$ is the mean vector of size $n_i\times 1$ for the respective $\mathbf{D}_i$ that can be found from **M**. Next, Eigendecomposition is performed on each computed covariance matrix of each $\mathbf{D}_i$. The overall projection matrix of the whole dataset is found by merging individual projection matrix of each $\mathbf{D}_i$ consecutively.

### C. FPCA for HSI

Another challenge is to obtain the covariance matrix using PCA and SPCA when the total number of pixels, $S$ is tremendously large, usually over 100K, which often causes software tools such as MATLAB crashed due to memory management problem [2]. Also, PCA treats all bands equally in obtaining the covariance matrix failing to pick up the distinct contributions of the featured $F$ bands and similarly SPCA treats all bands equally in a subgroup [2]. Thus, to reduce the size of covariance matrix and to extract the local structure from the entire hypercube spectral domain, FPCA is presented where the correlation between bands as well as band groups are extracted fruitfully [2].

In the implementation [2], every mean-adjusted spectral vector $\mathbf{I}_n$ in the zero–mean dataset is transformed into a matrix. Each row of the matrix contains a group of $W$ bands, where the total $F$ bands are folded into $H$ groups or segments. Mathematically, let $\mathbf{A}_n$ be the converted matrix of size $H\times W$ ($F=H*W$). Then, $\mathbf{A}_n=[\ \mathbf{a}_{n1}\ \ \mathbf{a}_{n2}....\mathbf{a}_{nH}]^T$, where, $\mathbf{a}_{nh}=[I_{n(1+W(h-1))}I_{n(2+W(h-1))}\ \ldots\ldots\ I_{n(W+W(h-1))}]$ and $h \in [1, H]$. The choice of different values for $H$ and $W$ may affect the results. The covariance matrix, denoted as $\mathbf{C}_n$, for each $\mathbf{A}_n$ is computed as $\mathbf{C}_n = \mathbf{A}_n{}^T\mathbf{A}_n$, where, the size of $\mathbf{A}_n$ is $H\times W$ and that of for $\mathbf{C}_n$ is $W\times W$. Finally, the overall covariance matrix, denoted as $\mathbf{C}_{FPCA}$, for the whole dataset is computed as:

$$\mathbf{C}_{FPCA} = \frac{1}{S}\sum_{n=1}^{S}\mathbf{C}_n = \frac{1}{S}\sum_{n=1}^{S}\mathbf{A}_n{}^T\mathbf{A}_n \tag{2}$$

Thus, the size of the overall covariance matrix is $W\times W$. The projection matrix is then calculated after performing Eigendecomposition on $\mathbf{C}_{FPCA}$.

### D. KPCA for HSI

Linear feature extraction methods may not be scale invariant. Also they may not guarantee good class separation in the transformed space since they reduce dimensions only in a linear fashion. Moreover, if the spectral data contains more complicated structures about the earth surface that cannot be well represented in a linear subspace, they may not be too useful [6], [16]. Fortunately, KPCA permits to generalize conventional PCA for nonlinear dimensionality reduction. Each spectral vector $\mathbf{x_i}$ is projected to a new vector $\emptyset(\mathbf{x}_i)$ in a new higher dimensional feature space, where $\emptyset$ is a nonlinear function. Conventional PCA can be performed in the new feature space, but this can be

tremendously costly and inefficient. Thus, kernel methods can be used to simplify the computation.

In the implementation, first the kernel matrix $\mathbf{K}$ is constructed from $\{\mathbf{x}_i\}$ as $\mathbf{K}_{i,j} = k(\mathbf{x}_i, \mathbf{x}_j)$, where, $k(\mathbf{x}_i, \mathbf{x}_j)$ is the kernel function which is defined as $k(\mathbf{x}_i, \mathbf{x}_j) = \emptyset(\mathbf{x}_i)^T \emptyset(\mathbf{x}_j)$. Then, the Gram matrix $\widetilde{\mathbf{K}}$ is computed using the following equation.

$$\widetilde{\mathbf{K}} = \mathbf{K} - \mathbf{1}_S\mathbf{K} - \mathbf{K}\mathbf{1}_S + \mathbf{1}_S\mathbf{K}\mathbf{1}_S, \tag{3}$$

where, $\mathbf{1}_S$is the $S\times S$ matrix with all elements equal to $1/S$. Next, the equation is used to solve for the vectors $\mathbf{a}_i$ ($\mathbf{K}$ is substituted with $\widetilde{\mathbf{K}}$ if the projected dataset $\{\emptyset(\mathbf{x}_i)\}$ does not have zero mean.).

$$\mathbf{K}\mathbf{a}_k = \mathbf{E}_k N \mathbf{a}_k, \tag{4}$$

where, $\mathbf{a}_k$ is the $S$ dimensional column vector of $a_{ki}$ i.e., $\mathbf{a}_k = [a_{k1} a_{k2} \ldots\ldots a_{kS}]^T$. The kernel principal components $\mathbf{y}_k(\mathbf{x})$ is then computed using the following equation.

$$\mathbf{y}_k(\mathbf{x}) = \emptyset(\mathbf{x})^T \mathbf{v}_k = \sum_{i=1}^{S} a_{ki} k(\mathbf{x}, \mathbf{x}_i) \tag{5}$$

The power of kernel methods is that $\emptyset(\mathbf{x}_i)$ should not be calculated explicitly. The kernel matrix can directly be constructed from the training dataset $\{\mathbf{x}_i\}$. The polynomial kernel, $k(\mathbf{x}, \mathbf{y}) = (\mathbf{x}^T\mathbf{y})^d$ or $k(\mathbf{x}, \mathbf{y}) = (\mathbf{x}^T\mathbf{y} + c)^d$, where c > 0 and the Gaussian kernel or Radial Basis Function (RBF), $k(\mathbf{x}, \mathbf{y}) = exp(-\frac{\|\mathbf{x}-\mathbf{y}\|^2}{2\sigma^2})$ with parameter $\sigma$ that can directly influence on the performance are the commonly used kernels. Ideally, $\sigma$ should be smaller than the interclass distances and larger than the inner-class distances if we want to separate classes in the new feature space. Since how many classes are there in the dataset is unknown while applying KPCA, thus it is uneasy to estimate the distances. Alternatively, the value of $\sigma$ can be set to a small value to capture only the neighborhood information of each data point. For the same, let the distance from each data point $\mathbf{x}_i$ to its nearest neighbor be $d_i^{\mathrm{NN}}$. Then, one way to find the parameter is $\sigma = a.mean\ (d_i^{\mathrm{NN}})$, where, $a$ is an arbitrary integer. This strategy is used in the experiment. The detail discussion on parameter selection and pre-image reconstruction is in [16].

### *E. KECA for HSI*

KECA, a successor of KPCA, exposes structure based on Renyi quadratic entropy of the input space dataset thus not on the eigenvalues and eigenvectors of the kernel matrix directly [17], [18]. This method performs data transformation and feature reduction by projecting onto those KPCA axes which give contribution to the entropy estimate. Usually, the axes will not essentially correspond to the highest eigenvalues and eigenvectors of the kernel matrix as in the case for KPCA dimensionality reduction. Thus, KECA may produce strikingly different transformed data than KPCA. In the implementation [17], as like KPCA, the kernel matrix $\mathbf{K}$ from $\{\mathbf{x}_i\}$ is constructed. Then, $V(p) = \int p^2(\mathbf{x})d\mathbf{x}$ is in concentration since the logarithm of the following original Renyi quadratic entropy estimation used in KECA is a monotonic function.

$$H(p) = -\log \int p^2(\mathbf{x})d\mathbf{x} \tag{6}$$

Where, $p(\mathbf{x})$ is the probability density function (*pdf*) generating the dataset, $\mathbf{D}=[\mathbf{x}_1,\ldots,\mathbf{x}_N]$ of dimensionality $d$. Then, the Renyi entropy estimator, $\hat{V}(p)$ in terms of the eigenvalues and eigenvectors of the kernel matrix is calculated that may be eigendecomposed as $\mathbf{K}=\mathbf{E}\mathbf{D}\mathbf{E}^T$, where, $\mathbf{D}$ is a diagonal matrix that stores the eigenvalues $\lambda_1,\ldots\ldots,\lambda_N$ and $\mathbf{E}$ is the matrix with the corresponding eigenvectors $\mathbf{e}_1,\ldots.,\mathbf{e}_N$ as columns using the following equation:

$$\hat{V}(p) = \frac{1}{N^2}\sum_{i=1}^{N}(\sqrt{\lambda_i}\mathbf{e}_i{}^T\mathbf{1})^2 \tag{7}$$

Using KPCA, the projection of defined $\Phi$ onto the $i^{\text{th}}$ principal axis $\mathbf{u}_i$ in the kernel feature space is as $P_{\mathbf{u}_i}\Phi = \sqrt{\lambda_i}\mathbf{e}_i{}^T$. Since KECA is defined as a $k$-dimensional data transformation obtained by projecting $\Phi$ onto a subspace $U_k$ spanned by those $k$ KPCA axes contributing most to the Renyi entropy estimate of the data. Hence, a subset of KPCA axes but not necessarily those corresponding to the top $k$ eigenvalues constitutes the $U_k$. The transformed data, $\Phi_{eca}$ for KECA is calculated as follows:

$$\Phi_{eca} = P_{U_k}\boldsymbol{\varphi} = \sqrt{\mathbf{D}_k}\mathbf{E}_k{}^T \tag{8}$$

## III. PROPOSED SEGMENTED-FPCA

SPCA performs conventional PCA on each of the highly correlated bands' segments of the dataset for extracting the global structures of the segments. On the other hand, FPCA extracts both global and local structures of the whole dataset with a 2D matrix based representation of each of the bands. Therefore, it is obvious that if both global and local structures of the entire dataset as well as the highly correlated bands' segments can be obtained to provide additional information for classification, then the accuracy may increase. Thus, SFPCA is proposed in which conventional FPCA will be performed on each of the highly correlated bands' segments of the dataset with a view to extracting both global and local structures of the segments as illustrated in Fig. 1.

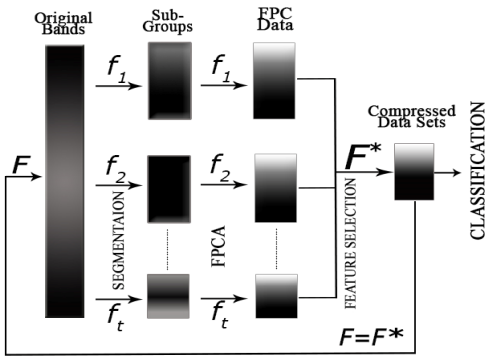


Fig. 1. Working procedure of SFPCA

In the implementation, the whole zero–mean dataset is first separated into $L$ subgroup datasets $\mathbf{D}_i$. The construction procedure of the $\mathbf{D}_i$ is described earlier in case of SPCA. Then, for each $\mathbf{D}_i$ of size $n_i\times S$, the calculation of the covariance matrix is described now assuming $\mathbf{D}= \mathbf{D}_i$ and $f= n_i$ for better understanding. Then, its every mean-adjusted spectral vector $\mathbf{I}_n$ is converted into a matrix in which each row contains a group of $w$ ($w<W$) bands, where the total $f$ ($f<F$) bands are folded into $G$ ($G<H$) groups or segments as shown in Fig. 2.

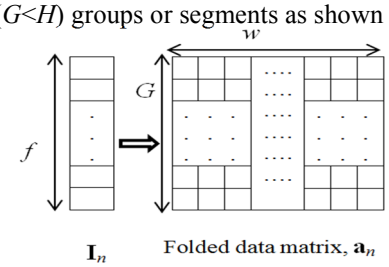


Fig. 2. Construction of a 2D matrix by folding a 1D spectral vector

Mathematically, let $\mathbf{a}_n$ be the converted matrix of size $G\times w$ ($f=G*w$). Then, $\mathbf{a}_n=[\ \mathbf{a}_{n1}\ \mathbf{a}_{n2}\ldots\mathbf{a}_{nG}]^T$, where, $\mathbf{a}_{ng}=[I_{n(1+w(g-1))}\ I_{n(2+w(g-1))}\ \ldots\ldots\ I_{n(w+w(g-1))}]$ and $g \in [1, G]$. In this case, the choice of different values for $G$ and $w$ may also affect the results. The covariance matrix, denoted as $\mathbf{c}_n$, for each $\mathbf{a}_n$ is computed as $\mathbf{c}_n = \mathbf{a}_n{}^T\mathbf{a}_n$, where, the size of $\mathbf{a}_n$ is $G\times w$ and that of for $\mathbf{c}_n$ is $w\times w$. Finally, the overall covariance matrix of the $\mathbf{D}_i$, denoted as $\mathbf{c}_i$ *of* size $w\times w$, is computed as:

$$\mathbf{c}_i = \frac{1}{S}\sum_{n=1}^{S}\mathbf{c}_n = \frac{1}{S}\sum_{n=1}^{S}\mathbf{a}_n{}^T\mathbf{a}_n \tag{9}$$

At last, Eigendecomposition is performed on each computed covariance matrix $\mathbf{c}_i$ for every $\mathbf{D}_i$. The overall projection matrix of the whole dataset can be found by merging individual projection matrix of each $\mathbf{D}_i$ consecutively.

## IV. Experimental Result

### A. Dataset Decription

The Indian Pine HSI acquired by Airborne Visible/Infrared Imaging Spectrometer (AVIRIS) sensor over the Indian Pine test site in North-western Indiana with 220 spectral reflectance bands is used in the experiment. Each band image is of 145×145 size with 20 meters geometric resolution/ground sampling distance (GSD). The wavelength range is 400-2500 *nm* (spectral resolution: 10 *nm*) having 16 ground classes [19].

### B. Performance Measure

Peak signal to noise ratio (PSNR) and space requirement have been calculated as a performance measure of the feature extraction methods. However, to evaluate the methods for HSI, overall classification accuracy has been considered. 2127 pixels of 14 different classes from the dataset have been used.

Twelve (12) principal components with highest eigenvalues are selected to accumulate approximately 100% cumulative variance for PCA, SPCA, FPCA and SFPCA to calculate the PSNR. However, the cumulative variance using 12 features of KPCA with RBF kernel is 63.34% since this method requires comparatively more, often all features to accumulate approximately 100% cumulative variance. Moreover, Renyi quadratic entropy measure is used for feature selection from KECA transformation with RBF kernel. The PSNR is defined as:

$$\text{PSNR} = 10\log_{10}\left(\frac{R^2}{MSE}\right) \tag{10}$$

Here, $R$ is the maximum fluctuation in the input image data type and can be found as $R$=*Maximum_element*($\mathbf{A_2}$)-*Minimum_element*($\mathbf{A_2}$) and *MSE* is the mean square error which can be calculated as follows:

$$\text{MSE} = \frac{\sum_{X,y,\lambda}[A_{1(x,y,\lambda)}-A_{2(x,y,\lambda)}]^2}{X*Y*F}, \tag{11}$$

where $A_{1(x,y,\lambda)}$and $A_{2(x,y,\lambda)}$are the values from the column $x$ of rows $y$ in the spectral band $\lambda$ in the input images $\mathbf{A_1}$ (transformed HSI) and $\mathbf{A_2}$ (original HSI) respectively.

Based on the correlation matrix of the dataset as shown in Fig. 3 in image form, SPCA is applied with 3 highly correlated segments of varying band-subgroups as shown in the Table I. FPCA has been applied on the dataset in five (5) different ways with five different folding options which is shown in Table II.

However, to apply the proposed SFPCA, the dataset is divided into three highly correlated bands' segments as like SPCA which is shown in Table I. Then, the probable combination of the folding options to perform the SFPCA transformation for the whole dataset using the three subgroup datasets $\mathbf{D}_1$, $\mathbf{D}_2$ and $\mathbf{D}_3$ is illustrated in Table III. From the projection matrix of each subgroup dataset $\mathbf{D}_i$, the first several PCs have been extracted. Merging the selected features from each subgroup dataset $\mathbf{D}_i$ consecutively, the overall projection matrix is formed for subsequent operation that contains both extracted local and global characteristics of the whole as well as subgroup datasets. The folding mechanism of uneven number of bands and feature selection constraints are broadly discussed in [2].

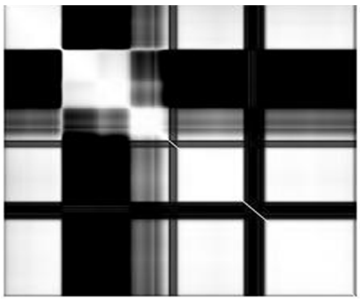

Fig. 3. Correlation matrix of the dataset

TABLE I. Segmentation of the Complete Set of Bands

| Subgroup dataset | Parameter | Values |
|---|---|---|
| 1 ($\mathbf{D}_1$) | Bands | 1-36 |
| | No. of bands | 36 |
| | Average correlation in diagonal | 0.9365 |
| 2 ($\mathbf{D}_2$) | Bands | 37-102 |
| | No. of bands | 66 |
| | Average correlation in diagonal | 0.6263 |
| 3 ($\mathbf{D}_3$) | Bands | 103-220 |
| | No. of bands | 118 |
| | Average correlation in diagonal | 0.7024 |

TABLE II. Folding Options for FPCA

| Option | $H$ | $W$ |
|---|---|---|
| 1 (FPCA-1) | 2 | 110 |
| 2 (FPCA-2) | 4 | 55 |
| 3 (FPCA-3) | 5 | 44 |
| 4 (FPCA-4) | 10 | 22 |
| 5 (FPCA-5) | 11 | 20 |

TABLE III. Combination of Folding Options for SFPCA

| Method | Folding Option for $\mathbf{D}_1$ ($G$, $w$) | Folding Option for $\mathbf{D}_2$ ($G$, $w$) | Folding Option for $\mathbf{D}_3$ ($G$, $w$) |
|---|---|---|---|
| SFPCA-1 | 2, 18 | 2, 33 | 2, 59 |
| SFPCA-2 | 2, 18 | 6, 11 | 2, 59 |
| SFPCA-3 | 3, 12 | 2, 33 | 2, 59 |
| SFPCA-4 | 3, 12 | 6, 11 | 2, 59 |
| SFPCA-5 | 4, 9 | 2, 33 | 2, 59 |
| SFPCA-6 | 4, 9 | 6, 11 | 2, 59 |
| SFPCA-7 | 6, 6 | 2, 33 | 2, 59 |
| SFPCA-8 | 6, 6 | 6, 11 | 2, 59 |

The PSNR values are shown in Fig. 4, where it can be seen that SFPCA produces better PNSR than PCA and FPCA but slightly smaller than SPCA with the same number of PCs.

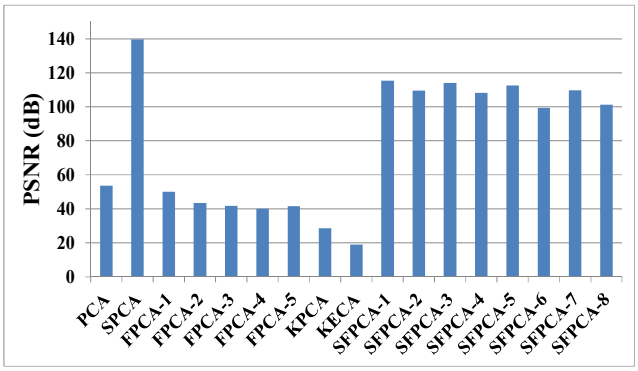


Fig. 4. PSNR of the feature extraction methods

In addition, the memory requirement for the methods over different stages is compared in the Table IV, where it is clear that SFPCA requires the least and KPCA and KECA require the most space in both stages.

TABLE IV. MEMORY REQUIREMENT

| Method | Stage | |
|---|---|---|
| | *Data Matrix* | *Covariance Matrix* |
| PCA | $S\times HW$ | $HW\times HW$ |
| SPCA | $S\times W$ | $W\times W$ |
| FPCA | $H\times W$ | $W\times W$ |
| KPCA | $S\times HW$ | $S\times S$ |
| KECA | $S\times HW$ | $S\times S$ |
| SFPCA | $G\times w$ | $w\times w$ |

## C. Classification Accuracy

To evaluate the performance of the feature extraction methods, classification accuracy has been calculated when support vector machine (SVM) with RBF kernel is applied. MATLAB LibSVM package is used [20]. The 10-fold cross validation scheme has been used to select the *C* and *gamma* parameters for the efficient training and testing. The training set contains 1121 pixels and the testing set contains 1006 pixels of 14 different classes as illustrated in Table V.

TABLE V. DETAIL OF THE TRAINING AND TESTING SAMPLES

| Class name | Training samples | Testing samples |
|---|---|---|
| Hay-windrowed | 165 | 135 |
| Soybean-notill | 109 | 85 |
| Woods | 279 | 248 |
| Wheat | 42 | 63 |
| Grass-trees | 96 | 80 |
| Soybean-min | 130 | 165 |
| Corn-min | 108 | 72 |
| Stone-Steel-Towers | 48 | 40 |
| Buildings-Grass-Trees-Drives | 48 | 44 |
| Grass-pasture | 15 | 14 |
| Corn-notill | 25 | 20 |
| Soybean-clean | 15 | 15 |
| Corn | 21 | 10 |
| Alfalfa | 20 | 15 |

Feature extraction methods for classification suffer from the major problem of searching the optimal number of PCs. In this experiment, the first PC calculated using the largest eigenvalue is used as the input of SVM to perform the classification. Then, the PCs are increased one by one corresponding to the largest eigenvalue at each step [12] and the overall classification accuracy (OA) is noted. The optimal number of PCs that produces the best OA for the dataset using SFPCA and other feature extraction methods is illustrated in Table VI.

TABLE VI. OVERALL CLASSIFICATION ACCURACY

| Method | Optimal number of image bands | Overall Accuracy (%) |
|---|---|---|
| PCA [13] | 46 | 93.7376 |
| SPCA [15] | 79 (31, 44, 4 ) | 93.837 |
| FPCA-1 [2] | 40 | 95.1292 |
| FPCA-2 [2] | 29 | 94.4334 |
| FPCA-3 [2] | 38 | 92.3459 |
| FPCA-4 [2] | 43 | 88.7674 |
| FPCA-5 [2] | 64 | 90.2584 |
| KPCA [6] | 107 | 95.9245 |
| KECA [18] | 147 | 95.6262 |
| SFPCA-1 | 60 (10, 20, 30) | 94.5328 |
| SFPCA-2 | 84 (20, 24, 34) | 93.837 |
| SFPCA-3 | 73 (15, 24, 34) | 93.4394 |
| SFPCA-4 | 75 (21, 24, 30) | 92.3459 |
| SFPCA-5 | 73 (20, 24, 29) | 95.6262 |
| SFPCA-6 | 74 (20, 24, 30) | 95.4274 |
| SFPCA-7 | 84 (24, 26, 36) | 94.5328 |
| SFPCA-8 | 84 (24, 24, 36) | 94.2346 |

From Table VI, it can be observed that the two variants of the improved unsupervised linear feature extraction method SFPCA, SFPCA-5 (95.6262%) and SFPCA-6 (95.4274%) outperform the other unsupervised linear methods PCA and all variants of SPCA and FPCA. Furthermore, the other variants of SFPCA have also produced satisfactory accuracy. The reason is that the both the local and global characteristics of the entire dataset as well as the highly correlated subgroup datasets have been extracted more minorly through applying FPCA on each of the highly correlated bands' segments.

Moreover, in comparison to unsupervised nonlinear feature extraction methods KPCA and KECA, SFPCA-6 attempts to beat KPCA having RBF kernel which produces the best classification accuracy (95.9245%) with $\sigma = 0.019$ and SFPCA also produces identical accuracy with entropy based KECA having RBF kernel and $\sigma$=0.011 for the given training and testing pixels of the dataset. Since only several bands of the dataset are nonlinear to each other as illustrated in Fig. 5 and Fig. 6 of scatter plots, KPCA tries to fix these nonlinear relationships through transforming the original dataset into a higher dimensional space for better classification. On the other hand, although Renyi quadratic entropy based KECA obtains strikingly different transformed data but it cannot fix the nonlinearity as much as KPCA can. Besides, SFPCA being linear method efforts to tackle several nonlinear relationships

through tremendously extracting the global and local structures of the dataset and its highly correlated subgroup datasets.

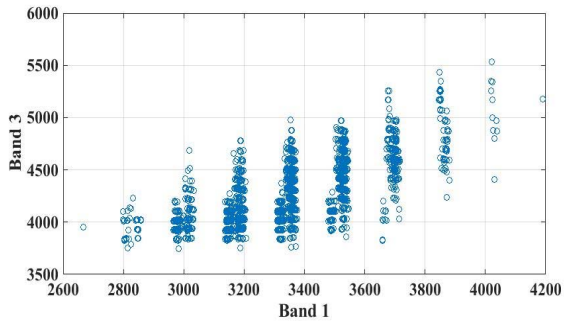


Fig. 5. Scatter plot of bands 1 and 3 showing nonlinear relationship

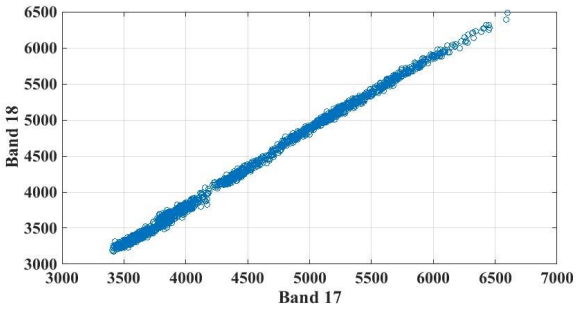


Fig. 6. Scatter plot of bands 17 and 18 showing linear relationship

Furthermore, any feature extraction method produces better accuracy than using the original dataset (70.2783%) which clarifies the need of feature reduction for efficient HSI classification. At the end, it is also observed that SPCA and FPCA effort to perform better over PCA as they also deal with the extraction of local characteristics in different ways.

## V. CONCLUSION

An improved feature extraction technique based on the specialty of both FPCA and SPCA, termed as segmented-FPCA (SFPCA), has been presented for extracting both local and global intrinsic characteristics of the entire dataset as well as the highly correlated bands' segments more appropriately with a view to supplying some additional information to the classifier for better classification result. The proposed feature extraction method SFPCA has been compared in terms of memory requirement and overall classification accuracy with its predecessor PCA, SPCA, and FPCA and nonlinear variants of PCA such as KCPA and KECA. The comparative outcome shows that SFPCA produces better classification accuracy than all investigated linear feature extraction methods with comparatively more input features and efforts to tackle with KPCA and KECA for fixing the several nonlinear relationships in the HSI. In addition, it offers the least space complexity. However, if the settings such as segmentation criteria, folding optimization strategies, kernel tricks, feature selection strategies etc. are altered, then the classification accuracy may fluctuate. Further improvement on classification accuracy may be possible through providing more training samples.

## REFERENCES


[1] J. A. Richards and X. Jia, *Remote Sensing Digital Image Analysis*, 4th edition, Berlin, Germany: Springer-Verlag, 2006.

[2] J. Zabalza, J. Ren, M. Yang, Y. Zhang, J. Wang, S. Marshall, and J. Han, "Novel folded-PCA for improved feature extraction and data reduction with hyperspectral imaging and SAR in remote sensing," *ELSEVIER ISPRS Journal of Photogrammetry and Remote Sensing*, vol. 93, pp.112–122, 2014.

[3] B. K. Mohan and A. Porwal, "Hyperspectral image processing and analysis," *Current Science*, vol. 108, no.5, pp. 833-841, 2015.

[4] B. Guo, S. R. Gunn, R. I. Damperand and J. D. B. Nelson, "Band Selection for Hyper spectral Image Classification Using Mutual Information," *IEEE Geoscience and Remote Sensing Letters*, vol. 3, no. 4, 2006.

[5] G. Hughes, "On the Mean Accuracy of Statistical Pattern Recognizers," *IEEE Transactions on Information Theory*, vol. IT-14, no.1, pp. 55–63, 1968.

[6] M. Fauvel, J. Chanussot and J. A. Benediktsson, "Kernel Principal Component Analysis for Feature Reduction in Hyperspectral Image Analysis," *IEEE 7th Nordic Signal Processing Symposium (NORSIG),* pp. 238-241, Iceland, 2006.

[7] X. Jia, B. Kua, and M. M. Crawford, "Feature Mining for Hyperspectral Image Classification," *Proceedings of the IEEE*, vol. 101, no. 3, pp. 676-679, 2013.

[8] C. Chang, D. Qian, T. L. Sun, and M. Althouse, "A Joint Band Prioritization and Band-decorrelation Approach to Band Selection for Hyperspectral Image Classification," *IEEE Transactions on Geoscience and Remote Sensing*, vol. 37, no. 6, pp. 2631–2641, 1999.

[9] F. Melgani and L. Bruzzone, "Classification of Hyperspectral Remote Sensing Images with Support Vector Machines," *IEEE Transactions on Geoscience and Remote Sensing*, vol. 42, no. 8, pp. 1778–1790, 2004.

[10] H. Peng, F. Long and C. Ding, "Feature Selection Based on Mutual Information Criteria of Max-dependency, Max-relecvance, and Min-redundancy," *IEEE Trans. Pattern Anal. Mach. Intell.*, vol. 27, no. 8, pp.1226–1238, 2005.

[11] P. Deepa and K. Thilagavathi, "Data Reduction Techniques of Hyperspectral Images: A Comparative Study," *IEEE 3rd International Conference on Signal Processing, Communication and Networking (ICSCN)*, 2015.

[12] L.J. Cao, K.S. Chua, W.K. Chong, H.P. Lee and Q.M. Gu, "A comparison of PCA, KPCA and ICA for dimensionality reduction in support vector machine," *ELSEVIER Neurocomputing*, vol. 55, issues. 1–2, pp. 321-336, 2003.

[13] C. Rodarmel and J. Shan, "Principal Component analysis for hyper-spectral image classification," *ACM Surveying and Land Information Science*, vol. 62, no. 2, pp. 115-122, 2002.

[14] A. Shabna, and R. Ganesan, "HSEG and PCA for Hyper-spectral Image Classification," *IEEE International Conference on Control, Instrumentation, Communication and Computational Technologies (ICCICCT),* 2014.

[15] X. Jia, and J. A. Richards, "Segmented Principal Components Transformation for Efficient Hyperspectral Remote-Sensing Image Display and Classification," *IEEE Transactions on Geoscience and Remote Sensing*, vol. 37, no. 1, pp. 538-542, 1999.

[16] Q. Wang, "Kernel Principal Component Analysis and its Application in Face Recognition and Active Shape Models," *ARXIV1207.3538*, 2012.

[17] R. Jenssen, "Kernel Entropy Component Analysis," *IEEE Transaction on Pattern Analysis and Machine Intelligence*, vol. 32, no. 5, pp. 847-860, 2010.

[18] L. Gómez-Chova, R. Jenssen and G. Camps-Valls, "Kernel Entropy Component Analysis for Remote Sensing Image Clustering," *IEEE Geoscience and Remote Sensing Letters*, vol. 9, No. 2, pp. 312-316, 2012.

[19] M. F. Baumgartner, L. Labial and D. A Landgrebe, "220 Band AVIRIS Hyperspectral Image Data Set: June 12, 1992 Indian Pine Test Site 3," *Purdue University Research Repository*, 2015.

[20] C. C. Chang and C. J. Lin, "LIBSVM: A library for support vector machines," *ACM Transactions on Intelligent Systems and Technology*, vol. 2, No. 3, pp. 27:1–27:27, 2011.

2017 3rd International Conference on Electrical Information and Communication Technology (EICT), 7-9 December 2017, Khulna, Bangladesh

# An Iterative Approach to Detect Region Boundary Eliminating Texts from Scanned Land Map Images

Md Omar Faruk Rokon[1], Md Rayhanul Masud[2] and Md Monirul Islam[3]
Department of Computer Science and Engineering
Bangladesh University of Engineering and Technology(BUET), Dhaka, Bangladesh
ofrokon@gmail.com[1], r.masudsaom@gmail.com[2], mmislam@cse.buet.ac.bd[3]

***Abstract*—Land map images are a complex document as it contains different kinds of information such as place names, the border of states or country etc. As texts may have different intensity value and size, it is not easy to extract these texts from land map images. This paper designs an iterative approach to extract texts from land map images. The approach deals with finding outlines using a mask in an iterative way to separate text and outlines. The proposed approach is tested on a set of land map images and the results are encouraging.**

***Keywords*—Land map, Iterative approach, Region, Texts.**

## I. Introduction

Traditionally, land maps, which are the geographical representation of a country, are paper based. These maps contain different text as geographical, historical, social and political information. In order to digitize these maps, it is must to detect text in map and after that to eliminate text from the map. Different types of text in different fonts, size and language have made it difficult to segment the text from map. As land map digitization is still a new technology to implement, literature on text extraction from map images is not so rich.

Researchers have proposed different approach to extract texts from map images. Some well-known techniques for text segmentation from natural scene images[1][2][3] exist which gives very satisfactory results. However, these techniques are mostly based on prior knowledge of text positions and connected components of image[4]. Since texts in images are usually more variant in size, fonts and orientation, and even they are sometimes overlapped with the region boundary, text segmentation from land map images is more complex.Tofani and Kasturi [5] segmented text from color map images. This process is started with the separation of each feature overlays according to their color. Then, it extracts the text from the black/pink pixel layer of the map image using area thresholding. Roy et al. [8], [9] partitioned the map into different layers according to color features where different size thresholds were used for initial layering. Then, the component features were connected, and to identify text characters it used skeleton information. Long straight lines were detected using Hough Transformation and curved lines were detected using major axis of partitioned components. Li et al. [6] analyzes connected components to separate texts and line arts from USGS topographic maps containing street lines and labels. Space width between two characters were the constraints for component separation. Cao et al. [7] separated characters from complex documents, which overlapped with lines, using differences of the length of line segments in character and line. Then neighboring areas of overlapping texts and lines were cut out manually, which was used to separate lines and text.

In this work, we have detected region boundary and eliminated Bengali texts namely place names and numbers in the region boundary from the map image using an iterative approach.

## II. Proposed Method

Since land map images represent region boundary and other land information, they can be converted into binary where text and outline of the areas/regions will be represented by black pixel. It is noted that outline of the regions are continuous throughout the map images. However, there are noise and discontinuity along the outlines. For this reason, no traditional edge/boundary detection techniques do not give a satisfactory result. However, the iterative approach has been proposed to extract these texts and to detect region boundary from land map images. It works on every pixel traversing the whole image in an iterative way. It uses a “Mask” to distinguish texts from the images which consequently results in finding text separated region contained in the map image.

Fig. 1: An example of Land Map image

The mask is a block of pixel containing some presumed characteristics to exemplify a text pixel. These texts are used to describe different parts of the image. Usually they are colored black like region boundary pixels surrounded by very closely distanced other neighboring text pixels. These characteristics are used to examine a pixel with the mask in order to separate text pixel from outline pixel.

978-1-5386-2307-7/17/$31.00 ©2017 IEEE

### A. Iterative Approach

Text extraction from land map images is difficult for it's low color intensity and connectivity issues. It consists of two main steps. First step is to locate non texts pixels in the image and second step is to get the texts by subtracting the non texts pixels from main image.

1) Locating Texts Pixels: A mask is assumed to be 13 dots in length having 2 5 dots discontinuity (maximum) and 4 6 columns in width. This dimension for Mask has been selected examining a considerable number of land maps. Maximum area of a single text has been found to support this dimension almost in every case. A block of pixel of variable length and height which is used to verify the characteristics of text, is used to identify whether a pixel lies on text or outline. Four sub steps are taken to ease the process.

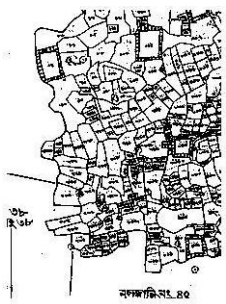

Fig. 2: Binarized Image of Map Figure 1

- Input image, $I$ is a rgb image. $I$ is converted from rgb to grayscale. Since rgb image is converted into gray scale image, color information and many text information are deleted. However, these information is not required to digitize the map image. This is because in order to digitize, region boundary is only required.
- The grayscale image $I$ is converted into binary image using a given Threshold and make a copy of $I$ and stored into $G$.
- Every pixel of the original image $I$ is traversed one by one and examined using aforementioned mask.

Fig. 3: Identified Texts from Map Image of Figure 2

- If all characteristics of the mask are satisfied, those text pixels are kept in a data structure $D$ and marked traversed. If a pixel is already in the data structure, it is ignored and searched for others. In case of region boundary pixel, they are colored white in image $G$ and marked traversed which makes image $G$ containing texts only.

**Algorithm 1** Render Text Free Image Using Iterative Approach

```
procedure ITERATIVE_APPROACH(image I)
    read the image, I
    do rgb2gray scale image conversion on I
    do binarize I
    take a base gray scale value V to be a black pixel
    take maximum black pixel count in mask T
    take a copy G of image I
    take empty data structure D
    while all pixel in G not traversed do
        take a pixel p
        if gray scale value (p) ≤ V then
            compute number of black pixel N around p
            considering mask in image G
            if N ≥ T then
                make all N pixels and p colored white in
                 image G
                mark them traversed
            else
                keep p and all N pixels in D
                mark them traversed
            end if
        else
            make pixel p colored white in image G
        end if
    end while
    produce text image W ← I − G
    binarize image W and produce Wb
    make closest neighbor black for discontinuity in Wb
    render connected text free image Wb
    return Wb
end procedure
```

2) Subtracting Region Boundary Pixel: When previous step is completed, pixels from image $G$ are subtracted from image $I$ in an iterative manner. Then, discontinuity is removed from produced image.This step needs two sub-steps to perform the task.

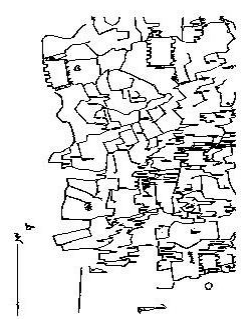

Fig. 4: Subtracted Texts Free Image

- An white image $W$ is taken with the same length and height as input image $I$. Pixels from image $G$ are subtracted from main image $I$ and resulted image is stored in $W$. $W$ is binarized to sharpen the edge outlines.

- Compare 8-neighbor for every pixel in image $Wb$ with main image and when closely distanced boundary pixels are found, make them strictly closed so that discontinuity found in the resultant image $Wb$ gets reduced.

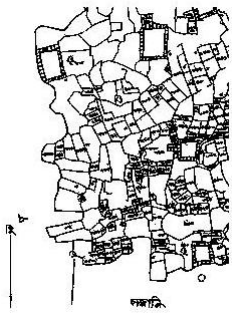

Fig. 5: Texts Free Image After Filling

## III. DATA SET DETAILS AND EXPERIMENT RESULTS

As there is no recognized set for map images, we have created our own data set for map images which are collected from different sources like websites, local land offices etc. and all of them are from Bangladesh. So, our main focus is to eliminate Bengali texts from image where we consider characters like place names and region number as texts.

(a) (b)

Fig. 6: a. Input Image b. Output Image - Texts Free Image

We experimented our algorithm using all the images and tried to find the reliability of our proposed algorithm. The reliability and accuracy are described followings. We detected region found by boundary. Actually detected region boundary (ARB) has been counted manually in each map from our data set. Truly detected region boundary (TDB) is truly found region boundary by the algorithm in the output map image. Falsely detected region boundary (FDB) is falsely detected region boundary by the algorithm in the output image. Incompletely detected region boundary (IDB) is incompletely or partially detected region boundary by the algorithm.

We computed False Positive Percentage (FPP), False Negative Percentage (FNP), True Detection Percentage (TDP) and Incomplete Detection Percentage (IDP) in order to estimate the efficiency of our proposed algorithm. They are computed as follows,

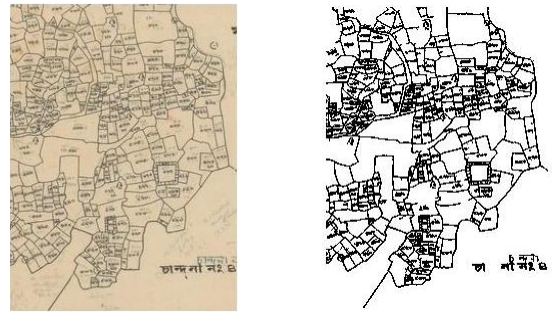

(a) (b)

Fig. 7: a. Input Image b. Output Image - Texts Free Image

$$TDP = \frac{TDB}{ARB} * 100\% \tag{1}$$

$$FPP = \frac{FDB}{TDB + FDB} * 100\% \tag{2}$$

$$FNP = \frac{ARB - TDB}{ARB} * 100\% \tag{3}$$

$$IDP = \frac{IDB}{TDB} * 100\% \tag{4}$$

TABLE I: EXPERIMENT RESULTS BASED ON THREE IMAGES FROM OUR DATA SET

| Map Images | ARB | TDB | FDB | IDB |
|---|---|---|---|---|
| Figure -5 | 157 | 98 | 45 | 14 |
| Figure -6 | 65 | 52 | 3 | 10 |
| Figure -7 | 205 | 123 | 60 | 22 |

TABLE II: REGION DETECTION PERCENTAGE OF THE PROPOSED ALGORITHM

| Map Images | TDP | FPP | FNP | IDP |
|---|---|---|---|---|
| Figure -5 | 62.42 | 31.47 | 37.58 | 14.29 |
| Figure -6 | 80.00 | 5.45 | 20.00 | 26.92 |
| Figure -7 | 60.00 | 32.79 | 40.00 | 17.89 |

Table I shows the results of experimental study for the proposed algorithm on three images from collected data set. Table II shows the accuracy and efficiency of the proposed method. It can truly detect region boundary 62.42% for Figure 5, 80.00% for Figure 6, 60.00% for Figure 7. We used our local images for the experiment and there is no common database. Moreover, very few related works have been discussed in the introduction. For this reason, we didn't compare our results with other because the comparison results could be biased. It is noted that our method has some limitations. When the map image contains very dense region and texts overlap with the boundary of region, the method doesn't give satisfactory results. The boundary lines are eliminated wrongly because the method assumes the lines as texts. Furthermore, when the map image is a low resolution image, the method can not detect all the region.

## IV. Conclusion

Considering different languages in the map images and scarcity of dataset, it is difficult to compare with other algorithms. It is still fancy to eliminate texts from the map image accurately due to its unpredictable nature. The iterative approach gives satisfactory results and can be used to eliminate texts from other type of images. The main contribution of this paper is that it can eliminate Bangla texts from land map images which is the prerequisite for land map digitization. The authors are currently working to compare with other approaches as a further research. There are scopes for future study in this field as it does not give efficient results when the image is small, low resolution and dense. It fails to eliminate text if text touches the region boundary.

## References


[1] S. M. Hanif and L. Prevost: *Text detection and localization in complex scene images using constrained adaboost algorithm,* In: ICDAR, 2009, pp. 15

[2] Y.-F. Pan, X. Hou, and C.-L. Liu: *Text localization in natural scene images based on conditional random field* In: ICDAR, 2009, pp. 610

[3] U. Bhattacharya, S. K. Parui, and S. Mondal: *Devanagari and bangla text extraction from natural scene images* In: ICDAR, 2009, pp. 171175

[4] B. B. Chaudhuri and U. Pal: *Skew angle detection of digitized indian script documents* In: IEEE Trans. Pattern Anal. Mach. Intell., vol. 19, no. 2, pp. 182186, 1997

[5] Tofani, P., Kasturi, R.: *Segmentation of text from color map images* In: Proceedings of the Fourteenth International Conference on Pattern Recognition, vol. 1, pp. 945947 (August 1998)

[6] Li, L., Nagy, G., Samal, A., Seth, S., Xu, Y.: *Cooperative text and line-art extraction from a topographic map* In: Proceedings of the Fifth International Conference on Document Analysis and Recognition, ICDAR 1999, pp. 467470 (September 1999)

[7] Cao, R., Tan, C.L.: *Text/graphics separation in maps* In: Proceedings of the 4th International Workshop on Graphics Recognition Algorithms and Applications, pp. 245254 (2001)

[8] Roy, P.P., Vazquez, E., Llados, J., Baldrich, R., Pal, U.: *A system to segment text and symbols from color maps* In: Liu, W., Llados, J., Ogier, J.-M. (eds.) GREC 2007. LNCS, vol. 5046, pp. 245256. Springer, Heidelberg (2008)

[9] Roy, P., Llados, J., Pal, U.: *Text/graphics separation in color maps* In: International Conference on Computing: Theory and Applications, ICCTA 2007, pp. 545551 (2007)

# Design and Implementation of Smart Taxi Fare Meter and Server Based Electronic Payment System

Md. Shahabuddin[±], Mohammad Rubaiyat Tanvir Hossain*, Mir Rifat Siyam[¥]
Department of Electrical and Electronic Engineering
Chittagong University of Engineering and Technology
Chittagong-4349, Bangladesh
E-mail: [±]shahab_cuet11@yahoo.com, *mrthhossain@cuet.ac.bd, [¥]siyam.rifat@yahoo.com

***Abstract*— An idea of development of a smart yet cost effective fare meter which can accurately measure the distance and also can give solution to the fare payment difficulties using a web server based dedicated smart card for fare payment, all accumulated in a single system has been proposed in this paper. Our main goal is to digitize the current system in such a way which would be of convenience both for the driver, vehicle owner and the passenger. The state of the art includes automatic online tariff upgradation system, to be controlled by the regulatory authority whenever there is a necessity to change the tariff due to various reasons. This makes it unique from the existing system as upgrading tariff becomes easier and comfortable which is too much time consuming in the present system. A miniature taxi has been developed having the proposed features onboard. The display unit displays the parameters by means of the number of rotations of the wheel and total waiting time using Infrared Ray receiver and emitters. This system mainly consists of an Arduino developing board, a Liquid Crystal Display, a Radio Frequency Identification Module, a GSM Module, an Encoder and a web server interface. Smart Card is used for payment via an onboard RFID reader which is an Active Reader Passive Tag system. GPRS feature of the GSM module has been used to transfer data between Arduino and web server.**

***Keywords*— *Web server, Infrared Ray, Arduino, Radio Frequency Identification, Liquid Crystal Display, Smart Card, Active Reader Passive Tag.***

## I. INTRODUCTION

Today, in context with the technological advancement in every sphere of life, digital taxi fare meter is not anymore an unfamiliar term. This whole process begins when the modern taximeter came into account, invented by German Friedrich Wilhelm Gustav Bruhn in 1891. Also the very first meter-equipped and gasoline-powered taxicab was invented by Gottlieb Daimler in 1897 [1]. Though smart taxi fare meter is being used all over the world for quite a long time, Bangladesh first came into the act in the year 2007 [2]. From then onwards, most of the meters are imported from India and some from China and others as it is not manufactured in Bangladesh. It takes roughly BDT 6000 per meter which is quite expensive. Moreover, reports have been recorded of damage of the circuitry most often. So reliability and robustness is a big question. The taxi meters which are used in our country are built with microcontrollers. The tariff is included in the microcontroller program. The display unit displays the fare counting the wheel rotation by means of any kind of sensor, a magnetic Hall Effect sensor particularly used in Bangladesh which costs BDT 600 and imported from China as well. Again whenever there is an update in the tariff due to price hike of gas, oil, etc. or any other reason, the meters has to be adjusted or calibrated with the revised microcontroller program having the new tariff. This calibration is done by some particular government authorized dealers and tested by Bangladesh Road Transport Authority (BRTA). All the vehicles have to rush to these particular points for calibration in a fixed time as per government regulation. It becomes difficult because of the large number of vehicles with respect to fewer numbers of calibration points. As we all know in the recent past there was a two time hike in the taxi fare in a very less span of time as the taxi drivers were averse to meters because of low tariff. Several statements from the government officials during the then period regarding the anarchy of system loss due to deadline extensions for the adjustment of meters, which have to be done from Dhaka, solely describes the whole scenario [3]. Again there are many problems related to the fare payment. People need to carry enough hard cash in order to make any journey. Again sometimes the driver doesn't have the change to return to the passenger in case of receiving big notes. So transaction becomes difficult. In a busy city like Dhaka this is often the major reason for traffic jam. . It's high time for a taxi card as the number of single public transport passenger like taxi, CNG auto rickshaw is huge [4]. Smart card for fare payment system is already a well-established thing in the outer world [5]. So, electronic payment system is a need in context with the present time frame in order to solve payment problems in Bangladesh. This again, is the practical example of the epoch making concept of **virtual money**.

## II. RELATED WORKS

Some distinct works have been done in the field of taxi fare meter in Bangladesh using microcontroller [6]. Again most of the work suggested the way to reduce taxi dispatching problem, keeping trace of vehicles on the road, forgery of license and other documents, reduce overpaying, etc [7-8].

978-1-5386-2307-7/17/$31.00 ©2017 IEEE

Again similar kind of work has been done in Iran where only electronic payment system was focused [9].

In Bangladesh a smart card for BRTC bus fare payment named SPASS had been introduced earlier but it failed miserably [10]. The reasons behind it were many. Now the system is proposed for private single passenger taxi cabs or CNG, but it can be implemented for other vehicles too with little modification [11]. Reference [12] described the whole working procedure and scenario of smart card system.

## III. METHODOLOGY

The implementation of the proposed system is done within 3 stages. First stage is the signal extraction stage, which is integrated with the wheel with the core purpose of only counting the rotations. Second stage is display and controlling stage, which contains the processing unit, display unit, controlling switches, GSM device, RFID reader and the RFID module. The third stage is the web section which contains the database management system and is linked with the second stage over GSM. So, first and second stages are wire connected and the third and second stages are connected wirelessly. The whole system block diagram is shown in Fig 1.

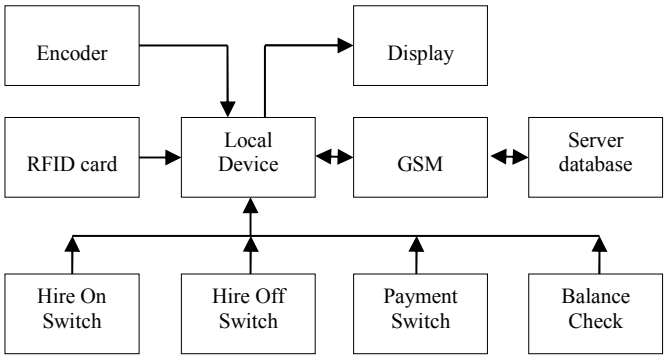


Fig. 1. Block diagram of the implemented system

### A. Distance Measurement

In this project, IR sensors have been used, mounted with a toothed shaft. IR radiation is non visible. The tooth blocks the signal from reaching the receiver. Thus, creating pulses of ones and zeros is fed to the Arduino. In figure 2 we can see that the shaft has 4 teeth. So for one full rotation of the wheel, the signal is as like shown in fig 03. So the equation is as follows

$$D=2*\pi*R*N$$

Where the symbols resemble, D= total distance covered, R= radius of the wheel, N= number of rotations.

### B. Fare Calculation

The fare is calculated in the server side. The tariff rate is included in the hosting files. It calculates the fare using the distance and waiting time data received from the Arduino via GSM module and calculates the fare. The fare data is then sent back to Arduino via GSM and displayed on the LCD.

Fig. 2. Encoder shaft

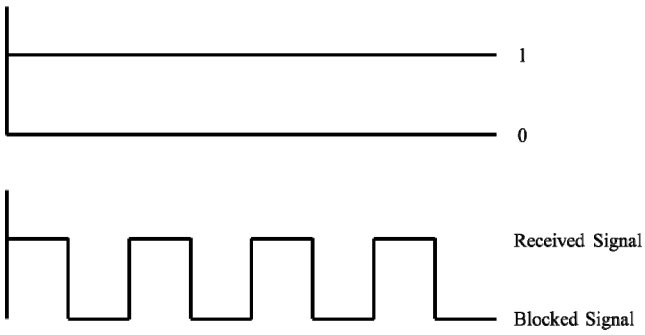


Fig. 3. Signal diagram of the working system

The equation as per present tariff is as follows

$$T=F+(R*C)$$

Where the symbols resemble, T= total fare in BDT, F= the fixed BDT 40 for initial 2 km, R= (D-2) km which is the rest of the distance after initial 2 km, C= BDT 12/km as per tariff.

### C. Control Switches

To operate the system 5 control switches are kept. The function of each switch is described below.

*1) Hire On Switch:* This switch is pressed when the passenger has hired the taxi. After pressing the switch the encoder starts counting the distance. Waiting time is calculated by the arduino when the taxi is stuck in jam.

*2) Hire Off Switch:* After reaching the destination the driver presses this switch. It then sends the data to the server. The total fare is then displayed in LCD after data received from the server.

*3) Payment Switch:* The RFID card is placed on the reader by the passenger in order to pay the fare. The unique ID is sent to the server and then the total fare amount is deducted

from his account linked with the ID. All the necessary information including last transaction, total amount availabe, etc are shown in the web page.

*4) Balance Check Switch:* Before making any journey one can check his available balance in the card by pressing this button.

*5) Driver ID Update Switch:* This is an optional switch for the driver. If the driver is changed, the new driver ID can be updated. This makes easier to create driver's account, track drivers licence and vehicle licence. So the driver must renew his licence time to time to make his account valid.

*6) Offline Payment Switch:* As every passenger will not carry smart card, there is an option named offline payment. Passenger can pay the fare in cash. The taxi driver has to press this button. By pressing this button the journey history will be saved in the server yet no online transaction is needed.

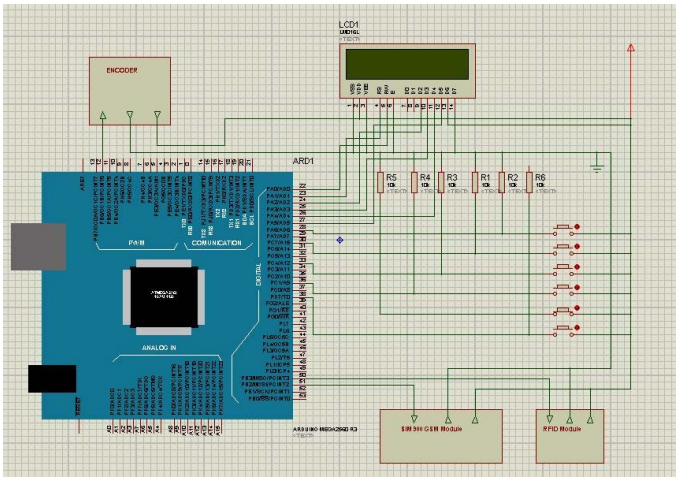


Fig. 4. Circuit Diagram of the proposed system

## D. Transaction

For transaction RFID card is used by the passenger. The RFID card holds value in taka. Passenger can add value to the card. Each RFID contains a unique ID. A website was built for hosting the necessary data. PHP script, MySQL, CSS and HTML5 has been used to develop the website. Apache, which is a web server application, responds to the request made by GSM module during transaction and fare calculation. All the personal data including balance, last transaction, and transit can be viewed on the web page. After each successful transaction the fare amount will be deducted from the passengers ID and added to the drivers ID.

# IV. RESULTS

A miniature taxi including the above feature has been developed. The performance is quite satisfactory though the process can be little bit slow due to the slow internet connection time to time. After pressing Hire on switch the meter started to measure the distance. The total distance and waiting time is displayed in the LCD given in fig 6. And then after pressing the hire off switch, the LCD displays the total fare which is accurate. Now to pay the fare the payment switch was pressed and RFID card was inserted into the reader. The transaction was successfully completed. And then the present balance was also checked. The last transaction and balance was updated into the webpage. All the results are shown in figure 5 and 6. The final outlook of the designed miniature taxi is shown in figure 7.

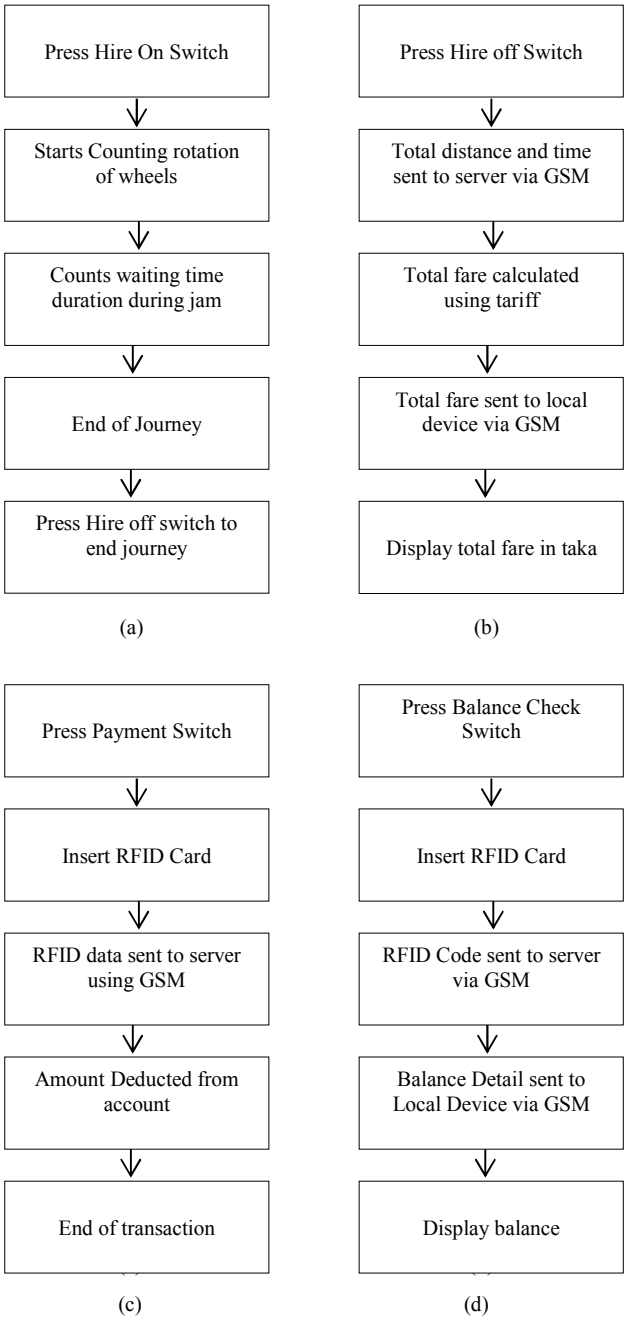


Fig. 5. Block diagram of the control switches (a) Hire on Switch, (b) Hire off Switch, (c) Payment Switch, (d) Balance Check Switch

Cost estimation is given in table 01. It shows the overall cost for this project. The cost can be reduced by 50% by using miniature GSM processor and microcontroller instead of GSM

module and Arduino developing board. IR sensors are used instead of the magnetic Hall Effect sensor which is less costly yet highly efficient. Again the tariff can be updated in the server side as it is included in the hosting files. So no need to rush to the BRTA or govt. authorized dealers for changing the tariff.

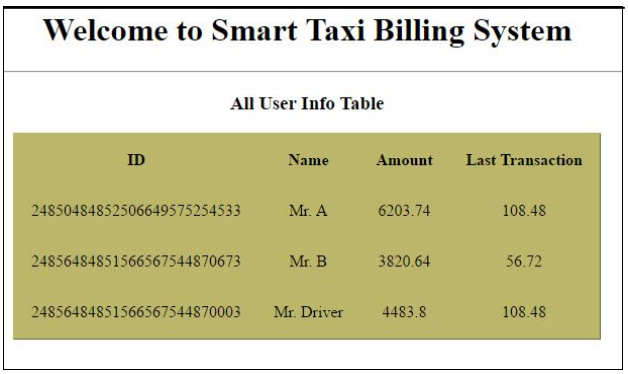

**Welcome to Smart Taxi Billing System**

**All User Info Table**

| ID | Name | Amount | Last Transaction |
|---|---|---|---|
| 248504848525066495752545 33 | Mr. A | 6203.74 | 108.48 |
| 248564848515665675448706 73 | Mr. B | 3820.64 | 56.72 |
| 248564848515665675448700 03 | Mr. Driver | 4483.8 | 108.48 |

Fig. 6. Home page data of the web server

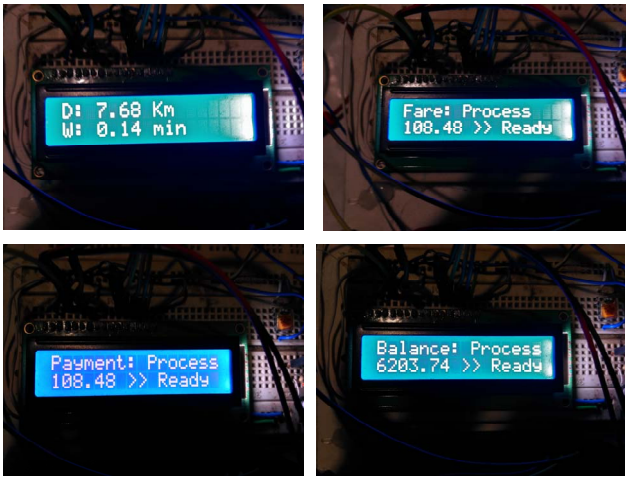


Fig. 7. Results of the system after a complete journey

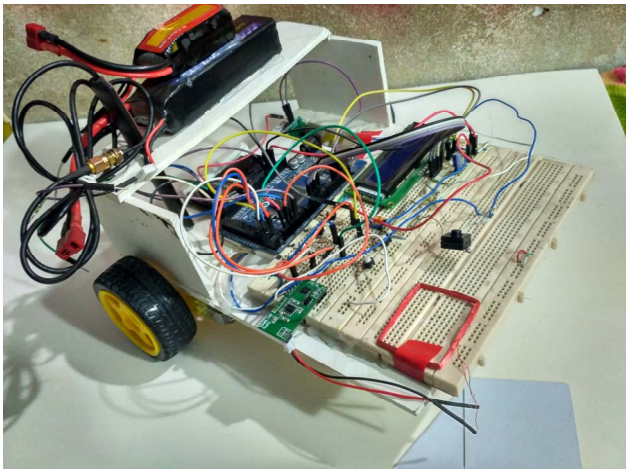

Fig. 8. Final outlook of the implemented system

TABLE I. COST ESTIMATION OF THE SYSTEM

| Sl. No. | Fare meter | | |
|---|---|---|---|
| | ***Name of the component*** | ***Quantity*** | ***Cost*** |
| 1 | ***Encoder*** | ***1*** | ***100 tk*** |
| 2 | ***Arduino Mega**** | ***1*** | ***1000 tk*** |
| 3 | ***LCD display*** | ***1*** | ***200 tk*** |
| 4 | ***12V Li-Po battery**** | ***1*** | ***1800 tk*** |
| 5 | ***DC motor with wheel**** | ***2*** | ***400 tk*** |
| 6 | ***Miscellaneous*** | | ***100 tk*** |
| | **Electronic Payment System** | | |
| 7 | ***GSM module*** | ***1*** | ***2000 tk*** |
| 8 | ***RFID module*** | ***1*** | ***1000 tk*** |
| Total Cost | | | 6700 tk |

*only used for this project. Will be excluded for implementation

## V. CONCLUSION

In this paper a system is described including the signal extraction method, online fare calculation and electronic payment system in a smart and cost effective way. Utilizing this small prototype is designed and built. And it successfully achieved the goals. The state of the art proposes online tariff upgradation in this paper.

The system can be made subject to future upgradation by using the GPS locating feature already available in the GSM module used. It can be used for various purposes such as tracking the vehicle, identifying the route, etc. Again the security can be enhanced for RFID payment by keeping a confirmation feedback method like sending SMS to the passenger for confirmation.

## REFERENCES

[1] Taximeter, Wikipedia, https://en.wikipedia.org/wiki/Taximeter, 11th March 2017.

[2] CNG auto-rickshaw, The Daily Star, Dhaka, http://www.thedailystar.net/news-detail-9829, 2nd Nov 2007.

[3] CNG AUTO-RICKSHAW: New fares come into effect in Dhaka today, New Age, Dhaka, http://archive.newagebd.net/171461/cng-auto-rickshaw-new-fares-come-into-effect-in-dhaka-today/, 1st Nov 2015.

[4] Possible causes and Solutions of Traffic Jam and their impact on the Economy of Dhaka City, https://www.researchgate.net/publication/266059210_Possible_Causes_Solutions_of_Traffic_Jam_and_Their_Impact_on_the_Economy_of_Dhaka_City, 26th September, 2107.

[5] Automated Fare Colletcion, Wikipedia, https://en.wikipedia.org/wiki/Automated_fare_collection, 30th October, 2017

[6] Md. Tofiqul Islam, "DESIGN AND FABRICATION OF FARE METER OF TAXICAB USING MICROCONTROLLER", Proceedings of the International Conference on Mechanical Engineering 2005 (ICME2005) 28- 30 December 2005, Dhaka, Bangladesh.

[7] Shahid Md. Asif Iqbal, Subrata Das, Shaikat Barua, Shamima Nasrin, "Smart Taxi Control System: Bangladesh Perspective", 18th International Conference on Computer and Information Technology(ICCIT), 21-23rd December, 2015

[8] Ms. Tejaswi Bhoite, Ms.Komal Jagadale, Ms.Kamini Jha, "GPS AND GSM BASED SMART TAXIMETER", National Conference on "Internet of Things: Towards a Smart Future" & "Recent Trends in Electronics & Communication" (IOTTSF-2016) In Association With Novateur Publication 17th -18th, Feb. 2016.

[9] Mozhgan Sadeghian, Soheila Dadjou, Majid Meghdadi, Leila Safari, Somayyeh Sadeghian, "The Design and Construction of an Intelligent Taxi Electronic Payment System Solution", *Journal of Intelligent Control and Automation, 2011, 2, 413-417, doi:10.4236/ica.2011.24047 Published Online November 2011 (http://www.SciRP.org/journal/ica)*

[10] BRTC's pre-paid smartcard plan falls flat, http://archive.dhakatribune.com/development/2013/aug/08/brtc%E2%80%99s-pre-paid-smartcard-plan-falls-flat, 8th August 2013.

[11] One card, many rides, http://www.theindependentbd.com/home/printnews/78403, 28th January 2017.

[12] Electronic Fare Payments Options, Chapter 6, http://www.tcrponline.org/PDFDocuments/TCRP%20RPT%2010-C.pdf

2017 3rd International Conference on Electrical Information and Communication Technology (EICT), 7-9 December 2017, Khulna, Bangladesh

# Design a Slotted Metamaterial Microstrip Patch Antenna by Creating Three Dual Isosceles Triangular Slots on the Patch and Bandwidth Enhancement

L. C. Paul[1*], M. A. Haque[1], M. A. Haque[2], M. M. U. Rashid[3], M. F. Islam[4], M. M. Rahman[2]
[1]Dept. of Electronic & Telecommunication Engineering
[1]Pabna University of Science & Technology, Pabna-6600, Bangladesh
[2, 3, 4] Dept. of Electrical and Electronic Engineering
[2]Daffodil International University, Dhaka, Bangladesh
[3]Rajshahi University of Engineering &Technology, Rajshahi-6204, Bangladesh
[4]Islamic University of Technology, Gazipur, Bangladesh
[*]litonpaulete@gmail.com

***Abstract*— The aim of this work is to design and analysis the performance of a metamaterial (MTM) based microstrip patch antenna (MPA) by introducing three dual isosceles triangular slots on the metallic patch. At First, a conventional microstrip patch antenna is designed using Isola FR-408 (loss free) substrate material having dielectric constant of 3.75. Then the slotted microstrip patch antenna has been designed and verified as left handed metamaterial (LHM) with the help of Nicolson Ross Weir (NRW) method. All the simulations have been accomplished by CST microwave studio 2011. The bandwidth of the proposed MTM antenna is enhanced by 464.93% compared to our designed conventional MPA (77 MHz for conventional MPA and 435 MHz for metamaterial MPA) and the return loss is reduced from -11.89 dB to -55.34 dB and directivity is increased from 6.713 dB to 7.187 dB. The voltage standing wave ratio (VSWR) of the proposed metamaterial antenna is of 1.0034 which is very close to unity.**

***Keywords—MTM; MPA; Slot; NRW; DNG***

## I. INTRODUCTION

Metamaterial (MTM) antenna is a special type of antenna loaded with metamaterial to ameliorate the performance like bandwidth, gain, return loss, efficiency of miniaturized microstrip patch antenna (MPA) [1]. Metamaterial is an artificial material which does not exist naturally [2]. The concept of MTM was introduced and proposed by Russian theorist Victor Vesalogo in 1967. It can be fabricated by changing the atomic structure of naturally available material [3] or modifying the physical structure of a piece of material in such way that leads to negative permittivity and permeability simultaneously and consequently it shows negative refractive index. The double negative (DNG) metamaterial property can be achieved by modifying physical structure in the following possible ways such as (i) modifying patch structure (split ring [4], slot on patch [5-6] etc), (ii) Modifying ground plane (defected ground structure [7], electromagnetic band-gap structure [8-9] etc.). Because of having distinct and extraordinary properties of this virtual material, the researchers are paying great attention in theoretical and experimental exploration on metamaterials (MTMs) in the recent years [6]. MTMs is alternatively familiar as left-handed metamaterials (LHMs) owing to its DNG properties i.e. both negative permeability and permittivity. Backward wave and the focusing effect inside the slab are supported by the MTMs but it instigates conduction loss and anisotropy [3]. Above mentioned exceptional nature of MTMs assists to alter the behavior of passing electromagnetic wave through it, which plays main role to ameliorate the performance of the metamaterial microstrip patch antenna (MMPA).

In this paper two microstrip patch antennas (MPAs) are presented, one is conventional MPA and another is metamaterial based MPA which is made by introducing three dual isosceles triangular slots on the copper patch of the conventional MPA. Metamaterial properties of the designed and proposed isosceles triangular slotted structure are investigated and proved as metamaterial by using Nicolson Ross Weir (NRW) approach. The proposed slotted structure exhibits double negative (DNG) property of metamaterial and the proposed metamaterial antenna shows improved bandwidth, greater directivity, lower return loss, comparatively more suitable VSWR than the conventional MPA.

The rest of the paper has been organized as following manner: section II contains the design specifications of conventional MPA and slotted metamaterial Antenna, metamaterial properties analysis and verification of proposed three dual isosceles triangular slotted structure with the help of NRW method and simulation results of both antennas. Section III reflects an abstract comparison between conventional MPA and metamaterial based slotted MPA. Finally, conclusion and discussions are figured out in the section IV. Some future scopes of this work have also been highlighted at the end of the section IV.

## II. SLOTTED METAMATERIAL ANTENNA

This section represents the designed structure and simulation results of slotted microstrip patch antenna (SMPA). The proposed SMPA structure has been also analyzed and

978-1-5386-2307-7/17/$31.00 ©2017 IEEE

verified as metamaterial antenna by using Nicolson Ross Weir (NRW) method.

### *A. Conventional and Slotted Antenna Design*

At first, we designed a conventional microstrip patch antenna (CMPA) then made three dual isosceles triangular slots on the patch of the previous designed CMPA. And finally the three dual isosceles triangular slotted microstrip patch antenna is characterized as metamaterial by using NRW method. For all the antenna configurations, we used Isola FR-408 (loss free) dielectric substrate having dielectric constant of 3.75, height of the dielectric substrate is of 1.6 mm and copper is used in both the patch and ground plane as well as the thickness of both is of 0.035 mm. Fig.1 shows the designed and optimized CMPA. All the necessary dimensions of the designed CMPA are listed in table I.

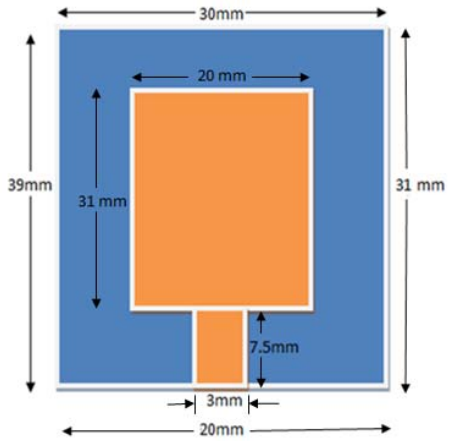


Fig.1. Front view of conventional MPA.

TABLE I DIMENSION OF THE CONVENTIONAL MPA

| Parameter Name | Dimension (mm) |
|---|---|
| Substrate length ($L_s$) | 39 |
| Substrate width ($W_s$) | 30 |
| Substrate height (t) | 1.6 |
| Patch Length ($L_p$) | 31 |
| Patch Width ($W_p$) | 20 |
| Patch Height ($t_r$) | 0.035 |
| Feeder Length ($L_f$) | 7.5 |
| Feeder Width ($W_f$) | 3 |

After making three dual isosceles triangular slots on the patch of the conventional MPA, the antenna can be represented as in Fig. 2 which is our proposed metamaterial antenna's front view that is proved as metamaterial structure in following subsection B by analyzing the metamaterial properties of the proposed structure with the help of widely used NRW method. The structure and dimensions of the single isosceles triangular shaped slot is shown in Fig. 3. Table II shows the dimensions of every dual isosceles triangular shaped slot.

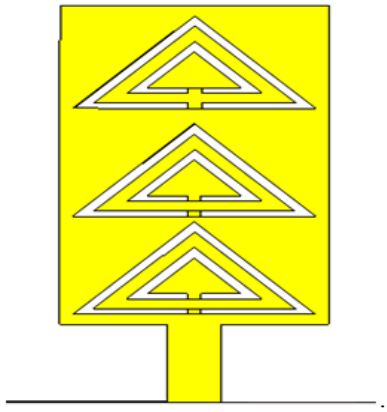

Fig.2. Front view of slotted MPA.

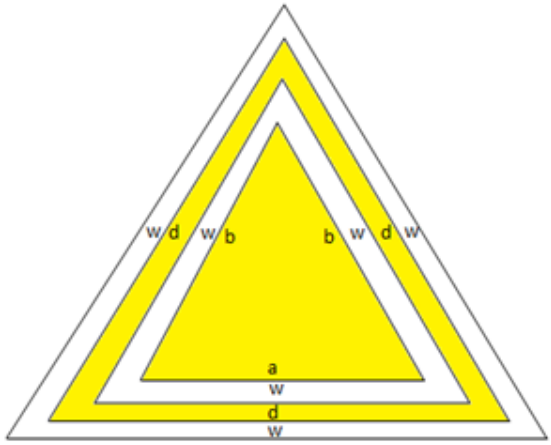


Fig. 3. Structure of single isosceles triangular shaped slot

where,

*a* and *b* are the side lengths of inner isosceles triangular slot.

*w* = width of both isosceles triangular slot

and *d* = distance between two isosceles triangular slot.

TABLE II DIMENSIONS OF EVERY DUAL ISOSCELES TRIANGULAR SHAPED SLOT

| Inner side lengths of isosceles triangular slot | | Width of isosceles triangular slot | Distance between two slots |
|---|---|---|---|
| *a* | *b* | *w* | *d* |
| 7 mm | 3.5 mm | 0.5 mm | 1 mm |

### *B. Metamaterial Properties Proof of the Proposed SMPA by NRW Method*

It is known that metamaterial is nothing but a virtual material. It is not a naturally available any extraordinary material but it can be produced by changing physical structure of any metal which leads to alter the electric and magnetic response of the EM wave travelling through the structure in such way that the modified metallic structure shows negative permittivity (ε), negative permeability (μ) as well as negative refractive index simultaneously. Any material having negative

refractive index does not exist in nature readily. Only after fulfilling the double negative properties of a modified metallic structure can be said to be as metamaterial.

In order to analyze and prove our proposed slotted structure as metamaterial the designed slotted on patch structure is settled in between a pair of waveguide ports as shown in Fig. 4. The excitation EM waves were fed from the waveguide port 1 to the waveguide port 2 to calculate the S parameters ($S_{11}$ and $S_{21}$). In that case, it is considered that the proposed structure was surrounded by air. The above mentioned two waveguide ports are placed along X-axis. Perfect electric boundary (PEB) and perfect magnetic boundary (PMB) were prescribed along the Y-axis and Z-axis respectively. Subsequently, the EM waves were incited in the direction of the Port 2 (positive X-axis) from the Port 1 i.e. negative X-axis. From this layout of the proposed slotted structure, complex valued S parameters ($S_{11}$ and $S_{21}$) were attained.

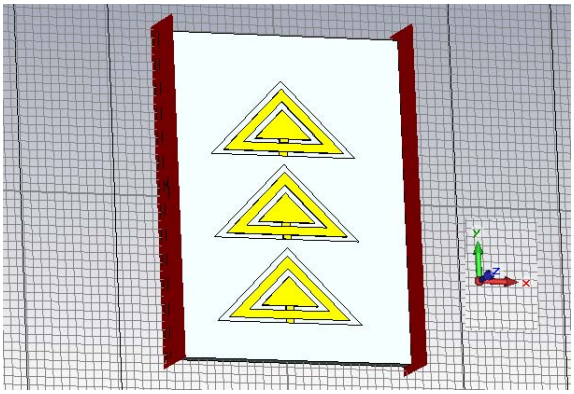

Fig. 4. Proposed slotted metamaterial structure settled between two waveguide ports

After getting $S_{11}$ and $S_{21}$ parameters, we used NRW method to calculate the permittivity (ε) and permeability (μ) of the slotted structure. NRW approach states the following formulas:

$$\mu_r = \frac{2c(1-v_2)}{\omega di(1+v_2)} \quad (1)$$

$$\varepsilon_r = \mu_r + \frac{2S_{11}ci}{\omega d} \quad (2)$$

where,

$$v_1 = S_{11} + S_{21} \quad (3)$$
$$v_2 = S_{21} - S_{11} \quad (4)$$

$\omega$ = angular frequency in radian
d = thickness of the substrate = 1.6 mm
c = velocity of the light = $3\times 10^8$ m/s
i = iota function
$v_1$ = voltage maxima
and $v_2$ = voltage minima

The values of permittivity (ε) and permeability (μ) are calculated by using above equations within the simulated frequency range and listed in the following table III.

TABLE III CALCULATED PERMITTIVITY (ε) AND PERMEABILITY (μ) OF THE PROPOSED SLOTTED METAMATERIAL STRUCTURE.

| $f$ (GHz) | $S_{11}$ (dB) | $S_{21}$ (dB) | $v_1$ | $v_2$ | $\mu_r$ | $\varepsilon_r$ |
|---|---|---|---|---|---|---|
| 0 | 0 | 0 | 0 | 0 | 0 | 0 |
| 0.5 | -4.74 | -10.53 | -15.27 | -5.79 | -10.6315 | -46.1815 |
| 1 | -0.41 | -15.85 | -16.26 | -15.44 | -4.26939 | -5.80689 |
| 1.5 | -0.12 | 18.46 | 18.34 | 18.58 | -2.24464 | -2.54464 |
| 2 | -0.08 | -20.01 | -20.09 | -19.93 | -2.0731 | -2.2231 |
| 2.5 | -0.05 | -20.6 | -20.65 | -20.55 | -1.65345 | -1.72845 |
| 3 | -0.04 | -20.34 | -20.38 | -20.3 | -1.37953 | -1.42953 |
| 3.5 | -0.05 | -19.01 | -19.06 | -18.96 | -1.19074 | -1.24431 |
| 4 | -0.13 | -16.02 | -16.15 | -15.89 | -1.06342 | -1.1853 |
| 4.5 | -0.63 | -9.8 | -10.43 | -9.17 | -1.03733 | -1.56233 |
| 5 | -3.06 | -4.36 | -7.42 | -1.3 | -5.75 | -8.045 |
| 5.5 | -0.15 | -15.66 | -15.81 | -15.51 | -0.7758 | -0.87807 |
| 6 | -0.04 | -20 | -20.04 | -19.96 | -0.69093 | -0.71593 |
| 6.5 | -0.01 | -24 | -24.01 | -23.99 | -0.62711 | -0.63288 |
| 7 | -0.01 | -27.14 | -27.15 | -27.13 | -0.57672 | -0.58208 |
| 7.5 | -0.03 | -29.74 | -29.77 | -29.71 | -0.53483 | -0.54983 |
| 8 | -0.49 | -41.3 | -41.79 | -40.81 | -0.4923 | -0.72199 |
| 8.5 | -0.41 | -25.03 | -25.44 | -24.62 | -0.47853 | -0.65942 |
| 9 | -0.05 | -24.9 | -24.95 | -24.85 | -0.45161 | -0.47244 |
| 9.5 | -0.05 | -24.95 | -25 | -24.9 | -0.42777 | -0.44751 |
| 10 | -0.07 | -23.41 | -23.48 | -23.34 | -0.40857 | -0.43482 |
| 10.5 | -0.2 | -20.11 | -20.31 | -19.91 | -0.39492 | -0.46634 |
| 11 | -1.2 | -13.84 | -15.04 | -12.64 | -0.39948 | -0.80858 |
| 11.5 | -1.33 | -14.73 | -16.06 | -13.4 | -0.37868 | -0.81238 |
| 12 | -0.38 | -21.35 | -21.73 | -20.97 | -0.3438 | -0.46255 |
| 12.5 | -0.23 | -25.04 | -25.27 | -24.81 | -0.3252 | -0.3942 |
| 13 | -0.22 | -27.83 | -28.05 | -27.61 | -0.31014 | -0.3736 |
| 13.5 | -0.3 | -27.74 | -28.04 | -27.44 | -0.29879 | -0.38212 |
| 14 | -0.45 | -23.8 | -24.25 | -23.35 | -0.29183 | -0.41236 |
| 14.5 | -0.58 | -19.72 | -20.3 | -19.14 | -0.28713 | -0.43713 |
| 15 | -1.67 | -16.83 | -18.5 | -15.16 | -0.28531 | -0.70281 |
| 15.5 | -2.69 | -19.51 | -22.2 | -16.82 | -0.27252 | -0.92333 |
| 16 | -0.81 | -30 | -30.81 | -29.19 | -0.251 | -0.44085 |

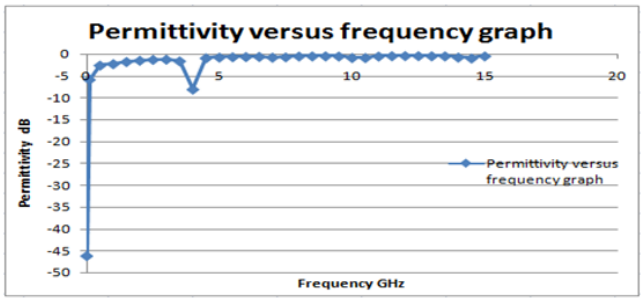


Fig. 5. Permittivity Vs. frequency curve of the proposed slotted structure.

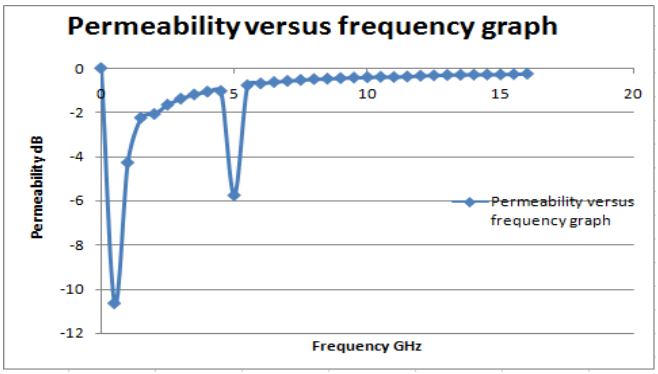


Fig. 6. Permeability Vs. frequency curve of the proposed slotted structure

Fig. 5 and Fig. 6 show the permittivity and permeability curve of the proposed slotted metallic structure. From the above figures it is clear that the proposed slotted metallic structure possesses both negative permittivity and negative permeability. That is the slotted structure has double negative properties and the slotted structure is functioning as a metamaterial.

### *C. Simulation Results of CMPA and Slotted Metamaterial Antenna*

In this subsection, we presented and analyzed the simulated results of both the conventional MPA and proposed slotted metamaterial antenna. All the simulations have been done by the CST microwave studio 2011 which is commercially available and very popular to the antenna researchers through all over the world. Fig. 7 and 8 shows the return loss curves of conventional MPA and metamateral antenna respectively. From the Figs, it is noticed that operating frequency of the antennas are of 7.3742 GHz and 6.489 GHz respectively. The conventional microstrip patch antenna possesses return loss of -11.89 dB and bandwidth of 77 MHz whereas the proposed metamaterial antenna shows return loss of -55.34477 dB and bandwidth of 435 MHz. So, the bandwidth of metamaterial antenna has been increased by 464.93% compared to our designed CPMA. Voltage standing wave ratio (VSWR) of conventional MPA is of 1.682 (shown in Fig. 9) whereas VSWR of metamaterial antenna is of 1.003 (shown in Fig. 10) which is the indication of perfection level of impedance matching because the desired VSWR of a perfect antenna is very close to unity at the operating frequency of it. Directivity of the CMPA is of 6.71 dB where as the directivity of metamaterial antenna is of 7.183 dB which indicates metamaterial antenna is slightly more directive than CMPA. 3D gain of CMPA and MTM antenna are presented in Fig. 13 and 14 respectively.

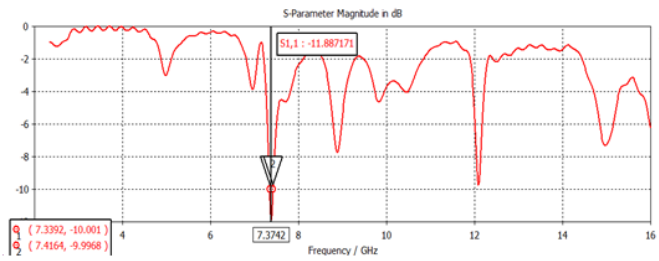


Fig.7. Return loss curve of conventional MPA.

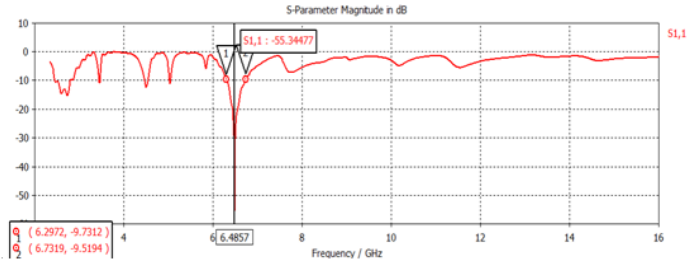


Fig.8. Return loss curve of slotted metamaterial antenna.

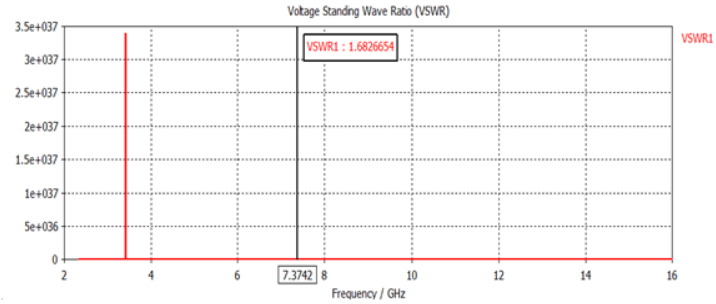


Fig.9. VSWR of conventional MPA.

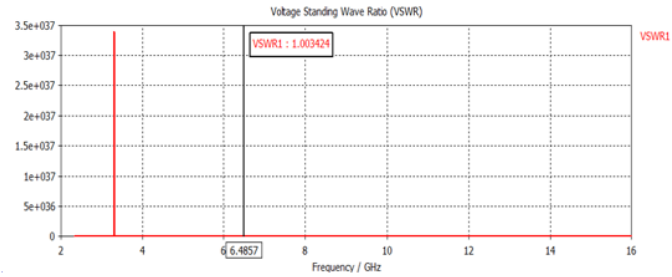


Fig.10. VSWR of slotted metamaterial antenna.

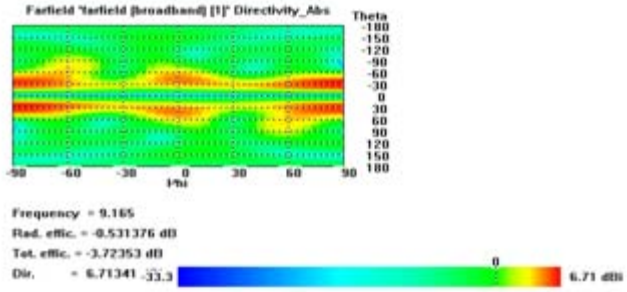


(a) 2D

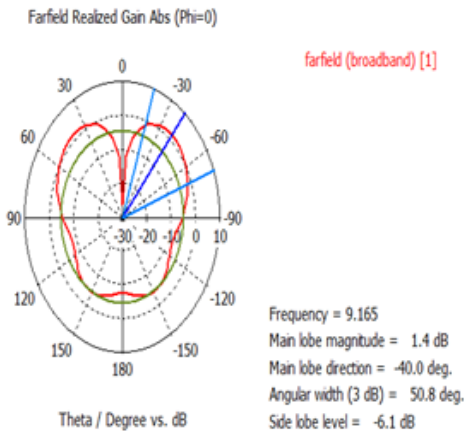


(b) Polar

Fig.11. 2D and polar directivity of conventional MPA

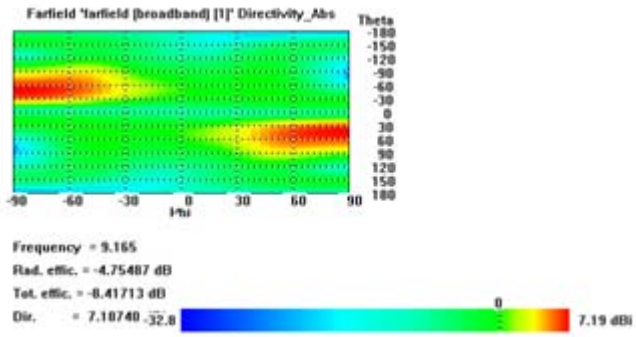


(a) 2D

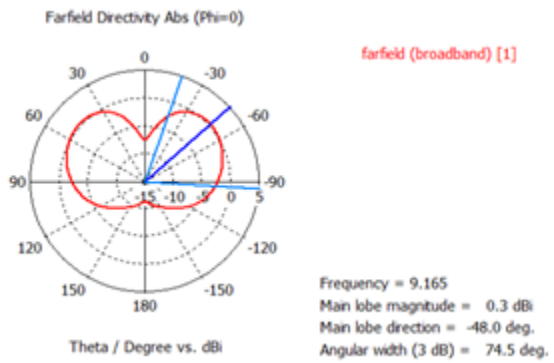


(b) Polar

Fig.12. 2D and polar directivity of slotted metamaterial antenna.

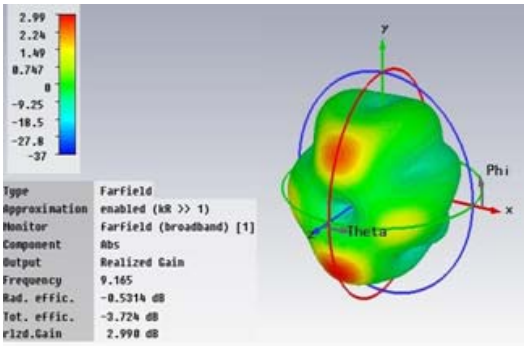


Fig.13. 3-D gain of conventional antenna.

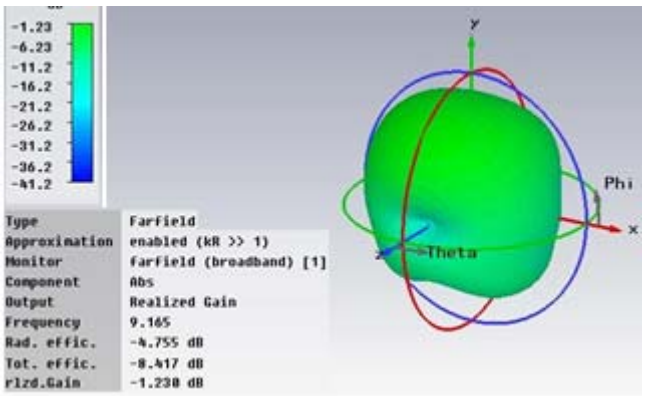


Fig. 14. 3-D gain of slotted metamaterial antenna.

## III. Comparative Study

In order to understand the performance improvement such as improvement of bandwidth, return loss, gain, directivity, VSWR etc of metamaterial antenna compared to conventional microstrip antenna, we designed and analyzed a conventional MPA and a metamaterial MPA by using CST microwave studio version 2011. The proposed metamaterial antenna provides the better performance than the same sized conventional antenna. All the simulated performance parameters of both conventional and metamaterial antennas are listed in table IV.

TABLE IV SUMMARY OF THE PERFORMANCE PARAMETERS

| Parameter | Conventional MPA | Metamaterial MPA |
|---|---|---|
| Return loss | -11.89 dB | -55.34 dB |
| BW | 77 MHz | 435 MHz |
| Gain | 2.99 dB | 1.23 dB |
| Directivity | 6.713 dB | 7.187 dB |
| Center frequency | 7.37 GHz | 6.486 GHz |
| VSWR | 1.6426 | 1.0034 |

From the above table, it is obvious that the bandwidth of metamaterial antenna has been increased by 464.93% compared to CPMA. The proposed MTM antenna also more directive, improved VSWR and reduced return loss than conventional MPA.

## IV. Conclusion and Discussion

In this research work, a microstrip antenna loaded with left handed metamaterial (LHM) has been designed and showed. It exhibits comparatively better performance than the conventional MPA having same size & same substrate material. Both the conventional and metamaterial MPA have been designed on Isola FR-408 (loss free) dielectric substrate having dielectric constant of 3.75. The three dual isosceles triangular slotted structure was analyzed and buttressed as metamaterial by using NRW method. From the NRW method it is seen that the slotted structure shows the double negative (DNG) property i.e. both negative permittivity and permeability which leads to negative refractive index. In case of our proposed metamaterial antenna, bandwidth is enhanced by 464.93% compared to our designed conventional antenna, return los is decreased from -11.89 dB (conventional) to -55.34 dB (metamaterial) and directivity is increased from 6.713 dB to 7.187 dB. The VSWR of the proposed metamaterial MPA is of 1.0034 which is very close to 1. All the simulations and analysis have been done by using CST and microsoft excel software. In near future, we are highly interested to fabricate the proposed slotted metamaterial antenna in our laboratory and want to compare between simulation results and experimental results.

## References

[1] V. I. Slyusar, "60 Years of Electrically Small Antennas Theory," *6th IEEE International Conference on Antenna Theory and Techniques*, Sevastopol, Ukraine, pp. 116 - 118, 17-21 Sep. 2007.

[2] R. W. Ziolkowski, "Double negative metamaterial design, experiments, and applications," *IEEE Antennas and Propagation Society International Symposium,* San Antonio, TX, USA, USA, pp. 396-399, 16-21 June 2002.

[3] Y. Li and N. Bowler, "Analysis of Double-Negative (DNG) Bandwidths for Metamaterials Composed of Three-Dimensional Periodic Arrays of Two Different Magnetodielectric Spheres Arbitrarily Arranged on a Simple Tetragonal Lattice," *IEEE Antennas and Wireless Propagation Letters*, Vol. 10 , pp. 1484 - 1487, 15 Dec. 2011.

[4] S. Gautam and A. Agrawal, "Directivity Improvement of Patch Antenna using Metamaterial," *IEEE Symposium on Colossal Data Analysis and Networking (CDAN)*, India, pp. 18-19 Mar. 2016.

[5] H. Kumar, R. K. Kanth, P. Liljeberg and H. Tenhunen, "Metamaterial based slotted patch antenna," *10th IEEE International Conference on Telecommunication in Modern Satellite Cable and Broadcasting Services (TELSIKS)*, Serbia, pp. 43-46, 5-8 Oct. 2011.

[6] S. Dwivedi, V. Mishra and Y.P. Kosta, "Slotted Patch Antenna Loaded with Metamaterial," *PIERS Proceedings*, Stockholm, Sweden, pp.508-510, 12–15 Aug. 2013.

[7] N. Ripin, W. M. A. W. Saidy, A. A. Sulaiman, N. E. A. Rashid and M. F. Hussin, "Miniaturization of microstrip patch antenna through metamaterial approach," *IEEE Student Conference on Research and Development (SCOReD)*, Malaysia, pp. 365-369, 16-17 Dec. 2013.

[8] N. Ripin, R. A. Awang, A. A. Sulaiman, N. H. Baba and S. Subahir, "Rectangular microstrip patch antenna with EBG structure," *IEEE Student Conference on Research and Development (SCOReD),* Malaysia, pp. 3266-271, 5-6 Dec. 2012.

[9] B. R. Behera and P. Suraj, "Rectangular Microstrip Patch Antenna for Wireless Fidelity Application: Design of a Wi-Fi Antenna using the concept of Metamaterials," *IEEE International Conference on Recent Trends in Electronics Information Communication Technology*, India, pp. 1933-1937, May 20-21, 2016.

# Design of an Improved QPSK Modulation Technique in Wireless Communication Systems

M. A. Noman Chowdhury[α1], M. R. Ullah Mahfuz[α2], S. Hoque Chowdhury[α3], and Md. Monirul Kabir[α4]
[α]Dept. of Electrical & Electronic Engineering, Dhaka University of Engineering & Technology (DUET), Gazipur, Bangladesh
[1]mdabunoman90@gmail.com, [2]mahfuzduet111@gmail.com, [3]saifulhoque.sabuj@gmail.com, [4]munir@duet.ac.bd

*Abstract*—**This paper proposes an improved QPSK modulation scheme, called as π/6-QPSK, which is an improvement of existing π/4-QPSK modulation technique in the wireless communication system in case of phase transition. The key aspects of π/6-QPSK are to consider three constellations apart by π/6 degree successively as well as incorporating a new constellation selection mode depending on input dibits. In order to facilitate these two key aspects, a set of new encoding rules has been designed. Finally, our π/6-QPSK provides the maximum and minimum phase transitions of ±90º and ±30º, respectively with reducing envelope variation. Simulation results of MATLAB Simulink confirm that the signal spectral performance of our proposed π/6-QPSK is better than that of conventional π/4-QPSK modulation scheme. On the other hand, the relative phase transition of π/6-QPSK is reasonably reduced comparing to the other conventional QPSK modulation schemes.**

***Keywords— Modulation, PSK, QPSK, π/4 QPSK, π/6 QPSK.***

## I. INTRODUCTION

Wireless communication is dominant everywhere in our everyday life like satellite television, navigation system, cellular telephones, global positioning system (GPS), and so on. The digital form of wireless communication is chosen over analog form due to the various advantages, such as, robustness, security, easy error detection and correction, improved performance in the communication system [1].

In digital transmission system, modulation scheme is an important part that is generally classified by three aspects: amplitude shift keying (ASK), frequency shift keying (FSK) and phase shift keying (PSK) [1]. Alternatively, PSK system sometimes is known as M-ary PSK. If M = 2 or 4, then it is called binary PSK (BPSK) or, quadrature PSK (QPSK). In selection of those modulation schemes, some factors must be considered, such as, power efficiency, bandwidth efficiency, low out-of band radiation, low sensitivity to multipath fading constant envelope, and so on [2]. Since each of the above-mentioned schemes has somewhat practical limitations and inter-related each other, it is not possible to select a modulation scheme for the all-time that simultaneously satisfies all of the above factors. Particularly, the performance of QPSK is better than that of BPSK in case of bandwidth but it has a limitation of 180º phase shift, which destroy the constant envelope property [3]. In order to reduce the transition limit, two advanced QPSK schemes, which are OQPSK and π/4 QPSK are introduced [4].

In this paper, we propose an improved QPSK scheme, called as π/6-QPSK, which is an improvement of π/4-QPSK in the sense of phase transition. In π/6-QPSK, phase transition is occurred one time in one symbol duration and the maximum phase transition is ±90º and minimum ±30º. Hence, the envelope variation of π/6-QPSK is lesser than π/4-QPSK and OQPSK.

According to our view, the performances of the modulation techniques are measured in some aspects, such as, bit error rate (BER) [5-6], signal spectra [4], bandwidth efficiency [4], and so on. Among these, the π/4-QPSK modulation technique is actually formulated based on the signal spectra. As our proposed modulation technique is the improvement of π/4-QPSK, the performance is measured on basis of the signal spectra and phase transition instead of BER.

## II. THEORETICAL BACKGROUND

### A. Phase Shift Keying

In Phase shift keying (PSK), the phase of carrier is changed with respect to the message data. The general analytical expression for PSK [5] can be defined as,

$$s_i(t) = \sqrt{\frac{2E}{T}} \cos\left[2\pi f_c t + \varphi_i(t)\right], \qquad 0 \le t \le T \tag{1}$$

$$i = 1,2,.....,M$$

Where, $E$ refers to transmitted signal energy per symbol, $T$ refers to symbol duration, $f_c$ is the carrier frequency, $\varphi_i(t)$ denotes the phase of the modulated signal having $M$ discrete values according to the expression:

$$\varphi_i(t) = \frac{2\pi}{M}(i-1) \qquad i = 1,2,.....,M \tag{2}$$

### B. Quadrature Phase Shift Keying

In QPSK modulation, the carrier signal phase can take four possible values as,

$$\varphi_i(t) = (2i-1)\frac{\pi}{4} \qquad i = 1,2,3,4$$

Therefore, the QPSK signal has four possible symbols; each of them carries two bits that are called dibits. These dibits and their corresponding signal phases are shown in Table I. Using Eq. (1) and (3), the QPSK signal can be expressed [7] as,

978-1-5386-2307-7/17/$31.00 ©2017 IEEE

$$s_i(t) = \sqrt{\frac{2E}{T}}\cos\left[(2i-1)\frac{\pi}{4}\right]\cos[2\pi f_c t] - \sqrt{\frac{2E}{T}}\sin\left[(2i-1)\frac{\pi}{4}\right]\sin[2\pi f_c t], \quad (4)$$

$$0 \le t \le T,\ i = 1.....4.$$

In the above equation, there are two quadrature carriers that having two orthogonal basis functions, $\varphi_1$ and $\varphi_2$ as,

$$\varphi_1(t) = \sqrt{\frac{2}{T}}\cos[2\pi f_c t] \qquad 0 \le t \le T \quad (5)$$

$$\varphi_2(t) = -\sqrt{\frac{2}{T}}\sin[2\pi f_c t] \qquad 0 \le t \le T \quad (6)$$

Because of these two basis functions, the signal space diagram of QPSK is two dimensional with four message points shown in Fig. 1.

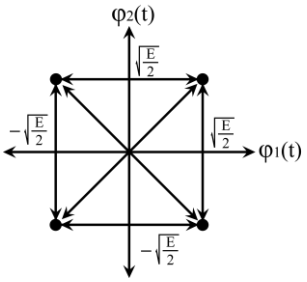


Figure 1. Signal space diagram of QPSK with signal constellation transition adapted from [5].

TABLE 1: Signal space characteristic of QPSK.

| Information of dibits | Phase of QPSK signal |
|---|---|
| 10 | π/4 |
| 00 | 3π/4 |
| 01 | 5π/4 |
| 11 | 7π/4 |

It is noted that, QPSK is considered as a constant envelope signal according to the literature. But, it is not technically a constant envelop signal because of its discontinuous phase shift, such as, 180º phase shift. This 180º phase shift is the major problem of QPSK, that is to say, the larger transition is a source of trouble for amplifier, which increases spectral side lobe. That's why, larger transition needs to be overcome [3]. To overcome such difficulty, reduced phase transition of QPSK modulation schemes, such as, OQPSK and π/4-QPSK are introduced [8].

### C. *Offset QPSK(OQPSK)*

Offset QPSK is a variant of QPSK, where the Q channel is delayed by half of a symbol time so that signal transition of *I* and *Q* channel do not occur at the same time. Due to this delay in quadrature arm, maximum phase transition is reduced by 90º in OQPSK [2], whereas in QPSK, the same quantity is π radians. The signal space diagram of the OQPSK shown in Fig. 2 is similar to QPSK except the elimination of possible state changes passing through the origin.

### D. *π/4-QPSK*

π/4-QPSK is a special type of QPSK scheme, which is introduced by Baker [4]. In π/4-QPSK system, two QPSK constellations are used that are π/4 shifted pattern apart by π/4-degree from each other. These two constellations can be denoted by constellation A and constellation B shown in Fig. 3. In π/4-QPSK, constellations are altered after every symbol. Precisely, k-th symbol is sent by the constellation A, while constellation-B is used to send the (k+1)th symbol [3] [8] [9]. As a result, successive symbols have a relative phase difference that is one of four angles ± π/4 and ±3π/4. Therefore, the signal space diagram of π/4-QPSK is two dimensional with eight message points shown in Fig. 4.

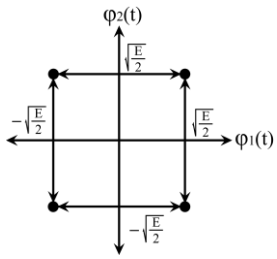


Fig. 2. Signal space diagram of OQPSK with signal constellation transitions adapted from [5].

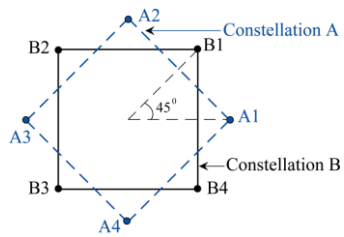


Fig. 3. Two constellations of π/4-QPSK.

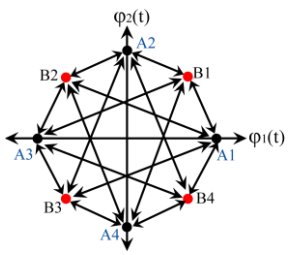


Figure 4. Signal space diagram of π/6-QPSK with signal constellation transition.

For more comprehensibility, an example is given here. If *k-th* symbol at message point $A_1$ then for the sequence 11→01→10→00→00→10→11→11, select the message point sequences, which are $B_1 \rightarrow A_3 \rightarrow B_2 \rightarrow A_1 \rightarrow B_3 \rightarrow A_3 \rightarrow B_3 \rightarrow A_4$.

The π/4-QPSK is a form of differentially encoded QPSK (DQPSK), in differential modulation technique the information dibits are represented by the phase differences $\Delta\theta_k$ from symbol to symbol [8]. Fig. 5 shows is the π/4-DQPSK modulator where ($I_k$, $Q_k$) and ($u_K$, $v_K$) are the uncoded and coded I-channel and Q-channel bits of $k$-th symbol duration. The differential encoder of π/4-DQPSK modulator encodes $I_k$ and $Q_k$ into signal $u_k$ and $v_k$ according to the following rules [8] as,

$$u_k = \frac{1}{\sqrt{2}}[u_{k-1}I_k - v_{k-1}Q_k] \tag{7}$$

$$v_k = \frac{1}{\sqrt{2}}[u_{k-1}Q_k + v_{k-1}I_k] \tag{8}$$

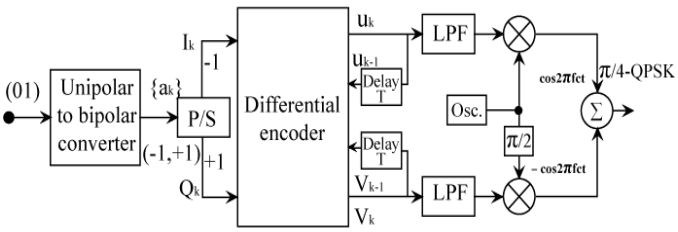


Figure 5. Block diagram of π/4 DQPSK modulator adapted from [10].

The output signal of the π/4-DQPSK modulator is,

$$s(t) = u_k \cos 2\pi f_c t - v_k \sin 2\pi f_c t$$
$$= A\cos(2\pi f_c t + \varphi_k) \qquad kT \le t \le (k+1)T$$

Where, $\varphi_k = \tan^{-1}\dfrac{v_k}{u_k}$ (9)

However, the output depends on the encoded data and $A$. Here, $A = \sqrt{u_k^{\,2} + v_k^{\,2}}$ that is the constant with respect to time index $k$. It means that, the signal has a constant envelope. The phase relationship between two successive symbols is,

$$\varphi_k = \varphi_{k-1} + \Delta\theta_k \tag{10}$$

$$\Delta\theta_k = \tan^{-1}\frac{Q_k}{I_k}$$

Where, $\Delta\theta_k$ is the phase difference determined by the input data. The dibit and corresponding phase difference of π/4-QPSK is shown in Table II.

TABLE II. π/4-QPSK SIGNAL PHASE ASSIGNMENT ADAPTED FROM [6].

| $I_k$ $Q_k$ | $\Delta\theta_k$ | $\cos\Delta\theta_k$ | $\sin\Delta\theta_k$ |
|---|---|---|---|
| 1 1 | π/4 | 1/√2 | 1/√2 |
| -1 1 | 3π/4 | -1/√2 | 1/√2 |
| -1 -1 | -3π/4 | -1/√2 | -1/√2 |
| 1 -1 | -π/4 | 1/√2 | -1/√2 |

## III. PROPOSED WORK

In this paper, an improved modulation scheme π/6-QPSK is proposed, which is an improvement of π/4-QPSK in case of phase transition. In π/4-QPSK, maximum transition is ± 135º and minimum transition is ± 45º. But, in π/6-QPSK, the maximum transition is ± 90º and minimum transition is ± 30º. Hence, π/6-QPSK provides the reduced envelope variation compared to π/4-QPSK and the side lobe power is lesser than π/4-QPSK after non-linear amplification.

### A. π/6-QPSK

In π/6-QPSK, three constellations are used, which are π/6 shifted pattern of the QPSK constellation, i.e., successive constellations are apart by π/6 degree. These three constellations denoted by A, B and C shown in Fig. 6. In π/6-QPSK, constellation is not changed after every symbol. The constellation selection is depended on input dibit. The selection of constellation is shown in Table III.

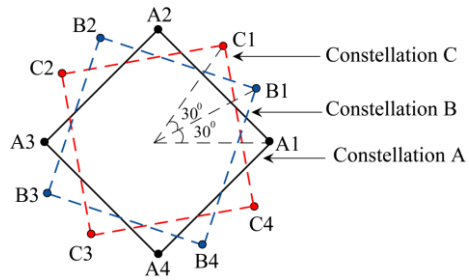


Figure 6. Three constellations of proposed π/6-QPSK scheme.

TABLE III. π/6-QPSK CONSTELLATION SELECTION AND PHASE TRANSITION FOR DIBIT.

| **Dibit** | **Constellation Selection** |
|---|---|
| 00 | Constellation is unchanged but message point shifted by -90º on existing constellation. |
| 01 | Constellation is unchanged but message point shifted by +90º on existing constellation. |
| 10 | Constellation is changed, the constellation changing sequence is ACBA cycle and message point shifted by -30º . |
| 11 | Constellation is changed, the constellation changing sequence is ABCA cycle and message point shifted by +30º . |

It is clear from Table III that, the π/6-QPSK is a differential modulation process, where the transmitted signal is chosen from one of three QPSK constellations, which are successively apart by π/6 degree. Hence, the phase transition between two successive symbols have the values in between {± π/6, ±π/2}. Here, the dibit with corresponding signal phase difference $\Delta\theta_k$ of π/6-QPSK is shown in Table IV. Therefore, the signal space diagram of π/6-QPSK is two-dimensional with twelve message points shown in Fig. 7.

TABLE IV. SIGNAL PHASE DIFFERENCES OF THE π/6-QPSK SCHEME.

| Dibit | $\Delta\theta_k$ |
|---|---|
| 00 | - π/2 |
| 01 | +π/2 |
| 10 | - π/6 |
| 11 | +π/6 |

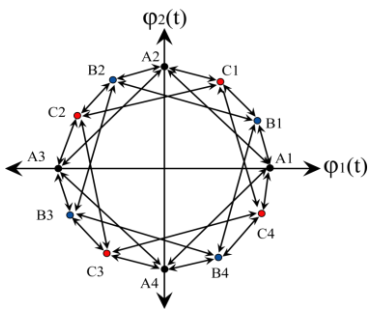


Figure 7. Signal space diagram of π/6 QPSK with signal constellation transition.

To clarify the above constellation transition, some examples are mentioned as follow:

*Example-1*:
If we consider that, $u_k = 1$ and $v_k = 0$ for the *k-th* symbol, then selected message point of *(k+1)-th* symbol depends on the dibit that is given below:

| Dibit | Selected point |
|---|---|
| 00 | $A_4$ |
| 01 | $A_2$ |
| 10 | $C_4$ |
| 11 | $B_1$ |

*Example-2*:
If the initial value of $u_k = 1$ and $v_k = 0$ for the sequence 11→01→10→00→00→10→11→11, then the selected message point sequences are:
$B_1 \rightarrow B_2 \rightarrow A_2 \rightarrow A_1 \rightarrow A_4 \rightarrow C_3 \rightarrow A_4 \rightarrow B_4$

*Example-3*:
If the initial value of $u_k = 1$ and $v_k = 0$, then the bit sequence are mentioned below with presenting the signal transition in Fig. 8.
a) 11 11 11 11……
b) 10 10 10 10……
c) 01 01 01 01……
d) 00 00 00 00……

*B. π/6- QPSK Modulator*

The π/6-QPSK is a differentially encoded and decoded system. The π/6-DQPSK modulator is shown in Fig.9. The differential encoder of π/6-DQPSK modulator encodes $I_k$ and $Q_k$ into signal $u_k$ and $v_k$ according to the following rules:

$$u_k = \frac{1}{2\sqrt{2}}[u_{k-1}(\sqrt{3+3I_k}) - v_{k-1}Q_k(\sqrt{5-3I_k})] \quad (11)$$

$$v_k = \frac{1}{2\sqrt{2}}[u_{k-1}Q_k(\sqrt{5-3I_k}) + v_{k-1}(\sqrt{3+3I_k})] \quad (12)$$

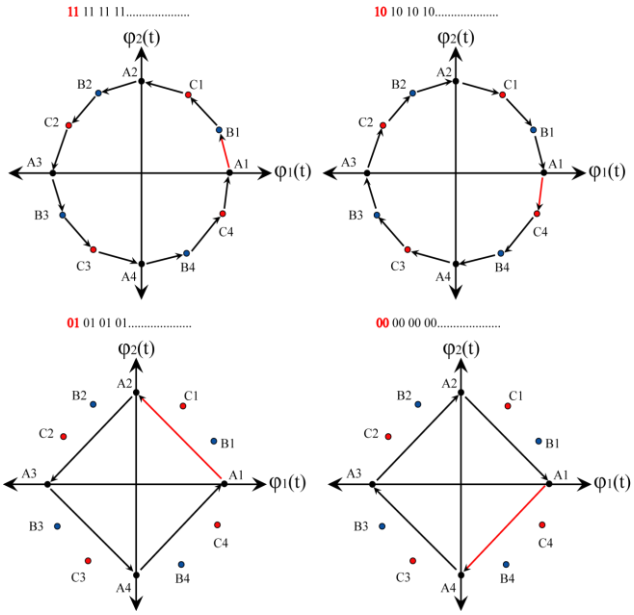


Figure 8. Example of transition routes. Here, red marked refers to start.

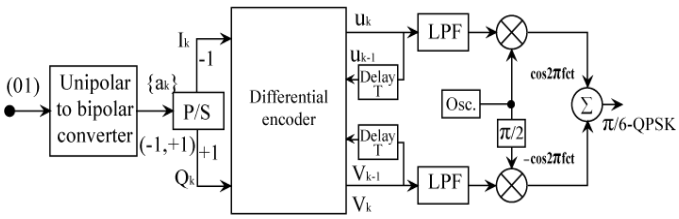


Figure 9. Block diagram of π/6-QPSK modulator.

The output signal of the π/6-QPSK modulator is similar to the formulation of π/4-DQPSK modulator presented in Eq. (9). Here, the phase difference $\Delta\theta_k$ determined by the input data as,

$$\left.\begin{aligned} \Delta\theta_k &= \sin^{-1}\{\frac{Q_k}{2\sqrt{2}}\sqrt{5-3I_k}\} \\ \Delta\theta_k &= \cos^{-1}\{\frac{1}{2\sqrt{2}}\sqrt{3+3I_k}\} \\ \Delta\theta_k &= \tan^{-1}\left\{\frac{Q_k(\sqrt{5-3I_k})}{\sqrt{3+3I_k}}\right\} \end{aligned}\right| \quad (13)$$

By combining Eqs. (11), (12) and (13), it can be written as,

$$u_k = u_{k-1}\cos\Delta\theta_k - v_{k-1}\sin\Delta\theta_k \quad (14)$$

$$v_k = u_{k-1}\sin\Delta\theta_k - v_{k-1}\cos\Delta\theta_k \quad (15)$$

*C. π/6-QPSK Demodulator*

The demodulation process of π/6-QPSK is similar to the π/4-QPSK. There are four ways to demodulate the π/4-QPSK [8] that can also be used as π/6-QPSK demodulation scheme. The main parts of such detection are:

a) Baseband Differential detection
b) IF band Differential detection
c) FM discriminator detection
d) Coherent detection

In detail, the baseband differential demodulator diagram is shown in Fig. 10. The output of the band pass filter (BPF) on absence of noise during the *k*-th symbol is,

$$r(t) = A_k \cos(2\pi f_c t + \phi_k + \theta) \qquad kT \le t \le (k+1)T \tag{16}$$

Due to the channel the random phase $\theta$ is introduced, which is almost constant in two consecutive symbols. The *I*-channel multiplier output in the k-th symbol duration is,

$$A_k \cos(2\pi f_c t)\cos(2\pi f_c t + \phi_k + \theta) =$$
$$\frac{1}{2} A_k [\cos(4\pi f_c t + \phi_k + \theta) + \cos(\phi_k + \theta)] \tag{17}$$

Now, ignoring the factor ½, the I-channel low-pass filter (LPF) output is,

$$w_k = A_k \cos(\phi_k + \theta) \tag{18}$$

Similarly, the Q-channel LPF output is,

$$z_k = A_k \sin(\phi_k + \theta) \tag{19}$$

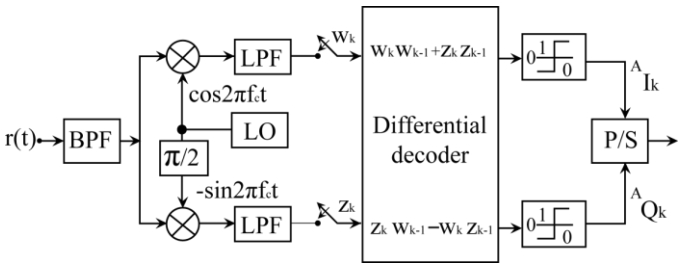


Figure 10. Baseband differential demodulator for π/6-QPSK.

Since, $\theta$ remain constant in two consecutive symbols then.

$$w_{k-1} = A_{k-1} \cos(\phi_{k-1} + \theta) \tag{20}$$

$$z_{k-1} = A_{k-1} \sin(\phi_{k-1} + \theta) \tag{21}$$

Thus, the decoding rules are:

$$x_k = w_k w_{k-1} + z_k z_{k-1} \tag{22}$$

$$y_k = z_k w_{k-1} - w_k z_{k-1} \tag{23}$$

Using the Eqs. (22) and (23), the above decoding rules become,

$$\begin{aligned} x_k &= A_k A_{k-1}[\cos(\phi_k + \theta)\cos(\phi_{k-1} + \theta) \\ &\quad + \sin(\phi_k + \theta)\sin(\phi_{k-1} + \theta)] \\ &= A_k A_{k-1} \cos(\phi_k - \phi_{k-1}) \\ &= A_k A_{k-1} \cos(\Delta\theta_k) \end{aligned} \tag{24}$$

$$\begin{aligned} y_k &= A_k A_{k-1}[\sin(\phi_k + \theta)\cos(\phi_{k-1} + \theta) \\ &\quad - \cos(\phi_k + \theta)\sin(\phi_{k-1} + \theta)] \\ &= A_k A_{k-1} \sin(\phi_k - \phi_{k-1}) \\ &= A_k A_{k-1} \sin(\Delta\theta_k) \end{aligned} \tag{25}$$

It is seen in Fig. 7 that, the signal space diagram of π/6-QPSK has twelve message points. However, at instant, π/6-QPSK works only on four message points and the decision region for selecting symbol of π/6-QPSK is shown in Fig. 11. Therefore, in π/6-QPSK, the following decisions can be made as,

$$I_k = \begin{cases} 1 & if\ \sqrt{3}x_k > |y_k| \\ 0 & if\ \sqrt{3}x_k < |y_k| \end{cases} \tag{26}$$

$$Q_k = \begin{cases} 1 & if\ y_k > 0 \\ 0 & if\ y_k < 0 \end{cases} \tag{27}$$

Where, $|y_k|$ is the absolute or modulus value of $y_k$.

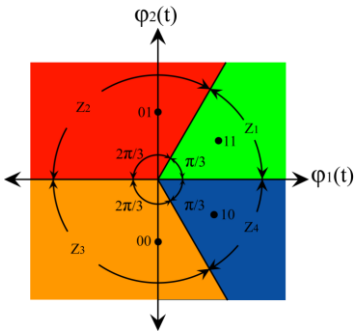


Figure 11. Decision region of π/6-QPSK for symbol selections.

## IV. Simulation Result

In order to evaluate our proposed π/6-QPSK, the simulation was done using MATLAB software. The software Simulink platform was used for simulation. In the simulation results, waveform performance of π/6-QPSK and signal spectral performance of π/6-QPSK were observed. Simulations were also performed for QPSK and π/4-QPSK. The simulation results are presented in the following figures.

### *A. Wave form performance of various QPSK modulation*

Simulation was performed here based on the Message bit of 00011011 and the Carrier frequency of 2 Hz.

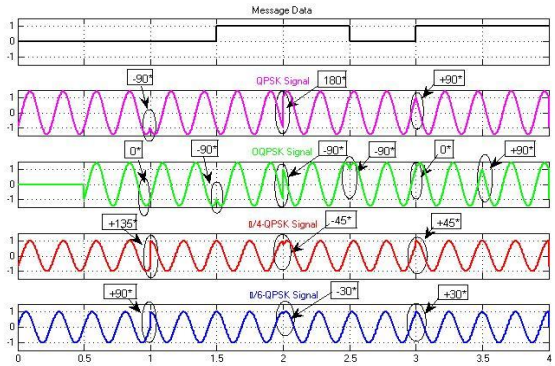


Figure 12. Wave form of QPSK, OQPSK, π/4-QPSK, and π/6-QPSK for same message data (00011011) and their relative phase transition.

### *B. Signal spectral performance*

a) Simulation was performed based on [11]:
Standard: WCDMA / UMTS (3G); Data Rate: 2 Mbps; Operating frequency: 1950 MHz; Filter: RRC (α= 0.5); Amplifier: Non-linear (Rapp model)

b) Simulation was done based on [11]:
Standard : IEEE 802.11g (WLAN)**;** Data Rate : 54 Mbp; Operating frequency: 2.4 GHz; Filter: RRC (α= 0.5); Amplifier: Non-linear (Rapp model)

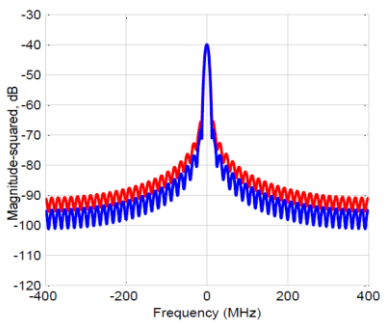


Figure 13. signal spectra after non-linear amplifier (Red: π/4-QPSK, Blue: π/6-QPSK).

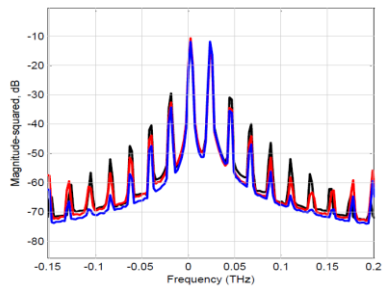


Figure 14. Signal spectra after non-linear amplifier (Red: π/4-QPSK, Blue: π/6-QPSK).

It can be observed from Fig. 12 that, at the same message data, the maximum and minimum phase transition of π/6-QPSK are ±90º and ±30º, whereas in π/4-QPSK are ±135º and ±45º. Although the maximum phase transition of OQPSK is same as π/6-QPSK, but in OQPSK the phase transition occur twice time in a symbol duration, whereas in π/6-QPSK occur one time. Furthermore, it is also observed from Figs. 13 and 14 that the side lobe power of π/6-QPSK is smaller than π/4-QPSK after non-linear amplification.

## V. CONCLUSION

In this paper, an improved QPSK modulation technique, π/6-QPSK has been presented. The proposed π/6-QPSK is modified from conventional π/4-QPSK. The focusing issue of π/6-QPSK has less phase transition compared to π/4-QPSK. Since, π/6-QPSK provides smaller phase transition, it obtains small envelope variation. As a result, after the non-linear amplificatio the spectral side lobe power of π/6-QPSK is less than π/4-QPSK. The MATLAB simulation has been carried out in this paper to evaluate the performances of our proposed technique. The relative phase transition of π/6-QPSK is reasonably reduced compared to that of other QPSK schemes (see Fig. 12). Furthermore, signal spectral performance of π/6-QPSK is better than that of π/4-QPSK after non-linear amplification (see Figs. 13 and 14). Thus, it can be concluded that our proposed π/6-QPSK is very much efficient in wireless communication for data transmission in terms of less phase transition, less envelope variation and less spectral side lobes power after non-linear amplification.

## REFERENCES

[1] Simon Haykin, *Digital Communication*, Wiley Press, 2013.
[2] J. Webber, N. Dahnoun, *Implementing a π/4-Shifted DQPSK Baseband Modem Using the TMS320C50*, ESIEE, Paris, September 1996.
[3] MNT Castle, *All About Modulation part-I*, Charan Langton, PP 1-38, 2002.
[4] Baker P. A., "Phase modulation data sets for serial transmission at 2000 and 2400 bits per seconds", AIEE Trans. on Communication Electronics, July 1962.
[5] D. Sai Brunda, B. Geetha Rani, "Design of QPSK Digital Modulation Scheme Using Turbo Codes for an Air Borne System", International Journal of Advanced Research in Computer and Communication Engineering (IJARCCE),vol. 5, issue 8, August 2016.
[6] R. Garg, Er. Ankita Mittal, Design & Implementation for Combination of QPSK & BPSK Modulation Techniques, International Journal of Advanced Research in Electronics and Communication Engineering (IJARECE), Volume 3, Issue 8, August 2014.
[7] Celal Dudak, *Effects of Solid State Power Amplifier Non-linearity on Various Phase Shift Keying Modulation Schemes*, Metu Publisher, 2001.
[8] Fuqin Xiong, *Digital Modulation Techniques (2nd Edition)*, Artech House, Jan 1, 2006.
[9] S.M.Haladik, S.Chennakeshu and G.J.Saulnier, "On ACIPR of π/4-Shifted-DQPSK for U.S. Digital Land Mobile Radio System", In Proc. IEEE Pacific Rim Conf. on Commun., Computers and Signal Processing, 1991, pp.530-533.
[10] Riddhi Pamar, Shilpi Gupta and Upena Dalal, "Comparison of BER Performance of Conventional and Non-conventional Mapping Schemes Used in OFDM", World Academy of Science, Engineering and Technology, vol.57, 2011.
[11] R. Shrestha, "RF Power Amplifier Techniques for Spectral Efficiency and Software-Defined Radio", Ph.D. thesis, University of Twente, November 2010.

# Low Complexity Carrier-Phase Estimation Based on Sign-Error Modified CMA for 16-QAM Coherent Optical Receivers

Md. Saifuddin Faruk
Department of Electrical & Electronic Engineering, Dhaka University of Engineering & Technology, Gazipur-1700, Bangladesh
faruk@duet.ac.bd

*Abstract*—**Carrier-phase estimation (CPE) is one of the key elements of the digital signal processing (DSP) unit of a coherent optical receiver. CPE is required to eliminate the effect phase noise, mainly stemming from transmitting laser and local oscillator (LO). In this paper, a simple CPE scheme for 16-QAM digital coherent receiver is proposed which is based on coordinate transformation and sign-error modified constant-modulus algorithm (CMA). Such CPE can be achieved with very low implementation complexity. Performance of the proposed CPE scheme is analyzed with intensive computer simulation. For a 32-Gbaud 16-QAM system, the combined laser linewidth tolerance of more than 2 MHz is found for 1-dB sensitivity penalty.**

***Keywords— Optical fiber communication, coherent detection, carrier-phase estimation, digital signal processing.***

## I. INTRODUCTION

The modern coherent optical receivers employing multilevel modulation formats utilize digital signal processing (DSP) techniques for equalization and synchronization purposes [1]. Carrier-phase estimation (CPE) is an important block of such DSP chain whose function is to estimate and compensate the laser phase noise from transmitting laser and local oscillator (LO). The Viterbi-Viterbi algorithm is a well-known algorithm for CPE purpose; however, it performs well only for constant-modulus modulation format such as quadrature phase shift keying (QPSK) format [2]. Further modifications with additional computational complexity is required to apply such algorithm for non-constant modulus format such as multilevel quadrature amplitude modulation (M-QAM) format [3]. Therefore, research on CPE for higher-order modulation formats has attracted a significant attention in recent years [4-5].

An alternate CPE approach is to use modified constant-modulus algorithm (CMA) based scheme [6]. However, such approach is again suitable for QPSK format only. In this paper, we modified such method to make it applicable for 16-QAM format. First, 16-QAM signal is converted to QPSK like signal using coordinate transform technique [7]. Then modified CMA is used to estimate the phase noise. Further, instead of using conventional modified CMA [8], the sign of the error function is used to get the updated estimated phase which makes the CPE process very low complexity. There are several benefits of the proposed methods. Firstly, the proposed method can be implemented with minimal computation complexity since we need only two real multiplications[1]. Secondly, there is no need of training sequences and thus can be implemented in a fully blind mode. Finally, there is no need of symbol decision for updating and thus can be implemented with minimal feedback latency.

Effectiveness of the proposed scheme is verified with intensive computer simulations. It is found that for a 32-Gbaud 16-QAM system, the proposed method can compensate the phase noise for a combined laser linewidth of more than 2 MHz with less than 1-dB sensitivity penalty.

## II. PRINCIPLE OF THE PROPOSED SCHEME

Consider the input signal at CPE stage after perfect clock recovery and equalization is given by:

$$u(n) = a(n)e^{j\theta(n)} + w(n), \tag{1}$$

where $n$ is the symbol-spaced sample index, $a(n)$ is the 16-QAM data symbol that belongs to the set $(\pm x \pm jy)$, $x, y \in \{1,3\}$, $\theta(n)$ is the laser phase noise and $w(n)$ is the additive white Gaussian noise (AWGN). The laser phase noise is modelled as Winner process with independent and identically distributed random Gaussian variables with zero mean and variance

$$\sigma_n^2 = 2\pi\delta_f T_s \tag{2}$$

where $\delta_f$ is summed linewidth of transmitting laser and LO and $T_s$ is the symbol period.

The task of CPE is to estimate $\theta(n)$ from Eq. (1). Considering the estimated phase as $\hat{\theta}(n)$, the proposed carrier-phase recovery scheme can be illustrated as in Fig.1. The phase recovered signal is obtained as $v(n) = u(n)e^{-j\hat{\theta}(n)}$ which represents the 16-QAM data symbols with AWGN. The 16-constattelion points of 16-QAM signal is then converted to 4-constellation points signal using coordinate transformation (CT) as below [7]:

[1] Multiplication is the costliest arithmetic operation for hardware implementation and therefore trimming the number of multiplications in algorithm design reduces the complexity significantly.

978-1-5386-2307-7/17/$31.00 ©2017 IEEE

$$v'(n) = [v_r(n) - 2sign\{v_r(n)\}] + j[v_i(n) - 2sign\{v_i(n)\}] \quad (3)$$

where, $v_r(n)$ and $v_i(n)$ are the real and imaginary part of $v(n)$, respectively and *sign* is the signum function which can be defined as:

$$sign(x) = \begin{cases} -1 & \text{if } x < 0 \\ 0 & \text{if } x = 0 \\ 1 & \text{otherwise} \end{cases} . \quad (4)$$

Such coordinate transformation changes 16-points of 16-QAM signals into QPSK like 4-points as shown in Fig. 2 (four points of same color in 6-QAM constellation transform into a single point).

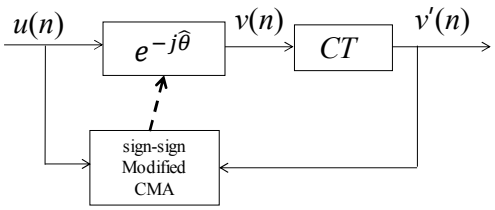


Fig.1: Schematics of the proposed carrier-phase recovery scheme. (CT: coordinate transformation)

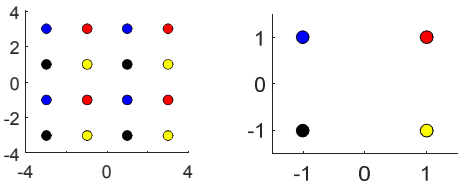

Fig. 2: Illustration of the coordinate transformation operation; before (left) and after (right) transformation.

Now the error function from $v'(n)$ can be calculated using modified CMA as [8]:

$$\varepsilon(n) = v_r'(n)(1 - v_r'(n)^2) + jv_i'(n)(1 - v_i'(n)^2) \quad (5)$$

Note that modified CMA calculate the error function from real and imaginary part of the output separately in contrast to the conventional CMA which uses absolute value of complex-valued output and thus modified CMA enables phase estimation [6]. The error signal is then used to update the estimated phase as [9]:

$$\hat{\theta}(n+1) = \hat{\theta}(n) - \mu \Im\{\varepsilon(n)u^*(n)\} \quad (6)$$

where, $\mu$ is the convergence parameter, $\Im\{.\}$ denotes imaginary part and superscript $(.)^*$ is the conjugate operation.

Now to reduce the number of multipliers, the value of $\mu$ is chosen as a power-of-two[2] and error function of Eq. (5) is modified by using the signum function as below [10]:

$$\varepsilon(n) = sign\{v_r'(n)\}sign\{1 - v_r'(n)^2\} + jsign\{v_i'(n)\}sign\{1 - v_i'(n)^2\}. \quad (7)$$

[2] Multiplication with a power-of-two value can be implemented with shift operation.

Herein, Eqs. (3), (7) and (6) constitute the proposed CPE scheme.

Since multiplication with 2 can be done with just shift operations, the coordinate transformation given by Eq. (3) can be implemented without any multiplication. Calculation of error function given by Eq. (7) requires only two real multiplications (to calculate the squared terms) and for such an error function the update equation given by Eq. (6) is multiplier-free. Therefore, the overall complexity of the proposed scheme is only two real multiplications. On the other hand, the conventional modified CMA based CPE [6] requires at least one more additional complex multiplication (i.e. four real multiplications).

## III. Simulation Resuts and Discussion

In order to verify the effectiveness of the proposed scheme, we conduct computer simulation considering 32-Gbaud 16-QAM signals. First, two million of random data symbols are generated and input signals to the CPE stage is produced using Eq. (1). Such signal is passed through the proposed carrier recovery circuit shown in Fig.1. The value of step size parameter is optimized for that gives the lowest BER. The phase recovered signal is then differentially decoded to avoid any cycle slips and bit-error-rate (BER) is measured using direct counting method.

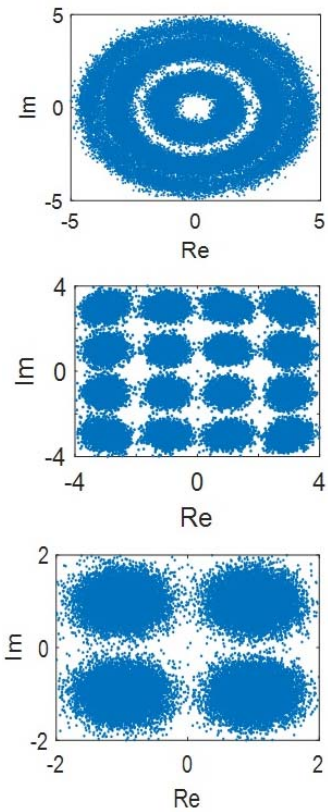


Fig.3: Constellation diagram of input signal of CPE (top), output after CPE (middle) and output after coordinate transformation (bottom).

Firstly, we observe the constellation diagrams at different stages of the proposed CPE for $\delta_f = 1$ MHz and $E_b/N_0$=12 dB. As shown in Fig.3, the input signal is phase rotated whereas the

output constellation is free from any phase rotation suggesting that laser phase noise is properly compensated. In addition, we also found that the coordinate transformation operation successfully transforms 16-point constellation (middle figure) to 4-point constellation (bottom figure) as expected in the theory.

As of the performance measure, the BER is evaluated as a function of the energy per bit to noise spectral-power-density ratio, $E_b/N_0$, for different laser linewidths ( $\delta_f$ ) as shown in Fig. 4. It is found that at the BER of $10^{-2}$ (20% FEC limit), the proposed method can tolerate more than 2 MHz linewidth with less than 1-dB of $E_b/N_0$ penalty. Thus, a commercially available distributed feedback (DFB) laser (usually having around 1 MHz 3-dB linewidth) can be used in the system when the proposed scheme is used.

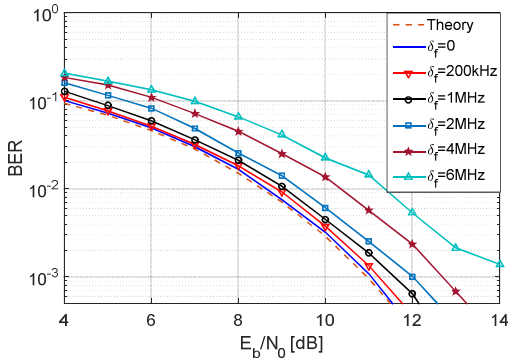


Fig. 4: BER characteristics as a function of $E_b/N_0$ for different laser linewidth.

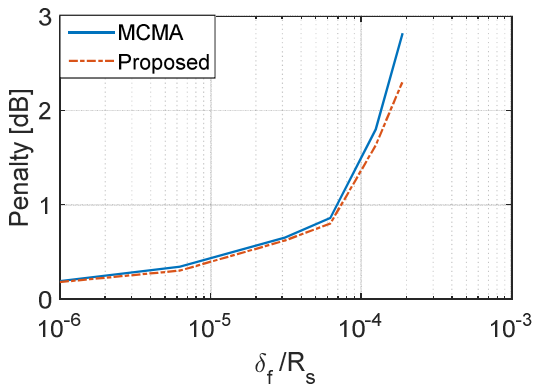


Fig. 5: Sensitivity penalty at BER of $10^{-2}$ as a function of laser linewidth normalized to symbol rate. (MCMA: modified CMA )

Finally, the linewidth tolerance of the proposed method is evaluated. In Fig. 5, the sensitivity penalty at BER of $10^{-2}$ is plotted as a function of normalized laser linewidth ( $\delta_f$ / $R_s$ , $R_s$ is the symbol rate) for modified CMA method (error signal given by Eq. (5)) and the proposed low complexity method (error signal given by Eq. (7)). For both the methods, almost identical performance is observed, albeit the later one requires only one-third of implementation complexity compare to former one. For a normalized laser linewidth of $10^{-4}$, the sensitivity penalty is found only around 1.5 dB.

## IV. Conclusion

We have proposed a low complexity CPE scheme for 16-QAM signals based on sign-error modified CMA and coordinate transformation. It requires only two real multiplications for the CPE purpose and thus can be implemented in a hardware-efficient manner. It is confirmed by means of computer simulation that proposed scheme can tolerate 2 MHz laser linewidth for 32-Gbaud system with less than 1-dB sensitivity penalty. Therefore, the proposed CPE scheme can be used in next generation high speed coherent optical receivers in an efficient manner.

## References


[1] M. S. Faruk and Seb J. Savory, "Digital signal processing for coherent transceivers employing multilevel formats." *J. Lightw. Technol.*, vol. 35, no. 5, pp. 1125-1141, Mar. 2017.

[2] A. J. Viterbi and A. M. Viterbi, "Nonlinear estimation of PSK-modulated carrier phase with application to burst digital transmission," IEEE Trans. Inf. Theory, vol. 29, no. 4, pp. 543–551, Jul. 1983.

[3] I. Fatadin, D. Ives, and S. J. Savory, "Laser linewidth tolerance for 16-QAM coherent optical systems using QPSK partitioning," IEEE Photon. Technol. Lett., vol. 22, no. 9, pp. 631-633, May 2010.

[4] X. Zhou, "Carrier recovery in coherent optical communication systems," in *Enabling Technologies for High Spectral-Efficiency Coherent Optical Communication Networks*, chap. 11, 2016.

[5] M. S. Llopis, M. S. Faruk, and S. J. Savory "Improved linewidth tolerant carrier phase recovery based on polar MAP metric estimate," In *Proc. Opt. Fiber Commun. Conf.*, paper Th4C-2, 2017.

[6] M. S. Faruk, "Blind equalization and carrier-phase recovery based on modified constant-modulus algorithm in PDM-QPSK coherent optical receivers" Opt. and Quantum Electron., vol. 48, no.1, p.3, Jan. 2016.

[7] W. Rao, Y. Kang-min, G. Ye-cai, and Y. Chao "A simple constant modulus algorithm for blind equalization suitable for 16-QAM signal," In *Proc. IEEE int. Conf. sig. process. (ICSP)*, pp. 1963-1966, 2008.

[8] K. N. Oh and Y. O. Chin, "Modified constant modulus algorithm: Blind equalization and carrier phase recovery algorithm," *Proc. ICC*, vol. 1, pp. 498 -502, 1995.

[9] I. Fatadin, D. Ives, and S. J. Savory, "Blind equalization and carrier phase recovery in a 16-QAM optical coherent system," *J. Lightw. Technol.,* vol. 27, no. 15, pp. 3042–3049, Aug. 2009.

[10] D. Lavery, B. C. Thomsen, P. Bayvel, and S. J. Savory, "Reduced complexity equalization for coherent long-reach passive optical networks [Invited]," *J. Opt. Commun. Netw.*, vol. 7, no. 1, pp. A16-A27, Jan. 2015.

# *Compact Dual S Shaped Slotted Multiband Patch Antenna*

M. Samsuzzaman[1,a], M. A. Rahman[1,,b], M. Z. Mahmud[2,c], M. Tarikul Islam[1,d], M.T. Islam[2,e]
[1]Patuakhali Science and Technology University, Patuakhali, Bangladesh
[2] Universiti Kebangsaan Malaysia, Malaysia
[a]sobuz@pstu.ac.bd, [b]atikur11@cse.pstu.ac.bd, [c]zulfikerm@siswa.ukm.edu.my, ,[d]mtarikulislam10@cse.pstu.ac.bd
[e]tariqul@ukm.edu.my

*Abstract*—**A compact patch antenna is designed and presented for the multiband application. The antenna is exclusively developed for multiband application such as Wireless Area Network (WLAN), Global Positioning System (GPS), GSM and WiMAX application. The overall dimension of the proposed antenna is 0.13 × 0.303 × 0.007 $\lambda^3$ at 1.3 GHz which has an S-shaped patch with an efficient size of 33.5 × 30 mm$^2$ and fed by 50Ω microstrip indication line. Simulated maximum gains, the radiation pattern, transmission return losses and efficiency are introduced in this conventional letter. The prototype is usually designed with the capability of covering multiple bands from 1.352-1.614 GHz for the GPS system, 1.77 GHz to 1.82 GHz for GSM application, 2.148-3.149 GHz for the WLAN programs, 3.522-3.754 GHz for the WiMAX system. The gain of 1.2dBi, 2.2dBi, 1.8dBi and also 4.2dBi are spotted for bands of desire. The detected properties advocate that the proposed antenna can be practiced in a present-day communication system having demands in dimension and weight.**

***Keywords—Multi-band antenna; Patch; S-shaped;***

## I. INTRODUCTION

More than the last years now, there has been an immediate improvement in the use of wireless compact tools. Now many professional products have come to light in order to cover the interest of products and services such as information/video transfer. For instance, the actual IEEE 802.11x methodologies are some being among the most largely put to use ones. It's encouraged by the need of antennas which might go over multiband purposes and can assist with large enough bandwidth at all working frequencies. Furthermore, current products tend to be small along with the area within the printed circuit board (PCB) for that antenna is limited. For that reason, compact antennas become more attractive. The main element benefits of the compact antenna might be wide bandwidth and effortless integration with various devices and is particularly a good choice for the style regarding multi-band antennas. The particular developments of numerous unique wireless communications specifications, it is truly appealing in order to incorporate numerous specifications as an illustration Global Positioning System (GPS), Global System for Mobile Communication, Wireless Specific geographic area Network standards as is feasible into a solitary wireless instrument. For this reason, different multi-band antennas had been studied.

Several antennae are designed for multiband application [1-3]. The actual dual T shaped antenna has been announced where two T-shaped and L-shaped antennas generate distinctive frequency band [4, 5]. A reconfigurable antenna is generally tougher, but its structure is challenging and requires shifting components [6]. These antennas are challenging in their geometry such as oval and T-slits patterns which have been acquired to gain multiband functions. The double U-shaped antenna with a tapered microstrip feeding line [7] and a different U-shaped monopole antenna, that is presented about the impact of numerous parameters on designed antenna [8] contains 2 GHz and 5 GHz twin band for WLAN applications. Some tri-band compact antenna is presented in [9, 10]. Those antennas only cover maximum three bands for wireless communication.

In this paper, a four-band compact antenna with geometry 70 × 30 mm$^2$ is presented. The antenna covers the frequency bands from 1.352-1.614 GHz for the GPS system, 1.77 GHz to 1.82 GHz for GSM application, 2.148-3.149 GHz for the WLAN systems and 3.522-3.754 GHz for the WiMAX system. CST and HFSS simulator are used to simulate the proposed antenna. The designed antenna is small dimensions, cost lessen and have decent features which make it suitable for using during multiband programs.

## II. ANTENNA CONFIGURATION

The following two equations (1) and (2) are used to calculate height and width of the proposed antenna [11]. Here, length is L, width is W, the center frequency is $f_0$, the dielectric constant is $\varepsilon_r$ and light velocity is C.

$$L = \frac{c}{2f_0\sqrt{\varepsilon_r}} - 2\Delta l \tag{1}$$

$$W = \frac{c}{2f_0}\sqrt{\frac{\varepsilon_r + 1}{2}} \tag{2}$$

The final design of the prototype is demonstrated in Fig 1. The patch is imprinted on both sides of the FR4 substrate which permittivity is 4.6 and substrate size is 33.5 × 30 mm$^2$. A 13.4 × 4 mm$^2$ feeding line is branded on the upper side of the substrate. After some modification of the patch on both side of the substrate, the final design comes out. At the first stage simple rectangle printed on both side of the substrate. This design covers two bands e.g. 1.4 GHz - 1.8 GHz for GPS system

and 2.1 GHz - 3.1 GHz for WLAN system. At the second stage cutting two rectangle slot from upper and lower end of both side patch. But the result is the same compared with the first stage. At the third stage making S-shape on the leading portion of the substrate and another side remains constant. This design also covers two bands but little different from above two results.

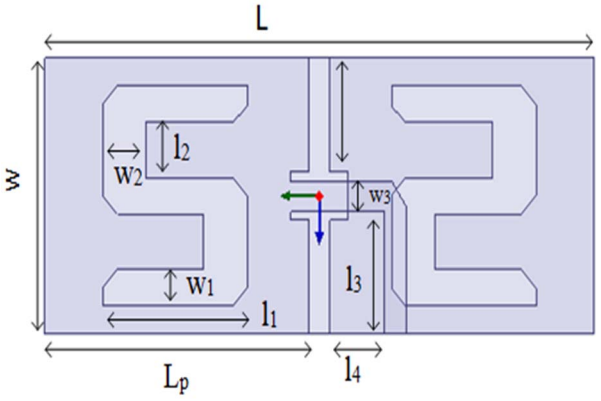


(a)

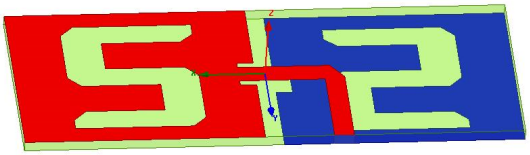

(b) 3D view

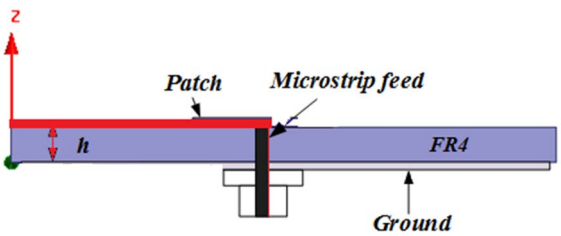


(c)

Figure 1. Geometry of proposed antenna (a) Top-view (b) 3D view(c) Side-view

The proposed antenna contains S-shape on both sides of the FR4 substrate. It covers three band e.g. 1.352-1.614 GHz for the GPS system, 1.77 GHz to 1.82 GHz for GSM application, 2.148-3.149 GHz for Wireless Local Area Network systems, 3.522-3.754 GHz for WiMAX application. The parameters of the prototype antenna are provided in Table 1.

TABLE I. DIMENSIONS OF PROPOSED ANTENNA

| Parameters | W | L | Lp | L1 | L2 | L3 | L4 | W1 | W2 | W3 | h |
|---|---|---|---|---|---|---|---|---|---|---|---|
| Size (mm) | 30 | 70 | 33.5 | 20 | 6 | 13.4 | 7.5 | 4 | 6 | 4 | 1.6 |

## III. RESULT AND DISCUSSION

Computer Simulation Technology (CST) and High-Frequency Structural Simulator (HFSS) software both are used to observed the performances and got the simulated result of proposed antenna. The antenna is fed by 50 Ω microstrip transmission line. The s11 result is carried out in four conditions: 1) simple rectangle on both side of the substrate, 2) cutting two rectangle slot from upper and lower end of both side patch, 3) S shape only top side, 4) the complete design, shows in Fig 2. The s11 result of the antenna simulated in two simulation software HFSS and CST is displayed in Fig 4. In order to get the final design, some parametric analysis has been done. The proposed antenna in Fig 1 has some parameters like w2, w3 and polyline which directly affect the frequency bands. In Fig 3(a) shows that, after increase width of w2 from 4 mm to 6 mm, band 1 is same but band 2 switches from 1.5 GHz to 1.8 GHz, band 3 switch from 1.8 GHz to 2.1 GHz, and band 4 switch from 3.0 GHz to 3.5 GHz. Thus w2 is set at 6mm. In Fig 3(b) shows that the antenna covers 4 bands after increasing the feed line width w2 from 3.2mm to 4mm. In Fig 3(c) indicates that 6 polylines are used to set the frequency band 2 which covers 1.7 GHz to 1.8GHz. Thus w3 is set to 4mm and total 12 polylines are used to get perfect frequency bands. In Fig 5 demonstrates the peak gain of the prototype which is simulated in both HFSS and CST software at different frequencies. The efficiency of the antenna is expressed in Fig 6. The simulated radiation pattern of the antenna at various frequencies such as 1.3 GHz, 1.7 GHz, 2.1GHz and 3.5 GHz is shown in Fig 7. According to the radiation pattern, it is said that the antenna is omnidirectional. At lower frequency, the antenna is totally omnidirectional, but when the frequency is increasing the characteristics of the antenna is changing. At 3.5 GHz, the antenna is directional. At 1.35 GHz the antenna is quite omnidirectional but at 2.1 GHz it turns to directional properties. The surface current distribution is shown in Fig 8 where the maximum radiating area is feed line and then the edge of S-shape. At lower frequency upper S-shape radiating most but at a higher frequency, the lower S-shape radiates larger than the upper side.

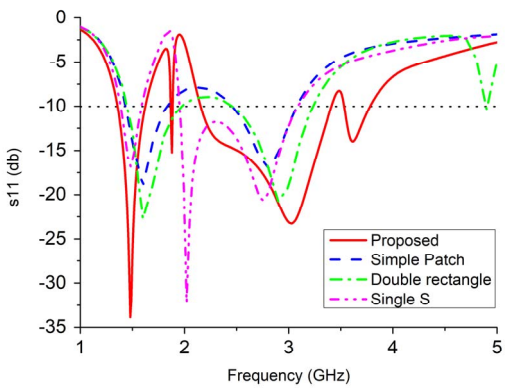


Figure 2. Simulated $s_{11}$ at various conditions of antenna

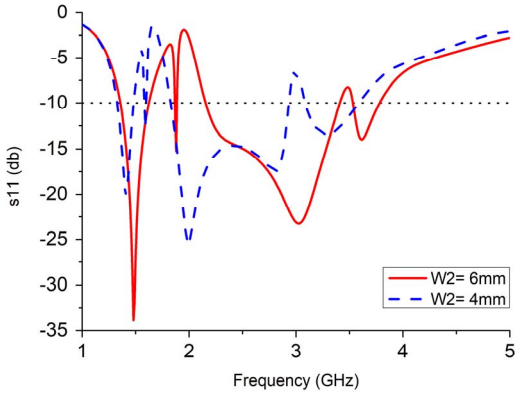


(a)

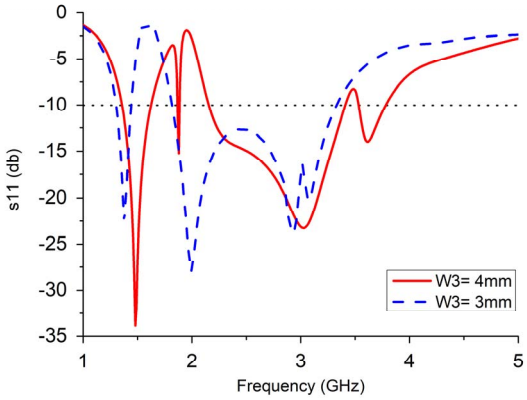


(b)

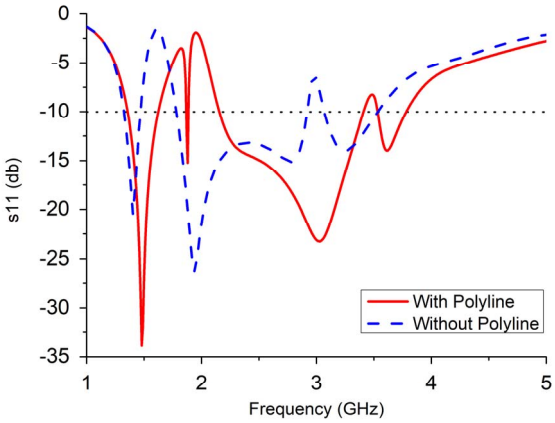


(c)

Figure 3. Simulated s11 at various values of (a) w2, (b) w3 and (c) polyline.

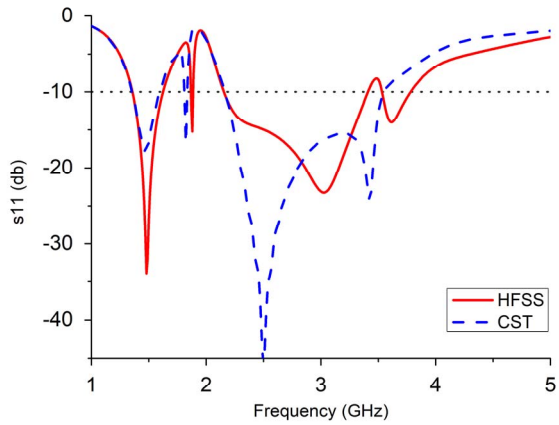


Figure 4. Simulated $s_{11}$ in HFSS and CST

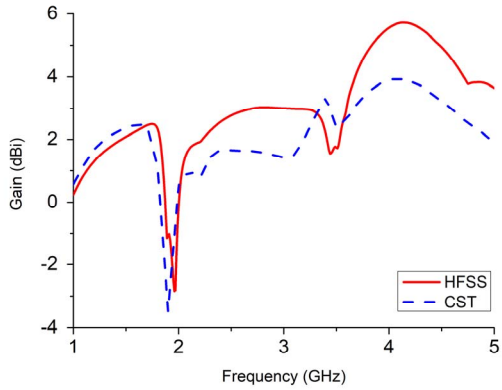


Figure 5. Simulated peak gain in HFS and CST

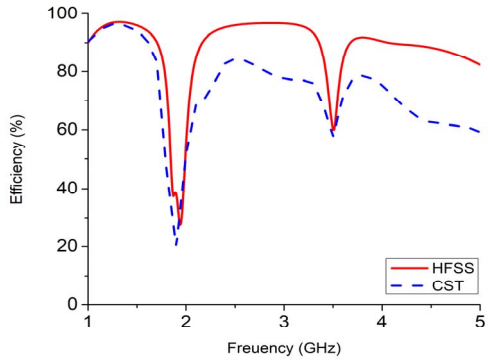


Figure 6. Simulated Efficiency in HFSS and CSS

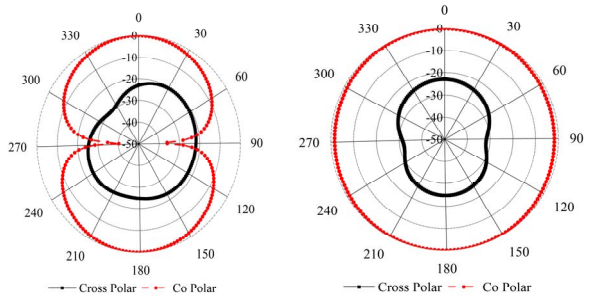


(a)

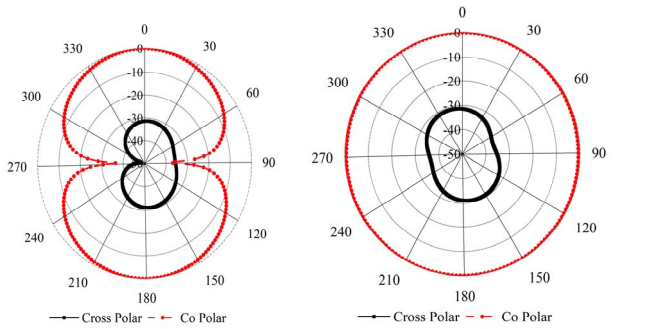


(b)

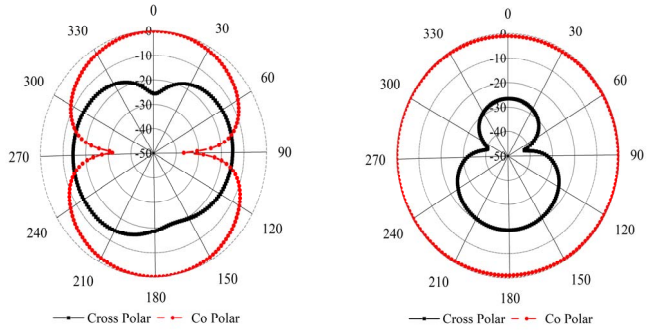


(c)

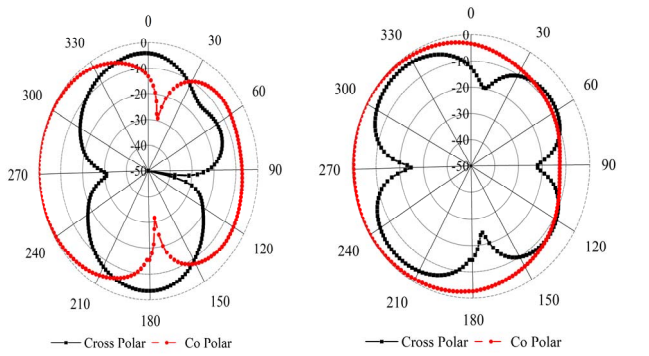


(d)

Figure 7. Simulated 2D radiation pattern at various frequency (a) 1.7 GHz, (b) 1.35 GHz, (c) 2.1 GHz (d) 3.5 GHz.

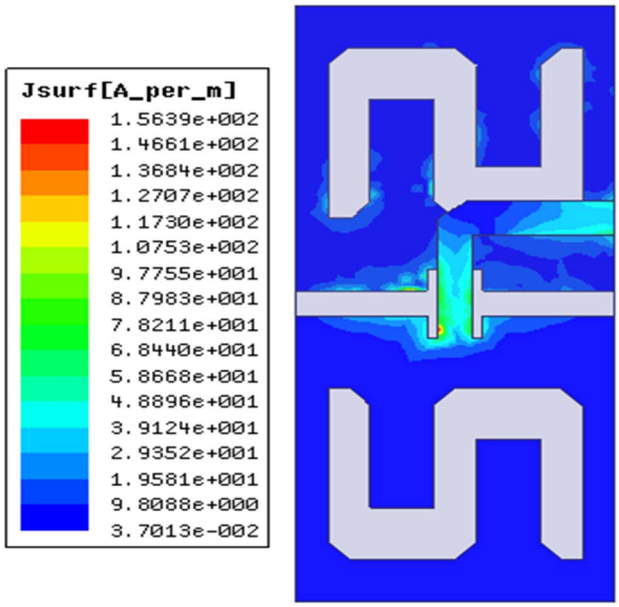


Figure 8 Surface current distribution at 3.5 GHz.

TABLE II. COMPARISON WITH OTHER WORKS

| Antenna | Dimension | Gain | Frequency Bands |
|---|---|---|---|
| [1] | 80 × 60mm$^2$ | - | 1.5 GHz<br>2.1 GHz<br>3.2 GHz |
| [9] | 46×50×0.16 mm3 | 6.69 (2.4 GHz)<br>1.89 (3.9 GHz)<br>2.53 (7.7 GHz) | 2.10 - 2.60 GHz<br>3.02 - 5.82 GHz<br>7.00 - 9.50 GHz |
| [12] | 28 × 16 × 0.8 mm$^3$ | - | 2.4 GHz<br>3.6 GHz<br>5.5 GHz |
| [13] | 25 × 28mm$^2$ | - | 1520 – 1590 MHz<br>1770 – 1840 MHz<br>2385 – 2490 MHz |
| Proposed | 70×30 mm$^2$ | 2.5 (1.6 GHz)<br>3.3 (1.8 GHz)<br>3.6 (3.1 GHz)<br>5.1 (3.7 GHz) | 1.352 - 1.614 GHz<br>1.77 - 1.82 GHz<br>2.148 - 3.149 GHz<br>3.522 - 3.754 GHz |

## IV. CONCLUSION

The structure of a compact multiband patch antenna for Global Positioning System, GSM, Wireless Local Area Network, WiMAX has been presented. The antenna consists of double S-shaped on FR4 substrate on both sides. The overall dimension of the prototype is 70 mm × 30mm. The antenna has four frequency bands i.e. 1.3 GHz, 1.75 GHz, 2.5GHz and 3.6 GHz. So that GPS, WLAN, and WiMAX systems are covered by the antenna. The obtained connection between studies has been used to help to propose a methodology of when using the design for other frequency bands. The prototype antenna is low cost, easy to design and fabricate for the multiband application.

## REFERENCES


[1] M. S. Garba and H.-x. Zheng, "Analysis and design of compact multiband patch antenna for wireless application," in *Microwave and Millimeter Wave Technology (ICMMT), 2016 IEEE International Conference on*, 2016, pp. 11-13.

[2] M. M. Islam, M. T. Islam, M. Samsuzzaman, M. R. I. Faruque, N. Misran, and M. F. Mansor, "A miniaturized antenna with negative index metamaterial based on modified SRR and CLS unit cell for UWB microwave imaging applications," *Materials,* vol. 8, pp. 392-407, 2015.

[3] R. Azim, M. T. Islam, and N. Misran, "Dual polarized microstrip patch antenna for Ku-band application," *Informacije MIDEM,* vol. 41, pp. 114-117, 2011.

[4] J.-H. Lu and B.-J. Huang, "Planar compact slot antenna with multi-band operation for IEEE 802.16 m application," *IEEE Transactions on Antennas and Propagation,* vol. 61, pp. 1411-1414, 2013.

[5] M. H. Ullah, M. T. Islam, J. Mandeep, and N. Misran, "A new double L-shaped multiband patch antenna on a polymer resin material substrate," *Applied Physics A,* vol. 110, pp. 199-205, 2013.

[6] J. Pei, A.-G. Wang, S. Gao, and W. Leng, "Miniaturized triple-band antenna with a defected ground plane for WLAN/WiMAX applications," *IEEE Antennas and Wireless Propagation Letters,* vol. 10, pp. 298-301, 2011.

[7] I.-F. Chen and C.-M. Peng, "Microstrip-fed dual-U-shaped printed monopole antenna for dual-band wireless communication applications," *Electronics letters,* vol. 39, pp. 955-956, 2003.

[8] C.-K. Hsu and S.-J. Chung, "Compact multiband antenna for handsets with a conducting edge," *IEEE Transactions on Antennas and Propagation,* vol. 63, pp. 5102-5107, 2015.

[9] M. I. Khan, M. A. Kabir, and A. Hira, "A simple multiband patch antenna for application in wireless communication," in *Electrical, Computer and Communication Engineering (ECCE), International Conference on*, 2017, pp. 615-618.

[10] M. Samsuzzaman, T. Islam, N. Abd Rahman, M. R. I. Faruque, and J. Mandeep, "Compact modified swastika shape patch antenna for WLAN/WiMAX applications," *International Journal of Antennas and Propagation,* vol. 2014, 2014.

[11] C. A. Balanis, *Antenna theory: analysis and design*: John Wiley & Sons, 2016.

[12] R. Saleem and A. Quddus, "Circular slotted reconfigurable multiband patch antenna for wireless applications," in *Applied Computational Electromagnetics Society Symposium-Italy (ACES), 2017 International*, 2017, pp. 1-2.

[13] M. Bod, H. Hassani, and M. S. Taheri, "Compact UWB printed slot antenna with extra bluetooth, GSM, and GPS bands," *ieee antennas and wireless propagation letters,* vol. 11, pp. 531-534, 2012.

# Abnormal Event Detection in Crowded Scenarios

Tahjid Ashfaque Mostafa, Jia Uddin, Md. Haider Ali
Department of Computer Science and Engineering, BRAC University
66 Mohakhali, Dhaka 1212, Bangladesh
atahjid@gmail.com, engrjiauddin@gmail.com, haider@bracu.ac.bd

*Abstract*— **This paper proposes an autonomous video surveillance system which analyzes footages of extremely crowded scenes and detects abnormal events in the context of that particular scene. The model analyzes the local spatial-temporal motion pattern and detects abnormal motion variations and sudden changes and it can be divided into two major parts, selecting a set of Points of Interest (POI) from given frames and tracking them across multiple frames and dividing the input video frame in a number of cubes and track the motion patterns in each of the cubes for spatial-temporal statistical deviations. To evaluate the performance of proposed model we utilize several datasets and compare the acquired results of the proposed model with various state-of-the art models. Experimental results demonstrate that the proposed model outperforms the other models by exhibiting an average of 96.12% accuracy using Convolutional Neural Network.**

***Keywords—Pattern Recognition, Abnormal Event, Feature Extraction, Convolutional Neural Network.***

## I. INTRODUCTION

With the recent decrease in the cost of video surveillance equipment, a large number of areas can be monitored constantly. However monitoring a place for abnormal and emergency situations is quite meaningless unless the situation can be identified and appropriate responses can be taken. Extremely crowded scenes require monitoring a large number of individuals engaged in various arbitrary actions, which is a significant challenge even for a human observer. It might include hundreds of people scattered across the frame and possibly thousands of individuals in the whole video sequence with extremely irregular motion patterns which might cause occlusions. The computation approach must be able to detect abnormal events in any specific area of the frame while maintaining the structural view of the entire scene. And the large number of subjects' cause analyzing the actions of the individual subjects to be a massive challenge, even with the computational prowess of the modern computers.

Abnormal events can be both spatial, an event which is abnormal in context of its surroundings and temporal, which is an event over duration of time which is abnormal [1]. It can also be divided into Local Abnormal Events where the behavior of an individual is different from its neighbors and Global Abnormal Events where the whole scenario is abnormal [2]. It takes sufficient computing power in order to analyze and detect the nature of an event in real time, because if the event cannot be identified in real time, the purpose of surveillance is not served. Many approaches have been undertaken in analyzing and classifying video events. For example, object tracking [3], pedestrian detection [4], crowd counting [5], background modeling [6], and action detection [7], estimation of crowd density based on texture and motion area ratio [8, 9, 10].

Approaches to abnormal event detection can mainly be divided in three types [1], (I) Macroscopic Models: Models that density and velocity of the whole crowd, (II) Microscopic Models: Models that focus on individual behavior and (III) Hybrid Models: Models which consider both overall and individual behavior. The usual approach used is to first define the normal behavior and its properties, and then classifying those behaviors which do not have similar properties as the predefined normal behavior as abnormal events. Samples of abnormal behaviors6 are infrequent and it is impractical to attempt to completely determine the types of abnormal events.

Determining the events in real time is a significant challenge as well. Bazmi *et al.* used a block-based Improved Centre Symmetric Local Binary Pattern method for feature extraction [11]. Tannouche *et al.* a Boosted Cascade of Simple Features for detection in real time [12]. Rani *et al.* used Fixed Thresholding and Histogram Based Edge Processing for real time tracking of vehicles [13]. A number of methods analyze the trajectory of the individuals with many well developed methods such as HOG [5] or motion patterns and appearances [14]. Mehran *et al.* used an optical flow based social force model and then use Latent Dirichlet Allocation (LDA) to detect abnormality [15]. Hua *et al* used Normalization Cut Clustering [16] and Benezeth *et al.* used a 3D spatial-temporal foreground mask using Markov random field [17]. Nacim *et al.* used a heatmap image as a mask for Harris Corner Detector to identify key Points of Interest [18]. Lagrangian Particle Dynamics is used in [19] for detection of flow instabilities which is very helpful in segmentation of high density crowd flows. A combination of Hidden Markov Models (HMM), spectral clustering and principal component analysis is used in [20, 21] to detect emergency scenarios. In this paper, we proposed a model for identifying abnormal events in extremely crowded scenarios by analyzing the motion patterns of a set of defined features and combining that with the overall motion structure within the frame.

The rest of the paper is organized as follows. Section II presents the required steps for feature vector generation from input frames and training a classifier, Section III describes the experimental results, compares the performance of the model on various datasets and finally compares the performance of various classifiers on the proposed model, Section IV presents conclusions for the paper.

978-1-5386-2307-7/17/$31.00 ©2017 IEEE

## II. PROPOSED MODEL

The proposed model can be divided in to 4 major blocks, and the detailed block diagram of the proposed model is depicted in Figure 1.

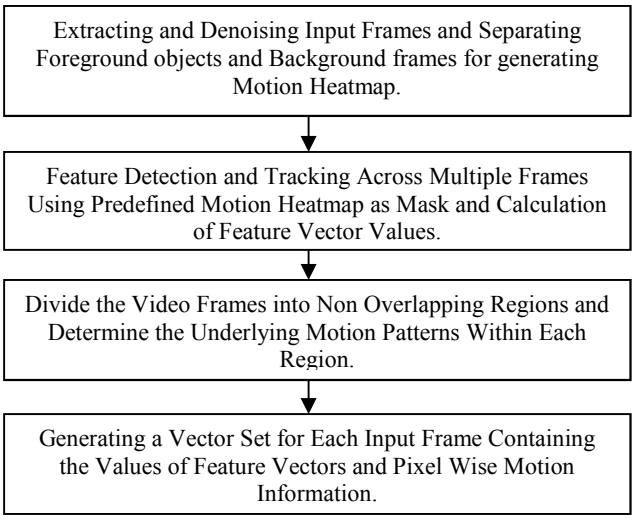


Figure 1: A detailed block diagram of the proposed model.

### A. De Noising Input Frames

First, confirm that you have the correct template for your paper size. This template has been tailored for output on the A4 paper size.

Surveillance videos contain a lot of noise, which might affect the accuracy of analysis. We use pixel wise Non Local Means (NLM) denoising to decrease the amount of blur and noise in the frames [22]. The mathematical equation of NLM is:

$$NLu(p) = \frac{1}{C(p)} \int f(d(B(p), B(q))u(q)\, dq \qquad (1)$$

Where, $d(B(p),B(q))$ represents the Euclidean distance between the image patches with centers respectively at $p$ and $q$, $C(p)$ is the Normalizing factor and $f$ represents the decreasing function. The denoising of a color image $u = (u_1, u_2, u_3)$ and pixel $p$ gives us:

$$\hat{u}_i(p) = \frac{1}{C(p)} \sum_{q \epsilon B(p,r)} u_i(q) w(p,q) \;\; and \; C(p) = \sum_{q \epsilon B(p,r)} w(p,q) \qquad (2)$$

Where $i$ = 1, 2, 3 and $B(p, r)$ represents a region with center at $p$ and size $(2r + 1)^2$pixels. $w(p, q)$ depends on the squared Euclidean distance $d^2 = d^2( B (p, f), B (q, f))$ of the $(2f + 1)^2$ color patches centered at $p$ and $q$.

$$d^2\big(B(p,f), B(q,f)\big) = \frac{1}{3(2f+1)^2} \sum_{i=1}^{3} \sum_{j \epsilon B(0,f)} \big(u_i(p+j) - u_i(q+j)\big)^2 \qquad (3)$$

Each of the pixels is replaced with an average value of the most resembling pixels. Weights $w(p, q)$ is computed using an exponential kernel.

$$w(p,q) = e^{-\frac{\max(d^2 - 2\sigma^2, 0.0)}{h^2}} \qquad (4)$$

(a) (b)

Figure 2: (a) A sample scenario, (b) After Denoising of 2(a) by NLM

Where $\sigma$ represents the standard deviation of the noise and $h$ is the filtering parameter set depending on the value of $\sigma$. Figure 2 gives an example of how NLM denoising works.

### B. Seperating Background Scenes and Foreground Objects

Separating the background from the foreground is a pivotal part of any event detection procedure. The abnormal event most often concerns subjects in the foreground such as people or vehicles, so we need to detect them. In this model we use a Gaussian Mixture-based Background [23] and Foreground segmentation algorithm [24]. This model selects appropriate number of Gaussian distributions for each pixel, which provides better adaptability for varying scenes due to illumination and other changes. This also detects shadows and separates them thus enabling us to ignore the movement of shadows in construction of motion heatmap and improving accuracy. Figure 3 shows an example of how our background/foreground segmentation algorithm works.

(a) (b)

Figure 3:(a) A sample scenario, (b) After Background Subtraction of Figure 3(a)

### C. Motion Heatmap Generation

Motion heatmap refers to a 2D histogram that indicates the regions that experienced any kind of motion activity in the video. Binary blobs of moving objects are extracted after background and foreground separation and later accumulated to form the motion heatmap. Region of Interest (ROI) for the next step is defined from the obtained heatmap which is used as a mask to increase the quality of the result and reduce computation time, especially in case of videos with long duration. The definition of what is normal and what is not might vary depending on the context, i.e. day/night, peak/off-peak hours etc. For example, low traffic on a road during night is considered to be normal, but during office hours it would be considered abnormal. A motion heatmap was built for all the available sample scenarios to

improve the performance of the model. Figure 4(a) shows a sample figure of generated motion heatmap.

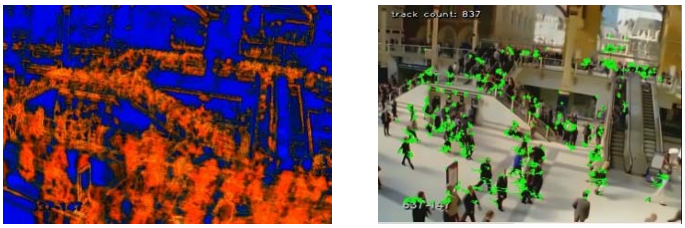


(a) (b)

Figure 4: (a) Generated Motion Heatmap of the loaction of Figure 3(a), (b) Detected Features in Figure 3(a)

### *D. Festure Detection and Tracking*

In this step, we define a set of POIs for each input frame. We use the heatmap obtained in the previous step and use it as a mask to define the ROI. Then we use ORB (Oriented FAST and Rotated BRIEF) feature detector to define the POIs [25]. First, ORB uses FAST (Features from Accelerated Segment Test) to find key points [26].Then the top *n* points are selected using Harris Corner [27]. We use the intensity centroid [28] as a measure of corner orientation. A corner's intensity is assumed to be an offset from its center, and this vector is used to compute an orientation. The moments of the patch are defined as:

$$m_{ab} = \sum_{a,b} j^a, k^b I(j,k) \tag{5}$$

Then the centroid is found using the following formula,

$$c = \left(\frac{m_{10}}{m_{00}}, \frac{m_{01}}{m_{00}}\right) \tag{6}$$

A vector is constructed from center of the detected corner *O* to centroid $\overrightarrow{OC}$, the orientation of the patch then becomes:

$$\theta = atan2(m_{01}, m_{10}) \tag{7}$$

Where, *I(j, k)* is the intensities of the image, *atan2* is the quadrant aware version of arctan. To improve rotation invariance we compute the moments while *j* and *k* remaining in a circular region of radius *g*, which is also chosen to be the patch size so that *j* and *k* run from *(-g, g)*. In our case, we defined *n* to be 500. Then BRIEF(Binary Robust Independent Elementary Features) descriptor is used for describing the identified key points [29], which gives a bit string description for an image patch constructed from a set of binary intensity tests. Let us assume *u* is a smoothed image, a binary test $\tau$ would be defined as equation (8):

$$\tau(u: j,k) = \begin{cases} 1: & u(j) < u(k) \\ 0: & u(j) \geq u(k) \end{cases} \tag{8}$$

Where *u(j)* is the intensity of *u* at point *j*. The feature is defined as vector of *t* binary tests.

$$f_n(u) = \sum_{1 \leq i \leq t} 2^{i-1} \tau(u: j_i, k_i) \tag{9}$$

A Gaussian distribution around the center of the patch was used as test. *t* had a vector length of 256. ORB is rotation invariant and resistant to noise, while it is also efficient and fast compared to other feature descriptors. Being rotation invariant, it can detect the same features from different angles. Once we detect the POIs, we track them across multiple frames. We use Kanade-Lucas-Thomasi feature tracker for this purpose [30, 31]. The key points might change with time. New subjects might enter the frame, or old ones might exit the frame, which will cause our previous key points estimation to be inaccurate. To address this issue, we redefine the points of interests (POI) at a fixed interval *k*. After matching features between the frames, we get a set of vectors for each frame:

$$V = \{V_1, \ldots\ldots, V_n | V_i = (x_i, y_i, d_i, \theta_i, r_i)\} \tag{10}$$

Where, $x_i$ and $y_i$ are coordinates for feature *i*, $d_i$ is the distance between the feature in the previous frame the matched feature in current frame, $\theta_i$ is the orientation or angle of the feature, it has a value between (0, 360) degrees, it is measured in relevance to the image coordinate system, that is in clockwise, $r_i$ is the response by which the strongest key points has been selected. A few static and noise features, i.e. features that moved less than 2 pixels were removed in this step. Noise features have a big angular and magnitude difference with their nearest neighbors. Figure 4(b) shows some detected features from Figure 3(a).

### *E. Identifying Motion Structure*

Identifying the motion structure in an extremely crowded scenario is difficult, because a large number of completely independent activities occur in different part of the frame. The motion between different local areas can be generated by different subjects and can have different rate of changing. However, the motion of the entire frame, such as the motion heatmap we generated earlier, might not always accurately portray the motion patterns of separate independent events going in different parts of the frame. We can isolate the local activities by dividing the video into local spatial-temporal volumes of fixed size. Then we identify a compact motion pattern for each volume, we capture the motion structure of the video [32]. For each input frame, we scale it to three sizes and divide every scaled frame in equal and non-overlapping regions. Corresponding regions in consecutive frames are stacked to form a 3D cube, which is shown in Figure 5. For every *k* frames, we identify non overlapping regions, and for

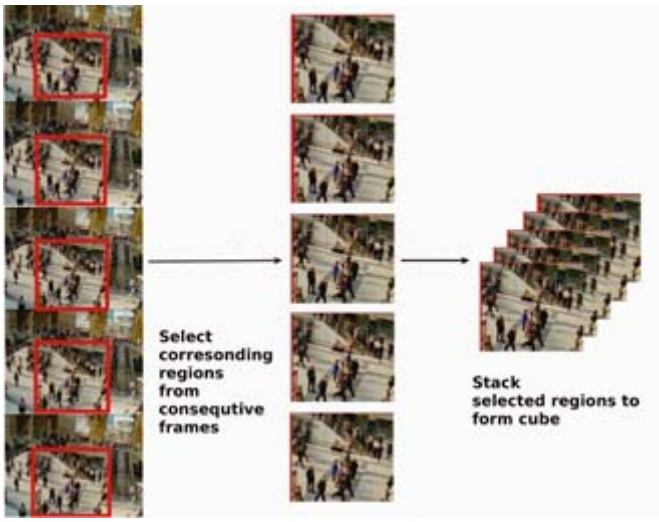


Figure 5: Spatio Temporal Cube Formation

every pixel $p$ in a non-overlapping region $R$, we calculate the spatial-temporal gradient $R_p$ using Sobel derivative function.

$$R_p = [R_{p,v}, R_{p,w}, R_{p,z}]^T = \left[\frac{\partial R}{\partial v}, \frac{\partial R}{\partial w}, \frac{\partial R}{\partial z}\right]^T \quad (11)$$

Where, $v$, $w$, $z$ are the horizontal, vertical and temporal dimensions of the video respectively. The collection of spatial-temporal gradient of every pixel within a region $R$ forms the dominant motion pattern within $R$. We model the gradient distribution as a three dimensional Gaussian distribution $G(\alpha, \beta)$; where,

$$\alpha = \frac{1}{N}\sum_1^N R_p \quad (12)$$

$$\beta = \frac{1}{N}\sum_1^N (R_p - \alpha)(R_p - \alpha)^T \quad (13)$$

Where $N$ is the total number of pixels. After this we have a four dimensional feature vector containing both the set of feature vectors and three dimensional gradient features for each pixel of the video, which we use later for classification purposes.After combining the detected features and underlying motion structure, we can define the final feature vector as:

$$S = \{V, G(\alpha, \beta)\} \quad (14)$$

### *F. Defining Criteria for Seperating Normal and Abnormal Events*

The specific threshold is determined based on comparison between the identified feature vectors and 3D gradient features in both abnormal and normal scenarios, which can be used in later cases in identification of abnormal events. The threshold might change based on camera position, time of the day, location etc. Therefore, special configuration might be necessary to determine the threshold. After we deploy the model, new captured footage once processed and checked for abnormalities, can be used for further learning thus increasing the accuracy with time.

### *G. Setting up Convolutional Neural Network*

Convolutional Neural Networks are a specific type of neural network which specialize in image classification. For our model we use a 2D convolutional neural network, with 1 x 1 shape and 64 output filters. On top of that we apply another 1 x 1 convolution with 32 output filters. We use rectifier activation function in first 2 layers and for the last layer we use SoftMax activation. We use sparse categorical cross entropy as our loss function efficient gradient descent algorithm [32] for optimizer. We use the 200 iterations and a batch size of 10 for CNN.

## III. EXPERIMENTAL SETUP AND RESULTS ANALYSIS

To evaluate the performance of our model, we used three datasets, Web Dataset [33] which contains a set of videos from twenty different urban scenarios, UMN Dataset [34] from University of Minnesota containing 11 scenarios from 3 different places both indoors and outdoors, and UCSD Anomaly Dataset [35, 36] which consists of videos acquired from a camera situated high above pedestrian walkways. These datasets contain various normal and abnormal events in both indoor and outdoor scenes in various times of the day. The events are both temporal and spatial as well as both local and global.

### *A. Experimental Setup*

All experiments were conducted in a personal computer with Intel Core i5 2.80 GHz CPU with 16 gigabytes of RAM with 64 bit Ubuntu 14.04 as operating system. We created a combined data file for all of the datasets containing the feature vectors of all of the frames for videos of the datasets. For each video, frames are extracted and then resized to three scales 20 x 20, 30 x 40 and 120 x 160. Then we divide the frames into 10 x 10 non overlapping regions. And corresponding patches in 5 overlapping frames are then used to form 10 x 10 x 5 3D cubes. For each cube, 3D gradient feature vector is generated. Combined with the features detected using ORB detector, we have a set of 3D feature vectors of shape [2, 2000, 500]. If in any case the number of detected features is not uniform, zeroes are used to make the size uniform. 50% of the generated features are used for training and 50% for testing purposes.

### *B. Experimental Result Analysis*

Performance of the proposed model for different datasets is depicted in Table 1.

TABLE I. ACCURACY OF CLASSIFICATION OF PROPOSED MODEL IN DIFFERENT DATASETS

| Dataset | Accuracy (%) |
|---|---|
| Web Dataset | 97.34 |
| UCSD Dataset | 94.28 |
| UMN Dataset | 96.74 |

The proposed model shows steady performance for all datasets and achieves an average accuracy of 96.12% for all datasets.

We tested our model with various classifiers and found out that CNN shows the best accuracy. Figure 6 shows the comparison among the accuracies in a bar chart form. CNN performs better with increased amount of data and specializes in processing visual data which increases the overall accuracy. CNN allows the networks to have fewer weights since these are shared between the neurons, and uses convolutions to increase the accuracy of the analysis.

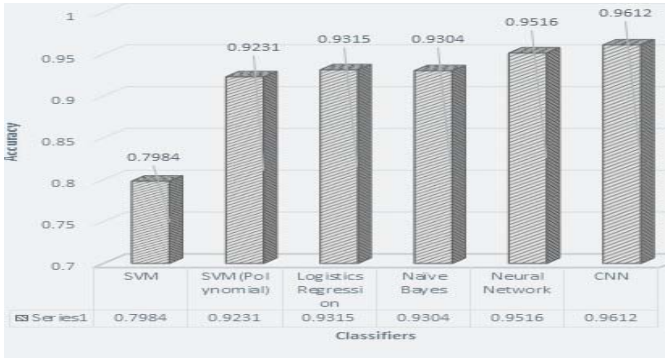


Figure 6: Comparison of performance among various classifiers

TABLE II. COMPARISON OF PERFORMANCE AMONG PROPOSED MODEL AND OTHER EXISTING MODELS

| Model | Accuracy (%) |
|---|---|
| Sparse Representation [2] | 46 |
| Sparse Representation+ LSDS(Large Scale Dictionary Selection) [2] | 46 |
| Pure Optical Flow [15] | 84 |
| Social Force Model [15] | 96 |
| Object Based Method [17] | 90.9 |
| Spatio-Temporal Co-Occurences [17] | 100 |
| Our Proposed Model | 96.12 |

Table 2 shows a comparison between the performance of our proposed model and various other existing models on some of the prominent video datasets in identifying abnormal events. Proposed model outperforms all other existing models except Spatial-Temporal Co-Occurrence method proposed by Benezeth *et al.* [17], which achieves 100% accuracy. But it's only been tested with singular events like illegal U-turns or abandoned luggage. But our proposed model can also detect overall abnormal situations based on overall behavior of the crowd or subjects within the video frame like an empty road in rush hour, or abnormal traffic during non-peak hours, people running or moving in higher speed than usual etc. Our model also identifies one or multiple separate events occurring in various regions of the video frame since it considers overall motion pattern as well as pixel wise motion information. For example, an accident occurring in one corner of a crowded place would be easily detected from the footage. In figure 6 we compared the performance of our model with various classifiers to justify the use of Convolutional Neural Networks. We tested our model with various classifiers to achieve the best accuracy and finally choose CNN based on the results.

## IV. CONCLUSIONS

In this paper we propose a pattern recognition method to determine abnormal situations in crowded scenarios. We proposed a model which can successfully identify both local and global abnormal models in temporal and spatial scenarios. The model is self-sufficient as once it is deployed with preliminary training it can further increase its accuracy by using the captured footages for learning as well. Our model calculates a motion heatmap of the region which is later used as mask for detecting and tracking features across multiple frames, while also dividing the video frame into multiple non-overlapping regions and calculating motion pattern within each separate region. Our model shows significant improvement over the previously proposed models in accuracy. It is also portable meaning it can be deployed in any situation with just a few days prior training to detect events, because it trains itself with time.

## REFERENCES


[1] Yen S-H, Wang C-H, "Abnormal Event Detection Using HOSF," 2013 International Conference on IT Convergence and Security (ICITCS)

[2] Cong Y, Yuan J, Liu J., "Abnormal event detection in crowded scenes using sparse representation," Pattern Recognition. 2013, vol. 46, no. 7, pp. 1851–64.

[3] Avidan S. Ensemble Tracking, "Ensemble Tracking," 2005 IEEE Computer Society Conference on Computer Vision and Pattern Recognition, 2005

[4] Cong Y, Gong H, Zhu S-C, Tang Y., "Flow mosaicking: Real-time pedestrian counting without scene-specific learning," 2009 IEEE Conference on Computer Vision and Pattern Recognition. 2009

[5] Dalal N, Triggs B. "Histograms of Oriented Gradients for Human Detection," 2005 IEEE Computer Society Conference on Computer Vision and Pattern Recognition.

[6] Stauffer C, Grimson W., "Adaptive background mixture models for real-time tracking," 1999 IEEE Computer Society Conference on Computer Vision and Pattern Recognition.

[7] Yuan J, Liu Z, Wu Y., "Discriminative subvolume search for efficient action detection," 2009 IEEE Conference on Computer Vision and Pattern Recognition.

[8] Ma R, Li L, Huang W, Tian Q., "On pixel count based crowd density estimation for visual surveillance," IEEE Conference on Cybernetics and Intelligent Systems, 2004.

[9] Marana A., "Estimation of crowd density using image processing," IEE Colloquium on Image Processing for Security Applications. 1997.

[10] Rahmalan H, Nixon M, Carter J., "On crowd density estimation for surveillance," IET Conference on Crime and Security. 2006.

[11] Bazmi A, Faez K., "Increasing the Accuracy of Detection and Recognition in Visual Surveillance," International Journal of Electrical and Computer Engineering, vol. 2, no. 3, 2012.

[12] Tannouche A, Sbai K, Rahmoune M, Agounoun R, Rahmani A, Rahmani A., "Real Time Weed Detection using a Boosted Cascade of Simple Features," International Journal of Electrical and Computer Engineering (IJECE). 2016, vol. 6, pp. 6, 2755.

[13] Rani NS, P. NO, Ponnath N., "Automatic Vehicle Tracking System Based on Fixed Thresholding and Histogram Based Edge Processing," International Journal of Electrical and Computer Engineering, vol.:8, pp. 69-78, 2015.

[14] V, J, S., "Detecting pedestrians using patterns of motion and appearance," Proceedings Ninth IEEE International Conference on Computer Vision. 2003.

[15] Mehran R, Oyama A, Shah M., "Abnormal crowd behavior detection using social force model," IEEE Conference on Computer Vision and Pattern Recognition, 2009.

[16] Zhong H, Shi J, Visontai M., "Detecting unusual activity in video," Proceedings of the 2004 IEEE Computer Society Conference on Computer Vision and Pattern Recognition, 2004

[17] Benezeth Y, Jodoin P-M, Saligrama V, Rosenberger C., "Abnormal events detection based on spatio-temporal co-occurences," 2009 IEEE Conference on Computer Vision and Pattern Recognition
[18] Ihaddadene N, Djeraba C., "Real-time crowd motion analysis," 2008 19th International Conference on Pattern Recognition
[19] Ali S, Shah M. A, "Lagrangian Particle Dynamics Approach for Crowd Flow Segmentation and Stability Analysis," 2007 IEEE Conference on Computer Vision and Pattern Recognition.
[20] Andrade E, Blunsden S, Fisher R., "Hidden Markov Models for Optical Flow Analysis in Crowds," 18th International Conference on Pattern Recognition, 2006.
[21] Andrade E, Blunsden S, Fisher R., "Modelling Crowd Scenes for Event Detection," 18th International Conference on Pattern Recognition, 2006.
[22] Buades A, Coll B, Morel J-M., "Non-Local Means Denoising," Image Processing On Line, vol. 1, 2011.
[23] Zivkovic Z. "Improved adaptive Gaussian mixture model for background subtraction," Proceedings of the 17th International Conference on Pattern Recognition, 2004 ICPR 2004.
[24] Zivkovic Z, Heijden FVD, "Efficient adaptive density estimation per image pixel for the task of background subtraction," Pattern Recognition Letters. 2006, vol. 27, no. 7, pp. 773–80.
[25] Rublee E, Rabaud V, Konolige K, Bradski G. ORB, "An efficient alternative to SIFT or SURF," 2011 International Conference on Computer Vision.
[26] Rosten E, Drummond T., "Machine Learning for High-Speed Corner Detection," Computer Vision – ECCV 2006 Lecture Notes in Computer Science, 2006, pp. 430-443.
[27] Harris C, Stephens M., "A Combined Corner and Edge Detector," Procedings of the Alvey Vision Conference, 1988.
[28] Rosin PL., "Measuring Corner Properties. Computer Vision and Image Understanding," 1999, vol. 73, no. 2, pp. 291-307.
[29] Calonder M, Lepetit V, Strecha C, Fua P., "BRIEF: Binary Robust Independent Elementary Features," Computer Vision –ECCV 2010 Lecture Notes in Computer Science, 2010, pp. 778-92.
[30] Shi J, T., "Good features to track," Proceedings of IEEE Conference on Computer Vision and Pattern Recognition CVPR-94. 1994.
[31] Lucas B.D., Kanade T., "An iterative image registration technique with an application to stereo vision," International Joint Conference on Artificial Intelligence, pp.674-679.
[32] P.Kingma, D., Ba, J. L. (2015). Adam: A Method For Stochastic Optimization. ICLR
[33] Kratz L, Nishino K., "Anomaly detection in extremely crowded scenes using spatio-temporal motion pattern models," 2009 IEEE Conference on Computer Vision and Pattern Recognition. 2009.
[34] Web dataset of unusual crowd activity, available at http://crcv.ucf.edu/projects/ Abnormal_Crowd/Normal_Abnormal_Crowd.zip
[35] Unusual crowd activity dataset of University of Minnesota, available from http://mha.cs.umn.edu/movies/crowd-activity-all.avi.
[36] UCSD anomaly dataset available at http://www.svcl.ucsd.edu/projects/anomaly /UCSD_Anomaly_Dataset.tar.gz

2017 3rd International Conference on Electrical Information and Communication Technology (EICT), 7-9 December 2017, Khulna, Bangladesh

# Design, Kinematic and Performance Evaluation of a Dual Arm Bomb Disposal Robot

Akib Jayed Islam[1*], Sadman Shahriar Alam[2], Khandoker Tanjim Ahammad[3], Fazllul Karim Nadim[4], Bithi Barua[5]
[1,4]Department of EEE, American International University-Bangladesh (AIUB), Dhaka, Bangladesh
[2]Department of Electronic Systems, Norwegian University of Science & Technology, Norway
[3]Department of Microelectronics and Microsystems, Technische Universität Hamburg, Germany
[5]Dept. of Electronics and Communication Engineering (ECE), Khulna University of Engineering & Technology, Bangladesh
*E-mail: akibjayedislam@gmail.com

*Abstract*— **This paper presents a dual arm bomb disposal robot that is designed to assist bomb disposal unit. Bomb disposal robot has been developed by different experts around the world to make an affordable and safe device designed to be used in emergency situations. Two segmented robotic arms (3 DOF and 3 DOF) are installed on a portable base with an IP camera to dispose bomb safely and easily from distance. The proposed model is controlled wirelessly with its main function to replace human in bomb disposal operation. The unique design and notable features introduced in this prototype add a new dimension in bomb disposal technology. Simulation-based direct kinematics is used to analyze performance along with mathematical modeling of the dual arm to develop an efficient, mobile and safe bomb disposal robot.**

***Keywords— Bomb Disposal, Dual Arm, Degrees of freedom (DOF), Kinematic***

## I. INTRODUCTION

The performances of robots with constant speed, accuracy and efficiency regardless the restrictions have made human lives more dependent on robots. With recent developments in the field of robotics, human behavior can be studied in details by the robots and can be imitated accordingly without the person's presence [1]. As the study of robotics is quite extensive, it requires different software development, multipurpose design, and persistent communication system. To reduce the human interference with life risking jobs, electronics devices as well as the programming languages are being developed to elevate the effectiveness of robots [2]. Although robotics has been developed significantly in the field of industry, life-threatening tasks such as disposing of bombs have been given immense priority in the research field only during past few years.

The current situations of bomb-disposing robots are not up to the mark in the developing countries due to factors such as high purchasing and maintenance cost. On the other hand, the first world countries have already added bomb disposal robots units more effectively even though the average cost of these bomb-disposing robots are very high [3]. The main reasons for third world countries to lack behind in this field are high costs electronic devices, restrictions on technological knowledge and lack of social awareness. Statistical data represents that, although the percentage of criminal activities has increased in the past few decades, the dependency on these types of robots have not been increased. Meanwhile, measures need to be taken on the issue as it is closely related to human lives. But due to higher production cost, it is not possible for all to afford such technology [4]. The robot which is proposed in this paper can be a solution of these problems in terms of its reliability, affordability, and features that reduce risks on human life. In recent years, several kinds of robots have been developed to perform in various extents such as autonomous navigated mobile robot [5], robots for boisterous gravel path [6-7], navigation and camera tacking systems [8], bomb disposing robots [9] with automatic navigation technology are already serving in different extent [10-11]. With highly equipped systems, the robots proposed in these papers are expensive.

A bomb disposal robot with 6 DOF single arm is presented in the literature [12]. The limitations of this literature are servo motor could not rotate smoothly because of the low PWM resolution and only one command is possible to send at the receiver end which means two movements are not possible to execute at a time by the servomotor. Literature [13] focuses on design and performance analysis of a low cost bomb-disposal robot named 'Muktibot'. The robot is subjected to various simulation test as well as real life experiment for evaluating the overall performance. The control and performance of the robot are satisfactory but no kinematic evaluation of this two degrees of freedom (DOF) bomb disposal robot are introduced in the paper.

Few techniques from previous research papers [12-20] are studied and an effort is made to reduce the limitation while designing the prototype with new modified techniques are shown in next segments. The limitations of these papers are overcome in this study. The dual arm, which is one of the unique designs in this study, ensures the precise workability. A mathematical formula is introduced to test the robot's performance. Life safety is the main purpose to build a robot and to do so it is mandatory to create an era to remote control system form bomb disposal robot. The cost of a prototype model comes second considering human safety. The model proposed by our team guarantees full safety during a bomb disposal mission. The robot is controlled wirelessly to ensure

978-1-5386-2307-7/17/$31.00 ©2017 IEEE

the security and to help the bomb disposal units. The notable design, performance and low cost of the prototype robot are designed to replace human life risk. The purpose of this big challenge is to find a trade of value with minimum cost with maximum efficiency along with a good environment to secure the betterment of mankind.

The rest of the paper is organized as follows. Simulation and hardware model design of the bomb disposal robot is discussed in section II. Section III summarizes the modeling and the architectural development of the robot where the mathematical modeling for different inverse kinematic and its performances are analyzed. In section IV, the design of the controller and the implementation of the prototype are discussed and explained to check the versatility of the robot. Cost analysis of the proposed model is explained in this section. Conclusion as well as future developments have been suggested in the last section.

## II. PROTOTYPE DESIGN

The prototype is designed with a dimension of a width of 33 cm, length 30cm and height 10 cm. First, a model is designed in the SOLIDWORKS software as shown in Fig.1. After the simulation of the design, the hardware is assembled. The base, the robotic arm and the wire cutter have been designed using polycarbonate sheet and aluminum angle. The design of the robotic arm is established considering the power to weight ratio as it has to be light enough to be moved by the DC motors and strong enough to be able to move nominal weights. A small IP camera is mounted at the upper part of the robotic arm for live feed.

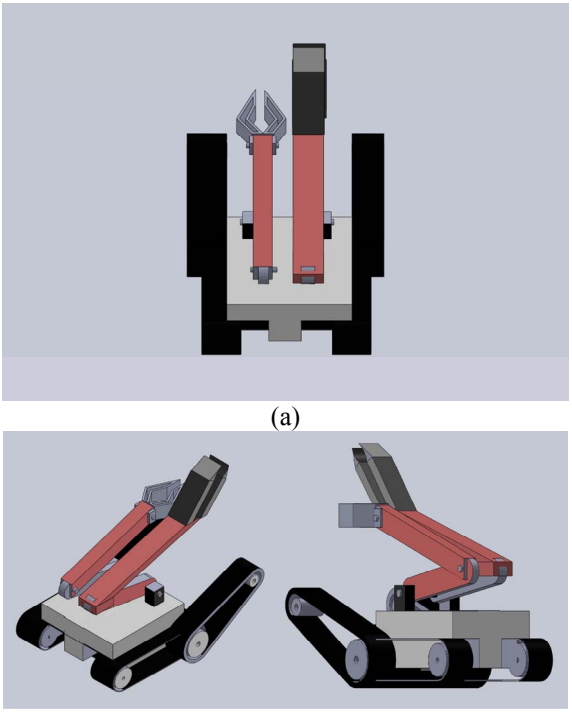

(a) (b) (c)

Fig. 1. Simulation prototype design (a) Top View (b) Left view (c) Right View

The wire cutter is constructed in a way that it will help to cut the wire perfectly. The dual arm of this prototype added a new dimension for disposing bomb easily. Two metallic strips have been installed onto a circular plate where a servomotor for the shoulder is mounted. The next joint is the elbow where a servomotor is connected and responsible for the pitch of the robotic arm. This servomotor controls the vertical movement of the arm. The movement of the gripper is controlled by a servomotor which is connected to the final joint. The gripper has two fingers using which it can pick up objects with ease. The robot can climb stairs due to its elevated continuous tracks and can perform a complete 360 degree rotation.

RF transmitter and receiver are used to control it. The total setup weight is about six kilograms. The robotic arm and the wire cutter both have three degrees of freedom (DOF). As a result, the robot can be moved to go up and go down to cut wire. The unique design and several methodologies are implemented so that the experiment can be reliable. To ensure the prototypes efficiency, few mathematical formulas was applied. The control panel consists of a radio transmitter and an Arduino board. Different other electronic components are used to precise the control system. To simulate the result, set of practical data was used. After examining the final result, a conclusion could be assumed that the practical system is a sustainable one.

## III. MATHEMATICAL MODELING FOR KINEMATICS

Since the robot is designed to be in a sensitive environment, the robot must have accurate and precise control over its movement as well as the movement of the arms. The robot accommodates two separate arms as it allows more control over a more difficult situation. The main arm which has 3 degrees of freedom allows a finer control of handling the bomb or removing objects in the way. The second arm is simply fit with a wire cutter which is used for cutting the wires connected to the timer of the bomb. The main arm holds the bomb firmly and brings out the wire that needs to be severed. Before designing the main arm, its kinematic structure was studied. The arm has two rotational joints and the third rotation comes from the movement of the rover around its axis.

For simulating the kinematics of the arm, the following flowchart was followed

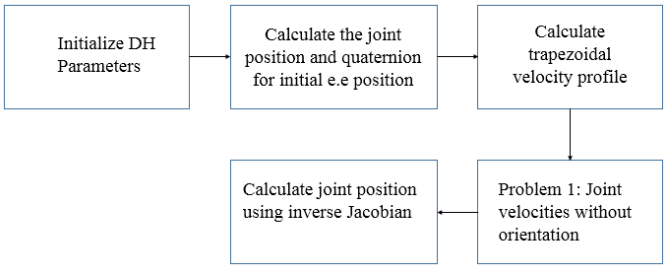


Fig. 2. Flowchart showing kinematics Simulation of the arm

The manipulator used in our case can be considered as a planar arm manipulator. It can be schematically represented from a mechanical viewpoint as a kinematic chain of links connected by means of revolute joints. One end is connected to the robot's frame while the other holds a mechanical gripper for grasping objects and this whole structure forms a kinematic chain. For the case of moving around the end effector of the arm, we are more interested in the final position of the end effector. Since the end effector can only be controlled by means of altering the degrees of the joint variables, direct kinematics allows the calculation of the final position based on the values of the joint variables. For calculation of the transformation matrix, in this project, the Denavit Hartenberg convention was used to find the final transformation matrix for the end effector from its initial position to its final position. DH convention allows the construction of direct kinematics function by composition of the individual coordinate transformations into a single homogeneous transformation matrix [21]. This allows the calculation of the open chain kinematics chain. One crucial aspect of DH convention is its ability to describe a rotation and translation matrix in terms of 4 parameters only for each link compared to the 6 parameters from a rotation matrix. The D-H parameter list for the main arm is as follows.

**TABLE I. D-H PARAMETER LIST OF THE MAIN ARM**

| Link | $a_I$ [m] | $\alpha_i$ [rad] | $d_i$ [m] | $\Theta_i$ [rad] |
|---|---|---|---|---|
| 1 | 0 | 1.57 | 0 | 0 |
| 2 | 1 | 0 | 0 | 0.7854 |
| 3 | 0.8 | 0 | 0 | -1.57 |

This DH table represents the posture of the arm in initial condition. With the initial position set, now, in order to move the arm to a new position, the joint variables must be changed accordingly. In order to have a smooth movement of the arm, a trapezoidal velocity profile is followed. A trapezoidal velocity profile is created over the total simulation time where the end effector slowly accelerates until the cruise velocity is achieved. The end effector then maintains a constant cruise velocity over the cruise time and then again finally de-accelerates constantly until the final position of the end effector is met.

Given, the initial and final position of the end effector and the total simulation time, the cruise velocity for the entire duration was calculated using the following formula.

$$\frac{|x_f - x_i|}{t_f} < |\dot{x}_c| \leq \frac{2|x_f - x_i|}{t_f} \quad (1)$$

Where, $x_f$ is the final desired position and $x_i$ is the initial position and $t_f$ is the simulation time for calculation the trapezoidal velocity profile and $x_c$ is the calculated cruise velocity.

From the Fig. 3, it can be seen the end effector follows a trapezoidal velocity profile, hence allowing a smooth movement and control of the end effector. Following such a smooth velocity profile is necessary especially in a sensitive environment. With the DH parameters initialized, now the next goal is to utilize inverse kinematics to find back the joint variables for every value of the desired position path taken following the trapezoidal velocity profile.

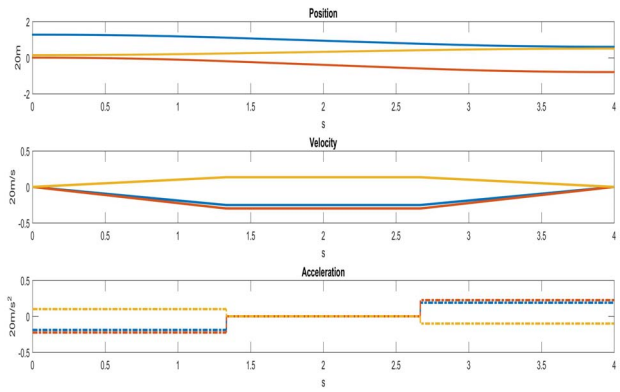


Fig. 3. Position, Velocity and Acceleration of the end effector following a trapezoidal velocity profile

Now for the mapping of the joint velocities which contributes to the overall velocity of the end effector, differential kinematics is used, The matrix that performs this mapping is known as the Jacobian Matrix given by J. The goal of utilizing differential kinematics is to allow the calculation of the relationship between joint velocities and end effector linear and angular velocity. Since orientation is not an issue for our work, only the linear velocity was taken into account.

In the following equation, $\dot{q}$ is the joint velocities and J(q) represents the Jacobian matrix. $v_e$ gives the overall angular plus linear velocity of the end effector. $J_P$ is only calculated as we are only interested in the linear velocity of the end effector given by $\dot{p}_e$

$$\dot{p}_e = J_{p(q)}\dot{q} \in R^3 \quad (2)$$

$$\omega_e = J_{o(q)}\dot{q} \in R^3 \quad (3)$$

$$v_e = \begin{bmatrix} \dot{p}_e \\ \omega_e \end{bmatrix} = \begin{bmatrix} J_{p(q)} \\ J_{o(q)} \end{bmatrix} = J_{q(\dot{q})} \quad (4)$$

Similarly, inverse Jacobean can be used to find back the joint velocities from the end effector velocity, $\dot{p}_e$, found from the trapezoidal velocity profile.

Joint velocity was computed using the following equation,

$$\dot{q} = J_A^{\dagger}(\dot{x}_d + K_e) \quad (5)$$

Where, $\dot{x}_d$ is the partial derivative of the desired position. And 'e' is the error between the computed translation and the

desired position of every frame. From the Fig. 4 it can be seen how the X, Y and Z axis error decreases over time for the end effector following the trapezoidal velocity profile.

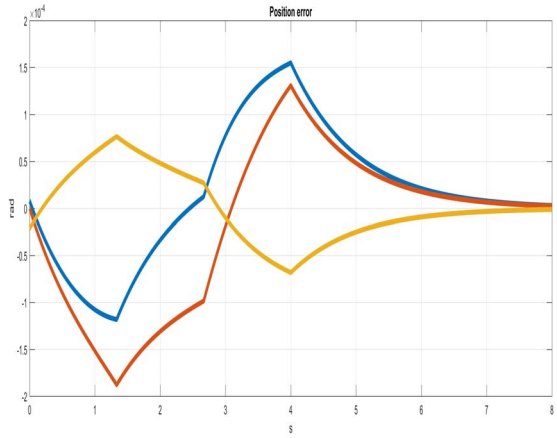


Fig. 4. Position error of the end effector

With the joint velocities calculated, the joint positions were found using the usual distance formula

$$q_i = q_{i-1} + T_s * \dot{q}_i \qquad (6)$$

This gave the values of each joint variable which was updated after every frame. This update of the joint variables for every frame contributes to the movement of the end effector following the trapezoidal velocity path.

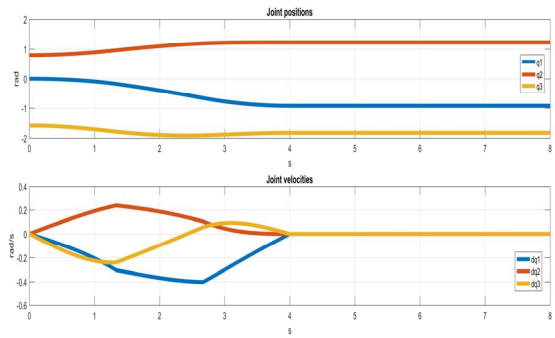


Fig. 5. Joint positions and joint velocity of simulation

The Fig. 5 represents the change in the values of each joint and the corresponding joint velocity over the time of simulation. The final joint position is reached when the joint velocity converges to zero.

The Fig.6 shows the initial and final position of the end effector of the robotic manipulator. From this kinematic study, we conclude that our arm is designed to have smooth and accurate motion and can be used to hand sensitive objects such as a bomb safely.

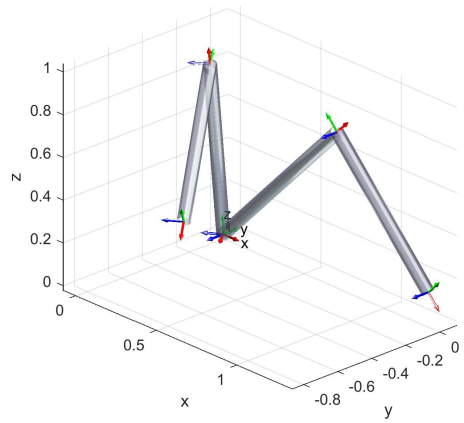


Fig. 6. Initial and final position of the end effector

## IV. CONTROLLER DESIGN & PERFORMANCE EVALUATION

Radio transmitter is used to control the robot. It is advantageous to use Radio Frequency (RF) because it covers a moderate distance and it is user friendly to setup with directional properties. Although Radio frequency is not entirely blocked by walls but obstructions can disrupt it. The faults of a wired system are like a handicap system which is diminished by the robustness of wireless radio frequency technology. Wireless transmission system can be used to control bomb disposal robots by operating it to perform the tasks with ease. Here, an electromagnetic wave is transmitted remotely to the receiver end. The device can be controlled manually from a distance place if that is connected to the receiver end. It can dispose any bomb or any explosive elements by pulling out the battery or cutting any wire with precision. The circuit area can be reduced by using the process of integration in the form of RF filtering function [22].

In the design, the Hobby King 6 Channel 2.4 GHz radio transmitter and receiver module is used. Only two out of six channels was allocated for helping the mobility of the robot. One channel was allocated for the forward and backward movement while another channel was used to move the robot sideways. The radio transmitter module data is sent to the receiver module while two channels are connected to the analog pins of the Arduino. The four motors speeds are controlled by the two motor driver ICs.

The two other channels are used to control the servo motor which is connected in the robotic arm. One robotic arm has three DOF which is designed to pick up any object with the gripper perfectly. Another arm of the robot is used as a wire cutter. The sharp edge of the wire cutter helps the robot to cut the wire completely.

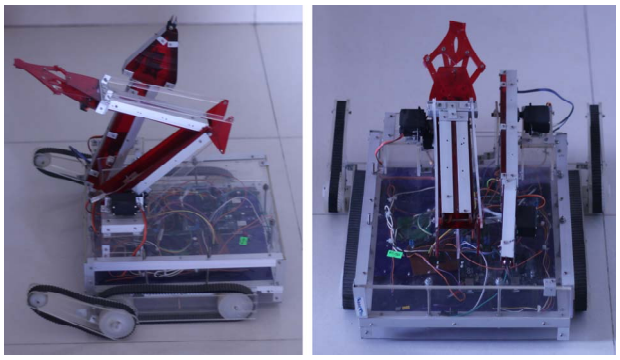

Fig. 7. Practical Prototype of Bomb Disposal Robot

The practical demonstration of the proposed model certifies its sustainability, reliability and efficiency. The final practical prototype of the bomb disposal robot is shown in Fig. 7. The high performance motors and the continuous track help the prototype to move on any surface. The advantage of using IP camera is that it enables human to observe things without being there physically. But it is most unfortunate for developing countries to afford such costly robot. The cost analysis of the prototype model is shown in table below

**TABLE II. COST ANALYSIS OF THE PROTOTYPE MODEL**

| Serial No. | Components | Price |
|---|---|---|
| 1. | Frame of the Model | $25 |
| 2. | Battery, Arduino, IP Camera, Radio Transmitter & Receiver | $85 |
| 3. | DC & Servo Motors, Motor Drivers | $70 |
| 4. | Robotic Arms and Continuous Track | $50 |
| 5. | Miscellaneous | $20 |
| | Total | $250 |

## V. FUTURE WORK AND CONCLUSIONS

The state of art design of the proposed dual arm bomb disposal robot will be suitable for disposing of the bomb because of its feasibility, DOF, dexterity. The low cost of the robot will increase the availability in the developing country. Further studies will help researchers for the benefit of mankind. The available bomb disposal robots have been investigated in detail before the hardware implementation of the prototype, it is tested in wireless manner with the operator center successfully. The experimental results ensure the system a sustainable one. Besides the IP camera, this robot can also be integrated with depth sensors which can allow a more informative scan of the environment around the robot's surroundings. Modern 3D scanning software is now able to use open source libraries and cheap Kinect sensors to reconstruct 3D models efficiently [23]. With the availability of such complete systems, a 3D visualization of the environment can also be added without increasing the overall cost. Finally, the proposed model can be implemented in real life applications.


## ACKNOWLEDGMENT

Authors would like to express gratitude to Mr. Tajwar Abrar Aleef, who is currently enrolled in Erasmus Mundus Joint Master Degree in Medical Imaging and Applications program, for his invaluable guidelines for exploring the facets of this work.


## REFERENCES


[1] Lin, Hsien-I., Yu-Cheng Liu, and Chi-Li Chen. "Evaluation of human-robot arm movement imitation." In *Control Conference (ASCC), 2011 8th Asian*, pp. 287-292. IEEE, 2011.

[2] Nikku, S. "Introduction to Robotics." (2011).

[3] Dallas Police's 'Bomb Robot' Raises Sticky Questions. [Online]. Available: www.huffingtonpost.com

[4] Navy to purchase MMP-30 bomb-disposal robots from The Machine Lab for use in Afghanistan. [Online]. Available: www.militaryaerospace.com/articles/2013/06/navy-bomb-robots.html

[5] S. Ginzburg, "Design and development of an autonomous navigation system for an omni-directional four-wheeled mobile robot," Master of Applied Science in Mechanical Engineering, Bachelor of Engineering, University of Ontario Institute of Technology, January 2012.

[6] P. Ben-Tzvi, S. Ito and A. A. Goldenberg, "A mobile robot with autonomous climbing and descending of stairs," Robotica, Cambridge University Press, United Kingdom, vol. 27, pp. 171-188, April 2008.

[7] I. Waheed and R. Fotouhi, "Trajectory and temporal planning of a wheeled mobile robot on an uneven surface," Robotica, Cambridge University Press, United Kingdom, vol. 27, pp. 481-498, Agust 2008.

[8] U. Gürel, "Navigation and camera tracking system for mobile robots" ("Gezgin robotlar için seyrüsefer ve kamera takip sistemi"), Master of Science Thesis, Osmangazi University Institute of Science, Eskişehir, June 2006.

[9] T. Denewiler, "Robot traffic school: Improving autonomous navigation in EOD robots," Master of Science, University of California, San Diego, 2011.

[10] N. R. Lavallee, "A multi-sensor system for a mobile robot for determining object location", Master of Science in Mechanical Engineering, University of Rhode Island, United States of America, 2012.

[11] E. S. Olson, "Analysis and design of a two-wheeled robot with multiple user interface inputs and vision feedback control", Master of Science in Mechanical Engineering, University of Texas at Arlington, United States of America, August 2010.

[12] A. K. B. Motaleb, M. B. Hoque and M. A. Hoque, "Bomb disposal robot," *2016 International Conference on Innovations in Science, Engineering and Technology (ICISET)*, Dhaka, 2016, pp. 1-5.

[13] H. U. Zaman *et al.*, "Design, control & performance analysis of Muktibot," *2016 IEEE 7th Annual Information Technology, Electronics and Mobile Communication Conference (IEMCON)*, Vancouver, BC, 2016, pp. 1-4.

[14] Judith L. Mwakalonge, Judy A. erkins, Erick C. Jones, Investigating Radio Frequency Identification (RFID) for Linear Asset Management, South Carolina State University, Orangeburg, USA, Public Works Management Policy April 2014 vol. 19 no. 2 164-179

[15] Ahmed El Oualkadi, J-M Paillot, Hervé Guegnaud, Rachid Allam, A novel Q-enhanced LC switched-capacitor bandpass filter for digital wireless RF applications, Radio Frequency Integrated Circuits (RFIC) Symposium, 2004. Digest of Papers. 2004 IEE, pp 659-662

[16] Y. M. (n.d.). The Bluetooth Based LED Control for Arduino Test Platform by Using Mobile APP. INTERNATIONAL JOURNAL OF SCIENTIFIC & TECHNOLOGY RESEARCH, 4(06), june 2015. ISSN 2277-8616

[17] Piyare, R. and Tazil, M. (2011) "Bluetooth Based Home Automation System Using Android Phones". IEEE 15TH International symposium on consumer electronics (ISCE), 14-17 june 2011, Singapure.

[18] DiVerdi, Rocco. "Miniature Robotic Hand for Bomb Disposal." (2012).

[19] Patoliya, Jignesh, Haard Mehta, and Hitesh Patel. "Arduino controlled war field spy robot using night vision wireless camera and Android application." 2015 5th Nirma University International Conference on Engineering (NUiCONE). IEEE, 2015.

[20] Narayanan, Siddharth, and C. Ramesh Reddy. "Bomb Defusing Robotic Arm using Gesture Control." International Journal of Engineering Research and Technology. Vol. 4. No. 02 (February-2015). ESRSA Publications, 2015.

[21] Siciliano, B., Sciavicco, L., Villani, L. and Oriolo, G., 2009. Robotics: modelling, planning and control, ser. Advanced Textbooks in Control and Signal Processing. *Springer*, *26*, p.29.

[22] El Oualkadi A, Paillot JM, Guegnaud H, Allam R. A novel Q-enhanced LC switched-capacitor bandpass filter for digital wireless RF applications. InRadio Frequency Integrated Circuits (RFIC) Symposium, 2004. Digest of Papers. 2004 IEEE 2004 Jun 6 (pp. 659-662). IEEE.

[23] Khawaldeh, S., Aleef, T. A., Pervaiz, U., Minh, V. H., & Hagos, Y. B. (2017). Complete End-To-End Low Cost Solution to a 3D Scanning System with Integrated Turntable. International Journal of Computer Science & Information Technology (IJCSIT), Volume 9, Number 4.

# A Comparative Analysis of PI and PID Controlled Bidirectional DC-DC Converter with Conventional Bidirectional DC-DC Converter

[1]Remon Das, [1]Humayun Rashid,[1] Iftekhar Uddin Ahmed
[1]Electrical and Electronic Engineering (EEE), International Islamic University Chittagong (IIUC), Chittagong-4314, Bangladesh
Email: remondas3@gmail.com

***Abstract*— The significance of the bidirectional DC to DC converter topologies is obtaining importance day by day due to the fact of the uncomplicated framework as well as its straightforward operation capability. This paper presents a comparative analysis between three Bidirectional DC to DC topologies of traditional, PI and PID controlled converter. It has been proved that Bidirectional DC-DC converter with PI controller is more efficient, comparatively with conventional and PID controlled topologies because of rhe stable output voltage given by the PI Controlled topology. The comparative analysis has been demonstrated in this paper to determine an efficient converter to achieve low steady state error and higher efficiency.**

***Keywords*— PI; PID; Conventional;Bi-Directional DC-DC Converter, Boost mode; Buck mode**

## I. Introduction

Bi-Directional DC to DC controllers are generally utilized to convert the energy in between a couple of DC sources in either course utilize in power supply charging as well as discharging as well as for stabilizing the voltage at the output[1]-[3]. Traditionally, PI, and PID controller happen to be most preferred controllers [4] as well as extensively employed in a large number of power electronic equipment because of its capability to be controlled in the buck mode and boost mode with different configuration and circuit arrangement [5]-[6]. Nevertheless, downsides of the traditional bidirectional dc-dc converter show significant transitioning deficits as well as the lengthy invert recuperation period of antiparallel diodes. In particular, throughout the restoration period of the diodes, it can be triggered by circuit deterioration as well as electromagnetic disturbance complications because of to excessive current surges [7]-[8].

In this paper, A Comparative Analysis of PI and PID Controlled Bidirectional DC-DC Converter with Conventional Bidirectional DC- DC Converter has been discussed for determination of the efficiency of different controllers. The simulation has been done using Simulink and the result was analyzed for determination of the converter with higher efficiency for achieving low steady state error.

## II. Modeling Of PI Controlled Bidirectional Dc - Dc Converter

### A. Designing of PI Controlled Converter

*a) Conversion of input:* The very first stage deals with the transformation of input DC into AC. A full bridge inverter circuit is certainly employed for execution of this particular steps as signifies in figure 1(a) which inverters the DC voltage into AC voltage. The inverter circuit comprises of four IGBT switches as well as passive components.

*b) Conversion of input Interfacing a Transformer:* In the following stage, a transformer is cascaded along with the Inverter circuit as demonstrated in Figure 1(b). The inverter circuit cascaded with a transformer is utilized to transforms the provided AC voltage to the preferred AC voltage.

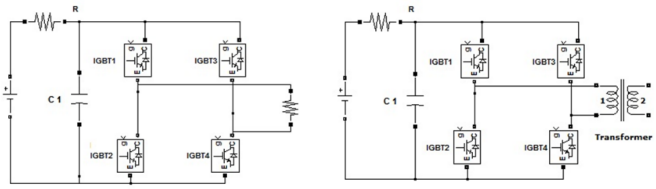


(a) (b)

Fig. 1. (a) Inverter (b)Inverter cascade with Transformer

*c) Development of Rectifier Circuit:* In phase three, A rectifier circuit is designed as well as linked to the secondary side of the transformer as demonstrated in figure 2. The intention of the cascaded rectifier circuit with the secondary side of the transformer is to transform the AC to DC voltage as well as a filter circuit is utilized for smoothing the DC voltages which is one of the key parts to complete Bidirectional DC to DC converter. Eventually, the designed system is composed of an input section, an inverter section, a rectifier section and an output section.

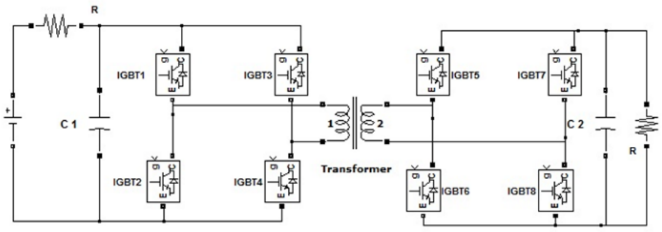


Fig. 2. Bidirectional DC to DC converter circuit without control circuit

*d) Development of PI control* Circuit:Designing a PI control circuit for delivering the triggering pulse to the IGBTS is essential as well as the control circuit is coupled along with either sides of the transformer.Figure 3 signifies the arrangement of a PI controlled bidirectional topology.

The circuit comprise with three differnet section of input, an inverter along with rectifier section as well as an output section. In input section ,electric battery is employed as a source. In both inverter section and rectifier section, eight IGBTs (four on each side) are utilized as inverter and rectifier element. The triggering pulse of IGBTs is operated by the PI controller. The circuit functions in two various mode of buck mode and boosts mode.

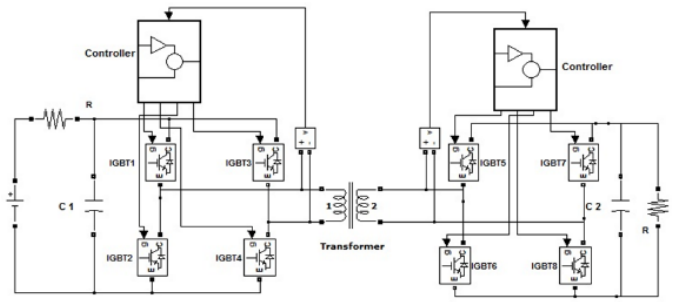


Fig. 3. PI implemented Bidirectional topology

## B. PI Control Circuit

A PI control circuit is employed to raising the operating performance as shown in figure 4. The circuit is implemented for transferring different pulse of triggers into the IGBTS.

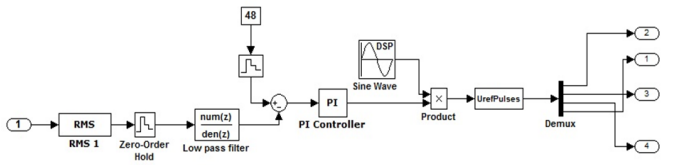


Fig. 4. PI Control Circuit

PI initially consider the parameter of output voltage to evaluate recommended output voltage as well as set predefined parameter for providing a trigger transmission for acquiring a predetermined parameter of output voltage by means of transformed input voltage of the particular topology.

## C. Circuit Diagram of Buck Operation

The buck operation of PI implemented bidirectional DC-to-DC controller is presented in figure 5. In buck operating mode, at the receiving end, the voltage becomes lesser compared to the supply end voltage as well as on the supply end, a battery as DC power source has provided 380 volts to transformer high voltage side. The inverter section in high voltage side inverts the DC voltage to AC voltage. The transformer is responsible for conversion of the higher AC voltage into lower AC voltage. Eventually, the rectifier segment in the transformer low voltage aspect tends to make the low AC voltage to low DC voltage.

## D. Circuit Diagram of Boost Operation

The boost mode of PI operated bidirectional topology is presented in figure 6. In boost operation, at the receiving end, voltage turn out to be higher as compared to the provided source end voltage and on the supply end, a power supply as DC source supplies 48 volts to transformer low voltage side. The inverter segment in low voltage side transforms low DC voltage into minimal AC voltage. The transformer converts the minimal AC voltage to high AC voltage as well as eventually, the actual rectifier sections in the transformer high voltage edge creates the high AC voltage to high DC voltage.

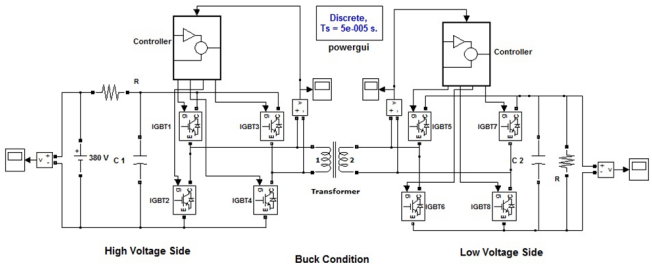


Fig. 5. Bidirectional DC to Dc converter with PI controller (Buck mode).

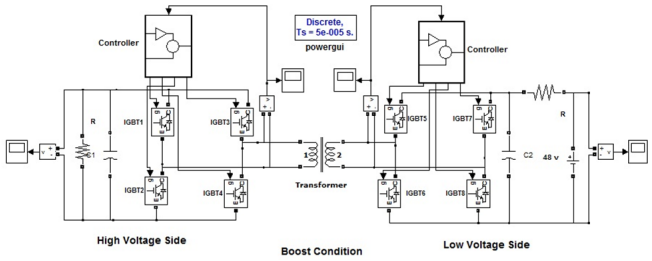


Fig. 6. Bidirectional DC to DC converter with PI controller (Boost mode)

## E. Simulation Output of Buck and Boost Operation

*a) Simulation Output of Buck Operation:* Figure 7 symbolize the Simulation Output of Buck Operation. The input curve of the voltage for 380 Volt is presented by **7(a).** The transformer primary side Output waveform wherever the optimum input voltage is 380 volt AC is demonstrated by Figure 7(b). Transformer secondary side produces 48 volt AC that is showed through the waveform of Figure 7(c). Figure 7(d) demonstrates the Output curve of PI implemented Bidirectional topology (buck mode) intended to output voltage 48 Volt DC.

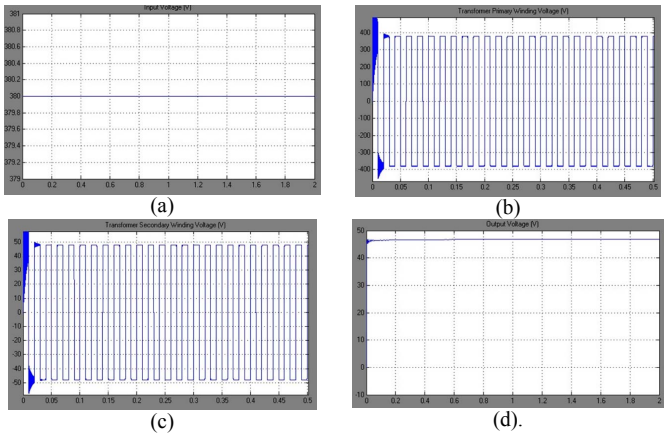


Fig. 7. (a) Input Curve (b)Transformer primary side output (Buck condition) (c)Transformer secondary side output at Buck condition.(d) Output Curve

*b)* Simulation Output of Boost Operation: Figure 8(a) exhibits the input curve of the voltage for 48 Volt DC. Figure 8(b) displays the Transformer primary side Output waveform where the peak input voltage is 48volt AC.Figure 8(c) demonstrates the Transformer secondary part Output waveform in which transformer secondary side supplies 380 volt AC. Figure 8(d) illustrates the Output curve of PI implemented Bidirectional topology (boost mode) in which the output voltage is 380 Volt DC. Data table of various output voltage with regard to the corresponding input voltage (PI Controlled Converter) is presented in Table I.

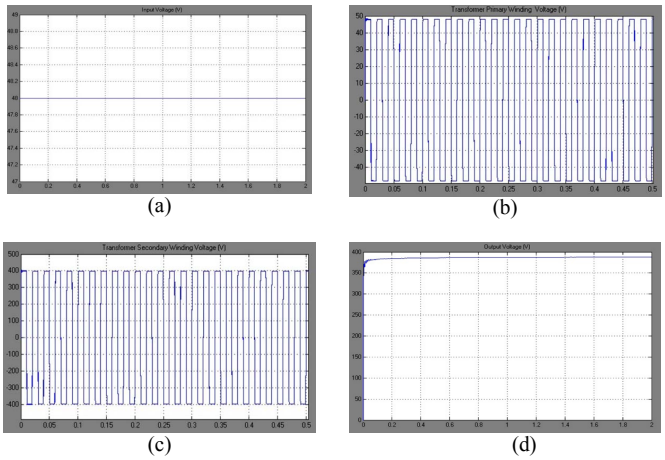


Fig. 8. (a)Input Curve (b)Transformer primary side output(boost condition) (c)Transformer secondary side output at boost condition. (d)Output Curve.

TABLE I. DATA TABLE FOR DIFFERENT OUTPUT VOLTAGE FOR THE CORRESPONDING INPUT VOLTAGE

| **Boost operation** | | **Buck operation** | |
|---|---|---|---|
| ***Input (V)*** | ***Output (V)*** | ***Input (V)*** | ***Output (V)*** |
| 45 | 379 | 375 | 47 |
| 48 | 380 | 380 | 47.5 |
| 50 | 381.5 | 385 | 48 |

## III. MODELING OF PID CONTROLLED BIDIRECTIONAL DC - DC CONVERTER

### *A. Designing of PID controlled Converter*

Figure 9 represents the arrangement of a PID controlled DC to DC controller topology consists of different sections of input, an inverter along with a rectifier as well as an output section. In input section, a DC battery is used as power supply.

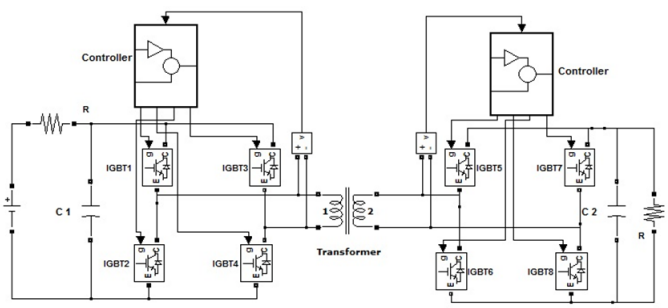


Fig. 9. PID implemented Bidirectional topology

In both inverter section and rectifier section, eight IGBTs (four on each side) is used as inverter and rectifier element. The triggering pulse of IGBTs is controlled by the PID controller. The circuit works in two different modes of buck and boost.

### *B. PID Control Circuit*

Figure 10 represents a PID Controller circuit to transfer the different pulse of triggering to the IGBTS. PID compares the output voltage parameters of the topology to the desired output voltage for providing a trigger signal to achieve a predetermined parameter for the voltage of output regarding the fact of varied input voltage of the controller.

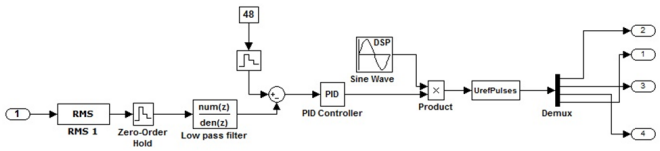


Fig. 10. PID Control Circuit

### *C. Circuit Diagram of Buck Operation*

Figure 11 represents the buck mode of PID controlled bidirectional DC-to-DC converter where at the receiving end, voltage becomes lower than the supply end voltage and on the supply end, a DC battery supplies 380 volt DC to transformer high voltage side.

The inverter section in high voltage side inverts the DC voltage into AC voltage and transformer transforms the higher AC voltage into lower AC voltage. Finally, the rectifier section in the transformer low voltage side makes the low AC voltage to low DC voltage.

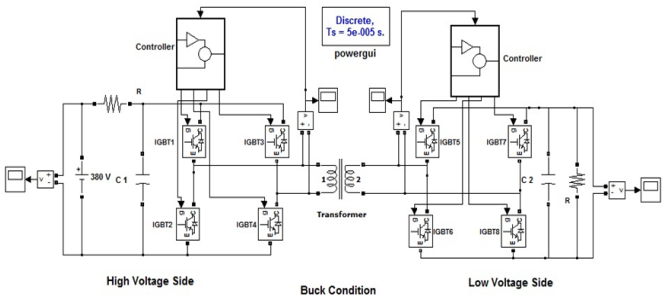


Fig. 11. Bidirectional DC to Dc converter with PID controller (Buck mode).

### *D. Circuit Diagram of Boost Operation*

Figure 12 demonstrates the boost mode of PID implemented bidirectional DC-to-DC converter. In boost mode, at the receiving end, voltage transforms into higher than the supply end voltage. On the supply end, a DC power supply supplies 48-volt DC to transformer low voltage side as well as the inverter section in low voltage side transform lower DC voltage into lower AC voltage.

The transformer converts the lower AC voltage into higher AC voltage and finally, the rectifier section in the transformer

high voltage side produces the high AC voltage to high DC voltage.

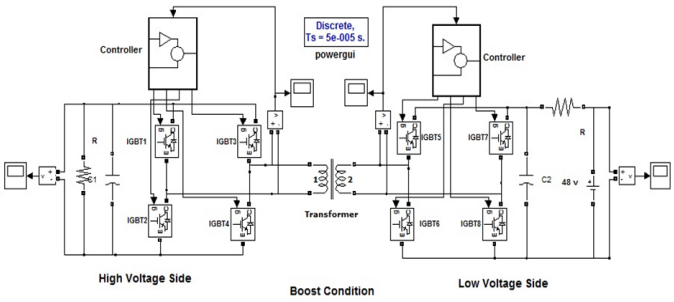


Fig. 12. Bidirectional DC to Dc converter with PID controller (Boost mode).

## E. Simulation Output of Buck and Boost Operation

*a) Simulation Output of Buck mode:* Figure 13(a) represents the input curve of the voltage for 380 volts and the figure 13(b) exhibits the transformer primary side output waveform where the peak input voltage is 380 volt AC.

The transformer secondary side output waveform is demonstrated in figure 13(c), where transformer secondary side supplies 44 volt AC. Figure 13(d) shows the output curve of buck operation for 380-volt input where the output voltage is 44 volt.

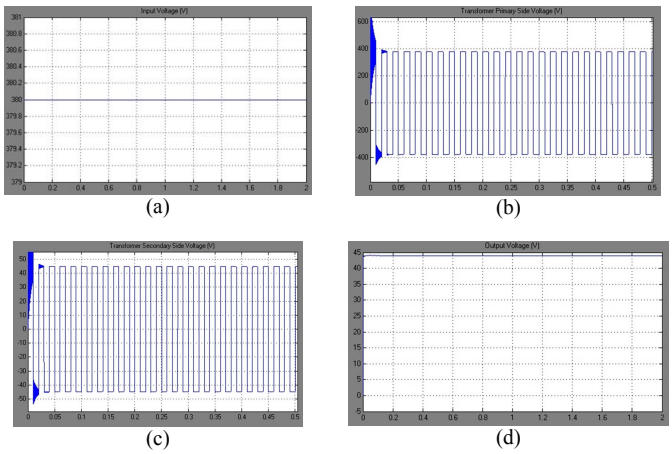


Fig. 13. (a) Input Curve (b)Transformer primary side output at Buck condition (c)Transformer secondary side output at Buck condition (d)Output Curve

*b) Simulation Output of Boost Mode:* Figure 14(a) shows the input curve of the voltage for 48 volts. And figure 14(b) represents the transformer primary side output waveform where the peak input voltage is 48 volt AC.

Figure 14(c) exhibits the transformer secondary side output waveform where transformer secondary side supplies 350-volt AC as well as the figure 14(d) represents the output curve of boost condition for 48-volt input where the Output voltage is 350 volt. Data table of different output voltage for the corresponding input voltage is shown in Table II.

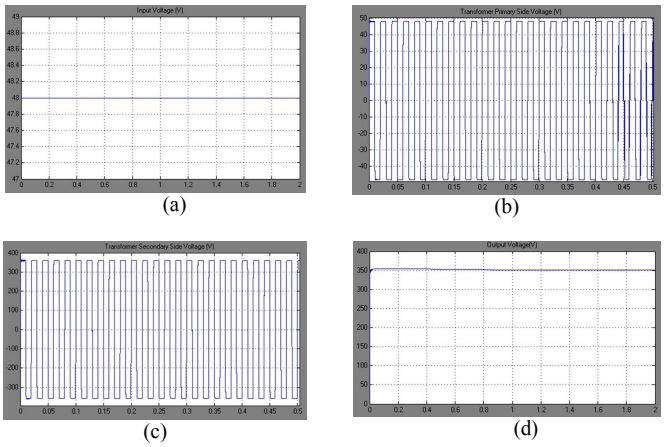


Fig. 14. (a) Input Curve (b)Transformer primary side output at boost condition (c)Transformer secondary side output at boost condition (d)Output Curve.

TABLE II. DATA TABLE FOR DIFFERENT OUTPUT VOLTAGE FOR THE CORRESPONDING INPUT VOLTAGE

| **Boost operation** | | **Buck operation** | |
|---|---|---|---|
| *Input (V)* | *Output (V)* | *Input (V)* | *Output (V)* |
| 45 | 340 | 375 | 43 |
| 48 | 351 | 380 | 44 |
| 50 | 360 | 385 | 46 |

# IV. MODELING OF CONVENTIONAL BIDIRECTIONAL DC TO DC CONVERTER

## A. Designing of Conventional Converter

*a) Conversion of input:* Figure 15(a) represents a full bridge inverter circuit consists of IGBT switches which is utilized for voltage transformation of DC voltage into AC voltage. The switches are utilized for transforming the input of DC voltage into AC voltage.

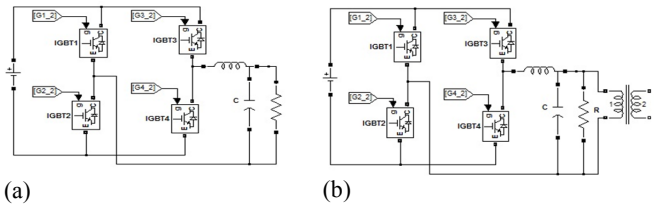


Fig. 15. (a)Inverter Figure (b) Inverter cascaded with transformer

*b) Interfacing of Transformer:* A transformer is cascaded with the Inverter circuit as represented in Figure 15(b) which transforms the supply AC voltage from inverter to the desired AC voltage.

*c) Development of Rectifier Circuit:* A rectifier circuit is added to the secondary side of the transformer as shown in Figure 16 at the conventional Bidirectional topology. A rectifier circuit is cascaded with secondary side of the transformer to converts the AC voltage to DC voltage and a filter circuit is added for smoothing the DC voltages. Finally, it consists of an input section, an inverter section, a rectifier section and an output section.

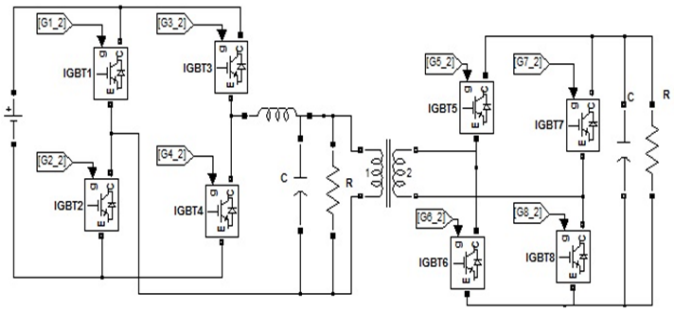


Fig. 16. Conventional Bidirectional topology

## B. Circuit Diagram of Buck Operation

Figure 17 represents the buck operation of Conventional topology where at receiving end, voltage tends to be lower with compare to the supply end voltage. On the supply end, a battery supplied 380-volt DC to transformer high voltage side.

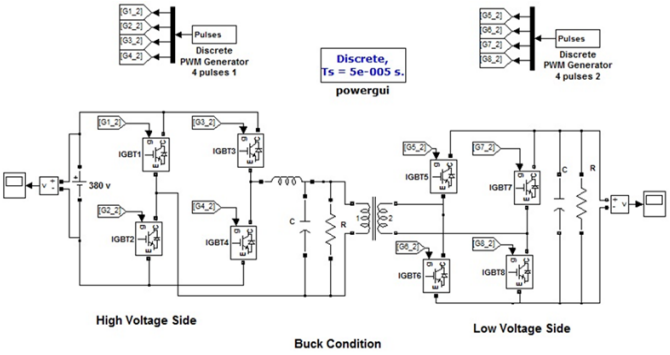


Fig. 17. Conventional Bidirectional DC to DC converter (Buck mode).

The inverter section in high voltage side consists with four IGBT that is responsible for conversation of the DC voltage to AC voltage. The transformer transforms the high AC voltage to low AC voltage and finally, rectifier section in the transformer low voltage side which consists with four IGBT converts the low AC voltage into low DC voltage and also responsible for the different pulse of triggers produced from two different PWM generators to the IGBTs.

## C. Circuit Diagram of Boost Operation

Figure 19 represents the boost mode of Conventional Bidirectional topology. voltage tends to be high at receiving the end of boost operation with compare to the supply end.A battery is used as DC power supply for providing 48-volt DC on the supply end. It is supplied to transformer low voltage side.

The inverter section consists of four IGBT in low voltage side converts the lower DC voltage to lower AC voltage. The transformer transforms the low AC voltage to high AC voltage. And finally, the rectifier section also consists of four IGBT in the transformer high voltage side makes the high AC voltage to high DC voltage. The different pulse of triggers produced from two different PWM generators to the IGBTs similarly like buck mode.

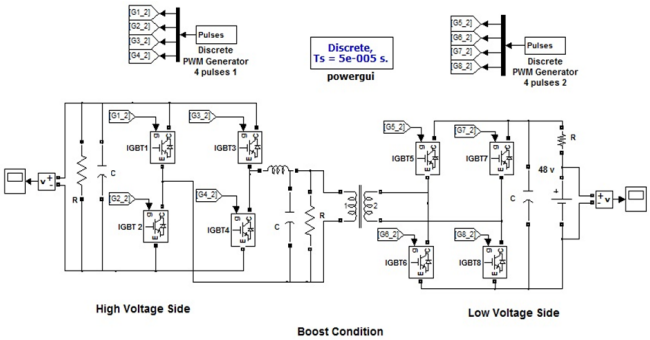


Fig. 18. Conventional Bidirectional DC to DC converter (Boost mode).

## D. Simulation Output of Buck and Boost Mode

*a) Simulation Output of Buck Mode:* Figure 18(a) shows the input curve of the voltage for 380 Volt. Figure 18(b)shows the Transformer primary side Output waveform where the peak input voltage is 380 volt AC.

Figure 18(c) shows the Transformer secondary side Output waveform where the transformer secondary side supplies 48 volt AC. Figure 18(d) shows the Output waveform of conventional Bidirectional DC to DC converter (buck mode) for peakvoltage of 32 volt DC.

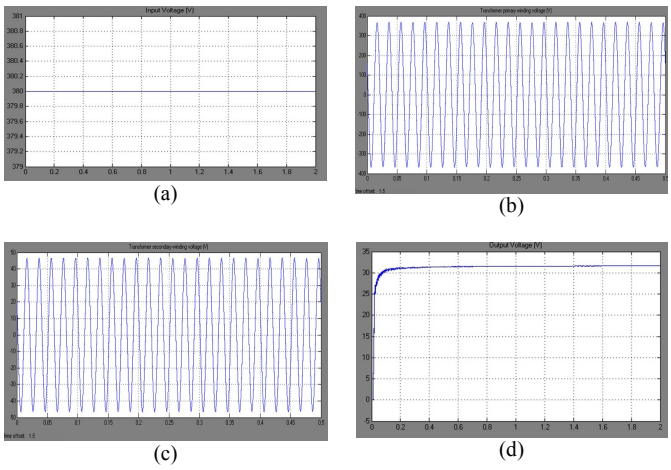


Fig. 19. (a) Input Curve (b)Transformer primary side Output (c) Transformer secondary side output (d)Output Curve.

*b) Simulation Output of Boost Mode:* Figure 20(a) shows the input curve of the voltage for 48 Volt. Figure 20(b) represents the transformer primary side Output waveform where the peak input voltage is 48 volt AC.

Figure 20(c) represents the transformer secondary side Output waveform for supplied 380-volt AC. Figure 20(d) shows the Output waveform of conventional Bidirectional DC to DC converter (boost mode) for the output voltage of 110 Volt DC. Data table of different output voltage for the corresponding input voltage of Conventionaltopology is shown in Table III.

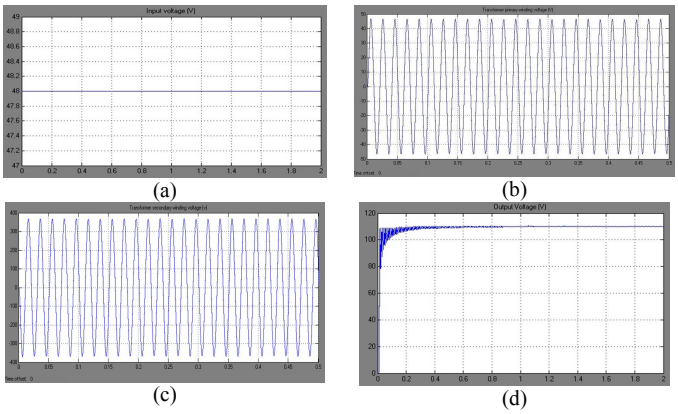

Fig. 20. (a)Input Curve (b)Transformer primary side output (c) Transformer secondary side output (d) Output Curve.

TABLE III. DATA TABLE OF DIFFERENT OUTPUT VOLTAGE FOR THE CORRESPONDING INPUT VOLTAGE

| Boost operation | | Buck operation | |
|---|---|---|---|
| ***Input (V)*** | ***Output (V)*** | ***Input (V)*** | ***Output (V)*** |
| 45 | 105 | 375 | 30 |
| 48 | 110 | 380 | 32 |
| 50 | 118 | 385 | 33.5 |

## V. COMPARISON BETWEEN CONVENTIONAL, PI AND PID CONTROLLED BI-DIRECTIONAL DC TO DC CONVERTER

The comparison study is demonstrated in Table IV and V shows that the PI implemented Bi-directional topology has more stability in comparison with PID and Conventional topology. For both buck and boost operation, output variation is less with the input variation for PI implemented controller with compare to another controller of PID and conventional. Figure 21 shows the Comparison of Output curve for 48 V boost condition and Figure 22 shows the comparison of Output curve for 375 Volt Buck condition. From both comparison, it is evident that PI controlled topology has more significant efficiency than the conventional and PID controlled topology.

TABLE IV. COMPARISON BETWEEN CONVENTIONAL, PI & PID CONTROLLED BI DIRECTIONAL DC-TO-DC CONVERTER (BOOST MODE)

| ***Topic*** | ***PI Controlled*** | | ***PID Controlled*** | | ***Conventional*** | |
|---|---|---|---|---|---|---|
| ***Output Voltage*** | ***Input (V)*** | ***Output (V)*** | ***Input (V)*** | ***Output (V)*** | ***Output (V)*** | ***Output (V)*** |
| | 45 | 379 | 45 | 340 | 45 | 102.3 |
| | 48 | 380 | 48 | 351 | 48 | 110 |
| | 50 | 381.5 | 50 | 360 | 50 | 118 |
| | ***Conversion Efficiency*** | | *Less Efficient* | | *Less Efficient* | |

TABLE V. COMPARISON BETWEEN CONVENTIONAL, PI & PID CONTROLLED BI DIRECTIONAL DC TO DC CONVERTER (BUCK MODE)

| ***Topic*** | ***PI Controlled*** | | ***PID Controlled*** | | ***Conventional*** | |
|---|---|---|---|---|---|---|
| ***Output Voltage*** | ***Input (V)*** | ***Output (V)*** | ***Input (V)*** | ***Output (V)*** | ***Output (V)*** | ***Output (V)*** |
| | 375 | 47 | 375 | 43 | 375 | 30 |
| | 380 | 47.5 | 380 | 44 | 380 | 32 |
| | 385 | 48 | 385 | 46 | 385 | 33.5 |

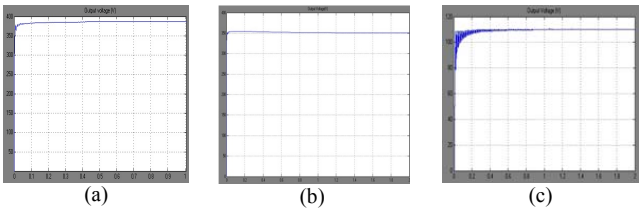

Fig. 21. Comparison of Output curve for 48 V boost condition (a)Pi Controlled (b)Pid Controlled (c)Conventional

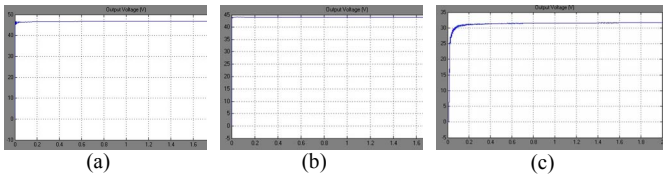

Fig. 22. Comparison of Output curve for 375 Volt Buck condition (a)Pi Controlled (b)Pid Controlled (c)Conventional

## IV. CONCLUSION

Bidirectional DC to DC converter with PI controller has exhibits more efficient output in comparison with conventional and PID controlled Bidirectional DC-DC converter. Due to the stable output voltage is given by the PI Controlled topology, the comparative analysis between conventional, PI and PID controlled Bidirectional DC-DC converter proves that PI controlled Bidirectional DC to DC converter is able to achieve low steady state error state as well as higher efficient output. PI controlled controller has also overcome downsides of the traditional bidirectional and PID topologies by ignoring significant transitioning deficits.

## REFERENCES


[1] S. Chiang, Y. Liao and K. Liu, "Capacity Limitation Control of Multiple Bi-directional DC-DC Converters for Micro Grid Application", *Studies in Engineering and Technology*, vol. 2, no. 1, 2015.

[2] H. Chiu, Y. Lo, S. Kuo, S. Cheng and F. Lin, "Design and implementation of a high-efficiency bidirectional DC-DC Converter for DC micro-grid system applications", *International Journal of Circuit Theory and Applications*, vol. 42, no. 11, pp. 1139-1153, 2013.

[3] "DC-DC Converter Based on PID Controller for Voltage Step- Down Application", *International Journal of Science and Research (IJSR)*, vol. 4, no. 11, pp. 1188-1189, 2015.

[4] L. Pan and C. Zhang, "An Integrated Multifunctional Bidirectional AC/DC and DC/DC Converter for Electric Vehicles Applications", *Energies*, vol. 9, no. 7, p. 493, 2016.

[5] K. Ramya and V. Jegathesan, "Comparison of PI and PID Controlled Bidirectional DC-DC Converter Systems", *International Journal of Power Electronics and Drive Systems (IJPEDS)*, vol. 7, no. 1, p. 56, 2016.

[6] E. Souza, G. Waltrich and I. Barbi, "Bidirectional Dual Active Clamping Push-pull Dc-dc Converter", *Eletrônica de Potência*, vol. 21, no. 4, pp. 322-331, 2016.

[7] Y. Wu, K. Huang and M. Li, "A bidirectional DC/DC converter charge/discharge controller for solar energy illumination system integrating synchronous rectification SEPIC converter and active clamp flyback converter", *International Journal of Circuit Theory and Applications*, vol. 44, no. 2, pp. 305-327, 2015.

[8] N. Xia and Y. Zhao, "Research on Multiple Bi-Directional DC/DC Converter in Wind Power Flow Optimization and Control System", *Advanced Materials Research*, vol. 383-390, pp. 7232-7237, 2011

# Fuzzy Logic Based Sensorless Adaptive Direct Torque Control of Surface Permanent Magnet Synchronous Motor (SPMSM) Drives

Shantanu Bose, Md. Rafiqul Islam, Tahmida Islam, and Md. Abdur Rafiq
Department of Electrical and Electronic Engineering
Khulna University of Engineering & Technology (KUET)
Email: shantanu67eee@gmail.com; rafiq043@yahoo.com; tahmida_eee@yahoo.com; mdabdurrafiq2003@yahoo.com

*Abstract*—**In this paper, a fuzzy logic based direct torque control method for permanent magnet synchronous motor has been proposed. Conventional direct torque control method may suffer from much torque ripple during command transients. The fuzzy logic based system proposed hereby is more accurate and can adapt quickly to varying conditions such as speed reversal, step change in torque or speed etc. In this research, a fuzzy inference system has been designed to make a human machine interface and the dynamic and steady state response error has been reduced to a much smaller value. Apart from this, the control system is made to cope with varying condition of loads during transients. The robustness to parametric uncertainty is substantiated by varying inertia, inductance, dc link voltage etc for a viscous load. A comparative study between conventional and fuzzy based direct torque control has been carried out for constant load to investigate the effectiveness of the proposed method. The system performance has been tested via computer simulation.**

***Keywords—Fuzzy Logic, Direct Torque Control, Permanent Magnet Synchronous Motor, Field Oriented Control, and Extended State Observer.***

## I. INTRODUCTION

In this neoteric years, high torque density permanent magnet synchronous motors (PMSMs) are becoming progressively widespread in variable speed motor drive applications in the industries. They can be a top-class choice for applications where torque density and speed regulations are critical. PMSMs have lower inductance and greater number of poles than induction motors which leads to smaller electrical time constant. This facility allows smoother stator current under high frequency commutation situation. They do not suffer from low power factor at low speed as induction motors. But problem may arise when phase current becomes high as it is in low speed application, the switching frequency of converters may decrease because of the thermal limitations of power electronic switching devices. Thus, it may lead to the problem of using highly constrained actuators.

In this paper, we have represented a Direct Torque Control (DTC) method that is capable of adapting itself to various torque demand while providing stability and assurance as well. Various techniques have been developed to control PMSM drives among which Field Oriented Control (FOC) was first proposed in [1] and again elaborated in [2]. It has good dynamic response but the FOC controllers have poor performance at high switching frequencies that leads to additional torque ripple and least adaptiveness. Extended state observers (ESOs) are also used in those drives to cope with disturbances [3], [4]. Again, the problem is that they need Fourier series based controller which is very complex to implement. Also many nonlinear techniques have been developed as in [5]-[9], they include huge computation procedure and solution of complex differential equations.

A preferable alternative to above mentioned techniques is DTC which has fast and precise dynamic response. It has faster flux control ability than FOC and other techniques [10], [11]. But it may suffer from torque ripple and switching losses at low frequency. To mitigate these problems, we propose a DTC technique using fuzzy logic and without position sensor that is capable of providing faster torque response, robustness to parametric uncertainty and faster dynamic response. Fuzzy controller provides more precise control of machines compared to PI or other conventional controllers [12]. They give faster dynamic response with minimum over and undershoot in the system response. Also, they are capable of responding quickly to any variation of command signal. Therefore, we will propose here a technique that combines DTC with Fuzzy logic control providing fast and stable dynamic and steady state response which eliminates the problem of attaching position sensor on rotor shaft.

The rest of this paper is organized as follows. Proposed model of PMSM along the mathematical analysis are discussed in Section II. Section III describes control technique of the system and the effect of fuzzy controller as well. Section IV illustrates simulation results along with graphical illustrations. Finally, conclusions are drawn in section V.

## II. MODEL OF PMSM

The mathematical model of PMSM can be derived and transformed into direct and quadrature field oriented reference frame applying Kirchoff's voltage law and Newton's second law in rotational form [2]. The model is given as

978-1-5386-2307-7/17/$31.00 ©2017 IEEE

$$\frac{di_d}{dt} = \frac{v_d}{L_d} - \frac{R}{L_d} i_d + p\omega_r \frac{L_q}{L_d} i_q - p\omega_r \frac{\phi_M}{L_d} \tag{1}$$

$$\frac{di_q}{dt} = \frac{v_q}{L_q} - \frac{R}{L_q} i_q - p\omega_r \frac{L_d}{L_q} i_d \tag{2}$$

$$\frac{d\omega_r}{dt} = -\frac{3p\phi_M}{2J} i_q - \frac{3p}{2J}(L_d - L_q) i_d i_q - \frac{\beta}{J}\omega_r + \frac{\tau_l}{J} \tag{3}$$

where d-axis and q-axis currents are $i_d$ and $i_q$ , rotational velocity is $\omega_r$ , d and q axis inductances are $L_d$ and $L_q$ , stator resistance is $R$ , number of magnetic pole pairs is $p$, magnetic flux is $\phi_M$ , damping coefficient is $\beta$ , load torque is $\tau_l$ and rotor moment of inertia is $J$ .Here $v_d$ and $v_q$ are two inputs and output can be defined as rotor velocity or torque. Here, the two inductances are equal and thus the second term of right hand side of equation (3) will disappear as follows-

$$\frac{d\omega_r}{dt} = -\frac{3p\phi_M}{2J} i_q - \frac{\beta}{J}\omega_r + \frac{\tau_l}{J}. \tag{4}$$

The error system can be defined as follows-

$$\Delta\tau_l = \tau_l - \tau_l^* \tag{5}$$

$$\Delta\psi_S = \psi_S - \psi_S^* \tag{6}$$

where, $\psi_S$ is the stator flux. This flux can be estimated using stator voltage, current and resistance as follows [13]

$$\psi_S = \int (v_S - R_S i_S) dt \tag{7}$$

where, all the quantities are of stator which are voltage, resistance and current respectively. The rotor position, $\theta_r$ can be estimated from the following equation.

$$\omega_r = \frac{d\theta_r}{dt}. \tag{8}$$

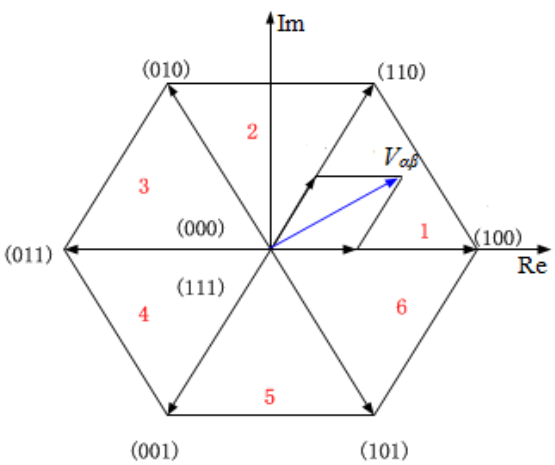


Fig. 1: Space vectors of the inverter.

## III. CONTROL SCHEME

### A. The Power Inverter

The power inverter used here is a two level three phase. As it has three phases and each leg has two switches, total states of switching will be $2^3$ that is 8. Among these two are zero which are [111] and [000]. The space vectors of switching are presented in Fig. 1. The sequence of switching can be described as [16]

$$(v_\alpha, v_\beta) \approx \frac{T_S - \eta_S - \sigma_S}{2}[000] + \eta_S[100] + \sigma_S[101] + \frac{T_S - \eta_S - \sigma_S}{2}[111] \tag{9}$$

where, $T_S$ is the sampling time and $\eta_S$ and $\sigma_S$ are two duty cycles assigned to nonzero switching states and must satisfy $\eta_S$, $\sigma_S \geq 0$. The converter can be represented in synchronous reference frame using rotor position as follows-

$$\begin{bmatrix} v_{dN} \\ v_{qN} \\ v_{oN} \end{bmatrix} = \frac{2}{3} \begin{bmatrix} \cos(\theta_e) & \cos(\theta_e - \frac{2\pi}{3}) & \cos(\theta_e + \frac{2\pi}{3}) \\ \sin(\theta_e) & \sin(\theta_e - \frac{2\pi}{3}) & \sin(\theta_e + \frac{2\pi}{3} \\ \frac{1}{2} & \frac{1}{2} & \frac{1}{2} \end{bmatrix} \begin{bmatrix} v_{AN} \\ v_{BN} \\ v_{CN} \end{bmatrix}. \tag{10}$$

### B. The Fuzzy Controller

A fuzzy controller is a combination of fuzzifier, fuzzy inference engine, defuzzifier and fuzzy rule base. The crisp sets are transformed into fuzzy sets through fuzzy membership function in the fuzzifier. The fuzzy inference engine uses product inference engine. The defuzzifier applies mean of maxima method for de-fuzzification. The fuzzy rule base consists of linguistic implication as described in Table I. The fuzzy sets are error in output torque $\varepsilon_\tau$ and error in stator flux $\varepsilon_\phi$. The intervals are defined as "ZERO (Z)", "POSITIVE SMALL (PS)" and "NEGATIVE SMALL (NS)". The resultant function is defined in the interval "NEGATIVE BIG (NB)", "NEGATIVE MEDIUM (NM)", NEGATIVE SMALL (NS)", "POSITIVE BIG (PB)", "POSITIVE MEDIUM (PM)" and "POSITIVE SMALL (PS)". The membership functions are triangular. The functions are defined with 50% overlap.

TABLE I
FUZZY RULE BASE

| $\varepsilon_\phi$ \ $\varepsilon_T$ | NS | Z | PS |
|---|---|---|---|
| Z | NB | NS | PM |
| PS | NM | PS | PB |

### C. Control Algorithm

The method of control explained above involves the following steps:

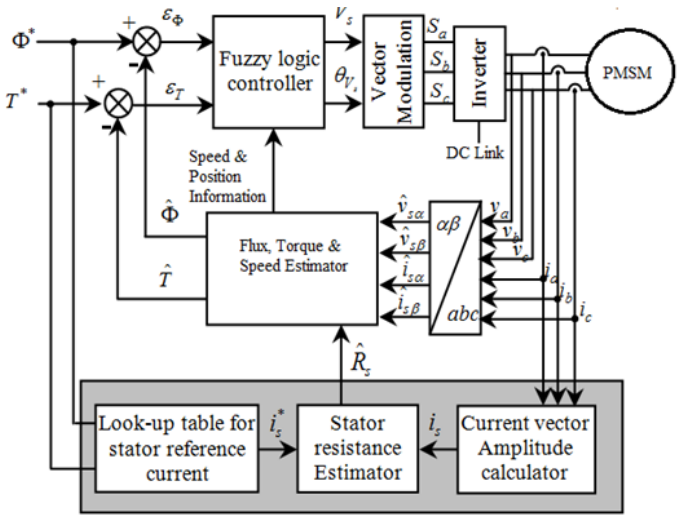


Fig. 2: Block diagram of the proposed system.

- Estimate the initial rotor position, $\theta r$ at every instant.
- Use $\theta r$ for the flux and torque estimation system.
- Estimate flux and torque with the rotor position information.
- Estimate stator current comparing measured and calculated value.
- Estimate errors $\varepsilon_T$ and $\varepsilon_\phi$ using flux linkage error $\Delta\Psi$ and torque error $\Delta T$. Give the information to the fuzzy controller which decides the switching state.
- Using corrected rotor position estimate flux again for speed correction.

The block diagram of the control system is shown in Fig. 2.

## IV. SIMULATION RESULTS

### A. System Response

The parameters used in the simulation are given in Table II. The sample time considered is 10 times the switching frequency. A fourth order Runge-Kutta method has been applied to solve the system equations and the whole system has been investigated through computer simulation using C++.

TABLE II
PARAMETERS CONSIDERED IN SIMULATION

| Parameters (Unit) | Value |
|---|---|
| DC Link Voltage (Volt) | 500 |
| Rated output power (kW) | 50 |
| Rated torque (Nm) | 200 |
| Rated speed (rpm) | 3000 |
| Rated phase current (Ampere) | 200 |
| Number of poles | 8 |
| Reference flux (Weber) | 1.00 |
| Switching frequency (kHz) | 10 |
| Stator inductance (mH) | 22.5 |
| Stator resistance (Ω) | 0.677 |

To investigate the proposed system response, first a slowly varying speed command that varies from 200 to -200 rpm, is given whereas the torque varies from 25 to -25 Nm in addition to a viscous load. These results are shown in Fig. 3 which shows good dynamic response with small error and overshoot that settles in less than 0.5 second.

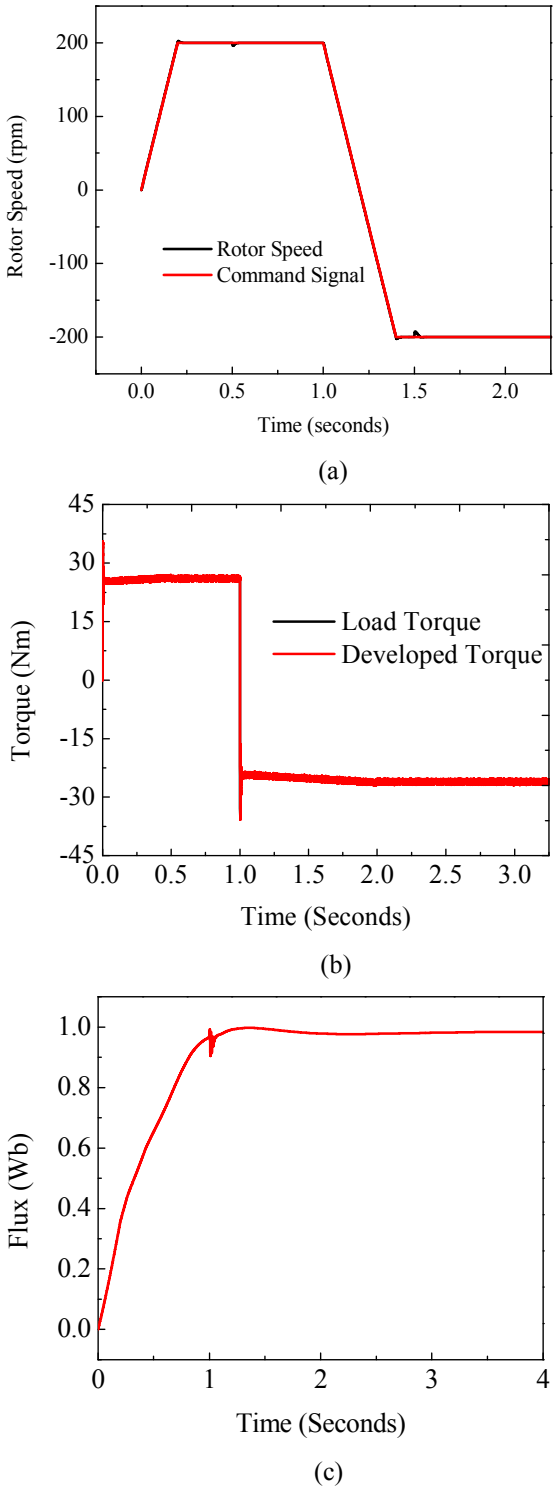


Fig. 3: Simulation results for (a) Rotor speed, (b) Torque, (c) Flux (slowly varying speed command)

These responses have some over and undershoots during command transitions but gains rapid regulation despite of the unknown and asymmetric load application. In order to show a more insightful investigation of the perfectness of the drive system, also a quickly varying command ranges from 0 to 500 rpm, is investigated that is represented in Fig. 4. The system shows quick response to this quickly varying load with less over and undershoots settling within a few microseconds with much less error in speed and torque.

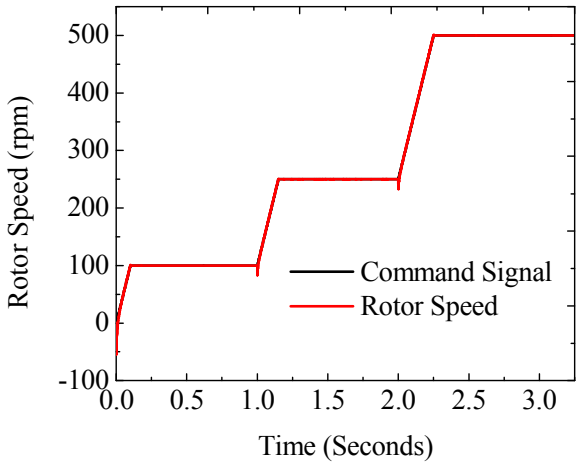


(a)

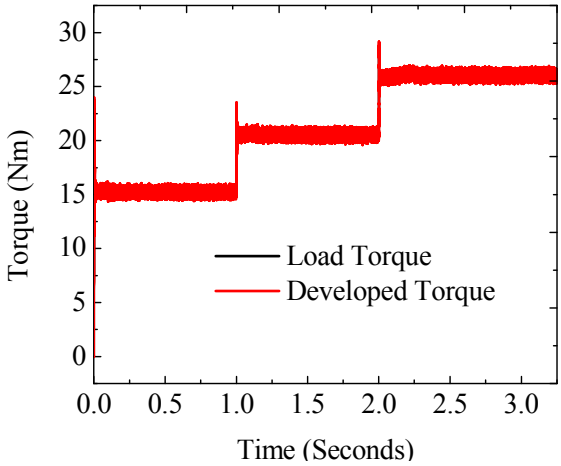


(b)

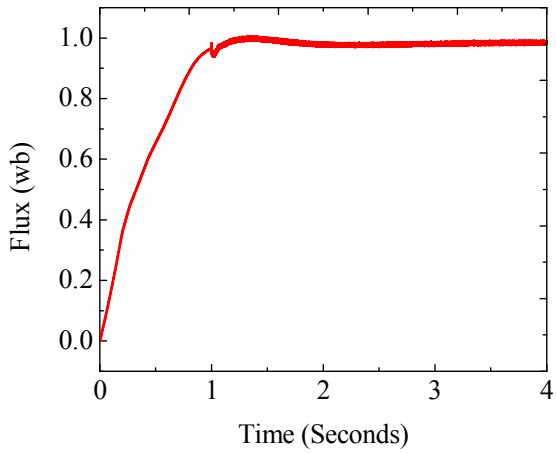


(c)

Fig. 4: Simulation results for (a) Rotor speed, (b) Torque, (c) flux (Quickly varying speed command)

*B. Robustness to uncertainty*

A very important and desirable quality of any control system is robustness to parametric uncertainty. This desirable quality is also investigated in this case and the results are given in Fig. 5. The inductance, DC link voltage, inertia and damping coefficients have been varied to prove the robustness of the proposed technique. The results show good robustness of the system and there is no adverse effect of parameter variations on the dynamic response which settles within approximately 0.2 second. A vast analysis of robustness of the system is afar the space of this paper, just sudden change of the aforementioned parameters has been applied to carry out the investigation. The system proposed here is a dynamic system and the data are much closer to one another. As a result, the curves look like a single one.

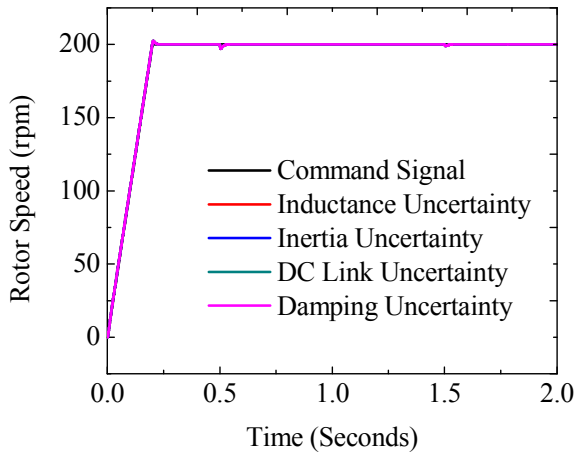


(a)

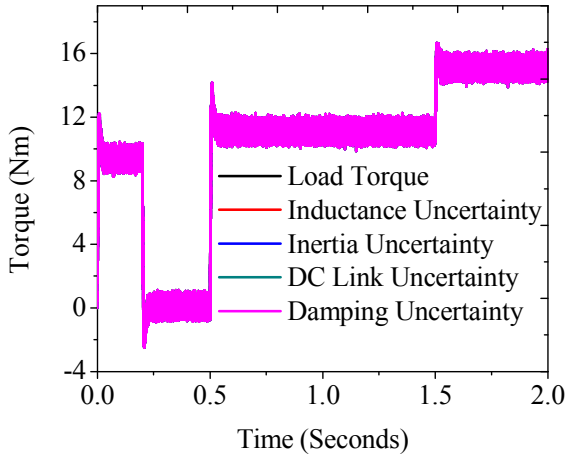


(b)

Fig. 5: Simulation results for parametric uncertainty (a) Rotor speed, (b) Torque

## V. CONCLUSION

In this paper, a fuzzy logic based direct torque control method has been represented which is adaptive to quick and slow variation of load torque and frequently changing speed. Also, this technique is robust to parametric uncertainties as the responses show smaller over and under shoots during transients which is very much desirable in practical drive applications where load variations are too much. The dynamic responses are good and steady state errors are less. The motor speeds up within much less time and produces smoother torque and flux during transients. The comparative study shows that the proposed method responses faster than the conventional method. Thus, the proposed system is much more adaptive and can respond quickly to any variation of speed and torque as it is demanded by the load.

## REFERENCES


[1] F. Blaschke, "The principle of field orientation as applied to the new transvector closed loop control for rotating field machines," *Siemens Rev.*, vol. 39, pp. 217–220, May 1972.

[2] P. C. Krause, O. Wasynczuk, and S. D. Sudhoff, *Analysis of Electric Machinery and Drive Systems*. Piscataway, NJ: IEEE Press, 2002.

[3] S. Li and Z. Liu, "Adaptive speed control for permanent-magnet synchronous motor system with variations of load inertia," *IEEE Trans. Ind. Electron.*, vol. 56, no. 8, pp. 3050–3059, Aug. 2009.

[4] J. Solsona, M. Valla, and C. Muravchik, "Nonlinear control of a permanent magnet synchronous motor with disturbance torque estimation," *IEEE Trans. Energy Convers.*, vol. 15, no. 2, pp. 163–168, Jun. 2000.

[5] M. Ouassaid, M. Cherkaoui, and Y. Zidani, "A nonlinear speed control for a PM synchronous motor using an adaptive backstepping control approach," in *Proc. IEEE Int. Conf. Ind. Technol.*, vol. 3. May 2004, pp. 1287–1292.

[6] M. Vilathgamuwa, M. Rahman, and K. Tseng, "Nonlinear control of interior permanent magnet synchronous motor," in *Proc. Ind. Appl. Conf.*, vol. 2. 2000, pp. 1115–1120.

[7] D. Dawson, J. Hu, and T. Burg, *Nonlinear Control of Electric Machinery*. New York: Marcel Dekker, 1998.

[8] D. Dawson, J. Carroll, and M. Schneider, "Integrator backstepping control of a brush DC motor turning a robotic load," *IEEE Trans. Control Syst. Technol.*, vol. 2, no. 3, pp. 233–244, Sep. 1994.

[9] Z. Cai, M. de Queiroz, and D. Dawson, "Robust adaptive asymptotic tracking of nonlinear systems with additive disturbance," *IEEE Trans. Autom. Control*, vol. 51, no. 3, pp. 524–529, Mar. 2006.

[10] N. Farid, B. Sebti, K. Mebarka, and B. Tayeb, "Performance analysis of field-oriented control and direct torque control for sensorless induction motor drives," in *Proc. Medit. Conf. Control Autom.*, Jun. 2007, pp. 1–6.

[11] H. Le-Huy, "Comparison of field-oriented control and direct torque control for induction motor drives," in *Proc. 34th IAS Annu. Meeting Conf. Ind. Appl.*, vol. 2. 1999, pp. 1245–1252.

[12] C. Xia, J. Zhao, Y. Yan, and T. Shi, "A Novel Direct Torque and Flux Control Method of Matrix Converter-Fed PMSM Drives," *IEEE Trans. Power Electronics*, vol. 29, no. 10, pp. 5417-5430, Oct. 2014.

[13] D. Liberzon, *Switching in Systems and Control*. Basel, Switzerland: Birkhäuser, 2003.

[14] M. P. Kazmierkowski, R. Krishnan, and F. Blaabjerg, *Control in Power Electronics*. New York: Academic, 2002.

[15] H. Y. Chung, C. C. Hou, and C. L. Chao, "Speed Control of a PMSM based on Integral-Fuzzy Control," proceedings of 2013*, Int. Conf. Fuzzy Theory and Its Application*, Dec. 2013, pp. 77-82.

[16] G. Prior, M. Krstic, "Quantized-Input Control Lyapunov Approach for Permanent Magnet Synchronous Motor Drives," *IEEE Trans. Control Systems Technology*, vol. 21, no. 5, pp. 1784-1794, Sept. 2013.

# Design And Implementation of A Robotic Technique Based Waiter

Md. Kamruzzaman, Md. Tareq
Department of Electrical & Electronic Engineering, Uttara University, Bangladesh
mkzamanmitdu@gmail.com, mtareq366@gmail.com

*Abstract*—**Life is going to be tough and challenging latterly without thinking anything bearing technology. For various robotic applications, our daily life is becoming smarter and handy day by day. Robotic waiter is one of the best examples of daily life automation. By this technology, a mobile robot can take order and serve food or beverage to the person in any environment of restaurant, hotel, office or household. This paper presents description about a robotic waiter technique along with the design of microcontroller based robot which works effectively in a restaurant and office environment within a certain area. A prototype design of a wheel based moveable robotic waiter has been shown in this paper. The prototype waiter robot has been designed and implemented to receive order-request via android apps, then to collect food/drinks(max600gram) from kitchen boy, then to travel to the destination (the person who send order-request) and again to come back to its source point completing the order of requested food/drinks.**

***Keywords— Robotic waiter, Microcontroller, step counting, location sensing.***

## I. INTRODUCTION

The robots are being designed to become a part of ordinary people to live for an increasing extent. To assist human with tedious tasks or difficult, their tasks may range from play or entertainments. The robot will closely interact with a human group in everyday environments, in these kinds of application. This means that it will be essential to create models, intuitive and natural communication between robots and humans [1].

Nowadays, robotic waiter is creating huge attraction in restaurants, hotels and offices. Considering robotic technique based waiter, there are numerous innovative technologies developed by researchers, to make easy ordering services like adopting mobile robot[2], collecting dining decisions[3], wireless call system[4], waiter-robot[5], self-service ordering system for restaurant[6] and automated menu-recommender[7].

In this paper, a robotic technique based waiter has been designed and implemented for an office having two rooms. The waiter robot has been designed to receive the order-request via android apps, collect food/drinks(max600gram) from kitchen boy, travel to the destination(the person who send order-request) and come back to its source point after the handover of requested food/drinks. The designed robot has been constructed by available local devices. As well as, the traveling technique from source to destination has been implemented in this waiter robot.

## II. BACKGROUND & LITERATURE REVIEW

The human waiter often create problems in restaurants, hotels and offices. They make mistakes in the most common blooper with customer's orders. Most of the time, waiters forget to make a change or add a precise item and also forget to place the customer's order to the kitchen. In addition, the customers also have to wait for the waiters to give their orders. The waiter is the one who remembers the food item and the customer is bound to depend on the waiter where there are so many possibilities of error occurrences. Sometimes, they also made wrong bills [8]. A robot waiter can solve these problems smartly. There are many projects and researches done on weightlifting robot, waiter robot, pion/MLSS robot and service robot.

Rupali Saple et al. [9] in his research proposed that the customer's can take their refreshment by pressing the buttons, where using the black line following technique the robot reaches the customer's table. When customers settled down in their chair of the restaurant they simply press a button to order for their refreshment. On switching the button a LED at the receiving side will make the robot to move to his destination (customer's table) which also had a LED that glows brightly creating a junction between the robot and the table. The robot headed towards the table following the black line and takes order of the customer. In the same way following the black line the robot comes back to source destination.

Neeti Malik, Neetu Rani, Alpana Singh, Pratibha, Srishti Pragya [10] proposed that the customer can gave orders via keypad. In the keypad the list of food items along with the prize has been provided so the customer can order from them easily without calling or waiting for someone. The LCD monitor shows the placed order on the screen. After taking the customer order, the robot will move towards the exact table location by the following black line. After serving the customers refreshment then the robot comes back towards the source position.

The development and design of a waiter robot, where the customer gave the order by using electronic menu bar and the bluetooth module transferred data to the kitchen from the customers table at a baud rate of 9600 bps has been shown by M. Asif et al. [11]. The robot waiter by using line following technique reaches the destined table. In the project four IR sensors were used where the two sensors installed on the sides for counting the table, the other two sensors in the center are used for line following where the robot has been always

978-1-5386-2307-7/17/$31.00 ©2017 IEEE

connected to internet. The reception point using the communication network sent order to the kitchen from the table. Then the robot waiter transferred the refreshment to the customer's table from the kitchen .

Sakari Pieska, Juhana Jauhiainen, Markus Liuska, Antti Auno [12] recently proposed in their paper that the customer's can order through application works on an Android tablet. The database connects to this application and download the real-time in the restaurant's menu. So the customer can easily browse the menu bar and order it. By pressing a button the customer can call the waiter. The waiter comes, for confirming the order and count the bill. In the kitchen's display this menu can be displayed. When this refreshment item is ready, then the kitchen staff can mark them as done. This refreshment item is visible in the cashier and also in the waiter application so that they can easily deliver them to the customer.

The studies by Harish Phapale, Prashant Patil, Sanjay Turate, Anshu Chaudhary, Prof. Mahesh Bhagwat [8] have shown that the advanced technology like touch screen menu display can play a vital role in the order process of the customer. It improves the efficiency and reduces the workload of the waiters by creating an intelligent restaurant. The system worked on an android tablet. The application of android, download real time menu bar list and access database. So the customer can easily browse and choice their items and order it.

Sakari Pieska et al. described a design of scalable service robot system for different groups of user in public and private environments. When the restaurant has been scanned by the sensors, the robot can give a voice command to go to the predefined location in the restaurant. There are different kinds of voice commands can be taught to the robot. The robot moves by using the voice commands or by interacting with other software. It has been used for delivery food to a table since the robot has been using a tray. The robot has a touch screen which is a service menu application and which contains the different applications for customers [13].

As the above mentioned all works, focuses on the serving task in the restaurant, here in this project it has been tried to create a prototype of robotic waiter which can serve customers after having the order given by the customer sitting on the table by only pressing a button. The robot designed in this project travel from the source point to the destination table by step counting of wheels revolution where the travelling distance has been measured and loaded in the robot. The designs and implementations of the robot waiter have been completed using existed appliances locally. These robot waiter can work in different areas such as restaurants, hospitals, office environment etc.

## III. Robotic Technique Based Waiter

Most of the waiter robot had designed by using line following technique. But in this design, wheel step counting have used in the programming of Arduino. To serve tea/coffee according to the user's order through wireless communication, an automated system is designed by using a ready-made microcontroller kit "Arduino mega". The Robot waiter designed with basic 6 units as :

- Main controlling unit (microcontroller)
- Motor Driver unit
- Apps: order receiving & Processing unit
- Bluetooth : Robot to user communication unit
- Load cell unit
- Robot position & travelling unit

The working floor layout for the robotic based waiter is shown in the figure 1. Here the room-1 & room-2 is the destination 1 & 2 respectively. Firstly, when the robot receives a command from room-1 or room-2 through android apps, the robot will follow some procedure. The robot asks for food to the kitchen boy and waits for the food to load on its load cell. After receiving food, robot travels to the destination following pre-programmed data (corresponding room) stored in its memory. Then the robot requests the person to receive his/her food. After handovering the food, it comes back to the destination. The complete process of operation & decisions are showing in the Figure 2.

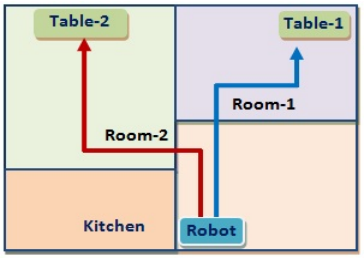


Figure 1. Floor layout where waiter robot will serve.

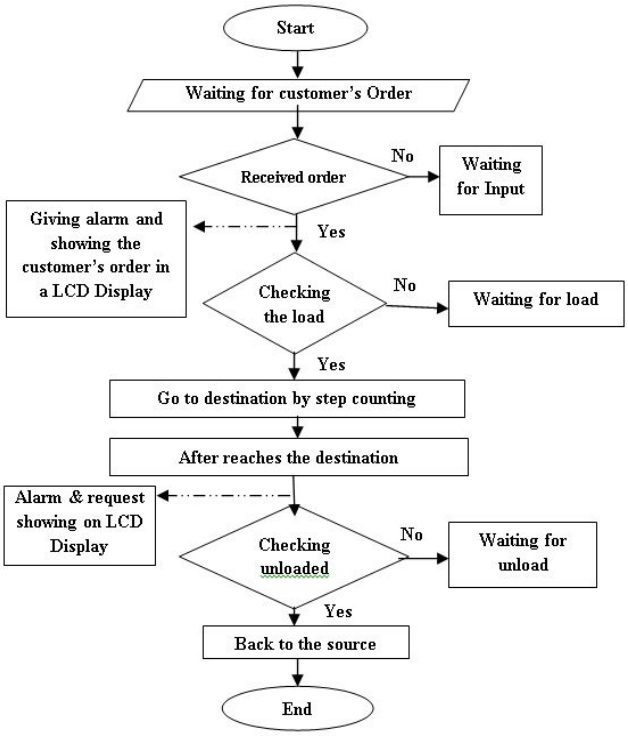


Figure 2. Step by step process flow diagram

978-1-5386-2307-7/17/$31.00 ©2017 IEEE

### *A. Operation Process*

The waiter robot will serve tea/coffee according to the user's order through wireless communication. The main controller is Arduino MEGA. After connecting the robot waiter to the DC power supply it will be waiting for customers command. When a customer selects a command for the robot by using android apps, that instantly the Bluetooth module will sense that command and through that command to the Arduino MEGA. Arduino MEGA has a microcontroller chip whose chip will be loaded by the program and it will do the work to follow the loaded program. When Arduino MEGA have the code (like as "A" or "B" anything that could be from "A" to "F") it will send data to the LCD display for displaying the drink's name (like as "Coffee", "Tea", "Water") along with displaying the location of the source of the command. At the same time an alarm will ring.

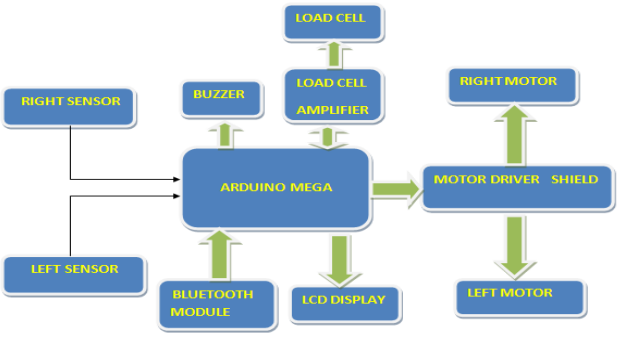


Figure 3. The process flow diagram of "Robot waiter".

The load cell sensor will connect to the digital port of Arduino MEGA and always give the feedback to the microcontroller. The robot will be waiting before to get a load. When the robot will get a load from the kitchen staffs then microcontroller will drive four DC gear motor with the help of the motor driver shield. The program will mention before that where is the room location or table location. Although the location will be mention in the program the robot will move easily towards the exact location by measuring step. This project will have to use rotary encoder for counting robot wheel revolution and this encoder will be connected to the digital pin of Arduino mega. When the robot will reach the exact location, then it will make an alarm and also show "Take your drink" on the LCD display. When the customer will receive their drink, then the robot will come back to the starting point or kitchen.

### *B. Incorporated Technologies*

The main components used to design the robot waiter are described below:

*1) Arduino :* Arduino is an open-source electronics prototyping platform, easy-to-use software and hardware. It's intended for designers, hobbyists, artists and anyone interested in creating interactive objects or environments [11]. Arduino has a 54 digital input/output pins. In this project Arduino takes the input from the motor encoder sensor and operate the motor by its wheel revolution counting. It also takes input from the load cell to sense the robot is loaded or unloaded. In this project lot of digital pins are needed to connect an additional device. Thus for this project the "Arduino MEGA 2560 board has been a suitable one.

*2) Motor Encoder :* In this project "rotary encoder" is used to count the robot wheel revolution. First of all it need to measure the exact room location in an office or a table located in a restaurant. After measuring that location, this measured value has to get mentioned in Arduino program. When the robot understands that measured value, it will go towards the exact location perfectly.

*3) Load Cell :* A load cell is a transducer which converts force into a measurable electrical output. In this project the sensor has been used to sense the load as the purpose to know when the robot is loaded and when it is not.

*4) Android Apps:* This robot will work by an android apps to operate this robot from a remote distance, shown in Figure 3. Hence, it will need to create an android app because the google play store has not availed this kind of apps. Here, in this project the app has been created for two rooms.

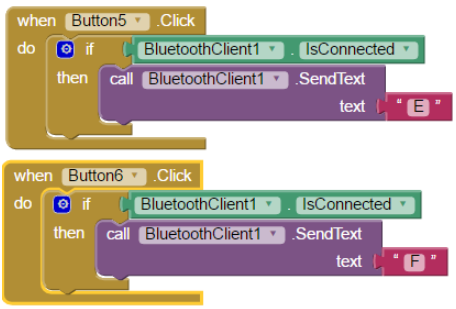


Figure 4. Android apps settings

Figure 5. User layout of Android apps

### *C. Implementation of Robotic Waiter*

To implement the robot waiter, travelling from source (kitchen) to destination (order requested person) is the major issue to discuss. Here we have design two packages for two rooms. Each package setup is for particular movement through a route and specific number of rotation of left wheel and right wheel. Table I describes the number of revolutions of back wheels need to reach destination.

978-1-5386-2307-7/17/$31.00 ©2017 IEEE

TABLE I. NUMBER OF REVOLUTIONS OF BACK WHEELS NEED TO REACH DESTINATION ROOM-1 AND ROOM-2

| Task | | Number of Revolution | |
|---|---|---|---|
| | | *Left Wheel* | *Right Wheel* |
| Destination Room-1 (PKG-1) | Robot Go Forward ( 10 ft) | 250 | 250 |
| | Robot Turn Right | 20 | 0 |
| | Robot Go Forward (4 ft) | 100 | 100 |
| | Robot Turn Left | 0 | 20 |
| | Robot Go Forward ( 2 ft) | 50 | 50 |
| Destination Room-2 (PKG-2) | Robot Go Forward ( 8 ft) | 200 | 200 |
| | Robot Turn Left | 0 | 20 |
| | Robot Go Forward (4 ft) | 100 | 100 |
| | Robot Turn Right | 20 | 0 |
| | Robot Go Forward ( 6 ft) | 150 | 150 |

Figure 5 shows the assembled Robot with motor encoder and Arduino mega. Figure 6 illustrates the final outlook of implemented robot waiter with a cup of drink. When the robot waiter has been connected to a DC power source it waited to get a customer's command. After a customer selects their drink by using android apps the command reached to the robot. Instantly the robot gave an alarm and showed the drink name along with the customer's location on the LCD display.

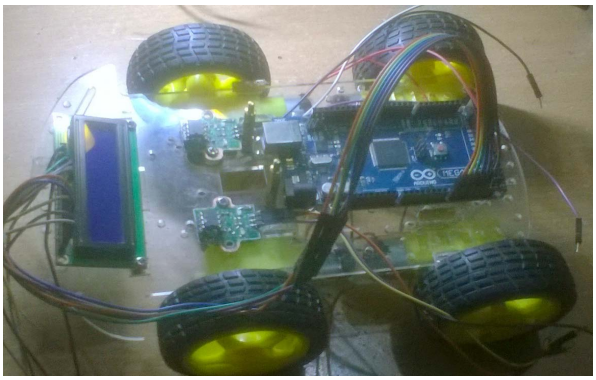

Figure 6. Robot with motor encoder and Arduino mega

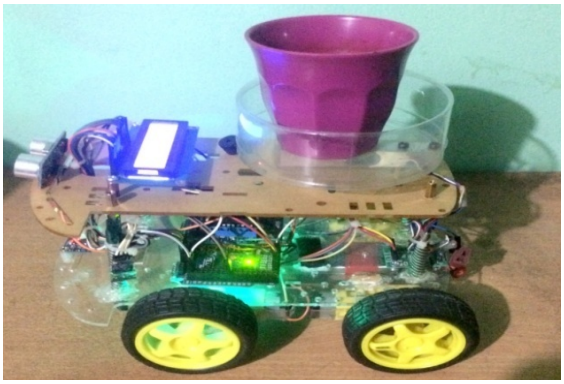

Figure 7. Complete setup of a robot waiter with a cup of drink

As a kitchen staff put the ordered drink on the robot it sensed the load and went to the exact location by counting its wheel revolution. When the robot arrived to the exact location, it made an alarm and showed "Take your drink" on the LCD display, as shown in Figure 5.

The robot waiter will never come back to the starting point or kitchen before the customer takes their drink. So, when the customer has taken their drink from the robot it came back to the starting point or kitchen following the same process of counting of wheels revolution.

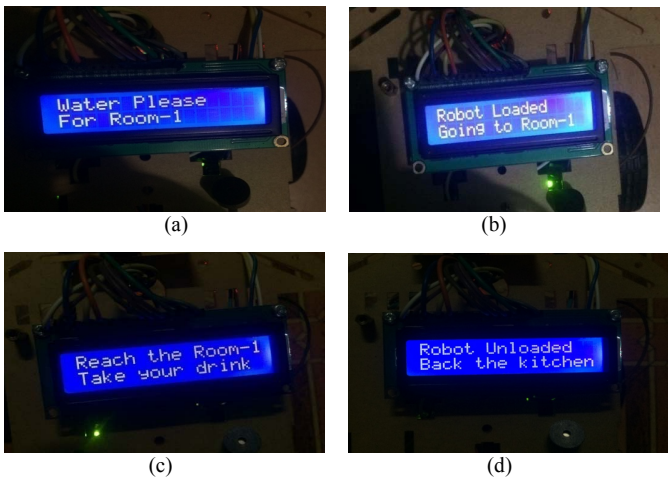


Figure 8. Display the information of job done by Robot Waiter ; (a) After order received & asking for load, (b) After load received, (c) After reach the destination, (d) After handover load to requester.

## IV. DISCUSSION

In this design, the waiter robot can receive and execute only one request at a time. There are no memories or buffering techniques to handle more than one request asking at the same time. It can be solved in future extension of this project. The structural design has not included in prototype model of waiter robot. It is implemented only for testing the logic operation. So the height of the robot was kept very short (8inch). The structural design of waiter robot can be the future extension of this project.

The errors of human waiters can be overcome by the robotic waiters. The robotic waiter can be very attractive, smart and cost effective. The approximate cost of the prototype waiter robot is 8000BDT only. The targeted advantages of designed robot are mentioned below.

- Reduce the extra manpower.
- No need to use noisy alarm/calling bell.
- Identify your refreshment smartly.
- Give the information about room location.
- Working at places 24/7 without any salary.
- It can perform tasks faster than humans and much more consistently and accurately.

978-1-5386-2307-7/17/$31.00 ©2017 IEEE

Some limitations of the design are

- Limited distance between source and destination
- Sometimes step counting does not work correctly due to change of wheel friction according to weight of load(food).
- Wheel friction is a barrier when the robot move.

The robots are used in developed countries for accomplishing precarious jobs, for example, coil mining, rescue people and such jobs which have a threat towards human lives. It is almost impossible to buy these robots for developing countries like Bangladesh because of the price. But some organizations and universities in Bangladesh are opening R&D sector to design and implement them in a cost effective way and in a small scale which signifies a promise in the evolution of technology. In the field of robotics to cope up with the advanced world, more concentration should be given to get the benefits of robotics. The products can't maintain the international standard due to the limitations of R&D sectors.

This design can be extented in size and also in weight lifting capacity. There is huge scope in design of the movement from source to destination. Here fixed code has been loaded in microcontroller which may create complexion in increasing number of destination.

## V. CONCLUSION

The robots can make our life easy and with the advancement of technology robots can be a part of our everyday life. Researchers and Engineers of developing countries like Bangladesh are working very hard to pull up the living standard of the country [14]. Robots can be seen everywhere like as in technical innovation, including self-educated technicians to educate researchers. Unfortunately, those innovations and researches could hardly effect our humanitarian developments and social life due to the lack of ability and opportunity of commercialization. This paper focused on designing a waiter robot and implemented this kind robot using simple technologies with equipments available in local market having very low cost. This robot has been designed to work effectively in restaurant, office and hospital environments. Some future work includes the use GPS module to call the robot. Another way would be giving command to the robot by using a smart android app, where the customer will give their command by typing in the apps. The project has been implemented for two rooms, but further it can be designed to operate for more rooms or destinations.

## REFERENCES

[1] Kerstin Severinson-Eklundh, Anders Green, Helge Hüttenrauch, Social and collaborative aspects of interaction with a service robot, International Journal Robotics and Autonomous Systems, 42 (2003) 223–234

[2] Tzou Jyh-Hwa, Wu-Feng, Su Kuo, L, "The development of the restaurant service mobile robot with a Laser positioning system," in Control Conference, 2008. CCC 2008. 27th Chinese, Kunming, China, July 16-18, 2008, pp. 662 – 666.

[3] National Restaurant Association (2014, May 14). New research shows restaurant technology plays part in dining decisions. [Online]. Available: http://www.restaurant.org/NewsResearch/News/New-research-shows-restaurant-technology-plays-par

[4] Zhu Bing, Xu-yan Zhou, Tan Bin, Peng Xu-Ge, "Research and design of restaurant service in wireless call system," in Artificial Intelligence and Education (ICAIE), 2010 International Conference, Hangzhou, China, Oct 29-30, 2010, pp.437-440.

[5] Franklin, D.F.; Kahn, R.E.; Swain, M.J.; Firby, R.J., "Happy patrons make better tippers: creating a robot waiter using Perseus and the Animate Agent architecture," in Automatic Face and Gesture Recognition, 1996., Proceedings of the Second International Conference, Killington, VT, Oct 14-16, 1996, pp. 253 – 258.

[6] Noor, M.Z.H.; Rahman, A.A.A.; Saaid, M.F.; Ali, M.S.A.M.; Zolkapli, M., "The development of Self-Service Restaurant Ordering System (SROS)," in Control and System Graduate Research Colloquium (ICSGRC), 2012 IEEE, Shah Alam, Selangor, July 16-17, 2012, pp.348 – 353.

[7] Tan-Hsu Tan, Ching-Su Chang, Yung-Fu Chen, "Developing an Intelligent e-Restaurant With a Menu Recommender for Customer-Centric Service," in Systems, Man, and Cybernetics, Part C: Applications and Reviews, IEEE Transactions, vol. 42, Sept, 2012, pp.775-787.

[8] Harish Phapale, Prashant Patil, Sanjay Turate, Anshu Chaudhary, Prof.Mahesh Bhagwat, E-RESTAURANT MANAGEMENT SYSTEM USING ZIGBEE and IoT, International Journal of Advanced Research in Computer Engineering & Technology (IJARCET), Volume 5, Issue 4, April 2016

[9] R upali Saple, Ketaki Zunjarrao, Siddhi Patil, Ketan Deshmukh, Robotic Waiter, International Journal for Innovative Research in Science & Technology, Volume 1 | Issue 11 | April 2015 ISSN (online): 2349-6010.

[10] Neeti Malik, Neetu Rani, Alpana Singh, Pratibha, Srishti Pragya, Serving Robot New Generation Electronic Waiter, International Journal for Innovative Research in Science & Technology| Volume 2 | Issue 11, April 2016, ISSN (online): 2349-6010.

[11] M. Asif, M. Sabeel, Mujeeb-ur-Rahman, Z. H. Khan, Waiter Robot, Solution to Restaurant Automation, MDSRC - 2015 Proceedings, 14-15 November, 2015 Wah/Pakistan.

[12] SakariPieska, Markus Liuska, JuhanaJauhiainen, AnttiAuno, Intelligent Restaurant System Smart- menu, 4th IEEE International Conference on Cognitive Info communications, December 2–5, 2013 , Budapest, Hungary.

[13] Sakari Pieska, Mika Luimula, Juhana Jauhiainen and Van Spiz, Social Service Robots in Wellness and Restaurant Applications, Journal of Communication and Computer 10 (2013) 116-123.

[14] Md. Khalilur Rhaman, Sabbir Ahmed Khan, and Shifur Rahman Shakil, State of Art in Robotics and Embedded Systems: Bangladesh Perspective, Journal of Automation and Control Engineering, Vol. 4, No. 1, February 2016.

978-1-5386-2307-7/17/$31.00 ©2017 IEEE

# Experimental Analysis of Harmonic and Power Factor for Various Lighting Loads

Khan Mohd. Mostafa Hasan[1], Dr. Muhammad Saifur Rahman[2], Dr. Md. Abdur Rafiq[2]
[1]Department of Electrical and Electronic Engineering (North Western University, Khulna, Bangladesh)
[2]Department of Electrical and Electronic Engineering (Khulna University of Engineering and Technology, Bangladesh)
mostafa_duet@yahoo.com, msrbitk@yahoo.com, mdabdurrafiq2003@yahoo.com

*Abstract—*

**Compact Fluorescent Lamps (CFL) and Light Emitting Diode (LED) Lamps are increasingly becoming popular as energy saving lamps among the consumers due to their long lifetime, good luminous output and encouragement from the governments of many countries.LEDs and CFLs are reported to be less real power consuming, energy efficient and economic than their counterpart incandescent lamps. However, as nonlinear loads, LEDs and CFLsdrawextremely distorted currents with poor power factor. Hence, a massive usage of LEDs and CFLs forlighting is likely togenerate important power qualitycrisis as well as loss for the power companies. This paper reports the experimental results of harmonicanalysis up to 50th order, power factor and luminous efficiency in terms of lumen per watt for some widely used CFL, LED, fluorescent and incandescent lamps for indoor lighting. Experimental results show that LED could be more economical, higher luminous efficiency with lower harmonic absorbing lighting source than CFL, fluorescent and incandescent lamps.**

***Keywords— CFL, LED, Harmonics, PowerFactor, Total Harmonic Distortion(THD), Lumen.***

## I. INTRODUCTION

In the developing countries, 20% to 50% of their total electricity consumption is used for lighting loadwhereas 19% of total electricity consumption in the world is used for indoor and outdoor lighting[3,5]. For lighting the indoor and outdoor space an enormous amount of energy is required. The population of the world increasing day by day and the technology is upgrading quickly thus the requirement of power for lighting also increasing. The increasing demand of power introduces different types of electronic lamps known as energy saving lamps. These lamps produces more light at less power and are replaces the incandescent lamps. Energy saving lamps requires considerably smaller amounts of active power than incandescent lamps when they have the same luminous flux. The price of ESL's are more than Incandescent Lamps (ISL) and Halogen Lamps but the low power consumption and longer life time is the main reason of using ESL [11]. All of the ESL's like compact fluorescent lamp (CFL) and Light Emitting Diode (LED) use electronic ballast which makes the power factor (PF) very low. The lower PF represents higher Reactive Power and lower active power. So a significant analysis becomes indispensable to find the most effective lighting technology.

The goal of this paper is to find the lighting technology which economizes the energy consumption and ensure stable power system. For doing this, an experiment was done with some available lamps of different types. CFL, LED, Fluorescent Lampand Incandescent lamps were randomly chosen and analyzed for electrical and optical indexes. The electrical indexes analyzed by connecting the lamps in series with a Digital Power Meter which is energized by an Ideal Power Source. For Optical characteristics a multi-Photometer was used. Finally a comparison was made to take a decision for most efficient lighting technology.

## II. MAIN INDEXES FOR ANALYSIS

In this experiment, amount of active power and the harmonics created by each lamp were tested. The active power is the power which is actually consumed by the consumers and only pays for the active power he consumes. The active power is the product of voltage and current multiplied a factor called Power Factor (PF), the active power is represented by

$$P = V * I * \cos\varphi$$

Where $V$ is the applied voltage across the load, $I$is the current through load and cosφ is the PF which determines the actual energy consumes by the load. The other important characteristic of ESL is the production of harmonics which create some adverse effect on power system like loss of power and instability of the power system.

### A. Power Factor

The factor $\cos\varphi_1$is the power factor which is the cosine angle of the displacement phase angle between 1st harmonic Voltage wave and the current wave. PF can also express as ratio of Active power (P) to Apparent Power (S).

$$PF = \frac{P}{S} = cos\varphi$$

The PF determines how much active power is used. The Energy saving lampsuses electronic ballast which produces low power factor. The low PF increases the reactive power which established some adverse effecton the power system like heating the cable, increasing the cable size, larger line loss, poor voltage regulation and the low efficient power system.

### B. Harmonics

Another important byproduct of ESL is the production of harmonics. The RMS value of voltage across and current through the ESL are decomposed of distorted wave which

978-1-5386-2307-7/17/$31.00 ©2017 IEEE

contain multiple frequency of the main frequency wave. The harmonics wave can be sub-divided into even and odd harmonics. The even harmonics produced by the ESLs tested in the laboratory was very low and neglected. The total amount of harmonics present in the main RMS voltage is called Total Harmonics Distortion (THD). So the total RMS voltage and current can be expressed as [2]

$$V_{rms}^2 = V^2 + V_{THD}^2$$

And $I_{rms}^2 = I^2 + I_{THD}^2$

Where $V$is the first harmonic component of the voltage wave and$I$is first harmonic component of the current wave. $V_{THD}$ and $I_{THD}$ are the distorted component contained with the main frequency signal or first harmonic wave.

### C. Luminus Flux

Luminous flux is the perceived power of visible light emitted by a light source measured in lumen. If 1 candela of luminous flux is imposed uniformly across a solid angle of one steradian, the total luminous flux is one lumen which is SI unit for measuring the intensity of the light.In this experiment luminous flux is expressed as lumen as the output of the Multi-Photometer is measured in lumen.

## III. EXPERIMENTAL METHOD

Experiments were conducted in an enhanced Laboratory. The lamps were tested individually for THD, % Voltage harmonics, % Current Harmonics, up to 50th order. Later PF and Lumen was also measured. There are 11 lamps of different types are used in this experiment. First 4 of them are CFL lamp and the next 4 is LED lamp. The 9th one is a Fluorescent Lamp and then an incandescent lamp was tested. The last one is an intelligent LED lamp which is an emergency light and can operate during load shading up to 3 hours. They are randomly chosen at their different rating and manufacturer.

### A. Rated operating condition

An Ideal ac testing source (DPS 1005) was used which is a product of everfine corporation. The power supply unit is a AC power supply and is based on SPWM (Sine-wave Pulse Width Modulation) technology. It has large load capability, low harmonic distortion, easy operation, and the output voltage and frequency are adjustable to meet the operator requirements. The testing source has voltage stability upto ≤0.2%,frequency stability upto ≤0.03% and THD anout ≤0.5% at ( 40.0Hz~65.0Hz). Allthe lamps are rated at 220V ac. So the power supply is made to supply 220 volt through a power meter. In this experiment a Digital Power Meter (DPM) "EVERFINE PF9800"was used to measure the Power, PF, THD and Harmonics up to 50th order. The accuracy of measuring the Voltage, Current and Power of the DPM are about ±0.5%, and PF and frequency can be measured ± 0.005% accurately. The Experimental setup for the experiment is shown in the figure 1.

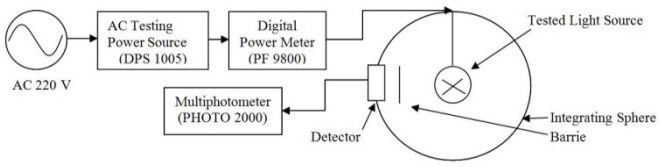


Figure 1: The Experimental Diagram

### B. Optical measuring condition

For measuring the luminance of the lamps an Intelligent Multi-photometer "PHOTO 2000" was used. The multi-photometer mainly consists of photometer head and display unit. The photometer head is fitted inside an integrating sphere coated by white phospor mixture. The tested lamp was fitted at the centre of the sphere and left for one hour at rated nominal voltage (220 Volt) for warm-up the phospor mixture. For operating at standerd temperature, the temperature was kept between 22ºC to 25ºC by airconditionar. After the warm-up phase all the electrical and optical parameters were measured.

Figure 2: Experimental set-up

### C. Data entry and analysing

The data were taken from the displays of the measuring instruments. For harmonics analysis the order of the harmonics need to be changed manually. The taken data were then analyzed with the help of Ms-Excel and the figures were drawn with the help of Origin lab software.

## IV. PERFORMANCE AT RATED VOLTAGE

The experiments were done in rated RMS 220 volt AC. To avoid any kinds of misunderstanding with the manufacturer of the lamps, the lamps were named from 1 to 11 with their type and power rated on the body of the lamps. All the CFL and LED lamps chosen were rated below 26W. The Incandescent lamp is chosen at 60W in order to get a good amount of light. A Fluorescent Lamp of 40W is 4 feet long and can't be fitted inside the integrating sphere of the Multi-Photometer. So a 20W Fluorescent Lamp of 2 feet long is chosen to fit the Fluorescent Lamp inside the integrating sphere. The rated power of the body of every lamp was not found. All the CFL and LED lamps have closer measured power to the rated power but are the measured power was little less than the rated power. In case of Incandescent and Fluorescent Lamp the measured power is more than the power they have rated in their body. So it can be said that the lamps does not represent the ideal one of respective types.

From all the taken data, only PF, Input power, Current, %THD, Lumen and Lumen/Watt were compared in the below Table 1 to make a significant comparison among them.

*Table 1:Comparison of different indexes among the tested lamps.*

| *Lamp details* | *PF* | *Input Power (W)* | *I (A)* | *%THD* | *Lumen* | *Lumen/ Watt* |
|---|---|---|---|---|---|---|
| CFL-1 (24 W) | 0.552 | 18.68 | 0.153 | 134.8 | 1326.4 | 71.01 |
| CFL-2 (23W) | 0.595 | 22 | 0.167 | 114.8 | 1355.2 | 61.60 |
| CFL-3 (26W) | 0.569 | 19.25 | 0.153 | 123.6 | 1311.5 | 68.13 |
| CFL-4 (14W) | 0.631 | 13.97 | 0.1 | 87.7 | 630.43 | 45.13 |
| LED-1 (12W) | 0.975 | 11.91 | 0.055 | 16.8 | 1107.4 | 92.98 |
| LED-2 (7W) | 0.958 | 6.25 | 0.029 | 18.4 | 721.74 | 115.48 |
| LED-3 (5W) | 0.198 | 2.75 | 0.062 | 27.3 | 195.23 | 70.99 |
| LED-4 (3W) | 0.471 | 2.91 | 0.027 | 52.2 | 289.1 | 99.35 |
| Fluorescent Lamp(20W) | 0.381 | 22.77 | 0.27 | 7.2 | 680.23 | 29.87 |
| Incandicent (60W) | 1 | 64.5 | 0.292 | 1.5 | 945.66 | 14.66 |
| Inteligent Emergency light (12W) | 0.499 | 5.91 | 0.053 | 156.4 | 468.2 | 79.22 |

From the above Table It is seen that the PF of Incandescent lamp is unity. It consumes more power as compared to the ESL's. The Lumen produced per Watt by incandescent lamp is only 14.66. This shows that the incandescent lamp has a very low efficiency. Fluorescent Lamp is also a less efficient lamp as the lumen produced per watt is only 29.87. It also creates a very low PF. On the other hand, the PF produced by the CFL lamps are ranged about 0.5 to 0.6 whereas highest PF of LED ranged about 0.95 to 0.98. So it can say that in PF index of Energy saving lamp is better than Fluorescent Lamp energy conversion technique. But ESL produces a big amount of THD. In CFL THD is about 90% to 140% whereas LED has minimum %THD index about 15% to 20%. CFL produced more lumen per watt than Fluorescent Lamp and Incandescent lamp. That's means CFL have better efficiency than Incandescent lamp. In case of LED lamps the PF is very high and also the lumen produced per watt is more than CFL lamps. The THD are also lower than the CFL, this means that the LED is more efficient than the other lighting technologies. The 11$^{th}$ one is an intelligent emergency light made with LED and battery combined circuit. This lamp has superior advantages of being operated without supply up to 3 hours depending on the charged condition of the battery. The production of harmonics is shown in Figure 3 to Figure 12 respectively. %Voltage and %Current harmonics are shown in the same figure using different bars. Black bars representing % Voltage harmonics contribution whereas crossed bars representing %Current harmonics contribution. %Voltage and % Current are taken along Vertical axis and the order of the harmonics is taken along horizontal axis. The even ordered harmonics are very low for every kind of lamps and are neglected and only Odd order harmonics were shown.The production of voltage harmonics are persists only for little order for every kind of lamps which is shown in the figures.The Current harmonics of odd order persists up to higher order in the ESL.

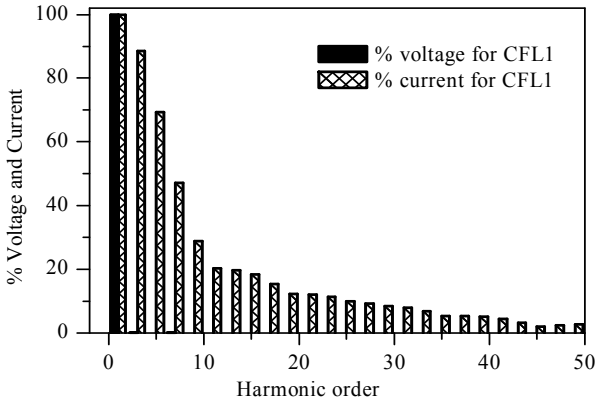


Figure 3: %Voltage and %Current for CFL-1

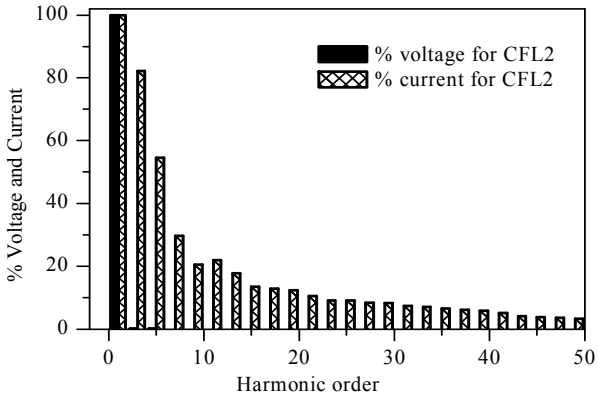


Figure 4: %Voltage and %Current for CFL-2

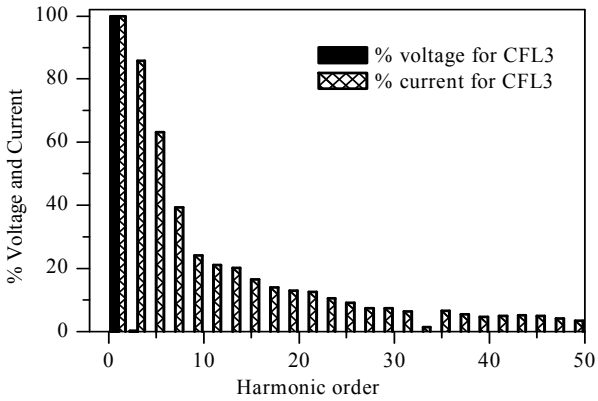


Figure 5: %Voltage and %Current for CFL-3

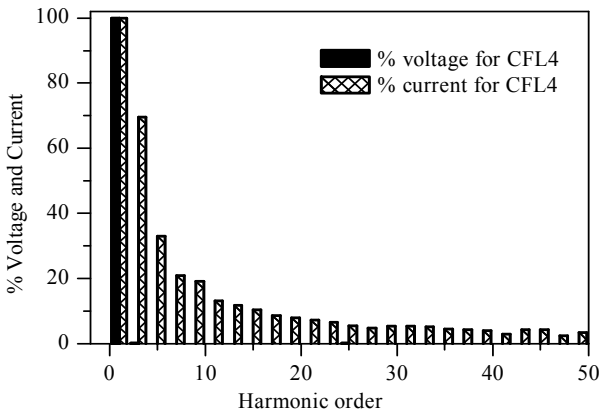


Figure 6: %Voltage and %Current for CFL-4

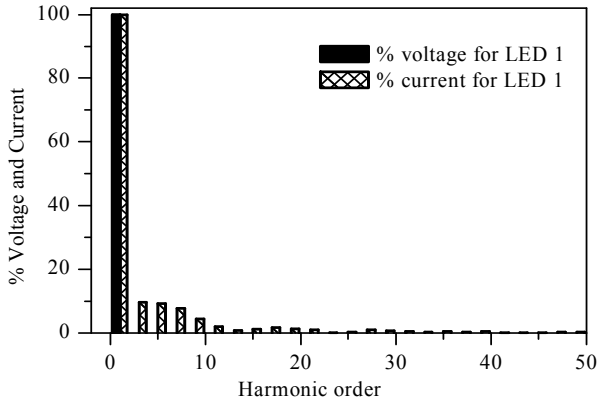


Figure 7: %Voltage and %Current for LED-1

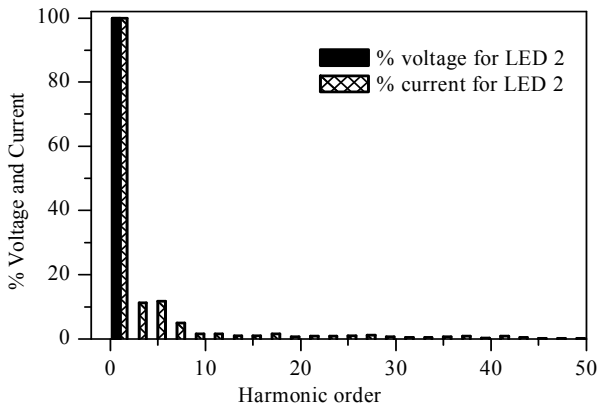


Figure 8: %Voltage and %Current for LED-2

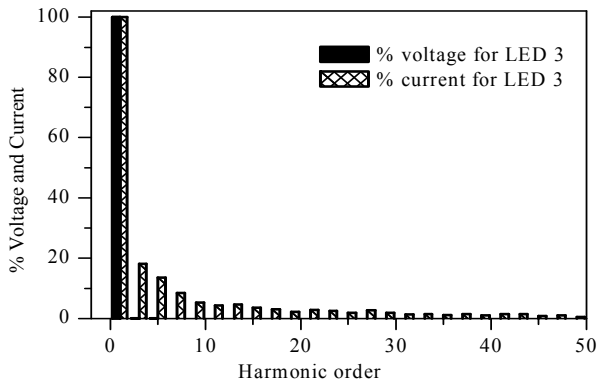


Figure 9: % Voltage and %Current for LED-3

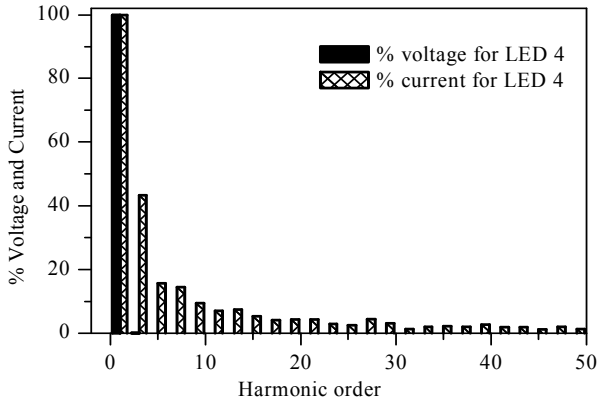


Figure 10: %Voltage and %Current for LED-4

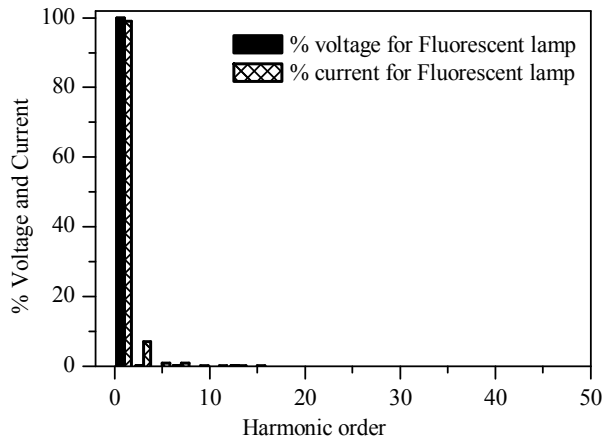


Figure 11: %Voltage and %Current for Fluorescent Lamp

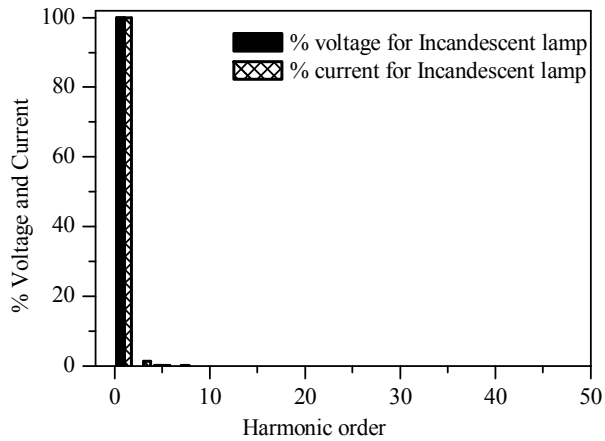


Figure 12: %Voltage and %Current for Incandescent Lamp

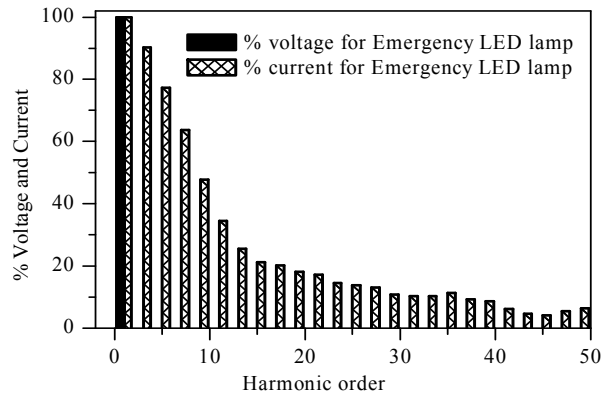


Figure 13: %Voltage and %Current for Emergency LED Lamp

## V. MEASUREMENT RESULT

From the above figure12, and the table 1, it is seen that Incandescent lamp has the best PF and THD index but the low optical efficiency makes the lamp less efficient. From the Figure 11 and Table 1, Fluorescent Lamp has a better THD index but the PF index and optical efficiency is very low. So the Incandescent and Fluorescent Lamp technology should be avoided for their lower efficiency. From Figure 3 to Figure 6, it is seen that the CFL technology creates current harmonic distortion up to a higher level and also their PF is very low. But the higher optical efficiency makes the technology more

efficient. In case of LED lamps Figure 7 to Figure 10 and Figure 13, it is seen that the production of current harmonics are lower than CFL technology. Its higher optical efficiency makes this technology superior than the other lighting technology.

## VI. FUTURE SCOPE AND CONCLUSION

From the above discussion, the LED technology is better than the other lighting technology. If the amount of harmonics in LED technology could be avoided, this technology would be more efficient. So an enormous amount of research is needed to reduce the harmonics in LED technology. On the other hand CFL technology may also be considered as future lighting technology if the PF and harmonics index could be improved. There are several methods available for PF correction and harmonic reduction. A capacitor may improve the PF and harmonic parameter up to a certain limit. For better performance PI controller may be good solution. So, there is huge scope for researching a better method of energy conversion in Energy Saving Lamps to make efficient and stable power system design.

## RFERENCES


[1] V. Ćuk, J.F.G. Cobben, W.L. Kling, and R.B. Timens "An Analysis Of Diversity Factors Applied To Harmonic Emission Limits For Energy Saving Lamps", Harmonics and Quality of Power (ICHQP), 2010 14th International Conference on, September 2010.

[2] Alberto Dolara and Sonia Leva, "Power Quality and Harmonic Analysis of End User Devices", Energies 2012, 5(12),5453-5466; doi:10.3390/en5125453, December 2012.

[3] GulShahzad, Heekwon Yang, ArbabWaheed Ahmad and Chankil Lee, "Energy-Efficient Intelligent Street Lighting System Using Traffic-Adaptive Control", IEEE Sensors Journal , Volume: 16, Issue: 13, July1, 2016

[4] Sheryl Nathan, Noel Shammas and Steve Grainger, "Energy Saving Using Light Emitting Diodes In Lighting Applications" Universities Power Engineering Conference, 2006. UPEC '06. Proceedings of the 41st International, 6-8 Sept. 2006.

[5] R. Simanjuntak, P. Dupuis, L. Canale, N.I. Sinisuka, G.Zissis,"Power Quality of Energy Saving Lamps under Wide Voltage Variations", Industry Applications Society Annual Meeting, 2014 IEEE, 5-9 Oct. 2014.

[6] ZahariIvanov, HristoAntchev, "Energy Saving Lamps as Sources of Harmonic Currents", American Journal of Electrical Power and Energy Systems, September 28, 2015.

[7] F.V. Topalis, "EFFICIENCY OF ENERGY SAVING LAMPS AND HARMONIC DISTORTION IN DISTRIBUTION SYSTEMS", IEEE Transactions on Power Delivery, Vol. 8, No. 4, October 1993

[8] Wan Norsyafizan W. Muhamad, MohamadYusof Mat Zain, NorfishahWahab, Noor HafizahAbdul Aziz, RosmaliniAbdKadir, "Energy Efficient Lighting System Design for Building", Intelligent Systems, Modelling and Simulation (ISMS), 2010 International Conference, February 2010.

[9] Craig DiLouie, "Advanced Lighting Controls", The Fairmont Press, 2006.

[10] Sohel UDDIN, Hussain SHAREEF, Azah MOHAMED, Mahammad A HANNAN," Harmonics and thermal characteristics of low wattage LED Lamps", PrzegladElektrotechniczny, 2012.

[11] F. G. Montoya and J. Castillo, " Power Quality in modern lighting: comparison of LED, microLED and CFL lamps", International Conference on Renewable Energies and Power Quality (ICREPQ'16) Madrid (Spain), 4th to 6th May, 2016.

[12] IEC Std 61000-3-2, Limits for Harmonic Current Emissions (Equipment Input Current ≤ 16A Per Phase), (Ed. 3.2, 2009).

# Model Reference Adaptive Control for Surface Permanent Magnet Synchronous Machine

Md. Kamal Hossain[1] and S.M.Rakiul Islam[2]
[1]Dhaka University of Engineering & Technology, Gazipur, Bangladesh
[2]University of Connecticut, Storrs, USA
k.hossain@duet.ac.bd

*Abstract*— **Sensorless rotor position estimators of permanent magnet synchronous machines (PMSMs) are extensively used in medium and high speed applications. In this paper, proposed a novel method of adaptive control based model reference motor speed estimator. The proposed control technique is designed considering a 0.2 kW surface permanent magnet synchronous motor and verified using MATLAB/Simulink environment. In this control technique, designed a model reference adaptive control (MRAC) observer for estimating the motor speed error. The control structure is designed considering the cascade control mechanism with the inner current and outer speed control loop using the decoupling control technique. The quadratic load is considered for simulation to verify the control approach. The result shows that the ability of MRAC controller performance to track the rotor position and convergence the actual motor speed of the PMSM.**

***Keywords— PMSM, MRAC, Quadratic load, Current controller, Speed estimation and speed control.***

## I. INTRODUCTION

THE permanent magnet synchronous machines (PMSMs) has been become very popular in the last few years for their higher efficiency, torque, high precision and maintenance free operation. At present, PMSMs are being broadly used in electric and hybrid electric vehicle systems due to their distinguishable advantages. PMSM can be operated in both motoring and generator mode. In motoring mode, it converts electric power to mechanical power and vice versa in generator mode. The PMSMs are used in different applications such as pumps, fans, propeller, hybrid electric vehicle, home appliances etc. So, the nature of load would be different based on the applications. In this paper, the motoring mode of PMSMs with quadratic loads has been considered only for estimating the motor speed [1]-[4].

In order to minimize the size, cost, enhance the functionality and the reliability of the drive system, to control the PMSM properly much research effort has gone and developed various control technique in the last 60 years. A field oriented vector control is required to achieve high performance PMSMs for precise rotor position information in the conventional PMSM drive systems. Usually, the optical encoders, resolvers and hall-effect sensors are used in PMSMs for achieving the motor speed information. The exact linearization of motor model has been provides to control rotor position through linear control techniques [5]. In recent years, the robust control has been developed by applying higher order sliding mode technique for obtaining the rotor position tracking difficulties [6]. The nonlinear adaptive control algorithm has been proposed regarding the state of art of the sensorless drives in industrial applications [7]. The dynamic performance of sensorless drive system has been developed in last decades compared to the development of sensor based drives system to estimate the rotor speed [8]. Usually, the above control technique developed based on the well established technique such as proportional integral derivative (PID), Extended Kalman Filter (EKF), Fuzzy logic, Neuron network, genetic algorithm etc. Meanwhile, new control theories were developed. So, new windows also have opened for controlling PMSMs [9].

Adaptive controls are established since 1960s [10]. The control parameters in adaptive control are updated regularly with respect to time. Model reference predictive control is an adaptive control method in which a model of the plant is developed and the parameters value are changed based on the actual systems output and the models output with respect to input [11]. The adaptive control is a general technique and has been extensively investigated both for linear and nonlinear systems [12]. The problem in adaptive control of parameter estimation for nonlinear system has been solved considering the time varying reference model both for the uncertainties of parameters and the input saturation [13]. On the other hand the difficulties of direct model reference adaptive control with actuator amplitude and rate saturation has discussed [14]. Therefore, in this paper the model reference adaptive control (MRAC) is introduced for controlling the surface permanent magnet synchronous motor speed and verifying the controller performance in order to track the rotor speed. The presented work is solved the adaptive control problem for rotor position estimation of PMSMs by developing the mathematical model of nonlinear system using dq model and considering all parameters are unknown. At first, the mathematical model for the PMSMs is developed and then the parameter is obtained for a 200 Watt motor using 220 Volt DC supply voltage. After obtaining the circuit parameters, the model of PMSM is simulated in the MATLAB/Simulink environment. The

978-1-5386-2307-7/17/$31.00 ©2017 IEEE

proposed rotor speed controller is designed based on MRAC algorithm and the performance of the controller is verified using the simulation result. The simulation result is compared with the previous study and validates the proposed model based adaptive control strategy for estimating the senseless rotor speed [15]. Rest of this paper is organized as follows: the mathematical model for PMSMs and the adaptive law of MRAC is described in section II & III respectively. The simulation block of PMSM and control blocks are presented in section IV. In section V, represents the simulation result with short description and finally the work is concluded in section VI.

## II. MATHMATICAL MODEL OF PMSM

### *A. Modeling of Machine Parameters*

The development of technology, semiconductor devices, and high quality magnetic materials into commercial production has incited several manufacturers to launch various PMSM with control mechanism into the market. Basically, PMSMs have been applied to servo drives for a long time. Recently, it has become popularity in industrial applications. Permanent magnet synchronous motor is propulsion set which transforms electrical energy to kinetic energy. Usually, the features of a permanent magnet machine are highly dependent on the rotor structure. A high switching frequency is required of a voltage source inverter in a surface magnet machine due to low inductance. The direct and quadrature inductance of the non salient pole machine are approximately equal. Therefore, in this paper consider the surface mounted PMSM. The vector control technique is a well established control technique for three phase systems. In order to achieve high torque sensitivity of a PMSM drive system the vector control is applied via decoupling the q-axis and d-axis components of stator currents in the synchronously rotating reference frame. Normally, the system is linearized by keeping the d-axis stator current, $i_d$ set to zero and the motor torque is linearly proportional to the q-axis current, $i_q$.

In the d-q frame the equation of the system can be represented by the following equations:

$$L_q \frac{di_q}{dt} = V_d - R_s i_q - n_p \omega \varphi \tag{1}$$

$$J \frac{d\omega}{dt} = \tau - \tau_L \tag{2}$$

$$\tau = n_p \varphi i_q \tag{3}$$

Where, $i_d$, $i_q$,, $V_d$ and $V_q$ are the d-axis and q-axis currents and voltages respectively. $L_q$ is the mutual inductance, $R_s$ is the stator resistance, J is the inertia constant, $n_p$ is the number of poles, $\omega$ is the motor speed, $\tau_L$ is the load torque, and $\varphi$ is the flux. The machine model of PMSM is-

$$J \frac{d\omega}{dt} = n_p \varphi i_q - \tau_L \tag{4}$$

In frequency domain the rotor speed of PMSM is represent as-

$$\omega(s) = \frac{n_p \varphi i_q - \tau_L}{Js} \tag{5}$$

The equation (5) represents the first order system under vector control method of a PMSM. The unknown load disturbance, temperature variation and other factors are making the first order system inaccurate. In addition, the mechanical time constant of PMSM is longer than electric time constant. Therefore, the permanent magnet synchronous machine drive model can be modeled as first order system with large inertia and parameters variation. As a result, the conventional PID controller cannot satisfy the requirement in high performance drive application [16]-[19].

If the load is quadratic then the equation will be slightly different represents by equation (6).

$$J \frac{d\omega}{dt} = n_p \varphi i_q - \tau_L - B_m \omega_m \tag{6}$$

Where, $B_m$ is viscous friction.

### *B. D-Q reference frame for current controller*

The permanent magnet synchronous machine is modeled by a well known d-q technique [20]. Since, the stator current of PMSM is only related to its rotating speed $\omega_r$, so we chose the model with calculation of currents as the reference model and choose the permanent magnet synchronous motor model as actual plants. The PMSM type used in this paper is surface type and the model of two phase rotating coordinate system (d-q) is as follows:

$$\frac{d}{dt}\begin{bmatrix} i_d + \frac{\varphi_f}{L} \\ i_q \end{bmatrix} = \begin{bmatrix} -\frac{R}{L} & \omega_r \\ -\omega_r & -\frac{R}{L} \end{bmatrix} \begin{bmatrix} i_d + \frac{\varphi_f}{L} \\ i_q \end{bmatrix} + \frac{1}{L}\begin{bmatrix} V_d + \frac{R\varphi_f}{L} \\ V_q \end{bmatrix} \tag{7}$$

Where, L is stator inductance in both b and q axis and these are equals as the rotor is round, $\Phi_f$ is flux linkage by permanent magnet, and, $\omega_r$ is the rotor speed.

$$\text{Let, } \acute{\imath}_d = i_d + \frac{\varphi_f}{L}, \quad \acute{\imath}_q = i_q, \; \acute{v}_d = v_d + \frac{R\varphi_f}{L}, \quad \acute{v}_q = v_q \tag{8}$$

Then, the reference model can be expressed as:

$$\frac{d}{dt}\begin{bmatrix} \acute{\imath}_d \\ \acute{\imath}_q \end{bmatrix} = \begin{bmatrix} -\frac{R}{L} & \omega_r \\ -\omega_r & -\frac{R}{L} \end{bmatrix} \begin{bmatrix} \acute{\imath}_d \\ \acute{\imath}_q \end{bmatrix} + \frac{1}{L}\begin{bmatrix} \acute{v}_d \\ \acute{v}_q \end{bmatrix} \tag{9}$$

Using the estimated parameters in above equation can be expressed as,

$$\frac{d}{dt}\begin{bmatrix} \widehat{\imath_d}' \\ \widehat{\imath_q}' \end{bmatrix} = \begin{bmatrix} -\frac{R}{L} & \widehat{\omega_r} \\ -\widehat{\omega_r} & -\frac{R}{L} \end{bmatrix} \begin{bmatrix} \widehat{\imath_d}' \\ \widehat{\imath_q}' \end{bmatrix} + \frac{1}{L}\begin{bmatrix} \acute{v}_d \\ \acute{v}_q \end{bmatrix} \tag{10}$$

## III. DESCRIPTION OF MRAC AND ADAPTIVE LAW

### A. Model Refrence Adaptive Control

Model reference adaptive system is a parameter estimation method based on the system stability theory and used to minimize the model errors. In 1960 MRAC was developed in MIT. The MRAC structure includes three parts: reference model, actual plant and adaptive law, as shown in Fig.1. The main idea is to construct the output model with the same physical meaning. One model is considered as the original plant with the equation of parameters known as adjustable model. Another model is known as reference model of PMSM with unknown parameters. The reference and the adjustable model are in parallel and excited by the same external input. The outputs of two different models are compared with each other to get the error signal. The $y_1$ and $y_2$ is the output state vector of the reference model and the actual model respectively. The reference model with its state vector $y_1$ provides a given performance index, and the performance index compared by the actual model of the vector $y_2$. The error of the comparison is adjusted by the adaptive law, and to update the parameters of the adjustable model. So, the output state of the adjustable model $y_2$ can be quickly and steadily close to the output state of the reference model $y_1$, which means that the difference vector "*e*" is close to zero. The following task is to find the reference model, the actual model and the adaptive law.

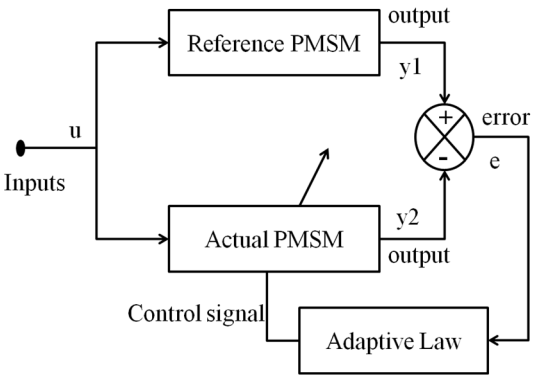


Fig.1. Block diagram of MRAC speed estimation

### B. Adaptive Law

In order to construct the MRAC algorithm with excellent performance, the selection of adaptive law is the key and the adaptive law is one kind of proportional integral (PI) controller with the combination of error estimation. The error is estimated by MRAC first and control algorithm is applied in latter. There are three design methods of adaptive law: local optimization, stability and super stability. In this paper, super stability method is proposed by Popov, which have strong logical reasoning and can get good results. According to the theory of Popov [21], if the feedback system is stable, it must meet the following two aspects:

a. The nonlinear time varying feedback link satisfies the Popov integral inequality:

$$\eta(0,t) = \int_0^t v^2 \omega d\tau \ \geq -\gamma^2 \tag{11}$$

$\forall t \geq 0$, $\gamma^2$ can be any finite positive real number.

b. Transfer matrix H(s) = C (sI - A)$^{-1}$ is strictly positive definite matrix.

Solve the Popov integral inequality through the reverse, then error is approximately to zero at initial state. The estimation speed is convergent to the true value, so the MRAC is asymptotically stable. The specific process of the reverse solution is follows:

$$v = e = i' - \hat{i}', \qquad \omega = J(\hat{\omega}_r - \omega_r)\hat{i}' \tag{12}$$

Take $v$ and $\omega$ into Popov integral inequality (11), then we can get:

$$\eta(0,t) = \int_0^t e^T J(\hat{\omega}_r - \omega_r)\hat{i}' d\tau \ \geq -\gamma^2 \tag{13}$$

In accordance with the general structure of the model reference adaptive parameters, $\hat{\omega}_r$ will be taken the proportion of the form as follows:

$$\hat{\omega}_r = \int_0^t F_1(v,t,\tau)d\tau + F_2(v,t) + \hat{\omega}_r(0) \tag{14}$$

Here, $\hat{\omega}_r(0)$ is the initial value. The above equation represents proportional integral structure with general meaning. After deformation and calculation, the following equation for PI controller can be derived,

$$\hat{\omega}_r = \int_0^t k_i \left[i_d\hat{i}_q - i_q\hat{i}_d - \frac{\varphi_f}{L}(i_q - \hat{i}_q)\right] d\tau + k_p \left[i_d\hat{i}_q - i_q\hat{i}_d - \frac{\varphi_f}{L}(i_q - \hat{i}_q)\right] + \hat{\omega}_r(0) \tag{15}$$

From equation (15) the angle, $\hat{\theta}_r$ can be estimated using equation (16). The equation for the rotor position angle is in below:

$$\hat{\theta}_r = \int_0^t \hat{\omega}_r d\tau \tag{16}$$

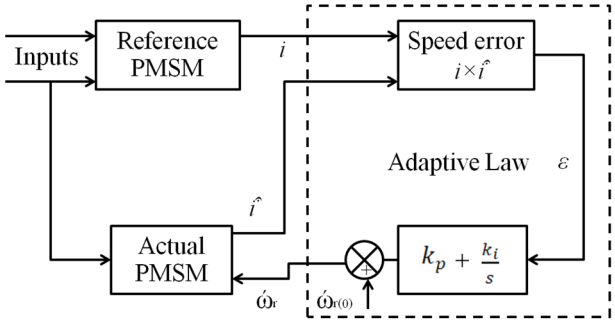


Fig.2. Block diagram of Adaptive control

The term $\left[i_d\hat{i}_q - i_q\hat{i}_d - \frac{\varphi_f}{L}(i_q - \hat{i}_q)\right] = \varepsilon$ is known as error signal. According to (15) the MRAC structure can be

constructed as shown in Fig.2. From (15) it is observed, that the estimated speed has the relationship with the angular deviation of the stator current vector '$i$' and '$\hat{i}$' are the reference and estimated current of PMSM respectively. Through, the adjustment of adjustable model the estimated current can be close to the reference model current. Therefore, the output of angular speed can be approximated to the actual speed of the machine.

## IV. SIMULATION AND CONTROL BLOCK

The block diagram of the overall system is shown in Fig.3. The overall control structure is based on the cascaded control mechanism with the inner current control loop and the outer speed control loop respectively. The outer PI controller is sets a reference for the torque producing in the quadarature axis stator current, $i_{_qref}$. On the other hand, the flux producing the direct axis current $i_{_dref} = 0$ as there is no flux linkage involved. The decoupling algorithm is introduced due to cross coupling between the d-axis and q-axis for implementing the controller in order to control the PMSM.

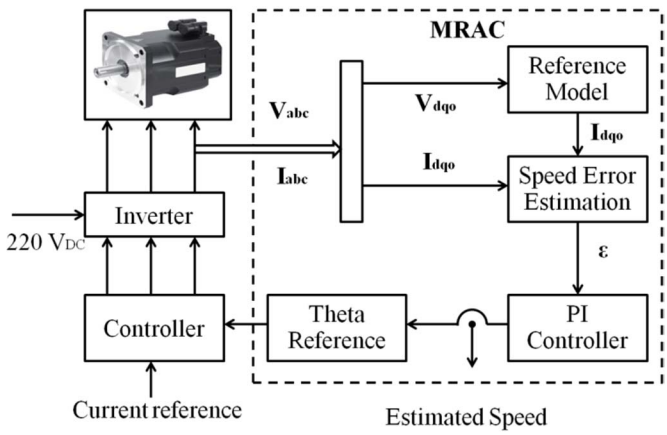


Fig.3. Overall block diagram of PMSM speed control

The voltage source inverter that uses the PWM switching technique for producing AC output from DC input. The magnitude and frequency of the inverter output can be controlled by controlling the PWM signals. The switching losses and harmonic reduction of an inverter are depends on the modulation technique. In this work, the sinusoidal pulse width modulation technique is used for controlling the inverter outputs. The modulation index used in the inverter is given as-

$$m = \frac{2 \times V_a}{V_{DC}} \tag{16}$$

The parameters used for simulation are shown in the Table.1. The simulation was done in MATLAB 2015b in Simulink version 8.6. In SIMULINK, the adaptive control based MRAC method is shown in Fig. (4), the major difficulties are to select the appropriate PI controller parameters in simulation process of rotor speed estimation. The suitable parameters value is not only make the estimation of the speed of PMSM but also it can reduce the current noise of the whole system.

Table.1. Parameters used for simulation

| | |
|---|---|
| Rated power, P (W) | 200 |
| Rated Voltage, V(DC) | 220 |
| Rated speed, ω (rpm) | 3000 |
| Stator resistance, R (ohm) | 2.875 |
| Stator inductance, L (H) | 8.5e-3 |
| Rotor flux linkage, ϕ (Wb) | 0.175 |
| Moment of Inertia, J (kgm2) | 8e-2 |
| Friction factor, B | 3.035e-6 |

In this paper, the PI controller parameters are designed by the application of the method using Ziegler Nichols approach. According to the principle of the PI design, first select the proportion controller value then the integration controller value. The optimal performance of the PMSM is achieved by the MRAC controller through repeating the debugging with tuning the PI controller value.

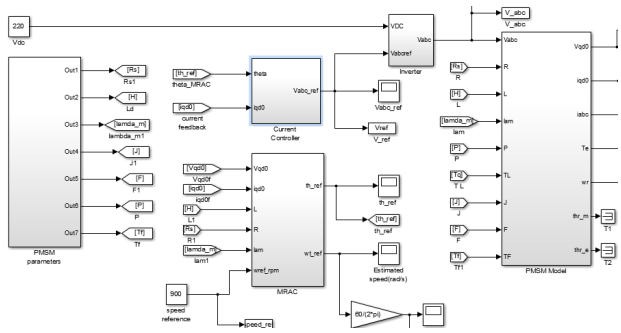

Fig.4. Overall simulation model of PMSM system based on MRAC method

Based on the above theory the simulation model of MRAC based method is built shown in Fig. (4). Overall simulation system is consists of the PMSM, inverter, abc to dq reference frame transformation, current regulation, speed regulation and speed estimation.

## V. SIMULATION RESULTS AND DISCUSSION

In order to verify the validity of the proposed speed control of PMSM based MRAC algorithm the simulation experiments are carried out in MATLAB Simulink environment. The motor parameters are constant without the inductance. The actual speed of the motor and the estimated speed of the motor are shown in Fig. 5-7. The green trace indicates the set value of speed reference, whereas the red trace is the measured speed and the blue trace indicates the estimated speed of the motor respectively. The speed is not steady at the starting time. However, several second later the machine runs with its synchronous speed. The estimated and the measured speed are also different in transient condition but the pattern of change of rotor speed is same in transient condition. The simulation result shows that after 5 sec the estimated speed obtained the actual motor speed. It is also indicates that both controller has the ability to tract the actual reference speed of the motor after few

sec running the simulation model. The speed error between the actual measured value and the estimation value are shown in Fig. 6. When the estimated speed is equal to the actual rotor speed the error signal become zero.

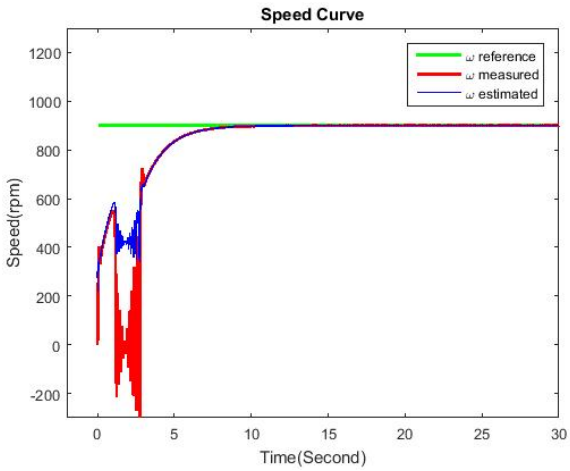


Fig.5 Actual speed, reference speed and estimated speed of PMSM

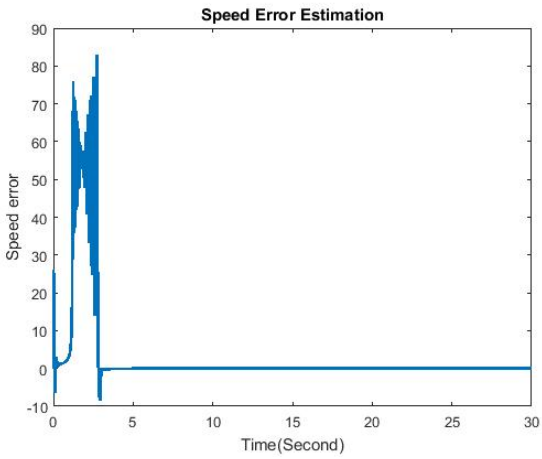


Fig.6 Speed error curve between actual and estimation

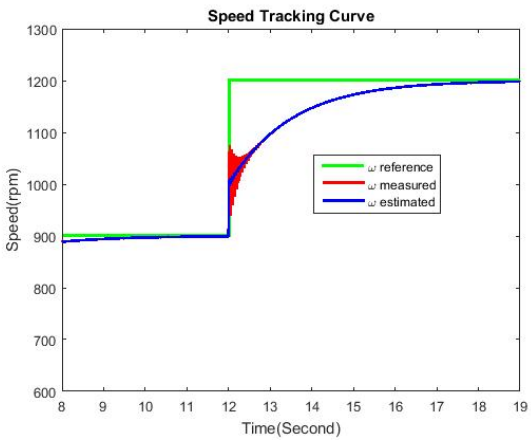


Fig. 7 Speed tracking capability of MRAC of PMSM

The controller performance of motor speed tracking is verified by motor speed variation after the stable operation of the rotating speed mutation: at t = 0 to 12 sec the speed of rotation, $\omega_r$ = 900r/min; when t≥ 12 sec the speed of rotation, $\omega_r$ = 1200 r/min. These conditions are shown in Fig.7. The motor torque versus speed curve is shown in Fig.8. The Toque becomes stable when it reaches the reference speed. The performance of current controller is shown in Fig.9.

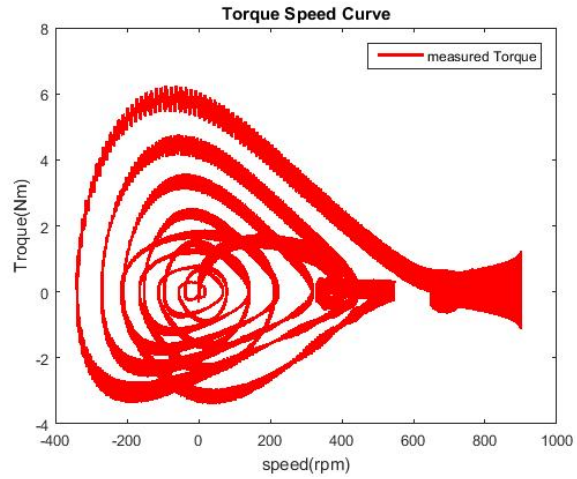


Fig.8 Torque versus Speed curve

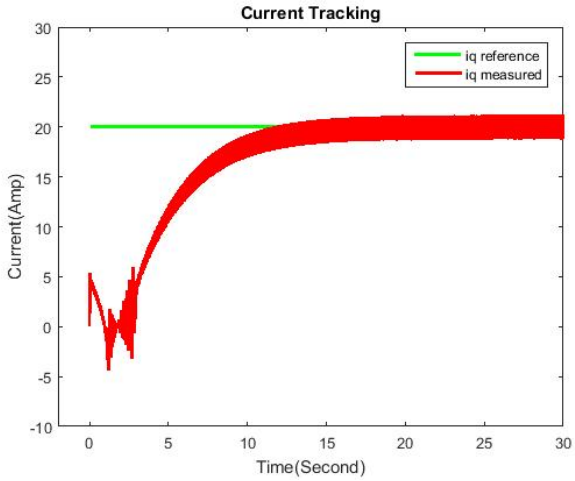


Fig.9 Current tracking capability of controller

## VI. CONCLUSION

In this paper designed the model reference adaptive controller based on the theory of Popov in order to speed control of PMSM. The performance of control ability of inner current controller and the outer speed controller have been verified by MATLAB/Simulink. The simulation result shows that, the speed of MRAC can estimate the motor speed and the controller can able to track the motor reference speed of the PMSM. This system completely omits the speed detection link, eliminates the error caused by the installation of speed sensor and also simplifies the overall system structure. The simulation performance of the proposed control system represents the validity of the MRAC system and it will have a very good research value in experimental test.

## ACKNOWLEDGMENT

The authors are like to express hearted deep gratitude to Prof. Dr. Ali M. Bazzi for his insightful comments and encouragement for successfully finished this project work.

## REFERENCES

[1] Bin Zhang, Yaohua Li, *'A PMSM Sliding Mode Control System Based on Model Reference Adaptive Control',*1990 IEEE Industry Application Society Annual. Meeting, Vol.1, pp 632-638.

[2] Haisheng Yu , Qingwei Wei, Dongqing Wang *'Adaptive Speed Control for PMSM Drive Based on Neuron and Direct MRAC Method'*, Intelligent Control and Automation, *The Sixth World Congress on*, Volume:2, pp 8117 - 8121, June 21 - 23, 2006, Dalian, China. WCICA 2006.

[3] N. Golea, A. Golea and M. Kadjoudj, "*Robust MRAC Adaptive Control of PMSM drive under General Parameters Uncertainties," 2006* IEEE International Conference on Industrial Technology*,* Mumbai, 2006, pp. 1533-1537.

[4] Xiaojun Ma, Liang Feng,' *Model Reference Adaptive Control for Permanent Magnet Synchronous Motor Servo System'*, Proceedings of IEEE, International Conference on Electrical Machines and Systems, pp 1483 - 1487, 2008. ICEMS 2008, Wuhan, China.

[5] M. Zribi and J. Chiasson, "*Position control of a pm stepper motor by exact linearization*," IEEE Transactions on Automatic Control, vol. 36, no. 5, pp. 620–625, 1991.

[6] M. Defoort, F. Nollet, T. Floquet, and W. Perruquetti, "*Higher order sliding mode control of a stepper motor*," in Proceedings of the 45th IEEE Conference on Decision and Control, December 2006, pp. 4002–4008.

[7] R. Marino, S. Peresada, and P. Tomei, "*Nonlinear adaptive control of permanent magnet stepper motors*," Automatica, vol. 31, no. 11, pp. 1595–1604, 1995.

[8] M. Pacas, "*Sensorless drives in industrial applications*," *IEEE Ind. Electron. Mag*., vol. 5, no. 2, pp. 16–23, Jun. 2011.

[9] Paul C. Krause, Oleg Wasynczuk, Scott D. Sudhoff, and Steven Pekarek, *Analysis of Electric Machinery and Drive Systems*, 3rd ed. Hoboken, NJ: Wiley, 2013.

[10] X. Yue, D. M. Vilathgamuwa and K.-J. Tseng, "*An observer-based robust adaptive controller for permanent magnet synchronous motor drive with initial rotor angle uncertainty*," IEEE Trans. Energy Convers., vol. 20, iss.1, pp. 115-120, Mar. 2005.

[11] Jen-Guey Chen, "*Adaptive PI Control to Realize Sinusoidal Ripple Current Charging in Battery Charger Systems*," M.S. thesis, Dept. Electrical. Eng., University of Connecticut., CT, 2015.

[12] L. Abida and H. Kaufman, "*Model reference adaptive control for linear time varying and nonlinear systems*," 1982 21st IEEE Conference on Decision and Control*,* Orlando, FL, USA, 1982, pp. 287-288.

[13] I. Y. Tyukin, D. V. Prokhorov, and C. van Leeuwen, "*Adaptation and parameter estimation in systems with unstable target dynamics and nonlinear parametrization*," IEEE transactions on automatic control, vol. 52, no. 9, pp. 1543–1559, 2007.

[14] A. Leonessa, W. M. Haddad, T. Hayakawa, and Y. Morel, "*Adaptive control for nonlinear uncertain systems with actuator amplitude and rate saturation constraints*," International Journal of Adaptive Control and Signal Processing, vol. 23, pp. 73–96, 2009.

[15] Li Yujie, Cao Shaozhong, "*Model Rreference Adaptive Contorl System Simulation of Permanent Magnet Synchronous Motor*," Advanced Information Technology, Electronic and Automation Control Conference (IAEAC) , 2015, pp. 498-502.

[16] K.-H. Kim and M.-J. Youn, "*A nonlinear speed control for a PM synchronous motor using a simple disturbance estimation technique*," IEEE Trans. on Ind. Electron., vol. 49, iss. 3, pp. 524-535, Jun. 2002.

[17] K.-T. Chang, T.-S. Low and T.-H. Lee, "*An optimal speed controller for permanent-magnet synchronous motor drives*," IEEE Trans. Ind.

[18] L. M. Grzesiak, T. Tarczewski and S. Mandra, "*Permanent magnet synchronous servo-drive with state position controller*," 13th Power Electronics and Motion Control Conference, EPE-PEMC 2008, pp. 1071-1076.

[19] A. Tewari, *Modern control design: with MATLAB and SIMULINK*, John Wiley and Sons, 2002.

[20] R. Krishnan, *Electric motor drivers - Modeling, Analysis, and Control*. Upper Saddle River, NJ: Prentice Hall, 2001.

[21] M. Chen Pengnian, Han Xianwei and Chen Shuzhong, "*Adaptive Control. Beijing",* Tsingua University press, 2011.

2017 3rd International Conference on Electrical Information and Communication Technology (EICT), 7-9 December 2017, Khulna, Bangladesh

# Word Sense Disambiguation of Bangla Sentences Using Statistical Approach

Saiba Nazah
Department of Computer Science & Engineering
Chittagong University of Engineering & Technology
Chittagong, Bangladesh
Email: saiba.nazah11@gmail.com

Mohammed Moshiul Hoque, Md. Rajib Hossain
Department of Computer Science & Engineering
Chittagong University of Engineering & Technology
Chittagong, Bangladesh
Email: mmoshiulh@gmail.com

***Abstract*— Word sense disambiguation is the process of identifying appropriate sense or meaning of a word in a sentence, when the word has multiple meanings. In this work, we propose a disambiguation system using Naïve Bayes classifier and ANN to disambiguate the Bangla words. Naïve Bayes classifier for training phase and using statistical information gained from the training dataset the unknown ambiguous words are predicted and gives detecting the correct sense using ANN. For the testing phase we used general regression neural network. The result of the evaluation shows that the proposed word sense disambiguation system can disambiguate the ambiguous Bangla word with 82% accuracy.**

***Index Terms*— Natural language processing, word sense disambiguation, Naïve Bayes classification, ambiguity, confusion matrix.**

## I. Introduction

There are lots of words are found in every natural languages that denote multiple meanings based on the contexts of their use within texts. Word sense disambiguation (WSD) is the technique of assigning sense labels to occurrences of an ambiguous word and computationally determining which sense of a word is activated by its use in a particular contextual scenario [1,2]. Like other languages, Bangla language also possesses a huge ambiguity problem. For example, the word "**কমলা** (orange)" may denote at least two senses based on its use in different types of construction, such as (i) in one sense it can be interpreted as a fruit (**ফল**) in the sentence, **আমি একটি কমলা খেতে চাই**. And (ii) in another sense, it can be treated as color (**রঙ**) in the sentence, **আমার জামা টি কমলা**. Therefore, words with multiple meanings are ambiguous in nature and they posit serious challenges in understanding a natural language text by machine.

Due to the inherent linguistic competence of humans, they can able to capture the substantial contextual sense of an ambiguous word within a specific syntactic structure. Since the machine does not hold such capabilities and competence, it requires some mechanism to do this disambiguation task successfully. WSD is one of the most appealing and challenging research problems in Bangla language processing. It is noticeably essential for language understanding and text processing applications. The WSD system can be used for disambiguation of content in various domains of Bangla language such as Bangla message understanding, human-computer communication, Bangla to other language machine translation system, Bangla information retrieval, Bangla speech processing and so on.

In this paper we provide a technique that can disambiguate Bangla ambiguous words from a sentence. To achieve this goal the whole task was divided into two phases; the training phase and the classification or prediction phase. In the training phase, a training corpus associated with proper senses of each ambiguous word is built that is used to statistically analyze the ambiguous words with the Naïve Bayes probabilistic technique. In the classification phase, ANN is used. With general regression neural network we have used the training model for retrieving the actual sense of a given sentence.

## II. Related Work

Although there is a plenty of research activities are conducted in word sense disambiguation in other language, there is very few work in Bangla language. A graph-based WSD system for Bangla is proposed by Das et al [3]. This system used for Bangla word sense disambiguation and applied to get correct lexical choice in Bengali-Hindi machine translation. It is evaluated for ten Bengali words only. Pandit et al. proposed an approach on WSD in Bangla using kNN algorithm [4]. The k-NN algorithm determines the classification of a new sample from its k nearest neighbors. Using k-NN they achieved an accuracy of over 71%. A Naïve Bayes classification algorithm is used to disambiguate the Bangla word [5]. The authors proposed a lemmatized system that achieved the accuracy of around 80%. Chakrabarty et al. proposed a system called BenLem that developed a lemmatization algorithm and shows its application for Bangla word sense disambiguation with 81% accuracy [6]. A dictionary based approach is used for Bangla WSD [7] with 82% accuracy. A statistical approach has been proposed for word sense disambiguation by Brown et al. [8]. A supervised AI based method proposed in [9] the used novel deep learning algorithm, namely, Deep Belief Networks (DBN) that makes an improvement to Word Sense Disambiguation (WSD) in term of accuracy. A corpus-based algorithm for performing word sense disambiguation is proposed in [10]. The algorithm

978-1-5386-2307-7/17/$31.00 ©2017 IEEE

does not need to train on many senses of each word; it uses instead probability that certain concepts will occur together. The role of multilingual features in improving word sense disambiguation is proposed in [11]. The use of semantic clues derived from context translation is used to enrich the intended sense and therefore reduce ambiguity. A supervised technique is used for word sense disambiguation in Bangla to English MT by Pasha [12]. We use statistical approach to develop a WSD technique for Bangla sentences due to better accuracy and efficiency.

## III. Proposed WSD Method

The main objective of our work is to develop a technique that can disambiguate the sense of a Bangla ambiguous word in a given sentence. The overall procedure of proposed WSD technique illustrates in Fig. 1.

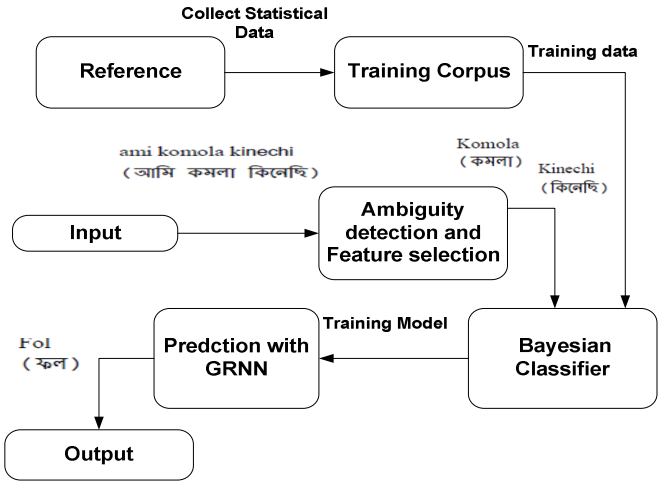


Figure 1. Proposed framework of Bangla WSD technique.

Firstly, we collect the sample data from several Bangla books, newspapers, blogs and web as reference and form a database. Based on these data a training corpus will build. The datasets will preprocess for converting into a desired format into the corpus from which the training model is developed. Naïve Bayes classifier will use to develop the training model based on the corpus. Apply general regression neural network (GRNN) to predict the correct sense of ambiguous word in the sentence with acceptable accuracy for unknown testing dataset.

### A. *Training Corpus*

Training corpus is a collection of texts, containing manually validated linguistic information, attributed to the original texts. The information is used by machine-learning programs to create a statistical model. Since there is no sense annotated Bangla corpus or sufficient amount of parallel corpus for Bangla, we had to create our own to use in our statistical approach for disambiguating word sense. In training corpus we have used a particular format from which the values are used in the training model. The format consists of three rows one for a particular representation. A segment of the training corpus is shown in Table I.

TABLE I. PORTION OF TRAINING CORPUS

| | |
|---|---|
| **Example 1** | |
| **1st row** | komola fol rong khai<br>(কমলা ফল রঙ খাই) |
| **2nd row** | 12 7 5 9 |
| **3rd row** | 8 1 |
| **Example 2** | |
| **1st row** | Paka dokho porepokko kaj<br>(পাকা দক্ষ পরিপক্ক কাজ) |
| **2nd row** | **10 6 4** 5 |
| **3rd row** | 3 1 |
| **Example 3** | |
| **1st row** | gorom tapmatra rag matha<br>(গরম তাপমাত্রা রাগ মাথা) |
| **2nd row** | 11 6 5 7 |
| **3rd row** | 2 5 |
| **Example 4** | |
| **1st row** | kushum dim halka gorom<br>(কুসুম ডিম হালকা গরম) |
| **2nd row** | 12 7 5 6 |
| **3rd row** | 1 5 |

In Table I, the first row represents ambiguous word, two different meaning and featuring word respectively. Number of occurrences is represented in the second row for each word of the first row. Third row represent the number of occurrence found for each meaning of the feature word.

### B. *Training Model*

The training model contains training algorithm to train the data which are each associated with a probabilistic estimated value and this trained data are send to the classifier block for comparing with the testing data. In the training model for learning step where a classification model is constructed there is a describing set of predetermined classes. We get the values from the training corpus for further calculation in model. We have used Naïve Bayes classifier for this model.

### C. *Naive Bayes Classification*

The probabilistic model of naive Bayes classifiers is based on Bayes' theorem. The idea of the Bayes classifier which we will present for word senses is that it looks at the words around an ambiguous word in a context window. Each content word contributes potentially useful information about which sense of the ambiguous word is likely to be used with it. The classifier does no feature selection. The supervised training of the classifier assumes that we have a corpus where each use of ambiguous words is labeled with its correct sense. A Bayes classifier applies the Bayes decision rule when choosing a class, the rule that minimizes the probability of error. Bayes decision rule is shown in (1).

Decide if $P(s'|c) > P(s_k|c)$ for $s_k \neq s'$ (1)

The Bayes decision rule is optimal because it minimizes the probability of error. This is true because for each individual case it chooses the class (or sense) with the highest conditional probability and hence the smallest error rate. The error rate for a sequence of decisions (for example, disambiguating all instances of w in a multi-page text) will

therefore also be as small as possible. We usually do not know the value of $P(s_k|c)$ but we can compute it using Bayes *rule* as (2).

$$P(s_k|c) = \frac{P(c|s_k)}{P(c)} P(s_k) \tag{2}$$

$P(s_k)$ is the prior probability of sense $s_k$, the probability that we have an instance of $s_k$ if we do not know anything about the context. $P(s_k)$ is updated with the factor $\frac{P(c|s_k)}{P(c)}$ which incorporates the evidence which we have about the context, and results in the posterior probability$P(s_k|c)$. If all we want to do is choose the correct class, we can simplify the classification task by eliminating $P(c)$ (which is a constant for all senses and hence does not influence what the maximum is). We can also use logs of probabilities to make the computation simpler. Then, we will assign $w$ to the sense $s'$ using (3).

$$\begin{aligned} s' &= argmax_{s_k} P(s_k|c) \\ s' &= argmax_{s_k} \frac{P(c|s_k)}{P(c)} P(s_k) \\ s' &= argmax_{s_k} P(c|s_k)P(s_k) \\ s' &= argmax_{s_k}[logP(s_k|c) + logP(s_k)] \end{aligned} \tag{3}$$

### D. *General Regression Neural Network*

This is the step where a model is used to predict class labels for given new data. For classifying future or unknown objects accuracy of the model is estimated. The known label of test sample is compared with the classified result from the model. In our system we have used general regression neural network for predicting the correct sense as the predictor. As there is less real data found for Bangla ambiguous words and thus our training set being not too large GRNN is preferred for prediction as it gives better performance in function approximation with less training set. Generalized regression neural networks are a kind of radial basis network that is often used for function approximation. GRNNs can be designed very quickly. $newgmn(x, T, SPREAD)$ takes $R_x Q$ matrix of column input vectors, $S_x Q$ matrix of column target vectors, and the SPREAD of the radial basis functions (default = 1.0), and returns a new generalized regression network. The larger SPREAD is, the smoother the function approximation will be. To fit data closely, use a SPREAD smaller than the typical distance between input vectors. To fit the data more smoothly use a larger SPREAD. Here a radial basis network is designed from inputs X and targets T, and simulated.

$net = newgrnn(x, t)$ ;

$y = sim(net\ x)$

In our framework, the model is trained based on the feature word. Suppose if we want to find the meaning of *komola(কমলা)* we take the feature words from the training model. All of the feature words of *komola (কমলা)* correspond to **x** in our system. The output **t** is determined based on the statistical observation by using Bayesian Network. The sense containing higher statistical value represents for the corresponding feature word.

## IV. Implementation

Implementing a system for word sense disambiguation of Bangla language is quite a challenging task due to its lack of resources on Bangla sense-annotate corpus and statistical data. A general purpose computer with Intel core i7 processor of 64 bit windows operating system along with 8GB RAM was used to develop the system in Matlab R2015a platform. Fig. 2 shows a GUI of the develop system that consists of four major parts: training corpus, training model, testing data and final classification.

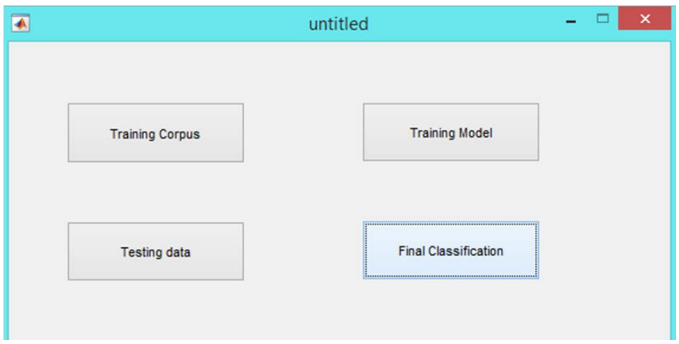


Figure 2. Graphical user interface of the proposed system.

Training corpus contains the training dataset that includes ambiguous words, their corresponding possible senses, and number of occurance with feaature words. Training model summerizes the ambigous words with possible sense and statistical information. Testing data contains the input Bangla sentences with unknown class. Correct meaning of input setences is also shown in this part. Final classifier contains all the training and testing values to predict the final sense with numeric information. This button is combines the whole work into one place to better understand how the disambigution process is happending and how the prediction works. Fig. 3 shows a sample snapshot for sense precition of some sentencse.

```
final_result_Store =

    'The sense of'    '  ami  komola  khabo '        'is'    'fol'
    'The sense of'    '  kaj  paka  koro '           'is'    'dokho'
    'The sense of'    '  kacha  fol  tok '           'is'    'opokko'
    'The sense of'    '  Karim  er  kacha  budhi '   'is'    'odokho'
    'The sense of'    '  holud  kine  ano '          'is'    'mosola'
```

Figure 3. Snapshot of the sense prediction.

From Fig. 3, we illustrates the input and corresponding output for an example sentence ami komola khabo (আমি কমলা খাবো) in the following way.

Input sentence: ami komola khabo (আমি কমলা খাবো)

Ambiguous word: komola (কমলা)

Predictable meaning: fol (ফল)

Original meaning: fol (ফল)

## V. Experimental Results

The proposed Bangla WSD consists of two main phases; learning/training phase and prediction/classification phase respectively.

### A. Trained Dataset

In the Naïve Bayes model the following prior and posterior probability equations (4) are used to calculate the senses of each word based on the dataset.

$$P(sense1) = \frac{total\ no\ of\ occurance\ of\ the\ ambigous\ word\ as\ sense1}{total\ no\ of\ occurance\ of\ the\ ambigous\ word}$$

$$P(sense2) = \frac{total\ no\ of\ occurance\ of\ the\ ambigous\ word\ as\ sense2}{total\ no\ of\ occurance\ of\ the\ ambigous\ word}$$

$$P(feature_{word}) = \frac{total\ no\ of\ occurance\ of\ feature\ word}{total\ no\ of\ occurance\ of\ the\ ambogous\ word}$$

$$P(feature_{word}|sense1) = \frac{occurance\ of\ featureword\ as\ sense1}{occurance\ of\ ambigous\ word\ as\ sense1}$$

$$P(feature_{word}|sense2) = \frac{ocurance\ of\ feature\ word\ as\ sense2}{occurance\ of\ the\ ambigous\ word\ as\ sense2}$$

$$P(sense1|feature_{word}) = \frac{P(feature_{word}|sense1) * P(sense1)}{P(feature_{word})}$$

$$P(sense2|feature_{word}) = \frac{P(fature_{word}|sense2) * P(sense2)}{P(feature_{word})} \quad (4)$$

Among all the entries let us consider one as an example. In the training corpus there are 12 ambiguous words for *'komola (কমলা)'* in a context where the first sense *'fol (ফল)'* is meant 7 times and second sense *'rong(রঙ)'* is meant 5 times and the feature word *'khai (খাই)'* occurred 9 times with the ambiguous word '*komola (কমলা)*' in the context. Where komola(কমলা) was meant as '*fol (ফল)*' 8 times and '*rong(রঙ)*' as 1. Using the above formulas with these statistical values we observe that the probability of the ambiguous word komola(কমলা) as sesnse1 is 0.8889 and sense2 is 0.1111. Table II represents the training model data. For example in the column one Komola (কমলা) is used as a ambiguous word. It has two meanings Fol(ফল) and Rong(রঙ) which represent in the column two and three. The feature word Khai(খাই) for this ambioguous word is used to represent in the column four which is very important for the prediction of the new word. The probability for this word is calculated by using Navie Bayas classifire which is represent in the column five and six. The sense 3 is sued for some words if that has other than two senses otherwise it is zero.

TABLE II: SAMPLE OF THE TRAINING DATASET

| Ambiguous Word | Sense1 | Sense2 | Feature Word | Sense1 PE | Sense2 PE |
|---|---|---|---|---|---|
| Komola (কমলা) | Fol (ফল) | Rong (রঙ) | Khai (খাই) | 0.88889 | 0.1111 |
| Paka (পাকা) | Dokho (দক্ষ) | Porepokko (পরিপক্ক) | Hat (হাত) | 1 | 0 |
| Valo (ভাল) | Shustho (সুস্থ) | Uttom (উত্তম) | Shorer (শরীর) | 0.75 | 0.25 |
| Hat (হাত) | Hosto (হস্ত) | Nipunota (নিপুণতা) | Shelai (সেলাই) | 0.66667 | 0.3333 |
| Boro (বড়) | Boyosh (বয়স) | Poreman (পরিমাণ) | Poribar (পরিবার) | 0.6667 | 0.3333 |

### B. Classification of Testing Dataset

The classification is mainly done in three steps.

- *Step1:* For a given input sentence, the system first determines the ambiguous word in the sentence. For example, the word *komola(*কমলা) detected as an ambiguous word in the sentence "Ami komola kinechi (আমি কমলা কিনেছি)".

  Ami komola kinechi (আমি কমলা কিনেছি) ⟹ komola (কমলা)

- *Step2:* After detecting the ambiguous word in a sentence the selection of the feature word (i.e., kinechi ) for that ambiguous word is done.

  Ami komola kinechi (আমি কমলা কিনেছি) ⟹ kinechi (কিনেছি)

- *Step3:* Finally for the corresponding ambiguous word, the system checks the training model and finds corresponding feature words with associated sense values. The GRNN uses these values for predicting the result of the sentence's ambiguous word and detecting the correct sense automatically. The GRNN follows the following function for result calculation.

$$net = newgrnn(X, F);$$

GRNN requires two parameters for calculation. $X$ is the input form the training model and $F$ is its corresponding output. In our system we took the input $X$ as the ambiguous word and $F$ as the corresponding feature word. As we require a numeric value the parameters we took was converted as numbers using double function. Then we simulate the network with the information for the result of an unknown X to give a value of $F$ as shown below.

| X | F |
|---|---|
| Kheyechi (খেয়েছি) | Fol (ফল ) |
| Jama (জামা) | Rong (রঙ) |
| ……. | …… |

The sense containing higher statistical value represents $\mathbf{F_{new}}$ for the corresponding feature word ($\mathbf{X_{new}}$) of the input sentence. The overall process is shown below:

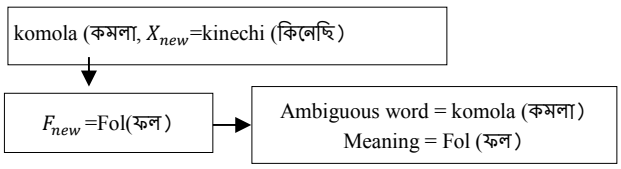


Table III represents the results of the prediction with the original meaning form few input sentences.

TABLE III: THE REPRESENTATION OF THE INPUT SENTENCE, AMBIGUOUS WORD, PREDICTED MEANING AND ORIGINAL MEANING

| Input Sentence | Ambiguous Word | Predicted Meaning | Original Meaning |
|---|---|---|---|
| Komola rong er deyal (কমলা রঙ এর দেয়াল) | Komola (কমলা) | Rong (রঙ) [0.35] | Rong (রঙ) |
| ami komola khabo (আমি কমলা খাবো) | Komola (কমলা) | Fol (ফল) [0.89] | Fol (ফল) |
| ami komola jama porechi (আমি কমলা জামা পরেছি) | Komola (কমলা) | Fol (ফল) [0.56] | Rong (রঙ) |
| paka am khete moja (পাকা আম খেতে মজা) | Paka (পাকা) | Porepokko (পরিপক্ক) [0.17] | Porepokko (পরিপক্ক) |
| kaj paka koro (কাজ পাকা কর) | Paka (পাকা) | Dokho (দক্ষ) [0.70] | Dokho (দক্ষ) |
| ..... | ..... | ..... | ..... |

## C. Evaluation Measurement

In order to evaluate the proposed Bangla WSD system, we use confusion matrix and ROC measures.

### 1) Confusion Matrix

The confusion matrix [13] is used to present the performance evaluation of our approach. We have taken each column of the matrix as the sense in a predicted class while each row represents the sense in an actual class. The confusion matrix of our results is shown in Table IV.

TABLE IV: CONFUSION MATRIX OF PROPOSED APPROACH

| | Predicted Sense1 | Predicted Sense2 | |
|---|---|---|---|
| *Actual Sense1* | TP=18 | FN=3 | 21 |
| *Actual Sense2* | FP=6 | TN=13 | 19 |
| | 24 | 16 | |

From confusion matrix we can calculate the accuracy or identify how often the classifier is correct by adding the true positive and true negative value then dividing the sum by the total number of input sentences. We measure the accuracy using (5), where TP represents true positive and TN true negative.

$$Accuracy = \frac{TP + TN}{total\ \ number\ of\ input\ sentences} \qquad (5)$$

We find the accuracy about 77.5% using confusion matrix. Moreover, we calculate the misclassification rate (22.5%), true positive rate (0.857), false positive rate (0.315), specificity (75%), precision (52.5%) and prevalence (68.4%) respectively. We collected a variety of sentences with ambiguous words from different sources and created our training set. We tested the system by checking how often it predicts correctly. However, our system does not depend on the length of any sentence rather the enrichment of the training dataset. Table.V summarizes the results.

TABLE.V: STATISTICS OF DATA SET

| Attributes | Number of count |
|---|---|
| *Number of sentences collected* | 160 |
| *Number of Ambiguous words* | 50 |
| *Number of training sentence* | 120 |
| *Number of testing sentence* | 40 |
| *Number of correct prediction* | 31 |
| *Sentence/ambiguous word* | 3.2 |
| *Average sense of ambiguous words* | 0.77 |

### 2) ROC Measure

In order to evaluate the system, we use the ROC measure [14]. Fig. 4 shows the ROC curve of the Bangla WSD system. The curve is created by plotting the true positive rate (TPR) against the false positive rate (FPR) with a threshold setting. For threshold point we took the values by subtracting 0.2 from both x and y axis. Thus, the true positive rate is plotted in function of the false positive rate for a cut-off point. From the curve we can see if we have higher x values that is the false positive rate the y value decreases and vice versa. In our classification we get true positive rates at a higher extend than false positive rate thus it indicates a better accuracy of predicting the correct sense.

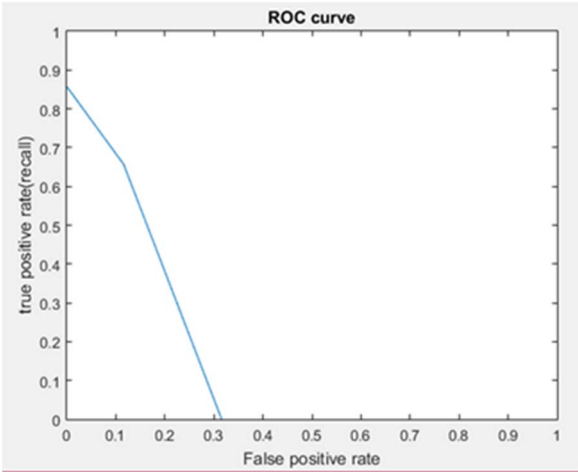


Figure 4. ROC curve on of the WSD system.

## D. Comparison with Existing Methods

The proposed WSD system is compare with two existing methods [4,12]. Pandit et al. [4] used unsupervised graph based method with 71% accuracy. A deep neural network based method is proposed by Pasha et al. [12] and their methods achieved the accuracy of 75%. In contrast to the previous work the proposed system provides the better

performance in term of accuracy (77.5%). Thebe VI summarizes the comparison analysis.

TABLE VI: COMPARISON OF PROPOSED WORD SENSE DISAMBIGUATION APPROACH WITH OTHER EXISTING APPROACHES

| WSD Methods | Learning Method | Classification Method | Accuracy (%) |
|---|---|---|---|
| *Proposed Statistical Based Approach* | Naïve Bayes Classification | General Regression Neural Network | **77.5%** |
| *Memory Based Approach [4]* | Unsupervised | The k-Nearest-Neighbor (k-NN) algorithm | 71% |
| *AI based Approach [12]* | The k-Nearest-Neighbor (k-NN) algorithm | Deep Neural Network | 75% |

The proposed WSD system is implemented on statistical based approach. All data are collected with real statistical value and applied to the classification. Comparing our system with other system on the basis of number of input output is difficult because we do not have the same dataset and there dataset are not online available. Therefore, we compared all approaches based on our own created dataset. We have also used statistical information to build the model which is more reliable to build it. This is the key point for which our approach is performing well than others. Another notable contribution is the introduction of GRNN model in the natural language processing system. It also handles the most difficult ambiguous words to predict accurately. This model does not require any environmental set up so no hazard or impact of noise, light and others.

## VI. CONCLUSION

Word sense disambiguation (WSD) is the task of assigning a meaning to an ambiguous word given the context in which it occurs. WSD serves as an intermediate step for many computing applications. Word sense disambiguation is an emerging research area in the context of Bangla language processing. This work provides an idea to detect Bangla ambiguous word in the sentence. The system is trained with Naïve Bayes algorithm and classified using general regression neural network. The combination of two learning algorithms shows the better accuracy. Evaluation performance with confusion matrix and ROC curve reveals the effectiveness of the proposed Bangla WSD technique. Inclusion of sense annotated corpora in complex sentence structure with more dataset will improve the performance of the WSD system that is left as future work.

## VII. REFERENCES


[1] N. Ide, and J. Veronis, "Word sense disambiguation: The state of the art," *J. Com. Ling.* vol. 24, no. 1, pp. 1-40, 1998.

[2] R. Navigli, "Word sense disambiguation: A survey," *ACM Computing Surveys*, vol. 41, no.2, ACM Press, pp. 1-69, 2009.

[3] A. Das and S. Sarkar. "Word Sense Disambiguation in Bengali applied to Bengali-Hindi Machine Translation" *In Proc. of International Conference on Natural Language Processing (ICON),* vol.10, pp. 20-28, 2013.

[4] R. Pandit and S. K. Naskar, "A memory based approach to word sense disambiguation in Bengali using k-NN method", in *Proc. of IEEE 2nd International Conference on Recent Trends in Information Systems (ReTIS)*, pp. 383-386, July 2015.

[5] A. R. Pal, D. Saha, S. Naskar, and N. S. Dash, "Word sense disambiguation in Bengali: A lemmatized system increase the accuracy of the result", in *Proc. IEEE International Conference on Recent Trends in Information Systems*, pp. 342-346, 2015.

[6] A. Chakrabarty, and U. Garain, "Benlem (A bengali lemmatizer) and its role in WSD", *ACM Trans. Asian Low-Resour. Lang. Inf. Process*, vol. 15, no. 3, February 2016.

[7] A. Haque, and M. M. Hoque, "Bangla word sense disambiguation using dictionary based approach", in *Proc. Int. Conf. on Advanced Information & Communication Technology*, 2016.

[8] P. F. Brown, S. A. D. Pietra, V. J. D. Pietra and R. L. Mercer, "Word-sense disambiguation using statistical methods", In *Proc. of 29th Annual Meeting on Association for Computational Linguistics*, pp. 264-270, 1991.

[9] P. Wiriyathammabhum, B. Kijsirikul, H. Takamura, and M .Okumura, "Applying deep belief networks to word sense disambiguation". *arXiv preprint arXiv:*1207.0396. Jul 2, 2012.

[10] A. Montoyo, A. Suárez, G. Rigau, and M. Palomar, "Combining Knowledge-and Corpus-based Word-Sense-Disambiguation Methods", *J. Artif. Intell. Res.(JAIR)*, vol.23, pp. 299-330, 2005.

[11] E. Fernandez-Ordonez, M. Rada and H. Samer, "Unsupervised word sense disambiguation with multilingual representations", in *Proc. of LREC*, pp. 847-851, 2012.

[12] M. U. R. Pasha, "An analysis of word sense disambiguation in Bangla and English using supervised learning and a deep neural network classifier", B. Sc. Engg. Thesis Report, Dept. of CSE, Brac University, Bangladesh, August 2016.

[13] H. G. Lewis, and M. Brown, M., "A generalized confusion matrix for assessing area estimates from remotely sensed data", *International Journal of Remote Sensing*, vol. *22, no.* 16, pp. 3223-3235. 2001

[14] T. Fawcett, "An introduction to ROC analysis", *Pattern recognition letters*, vol. *27, no.* 8, pp.861-874, 2006.

# A Novel Design of an Intangible Hand Gesture Controlled Computer Mouse using Vision Based Image Processing

Rokhsana Titlee, Ashfaq Ur Rahman, Hasan U. Zaman, and Hafiz Abdur Rahman
Department of Electrical and Computer Engineering, North South University, Dhaka, Bangladesh
rokhsanatitlee@gmail.com, ashfaqnadim@yahoo.com, hasan.zaman@northsouth.edu, hafiz.rahman@northsouth.edu

*Abstract*— **In this paper we presented an intangible hand gesture based computer mouse control system. Our approach uses a novel skin color segmentation technique to control mouse movement. The system uses morphological operations like structuring elements and blob counting. Our system can remove other skin like objects from the background. One of the key features of the system is its simplicity. We have successfully tested our system for an intangible interface between human hand and computer mouse without any complex processing. Various mouse operations like cursor movements, right click and left click have been performed. The system has been implemented using webcam and MATLAB.**

***Keywords— Computer vision, Hand gesture, YCbCr, Skin color detection, blob, structuring element.***

## I. INTRODUCTION

The technological infusion into our lifestyles is unavoidable and in this 21st century it is happening in the massive form. From office room to our bedroom there could be a range of electronic devices that need commands from us to perform their tasks. People always seek the easiest and natural way. In the beginning, we used to command the devices manually, then using the remote controller, after that, the touch and voice controlled technologies came. Now people are trying to use one of the most natural communication modes of human being, which is gesture [1]. It would be a great matter of comfort and joy if we could control our devices just with body movement as hand gesture [2][3][4]. Communication between human and robot (machine) instinctively and directly is still a challenging task. Using gestures for controlling devices is a technology yet to be exploited. In everyday life, our hand is used widely as a natural human to human interaction by gesturing. Hence, it could be also exploited for the communication between human and machine.

The application is countless: virtual gaming, recognition of sign language, robot controlling, smart house or office, controlling TV, driving vehicles, making young children to interact with devices, robot control, lie detection, augmented reality, etc. Hollywood movies already simulated the idea of hand gesture controlled mega-robots and war machine.

Hand gestures are mainly categorized as static gestures and dynamic gestures [5]. Static gestures make use of the hand shape and feature. Dynamic gestures make use of the hand movements. Former gesture recognition technique uses computer vision, whereas the later uses accelerometer.

Vision based recognition is contactless and most natural. It is becoming popular and many works have been done using this method [6][2][7]. However, there are some difficulties in this approach due to the difference in hand sizes, hand position and orientation and the lighting conditions etc. In most of the works, color pointer, gloves, color stickers or other devices are being used [8][10] which are not flexible for interacting in real-time environment. Moreover, these methods also have consequences like additional cost, lack of availability among common people, more amount of maintenance etc. The intangible interfaces with devices would be a major help for taking care of aged and handicapped people since in future the uses of robots will be feasible in human social environment. It would also help to reduce the disadvantages [9] of the usage of tangible devices like mouse, keyboard etc.

In our work, an intangible interface is designed and implemented using vision based real time dynamic hand gestures to perform mouse operations like moving the mouse pointer, clicking left, clicking right with hand gesture. The 2D hand images of bare hand [3] are captured using the computer web camera and are processed using feature extraction algorithm implemented in MATLAB in real-time, so that a mouse can interact with its user in fraction of a second. Since webcam is easily available device, it has been used as an initial testing device for our system.

## II. RELATED WORK

There have been many approaches developed to control mouse movement using video devices with different methods. In [10] the authors have tried to control the mouse pointer using a color detection technique based camera. However, the user needs to wear colored tapes to provide information to the system. In [8] gesture control is performed using the color based segmentation technique. Here red glove is used which makes segmentation easier but the drawback is it adds an extra cost and could be a discomfort to the users. In [11] color pointers have been used. Here, 'Flipping of Image' was needed. Use of color pointer might not be comfortable and it also increases the cost. In [12] the background is very simple, and no dynamic gesture was being performed. We are inspired by a work by Alisha Pradhan and B.B.V.L Deepak [8] where they have designed an interface for mouseless computer handling. However, they have used colored glove for performing the hand gestures. In our

978-1-5386-2307-7/17/$31.00 ©2017 IEEE

work, we have avoided the use of any glove. Rather we used our bare hand and simpler algorithms for controlling the mouse.

## III. Proposed Method

Our system for real-time vision-based gesture controlled mouse contains several stages that are explained in the flowchart of Fig. 1.

### A. Flowchart

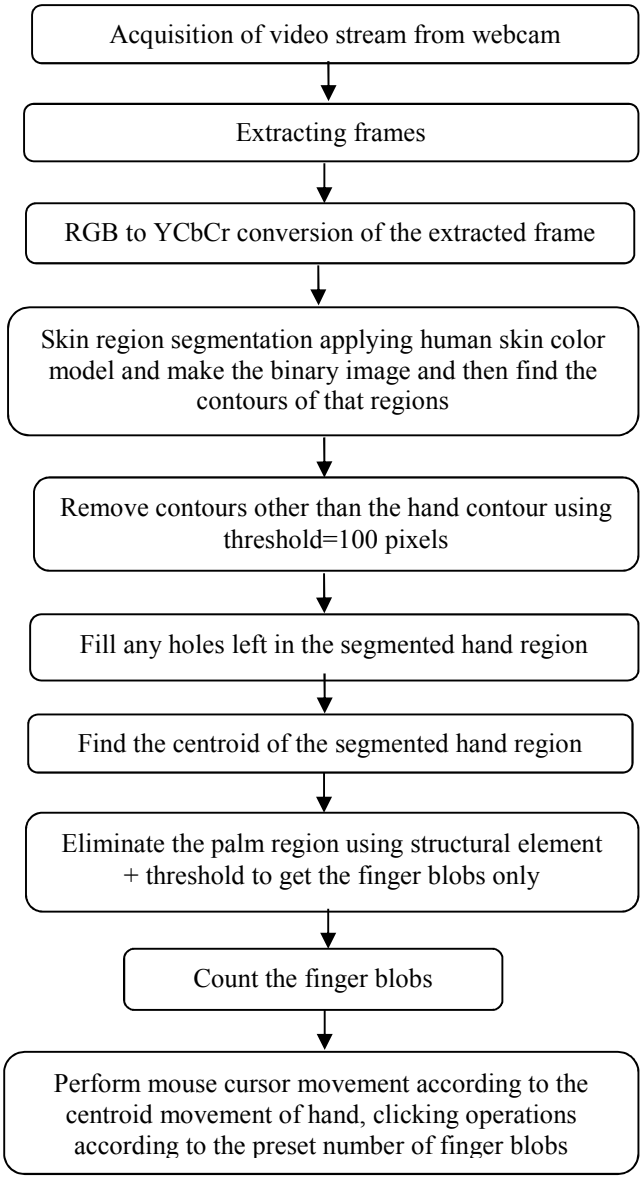


Fig. 1. Flowchart of the proposed method.

### B. Hand Segmentation using YCbCr and Skin Color Modeling

One of the most important steps in our work is image segmentation. There are several processes for hand segmentation. We have used the color based segmentation explained below.

*YCbCr* color space is commonly used in digital video processing and for image and video compression work. It makes the process easy to get rid of some redundant color information. The Y, Cb and Cr values are as follows

$$Y = 0.299R + 0.587G + 0.114B \quad (1)$$
$$Cr = R - Y \quad (2)$$
$$Cb = B - Y \quad (3)$$

Here R, G and B are the red, green and blue components of an RGB image. This color space is popular for skin color modelling due to its transformation simplicity and easier process for separating the luminance component and the chrominance component.

A MATLAB function rgb2ycbcr is used for this conversion. Human skin detection model is a two-class classifier: Skin pixel and non- skin pixel. We assume a pixel $p(x, y)$ in an image $I$. It will be considered as skin if it follows the conditions below:

The luma component: $pY(x, y) > 80$, and
The blue component: $85 < pCb(x,y) < 135$, and
The red component: $135 < pCr(x,y) < 180$

After that we have created a binary image as of same dimension where each pixel's color is either black if it is not considered as a skin color or white if it is considered as a skin color pixel. In Fig. 4, the skin like other objects are being segmented as like a portion of dress of the user.

Fig. 2. RGB image

Fig. 3. YCbCr image

Fig. 4. Skin color segmented image

### C. Contour extraction

After getting the binary image, contour extraction is performed to get the boundary information of the desired regions. The different characteristics of a contour are examined and used as features. So, correct extraction of contour produces accurate feature.

### D. Region filling

Regions are filled to improve accuracy. This completes the hand portion where due to bad lighting conditions erroneous or bad image of gestures were captured. This actually fills the holes left in the gestures. Here 8-connected filling procedure was

applied. There is a function called "imfill" in MATLAB to accomplish this task.

### E. Smaller regions reduction

The object of interest here is the hand. Since, there might be other objects than hand at the background, a threshold area is defined which approximately matches with the hand area. Other objects with skin color are smaller and counted as a noise. Here the skin color objects are represented as blobs and hand is the biggest blob in this case. In this step a threshold of 100 was used, that removed all the connected components that have pixel size lower than 100, it means remove all the objects that have pixels smaller than 100. As a result, only the biggest object is extracted, which is hand in this case. This uses 8-connected neighbors. The functions "bwareaopen" and "bwconncomp" in MATLAB were used.

### F. Calculating the Centroid of the hand region

It is important to find the centroid of the segmented hand region for performing the morphological operations like blob counting and using the structural elements. To find the geometric moments of an $M \times N$ image $i(x, y)$ for the moment of order $(p + q)$, the formula is as follows:

$$\sum_{x=0}^{m} \sum_{y=0}^{n} X^p \, Y^q I(x, y)$$

$m_{00}$: Moment of zero order. It is equivalent to the total intensity of the image.
$m_{10}$: 1st order moment about the $X$- axis.
$m_{01}$: 1st order moment about the $Y$-axis.
Intensity centroid gives the geometric center of the image. It is given by:

$$\bar{X} = \frac{m_{10}}{m_{00}} \qquad \bar{Y} = \frac{m_{01}}{m_{00}}$$

This formula was implemented using the MATLAB procedure "regionprops".

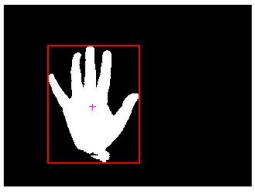

Fig. 5. Centroid of the hand region after performing contour extraction, region filling and smaller regions reduction processes.

### G. Morphological Operations

The objective of this section is to remove the palm region from the segmented hand region so that only the fingers remain in the image. This was done using structural elements. MATLAB has various structuring element shapes like diamond, disk, octagon, square, rectangle, cube etc. Here, we have used "disk". Here disk size is dynamically selected upon minimum distance on the contour area from the centroid. Because depending on distance, the hand image exhibited different sizes.

The structural element was calculated as

strel('disk', r), where

$$r = radius = MinimumDistance + \delta$$

Where $\delta$ = 50% of minimum distance

Here MinimunDistance was calculated as the distance of the first black pixel from the centroid. We added $\delta$ to ensure the blobs created after the operation are separate enough. So, we increased the radius of the structural element by 50%

Fig. 6. Palm region removal using Structuring element

### H. Blob counting

A blob is a region of an image in which some properties are constant or approximately constant; all the points in a blob are considered in some sense similar to each other. Here, the number of finger blobs in the hand gesture was counted out. For this, the "bwlabel" function of MATLAB was used.

Fig. 7. Blob counting and showing

### I. Set hand gestures to control the mouse functions

The mouse functions was performed according to the predefined gestures. Here, it was depended on the number of finger blobs counted in the previous part.

No. of blob = 1, perform movement of the cursor on the screen
No. of blob = 4, perform left click.
No. of blob = 5, perform right click

### J. Interfacing and Controlling the mouse pointer

The java class "java.awt.Robot" was used to access the mouse driver after calculating the center coordinates of hand. The mouse cursor moved according to these coordinates. The MATLAB function "set(0,'PointerLocation',[x,y])" was used for the moving operation. The clicking operations were performed according to the blob counting. Resolution of camera was also an important issue, since it was directly proportional to the resolution of mouse pointer. In our project, the resolution of the input image was 320x240 and the resolution of the laptop monitor was 1280x800.

## IV. Results

The system was tested indoor (classroom and reading room) with good lighting condition during day and night. The distance

of the hand was about 1-2 feet from the screen/webcam, for which we got about 97% accuracy as we have tested the system with different people and with several trials (ex. For testing 10 times, 9 trials were accurate). At 5-6 feet distance, its accuracy was about 60%. This limitation we expect to improve in future so that gesture can be recognize from more practical scenarios. We tested with different people. In Fig. 8, the mouse cursor movement is shown.

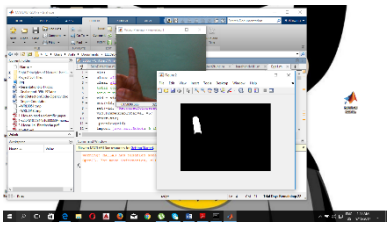

Fig. 8. Movement of mouse pointer on screen

The video preview window and the figure window show us the movement of mouse cursor according to the hand movement. The "PrntScr" command was used to get the snapshot. The pictures in Fig. 9 and Fig. 10 show the mouse on the screen from these screen shots.

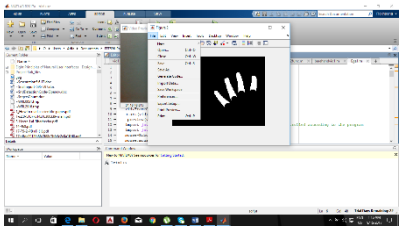

Fig. 9. Left click

In Fig. 9, the left cllick is shown on the figure window as the number of finger blob is 4. Here, the user cllicked on the "File" menu.

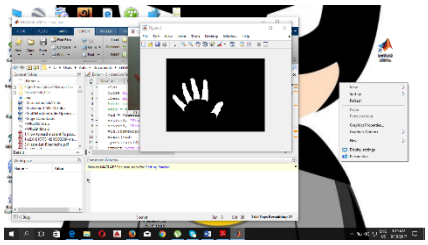

Fig. 10. Right click

In Fig. 10, the right click of mouse is shown as the number of finger blob is 5. To show it clearly, the clicking was performed on the screen.

## V. Conclusion

In this paper we have presented the theoretical model and implementation of a real time vision based bare hand gesture controlled mouse system. Our system works using bare hand and built-in webcam. Mouseless computing is not far from reality anymore. Hand gesture recognition system has its own advantages over other intangible interfacing system like touch and voice controlling computers or other devices in certain scenarios and distance and noise conditions.

## VI. Future Work

Our hand gesture recognition system is not limited for only mouse. It can be used for controlling many other devices, such as TV, robots inside a hazardous nuclear reactor in a convenient way for human and also in some other industrial setup. It can further be applied to control multimedia applications, multiplayer gaming etc. Sensibility of the system to lighting and background conditions can also be improved.

## References


[1] Stefan Reifinger, Frank Wallhoff, Markus Ablassmeier, Tony Poitschke, Gerhard Rigoll, "Static and Dynamic Hand-Gesture Recognition for Augmented Reality Applications," Intl. Conf. Human-Computer Interaction, pp. 727-737, 2007.

[2] Cristina Manresa-Yee, Javier Varona, Ramon Mas and Francisco J. Perales, "Real –Time Hand Tracking and Gesture Recognition for Human-Computer Interaction," Electronic Letters on Computer Vision and Image Analysis, ISSN 1577-5097 E(1):1, Jan. 2000.

[3] Heera Lal Bhadrecha, "Finger Gesture Control Computer Mouse With Image Processing," InternatIonal Journal of electronIcs & communIcatIon technology IJECT, Vol. 6, Issue 1, Jan. – Mar. 2015.

[4] Randeep Singh, Bhartendu Seth, Bhartendu Seth, "A Real-Time Framework for Vision based Human Robot Interaction," Intl. Conf. Intelligent Robots and Systems, Oct. 9 - 15, 2006, Beijing, China.

[5] Erdem Yörük, Ender Konukoglu, Bülent Sankur, and Jérôme Darbon, "Shape-Based Hand Recognition," IEEE Trans. Image Processing, Vol. 15, No. 7, July 2006.

[6] Pragati Garg, Naveen Aggarwal and Sanjeev Sofat,"Vision Based Hand Gesture Recognition," World Academy of Science, Engineering and Technology, International Journal of Computer, Electrical, Automation, Control and Information Engineering, Vol.3, No.1, 2009.

[7] David J. Rios-Soria, Satu E. Schaeffe, Sara E. Garza-Villarreal, "Hand-gesture recognition using computer-vision techniques," 21st International Conference on Computer Graphics, Visualization and Computer Vision, 2013.

[8] Alisha Pradhana, B.B.V.L. Deepak, "Design of Intangible Interface for Mouseless Computer Handling using Hand Gestures," Procedia Computer Science 79 ( 2016 ) 287 – 292, 7th International Conference on Communication, Computing and Virtualization 2016. Available [online]: www.sciencedirect.com.

[9] Radhika Bhatt, Nikita Fernandes, Archana Dhage, "Vision Based Hand Gesture Recognition for Human Computer Interaction," International Journal of Engineering Science and Innovative Technology (IJESIT), Vol. 2, Issue 3, May 2013.

[10] R. Lulu, Vanshri Kurhade, Neha Pande, Rohini Gaidhane, Nikita Khangar, Priya Chawhan, Ashwini Khaparde, "Web Camera Based Mouse Controlling Using RGB Colours," International Journal of Advanced Research in Computer Engineering & Technology (IJARCET), Vol. 4, Issue 2, Feb. 2015.

[11] Shridhar Kolap, Madhu Khaparkhande, Pooja Latane, "Mouse Control Using Image Processing," International Journal Of Engineering And Computer Science, ISSN: 2319-7242, Vol. 5, Issue 09, Sep. 2016.

[12] Ram Pratap Sharma and Gyanendra K. Verma, "Human Computer Interaction using Hand Gesture", 11th Intl. Multi-Conference on Information Processing (IMCIP-2015), Haryana, India, 2015.

# Barriers of biomass energy and their potential solutions for remote areas of Bangladesh

Jitu Prakash Dhar[1] and Adharaa Neelim Dewanjee[2]
[1]Lecturer, Dept. of EEE, CUET, Bangladesh
[2]Lecturer, Dept. of EEE, CUET, Bangladesh
jituprakashdhar@gmail.com, adharaa_eee@yahoo.com

***Abstract*—This paper presents an analytical view of the barriers against the biomass energy development in Bangladesh and suggests some possible solutions to overcome them. The barriers are classified into different categories and then investigated to provide some solutions with the current technologies and government investment plans available in Bangladesh. According to the plans and strategies, the net output energy can be increased which can minimize the operating cost and solve the energy crisis for remote areas of Bangladesh by attracting more investment plans from the government.**

***Keywords—Biomass energy sources, Financial Barriers, Technical Barriers, Investment plans, Policies, Gasification, Proposed Solutions.***

## I. Introduction

The main cause of energy security interruption of Bangladesh is generation supply shortage and poor natural resources availability [1]. The poverty rate in remote areas is higher than the urban areas. About 43.80% people of remote areas are living below the upper poverty level, while 28.60% of urban people live below the poverty level [2]. All the socio economic and industrial developments are related to the electricity access of remote areas. The common solution of this crisis is the introduction of renewable energies. Biomass energy resource availability can be the potential solution for the country. Installed renewable energy harnessed from biogas is 5MW and from other biomass sources is 1MW [1]. This is a very small portion of total renewable sources. The reasons behind this shortage are some financial, technical and economic barriers.

The main resources of biomass in Bangladesh are rice husks, sugarcane bagasse, wheat straw, jute stalks, coconut shells, animal waste, poultry droppings, municipal solid waste, fuel wood, tree residues, maize and groundnuts. The rice mill industries generates a huge amount of rice husks as a by-product everyday but the major issue associated with it is that it is treated as waste material [3]. The ash content produced from the rice husk is also a potential source of amorphous silica. The energy obtained from biomass is clean and environment friendly. The cost of the above biomass sources is also low [2]. It is possible to achieve the 5% target of total energy production from renewable sources if the barriers of the biomass energy are prevented by taking proper planning and strategies [4].

The rest of the paper is organized as follows. In section-II, different biomass energy sources are discussed. Section-III describes the barriers against biomass energy. In Section-IV, the potential solutions to these barriers are analyzed. Finally, section-V concludes the most efficient plans and strategies that should increase the energy efficiency from this sector.

## II. Biomass Energy Sources

### A. Crop Residues From Agricultural sectors

The agricultural crop residues such as rice husks, jute stalks are used as cooking fuel in the remote areas. The total residues obtained each year from these areas can be used in biomass gasification process, which generates syngas. The process is accomplished under high temperature and the generated gas can be used in producing electricity by gas turbine-generators. Table-1 shows the generation and recoverable rates of agricultural crop residues in 2012-13 [5]:

Table 1: Recovered energy of agricultural residues in 2012-13

| *Crop Residues* | *Moisture content (%)* | *Dry Residues Recovery($10^3$tons)* | *Recovered Energy(PJ)* |
|---|---|---|---|
| Rice Straw | 12.7 | 17831.55 | 290.65 |
| Rice Husks | 12.4 | 8052.90 | 131.26 |
| Sugarcane Bagasse | 49 | 1079.67 | 19.54 |
| Wheat Straw | 7.5 | 586.96 | 9.25 |
| Jute Stalks | 9.5 | 1574.56 | 26.63 |
| Groundnut straws | 12.1 | 89.16 | 1.57 |
| Groundnut husks | 8.2 | 55.17 | 0.86 |
| Coconut shells | 8 | 35.99 | 0.67 |
| Coconut husks | 11 | 118.96 | 2.20 |
| Maize stalks | 12 | 1257.87 | 18.49 |
| Maize cob | 15 | 473.85 | 6.63 |

### B. Municipal Solid Waste

Municipal solid waste management has become a burning issue in different regions in Bangladesh. Since they contribute to the environment pollution, they should be managed, recycled and processed for power generation. Table-2 shows the total waste generation in major cities of Bangladesh [6]:

978-1-5386-2307-7/17/$31.00 ©2017 IEEE

Table 2: Waste Generation in Major Cities of Bangladesh in 2005

| *City* | *Population* | *Daily Average Generation(tons)* |
|---|---|---|
| Dhaka | 6,728,404 | 4,634.52 |
| Chittagong | 2,622,098 | 1,548.09 |
| Rajshahi | 468,378 | 172.83 |
| Khulna | 967,365 | 321.26 |
| Barisal | 437,009 | 134.38 |
| Sylhet | 386,896 | 142.76 |
| Pourashavas | 15,214,306 | 4,678.40 |
| Other Centers | 9,217,612 | 1,700.65 |
| Total | 36,042,067 | 13,332.89 |

### C. Animal Manure

Animal manure is mainly used as fertilizer in remote areas of Bangladesh. But the can be processed and decomposed into organic materials and then can be used for the production of different gas like methane and carbon-di-oxide. These gases can run a gas turbine-generator set to produce power. Table-3 shows the generation and recovery rates of different animal wastes in Bangladesh in 2008–09 [2]:

Table 3: Generation and recovery rates of different animal wastes in Bangladesh in 2008–09

| *Animal Waste* | *Generation (kton/yr)* | *Recovery (kton/yr)* |
|---|---|---|
| Cattle | 23,978.38 | 14,387.03 |
| Buffalo | 1195.74 | 717.44 |
| Goat | 4496.8 | 2698.08 |
| Sheep | 345.69 | 207.41 |
| Poultry Waste | 1917.12 | 958.56 |
| Total | 31,933.73 | 18,968.52 |

### D. Forest Residues

Forest residues are potential biomass sources for producing electricity. The Major issue associated with them is the by-product utilization problem. Traditional uses of forest residues in remote areas are as cooking fuels. Controlled collection of forest residues can be effectively used for power generation which will not harm the environment. Tropical and mangrove forests of the country can supply this collection. The recoverable rate of forest residues as fuel in power generation is approximately 80% [2]. Table-4 shows the estimated production of wood and bamboo in Bangladesh till 2020 [2]:

Table 4: Estimated Production of Wood & Bamboo in Bangladesh from 1990-2020:

| *Year* | *Wood(million $m^3$)* | *Bamboo(million $m^3$)* |
|---|---|---|
| 1990 | 4.88 | 70.51 |
| 2000 | 6.25 | 78.61 |
| 2010 | 8.96 | 63.45 |
| 2020 | 14.24 | 65.68 |

## III. Barriers of Biomass Energy

Biogas plant at kapasia, Gazipur shows the bright future of biomass energy for remote areas. However, in most remote areas, power generation from the biomass resources is not fruitful due to the following barriers:

*1) Limited Availability of Loans*

In general, the commercial banks of our country don't provide any loan for the promotion of renewable energy [1]. So they consider the loans as risky investments. Also the private sector financing track records are not satisfactory. Although Infrastructure Development Company Limited (IDCOL) and other participating organizations are providing short loans, the interest rate is high.

*2) High Cost of Installation*

Biogas plants in Bangladesh require high installation cost due to fixed construction and poor design. They require earth excavation and masonry which needs external experts to operate [10]. Portable biogas plant is also introduced in some areas, but their installation cost is still undetermined.

*3) Unavaiability of Fuel Type To be Used*

Most of the biomass fuels are used for cooking purpose in remote areas, which shortens the fuels for power generation. For example, a huge amont of rice husks can not be used for the traditional gasifiers because they contain considerable amount of moisture. They should be treated with pyrolysis and other drying techniques before the use which requires additional cost and complexity of the system increases. Besides in rainy season the rice mills can not produce enough rice husks [11]. Also the mill owner are not willing to sell the rice husk at cheaper rate because they want to use them for their own fuel use.

*4) Poor Efficiency of Biomass Energy Conversion Decices*

The traditional biomass energy conversion devices do not contain sophisticated modern technologies. Hence, the gas turbines, generators and other auxiliary devices used for power generation are not as efficient as conventional power plants [11]. Besides, moisture content of the biomass fuels adds to this problem severely.

*5) By-product Utilization Problems*

By-products such as fly ash and other residue materials from biomass remain unused and hence add to the environmental pollutions. The most common use of them is as fertilizer in remote areas. But fly ash contains carbon-rich materials which become wasted if they are not properly utilized by suitable techniques [12].

*6) Poor Technical Knowledge of Rural people*

Rural people do not have sufficient knowledge about the infrastructures of biomass power plants. They are not

978-1-5386-2307-7/17/$31.00 ©2017 IEEE

concerned about the long term policy incentives and regulations of renewable energy [11].

## IV. Solutions to the barriers

Government along with the private investors can take steps to promote biomass energy in rural areas. Therefore, the following solutions can be done in this respect:

*Step-1: Availability of Loans*

Bangladesh represents an early style market approach at the moment. A number of advancements need to be made before it is really viable however a number of developers and investors are assessing the market [7]. Clean Development Management Process along with IDCOL can help to make the loans available at low interest rate for rural areas. Considering the risk mitigation, they should develop a unique asset finance model for biogas plants. They should provide low-cost financing and technical capacity-building support to the POs, which interact directly with customers. Certain components are essential to its success: ownership; multi-party financial contribution; market price determination; independent selection of POs and suppliers; and indirect subsidy to the consumers [9]. Capital used for project financing energy projects can be raised through a combination of debt and equity investment [8]. Rural people should be informed about the micro credit support systems for purchasing equipments.

*Step-2: Reduction of Installation cost*

Government subsidy can be provided to the equipments of biomass plants. Gasification and internal combustion with low energy content can sufficiently reduce the cost if the biogas is cleaned up before combustion. Long term feedstock supply chain is necessary for any biomass plant [13]. Potential of resources, deforestation risks and availability of land should be taken into account for decreasing the cost. Sustainable harvesting techniques like one pass harvesting can reduce the fuel cost. More commercial funding experiences are required for the less mature technologies.

*Step-3: Biomass Projects Launched By Various Institutions*

Currently IDCOL is financing some biomass projects in different parts of the country. Grameen Shakti had installed 12795 biogas plants till 2012. Other organizations like SOUL, LGED, SREDA, REB and RB should launch more projects in remote areas [2].

*Step-4: Mass-Media Utilization*

Radio, Television, Newspapers and other mass media can be used for the promotion of biomass technologies by updating the rural people about the advantages, renewable energy loans and cost reduction incentives [2]. Rice mill owners should be motivated to use their rice husk and other residues in biomass gasification and other modern technologies.

*Step-5: Organizing Training Courses and Exhibitions*

Private institutions and government can organize training courses for the unemployed young people in the rural areas. Seminars and exhibitions should be regularly organized by the Ministry of Science and Information & Communication Technology in remote areas [2].

*Step-6: Increasing Efficiency of Biomass Conversion Devices*

Modern conversion technologies can increase efficiency significantly. Three of them are: pyrolysis, gasification, and liquefaction [14]. The two main technologies presently used to convert biomass into energy are thermo-chemical and biochemical. Selection of a conversion technology for biomass depends upon the form in which the energy is required. Pyrolysis, fermentation and mechanical extraction (trans-esterification) all produce liquid fuels suitable for use as transportation fuels. Other conversion processes produce energy in a form that is best used at the point of production i.e. hot air or steam or a gas. Pyrolysis oils and liquid fuels are suitable only for diesel cycle engines. Alcohol-based liquid fuels and combustible gases are suitable for use in Spark Ignition Gas Engine (SIGE). Alcohol-based liquid fuels produced by fermentation are considered too costly for use in stationary SIGE. Only gas from gasification/pyrolysis and Anaerobic digestion (AD) is currently a cost-effective fuel for use in static SIGE. Having identified that gasification, pyrolysis and AD are the most likely cost-effective processes to produce a fuel suitable for an SIGE, further consideration indicates that while all of the processes are (technically) able to produce a suitable fuel, only gasification is likely to be commercially viable. Using AD, cost reductions of 17% to 19% might be possible by 2020, with cost reductions of 5% to 8% by 2015. This finding is based on consideration of the greater overall conversion efficiency of gas production via gasification and the proven operational history and performance of gasifiers using biomass feedstock. Pyrolysis is a rapidly developing technology with great potential but the process is inherently better suited to producing a fuel oil, more suited to use in diesel engines and gas turbines. AD also has its place both as a conversion process to provide a gaseous fuel and as a treatment process for high moisture content industrial organic wastes, such 'difficult' or wet biomass wastes like MSW and sewage sludge. In terms of providing a cost-effective process route to produce a gaseous fuel for stationary SIGE, gasification is the preferred conversion process [15]. For electricity generation, efficient processes are thermal gasification combined cycle, supercritical water gasification combined cycle, and direct combustion in order of efficiency for low moisture content biomass [16].

*Step-7: Byproduct utilization*

Waste wood can be reused as a fuel and raw material for a variety of applications based on regulatory promotion. The most commonly used end use is to directly utilize it as an auxiliary fuel in industrial utilities (e.g., boilers, heaters and furnaces) for the purpose of co-firing with coal/fuel oil. Byproducts can be used in olive oil industry by proper treatment technologies [17]. Fly ash can be further used as

978-1-5386-2307-7/17/$31.00 ©2017 IEEE

fertilizer. The materials resulting from the high temperature combustion of fuel are highly oxidized and can be reactive components of a variety of construction materials like concrete. Combustion of biomass fuels also produces a biomass-derived fly ash, and the engineering properties of this material are less well-defined when compared to the properties of coal-derived fly ash [18]. Amorphous silica is produced as a byproduct from Rice husk based power generation plants. Therefore, it can be used in glass and ceramic industries.

*Step-8: Motivating Research Works*

BCSIR, LGED, BRAC, GS, Bangladesh Agriculture University (BAU) and Bangladesh University of Engineering & Technology (BUET) are undertaking researches on cost reduction, proper methods of utilizing slurry, increasing efficiency on biogas technology and modeling biogas plants etc [2]. Research on pyrolysis is improving in RUET since 2000. Bangladesh Rice Research Institute (BRRI) should conduct more research activities on rice husk gasification.

## V. Conclusion

Bangladesh has huge resources of biomass energy to mitigate the energy crisis. In this paper, the barriers against the biomass resources are focused and possible solutions are suggested for the remote areas. From the analysis, it can be concluded that the government should play the key role along with the commercial banks. Besides more importance should be given on implementing the projects, monitoring them and consulting with other private sector to motivate and invest in those projects. More research works should be conducted by the technical institutions to reduce the cost of equipments and process. In addition, the rural people should also increase their knowledge from the training courses and implement them properly. They need to understand that energy from biomass resources is cost effective and advantageous to them. In the same time, some unemployed people can get job in these projects conducted by the organization and the unemployment rate of the country can be declined by a large margin. The ultimate pressure on fossil fuels will be decreased if we can utilize more biomass resources.

## Acknowledgment

This work is supported by Chittagong University of Engineering & Technology.

## References

[1] Sustainable and Renewable Enegry Development Authority: Scaling up Renewable Enegry in low income countries (SREP). [Online]. Available: www.sreda.gov.pdf

[2] A.S.N.Huda, S.Mekhilef, A.Ahsan,"Biomass energy in Bangladesh: Current status and prospects", journal homepage: www.elsevier.com/locate/rser.

[3] M. S. Islam & T. Mondal," Potentiality of Biomass energy for electricity Generation in Bangladesh", Asian Journal of Applied Science and Engineering, Volume 2, No 2 (2013) ISSN 2305-915X.

[4] Md. Shafayat Hossain, Mohammad Wahidur Rahman, Ahmedullah Aziz & Farseem Mannan Mohammedy, "Prospect of Biogas & Biomass as Potential Sources of Renewable Energy in Bangladesh", IEEE/OSA/IAPR International Conference on Infonnatics, Electronics & Vision (ICIEV)-2012.

[5] P. K. Halder, M. A. Hossain, N. Paul, I. Khan, "Agricultura Residue Potential for Electricity Generation in Bangladesh", IOSR Journal of Mechanical and Civil Engineering (IOSR-JMCE) e-ISSN: 2278-1684,p-ISSN: 2320-334X, Volume 11, Issue 2 Ver. III (Mar- Apr. 2014), PP 89-95, Available at www.iosrjournals.org.

[6] Community Based Solid Waste Management Through Public-Private-Community Partnerships: Experience of Waste Concern in Bangladesh-3R Asia Conference Tokyo, Japan, October 30 to November 1, 2006, available at www.wasteconcern.org.

[7] Available at http://www.lexology.com/library/detail.aspx?g=cba68495-1230-4aed 9567-1090bf2b3c11.

[8] Renewable energy project financing of infrastructure development company limited (idcol) in bangladesh. Available: https://www.slideshare.net/mehdihassanonline1/renewable-energy-project-financing-of-infrastructure-development-company-limited-idcol-in-bangladesh.

[9] arcfinance website. [Online]. Available: http://arcfinance.org/news/blog/going-all-in-on-solar-finance-how-idcol-incubates-a-growing-industry-in-bangladesh/

[10] NEWAGE Opinion (January 23, 2017), Low Cost Energy Solution for Rural Area. [Online]. Available: http://www.newagebd.net/article/7568/low-cost-energy-solution-for%20rural-area

[11] Md. Risat Abedin, Himadry Shekhar Das, "Electricity from Rice Husk: A Potential Way to Electrify Rural Bangladesh", INTERNATIONAL JOURNAL of RENEWABLE ENERGY RESEARCH *Himadry hekhar Das et al.* , Vol.4, No.3, 2014.

[12] Jan R. Pels, Danielle S. de Nie, Jacob H. A. Kiel, "Utilization of ashes from biomass combustion and gasification" 14th European Biomass conference and Exhibition, October 2015.

[13] "Biomass for Power Generation", Renewable Energy Technologies: Cost analysis series, IRENA, vol.1: Power Sector, June 2012. Available: https://www.irena.org/DocumentDownloads/Publications/RE_Technologies_Cost_Analysis-BIOMASS.pdf

[14] A. DEMIRBAS, "Modernization of Biomass Energy Conversion Facilities", Energy Sources, Part B, 2:227–235, 2007 Copyright © Taylor & Francis Group, LLC ISSN: 1556-7249 print/1556-7257 online DOI: 10.1080/15567240500402784

[15] Peter McKendry," Energy production from biomass (part 2): conversion technologies", Applied Environmental Research Centre Ltd, Tey Grove, Elm Lane, Feering, Colchester CO5 9ES, UK.

[16] Yoshikuni Yoshidaa, Kiyoshi Dowakib, Yukihiko Matsumurac, Ryuji Matsuhashid, Dayin Lie, Hisashi Ishitanif , Hiroshi Komiyamae," Comprehensive comparison of efficiency and CO2 emissions between biomass energy conversion technologies—position of super critical water gasification in biomass technologies", available at www.sciencedirect.com, Biomass and Bioenergy 25 (2003) 257 – 272.

[17] Antonio C.Caputo, Federica Scacchia, Pacifico M.Pelagagge, "Disposal of by-products in olive oil industry: waste-to-energy solutions" Journal of Applied Thermal Engineering, vol. 23, no. 2, pp. 197-214, 2003.

[18] GeorgiaTech website. [Online]. Available: https://ce.gatech.edu/node/24.

# ATP-EMTP Modeling and Performance Test of Different Type Lightning Arrester on 132kv Overhead Transmission Tower

Md. Zoyheroul Islam[1], Md. Rasheduzzaman Rashed[2] and Md. Salah Uddin Yusuf[1]
[1]Affiliation (Khulna University of Engineering & Technology, Bangladesh)
[2]Affiliation (Bangladesh Navy, Bangladesh)
shourov1688@yahoo.com

*Abstract*— **Lightning and switching surges are the main causes of over voltages in power system. If any high voltage transmission tower stroked by lightning the insulation of the line and equipment connected to the power system can be damaged. Metal Oxide Varistor (MOV) type surge arrester might be used for protecting the transmission line insulations and equipment of the power system connected to the transmission tower. To simulate the dynamic properties of MOV type arrester several types of models are proposed. In this research IEEE model, Pinceti model and Fernandes model of MOV type surge arrester are simulated with ATP-EMTP transient simulator. A 900m single line of 132kv with three tower are designed and simulated with ATP-EMTP program and evaluate the performance of different models of lightning arrester for protecting the towers and transmission line from direct and indirect strike.**

***Keywords—lightning; surge arrester; ATP; MOV, Transmission Tower***

## I. INTRODUCTION

Lightning is the phenomenon of electrical discharge between charged cloud to ground, between clouds or between the different charge centers of the same cloud. Lightning is the most common and frequent cause of over voltage and insulation failure in power system. Lightning and switching surge are the main reasons for outage in power transmission and distribution system [1]. Characteristics of lightning over voltage is important to be studied to design protection scheme for the power system. It is well known that the probability of a structure being strike by lightning will increase with the increasing of its height. Modeling of transmission lines and Lightning performance analysis of transmission lines using the EMTP was investigated by J. A Martinez[2][3]. The height of high voltage transmission tower is another major issue for which lightning got enough short distance for direct strike on tower top. M. Ishii and T. Hara designed multistory transmission tower for lightning performance analysis [4][5]. For designing protection scheme for high voltage transmission tower it is necessary to calculate the surge current parameters which was successfully done by F. Heidler[6]. Tower surge impedance was calculated by M.A. Sargent [7]. Simulation of lightning transients on 110kV overhead transmission line using ATP- EMTP was done by K. Fekete[8]. Recently X Pejtemalli has been analyzed transient process during direct lightning strike to the telecommunication tower using ATP[15]. ATP- EMTP software is one of the most commonly used simulation tool for modelling transmission and distribution-line systems. Nowadays, many researchers widely use ATP-EMTP software for simulating power system transient. In this paper a segment of single transmission line which is 900m in length with three towers was developed by using ATP-EMTP software. Three most commonly used lightning arrester models were implemented by ATP-EMTP software and evaluate their performance on the transmission line which was stroked by direct lightning.

## II. MODELING OF TRANSMISSION SYSTEM

### A. Modeling of Transmission Line

In this research a 132kv three phase line with overhead ground wire was modeled with three towers which are apart 300m from each other. Phase wires and ground wire are explicitly modeled between the towers where three tower spans were used. Line termination at each side of the model was to avoid any reflection that might affect the simulated high-voltages around the point of impact [3]. This has been done by terminating the phase conductors with AC operation voltages, and by grounding the sky wire. Fig.1 shows the span of three towers with line termination of the model.

### B. Parameters of Transmission Tower

There are different types models of transmission tower proposed by the researchers at last few years. One of the more well-known models is the multistory model designed by Masaru Ishii in 1991[4]. A multistory tower model basically is a composition of distributed parameter lines with parallel RL circuits and has been recommended by the Japanese Guideline of insulation design/coordination against lightning [9]. In Japan and other countries this model is widely used for analyzing lightning-surge characteristics. Fig.2 shows the proposed multistory tower model. However, the design of the multistory tower model was based on high voltage transmission line. Thus, multistory tower model is not relevant to Mal -voltage transmission line system (such as 132kV and 230kV). Based on the investigation done by Takamitsu [10], a simple distributed line model is adequate enough to represent a low-voltage transmission line model in ATP-EMTP software. Therefore, this model has been used for designing the transmission tower for this work.

978-1-5386-2307-7/17/$31.00 ©2017 IEEE

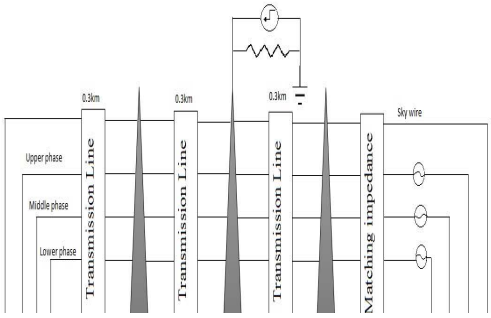


Figure 1. Model of 900m single line transmission line with three tower.

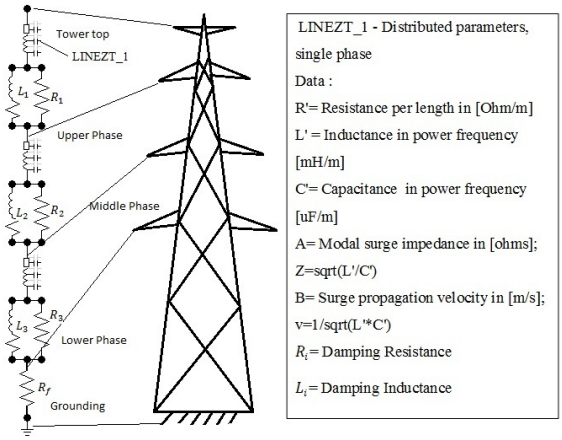


Figure 2. Parameters of multistory tower

## III. Simulation of the ATP Equivalent Circuit of Proposed Transmission Line

In this study ATPDraw is used for selecting lightning protection scheme of a 900m long 132KV transmission line which is accumulated with three towers. The simulated incident is a single-phase back-flashover caused by a lightning strike to the tower structure 900 m away from the substation. The most severe Heidler's type current source and lightning parameters were chosen with 500kA amplitude and 4/50µs front/tail times. The ATPDraw circuit of the complete network is shown in Fig.3. The line spans are represented by 4-lines (3 are phase conductor and another one is sky wire). The surge propagation along the transmission tower structure has been considered in this model by representing the vertical pylon sections as single-phase transmission lines with constant parameter. The tower grounding impedance has been simulated by the R-L branches below the tower model. The front of wave flashover characteristic of the line insulators plays a significant role in such a back-flashover study. The effect of the power frequency voltage on the back-flashover possibility can't be ignored either at this voltage level. In Fig.3.a and Fig. 3.b the voltage and current waveform without surge protector were shown respectively.

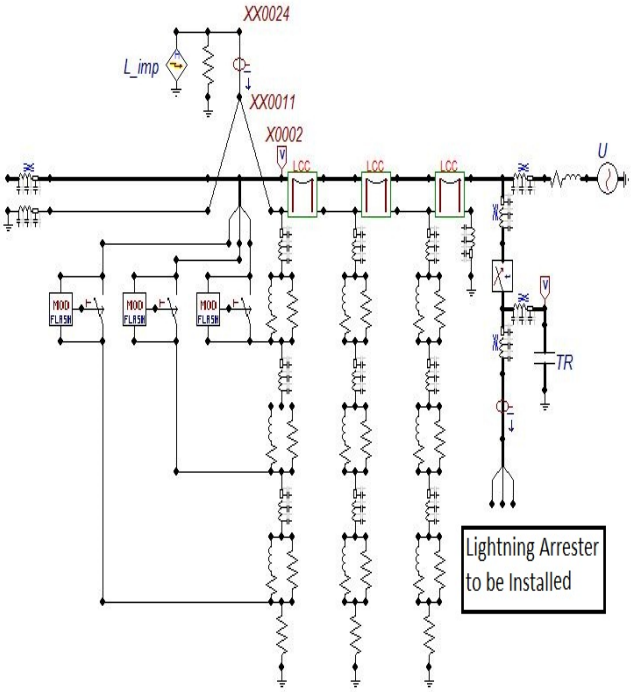


Figure 3.a. ATP equivalent circuit of the transmission line system to be protected

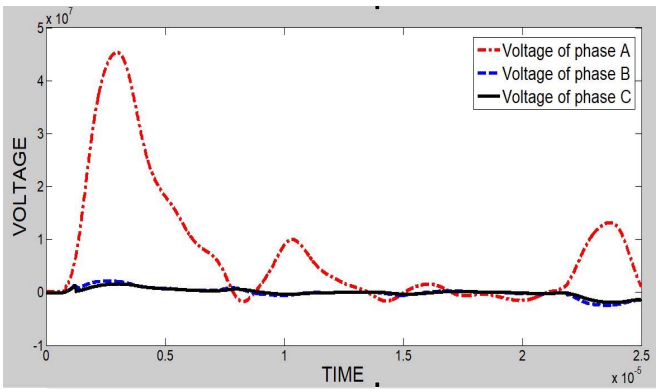


Figure 3.b. 3-phase voltage waveform without surge protection

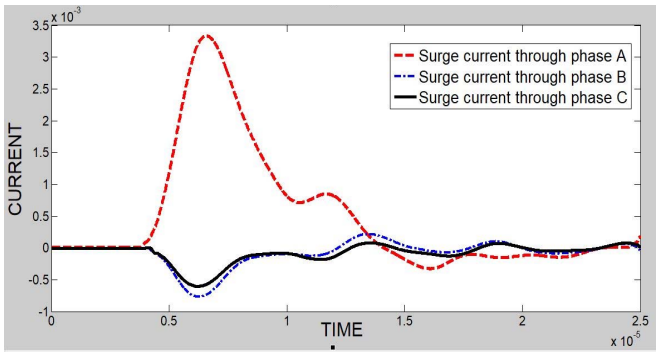


Figure 3.c. 3-phase current waveform without surge protection

## IV. Proposed Models for Three Types of MOV Surge Arrester

The dynamic models of surge arrester are very important for insulation coordination and reliability studies of several models in power system at different voltage levels, are proposed to represent the frequency depended characteristic of MOV type surge arresters. IEEE, Fernandez, Pinceti and Popov models are the established models of surge arresters. Frequency-dependent characteristic of arrester have been simulated by IEEE, Pinceti and Fernandez models which are used in this work for designing proper protection scheme of transmission tower. The equivalent ATP model has been drawn for all the models and find the voltage and current across the MOV. For determining the performance of the three models the time of bypassing surge has been found from the Matlab figure which were generated by compilation of the ATP circuit of each. In Fig.4 ATP equivalent circuit three models are shown. Fig.4.a shows the surge arrester model proposed by the IEEE Working Group 3.4.11 [11]. It has two nonlinear *varistor* known as $A_0$ and $A_1$ separated by $R_1$-$L$ filter. External capacitance given by a capacitor related with the height of the arrester. The stability can be improved by adding an parallel inductance $L_0$ with resistance. For the fast rising current, the impedance of RL filter becomes more significant which means current passes through the non-linear branch$A_0$. So, $A_0$ has a higher voltage than $A_1$. The model of arrester will generate higher voltages which then match the dynamic behaviour of metal oxide surge arrester. Pinceti model is related to IEEE model which is shown in Fig.4.b but a few modifications are done in Pinceti model [12]. The difference is that no capacitance between the one terminal to other terminal and nonlinear resistance $A_0$. R is replaced by nearly about 1MΩ resistance. The higher value of R is used to avoid numerical oscillation. Fernandez and Diaz model is also based on the IEEE model. In Fernandez and Diaz model $A_0$ and $A_1$ are separated by $L_1$ and $L_0$ is neglected. This is shown in Fig.4.c. Capacitance is included in this model and it represents terminal to terminal capacitance of arrester [13]. In Table-1 the initial computed parameters for the above three models are shown, the optimum parameter values obtained using the genetic algorithm [14].

TABLE I. PARAMETERS OF SURGE ARRESTER MODELS

| Name of the model | $R_0$(Ω) | $R_1$(Ω) | $L_0$(μH) | $L_1$(μH) | C(pF) |
|---|---|---|---|---|---|
| IEEE model | 25.43 | 17.85 | 0.278 | 1.017 | 967.21 |
| Pinceti-Gianettoni model | $0.895\times10^6$ | - | 0.376 | 0.0435 | - |
| Fernandez-Diaz model. | $1.465\times10^6$ | - | - | 1.371 | 675.5 |

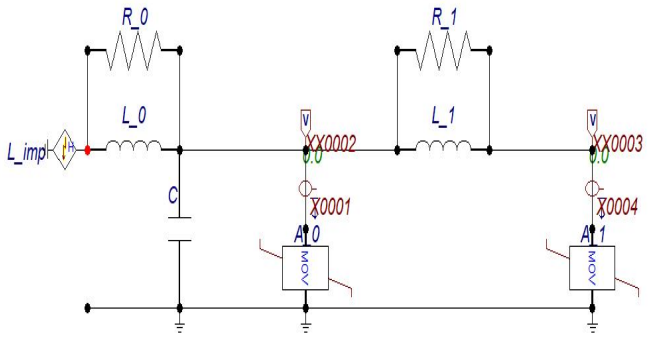


Figure 4.a. ATP equivalent circuit of IEEE model

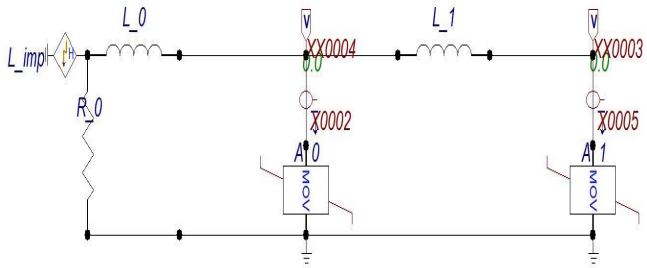


Figure 4.b. ATP equivalent circuit of Pinceti model

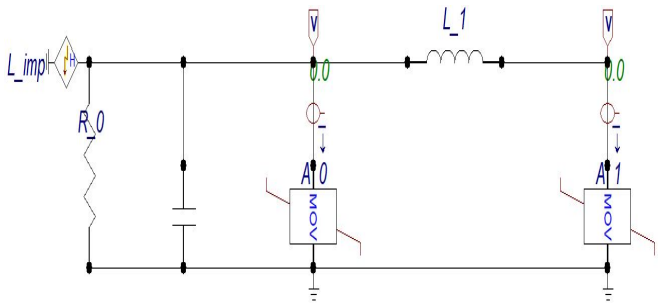


Figure 4.c. ATP equivalent circuit of Fernandez and Diaz model

## V. Performance Evaluation of Different Arrester Models by ATP Simulation

### A. IEEE model

Transmission line is protected with the lightning arrester designed according to IEEE model of MOV type surge arrester is shown in Fig.5.a. The performance of the surge arrester can be evaluated from the simulation outputs which are shown in Fig.5.b and Fig.5.c. From the Fig.5.b the waveform of surge current of $A_0$ varistor of ABC phase is found maximum amplitude of surge current found 100kA at phase A at the time of 5μsec. For the $A_1$ varistor the maximum amplitude of surge current is found 160kA for phase A at 7.5 μsec. For B and C phase maximum amplitude have found at 100kA at 6μsec and 70kA at 6.5 μsec respectively.

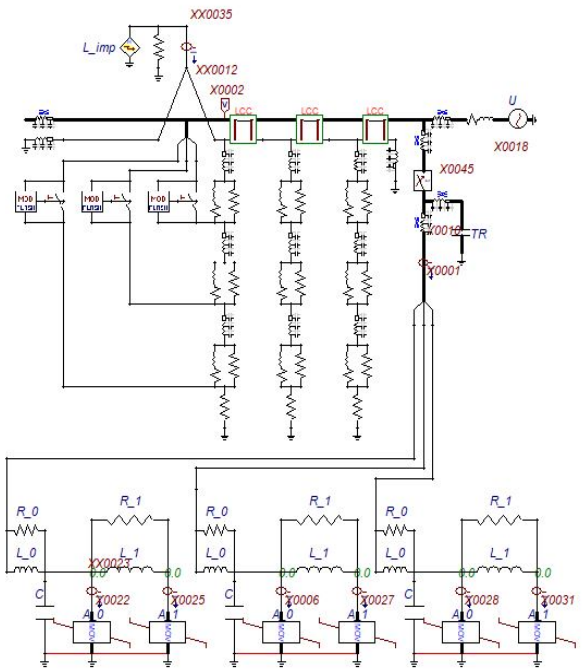


Figure 5.a. ATP equivalent circuit of the transmission system protected with MOV type surge arrester modeled according to IEEE model.

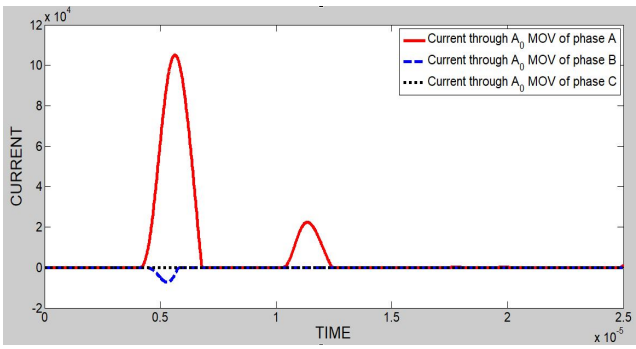


Figure 5.b. Current waveform of the $A_0$ varistor of IEEE model.

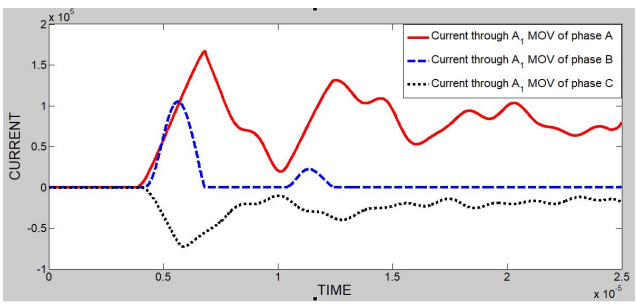


Figure 5.c. Current waveform of the $A_1$ varistor of IEEE model.

## B. Pinceti-Gianettoni Model

The transmission line is protected with the lightning arrester designed according to Pinceti-Gianettoni model of MOV type surge arrester shown in Fig.6.a. For Pinceti-Gianettoni model the only 6A current at 6 µsec for phase A and for remaining two phase the amplitude of surge current is very small at $A_0$ varistor which is shown in Fig.6.b. For $A_1$ varistor maximum 200kA amplitude of surge current is found at phase A and for phase B and C the surge current amplitude is negative 60KA at 7 µsec and 50kA at 6.5 µsec respectively shown in Fig.6.c.

## C. Fernandez-Diaz model Model

$A_0$ MOV and $A_1$ MOV are separated by $L_1$ and the capacitor represents terminal to terminal capacitance of the MOV. In Fig.7.a it is shown that the transmission line is protected with the lightning arrester designed according to Fernandez-Diaz model of MOV type surge arrester. From Fig.7.b it is observed that amplitude of surge current is 130kA at 6 µsec and 22kA surge current amplitude at 12 µsec at phase A. For phase B and C amplitude of surge currents are found 18kA at 6 µsec and 8kA at 6 µsec respectively and also the harmonics for B and C phase can be ignored as compared with phase A. Fig.7.c shows the surge current waveform of $A_1$ varistor. At phase A maximum amplitude found 150kA at 7.5 µsec, for phase B and C surge current amplitude found 60kA at 5 µsec and 50kA at 5 µsec.

# VI. Results

It was carrying out a comparative study among the results provided by the IEEE model, Pinceti model and Fernandez models. In TABLE II the computed peak value of the surge current for each model are given also computed duration and front time of the surge current waveforms. For the simplicity of calculating peak value the harmonics of the phase B and C are not considered. From the above figures it has been cleared that surge current is maximum at upper phase so different arrester at different phase is not necessary for comparison of different arrester performance at different phase.

TABLE II. PERFORMANCE EVALUATION OF THREE TYPES OF ARRESTER MODEL

| **Models** | **Maximum amplitude and discharge time of surge current at phase A** | | **Maximum amplitude and discharge time of surge current at phase B** | | **Maximum amplitude and discharge time of surge current at phase C** | |
|---|---|---|---|---|---|---|
| | **$A_0$ MOV** | **$A_1$ MOV** | **$A_0$ MOV** | **$A_1$ MOV** | **$A_0$ MOV** | **$A_1$ MOV** |
| IEEE model | 100kA and 5µsec | 160kA and 6 µsec | -10kA and 2.5 µsec | 100kA and 2 µsec | 0kA and 0 µsec | 70kA and4 µsec |
| Pinceti model | 6A and 2.5 µsec | 200kA and 5 µsec | -1A and 2 µsec | 60kA and 3 µsec | -0.5A and 1 µsec | 50kA and 3 µsec |
| Fernandez-Diaz model | 130kA and 5 µsec | 150kA and 6 µsec | 18kA and 2 µsec | 60kA and 4 µsec | 8kA and 1.25 µsec | 50kA and 3 µsec |

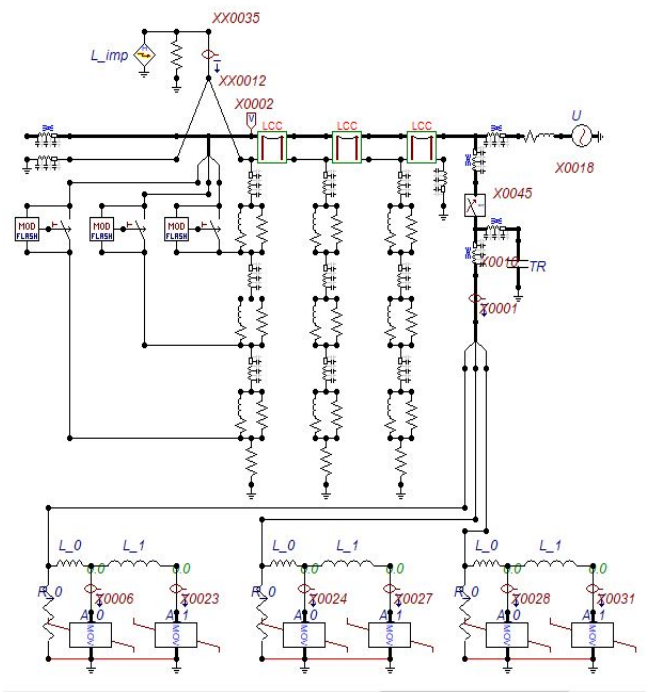


Figure 6.a. ATP equivalent circuit of the transmission system protected with MOV type surge arrester modeled according to Pinceti model.

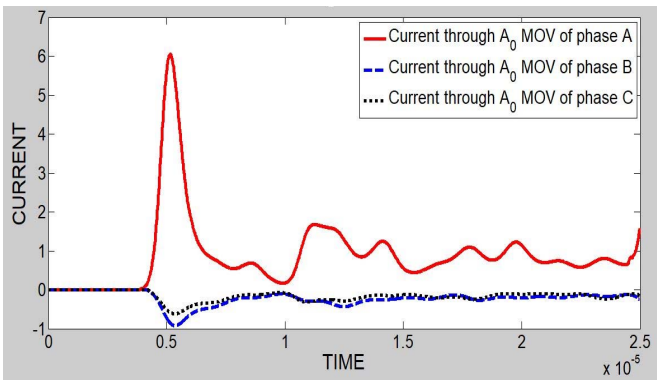


Figure 6.b. Current waveform of the $A_0$ varistor of Pinceti model.

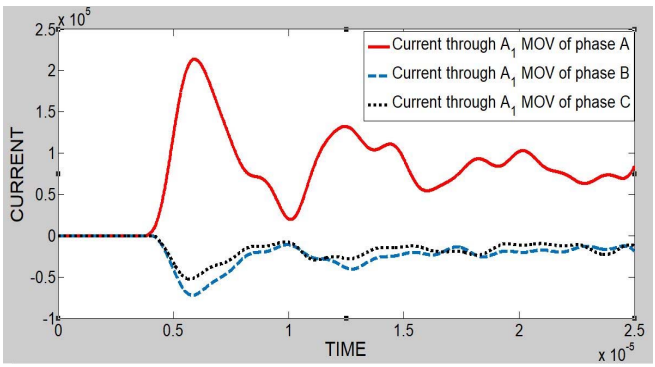


Figure 6.c. Current waveform of the $A_1$ varistor of Pinceti model.

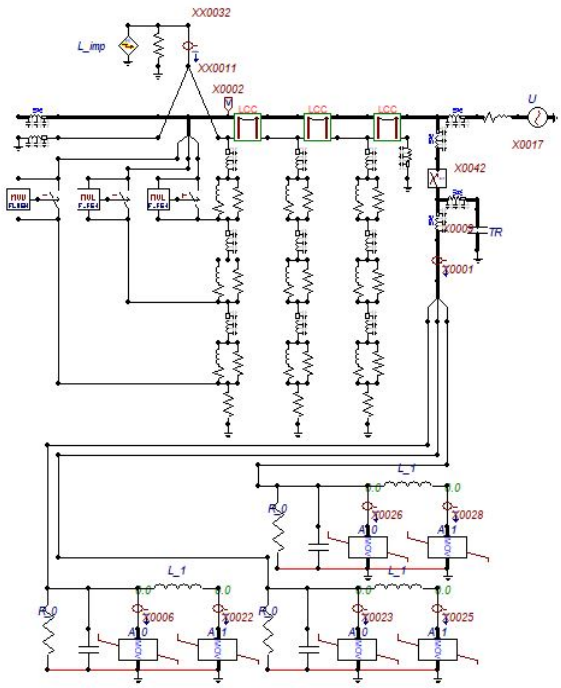


Figure 7.a. ATP equivalent circuit of the transmission system protected with MOV type surge arrester according to Fernandez-Diaz model.

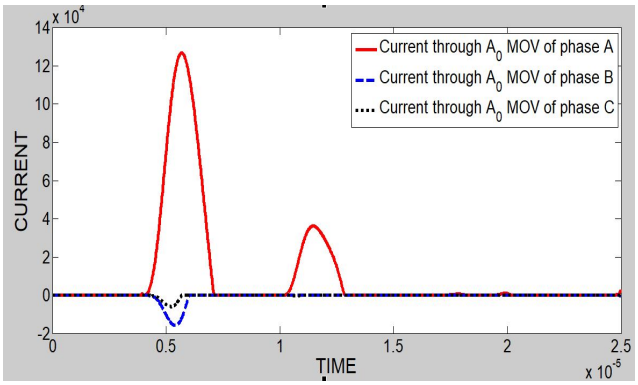


Figure 7.b. Current waveform of the $A_0$ varistor of Fernandez-Diaz model.

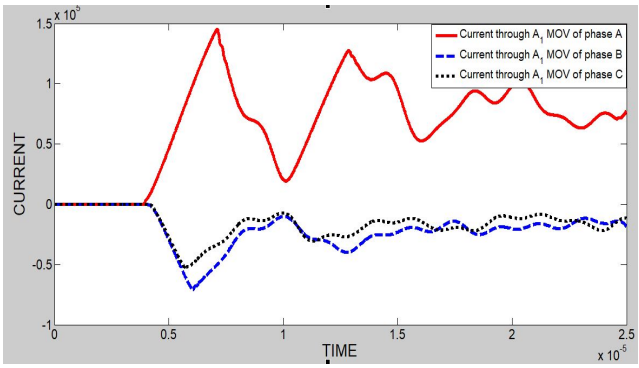


Figure 7.c. Current waveform of the $A_1$ varistor of Fernandez-Diaz model.

## VII. CONCLUSION

In this work a 132kV single line transmission system with three towers was developed in order optimum surge arrester equivalent circuit model parameters to be determined for designing proper protection scheme for the power network. ATP-EMTP circuit for three most popular MOV type surge arrester model were developed and evaluated their performance. From the simulation result the characteristics of parameter identification for high current impulses can be easily evaluated also. All the models can reproduce the property of metal oxide arresters precisely. In pinceti model, nine parameters must be estimated and in IEEE model, eleven parameters must be estimated, so Pinceti's convergence speed is faster than IEEE and Fernandez model. From the above figure it can also be clearly estimated that Pinceti's model is more faster and when the amplitude of current is higher than the surge arrester exhibit shorter time to peak than at higher amplitude. From the current wave form of across the two MOV it is clear that at higher amplitude of current, the MOV type surge arrester exhibit shorter time to peak than at higher amplitude. From the output of simulation and perception the Pinceti model gives profoundly agreeable results will all dynamic properties and show the shortest quenching time contrasted with IEEE and Fernandez model.

## REFERENCES


[1] GREENWOOD, A. Electrical Transients in Power Systems. New York: John Wiley & Sons, 1991. ISBN 978-0471620587.

[2] J. A Martinez, F. Castro- Aranda. (2003). Lightning Performance Analysis of Transmission Lines Using the EMTP. Power Engineering Society General Meeting, IEEE. pp. 295 300, Vol. 1.

[3] Juan A. Martinez- Velasco and Ferley Castro- Aranda. (June 19-23, 2005). Modeling of Overhead Transmission Lines for Lightning Studies. International Conference on Power System Transients(IPST'05) in Montreal, Canada.

[4] M. Ishii, T. Kawamura, T. Kouno, E. Ohsaki, K. Shiokawa, K. Murotani, T. Higuchi. (1991). Multistory transmission tower model for lightning surge analysis. IEEE Transactions on Power Delivery. Vol: 6. Issue: 3. Page(s): 1327- 1335.

[5] T. Hara, O. Yamamoto. (1996). Modeling of a transmission tower for lightning surge analysis. IEE Proceedings on Generation, Transmission and Distribution. Volume: 143. Issue: 3. pp. 283-289.

[6] F. Heidler, J.M. Cvetic, B.V. Stanic. (1999). Calculation of Lightning Current Parameters. IEEE Transactions on Power Delivery. Volume: 14. Issue: 2. pp. 399- 404.

[7] M.A. Sargent, M. Darveniza. (May, 1969). Tower Surge Impedance. IEEE Transactions on Power Apparatus and Systems. Vol: PAS-88. Issue: 5, Part-1.

[8] K. Fekete, S. Nikolovski, G. Knezevic, M. Stojkov, Z. Kovac. (2010). Simulation of Lightning Transients on 110kV Overhead- Cable Transmission Line using ATP- EMTP. MELECON 2010- 2010 15 th IEEE Mediterranean Electrotechnical Conference. pp. 856- 861.

[9] J. A Martinez, F. Castro- Aranda. (2003). Lightning Performance Analysis of Transmission Lines Using the EMTP. Power Engineering Society General Meeting, IEEE. pp. 295 300, Vol. 1.

[10] Takamitsu Ito, Toshiaki Ueda, Hideto Watanabe, Toshihisa Funabashi, and Akihiro Ametani. (2003). Lightning flashover on 77-kV systems: observed voltage bias effects and analysis. IEEE Transactions on Power Delivery, Vol: 18, Issue: 2, pp. 545 550.

[11] IEEE Working Group 3.4.11 "Modelling of metal oxide surge arrester", IEEE Trans. On Power Delivery, vol.7, No 1, pp. 302-309,1992.

[12] PINCETI, P., & GIANNETTONI, M. (1999). "A simplified model for zinc oxide surge arresters". Power Delivery, IEEE Transactions on, 14(2), 393-398.

[13] FERNANDEZ, F., & DIAZ, R. (2001, June). "Metal oxide surge arrester model for fast transient simulations". In The Int. Conf. on Power System Transients.

[14] P.F. Evangelides, C.A. Christodoulou, I.F. Gonos, I.A. Stathopulos. "PARAMETERS' SELECTION FOR METAL OXIDE SURGE ARRESTERS MODELS USING GENETIC ALGORITHM". 30th International Conference on Lightning Protection - ICLP 2010 (Cagliari, Italy - September 13th -17th, 2010).

[15] X Pejtemalli, P Cipo and A Muçka, "ATP Analysis of Transient Process during Direct Lightning Strike to the Telecommunication Tower, " Asian Transactions on Engineering (ATE ISSN : 2221-4267) Volume 05, Issue 03, June. 2015.

[16] B. Filipović-Grčić, B. Franc, I. Uglešić, "Lightning overvoltage protection of combined overhead line and underground cable distribution network," International Colloquium on Lightning and Power System, 21, rue d'Artois, F-75008 PARIS, 2016

# Optimal Design of a Standalone Hybrid System for Supporting Sajek Valley, a Remote Tourist Spot of Bangladesh

Faisal Bin Kashem[1], Md. Didarul Alam[2]
Department of Electrical and Electronic Engineering
University of Chittagong, Chittagong, Bangladesh
[1]fbk835@gmail.com, [2]didar.apece@cu.ac.bd

*Abstract*— **Advancement of a country is reflected by the advancement of that country in technology. For proper growth in technology, it is necessary to ensure electricity for every people of the country. In Bangladesh, lots of people do not have the access to grid electricity as they live in remote areas. Sajek Valley is one of the remotely located tourist spots of Bangladesh, where grid connection is not available. In last few years, this area has drawn the attraction of many tourists for its scenic beauty. Ensuring electricity at that locality can increase the income of the people of that locality and so it can give pace in the economic growth of the country. In this paper, we have designed a standalone hybrid system for the locality of Sajek Valley considering the load profile for the people of that locality as well as tourists. HOMER software is used to find out an optimal design of the system for the available resources on that locality. Such design can be helpful to serve electricity at the remote location of the country.**

***Keywords— Renewable Energy; Hybrid System; PV; Optimal Design; Sajek Valley***

## I. INTRODUCTION

Bangladesh is a densely-populated developing country with a population of over 170 million people. A large number of people live in village and more than 70% people do not get grid electricity on a regular basis. In some rural and remote areas, grid connection is not available and even if grid connection is available in some of the areas, load shedding occurs frequently at remote and rural areas [1]. In this era of globalization, it is impossible to think of a day without electricity. The energy reserve reflects the national security of a country and the amount of electricity use, which increases GDP rate, shows the economic growth [2]. So, it is necessary to ensure electricity for all without any discrimination about the location. But it is not always possible and economically feasible to serve grid connection at every community as many of them are located in very remote areas with comparatively low population. Besides, the electricity production is not satisfactory in Bangladesh considering the increasing demand growth of about 10% [3]. For such cases, off grid hybrid system is a relief for the people of those locality.

Thermal plants are dependent upon fossil fuels which is limited and nuclear plant is a white elephant for a developing country like Bangladesh. In this situation, for its environmental friendly nature, renewable and hybrid system is great relief. Two or more manners of power generation are combined in hybrid power generation system and such systems are assessed in different areas [4].

In present world, when the upcoming shortage of fossil fuel is a matter of great concern, moving towards renewable energy is a great relief. Though a solely renewable hybrid energy system can be designed, it may not perform well due to the ambiguous behavior of renewable resources. In that case, the preferable choice becomes limited to generator powered by fossil fuel and grid electricity. It is not economically suitable and preferable to supply electricity at a distant place like Sajek Valley. So, that choice limits our capability to design the model using generator as the backup source. A standalone hybrid energy system can enlighten the homes of Sajek Valley with the light of hope that they are not discriminated by the people with better facilities living at large cities.

In the next section of this paper, we have given an overview on Sajek Valley along with the load profile of this area. Section III describes the available renewable resources at Sajek Valley. The following section describes the simulated model in HOMER simulation software where we have discussed the reason to choose the components and their effect on the designed system along with particular cost analysis. In section V, we have analyzed the optimized results based on cost and emission. Finally, we have concluded this paper discussing the significance and limitations of this work.

## II. SAJEK VALLEY: AN OVERVIEW

### A. Location Details

Sajek Valley (23°22.9'N, 92°17.6'E), a part of Sajek union, located in Chittagong Hill Tracts near the Mizoram border edge area [5]. It is situated in the verdant hills of Kasalong range of mountain under Baghaichari Upazila at Rangamati district. Sajek Valley has become a great tourist attraction for the last few years. People from distant places are visiting this place to enjoy the scenic beauty of this place. As a result, some government and privately-owned hotels, resorts and rest houses have been introduced for tourists. People visit Sajek Valley and Konglak Para, a neighborhood very close to Sajek Valley, in a regular basis, especially in winter season. The area of Sajek Valley, shown in Fig. 1, is about 7 square kilometer including Konglak Para [6].

978-1-5386-2307-7/17/$31.00 ©2017 IEEE

Figure 1. Area of Sajek Valley including Konglak Para [6]

## B. *Load Profile*

The population density at Sajek Valley and Konglak Para is very low. About 65 people lives per square kilometer in the considered area. Based on seasonal variation, the load of Sajek Valley has been divided into four categories. We considered November to February as Winter season. March to June is considered as Summer, July to August is considered as Rainy season, and finally September and October is measured as Autumn. Though the main tourist season is winter, a considerable number of tourists visit Sajek Valley during rainy season.

There are several types of consumer in Sajek Valley. Hotels, resorts, rest houses are considered as high consumers. They require a high amount of electricity during tourist season. Most of the residents of Sajek Valley do not have a good economic condition. As a result, they are not able to have a high number of electrical appliances. The load variations for Sajek Valley throughout the year is provided in Fig. 2. The average load is about 8 kW with the peak load of about 12 kW in Summer.

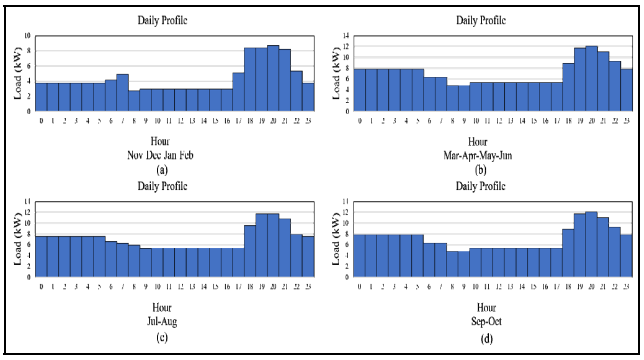


Figure 2. Load profile at Sajek Valley throughout the year

# III. Renewable Resources at Sajek Valley

HOMER simulation software requires some input data to evaluate the optimized model from various combinations. In this section, we have discussed on the available natural resources in Sajek Valley.

## A. *Solar Resource*

The rays of the sun that reach to the earth is a converted form of energy known as solar energy. Solar irradiance, the amount of incoming radiation from sun, is a necessary measure to calculate electrical energy that can be achieved from the photovoltaic systems used in solar cells or panels [7]. The monthly average solar irradiation data has been obtained from National Aeronautics and Space Administration (NASA) for Sajek Valley which is summarized in Table I.

TABLE I. Solar Irradiation and Clearness Index at Sajek Valley

| Month | Clearness Index | Daily Radiation ($kWh/m^2/day$) |
|---|---|---|
| January | 0.650 | 4.530 |
| February | 0.633 | 5.100 |
| March | 0.594 | 5.570 |
| April | 0.529 | 5.530 |
| May | 0.452 | 4.980 |
| June | 0.401 | 4.480 |
| July | 0.391 | 4.320 |
| August | 0.421 | 4.470 |
| September | 0.445 | 4.320 |
| October | 0.520 | 4.380 |
| November | 0.599 | 4.310 |
| December | 0.651 | 4.310 |

Table I shows that maximum amount of solar radiation availing on the month of March is 5.570 $kWh/m^2/day$ and minimum on November and December is 4.310 $kWh/m^2/day$, with an average of 4.69 $kWh/m^2/day$. Fig. 3 shows the average monthly solar irradiation data with respective clearness index and Fig. 4 displays the graphical representation of average sunshine at Sajek Valley.

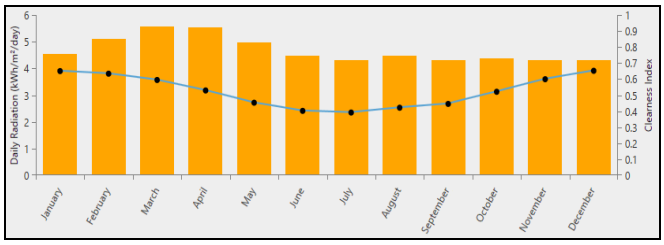


Figure 3. Monthly solar radiation and clearness index at Sajek Valley

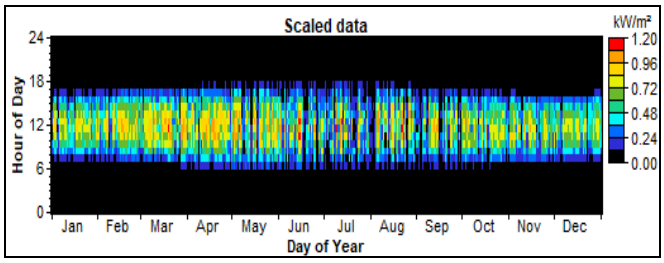


Figure 4. Average sunny hour at Sajek Valley

### B. *Wind Resources*

At different height the average velocity over Bangladesh reach up to 9 m/s during March to September, especially in coastal region [4]. According to the studies of Bangladesh Meteorological Department (BMD), during Monsoon, extended from March to September in Bangladesh, the monthly average wind speed is high and it is too low for the rest of the year [7]. In Sajek Valley, the annual average wind speed is 2.43 m/s which is shown in Fig. 5.

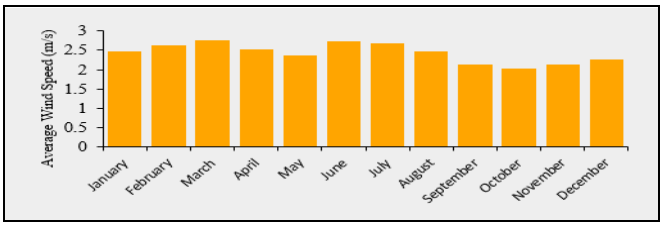


Figure 5. Average wind speed at Sajek Valley throughout the year

As the load requirement of Sajek Valley is comparatively low, setting up wind turbine won't be cost effective. So, we have not considered wind resource as energy source.

### C. *Biomass*

The population density of Sajek Valley is very low and the residents do not have much cattle to produce enough manure to run biomass generator which removes biomass from our list as renewable resource.

## IV. Simulation Model

In this simulation model, we have considered solar energy as the only renewable source. But solar energy is not capable of meeting the required load solely. So, a diesel generator is used along with PV array to support the system. Fig. 6 shows the designed hybrid power system which consists of PV array, diesel generator, battery, converter, and load. PV array and the battery are connected to a DC-bus where the diesel generator is connected to an AC-bus. A bi-directional converter creates the bridge between both buses. Though the load demand can be AC or DC, in this simulation model, we have assumed the load to be AC.

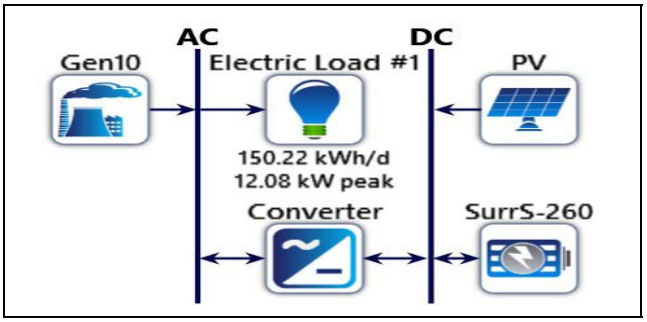


Figure 6. Schematics of simulated model

HOMER estimates the system performance under different situations simulating the arrangement at the same area and same load based on different costs such as the estimated installation cost, operation and maintenance cost, replacement cost, interest etc. [8].

### A. *Solar Photovoltaic*

Solar PV panels use the incident photon from solar radiation to generate electricity [9]. The PV panel used in this model are connected to a DC output. The initial installation cost is considered as 4500$ for 3 kW Generic flat plate PV modules. The sun tracking system with the PV panels moves on horizontal axis in daily basis. The details of PV module are provided in TABLE II.

TABLE II. Cost Estimation & Technical Details of Solar Photovoltaics

| Parameter | Unit | Value |
|---|---|---|
| Capacity | kW | 3 |
| Capital Cost | $/W | 1.5 |
| Replacement Cost | $/W | 1.17 |
| O & M Cost | $/year | 10 |
| Derating Factor | % | 80 |
| Ground Reflectance | % | 20 |
| Lifetime | Years | 25 |

### B. *Diesel Generators*

A generator is required to support an off-grid electricity system and diesel generator is a reliable source for such regions. In this simulated model, a 10 kW diesel generator supplies partial load. It consumes about 14000 liter diesel with an average of 39 liter per day. Fig. 7 represents the average fuel consumption by the diesel generator for the optimized model throughout the year.

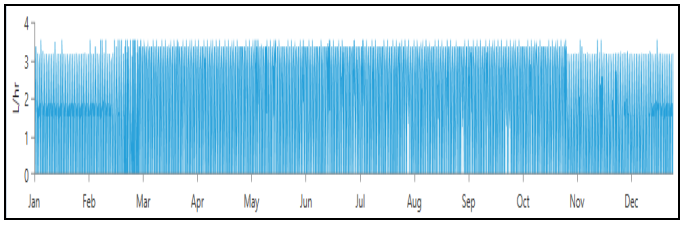


Figure 7. Average fuel consumption by diesel generator throughout the year

Several parameters like capital, replacement, and operation & maintenance cost, lifetime, fuel price etc. define the performance of generator and cost of electricity production. TABLE III shows the cost assumptions and other technical parameters for the diesel generator used in this model.

TABLE III. Cost Estimation & Technical Parameters of Diesel Generator

| Parameter | Unit | Value |
|---|---|---|
| Capital Cost | $/kW | 500 |
| Replacement Cost | $/kW | 400 |
| O & M Cost | $/hour | 0.3 (10 kW) |
| Fuel Price | $/L | 0.82 |
| Lifetime | Hours | 15000 |

### C. Battery

Sporadic behavior of renewable energy sources creates the requirement to use energy storage unit in the modeled design [10]. In this model, we have used Surrette S-260 energy storage unit, with 12V nominal voltage, to maintain the uniform voltage during peak load and in the occurrence of any deficit. Nominal capacity of this battery is 3.12 kWh and lifetime throughput is about 1700 kWh. The roundtrip efficiency of Surrete S-260 is 80%. Installation cost for per battery is 480$ and we have used 10 batteries in this hybrid system.

### D. Converter

Converter can be used both as inverter and rectifier to convert DC to AC and AC to DC respectively. As, in our designed system, DC voltage supplied by PV module and batteries are used by the AC load, a converter is required [9]. In this simulated model, we have used a 10kW converter with an installation cost of 1000$. The converter has a lifetime of 15 years and after that it needs to be replaced with a replacement cost of 800$. The inverter efficiency of this converter is 95% where the rectifier efficiency is 90%. The operation and maintenance cost of the converter is 10 $/year.

### E. Energy System Constraints and Parameters

This energy system is designed considering a project lifetime of 25 years with an annual interest rate of 10%. The constraints that is applied in this model are: minimum renewable fraction is 20%, operating reserve is 10% of the hourly load and maximum annual capacity shortage is 0%.

## V. Results and Discussion

HOMER software found 96 feasible solutions simulating the designed model. HOMER analyses the system based on the available resources, provided components, renewable energy factor etc. and then presents the optimized model based on cost of electricity (COE). Other factors which influence the selection of optimized model, includes capital cost, operating cost, net present cost (NPC), diesel consumption rate etc. Some sensitivity factors like diesel price, minimum load ration etc. also influence the optimized model and so do the COE [11].

The optimized system contains solar panel and diesel generator for electricity generation. Batteries and converter are respectively used as energy storage device and to convert DC supply to AC supply for the load. The architecture of the optimized system is provided in Table IV.

TABLE IV. Architecture of Optimized System

| Parameter | Value |
|---|---|
| Solar PV | 17.8 kW |
| Battery | 10 Surrette S-260 |
| Diesel Generator | 10 Kw |
| Converter | 7 Kw |

The production ratio shows that total 68,718 kWh electricity is produced every year where 40.9% energy is produced by solar PV and the rest 59.1% is supplied by diesel generator. Fig. 8 shows the monthly average electric production by different components of the optimized system.

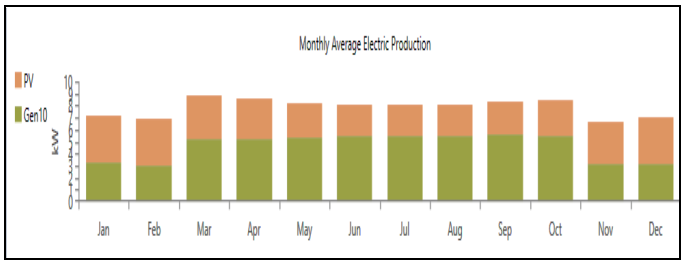


Figure 8. Monthly average electric production by different componenets

### A. Cost Summary

As HOMER provides optimization results of the system based on COE, the optimized model, with the available resources, can meet the demand for electricity at lowest possible cost. The optimization result is simulated based on the price of the components and fuel mentioned in the previous section. The cash flow for this system, by cost type, is shown in Fig. 9, which represents that the major cost for this system is its installation cost. Besides, there is a regular cost of the fuel for the diesel generator. This regular expense increases COE to 0.334$. This cost would be reduced if there would be available renewable resource to meet the demand or a higher load requirement by the consumer. But the limited resources at Sajek Valley has given rise on the cost of electricity which is the minimum possible rate to serve the electricity to the consumer on this configuration.

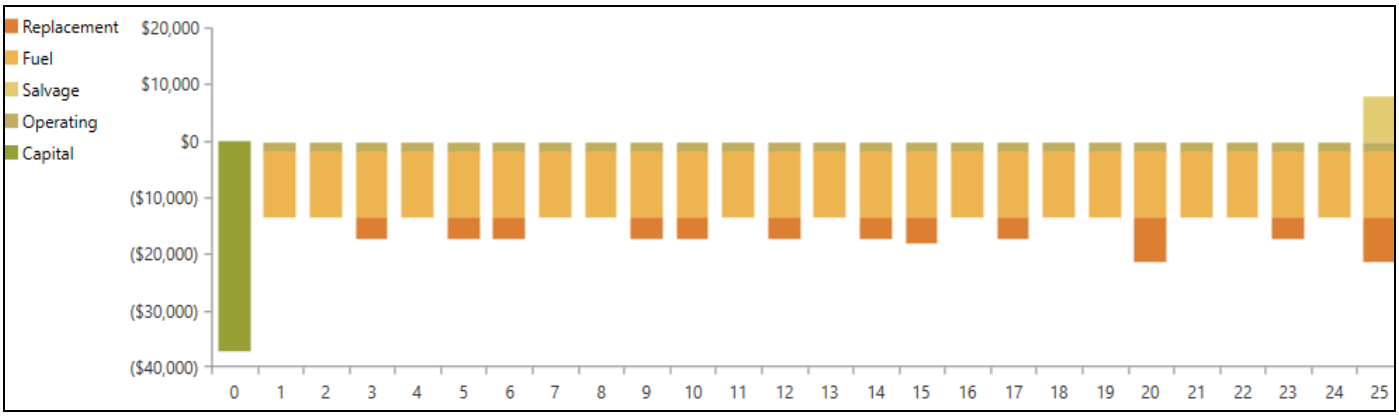


Figure 9. Monthly average electric production by different componenets

### B. Emission Analysis

Combustion of fossil fuels results in emission of various types of pollutants like $CO_2$, CO, $NO_x$, $SO_2$, unburned hydrocarbon etc. [12] The amount of emission from different types of pollutants is shown in TABLE V.

TABLE V. EMISSION SUMMARY

| Quantity | Value | Unit |
|---|---|---|
| Carbon Dioxide | 37.163 | tonne/yr |
| Carbon Monoxide | 0.281 | tonne/yr |
| Unburned Hydrocarbons | 0.010 | tonne/yr |
| Particulate Matter | 0.017 | tonne/yr |
| Sulfur Dioxide | 0.091 | tonne/yr |
| Nitrogen Oxides | 0.319 | tonne/yr |

The emission due to production of the required electricity via grid would be about 48.10 tonne/year considering the emission factor for Bangladesh as 0.7 [12]. In our proposed system, this emission is reduced to 37.88 tonne/year making the model environment friendly.

## CONCLUSION

Modern civilization is running based on electricity. The advancement of a country largely depends upon it. So, we cannot think to proceed forward keeping a portion of our population in dark. So, to ensure the availability of electricity for the people of Sajek Valley, our proposed system can be the light of hope and start of prospect. Besides, if electricity is available at Sajek Valley, it will be possible to provide better facility to the tourists and the income of the people at that place will be increased. In remote areas, where grid connection is not feasible, such standalone model can be a good solution for the people of those locality.

## REFERENCES


[1] M. S. Kaiser, and A. R. M. Siddique, "Optimal Hybrid Option Analysis for a Remote Location in Bangladesh," *International Journal of Advanced Renewable Energy Research*, vol. 2, no. 2, pp. 777-784, September, 2013.

[2] A. S. Pranti, A. M. S. Iqubal, and A. Z. A. Saifullah, "Conceptual Design of Solar-micro Hydro Power Plant to Increase Conversion Efficiency for Supporting Remote Tribal Community of Bangladesh," *American Journal of Engineering Research (AJER),* vol. 3, no. 11, pp. 167–197, 2014.

[3] A. Zubair, A. A. Tanvir, and M. Hasan, "Off-Grid Hybrid Energy System Incorporating Renewable Energy: The Case of Remote Coastal Area of Bangladesh," *Journal of Modern Science and Technology,* vol. 1, no. 1, pp. 188–198, 2013.

[4] A. K. Sikder, N. A. Khan, and A. Hoque, "Design and optimal cost analysis of hybrid power system for Kutubdia island of Bangladesh," *8th International Conference on Electrical and Computer Engineering*, Dhaka, 2014, pp. 729-732.

[5] Sajek Valley. (2017) Wikipedia. [Online]. Available: https://www.wikipedia.org/wiki/Sajek_Valley

[6] Google Maps. (2017) [Online]. Available: https://www.google.com.bd/maps/place/Sajek+Valley/@23.38,92.29

[7] A. Zubair, A. A. Tanvir, and M. Hasan, "Optimal Planning of Standalone Solar-Wind-Diesel Hybrid Energy System for a Coastal Area of Bangladesh," *International Journal of electrical and computer engineering,* vol. 2, no. 6, pp. 731–738, 2012.

[8] M. Nurunnabi and N. K. Roy, "Grid connected hybrid power system design using HOMER," *2015 International Conference on Advances in Electrical Engineering (ICAEE)*, Dhaka, 2015, pp. 18-21.

[9] S. Salehin, A. K. M. S. Islam, R. Hoque, M. Rahman, A. Hoque and E. Manna, "Optimized model of a solar PV-biogas-diesel hybrid energy system for Adorsho Char Island, Bangladesh," *2014 3rd International Conference on the Developments in Renewable Energy Technology (ICDRET)*, Dhaka, Bangladesh, 2014, pp. 1-6.

[10] S. Ghaem *et al.*, "Feasibility study of using a biogas engine as backup in a decentralized hybrid ( PV / wind / battery ) power generation system e Case study," *Energy*, vol. 90, no. 2, pp. 1830–1841, October, 2015.

[11] R. Mirza *et al.*, "Design of a Cost Effective Off-Grid Wind-Diesel Hybrid Power System in an Island of Bangladesh," *International Journal of Electrical, Computer, Energetic, Electronic and Communication Engineering,* vol. 5, no. 12, pp. 1646–1649, 2011.

[12] M. Shahadat, H. Lipu, S. Uddin, M. Ahad, and R. Miah, "A feasibility study of solar-wind-diesel hybrid system in rural and remote areas of Bangladesh," *International Journal of Renewable Energy Research*, vol. 3, no. 4, pp. 892-900, 2013.

# Optimal Design of Hybrid Microgrids for Readymade Garments Industry of Bangladesh: A Case Study

Udoy Paul[1], Md Mehedi Hasan[2], Labib Labib[3], and Naruttam Kumar Roy[1,2]
[1] Khulna University of Engineering & Technology, Bangladesh
[2] Khulna University of Engineering & Technology, Bangladesh
[3] Saint Mary's University, Canada
udoy.eee@gmail.com

*Abstract*— **Bangladesh, the world's second-largest apparel exporter of western brands is facing daunting energy crisis as the existing natural resources are shrinking. To maintain the current economic growth, it is crucial to meet the incremental energy demand. Integration of renewable energy resources could possibly help meeting the accumulative energy demand, thus ensuring stable economic growth. This paper represents a case study of integrating a solar microgrid and associated energy storage system in a RMG factory where the economic and environmental impacts are studied. System optimization, cost calculation, and emission profile analysis was carried out with the help of Hybrid Optimization Model for Electric Renewables (HOMER) software. The case study concludes that the integration of solar microgrid could offer less environmental pollution as well as higher economic benefits.**

***Keywords— Bangladesh; solar microgrids; renewable energy; readymade garments; economic development; environmental pollution, HOMER.***

## I. Introduction

Bangladesh is one of the developing countries in South Asia, having an estimated population of about 170 million with an area of 147,570 km2 and geographical location is between 24°34 to 26°38 north latitude and 88°01 to 92°42 east longitude [1]. The Ready-Made Garments (RMG) industry occupies a remarkable position in the Bangladesh economy. It is the largest foreign currency earning industry in Bangladesh, which experienced outstanding growth during the last 25 years. Textiles & Clothing account for about 85% of total export earnings of Bangladesh [2]. Electricity demand in Bangladesh is currently increasing at a rate of about 8% annually. The demand is expected to be 22,500 MW in 2021 where near about 40% of the energy is consumed in the industrial sector in Bangladesh [3].

During the last few decades, the massive use of fossil fuels and related polluting emissions has grown exponentially and made the environmental situation very difficult since relationship between temperature rise and $CO_2$ emissions has always been a direct relationship [4]. The consequences of the increase in atmospheric temperature also contribute to an increased frequency of natural disasters, corrosion of buildings and faster growth of bacteria and the spread of disease. The only possible way to limit such occurrences, is to reduce man-made $CO_2$ emissions; either by consuming reduced amount of energy or by adopting renewable energy resources that emit less $CO_2$ [5], [6]. Solar microgrids with a series of advantages like lower financial commitment, lower $CO_2$ emission, and less maintenance requirements can be a good option.

## II. RMG Sector and Captive Power Generation

Bangladesh has been the one of the largest export trade countries of RMG and apparel in the world market. The number of factories in RMG industry has gone manifold increase over the last 3 decades and currently this industry comprises near about 4222, garment factories with up to 10 million livelihoods dependent on it while earned about 31 billion USD in 2014-2015 [2], [13]. Present value added by different sub-sector in the manufacturing sector of Bangladesh is shown in Fig. 1. As is evident from the figure, textile industry is the largest in the manufacturing sector and accounts for approximately 60% of total value added in the sector. Besides, there exist some other industries like machineries and parts, processed foods, footwear, plastic products, and metal products in the manufacturing sector, but these industries' share in value added is still limited [14].

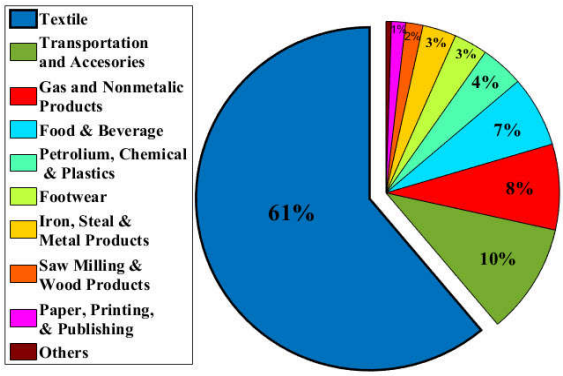


Figure 1: Value added by various manufacturing industries in Bangladesh

In Bangladesh, most of the textile industries do not take power from the national grid rather they produce their own power usually by gas or diesel generator to avoid interruption in the power supply [7]. This power is known as captive power. As on 2014, according to the data found from statistical approximation, Bangladesh had a supply of captive power for at least 2700 MW in textile industries [10]. Annual $CO_2$

978-1-5386-2307-7/17/$31.00 ©2017 IEEE

emission of Bangladesh is approximately 50 megatons per year whereas the absolute quantity the $CO_2$ emissions related to the manufacturing sector is about 10 million metric tons per year throughout the first decade of the 21st century. Almost 45% of all $CO_2$ emissions are by product of the electricity and heat production [12].

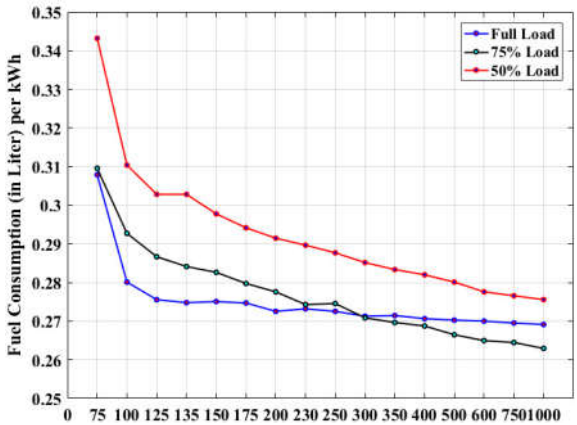


Figure 2: Fuel consumption for different generator size and load condition

Fig. 2 represents the fuel consumption for different generator sizes at different loading condition [15]. With the increase in generator size and loading condition fuel consumption decreases for per kWh of energy production. Fuel consumption and $CO_2$ emission are almost linearly correlated [16]. During the process of captive power generation, the consumption of one-liter diesel emits about 2.7 kg of $CO_2$. However, the number of kg of $CO_2$ produced per liter of diesel consumed by the diesel generator varies slightly depending on the characteristics of the diesel generator, ambient temperature, maintenance factor, and on the characteristics of the fuel, and it is usually falls in the range of 2.4~2.8 kg/l [15]. At an average 0.263~0.345 liter of diesel is burnt for 1kWh of power generation depending on the size, loading condition and other factors which emits approximately 0.710~0.932 kg of $CO_2$ [9], [11].

## III. Background and Scope of the Study

According to the Renewable Energy Policy of Bangladesh 2008, there is a strong potential for solar energy within the country but an efficient utilization of renewable energy resources is yet to assume commercial dimensions and hence, rational policy dissemination on renewable energy usage is essential. The objectives of Renewable Energy Policy 2008 are to [17]:

- Develop sustainable energy supplies to substitute indigenous non-renewable energy supplies;
- Promote appropriate, efficient and environment friendly use of renewable energy and facilitate the use of renewable energy at every level of energy usage.
- Scale up contributions of renewable energy to electricity production and achieve the targets for developing renewable energy resources to meet five percent of the total power demand by 2015 and ten percent by 2020.

For remote, rural isolated regions due to high transmission expenses, transmission losses and load dispatch bottlenecks, renewable energy resources are being increasingly recognized as reliable and cost-effective power generation sources. Till date, 4.5 million families in the rural area of Bangladesh are using the solar photovoltaic technology in their household which has an aggregated capacity of 179.27 MW [22]. Several studies have been carried out for evaluating the optimal hybrid renewable system for such isolated systems are as mention below.

In paper [18], the ways of reducing fuel usage and minimizing $CO_2$ emission was discussed. Higher degree of system reliability and power quality were maintained for the microgrids and minimal $CO_2$ emission was ensured by reduced fuel usage. This is achieved by increasing the renewable fraction of the generated electric power for the approximated load of a system and scheduling optimal efficiency operating points for generators. An additional energy storage system was also proposed to reduce the dependency on the utility grid. A case study of microgrid for electrification of a rural village was presented in [19]. Economic feasibility and environmental advantages of off grid renewable based hybrid power generation was also presented on that study. The authors in [20], demonstrated a mathematical model, optimization algorithm and software based optimization approach for the identification of optimal microgrid configuration and optimal generation of the combined configuration. The study showed that the optimal selection of renewable energy sources and energy storage units along with proper dispatch strategy while in grid-connected mode can significantly reduce the microgrid lifetime cost and greenhouse gas emission. Feasibility analysis of an off-grid stand-alone renewable energy technology system for remote areas in Senegal was presented in [21]. This paper presented a comparative study of cost savings and environment friendliness of the grid extension with renewable energy technology. Most of these studies are hypothetical in nature particularly because of the hypothetical load estimation and stereotyping one or few of the total possible load profiles for the study of a larger system comprising many such units. Also, to serve the objective of Renewable Energy Policy of Bangladesh, 2008, it is crucial to promote green energy supply to substitute non- renewable energy supplies.

The purpose of this paper is to present an optimal design and planning of a renewable energy and associated energy storage facility based microgrid. This study was carried out considering the load conditions and capacity information of a readymade garment factory named Mondol Fashions Ltd. A comparative study for economic and environmental impacts is carried out among the existing diesel generator based power system and three different hybrid microgrid configurations.

## IV. Definition and Practical Considerations

### A. *Electrical System of Mondol Fashions Ltd*

The *Mondol Fashion Ltd.* factory located at Tongabari, Ashulia, savar, Dhaka (23°54'21.1"N 90°19'20.9"E) is

established in a rented six storied building. The total floor area of the building is 58,000 square ft with building height of 71.2 feet. Approximately 1050 workers are working in the factory on a regular basis. The factory has one diesel generator of 500kW and its output is connected to a 440 volts Low Tension (LT) panel. The LT outputs are fed to the panels on ground, 1st, 2nd, 3rd, 4th and 5th floor. Total connected electrical load for the whole unit is about 412.06 kW. The information collected and approximate load profile for the factory was based on field inspection.

### *B. The Hybrid Optimisation Platform: HOMER*

The optimization software, Hybrid Optimization Model for Electric Renewables (HOMER) is developed by the U.S. National Renewable Energy Laboratory (NREL). It is a simulation tool developed to assist in the planning and design of renewable energy based microgrids. The physical behavior of different grid connected and standalone microgrid system and their net percent cost (capital cost + operating cost over lifespan) can be modeled using HOMER [18].

### *C. Economic Analysis*

In this study, the economic analysis is performed based on the Net Percent Cost (NPC). The net present cost of a component or a system is the summation of present value of all the costs over the project lifetime. HOMER calculates the NPC of each component in the system, which includes the initial system component's cost, maintenance, fuel and replacement cost within the project life [23].

$$NPC = \frac{\textit{Total Annualized Cost}}{\textit{Capital Recovery Cost}} \quad (1)$$

Where, total annualized cost is defined as the sum of annualized cost of each system component and the capital recovery cost (CRF) is obtained from the following equation:

$$CRF = \frac{i\,(1+i)^n}{(1+i)^n \quad 1} \quad (2)$$

Here '*i*' is the interest rate and '*n*' is the project length in year. For this study, a 6 % interest rate and 20 year of project life has been considered.

### *D. Renewable Fraction*

The renewable fraction is the ratio of annual electrical power production from renewable resources to the total annual electrical power generation per annum [8].

### *E. Demand Analysis*

Demand analysis is carried out mainly by field inspection and summarizing the total connected load in the factory. The production process includes various electrical load types like sewing machines, lights, fans, air conditioning unit, air compressor, iron unit, etc. Workers of *Mondol Fashion Ltd* work in one shift from 8 a.m. to 6 p.m. with one hour of lunch break 1 p.m.-2 p.m. During this 10-hour period the factory runs on full load except for the lunch break. The electrical system is connected to the national grid but due to frequent power outages and because many of the production process require uninterrupted power supply, a diesel generator of 500 kW is the used as the primary power source for more reliable operation. According to National Fire Protection Association (NFPA) 70E [25], article 220.42 and 430.24 considering the demand factor for industrial appliances as 1.0 the following table summarizes the total load of *Mondol Fashions Ltd.*

TABLE I. ELECTRICAL LOAD SCHEDULE

| Type of the Load | Load Details | | | |
|---|---|---|---|---|
| | *Load Size (kW)* | *Quantity* | *Time (Hour)* | *Total load (kW)* |
| Embroidery Unit | 6.40 | 02 | 09 | 12.80 |
| Washing Machine | 2.30 | 03 | 09 | 06.90 |
| Dryer Machine | 2.30 | 06 | 09 | 13.80 |
| Lift | 4.30 | 01 | 11 | 04.30 |
| Fan | 0.08 | 301 | 09 | 24.08 |
| Light | 0.04 | 1329 | 10 | 53.16 |
| Exhaust Fan | 1.50 | 25 | 09 | 37.50 |
| Utility Pump | 4.00 | 01 | 10 | 04.00 |
| Iron Unit | 0.75 | 45 | 09 | 33.75 |
| Sewing Machine | 0.36 | 397 | 09 | 142.92 |
| Computer | 1.00 | 28 | 10 | 28.00 |
| Air Compressor | 7.50 | 1 | 09 | 07.50 |
| Air Conditioner | 2.00 | 21 | 10 | 42.00 |
| Emegency Light | 0.01 | 145 | 24 | 01.45 |
| **Total electric load for the whole unit** | | | | **412.06** |

Fig. 3 shows the daily load profile of the factory. The daily load profile represents the loading pattern during a typical workday.

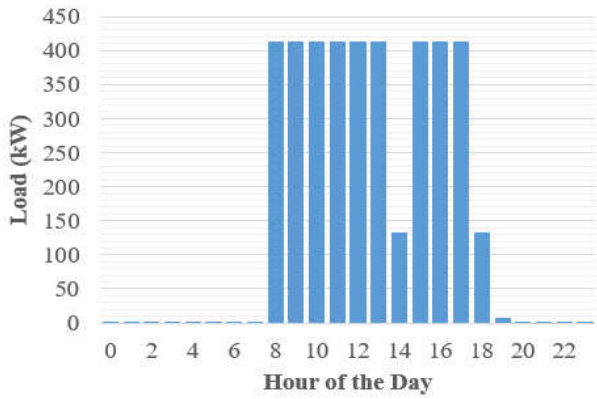


Figure 3: Daily load profile of *Mondol Fashions Ltd.*

### *F. Solar Resource*

The National Renewable Energy Lab's (NREL's) PV-watt calculator has been used for the determination of solar

radiation profile for Dhaka region. The PV-watt estimates the PV energy production throughout the world. The annual average solar radiation for this region is 5.57 kWh/m²/day [4]. Monthly average solar horizontal irradiance is presented in Fig.4.

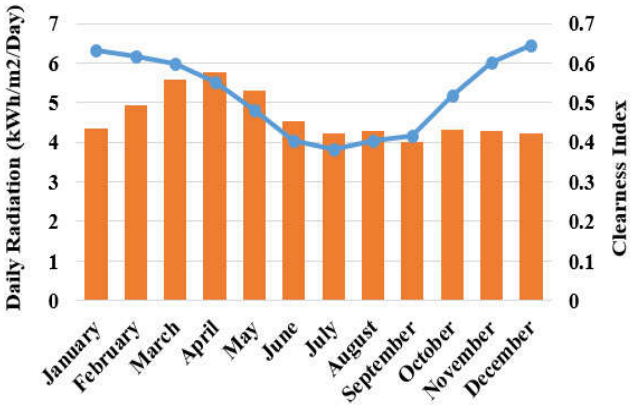


Figure 4: Monthly average solar horizontal irradiance

## V. Assumptions and Microgrid Configurations

HOMER analyzes the feasible systems with their configurations under the user defined search space. Four different cases have been analyzed in this study. Case 1 represents the existing electrical system in *Mondol Fashions Ltd.* where a 500-kW diesel generator is used as the main electric power source. In Case 2 and Case 3, a solar microgrids and associated converter and storage unit was considered along with the existing electrical system in the garments factory. In case 4, the 100 percent renewable sources are considered instead of the diesel generator. For the optimization modeling, generic HOMER components have been used. For all cases, a 6 % annual interest rate and built in constraints have been considered. Tables II and III show different input data considered for sizing cost and other parameters [20]. Based on the parameters listed in the following tables, HOMER analyzes various parameters and identifies the optimal solution option based on the NPC. The analysis was carried out using the same PV and diesel parameters for all the cases.

TABLE II. Input Data for Cost Analysis

| *Options* | *Capital Cost* | *Replacement Cost* | *O& M Cost* |
|---|---|---|---|
| Diesel Generator | $500/kW | $500/kW | $0.15/Hour |
| Battery | $75/Battery | $75/Battery | $2/Battery/Year |
| PV | $7.5/W | $7.5/W | - |
| Converter | $1000/kW | $1000/kW | $100/Year |

TABLE III. Input Data for Sizing and Other Parameters

| *Options* | *Size and unit numbers* | *Life* | *Additional Information* |
|---|---|---|---|
| Diesel Generator | 500 kW | 15000 h | Minimum load ratio = 30% |
| Battery | 50, 100, 120, 135, 150 | 845 kWh | Nominal capacity = 225Ah |
| PV | 1, 5, 10, 15, 20, 30, kW | 20 Years | Derating factor = 90% |
| Converter | 5, 7, 10, 15, 20, 30 kW | 15 Years | Efficiency= 90%<br>Rectifier Efficiency=85% |

### A. Case 1

The existing electrical system in *Mondol Fashions Ltd.* and its NPC value and emission profile was simulated using HOMER. It is a standalone diesel generator scenario with an average energy consumption of 2869.63 kWh/day where the peak load is 412.06 kW. Fig. 5 shows the existing battery-diesel configuration of the factory.

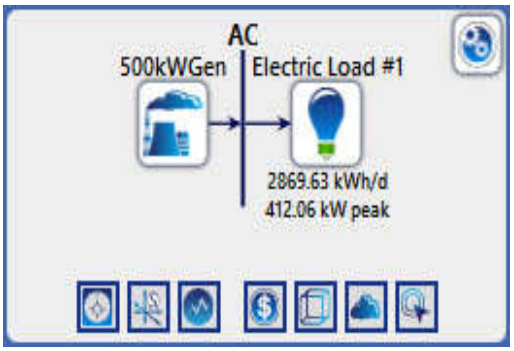


Figure 5: Diesel only configuration (Case 1)

### B. Case 2

A PV-battery-diesel hybrid model that selects a solar microgrid sized 1 kW and associated storage and converter unit along with the existing 500 kW diesel generator is presented in Case 2. The average energy consumption and peak load was considered same for this case.

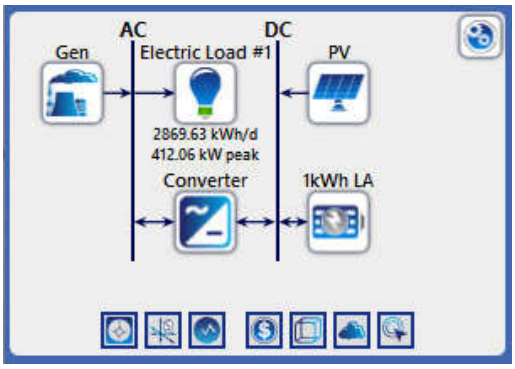


Figure 6: PV-diesel-battery hybrid microgrid configuration (Case 2 & Case 3)

### C. Case 3

Case 3 is also a PV-battery-diesel hybrid model like Case 2 except a 15 kW solar microgrid and associated converter and storage is considered in Case 3 instead of 1 kW solar microgrid in Case 2.

### D. Case 4

The electrical system in Case 4 completely relies on solar PV. Considering the same load profile and energy consumption, the NPC, initial cost, converter and battery size, and other parameters are determined with the help of HOMER.

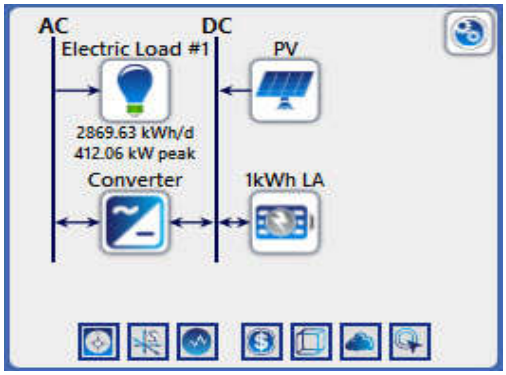


Figure 7: Solar PV only configuration (Case 4)

## VI. Results and Discussion

Table IV shows the comparison among all the four cases for NPC, $CO_2$ emission, and other elated parameters related to net percent cost. Case 1 involves an initial cost of $0.15 million which is the lowest initial cost amongst the 4 cases. Since the system totally depends on renewable resources in Case 4, the involvement of large number of storage unit and battery led to a greater initial cost. As smaller solar microgrid integration is considered in Case 2, the initial cost has not increased significantly and only accounted for $0.177 million whereas Case 3 accounted for almost twice as much initial cost as Case 1.

TABLE IV. Solution generated by HOMER

| Item | Case 1 | Case 2 | Case 3 | Case 4 |
|---|---|---|---|---|
| PV (kW) | 0 | 1 | 15 | 1038 |
| Diesel Generator (kW) | 500 | 500 | 500 | 0 |
| Lead Acid Battery (kWh) | 0 | 135 | 97 | 22171 |
| Converter (kW) | 0 | 10 | 07 | 484 |
| Initial Cost ($) | 0.15M | 0.177M | 0.276M | 9.93M |
| Fuel Cost ($) | 0.306M | 0.277M | 0.272M | 0 |
| NPC ($) | 5.75M | 2.9M | 3.01M | 13.8M |
| CO2 Emission (Kg/ Year) | 1295478 | 725118 | 713056 | 0 |
| Excess Electricity (%) | 40.9 | 0.05 | 0.34 | 22.2 |
| Renewable Fraction (%) | 0 | ≈ 0 | 1.56 | 100 |

Of the four cases, the highest fuel cost is involved with the diesel generator only system. With the increase in renewable fraction in Case 2 and Case 3 the fuel cost reduced. In the same way, the diesel generator only system was responsible for the highest $CO_2$ emission. Approximately 725118 kg of $CO_2$ is estimated to be emitted per year from the PV-diesel-battery hybrid microgrid configuration in Case 2 whereas 15 kW solar PV accompanied by the diesel generator and battery is supposed to emit 713056 kg of $CO_2$ every year. Neither the fuel cost nor $CO_2$ emission is associated with the solar PV only microgrid configuration. Owing to no fuel cost and negligible maintenance cost for the solar PV only microgrid, it has the highest NPC compared to the other cases mainly due to the high initial cost. The hybrid microgrid configuration in Case 2 and Case 3 has much lower NPC than the other two. 1 kW solar PV and 500 kW diesel generator base configuration is supposed to encounter the least NPC among the four-configurations studied.

Although 100 percent solar photovoltaic configuration is the most environment friendly configuration, the core problem with it is higher initial investment and greater NPC. The diesel only configuration offers least initial investment but is responsible for the highest $CO_2$ emission. The hybrid microgrid configurations in Case 2 and Case 3 are more economical system in term of net percent cost albeit they account moderate $CO_2$ emission.

## VII. Conclusions

This paper presents the study of four different microgrid configurations for optimal design of a PV-diesel-battery hybrid microgrid for a RMG factory. A comparative study of energy economy and $CO_2$ emission for the existing diesel generator based electrical system, PV-diesel-battery microgrid systems and solar PV only system was carried out using the HOMER software. The study reveals that the diesel-renewable mixed microgrid has the lower NPC, lower fuel cost and a less carbon footprint, when compared to that of a diesel generator based microgrid. To comply with objectives of Renewable Energy Policy of Bangladesh 2008, inclusion of renewable microgrid at the industrial level is crucial. A proper planning and optimization can help minimizing the electricity production cost and environmental pollution and eventually that would boost up the industry itself and the national economy.

## References

[1] H. S. Das, A. Yatim, C. W. Tan, and K. Y. Lau, "Proposition of a pv/tidal powered micro-hydro and diesel hybrid system: A southern Bangladesh focus," *Renewable and Sustainable Energy Reviews*, vol. 53, pp. 1137-1148, Jan. 2016.

[2] K. M. F. Hasan, M. S. Mia, Ashaduzzaman, M. M. Rahman, A. N. M. A. Ullah, M. S. Ullah, "Role of Textile and Clothing Industries in the Growth and Development of Trade & Business Strategies of Bangladesh in the Global Economy," *International Journal of Textile Science 2016*, vol. 5(3), pp. 39-48, May. 2016.

[3] M. A. Habib, M. Hasanuzzaman, M. Hosenuzzaman, A. Salman, Md R. Mehadi, "Energy consumption, energy saving and emission reduction of a garment industrial building in Bangladesh," *Energy*, vol. 112, pp. 91-100, Oct. 2016.

[4] M. M. Biswas, K. K. Das, I. A. Baqee, M. A. H. Sadi, H. M. S. Farhad, "Prospects of Renewable Energy and Energy Storage Systems in

Bangladesh and Developing Economics," *Global Journal of Research In Engineering*, vol. 11, no. 5, pp. 23-32, Jul. 2011.

[5] M. Z. Rahman, M. N. Sajib, M. M. S. H. Rifat, M. H.-E-Haider, M. A. A. Khan, "Forecasting the Long Term Energy Demand of Bangladesh Using SPSS from 2011-2040," in *Proc.* 3rd Int. *Conf. on Electrical Engineering and Information Communication Technology,* Sep. 2016.

[6] S. Bigerna, C. A. Bollino, S. Micheli, *The Sustainability of Renewable Energy in Europe*, Springer International Publishing Switzerland, 2015.

[7] Tetra Tech ES India Limited, "Bangladesh: Industrial Energy Efficiency Finance Program," Asian Development Bank, Tech. Assistance Consultant's Rep, 2014.

[8] Y. V. P. Kumar, R. Bhimasingu "Renewable energy based microgrid system sizing and energy management for green buildings," *Journal of Modern Power Systems and Clean Energy*, vol. 3, pp 1–13, Mar. 2015.

[9] R. J. North, "Assessment of real-world pollutant emissions froma light-duty diesel vehicle," Ph. D. thesis, Imperial College London, 2006.

[10] M. Chowdhury, "Study on Implications of the Inadequate Electricity and Gas Supply in the RMG Industry in Chittagong EPZ" M. Sc. thesis, Bangladesh University of Engineering and Technology, Bangladesh, Jul. 2014

[11] P. Jaramillo, W. M. Griffin, H. S. Matthews "Comparative Life-Cycle Air Emissions of Coal, Domestic Natural Gas, LNG, and SNG for Electricity Generation," *Environmental Science & Technology*, vol. 41, no. 17, pp. 6290-6296, Jul. 2007

[12] R. Zaman, "$CO_2$ Emissions, Trade Openness and GDP Percapita: Bangladesh Perspective," MA in Economics thesis, University of Bari, Italy, Nov. 2013.

[13] ATM. Adnan, A. Rakib, M. Rahman, "Export trend of Bangladesh: the dominance of ready-made garments industry," *Research Journal of Economics, Business and ICT*, vol. 10, 2015.

[14] "People's Republic of Bangladesh Survey on Power System Master Plan 2016" Japan International Cooperation Agency (JICA), Jun. 2016.

[15] Approximate Fuel Consumption Chart. [Online]. Available: http://www.dieselserviceandsupply.com/Diesel_Fuel_Consumption.aspx

[16] N. G. Zacharof, G. Fontaras, "Review of in use factors affecting the fuel consumption and $CO_2$ emissions of passenger cars," JRC Science for policy report, 2006.

[17] *Renewable Energy Policy of Bangladesh, 2008,* Ministry of Power, Energy and Mineral Resources, Government of the People's Republic of Bangladesh, Dec. 2008.

[18] A. Prasai, A. Paquette, Y. Du, R. Harley, D. Divan. "Minimizing emissions in microgrids while meeting reliability and power quality objectives," in *Proc. of 2010 Int. Power Electronics Conf.*, pp. 726-733, Jun. 2010.

[19] S. M. Basnet, H. Aburub, W. Jewell, A. Poudel, "Case Study of Microgrid for Electrification and its Benefits in Rural Nepal," in *Proc. of IEEE 2015 Global Humanitarian Tech. Conf.,* pp. 33-39, Oct. 2015.

[20] S. Mizani, A. Yazdani, "Optimal design and operation of a grid-connected microgrid," in *Proc. of IEEE Electrical Power and Energy Conf.,* pp. 1-6, Oct. 2009

[21] D. Thiam, "Renewable decentralized in developing countries: appraisal from microgrids project in Senegal," *Renewable Energy*, vol. 35, pp. 1615-1623, Aug. 2010.

[22] Renewable Energy/Energy Efficiency Status Report (Installed). [Online]. Available: http://www.sreda.gov.bd/index.php/site/re_present_status

[23] F. A. Farret, M. G. Simoes, "*Integration of Alternative Sources of Energy*", John Wiley & Sons, 2006.

[24] Energy Storage Location and Cost, Independent Statistics and Analysis, US Energy Information Administration, June29, 2012, [Online]. Available: http://www.eia.gov/todayenergy/detail.cfm?id=6910#

[25] *NFPA 70E, Standard for Electrical Safety in the Workplace*, National Fire Protection Association, 2014.

# Design and Analysis of Grid Connected Biomass System Utilizing Chittagong Municipal Food Waste

Kazi Meharajul Kabir[1*], Mahmud Abdul Matin Bhuiyan[2], Md. Sarwar Uddin Chowdhury[3], Riku Chowdhury[3,]
[1]Post graduate student, IET, Chittagong University of Engineering & Technology, Bangladesh
[2]Professor, EEE, Chittagong University of Engineering & Technology, Bangladesh
[3]Assistant Professor, EEE, University of Science & Technology Chittagong, Bangladesh
*kazimeharajul_kabir@yahoo.com

*Abstract*— **An agricultural country like Bangladesh is facing insufficient electricity production system. All of the expert bodies are trying to upgrade our electricity production system also trying to create various scopes for producing electricity. Therefore, we are offering a grid connected food wastage based biomass power plant because we have a lot of wastage and maximum of the wastage are vegetables and foods. We proposed renewable energy based power plant because it is environment friendly with less emission of carbon about 2% as well as others conventional power plant. For design and analysis, we have chosen Chittagong City Corporation because there are lot of food wastage in Chittagong. Also, the system is connected to national grid for upgrading our nation.**

***Keywords— Green energy; Bio-mass generator; Grid connection; Food wastage;***

## I. INTRODUCTION

A developing country like Bangladesh where energy is required for upgrading the nation. The generation of electricity in Bangladesh is mainly depends on fossil fuels and about 66% power stations fuel are natural gas [1]. This reserve may be finished within 10 to 20 years [2]. So, this situation is very alarming for us. If we do not find out new resources or alternate resources, it will be disaster for our nation. For this instance our governing body takes few step to overcome this situation. For instance, establishing different resources based on power plants such as oil, gas, coal based plants, and many more. In addition, government establishing a 1000MW nuclear based power plant in Ruppur. However, nuclear power plants needs advance technological safety. If any kinds of mistake would happen,it would be very devastating for us. Besides this Our Government also has taken steps to establish about 1320MW thermal coal based power plant in Rumpal & 1200MW power plant in Moheshkhali also, 1200MW power plant in Baskhali [3]. It's also dangerous for our climate. In addition, Government established furnaces oil based quick rental power plant for quickly solving power situation, but per units cost of this types of power plant is very high. Therefore, we can't effort this types of power plant for longer period. Because Bangladesh has a population of 159.9 million[4] people spread across a land of 1,47,570 sq km. Due to rapid urbanization and increasing industrialization, the country's electricity demand will increase. To meet the growing electricity demand the use of furnaces oil based power plant has negative impact on our environment. This type of power plant contributes to 40% $CO_2$ emission in Bangladesh [5]. For this reason, to ensure our environment security, it is very necessary for us to find out new resources for producing environment friendly electricity. The natural resources of alternative energy create new opportunities of growth in power sector. In Bangladesh, about 72% of the population lives in the rural areas and renewable energy is the right choice for providing green energy [6].Government also takes few steps to establish renewable power plant for producing electricity. Government has issued its Vision and Policy Statement in February 2000 to bring the entire country under electricity service by the year 2020 in phases [7].

So, we are offering a grid connected renewable food waste based biomass power plant. Waste production is 1113.939 ton/day in Chittagong City Corporation. 80% wastage is food & vegetables. So, based on biomass energy, it is easy to implement a grid connected biomass power system in the area which will solve energy crisis in our country. Also, manage our regular wastage. This types of power plant also established in Germany.

## II. PROPOSED BIOMASS SYSTEM

We are offering a grid connected biomass system which is consists of biomass generator with gasification technology and resource is Chittagong municipal food wastage, load. Table I Shows propose system component specification. Fig. 1 shows biomass system by Homer

TABLE I. PROPOSED SYSTEM COMPONENETS SPECIFICATION

| | | | |
|---|---|---|---|
| Biomass | Generic Biomass Generator | 5*4=20 | MW |
| National Grid | Extension | 2 | Km |

978-1-5386-2307-7/17/$31.00 ©2017 IEEE

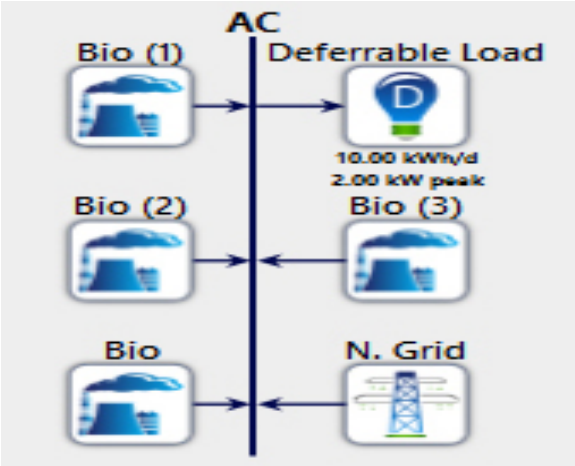


Fig. 1 Proposed Biomass System

## III. BIOMASS ENERGY ANALYSIS

The main process of biomass is photosynthesis [8].The photosynthetic efficiency is the fraction of light energy converted into chemical energy during photosynthesis in food & vegetables. Photosynthesis can be described by the simplified chemical reaction-

$$C_6H_{12}O_6 + 6\ O_2 \text{ ---> } 6\ CO_2 + 6\ H_2O + 17.5\ MJ\ /Kg \qquad (1)$$

$C_6H_{12}O_6$ represents biomass resource [9]. Biomass resources data collected from Bangladesh Municipal Development Fund (BMDF). Table II. Shows the Chittagong city corporation municipal waste [10-11].

TABLE II. WASTE OF CHITTAGONG CITY CORPORATION (CCC)

| Description | LOW | MEDIUM | HIGH |
|---|---|---|---|
| Per Capita Domestic Waste Generation Rate (kg/capita/day) | 0.25703 | 0.25703 | 0.25703 |
| Total Domestic Waste (ton) | 765.629 | 846.507 | 876.828 |
| Market Waste (ton) | 146.050 | 146.050 | 146.050 |
| Street Sweeping Waste (ton) | 138.234 | 138.234 | 138.234 |
| Total Waste (ton) | 1049.913 | 1130.791 | 1161.113 |
| Average Waste (ton/day) | **1113.939** | | |

We used compostable wastage for using biomass resources. 80 % wastage is vegetable & food. So, average food wastage is about 891.15ton/day [09-10].

## IV. SYSTEM SIMULATION & RESULTS

We chose HOMER software to simulate the proposed system [12-14].

### *A. Component Specification for Simulation*

The capacities of each Biomass system are 5MW. The system parameters presents in Table III. Also fig. 2 shows the Biomass resource. The lower heating value of the fuel is 5.5MJ/kg which is presents in table IV. We used 500 ton/day Chittagong municipal food wastage. Fig. 3 shows the Biomass generator efficiency curve.

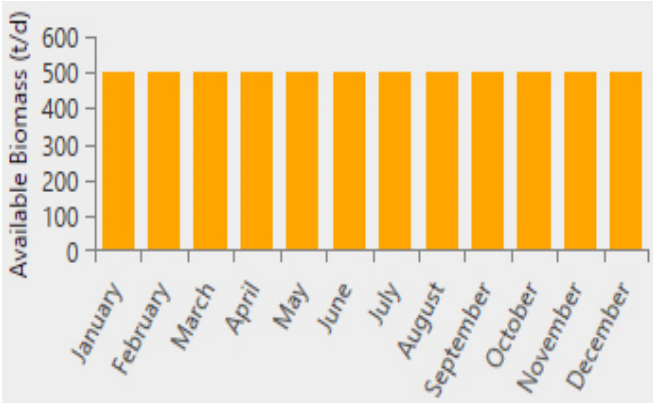


Fig. 2 Biomass resource

All of the biomass generators are of same specification

TABLE III. BIOMASS GENERATOR

| | |
|---|---|
| Sizes to consider | 5 MW |
| Lifetime | 20,000 hrs |
| Gasification Ratio | 0.70 kg |
| Fuel used | Biomass |
| Fuel curve intercept | 0.1000 L/hr/kW |
| Fuel curve slope | 2.0000 L/hr/kW |

TABLE IV. FUEL SPECIFICATION

| | |
|---|---|
| Lower heating value | 5.5 MJ/kg |
| Density | 0.72 kg/m3 |
| Carbon content | 2.0% |
| Sulfur content | 0.0% |

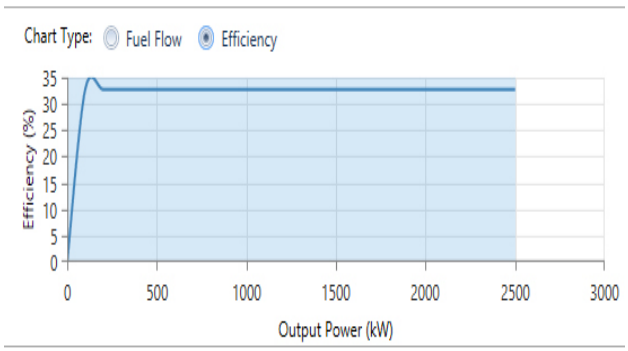


Fig. 3 Biomass Generator Efficiency Curve

We use some electrical load, such as light and fan using for control room of the system. The average load in a day is 10kWh. Also, 2km grid extension needed for the system connected to national grid. Table V. Shows Electrical load demand.

TABLE V. ELECTRICAL LOAD DEMAND

| | |
|---|---|
| Scaled annual average | 10kWh/day |
| peak load | 2kw |
| Load factor | 0.68 |
| Total annual load | 3650 kWh/yr |

*B. Simulation Results*

All of the biomass generators are given equal output.The rated capacity of a biomass generator is 5MW and total electrical production is 14991.867MWh/yr and the mean output production is 3.828 MW. The fuel consumption is 45631L/yr. The mean efficiency of the biomass generator is 31%.
Table VI. shows generic biomass generator output.
Fig. 4 shows the biomass generator output.

TABLE VI. BIOMASS GENERATOR OUTPUT

| Quantity | Value | Units |
|---|---|---|
| Hours of operation | 3916 | hrs/yr |
| Number of starts | 3603 | starts/yr |
| Operational life | 5 | Yr |
| Fixed generation cost | 220.83 | $/hr |
| Electrical production | 14991867 | kWh/yr |
| Mean electrical output | 3828 | kW |
| Min. electrical output | 2501 | kW |
| Max. electrical output | 5000 | kW |
| Fuel consumption | 45631 | L/yr |
| Specific fuel consumption | 2.13 | L/kWh |
| Fuel energy input | 48799873 | kWh/yr |
| Mean electrical efficiency | 31 | % |

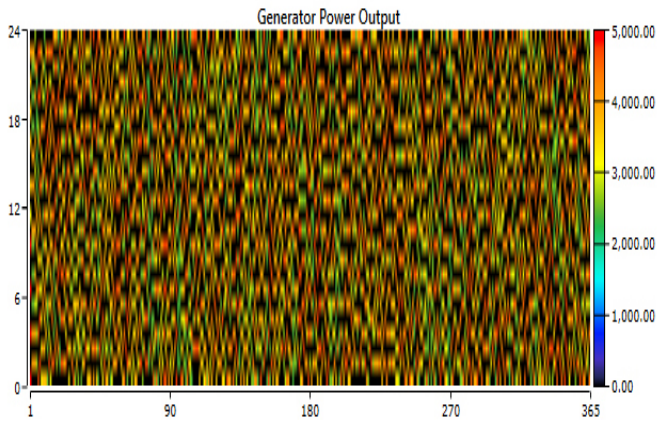

Fig. 4 Biomass Generator output Curve

Table VII. Shows Total Electricity Production.
Fig. 5 shows total Electricity Production.

The following results are obtained

TABLE VII. TOTAL ELECTRICITY PRODUCTION

| Component | Production (yr) | Fraction (%) |
|---|---|---|
| Biomass Generator | 14,991,867KWh | 25 |
| Biomass Generator 1 | 14,991,867KWh | 25 |
| Biomass Generator 2 | 14,991,867KWh | 25 |
| Biomass Generator 3 | 14,991,867KWh | 25 |
| Total | 59,967,470 KWh | 100 |

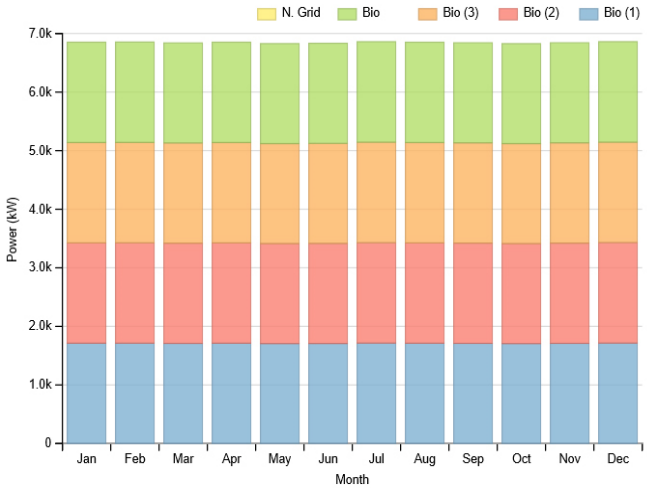

Fig. 5 Total Electricity Production

The main target of the system is reducing national power crisis. In this system, we contributed 7MW/hr and total production in a year is 59967.470MWh. Electrical load consumption is 3650KWh/yr and Electrical power cell to grid is 59963.820MWh. Table VIII. Shows Electricity Consumption. Fig. 6 Shows National Grid Purchase & Sell output.

TABLE VIII. ELECTRICITY CONSUMPTION

| Component | Production (yr) | Fraction (%) |
|---|---|---|
| Electrical load | 3650KWh | 0.01 |
| Grid Sell | 59,963, 820KWh | 99.99 |
| Total | 59,967,470 KWh | 100 |

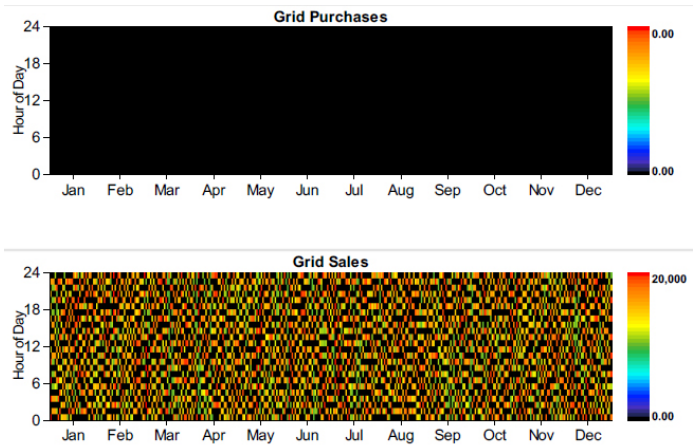

Fig. 6 National Grid Purchase & Sell output

## V. COST ANALYSIS

The initial cost of the system is $40,025,000 and the annualized cost is $2,924,692.00. Table IX. Shows net present cost. Table X. Shows annualized cost. Fig. 7 shows total Cost Summary of the system.

TABLE IX. NET PRESENT COSTS

| Component | Initial Capital($) | Replacement ($) |
|---|---|---|
| Biomass Technology | 10,000,000 | 13,675,996.84 |
| Biomass Technology 1 | 10,000,000 | 13,675,996.84 |
| Biomass Technology 2 | 10,000,000 | 13,675,996.84 |
| Biomass Technology 3 | 10,000,000 | 13,675,996.84 |
| National Grid | 25,000 | 0.0 |
| System | 40,025,000 | $54,703,987.34 |

TABLE X. ANNUALIZED COSTS

| Component | Initial Capital($) | Replacement ($) |
|---|---|---|
| Biomass Technology | 730,716.30 | 999,327.38 |
| Biomass Technology 1 | 730,716.30 | 999,327.38 |
| Biomass Technology 2 | 730,716.30 | 999,327.38 |
| Biomass Technology 3 | 730,716.30 | 999,327.38 |
| National Grid | 1,828 | 0.0 |
| System | $2,924,692.00 | $3,997,309.53 |

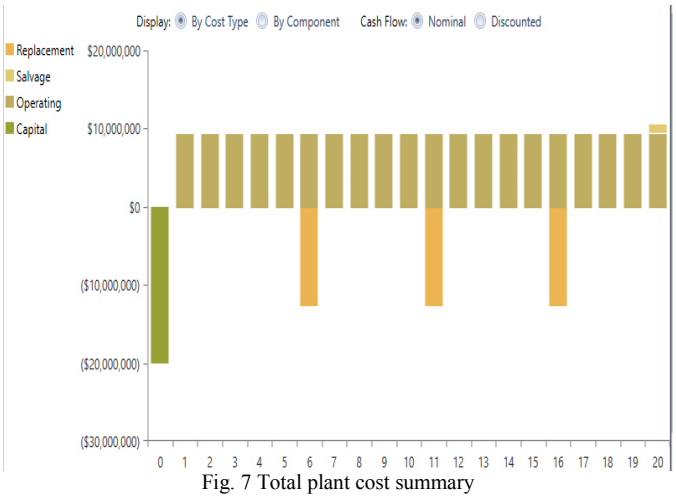

Fig. 7 Total plant cost summary

## VI. CONCLUSIONS

In this proposed system we can easily manage our wastage. We proposed a system for Chittagong City Corporation area, but we can easily use this system at any areas in Bangladesh. The system is green and $CO_2$ emissions about 2% which is negligible. This system is mainly designed for reducing national power demand crisis also to utilize our regular wastage. Initially the cost of the system is $40,025,000, but the cost of energy of the system is $0.145/KWh. If we sell energy to national grid into $0.18/KWh, after 20 years overall profit would be $51,340,353.59. Also, we can use this system for the replacement of quick rental coal or oil based power plant of Bangladesh.

## *REFERENCES*


[1] N.U.R. Chowdhury"Present Scenario of Renewable Energy in Bangladesh and a Proposed Hybrid System to Minimize Power Crisis in Remote Areas" *International journal of renewable energy research Vol.2, No.2,(2012).*

[2] M.S.H. Lipu "A Feasibility Study of Solar-Wind-Diesel Hybrid System in Rural and Remote Areas of Bangladesh" *International journal of renewable energy research, Vol.3, No.4, (2013).*

[3] (2016) Ministry of Power, Energy and Mineral Resources, Government of the Peoples Republic of Bangladesh *http://www.powerdivision.gov.bdl*

[4] (2016) "Bangladesh Economic Survey" *http://cpd.org.bd/wp-content/uploads/2016/05/IRBD-FY16-Third-Reading-FINAL_Revised.pdf*

[5] R. M. Shrestha, G. Anandarajah, M. H. Liyanage, "Factors affecting CO2 emission from the power sector of selected countries in Asia a nd the Pacific,"*Energy Policy,* vol. 37, pp. 2375-2384, Jun (2009).

[6] M.M. Rhaman "Hybrid Renewable Energy System for Sustainable Future of Bangladesh" *International journal of renewable energy research,Vol. 3, No. 4,(2013).*

[7] (2008) "Bangladesh Gazette: Renewable Energy Policy of Bangladesh", published in November 06, 2008. http://lib.pmo.gov.bd/.pdf

[8] (2005) Stanford University Global Climate & Energy Project, Annual Report, An Assessment of Biomass Feedstock and Conversion Research Opportunities. [Online]. Available*: http://gcep.stanford edu/pdfs/assessments/biomass_assessment.pdf*

[9] I.A. Gondal "Model for Biomass-based Renewable Hydrogen Supply Chain" *International journal of renewable energy research* al., Vol.2, No.3,( 2012).

[10] (2014)Bangladesh Municipal Development Fund (BMDF) http://www.bmdf-bd.org/

[11] M.R. Abedin, A. Muhtasim, F. Alam "Electricity from Municipal Waste: A Potential Way to Meet up the Electricity Demand in Urban Bangladesh " Volume 14 Issue 9 Version 1.0 Year (2014) Global Journals Inc. (USA) [Online] ISSN: 2249-4596 & Print ISSN: 0975-5861

[12] Kabir, K. M., Nath, A., Mazumder, S., & Islam, M. O. (2016, December). Modelling & simulation of a grid connected hybrid power plant with photovoltaic, wind & diesel power for Cox's Bazar. In *Electrical, Computer & Telecommunication Engineering (ICECTE), International Conference on* (pp. 1-4). IEEE.

[13] Kabir, K. M., & Matin Bhuiyan, M. A. (2017). Design & simulation of hydrogen based hybrid green power system using sea water for Cox's Bazar. *Cogent Engineering*, *4*(1), 1347029.

[14] Kabir, K. M., Mazumder, S., Chowdhury, S. U., & Haq, M. R. (2015, December). Design & simulation of photovoltaic, wind, battery, grid connected hybrid power system for Patenga, Chittagong, Bangladesh. In *Advances in Electrical Engineering (ICAEE), 2015 International Conference on* (pp. 1-4). IEEE.

# Modeling of High Efficient Perovskite-Si Tandem Solar Cell

M. N. Hasan[1], M. M. Habib[1] , M. A. Matin[1], N. Amin[2]
[1]Dept. of EEE,Chittagong University of Engineering and Technology, Chittagong-4349
[2] Department of Electrical, Electronic and Systems Engineering, National University of Malaysia
1.mnhasan.eee@gmail.com
2. mahedihabibchowdhury@gmail.com
3. mamatin@cuet.ac.bd

Abstract— **Tandem solar cells combining silicon and perovskite absorbers have the potential to outperform state-of-the-art high efficiency silicon single junction devices. Organic-inorganic lead halide Perovskites have significant role in the photovoltaic (PV) technology due to its high efficiency, lightweight and cost effectiveness especially methyl ammonium lead iodide. This can act as absorber layer which has a band gap of 1.65 eV is compatible to be paired with silicon (Si) solar cell with energy gap of 1.124 eV as a tandem solar cell. This tandem approach is a refined solution to improve the efficiency of Si solar cell that has been stuck around 25 % for 15 years. This study focuses on the development of the device configuration model for Si-perovskite tandem solar cell by using WX-Amps simulation. The thickness and dopant concentration of perovskite layer have affected the solar cell parameters performance. The efficiency result obtained from WX-Amps simulation is 31.85 % for Si-perovskite tandem solar cell with an open circuit voltage of 0.9995 V, short circuit current 38.24 mA/cm$^2$ and fill factor 83.34 %.**

Keywords— **Perovskite solar cells, Silicon solar cells, tandem solar ells, tuneable bandgap, wx AMPS simulation.**

## I. INTRODUCTION

A secured and sustainable supply of energy is a key to the prolongation and development of prosperous and modern society. As energy consumption has been increased steadily with civilization development, in the future the energy consumption will be further increased to sustain the current human development. So the best alternative to this energy crisis might be solar energy and the solar cell technology. But the lower efficiency and high cost of the photovoltaic solar cells has limited its use. Thus, increasing efficiency and decreasing cost of solar cell is the major challenge to the researchers. Already single junction solar cell have reached to its peak by 26.1% (Single junction Si solar cell) and by single junction it could be maximized up to 30% efficiency. Now to surpass that limit, multi-junction solar cell was introduced. But at first these solar cells were used for satellite purposes. These multi-junction solar cells were constructed using high grade material such as GaAs whose cost is unimaginably high for terrestrial purposes. That is why our team has worked on low cost solar cell with high efficiency by making tandem solar cell with c-Si and Perovskite solar cells.

The power conversion efficiency of silicon (Si) solar cell has been stuck around 25 % for 15 years, Since the Si is stable, non-toxic and abundant, best way to improve the cell is by developing it in a tandem solar cell. By using a higher bandgap material as top cell which higher than 1.124 eV of silicon band gap [1]. The higher energy photons generates a voltage that can generate approximately twice than silicon. Then developments in organic-inorganic lead halide-based Perovskite solar cells have been very fast over the last 2 years, with efficiencies reaching 20% on small-area devices and 13% on series-type modules respectively, making this material competitive with PV thin film technology [2-6]. The Perovskite cell demonstrated higher built in voltage as well as higher open circuit voltage (Voc), relative to the bandgap of l.6 eV, than a single c-Si junction under the sunlight visible spectrum (400- 800nm). Furthermore, the tandem architecture can be optimized tuning the band gap of the Perovskite by inserting Br atoms in the final crystalline structure [6].

In Silicon-Perovskite tandem device, the high energy photons will be absorbed by the top cell of perovskite, while the low energy photons will be absorbed by the Si bottom cell. Recently, the perovskite with ~1.6 eV bandgap is a compatible contender as a material for the top cell in tandem configuration [7], [8]. This is due to its flexible chemical and physical properties. This kind of Perovskite solar cell is promising due to its high efficiency, lightweight, cost-effective option to be fabricated at low temperatures with simple deposition process such as solution-processing and vapor processing method.

Organic-inorganic perovskite materials are promising solar cell absorbers as they show unique optoelectronic properties and can be processed from solution enabling low lost, high throughput fabrication at low temperatures on flexible substrates. The optical band-gap of $CH_3NH_3PbI_3$ is 1.57 eV and can be tuned via halide replacement or cation exchange [11]. The perovskite material has a high absorption coefficient across the entire visible range together with a sharp onset and very low sub band-gap absorption. Thus, a perovskite layer thickness of around 500 nm is sufficient to absorb a very high portion of the incident light. Due to the negligible exciton binding energy at room temperature, the long carrier diffusion length, the bipolar

978-1-5386-2307-7/17/$31.00 ©2017 IEEE

charge transport with high charge carrier mobilities, and the strongly reduced recombination in the bulk and at the surface, free charge carriers are formed directly upon photo-excitation. These are, in turn, effectively collected at the selective contacts, enabling internal quantum efficiencies close to 100%,a high fill factor (FF), and open circuit voltage ($V_{OC}$) resulting in a record efficiency over 22.1%.

In the c-Si/perovskite tandem cell, higher energy photons are absorbed within the perovskite sub-cell and converted at a high voltage without significant losses from thermalization. Infrared photons are transmitted through the perovskite and lead to photo generation in the c-Si sub-cell, covering a wide spectral range up to 1.12 eV defined by the band-gap of c-Si. This tandem design has a detailed balance limit of 40%, thus, overcoming the Shockley-Queisser limit of silicon single junctions [11]

The Si-perovskite tandem solar cell is reliable material due to its potential to raise the efficiency up to 30 %.However this study will focus on the improvement of that can enhance the efficiency of Si-perovskite tandem solar cell. The simulation will be carried out using the wxAMPS to study the Si-perovskite tandem solar cell configuration in order to indicate the electrical properties dependency on the thickness and dopant concentration of $CH_3NH_3PbI_3$. The wxAMPS program is a newly developed solar cell simulation software based on the original AMPS code [12].

The improvement of Si-perovskite tandem solar cell performance is promising when applying the $CH_3NH_3PbI_3$ as a top cell and Si wafer substrate as a bottom cell.

## II. Device Structure & Modeling

In this section we describe the device structure and methodology used for obtaining the Perovskite/Si solar cell characteristics .For a two bandgap system, it is known that the top cell material band gap needs to be higher than the bottom cell for optimum operation. [1] As mentioned in the previous section, Perovskite has the property of tunable bandgap ranging from 1.6 to 1.9 eV(higher than Si).Which is close to top cell bandgap of an optimum two bandgap system. Besides the selection of energy gap ($E_g$) value of the absorber layer of the top cell is essential to enhance to attain record efficiency higher than single silicon junction [9]

To obtaining the current voltage (J-V) characteristics of the given two terminal tandem cell, where the cells are configured in series. At first we have optimized the top perovskite cell. Then we have used the Si cell to match its current density or maximize the efficiency. Different physical parameters of both cells have been varied to see their effects on the performance of tandem cell and get the insight on the optimization of such cell.For top solar cell the best band gap is 1.5 eV. We have designed a cell of which consist single absorber layer. We choose $CH_3NH_3PbI_3$ as absorber for single absorber cell. This material has direct band gap. The band gap of $CH_3NH_3PbI_3$ is 1.65 eV. MAPbI3 has high power conversion efficiency and high current density ($J_{SC}$). Thus for structure with $CH_3NH_3PbI_3$ i.e. with single absorber layer, we get high $J_{SC}$ and high power conversion efficiency.

The structure of the employed device here is an n-i-p solar cell where ZnO is used as n-type and $Cu_2O$ is used as p-type material. As intrinsic layer $CH_3NH_3PbI_3$ is used. The p-type $Cu_2O$ has good transparency, high hole mobility and good chemical stability. Also it is nontoxic and abundantly available on the earth. By adjusting the thickness of perovskite layers, the PCE of the cell can be improved [1].

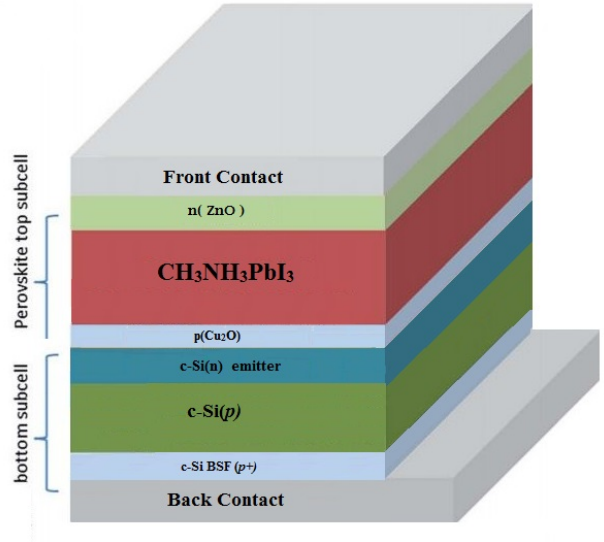


**Fig. 1. 3D schematic view of Perovskite/Si tandem cell**

ZnO has an energy-band structure and physical properties similar to those of $TiO_2$. But ZnO has substantially higher electron mobility than that of $TiO_2$, which would make it an ideal kind of n-type material. Therefore, $Cu_2O$ as HTM and ZnO as ETM are widely utilized to Perovskite solar cells.

The basic structure of c-Si solar cell consisted of front contact/c-Si (*n*) emitter/c-Si (*p*)/c-Si BSF (*p*+)/metal back contact. Infrared photons are transmitted through the perovskite and lead to photo generation in the c-Si sub-cell, covering a wide spectral range up to 1.12 eV defined by the band-gap of c-Si. This is a n-p-p+ solar cell structure. The c-Si (n) emitter is highly doped and acts as hole transport layer when combined with Perovskite top cell. The c-Si absorber layer is thick and has high light absorption coefficient.

Now, by combining these two cells we get the tandem structure. Tandem architecture can be optimized tuning the band gap of the Perovskite. In this structure the Perovskite layer acts as a light harvester sandwiched between a hole transport material and electron transport layer. The advantages of this cell architecture are highest silicon based single junction efficiency, high potential inferred by the band structure of the thin-film emitters and these features reflect in higher $V_{OC}$ values than that of conventional c-Si based homojunction. This effect represents an advantage in a tandem cell configuration i.e voltage gain is due to the sum of the two stacked cell.

978-1-5386-2307-7/17/$31.00 ©2017 IEEE

**TABLE 1.** Input parameters Perovskite-Si solar cell.

| Parameters | n ZnO | $CH_3$ $NH_3$ $PbI_3$ | P ($Cu_2O$) | c-Si(n) emitter | c-Si(*p*) | c-Si BSF (*p+*) |
|---|---|---|---|---|---|---|
| Thickness | 10nm | 6µm | 0.8 µm | 50nm | 280µm | 30nm |
| Bandgap (eV) | 3.37 | 1.65 | 2.1 | 1.124 | 1.124 | 1.124 |
| Electron affinity (eV) | 4.35 | 3.93 | 3.6 | 3.9 | 4.05 | 3.9 |
| Dielectric Permittiviy (relative) | 10 | 30 | 10 | 11.9 | 11.9 | 11.9 |
| CB effective density of states ($cm^{-3}$) | 2.22 x $10^{18}$ | 2.5 x $10^{20}$ | 1 x $10^{19}$ | 2.8 x $10^{19}$ | 2.8 x $10^{19}$ | 2.84 x $10^{19}$ |
| VB effective density of states ($cm^{-3}$) | 1.78 x $10^{19}$ | 2.5 x $10^{20}$ | 1x $10^{19}$ | 2.6 x $10^{19}$ | 2.6 x $10^{19}$ | 2.68 x $10^{19}$ |
| Electron mobility ($cm^2$/Vs) | 100 | 50 | 30 | 1250 | 1010 | 1212 |
| Hole mobility ($cm^2$/Vs) | 25 | 50 | 30 | 443 | 443 | 421 |
| Donor Concentration ($cm^{-3}$) | 1 x $10^{20}$ | 0 | 0 | 8 x $10^{20}$ | 0 | 0 |
| Acceptor Concentration ($cm^{-3}$) | 0 | 0 | 2.5 x $10^{16}$ | 0 | 5 x $10^{18}$ | 9.5 x $10^{20}$ |

## III. RESULT AND DISCUSSION

In this section we analyze the performance of tandem configuration within our proposed modeling under AM1.5 illumination. The physical parameters of the solar cell has been taken from table 1.The highest efficiency was recorded via changing thickness and keeping it under optimum limit. At first the single junction perovskite solar cell is simulated. The output J-V characteristic curve is plotted in fig. 2.

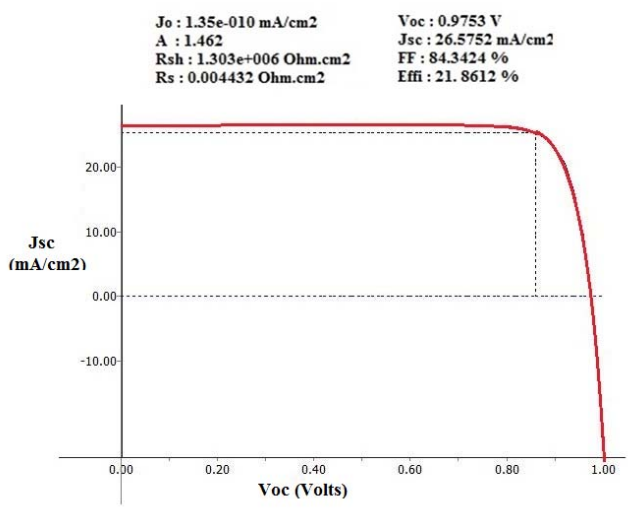


**Fig. 2. J-V Characteristics of single junction Perovskite cell in wx-AMPS in AM 1.5G.**

From the J-V characteristic curve we got an efficiency of 21.82%, $J_{SC}$= 26.5752mA/$cm^2$, $V_{oc}$ = 0.9753V, fill factor = 84.3424% for single junction Perovskite cell (Fig.2).
In the first cell, the Perovskite cell has a thickness of total 6.81µm with the thickness of 6µm Perovskite layer ($CH_3NH_3PbI_3$), 0.01µm ZnO layer and 0.8µm $Cu_2O$ layer.

Now, fig. 3 shows the J-V characteristic curve by simulating single junction c-Si solar cell.

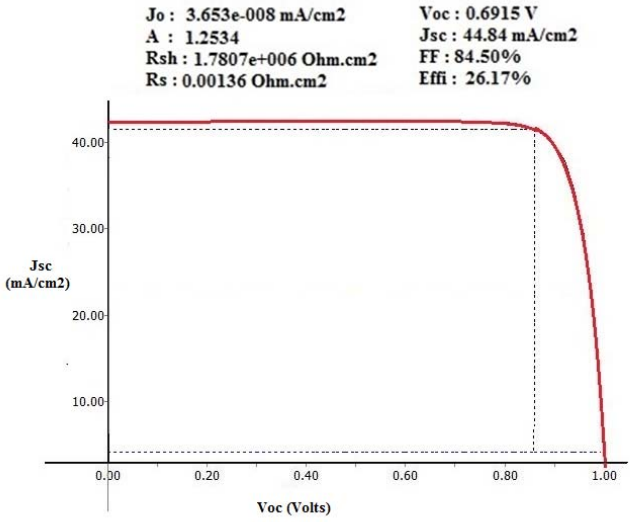


**Fig. 3. J-V Characteristics of single junction C-Si cell in wx-AMPS in AM 1.5G.**

The single junction c-Si solar cell has an efficiency of 26.17% , $J_{SC}$= 44.84mA/$cm^2$, $V_{oc}$= 0.69V, fill factor = 84.50% .
The silicon solar cell has a thickness of total 280.08µm with the thickness of 280µm c-Si absorber layer, 0.05µm c-Si emitter layer and 0.03µm c-Si BSF layer.
We analyzed the performance of the structures by changing the thickness of different layers of the structures, by varying the doping concentration of the N-type and P-type materials and by varying the operating temperature.
Then the two cell are joined each other to form the tandem device. In Fig. 4 it is reported that the experimental J-V characteristic of the tandem device measured under AM1.5G sunlight condition at 25°C of temperature in wx-AMPS simulator. Table 2 shows the output parameters of the perovskite/c-Si tandem structure

**TABLE 2.** Output parameters Perovskite-Si solar cell.

| Cell Type | Voc(V) | Jsc(mA/cm2) | Fill Factor % | Efficiency % |
|---|---|---|---|---|
| Perovskite/ c-Si tandem Solar cell | 0.9995 | 38.2395 | 83.3487 | 31.8547 |

978-1-5386-2307-7/17/$31.00 ©2017 IEEE

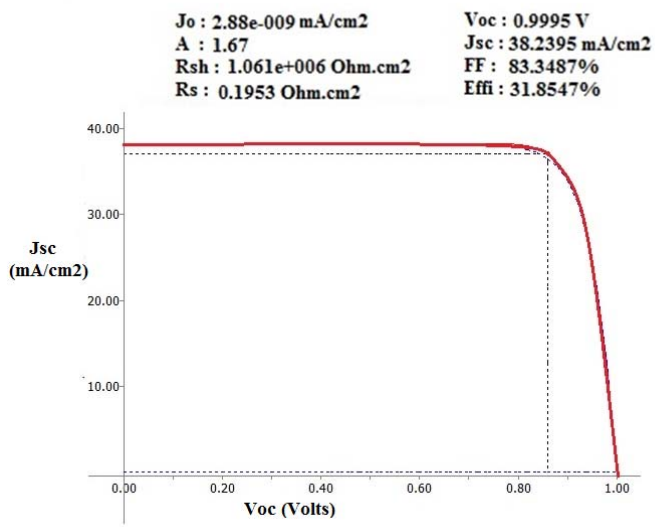


**Fig. 4. J-V Characteristics of Perovskite/Si tandem cell in wx-AMPS in AM 1.5G.**

These preliminary results of properly working device, demonstrates the feasibility of the tandem structure. Indeed $V_{OC}$ value as high as 0.9995V has been achieved in that is higher than the two $V_{OC}$ values of each cell reported. Efficiency up to 31.8547% has been reached using thicker perovskite absorber film for the top cell and c-Si as bottom. This tandem structure shows short circuit current $J_{SC}$=38.2395mA/cm$^2$ and fill factor of 83.3487 %.

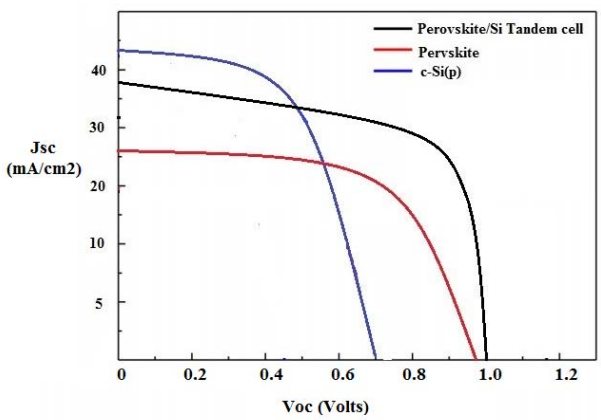


**Fig. 5. J–V characteristics of Pervskite/Si tandem solar cell and Perovskite and Si single-junction solar cells**.

As from fig. 5 it can be seen that the tandem structure has an overall open circuit voltage (Voc) higher than both single junction perovskite and c-Si solar cells.The tandem solar cell has a higher short circuit current density(Jsc) than single junction perovskite solar cell, but slightly lower Jsc than single junction c-Si solar cell.

We analyzed the performance of the structures by changing the thickness of different layers of the structures, by varying the doping concentration of the N-type and P-type materials and by varying the operating temperature.

The thickness of $CH_3NH_3PbI_3$ was varied from 1µm to 17 µm for the Si-Perovskite tandem solar cell and the simulated results obtained efficiency by thickness variation of the $CH_3NH_3PbI_3$ is plotted in graph that shown in fig. 6(a). The optimum thickness was chosen 6µm as after that point efficiency is quite stable while optimum thickness can minimize the materials used as well.

The c-Si absorber layer thickness varied from 50µm to 350 µm and the optimum thickness is chosen as 280µm for the tandem structure as shown in Fig. 6(b).

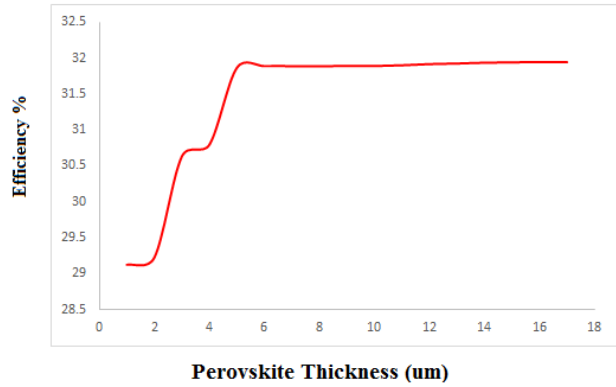


(a)

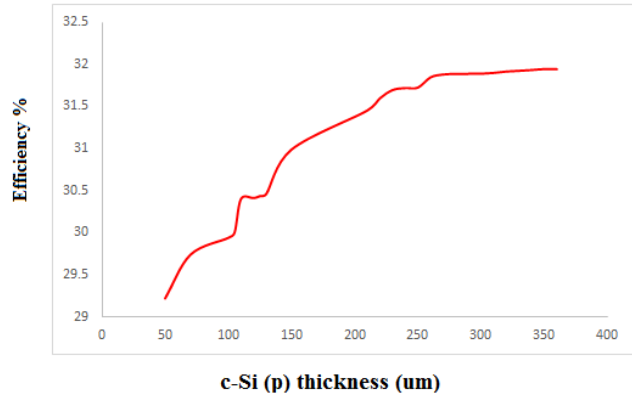


(b)

**Fig. 6. Numerical simulation of efficiency related to the Perovskite/Si tandem cell a) as a function Perovskite layer thickness. b) as a function of Si layer thickness.**

Now, fig. 6 shows the numerical simulation of tandem cell as a function of thickness of perovskite and c-Si absorber layer. Fig.6 (a) shows that the efficiency performances increased with the increase in the thickness of perovskite layer. This is because as the thickness of absorber layer increases, the absorber layer can absorb more photons and which in turn generates more electron hole. This increases

978-1-5386-2307-7/17/$31.00 ©2017 IEEE

the Voc and Jsc significantly so the efficiency increases as well. For the thickness increase in c-Si absorber layer, the efficiency performance increases because, the c-Si absorber layer absorbs photons in higher amount and which in turn generates more electron hole. This increases the Voc and Jsc. So the efficiency increases as shown in the graph of fig. 6(b).

The study obtained that $V_{oc}$ is increased, but the FF is decreased by adding the $CH_3NH_3PbI_3$ as top sub-cell layer to the Si bottom sub-cell layer. This is due to the characteristic of $CH_3NH_3PbI_3$ as an absorber which can absorb sufficient sunlight and enhance the efficiency.$Cu_2O$ is functioned as hole transporting material (HTM), which eases the hole transport from the absorber layer into the Si bottom layer and works as Hole Transport Layer (HTL). In addition, c-Si emitter works as an electron transport material (ETM), which is also a good electron-selective and compatible for c-Si absorber layer and works as Electron Transport Layer (ETL).

With the aid of simulations it was possible to evaluate the maximum efficiency value obtainable from the proposed structure.

## IV. Conclusion

In conclusion, we have presented a theoretical framework for modeling two terminal perovskite/c-Si tandem solar cell. The developed model proved that the efficiency can be improved by making the tandem incorporating Si and Perovskite. The Si-Perovskite tandem solar cell recorded the highest efficiency performance of 31.8547 % , $V_{OC}$ = 0.9995V ,$J_{SC}$ = 38.2395 mA/cm$^2$, FF= 83.3487 %). The optimum thickness of $CH_3NH_3PbI_3$ was determined to be 6μm for the tandem solar cells because a good electrical property can be demonstrated at that point. Moreover, the donor dopant concentration of $CH_3NH_3PbI_3$is the most influence factor for the Si-Perovskite tandem. Current matching condition has also been fulfilled by varying these parameters. There is a vital effect of the transport layer parameters that have on the performance of tandem cell and open up the possibilities of analyzing and designing low cost, high efficiency tandem solar cell with stability.

## V. Acknowledgment

The research was partially supported by Renewable Energy Lab, CUET. We would like to show our gratitude to the lab for sharing their pearls of wisdom with us during the course of this research and providing us with necessary software and books.

## VI. .References

[1] Noor Fadhilah Ramlia, Suhaila Sepeaib, Nur Fairuz Mohd Rostanc, Norasikin Ahmad Ludind, Mohd. Adib Ibrahim , Mohd Asri Mat Teridif) and Salem H. Zaidig. “Model Development of Monolithic Tandem SiliconPerovskite Solar Cell by SCAPS Simulation” (2017)

[2] H. 1 Snaith. Perovskites: the emergence of a new era for low cost, high-efficiency solar cells. J. Phys. Chem. Lett. Vol. 4 pp.3623-3630 (2013).

[3] G. Hodes and D. Cahen, Perovskite cells roll forward. Nat. Phot., vol.8, pp.87-88 (2014).

[4] M. Liu, M. B. Johnston, H. 1. Snaith. Efficient planar heterojunction perovskite solar cells by vapour deposition. Nature, vo1.7467, pp.395-398 (2013).

[5] J. Burschka, N. Pellet, S.J. Moon, R.H. Baker, P. Gao, M. K. Nazeeruddin, M. Gratzel. Sequential deposition as a route to high-performance perovskite-sensitized solar cells. Nature, vo1.499, pp. 316-319 (2013).

[6] J.H. Noh, S. H. 1m, J. H. Heo, T.N. MandaI, Sang II Seok, Chemical management for colorful, efficient, and stable inorganic-organic hybrid nanostructured solar cells. Nano Lett., vol.13 (4), pp. 1764-1769 (2013).

[7] J. P. Mailoa, C. D. Bailie, Er. C. Johlin, E. T. Hoke, A. 1. Akey,I W. H. Nguyen, M. D. McGehee and T. Buonassisi A 2-
terminal perovskite/silicon multijunction solar cell enabled by a silicon tunnel junction, Appl. Phys. Lett. 106, 121105 (2015).

[8] T. Todorov, T. Gershon, O. Gunawan, C. Sturdevant, and S. Guha, Perovskite-kesterite monolithic tandem solar cells with high open-circuit voltage. Appl. Phys. Lett. 105, 173902 (2014).

[9] Almansouri, A. Ho-Baillie, S. P. Bremner, and M. A. Green Supercharging Silicon Solar Cell Performance by Means of Multijunction Concept IEEE Journal of Photovoltaics, vol. 5, n.3, pp.968-976 (2015).

[10] Noor Fadhilah Ramlia, Suhaila Sepeaib, Nur Fairuz Mohd Rostanc, Norasikin Ahmad Ludind, Mohd. Adib Ibrahim , Mohd Asri Mat Teridif) and Salem H. Zaidig. “Model Development of Monolithic Tandem SiliconPerovskite Solar Cell by SCAPS Simulation” (2017)

[11] Steve Albrecht , Michael Saliba , Juan Pablo Correa Baena , Felix Lang , Lukas Kegelmann , Mathias Mews , Ludmilla Steier , Antonio Abate , Jörg Rappich , Lars Korte , Rutger Schlatmann , Mohammad Khaja Nazeeruddin , Anders Hagfeldt ,Michael Grätzel and Bernd Rech ¨Monolithic perovskite/silicon-heterojunction tandem solar cells processed at low temperature” (2015).

[12] Y. Liu, D. Heinzel, and A. Rockett, "A revised version of the AMPS simulation code ", in Photovoltaic Specialists Conference (PVSC), 2010 35th IEEE, 2010, pp. 001943-001947.

[13] Yiming Liu1,2, Dan Heinzel2, and Angus Rockett2, “A NEW SOLAR CELL SIMULATOR: wxAMPS’’, Institute of Photo-Electronic Thin Film Devices and Technology, Nankai University, Tianjin 300071, P.R. China2 Department of Materials Science and Engineering, University of Illinois, 1304 W. Green St., Urbana Illinois Illinois 61801, USA.

[14] D.L Pulfrey, “ Understanding modern transistors and diodes”, Cambridge University Press, New York, 1st Edition, 2010.

# Numerical Analysis of Efficient Cadmium Selenide Solar Cell

Mrinmoy Dey[1,2*], Mahmudul Hasan[1], Rahat Amin[1], Rishita Chakma[1], Maitry Dey[1,2], N. K. Das[1,2], A. K. Sen Gupta[1,2], M. A. Matin[1,2] and Nowshad Amin[3,4]

[1]Department of Electrical and Electronic Engineering, Chittagong University of Engineering and Technology, Chittagong-4349, Bangladesh

[2]Renewable Energy Laboratory (REL), Chittagong University of Engineering and Technology, Chittagong-4349, Bangladesh

[3]Solar Energy Research Institute (SERI), The National University of Malaysia, 43600 Bangi, Selangor, Malaysia

[4]Department of Electrical, Electronic and Systems Engineering, The National University of Malaysia, 43600 Bangi, Selangor, Malaysia

*mrinmoycuet@gmail.com

**Abstract—Performance of CdSe solar cell along with ZnS as an n-type buffer layer was numerically analysed by using AMPS 1D simulator. In the proposed cell, variation of layer thickness, doping concentration and temperature of the CdSe absorber layer were studied. The best cell performance was found for ITO/ZnS/CdSe structure where p-type CdSe was used as an absorber layer. The structure ITO/ZnS/CdSe gives the high efficiency of 17.35% at only 1.2 µm layer thickness of absorber layer material. The other cell performance parameters are *Jsc* =13.82 mA/cm$^2$, *Voc* = 1.38 V and FF = 0.908. The power conversion efficiency is 22.49% with 10 µm thickness of absorber layer. The proposed cell is designed 1.2 µm thickness of absorber layer to preserve the materials used for generation of solar energy.**

***Keywords—CdSe solar cell; ZnS buffer layer; AMPS 1D; High efficiency; Performance parameters.***

## I. INTRODUCTION

Solar energy is the most feasible and enormous complexion of renewable energy which acts as a substitute arrangement of energy for growing need of power consumption. The need of energy is rising at a rapid rate and as a result the energy cost is rising too. Now, it is inevitable to search for the substitute source of energy that is environment friendly, clean, sustainable and cost effective. All of these requirements can be fulfilled by renewable energy. Among all the renewable energy resources, solar energy is the most abundant in nature and this energy can be converted into electrical power by using solar PV modules. To compete with commercial energy resources, industrial cost of solar PV modules needs to be reduced. The cost of the solar cells can be minimized through optimization by varying different layer thickness, doping concentration, increasing proficiencies or by reducing production cost.

Through comparative study with various materials it is found that ZnS, $TiO_2$ and CdS as buffer layers and CdSe as an absorber layer have satisfactory optoelectronic properties for photovoltaic conversion. CdS and CdSe are fascinating because of their higher potential in harvesting of light in the region of visible light [1-2]. Amazing power conversion proficiency about 5.21% is presented in the research work of Wang et al. [3] which emphasize upon CdSe and $TiO_2$ solar cells. The optical absorption of solar cells can be broaden by using CdSe and improvement in adsorption of CdSe can be done by using CdS [4-5]. Mn-doped CdS/CdSe attained power conversion proficiency of 5.4% which is claimed by Santra and Kamat [6]. PbS [7-8], CdSe [9], CIS [10], PbSe [11-12], CdTe [13-14] are the available nanocrystals semiconductor materials for effective solar energy harvesting. Among the effective nanocrystals, CdSe is used as p-type absorber layer in this research work. Though manufacturing cost is less, power absorption is minimum for thin film solar cell. On the other hand, silicon solar cells are high cost and low efficient. Almost 70% energy is lost as heat. Hybrid solar cells reduce the problems. It has superior electronic properties, reduce cost and flexibility. CdSe is a hybrid solar cell material. High electron mobility of CdSe ensures speedy electron transport and detachment of electron hole pair [15]. As a p type absorber layer CdSe material is superior.

Indium Tin Oxide (ITO) is a transparent conducting oxide (TCO) material which is used in solar cell for increasing conductivity. ZnS has been used as a buffer layer in this study. The thickness of this n-type ZnS layer was considered as 50 nm for better cell performance. Higher band gap of the materials bears higher operating temperatures. This thermal consideration plays a vital role for device. In this research work, the high performance have been achieved as *Voc*=1.38 V, *Jsc*=13.82 mA/cm$^2$, *FF*=0.908 and η=17.35% for ITO/ZnS/CdSe cell structure.

## II. MODELING AND SIMULATION

The solar cell model and numerical analysis in this research work with ITO/ZnS/CdSe structure were done by AMPS 1D simulator. At 100 nm thickness of ITO as TCO layer with 50

nm thickness of ZnS as buffer layer were used in the study. The schematic arrangement of the proposed ITO/ZnS/CdSe cell structure is shown in Fig. 1.

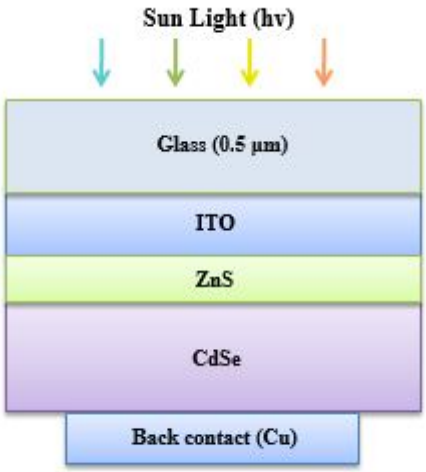


Fig.1 The structure of CdSe solar cell

To observe the output performance parameters of proposed cell structure in the simulator, material parameters of ITO, ZnS and CdSe must be needed. So the material parameters which are used in this research work are shown in Table I taken from previous research work and literature review.

TABLE I MATERIAL PARAMETERS OF CDSE SOLAR CELL.

| Parameters | i-ITO | n-ZnS | p-CdSe |
|---|---|---|---|
| Thickness, W (nm) | 100 | 50 | 100-10000 |
| Permittivity, $\varepsilon/\varepsilon_0$ | 9 | 10 | 10.6 |
| Band gap, Eg (eV) | 3.6 | 3.50 | 1.74 |
| Electron mobility, µc ($cm^2/Vs$) | 100 | 50 | 650 |
| Hole mobility, µp ($cm^2/Vs$) | 25 | 20 | 50 |
| Carrier concentration, n, p ($cm^{-3}$) | $1.7\times10^{17}$ | $1.0\times10^{15}$ | $1.0\times10^{17}$ |
| Density of state in conduction band, Nc ($cm^{-3}$) | $2.2\times10^{18}$ | $1.8\times10^{18}$ | $2.75\times10^{18}$ |
| Density of state in valence band, Nv ($cm^{-3}$) | $1.8\times10^{19}$ | $1.5\times10^{18}$ | $2.8\times10^{19}$ |
| Electron affinity, χ (eV) | 4.50 | 4.50 | 4.56 |

## III. RESULT AND DISCUSSION

### A. *Impact of Absorber Layer Thickness*

The variation of absorber layer thickness changes the output cell performance parameters of solar cell. The increases in layer thickness of CdSe, the output parameters $J_{sc}$ and power conversion efficiency increase also. On the contrary, Fill Factor (*FF)* and open circuit voltage ($V_{oc}$) decrease. Fill factor decreases a little bit like constant value. At 100 nm layer thickness, the FF is about 0.909 and it is decreased to 0.901 when the layer thickness is increased to 10 µm. At 1 µm layer thickness the FF=0.908, at 2 µm layer thickness the FF=0.907, at 3 µm layer thickness the FF=0.906, at 7 µm layer thickness the FF=0.903. Similarly, at 100 nm layer thickness of CdSe, the $V_{oc}$ is 1.44 V and it is decreased to 1.33 V at 10 µm layer thickness. At 1 µm layer thickness the $V_{oc}$=1.38 V, at 2 µm layer thickness, the $V_{oc}$=1.37 V, at 3 µm layer thickness the $V_{oc}$=1.36 V and at 7 µm layer thickness the $V_{oc}$=1.34 V. On the other hand, at 100 nm layer thickness the Jsc is 9.22 $mA/cm^2$ and it increases to 18.66 $mA/cm^2$ at 10 µm layer thickness of absorber layer. Finally, at 100 nm layer thickness the cell efficiency is 12.10%, at 1200 nm thickness the efficiency is 17.35% and at 10 µm thickness the PCE is 22.49%.

The thick layer thickness of CdSe material will be costly to implement. So, a reasonable thickness of 1.2 µm is chosen. At highest cell performance, the output parameters are: Voc= 1.38 V, Jsc= 13.82 $mA/cm^2$, FF= 0.908 and η= 17.35%. The efficiency is mainly affected by Voc and Jsc during the layer thickness variation. The cell performance for variation of layer thickness of CdSe absorber layer from 0.1 µm to 10.0 µm is given is shown in Fig. 2.

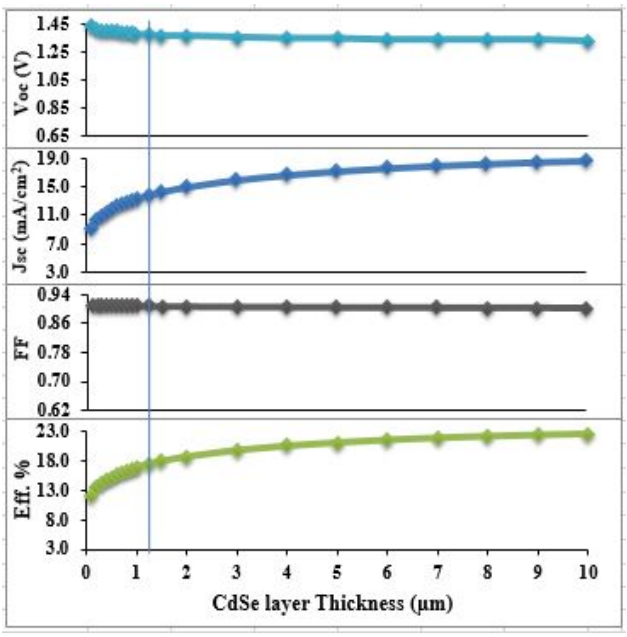


Fig.2: Effect of CdSe absorber layer thickness for the proposed solar cell structure.

### B. Effect of Doping Concentration

The doping concentration of CdSe absorber layer is varied from $1.0\times10^{13}$ to $1.0\times10^{20}$ $cm^{-3}$. It can be observed that *Voc* and *FF* increase with the increase of doping concentration. The short circuit current density (*Jsc*) shows the constant result. This research work was done at $1.0\times10^{17}$ $cm^{-3}$ doping concentration considering the present solar cell technology. Though the performance increases after that doping, the Voc increase at a significantly. At $1.0\times10^{15}$ $cm^{-3}$ doping, the output cell performance parameters are: *Voc*= 1.27 V, *Jsc*= 13.82 mA/cm$^2$, *FF*= 0.869 and $\eta$= 15.35%. At $1.0\times10^{17}$ $cm^{-3}$ doping the cell performance output parameters are: *Voc*= 1.38 V, *Jsc*= 13.82 mA/cm$^2$, *FF*= 0.908 and $\eta$= 17.35%. And at $1.0\times10^{19}$ $cm^{-3}$ doping the output cell performance parameters are: *Voc*= 1.50 V, *Jsc*= 13.81 mA/cm$^2$, *FF*= 0.913 and $\eta$= 18.97%.

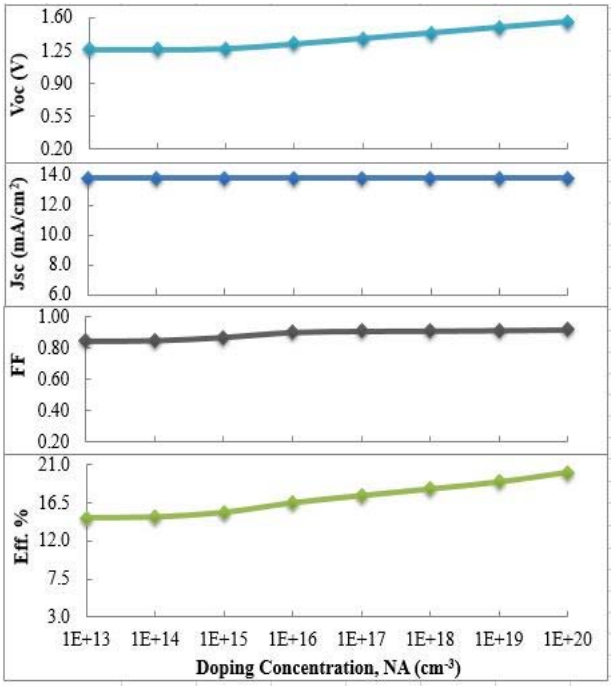


Fig. 3: Effect of the CdSe doping concentration on performance parameters.

### C. Effect of Temperature

The cell performance mostly depends on operating temperature. The temperature variation is needed to test the thermal stability of solar cells. In this research work, performance of this cell is examined for higher temperature. High operating temperature affects the electron-hole mobility, carrier concentration, density of states and band gap of the materials. This research work incorporated the operating temperature ranging from 25°C to 105°C. The cell performance decreases with the increase of operating temperature. Open circuit voltage (*Voc*) and Fill Factor (*FF*) decrease but short circuit current density (*Jsc*) remains constant. So, overall cell efficiency decreases with the increases of operating temperature. At 25°C temperature, the *Voc* is 1.38 V, *Jsc* is 13.82 mA/cm$^2$, *FF* is 0.908 and power conversion fficiency is 17.35%. Again at 50°C temperature, the cell performance parameters are: *Voc*=1.35 V, *Jsc*=13.82 mA/cm$^2$, *FF*=0.90 and power conversion efficiency= 16.83%. Finally, at 105°C temperature the output values are: *Voc*=1.28 V, *Jsc* = 13.82 mA/cm$^2$, *FF*=0.883 and Efficiency= 15.71%. The cell performance results at temperature ranging from 25°C to 105°C is shown in Fig. 4.

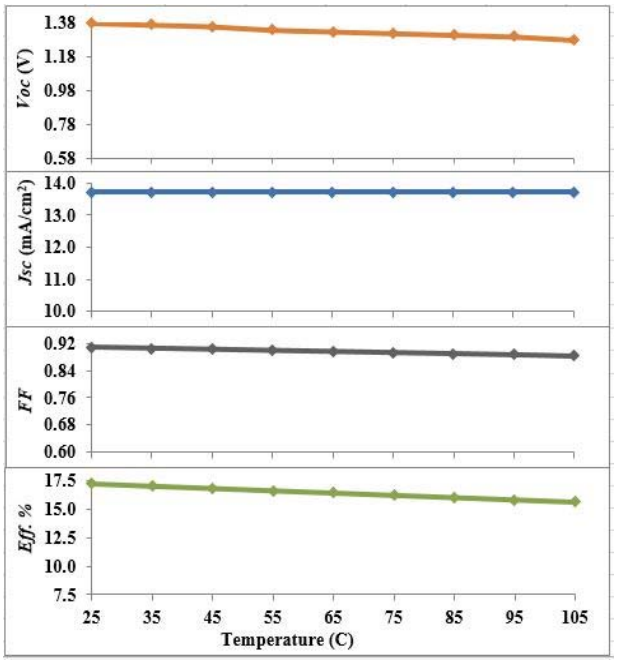


Fig. 4: Effect of the operating temperature on cell performances.

The Fig. 5 shows normalized efficiency in response of different operating temperature. The cell efficiency linearly decreased with the increase of temperature. Normalized value of efficiency 1 is selected for 25°C operating temperature. At 50°C temperature the normalized value is 0.97, at 80°C temperature the value is 0.94 and at 105°C the normalized value of temperature is 0.91. This result shows that the degradation of performance is in tolerable limit.

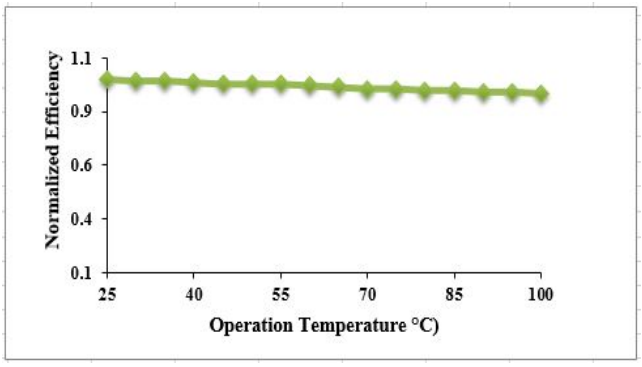


Fig. 5: Effect of operating temperature on normalized efficiency.

### D. Effect of the TCO Layer

Indium Tin Oxide (i – ITO) was used in the proposed cell as TCO layer for transparency and conductivity of solar light. Naturally, the output performance increases if the TCO is inserted in the cell structure. Over 3 eV band gap of TCO

layer can cover the visible wavelength range of light radiation and the resistivity of layer should be as low as possible [16]. In this cell, TCO layer has no effect. Without TCO layer the performance is remain constant. Table II shows the performance of CdSe solar cell with and without TCO layer.

TABLE II COMPARISON OF OUTPUT PERFORMANCE WITH AND WITHOUT TCO LAYER

| **Parameters** | ***Voc* (V)** | ***Jsc* (mA/cm²)** | ***FF*** | ***Eff. (%)*** |
|---|---|---|---|---|
| With TCO | 1.38 | 13.815 | 0.908 | 17.35 |
| Without TCO | 1.38 | 13.824 | 0.908 | 17.35 |

### *E. J-V characteristics curve of CdSe solar cell*

Short circuit current (*Jsc*) will be maximum when open circuit voltage (*Voc*) is zero. The maximum short circuit current is 13.82 mA/cm$^2$. Again Voc will be maximum at zero *Jsc*. The maximum *Voc* of this proposed cell structure is 1.38 V. The *J-V* characteristic curve is shown in figure 6.

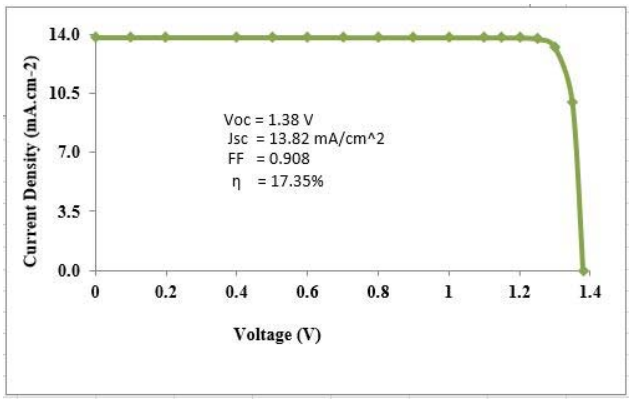


Fig. 6: J-V characteristics curve of proposed CdSe solar cell.

## IV. CONCLUSION

The ZnS buffer layer (50 nm) with transparent ITO layer (100 nm) showed higher cell performances were found for 1.2 µm layer thickness of CdSe material. This cell structure gives the better performance than the other buffer layers based CdSe solar cell. The better conversion efficiency is 17.35% with *Jsc* =13.82 mA/cm$^2$, *FF* =0.908, *Voc* =1.38V. This cell also shows better thermal stability at high temperature.

## ACKNOWLEDGMENT

This work has been supported by the Department of Electrical and Electronic Engineering (EEE) and Renewable Energy Laboratory (REL), Chittagong University of Engineering and Technology (CUET), Bangladesh.

## REFERENCES

[1] Zhu G Pan, L Xu T and Sun Z, "Acs Appl. Mater. Inter," vol. 3, pp. 3146 −3151, 2011.

[2] Lee Y H, Im S H, Chang J. A, Lee J. H and Seok, S. I. Org. Electron, vol. 13, pp. 975 −979, 2012.

[3] Hossain Md. Anower, Jennings, James Robert, Shen Chao, Pan Jia Hong, Yu Koh Zhen, Nripan Mathews and Qing, W. J. Material Chemistry, vol. 22, pp. 16235 −16242, 2012.

[4] Chong L. W., Chien H. T. and Lee, "Y.-L. J. Power Sources," vol. 195, pp. 5109 −5113, 2010.

[5] Zarazua I., De la Rosa E., Lopez-Luke T., Reyes-Gomez J., Ruiz S., Angeles Chavez C. and Zhang, "J. Z. J. Phys. Chem. C," vol. 115, pp. 23209 −23220, 2011.

[6] Santra P. K. and Kamat, "P. V. J. Am. Chem. Soc." vol. 134, pp. 2508−2511, 2012.

[7] M. Yuan, K. W. Kemp, S. M. Thon, J. Y. Kim, K. W. Chou, A. Amassian and E. H. Sargent, "*High-Performance Quantum-Dot Solids via Elemental Sulfur Synthesis,"* Adv. Material," vol. 26, pp. 3513-3519, 2014.

[8] Z. Ning, O. Voznyy, J. Pan, S. Hoogland, V. Adinolfi, J. Xu, M. Li, A. R. Kirmani, J.Sun, J. Minor, K. Kemp, H. Dong, L. Rollny, A. Labelle, G. Carey, B. Sutherland, L. Hill, A. Amassian, H. Liu, J. Tang, O. Bakr and E. H. Sargent, "*Air-stable n-type colloidal quantum dot solids. Nature Mater*," vol. 13, pp. 822-828, 2014.

[9] G. H. Carey, A. L Abdelhady, Z. Ning, S. M. Thon, O. M. Bakr and E. H. Sargent, "*Colloidal Quantum Dot Solar Cells*," Chem. Rev, vol. 115(23), pp. 12732-12763, 2015.

[10] K. Kim, Y. J. Eo, A. Cho, J. Gwak, J. H. Yun, K. Shin, S. K. Ahn, S. H. Park, K. Yoon and S. Ahn, "*Role of chelate complexes in densification of $CuInSe_2$ (CIS) thin film prepared from amorphous Cu-In-Se nanoparticle precursors*," J. Mater. Chem, vol. 22, pp. 8444-8448, 2012.

[11] R. W. Crisp, D. M. Kroupa, A. R. Marshall, E. M. Miller, J. Zhang, M. C. Beard and J. M. Luther, "*Metal Halide Solid-State Surface Treatment for High Efficiency PbS and PbSe QD Solar Cells*," SCIENTIFIC REPORT, vol. 5, pp. 9945, 2015.

[12] J. Zhang, J. Gao, C. P. Church, E. M. Miller, J. M. Luther, V. I. Klimov and M. C. Beard, "*PbSe Quantum Dot Solar Cells with More than 6% Efficiency Fabricated in Ambient Atmosphere*," Nano Lett., vol. 14, pp. 6010-6015, 2014.

[13] Y. Tian, Y. Zhang, Y. Lin, K. Gao, Y. Zhang, K. Liu, Q. Yang, X. Zhou, D. Qin, H. Wu, Y. Xia, L. Hou, L. Lan, J. Chen, D. Wang and R. Yao, "*Solution-processed efficient CdTe nanocrystal/CBD-CdS hetero junction solar cells with ZnO interlayer*," J Nanopart Res, vol. 15, pp. 2053, 2013.

[14] J. Jasieniak, B. I. MacDonald, S. E. Wakins and P. Mulvaney, "*Solution-processed Sintered Nanocrystal Solar Cells via Layer-by-Layer Assembly*," Nano Lett., vol. 11, pp. 2856-2864, 2011.

[15] Dr.Mrunal Deshpande and Dr.R.Seyezhai, "*Review of Hybrid Solar Cells Based on CdSe and $TiO_2$ Materials*," International Journal of Innovative Research in Computer and Communication Engineering, vol. 2, 2014, pp 3387-3392.

[16] E. Fortunato, D. Ginley, H. Hosono and D. C. Paine, "*Transparent conducting oxides for photovoltaics*," MRS Bulletin, vol. 32, pp. 242-247, March 2007.

# Numerical Investigation on the performance of new ultra-thin CZTS solar cell using SCAPS

Sudipto Saha[1], Sourav Kumar Ukil[2], Muhammad Rashedul Haq Rashed[3]
[1]North Dakota State University, United States of America
[2]Chittagong University of Engineering & Technology, Bangladesh
[3]Bangladesh University of Engineering & Technology, Bangladesh
sudipto.saha@ndsu.edu[1], souravkumarukil@gmail.com[2], rashed.eee09@gmail.com[3]

*Abstract*—**This paper suggests an upgraded structure for CZTS solar cells by simulating an ultra-thin one dimensional CZTS cell with an added absorber layer of silicon and analyzing the cell for several parameters like operating temperature, thickness of absorber layer and concentration of acceptor carrier. Simulation result denotes that with a given extra silicon absorber layer, efficiency of CZTS solar cell shows positive, negative and varying correlation against respective changes in thickness, temperature and concentration. In case of increased concentration of the absorber layer, initially it pushes the efficiency up but eventually falls back after achieving the maximum level. Overall the best conditions of different parameters and respective changes in efficiency of the CZTS solar cell are presented in this work.**

***Keywords—CZTS; SCAPS-1D simulation program; ultra-thin; thin flim; solar cells.***

## I. INTRODUCTION

The balancing between conversion efficiency and material cost is one of the key challenges in solar cell fabrication process, which alternatively makes this an attractive research field as well. Here, utmost attention is required on three important factors while selecting the fabrication materials; cost, conversion efficiency and longevity.

Polycrystalline Chalcopyrite $Cu(In,Ga)Se_2$ (CIGS) material seems to be way ahead of competition on efficiency standpoint of solar cells than any other material with a conversion efficiency of 20.4% [1]. Appropriate band gap and high absorption co-efficiency of solar radiation have helped the CIGS cell to outstrip the bulk silicon devices [2]. However, when it comes to the mass production of electrical power, CIGS technology can prove to be rather expensive in terms of cell material cost [2]. Indium (In) and gallium (Ga) increase the fabrication cost of CIGS solar cell as they both are scarce elements. One possible solution to this could be the reduction of the absorber thickness, and in return, minimizing the material cost. Nevertheless, this method appeared to have a significantly high trade-off in efficiency than the conventional CIGS cells [3]-[5]. Using CIGS material has one more major drawback. Indium is a toxic element and hence is threatening for the ecosystem. For these reasons, a cheaper and eco-friendly substitute of CIGS is of great interest now.

Quaternary semiconductor $Cu_2ZnSnS_4$ (CZTS) solar cells have the potential to be exactly that substitute. All the elements of CZTS material are abundant in earth, ensuring much lesser cell material cost. The conversion efficiency of CZTS is also fair for mass production of electricity [6]. Moreover, CZTS is eco-friendly, because it doesn't contain any toxic element.

However, there are few challenges in using CZTS thin films. Among them, imperfect morphology [7], open circuits voltage deficit relative to the absorber bandgap energy [8], non-ohmic back contact [9], narrow kesterite phase stability region and subtle and critical controllability over composition and phase [10] have made it problematic to use CZTS materials. Moreover, high quality CZTS absorbers usually requires sulfurization at high temperatures (540-590$^0$C) which eventually destroy highly reducible Indium Tin Oxide (ITO) at temperatures higher than 500$^0$C [9]. These issues have made it necessary to reduce the thickness of CZTS absorber layer.

Here in this paper, inspired from the work of Vermang et al. [5] (on CIGS solar cell with an added Si absorber layer), an alternative structure for CZTS solar cells has been suggested. Process initiates with the consideration of a CZTS cell with an added extra absorber layer of silicon and then simulating it in SCAPS by setting precise experimental conditions. In the later parts, performance based analysis for the new ultra-thin CZTS cell are presented for varied values of the following parameters; operating temperature, absorber layer thickness and acceptor carrier concentration.

## II. METHODOLOGY

### *A. SCAPS-1D Simulation Program*

SCAPS (a Solar Cell Capacitance Simulator) is an extensively used simulation software for analyzing one dimensional solar cells. The software is capable of simulating solar cells up to seven semiconductor layers. This simulation uses Poisson equation and the electron and hole continuity equations for estimating the steady state band diagram, carrier transport and recombination profile. To calculate the recombination currents for bulk defects and the defects of interface, Shockley-Read-Hall (SRH) model and its extension are used. This software operates with the following working points for calculations: voltage, frequency and temperature. It can calculate current-voltage characteristics, as well as ac characteristics, spectral response, energy bands, concentrations and currents at a given working point. All the simulation works in this work have been done with the SCAPS 3.2 software. The

978-1-5386-2307-7/17/$31.00 ©2017 IEEE

software can be availed through an e-mail request to the address mentioned in [7].

### *B. Device Structure and Simulation*

A solar cell structure of Substrate | Back metal contact (Mo) | Absorber layer | Cds | ZnO:Al | Flat front contact model is chosen for the simulation. In this model, p-type absorber layer of CZTS is used for formulating the cell structure. Additionally, an extra absorber layer of p-Si has been added between the back metal contact and the CZTS absorber layer of the cell structure. A comparative study of the photovoltaic cell structure has been numerically investigated using the SCAPS-1D simulation tool (version 3.2). Figure 1 demonstrates the schematic cross-section of the solar cell with CZTS in the absorber layer.

In this new ultra-thin CZTS cell structure, n- ZnO:Al has been taken as the window layer, n- CdS as the buffer layer and Molybdenum (Mo) as the back metal contact. A constant p-Si layer of 1µm has been used in this structure. The experimental conditions for the simulation has been set carefully. The main parameters of interest are temperature, illumination, bias voltage etc. For cell illumination, a solar spectrum of 1kW/m2 (AM 1.5) is considered. Furthermore, in some special cases intelligent estimations have been made. However, rest of the parameters followed the standard values used in the preceding literatures. A summary of the device parameters used in the simulation is depicted in the Table I.

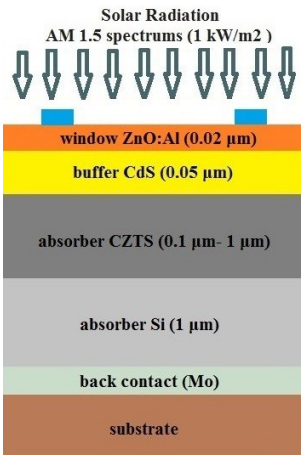


Figure 1. Schematic View of new ultra-thin CZTS Structure

TABLE I. DEVICE PARAMETERS USED IN THIS ARTICLE [6]

| | | |
|---|---|---|
| **Cell Properties** | Cell temperature (K) | 300 |
| | Series resistance, $R_S$ (Ω) | 4.25 |
| | Shunt resistance, $R_{SH}$ (Ω) | 400 |
| **Front metal contact properties** | SRV* of electron (cm/s) | 1.0 x $10^7$ |
| | SRV of hole (cm/s) | 1.0 x $10^5$ |
| | Electron work function (eV) | Flat band |
| **Back metal contact properties** | SRV of electron (cm/s) | 1.0 x $10^5$ |
| | SRV of hole (cm/s) | 1.0 x $10^7$ |

*SRV stands for Surface Recombination Velocity

The effects of radiative recombination and Auger electron/hole captures have been considered in this simulation throughout all the cases. The radiative recombination coefficient and the Auger electron capture coefficient was estimated to be 5 x $10^{-9}$ $cm^3/s$ and 1 x $10^{-29}$ $cm^6/s$ respectively [6]. Similarly, considered absorption coefficient for the thin film was 2.5x$10^4$ $cm^{-1}$ and Electron/hole thermal velocity was $10^7$ cm/s. In this new ultra-thin CZTS solar cell structure, the material property of window layer, buffer layer and Si absorber layer have been kept identical. The used material parameters in the simulation are listed in Table II.

## III. RESULTS AND DISCUSSIONS

In the process of SCAPS-1D Simulation on the new ultra-thin CZTS cell of Figure 1, 1µm width of CZTS absorber layer, 300K cell temperature and 2.00 x $10^6$ $cm^{-3}$ concentration of absorber layer acceptor have been taken into account. At the

TABLE II. MATERIAL PROPERTIES OF DIFFERENT LAYERS [12]-[15]

| **Material Properties** | n- ZnO:Al | n- CdS | p- CZTS | p- Si |
|---|---|---|---|---|
| Thickness (µm) | 0.020 | 0.050 | 1.000 | 1.000 |
| Energy bandgap (eV) | 3.300 | 2.450 | 1.460 | 1.120 |
| Electron affinity (eV) | 4.600 | 4.400 | 4.500 | 4.050 |
| Dielectric permittivity (relative) | 9.000 | 10.000 | 10.000 | 11.900 |
| Conduction band effective density of states ($cm^{-3}$) | 2.20 x $10^{18}$ | 2.20 x $10^{18}$ | 2.20 x $10^{18}$ | 2.80 x $10^{19}$ |
| Valence band effective density of states ($cm^{-3}$) | 1.80 x $10^{19}$ | 1.80 x $10^{19}$ | 1.80 x $10^{19}$ | 1.65 x $10^{19}$ |
| Electron mobility ($cm^2/Vs$) | 1.00 x $10^2$ | 3.50 x $10^2$ | 1.00 x $10^2$ | 1.45 x $10^3$ |
| Hole mobility ($cm^2/Vs$) | 2.50 x $10^1$ | 5.00 x $10^1$ | 2.50 x $10^1$ | 5.00 x $10^2$ |
| Donor density, $N_D$ ($cm^{-3}$) | 1.00 x $10^{20}$ | 1.10 x $10^{20}$ | 1.00 x $10^1$ | 1.00 x $10^1$ |
| Acceptor density, $N_A$ ($cm^{-3}$) | 0.00 | 1.00 x $10^1$ | 2.00 x $10^6$ | 1.00 x $10^{20}$ |
| Defect density ($cm^{-3}$) | 1.00 x $10^{14}$ | 1.00 x $10^{14}$ | 1.00 x $10^{14}$ | 1.00 x $10^{14}$ |

same time, for the photovoltaic parameters simulation, a 4.25Ω of series resistance and a 400Ω of shunt resistance have been considered. The simulation results on the cell is depicted in Table III.

TABLE III. PERFORMANCES OF CZTS SOLAR CELLS

| PV Performance Parameters | Solar cell with CZTS layer (1μm) |
|---|---|
| Efficiency (%) | 9.21 |
| Short Circuit Current Density, $J_{sc}$ (mA/cm$^2$) | 21.147445 |
| Open Circuit Voltage, $V_{oc}$ (V) | 0.6727 |
| Fill Factor, FF (%) | 64.73 |

### A. *Effect of Varying Operating Temperature*

The effect of varying operating temperature has been studied in this segment. Operating temperature plays a crucial role in the performance of solar cells. Usually solar cells are exposed to the temperatures ranging from 288K to 323K [9]. A fixed absorber layer thickness of 2μm has been considered for the cell of Figure 1 and their performances for varying operating temperatures are studied. Here, a synopsis of the simulation has been presented in Figure 2. It can be realized from the Figure 2(a) that the efficiency of the new ultra-thin CZTS solar cell has a negative correlation with the varying operating temperature, means efficiency decreases with the increase of temperature. The underlying physics behind this decrease of efficiency is pretty straightforward. Cell parameters like carrier concentrations, band gaps and also electron and hole mobility of cell materials are affected by temperature increase. These result in decrease in cell efficiency. The simulation on the CZTS solar cell of Figure 1 results in the efficiency 9.43% for the operating temperature of 288K and 8.68% for the operating temperature of 323K.

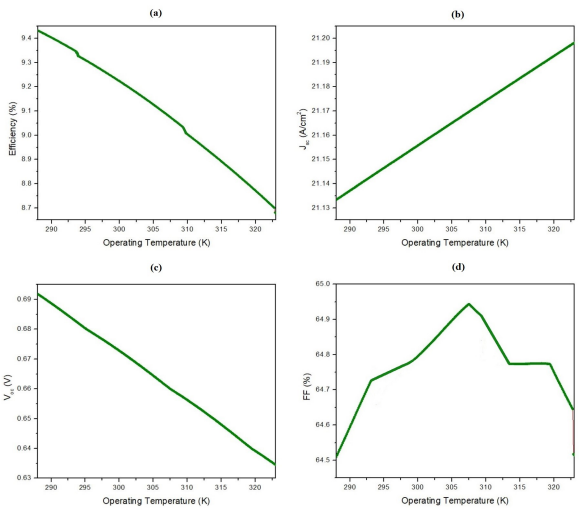


Figure 2. New ultra-thin CZTS solar cell performance analysis: (a) Efficiency vs Operating Temperature, (b) Short Circuit Current Density, $J_{sc}$ vs Operating Temperature, (c) Open Circuit Voltage, $V_{oc}$ vs Operating Temperature, (d) Fill Factor, FF vs Operating Temperature

Again, Figure 2(b) indicates that the short circuit current density, $J_{sc}$ of the new ultra-thin CZTS solar cell increases with the increase of operating temperature. Temperature has inverse relation with band-gap energy. The higher the temperature, the narrower the band-gap energy of the cell. The resultant being- more photons are able to overcome the energy barrier to create electron-hole pairs. The simulation result indicates that, for the CZTS solar cell in Figure 1, short circuit current density, $J_{sc}$ is 21.1 mA/cm$^2$ for operating temperature of 288K and 21.2 mA/cm$^2$ for operating temperature of 323K. Furthermore, it can also be realized from the Figure 2(c) that the open circuit voltage, $V_{oc}$ of the cell decreases with the increase of temperature. The saturation current decreases swiftly with the increase in temperature. This is the reason behind the decrease in $V_{oc}$. The simulation result indicates that, for the new ultra-thin CZTS solar cell, open circuit voltage, $V_{oc}$ is 0.692V for operating temperature of 288K and 0.635V for operating temperature of 323K.

### B. *Effect of Varying Absorber Layer Thickness*

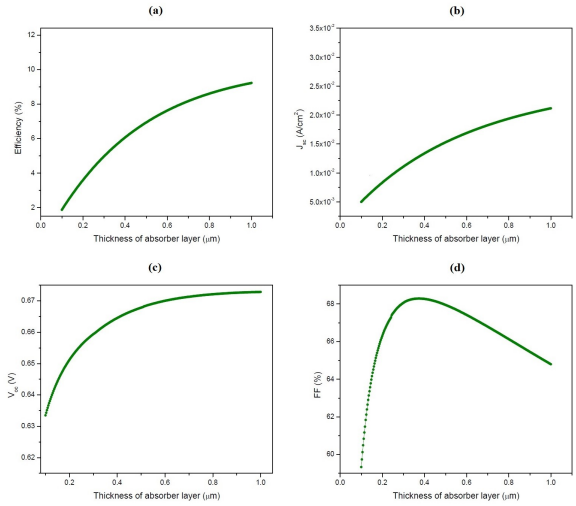


Figure 3. New ultra-thin CZTS solar cell performance analysis: (a) Efficiency vs Absorber Layer Thickness, (b) Short Circuit Current Density, $J_{sc}$ vs Absorber Layer Thickness, (c) Open Circuit Voltage, $V_{oc}$ vs Absorber Layer Thickness, (d) Fill Factor, FF vs Absorber Layer Thickness.

In this section, SCAPS simulations have been conducted on the cell of Figure 1 considering a fixed silicon absorber layer thickness of 1μm and a varying absorber layer thickness of CZTS. The CZTS layer thickness is varied from 0.1μm to 1μm and found that the resultant efficiency has a positive correlation with the absorber layer thickness. From the Figure 3(a), it can be seen that the efficiency is 1.87% for thickness of 0.1μm, while it is 9.22% for thickness of 1μm. The physics behind this phenomenon being- the more is the width of the absorber layer, the more will be the absorption of photons. Hence the resultant will be the increase in efficiency. A clear idea about the respective change of short circuit current density, $J_{sc}$, open circuit voltage, $V_{oc}$ and fill factor, FF with the change of absorber layer thickness can also be observed from Figure 3(b), 3(c) and 3(d). For a CZTS layer thickness of 0.1μm, the short circuit current density, $J_{sc}$ is found to be 4.99 mA/cm$^2$, while

the open circuit voltage, $V_{oc}$ is 0.634V. When the CZTS layer thickness is increased up to 1μm, the short circuit current density, $J_{sc}$ also moves up to 21.2 mA/cm$^2$, and the open circuit voltage, $V_{oc}$ becomes 0.673V. With the change of thickness of the absorber layer from 0.1μm to 1μm, the fill factor, FF goes from 5.93% to 64.8%.

### *C. Some Effect of Varying Acceptor Carrier Concentration*

The effect of acceptor carrier concentration on the solar cell performances is discussed in this segment. The simulation is performed in the new ultra-thin CZTS solar cell by assuming a fixed absorber layer thickness of 2μm and a fixed operating temperature of 300K. The simulation results are obtained by varying the acceptor carrier concentration from 5.00 x $10^{14}$ cm$^{-3}$ to 6.56 x $10^{16}$ cm$^{-3}$. Figure 4 demonstrates the summary of the simulation results. Simulation Result in Figure 4(a) shows that

the efficiency of the CZTS solar cell in Figure 1 starts increasing from 9.25% for acceptor concentration of 5.00 x $10^{14}$ cm$^{-3}$ and reaches maximum efficiency of 9.45% for acceptor concentration of 2.02 x $10^{15}$ cm$^{-3}$. The maximum efficiency sustains up to acceptor concentration of 3.11 x $10^{15}$ cm$^{-3}$, and beyond that, the efficiency starts decreasing and reaches a minimum of 7.22% for acceptor concentration of 6.56 x $10^{16}$ cm$^{-3}$.

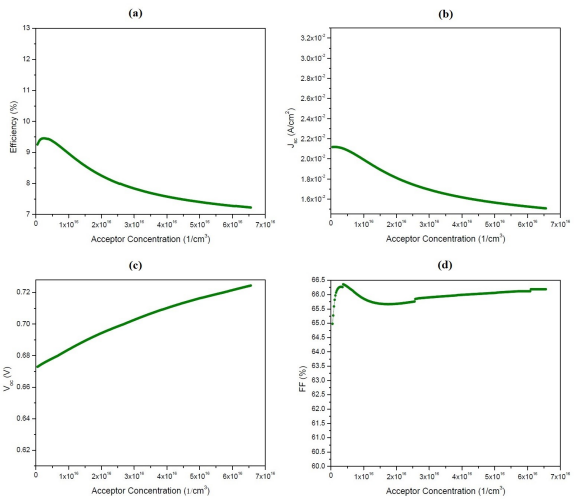


Figure 4. New ultra-thin CZTS solar cell performance analysis: (a) Efficiency vs Acceptor Carrier Concentration, (b) Short Circuit Current Density, $J_{sc}$ vs Acceptor Carrier Concentration, (c) Open Circuit Voltage, $V_{oc}$ vs Acceptor Carrier Concentration, (d) Fill Factor, FF vs Acceptor Carrier Concentration

Figure 4(b) indicates that the short circuit current density decreases with the increase of acceptor carrier concentration. From the simulation it has been seen that the short circuit current density, $J_{sc}$ for the CZTS solar cell of Figure 1 is 21.17 mA/cm$^2$ for acceptor concentration of 5.00 x $10^{14}$ cm$^{-3}$ and 15.07 mA/cm$^2$ for acceptor concentration of 6.56 x $10^{16}$ cm$^{-3}$. The respective change of open circuit voltage, $V_{oc}$ with the change of acceptor carrier concentration can be observed from Figure 4(c), where $V_{oc}$ increases with the increase in acceptor carrier concentration. The building of electric field within the space charge region is stirred up by the acceptor concentration. Hence, when the acceptor concentration is increased, the electric field also increases. This is the reason behind the increase in open circuit voltage. From the simulation it can be seen that the open circuit voltage, $V_{oc}$ for the CZTS cell of Figure 1 is 0.67V for acceptor concentration of 5.00 x $10^{14}$ cm$^{-3}$ and 0.72V for acceptor concentration of 6.56 x $10^{16}$ cm$^{-3}$.

## IV. CONCLUSION

This paper exhibits the simulation result for electrical properties and performances of new ultra-thin CZTS solar cell structures with an added Si absorber layer of 1μm thickness. Here, in comparison with conventional ones, cells with the added Si absorber layer have acceptable efficiency [11], and also is a more cost effective alternative. While balancing the material cost with the efficiency return, the suggested model shows promise as a viable option for replacing the costly conventional cells.


## ACKNOWLEDGMENT

The authors would like to thank all the researchers and developers who are behind the simulation tool, A Solar Capacitance Simulator (SCAPS). This research work would not be possible without this free and very user friendly software.


## REFERENCES


[1] N. Khoshsirat, N. A. M. Yunus, M. N. Hamidona, S. Shafie, and N. Amin, “Analysis of absorber layer properties effect on CIGS solar cell performance using SCAPS.” Optik 2015; 126:681-6.

[2] H. Katagiri, K. Jimbo, W. S. Maw, K. Oishi, M. Yamazaki, H. Araki, and A. Takeuchi, “Development of CZTS-based thin film solar cells.” Thin Solid Films 2009; 2455–2460.

[3] H. Heriche, Z. Rouabah, and N. Bouarissa, “New ultra-thin CIGS structure solar cells using SCAPS simulation program.” Hydrogen Energy 2017; 9524-9532.

[4] N. Amin, P. Chelvanathan, M. I. Hossain, and K. Sopian, “Numerical modelling of ultra-thin Cu(In,Ga)$Se_2$ solar cells.” Energy Procedia 2012; P 15:291-8.

[5] B. Vermang, J. T. Wätjen, V. Fjällström, F. Rostvall, M. Edoff, R. Kotipalli, F. Henry, and D. Flandre, “Employing Si solar cell technology to increase efficiency of ultra-thin Cu(In,Ga)$Se_2$ solar cells.” Prog Photovolt Res Appl 2014; P 22:1023-9.

[6] M. Patel and A. Ray, “Enhancement of output performance of $Cu_2ZnSnS_4$ thin film solar cells - A numerical simulation approach and comparison to experiments.” Physica B 2012; P 4391–4397.

[7] Y. Zhang, K. Tse, X. Xiao, and J. Zhu, "Controlling defects and secondary phases of CZTS by surfactant potassium", Physical Review Materials 1 2017; 045403.

[8] E. Garcia-Llamas, J. M. Merino, R. Gunder, K. Neldner, D. Greiner, A. Steigert, S. Giraldo, V. Izquierdo-Roca, E. Saucedo, M. León, S. Schorr, and R. Caballero, "Cu2ZnSnS4 thin film solar cells grown by fast thermal evaporation andthermal treatment", Solar Energy 141 2017; 236-241.

[9] J. Ge, Y. Yu, W. Ke, J. Li, X. Tan, Z. Wang, J. Chu, and Y. Yan, "Improved Performance of Electroplated CZTS Thin-Film Solar Cells with Bifacial Configuration", ChemSusChem 2016; 9, 1-11.

[10] J. Tao, J. Liu, L. Chen, H. Cao, X. Meng, Y. Zhang, C. Zhang, L. Sun, P. Yanga, and J. Chu, "7.1% efficienct co–electroplated Cu2ZnSnS4 thin film solar cellswith sputtered CdS buffer layers", Green Chem2015; 045403.

[11] M. Burgelman, P. Nollet, and S. Degrave, “Modelling polycrystalline semiconductor solar cells,” Thin Solid Films 2000; P 527–532.

[12] S. Saha, M. Z. E. Rafique, and M. M. S. Hassan, “Performance of CZTSxSe1−x solar cell with various mole fractions of sulfur for

different buffer layers." 4th International Conference on the Development in the in Renewable Energy Technology, 2016.

[13] S. Saha, R. Chowdhury, and M. M. S. Hassan, "Improvement of the output performance of CZTS thin film solar cell." 2nd International Conference on Electrical, Computer & Telecommunication Engineering, 2016.

[14] N. Khoshsirat, and N. A. M. Yunus, "Numerical simulation of CIGS thin film solar cells using SCAPS-1D", IEEE Conference on Sustainable Utilization and Development in Engineering and Technology 2013.

[15] A. Bouloufaab, K. Djessasb, A. Zegadia, "Numerical simulation of CuInxGa1 − xSe2 solar cells by AMPS-1D", Thin Solid Films 2007; 6285-628

# 3D Simulation of Impact Ionization Induced Kink Effect in AlGaN/GaN HEMTs: A Novel Split Channel Design with Asymmetric Double Gate for Kink Suppression

Sharadindu Gopal Kirtania[1], Muhammad Navid Anjum Aadit[2], and Md. Kawsar Alam[3]
Department of Electrical and Electronic Engineering
Bangladesh University of Engineering and Technology
Dhaka-1205, Bangladesh
Email: [1]sharadindugopal@gmail.com, navidanjumaadit@gmail.com[2], and [3]kawsaralam@eee.buet.ac.bd

***Abstract*—In this paper, we present 3D simulation of AlGaN/GaN High Electron Mobility Transistors (HEMTs) to demonstrate impact ionization generated kink effect on current-voltage characteristics. We use an in-house built self-consistent simulator coupled with impact ionization model to obtain kink voltage and total drain current by iterations. Dependence of kink voltage on applied gate bias is also studied. From the results, we suggest a simple technique to suppress kink effect by reducing Al mole fraction. However, this technique has a trade-off that it reduces electron mobility too, making the device inappropriate for high frequency applications. Finally, a novel asymmetric double gate design with split channel is proposed. It is shown that the design effectively suppresses kink effect with no need to reduce mole fraction or electron mobility. The proposition would be useful in designing kink-free devices suitable for high frequency applications.**

***Keywords*—Double Gate HEMT, Impact ionization, Kink effect, Split channel**

## I. Introduction

High Electron Mobility Transistors (HEMTs) are high speed devices which are being immensely researched at present for their improved mobility by separation of majority carriers [1]. Under high temperature and high frequency, AlGaN/GaN HEMTs exhibit superior performance compared to other III-V semiconductor based HEMTs. These transistors offer high power [2], high breakdown voltage [3], high drain current [4] and low gate leakage current [5]. Moreover, high 2-Dimensional Electron Gas (2DEG) density induced at AlGaN/GaN interface enhanced by polarization charge is a primary requirement for power transistors, and next generation wireless base station applications [6], [7]. Despite these noteworthy characteristics, AlGaN/GaN HEMTs have some drawbacks regarding current dispersion and device reliability which degrade performance of the device [8].

Kink effect, an abrupt rise in drain current at a certain drain to source voltage is one of the major degradation mechanisms for AlGaN/GaN HEMTs causing low breakdown voltage and abnormal increase in output characteristics as well as anomaly between dc and RF characteristics [9]. Many researchers suggest that, kink phenomenon happens due to different layer traps and impact ionization. Thus, it is an electron trapping-detrapping process which is activated by high drain-source voltage [10]. Different physical, numerical and experimental models are found in literature to explain this phenomenon and its effect on current-voltage characteristics of different types of HEMTs. Suemitsu *et al.* proposed a 2D device simulation method for modeling kink effect in InAlAs/InGaAs HEMTs [11]. Another 2D device simulation is presented to investigate kink effect in similar types of HEMTs considering impact ionization [12]. Somerville *et al.* proposed a novel physical model which provides evidence of relation between kink effect and impact ionization [13]. Apart from physical models and device simulations, some extensive experimental works are also done to demonstrate this anomalous phenomenon [14]. Light sensitivity in substrate related kink effect in AlGaAs/InGaAs pHEMTs is shown and corresponding change in substrate potential is experimentally reported [15]. Temperature based analysis to show thermal variation of kink effect is also presented [16].

Kink effect is a detrimental phenomenon for the current-voltage characteristics of the device as it causes an abnormal rise in drain current and thus gate control is lost [9]. Moreover, it reduces threshold voltage of the device and contributes to leakage current. It further lowers breakdown voltage of the device leading to high voltage instability [17]. Therefore, kink suppression is practically important for device control and stability and many research works are going on to propose effective kink-free models or methods to suppress it. Georgakilas *et al.* showed that buffer layer grown at a specific temperature can reduce kink effect [18]. Sawada *et al.* also eliminated kink effect by using direct ohmic contact in InGaAs channel [19]. Using Pt buried gate technology, a new Y shaped gate to suppress kink effect is proposed [20]. However, most of the works to demonstrate and suppress kink effect on HEMTs are found for InAlAs, InGaAs or InP materials [21], [22]. There is not much work suggesting suppression of kink effect in AlGaN/GaN HEMTs although it exhibits many superior performances over other III-V HEMTs, as mentioned earlier. Kink effect in AlGaN/GaN HEMTs related to electrical stress

978-1-5386-2307-7/17/$31.00 ©2017 IEEE

is reported by Xiao-Hua *et al.* by measuring DC performance [23]. Another work by Wang *et al.* shows kink effect in similar HEMTs enhanced by pumping of drain and gate [24]. However, as in the case for InAlAs/InGaAs HEMTs [11], it may be predicted that impact ionization plays a prominent role to initiate kink phenomenon in AlGaN/GaN HEMTs too at high drain to source voltages. 3D simulation work which incorporates impact ionization to investigate kink effect of AlGaN/GaN HEMTs is yet to be done. Moreover, to the best of our knowledge, very few works are found in literature suggesting suppression of kink effect in AlGaN/GaN HEMTs; specially suppression of impact ionization and accumulation of holes are not reported yet for these HEMTs.

In this paper, we present kink effect on current-voltage characteristics of AlGaN/GaN HEMTs owing to impact ionization. Drain current is calculated by solving 3D Poisson and 2D Schrödinger equations self-consistently as described in the next section. We simulate the device using COMSOL Multiphysics linked with MATLAB software. We show the variation of kink voltage with gate bias voltage and suggest a way to minimize kink effect by reducing Al mole fraction in AlGaN layer. This method imposes a limitation of low electron mobility. Taking inspiration from a dual-gate kink suppressed model for Thin Film Transistors (TFTs) by Lee *et al.* [25], we propose a novel split channel AlGaN/GaN HEMT design with asymmetric double gate which suppresses the kink phenomenon effectively and also overcomes the low electron mobility limitation.

The rest of the paper is organized as follows. In Section II, we propose the split channel asymmetric double gate structure and compare it with the conventional single gate structure. This section also presents the device simulation technique including necessary equations. Finally, Section III shows the results and discussions on kink effect and suggests how it is suppressed in the proposed design.

## II. Device Structure and Modeling

### A. Device Structure

We simulate traditional single gate AlGaN/GaN HEMT using a simplified device structure as shown in Fig. 1. The structure contains only the basic layers for faster device simulation- buffer, channel, spacer and donor layers. However, such traditional single gate AlGaN/GaN HEMTs exhibit kink effect at higher drain to source voltages. To suppress kink effect, we propose a novel split channel AlGaN/GaN HEMT design as shown in Fig. 2. The main feature of the design is that it has two separate gates of different lengths which are connected by a floating $n^+$ region only. The gate length on the source side, $L_1$ is much larger than the gate length on the drain side, $L_2$ and the channel lengths are equivalently adjusted on both sides. To get comparative insight from simulation, we set $L_1$ and $L_2$ in such a way that the sum $L_1 + L_2$ equals the gate length of the single gate design. The purpose of the floating region is that it electrically floats the two split channels. However, as it is heavily doped, it develops a voltage in itself. This voltage virtually works as operating drain voltage and current flows from floating $n^+$ region to the source region where the channel length is 80 $nm$. Impact ionization may initiate near the drain region, where the channel length is also relatively small (40 $nm$). However, as the generated holes recombine with abundant electrons in the floating $n^+$ region and cannot propagate towards the source region, hole accumulation beneath the source region cannot be induced by such impact ionization. As a result, reduction of source resistance becomes suppressed and kink current flow is minimized. Since the voltage remains continuous from drain to source region, we get current flow from drain to source where kink effect is effectively suppressed.

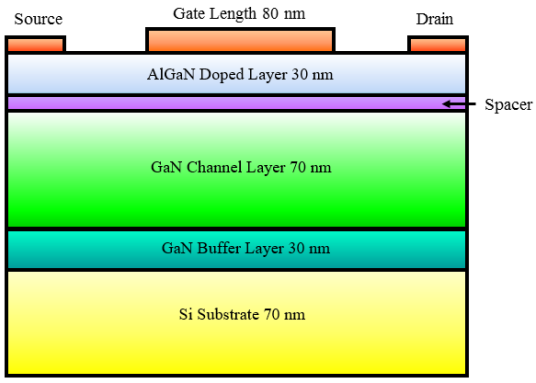


Fig. 1. Simplified schematic model of single gate AlGaN/GaN HEMT

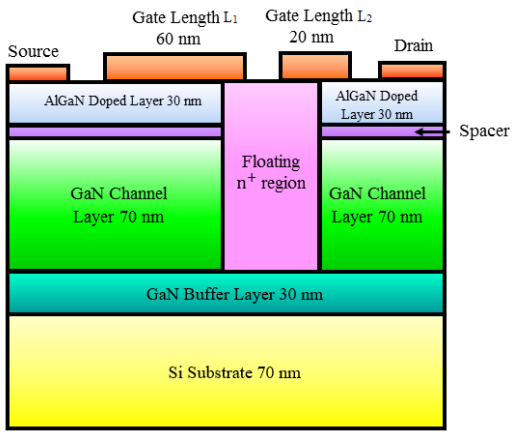


Fig. 2. Schematic of proposed kink suppressing split channel AlGaN/GaN HEMT with asymmetric double gate ($L_1 > L_2$)

### B. Modeling

To demonstrate kink effect on current-voltage characteristics of AlGaN/GaN HEMTs, at first, the above mentioned single gate structure is simulated in an in-house built quantum mechanical simulator that solves 3D Poisson and 2D Schrödinger equations self-consistently. The design of the simulator is based on the work presented by Wang *et al.* for silicon nanowire transistors [26].

The 3D Poisson's equation which is solved can be expressed as,

$$-\nabla(\varepsilon\nabla U) = \rho, \tag{1}$$

where,
$\nabla \equiv \left(\hat{x}\frac{d}{dx} + \hat{y}\frac{d}{dy} + \hat{z}\frac{d}{dz}\right)$,
$U$ is the electrostatic potential,
$\rho$ is the charge density,
$\varepsilon$ is the permittivity.
In three dimension, (1) can be written as,

$$\left(\frac{d^2}{dx^2} + \frac{d^2}{dy^2} + \frac{d^2}{dz^2}\right)U = -\frac{\rho}{\varepsilon}, \quad (2)$$

We also consider polarization effect at the AlGaN/GaN interface in our simulation by adding additional constant polarization charge density with $\rho$. This is particularly important if the mole fraction, $x$ of Al in $Al_xGa_{1-x}N$ is relatively high and strain occurs at the interface. However, in this paper, we generally assume $x$ to be 20%, unless it is mentioned otherwise.

The 2D Schrödinger equation which is solved can be expressed as,

$$\Big[-\frac{\hbar^2}{2}\frac{\partial}{\partial y}\Big(\frac{1}{m_y^*(y,z)}\Big)\frac{\partial}{\partial y} - \frac{\hbar^2}{2}\frac{\partial}{\partial z}\Big(\frac{1}{m_z^*(y,z)}\Big)\frac{\partial}{\partial z} + \overline{U}(y,z)\Big]\overline{\xi^m}(y,z) = \overline{E_{sub}^m}.\overline{\xi^m}(y,z), \quad (3)$$

where,
$\hbar$ is reduced Planck's constant,
$\overline{U}(y,z)$ is average conduction band-edge,
$m_y^*(y,z)$ is effective mass of electrons in the y direction,
$m_z^*(y,z)$ is effective mass of electrons in the z direction,
$\overline{\xi^m}(y,z)$ is eigen function,
and $\overline{E_{sub}^m}$ is sub-band energy of mode $m$.

Once self-consistent solution is achieved, ballistic drain current is computed by,

$$I_{d_0} = \frac{q}{\pi\hbar}\int_{-\infty}^{+\infty} T(E)[f(\mu_S,E) - f(\mu_D,E)]dE, \quad (4)$$

where,
$T(E)$ is the transmission coefficient calculated using Non-equilibrium Green Function (NEGF) approach [26],
$q$ is charge of electron,
$f$ is the Fermi function,
$\mu_S$ is source Fermi level,
$\mu_D$ is drain Fermi level,
and $E$ is eigen energy.

It is to be noted that both $\mu_S$ and $\mu_D$ are pinned at a constant Fermi level determined by gate bias voltage. This eventually ensures surface Fermi level pinning which is required in the simulation for side-etching surface as suggested by Suemitsu *et al.* [11]. The current we calculate by (4) does not include any kink effect. In this paper, we assume that kink effect occurs for impact ionization which is initiated by hot electrons and accumulates holes beneath the source region. As a result, source resistance is reduced and drain current is abnormally increased. To show kink effect on current-voltage characteristics, we need to calculate kink voltage. Calculation of kink voltage and kink current presented in this paper is based on the equations proposed by Somerville *et al.* [27] to describe kink effect in InAlAs/InGaAs HEMTs. Accordingly, kink voltage of the channel can be expressed as,

$$V_{kink} = \frac{k_BT}{q}\ln\left(\frac{n_{p_0} + n_p'}{n_{p_0}}\right), \quad (5)$$

where,
$k_B$ is Boltzmann constant,
$T$ is temperature in Kelvin,
$n_{p_0}$ is pre-kink hole concentration of the extrinsic channel,
and $n_{p'}$ is excess hole concentration in the channel for kink effect.
Kink current is then given by,

$$\Delta I_d = g_{m_0}V_{kink}, \quad (6)$$

where,
$g_{m_0}$ = pre-kink transconductance.

From impact ionization theory, excess hole concentration can be calculated as,

$$\frac{n_p'}{n_{p_0}} = AI_de^{\left(\frac{-B}{V_{ds}-V_{ds_sat}}\right)}, \quad (7)$$

where,
$V_{ds}$ is drain to source voltage,
$V_{ds_sat}$ is drain to source voltage for current saturation,
and $A$ and $B$ are time dependent constants.
For simulation, we use values of $A$ and $B$ as described by Tut *et al.* for AlGaN/GaN avalanche photodiodes [28].

Combining (5), (6) and (7), kink current can be approximated as,

$$\Delta I_d \approx g_{m0}\frac{k_BT}{q}ln\left[1 + AI_de^{\left(\frac{-B}{V_{ds}-V_{ds_sat}}\right)}\right], \quad (8)$$

Finally, we can obtain total drain current including kink effect as,

$$I_d = I_{d_0} + \Delta I_d \quad (9)$$

where, $I_{d_0}$ is kink-free drain current as calculated by (4).

Kink current $\Delta I_d$ is relatively small compared to saturated drain current $I_{d_0}$. Assuming $\Delta I_d << I_{d_0}$, we evaluate $\Delta I_d$ from (8) taking $I_d = I_{d_0}$. The result can be updated iteratively using (9) to find new $I_d$. Eventually, we can calculate $I_d$ accurately for different drain to source voltages which includes kink effect considering impact ionization.

## III. Results and Discussions

The simplified single gate structure as shown in Fig. 1 is simulated in COMSOL Multiphysics for self-consistent solution of 3D Poisson and 2D Schrödinger equations and the obtained data are transferred to MATLAB for transport (current) calculation. Fig. 3 shows the current-voltage characteristics of the device with both $V_g$ and $V_{ds}$ sweeps. The flat, saturated currents are found for different $V_g$ values when impact ionization effect is not considered and current is calculated using NEGF formalism according to (4). These curves represent currents without kink effect, $I_{d_0}$. When impact ionization is considered, we calculate kink current, $\Delta I_d$ using (8) and total drain current, $I_d$ using (9) iteratively. Drain

currents including kink effect are also shown in the figure and it is found that this effect is dominant at higher $V_g$ values. Also, the figure shows that as we increase $V_g$, the locus of kink voltages shifts towards right. Therefore, kink voltage is higher for higher gate bias voltages. Dependence of kink voltage on gate bias is shown in Fig. 4. As we increase gate voltage, $V_g$ from -0.3 V to 0.7 V, kink voltage also rises from 0.66 V to 0.81 V. Both of the figures confirm that kink effect in AlGaN/GaN HEMTs is a strong function of gate bias voltage.

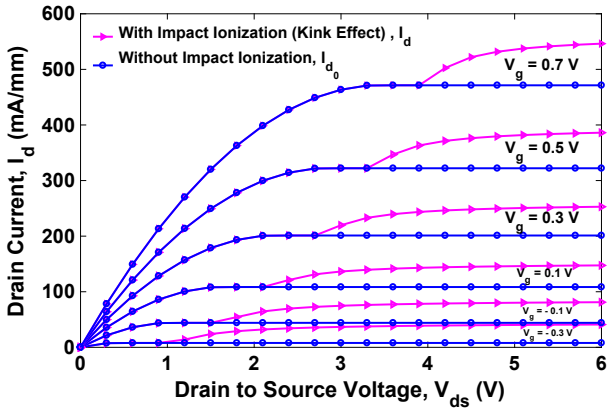


Fig. 3. I-V characteristics of AlGaN/GaN HEMTs (legend indicates whether impact ionization initiated kink effect is considered or not)

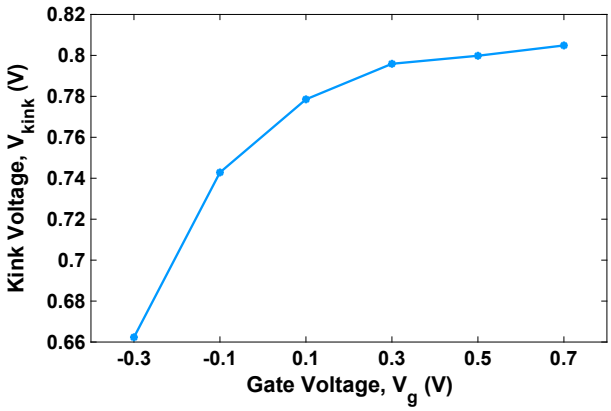


Fig. 4. Dependence of kink voltage on applied gate bias voltage: kink voltage rises as gate voltage increases

However, AlGaN/GaN HEMT drain current, $I_d$ is a function of difference between gate voltage, $V_g$ and threshold voltage, $V_{th}$ [29]. Therefore, it is expected that improved $V_{th}$ may suppress kink effect. One common technique to improve $V_{th}$ of AlGaN/GaN HEMTs is to minimize Al mole fraction, $x$ [30]. To investigate whether it works to suppress kink effect, we vary Al mole fraction, $x$ in the simulator and show the I-V characteristics result in Fig. 5. The figure shows that low $x$ values (suppose, $x = 0.05$) shifts the locus of kink voltages to even more rightward, suggesting rise in kink voltage and kink current. However, it conversely suggests that higher drain to source voltage is required to initiate kink effect. The figure shows that kink effect for $x = 0.05$ is actually much less than that for $x = 0.2$, although kink voltage is higher. This is due to the fact that $x = 0.05$ refers to a much higher $V_{th}$ value than that for $x = 0.2$ as suggested by Tsai *et al.* for normally-off HEMTs [30] which offsets the effect of kink voltage to a great extent. As a result, $V_g - V_{th}$ decreases and so does $I_d$. Therefore, kink effect can be suppressed by lowering Al mole fraction, $x$.

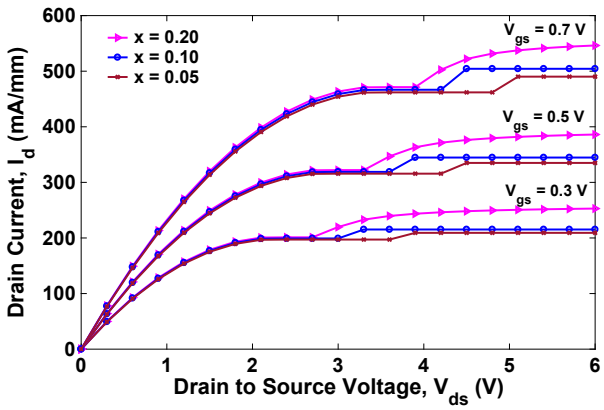


Fig. 5. I-V characteristics of AlGaN/GaN HEMTs including kink effect in the simulation with varying Al mole fraction, $x$ (indicated in the legend)

One major disadvantage of low $x$ values ($x < 0.2$) is that it reduces electron mobility too which makes the device inappropriate for high frequency applications [31]. To overcome this issue, in this paper, we propose a novel split channel AlGaN/GaN HEMT design with asymmetric double gate that is described in Section II. The design can suppress kink effect while keeping Al mole fraction, $x = 0.2$. In Fig. 6, the 3D

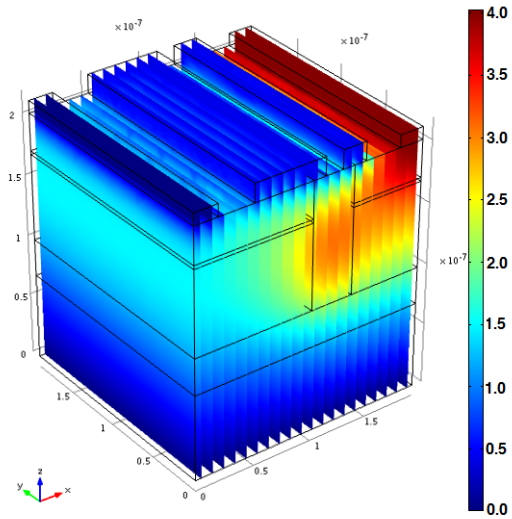

Fig. 6. 3D potential distribution of the proposed device after convergence with gate voltage, $V_g$ = 0.4 V, drain to source voltage, $V_{ds}$ = 4 V and doping concentration, $N_d$ = $10^{24}$ $m^{-3}$

electrostatic potential distribution of the proposed device is shown after the convergence of the self-consistent simulation with doping concentration, $N_d$ = $10^{24}$ $m^{-3}$, applied gate bias, $V_g$ = 0.4 V, and drain to source voltage, $V_{ds}$ = 4 V. From this figure, it is found that the drain voltage is 4 V, whereas the built-in voltage of the floating $n^+$ region is above 3 V. So, it effectively becomes a virtual drain and current flows from this virtual $n^+$ drain to the source region. The longer gate (gate length = $L_1$) near the source region controls the current flow.

Fig. 7 shows the electrostatic potential distribution of the proposed device from a different view by taking cut line from source to drain along the channel. The figure clearly shows that the $n^+$ region with more than 3 V is at higher potential than the source region with 0 V and there is a smooth trap-free path for current flow between these two regions. The channel length is 80 $nm$ for this current flow. Also, there will be a current flow from the drain region to the $n^+$ region (channel length = 40 $nm$) as the drain is at higher potential with 4 V. Due to smaller channel length, impact ionization of electrons may occur in this region. However, these hot electrons cannot induce accumulation of holes in the source region as the channels are split by the $n^+$ region where the holes are recombined with excess electrons. Since the source resistance is not decreased by accumulation of holes, we expect to obtain kink-free current from drain to source.

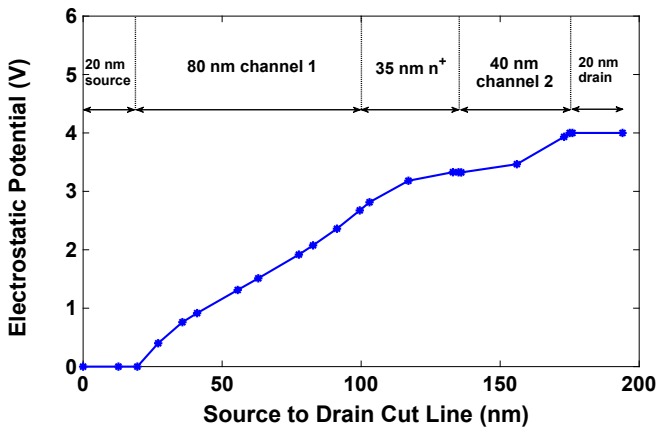


Fig. 7. Electrostatic potential distribution of the proposed device taking cut line from source to drain along the channel

The I-V characteristics (considering impact ionization in simulation) of the proposed device is shown in Fig. 8 and compared with the results obtained for the traditional single gate device (gate length = 80 $nm$). For the proposed double gate design with $L_1$ = 50 $nm$ and $L_2$ = 30 $nm$, there is no sharp rise in drain current and thus smooth current is found at higher $V_{ds}$ values. Therefore, kink effect is suppressed for the proposed design, as expected. The figure also suggests that the result can be even better if the gate near the source region is made much longer ($L_1$ = 60 $nm$) than the gate near the drain region ($L_2$ = 20 $nm$) and the channel lengths are adjusted equivalently so that the longer channel can minimize the probability of hole accumulation under the source. Thus, asymmetric double gate ($L_1 > L_2$) design that splits the channel into equivalent lengths by floating $n^+$ region keeping Al mole fraction, $x = 0.2$ is a suitable solution to suppress kink effect even at high frequency applications.

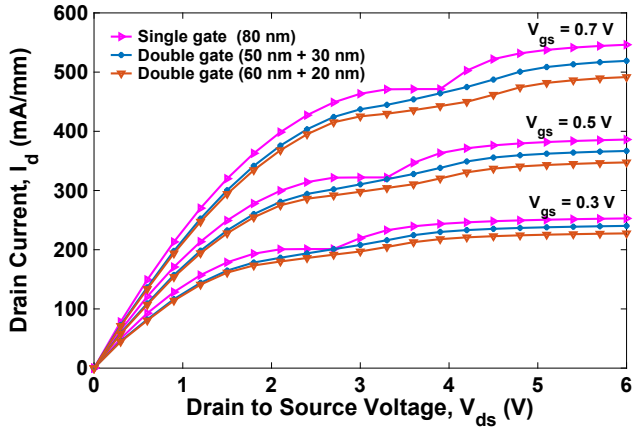


Fig. 8. I-V characteristics of AlGaN/GaN HEMTs for different gate lengths including kink effect in the simulation (legend indicates gate length of single gate or double gate design)

## IV. Conclusion

We have shown kink effect on current-voltage characteristics of AlGaN/GaN HEMTs. It is found that kink effect is dominant for higher gate bias voltages. It is suggested that improvement of threshold voltage would minimize kink effect. The device is simulated with variation of Al mole fraction and it is found that lower mole fraction provides kink-suppressed I-V characteristics. However, lower electron mobility is a limitation of this technique. Therefore, we have proposed a new kink-free design that suppresses kink effect and at the same time, ensures high electron mobility. The design is based on asymmetry in gate lengths and separation of channels. The effectiveness of the design with different asymmetric gate lengths is also studied and it is found that longer gate length near the source region provides a better kink-free device. Thus, the new design would help to improve the current-voltage characteristics and performance of the device.

## References


[1] A. Adikimenakis, K. Aretouli, E. Iliopoulos, A. Kostopoulos, K. Tsagaraki, G. Konstantinidis, and A. Georgakilas, "High electron mobility transistors based on the AlN/GaN heterojunction," *Microelectronic Engineering*, vol. 86, no. 4, pp. 1071–1073, 2009.

[2] Y. F. Wu, A. Saxler, M. Moore, R. P. Smith, S. Sheppard, P. M. Chavarkar, T. Wisleder, U. K. Mishra, and P. Parikh, "30-W/mm GaN HEMTs by field plate optimization," *IEEE Electron Device Letters*, vol. 25, no. 3, pp. 117–119, March 2004.

[3] J. Du, N. Chen, P. Pan, Z. Bai, L. Li, J. Mo, and Q. Yu, "High breakdown voltage AlGaN/GaN HEMT with high-K/low-K compound passivation," *Electronics Letters*, vol. 51, no. 1, pp. 104–106, 2015.

[4] M. N. A. Aadit, S. G. Kirtania, and M. K. Alam, "Dependence of threshold voltage on doped layer thickness in AlGaN/GaN HEMT: An improved split donor E-mode design," in *Informatics, Electronics and Vision (ICIEV), 2016 5th International Conference on.* IEEE, 2016, pp. 681–686.

[5] X. Xin, J. Shi, L. Liu, J. Edwards, K. Swaminathan, M. Pabisz, M. Murphy, L. F. Eastman, and M. Pophristic, "Demonstration of Low-Leakage-Current Low-On-Resistance 600-V 5.5-A GaN/AlGaN HEMT," *IEEE Electron Device Letters*, vol. 30, no. 10, pp. 1027–1029, Oct 2009.

[6] K. Joshin and T. Kikkawa, "Recent progress of high power GaN-HEMT for wireless application," in *2006 Asia-Pacific Microwave Conference*, Dec 2006, pp. 1027–1032.

[7] M. N. A. Aadit, S. G. Kirtania, and M. K. Alam, "Estimation of polarization charge in nitride based MODFETs using differential threshold voltage technique," in *Electrical Engineering and Information Communication Technology (ICEEICT), 2016 3rd International Conference on*. IEEE, 2016, pp. 1–6.

[8] S. Faramehr, P. Igic, and K. Kalna, "TCAD modelling of current dispersion in a 0.25$\mu$m gate length GaN HEMT," in *Advanced Semiconductor Devices Microsystems (ASDAM), 2012 Ninth International Conference on*, Nov 2012, pp. 11–14.

[9] O. Pajona, C. Aupetit-Berthelemot, and J. M. Dumas, "Electrical models for detrimental effects in metamorphic HEMTs," in *2006 International Conference on Indium Phosphide and Related Materials Conference Proceedings*, 2006, pp. 332–335.

[10] M. Xiao-Hua, L. Min, P. Lei, J. Yuan-Qi, Y. Jing-Zhi, C. Wei-Wei, and L. Xin-Yu, "Kink effect in current-voltage characteristics of a GaN-based high electron mobility transistor with an AlGaN back barrier," *Chinese Physics B*, vol. 23, no. 2, p. 027302, 2014.

[11] T. Suemitsu, T. Enoki, N. Sano, M. Tomizawa, and Y. Ishii, "An analysis of the kink phenomena in InAlAs/InGaAs HEMT's using two-dimensional device simulation," *IEEE Transactions on Electron Devices*, vol. 45, no. 12, pp. 2390–2399, Dec 1998.

[12] ZhimingWang, XiaobinLuo, W. Yu, and XinLv, "2D Simulations of Kink phenomenon in InAlAs/InGaAs/InP HEMTs," in *Microwave Technology Computational Electromagnetics (ICMTCE), 2013 IEEE International Conference on*, Aug 2013, pp. 320–323.

[13] M. H. Somerville, J. A. del Alamo, and W. Hoke, "A new physical model for the kink effect on InAlAs/InGaAs HEMTs," in *Electron Devices Meeting, 1995. IEDM '95., International*, Dec 1995, pp. 201–204.

[14] G. Crupi, A. Raffo, Z. Marinkovi, G. Avolio, A. Caddemi, V. Markovi, G. Vannini, and D. M. M. P. Schreurs, "An Extensive Experimental Analysis of the Kink Effects in $S_{22}$ and $h_{21}$ for a GaN HEMT," *IEEE Transactions on Microwave Theory and Techniques*, vol. 62, no. 3, pp. 513–520, March 2014.

[15] J. Haruyama, H. Negishi, Y. Nishimura, and Y. Nashimoto, "Substrate-related kink effects with a strong light-sensitivity in AlGaAs/InGaAs PHEMT," *IEEE Transactions on Electron Devices*, vol. 44, no. 1, pp. 25–33, Jan 1997.

[16] T. Akazaki, H. Takayanagi, and T. Enoki, "Kink effect in an InAs inserted-channel InAlAs/InGaAs inverted HEMT at low temperature," *IEEE Electron Device Letters*, vol. 17, no. 7, pp. 378–380, July 1996.

[17] R. Suemitsu, T. Enoki, and Y. Ishii, "Body contacts in InP-based InAlAs/InGaAs HEMTs and their effects on breakdown voltage and kink suppression," *Electronics Letters*, vol. 31, no. 9, pp. 758–759, Apr 1995.

[18] A. Georgakilas, K. Zekentes, N. Kornilios, G. Halkias, A. Dimoulas, A. Christou, F. Peiro, A. Cornet, T. Benyattou, A. Tabata, and G. Guillot, "Suppression of the kink effect in InGaAs/InAlAs HEMTs grown by MBE by optimizing the InAlAs buffer layer," in *Indium Phosphide and Related Materials, 1992., Fourth International Conference on*, April 1992, pp. 97–100.

[19] K. Sawada, T. Arai, T. Takahashi, and N. Hara, "Elimination of kink phenomena and drain current hysteresis in InP-based HEMTs with a direct ohmic structure," *IEEE Transactions on Electron Devices*, vol. 50, no. 2, pp. 310–314, Feb 2003.

[20] D.-H. Kim, T.-W. Kim, H.-H. Noh, J.-H. Lee, W. Feng, X. Xie, Q. Du, J. Jian, J.-I. Song, and K.-S. Seo, "Suppression of kink phenomenon in ultra-high-speed strained InAs- inserted E-mode HEMTs with a new 0.1 $\mu$m Y-shaped Pt-buried gate and their impacts on device performance," in *Electron Devices Meeting, 2004. IEDM Technical Digest. IEEE International*, Dec 2004, pp. 1027–1030.

[21] W. Kruppa and J. B. Boos, "Examination of the kink effect in InAlAs/InGaAs/InP HEMTs using sinusoidal and transient excitation," *IEEE Transactions on Electron Devices*, vol. 42, no. 10, pp. 1717–1723, Oct 1995.

[22] H. Rodilla, J. Schleeh, P. . Nilsson, and J. Grahn, "Cryogenic Kink Effect in InP pHEMTs: A Pulsed Measurements Study," *IEEE Transactions on Electron Devices*, vol. 62, no. 2, pp. 532–537, Feb 2015.

[23] M. Xiao-Hua, M. Ji-Gang, Y. Li-Yuan, H. Qiang, J. Ying, M. Ping, and H. Yue, "Kink effect in AlGaN/GaN high electron mobility transistors by electrical stress," *Chinese Physics B*, vol. 20, no. 6, p. 067304, 2011.

[24] M. Wang and K. J. Chen, "Kink Effect in AlGaN/GaN HEMTs Induced by Drain and Gate Pumping," *IEEE Electron Device Letters*, vol. 32, no. 4, pp. 482–484, April 2011.

[25] M.-C. Lee and M.-K. Han, "Poly-Si TFTs with asymmetric dual-gate for kink current reduction," *IEEE Electron Device Letters*, vol. 25, no. 1, pp. 25–27, Jan 2004.

[26] J. Wang, E. Polizzi, and M. Lundstrom, "A three-dimensional quantum simulation of silicon nanowire transistors with the effective-mass approximation," *Journal of Applied Physics*, vol. 96, no. 4, pp. 2192–2203, 2004.

[27] M. H. Somerville, A. Ernst, and J. A. del Alamo, "A physical model for the kink effect in InAlAs/InGaAs HEMTs," *IEEE Transactions on Electron Devices*, vol. 47, no. 5, pp. 922–930, May 2000.

[28] T. Tut, M. Gokkavas, B. Butun, S. Butun, E. Ulker, and E. Ozbay, "Experimental evaluation of impact ionization coefficients in $Al_xGa_{1-x}N$ based avalanche photodiodes," *Applied physics letters*, vol. 89, no. 18, p. 183524, 2006.

[29] D. A. Neamen, *Semiconductor physics and devices*. McGraw-Hill Higher Education, 2003.

[30] J. R. Tsai, Y. S. Chang, K. S. Wei, and T. T. Wen, "Engineered threshold voltage in AlGaN/GaN HEMTs for normally-off operation," in *2015 International Symposium on Next-Generation Electronics (ISNE)*, May 2015, pp. 1–2.

[31] S. Keller, G. Parish, P. Fini, S. Heikman, C.-H. Chen, N. Zhang, S. DenBaars, U. Mishra, and Y.-F. Wu, "Metalorganic chemical vapor deposition of high mobility AlGaN/GaN heterostructures," *Journal of applied physics*, vol. 86, pp. 5850–5857, 1999.

# Numerical Simulation of Vibrational Properties of AGNR with Vacancy and Stone Wales Defects

A. S. M. Jannatul Islam, Md. Rasidul Islam, Md. Sherajul Islam, A. G. Bhuiyan
Department of Electrical and Electronic Engineering, Khulna University of Engineering & Technology, Khulna, Bangladesh
syed.113.kuet@gmail.com, sheraj_ruet@yahoo.com

*Abstract*— **This paper reports the effects of vacancy and stone wales defects on the vibrational properties of armchair graphene nanoribbon (AGNR) using molecular dynamic simulation. The optimized Tersoff and Brenner empirical potential has been used to calculate the phonon density of states (PDOS) using atomistic toolkit (ATK) force-field method, which provides a very good agreement with the Raman spectra of graphene related systems. The calculated results show a downshift of the PDOS peaks with the decrease of AGNR width. The vacancy and stone wales defects strongly affect the PDOS peaks of AGNR. Due to vacancy defects some new peaks are appeared in the low frequency region while stone wales defects produce some new peaks in the high frequency region. However, due to both vacancy and stone wales defects, a localized in-plane optical mode phonon is appeared near the edge and defect sites. This paper also discusses the effects of defects on the phonon transmission spectrum which is responsible for thermal conductivity and electron transport properties of AGNRs.**

**Keywords**— ***Armchair, Zigzag, GNR, Phonon mode, PDOS, Localized mode, Phonon transmission spectrum.***

## I. INTRODUCTION

Graphene, a carbon based nanomaterials has been considered as the promising candidate for next generation nanoelectronics [1] because of its outstanding electronic, thermal and mechanical properties. The ultra-high electron mobility (200,000 $cm^2/V.s$), unbelievable current density ($10^8$ $A/cm^2$), strongest structural quality (200 times of steel) and tunable electron/hole transport properties make it promising for future nanoelectronic applications [2]. Although graphene shows outstanding properties, it cannot be used in semiconductor IC fabrication technology, due to its zero bandgap [3]. Various approaches have been used to tune a finite bandgap in graphene structure. It is well known that, confinement of the electronic wave function in a quasi 1D system can open the bandgap in graphene [4]. When graphene is patterned into a finite width, a bandgap is opened due to the quantum confinement effect. Therefore, graphene nanoribbon (GNR) can be the candidate for the fabrication of nanoelectronic devices.

Depending on the edge structure, graphene nanoribbons may be armchair or zigzag types [5]. The electronic properties of nanoribbon depend on the types of edge structure and the width of the ribbon. For example, localized edge states and intervalley backscattering are found in zigzag and armchair edges, respectively that affect the electronic as well as vibrational properties of the nano devices [6]. Therefore, edge related phenomena are of great interest for future nanolectronics. GNR structure with armchair shaped edge are known as the promising candidate for IC fabrication technology rather zigzag types because it introduces relevant band gaps for nanelectronic devices [7].

From a practical viewpoint, when armchair graphene nanoribbon (AGNR) are experimentally fabricated, various structural defects such as atomic vacancies, stone wales defect and ad-atom vacancy defect [8] are formed that may alter the vibrational as well as electronic properties of GNRs. Due to the strong electron-phonon interaction in the graphene related allotropes, the electron transportation of AGNRs strongly depend on the behavior of the edge dependent phonon modes in addition to the orientation of the atoms of nanoribbon with different defects [9]. Therefore, we require a clear conception of the effects of vacancy and stone wales defects on the phonon modes which noticeably change the electron transport properties of GNR based nanodevices.

Although several investigations have been performed on the phonon properties of AGNRs using different theoretical approaches such as force constant fittings [1], DFT theory [10], first-principles calculations [11] and force vibrational method [12,13], most of these are worked mainly on the pure GNR. However, when defects present in a system, the symmetry of elemental topological arrangements has been brokendown, which create very complex lattice structures. As a result, the dynamical matrix technique needs huge computational resources.

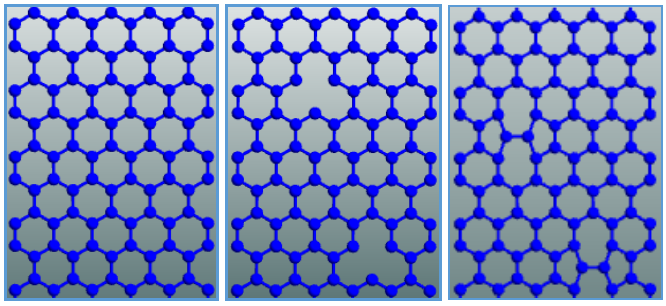

a b c

Fig. 1. Structure of a) pure AGNR, b) AGNR with vacancy defect, c) AGNR with stone wales defect

978-1-5386-2307-7/17/$31.00 ©2017 IEEE

These long computational times and convergence problems in the dynamical matrix techniques limit the systems of interest to benchmark molecules. Therefore, a significantly reliable model is essential for in depth understanding of the vibrational properties of defective atomic structures.

In this work, molecular dynamic simulation has been used with optimized Tersoff and Brenner empirical potential [14] to find out the vibrational properties of vacancy and stone wales defected AGNR. The molecular dynamic simulation is implemented on the virtual nanolab using atomistic toolkit (ATK) force–field calculator. The benefits of ATK force–field method is that there is no computational and convergence problem and it shows the result, which are very much comparable to first principle calculations using DFT theory and the peaks of Raman spectra. For disordered AGNR with defects, there may observe phonon modes lying outside of the permissible frequency range of the pristine crystal. These modes are known as localized phonon modes. To observe the localized phonon modes, we have calculated the typical vibrational pattern of AGNRs considering the effects of stone wales and vacancy type defects. We mainly analyze the K point in-plane transverse optical mode phonon due to its importance in the D band of Raman spectra that suggest that the armchair edge behaves as a defect.

## II. COMPUTATIONAL DETAILS

The analysis of the present work is performed on the AGNR with vacancy and stone wales defect as shown in Fig.1. using molecular dynamic simulation with optimized Tersoff and Brenner empirical potential. According to the molecular dynamic simulation the local vibrational density of state (LVDOS) on an atomic site $i$ for a frequency ω is given by,

$$\rho_i(\omega) = 2\omega \sum_{\nu} \sum_{\alpha} \left| u_{i,\nu}(\alpha) \right|^2 \delta(\omega^2 - \omega_\nu^2) \tag{1}$$

where, the summation is performed over all the modes ν and the space directions α, $\omega_\nu$ and $u_{i,\nu}(\alpha)$ are the frequency and the ($i$,α) component of the νth phonon eigenvector, respectively. These parameters are calculated by using the lattice-dynamics equations as,

$$\sum_{j,\beta} D_{ij}(\alpha,\beta) u_{j,\nu}(\beta) = \omega_\nu^2 u_{i,\nu}(\alpha) \tag{2}$$

where, β means the direction along the Cartesian coordinate and $D$ represent the dynamical matrix expressed by [10],

$$D_{ij}(\alpha,\beta) = \frac{\Phi_{ij}(\alpha,\beta)}{\sqrt{M_i M_j}} \tag{3}$$

where, $M$ denotes the masses of $i^{th}$ and $j^{th}$ atoms and $\Phi_{ij}$ is the force constant tensor representing the full information of the interactions between these atoms of the structure. The phonon density of states is thus calculated by the summation of LVDOS as defined by $\rho_i(\omega)$ in Eq. (1). From Eq. (3), it is known that $\Phi_{ij}$ are the dominant quantities to be obtained in order to calculate the LVDOS [10]. These force constant tensors have been calculated with the help of optimized Tersoff and Brenner empirical potential. The total energy for AGNR can be expressed as [10],

$$E = \sum_i \sum_{j>i} f_c(r_{ij})[V_R(r_{ij}) - b_{ij} V_A(r_{ij})] \tag{4}$$

where, $f_c(r_{ij})$ is called the cut-off-distance function between the atoms and $V_R(r)$ is repulsive and $V_A(r)$ is attractive parts of the potential. The $b_{ij}$ is a coefficient determined by the angles between the bond $i$ and $j$ and all other bonds made from the $i$ and $j$ sites. The parameters of the empirical potential depend on the local coordination number. A lot of calculations represent the validity of this potential when addressing structural properties of carbon based systems, such as fullerenes, nanotubes and graphene [10]. The optimized Tersoff and Brenner empirical potential is used to optimize the force constant tensor. In optimizing geometry the Limited memory Broyden Fletcher Goldfarb Shanno (LBFGS) optimizer method is used, where the force tolerance is 0.01 eV/Ang. and stress tolerance is 0.0001 eV/Ang.$^3$ and maximum number of steps is 200. In the dynamical matrix we have used central finite difference method with an atomic displacement of 0.01 Ang. In the PDOS calculation, the C-C bond length is 1.42086 Ang. and the Brillouin zone is sampled by Monkhorst pack-grid with 51×1×1 k-point grid whereas for transmission spectrum it is 60×1×1 k-point grid. The phonon transmission spectrum has been calculated by a recursive technique where the average Fermi level is $1\times10^{-6}$ eV.

## III. RESULTS AND DISCUSSION

Fig. 2 represents the calculated phonon density of states of 32, 24, 18 and 13 atoms wide pure AGNR as a function of frequency. From PDOS peaks, it is seen that three characteristic peaks are appeared around 370 cm$^{-1}$, 830 cm$^{-1}$ and 1580 cm$^{-1}$ frequency. The PDOS peaks of wider AGNR approaches to that of infinite graphene sheet and the peaks are softened and broadened with the decrease of ribbon width. Generally, a group of six phonon modes are observed at the Γ point of GNRs. The physical origin of G peaks around 1580 cm$^{-1}$ of Raman spectra comes from the longitudinal optical (LO) and transverse optical (TO) phonon modes at the Brillouin zone center. Here, our results provide sharp peak around 1580 cm$^{-1}$ (LO mode for AGNR) which is very good outcomes of the used method in comparing with Raman spectra results [12, 13]. From PDOS curves, it is found that Γ point LO and TO mode is non-degenerate and shifted down with the decrease of GNR width. In AGNRs, only the longitudinal optical (LO) modes are Raman active and the graphene (G) peak of Raman spectra near the edge side shows a down shift of the longitudinal optical (LO) mode phonon. Nevertheless, the transverse optic (TO) phonon modes is decoupled from electron/hole pairs.

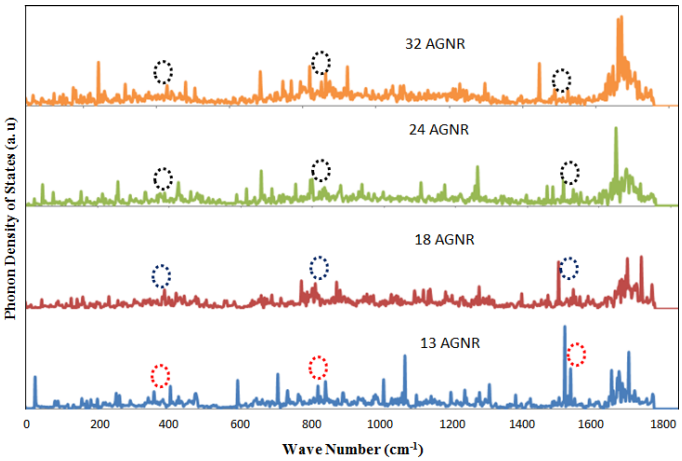


Fig. 2. Width dependent PDOS of pure armchair graphene nanoribbon as a function of frequency.

As a result, the TO mode phonon remain same as the original Γ point frequencies of infinite graphene sheet. Hence, it is predicted that LO mode phonon has the significant contribution to the transport of electron in comparing with TO mode phonon for GNR based nanodevices.

Fig. 3 shows the effect of vacancy defect on the PDOS peaks of different atoms wide AGNR. Here, it is found that some edge localized phonon modes are located around 410 $cm^{-1}$, which denotes the characteristic of AGNRs. It is observed that some new peaks are appeared in the low frequency region due to vacancy types defect with respect to pure AGNR. It is also found that the PDOS peaks are softened with the decrease of ribbon width. A localized phonon mode (Fig. 3.) is observed in the defect sites around 1355 $cm^{-1}$ which is very good agreement with the D peaks comes from Raman spectra of disordered GNR. For stone wales defect, we also calculate the PDOS of 32, 18, 15 and 14 atoms wide AGNRs. When there is a rotation of $90^0$ of the two atoms, there occurs stone wales defect. From Fig. 4. it is found that the stone wales defects dominate the AGNR with small width. Here we observe that the PDOS peaks are shifted down with the decrease of ribbon width in the stone wales defected AGNR. We observe a new peak near 450 $cm^{-1}$, which may also due to the stone wales defects. Armchair edge phonon mode (peaks) are also observed at 1580 $cm^{-1}$ which are well agreed with the Raman G peaks come from the LO mode phonon for AGNRs. From Fig. 4. it is also observed that for stone wales defect, some new peaks are appeared in the high frequency region.

The vibrational patterns for pure and disordered AGNRs have also been calculated as depicted in Fig. 5. The results show that the K-point TO mode phonon is distributed through the whole system in the pure AGNR as shown in Fig. 5(a). However, due to the vacancy or stone wales for both types of defects phonon propagations is constrained into a particular region which are clearly observed in Fig 5(b) and 5(c). It is expected that this localization of phonon strongly affects the electronic as well as vibrational properties of GNR based devices. For example, due to the localized phonon mode, the thermal conductivity of GNR will be reduced significantly.

Fig.6 shows the phonon transmission spectrum for pure and defective AGNRs. The results demonstrate that, stone wales defect is more sensitive than vacancy type defect. We obtain a very high value (30) of phonon transmission coefficient for pure AGNR. However, this value is reduced to 15 and 8.5 for vacancy and stone wales defects, respectively.

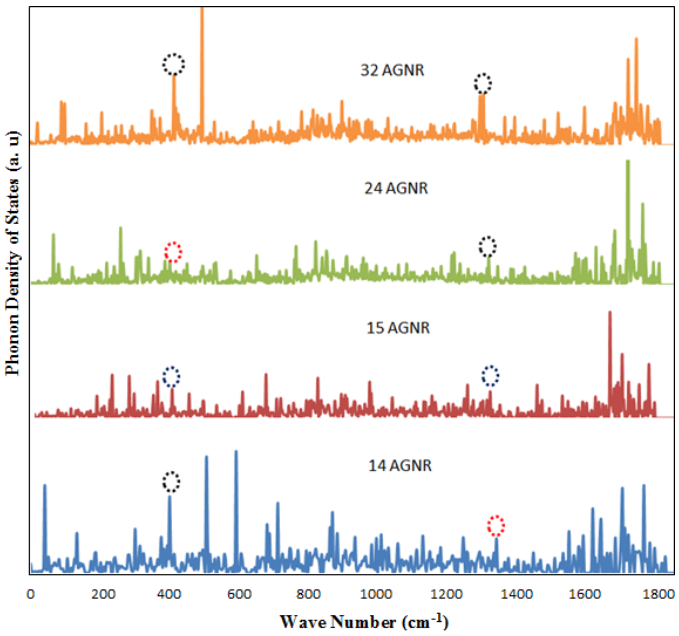


Fig. 3. PDOS of armchair graphene nanoribbon with vacancy defect.

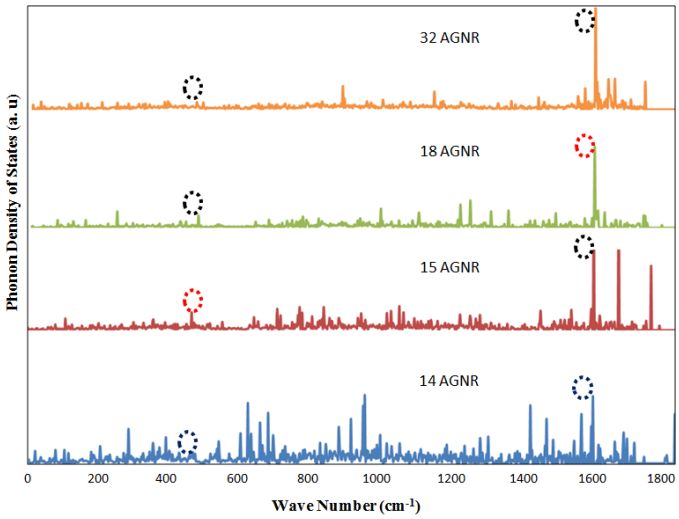


Fig. 4. PDOS of armchair graphene nanoribbon with stone wales defect.

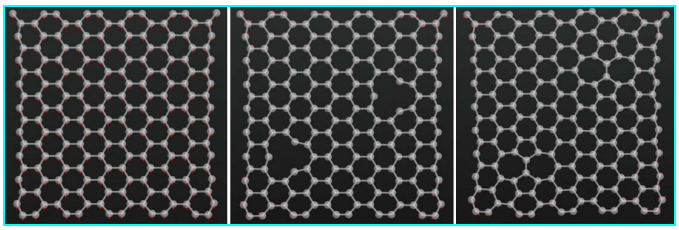

a) b) c)

Fig. 5. K point i-TO mode phonon for a) pure AGNR, b) AGNR with vacancy defect, c) AGNR with stone wales defect.

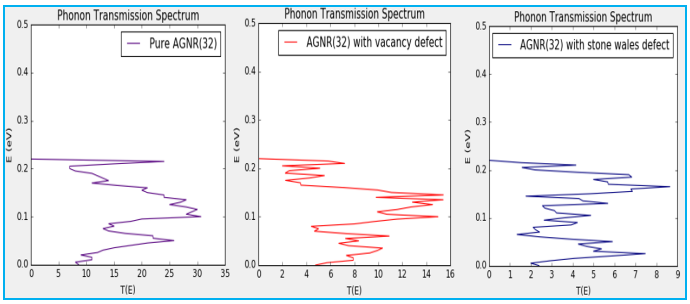


Fig. 6. Phonon transmission spectrum for 32-atoms wide AGNR a) pure AGNR, b) AGNR with vacancy defect c) AGNR with stone wales defect.

Thermal properties of AGNR change when the structure is changed due to impurities or defects. The three phonon transmission spectra in the above Fig. 6 (purple: pure AGNR, red: AGNR with vacancy defect, dark blue: AGNR with stone wales defect) are significantly different. The difference is caused by phonon scattering by the defects. At low energy (long wavelength) the spectrum is unchanged, while the main difference is at higher energies (shorter wavelength). Comparing the results we found that, the transmission spectra for the distorted GNR are strongly suppressed due to scattering by the defects.

## IV. CONCLUSIONS

In this work, vibrational properties of armchair graphene nanoribbon with vacancy and stone wales defects are studied. Molecular dynamic simulation has been used for investigating the phonon properties of defective AGNR using optimized Tersoff and Brenner empirical potential in the virtual nanolab. We observe a softening and broadening of the LO mode phonon due to the defects and the reduction of the ribbon width of AGNR. Localized K-point TO mode phonon is perceived for both vacancy and stone wales defected AGNR. The K-point TO mode phonon is distributed through the whole system in the pure AGNR. However, due to the vacancy or stone wales for both types of defects phonon propagations is constrained into a particular region. It is expected that this localization of phonon strongly affects the electronic as well as vibrational properties of GNR based devices. The phonon transmission spectrum for 32 atoms wide pure AGNR and defective AGNR are also analyzed. Our results show the disordered AGNRs have the small value of phonon transmission coefficients. These findings are very much important to understand the heat transport phenomena in GNR based nanoelectronic devices as well as to apply phononic engineering by defect to manipulate thermal and electronic properties in AGNR.

## REFERENCES


[1] F. Mazzamuto, J. Saint-Martin, A. Valentin, C. Chassat, and P. Dollfus, “Edge shape effect on vibrational modes in graphene nanoribbons: A numerical study,” J. Appl. Phys., vol. 109, no. 6, pp.064516, March 2011.

[2] M. S. Islam, S. Tanaka, and A. Hashimoto, “Effect of vacancy defects on phonon properties of hydrogen passivated graphene nanoribbons,” Carbon, vol. 80, pp. 146-154, December 2014.

[3] Y.Y. Li, M.X. Chen, M. Weinert, and L. Li, “Direct experimental determination of onset of electron-electron interactions in gap opening of zigzag graphene nanoribbons,” Nat. Commun., vol. 5, pp. 4311, July 2014.

[4] Z. Chen, Y.M. Lin, M.J. Rooks, and P. Avouris, “Graphene nanoribbon electronics,” Physica E, vol. 40, pp. 228-232, December 2007.

[5] J.Cai, P. Ruffieux, R. Jaafar, M. Bieri, T. Braun, and S. Blankenburg et al., “Atomically precise bottom-up fabrication of graphene nanoribbons,” Nature, vol. 466, pp. 470-473, July 2010.

[6] L.G. Cancado, M.A. Pimenta, B.R.A. Neves, M.S.S. Dantas, and A. Jorio, “Influence of the Atomic Structure on the Raman Spectra of Graphite Edges,” Phys. Rev. Lett., vol. 93, pp. 247401, December 2004.

[7] YW Son, ML Cohen, SG. Louie, “Energy gaps in graphene nanoribbons,” Phys. Rev Lett., vol. 98, pp.216803, November 2006.

[8] A Hashimoto, K Suenaga, A Gloter, K Urita, S Iijima, “ Direct evidence for atomic defects in graphene layers,” Nature, vol. 430, pp.870–873, August 2004

[9] M Droth, G. Burkard, “Acoustic phonons and spin relaxation in graphene nanoribbons,” Phys Rev B, vol. 84, pp. 155404, October 2011.

[10] M Vandescuren, P Hermet, V Meunier, L Henrard, P. Lambin, “ Theoretical study of the vibrational edge modes in graphene nanoribbons,” Phys. Rev B, vol.78, pp.195401, November 2008.

[11] R Gillen, M Mohr, C Thomsen, J. Maultzsch, “ Vibrational Properties of graphene nanoribbons by first-principles calculations,” Phys Rev B, 2009; vol.80, no. 15, pp. 155418, October 2009

[12] M. S. Islam, AG Bhuiyan and A. Hashimoto, “Realistic edge shape effects on the vibrational properties of graphene nanoribbons,’’ in proc. *IEEE* 2nd EICT, KUET, Khulna, Bangladesh, December 2015, pp. 412 – 415.

[13] M. S. Islam, K. Ushida, S. Tanaka and A. Hashimoto,“Numerical analysis on vacancy induced vibrational properties of graphene nanoribbons,” Computational Materials Science, vol. 79, pp. 356-361, Nov. 2013.

[14] L. Lindsay and D. A. Broido, “Optimized Tersoff and Brenner empirical potential parameters for lattice dynamics and phonon thermal transport in carbon nanotubes and graphene,” Phys. Rev. B, vol. 81, pp.205441, May 2010.

# Study and Suppression of Ambipolar Effect in Multilayer Phosphorene Tunnel Field Effect Transistors Using Double Gate Structure

Muhammad Navid Anjum Aadit[1], Shamima Nasrin Juthi[2], and Sharadindu Gopal Kirtania[3]
Department of Electrical and Electronic Engineering
Bangladesh University of Engineering and Technology
Dhaka-1205, Bangladesh
Email: [1]navidanjumaadit@gmail.com, [2]juthishamimanasrin@gmail.com, and [3]sharadindugopal@gmail.com

***Abstract*—We present a comprehensive study of ambipolar effect in multilayer phosphorene tunnel field-effect transistors (TFETs). Phosphorene is a promising 2D material with tunable bandgap and high mobility but ambipolarity limits many of its potential applications. We explain the ambipolar effect with energy band diagram which results in undesirable off state drain current. This work uses an in-house built simulator and suggests a technique to suppress the ambipolar current by using different gate oxide materials. However, this method has a trade-off that it reduces on-current too. Therefore, in this paper, we present a novel double gate structure of multilayer phosphorene TFETs which not only minimizes the off-current but also sustains the on-current at its desired level. The proposed design is very efficient in suppressing ambipolarity up to a certain number of layers. The simulated results are presented in tabular form which would be helpful for any further study on ambipolarity of phosphorene TFETs. The proposition can be extended to other 2D material TFETs too where ambipolarity limits device performance.**

***Keywords*—Ambipolar, Double gate, Multilayer, Phosphorene, TFET.**

## I. Introduction

Transistors are widely used electronic devices offering applications of switching and amplification in analog and digital circuits, and in optical as well as communication sectors. The characteristics of immunity to radiation, producing less noise, and better thermal stability make Field Effect Transistor (FET) an essential electronic transistor device in almost all sorts of amplifications, noise sensitive applications, extremely low power switching, chopper multiplication, multiplexing and so on [1]–[4]. Tunnel FETs (TFETs) are special types of FETs in which the source and drain are oppositely doped to exploit the quantum tunneling of charge carriers to enhance current flow [5]. However, due to ambipolar effect, some TFETs conduct for both positive and negative values of gate voltage making the devices unsuitable for complementary logic circuits which are commonly required to design digital circuits [6]. This effect is largely undesirable in the conventional applications of transistors.

Two dimensional (2D) crystals with novel properties such as graphene, Transition Metal Dichalcogenides (TMDs), Black Phosphorous (BP) have emerged to impact future technologies. Although graphene is considered as an effective material for optical devices, due to the absence of bandgap, its application is limited to many device applications such as logic device and current saturation for power gain [7]. On the other hand, the carrier mobility of TMDs is comparatively lower than other available semiconductors [8]. In order to overcome all these limitations, it has become mandatory to explore other 2D semiconductors which can substitute graphene or TMDs. Apart from graphene, phosphorene is the best choice as a 2D layer material having the unique properties of mechanical exfoliation due to the Van der Waals force reinforced honeycomb structure of black phosphorous [9]. It has tunable bandgap, making it superior to graphene and high carrier mobility, making it superior to TMDs. Generally, black phosphorous exhibits a direct bandgap of 0.3 eV [10] but it is tunable up to 2 eV [11]. Black phosphorus is preferred in designing FETs because of its superior stability over red and white allotropes. [12].

In Phosphorene FETs, the term “Phosphorene” represents multilayer black phosphorus in 2D structure [13]. These devices are viable candidates for optoelectronic applications and optimized electronics. Eventually, economic yield of phosphorene on large scale as well as mass reproduction has become an inevitable research trend [14]. Initially unpassivated phosphorene FETs were used to demonstrate promising performance characteristics [15], [16]. Next, passivated ones with top gate structure have come to interest in search of high frequency device performance. Analytical properties of phosphorene FETs with possible applications have been reported too [17]. Moreover, Yin *et al.* defined scaling limit of phosphorene FETs presenting simulation based study [18]. Apart from conventional FET structures, performance of phosphorene TFETs has also been studied and multilayer phosphorene is found to be a promising material for TFETs [19], [20]. Chen *et al.* investigated phosphorene TFETs by engineering thickness of layers with different bandgaps [21]. Another related work extensively studied the transfer characteristics of monolayer and multilayer phosphorene FETs in both conventional FET and TFET structures where it is obvious that multilayer phosphorene TFETs suffer from undesirable ambipolar effect due

978-1-5386-2307-7/17/$31.00 ©2017 IEEE

to smaller bandgap [22]. It has been already investigated that the number of layers plays a vital role in the ambipolar transfer characteristics of phosphorene based FETs [14]. However, effective methods to suppress ambipolar current in multilayer phosphorene TFETs are yet to be reported. Ambipolar current tends to flow over a wide range of positive and negative gate bias values when the barrier heights for both electrons and holes become identical. In such cases, leakage saturation current is merely dependent on number of layers or bandgap, not on gate bias. Although significant number of research works are found in literature aiming to convert ambipolar FETs to unipolar ones that use graphene [23] or Carbon Nanotube (CNT) [24] as channel material, to the best of our knowledge, no such work has been done so far with multilayer phosphorene TFETs.

In this paper, we present an extensive study of ambipolarity in multilayer phosphorene TFETs. Transfer characteristics of tri, tetra and penta-layer phosphorene TFETs have been explored to demonstrate ambipolar effect and a method to reduce ambipolarity using low dielectric gate oxide is presented. It is shown that this method has a trade-off with reduced on-current. Therefore, the objective of this work is to suppress ambipolar effect in such devices as much as possible with no loss of on-current by using double gate structure with one gate extending over the drain region. Ambipolar current flows when electrons flow at positive gate bias (n-type) and holes flow at negative gate bias (p-type) for the same device. This phenomenon occurs due to the lowering of tunneling barrier height of electron and hole injection alternatingly with switching of polarity of gate voltage. In the proposed design of multilayer phosphorene TFETs, tunneling of holes at negative gate bias will be controlled by increasing barrier height at the drain-channel interface. Thus, the device will conduct only at positive gate bias as an n-type device with electrons being the charge carriers. The improved results are also shown for tri, tetra and penta-layer phosphorene TFETs and presented in tabular form for quick comparison.

The rest of the paper is organized as follows. Section II presents the conventional phosphorene TFET structure with single gate and the proposed structure with double gate with brief description of the simulation technique. Finally, Section III explains the results found and shows how ambipolar current can be suppressed effectively using an extra gate extended over drain.

## II. Device Structure and Modeling

### A. Device Structure

For faster device simulation, we present a simplified phosphorene TFET structure which includes the layer of black phosphorous or phosphorene as the active channel material. Although monolayer is preferable for low power switching devices, we prefer multilayer phosphorene due to its additional advantages of optimum bandgap and comparatively less effective mass which in turn lead to high performance applications.

Two different phosphorene TFET structures are considered. In Fig. 1, the schematic view of conventional single gate phosphorene TFET structure and in Fig. 2 the proposed double gate phosphorene TFET structure are shown. In both structures, we use $Si$ as substrate, and $SiO_2$ as insulator. Here, we use multilayer phosphorene (tri, tetra and penta-layer in simulation) as channel material where the channel length is about 30 nm and $HfO_2$ (dielectric constant, $k$ = 25) as gate oxide. In both structures, the equivalent oxide thickness is around 3 nm, source-drain extensions are of 15 nm and the dielectric constant of phosphorene is 10. The source is p-doped and the drain is n-doped and the doping concentration at source and drain is $2 \times 10^{20} cm^{-3}$. The drain to source voltage, $V_{DS}$ is set to be 1 V throughout all analysis in this paper. The gate length, $L_G$ is 10 nm for both the devices while the proposed device has an extra gate extended over the drain region with a gate length, $L_{new}$ of 10 to 20 nm, depending on design requirements. During our simulation, scattering is ignored since it is expected that due to short channel length consideration, the effect of scattering is almost negligible. The device operating temperature is assumed to be 300 K.

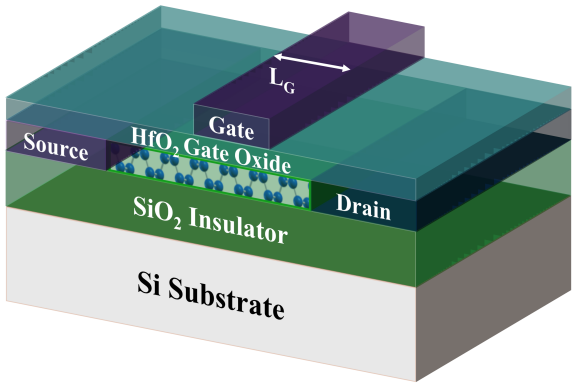


Fig. 1. Simplified schematic diagram of conventional single gate multilayer phosphorene TFET structure

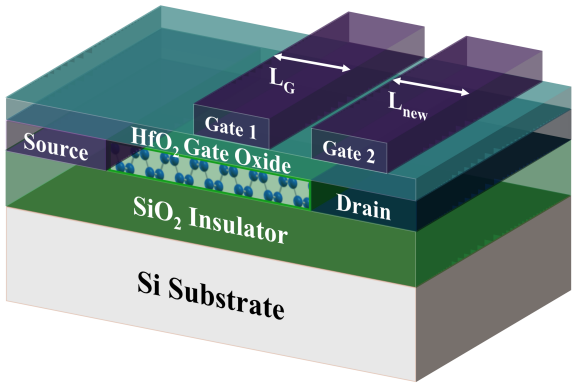


Fig. 2. Schematic diagram of the proposed double gate multilayer phosphorene TFET structure to suppress ambipolar current

### B. Modeling

In the conventional single gate structure, when gate voltage $V_G$ is positive, the tunneling barrier at the source-channel

interface becomes lower and current flows due to electron flow. Besides, when $V_G$ becomes negative crossing the Dirac point, the tunneling barrier at the drain-channel becomes lower which in turn leads to current flow due to hole flow. Thus, ambipolar effect is evident in this structure. On the contrary, in our proposed double gate structure, including an extra gate over the drain region, the situation remains identical for positive values of $V_G$. But for negative values of $V_G$, the case is different because this makes the tunneling barrier at the drain-channel interface comparatively higher. Thus, the overall hole flow path offers less steepness, and current flow due to hole flow becomes limited. In this way, it results in suppression of ambipolar effect in the proposed multilayer phosphorene TFET structure to a great extent.

We investigate the electronic states of the device at atomistic level by using tight binding approximation that can precisely describe multilayer phosphorenes [25]. Ten intra-layer and four inter-layer hopping parameters have been used and armchair transport direction is selected [22]. Both the conventional and the proposed structures have been simulated using NanoTCAD ViDES [26] and data have been processed in MATLAB [27]. Non Equilibrium Green Function (NEGF) formalism is invoked to find the transport characteristics where the Hamiltonian matrix has been formed using a suitable supercell consisting of two unit cells of phosphorene. Self-consistent simulation of Poisson's and Schrödinger equations is performed to find device potential and charge distribution [28]. Ballistic current has been calculated using transport equation taking summation of charge carriers of all modes [29]. The properties of channel material such as band gap and effective mass are changed in the simulator to represent tri, tetra and penta-layer phosphorene TFETs.

## III. Results and Discussions

At first, we consider the conventional single gate multilayer phosphorene TFET structure and simulate it according to the simulation technique mentioned above. Fig. 3 shows the transfer characteristics of this structure where the legend indicates the number of layers used. For gate voltages above $V_G$ = 0.3 V, drain current, $I_D$ increases significantly as the gate voltage increases. This is typical n-type characteristics of a device where electrons are the major charge carriers. Such behavior of on-current is identical irrespective of number of layers although drain current is higher when number of layers is also greater. However, getting backward from $V_G$ = 0.3 V, decreasing gate voltage also gives rise to drain current which continues even below $V_G$ = 0 V. This off-current occurs due to hole flow which is a result of lowering of tunneling barrier at the drain-channel interface with a negative voltage applied at the gate above the channel. The device behaves like a p-type device with current flow at negative gate bias resulting from hole flow. Once again the effect is similar irrespective of number of layers although the off-current increases when number of layers is greater. Within the simulation range, the maximum off-current for tri-layer phosphorene TFET is 0.4229 $\mu$A/$\mu$m and for tetra and penta-layer TFETs, it is 3.001 $\mu$A/$\mu$m and 29.84 $\mu$A/$\mu$m respectively. Thus, the conventional single gate multilayer structure shows obvious ambipolarity irrespective of number of layers.

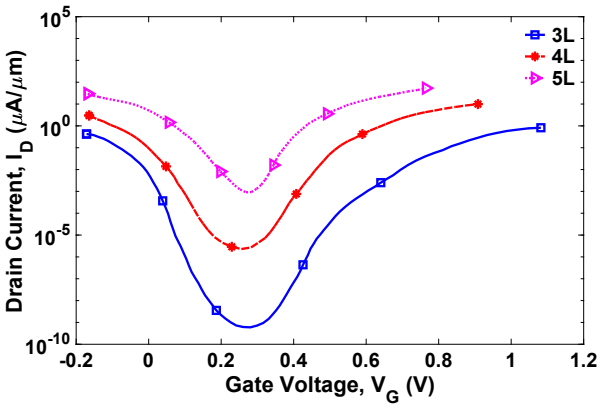


Fig. 3. Transfer characteristics of conventional multilayer phosphorene TFETs for tri, tetra and penta-layers

The physics behind ambipolarity can be explained with the simulated energy band diagram of the tri-layer phosphorene TFET as shown in Fig. 4. With gate to source voltage, $V_{GS}$ = 1.2 V, the device allows electron flow by lowering the tunneling barrier height at the source-channel interface and introduces drain current. When a negative gate to source voltage is applied ($V_{GS}$ = -0.2 V), the tunneling barrier height at the channel-drain interface is reduced and hole conduction through this tunnel once again introduces drain current. Eventually, the device conducts with both positive and negative values of $V_{GS}$ and exhibits ambipolarity.

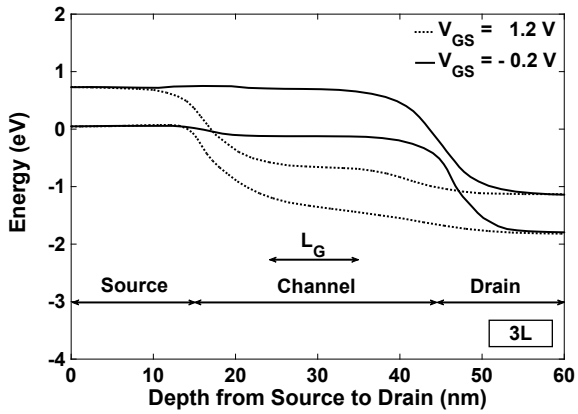


Fig. 4. Simulated energy band diagram of conventional tri-layer phosphorene TFET with $L_G$ = 10 nm

To retain control over off-current, a trivial approach can be employed using different gate dielectric materials. Changing the dielectric constant of the oxide in the simulator, a plot of transfer characteristics of the conventional tri-layer phosphorene TFET structure is depicted in Fig. 5. Three different gate oxides- $HfO_2$, $Al_2O_3$ and $SiO_2$ have been used with

dielectric constant, $k$ = 25, 9 and 3.9 respectively [30]. It is found that low dielectric gate oxide offers reduced off-current. The maximum off-current reduces to 0.0126 $\mu$A/$\mu$m for $Al_2O_3$ from 0.4229 $\mu$A/$\mu$m for $HfO_2$. It is further reduced to 0.0014 $\mu$A/$\mu$m for $SiO_2$. However, it is also noticeable that the maximum on-current is substantially reduced from 0.8219 $\mu$A/$\mu$m for $HfO_2$ to 0.0856 $\mu$A/$\mu$m for $Al_2O_3$ and to 0.0479 $\mu$A/$\mu$m for $SiO_2$. Therefore, this approach is not a suitable one for suppressing ambipolarity which limits on-current significantly.

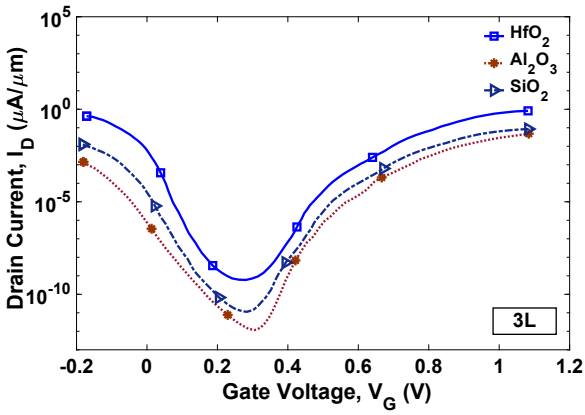


Fig. 5. Transfer characteristics of conventional tri-layer phosphorene TFET with different gate oxides

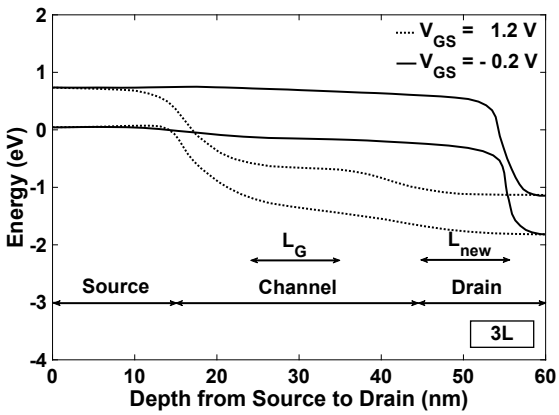


Fig. 6. Simulated energy band diagram of proposed tri-layer phosphorene TFET with $L_G$ = 10 nm and $L_{new}$ = 10 nm

To overcome the trade-off between on-current and off-current, the proposed TFET structure uses a double gate structure where an extra gate is overlapped over the drain. Fig. 6 shows the simulated energy band diagram of the proposed double gate tri-layer phosphorene TFET with $L_G$ = 10 nm and $L_{new}$ = 10 nm. The energy band diagram is identical to that of Fig. 4 for positive gate voltage, $V_{GS}$ = 1.2 V applied at both gates. However, at negative gate voltage, $V_{GS}$ = -0.2 V applied at both gates, the energy band diagram cannot bend at the drain-channel interface and so tunneling barrier height at this interface is maintained at the same level to that of the source-channel interface which provides resistance to hole flow. As a result, flow of drain current at negative bias due to hole flow becomes essentially limited and ambipolarity is expected to be reduced.

Fig. 7 shows the transfer characteristics of tri-layer phosphorene TFET structure where $L_{new}$ = 0 nm indicates the conventional single gate structure and $L_{new}$ = 10 nm and 15 nm indicates the proposed double gate structure. It is found that above $V_G$ = 0.3 V, the on-currents for all the three configurations are almost identical. However, below this point and with negative gate bias, the conventional TFET exhibits a maximum off-current of 0.4229 $\mu$A/$\mu$m as shown earlier. The proposed TFET with $L_{new}$ = 10 nm shows a maximum off-current of 0.0015 $\mu$A/$\mu$m and with $L_{new}$ = 15 nm shows a maximum off-current of $2.548 \times 10^{-6}$ $\mu$A/$\mu$m. An extra gate with $L_{new}$ = 15 nm over the drain region has reduced the off-current to $10^{-6}$ range which is better than any of the results obtained with different gate oxides. Moreover, the double gate tri-layer TFET retains the on-current to its usual level. Thus, the proposed double gate structure is a very efficient design to suppress ambipolar effect in tri-layer phosphorene TFETs.

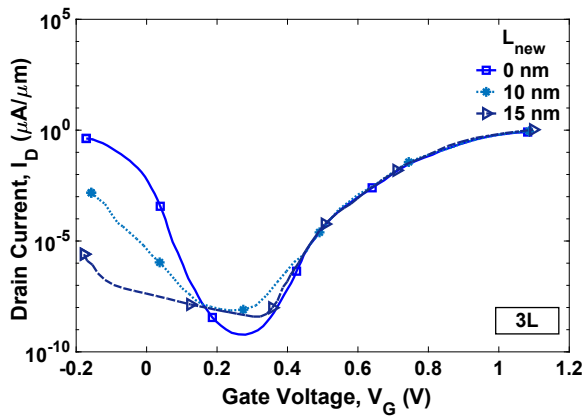


Fig. 7. Transfer characteristics of conventional single gate ($L_{new}$ = 0 nm) and proposed double gate ($L_{new}$ = 10 nm and 15 nm) tri-layer phosphorene TFET

We extend our simulation to tetra and penta-layer phosphorene TFETs and the transfer characteristics of these devices are shown in Fig. 8 and Fig. 9 respectively. The tetra-layer TFET exhibits maximum off-currents of 3.001, 0.7044, and 0.1399 $\mu$A/$\mu$m for $L_{new}$ = 0, 10, and 15 nm respectively. The maximum on-current is 9.318 $\mu$A/$\mu$m for all three configurations. It is to be noted that both the on-current and off-current for tetra-layer TFETs are higher than those of tri-layer TFETs which is consistent with the related work [22]. Although the off-current is not reduced to $10^{-6}$ range, it is still quite low in comparison with the conventional structure. However, the penta-layer phosphorene TFETs give rise to on and off-currents even more than that of tetra-layer ones. The maximum off-currents in Fig. 9 are 29.84, 14.23 and 8.895 $\mu$A/$\mu$m for $L_{new}$ = 0, 10, and 15 nm respectively along with maximum on-current of 44.67 $\mu$A/$\mu$m for all three configurations. These results indicate that even double gate structure will lose control

over ambipolar current if the number of layers is increased further. This is due to the fact that increasing number of layers reduces the bandgap even more which leads lowering of tunneling barrier height irrespective of single gate or double gate structure. However, for practical low-power applications, the proposed structure has fine control over ambipolarity if the number of layers is limited between 3 to 5. Keeping the on-current unchanged to its optimum value, the proposed multilayer double gate phosphorene TFET suppresses the off-current and ambipolar effect to a great extent.

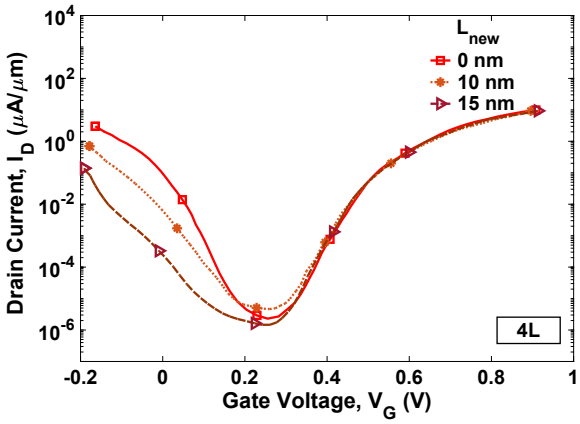


Fig. 8. Transfer characteristics of conventional single gate ($L_{new}$ = 0 nm) and proposed double gate ($L_{new}$ = 10 nm and 15 nm) tetra-layer phosphorene TFET

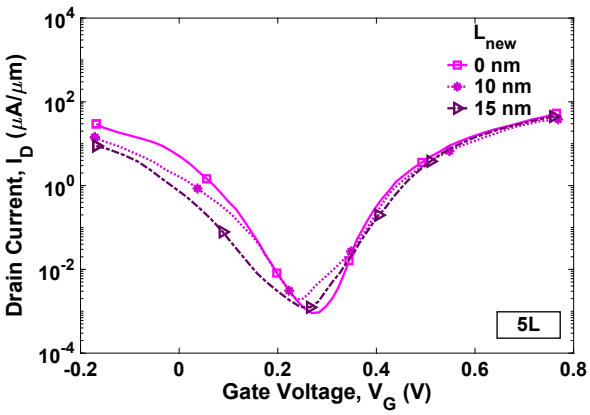


Fig. 9. Transfer characteristics of conventional single gate ($L_{new}$ = 0 nm) and proposed double gate ($L_{new}$ = 10 nm and 15 nm) penta-layer phosphorene TFET

Table I summarizes the results obtained in terms of maximum off-currents found for multilayer phosphorene TFETs with conventional single gate ($L_{new}$ = 0 nm) and proposed double gate ($L_{new}$ = 10 nm and 15 nm) structures. It is obvious that increasing number of layers increases off-current and increasing length of the extra gate, $L_{new}$ reduces off-current. Therefore, the best result in suppressing ambipolarity is found for tri-layer phosphorene TFET with $L_{new}$ = 15 nm which exhibits very low off-current making it suitable for low-power applications.

TABLE I
COMPARATIVE ANALYSIS OF OFF-CURRENTS ($\mu$A/$\mu m$)

| | Tri-layer | Tetra-layer | Penta-layer |
|---|---|---|---|
| $L_{new}$ = 0 nm | 0.4229 | 3.001 | 29.84 |
| $L_{new}$ = 10 nm | 0.0015 | 0.7044 | 14.23 |
| $L_{new}$ = 15 nm | $2.548 \times 10^{-6}$ | 0.1399 | 8.895 |

## IV. CONCLUSION

We have simulated multilayer phosphorene tunnel field-effect transistors (TFETs) to explain ambipolar behavior of drain current due to smaller bandgap of channel material. It is shown that the maximum off-current increases with increased number of layers. A trivial technique to suppress this off-current and ambipolarity is suggested which has a limitation of reduced on-current. To overcome this limitation, an improved double gate multilayer phosphorene TFET structure has been proposed. It is found that with an extra gate extended over the drain region, the proposed design successfully reduces ambipolar current to a great extent. However, increasing number of layers may limit the efficiency of the proposed system. Finally, the results are presented in tabular form for quick investigation. This study of ambipolar effect and the proposed off-current suppression technique may be extended to other similar 2D materials too.

## REFERENCES


[1] A. Dubey, A. Singh, R. Narang, M. Saxena, and M. Gupta, "Modeling and Simulation of Junctionless Double Gate Radiation Sensitive FET (RADFET) Dosimeter," *IEEE Transactions on Nanotechnology*, vol. PP, no. 99, pp. 1–1, 2017.

[2] M. Hua, Z. Zhang, J. Wei, J. Lei, G. Tang, K. Fu, Y. Cai, B. Zhang, and K. J. Chen, "Integration of LPCVD-$SiN_x$ gate dielectric with recessed-gate E-mode GaN MIS-FETs: Toward high performance, high stability and long TDDB lifetime," in *2016 IEEE International Electron Devices Meeting (IEDM)*, Dec 2016, pp. 10.4.1–10.4.4.

[3] F. A. Levinzon, "Ultra-Low-Noise Seismic Piezoelectric Accelerometer with Integral FET Amplifier," *IEEE Sensors Journal*, vol. 12, no. 6, pp. 2262–2268, June 2012.

[4] D. Im, B. K. Kim, D. K. Im, and K. Lee, "A Stacked-FET Linear SOI CMOS Cellular Antenna Switch with an Extremely Low-Power Biasing Strategy," *IEEE Transactions on Microwave Theory and Techniques*, vol. 63, no. 6, pp. 1964–1977, June 2015.

[5] Wikipedia. (2017) Tunnel Field-Effect Transistor. [Online]. Available: https://en.wikipedia.org/wiki/Tunnel_field-effect_transistor

[6] N. Bagga, S. Sarkhel, and S. K. Sarkar, "Recent research trends in gate engineered tunnel FET for improved current behavior by subduing the ambipolar effects: A review," in *Computing, Communication & Automation (ICCCA), 2015 International Conference on*. IEEE, 2015, pp. 1264–1267.

[7] S. Das, W. Zhang, M. Demarteau, A. Hoffmann, M. Dubey, and A. Roelofs, "Tunable transport gap in phosphorene," *Nano letters*, vol. 14, no. 10, pp. 5733–5739, 2014.

[8] S. Das, M. Demarteau, and A. Roelofs, "Ambipolar phosphorene field effect transistor," *ACS nano*, vol. 8, no. 11, pp. 11 730–11 738, 2014.

[9] R. Hultgren, N. Gingrich, and B. Warren, "The atomic distribution in red and black phosphorus and the crystal structure of black phosphorus," *The Journal of Chemical Physics*, vol. 3, no. 6, pp. 351–355, 1935.

[10] S. Endo, Y. Akahama, S.-i. Terada, and S.-i. Narita, "Growth of large single crystals of black phosphorus under high pressure," *Japanese Journal of Applied Physics*, vol. 21, no. 8A, p. L482, 1982.

[11] R. W. Keyes, "The electrical properties of black phosphorus," *Physical Review*, vol. 92, no. 3, p. 580, 1953.

[12] Y. Akahama, S. Endo, and S.-i. Narita, "Electrical properties of black phosphorus single crystals," *Journal of the Physical Society of Japan*, vol. 52, no. 6, pp. 2148–2155, 1983.

[13] R. V. Gold, K. Loening, A. McNaught, and P. Sehmi, *Compendium of Chemical Terminology. IUPAC*. JSTOR, 1987.

[14] C. Guo, L. Wang, H. Xing, and X. Chen, "The study of ambipolar behavior in phosphorene field-effect transistors," *Journal of Applied Physics*, vol. 120, no. 21, p. 215701, 2016.

[15] H. Liu, A. T. Neal, Z. Zhu, Z. Luo, X. Xu, D. Tománek, and D. Y. Peide, "Phosphorene: an unexplored 2D semiconductor with a high hole mobility," 2014.

[16] S. P. Koenig, R. A. Doganov, H. Schmidt, A. Castro Neto, and B. Özyilmaz, "Electric field effect in ultrathin black phosphorus," *Applied Physics Letters*, vol. 104, no. 10, p. 103106, 2014.

[17] A. Carvalho, M. Wang, X. Zhu, A. S. Rodin, H. Su, and A. H. C. Neto, "Phosphorene: from theory to applications," *Nature Reviews Materials*, vol. 1, p. 16061, 2016.

[18] D. Yin, G. Han, and Y. Yoon, "Scaling limit of bilayer phosphorene fets," *IEEE Electron Device Letters*, vol. 36, no. 9, pp. 978–980, 2015.

[19] T. A. Ameen, H. Ilatikhameneh, G. Klimeck, and R. Rahman, "Few-layer phosphorene: An ideal 2D material for tunnel transistors," *Scientific reports*, vol. 6, p. 28515, 2016.

[20] J. Seo, S. Jung, and M. Shin, "The Performance of Uniaxially Strained Phosphorene Tunneling Field-Effect Transistors," *IEEE Electron Device Letters*, 2017.

[21] F. W. Chen, H. Ilatikhameneh, T. A. Ameen, G. Klimeck, and R. Rahman, "Thickness engineered tunnel field-effect transistors based on phosphorene," *IEEE Electron Device Letters*, vol. 38, no. 1, pp. 130–133, 2017.

[22] D. Yin and Y. Yoon, "Design strategy of two-dimensional material field-effect transistors: Engineering the number of layers in phosphorene FETs," *Journal of Applied Physics*, vol. 119, no. 21, p. 214312, 2016.

[23] H. Li, Q. Zhang, C. Liu, S. Xu, and P. Gao, "Ambipolar to unipolar conversion in graphene field-effect transistors," *ACS nano*, vol. 5, no. 4, pp. 3198–3203, 2011.

[24] Y.-M. Lin, J. Appenzeller, and P. Avouris, "Ambipolar-to-unipolar conversion of carbon nanotube transistors by gate structure engineering," *Nano Letters*, vol. 4, no. 5, pp. 947–950, 2004.

[25] E. T. Sisakht, M. H. Zare, and F. Fazileh, "Scaling laws of band gaps of phosphorene nanoribbons: A tight-binding calculation," *Physical Review B*, vol. 91, no. 8, p. 085409, 2015.

[26] G. I. Gianluca Fiori. (2017) NanoTCAD ViDES. [Online]. Available: http://vides.nanotcad.com/vides/

[27] I. The MathWorks. (2017) MATLAB. [Online]. Available: https://www.mathworks.com/products/matlab.html

[28] M. N. A. Aadit, S. G. Kirtania, and M. K. Alam, "Dependence of threshold voltage on doped layer thickness in AlGaN/GaN HEMT: An improved split donor E-mode design," in *Informatics, Electronics and Vision (ICIEV), 2016 5th International Conference on*. IEEE, 2016, pp. 681–686.

[29] J. Wang, E. Polizzi, and M. Lundstrom, "A three-dimensional quantum simulation of silicon nanowire transistors with the effective-mass approximation," *Journal of Applied Physics*, vol. 96, no. 4, pp. 2192–2203, 2004.

[30] A. Huang, Z. Yang, and P. K. Chu, "Hafnium-based high-k gate dielectrics," in *Advances in solid state circuit technologies*. InTech, 2010.

# Phonon Transmission of Vacancy Defected (10,0) Carbon Nanotube

Ashraful Hossain Howlader and Md. Sherajul Islam
Khulna University of Engineering and Technology, Bangladesh
ahhowlader.eee@gmail.com, sheraj_ruet@yahoo.com

*Abstract*— **Carbon nanotubes (CNTs) are envisaged as the nano-building blocks in the next generation electronic devices due to their versatile potentialities. Here, the phonon properties of vacancy defected semiconductor (10,0) zigzag carbon nanotube (ZCNT) are explored using empirical interatomic potentials (EIPs). It is found that phonon modes become non-degenerate at the *Γ* point of Brillouin zone due to vacancies. The small changes in defect concentrations give rise to a large variation in the entropy and phonon transmission properties of the system. The thermal conductivity reduces about 50% with only 1% vacancy defects. We also address the issue of temperature effects on thermal conductivity. Moreover, quasi-ballistic low-frequency acoustic phonon transport is observed.**

***Keywords—Zigzag carbon nanotube, vacancy defects, entropy, thermal conductivity.***

## I. INTRODUCTION

The nanotechnology paves the way to manufacture electronic devices with reduced sizes. These miniature electronic devices cause to an exponential increase of power densities in the large scale integrated circuits. With the present trend of continuous miniaturization of electronic devices, thermal management has become a crucial issue in those devices due to heat dissipation and self-heating effects. The recent advances in processing nanostructured materials give wider possibilities of controlling the thermal transport within those nanodevices. The CNT, with unusually high thermal conductivity, claims to be a promising candidate for future high-frequency molecular electronics [1]-[5]. CNT can be a potential thermal management unit in those nanoelectronic devices due to ballistic carrier transport property with remarkable thermal stability.

The thermal conductivity in carbon-based low dimensional materials entirely depends on atomic vibrations. Moreover, other fundamental characteristics of CNT are related to its vibrational properties and phonon spectrum, from which one can derive several physical properties. Phenomena such as heat transport [6], specific heat capacity [7], electron-phonon scattering [8], resistivity and superconductivity [9] can be explained with a detailed knowledge of the phonon properties.

During the synthesis or purification processes of CNT the vacancy defects might have appeared. Due to low dimensionality of CNT structures, even a small numbers of vacancies can influence on the vibrational properties noticeably. The lack of proper investigation of the phonon properties of non-ideal vacancy defected CNTs, hampers the employment of CNTs in practical thermal management applications and make difficult the nanodevice design.

The previous theoretical analyses are based on tight binding method [10], first principle calculations [11]-[13], and force constant model [14]. These approaches are considerably more difficult and presented for perfect structures of CNTs. In the present paper we are interested to explain the discrepancies of vibrational properties between pristine and imperfect semiconductor (10,0) ZCNTs using EIPs. A systematic numerical analysis has been carried out in order to find how the presence of vacancy defects affects the phonon band structure, entropy and phonon transmission spectrum. The relations of the lattice thermal conductivity with the vacancy and temperature are inspected. The low-frequency in-plane longitudinal acoustic (iLA) phonon transport property in the presence of vacancies is also visually represented.

## II. (10,0) ZCNT MODEL

The simulation model of a single wall (10,0) ZCNT as shown in Fig. 1 has a diameter of 0.78 nm with carbon-carbon (C–C) bond length of 0.142 nm. The unit cell of (10,0) ZCNT consists of 40 carbon atoms. We have taken 5 unit cells consisting of 200 atoms for simulation. The vacancy defects are induced randomly. The atomic vacancies are very persistent in ZCNTs. They can create local deformation to the stable molecular structures of ZCNTs and as a result the stability of system declines sharply. The vacancies will perturb the ideal hexagonal structure. Therefore, the C–C bonds interactions among the neighboring atoms become weaker and result a higher degree of freedom for those atoms around vacancy regions.

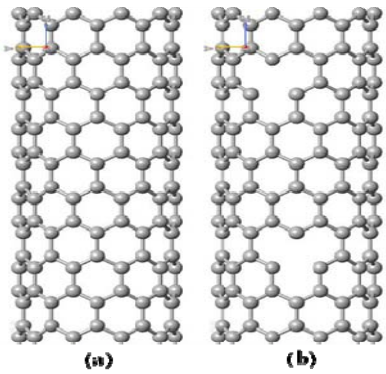


Figure 1. Model of single wall (10,0) ZCNT. (a) Pristine (b) Defective ZCNT.

978-1-5386-2307-7/17/$31.00 ©2017 IEEE

## III. SINMULATION METHOD

All the calculations in this work have been carried out using the Virtual NanoLab (VNL). The phonon dispersion relation, entropy of the system, phonon transmission spectrum, and phonon modes are numerically investigated by EIPs. EIPs are commonly employed in vibrational property calculations in CNTs. The most frequently used EIPs are those developed by Tersoff [15]-[16] and Brenner [17]-[18]. The Tersoff and Brenner EIPs are short ranged and cannot accurately fit the CNT dispersion over the entire Brillouin zone. Specially, they do not exactly obtain the velocities of the three acoustic branches near the $\Gamma$ point of the Brillouin zone. Therefore, VNL uses optimized parameter sets for the Tersoff and Brenner EIPs by Lindsay et al. [19], which better represent the lattice dynamical properties of CNTs.

The thermal conductivity of ZCNTs is calculated using the Fourier's law:

$$\kappa = \theta/\Delta T \quad (1)$$

where, $\kappa$ stands for the thermal conductivity, and $\Delta T$ represents the temperature gradient along the ZCNT length. The average heat flux $\theta$ along the ZCNT can be established as:

$$\theta = 1/A\ [\{\textstyle\sum_{\varphi=1....\nu} \Delta E\ (\varphi)\}/\tau] \quad (2)$$

where, A represents the cross-sectional area, $\nu$ represents the number of atoms, and $\tau$ refers to the total time, and $\Delta E$ expresses the energy change in the thermostat area. The average temperature depends on the average kinetic energy of all carbon atoms in the system. The average temperature can be determined as follows:

$$T = \{[\{\textstyle\sum_{\varphi=1....\nu} \mu_\iota\ (\varpi_\iota)^2\}/3N\kappa_B \quad (3)$$

where, $\mu_\iota$ is the atomic mass of carbon, $\varpi_\iota$ is the velocity of the $\iota^{th}$ carbon atom, N and $\kappa_B$ represent the Avogadro and the Boltzmann constants, respectively.

## IV. RESULTS AND DISCUSSION

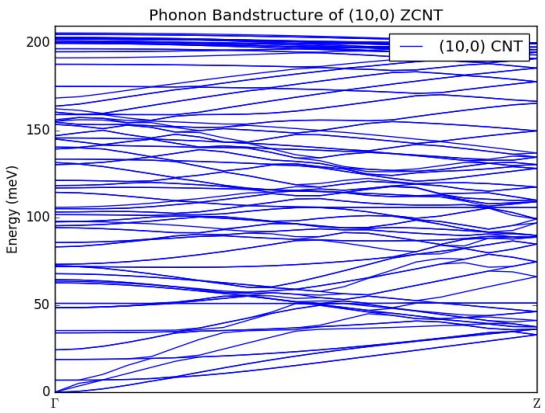


Figure 2. Phonon bandstructure of pristine (10,0) ZCNT. There are 66 distinct phonon modes, of which 12 modes are non-degenerate and 54 modes are degenerate.

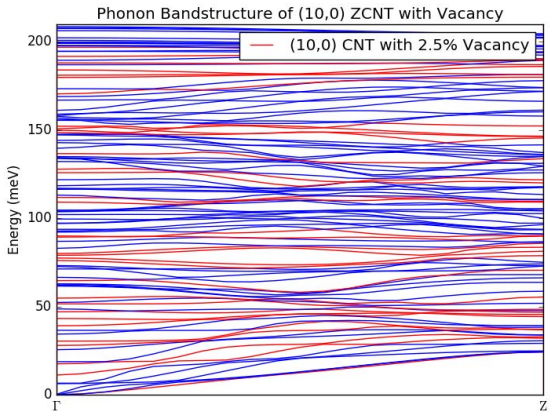


Figure 3. Phonon bandstructure of (10,0) ZCNT with vacancy defects. Phonon branches become non-degenerate due to vacancy defects (red lines).

The phonon dispersion relation for pristine and vacancy defected (10,0) ZCNTs have been simulated. If a CNT has N number of hexagons per unit cell, there will be 6N degree of vibrational freedom and 6N distinct phonon branches. (10,0) ZCNT consists of 20 number of hexagons per unit cell and 120 distinct phonon branches at the center of the Brillouin zone. Because of low dimensionality there exist only 66 distinct phonon branches, of which 12 modes are non - degenerate and 54 modes are degenerate as depicted in Fig. 2. When vacancies are induced in the system, the long range crystalline order is disturbed and phonon branches become non-degenerate as shown in Fig. 3.

The entropy of a system indicates how much it is disordered. The greater the value of entropy of a system, the more disordered the system. Fig. 4 illustrates that the entropy of disordered ZCNT increases linearly with increasing defect densities. The value of entropy increases about 50% per 1% defect density variation. The simulation temperature is taken as 300 K.

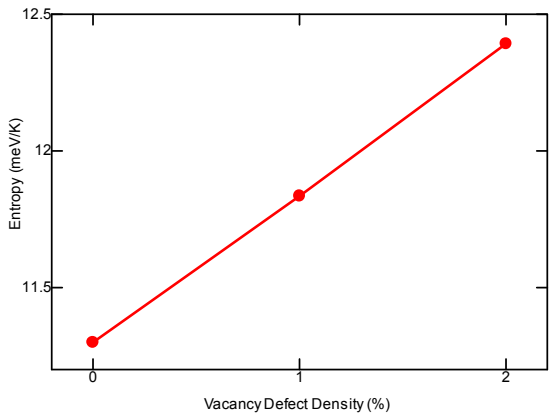


Figure 4. Entropy vs. vacancy defect density of (10,0) ZCNT. The value of entropy increases linearly with vacancies.

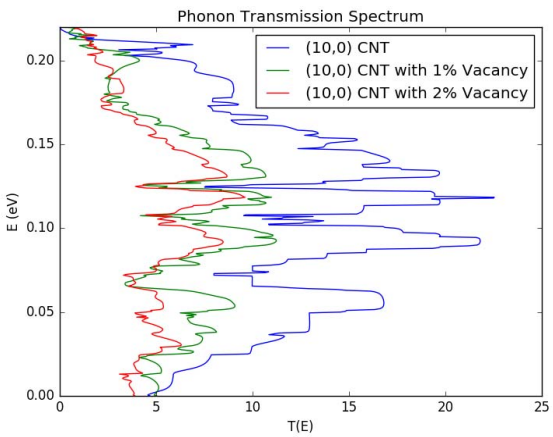


Figure 5. Phonon transmission spectrum of (10,0) ZCNT with different vacancy concentrations.

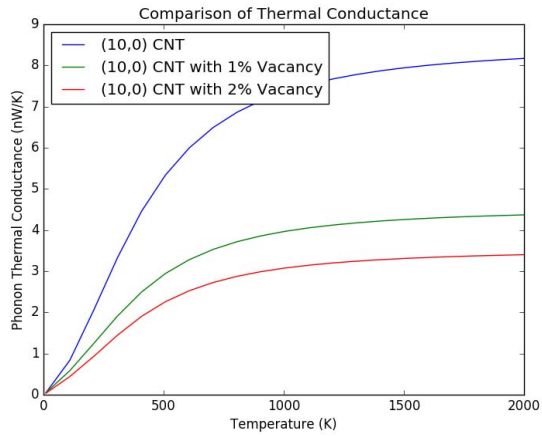


Figure 6. Thermal conductivity of (10,0) ZCNT with variation of vacancy concentrations with respect to temperature.

The influence of vacancies on phonon transmission spectrum of (10,0) semiconductor ZCNT is investigated. The main focus of this investigation is to inspect the effects of vacancy disorder on different parts of the phonon spectrum. From Fig. 5, it is shown that, phonons transport thermal energy throughout the entire phonon energy spectrum. With the introduction of atomic vacancies, the phonon transmission is significantly reduced. The decline of the phonon transmission is strong over the whole energy spectrum. In case of 1% defect densities, the phonon transmission becomes almost half as compared the ideal case. The simulation results demonstrate that vacancy defects suppress both low and high-energy phonon transmission noticeably. It is also noticed that the vacancy defects affect severely, particularly on the high-energy optic phonon transmission.

Fig. 6 shows changes of thermal conductivity with temperature and defect densities. The temperature is varied from 0K to 2000 K. It is found that with the increase of temperature up to 500 K, the thermal conductance of pristine (10,0) ZCNT rises linearly. Interestingly the disordered ZCNT shows almost the same linear characteristics up to 500K temperature. Above the 500 K temperature the thermal conductivity remains almost constant for both non-defective and defective ZCNTs. The atomic vibrations are responsible for thermal conductance in any system. Thus, these findings imply that after increasing certain value of temperature the atomic vibrations reach their saturation limit, even there are atomic vacancies. Moreover, the characteristics of thermal conductivity in vacancy defective ZCNTs are also analyzed. The analysis reveals that with 1% vacancy defects the thermal conductivity decreases about 50% from normal value. It is quite intriguing that for 2% vacancy defects the thermal conductivity reduces only 25% from the thermal conductivity of 1% vacancy defective ZCNT. Therefore, we can assume that, increasing atomic vacancy defects will not affect the thermal conductivity of (10,0) semiconductor ZCNT significantly.

Low-energy iLA phonons are the main contributor for thermal conduction through the ZCNT. The iLA phonon vibrational direction is visualized in Fig. 7 for both pristine and defective ZCNTs. For pristine ZCNT, it is observed that all the atoms are vibrating in the same direction uniformly. In vacancy defective ZCNT, all the atoms are vibrating with different amplitude and direction. There is no phonon localization effect, while phonon localization effect is detected in case of high-energy in-plane transverse optical (iTO) phonons [20]-[23]. In recent time, Sevik et al. [24] reports that, in vacancy defective ZCNT intermediate and high-frequency phonons are filtered out by defect scattering, while low-frequency phonons are transmitted quasi-ballistically. Our simulated results support the quasi-ballistic nature of low-frequency iLA phonon. The $sp^2$ C-C bonds are very strong, even stronger than the $sp^3$ C-C bonds in diamond. Thus, low-frequency iLA phonons can transmit thermal energy even in the defective ZCNT.

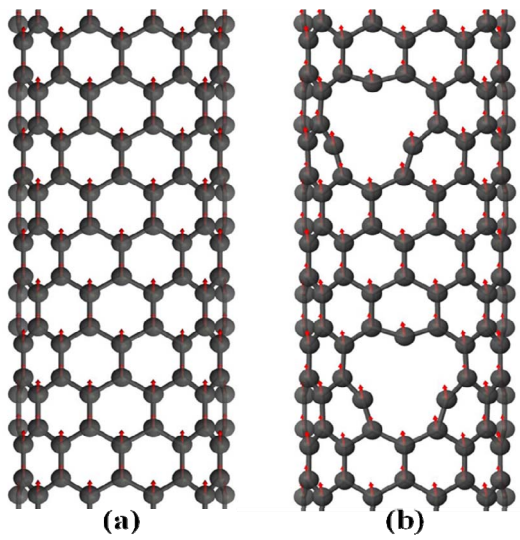


Figure 7. The atomic vibrational direction (red arrows) of iLA phonon mode for (a) pristine (b) vacancy defective (10,0) ZCNT.

## V. CONCLUSION

A systematic computer simulation is carried out to understand phonon properties of vacancy defective semiconductor (10,0) ZCNT. The phonon bandstructure for the entire Brillouin zone of ZCNT is extracted. In pristine ZCNT there are many degenerate phonon modes. Vacancies in the disordered ZCNT create non-degenerate phonon modes. The entropy of the vacancy disordered ZCNT shows linear increment with vacancy concentration. The entropy increases about 50% with 1% increase of vacancies. From the phonon transmission spectrum, it is noticed that phonon transport suppresses significantly over the whole energy range due to vacancy defects. Particularly high-energy optic phonon transmission reduces extensively. The thermal conductance of ZCNT rises linearly for certain value of temperature. Above that temperature no considerable changes of thermal conductance are observed. The thermal conductance decreases about 50% with only 1% vacancy defects. The most attention-grabbing finding is that the thermal conductance falls slowly with increasing vacancies because of the quasi-ballistic nature of low-frequency iLA phonons in vacancy defective ZCNT.

## REFERENCES


[1] S. Abdalla, F. Al-Marzouki, A. Ahmed, Al-Ghamdi, and A. Abdel-Daiem, ''Different technical applications of carbon nanotubes,'' *Nanoscale research letters*, vol. 10, no. 1, pp. 358, Sep. 2015.

[2] L.-M. Peng, Z. Zhang and S. Wang, "Carbon nanotube electronics: recent advances," *Materials Today*, vol. 17, no. 9, pp. 433-442, Nov. 2014.

[3] M. M. Shulaker, G. Hills, N. Patil, H. Wei, H.-Y. Chen, H.-S. P. Wong, and S. Mitra, "Carbon nanotube computer," *Nature*. vol. 501, no. 7468, pp. 526-530, Sep. 2013.

[4] C. Wang, K. Takei, T. Takahashi and A. Javey, "Carbon nanotube electronics-moving forward," *Chemical Society Reviews*, vol. 42, no. 7, pp. 2592-2609, 2013.

[5] M. F. L. De Volder, S. H. Tawfick, R. H. Baughman, and A. J. Hart, "Carbon nanotubes: present and future commercial applications," *Science*, vol. 339, no. 6119, pp. 535-539, Feb. 2013.

[6] S. Berber, Y.-K. Kwon and D. Tomanek, "Unusually high thermal conductivity of carbon nanotubes," *Physical Review Letters*, vol. 84, no. 20, pp. 4613, May 2000.

[7] L. X. Benedict, S. G. Louie and M. L. Cohen, "Heat capacity of carbon nanotubes," *Solid State Communications*, vol. 100, no. 3, pp. 177-180, Oct. 1996.

[8] K.-P. Bohnen, R. Heid, H. Liu and C. T. Chan, "Lattice dynamics and electron phonon interaction in (3, 3) carbon nanotubes," *Physical Review Letters*, vol. 93, no. 24, pp. 245501, Dec. 2004.

[9] Z. Tang, L. Zhang, N. Wang, X. X. Zhang, G. H. Wen, G. D. Li, J. N. Wang, C. T. Chan and P. Sheng, "Superconductivity in 4 angstrom single-walled carbon nanotubes," *Science*, vol. 292, no. 5526, pp. 2462-2465, Jun. 2001.

[10] J. Yu, R. Kalia and P. Vashishta, "Phonons in graphitic tubules," *EPL* (*Europhysics Letters*), vol. 32, no.1, pp. 43, Oct. 1995.

[11] D. Sanchez-Portal, E. Artacho, J. M. Soler, A. Rubio, and P. Ordejon, "Ab initio structural, elastic, and vibrational properties of carbon nanotubes," *Physical Review B*, vol. 59, no.19, pp. 12678, May 1999.

[12] O. Dubay and G. Kresse, "Accurate density functional calculations for the phonon dispersion relations of graphite layer and carbon nanotubes," *Physical Review B*. vol. 67, no. 3, pp. 035401, Jan. 2003.

[13] L.-H. Ye, B.-G. Liu, D.-S. Wang, and R. Han, "Ab initio phonon dispersions of single-wall carbon nanotubes," *Physical Review B*, vol. 69, no. 23, pp. 235409, Jun. 2004.

[14] R. Saito, T. Takeya, T. Kimura, G. Dresselhaus, and M. S. Dresselhaus, "Ramanintensity of single-wall carbon nanotubes," *Physical Review B*, vol. 57, no. 7, pp. 4145, Feb. 1998.

[15] J. Tersoff, "New empirical approach for the structure and energy of covalent systems," *Physical Review B*, vol. 37, no. 12, pp. 6991, Apr. 1988.

[16] J. Tersoff, "Empirical interatomic potential for carbon, with applications to amorphous carbon," *Physical Review Letters*, vol. 61, no. 25, pp. 2879, Dec. 1988.

[17] D. W. Brenner, "Empirical potential for hydrocarbons for use in simulating the chemical vapor deposition of diamond films," *Physical Review B*, vol. 42, no. 15, pp. 9458, Nov. 1990.

[18] D. W. Brenner, O. A. Shenderova, J. A. Harrison, S. J. Stuart, B. Ni and S. B. Sinnott, "A second-generation reactive empirical bond order (rebo) potential energy expression for hydrocarbons," *Journal of Physics: Condensed Matter*, vol. 14, no. 4, pp. 783, Jan. 2002.

[19] L. Lindsay and D. Broido, "Optimized Tersoff and Brenner empirical potential parameters for lattice dynamics and phonon thermal transport in carbon nanotubes and graphene," *Physical Review B*, vol. 81, no. 20, pp. 205441, May 2010.

[20] M. S. Islam, K. Ushida, S. Tanaka and A. Hashimoto, "Numerical experiments on phonon properties of isotope and vacancy-type disordered graphene," *Diamond and Related Materials*, vol. 40, pp. 115-122, Nov. 2013.

[21] M. S. Islam, K. Ushida, S. Tanaka, T. Makino and A. Hashimoto, "Effect of boron and nitrogen doping with native point defects on the vibrational properties of graphene," *Computational Materials Science*, vol. 94, pp. 35-43, Nov. 2014.

[22] M. S. Islam, K. Ushida, S. Tanaka and A. Hashimoto, "Numerical analysis on vacancy induced vibrational properties of graphene nanoribbons," *Computational Materials Science*, vol. 79, pp. 356-361, Nov. 2013.

[23] M. S. Islam, S. Tanaka and A. Hashimoto, "Effect of vacancy defects on phonon properties of hydrogen passivated graphene nanoribbons," *Carbon*, vol. 80, pp. 146-154, Dec. 2014.

[24] C. Sevik, H. Sevinçli, G. Cuniberti and T. Çağın, "Phonon engineering in carbon nanotubes by controlling defect concentration," *Nano Letters*, vol. 11, no. 11, pp. 4971-4977, Oct. 2011.

# Supplementary Frequency Control Mechanism to Ensure Reliability of Power System: Based on an International Comparison

Md Saleh Ebn Sharif[1,*], Mahmud-Ul-Tarik Chowdhury[2], Md. Moniruzzaman[1], Masud Reza[1]

[1]Department of Electrical & Electronic Engineering, Bangladesh University of Engineering and Technology, Bangladesh

[2]Department of Electrical and Computer Engineering, Northeastern University, Boston, MA

* saleh.electrical07@gmail.com

*Abstract*— **In this paper, as a part of comprehensive frequency control mechanism, the supplemental frequency control mechanisms to stabilize the power system during severe contingencies has been presented. From the regulatory, operational and technical perspective, a worldwide international practice among the different countries also has been discussed. In general, for resourceful countries, adequate operating reserve including spinning & non-spinning can restore system frequency within the shortest possible time frame. But, for a developing country with high energy demand and limited fuel resources, during severe contingencies an additional frequency control mechanism is also required to avoid cascading blackout. In this paper, based on international practice and considering developing countries electricity market a four layer supplemental frequency control mechanism is proposed. These four layer mechanisms – reserve, contingency-based load shedding, under frequency load shedding and islanding can be added on grid code with the alignment of policy.**

***Keywords— Frequency Control, System Operation, Contingency, System Stability, Cascading Blackouts, Protection Scheme.***

## I. INTRODUCTION

Sometimes, in power system an unbalance condition between generation and load happens and each part of the power system is confronted with serious problems. Loss of generation is one of the main causes of unbalancing between generation and load. In this condition, the prime movers of other units begin to slow down to compensate lack of generation. Moreover, tie lines take part in compensation by drawing power from other areas. However, this situation may lead to overloading the tie lines which causes protection functions to operate due to constraints of power swings and stability [2], [3]. Finally, if reliable frequency procedures are not used, the cascading events may lead to the blackout. Therefore, using a reliable procedure is required in order for alleviating any unbalance condition to avoid isolation. In this paper, alongside operating reserve for power system, additional frequency control framework is discussed based on worldwide international practice. To avoid total blackout following a grid disturbance, a number of defense mechanisms and system protection schemes mainly comprising of generation backing down, contingency based load shedding, under frequency load shedding, df/dt load shedding etc. already exist [4]. The success of these schemes in avoiding grid disturbances to a large extent depends upon the severity, area of disturbance and system conditions prior to the disturbance. Also as a last resort, some islanding schemes to save the generating stations are also in existence [5]. The aim of this report is to present and compare additional frequency control mechanism in different regions and propose a suitable frequency control mechanism during severe contingency. A case study of supplementary frequency control mechanism at severe contingency has also been assessed for Bangladesh Grid. DIgSILENT Power factory software is used for simulation of the power system.

In the following subsections, the additional frequency control mechanisms are introduced. In second section, a short description of frequency control mechanism is discussed. In the third section, a survey of these mechanisms utilized in India, New Zealand and USA (WSCC) with complete details is presented. The essential matters in frequency control guidelines are indicated in the fourth section and finally, a case study is shown in fifth section.

## II. ADDITIONAL FREQUENCY CONTROL MECHANISM PROGRAMS

### A. Load Shedding

For reliable operation of power system and in order to prevent collapse of network frequency, some actions should be taken. Under Frequency Load Shedding (UFLS) and Contingency Based Load Shedding (CBLS) are used to automatically shed predetermined load to balance the load to the available generation. These actions taken must be sufficient to conserve essential load and enable the remainder of the system to recover from the under frequency condition.

*1) Contingency Based Load Shedding (CBLS):* CBLS (named as fast load shedding in some documents) involves fast load shedding that is automatically and instantaneously activated in presence of recognized contingency events and trips load immediately without waiting for observing the frequency declines. Generally, contingency-based load shedding is designed for severe contingency events [6]. In other words, system's dynamic response to contingencies under a variety of operating conditions, such as generation configuration and load level and respective loads must be evaluated in advance in order to determine contingencies for which CBLS is necessary as well as the level of load shedding, if any [7].

*2) Under Frequency Load Shedding (UFLS):* More severe contingency events with less probability are taken into consideration for designing of response driven load shedding (UFLS) which is used as backup for fast load shedding. In fact, the goal in fast load shedding is to protect the grid, among other things, the triggering of UFLS [7], [8]. UFLS operation criterion may be based on the following variables [9]:

- Only frequency drop: this scheme is very common and also exists in traditional relays
- df/dt amount (named as 'RoCoF- Rate of change of frequency' in some documents): this scheme is not common to be used individually.
- Combination of frequency and df/dt: this scheme is the last approach for UFLS. That's because the settings for the df/dt relays are finite, while decay rate of frequency is not finite. Hence, the df/dt UFLS is a backup for frequency elements.

### B. Islanding

If in a very severe event, the UFLS scheme is not sufficient to return the frequency to appropriate range, system islanding is the last solution [7]. These events may occur because of one or combination of the following reasons:

- Unsound UFLS settings
- Wrong operation of UFLS relays
- Circuit breaker failure
- Severe (N-n) contingency for ( $n \geq 2$)

### C. Restoration

After a successful load shedding, the system frequency will be stabilized and enters into a safe margin of the nominal frequency. The recovery of system frequency to normal is likely to be quite slow and may extend over a period of several minutes. In this situation, the shed loads can be restored which can be accomplished automatically. If loads are manually reconnected, they shall be restored only by direct action or order of the power system dispatcher, as generating capacity becomes available and transmission ties are reconnected. It is necessary to restore a reasonable amount of load in each step, in order to prevent further frequency drop. The criterion is that the available generation must always exceed the amount of load being restored. A severe frequency drop could lead to undesirable load shedding repetition and shed/restoration oscillation. Load restoration program usually incorporates time delay.

## III. Worldwide Practice of Supplementary Frequency Control

From international practice, the approach of UFLS and islanding in three power grids with specific conditions will be addressed in this section. However frequency control mechanism schemes between power systems cannot be directly compared since different power systems have different reserve management schemes, load pattern, network configuration and operate by different frequency standards. Study of worldwide schemes will provide guidelines about methods and methodology. In this section, the general and valuable lessons from previous networks frequency control mechanisms will be described and the most important findings are presented. Because of different terminologies for frequency control schemes, following terms are used:

- CBLS: Contingency Based Load Shedding. This term in some documents is known as a type of SPS (Special Protection System).
- UFLS: Under Frequency Load Shedding. This term in some documents is known as AUFLS (Automatic UFLS).
- df/df: a type of UFLS decision logic which is based on the rate of change of system frequency. This term in some documents is known as RoCof (Rate of Change of Frequency).

### A. India

*1) UFLS:* In Indian power grid, 3 stages for UFLS in both frequency and df/dt based decision are recommended. The frequency settings of UFLS is the same for all sub-networks, while, load shed amounts are different [10],[21]. The first UFLS frequency setting is 48.8 Hz and shedding steps are distinguish with 0.2 Hz difference [10]. System operator should ensure that the UFLS schemes are always functional. Indian regulatory has great emphasis on frequently report of load shedding/restoration operation and performance monitoring. Also, they recommend keeping comparative records of expected load relief and actual load relief obtained in real time system operation. Interruptible loads should be arranged in four groups of loads [11]:

- For scheduled power cuts/load shedding;
- Loads for unscheduled load shedding;
- Loads to be shed through under frequency relays/ (df/dt) relays and;
- Loads to be shed under any SPS.

These loads shall be grouped in such a manner, that there is no overlapping between them.

*2) Islanding*: For islanding scheme, three main objectives are defined:

- Prevention from total black out by avoiding effect of cascade tripping in the power system;
- Fast restoration of supply to the affected areas;
- Supply to Important Loads/essential services should be maintained or can be restored on priority.

In India two layers of islanding scheme are defined. First, if frequency drops to 47.9 Hz, islands comprising of more than one generating stations are formed. Second, if frequency drops to 47.7 Hz, the mentioned islands could be further broken into smaller islands [12]. There would be need to review the scheme on seasonal basis. Peak and off peak operating conditions are minimum season. The load and generation of islands should match and also generators within the island are operated with governor system in active mode [12],[13]. Formation of islands should be initiated as a last resort, if other defense mechanisms fail to stop frequency decline to dangerously low levels [7]. For continuous monitoring of the generation (including regulating reserve of the generating units) and load at substations, an intelligent system through existing or stand-alone SCADA system is proposed. This system for real time decision for islanding and restoration is

beneficial. To assess stability and evaluation of proposed islands under different scenarios, dynamic network simulation studies and stability analysis would be required. The islanding scheme shall be reviewed periodically, at least once a year [13].

### B. New Zealand

The minimum frequency of grid is defined based on the generators limitations. The reserve is procured to ensure that the frequency remains higher than 48 Hz in contingent events (Contingent events are events that happen regularly). For larger events, UFLS scheme is considered [14]. It is obvious that for extended contingent (events that occur much less frequently), it is not cost efficient to procure sufficient reserves to cover such an event. The System Operator should ensure that there is sufficient reserve and AUFLS to prevent the system frequency from falling below minimum desired frequency (47 Hz and 45 Hz for the North and South Islands respectively) [15]. For very extreme contingencies (occasionally), New Zealand engages CBLS.

*1) CBLS*: A CBLS could be set up to trip a pre-determined load following a severe contingency (like HVDC tripping). Such CBLS would operate faster than UFLS, and trip load that is closer to the source of the disturbance. This may have the result of the frequency not dropping as low as under the existing frequency load shed scheme and would remove the need to shed load across the entire island. In fact, it is considered that a CBLS should complement UFLS; UFLS may still be required to:

- Cover other undefined events
- Assist in creating a successful electrical island following a system split
- Provide a backup to any existing CBLS

*2) UFLS:* The traditional UFLS relay of New Zealand consist of two steps, with 0.2 Hz frequency difference and the first step is set for 48 Hz. UFLS load shed amount is differ in north and south islands and relay time delay is considered 0.4 sec [15]. HVDC links as well as any wind generators are modeled as constant power in frequency studies. Hence, for any contingent events, there will be no frequency response from these. Also, tripping of HVDC link should accounted for frequency control mechanisms. It is obvious that the larger the load shed, the more the generation loss can be balanced by the UFLS. For designing the size of the UFLS blocks, consideration is given to the frequency overshoot [21],[24]. The df/dt function of UFLS does not eliminate the need for under frequency elements. This is because the settings for the UFLS relays are finite but the system frequency rate of decay is not [23]. If the system frequency decays at a slightly higher rate than the settings, the under frequency elements must be present to operate the UFLS to arrest the system frequency [16]. Re-evaluation of New Zealand UFLS reached a number of valuable conclusions. New UFLS scheme should:

- Sheds less percentage of total load at each step
- Has more steps
- Trips load at higher frequency

In new UFLS setting, use narrow frequency band (under 48.5Hz) and more load shedding steps. The time delay is still 0.4 sec [15]. Also it is proposed to use df/dt with combination of traditional frequency based relays. Finally after comparing the results of different studies, deployment of CBLS and UFLS (combination of frequency and df/dt based shedding) are proposed [25].

*3) Restoration:* The main constraint for load restoration depends mostly on the availability of transmission and generation capacity.

### C. Western Systems Coordinating Council (WSCC)

*1) UFLS:* The objective of the proposed scheme in WSCC is to arrest frequency from declining under 58Hz and recovering frequency to a level upper than 59.5Hz (and lower than the upper permissible frequency band). The minimum endurance frequency of system is 56.4Hz. Following assumptions are roots of WSCC guidelines [17]-[19], [24]:

- The UFLS should coordinate with the 5% loss of life of turbine blades recommendations as determined by generator manufacturers;
- The UFLS should provide coverage during a substantial loss of generation or resources (e.g. 25-33%);
- The minimum and maximum permissible dynamic frequency during a disturbance is 57.9 Hz. and 61.0 Hz respectively;
- UFLS scheme can utilize about 5-6 steps with minimum 0.1 Hz separation between steps;
- Maximum operating time of UFLS relays is considered 6 cycles. This time for distribution circuit breakers are 12 cycles;
- If there is any discretion allowed, the preferred option is to have the post-disturbance frequency settle out above 60 Hz, as opposed to below 60 Hz.

The first UFLS step in WSCC is defined 59.3Hz and load sensitivity to frequency is defined as low as 1.0 and as high as 2.0. This guide for frequency control recommends considering maximum generation outage and introduces procedures for load restoration after sufficient load shedding [18]. Also, the UFLS plan should be designed to meet losses of generation of 1%, 2%, 3%, 4%, 5%, 10%, 15%, 20%, 25%, and 30%. The UFLS should not trip generating station auxiliary power. WSCC also defined a load shedding group for correct under-frequency stalling with longer delay time (15 sec to 60 sec). Also it employs automatic load restoration to correct frequency overshoot when the frequency exceed 60.5Hz [19].

*2) Load Restoration*: Loads which have been shed by UFLS should be restored when system conditions have recovered to marginal safety without creating adverse effects. In other word, restoring depends on the availability of generation and transmission facilities. Restoration could be performed in one of the following methods [19]:

- Manual restoration
- Automatic restoration

If loads are restored manually or by supervisory control, they shall be restored only by direct order of the dispatcher (System Operator) to ensure generating capacity becomes available and transmission ties are reconnected**.** The delay time

for load restoration is about ten minutes. If loads are restored automatically, it should be accomplished through a comprehensive study to insure coordination with neighboring systems and avoid the possibility of recreating under-frequency, overloading ties, or burdening neighboring systems [20]. These relays should be set with relatively long time delays, except in those cases where automatic load restoration is designed to protect against frequency overshoot. Automatic load restoration shall begin later than thirty minutes after the frequency has been restored to levels above 59.95 Hz and lower than 2% of the system load every five minutes [19]. If the amounts of UFLS steps are large (e.g. 2% or 3% system total load), the frequency at the restoration node should be higher and the time between steps should be longer. The brief compression of frequency control mechanism of India, New Zealand and USA is shown in table 1.

TABLE I. BRIEF COMPARISSION OF SUPPLEMENTARY FREQUENCY CONTROL MECHANISM OF INDIA, NEW ZEALAND AND USA

| Country | CBLS | | UFLS | | Islanding | |
|---|---|---|---|---|---|---|
| India | Not in function | | ***Stages*** | 3 | ***Layers*** | 2 |
| | | | ***Frequency stage*** | 48.8 Hz | ***Frequency stage -1*** | 47.9Hz |
| | | | ***Step size (at least)*** | 0.2 Hz | ***Frequency stage -2*** | 47.7 Hz<br>Broken into smaller zone |
| | | | ***Active time*** | Always | | |
| New Zealand | ***Function*** | Fast | ***Stages*** | 2 | Not in Action | |
| | ***Trip location*** | Close to source | ***Step size*** | 0.2 Hz | | |
| | | | ***1st Stage*** | 48Hz | | |
| | ***Back up*** | UFLS | ***Time delay*** | 0.4 Sec | | |
| USA | Not in Action | | ***Stages*** | Up to 6 | Not in Action | |
| | | | ***Start timing*** | 58Hz | | |
| | | | ***Active until*** | 56.4 Hz | | |
| | | | ***Step size*** | 0.1 Hz | | |
| | | | ***Percentage of Generation meet up*** | Loss of 30% generation | | |

## IV. PROPOSED ADDITIONAL FREQUENCY CONTROL MECHANISM

The system operator provides sufficient instantaneous reserves to meet the risk in a least cost manner to prevent the system frequency from falling below minimum desired frequency following a contingent event. Extended contingent events are events that occur much less frequently, and due to this, it is not cost efficient to procure sufficient reserves to cover such an event. Also, in a severe event with fast frequency drop, governors could not adjust load generation balance in short time. So, the frequency will further drop in accordance with the system inertial response characteristic and dependency of load to frequency.

As well as instantaneous reserves, the system operator also relies on Under Frequency Load Shedding (UFLS) to cover the risk of an extended contingent event. The operator will ensure that there is sufficient reserve and UFLS to prevent the system frequency from falling below minimum desired frequency following an event. These tools should be procured to ensure that the frequency remains higher than desired minimum frequency in certain types of events known as contingent events. For very severe and rare contingency, a very fast action is requiring to shed loads for predetermined contingencies. This scheme is Contingency Based Load Shedding (CBLS). Also, it recommends that some methods and procedures for load restoration after sufficient load shedding are defined. If the UFLS could not bring the frequency into desired range, the network should be separated into independent islands. So, the frequency control mechanisms are depicting four layers:

- Reserve management
- CBLS
- UFLS
- Islanding

The first layer (reserve) is beyond of this study. In our work [1], a detailed reserve management scheme and methodology to determine operating reserve are discussed in details. Inside operating reserve the frequency control mechanism is shown in figure 1.

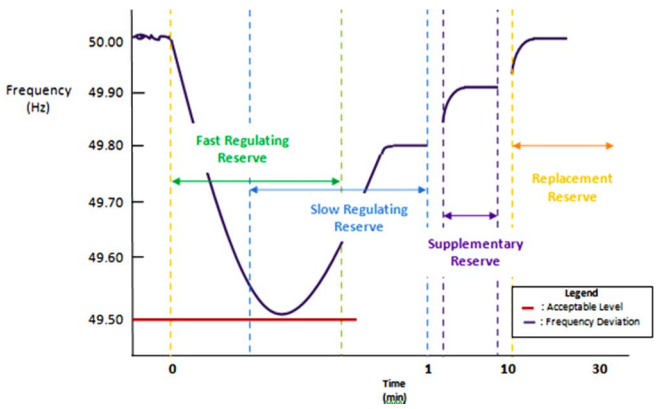


Figure 1. Contribution of operating reserve at different frequency level.

The relation between frequency control mechanisms is shown in figure 2. The terminologies of the used terms are described in the following:

- Extreme Contingency: a contingency leading to drastic frequency drop
- CBLS: Contingency Based Load Shedding
- UFLS: Under Frequency Load Shedding
- Secure Condition: stable frequency in desired range

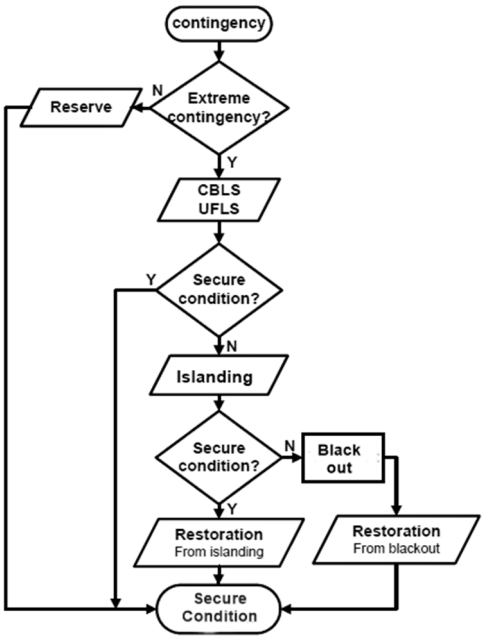


Figure 2. Schematic of frequency control mechanisms position.

Before starting frequency studies, determination of minimum and maximum acceptable value of frequency is the first step. These values are more dependent on allowable off-nominal operating frequency range of generating units. Hence, for example if there is a nuclear power plant in the network, this unit will limit the bound range of allowed frequency deviations. Determination of desired range for final frequency decline is next step.

At the third step, interruptible loads should be predetermined in the following groups, so that there is no overlap between them:

- CBLS load shedding: for severe pre-defined events;
- UFLS load shedding: as a backup for whole events.

The interruptible loads should be distributed in all zones of the transmission network. It is important to notice that the optimize frequency control mechanisms needs integrated data base, system study and engineering knowledge. To conduct in depth frequency control study, a centralized dataset is an essential perquisite. The model used in simulation studies needs data related to the network static and dynamic variables and parameters. The most important items for such studies are: generator controllers (governors, AVRs etc.), and load dynamic characteristics (Especially load sensitivity to frequency: the percent load that change due to one percent change in frequency). For real time frequency monitoring and frequency control, a proper tool for online measuring of system frequency is required.

The cases estimated should adequately represent the worst case for connected system inertia, regulating reserve and reserves requirement. HVDC link and wind generators should be modeled as constant power. For any contingent events, there will be no frequency response from governor system of generating units in frequency control mode. However, loss of HVDC link should be considered as a credible contingency in frequency response studies.

### *A. CBLS*

- CBLS is predetermined for large contingencies which lead to desired minimum frequency (the minimum frequency of grid defined by generators which usually is 47 Hz);
- CBLS should be faster than UFLS and trip loads that are closer to the source of the disturbance. In fact, it is considered as a complementary Special Protection System (SPS) to UFLS;
- The CBLS should be activated immediately after the onset of determinate events;
- Result of CBLS should lead to secure frequency and not dropping as low as under the trigger point of the UFLS scheme;
- The power system operator should ensure that the CBLS schemes are functional;
- The CBLS scheme should be updated frequently.

### *B. UFLS*

In addition to CBLS, UFLS still will be required to:

- Cover other undefined events;
- Assist in creating a successful electrical island following a system split;
- Provide a backup to any existing CBLS;
- UFLS is for probable events such as (N-1) contingencies and regular events;
- UFLS scheme should account for the off-nominal frequency at which damages to turbine blades are kept to minimum, as recommended by the manufacturer;
- Sufficient load should be dropped by UFLS scheme to restore the system frequency to continuous operating range of the generating units;
- UFLS delay time should be chosen such that to ensure it is triggered only for cases where the system frequency would not return back to safe boundary (e.g. $T_d$=0.4sec). The system frequency may return from dropping because of network inherent characteristic;
- UFLS schemes are usually designed with 5-6 stages of interruptible loads;
- The minimum separation frequency between steps should be determined based on the network configuration, generating units and load characteristics (e.g. 0.3 Hz). The frequency setting could become narrow following some experiences and confident UFLS settings (e.g. reach to 0.1 Hz);
- The total amount of shed load and step sizes should be set depending on the static and dynamic characteristics of the network;
- The UFLS operation should not cause over frequency, which means over-shedding;
- Generating station auxiliary power should not be shed in UFLS**;**
- UFLS design and operation criterion could be based on one of the following classifications (i) only frequency drop (traditional relays), (ii) df/dt amount

(not common to be used on its own); and (iii) Combination of frequency and df/dt (new approach).

- The frequency rate function (df/dt) of UFLS does not eliminate the need for under frequency elements;
- If there is any discretion allowed, the preferred option is to have the post-disturbance frequency settle out above nominal frequency (and below permissible upper frequency band), as opposed to below nominal frequency;
- Also it is possible to define additional UFLS relays to correct under frequency stalling. In this case, the operation time of relays is much bigger than traditional UFLS (several tens of seconds);
- The power system operator should ensure that the UFLS schemes are always functional and shall furnish frequently report of UFLS operation;

### C. Islanding

- If all of the above remedial actions are not enough to emend power system frequency, it becomes inevitable to separate the network into islands;
- Proposed islands shall achieve the following objectives- (i) prevention of total black out and cascade tripping, (ii) supplying Important Loads and essential services in created islands, and (iii) Restoring shed loads after safe conditions are reached.
- Load and generation of desired islands should match together;
- Also it is recommended that there is adequate reserve in each island and the generators within the islands are operated with governor systems in active mode;
- Load-generation balancing in any specific islands may change based on the season. Therefore revision of the islanding scheme on seasonal basis is necessary;
- To assess stability and validation of each island configuration/boundary under different scenarios, simulation studies must be performed;
- The power system operator should ensure that the islanding schemes are functional;
- Islanding schemes should be updated frequently after major changes in system configuration.

### D. Restoration

- Attempts to restore interrupted load shall not be done until enough transmission and generation capacities are made available;
- The load restoration may not lead to violation from desired range of frequency, voltage and line loading. In other words, restoration may not lead to frequency drop, voltage drop or line over loading;
- Load restoration can be performed manually (by dispatcher order) or automatically (by load restoration relays);
- Relays installed to restore load automatically should be set with varying and relatively long time delays, except in those cases where automatic load restoration is designed to protect against frequency overshoot;
- The amount of load restored (per step) should be small enough in order to prevent wide frequency fluctuations and the possibility of load shedding/restoration oscillation;
- Restoring of Important Loads and essential services have higher priority, if they are shed inevitably;

## V. Case Study

In this section, a case study of supplementary frequency control mechanism at severe contingency has been assessed for Bangladesh Grid. Islanding and Under-Frequency Load Shedding (UFLS), alongside reserves, are used to help the power system recovery from severe contingency events, and to protect against other rare events such as cascading outages. Severe contingency events could readily lead to total outage of the Bangladesh power grid such as tripping of HVDC links. Therefore, some remedial actions are required to allow the Bangladesh power grid survive severe contingency events. Based on the studies performed and reported in this report, a solution is recommended to maintain the integrity of the Bangladesh power grid under some disturbances. The first part of the solution involves "Contingency-Based Load Shedding (CBLS)" or "fast load shedding" which automatically and instantaneously drops load as soon as certain contingencies are detected in the network. The second part of the solution involves the UFLS, or response-driven load shedding, scheme as a backup to contingency-based load shedding and last resort is islanding. CBLS involves fast load shedding that is automatically and instantaneously activated in presence of recognized contingency events and trips load immediately without waiting for observing the frequency declines. In small power system with large contingencies such as Bangladesh power grid, contingency-based load shedding is necessary and sometimes, inevitable in order to maintain power system operational security. In Bangladesh power grid, loss of HVDC links (500 MW and 1000 MW) are considered as credible contingency events, in which cases the specified reserves cannot satisfy the frequency requirements. The detail of operating reserve determination methodology to control frequency is described in our previous works [1], [26]. According to the conducted studies, increase in the regulating reserve and decrease of the imports can handle the loss of 500 MW HVDC link [1]. However, they are not economical. Therefore, designing some CBLS plane for loss of HVDC links (500 MW and 1000 MW) is necessary in the Bangladesh power grid. Based on the performed studies, the required CBLS plan for Bangladesh power grid are summarized in table II:

TABLE II. Credible contingency and Load levels

| Credible Contingency | Load Level |
|---|---|
| Loss of import from NEI (1000 MW) | All load levels |
| Loss of import from Bheramara (500 MW) | All load levels |
| Loss of import from Tripura (300 MW) | Load level<8500 MW |
| Loss of Haripur GT unit (273 MW) | Load level<8500 MW |

Figure 3 and Figure 4, show the impact of loss of Bheramara import of 500 MW on power system frequency with and without CBLS plane in the light load level. It can be seen that although there are sufficient reserves in the light load level, the frequency requirements are not satisfied due to low regulating reserve of the units.

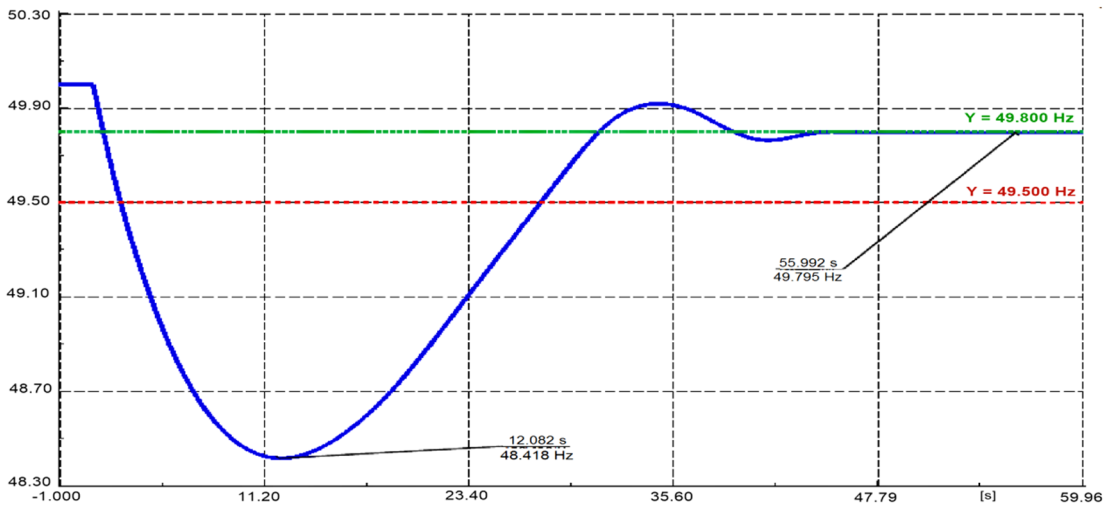


Figure 3. System frequency with loss of 500 MW in grid at 440 MW of regulating reserve without CBLS plane

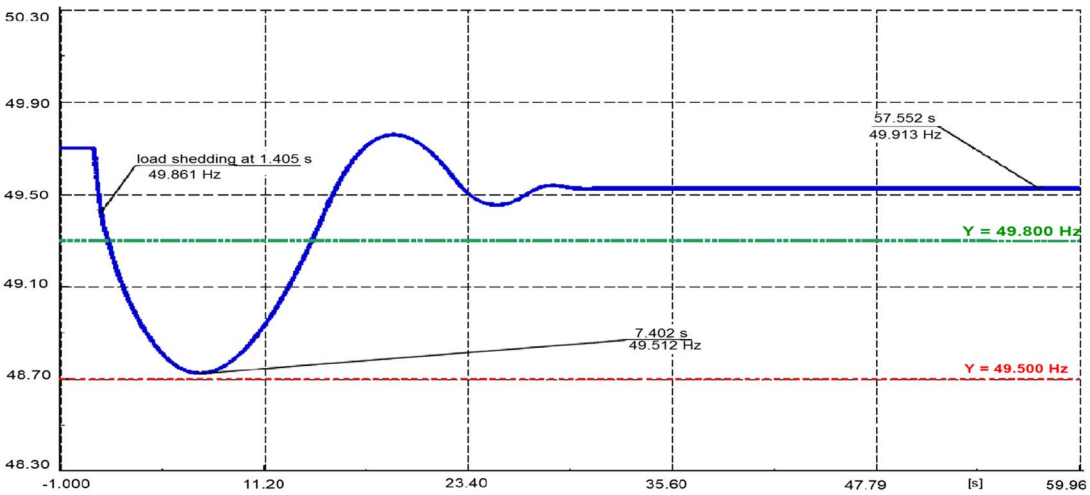


Figure 4. System frequency with loss of 500 MW in grid at 440 MW of regulating reserve with CBLS plane

It is seen from the above two figures that, system frequency is controlled and sustained in CBLS scheme. According to proposed guideline described in our previous work, in case of the largest credible loss, the frequency should be restored to 49.80 Hz within one minute and to 49.90 Hz within 10 minutes [1]. The amount of regulating reserve for the loss of 500 MW cannot pull up the frequency to 49.80 Hz within one minute. But on the other hand, at same scenario, CBLS scheme with same regulating reserve is capable of control the level of frequency during contingency of 500 MW.

In under frequency load shedding study, the percentage of load shedding based on substation load is necessary for simulation studied. The substation load varies in different times. So, we assumed that the received values are based on maximum loading of each substation. The UFLS operation can control the frequency in a safe band. This band is aver the first UFLS stage (48.9Hz) and under 50.5 Hz. Also, the UFLS should shed a specific percentage of system load. This amount is not a fixed value in all operation conditions. The performances of under frequency load shedding (UFLS) relays are examined. It assumed that all of UFLS relays operate correctly. After that the performance of these relays are simulated for a large disturbance caused by the outage of HVDC connection with India. The result of power system frequency response without any UFLS relay action (as a sample) is shown in figure 5. As the figure 5 shows, without UFLS action, the frequency will drop to 47.65 Hz (after 50 sec). The result of frequency variation with under frequency load shedding relay is shown in figure 6. As the figure 6 shows, with UFLS action, the frequency will drop to 48.91Hz (after 50 sec) and improve the system frequency by 1.14Hz. The first stage setting is for 48.9Hz and second stage is 48.85HZ. As the results show, the final frequency is 48.91Hz. If the UFLS relays operate expected and designed, 258 MW should be shed, but actually only 239 MW is shed. This is because in load shedding, a feeder will disconnect and the related MW is not equal to prospected shed. Now if the amounts of load shedding are identically equal to prospected values, the final frequency becomes 49.05 HZ. Now, if the abovementioned procedures be done for different load and generation outage following results will be outcome. This should mention that the outage of 2000MW is only for screening the performance of UFLS and is not a real contingency. The UFLS operation at different

contingency, frequency stage and load shed are summarized in table III.

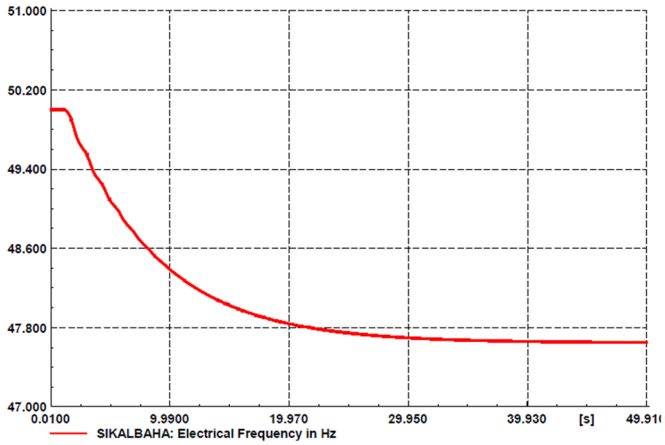


Figure 5. Frequency variation without UFLS action

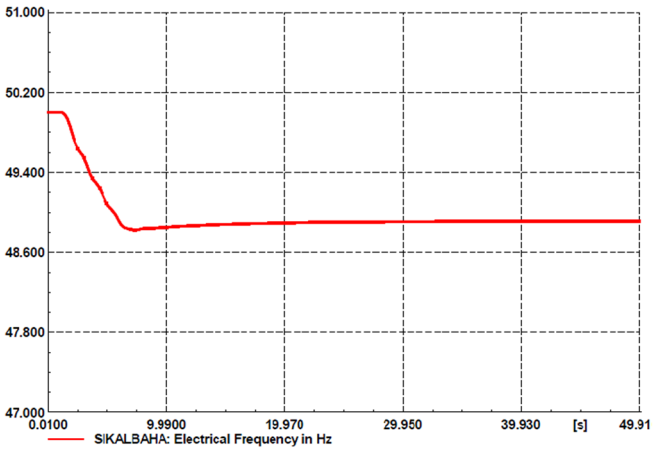


Figure 6. Frequency variation with UFLS action

TABLE III. UFLS OPERATES RELAYS FOR DIFFERENT LOAD AND GENERATION OUTAGE

| Scenario | Contingency [MW] | Shed stage [Hz] | Shed [MW] | Final [Hz] |
|---|---|---|---|---|
| peak | 100 | - | 0 | 49.566 |
| peak | 419 (HVDC) | 48.85 (step 2) | 239.4 | 48.91 |
| peak | 2029 | 48.5 (all steps) | 759.8 | 48.382 |
| light | 100 | - | 0 | 49.383 |
| light | 264 (HVDC) | 48.8 (step 3) | 211.1 | 48.653 |
| light | 2068 | 48.5 (all steps) | 748.15 | - |

The results show that:

- In 100 MW outage, both in peak and light load, the final frequency is above UFLS operation and the performance assess correct.
- Also, in the peak load and HVDC outage the performance of UFLS is proper.
- Now, if 2000 MW outage issued in peak load condition, all the UFLS stages will be operate and frequency reach to 48.38 Hz. This frequency is below the first shedding target. So, this performance is not correct. It needs CBLS.
- If HVDC with 264 MW outage issued in light load condition, the final frequency is 48.65 and again below the first shedding target.
- Now, if 2000 MW outage issued in light load condition, all the UFLS stages will be operate and unable to stabilize frequency response. In this condition, the frequency is drop drastic and network generations become unstable.

Finally based on results, following points can be stated:

- The amount of load shedding in some cases is not sufficient and final frequency is not in the assumed bound. Hence there is a need of islanding scheme.
- In some cases, the UFLS operation is not accurate and cannot prevent system instability. So it needs CBLS.
- The amount of load shedding MW, should not fixed value in all operation condition and different load.
- The UFLS stages should optimize in order to correct operation.

## VI. CONCLUSION

The proposed supplemental frequency control mechanisms are four layers- Reserve, CBLS, UFLS and Islanding. In operating reserve, spinning & non spinning reserve contribute to restore frequency. For very severe and rare contingencies, a very fast action is required to shed loads for predetermined events. CBLS scheme should be faster than UFLS and activated immediately after the onset of determinate events. UFLS scheme covers the risk of frequency drop in all events. UFLS is usually designed with 5-6 stages with an appropriate time delay and frequency setting. The amount of load shed in each step and the total load shed should be determined carefully. Also, these loads should be dispatched in different zones of the network. The UFLS design could be based on combination of frequency and df/dt (the rate of change of frequency). The operator should ensure that there is sufficient reserve, CBLS and UFLS load shed to prevent the system frequency from falling below minimum desired frequency following any event. If these three mechanisms could not bring the frequency into desired range for any reason, the network should be separated into independent islands. Each island should create load-generation balance and has adequate reserve and frequency regulation provided by generating unit's governors. After returning of the system frequency to secure condition, restoration schemes are needed to restore shed loads without any violation from desired range of frequency, voltage and line loading. So, this restoration should be done in small steps and long time period. Finally, the system operator should ensure that all of the above schemes are functional and updated. For further study and validation, comprehensive record of frequency control mechanisms should be kept.

## VII. FUTURE WORKS

Although decreasing the magnitude of frequency fluctuation can inherently reduce the maintenance and operating costs of power plant, regarding international experiences, power plant's owner prefers not to participate in frequency control program while there is no payment for covering the missed opportunities of selling generated power.

In addition, being on dispatch bar with head rooms can lead to increase the marginal cost of generating units. So, it is extremely recommended to anticipate a proper motivation method for activating governors as well as testing and monitoring their responses to different type of events when they play the vital role for alleviating the transient frequency deviations with automatically increasing/decreasing their generation. In our future works, a study on an incentive mechanism for participating in frequency control program (both of steady and transient segments) will be conducted.

## REFERENCES


[1] Md Saleh Ebn Sharif, Mahmud-Ul-Tarik Chowdhury, Md. Moniruzzaman, Abdullah- Al- Mohit, "An Efficient Method for Power System Frequency Control and Optimal Reserve Determination Considering Probabilistic Loss-of-Load Expectation Risk Index," *3rd International Conference on Electrical Information and Communication Technology (EICT)*, December, 2017.

[2] Jan Machowski, Janusz W. Bialek, James R. Bumby, *Power System Dynamics and Stability*, John Wiley & Sons, 1997.

[3] Allan, R. N, *Reliability evaluation of power systems*, Springer Science & Business Media, 2013

[4] S. Mukhopadhyay, S. K. Soonee, S. R. Narasimhan and R. K. Porwal, "An Indian experience of defense against blackouts and restoration mechanism followed," *2008 IEEE PES General Mee*ting, Pittsburgh, PA, 2008, pp. 1-7.

[5] H. M. Dola and B. H. Chowdhury, "Intentional islanding and adaptive load shedding to avoid cascading outages," *2006 IEEE Power Engineering Society General Meeting,* Montreal, Que., 2006, pp. 8

[6] F. Shokooh et al., "Intelligent Load Shedding," in *IEEE Industry Applications Magazine*, vol. 17, no. 2, pp. 44-53, March-April 2011.

[7] B. Cho, M. Almulla, H. Kim, and N. Seeley, "The Application of a Redundant Load-Shedding System for Islanded Power Plants," proceedings of *the 35th Annual Western Protective Relay Conference*, Spokane, WA,October 2008.

[8] A. Atputharajah and T. K. Saha, "Power system blackouts - literature review," *2009 International Conference on Industrial and Information Systems (ICIIS)*, Sri Lanka, 2009, pp. 460-465.

[9] M. Karimi, H. Mohamad, H. Mokhlis, A.H.A. Bakar, "Under-Frequency Load Shedding scheme for islanded distribution network connected with mini hydro", *International Journal of Electrical Power & Energy Systems*, Volume 42, Issue 1, 2012, Pages 127-138.

[10] *NRPC standard for UFLS: Under frequency load shedding scheme in Northern Region (NR) January, 2010, New Delhi.*

[11] *CERC Indian gridcode: Central Electricity Regulatory Commission, Indian Electricity Grid Code Regulations, 2010.*

[12] *UPPTCL standard for Islanding scheme in India: Islanding scheme uttar pradesh, February, 2013.*

[13] *The Indian Electricity Grid Code. Technical Report L-1/18/2010-CERC; Central Electricity Regulatory Commission: New Delhi, India, 2010.*

[14] K. U. Z. Mollah, M. Bahadornejad and N. K. C. Nair, "Automatic under-frequency load shedding in New Zealand power system — A systematic review," *AUPEC 2011*, Brisbane, QLD, 2011, pp. 1-7.

[15] *Transpower standard for Transmission Code: Transmission Code of Practice, TP.DG 25.01 Issue 4 Jan 2013.*

[16] *WECC standard of Load sheeding plan: Off-Nominal Frequency Load Shedding Plan. May 2011.*

[17] WECC Underfrequency Load Shedding Review Group, "Underfrequency Load Shedding Assessment Report Western Interconnection", December 2013.

[18] Underfrequency Issues Work Group WSCC Technical Studies Subcommittee, "WECC Coordinated Off-Nominal Frequency Load Shedding and Restoration Requirements ( Technical report)", 2003.

[19] Underfrequency Load Shedding Review Group, "Underfrequency Load Shedding Program Assessment Report", 155 North 400 West, Suite 200 Salt Lake City, Utah, 2015.

[20] M. M. Adibi, Nelson Martins, "Impact of Power System Blackouts," *2015 IEEE Power & Energy Society General Meeting,* Denver CO, July 2015.

[21] M. Lu, W. A. W. ZainalAbidin, T. Masri and D. H. A. Lee, S. Chen, "Under-Frequency Load Shedding (UFLS) Schemes – A Survey," *International Journal of Applied Engineering Research,* Volume 11, Number 1 (2016) pp 456-472.

[22] A. Sauhats, V. Chuvychin, V. Strelkovs, R. Petrichenko, and E. Antonov, "Underfrequency Load Shedding in Large Interconnection", *IEEE Grenoble Power Tech (POWERTECH)*, 2013.

[23] Scott Manson, Greg Zweigle, Vinod Yedidi, "Case Study: An Adaptive Underfrequency Load-Shedding System," *60th Annual Petroleum and Chemical Industry Technical Conference*, Chicago, Illinois, September 23–25, 2013.

[24] *NRPC standard for UFLS: Standard PRC-006-2 — Automatic Underfrequency Load Shedding, November 10, 2017,USA.*

[25] Electricity Authority, "*Electricity in New Zealand,"* EA, 2016.

[26] Md Saleh Ebn Sharif, Mahmud-Ul-Tarik Chowdhury, Md Janatul Ferdous, Md Moniruzzaman, Md Monower Zahid Khan, "An Overview of Frequency Control as a Criterion of Power System Reliability and International Survey of Determining Operating Reserve," *American Journal of Modern Energy*. Vol. 3, No. 5, 2017, pp. 101-114.

# A Probabilistic LOLE based Method to Determine Optimal Reserve and Control Power System Frequency

Md Saleh Ebn Sharif[1,*], Mahmud-Ul-Tarik Chowdhury[2], Md. Moniruzzaman[1], Abdullah- Al- Mohit[3]

[1]Department of Electrical & Electronic Engineering, Bangladesh University of Engineering and Technology, Bangladesh
[2]Department of Electrical and Computer Engineering, Northeastern University, Boston, MA
[3]Department of Electrical & Electronic Engineering, Ahsanullah University of Science and Technology, Bangladesh
[*]saleh.electrical07@gmail.com

***Abstract*— This paper presents methodology that can be adopted in evaluation of power system reliability and optimization of resources for future power system planning. As a part of reliability evaluation, it is important to determine the adequate operating reserve to maintain power system frequency in an acceptable range. In order to determine sufficient operating reserve, the North American Electric Reliability Corporation standard of one day outage in ten years has been used for this study. So, Loss of Load Expectation (LOLE) of 0.1 day per year has been set as standard. The total operating reserve of power grid against LOLE of 0.1 day/year is calculated using probabilistic Chronological Monte Carlo method. The stochastic optimization algorithm has been applied to determine the least cost economic dispatch and unit commitment. The resulted unit commitment was checked and corrected in an iterative process by dynamic simulation in PowerFactory to analyze voltage level and line loading under normal and N-1 contingency conditions to evaluate potential reliability problems. After simulation in difference loading scenarios it showed the determined operating reserve is adequate to control the system frequency in acceptable level as well as reliability of system was ensured.**

***Keywords—Reliability analysis, Unit commitment, Operating margin, Frequency control, Transmission planning, Probabilistic method.***

## I. Introduction

In power system, it is required to keep balance between the electrical load on the system and the available power generation to maintain system frequency in an acceptable range. Within very short time frame, power system reliability is almost entirely maintained by natural inertia, generators governor system and the power system's automatic generation control (AGC) [1]. In the intermediate to longer time frames, economic dispatch mechanisms and operational planning become the key factors in maintaining power system reliability. In order to keep a balance between generation and consumption at all times, the load is forecasted and sufficient generation is committed and dispatched to maintain supply/demand balance [4]. However, since the demand forecast is never hundred percent accurate and since unpredictable contingencies (forced outages) like generator and transmission line trips may occur in power systems, the generation and consumption will experience mismatch on regular basis. This unbalance can cause instability of system frequency and reliability of power system [5]. Consequently, the system operator needs committed generation units to maintain system frequency and guarantee security and stability (reliability) of power system operation. These resources, commonly referred to as reserves should be available at the right time in order to keep power system frequency in an acceptable range [2], [3]. So, in order to control frequency or, in other words, to maintain balance between generation and demand, adequate amount of generation reserve is required. Generally, reserve consists of upward and downward reserves that both of them are required for maintenance of stability and frequency [6]. In the following subsections, the operating reserve determination and frequency control mechanisms are illustrated. In second section, a short description of reliability indices is discussed. In the third section, methodology to determine operating reserve is presented. In fourth and fifth section proposed guidelines and a case study is examined respectively.

## II. Reliability Indices

The indices used to measure generation reliability are probabilistic estimates of the ability of a particular power system configuration, mainly in the form of available generation, to supply the demand [3]. The deterministic method is simple but probabilistic methods for the determination of operating reserve levels can provide more meaningful information to be used in planning and allocation of system resources [7]. There are a number of reliability indices which evaluate generation system reliability, for example, Loss of Load Probability (LOLP), Loss of Load Expectation (LOLE), Loss of Energy Probability (LOEP), Loss of Energy Expectation (LOEE) etc. The LOLE risk index is the most widely accepted a used probabilistic method in system reliability evaluation for generating systems [8]. LOLE is the expected number of days or hours in a specified period in which the load exceeds the available generating capacity [9],[10]. The LOLE evaluation method is expressed in the following mathematical formula [10]:

$$LOLE = \sum_{i=1}^{n} ti\ Pi\ \left(\frac{d}{y}\right)(Lmax > C)$$

Pi = the probability of this $i^{th}$ outage and ti = the time duration of that outage. LOLE of one day in 10 years, or 0.1

days/year, is commonly used across different systems including the power systems affiliated to the North American Electric Reliability Corporation (NERC) [11], [12], [17].

## III. Methodology of Operating Reserve Determination

The Operating Margin (OM) of power system is the combination of Operating Reserve (OR) and Contingency Reserve. Operating Reserve is the additional generating capacity available from synchronized generators and/or interruptible demand. The spinning reserve is the extra generating capacity that is available by increasing the power output of generators that are already connected to the power system [13],[18]. Spinning reserve consists of Regulating Reserve (RR) and the capacity that could be available within 10 minutes, from generators synchronized to the bars (That is called in this report as Supplementary Reserve (SR)). Supplemental reserves are used for longer timescale events; note that the timescales may vary by system [6], [19]. Contingency Reserve is the reserve power provided by generators that require a longer start-up time (typically 30 to 60 minutes) to relieve the generators providing the spinning or non-spinning reserve and thus restore the operating reserve. Non-spinning reserve is generating capacity which is capable of being brought online within 10 minutes if it is offline. Different types of reserve are shown in figure 1.

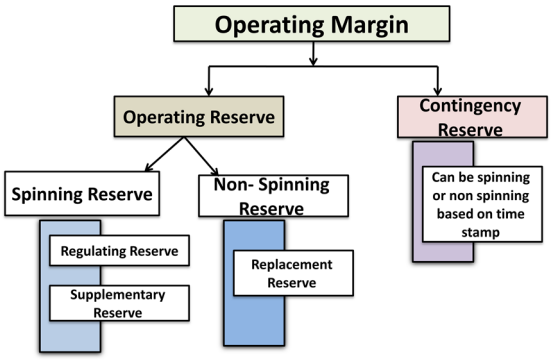


Figure 1. Operating Margin: and different types of reserve

The total Operating Reserve (OR) level, consisting of both spinning and non-spinning reserves, was determined in such a way that the system reliability indicator (LOLE) that would comply NERC's standard of LOLE of one day outage in ten years or 0.1 days/year [13],[14]. The amount of operating reserve was determined by the chronological Monte Carlo simulation of future power system plan using the PLEXOS software. The simulation runs were used to estimate the reliability indices of this power system by simulating the actual random behavior of that system. It should be mentioned that system operator can consider the lesser amount than LOLE of 0.1 days/year for determination of operating reserve. Some assumptions are required for reliability analysis. Firstly, all generation station and loads are assumed to be connected in one bus bar. Secondly, there is no transmission network in this system. PLEXOS PASA module requires information of forced outage rate (FOR), maintenance plan, load data, heat rate, energy demand, generation availability, fuel constraints, tariff, startup cost, boiler efficiency, unit commitment, must run units, transmission data etc to compute reliability statistics (LOLE, LOLP, EENS etc), capacity reserve margin, system adequacy, maintenance plan (up to 10 years) etc .

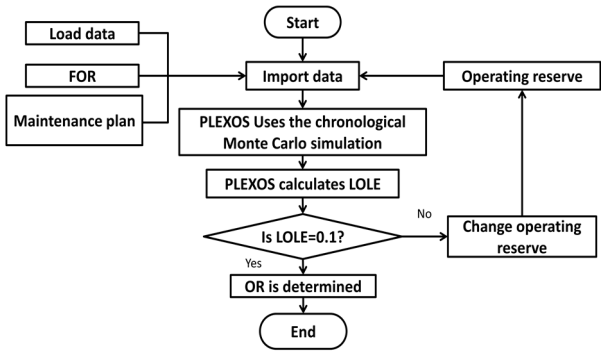


Figure 2. The methodology of OR margin determination.

PLEXOS calculated adequate amount of operating reserve when LOLE is near 0.1 day/year. If LOLE was not equal to 0.1 day/year, the whole procedure is repeated until LOLE of 0.1 day/year found. The amount of operating reserve was also tuned; hence the whole process is iterative process. The Figure.2 shows the systematic steps followed in the evaluation of the reliability level (LOLE) in order to determine the appropriate operating reserve margin in this step. The LOLE target is set in this study according to NERC standard (i.e. 0.1 day in year).

### A. *Determination of Spinning and Non-spinning Reserve:*

Operating reserve capacity comprises of spinning and non-spinning reserve capacities. Firstly, it is required to determine the operating reserve capacity. Then, spinning and non-spinning reserve capacity is determined. For this particular case study, two load levels have been considered. For different load levels, the spinning reserve and non-spinning reserve portions of the OR were determined after determination of Regulating Reserve and Supplementary Reserve.

*1) Determination of Regulating Reserve:* PLEXOS software is used for determination of Regulating Reserve. The Unit commitment (UC) to minimize total system cost was determined for every load level by this software. Then obtained results were collected to use in dynamic simulation studies in DIgSILENT. The collected information included unit commitment/ dispatch and reserve level for each generating unit. Then, violation of voltage level and line loading was checked under normal and N-1 contingency conditions by DIgSILENT. The results from DIgSILENT revealed potential reliability issues if existed and based on dynamic studies some corrective measures were taken for unit commitment/ dispatch algorithm. For example, in order to consider economic viability, least cost operation, fuel price constraints and eliminate voltage violation and line loading problems some generation units are needed to operate as 'must-run' units. In other word, generating units which should be on-line based on the studied load condition in order to improve system stabilities from static point of views are called as must-run units in this study. It should mention that the Imports from cross border are considered as Must-Run units in all studies not regarding the technical issues. After required

corrective measures, the updated information imported to PLEXOS for correct unit commitment/ dispatch. Then updated dispatch information from PLEXOS is extracted and the applied again in DIgSILENT to complete dynamic study. At the final stage, various types of contingency analysis applied to power system to find out frequency variations. The frequency variations are monitored and compared with allowed limits according to standard. In an iterative process, at the worst contingency condition the final amount of regulating reserve capacity was found out to maintain the frequency at an acceptable limit. Based on the standard and grid code, the acceptable range of frequency is 50±0.05 Hz and System frequency should return to 49.8 Hz within one minute. More detailed of the proposed guideline is described on Section IV.

*2) Determination of Supplementary Reserve:* Supplementary Reserve Capacity (SR) is frequency dependent reserve. Supplemental Reserve is that amount of operating capacity, some or all of which may not be connected to the interconnected network but which can be connected within 10 minute and fully applied to meet the requirements [6], [15]. It is the amount of reserve required for returning system frequency to 49.9 Hz and can be calculated by equation (1), hence the name is supplemental reserve.

$$SR\ (MW) = \Delta f\ (p.u.)\ X\ \boldsymbol{D} \ldots\ldots\ldots\ldots\ldots (1)$$

In DIgSILENT, ***D*** is defined as frequency dependency co-efficient of load [16]. ***D*** is assumed 1.3 for this particular study based on following evidence. For dynamic and especially frequency study, load modeling is a vital assumption. For this purpose, the criterion 0.1 Hz per 7 MW is set as the basis after studying six different scenarios. The frequency dependency of load, ***D*** is varied from 1 to 2. Finally the ***D*** for overall loads of Bangladesh for case study is set as 1.3.

*3) Determination of Supplementary Reserve:* The amount of spinning reserve and non-spinning reserve could be determined from following equations:

$$Spinning\ Reserve = RR + SR \ldots\ldots\ldots.(2)$$

&

$$Operating\ Reserve = Spinning\ Reserve + NonSpinning\ Reserve \ldots\ldots\ldots\ldots\ldots\ldots\ldots\ldots(3)$$

For allocating Non-spinning Reserve (NSR), at first the total capacity reserve will be evaluated. Capacity reserve is considered as the total of head room of each unit minus its assigned spinning reserve if this unit is set on dispatch bar. If NSR is lower than capacity reserve in a case, the value of required NSR will be reported as zero, otherwise the difference of NSR between capacity reserve is reported as the required NSR in this report.

## IV. Proposed Guideline and Constraints

The guideline and constraints of acceptable levels for frequency are as follows:

- In normal operation, the frequency should be maintained in 50±0.05 Hz range;
- In event of N-1 contingency the frequency should not fall below 49.50Hz;
- The frequency should not drop below lowest UFLS setting, even for very severe disturbances;
- In case of the largest credible loss, the frequency should be restored to 49.80Hz within one minute and to 49.90 Hz within 10 minutes;
- After a disturbance, the OR level in the system should be restored to normal level within 30 minutes;
- The transmission system voltage levels within the lower limit of -5% and the upper limit +5 % of their rated voltages;
- Under contingency conditions, transmission lines and transformers loading is 120% of the normal rating.

In this study, it was assumed that the governors of the Gas turbine units having capacity upper than 100 MW are in service for 2021. The governor of those units is modeled in DIgSILENT software. Based on those models, the maximum regulating reserve capacity for each unit which participates in frequency control program via its governor is considered as 10% of its capacity.

## V. Case Study : Operating Reserve Margin Determination

### A. Operating Reserve

This section presents the results of calculating the operating reserve level for Bangladesh power system. The reliability index, LOLE was used for calculating operating reserve level. The LOLE was calculated using PLEXOS to determine the adequate level of operating reserve. Figure 3 shows the result of the analyses done by probabilistic Chronological Monte Carlo method in PLEXOS software which represents the fact- the LOLE is higher when the capacity reserve is low. Shown in the figure 6, the operating reserve level which complies with LOLE target of 0.1 days per year is 11.2% of the daily peak load of power system. The amount of operating reserve for specified operating hour is measured by optimal unit commitment and dispatch algorithm and this operating reserve should not be lower than 11.2% of the load for that hour. But, the operating reserve can be higher than 11.2% of peak load based on system characteristics and requirements. So, it is concluded that 11.2% operating reserve of peak load is optimal and most economic for this particular case study.

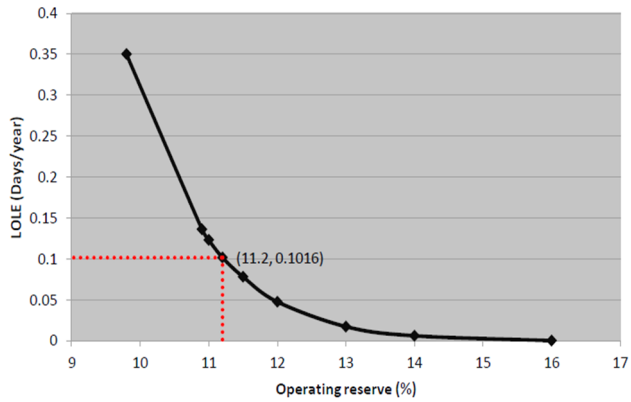


Figure 3. Relationship between LOLE and OR

### B. Spinning And Non-Spinning Reserve In Different Level of Load Condition

In this section, spinning and non-spinning reserve capacity were determined for the Bangladesh system for the peak load

condition. All studies will be done based on collected data, proposed methodology, assumptions and considerations. It should be noted that the contingency considered for dynamic simulation was the outage of 300 MW HVDC link. For the peak load condition in the Bangladesh system, which is a forecasted day in 2021, the load varies between 10960 MW to 14600 MW. Figure 4 shows the hourly load profile for this day.

Figure 4. Hourly load profile in peak load condition

To determine the spinning and non-spinning capacity portions of the OR, at first based on operational experience, it was assumed that the regulating reserve (RR) level could be 190 MW in the peak load hour and different resources were committed and dispatched for this hour by PLEXOS software. Next, the system's static performance was verified using DIgSILENT software to assure that the power system's voltages and line loadings remain within their acceptable ranges and some modifications were applied to further improve static adequacy. These changes include defining some generation units as 'Must-Run' units and some lines should be opened just in this load condition in order to avoid overloading problem (referred to section III). Finally, the system frequency variation was checked using a dynamic study for this regulating reserve level and in this particular case study, it was determined that this level of regulating reserve was insufficient. Therefore, the amount of regulating reserve was increased to 210 MW. These steps were also performed for the light load hour. In conclusion, it was determined that the Bangladesh system needed 250 MW worth of regulating reserve and 34 MW of Supplemental Reserve (SR) for the peak load hour and 320 MW of regulating reserve and 12.5 MW for SR for the light load hour. The amount of regulating and supplementary reserve for peak and light load hours of each load level were specified and the maximum of these amounts were taken into account for daily scheduling. Therefore, for the peak load condition, 320 MW of regulating reserve and 34 MW of SR were scheduled for the Bangladesh system. Under these circumstances (for 320 MW as regulating reserve and 34 MW of SR), given that the operating reserve should be 11.2% (14600 × 0.112=1635 MW in peak hour and 10960 × 0.112= 1228 MW in light hour), the required Non-Spinning Reserve (NSR) capacity for these hours would be about 373 MW and 77 MW, respectively (according to equation 2 and 3). The summary of results for this load condition can be found in Table I. The detailed calculation of table I is also shown below.

Operating reserve (OR)= 11.2 %
<u>Peak load condition:</u>
Load at peak hour= 14600 MW
OR (peak hour)= 14600 × 0.112 = 1635 MW
RR = 320 MW [ from trial and error simulation]
Supplemental Reserve (SR) = 34 MW [Frequency behavior during blackout]
Spinning Reserve = 320 + 34 = 354 MW
NSR= OR - Spinning Reserve = 1635- 354 = 1281 MW
Planned capacity reserve= 908 MW
Required NSR= 1281-908= 373 MW

<u>Light load condition:</u>
Load at light hour= 10960 MW
OR (light hour)= 10960 × 0.112 = 1228 MW
RR= 320 MW [maximum amount taken into consideration]
SR = 12.5 MW [Frequency behavior during blackout]
Spinning Reserve = 320 + 12.5 = 332.5 MW
NSR= OR - Spinning Reserve = 1228- 332.5 = 895.5 MW
Planned capacity reserve= 818 MW
Required NSR= 895.5 -818= 77.5 MW

TABLE I. THE SPINNING AND NON-SPINNING RESERVES IN PEAK LOAD CONDITION

| Scenario | Number of Governors | RR (MW) | SR (MW) | Capacity Reserve (MW) | Required Non Spinning Reserve (MW) | Operating Reserve (MW) |
|---|---|---|---|---|---|---|
| a | b | c | d | e | f | g =(c+d+e+f) |
| Peak load hour in the peak load condition | 25 | 320 | 34 | 908 | 373 | 1635 |
| Light load hour in the peak load condition | 27 | 320 | 12.5 | 818 | 77.5 | 1228 |

Figure 5 and Figure 6 show the system frequency in different reserve levels in peak and light hours of peak load condition. It is observed from the figures; proposed regulating reserve (summarized in Table.1) is capable of controlling frequency in an acceptable range and stabilizes the system within predefined time. During peak hour of peak load condition 320 MW of regulating reserve pull up the frequency above 49.8 Hz within one minute without any violation (Figure.5) while 190 MW and 210 MW of regulating reserve was inadequate for the system to restore to 49.8 Hz. 250MW of regulating reserve is also good choice for peak hour of peak load condition but maximum of 320 MW has been selected. Again, during light hour in peak load condition 320 MW of regulating reserve was capable of restoring frequency above 49.8 Hz within one minute and also 250 MW of regulating reserve was good choice (Figure.6). The amount of regulating reserve and Supplementary reserve for peak and light load hours of each load condition were specified and the maximum of these amounts were taken into account for daily scheduling. So, 320 MW of regulating reverse was the perfect choice for light hour in peak load condition.

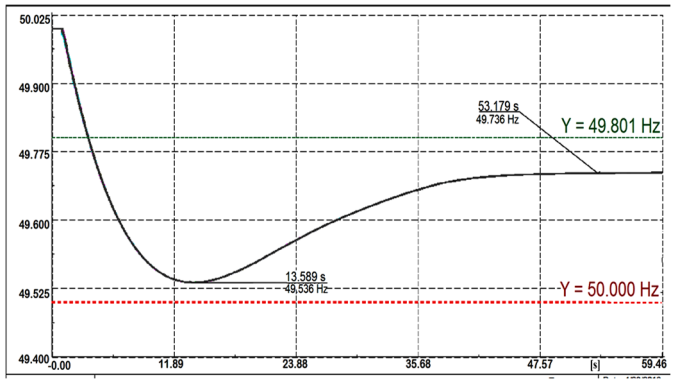


a

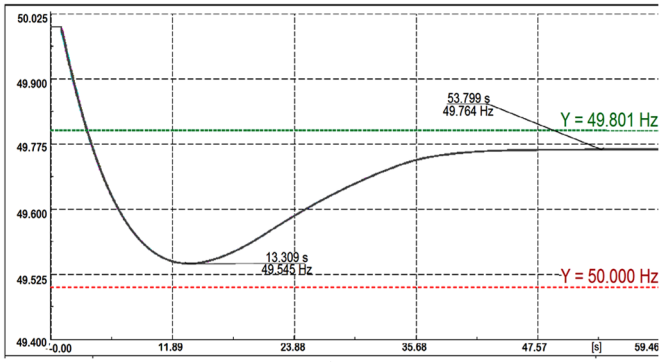


b

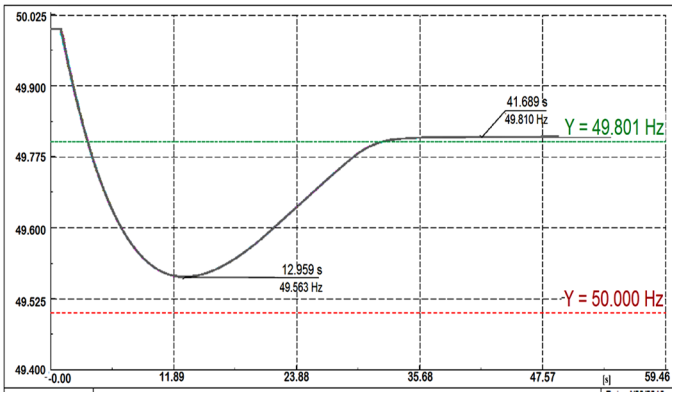


c

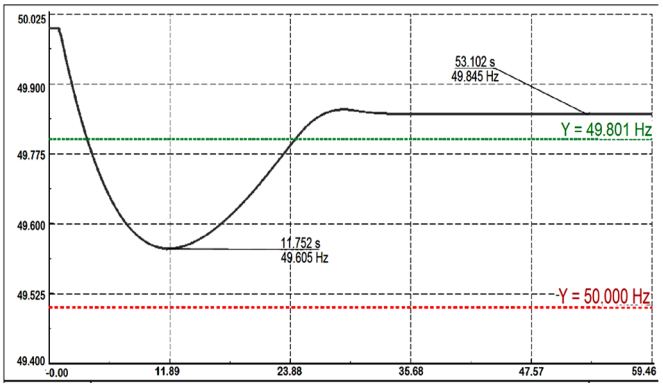


d

Figure 5. System frequency in peak hour of peak load condition at (a) 190, (b) 210, (c) 250 and (d) 320 MW of regulating reserve

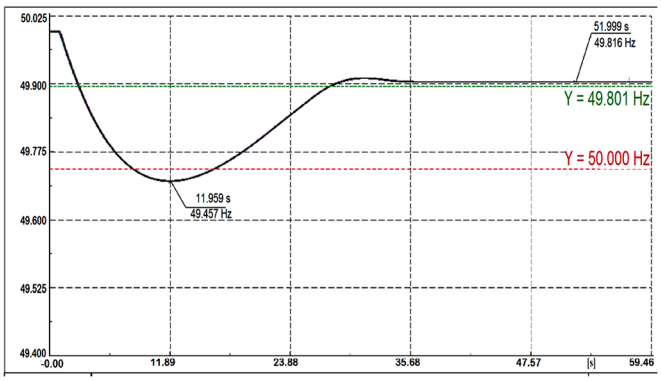


a

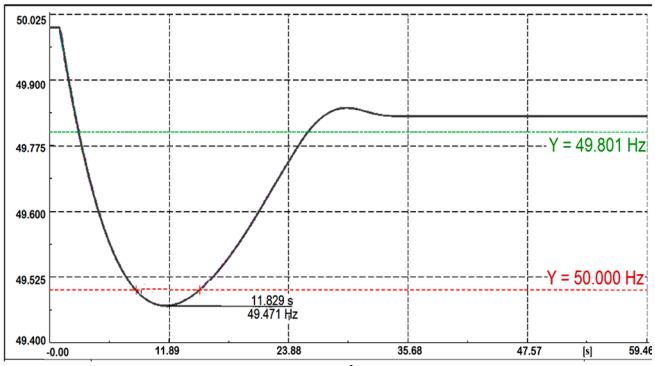


b

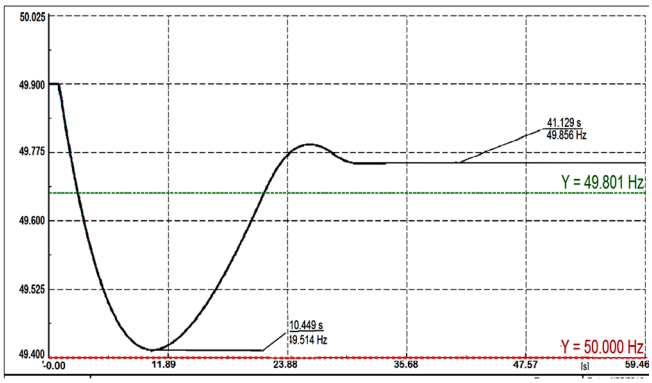


c

Figure 6. System frequency in light hour of peak load condition at (a) 250, (b) 270 and (c) 320 MW of regulating reserve

During simulation in DIgSILENT, 10% of plant capacities of large turbine plants are considered for frequency control program. After large contingency of 300 MW HVDC, the active power of plants participating in frequency control program is shown in the figure 7. It is clear that plants participating in frequency control program had change of active power immediate after contingency. It is worth mentioning that all simulations are done for 300 MW HVDC trip. Contingency bigger than 300 MW, for example 500 HVDC, should be avoided as frequency drops below 48.9 Hz. However, frequency control program can stabilize the system 49.7 Hz but it is can be very risk. At this circumstance, special protection scheme is required for large HVDC interconnections [20].

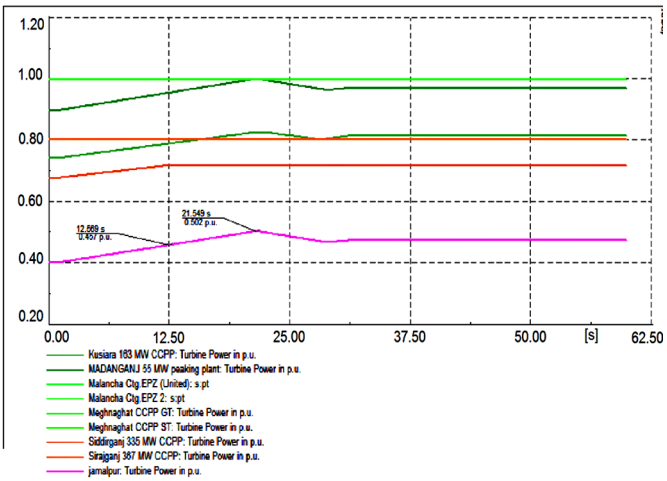


Figure 7. Active Power Governor Response of Some Generation Units after outage of 300 MW HVDC

## VI. CONCLUSIONS AND FUTURE WORKS

According to proposed Reserve policy in this paper, the system frequency can be controlled in acceptable range for load forecast errors and generation capacity outages less than 300 MW in 2021. The active governors of generating units can extremely assist to satisfy the proposed Frequency Control Mechanism. The data of "Grid Inertia" and "Load Dependency to Frequency" should continuously be monitored, calculated, and also recorded for different seasons and hours, and the proposed procedures for calculation of reserve should be repeated for new values. Another important issue should mention is to consider Hydro power plant as the main regulating frequency tool in frequency control program. In this case study, it is assumed that the water is available and simulations show that the effect of these existing hydropower units on the power system frequency control is negligible in comparison with thermal generating units' participation due to their small capacity and consequently regulating reserve. The fact that these contingencies require a very high reserve capacity that is not economically viable (for large hydro units) but very essential for system stability & frequency control purpose. Therefore, it is concluded that, special protection scheme is required to satisfy frequency limit for these outages. As a continuation of this work, we are working to study the impact of Hydro units in frequency regulation & operating reserve and international comparison of protection mechanism.

## REFERENCES


[1] Jaleeli, Nasser, Louis S. VanSlyck, Donald N. Ewart, et al., "Understanding automatic generation control." *IEEE transactions on power systems* 7, no. 3 (1992): 1106-1122.

[2] Berkel, Felix, Daniel Gorges, Steven Liu, "Load-frequency control, economic dispatch and unit commitment in smart microgrids based on hierarchical model predictive control" *Decision and Control (CDC), 2013 IEEE 52nd Annual Conference*. IEEE, 2013.

[3] Jan Machowski, Janusz W. Bialek, James R. Bumby, "Power System Dynamics and Stability", *John Wiley & Sons*, 1997.

[4] Allan, R. N,"Reliability evaluation of power systems," *Springer Science & Business Media*, 2013

[5] *NERC standard for relaibility, Special Reliability Assessment: Maintaining Bulk Power SystembReliability While Integrating Variable Energy Resources – CAISO Approach,* NERC, 2013.

[6] Milligan, Michael, et al, "Operating reserves and wind power integration: An international comparison," proc. *9th International Workshop on large-scale integration of wind power into power systems*. 2010.

[7] Dawes, Brett, Kwan-Wu Chin, "A comparison of deterministic and probabilistic methods for indoor localization," *Journal of Systems and Software* 84.3 (2011): 442-451.

[8] Al-Alawi, Ameer, Makarand Nagle, and Jinxiang Zhu, "Utilizing reliability indices to study generation adequacy," *In Transmission and Distribution Conference and Exposition, 2010 IEEE PES*, pp. 1-5. IEEE, 2010.

[9] Al-Shaalan, Abdullah M, "Reliability evaluation in generation expansion planning based on the expected energy not served," *Journal of King Saud University-Engineering Sciences* 24, no. 1 (2012): 11-18.

[10] Al-Shaalan, Abdullah M, "Essential aspects of power system planning in developing countries," *Journal of King Saud University-Engineering Sciences* 23, no. 1 (2011): 27-32.

[11] Sanghvi, Arun P, "Neal J. Balu, and Mark G. Lauby.: 'Power system reliability planning practices in North America," *IEEE transactions on power systems* 6, no. 4 (1991): 1485-1492.

[12] *NERC standard for Reliability, Reliability Standards for the Bulk Electric Systems of North America, NERC, November 2009*.

[13] NERC (2014), Long-Term Reliability Assessment - NERC, 2014. [Online] . Available at: https://www.eenews.net/assets/2014/11/12/document_gw_03.pdf

[14] *NERC standard for adequacy analysis, BAL-502-RFC-02: Planning Resource Adequacy Analysis, Assessment and Documentation, NERC, 2011.*

[15] Southwest Power Pool, Inc., "Operating Criteria, Revision 1.0", SPP, 2015.

[16] DIgSILENT (2013), PowerFactory V-15.1 User Manual, [Online], Available at: http://www.digsilent.de.

[17] K. Debnath, L. Goel, "Power system planning — a reliability perspective*", In Electric Power Systems Research*, Volume 34, Issue 3, 1995, Pages 179-185, ISSN 0378-7796.

[18] ENTSO-E,European Network of Transmission System Operators for Electricity, "Operation handbook", Tech. rep., ENTSO-E, 2012 .

[19] Kirby, Brendan J,"Spinning reserve from responsive loads," *United States. Department of Energy*, 2003.

[20] MdSalehEbn,Sharif, Mahmud-Ul-Tarik Chowdhury,Md Moniruzzaman, Masud Reza, "Supplementary Frequency Control Mechanism to Ensure Reliability of Power System: Based on an International Comparison," *3rd International Conference on Electrical Information and Communication Technology (EICT)*, 7-9 December 2017.

# Power Quality Analysis of Distributed Wind Generation Systems

A. Das[1], N. K. Roy[1], and H. R. Pota [2]
[1] Dept. of Electrical and Electronic Engineering, Khulna University of Engineering &Technology, Bangladesh
[2]School of Engineering & IT, The University of New South Wales, Australia
aparupa.das92@gmail.com; nkroy@eee.kuet.ac.bd; h.pota@adfa.edu.au

**Abstract—This paper analyzes one of the most crucial problems related to the harmonics pollution of distributed generators connected to distribution networks which contain non-linear loads. A wind-based distributed generation system is considered here which generates harmonics due to its power electronics interface to the grid. To investigate the interactions between distributed generation and loads, different types of non-linear loads, which are also a source of harmonics, are connected to the distribution network. When distributed generation and non-linear loads both are connected to establish a technologically upgraded system, then the harmonics from both ends merge in such a way that the resultant harmonics become extremely high that is very much deleterious for any system. This research examined the impact of the resultant harmonics in various possible conditions and pointed out that the harmonics nature and magnitudes are different for different types of loads. The system is also tested under different fault conditions and significant voltage sags and swells are observed. To analyze the effects, a model is considered encompassing a permanent magnet synchronous generator based wind turbine, an AC/DC/AC converter with current controller which is dependent on a straight line method and the total setup is connected to a 12 bus radial system to investigate the power quality issues. This power quality analysis is conducted on the PSCAD/EMTDC environment.**

***Keywords—Distributed generation, Permanent magnet synchronous generator, AC/DC/AC converter, Adjustable speed drive, Arc furnace, Harmonics, Voltage sag.***

## I. INTRODUCTION

The universe today is using an excessive amount of fossil fuel which will lead the world towards a huge crisis of environmental disaster in the near future. Scientists, researchers and planners have no alternative option rather than shifting to renewable and green energy sources to minimize greenhouse gas emissions and thus, preventing the rise of sea level due to the melting of ice-berg by increased global temperature. The technologies should be remolded to diversify the energy consumption and generation concepts to link with sustainable world. Among the various sources of renewable energy, wind turbines recently have gained the attraction and become famous due to their availability, structure and design [1].

Nowadays, the distributed generation (DG) plays an important role in energy sector because it not only provides sufficient power support to the distribution network (DN) but also reduces the cost of power generation [2]. DNs previously only deal with delivering electricity to the customer and this trend has changed a lot as the connection of DG is introduced and they are being used for the collection of power from different DGs [3]. With the development of wind technologies, the trend of using the fixed speed wind turbine (FSWT) is shifted towards the variable speed wind turbine (VSWT) to utilize the aerodynamics of the wind more significantly within a wide range of wind velocity and to maintain the stable torque [4], [5]. Not only this, the VSWT can maintain a tip speed ratio at the time of low wind velocity and, when the velocity of the wind is strong, it only generates the rated power output without being damaged by the high speed [6]. The VSWT generators can be categorized into two categories such as doubly fed induction generator (DFIG) and permanent magnet synchronous generator (PMSG). After comparing DFIGs and PMSGs, it is found that PMSGs are optimum in generation with a wide range of varying wind speed and they have other benefits like low loss, stable and comparatively high magnitude of power is generated [7], [8]. All the development in wind power technologies have made it more popular.

An AC/DC/AC converter has to be connected when the PMSG based wind turbine system is used because, without this device, it is difficult to push the power into the DN due to the voltage and frequency issues and it can sweep the maximum amount of power. The AC/DC/AC converter has non-linear characteristics and this is one of the reasons behind the generation of harmonics in the system. These harmonics generate heat, damage equipment, reduce power quality and increase losses of energy. On the other hand, several non-linear loads are present in the DN and the level of harmonics of the DN may dramatically increase when the converter connected DGs are employed. The interaction of these harmonics can hamper the setup of the system. The other major power quality problems are voltage sags and swells, which take place in the system when any fault or disturbance occurs. Previously, various analyses and calculations were made on the level and nature of harmonics that deal with only the issues related to non-linear loads [9]-[11]. However, the issues related to DG are not extensively studied. Before integrating large-scale power electronics interfaced DG into existing DNS, the problems must be precisely understood and critically analyzed. Therefore, the main goal of this research is to analyze the harmonics issues of the DN in the presence of DG and non-linear loads. The entire research has been planned to explore the problems and situations more intensely. Thus, it

978-1-5386-2307-7/17/$31.00 ©2017 IEEE

will help the other academicians to solve the problems and to find a perfect solution and pave a pathway to ensure the mass usage of wind based DG around the globe, to adopt these technologies commercially and to ensure a sustainable world.

In this paper, Section II contains the wind-based DG model where the PMSG and the converter models are given in detail. In the next section, the power quality problems and non-linear load models are shown and harmonics, voltage sag and swell analyses are conducted considering different cases. Lastly, in section IV the conclusion is drawn based on the entire analysis.

## II. DG MODEL

The DG is a method of producing power from a small-scale energy source which is fed to the DN directly. Sometimes this system is called as decentralized energy generation system or onsite generation. The conventional or centralized power systems are often required to cover a long distance to transmit electricity which increases the transmission loss as well as the cost and these problems are often highlighted in power distribution sectors. To minimize such situations, a DG system is the perfect solution which is generally located near the load or in the distribution network.

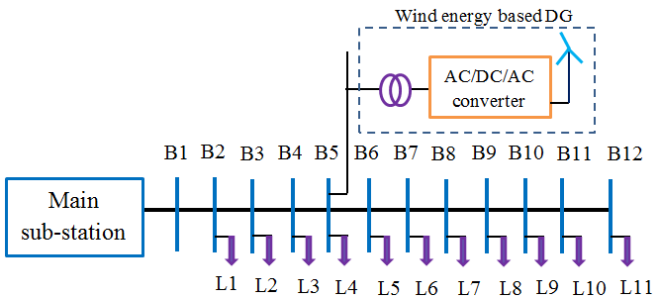


Figure 1. A 12 bus radial network with wind power based DG.

TABLE I. LINE DATA FOR 12 BUS RADIAL SYSTEM

| From bus | To bus | Resistance, R (in Ω) | Reactance, X (in Ω) |
|---|---|---|---|
| 1 | 2 | 1.093 | 0.455 |
| 2 | 3 | 1.184 | 0.494 |
| 3 | 4 | 2.095 | 0.873 |
| 4 | 5 | 3.188 | 1.329 |
| 5 | 6 | 1.093 | 0.455 |
| 6 | 7 | 1.002 | 0.417 |
| 7 | 8 | 4.403 | 1.215 |
| 8 | 9 | 5.642 | 1.597 |
| 9 | 10 | 2.890 | 0.818 |
| 10 | 11 | 1.514 | 0.428 |
| 11 | 12 | 1.238 | 0.351 |

In this paper, a DG system is designed with a PMSG based wind turbine and an AC/DC/AC converter is incorporated while connecting to the DN. A current controller mechanism with voltage dependent current limiter is employed for controlling the converter. A 12 bus radial DN is considered for the analysis as shown in Fig. 1, where B represents bus and L represents load [12]. In this model, a wind energy based DG is connected at bus 5. At this bus, different types of non-linear loads are connected to examine different situations of harmonics generation in the system. The 12 bus radial system's line data and load data are given in Table I and Table II, respectively [12].

TABLE II. LOAD DATA OF 12 BUS RADIAL SYSTEM

| Bus no. | Active power load, PL (kW) | Reactive power load, QL (kVAR) |
|---|---|---|
| 1 | 0 | 0 |
| 2 | 60 | 60 |
| 3 | 40 | 30 |
| 4 | 55 | 55 |
| 5 | 30 | 30 |
| 6 | 20 | 15 |
| 7 | 55 | 55 |
| 8 | 45 | 45 |
| 9 | 40 | 40 |
| 10 | 35 | 30 |
| 11 | 40 | 30 |
| 12 | 15 | 15 |

### A. *PMSG based wind turbine*

The latest wind generation technologies around the world are following the trend of using PMSGs. In past, generators had exciters like coils but due to the recent advancement they use a permanent magnet in the place of an exciter. The permanent magnet in this generator is mounted to a shaft. When the system is at work, then the rotor's and stator's magnetic fields have same angular speed and the electricity is generated at the stator end. The rating of the PMSG in this analysis is 3 MVA.

The frequency (Hz) of the stator is directly proportional to the speed (RPM) of the rotor. The equation for power of the wind turbine is [13]:

$$P_w = 0.5\rho A C_p V_w^3, \tag{1}$$

here, $P_w$ = wind power [W], $V_w$ = wind speed (m/s), $C_p$ = power co-efficient, $\rho$ = air density (kg/m$^3$), $A$ = area swept by the rotor [m$^2$] .

### B. *AC/DC/AC Converter*

Generally, an AC/DC/AC converter is set to sweep the maximum amount of power from the generator; however, the matter of concern is that it produces harmonics due to the non-linear characteristics. It has three important components, such as diode rectifier, dc bus with a storage capacitor, and 6-pulse bridge thyristor inverter. The rectifier is an important component of this converter system which has a higher inductance in the dc side than its ac side. Therefore, the dc current gives a constant value in dc side. As a result, it works like a harmonics voltage source at its dc side whereas it acts like a harmonic current source in its ac side. The rate of harmonics generation depends on the number of pulses. The total current and voltage harmonic distortions are mathematically expressed as [14], [15],

$$I_{\text{thd}} = \frac{\sqrt{\sum_{n=2}^{\infty} I_n^2}}{I_1} \times 100\% = \frac{\sqrt{I_2^2 + I_3^2 + \ldots\ldots + I_n^2}}{I_1} \times 100\%, \tag{2}$$

$$V_{\text{thd}} = \frac{\sqrt{\sum_{n=2}^{\infty} V_n^2}}{V_1} \times 100\% = \frac{\sqrt{V_2^2 + V_3^2 + \ldots\ldots + V_n^2}}{V_1} \times 100\%, \quad (3)$$

here, $V_{\text{thd}}$ = total voltage harmonic distortion, $I_{\text{thd}}$ = total current harmonic distortion and they are calculated by RMS values ($V_1, V_2, \ldots V_n$) and ($I_1, I_2, \ldots\ldots I_n$).

For controlling the voltage collapse mechanism, the voltage dependent current limiter (VDCL) is used. When any short circuit occurs in the ac system, voltage will be collapsed. The VDCL will identify it and set the current order in a certain level. The VDCL only allows the flow of current with in a predetermined value. There are two limiting parameters, one is volts for applying limit ($V_{\text{on}}$) and another one is volts for removing limit ($V_{\text{off}}$) that must be in the same polarity as the measured voltage and $V_{\text{off}}$ is always greater than $V_{\text{on}}$.

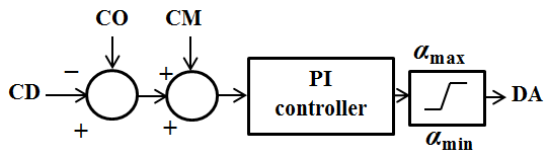


Figure 2. Current controller model of AC/DC/AC converter.

The system is designed through the straight line method [16]. For limiting the system's current, two conditions are implemented so that the over and under current situations can be avoided which not only protect the system but also reduce the generation rate of harmonics. In this system, input parameters are the measured dc bus voltage ($V_d$) and reference current (CI) whereas the output parameter is the current order (CO). When, $V_d > V_{\text{off}}$ then, CO=CI; which is the current for the rated power. When $V_d < V_{\text{on}}$ then, CO=current limit; which is the minimum current in the inverter.

To act on the error between CO and measured dc current (CD), the current controller is employed in the system as shown in Fig. 2. For producing firing angle, this controller generates a desired alpha order (DA). The current margin (CM) usually has a fixed value and in normal operating condition, it is zero. If under normal operating condition, the converter is not controlling current, then it is forced into establishing dc voltage by setting CM positive for an inverter or negative for a rectifier. This force takes the desired firing angle of the inverter to the maximum level of alpha ($\alpha_{\max}$). At the rectifier, a negative CM forces the firing angle to alpha minimum limit ($\alpha_{\min}$).

## III. Power Quality Problems

In DNs, several kinds of power quality issues are raised like harmonics, voltage sag and swell. In faulty condition, the voltage sag is notified in the system whereas harmonics are generated from the converter connected DG and non-linear loads.

### A. Harmonic distortion

Nowadays, harmonic distortion is being very crucial and significant crisis in power sector, which is assumed to be much higher in the future as the non-linear power electronics devices are used all over the globe. In power equipment and components, the harmonic causes various problems like it increases skin effect which causes $I^2R$ losses and generates heat in the circuit. The eddy current losses in the transformers will be increased if the harmonics increased. When the level of harmonic rises, the capacitor will be overheated and dialectic stress will take place. Moreover, it hampers the effectivity of circuit breaker. In this paper, different types of non-linear loads are designed for harmonics analysis.

A 40 HP induction motor with an adjustable speed drive (ASD), as shown in Fig. 3 is designed, and connected at bus 5 for the analysis. In this motor drive, the PWM technique is applied for controlling the 6-pulse inverter of the ASD which is the main source of harmonics generation. Generally, for its construction, in an induction motor two types of harmonics are introduced; one is space harmonic and the other one is time harmonic [17]. Space harmonics are generated in the circuit for the interaction of different phase winding at the time of rotating magnatic field generation. This space harmonics cause various problems like generation of noise, viabration and affect the starting of the motor. On the other hand, the time harmonics generate heat which is very harmfull for the system. The addition of ASD's harmonics, this harmonics pollution reached to an extreme level. In this system, a 6-pulse bride rectifier and a dc link capacitor is also used. The inverter of the ASD converts the dc voltage to ac voltage to control the motor's speed.

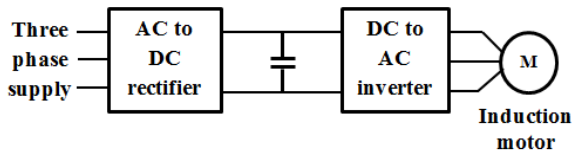


Figure 3. Model of induction motor with ASD.

The electric arc furnace is another major non-linear load which is commonly used in steel industry for melting and refining purposes. This device is used for melting metal by converting the electrical energy to an electric arc. However, it produces harmonics in the system for the highly non-linear V-I characteristics of arc. The harmonic effect is large because of its large capacity lumped together at one place. When this load is connected to the system, it hampers the power quality of the system. Voltage harmonic distortion is prominent in this load than the current harmonics [18]. Practically, the V-I characteristic gives more noise due to the unpredictable and chaotic nature of the load. This model of arc furnace is based on a non-linear differential equation [16], [19].

$$k_1 \cdot r^n + k_2 r \frac{dr}{dt} = \frac{k_3}{r^{m+2}} \cdot i^2, \quad (4)$$

$$v = \frac{k_3}{r^{m+2}} \cdot i, \quad (5)$$

here, $i$ = arc current, $v$ = arc voltage, $r$ = arc radius. The parameters $k_i$ ($i=1, 2, 3$), $r$ and $n$ characterize the arc under a given operating condition.

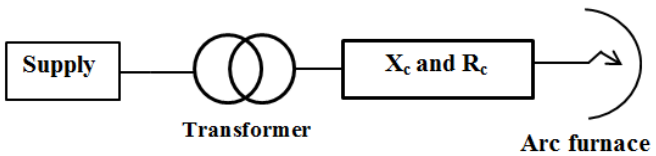


Figure 4. Online diagram of an arc furnace.

An arc furnace is connected at bus 5 of the DN as shown in Fig. 4. Here, $X_c$ and $R_c$ are the reactance and resistance, respectively of the connecting line to the arc furnace electrodes.

For understanding the harmonics generation rate in the system, various situations are examined.

**Case 1:** When the RL load is implied with the system at bus 5, the harmonics of the DG's converter and RL load are merged and the resultant harmonics go beyond the tolerable limit. In normal operating condition, an RL load produces less harmonics and the individual harmonic of the system mostly comes from the converter of DG. From this analysis, it is observed that in case of RL load, the current harmonics are higher than the voltage harmonics. The distorted current waveform in this case is shown in Fig. 5. Generally, in DN several DGs are connected, for collecting more power. If the number of DG is increased in the system then the harmonic level is also increased, as shown in Table III, because of increasing the number of power electronics based converters.

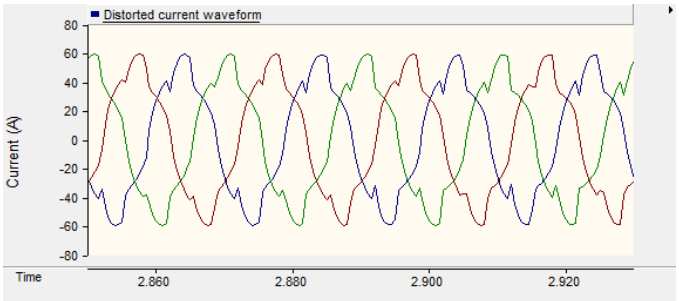


Figure 5. Distorted current waveform due to RL load and DG's converter.

TABLE III. INDIVIDUAL HARMONIC DISTORTION (IN %) OF THE SYSTEM DURING RL LOAD WITH SINGLE AND THREE DG UNIT.

| Harmonic Order | RL load with single DG unit | | RL load with three DG unit | |
|---|---|---|---|---|
| | Individual current harmonic distortion (in %) | Individual voltage harmonic distortion (in %) | Individual current harmonic distortion (in %) | Individual voltage harmonic distortion (in %) |
| 3rd | 3.925 | 2.331 | 11.761 | 9.843 |
| 5th | 19.148 | 15.394 | 63.653 | 49.975 |
| 7th | 16.921 | 13.283 | 46.212 | 38.274 |
| 9th | 14.991 | 9.937 | 28.559 | 20.345 |

**Case 2:** If the induction motor with ASD is incorporated in the system, an excessive magnitude of harmonic is generated because this ASD contains a power electronic inverter. In this case, the current is more affected by the harmonics as shown in Fig. 6 and both current and voltage harmonics are more than that of the RL load. The combination of the induction motor's harmonics, ASD's harmonics and the DG converter's harmonics create a vulnerable situation in the system.

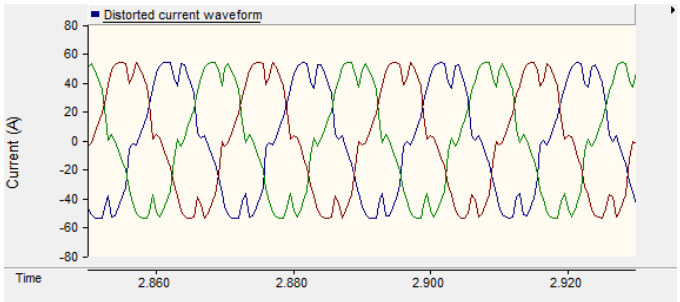


Figure 6. Distorted current waveform due to induction motor with ASD and AC/DC/AC converter of DG.

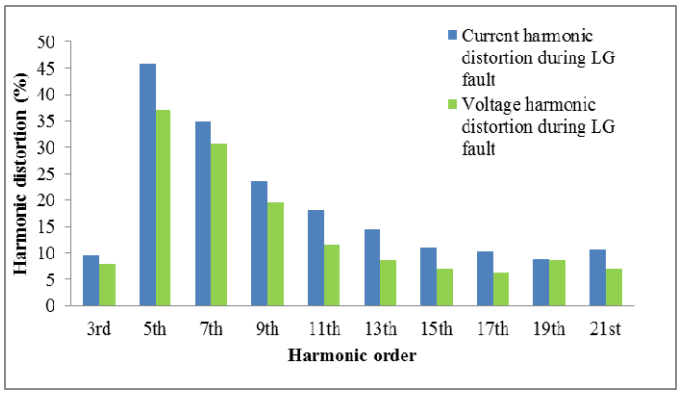


(a)

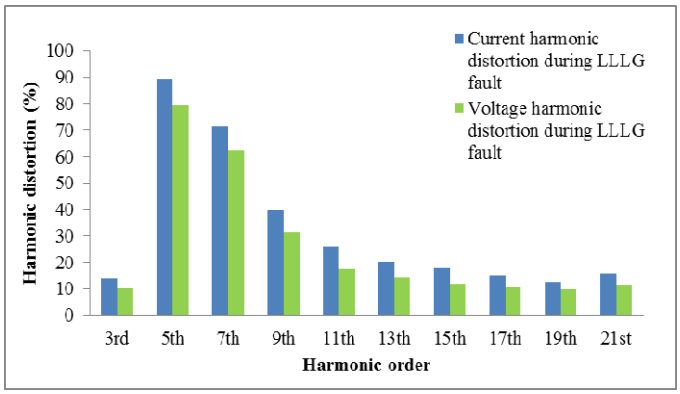


(b)

Figure 7. Individual current and voltage harmonic distortion (in %) of induction motor with ASD and DG's converter during (a) LG fault and (b) LLLG fault.

**Case 3:** The level of interrupted harmonics of the converter and the non-linear loads is increased when the system faces any kinds of faults as shown in Fig. 7. During single line to ground (LG) fault the level of harmonic is raised but it reaches to the extreme level in case of three-phase (LLLG) fault which may damage a significant portion of the system. This representation again proves that an LLLG fault is the most severe fault in case of harmonics. In the system, a fault is applied at bus 12 for 0.2 second.

**Case 4:** The positioning of the DG is an important factor in harmonics analysis. The position of it determines the magnitude of harmonics. The far the DG from the non-linear load, the minimum amount of harmonics is generated and vice-versa. If the non-linear load and the DG are connected at the same bus that is bus number 5, then the highest magnitude

of harmonics is generated. If the DG is connected at the far corner that is bus number 12, the harmonics are minimum. And, connecting the DG unit in a mid-position that is bus number 3, the generated harmonics also lie in the mid-range as shown in Fig. 8.

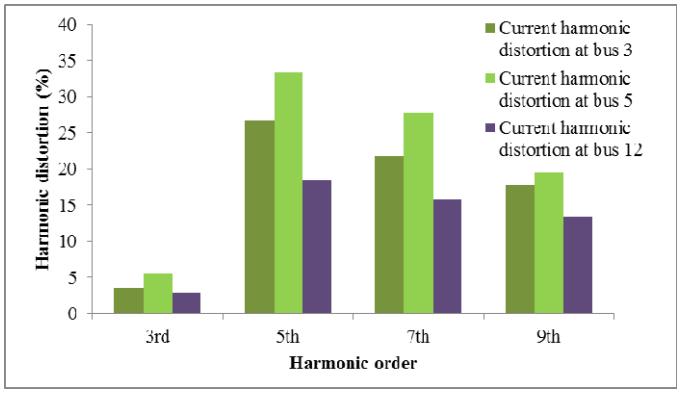


(a)

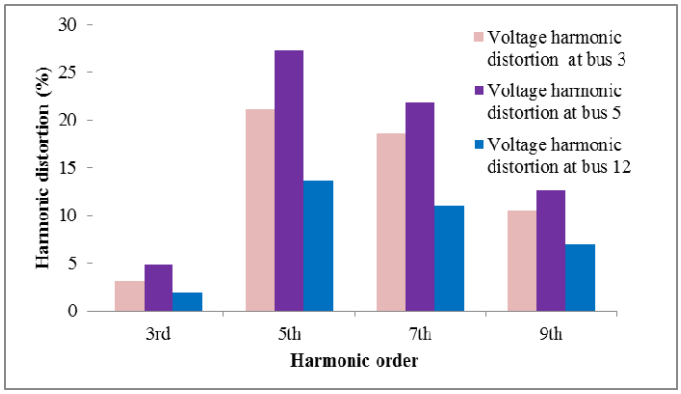


(b)

Figure 8. Individual (a) current and (b) voltage harmonic distortion (in %) of induction motor with ASD and DG's converter depending on DG's position.

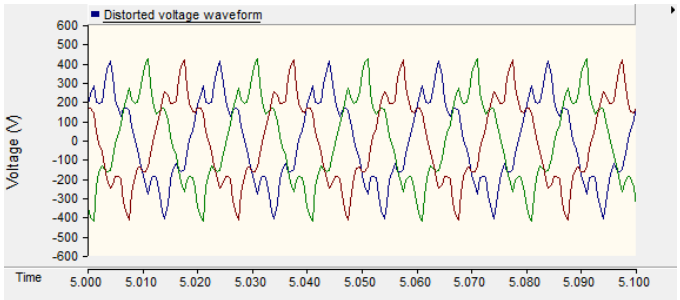


Figure 9. Distorted voltage waveform due to arc furnace and AC/DC/AC converter of DG.

**Case 5:** In this part, an arc furnace is taken into consideration for harmonic analysis. It is connected at bus 5. The voltage harmonics are the major harmonics in this case. From Fig. 9, it is seen that the voltage wave form is seriously affected by the harmonics. The DG's converter adds more contribution in harmonics pollution.

**Case 6:** In this part of the analysis, a comparison among the RL load, induction motor load and arc furnace load is overviewed and through graphical expression, it has been depicted. From Fig. 10, it is found that the induction motor is the most current harmonics generating device in comparison with RL load and arc furnace. On the other hand, the arc furnace produces more voltage harmonics than the other two types of loads. The RL load contributes less harmonics in both cases of current and voltage. From Fig. 10, it is observed that $5^{th}$ and $7^{th}$ are the most prominent harmonics in this system. According to IEEE Std 519-1992, the allowable individual voltage and current harmonic distortion are 3% and 4%, respectively [15]. In this test setup, voltage and current harmonic distortions of three types of loads exceed the tolerable limit set by the IEEE.

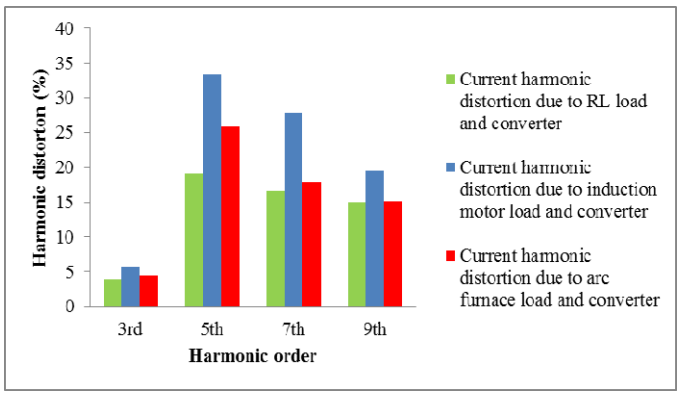


(a)

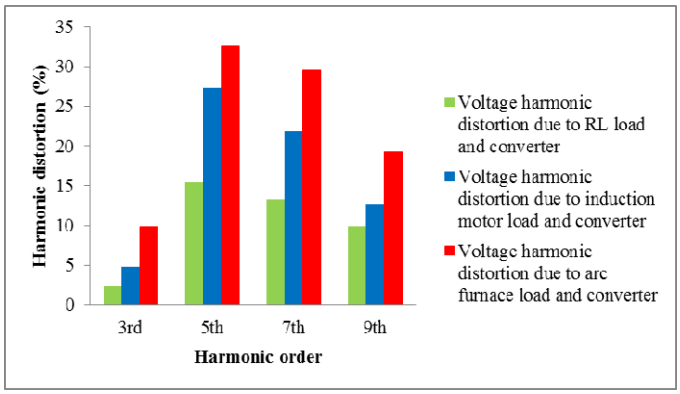


(b)

Figure 10. Individual (a) current and (b) voltage harmonic distortion (in %) due to three different non-linear loads with DG's converter.

## B. *Voltage sag and swell*

The voltage sag is another most common power quality problem which is caused for the unexpected fault, motor startup and short-circuit. It is also known as voltage sag which is the short term reduction of voltage from its rated value [20]. It is measured by seeing the depth and duration. For voltage sag analysis purpose, an induction motor with ASD is taken into consideration with the DG connection. If, after 3.7 second, an LG fault occurred in the test system at bus 12 for two-cycle then voltage sag is notified in the system as shown in Fig. 11. From this figure it can be observed that, only faulty phase A has fallen down during this time where the other two phases are also disturbed but it faces voltage swell which is the sudden increase of voltage from its rated value. This voltage swell problem is also taken place during the total time of voltage sag [21].

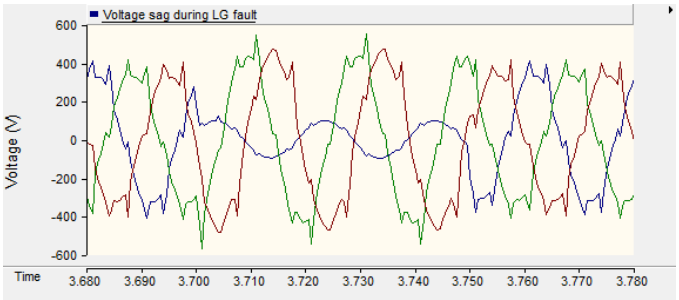


Figure 11. Voltage sag and swell during LG fault.

Figure 12 potrays the voltage sag in case of a double line to ground (LLG) fault and an LLLG fault. If the LLG and LLLG faults are occurred repetitively for 0.2 second at bus 12 then in case of LLLG fault the largest voltage sag is notified that is 53% sag whereas during an LLG fault, it is 58% sag.

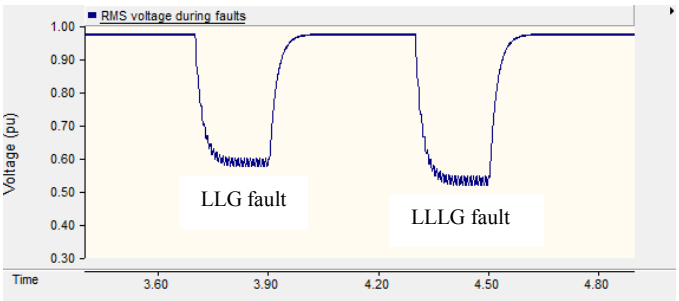


Figure 12. Voltage sag during repetitive LLG and LLLG faults.

## IV. CONCLUSION

From the discussion and analysis, it can be said that this research elaborates and clarifies the concepts and conditions regarding DG connected system with DNs. The designed model is critically examined under some important load conditions and it is found with proper evidence that every load characteristics causes different level of harmonics within the system. The current harmonics, which are the most harmful harmonics, are reached to a higher level in case of an induction motor whereas the voltage harmonic are larger in an arc furnace. In this system, it is found that 5$^{th}$ and 7$^{th}$ order harmonics are the prominent harmonics in this type of non-linear loads. The position and the number of DG units play a crucial role in harmonics generation. The level of harmonics generation goes upward as the number of the DG unit gets increased. When the DG is connected with the non-linear load at the same bus the generated harmonics become the maximum and if the position of the DG shifts away from the non-linear load, the generated harmonics gets reduced with distance increased. However, the worst case may take place if the system faces any fault, which takes the generated harmonics at a drastic level, even may collapse any part of the system. Not only this, fault in the system causes voltage sag and it also creates a challenging situation for the total system. This paper aims to identify and objectify the critical problems related to DG-integrated systems which have been successfully enlightened by this work. The solution of power quality issues with DG connected DNs is the future aim of this research to upgrade the current technological order to a new dimension.

## REFERENCES


[1] T. Agarwal, S. Verma, and A. Gaurh, "Issues and challenges of wind energy," International Conference on Electrical, Electronics, and Optimization Techniques (ICEEOT), Chennai, 2016, pp. 67-72.

[2] N. K. Roy and H. R. Pota, "Current status and issues of concern for the integration of distributed generation into electricity networks," IEEE Systems Journal, vol. 9, no. 3, pp. 933-944, 2015.

[3] N. K. Roy, H. R. Pota, and A. Anwar, "A new approach for wind and solar type DG placement in power distribution networks to enhance systems stability," IEEE International Power Engineering and Optimization Conference, Malaysia, 2012, pp. 296-301.

[4] S. S. Murthy, B. Singh, P. K. Goel, and S. K. Tiwari, "A comparative study of fixed speed and variable speed wind energy conversion systems feeding the grid," 7th International Conference on Power Electronics and Drive Systems, Bangkok, 2007, pp. 736-743.

[5] M. R. R. Mojumdar, M. S. H. Himel, M. S. Rahman, and S. J. Hossain, "Electric machines & their comparative study for wind energy conversion systems (WECSs)," Journal of Clean Energy Technologies, vol. 4, no. 4, Jul. 2016.

[6] S. Bhowmik and R. Spee, "Wind speed estimation based variable speed wind power generation," Industrial Electronics Society, 1998, Proceedings of the 24th Annual Conference of the IEEE, Aachen, 1998, pp. 596-601 vol.2.

[7] V. Yaramasu, A. Dekka, M. J. Duran, S. Kouro, and B. Wu, "PMSG-based wind energy conversion systems: survey on power converters and controls," IET Electric Power Applications, vol. 11, no. 6, pp. 956-968, 2017.

[8] E. Hamatwi, M. N. Gitau, and I. E. Davidson, "Control of a direct-driven permanent magnet synchronous generator-based wind turbine to achieve maximum wind-power extraction," IEEE PES PowerAfrica, Accra, 2017, pp. 65-74.

[9] M. J. H. Rawa, D. W. P. Thomas, and M. Sumner, "Simulation of non-linear loads for harmonic studies," 11th International Conference on Electrical Power Quality and Utilisation, Lisbon, 2011, pp. 1-6.

[10] W. Su, Z. Li, and Z. Shao, "The harmonic calculation model of non-linear load," 2014 China International Conference on Electricity Distribution (CICED), Shenzhen, 2014, pp. 866-872.

[11] K. C. Umeh, A. Mohamed, and R. Mohamed, "Determining harmonic characteristics of typical single phase non-linear loads," Proceedings. Student Conference on Research and Development, 2003, pp. 413-419.

[12] D. Das, H. S. Nagi, and D. P. Kothari, "Novel method for solving radial distribution networks," IEE Proceedings - Generation, Transmission and Distribution, vol. 141, no. 4, pp. 291-298, Jul 1994.

[13] A. Rolan, A. Luna, G. Vazquez, D. Aguilar, and G. Azevedo, "Modeling of a variable speed wind turbine with a permanent magnet synchronous generator," IEEE International Symposium on Industrial Electronics, Seoul, 2009, pp. 734-739.

[14] N. Shah, "Harmonics in power systems causes, effects and control," Siemens, USA, 2013, pp.1-24.

[15] "IEEE recommended practices and requirements for harmonic control in electrical power systems," in IEEE Std 519-1992, pp.1-112, 1993.

[16] The PSCAD/EMTDC user's guide v4.2.0, 2005.

[17] X. Liang and Y. Luy, "Harmonic analysis for induction motors," Canadian Conference on Electrical and Computer Engineering, Ottawa, Ont., 2006, pp. 172-177.

[18] P. Chittora, A. Singh, and M. Singh, "Modeling and analysis of power quality problems in electric arc furnace," Annual IEEE India Conference (INDICON), New Delhi, 2015, pp. 1-6.

[19] E. Acha, A. Semlyen, and N. Rajakovic, "A harmonic domain computational package for nonlinear problems and its application to electric arcs," IEEE Transactions on Power Delivery, vol. 5, no. 3, pp. 1390-1397, Jul 1990.

[20] M. H. Bollen, Understanding power quality problems: voltage sags and interruptions. USA: Wiley-IEEE Press, 1999.

[21] R. Sedaghati, N. M. Afroozi, Y. Nemati, A. Rohani, A. R. Toorani, N. Javidtash, A. Heydarzadegan, and H. Sedaghati, " A survey of voltage sags and voltage swells phenomena in power quality problems," International Journal of Scientific Research and Management , vol. 1, no. 9, pp. 458-462, 2013.

2017 3rd International Conference on Electrical Information and Communication Technology (EICT), 7-9 December 2017, Khulna, Bangladesh

# A Comparative Study of LQR, LQG, and Integral LQG Controller for Frequency Control of Interconnected Smart Grid

Mizanur Rahman*, Subroto K. Sarkar* Sajal K. Das* and Yuan Miao†
*Department of Mechatronics Engineering, Rajshahi University of Engineering & Technology, Bangladesh.
†Department of Information Technology, College of Engineering and Science, Victoria University, Australia.
Email: mizan138027@gmail.com ; skshuvo138008@gmail.com; das.k.sajal@gmail.com; yuan.miao@vu.edu.au

***Abstract*—Renewable energy plays the vital role to increase the power generation of smart grid. A smart grid consists of smart meters, smart appliances, energy efficient resources and renewable energy resources. The integration of renewable energy in a smart grid is challenging because of its frequency fluctuation in the power grid. The Plug-in hybrid electric vehicles (PHEV) are expected to install in customer side. The PHEV can be applied to stabilize the power and frequency fluctuation. This paper shows a comparative study of Linear Quadratic Regulator (LQR), Linear Gaussian Control (LQG) and Integral Linear Quadratic Gaussian Controller (ILQG) to control the frequency of interconnected power systems. In order to maintain the frequency stabilization, the three controllers are developed in this paper. The performance of these controllers is presented using Matlab simulation. The simulation results show that the integral linear quadratic gaussian controller provides best as compared to LQR and LQG controller.**

***Keywords:*** **Load-frequency control, LQR, LQG, Integral Linear Quadratic Regulator, Smart grid, Plug-in hybrid electric vehicles.**

## 1. Introduction

Over the past few decades, there have been a significant change in the way to produce and transmit electricity [**?**]. A traditional grid uses electromechanical and solid state devices to produce power which distributes through the communication and protection equipment. The generation of power from grid faces several problems [**?**]. In order to remove the problems, a hub is investigated to connect the generation of power, transmission and consumption equipment which caries the high amount cost. Smart power grid is a great solution to achieve efficient, reliable, and communication-rich system. A smart grid is one kind of electrical grid which can deliver electricity from multiple suppliers to end user using two way communication, multiple distributed intelligent entities and large scale real time data collection. Smart grid technology is a multidisciplinary technology as power engineering, information communication control and instrumentation.

The components use in a smart grid are electric power generators, electric power substation, transmission and distribution lines, controllers, smart meter and collector nodes [**?**]. Electronic controller uses in power generators and electric power substation to control the generation and flow of electric power. The collector nodes communicate with each of other using Zigbee or two way mesh wireless communication network. Advanced Metering Infrastructure (AMI) uses to communicate with collector nodes and utility grid. Smart grid uses a control system that allows intelligent monitoring mechanism and it makes electric power flow flexible and detail.

PHEV is connected to smart grid due to excessive usage of smart grid power [**?**]. It makes additional load on a smart grid and increases time distribution and reduces the life of the power equipments. The function of PHEV is to reduce the transportation cost and integrates the energy storage unit in power grid. The renewable energy penetrates in a smart grid and it causes frequency fluctuation. The frequency fluctuation makes system unstability. The energy storage units increase the reliability and efficiency of grid and store energy from grid and renewable sources. During stored energy period, the performance of PHEV can be deviated due to variation of renewable energy sources such as wind power and solar strength. The variation of these factors ensures the frequency fluctuation that makes the grid instability [**?**].

A number of researches have been done to control the frequency stabilization of plug-in hybrid electric vehicles during charging period. The bidirectional charging and discharging power control of PHEV has been proposed to control the power fluctuation. The design of charging controller is done based on proportional control theory. It ensures the system stability only when the generation of power is greater than the demand of power, whereas it can not control the system stability. This limitation restricts the application of charging controller. The charging or power controller also presents the unbalance frequency in the presence of various uncertainty such as the variation of wind power parameters [**?**]. However, the lack of robustness is another drawback of

charging controller.

Robust $H_\infty$ [**?**] controller has been proposed to overcome the limitation of charging controller. The advantage of $H_\infty$ controller over other controller is that it can applicable to problem involving a multivariate systems. The design of $H_\infty$ controller is done using $H_\infty$ norms minimization which deals with the require of high level of mathematical knowledge. However, in many practical control constraints, the design of $H_\infty$ controller is challenging. Fuzzy logic controller has been used for frequency stabilization for two area interconnected system. The fuzzy logic can deal with change in system parameter. Since the parameters of controller can be generally changed very quickly, which make control algorithm complicated and unstable transient response. Model predictive controller (MPC) can be applied for desirable performance in multi area power system. The MPC controller can give fast response and robustness against system parameter uncertainties but MPC suffers calculation burden problem.

The linear quadratic regulator (LQR) is an optimal controller that provides practical feedback gain. The controller has been proposed for frequency stabilization and it can minimize the cost function. The performance of LQR may be deviated due to the presence of system noise. The LQG controller is quite similar with LQR controller. It is able to provide stable performance under system noise and uncertainty. However, integral LQG controller can give better performance than the others. The motivation for designing a integral LQG controller is to provide large bandwidth, large gain and phase margin.

In this paper the comparative study of LQR, LQG and integral LQG controller is presented for frequency stabilization of a two area interconnected system. The aim of this paper is to develop high performance controller for frequency stabilization within interconnected power system. The goal of designing controller is to achieve fast transient response, zero steady state error and remove the frequency fluctuation problem. The contribution of this paper is to find the robust control strategy for frequency stabilization of smart grid within PHEV. The controller is designed to achieve the robust performance of frequency stabilization. The results presented in this paper provide the optimum frequency stabilization for the interconnected system. The comparison analysis is important for smart grid as it paves the way for frequency stabilization for high performance.

The rest of the paper is organized as follows. Section 2 presents the modeling of smart grid. Controller design for the system is carried out in Section 3. Performance evaluation of the controllers for smart grid is presented in Section 4. The paper is concluded in Section 5.

## 2. System Modelling

Two area interconnected power system shown in Figure 1 is used for the study of smart grid. Each area consists of wind farm (WF), thermal power plant (THP), load frequency control (LFC), PHEV and load. In area 1, Power capacities of WF, THP and load are 12038 MW, 33090 MW and 7090 MW respectively. The power capacities of WF, THP and load in area 2 are 2530 MW, 5560 MW and 7090 MW respectively [**?**]. The number of PHEV in area 1 is 640000 and the number of PHEV in area 2 is 200000 respectively. The rated power capacity for one PHEV is 5 KW. Hence total power capacities of PHEV in both areas are 3200 MW and 100 MW respectively.

**TABLE 1:** System parameter values

| Parameters | Area 1 | Area 2 |
|---|---|---|
| Reference frequency $f_0$(Hz) | 50 | 50 |
| Inertia Constant $M$(s) | 9 | 9 |
| Frequency characteristic of load except PHEV$D$(pu) | 2 | 2 |
| ACE calculation time constant $T_{ACE}$(s) | 10 | 10 |
| Frequency bias factor $K_{(system)}$ | 10 | 10 |
| Frequency Characteristic per PHEV (KW/Hz) | 2.5 | 2.5 |
| Number of PHEV | 640000 | 640000 |
| Total frequency characteristic $K_{PHEV}$ | 1600 | 1600 |
| Time constant of PHEV $T_p$ | 1 | 1 |
| Tie-line stiffness coefficient $T$(s) | 5 | 5 |
| Area capacity ratio $a_{(21)}$ | 0.17 | 0.17 |

The PHEV is in charge of seducing the peak value of frequency deviation against the abrupt load changes. Linearized model of two area interconnected power system is shown in Figure 1. In both areas of Figure 1 the generator and the frequency sensitive load are represented by the first order transfer function with inertia constant M and damping coefficient D. Using first order transfer function with gain $K_{PHEV}$, i =1,2 and time constant $T_p$ is in series with controller with gain and time constant. The model of wind power and load changes are considered as $\Delta P_W$ and $\Delta P_L$ respectively. In both areas the presented controller is $1^{st}$ order transfer function with time constant $T_{ACEi}$ and the area control error is $(ACE_i)$. Here,
$ACE_1 = f_o K_{system1} \Delta f_1 - \Delta P_{21}$
$ACE_2 = f_o K_{system2} \Delta f_2 - a_{21} \Delta P_{21}$
where, $K_{system1}$ and $K_{system2}$ are the system constant of area 1 and 2 respectively, $f_o$ is the normal system frequency, $a_{21}$ is the area capacity ratio, $\Delta P_{21}$ is the deviation of tie line power from area 2 to area 1, $\Delta f_1$ and $\Delta f_2$ is the deviation of frequency in area 1 and area 2 and T is synchronizing power coefficient. The area control error $(ACE_i)$ sends the signal from controller to PHEV using smart meters. Signal is sent to PHEV via the smart meter. The load frequency control (LFC) $f_{LFC1}, f_{LFC2}$ is considered as a input signal for the area 1 and area 2 respectively. The system parameters are given in Table 1.

Consider the following state space model for two area interconnected linear time invariant system

$$\Delta \dot{X} = A\Delta X + B\Delta u \tag{1}$$

$$\Delta Y = C\Delta X \tag{2}$$

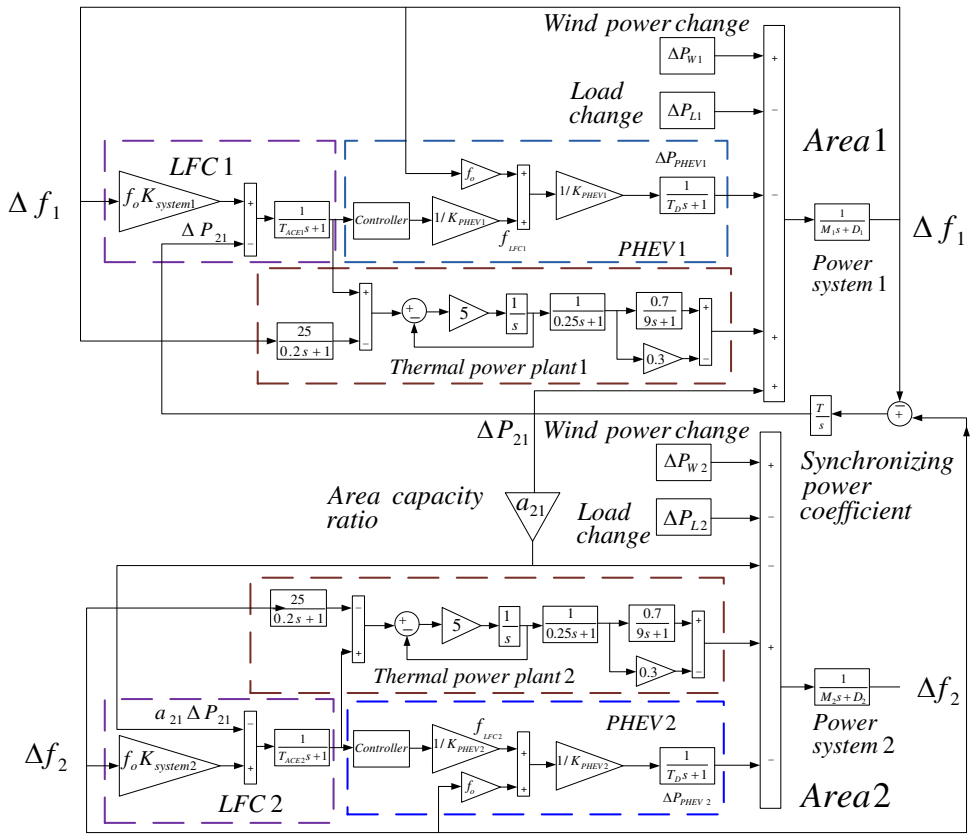


**Figure 1:** Linearized model of two-area interconnected system

Where A is the system matrix, B is the input matrix and C is the output matrix as follows:

$$A = \begin{bmatrix} \frac{-D_1}{M_1} & 0 & \frac{-1}{M_1} & \frac{-1}{M_1} & 0 & 0 & 0 \\ \frac{-f_o K_1}{T_1} & \frac{-1}{T_1} & 0 & \frac{-1}{T_1} & 0 & 0 & 0 \\ K_3 f_o & 0 & -1 & 0 & 0 & 0 & 0 \\ -T & 0 & 0 & 0 & T & 0 & 0 \\ 0 & 0 & 0 & \frac{-a_{21}}{M_2} & \frac{-D_2}{M_2} & 0 & \frac{-1}{M_2} \\ 0 & 0 & 0 & \frac{-a_{21}}{T_2} & \frac{-f_o K_1}{T_2} & \frac{-1}{T_2} & 0 \\ 0 & 0 & 0 & 0 & K_4 f_o & 0 & -1 \end{bmatrix};$$

$$B = \begin{bmatrix} 0 & 0 \\ 0 & 0 \\ K_3 & 0 \\ 0 & 0 \\ 0 & 0 \\ 0 & 0 \\ 0 & K_4 \end{bmatrix}; C = \begin{bmatrix} 0 & 1 & 0 & 0 & 0 & 0 & 0 \\ 0 & 0 & 0 & 0 & 0 & 1 & 0 \end{bmatrix}$$

Here, $K_1 = K_{system1}$, $K_2 = K_{system2}$, $K_3 = K_{PHEV1}$, $K_4 = K_{PHEV2}$ and $T_2 = T_{ACE2}$ the state vector $\Delta X = [\Delta f_1, ACE_1, \Delta P_{PHEV2}]^T$. The input vector and the output vector for the two area system is $\Delta u = [f_{LFC1}, f_{LFC2}]^T$ and $\Delta Y = [ACE_1, ACE_2]^T$, respectively.

## 3. Controller Design

### 3.1. LQR Controller Design

The LQR is defined as where the system dynamics are described as set of differential equations and the cost function is described as quadratic function [**?**]. Using mathematical algorithm the cost function has been minimized with weighting factors. The performance criterion of equation (1) and (2) determined by the cost function is as follows:

$$J_\infty = \int_0^\infty [x^T(t)Qx(t) + u^T(t)Ru(t)]dt \tag{3}$$

where Q is non negative definite and R is positive definite. Now the optimal control position of $J$ is found using the state feedback law. $u(t) = -Kx(t)$ where k is the controller gain that is determined by following way

$$K = R^{-1}B^T P \tag{4}$$

and here P is the unique positive definite solution to Algebric Riccati Equation (ARE). The ARE is as follows

$$A^T P + PA - PBR^{-1}B^T P + Q = 0 \tag{5}$$

**TABLE 2:** Design parameter values for integral LQG

| Design parameter | $\gamma_1$ | $\gamma_2$ | $\gamma_3$ | $Q$ | $R$ |
|---|---|---|---|---|---|
| Value | $1 \times 10^{12}$ | $1 \times 10^{-8}$ | $1 \times 10^{6}$ | $1 \times 10^{7}$ | $5 \times 10^{-3}$ |

### 3.2. LQG Controller Design

The LQG controller is the combination of Kalman filter with Linear Quadratic Regulator (LQR). LQG control can be applied to linear time invariant systems as well as linear time variant systems. It deals with uncertain linear systems disturbed by additive white gaussian noise, having incomplete state information [**?**]. Practically it is used for predicting future courses of dynamic systems that are likely as:

$$\dot{x} = Fx + Gu + w \tag{6}$$

the measurement may be linearly related.

$$z = Hx + v \tag{7}$$

The process noise matrix $Q$ with noise vector w and measurement noise matrix $R$ is related to the measurement noise vector v according to

$$\begin{aligned} Q &= E[ww^T] \\ R &= E[vv^T] \end{aligned} \tag{8}$$

Here, $E$ represents expected value or average value of the parameter of the system.

A kalman filter is optimal recursive data processing algorithm. It computes all avilable data, regardless of their precession, to estimate the current value of the variable of interest. Operation of kalman filter can be divided with few steps: (1) state vector propagation, (2) parameter covariance matrix propagation, (3) Compute Kalman Gain, (4) State vector update, (5) Parameter Covariance Matrix update

**Step 1:** State Vector Propagation:

$$\begin{aligned} \hat{x}^-(t_n) &= \phi.(\tau)\hat{x}^+ + t_{n-1} \\ R &= E[vv^T]. \end{aligned} \tag{9}$$

where $\hat{x}^-(t_n)$ estimate of state vector at iteration n and $\phi(\tau)$ is state propagation matrix and $\hat{x}^+(t_n)$ estimate of the state vector at iteration n-1 including measurement n-1.

**Step 2:** parameter covariance matrix propagation from iteration n-1 to n:

$$\hat{P}^-(t_n) = \phi.(\tau)P^+t_{(n-1)}\phi.(\tau) + Qt_n \tag{10}$$

where $\phi(\tau)\phi(\tau)^T$ is the state propagation matrix and the transpose calculated for time spacing t. $P^-(t_n)$ is the parameter covariance matrix at iteration n not including measurement n. $Q(t_n)$ is the process covariance matrix.

**Step 3:** Kalman gain computation:

$$K(t_n) = P^-(t_n)H^T[HP^-(t_n)H^T + R(t_n)]^{-1} \tag{11}$$

where $P^-(t_n)$ is the parameter covariance matrix at iteration n not including measurement n. The design matrix transpose is $HH^T$. The Kalman Gain and measurement covariance matrix are $K(t_n)$ and $R(t_n)$ respectively.

**Step 4:** state vector update:

$$\hat{x}^+(t_n) = \hat{x}^-(t_n) + K(t_n)[y(t_n) - H\hat{x}^-(t_n)] \tag{12}$$

where the estimate of the state vectors at iteration n and not including measurement n are $\hat{x}^+(t_n)$ and $\hat{x}^-(t_n)$ respectively. The measurement vector is represented as $y(t_n)$. The kalman gain is $K(t_n)$ and The design matrix is shown as $H$.

**Step 5:** Parameter covariance matrix update:

$$P(t_n^+) = [I - K(t_n)H]P(t_n^-) \tag{13}$$

where $P(t_n^+)$ and $P(t_n^-)$ is the parameter covariance matrix at iteration n, not including measurement n. If kalman gain is deliberately set sub-optimal then use

$$P(t_n^+) = [I - K(t_n)H]P(t_n^-)[I - K(t_n)H]^T \tag{14}$$

Time Update(Predictor): update expected value of x is shown as follows

$$\hat{x}^+ = A\hat{x}_{(k-1)} + Bu_k \tag{15}$$

The update error covariance matrix is p represented as

$$P_k^-(+) = AP_{(k-1)}A^T + Q \tag{16}$$

The optimal kalman gain $K_k$ is as

$$K_k = P_k^- H^T(HP_kH^T + R)^{-1} \tag{17}$$

### 3.3. Integral Linear Quadratic Gaussian Controller Design

First consider the state space model for the system is

$$\dot{x}(t) = Ax(t) + Bu(t) + D_1w(t) \tag{18}$$

$$y(t) = Cx(t) + D_2\overline{w}(t) \tag{19}$$

where $x$ represents state vector, $u$ is the input to the system, $y$ is the measured output from the plant and $w$ is a gaussian white noise disturbance acting on the system. $A$ represents the system matrix, $B$ is the input matrix, $C$ is the output matrix, and $D_1$ and $D_2$ is the system noise matrices. An optimal LQG controller design will begin form that state space model. Desiging of optimal LQG controller with the feedback controller designed in such a way that it minimizes cost function.

$$J = \lim_{T \to +\infty} \mathbf{E}\Big[\frac{1}{T}\int_0^T (x(t)^TQx(t) + u(t)^TRu(t))dt\Big]. \tag{20}$$

Here, $Q \geq 0$ and $R > 0$ are symmetric weighting matrices. $\mathbf{E}[.]$ is the expected value. In the cost function (**??**), the term $x^TQx$ corresponds to a requirement to minimize the

states of the system. the term $u^T Ru$ corresponds to the requirement to minimize the size of control inputs. The selection of matrices $Q$ and $R$ in the cost function (**??**) depends on the desired performance objective of the system. Minimizing the tracking error between the command signal and measured output is the main control objective. Integarl controller can be used in smart grid, because it has excellent low frequency tracking performance. The updated plant with an integral controller of the plant can written as

$$\dot{x_f}(t) = A_f x_f(t) + B_f u(t) + B_f w_1 \tag{21}$$

$$z_f(t) = C_f x_f(t) + v \tag{22}$$

Here, $v = [w_2 \ w_3]^T$ is the augmented state and output vectors are $x_f = [x \ \int y dt]^T$ and $z_f = [z_1 \ z_2]^T$ . The matrices for the augmented system are defined as $A_f = \begin{bmatrix} A & 0 \\ C & 0 \end{bmatrix}$, $B_f = \begin{bmatrix} B \\ 0 \end{bmatrix}$, and $C_f = \begin{bmatrix} C & 0 \\ C & I \end{bmatrix}$ where $A$, $B$, $C$ are defined in (**??**)-(**??**).

The quantity $w_1$ is the mechanical noise entering into the system which is assumed as the gaussian white noise with variance $\gamma_1^2$. The quantity $w_2$ is the sensor noise from the output $y$ of the system which is also assumed to be gaussian white noise with variance $\gamma_2^2$. For the augmented plant outlined in (**??**)-(**??**), the integral LQG controller is designed by defining a quadratic cost function of the form

$$J = \lim_{T \to +\infty} \mathbf{E} \frac{1}{T} \int_0^T (x^T Q x + f(y)^T Q_I f(y) + u^T R u) dt, \tag{23}$$

where $f(y) = \int_0^T y(\tau) d\tau$, $Q \geq 0$, $Q_I \geq 0$, and $R > 0$ are weighting matrices associated with the state, the integral state, and the control input respectively.

The integral LQG controller is represented as

$$\dot{\widehat{x}}_f(t) = A_f \widehat{x}_f(t) + B_f u(t) + K(z_f - C_f \widehat{x}_f) \tag{24}$$

$$u(t) = -L \widehat{x}_f. \tag{25}$$

Here, $\widehat{x}_f$ is the augmented state vector estimated by linear Kalman filter and $K$ is the associated Kalman gain defined as

$$K = P_K C_f^T R_K^{-1} \tag{26}$$

where $P_K \geq$ is the solution of the following Riccati equation:

$$\dot{P_K} = A_f P_K + P_K A_f^T - P_K C_f^T R_K^{-1} C_f P_K + Q_K \tag{27}$$

Here, $Q_K \geq 0$ and $R_K > 0$ are process and measurement noise matrices defined as

$$Q_K = \gamma_1^2 \quad R_K = \begin{bmatrix} \gamma_2^2 & 0 \\ 0 & \gamma_3^2 \end{bmatrix} \tag{28}$$

where $\gamma_1$ is the standard deviation associated with the process noise $w_1$. $\gamma_2$ and $\gamma_3$ are the standard deviation associated with the output sensor noise $w_2$ and the augmented integral output sensor noise is $w_3$.

The feedback gain matrix $L$ in (**??**) is given by

**TABLE 3:** Settling Time Comparison

| **Controller** | **settling time for input 1 to output 1 (in sec)** | **settling time for input 1 and output 2 (in sec)** | **settling time for input 1 and output 3 (in sec)** | **settling time for input 1 and output 4 (in sec)** |
|---|---|---|---|---|
| LQR Controller | 4.16 | 347 | 374 | 0.675 |
| LQG Controller | 4.77 | 6.83 | 11.5 | 8.26 |
| ILQG Controller | 0.0761 | 1.03 | 1.3 | 1.38 |

$$L = R_C^{-1} B_f P_C \tag{29}$$

where $P_C \geq 0$ is the solution of the following matrix riccati equation:

$$\dot{P_C} = A_f P_C + P_C A_f^T - P_C C_f^T R_C^{-1} C_f P_C + Q_C \tag{30}$$

Here, $R_C = r$ is the controller weighting matrix and

$$Q_C = C_f^T \begin{bmatrix} 1 & 0 \\ 0 & q \end{bmatrix} C_f \tag{31}$$

The controller design parameters $\gamma_1$, $\gamma_2$, $\gamma_3$, $r$ and $q$ are adjusted for good controller performance. This includes a requirement that the control system has a suitable gain and phase margins and a reasonable controller bandwidth.

## 4. Performance Evaluation

The performance of the controllers is investigated in this section. The simulation results of the proposed controllers are presented using Matlab. The results are shown for individual controller. The parameter values of Table 1 is used to measure the performance of proposed system. The performance of the controller can be varied due to change in system parameter, renewable energy source that ensures the instable performance of smart grid.

The open-loop step response for two area interconnected system is shown in Figure 2(a) that provides undesirable nature of responses. This causes poor frequency stabilization for the system. The closed-loop step response for two area interconnected system given in Figure 2(b). The comparison results are reported in Table 3. The settling time for integral LQG is very small for every output with respect to every input and makes it superior controller in compared with LQR and LQG controller. The integral LQG controller has zero steady state error and less rising time for the system. The transient time period is also very small of integral LQG controller in comparison with others.The closed-loop frequency response of two area interconnected system is shown in Figure 3. The proposed controllers have stable poles for the nominal system. The integral LQG controller is able to provide high gain and phase margin for each output with its corresponding input. For all cases, the integral LQG controller shows the high performance compared to others

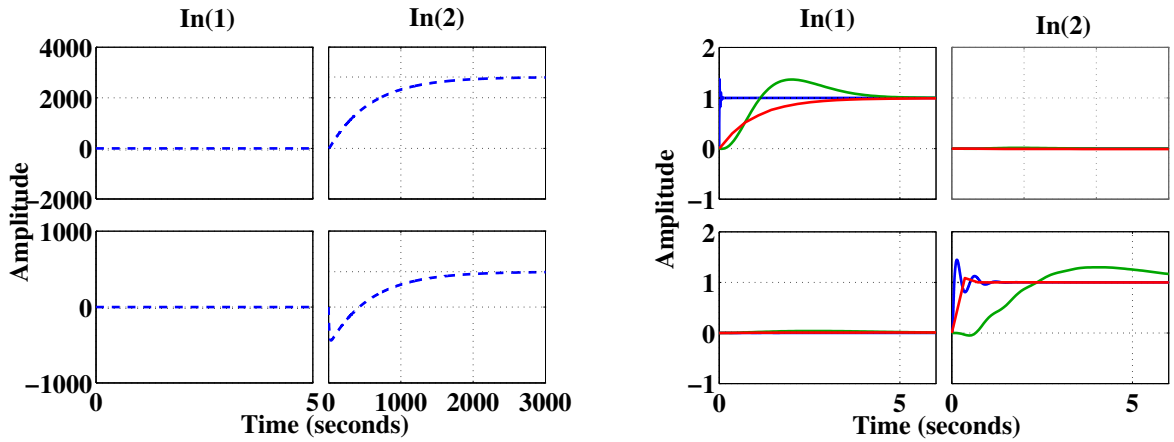


(a) (b)

**Figure 2:** (a) The dashed line (- -) represent open-loop step response for the plant, (b) The blue (- -) solid line , green solid line (-) and red solid (-) line represent closed-loop step response of integral LQG , LQG and LQR controller respectively

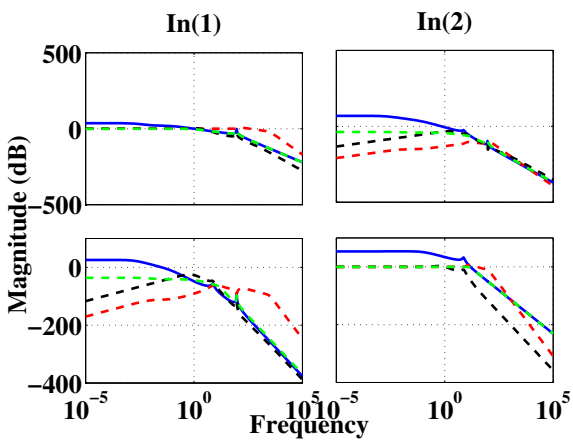


**Figure 3:** Comparison of bode diagram. The green (- -) dashed line represents LQR controller. The black (- -) dashed line shows LQG controller and red (- -) dashed line represents integral LQG controller. The blue (-) solid line line represents open loop system response.

proposed controllers for frequency stabilization of two area interconnected power system.

## 5. Conclusion

The design of robust frequency controller is presented in this paper for frequency stabilization control for a two area interconnected system . The comparative study of controllers is designed for stabilization of frequency fluctuation in the smart grid with renewable energy. The results of this paper is of interest to engineering community because the comparative study presented in the paper provides the way of optimum frequency stabilization for a two area interconnected power system. Simulation results in two area interconnected power system and comparison study shows the superior robustness has integral linear quadratic gaussian controller. The controller has superior performance against system parameter variation in comparison with conventional controllers.

## References


[1] A.B.M.Shawkat Ali, "Smart Grids opportunities,Developments and Trends," Springer, 2013.

[2] Subroto K. Sarkar, Faisal R. Badal and Sajal K. Das, "A comparative study of high performance robust PID controller for grid voltage control of islanded microgrid," *International Journal of Dynamics and Control*, pp. 1-11, Springer, 2017.

[3] A. Yokoyama, "Smarter grid II," *IEEJ Journal*, vol.30, no.3, pp.163-167, 2010.

[4] Maniza Armin, Priyo Nath Roy, Subroto K. Sarkar and Sajal K. Das, "LMI Based Robust PID Controller Design for Voltage Control of Islanded Microgrid,"*Asian Journal of Control*, 2017.

[5] Issarachai Ngamroo, "Specified structure mixed $H_2/H_\infty$ control-based robust frequency stabilization in a smart grid by plug-in hybrid electric vechiles," *International Journal of Innovative Computing, Information and Control*, vol.9, no.1, pp.81-97, 2013

[6] Subroto K. Sarkar and Sajal K. Das, "High performance nonlinear controller design for AC and DC machines: partial feedback linearization approach," *International Journal of Dynamics and Control*, pp. 1-15, Springer, 2017. 2005.

[7] Subroto K. Sarkar and Sajal K. Das, "Nonlinear modeling and control of DC machines: A partial feedback linearization approach," vol.4, *Electrical, Computer & Telecommunication Engineering (ICECTE), International Conference on*, pp. 1-4, 2016.

[8] M. Takagi, K. Yamaji and H. Yamamoto, "Power system stabilization by charging power management of plug-in hybrid electric vehicles with LFC signal," *Proc. of IEEE Vehicle Power and Propulsion Conf.*, pp.822-826, 2009.

[9] H.S.Koak.Y.LeebH.C.Kim, "An intelligent based LQR controller design to power system stabilization,"*Electric Power Systems Research*, vol. 4 pp.19,2004

[10] Sajal K. Das, Hemanshu R. Pota and Ian R. Petersen, "Passive Damping Controller Design for Nanopositioners," *American Control Conference (ACC)*, 2014.

# A New Method for Smooth Trajectory Planning for 3R Robot Arm Using Enhanced Particle Swarm Optimization Algorithm

Soniya Yeasmin, Fatematuzzohura Karima, Shahnaz Kabir and Pintu Chandra Shill
Department of Computer Science and Engineering
Khulna University of Engineering and Technology
Khulna-9203, Bangladesh
soniya.cse08@gmail.com, kareema.zohra@gmail.com, sshahnazkabir@yahoo.com, and lpintucskuet@yahoo.com

*Abstract*— **Optimum trajectory planning for robot arm plays an important role in the area of robotics. In this study, we propose the novel point-to-point motion and trajectory planning in obstructed dynamic environments for a three link robot arm using the enhanced particle swarm optimization (EPSO) algorithm. Trajectory planning for a three link robot arm finds an optimal path from a source node to a destination node in an obstructed environment. The developed EPSO has been widely used for constructing an optimal trajectory by utilizing its strong optimization capability. The proposed method significantly reduce the traveling time and space for generating the optimal path, does not exceed a given maximum torque without colliding obstacles in the robot work area. Quadrinomial and quintic polynomials are used to illustrate the parts which join the initial, intermediate and final points at joint-space. Direct kinematics is used in order to handle the configuration of robot arm. The results of simulation and comparison studies depict the capability and performance of the suggested method.**

***Keywords— Trajectory and motion Planning, 3R robot arm, Enhanced particle swarm optimization, Collision avoidance.***

## I. INTRODUCTION

Motion planning is the process of generating a sequence of actions that moves an object from an initial state space to a goal state space while satisfying a set of constraints. Many challenging tasks related to robot arm motion planning have been applied successfully in several fields such as machine production[1], medical robotics[2] to aerospace robotics[3]. In this study, robotics field, particularly the PTP and trajectory planning for robot arm are addressed. Several traditional techniques[4]–[5] have been employed for trajectory and motion planning of robot.

S. G. Yue et al.[6] proposed a method for robot trajectory to reduce the vibration for redundant robot arm in joint space according to genetic algorithms(GAs).The authors used kinematics redundancy as design variables and quadrinomial and quintic polynomial to define the point-to-point trajectory. Zhe Tang et al. [7] introduce a technique for robot trajectory on the basis of third–order spline interpolation in order to achieve a smooth biped swing leg trajectory.This trajectory is generated to minimize the change of quick velocity that can be occurring during the collision of the biped swing leg with the ground. Their method illustrate that the effect impacts can be maintained when the swing foot's heel touches the ground.

Savsani and Jhala [8] introduce an optimal trajectory planning method for robot arm through artificial bee colony(ABC). Ang, Pham and Ng propose a motion planning method under obstacles [9] through the Bees Algorithm. The target function for both propose algorithm is to reduce the trajectory time-space, does not exceed a given maximum torque avoiding obstacles in the robot work area.

Moreover, a sustainable number of methods based on evolutionary algorithms (EAs) have been applied for robot manipulators under obstacles [10]–[12] successfully. Tuncer et. al proposed a technique to generate an optimal pathway for mobile robot in a progressive surrounding with obstacle based on a GA[10]. They used the numbered grid representation model that is widely used for motion area of mobile robot. His technique further will be extended to an n-dimensional space.

Yano and Tooda introduce method based on the GA to tackle the movement and position of an end-effector on the edge of a two-joint robot arm [11]. In their method, they used the Cartesian space and joint space objective functions and combined these objective functions in order to optimize the robot trajectory. In this way, generate the optimal trajectories and to minimize the joint rotation. Shintaku [12] introduce a technique on the basis of a GA for an underwater manipulator to solve the collision free trajectory. Shintaku use a polynomial to approximate the joint space trajectory time. They used the GA to determine polynomial parameters in order to reduce the fitness value of the objective function.

Here, we came up with the idea of a point-to-point trajectory and motion planning of a 3R robot arm in obstructed environments based on developed PSO with adopting the inverse dynamics and the direct kinematics. The optimum collision-free trajectory and motion is the one that lessen trajectory time and space, without surpassing the highest torque, can avoid obstacles in the workspace of robot. Also, a number of simulations and experiments for trajectory planning of robot arm are carried out, which illustrate the power and efficiency of the proposed algorithm. The main differences between the previous approaches lie mainly in the type of PSO

978-1-5386-2307-7/17/$31.00 ©2017 IEEE

coding and how the parameters of dynamics of 3R robot are optimized.

Bearing these concepts, the remaining part of the study is arranged as shown below: Section II introduces trajectory planning of 3R robot arm, Section III presents how PSO can be used to optimize the parameters of 3R robot arm motion and trajectory planning scheme. Section IV presents some evolution criteria. Based on this conception, section V presents the simulation results. Finally, section VII sketches the key points of our proposed method referred to as conclusions.

## II. THE TRAJECTORY AND MOTION PLANNING

The motion and trajectory planning is the process of finding the possible link configuration and trajectories in a way so that end effector moves from starting node to target node satisfying with given constraints. In Fig. 1, it is shown that the various segments and sub-segments with continuous acceleration through intermediate points are connected on point-to-point (PTP) trajectory and motion.

In the case of robot, n and m are the amount of manipulator degree of freedom and the amount of degree of freedom of end-effectors respectively. The robot position is represented by a quadrinomial and a quintic polynomial and velocity and acceleration at the starting and end of a path space is used to specify the position. Let us consider $m_p$ is the intermediate points via in-between the start and end nodes.

From the initial points to intermediate point, $m_p$ through points, these segments is defined by a quadrinomial as follows:

$$\theta_{i,i+1}(t) = a_{i0} + a_{i1}t_i + a_{i2}t_i^2 + a_{i3}t_i^3 + a_{i4}t_i^4, (i = 0,....., m_p - 1) \quad (1)$$

Here $(a_{i0},.....,a_{i4})$ are used as constants and the constraint are given as:

$$\theta_i = a_{i0} \quad (2)$$

$$\theta_{i+1} = a_{i0} + a_{i1}T_i + a_{i2}T_i^2 + a_{i3}T_i^3 + a_{i4}T_i^4 \quad (3)$$

$$\dot{\theta}_i = a_{i1} \quad (4)$$

$$\dot{\theta}_{i+1} = a_{i1} + 2a_{i2}T_i + 3a_{i3}T_i^2 + 4a_{i4}T_i^3 \quad (5)$$

$$\ddot{\theta}_i = 2a_{i2} \quad (6)$$

Here $T_i$ is the parameter used for execution time from point i to point i+1.The solution for the five unknown parameters can be achieved using the equations given below:

$$a_{i0} = \theta_i \quad (7)$$

$$a_{i1} = \dot{\theta}_i \quad (8)$$

$$a_{i2} = \ddot{\theta}/2 \quad (9)$$

$$a_{i3} = (4\theta_{i+1} - \dot{\theta}_{i+1}T_i - 4\theta_i - 3\ddot{\theta}_i T_i^2)/T_i^3 \quad (10)$$

$$a_{i4} = (\dot{\theta}_{i+1}T_1 - 3\theta_{i+1} + 3\theta_i + 2\dot{\theta}_i T_i + \ddot{\theta}_i T_i^2/2)T_i^4 \quad (11)$$

The acceleration of intermediate point (i+1) which can be calculated as follows:

$$\ddot{\theta}_{i+1} = 2a_{i2} + 6a_{i3}T_i + 12a_{i4}T_i^2 \quad (12)$$

Between the numbers of $m_p$ intermediate points to the final via points, quintic polynomoial is used to explain these portions:

$$\theta_{i,i+1}(t) = b_{i0} + b_{i1}t_i + b_{i2}t_i^2 + b_{i3}t_i^3 + b_{i4}t_i^4 + b_{i5}t_i^5, (i = mp) \quad (13)$$

Where these constants are given as:

$$\theta_i = b_{i0} \quad (14)$$

$$\theta_{i+1} = b_{i0} + b_{i1}T_i + b_{i2}T_i^2 + b_{i3}T_i^3 + b_{i4}T_i^4 + b_{i5}T_i^5 \quad (15)$$

$$\dot{\theta} = b_{i1} \quad (16)$$

$$\dot{\theta}_{i+1} = b_{i1} + 2b_{i2}T_i + 3b_{i3}T_i^2 + 4b_{i4}T_i^3 + 5b_{i5}T_i^4 \quad (17)$$

$$\ddot{\theta} = 2b_{i2} \quad (18)$$

$$\ddot{\theta}_{i+1} = 2b_{i2} + 6b_{i3}T_i + 12b_{i4}T_i^2 + 20b_{i5}T_i^3 \quad (19)$$

Where $T_i$ depicts the execution time from point i to point i+1. The six unknown parameter can be calculated as:

$$b_{i0} = \theta_i \quad (20)$$

$$b_{i1} = \dot{\theta}_i \quad (21)$$

$$b_{i2} = \ddot{\theta}_i/2 \quad (22)$$

$$b_{i3} = (20\theta_{i+1} - 20\theta_i - (8\dot{\theta}_{i+1} + 12\dot{\theta}_i)T_i - (3\ddot{\theta}_i - \ddot{\theta}_{i+1})T_i^2)/2T_i^3 \quad (23)$$

$$b_{i5} = (12\theta_{i+1} - 12\theta_i - (6\dot{\theta}_{i+1} + 6\dot{\theta}_i)T_i - (\ddot{\theta}_i - \ddot{\theta}_{i+1})T_i^2)/2T_i^5 \quad (24)$$

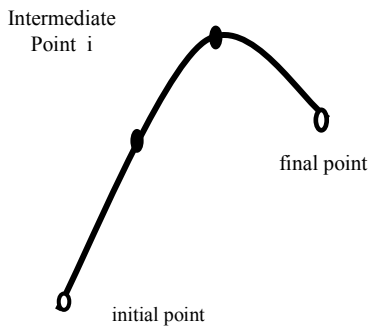


Figure 1. PTP trajector with intermediate points

From the above equation, we have derived the following parameters: the joint angles, each intermediate points joint angular velocities, defined by ( n * $m_p$ parameters), each path segment execution time specify by ($m_p$ + 1 parameters) and the ending configuration position (n – m).

For 3-link robot, consider $m_p$=1 and n=3. It should be noted that each intermediate point joint angular acceleration can be determine using equation (12). There will be eight parameters if intermediate points are joined through quintic polynomial which is time consuming. For this reason we adopt both quadrinomial and quintic polynomial to produce path segment.

## III. THE DEVELOPED PSO BASED MOTION PLANNING SCHEME

The conventional particle swarm optimization (PSO) is considered as an iterative and stochastic computational optimization problem solving process and all the particles are initialized randomly. The particles are flying by the problem space through learning from particles which have the best experiences. For this reason, according to the searching criteria, the particle has a property for flying to the better search field.

The ith particle velocity $v_i^d$ and position $x_i^d$ are updated over dth dimension as follows [13]-[14]

$$_{n+1}v_i^d = \omega_n v_i^d + c_1 r_{1_i}^d (pbest_i^d - {}_n x_i^d) + c_2 r_{2_i}^d (gbest^d - {}_n x_i^d),$$

$$_{n+1}x_i^d = {}_n x_i^d + {}_{n+1} v_i^d$$

where $n$ is the migration number. $c_1$ and $c_2$ defined as the acceleration constants used for the weighting of stochastic acceleration terms. The acceleration terms are used to move the particle to the direction of pbest and gbest positions. The parameters $r_1$ and $r_2$ are used as two random functions between 0 and 1 and $x_i = (x_i^1\ x_i^2, x_i^3, ....., x_i^D)$ is the position vector of ith particle .The best previous position of the ith particle having the best fitness value, $pbest_i$ is represented through the vector, $pbest_i = (pbest^1, pbest^2, pbest^3, ....pbest^D)$, $gbest_i = (gbest^1, gbest^2, gbest^3, ....gbest^D)$ is the best position discovered by the whole population. The ith particle rate of position change defined as velocity is $v_i = (v_i^1\ v_i^2, v_i^3, ....., v_i^D)$. The inertia weight $\omega$ is used for balancing the search ability between the global search and local search. Fig. 2 shows the flowchart of developed enhanced PSO with 3R robot arm.

**Enhanced PSO (EPSO):** The conventional PSO suffers premature convergence' is typically caused by quick loss of diversity. In order to achieve a trade-off between exploration and exploitation abilities, an enhancing diversity mechanism is included. The diversity mechanism which improves the performance of the conventional PSO as follows:

$$Diversity = \frac{1}{N}\sum_{i=1}^{N}\sqrt{\sum_{j=1}^{D}(x_{ij}(t) - \bar{x}_j(t))^2}$$

$$\text{Where } \bar{x}_j(t) = \frac{\sum_{i=1}^{N} x_{ij}(t)}{N}$$

The EPSO planning scheme presents an optimized trajectory and motion planning with minimum time and space which does not exceed a given maximum torque without colliding obstacles in the robot work area. The motion planning chooses direct kinematics in order to handle the configuration of robot arm.

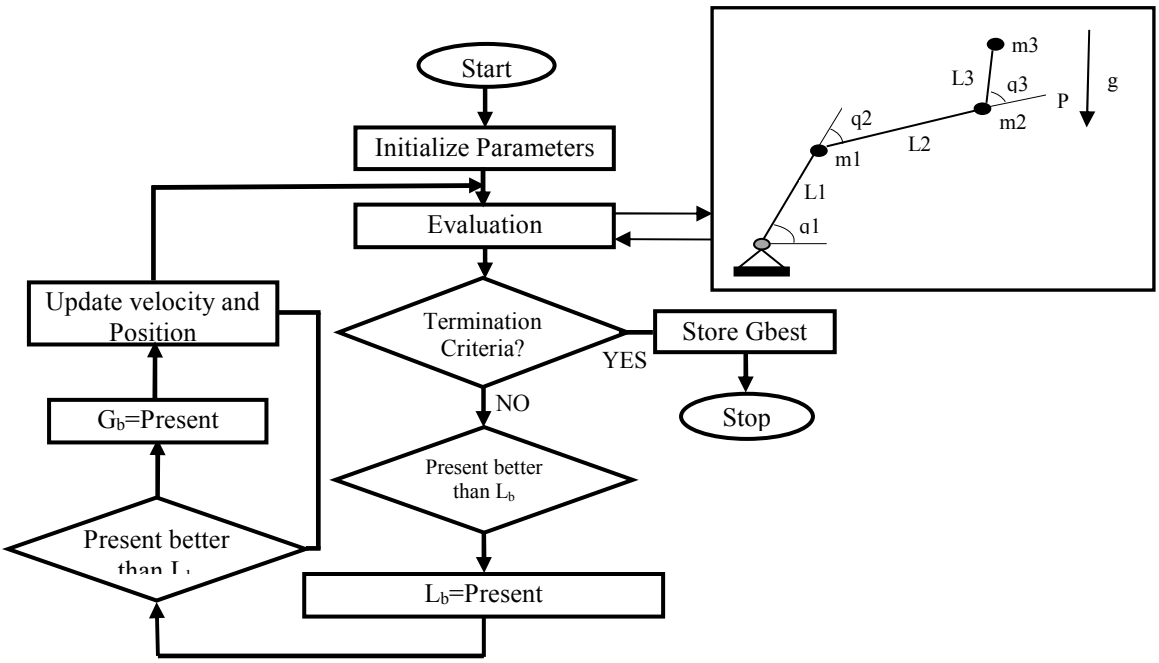


Figure 2. Flow Chart of Developed EPSO with 3R robot Arm

The nine parameters for 3-link robot arm must be optimized as shown in the below:

$$[q_1, q_2, q_3, q_g, \dot{q}_1, \dot{q}_2, \dot{q}_3, t_2, t_2]$$

Where $q_i$ and $\dot{q}_i$ are the ith joint angle and velocity of intermediate joint, $q_g$ represents the final configuration of the end-effectors global angle. The global angle is equal to the sum of joint angles of manipulator [15], $t_1$ and $t_2$ are execution time from starting point to intermediate via point and intermediate to ending point respectively.

## IV. EVOLUTION CRITERIA

Four evolution criteria are acclimated to qualify the developing trajectory robotic manipulators in the obstacle work area. All evolution criteria are converted into penalty function which is to be reduced. Every criterion is calculated severally and is combined with evaluation of fitness function. For calculating the candidate trajectories fitness function, $f_f$ is defined as:

$$f_f = \beta_1 f_{ot} + \beta_2 f_q + \beta_3 f_c + \beta_4 t_T \tag{25}$$

The optimization objective consists for finding a arrangement of parameters which are used to minimize $f_f$ as per the needs generated from the weighting factors $\beta_i$ (i =1,..,4), where every $\beta_i$ is specify in a different way. The $f_{ot}$ is called a cost function [16] denoted in (28) that explains over driving amount in connection with the maximum torque $\tau_{i\max}$ which is requested for the ith link motor for the trajectory.

$$f_{ot} = \sum_{j=1}^{b} \sum_{i=1}^{a} f_i^j \tag{26}$$

Where a, b are the robot links number and joint position from starting to ending point.

$$f_i^j = \begin{cases} 0, & \left|\tau_i^j\right| < \tau_{i\max} \\ \left|\tau_i^j\right| - \tau_{i\max}, & \text{otherwise} \end{cases} \tag{27}$$

Where $\tau_{i\max}$ and $\tau_i^j$ represents the maximum torque and the torque of ith link, respectively.

The $f_q$ represents as the distance of total joint traveling of the robot arm is defined by the equation as follows:

$$f_q = \sum_{i=1}^{a} \sum_{j=2}^{b} \left| q_{ij} - q_{ij-1} \right| \tag{28}$$

The total Cartesian trajectory length, $f_c$ is defined as:

$$f_c = \sum_{j=2}^{b} d(p_j, p_{j-1}) \tag{29}$$

Where $p_j$ represents the robot $j$th intermediate arm Cartesian position .The distance between the two parameters is calculated by the function d(.,.). The term $t_T$ defines as total depleted time for robot motion, can be expressed below:

$$t_T = t_1 + t_2 \tag{30}$$

Here, $t_1$ symbolizes the execution time from the starting to intermediate composition. On the other hand, $t_2$ refers to the time from intermediate to the ending composition.

The following function is a combination of two functions. One is for obstacle avoidance and the other is for freeing space fitness represented by $f_{ob}$ and $f_f$ respectively. The combined function representing the obstacle existence workspace is expressed as:

$$f = f_f / f_{ob} \tag{31}$$

With the capacity to avoid the obstacle encountering, the robot manipulator moves from point to point in the work area using the function $f_{ob}$ and it can be illustrated as [17], all the connections in the configuration which are constructed by the joint positions in-between the starting and the ending robot configuration do not converge at any point in the obstacle area. Here, $f_{ob}$ = 1 is the fitness value.

$$f_{ob} = \begin{cases} 1, & \sum_{j=1}^{b} \sum_{i=1}^{a} (link_{ij} \cap obstacle) = 0 \\ 0, & \text{otherwise} \end{cases} \tag{32}$$

## V. SIMULATION AND RESULTS

To verify the success of the suggested approach, it is applied to a 3R robot arm with obstructed dynamic environments. Moreover, we have conducted several experiments to evaluate our approach with different parameter setting both in PSO and 3R robot arm.

The first experiment is conducted while moving the 3R robot arm from the start point ($x$=0m, y=2.3m, $q_g$=80°) to the destination point ($x$=-2 m, y=0 m). The length and mass of the robot links are as follows: $l_1$=1m, $l_2$=1m and $l_3$=0.5m and $m_1$=1kg, $m_2$=1kg and $m_3$=0.5kg. The 3R robot joint 1, 2 and 3 the maximum torques for are as follows: $\tau_{1\max}$ = 45 Nm, $\tau_{2\max}$ = 20 Nm and $\tau_{3\max}$ =5 Nm.

The initial and final configuration of the joint velocity and acceleration are assumes to be zeros and all robot joints are free to rotate to $2\pi$. In this study, we consider the obstacle has circular shape with radius 0.35m. The weight factors set [$\beta_1$,$\beta_2$,$\beta_3$,$\beta_4$] = [1,2,2,1] is used for fitness function.

The parameters of EPSO were considered during the experiment as follows: Inertial weight: 0.9 to 0.4, acceleration factors (c1 and c2): 2 to 2.05, population size: 40, maximum iteration: 80 and initial velocity: 8% of position.

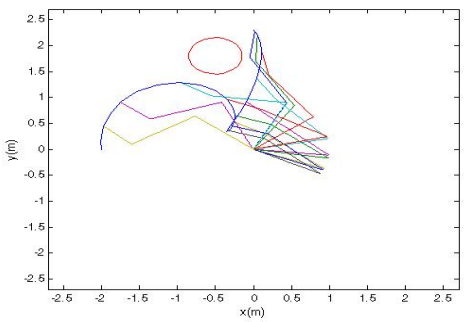


Figure 3. Samples of successful optimized Cartesian path of end effector of robot arm with the obstacle

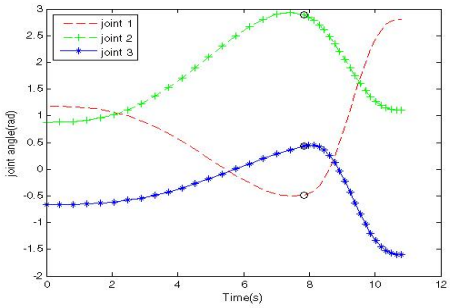


Figure 4. The Joint angles response with respect to time when avoid the obstacle

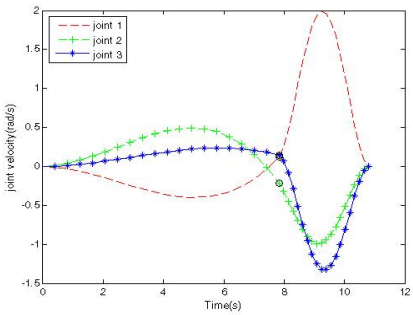


Figure 5. The Joint velociy response while avoiding the obstacle

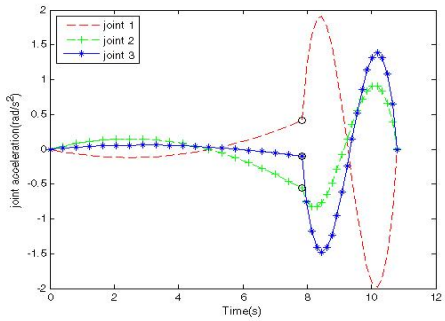


Figure 6. Joint acceleration response with respect to time while avoiding the obstacle

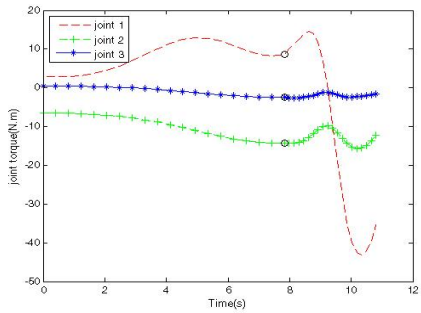


Figure 7. Joint torque response with respect to time while avoiding the obstacle

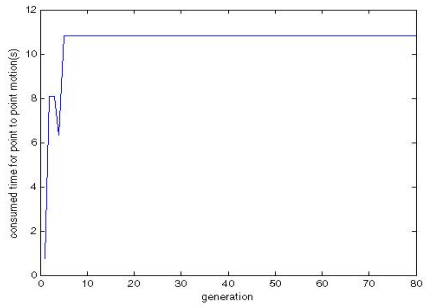


Figure 8. Generation by generation consumed time for point to point motion

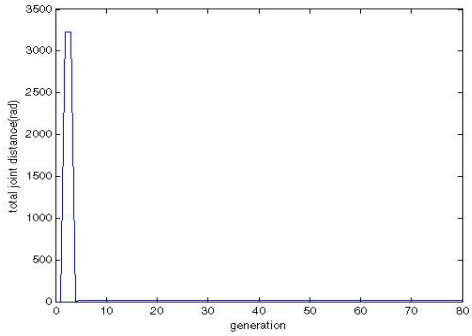


Figure 9. Generation Vs Generation total joint distance of each generation

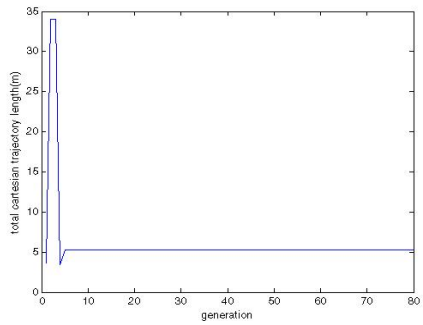


Figure 10. Generation Vs generation total cartesian trajectory length

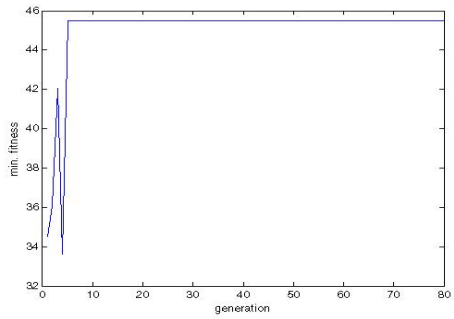


Figure 11. Generation Vs generation fitness

In Fig. 3, we have shown the obstacle position defined by the circle, robot's hand position and sample trajectory path of the hand's end effector. It demonstrates the capacity of the developed EPSO to optimize the parameters which produce the smaller Cartesian path in the obstacle work area with respect the other defined functions.

Fig. 4, 5 and 6 depicts the improved intermediate joint angle, joint velocity and joint acceleration respectively by plotting a small circle. As shown in Fig.7, the torque that determined from the environment with obstacle work area does not exceed the predefined maximum torque. Figure 8, 9 and 10 shows the generation by generation consumed time for PTP motion, total joint distance and total Cartesian trajectory length respectively. Direct kinematics has suggested for handling the configuration of robot arm, for this reason tool configuration is not used [14]. In Fig. 11 we have shown that the fitness is improved through generation by generation.

Finally, table I shows the overall performance of the propose methods that illustrate the proposed algorithm is robust changing the locations of the obstacles.

TABLE I. SIMULATED OPTIMIZED RESULTS FOR ROBOT ARM WHILE OBSTACLES IS EXISTS IN THE WORKSPACE

| Criteria | Obstacles in robot work area |
|---|---|
| Trajectory time in sec (Total) | 10.8087 |
| Joint traveling distance in rad | 5.0070 |
| Cartesian trajectory length in meter | 3.4702 |

## VI. CONCLUSION

In this paper, we proposed the point to point trajectory planning of the 3 link robot arm using the developed EPSO which generate an efficient optimal trajectory on the obstructed robotic environment. The EPSO determines the optimal parameters that are used to devise the polynomial specify the point to point trajectory, in order to reduce the fitness value of the desired objective function. Simulation results illustrate that the method still can generate an optimal trajectory for the 3-link (redundant) robot arm even under different conditions and complicated dynamic environment. A developed EPSO finds the optimal trajectory far too many times and converges more rapidly.

## REFERENCES


[1] E. Hultman and M. Leijon, "Utilizing cable winding and industrial robots to facilitate the manufacturing of electric machines," Robotics and Computer-Integrated Manufacturing, Vol. 29, Issue 1, pp.246-256, 2013.

[2] L.Y. Qin, J. Z. Wen, C.S.Chui, and K.-S. Leung, "Housing design and testing of a surgical robot developed for orthopaedic surgery," Journal of Orthopaedic Translation, vol. 5, pp. 72-80, 2016.

[3] A. Abad, O. Ma, K. Pham, and S. Ulrich, "A review of space robotics technologies for on-orbit servicing," Progress in Aerospace Sciences, vol. 68, pp. 1-26, 2014.

[4] M.S.Ganeshmurthy and G.R.Suresh, "Path Planning Algorithm for Autonomous Mobile Robot in Dynamic Environment," *in Proc. 3rd International Conference on Signal Processing, Communication and Networking (ICSCN)*, 2015.

[5] O. Montiel, R. Sepúlveda, and Ulises Orozco-Rosas, "Optimal Path Planning Generation for Mobile Robots using Parallel Evolutionary Artificial Potential Field," *Journal of Intelligent & Robotic Systems*, Vol. 79, Issue 2, pp 237–257, 2015.

[6] S.G. Yue, D. Henrich, X. L. Xu, and S.K. Toss, "Point-to-Point Trajectory Planning of Flexible Redundant Robot Manipulators Using Genetic Algorithms," *Journal of Robotica*, vol.20, pp. 269-280, 2002.

[7] Zhe Tang, Changjiu Zhou and Zenqi Sun, "Trajectory Planning For Smooth Transition of A Biped Robot," *in Proc. IEEE International Conference on Robotic & Automation*, 2003, pp. 2455-2460.

[8] P.V. Savsani and R.L. Jhala, "Optimal Path Planning for a Robot Arm by using Artificial Bee Colony(ABC) Algorithm," *International Journal of Modern Engineering Research(IJMER)*, vol.2, no. 5, pp. 4434-4438, 2002.

[9] M.C. Ang, D.T. Pham and K.W.Ng "Minimum Time Motion Planning for a Robot Arm Using the Bees Algorithm," *in Proc. 7th International Conference on Industrial Informatics (INDIN)*,2009, pp. 487-492.

[10] A.Tuncer and M. Yildirim, "Dynamic path planning of mobile robots with improved genetic algorithm," *Computers & Electrical Engineering*, vol. 38, no. 6, pp. 1564-1572, 2012.

[11] F.Yano and Y. Tooda, "Preferable movement of a multi-joint robot arm using genetic algorithm," *in Proc. In: Part of the SPIE Conf. on Intelligent Robots and Computer Vision*, 1999. pp. 80–88.

[12] E. Shintaku, "Minimum energy trajectory for an underwater manipulator and its simple planning method by using a genetic algorithm," *Adv Robotics*, vol. 13, pp. 115-138, 1999.

[13] R.C Eberhart and J. Kennedy "A new optimizer using particle swarm theory" *in Proc. of the sixth international symposium on micromachine and human science*, Nagoya, Japan, 1995. pp. 39 – 43.

[14] J. Kennedy and RC. Eberhart "Particle swarm optimization," *in Proc. of IEEE Int. conference on neural networks*, Piscataway, NJ, 1995. p. 1942 – 1948.

[15] T. Lung-Wen, Robot Analysis, the Mechanism of Serial and Parallel Manipulators, John Wiley &Sons, Inc., 1999.

[16] D. E. Goldberg, *Genetic Algorithm in Search, Optimization, and Machine Learning*, Addison-Wesley Longman Publishing Co., Inc. Boston, MA, 1989.

[17] D. Xin, C. H. Hua and G. W. Kang, "Neural Network And Genetic Algorithm Based Global Path Planning In A Static Environment," *Journal Of Zhejiang University Science*, vol. 6A, no. 6, pp. 549- 554, 2005.

# Ranking of Bangla Word Graph using Graph based Ranking Algorithms

S. M. Rafiuddin
Department of Computer Science and Engineering
Bangladesh University of Engineering and Technology
torifat@outlook.com

***Abstract*— Ranking words is an important way to summarize a text or to retrieve information. Word graph is a way to represent the words of a sentence or a text as vertices of a graph and to show the relationship among the words. It is also useful to determine the relative importance of a word among the word graph. In this research, the ranking of Bangla words are calculated representing Bangla words from a text in a word graph using various graph based ranking algorithms. There is a lack of standard Bangla word database. In this research, Indian Language POS-tag Corpora is used that has a rich collection of Bangla words as a form of sentences with their parts of speech tag. For applying a word graph to various graph based ranking algorithms, several standard procedures are applied. The preprocessing steps are done in every word graph and then applied to graph based ranking algorithms to make a comparison among these algorithms. This paper illustrate the entire procedure of calculating the ranking of Bangla words including the construction of word graph from text. Experimental result analysis on real data reveals the accuracy of each ranking algorithms in terms of F measure.**

***Keywords—bangla word; ranking word; word graph; graph; ranking algorithms.***

## I. Introduction

Natural Language Processing for a machine is an AI complete problem. To represent Natural Language to a machine or a computer, a graph is an important data structure. Various algorithms that are used for Natural Language Processing has the input in a notion of a chart, which is a kind of graph. Word is the fundamental building block in Natural Language. Ranking word is a measurement of text classification, page ranking, text summarization and various other applications. There are two types of ranking procedures. One is statistical methods and other is using graph based methods [1]. In this research, several graph based ranking methods are applied to Bangla word, which are represented by word graph data structure, then the ranking accuracy are measured.

There are huge amount of unstructured data floating around World Wide Web (WWW) that need to be processed. To find the relevant terms and to extract the required information we need to find the right terms associated with that required information. To do this, the relevant terms need to be ranked. However extracting the relevant terms manually is an extremely time consuming process. So, to extract the relevant information from various documents, first we need to extract the relevant terms and form a word graph of these terms then rank the relevant terms using graph based ranking algorithms.

Graph based ranking algorithms that are used to measure the accuracy of word graph are HITS [2], positional power function [3], PageRank algorithms [4]. In the recent past, many researcher has used graph theory based algorithms to analyze Natural Language Processing. Although, graph theory and computational linguistics are two distinct fields of Computer Science, but some recent research work shows that graph theory can be very useful and sometimes connected to various aspects of Natural Language Processing.

Another importance of this research work is to apply this ranking algorithms to Bangla words that are represented via word graph. This technique can be applied to Bangla word based search engine. In this context of Bangla word ranking, there are scarcity of standard dataset. So, in this research Indian Language POS-tag corpora dataset is used for the ranking procedure.

So, the steps of the procedure of word ranking from different documents using Bangla word graph are as follows—

*a)* Read Documents
*b)* Tokenization of Texts
*c)* Stemming
*d)* Stop Word deletion
*e)* Build Word Graph
*f)* Apply graph based ranking algorithms to word graphs
*g)* Measure ranking accuracy

Here, Stemming means find the root word from the derived words and stop word deletion means remove the irrelevant words that are not necessary for the consideration of ranking.

Word graphs are graph based syntactic representation of word and text. The graphs are directed, acyclic where edges represents acoustic relations among the words. The word graph contains unique start vertex and end vertex. These properties follow that the word graph is loosely connected. Edge labels denote words and weights denote acoustic numbers [5].

## II. Literature Review

Rada Mihalcea (2004) represents an unsupervised method for automatic text extraction for summarization process. In this research graph based ranking algorithms are applied to rank the words for summarization process [6]. This paper investigates a

978-1-5386-2307-7/17/$31.00 ©2017 IEEE

range of standard algorithms and evaluates their applications to text summarization.

Florian Boudin (2013) presents various centrality measures for keyphrase extraction using graph based methods. Keyphrase of a text documents means words or phrases that precisely represent the associated document [7]. Also this paper compares centrality measures of the experiments and results with related works of the recent past.

Litvak and Last (2008) introduce supervised and unsupervised approach of keyword extraction for single document. This method used graph based syntactic representation of text that enhances traditional vector space model. They also used HITS algorithm assuming that top ranked nodes of word graph represents most relevant terms of words [8]. Then they represent their keyword identification accuracy using $F_1$ score.

Khan et al. (2016) proposed an approach to extract domain relevant terms from an unstructured corpus. Their paper emphasized on minimizing the impact of term frequency to improve the precision of top k-terms. They also used unstructured data for categorization and information retrieval [9]. This paper also estimated term or word similarities based on term embedding.

Shams and Haratizadeh (2017) used collaborative ranking in graph based representation for item recommendation. They calculated users similarities based on ranking data. In this paper, a graph based approach called GRank is proposed and recommendation quality is compared with other collaborative ranking techniques [10].

Sidiriopoulos and Manolopoulos (2006) used graph based ranking algorithms for publications and authors using citations and worked on the impact of scientific collections and authors [11].

## III. Methodologies

Graph based word ranking from a word graph is a procedure for deciding which vertex that represent the words with ranking that are relatively more relevant to the text. Let $G(V, E)$ be a graph. An edge $vv' \in E$ is called incident from $v$ and incident to $v'$. For a vertex $v$ of the graph $G$, the in-degree is defined as number of edges incident to $v$ [12]—

$$\#in(): V \to \mathbb{N}, \#in(v) \coloneqq \#\{e \in E | \beta(e) = v\}$$

The out-degree of a vertex $v$ is defined as the number of edges incident from $v$ —

$$\#out(): V \to \mathbb{N}, \#out(v) \coloneqq \#\{e \in E | \alpha(e) = v\}$$

Here, $\alpha$ as access function to the start vertex of an edge defined as—

$$\alpha: E \to V, \alpha(e) \coloneqq v$$

$\beta$ as access function to the end vertex of an edge defined as—

$$\beta: E \to V, \beta(e) \coloneqq v'$$

A word graph is a directed, acyclic graph $G(V, E, L, W)$ with edge labels and edge weights, if the following conditions hold [12]—

$$\exists v^{(r)} \in V: \#in(v^{(r)}) = 0 \wedge \forall v \in V: \#in(v) = 0 \Longrightarrow v = v^{(r)}$$

$$\exists v^{(f)} \in V: \#out(v^{(f)}) = 0 \wedge \forall v \in V: \#out(v) = 0 \Longrightarrow v = v^{(f)}$$

Here, $l$ as access function to the label of an edge defined as—

$$l: E \to L, l(e) \coloneqq l$$

And, $w$ as access function to the weight of an edge defined as—

$$w: E \to W, w(e) \coloneqq w$$

Applying topological ordering to Bangla word graph, as the word graph is a directed acyclic graph that has the mapping defined as—

$$\tau: V \to \mathbb{N}\ with\ \forall e \in E: \tau(\alpha(e)) < \tau(\beta(e))$$

### A. Processing of Word Graph

***Algorithm 1.*** Computing the topological order of word graph [12]

```
begin
    Stack s;
    for each vertex v ∈ V(G), do
        inE_v := #in(v)
    s.Push(v^(r))
    order ← nil
    while v ← s.Pop() do
        order ← order. v
        for each edge e = (v, v') starting in v do
            inE_v' ← inE_v' − 1
                if inE_v' == 0 then
                    s.Push(v')
    return order
end
```

***Algorithm 2.*** Computation of the transcript independent density of a word graph [12]

```
begin
    dens ← 0
    totalDens ← 0
    for each vertex v ∈ V, taken in topological order, do
        totalDens ← totalDens + dens
        dens ← dens - #in(v) + #out(v)
    return totalDens / (|V| − 1)
end
```

***Algorithm 3.*** Calculation of the number of path in a word graph [12]

**begin**

**for** each vertex $v \in V(G)$, taken in topological order, **do**
    $p^{(v)} := \sum p^{(w)} : wv \in E$
    $p[v] \leftarrow 0$
    **for** each vertex $e = wv \in E$ ending in $v$ **do**
        $p[v] \leftarrow p[v] + p[w]$
$p^{(G)} \leftarrow p^{(v^{(f)})}$
**return** $p^{(G)}$
**end**

***Algorithm 4.*** Reducing a graph to unique label sequences [12]

**begin**

**for** each vertex $v \in V(G)$, taken in topological order, **do**
    **for** each pair of identically labeled edges $e_1, e_2$ **do**
        Create a new vertex $v$ having $t(v) := \min\left(t(\beta(e_1)), t(\beta(e_1))\right)$, inserting $v$ into the topological order
        **for** each edge $e = (\beta(e_1), w, s, y)$ **do**
            Create a new edge $e' := (v, w, s, y)$
        **for** each edge $e = (\beta(e_2), w, s, y)$ **do**
            Create a new edge $e' := (v, w, s, y)$
**end**

***Algorithm 5.*** Merging two vertices [12]

**begin**

**for** each edge $e = (x, w, s, l)$, **do**
    **if** $\exists e' = (x, v, s', l)$, **then**
        $s' \leftarrow \min(s, s')$
    **else**
        Create a new edge $e'' = (x, v, s, l)$
**for** each edge $e = (w, x, s, l)$, **do**
    **if** $\exists e' = (v, x, s', l)$, **then**
        $s' \leftarrow \min(s, s')$
    **else**
        Create a new edge $e'' = (v, x, s, l)$
**end**

***Algorithm 6.*** Calculation of the number of steps of a fictitious parser for a word graph [12]

**begin**

totalderiv ← 0
**for** each vertex $v \in V(G)$, taken in topological order, **do**
    $\text{deriv}_v[1] \leftarrow \#in(v)$
    **for** all $i \in \{2, \ldots, |V|\}$ **do**
        **for** each edge $e = (w, v, x, y)$ ending in $v$ **do**
            $\text{deriv}_v[i] \leftarrow \text{deriv}_v[i] + \text{deriv}_w[i-1]$
        totalderiv ← totalderiv + $\text{deriv}_v[i]$
**return** totalderiv
**end**

## B. *Compute rank using Graph based Ranking Algorithms*

***Algorithm 7.*** Computing rank using minimum and maximum prefix scores [12]

**begin**

**for** each vertex $v \in V(G)$, taken in topological order, **do**
    $S_{v,min} \leftarrow \infty$
    $S_{v,max} \leftarrow 0$
    **for** each edge $e = (w, v, s_c, y)$ ending in $v$ **do**
        $S_{v,min} \leftarrow \min(S_{w,min} + S_e, S_{v,min})$
        $S_{v,max} \leftarrow \min(S_{w,max} + S_e, S_{v,max})$
$r \leftarrow \boldsymbol{ComputeRank}(v_f, s_{ref})$
**return** $r$
**end**

***Algorithm 8.*** Computing rank if the reference score is lower than or equal to the minimum score [12]

**begin**

if $s_{ref} \leq s_{v,min}$
    return 0
if $s_{ref} \geq s_{v,max}$
    return $p^{(v)}$
$r_{tmp} \leftarrow 0$
**for** each edge $e = (w, v, s_e, y)$ ending in $v$ **do**
    $r_{tmp} \leftarrow r_{tmp} + \boldsymbol{ComputeRank}(w, s_{ref} - s_e)$
**return** $r_{tmp}$
**end**

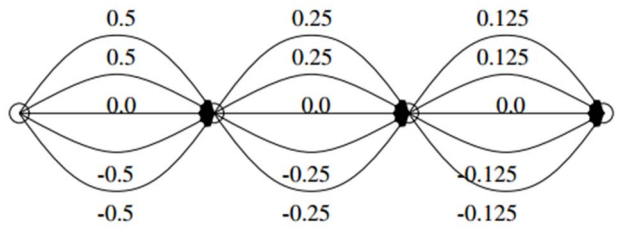


Fig. 1. A word graph for rank computation.

***Algorithm 9.*** Hyperlinked Induced Topic Search (HITS) [2]

This is an iterative algorithm developed by Kleinberg in 1999 [2]. It ranks web pages using authority measurements. Authority is measured using the number of incoming links. This algorithm recursively assign a weight of each vertex determining how relevant the word graph vertex is. For each vertex in a word graph we would calculate two types of scores. One is authority

score and another is hub score. Calculate ranking of a vertex in a word graph using HITS algorithm is an unsupervised approach. It was mainly developed to increase search performance on the Web.

Authority score of HITS algorithm is defined as—

$$HITS_A(V_i) = \sum_{V_j \in \#In(V_i)} HITS_H(V_j) \quad (1)$$

Hub score of HITS algorithm is defined as—

$$HITS_H(V_i) = \sum_{V_j \in \#Out(V_i)} HITS_A(V_j) \quad (2)$$

To calculate rank of a vertex the following four methods are used—

1. Rank associated with the authority score, defined as—
$$H(V_i) = HITS_A(V_i)$$
2. Rank associated with the hub score, defined as—
$$H(V_i) = HITS_H(V_i)$$
3. Rank associated with the average between two score—
$$H(V_i) = avg\{HITS_A(V_i), HITS_H(V_i)\}$$
4. Rank associated with the maximum between two score—
$$H(V_i) = max\{HITS_A(V_i), HITS_H(V_i)\}$$

***Algorithm 10.*** Positional Power Function Algorithm [3]

This is a ranking algorithm introduced by Herring et al. in 2001 [3]. This algorithm determines the ranking of a vertex as a function the number and score of its successor. Positional Power function is defined as [3]—

$$POS_P(V_i) = \frac{1}{|V|} \sum_{V_j \in \#Out(V_i)} (1 + POS_P(V_j)) \quad (3)$$

***Algorithm 11.*** PageRank Algorithm [4]

This is a ranking algorithm developed by Brin and Page in 1998. This algorithms integrates the impact of both incoming and outgoing paths of a single vertex [4] is defined as—

$$PR(V_i) = (1 - d) + d * \sum_{V_j \in \#In(V_j)} \frac{PR(V_i)}{|\#Out(V_j)|} \quad (4)$$

Here, d is a parameter between 0 and 1. Initially arbitrary values are set for each of the vertex. The computation of rank continues until the convergence reaches.

## IV. Experiments and Results

### A. Dataset Description

The experiment of this research project is Indian Language POS-tag corpus [13]. The corpora has several language e.g. Bangla, Hindi, Marathi and Telegu. This research is working with bangla.pos file inside of this corpora. This database is completely publicly available and accessible via Natural Language Processing Toolkit. The database is compiled with XML file and has 895 Bangla sentence e.g. sentence number 808 has the following form in the database—

$$< Sentence\ id = 808 >$$

$$\text{এ_}PRP\ \text{যেন_}RP\ \text{একটা_}QC\ \text{উপন্যাসের_}NN\ \text{প্লট_}NN\ \text{।_}SYM$$

$$</Sentence >$$

### B. Experimental Setup

Hardware Setup:
Processor: AMD X4 Phenom II 965 BE 3.4GHz
RAM: 8GB DDR3 1333MHz
HDD: 1TB
Software Setup:
Operating System: Linux Mint XFCE 18.2
Programming Language: Python Programming Language
Version: Python 3.4.1
Used packages: Natural Language Toolkit (NLTK)

### C. Results

The metric of accuracy has four distinct features [14]. They are defined as follows—

i) **True positives** are relevant terms that are correctly ranked.

ii) **True negatives** are irrelevant terms that are correctly ranked.

iii) **False positives** are irrelevant terms that are incorrectly ranked.

iv) **False negatives** are relevant terms that are incorrectly ranked.

By these four features, two parameters of F measure is calculated. First parameter i.e. Precision, is calculated as how many terms that are ranked properly, i.e.—

$$\frac{True\ Positive}{True\ Positive + False\ Positive}$$

Second parameter i.e. Recall, is calculated as how many relevant terms that are identified, i.e.—

$$\frac{True\ Positive}{True\ Positive + False\ Negative}$$

From Precision and Recall, the metric of accuracy, i.e. $F_1$ is calculated as—

$$\frac{2 \times Precision \times Recall}{Precision + Recall}$$

Using $F_1$ score, the accuracy of ranking from word graph derived from Indian Language POS-tag Corpora, by graph based ranking algorithms are presented below—

TABLE I. RESULT ANALYSIS OF RANKING ALGORITHMS FROM BANGLA WORD GRAPH

| Ranking Algorithms | Number of Words | Precision | Recall | $F_1$ Score |
|---|---|---|---|---|
| Rank using minimum and maximum prefix | 1234 | 0.36 | 0.40 | 0.37 |
| Rank considering reference score | 1259 | 0.32 | 0.38 | 0.33 |
| HITS | 1435 | 0.31 | 0.37 | 0.32 |
| Positional Power Function | 1278 | 0.30 | 0.35 | 0.31 |
| PageRank | 1546 | 0.29 | 0.36 | 0.31 |

The following figure depicts the ranking algorithm accuracy in column graph—

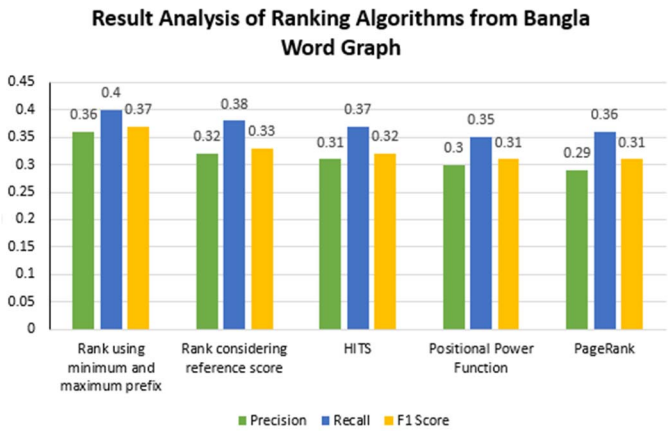


Fig. 2. Result Analysis of Ranking Algorithms Accuracy from Bangla Word Graph

## V. CONCLUSION

This research has the goal of accuracy measurement of the ranking algorithms of Bangla word using graph based ranking algorithms. Bangla is the 7th ranked most spoken language in the world. The text containing Bangla words are increasing at a very high rate in newspaper, blogs and social media. So, searching the documents containing Bangla words are getting important in recent research field. For searching, summarizing, information retrieval of Bangla text, ranking Bangla word using graph based ranking algorithms are important. So, Bangla word ranking will grow more attention in Natural Language Processing field of Bangla Language. There are some scarcity of Bangla word database. This research has used Indian Language POS-tag Corpora for Bangla word. To represent the words in a data structure, using graph word is very useful. So, to process Bangla word, several graph word methods and techniques are used to process the work in the text that has been discussed in methodologies portion. The future work of this research is to optimize ranking algorithm up to a certain level and to improve these algorithm for Bangla word ranking process.

## ACKNOWLEDGMENT

The author(s) would like to thank Professor Dr. Mohammad Kaykobad, Department of Computer Science and Engineering (CSE), Bangladesh University of Engineering and Technology (BUET), for his kind support and enthusiasm. Also this research work is very much grateful to Dr. Sarada Herke, Postdoctoral Research Fellow, School of Mathematics and Physics, University of Queensland, Australia for her tutorials on Graph Theory in Youtube.

## REFERENCES

[1] Frakes, William B., and Ricardo Baeza-Yates. "Information retrieval: data structures and algorithms." (1992).

[2] Kleinberg, Jon M. "Authoritative sources in a hyperlinked environment." *Journal of the ACM (JACM)* 46.5 (1999): 604-632.

[3] Herings, P., Gerard Van der Laan, and Dolf Talman. "Measuring the power of nodes in digraphs." (2001).

[4] Page, Lawrence, et al. The PageRank citation ranking: Bringing order to the web. *Stanford InfoLab,* 1999.

[5] Oerder, Martin, and Hermann Ney. "Word graphs: An efficient interface between continuous-speech recognition and language understanding." *Acoustics, Speech, and Signal Processing, 1993. ICASSP-93., 1993 IEEE International Conference on.* Vol. 2. IEEE, 1993.

[6] Mihalcea, Rada. "Graph-based ranking algorithms for sentence extraction, applied to text summarization." *Proceedings of the ACL 2004 on Interactive poster and demonstration sessions. Association for Computational Linguistics,* 2004.

[7] Boudin, Florian. "A comparison of centrality measures for graph-based keyphrase extraction." *International Joint Conference on Natural Language Processing (IJCNLP).* 2013.

[8] Litvak, Marina, and Mark Last. "Graph-based keyword extraction for single-document summarization." *Proceedings of the workshop on Multi-source Multilingual Information Extraction and Summarization. Association for Computational Linguistics,* 2008.

[9] Khan, Muhammad Tahir, Yukun Ma, and Jung-jae Kim. "Term Ranker: A Graph-Based Re-Ranking Approach." *FLAIRS Conference.* 2016.

[10] Shams, Bita, and Saman Haratizadeh. "Graph-based collaborative ranking." *Expert Systems with Applications* 67 (2017): 59-70.

[11] Sidiropoulos, Antonis, and Yannis Manolopoulos. "Generalized comparison of graph-based ranking algorithms for publications and authors." *Journal of Systems and Software* 79.12 (2006): 1679-1700.

[12] Amtrup, Jan Willers. *Incremental speech translation. Springer*-Verlag, 1999.

[13] "http://nltk.org/", Indian Language POS-Tagged Corpus Collected by A Kumaran, Microsoft Research, India Distributed with permission.

[14] Mishu, Sadia Zaman, and S. M. Rafiuddin. "Performance analysis of supervised machine learning algorithms for text classification." *Computer and Information Technology (ICCIT), 2016 19th International Conference on.* IEEE, 2016.

# Towards Developing a Tool for UX Evaluation Using Facial Expression

Kazi Md. Munim[1], Iyolita Islam[2], Mahmuda Khatun, Md Mahboob Karim, Muhammad Nazrul Islam[3]
Department of Computer Science and Engineering, Military Institute of Science and Technology, Dhaka, Bangladesh
Email: [1]kazimunim2014@gmail.com, [2]iyolita2011@gmail.com, [3]nazrulturku@gmail.com,

***Abstract*— User Experience (UX) can be considered as a quality attribute of a system, defining whether the system is easy to adapt, efficient to use and comfortable. User experience evaluation can be used as a tool for determining the degree of user experience for a system or service. Among many existing UX evaluation tools, only a few are online based, easily usable and conducts real time analysis. Therefore, the objective of this paper is to design and develop a web based user experience evaluation tool using measurement of user emotions. To attain these, firstly we have gone through the existing literature. Secondly, we have proposed a conceptual framework. Thirdly, we have implemented the system using Affdex SDK. Finally, we have tested our tool with four participants. The evaluation study showed that our tool is effective and efficient.**

***Index Terms*—User experience (UX), human computer interaction (HCI), UX evaluation, emotion detection, facial expressions.**

## I. Introduction

When a system is used, the user faces an environment, gathers certain knowledge and gets impression about the system. For the user, the whole association with the system and the impression to the system is User Experience (UX). In other words, the experience of the user to use a the system like- a application or a website, product or services, is called UX [1] [2]. So, this experience mainly denotes impression, emotions, preferences, beliefs, points of focus, physical and psychological responses and attitudes of the user.

"UX evaluation encompasses all aspects of the end-user's interaction with the company, its services, and its products" [3]. UX evaluation can also be used to form structure and to frame the designing attributes of a system. Basically, UX evaluation or User experience assessment (UXA) includes a set of procedures or methods to evaluate user performance against the targeted features.

There are many existing methods which have been introduced to assess the level of UX of a system. As emotion of the user during using a system is a multifaceted phenomenon, it can be very helpful for the area of the development of software. A majority of human interaction with a system comes from non-verbal communication and user emotion detection is one of the directions that can be used to improve the overall user experience. Mehrabian [4] stated that the non-verbal expression contributes 55% to the overall impression or perception of a product. So, we focused on non-verbal languages (i.e. facial expressions) to assess the degree of UX.

Humans are largely motivated by their emotions. Emotion primarily controls customers' decisions about any service or product. So, UX professionals are interested to use new technologies and methods to get a better picture of how a person feels about their products and services. Using UX evaluation we can determine the state of the user (positive or negative), the responsible feature or portion of the system for the state, the facial expression of the user, the possible new update which can improve the state.

The relation between emotions and user response can be stated as emotional states that denotes the user attitude [5]. For example, emotion during using the gaming application, emotion can reflect the user's enjoy, excitement and sorrow [6]. Thus, the user experience converts into player experience. User's facial expression denotes whether he is actually enjoying while using the gaming application. So emotions can be considered to evaluate UX evaluation in gaming, interactive learning, distance learning applications.

Again, design of a system plays a key role in achieving good user experience. To achieve some degree of success and to optimize specific aspect of UX, the design should be dynamically changed according to the interaction of the users with the application. For this we need to consider- motivation of the users, the experience and skills of them and to identify where changes are needed [7]. Understanding how a user truly feels in reaction to an experience can help us to optimize specific aspects of the experience to extract certain expressive states. In fact, to assess the system usability, UX measure is essential and to assess the UX, emotions plays a key role that can be evaluated using the facial expression.

Therefore, the objective of this paper is to develop a tool to evaluate user experiences of a system from facial expression. In order to attain this objective, a conceptual design is proposed and materialized using Affdex SDK. An evaluation study with five participants has been also carried out to assess the performance of the tool.

The remaining sections of this paper are organized as follows: a brief overview of the related work is presented in section II. The design and development of proposed UX evaluation tool with the conceptual framework are discussed in section III. In section IV, the evaluation of the tool is discussed, followed by a discussion and conclusion in section V.

## II. Literature Review

The research focused to the field of user experience, usability evaluation and emotion detection. To find out the related literature we have conducted search in the major scholar

databases including ACM scholar, Google scholar, IEEE explorer, ScienceDirect and SpringerLink. For searching, we have used the following search-strings- user experience, facial expression, UX evaluation, usability evaluation and emotion, HCI evaluation and emotion detection.

Topics that are that are mostly related to this research can be divided into the following categories: (a) Emotion Detection and (b) Emotion and UX Evaluation.

### A. Emotion Detection

Many papers propose algorithms to detect emotions from the facial expressions. For example, Rajeshkumar [8] found the relation between UX and usability by working with the UX evaluation taxonomy.

Supavich [5] used sentimental analysis to detect emotions and found that a combination of three salient emotions- anger, trust and joy can influence the number of downloads of an application. His research highlights that emotion can be an important issue to materialize UX to evaluate a system. Whereas, Filko [9] detected 7 emotions by analyzing key facial regions using principal component analysis and neural networks. After being trained with samples, the system could automatically detect user emotions from still images. By converting each individual image to binary image, it generates a recognition matrix for 7 neural networks(1 for each universal emotion). The matrix values are used for emotion detection. But the research had two limitations: i) It couldn't detect the actual emotion different from the expression accurately. ii) There was a chance to be confused to differentiate the emotions like anger and disgust, sadness and fear etc. Maia [10] and Georges [11] found by conducting several studies that psychophysiological and physiological measures can be used to measure UX respectively each of which can provide more reliable evaluation. Again, to improve the accuracy, Landowska [12] also placed biometric sensors in non-disturbing locations rather than finger to monitor HCI. The sensor measurements of body temperature, blood-volume pulse and skin conductance proved that reading from alternative location is a good proxy as typical (finger) location. But conducting bio-measurements in one location and using a small group of convenience might change the accuracy of result.

In other studies [13]–[17], measurement of facial expression detecting muscle activity by electromyography (EMG) showed a better accuracy. Though they used different strategy, all of them concluded that facial muscle activity can be used to track facial expressions as well as emotions over time. In another research, Sharma [18] used ANN (Artificial Neural Network) approach to detect emotion from 5 facial expressions.

Another approach based on smartphone app were conducted by Bachmann [19] to detect mood of the user when any specific event occurred. In this app, the user had to select the level of three dimensions: Mood, Tiredness and Stress and after some predefined steps the user's mood were recognized. The author also conducted a field study which resulted in an acceptable accuracy.

Some other studies introduces tools for emotion detection. For example, Staiano [20] introduced a tool named UX_Mate which interprets user's facial expressions into emotions using some pre-set rules. It could detect dynamic user emotional state automatically at the time of interaction with a system. The author, also conducted a pilot run of the system and validated the prediction of error, comparing it with annotation of errors by experts. Moreover, Dupre [21] developed another open-source annotation software, "Oudjat", which integrates all required options for various kinds of experiments. It is configurable and easily evolves with the investigator's needs. Gaffney [22] represented an tool named "The AMAS Authoring Tool 2.0" for UX design evaluation for an application.

### B. Emotion and UX evaluation

Some studies in the human-computer interaction (HCI) show theoretical motivations between emotion and UX evaluation. Ethier [23] and Heijden [24] worked on user experience and they found that emotions are inalienable part of UX while interacting with a system.

Research in psychology and emotions summarized that facial expressions has a feasible correlation with self-reported emotions [25] and with physiological measurements of emotion [26]. As an implementation, including 3 case studies, Saariluomaand [27] proposed a model which investigates user psychology to determine emotional aspects of UX. The experiments considered two factors: "Competence" and "Frustration" (Competence and Frustration were used to denote positive UX generated for ability and negative UX generated for inability respectively to use the technology). The resulting factor matrix denoted the relevancy between individual emotion and UX.

The degree of accuracy of emotion recognition from psychological measurements as well as voice signals and facial expression of a user proved so high in [28]. This research included a study on user interaction with system and a questionnaire for the participants. Using cameras, the user expression were taken. But if there is any noise, the voice signal will give incorrect result.

Altrabsheh [29] detected specific emotions from students' real-time feedback: amuse, anxiety, bored, confusion, engagement, enthusiasm, excitement and frustration in his research which helped the teachers to understand the student's emotion while learning. Bosch [30] conducted another experiment on the students using the computer vision and machine learning techniques to detect students' affect while using an educational game designed to teach fundamental principles of Newtonian physics. So, emotion detection can be used for evaluate a system or procedure.

Bernhaupt [31] also described the challenges to be faced while conducting UX evaluation in the area of gaming. Gilleade [7] showed how the emotion "frustration" can be used as an indicator of change in the design of an adaptive video game. He identified two dimensions from a gaming context: in-game and at-game. He detected the frustration of the player from some events like- button pressure, game-pad grip, game-pad tilt etc. and game progression.

In sum, though a number of studies has been carried out related to this field, most of the UX evaluation tools are not explicitly focused on developing an online, user friendly

and cost effective tool with a report instantly for usability evaluation. Therefore, our research work will focus to develop a tool that will achieve these features.

## III. Tool Design and Development

Our objective is to develop this tool for capturing the user's facial expressions, detecting his emotions and based on his emotions generating a report to assess the UX of the studied application. For design and development we followed two steps: (a) Construction of a conceptual framework; (b) Development of the system

### A. Conceptual Framework

Conceptual framework of the whole system is depicted in Figure 1. The system will take two inputs: user face video feed (recorded by webcam) and screen recording (of the PC/laptop on which the tested application is running) also will be taken as input in the system. The inputs will be uploaded in the database server which can be accessed from the web terminal by the authorized personnel (i.e. project manager, software developers, testing team, UX evaluator, quality control technicians etc.). Besides, the detected percentage of the different emotions along with the user's gender (at the user end) will be stored in the database which will be presented as a graph in the web terminal.

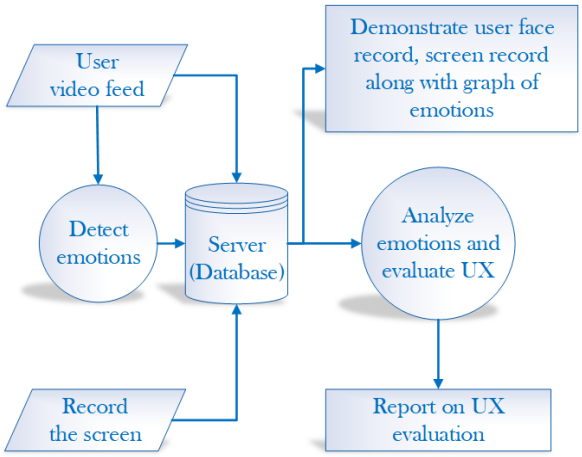


Figure 1: Conceptual Framework

After the evaluation process a report on UX evaluation will be generated by server automatically which will be observable from the web terminal. The human evaluator team can evaluate UX manually from the recorded video of user and the screen. From the graph of different emotions they will be able to know at which time the user emotion was not good. Then the evaluator can directly access to that time of the video. It will save time and effort of the evaluator team to prepare UX evaluation report with the help of the data from the system and their knowledge and experience. They evaluator can also compare his report with the report generated by the system.

The system will acclimatize itself with the value of the manual report for some test participants. These adjustments will be stored in the server database.

Input module consists of the user, application on a computer and webcam. The screen of the application will be recorded as well as the user face as input for the system along with the emotions of the user.

Store module is responsible for storing all the necessary data for the video streaming, presenting graphs, generating reports etc. This module will store the facial record of the user, screen record of the application and the different user emotion values in the server.

Processing module is the backbone of the system since it performs all the processing, analysis, calculation. Affdex SDK is one component of the processing module which can analyze spontaneous facial expressions that the user shows in his interactions along with the gender and some physical parameters. It will do the processing to show the graph of emotions and generate the report on UX of the application.

Output module will be active on a web terminal to represent and organize all the required outputs. The web terminal is the platform from where the authorized personnel can access the data to use for evaluation and other necessary task. This module will present the continuous graph in a user understandable manner including the facial record of the user, screen record of the application and report on UX evaluation.

### B. Tool Development

The client side tool is mainly divided into three sub-applications: one that records user face, another that records user emotions and the last one records screen of the application. The tool is developed in Microsoft Visual Studio 2017 on windows 10 and programming language C Sharp is us

To record user face AForge.NET is used. AForge.NET is a computer vision and artificial intelligence library originally developed by Andrew Kirillov for the .NET Framework [32]. It uses a webcam connected with the computer. The video is saved as AVI file. The video file is stored in the computer file system temporarily. After finishing the recording the video is uploaded automatically in the web server.

To detect user emotions Affdex SDK and the webcam was used. Affdex has rich knowledge base and its dll file is used for developing the application. This SDK can detect the gender of the user and other emotions like engagement, valence, contempt, surprise, anger, sadness, disgust, fear and joy. All the emotions are wrote into a text file. After the recording the emotions will be wrote into the text file by separating the emotion value by comma. This text file is uploaded in the server file system after stopping the emotion detection.

To record the screen of the device the AForge.NET is used again. This application can record the screen with high definition. The video is saved as AVI file. This file is also uploaded in the server file system.

These three sub-applications are merged together and all the files are uploaded to the server for future use. The upload function uses HttpWebRequest to connect with the server. In the merged application - the user face record application and emotion detection application both needs access of the webcam at the same time. But one resource can't be given to two different sub-program. Therefore two webcams were used.

To show the results and report web terminal is used. The website is developed using HTML, CSS, PHP and JavaScript language. To demonstrate the graph a JavaScript plotting library named "Flot" is used. The website access the server and use the files uploaded from the desktop application. In the dashboard user face recording, screen recording and the emotion graph is presented.

In summary, the tools used in our system are described in Table I

Table I: TOOLS USED TO DEVELOP THE FEATURES

| Purpose | Tool Name |
|---|---|
| Windows application | Microsoft Visual Studio (C Sharp) |
| To record user face | AForge.NET |
| To detect User Emotion | Affdex SDK |
| To record user screen | AForge.NET |
| To show graph | Flot library |
| To show report and others in web terminal | HTML, CSS, PHP, JavaScript |

A screen shot of the website is depicted in Figure 2.

## IV. EVALUATION OF THE TOOL

The tools was evaluated in an academic environment.

### A. Participants Profile

A total of 4 participants were invited in software engineering laboratory. Participants' mean age was 30 years. They had experience of 3-4 years of using ICT applications and gaming system. One of them had the previous experience of playing the studying game, others played for the first time.

### B. Study Procedure

During the evaluation study, a short brief was provided to our participants about how the tests will be conducted and what's the purpose of this study. We also ensured that we were going to evaluate the system, not the participants. For this test, we chose a game named "Zombie Tsunami" [33] and the participants were asked to play the game for 3 minutes. During their playing session, the system recorded the user face and screen along with the emotions.

### C. Analysis and Study Findings

The system took user video feed and screen recording as inputs and analyzing them generated the graphs which were viewed from the web terminal. Two evaluators (first two author of this paper) evaluated their 5 emotions (joy, surprise, fear, engagement and anger) manually and compiled the evaluation report graphically. By superimposing these two graphs for different emotions we found a combined graph for each user. Among them one example case is demonstrated in Figure 3 for four emotions (a) Joy, (b) Engagement, (c) Surprise and (d) Anger.

However, analyzing and combining data of all four participants, we have found two concerns: effectiveness and efficiency of the system.

For the *Effectiveness* we have found that the system generates almost the same graphical view as that of the manual evaluation. The external evaluation requires hard labor, too expert cost and is time consuming. On the other hand, our system generates an on time evaluation on a click and no expertise cost is required. Besides, the manual evaluation has a chance of error or biasness to the system whereas our system has a very less chance of error and no possibility of biasness.

To define the *Efficiency* of our system we figured out from the generated graph that the system mostly keeps the user engaged though he feels also the fear and surprise for a specific time which can be understood from the user face video. In this game, at different stage user have different emotions, like when he is in a critical point he has engagement or when he has a chance to lose he has fear or when he can complete his goal he is happy. From the graph, it can be easily depicted that for which time being the user has a specific type of emotion. So, the system generates an overall evaluation on the game also. It can suggest the developer where revision or improvement is required. For example, the engagement of the user is not sufficient, it needs to be increased or the user gets angry frequently, so the stages can be redesigned. In other words, the system can generate a comprehensive recommendation about the UX evaluation by treating the user emotions at different phases of the game.

## V. DISCUSSION AND CONCLUSIONS

In this paper we have proposed a system to evaluate user experience from facial expressions. An evaluation study is also conducted to assess the effectiveness and efficiency of the proposed system. UX evaluators and UI designers may use this system to assess the UX of their system and to get the necessary recommendation of redesigning the system to improve it's UX.

The working principle of our tool is based on detecting facial expression. In comparison with various kinds of UX evaluation tool, our tool will assist to evaluate the applications which are entertainment applications like- gaming which can play a significant role to frame the exact user sentiment. There are some existing tools which uses facial expression to evaluate the UX. But in some context this one is different from them. Table II shows a comparison among the existing UX evaluation tools based on their features.

We have conducted a lab based validation test that has been replicated with a few participants. In future we will conduct an extensive study to improve performance of our tool. Future research will be carried out by recruiting more participants to refine an update of system performance. However in such case, we may include evaluators for manual evaluation from the industries. An usability evaluation can be carried out to improve the user interface of the system.

The Human-Computer Interaction (HCI) and the design communities has been agreed to the point of accepting UX as a key concern of a system. Our tool combines affinity between user's facial expression and screen recording during the interaction period and generates a graph for the ease of evaluation. We hope our UX evaluation tool can be a key to

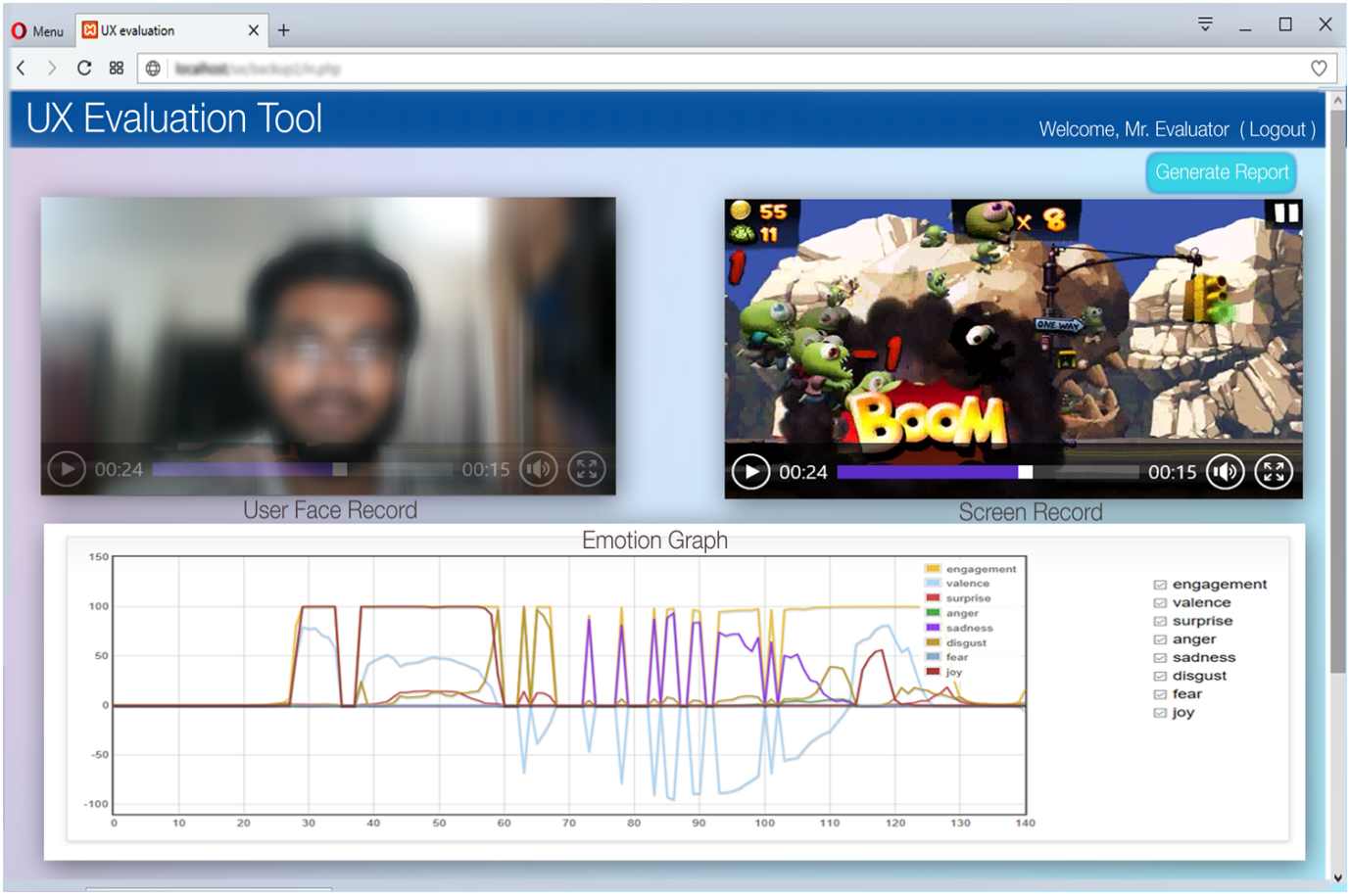


Figure 2: Demonstration of the website

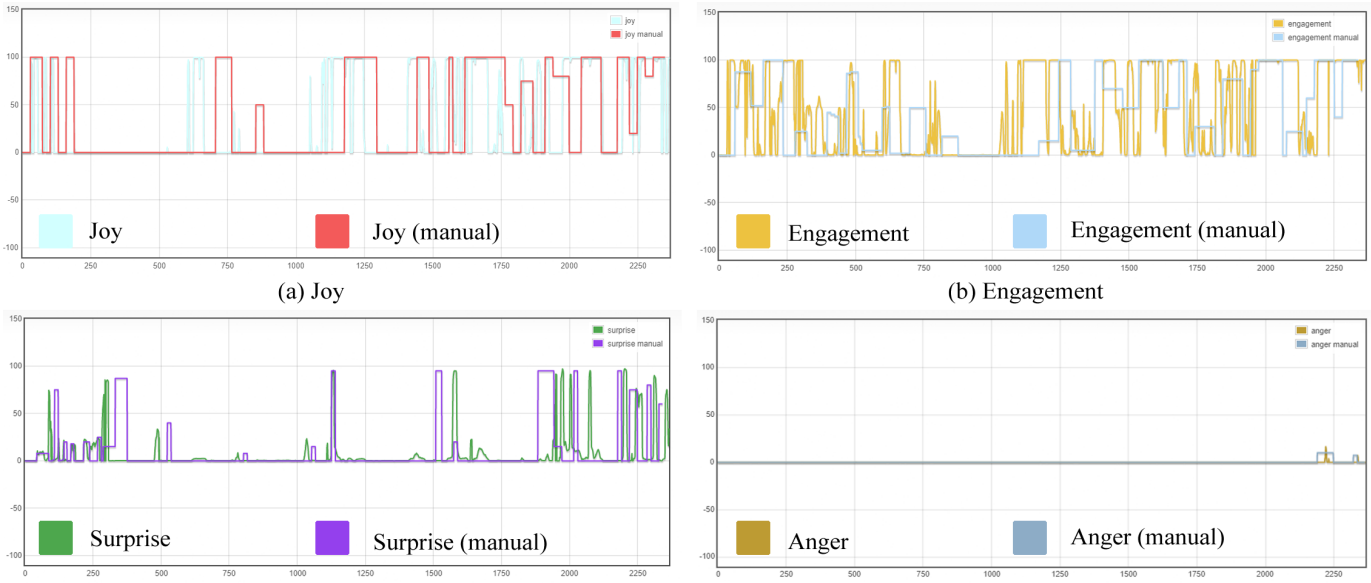


(a) Joy (b) Engagement

(c) Surprise (d) Anger

Figure 3: Comparative views of emotion states predicted by the system and manual evaluator

Table II: COMPARISON OF FEATURES AMONG EXISTING TOOLS AND OUR TOOL

| Features | Fac-eReader [34] | UX_Mate [20] | Oudjat [21] | Our System |
|---|---|---|---|---|
| Emotion detection in real Time | ✓ | ✓ | - | ✓ |
| Discrimination of mixed User Emotion | ✓ | ✓ | ✓ | ✓ |
| Training through Machine learning | - | ✓ | - | - |
| Display user emotion in graph | ✓ | - | - | ✓ |
| Generate Report on UX evaluation | - | - | - | ✓ |
| Validation Study | ✓ | ✓ | - | ✓ |

overcome the designing limitations caused by lack of concern about UX and design methods and UX evaluation tools.

## REFERENCES


[1] N. McNamara and J. Kirakowski, "Functionality, usability, and user experience: Three areas of concern," *interactions*, vol. 13, no. 6, pp. 26–28, Nov. 2006. [Online]. Available: http://doi.acm.org/10.1145/1167948.1167972

[2] N. Bevan, "Ux, usability and iso standards," in *CHI 2008 Workshop on User Experience Evaluation Methods in Product Development*, 2008, pp. 1–5.

[3] "The definition of user experience (ux)," https://www.nngroup.com/articles/definition-user-experience/.

[4] A. Mehrabian, "Communication without words," *Communication theory*, pp. 193–200, 2008.

[5] S. F. Pengnate and D. Delen, "Evaluating emotions in mobile application descriptions: Sentiment analysis approach," 2014.

[6] K. Isbister and N. Schaffer, *Game usability: Advancing the player experience*. CRC Press, 2015.

[7] K. M. Gilleade and A. Dix, "Using frustration in the design of adaptive videogames," in *Proceedings of the 2004 ACM SIGCHI International Conference on Advances in computer entertainment technology*. ACM, 2004, pp. 228–232.

[8] S. Rajeshkumar, R. Omar, and M. Mahmud, "Taxonomies of user experience (ux) evaluation methods," in *Research and Innovation in Information Systems (ICRIIS), 2013 International Conference on*. IEEE, 2013, pp. 533–538.

[9] D. Filko and G. Martinović, "Emotion recognition system by a neural network based facial expression analysis," *automatika*, vol. 54, no. 2, pp. 263–272, 2013.

[10] C. L. B. Maia and E. S. Furtado, "A study about psychophysiological measures in user experience monitoring and evaluation," in *Proceedings of the 15th Brazilian Symposium on Human Factors in Computer Systems*, ser. IHC '16. New York, NY, USA: ACM, 2016, pp. 7:1–7:9. [Online]. Available: http://doi.acm.org/10.1145/3033701.3033708

[11] V. Georges, F. Courtemanche, S. Sénécal, P.-M. Léger, L. Nacke, and R. Pourchon, "The adoption of physiological measures as an evaluation tool in ux," in *International Conference on HCI in Business, Government, and Organizations*. Springer, 2017, pp. 90–98.

[12] A. Landowska, "Emotion monitoring–verification of physiological characteristics measurement procedures," *Metrology and measurement systems*, vol. 21, no. 4, pp. 719–732, 2014.

[13] H. Van Kuilenburg, M. Wiering, and M. Den Uyl, "A model based method for automatic facial expression recognition," in *Proceedings of the 16th European Conference on Machine Learning (ECML'05)*. Springer, 2005, pp. 194–205.

[14] T. Lavie and N. Tractinsky, "Assessing dimensions of perceived visual aesthetics of web sites," *International journal of human-computer studies*, vol. 60, no. 3, pp. 269–298, 2004.

[15] I. Lopatovska and I. Arapakis, "Theories, methods and current research on emotions in library and information science, information retrieval and human–computer interaction," *Information Processing & Management*, vol. 47, no. 4, pp. 575–592, 2011.

[16] S. Mahlke, M. Minge, and M. Thüring, "Measuring multiple components of emotions in interactive contexts," in *CHI'06 extended abstracts on Human factors in computing systems*. ACM, 2006, pp. 1061–1066.

[17] B. McDaniel, S. D'Mello, B. King, P. Chipman, K. Tapp, and A. Graesser, "Facial features for affective state detection in learning environments," in *Proceedings of the Cognitive Science Society*, vol. 29, no. 29, 2007.

[18] M. Sarma and K. Bhattacharyya, "Facial expression based emotion detection-a review," *ADBU Journal of Engineering Technology*, vol. 4, 2016.

[19] A. Bachmann, C. Klebsattel, M. Budde, T. Riedel, M. Beigl, M. Reichert, P. Santangelo, and U. Ebner-Priemer, "How to use smartphones for less obtrusive ambulatory mood assessment and mood recognition," in *Adjunct Proceedings of the 2015 ACM International Joint Conference on Pervasive and Ubiquitous Computing and Proceedings of the 2015 ACM International Symposium on Wearable Computers*. ACM, 2015, pp. 693–702.

[20] J. Staiano, M. Menéndez, A. Battocchi, A. De Angeli, and N. Sebe, "Ux_mate: from facial expressions to ux evaluation," in *Proceedings of the Designing Interactive Systems Conference*. ACM, 2012, pp. 741–750.

[21] D. Dupré, D. Akpan, E. Elias, J.-M. Adam, B. Meillon, N. Bonnefond, M. Dubois, and A. Tcherkassof, "Oudjat: A configurable and usable annotation tool for the study of facial expressions of emotion," *International Journal of Human-Computer Studies*, vol. 83, pp. 51–61, 2015.

[22] C. Gaffney, O. Conlan, and V. Wade, "The amas authoring tool 2.0: A ux evaluation," in *Proceedings of the 25th ACM Conference on Hypertext and Social Media*, ser. HT '14. New York, NY, USA: ACM, 2014, pp. 224–230. [Online]. Available: http://doi.acm.org/10.1145/2631775.2631827

[23] J. Éthier, P. Hadaya, J. Talbot, and J. Cadieux, "Interface design and emotions experienced on b2c web sites: Empirical testing of a research model," *Computers in Human Behavior*, vol. 24, no. 6, pp. 2771–2791, 2008.

[24] H. Van der Heijden, "User acceptance of hedonic information systems," *MIS quarterly*, pp. 695–704, 2004.

[25] D. Keltner, "Signs of appeasement: Evidence for the distinct displays of embarrassment, amusement, and shame." *Journal of personality and social psychology*, vol. 68, no. 3, p. 441, 1995.

[26] R. J. Davidson, P. Ekman, C. D. Saron, J. A. Senulis, and W. V. Friesen, "Approach-withdrawal and cerebral asymmetry: Emotional expression and brain physiology: I." *Journal of personality and social psychology*, vol. 58, no. 2, p. 330, 1990.

[27] P. Saariluoma and J. P. Jokinen, "Emotional dimensions of user experience: A user psychological analysis," *International Journal of Human-Computer Interaction*, vol. 30, no. 4, pp. 303–320, 2014.

[28] A. Landowska, "Towards emotion acquisition in it usability evaluation context," in *Proceedings of the Mulitimedia, Interaction, Design and Innnovation*. ACM, 2015, p. 5.

[29] N. Altrabsheh, M. Cocea, and S. Fallahkhair, "Predicting students emotions using machine learning techniques," in *International Conference on Artificial Intelligence in Education*. Springer, 2015, pp. 537–540.

[30] N. Bosch, S. D'Mello, R. Baker, J. Ocumpaugh, V. Shute, M. Ventura, L. Wang, and W. Zhao, "Automatic detection of learning-centered affective states in the wild," in *Proceedings of the 20th international conference on intelligent user interfaces*. ACM, 2015, pp. 379–388.

[31] R. Bernhaupt and F. F. Mueller, "Game user experience evaluation," in *Proceedings of the 2016 CHI Conference Extended Abstracts on Human Factors in Computing Systems*, ser. CHI EA '16. New York, NY, USA: ACM, 2016, pp. 940–943. [Online]. Available: http://doi.acm.org/10.1145/2851581.2856683

[32] "AForge.NET," available on: https://en.wikipedia.org/wiki/AForge.NET, last accessed: 29 Aug 2017.

[33] "Zombie tsunami," [PC CD-ROM], Mobigame, 2014.

[34] K.-I. Benţa, H. Van Kuilenburg, U. X. Eligio, M. den Uyl, M. Cremene, A. Hoszu, and O. Creţ, "Evaluation of a system for realtime valence assessment of spontaneous facial expressions," in *Distributed environments adaptability, semantics and security issues international romanian-french workshop, Cluj-Napoca, Romania*, 2009, pp. 17–18.

# Developing a Multi-Channel Military Application Using Interactive Dialogue Model (IDM)

Muhammad Nazrul Islam[1], Sahrima Jannat Oishwee[2], Shifat Zaman Mayem, A S M Nur Mokarrom, Md Abdur Razzak, A B M Humayun Kabir
Department of Computer Science and Engineering
Military Institute of Science and Technology, Dhaka, Bangladesh
Email: {[1]nazrulturku, [2]sjoishwee}@gmail.com

***Abstract*—Software systems and applications developed in the modern era are created using various design techniques. These designs are specially created on specific themes and purposes. Present day military applications demand effective, efficient and satisfactory outputs in a highly portable package. Designing an efficient application exclusively for military use demands a professionally applicable design technique. In the existing literature, no specific design technique is proposed to implement a multi-channel (web and mobile version) military application. However, Interactive Dialogue Model (IDM) is a design technique specifically tailored for multi-channel (web, mobile) applications. As military applications need versatile use in multiple platforms, therefore, the objective of this paper was to assess the applicability of IDM to develop a multi-channel military application. As outcome, we developed a military software system for battlefield communication using IDM. An evaluation was carried out with eleven participants. As outcome, we found that the proposed system was effective, flexible, easy to use and supports multi-channel features.**

***Keywords*—Military communication system; multi-channel application; military application; interactive dialogue model; web design, usability***

## I. Introduction

The Internet, the biggest innovation, is the result of a military research [1]. Along with Internet, numerous inventions and discoveries were also possible due to military investments and requirements. In this era, information technology is advancing in an exponential speed. In parallel pace, military equipment and requirements are also progressed quiet a long way. Modern technology has always influenced the outcome of the battle. Present day military applications demand more outputs in a fast and highly portable package. So, designing an efficient application exclusively for military use demands a high degree of precise and professional skill-set.

Military Forces need to deal with diverse and unexpected situation arousing from the thick of the battle. A decision may lead to win or lose the battle. Enriched information from different and multiple platforms enhance the decision making. Battlefield scenario develops laterally and vertically in a scalable environment. Commanders and troops traverse the length and breadth of such environment. A military application thus demands versatile use in multiple platforms. Therefore, a multi-channel approach can satisfy the need of military application. A multi-channel application ensures the use of same services from various devices. e.g. communication between a soldier with the mid-level commander in mobile platform whereas the same communication between the mid-level commander to higher commander in web platform.

The IDM [2] is a novel design model specifically tailored for multi-channel applications. The background research, moving from linguistic theories and practices, has led to the development of a channel independent design model (based on dialogue primitives). IDM approach suggested to start the design in a conceptual channel-independent fashion, and then proceed into a further logical design for a specific channel (e.g. mobile, web). These sequence of technique offers many advantages without complexity. IDM has additional distinctive features: it is lightweight, provides a few sets of primitives (and a simple graphic notation), which are easy to learn and teach. Moreover, it is suitable for brainstorming and generating ideas at early stage during design (or during the shift from requirements to design). Finally, it is cost-effective (it requires little effort from designers) and modular (designers can take the part they wish, not being forced to all or nothing). IDM has been validated both in the academic and industry environments by designing the information intensive application like museum and e-governance sites.

The objective of this paper is to assess the applicability of IDM for implementing a multi-channel military application. To attain this objective, we have developed a multi-channel (web and mobile) military application following each step of IDM. Finally, the application was evaluated to assess the performance and usability standard with eleven military personnel.

The rest of the paper is organized as follows: the existing design techniques used for designing the general and military application are presented in Section II. Section III discussed the design of Advanced Battle Field Communication System using IDM. In Section IV, the development of the system is enumerated. Section V presented the evaluation of the system. The discussion and conclusion are presented in Section VI.

## II. Related Works

This section briefly presents the related studies, which focused the design and development techniques of both general & military purpose applications. First, design techniques of general-purpose applications are discussed.

F. Garzotto and P. Paolini [3] proposed the Hypertext Design Model (HDM) to describe hypertext systems. This system describes to develop hypertext application in a system independent manner. This model has some similarities with the Entity Relationship (E-R) model. HDM is mainly used for large-scale hypermedia applications where regularity, organization, modernization and consistency are contributing factors.

In [4], a Unified Modeling Language (UML)-based navigation design approach for modeling complex interactions in web applications is proposed called UML Extension Web Design Model (UEWDM). In this approach, navigation design is done through two design models- Navigation Space Model and Navigation Access Model. Navigation space model defines what the users will see and the relationships among navigation classes. Navigation access model defines how the web users reach those classes.

The web page design method proposed by Q Liu et el [5] obtains the client resolution adaptive table to calculate the best-visual-effect size of character by the clients mainstream device resolution adaptation.

Another model named Web Site Design Method (WSDM) is proposed in [6] which is a user-centered method for designing websites. It starts from dividing the users into user classes and data is modeled depending on the different viewpoints of user classes. Then the conceptual design is made which has no dependency on the implementation details. During implementation, the implementation model is converted into files containing the source code written in the programming language to be used for implementation.

Relationship Management Methodology (RMM) proposed in [7] is applicable mostly for hypermedia applications and its design process consists of several steps. The steps are entity-relationship design, slice design, navigational design, conversion design, user interface design, run-time behavior design and construction and testing.

Object Oriented Hypermedia Design Model (OOHDM) proposed in [8] is an Object-oriented design model. OOHDM allows the navigational views rather than a conceptual view in the Hypertext Design Models. Navigation links are mapped onto relationships of the conceptual model. The designers can design an early prototype using this design technique and later removes the faults generated from the initial design.

The enhanced object-relationship model (EORM) proposed in [9] is an Object-oriented methodology based on three frameworks: Class framework, Composition framework and GUI framework. Class framework expresses the underlying information structure of the application. Composition framework expresses the rules through which navigation capabilities can be defined based on the class framework, and the GUI framework defines how the information and navigation elements are presented to the user.

A few other methods based on semiotic theory (sign theory) have been proposed to design and evaluate the web and mobile applications. For example, Speroni [10] proposed the W-SIDE (Web-Semiotic Interface Design and Evaluation) framework and the Islam & Bouwman [11][12] proposed the SIDE (Semiotic Interface sign Design and Evaluation) framework to design the intuitive interface signs (that encompassed the UIs of web and mobile applications) as well as to evaluate the intuitiveness of interface signs in order to improve the overall system usability.

For a military application we need high portability, user friendliness and fast response time. Some studies that focus to the design techniques and usability concept of military applications are presented below.

Sungho Kim et el [13] described their study on improved graphic user interface (GUI) in terms of usability for military Computer-Based Training (CBT). In this study, a comparative evaluation in terms of ten usability criteria was conducted i.e. attractiveness, simplicity, responsiveness, informativeness, accessibility etc. As an outcome, they found the hierarchy and context type in term of accessibility and informativeness for the proposed GUI, which was highly appreciated, apart from the simplicity part.

In another study U. S. Army developed Command, Control, Communications, Computers, intelligence, surveillance, and reconnaissance (C4ISR) to identify human performance and human-system interaction using an iterative user-centered design process [14]. It focuses to work on seven domains, which are: manpower, personnel, training, human factors engineering (HFE), soldier survivability, system safety and health hazards. This system tried to improve the soldier-centered design activities.

The Linguistic Geometry Real-time Adversarial Intelligence and Decision-making (LG-RAID) [15] is a computer based training simulation, designed for Army personnel undergoing training on the development of tactically correct courses of action. They have evaluated the system based on some heuristic. i.e. Software-User Interaction, Learnability, Graphic Design, Software-System Interaction etc. In the study they have identified four critical shortcomings of the gaming simulation.

In sum, though a few studies focused on design issues to develop military applications, but they are mainly discussed on the usability evaluation and the user-centered design process. No specific design techniques are suggested or recommended to develop a military application. On the other hand, though a number of design techniques are proposed to develop general-purpose applications, only one technique (IDM) is proposed to design multi-channel applications (See Table I). Thus, for developing a military application where multi-channel feature is a key concern, IDM can be a suitable design technique. It also provides maximum number of positive attributes, which are required for a military application (See Table I). This work thus focused to assess the viability of IDM in designing and evaluating a multi-channel military application.

## III. Designing Advanced Battle Field Communication System Using IDM

A prototype of Advanced Battlefield Communication System was developed using IDM. In this application we tried to provide an exclusive battlefield scenario to the higher echelon of military through the eye of a front line soldier. We

TABLE I
COMPARATIVE STUDY OF DIFFERENT DESIGN TECHNIQUES

| Factors | HDM | UEWDM | WSDM | OOHDM | EORM | IDM |
|---|---|---|---|---|---|---|
| Easy to navigate | ✓ | ✗ | ✗ | ✓ | ✗ | ✓ |
| Maintain consistency | ✓ | ✗ | ✓ | ✗ | ✓ | ✓ |
| Support responsiveness | ✗ | ✗ | ✗ | ✗ | ✗ | ✓ |
| Support multiple languages | ✓ | ✓ | ✓ | ✓ | ✓ | ✓ |
| Can it be used for both informational website & application based website | ✗ | ✗ | ✗ | ✗ | ✗ | ✓ |
| Need high skill set of designers | ✓ | ✗ | ✓ | ✗ | ✗ | ✗ |
| Can it differentiate between channel independent and channel dependent applications | ✗ | ✗ | ✗ | ✗ | ✗ | ✓ |
| Portability | ✗ | ✗ | ✗ | ✗ | ✗ | ✓ |
| Supports multi-channel feature | ✗ | ✗ | ✗ | ✗ | ✗ | ✓ |

Legend: Present feature: ✓& Missing feature: ✗

have integrated video streaming, audio & text communication portals with a group of front line troops and generated those portals in our web page. The detail design methodology for developing the application is discussed in the subsequent sections:

### A. Designing the Conceptual-IDM (C-IDM)

The C-IDM is the first step of IDM. It's a channel independent design, which can be viewed as a model for conceptual schema. The C-IDM of the proposed application is shown in Fig. 1.

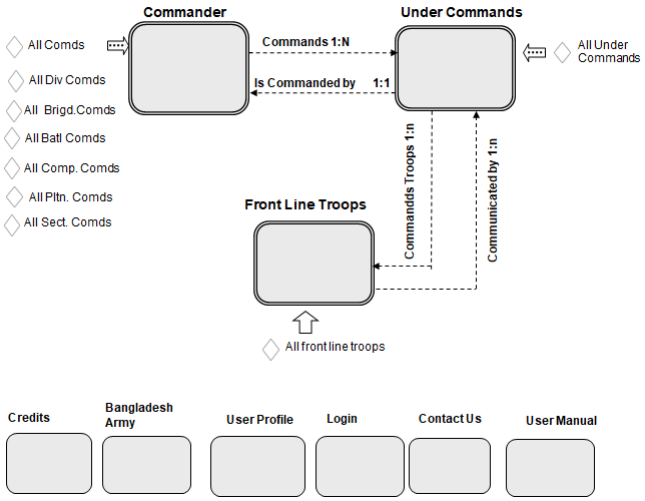


Fig. 1. C-IDM of Advanced Battlefield Communication System

The C-IDM consists of three design elements: Topic, Relationship and Group of Topic. Topic is something that can be viewed as the subject of conversation between the user and the system. Kind of topics are topics with multiple instances. There are three kind of topics in the C-IDM for our proposed system: *Commander, Under Commands* and *Front Line Troops. Single Topics* have single instance. There are few single topics in the C-IDM of our proposed system like Credits, User profile, etc. Relevant relations indicate the relations between two multiple topics with cardinality. For example, in our system each Commander can command multiple Under Commands but one Under Command can communicate with only one Commander. Similarly, One Under Command commands several Front Line Troops whereas each Front Line Troop can communicate with only one Under Commander. Therefore, the multiple topic *Commander* is connected to Under Commands with relevant semantic relationship with 1: n cardinality. *Group of topics* defines a specific group of topics. For example, all division commanders indicate commanders who are divisional commanders.

### B. Designing the Logical-IDM (L-IDM)

The L-IDM is a more detailed version of C-IDM with dialogues. It is a channel dependent design where details are decided on the basis of a variety of channel-dependent factors. The constraints imposed on designing L-IDM are: by the type of device available on a given channel (e.g. screen size), by pointing devices (e.g. keyboard, smart pen, mouse, scroll, audio input, touch pointers, eye-tracking pointers), by the media which can be used (e.g. audio, visual text, images, graphics, or video), by the expected performance, and the typical scenarios of use (e.g. home or office desktop use, walking or standing contexts, mobile use on car, etc.) Desktop version of L-IDM for our proposed system is given in Fig. 2. The hand held (mobile) version is given in Fig. 3.

Logical design contains the same Kind of Topics, Group of Topics, Single Topics and semantic relationships as the conceptual design. Each topic includes single or multiple dialogue acts. A dialogue act is a unit or move of the dialogue within a topic. Each dialogue act can be converted to a page later. For example, in L-IDM for our proposed system the topic Front Line Troop has three dialogue acts: Name & Profile, Photo, and Inventory Status. Transition acts are used when switching from one kind of topic to another with multiple instances. "Commands" is a transition act here, which is used while switching from Commander to Under Commands. Single topics might also include several dialogue acts. For example, the single topic User Profile has three dialogue acts: Name and Profile, Photo and Contact Details. While designing the hand-held version of L-IDM only crucial and necessary contents from the desktop version were included.

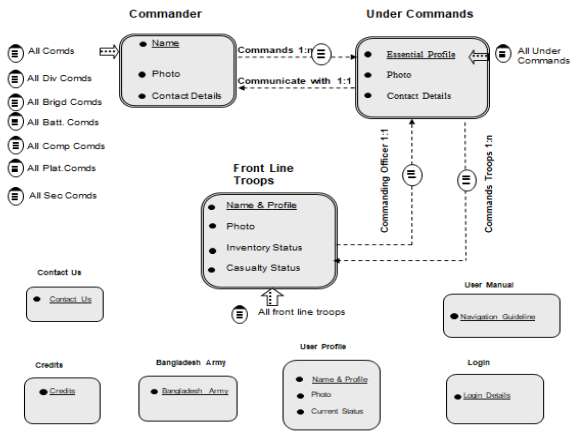


Fig. 2. L-IDM (Desktop Version)

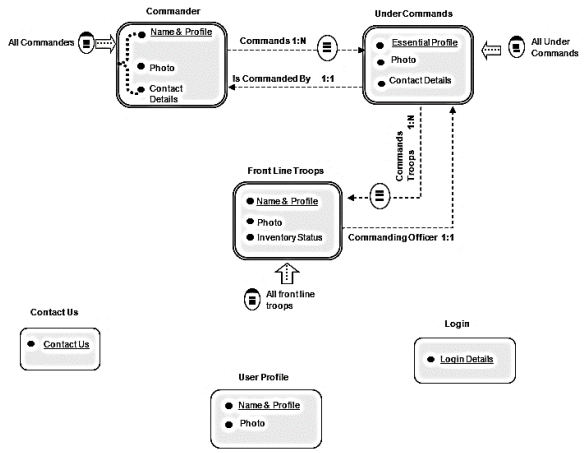


Fig. 3. L-IDM (Mobile Version)

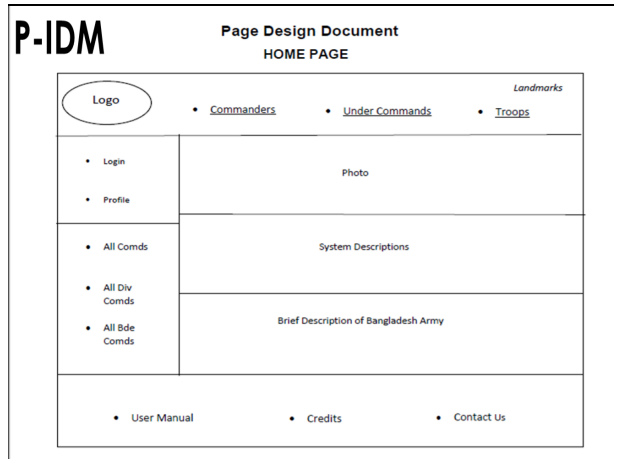


Fig. 4. Page Design (Home Page)

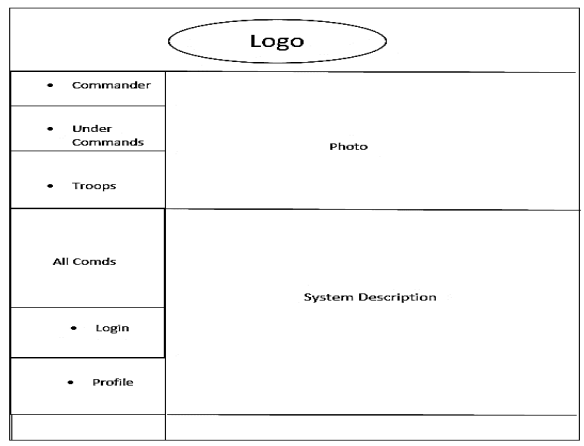


Fig. 5. Page Design Mobile Version (Home Page)

### C. Desigining the Page-IDM (P-IDM)

The P-IDM defines the elements to be used for interaction between the user and the application in a single dialogue act. Based on the information proposed in L-IDM we completed the page design (P-IDM) for our application.

In Fig. 4 & 5 page design (P-IDM) of the home page of our application is given. This is the landing page once any user enters the application. All the necessary links are combined in this single page so that any user can easily navigate to their desired destination from this page. Landmarks of the page are kind of topics (Commanders, Under Commands and Front Line Troops). The P-IDM is designed for both the mobile and web version. The communication between a Front Line Troop and the mid level Under Command, will be on portable devices like mobile phone or soldier data terminal (SDT). A mid level Under Command might receive any command decision from the higher authority from a portable device or from a web-page version too. It proves a multi-channel environment that is highly required for the flexible and smooth operation of the application.

## IV. Developing The System

We developed Advanced Battlefield Communication System application based on the designs we obtained in P-IDM (page design) phase. As mentioned in the previous sections, each page design obtained in P-IDM phase was converted into a web-page using preferred language. We used Hypertext Markup Language (HTML) for front end design and PHP (a server scripting language) with MySQL database for backend to make it a dynamic and interactive website.

Fig. 6 & 7 displays the web & mobile version of the application respectively. A soldier can use his SDT device to update any latest information through this multi-channel facilities.

Fig. 8 shows the live video feed coming from the cameras which are placed on the helmets of the troops. The links and pages could be created easily because of the cardinalities stated in the conceptual design. Using the web-version of the application any operation room can get the latest update of any soldier who is streaming his live video, audio and text feed.

Fig. 6. Page Design (Home Page)

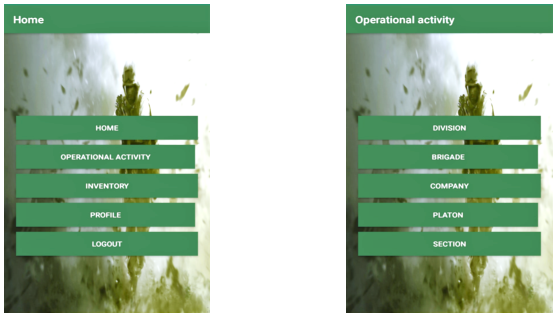


Fig. 7. Page Design (Mobile Version)

Fig. 9. is the mobile version of the communication portal. Again, we can feel the ease of use of IDM. As our design was channel independent and fit for multi-channel use so a soldier can stream his view through the mobile too. Moreover, anyone can observe this stream using his/her mobile or a web page.

## V. Evaluating The System

### A. Participant Profile

We have invited about 20 military personnel from the rank of Captain to Colonel to participate in the evaluation study. Finally eleven military personnel participated. All participants were male having age $34 \pm 6.7$ (Mean $\pm$ Standard Deviation). Their service length ranged from 7 to 26 years. Two participants had about 1-2 years, four participants had 3-5 years, three participants had 9-10 years and rest of them had more than 10 years of experiences of using ICT related applications and tools.

### B. Study Procedure

They study was conducted in the software engineering laboratory of CSE department of authors institution. At the beginning of the study the participants were assured that the evaluation process is not to judge the individual participants but the system itself. After that, a short demonstration and presentation was presented on the developed system. They were also briefed about their role and the objective of the system. Later, they were given fifteen minutes time to get acquainted with the system. Then they were asked to rate a few statements (questionnaires) for assessing the performance and usability standard. We assigned ratings 1-7 where 1 being strongly disagree and 7 being strongly agree of the studied system.

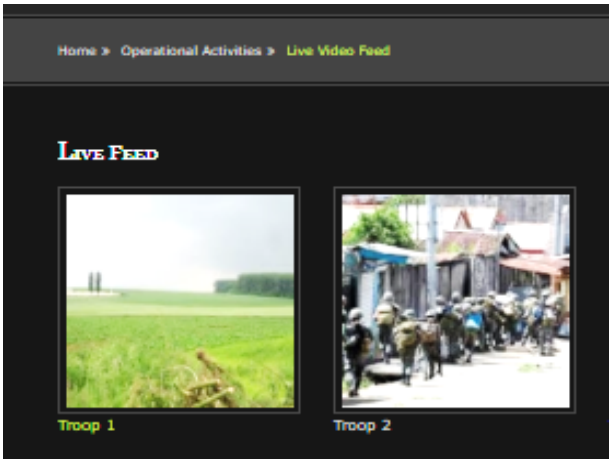


Fig. 8. Communication Portal (Web Version)

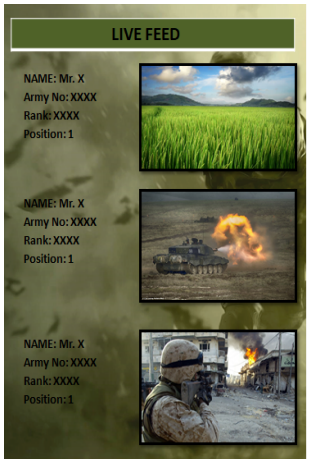


Fig. 9. Communication Portal (Mobile Version)

### C. Analysis and Result

Study data have been analyzed using the descriptive statistics where we have calculated the mean and standard deviations and showed how much the users are aligned with the quality factors of this application. The result is showed in in Fig. 10. The results indicate that all the evaluating factors attained more than the average standard. However, ease of use and effectiveness were comparatively highly appreciable than maintainability and reliability. On the other hand, robustness and integrity were not much appreciated compared to attractiveness and flexibility. Remaining factors like, portability, effectiveness and availability were also appreciated judiciously. In a nutshell, the result showed that, the application was treated as an effective and efficient application.

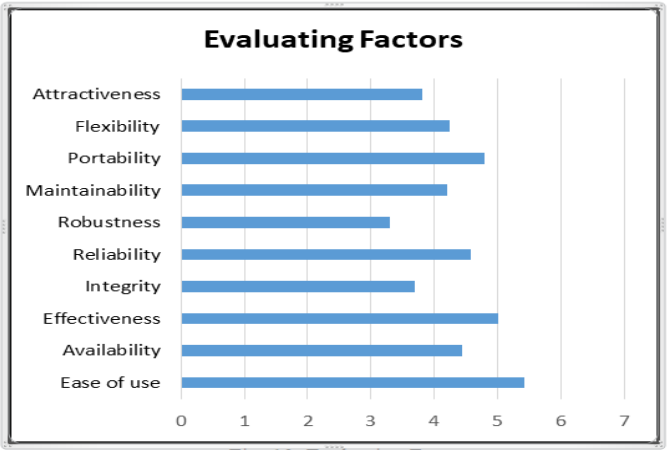


Fig. 10. Mean scores to usability factors

## VI. Discussion And Conclusion

In this paper, we have developed a multi-channel military application. The study showed that IDM is an effectively applicable technique to design a multi-channel military application. The evaluation study also showed that the system developed using IDM is effective and easy to use. The study outcome will greatly contribute to develop successful military applications. The user interface (UI) designers and Human Computer Interaction (HCI) practitioners can be aware about the diversity of the uses of IDM and the fact that IDM can be used in design and development of military related applications.

This study has a few limitations as well. Firstly, the software part of the system was developed, but the hardware part is yet to be integrated with the system. Secondly, the evaluation process was replicated by only eleven participants and conducted by explorative study and finally, only ten factors were considered in the study to evaluate the effectiveness and usability of the system. However, there were few more evaluating factors stated in [16] to assess the performance and usability standards of a military system. The first limitation will not have a lot of impact on the results because IDM mainly focuses on the software design part which was carried out properly in this study. Therefore, this research is barely affected by the yet to be integrated hardware part.

In future, we will consider developing the full system along with the hardware integration to conduct a consolidated and extensive evaluation study to explore more detailed findings.

## References

[1] B. K. Kim "Internationalising the Internet the Co-evolution of Influence and Technology," Edward Elgar. pp.5155.ISBN 1845426754,2005.

[2] D. Bolchini & P. Paolini, "Interactive Dialogue Model: A Design Tecnique for Multi-channel Applications," IEEE transactions on multimedia, vol 8, no 3, june 2006.

[3] F. Garzotto and P. Paolini, "A model-based approach to hypertext application design," ACM Trans. Inform. Syst., vol. 11, no. 1, pp. 126, Jan. 1993.

[4] S. A. Mubin, A. H. Jantan, R. Abdullah and A. Kamaruddin, "UML-based navigational design approach for modeling complex interactions in web applications," 2015 9th Malaysian Software Engineering Conference (MySEC), Kuala Lumpur, 2015, pp. 60-63.

[5] Q. Liu, J. Hu, L. Wu and J. Huang, "A Web Page Design Method for Multi-Terminal Devices," 2015 International Symposium on Educational Technology (ISET), Wuhan, 2015, pp. 3-7. doi: 10.1109/ISET.2015.10.

[6] O. De Troyer and C. Leune, "WSDM: a user-centered design method for web sites," in Proc. 7th Int. World Wide Web Conf., Brisbane, Australia,1997.

[7] T. Isakowitz, E. A. Stohr, and P. Balasubramanian, "RMM: a design methodology for structured hypermedia design," Commun. ACM, vol. 38, no. 8, pp. 3444, Aug. 1995.

[8] G. Rossi, D. Schwabe, and R. Guimaraes, "Designing personalized web applications," in Proc. WWW10, Hong Kong, May 2001.

[9] D. B. Lange, "An object-oriented design method for hypermedia information systems," J. Org. Comput. Electron. Commerce, vol. 6, no. 3, 1996.

[10] M. Speroni, "Mastering the semiotics of information-intensive web interfaces," Doctoral dissertation. University of Lugano, Lugano, 2006

[11] M. N. Islam and H. Bouwman, "Towards userintuitive web interface sign design and evaluation: A semiotic framework,"International Journal of Human-Computer Studies, vol. 86, pp. 121137, 2016.

[12] M. N. Islam and H. Bouwman, "An assessment of a semiotic framework for evaluating user-intuitive Web interface signs,"Universal Access in the Information Society, vol. 14, no. 4, pp. 563582, 2015.

[13] S. Kim, S. Lee, K. Kee, B. Lee, J. Lee, S. Park, H. You, "Usability Evaluation of Graphic User Interfaces for a Military Computer-Based Training System," in J Ergon Soc, Korea 2015.

[14] P. S. Knepshield, "Designing the User Experience (UX) for C4ISR systems in the U. S. Army," in HCI International, 25th June 2014.

[15] S. R. Serge, J. A. Stevens & L. Eifert, "Make it Usable: Highlighting the Importance of Improving the Intuitiveness and Usability of a Computer-Based Training Simulation," in Winter Simulation Conference-2015.

[16] M. A.Razzak & M. N. Islam, "Exploring the Usability Factors of Military Application: A User Study," accepted in 4th Asian Conference on Defence Technology,Japan, 2017.

# Fuzzy Logic Based Algorithm to Classify Tumor Categories with Position from Brain MRI Images

Rasel Ahmmed[1], Md. Asadur Rahman[2], and Md. Foisal Hossain[3]
[1,3]Department of Electronics and Communication Engineering, [2]Department of Biomedical Engineering,
[2,3]Khulna University of Engineering & Technology (KUET), Bangladesh
[1]East West University, Dhaka, Bangladesh
rsa@ewubd.edu, bmeasadur@gmail.com, foisalkuet@yahoo.com

*Abstract*—**Early tumor detection is a vital issue and tumor position, tumor area, and tumor categories evaluation are also mandatory concerns for the proper medication. This paper proposes fuzzy logic based tumor classification method which can identify the tumor position as well. A database is prepared with normal and tumor affected brain MRI images. The integration of Temper based K-means and modified Fuzzy C-means (TKFCM) clustering algorithm is used to segment the MRI images regarding gray level intensity in small portion of brain images. The values of K which signifies the number of classifying contour in Temper based K-means algorithm is more than the conventional one and automatically updated membership of FCM eradicates the contouring problem between these two methods. Then, from the segmented images two types of features, i.e., first order statistic features and region property based features are extracted. The first features are used to detect and isolate tumor and second kind features are used to design Fuzzy expert logic with 93 rules to classify the tumor. In this process three inputs and one output variable are used with several membership functions to obtain the six categories of tumor. The orientation of the tumor provides position of tumors. The performance parameters of the proposed algorithm show substantial results which are effective in classifying tumors in multiple intensity based brain MRI image.**

***Keywords*— Magnetic resonance imaging (MRI); temper based k-means and modified fuzzy c-means clustering (TKFCM); fuzzy logic system; defuzzified values.**

## I. INTRODUCTION

Brain tumor is occurred because of the abnormal and uncontrolled cell division activity of the brain tissue. Brain tumors are categorized as benign and malignant. There are several ways to diagnose brain tumors, among which most popular and effective is MRI image. In MRI technique, brain is imaged on the basis of density of water in soft tissue which is higher compared to other tissues such as bone [1]. Through the MRI images, the radiologist can see the brain anatomy without performing surgery. However, this process is still done manually and could lead to misdiagnoses. In addition, the different complex characteristics of brain tumor make diagnosis more difficult [2]. Therefore, system of Computer Aided Diagnostic (CAD) is indispensable that can be helpful for radiologist in identifying and classifying brain tumors.

Now a days, different methods are introduced to aid the radiologist in point of segmenting, detecting, positioning, and classifying exact brain tumor in brain MRI images. For the classification of any brain tumor categories, the region growing algorithm is introduced in [3] based on the statistical test data for the brain MRI images. The results are acquired regarding some predefined criteria *i.e.* intensity information and/or edges, and the connected region of an image. The primary limitation of this method is that, its seed points are found through manual interaction. Support Vector Machine (SVM) is discussed in [4] and showed better precision but the increased number of features and samples cause time consumption and inaccuracy in results [5]. The classification with K-means clustering which is announced for CT-Liver image along with experimental application in Brain MRI explained that proper segmentation can be possible with exact thresholding [6]. Again the K-value does not exceed greater than 3 if there is any gray level intensity more than that. Deng et al in [7] has presented a masking algorithm for the classification with the aid of any classifier algorithm. It is effective in finding automatic seed point and neighbors but the dimension of mask is to change manually for different brain MRI images [7].

The Fuzzy C-means algorithm is introduced in [8]-[10] has accomplished segmentation, and then introduces an expert system with defined membership and clustered centroid to locate a landmark tissue by matching them with a prior model. FCM mentioned in [8] has limitation of noise sensitivity and imperfection to the abnormality of brain *e.g.* tumor, edema, and cyst. Mostly used technique for classification of brain MRI image is Artificial Neural Network (ANN). An ANN technique is offered in [11] that showed good results with large data with the changing of some characteristics parameter for training and test of the network. This process requires a perfect pixel classifier, training data and huge time to proceed which cause a vulnerable conditions for the critical patients. From the above discussion, there arises scopes to propose a new method which can be able to detect the tumor size, its position, and categories automatically with high accuracy and specificity. In addition, the method should have the minimum time requirement for process to result representation.

In this paper, a new approach for tumor classification along with position evaluation from brain MRI image is introduced. For this normal and abnormal brain MRI images are firstly enhanced through wiener & median filter. Therefore, for the position detection of the tumor presence in the brain, there be an incorporated segmentation process namely Temper based K-

978-1-5386-2307-7/17/$31.00 ©2017 IEEE

means and modified Fuzzy C-means (TKFCM) clustering algorithm [12]. In this technique, the K-values varies from 1 to 8 which was limited to only 1 to 3 in conventional K-means and the automatically updated membership function eradicates limitation of FCM. There are two kinds of feature which are extracted from the segmented MRI images. The first order statistical feature i.e. contrast, correlation, homogeneity, entropy & energy are used to detect tumor. If there is a presence of tumor in images then fuzzy membership for tumor classification is defined by second order region based feature like area, eccentricity and perimeter. The defuzzified value is obtained from the specified rules for classifying tumor. The orientation of tumor is used to define position of tumor in brain images.

This paper is organized as follows. In section II methodology is described step by step .The results and discussion is shown throughout in section III and finally the whole work is concluded in section IV.

## II. METHODOLOGY

### A. Image data collection

Image data of brain MRI is taken from internet public repository. The image of normal brain and tumor brain with Lower Grade Glioma or Glioblastoma Multiforme is collected from [13]-[15]. The number of the used data for the classification is of 3 normal brains, 22 malignant tumors, and 5 benign tumors totally are of 30 MRI images.

### B. Image processing

The transform the MRI brain image to make it more suitable for the next process is concerned through some steps which are like following steps.

1) The conversion of Image to JPG and Image Orientation Setting: The image is converted from *.mha* format and *.dicom* format into *.jpg* by using MATLAB conversion Tools application. After the conversion, the size and direction resetting is conducted in order to have the same size and direction. The process is done manually by using Photoshop CS5 application with $256\times256$ pixels.

2) Image Enhancement: The obtained images firstly are converted to L*a*b* image for better view and quality. That is why the values of luminosity can span a range from 0 to 100 which should be scaled to [0 1] range (appropriate for MATLAB(R) intensity images of class double) before applying the three contrast enhancement techniques like adjusted, adaptive thresholded, and histogram imaging using both weiner2 and median2 filter.

### C. TKFCM based segmentation:

In this segmentation process K-means algorithm is used to segment MRI images on the basis of gray level. This gray level is selected depending on the temper of the image. Then the modified Fuzzy c-means algorithm which depends on the updated membership is applied to segment the temper based K-means segmented image. The membership of modified Fuzzy c-means is updated with the cluster distances from centroid defining by the features of the tumor MRI image. The TKFCM algorithm [12] is integration of the K-means and Fuzzy c-means with some modification. The temper is added along with the conventional K-means, which is identified by the temper or gray level intensity in the brain image. Besides, the Fuzzy c-means membership and Euclidian distance is modified by the image features.

Here, the coarse image $B\left(x_i, y_j\right)$ which is marked in describing desired temper for the K-means could be found through convolution of gray level based temper and image shown in below equation (1):

$$B\left(x_i, y_j\right) = \sum_{i=n+1}^{M+n} \sum_{j=n+1}^{N+n} P(x_i, y_j) \oplus T_{MN(resize)} \tag{1}$$

Temper based window is selected by $T_{MN}$ which is given as:

$$T_{MN} = \sum_{i=n+1}^{M-n} \sum_{j=n+1}^{N-n} P(x_i, y_j) \tag{2}$$

In the equation (2), there is an temper based image matrix with number of gray level intensity, $G$ and number of bins, $S$ which is used to detect the temper of the image $P\left(x_i, y_j\right)$. Where the $n$ is defined as $n = (winsize - 1)/2$ . With exact value of the temper, row and column, the desired temper is obtained.

Separately Temper based K-means and modified Fuzzy c-means clustering algorithm for segmentation can be written in equation as below:

$$J_k = \sum_{i=1}^{C} \sum_{j=1}^{K} B(x_i, y_j) \| x_i - c_j \|^2 \tag{3}$$

$$J_m = \sum_{j=1}^{N} \sum_{i=1}^{K} (U_{ij})^m (d_{ij})^2 \tag{4}$$

Then, from the equation (3) and (4) the contour through which the exact location of and tumor portion in any image can be find is

$$J_{km} = \oint_c \left(J_k, J_m\right) \tag{5}$$

Where, $M$ and $N$ are the row and column of $B(x_i, y_j)$ a binary coarse image matrix. The centroid of the cluster, number of data points in clusters and number of cluster is defined by $N$, $C$ and $K$ respectively. In the equation (5) which shows a contour integral of Temper based K-means image and updated membership based FCM image, where $c$ is the contour value. The last portion of equation (5) is defined as modified Fuzzy C-means whose Euclidian distance is depended on the image features and the first portion is used as the conventional K-means algorithm, which is defined by the distance from each point to cluster center.

*D. Feature Extraction:*

The system will extract the first and second order statistic. The first order statistic feature is used to detect exact tumor and it position in the brain MRI image and second order region based statistic feature is required for distinguishing the malignant tumor and benign tumor. Those are the parameters that will be taken as first order; contrast, correlation, entropy, energy and Homogeneity. The region properties of the segmented MRI image provide area, eccentricity, and perimeter. These values are used as the input of the Fuzzy Inference System (FIS) and provide desired defuzzified value for classification.

*E. Fuzzy Logic Approach:*

In a FIS it is required that there be input variables of the given features used to classify the tumor categories and the output should be made for the defuzzification values to obtained desired results. There are three input variables which exhibits the feature values acquired from region based statistical feature extraction process and one output variable of tumor categories. The membership functions of each input variables are finalized based on the range of the each feature value and there will be six membership functions for the output variable.

The whole method is described by the following flow chart.

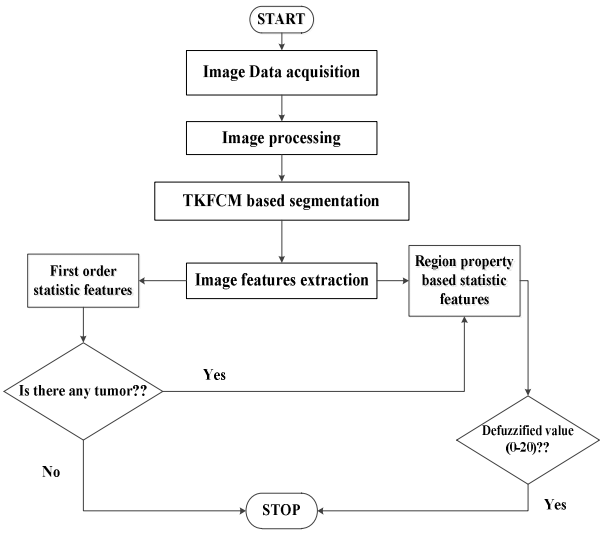


Figure 1. The flowchart of proposed algorithm

## III. Results and Discussions

For Magnetic Resonance Imaging (MRI), it is quite difficult to classify the tumor since, MRI image rarely color image. MRI imaging technique has good contrast value over different technique and gold accepted technique of imaging. The image of normal brain and tumor brain is collected from [13]-[15]. The numbers of the used data for the classification are of 30 MRI images in total.

The preprocessing steps include filtration, increase of luminosity and adjust of contrast. Then the images are goes through the TKFCM based segmentation process which can be shown in Fig 2. The figure describes that the input image firstly processed and segmented through TK-segmentation and modified FCM. Finally the extracted tumors are acquired which is used to determine the region property based statistical features.

A very well-known example of Mamdani Fuzzy Inference System (FIS) with three input variables of Eccentricity, Mean and Standard deviation is shown Fig. 3(d). The sample membership functions for the input variables area, eccentricity, and perimeter along with output variable tumor type are shown in Fig. 3(a), 3(b), 3(c, and 3(e). The input and output membership function is in triangular form. The defuzzified values which are obtained from the rule based fuzzy logic expert system are defined for the tumor classification [11]. Here, 93fuzzy rules (i.e. Using 'AND' & 'OR' operand) are used to recognize the tumor type. The logical defuzzified value of 0 to 3 belongs to normal brain image, the value of greater than 3 to less than or equal 6 describes benign tumor and above this values fits to the malignant tumor. Again, the greater than 6 to less than or equal 9 refers to malignant stage I. Malignant stage II includes the value between greater than 9 to 12, malignant stage III comprises of values between 12 to 15. Finally, the malignant stage IV tumors are find if the crisp value stands from 15 to 20 which is describes in TABLE I.

The TABLE I shows that which is usually found to be malignant stage I with the value of area referred in [16]. But it is actually belonging in malignant stage II considering other two parameters along with area which is shown in 1st row of the table. Like this example tumor images whose area, eccentricity, and perimeter are belonging in the range malignant or benign are correctly classified. This table also shows that with the change of the orientation the tumor lobe is identified whether it is accumulated at right, left or center position. Here, the positive orientation defines that the tumor belongs to right lobe and negatively oriented angle refers left lobe based tumor. The orientation angle approximately zero and perfectly zero mention as centered tumor and normal brain respectively.

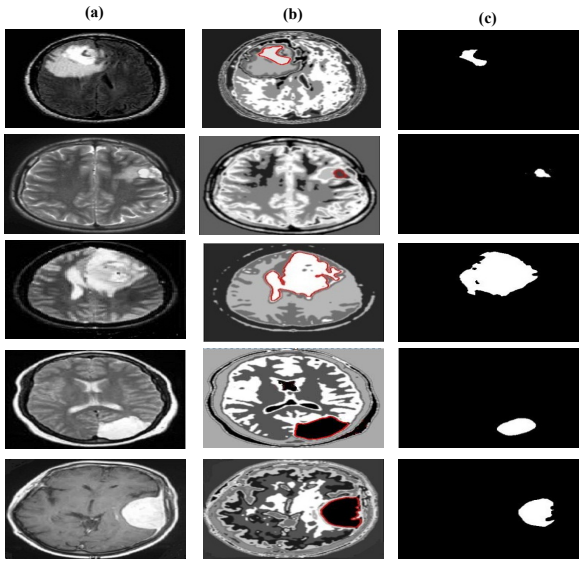


Figure 2. (a) Input images for TKFCM, (b) Detected brain tumor images using TKFCM, and (c) Extracted tumor through TKFCM

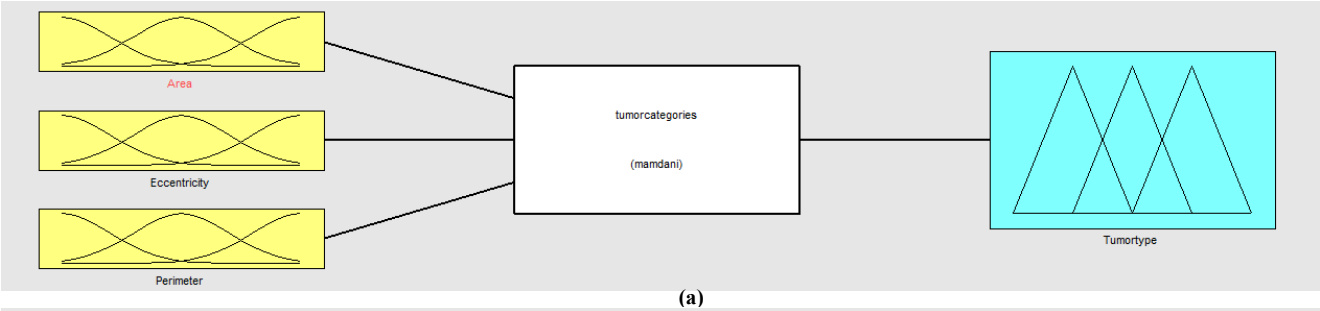


**(a)**

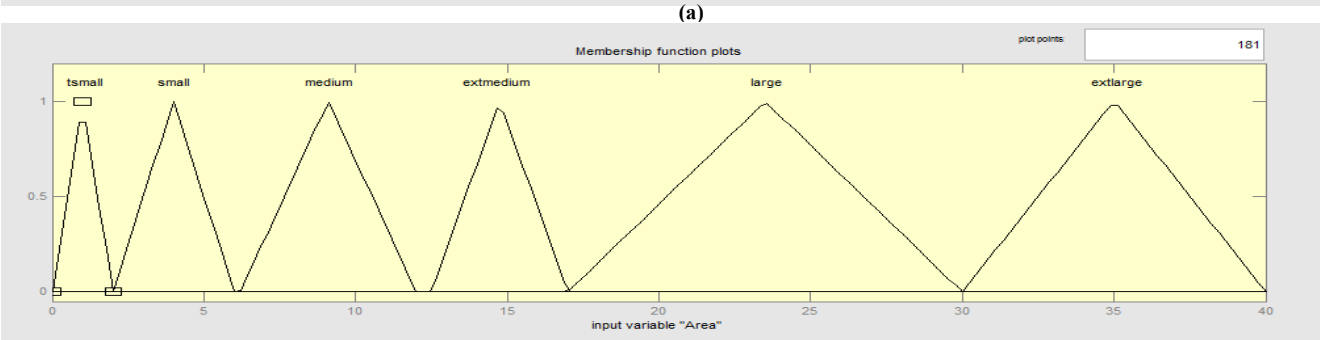


**(b)**

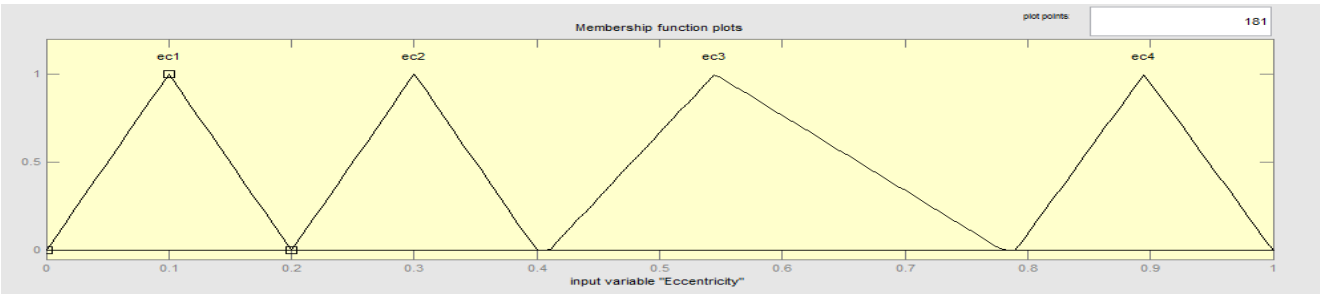


**(c)**

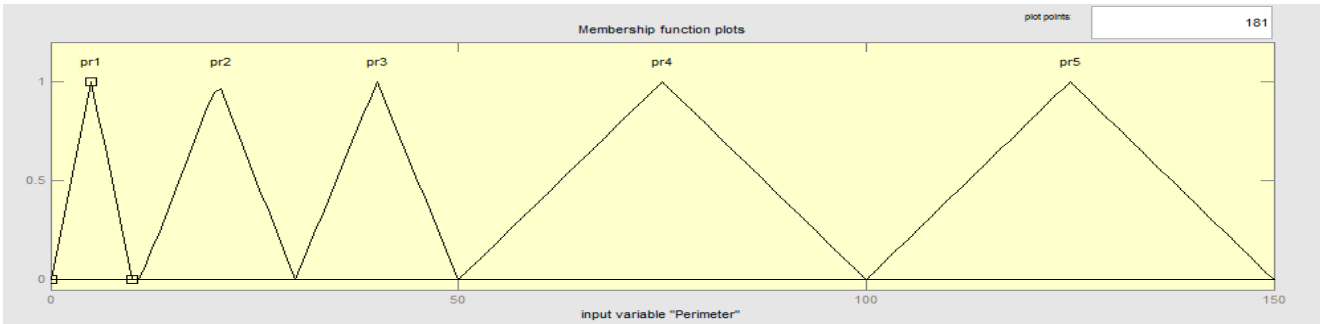


**(d)**

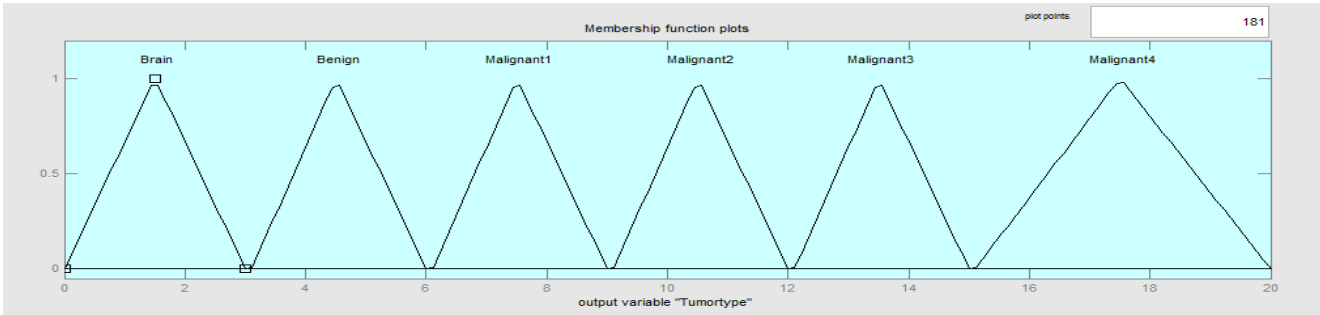


**(e)**

Figure 3. (a) Mamdani FIS for tumor classification, (b) Sample membership function of input variable area, (c) Sample membership function of input variable eccentricity, (d) Sample membership function of input variable perimeter, and (e) Sample membership function of output variable tumor type.

TABLE I. CLASSIFICATION OF TUMOR CATEGORIES AND IDENTIFICATION TUMOR POSITION USING FEATURES BASED FUZZY LOGIC APPROACH

| Area in $mm^2$ | Eccentricity in mm | Perimeter in mm | Defuzzified value | Tumor type | Orientation in degree | Tumor position in lobe |
|---|---|---|---|---|---|---|
| 9.9167 | 0.9754 | 60.275424 | 11.7252 | Malignant II | -84.1794 | Left |
| 6.472 | 0.9213 | 33.55836 | 9.0327 | Malignant I | -100.0502 | Left |
| 8.2561 | 0.8402 | 40.736784 | 8.7055 | Malignant I | -54.547 | Left |
| 9.5952 | 0.9414 | 36.863376 | 8.8824 | Malignant I | -57.7349 | Left |
| 6.1 | 0.8464 | 20.64 | 4.56 | Benign | 72.1398 | Right |
| 8.6719 | 0.7084 | 31.913904 | 11.0431 | Malignant II | 0.404 | Centered |
| 10.2451 | 0.6974 | 41.258448 | 10.4773 | Malignant II | -32.196 | Left |
| 21.5625 | 0.793 | 82.645728 | 12.9462 | Malignant III | 0.6467 | Centered |
| 9.7787 | 0.6381 | 37.249872 | 11.3492 | Malignant II | -88.0731 | Left |
| 8.1541 | 0.8617 | 32.143056 | 9.034 | Malignant I | 69.189 | Right |
| 7.0295 | 0.7793 | 25.955424 | 7.61 | Malignant I | 14.0189 | Right |
| 7.9814 | 0.9886 | 18.599592 | 7.9451 | Malignant I | 85.0421 | Right |
| 22.4633 | 0.6164 | 135.3689 | 13.5718 | Malignant III | 60.2044 | Right |
| 0 | 0 | 0 | 0 | Brain | 0 | No tumor |
| 8.0379 | 0.4214 | 28.77864 | 9.612 | Malignant II | -59.6895 | Left |
| 6.5788 | 0.9625 | 1.03488 | 5.856 | Benign | -36.3963 | Left |
| 0 | 0 | 0 | 0 | Brain | 0 | No tumor |
| 8.7599 | 0.8547 | 36.848064 | 8.9385 | Malignant I | 1.3184 | Right |
| 4.5726 | 0.99 | 28.009608 | 3.97 | Benign | -85.4523 | Left |
| 24.4937 | 0.8675 | 135.78576 | 14.2 | Malignant III | -77.2517 | Left |
| 7.7914 | 0.7926 | 36.24984 | 9.0316 | Malignant I | -49.5862 | Left |
| 13.3835 | 0.8289 | 49.570752 | 9.0528 | Malignant I | 12.2018 | Right |
| 15.8158 | 0.8813 | 75.392592 | 11.58 | Malignant II | 44.3799 | Right |
| 11.0597 | 0.625 | 89.080464 | 11.1849 | Malignant II | -55.4867 | Left |
| 0 | 0 | 0 | 0 | Brain | 0 | No tumor |
| 4.967 | 0.79 | 10.77912 | 4.535 | Benign | 75.2136 | Right |
| 5.82 | 0.9288 | 7.521624 | 4.834 | Benign | -4.3858 | Left |
| 36.9817 | 0.4032 | 141.77 | 17.5357 | Malignant IV | -82.9364 | Left |
| 15.7074 | 0.671 | 58.995552 | 12.9839 | Malignant III | 89.6919 | Right |
| 12.3489 | 0.8206 | 58.698816 | 11.7311 | Malignant II | -82.3899 | Left |

TABLE II. COMPARISON OF PROPOSED ALGORITHM WITH CONVENTIONAL METHODS

| Algorithms | Sensitivity (%) | Specificity (%) | Accuracy (%) | BER | Computational time |
|---|---|---|---|---|---|
| Thresholding | 85 | 80 | 83.3 | 0.175 | ~5-7 min |
| Region Growing | 88.46 | 75 | 86.7 | 0.182 | ~10 min |
| ANN | 95.42 | 100 | 96.67 | 0.022 | ~15 min |
| FCM | 86.95 | 85.7 | 87 | 0.136 | ~5 min |
| K-means | 75 | 92.85 | 83.3 | 0.160 | ~160-170 sec |
| TKFCM | 88.9 | 100 | 93.3 | 0.055 | ~100 sec |
| Proposed Method | **96.3** | **100** | **96.667** | **0.018** | **~ 120 sec** |

Image size=256x256, Software=MATLAB2014a, Processor= Core2duo, RAM=2GB, windows=7

There is some error rate on the basis of identifying or not identifying any abnormal tissue in all brain tumor MRI image. This can be calculated depending on the value of true positive, false positive, true negative, and false negative [17].The performance parameters can be calculated for the 40 brain tumor images through following formula

$$Sensitivity = \frac{TP}{(TP+FN)} \times 100 \quad (6)$$

$$Specificity = \frac{TN}{(TN+FP)} \times 100 \quad (7)$$

$$Accuracy = \frac{(TP+TN)}{(TP+TN+FN+FP)} \times 100 \quad (8)$$

$$BER = \frac{1}{2}\left(\frac{(FN)}{(TP+FN)} + \frac{(FP)}{(FP+TN)}\right) \quad (9)$$

*Where, TP*=True Positive, *TN*=True Negative, *FP*= False Positive, *FN*= False Negative.

In TABLE II, a comparison chart is prepared among the conventional brain tumor classification processes and proposed method. The performance analysis is comprehended through True Positive (TP), True Negative (TN), False Positive (FP), and False Negative (FN). In proposed technique there are 30 brain MRI images are taken and from the equation (6), (7), (8) and (9) the sensitivity of 96.1%, 100% specificity, accuracy of 96.67%, and BER 0.018 are obtained which is better than the conventional methods like thresholding, region growing, ANN, FCM, and K-means. As the ANN comprehends the value of accuracy of 96.67%, but the

computational time is so high. On the other hand, the proposed method sensibly pursues a computational time of ~120 sec, which is good enough for the medical diagnosis applications.

## IV. Conclusion

According to the objectives of the proposed method, the applicability of the proposed algorithm is tested and compared to the other existing methods. From the results we found that the classification accuracy of the proposed method is the highest compared to the others except ANN. On the other hand, though the classifying accuracy of ANN is similar to the proposed algorithm, its time requirement is greater than the proposed method. From the other metrics of the effectiveness of the proposed algorithm such as, specificity, sensitivity, and BER it is found that the proposed algorithm is better than the other conventional methods. The extra feature of the proposed algorithm is to find the position of the tumor which is also identified by the sign of orientation angle value. Hopefully, this algorithm will be helpful for automatic medical diagnosis applications.

For the better performance of the proposed algorithm, it is necessary to arrange the brain MRI images of non-distorted form.

## References


[1] R. Rana, H. S. Bhadauria, and A. Singh, "Study of various methods for brain tumor segmentation from MRI images", International Journal of Emerging Technology and Advanced Engineering, vol. 3, no. 2, pp. 338-342, 2013.

[2] J. Joshi and A. Phadke, "Feature extraction and texture classification in MRI" In Special Issue of IJCCT, pp. 130-136, 2010.

[3] A. Ahirwar, "Study of techniques used for medical image segmentation and computation of statistical test for region classification of brain MRI", International Journal on Information Technology and Computer Science, pp. 44-53, 2013.

[4] Richika et al, "A novel approach for brain tumor detection using support vector machine, K-means and PCA algorithm" International Journal of Computer Science and Mobile Computing, vol.4 issue.8, pp. 457-474, August- 2015.

[5] D. L. Pham, C. Xu, and J. L. Prince, "Current methods in medical image segmentation," Annual review on Biomedical Engineering, vol. 2, pp. 315-337, 2000.

[6] W. Narkbuakaew, H. Nagahashi, K. Aoki, and Y. Kubota, "Integration of modified K-Means clustering and morphological operations for multi-organ segmentation in CT Liver-Images," Recent Advances in Biomedical & Chemical Engineering and Materials Science, pp.34-39, March.2014.

[7] G. Deng, "A generalized unsharp masking algorithm", IEEE Transactions on Image Processing, vol. 20, no. 5, pp. 1249-1261, May 2011.

[8] S. R. Kannana, S. Ramathilagam, R. Devi, and E. Hines, "Strong fuzzy C-means in medical image data analysis," Article in The Journal of Systems and Software, vol. 85, pp. 2425– 2438, December, 2011.

[9] V. Harati, R. Khayati, and A. R. Farzan, "Fully automated tumor segmentation based on improved fuzzy connectedness algorithm in brain MR images," Article in Computers in Biology and Medicine, vol. 41, pp. 483–492, April, 2011.

[10] H. R. Shally, and K. Chitharanjan, "Tumor volume calculation of brain from MRI slices", International Journal of Computer Science & Engineering Technology (IJCSET), vol. 4, no. 8, pp. 1126-1132, 2013.

[11] M. Lugina, N. D. Retno, and R. Rita, "Brain tumor detection and classification in magnetic resonance imaging (MRI) using region growing, fuzzy symmetric measure, and artificial neural network back propagation", International Journal on ICT, vol. 1, pp. 20-28, December, 2015.

[12] R. Ahmmed, A. S. Swakshar, M. F. Hossain, and M. A. Rafiq, "Classification of tumors and it stages in brain mri using support vector machine and artificial neural network", Proceedings of International Conference on Electrical, Computer and Communication Engineering (ECCE-17), pp. 229-234, February 16-18, 2017, Cox's Bazar, Bangladesh.

[13] (2015) PE- Brain tumor website. [Online]. Available: http:// www.mayfieldclinic.com /

[14] University of Maryland Medical Center (2015) homepage. Primary brain tumor [Online]. Available: http://umm.edu/health/medical/reports/articles/brain-tumors-primary

[15] Oncology (2015) homepage. Tumor type [Online]. Available: http://www.oncolink.org/types/article.cfm?c=52&aid=247&id=9534

[16] J. Selvakumar, A. Lakshmi, and T. Arivoli, "Brain tumor segmentation and its area calculation in brain MR images using K-mean clustering and fuzzy C-mean algorithm," International Conference on Advances in Engineering, Science and Management (ICAESM), pp.186-190, 30-31 March, 2012.

[17] X. Descombes, F. Kruggel, G. Wollny, and H. J. Gertz, "An object-based approach for detecting small brain lesions: Application to Virchow-robin spaces", IEEE Transaction on Medical Imaging, vol.23, no.2, pp.246–255, 2004.

# Implementation of Biochip on Multirate System for EEG signal on ALTERA Cyclone Device

[1]Nazifa Tabassum, [1]Sheikh Md. Rabiul Islam, [2]Xu Huang
[1]Dept. Electronics and Communication Engineering
Khulna University of Engineering & Technology, Bangladesh
[2]Faculty of ESTeM, University of Canberra, Australia,
Email: nazifa.ece12@gmail.com; robi@ece.kuet.ac.bd; Xu.Huang@canberra.edu.au

*Abstract* –**EEG signal needs to be analyzed for various medical purposes. As there may be noises and artifacts in EEG raw data, we need to denoise it and amplify the EEG signal for better analysis. We propose a new biochip for EEG signal amplification on multirate system. This system uses ALTERA Cyclone DE II field-programmable gate array (FPGA) development board for the proposed biochip implementation. This FPGA development board is interfaced with processors EP2C35F672C6 for designing the proposed bio-chip in real-time for the proper data accuracy. In this case, Modelsim is used for simulation of biochip design in Verilog HDL. The proposed biochip is designed on multirate system with support of up-sampler or interpolation, polyphase filter and down-sampler or decimation for amplifying the EEG signal. This biochip shows good enough electrical characteristics such as low voltage & current, enough memory storage spaces, less power and area.**

*Keywords* – ***EEG, FPGA, Bio-chip, multirate.***

## I. INTRODUCTION

Electroencephalography (EEG) is a method to record brain's spontaneous electrical activity over a period of time. EEG [1]. contains some noise and artifacts causing from electrocardiogram (ECG), electromyogram (EMG), electro-oculogram (EOG). These artifacts are totally unwanted capacities which originates from non-cerebral activities such as eye blinking that infect the EEG signal. EEG artifacts originate from two sources namely, technical and physiological. Technical artifacts can be avoided through proper apparatus setup, consistent monitoring and meticulous inspection of equipment. Physiological artifacts arise from a variety of body activities that are either due to movements, skin resistance fluctuations or other bioelectrical potentials. Different types of EEG waves are categorized by the frequency namely Alpha waves (7.5-14 Hz), Beta waves (14-40 Hz), Gamma waves (above 40 Hz), Theta waves (4- 7.5 Hz), Delta waves (0.5-4 Hz). All the waves represent different mental states of the patient.

These noises need to be removed for proper diagnosis of patient using recorded EEG signals [2] - [4]. Again, some cerebral activities produce signal which can't be analyzed with raw EEG data. Some medical diagnosis also requires signal amplification. So, for removing these noises and amplifying the signal, we need to design a proper filter.

Polyphase filter is used in this case because it is a multi - phase filter using multi-branch. Again, polyphase filter reduces signal saturation. Moreover, Multirate system [5], [6] based denoising method is most promising field now a day. In this paper, we have developed a biochip which is implemented on ALTRA Cyclone DE II FPGA board**.** This bio-chip consist on three units such as interpolation or up-sampling, polyphase filter designing and decimation or down-sampling.

The system uses a computer in which the design can be programmed and simulated on Xilinx[@] Integrated Software Environment (ISE) Suite 14.7 or Quartus II software with interface to ALTRA Cyclone DE II board of FPGA device**.** From the implementation side, references [7], [8], [9], use Xilinx chips and Altera devices [10].

## II. MATERIALS AND METHODS

### A. Database

The set of EEG data is collected from BME (Biomedical Engineering) signal processing laboratory. The data is taken on *biopac* system which interfaces with human body and PC. The patients age was around 20-23 and they all are students. For further processing an Analog to Digital Converter(ADC) is applied to generate discrete data set from the continuous data set. In this case, the ADC operation have been performed manually.

### B. Proposed Methodology

A simple block diagram of the proposed biochip is shown in Fig. 1 below.

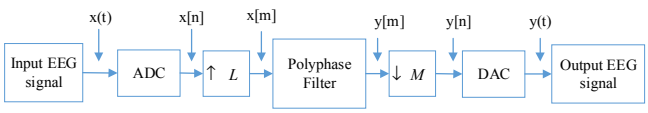


Fig. 1. Block diagram of proposed biochip.

The proposed biochip using polyphase filter have considered sampling rate conversion (SRC) using Multirate system. Firstly, EEG data is passed to the ADC block in order to make the discrete data x[n] from continuous data x(t). This input signal x[n] is fed into the interpolator so that the data is up-sampled by L. This block inserts L-1 samples containing zero values after each input sample. These samples are denoted as x[m] as & in Fig. 1 & in the equation (1) below.

Up-sample output,

$$x(m) = x(n) = \begin{cases} x\left[\frac{n}{L}\right], & n = 0, L, 2L \\ 0, & \text{otherwise} \end{cases} \quad (1)$$

The sampling frequency of the input signal is increased from fs to $L * f_s$ by the interpolator. One implication of inserting L-1 zeroes after each sample is that the energy of each input sample is spread across L output samples. Thus, the interpolator has a gain of $1/L$.

These samples are filtered by using polyphase filter. The polyphase filter is an FIR (Finite Impulse Response) filter. After filtering we get the filtered output y[m] as shown in Fig. 1. The N=8th order polyphase filter consists mainly of the followings:

i. the input x[m], its one-unit delayed version $x[m-1]$ and two-unit delayed version $x[m-2]$.
ii. for filter order N=8, the filter coefficients are $h(0), h(1) \ldots\ldots\ldots h(8)$.
iii. The multiplication of $h(0), h(1), h(2)$ with x[m]; $h(3), h(4), h(5)$ with $x[m-1]$; $h(6), h(7), h(8)$ with $x[m-2]$ is performed and $y_0[m]$, $y_1[m]$ and $y_2[m]$ are calculated using the equations (2) to (4). y[m] is calculated by adding these three components $y_0[m]$, $y_1[m]$ and $y_2[m]$ as in the equation (5) and shown in Fig. 2, where y[m] is our desired filter output.

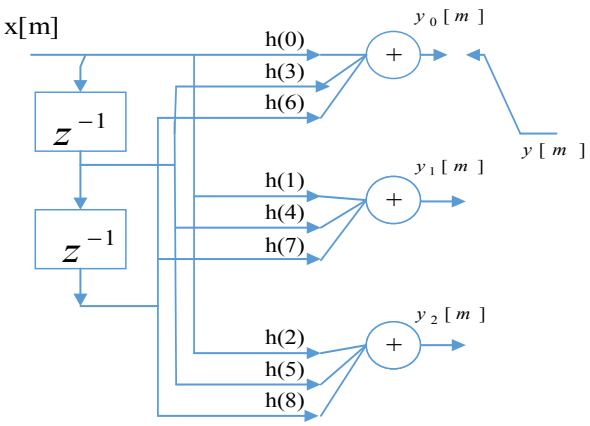


Fig. 2. Basic Polyphase filter structure.

The equation of polyphase filter with order $N = 8$, is written below;

$$y_0[m] = \{h(0) + h(3) + h(6)\} * x[m] \quad (2)$$

$$y_1[m] = \{h(1) + h(4) + h(7)\} * x[m-1] \quad (3)$$

$$y_2[m] = \{h(2) + h(5) + h(8)\} * x[m-2] \quad (4)$$

$$y[m] = y_0[m] + y_1[m] + y_2[m] \quad (5)$$

y[m] is desired polyphase filter output which is the amplified version of input EEG signal. Here the filter coefficient h[n] values are optimized for polyphase filter as shown in Table I and its frequency response is shown in Fig. 3. It is clear from Fig. 3 that It has the response of a Band pass filter(BPF) which has cut-off frequencies -1 Hz to 1 Hz.

TABLE I. THE IMPULSE RESPONSE h(n) OR FILTER COEFFICIENTS OF POLYPHASE FILTER (N = 8).

| h(n) | Value |
|---|---|
| h (0) | 1 |
| h (1) | 5 |
| h (2) | 60 |
| h (3) | 80 |
| h (4) | 100 |
| h (5) | 80 |
| h (6) | 60 |
| h (7) | 5 |
| h (8) | 1 |

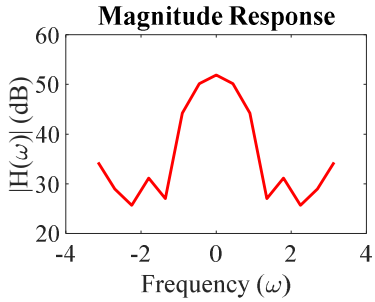


Fig. 3. Frequency response of designed polyphase filter.

Our next operation is to perform down-sampling by $M$. In this case we have used $M = 2$. In Down-sampling the signal {y[m]} is multiplied by the sampling function $\{s_P[n]\}$ defined as,

$$s_P[n] = \begin{cases} 1, & n = 0, \pm P, \pm 2P, \ldots. \\ 0, & \text{otherwise} \end{cases} \quad (6)$$

Now, if we multiply{y[m]} by the sampling function $\{s_P[n]\}$ results the down sampled signal $\{y[n]\}$

$$y[n] = y(m)s_P[n] = \begin{cases} y(m), & n = 0, \pm P, \pm 2P, \ldots. \\ 0, & \text{otherwise} \end{cases} \quad (7)$$

The input y[m] is fed into the delay line one sample at a time. For every M samples of y[m] applied to the delay line one output sample y[n]. This involves keeping the first sample of y[m], discarding the next $M-1$ samples, keeping the next sample, and discarding the next M-1 samples, and so on. Finally, this discrete data (y[n]) are passed through a DAC block to get the continuous data y(t).

### C. *Flowchart of proposed biochip on multirate system*

Fig. 4 shows the flowchart of the proposed biochip using polyphase filter on multirate system with interface to ALTERA Cyclone DE II Device. The equation (1) is used for up sampling operations; where EEG signal is converted to binary by ADC and up sampled or interpolator by L which is also binary. The polyphase filter operation is obtained by using the equation (2) to (5). Lastly, the equation (6) & (7) have been used for down sampling operation by M and used DAC to get continuous output y(t) of EEG signal.

## III. EXPERIMENTAL RESULTS AND DISCUSSION

### A. Algorithm and Flowchart

Basically, this proposed Biochip has three individual operations working on multirate system which are Up-sampling, polyphase filter, Down-sampling. These operations in the biochip are described below.

#### i. *Up-sampling*

Up-sampling is a process by which the number of samples is increased by a definite rate L. If the original number of samples are 100, then using L=2 up-sampling, the number of samples becomes 100*2=200. The main concept is to insert zero valued data in the middle of every samples of data. Thus, inserting L-1 zeros, the up-sampling process is obtained. For example, if the original sequence of data is (60,58,55,52……), the resulting sequence after up-sampling is (60,0,58,0,55,0,52,0…….). This operation is done by altering integer value *i* as shown in Fig.5 in biochip design. The input EEG data (x[n]) is denoted as *data_in* and the data after up-sampling process is stored in a register and denoted by *data_out1*.

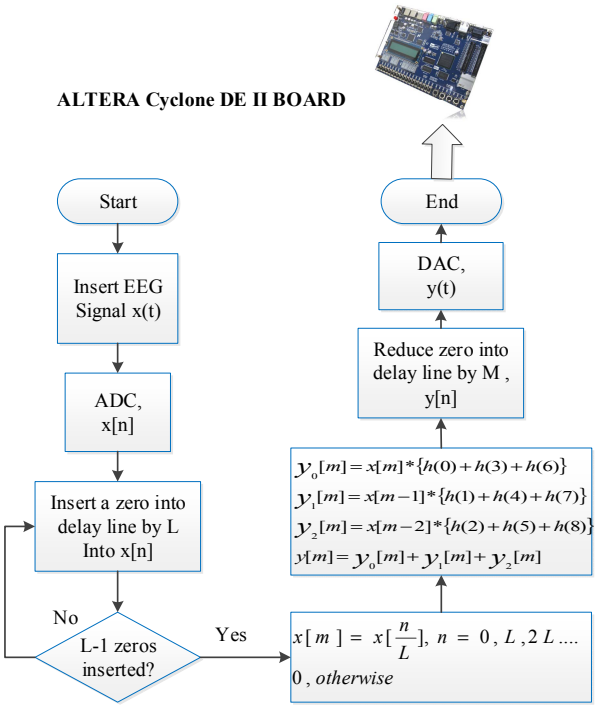


Fig. 4. A simplified flowchart of proposed biochip interface with ALTERA Cyclone DE II Board.

#### ii. *Polyphase Filter Design*

After being up-sampled the data are passed through a polyphase filter so that we can get a better representation of data with huge amplification. A polyphase filter with order N=8 has been used here. Two D-flip-flops have been used for delay operations. Fig. 6 shows the designed filter.

- The input of 1st D-Flip-Flop is the data input(*x[m]*).
- Output of 1st D-FF is one-unit delayed version of input and denoted as d11(*x[m-1]*).
- Input of 2nd D-FF is the output of 1st D-FF.
- Output of 2nd D-FF is two units delayed version of original input and denoted as d12(*x[m-2]*).
- $h(0), h(1), h(2) \ldots\ldots h(8)$ are the coefficients of the polyphase filter.
- $y_0[m]$, $y_1[m]$, $y_2[m]$ are calculated by using equation no (2) to (5).
- Finally, y[m] is calculated by adding $y_0[m]$, $y_1[m]$ and $y_2[m]$.

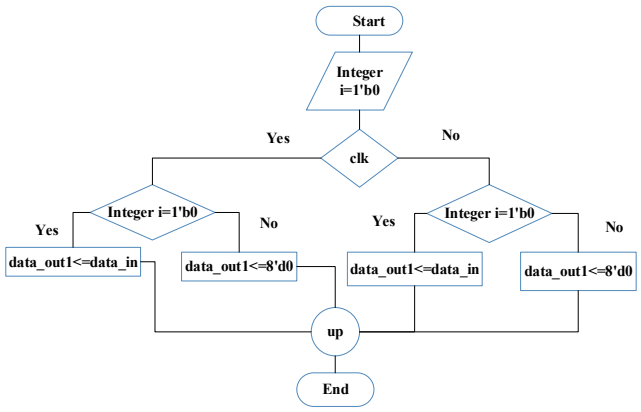


Fig. 5. Flowchart of Up-sampling process in Biochip.

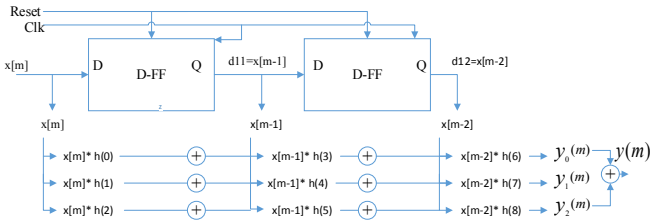


Fig. 6: Basic Diagram of designed polyphase filter.

#### iii. *Down-sampling*

In down-sampling process, the number of samples is decreased by a definite rate M. If the original number of samples are 300, then using M=2 down-sampling, the number of samples becomes 300/2=150. The main concept is to omit sample of data one after another. Thus, removing M-1 samples, the down-sampling process is obtained.

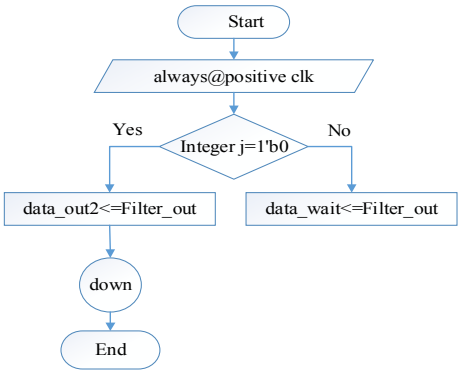


Fig. 7. Flowchart of down-sampling process in Biochip.

For example, if the original sequence of data is (60,58,55,52,50,47……) then the resulting sequence after

up-sampling is (60, 55,50…….). Here the down-sampling is done by altering integer value *j* as shown in Fig. 7. The filtered EEG data (y[m]) is denoted as *Filter_out* and the data after down-sampling process is stored in a register and denoted by *data_out2* which is the desired output as shown in Fig. 7.

### *B. RTL diagram of proposed Biochip*

The overall RTL diagram consists of basic three parts (up-sampling, polyphase filter, down-sampling parts).

At first, input EEG data has been passed by input buffers(IBUF) as shown in Fig.8. Every data is stored in registers. For every two consequent clock pulses, an input data has been taken and the input is stored in an intermediate register. Original data is stored in first clock pulse and data containing zero value is inserted into register in the next clock pulse. After performing up-sampling operation, the data is stored in FDR (D Flip-flop with synchronous reset) as shown in Fig. 9. For polyphase filter operation, D flip-flops have been used as memory element and two D Flip-flops are connected in series in order to obtain one and two-units delay operation of input where input clock and reset value controls the D flip-flops. The X-OR gates, Multiplexers (MUX) and Lookup Tables (LUT) have been used for logic operations in the Total RTL block as in Figs. 10 and 11. After filter operation, the down-sampling operation is performed and the values are stored in registers. The *clk* and *reset* keys controls the flip-flops. The overall RTL block diagram is shown in Fig. 12.

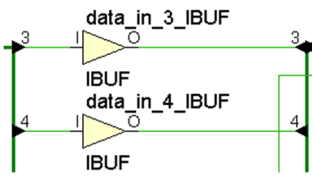


Fig. 8. IBUF of RTL block.

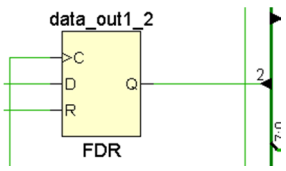


Fig. 9. Data storage element (FDRE).

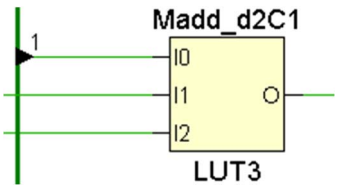


Fig. 10. Used LUT for logic operation.

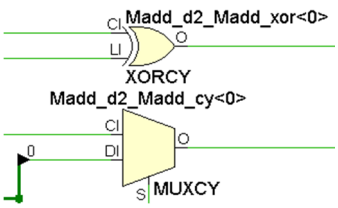


Fig. 11. Used X-OR gate and MUX (2:1) for carry logic operation.

The Advanced HDL Synthesis Report (Macro statistics) is shown in Table II. Also, the power analyzer report is shown in Table III.

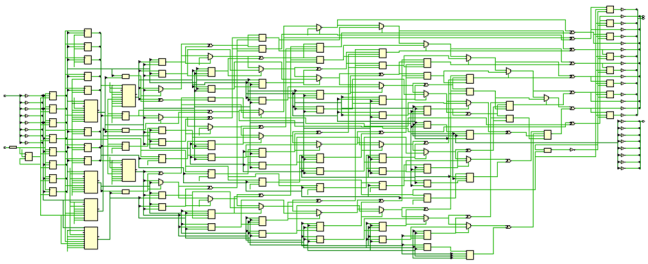

Fig. 12. Overall RTL block diagram of proposed Biochip.

TABLE II. ADVANCED HDL SYNTHESIS REPORT (MACRO STATISTICS) OF PROPOSED BIOCHIP.

| | |
|---|---|
| Adders | 14 |
| Registers (D Flip-Flops) | 28 |
| Multiplexers | 65 |
| Comparators | 10 |
| Total Memory usage | 278264 kB |

TABLE III. POWER ANALYZER REPORT OF PROPOSED BIOCHIP.

| | |
|---|---|
| Total Power | 0.081 W |
| Total Current | 0.018 A |
| Voltage supply($v_{cc}$) | 2.5V |
| Core junction temp. | $27.1^{\circ}C$ |

It is clear from Table II & III that, the number of Adders, Registers, Multiplexers, Comparators are very reasonable and easily manageable. Moreover, the total power consumption is only 81mW, the required current is 18mA, voltage supply is 2.5V and core temperature was $27.1^{\circ}C$. So, from the power analyzer report it is noticeable that, this biochip design would be power and cost effective. Lastly, the memory usage was moderate (271.74 Mega Bytes only) so that we could design a reliable and efficient biochip.

### *C. Timing diagram analysis*

The Fig. 13 illustrates the timing diagram of proposed biochip design where we have used L=2 and M=2.

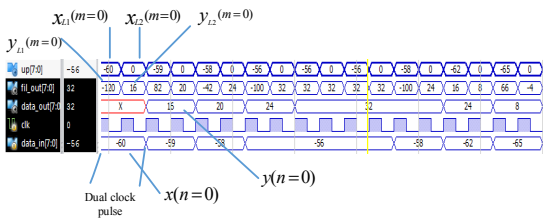


Fig. 13. Timing diagram of proposed Biochip.

The timing diagram clearly shows that data has been up-sampled by L=2, and then filtered using polyphase filter, then down-sampled by M=2. Here, *data_in* is the EEG input which is taken in every two consequent clock pulses. x(n=0) is the first input for n=0. Next, for performing up-sampling, Original data

is stored in first clock pulse [$x_{L1}(m=0)$] and data containing zero value is inserted into register in the next clock pulse [$x_{L2}(m=0)$]. The $y_{L1}(m=0)$ and $y_{L2}(m=0)$ are the polyphase filter outputs of $x_{L1}(m=0)$] and $x_{L2}(m=0)$] respectively. Having a delay of two clock pulses, our desired down-sampled data is y(n=0). Similarly, for $n = 1,2,3 \ldots\ldots$ ; EEG data set is passed and filtered on multirate system.

Table IV shows the timing summary of proposed biochip. Here, Clock cycles are needed twice the inputs. For example: If 200 data are used, then total 400 clock pulses are needed. Again if each clock cycle requires 4ns, Then total timing is 4*400=1600 ns= 1.6 µs.

TABLE IV. TIMING SUMMARY SF DESIGNED BIOCHIP.

| | |
|---|---|
| Clock Frequency | 102.564 MHz |
| Clock period | 9.750 ns |
| Minimum input arrival time before clock | 0.285 ns |
| Maximum output required time after clock | 5.156 ns |
| Maximum combinational path delay | Null |

### *D. Result Analysis*

Table-V shows the first ten input data and their corresponding outputs. Here up-sampling makes the input data twice (L=2) the original data. Again, the up-sampled data is filtered by polyphase filter (for amplification purposes) and finally we get the down-sampled (M=2) data which is our desired data and contains the same number of samples of input data.

TABLE V. FIRST 10 EEG DATA FOR L=2 AND M=2.

| Serial No. | Data input | Up-sampled value | Polyphase filter output | Down-sampled value/ Data output |
|---|---|---|---|---|
| 1 | -60 | -60 | -120 | 16 |
| | | 0 | 16 | |
| 2 | -59 | -59 | 82 | 20 |
| | | 0 | 20 | |
| 3 | -58 | -58 | -42 | 24 |
| | | 0 | 24 | |
| 4 | -56 | -56 | -100 | 32 |
| | | 0 | 32 | |
| 5 | -56 | -56 | 32 | 32 |
| | | 0 | 32 | |
| 6 | -56 | -56 | 32 | 32 |
| | | 0 | 32 | |
| 7 | -58 | -58 | -100 | 24 |
| | | 0 | 24 | |
| 8 | -62 | -62 | 16 | 8 |
| | | 0 | 8 | |
| 9 | -65 | -65 | 66 | -4 |
| | | 0 | -4 | |
| 10 | -68 | -68 | -74 | -16 |
| | | 0 | -16 | |

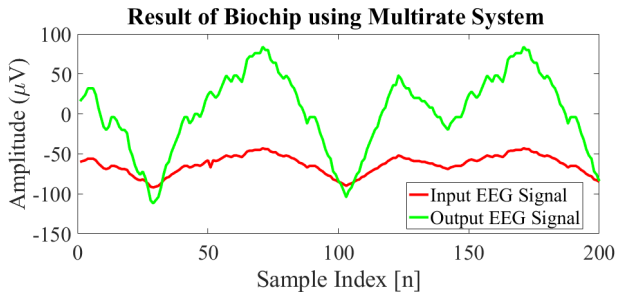


Fig. 14. Input and Output data comparison of proposed biochip for L=2 and M=2.

The final and overall data comparison is shown in Fig. 14. The red signal is the input EEG signal, the green signal shows the output of Polyphase Filter with L=2 and M=2. It is easily noticeable from Fig. 14 that this polyphase filter with multirate system is very good at amplifying signals. Moreover, this biochip can also reduce the artifacts as shown in the following Figure(near the sample index 50). This EEG dataset is only one portion of a large data set of a single patient. A full set of data can be used in practical medical applications and patient monitoring system. That means, if we apply this biochip, the EEG signal can be scrutinized more easily.

## IV. CONCLUSION

This paper proposes a Biochip for EEG signal amplification using polyphase filter and is based on multirate system. This system supports ALTRA Cyclone II FPGA board. In this proposed biochip, the EEG signal is amplified so that the signal can be analysis more easily. The system characteristics such as performance parameters: speed, clock frequency, power consumption on HDL synthesis report, power analysis and timing diagram have also been checked and analyzed. This system requires moderate power and frequency. In this case a few data have been considered (200 data) for checking operations. But in future, this model can be elaborated with larger dataset and fabricated for EEG signal amplification purposes and to apply into patient monitoring system. So, it will be fascinating to see how medical technology uses this biochip for EEG signal diagnosis in patient monitoring system.

## REFERENCES


[1] E. Niedermeyer, F. H. Lopes da Silva, **"**Electroencephalography**:** Basic Principles, Clinical Applications, and Related Fields" *Lippincott Williams & Wilkins*, 2005 Sixth edition, ISBN-13: 978-0781789424

[2] A. Mouraux_, G. D. Ineetti "Across-trial averaging of event-related EEG responses and beyond," *Magnetic Resonance Imaging*, September 2008, Volume 26, Issue 7, pp. 1041-1054.

[3] M. Teplan "Fundamentals of EEG measurement," *Measurement Science Review*, Volume 2, Section 2, 2002, pp.1-11.

[4] V. Sakkalis, T. Oikonomou, E. Pachou, I. Tollis, S. Micheloyannis and M. Zervakis, "Time-significant Wavelet Coherence for the Evaluation of Schizophrenic Brain Activity using a Graph theory approach," *2006 International Conference of the IEEE Engineering in Medicine and Biology Society*, New York, NY, 2006, pp. 4265-4268.

[5] L. Milic, "Multirate Filtering for Digital Signal Processing: MATLAB Applications" *Publisher***:** *Information Science Reference*; 1st edition December 26, 2008.

[6] E. Ifeachor. and B. WQ. Jervis, "Digital Signal Processing: A Practical Approach, 2/E" Publisher," *Pearson Education India*, 2002, ISBN 813708241, 9788131708248.

[7] C. Chou, S. Mohanakrishnan, and J. B. Evans, “FPGA Implementation of Digital Filters”, *Proc. Int. Conf. Signal Proc. Appl. & Tech*. (ICSPAT’93), 1993.

[8] J. B. Evans, "Efficient FIR filter architectures suitable for FPGA implementation," *IEEE Transactions on Circuits and Systems II: Analog and Digital Signal Processing*, vol. 41, no. 7, pp. 490-493, Jul 1994.

[9] K. Sundaram, M. Pradeepa, "FPGA based filters for EEG pre-processing," *2016 Second International Conference on Science Technology Engineering and Management (ICONSTEM)*, Chennai, 2016, pp. 572-576.

[10] S. M. Rabiul Islam, R. Sarker, S. Saha and A. F. M. Nokib Uddin, "Design of a programmable digital IIR filter based on FPGA," *2012 International Conference on Informatics, Electronics & Vision (ICIEV)*, Dhaka, 2012, pp. 716-721.

[11] S. M. R. Islam, R. Sarker and M. S. Monsur Hossain, "Design a digital system for detection of abnormality condition of heart from ECG waveforms," *14th International Conference on Computer and Information Technology (ICCIT 2011)*, Dhaka, 2011, pp. 24-29.

[11] S. M. R. Islam, S. Saha, M I. Khan “FPGA Based Digital System for Detection of Dicrotic Notch in the Carotid Pulse Signal” *International Journal of Information and Communication Technology Research*, Vol.2 No.12, pp. 872-880, December 2012.

[12] S. M. Rabiul Islam, A. F. M. N. Uddin, M. B. Hossain, M. I. Khan “FPGA based Heart Arrhythmia’s Detection Algorithm” *ACEEE International Journal of Information Technology* ,Vol. 3, No. 1, pp**.** 9-14, March 2013.

[13] G. Goslin. “A Guide to Using FPGAs for Application-Specific Digital Signal Processing Performance.” *Xilinx Inc*.

[14] A. Aggarwal, "FIR Filter Designing using XIllinx System Generator" *International Journal of Computer Applications* , Volume 68- No.11, , April 2013, pp. 37-41.

[15] N. M. Bhagyalakshmi., "Modified DA based FIR Filter in Multirate DSP systems on FPGA," *International Journal on Recent and Innovation Trends in Computing and Communication*, Volume 4, Issue 5, May 2016, pp.474-478.

[16] Y. Sanada, , T. Ohira, S. Chikuda, M. Igarashi, , M. Ikebe, , T. Asai, , M. Motomura, "FPGA Implementation of Single-Image Super-Resolution Based on Frame-Bufferless Box Filtering," *Journal of Signal Processing*. 17. 111-114. 10.2299/jsp.17.111, 2013.

[17] B. Shenoi, “Introduction to Digital Signal Processing and Filter Design” *John Wiley & Sons, Inc.* 2006, ISBN: 978-0-471-46482-2.

[18] P. Sovili, " FPGA based model of processing EEG signal,″ *Telekonmikacioni forum TELFOR*. Srbija, Beograd, pp. 677-680, Novembar 24.-26., 2009.

[19] W. Huang, S. Hung, J. Chung, M. Chang, L.Van and C. Lin, "FPGA implementation of 4-channel ICA for on-line EEG signal separation," *2008 IEEE Biomedical Circuits and Systems Conference*, Baltimore, MD, 2008, pp. 65-68.

# Baseline Wandering Removal from ECG Signal by Wandering Path Finding Algorithm

Md. Asadur Rahman[1], Md. Mahmudul Haque Milu[1], Anika Anjum[1], Farzana Khanam[1], and Mohiuddin Ahmad[2]
[1]Department of Biomedical Engineering,
Khulna University of Engineering & Technology (KUET), Bangladesh
[2]Department of Electrical and Electronic Engineering,
Khulna University of Engineering & Technology (KUET), Bangladesh
bmeasadur@gmail.com, mahmudhmilu@gmail.com, anikaanjum123@gmail.com, farzana0703047@gmail.com, mohiuddin0ahmad@gmail.com

*Abstract*—**This work investigates to remove highly wandered path from ECG signal. In normal condition, ECG signal contains a very little amount of baseline wandering which can easily be removed by high pass filtering. On the other hand, acquired ECG signal during walking, running, push-up or pull-up the body contain different shapes of baseline wandering which cannot be possible to remove by conventional filtering concept. To meet the challenge, in this paper we have proposed a baseline wandering removal technique based on baseline wandering path finding (BWPF) algorithm. This BWPF algorithm works by piecewise polynomial fitting. In this paper, the impact of this algorithm on wandered ECG signal is discussed elaborately with graphical interpretations. In addition, it is also shown that why this algorithm works better than the conventional polynomial baseline wandering removing technique.**

***Keywords— Electrocardiogram (ECG), baseline wandering, baseline wandering path finding (BWPF) algorithm, polynomial fitting.***

## I. INTRODUCTION

Electrocardiogram or ECG refers to the recording and graphical representation of the functionalities of human heart. ECG is the most applying biomedical signal compared to the others. It is an important tool to identify the abnormalities of heart and therefore most of the doctors prefer to observe the ECG report before prescribing a cardiac patient. A typical ECG signal with its prominent peaks is given in Figure 1. From the figure we can see that there are some peaks of different shape those are named as P wave, QRS complex, T wave and U wave sometimes as given in figure. These waves carry different information about heart's functionality and shows significant change in case of abnormalities. Since this is a noninvasive and easy way to get this signal from human body, doctors are depending on ECG for cardiac treatment from 1901[1].

Based on ECG, huge research works have been done by a lot of researchers during last 100 years. Almost all findings have already been discovered as well as signal processing related different problems are also solved with a number of methods. Nonetheless, in this paper, we would like to share an interesting problem. In our laboratory we use world's most popular module BIOPAC MP36 [2] to acquire ECG signal. BIOPAC MP36 gives proper ECG graphs through BSL (Biopac Student Laboratory) software when body is at rest or static condition. The problem arises when we would like to acquire ECG for some conditions or research purposes such as running, walking, push-up, or pull-up the body. In these cases, the ECG signals we get are drifted with a high degree from baseline. This drift from baseline is also known as baseline wandering. Baseline wander means the effect where the base axis of ECG signal appears to 'wander' or move up and down rather than being straight. The post processing of the ECG signal is necessary to get different information like heart rate, cardiac output, stroke volume, and other features. It is not possible to write an algorithm to get these features from ECG signal without removing baseline wander. In addition, BIOPAC software does not provide any solution to this problem. Therefore, baseline wandering removal becomes the first step among the other post processing steps.

There exists a lot of research works based on removal of baseline wandering. Most of the research works are based on the filtering techniques. In [3] finite impulse response (FIR) filter is used to remove baseline fluctuations. A suitable impulse response is designed with a pass-band ripple of less than 0.5 dB and high stop-band attenuation is considered in this case. The non-adaptive filtering approaches mainly include IIR filter, FIR filter and notch filter. The high pass filter with 0.5Hz cut-off frequency can be used to remove the interference of baseline wander, which can filter out signal component with frequency below 0.5Hz while frequency above 0.5Hz are preserved. Furthermore this type of filter faces a drawback of time delay to get the filtered signal. Thus, the meaningful information contained in the initial stage of getting ECG signal can't be resolved or can be lost due to the failure of correcting baseline distortion [4].

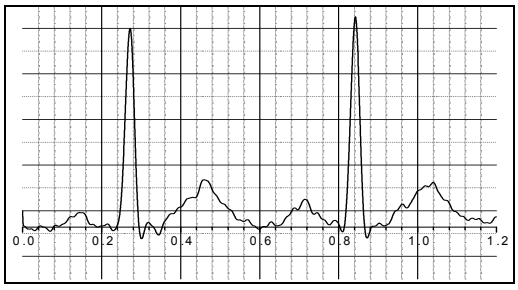


Figure 1. A typical ECG signal.

978-1-5386-2307-7/17/$31.00 ©2017 IEEE

A number of research works proposed different methods of adaptive filter to remove the baseline wandering such as, cascade adaptive filter in two phases in [5] & [6], adaptive filter based on error nonlinearity least mean square (LMS) algorithm in [7], constrained stability least mean square algorithm was applied to decrease mean-square error of LMS algorithm in [8]. Adaptive filtering approach usually does not interrupt the ECG frequency spectrum but it requires reference signal, which adds to the complexity of hardware and software. On the other hand, authors in [9] considered many adaptive linear neurons artificial neural network model to delete ECG baseline wander. The artificial neural network model requires a proper training stage to solve the baseline wandering problem and it is definitely a difficult way to handle the persistent non-stationary trend especially in a long-term ECG signal [4].

There are some other approaches as well to remove baseline wander. The wavelet transform is used to eliminate baseline wandering of ECG by implementing a search algorithm based on computing wavelet packet coefficients [10]. Baseline wander removal process using EMD cannot be automated because baseline wander noise may be interrupted over a number of intrinsic mode functions [11]-[12]. A similar problem arises with the wavelet approach where we cannot determine the amount of baseline wander noise present in different levels of detail coefficients [13].

Finally, in all cases one thing is common and that is, considering the cause of baseline wandering is due to movements, breathing, coughing, anxiety, stress or pain, and motion of electrodes. The aspect of our research problem is quite different on the basis of the cause of baseline wandering. We are interested to find the effect of ECG during a strong movement such as walking, running on treadmill, up and down, push up, etc. Due to these physical activities the frequency of baseline wandering cannot be within 0.05 to 0.5~0.7 assuredly, that is considered generally. Therefore, the best way is to find the accurate wandering path due to movement.

In this paper, we have proposed a baseline wandering path finding (BWPF) algorithm based on piecewise polynomial fitting. Polynomial fitting method is partially discussed in [14] where it is approached that considering a prominent knot corresponding every ECG QRS complex, wandering path can be fitted with higher order polynomial. In this case, there may arise two types of problems: 1) over fitting (due to less wandering) and 2) under fitting (due to very high drift of wandering). As a result, in our proposal to solve this problem, piecewise polynomial fitting is implemented with a satisfactory error threshold. Our proposed BWPF algorithm is also capable of maintaining the optimal polynomial order for the piecewise fitting. By the result of BWPF algorithm, the baseline wander can be easily removed by subtracting from the original noisy data.

The rest of the paper is organized as followings: i) Proposed methodology is described with mathematical clarifications in section II, ii) Results and Corresponding discussions are presented with graphical and numerical representation in section III, and iii) our total work is concluded in section IV.

## II. PROPOSED METHODOLOGY

### A. *Proposed Processing Methodology*

Since this paper investigates highly wandered ECG signal due to physical movements, a complete ECG signals of several minutes contain different types of wandering path. Therefore, total signal cannot be considered for polynomial fitting. This is because with a very high degree of polynomial will also be unable to trace the path of wandering. Considering this fact, after loading the full length ECG signal, it is divided into several segments which help to divide the wandered path into several limited ordered wandered ECG signals. In our proposed algorithm, this segmentation number will be taken as user or operator input based on the wandering path existed in ECG signal. Polynomial fitting order is self-assessed in our proposed methodology based on the threshold value of fitting. The algorithm will be started from order 1 to fit the ECG wandering path and compute its fitting error to compare the standard value given as threshold. If the error is greater than the threshold value the process will be repeated with the order=previous_order+1 and will continue the process to achieve the error value less than or equal to the threshold value.

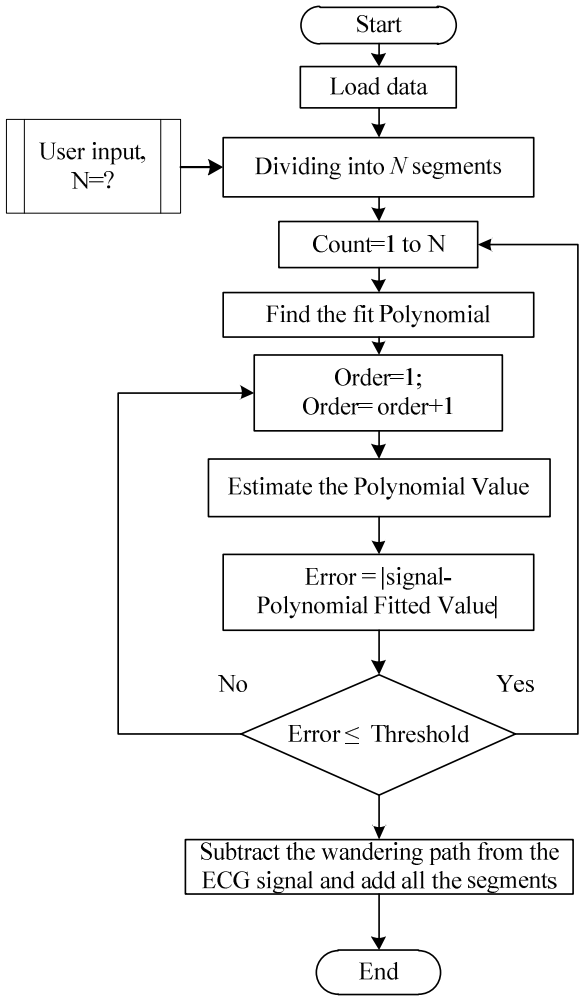


Figure 2. Block diagram of proposed baseline wandering removal algorithm

Suppose we have an ECG signal, $X(n)$ that contains $N$ number of samples. Consider that this signal is too long and there exists wide range of baseline drift in positive and negative direction with respect to original baseline. Sometimes with a conventional polynomial fitting this type of baseline wandering cannot be estimated due to its very high degree of wander. To solve such problem, our proposed method piecewise polynomial fitting can be a solution. According to the piecewise polynomial fitting following steps have been performed:

1. Divided the signal into $K$ equal space and form a matrix, $G(n)$ of order $K\times(N/K)$ from the original signal of order $1\times N$. Therefore, every row of the matrix represents the sub-signal of the original signal.
2. Now, fit all the rows of the matrix separately with a suitable lower order polynomial. Polynomial order can be chosen as iterative method based on a satisfactory threshold level of error. So, a matrix of fit polynomial coefficient $P[a^0, a^1, a^2, \ldots, a^k]$ will be found as ascending polynomial order.
3. Estimate the polynomial value for all the rows by applying the rule *PoG*. For each row, the wandering path will be found as a matrix, $E_1$ of $1\times(N/K)$ order.
4. Rearrange the estimated row wise wandering path as following,

$$S_1 = [[E_1]_{1\times(N/K)}, [0]_{1\times(N/K)}, [0]_{1\times(N/K)}, \ldots, [0]_{1\times(N/K)}]$$

$$S_2 = [[0]_{1\times(N/K)}, [E_1]_{1\times(N/K)}, [0]_{1\times(N/K)}, \ldots, [0]_{1\times(N/K)}]$$

$$S_k = [[0]_{1\times(N/K)}, [0]_{1\times(N/K)}, [0]_{1\times(N/K)}, \ldots, [E_1]_{1\times(N/K)}]$$

5. Now sum all the matrix to make a single signal as,

$$S[n] = \sum_{i=1}^{k} S_i$$

Here, $S[n]_{1\times(N/K)}$ represents the path of baseline wander.

6. Therefore, baseline wander removed signal can be easily achieved as, $\hat{X}(n) = X(n) - S(n)$ .

Now, the signal can be simply filtered to prepare it for the further processing like heart rate calculation, peaks identification, ischemia detection, angina pectoris identification, etc.

### *B. Mathematical Explanation of Polynomial Fitting*

To model a time series of data by polynomial fitting we generally consider a polynomial equation as an estimation function of the predictive model of the given data. Suppose the estimation function, E(s) is of $k^{th}$ degree polynomial and can be presented as,

$$E(s) = a_0 + a_1 x + a_2 x^2 + \ldots + a_k x^k \tag{1}$$

Therefore the difference between actual value, y and estimated vale derived by the proposed model estimating equation, E(s) is termed as residual, $R^2$ which can be formulated as given (2).

$$\begin{aligned} R^2 &= \sum_{i=1}^{n} [y_i - E(s)]^2 \\ &= \sum_{i=1}^{n} [y_i - (a_0 + a_1 x + a_2 x^2 + \ldots + a_k x^k)]^2 \end{aligned} \tag{2}$$

For achieving the best fitted estimated model equation, it is the foremost target is to minimize the value of $R^2$ and we know that in the minimum value of $R$ for the different coefficient $a^i$, the partial derivative of $R$ is zero which means,

$$\frac{\partial}{\partial a_i}(R^2) = 0 \tag{3}$$

From (3) we get that,

$$\frac{\partial}{\partial a_0}(R^2) = -2\sum_{i=1}^{n} [y_i - (a_0 + a_1 x + a_2 x^2 + \ldots + a_k x^k)] = 0 \tag{4}$$

$$\frac{\partial}{\partial a_1}(R^2) = -2\sum_{i=1}^{n} [y_i - (a_0 + a_1 x + a_2 x^2 + \ldots + a_k x^k)]x = 0 \tag{5}$$

$$\frac{\partial}{\partial a_k}(R^2) = -2\sum_{i=1}^{n} [y_i - (a_0 + a_1 x + a_2 x^2 + \ldots + a_k x^k)]x^k = 0 \tag{6}$$

From the relations given in (4)-(6), we get a vandermonde type matrix that can be solved for least square fitting and finally we get,

$$\begin{aligned} & y = Xa \\ or,\ & X^T y = X^T X a \\ or,\ & a = (X^T X)^{-1} X^T y \end{aligned}$$

Since we get the coefficients of the polynomial by the previous equation, the polynomial fitted valuation of the function can be easily done by multiplying these coefficients with their orders given in (1).

## III. Data Collection and Processing Environment

The sole scope of this paper is to remove high degree of baseline wandering. To achieve this goal, ECG signal is acquired in Biomedical Signal Processing Laboratory of the department of Biomedical Engineering of Khulna University of Engineering & Technology (KUET). During signal acquisition, participant is requested to move their hands, legs, push up, etc. Due to these types of physical movements acquired ECG signal was corrupted with high degree of baseline wander. ECG signal was acquired by Biopac MP36 hardware and Biopac Student Laboratory (BSL) software. ECG data acquisition is performed by three leads system from two hand and one foot configuration. Data acquisition procedure from the participant is illustrated by the Fig. 3. From the figure it is observable that the acquired ECG signal contains high degree of baseline wander.

The baseline wandered signal is converted to .mat file and all processing regarding this proposed algorithm are performed by MATLAB as an offline signal processing scheme.

Figure 3. Data acquisition procedures in our laboratory for incorporating high degree of baseline wandering in ECG signal

## IV. Results and Discussions

Baseline wandering affects the regular shape of ECG signal and this effect can be of different kinds. In Fig.4, three types of baseline wandered signals are given. ECG signal corresponding to Fig.4 (a) contains a baseline with constant lag from baseline. This lag can be either positive or negative. In this case, the constant baseline lag is negative and this type of baseline wandering can be easily removed by band-pass filtering. On the other hand the ECG signal corresponding to Fig.4 (c) contains a baseline wandering of very slow frequency oriented drift. This type of problem is also removed by filtering technique. Nonetheless, very high degree baseline wandering is presented in Fig.4 (b). This signal is acquired in our laboratory to create this difficulty in ECG signal and this problem cannot be solved by simple filtering technique. This paper solely scopes to remove such highly drifted baseline from affected ECG signals.

Therefore in this work, very high degree of baseline drifted ECG signal is considered. Generally polynomial fitting technique can be applied to remove baseline wandering but for the very long ECG signal, a high degree of polynomial fitting often fails to achieve the fitting assumption. In addition with that, high degrees of polynomial increases computational complexity. Such problems are given in Fig. 5. Where a long ECG signal is considered with different baseline wandering at different section which is unable to remove by conventional polynomial fitting algorithm.

Fig. 5(a) represents the baseline wandered ECG signal from which baseline wandering is removed by polynomial fitting algorithm with different polynomial order. Fig.5 (b), Fig.5 (c), Fig.5 (d), and Fig.5 (e) are baseline wander removed signal by polynomial order of 5, 10, 15, and 30, respectively. From the results given in Fig.5, we can observe that for polynomial order of 5 and 10 are completely failed to remove the baseline wander. On the other hand polynomial order 15 removes almost all the baseline wandering but order 30 is the best in this action. Therefore, we can understand from this result that very high polynomial order is necessary to remove higher order baseline wander. Into this bargain, it is easily perceivable that this high polynomial order may be a cause or increasing the computational complexity in algorithm and it may also face the over fitting problem because of high polynomial order. Hence, conventional polynomial fitting cannot be a solution.

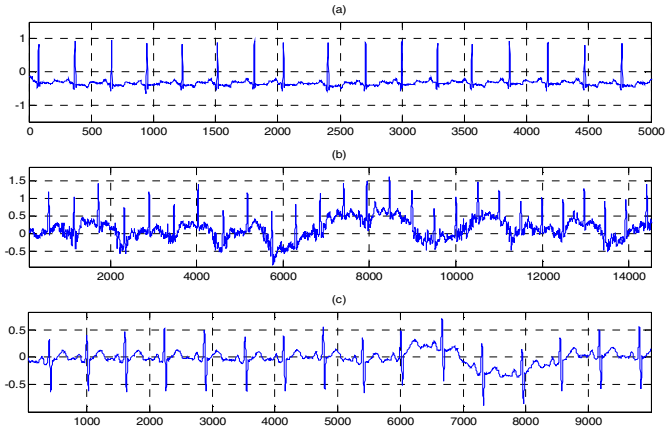


Figure 4. Examples of different types of baseline wandering. (a) & (c) ECG signals are collected from MIT Arrythmia database [15] and (b) ECG signal is acquired by the authors while participant performs physical movements.

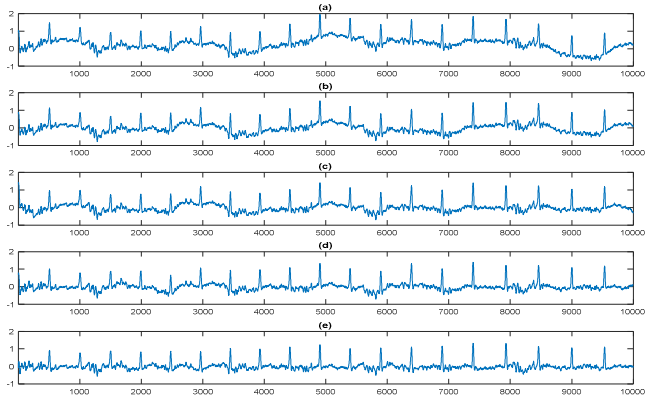


Figure 5. Baseline wandering removal by polynomial fitting based algorithm with different polynomial orders

To overcome this problem, we have proposed the BWPF algorithm which is able to apply the piecewise polynomial fitting with necessary polynomial order. Using our proposed algorithm, very highly baseline wandered signal is corrected which is given in Fig. 6. The raw ECG signal is contaminated with a very high degree of baseline wandering with different shapes in different area of ECG signal. According to our proposed algorithm BWPF, this raw ECG signal was divided into 30 equal pieces of signal and create a matrix with 30 columns. Thereafter, each column was considered as separate signal and fitted the piece of each signal with their appropriate polynomial order. The order was selected from 1 and increased to achieve the least fitting error which was previously provided to the algorithm as threshold error (0.15). Therefore the polynomial fitted results created another matrix of column 30. Then the original signal's matrix and polynomial fitting matrix were reconstructed to single dimensional signal. Therefore, mathematically, the reconstructed polynomial fitted signal is actually the baseline wandering path of the total raw ECG signal. Eventually, this algorithm finds the baseline travelling path. The baseline travelling path is finally subtracted from the raw ECG signal which gives us the baseline corrected signal. The third signal representation of Fig. 6 is the Gaussian windowing filtered of baseline wander removed signal.

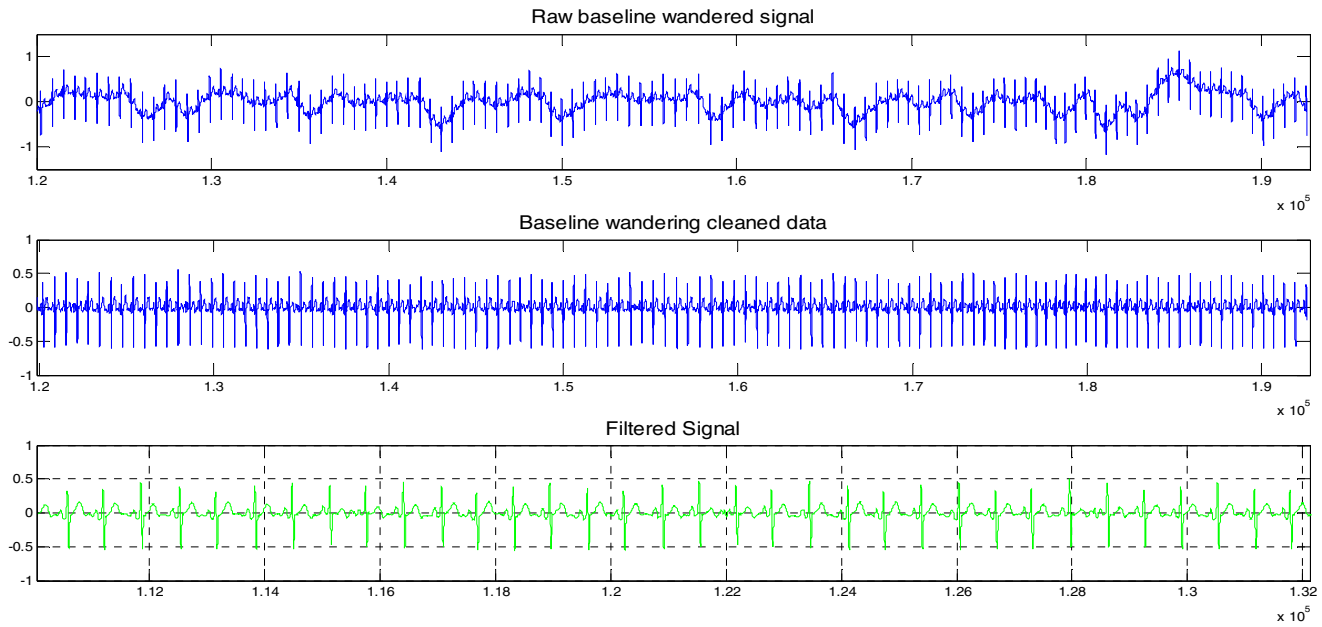


Figure 6. Results of proposed BWPF algorithm in case of very long and highly drifted baseline wander contaminated ECG signal. The first signal is raw ECG signal. Second one is baseline wander corrected signal. The third one is filtered signal of the second one and it is shown as slightly zoomed for clear appearance.

## V. Conclusion

The proposed baseline wandering path finding (BWPF) algorithm provides the benefit to the user to choose the number of division of the raw signal. In addition, proposed algorithm selects the polynomial order, itself based on the threshold error rate which is able to reduce the computational complexity. From the results, it is clear that the BWPF algorithm is better than the conventional polynomial fitting algorithm in case of removing baseline wander from ECG signal. This algorithm is also applicable to the other signals having baseline wandering. BWPF algorithm will be helpful before all kinds of ECG signal processing.

## Acknowledgment

This work was supported by Higher Education Quality Enhancement Project (HEQEP), UGC, Bangladesh under Subproject "Postgraduate Research in BME", CP#3472, KUET, Bangladesh.

## References

[1] M. R. Ruiz, C. Cajavilca, and J. Varon "Einthoven's String Galvanometer: The First Electrocardiograph," Texas Heart Institute journal, vol. 35, no. 2, pp. 174–178, September 1927.

[2] Available in: https://www.biopac.com/product/upgrade-to-mp36-system/

[3] J. A. V. Alste and T.S. Schilder, "Removal of base-line wander and power-line interference from the ECG by an efficient FIR filter with a reduced number of taps," IEEE Transaction on Biomedical Engineering vol. 32, pp.1052–1060, December 1985.

[4] S. W. Shin, K. S. Kim, C. G. Song, J. W. Lee, J. H. Kim, and G. W. Jeung, "Removal of baseline wandering in ECG signal by improved detrending method," Bio-Medical Materials and Engineering, vol. 26, pp. S1087–S1093, 2015.

[5] P. Laguna, R. Jane, and P. Caminal, "Adaptive filtering of ECG baseline wander," IEEE Engineering in Medicine and Biology Society, vol. 2, pp. 508–509, November 1992.

[6] R. Jane, P. Laguna, N. V. Thakor, and P. Caminal, "Adaptive baseline wander removal in the ECG: Comparative analysis with cubic spline technique," Proceedings of Computers in Cardiology, Durham, North Carolina, 1992, pp. 143–146.

[7] M. Z. U. Rahman, R. A. Shaik, and D. V. R. K. Reddy, "Baseline wander and power line interference elimination from cardiac signals using error nonlinearity LMS algorithm," International Conference on Systems in Medicine and Biology, Kharagpur, 2010, pp. 217–220.

[8] K. Manivel and R. S. Rabindran, "Noise removal for baseline wander and power line in electrocardiograph signals," International Journal of Advanced Research in Electrical, Electronics and Instrumentation Engineering, vol. 4, pp. 1114–1122, 2015.

[9] J. Mateo, C. Sanchez, C. Vaya, R. Cervigon, and J. J. Rieta, "A new adaptive approach to remove baseline wander from ECG recordings using madaline structure," Computers in Cardiology, Durham, North Carolina, 2007, pp. 533–536.

[10] M. A. Tinati and B. Mozaffary, "A wavelet packets approach to electrocardiograph baseline drift cancellation," International Journal of Biomedical Imaging, pp. 1–9, September 2006.

[11] N. Pan, V. M. I, M. P. Un, and P. S. Hang, "Accurate removal of baseline wander in ECG using empirical mode decomposition," Proceedings of NFSI-Joint Meeting of the 6th International Symposium on Non-invasive Functional Source Imaging of the Brain and Heart and the International Conference of Functional Biomedical Imaging, October 2007, pp.177–180.

[12] B. Narsimha, E.Suresh, K. Punnamchandar, and M. S. Reddy, "Denoising and QRS detection of ECG signals using Empirical Mode Decomposition," Proceedings of International Conference on Communications and Signal Processing, February 2011, pp.439–442.

[13] S. Agrawal and A. Gupta, "Fractal and EMD based removal of baseline wander and powerline interference from ECG signals," Computers in Biology and Medicine, vol. 43, pp. 1889–1899, November 2015.

[14] Manpreet Kaur, Birmohan Singh, and Seema. "Comparisons of Different Approaches for Removal of Baseline Wander from ECG Signal," Proceedings on International Conference and workshop on Emerging Trends in Technology (ICWET), 2011, vol. 5, pp. 30-34.

[15] MIT-BIH Arrhythmia Database Directory, Available in: https://www.physionet.org/physiobank/database/html/mitdbdir/mitdbdir.htm.

# Spinal Cord Injured (SCI) Patients' Length of Stay (LOS) Prediction Based on Hospital Admission Data

Tabib Ibne Mahzar[1], Nusrat Jahan Suha[2], Dipankar Chaki[3], and Dr. Md. Haider Ali[4]
Department of Computer Science and Engineering
School of Engineering and Computer Science
BRAC University, Dhaka, Bangladesh
Email: [1]tabibibnemazhar@gmail.com,[2]njsuha@gmail.com,[3]joy.dcj@gmail.com,[4]haider@bracu.ac.bd

*Abstract*—**In order to take better care and to ensure better facilities to the inpatients, predicting length of stay serves a great importance. Since, the resources and the doctors are limited in the hospital, especially in a developing country like Bangladesh, it is quite difficult to provide proper healthcare to the inpatients. Not only the hospital resources are limited but also, it is difficult for the inpatients to bear the expense for a long period of time. In addition to that, if doctors can predict length of stay at the early stage of pre-admission, they can map a well instructed way for example, which treatment, which instrument will treat patients best. As a result, the patient can start his treatment with a slight assumption of the expenses. If we can predict accurate length of stay, patients do not have to leave in between the treatment without medical advice. Keeping all these points in mind, we develop a system using machine learning algorithms to predict Spinal Cord Injured (SCI) patient's length of stay. For this purpose, we choose Centre for the Rehabilitation of the Paralyzed (CRP) to collect data. They provide us around 600 inpatients' admission data who have been admitted to the hospital. After that we successfully build a model for predicting length of stay (LOS) with 81.62% accuracy.**

***Keywords—Multiple Linear Regression; Early Prediction; Length of Stay; Spinal Cord Injury; Natural Logarithmic Transformation.***

## I. INTRODUCTION

Have you ever thought of a life that is confined to wheelchair for the whole life? Have you ever thought of that person, who has to depend on others for every movement? Well, that's the life of most of the people who are suffering from spinal cord injury. The spine consists of spinal cord and the spinal cord is made of different nerves which are secured by the selected vertebrae of the spine. The primary function of spinal cord is to transfer signal to the various sections of the body from the brain. It is the primary dispatcher all through the body. Any kind of harm that is either for a short period of time or a long period of time to the spinal cord which can alter its function is called spinal cord injury (SCI) and can cause a range of symptoms, including weakness, loss of muscle function, and also loss of sensation. Spinal cord injury effect can be classified into two types, one is complete and another one is incomplete. If a patient is unable to feel any sensation or have no function or voluntary movement past the point of the injury, then the injury is defined as complete injury. This affects the body on the both sides equally. In terms of incomplete injury, people can move parts of their body. They can feel their paralyzed body parts which cannot be moved or people can move some parts of their body but cannot move other parts. A lot of body parts are affected from the complications of the spinal cord injury. Respiratory problems, bed sores or pressure sores (P.sore) or pressure ulcers and muscle atrophy are the most common problems caused by spinal cord injuries. Sometimes bladder stops working properly due to neurogenic problem which is a common consequences of Spinal Cord Injury [1].

For the past several years, length of stay prediction has become a very important topic. The main benefit of predicting length of stay is, we can utilize our limited resources by serving huge number of patients. For instance, effective bed allocation is one of the principal factors in the case of boosting up accurate uses of health care facilities [2]. Generally, the shorter time a patient has to stay at the hospital, the more cost effective it will be. In addition to that, it plays a vital role in terms of efficient hospital resources management [3]. Moreover, in order to achieve cost-effective treatment and elevated flexibility in bed allocation, precise estimation of LOS can be used [4, 5].

It is really unfortunate if a patient has to stop his/her care in the middle of the ongoing treatment due to financial reason or because of unavailability of enough resources. Since spinal cord act as a breeze between body and brain through which motor and sensors passes signals, spinal cord injury should be treated with special care [6]. If we are able to predict the LOS, patients and doctors both can come up with better preparation. Sometimes LOS depends on some factors such as hospital management system, resource system. A close relationship has been found between hospital resources and patient's LOS at the hospital [7, 8]. Guardian association such as problem

978-1-5386-2307-7/17/$31.00 ©2017 IEEE

management, communication, cooperation among nurse and physicians are greatly correlated with low LOS [8]. We propose to develop a study to estimate the Length of Stay for Spinal Cord Injured Patients using multiple linear regressions. The main purpose of this study is to develop a model for predicting the LOS at the early admission stage using all the admission data. We use multiple linear regressions for this study in order to predict length of stay (LOS). For our study, we collected a dataset from Centre for the Rehabilitation of the Paralyzed (CRP). We modified the data and used statistical analysis to apply linear regression.

The rest parts of the paper are arranged as follows: section II covers the existing works regarding this topic, section III describes the research methodologies that we approach and section IV presents the experimental evaluation of the study. Finally, section V concludes the paper with general remarks.

## II. EXISTING WORKS

Length of stay prediction is playing very important role these days in order to allocate resources efficiently. Since Bangladesh is a developing country, this study will play vital role in this perspective. To analyze the huge amount of medical data, machine learning algorithm can be named first.

In [1], the purpose of this study was to identify how bladder behaves after severe spinal cord injury. They used multivariate logistic regression on the data to develop prediction model of urinary continence and bladder emptying completely and an external validation in 111 patients was calculated. Early prediction of bladder control is important for advising at the early stage and introduction to patient-tailored rehabilitative interventions which will result in a higher level of supervision, responsibility and in future hospital researches it may also increase patients gratification. External validation of the modes showed excellent results: the eROC were 0.965(95% CI: 0.934-0.996) and 0.972 (95% CI 0.943-0.999), respectively.

Tsai et al. proposed a model to predict the Length of Stay for cardiology patients analyzing the data before admitting him/her at the hospital. The purpose is to develop an Artificial Neural Network (ANN) for prediction using three primary diagnoses, coronary atherosclerosis (CAS), heart failure (HF), and acute myocardial infarction (AMI). Pearson correlation coefficient has been used to visualize the relation between data. Along with that, to develop the study, Artificial Neural Network and linear regression has also been applied. It has been observed for CAS patients, the accuracy for these models is ranged from 88.07% to 91.53%. Again linear regression's performance is better than ANN with LOS of 2 days for CAS patients. For HF and AML patients, LR and ANN models performed better in predicting LOS between 8 and 11 days. ANN performs better than LR model for patients with LOS of 3, 5, 6 or 7 days, which is about 60% of the dataset [9].

Jiminez et al. in their study, they targeted to develop an efficient model to predict the length of stay for the acute psychiatric patients and then identify the inefficient care for the different Observed-Predicted LOS. The total groups of data were divided into two parts, first group was used for the prediction of LOS and the second group has been worked to identify the problems when the patients were staying at the hospitals. Multiple linear regressions have been used in order to build the LOS prediction model [10].

In [11], they propose to predict the length of stay for acute psychiatric patients and, whether negligence is reason for longer length of stay. In order to predict the effect of each variable individually on Length of stay, multiple linear regressions have been. An assurance coefficient was acquired which indicates the qualification for the next step. After that this function has used to predict the LOS of the second group. The difference of LOS-PLOS is secured as well. They developed a Receive Characteristic (ROC) curve to examine new difference of LOS-PLOS for predicting the inefficiency issues.

In [12], they developed this study for the purpose of predicting the LOS of spinal cord injured (SCI) patients. For this purpose, their included features were age, sex, neurological level of lesion, number injuries, number of surgeries and so on. Firstly, they applied multiple linear regressions. They built 3 different models with, actual LOS, root square LOS and log transformation LOS of their actual LOS to find out the normal distribution of LOS, as their data was not normally distributed. In the end, the log transformation was successful to produce their desired data.

In [13], they have proposed a model to estimate the performance in terms of money of a movie before its theatrical release in the theater. They presented the result using two performance measures: success rate of classifying a movie's success exactly (Bingo) or the success rate of classifying within one class of its actual performance. They used Neural Network, C&RT, Discriminant Analysis and Logistic Regression for the prediction.

Qian et al. build a model for predicting Length of Hospital Stay after severe myocardial violation in the Myocardial Infarction Triage and Intervention Project Registry. The purpose of this study was to point out both clinical and nonclinical reason that has great impact on length of stay. They also included researching the attribute that has caused length of stay reduction during the observation period of 7 years. Natural logarithmic transformation for length of stay was used as predictor feature, since the length of stay was not normally distributed. To observe the effect of demographic, institutional and clinical on LOS, univariate comparison was considered. A multivariate model has also developed for this model. Linear regression was used to analyze the reason and component that affected LOS. For this study only those patients were included who has less complex issues in their cases [14].

Awal et al. developed a model for predicting future crime trend in Bangladesh. They have developed linear regression model for this purpose. To find out all the linear regression parameters, gradient descent algorithm has been used. In this study, linear regression performance is outstanding. The dataset has been divided into two portions, one is metropolitan region

and other is divisional region. For both portions, they have analyzed the prediction for individual crime. In the conclusion it has been proved in their study that, with the growing population, the number of crime is also on increase [15].

In [16], they aimed to develop a study to forecast gold price based on available economic factors. They used linear regression to develop a model. They made 4 models, first one is developed by gathering all related factor in account. After that, stepwise regression is applied for reducing the number of variable and solving the multi collinearity problem as well. Then model 3 was developed consisting the lagged variable and removed the variables having coefficients which are indifferent from zero. Then, Prais-Winsten procedure was followed to re calculate the coefficient and estimate model 4. Lastly, the lagged variable model which has smaller MSPR was selected. For comparing the models and to derive the output, "forecast-1" was used which is a naive process.

## III. METHODOLOGY

Nowadays, data mining is one of the most popular methods for analyzing data. This process is wrapped into few steps, data collection, analyzing data behavior and finally reaching to a conclusion. Real time mining for example, medical data, business data, and crime data is used for this process. In this paper, medical data is used. Below, data set behavior and the methodology has been described.

### *A. Dataset Description*

In order to develop this study, a data set is collected from Centre for the Rehabilitation of the Paralyzed (CRP). Initially the dataset contained around 600 patients' details. After that, the patients who was referred to another organization for better treatment, patients who stopped their treatment willingly without doctor's advice, those who died in between the treatment, we excluded those details since their treatment was incomplete and did not conclude to any result. In this case we find 75 number of referred inpatient, people has stopped the treatment willingly, people who died. So we exclude all those data. Moreover, some patients' data were incomplete. After excluding those data, we have around 377 patient's details. For this study, we have 9 predictors and 1 target class. Our features are- age, sex, duration between injury and admission, P.sore, diagnosis type, admission ASIA, admission SCIM, S/L, admission N/L. In table I, details of all variables are described.

The diagnosis feature explains the types of Diagnosis. Basically there are 4 types of diagnosis. In table II, the types of diagnosis are explained.

ASIA means, American Spinal Injury Association by whom spinal cord has been classified and the levels are determined. Its classification system is divided into 5 points on a scale of A to E [6] and shown in table III.

TABLE I. INPATIENT DATA TYPE AND THE ASSOCIATED LOS DATA

| **Attribute Description** | **Type** | **Permissible Values** |
|---|---|---|
| Age | Numerical | *2-75* |
| Sex | Binary | *Male*<br>*Female* |
| Late Admission | Numerical | *0-1200 days* |
| P.sore | Binary | *Yes*<br>*No* |
| Diagnosis type | Categorical | TT<br>TP<br>NTT<br>NTP |
| Admission ASIA | Categorical | *A*<br>*B*<br>*C*<br>*D*<br>*E* |
| Admission SCIM | Numerical | *0-100* |
| Admission S/L | Categorical | *C1-C5*<br>*T1-T12*<br>*L1-L5*<br>*S1-S5* |
| Admission N/L | Categorical | *C1-C5*<br>*T1-T12*<br>*L1-L5*<br>*S1-S5* |
| Length of Stay(LOS) | Numerical | *8-408 days* |

TABLE II. DESCRIPTION OF DIAGNOSIS TYPES

| | |
|---|---|
| TT | Traumatic Tetraplegia |
| TP | Traumatic Paraplegia |
| NTP | Non Traumatic Tetraplegia |
| NTP | Non Traumatic Paraplegia |

TABLE III. DESCRIPTION OF ASIA

| | |
|---|---|
| A | Complete, below the affected portion lack of motor and sensory function. |
| B | Incomplete sensor. |
| C | Some sensation beneath the level of the damage, including anal sensations. |
| D | Around half of the muscles that are saved underneath the damage level are sufficient amount of powerful and able to move against gravity. |
| E | Restored all sensational capacity. |

### B. *Working methods*

Initially we have used the Pearson Coefficient method to analyze the relationship between variables. In order to present a clear picture of significance of the features, a correlation matrix has been given in table IV. * Correlation is significant at the 0.05 and ** Correlation is significant at the .01, level (2-tailed). In the table, the diagonal variables are always 1 since relation between variables with itself is 1. And the other values indicate how strongly they are connected with each other.

Again we also want to show whether the variables are normally distributed or not. According to the fig. 1, data are not normally distributed. And finally, Multiple Linear Regression (MLR) has been used to develop prediction model.

Linear regression predicts the relationship between the predictors who have cause and effect relation. Usually there is one dependent variable, which depends on other independent variable. If one or more conditions cause a certain event, linear regression is a suitable for that study. In other words, it can be said, linear regression is preferable for prediction study. The main concentration of linear regression study is to research the relation between dependent and independent variable and to produce a linear equation which defines the relation between them [15]. When one dependent predictor depends on more than a one independent predictor, the study is called Multiple Linear regression (MLR). Multiple linear Regression hypothesis can be expressed as,

$$y = \theta_0 + \theta_1 x_1 + \theta_2 x_2 + \theta_3 x_3 + \cdots + \theta_n x_n \quad \ldots\ldots \text{(i)}$$

Where the $\theta_0$, $\theta_1$, $\theta_2$..... $\theta$n is regression parameter, $x$ is predictor and $y$ is predicted value.

TABLE IV. CORRELATION MATRIX

| | v1 | v2 | v3 | v4 | v5 | v6 | v7 | v8 | v9 | v10 |
|---|---|---|---|---|---|---|---|---|---|---|
| v1 | 1 | -0.118* | -0.072 | 0.068 | 0.081 | 0.057 | .150** | 0.003 | -0.046 | 0.018 |
| v2 | | 1 | 0.028 | .227** | 0.038 | 0.087 | -0.028 | -0.045 | 0.049 | -.193** |
| v3 | | | 1 | .188** | -0.088 | 0.05 | -0.012 | -0.03 | .266** | -0.055 |
| v4 | | | | 1 | -0.008 | 0.215** | .239** | -0.008 | -0.055 | -0.095 |
| v5 | | | | | 1 | .283** | -0.038 | -.156** | .132* | -.363** |
| v6 | | | | | | 1 | 0.055 | -.148** | .173** | -.521** |
| v7 | | | | | | | 1 | .190** | -.111* | -0.037 |
| v8 | | | | | | | | 1 | -0.064 | 0.056 |
| v9 | | | | | | | | | 1 | -.325** |
| v10 | | | | | | | | | | 1 |

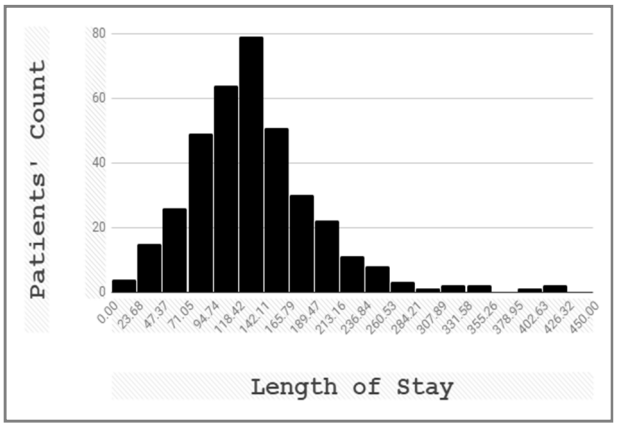


Figure 1. Histogram of Un-transformed data.

## IV. EXPERIMENTAL EVALUATION

In this section, the outcome that we have achieved from MLR has been discussed. As we wanted to develop a prediction model, MLR is chosen. Since the data are not normally distributed we also developed a model with natural logarithmic transformation [12]. In the table-V we can see two initial models. Both of the models are significant.

We also plot a histogram with logarithmic transformed data to check the data distribution in fig. 2.

Fortunately, the transformed model is able to predict the LOS more accurately. And the model also stands with greater value of adjusted R-squared. Adjusted R-squared is a number, which is adjusted for a model. The value of R-squared increases only when the features improve the model more than the expected chance. A greater number of adjusted R-square indicates a better model.

In table VI, we can see that, the R-squared value (0.381) of transformed model is significantly better than the R-squared value (0.316) of un-transformed data which shows that the transformed data model is better.

TABLE V. INITIAL TWO MODELS

| | Transformed model | | | Un-Transformed Model | | |
|---|---|---|---|---|---|---|
| | Co-efficient | t-value | Sig. | Co-efficient | t-value | Sig. |
| Constant | 5.863 | 28.167 | 0 | 261.733 | 16.182 | 0 |
| Age | 0.045 | 0.957 | 0.339 | 0.196 | 0.999 | 0.318 |
| Sex | -0.21 | -3.3 | 0.001 | -24.275 | -3.072 | 0.002 |
| Admission | 2.81E-05 | 0.166 | 0.869 | 0.006 | 0.297 | 0.766 |
| P.sore | 0.014 | 0.453 | 0.651 | 7.982 | 2.01 | 0.045 |
| Diagnosis | -0.232 | -5.075 | 0 | -33.192 | -5.843 | 0 |
| ASIA | -0.216 | -9.354 | 0 | -20.593 | -7.202 | 0 |
| SCIM | -0.025 | -1.189 | 0.235 | -0.823 | -2.696 | 0.007 |
| S/l | -0.034 | -1.21 | 0.227 | -0.467 | -1.297 | 0.195 |
| N/L | -0.008 | -5.101 | 0 | -0.796 | -3.901 | 0 |

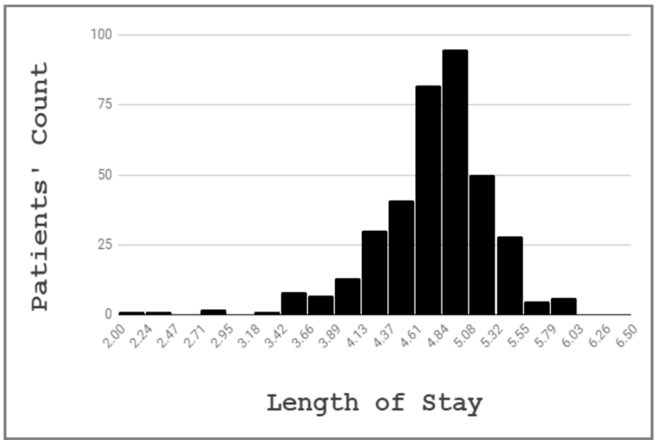


Figure 2. Histogram of logarithmic transformed data

TABLE VI. COMPARISON OF ADJUSTED R-SQUARED VALUE

| Method Name | Un-Transformed Model | Transformed Model |
|---|---|---|
| Adjusted R-square | 0.316 | 0.381 |

For this model, we trained with the whole data set and for testing purpose, use the same values. In terms of that, 370 patients' details were used. To develop this study, the model which is built with multiple linear regressions is,

$$y = 5.863 + 0.045 * x_1 + (-0.210) * x_2 + 2.814E - 5 * x_3 + 0.014 * x_4 + (-0.232) * x_5 + (-0.216) * x_6 + (-0.025) * x_7 + (-0.034) * x_8 + (-0.008) * x_9$$

Here, the regression parameters are, $\theta_0 = 5.863$, $\theta_1 = 0.045$, $\theta_2 =$ -0.210, $\theta_3 = 2.814E - 5$, $\theta_4 = 0.014$, $\theta_5 =$ -0.232, $\theta_6 =$ -0.216, $\theta_7 =$ -0.025, $\theta_8 =$ -0.034, $\theta_9 =$ -0.008.

Fig. 3 demonstrates Predicted Length of Stay vs. Actual Length of Stay in a scatter plot. From the graph we can see that after logarithmic transformation the accuracy increases. The Predicted vs. Actual plotting almost becomes linear line. We use the prediction model to predict the length of stay of the test data with an error of +/- 0.5 or +/- 25-50 days and find that the accuracy of Length of Stay prediction of the logarithmic transformed data is 81.62% which shows a significant improvement over the un-transformed data.

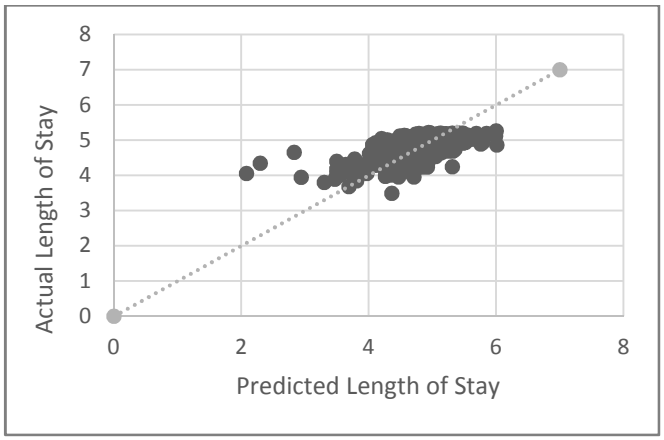


Figure 3. Scattered plot showing Predicted Length of Stay vs. Actual Length of Stay

## V. Conclusion And Discussion

This study proposes the use of multiple linear regressions for the prediction hospital stay of spinal cord injured patient at the early admission state. Our contribution here is to develop a model on the SCI patients which will help better patient care in the future and help the hospital for the better resource management. We selected CRP in purpose of collecting data and provided with around 600 patients information. After modifying the data, around 377 patients' data was selected for analysis. Firstly, we used Pearson correlation to see the significance between our features. We plot a histogram to check whether they are normally distributed or not. After that, we build two types of model, one is logarithmic transformed data model and another one is un-transformed data model. As logarithmic results were better, we chose that as final model. The accuracy of logarithmic transformed is much satisfying. But, for better accuracy level, the data set needed to be larger and more attributes are needed. Though the logarithmic transformed model was better, the model is not able to predict the LOS with greater number of days i.e. more than 250 days. For the future work of the study, we will implement neural network for building models which have also shown great accuracy level on different kinds of predictions.

## References


[1] C. Pavese, M. Schneider, M. Schubert et al, "Prediction of Bladder Outcomes after Traumatic Spinal Cord Injury: A Longitudinal Cohort Study", PLOS medicine journal, June 21, 2016.

[2] Walczak, S., Pofahl, W. and Scorpio, R. (2003). A decision support tool for allocating hospital bed resources and determining required acuity of care. *Decision Support Systems*, 34(4), pp.445-456.

[3] Development, *Health at a Glance 2011*. Paris: OECD Publishing, 2011.

[4] C. Lin, P. Lin, L. Chou, S. Lan, N. Meng, S. Lo and H. Isaac Wu, "Model-based Prediction of Length of Stay for Rehabilitating Stroke Patients", *Journal of the Formosan Medical Association*, vol. 108, no. 8, pp. 653-662, 2009.

[5] M. Rowan, T. Ryan, F. Hegarty and N. O'Hare, "The use of artificial neural networks to stratify the length of stay of cardiac patients based on preoperative and initial postoperative factors", *Artificial Intelligence in Medicine*, vol. 40, no. 3, pp. 211-221, 2007.

[6] S. Kirshblum, S. Burns, F. Biering-Sorensen, W. Donovan, D. Graves, A. Jha, M. Johansen, L. Jones, A. Krassioukov, M. Mulcahey, M. Schmidt-Read and W. Waring, "International standards for neurological classification of spinal cord injury (Revised 2011)", *The Journal of Spinal Cord Medicine*, vol. 34, no. 6, pp. 535-546, 2011.

[7] H. Imai, J. Hosomi, H. Nakao, H. Tsukino, T. Katoh, T. Itoh and T. Yoshida, "Characteristics of psychiatric hospitals associated with length of stay in Japan", *Health Policy*, vol. 74, no. 2, pp. 115-121, 2005.

[8] S. Shortell, J. Zimmerman, D. Rousseau, R. Gillies, D. Wagner, E. Draper, W. Kanus and J. Duffy, "The Performance of Intensive Care Units: Does Good Management Make a Difference?", *Medical Care*, vol. 32, no. 5, pp. 508-525, 1994.

[9] P. Tsai, P. Chen, Y. Chen, H. Song, H. Lin, F. Lin and Q. Huang, "Length of Hospital Stay Prediction at the Admission Stage for Cardiology Patients Using Artificial Neural Network", *Journal of Healthcare Engineering*, vol. 2016, pp. 1-11, 2016.

[10] R. Jiménez, R. Lam, M. Marot and A. Delgado, "Observed-predicted length of stay for an acute psychiatric department, as an indicator of inpatient care inefficiencies. Retrospective case-series study.", *BMC Health Services Research*, vol. 4, no. 1, 2004.

[11] R. McLay, A. Daylo and P. Hammer, "Predictors of Length of Stay in a Psychiatric Ward Serving Active Duty Military and Civilian Patients", *Military Medicine*, vol. 170, no. 3, pp. 219-222, 2005.

[12] R Fine, P & L Stover, S & DeVivo, Michael. "A methodology for predicting lengths of stay for spinal cord injury patients. Inquiry: a journal of medical care organization", *provision and financing*. 24. 147-56, 1987.

[13] S. Ramesh, D. Dursun, "Predicting box-office success of motion pictures with neural networks", pp 243-254, 2006.

[14] Q. Li, Z. Lin, F. Masoudi, J. Li, X. Li, S. Hernández-Díaz, S. Nuti, L. Li, Q. Wang, J. Spertus, F. Hu, H. Krumholz and L. Jiang, "National trends in hospital length of stay for acute myocardial infarction in China", *BMC Cardiovascular Disorders*, vol. 15, no. 1, 2015.

[15] Abdul Awal, Md & Rabbi, Jakaria & Hossain, Sk & Hashem, M.M.A. "Using Linear Regression to Forecast Future Trends in Crime of Bangladesh" . 10.1109/ICIEV.2016.7760021, 2016.

[16] Ismail, A. Yahya and A. Shabri, "Forecasting Gold Prices Using Multiple Linear Regression Method", *American Journal of Applied Sciences*, vol. 6, no. 8, pp. 1509-1514, 2009.

# Bangla Sign Language Interpretation using Bag of Features and Support Vector Machine

Jia Uddin, Fahmid Nasif Arko, Nujhat Tabassum, Taposhi Rabeya Trisha and Fariha Ahmed
Department of Computer Science and Engineering, BRAC University, Dhaka, Bangladesh
{engrjiauddin, arkoocse, tabassum1125, trtrisha2217, fariha.ahmed3456}@gmail.com

*Abstract*—**To complete any process, communication is necessary. Deaf and dumb people use special language to communicate which is known as Sign Language. In this paper, we propose an image processing based model for interpretation of Bangla sign language. In the model, initially $YC_BC_R$ color components are used to detect the skin color of the user and then extract the Bag of features for each input image. Finally extracted features are feed to the Support Vector Machine (SVM) for training and testing. To validate the proposed model, we use our own dataset where both male and female hand gestures are used. Experimental results show that the proposed model exhibited average 86% accuracy for our tested dataset. In addition, the proposed model outperforms than other state-of-art models by exhibiting higher accuracy.**

***Keywords—Sign Language, Bag of Features, Support Vector Machine, Classification Accuracy.***

## I. INTRODUCTION

Human can portray their languages using their all six senses. Like listening organ, seeing organ can also make sense of communication. Sign language is one of those methods [1]. Sign language is a popular way of communication among listening and hearing impaired people all over the world. By using hands, facial expressions and body languages communication is made in sign language. Different countries have different sign languages. Among them American sign language is considered as International sign language [2]. In Bangladesh, Bangla is mother tongue, Bengali sign language is widely used by its listening and hearing disable people. But general people are not so capable of understanding the sign language. So there comes the demand of an interpreter by who or which those special people can communicate with general people. But a human interpreter is not always available or affordable. On the other hand, the number of interpreter device in Bangladesh is very less and they are also very costly.

Hence, we are trying to develop a system that will interpret Bangla sign language [3]. This will make a great help for the special people to communicate with every common people easily. The field of image processing for any data or image recognition is growing every day. A lot of researchers are working on this sign language interpretation and use different tools, such as Kinect [12], machine deep learning, etc. In [9], Microsoft Kinect device is used to translate sign language into spoken language. The limitation of this method, a system that uses Sigma NIL framework that delivers hand shape recognition which is not supported by official and other SDKs (Software Development Kit) for Kinect. In addition, the system can only translate limited vocabulary. In [7], Arab sign language has an interpreter using motion detector.

In recent years, few researchers work on Bangla Sign language recognition. In [8], authors proposed a Bangla sign recognition method using Gabor filter. In the method, firstly they converted all the hand gesture images into HSV from RGB images and then use Gabor filter. The limitation of the method is, the extracted feature dimension is high and use PCA (Principal Component Analysis) as dimension reduction tool [5]. To overcome the limitation of the proposed model, this paper proposed an efficient method for interpreting Bangla sign language using Bag of feature and Support Vector Machine, SVM.

Rest of the paper is organized as follows. Chapter II describes the detail of proposed model. The performance analysis of proposed model is depicted in chapter III. Finally conclude the paper in chapter IV.

## II. PROPOSED MODEL

Figure 1 shows a detail block diagram of proposed model. This method stems from two principal application areas: (i) upgrading pictorial data for human interpretation, and (ii) processing of scene data for autonomous machine perception.

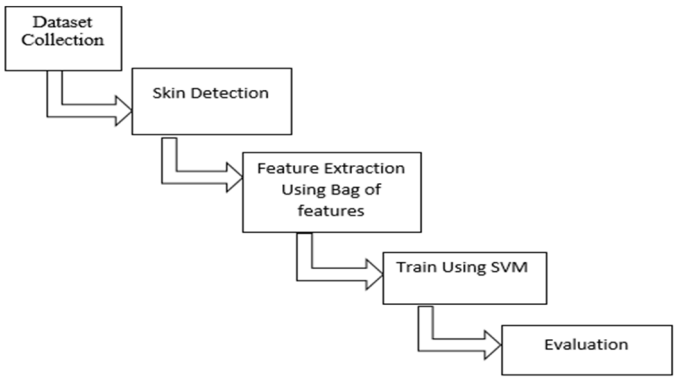


Figure 1. Proposed model of our system

In the first phase, data acquisition we had to make our own dataset as there has not been many research on Bangla Sign Language interpretation. In our dataset we acquired images of fifteen Bangla different consonant signs. In total eight hundred images are acquired for the system implementation. Each class of sign has fifty two to fifty six images of twenty nine different bare hands. Where thirty percentage of the dataset has been used for training the system and with the rest seventy

978-1-5386-2307-7/17/$31.00 ©2017 IEEE

percent we tested our system. In the second phase we used $YC_BC_R$ skin detection algorithm [10]. For applying this method we converted the image in 400 × 400 pixels, which gives very faster response in conversion.

The formula we have used for the conversion of RGB to $YC_BC_R$ color space are:

$$Y' = 16 + (65.481.R' + 128.553.G' + 24.966.B')$$

$$C_B = 128 + (-37.797.R' - 74.203.G' + 112.0B')$$

$$C_R = 128 + (112.0.R' - 93.786.G' - 18.214.B') .$$

Here, Y is the luminance information as a single component. Chrominance difference are stored as two color-difference component $C_B$ and $C_R$. $C_B$ represents the difference between the blue component and a reference value and $C_R$ difference between the re component and reference value [13]. After detecting the skin this algorithm is making the image binary and subtracting noise from image.

The next phase is Feature Extraction, where we use Bag of features method that is also known as Bag of words. The process is done in four steps- extracting features, learning visual vocabulary, quantize feature using visual vocabulary and representing images by frequencies of visual words. The bag of feature uses SURF (Speeded up Robust Feature) to compute the local features from the training set [11]. SURF uses a blob detector based on Hessian matrix to find interest points to extract features [17]. To describe the region around the point, a square region is extracted, centered on the interest point and weighted sums in rectangular sub windows are calculated to describe the interest point and the feature descriptor is then put into the feature vector. Figure 2 shows the feature extraction process.

With the help of Hessian matrix it is detecting the curve points in the hand where the pixel color is changing. Local features are being detected according to the property count, location, scale, sign of Laplacian and orientation. These Local features are being stored in a 1×64 vector. If we find 82 features in a binary image then the vector size will be 82×64.

To find the local features the algorithm uses three types of filter size including 9×9, 15×15 and 21×21. Different types of filter size are being used to find all the interest points correctly. From each of 15 classes the total potential point is 46,656. So the total vector size will be 46,656 × 64 for each class, which is very large in number. Then k-means clustering is used to minimize features and calculate the visual words K-means clustering process selects initial centroids from the graph randomly and assign each object to the cluster with nearest centroid. After that calculation, each centroid as the mean of the objects assigned to it.

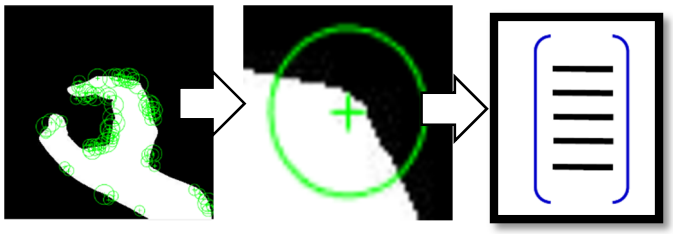

(a) (b) (c)

Figure 2. Process for Bag of Features Image Representation, (a) Interest point detection, (b) SURF descriptors being calculated, (c) Descriptors stored in feature vector

Visual vocabulary should not be too big or too small. For this computational efficiency Vocabulary Tree [4] is used. Vocabulary tree performs instance object recognition. It does not perform recognition at category level.

After that for image classifier we used SVM linear multiclass classifier. The SVM plot each data item as a point in n-dimensional space (where n is the number of features) with the value of each feature. Then the classification is performed by finding the hyper-plane that separate different classes very well.

## III. Experimental Evaluation of Proposed Model

The proposed model was tested with different types hand color, shapes and gender. For tested dataset, we collected data from different ages of people including male and female and got different skin colors. In the fifteen classes of data in each class we used sixteen to seventeen images for training the system and with thirty-seven to forty images we tested individual classes. Figure 3 shows some of our dataset classes accordingly 'Ka', 'Kha' and 'Ga'. Table I shows the train set accuracy and evaluation set accuracy for individual class.

(a) (b) (c)

Figure 3. Some sign images from the dataset (a) Ka , (b) Kha , (c) Ga

TABLE I. TEST AND EVALUATION SET ACCURACY FOR EACH CLASS

| Class Name | Train Set Average Accuracy | Evaluation Set average Accuracy | Class Name | Train Set Average Accuracy | Evaluation Set average Accuracy |
|---|---|---|---|---|---|
| Ka (ক) | 100% | 82% | Tho(থ) | 94% | 95% |
| Kha (খ) | 94% | 89% | Do (ড) | 100% | 87% |
| Ga (গ) | 94% | 92% | Dha (ঢ) | 94% | 87% |
| Gha (ঘ) | 94% | 79% | Da (দ) | 100% | 82% |
| Umo(ঙ) | 100% | 58% | Murdho-Na (ণ) | 100% | 100% |
| Cha(ছ) | 88% | 63% | Ba (ব) | 88% | 87% |
| Jo(জ)) | 94% | 95% | Anusshar (ং) | 88% | 92% |
| Jha(ঝ) | 100% | 97% | | | |

The average accuracy for training set is 95% and the average accuracy for evaluation set is 86%. Plotting the accuracy rate in the graph it is visible that for train set most of the accuracy rate is fluctuating between ninety four to hundred percent. From this it can be said that the system is trained in proper calculative way. Even in some classes like 'Ka', 'Umo', 'Jha', 'Do', 'Da' and 'Murdho-No' the accuracy rate was hundred percent. From the Figure 4, it is visible that most sets of class has an accuracy above eighty two percent but only in 'Umo' and 'Cha' it got very low accuracy where in its train set it achieved higher accuracy. As most of the Bangla signs are almost similar it was very difficult to identify each patch in feature vector in different classes.

Table II shows comparison between the proposed system and other system were the researchers used different techniques to interpret sign language. In [15], for Bengali Sign Language recognition they used Artificial Neural Network and it shows 80.902% accuracy. Their dataset was not enough for getting a better output from ANN recognition method.

In [15, 16], multilayer feedforward ANN is used and it shows around 80% accuracy for both Bangali and Amedican sign languages. The limitations of ANN is that, for learning Neural Network (NN) the feature vector should have been integer values. In addition, the Table II shows that the proposed model shows better accuracy than other existing models.

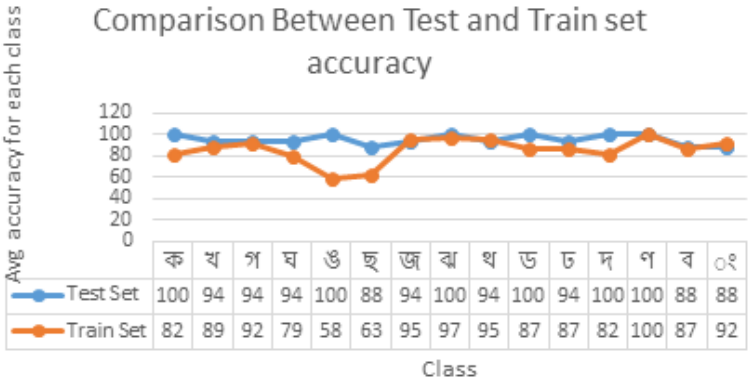


Figure 4. Graph showing comparison between test and evaluation set

TABLE II. COMPARISON BETWEEN PROPOSED MODEL AND OTHER SYSTEMS

| Technique Used | Sign Language | Average Accuracy |
|---|---|---|
| Matching signs with previously used knowledge based [14] | Bengali | 82% |
| Multillayer Feedforward ANN [15] | Bengali | 80.9% |
| Multillayer Feedforward ANN [16] | American | 79.33% |
| Proposed model | Bengali | 86% |

## IV. CONCLUSIONS

This paper presents a model for Bangla sign language interpretation. YCbCr skin detection method was used to detect skin. The system successfully extracted features by using Bag of Features. As a classifier, SVM is used for training and testing. The implemented system achieved average 86% of accuracy for tested dataset that consists of eight hundred images of hand gestures of both male and female.

## REFERENCES


[1] C. Zhang, Y. Tian and M. Huenerfauth, "Multi-modality American Sign Language recognition," in *Proc. 2016 IEEE International Conference on Image Processing (ICIP)*, Phoenix, AZ, 2016, pp. 2881-2885.

[2] C. M. Lange, S. Lane-Outlaw, W. E. Lange, and D. L. Sherwood, "American Sign Language/English Bilingual Model: A Longitudinal Study of Academic Growth," J*ournal of Deaf Studies and Deaf Education*, vol. 18, no. 4, pp. 532–544, May 2013.

[3] Juthy, N. S., Shaha, B. G., and Ali, M. S., Shojol. (2011). Ishara Bhashay Jogajog (Communicating through Sign Language).

[4] D. Nist´er and H. Stew´enius, "Scalable Recognition with a Vocabulary Tree," 2006.

[5] M. A. Uddin and S. A. Chowdhury, "Hand sign language recognition for Bangla alphabet using Support Vector Machine," Oct. 2016.

[6] C.Louder,"Mathematical Techniques of Image Processing," Oct. 2012.

[7] M. Hassan, K. Assaleh, and T. Shanableh, "User-Dependent Sign Language Recognition Using Motion Detection," in *Proc. 2016 International Conference on Computational Science and Computational Intelligence (CSCI)*, 2016.

[8] X.-X. Gao, L. Cao, and G.-R. Chang, "Edge detection algorithm based on odd Gabor filter," *Journal of Computer Applications*, vol. 28, no. 10, pp. 2625–2627, 2009.

[9] E. Mustafa and K. Dimopoulos, "Sign Language recognition using Kinect".

[10] K. B. Shaik, P. Ganesan, V. Kalist, B. Sathish, and J. M. M. Jenitha, "Comparative Study of Skin Color Detection and Segmentation in HSV and YCbCr Color Space," *Procedia Computer Science*, vol. 57, pp. 41–48, 2015.

[11] B. Herbert, T. Tuytelaars, and L. V. Gool, "Surf: Speeded up robust features," *Computer vision–ECCV* 2006, pp. 404-417, 2006.

[12] A. Singh, "Hacking the Kinect," in Introduction to Kinect (RGB-D Image Processing).

[13] Mahmoud, Tarek M. A New Fast Skin Color Detection Technique. 2nd ed. 2008. Print.

[14] A. Eshaque, T. Hamid, S. Rahman, and M. Rokonuzzaman, "A Novel Concept of 3D Animation Based 'Intelligent Assistant' for Deaf People: for Understanding Bengali Expressions," in *Proc. International Conference on Computer and Information Technology*, East West University, Dhaka, Bangladesh, pp 252-256, 2002.

[15] M. A. Rahman, Ahsan-Ul-Ambia, M. I. Abdullah, and S. K. Mondal, "Recognition of Static Hand Gestures of Alphabet in Bangla Sign Language," *IOSR Journal of Computer Engineering (IOSRJCE)*, vol. 8, no. 1, pp. 07-13, 2012.

[16] M. Manar, A. Z. Farid, M. Dhyabat, and R. A. Zitar, "Recognition of Arabic Sign Language (ArSL) Using Recurrent Neural Networks," *Journal of Intelligent Learning Systems and Applications*, vol. 4, pp. 41-52, 2012.

[17] H. Urruty, J. Baptiste, J.J. Strodiot, and V. H. Nguyen, "Generalized Hessian matrix and second-order optimality conditions for problems withC 1, 1 data," *Applied Mathematics and Optimization* 11.1 (1984): 43-56.

# Cataract Detection using Smartphone

Juyel Rana[1*], Syed Md. Galib[2]
[1]Faculty of Computer Science and Engineering,
Patuakhali Science and Technology University, Bangladesh
[2]Department of Computer and Information Technology,
Patuakhali Science and Technology University, Bangladesh
*mjuyelrana@gmail.com

***Abstract*— A cataract could be an evaporation of the ordinarily clear lens of the eye. Those having cataracts may experience seeing through their cloudy lenses which could be a bit like exploring through a frosty a fogged up window. Clouded vision caused by cataracts will create it tougher to browse websites, drive an automobile (especially at night) or see the expression on a friend's face. Most cataracts develop slowly and do not disturb sight early. However, with time, cataracts can eventually interfere with vision. There are some manual techniques to detect a cataract. An ophthalmologist or optometrist diagnoses a cataract by doing a comprehensive eye examination. The ophthalmologist uses a slit lamp camera to diagnose a cataract. By the lacking of ophthalmologist and slit lamp camera in rural areas, especially in developing country like Bangladesh are the main problem of diagnosing a cataract. There also have some automated smartphone based cataract detection techniques that will overcome these problems. In these research, we proposed a methodology that will be implemented on a smartphone (Android, iOS, Windows). This paper presents a proof-of-concept self-screening cataract detecting mobile application. It enables the public to carry out early detecting by using a smartphone with a well focusing front camera that allows self-screening to be performed by almost anyone, anytime, anywhere.**

**Keywords—** ***Cataract, SDK, NDK, OpenCV, Image Processing, Smartphone.***

## I. INTRODUCTION

The expanding evaluation of smartphones with detecting ability is giving developers the chance to plan and create versatile applications. Especially, portable advancements are opening new doors to human services. For example, handheld gadgets and smartphones have significantly changed the present world. With the new era of portable working, applications have been generous expanding improvements and selections of versatile applications. To date, more than 100,000 therapeutic and medicinal services applications are devoted to smartphone and several other handheld gadgets [1].

About 285 million individuals are assessed to be outwardly disabled around the world: 39 million are visually impaired and 246 million have low vision. Around 90% of the world's apparently weakened live in low-wage settings. 82% of individuals living with visual impairment is 50 years old. All inclusive, uncorrected refractive blunders are the fundamental driver of direct and extreme visual impedance; cataract remains the main source of visual deficiency developing countries. The number of individuals apparently weakened from irresistible ailments has lessened over the most recent 20 years as indicated by worldwide assessments work[2].

There are various approaches to screen cataract, for example, utilizing opening light examination, red reflex, and light scrambling techniques. The ophthalmologist will put the ophthalmoscope 30cm/1 foot far from the eye's retina and watch the ruddy orange reflection (red reflex) of light. The red reflex from ophthalmoscope decides the seriousness of the cataract. The red reflex happens on the grounds that the transmission of light from an ophthalmoscope through all the typically straightforward parts of a subject's eye. Any factor that hinders or obstructs this optical pathway will bring about a variation from the norm of the red reflex.

There are few difficulties for consistent screening. Initially, screenings are done by therapeutic professionals, and their accessibility will be a factor. Furthermore, legitimate sorts of hardware are required for the screening, and they are not shabby. The expenses and time required to do eye examination from restorative professionals are likewise conceivable why some are doing the screening as customary as could reasonably be expected. These difficulties are much more troublesome with regards to screening for individuals from the provincial range. For screening cataract, patients ought to be done in the beginning periods as the specialist may require time to plan for the patient's surgery and furthermore patients may require time to get ready mentally.

We propose to build up an answer utilizing versatile innovation that explains the above difficulties. The thought is to use a smartphone with a fitting application as an options screen instrument. This device ought to be intended for the use by overall population. As it were, nearly anybody ought to have the capacity to work the application and do cataract screening without the help of a therapeutic professional. This paper displays the thought and an original model to show the believability of the thought. The proposition does not mean to supplant the expert screening method. The application should fill in as a non-therapeutic self-screening administration so that with early discovery, the patient would then be able to look for proficient screening to affirm and thus ready to avoid potential risk ventures by having early treatment. As smartphone turns out to be practically universal in most urban spots since the earlier years, cataract self-screening with smartphone expels the boundaries like screening cost and travel/time bothers for patients who are associated with having a cataract. As cataract

978-1-5386-2307-7/17/$31.00 ©2017 IEEE

event increments with age, visit self-screening can distinguish cataract right in time to decrease preventable visual impairment. Our proposed method is to detect cataract using a smartphone like Android, iOS, Windows. First developed customize camera using Open CV, Java Camera View which give real-time camera application. When the patients or users launch the application its open the customize camera. The camera detects two eyes, crop eyes on running time and shows the different layout in the camera view. When cropping the pupil from two eyes on running time, then two pupils are stored in a matrix. Analyze two matrices using the help of NDK, which provide C/C++ coding on android platform. Some color detection method is applied to detect the pupils color then take the decision, eyes are a cataract or not.

## II. RECENT WORKS

Cataracts are the most common cause of vision loss in people over age 40 and are the principal cause of blindness in the world. In fact, there are more cases of cataracts worldwide than there are of glaucoma, macular degeneration and diabetic retinopathy combined, according to Prevent Blindness America (PBA). Today, cataracts affect more than 22 million Americans age 40 and older. And as the U.S population ages, more than 30 million Americans are expected to have cataracts by the year 2020 [3].

Several research works have been performed to detect cataract using retinal images. Some related reviews have been presented here under the following sub-heads. A Bourouis, M. Feham, M.A. Hossain and L. Zhang (2014) proposed a retinal disease diagnosis using a Feedforward Neural Network (NN). The NN used to break down patient's retinal images and perform infection determination. The Neural Network is at first prepared with solid and tainted retinal pictures on a PCs and after that installed in an Android domain. After retinal pictures are caught by the minuscule focal point joined with a smartphone, a progression of Android's picture handling API's is likewise used to investigate the crude pictures. The exploration is composed and created to find anomalous retinal from typical cases. They used two therapeutic picture databases DIARETBO and STARE, for the assessment of the savvy versatile based conclusion framework. The assessment comes about prove that the framework indicates focused retinal sickness identification exactness (>87 %) [1].

Jaspreet kaur and Ravinder kaur (2015) proposed low-cost cataract detection system using smartphones. The authors proposed a minimal effort cell phone based keen framework mix and miniaturized scale focal points enable patients in remote zones to have standard eye checks and inventive advancement of ailment determination. The official portable demonstrative framework for the investigation of retinal pictures taken by minuscule focal point to recognize retinal infection conditions. The neural system constructs approach can be kept running in light of both desktop PC strange/typical retina picture characterization for Android-based cell phones. Feedforward neural system calculation ready to carry out ongoing proficient arrangements, as a matter of first importance the sound and tainted stages. At that point utilizes the dataset of the retina, on a desktop PC testing neural system INA cell phone introduced Android in the ready framework (OS). Testing stage, utilizing miniaturized scale focal point and gather clients, which is utilizing retinal pictures, indicative, Android smartphone, is joined. The advantages of utilizing magnifying instrument focal point, execution for the conclusion of enabling the framework to take clear retinal pictures. To give shrewd answers for portable based proficient to do different streamlining strategies, continuous determination, considered their examination. Coordination of the outer magnifying lens by utilizing an industrially accessible smartphone introduced to clever portable based retinal infection discovery technique. The proposed technique was produced for the Android working stage. The application is anything but difficult to work with any portable clients could be used remotely as a productive minimal effort versatile for wellbeing checking framework when [4].

Yunendah Nur Fuadah, Agung W. Setiawan, Tati L.R. Mengko and Budiman (2015) proposed mobile cataract detection using the ideal combination of texture analysis. The authors proposed optimal combination candidate of statistical texture features that provides the highest accuracy for cataract detection. They use K-Nearest Neighbor (KNN) as grouping technique that is actualized on Android telephone. The principal procedure of the framework consists of preparing and testing process. Both of the preparation and testing process have the means, specifically, reprocessing, highlight extraction and order. They utilize the factual surface examination highlight extraction to distinguish waterfall and K-NN as grouping technique. The framework configuration is executed in MATLAB and dissect the execution of factual surface components (Uniformity, Contrast, Dissimilarity, Correlation, and Homogeneity), at that point find the ideal estimation of K-NN. After the surface components and the ideal k esteem, execute the framework on Android Smartphone. The most astounding exactness of their proposed framework is 97.5% [5].

Stewart Jordan et al., (2014) proposed a smartphone based ophthalmoscope. A minimal effort contrasting option to the immediate ophthalmoscope, a straightforward optical connector for a cell phone. It can beat a large part of the specialized difficulties of fundus duplicate, giving a high determination perspective of the retina through an unengaged student. Correlation of optic nerve pictures from business retina screening cameras with the cell phone connector exhibits solid confirmation for no distinction in execution in glaucomatous plate evaluating [6].

Prateek Prasanna, Shubham Jain, Neelkshi Bhagat and Anant Madabhushi (2013) proposed decision support system for diabetic retinopathy using smartphones. The authors proposed model needs a smartphone to be attached to a direct hand-held ophthalmoscope. The phone is used to capture fundus images as seen through the direct ophthalmoscope. The algorithm performance is characterized by testing an existing database. The system has been designed to be used by Ophthalmologist, general practitioners, emergency room physicians, and other healthcare people alike. They able to diagnose conditions with an average sensitivity of 86% [7].

S. Pathak and B. Kumar (2016) proposed a robust automated cataract detection algorithm using diagnostic

opinion based factor threshold for telemedicine application. The authors proposed an algorithm to automatically detect cataracts from color images in adult human subjects. The main motive behind their research work is to develop an inexpensive, robust and convenient algorithm which in conjugation with suitable devices will be able to diagnose the presence of cataract from the true color images of an eye. An algorithm is proposed for cataract screening based on texture features: uniformity, intensity and standard deviation. These features are first computed and mapped with a diagnostic opinion by the eye expert to define the basic threshold of screening system and later tested on real subjects in an eye clinic. Finally, a teleophthalmology model using their proposed system has been suggested, which confirms the telemedicine application of the proposed system [8].

A large number of works have been done to estimate the detection of cataract using digital image processing. Also, some algorithm has been implemented for feature choice. The goal of my research is to develop an Android Application Software for detecting cataract on running time camera.

## III. METHOD

In our proposed model, we want to develop an Android Application. Today's Google's Android provides better features for developers. Every day's programmer builds some library to make the development works easy. Our research work, we used Android Studio, SDK, NDK, and OpenCV.

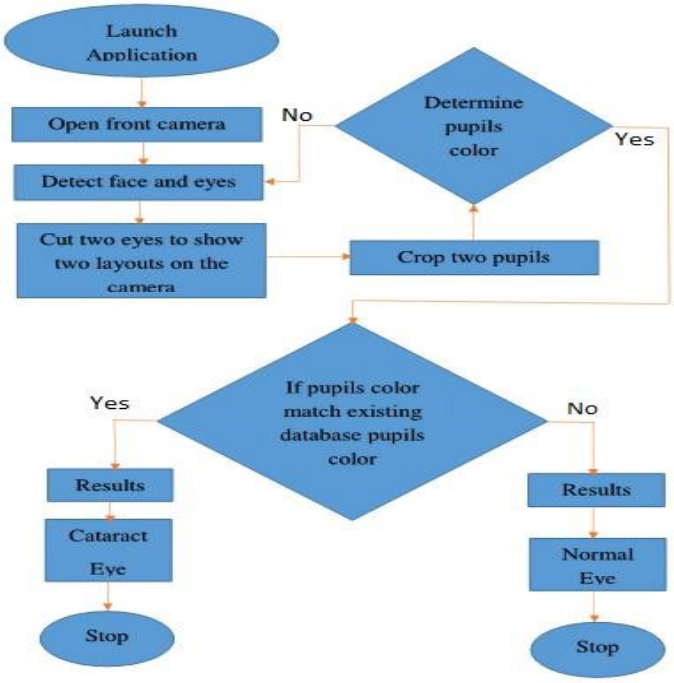


Figure 1: Flow diagram of proposed model

At first, the patient launches the application. When the app is launched, it opens a customized camera which provides OpenCv an image processing library. The phone is placed in front of the eye with the maximum distance of 30 cm. The camera first detects the patient's face with a colored rectangle. The two eyes are also shown in two different rectangular views. Here only two eyes are shown clearly so that the patient can see his own eyes problem. Now the two frame detect and cut the pupil using Cascade Classifier.

Cascade Classifier is a library that has some functionality to detect pupil. Then the pupil image is stored in a temporal matrix. The matrix stored the values as RGB format. Now the two frame detect the pupil using Cascade Classifier. Then the pupil image is stored in a temporal matrix as an RGB value.

**Algorithm 1**. Pseudo code for detecting cataract

**Algorithm 1. Pseudo code for detecting cataract**

start

1. Launch application, open front camera and detect face and eyes
2. Cut two eyes and show two different layouts on the camera screen.
3. Detect two pupils from two different layouts and crop only pupils region.
4. Determine pupils color;
5. repeat

   {

   5.1 if (determine pupil color)

   {

   - Check pupils color on existing database pupil color
   - If pupils color match then classify the into three stages- Cataract stage 1, Cataract stage 2 and Cataract stage 3.
   - If doesn't match pupil color, it classify to normal eye.

   }

   else {

   - GOTO step 3

   }

   until (stop the application)

   }

end

## IV. RESULTS AND DISCUSSION

After pupil detection and crop automatically it will send to OpenCv C++ coding part. OpenCv provide some methodology to determine the pupil color. In the following section, described the pupil color detection.

```
cv: Mat img = cv::imgread("pupliImage")
int pixelValue = 0, int m = 0;        for ( int j =
0; j <= img.rows; j++){
            for( int I = 0; I <= img.cols; i++){
```

```
                pixelValue = (int) img.at<uchar>(i,j);
                n++;
            }
        }
```

int pupilColor = $\frac{pixelValue}{n*255}$

Now we can determine the four stages of cataract detection.

**Stage 1:** If pupilColor is less than OR equal to databaseCataractPupilColor AND less than OR equal to 50. This is dark gray and Normal eye.
**Stage 2:** If pupilColor is less than OR equal to databaseCataractPupilColor AND the pupilColor is greater than 50 AND pupilColor less than 120. This is medium gray and Cataract stage-1.
**Stage 3:** If pupilColor is less than OR equal to databaseCataractPupilColor AND the pupilColor is greater than 120 AND pupilColor less than 200. This is light gray and Cataract stage-2.
**Stage 4:** If pupilColor is less than OR equal to databaseCataractPupilColor AND the pupilColor is greater than 200. This is light gray and Cataract Stage-3 (Glucoma).

We presented an experiment using 50 people. Those are 20 having cataract and 30 are normal. The evaluation results indicate that the system shows competitive retinal disease detection accuracy rates greater than 90%.

## V. CONCLUSION

The cataract is the leading cause of blindness and affecting people age 40 and older. Multiple studies have also been shown that cataract increases changes in automobile crashes and also accidental injuries sustained to the elderly. This research work presents a proof-of-concept self-screening cataract mobile application. It enables the general public to carry out early detection by using a smartphone with a camera and flash. This is not only allows self-screening to be performed by almost anyone, anytime, anywhere, it also can be used as a portable screening solution in places with limited medical facilities or professional. The research has shown that such the approach is possible.

## REFERENCES


[1] A. Bourouis, M. Feham, M. A. Hossain, and L. Zhang, "An intelligent mobile based decision support system for retinal disease diagnosis," *Decision Support Systems,* vol. 59, pp. 341-350, 2014.

[2] WHO. (2017). *Vision impairment and blindness*. Available: http://www.who.int/mediacentre/factsheets/fs282/en/

[3] G. Bailey. (2017, October,17). *Cataracts*. Available: http://www.allaboutvision.com/conditions/cataracts.htm

[4] M. Kaur, J. Kaur, and R. Kaur, "Low cost cataract detection system using smart phone," in *Green Computing and Internet of Things (ICGCIoT), 2015 International Conference on*, 2015, pp. 1607-1609.

[5] Y. N. Fuadah, A. W. Setiawan, and T. L. Mengko, "Mobile cataract detection using optimal combination of statistical texture analysis," in *Instrumentation, Communications, Information Technology, and Biomedical Engineering (ICICI-BME), 2015 4th International Conference on*, 2015, pp. 232-236.

[6] M. E. Giardini, I. A. Livingstone, S. Jordan, N. M. Bolster, T. Peto, M. Burton*, et al.*, "A smartphone based ophthalmoscope," in *Engineering in Medicine and Biology Society (EMBC), 2014 36th Annual International Conference of the IEEE*, 2014, pp. 2177-2180.

[7] P. Prasanna, S. Jain, N. Bhagat, and A. Madabhushi, "Decision support system for detection of diabetic retinopathy using smartphones," in *Pervasive Computing Technologies for Healthcare (PervasiveHealth), 2013 7th International Conference on*, 2013, pp. 176-179.

[8] S. Pathak and B. Kumar, "A Robust Automated Cataract Detection Algorithm Using Diagnostic Opinion Based Parameter Thresholding for Telemedicine Application," *Electronics,* vol. 5, p. 57, 2016.

# Reconstruction Algorithm for Pigeon Hole Imaging (PHI)

Rushdi Zahid Rusho[1,2] and M Abdul Kadir[1]
[1]Department of Biomedical Physics and Technology, University of Dhaka, Dhaka-1000, Bangladesh
[2]Department of Biomedical Engineering, Khulna University of Engineering and Technology, Khulna-9203, Bangladesh
rushdizahid@gmail.com, kadir@du.ac.bd

*Abstract*— **Pigeon Hole Imaging (PHI) is a non-ionizing imaging modality that maps spatial distribution of electrical conductivity within a volume conductor. In PHI, electrical impedance is measured placing an electrode array on the surface of a volume conductor and the conductivity distribution in a plane parallel to the electrode array is obtained. This paper describes an image reconstruction algorithm for PHI based on 4-electrode Focused Impedance Measurements (FIM). The impedance measurements were simulated in a finite element based simulation software COMSOL Multiphysics for 5×5 and 6×6 PHI matrices. The measured impedance on the volume conductor surface just above an object of different conductivity compared to the volume conductor was found to be different than that in the neighbouring regions which is the basis of the image reconstruction algorithm. The developed algorithm was tested by modelling volume conductors containing multiple objects of different conductivities at different depths. It was found that PHI has 3D sensitivity and the developed algorithm can fairly detect objects with diameter at least of the order of half the electrode separation with depth equal to or less than electrode separation. Being a low cost and non-ionizing method, there is a potential of using PHI in the imaging of organs, tumors and blood vessels in human body although the image resolution is low.**

***Keywords— Electrical bioimpedance, Pigeon Hole Imaging, Conductivity Imaging, Image Reconstruction, FIM, EIT.***

## I. INTRODUCTION

Bioimpedance deals with the passive electrical properties of biological tissues. It is the property that impedes or opposes flow of electric current through biological tissues. Bioimpedance analysis is a broadly applied approach used in body composition measurements and healthcare assessment systems [1]-[2]. There is a potential of using bioimpedance techniques in the detection and diagnosis of many disorders and diseases in the human body. In two electrode method, the impedance is measured by passing a current through the tissue via two terminals of a conductor and measuring the potential difference across the same set of electrodes. However, if the contact impedance is comparable to the impedance of the tissue then this two electrode configuration will produce inaccurate result. To eliminate the effect of contact impedance, two separate pairs of electrodes are usually used for current injection and voltage measurements. This method is known as tetrapolar impedance measurement (TPIM). However, conventional TPIM has a rather broad region of spatial sensitivity, and hence not suitable for localization of a small region of interest or a specific target organ [3]. Electrical Impedance Tomography (EIT) uses a number of electrodes fixed circumferentially around the boundary of a volume conductor in a particular plane and images the two dimensional conductivity distribution in that plane under consideration [4]. However, since current flows in 3D, there is significant and complex contribution to the image from points in the 3rd dimension [5]. Thus the individual pixel values of the reconstructed image do not give resistivity distribution expected. In many applications including the study of stomach emptying, pulmonary function study, a region of interest is usually marked out in the EIT image and the time progression of the sum of all the pixels within the region is followed for a dynamic study [6]. In some applications, a single target object may be studied at different frequencies if its impedance has frequency dependence comparted to that of the background [7]. For localized impedance measurement on a region of interest minimizing contribution from neighbouring regions, a new impedance measurement technique is proposed known as Focused Impedance Method (FIM) [8]-[9]. In FIM two traditional TPIM systems are placed orthogonally around a region of interest as shown in Fig. 1. FIM has so far three variants namely 8, 6 & 4-electrode FIM. Pigeon hole imaging (PHI) is an extension of 6 or 4 electrode FIM techniques [10]-[12]. Fig. 2 shows a schematic of PHI as a matrix of many 4-electrode FIM.

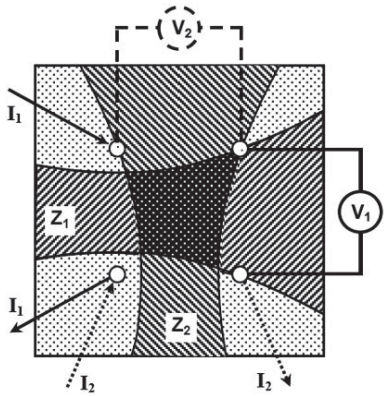


Figure 1. Four electrode configuration of FIM [13]

978-1-5386-2307-7/17/$31.00 ©2017 IEEE

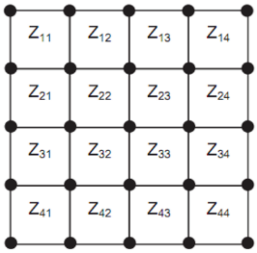


Figure 2. 4×4 PHI imaging matrix based on 4 electrode FIM [12]

In PHI, spatial distribution of conductivity along the surface of a volume conductor giving information to a certain depth can be obtained by measuring the voltage on its surface. The voltage is excited by a small constant current that flows through the surface in various directions including the third dimension. Thus, PHI is a bridge between more complex EIT and simpler FIM. Because of the 3D distribution of electrical currents, organs within certain depths, typically of the order of the electrode separation, can be detected and monitored using skin surface electrodes [14]-[15]. The reconstruction algorithm of PHI aims to obtain an image of an unknown impedance distribution from surface measurements. Previously, there was an attempt to detect the position of an object inside the volume conductor using PHI [16]. However, there was no indication of the depth and shape information of the object. Moreover, all negative sensitivity values were ignored. The object detection and localization process requires careful understanding of the 3D sensitivity distribution within a volume conductor and based on this information a method could be developed to reconstruct the image. There is some inherent problem in PHI imaging such as the object to be located can either have higher or lower impedance within the volume conductor. The objective of this work is to develop a suitable reconstruction algorithm in order to improve PHI imaging performance in terms of image quality and robustness. The motivation is to provide a reliable, real-time, portable and cost efficient imaging tool.

## II. MATERIALS AND METHODS

### *A. Model Description*

The present work was performed on finite element method (FEM) based multi-physics simulation software COMSOL Multiphysics (5.1). Fig.3 shows the Comsol model of a volume conductor together with the placement of electrode array and the corresponding FEM mesh representation for simulation of impedance measurements. The mesh type used in this study was 'fine' generated using the meshing tool of Comsol Multiphysics software. The volume conductors representing body fluid were modeled as cubes of size 30cm×30cm×30cm and 50cm×50cm×50cm for 5×5 and 6×6 PHI matrix respectively.

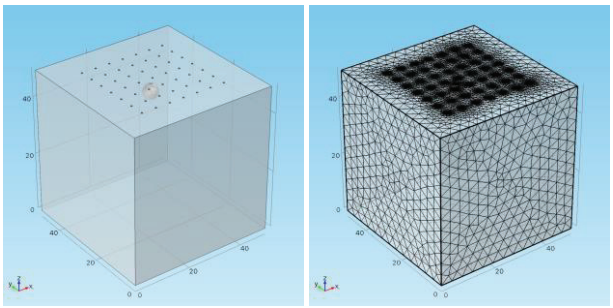

(a) (b)

Figure 3. (a) COMSOL model of the phantom with object below the surface and electrodes on top (b) Corresponding mesh representation of FEM Model

Inhomogeneity in the form of spherical objects (representing body organ e.g. liver, muscle) of different diameter and different conductivity were embedded within the volume conductor. The cross sectional view of the model setup is shown in Fig. 4. For current injection and voltage measurement, electrodes were used which are modeled as cylindrical in shape. The dimension of electrodes are 0.25 cm radius and height of 0.1 cm. COMSOL AC/DC module is used for current injection and voltage measurement.

### *B. Electrode Placement for Impedance Measurement*

In this study, 5×5 and 6×6 matrix of 4 electrode FIM are used to obtain PHI. A total of 36 and 49 electrodes are placed on the surface of the volume conductor in case of 5×5 and 6×6 PHI respectively. The electrode separation is kept 5 cm and the distance between the edge of the volume conductor and the nearest electrode is kept 2.5 cm and 10 cm for 5×5 and 6×6 PHI respectively. Here, electrical impedance is measured twice and the arrangement is depicted in Fig. 5. At first, current ($I_1$=I) is injected on electrode 1 and 2 as shown in Fig. 5 and the voltage ($V_1$) is measured on electrode 3 and 4. Then the whole arrangement is shifted by 90 degrees where current ($I_2$=I) is applied in electrode 2 and 3 and voltage ($V_2$) is measured on electrode 1 and 4. The impedance (Z) is calculated by $Z_1=V_1/I_1$ and $Z_2=V_2/I_2$. The average of these two values is taken as the focused impedance (FZ) reading. Here, I=1A current is applied on the electrodes and frequencies were 10, 20 & 40 kHz.

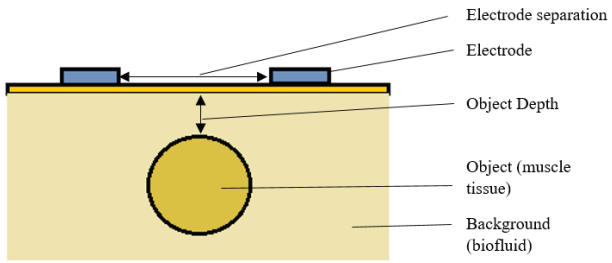


Figure 4. Cross sectional view of the study setup

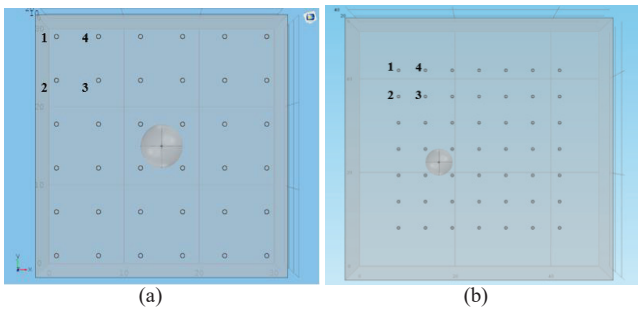


(a) (b)

Figure 5. Electrode placement for impedance measurement (a) for 5×5 PHI and (b) for 6×6 PHI

### C. *Material Properties*

The electrical properties, i.e., permittivity and conductivity of the body fluid, the liver tissue, the muscle tissue and the steel electrodes were taken into consideration. The conductivity and relative permittivity values of the materials used at different frequencies are listed in Table I. These data are collected from an internet resource for the calculation of the dielectric properties of body tissues [17].

TABLE I. CONDUCTIVITY AND RELATIVE PERMITTIVITY OF THE MATERIALS USED IN THE MODEL AT DIFFERENT FREQUENCIES

| Name of the Material | Frequency (kHz) | Conductivity (S/m) | Relative Permittivity |
|---|---|---|---|
| Body fluid | 10 | 1.5 | 98.919 |
| | 20 | 1.5 | 98.837 |
| | 40 | 1.5 | 98.657 |
| Liver tissue | 10 | 0.053495 | 28930 |
| | 20 | 0.060719 | 18516 |
| | 40 | 0.068968 | 12100 |
| Muscle tissue | 10 | 0.34083 | 25909 |
| | 20 | 0.34488 | 15521 |
| | 40 | 0.34977 | 10988 |
| Steel AISI 4340 (electrode) | - | 4.032×10^6 | 1 |

### D. *Variation of Position, Depth and Diameter of the Object*

Position of object is varied inside the volume conductor keeping depth and diameter fixed. At first, single object is placed at various position inside the volume conductor. After that multiple objects are placed at various positions inside the volume conductor. The diameter of the object is also varied keeping position and depth of center fixed in this work. For 5 cm electrode separation, the diameter of the object is varied from 0.5 cm to 5 cm with center depth fixed at 2.5 cm. Measurement is also performed for 6 cm and 10 cm diameter of the object keeping 5 cm electrode separation and object center depth at 3 cm and 5 cm respectively.

### E. *Image Reconstruction Algorithm*

The aim of this work was to develop an effective algorithm for pigeon hole imaging. The impedance values obtained by the surface electrodes for the body fluid i.e. the volume conductor without any object is shown in Fig. 6. Since there is no object placed inside the volume conductor, the measured impedance values should be same with minor deviations.

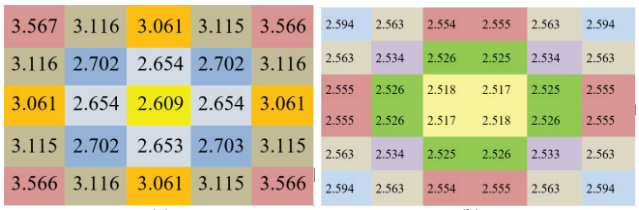


(a) (b)

Figure 6. Impedance values obtained for volume conductor without any objects (a) for 5×5 PHI and (b) for 6×6 PHI

But a definitive pattern is observed in the measured impedance values for the volume conductor without any object. This happens due to the fact that the PHI electrodes are placed very close (in case of 5×5 PHI only 2.5 cm from the edges) to the edges or boundaries of the volume conductor. This boundary effect causes distortion in the current paths and since the volume conductor is cubic which is symmetrical, the current lines and equipotential lines in the cube will have definite patterns which in turn results in this observed pattern in the measured impedance values. The boundary effect is depicted in Fig. 6 by assigning a unique color to similar values of the impedance. This effect is more intense in case of 5×5 PHI than 6×6 PHI due to the fact that the distance between the boundary of the volume conductor and the nearest electrode is kept 2.5 cm and 10 cm for 5×5 and 6×6 PHI respectively. This effect is considered while developing an imaging algorithm. To minimize this effect, the boundary of the volume conductor should be, if possible, kept as far as the measurement setup (at least twice the electrode separation as this study suggests). Additionally, a simple compensation method is proposed in this work for calibration, if the shape or dimension of the volume conductor as well as electrode position is known prior to the measurement. The respective weighted values for each pixel corresponding to a uniform background can be determined from an electrically homogeneous volume conductor having same dimension or shape as the actual volume conductor in which the measurement is to be performed. These weights can be used to determine the weighted average of the impedance values of the actual measurement. The reconstruction algorithm is developed considering the fact that the impedance of the object to be located will have higher or lower value than the surrounding regions. If the arithmetic average of all the pixel values of the PHI matrix is calculated, then the pixel containing the object will have different value than this arithmetic average. Each pixel value is subtracted from the weighted (in case of boundary effect) or arithmetic average values to generate color scaled PHI image using MATLAB software. The process is described in Fig. 7. This method was used to obtain images for different placement of objects for both the 5×5 and the 6×6 PHI systems and the results are given in the next section.

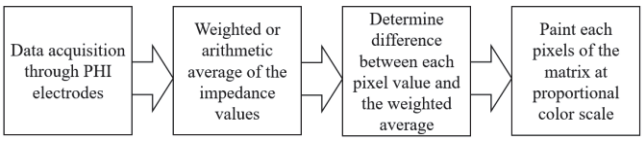


Figure 7. Proposed method for PHI imaging

## III. RESULTS

Fig. 8 shows 6×6 PHI image of muscle tissue placed at position (2,4) inside the body fluid obtained through the proposed algorithm with the matrix positions described as (row, column).

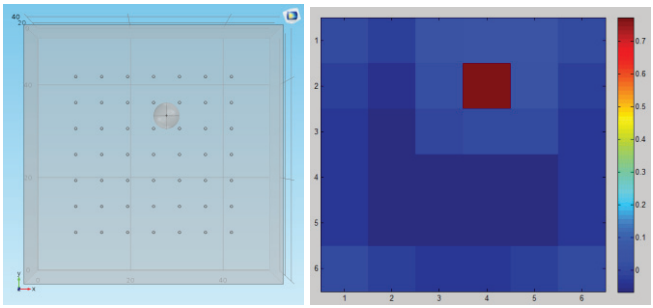

Figure 8. 6×6 PHI for one object placed inside the volume conductor

The effect of calibration is shown in Fig. 9. In case of 5×5 PHI object was placed at (3,4) and for 6×6 PHI, at (4,2). Since the distance between the boundary of the volume conductor and the nearest electrode is kept half the electrode separation in case of 5×5 PHI and twice the electrode separation in case of 6×6 PHI, no significant improvement was observed after calibration of 6×6 PHI but without calibration 5×5 PHI image was distorted and gives incorrect result. The 6×6 PHI images produced from four simulated data sets following the scheme mentioned above are shown in Fig. 10 for objects placed at different positions. These images were generated without calibration i.e. taking arithmetic mean only. Top left of Fig. 10 shows two muscle tissues placed at positions (2,5) & (4,2) and top right of the same figure shows liver and muscle tissues placed at positions (2,4) & (4,2) respectively. Bottom left of the Fig. 10 shows three muscle tissues placed at positions (2,2), (2,3) and (5,6). Here, each object slightly increases impedance in their neighboring regions so in this case two adjacent objects increases each other's impedance value and gives more red than the object at position (5,6).

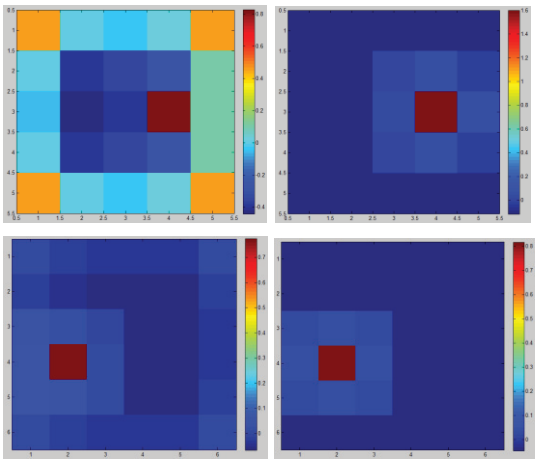

Figure 9. Effect of calibtration on PHI, top left and top right shows 5×5 PHI without and with calibration respectively; bottom left and bottom right shows 6×6 PHI without and with calibration respectively

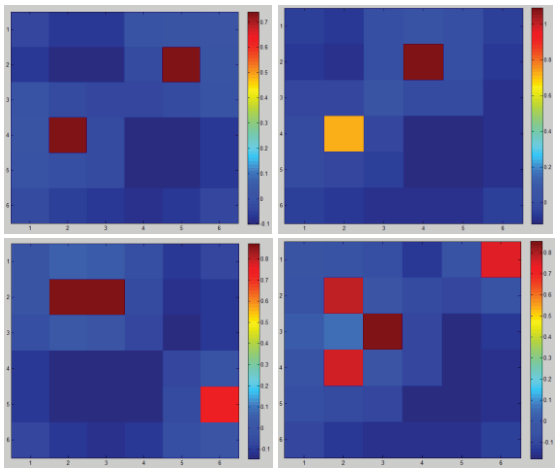

Figure 10. 6×6 PHI for two, three and four objects placed at different positions without performing calibration

Similar situation is observed in case of four muscle tissues in the bottom right image of Fig. 10. The effect of higher and lower impedance of the object than the volume conductor is depicted in Fig. 11. Four muscle tissues having higher impedance than body fluid are placed at (1,6), (2,2), (3,3) and (4,2) position and steel having lower impedance than body fluid is placed at (5,5) position. The color scale clearly shows higher and lower impedance values. It is observed that PHI has 3D sensitivity just like FIM. This phenomenon is shown in Fig. 12. At a particular depth, the differences of the impedance at different positions is due to the boundary effect mentioned earlier. The arithmetic average value for background i.e. biofluid for 6×6 PHI is 2.548 ohms. From Fig. 12 it can be observed that the muscle tissues having minimum impedance that can be distinguished from body fluid are at least 5 cm deep from the surface. This distance is also equal to electrode separation. Diameter of the object was also varied keeping a fixed center and position. The resulting graph is shown in Fig. 13. Also due to boundary effect, different impedances were observed at a particular diameter at different positions. The minimum diameter of the muscle tissue to have a distinguishable impedance than the body fluid is 2 cm which is of the order of half the electrode separation. Simulated data sets were also generated by varying the frequency of the injecting current from 10 kHz to 40 kHz but no significant change in the PHI image was observed.

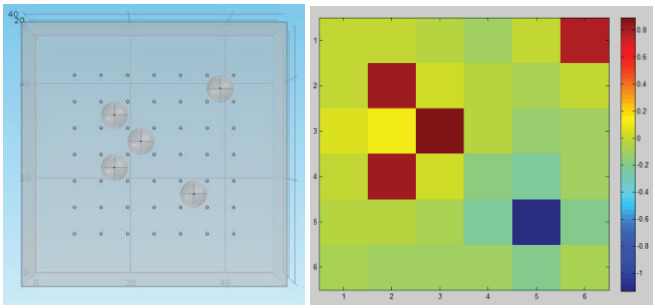

Figure 11. 6×6 PHI image showing objects with higher (red) and lower (blue) impedance with respect to that of background (green) corresponding to the different object placement in the volume conductor (left)

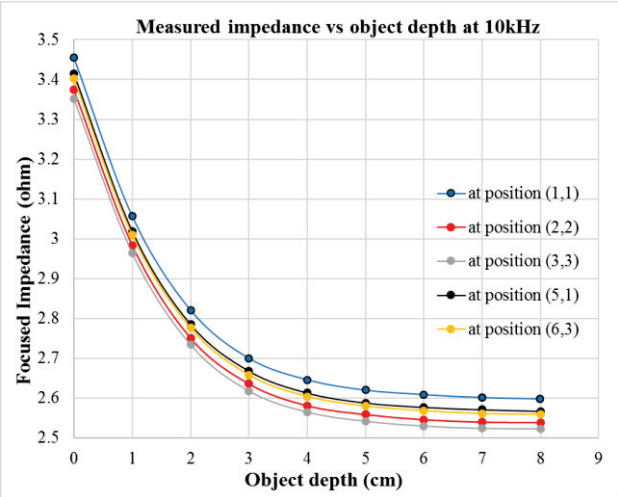


Figure 12. Measured impedance vs. object depth at fixed positions at 10kHz with 5cm object diameter and 5cm electrode separation for 6×6 PHI

## IV. DISCUSSION

The newly developed algorithm fairly detects objects placed at various positions in the PHI matrix. Based on this study it is suggested that the minimum impedance difference should be 0.1 ohms to give meaningful PHI image. Since only a few materials were used to perform this simulation work, no conclusive decision can be made about the depth and diameter of the object inside the volume conductor. But it can be inferred that if any object is detected at a particular position, then it must be at least 5 cm deep from the surface and its diameter is at least 2 cm where electrode separation was kept at 5 cm. Although for the simulation using COMSOL MPH a sinusoidal current amplitude of 1A was used for convenience, for practical measurements on human subjects a safe value of current-amplitude at a particular frequency should be used according to IEC [18].

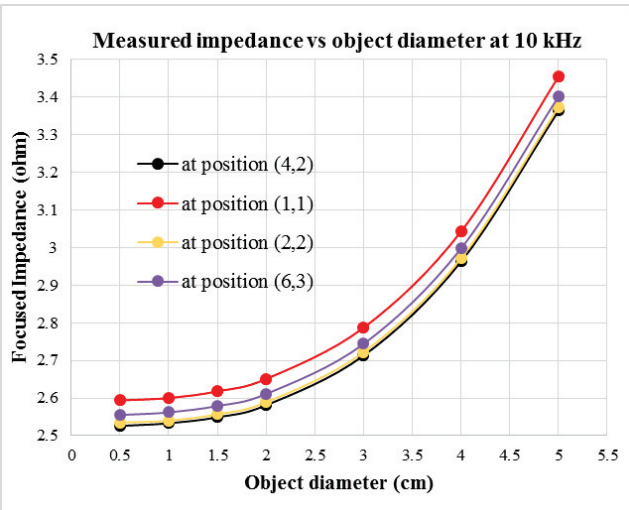


Figure 13. Measured impedance vs. object diameter at fixed positions at 10kHz with object center at 2.5 cm and 5cm electrode separation for 6×6 PHI

If two adjacent objects were detected than it should be confirmed by moving PHI electrodes along the surface of the volume conductor as one object may be positioned in between the two adjacent pixels of PHI image. To minimize the boundary effect, the volume conductor should be kept at least twice the electrode separation as this study suggests. Moreover, the weighted values for the calibration for some common shapes like cubic, spherical or cylindrical for different electrode placements can be calculated and stored in the PHI device prior to perform actual measurement. The shape information of the object can be improved by repeating block of n×n PHI matrix or increasing PHI matrix size and decreasing the electrode separation to cover a fixed surface area. However, this will cause the loss of depth sensitivity as suggested by this work as well as previous work on 4 electrode FIM [3]. So, based on the objective, a trade off should be made or a separate set of the electrode should be used to extract information about the depth of the object. However, this will require a more complex algorithm and instrumentation to be developed. However, any electrode system other than two electrode method, actually measures the transfer impedance between drive and receive electrodes. It should be noted that the measured transfer impedance may not represent the actual value of bioimpedance [19]. Electrode uncertainty is another degradation of PHI performance. For example, electrode movement, variable electrode contact impedance, and drift in the electronics can produce dramatic artefacts in images. Other than hardware improvements, reconstruction algorithms need to be upgraded to compensate model errors and be robust against electrode uncertainty. This is a prerequisite to bring PHI, a promising medical imaging modality, into routine clinical applications. Extensive research work must be performed by varying frequency of the applied current, materials, electrode separation and geometry of the electrode as well as volume conductor in order to extract more information from PHI image. Moreover, machine learning algorithms may also be used to improve PHI image quality. There exist many imaging modalities including ultrasound, X-ray, CT, MRI, EIT that are used for diagnostic purposes. However, these modalities are either sophisticated, or lack portability and not appropriate for real time imaging because of ionizing exposure. As the method is technically simple and of potentially low cost, the technology can be adopted easily for local manufacture, making its service affordable and sustainable.

## V. CONCLUSION

Impedance measurements for PHI were simulated using the FEM based software COMSOL Multiphysics. A robust algorithm was developed for imaging the conductivity distribution beneath the PHI electrode array by analyzing impedance values measured by placing electrodes on the surface of a volume conductor. The developed algorithm can detect the presence and location of embedded objects within a volume conductor. The algorithm is more effective for objects with diameter at least of the order of half the electrode separation with depth equal to or less than electrode separation. Again, shape of the objects is not evident in the reconstructed image. Still, the presence and localization of objects is useful in many applications including organ localization and subcutaneous vein detection [20]. Being a non-ionizing method

there is a potential of PHI in long term monitoring of physiological events. However, the proposed algorithm needs to be evaluated in phantom and human subjects to justify its application in practice.

## ACKNOWLEDGMENT

The authors acknowledge the financial support of the International Science Programme (ISP) of Uppsala University, Sweden through which the COMSOL Multiphysics software license was procured.

## REFERENCES

[1] A. Pietrobelli, F. Rubiano, M. P. St-Onge, and S. B. Heymsfield. "New bioimpedance analysis system: improved phenotyping with whole-body analysis." *European journal of clinical nutrition, vol.* 58, no. 11, pp. 1479-1484, 2004.

[2] A. Piccoli, B. Rossi, L. Pillon, and G. Bucciante. "A new method for monitoring body fluid variation by bioimpedance analysis: the RXc graph." *Kidney international, vol.* 46, no. 2, pp. 534-539, 1994.

[3] S. P. Ahmad, M. A. Kadir, G. D. Al-Quaderi, R. Rahman and K. S. Rabbani, "Improved understanding of the sensitivity of linear tetrapolar impedance measurement (TPIM) and 8-electrode focused impedance method (FIM) in a volume conductor," *Bangladesh Journal of Medical Physics*, vol. 8, pp. 22–31, 2015.

[4] D. C. Barber, B. H. Brown and I. L. Freeston, "Imaging spatial distributions of resistivity using applied potential tomography," *Electron. Lett. 19,* pp. 933–5, 1983.

[5] K. S. Rabbani, and A. M. B. H. Kabir. "Studies on the effect of the third dimension on a two-dimensional electrical impedance tomography system." *Clinical Physics and Physiological Measurement, vol.* 12, no. 4, pp. 393, 1991.

[6] N. D. Harris, A. J. Suggett, D. C. Barber and B. H. Brown, "Applications of applied potential tomography (APT) in respiratory medicine," *Clin. Phys. Physiol. Meas. 8 (Suppl. A)*, 1987 pp. 155-65.

[7] D. C. Barber, B. H. Brown, W. Wang, L. Lu, A. D. Leathard, R. H. Smallwood, A. R. Hampshire, R. Mackay and K. Hatzigalanis, "Multi-frequency imaging and modelling of respiratory related electrical impedance changes," *Physiol. Meas. suppl. A 15*, 1994, pp. A1–A12.

[8] K. S. Rabbani, M. Sarker, M. H. R. Akond and T. Akter, "Focused impedance measurement (FIM) – a new technique with improved zone localization in "Electrical Bioimpedance methods"," *Annals of the New York Academy of Sciences,* vol. 873, pp. 408–420, 1999.

[9] K. S. Rabbani and M. A. S. Karal, "A new four-electrode focused impedance measurement (FIM) system for physiological study," *Annals of Biomedical Engg. (Springer, US)*, vol. 36, no. 6, pp. 1072–1077, 2008.

[10] K. Afroj, N. Alam, M. Rahman and K. S. Rabbani, "Pigeon hole imaging (PHI) – an electrical admittance backprojection technique," *Bangladesh Journal of Medical Physics*, vol. 3, pp. 7–13, 2004.

[11] K. Afroj and K. S. Rabbani, "An image smearing technique to improve pigeon hole imaging (PHI)," *Bangladesh Journal of Medical Physics*, vol. 4, no. 1, pp. 11–20, 2011.

[12] A. R. Abir, I. A. Khan and K. S. Rabbani, "Graphical implementation of a new pigeon hole imaging (PHI) technique," in *Proc. of the 4th Int. Symposium on Applied Sciences in Biomedical and Communication Technologies (ISABEL)*, Oct. 2011.

[13] K. S. Rabbani and M. A. Kadir, "Possible applications of focused impedance method (FIM) in biomedical and other areas of study," *Bangladesh Journal of Medical Physics*, vol. 4, no. 1, pp. 67–74, 2011.

[14] A. H. M. Iquebal and K. S. Rabbani, "3D sensitivity of 6-electrode focused impedance method (FIM)," *Journal of Physics: Conference Series*, 224, 012156, 2010.

[15] M. A. Kadir, S. P. Ahmed, G. D. Al-Quaderi, R. Rahman and K. S. Rabbani, "Application of the focused impedance method (FIM) to determine the volume of an object within a volume conductor*," in Proc. COMSOL Conference, Bangalore*, India 2013.

[16] A. R. Abir and K. S. Rabbani, "Sensitivity study for a 4-electrode focused impedance method (FIM) using finite element method analysis," *Bangladesh Journal of Med. Physics*, vol. 7, pp. 1–7, 2014.

[17] (2017) An internet resource for the calculation of the dielectric properties of Body Tissues in frequency range 10 Hz-100 GHz. [Online]. Available: http://niremf.ifac.cnr.it/tissprop/

[18] *Safety of Medical Electrical Equipment: Part 1, General requirements Publ., 601–1*, International Electrotechnical Commission (IEC), 2015.

[19] Ø. G. Martinsen and S. Grimnes, "The concept of transfer impedance in bioimpedance measurements," *IFMBE Proceedings* 22, pp 1078-1079, 2008.

[20] R. Z. Rusho and M. A. Kadir, "Subcutaneous vein detection using pigeon hole imaging: simulation study", in *Proc. The fifth IEEE Region 10 (Asia Pacific) Humanitarian Technology Conference (R10HTC)*, Dhaka, December 2017. "in press"

# A New Approach of Brain MRI Analysis for Identifying Creutzfeldt-Jakob Disease (CJD)

Akib Jayed Islam[1*], Khandoker Tanjim Ahammad[2], Bithi Barua[3], Sadman Shahriar Alam[4], Akash Biswas[5]
[1,5]Department of EEE, American International University-Bangladesh (AIUB), Dhaka, Bangladesh
[2]Department of Microelectronics and Microsystems, Technische Universität Hamburg, Germany
[3]Dept. of Electronics and Communication Engineering (ECE), Khulna University of Engineering & Technology, Bangladesh
[4]Department of Electronic Systems, Norwegian University of Science & Technology, Norway
*E-mail: akibjayedislam@gmail.com

*Abstract*— **Creutzfeldt-Jakob disease (CJD) is an uncommon, degenerative, invariably destructive brain infection which is difficult to analyze, especially during its early stages. CJD is considered as prion infection and can do harm in the brain when it is developing as a misshapen form. By analyzing the characteristic of Magnetic Resonance Imaging (MRI) signal changes, prion disease can be identified. But till now in the diagnosis of Creutzfeldt-Jakob disease, MRI images are rather not utilized. By further processing brain MRI, advance CJD can be detected and pinpointed more efficiently. To have a mean of comparison, MRI scans of both a healthy patient and symptomatic patient are reviewed in this study. This paper is focused on CJD MRI analysis of head scans in order to determine caudate and putamen for identifying the existence of brain tissue using a new algorithm. To determine the difference of brain tissue between the MRI of healthy and CJD affected image with the help of pixel counting approach by analyzing the image block by block. The proposed algorithm performs to identify a CJD diseased image from a healthy image of brain MRI, image segmentation is partitioned by image preprocessing stage, image enhancement stage and pixel counting stage. To determine the parts of the brain affected by CJD, MRI scans of infected patients was taken as input. The healthy patients' scans are also later tested with the proposed program to check if the proposed algorithm produces any false positives or not.**

**Keywords— Creutzfeldt-Jakob disease, Dementia, Prion, MRI, Pixel counting.**

## I. INTRODUCTION

Creutzfeldt-Jakob disease (CJD) is caused by the cerebral accumulation misshapen protein. This protein is devoid of typical hereditary component and habitually deadly [1]. It is demanding to recognize in the early stage [2]. CJD is also known as human prion disease and it is a rare one which is hastily growing structure of dementia generated by infectious proteins called prions. Prion proteins affected brain and annihilate brain cells while changing their shapes [3-4]. CJD can be destructive as an iatrogenic, sporadic and genetic fatal neurodegenerative disorder [5]. Three types of CJD have been identified as sporadic, genetic and acquired. Parents who are affected by genetic types of CJD, have a fifty percent chance of transferring it to their children. Sporadic CJD precipitated patient generally die within a year without showing any warning. Acquired CJD is created by tissue contamination from a diseased person. Blood transfusion, gonadotropin hormone therapy, and corneal and meningeal transplants from an infected person are the main reasons of transforming CJD [6].

By performing tissue investigation, CJD can be diagnosed except the genetic types. Brain biopsy or autopsy can be performed to diagnose this disease. WHO has explained the symptoms of a CJD patient by using clinical and scrutinize criteria. The genuine criteria contain neurological signs of dementia and the existence of 14.3.3 proteins in characteristic EEG with pseudo-periodic complexes and the Cerebrospinal fluid (CSF). Nowadays, MRI findings are able to provide the sensitivity and more than 90% specificity for portable CJD [7]. These changes comprise alterations on Diffusion-Weighted Image (DWI) and FLAIR images in the basal ganglia, thalamus, and cortex [8-9]. However, the MRI data can be subtle and can easily be unrecognized by a physician unfamiliar with this kind of infrequent infection. Consulting the specialists, in contemplation of altering the natural history of the disease, early diagnosis is the best criterion to give the highest chance of recovering functional brain tissue [10]. Sometimes MRI findings provide noninvasive test assisting recognition so the introduction of imaging features, new algorithms would help the experts to procure the disease more effectively. At present, it is unknown that how often radiologists report about the MRI abnormalities in the cases of definite CJD.

The identification of diagnostic markers is a major challenge in the clinical care of patients with CJD. The literature [11-15] presented notable divergences between diagnosis of CJD and the analysis of the data abnormality in the deep grey matter internal nuclei in MRI of the brain. In this paper, comparisons between CJD and healthy brain MRI are processed. By processing the MRI, CJD can easily be identified. Different strategies can be adopted for recognizing infected area covering the head of putamen using the proposed algorithm. The main objective of this study is to identify the

978-1-5386-2307-7/17/$31.00 ©2017 IEEE

CJD more efficiently, using noninvasive medical imaging techniques and hence provide the infected patient with an accurate medical diagnosis.

## II. MAGNETIC RESONANCE IMAGING (MRI)

The principle of Magnetic resonance imaging (MRI) is based on magnetization properties of atomic nuclei. Typically MRI systems have magnetic field strength of 1.5T. MRI is widely used for noninvasive diagnosis of neurological disease patients. The studies and evidence over fifteen years of MRI hyper-layer signals in CJD patients have been found which presented the early stage diagnosis of CJD [16-17]. MRI is a valuable tool for imaging the brain and adaptations are needed for hardware and sequences. It is very advantageous to perceive brain tissue examinations.

### *A. MRI IMAGING SEQUENCES*

The MRI sequence provides a set of images containing miscellaneous appearance.

#### *1) T1-weighted:*

T1-weighted images are the most basic MRI images consisting of radio frequency pulses. Short TE and TR are required to produce these images. With the help of the dark and bright criterion, the T1 properties of the images can be determined. The fat and fluid of the MRI image is marked as light and dark respectively. For identification process, the magnetization vector of the brain tissues are obtained from the longitudinal relaxation times of brain tissues. Actually, an external magnetic field aligns all the spins of vector and the RF pulses put them on the traverse plane. Then the spins again slide away to their equilibrium condition of external field quickly. Because of this process, T1 weighted images are also regarded as “spin-lattice” relaxation time images. The brain tissues like fat which quickly performs this realignment to the longitudinal magnetization with applied external field appears bright on T1 weighted images. Conversely, the fluid shows as dark because of the slow realignment process. The gandolinium containing compounds in the MRI can be best detected with the help of T1 weighted images [18-19].

#### *2) T-2 weighted:*

T2 weighted images are another type of MRI images producing on the basis of spin echo sequences. Longer TE and TR are essential for identifying the T2 properties of the images. The recognition of the fat and fluid is done by the intermediate bright and bright color in the images. Basically, the relaxation of the magnetization vector of the tissues on the transverse plan produce longer TE and TR. Thus the images are known as “spin-spin” relaxation time images. The detection of tumor surrounded by bright signal of edema can be best detected through T2 sequences. Again the size and the symmetry of ventricles and the “sclerosis” which is the bright signal of the myelin sheath can be diagnosed usingT2 weighted images [19].

In our proposed approach, we have evaluated the task of detecting CJD using T2 weighted MRI images. Here T2 weighted images have been processed as the identification of intermediate bright and the bright properties are required in this approach. Considering the intermediate bright and bright properties, proper identification of the number of fluid and fat presence in the brain tissues is allocated in this task.

## III. PROPOSED APPROACH

In order to identify a CJD image from a healthy image of brain MRI, image segmentation is followed in this work. This is the primary task for image analysis. We have used T2 weighted images in this work as these images are useful in indicating the structure filled with water and localizing the inflammation which results higher volume of water because of the affected tissue. For the case of brain MRI analysis, image segmentation mainly used for dividing the whole image into small partitions to determine and observe the presence of tissue, analyzing the changes in the brain [20].

### *A. Image Segmentation:*

Image segmentation is a computer related task done in the research areas. Many sequential tasks like the extractions of features, recognitions of patterns, registration and compression of images etc. are done in this process, depended on the quality of the segmented image. It is an image-dependent problem.

In this approach, the location identification of a CJD affected image is proposed by the procedure for brain image segmentation.

The classification of a CJD image from a healthy one includes the following stages:

- Image preprocessing stage
- Image enhancement stage
- Pixel counting stage

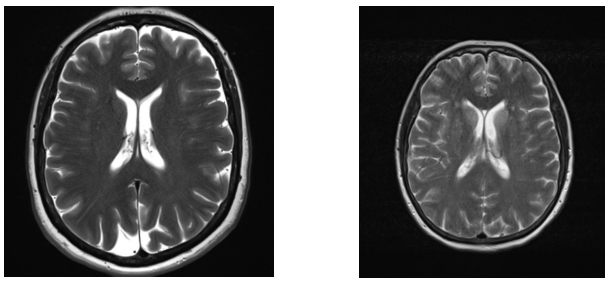

(a) (b)

Fig.1: T2 weighted grayscale image (a) Healthy MRI (b) CJD MRI

(a) (b)

Fig.2: Binary mask from binary image (a) Healthy MRI (b) CJD MRI

(a) (b)

Fig.3: Basic line detection of image after canny edge algorithm (a) Healthy MRI (b) CJD MRI

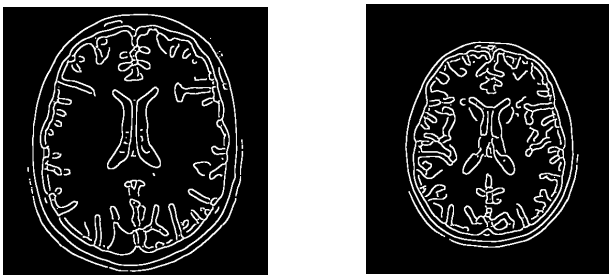

(a) (b)

Fig.4: Dilated images (a) Healthy MRI (b) CJD MRI

*1) Image preprocessing stage:*

In our approach, the segmentation is done in order to extract the brain tissue containing in a brain MRI image. At first the input grayscale T2 weighted image [18-19] shown in Fig.1 which are converted into the binary image. Binary image is the image which represents pixel value of 1 and 0 indicating white and black pixel respectively. Then the binary image is used to produce a filter known as the binary mask shown in Fig.2. This filter is helpful in to smooth the image so that the edges can be extracted from it. After the filtering procedure, canny edge algorithm is used and is applied to detect the basic lines in the image. The basic line detected image is shown in Fig.3. In our work, the edges of white pixels are considered as the brain tissues along with the presence of water in MRI.

*2) Image enhancement stage:*

When the basic line detection is done, the enhancement of the image is applied to the brain MRI by using the dilation procedure. This dilation is helpful for visualizing the white and black pixels perfectly. The amount of dilation should be done in a same proportion to both the healthy and CJD brain MRI. Otherwise the identification of the pixel variation cannot be measured properly. The dilated images for both healthy and CJD images are shown in Fig.4.

*3) Pixel counting stage:*

Pixel counting is the main task of our approach. After enhancing the image, at first the white and black pixel of the whole image is counted.

Here, we have found notable difference of the white pixels. In a healthy brain MRI, the number of the white pixels is higher than a CJD. It evaluates the fact that a CJD affected person's brain MRI contains less brain tissues than a healthy person's. The total counting of pixels from healthy and CJD image is included in TABLE I.

TABLE I. TOTAL NUMBER OF PIXELS FROM HEALTHY AND CJD IMAGES

| **Pixel Type** | **Pixel Number from CJD image** | **Pixel Number from Healthy image** |
|---|---|---|
| Black Pixel | 858601 | 857245 |
| **White Pixel** | **91671** | **93027** |

For our further analysis we have applied Algorithm 1: Pixel counting approach [19] in the brain MRI with a different measurement.

**Proposed Algorithm: Pixel counting for tissue analysis**

**Step 1:** Input image is the dilated image of 1024×928.
**Step 2:** Select a block size of 200×200 to divide the whole image.
**Step 3:** Start the process of pixel counting from block 1.
**Step 4:** Count the number of white and black pixels from every block.
**Step 5:** Continue the procedure for whole partitioned image.

In this approach, the whole image gets allocated with 20 blocks. This block by block analysis is followed in this approach in order to find from which position the disease is formulated as the number of the white pixels have a significant low value in that area. The data of pixel counting from the MRI images are included in TABLE II.

TABLE II. NUMBER OF PIXELS FROM BLOCKS OF HEALTHY AND CJD IMAGES

| Block Number | Pixel Number from CJD Image | | Pixel Number from Healthy image | |
|---|---|---|---|---|
| | Black | White | Black | White |
| 1 | 40000 | 0 | 39804 | 196 |
| 2 | 38713 | 1287 | 34152 | 5848 |
| 3 | 36226 | 3774 | 33009 | 6991 |
| 4 | 39530 | 470 | 35806 | 4194 |
| 5 | 39639 | 361 | 37116 | 2884 |
| 6 | 31930 | 8070 | 35707 | 4293 |
| 7 | 32225 | 7775 | 34887 | 5113 |
| 8 | 33223 | 6777 | 33288 | 6712 |
| 09 | 37935 | 2065 | 35775 | 4225 |
| 10 | 31620 | 8380 | 39158 | 842 |
| 11 | 33524 | 6476 | 35020 | 4980 |
| 12 | 30955 | 9045 | 36956 | 3044 |
| 13 | 37935 | 2065 | 35090 | 4910 |
| 14 | 32995 | 7005 | 37644 | 2356 |
| 15 | 34462 | 5538 | 35874 | 4126 |
| 16 | 32715 | 7285 | 34274 | 5726 |
| **17** | **40000** | **0** | **38611** | **1389** |
| 18 | 35276 | 4724 | 32599 | 7401 |
| 19 | 33047 | 6953 | 32243 | 7757 |
| 20 | 36748 | 3252 | 33804 | 6196 |

In our simulation we have found 20 blocks for both the cases of the images. Comparing the results, we have estimated that on average the number of white pixels is lower in CJD than healthy image. A significant result can be observed at block 17 where the number of white pixels is 0 compared to 1389 white pixel is present in healthy image. It indicates that the area of block 17 is highly affected by CJD as the amount of brain tissues has been lessened greatly. This result gives a conclusion that the localization of CJD affected area of brain MRI can be allotted using the block by block analysis.

## IV. FUTURE WORK

Our proposed approach is evaluated on the basis of image data analysis both for CJD and healthy images. T2 weighted image is examined for our approach initially. But in future this approach can be applied to the other imaging sequences of MRI like T1 weighted image, Flair and DWI. Gathering all the image data from different sequences of imaging, a 3D model of brain MRI can be generated locating the common positions of CJD affected areas.

## V. CONCLUSION

MRI is a valuable device in the identification of CJD. However variations in signal are often missed at the first stage of scan. Even after the initial imaging, advanced diagnosis of CJD should be examined with the help of expert MRI analyst or by an experienced neuroradiologist. The main purpose of this research is to identify CJD more easily and effectively. Using the proposed feature analysis, CJD affected MRI data are evaluated and the proposed algorithm is developed to detect the affected parts by CJD. The reports for a healthy brain MRI as well as the CJD injured MRI are differentiated to see if the proposed algorithm works perfectly or not.


## ACKNOWLEDGMENT

Authors would like to express gratitude to Mr. Tajwar Abrar Aleef, who is currently enrolled in Erasmus Mundus Joint Master Degree in Medical Imaging and Applications program, for his invaluable guidelines for exploring the facets of this work.


## REFERENCES


[1] Wille, Holger, Melissa D. Michelitsch, Vincent Guénebaut, Surachai Supattapone, Ana Serban, Fred E. Cohen, David A. Agard, and Stanley B. Prusiner. "Structural studies of the scrapie prion protein by electron crystallography." *Proceedings of the National Academy of Sciences* 99, no. 6 (2002): 3563-3568.

[2] Geschwind, Michael D., Huidy Shu, Aissa Haman, James J. Sejvar, and Bruce L. Miller. "Rapidly progressive dementia." *Annals of neurology* 64, no. 1 (2008): 97-108.

[3] Perry, David C., and Michael D. Geschwind. "Prion disease: thorough work-up and new diagnostic criteria needed for CJD." *Nature Reviews Neurology*7, no. 9 (2011): 479-480.

[4] Public Health Agency of Canada (2007). CJD and human prion diseases. [Online: Accessed June 9, 2017] Available: http://www.phac-aspc.gc.ca/index-eng.php.

[5] Collinge, John. "Prion diseases of humans and animals: their causes and molecular basis." Annual review of neuroscience 24, no. 1 (2001): 519-550.

[6] Creutzfeldt-Jakob disease | Alzheimer Society of Canada [Online: Accessed March 2016]. Available: http://www.alzheimer.ca

[7] Zerr, Inga, K. Kallenberg, D. M. Summers, C. Romero, A. Taratuto, U. Heinemann, M. Breithaupt et al. "Updated clinical diagnostic criteria for sporadic Creutzfeldt-Jakob disease." *Brain* 132, no. 10 (2009): 2659-2668.

[8] Young, Geoffrey S., Michael D. Geschwind, Nancy J. Fischbein, Jennifer L. Martindale, Roland G. Henry, Songling Liu, Ying Lu et al. "Diffusion-weighted and fluid-attenuated inversion recovery imaging in Creutzfeldt-Jakob disease: high sensitivity and specificity for diagnosis." *American Journal of Neuroradiology* 26, no. 6 (2005): 1551-1562.

[9] Tschampa, Henriette J., Kai Kallenberg, Horst Urbach, Bettina Meissner, Claudia Nicolay, Hans A. Kretzschmar, Michael Knauth, and Inga Zerr. "MRI in the diagnosis of sporadic Creutzfeldt–Jakob disease: a study on inter-observer agreement." *Brain* 128, no. 9 (2005): 2026-2033.

[10] Collinge, John, Michele Gorham, Fleur Hudson, Angus Kennedy, Geraldine Keogh, Suvankar Pal, Martin Rossor et al. "Safety and efficacy of quinacrine in human prion disease (PRION-1 study): a patient-preference trial." *The Lancet Neurology* 8, no. 4 (2009): 334-344.

[11] Chitravas, Numthip, Richard S. Jung, Diane M. Kofskey, Janis E. Blevins, Pierluigi Gambetti, R. John Leigh, and Mark L. Cohen. "Treatable neurological disorders misdiagnosed as Creutzfeldt-Jakob disease." *Annals of neurology* 70, no. 3 (2011): 437-444.

[12] Peden, A., L. McCardle, M. W. Head, S. Love, H. J. T. Ward, S. N. Cousens, D. M. Keeling, C. M. Millar, F. G. H. Hill, and J. W. Ironside. "Variant CJD infection in the spleen of a neurologically asymptomatic UK adult patient with haemophilia." *Haemophilia* 16, no. 2 (2010): 296-304.

[13] Chohan, Gurjit, Catherine Pennington, Jan M. Mackenzie, M. Andrews, Dawn Everington, Robert G. Will, R. S. G. Knight, and A. J. E. Green. "The role of cerebrospinal fluid 14-3-3 and other proteins in the diagnosis of sporadic Creutzfeldt–Jakob disease in the UK: a 10-year review." *Journal of Neurology, Neurosurgery & Psychiatry* (2010): jnnp-2009.

[14] Heinemann, U., A. Krasnianski, B. Meissner, D. Varges, K. Kallenberg, W. J. Schulz-Schaeffer, B. J. Steinhoff, E. M. Grasbon-Frodl, H. A. Kretzschmar, and I. Zerr. "Creutzfeldt–Jakob disease in Germany: a prospective 12-year surveillance." *Brain* 130, no. 5 (2007): 1350-1359.

[15] Vitali, Paolo, Elio Maccagnano, Eduardo Caverzasi, R. G. Henry, A. Haman, C. Torres-Chae, D. Y. Johnson, B. L. Miller, and M. D. Geschwind. "Diffusion-weighted MRI hyperintensity patterns differentiate CJD from other rapid dementias." *Neurology* 76, no. 20 (2011): 1711-1719.

[16] MD. David C Preston, "MRI Basics." [Online: Accessed: 13-Feb-2017]. Available: http://case.edu/medicine.

[17] Teitelbaum, George P., et al. "MR imaging of neurocysticercosis." *American Journal of Roentgenology* 153.4 (1989): 857-866.

[18] ."Creutzfeldt-Jakob disease (CJD) | Radiology Case | Radiopaedia.org." [Online]. Available: https://radiopaedia.org/cases/creutzfeldt-jakob-disease-cjd-3. [Accessed: 01-May-2017].

[19] "Normal brain: MRI | Radiology Case | Radiopaedia.org." [Online]. Available: https://radiopaedia.org/cases/normal-brain-mri-3. [Accessed: 01-May-2017].

[20] B. Barua and M. M. Hasan, "A new approach of detection and segmentation of blood vessels for the classification of healthy and diseased retinal images," *2016 3rd International Conference on Electrical Engineering and Information Communication Technology (ICEEICT)*, Dhaka, 2016, pp. 1-6.

2017 3rd International Conference on Electrical Information and Communication Technology (EICT), 7–9 December 2017, Khulna, Bangladesh

# Modified High Frequency Phase Disposition Pulse Width Modulation for Modular Cascaded H-bridge Multilevel Converters

Md. Ashib Rahman* and Md. Rabiul Islam*
*Department of Electrical and Electronic Engineering
*Rajshahi University of Engineering & Technology, Rajshahi-6204, Bangladesh
Email: m.rahman.bd@ieee.org and rabiulbd@hotmail.com

***Abstract*—Modulation plays a vital role for the proper and reliable operation of power converters. For high power and medium voltage applications, cascaded H-bridge (CHB) multilevel converters (MLC) are becoming industry standard. In this article, a modified high frequency phase disposition pulse width modulation (PDPWM) technique is proposed. The proposed technique is applied to 1.0 MVA 3.0 kV, 3-phase 5-level CHB converter to validate the improved performance regarding total harmonic distortion (THD), suppression of lower order harmonics and less bulky filtering circuitry. As a reference for modulation, third harmonic injected sixty degree bus clamped signals are applied to the proposed phase disposed carrier signals. All the simulation works are carried out in MATLAB/Simulink environment.**

***Keywords*—Modulation, multilevel converter, H-bridge.**

## I. Introduction

Since the first proposal of multilevel converter (MLC) in 1975 [1], they (2.3–30 kV, 0.3–32 MVA) are replacing the conventional two or three level converters and becoming industry standard for the implementation of most modernized, medium (0.1–5.0 MW) to large scale (6.0–50 MW) micro-grid system. The MLC can be designed to operate in particular higher voltage levels which completely eliminates the use of any low frequency, heavy step-up transformers (50–70% of converter weight and 30–50% of drive size are characterized by transformer [2]) and removes bulky filtering circuitry (43 level MLC) [3]. In this work, the cascaded H-bridge (CHB) MLC is selected for its superior qualities. Since the first appearance of CHB in 1988 [4], this technology is standardized with a power range of 0.15–120 MW and frequencies up to 330 Hz [5]. Currently, the CHB MLCs are applied in medium voltage, high power drive markets with maximum rating of 13.8 kV, 1400 A and 31.0 MVA [6].

Modulation plays a crucial role for extracting proper outcome from MLC. $L$ level converter utilizes $L-1$ carrier signals. So, there exists certain 'control freedom degree (CFD)' in choosing different parameters of carrier and reference signals like: frequency, amplitude, phase angle, offsets between carries and adding zero sequence voltage (triplen harmonics) or not [7]. Therefore, based on the combination of various parameters mentioned above, diverse modulation techniques have been investigated [8]. Normally, pulse width modulation (PWM) methods are classified as low frequency and high frequency modulation. Carrier based modulation is termed as high frequency modulation where the high frequency carrier signals are compared to fundamental frequency reference signals for gate pulse generation.

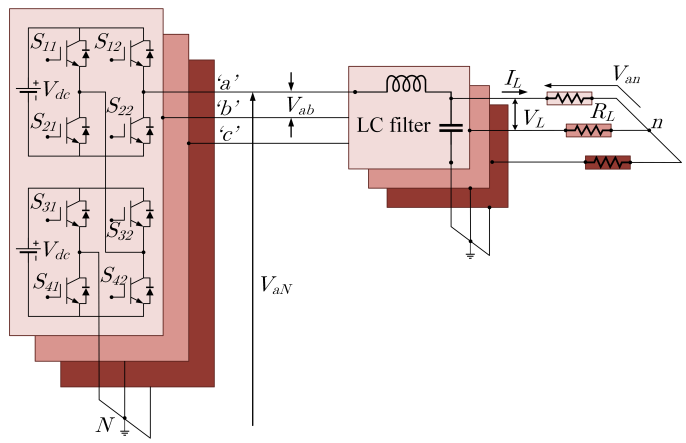


Fig. 1. Simplified diagram of 5-level cascaded H-bridge converter with LC filter and resistive load.

In carrier based PWM, high frequency triangular waves are level shifted or phase disposed in variety of manners and certain PWM schemes are introduced. Three types of sub-harmonic PWM (SHPWM) methods like, phase disposition PWM (PDPWM), phase opposition disposition PWM and alternate phase opposition disposition PWM were proposed by G. Carrara [9]. Where, three techniques to dispose the carrier signals at different amplitude levels and certain phase shifting strategies among the carrier signals were shown. Variable frequency PWM technique was suggested by L. M. Tolbert [10], where the upper and lower level carriers have comparatively less frequency than the intermediate ones to balance the number of switching in all the switching devices of the converter [10]. Carrier overlapping PWM method utilizes vertical offsetting parameters of CFD and presents better output voltage harmonic profile than SHPWM, under low modulation index (MI) but has high total harmonic distortion

978-1-5386-2307-7/17/$31.00 ©2017 IEEE

(THD) in high MI [7]. Among the mentioned modulation techniques, PDPWM offers best THD performance and comparable fundamental gain [11].

On the other hand, in reference signal modulation category, pure sinusoidal PWM is the most applied, investigated with traditional features, ranging from two-level to MLCs. Trapezoidal PWM technique was offered by K. Taniguchi in 1986 [12], which takes advantage of the flat top of the signal to minimize switching loss. In third harmonic PWM, third harmonic signal is injected to fundamental signal which offers less THD and higher fundamental gain [13]. In the process of 60° PWM, top of the sinusoidal signal is kept flat from 60° to 120° and 240° to 300°. Switching devices will work for one third of the cycle with lower switching losses [14]. To carry forward the legacy of bus clamping PWM (BCPWM) techniques, third harmonic injected sixty degree BCPWM (THSDBCPWM) and third harmonic injected thirty degree BCPWM methods are introduced recently in [15], to show better harmonic spectra than the other conventional PWM mehtods.

In this article, conventional PDPWM scheme, is taken to compare the performance of the proposed modulation scheme, combined with THSDBCPWM method. Results are compared in terms of THD, fundamental gain and capability of efficient filtering property. The structure of this article is as follows. Section II slightly describes about the basic operating mechanism of CHB. Section III presents brief knowledge on conventional PDPWM method. Section IV gives detailed mathematical and graphical demonstration on the proposed PDPWM approach. Section V covers simulation and results. Finally, section VI contains the conclusion part.

## II. Cascaded H-Bridge Multilevel Converter

Fig. 1, showing a 5-level CHB converter, has two H-bridge cells and each cell has four switches. For the first cell in phase '$a$', four switches are identified as $S_{11}$, $S_{12}$, $S_{21}$ and $S_{22}$. Two cells are series connected or cascaded and the summation of voltages $V_{a1}$, $V_{a2}$ is taken as $V_{aN}$. Summation of the cell voltages per phase leg can be mathematically represented as [16],

$$V_{pN} = \sum_{i=1}^{Y} V_{pi} = \sum_{i=1}^{Y} V_{dc}(S_{i1} - S_{i2}) \tag{1}$$

where, $p$ represents phases $a, b, c$ and $Y$ defines total H-bridge cells per phase leg.

## III. Conventional Phase Disposition Pulse Width Modulation

In regular PDPWM technique, all carrier signals should have equal amplitude $A_{cr}$ and equal frequency $f_{cr}$, so that their occupying bands remain in closed periphery [9]. The amplitude modulation index (AMI) $m_a$, can be calculated from (2), where $A_r$ and $A_c$ denote peak-to-peak amplitude

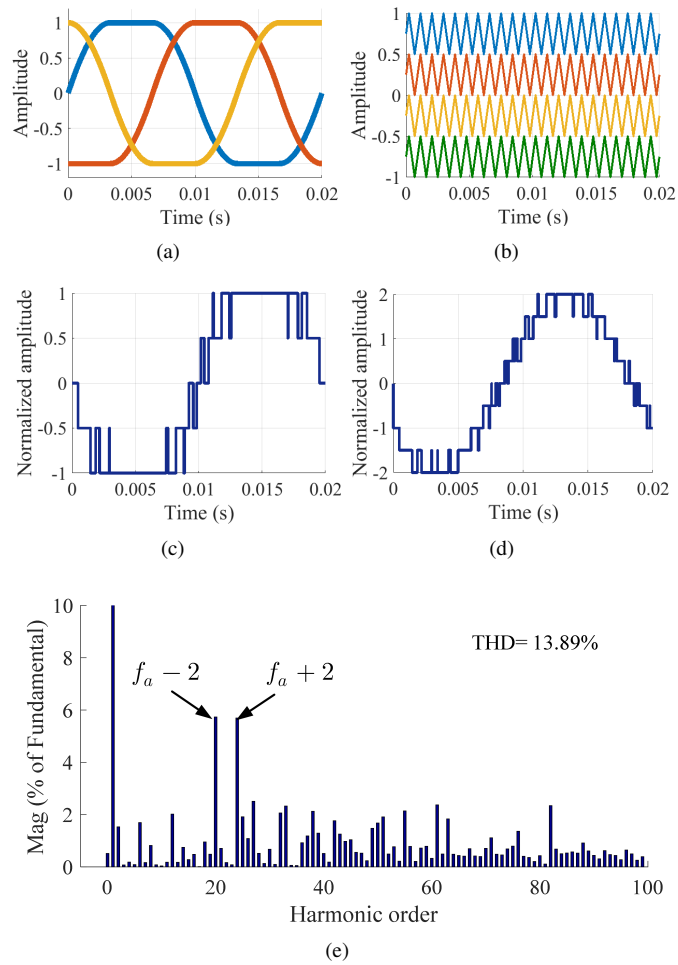


Fig. 2. Waveforms and harmonic profile in case of regular PDPWM for 5-level converter: (a) third harmonic injected 60° bus clamped reference signals, (b) four phase disposed high frequency carrier signals, (c) line to neutral voltage ($V_{aN}$), (d) line to line voltage ($V_{ab}$), and (e) harmonic profile of $V_{ab}$.

of reference signal and carrier signal respectively. Also, the frequency modulation index (FMI) $f_a$ will be found from (3), where $f_r$ and $f_c$ refer to the frequency of reference and carrier signal respectively. If $m_a$ is taken to be 1.0, the peak-to-peak amplitude of the carrier signals can be calculated by (4) [17].

$$m_a = \frac{A_r}{(L-1)A_c} \tag{2}$$

$$f_a = \frac{f_c}{f_a} \tag{3}$$

$$A_c = \frac{\pm A_r}{(L-1)} \tag{4}$$

Fig. 2 exhibits line to neutral voltage, line to line voltage and the harmonic spectra of line voltage in case of regular PDPWM with third harmonic injected 60° bus clamped signal.

## IV. Proposed Phase Disposition PWM

In the proposed method, the disposed carrier signals are not placed in contiguous form, rather they are settled to keep an

TABLE I
SIMULATION PARAMETERS

| Parameters | Value |
|---|---|
| Rated power | 1.00 MVA |
| Rated voltage | 4.30 kV |
| Rated load, $R$ | 17.00 Ω |
| Cell voltage | 1.10 kV |
| Filter components | $L = 50$ mH and $C = 70$ $\mu$F |
| Carrier frequency | 1.10 kHz |
| Fundamental frequency | 50 Hz |
| Modulation index | 1.0 |
| Carrier band gap, $B_{cr}$ | 0.20 |
| Ratings of IGBT switches | 2.50 kV, 1500 A |

even band gap $B_{cr}$ ($0 < B_{cr} < 1$ and $B_{cr} \in \Re$) among them, as shown in Fig. 3(a). First to accommodate $L-1$ carrier signals in a required peak to peak (p-p) band (amplitude band $= 2.0$) for $L$ level converter, the p-p amplitude of carrier signals $A_{cr}$ is calculated as,

$$(L-1)A_{cr} + (L-2)B_{cr} = 2 \tag{5}$$

or,

$$A_{cr} = \frac{2-(L-2)B_{cr}}{L-1} \tag{6}$$

Then the carrier signals are multiplied by the multiplication factor $C_m$, as calculated by,

$$C_m = \frac{A_{cr}}{2} \tag{7}$$

After that, for the proper disposition of the $L-1$ carriers, the upper $(L-1)/2$ carriers and the lower $(L-1)/2$ carriers are positively and negatively summed respectively with the multiplied carriers, as shown in Fig. 4. The disposition factor $F_R$ for required shifting of the carrier signals are determined as,

$$F_1 = 1 - C_m \tag{8}$$

$$F_2 = 3F_1 - B_{cr} - 2 \tag{9}$$

$$F_3 = 5F_1 - 2B_{cr} - 4 \tag{10}$$

Similarly for $L$ level converter,

$$F_R = (2R-1)F_1 - (R-1)B_{cr} - (2R-2) \tag{11}$$

which could be modified as,

$$F_R = [2F_1 - (B_{cr}+2)]R - [F_1 - (B_{cr}+2)] \tag{12}$$

where,

$$R = 1, 2, 3, ....., \frac{L-1}{2} \tag{13}$$

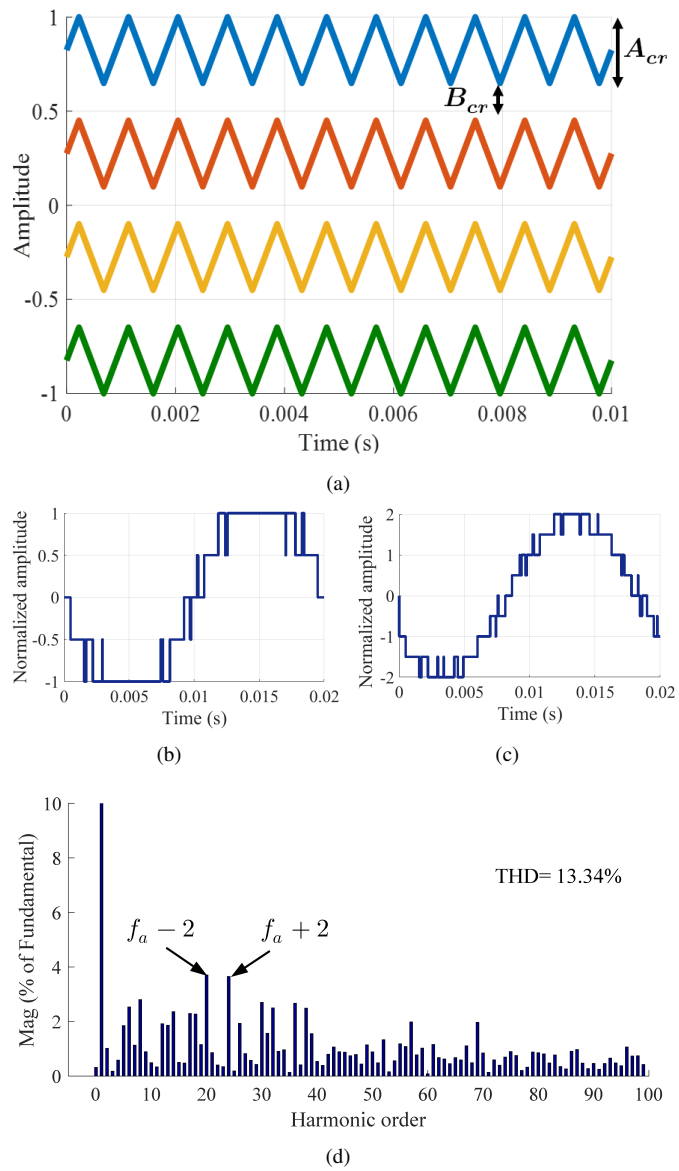


Fig. 3. Waveforms and harmonic profile in case of proposed PDPWM for 5-level converter: (a) four evenly disposed high frequency carrier signals with band gap $B_{cr}$ and p-p amplitude $A_{cr}$, (b) line to neutral voltage ($V_{aN}$), (c) line to line voltage ($V_{ab}$), and (d) harmonic profile of $V_{ab}$.

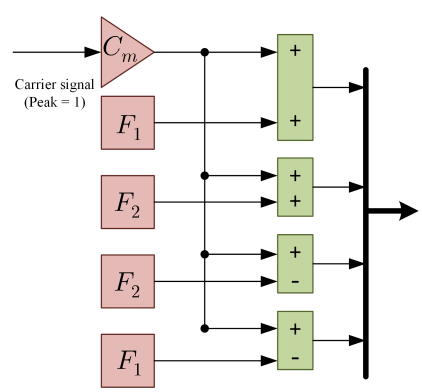


Fig. 4. Phase disposed carrier signal generation for 5-level converter.

TABLE II
COMPARISONS OF REGULAR AND PROPOSED PDPWM REGARDING DIFFERENT PARAMETERS

| Type of modulation | Phase voltage ($V_{aN}$) THD | Phase voltage ($V_{bN}$) THD | Line voltage ($V_{ab}$) (RMS) | Fundamental ($V_{ab}$) | THD of $V_{ab}$ | Harmonics at $[f_a - 2]$ (% of fundamental) | Harmonics at $[f_a + 2]$ (% of fundamental) |
|---|---|---|---|---|---|---|---|
| Conventional | 23.70 % | 23.38 % | 3140.91 kV | 4394.00 kV | 13.89 % | 5.70 % | 5.70 % |
| Proposed | 20.65 % | 20.34 % | 3062.00 kV | 4289.00 kV | 13.34 % | 3.70 % | 3.65 % |

TABLE III
COMPARISONS OF REGULAR AND PROPOSED PDPWM REGARDING LOAD VOLTAGES AND CURRENTS

| Type of modulation | Load voltage ($V_L$) | Fundamental ($V_L$) | Load current ($I_L$) | Fundamental ($I_L$) | THD of $I_L$ |
|---|---|---|---|---|---|
| Conventional | 2.75 kV | 3.88 kV | 93.40 A | 131.90 A | 4.43 % |
| Proposed | 2.70 kV | 3.80 kV | 91.14 A | 128.80 A | 3.17 % |

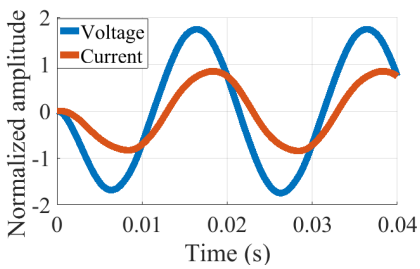


Fig. 5. Normalized load voltage and current after filtering (single phase).

## V. SIMULATION AND RESULTS

Simulation is done for 5-level modular H-bridge converter. Voltage values are normalized by two times of converter cell voltage and current values are normalized by 150 A. Table I shows all the parameters used for simulation. It can be seen from the Table II that, in proposed technique, THD of phase voltages $V_{aN}$ and $V_{bN}$ decreased around 13% and THD of line voltage $V_{ab}$ decrease around 4.0% than the existing technique. The harmonic components at $f_a - 2$ and $f_a + 2$ are approximately 37% lower than that of the conventional one, which has a direct impact on the requirements of the filter circuitry (harmonic amplitudes less than 3.0% of the fundamental are overlooked in this case). This consequence can be easily observed from Table III. The $LC$ filter is designed such that the THD of converter load voltage and current remains under 5.0%. Table III demonstrates that in proposed modulation scheme with the same filtering circuitry, load current offers THD of 3.17% instead of 4.43% for the traditional one. This signifies about 28.5% performance improvement in terms of converter load current in the suggested modulation approach.

Moreover, converter phase voltage $V_{aN}$ shown in Fig. 4(b) has less switching transition than that of the regular one shown in Fig. 2(c). Which, infers upon less switching loss and higher efficiency of the converter. Converter load voltage and current after filtering are shown in Fig. 5. An interesting fact can be observed from Table III that converter output voltage and current as well as their fundamental components get reduced due to the presented modulation process. This in turn reduces the fundamental gain. But, in this work, switching and conduction losses of the converter as well as converter efficiency are not considered (which will be an extension of this work). With the increase of current, conduction losses tend to increase and decrease the converter efficiency. Therefore, the internal impact of the increased voltage and current components on the converter overall performance is yet to be investigated.

## VI. CONCLUSION

Cascaded H-bridge modular multilevel converters are highly efficient in many practical applications. Suitable number of levels, switching patterns as well as proper modulation scheme can demonstrate better converter performance. In the proposed PDPWM method with the combination of THSDBCPWM technique, performance of the CHB converter gets improved in terms of THD of phase voltage, line voltage, load voltage and line current. Harmonic spectra of the line voltage demonstrates the claimed performance in the proposed modulation approach. It is also shown that with the same size of filtering circuitry, suggested modulation scheme offers better performance in terms of load voltage and current. Though, regular PDPWM offers slightly higher fundamental voltage and current than the proposed one, their inherent impact on the converter switching and conduction losses as well as on the overall efficiency is yet to explore.

## REFERENCES


[1] M. R. Islam, Y. Guo, and J. Zhu, "A multilevel medium-voltage inverter for step-up-transformer-less grid connection of photovoltaic power plants," *IEEE J. Photovoltaics*, vol. 4, no. 3, pp. 881–889, 2014.

[2] H. Abu-Rub, J. Holtz, J. Rodriguez, and G. Baoming, "Medium-voltage multilevel converters – state of the art, challenges, and requirements in industrial applications," *IEEE Trans. Ind. Electron.*, vol. 57, no. 8, pp. 2581–2596, Aug 2010.

[3] M. R. Islam, Y. Guo, M. Jafari, Z. Malekjamshidi, and J. Zhu, "A 43-level 33 kV 3-phase modular multilevel cascaded converter for direct grid integration of renewable generation systems," in *Proc. 2014 IEEE Innovative Smart Grid Technology-Asia (ISGT ASIA)*, 2014, pp. 594–599.

[4] M. Marchesoni, M. Mazzucchelli, and S. Tenconi, "A non conventional power converter for plasma stabilization," in *Proc. Power Electron. Spec. Conf.*, vol. 1, April 1988, pp. 122–129.

[5] J. I. Leon, S. Kouro, S. Vazquez, R. Portillo, L. G. Franquelo, J. M. Carrasco, and J. Rodriguez, "Multidimensional modulation technique for cascaded multilevel converters," *IEEE Trans. Ind. Electron.*, vol. 58, no. 2, pp. 412–420, Feb 2011.

[6] M. Malinowski, K. Gopakumar, J. Rodriguez, and M. A. Perez, "A survey on cascaded multilevel inverters," *IEEE Trans. Ind. Electron.*, vol. 57, no. 7, pp. 2197–2206, July 2010.

[7] H. Wang, R. Zhao, Y. Deng, and X. He, "Novel carrier-based PWM methods for multilevel inverter," in *Proc. 29th Annu. Conf. IECON*, vol. 3. IEEE, 2003, pp. 2777–2782.

[8] J. I. Leon, S. Kouro, L. G. Franquelo, J. Rodriguez, and B. Wu, "The essential role and the continuous evolution of modulation techniques for voltage-source inverters in the past, present, and future power electronics," *IEEE Trans. Ind. Electron.*, vol. 63, no. 5, pp. 2688–2701, May 2016.

[9] G. Carrara, S. Gardella, M. Marchesoni, R. Salutari, and G. Sciutto, "A new multilevel PWM method: A theoretical analysis," *IEEE Trans. Power Electron.*, vol. 7, no. 3, pp. 497–505, 1992.

[10] L. M. Tolbert and T. G. Habetler, "Novel multilevel inverter carrier-based PWM method," *IEEE Trans. Ind. Appl.*, vol. 35, no. 5, pp. 1098–1107, 1999.

[11] M. A. Rahman and M. R. Islam, "Performance evaluation of carrier-based modulation strategies for modular cascaded H–bridge multilevel converters," in *Proc. 2017 Int. Conf. Elec. Comput. Commun. Eng. (ECCE)*, Feb 2017, pp. 533–538.

[12] K. Taniguchi and H. Irie, "Trapezoidal modulating signal for three-phase PWM inverter," *IEEE Trans. Ind. Electron.*, vol. 2, no. IE-33, pp. 193–200, 1986.

[13] J. K. Steinke, "Switching frequency optimal PWM control of a three-level inverter," *IEEE Trans. Power Electron.*, vol. 7, no. 3, pp. 487–496, 1992.

[14] M. H. Rashid, *Power Electronics: Circuits, Devices & Applications*, 4th ed. Upper Saddle River, New Jersey, US: Pearson, 2013.

[15] M. R. Islam, A. M. Mahfuz-Ur-Rahman, M. M. Islam, Y. Guo, and J. Zhu, "A modular medium voltage grid connected converter with improved switching techniques for solar photovoltaic systems," *IEEE Trans. Ind. Electron.*, 2017, in press.

[16] J. Rodríguez, S. Bernet, B. Wu, J. O. Pontt, and S. Kouro, "Multi-level voltage-source-converter topologies for industrial medium-voltage drives," *IEEE Trans. Ind. Electron.*, vol. 54, no. 6, pp. 2930–2945, 2007.

[17] M. R. Islam, Y. Guo, and J. Zhu, "A high-frequency link multilevel cascaded medium-voltage converter for direct grid integration of renewable energy systems," *IEEE Trans. Power Electron.*, vol. 29, no. 8, pp. 4167–4182, Aug 2014.

# A Novel Flux Estimation Algorithm Based Position Sensorless Field Oriented Vector Controlled Permanent Magnet Brushless DC Motor Drive

Protik Chandra Biswas and Bashudeb Chandra Ghosh
Department of Electrical and Electronic Engineering
Khulna University of Engineering & Technology (KUET), Khulna-9203, Bangladesh
Email: protikpc07@gmail.com

*Abstract*— **Permanent Magnet Brushless DC (PMBLDC) motor is a permanent magnet synchronous machine with solid state commutation system having huge scope to be used as an industrial motor in future. For proper commutation of the phase currents, rotor position information must be obtained from the position sensors. But there are some vital disadvantages of position sensors. Instead of using position sensors, a novel flux estimation algorithm is proposed in this paper to estimate the rotor position and speed to perform the operation of position sensorless field oriented control (FOC) of a PMBLDC motor. Comparison between the actual and estimated quantities is analyzed through the results for evaluating the performance of proposed flux estimation algorithm, rotor position estimator and speed estimator. Though there is no rotor position or speed sensor in the proposed control drive, the performance of this drive remains unchanged comparing to the position sensored control drive.**

***Keywords—Permanent Magnet Brushless DC motor drive, field oriented control, position sensorless, rotor flux estimation algorithm.***

## I. INTRODUCTION

During the last several decades, electrical AC machines have been considered mainly as work horse of industry. Permanent Magnet Brushless DC (PMBLDC) motor is extensively used in industry as the replacement of AC machines due to their advantages including low maintenance due to low friction, long operating life, noiseless operation, compact form, silent operation, high power density, fast dynamic response, high power factor, increased reliability, higher speed ranges and better controllability [1]-[3].

Since PMBLDC motor does not use brushes for commutation. For proper commutation of the phase currents of conventional PMBLDC motor, rotor position must be obtained by the position sensors [4]. Generally Hall-effect sensors or optical encodes are employed as position sensor to provide rotor position information for commutation [5]. Hall sensors used as rotor position encoder are advantageous for simple control algorithm and mature application [6]. But considering the high cost, poor reliability and installation difficulty of high resolution position sensor, it is the right time to think about a position sensorless PMBLDC motor drive for industrial applications [4], [6].

In the last two decades, many sensorless motor drives have been proposed to eliminate the costly and fragile position sensor for PMBLDC motors with trapezoidal back-EMF. Sensorless control based on a hysteresis comparator of terminal voltage and a potential start-up method with a high starting torque is presented in paper [7]. In lieu of position sensors, zero crossing points (ZCPs) of back EMFs with 30° phase shift is used in [8]. Commutation instants are estimated by using ZCPs detection of the three-phase line-to-line voltages without 30° phase shift in [9]. A simple technique to detect back EMF zero crossings for a PMBLDC motor using the line voltages is proposed in [9]. The motor neutral voltage is required to get the ZCP of phase back EMFs [8], but the neutral line of the motor is usually not extracted. To obtain the virtual neutral voltage, a resistance network composed by three resistors is used [10].

An offline finite element method assisted position and speed observer for PMBLDC motor drive is investigated in [11]. By using disturbance observer structure, a new 12-step sensorless drive for brushless dc motor based on back EMF differences is presented in [12]. Integration of third harmonic back EMF and the phase-locked loop technique are used in [13] and provides controllable advanced commutation to the PMBLDC motor. These existing methods for position sensorless operation of PMBLDC motor drives require costly additional circuitry arrangements and complex algorithms. But the performance of these drives to estimate the rotor position is not satisfactory.

In this paper, instead of using rotor position or speed sensor, a simple control algorithm is proposed to estimate the rotor position and speed without the necessity of any additional circuitry arrangement to perform the operation of position sensorless field oriented vector control of a PMBLDC motor. This paper proposes field oriented control for PMBLDC motor drive with current fed inverters. An Adaptive PI controller based on motor speed error is considered. A hysteresis type current controller is implemented. Transient response and loading capability of the motor are studied to compare the performance of the proposed position sensorless FOC drive with the conventional position sensored FOC drive.

978-1-5386-2307-7/17/$31.00 ©2017 IEEE

## II. MATHEMATICAL MODEL OF PMBLDC MOTOR

The *d-q* orthogonal synchronously rotating reference frame model is not suitable to model PMBLDC motor, because the flux distribution of this motor is trapezoidal in nature. Phase variables have to be considered for mathematical modeling of PMBLDC motor for this non-sinusoidal flux distribution as shown in (1).

$$\begin{bmatrix} V_{as} \\ V_{bs} \\ V_{cs} \end{bmatrix} = \begin{bmatrix} R_s & 0 & 0 \\ 0 & R_s & 0 \\ 0 & 0 & R_s \end{bmatrix} \begin{bmatrix} i_{as} \\ i_{bs} \\ i_{cs} \end{bmatrix} + \frac{d}{dt} \begin{bmatrix} L_{aa} & L_{ab} & L_{ac} \\ L_{ba} & L_{bb} & L_{bc} \\ L_{ca} & L_{cb} & L_{cc} \end{bmatrix} \begin{bmatrix} i_{as} \\ i_{bs} \\ i_{cs} \end{bmatrix} + \begin{bmatrix} e_a \\ e_b \\ e_c \end{bmatrix} \quad (1)$$

Where, $V_{as}$, $V_{bs}$, $V_{cs}$ are stator phase voltages, $i_{as}$, $i_{bs}$, $i_{cs}$ are phase currents of stator, $R_s$ is per phase stator resistance, $L_{aa} = L_{bb} = L_{cc} = L$ are self-inductance of phase *a, b* and *c* respectively, $L_{ab} = L_{bc} = L_{ac} = M$ are mutual inductance between the phases. Three phase back EMF of the PMBLDC motor is given in (2), which is trapezoidal in nature.

$$\begin{bmatrix} e_a \\ e_b \\ e_c \end{bmatrix} = \omega_m \lambda_m \begin{bmatrix} \varphi_a(\theta_r) \\ \varphi_b(\theta_r) \\ \varphi_c(\theta_r) \end{bmatrix} \quad (2)$$

$$\varphi_a(\theta_r) = \begin{cases} \theta_r \dfrac{6}{\pi}, & 0 \le \theta_r < \dfrac{\pi}{6} \\ 1, & \dfrac{\pi}{6} \le \theta_r < \dfrac{5\pi}{6} \\ (\pi - \theta_r)\dfrac{6}{\pi}, & \dfrac{5\pi}{6} \le \theta_r < \dfrac{7\pi}{6} \\ -1, & \dfrac{7\pi}{6} \le \theta_r < \dfrac{11\pi}{6} \\ (\theta_r - 2\pi)\dfrac{6}{\pi}, & \dfrac{11\pi}{6} \le \theta_r < 2\pi \end{cases} \quad (3)$$

Where, $\lambda_m$ is flux linkage constant, $\omega_m$ is rotor speed (rad/s), $\theta_r$ is rotor position (radian) and $\varphi_a(\theta_r), \varphi_b(\theta_r), \varphi_c(\theta_r)$ are three phase rotor flux. Only the rotor flux function $\varphi_a(\theta_r)$ is given by (3). The $\varphi_b(\theta_r), \varphi_c(\theta_r)$ are 120° and 240° phase displaced from $\varphi_a(\theta_r)$ respectively.

## III. POSITION SENSORLESS FIELD ORIENTED CURRENT FED PMBLDC MOTOR DRIVE

Sensorless means that, rotor position encoder or speed sensors are absent in this proposed system. No Hall sensors or optical encoders are used to detect the rotor position for the purpose of stator current commutation. The proposed control drive is shown in Fig. 1.

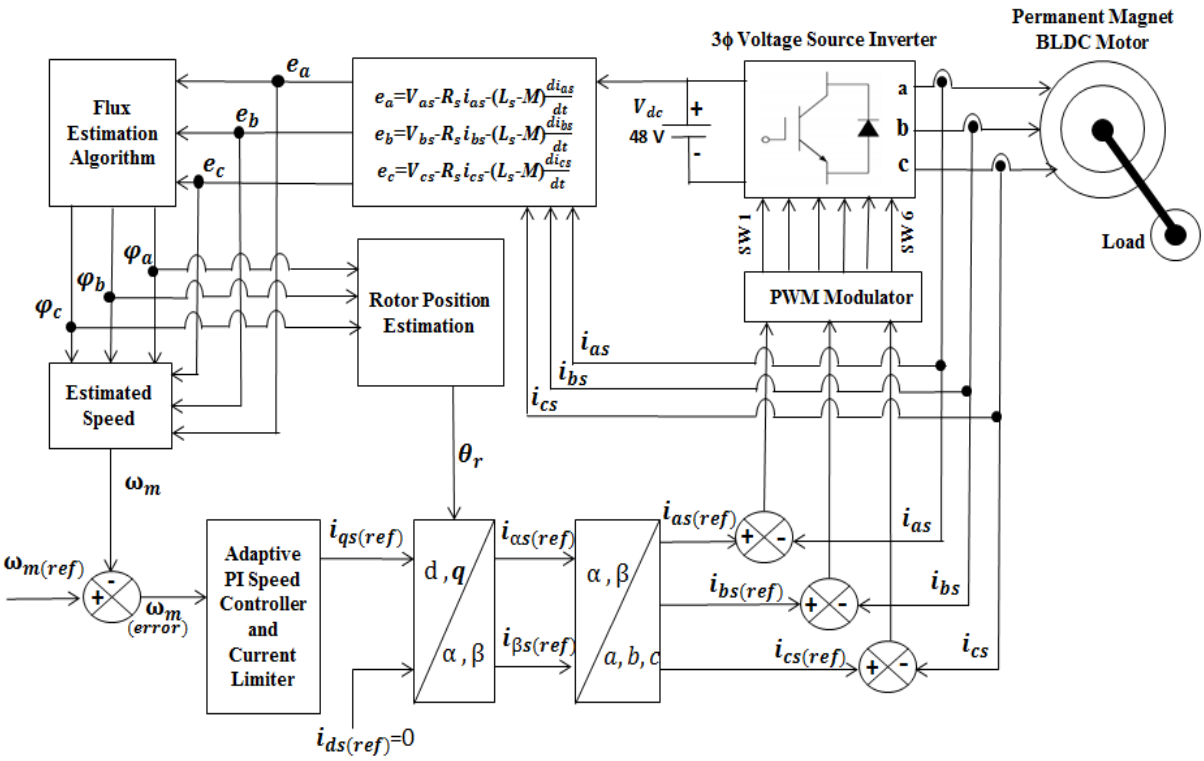


Figure 1. Block diagram of field oriented vector controlled PMBLDC motor drive without rotor position or speed sensor.

### A. Rotor Flux Estimation Algorithm

Novel flux estimation algorithm is proposed. Three phase back EMF $e_a, e_b, e_c$ have to be calculated for the rotor flux estimation algorithm as shown in Fig. 1. Three phase rotor flux linkage $\varphi_a, \varphi_b, \varphi_c$ can be estimated by using three phase back EMF $e_a, e_b, e_c$ according to the algorithm as shown in Fig. 2. Where $i$ is the iteration number. Hysteresis-band used for this delta modulated PWM is 0.001. As a result, the actual stator phase currents oscillate around the reference current with maximum oscillation width 0.001 A. Since back EMF $e_a, e_b, e_c$ are calculated by using the stator phase currents $i_{as}$, $i_{bs}$ and $i_{cs}$ as shown in Fig. 1. The oscillation of stator phase currents incorporate in three phase calculated back EMF. For this reason a band is used in flux estimation algorithm to compare per phase back EMF with previous iteration. In this algorithm, main objectives are to find out the value of back EMF $e_{ac}, e_{bc}, e_{cc}$ at constant back EMF region as shown in Fig. 3. Thus the rotor flux linkage can be estimated in per unit value by using $e_{ac}, e_{bc}, e_{cc}$ as given in Fig. 2. To understand this proposed flux estimation algorithm, graphical representation of 3-phase back EMF and per unit estimated rotor flux linkage according to the back EMF is illustrated in Fig. 3.

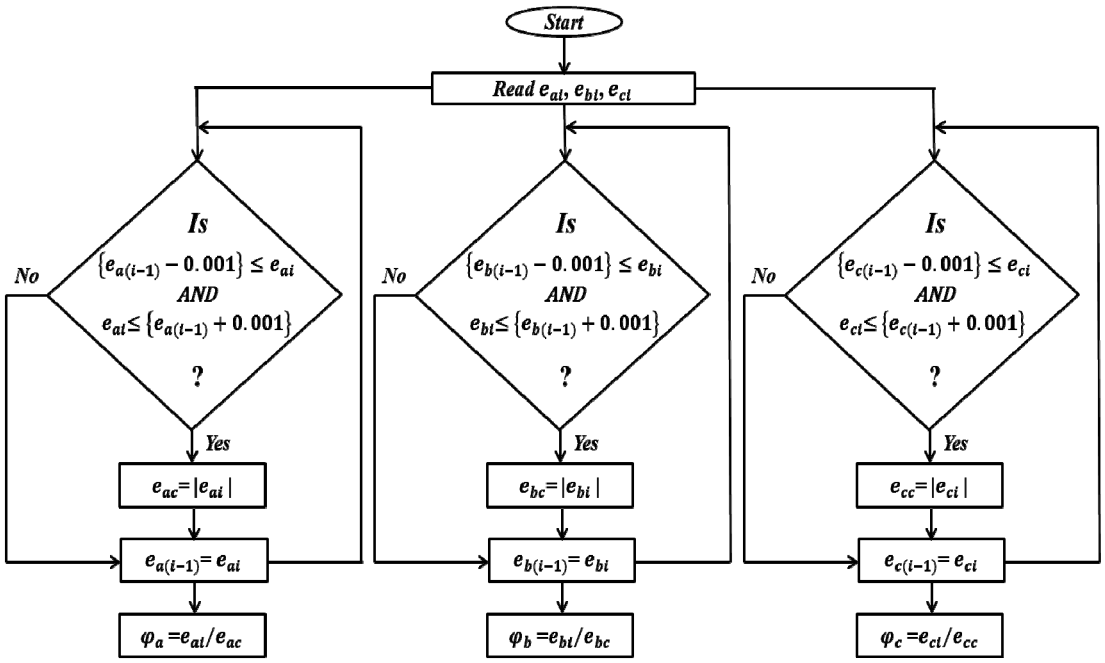


Figure 2. Flowchart for rotor flux estimation algorithm.

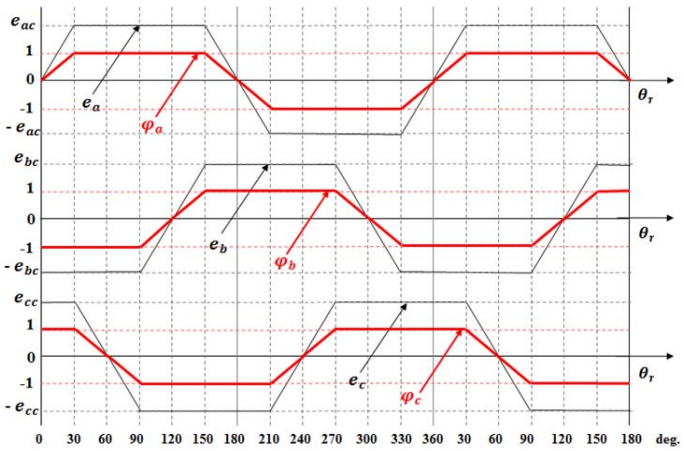


Figure 3. 3-phase back EMF and per unit estimated rotor flux linkage according to the back EMF.

### B. Rotor Position Estimation

Rotor position $\theta_r$ is estimated by using estimated rotor flux $\varphi_a, \varphi_b, \varphi_c$ according to Table I. At a specific time, rotor position is determined only by using estimated flux of a single phase as tabulated in Table I. This phase is selected on the basis of a simple rule. From Fig. 3, it is seen that, at every instant, flux of any two phases have constant value and flux of other phase changes with rotor position. This phase have to be chosen to determine the rotor position according to the value of flux of that phase.

TABLE I. ROTOR POSITION CORRESPONDING TO THREE PHASE ROTOR FLUX LINKAGE

| Condition of Rotor Flux Linkage | | | Rotor Position, $\theta_r$ (radian) |
|---|---|---|---|
| $\varphi_a \geq 0.0$ | $\varphi_b \leq -1.0$ | $\varphi_c \geq 1.0$ | $\theta_r = (\varphi_a \times \frac{\pi}{6})$ |
| $\varphi_a \geq 1.0$ | $\varphi_b \leq -1.0$ | – | $\theta_r = \frac{\pi}{3} - (\varphi_c \times \frac{\pi}{6})$ |
| $\varphi_a \geq 1.0$ | – | $\varphi_c \leq -1.0$ | $\theta_r = \left(\varphi_b \times \frac{\pi}{6}\right) + \frac{2\pi}{3}$ |
| – | $\varphi_b \geq 1.0$ | $\varphi_c \leq -1.0$ | $\theta_r = \pi - (\varphi_a \times \frac{\pi}{6})$ |
| $\varphi_a \leq -1.0$ | $\varphi_b \geq 1.0$ | – | $\theta_r = \left(\varphi_c \times \frac{\pi}{6}\right) + \frac{4\pi}{3}$ |
| $\varphi_a \leq -1.0$ | – | $\varphi_c \geq 1.0$ | $\theta_r = \frac{5\pi}{3} - (\varphi_b \times \frac{\pi}{6})$ |
| $\varphi_a < 0$ | $\varphi_b \leq -1.0$ | $\varphi_c \geq 1.0$ | $\theta_r = \left(\varphi_a \times \frac{\pi}{6}\right) + 2\pi$ |

### C. *PMBLDC Motor Speed Estimation*

Generally motor speed can be determined by the differentiation of the rotor position of a motor. But this conventional approach is not applicable for estimated rotor position of a PMBLDC motor for delta modulated PWM current fed field oriented control drive. Because there exists oscillation in estimated rotor position which is incorporated from delta modulated stator phase currents as discussed earlier. PMBLDC motor speed can be estimated by using the estimated flux linkage $\varphi_a$ , $\varphi_b$ , $\varphi_c$ and calculated back EMF $e_a$ , $e_b$ , $e_c$ according to the Table II. Flux of one phase and the calculated back EMF of that phase are used to determine the motor speed. Similar to the rotor position estimation, the phase has to be selected to determine the motor speed according to a rule that, the value of rotor flux of selected phase, changes with rotor position and other two phases have constant value of flux.

TABLE II. ESTIMATED SPEED CORRESPONDING TO ESTIMATED THREE PHASE ROTOR FLUX LINKAGE

| Condition of Rotor Flux Linkage | | | Motor Speed, $\omega_m$ (radian/s) |
|---|---|---|---|
| $\varphi_a \geq 0.0$ | $\varphi_b \leq -1.0$ | $\varphi_c \geq 1.0$ | $\omega_m = e_a/(\lambda_m \times \varphi_a)$ |
| $\varphi_a \geq 1.0$ | $\varphi_b \leq -1.0$ | - | $\omega_m = e_c/(\lambda_m \times \varphi_c)$ |
| $\varphi_a \geq 1.0$ | - | $\varphi_c \leq -1.0$ | $\omega_m = e_b/(\lambda_m \times \varphi_b)$ |
| - | $\varphi_b \geq 1.0$ | $\varphi_c \leq -1.0$ | $\omega_m = e_a/(\lambda_m \times \varphi_a)$ |
| $\varphi_a \leq -1.0$ | $\varphi_b \geq 1.0$ | - | $\omega_m = e_c/(\lambda_m \times \varphi_c)$ |
| $\varphi_a \leq -1.0$ | - | $\varphi_c \geq 1.0$ | $\omega_m = e_b/(\lambda_m \times \varphi_b)$ |
| $\varphi_a < 0$ | $\varphi_b \leq -1.0$ | $\varphi_c \geq 1.0$ | $\omega_m = e_a/(\lambda_m \times \varphi_a)$ |

## IV. SIMULATION RESULTS AND DISCUSSION

Field oriented controlled current fed PMBLDC motor drive without rotor position or speed sensors has been simulated in C++ platform. The sampling time used for this simulation is 0.0000025 second. The specifications of the simulated brushless DC motor are given in Table III.

TABLE III. NAME PLATE DATA OF PMBLDC MOTOR

| Specifications | Quantity |
|---|---|
| No. of Poles | 8 |
| Rated Voltage | 48 V |
| Peak Value of Rated Current | 2.5 Amp |
| Rated Speed | 150 rad/s |
| Rated Torque | 1.55 Nm |
| Initial Torque | 0.4 Nm |
| Flux linkages constant | 0.105 |
| Moment of Inertia | 0.0048 kg-m$^2$ |
| Damping constant | 0.002 N-m/rad/sec |
| Per Phase Stator Resistance | 0.36 Ω |
| Per Phase Self-Inductance | 2.1 mH |
| Mutual inductance | 1.5 mH |

### A. *Starting Characteristics*

The initial load torque on the PMBLDC motor is 0.4 Nm at the time starting. From Fig. 4, it is seen that, PMBLDC motor takes 0.55 second for the proposed position sensorless FOC drive to gain rated speed (150 rad/s). Field oriented controlled sensored PMBLDC motor drive also takes 0.55 second to gain its rated speed. There exists negligible amount of speed deviation between the actual and estimated speed at the initial time of starting. Because at initial transient state (before 0.085 second), there exists deviation between the actual and estimated flux and rotor position as shown in Fig. 6 and Fig. 7. After 0.085 seconds estimated speed follows actual speed very sharply i.e. at steady state there is no error for speed estimation both for the proposed position sensorless field oriented controlled PMBLDC motor drive.

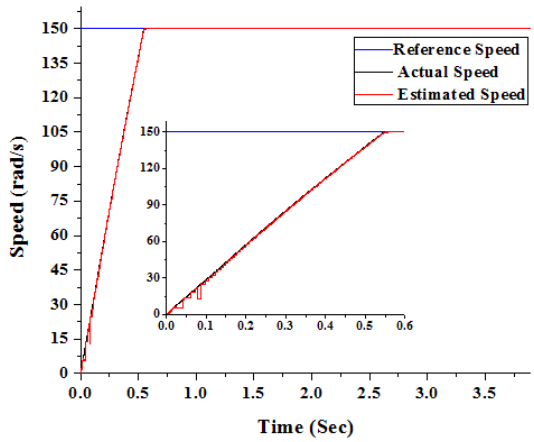


Figure 4. Starting characteristics of PMBLDC motor drives for field oriented control without position sensor.

Phase currents of PMBLDC motor at the time of starting for field oriented current fed drives for the proposed sensorless operation are depicted in Fig. 5. It shows that the amplitude of 3-phase current is 2.5 Amp (rated current of the motor) at the transient time of starting. Fig. 5 also describes that after gaining rated speed, motor takes maximum 1.0 Amp current for initial torque 0.4 Nm. Same scenario is noticed for position sensored field oriented vector controlled PMBLDC motor drive.

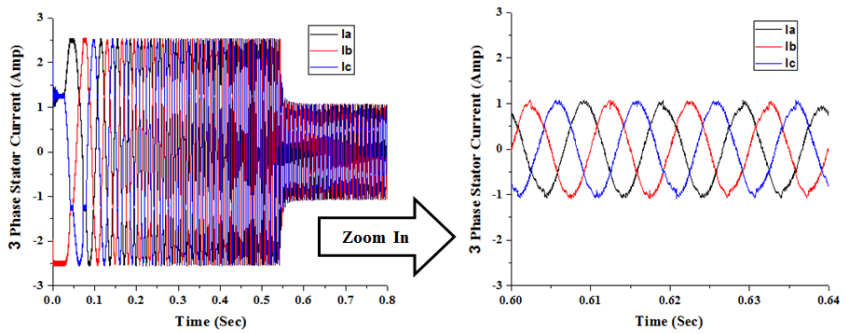


Figure 5. Stator current of PMBLDC motor for field oriented current fed drive without position sensor.

Comparison of actual and estimated rotor flux for sensorless field oriented vector controlled PMBLDC motor drive is depicted in Fig. 6. At the initial transient time of starting of PMBLDC motor (before 0.085 second), there exists little mismatch between the actual flux and estimated flux. Actual and estimated rotor position for sensorless field oriented vector controlled PMBLDC motor drive are depicted in Fig. 7. Since rotor positions are calculated by using the estimated rotor flux. So, there exits little misalignment between the actual and estimated rotor position at the initial time of starting as shown in Fig. 7. After 0.085 second, estimated flux fully traced actual flux. So, estimated rotor position can be fully matched with actual rotor position. It is one of the novelties of the proposed algorithms.

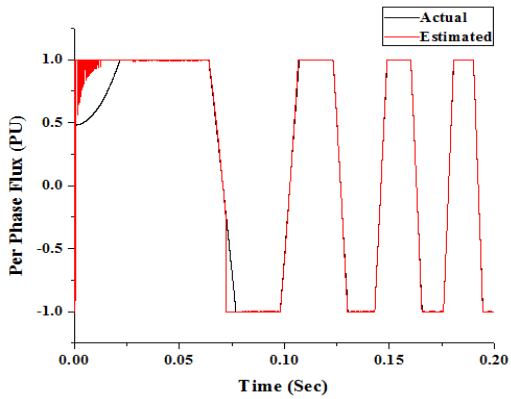


Figure 6. Actual and estimated rotor flux in per unit value for position sensorless field oriented control drive.

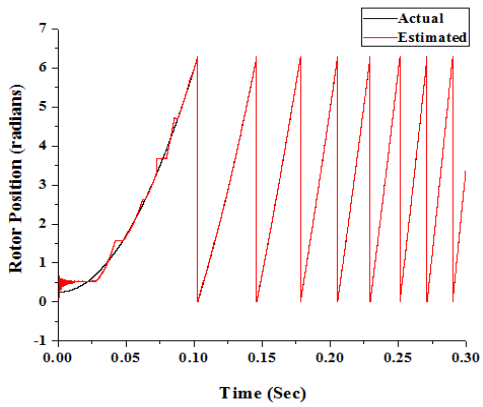


Figure 7. Actual and estimated rotor position for position sensorless field oriented control drive.

Stator flux linkage trajectory for position sensorless field oriented vector controlled PMBLDC motor drive is shown in Fig. 8, which ensures field oriented control.

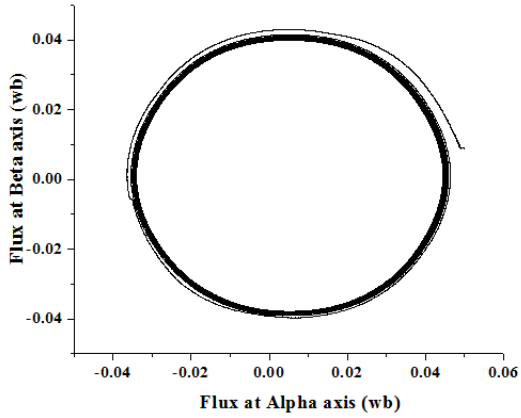


Figure 8. Stator flux linkage in the stationary αβ axes reference frame for position sensorless field oriented controlled PMBLDC motor drive.

## B. *Dynamic Speed Changing Characteristics*

For dynamic speed changing condition, estimated speed nearly follows the actual speed of PMBLDC motor according to the reference speed as shown in Fig. 9. At 1.0 second, speed command is changed from 100 rad/s to 75 rad/s with load torque 0.4 Nm and there is a small amount of mismatch between the actual speed and estimated speed at transient time interval 1.0 second to 1.05 second. When speed command is changed from 75 rad/s to 150 rad/s at 1.5 second, there is no noticeable error between the estimated and actual motor speed for the proposed position senrsorless FOC drive. At steady state condition, estimated speed exactly traced out the actual speed of the motor for the proposed algorithm.

## C. *Motor Characteristics due to Load Torque Variation*

Initial load torque of PMBLDC motor at 150 rad/s rated speed is 0.4 Nm. Motor is loaded with 1.55 Nm rated load torque at 1.5 second. Fig. 11 depicts that, there is no change in speed characteristic at the time 1.5 second when the motor is loaded with 1.55 Nm. Both actual and estimated motor speed sharply follows the given reference speed command. Maximum 1.55 Nm load torque have to be applied to a field oriented control drive for the specific simulated PMBLDC motor for both position sensored and position sensorless operation.

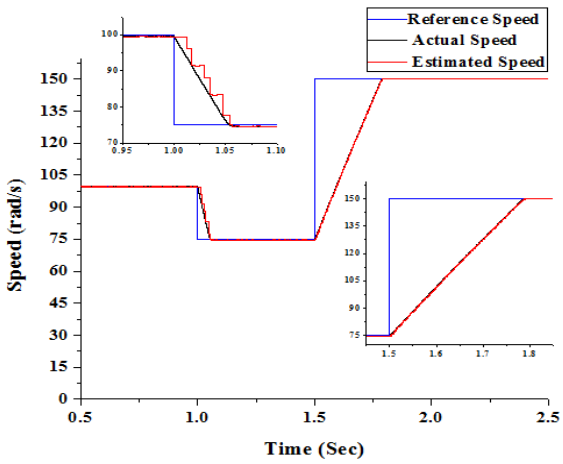


Figure 9. Actual and estimated speed response of PMBLDC motor for position sensorless field oriented control drive at dynamic speed changing condition.

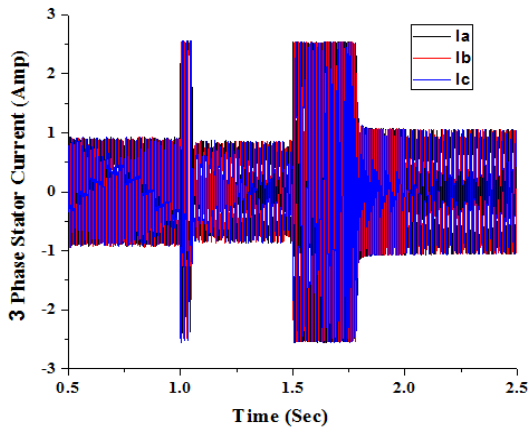


Figure 10. Three phase stator current of PMBLDC motor for position sensorless FOC drive considering transient current at the interface of speed changes.

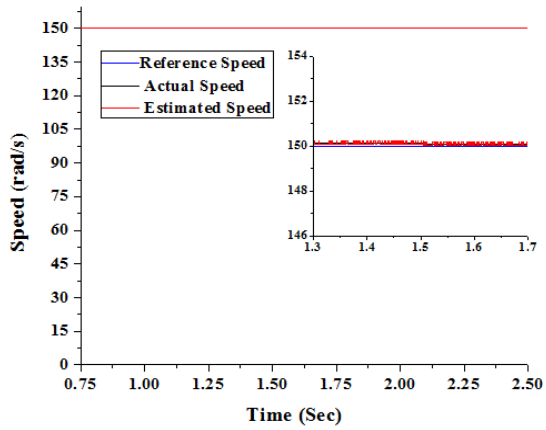


Figure 11. Response of speed of PMBLDC motor for sudden load torque change to 1.55 Nm (rated) from 0.4 Nm (initial load) at 1.5 second for position sensorless field oriented control drive.

## V. CONCLUSION

Position sensorless field oriented vector controlled current fed delta modulated PMBLDC motor drive is proposed in this paper. Instead of using position sensor, novel rotor flux estimation algorithm is proposed to estimate rotor position and speed. Excluding initial starting time (before 0.085 second) negligible error, estimated rotor flux exactly traced out the actual flux linkage of the PMBLDC motor for the proposed control drive. Similar to the estimated flux, there is no mismatch between actual and estimated rotor position. The performance of rotor flux, rotor position and motor speed estimators are very satisfactory. The lowest speed handling capacity of the proposed position sensorless control drive is 2 rad/s. Both the transient and steady state characteristics of the proposed position sensorless FOC drive are similar to the position sensored FOC drive. Though position sensors are not used, the performance of the proposed control drive does not degrade.

## REFERENCES


[1] A. Lee, S. Wang, and C. Fan, "A Current index approach to compensate commutation phase error for sensorless brushless DC motors with nonideal back EMF," *IEEE Trans. Power. Electron.*, vol. 31, no. 6, Jun. 2016.

[2] C. Lin, C. Hung, and C. Liu, "Position sensorless control for four-switch three-phase brushless DC motor drives," *IEEE Trans. Power. Electron.*, vol. 23, no. 1, pp. 438-444, Jan. 2008.

[3] S. B. Ozturk, W. C. Alexander, and H. A. Toliyat, "Direct torque control of four-switch brushless DC motor with non-sinusoidal back EMF," *IEEE Trans. Power. Electron.*, vol. 25, no. 2, pp. 263-271, Feb. 2010.

[4] G. Liu, C. Cui, K. Wang, B. Han, and S. Zheng, "Sensorless control for high-speed brushless DC motor based on the line-to-line back EMF," *IEEE Trans. Power. Electron.*, vol. 31, no. 7, Jul. 2016.

[5] H. Li, S. Zheng, and H. Ren, "Self-correction of commutation point for high-speed sensorless BLDC motor with low inductance and nonideal back EMF," *IEEE Trans. Ind. Electron.*, vol. 32, no. 1, pp. 642-651, Jan. 2017.

[6] W. Li, J. Fang, H. Li, and J. Tang, "Position sensorless control without phase shifter for high-speed BLDC motors with low inductance and nonideal back EMF," *IEEE Trans. Power. Electron.*, vol. 31, no. 2, Feb. 2016.

[7] T. Chun, Q. Tran, H. Lee, and H. Kim, "Sensorless control of BLDC motor drive for an automotive fuel pump using a hysteresis comparator," *IEEE Trans. Power. Electron.*, vol. 29, no. 3, Mar. 2014.

[8] Y. Wang, X. Zhang, X. Yuan, and G. Liu, "Position-sensorless hybrid sliding-mode control of electric vehicles with brushless DC motor," *IEEE Trans. Vehicul. Techn.*, vol. 60, no. 2, pp. 421–432, Feb. 2011.

[9] P. Damodharan and K. Vasudevan, "Sensorless brushless DC motor drive based on the zero-crossing detection of back electromotive force (EMF) from the line voltage difference," *IEEE Trans. on Energy Conversion*, vol. 25, no. 3, pp. 661-668, Sep. 2010.

[10] C. Cui, G. Liu, K. Wang, and X. Song, "Sensorless drive for high-speed brushless DC motor based on the virtual neutral voltage," *IEEE Trans. Power. Electron.*, vol. 30, no. 6, Jun. 2015.

[11] A. Stirban, I. Boldea, and G. Andreescu, "Motion-sensorless control of BLDC-PM motor with offline FEM-Information-Assisted position and speed observer," *IEEE Trans. Power. Electron.*, vol. 48, no. 6, Dec. 2012.

[12] S. Wang and A. Lee, "A 12-step sensorless drive for brushless DC motors based on back-EMF differences," *IEEE Trans. Energy Conversion*, vol. 30, no. 2, Jun. 2015.

[13] J. X. Shen and S. Iwasaki, "Sensorless control of ultrahigh-speed PM brushless motor using PLL and third harmonic back EMF," *IEEE Trans. Ind. Electron.*, vol. 53, no. 2, Apr. 2006.

# A Study of THD Minimization of Three Phase Inverter Using Modified THPWM

Airin Rahman[1], Md. Moshiur Rahman[2], Md. Rabiul Islam[3]
[1,2]Department of Electrical and Electronic Engineering, Prime University, Dhaka, Bangladesh.
[3]Department of Electrical and Electronic Engineering, Rajshahi University of Engineering & Technology, Rajshahi, Bangladesh.
airin.r82@gmail.com, moshiur.r10@gmail.com, rabiulbd@hotmail.com

*Abstract*— **The output current of inverter should contain lower harmonic component. In order to reduce the harmonic component or total harmonic distortion (THD) different types of pulse width modulation (PWM) techniques are used. Among these techniques third harmonic injected PWM (THPWM) is widely used for lower THD. This paper studies THD variation for THPWM technique by varying the modulation index and frequency of the carrier signal. From the analysis, an optimum condition is suggested which offers lowest THD for that optimum condition. In this paper, a modified THPWM technique is proposed. This proposed modulation technique helps to reduce the THD to the lowest value than the THPWM technique. All the simulation work is done by MATLAB/Simulink software. Here the THPWM technique is compared with the modified THPWM and justifies that the modified THPWM is better than the THPWM technique.**

***Keywords— Total harmonic distorsion, pulse width modulation, third harmonic injected pulse width modulation.***

## I. INTRODUCTION

Pulse width modulation (PWM) switching technique for inverter is widely used for dc signal to ac signal conversion. For fixed switching frequency, low ripple current and well defined harmonic spectrum characteristics, PWM techniques are popularly used for different types of inverter [1], [2]. The PWM signals are generated by comparing a reference signal with a carrier signal. The reference signal is in the form of sinusoidal or square wave and the carrier signal may be triangular or saw tooth wave where the carrier signal frequency is greater than the reference signal frequency [3]. By comparing the reference signal and carrier signal, the triggering pulses are generated which turn on and turn off the inverter leg switches. According to the different types of major reference signals, PWM techniques can be divided into different categories such as sine PWM, third harmonic injected PWM, sixty degree PWM, trapezoidal PWM etc. These techniques reduce the number of switching which reduces the switching loss [4]. Based on the total harmonic distortion (THD) analysis, third harmonic injected PWM (THPWM) is better among them [5]. THD is the measurement of harmonic distortion present in the output signal of the inverter. THD should be kept as low as possible because higher THD has unfavorable effect on power supply. Lower THD offers higher power factor, lower pick current and higher efficiency. So it is important to reduce the THD of power system. The THD of power system can be reduced by minimizing harmonics present in the output waveform of inverter. The aim of this paper is to analyze how to reduce the THD of inverter output.

This paper studies details about THPWM and tries to reduce THD effect of the output waveform of inverter. To reduce the harmonic effect, one easy way is to insert a filter in the output of the inverter which will help to get pure sinusoidal output. But the filter arrangement is costly and makes the inverter bulky. Hence to skip the filter arrangement, this paper proposes a modified THPWM technique. In this paper, these two techniques are compared. From the comparison it is shown that this modified technique is able to minimize the THD at lower level without using a filter.

## II. THREE PHASE INVERTER

Fig. 1 indicates a standard layout of three phase two level inverter. The inverter consists of six controlled semiconductor switches. IGBT is most popularly used as controlling switches for inverter. At the time of conversion process from dc signal to ac signal, these semiconductor switches regulate the duration and direction of the output waveform. The line currents and output ac voltage can be obtained as pure sinusoidal by controlling the switching pattern [6].

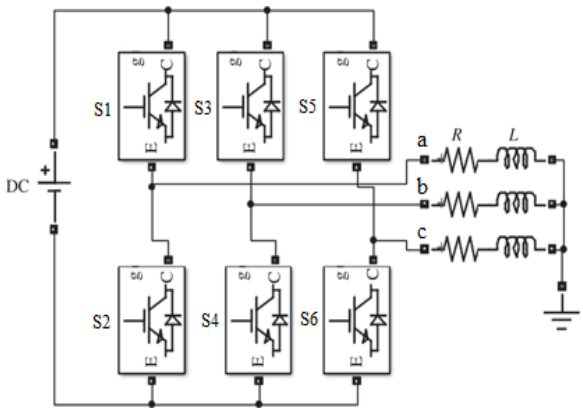


Fig. 1 Three phase inverter

## III. THIRD HARMONIC INJECTED PWM

The third harmonic injected PWM is widely preferred for three phase system than single phase system [7]. In THPWM, the reference signal is generated by adjoining two sine wave where the frequency of a sine wave is three times of another. By

978-1-5386-2307-7/17/$31.00 ©2017 IEEE

comparing the reference signal with the carrier signal, triggering pulses are generated. The third harmonic injected reference signal controls the amplitude of the third harmonic component to obtain the desired quality output. Switching loss of the inverter is thus reduced due to the flatting top of the reference signal [4]. THPWM offers better utilization of dc supply by cancelling the third harmonic component. The Fig. 2 shows the generation of reference signal for THPWM technique.

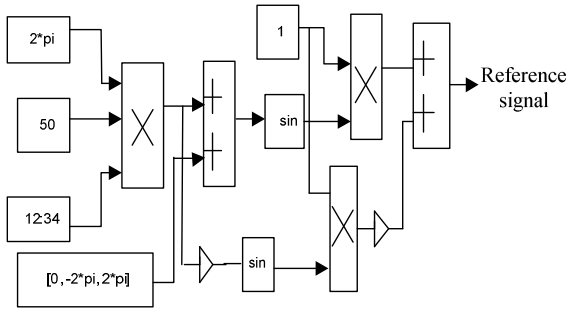


Fig. 2 Reference signal generation for THPWM technique

And Fig. 3 shows the gate pulse generation process.

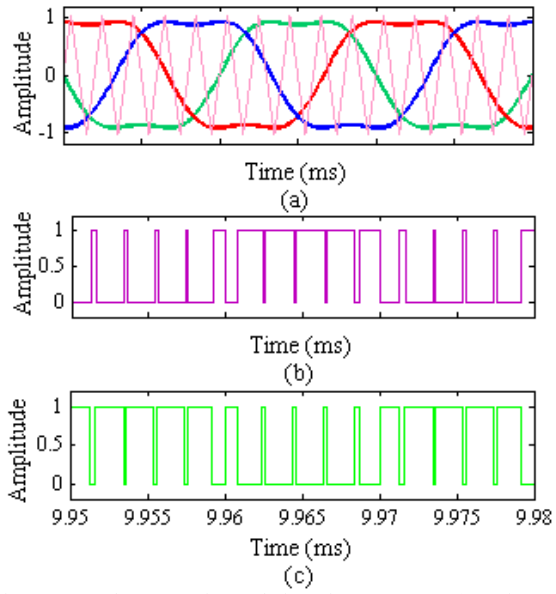


Fig. 3 Gate pulse generation technique for THPWM: (a) carrier and reference signal, (b) generated gate pulse and (c) inverted gate pulse

## IV. Modified Third Harmonic Injected PWM

This modulation technique is proposed by modifying the THPWM technique. The modification is done by replacing the sine wave whose frequency is three times of the fundamental frequency with a triangular wave. The following Fig. 4 shows the generation of reference signal for modified THPWM technique.

Here the reference signal is generated by adding a sine wave with a triangular wave whose frequency is three times than the sine wave frequency. This reference signal is compared with the triangular carrier signal to generate the gate pulses.

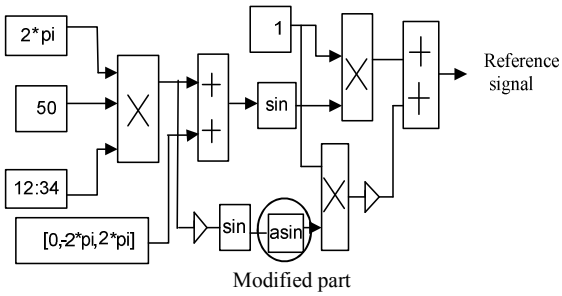


Fig. 4 Reference signal generation for modified THPWM technique

And Fig. 5 shows the generation process of gate pulse.

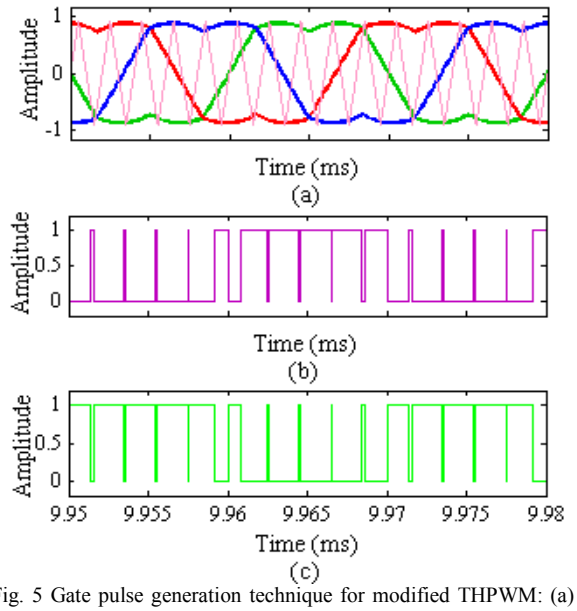


Fig. 5 Gate pulse generation technique for modified THPWM: (a) carrier and reference signal, (b) generated gate pulse and (c) inverted gate pulse

## V. Simulation and Performance Analysis

The modulation techniques stated above are analyzed for three phase two level inverter using MATLAB/Simulink software. This paper presents sample of the obtained result to compare both modulation techniques. The obtained result will help us to verify our proposed modified THPWM model and also helps to prove that the modified model is better than the THPWM model. The following Fig. 6, Fig. 7 and Fig. 8 indicates the output current, line voltages and frequency spectrum of three phase two level inverter respectively.

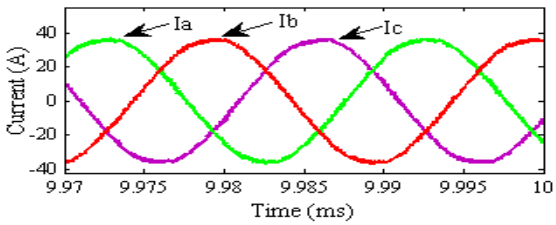


Fig. 6 Output current of three phase two level inverter

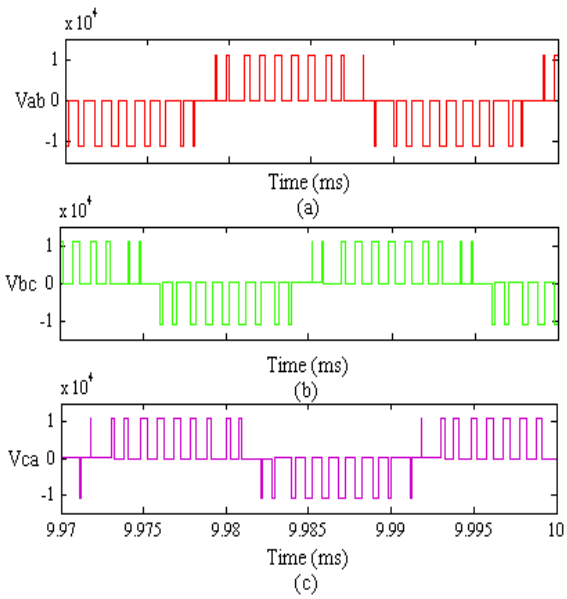


Fig. 7 Output line voltages of three phase two level inverter: (a) voltage of line a-b, (b) voltage of line b-c and (c) voltage of line c-a

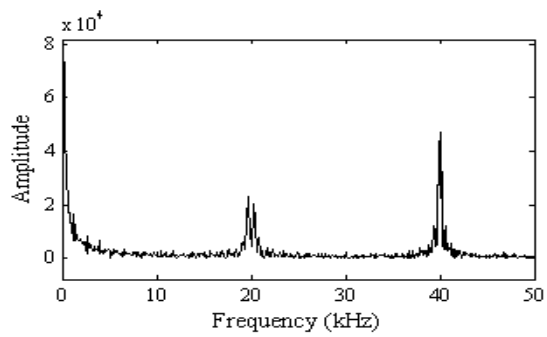


Fig. 8 Frequency spectrum of output voltage

The performance of the two models are analyzed based on the percentage THD. The variation of THD is observed by varying the modulation index and frequency of the carrier signal.

### *A. THPWM Technique*

Fig. 9(a) and Fig. 9(b) shows the calculated THD of THPWM technique for frequency variation and modulation index variation respectively. Frequency is varied from 10 kHz to 40 kHz and modulation index is varied from 0.5 to 1. For frequency variation the lowest THD is 3.99% when the modulation index is fixed at 1. Again for modulation index variation the lowest THD is also 3.99% when the frequency is fixed at 20 kHz.

### *B. Modified THPWM Technique*

The THD variation of modified THPWM technique is indicated in Fig. 9(c) for frequency variation and Fig. 9(d) for modulation index variation. Here the lowest THD 2.97% is obtained for frequency 20 kHz when the modulation index is fixed at 1. Again for modulation index variation the lowest THD is same as 2.97% obtained for modulation index 1 and constant frequency 20 kHz.

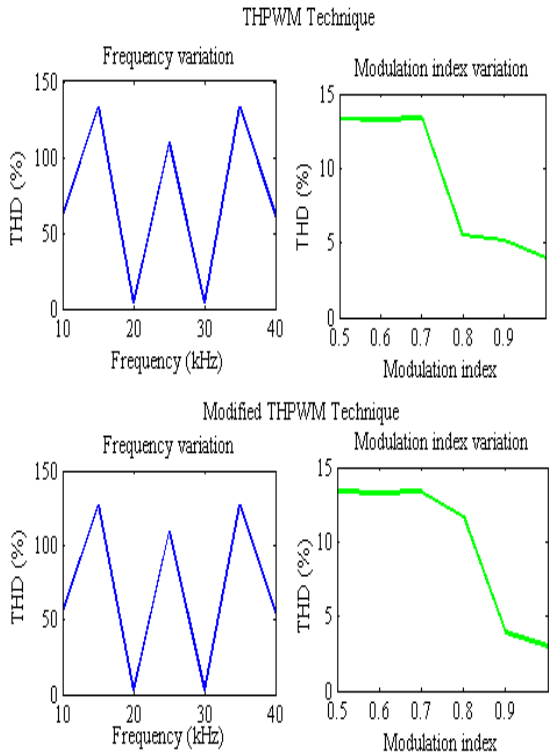


Fig. 9 Calculated THD for THPWM and modified THPWM technique: (a) frequency variation for THPWM, (b) modulation index variation for THPWM, (c) frequency variation for modified THPWM and (d) modulation index variation for modified THPWM

### *C. Comparison between THPWM and Modified THPWM*

All the comparisons are done by varying the frequency and modulation index while one of the parameter is kept constant. The obtained results from the simulation are presented in the tables below. The following tables will provide better understanding about the justification of our proposed model.

TABLE I
COMPARISON OF THD FOR FREQUENCY VARIATION AT MODULATION INDEX 1

| Frequency ( kHz) | THPWM | Modified THPWM |
|---|---|---|
| 10 | 61.28 | 55.33 |
| 15 | 132.7 | 126.6 |
| 20 | 3.99 | 2.97 |
| 25 | 109.1 | 109.1 |
| 30 | 4.11 | 3.17 |
| 35 | 132.7 | 126.6 |
| 40 | 61.28 | 55.33 |

The above simulated data in Table I shows that the THD is lower for modified THPWM than the THPWM technique. For the fixed modulation index 1 the lowest level of THD is obtained at 20 kHz and 30 kHz frequency. For this two frequencies the THD of our proposed model is lower than THPWM. Also for the other frequency our proposed model can minimize the THD level.

TABLE II
COMPARISON OF THD FOR MODULATION INDEX VARIATION AT FREQUENCY 20 KHZ

| Modulation Index | THPWM | Modified THPWM |
|---|---|---|
| 0.5 | 13.38 | 13.38 |
| 0.6 | 13.28 | 13.28 |
| 0.7 | 13.38 | 13.38 |
| 0.8 | 5.51 | 11.64 |
| 0.9 | 5.14 | 3.92 |
| 1.0 | 3.99 | 2.97 |

Table II shows modulation index variation for certain constant frequency at 20 kHz and here modulation index around 1 offers lower THD. And for modulation index 1 THD is lower for both the techniques but modified THPWM offers the lowest THD.

TABLE III
COMPARISON OF THD FOR MODULATION INDEX VARIATION AT FREQUENCY 35 KHZ

| Modulation Index | THPWM | Modified THPWM |
|---|---|---|
| 0.5 | 4.40 | 3.40 |
| 0.6 | 3.32 | 3.75 |
| 0.7 | 4.56 | 5.01 |
| 0.8 | 144.1 | 165.1 |
| 0.9 | 139.5 | 132 |
| 1.0 | 132.7 | 126.6 |

Again for modulation index variation in Table III keeping frequency constant at 35 kHz, the lower level THD is obtained for modulation index around 0.6. If any inverter needs to operate at lower modulation index then modified THPWM helps to reduce the THD at fixed frequency 35 kHz and modulation index around 0.6.

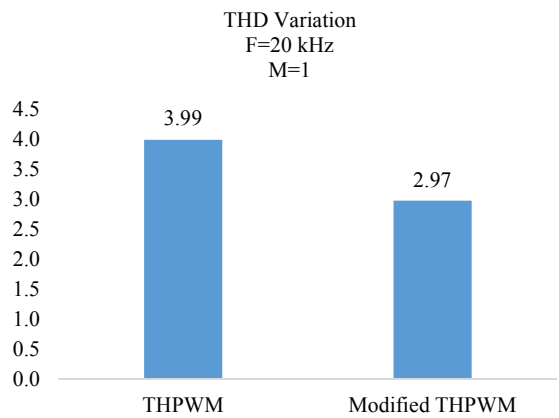


Fig. 10 THD variation for optimum condition (in percentage)

From the simulated data it can be easily found that THD is less at frequency 20 kHz and modulation index 1. This is the optimum condition for the above simulation. At that optimum condition the lowest THD is 3.99% for THPWM and 2.97% for modified THPWM. Fig. 10 represents the lowest THD for THPWM and modified THPWM in bar graph.

## VI. CONCLUSION

The performance of inverter is analyzed based on the level of THD present in the output signal. The lower THD indicates better performance of inverter. According to the analysis and comparative study by varying modulation index and frequency, this paper suggests an optimum condition for THD analysis. This optimum condition belongs to modulation index 1 and frequency 20 kHz. The given tables provide the necessary information for this optimum condition. At this optimum condition the THD for both THPWM and modified THPWM is shown in the bar graph. The bar graph justifies that the modified THPWM offers lowest THD than THPWM at that optimum condition. From the analysis and simulated data we can conclude that the modified THPWM technique provides better performance than THPWM. Hence the efficiency of inverter can be improved by using this modified THPWM technique.

## REFERENCES

[1] J. Jose, G. N. Goyal and M. V. Aware, "Improved inverter utilization using third harmonic injection," in *Proc. Joint Int. Conf. Power Electronics, Drives and Energy Systems (PEDES)*, 2010, New Delhi, India, Dec. 20-23, pp. 1-6.

[2] J. A. Houldsworth and D. A. Grant, "The use of harmonic distortion to increase the output voltage of a three phase PWM inverter," *IEEE Trans. industry applications*, vol. IA-20, no. 5, pp. 1224-1228, Sept/Oct. 1984.

[3] U. Bose, K. Divya, V. Jyothi and S. Sreejith, "Performance analysis of four-switch three-phase inverter-fed induction motor drive," in *Proc. Power and Energy Systems Conf. Towards Sustainable Energy*, Bangalore, India, Mar. 13-15, 2014.

[4] M. R. Islam, Y. G. Guo and J. G. Zho, "Power Converter Topologies for Grid-Integrated Medium-Voltage," in *Power converters for medium voltage networks*, Springer-Verlag Berlin Heidelberg, 2014.

[5] S. K. Sahoo, A. Ramulu, S. Batta and S. Duggal, "Performance Analysis and Simulation of Three Phase Voltage Source Inverter using basic PWM Techniques," in *Proc. IET Chennai 3rd Int. Conf. Sustainable Energy and Intelligent Systems (SEISCON 2012)*, Tiruchengode, India, Dec. 27-29, 2012.

[6] M. A. A. Younis, N. A. Rahim and S. Mekhilef, "Simulation of Grid Connected THIPWM-Three-Phase Inverter Using SIMULINK," in *Proc. IEEE Symp. Industrial Electronics and Applications (ISIEA2011)*, 2011, Langkawi, Malaysia, Sep. 25-28, pp. 133-137.

[7] I. Colak, R. Bayindir and E. Kabalci, "A modified harmonic mitigation analysis using Third Harmonic Injection PWM in a multilevel inverter control," in *Proc. 14th Int. Power Electronics and Motion Control Conf., EPE-PEMC*, 2010, Ohrid, Macedonia, Sep. 6-8, pp. 215-220.

# Comparative Analysis and Simulation of Active Inductors for RF Applications in 90 nm CMOS

Omar Faruqe, Md. M. M. Saikat, Md. A. K. Bulbul and Md. Tawfiq Amin, *Member, IEEE*
Department of EECE, Military Institute of Science and Technology (MIST), Dhaka-1216, Bangladesh
Email: ofaruqe20@gmail.com; tawfiqamin@gmail.com

***Abstract*—This paper presents the comparative analysis of active inductor design for high quality factor at high frequency applications on the selection of active inductor topologies. Inductor based circuits are commonly used in integrated circuits where the quality factor of the inductor dominates the performance of the designed circuits. Since planner spiral inductor occupies a large area and shows low quality factor, active inductor is a good option to overcome the drawbacks of the spiral inductors. This paper summarizes the analysis and simulation results to select the best active inductor topology for high quality factor at high frequency applications (RF applications). Simulated in Cadence 6.16 environment using the 90 nm CMOS technology, Weng-Kuo active inductor topology shows the higher quality factor as well as high frequency range.**

***Keywords*—Active Inductor, RF Integrated Circuits, Voltage-controlled oscillator (VCO), quality factor, *LC* tank, planner spiral inductor.**

## I. Introduction

In the encompassing range in various applications such as RF transceivers, low-noise amplifiers, power amplifiers, filters, LC tank voltage-controlled oscillators (VCOs), bandwidth extension circuits, clock drivers, power distribution modules, microwave integrated circuits. Fundamentally planner spiral inductors are usually applied mainly because of their outstanding phase noise [1]-[5]. The usage of the spiral inductors exhibits several drawbacks: large chip area, complexity to achieve high inductive values in association with low values in quality factor and its geometry is not that much efficient leading to discourage to use at high density integration [1]. In order to overcome the drawbacks, active inductors can be used in an efficient way to achieve the objectives like low cost, low supply voltage, suitable operational frequency which are the important parameters for designing circuits. An implementation of the active inductor is a methodology called the Gyrator-C configuration [6]-[7]. Recombining circuit elements such as resistor, capacitor, transistor in a benefitting manner which will act as an equivalence of impedance. This Gyrator-C configuration exhibits much higher values of inductance and quality factor in quantitative comparison to traditional spiral inductors [8]-[9]. Gyrator-C network configured in different ways and have variations in parameters such as frequency range, power consumption, inductance tunable range, requirement of silicon area for physical implementation [11].

Moreover, Yodprasit-Ngarmnil, Thanachayanont-Payne cascode, Weng-kuoCascode, Lin-Payne active inductors are also several active inductor topologies [10]-[14]. Thanachayanont-Payne active inductor is based on low voltage topology that can achieve high Q with least circuit multifaceted nature, in this manner limiting noise and power utilization [14]. In addition, Lin-Payne active inductor fulfills noteworthy purposes like making conceivable high frequency circuit operation and maximizing the dynamic range through adequate voltage headroom [13]. In Weng-Kuo active inductor, the constrains of not being able to vary the inductance and quality factor are invalidated [10]-[11]. Yodprasit-Ngarmnil active inductor is based on double feedback transconductance topology for enhancing Q [12].

This paper summarizes different active inductor models with quantitative analysis to sort out which has better quality factor, relatively low level of power consumption, tunable frequency ensuring higher performance in the active inductor based practical circuitry.

## II. Active Inductor Topology

### A. *Lossless Single Ended Gyrator-C Active Inductor*

A Gyrator-C network is back-to-back transconductors having one port associated with a capacitor. When the input and output impedances of the transconductors are infinite the network is said to be lossless. Single ended indicates that any one end of the network is connected to a ground. That's the reason the definitive name of the network is Lossless Single Ended Gyrator-C Active Inductor. Fig.1 shows the lossless single ended Gyrator-C active inductors where, at node (2), applying KCL

$$I_{in} + G_{m2}V_1 = 0, I_{in} = \frac{\frac{V_2}{sC}}{G_{m2}G_{m1}} \quad (1)$$

where $V_1 = -G_{m1}V_2 \times \frac{1}{sC}$ is used

The admittance of the Gyrator-C network at port 2 is given by

$$Y = \frac{I_{in}}{V_2}, \quad Y = \frac{1}{s(\frac{C}{G_{m1}G_{m2}})} \quad (2)$$

From the denominator of the equation (2)

978-1-5386-2307-7/17/$31.00 ©2017 IEEE

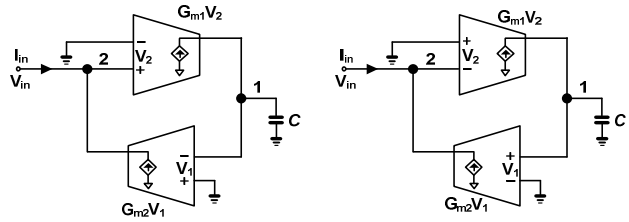


Figure 1. Lossless single ended Gyrator-C active inductors
(a) Positive transconductance in forward path and negative in the feedback path (b) Negative transconductance in forward path and positive in feedback path.

$$\frac{C}{G_{m2}G_{m1}} = \frac{QV}{I^2} = \frac{V}{\frac{I}{\frac{Q}{I}}} = \frac{V}{\frac{I}{t}} = L, [Q = It]$$

Thus a single ended lossless inductor is emulated at the port 2 of Gyrator-C network which is known as Gyrator-C active inductor of which inductance is proportional to the load capacitance and inversely proportional to the product of the transconductance of the tranconductors has an inductance of

$$L = \frac{C}{G_{m1}G_{m2}} \tag{3}$$

The impedance due to inductance is $X_L = sL$where $s = 2\pi f$. Both Fig. 1(a) and Fig. 1(b) will work as a single ended inductor where the basic difference is, Fig. 1(a) has a positive transconductance in the forward path and a negative transconductance in the feedback path but Fig. 1(b) has a negative transconductance in the forward path and a positive transconductance in the feedback path. In a shortsighted manner, with the increment of the applied input voltage, the output current of a transconductor enhances and at that point it might be said that the transconductor has a positive transconductance. On the contrary, the decrement of the output current of a transconductor can be illustrated as a transconductor having negative transconductance.

### *B. Lossy Single Ended Gyrator-C Active Inductor*

Inductors are called lossy when the input and output inpedances of transconductors of Gyrator-C configuration are finite. Implementing MOS transistor, the input and output impedances of the network become finite. The lossy network is inductive upto self-resonant frequency [11].

The common-source configuration exhibits the negative transconductance while the common-drain configuration exhibits

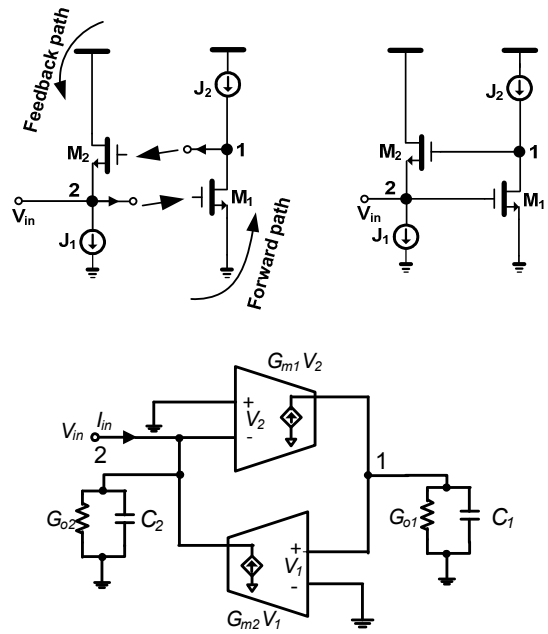


Figure. 2. Simplified schematic of Basic Gyrator-C active inductor (up) and Lossy single-ended Gyrator-C active inductors (down)

positive transconductance. Therefore a common source configuration in the forward path and a common gate configuration in the feedback path are applied to emulate the basic Gyrator-C configuration as shown in Fig. 2. Applying KCL at node 1 and 2 of Fig. 2

$$G_{m1}V_2 = (sC_1 + G_{01})V_1 \tag{4}$$

$$I_{in} + G_{m2}V_1 = (sC_2 + G_{02})V_2 \tag{5}$$

Solving (4) and (5)

$$Y = sC_2 + G_{02} + \frac{1}{s(\frac{C_1}{G_{m1}G_{m2}}) + \frac{G_{01}}{G_{m1}G_{m2}}} \tag{6}$$

Equation (6) represents a RLC networks and its parameters are given by $R_p = \frac{1}{G_{02}}$ and $Cp = C_2$where $R_P$ and $C_P$ are the parallel resistance and parallel capacitance respectively. Series resistance with inductor,$R_s = \frac{G_{01}}{G_{m1}G_{m2}}$ and the inductance, $L = \frac{C_1}{G_{m1}G_{m2}}$.

## III. Different Active Inductor Models

### *A. Yodprasit-Ngarmnil Active Inductor*

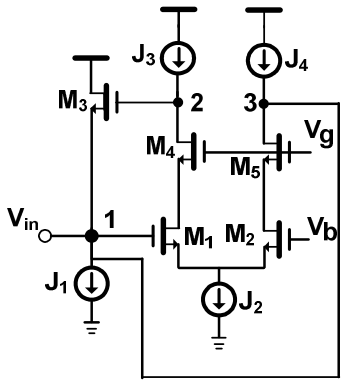


Figure 3. Yodprasit-Ngarmnil active inductor.

This model is developed on double feedback transconductane topology. Here positive feedback is used to raise a resistance for negating the inductor loss and the negative feedback is to conceive inductive input impedance so that the Q factor can be enhanced. In the circuitry shown in Fig. 3, for producing positive feedback, the active inductor input terminal and drain of $M_5$ is connected electrically. As there is resistive loss in the Yodprasit-Ngarmnil active inductor, a negative resistor with resistance of $-R_{P,total}$ is connected in parallel with $R_{P,total}$. By this way, the net resistive loss of designed active inductor demolishes. To analyze the performance of this type of inductor, quality factor can be defined as

$$Q = \frac{\sqrt{g_{m_3} g_{m1} C_{gs_3} C_{gs_1}}}{\frac{C_{gs_1}}{r_{o_1}} + 2\frac{C_{gs_1}}{r_{o_3}}} \tag{7}$$

Q can be tuned by varying $g_{m_{1,2}}$ or $r_{o1,2}$. As the preceding parameters change the inductance,$r_0$of $M_1$and $M_2$can be changed and this variation can be achieved by employing the cascade configuration [11]-[12].

*B. Lin-Payne Active Inductor*

Lin-Payne active inductor methodology satisfies two major purposes. i) Under low parasitic, it has made possible high frequency circuit operation, and ii) Maximize the dynamic range through sufficient voltage headroom. For this design requirement, a minimum level of supply voltage is expressed as

$$V_{DD_{min}} = V_{GSp} + V_{DSat}$$

This minimum supply voltage for outer transistor $M_2$ is higher with a quantitative comparison to inner transistor branch $M_1$. For $M_1$,

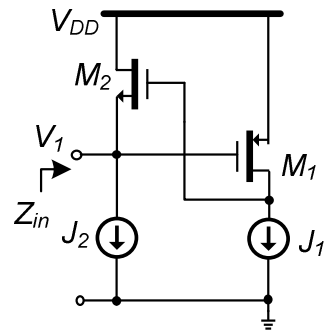


Figure 4. Lin-Payne active inductor.

$$V_{DD_{min}} = V_{GSp} - V_{GSn} + V_{DSat}$$

This equation connotes that for the current source $I_1$ a considerably large voltage headroom is left which is the key factor for varying tuning range. [11]-[13].

*C. Thanachayanont-Payne Active Inductor*

For the low phase noise and low power performance of the LC-VCO, the LC-tank should have high Q. It was indicated out before that amplify the frequency range of dynamic inductors, $\omega_z$ ought to be limited and $\omega_0$ ought to be amplified. Expanding $\omega_0$ is fairly troublesome in light of the fact that $\omega_0$ of dynamic inductors is set by the cut-off frequency of the transconductors constituting the dynamic inductors. The frequency of the zero of dynamic inductors given by $\omega_z = \frac{g_{01}}{C_{gs2}}$ , then again, can be brought down by either increasing $C_{gs2}$ or diminishing $g_{01}$. The previous is at the cost of bringing down $\omega_0$ and ought to in this way be kept away from. To diminish $g_{01}$, Thanachayanont and Payne proposed the cascode dynamic inductors appeared in Fig 5.

Cascode can be executed in both of the two transconductors, as appeared in Fig. 5. The impedance of Thanachayanont-Payne cascode dynamic inductor is given by

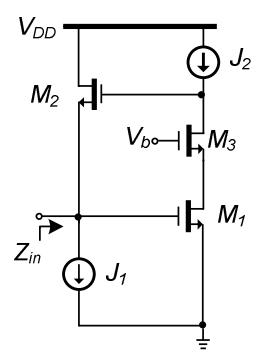


Figure 5. Thanachayanont-Payne active inductor

$$Z \approx \left(\frac{g_{01}g_{03}}{C_{gs1}C_{gs2}g_{m3}}\right)\frac{s\left(\frac{C_{gs2}g_{m3}}{g_{01}g_{03}}\right)+1}{s^2+s\left(\frac{g_{01}g_{03}}{C_{gs2}g_{m3}}+\frac{g_{01}}{C_{gs1}}\right)+\frac{g_{m1}g_{m2}}{C_{gs1}C_{gs2}}} \quad (8)$$

The self-resonance frequency of the dynamic inductor is given by

$$\omega_0 = \sqrt{\frac{g_{m1}g_{m2}}{C_{gs1}C_{gs2}}}$$

and it stays unaltered. It ought not be astounded to see that cascodes try not to change $\omega_0$ . This is on account of cascodes are not subject to Miller impact and has no impact on the transmission bandwidth. Cascode designs therefore can successfully enhance the frequency range scope of dynamic inductors by bringing down the lower bound of the frequency range of dynamic inductors [11]-[14].

### *D. Weng-Kuo Cascode Active Inductor*

Weng-Kuo cascode active inductor negates the limitation of that the inductance and the quality factor can't be varied. The simplified schematic of Weng-Kuo active inductor is shown in Fig. 6 where $g_{m1}$ is proportional to $J_1$+$J_3$ while $g_{m3}$ is only proportional to $J_1$. The parameters are defined as

$$L = \frac{C_{gs2}}{g_{m1}g_{m2}}, R_S = \frac{g_{01}g_{03}}{g_{m1}g_{m2}g_{m3}}, C_P = C_{gs1} \text{and } R_P = \frac{1}{g_{o2}},$$

And

$$Q(\omega_0) = \frac{\omega_{oL}}{R_s} = \frac{g_{m3}}{g_{01}g_{03}}\sqrt{\frac{g_{m1}\,g_{m2}C_{gs2}}{C_{gs1}}} \quad (9)$$

$\omega_0$ can be tuned by varying $g_{m1}$ and $g_{m2}$while Q can be tuned by varying $g_{m3}$ only. So the tuning of Q can be made independent of $\omega_0$. For the tuning of $\omega_0$, Q will be affected [10]-[11].

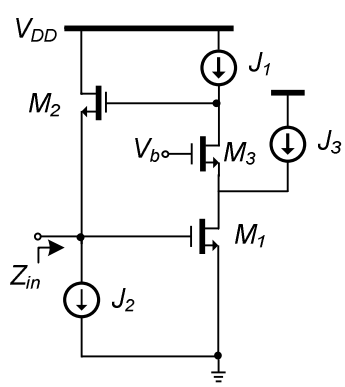


Figure 6. Weng-Kuo cascade active inductor

## III. Simulation Results

To compare the performance of different active inductor topologies, simulations have been performed in Cadence 6.16 environment using the 90 nm CMOS technology. In the simulations, channel length of all NMOS and PMOS transistors areset at 200 nm and the width of NMOS and PMOS are set at 10µm and 20µm respectively. The s parameter simulation has been performed for obtaining the inductance and quality factor of the investigated models of active inductor. The s-parameter simulation has been accomplished with an ac source in series with a resistance of 50 ohm and a capacitor of 100pF for dc isolation. For less-loss active inductors, the ideal current source of 300µA has been used. NMOS at the $V_{DD}$ to input terminal (according to maximum Q factor based on Gyrator-C network) has width of 30µm and length of 200nm. Supply $V_{DD}$ voltage was set at 1.8V .

The comparison has been performed based on different parameters like quality factor, inductance, power consumption and self-resonant frequency. Fig. 7 shows the variation of Q factor for different models where Fig. 8 shows the variation of inductance. In Fig. 7(a) and 7(b) stated below, it is comprehensively noticed that quality factor has been increased linearly at low frequency and reached to maximum level. Afterwards, attaining maximum value, the factor has started to decrease owing to finite output impedance and the self-resonance of the inductor. The quality factor is annihilated at the point when the frequency is proceeded the cut off or self-resonance frequency of the inductor. In Fig. 7(a), constant current source has been employed for biasing. As a result, the net loss emerged from the parasitic resistance is less. On the contrary, in Fig.7(b),loss emerged from parasitic resistance increases on account of inserting MOS device which degrades the quality factor. In spite of the drawback, the insertion of MOS enhances the frequency range as well as inductance.

Yodprasit-Ngarmnil introduced parallel negative resistance for enhancing the Q factor which reduces parallel parasitic resistance of active inductors. Nevertheless employing MOS as current source does not affect significantly since the appeared value of quality factor is 0.5806 which is much lower comparing to others. On the other hand, for constant current source the quality factor improves but not capable of exceeding the outcome of Weng-Kuo. In addition, the power consumption is greater than Weng-kuo active inductor.

Weng-Kuo active inductor is the modified version of Thanachynont-Payne. But both have unique property of enhancing the frequency range by a cascaded MOS. But Weng-Kuo model has wider frequency range than Thanachynont-Payne which are 7.5 GHz and 11.87 GHz. In addition, Weng-Kuo is preferable than other models of having the property of tunability of the quality factor and inductance which have been

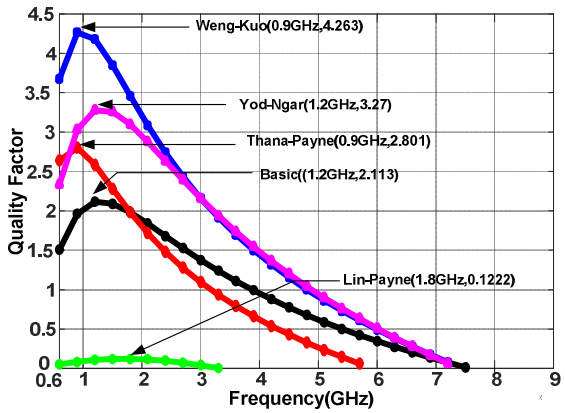


(a)

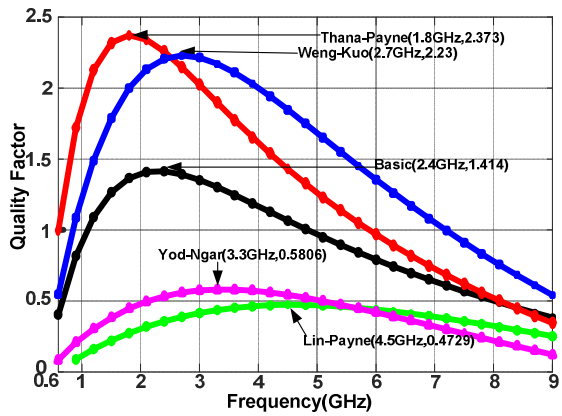


(b)

Figure 7. Variation of quality factor with frequency for different topologies. (a) Active inductors with constant current source, and (b)
Active inductors with saturated MOS as current source.

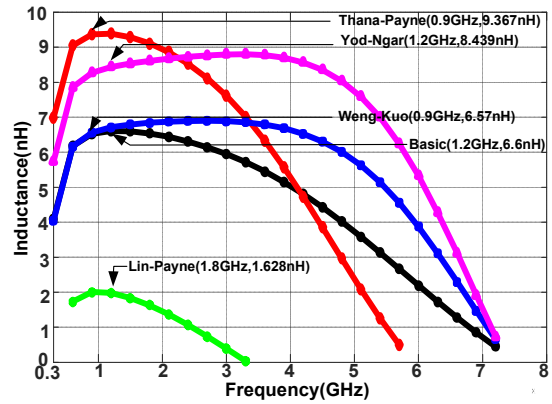


(a)

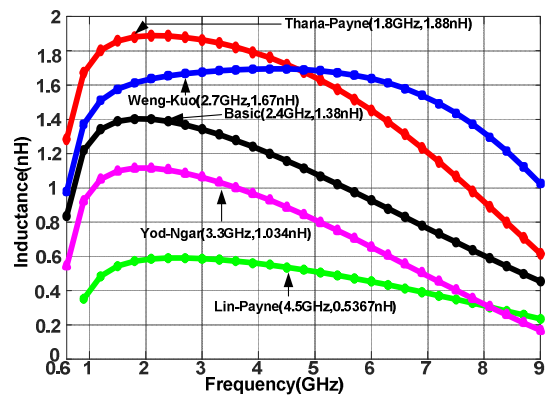


(b)

Figure 8.Variation of Inductance with Frequency for different topologies. (a) Active inductors with constant current source, and (b) Active inductors with saturated MOS as current source.

made possible for introducing an additional current source in the circuitry. Though the power consumption of this type active inductor is 10.63 mW which more than other topologies due to the additional current source. In spite of this demerit, it is highly advantageous with increasing quality factor having the numerical values of 4.263 and 2.23. TABLE I and TABLE II summarizes the simulation results.

TABLE I.
ACTIVE INDUCTOR WITH CONSTANT CURRENT SOURCE

| | Basic Gyrator-C | Yodprasit-Ngarmnil | Lin-Payne | Thanachayanont-Payne | Weng-Kuo |
|---|---|---|---|---|---|
| **Quality Factor** | 2.113 @1.2GHz | 3.27 @1.2GHz | .1222 @1.8 GHz | 2.801 @0.9GHz | 4.263 @0.9GHz |
| **Inductance (nH)** | 6.6 @1.2 GHz | 8.439 @1.2GHz | 1.628 @1.8GHz | 9.367 @0.9GHz | 6.57 @0.9GHz |
| **Power (mW)** | 1.08 | 2.34 | 1.08 | 1.08 | 1.62 |
| **$f_0$ (GHz)** | 7.57 | 7.40 | 3.332 | 5.923 | 7.462 |

TABLE II.
ACTIVE INDUCTOR WITH SATURATED MOS AS CURRENT SOURCE

| | Basic Gyrator-C | Yodprasit-Ngarmnil | Lin-Payne | Thanachayanont-Payne | Weng-Kuo |
|---|---|---|---|---|---|
| **Quality Factor** | 1.414 @2.4GHz | 0.5806 @3.3GHz | 0.4729 @4.5GHz | 2.373 @1.8GHz | 2.23 @2.7GHz |
| **Inductance (nH)** | 1.38 @2.4GHz | 1.034 @3.3GHz | 0.5367 @4.5GHz | 1.88 @1.8GHz | 1.67 @2.7GHz |
| **Power (mW)** | 8.18 | 12.6 | 14.35 | 8.38 | 10.63 |
| **$f_0$ (GHz)** | 13.177 | 10.294 | 12.317 | 11.362 | 11.868 |

## IV. CONCLUSIONS

A comparative analysis on active inductor topologies based on quality factor, frequency range of applications, power consumptions and inductance values have been presented in this paper. The analysis is validated by computer simulations using Cadence Software in 90 nm CMOS technology. Based on the simulation results, Weng-Kuo active inductor shows the wider frequency range which are 7.5 GHz and 11.87 GHz with high Q factor of 4.263 and 2.23 and preferable for tunability of the quality factor and inductance.


## ACKNOWLEDGEMENT

Authors would like to thank Military Institute of Science and Technology (MIST) to give support for simulation at VLSI lab of EECE Department.


## REFERENCES


[1] Krzysztof Iniewski, Advanced Circuits for Emerging Technologies, New Jersey: John Wiley & Sons, Inc, 2012.

[2] N. Nguyen and R. Meyer, "SI IC-compatible inductors and lc passive filters," *IEEE Journal of Solid-State Circuits*, Vol. 25, No. 4, pp. 1028–1031, 1990.

[3] Md. Tawfiq Amin, "On the selection of passive elements for low phase noise LC tank VCO in 65 nm process," *Proceedings, 3rd International Conference on Electrical Engineering and Information & Communication Technology (iCEEiCT-2016)*., Dhaka, Bangladesh, 2016.

[4] V. L. Belini and M. a. Romero, "Design of active inductors using CMOS technology," *Proceedings. 15th Symp. Integr. Circuits Syst. Des.,* no. February 2002, pp. 5–10, 2002.

[5] S. Vallabhbhai and P. Polytechnic, "Quality-Factor Improvement of 0 . 18-µm Active Inductor by a Current Reuse Design," pp. 202–205, 2015.

[6] Wai-Kai Chen, "Passive, Active and Digital Filters", Boca Raton : CRC Press LLC, 2005

[7] T. Deliyannis, Yichuang Sun and J.K. Fidler, Continuous-Time Active Filter Design, Boca Raton: CRC Press LLC, 1996

[8] H. U. Uyanik and N. Tarim, "Compact low voltage high-Q CMOS active inductor suitable for RF applications," *Analog Integr. Circuits Signal Process.,* vol. 51, no. 3, pp. 191–194, 2007.

[9] R. L. Geiger and E. Sânchez-sinencio, "Active Filter Design Using Operational Transconductance Amplifiers: A Tutorial," 1985.

[10] R. M. Weng and R. C. Kuo, "An ω0-Q tunable CMOS active inductor for RF bandpass filters," *Conf. Proc. Int. Symp. Signals, Syst. Electron., pp.* 571–574, 2007.

[11] Fei Yuan, CMOS Active Inductors and Transformers: Principle, Implementation, and Applications , New York: Springer, 2008.

[12] U. Yodprasit and J. Ngarmnil, "Q-enhancing technique for rf CMOS active induor," *2000 IEEE Int. Symp. Circuits Syst. Emerg. Technol. 21st Century. Proc. (IEEE Cat No.00CH36353),* vol. 5, pp. 589–592, 2000.

[13] T. Y. K. Lin and a. J. Payne, "Design of a low-voltage, low-power, wide-tuning integrated oscillator," *2000 IEEE Int. Symp. Circuits Syst. Emerg. Technol. 21st Century. Proc. (IEEE Cat No.00CH36353),* vol. 5, pp. 629–632, 2000.

[14] A. Thanachayanont and A. Payne, "VHF CMOS integrated active inductor," *Electron. Lett*., vol. 32, no. 11, p. 999, 1996.

# Design and Performance analysis of 0.6Tb/s VCSEL based optical link

Mohammad Tanvir Hannan*, Mohammad Istiaque Reja and Jobaida Akhtar
Department of Electrical and Electronic Engineering,
Chittagong University of Engineering and Technology, Chittagong-4349, Bangladesh.
tanvirhannan145@gmail.com*

*Abstract*—An error free (BER < $10^{-12}$) data transmission system model over 50km distance using single mode fiber (SMF) is demonstrated at 0.6Tb/s in this paper. This Vertical Cavity Surface Emitting Laser (VCSEL) based system is designed to operate at room temperature (25ºC). The performance of this model is analyzed at 683nm, 863nm, 1550nm wavelengths. By varying the bit rate the overall performances including Q-factor, bit error rate (BER), output power are analyzed. The analysis also includes fiber amplifiers namely Semiconductor Optical Amplifier (SOA) and Erbium Doped Fiber Amplifier (EDFA) respectively in the system. With the proposed system error free data transmission is achieved over 50km distance with maximum Q-factor of 33.56, bit rate of 0.6Tb/s at 863nm and also the maximum output power of 125.2mW at room temperature at 683nm.

***Keywords— VCSEL; EDFA; Error free data transmission; SOA; Optical link.***

## I. INTRODUCTION

Vertical Cavity Surface Emitting Laser (VCSEL) based data transmission system creates a new era for high speed error free data transmission over long distances. Low temperature dependency and high speed data transmitting ability with relatively high output power production make it ahead of Edge Emitting Laser (EEL) based system [1-2]. Long distance error free data transmission was always a big challenge for VCSEL based system. And also meeting up the ever growing demand of high speed communication makes this system more and more challenging than before. Numerous researches are going on to achieve minimum bit error rate (BER) and better quality output from VCSEL based system for transmitting high speed signals over long distance. Fiber amplifiers are used in the VCSEL based system as they can provide all optical amplification that reduces the necessity of using electrical components. VCSEL provides numerous unique advantages like higher temperature sustainability and error free operation at 25Gb/s [3-4] to 50Gb/s range [5] at frequencies near infrared wavelength region where VCSELs having frequencies near red wavelength region can provide high output power [6]. Some studies reported temperature sensing and compensation for VCSEL driver ICs [7], self-heating control [8], temperature analysis of infrared VCSEL [9], thermal effect of gain-guided VCSEL [10], modeling temperature effects and spatial hole burning [11] to make it more efficient as a transmitter. Up to 105ºC temperature sustainable and 14mW output power producer VCSEL transmitter is reported by using red VCSEL (680nm) [12].

As the aim of this work was to design a VCSEL based error free (BER < $10^{-12}$) ultra high speed data transmission system and analyze it's performance at room temperature, so firstly a VCSEL based system has been demonstrated over 50km distance at 0.6Tb/s. After that, at room temperature the output power, quality factor, bit error rate performance of the system at wavelengths of 683nm, 863nm, 1550nm are analyzed. The focus was to design the VCSEL based system at red and infrared wavelengths (first and third window), that was the reason which played a vital role for choosing those wavelengths. Fiber amplifiers namely SOA and EDFA are incorporated in the data transmission system over a span of 50km and their performance is also analyzed in terms of BER and quality factor for different bit rates. Also Performance analysis of both RZ modulated and NRZ modulated VCSEL in terms of output power has been done here. Finally, it is found that the highest bit rate operation is achieved from the 863nm VCSEL based system at room temperature and the performance is far beyond in terms of bit rate of any existing VCSEL based system at room temperature [13].

## II. VCSEL DESIGN

Optisystem software is used to design the VCSEL and to analysis the system performance. To develop error free data transmission VCSEL of 863nm has been used whose parameters are listed below-

Table 1. Optimized parameters set for VCSEL

| Parameters | Value |
|---|---|
| Thermal Impedance | 2600C/W |
| Thermal Time Constant | 1E-6 |
| Scaling Factor | 2.6E-8W |
| Gain coefficient | 16000$s^{-1}$ |
| Carrier number of transparency | 19400000 |
| Carrier lifetime | 1E-9s |
| Photon lifetime | 3E-12s |
| Spontaneous emission factor | 3E-5 |
| Max. Input current | 40mA |
| Bias current | 5mA |
| Modulation peak current | 10mA |
| Injection efficiency | 1 |
| a- $I_{off}(T)$ | 1.25e-3 -2.55e-5 2.91e-7 -2.53e-10 1.02e-12 |
| b- V(T) | 1 |
| c- V(I) | 1.721 275 -2.44e4 1.34e6 -4.15e7 6.68e8 - 4.27e9 |

978-1-5386-2307-7/17/$31.00 ©2017 IEEE

## III. System Design

This VCSEL based system is designed for transmitting error free data over 50km distance by varying temperature and wavelengths in presence of EDFA and SOA. Our proposed system is a combination of three sections.

### *A. Transmission Section Design*

In transmitting section RZ modulated VCSEL of 1550nm, 863nm, 683nm is used for analyzing system performance at room temperature. VCSEL is driven by bias generator which provides proper stability and reduces non-linear effect from it. Pseudo Random Bit Sequence (PRBS) is used in this model to generate digital data. Mach-Zehnder modulator of an extinction ratio of 6dB mixes the electrical signal with the input signal to produce optical output signal. The output signal is then sent through single mode optical fiber link.

### *B. Channel Section Design*

A single mode optical fiber of 50km length has been used in the channel section of the model. The optical fiber is designed with dispersion of 16.75ps/nm/km and attenuation of 0.2dB/km. Optical amplifiers (SOA and EDFA) are used at wavelengths under consideration for achieving less distorted and better output performance.

### *C. Receiver Section Design*

In the receiver section an optical receiver is used to receive the data which is transmitted from transmitter section. The optical receiver consists of an APD photo detector and a low pass filter. Photo detector receives the transmitting data and sends it to low pass filter for discarding the high frequency signals. We have accounted the effect of shot noise, thermal noise and estimated receiver noise at the receiver end of the system.

## IV. Results and Discussion

The proposed system represents error free data transmission at room temperature at wavelengths under consideration. Quality factor (Q-factor) is a dimensionless measurement which indicates the quality of the system. For given SNR, Q-factor can be calculated using equation (1) where T= bit period, SNR= signal to noise ratio, $B_{opt}$= bandwidth of the optical filter used [14].

$$Q= SNR\sqrt{(2TB_{opt})}/\{1+\sqrt{(1+2SNR)} \qquad (1)$$

Bit error rate (BER) is also an essential measuring parameter for optical data transmission system which measures the number of error bits received as a proportion of the number of good bits. Optisystem uses following equation for calculating BER [14].

$$BER= erfc(Q/\sqrt{2})/2 \qquad (2)$$

BER for this model is considered $BER<10^{-12}$ as a standard, which means that in every $10^{12}$ bits, one bit was error. Eye diagram for wavelengths under consideration represents system's performance.

Fig. 1 represents widely open eye pattern for 863nm wavelengths which shows less distorted system behavior with high signal to noise ratio (SNR) and small amount of jitter. A high Q-factor of 34.55 is also found for 863nm which is shown in Fig. 1 with red color curve that represents better quality output of the system. For 1550nm we have got almost similar amount of SNR and jitter with less distorted behavior and high Q-factor of 31.9 which is slightly lesser than 863nm shown in Fig. 2.

For 683nm from the eye diagram we have got comparatively highly distorted response with lower SNR and higher jitter than 1550nm and 863nm system as shown in Fig. 3. A moderate Q-factor of 26.5 is described by the red curve as shown in Fig. 3.

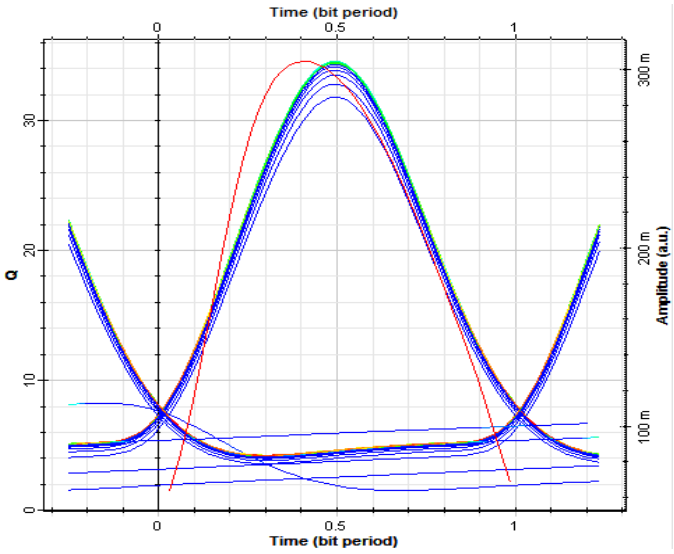


Fig. 1. Eye diagram for maximum Q-factor and minimum BER at 863nm

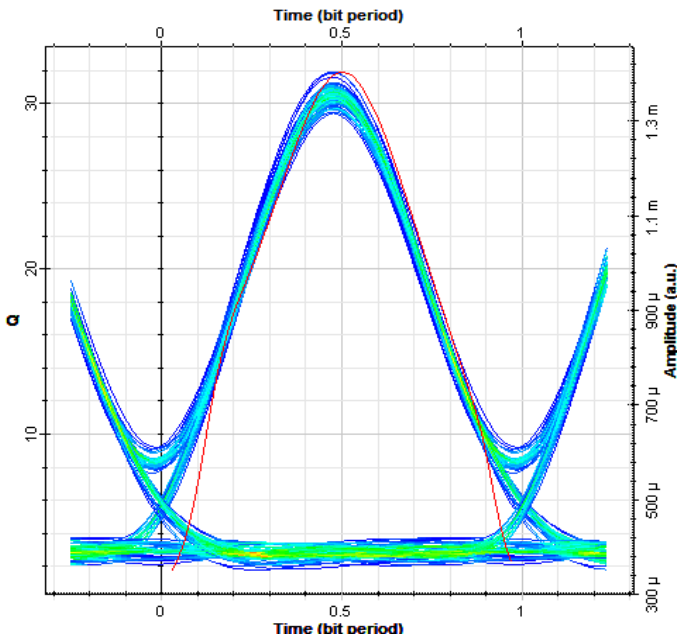


Fig. 2. Eye diagram for maximum Q-factor and minimum BER at 1550nm.

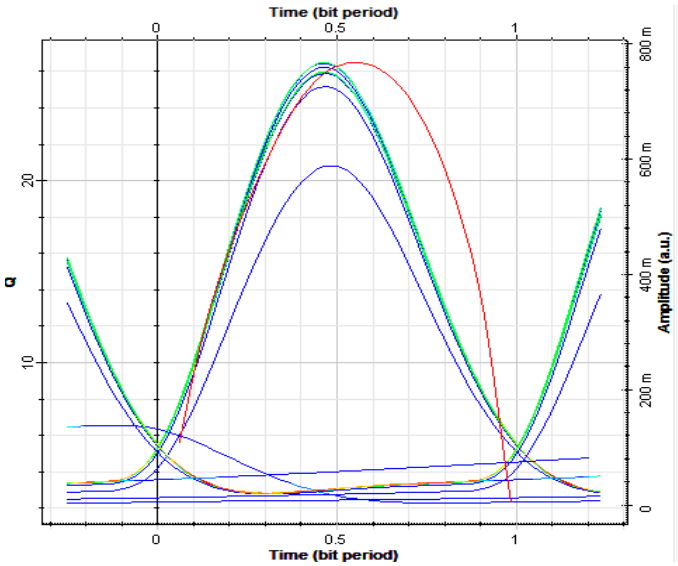


Fig. 3. Eye diagram for maximum Q-factor and minimum BER at 683nm.

Performance parameters of the proposed system i.e. output power, quality factor performance, bit error rate at different bit rates are analyzed at wavelengths under consideration. The system performance is analyzed in several conditions like without amplifier or by incorporating EDFA and SOA with the system separately at room temperature.

At 1550nm we have got system operation up to 480GB/s at room temperature by using SOA and also got small variation of quality factor with the increase of bit rates. On the other hand with EDFA and without amplifier system we have found lesser bit rate operation with drastic fall of Q-factor as shown in Fig. 4.

At 863nm by using SOA we have got highest bit rate operation of 0.6Tb/s. We also have got better quality factor (34.55) with SOA at 100Gb/s shown in Fig. 5. The system at 863nm suits the best for 100Gb/s operation after incorporating SOA, an increasing trend of quality factor is achieved here up to this bit rate. On the other hand we have got exponentially decreased quality output from without amplifier and EDFA based system with the rise of bit rate which is shown Fig. 5.

At 683nm we have achieved almost equal quality output with EDFA and without amplifier system with bit rate operation of nearly 250GB/s. But the inclusion of SOA in the system reduces its bit rate performance range and a drastic fall of quality factor with the increase of bit rate is shown in Fig. 6.

When system is designed without any amplifier we have got better bit rate operation range and quality factor performance at 863nm than the other two as illustrated in Fig. 7.

Almost identical performance as in the system without amplifier is found from the system with EDFA which is shown in Fig. 8 where 863nm is dominating the 683nm and 1550nm system in terms of better quality of output and higher bit rate operation.

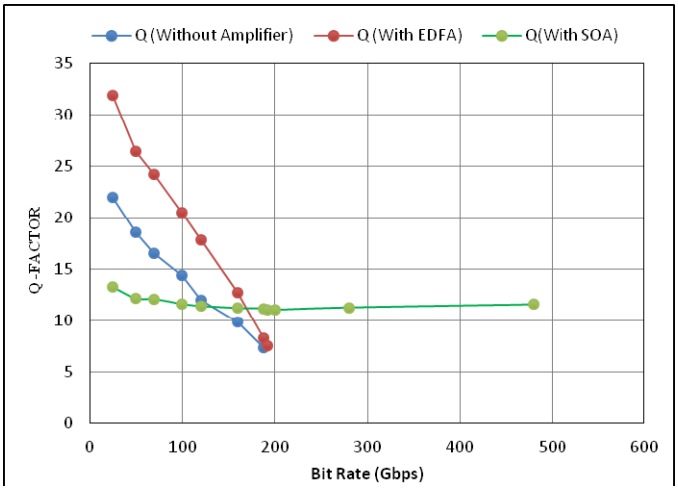


Fig. 4. Q-factor vs Bit rate curve at 1550nm.

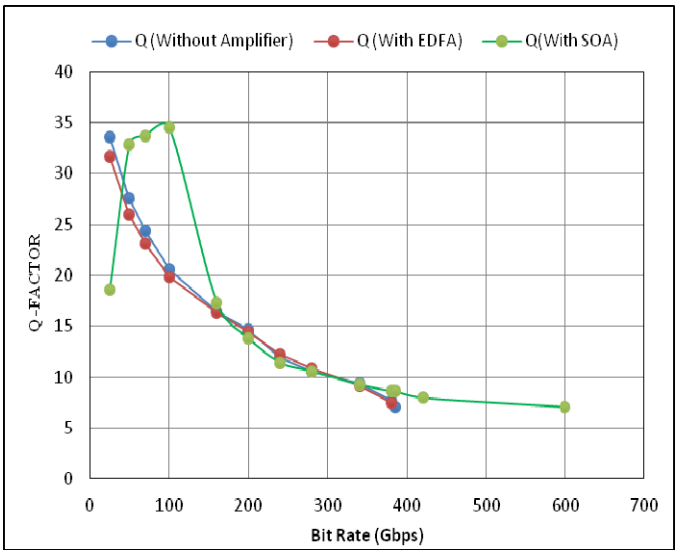


Fig. 5. Q-factor vs Bit rate curve at 863nm.

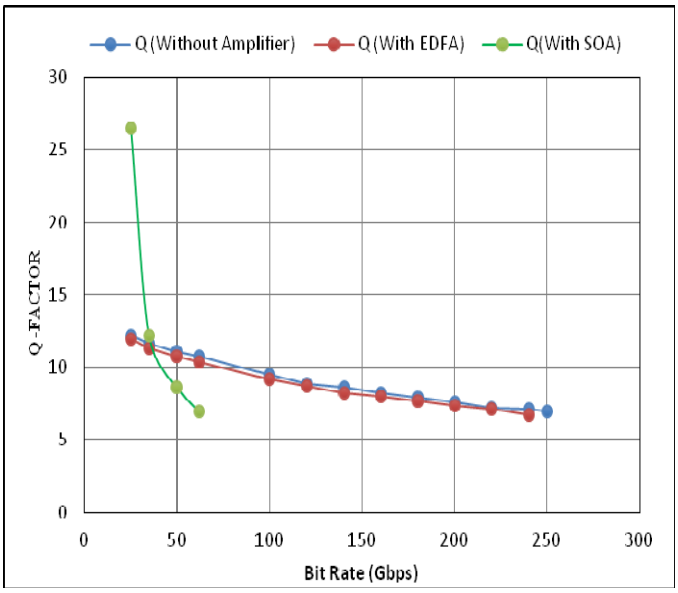


Fig. 6. Q-factor vs Bit rate curve at 683nm.

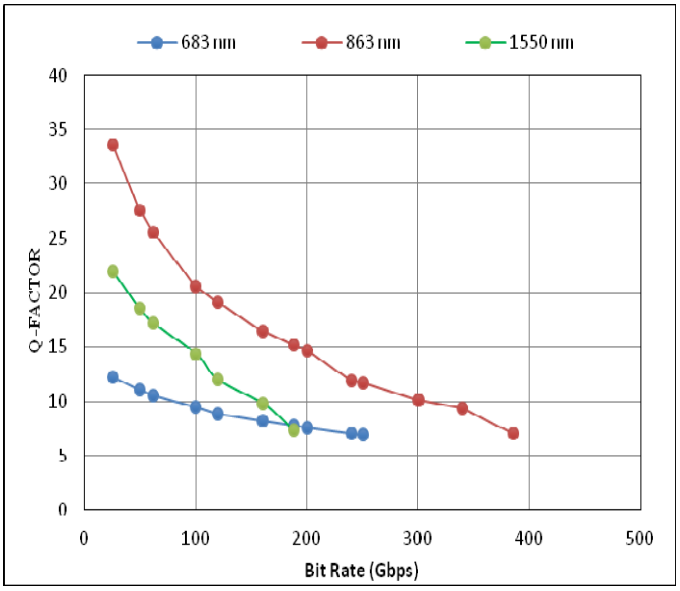


Fig. 7. Q-factor vs Bit rate curve at wavelengths under consideration (without amplifier).

From Fig. 9 we have got better quality output and bit rate operation by using SOA in the 863nm based system and also found a drastic fall of quality factor with the increase of bit rate from 683nm based system.

We have found the highest Q factor at 100 Gb/s bit rate from 863nm based system, which indicates that the designed VCSEL based system with SOA performs best at this wavelength.

In Fig. 10 we have demonstrated the power performance with respect to bit rate when SOA is used in the system model at wavelengths under consideration. From the figure it can be seen that 683nm provides very high performance of 125.2mW than the other two wavelengths of 863nm and 1550nm at room temperature.

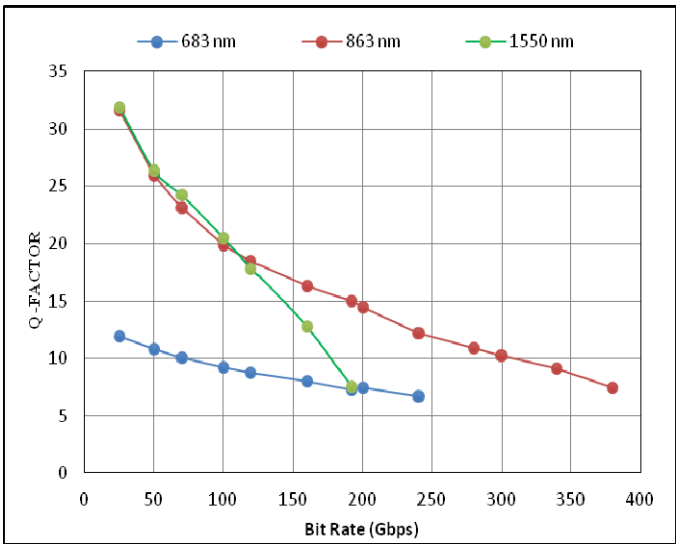


Fig. 8. Q-factor vs Bit rate curve at different wavelengths (EDFA used).

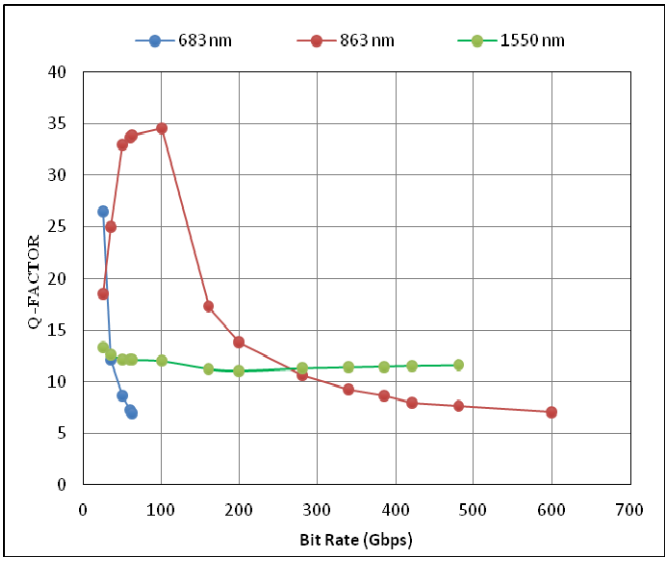


Fig. 9. Q-factor vs Bit rate curve at different wavelengths (SOA used).

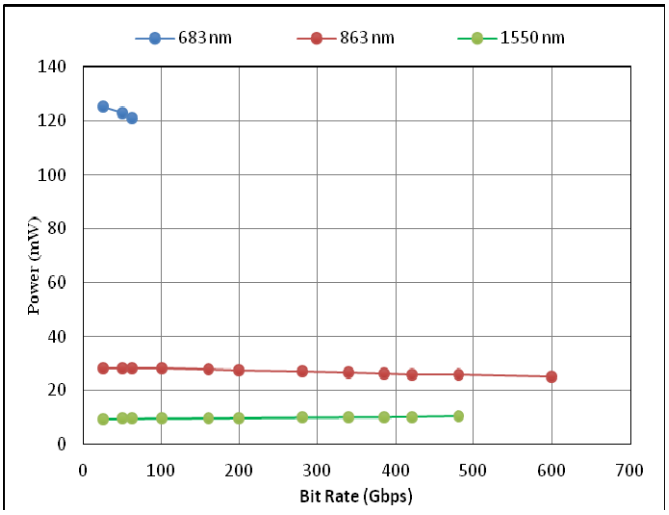


Fig. 10. Power vs Bit rate curve at different wavelengths (SOA used).

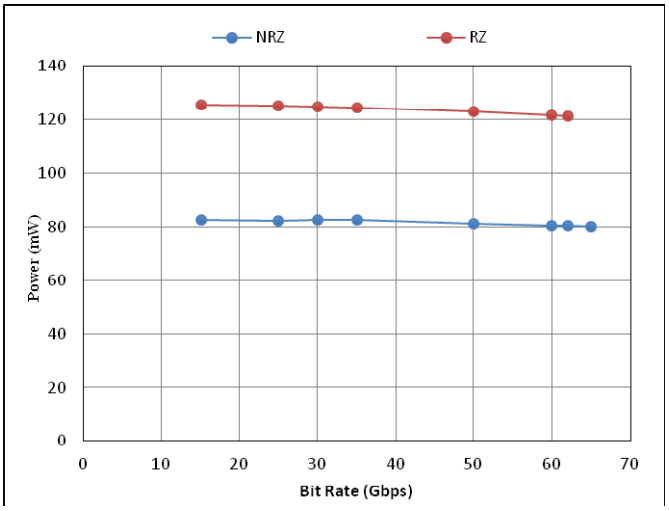


Fig. 11. Power vs Bit rate curve for NRZ and RZ modulated VCSEL model (SOA used).

In Fig. 11 output power and bit rate performance of NRZ and RZ modulated VCSEL system are presented and we have better output power from RZ modulated system. On the other hand slightly better bit rate operation is found from NRZ modulated system.

## V. CONCLUSION

We have achieved 0.6Tb/s data transmission at room temperature by incorporating SOA at 863nm in our system. And we also have achieved record 125.2mW output power at 25Gb/s at room temperature for single mode fiber by incorporating SOA at 683nm. The maximum quality factor of 34.55 was found at 100Gb/s for error free operation by incorporating SOA at 863nm. In future, we will work on highest temperature operation at wavelengths under consideration by incorporating the fiber amplifiers and also by using Return Zero (RZ) pulse generator at transmitter end. We also will work on material challenges of red VCSEL system. Short reach Ultra-high speed data communication by using multimode fiber at the wavelengths under consideration is also our point of interest to work on future.

## REFERENCES


[1] K. Iga, *Fundamentals of Laser Optics*. New York: Plenum Press, 1994.

[2] Rainer Michalzik and Karl Joachim, "Operating Principles of VCSELs", University of Ulm, Optoelectronics Department, D-89069 Ulm, Germany.

[3] S. Masumi, "CMOS VCSEL driver circuit for 25+Gbps/channel short-reach parallel optical links", Master's thesis, University of Toronto, Ontario, Canada, 2015.

[4] Nikolaos Bamiedakis, Jian Chen, Richard V. Penty, "Bandwidth Studies on Multimode Polymer Waveguides for ≥25 Gb/s Optical Interconnects", *IEEE photonics technology letters*, vol. 26, no. 20, october 15, 2014.

[5] Daniel M. Kuchta, Alexander V. Rylyakov, "A 50 Gb/s NRZ Modulated 850 nm VCSEL Transmitter Operating Error Free to 90°C", *Journal of lightwave technology*, vol. 33, no. 4, february 15, 2015.

[6] Jean-Francois Seurin, Viktor Khalfin, Guoyang Xu, Alexander Miglo, "High-power red VCSEL arrays", Princeton Optronics, Electronics Drive, Mercerville, NJ, USA 08619, 2013.

[7] P. T. Woan, "In-chip temperature sensing and compensation for VCSEL driver ICs", Master's thesis, Korea Advanced Institute of Science and Technology, Korea, 2012.

[8] Yu Zhang, "Self-heating control of Edge Emitting and Vertical Cavity Surface Emitting Lasers", PhD work, University of Central Florida, Orlando, Florida, 2012.

[9] Chen Chen, Paul O. Leisher, Kent D. Choquette, Andrew A. Allerman, Kent M. Geib, "Temperature Analysis of Threshold Current in Infrared Vertical-Cavity Surface-Emitting Lasers", *IEEE journal of quantum electronics*, vol. 42, no. 10, october 2006.

[10] J. Piprek, H. Wenzel and G. Sztefka, "Modeling Thermal Effects on the Light vs. Current Characteristic of Gain-Guided Vertical-Cavity Surface-Emitting Lasers", *IEEE photonics technology letters*, vol. 6, no. 2, february 1994.

[11] Jeff W. Scott, Randall **S.** Geels, Scott W. Corzine and Larry A. Coldren, "Modeling Temperature Effects and Spatial Hole Burning to Optimize Vertical-Cavity Surface-Emitting Laser Performance", *IEEE journal of quantum electronics*, vol 29, no. 5. may 1993.

[12] K. Johnson, W. Hogan, M. Dummer and G. Breg, "Record high temperature, high power red VCSELs", 15350 25th Ave N, Suite 110, Plymouth, MN 55447 USA, 2011.

[13] Daniel M. Kuchta, Alexander V. Rylyakov, "A 71 Gb/s NRZ Modulated 850 nm VCSEL-based optical link", *IEEE photonics technology letters*, vol. 27, no. 6, march 2015.

[14] J. Zweck, I. Lima Jr., Y. Sun, A. Lima, C. Menyuk and G. Carter, "Modeling Receivers in Optical Communication Systems With Polarization Effects", *Optics & Photonics News*, vol. 14, no. 11, p. 30, 2003.

2017 3rd International Conference on Electrical Information and Communication Technology (EICT), 7-9 December 2017, Khulna, Bangladesh

# Nonlinear Coupling of Whispering Gallery Mode Silica Microcavity for Sensing Application

Shovasis Kumar Biswas*, Abdullah al Noman, S. M. Rakibul Islam, Md. Rubayet Islam, Md. Tawhid Islam Opu, Feroz Ahmed
Department of Electrical and Electronic Engineering
Independent University, Bangladesh
*Email: shuvoapece@gmail.com

***Abstract*—An analytical expression for the coupling of whispering gallery mode is derived by adding coupling and intrinsic loss terms. We found smaller negative frequency shift for higher order mode when nonlinear coefficient is smaller consistent with the reported experimental observations. This result opens up a range of new applications in nonlinear sensing and quantum optics.**

**Keywords - Coupled-mode theory, microcavity, microsphere, resonator.**

## I. Introduction

Whispering gallery modes (WGM) microcavity have played an ubiquitous role due to their high quality factor Q and small effective mode volume $V_{eff}$. They are suitable for different applications and scientific research which includes quantum electrodynamics (QED) [1], microlasers [2], [3], Raman lasers [4], [5], sensing [6]–[8], parametric oscillation [9], frequency comb [10], [11] and so forth. In huge numbers of these applications, light should be coupled into the microsphere without any changing of high quality factor, Q. There are a number of methods to couple light into the micro sphere. Among all of the methods, tapered fiber [12], prism coupler [13], and polished half-block coupler are used widely. Tapered fibers are widely used for device applications. The main goal of this paper is to derive an analytical formula for coupling Whispering gallery mode by taking into account the intrinsic loss and coupling loss terms.

We developed a theoretical framework to describe the impact of Kerr nonlinearity by taking tensor components in spherical coordinates and showed that the amount of negative frequency shift is proportional to the mode energy [14], [15]. Recently, We also investigated the Kerr effect in whispering gallery modes (WGMs) due to SPM, XPM and stimulated Raman scattering (SRS) and showed that the frequency shift depends on the injected energy of both modes. Taking into account the delayed Raman response, analytical coupled mode equations are developed to describe the transfer of energy between pump wave and Stokes wave. The analytical model is found to be in good agreement with numerical results in situations where the pump depletion is negligible.

In this paper, we present a new extension of the impact of Kerr effect on microcavity to study the single mode coupling of Whisperring gallery mode due to self-phase modulation (SPM). We develop an analytical expression for the coupling of whispering gallery mode is by adding the coupling and intrinsic loss terms. We found large negative frequency shift depending on injected power. Our result show that frequency shift is large when mode order is smaller. However, to the best of our knowledge, coupling of Whispering gallery mode has not been analytically modeled previously to explain the spm effect in microsphere by taking tensor components in spherical co-ordinates.

## II. Mathematical description of coupling to whispering gallery mode microcavity resonators

In a microsphere resonator, the optical transfer of energy between waveguide and cavity resonator can be described through a simple model, as shown in Fig. (1). Figure (1) represents the whisperring gallery mode resonator coupled to a waveguide. The coupling between waveguide-resonator is described by the following three important parameters, the resonant frequency $\omega_0$, decay rate due to cavity internal loss $\tau_p^{-1}$ and decay rate due to coupling to the waveguide $\tau_{ex}^{-1}$.

According to the H. Haus, coupling of modes can be described by the following equation [17]–[19]

$$\frac{dq}{dt} = -\frac{1}{2}\left(\frac{1}{\tau_0} + \frac{1}{\tau_{ex}}\right)q + i\kappa_0 s \tag{1}$$

where q signifies the slowly varying amplitude in the cavity resonator and s denotes the input wave. The coupling into the waveguide is denoted by $\tau_{ex}$ (external lifetime). The coupling coefficient $\kappa_0$ is related to the $\tau_{ex}$ which denotes the coupling in to the waveguide and is given by

$$\kappa_0 = \sqrt{\frac{1}{\tau_{ex}}} \tag{2}$$

Depending on the relation between $\tau_0$ and $\tau_{ex}$, the transmission through the waveguide can be described by the following equation

$$T = \left(\frac{\tau_{ex} - \tau_0}{\tau_{ex} + \tau_0}\right)^2 = \left(\frac{1-K}{1+K}\right)^2 \tag{3}$$

where $K$ is the dimensionless coupling parameter which is defined as the ratio of coupling between resonator and waveguide to intrinsic resonator loss. Depending on $K$, the

978-1-5386-2307-7/17/$31.00 ©2017 IEEE

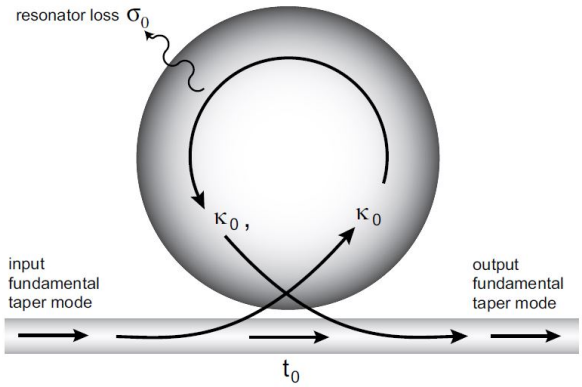


Fig. 1. Schematic of a waveguide coupled resonator.

transmission profile can be characterized by the three coupling regime.

Under coupling ($K = 1$): Under coupling means the waveguide coupling is weak and the rate of cavity decay $\tau_0^{-1}$ exceeds the cavity coupling rate $\tau_{ex}^{-1}(\tau_0^{-1} > \tau_{ex}^{-1})$. This regime is called undercoupled due to the fact that in this regime coupling is less than the cavity loss.

Over coupling ($K > 1$): Over coupling refers to the regime where output coupling dominates the loss. In this case cavity coupling loss larger than the cavity internal loss.

Critical coupling ($K = 1$): At critical coupling, input coupling or waveguide coupling just balances the cavity internal loss ($K = 1$). As there is no waveguide transmission at critical coupling, so complete power is coupled into the microcavity. The primary goal for nonlinear devices is to obtain complete power transfer into the microcavity.

## III. Coupling of WGMs resonators

We developed an analytical model to describe the impact of Kerr nonlinearity on spherical microcavity by taking tensor components in spherical coordinates. Loss and Kerr nonlinear effect is considered as perturbations [14].

$$i\Big(\frac{\partial q}{\partial t} + \frac{q}{2\tau_p}\Big) = \gamma|q|^2 q, \tag{4}$$

where $\tau_p$, denote the photon lifetime with the resonant frequency $\omega$.

If the resonator is coupled to an external waveguide or to the outside space, one can easily proceed and add coupling and intrinsic loss terms in Eqs. (4) Now, considering the input wave $s$ and coupling coefficients $\kappa_0$, Eq. (4) may be written as

$$i\Big(\frac{\partial q}{\partial t} + \frac{q}{2\tau_p}\Big) = \gamma|q|^2 q + i\kappa_0 s, \tag{5}$$

To solve Eq. (5), let

$$q(t) = B(t)e^{i\theta(t)}, \tag{6}$$

where $B(t)$ and $\theta(t)$ are amplitude and phase, respectively. Subtituting Eq. (6) in Eq. (5), we find

$$\frac{dq}{dt} = \big(\frac{dB}{dt} + i\frac{d\theta}{dt}B\big)e^{i\theta}. \tag{7}$$

From Eq. (5), we have

$$i\frac{dB}{dt} - \frac{d\theta}{dt}B + i\frac{B}{2\tau_p} = \gamma B^2 B + i\kappa_0 s. \tag{8}$$

Separating real and imaginary parts of Eq. (8), we obtain

$$\frac{dB}{dt} + \frac{B}{2\tau_p} = \kappa_0 s, \tag{9}$$

$$\frac{d\theta}{dt} = -\gamma B^2(t). \tag{10}$$

Integrating Eqs. (9) and (10), we obtain

$$B(t) = 2\kappa_0 s\tau_p(1 - e^{-t/2\tau_p}), \tag{11}$$

$$\theta(t) = -\gamma\Big[4\kappa_0^2 s^2\tau_p^2\big\{t + \big(1 - e^{-t/\tau_p}\big)\tau_p - \big(1 - e^{-t/2\tau_p}\big)4\tau_p\big\}\Big], \tag{12}$$

Instantaneous frequency shift is defined as

$$f(t) = -\frac{\gamma}{2\pi}\Big[4\kappa_0^2 s^2\tau_p^2\big(1 + e^{-t/\tau_p} - 2e^{-t/2\tau_p}\big)\Big]. \tag{13}$$

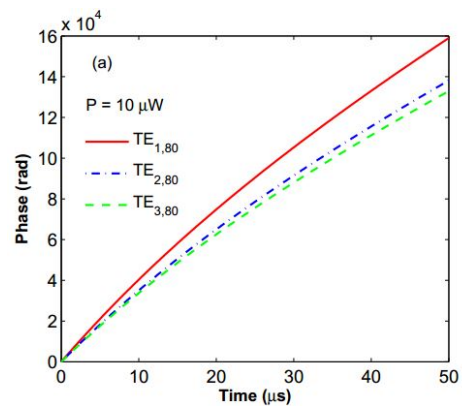


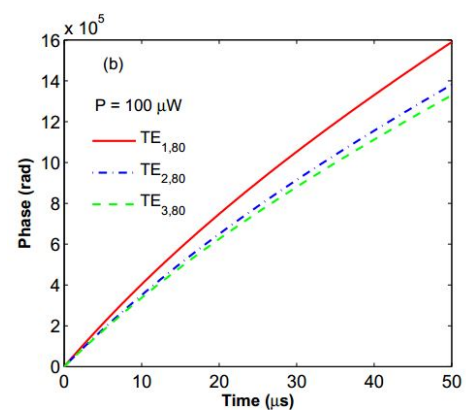

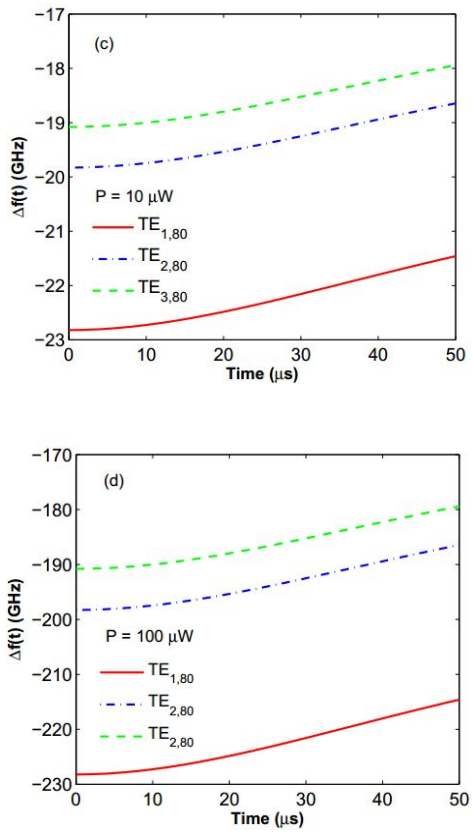


Fig. 2. Observation of phase change and frequency shift as a function of time for different injected powers in the microsphere with a radius of $15\mu m$.

## IV. Results and Discussion

Figs. (2) shows the phase $\theta(t)$ and corresponding instantaneous frequency shift $\Delta f(t)$ calculated using Eq. (12) and Eq. (13) respectively for different injected powers. As can be seen in the Fig. (2), the frequency shift increases with time due to the presence of input power. It can also be seen that negative frequency shift is increasing with time from higher order mode to lower order mode because lower order mode coupled more power as compared with higher order mode. More importantly mode order is inversely related to nonlinear coefficient. So, smaller mode order provides larger nonlinear coefficients and hence we found larger negative frequency shift.

These results can be used to analyze the experimental work related to frequency comb, third harmonic generation and parametric oscillation. WGMs have been used for sensing applications in which the object placed in the microcavity alters the refractive index profile of the microcavity which leads to the frequency shift of the WGMs. In addition, the object changes the nonlinear polarization properties of the microcavity and it could lead to additional frequency shifts due to SPM as discussed in this paper and hence, the analysis developed in this paper could be used for nonlinear sensing applications.

## V. Conclusion

In this paper, coupling equations for WGMs microsphere are derived by adding coupling and intrinsic loss terms. We found that radial mode order is inversely related to frequency shift. As the mode order increased, effective nonlinear coefficient decrease considerably hence we obtain large negative frequency shift. These results can be used for sensing applications in which the object placed in the microcavity alters the refractive index profile of the microcavity which leads to the frequency shift of the WGMs.

## References

[1] D. K. Armani, T. J. Kippenberg, S. M. Spillane & K. J. Vahala, "Ultra-high-Q toroid microcavity on a chip, Nature, 421(6926), 925 (2003).

[2] F. Treussart, V. S. Ilchenko, J. F. Roch, P. Domokos, J. Hare, V. Lefevre, & S. Haroche, "Whispering gallery mode microlaser at liquid helium temperature, Journal of luminescence, 76, 670-673 (1998).

[3] K. An, J. J. Childs, R. R. Dasari, & M. S. Feld, "Microlaser: A laser with one atom in an optical resonator, Physical review letters, 73(25), 3375 (1994).

[4] S. K. zdemir, J. Zhu, X. Yang, B. Peng, H. Yilmaz, & L. Yang, "Highly sensitive detection of nanoparticles with a self-referenced and self-heterodyned whispering-gallery Raman microlaser Proceedings of the National Academy of Sciences, 111(37), E3836-E3844 (2004).

[5] T. Carmon, T. J. Kippenberg, L. Yang, H. Rokhsari, S. Spillane, & K. J. Vahala, "Feedback control of ultra-high-Q microcavities: application to micro-Raman lasers and micro-parametric oscillators," Optics Express, 13(9), 3558-3566 (2005).

[6] L. Maleki & V. Ilchenko, "U.S. Patent No. 6,490,039" Washington, DC: U.S. Patent and Trademark Office (2002).

[7] M. R. Foreman, J. D. Swaim & F. Vollmer, "Whispering gallery mode sensors. Advances in optics and photonics," 7(2), 168-240 (2015).

[8] E. Krioukov, D. J. W. Klunder, A. Driessen, J. Greve & C. Otto, "Sensor based on an integrated optical microcavity. Optics letters, 27(7), 512-514 (2002)

[9] A. A. Savchenkov, A. B. Matsko, D. Strekalov, M. Mohageg, V. S. Ilchenko & L. Maleki, "Low Threshold Optical Oscillations in a Whispering Gallery Mode C a F 2 Resonator," Physical review letters, 93(24), 243905 (2004)

[10] T. J. Kippenberg, R. Holzwarth & S. A. Diddams, "Microresonator-based optical frequency combs," Science, 332(6029), 555-559 (2011).

[11] T. Herr, K. Hartinger, J. Riemensberger, C. Y. Wang, E. Gavartin, R. Holzwarth & T. J. Kippenberg, "Universal formation dynamics and noise of Kerr-frequency combs in microresonators. Nature Photonics, 6(7), 480-487 (2012).

[12] J. C. Knight, G. Cheung, F. Jacques, and T. A. Birks, Phase-matched excitation of whispering-gallery-mode resonances by a fiber taper, Opt. Lett., vol. 22, pp. 11291131, 1997.

[13] L. Collot, V. Lefevre-Seguin, M. Brune, J. M. Raimond, and S. Haroche, Very high-Q whispering-gallery mode resonances observed on fused silica microspheres, Europhys. Lett., vol. 23, pp. 327334, 1993.

[14] S. K. Biswas and S. Kumar, "Impact of Kerr nonlinearity on the whispering gallery modes of a microsphere," Optics Express **23**, 26738-26753 (2015).

[15] S. K. Biswas, "Impact of Kerr and Raman Nonlinear Effects on the Whispering Gallery Modes of a Spherical Microcavity," M.A.Sc. thesis (McMaster University, 2016).

[16] S. Kumar, & S. K. Biswas "Impact of Kerr nonlinearity and stimulated Raman scattering on the whispering gallery modes of an optical microsphere. JOSA B, 33(8), 1677-1687(2016).

[17] H. A. Haus, Waves and Fields in Optoelectronics (Prentice-Hall series in solid state physical electronics, 1984).

[18] M. L. Gorodetsky and V. S. Ilchenko, "Optical microsphere resonators: optimal coupling to high-Q whispering-gallery modes," JOSA B, 16(1), 147-154 (1999).

[19] M. L. Gorodetsky, A. D. Pryamikov and V. S. Ilchenko, "Rayleigh scattering in high-Q microspheres," JOSA B, 17(6), 1051-1057 (2000).

2017 3rd International Conference on Electrical Information and Communication Technology (EICT), 7-9 December 2017, Khulna, Bangladesh

# Design of a Compact Triple-band Antenna for WLAN/WiMAX Applications

Mohammad Shuhrawardy[1], Md. Halim Miah Chowdhury[2] and Rezaul Azim[3]
[1,3]University of Chittagong, Chittagong-4331, Bangladesh
[2]University of Rajshahi, Rajshahi-6205, Bangladesh
mswardy@cu.ac.bd, halimice08@gmail.com, rezaulazim@cu.ac.bd

***Abstract*—This paper represents a simple planar antenna, with a very compact size of $28 \times 14 \times 0.8$ mm$^3$, for WLAN and WiMAX applications. The proposed antenna comprises an inverted L-shaped, an inverted U-shaped and a T-shaped patch elements with a defected ground structure. By modifying and optimizing the dimensions of the patch elements and the ground plane, the antenna is designed to operate at three different frequency bands having -10dB impedance bandwidths of 95 MHz (2.395-2.490 GHz), 580 MHz (3.35-3.93 GHz) and 1430 MHz (4.78-6.21 GHz), which cover WLAN 2.4/5.2/5.8 GHz bands and WiMAX 3.5/5.5 GHz bands. The proposed antenna possesses compact size, simple structure, achieves high gain and exhibits omnidirectional radiation pattern which make it a suitable candidate to be used in small/portable WLAN/WiMAX devices.**

***Keywords*—Triple-band, Mobile Broadband, WLAN/WiMAX, Defected Ground Structure (DGS), Radiation Pattern.**

## I. Introduction

Due to the growing demand of mobile broadband access, the deployment of WLAN and WiMAX is increasing rapidly. On the other hand, considering the size limitation of wireless devices, compact and multiband antennas are required. Various structures are used for designing multiband antennas such as planar inverted-F antenna (PIFA), defected ground structure (DGS), slotted radiating patch and coplanar waveguide (CPW) feed-line. Compared to normal ground plane, the defected ground structure method increases the surface current and improves the impedance bandwidths [1], [2].

As specified by the Federal Communication Commission (FCC), the WLAN spectrum is centered at 2.4, 5.2 and 5.8 GHz where WiMAX spectrum is at 2.5, 3.5 and 5.5 GHz [3]. In the recent years, a considerable number of multiband antennas of different structures have been investigated for WLAN and/or WiMAX applications. A dual-band slotted circular patch antenna has been proposed in [4] that covers only two WLAN bands of 2.4/5.2 GHz. A CPW-fed microstrip antenna operating in the frequency ranges 2.36-2.485 GHz and 5.14-6.43 GHz has been developed in [5] covering all WLAN 2.4/5.2/5.8 GHz bands with a complex structure and low gain. Antenna covering WiMAX 2.5/3.5 GHz bands has been presented in [6]. The same frequency bands have also been covered by a dual-band antenna of the size of $96 \times 96 \times 1.6$ mm$^3$ with RT Duriod 5880 substrate [7]. A metamaterial-inspired dual-band antenna resonating at the frequencies of 2.45 and 3.5 GHz has been proposed in [8] which cover 2.4/3.5 GHz WLAN/WiMAX bands only. Two triple-band antennas covering WLAN/WiMAX bands of 2.4/3.5/5.8 GHz have been presented in [9] and [10] respectively. The antenna reported in [11] also covers these frequency bands with a high gain but uses expensive dielectric substrate. A CPW-fed planar antenna of the size of $29 \times 21 \times 1.6$ mm$^3$ has been presented in [12] that achieves three resonant modes for covering the 2.4/5.2/5.8/3.5/5.5 GHz WLAN/WiMAX bands. Antenna proposed in [13] use the similar method to cover the same WLAN/WiMAX bands. A rectangular-shaped planar antenna using two open-ended slots has been presented in [14] that excite in the frequency ranges 2.4-2.5 GHz, 3.25-3.75 GHz and 5.22-5.83 GHz and covers the WLAN 2.4/5.2/5.8 GHz bands and WiMAX 3.5/5.5 GHz bands. However all of the above mentioned antennas have the disadvantage of having a relatively larger size and either operate for a limited frequency bands or have a lower gain and even some of them have complex structures.

This article develops a very compact planar antenna containing a defected ground plane that exhibits multifrequency band functionality. The antenna resonates at three distinct frequency ranges covering the WLAN bands of 2.4/5.2/5.8 GHz and WiMAX bands of 3.5/5.5 GHz. The overall size of the proposed antenna is $28 \times 14 \times 0.8$ mm$^3$, which could be an excellent competitor in the field of present and future generation WLAN/WiMAX devices.

## II. Design of The Antenna

### A. Structure of the Antenna

The optimized layout of the proposed antenna with the dimensional details is shown in Fig. 1. The antenna is composed of inverted L-shaped, inverted U-shaped and T-shaped patch elements and a defected ground plate. The patch of the proposed antenna is printed on the front face of an inexpensive FR4 substrate ($\varepsilon_r$ = 4.4 and tan $\delta = 0.02$) with a thickness of 0.8mm. The back face of the substrate contains the ground plate (size:

978-1-5386-2307-7/17/$31.00 ©2017 IEEE

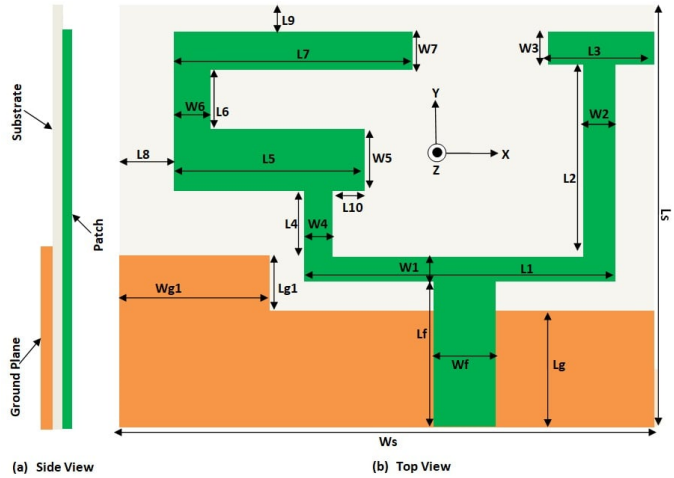


Fig. 1. Optimized layout of the proposed triple-band antenna.

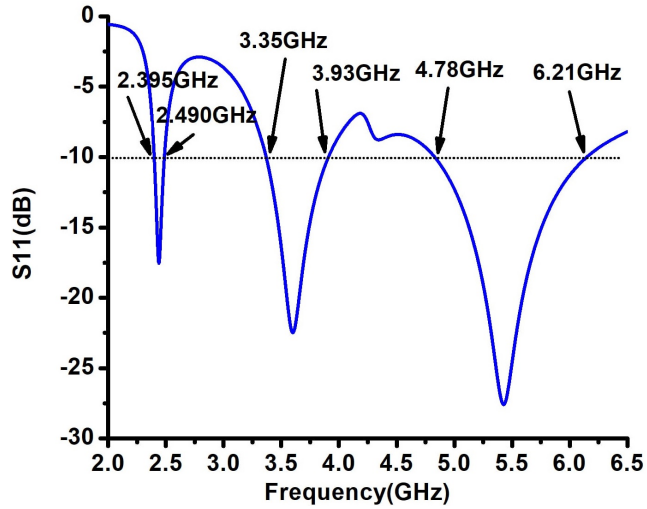


Fig. 2. Simulated return loss (S11) of the proposed triple-band antenna.

$28 \times 3.9$ mm$^2$) of the antenna. To feed the antenna a $2 \times 4.7$ mm$^2$ 50 $\Omega$ microstrip line is used on the substrate. The proposed antenna is designed, optimized and analyzed with the simulation software ansoft High Frequency Structural Simulator (HFSS) version 13. All the optimal parameter values are given in Table I.

TABLE I
OPTIMAL PARAMETER VALUES

| Parameter | Values (mm) | Parameter | Values (mm) |
|---|---|---|---|
| $L_s$ | 14 | $L_5$ | 10 |
| $W_s$ | 28 | $W_5$ | 1.8 |
| $L_f$ | 4.2 | $L_6$ | 2.8 |
| $W_f$ | 2 | $W_6$ | 1 |
| $L_1$ | 16.3 | $L_7$ | 12.8 |
| $W_1$ | 0.7 | $W_7$ | 1.1 |
| $L_2$ | 7.8 | $L_8$ | 2 |
| $W_2$ | 0.8 | $L_9$ | 0.3 |
| $L_3$ | 4.2 | $L_{10}$ | 1.3 |
| $W_3$ | 1 | $L_g$ | 3.9 |
| $L_4$ | 3.1 | $L_{g1}$ | 1.6 |
| $W_4$ | 0.7 | $W_{g1}$ | 7.8 |

The simulated return loss (S11) of the proposed antenna is shown in Fig. 2. The proposed antenna can achieve the bandwidths 2.395-2.490 GHz (95 MHz), 3.35-3.93 GHz (580 MHz) and 4.78-6.21 GHz (1430 MHz) for $S11 < -10dB$ and $VSWR < 2$.

### B. Operating Principle of the Antenna

The design evolution process of the antenna to meet the WLAN/WiMAX triple-band operation is analyzed in Fig. 3

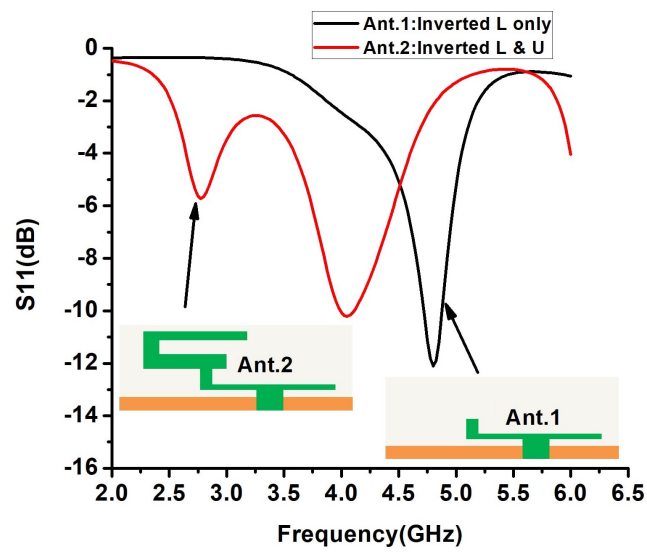


Fig. 3. Return loss characteristics for (i) Ant.1 and (ii) Ant.2.

and Fig. 4 corresponding with simulated reflection coefficient. The different dimensions in Ant.1, Ant.2, Ant.3 and Pro.Ant are similar to that of the optimized values in Table I. At first only an inverted L-shaped element is considered for which a resonant mode is found at about 4.8 GHz (Ant.1). From the feed point it's length is about 16 mm which excites a resonant mode at quarter-wavelength ($\lambda$/4). The second resonant mode of the antenna is occurred at 2.8 GHz by adding an inverted U- shaped element of the length of 27 mm ($\lambda$/4). However, the inverted U-shaped element has an influence on the first resonant mode and causes it to shift towards 4.2 GHz (Ant.2). Then a T-shaped element is applied in the right side of the antenna that

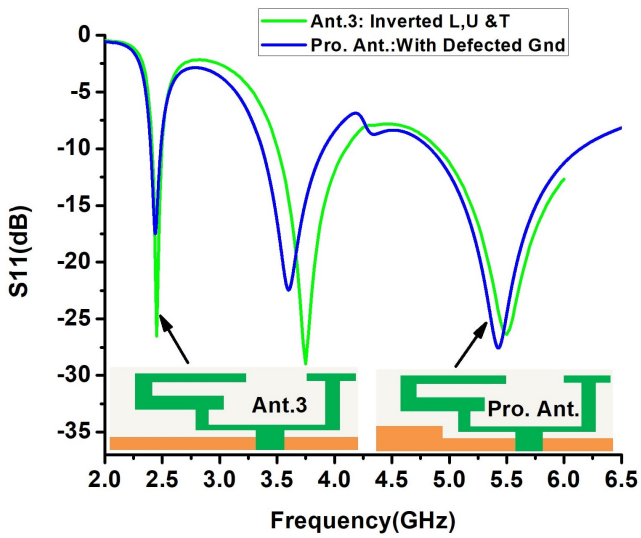


Fig. 4. Return loss characteristics for (i) Ant.3 and (ii) Pro.Ant.

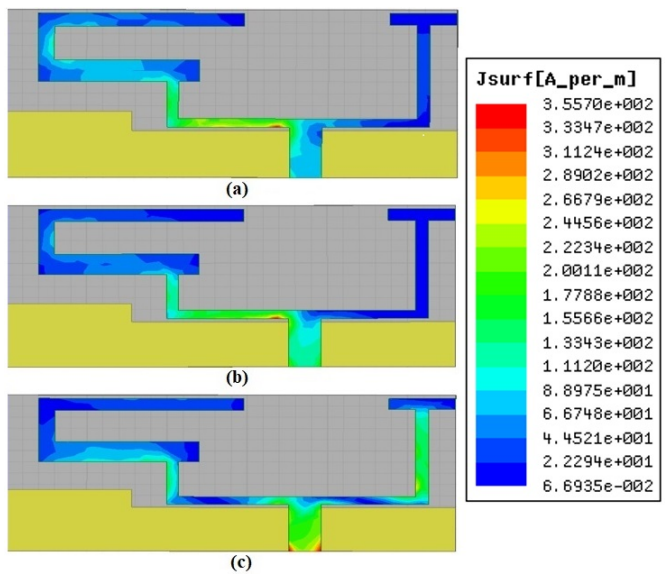


Fig. 5. Simulated surface current distributions of the proposed antenna at (a) 2.4 GHz, (b) 3.5 GHz and (c) 5.5 GHz.

generates a third resonant mode at 5.5 GHz and also improves the impedance bandwidths (Ant.3). The length of this T-shaped element is about 26.50 mm from the feed point which causes the resonant mode to occur at half-wavelength ($\lambda/2$). Finally, defection of ground plane shifts all the frequency bands towards left to meet the desired responds (Pro. Ant.).

To further observe the frequency response of the proposed antenna, the simulated surface current distributions at different resonant frequencies are illustrated in Fig 5. It is shown from

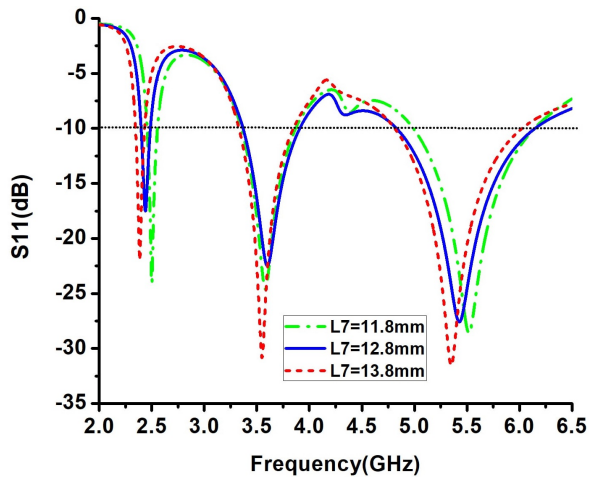


Fig. 6. Effect of L7 on return loss of the proposed antenna.

the figure that at 2.4 GHz, almost all of the electric current flows along the inverted L-shaped and inverted U-shaped elements where for 3.5 GHz, the surface current is mainly concentrated on the L-shaped element of the antenna. For 5.5 GHz, the most of the current is distributed along the T-shaped element. From the above study, it can be concluded that the left portion of the antenna (inverted L-shaped and inverted U-shaped elements) is responsible for the lowest and the median resonant modes while the right portion (T-shaped element) affects the highest resonant mode.

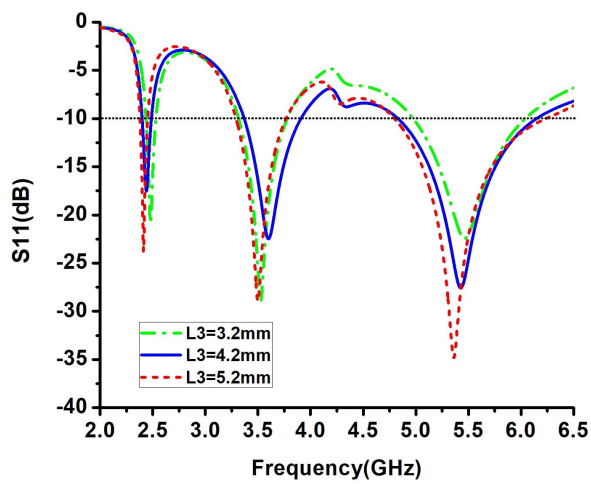


Fig. 7. Effect of L3 on return loss of the proposed antenna.

## III. Result and Discussion

### A. Parameter Study

The effect of different values of L7 on return loss is illustrated in Fig. 6 where Fig. 7 and Fig. 8 give the effect on the same for

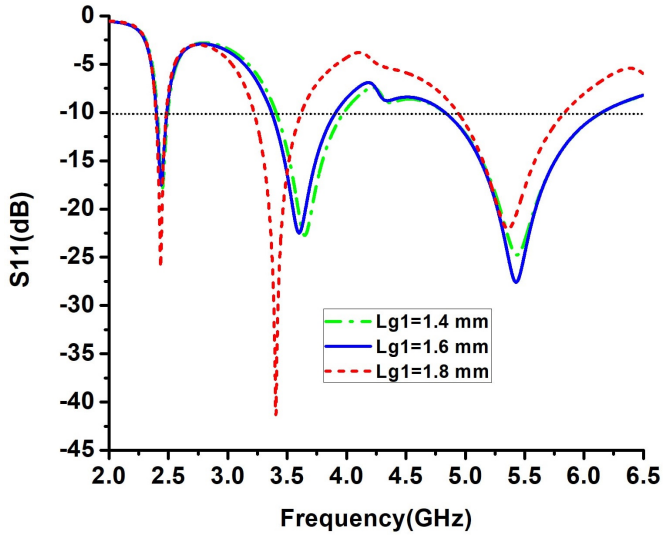


Fig. 8. Effect of Lg1 on return loss of the proposed antenna.

variation in the values of L3 and Lg1 respectively. It is observed that the lower band shifted left with increase in L7 and has a better return loss with L7=12.8 mm (Fig. 6).

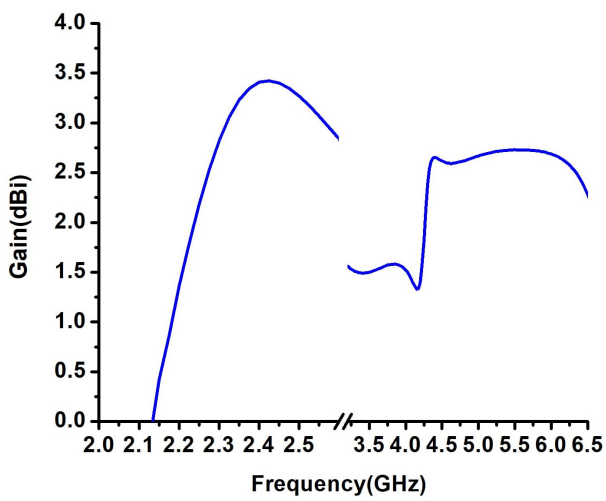


Fig. 9. Simulated antenna gain.

The value of $|S11|$ for the higher band increases with increase in L3 (Fig. 7). Fig.8 shows that impedance matching of the middle band is mostly affected by Lg1 and finally the desired impedance match is found for the defected ground plane with Lg1=1.6 mm.

### B. Antenna Gain

The antenna gain against frequencies is plotted in Fig. 9. At the lower band the variation of the peak gain is in the range of 3.35-3.45 dBi and between 1.4 dBi to 1.6 dBi of the middle band where the range is 2.6 to 2.8 dBi for the upper band.

Table II presents a comparison between the proposed antenna and some previously reported designs. It can be observed that the proposed antenna can cover WLAN and WiMAX bands with very compact size and high gain.

TABLE II
COMPARISON OF SOME RECENT DESIGNS WITH THE PROPOSED DESIGN

| Multiband antennas | Dimensions ($mm^3$) | Frequency bands | | Peak Gain (At 2.4,3.5, 5.5 GHz) |
|---|---|---|---|---|
| | | WLAN (2.4/5.2/5.8 GHz) | WiMAX (2.5/3.5/5.5 GHz) | |
| [4] | $44 \times 40 \times 1.5875$ | 2.4/5.2/5.8 | - | 0.85 dBi<br>-<br>2.60 dBi |
| [7] | $40 \times 12 \times 1.6$ | 2.4 | 3.5 | 0.30 dBi<br>1.10 dBi<br>- |
| [8] | $16 \times 30 \times 1.0$ | 2.4/5.8 | 3.5 | 1.00 dBi<br>2.20 dBi<br>1.80 dBi |
| [12] | $21 \times 24 \times 0.8$ | 2.4/5.2/5.8 | 3.5/5.5 | 0.75 dB<br>2.05 dBi<br>3.10 dBi |
| [13] | $30 \times 20 \times 1.0$ | 2.4/5.2/5.8 | 3.5/5.5 | 1.58 dBi<br>1.72 dBi<br>2.15 dBi |
| Proposed antenna | $28 \times 14 \times 0.8$ | 2.4/5.2/5.8 | 3.5/5.5 | 3.45 dBi<br>1.60 dBi<br>2.80 dBi |

### C. Radiation Patterns

The simulated radiation patterns (E-field and H-field) for the proposed antenna at the frequencies of 2.4, 3.5 and 5.5 GHz are plotted in Fig.10. From this figure, it is obvious that the proposed antenna has an omnidirectional radiation pattern.

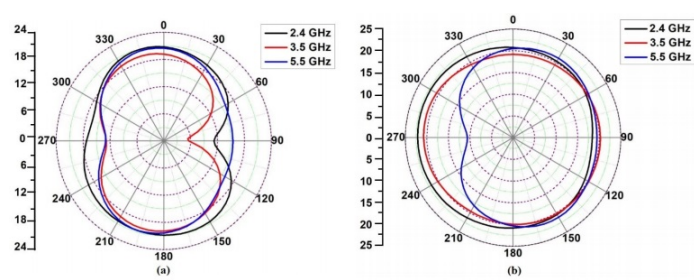


Fig. 10. Radiation patterns for the proposed antenna (a) E-field and (b) H-field.

## IV. CONCLUSION

A very compact triple-band antenna has been presented. With the optimized parameters of the strips, the proposed antenna is able to excite at three distinct frequency ranges covering WLAN/WiMAX bands of 2.4/5.2/5.8/3.5/5.5 GHz. The designed

antenna has a simple structure with a very compact size of $28 \times 14 \times 0.8$ mm$^3$. The results also show that the proposed antenna achieves high gain and exhibits omnidirectional radiation pattern. Because of its smaller size and better performance, the proposed antenna would be a promising competitor in WLAN/WiMAX devices such as Wireless Bridge, Access Point, Gateways, External modems, Mobile phones etc.

## REFERENCES


[1] K. Pedram, J. Nourinia, and C. Ghobadi, "A small dual band antenna with simple structure for WLAN/WiMAX application," in *Telecommunications (IST), 2016 8th International Symposium on*. IEEE, 2016, pp. 349–352.

[2] K. L. Wong, *Planar Antennas for Wireless Communications*. New York: Wiley, 2003.

[3] A. K. Gautam, L. Kumar, B. K. Kanaujia, and K. Rambabu, "Design of compact F-shaped slot triple-band antenna for WLAN/WiMAX applications," *IEEE Transactions on Antennas and Propagation*, vol. 64, no. 3, pp. 1101–1105, 2016.

[4] S. Ismail, S. Rahim, A. Ibrahim, M. Sabran, and H. Mohamad, "Dual band inverted H-shaped slot monopole antenna for WLAN applications," in *Communications (MICC), 2015 IEEE 12th Malaysia International Conference on*. IEEE, 2015, pp. 197–200.

[5] A. Kundu, U. Chakraborty, and A. K. Bhattacharjee, "Design of compact dual-band co-axially fed microstrip antenna for 2.4/5.2/5.8 GHz WLAN applications," *Journal of Electromagnetic Waves and Applications*, vol. 29, no. 12, pp. 1535–1546, 2015.

[6] W. Shi, Z. Qian, and W. Ni, "Dual-band stacked annular slot/patch antenna for omnidirectional radiation," *IEEE Antennas and Wireless Propagation Letters*, vol. 15, pp. 390–393, 2016.

[7] I. Ali and R. Y. Chang, "Design of dual-band microstrip patch antenna with defected ground plane for modern wireless applications," in *Vehicular Technology Conference (VTC Fall), 2015 IEEE 82nd*. IEEE, 2015, pp. 1–5.

[8] S. K. Sharma, M. A. Abdalla, and R. K. Chaudhary, "An electrically small sicrr metamaterial-inspired dual-band antenna for WLAN and WiMAX applications," *Microwave and Optical Technology Letters*, vol. 59, no. 3, pp. 573–578, 2017.

[9] J. Bao, Q. Huang, X. Wang, and X. Shi, "Compact multiband slot antenna for WLAN/WiMAX operations," *International Journal of Antennas and Propagation*, vol. 2014, 2014.

[10] T. Ali, R. Biradar *et al.*, "A compact multiband antenna using $\lambda/4$ rectangular stub loaded with metamaterial for IEEE 802.11 N and IEEE 802.16 E," *Microwave and Optical Technology Letters*, vol. 59, no. 5, pp. 1000–1006, 2017.

[11] H.-R. Kou, B.-Z. Zhang, J.-P. Duan, and S.-L. Ge, "Triple-band monopole planar antenna designed for WLAN/WiMAX application," in *Microwave and Millimeter Wave Technology (ICMMT), 2016 IEEE International Conference on*, vol. 2. IEEE, 2016, pp. 555–557.

[12] H. Chen, X. Yang, Y. Yin, S. Fan, and J. Wu, "Triband planar monopole antenna with compact radiator for WLAN/WiMAX applications," *IEEE Antennas and Wireless Propagation Letters*, vol. 12, pp. 1440–1443, 2013.

[13] V. K. Pandit and A. Harish, "A compact CPW-fed triple band monopole antenna for WLAN/WiMAX applications," in *Microwave Conference (APMC), 2016 Asia-Pacific*. IEEE, 2016, pp. 1–4.

[14] H. Wang and H. Li, "A compact triple-band monopole antenna for WLAN/WiMAX," *International Journal of Simulation–Systems, Science & Technology*, vol. 17, no. 17, 2016.

2017 3rd International Conference on Electrical Information and Communication Technology (EICT), 7-9 December 2017, Khulna, Bangladesh

# Performance Analysis of Cognitive Radio: Netsim Viewpoint

Khaled Mohammed Saifuddin[1], Abu Shakil Ahmed[2], Kazi Fahid Reza[3], Sk Shariful Alam[4], Sharmina Rahman[5]
Khulna University of Engineering & Technology, Khulna-9203, Bangladesh
hamim026@gmail.com[1], shakil.ahmed.bd71@gmail.com[2], fahidreza2708@gmail.com[3], ssa1996@gmail.com[4], sharminalima@gmail.com[5]

*Abstract*—**Electromagnetic spectrum is very precious as it is limited and performance of a communication system degrades if it is used inefficiently. Cognitive Radio (CR) ensures proper utilization of the available licensed spectrum of Primary User (PU) by allocating the temporary unused portion of it to a Secondary User (SU). In this paper, we have analyzed the impact of PU activities on the SU throughput and assessed the spectral efficiency. Moreover, the performance of CR has been evaluated for different cooperative approaches and compared considering the corresponding fading effects. Furthermore, security threat in Cognitive Radio Network (CRN) due to PU emulation attack from malicious users has been addressed as well as the corrective measure has been proposed to mitigate the risk.**

***Keywords—CRN, IFQP cycle length, Congestion control, PUE attack, Throughput, Spectral efficiency, Cooperative spectrum sensing, Channel allocation.***

## I. INTRODUCTION

Progressively we are getting more accustomed to wireless communication to keep abreast with the dynamic life. The efficiency of the communication system is subject to optimum consumption of electromagnetic spectrum. CR, one of the most trending concepts in wireless communication, ensures the proper utilization of licensed spectrum of PU when it is not in use. The unused spectrum is shared with SU until the PU starts using it once again. Throughput and spectral efficiency of SU are two decisive factors for the performance of CR as they assess the quality of communication over a limited frequency spectrum. Throughput is a measure of successful transmission of data packets, and spectral efficiency refers to the data transmission rate over a given bandwidth. Different parameters have an impact on throughput and spectral efficiency such as the operation of PU, frequency allocation, and congestion control. Moreover, security is one of the primary concern for CRN as illegitimate users may temper the air interface of CR to imitate PU signal characteristics which SUs erroneously identify as legitimate. CRN is venerable for PU Emulation (PUE) attack since it is highly reconfigurable due to its software-based air interface.

A brief overview of some significant approaches towards the improvement of spectrum sensing, better throughput, and enhancement of system performance has been mentioned in TABLE I referring to the respective author/s along with the methodology they have proposed, and the contributions they have offered.

TABLE I. LITERATURE REVIEW ON CRN AND ITS DIFFERENT ASPECTS

| *Author/s* | *Methodology* | *Contribution* |
|---|---|---|
| Dhanalakshmi P. et al. [1] | In this paper, normalized throughput has been calculated for both single and multiple SUs under multiple PU using optimal *K*-of-*N* rule. | It has been observed that among cooperative and non-cooperative spectrum sensing techniques, the cooperative one is more efficient. |
| V. Tumuluru et al. [2] | Spectrum handoff prioritization technique has been used for various Dynamic System Access (DSA) under different CRN topology. | Outcomes of this paper suggest that the handoff buffer has managed to improve the call completion rate of SU. |
| A. El-Toukhey et al. [3] | The impact of the variation in both arrival rate and service rate of the priority based SUs has been evaluated using three-dimensional Markov model. | The priority of SUs has been capable of enhancing the system performance of CR, and the model has prioritized highest SUs to have channel access for a longer period. |
| R. Bouraoui et al. [4] | Cooperative spectrum sensing based on censored energy detection has been employed in this paper to enhance the decision accuracy. | The reliability of sensing has been improved using decision fusion rules based on sensor energy detection method. |
| S. Alam et al. [5] | Energy detection method over different fading channels has been incorporated as well as the dependency of the throughput on the fading channel has been analyzed. | The throughput has been improved by applying this model as it has been observed that throughput in the conventional model decreases rapidly with the increase in time. |
| S. Alam et al. [6] | In this paper, cooperative detection technique has been utilized for the radio nodes to improve the detection performance. | Cooperative detection technique improves system performance as better throughput has been obtained. |
| I. Akyildiz et al. [7] | An improved detection scheme using cooperative sensing technique has been proposed that applies hypothesis testing, data fusion, control channel and reporting, and user selection. | Result suggests that the evaluation has been able to improve the detection performance by means of analyzing spatial diversity at the expense of cooperation overhead. |
| W. Stevens et al. [8] | Four different algorithms have been implemented in this paper such as slow start, congestion avoidance, fast retransmit, and fast recovery. | The implementation of the algorithms have been elaborated, and the pros and cons have been discussed. |

978-1-5386-2307-7/17/$31.00 ©2017 IEEE

| *Author/s* | *Methodology* | *Contribution* |
|---|---|---|
| X. Xie et al. [9] | In this paper, physical layer network coding technique has been applied to detect the emulators, as well as the starting point of collision, has been determined using the distances between the receiver and the senders. | The difference between the starting points of interference at two receivers is restricted by the positions of the senders. The system has been able to determine the hyperbolas on which the desired sender resides. |
| J. Unnikrishnan et al. [10] | The paper has proposed a linear-quadratic (LQ) fusion strategy to detect PU based on a deflection criterion for low signal to noise ratio. | The proposed system provides better performance over counting rule and suggests the correlation between the nodes should not be ignored. |

In this paper, the impact of PU activity on the SU throughput has been analyzed as well as the spectral efficiency has been assessed. Besides, we have evaluated the performance of CR for different cooperative approaches and made a comparison among them considering the corresponding fading effects. Furthermore, security threat in Cognitive Radio Network (CRN) due to PU emulation attack from malicious users has been addressed as well as the corrective measure has been proposed to mitigate the risk.

We have arranged the paper in an orderly manner. In section II, the performance parameters such as PU operation and IFQP cycle length have been explained with emphasis on their effects on the system performance. In section III, we have proposed a TCP congestion control technique with its different variants like Old Tahoe, Tahoe, Reno, and New Reno as well as the related algorithms to prevent congestion in CRN. In section IV, the PUE attack on CRN and the necessary corrective measure to mitigate the risk have been mentioned. In section V, two different cooperative sensing techniques, i.e., centralized and distributed approaches have been described in brief. We have specified the outcomes in section VI after simulating the effects of PU operation, channel allocation, congestion window as well as the system performance for PU detection, PUE attack detection, and cooperative operation. To conclude the paper the entire work has been summarised in section VII.

## II. Performance Parameters

### A. PU Operation

Throughput and spectral efficiency of SU are two performance parameters of CRN. As PU is the licensed user of spectrum, SU cannot use it when the PU is active. Hence the throughput and spectral efficiency of SU is zero in this condition. SU can use the spectrum only when PU is inactive, and it is an obligation for SU to comply. In case both the PU and SU are allocated to the same frequency band, there is no presence of spectrum hole. As a result, the throughput and spectral efficiency of SU will be negligible.

### B. IFQP Cycle Length

The available radio spectrum is divided into several nonoverlapping channels with a view to minimizing adjacent channel interference, especially for traffic channels. CRN aims to provide quality service to as many clients as possible by the efficient allocation of the available bandwidth. Inter Frame Quiet Period (IFQP) indicates the spacing between super-frames for which the intra-frame quiet period specification is valid. For example, if the field is set to 1, the cycle of quiet period repeats for each super-frame. If it is set to 2, the cycle repeats for every two super-frames while for 0, no intra-frame quiet period is scheduled, i.e., the current IFQP is canceled.

## III. TCP Congestion Control

TCP stands for Transport Layer Protocol and defines the way to establish and maintain connection within a network. It is a connection-oriented and reliable end-to-end protocol that supports a variety of network applications. When too many packets are exchanged, the load of the system goes beyond the capacity and congestion occurs. It leads to performance degradation that TCP takes into consideration. For better throughput and spectral efficiency, congestion must be controlled before or after it occurs. We have used four variants of TCP and a congestion control algorithm to keep the congestion in check. Fig. 1 represents the control algorithm for TCP congestion where cwnd implies congestion window, SMSS stands for Sender Maximum Segment Size, and MSS denotes Maximum Segment Size.

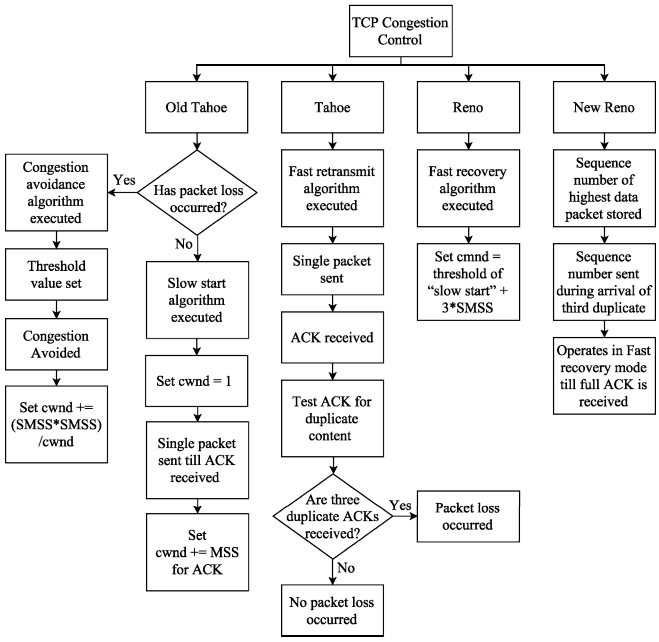


Figure 1. TCP congestion control technique.

### A. Old Tahoe

Being one of the earliest variants of TCP, Old Tahoe incorporates slow start and congestion avoidance algorithm in order to update the congestion window (cwnd). When no packet loss occurs, the slow start algorithm is executed. As per the algorithm, cwnd refers to the maximum size of a packet that can be transmitted without any acknowledgment (ACK). In the beginning, TCP can send one packet until it receives an

ACK. When the ACK is received, the size of cwnd increases exponentially. We have used congestion avoidance algorithm when packet loss occurs. At first, a threshold value is set to avoid the congestion. In this case, congestion window size is increased linearly.

### B. Tahoe

Tahoe, an enhanced edition of Old Tahoe, uses fast retransmit algorithm for quicker response. Fast retransmit detects packet loss by checking the number of duplicate ACKs. If the system receives three duplicate ACKs, it indicates packet loss.

### C. Reno

Reno preserves the core principles of Tahoe though it is less destructive than the later one to reduce the congestion window. Reno based TCP uses fast recovery algorithm for congestion control. A slow start threshold value is set to half of the congestion window where the cwnd is equal to the summation of slow start threshold and three times of the SMSS [8].

### D. New Reno

New Reno is preferable to Reno based TCP as it improves throughput in case of multiple packet loss. New Reno based TCP congestion control stores the sequence number of the highest data packet and sends it during the arrival of the third duplicate packet in order to avoid packet loss [8]. TCP keeps executing fast recovery algorithm until it receives a full ACK.

## IV. PUE Attack

The security of CRN is often in jeopardy for access of illegitimate malicious users as they may temper the air interface of CR to imitate PU signal characteristics which SUs erroneously identify as legitimate. PUE attack on CRN poses a severe threat to its implementation since CR is highly reconfigurable due to its software-based air interface [7]. We have proposed a method to create and detect a PUE attack in CRN. Detection of the position of the transmitter is a prerequisite for identifying an attacker, and then effective countermeasures can be carried out. We have simulated a PUE attack in NetSim by adding two PUs one of which is a real and the other is malicious in the scenario. After carrying out PUE attack, we have evaluated the detection accuracy of SU.

## V. Cooperative Operation

Multipath fading, shadowing, and uncertainty of receiver affect the detection performance of CRN. Cooperative spectrum sensing is an effective method to mitigate these impacts as it provides a better perception of the spectrum usage over the area where the CRs are located [9]. Cooperative operation refers to sharing individual sensing information about the unused spectrum by the CR nodes with a master node or every other node with a view to improving the detection performance. We have evaluated the detection performance for different types of cooperative approach and compared between the centralized and distributed ones on the basis of fading.

### A. Centralized Approach

In centralized sensing approach, a master node collects individual sensing data from other nodes and broadcasts information about available spectrum to the nodes after detection. The master or central node further analyzes and determines the usable frequencies those are not in use by PU. Due to security concerns, the central unit collects information only from the reliable nodes and processes it. In a simulation environment, various numbers of nodes can be introduced to find out the optimized performance of centralized cooperation under different parameters.

### B. Distributed Approach

In distributed sensing approach, CR nodes share their sensing information with one another instead of providing it to the master node and make individual decisions for usage of the unused spectrum. Unlike centralized approach, distributed approach employs individual radios having much higher level of autonomy in place of a backbone infrastructure [10]. Moreover, some overheads are considered for the approach such as sensing delay, throughput, and packet loss. We have examined the overheads of packet loss and throughput for both centralized and distributed approaches and determined their performance limits.

## VI. Simulation Result

We have carried out the simulations in NetSim by creating network scenarios, modeling traffic, and analyzing performance metrics. The CRN topology has been shown in Fig. 2.

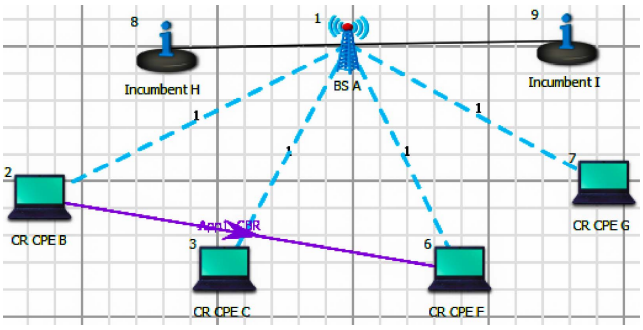


Figure 2. CRN topology.

We have designed the topology incorporating two PUs, four SUs, and one Base Station and considered the default properties for each device, physical layer, and data link layer.

### A. Effect of PU Operation

We have taken three samples with different operational interval time to observe the effect of PU Operation. The samples have been set as shown in TABLE II and each of them has been simulated for 100s. Besides, we have calculated the throughput and spectral efficiency of SU. A comparative analysis of spectral efficiency and throughput with operational intervals of PU have been shown in Fig. 3. In the first sample, PU constantly uses the entire spectrum as the operational interval is set 0s. Hence the value of throughput and spectral

efficiency is almost zero. With the increment of the operational interval, the values of both throughput and spectral efficiency increase sharply.

TABLE II. SAMPLES AND THE OPERATIONAL INTERVALS

| Sample | sample 1 | Sample 2 | Sample 3 |
|---|---|---|---|
| Operational interval | 0s | 10s | 15s |

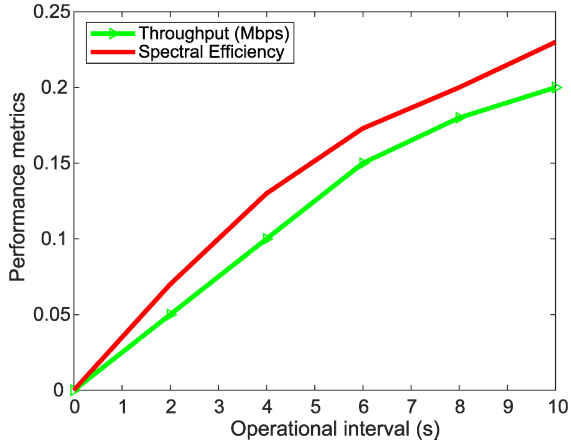


Figure 3. Variation of throughput and spectral efficiency with operational intervals of PU.

## B. *Effect of Channel Allocation*

In a CRN system, channels are allocated by varying cycle lengths of IFQP. We have compared the throughput with the IFQP cycle length which has been ranged from 1 to 15 as shown in Fig. 4.

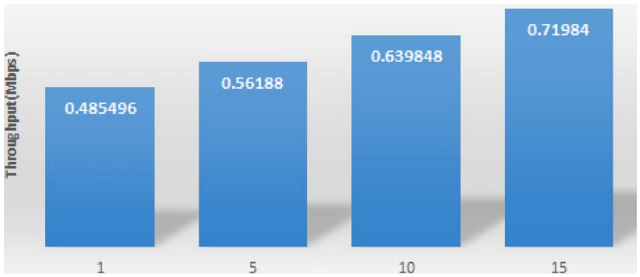


Figure 4. Effect of channel allocation on throughput.

This simulation suggests the throughput increases with the cycle length of IFQP.

## C. *Effect of Congestion Window*

By default, NetSim uses Old Tahoe for TCP congestion control that depends on the timer to expire before retransmission of a packet is allowed. Hence, we have used several variations of TCP such as Tahoe, Reno, and New Reno along with Old Tahoe for simulation.

Fig. 5 shows New Reno and Tahoe offer more spectral efficiency than Reno and Old Tahoe respectively. The New Reno offers the best spectral efficiency while Old Tahoe offers the least on the contrary.

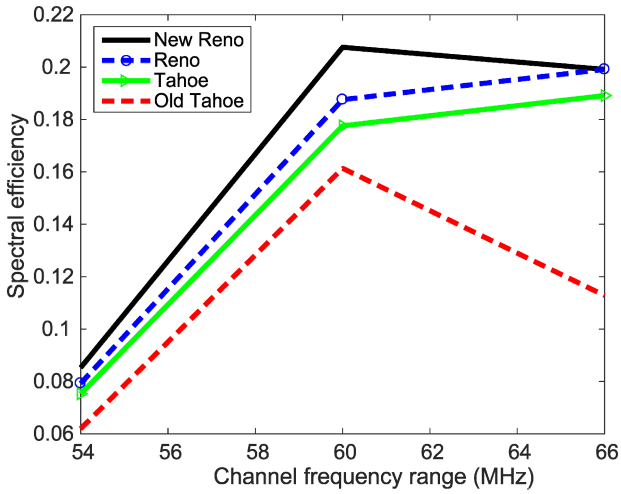


Figure 5. Spectral efficiency vs. Channel Frequency for different congestion control technique

## D. *PU Detection*

We have ensured the detection of PU or incumbent before simulating and detecting a PUE attack in order to keep PU activity free from interference. Hence different operational intervals have been set for both the SUs and the PUs so that no interference can occur. Fig. 6 shows the variation of sensing delay with different operational intervals. The runtime of the simulation is 100s. Here SU has higher sensing delay than PU.

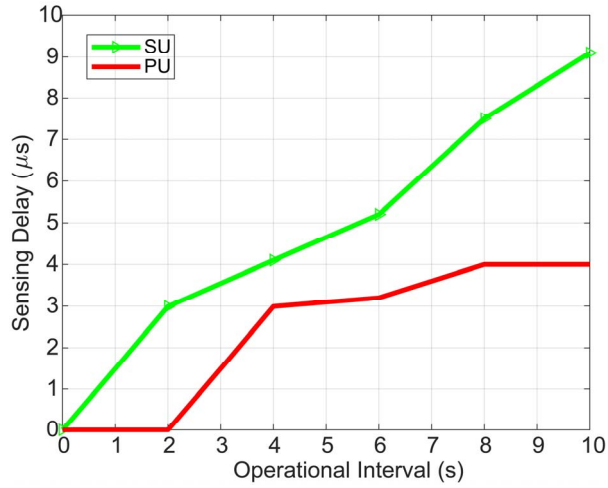


Figure 6. Incumbent detection in a CRN.

## E. *PUE Attack Detection*

We have simulated a PUE attack in NetSim with two PUs one of which is real and the other is malicious along with two SUs, and a base station as shown in Fig. 7.

The detection time has been set proportional to the distance of the SUs from the malicious PU and the appropriate operational interval for both PUs has been selected. Here initially additional delay has been considered to be the one tenth of the value of distance and varied for one hundredth and one thousandth to analyze the effect of the time delay.

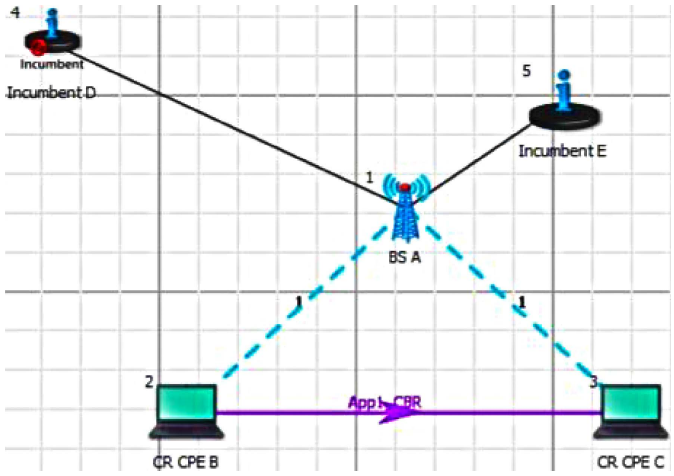


Figure 7. PUE attack topology.

The operational time for real and malicious PU has been set 9s and 4s respectively, and the operational interval has been set 9s and 10s for them in sequence. The active and inactive states for both real and malicious PUs have been shown in TABLE III.

TABLE III. ACTIVE AND INACTIVE STATES OF PUS

| Real PU (OFF) | Real PU (ON) | Malicious PU (OFF) | Malicious PU (ON) |
|---|---|---|---|
| 0s to 9s | 9s to 18s | 0s to 10s | 10s to 14s |
| 18s to 27s | 27s to 36s | 14s to 24s | 24s to 28s |
| 36s to 45s | 45s to 54s | 28s to 38s | 38s to 42s |
| 54s to 63s | 63s to 72s | 42s to 52s | 52s to 56s |
| 72s to 81s | 81s to 90s | 56s to 66s | 66s to 70s |
| 90s to 99s | 99s to 108s | 70s to 80s | 80s to 84s |
| - | - | 84s to 94s | 94s to 98s |
| - | - | 98s to 108s | - |

TABLE IV. TIME VARIATIONS FOR PUE ATTACK DETECTION

| Detected By | Detected | Delay time (micro second) |
|---|---|---|
| CPE2 | Incumbent 1 | 9129743 |
| CPE3 | Incumbent 1 | 9129741 |
| CPE2 | Incumbent 2 | 24049746 |
| CPE3 | Incumbent 2 | 24049746 |
| CPE2 | Incumbent 2 | 38129746 |
| CPE3 | Incumbent 2 | 38129746 |
| CPE2 | Incumbent 1 | 4500974 |
| CPE3 | Incumbent 1 | 45009741 |
| CPE2 | Incumbent 1 | 63049743 |
| CPE3 | Incumbent 1 | 63049743 |
| CPE2 | Incumbent 2 | 63049743 |
| CPE3 | Incumbent 2 | 80049746 |
| CPE2 | Incumbent 2 | 94049746 |
| CPE3 | Incumbent 2 | 94049746 |

NetSim generates a text file after the simulation that contains the required time to detect the PUE attack. Point to be noted that the throughput of the PU may be affected by the mobility of the SU. The time variation for detection of PUE attack has been presented in TABLE IV.

### *F. Cooperative Operation*

We have compared between the performances of centralized and distributed cooperative sensing by using the topology shown in Fig. 8. The aim of using centralized sensing is to mitigate the fading effects of the channel and increase the detection performance. According to Fig. 9, centralized cooperative sensing concedes less packet loss and hence provides better performance than the decentralized one for the same number of nodes. Moreover, the occurrence of packet loss decreases in centralized cooperative sensing with increasing number of nodes while quite the opposite nature has been observed for the decentralized or distributed approach.

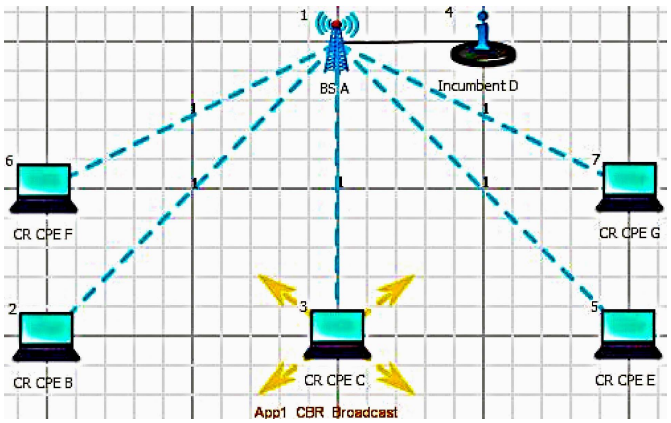


Figure 8. Topology for cooperative CRN.

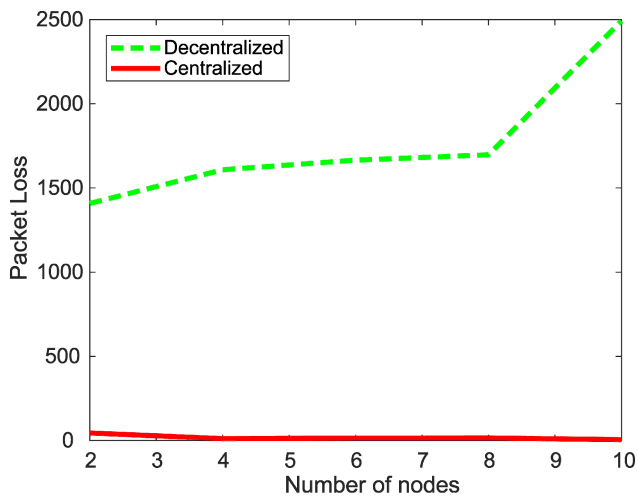


Figure 9. Comparison between fading effects in different cooperation.

In case of throughput, centralized sensing approach yields better performance than the decentralized one as per Fig. 10 suggests.

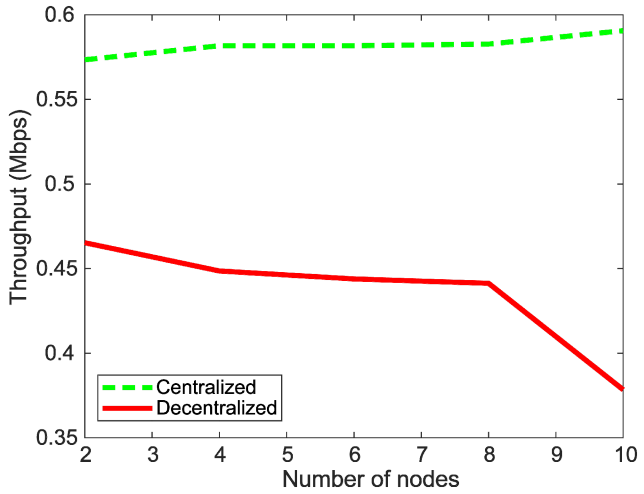


Figure 10. Obtained throughput in different cooperation technique.

## VII. Conclusion

CR is a wireless communication technique that ensures proper utilization of the available licensed spectrum of PU by allocating the temporary unused portion of it to SUs. However, SUs can use the spectrum only when PU is inactive, and it is an obligation for SUs to comply. In this paper, we have conducted comparative analysis among several performance parameters of CRN through simulation, and different topologies have been designed with performance appraisal. The channels have been allocated by varying the cycle length of IFQP with which the throughput varies proportionally. Moreover, four variants of TCP control algorithm such as Old Tahoe, Tahoe, Reno, and New Reno have been employed to reduce the congestion in CRN. We have observed that both the throughput and the spectral efficiency increase notably with the rise in the operational interval of PU. The SUs are more sensitive to operational interval than PU in case of sensing delay. Different operational intervals have been set for both the SUs and the PUs in order to prevent interference to PU activity. As security assessment, a PUE attack has been modeled in NetSim and the time variation for detection of the attack has been presented. In case of spectrum sensing method, the centralized cooperative sensing technique is preferable to decentralized one as it concedes less packet loss and provides better throughputs for the same number of nodes. Furthermore, the occurrence of packet loss decreases in centralized cooperative sensing with increasing number of nodes while quite the opposite behavior has been perceived as the decentralized approach. In CRN, centralized cooperative sensing technique, greater cycle length, wider operational interval, and New Reno congestion control protocol offers better performance for proper utilization of electromagnetic spectrum.

## References


[1] Dhanalakshmi P., Divya S., Kamila S.A., Muthumeenakshi K. and Radha S., "Modeling and analysis of Cognitive Radio with multiple primary/Secondary users and imperfect sensing", *2014 International Conference on Recent Trends in Information Technology*, 2014.

[2] V. Tumuluru, P. Wang, D. Niyato and W. Song, "Performance analysis of cognitive radio spectrum access with prioritized traffic", *IEEE Transactions on Vehicular Technology*, vol. 61, no. 4, pp. 1895-1906, 2012.

[3] A. El-Toukhey, A. Ammar, M. Tantawy and I. Tarrad, "Performance analysis of different opportunistic access based on secondary users priority using licensed channels in cognitive radio networks", *2017 34th National Radio Science Conference (NRSC)*, 2017.

[4] R. Bouraoui and H. Besbes, "Cooperative spectrum sensing for cognitive radio networks: fusion rules performance analysis", *2016 International Wireless Communications and Mobile Computing Conference (IWCMC)*, 2016.

[5] S. Alam, J. Chowdhury, M. Rashed, S. Anjuman and R. Zaman, "Throughput analysis of narrowband cognitive radio networks for fading channel", *2016 3rd International Conference on Electrical Engineering and Information Communication Technology (ICEEICT)*, 2016.

[6] S. Alam, M. Lucio and C. Regazzoni, "opportunistic spectrum access of sparse wideband in stand-alone and cooperative cognitive radio networks", *2015 IEEE International Conference on Smart City/SocialCom/SustainCom (SmartCity)*, 2015.

[7] I. Akyildiz, B. Lo and R. Balakrishnan, "Cooperative spectrum sensing in cognitive radio networks: a survey", *Physical Communication*, vol. 4, no. 1, pp. 40-62, 2011.

[8] W. Stevens, "TCP slow start, congestion avoidance, fast retransmit, and fast recovery algorithms," *RFC 2001*, Jan. 1997.

[9] X. Xie and W. Wang, "Detecting primary user emulation attacks in cognitive radio networks via physical layer network coding", *Procedia Computer Science*, vol. 21, pp. 430-435, 2013.

[10] J. Unnikrishnan and V. Veeravalli, "Cooperative sensing for primary detection in cognitive radio", *IEEE Journal of Selected Topics in Signal Processing*, vol. 2, no. 1, pp. 18-27, 2008.

2017 3rd International Conference on Electrical Information and Communication Technology (EICT), 7-9 December 2017, Khulna, Bangladesh

# A User Rating Based Collaborative Filtering Approach to Predict Movie Preferences

Md. Asif Shahjalal[1], Zubaer Ahmad[2], Mohammad Shamsul Arefin[3], Mohammad Rubaiyat Tanvir Hossain[4]
Department of Electrical and Electronic Engineering[1 4]
Department of Computer Science and Engineering [2 3]
Chittagong University of Engineering and Technology
Chittagong-4349, Bangladesh
asif.cuet93@gmail.com[1], mail2zubaer@gmail.com[2], sarefin@cuet.ac.bd[3], mrthossain@cuet.ac.bd[4]

***Abstract*—Recommender systems are arguably one the most successful and widely popular commercial application of machine learning. This paper discusses and presents a collaborative filtering based movie recommender system. One of the most challenging issues in machine learning is choosing perfect features for learning algorithms. However, choosing features manually can be quite difficult and tiresome work in many complex situations. The traditional content-based recommender systems require well-defined feature matrix for the movies. However, such features are not readily available for a large dataset of movies. This is where collaborative filtering comes to rescue. It can select and learn the features all by itself. Here prediction is based on user behavior. The real advantage is that the features learned by the algorithm do not need to be human defined. A user rating based low-rank matrix factorization collaborative filtering approach has been selected for this research. MovieLens 100k dataset [1] from GroupLens research has been used in this research. To minimize the squared error of the cost function gradient descent algorithm has been used in this approach. Here all the users collaboratively contribute to the development of different features that will help new users in the future. This approach saves the time consuming, expensive and difficult nature of content based recommender as well as saving the user from a lot of hassles like filling up a long survey form. This paper is based on the study of popular Coursera course "Machine Learning" [2] by professor Andrew Ng from Stanford University. The cost function minimization to minimize the squared error is done using gradient descent algorithm which ensured the visual confirmation of the cost minimization and to provide a visual representation of the cost minimization. Also, the outliers in the prediction matrix are eliminated using a threshold value. A prototype has been proposed and implemented with the help of Matlab.**

***Keywords*—Machine learning, movie recommender system, collaborative filtering, gradient descent, mean normalization.**

## I. Introduction

Popular technology companies in Silicon Valley have agreed on the fact that the most popular and important application of machine learning in the business is product recommender system. Sites like Amazon, Netflix, eBay, or iTunes Genius from Apple are a few well-known examples of product recommender systems in our everyday use. These types of recommenders look at what books a user have purchased previously, or the movies they have previously rated and make predictions based on what the user may be interested in to buy in the future. These systems are responsible for a considerable amount of these companies revenue. With the advent of internet and e-commerce recommender systems are making the user experience a lot easier. These facts easily describe why even a slight improvement to a recommender system can benefit these companies.

The most popular recommender systems are content based filtering and collaborative filtering. There are even hybrid techniques which utilize both of the above methods. Each type of systems has both its pros and cons. Usually in case of collaborative filtering approach a huge quantity of data is needed to make an accurate prediction while content-based filtering systems are generally too limited in scope.

Content-based systems make prediction from a users past activity [3], [4]. All the items are compared with users previous ratings on other items. The top items that are matched are recommended. Features describing the users tastes and preferences are collected. Users previous ratings are detected and analyzed to attain these features. The content-based recommendation depends on the advancement of information retrieval [5] and information filtering [6] research. These earler advancements mentioned along with emergence of various text-based applications have paved the way for numerous content-based systems focusing on recommending products which generally involves textual information like articles, websites, news, messages. Here the user profiles define the user preferences and their needs and help to improve the information retrieval approaches. It can be easily presumed that the content in these systems are mostly keywords. Fab system [7], is an ideal example which recommends websites to users. It creates page content based on top 100 words. Similarly, Syskill and Webert system [4] use 128 most useful words to epitomize an article. Bayesian classifiers [8] as much as machine learning algorithms like clustering and neural

978-1-5386-2307-7/17/$31.00 ©2017 IEEE

networks [4] are also significant content-based recommendation which analyze utility estimation based on a model trained through underlying data by use of machine learning algorithms, e.g. by categorizing users rating on a group of web sites as relevant or irrelevant[4], unrated web pages are classified using naive Bayesian classifier.

For a new user a huge quantity of items are needed to be viewed and rated by him so that content-based system can learn the user's likings and predict reliable recommendations. But collaborative filtering has an interesting property that it can learn the features all by itself. Collaborative filtering filters a user's preference automatically by gathering preferences data from numerous users. The primary assumption states that two person sharing same view on a common issue are more likely to share the same view on a diverse situation than a randomly chosen person. This way each user contributes to the learning of new features and what features to choose. This makes sense for the name collaborative. In contrast with the content-based recommendation, it tries to recommend an item for a particular user depending on items which were earlier rated by distinct users.

The initial recommender system known as the Grundy system [9] proposed a method for building user models from a limited data on each distinct user, built distinct user models, using them to suggest relevant books to particular user. Following, the Tapestry system used individual user data to classify similar users physically [10]. GroupLens and Ringo [11] were the very first automatic prediction systems which utilized collaborative filtering systems. Amazons book recommendation system is a popular one of this kind. Other popular examples are the PHOAKS system associating people to discover related information on the web [12] and a recommender scheme named Jester [13] which suggests joke.

A certain type of collaborative filtering uses matrix factorization which involves low-rank matrix approximation method [14]. Collaborative filtering schemes are broadly categorized in two types - memory-based and model based. A famous example of memory-based tactics is user-based algorithm[15]. Similarly, a popular model-based method is Kernel-Mapping Recommender. Memory-based algorithms [16] are approaches that predicts ratings depending on the history of items rated by different users. The unidentified rating for a user and item is typically computed as an amalgamation of the ratings by other similar users. On the contrary model-based algorithms [17], [13], [18] utilize the group of ratings to train a model, that is used to make predictions of ratings. In this approach, models are established using different machine learning and data mining algorithms to predict user's rating of unrated items. Popular model-based systems are Bayesian networks, singular value decomposition, clustering models, latent Dirichlet allocation, multiple multiplicative factor and Markov decision based models [19]. Dimensionality reduction methods are also used as complementary technique to improve efficiency of memory-based approach. Processes like SVD, PCA compress user-item matrix into a low-dimensional representation.

A few other works on movie recommendation system used are also studied. An internet based movie recommender which predicts from text categorization (TC) [20] to learn from movie summaries. The efficiency of different feature illustrations, feature pickers, feature weighting methods and classifiers are assessed and conferred. It seemed to work better than the feature based approach. An inductive learning algorithm [21] was introduced to the recommendation process. Instead of computing users or items similarities, it constructed a decision tree to represent user preference. There are also works on clustering approach based on semi-supervised learning [22]. Besides, Coursera shows a very intelligent recommendation system in their machine learning MOOC [2]. In this paper a low rank matrix factorization collaborative filtering approach is presented and implemented. It has used the popular MovieLens dataset. There have been four MovieLens datasets released, known as 100k, 1m, 10m, and 20m reflecting the approximate number of ratings in each dataset. However in our work, the 100k dataset has been used. The MovieLens data sets are extensively used in research, education and commerce. They are downloaded numerous times each year and are being used in coding books, online courses. This method shows great efficiency from the user standing and reduces complexity.

## II. Proposed Methodology

### A. Problem Formulation

TABLE I
MOVIE RATINGS BY USERS

| Movies | User A | User B | User C | User D |
|---|---|---|---|---|
| P | 5 | 5 | 1 | 1 |
| Q | 5 | ? | ? | 1 |
| R | ? | 4 | 1 | ? |
| S | 1 | 1 | 5 | 4 |
| T | 1 | 1 | 5 | ? |

Let us first define the problem statement. As seen from table-I the users rate various movies on a rating based on 1 to 5. There are 5 movies. P, Q, R, S, T and we have 4 users, A, B, C, and D. Suppose, A is really fond of movie P and gives it a rating of 5. He also likes movie Q and gives it top rating. R is a new movie to him. So, we don't know the rating for that. A was not fond of movie S and T and rated them 1. And a different user B, rated a different set of movies. He likes P, did not watch Q. Thus, we can see that we don't have the ratings of all the movies for all the user. Our task is to guess the ratings for the movies for each user which they still haven't watched. In Fig. 1 the approach to solve this problem is shown in a diagram.

We are given the following data :

$r^{(i,j)}$ = 1 ; whether user j has rated movie i, 0 otherwise

$y^{(i,j)}$ = rating user j has given to movie i

So, our job here is to develop a learning algorithm to automatically predict these missing values in order to find out the movies that are not watched by users and recommend him new movies that will be interesting to him.

And to predict that we have to find out :

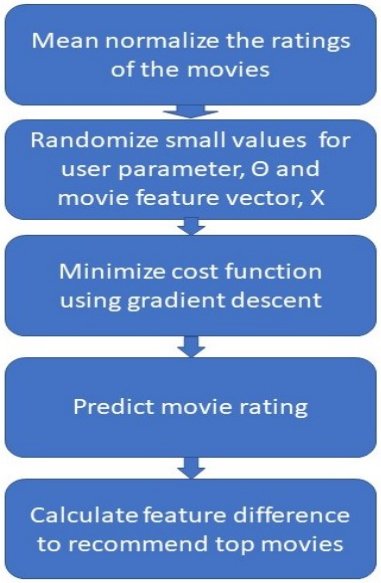


Fig. 1. Recommender system algorithm

$\theta^j$ = parameter matrix for user j
$X^i$ = feature matrix for movie i

Here, $\theta^j$ represents a users preferences like whether he likes romantic movie or action movie. $X^i$ refers to features of a movie like how much action does it have or how many explosive scenes does it involve.

### B. Preprocessing : Mean Normalization

If a new user is added to the system then he does not have any user preference vector associated with him. So it gets quite difficult to suggest movie to him. This is known as a cold start problem. To deal with this problem mean normalization technique is used. In this way, the mean rating of each movie is subtracted from that movie rating. So the movie ratings are now normalized and each movie has a mean rating of zero. This improved the efficiency of the algorithm a lot better.

### C. Optimization Objective

The collaborative filtering algorithm in case of movie recommendations defines a group of n-dimensional movie feature vectors $x(1).....x(n_m)$ and user weight vectors $\theta(1).....\theta(n_u)$, by which the system forecasts the rating for movie i by user j as $y(i;j) = (\theta(j))^T x(i)$. If a dataset is provided which contains a group of ratings produced by different users on random movies, then the goal is to learn the feature vectors $x(1)....x(n_m), \theta(1)....\theta(n_u)$ which yields the best fit (minimizes the squared error). On the other hand if movie feature vectors $x(1), ...., x(n_m)$ are given then we can predict user weight vectors $\theta^j, ...., \theta^(n_u)$ using the following optimization (1):

$$\min_{\theta^1,....,\theta^{n_u}} \frac{1}{2}\sum_{j=1}^{n_u}\sum_{i:r(i,j)=1}((\theta^j)^T x^i - y^{(i,j)})^2 + \frac{\lambda}{2}\sum_{j=1}^{n_u}\sum_{k=1}^{n}(\theta_k^j)^2 \tag{1}$$

Here, $\frac{\lambda}{2}\sum_{j=1}^{n_u}\sum_{k=1}^{n}(\theta_k^j)^2$ term is known as the regularization term where $\lambda$ is the regularization constant. Similarly given a set of user parameters $\theta(1), ...., \theta(n_u)$ we can learn feature vector $x(1), ...., x(n_m)$ from (2):

$$\min_{x^1,....,x^{n_m}} \frac{1}{2}\sum_{i=1}^{n_m}\sum_{i:r(i,j)=1}((\theta^j)^T x^i - y^{(i,j)})^2 + \frac{\lambda}{2}\sum_{i=1}^{n_m}\sum_{k=1}^{n}(x_k^i)^2 \tag{2}$$

The most basic solution to this problem is that we may first assume some values for $\theta$ and then find out $x$. Then we can keep estimating $\theta$ and $x$ in an iterative way. However, that is not our approach. We have taken both of the above objectives and combine them in the same objective. So, a new optimization objective to reduce the cost function is found which is both a function of features x and parameter $\theta$.

$$J(x^1, .., x^{n_m}, \theta^1, .., \theta^{n_u}) = \frac{1}{2}\sum_{(i,j):r(i,j)=1}((\theta^j)^T x^i - y^{(i,j)})^2 + \frac{\lambda}{2}\sum_{i=1}^{n_m}\sum_{k=1}^{n}(x_k^i)^2 + \frac{\lambda}{2}\sum_{j=1}^{n_u}\sum_{k=1}^{n}(\theta_k^j)^2 \tag{3}$$

And it is basically the previous two optimization objectives put together.

### D. Cost Function Minimization

After establishing the cost function then arises the question of minimizing it. Minimization means to reduce the squared error rate in the cost function to make it most efficient. The gradient descent algorithm has been used to minimize the cost function. The $X$ and $\theta$ matrices have been initialized to small random values and they are simultaneously updated for a suitable number of iteration. A perfect learning rate is selected by a number of trials. Finally to solve the problem of overfitting a regularization term is added.

$$x_k^i := x_k^i - \alpha\Big(\sum_{j:r(i,j)=1}((\theta^j)^T x^i - y^{(i,j)})\theta_k^j + \lambda x_k^i\Big) \tag{4}$$

In the above equation, the $\lambda x_k^i$ term is the regularization term. $\alpha$ signifies the learning rate of the algorithm.

$$\theta_k^j := \theta_k^j - \alpha\Big(\sum_{i:r(i,j)=1}((\theta^j)^T x^i - y^{(i,j)})x_k^i + \lambda\theta_k^j\Big) \tag{5}$$

The $\lambda\theta_k^j$ term solves the overfitting problem in above equation.

### E. Recommend Top Movies

Finally after minimizing X and $\theta$ matrices the predicted rating for a user with parameter $\theta$ and a movie with feature $X$ is made from $\theta^T X$ formula. Another approach to recommend movies is to calculate the feature difference between movies. The movies with the least difference is recommended to a user. For example, a small difference $|X^i - X^j|$ between movies i and j means that they are similar.

## III. Result

The movielens 100k dataset was used for the movie recommender. It contained a matrix of 1682 movies and 943 users. Each users rated at least 20 movies. Total 100000 ratings are available in the dataset. The dataset was first rearranged for further analysis. The ratings matrix can be visualized in Fig. 2.

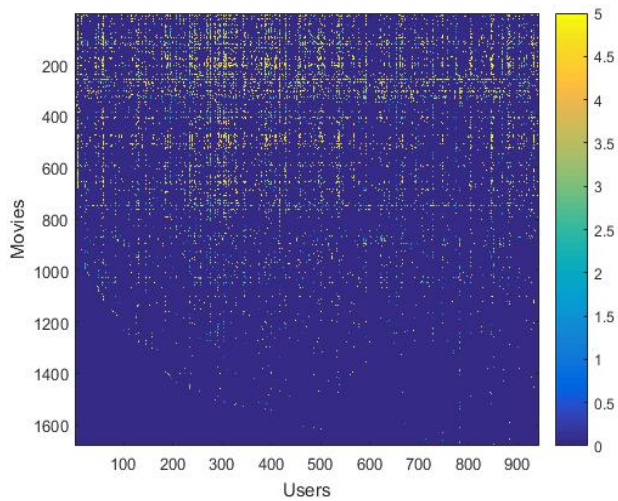


Fig. 2. Visualization of the ratings matrix

The learning rate for the gradient descent algorithm was selected by trial method. Learning rate, $\alpha$ was tested with different values like 0.3, 3, 0.03 values. 0.0001 was found to be the best learning rate for our case. 100 iterations were made to find out the optimum value for $\theta$ and $X$. The cost function vs iteration plot that is the cost function minimization plot can be seen from Fig. 03.

To evaluate the performance root mean square error(RMSE) and mean square error(MSE) was calculated for the given data set and the predicted ratings. The RMSE was found to be 0.7761 and the MSE was calculated to be 0.6023. Both these error rates are considerable and seemingly provide a good prediction. A visualization of the prediction matrix is shown in Fig. 4.

Another performance measure was taken. 82 users were asked to rate 20 of the movies from the data set. According to their rating top 20 movies were suggested for them. 58 users said that the recommendations were 95 - 100% satisfactory. Another 14 users notified about 80-85% of satisfaction. However the other 10% users stayed on 70 - 80 percent perfection.

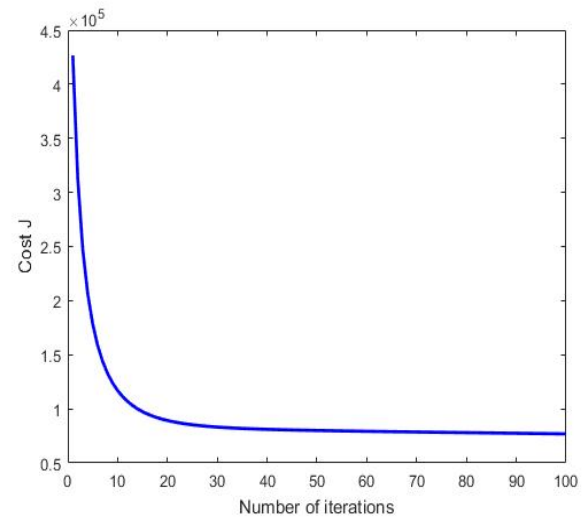


Fig. 3. Minimizing the cost function

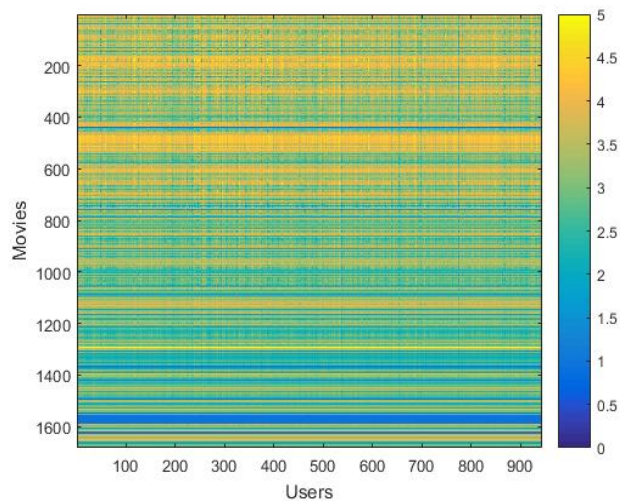


Fig. 4. Visualization of the prediction matrix

This statistics showed that the predictions are quite efficient. Fig. 5 and Fig. 6 shows a user's rating of some movies and which movies are then recommended to him.

The overall important data are mentioned in Table - II.

TABLE II
Data summary

| | |
|---|---|
| Number of movies | 1682 |
| Number of users | 943 |
| Number of features | 10 |
| Learning rate, $\alpha$ | 0.0001 |
| Regularization parameter, $\lambda$ | 10 |
| Mean square error | 0.6023 |
| Root mean square error | 0.7761 |

```
Command Window
New to MATLAB? See resources for Getting Started.

Original ratings provided:
Rated 5 for Toy Story (1995)
Rated 4 for Seven (Se7en) (1995)
Rated 5 for Usual Suspects, The (1995)
Rated 5 for Braveheart (1995)
Rated 5 for Taxi Driver (1976)
Rated 4 for Desperado (1995)
Rated 4 for Star Wars (1977)
Rated 3 for Pulp Fiction (1994)
Rated 5 for Shawshank Redemption, The (1994)
Rated 5 for Forrest Gump (1994)
Rated 5 for Lion King, The (1994)
Rated 4 for Carlito's Way (1993)
Rated 4 for Jurassic Park (1993)
Rated 4 for True Romance (1993)
Rated 4 for Terminator 2: Judgment Day (1991)
Rated 5 for Godfather, The (1972)
Rated 4 for Gone with the Wind (1939)
Rated 5 for GoodFellas (1990)
Rated 4 for Psycho (1960)
Rated 5 for Godfather: Part II, The (1974)
Rated 3 for Terminator, The (1984)
fx >>
```

Fig. 5. Ratings by a user

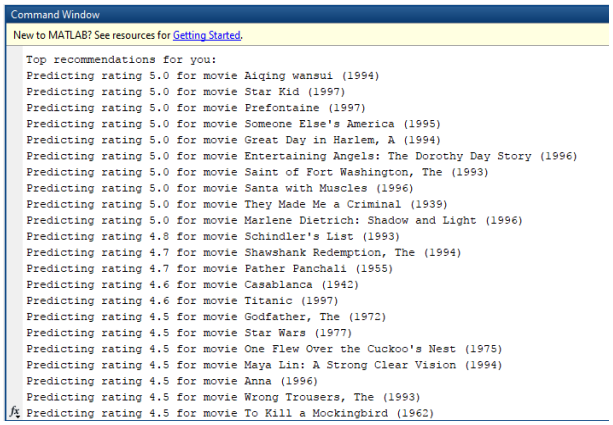

```
Command Window
New to MATLAB? See resources for Getting Started.

Top recommendations for you:
Predicting rating 5.0 for movie Aiqing wansui (1994)
Predicting rating 5.0 for movie Star Kid (1997)
Predicting rating 5.0 for movie Prefontaine (1997)
Predicting rating 5.0 for movie Someone Else's America (1995)
Predicting rating 5.0 for movie Great Day in Harlem, A (1994)
Predicting rating 5.0 for movie Entertaining Angels: The Dorothy Day Story (1996)
Predicting rating 5.0 for movie Saint of Fort Washington, The (1993)
Predicting rating 5.0 for movie Santa with Muscles (1996)
Predicting rating 5.0 for movie They Made Me a Criminal (1939)
Predicting rating 5.0 for movie Marlene Dietrich: Shadow and Light (1996)
Predicting rating 4.8 for movie Schindler's List (1993)
Predicting rating 4.7 for movie Shawshank Redemption, The (1994)
Predicting rating 4.7 for movie Pather Panchali (1955)
Predicting rating 4.6 for movie Casablanca (1942)
Predicting rating 4.6 for movie Titanic (1997)
Predicting rating 4.5 for movie Godfather, The (1972)
Predicting rating 4.5 for movie Star Wars (1977)
Predicting rating 4.5 for movie One Flew Over the Cuckoo's Nest (1975)
Predicting rating 4.5 for movie Maya Lin: A Strong Clear Vision (1994)
Predicting rating 4.5 for movie Anna (1996)
Predicting rating 4.5 for movie Wrong Trousers, The (1993)
fx Predicting rating 4.5 for movie To Kill a Mockingbird (1962)
```

Fig. 6. Recommended movies for a user

## IV. Conclusion

In this collaborative filtering we have used a linear regression approach to optimize the feature vector and user parameter vector. Gradient descent algorithm has been used to minimize the cost function. This could be substituted with much advanced algorithms like Conjugate gradient, BFGS, and L-BFGS.

Matlab was used for prototyping, as Matlab has always been proved to be the fastest tool to compute matrices. However this can be further implemented in python to create a more sophisticated recommender system. [23]

The data set contained very few movie ratings by users. An enriched data set would have provided even better predictions. The cold-start problem associated with the collaborative filtering is dealt in this approach using mean normalization. The 1 million data set by MovieLens would have yielded a lot better recommendation. However, due to the limitation of computing such a huge data set, the 100k data set was selected. Using a much powerful machine the 1 million data set could be experimented with. This paper demonstrate a very simplified yet efficient recommender system.

## References


[1] F. M. Harper and J. A. Konstan, "The movielens datasets: History and context," *ACM Transactions on Interactive Intelligent Systems (TiiS)*, vol. 5, no. 4, p. 19, 2016.

[2] A. Ng, "Machine learning," https://www.coursera.org/learn/machine-learning/.

[3] R. J. Mooney and L. Roy, "Content-based book recommending using learning for text categorization," in *Proceedings of the fifth ACM conference on Digital libraries*. ACM, 2000, pp. 195–204.

[4] M. Pazzani and D. Billsus, "Learning and revising user profiles: The identification of interesting web sites," *Machine learning*, vol. 27, no. 3, pp. 313–331, 1997.

[5] R. Baeza-Yates, B. Ribeiro-Neto *et al.*, *Modern information retrieval*. ACM press New York, 1999, vol. 463.

[6] N. J. Belkin and W. B. Croft, "Information filtering and information retrieval: Two sides of the same coin?" *Communications of the ACM*, vol. 35, no. 12, pp. 29–38, 1992.

[7] M. Balabanović and Y. Shoham, "Fab: content-based, collaborative recommendation," *Communications of the ACM*, vol. 40, no. 3, pp. 66–72, 1997.

[8] R. J. Mooney, P. N. Bennett, and L. Roy, "Book recommending using text categorization with extracted information," in *Proc. Recommender Systems Papers from 1998 Workshop, Technical Report WS-98-08*, 1998.

[9] E. Rich, "User modeling via stereotypes," *Cognitive science*, vol. 3, no. 4, pp. 329–354, 1979.

[10] D. Goldberg, D. Nichols, B. M. Oki, and D. Terry, "Using collaborative filtering to weave an information tapestry," *Communications of the ACM*, vol. 35, no. 12, pp. 61–70, 1992.

[11] U. Shardanand and P. Maes, "Social information filtering: algorithms for automating word of mouth," in *Proceedings of the SIGCHI conference on Human factors in computing systems*. ACM Press/Addison-Wesley Publishing Co., 1995, pp. 210–217.

[12] L. Terveen, W. Hill, B. Amento, D. McDonald, and J. Creter, "Phoaks: A system for sharing recommendations," *Communications of the ACM*, vol. 40, no. 3, pp. 59–62, 1997.

[13] K. Goldberg, T. Roeder, D. Gupta, and C. Perkins, "Eigentaste: A constant time collaborative filtering algorithm," *Information Retrieval*, vol. 4, no. 2, pp. 133–151, 2001.

[14] I. Markovsky, *Low rank approximation: algorithms, implementation, applications*. Springer Science & Business Media, 2011.

[15] J. S. Breese, D. Heckerman, and C. Kadie, "Empirical analysis of predictive algorithms for collaborative filtering," in *Proceedings of the Fourteenth conference on Uncertainty in artificial intelligence*. Morgan Kaufmann Publishers Inc., 1998, pp. 43–52.

[16] J. Delgado and N. Ishii, "Memory-based weighted majority prediction," in *SIGIR Workshop Recomm. Syst. Citeseer*, 1999.

[17] D. Billsus and M. J. Pazzani, "Learning collaborative information filters." in *Icml*, vol. 98, 1998, pp. 46–54.

[18] L. H. Ungar and D. P. Foster, "Clustering methods for collaborative filtering," in *AAAI workshop on recommendation systems*, vol. 1, 1998, pp. 114–129.

[19] X. Su and T. M. Khoshgoftaar, "A survey of collaborative filtering techniques," *Advances in artificial intelligence*, vol. 2009, p. 4, 2009.

[20] H. Mak, I. Koprinska, and J. Poon, "Intimate: A web-based movie recommender using text categorization," in *Web Intelligence, 2003. WI 2003. Proceedings. IEEE/WIC International Conference on*. IEEE, 2003, pp. 602–605.

[21] C. Basu, H. Hirsh, W. Cohen *et al.*, "Recommendation as classification: Using social and content-based information in recommendation," in *Aaai/iaai*, 1998, pp. 714–720.

[22] C. Christakou, L. Lefakis, S. Vrettos, and A. Stafylopatis, "A movie recommender system based on semi-supervised clustering," in *Computational Intelligence for Modelling, Control and Automation, 2005 and International Conference on Intelligent Agents, Web Technologies and Internet Commerce, International Conference on*, vol. 2. IEEE, 2005, pp. 897–903.

[23] M. R. T. Hossai, M. A. Shahjalal, and N. F. Nuri, "Design of an iot based autonomous vehicle with the aid of computer vision," in *Electrical, Computer and Communication Engineering (ECCE), International Conference on*. IEEE, 2017, pp. 752–756.

# Improved Optimum Dynamic Time Slicing Round Robin Algorithm

Shihab Ullah[1]
[1]Department of Computer Science and Engineering (BRAC University, Bangladesh)
shihabullah@outlook.com

*Abstract*—**In time-shared systems, selection of the time quantum plays a pivotal role in performance of CPU. In this paper, the static use of dynamic time quantum as CPU Time Slice is reviewed and a new algorithm for CPU scheduling named Improved Optimum Dynamic Time Slicing Round Robin Algorithm (IODTSRR) is proposed for process and thread scheduling. The proposed algorithm is based upon dynamic nature of allocation, calculation of the value of time quantum which varies according to the state of queue along with the capability of executing ready processes arriving at the same or different time. The concept of multi-threading by using Dummy Thread is introduced to hold the added processes in the queue during all arrival time intervals respectively. The performance is compared with Optimum Dynamic Time Slicing Using Round Robin (ODTSRR) and the results revealed that the proposed algorithm is much better specifically in response time and turnaround time. As process gets fully or partially executed while others arrive simultaneously, the context switch rates, waiting time and throughput improves hence resulting in optimized CPU performance.**

***Keywords—Time quantum, context and thread switches, arrival time interval, dynamic queue, first come shortest job first (FCSJF), improved optimum dynamic time slicing round robin algorithm (IODTSRR), optimum dynamic time slicing using round robin (ODTSRR).***

## I. INTRODUCTION

Process Management is one of the primary tasks achieved by the Operating Systems. The system's performance sententiously depends upon CPU scheduling algorithms. Operating systems today, are moving towards multitasking environments. In single processor system, only one process can be executed at a time, any other process or processes must wait until the CPU becomes free. The primary objective of multiprogramming is to maximize CPU utilization by having some processes running all the time. For multiprogramming systems, scheduling becomes an elemental activity of the operating system. Imprudent use of the CPU can dwindle the efficiency of system in multiprogramming environments. More than one processes are being kept in memory to achieve maximum CPU utilization. CPU scheduling controls which processes will execute when there are multiple executable processes. CPU scheduling is imperative because it can have immense impact on CPU utilization and inclusive performance of the system. Scheduling requires conscientious consideration to ensure fairness and avert process starvation in the CPU. This allocation involves a scheduler and dispatcher of long-term, middle-term, short-term basis respectively [1].

## II. METHODOLOGIES

### A. Scheduling Terminologies

It is necessary to be familiar with different scheduling terminologies defined below [1]:

- **Ready Queue:** The processes which reside in Main Memory and waiting for the CPU time are put in a queue called ready queue.
- **Concurrent Queue:** A ready queue that additionally supports operations that wait for the queue to become non-empty when retrieving an element, and wait for space to become available in the queue when storing an element.
- **CPU Utilization:** It is defined as the amount of time CPU is in use. Maximizing CPU utilization is usually the aim of any scheduling algorithm.
- **Context Switch:** Context switch is a process of keeping and restoring context of a pre-empted process, so the execution can be carried on from the same position at later time. Context switching is wastage of time and memory which results in increasing overhead of the scheduler.
- **Turnaround Time:** It is defined as the total time which is used to complete the process, from entering in to the ready queue till its complete execution.
- **Waiting Time:** It is defined as the total amount of time a process waits in ready queue.
- **Response Time:** It is defined as the time consumed by the system to give first response to a particular process.
- **Starvation:** It means the long process blocks the way of short process vice versa and the higher priority process out run the lower priority processes.
- **Priority:** Give preferential treatment to processes with higher priorities.

### B. Scheduling Criteria

The Characteristics of good scheduling algorithms are mentioned as follows [1]:

- Minimum number of context switches and waiting, turnaround, response time.

978-1-5386-2307-7/17/$31.00 ©2017 IEEE

- Maximum CPU utilization and throughput.
- Avoid indefinite blocking or starvation.
- Enforcement of priorities

### C. *Algorithmic Sypnosis*

The FCFS is better for a small burst time. The SJF is better if the process comes to processor simultaneously. While Round Robin is better to adjust the average waiting time desired [2], I have considered the above relative insights correspondingly. The processes are arranged in ascending order according to their burst times upon early arrival in the ready queue. Instead of using static time slices. I also used optimum time slicing approach where heuristic and multi-level programming reformation dynamically changes the basis of calculating Time Quantum. For scheduling and executing the ready queue where all the process have same arrival time, I modified and used ODTSRR algorithm where my proposed modified median is calculated and used only if there exist even number of processes in the queue respectively.

It might be considered as modified form of existing Optimum Dynamic Time Slicing Using Round Robin Scheduling Algorithm (ODTSRR). Rather than the use of different queues during scheduling, I used a concurrent dynamic queue as both ready and blocking queue respectively. The CPU Time Slice for process execution is calculated dynamically on basis of complete arrival of processes.

## III. LITERATURE REVIEW

Round Robin is the simplest, fairest and most widely used scheduling technique in timeshared systems. Use a fixed time slice for scheduling also known as time quantum. It choose process from head of ready queue and run that process for at most 1 time slice, and if it is not completed, add it to the end of the ready queue. If that process terminates or blocks before its time slice is completed, choose another process from the head of the ready queue, and run that process for at most 1 time slice. It achieves the fairness of resource allocation and result in minimized response time as compared to the Shortest Job First and First Come First Serve algorithms. But, due to the static time quantum concept it increases the turnaround time and waiting time resulting in dilapidation of system performance. Response time is good for short processes, while long processes may have to wait. Fairness factor which penalizes I/O-bound processes (may not use full time slice). Starvation is not possible as every process is getting the equal share of time, and the CPU Overhead is low [1].

Aashna Bisht et al. [1] proposed Enhanced Round Robin algorithm (ERR). ERR allocates CPU to a process for designated time quantum after the completion of which, it checks the remaining CPU burst time of the process currently in execution, if the remaining CPU burst time of the currently running process is less than (average burst time/time quantum) value, then CPU is again allocated to the currently running process for remaining CPU burst time.

Rami J. Matarneh et al. [1] proposed an algorithm named "Self- Adjustment Time Quantum in Round Robin Algorithms Depending on Burst Time of the Now Running Processes algorithm the time quantum is repetitively adjusted according to the burst time of the currently running processes using median.

Lalit Kishor and Dinesh Goyal [1] proposed median based round robin algorithm. This algorithm is a blend of two techniques, the processes are arranged in ascending order first, and then the time quantum is set according to the value of median.

H.S. Behera and Brajendra Kumar Swain [1] proposed an algorithm named "A New proposed precedence based Round Robin with dynamic time quantum scheduling algorithm for soft real time systems" in which precedence value is allocated to all the processes according to their priority and burst time. RR algorithm is then applied on the processes on the basis of their precedence. This Proposed algorithm is developed by taking dynamic mean time quantum in to account. Time quantum is computed dynamically by taking the mean of priority values and burst times.

Ali Jbaeer Dawood et al. [1] proposed an algorithm "Improved Efficiency of Round Robin Scheduling Using Ascending Quantum and Minimum-Maximum Burst Time" in which processes were arranged in ascending order with shortest remaining burst time and calculated the time quantum by multiplying the average summation of minimum and maximum burst time by (80) percentage. The (80) percentage is chosen depending to two reasons: First, if the TQ calculated depending only on the summation the algorithm is become as the Short Job First (SJF). Second, the rule of thumb is that 80 percent of the CPU bursts should be shorter than the time quantum.

Radhe Shyam and Parmod Kumar [3] on the article "Improved Round Robin with Shortest Job First Scheduling" proposed an algorithm combining Round Robin with shortest Job first scheduling. The TQ studied to improve the efficiency of RR and performs degrades with respect to context switching, Average Wait Time and Average turned around time. The processes were ascending with shortest remaining burst time and then TQ are given to that ascending process to CPU and also continue to allocate TQ again if the remaining burst time is less than 1 time quantum. While ready queue is not empty or any new process enter in the queue, the execution is regulated. The proposed algorithm (IRRSJF) performs better than Round Robin (RR), Improved Round Robin (IRR), FCFS and some other scheduling algorithm in terms of reducing the number of context switches, average waiting time and average turnaround time.

Anju Muraleedharan et al. [4] lodged an article "Dynamic Time Slice Round Robin Scheduling Algorithm with Unknown Burst Time" where their approach mainly focuses on how round robin will perform if the processes burst times are unknown at the beginning. They propose a refinement to simple RR by altering the time quantum while execution. First and foremost, put a small value to initial time quantum, and carry through the first cycle with this time quantum. In succeeding cycles, they multiply the time quantum by two if no processes finished its work. It will scrutinize the number of processes completed in each cycle. If at least one of them is completed, then continue the next iteration with an

unchanged time quantum. By this method, some of the problems with static time quantum are partially solved. If the time slice used is larger, then the average waiting time will reduce, in normal cases. But a factor that affects the average waiting time of the RR is the arrival time of the jobs – if several new processes arrived in during the execution, then it may cause an increase in the average waiting time.

Wasim Firuj Ahmed and Sahana Parvin Muquit [5] brought up a new method in their article named "Improved Round Robin Scheduling Algorithm with Best Possible Time Quantum and Comparison And Analysis with the RR Algorithm" to find the best possible time quantum to make the traditional Round-Robin algorithm an efficient one. Instead of usual fixed time quantum, calculated value of the time quantum unit becomes a rounded-up magnitude of the square root of the multiple of the median and highest burst time respectively applied in RR algorithm.

Mohammad Salman Hafeez and Farhan Rasheed [1] proposed an algorithm in "An Optimum Dynamic Time Slicing Scheduling Algorithm Using Round Robin Approach" article where the time quantum is determined dynamically with median value and the continuity of the execution of a process with the remaining burst time lesser than the time quantum set by the median value.

Following that, an article paper called "An Enhanced Round Robin CPU Scheduling Algorithm", Jayanti Khatri [6] proposed an algorithm is similar to traditional Round Robin algorithm with a small improvement. The proposed algorithm (ERR) allocates the processor to the first process of the ready queue for a time interval of up to 1 time quantum. Then it checks the remaining burst time of the currently running process and if the remaining burst time is less than or equal to 1 time quantum, the processor again allocated to the same process. After completing the execution, this process is removed from the ready queue. If the remaining burst time of the currently running process is longer than 1 time quantum, the process will be added at the tail of the ready queue.

Omar Hani Mohammad Dorgham and Dr. Mohammad Othman Nassar [7] came up with attempts to introduce an alternative method in RR algorithm in the paper "Improved Round Robin Algorithm: Proposed Method to Apply SJF using Geometric Mean" which combines two algorithms together and calculate a dynamic time quantum using the geometric mean method to enhance the CPU utilization and minimize the waiting and turnaround time in CPU scheduling. Geometric Mean can be calculated by applying the nth root of the product of n numbers, where these numbers is considered as the burst times of the processes, and then take the ceil of the result as a time quantum. On the other hand, the proposed algorithm will take into consideration two cases, first one, when the processes have an arrival times, and the second case, when there is no arrival time. Algorithm will depends on the arrival time, and here the proposed algorithm applies the second algorithm which it is First Come First Serve to take the proper process, where the first process enter the ready queue will be execute first. Accordingly, if there exist a process which need more than 1 time quantum, the remaining burst time will be compared with the other processes burst times by applying the SJF algorithm to choose the proper process to start execution in the CPU. Without Arrival Time, the algorithm applies the SJF only to choose the lowest burst time between all processes, where the shortest burst will enter the CPU for the execution and if the lowest burst time needs more than 1 time quantum, the remaining burst time will be compared between other burst times by applying the SJF algorithm, then it will choose the lowest burst time again.

## IV. ALGORITHMIC DESIGN

When the list of processes to be scheduled has same arrival time, time quantum is also calculated dynamically using the proposed calculation of median. The processes are arranged in ascending order with the shortest remaining CPU burst time and placed accordingly in the priority queue. The median value is set as the time quantum which will be the value of CPU Time Slice. If the process is in its execution state and consumed its time slice and its remaining CPU burst time is less than or equal to the time quantum, the CPU will continue its execution till it finishes, Otherwise the process will be placed at the end of the dynamic queue (Here, it is performing like a Synchronized Ready queue). After all the processes in the ready queue are at least once attended by the CPU, it will again sort the process in ascending order with shortest remaining burst time. If a process is suspended by CPU for I/O wait or other reasons, the very same queue will dynamically perform as a Synchronized Blocking queue where the process will be placed in and will stay there until the waiting state is over.

If the list of processes to be scheduled has different arrival times, time quantum for executing processes is calculated differently before and after all the processes arrived in the queue. Let, N be the total time required for the arrival of all the processes and k be the arrival interval of the processes arrived already. At first, add the processes in the queue (one or multiple) arriving in $k^{th}$ interval (where $k<=N$ and initially $k = 0$). The queue execute those processes based on my modified FCSJF algorithm till the next $(k+1)^{th}$ time interval arrives. When the summation of the arrival interval of the processes become equivalent to the total arrival time of all processes, I perform ODTSRR with my modified median to the processes either added or have remaining CPU Burst Time existing in the same queue.

### A. *First Come Shortest Job First (FCSJF)*

The time quantum for executing the process is also calculated dynamically using the proposed calculation of median. The process ready for the execution are placed in the dynamic queue. At first processes are arranged in ascending order with the shortest remaining CPU burst time on basis of early arrival. After sorting, if the processes is in its execution state and consumed its time slice, the processes only with remaining CPU burst times will be placed at the end of the queue. After all the processes in the queue are at least once attended by the CPU, it will again sort the process in ascending order with shortest remaining burst time respectively.

## V. ASYMPTOTIC COMPLEXITY

IODTSRR calculates the value of median in O (n (log n)) in both average and worst cases respectively for total n number of processes in the queue respectively [8].

When one or more processes in the scheduler all arrives at the same time, IODTSRR and ODTSRR will be executed in O (n (n+1) (log n)) for all n > 0 in every cases.

When processes arrives at different times, ODTSRR runs in total of O (n^2(n+1) log n) and O (n (n+1) log n) during worst cases (i.e. neither one nor multiple processes arrives at the same time). Thus, exponential growth of total runtime occurs when there are large number of processes to be scheduled.

Whereas, complete execution of processes arriving at different times with IODTSRR will be in O (n^2 (log n)) in best and average cases. In worst case scenarios, the runtime complexity will be equal to either (n^2 (log n)) or (n (n+1) (log n)) + (n^2 (log n)) which fairly depends on the pattern of arrival of the process along with the variance of its burst time. Consequently, quick but constant rate of improvement in scheduling performance can be further noticed. In the Table 1, the total amount of runtime cost occur when both algorithm is scheduled for 5<= ∑ n <=200 are given as follows.

TABLE I. ASYMPTOTIC COMPLEXITY OF ODTSRR AND IODTSRR

| Amount of Processes | ODTSRR | IODTSRR |
|---|---|---|
| 5 | 125.81 | 38.44 |
| 10 | 1210 | 210 |
| 20 | 11475.08 | 1066.84 |
| 50 | 220951.05 | 8579.8 |
| 75 | 812276.54 | 21235.07 |
| 100 | 2040200 | 40200 |
| 150 | 7442558.52 | 184542.61 |
| 200 | 18592782.57 | 184542.61 |

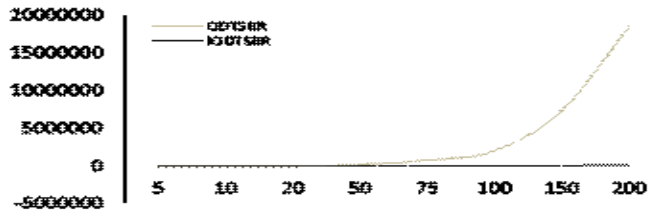


Figure 1. Difference of the asymptotic complexities between ODTSRR and IODTSRR. (for 5 <= ∑n <= 200)

The above presentation of data in tabular format (Table 1) and graph chart (Fig 1) both theoretically conclude promising performance results of IODTSRR having not only constant but also quadratic rate of improvement in each and every cases comparative to ODTSRR. Specifically, when there are 50 or more than that number of processes assumed to be of same priority have to be executed fairly while taking lesser time.

## VI. EXPERIMENTAL DETAILS

In-depth experimentation are purely based on considering overall and average performances of most of the state of the art variations in RR algorithms published especially before and after ODTSRR respectively.

### A. Estimations

The processes are independent of both full and reduced level of computational time requirements, specifically that supporting hardware virtualization. The system runs the algorithm only when it is in a stable state, that is, p < l/R. Irrespective of I/O bound, all processes are CPU bounded .The time unit is considered to be millisecond (ms). All attributes like burst time, number of processes and the time slice of all the processes are known before submitting the processes to the processor as performance metrics.

### B. Experimental Framework

The experiment consists of a number of input and output parameters. The input parameters consist of Burst Time<BT>, arrival time<AT>and total number of processes <Tn>. The output parameters consist of average response time, average waiting time, average turnaround time and number of context switches, fairness factor, throughput and CPU overhead.

### C. Procedure

Suggested algorithm is experimented thoroughly and effectively with large number of data input and cases. In this algorithm, the processes are arranged in ascending order according to their burst time's existent upon early arrival in the ready queue. Instead of using static time slices. I also used optimum time slicing approach where heuristic and multi-level programming reformation dynamically change the basis of calculating Time Quantum. In order to prove the correctness of performances along with stated efficiency and potential consistency of IODTSRR, same data set used in the experimentation of ODTSRR along with mentioned RR variations are used exactly as that of by being majority of test cases for proposed algorithm.

### D. Illustration

Let five processes labeled as P1, P2, P3, P4 and P5 all are arriving at zero millisecond (ms) with their burst time of 140, 75, 320, 280 and 125 ms respectively. Gantt chart of ODTSRR and my proposed algorithm are shown in Table 2 and 3 perceptively.

TABLE II. GANTT CHART (ODTSRR)

| ODTSRR | | | | | | | |
|---|---|---|---|---|---|---|---|
| *P2* | *P5* | *P1* | *P4 (140)* | *P3 (180)* | *P4* | *P3* | |
| 0 | 75 | 200 | 340 | 480 | 620 | 760 | 940 |

TABLE III. GANTT CHART (IODTSRR)

| IODTSRR | | | | | | |
|---|---|---|---|---|---|---|
| *P2* | *P5* | *P1* | *P4* | *P3 (180)* | *P3* | |
| 0 | 75 | 200 | 340 | 620 | 760 | 940 |

In accordance with, the comparison of average of turn-around, waiting and response times of every process are mentioned in the above Table 4.

TABLE IV. COMPARISON TABLE

| Name | Average Turnaround Time | Average Waiting Time | Average Response Time | No. of Context Switches |
|---|---|---|---|---|
| ***ODTSRR*** | 463 ms | 275 ms | 219 ms | 2 |
| ***IODTSRR*** | 435 ms | 247 ms | 247 ms | 1 |

Now, consider eight processes labeled as P1, P2, P3, P4, P5, P6, P7, and P8 arriving at 1st, 2nd, 3rd, 4th, 5th, 6th, 7th and 8th ms with burst time of 140, 75, 320, 280 and 125 ms consecutively. Gantt chart of ODTSRR and IODTSRR along with its comparison are given in the following Table 5, 6 and 7 respectively.

TABLE V. GANTT CHART (ODTSRR)

| ODTSRR | | | | | | | |
|---|---|---|---|---|---|---|---|
| ***P1*** | ***P8*** | ***P6*** | ***P3*** | ***P2*** | ***P5*** | ***P4*** | ***P7*** |
| 1 21 | 28 | 64 | 117 | 186 | 268 | 362 | 462 |

TABLE VI. GANTT CHART (IODTSRR)

| IODTSRR | | | | | | | | |
|---|---|---|---|---|---|---|---|---|
| ***P1(13)*** | ***P8*** | ***P1*** | ***P6*** | ***P3*** | ***P2*** | ***P5*** | ***P4*** | ***P7*** |
| 1 8 | 15 | 28 | 64 | 117 | 186 | 268 | 362 | 462 |

TABLE VII. COMPARISON TABLE

| Name | Average Turnaround Time | Average Waiting Time | Average Response Time | No. of Context Switches |
|---|---|---|---|---|
| ***ODTSRR*** | 184 ms | 126.25 ms | 126.38 ms | 0 |
| ***IODTSRR*** | 183.25 ms | 125.63 ms | 124.75 ms | 3 |

Cost of context switches in IODTSRR can often be compared as that of thread switches which is lesser and faster without falling in dead-lock conditions

## VII. COMPARATIVE ANALYSES AND RESULTS

I have compared our proposed algorithm on basis of all mandatory performance metrics and results with only that of ODTSRR as it's the considered standard algorithm in respective analyses.

### *A. Research Feasibilities*

While applying Little's Law in series of test case simulation, IODTSRR sounds highly feasible for scheduling, better than other RR variations respectively. Also by avoiding process starvation, no aging required due to fixed standard of prioritization. Most of the processes to be scheduled have shorter burst time i.e. less than 10 milliseconds respectively [9]. Hence, proper resource and time slice allocation may impose probability of more efficiency in scheduling processes in fixed priorities.

### *B. Algorithmic Analysis*

One or multiple processes can be scheduled in the queue upon instant arrival while the current process gets fully or partially executed. Unlike ODTSRR where no other processes can be scheduled in the queue before the execution of the current processes is fully completed, scheduling and execution can be done simultaneously. Due to dynamic nature of the calculation of time quantum and process handling in the queue, lesser CPU overhead and higher throughputs are unavoidable for larger input respectively. Whereas, the performance of ODTSRR decreases significantly and gradually when scheduling processes arriving in different times as both scheduling and execution cannot be done at the same time.

Importantly, in IODTSRR, if multiple processes with same remaining CPU burst time are scheduled, the processes with earlier arrivals will get the chances to be executed foremost. Hence, CPU will be implementing real time enforcement of priorities to always avoid Dead-lock condition and starvation as being functioned like a blocking queue respectively.

Consequently, instead of the traditional approach where the processes in blocking and ready state are stored in two separate queues, a concept of only one synchronized blocking queue is considered. Time Quantum is calculated differently before and after the completion of arrival of all the processes to be scheduled.

### *C. Experimental Analytics*

Overall projection of the performance gap between my proposed algorithm and ODTSRR when both are executed on the list of processes in queue (where at least one or more process arrives in different time) are stated as follows in Table 8 along with corresponding graph chart in Figure 2 respectively.

TABLE VIII. CUMULATIVE DIFFERENCE OF SUM OF AVERAGE TURN-AROUND, WAITING AND RESPONSE TIME OF LIST OF PROCESSES SCHEDULED IN DISSIMILAR ARRIVAL TIMES

| Metrics | ODTSRR | IODTSRR |
|---|---|---|
| ***Mean Turnaround Time*** | 216.97 | 212.3 |
| ***Mean Waiting Time*** | 154.64 | 149.83 |
| ***Mean Response Time*** | 153.95 | 148.58 |

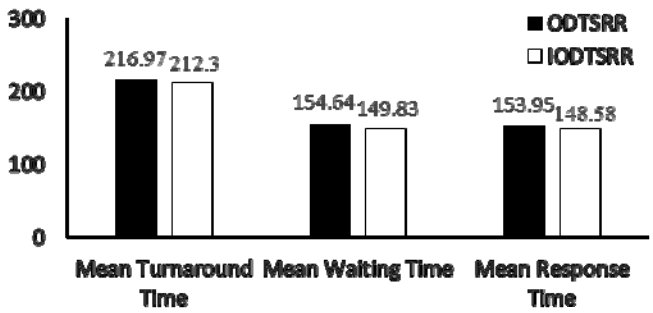


Figure 2. Cumulative difference of sum of the average turn-around,waiting and response time of n number of test cases scheduled in dissimilar arrival times. (for $\sum n = 21$ )

Last but not the least, overall performance of proposed IODTSRR on all types of input dataset used for analysis are stated in Fig 3 and Table 9 respectively. The test cases are used as input individually in respect of its types and complexities, where each test cases represent any queues or list of processes to be scheduled and executed.

TABLE IX. COMPLETE PROJECTION OF SUM OF AVERAGE TURN-AROUND, WAITING AND RESPONSE TIME OF ALL TEST CASES

| Metrics | ODTSRR | IODTSRR |
|---|---|---|
| ***Mean Turnaround Time*** | 79.15 | 75.08 |
| ***Mean Waiting Time*** | 52.66 | 48.06 |
| ***Mean Response Time*** | 41.95 | 41.73 |

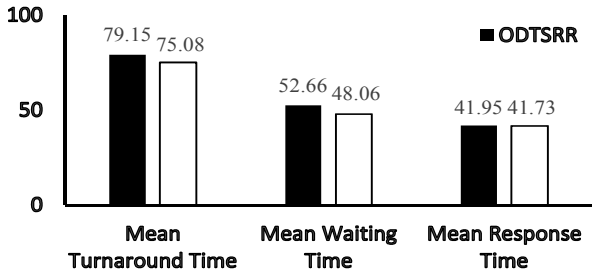


Figure 3. Complete projection of sum of the average turn-around,waiting and response time for n amount of testcases. (where $\Sigma$ n = 32)

Thus, all the tabular data and graphs resulted above from competitive test cases ensures that my proposed method ultimately takes lesser turn-around, waiting and response time than ODTSRR for scheduling processes at the same or different time period of their arrivals. Especially when there are large amount of processes in queue to be executed, no matter it have same or different priorities or extreme variation of their burst time consequently.

## VIII. CONCLUSION

I believe, from the above illustration of results and comparative analysis, IODTSRR as "complete" CPU scheduling algorithm has overall ascending performances not specifically scheduling and executing processes arriving in different times than other but also that of one or multiple processes arriving at the same time respectively. The suggested architectural implementation of a singular dynamic queue rather than handling that of both ready and block queue shows significant possibilities of decreasing but consistent run-time complexity of executing and scheduling processes. Unlike other variations of RR algorithm, the approached method effectively calculates the Time Quantum being feisty and performs its dynamic allocation as CPU time slice unit too. It ensures lower-cost along with decrease of context switches between longer processes due to CPU resources utilization by multi-threading programming. Despite of hardly sufficient input cases available i.e., both custom and derived for testing the benchmarks, the stated performance can be observed by operating in the offered dynamic queue architecture. For very long list of process scheduling, the trade-off with space and negligible cost in thread and context switches against CPU idleness can be worth considering. Further extension of research in the future, faster modification of the algorithm with intelligent CPU resource utilization and con-currency handling of scheduling can be possible. IODTSRR may have practical employment and fruitful experimentation when accordingly imposed in the real time operating systems and along with other version of known OS platforms such as Windows, Linux, MacOS etc.

## REFERENCES

[1] M. S. Hafeez and F. Rasheed, "An optimum dynamic time slicing scheduling algorithm using Round Robin approach," *IJCSIS*, vol. 14, no. 6, pp. 778–798, Jun. 2016.

[2] A. Putera and U. Siahaan, "Multiuser Comparison analysis of CPU Scheduling: FCFS, SJF and round robin," *IJEDR*, vol. 4, no. 3, pp. 124–131, Jul. 2016.

[3] R. Shyam and P. Kumar, "Improved Round Robin with shortest job first scheduling," *IJARCSSE*, vol. 5, no. 3, pp. 156–162, Mar. 2015.

[4] A. Muraleedharan, N. Antony and R. Nandakumar, "Dynamic time slice Round Robin scheduling algorithm with unknown burst time," *IJST*, vol. 9, no. 8, pp. 1–6, Feb. 2016.

[5] W. F. Ahmed and S. P. Muquit, "Improved Round Robin scheduling algorithm with best possible time quantum and comparison and analysis with the RR algorithm," *IRJET*, vol. 3, no. 3, pp. 1357–1361, Mar. 2016.

[6] J. Khatri, "An enhanced Round Robin CPU scheduling algorithm," *IOSRJCE*, vol. 18, no. 4, pp. 20–24, Aug. 2016.

[7] O. H. M. Dorgham and Dr. M. O. Nassar, "Improved Round Robin algorithm: Proposed method to apply SJF using geometric mean," *IJASCSE*, vol. 5, no. 11, pp. 112–119, Nov. 2016.

[8] M. Naftalin and P. Wadler, *Java Generics and Collections Handbook*, Sebastopol, CA: O'Reilly Media, 2006.

[9] A. Silberschatz, P. B. Galvin and G. Gagne, *Operating System Concepts*, Danvers, MA: John Wiley & Sons, 2009

# A New Approach to Hide Data in Color Image Using LSB Steganography Technique

Zinia Sultana[1], Fatima Jannat[2], Sadman Sakib Saumik, Niloy Roy, Nishith Kumar Datta, Muhammad Nazrul Islam[3]
Department of Computer Science and Engineering
Military Institute of Science and Technology, Dhaka, Bangladesh
Email: {[1]sultana.hiramony, [2]fj.jannat20, [3]nazrulturku}@gmail.com

***Abstract*—With the advancement of information technology, almost everything in this digital world evolves with information and data. The importance of security and secrecy of data is also increasing enormously. Steganography presents the practice of hiding data or information in any sort of cover medium, e.g image, audio, video. In most of the existing procedures, with the exposure of the keys intruders get successful in picking their required bits. The objective of this paper is to propose and implement a tool for increasing the secrecy of data transmission using steganography. In this paper, firstly we have proposed a technique which adds double layer security to hide data in image using LSB algorithm, AES-128 encryption and a new approach of choosing index of image pixel. Secondly, we have developed a steganography tool using our proposed technique. Finally, we have evaluated the performance of the proposed technique using Mean Square Error (MSE) method, Peak Signal to Noise Ratio (PSNR) and by measuring payload capacity. A comparative analysis of the developed tool with the some existing tools has showed that our tool performs better comparing with some other tools.**

***Keywords*—Steganography, LSB, AES (Advanced Encryption Standard), MSB, MSE (Mean square Error)***

## I. Introduction

Information security prevents any sort of unauthorized and illegal access of data. Now-a-days, the key concern of the information technology industries (IT) is to protect information and data from being stolen. There are a number of techniques in the information technology that maintain the confidentiality, secrecy and concealment of data. Among them, one of the popular techniques is steganography which ensures the security of the hidden commutation between the sender and the receiver.

Steganography is the craft of hiding data within images, videos and texts through transmission channels. It is aimed to ensure the confidentiality of the sent information through two levels of security: avoidance of detection and decryption. Avoiding detection covers both software & visual detection i.e. the secret text needs to embedded in the image in such a manner that it is not noticeable. One must confuse the intruder that the cover image can contain any hidden data. Decryption covers the part that even by any chance it is detected that an image is carrying any confidential data the intruders cannot decrypt it i.e. get the actual plain text.

In steganography, the hiding techniques will fail if an intruder can suspect the cover medium [18]. While using a steganography tool, one should ensure whether the hiding technique used by the tool is prevailing all sort of detection by the intruder. In some cases, after hiding an information or data in an image, people can understand that there is some distortion in the image. The more the success rate of avoiding detection of a steganography tool is, the more trustworthy the tool will be.

The objective of this paper is to propose a good performing steganography tool with a new hiding technique and to evaluate the performance of the proposed tool using Mean Square Error (MSE) method, Peak Signal to Noise Ratio (PSNR) and payload capacity.

The remaining sections of this paper are organized as follows. A brief overview of the related work and literature review is presented in section 2. The development framework of proposed steganography tool with the new technique and implementation processes are discussed in section 3. In section 4, the evaluation of tool is discussed, followed by conclusion and future work in section 5.

## II. Literature Review

This section discusses about the related prior works of different stegenography data hiding techniques and tools.

In [2], an analysis of different algorithms for data hiding has been presented. This paper describes some of the mostly used stegnography algorithms briefly. They are Blindhide, Pixelswap, Hide Seek, Filter First, and Battle Steg. After that 2 types of filters (i.e. Laplace & Sobel) used for finding the best zones in images to hide have been mentioned. These are followed by a comparative analysis of performance among algorithms in terms of machine learning accuracy as a function of embedding rate. It concludes with the proposal and mathematical representation of a plausible deniability scheme.

Blowfish algorithm and LSB technique have been used respectively to encrypt the secret message and to hide the cipher into the bits of the frames of videos in [3]. Authors claimed the blowfish algorithm to be better than the other ones and evaluated their work of hiding into frames of videos as a new dimension in the steganographic field.

The work described in [4] is potentially in the field of cryptography. The idea of play fair method has been implemented in encrypting messages which resulted in MSA method (named after the names of designers). They have evaluated

their way of encrypting with experiments and have considered it best for watermarking.

In [5], modified versions of AES encryption algorithm have been proposed. The work is supported with adequate experimental data. It also compares AES+A5/1 and AES+W7 in terms of the performance parameters like correlation vertical, correlation horizontal, PSNR value and entropy.

Instead of following the common method of modifying an existing image the work in [6] has chosen the time of synthesizing of a texture image to hide the text in that. Also claims the capability of dealing with JPEG compression.

The process of maintaining confidentiality evolved around steganography has been tried in the field of electronic voting in [7]. The techniques are LSB and the Minimal Impact Decimal Digit Embedding (MIDDE). Personal identification number and fingerprint are the keys here.

The paper [8] tells about an approach to detect LSB steganography. This approach is based on statistical measures of sample pairs. Bounds on estimation errors of this simple and fast approach have also been measured.

Paper [9] just tells about another hiding scheme consisting of parity-bit pixel value difference and improved right most digit placement which promises not only good visual quality but also security.

OpenStego [16] is an open source steganography software which is distributed under GNU general public license v2.0. In this software the authors have provided two main functionalities: data hiding and watermarking (beta). This Java based tool supports password-based encryption of data for additional layer of security. DES algorithm is used for data encryption, along with MD5 hashing to derive the DES key from the password provided. It uses a plugin based architecture, where various plugins can be created for different kind of steganography algorithms.

QuickCrypto [17] is another paid steganography tool for windows operating system. It uses DES algorithm to encrypt and decrypt.

In sum, the existing literature shows that the mostly used and popular hiding technique is the LSB and the best hiding places can be found using filters and laplace equations. The review study also showed that different algorithms have different fields of application where they fit most (i.e. some are best for watermarking and some are best for steganography). The earlier researches also showed that the performance of any steganographic tool can be measured based on Embedding rate, Robustness, Imperceptibility, Mean Square Error and Peak Signal to Noise Ratio. This work thus will focus on a new hiding technique where we will use the LSB hiding technique and AES encryption technique and measure the performance of the tool using some metrics that has been used in the existing literature.

## III. Tool Development

This section discusses briefly about the total procedure of the new technique and how the tool has been implemented step by step.

### A. Developing the Technique

The complete technique is divided into two major parts: Firstly, embedding secret data in a cover image avoiding detection and decryption of data from the image. To avoid the detection of data we have used LSB algorithm and a new approach of choosing pixel index in the cover image. On the other hand, to avoid decryption we have used AES-128 encryption technique to encrypt the secret text.

LSB (Least Significant Bit) algorithm insert bits of the secret text in the least significant bit of a pixel value so that the distortion is not detectable. In this paper, we have used two number series and MSB of the pixel value to get a random distance from one hidden bit to another. So that detection become more difficult.

To avoid decryption we have used cryptography technique. Among different types of cryptography techniques we have chosen symmetric key algorithm, AES-128 to encrypt the secret text before embedding it in the image using LSB. The strength of AES-128 bit is very high. It takes billions of years to break the encrypted text. [1]

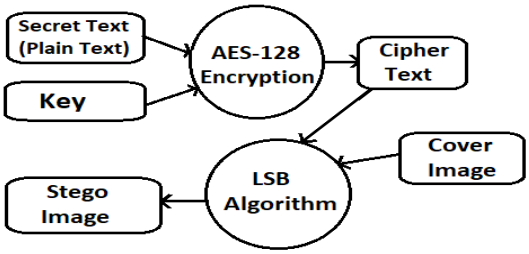


Fig. 1. Overview of Steganograohy Technique

The next part of the paper presents the algorithm 1 used to embed data in the image. While implementing algorithm 1 we have integrated our new technique (Algorithm 3) for choosing pixel index of cover image.

**Algorithm 1:** Algorithm for embedding Data in cover image

Step-1: Take input of secret text, cover image and a key.
Step-2: Check image quality according to the text. If not good enough then give warning to increase.
Step-3: Get byte array from the image and form pixel array using only blue color value of each pixel of the image.
Step-4: Encrypt the given secret text using AES algorithm with the given key known as **cipher text**.
Step-5: Apply **Algorithm 3** on the pixel byte array.
Step-6: Save the Steg Object.

Secondly, the next major part is to extract the secret data from the image. Counter part of the previous algorithm extracts the hidden data. In this case we give input of the key with the stego image known as stego-object and use AES-128 bit decryption mode as shown in algorithm 2.

In case of LSB algorithm one of the most important parts is finding the exact pixels of the cover image where the data

**Algorithm 2:** Algorithm for extracting hidden data from the stego-object

Step 1: Take inputs: stego-object & the key.
Step 2: Apply counter part of the **Algorithm 3** to get hidden bit stream.
Step 3: Get char value of the bit steam.
Step 4: Decrypt using AES decryption using the key.
Step 5: Outputs the secret Text.

would be hidden. For algorithm 1 and algorithm 2 we need to find the index of cover image pixel. Our proposal of a new approach for finding the desired index value of pixels in the cover image while inserting the secret data is described in Algorithm 3. This approach makes the detection more difficult for the intruders. For this purpose we consider two series randomly. They are,

1) Byte jumping series
2) Zero case series

First, we consider a **byte jumping series** which is used to traverse through the pixel indices of the image. It is used to get the next position or index of the byte array (pixel) where next bit of the cipher text is inserted. Byte jumping series is hard coded. Using its value we get the decimal value of the number of bits of the MSB of that byte. By adding the decimal value with the current positions column, we get the next byte where insertion takes place.

Second, we consider a **zero series** for a special case. As we use a byte series to get the next byte, there may be a case that the decimal value of the MSB is zero. In that case we get the next byte using zero case series.

An example case to describe the approach of finding pixel indices and then inserting data into that pixels are presented below: At first we consider the following two series as byte jumping series and zero case series.

1) Byte jumping series: [ 2 3 2 3 3 3 2 2 ]
2) Zero case series: [ 7 3 5 4 2 6 1 ]

Let the cipher text which will be converted in cipher bit stream is, 101110101 Let the byte array of an 8-by-8 image is the following figure 2.

| | j= 1 | 2 | 3 | 4 | 5 | 6 | 7 | 8 |
|---|---|---|---|---|---|---|---|---|
| i = 1 | 10110111 | 00111001 | 10101010 | 11110000 | 10101010 | 01010101 | 11100111 | 10110100 |
| i = 2 | 10111101 | 01111000 | 10011001 | 00010101 | 10110101 | 01010101 | 10111001 | 10001010 |
| i = 3 | 11010111 | 10110101 | 10110001 | 10101010 | 10110001 | 11010011 | 10110011 | 11101001 |
| i = 4 | 10010010 | 10010010 | 10110110 | 10110010 | 11010010 | 10010101 | 01011001 | 01001010 |
| i = 5 | 10101010 | 11010101 | 10101011 | 11010101 | 10110110 | 10001001 | 10101010 | 01001100 |
| i = 6 | 01010011 | 10100101 | 01010100 | 00000010 | 00000000 | 10010101 | 00011110 | 00101001 |
| i = 7 | 10101111 | 10101110 | 10101011 | 00111101 | 10101001 | 10111010 | 10001010 | 10100001 |
| i = 8 | 00110101 | 01010111 | 11010111 | 01010010 | 11111111 | 01011111 | 00010101 | 10100100 |

Fig. 2. Byte array of an 8-by-8 image

Initialize all the necessary variables i.e i=1, j=1,m = 1, jumping_series_index = 1 and zero_series_index = 1 and cipher_text_index = 1.

**Algorithm 3:** Pseudo algorithm for finding index of pixel from image and inserting cipher bits

```
Input: image, secret_text
Initialization: set: i=1 , j=1, jumping_series_index = 1,
  zero_series_index = 1, cipher_bits_index = 1,
  jumping_series = [ 2 3 2 3 3 3 2 2 ], zero_series = [ 7
  3 5 4 2 6 1 ] ;
Find: cipher_text = aes(secret_text); cipher_len = length
  (cipher_text); [ row, col ] = size (image);
while i ≤ row do
    while j ≤ col do
        insert cipher_text[cipher_bits_index] in the LSB
          of image[i, j] ;
        cipher_bits_index ++ ;
        if cipher_bits_index > cipher_len then
            break ;
        end
        n1 = jumping_series[jumping_series_index] ;
        if n1 == 2 then
            Take decimal value of 2 MSB bits by setting:
              n = image[i, j] / 64 ;
        else
            Take decimal value of 3 MSB bits by setting:
              n = image[i, j] / 32 ;
        end
        if n == 0 then
            n = zero_series[zero_series_index] ;
            if zero_series_index < length(zero_series)
              then
                zero_series_index ++ ;
            else
                zero_series_index = 1 ;
            end
        end
        if jumping_series_index < length
          (jumping_series) then
            jumping_series_index ++ ;
        else
            jumping_series_index = 1 ;
        end
        update: j = j + n ;
    end
    update: i= i + 1 ;
    update: j = n ;
    if cipher_bits_index > cipher_len then
        break ;
    end
end
```

At first, ( row, column ) = (i, j) = (1, 1) = first binary value of the byte array (10110111) of Figure 2. Next, cipher_text_index$^{th}$ bit of the cipher bit stream is 1, so insert 1 in the LSB of the value of (1, 1). As the LSB of 10110111 is 1, so no change takes place. If the LSB would be 0, then we

would change it into 1. Next, jumping_series_index$^{th}$ value of the byte jumping series = 2. So consider 2 bits from the most significant bit (MSB) that is '1 0'. Decimal value of $(10)_2$ = $(2)_{10}$. So, n = 2. As n $\neq$ 0, so nothing needs to do. Calculate m = j + n = 1 + 2 = 3 Next, check whether m > **col** or not. As the byte array is 8-by-8, col = 8. So m < col and j = m = 3. Now (i, j) = (1, 3). Then, increment value of cipher_text_index and jumping_series_index. The above steps are continued until we reach the last bit of the cipher bit stream. Doing this the byte jumping series or the zero case series may finish. In that case we start from the beginning. After 4$^{th}$ iteration m > **col**.

Then new (i, j) = (i++, n).

Now consider the value of index(i, j) = (2, 4). It is 00010101. Here we see that decimal value of 3 MSB ('000') is 0. In this case position does not change, that means value of i and j is remained same. But we need a different index position to insert the next bit of the cipher bit stream. For this case the concept of zero case series comes. Upgrade the value of n with the 1st value of zero case series and increment zero_series_index. Table I shows the iterations to embed the cipher bit stream

TABLE I
ITERATION TO HIDE CIPHER BIT STREAM

| **Iteration** | **i** | **j** | **Byte jumping series value** | **MSB** | **Zero case series value** | **n** | **m = j + n** |
|---|---|---|---|---|---|---|---|
| 1 | 1 | 1 | 2 | 10 | 7(No need) | 2 | $3 \leq 8$ |
| 2 | 1 | 3 | 3 | 101 | - | 5 | $8 = 8$ |
| 3 | 1 | 8 | 2 | 10 | - | 2 | $10 \geq 8$ |
| 4 | 2 | 2 | 3 | 011 | - | 3 | $5 \leq 8$ |
| 5 | 2 | 5 | 3 | 101 | - | 5 | $10 \geq 8$ |
| 6 | 3 | 5 | 3 | 101 | - | 5 | $10 \geq 8$ |
| 7 | 4 | 5 | 2 | 11 | - | 3 | $8 = 8$ |
| 8 | 4 | 8 | 2 | 01 | - | 1 | $9 \geq 8$ |
| 9 | 5 | 1 | 2 | 10 | - | 2 | $3 \leq 8$ |

in the 8-by-8 byte array. As the length of cipher bit stream is 9, so the number of total required iteration to insert the bits in the LSB is 9.

In Table I we see that zero case series is not used, as there is no MSB value with 0. But it plays a vital role when the MSB value will result in 000 or 00 to get the next position to insert the next cipher bit.

### *B. Developing the Tool*

This section gives the broad view of our implemented steganography tool using the methodology that is proposed in this paper. The tool is implemented in MATLAB (Matrix Laboratory)[15] (The source code can be found by e-mail request from the corresponding authors). There are two main parts: embedding data and extracting data

#### *i) AES Encryption / Decryption*

To avoid detection first we encrypt the plaintext i.e. the given secret text as input with AES-128 encryption using a key. This key is an input given by user which acts like a password. To use AES-128 bit the key needs to contain 16 characters. To make users unaware of AES-128 and its working process, we have written a section of code so that if the key is less than 16 character, then we have filled it with additional stars (*) to make the key length 16.

In this paper, Electronic Codebook Mode (ecb) [14] has been used to encrypt and decrypt data using AES. It is a mode of block cipher. In this mode the plaintext is divided in blocks and then each block is encrypted separately. Using the following segment of code we encrypt plaintext i.e. secret text.

```
Plaintext = double(secret_text);
key = double(key);
s = aesinit(key);
cipher_text = aes(s,'encrypt','ecb', Plaintext);
```

First we make both plaintext and key in double data type. Then we call aseinit() function. This function mainly generate the substitute box also named as S-box using the key and return the S-box. Then we call the aes() function which does the encryption of the plaintext and return the cipher text. In the aes() function we also mention the mode of block cipher. Thus we get the desired cipher text. Again the counterpart does the decryption as shown below which is needed after extracting LSB bits from the image byte array.

```
plaintext = aes(s,'decrypt','ecb', cipher_text);
```

#### *ii) Embedding Secret Data*

Embedding secret data follows the steps of algorithm 1. First we take input of the secret text and a key. Then we encrypt it using AES-128. Next we convert the encrypted text in a bit stream and take the cover image of BMP file format. After that we get the byte array of the image. The byte array (pixels) of the image contain three values of red, green and blue component of each pixel as the image is a color image. We only consider the blue color matrix to hide cipher bit stream. Then according to the LSB algorithm and our pixel index choosing technique (algorithm 3), we insert the bits. In case of insertion if we have cipher bit 1 need to insert, and the byte value is even, we increment it by one, as a number even means in binary it contains zero (0) in the LSB. If byte value is odd, then nothing needs to do. And if we have cipher bit 0 and the byte value is odd, then we decrement it by one. Otherwise do nothing. We also insert an end of file (EOF) 00000 after inserting the cipher bits. To insert this EOF, we ensure that, the main cipher bits do not contain 5 consecutive zeros. To ensure this, one 1 is inserted after every consecutive 4 zeros. This procedure is called bit stuffing.

After inserting all the bits in the blue color matrix, we reconstruct the full image and saved it as a BMP file which is the desired stego object.

#### *iii) Extracting the Secret Data*

The extracting part follows the steps of algorithm 2. At first we take input of the stego image and the key. Then we collect the LSB value using the counter part of algorithm 3 until we get the EOF which is encrypted using AES. From

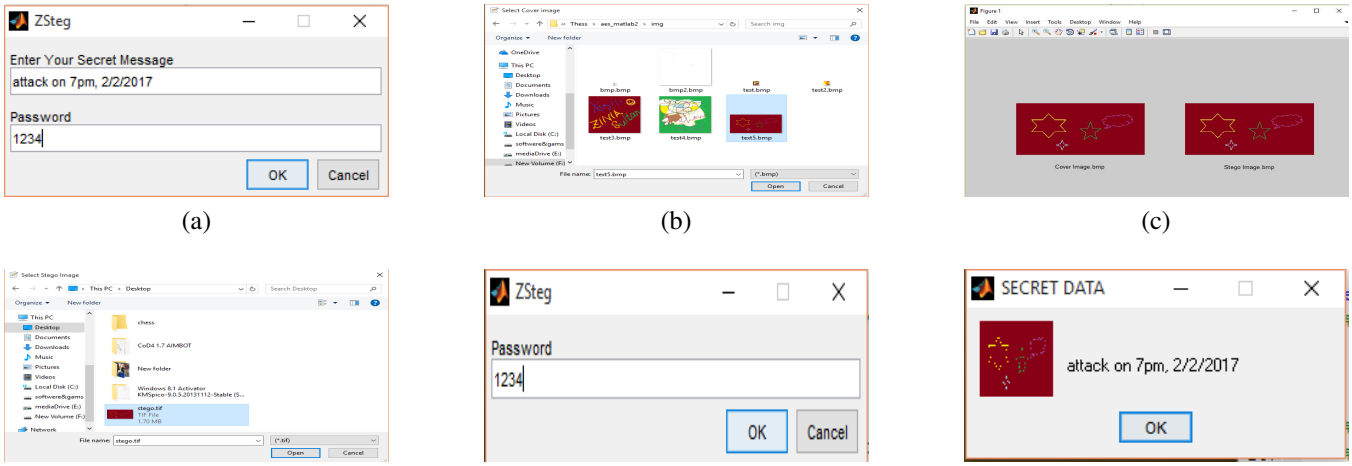


(a) (b) (c)

(d) (e) (f)

Fig. 3. Snippets of embedding and extracting secret data. (a) Giving input of secret text and the password (key). (b) Selecting a bmp image to hide the secret text. (c) Showing the cover image and stego image together. (d) Selecting the stego image to extract the secret data. (e) Giving password (key) at the rime of extracting. (f) Extracted secret text.

this cipher text, the 1's are removed after every consecutive 4 zero's which have been inserted during the embedding stage. Then using the AES decryption we get the plaintext.

Figure 3 shows some screenshots of the implemented tool. In fig 3. (a) an user enters the secret text and the password (key). Then in fig 3. (b) a bmp image needs to be selected where the text will be hidden. Thus the stego image embedded with secrect text will be found which is shown in fig 3. (c). In case of extracting secret data part, at first the user needs to select the stego image from its destination folder (fig 3. (d)). Then like 3. (e) user will have to enter the password(key). Finally if the password is correct, the secret data will be extracted like 3. (f)

## IV. Evaluation of Implemented Tool

There are many ways to measure the performance of an implemented tool. There are many performance metrics like Mean Absolute Error (MAE), Mean Square Error (MSE), Peak Signal to Noise Ratio (PSNR), Time Complexity, Qualitative Analysis, Normalized Color Deviation (NCD), Normalized Histogram Intersection Coefficient, Bhattacharyya Coefficient and Universal Image Quality Index (UIQI)[12]. Among these, we have analyzed our implemented tool in three criteria. They are Mean square error (MSE), Peak Signal to Noise Ratio and payload capacity.

### A. Mean Square Error (MSE)

Mean square error is calculated by dividing sum of the square of all pixel values difference of the cover image and stego image by the total number of pixel. The following equation will give a better understanding. A steganography tool will be better if the MSE value becomes less.

$$MSE = \sum_{i=1}^{n} \frac{(x_i - y_i)^2}{N} \tag{1}$$

Where, i = 1, 2, 3 . . . . . n, up to the last pixel, e.g. for all pixels.

x is color value of $i^{th}$ pixel in the cover image.

y is color value of $i^{th}$ pixel in the stego image.

N is the total number of pixel. We calculate the MSE value

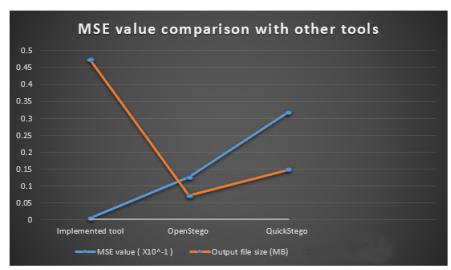


Fig. 4. Graph showing the comparison of MSE values and output file size among different tools.

TABLE II
MSE value comparison with other tools

| Tools name | MSE value | Output file type | Output file size |
|---|---|---|---|
| Implemented tool | 0.00041875 | .bmp/.tiff | 473 KB |
| OpenStego | 0.012436427209154482 | .bmp | 70.3 FB [13] |
| QuickStego | 0.03176652892561983 | .bmp | 147 KB [13] |

of our implemented tool using the above formula. The MSE value (0.00041875) of the tool is relatively low comparing with the other two tools (Table II).

### B. Peak Signal to Noise Ratio (PSNR)

PSNR is calculated in decibel. The more will be the PSNR value, the tool will be better than other. PSNR is calculated by the following formula,

$$PSNR = 10log_{10}\frac{MAX_I^2}{MSE} \tag{2}$$

Here $MAX_I$ is the maximum intensity value of each color component of a pixel. For color depth 24 bit, each component

of a pixel holds 8 bits. So $MAX_I$ will be 255 for 8 bit. The following Table III shows the PSNR value of our tool and other available tool. It is based on Table II.

TABLE III
SHOWING PSNR VALUE OF DIFFERENT TOOLS

| Tools name | PSNR value |
|---|---|
| Implemented tool | 81.91125541 |
| OpenStego | 67.18384729 |
| QuickStego | 63.11110598 |

### C. Payload Capacity

Payload capacity measures how much data can be hidden in an image using the steganography tool. A 'text to image' ratio in percentage is needed to measure this payload capacity (equation 3). Let, Secret text size (in byte) = x, Total number of pixels in Image = y

$$x <= \frac{y}{8 * 8} = \frac{y}{64} \tag{3}$$

As byte jumping series or zero case series have been used to jump from one pixel position to another, according to the values of series's at most 7 bytes can be jumped over at once. Considering 8, the number of available pixels $y/8$. Again one byte of the secret data will be hidden in 8 pixels of the cover image. So again divide it by 8. Thus the ratio becomes that secret data bits size should be less or equal to the quotient of the total number of pixel in the image divided by 64. So during implementation, a warning is given requesting to increase the image size or decrease the secret text size, if the ratio is not maintained. The payload capacity can be measured from equation 3,

$$x : y = 1 : 64 \tag{4}$$

In percentage,

$$x : y = 1.5625 : 100 \tag{5}$$

So the calculation indicates that the payload capacity of the proposed technique is 1.6% with respect to image size. This plays a vital role. Whatever the image size is, only 1.6% will be affected after applying steganography. The more payload capacity is, the more secret data can be hidden in an image. But there should be a threshold or it may be perceptible that a particular image is having some sort of secret data. MSE value will also be greater for greater payload capacity which is supposed to keep low for less distortion of stego-image with original image.

## V. CONCLUSION AND FUTURE WORK

This paper proposed a technique to choose the pixel index in the cover image of steganography for doubling the data security at the detection level. LSB algorithm and AES-128 encryption method have been integrated with this new technique. We have developed a steganography tool incorporating this proposed technique. The performance of our tool has been tested using MSE, PSNR method and measuring payload capacity. Since the proposed technique is not solely based on secrecy of keys, so even if the keys (series) are detected, it will be still difficult for intruder to pick up the desired bits. An intruder will face extream difficulty to reveal the message due to the procedure of dynamically choosing the bits to hide as a function of the values of pixel bits. Our future plan includes: a) measuring the performance of our tool in some other metrics (like NDC) to compare with the performance of exsisting tools, b) comparing the Payload capacity with other methods, c) addition of an interface for the users to add keys so that after a certain time, keys can be updated and d) update the tool for the compressed images e.g. jpeg, png etc.

## REFERENCES


[1] "Advanced Encryption Standard". [Online]. Available: https://en.wikipedia.org/wiki/Advanced_Encryption_Standard. Accessed: Jan 14, 2017.

[2] Umamaheswari, M.,Sivasubramanian, S. and Pandiarajan, S., "Analysis of different steganographic algorithms for secured data hiding," in IJCSNS International Journal of Computer Science and Network Security 10.8 (2010): 154-160.

[3] Sharma, Ms. H.,MithleshArya, Ms. and Goyal, Mr. D., "Secure Image Hiding Algorithm using Cryptography and Steganography," in IOSR Journal of Computer Engineering (IOSR-JCE) e-ISSN (2013): 2278-0661.

[4] Nath, J. and Nath, A., "Advanced Steganography Algorithm using encrypted secret message," in International journal of advanced computer science and applications 2.3 (2011).

[5] Zeghid, M., Machhout, M.,Khriji, L.,Baganne, A. and Tourki, R. "A modified AES based algorithm for image encryption," in International Journal of Computer Science and Engineering 1.1 (2007): 70-75.

[6] Owada, M., Nagashima, Y. and Kimura, T., "Image processing apparatus and method for synthesizing first and second image data," in U.S. Patent No. 5,857,038. 5 Jan. 1999.

[7] Dutta, S., Das, X., Ganguly, R. and Mukherjee, I., "A Novel Approach to E-Voting Using Multi-bit Steganography," in Proceedings of the First International Conference on Intelligent Computing and Communication. Springer Singapore, 2017.

[8] Dumitrescu, S., Wu, X., and Wang, Z., "Detection of LSB steganography via sample pair analysis," in IEEE transactions on Signal Processing 51.7 (2003): 1995-2007.

[9] Wu, H-C., Wu, N-I., Tsai, C-S. and Hwang, M-S. , "Image steganographic scheme based on pixel-value differencing and LSB replacement methods," in IEEE Proceedings-Vision, Image and Signal Processing 152.5 (2005): 611-615.

[10] "Root: En: Projects [RFMLabWiki]," 2014. [Online]. Available: http://radio.feld.cvut.cz/personal/matejka/wiki/doku.php?id=root:en:projects. Accessed: Jan. 14, 2017.

[11] "Why does the human eye see more shades of green than any other colour?," [Online]. Available: https://www.quora.com/Why-does-the-human-eye-see-more-shades-of-green-than-any-other-colour. Accessed: Jan. 14, 2017.

[12] Dhall, S., Bhushan, B. and Gupta, S., "An In-depth Analysis of Various Steganography Techniques." International Journal of Security and Its Applications 9.8 (2015): 67-94.

[13] V, V. and Sebastian, S., "Comparative Study Of Steganography Tools." in International Journal of Innovations & Advancement in Computer Science IJIACS, ISSN 2347 - 8616, Volume 2, Issue2, February 2015.

[14] "Electronic Codebook (ECB)". [Online]. Available: https://en.wikipedia.org/wiki/Block_cipher_mode_of_operation#Electronic_Codebook_.28ECB.29. Accessed: Sep 25, 2017.

[15] "MATLAB- MathWorks". [Online]. Available: https://www.mathworks.com/products/matlab.html. Accessed: Sep 25, 2017.

[16] "OpenStego," [Online]. Available: http://www.openstego.com. Accessed: Sep. 27, 2017.

[17] "Free Steganography software - QuickStego," 2015. [Online]. Available: http://quickcrypto.com/free-steganography-software.html. Accessed: Sep. 27, 2017.

[18] Provos, N. and Honeyman, P., "Detecting Steganography Content on the Internet". CITI Technical Report 01 -11, 2001.

# A Model for Ensuring Data Security to Distributed Financial System in Cloud Storage

Miraj Hossain[1], Md. Rafiqul Islam[2]
Khulna University, Bangladesh
mirajhossaincse@gmail.com, dmri1978@gmail.com

***Abstract*—Cloud storage enables users to access their data from the cloud server and data needs to be secured in the cloud storage. One security service is not enough for ensuring adequate security to the financial data. In order to provide strong security, the proposed model introduces authentication and authorization method, encryption process, classification of data using decision tree and access control mechanism to the distributed financial system. For authentication and authorization purpose, we have proposed multilevel authentication and authorization method. For access control, we have proposed user-view mapping technique to restrict the user to a specific operation. For our proposed model SSE can be implemented to protect financial data. We have classified financial data according to the business value of data using a decision tree. High business valued data can be treated as private data, medium valued data can be treated as moderate and low valued data can be treated as public data. In this paper, we show that data classification together with other three level of security leads to improve the security of the distributed financial system in cloud storage. We have also analyzed data to do data classification that saves data processing overhead and enhance system performances.**

***Keywords—data security; searchable encryption; DFS;data classification; access control; secure authentication***

## I. Introduction

Nowadays, the distributed financial system becomes more and more popular as business is growing day by day all over the world. For organizations throughout the world whether governments, nonprofitable or private companies cloud computing or remote hosting has become a key part of their IT strategy. Many enterprises and individuals are outsourcing their databases to the remote servers, in order to enjoy the lower data management cost than maintaining their own server and speed up operations [1], [2]. A variety of users/clients could easily access or share information stored on the server such as cloud server, independent of their locations. But data owners face some serious security and privacy concerns when outsourced their data to the remote server. Some of their outsourced data may contain highly sensitive information. A third party provider can easily access those data and leak out information to others company [2], [3]. Besides, a distributed financial system can easily be used by a broad range of clients including browsers, mobiles, iPhone, and tablets. A web based application can be accessed from various devices to fulfill customers demand. People are using smart devices such as iPhone, mobile, tablets etc. in their daily lives. If we want to access web application from these devices easily, we should have APIs. For example, Twitter, Facebook and Google API for the web application and phone apps. Application programming interface (APIs) have been a standard method of interconnection system components for decades. APIs are the heart of Smartphone applications and service-driven financial applications because they allow the app to pull in data from multiple sources and manipulate it in different ways [4].

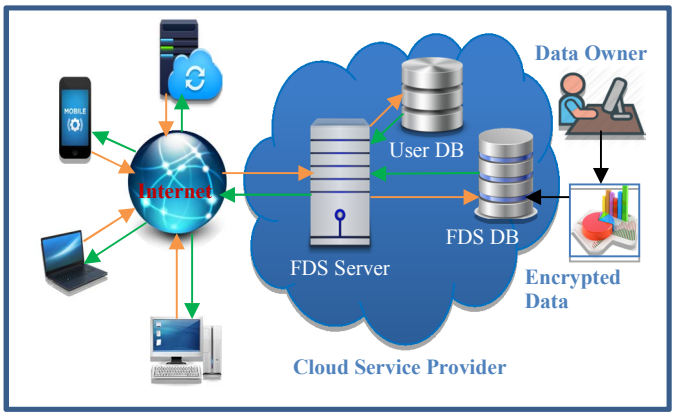


Fig. 1. Distributed Financial System

Financial Application Programming Interfaces (APIs) provide a standard way for software applications to exchange financial data such as user investment portfolios, spending patterns, and risk preferences, and perform requested transactions such as making payments, money and stock transfers and loans, buying insurance, and recording financial documents. There are two types of APIs: private and open. Private APIs are accessible only to customers or in-house or contracted developers. Open APIs sit on the programmable web and a developer or business doesn't need to log into the provider site or be a customer to access them [5].

Classification of data is a critical part of data management which ensures all sensitive information is protected. Data classification is the process of categorizing data assets based on nominal values according to its sensitivity. For example, data might be classified as public, private and moderate. In the process of data classification following roles and responsibilities are involved.

Data Owner: A data owner is a person who correctly defined the encryption aspect of their organizations. The data owner is responsible for assigning individuals to the following roles. For example,the super user can assign admin and general user's roles in a system.

Data Manager: The data manager develops general procedures and guidelines for the management, security, and access to data. For example, the system admin can act as a data manager in a system.

978-1-5386-2307-7/17/$31.00 ©2017 IEEE

Data User: A data user is any individual who is eligible and authorized to access and use the data such as a general user in a system.

A financial system contains different categories of data. Some data are highly sensitive such as trade secrets, financial transactions, loan information, employee salary etc. Some are medium sensitive or moderate (internal use) such as acquisition plans, supplier, and customer information. Some are low sensitive or public (general use) should be thought of as being for general use such as annual reports, chart of accounts, voucher information etc. These three categories of data do not need the same level of security. Highly sensitive data need a top level of security and we have to apply strong security mechanisms to this group of data. Moderate data need security, but we can consider the medium level of security for them. Consequently,a moderate standard security mechanism is enough for this group of data. For public data, we can apply only identification and usual authentication method. In Distributed Financial System (DFS), more security is needed as it exposes APIs for a broad range of client. To prevent unauthorized access we need to apply token based authentication in all private APIs. On the other hand, along with many benefits provided by cloud storage, some security problems arise in cloud storage which prevents enterprises migrate their financial data to cloud storage. To prevent leak out data in remote cloud storage we need to apply data encryption technique but this technique degrades the performance to read data from the application level. So, in this situation, we need to apply searchable encryption scheme to read encrypted data directly from application level without decrypting it [12]. If we want to secure financial data properly we have to provide data security using different security mechanism altogether such as encryption, token based authentication, role based authentication and data classification etc. In order to provide proper security to the distributed financial system, we proposed a secure model based on multilevel authentication and authorization method, encryption, access control and data classification.

Data security is a when data stored in the cloud storage. Many organizations are making the distributed financial systems to run their business smoothly. But their financial data remains insecure in the cloud. To secure their data we have proposed a model that will help data owner to store their data safely. Also, this model will help application developer to develop the secure financial system. The problem statement consists of three services related to data security. They are followings:

a) Authentication b) Access control c) Encryption

We consider that one service is not enough for data security and more services can solve data security problem properly.

## II. RELATED WORKS

Rizwana Shaikh and Dr. M. Sasikumar proposed a data classification technique that defines various parameters. Parameters are defined based on various dimensions. Data security can be provided bassed on the level and the required protection on data set classified based on dimensions [6]. Runhua Xu and James B.D. Joshi, propose an integrated user-centric (or an organization-centric) privacy preserving attribute based access control approach to protect the security and privacy of a user's (or organization's) data stored by a cloud service provider. The proposed approach includes a novel privacy preserving revocable ciphertext policy attribute-based encryption scheme [7]. In paper [8] the author proposed a framework to accommodate the protection of sensitive data in cloud computing environment. This framework consists of three levels authorization, security, and privacy. Deepak Singh and Harsh K Verma proposed a new framework to protect Confidentiality and Integrity of data stored in the cloud. In this framework, they used AES, SHA-I, and station-to-station key agreement protocol [9]. In paper [10], the author proposes a secure cloud computing model based on data classification. The proposed cloud minimizes the overhead and processing time needed to secure data through using different mechanisms with variable key sizes to provide appropriate confidentiality level required for the data. A novel method to protect privacy information for the cloud based video storage system, which not only distribute the CVSS geographically, but also use different privacy protection key algorithm for different CVSS to encode/decode the actual video data itself stored in the storage with the subscriber key for the privacy protection so that the system even under the hacking of the CVSS systems, still provide the privacy protection of video data [11]. Another work shows a client-server prototype implementation of the adaptive-secure scheme by Syh-Yuan Tan and others. Utilizing only open source software on both client and server side. They show that their implementation runs in reasonable time and provides confidential search functions as defined by SSE schemes [12].

## III. PROPOSED MODEL

In this section, various security levels of the proposed model have been described.

### *A. User Authentication*

In DFS (Distributed Financial System) we have used two data storage: one is for storing user information and another is for storing business data (financial data). User Database contains three categories of users:

- Super User: here super user acts as a data owner. High sensitive, moderate and public data is visible only for this type of user. This type of user remains at top hierarchical level in security suite and no need to provide permission to gain access to the system byte system admin. Data owner can control others users that remains under Superuser in hierarchical level.
- Admin User: here admin user acts as a system admin in an organization. Public and moderate data is visible only for this type of user except for high sensitive or private data. The Superuser can decide what activities are performing by this type of user. Data classification rules are applicable for this type of user.
- General User: here general user acts as a general employee in an organization. If system admin accepts access request of general user s/he will gain access for logged in DFS. Only public and moderate data is accessible by these types of users if they are permitted.

Also, data classification rules have been applied to this type of user.

. In a distributed financial system, very strong authentication and authorization method must be applied. We have proposed a multi-level authentication and authorization method here. If any user wants to access data in a specific class, he must go through usual authentication first. This process uses id and password of the user only. If the user wants to get access to confidential and moderate classes he must go through the further authentication and authorization process as stated below. The server creates two numbers using the cryptographic hash function:

LN = H (pwd || IDu || Kss || IDs ||TS1)
LA = H (pwd||IDu || LB||TS1)

The server produces encrypted token for the users as follows:

CL = E (Kss, [LN||LA||TS2||LT])
CT = E (Kss, [CL||TS3])

Here CT is a token (encrypted text) for the user created by the server. The server encrypts the token using the public key of the user and sends it to the user.

Cu = E (Kpu, [N||CT||N1])

The user decrypts Cu as follows:

D (Ksu, Cu) and gets CT and N1.

The user opens Cu using his secret key and gets CT with N1 but he does not know what is inside CT. He sends a request with CT to the server as follows:

Cs = E (Kps, [IDu ||CT||N1||TS4]

The server decrypts Cs using D (Kss, Cs) and gets CT with N1 and ensures that the user is a valid one.

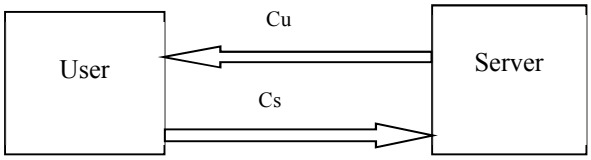


Fig. 2. shows the dialogue between user and server.

The descriptions of all symbols are described in Table I. For further authentication on the server decrypts CT and finds N'(say) and CL. If N = N', the user gets permission to enter into the server. For authorization purpose, the server opens CL that contains LN' and LA'. If LN' = LN and LA' = LA then according to these two numbers, the user gets permission to access data of a specific class. Otherwise, the server rejects the request to enter into a specific class.

TABLE I. DESCRIPTION OF THE SYMBOLS

| Symbol | Description |
|---|---|
| H | Hash function such as SH3 |
| IDs | ID of the server |
| IDu | ID of the user |
| pwd | Password of the user |
| TSi | The ith Time stamp |
| N | A nonce |
| N1 | Another nonce |
| Kss | Secret key of the server |
| Kpu | Public key of the user |
| Kps | Public key of the server |
| E | Encryption method |
| D | Decryption method |
| \|\| | Concatenation |

LN and LA are two unique numbers derived by the hash function, which helps to find aspecific user and LA contains a level number (LB) for the class of data such as 01 or other large number or label for the data in confidential class. CL also contains lifetime, after getting Cu, he must use it within the specific time period mention in CL. This is secure authentication and authorization method because without knowing secret key of the user Cu cannot be decrypted. Another point is that without knowing Kss, Cs cannot be decrypted or CT cannot be produced and sent to the user. The above method depicts a strong user authentication and authorization process. After entering into the area of a specific class of data to access specific data object (file) he must have proper access right to the object. As for example, if a user, Ui wants to modify an object, Ocj, which is an object in the confidential class, Ui must have write/modify access right to Ocj. This process can be ensured by applying access control to the users. Sequence diagram of data access is shown in Fig. 6.

### *B. Data access control*

For access control purpose, we have proposed user-view mapping relationship and data should be classified based on business value. Suppose, a set of view V= {$v_1$, $v_2$, $v_3$, $v_4$……$v_n$} and set of user U= {$u_1$, $u_2$, $u_3$….$u_n$} and Domain of a function is shown in Fig. 3.

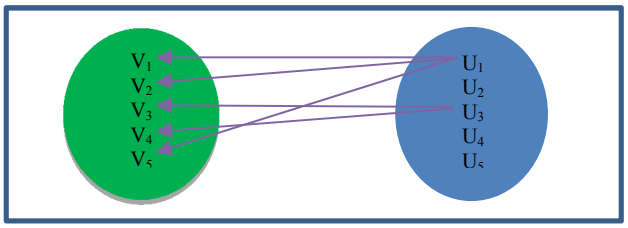


Fig.3. User-View mapping

In the above figure user $u_1$ is permitted for $v_1$, $v_2$, $v_5$ and $u_3$ is permitted for $v_3$, $v_4$ respectively. Here view represents one or more object, Ocj. And in individual view which action can perform an authorized user depends on decision-making. The decision tree based classification is shown in Fig.4.

### C. Data classification

Data classification is the process of identifying data elements according to its value in the business. For our DFS system data has been classified based on its business value and confidentiality. High valued the data has been considered as highly sensitive or private data (for confidential use only) and medium valued data has been considered as moderate data (for specific use only) and low valued data has been considered as public data (for general use only). Consistent use of data classification will facilitate more efficient business activities and lower the costs ensuring adequate information security. By classifying data, the company can prepare generally to identify the risk and impact of an incident based on what type of data is involved. The classification as listed (public, moderate, private) to give a basis for determining the impact based on the level and type of access to data. The decision tree based data classification is shown in Figure.4. In the decision tree, FD means Financial Data, BV denotes Business Value.

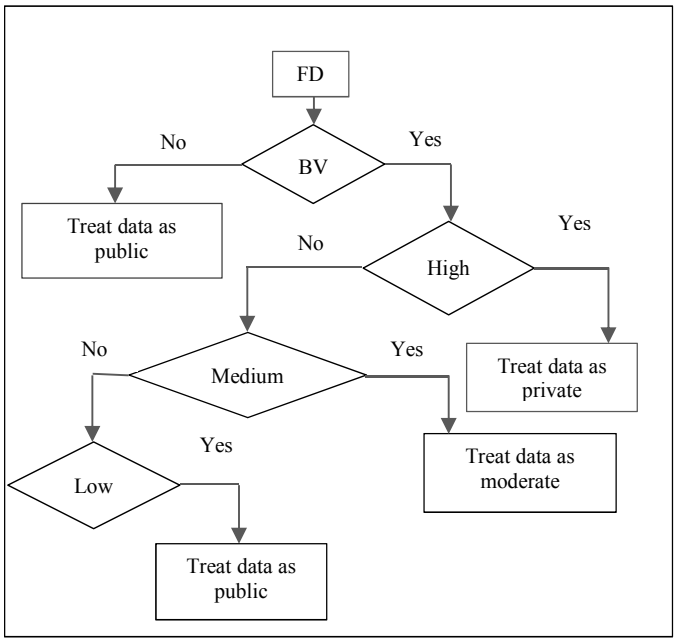


Fig. 4. Decision tree for data classification

Let us consider that there are some objects in a system each object contains several attributes. Each attribute has any of the business values such as 1, 0.5 and 0. Now we have to calculate whether an object will go to which class (private, moderate, and public). If an object has such an attribute that has business value 1 then this object is considered as in private class (even if there is any attribute in the object that has business value 0). If an object has any attribute that has business value 0.5, so it will be considered as an object of the moderate class. If there is an object where all the attributes have values 0 that it will go to the public class. The value of any attribute can be selected by the authority of the organization. Now we can see a simple example:

Suppose that there are three objects in a system such as FS = ($O_1$, $O_2$, $O_3$). Since all the object will not contain the same number of attributes so can represent them as $O_1$ = ($A_{11}$, $A_{12}$, $A_{13}$), $O_2$ = ($A_{21}$, $A_{22}$, $A_{23}$, $A_{24}$). $O_3$ = ($A_{31}$, $A_{32}$, $A_{33}$). In Table II we have shown the classification process according to business value of each attribute of the objects. In Table II, x denotes no respective attribute of the respective object in that column of the row.

TABLE II. AN EXAMPLE OF DATA CLASSIFICATION

| Object | Value of respective attribute | | | | Class |
|---|---|---|---|---|---|
| $O_1$ | 0.5 | 0.5 | 0 | x | Moderate |
| $O_2$ | 1 | 0.5 | 0 | 0.5 | Private |
| $O_3$ | 0 | 0 | 0 | x | Public |

### D. Searchable Encryption

It is important to restrict unauthorized access to financial data and for this data encryption is necessary. Since sensitive data can be stored in one or more columns of a table or in a whole table, it does not need to encrypt the whole database. In our system we have considered encryption of a complete table if it belongs to the private class, encrypt only column when it belongs to a moderate class. We have not encrypted the data if the table is in public class.

Here we consider searchable encryption for data privacy and security. At present, many users consider data outsourcing to the cloud to mitigate the overhead of local storage. However, storing sensitive data on remote servers may face privacy challenges and it is a matter of concern. Searchable Encryption is a process to protect users' sensitive data, which gives facility to search on the server side. This encryption enables the server to search encrypted data without leaking information in plaintext form. The two main branches of SE are Searchable Symmetric Encryption (SSE) and Public key Encryption with Keyword Search (PEKS). SSE gives facility only to private key holders to produce ciphertexts and to create trapdoors for searching, whereas PEKS enables a number of users who has the public key to produce ciphertexts but allows only the private key owner to create trapdoors. For our proposed approach SSE can be implemented to protect the financial data.

There are three parties in a searchable encryption such as data owner, data user and server. The data owner outsources her/his objects/documents along with some keywords. The owner needs to encrypt the objects in a specific way so that user can perform searching on them. Next, s/he sends the ciphertexts to the server. When a data user wants to perform searching the objects containing a specific keyword, s/he submits the trapdoor of this query keyword to the server. The server returns the respective objects to the user. A server performs searching for the user. After receiving a trapdoor of a query keyword from the user the server searches over ciphertexts and return the respective object to the user.

## IV. IMPLEMENTATION DETAILS

In this section detailed descriptions of our proposed model have been described. For the implementation of our proposed model, we have chosen Microsoft's.Net Platform, C# programming language and Java script, ASP.NET Web API to develop distributed financial system. We have chosen MS SQL Server as the database.

In order to implement secure token based authentication, we have used multilevel authentication and authorization model. For data classification, we have used decision tree based classification. For access control, we have used user-view mapping technique to give permission of a specific user to specific view for performing creates, read and update operation. We have used SSE scheme for implementation searchable encryption to protect financial data.

The system architecture of the implementation for proposed model is shown in Fig. 5.

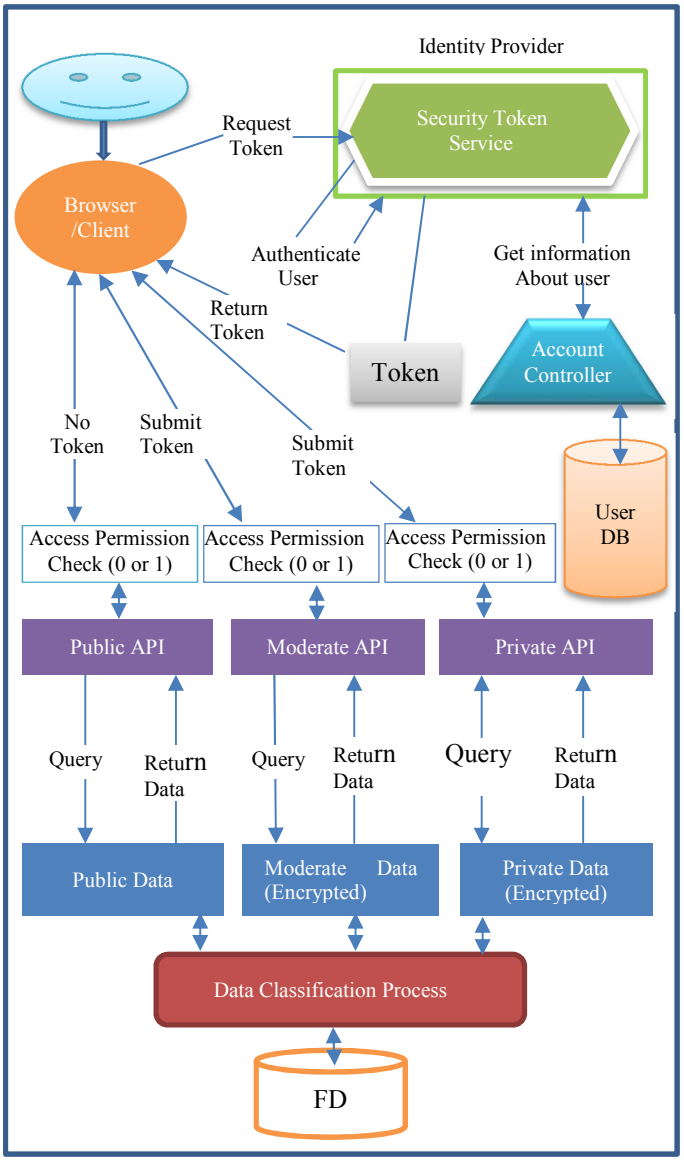


Fig. 5. System Architecture

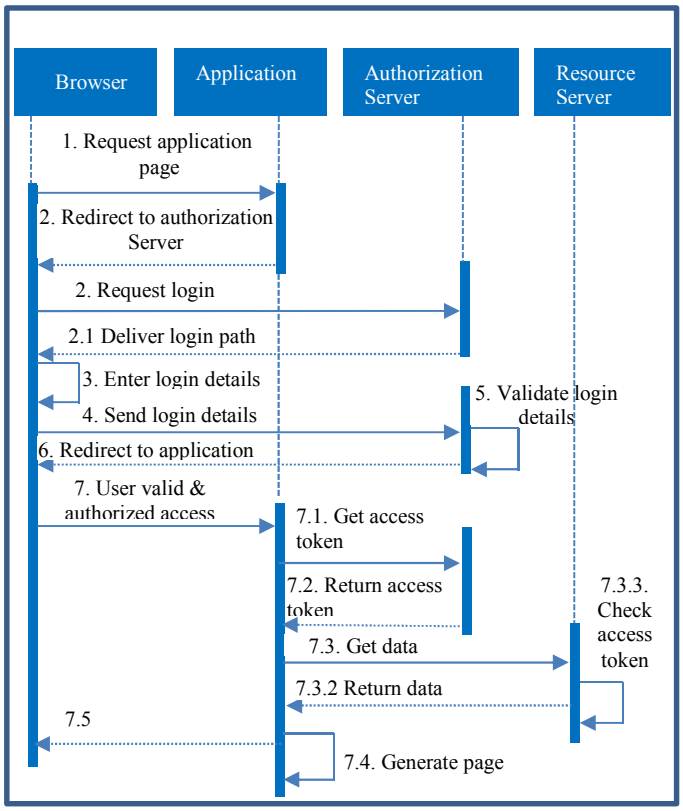


Fig. 6. Sequence Diagram of Data access

## V. SURVEY AND ANALYSIS

We have done a survey and collected data from various organizations. There are three categories of data such as public, moderate and private in the percentage that has been used in an individual organization. The data of four organizations in three categories are shown in Table III.

TABLE III. CLASSIFICATION OF DATA OF DIFFERENT COMPANIES

| Organization Name | Data Set | Private (%) | Moderate (%) | Public (%) |
|---|---|---|---|---|
| Paradise Group | Dpg | 30 | 50 | 20 |
| Orion Group | Dog | 35 | 40 | 25 |
| AL Fatah Publications | Dafp | 20 | 35 | 45 |
| Idea Solutions Ltd | Disl | 40 | 0 | 60 |

We consider that data in private class need all the security services such as cryptography, access control, Authorization, hash function, password authentication scheme. The data in Moderate needs services except for cryptography. The data in public need services such as access control, hash function, and password. Using cryptography service data have been encrypted in the database and show data in plaintext format to the user. Access control scheme used to check data access right for an individual user. The hash function and password are used when the user wants to login to the system. Overhead of the security services are shown in Table IV.

TABLE IV. THE OVERHEAD OF THE SECURITY SERVICES

| Service Type | Crypto-graphy | Authoriza-tion | Access-control | Hash Function | Pass-word |
|---|---|---|---|---|---|
| Overhead | 0.3 | 0.3 | 0.2 | 0.1 | 0.1 |

Since the data in private class need all services, so the data in private class require more overhead compared to others class is as follows:

$OH_{pri}$= 1(0.3+0.3+0.2+0.1+0.1).

The overhead of the data in a moderate class is as follows:

$OH_{mod}$= 0.7(0.3+0.2+0.1+0.1).

The overhead of the data in public class require less overhead,

$OH_{pub}$= 0.4(0.2+0.1+0.1).

Total overhead of class of data is shown in Table V.

TABLE V. TOTAL OVERHEAD OF DATA CLASS

| Data Class | Private | Moderate | Public |
|---|---|---|---|
| Overhead | 1 | 0.7 | 0.4 |

Let, $P_{pri}$ be the probability of data to be in private class,$P_{mod}$the probability of data to be in moderate class, and $P_{pub}$be the probability of data to be in public class. The overhead of security services for the private, moderate and public class are $OH_{pri}$, $OH_{mod}$ and $OH_{pub}$ respectively. So, we can compute the overhead for a data set (FD) of an organization is as follows:

$$OH\ (DS) = P_{pri}\times OH_{pri} + P_{mod}\times OH_{mod} + P_{pub}\times OH_{pub} \quad (1)$$

By using above equation (1), we can calculate the overhead of data set $D_{pg}$ of Table I as follows:

$$OH\ (D_{pg}) = 30\times 1 + 50\times 0.7 + 20 \times 0.4 = 30 + 35 + 8 = 73$$

If we provide all the security services to all the data, the overhead will be as follows:

$$OH\ (D_{pg}) = 30\times 1 + 50\times 1 + 20 \times 1 = 30 + 50 + 20 = 100$$

Therefore, overhead savings for data set $D_{pg}$=100-73=27. Similarly, we can calculate overhead savings for others data sets listed in Table III. The overhead savings for individual data set of an organization is shown in Table VI. From Table VI, it can be conclude that, we can save at most 37.5% overhead of the system using data classification, which means system performance will be enhanced for this overhead savings. If we used encryption to all data in FDS Sever it increased overhead of the system and degraded its performances.

TABLE VI. OVERHEAD SAVINGS IN PERCENTAGE

| Data Set | Private | Moderate | Public | OH(DS) | Savings % |
|---|---|---|---|---|---|
| Dpg | 30 | 50 | 20 | 73 | 27 |
| Dog | 35 | 40 | 25 | 73 | 27 |
| Dafp | 20 | 35 | 45 | 62.5 | 37.5 |
| Disl | 40 | 0 | 60 | 64 | 36 |

## VI. CONCLUSIONS

Data privacy and security are the crucial issues when data stored in the cloud. To maintain privacy preserving of stored financial data we proposed a model that deals with the different security services of financial systems instead of single service. The different services are multilevel authentication and authorization, access control, and searchable encryption. Data classification together with these three services, a system can be secured for ensuring data security. We have also analyzed data for data classification that saves the system overhead and enhances the performances.

## REFERENCES


[1] Ming Li, Shcheng Yu, Ning Cao, Wen, "Authorized Private Keyword Search over Encrypted Data in Cloud Computing".

[2] http://www.bbc.com/news/business-36151754

[3] Miyoung Jang, MinYoon, Youngho Song, Jae-Woo Chang,"A Signature-based Data Authentication Method with Bitmap-based Transformed Data in Database Outsourcing"The 6th International Conference on Ambient Systems, Networks and Technologies (ANT 2015).

[4] http://www.bankingtech.com/383591/is-everybody-api/

[5] http://www.fsroundtable.org/cto-corner-open-finance-application-programming-interfaces-api-why-they-matter/

[6] Rizwana Shaikh, Dr. M. Sasikumar, "Data Classification for achieving Security in Cloud Computing" Procedia Computer Science 45 (2015) 493-498.

[7] Runhua Xu, James B.D Joshi, "An Integrated Privacy Preserving Attribute Based Access Control Framework" 2016 IEEE 9th International Conference on Cloud Computing.

[8] Haifaa Jassim Muhasin, Rodziah Atan, Marzanah binti A.Jabar, Salfarina binti Abdullah, "Cloud Computing Sensitive Data Protection using Multi Layered Approach" 2016 2nd International Conference on Science in Information Technology (ICSITech).

[9] Deepak Singh, Harse K Verma, "A New Framework for Cloud Storage Confidentiality to Ensure Information Security" 2016 Symposium on Colossal Data Analysis and Networking (CDAN).

[10] Lo'ai Tawalbeh, Nour S. Darwazeh, Raad S. Al-Qassas and Fahd AlDosari, "A Secure Cloud Computing Model based on Data Classification" First International Work Shop on Mobile Cloud Computing Systems, Management, and Security (MCSMS-2015).

[11] Kang Choi, Jung Hee Lee, Bhum Cheol Lee, "A Distributed Cloud based Video Storage System with Privacy Protection" ICACT Transactions on Advance Communications Technology (TACT) Vol.5, Issue 3, May 2016.

[12] Syh-Yuan Tan, Ji-Jian Chin, Geong-Sen Poh, Yvonne H.S Kam, Wei-Chuen Yau, "A Client-Server Prototype of a Symmetric Key Searchable Encryption Scheme Using Open-Source Applications".

[13] Zhao F., Nishide T. (2016) Searchable Symmetric Encryption Supporting Queries with Multiple-Character Wildcards. In: Chen J., Piuri V., Su C., Yung M. (eds) Network and System Security. NSS 2016. Lecture Notes in Computer Science, vol 9955. Springer, Cham.

# An adaptive flower pollination algorithm for software test suite minimization

Muhammad Nomani Kabir*, Jahan Ali, AbdulRahman A. Alsewari and Kamal Z. Zamli
Faculty of Computer Systems & Software Engineering, University Malaysia Pahang, 26300 Gambang, Pahang, Malaysia
*Corresponding author: nomanikabir@ump.edu.my

*Abstract*—**Optimization is the selection of a best set of parameters from available alternative sets. Global optimization is the task of finding the absolutely best set of parameters. In this paper, we present an adaptive flower pollination algorithm for solving an optimization problem, i.e., minimization of software test suite for interaction testing. In software testing, test engineers generate a set of test cases to validate against the requirements to avoid failure of the software. Testing all the interactions for modern software with many system inputs is impractical due to huge number of possible combinations of the inputs. In order to tackle the issue, global optimization algorithms are used to systematically minimize the test suite for interaction testing. Using the proposed adaptive flower pollination algorithm, we carried out some experiments for minimizing software test suite for interaction testing. The results were compared with the results of some existing algorithms to demonstrate the strength of our algorithm. Comparison shows that our algorithm performs slightly better than the existing algorithms and thus, the proposed algorithm can potentially be used by researchers and test engineers to obtain optimal test suite.**

***Keywords— Global optimization, stochastic optimization method, software test suite, interaction testing.***

## I. INTRODUCTION

Optimization is the process of finding the minimum value of a cost function. Global optimization is the task of searching the absolute minimum value. The tasks of minimization and maximization are trivially related to one another. In practice, optimization can mean to accomplish a task in the most efficient way or with the highest quality or to produce the maximum yield with given limited resources. For example, a manager may need to decide an appropriate investment portfolio according to the specific investment objective; or an automobile industry wants to build the most fuel-efficient car [1].

In this work, our scope is software test suite minimization for interaction testing. In the present era, software and its diffusion into many applications are growing and thus complexity is increasing, which in turn, causes huge number of test cases. In software interaction test-cases generation, a test suite should be generated with less number of test cases that cover the required combinations [2], [3], [4]. Test-suite size increases with higher number of test cases which substantially elevate the overall testing time and cost. Thus, minimization of test suite is important in order to obtain a minimum number of test cases that suffice for satisfying the interactions of test requirements.

Global optimization methods are solved using the several algorithms based on stochastic approach such as Particle Swarm Optimization (PSO), Simulated Annealing (SA) and Genetic Algorithm (GA). As the problem of test suite minimization often contains multiple solutions (local minima), no single strategy e.g., PSO, SA or GA can do well in all scenarios. Each method has advantages and disadvantages in terms of convergence and complexity. PSO does not often perform well to find a global optimal solution when the optimizing variables in objective function are of a large dimension [5], [6]. SA is preferable for problems in which the global optimum with the best solution is less important than a local optimum with an acceptable solution in a certain time [7]. For higher dimensions, complexity of GA exponentially grows [8]. To develop an algorithm that has less complexity, but provides higher convergence rate is always challenging.

In this work, we scrutinized an optimization technique - flower pollination algorithm and reformulated a new algorithm to obtain better convergence. Our proposed technique is a modified flower pollination algorithm (MFPA) that is developed by devising a new strategy through updating the parameters (step lengths) at each iteration. The step lengths are set to increase if the convergence is satisfactory. On the other hand, they are reduced if the convergence is weak. This new strategy is aimed at accelerating the convergence. Performance and efficiency of the proposed algorithm were tested on minimization problems of software interaction testing by comparing the results with the results of existing algorithms to demonstrate the strength of the proposed algorithm. Thus, the implemented code of the algorithm can be useful to generate a minimum test suite for interaction testing. Researchers and test engineers will have a tool to obtain satisfactory test cases and the generated test suite will require the minimum time for software interaction testing.

The rest of the paper is organized as follows. Section II presents the related works on different stochastic methods for software test-cases minimization. The next section describes the methodology of building the proposed algorithm MFPA. The test results are provided in section IV and finally, conclusion is made in section V.

978-1-5386-2307-7/17/$31.00 ©2017 IEEE

## II. RELATED WORKS

In software testing, test engineers generate a set of test cases to validate against the requirements to avoid the software defect. A large number of system inputs that result in a extremely large number of combinations of inputs increase the possibility of defects of the software. However, testing all the interactions is impossible due to time constraints. In order to tackle the issue, global optimization algorithms are used to systematically minimize the test suite for software interaction testing. Since test suite minimization is an optimization problem with multiple solutions, Genetic Algorithm (GA), Particle Swarm Optimization (PSO), Simulated Annealing (SA) can be used to find the best solution [2], [3], [4].

GA is an iterative technique that solves the optimization problems using techniques inspired by natural evolution, such as inheritance, mutation, selection, and crossover. Repeated fitness function evaluation for complex problems is often a bottleneck with GA. With higher number of elements which are exposed to mutation, there is often an exponential increase in search space size [8]. GA is used by Fraser and Arcuri [9] for their work on scalable mutation-based generation of whole software test suites. Moreover, Patrick [10] used metaheuristic optimization approach with combination for mutation-based test data generation.

Particle Swarm Optimization is a population-based stochastic algorithm which follows the social behavior of animals e.g., bird flocking and fish schooling. PSO has the properties of simple computation with rapid convergence rate. The algorithm requires to adjust a few parameters. This is an advantage with PSO. The algorithm tries to attain the best value from the interactions among particles. However, if the search space is high, the convergence rate slows down near the global optimum. The algorithm performs poor when the optimization problem consists of a large and complex data set. As mentioned before, the algorithm fails to attain a global optimum if the objective function contains a large number of optimizing variables [6]. Ahmed et al. [11] introduced a modified version of PSO algorithm called Cuckoo search algorithm for configuration-aware software test. Jin et al. [12] combined artificial neural network and quantum particle swarm optimization. Gosciniak [5] proposed a new approach of PSO algorithm. Jensi and Jiji [13] investigated a modified version of PSO using a levy flight for global optimization. Ouyang [14] presented a hybrid harmony search technique with PSO using global dimension selection.

Simulated annealing (SA) is a stochastic algorithm that imitates the forging process of metal when the metal is rapidly heated followed by gradual cooling process. SA can often find a good solution even in the presence of noisy data; however, the global solution may not be found by this technique. SA may be preferable to alternatives e.g., brute-force search or gradient descent, for finding the solutions of the problems in a certain time where the precise global optimum is less important than an acceptable local optimum [7].

Combinatorial techniques are alternatives to solve the software interaction testing problems. Some of the combinatorial techniques [15], 16] are tried to minimize software test suite minimization.

As the problem of software test suite minimization may contain multiple solutions (i.e., local minima), no single strategy can work well for all the problems. In software test-cases, a test suite can be constructed by a sequence of permutation of test cases where the test cases can be formulated in any order. Note that one of the (concatenated) permutations can minimally satisfy all the requirements using an exhaustive permutation. Nonetheless, for a large problem, exhaustive permutation may be expensive and difficult to manage. Hence, this work presents a global optimization algorithm - an adaptive flower pollination algorithm for solving the problem of software test suite minimization.

## III. METHODOLOGY

The proposed algorithm modified flower pollination algorithm (MFPA) is a metaheuristic algorithm which can be used for solving the problem of software suite minimization. Flower pollination algorithm was originally formulated by Yang [17] based on the flower-pollination process. This algorithm was developed considering four rules:

**Rule 1:** Global pollination is represented by biotic and cross-pollination, where a pollinator maintains a Levy flight.

**Rule 2:** Local pollination is designated by abiotic and self-pollination.

**Rule 3:** A reproduction probability that is proportional to the similarity between two flowers is used to measure the flower constancy.

**Rule 4:** Switching between local and global pollinations is performed with a probability $p \in [0,1]$ value. Local pollination is slightly dominant over global pollination because of the physical closeness and other factors e.g., wind.

Above four rules can be formulated as equations. First the local pollination: rule 2 is expressed as

$$x_{t+1}^{i} = x_t^{i} + c\left(x_t^{j} - x_t^{k}\right) \tag{1}$$

where $x_t^i$ denotes the current pollen (i.e., the current solution at iteration $t$; $x_t^j$ and $x_t^k$ are the solution vectors which are the selected pollens from two different flowers of the same plant-species with $c \in [0,1]$ i.e., the value of c obtained from a uniform distribution in [0, 1]. In our case of software test-cases minimization, $x_t^j$ and $x_t^k$ are the test cases that are selected randomly in the list.

Rule 1 can be translated as

$$x_{t+1}^{i} = x_t^{i} + aL(b)\left(g^* - x_t^{i}\right) \tag{2}$$

where $g^*$ denotes the best solution at iteration $t$, $a > 0$ represents the step size and $L(b)$ implies a Levy flight. For our problem, $g^*$ is best test case in the list. Levy flight imitates the characteristics of long move of the pollinators. Thus, $L$ is deduced from a Levy flight as follows:

$$L(b) = \frac{b\Gamma(b)\sin(\pi b/2)}{\pi}\frac{1}{s^{1+b}} \quad (3)$$

where $s >> s_0 > 0$; $b$ is the Levy exponent and Γ(b) is the gamma function. The formula (3) of $L$ is valid for a large step $s$. The proposed algorithm MFPA is shown in Algorithm 1. Note that in the algorithm, we use the value of $c \in [0.25, 0.75]$, since if the value of $c$ is close to 0 or 1, then the next iterate with (1) will not significantly progress. Furthermore, we modify $a$ in equation (2) depending on the steps.

If $s > 1.5R$, then

$a = \max(2a, 1)$ and $R = \max(2R, R_{\max})$;

If $s < 0.5R$, then

$a = \min(a/2, 1.0e\text{-}4)$, and $R = \max(R/2, R_{\min})$;

where $R$ is the trust-region radius. $R_{\max} = 1000$, $R_{\min} = 10^{-4}$ with an initial $R = 1$;

ALGORITHM 1. MODIFIED FLOWER POLLINATION ALGORITHM (MFPA)

**Input:** Parameters, $P$ and Set of values for each parameter, $V = \{V_0 \ldots V_j\}$;
**Output:** Final test suite;

```
Initialize a set of n-candidate tests;
Find the best solution g* of n-candidate tests.
Generate all possible interactions based on P and V and
  set the results in a list T
while (T is not empty) do
  while (t < MaxGeneration) do
    for i = 1 : n (all n flowers in the population)
      if rand() < p,
        Compute L using (3)
        Compute x_{t+1}^i using (2)
      else
        Draw c from a uniform distribution in [0,1]
        Compute x_{t+1}^i using (1)
      end if
      Evaluate new solutions
      If new solutions are better, update them in the
      population
    end for
    Find the current best solution g*
  end while
  Add the best test case, g* in final test cases.
  Remove covered interactions from T.
end while
```

## IV. TEST RESULTS

The adaptive flower pollination algorithm was implemented in Java with NetBeans environment under Windows 7 operating system. The implemented program was run on *intel core i*7-2640 CPU with 4GB RAM. We tested the program on two experiments in software test suite reduction. The following values are used in the algorithm: $a = 1$, $b = 1.5$ and $p = 0.8$. Two experimental results are presented to demonstrate the efficacy of our algorithm. Tables I and III provide the experimental setups where the problems PB1 to PB5 are defined according to the $t$-way of interactions with $t$ = 2 to 6 which are used for the experiments. The term $t$-way of interactions is used to indicate that $t$ parameters are involved in the interactions. Column 3 of the tables provides the input specifications. For example, the number of parameters $P$ in Table I is 7 while each parameter consists of a set of 3 values i.e., $V = \{V_0, V_1, V_2\}$.

Table III lists the test suite size for different problems with different degree of interactions given in Table I. In the table, columns 3-7 provide the test suite size from existing algorithms, i.e., HSS, IPOG, WHITCH, Jenny and TConfig [18], [19], [20]. The result of the proposed algorithm is reported in column 8. Best of the results obtained from all the algorithms is given in column 9. It can be noticed that our algorithm performs slightly better than the other algorithms. This can be checked by the total values given in the last row of the table. For the problems PB1, PB3-PB5, our algorithm outperforms the others. The second best results are achieved by HSS while WHIPBH even fails to execute on problems PB4-PB5, performing the worst.

TABLE I. EXPERIMENTAL SETUP FOR EXPERIMENT 1

| Problem No. | *t* | Input Specifications |
|---|---|---|
| PB1 | 2 | 7 3-valued parameters |
| PB2 | 3 | 7 3-valued parameters |
| PB3 | 4 | 7 3-valued parameters |
| PB4 | 5 | 7 3-valued parameters |
| PB5 | 6 | 7 3-valued parameters |

TABLE II. TEST SUITE SIZE FOR DIFFERENT *t*-WAY INTERACTION FOR EXPERIMENT 1 WITH SEVEN INPUT PARAMETERS WITH THREE VALUES FOR EACH PARAMETER

| Problem No. | *t* | HSS | IPOG | WHIPBH | Jenny | PConfig | MFPA | Best |
|---|---|---|---|---|---|---|---|---|
| PB1 | 2 | **14** | 17 | 15 | 16 | 15 | **14** | **14** |
| PB2 | 3 | 50 | 57 | **45** | 51 | 55 | 50 | **45** |
| PB3 | 4 | **157** | 185 | 216 | 169 | 166 | **150** | **150** |
| PB4 | 5 | 437 | 561 | NA | 458 | 477 | **425** | **425** |
| PB5 | 6 | **916** | 1281 | NA | 1087 | 921 | **905** | **905** |
| Total | | 1574 | 2101 | | 1781 | 1634 | 1544 | 1539 |

TABLE III. EXPERIMENTAL SETUP FOR EXPERIMENT 2

| Problem No. | *t* | Input Specifications |
|---|---|---|
| PB1 | 2 | 10 2-valued parameters |
| PB2 | 3 | 10 2-valued parameters |
| PB3 | 4 | 10 2-valued parameters |
| PB4 | 5 | 10 2-valued parameters |
| PB5 | 6 | 10 2-valued parameters |

TABLE IV. TEST SUITE SIZE FOR DIFFERENT *t*-WAY INTERACTION FOR EXPERIMENT 2 WITH TEN INPUT PARAMETERS WITH TWO POSSIBLE VALUES FOR EACH PARAMETER

| Problem No. | *t* | HSS | IPOG | WHIPBH | Jenny | PBonfig | MFPA | Best |
|---|---|---|---|---|---|---|---|---|
| PB1 | 2 | 8 | 10 | **6** | 10 | 9 | **7** | **6** |
| PB2 | 3 | **16** | 19 | 18 | 18 | 20 | 17 | **16** |
| PB3 | 4 | **37** | 49 | 58 | 39 | 45 | 38 | **37** |
| PB4 | 5 | **81** | 128 | NA | 87 | 95 | **78** | **78** |
| PB5 | 6 | 158 | 352 | NA | 169 | 183 | **155** | **155** |
| Total | | 300 | 558 | | 323 | 352 | 295 | 292 |

Table IV provides the results from experiment 2, of which setup is given in Table III. Similar to Table II, Table IV shows the test suite size for some existing algorithms along with our algorithm MFPA. The total value of suite size for MFPA is slightly better than its nearest competitor HSS. Again, WHIPBH makes the worst performance, failing to execute problems PB4-PB5. Bearing in mind that these are the stochastic approaches, no single method works with the best performance for all problems. We can adopt some strategies (as we made a strategy to update the parameters at each iteration) to enhance the performance; however these strategies are limited.

Evaluating the experimental results, one can summarize that MFPA performs better than other algorithms and thus MFPA is a good candidate for using in reduction of test cases.

## V. CONCLUSION

In this paper, we proposed an optimization technique MFPA by modifying the original flower pollination algorithm. MFPA provides an optimal test suite for software interaction testing with the minimum suite size. This proposed algorithm has faster convergence rate than the original algorithm. The test results of our algorithm were compared with existing results of some existing algorithms to demonstrate the strength of our algorithm. Comparison shows that our algorithm performs slightly better than the existing algorithms and thus, the proposed algorithm can potentially be used by researchers and test engineers to obtain optimal test suite requiring the minimum time for software testing. However, more efficient optimization algorithm is needed to solve the large problem with massive computational cost and to meet the requirements of accuracy and convergence. Therefore, new ideas, strategies and algorithms are necessary to improve the current state-of-the-art research in the area of global optimization.

## ACKNOWLEDGMENT

This work was supported by Fundamental Research Grant Scheme (FRGS) No. RDU160102 from Ministry of Higher Education, Malaysia.

## REFERENCES

[1] M. N. Kabir, A. Issa-Salwe, and M. Ahmed, "Simplified model of combustion process in a diesel engine for real-time operation," *International Journal of Vehicle Systems Modelling and Testing,* vol. 5, no. 4, pp. 347-357, 2010.

[2] A. A. Alsewari and K. Z. Zamli, "Design and implementation of a harmony-search-based variable-strength t-way testing strategy with constraints support," *Information and Software Technology,* vol. 54, no. 6, pp. 553-568, 2012.

[3] A. Hervieu, D. Marijan, A. Gotlieb, and B. Baudry, "Practical minimization of pairwise-covering test configurations using constraint programming," *Information and Software Technology,* vol. 71, pp. 129-146, 2016.

[4] K. Z. Zamli, B. Y. Alkazemi, and G. Kendall, "A Tabu Search hyper-heuristic strategy for t-way test suite generation," *Applied Soft Computing,* vol. 44, pp. 57-74, 2016.

[5] I. Gosciniak, "A new approach to particle swarm optimization algorithm," *Expert Systems with Applications,* vol. 42, no. 2, pp. 844-854, 2015.

[6] T. Mahmoud and B. S. Ahmed, "An efficient strategy for covering array construction with fuzzy logic-based adaptive swarm optimization for software testing use," *Expert Systems with Applications,* vol. 42, no. 22, pp. 8753-8765, 2015.

[7] S. Yoo and M. Harman, "Regression testing minimization, selection and prioritization: a survey," *Software Testing, Verification and Reliability,* vol. 22, no. 2, pp. 67-120, 2012.

[8] B. Galeebathullah and C. Indumathi, "A novel approach for controlling a size of a test suite with simple technique," *International Journal on Computer Science and Engineering,* vol. 2, no. 3, pp. 614-618, 2010.

[9] G. Fraser and A. Arcuri, "Achieving scalable mutation-based generation of whole test suites," *Empirical Software Engineering,* vol. 20, no. 3, pp. 783-812, 2015.

[10] M. Patrick, "Metaheuristic optimisation and mutation-driven test data generation," in *Computational Intelligence and Quantitative Software Engineering*, Springer, 2016, pp. 89-115.

[11] B. S. Ahmed, T. S. Abdulsamad, and M. Y. Potrus, "Achievement of minimized combinatorial test suite for configuration-aware software functional testing using the Cuckoo Search algorithm," *Information and Software Technology,* vol. 66, pp. 13-29, 2015.

[12] C. Jin and S. W. Jin. "Prediction approach of software fault-proneness based on hybrid artificial neural network and quantum particle swarm optimization," *Applied Soft Computing,* vol. 35, pp. 717-725, 2015.

[13] R. Jensi and G. W. Jiji, "An enhanced particle swarm optimization with levy flight for global optimization," *Applied Soft Computing,* vol. 43, pp. 248-261, 2016.

[14] H. B. Ouyang, L. Q. Gao, X. Y. Kong, S. Li, and D. X. Zou, "Hybrid harmony search particle swarm optimization with global dimension selection,". *Information Sciences,* vol. 346, pp. 318-337, 2016.

[15] L. Yu, Y. Lei, M. Nourozborazjany, R. N. Kacker, and D. R. Kuhn, "An efficient algorithm for constraint handling in

combinatorial test generation," in *Software Testing, Verification and Validation (ICST), 2013 IEEE Sixth International Conference on*, 2013, pp. 242-251.

[16] Z. Zhang, J. Yan, Y. Zhao, and J. Zhang, "Generating combinatorial test suite using combinatorial optimization," *Journal of Systems and Software,* vol. 98, pp. 191-207, 2014.

[17] X. S. Yang, "Flower Pollination Algorithm for Global Optimization," in *Unconventional computation and natural computation*, Springer, 2012, pp. 240-249.

[18] B. S. Ahmed, K. Z. Zamli, and C. P. Lim, "Constructing a t-way interaction test suite using the particle swarm optimization approach," *International Journal of Innovative Computing, Information and Control,* vol. 8, no. 1, pp. 431-452, 2012.

[19] T. Shiba, T. Tsuchiya, and T. Kikuno, "Using artificial life techniques to generate test cases for combinatorial testing," in *Computer Software and Applications Conference (COMPSAC), 2004. Proceedings of the 28th Annual International*, 2004, pp. 72-77.

[20] A. A. Alsewari and K. Z. Zamli, "Interaction test data generation using harmony search algorithm," in *Industrial Electronics and Applications (ISIEA), 2011 IEEE Symposium on*, 2011, pp. 559-564.

# Estimation of Energy Potential of Point Absorber Buoy type Wave Energy Converter

Abdullah Al Mahfazur Rahman[1], Md. Moniruzzaman[2], and M. Al Mamun[3]
[1]Lecturer (Southeast University, Bangladesh)
[2]Sr. Lecturer (Southeast University, Bangladesh)
[3]Lecturer (Southeast University, Bangladesh)
rajib.aust.eee@gmail.com

*Abstract*— **Wave energy has a huge potential compared to other renewable energy resources. The energy of sea wave can be converted into other form of energy like electrical energy using a Buoy wave energy converter. The converted power is collected by a Power take off device. This paper aimed to model a wave energy converter (WEC) and analyze its potential. It's mainly focus is on the construction and operation of point absorber buoy type wave energy converter and the responses of the converter when sea wave appears on it. The simulation is done in MATLAM/Simulink.**

***Keywords— Wave Energy Converter (WEC);Point Absorber Buoy, Power Take off Device(PTO).***

## I. INTRODUCTION (HEADING 1)

The world energy demand has increased extensively in the last decade because of human need for better living standards. The establishment of the Kyoto protocol to decrease the $CO_2$-concentartion in the atmosphere spurred the need for alternative renewable energy sources with zero carbon footprints. Inventors and researchers worldwide are busy working on the ways of Electric Power generation without creating greenhouse gases. Due to lack of proper engineering solution the potential of wave energy converter has not been addressed effectually. According to [1] this type of energy converter provides high power density, relatively high utilization factor, low visual impact and presumed low impact on environment compared to other renewable sources. Wave energy is produced when electricity generators are placed on the surface of the ocean. The energy provided is most often used in purification plants, power plants and water pumps. Energy output is determined by wave height, speed, wavelength, and water density. As mentioned in [2], a wave energy converter has to deal with the natural characteristics of ocean wave as well as the transmission mechanism of point absorber to the PTO and the electromagnetic force of the generator.

According to [3] many research studies are focusing on the design of generators for this application or on the process of electric power conversion to optimize the wave energy extraction system, while few investigate the motion of the buoy, which drives the linear generator. It is very difficult to analyze the behavior of heavyweight buoy when it is exposed to the nonlinear motion of ocean waves.

This article contains an estimation of the wave energy potential for the sea surface using Point Absorber Buoy with Linear Generator. This type of system can be used to extract large renewable energy from the ocean waves. It is very new and highly efficient technology. It has the unique ability to generate electricity during both the rise and fall of a wave. A wave energy converter should have at least two devices which are the surface float and a submerged body.

## II. BASIC WAVE ENERGY CONVERTER

### *A. Point Absorber Buoy with Linear Generator*

The basic design of a Point Absorber Buoy with Linear Generator is shown in Fig.1. The point absorber buoy is a vertical cylinder. It is a floating mass which is allowed to move vertically following sea waves. The linear generator on the seabed has limited stroke length as mentioned in [4]. The buoy and the linear generator are connected through a string as shown in Fig.1. Note that the string is modeled as a stiff mass-less piston. One end of the piston is connected to the buoy through string and the other end is connected to the support through a spring.

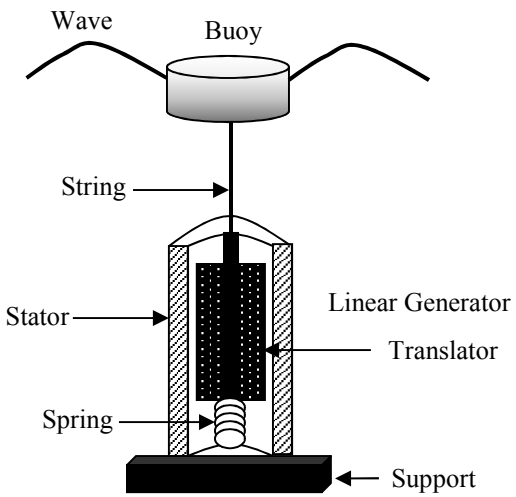


Figure 1. Basic design of a Piont Absorber Buoy with Linear generator.

When sea wave appears on the buoy it starts to move. The speed of movement of the buoy depends on the nature of appeared ocean wave. The movement of the buoy is transferred

978-1-5386-2307-7/17/$31.00 ©2017 IEEE

to the moveable part of the linear generator. Thus the potential wave energy can be transformed to the electrical energy as indicated in [5]. The generated electrical energy is transferred to the land station through cable. The selection of linear generator is very crucial in the design of point absorber wave energy converter. According to [6, 7], synchronous generator, induction generator and switched reluctance generator can be selected as the linear generator for the energy conversion process.

The advantages of Point Absorber type wave energy converter compare to other types of wave energy converter as mentioned in [8] can be summarized as:

- It can absorb wave energy from every direction. As a result it can work actively except during extreme wave conditions.
- The design of the system is very simple and small compared to other types of energy converter.
- It is more cost effective in terms of manufacturing, installation and maintenance.
- Power Extraction, focusing mainly on studying the efficiency of different PTO devices, evaluating their performance and energy losses.

### *B. Motion EquationActing on the Floating Buoy*

As in Fig.2 a vertical cylinder floating buoy has been considered with mass including the piston is $\mathbf{m_b}$. The radius and height of the cylinder are **r** and **h** respectively. Due to the influence of the sea wave the displacement of the sea level with respect to sea surface from the equilibrium is **y** and the displacement of the buoy is x. It is indicated in [9, 10] that the nature of ocean wave is nonlinear and continuously changing, which depends on the climate of the sea. But for ease of the analysis the effects of wind and tide have been ignored in the motion equation and a monochromatic sinusoidal wave has been considered.

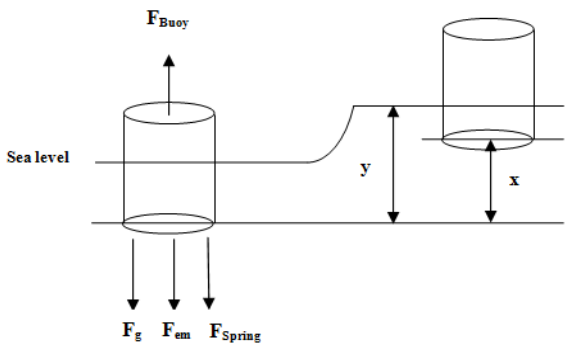


Figure 2. Reaction diagram (the active forces on the Buoy).

From the reaction diagram of Fig.2 the motion equation of the buoy can be written as,

$$m_b \frac{d^2x}{dt^2} = F_{Buoy} - F_g - F_{em} - F_{Spring} \quad (1)$$

Where, $F_{Buoy}$ is the hydrostatic reaction force, $F_g$ is the gravity force, $F_{em}$ is the electromagnetic force and $F_{Spring}$ the mechanical-spring force acting on the buoy.

As the hydrostatic reaction force acting on the buoy depends on the density of water, gravity constant g, dimension and vertical displacement of the buoy from its original position, the equation of $F_{Buoy}$ can be written as,

$$F_{Buoy} = \pi r^2 \rho g(y - x) \quad (2)$$

Where, ρ is the density of salty sea water (1020 kg/m$^3$) and g =9.81 m/s$^2$.

The gravity force acting on the buoy is given by,

$$F_g = m_b g \quad (3)$$

The electromagnetic force can be written as,

$$F_{em} = k_e \frac{dx}{dt} \quad (4)$$

Where, $k_e$ is the electromagnetic constant. The nature of the linear generator determines the value of $k_e$. As explained in [11] the characteristics of generator and its connection affect the dynamic behavior of the buoy.

The spring behaves like an mechanical energy storage system. For this involving force equation can be written as,

$$F_{spring} = (F_{Static} + k_s x) \quad (5)$$

Where, $F_{Static}$ is the static spring force and $k_s$ is the spring constant.

## III. SIMULATION MODEL

Based on the concept of the equations explained in the previous section a simulation model has been created in MATLAB/Simulink. The wave shape from the sea has been considered as a sinusoidal wave with amplitude of wave height/2 and frequency of 1/wave period. When sea wave has imparted on the floating buoy connected to a linear generator produces electricity. Different parameters have been observed from the simulation model which is shown in Fig.3.

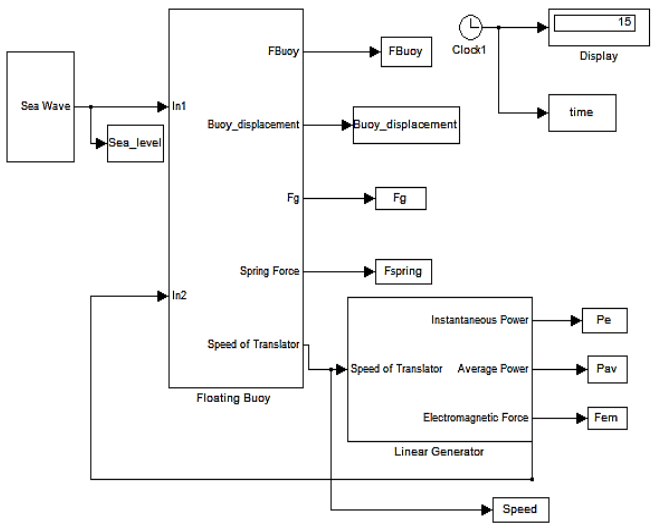


Figure 3. Wave Energy Converter's (WEC) simulation model.

In this study, the wave parameters have been selected which are given in TABLE I. The parameters of buoy and the

generator have been given in TABLE II. Spring is sized to have about equal energy at the upward and the downward piston motion as mentioned in [12]. The instantaneous power and average power output of the system also have been obtained from this study.

TABLE I. A SELECTION OF WWAVE PARAMETERS

| Wave parameters | *Quantity* |
|---|---|
| Wave amplitude (H) | 1.75 meters |
| Wave period (T) | 3.5 Seconds |
| Phase angle (Θ) | 0 |

TABLE II. A SELECTION OF BUOY PARAMETERS

| WEC parameters | *Quantity* |
|---|---|
| Height (h) | 0.5 meters |
| Radius (r) | 2.5 meters |
| Mass ($m_b$) | 250 kg |
| Static Spring force ($F_{Static}$) | 10kN |
| Spring Constant ($k_s$) | 10kNs/m |
| Electromagnetic Constant ($k_e$) | 15kNs/m |

## IV. RESULT ANALYSIS

Several analyses have been carried out in this section based on different parameters of the system.

### A. Observation on Buoy Position and Sea Surface

The buoy follows the pattern of movement of sea surface as shown in the Fig.4 but with little less amplitude than the sea surface.

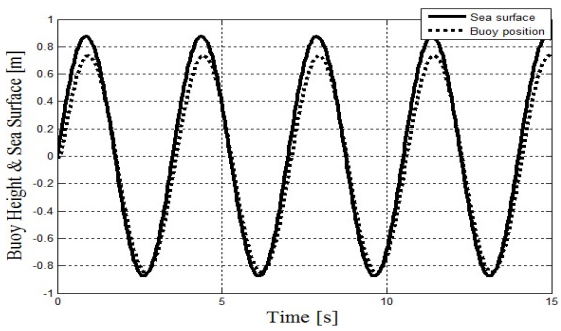


Figure 4. Buoy height & sea surface.

### B. Influences of Different Forces on the Buoy

The influence of different forces on the Buoy is shown in Fig.5. Both hydrostatic reaction force $F_{Buoy}$ and spring force, $F_{Spring}$ are acted opposite to each other, as expected. As the buoy wants to go up due to the hydrostatic reaction force, the spring resists. The gravity force is constant for the total duration of simulation. The electromagnetic force varies with the position. $F_{Buoy}$ and $F_{Spring}$ are a bit shifted compared to the position and the electromagnetic force, $F_{em}$ due to the initial value of $F_{Buoy}$ which is not applicable for $F_{em}$.

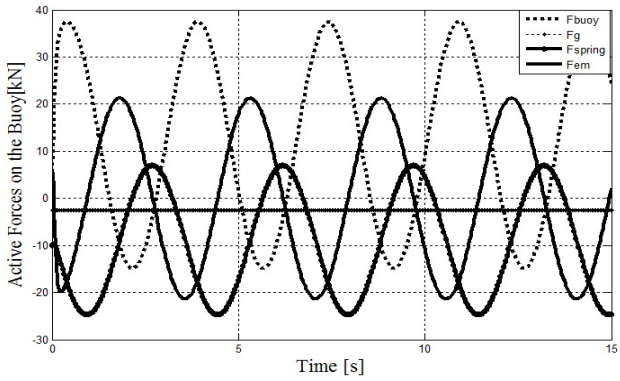


Figure 5. Influence of different forces on the Buoy.

### C. Effect of Translator speed on the Electromagnetic Force

In this simulation the speed of translator has been measured. Fig.6 has been plotted for electromagnetic force and speed. As $F_{em}$ act opposite to the translator, this can be seen from the Fig.6.

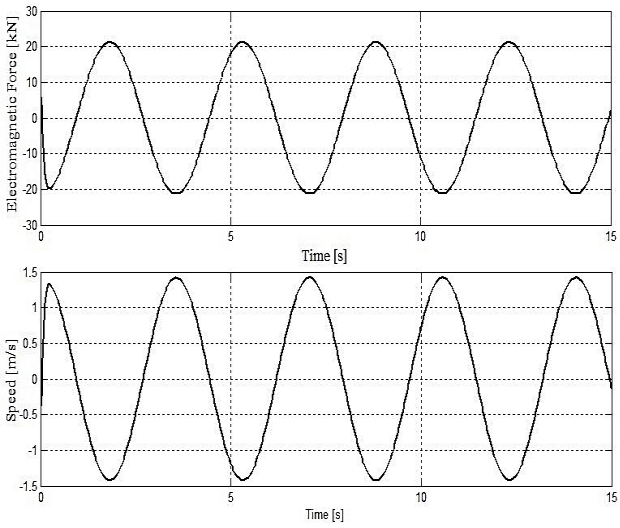


Figure 6. Effect of Translator's speed on the Buoy.

### D. Observation on Instantaneous Power and Average Power

The instantaneous power as shown in Fig.7 has low peak in the first cycle because of the settling of the hydrostatic reaction force at the start of the simulation. After that it has a peak where the slope of the position is maximal, due to the relation between electromagnetic force and the derivative of the position (speed). The average power generated is 15 kW.

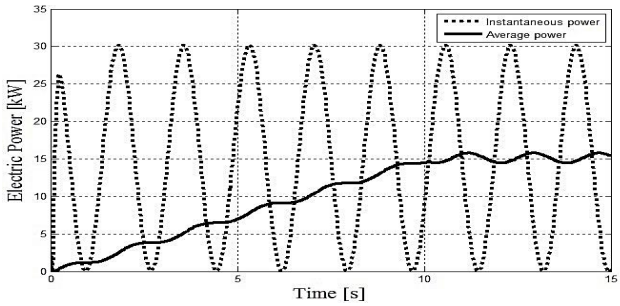


Figure 7. Instantaneous Power and Average Power curves.

### E. Influence of Electromagnetic Constant on Average Power

There is a linear relation between electromagnetic constant and average output power. The values of $k_e$ have been changed from 1kNs/m to 15kNs/m and the corresponding values of output power have been recorded. Fig.8 has elucidated the influence of $k_e$ on output power.

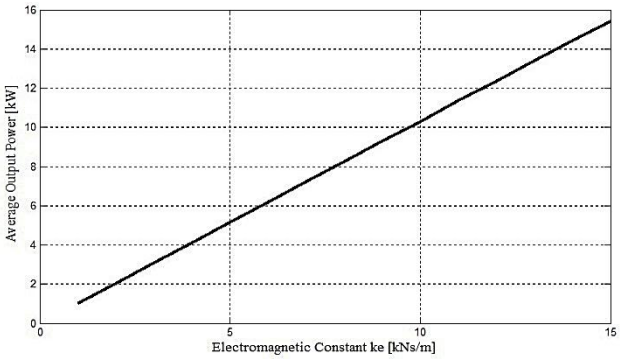


Figure 8. Influence of Electromagnetic Constant on Average Output Power.

### F. Variation of Electric Power on Wave Height

There is a significant impact of wave height on the output power of the wave energy converter, which is shown in Fig.9. According to TABLE III, Fig.9 has been plotted. From this plot, it is seen clearly that the instantaneous and average output power have the changing nature. At the instant when wave height has changed, a sharp spike of instantaneous power occurred which settled down very quickly.

TABLE III. WWAVE HEIGHT FORDDIFFERENT TIME DURATION

| Wave Height [m] | Operating Time [Sec] | Average Power [kW] |
|---|---|---|
| 1.75 | 0 to 10 | 15 |
| 1.5 | 10 to 20 | 11 |
| 2 | 20-40 | 20 |

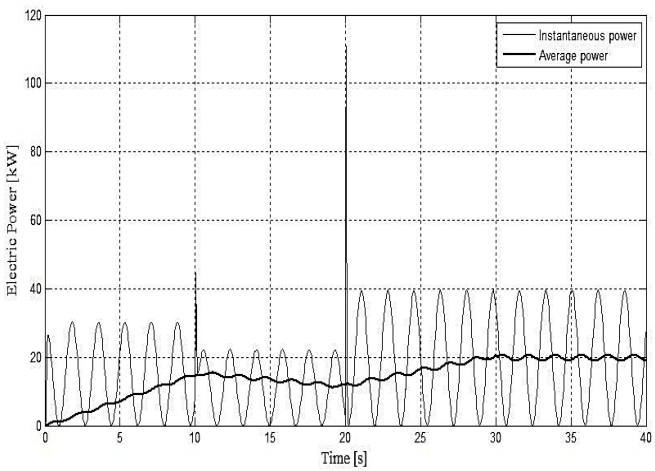


Figure 9. Variation of Electric Power on Wave Height.

### G. Variation of Electric Power on Wave Frequency

The frequency of appeared sea wave has influenced on the generation of electric power as it has a direct impact on the vibration frequency of the linear generators translator, as is shown in Fig.10. TABLE IV is used to simulate this behavior and plot of Fig.10.

TABLE IV. WWAVE PERIOD FORDDIFFERENT TIME DURATION

| Wave Period [Sec] | Operating Time [Sec] |
|---|---|
| 3.5 | 0 - 4 |
| 4 | 4 - 8 |
| 4.5 | 8-10 |
| 3.5 | 10-14 |
| 4 | 14-18 |
| 4.5 | 18-20 |
| 3.5 | 20-24 |
| 4 | 24-28 |
| 4.5 | 28-30 |

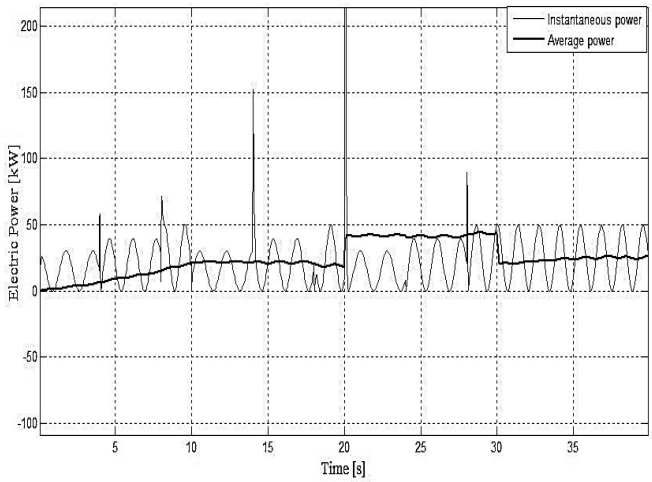


Figure 10. Variation of Electric Power on Wave frequency.

## V. CONCLUSION

Energy production from wave energy has recently explored new horizon towards the finding of alternative energy sources. It has high potential compare to other green energy sources. The major area of concern in this respect is the energy distribution of wave, which is not uniform throughout the globe. So the technologies of the energy conversion device play a vital role to overcome this problem. In this paper a simple wave energy conversion process has explained. The aim of this work is to evaluate the influence of different forces and enhancement of electrical power output under different condition of the electromagnet force of the linear generator. The model work as it is expected. In future a modified version of this model can be implemented to evaluate the influence of other parameters like the parameters of linear generator for efficient electric power production.

## REFERENCES


[1] U. Henfridssona, V. Neimanea, K.Stranda, R. Kappera, H. Bernhoffb, O. Danielssonb, M. Leijonb, J. Sundbergb, K.Thorburnb, E. Ericssonc,andK.Bergmanc, "Wave energy potential in the Baltic Sea and the Danish part of the North Sea, with reflections on the Skagerrak," pp. 272-284, December 2006. Elsevier Ltd. Renewable Energy 32 (2007) 2069–2084.

[2] Yung-Lien Wang, "A wave energy converter with magnetic gear," pp. 101-108, April 2015, Elsevier Ltd., Ocean Engineering 101 (2015) 101–108.

[3] Q.Guodong, P. Quanru and C. Zhongxian, "A Wave Energy Extraction System in Experimental Flume,"pp. 1-4, June 2016,Hindawi Publishing Corporation,International Journal of Rotating Machinery, Volume 2016, Article ID 2573174.

[4] Halvar Gravrakmo , ErlandStromstedt,AndrejSavin,OlleSvensson and Mats Leijon "Measurements of extreme forces on a wave energy converter of point absorber type and estimation of added mass of cylindrical buoy," Proceedings of the ASME 2014 33rd International Conference on Ocean, Offshore and Arctic Engineering, OMAE2014, June 8-13, 2014, San Francisco, California, USA.

[5] LorandSzabo, ClaudiuOprea, Joan-Adrian Viorel, andKairolyAgoston Biro,"Novel Permanent Magnet Tubular LinearGenerator for Wave Energy Converters" Proceedings ofthe IEEE International Electric Machines & Drives Conference,Antalya, Turkey, 16 July 2007.

[6] Rickard Ekström, BoelEkergård, Mats Leijon , "Electrical damping of linear generators for wave energyconverters-A review", pp.116-128, October2014, Elsevier Ltd., Renewable and Sustainable Energy Reviews 42 (2015) 116–128.

[7] Polinder H, Mecrow B, Jack A, Dickinson P, Mueller M., "Conventional and TFPM linear generators for direct-drive wave energy conversion". IEEE Trans Energy Convers 2005;20(2):260–7.

[8] FilipposKalofotias,"Study for the Hull Shape of a Wave Energy Converter-Point Absorber,"A thesis presented for the degree of Master of Science Water Engineering & Management University of Twente The NetherlandsJune 2016.

[9] Terry Lettenmaier, Annette von Jouanne, and Ted Brekken,"A new maximum power point tracking algorithm for ocean",pp.40–55,January 2017, Elsevier Ltd., International Journal of Marine Energy17 (2017) 40–55.

[10] J Q Wang, X C Zhang, Y Zhou, Z C Cui and L S Zhu, "A maximum power point tracking algorithm for buoy-rope-drum wave energy converters" , Proceedings of the International Conference on New Energy and Future Energy System (NEFES), 2016.

[11] M. Eriksson, R. Waters, O. Svensson, J. Isberg, and M. Leijon, "Wave power absorption: Experiments in open sea and simulation", Journal of Applied Physics 102, 084910, October 2007.

[12] I.A. Ivanova, H. Bernhoff, O. Agren, M. Leijon,"Simulated generator for wave energy extractionin deep water ,"pp. 1664-1678, April 2005. Elsevier Ltd.,Ocean Engineering 32 (2005) 1664–1678.

# Energy-Cost Aware Hybrid Power System for Off-Grid Base Stations Under Green Cellular Networks

[1]Abu Jahid and [2]Md. Sanwar Hossain
[1,2]Department of Electrical, Electronic and Communication Engineering, MIST, Dhaka-1216, Bangladesh
Email: [1]setujahid@gmail.com, [2]sanwareee@gmail.com

***Abstract*—Growing concern about global warming and energy consumption, utilizing green energy to power cellular base stations (BSs) is an attractive solution to reduce operational expenditure and global carbon emissions. With the advancement of renewable energy (RE) generation technology, cellular operators are increasingly deployed solar energy system that could be made financially viable in cellular industry with the added merits of minimum maintenance. The random and dynamic nature of green energy generation could lead deterioration of the quality of service (QoS) and impose severe challenges to design reliable cellular systems. To increase the self-reliance, the integration of diesel generator (DG) with the solar energy harvester (EH) has drawn intensive attention for the envisaged off-grid BSs. In this paper, we extensively explore the energy sustainability, cost-effectiveness, energy efficiency and reliability of the proposed hybrid power sources for cellular communications taking advantages of photovoltaic (PV) technology. The prime intention of adopting solar energy in telecom sectors is to minimize the diesel consumption as well as meet the challenges of climate changes. Simulation results demonstrate the validity of the proposed technique and sustainability can be ensured with better planning by providing cleaner energy.**

***Index Terms*—Green communication, Energy harvesting, Sustainability, Energy efficiency, Renewable energy, Hybrid supplies.**

## I. Introduction

Cellular networks are growing at an enormous pace due to the recent rapid growth in the number of user terminals and the ubiquitous availability of internet access. Such tremendous growth of mobile data traffic in cellular industry has escalated massive inflation in energy consumption and exerting a detrimental effect on both the environmental implications and the economic aspects [1]–[3]. It has been estimated that global mobile traffic has grown exponentially 12 times from 2010 to 2014 and is also expected to raise 10 times much of global traffic by 2020. Accordingly, global energy demand is expected to rise by 37% from 2013 to 2035, or by an average of 1.4% per year. Another downside, mobile sectors are responsible for 2-3% global carbon emissions and expected to increase by a growth of 6% every year through 2020. Base stations (BSs) in the radio access network (RAN) contribute more than 50% of the total energy expenditure and placing the mobile operator under immense pressure to solve the problem of reliable power supply in a cost-effective way [4]–[6]. Under the pressure from economic and environmental aspects, green cellular communications have thereby become an inevitable trend for next generation wireless network.

Being inspired by energy cost savings considerations, mobile network operators (MNO) worldwide are deploying renewable energy sources e.g., solar panels, wind turbines, etc., at the sites of their BSs to obtain clean electricity [7]–[9]. Huawei [9] has developed green power BSs solution to curtail grid electricity consumption and thereby reducing carbon footprints. The integration of RE sources at BSs offers to MNO the possibility to obtain low cost electricity and also reduces its dependence on external energy suppliers. Despite the potential advantages, the inherent randomness and intermittency of RE generation pose significant technical challenges to design large-scale cellular networks. Additionally, the mismatch between harvested energy and traffic distributions (i.e., BS load) may degrade the energy sustainability performance.

Diesel generators (DG) are widely used for powering off-grid BSs sites where the electricity grid is not reliable or is not an economically attractive option. The concept of using DG as a primary power supply has become less favorable due to the challenges linked to their reliability, technical issues, high operational & maintenance costs [11]. As the cellular systems are expected to provide reliable services with guaranteed QoS, envisioning BSs to be powered by hybrid supplies combining solar energy sources with DG power source has become a promising alternative and stimulated the current work. Such hybrid power solutions are feasible due to mitigating the intermittent nature of RE sources and have become favorable in areas where the grid electricity is not uninterruptedly available to cover a continuous power supply. The additional advantage is that the high capital cost of PV arrangements may be compensated by the low cost DG and the standby DG supply can help prolong the battery lifetime. The benefit of using RE focusing increasing reliability of cellular networks has been thoroughly studied in the literature [11], [12]. Authors [11], [12] analyzed the hybrid power solutions for a remote cellular system without considering the actual traffic demand to be served by BS. This design could lead the mismatch between the dimensioning of hybrid installed capacity according to BS demand and energy utilization efficiency.

Motivated by the above analysis, this paper investigates the potential of hybrid power system solution for green Long-term Evolution (LTE) cellular networks. Each individual BS is equipped with PV energy harvester, DG power supply, and adequate energy storage devices such as batteries in case of excess RE generation. The ultimate goal is to maximize the green energy utilization resulting minimization of DG energy as well as fuel consumption. Particularly, five key aspects have been examined in this study: (i) optimum system architecture, (ii) technical criteria, (iii) energy yield, (iv) economic factors and (v) carbon footprints. In the proposed paradigm, temporal variation of both solar energy generation and mobile traffic intensity are considered. Extensive simulations are carried

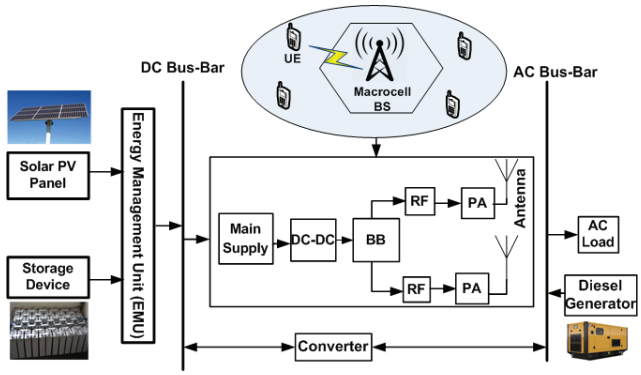


Fig. 1. Hybrid SPV/DG powered LTE BS architecture.

out to evaluate the system performance in terms of per unit electricity cost, contribution of each individual power supply components, diesel consumption with price and greenhouse gas (GHG) emissions effects along the net present cost. A hybrid optimization model for electric renewables (HOMER) software is used to critically analyze the optimization of the techno-economic feasibility of LTE macro BSs.

The rest of the paper is organized as follows. Section II outlines the architecture of the proposed hybrid solar/DG driven LTE macro BS system. Section III presents the cost modeling and optimization objectives. Section IV demonstrates the simulation setup and the numerical results with insightful analysis. Section V concludes the paper summarizing the key findings.

## II. System Model

We consider LTE cellular networks whose BSs are powered by hybrid supplies combining PV solar energy and diesel generator sources. Macro BSs are assumed to be deployed using 2/2/2 antenna pattern in hexagonal layout and user equipment (UEs) are uniformly distributed throughout the network. Each BS has independent on-site solar energy harvester, a DG set and backup energy storage device such as battery bank with energy management unit (EMU). PV solar energy acts as the primary energy source, while DG is kept as a standby supply. Fig. 1 is a schematic diagram depicts the architecture of the system model consisting two subsystems, the telecommunication load and the hybrid power system. An EMU consists of battery regulator unit that is used to prevent overcharging and restricts deep discharging of the battery bank, to protect battery life. The nomenclature 2/2/2 represents a three sector macrocell with 2 antennas per sector.

### A. PV System

The solar energy harvester contains multiple solar modules interconnected in series/parallel to form a PV array. Solar panels absorb sunlight irradiance and convert it into DC power electricity. The amount of solar energy produced is heavily depends on the geographic location, panel materials, environmental implications, PV panels's tilt, tracking mode and generation technology. HOMER calculates the annual energy output of the solar PV (SPV) array expressed as [12]

$$E_{SPV} = \gamma_{SPV} \times PSH \times \eta_{SPV} \tag{1}$$

where $\gamma_{SPV}$ is the rated capacity of the SPV array (kW), $PSH$ is the peak solar hour which is equivalent average daily solar radiation in kWh/$m^2$/day and $\eta_{SPV}$ is the derating factor of the SPV is used to account the effects of dust, wire losses, temperature, and other factors that can affect output energy of the solar array. However, the panels are modeled on a two-axis tracking mode, thereby increasing the total annual energy contribution of the PV array by 25%, as well as enabling wind, rain, and gravity to naturally remove most of the debris and dust [12].

### B. Battery Model

A battery bank is used as a backup system which is not immediately used to run the BS and also store excess electricity for future consumption by the BS during night, load-shedding, or if solar energy is failed to feed the BS demand completely. The battery charging and discharging is modeled based on the state of charge (SOC) condition and the nominal capacity of the battery bank is the maximum SOC. The minimum SOC of the battery $B_{SOC_{min}}$ is the lower threshold limit that does not discharge below the minimum state of charge. The depth of discharge ($B_{DOD}$) indicates the maximum discharge energy that can be delivered from the battery and can be expressed as [12]

$$B_{DOD} = (1 - \frac{B_{SOC_{min}}}{100}) \tag{2}$$

However, battery bank autonomy ($B_{aut}$) is a significant factor that implies the potential number of days that the battery bank can provide the necessary energy to drive BS load if the PV array malfunctions. This value is expressed as the ratio of the battery bank size to the daily BS load [12]

$$B_{aut} = \frac{N_{batt} \times V_{nom} \times Q_{nom} \times B_{DOD} \times (24h/day)}{L_{BS}} \tag{3}$$

where $N_{batt}$ is the number of batteries in the battery bank, $V_{nom}$ is the nominal voltage of a each battery cell (V), $Q_{nom}$ is the nominal capacity of a single battery (Ah) and $L_{BS}$ is the average daily BS load in kWh. Without losing the generality, Trojon L16P battery model is used in cellular infrastructure due to their large capacity and high reliability.

On the other hand, battery lifetime is another crucial parameter that has a direct impact on replacement costs over the project duration.

### C. Converter

An inverter convert a low DC voltage into a usable 220V AC voltage with the desired frequency of the load. The inverter capacity ($C_{inv}$) is computed as following [12]

$$C_{inv} = (\frac{L_{ac}}{\eta_{inv}}) \times S_f \tag{4}$$

where $L_{ac}$ is the maximum AC load in kW, $\eta_{inv}$ is the inverter efficiency in %, and $S_f$ is the safety factor. On the other hand, rectifier convert electrical energy from the AC form into the DC form with the compatible bus voltage.

### D. Diesel Generator

The energy produced by a DG ($E_{DG}$ in kWh) with a given rated power output ($P_{DG}$) is expressed as [11]

$$E_{DG} = P_{DG} \times \eta_{DG} \times t_{op} \tag{5}$$

where $\eta_{DG}$ is the efficiency of the DG and $t_{op}$ operational time. However, the fuel consumption ($F_C$) is calculated as follows

$$F_C = E_{DG} \times F_{sp} \tag{6}$$

where $F_{sp}$ is the specific fuel consumption (L/kWh).

TABLE I
BS APPROXIMATE POWER CONSUMPTION MODEL PARAMETERS [13]

| BS Type | $N_{TRX}$ | $P_{MAX}$ $[W]$ | $P_0$ $[W]$ | $\triangle_P$ |
|---|---|---|---|---|
| Macrocell | 6 | 20 | 130 | 4.7 |

### E. BS Power Consumption Model

The BSs energy consumption is directly related to the traffic load. Practically, incoming traffic arrival rate in a cellular network is time-inhomogeneous and not all subscribers are always active. Hence, traffic volume at individual BSs are highly dynamic over time. It is essential to investigate the traffic demand to be served by the BSs in order to analyze the energy consumption of the network to implementing hybrid power system. An approximate traffic pattern is shown in Fig. 2 can be estimated by using Poisson distribution model as follows

$$p(t,\alpha) = \frac{\alpha^t}{t!}e^{-\alpha} \tag{7}$$

where, $p$ is the Poisson distribution function of traffic demand for a given period of time, and $\alpha$ is the mean value where peak number of traffic arrivals occur at 5 PM.

The total approximate power consumption considering number of transceivers ($N_{TRX}$) and actual traffic intensity ($\chi$) is defined as [13]

$$P_{in} = N_{TRX}(P_1 + \triangle_p P_{MAX}(\chi - 1)), \quad \text{if } 0 < \chi \leq 1 \tag{8}$$

where $P_1 = P_0 + \triangle_p P_{MAX}$ and $P_0$ is the consumption at idle state. The load dependency is accounted for by the power gradient, $\triangle_p$. The scaling parameter $\chi = 1$ indicates that a fully loaded system. The dynamic power consumption is varied with traffic loading parameter $\chi$ as seen from Fig. 4. The parameters of BS load are summarized in Table I.

The power consumption of the air-conditioning unit depends on the internal temperature of the BS cabinet and approximately consumes 10% of total power consumption in the macrocell [12]. We assume that air conditioner run 18 hours in a day with 6 hours running and 2 hours shut off, and so on. Also, an auxiliary 25 W lamp is connected to BS running from 7 PM to 6 AM. The total annual energy consumption and percentage of DC load and AC load contribution for the two different LTE BS are listed in Table II.

TABLE II
ANNUAL ENERGY CONSUMPTION OF LTE BS IN KWH AND CONTRIBUTION OF DC LOAD AND AC LOAD SHARING

| BS Type | Annual demand(kWh) | DC load(kWh) | AC load(kWh) |
|---|---|---|---|
| Macro | 9,213 | 8,404 (91.2%) | 809 (8.8%) |

The schematic diagram of LTE 2/2/2 macro BS architecture in HOMER platform and its seasonal AC load profile are shown in Fig. 3 and Fig. 5 respectively.

## III. COST MODELING AND OPTIMIZATION

HOMER is the optimization software used in this study to evaluate the optimal hybrid SPV/DG power system that satisfies user-specified constraints with the lowest net present cost (NPC) including the capital costs ($CC$), replacement costs ($RC$), O&M costs ($OMC$), fuel costs ($FC$), and salvage value ($S$) within the project duration. The NPC is computed as follows [12]

$$NPC = \frac{TAC}{CRF} = CC + RC + OMC + FC - S \tag{9}$$

Total annualized cost (TAC) value and capital recovery factor (CRF) is described as follows

$$TAC = TAC_{CC} + TAC_{RC} + TAC_{OMC} \tag{10}$$

$$CRF = \frac{i(1+i)^N}{(1+i)^N - 1} \tag{11}$$

where $N$ is the project duration and $i$ is the annual real interest rate.

The salvage value is usually computed at the end of the project lifecycle and applies to components that have longer lifetimes than the project lifecycle.

$$S = rep(\frac{rem}{comp}) \tag{12}$$

where rep, rem, and comp are the replacement cost of the component, the remaining lifetime, and the lifetime of the component respectively.

However, the objective function of optimization is to minimize the $NPC$, subject to

$$E_{SPV} > 0 \quad and \quad E_{DG} > 0 \tag{13}$$

$$E_{SPV} + E_{DG} > E_{BS} \tag{14}$$

$$E_{SPV} + E_{batt} + E_{DG} = E_{BS} + E_{losses} \tag{15}$$

where $E_{losses}$ comprises with battery losses and converter losses, $E_{BS}$ and is the annual BS load consumption in kWh and $E_{batt}$ is the energy supply from battery. The constraints implies the annual cumulative hybrid energy production carry the BS load consumption along with different losses.

## IV. PERFORMANCE ANALYSIS

### A. Simulation Setup

The lifetime of the project is 15 years and the annual interest rate considered in this study is 6.75% [14], which affects the total project cost. Moreover, 10% back power is reserved to serve the BS load, even if the solar energy generation suddenly decreases. HOMER decides at each time step to meet the energy requirements at the lower net present cost, subject to the constraint from the dispatch strategy chosen in the simulation. Techno-economic specifications and system constraints are presented in Table III.

TABLE III
SIMULATION SETUP OF SPV/DG POWER LTE CELLULAR NETWORKS [12]

| System Components | Parameters | Value |
|---|---|---|
| SPV | Operational lifetime | 25 years |
| | PV derating factor | 0.9 |
| | Capital cost | $1/W |
| | Replacement cost | $1/W |
| | O&M cost/year | $0.01/W |
| Battery | Round trip efficiency | 85% |
| | $B_{SOC_{min}}$ | 30% |
| | $V_{nom}$ | 6V |
| | $Q_{nom}$ | 360 Ah |
| | Lifetime throughput | 1075 kWh |
| | Capital cost | $300/unit |
| | Replacement cost | $300/unit |
| | O&M cost/year | $10 |
| Inverter | Efficiency | 95% |
| | Operational lifetime | 15 years |
| | Capital cost | $0.4/W |
| | Replacement cost | $0.4/W |
| | O&M cost/year | $0.01/W |
| Diesel Generator | Efficiency | 40% |
| | Capital cost | $0.66/W |
| | Replacement cost | $0.66/W |
| | O&M cost | $0.05/h |
| | Operational lifetime | 25,000h |

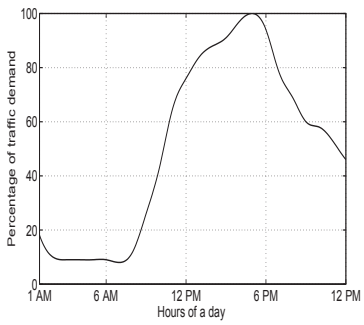


Fig. 2. Daily traffic load profile.

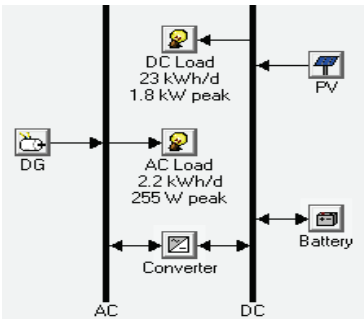


Fig. 3. Schematic diagram for 2/2/2 macro BS architecture in HOMER.

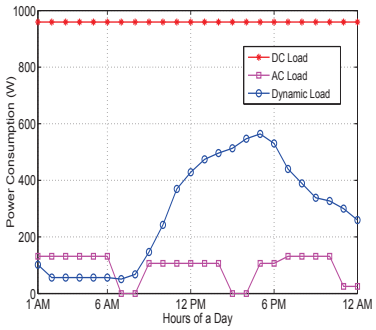


Fig. 4. Hourly load profile.

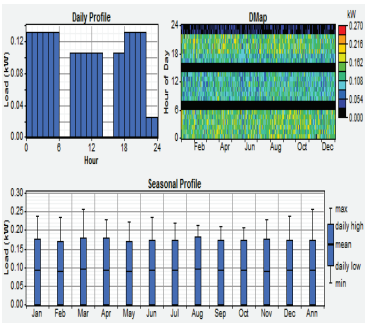


Fig. 5. Seasonal AC load profile.

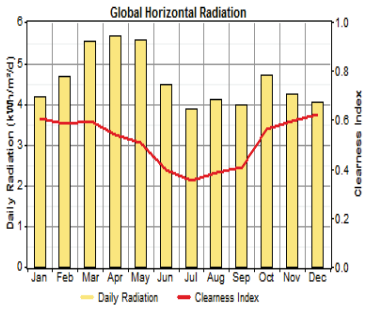


Fig. 6. Average annual profile of solar irradiation in Bangladesh.

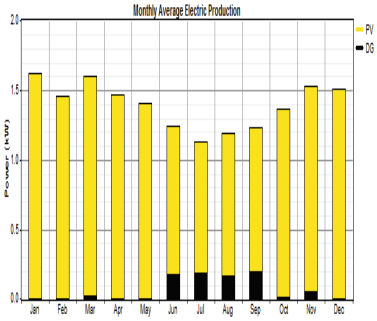


Fig. 7. Monthly power contribution at an average solar irradiation of 4.59 kWh/$m^2$/day.

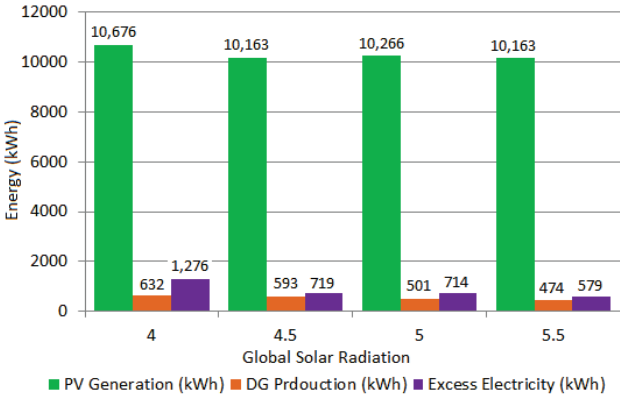


Fig. 8. Annual energy contribution and surplus energy of SPV/DG system in kWh for various solar radiation.

TABLE IV
OPTIMAL SYSTEM ARCHITECTURE FOR AVERAGE SOLAR RADIATION OF 4.59 KWH/$m^2$/DAY USING HOMER SIMULATION

| SPV (kW) | DG (kW) | Battery (Units) | Converter (kW) |
|---|---|---|---|
| 5.5 | 1 | 32 | 0.3 |

## B. Optimal System Architecture

The annual average solar irradiation is 4.59 kWh/$m^2$/day. Fig. 6 illustrates the solar resource profile for a one-year period. Table IV includes a summary of the technical criteria for the optimal system design of the hybrid powered LTE BS at an average solar radiation. Fig. 7 shows the monthly average of hybrid power production including the PV array output power and DG power. The result is axiomatic and the battery bank and DG are used to compensate the energy deficit during PV malfunctioning or low power output from PV array.

A summary of the optimum size of the components under the proposed hybrid power system identified by the HOMER simulation based on the different daily solar radiation values, are presented in Table V. As observed, the optimal size of solar array decreases with the increasing of solar radiation.

TABLE V
SUMMARY OF THE TECHNICAL CRITERIA FOR THE HYBRID POWER CELLULAR NETWORKS

| kWh/$m^2$/day | PV (kW) | DG (kW) | Battery | Conv. (kW) |
|---|---|---|---|---|
| 4.0 | 6.5 | 1 | 32 | 0.3 |
| 4.5 | 5.5 | 1 | 32 | 0.3 |
| 5.0 | 5.0 | 1 | 32 | 0.3 |
| 5.5 | 4.5 | 1 | 32 | 0.3 |

## C. Energy Yield Analysis

*PV Array:* The Sharp ND-250QC module (polycrystalline) with a nominal voltage of 29.80 V, nominal current of 8.40 A and power of 250 W is used in the simulation. For instance, SPV array consists of 22 Sharp modules are required for macro BS for the capacity of the PV array is 5.5 kW. The annual energy contribution of the SPV array is computed using (1); 5.5 kW $\times$ 4.59 $\times$ 0.90 $\times$ 365 days/year = 8,293 kWh. However, a dual-axis tacker increases the total amount of energy by 25% to be 10,366 kWh.

*Diesel Generator:* According to (5), 1 kW DG generates 542 kWh/yr (5% of total energy generation); (1 kW DG $\times$ $\eta_{DG}$ = 0.4 $\times$ $t_{op}$ = 1,355 hrs). HOMER calculates the battery loss ($B_{loss}$) and converter loss ($C_{loss}$) is 795 kWh/year and 35 kWh/year respectively. Hence, the annual excess electricity ($E_{excess}$) can be computed as 10,366 kWh + 542 kWh - 9,213 kWh - 795 kWh - 35 kWh = 865 kWh/year (7.93%).

*Battery Bank:* The total number of batteries is 32 connected 8 in series and 4 in parallel to be compatible with the 48 V DC bus bar for the LTE BS. The battery bank autonomously support the BS 46.4 hours, which is calculated using (3); (32 batteries $\times$ $V_{nom}$ = 6 V$\times$ $Q_{nom}$ = 360 Ah$\times$ $B_{DOD}$ = 0.7$\times$24h)/daily average BS load 25.24 kWh. Moreover, HOMER calculates the expected battery life of 6.59 years.

Table VI presents the statistical analysis of yearly energy contribution from two different energy sources including re-

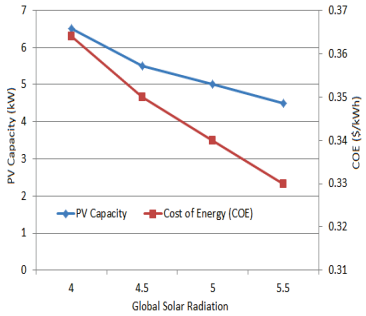


Fig. 9. Variation of PV array capacity and per unit energy cost with different solar radiation.

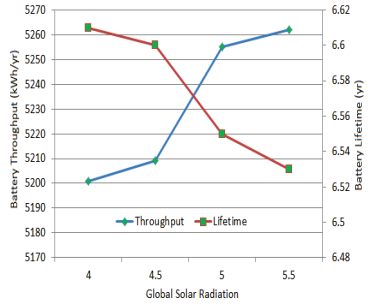


Fig. 10. Annual battery throughput and battery lifetime variying global solar radiation.

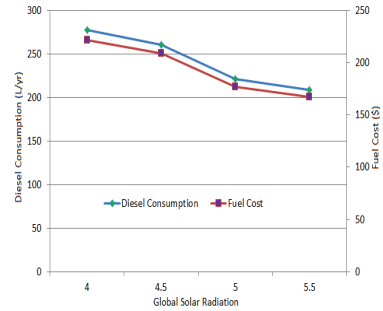


Fig. 11. Comparison of annual diesel consumption and corresponding fuel cost varying solar radiation.

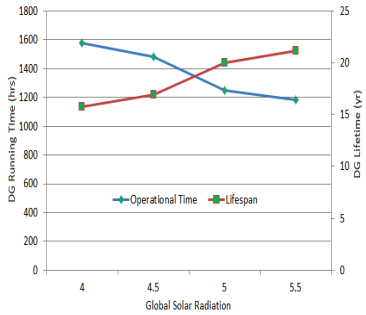


Fig. 12. Comparison of DG operational time and lifespan varying global solar radiation.

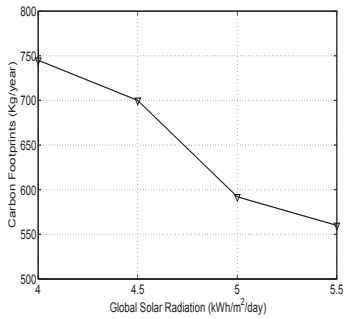


Fig. 13. Pollutant carbon emissions vs. global solar radiation rate.

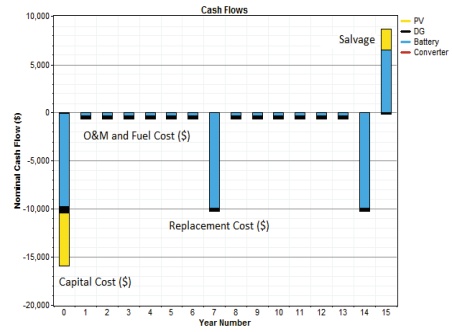


Fig. 14. Cash flow summary of the hybrid SPV/DG power system for solar radation of 4.59 kWh/$m^2$/day.

TABLE VI
ENERGY CONTRIBUTION AND EXCESS ELECTRICITY IN KWH FOR THE HYBRID SPV/DG POWER SYSTEM

| kWh/$m^2$/day | $E_{SPV}$ | $E_{DG}$ | $B_{loss}$ | $C_{loss}$ | $P_{excess}$ | $B_{aut}$ |
|---|---|---|---|---|---|---|
| 4.0 | 10,676 | 632 | 785 | 34 | 1,276 | 46.4 |
| 4.5 | 10,163 | 593 | 790 | 34 | 719 | 46.4 |
| 5.0 | 10,266 | 501 | 805 | 35 | 714 | 46.4 |
| 5.5 | 10,163 | 474 | 810 | 35 | 579 | 46.4 |

TABLE VII
TECHNICAL CRITERIA FOR DG POWER SYSTEM

| kWh/$m^2$/day | DG (hr) | Diesel (L) | DG Life (yr) | $CO_2$ (kg/yr) |
|---|---|---|---|---|
| 4.0 | 1,580 | 278 | 15.8 | 745 |
| 4.5 | 1,482 | 261 | 16.9 | 700 |
| 5.0 | 1,252 | 221 | 20 | 592 |
| 5.5 | 1,184 | 209 | 21.2 | 560 |

served electricity and battery autonomy. Fig. 8 shows the annual energy contribution of the hybrid PV/DG system for the different solar radiation values. As expected, the energy contribution of solar power system increases continually with the higher value of solar radiation except at a point of 5.5 kWh/$m^2$/day. At this point, the combination PV array capacity and solar radiation overlap with the first case leading to same solar energy generation as obtained from (1). Meanwhile, the DG produces less amount of energy resulting in minor consumption of diesel which reflects our optimization objectives. In addition, the graph also includes the reserved surplus electricity that signifies the proposed hybrid power system could meet the required BS energy demand independently without support from the battery bank. However, the batteries are integrated to the system in order to ensure zero outage and further enhance the sustainability.

A comparison of PV array capacity and levelized cost of electricity (COE) is demonstrated in Fig. 9. According to optimal architecture presented in Table V, PV array capacity decreases with the higher value of solar radiation. Additionally, the unit cost of electricity is seems to decreased with the higher value of global irradiation. The annual battery throughput follows an increasing trend to reach at maximum value whereas battery lifetime gradually decreased with the various solar radiation as seen from Fig. 10.

The statistical analysis of DG system including DG operating hours, diesel consumption and associated carbon emissions are listed in Table VII. Consequently, a details comparison of fuel consumption and corresponding annual diesel cost based on the DG energy production is clearly shown in Fig. 11. The both curve follows the similar pattern of decreasing trend with the increasing value of daily solar radiation. A higher value of average global radiation indicates the small DG production and hence incurs less diesel consumption. This in turn reduces the fuel cost as well as toxic gas emissions. On the other hand, DG lifespan and running hours are clearly presented in Fig. 12. The DG operational time continually falls down with the global daily radiation, whereas DG lifecycle follows the opposite manner as evident from the figure. The intuition state that the lower DG operational time certainly improves the DG lifetime. Therefore, a significant enhancement of DG lifetime is attained for the larger value of solar radiation.

### D. Carbon Footprints

Typically, a diesel generator emit $CO_2$ emission 2.68 kg/L and fuel consumption is 0.44 L/kWh [12]. Fig. 13 demonstrates the annual greenhouse gas emission contributed by a diesel generator. The pollution rate decreases with the increment of solar radiation because the operating period of the DG step downs. It is clearly evident that hybrid SPV/DG powered LTE cellular networks can significantly diminish carbon footprints compared to only DG enabled cellular systems and ensure better sustainability of the ICT sector through green engineering solutions.

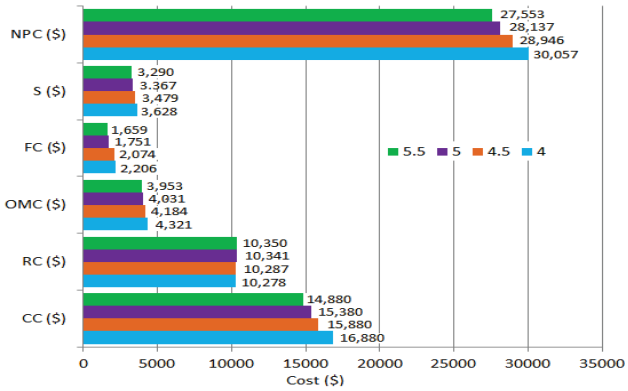


Fig. 15. Comparison of cost analysis for hybrid SPV/DG powered LTE BS with different solar radiation.

### E. Economic Analysis

The breakdown of the gross capital cost, O&M cost, replacement cost, and fuel cost incurred within the project lifetime are calculated using data from Table II. The diesel price in Bangladesh is $0.79 per liter [15]. Table VIII summarizes the cost analysis breakdown of different components of the hybrid system. However, this cost analysis can be extended for various exposure of global daily irradiation and the data presented in Table IX can be obtained similarly using Table VIII. The capital cost is paid once at the beginning of the project, is directly proportional to the size of the system. Besides, the bulk of the replacement costs goes to the components having short lifetimes such as battery bank (i.e., 6.6 years). The cost analysis breakdown discusses the nominal cash flow based on several solar radiation profiles as shown in Fig. 14.

TABLE VIII
COST ANALYSIS BREAKDOWN OF DIFFERENT COMPONENTS FOR MACRO BS WITH SOLAR RADIATION EXPOSURE OF 4.59 KWH/$m^2$/DAY

| Components | CC | RC | OMC | FC | S | NPC |
|---|---|---|---|---|---|---|
| SPV | 5,500 | 0 | 509 | 0 | 1216 | |
| DG | 660 | 0 | 627 | 1,895 | 46 | |
| Battery | 9,600 | 10,337 | 2,961 | 0 | 2,560 | **28,805** |
| Converter | 120 | 0 | 28 | 0 | 0 | |
| **Total cost** | 15,880 | 10,337 | 4,125 | 1,895 | 3,432 | |

To this end, Fig. 15 illustrates the summary of cost analysis for the entire cellular system with hybrid supplies under 15 years project lifetime. The NPC clearly decreases with increasing solar radiation due to the increase of solar energy contribution and thus, minimize the energy sharing by the DG. As a consequence, the operating period of DG decreases, resulting a noticeable amount of O&M cost reduction and also improves DG life hours.

TABLE IX
SUMMARY OF THE ECONOMIC CRITERIA FOR THE OPTIMAL HYBRID SPV/DG ENABLED POWER SYSTEM FOR LTE BS

| kWh/$m^2$/day | CC ($) | Operating ($/yr) | NPC($) | COE ($/kWh) |
|---|---|---|---|---|
| 4.0 | 16,880 | 1,424 | 30,057 | 0.36 |
| 4.5 | 15,880 | 1,412 | 28,945 | 0.35 |
| 5.0 | 15,380 | 1,379 | 28,137 | 0.34 |
| 5.5 | 14,880 | 1,369 | 27,553 | 0.33 |

## V. CONCLUSIONS

In this paper, we examined the feasibility of the incorporation of hybrid solar power system with a DG to powering off-grid cellular BSs and demonstrated the viability of the proposed system using HOMER software. The simulation results revealed that the combined SPV/DG power system could meet the BS energy requirements fully without support from the battery bank or any external retailers. The amount of surplus electricity guarantees zero outage and improves the system reliability. Moreover, the battery bank can easily feed the BS load autonomously about 2 days which is a sufficient time to fix hybrid system malfunctions. A profound impact of solar radiation variation is observed in energy yield analysis as well as cost analysis. With the increment of solar radiation, the energy produced from DG set decreases which have the positive impact of reducing the pollutant greenhouse gas emissions. Meanwhile, the overall cost of the entire system is considerably reduced due to the higher rate of solar radiation. The costs of the system should be taken into consideration while designing optimal power hybrid system, as the bulk of initial cost is higher for solar panels which tends to increase with solar panel size. Thus, this study examines the long-term energy balance among the dimension of the hybrid system, DG energy contribution, fuel consumption, cost of electricity, carbon footprints and overall system costs (NPC) with guaranteed sustainability. In summary, the proposed hybrid power system provides an increased level of reliability with lower carbon footprints and identified as an attractive long-term economical solution for LTE cellular networks.

## REFERENCES

[1] M. J. Farooq, H. Ghazzai, A. Kadri, H. ElSawy and M-S. Alouini, "A hybrid energy sharing framework for green cellular networks, *IEEE Transactions on Communications*, vol. 65, no. 2, pp. 918-934, Dec 2016.

[2] A. Jahid, A. B. Shams and M. F. Hossain, "Energy cooperation among BS with hybrid power supply for DPS CoMP based cellular networks," *IEEE International Conference on Electrical, Computer and Telecommunication Engineering (ICECTE)*, Rajshahi, Bangladesh, pp. 1-4, Dec 2016.

[3] Jahid *et. al.*, "Energy Efficiency of JT CoMP Based Green Powered LTE-A Cellular Networks," *IEEE Int. Conf. on Wireless Communications Signal Processing & Networking (WiSPNET)*, Chennai, India, Mar 2017.

[4] Rached *et. al.*, "Energy management optimization for cellular networks under renewable energy generation uncertainty," *IEEE Transactions on Green Commun. and Networking*, vol. 1, no. 2, pp. 158-166, Jun 2017.

[5] F. Ahmed, M. Naeem and M. Iqbal, "ICT and renewable energy: a way forward to the next generation telecom base stations," *Telecommunication Systems*, vol. 64, no. 1, pp. 43-56, Jan 2017.

[6] E. Oh, B. Krishnamachari, X. Liu and Z. Niu, "Toward dynamic energy-efficient operation of cellular network infrastructure," *IEEE Communication Magazine*, vol. 49, no. 6, pp. 5661, Jun. 2011.

[7] V. Chamola and B. Sikdar, "Solar powered cellular base stations: Current scenario, issues and proposed solutions," *IEEE Communication Magazine*, vol. 54, no. 5, pp. 108114, May 2016.

[8] A. Jahid, A. B. Shams and M. F. Hossain, "PV-powered CoMP-based green cellular networks with a standby grid supply," *International Journal of Photoenergy*, vol. 2017, Article ID 6189468, 14 pages, Mar 2017.

[9] Huawei Energy Efficiency Solution, "Improving energy efficiency, lower CO2 emission and TCO," White Paper, Huawei Technologies Co. Ltd., pp. 113, 2011.

[10] A. Jahid and M. S. Hossain, "Feasibility Analysis of Solar Powered Base Stations for Sustainable Heterogeneous Networks," *IEEE Region 10 Humanitarian Technology Conference*, Dhaka, Bangladesh, Dec 2017.

[11] M. H. Alsharif, R. Nordin and M. Ismail, "Energy optimization of hybrid off-grid system for remote telecommunication base stations deployment in Malaysia," *EURASIP Journal on Wireless Communication and Networking*, vol. 2015, no. 1, pages 64, Mar 2015.

[12] M. H. Alsharif and J. Kim, "Hybrid Off-Grid SPV/WTG Power system for remote cellular base stations towards green and sustainable cellular networks in South Korea," *Energies*, vol. 10, no. 1, 2017.

[13] A. Jahid, A. S. Ahmad and M. F. Hossain, "Energy efficient BS cooperation in DPS CoMP based cellular networks with hybrid power supply," *IEEE International Conference on Computer and Information Technology (ICCIT)*, pp. 93-98, Dhaka, Bangladesh, Dec 2016.

[14] Bangladesh Bank Monetary Policy. [Online]. Available: https://tradingeconomics.com/country-list/interest-rate?continent=asia

[15] Global Petrol Prices. [Online]. Available: https://www.globalpetrolprices.com/Bangladesh/dieselprices/

# Design of Efficient Triple-junction Organic Solar Cell

Md Sharjis Ibne Wadud[1], Md. Rafiqul Islam[2]
Electrical and Electronic Engineering (Khulna University of Engineering & Technology, Bangladesh)
sharjisibnewadud@gmail.com[1], mri@eee.kuet.ac.bd[2]

*Abstract*— **Organic Photovoltaics have become a promising alternative to today's silicon-based technologies with the potential of providing low-cost, large-scale production. However, Organic Solar Cells (OSC) still suffer from lower efficiencies than their inorganic counterparts due to the narrow absorption band of single cell OSC. In this work, the performance of the several active materials available for OSCs has been analyzed in search of materials having complementary absorption band to obtain better light harvest and in turns efficient tandem OSC. For the performance analysis, an analytical model for the external voltage-dependent photocurrent in Bulk Heterojunction OSCs has been used, which incorporates exponential photon absorption, dissociation efficiency of bound electron-hole pairs (EHPs), carrier trapping, and carrier drift and diffusion in the photon absorption layer. Considering current matching, the optimized thickness of the individual cells has been obtained to design better performing double and triple-cell tandem OSCs. An efficiency of 8.29% has been obtained from a double-cell (junction) OSC by series connecting P3HT:PCBM (front cell) and pBBTDPP2:PCBM (back cell). A completely new low-bandgap (1.59 eV) material has been introduced as a middle cell to design a triple-junction(cell) tandem OSC which provided a PCE of about 14%, which is a great enhancement in PCE.**

***Keywords—Triple-junction Solar Cell, Organic Solar Cell, Efficient OPV, PDTBT-TT:PC$_{71}$BM blend, Low Band Gap Polymer***

## I. INTRODUCTION

This Organic Solar Cells (OSCs), an emerging solar technology have drawn much attention during the past decade due to its low-cost solution processability, flexibility, transparency, light weight as well as considerable power conversion efficiency [1], [2]. As the name suggests, the OSCs are based on organic materials, such as polymers and small molecules, hence it is environment friendly as well as widely available. Despite of these features, OSCs couldn't outnumber conventional inorganic solar technologies due to its low efficiency. Hence increasing the efficiency of OSC is one of the major concerns. Continuous research is being performed to increase the efficiency of OSCs. Recently, the use of bulk heterojunctions (BHJ) as an active material has offered enhanced power conversion efficiency (PCE) compared to the earlier single layer or double layer structure of OSCs. Bulk heterojunction is a blend of donor-acceptor material which offers more charge separation interface then the layered structure. The blend of ploy 3-hexylthiophene-2,5-diyl (P3HT) and [6, 6]-phenyl C61-butyric acid methylester (PC$_{61}$BM) i.e. P3HT:PCBM is the one of the efficient and most extensively researched OSC which offers PCE up to 5% [3],[4]. Another prospective material is the poly [3,6-bis-(40-dodecyl- [2,20] bithiophenyl-5-yl)-2,5-bis-(2-ethyl-hexyl)-2,5 dihydropyrrole [3,4] pyrroledione] (pBBTDPP2) [5]. This narrow bandgap material covers a broad range of solar spectrum that offers an efficient light harvest. Another recently developed low-bandgap donor polymer. 3,6-dialkyl-thienothiophene and 4,7-bis(thien-2-yl)-2,1,3-benzothiadiazole (PDTBT-TT) has a bandgap of 1.59 eV with a relatively higher HOMO level of -5.27 eV. The device using PDTBT-TT as the donor gives a $V_{oc}$ in excess of 0.7 V [6].

However, most of the active materials suffer from low PCE either due to narrow absorption range that limits efficient light harvest, or due to low carrier mobility that limits efficient charge extraction. The efficiency of organic solar cells must be enhanced to sustain as a better alternative of the conventional photovoltaic technologies. Towards achieving this efficiency goal, the tandem or multijunction solar cell technology is one of the promising technologies that features the efficient use of the available solar spectrum. Tandem solar cell is a stack of two or more cells having active materials of different bandgap interconnected by recombination layer. Each individual sub-cell absorbs different part of the available solar spectrum. PCE of series connected tandem organic solar cell up to 7% has been reported yet [7].

Despite being a promising solar technology for low cost eco-friendly energy production, organic solar cell has not find its way to the market due to its low power conversion efficiency. So, there is enough scope to work on the efficiency enhancement of OSC to make it a competitive alternative to the present inorganic solar technologies. Hence, this research was devoted to model an OSC to achieve notable efficiency improvement. First of all, the performance of the single junction(cell) organic solar cells such as P3HT:PCBM, PDTBTT-TT:PC$_7$1BM and pBBTDPP2:PCBM was analyzed using an analytical model [8]. After that, the tandem of P3HT:PCBM and pBBTDPP2:PCBM was analyzed to observe the notable efficiency improvement as reported in [9]. But that even didn't capture the full spectrum to offer more power conversion efficiency. So, in order to ensure more efficient light harvest to capture the most of the available solar spectrum a triple junction tandem organic solar cell has been designed. Where three materials having complementary absorption-spectrum have been stacked together. The triple junction OSC has been designed maintaining two conditions. One is the photo current matching of the individual sub-cells and another one is the addition of the open circuit voltages of the individual sub-cells.

978-1-5386-2307-7/17/$31.00 ©2017 IEEE

## II. MODELING

### A. Single Junction Organic Solar Cells

Single junction organic solar cell consisting of the P3HT:PCBM blend as an active material is shown in Fig. 1. This is the regular geometry of organic solar cell. P3HT can absorb solar spectrum having wavelength up to 650 nm owing to its high band gap of 1.9 eV. P3HT is blended with fullerene derivative PCBM to form the bulk heterojunction where P3HT serves as donor and PCBM acts as an acceptor. P3HT: PCBM is the most extensively researched active material and is the first organic solar cell material to offer a short circuit current density, $J_{sc}$ of 8.7 mA/cm$^2$ [10]. The hole mobility of P3HT is also high which is up to 0.1 cm$^2$/Vs [11]. So, the active layer can be thick enough to facilitate better light absorption. But, the P3HT:PCBM blend has reached an efficiency limit of about 5% due to its high-lying HOMO of about 4.9 eV that gives a maximum open circuit voltage of about 0.6 V [12]. Most commonly used Hole Transport Layer (HTL) for P3HT:PCBM is PEDOT:PSS which also acts as an anode, and ZnO serves the purpose of electron transport layer (ETL).

The combination of electron-poor diketo pyrrolo-pyrrole (DPP) with electron-rich quaterthiophene (BBT) segments results in a new low bandgap organic solar cell material named as pBBTDPP2. Which has an optical band gap as low as 1.4 eV [13]. The absorbance of the pBBTDPP2:PCBM blend ranges up to 900 nm that helps to absorb the photons having longer wavelength. The active layer thickness of the blend ranges between 100 and 120 nm. An effective weight ratio of 1:2 of pBBTDPP2:PCBM has offered best results as an OSC active material. The regular structure of the pBBTDPP2:PCBM based OSC is shown in Fig. 1.

A recently developed low-band gap polymer PDTBT-TT has shown great promise in terms of power conversion efficiency. When blended with $PC_{71}BM$ it covers a wide range of spectrum with the main absorption band in the wavelength range from 600-700 nm. Fig. 4 shows the absorption spectrum of PDTBT-TT:$PC_{71}BM$. The blend of PDTBT-TT and $PC_{71}BM$ have yielded promising PCE of the highest 6.71%, [6]. PDTBT-TT forms longer and better-connected pathways when the weight ratio of PDTBT-TT:$PC_{71}BM$ blend is 1:1 for low molecular weight and 1:1.5 for high molecular weight. PDTBT-TT organic solar cells have well balanced hole to electron mobility ratio of 1.5. It also offers low charge transfer resistance and suppressed bimolecular recombination. [6].

### B. Multi-junction Organic Solar Cells

The power conversion efficiency of the single junction solar cells is low as they capture only a part of the available solar spectrum. So, incorporating several single junction solar cells by stacking them together may be an effective way to improve PCE if materials are chosen effectively so that they can capture different parts of the available solar spectrum. That is, the materials should have complementary absorption band. The active material P3HT:PCBM can absorb solar spectrum up to 650 nm leaving the lights of longer wavelengths uncaptured. That region can be partly captured by the low bandgap material pBBTDPP2:PCBM that has an extended absorption range up to 900 nm. The absorption coefficients of the two active materials are shown in Fig. 2.

The model of the double junction OSC is shown in Fig. 3 where P3HT:PCBM acts as a front cell to absorb high energy photons and pBBTDPP2:PCBM absorbs the low energy photons as a rear cell.

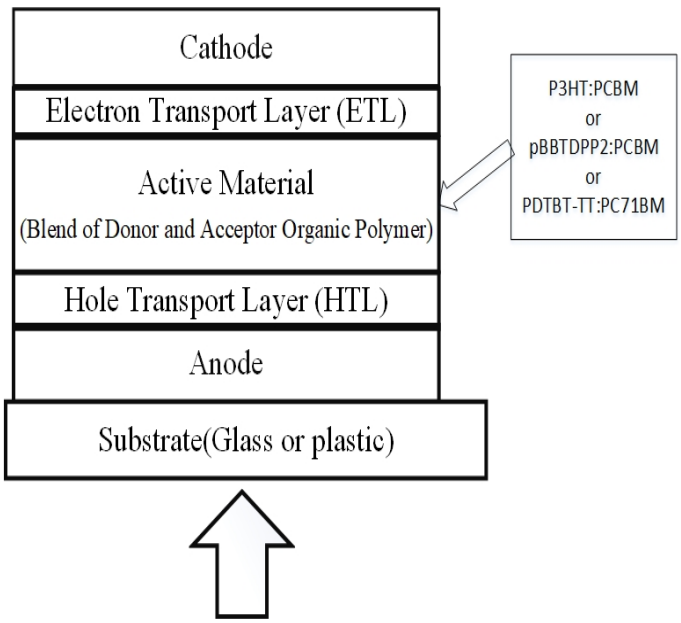


Fig. 1. Schematic of Single Junction Organic Solar Cell.

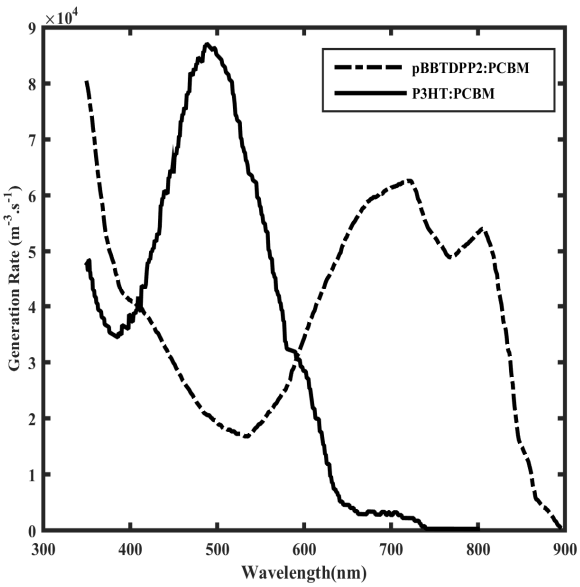


Fig. 2. The absorption coefficients of P3HT:PCBM and pBBTDPP2:PCBM

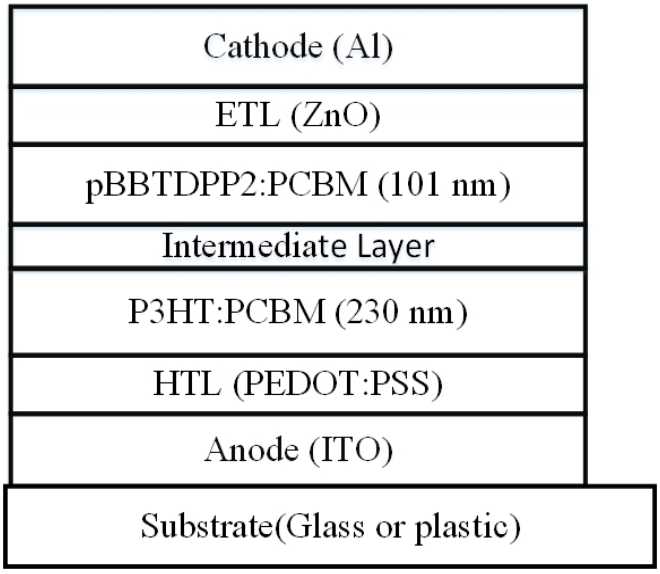


Fig. 3. Schematic of double-junction organic solar cell

From the model of double junction organic solar cell, it was observed that two materials of different bandgap cover more solar spectrum than the single junction solar cell. But still they cannot cover the maximum of the available spectrum. From Fig. 2 it is observed that P3HT: PCBM covers roughly 400 nm to 550 nm and pBBTDPP2:PCBM covers from 680 nm to 850 nm that means the generation rate is higher in this range. So, the solar spectrum in between 530 nm to 680 nm is not being captured properly by the cells. So, it is evident that another intermediate cell is needed to cover the unattained solar spectrum. To meet this necessity, extensive search for materials has been performed to find material that at least cover the solar spectrum of that uncaptured region. Finally, a material with bandgap 1.59 eV 'PDTBT-TT' has been found which not only covers the spectrum in the range of 530 nm to 680 nm but also absorbs sufficient amount of light over the available spectrum when blended with $PC_{71}BM$. The absorption coefficient and generation rate of P3HT:PCBM, pBBTDPP2:PCBM and PDTBT-TT:$PC_{71}BM$ altogether is shown in Fig. 4 and Fig. 5. Fig. 4 suggests that P3HT absorbs high energy photons of smaller wavelength, pBBTDPP2 absorbs the photons with large wavelength and the PDTBT-TT helps to absorb the photons which are not captured by the other two cells. As the high energy photons having smaller wavelength travels small distance in the active material and get absorbed near the front end, the P3HT:PCBM is employed for absorbing smaller wavelength photons as front cell.Similarly, pBBTDPP2:PCBM is employed as back cell to absorb photons of red region having larger wavelength. And the PDTBT-TT:$PC_{71}BM$ is placed in the middle. The proposed model of the triple-junction organic solar cell is shown in Fig. 6. This model offers sufficient generation over the range from 400 nm to 840 nm (Fig. 5) which will lead to enhanced power conversion efficiency. The thickness of the materials has been optimized to ensure proper current matching. The effect of intermediate layer has not been considered during performance analysis. So, intermediate layer has been taken arbitrarily. Reference [14] better explains different types of intermediate layers for OSC.

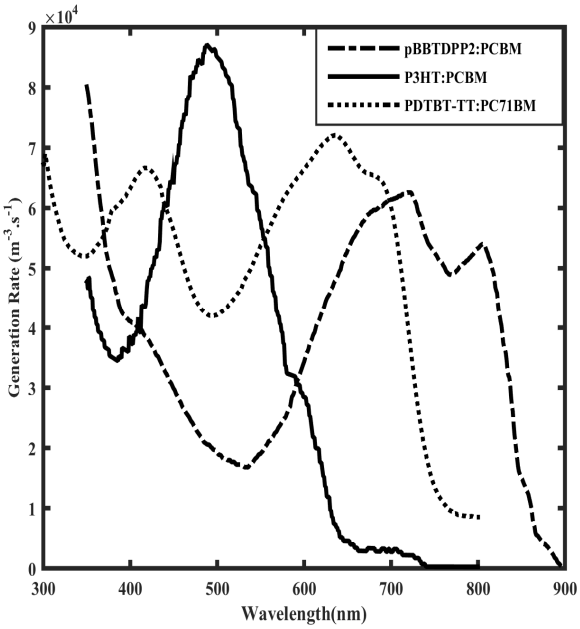


Fig. 4. Absorption coefficients of the cells used to design triple junction solar cell.

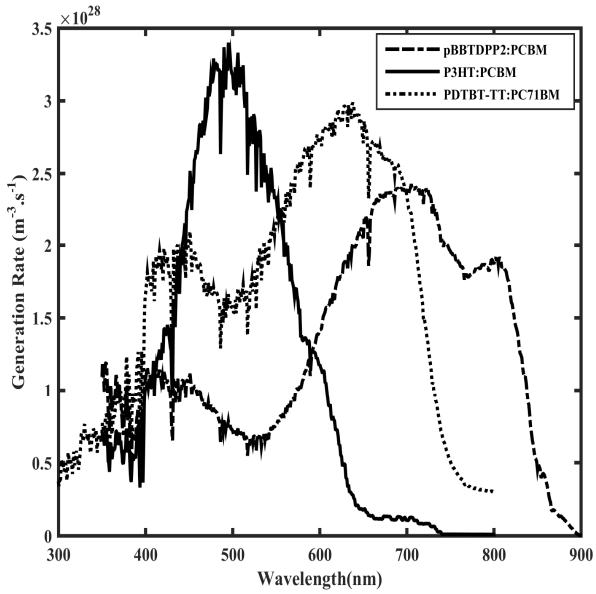


Fig. 5. Carrier generation rate of the cells used to design triple junction solar cell.

### *C. Short Circuit Current Density*

The short circuit current density, $J_{sc}$ of a tandem OSC is obtained from the photocurrent densities produced by individual sub-cell. An analytical model based on carrier continuity equation has been considered where the carrier transport through active layer depends on the electric field.

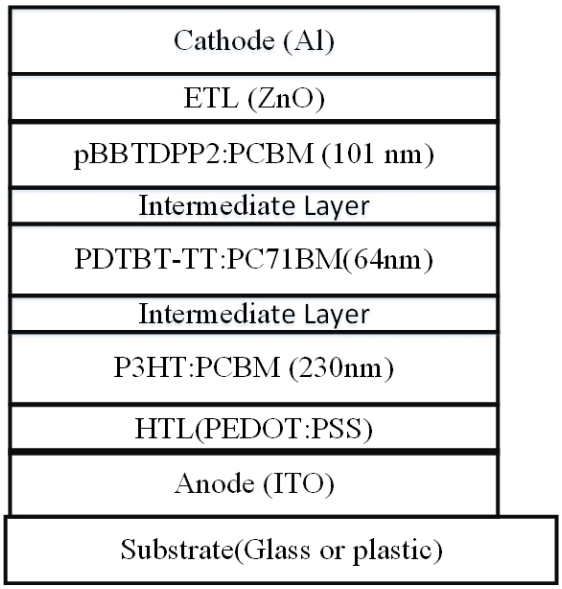


Fig. 6. Schematic of the proposed triple-junction organic solar cell

The photo current density due to the incident solar radiation can be written as [8].

$$J_{ph}(V) = \int_0^\infty \{J_p(\lambda, V) + J_n(\lambda, V)\} d\lambda \quad (1)$$

Where $J_p$ and $J_n$ denotes the photocurrent density for holes and electrons respectively.

The steady-state continuity equation for hole is

$$\frac{\partial}{\partial t}(\delta_P) = \mu_p F \frac{\partial}{\partial x}(\delta_P) + D_p \frac{\partial^2 \delta_P}{\partial x^2} + G e^{-\alpha(\lambda)x} - \frac{\delta_P}{\tau_p} = 0 \quad (2)$$

Where $\delta_p$ is photo generated hole concentration, x is the distance from the front contact along the active layer, $\mu_p$ is the hole mobility, λ is the hole lifetime, $D_p$ the hole diffusion coefficient defined by the Einstein relation, $D_p = (\mu_p K_B T)/q$. The electric field F is defined by $F = V_{bi}/T_b$, where $V_{bi}$ is the built-in potential and $T_b$ is the thickness of the blend. Solving the equation photocurrent density for hole is

$$J_p(\lambda, V) = \frac{e}{T_b}\left\{\mu_p F \int_0^{T_b} \delta_P \, dx - D_p \int_0^{T_b} \frac{\partial \delta_P}{\partial x}\right\} \quad (3)$$

where the subscript p represents holes.

Similarly, the photocurrent density for electron becomes

$$J_n(\lambda, V) = \frac{e}{T_b}\left\{\mu_n F \int_0^{T_b} \delta_n \, dx - D_n \int_0^{T_b} \frac{\partial \delta_n}{\partial x}\right\} \quad (4)$$

where the subscript n represents electrons.

### D. *Open Circuit Voltage*

The open circuit voltage of a multi-junction or multi-cell organic solar cell is considered to be equivalent to the sum of the open circuit voltages of individual sub-cells.

$$V_{oc} = \sum_{i=1}^{N} V_{oc}(i) \quad (5)$$

i = 1, 2 ……N, N is number of junction incorporated in the tandem cell.

Therefore, the open circuit voltage is given by [8]

$$V_{oc}(V) = \left(\frac{nK_B T}{q}\right) \ln\left(1 + \frac{J_{ph}}{J_0}\right) \quad (6)$$

$J_0$ is the saturation or dark current density, $K_B$ is the Boltzmann constant, T is the temperature usually taken as 300°K, q is elementary electron charge density, n is the ideality factor.

## III. Results and Discussions

Fig. 7 shows the J-V curves of P3HT:PCBM solar cell for 1 sun intensity taking the active layer thickness, $T_b$=230 nm. The value of short circuit current ($J_{sc}$) is found to be 8.216 mA/cm$^2$ and $V_{oc}$ is 0.5627V. The power conversion efficiency for 1 sun intensity is 3.37%. In this analysis, the hole and electron lifetimes have been kept fixed at $6\times10^{-5}$ s and $3\times10^{-5}$ s, respectively. The values of other fitting parameters are $\mu_p=2\times10^{-4}$ cm$^2$/Vs, $\mu_n=5\times10^{-3}$ cm$^2$/Vs, $J_0=8.76\times10^{-9}$ A/cm$^2$, n=1.58, [8]. It can be intercepted from Fig. 4 that the efficiency of P3HT: PCBM is low as it has a narrow absorption band. That is, it cannot sufficiently absorb the available solar spectrum.

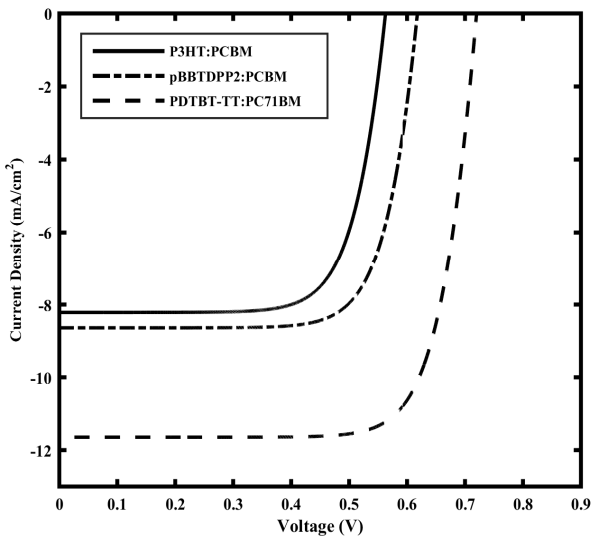


Fig. 7. J-V characteristics of P3HT: PCBM, pBBTDPP2: PCBM and PDTBT-TT:$PC_{71}$BM organic solar cell at 1 sun intensity.

Fig. 7 shows the J-V characteristics of the single junction pBBTDPP2: PCBM. It presents a $J_{sc}$ of 9.44mA/cm$^2$ and $V_{oc}$ of 0.6213 V and efficiency of 4.36% with the active layer thickness 120nm. In order to ensure the best fit with the experimental results, some parameters have been assumed with an acceptable range as the values of different fitting parameters needed for the analytical model simulation for the pBBTDPP2:PCBM based OSC is not available in literature. The electron and hole lifetimes have been kept fixed at $3\times10^{-5}$ s and $5\times10^{-5}$ s respectively, hole mobility $\mu_p=5\times10^{-4}$ cm$^2$/Vs, electron mobility, $\mu_n= 6\times10^{-3}$ cm$^2$/Vs, reverse saturation current density $J_0=2.24\times10^{-9}$ A/cm$^2$ [15]. Its offers slightly better efficiency than P3HT:PCBM cell. But the notable fact is that they separately absorb different part of the solar spectrum which makes them suitable candidate to make a double junction tandem solar cell.

The single junction solar cell PDTBT-TT:$PC_{71}BM$ presents a short circuit current density of 11.6448 mA/cm$^2$ and $V_{oc}$ of 0.7199 V with a power conversion efficiency of 6.39% at active layer thickness of 100 nm. Fig. 7 shows the performance characteristics of PDTBT-TT: $PC_{71}BM$ OSC. The fitting parameters like carrier mobility, lifetime, series and parallel resistances are obtained from literature [6]. The electron and hole mobilities are $1.5125\times10^{-4}$ cm$^2$/Vs and $2.268\times10^{-4}$ cm$^2$/Vs respectively. The electron and hole lifetimes are kept fixed at $7\times10^{-5}$ s and $9\times10^{-5}$ s. To ensure best fit with the experimental results some parameters have been assumed at an acceptable range considering P3HT:PCBM as a reference [6].

To justify the above statement P3HT:PCBM and pBBTDPP2:PCBM have been stacked together and analyzed keeping the parameters and conditions same as of the single junction cells. The double junction solar cell with a series connected 230 nm thick P3HT:PCBM front sub-cell and a 101 nm thick pBBTDPP2:PCBM back sub-cell gives a $J_{sc}$ of 8.216 mA/cm$^2$,$V_{oc}$ of 1.184 V, and PCE 8.29%. Fig. 8 shows the overall device performance considering the double junction short circuit current density and open circuit voltage. Where short circuit current density of double junction OSC is the minimum of the photocurrents of the individual cells and the open circuit voltage is the summation of the open circuit voltages of the individual cells. Current matching has been obtained to minimize ohmic loss at the intermediate layer and to hold the above statement true. The performance parameters are shown in Table I. It is evident that there is a significant improvement of PCE from 3-4 % to around 8%.

**Table I** Simulation results of power conversion efficiencies of single junction and double-junction organic solar cell based on P3HT:PCBM as front cell and pBBTDPP2:PCBM as back cell

| Organic Solar Cells | $J_{sc}$ (mA/cm$^2$) | $V_{oc}$(Volt) | PCE (%) |
|---|---|---|---|
| P3HT:PCBM | 8.216 | 0.5627 | 3.37 |
| pBBTDPP2:PCBM | 9.44 | 0.6213 | 4.36 |
| Double Junction | 8.216 | 1.184 | 8.29 |

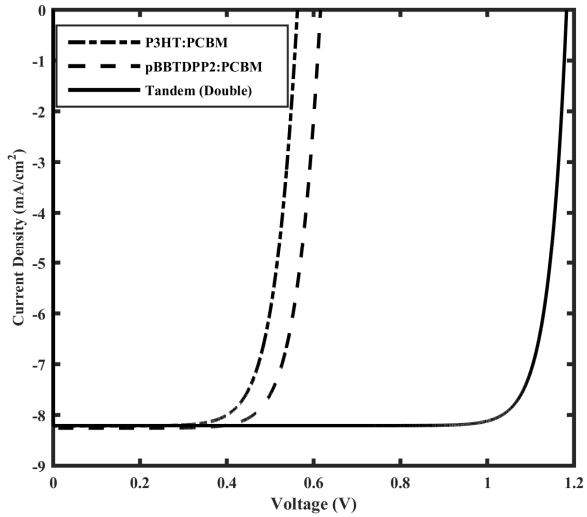


Fig. 8. J-V characteristics of double junction organic solar cell (P3HT:PCBM as front cell and pBBTDPP2:PCBM as back cell)

But there still remains available solar spectrum which is not captured by the two cells of double junction solar cell. The spectrum between 530 nm and 680 nm is not being properly absorbed to give rise to sufficient generation of carriers as shown in Fig. 2. For this reason extensive material search has done and a mid-bandgap material PDTBT-TT:$PC_{71}BM$ was found suitable for capturing the solar spectrum of that region. Fig. 7 shows that incorporation of a mid-bandgap material PDTBTT-TT helps to capture the spectrum between 530 nm and 680 nm. Which ensures more efficient light harvest covering almost the whole visible spectrum 350 nm to 860 nm. While modelling the triple junction organic solar cell it was assumed that ohmic losses in recombination layer is negligible and the recombination layers offer uniform transmittance and negligible reflection of light. To minimize the ohmic loss at the intermediate layer due to the mismatch of photo current, current matching among the cells was obtained so that all individual cells provide equal amount of current in a series connected triple junction solar cell. To obtain proper current matching, the well-established active material P3HT:PCBM has been considered as the reference , which offers a short circuit current density of 8.216 mA/cm$^2$ though utilizes a relatively large thickness of 230 nm. To match the current density of the other cells with the $J_{sc}$ of 8.216 mA/cm$^2$, the thickness of the pBBTDPP2:PCBM and PDTBT-TT:$PC_{71}BM$ has been tuned. The short circuit current of pBBTDPP2:PCBM which closely matches with the $J_{sc}$ of P3HT is found to be 8.261 mA/cm$^2$ at an active layer thickness of 101nm . And for PBTBT-TT:$PC_{71}BM$ matched current density 8.207 mA/cm$^2$ has been obtained at an active layer thickness of 64 nm. So, the proposed triple junction solar cell as shown in Fig. 6 has been designed considering the complementary absorption band matching and optimizing the active layer thickness of the sub-cells for proper current matching. And it has presented a short circuit current density of 8.207 mA/cm$^2$, the minimum among

**Table II** Simulation results of power conversion efficiencies of Single-junction, Double-junction and the proposed Triple-junction OSC**.**

| Organic Solar Cells | Jsc (mA/cm2) | Voc (Volt) | PCE (%) |
|---|---|---|---|
| P3HT:PCBM | 8.216 | 0.5627 | 3.37 |
| pBBTDPP2:PCBM | 9.44 | 0.6213 | 4.36 |
| PDTBT-TT:PCBM | 11.6448 | 0.7199 | 6.39 |
| Double-Junction (Fig. 3) | 8.216 | 1.184 | 8.29 |
| Triple-Junction (Fig.6) | 8.207 | 1.9 | 14.02 |

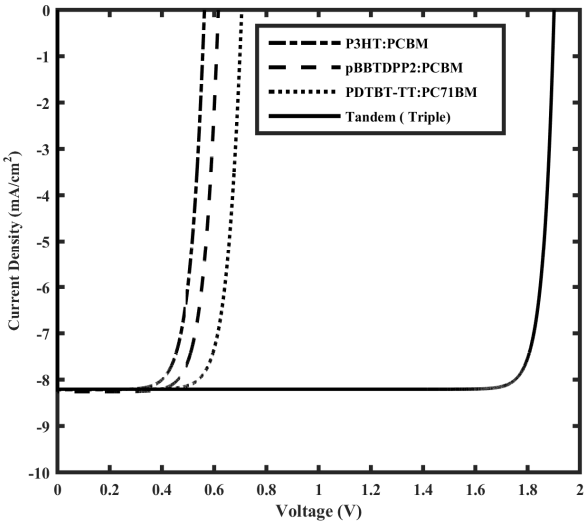


Fig. 9 J-V characteristics of the proposed Triple-junction Organic Solar Cell along with the sub-cells.

the matched currents and $V_{oc}$ of 1.9 V with an immense improvement in power conversion efficiency of 14.02%. To the best of our knowledge, this represents the highest efficiency in the organic photovoltaic field. The performance characteristics curve of the triple junction solar cell is shown in Fig. 9. The performance parameters of the organic solar cells have been tabulated in Table II.

## IV. Conclusions

The lower efficiency of single junction organic solar cells is attributed by the inefficient light harvesting due to narrow solar spectrum absorption band. This problem has been effectively addressed and a high efficiency triple junction organic solar cell has been designed. The proposed triple junction solar cell employs large, mid and small bandgap organic material having complementary absorption band. That ensures efficient light harvesting by the organic solar cell resulting in efficiency as high as 14.02% which is a great enhancement of power conversion efficiency. The optimized design of the triple junction solar cell has been obtained by proper current matching among the sub-cells that has been achieved by effectively tuning the thickness of the middle and the back sub-cell taking the current density of the front cell P3HT:PCBM as a reference. The optimized device demonstrates short circuit current density, $J_{sc}$ of 8.207 mA/cm$^2$ along with a $V_{oc}$ of 1.9 V under 1 sun intensity. In conclusion, the proposed design could be one the best possible ways to achieve efficient organic solar cell.

## References


[1] P. Peumans, A. Yakimov, and S. R. Forrest, “Small molecular weight organic thin-film photodetectors and solar cells,”J. Appl. Phys., vol. 93, no. 7, pp. 3693–3723, Jul. 2003.

[2] N. S. Sariciftci, L. Smilowitz, A. J. Heeger, and F. Wudl,“Photoinduced electron transfer from a conducting polymer to buckminsterfullerene,” Science, vol. 258, no. 27, pp. 1474–1476, Nov. 1992.

[3] S. H. Park, A. Roy, S. Beaupre, S. Cho, N. Coates, J. S. Moon, D. Moses, M. Leclerc, K. Lee, and A. J. Heeger, “Bulk heterojunction solar cells with internal quantum efficiency approaching 100%,” Nat. Photonics 3, 297 (2009).

[4] Florent Monestier, Jean-Jacques Simon, Philippe Torchio, Ludovic Escoubas, Franc ois Flory, Sandrine Bailly, Remi de Bettignies, Stepene Guillerez, Christophe Defranoux, “Modeling the short-circuit current density of polymer solar cells based on P3HT:PCBM blend,” Elsevier doi: 10.1016/j.solmat.2016.10.019.

[5] M. M. Wienk, M. Turbiez, J. Gilot and R. A. J. Janssen, Adv. Mater, 20, p.2556 (2008).

[6] X. Li, X. Tang, F. Wang, V. Chellappan, "Investigations of a new high-performance low-band-gap photovoltaic polymer semiconductor", IEEE J. Photovolt., vol. 6, no. 3, pp. 696-704, May 2016.

[7] V. S. Gevaerts, A. Furlan, M. M. Wienk, M. Turbiez and R. A. J. Janssen, Adv. Mater., 2012, 1–5.

[8] Salman M. Arnab, M. Z. Kabir, “An analytical Model for analyzing the current-voltage characteristics pf bulk heterojunction organic soalr cells,” J. Appl. Phys., 115, 035404 (2014).

[9] N. Karim, F.I. Mime, M.R. Islam, and I.M. Mehedi, “Tandem Organic Solar Cells with Improved Efficiency,” in *Proc. IEEE Int. Conf. ECCE.*, Feb. 2017, pp. 5126–5131.

[10] P. Schilinsky, C. Waldauf, and C. J. Brabec, “Recombination and loss analysis in polythiophene based bulk heterojunction photodetectors,” Appl. Phys. Lett., vol. 81, no. 20, pp. 3885–3887, Nov. 2002.

[11] H. Sirringhaus et al., “Two-dimensional charge transport in self organized, high-mobility conjugated polymers,” Nature, vol. 401, pp. 685–688, 1999.

[12] J.-J. Yun et al., “Chlorophyll-layer-inserted poly(3-hexyl-thiophene) solar cell having a high light-to-current conversion efficiency up to 1.48%,” Appl. Phys. Lett., vol. 87, no. 12, pp. 123102, Sep. 2005.

[13] Ikerne Etxebarria, Jon Ajuria, Roberto Pacios, “Polymer:fullerene solar cells: materials, processing issues, and cell layouts to reach power conversion efficiency over 10%, a review,” J. Photon. Energy. 5(1), 057214 (Feb 16, 2015). doi:10.1117/1.JPE.5.057214.

[14] Yuan, Y., Huang, J. & Li, G. (2011). Intermediate Layers in Tandem Organic Solar Cells. Green, 1(1), pp. 65-80. Retrieved 17 Nov. 2017, from doi:10.1515/green.2011.009

[15] Chunfu Zhang, Yue Hao, Dazheng Chen, Zhizhe Wang and Zhenhua Lin, “Investigation of Organic Bulk Heterojunction Solar Cells from Optical Aspect”, http://dx.doi.org/10.5772/52819.

# Device Modeling and Numerical Simulation of Highly Efficient Gallium Arsenide Solar Cells

Mrinmoy Dey[1,2*], Nazia Rahman[1], Iffat Tasnim[1], Rishita Chakma[1], Maitry Dey[1,2], N. K. Das[1,2], A. K. Sen Gupta[1,2], M. A. Matin[1,2] and Nowshad Amin[3,4]

[1]Department of Electrical and Electronic Engineering, Chittagong University of Engineering and Technology, Chittagong-4349, Bangladesh

[2]Renewable Energy Laboratory (REL), Chittagong University of Engineering and Technology, Chittagong-4349, Bangladesh

[3]Solar Energy Research Institute (SERI), The National University of Malaysia, 43600 Bangi, Selangor, Malaysia

[4]Department of Electrical, Electronic and Systems Engineering, The National University of Malaysia, 43600 Bangi, Selangor, Malaysia

*mrinmoycuet@gmail.com

*Abstract*— **Gallium Arsenide (GaAs) has recently drawn the attention of researchers because of its' several unique advantages. It is lightweight, flexible and has a band gap of 1.42 eV which is both wide and direct. Subsequently, it can absorb more photons and obtain high power conversion efficiency. A simple and new structure of GaAs solar cell with Cadmium Sulfide (CdS) as buffer layer is proposed in this research work which is numerically analyzed by AMPS-1D software. The main purpose is to reduce the cost of fabrication by using lesser material. In this research work, an efficiency of 24.20% (Jsc = 26.24 mA/cm², FF = 0.89, Voc=1.04 V) has been found. Moreover, the attenuation of the normalized efficiency of the proposed model is observed with the increase of operating temperature, thermal stability of the GaAs solar cell has been analyzed and found that the temperature gradient is -0.043%/°C.**

***Keywords— GaAs solar cell; CdS buffer layer; reduced cost, photon absorption; Thermal stability.***

## I. INTRODUCTION

To meet the demand of excessive population, more energy is required. This energy is continuously produced from different natural resources such as coal, oil, gas etc. Coal is used to produce 28% of the total energy required for the world [1]. If it continues then one day this source will be exhausted. This condition is similar for other fossil fuels. These fossil fuels are not only rapidly depleting but also result in irreversible climate change by emitting different greenhouse gases. So, it is necessary to find out alternative sources of energy and one of the hopeful solutions found for the global energy crisis is solar energy. Among different renewable energy, solar energy is the most authentic and profuse source because of its' some unique advantages such as it is pollution free, cost effective and sustainable. More energy from the sun falls on the earth than is used by everyone in the world in one year.

Thin film solar cell is both trifling and whippy so researchers now are more interested to develop solar cell with it. Among different thin film materials, GaAs has become a good competitor because of its unique property and higher power conversion efficiency than others. It is an important semiconductor material in thin film solar cell market which is used for both single crystalline and multi crystalline solar cell.

Global production of PV cells was increased from 12.3 GW to 20 GW in one year difference in 2009 [2, 3]. Different types of solar cell are recently designed and developed with Si, thin film and organic materials. But it will be economical only when cost can be deduced to $0.33 per watt peak according to US Department [4]. The base of solar cell had been made about 175 years ago by Alexandre Edmond Becquere by observing the PV effect by an electrode in a conductive solution. After that, it is continuously being developed day by day. The 1st hetero-structure of GaAs was developed by the team of Zhores Alferov in the USSR in 1970 [5, 6, 7]. At first, the highest efficiency was achieved by using crystalline silicon in the early 1980s. As the time passes GaAs solar cell took this place because of its unique property in the early 1990s. It was mainly suitable for satellite applications. Subsequently, Ge and InGaP materials were used with GaAs to develop dual and triple-junction solar cell. The highest efficiency recorded for GaAs based single junction solar cell is 28.8% [8]. To achieve higher efficiency photon recycling method was developed in the thin film design [9]. Alta device Inc. fabricated 27.6% efficient GaAs single junction solar cell which is practically feasible [10]. Many other numerical analysis of GaAs solar cell both single and multi-junction had been carried out using AMPS-1D software. Among them in 2013, graded and non-graded AlGaAs was used as buffer layer with GaAs absorber layer and efficiency was improved by 3.8% with graded interface [11]. Then, a new model of GaAs solar cell with Graphene as buffer layer is simulated and 14.46% conversion efficiency was achieved in 2014 [12]. In the same year, tunnelling of cascaded GaAs with Ge was simulated using the same software and 33.5% efficiency was obtained [13]. Recently in 2017, a comparison of dual and triple-

junction herero-structure of GaAs solar cell was investigated using TCAD silvaco software. It was found that for dual-junction 23.33% and for triple-junction 32.11% efficiency was achieved [14].

In this research work, numerical analysis has been performed using AMPS-1D software to analysis different parameters such as thickness of absorber layer, temperature, doping concentration, lifetime etc,. All these parameters are investigated to obtain higher performance of GaAs solar cell.

## II. MODELING AND SIMULATION

Structural diagram of the proposed cell CdS/GaAs is given in Fig. 1 and this cell is numerically analysed by using AMPS-1D software for the purpose of modelling. In the AMPS-1D software, lifetime model is used among two different approaches of device modelling: DOS model. A 60 nm buffer layer (CdS) is designed with a 1 µm absorber layer thickness of GaAs solar cell.

In the proposed model, CdS is used as buffer layer because it can be deposited as intermediate layer to improve the interface properties [15]. CdS is considered one of the best materials among possible alternative buffer layers having a higher band gap of 2.3 eV. Because of this higher band gap, light absorption can be increased in the absorber layer by transmitting higher energy photons in the conduction band. If isolation cannot be created properly between TCO and absorber layer then it arises shunt problem. Besides, when it is used as buffer layer it increases the shunt resistance which results the increase of the open circuit voltage and power conversion efficiency. Moreover, it has a higher current density due to thinner thickness which improves the efficiency by around 6.1% with less demand of material. In the early of 2001, CdS was used with CdTe to form hetero-structure and obtained efficiency upto 16.5% in the lab scale [16]. On the contrary, in the proposed model GaAs solar cell is used as absorber layer instead of CdTe material. This model improves the efficiency to 24.20 %.

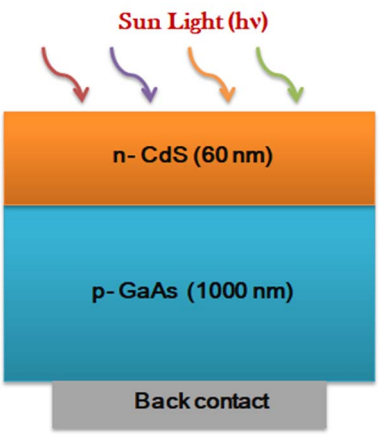


Fig.1: Schemed model of GaAs solar cell

The material parameters of CdS and GaAs found from data base value, hypothesis value and in some cases from approximation from literature review are given in Table I.

TABLE I. MATERIAL PARAMETERS OF THE SCHEMED MODEL OF SOLAR CELL USED IN SIMULATION

| Parameters | n-CdS | p-GaAs |
|---|---|---|
| Band gap (eV) | 2.80 | 1.42 |
| Electron mobility ($cm^2/Vs$) | 350 | 8500 |
| Hole mobility ($cm^2/Vs$) | 50 | 400 |
| Carrier concentration ($cm^{-3}$) | $1\times10^{17}$ | $1\times10^{17}$ |
| Density of state in conduction band ($cm^{-3}$) | $1.8\times10^{19}$ | $4.77\times10^{17}$ |
| Density of state in valence band ($cm^{-3}$) | $2.4\times10^{18}$ | $9\times10^{18}$ |
| Permittivity | 9 | 12.90 |
| Electron affinity (eV) | 4.50 | 4.07 |
| Thickness (nm) | 10-100 | 500-3000 |

From the numerical analysis, GaAs solar cell with 24.20 % power conversion efficiency, 1.04 V open circuit voltage (Voc), 26.24 mA/cm² short circuit current density (Jsc) and 0.89 fill factor (FF) are found.

## III. RESULT AND DISCUSSION

### A. *Event of GaAs Layer Thickness*

The proposed model has been numerically analysed and the effect of absorber layer thickness on cell efficiency and other parameters has been observed. From the Fig. 2, it can be seen that cell performance parameters are improving with the increasing of the layer thickness of absorber layer which depicts the performance of solar cell in response to the improve of absorber layer thickness.

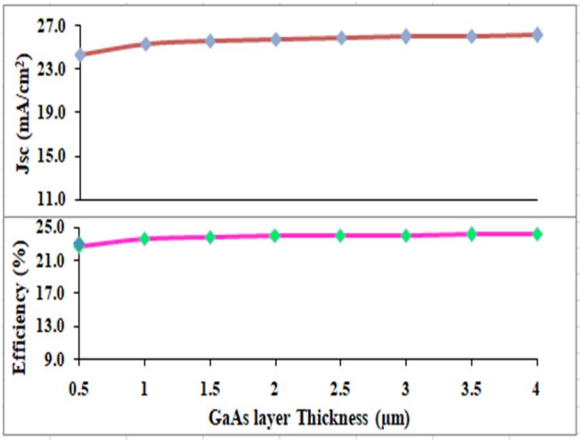


Fig. 2 Variation of GaAs thickness with efficiency and current density

From Fig. 2, it can be seen that efficiency and current density are increased upto 1500 nm and then after a certain thickness of absorber layer, the performance is almost constant. To reduce the fabrication cost and considering the material preservation 1000 nm is taken as optimum thickness to investigate the performance of GaAs solar cells.

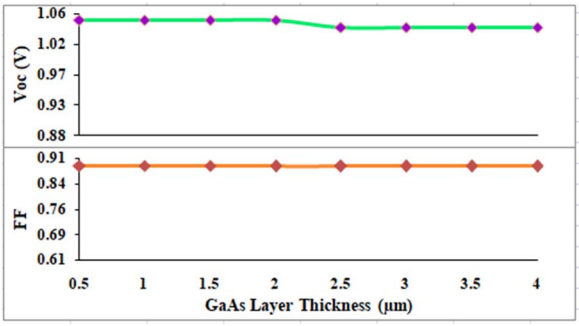


Fig. 3 Variation of GaAs thickness with fill factor and Voc

Fig. 3 shows the performance of GaAs solar cell with the increase of absorber layer thickness. The cell performance parameter *Voc* remains constant upto 2000 nm and after that then decreases slightly with constant magnitude of open circuit voltage whereas fill factor remains constant.

### *B. Event of Doping Concentration*

In the proposed model, doping concentration is selected for GaAs absorber layer is p type which is examined from $1\times10^{12}$ to $1\times10^{17}$ $cm^{-3}$. From Fig. 4, it is observed that conversion efficiency has an increasing trend after $1\times10^{13}$ $cm^{-3}$ but current density remains constant.

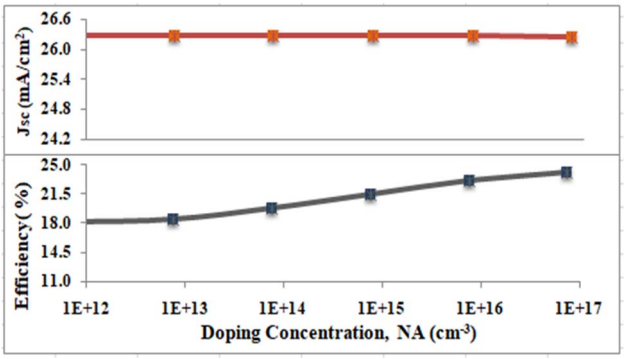


Fig.4 Event of doping concentration on Jsc and efficiency

With the increasing doping concentration, the reverse saturation current decreases leading to an increase of open circuit voltage which consequently increase the power conversion efficiency. This increasing trend remains until the reverse effect of high doping concentration is observed which means reduction of band-gap and minority carrier lifetime. So, $1\times10^{17}cm^{-3}$ is taken as optimum level of doping concentration.

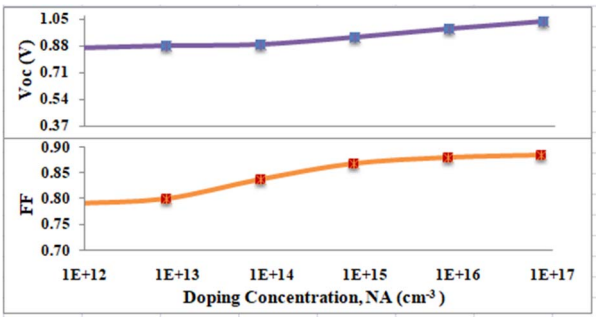


Fig. 5 Event of doping concentration on FF and Voc

FF shows an increasing nature after a certain amount of doping concentration like as efficiency curve and Voc has an increasing trend with the doping concentration. So, by observing the output of Fig. 4 and Fig. 5, an improved performance is achieved at $1\times10^{17}$ $cm^{-3}$ doping concentration.

### *C. Event of Temperature*

To check the performance of the cell at higher temperature and to find thermal stability, numerical analysis is carried out by varying the temperature from 20°C to 100°C. Generally, with the increase of temperature band-gap reduces and excessive heat is produced which shows a negative effect towards the performance of the cell.

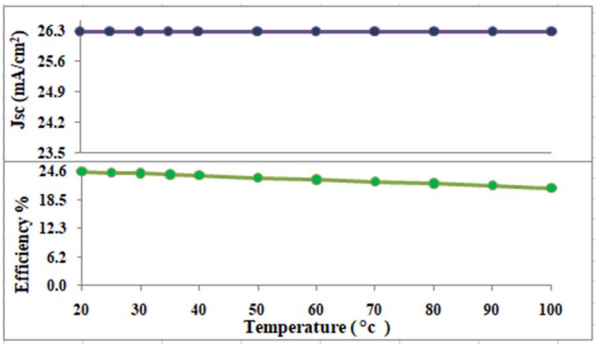


Fig.6 Event of temperature variation on efficiency And Jsc

By observing the performance of GaAs solar cell with numerical analysis result from Fig. 6 and Fig. 7, it is found that conversion efficiency, open circuit voltage and fill factor are proportionally decreased but current density remains constant.

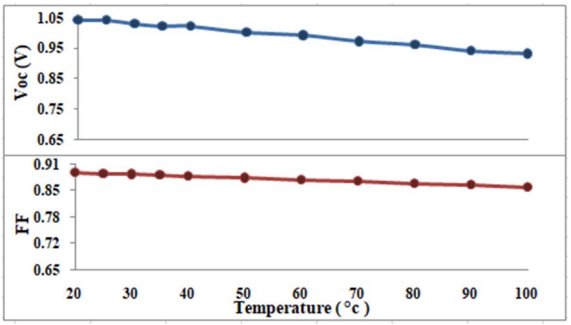


Fig.7 Event of temperature variation on FF and Voc

From Fig. 7, it is seen that the higher cell conversion of GaAs solar cell is found at 20°C. But by considering the ambient condition, it is kept at 25°C and the temperature coefficient (TC) is -0.043%/°C in GaAs solar cell that shows better thermal stability.

### *D. Event of Lifetime*

To find out the performance of GaAs solar cell, lifetime is varied from 10 ns to 100 ns in order to investigate cell performance parameters. The increased in minority carrier lifetime reduces the recombination rate which in turn improves the overall cell performance through improving the cell performance parameters.

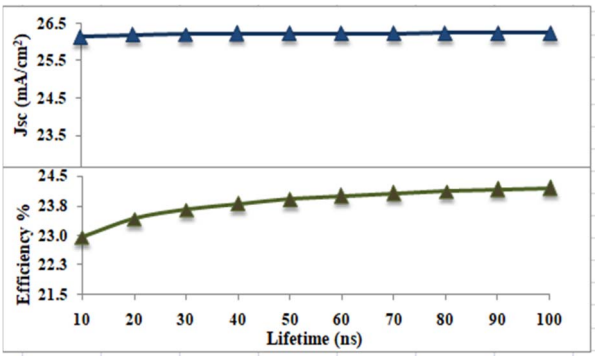


Fig. 8 Event of lifetime variation on Efficiency and Jsc

Fig. 8 shows that power conversion efficiency is increased in proportion with the increase of lifetime whereas short circuit current density remains constant.

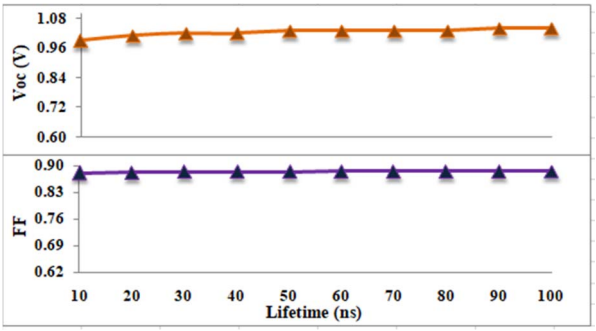


Fig. 9 Event of lifetime variation on Voc and FF

The J-V characteristics curve is shown in Fig. 10 and it can be seen that current density is approximately constant up to 0.98 V and then suddenly drops to zero for maximum value of open circuit voltage whereas maximum current density is found at zero open circuit voltage.

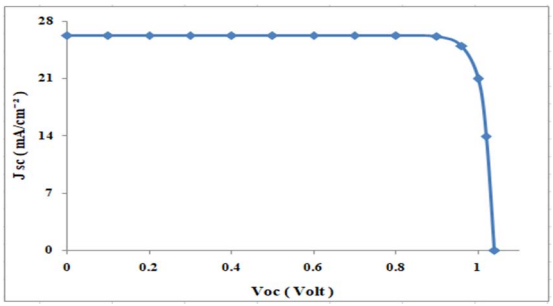


Fig.10 J-V characteristics curve of proposed GaAs cell

## IV. Optimized Results

The performance of the optimized GaAs solar cell consists of 1 µm thickness of absorber layer along with 60 nm thickness of CdS layer. The result of the optimized cell is shown in Table II.

TABLE II OPTIMIZED RESULT OF THE SCHEMED CELL

| *Jsc* (mA/cm$^2$) | Efficiency (%) | FF | Voc ( V) |
|---|---|---|---|
| 26.24 | 24.20 | 0.89 | 1.04 |

## V. Conclusion

The potential buffer layer material CdS with GaAs absorber layer is simulated and investigated using AMPS-1D software and a cost effective efficiency is obtained for 1000 nm GaAs absorber layer and 60 nm CdS buffer layer. It is found that the best conversion efficiency is 24.20 % (*Jsc* = 26.24 mA/cm$^2$, FF = 0.89, *Voc* = 1.04 V). The temperature coefficient of the proposed cell was found -0.043%/°C.


## Acknowledgment

This work has been supported by the Department of Electrical and Electronic Engineering (EEE) and Renewable Energy Laboratory (REL), Chittagong University of Engineering and Technology (CUET), Bangladesh.


## References


[1] Ideas for an Essay on Renewable Energy or Alternative Energy Essay Posted on July 23, 2012 by Essay Shark.

[2] W. P. Hirshman, "Surprise, surprise (cell production 2009: survey)," *Photon International*, pp. 176–199, 2010.

[3] A. Sharma, "PV demand database—quarterly," *IMS Research*, 2011.

[4] T. P. Kimbis, "Solar energy technology program," *US Department of Energy,* 2011.

[5] Alferov, Zh. I., V. M. Andreev, M. B. Kagan, I. I. Protasov and V. G. Trofim, ''Solar-energy converters based on p-n AlxGa1−xAs-GaAs heterojunctions,'' Fiz. Tekh. Poluprovodn, 1971.

[6] Nanotechnology in energy applications. im.isu.edu.tw. 16 November 2005.

[7] Nobel Lecture by Zhores Alferov at nobelprize.org

[8] E. Yablonovitch, O. D. MilleR, S.R. Kurtz, "The opto-electronic physics that broke the efficiency limit in solar cells," *38th IEEE Photovoltaic Specialists Conference,* 2012.

[9] Wang, X.; et al. "Design of GaAs Solar Cells Operating Close to the Shockley–Queisser Limit," *IEEE Journal of Photovoltaics,* vol.3*, no.*2, pp. 737, 2013.

[10] Brendan M. Kayes, Hui Nie, Rose Twist, Sylvia G. Spruytte, Frank Reinhardt, Isik C. Kizilyalli, and Gregg S. Higashi, "27.6% Conversion efficiency, a new record for single-junction solar cells under 1 sun illumination," *Photovoltaic Specialists Conference (PVSC), 37th IEEE,"* vol.11, pp.000004-000008, 2011.

[11] Hassane Ben slimane1, B. Dennai, A. Helmaoui, "Numerical simulation of graded band gap GaAs/AlGaAs heterojunction solar cell by AMPS-1D," *Advances in Physics Theories and Applications,* vol. 22, 2013.

[12] S. J. Gong, Q. C. Peng and X. W. Zhao, "Simulation of graphene-GaAs schottky barrier solar cell with AMPS-1D," *Materials Research Innovations,* vol. 19, 2015.

[13] Benmoussa Dennai, H. Ben Slimane, A. Helmaoui, "Simulation of Tunnel Junction in Cascade Solar Cell (GaAs/Ge) Using AMPS-1D," *JOURNAL OF NANO- AND ELECTRONIC PHYSICS,* vol. 6**,** no. 4, 2014.

[14] F. Djaafar, B. Hadri, G. Bachir, "Comparison between the Efficiency of Heterojunction Thin Film InGaP\GaAs\Ge and InGaP\GaAs Solar Cell," *International Journal of Electrical, Computer, Energetic, Electronic and Communication Engineering*, vol.11, no.3, 2017.

[15] Ashrafalsadat S. Mirkamali1 and Khikmat Kh. Muminov, "Simulation of the Efficiency of CdS/CdTe Tandem Multi-Junction Solar Cells," *Journal of Optoelectronical Nano Structures,* vol. 2, no. 2, pp. 13-24, 2017.

[16] X. Wu, J. C. Keane, R. G. Dhere et al., "16.5%-efficient CdS/ CdTe polycrystalline thin-film solar cells," *Proceedings of the 17th European Photovoltaic Solar Energy Conference and Exhibition (PVSEC '01)*, pp. 995–1000, 2001.

# Design and Implementation of Protective Relay Testing Device Using Microcontroller and Servo-Motor

Md. Shamim Rahman[1], Nazmus Saqib[2], Sarafat Hussain Abhi[3] and S. M. Ishraqul Huq[4]
[1,2,3]European University of Bangladesh (EUB), Bangladesh
[4]Ahsanullah University of Science and Technology (AUST), Bangladesh
[1]shamim.ruet.93@gmail.com, [2]nazmussaqib7@gmail.com, [3]sarafat.rueteee@gmail.com, [4]ishraqulhuq.eee@aust.edu

***Abstract*—One of the major elements in power system protection is a protective relay. Prior to its installation and continuous use in the system, the relay needs to be tested accurately. Many capable devices are available in the market for this purpose which are costly. In this paper, a cost-efficient relay testing device is designed and implemented using microcontroller and servo-motor. The device is capable of accurately testing a protective relay in system frequency for under-voltage and over-voltage conditions with a maximum error of 2%.**

***Keywords—Protective relay; over-voltage; under-voltage; time-test; microcontroller; servo-motor.***

## I. INTRODUCTION

Protective relays are frequently found device in high voltage or medium voltage power system. Their main duty is to isolate a faulty section within few cycles by ensuring minimum interruption to healthy sections [1]. Therefore an ideal relay is a unit which is cost effective and performs correctly as its setting. With usage the connections of relay gets deteriorated or contaminated with carbon particles, etc. Properly working protection devices help to maintain the safety of the system and to safeguard assets from damage. In order to ensure reliable operation, protective relays as well as re-closer controls must be tested throughout their life-cycle, from their initial development through production and commissioning to periodical maintenance during operation.

Basic connections of a protective relaying system is shown in Fig. 1. The protective relay detect the abnormal conditions in the electrical circuits by constantly measuring the electrical quantities which are different under normal and fault conditions. Whenever a fault occurs on the feeder, the current transformer (CT) transmits the fault current to current coil of the protective relay and the potential transformer (PT) transmits the voltage under fault conditions to the potential coil of the relay, if the relay is a two quantity relay. Thus the relay operates and closes the trip circuit of the breaker.

There are different methods of testing a relay, depending on the availability of equipment. These methods include steady-state, dynamic-state and transient tests [2]. In our device, we incorporated the steady-state method, which is usually for checking the relay pick-up. Injected current, voltage or frequency is held at predetermined value for duration longer than the planned time for relay. Then the parameter is varied gradually at a rate much smaller than the resolution of relay, either manually turning a knob or by an automated system.

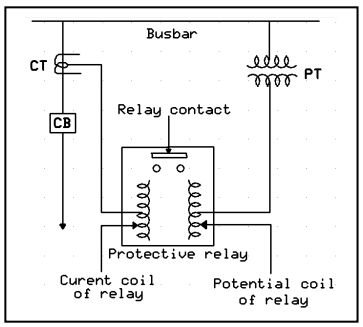


Figure 1. Basic Protective relay system.

There are two testing principles which can be followed to test a relay: primary injection and secondary injection [3]. Primary injection involves relay unit to be disconnected from the system, and a high voltage (or current) is injected to the primary of PT (or CT). For the secondary injection principle, the relay is disconnected from the PT and CT and the stepped-down voltage (or current) is directly injected to the relay. We selected the secondary injection principle to test the relay, for which a stepped-down variable voltage is generated using variable autotransformer.

In this paper, we designed a relay testing device to test the performance of a protective relay for over-voltage and under-voltage conditions. We also carried out a time test for the relay where it was allowed to run on over-voltage condition for a fixed duration. Our objective is to design a cost-efficient device which can accurately test the performance of a relay for voltage instability. The following section discusses the overall system and working principle of the device. Section III depicts the system circuit and section IV discusses the results of the test. Finally, section V concludes the paper.

## II. SYSTEM MODEL AND METHODOLOGY

The overall system layout is shown in Fig. 2. Block diagram of the system model can be divided into three parts:

a. Main power supply
b. Main working circuit

978-1-5386-2307-7/17/$31.00 ©2017 IEEE

c. Auxiliary DC power supply

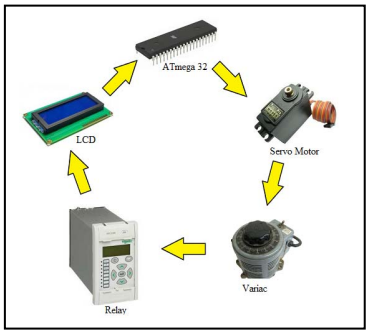


Figure 2. System Layout

## A. Main Power Supply

The main power supply consists of a step-down transformer, a bridge rectifier and filtering capacitor, and three levels of voltage regulator: 5V, 6V and 12V. The 5V powers the microcontroller, LCD, buttons and other peripherals. The 6V powers the servo-motor and the 12V powers the miniature relay inside the device.

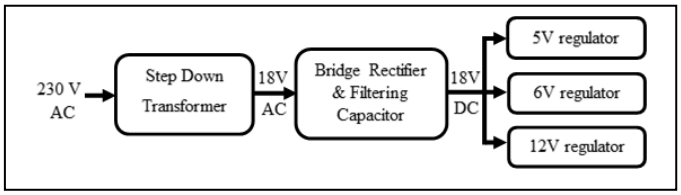


Figure 3. Block diagram of the main power supply circuit.

## B. Main Working Circuit

The main working circuit consists of all the main components of the device i.e. microcontroller, servo-motor, variac, gear system, input buttons, LCD, etc. Buttons are for inputting operating commands and changing parameter values like set voltage, set time, tolerance, etc. Microcontroller is the brain of the system which controls the servo-motor. The servo-motor is connected with the variac through gear mechanism which can control the applied voltage to the testing terminal of the protective relay. A feedback path sends the final applied voltage value and a separate path sends a trip signal to the microcontroller after which the result is displayed in the LCD.

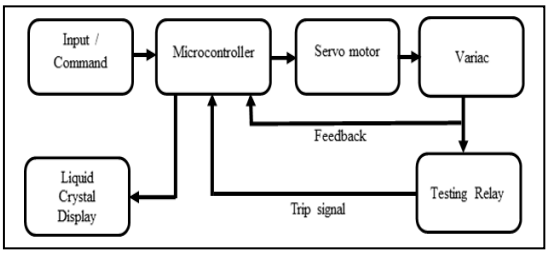


Figure 4. Block diagram of the main working circuit.

## C. Auxiliary Power Supply

The auxiliary power supply consists of a 230/110V step-down transformer, bridge rectifier and a filtering capacitor. The output DC voltage powers the relay to be tested.

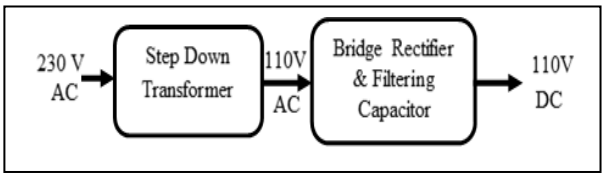


Figure 5. Block diagram of the auxiliary power supply.

## D. Program Flow Charts

The device mainly has four modes of operations: automatic over-voltage test mode, automatic under-voltage test mode, manual voltage test mode and automatic time test mode. The algorithm or program that the four modes of operation follow are shown using flow charts in Fig. 6.

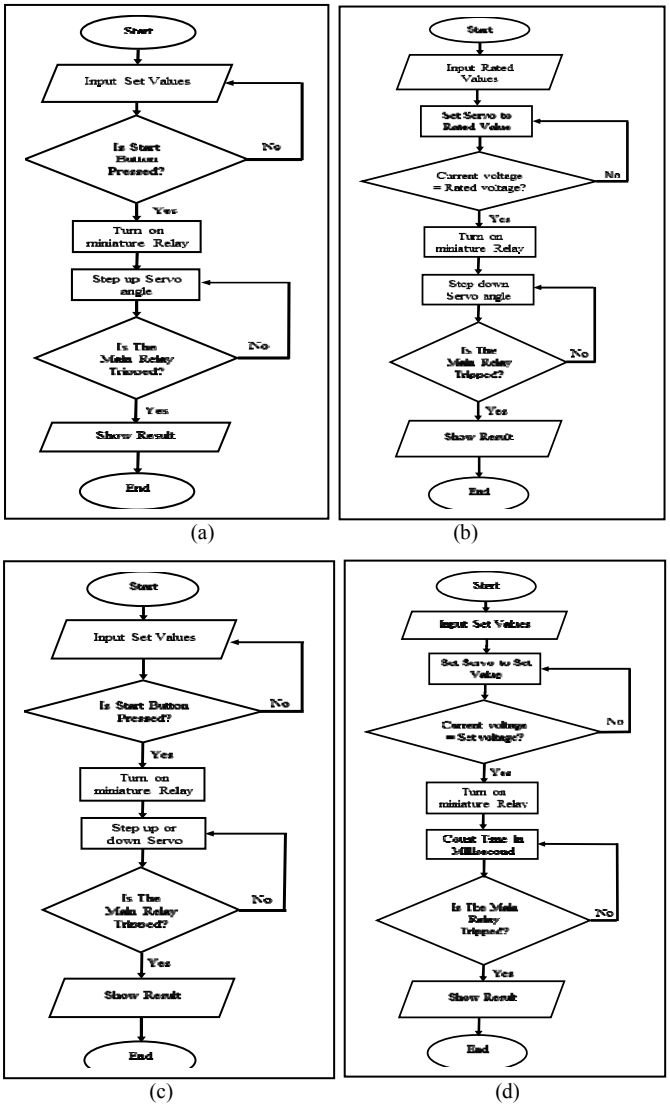


Figure 6. Flow charts of (a) automatic over-voltage, (b) automatic under-voltage, (c) manual over-voltage, and (d) automatic time test modes.

## III. Schematic Diagrams and Circuit Components

The schematic diagram and PCB layout of the overall device circuit is drawn using ExpressPCB software and are shown in Fig. 7-13. Table I shows the list of components and their specifications used in the device circuit.

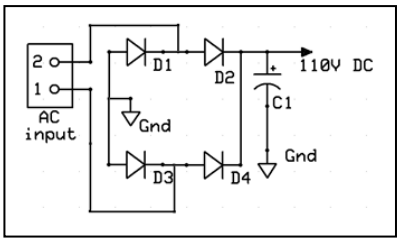


Figure 7. Schematic diagram of auxiliary power circuit.

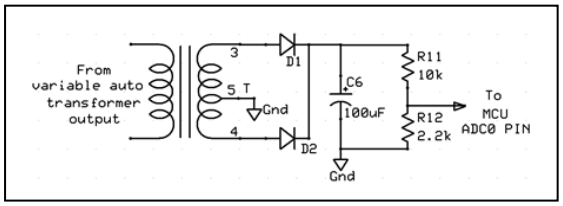


Figure 8. Schematic diagram of high voltage measuring circuit.

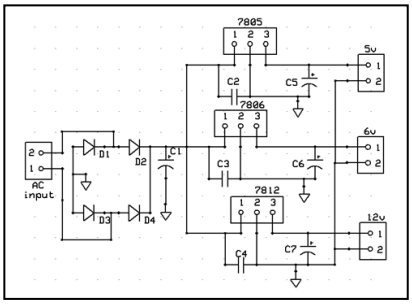


Figure 9. Schematic diagram of main power circuit.

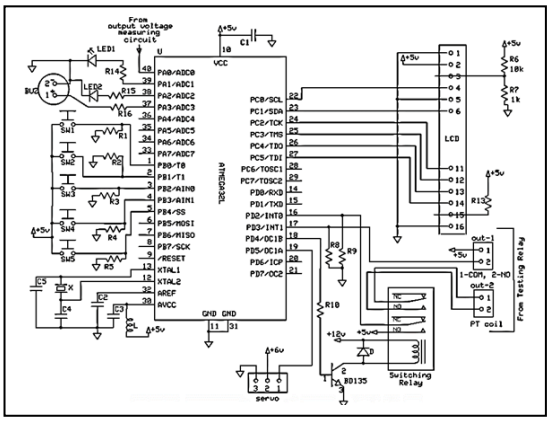


Figure 10. Schematic diagram of main control circuit.

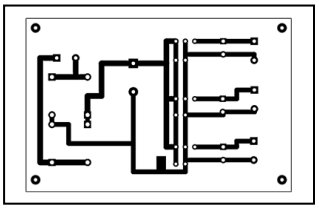

Figure 11. PCB layout of main power circuit.

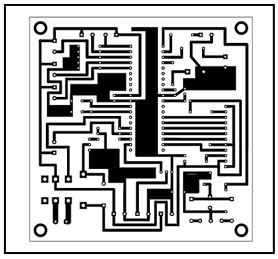

Figure 12. PCB layout of main working circuit.

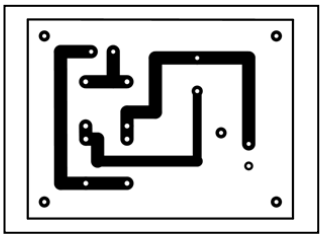

Figure 13. PCB layout of auxiliary power circuit.

TABLE I. Circuit Components and Specifications

| Component | Specification |
|---|---|
| Microcontroller | ATmega32 |
| Servo-motor | MG995 |
| Variac | 0-280V, 1A, 50Hz |
| LCD | HD44780 |
| Transformers | 230/12V, 230/18V, 230/110V; 1A |
| Voltage regulators | LM7805, LM7806, LM7812 |
| Transistor | BD135 |
| Switching relay | OMRON-LY2NJ |
| Diodes | D1N4007 |
| Resistors | - |
| Capacitors | - |
| Others | - |

## IV. Results and Discussion

The complete system is fit into a rectangular device having dimension of 12”x10”x8”. The front side of the device contains the control panel and the connecting points of all kind and the back side contains the main power port and the cooling fan. The front view of the device is shown in Fig. 8(a) and the isometric view of the device is shown in Fig. 8(b).

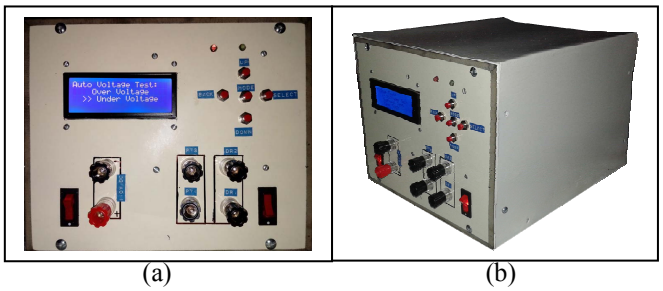


(a) (b)

Figure 8. (a) Front side view of device, (b) isometric view of device.

The relay to be tested is a numerical relay from MiCOM, model no: P127. The nominal ratings of the relay are given in [4]. The four modes of test, i.e. automatic over-voltage and under-voltage, manual over voltage, and automatic time test,

are carried out to see the performance of the relay. For the automatic and manual over-voltage tests, the set voltage is 110V. For the automatic under-voltage test, the set voltage is 100V and for the automatic time test, the set voltage and set time are 110V and 5s respectively. The tolerance of the relay to be tested is set to 5%. For the voltage tests, the tripping voltage is obtained and for the time test, the tripping time is obtained. Error is calculated using the equation,

$$\text{Error} = (|\text{set value} - \text{trip value}|/\text{set value}) \times 100\%$$

Results of the experiment is given in Table II. The error of the results are all within 5% tolerance level, so the relay has passed all the tests. The device has accurately tested the performance of the relay for voltage and time tests. The device can therefore be said to be working perfectly.

TABLE II. TEST RESULTS

| Test | Set Value | Trip Value | Error (%) |
|---|---|---|---|
| Automatic over-voltage | 110V | 112V | 1.8 |
| Automatic under-voltage | 100V | 102V | 2 |
| Manual Over-voltage | 110V | 112V | 1.8 |
| Automatic time | 110V, 5s | 5.049s | 0.98 |

Existing devices in the market use microprocessor and microcomputer for operation, which use extra peripherals like RAM, EPROM, flash memory, etc. As a result, cost and weight both increases. Use of microcontroller and variac makes the designed device more cost-efficient and less bulky. Table III gives a comparison between available devices with the designed device of this paper.

TABLE III. COMPARISON OF OUR DESIGN WITH OTHER DEVICES

| Company | Model | Weight (Kg) | Price (US$) |
|---|---|---|---|
| CNHV | HRWJC-6 [5] | 16 | 8,800 |
| ZHENHUAN | HDJB [6] | 22 | 19,000 |
| GFUVE | Test-750 [7] | 18 | 20,000 |
| Our Device | - | 10 | 75 |

## V. CONCLUSION

For ensuring the accurate operation and credibility in industries and in power system, regular checking of a protective relay is mandatory. So a relay testing device is designed and discussed in this paper which can check the performance of a protective relay. The device is cheap, light-weight and simple for use in laboratory experiments. The device successfully tested the performance of the relay for different conditions with an error of 2%, which is well within the tolerance level of 5%. The device uses an autotransformer for varying the applied voltage to the relay coil. However, use of autotransformer makes the device bulky and so can be replaced with a PWM voltage controller to further decrease the weight and bulkiness of the device. A major limitation of the device is the absence of current test method. Further research will be carried out to add current test mechanism and other features in the device, while keeping the device cost-efficient.

## REFERENCES


[1] B. A. Oza, N. K. C. Nair, R. P. Mehta and V. H. Makwana, *Power System Protection and Switchgear,* McGraw Hill Education (India) Pvt. Ltd. , 2010.

[2] Chris Werstiuk, *The Relay Testing Handbook: Relay Testing Fundamentals,* Valence Electrical Traning Services LLC, 2007, pp.19-21.

[3] (2010) Engineering 360 weibsite. [Online]. Available: www.globalspec.com

[4] *MiCOM P125, 126 & 127 Technical Manual,* Schneider Electric, 2011.

[5] Alibaba website. [Online]. Available: http://www.alibaba.com/product-detail/Microcomputer-relay-Protection-tester_473164387.html?spm=a2700.7724838.0.0.nBYGS5&s=p

[6] Alibaba webisite. [Online]. Available: http://www.alibaba.com/product-detail/-6-phase-of-voltage-6_60434372949.html?spm=a2700.7724838.0.0.HQxs3Q

[7] Alibaba website. [Online]. Available: http://www.alibaba.com/product-detail/Test-750-Secondary-Injection-Tester-Relay_1047491034.html?spm=a2700.7724838.0.0.IHMwB

# Modeling and Comparative Analysis of Cost Effective Hybrid AC/DC Micro-grid in Coastal Area of Bangladesh using AVR and LFC System

Afsana Hossain Rima[1], Rezwan Mohammad Sayeed[2]
[1, 2] Lecturer (Dept. of EEE, Daffodil International University, Bangladesh)
[1]rima.eee@daffodilvarsity.edu.bd
[2]rezwan.eee@diu.edu.bd

***Abstract*— This paper highlights about the cost effective optimal modeling of hybrid AC/DC micro-grid for the coastal area of Bangladesh, where distributed energy sources like solar PV, wind energy as well as bio-mas energy are available. For the purpose of research Kuakata is chosen, which is one of the attractive tourist spot of Bangladesh. However, despite being a tourist spot, the electricity generation of this place has not yet been any self-reliance. The discussion of this paper not only circumscribed by the modeling of micro-grid, but also shows the detail of optimizing result with sensitivity analysis. This modeling with its optimal analysis is simulated via HOMER software. The micro-grid can operate on both grid connected mode and islanded mode. This paper proposes an off-grid or standalone micro-grid. In off-grid mode, the voltage and frequency does not remain balanced like grid connected mode. Hence, a new seamless control strategy for islanded mode voltage and frequency control is being proposed in this paper. Automatic voltage regulator (AVR) can be treated as a good solution for voltage control and load frequency control (LFC) technique can be used for frequency tuning. The control strategies applied in this research are simulated via MATLAB Simulink software.**

***Keywords—Micro-grid; AVR; LFC; Islanded mode operation; Control strategy; HOMER; MATLAB simulink.***

## I. INTRODUCTION

Bangladesh is not well endowed with the most sources of energy. The energy resources like coal, oil natural gas are so negligible in Bangladesh. Though it is a land of river, but still it cannot utilize its hydro potential. Nuclear power is not a best way for power generation as it requires a good financial capacity. Of traditional energy, it has sufficient forest areas for wood production and its dominant agricultural sector does produce substantial biomass waste, but this substantial amount of biomass feedstock is not utilized in energy sector. Existing power plants of Bangladesh are mainly based on the fuel of natural gas and oil. As required oil is not sufficient in our country, oil has been imported from other countries. Gas has been taken from internal resources for gas fired power plant. At the moment, it is no longer possible to depend on gas fired power plant. Apart from this, the Government pays more attention for alternative resources as oil or gas fired power plant cannot be the solution for meeting up energy demand in near future [1]. Clearly, Bangladesh must move on for hybrid energy with distributed energy sources if energy is not to constrain economic development. The challenge is how best to do this. The best possible way can be self-dependent micro-grid based power generation system which will be optimum in cost as well as environment friendly.

Kuakata sea beach is renowned for its panoramic beauty. The location of Kuakata is south-eastern part of Bangladesh. Kuakata beach is 18 kilometers (11 mi) long and 3 kilometers (1.9 mi) wide. An unobstructed view of both sunrise and sunset over the Bay of Bengal can be relished from there. The study area lies between latitude N21°48'05" to N21°51'36" and longitude E90°05'06" to E90°15'07". According to the 2011 Bangladesh census, Kuakata had 2,065 households and the total population of Kuakata is 174921. An optimum cost effective hybrid micro-grid is being designed here by taking a sample of 50 households [2].

## II. CONCEPTS OF MICRO-GRID

A micro-grid is a local distributed energy source based network, which offers the integration of those distributed energy sources with local loads (such as distributed generators, storage devices, or controllable loads). This concept reflects a new way of thinking about designing and building smart grids. Specifically, the Micro-grid concept focuses on creating a design and plan for local power delivery that meets exact needs of the constituents being served. The Micro-grids integrate customers and buildings with electricity distribution and generation very efficiently and economically. A micro-grid operation can be classified as grid connected mode operation and islanded mode operation. A grid connected mode operation means when the entity operates parallel with the grid and in this case the system remains balanced. Another one is the islanded mode or disconnected mode operation which means the micro-grid gets isolated from the grid and operates like a single entity [4]. The later system incorporates voltage and frequency fluctuations that cause serious harm to power system. This paper focuses on off grid system with its control scheme. Fig. 1 shows a typical hybrid AC/DC micro-grid with distributed energy system.

978-1-5386-2307-7/17/$31.00 ©2017 IEEE

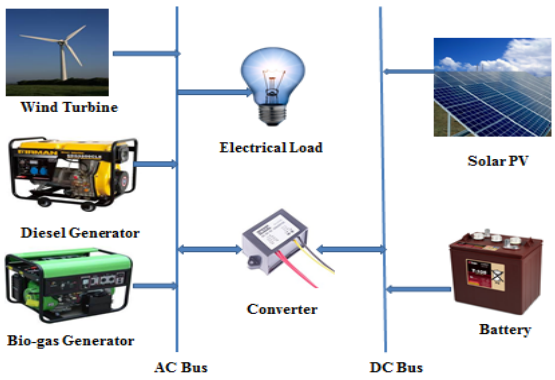


Fig. 1. Typical hybrid AC/DC micro-grid.

## III. Modelling of Micro-grid

For modeling of micro-grid the first thing that must take into account is the availability of distributed energy resources (DER) of the targeted place. After that the total load demands are calculated to find the average KWhr/day and KW of peak demand. After that the renewable resources data is collected and calculated for further modeling. Finally the hybrid micro-grid modeling is completed with all available renewable resources and a diesel generator. HOMER software is used for modeling an optimum cost effective micro-grid by analyzing its optimization result along with sensitivity analysis.

### *A. Load Calculation*

The coastal area residential unit is very simple and does not require expansive amounts of electrical vitality utilized for lighting and electrical machines. The proposed load profile is considered as the general hourly based load utilization. At midnight hours, the residential unit power consumption comes down whereas only basic electrical appliances are consuming power. During morning hours, when everybody gets ready either to leave for schools or working, the load demand rises up. At noon hours, when most of the family members are outside, the load demand levels are comparatively less. During the evening hours, all the family members come back and the power consumption rises as everyone switches on various entertainment appliances. For modeling a simple off grid micro-grid a sample of 50 households have taken into consideration. The average energy consumption of electrical appliances of a typical residential unit is found by calculating load profile is 46.2 KWhr/day and the peak demand is 11KW [6]. Fig. 2 shows the daily load profile of the month of June.

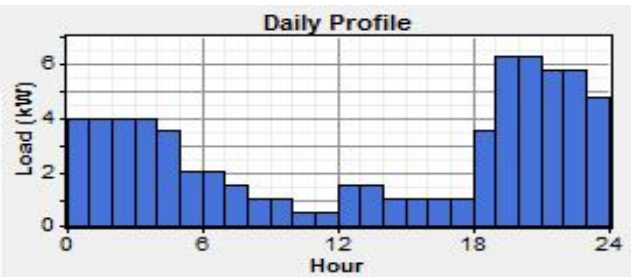


Fig. 2. Daily load profile for the month of June.

### *B. Adding Diesel Generator*

Diesel generators used in remote areas are mostly in the range of (12 - 20 KW). In this analysis, a 12 KW generator is considered and the cost is taken $2000 (160,000BDT). The rating lifetime is taken to be (15000 hr) and the price diesel is $ 0.79/L (63.2BDT).

### *C. Adding Battery and converter*

A combination of a diesel generator and a battery bank can sometimes supply power more cheaply than a generator alone. Such a system typically supplies power using the generator during times of high load, and using the battery bank during times of low load. When the generator operates, it produces extra power to charge the battery bank. This allows the generator to avoid running at very low load, where it is least efficient. A Trojan T-105 battery is selected for use, as T-105 is a common deep-cycle lead-acid battery. The installment cost is considered $150 (12000BDT) per battery and the maintenance cost would be 4$/yr (320BDT/yr) per battery.

Batteries operate on DC power and the rest of the system operates on AC power, so to add a battery bank an AC/DC converter is needed. The installed cost of a 12 KW converter is $3250 (260,000BDT).

### *D. Adding PV Array*

The first renewable energy that is used in model is PV array. For location between latitude N21°48'05" to N21°51'36" and longitude E90°05'06" to E90°15'07" the twelve month solar radiation is found from NASA satellite [5,6]. Fig.3. presents the twelve months solar radiation graph of Kuakata. The average solar insolation is found 4.67 KWh/m$^2$/d.

The installed cost of 2.5KW solar PV array is $4000 (320,000BDT) and the maintenance cost is 20$/yr (1,600BDT/yr). The chosen PV has no tracking system included and life time considered for the PV array is 25 years.

### *E. Adding Wind Turbine*

In Kuakata the average annual wind speed is found 6.742m/s [3]. Altitude from sea level is chosen 10m and anemometer height is chosen 30m. Fig.4. shows the annual wind speed variations in Kuakata.

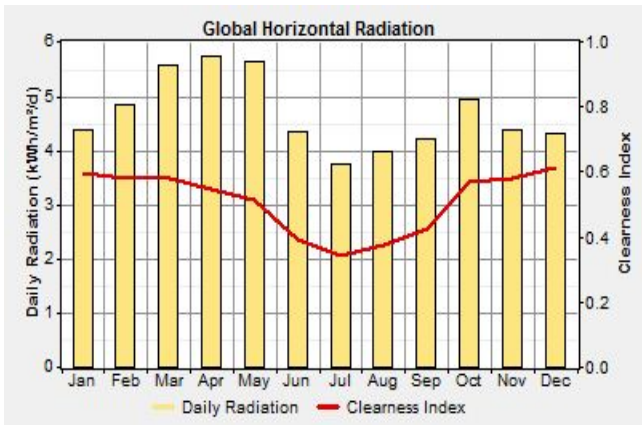


Fig. 3. Twelve months solar radiation graph of Kukata.

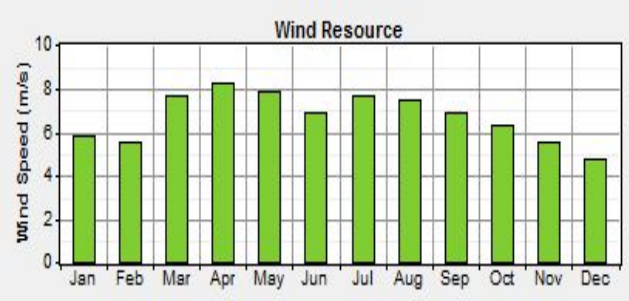


Fig. 4. Annual wind speed variation graph of Kukata.

For modeling the wind turbine Fuhrlander AG (FL 30) is selected. The capacity of this kind of wind turbine is 1.5KW. The installment cost is $600 (48,000BDT).

### F. Adding Bio-gas Generator

Finally a bio-gas generator is used in the modeling. I have included the proper input such as 1kw output need 1.18 L/hr fuel and 1000kw need 1200 L/hr fuel. Here the capital cost is $2500 (200,000BDT) and replacement cost is $2300 (184,000BDT) and O&M cost 0.3$/hr (24BDT/hr). And 12kw size is considered. Biomass resource data is entered month wise. The annual average is calculated by HOMER [6]. Fig.5. shows the annual biomass resource graph of Kuakata.

After adding all these components and in the HOMER, it can be concluded as an off grid micro-grid using DERs. The costing of each component must be added to complete full schematic. Fig.6. presents the full schematic of proposed hybrid AC/DC micro-grid system.

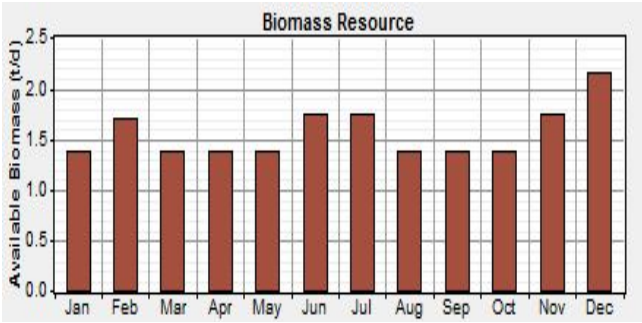


Fig. 5. Annual biomass resources of Kukata.

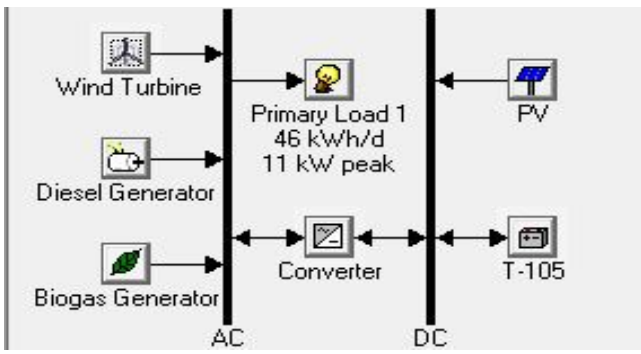


Fig. 6. Schematic diagram of the proposed hybrid AC/DC micro-grid.

## IV. Simulation Results

After the completion of the modeling of micro-grid the simulation result is carried out by HOMER software. The HOMER finds a feasible modeling by analyzing the cost. The sensitivity analysis is also done by HOMER software. A sensitivity analysis allows seeing how changes in an input variable affect the outputs. In HOMER, almost any variable that is not a decision variable can be a sensitivity variable i.e. solar radiation, wind speed variation and bio mass resources.

### A. Optimization Result

HOMER simulates hundreds of simulation to find the most optimum result. From the simulation result it is observed that a net present cost of the proposed system is $44,279 (3,542,320 BDT) and the operating cost per year is 2357$/yr (188,560 BDT/yr). The cost of energy observed from the result is 0.205$/KWh (16.4BDT/KWh). If cycle charging (CC) system is considered rather than load flow (LF) system then the proposed system cost will be increased a little bit. For the CC dispatch system the net present cost will be $50,465 (4,037,200BDT) and the operating cost will be 2,841$/yr (227,280BDT/yr). The cost of energy will be increases from 0.205$/KWh (16.4BDT/KWh) to 0.234$/KWh (18.72BDT/KWh). Fig.7. shows the overall simulation result of the system [3].

### B. Cash Flow of the System

From the simulation result the cash flow summary can be observed. From there it is focused that biogas generator carries most of the operating cost than others; but the installment cost and maintenance is less. Moreover, sometimes wind turbine is not reliable for large wind speed variations and PV is not a suitable solution for winter season as well as night time. In that case biogas generator can be a good solution for production of electricity. On the other hand diesel generator requires least cost in the proposed hybrid system, as it is used only in the case of backup. Fig.8. shows the cash flow summery of the proposed system.

### C. Electricity production

From HOMER simulation results, the monthly average electricity production can also be observed. Here it is also focusable that biogas produce around 50% of monthly average electricity and another 50% electricity production is by PV and wind. Excess electricity production is found 7237KWh/yr which is 28.7% and unmet electricity production is almost 0%. The renewable fraction found in this hybrid proposed system is 1. That means, the system's total electricity production originating from renewable power sources. Fig.9. presents the monthly average electricity production of the proposed system.

### D. Economics

HOMER estimated the possible pollutant emissions of the proposed system [5]. Table I shows the pollutant emission information.

Double click on a system below for simulation results. Categorized Overall

| PV (kW) | WT | DG (kW) | BG (kW) | T-105 | Conv. (kW) | Disp. Strgy | Initial Capital | Operating Cost ($/yr) | Total NPC | COE ($/kWh) | Ren. Frac. | Diesel (L) | Biomass (t) | DG (hrs) | BG (hrs) |
|---|---|---|---|---|---|---|---|---|---|---|---|---|---|---|---|
| | 1 | | 12 | 12 | 12 | LF | $ 8,150 | 2,528 | $ 40,464 | 0.188 | 1.00 | | 47 | | 3,571 |
| | 1 | 12 | 12 | 12 | 12 | LF | $ 10,150 | 2,496 | $ 42,055 | 0.195 | 1.00 | | 47 | 0 | 3,571 |
| 2.5 | 1 | | 12 | 12 | 12 | LF | $ 12,150 | 2,389 | $ 42,688 | 0.198 | 1.00 | | 41 | | 3,103 |
| 2.5 | 1 | 12 | 12 | 12 | 12 | LF | $ 14,150 | 2,357 | $ 44,279 | 0.205 | 1.00 | | 41 | 0 | 3,103 |
| | 1 | | 12 | 12 | 12 | CC | $ 8,150 | 2,987 | $ 46,330 | 0.215 | 1.00 | | 57 | | 3,995 |
| 2.5 | | | 12 | 12 | 12 | LF | $ 11,550 | 2,734 | $ 46,495 | 0.216 | 1.00 | | 54 | | 3,946 |
| | | | 12 | 12 | 12 | LF | $ 7,550 | 3,095 | $ 47,112 | 0.219 | 1.00 | | 66 | | 4,852 |
| | 1 | 12 | 12 | 12 | 12 | CC | $ 10,150 | 2,955 | $ 47,921 | 0.222 | 1.00 | | 57 | 0 | 3,995 |
| 2.5 | | 12 | 12 | 12 | 12 | LF | $ 13,550 | 2,708 | $ 48,173 | 0.223 | 1.00 | 6 | 54 | 1 | 3,946 |
| | | 12 | 12 | 12 | 12 | LF | $ 9,550 | 3,063 | $ 48,703 | 0.226 | 1.00 | | 66 | 0 | 4,852 |
| 2.5 | 1 | | 12 | 12 | 12 | CC | $ 12,150 | 2,873 | $ 48,874 | 0.227 | 1.00 | | 52 | | 3,707 |
| 2.5 | 1 | 12 | 12 | 12 | 12 | CC | $ 14,150 | 2,841 | $ 50,465 | 0.234 | 1.00 | | 52 | 0 | 3,707 |
| 2.5 | | | 12 | 12 | 12 | CC | $ 11,550 | 3,191 | $ 52,347 | 0.243 | 1.00 | | 64 | | 4,296 |
| | | | 12 | 12 | 12 | CC | $ 7,550 | 3,509 | $ 52,401 | 0.243 | 1.00 | | 73 | | 4,996 |
| 2.5 | | 12 | 12 | 12 | 12 | CC | $ 13,550 | 3,159 | $ 53,938 | 0.250 | 1.00 | | 64 | 0 | 4,296 |
| | | 12 | 12 | 12 | 12 | CC | $ 9,550 | 3,477 | $ 53,993 | 0.250 | 1.00 | | 73 | 0 | 4,996 |
| 2.5 | 1 | 12 | | 12 | 12 | LF | $ 11,650 | 21,546 | $ 287,079 | 1.332 | 0.51 | 14,573 | | 3,103 | |
| | 1 | 12 | | 12 | 12 | LF | $ 7,650 | 24,579 | $ 321,855 | 1.493 | 0.39 | 16,777 | | 3,571 | |
| 2.5 | 1 | 12 | | 12 | 12 | CC | $ 11,650 | 26,193 | $ 346,486 | 1.607 | 0.44 | 17,771 | | 3,697 | |
| 2.5 | | 12 | | 12 | 12 | LF | $ 11,050 | 27,300 | $ 360,036 | 1.670 | 0.18 | 18,709 | | 3,946 | |
| | 1 | 12 | | 12 | 12 | CC | $ 7,650 | 27,830 | $ 363,409 | 1.686 | 0.34 | 18,955 | | 3,939 | |
| 2.5 | | 12 | | 12 | 12 | CC | $ 11,050 | 30,605 | $ 402,285 | 1.866 | 0.15 | 20,903 | | 4,297 | |
| | | 12 | | 12 | 12 | CC | $ 7,050 | 33,123 | $ 430,478 | 1.997 | 0.00 | 22,737 | | 4,673 | |
| | | 12 | | 12 | 12 | LF | $ 7,050 | 33,229 | $ 431,827 | 2.003 | 0.00 | 22,947 | | 4,852 | |

Fig. 7. Overall simulation results of the hybrid system.

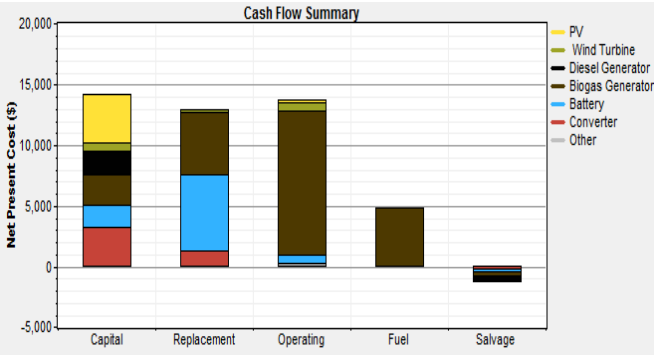


Fig. 8. Categorized cash flow summery of the proposed system.

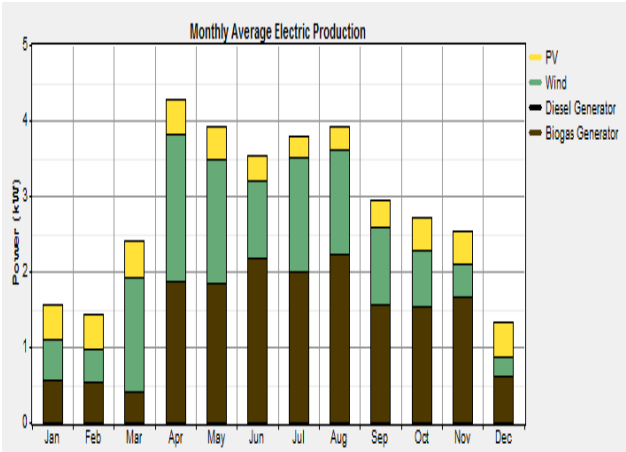


Fig. 9. Monthly average electric production of the proposed system.

TABLE I. POLLUTANT EMISSION OF THE SYSTEM

| Pollutants | Emissions (Kg/yr) |
|---|---|
| Carbon dioxide | 115 |
| Carbon monoxide | 0.264 |
| Unburned hydrocarbons | 0.0293 |
| Particulate matter | 0.0199 |
| Sulfur dioxide | 0 |
| Nitrogen oxides | 2.36 |

## V. CONTROL STRATEGIES OF MICRO-GRID

Various control strategies had been proposed previously for off grid micro-grid system as in isolated mode the electrical quantity of the system does not remain balanced like grid connected mode. Load sharing concept was proposed for islanded mode operation; in that case the system will be run on critical load rather than non-critical load of the balanced system [5]. Multi-agent system was proposed where functionalities, interconnection and effective agent protocol is required [7]. A fuzzy logic frequency controller was developed for autonomous operation of micro-grid. A droop control technique was most common where PQ control is consider in grid connected mode and V/F control is consider in islanded mode operation [6].

A well planned and maneuvered power system must subsist with load variation and with system disturbances. While maintaining both voltage and frequency within tolerable limits it should provide acceptable high level of power quality. Despite all of the above control strategies, this paper proposes a new seamless control strategy which can be an effective way of

controlling the unbalanced voltage and frequency in case of off-grid system. Here, the proposed control strategy has not been synchronized with the proposed system. The synchronization can be done in software named Etap.

## VI. Automatic Volatge Regulator

When the micro-grid is in islanded mode, there might be a possibility of voltage fluctuation. The power system equipment is damaged by this voltage variation. This paper also describes about how to control this voltage fluctuation and how to achieve voltage stability. In this regard, automatic voltage regulator can be used with generator which ensures the generated voltage running smooth to maintain the stable voltage in specified limit [8].

The AVR system operates based on the principle of detection of errors. After obtaining the output voltage, it is rectified, filtered and then compared with the reference value. The error voltage is found by the difference of actual voltage value and the reference voltage value. An amplifier is used to amplify the error voltage; after that the amplified signal is fed to the exciter. The excitation maintains the VAR in the network. Fig.10. presents the AVR system, which is simulated in MATLAB Simulink. A PID controller is used in this case to observe better performance [12].

### *A. Simulation Outcome*

The performance analysis without a PID controller and with a PID controller is shown in Fig.11. The blue colored curve presents the performance of AVR system without a PID controller; whereas the red colored curve presents the performance with a PID controller. It is observed that the red curve shows better performance with less % overshoot and settling time.

## VII. Load Frequency Control

Load frequency control is a system reasonably uniforms the frequency, divide it to the generators. When the micro-grid is in off grid mode, the load suddenly increases then the speed of turbine drops before the governor adjust the input to new load [8].

The rotor angle determines the changes in frequency. The real power command signal transform the error signal that is sent to prime mover for increment of torque. Changes in the generator output with its specified tolerance are brought by the prime mover [12]. Fig. 12 presents the LFC system simulated by MATLAB Simulink. Here also PID controller is used to observe better performance.

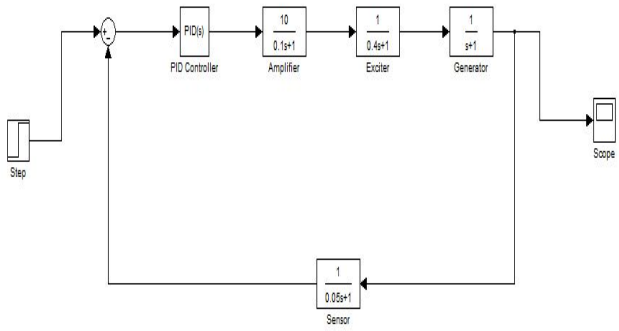


Fig. 10. AVR system with PID controller.

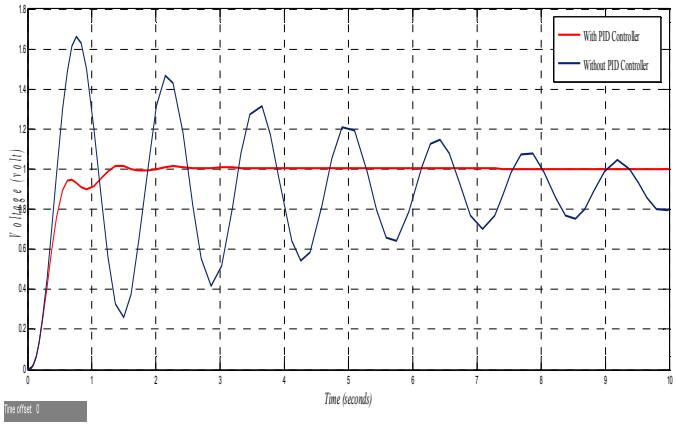


Fig. 11. Comparative performance analysis of AVR system with and without PID controller.

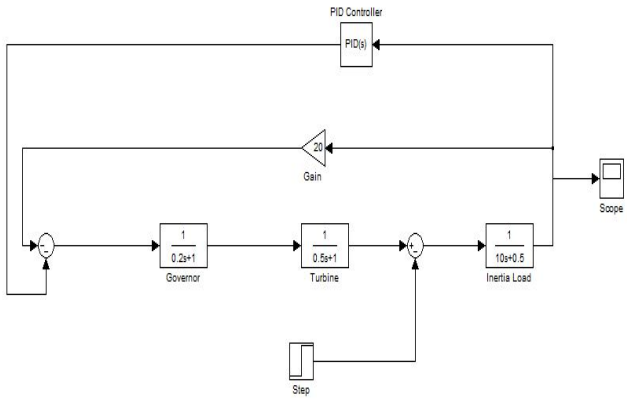


Fig. 12. LFC system with PID controller.

### *A. Simulation Outcome*

Fig.13. shows the performance analysis of LFC system with and without a PID controller. Here, also the blue colored curve presents the performance of LFC system without a PID controller; whereas the red colored curve shows the performance with a PID controller. A PID controller in LFC system provides a better performance than a LFC system without a controller.

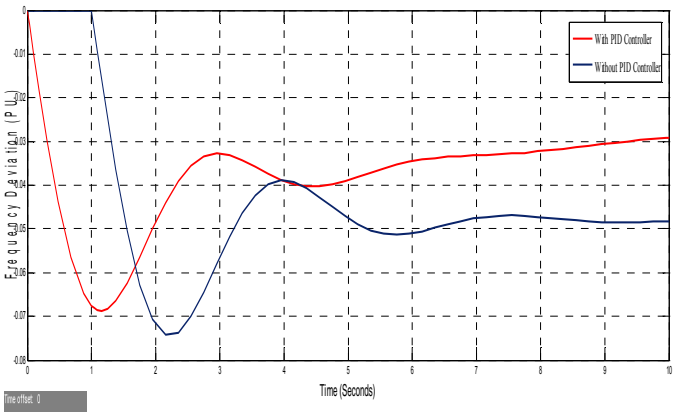


Fig. 13. Comparative performance analysis of LFC system with and without PID controller.

## VIII. CONCLUSION

The modeling of the (PV/Wind/Diesel/Biogas) hybrid power system has been discussed in this paper. From results, it is observed that this system can give good profit with a reasonable investment due to the amount of renewable energy generated. It utilizes all renewable energy with 1 renewable fraction. However, the system reliability cannot be ensured due to variable nature of solar radiation availability and lack of adequate wind speed in winter unless the control strategy is considered. Implementation of AVR and LFC system with the off-grid system will highly ensure the seamless operation on that unreliable condition. The hybrid power system solution for off-grid electricity supply to a remote coastal area such as Kuakata resulted in a least-cost combination of PV, Wind, Diesel and Biogas generator that can meet the demand in a dependable manner at a cost of energy 0.205$/kWh (16.4BDT/KWh) . The proposed hybrid system is simulated by taking 50 households samples, but this off-grid hybrid system can be used for whole Kuakata as well as any coastal area of Bangladesh with a least cost of energy. Moreover, we like to extend further our research work to any place of Bangladesh by collecting the real time data; that unquestionably reduces the pressure of conventional electrical energy generation. Where the question of control comes in case of off-grid system, AVR and LFC system with PID controller can be the best solution for dynamic performance of islanded mode micro-grid.

## ACKNOWLEDGMENT

The authors would like to thank their thesis supervisor for his valuable suggestions and guidelines. The authors are also grateful to their colleagues, friends for their constant support to continue with this work. They also like to thank their parents for their understanding and bearing with them for the whole period of this task.

## REFERENCES

[1] Islam, S. and Khan, M. (2017). A Review of Energy Sector of Bangladesh. *Energy Procedia*, 110, pp.611-618.

[2] Rahman, M. M., Rahman, M. A., & Nahar, A. (2015). STATUS OF "KUAKATA" A NEGLECTED NATURAL SCENIC RESOURCE OF BANGLADESH. *European Scientific Journal, ESJ, 11*(5).

[3] Zubair, A., Abdulla Tanvir, A. and Hasan, M. (2012). Optimal Planning of Standalone Solar-Wind-Diesel Hybrid Energy System for a Coastal Area of Bangladesh. *International Journal of Electrical and Computer Engineering (IJECE)*, 2(6).

[4] Nazir, R., Laksono, H. D., Waldi, E. P., Ekaputra, E., & Coveria, P. (2014). Renewable energy sources optimization: a micro-grid model design. *Energy Procedia*, *52*, 316-327.

[5] Khadem, S. K. (2006). Feasibility study of wind home system in coastal region of Bangladesh. *energy, 4,* p.5.

[6] Amin, M., Roy, R. and Hasan, M. (2014). Modeling and Optimization of Decentralized Microgrid System for St. Martin's Island in Bangladesh. *International Journal of Energy, Information and Communications*, 5(5), pp.1-12.

[7] Das, H. S., Dey, A., Tan, C. W., & Yatim, A. H. M. (2016). Feasibility analysis of standalone PV/wind/battery hybrid energy system for Rural Bangladesh. *International Journal of Renewable Energy Research (IJRER), 6*(2), 402-412.

[8] NASA Surface Meteorology and Solar Energy. 2015; Available from: https://eosweb.larc.nasa.gov/sse/.

[9] Basak, P., Saha, A. K., Chowdhury, S., & Chowdhury, S. P. (2009, September). Microgrid: Control techniques and modeling. In *Universities Power Engineering Conference (UPEC), 2009 Proceedings of the 44th International* (pp. 1-5). IEEE.

[10] Tahim, A. P. N., Pagano, D. J., Lenz, E., & Stramosk, V. (2015). Modeling and stability analysis of islanded DC microgrids under droop control. *IEEE Transactions on Power Electronics, 30*(8), 4597-4607.

[11] Kim, H. M., Lim, Y., & Kinoshita, T. (2012). An intelligent multiagent system for autonomous microgrid operation. *Energies, 5*(9), 3347-3362.

[12] Singh, A., Singh, R., & Kushwah, R. Automatic Voltage Regulator and Automatic Load Frequency Control of Electrical Power Plant with Optimal Tuning Controller PID. *International Journal for Research in Applied Science & Engineering Technology (IJRASET)*, *3*.

# Assessment of the Health Condition of Oil-Immersed Transformers Using Logistic Regression and Poisson Distribution

Sultanul Areffin, Mohammed Imamul Hasan Bhuiyanand Aongti Chowdhury

Department of Electrical and Electronic Engineering, Bangladesh University of Engineering and Technology, Dhaka-1205, Bangladesh
E-mail: areffinrhythm@gmail.com

***Abstract*—In this paper, a method is proposed to assess the health condition of oil-immersed transformers using a logistic regression analysis and Poisson distribution. The parameters of the regression model are estimated by using a maximum-likelihood cost function developed based on Poisson distribution for modeling transformer health condition that include oil breakdown voltage (BDV), acidity of oil, 2-Furaldehyde content, water content in oil, dissolved combustible gas (DCG), and dissipation factor (DF). The minimization of the criterion function is carried out by the Gradient Descent technique. The values of the health indices of 30 working power transformers below 110 kV are obtained from the regression model. Using preset ranges of health indices, the transformers are classified into four different health conditions. It is shown that the results are close to expert evaluations and on par with recently reported ones in the literature, thus signifying a reliable and effective assessment of transformer health.**

***Keywords— Power Transformer, Health Index (HI), Weighing factor, Regression model, Poisson distribution.***

## I. INTRODUCTION

Power transformers are among the most expensive components in power systems. Faults and degradation occurring in power transformers damage a power distribution system leading to a substantial amount of loss [1], [2]. To avoid this, monitoring and proper maintenance of transformers are required. Typical age limit of transformers is between 25-40 years, but it varies from plant to plant and depends upon proper maintenance. Considering these in conjunction with the continuous expansion of electrical networks, aging of electrical equipment including transformers and the increasing demand for technical performance, many power utilities are facing the need to evaluate the actual technical condition of their transformers. The evaluation is required to provide economic and technical justifications regarding crucial engineering decisions and capital investments on transformers for replacement, repair, maintenance plan etc.

Recently, the idea of Health Index (HI) has been introduced as a suitable indicator of the overall health condition of a transformer [3]-[7]. It helps a power utility to identify whether a transformer is near its life end or brand new or still repairable. Traditionally, the health of transformers is assessed by the weighted combination of various electrical, mechanical and chemical test data. A disadvantage of this approach is that the weighing factors are provided by experts and thus, may be error -prone as it is subjective and based on the experience of the transformer expert and can be different from one expert to another. A number of methods have been proposed to overcome the shortcomings of traditional approach in assessing transformer health [3]-[7]. In [3], a multi-criteria –based method is proposed to combine various typical test data with different condition parameters to obtain the health index. In [4], real measurements of several working transformers are used to train a feed-forward neural network which subsequently provides the health index. A fuzzy support-vector machine is used in [5] to derive the health index of a transformer. In [5], 33 fuzzy-based rules are used to derive the health indices of transformers. Transformers are categorized using the indices and fuzzy membership function into four classes, Good (*G*), Moderate (*M*), Bad (*B*), and Very Bad (*VB*). A logistic regression model is used in [6] to calculate the health index of a transformer. The values of the indices obtained from various transformers are used to classify them into four categories as above. The parameters of the regression model are estimated by minimizing a maximum-likelihood (ML) criterion based on modeling the observed data with a Gaussian distribution. Since the number of transformers in a power system is large, while the probability of a transformer being unhealthy is rather low and our objective is to find if a transformer is healthy or unhealthy, a Poisson distribution could be a better choice for modeling the test data of transformers. In this paper, a regression model [6] is employed to determine the health index. Unlike [6], the parameters of the model are derived using a ML criterion developed based on modeling the test data with a Poisson distribution. The solution process of the ML-function is carried out by the Gradient Descent method. Using preset ranges on the calculated health indices, the transformers are categorized into the classes G, M, B and VB. The obtained results are compared with expert

978-1-5386-2307-7/17/$31.00 ©2017 IEEE

evaluations from an asset management and health assessment consulting company referred to as AMHA and those of recently reported method of [5], [6].

## II. MATERIALS

In this Section, the input data for HI calculation is briefly described. The same data has also been used in [5] and [6]. The health indices of total 30 transformers are calculated, that are selected from, a group of 90 transformers, 81 being installed between 1980 and 1981. The samples are taken in 2006, thus the ages of the majority of the transformers range between 25 and 26 years. Six transformers are installed between 1986 and 2000 and the rest around 1970 [5]. The obtained values are then classified using a preset range of values. Six major variables among numerous test components of transformer oil are considered that are shown in Table I. The reference values [8], [9], [10] for each variable for the transformer to be in healthy condition are also provided in the same table.

TABLE I. INPUT DATA FOR HI CALCULATION

| No. | Variable | Component name | Reference values |
|---|---|---|---|
| 1. | $x_1$ | Water content in oil | 30 to 35 ppm |
| 2. | $x_2$ | Total acidity of oil | 0 to 0.25 mgKOH/g |
| 3. | $x_3$ | Oil breakdown voltage (BDV) | Minimum 30 KV |
| 4. | $x_4$ | Dissipation factor (DF) | 0 to 0.1 % |
| 5. | $x_5$ | Dissolved combustible gases (DCG) | 0 to 500 ppm |
| 6. | $x_6$ | 2-Furfuraldehyde content | 0 to 0.1 mg/L |

The details of the input data are given in the appendix of this paper.

## III. METHOD

### A. Logistic Function from Bernoulli's Differential Equation

Logistic regression is widely used to model the outcomes of categorical dependent variables. It is inappropriate to use linear regression model for categorical variables as the response values are not estimated on a ratio scale and the erroneous terms are not normally distributed. Moreover, linear regression can generate any real integer values but categorical variable can only take a limited number of discrete values within a specified range. For a given input *(x)* the output *(y)* of the logistic regression can be given by Bernoulli's differential equation as

$$y = \frac{e^x}{C+e^x} \tag{1}$$

where $C$ is an arbitrary constant. The logistic function is obtained for $C = 1$ in (1) and given by

$$y = \frac{1}{1+e^{-x}} \tag{2}$$

The reasons behind using this function are that it is real valued, monotonic, differentiable and constrained by a pair of horizontal asymptotes.

In this paper, $x$ is defined by a multinomial equation [11] and given by

$$x = \theta_0 + \sum_{i=1}^{m} \theta_i x_i;\ m=1,2,3,\ \ldots,N \tag{3}$$

where $\theta_0$ is a constant and $\theta_i$ is the assigned weighing factor for the input $x_i$; $m$ represents the transformer test data variable and $N$ the number of such variables. In this paper, since the no. of input variable is six, $m=6$ and thus, (3) is written as

$$x = \theta_0 + \theta_1 x_1 + \theta_2 x_2 + \theta_3 x_3 + \theta_4 x_4 + \theta_5 x_5 + \theta_6 x_6 \tag{4}$$

Subsequently, the health index of a transformer from (2) is given by [6]

$$HI = \frac{1}{1+e^{-(\theta_0+\sum_{i=1}^{6}\theta_i x_i)}} \tag{5}$$

### B. ML criterion from Poisson Distribution

Consider a random variable $y$ that can take two possible values; '$y$=1' indicates 'healthy' and '$y$=0' signifies 'unhealthy' condition of transformers.

Let, **X** be a $k\times m$ matrix where, $x_{ki}$ denotes the $i$-th variable of the $k$-th transformer and the maximum value of $k$ and $m$ are 30 and 6 respectively as test data of 30 transformers with 6 variables are used. **X** is given by

$$\mathbf{X}=\begin{bmatrix} x_{1,1} & x_{1,2} & \cdots & x_{1,6} \\ x_{2,1} & x_{2,2} & \cdots & x_{2,6} \\ \vdots & \ddots & \ddots & \vdots \\ x_{30,1} & x_{30,2} & \cdots & x_{30,6} \end{bmatrix} \tag{6}$$

Now, define a column vector $\boldsymbol{n_i}$ of length $k$ as

$$\boldsymbol{n_i}=[x_{1,i} \quad x_{2,i} \quad \cdots \quad x_{30,i}]^{\boldsymbol{T}} \tag{7}$$

Obviously, $\boldsymbol{n_i}$ denotes the values of the $i$-th test data variable of different transformers. Let $\boldsymbol{\pi_i}$ be a column vector also of length $i$ with elements $\pi_i = P(y_i = 1|i)$ where, $\boldsymbol{y_i}$represents the health condition of transformers in column. The logistic regression model equates the logit transform, the log-odds of the probability of a success, to the linear component as

$$\ln\left(\frac{\boldsymbol{\pi_i}}{\boldsymbol{1-\pi_i}}\right) = \theta_0 + \sum_{k=1}^{k} x_{ki}\theta_i \tag{8}$$

From (8), one can obtain [11]

$$\boldsymbol{\pi_i} = \frac{\exp(\theta_0+\sum_{k=1}^{k} x_{ki}\theta_i)}{1+\exp(\theta_0+\sum_{k=1}^{k} x_{ki}\theta_i)} \tag{9}$$

Using Poisson distribution to model $\boldsymbol{y_i}$, one can write the ML criterion as [11]

$$\boldsymbol{J}(\boldsymbol{y_i}|\boldsymbol{n_i})=\frac{1}{m}\sum_{i=1}^{m}\frac{e^{-n_i}(n_i)^{y_i}}{y_i!} \quad (10)$$

that can be further modified as [11]

$$\boldsymbol{J}(\boldsymbol{y_i}|\boldsymbol{\theta}) = \frac{1}{m}\sum_{i=1}^{m}\frac{n_i!}{y_i!(n_i-y_i)!}\pi_i^{y_i}(1-\pi_i)^{n_i-y_i} \quad (11)$$

Factorial terms do not contain $\pi_i$ and thus can be ignored. Thus, from (11) one obtains

$$\boldsymbol{J}(\boldsymbol{y_i}|\boldsymbol{\theta}) = \frac{1}{m}\sum_{i=1}^{m}(\frac{\pi_i}{1-\pi_i})^{y_i}(1-\pi_i)^{n_i} \quad (12)$$

Substituting $\pi_i$ from (9), (12) is written as

$$\boldsymbol{J}(\boldsymbol{y_i}|\boldsymbol{\theta}) = \frac{1}{m}\sum_{i=1}^{m}(\theta_0+\sum_{k=1}^{k}x_{ki}\theta_i))^{y_i}(1-\frac{\exp(\theta_0+\sum_{k=1}^{k}x_{ki}\theta_i)}{1+\exp(\theta_0+\sum_{k=1}^{k}x_{ki}\theta_i)})^{n_i} \quad (13)$$

Using function $h_\theta(x_i) = g(\sum_{k=0}^{K}x_{ki}\theta_i)$and $g(z) = \frac{1}{1+e^{-z}}$ (13) can be written as

$$\boldsymbol{J}(\boldsymbol{y_i}|\boldsymbol{\theta}) = \frac{1}{m}\sum_{i=1}^{m}[-y_i\ln\big(h_\theta(x_i)\big)-(1-y_i)\ln(1-h_\theta(x_i))] \quad (14)$$

Equation (14) is the cost function for the ML criterion which is minimized to calculate $\boldsymbol{\theta}$.

### C. Minimization by Gradient Descent method

Vectorizing the gradient of cost function is needed for Gradient Descent algorithm. Recall that the gradient of the (unregularized) logistic regression cost is a vector where the *j*th element is defined as

$$\frac{\partial \boldsymbol{J}}{\partial \boldsymbol{\theta_i}} = \frac{1}{m}\sum_{i=1}^{m}[(h_\theta(x_i)-y_i)x_{ki}] \quad (15)$$

To vetorize this operation over the dataset, we start by writing out all the partial derivatives explicitly for all $\theta_i$

$$\begin{bmatrix}\frac{\partial J}{\partial\theta_0}\\ \frac{\partial J}{\partial\theta_1}\\ \frac{\partial J}{\partial\theta_2}\\ \vdots\\ \frac{\partial J}{\partial\theta_i}\end{bmatrix}=\frac{1}{m}\begin{bmatrix}\sum_{i=1}^{m}[(h_\theta(x_i)-y_i)x_{k0}]\\ \sum_{i=1}^{m}[(h_\theta(x_i)-y_i)x_{k1}]\\ \sum_{i=1}^{m}[(h_\theta(x_i)-y_i)x_{k2}]\\ \vdots\\ \vdots\\ \sum_{i=1}^{m}[(h_\theta(x_i)-y_i)x_{ki}]\end{bmatrix}$$

$$=\frac{1}{\mathrm{m}}\mathbf{X^T}(\mathbf{h_\theta}(\mathbf{x})-\mathbf{y}) \quad (16)$$

where

$$\mathbf{h_\theta}(\mathbf{x})-\boldsymbol{y}=\begin{bmatrix}\mathrm{h}_\theta(x_1)-y_1\\ \mathrm{h}_\theta(x_2)-y_2\\ \vdots\\ \mathrm{h}_\theta(x_m)-y_m\end{bmatrix} \quad (17)$$

For 30 transformers, a total of 30 equations are obtained. The subsequent steps to solve for $\theta_i$ using the 30 equations by the Gradient Descent technique are:

**Step 1:** Binary responses (1, 0) are obtained from the logistic function using the reference values given in Table I. Response '1' indicates healthy and '0' unhealthy condition.

**Step 2:** Set *k*=1 in (16) to start the loop.

**Step 3:** Set *i*=1 in (16) to start a subordinate loop for the first loop.

**Step 4:** Binary responses and the values of variables are put in (16) with the increment of (k, i).

**Step 5:** When, *k*=30 the first loop stops and when *i*=6 the subordinate loop stops.

**Step 6:** Set each gradient in (16) to zero and thus, total 30 equations are obtained.

**Step 7:** The equations are solved by multiple linear regression and the unknown values of $\boldsymbol{\Theta}$ are obtained.

**Step 8:** The values of $\boldsymbol{\Theta}$ and $\boldsymbol{x}$ are used in (5) to obtain HI.

## IV. Results

The performance of the proposed method is compared with those of AMHA and [5], [6]. The results of the latter methods are obtained from [6]. Note that AMHA classifies the transformers into three classes, Good (*G*), Moderate (*M*) and Bad (*B*). Thus, in our case we consider the *VB* and *B* classes as equivalent to *B* in AMHA during performance comparison. The test results of the water content, acidity content, BDV, DF, DCG and 2-Furfuraldehyde content and the estimated values of the weighing factors are shown in Table II.

TABLE II. Values of $\theta_0$ and $\theta_i$ with corresponding variables (test data)

| Variables | Weighing factor ($\boldsymbol{\theta}$) | Parameters |
|---|---|---|
| Constant | 2.6185 | $\theta_0$ |
| $x_1$, Water | 0.0004 | $\theta_1$ |
| $x_2$, Acidity | -1.1673 | $\theta_2$ |
| $x_3$, BDV | 0.0673 | $\theta_3$ |
| $x_4$, DF | -5.8187 | $\theta_4$ |
| $x_5$, DCG | -0.0041 | $\theta_5$ |
| $x_6$, 2-Furfuraldehyde | -0.5838 | $\theta_6$ |

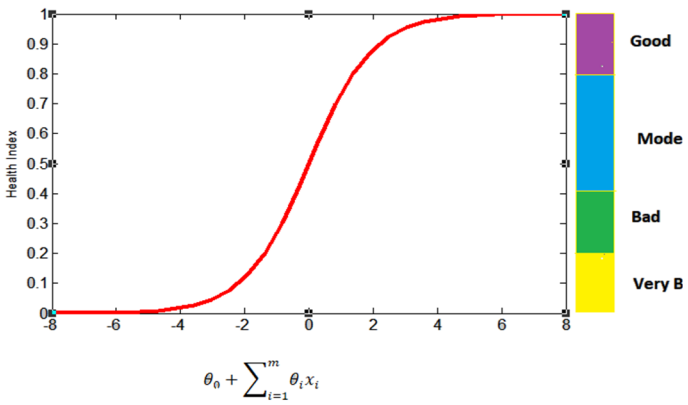


Figure 1. Plot of HI values and their classification, range

Using the weighing factors estimated as above in (6), the corresponding values of HI are obtained. The transformers are classified into four classes: G, M, B and VB, if the values of HI are between 0.8 to 1.0, 0.4 to 0.8, 0.2 to 0.4, and 0 to 0.2, respectively, as shown in Figure 1. The health indices of 30 transformers and their health conditions as determined by the proposed method are shown in Table III. The corresponding classifications from AMHA and [5], [6] are also provided in the same table.

TABLE III. VALUES OF HI AND CLASSES OF TRANSORMERS FOR THE PROPOSED METHOD AND THE CLASSES GIVEN BY AMHA, [6] AND [5]

| No. | Proposed method | | AMHA | [6] | [5] |
|---|---|---|---|---|---|
| | HI values | Class | Class | Class | Class |
| 1. | 0.8670 | *G* | *G* | *M* | *G* |
| 2. | 0.2013 | *B* | *G* | *G* | *G* |
| 3. | 0.9945 | *G* | *G* | *G* | *G* |
| 4. | 0.2824 | *B* | *B* | *VB* | *B* |
| 5. | 0.9984 | *G* | *G* | *G* | *VG* |
| 6. | 0.9976 | *G* | *G* | *G* | *G* |
| 7. | 0.9901 | *G* | *G* | *G* | *G* |
| 8. | 0.9952 | *G* | *G* | *G* | *G* |
| 9. | 0.9975 | *G* | *G* | *G* | *VG* |
| 10. | 0.8827 | *G* | *G* | *G* | *G* |
| 11. | 0.0914 | *VB* | *B* | *VB* | *VB* |
| 12. | 0.3627 | *B* | *B* | *VB* | *VB* |
| 13. | 0.0617 | *VB* | *B* | *VB* | *VB* |
| 14. | 0.6959 | *M* | *B* | *B* | *B* |
| 15. | 0.3692 | *B* | *B* | *VB* | *B* |
| 16. | 0.9840 | *G* | *G* | *G* | *G* |
| 17. | 0.7668 | *M* | *M* | *B* | *M* |
| 18. | 0.9740 | *G* | *G* | *G* | *G* |
| 19. | 0.0000 | *VB* | *B* | *VB* | *VB* |
| 20. | 0.9940 | *G* | *G* | *G* | *G* |
| 21. | 0.9775 | *G* | *M* | *G* | *VG* |
| 22. | 0.9986 | *G* | *G* | *G* | *VG* |
| 23. | 0.2702 | *B* | *B* | *VB* | *VB* |
| 24. | 0.9904 | *G* | *G* | *G* | *G* |
| 25. | 0.9017 | *G* | *M* | *G* | *M* |
| 26. | 0.9977 | *G* | *G* | *G* | *VG* |
| 27. | 0.4668 | *M* | *G* | *G* | *M* |
| 28. | 0.9887 | *G* | *G* | *G* | *G* |
| 29. | 0.9740 | *G* | *G* | *G* | *G* |
| 30. | 0.6706 | *M* | *M* | *M* | *M* |

As seen in Table III, there are 5 transformers (2, 14, 21, 25, 27) that show mismatch with the results of AMHA. In [6], 4 transformers (1, 17, 21, 25) and in [5], 2 transformers (21, 27) show mismatches, respectively. It is to be noted that, the proposed method categorizes only 3 transformers (11, 13, 19) in *VB* class. On the other hand, the number of transformers categorized in *VB* class is 7 (4, 11, 12, 13, 15, 19, 23) in [6] and 5 (11, 12, 13, 19, 23) in [5], respectively. The no. 11 transformer is installed in 1970, about 36 years old and thus, expected to be near the end of it's life. Rightfully, the method in [5], [6] as well as the proposed method calssify it as *VB*. However, the other transformers being installed in 1980, are about 26 years old. Thus, they are less likely to be near the end of their lives. Also, AMHA classifies them as *B*.Thus, these transformers are more likely to be in class *B* rather than *VB*. Note that a transformer in *VB* might require replacement whereas those in class *B* could be kept in operation thorugh ncessary repair or maintenance. Obviously, the latter involves less cost and reduced interuption in power. The accuracy of the assessment by the proposed method is $\frac{25}{30} \times 100$ %=83.33%, indicating a highly effective transformer health identification.

## V. CONCLUSION

Transformer health index is a comprehensive value for describing the health of a transformer which has both technical and economic implications. In this paper, the health indices of oil-immersed transformers have been obtained using a logistic function. Unlike existing methods, a Poisson distribution has been used to model the health conditions of transformers. The resulting ML criterion is minimized by the Gradient Descent technique to obtain the weighing parameters of the logistic function. Using preset ranges, 30 working power transformers (from 3.15 KVA to 25.6 MVA) have been classified as good, moderate, bad, and very bad. Out of thirty, 25 transformers' health conditions have matched with those of expert assessments. Our results are also quite close to those of existing reports in the literature. In addition, in many cases the proposed method avoids categorizing a moderately old transformer as very bad. Thus, unnecessary replacement cost and power interruption can be avoided. Overall, the proposed method has been shown to provide a reliable and effective evaluation of the health of oil-immersed transformers.

## VI. APPENDIX

The sample 30 transformers are from the 90 working transformers [5]. Their test variables including installation year and KVA rating are given in Table IV.

## VII. REFERENCES

[1] Brian Sparling and Jacques Aubin "Determination of Health Index for Aging Transformers in view of Substation Asset Optimization", *GE Energy*, pp. 6-13, January, 16, 2010.

[2] A. Naderian, S. Cress, R. Piercy, F. Wang, and J. Service, "An approach to determine the health index of power transformers," in *Proceedings of the IEEE International Symposium on Electrical Insulation*, pp. 192–196, Vancouver, Canada, June 2008.

[3] A. E. B. Abu-Elanien, M. M. A. Salama, and M. Ibrahim, "Determination of transformer health condition using artificial neural networks," in *Proceedings of the International Symposium on Innovations in Intelligent Systems and Applications*, pp. 1–5, Istanbul, Turkey, June, 2011.

[4] A. D. Ashkezari, H. Ma, T. Saha, and C. Ekanayake, "Application of fuzzy support vector machine for determining the health index of the insulation system of in-service power transformers," *IEEE Transactions on Dielectrics and Electrical Insulation*, vol. 20, no. 3, pp. 965–973, 2013.

[5] A. E. B. Abu-Elanien, M. M. A. Salama, and M. Ibrahim, "Calculation of a health index for oil-immersed transformers rated under 69 kV using fuzzy logic," *IEEE Transactions on Power Delivery*, vol. 27, no. 4, pp. 2029–2036, 2012.

[6] W. Zuo, H. Yuan, Y. Shang, Y. Liu and T. Chen, "Calculation of a Health Index of Oil-Paper Transformers Insulation with Binary Logistic Regression", *Mathematical Problems in Engineering*, Article ID 6069784, pp.1-9, 2016.

[7] I. G. N. S. Hernanda, A. C. Mulyana, D. A. Asfani, I. M. Y. Negara, and D. Fahmi, "Application of health index method for transformer condition assessment," in *Proceedings of the IEEE Region 10 Conference (TENCON '14)*, pp. 1–6, Bangkok, Thailand, October, 2014.

[8] P. J. Griffin, C. M. Bruce, and J. D. Christie, "Comparison of Water Equilibrium in Silicone and Mineral Oil Transformers," *Minutes of the Fifty Fifth Annual International Conference of Doble Clients*, Sec. 10-9.1, 1988.

[9] Lars E. Lundgaard, Walter Hansen, Dag Linhjell, and Terence J. Painter, "Ageing of oil-impregnated paper in power transformers" *Proc. of IEEE Trans. on Power Delivery,* vol. 19, no. 1, pp. 230-239, 2004.

[10] Kanika Shrivastava and Ashish Choubey, "A Novel Association Rule Mining with IEC Ratio Based Dissolved Gas Analysis for Fault Diagnosis of Power Transformers," *International Journal of Advanced Computer Research (ISSN (print): 2249-7277 ISSN (online): 2277-7970) Volume-2 Number-2 Issue-4 June-2012.*

[11] Ronald E. Walpole, Raymond H. Myers, Sharon L. Myers, and Keying Ye, *Probability and Statistics for Engineers and Scientists*, 8th Edition, Pearson Education International, 2001.

TABLE IV. VALUES OF TEST VARIABLES FOR 30 SAMPLE TRANSFORMERS

| No | Year of installation | Voltage ratio(KV) and power rating(KVA) | Water (ppm) $x_1$ | Acidity (mgKOH/g) $x_2$ | BDV (KV) $x_3$ | DF % $x_4$ | DCG (ppm) $x_5$ | 2-Furfuraldehyde (mg/L) $x_6$ |
|---|---|---|---|---|---|---|---|---|
| 1. | 1980 | 22/6.9;5000 | 21.7 | 0.024 | 32.5 | 0.075 | 483 | 0.86 |
| 2. | 1980 | 22/6.6;3.15 | 26.9 | 0.098 | 40.5 | 0.894 | 254 | 0.65 |
| 3. | 1980 | 22/6.6;8 | 14.5 | 0.033 | 58 | 0.14 | 78 | 0.26 |
| 4. | 1980 | 22/6.9;8 | 21.2 | 0.226 | 48.7 | 0.424 | 215 | 5.53 |
| 5. | 2000 | 22/6.6;5000 | 10 | 0.01 | 75 | 0.111 | 126 | 0.06 |
| 6. | 1981 | 22/6.6;4 | 15.5 | 0.075 | 71 | 0.143 | 38 | 0.53 |
| 7. | 1981 | 22/6.6;10 | 16.8 | 0.167 | 70.1 | 0.255 | 149 | 0.78 |
| 8. | 1980 | 22/7.2;15 | 15 | 0.092 | 67.8 | 0.211 | 28 | 0.69 |
| 9. | 1980 | 22/6.9;8000 | 17 | 0.035 | 62.7 | 0.113 | 9 | 0.21 |
| 10. | 1981 | 22/3.3;3.15 | 30 | 0.088 | 37.6 | 0.353 | 197 | 0.31 |
| 11. | 1970 | 22/6.9;8000 | 16.2 | 0.181 | 25.5 | 0.201 | 35 | 8.76 |
| 12. | 1980 | 23.5/11;25600 | 15 | 0.155 | 37.5 | 0.182 | 53 | 7.29 |
| 13. | 1980 | 11/23.5;25600 | 16.8 | 0.115 | 25.6 | 0.174 | 78 | 96 |
| 14. | 1980 | 11/23.5;25600 | 15 | 0.21 | 57.2 | 0.22 | 53 | 6.69 |
| 15. | 1980 | 22/6.6;8 | 27.6 | 0.089 | 30.4 | 0.128 | 336 | 5.12 |
| 16. | 1980 | 21.45/6976;5000 | 23.5 | 0.106 | 45.8 | 0.207 | 30 | 0.24 |
| 17. | 1980 | 21.45/6.9;8000 | 24.8 | 0.012 | 29.9 | 0.068 | 504 | 1.68 |
| 18. | 1980 | 21.45/7.2;15000 | 23.6 | 0.07 | 39.2 | 0.203 | 22 | 0.5 |
| 19. | 1980 | 21.45/6.9;8000 | 30.5 | 0.073 | 28.7 | 67 | 30 | 15.7 |
| 20. | 1980 | 21.45/6.9;8000 | 18.4 | 0.063 | 64.5 | 0.243 | 69 | 0.15 |
| 21. | 1980 | 22/0.4;1600 | 21.1 | 0.019 | 28.4 | 0.025 | 144 | 0.02 |
| 22. | 1981 | 22/0.4;630 | 8.1 | 0.01 | 66.9 | 0.042 | 71 | 0.05 |
| 23. | 1980 | 23.5/11;25600 | 19.6 | 0.216 | 41.1 | 0.264 | 48 | 7.54 |
| 24. | 2000 | 22/6.98;5000 | 6 | 0.01 | 67.6 | 0.126 | 427 | 0.08 |
| 25. | 1981 | 22/6.6;10 | 18.4 | 0.152 | 37.2 | 0.299 | 81 | 1.14 |
| 26. | 1997 | 6.6/0.4;1600 | 11.1 | 0.032 | 67.2 | 0.089 | 119 | 0.04 |
| 27. | 1980 | 22/6.6;3.15 | 21.5 | 0.147 | 60.8 | 0.938 | 168 | 0.92 |
| 28. | 1986 | 22/6.6;4 | 7.5 | 0.16 | 70.1 | 0.448 | 10 | 0.06 |
| 29. | 1981 | 0.38/19.2;100 | 13 | 0.091 | 51.6 | 0.369 | 8 | 0.32 |
| 30. | 1981 | 0.38/19.2;100 | 35.7 | 0.229 | 41.4 | 0.639 | 24 | 1.07 |

# Feasibility Analysis of Grid Connected Mini Hybrid Energy System in Coastal Region of Chittagong, Bangladesh

Faisal Bin Kashem[1], Mohammed Shahriar Arefin[2]
[1]Department of EEE, University of Chittagong, Chittagong, Bangladesh
[2]Department of EEE, CUET, Chittagong, Bangladesh
[1]fbk835@gmail.com, [2]shahriar.cuet2013@gmail.com

*Abstract*— **In current world, it is tough to think of a moment without electricity but in Bangladesh, especially in rural areas, power crisis is a major constraint to the advancement. Parki, a coastal region of Chittagong, Bangladesh, has abundance of different renewable energy. This paper presents the model and the economical convenience of a grid connected hybrid energy system for Parki area. HOMER software is used to find out the optimized model via analyzing several sets of system for the available resources. Optimized grid connected model is compared with standalone system and grid to find out the feasible model for the consumers. This renewable resource based grid connected hybrid energy system will be helpful to reduce load demand from the grid and hence the energy shortage in national grid. Besides, renewable energy based energy system ensures the reduction of greenhouse gas by a significant amount.**

***Keywords— Parki; HOMER; Renewable energy; Hybrid System; PV; Wind energy; Biomass; Optimization***

## I. INTRODUCTION

About 80% of the total energy consumption around the world is fossil energy like oil, natural gas and coal [1]. But fossil fuel is limited and so the depletion of fossil fuel reserve has become a burning question in last few decades as new fossil energy sources are not being available compared with consumption rate. According to study, current fossil fuel reserves will be depleted at the end of this century if fuel consumption continues at this rate [1]-[2]. Besides, burning of fossil fuel is the leading reason of increasing amount of greenhouse gases in the environment which is also a great concern. Renewable and hybrid system can be a great relief in this situation for its environment friendly nature.

Recently, renewable energy technologies have become popular around the world to ensure sustainable development. Many countries are implementing renewable energy system instead of conventional system. Besides, use of renewable energy ensures a healthier environment by decreasing pollution as well as it saves the fossil fuel and coal which are used a lot to produce electricity. It serves the best interest as an effective solution to the global warming and high fuel cost [3].

Bangladesh is a developing country with a population of over 170 million people within 147,570 km$^2$ area. The conventional power sources are used in Bangladesh to generate electricity. About 76% of the total generated energy is fueled by natural gas which will be depleted by the end of the decade [4]. So, like many other countries, using renewable energy to generate electricity will be beneficial to Bangladesh.

Bangladesh has a 270 km long coastal line which provides a prodigious prospect of harnessing wind energy to produce electricity [5]. Besides, the amount of solar irradiation at the coastal area is comparatively high which can also be used to generate electricity. Hydro energy and biomass resources are also being considered to design hybrid systems where significant amount of these resources are available [6]-[8]. Hybrid energy system comprises of two or more sources of energy to generate electricity [1]. This kind of energy system is more reliable and stable than standalone system based on single resource. Many studies have been done on different coastal region on Bangladesh. Several hybrid and standalone system have been designed for St. Martin island, Kutubdia Island, Nijhum Dwip etc. [8]-[10].

Parki (22°12.06'N, 91°48.83'E), an area of Barasat Union in Chittagong, Bangladesh, is a coastal area near Bay of Bengal. Load shedding is a common occurrence at the rural areas of Bangladesh and Parki is not an exception. In this paper, we have discussed the feasibility of a grid connected mini hybrid energy system for Parki area and designed an optimized mini hybrid energy system. Simulation is carried out by HOMER software to determine the best possible combination to minimize the cost of energy (COE). This optimized hybrid energy system can be a relief for the dwellers of Parki as well as excess electricity can be sold to the grid which will help to reduce the cost of energy and this extra amount of electricity added to the grid will be helpful for a broader community.

## II. LOAD CALCULATION

We went through an on-sight survey and based on the collected data, we have categorized the load of the area into two groups as residential and non-residential load. To calculate residential load at Parki and nearby areas, we divided the families into 3 sub-categories based on their economic condition and calculated the load for each group. Among 6000 families of Parki, there are 2000 families who have yearly income of less than 70000 BDT who have been placed on

978-1-5386-2307-7/17/$31.00 ©2017 IEEE

"Poor" category, 3000 families have been placed on "Solvent" category with yearly income of 70000 to 150000 BDT range and the third category is "Very Solvent" with 1000 families where yearly family income is more than 150000 BDT. From our survey data, we found that 10% of total families hold refrigerators, all of the families under "Very Solvent" category and two-third families of "Solvent" category hold television. The load division for each category is shown below in TABLE I.

TABLE I. LOAD DESCRIPTION FOR DIFFERENT FAMILY CATEGORIES

| Categories | Number of Family | Description of Necessary Loads Per Family | Description of Extra Loads on Different Category |
|---|---|---|---|
| Poor | 2000 | 2 CFL,1 Fan | - |
| Solvent | 3000 | 3 CFL, 2 Fan | 2000 TV |
| Very Solvent | 1000 | 4 CFL, | 1000 TVs & 60 Pumps |

For calculation of non-residential load, we considered schools, colleges, shops, places of worship, health care center, administration building, restaurants and shops near beach area etc. Based on seasonal variation, we divided the load of the whole year in two groups-Summer and Winter. Fig. 1 and Fig. 2 respectively shows the graphical representation of daily load profile for summer and winter.

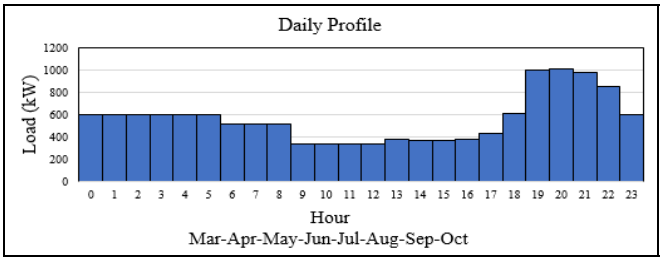


Figure 1. Daily load profile of Parki in summer

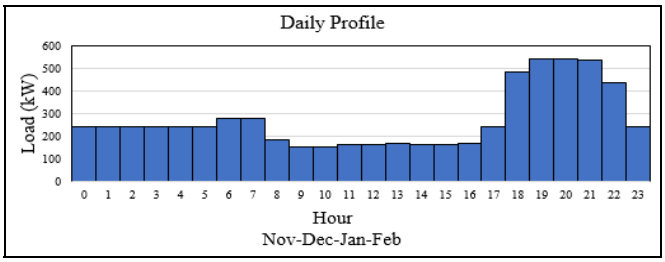


Figure 2. Daily load profile of Parki in winter

## III. RESOURCE DATA ANALYSIS IN PARKI

In this study, we have found that use of standalone system with a single resource will not be enough to produce the required amount of energy and it won't be cost effective. So, we have designed a hybrid system where the renewable resources, we considered, are solar, wind, biomass system. As our design comprises grid electricity along with renewable sources, we have considered to energize the place with a minimum of 65% renewable energy to ensure high use of renewable resources.

### A. *Solar Resource*

HOMER requires solar irradiation data to calculate the solar energy produced by the panel used. Due to the unavailability of hourly data, we have used monthly averaged global radiation data from NASA Surface Meteorology and Solar Energy. It has monthly averaged global horizontal radiation for a period of 22 years. The monthly variations of solar data and clearness index is summarized in TABLE II.

TABLE II. SOLAR RESOURCE OF PARKI

| Month | Clearness Index | Daily Radiation ($kWh/m^2/day$) |
|---|---|---|
| January | 0.618 | 4.420 |
| February | 0.607 | 4.980 |
| March | 0.574 | 5.440 |
| April | 0.526 | 5.510 |
| May | 0.465 | 5.110 |
| June | 0.375 | 4.160 |
| July | 0.367 | 4.040 |
| August | 0.394 | 4.180 |
| September | 0.411 | 4.020 |
| October | 0.501 | 4.280 |
| November | 0.577 | 4.250 |
| December | 0.629 | 4.280 |

Fig. 3 shows the visual representation of solar radiation and clearness index data throughout the year.

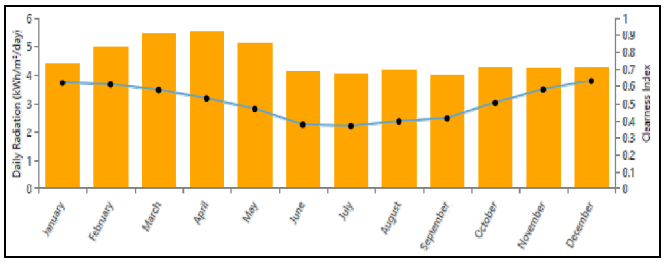


Figure 3. Solar radiation data throughout the year

### B. *Wind Resources*

Wind is a great source of renewable energy which provides a comparatively higher fraction of renewable energy in this model. According to the study of Bangladesh Center of Advance Studies (BCAS), by utilizing the wind velocity at the coastal area of Bangladesh, it is possible to generate power in both summer and winter season over the year [1]. As Parki is located at the coastal line of Bay of Bengal, the average wind speed is comparatively good at Parki Saikat throughout the year. According to the data from NASA Surface Meteorology and Solar Energy, for a height of 50 meter above sea level, yearly average wind speed at Parki Saikat is 2.74 m/s with a maximum speed of 3.420 m/s at June and minimum speed of 2.040 m/s at October. Fig. 4 presents the variation of average wind speed at Parki throughout the year.

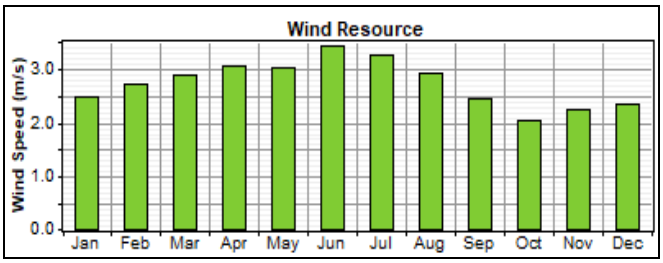


Figure 4. Variation of average wind speed at Parki throughout the year

### C. *Biomass Resource*

Biogas can be a source to produce electricity at Parki as a good amount of manure is produced from the cattle kept by the dwellers of Parki. Generally, the amount of produced manure doesn't vary too much with time to make an impact on electricity production. Everyday a cow and a bull produce an average of 7.5kg and 10kg dung, respectively which results in a total collection of 2 tonne manure per day at Parki estimating 25% collection factor. This amount of biomass can provide 1.4 tonne biogas considering 70% gasification ratio.

## IV. HYBRID RENEWABLE ENERGY SYSTEM

As we mentioned at section III, we have considered solar, wind and biomass as renewable resources to generate electricity at Parki. So, our designed system comprises biogas generator, photovoltaic(PV) array and wind turbine to generate electricity. It also consists of grid as backup source and excess energy absorber. Fig. 5 shows the hybrid energy system designed to meet the demand at Parki. Biogas generator, wind turbine and grid are connected to AC bus while PV array and battery, used to store energy, are connected to DC bus. A bi-directional converter is used to create bridge between AC and DC bus. The load is also connected to the AC bus as we mostly use AC loads in our daily life.

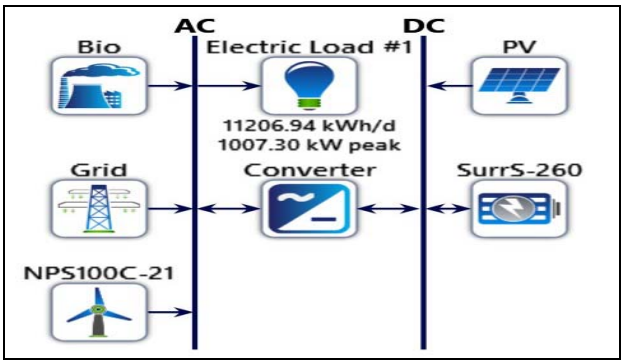


Figure 5. Design of hybrid energy system for Parki

### A. *Solar PV Modules*

Generic flat plate PV has been used in this system to generate electricity from solar energy. The PV array with a rated capacity of 3025 kW is used here which capacity factor is 17.3% and that results in a mean output of about 523 kW. Fig. 6 represents the power output of the PV array used in this model.

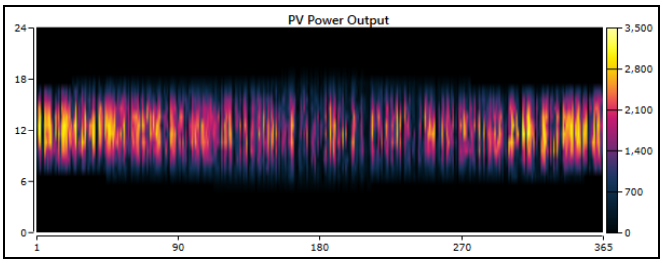


Figure 6. Power output of Generic flat plate PV

The installation cost for the PV array is about 4,538,160$ with a lifetime of 25 years and about 130,000$ costs for operation and maintenance of this PV array. The sun tracking system with the PV panels moves on horizontal axis in daily basis to ensure the best use of daylight. Solar PV modules generates about 4,580,071 kWh every year in the optimized model which is 58.1% of the total electricity generated by the system.

### B. *Wind Turbines*

We have used Northern Power NPS100C-21 wind turbine in this hybrid model to convert wind energy to electrical energy. Each of the turbine has a rated capacity of 100 kW and the mean output of each turbine is 70.9 kW with a capacity factor of 2.84%. 25 wind turbines have been used in this system with a project lifetime of 25 years. The installation cost for 25 wind turbines is 53,333$ and maintenance cost is about 215$/year. In optimized model, these 25 wind turbines produced about 621,330 kWh electricity every year via operating for 5209 hours.

### C. *Biogas Generator*

To generate electricity from the biogas Generic Biogas Genset has been used. Minimum load ratio of this biogas generator is 50%. The initial installation cost for this generator is 400$/kW with an O&M cost of 5$/hour for each generator. Lifetime of each generator is about 20000 hours. Lower heating value of the biogas, generated from cattle manure, is 5.5 MJ/kg and this biogas contains 5.5% carbon content.

### D. *Battery*

Though renewable resources provide an average amount of energy for a long period of time, it doesn't follow any regularity and for this reason it is required to use energy storage unit to support the consumers when the resource provides low amount of energy [11]. We have used Surrette S-260 energy storage unit to store the energy of PV panel which can supply stored energy at a nominal voltage of 12V. Two units are used in each string to ensure 24V bus voltage. Primary installation cost for each battery is 50$ and the replacement cost for each battery is 45$.

### E. *Converter*

Converter can be used to covert AC to DC and vice versa which means that it can be used both as rectifier and inverter. In the designed model, it is needed to convert the DC voltage supplied by PV module and batteries as the supplied energy is

used by AC load [12]. So, we have used 10 kW converter for the conversion of energy. The capital required to install 251 converters is 250,153$ and the replacement cost for the converter is 84,907$. This converter has 95% inversion efficiency and 90% rectification efficiency. The O&M cost for the converter is about 1300$/year.

### *F. Grid Electricity*

In this model, grid is used as a backup source of electricity and it also serves as the absorber when more electricity is produced from renewable resources. Electricity is supplied from the grid if the energy production by renewable resources is not sufficient to meet the demand of the consumer. Selling excess electricity reduces cost of energy as well as reduce load shedding in national grid. The price of grid power is 0.065$/kWh and grid sellback price is 0.050$/kWh. In the optimized model about 815,428kWh net energy is sold to the grid per year. In optimized model, maximum amount of electricity is purchased from grid at October and maximum amount of electricity is sold to grid at December.

### *G. Constraints*

This model is designed for 25 years with 10% interest rate. To ensure more use of renewable energy and less amount of pollution, we have kept the minimum renewable fraction at 65%. We also wanted to relieve the consumers from the burden of load shedding and so we have fixed the maximum annual capacity shortage at 0%.

## V. RESULTS AND DISCUSSION

HOMER software simulates 4118 solutions for the provided load profile and different hybrid models among which 2034 solutions are feasible. The system is analyzed in HOMER software based on various sensitivity variables and economic constrains like minimum renewable fraction, interest rate, capacity shortage, battery life, available resources and then optimized model is presented based on cost of energy (COE) [5], [13]. Factors like net present cost (NPC), operation and maintenance cost, capital cost, etc. also influence the selection [13]. Among 2034 feasible solutions, the optimized architecture comprises of 2987 kW PV, 25 wind turbines, 2286 batteries, 2502 kW converter and grid connection as backup source when renewable resources are not sufficient to meet the load demand. TABLE III represents the optimized system architecture for the designed model.

TABLE III. OPTIMIZED SYSTEM ARCHITECTURE

| Parameter | Value |
|---|---|
| Solar PV | 2987 kW |
| Battery | 2286 Surrette S-260 |
| Wind Turbine | 25 NPS100C-21 |
| Converter | 2502 kW |
| Grid | Backup |

Monthly average electricity production is shown in Fig. 7 which represents that maximum amount of electricity is purchased from the grid at October. The consumption ratio shows that 54.3% of the produced energy is consumed by the AC electric load and rest 45.7% electricity is sold to the grid which reduced COE for the optimized model.

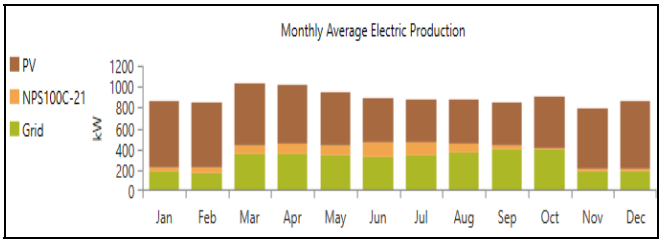


Figure 7. Monthly average electricity production by different components

### *A. Economic Analysis*

The optimized model, with the available resources, can meet the load demand at lowest possible cost. Fig. 8 represents the cost summary for the optimized system architecture by different cost type for different components. The major cost to implement the system is capital cost which is about 4.5 million USD. Though the installation cost seems high, for 25 years plan this cost become the minimal as it serves the energy at a minimum cost of 0.0518$ considering all cost of installment and maintenance of the system for the mentioned period.

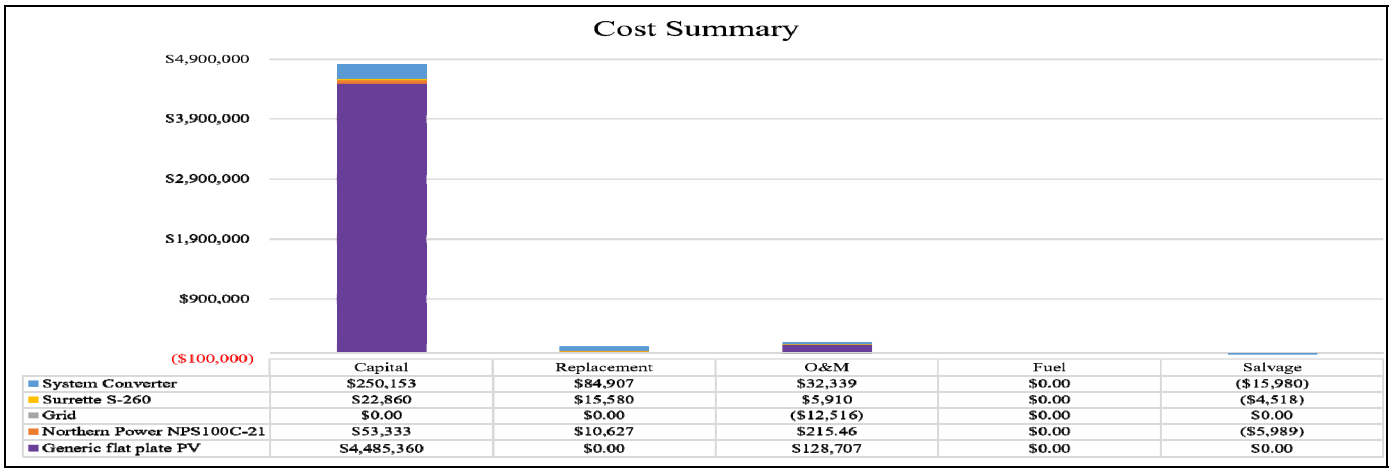


Figure 8. Cost summary of the designed system for different components

### B. *Environmental Effect*

In this modern world, emission of greenhouse gases has increased at a concerning rate and so it is necessary to reduce the amount of release in nature. This can be attained by the generation of power using renewable resources. If the total load is supplied via grid, then the amount of $CO_2$ emission will be about 5300 tonne/year as the emission factor for Bangladesh is 0.7 [1]. Using renewable energy sources ensures the significant reduction of emission of $CO_2$, $SO_2$, $NO_x$ to the environment [9]. In this model, larger portion of electricity is generated from renewable resources and the net amount of energy sold to the grid is about 815,428 kWh, according to the data from HOMER software which results in a possible reduction of 511.81 tonne $CO_2$ every year. It also reduces $SO_2$ emission by 2.22 tonne/year and the emission of $NO_x$ by an amount of 1.089 tonne/year. This substantial reduction of greenhouse gas emission guarantees a healthier environment.

## CONCLUSION

Due to shortage of power generation, rural areas like Parki are being deprived from the full facilities of technology and industrialization. This shortage can be neutralized with the use of renewable energy. Our paper shows that grid connected hybrid renewable energy system can be a good solution for Parki area. Proposed system is reliable as it has necessary backups in case of low production of energy by renewable resources or failure in grid. The COE being only 0.0518$ (4.25 BDT) which ensures electricity for everyone at comparatively low price. Proposed system also curtails the amount of Carbon emission by 9.66% which is a step forward to green energy.

## REFERENCES


[1] M. Shahadat, H. Lipu, S. Uddin, M. Ahad, and R. Miah, "A feasibility study of solar-wind-diesel hybrid system in rural and remote areas of Bangladesh," *International Journal of Renewable Energy Research*, vol. 3, no. 4, pp. 892-900, 2013.

[2] Noam Lior, "Energy resources and use: The present situation and possible paths to the future," *Energy*, vol. 33, no. August 2006, pp. 842–857, 2008.

[3] M. Nurunnabi and N. K. Roy, "Grid connected hybrid power system design using HOMER," *2015 International Conference on Advances in Electrical Engineering (ICAEE)*, Dhaka, 2015, pp. 18-21.

[4] A. Zubair, A. A. Tanvir, and M. Hasan, "Optimal Planning of Standalone Solar-Wind-Diesel Hybrid Energy System for a Coastal Area of Bangladesh," *International Journal of electrical and computer engineering,* vol. 2, no. 6, pp. 731–738, 2012.

[5] Alam, M., & Bhattacharyya, S., "Decentralized renewable hybrid mini-grids for sustainable electrification of the off-grid coastal areas of Bangladesh," *Energies,* vol. 9, no. 4, pp. 268, 2016.

[6] A. S. Pranti, A. M. S. Iqubal, and A. Z. A. Saifullah, "Feasibility study of small Hydro/PV/Wind hybrid system for off-grid rural electrification in Ethiopia," *Applied Energy,* vol. 97, pp. 5-15, 2012.

[7] A. S. Pranti, A. M. S. Iqubal, and A. Z. A. Saifullah, "Conceptual Design of Solar-micro Hydro Power Plant to Increase Conversion Efficiency for Supporting Remote Tribal Community of Bangladesh," *American Journal of Engineering Research (AJER),* vol. 3, no. 11, pp. 167–197, 2014.

[8] M. M. Hossain, S. Barua and M. A. Matin, "A pre-feasibility study for electrification in Nijhum Dwip using hybrid renewable technology," *2015 International Conference on Electrical & Electronic Engineering (ICEEE)*, Rajshahi, 2015, pp. 225-228.

[9] A. K. M. S. Islam, M. Rahman, A. H. Mondal, and F. Alam, "Hybrid energy system for St. Martin Island, Bangladesh: An optimized model," *Procedia Engineering*, vol. 49, pp. 179-188, 2012.

[10] A. K. Sikder, N. A. Khan and A. Hoque, "Design and optimal cost analysis of hybrid power system for Kutubdia island of Bangladesh," *8th International Conference on Electrical and Computer Engineering*, Dhaka, 2014, pp. 729-732.

[11] S. Ghaem *et al.*, "Feasibility study of using a biogas engine as backup in a decentralized hybrid (PV/wind /battery) power generation system e Case study," *Energy*, vol. 90, no. 2, pp. 1830–1841, October, 2015.

[12] S. Salehin, A. K. M. S. Islam, R. Hoque, M. Rahman, A. Hoque and E. Manna, "Optimized model of a solar PV-biogas-diesel hybrid energy system for Adorsho Char Island, Bangladesh," *2014 3rd International Conference on the Developments in Renewable Energy Technology (ICDRET)*, Dhaka, Bangladesh, 2014, pp. 1-6.

[13] R. Mirza *et al.*, "Design of a Cost Effective Off-Grid Wind-Diesel Hybrid Power System in an Island of Bangladesh," *International Journal of Electrical, Computer, Energetic, Electronic and Communication Engineering,* vol. 5, no. 12, pp. 1646–1649, 2011.

# Measurement of weak low frequency pressure signal using stretchable polyurethane fiber sensor for application in wearables

Md Rejvi Kaysir[1,2,*], Alessio Stefani[1,3], Richard Lwin[1], and Simon Fleming[1,**]
[1]Institute of Photonics and Optical Science (IPOS), School of Physics, The University of Sydney, NSW 2006, Australia
[2]Department of EEE, Khulna University of Engineering and Technology, Khulna 9203, Bangladesh
[3]DTU Fotonik, Department of Photonics Engineering, Technical University of Denmark, DK-2800 Kgs. Lyngby, Denmark
*rejvi@eee.kuet.ac.bd, **simon.fleming@sydney.edu.au

*Abstract*— **The practical realization of low Young's modulus Polyurethane (PU) based optical fibers offers new possibilities for sensing on bodies due to its bio-compatibility and high material sensitivity. Here, we experimentally demonstrate a PU fiber pressure sensor using the simplest possible structure (i.e. a capillary) to measure a weak low frequency signal comparable to respiration/heart rate. We characterized the fiber and measured the sensitivity of a PU capillary using a speaker connected to a function generator. The frequency of the modulated signal was recovered using Fourier Transform (FT). This bodes well for applying more sophisticated structures to wearable devices.**

***Keywords—Polyurethane, fiber optic sensors, fiber drawing and fabrication, stretchable waveguide, biomedical signal.***

## I. INTRODUCTION

The detection/measurement of low frequency signals (such as vibration) is important in many applications, such as aerospace, automotive, architectural, security, and biomedical [1-4]. Measurement of pressure in the environment often involves low frequency signals. There exist different sensors, which convert pressure induced mechanical deformation into an electrical signal, based on their principle of operation such as piezoresistive or piezoelectrical, inductive or capacitive, thermo-electrical or acoustic [5]. These principles have many technological limitations including electromagnetic interference, higher temperature deformation, harsh chemicals or explosion sensitivity that restrict their complete utilization in sensing pressure in various environments.

Optical fiber sensors (OFSs) are an existing technology that overcomes most of those constraints and often also offers better long-term reliability. This technology is also particularly attractive for application in wearable, implantable, and human-friendly devices as it allows both sensing and signal transmission. There are three technologies which are commercially available for pressure measurement with fiber optics sensors: intensity based, fiber Bragg grating and Fabry-Perot [5,6], where the latter two use complicated light detection systems. All these currently used commercial OFS technologies for measuring pressure rely on optical fibers made of high (e.g. >1 GPa) Young's modulus (YM) materials (e.g. glass or PMMA), and their intrinsic sensitivity (which comes from these materials) to the external pressure is very low. Thus, high YM materials limit the maximum response of the overall pressure sensing system and the intrinsic sensitivity could effectively be increased by using low YM materials with good optical properties. Such low YM materials can also be used in stretchable human friendly environments where the fiber can be integrated into the fabrics of garments, which can permit bending and twisting with the human body. One such material is polyurethane which has YM as low as 10 MPa and can be elongated to 600% [7].

Recently, we demonstrated pressure sensing using hollow core PU fiber (outer and inner diameters of ~2100 μm and ~400 μm, respectively) for the application of detecting human movement, such as bed-ridden patients [8]. A comparatively rigid structure with a jacket of the PU material was chosen for this application. We are now interested in monitoring respiration/heart rate signal, which is generally required for either medical diagnosis or daily health monitoring. To demonstrate the suitability of the PU fiber as a sensor for monitoring respiration/heart rate, we used a simple laboratory set-up comprising a speaker connected to a function generator to introduce very low pressure on the fiber surface as a proof of the principle. This problem has been already investigated with the use of optical fiber sensors of high YM materials, but mostly using glass fibers and fiber Bragg gratings [9,10]. Both the material used and the costly detection method make impractical utilizing this technology as a wearable device.

In this work, we demonstrate the detection of a low frequency (e.g. 1 Hz) pressure signal, generated from a speaker connected to a function generator, using a simple PU capillary. The capillary fiber was used here due to its simple structure and ease of characterization (i.e. making a relationship between the transmission loss and the deformation of the fiber caused by applied force). A capillary optical fiber consists of low index air core surrounded by a high index dielectric cladding (PU material in this case), where the light is guided in the air hole by grazing incidence reflection of the waves between the air and dielectric medium. As the loss of this capillary fiber originates from individual reflections, the waveguide needs to be straight to minimize loss. The biggest problem of having capillary guidance is that the loss will

978-1-5386-2307-7/17/$31.00 ©2017 IEEE

increase abruptly with small microbending or gradual bending caused by any external factors/noise. The fiber was kept straight in the laboratory setup to minimize any additional losses during the measurement.

The flexibility of PU allows high levels of deformation of the air core of the capillary fiber that directly induce transmission losses. The response of the PU fiber can be related to the applied force and the sensitivity is much higher than that of the same fiber made of a higher YM material (e.g. PMMA). The frequency of the speaker head was recovered by using the FT signal. This analysis provides a pathway for characterizing more sophisticated PU fiber structures, which is a potential candidate for wearable devices.

## II. Sensor Fabrication and Characterization Method

### A. Fiber fabrication

We used a simple PU capillary for the experiments. The final capillary was realized by standard fiber drawing and the final dimension determined by the ratio between feeding and drawing. The simple structure helps to elucidate the loss mechanism and determine the relationship between the transmission loss and corresponding deformation of the fiber. The fabricated capillary was 30 cm long having inner and outer diameters 613 µm and 892 µm, respectively.

### B. Experimental setup for dynamic response measurement

The fiber was characterized in terms of sensitivity (*S*) that is defined as a change in transmission loss (in dB) of the fiber per unit change in the force (in N) applied on the fiber. As a PU capillary is used here, the light guides in the air core of the capillary. In the experimental setup, the fiber was kept straight by fixing at the input and output terminals and the force was applied on a small area of the fiber. Thus, the variable loss mainly originates from the deformation of the core by the applied force. To minimize the effect of other static losses in the system including launching, scattering and coupling to the detector, we kept the setup fixed throughout the measurement. Thus, the dominant loss in the system is the deformation of the core which modulates the transmission loss. To measure the low frequency signal, we investigated the dynamic response of the fiber, described in the following section.

Light from an inexpensive (~$1/unit) 655-nm laser diode was launched into the fiber through a 4X lens. This laser was driven by a laboratory power supply, however a 3V battery could be used as a power source for intended wearable devices. The output of the fiber was coupled to a Si-photodetector (THORLABS-SV2) that is connected to an oscilloscope. The dynamic force implementation was achieved using a speaker connected to a function generator. The head of the speaker (1 cm diameter) was in contact with the fiber surface, whereby modulations of the speaker head caused deformation on the air core fiber, thus causing loss.

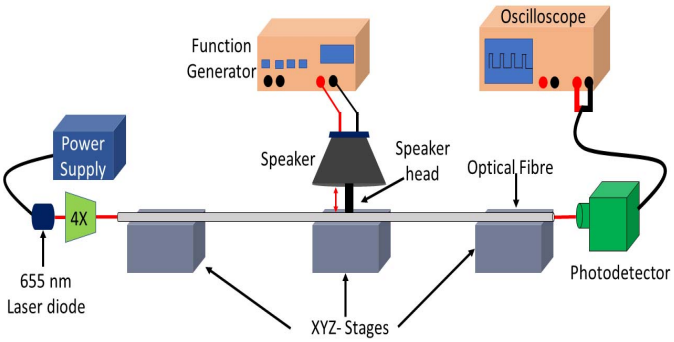


Figure 1. Schematic diagram of the experimental setup for the dynamic response measurement of the PU capillary.

The fiber was located on three XYZ stages of which two stages were fixed for launching to the input of the fiber and coupling to the detector. The middle stage was used to apply dynamic force from the speaker head. The fiber was secured using adhesive tape on the middle stage. This also ensured that the deformation of the air core does not create propagating waves along the fiber resulting in transients, spurious responses and other losses.

## III. Experimental Results

### A. Fiber characterization

We characterized the fiber in terms of sensitivity using the setup shown in Fig. 1. The change in the output power from the fiber with the applied force by the speaker head was measured by using both the Si-Photodetector (SV-2) connected to an oscilloscope and a THORLABS (PM100D) power meter (not shown in Fig. 1). Direct power measurements by the power meter would assist in determining the right detector for any specific applications.

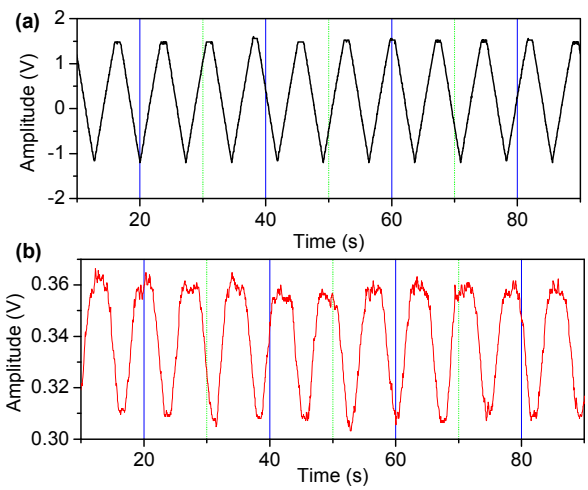


Figure 2. (a) Input signal to the speaker from a function generator for characterizing the PU capillary fiber and (b) the corresponding response of the fiber taken from the oscilloscope. There is a saturation effect shown at the top and bottom of the response signal as the speaker did not have enough strength to apply more force to deform the fiber.

We first used a triangular wave signal from the function generator to modulate the speaker head (i.e. modulate the force on the fiber) to determine the maximum dynamic range of the output signal change due to the applied force. Figure 2 (a) shows the input signal to the speaker in which the positive signal means the speaker head moving downwards, hence compressing the air core of the fiber. On the other hand, the negative signal moves the speaker head upwards and releases the compression on the fiber. Figure 2(b) shows the corresponding response of the fiber with the applied force. When the input signal to the speaker is maximum, the output signal reaches the lowest value, as expected due to increasing transmission loss caused by deforming the air core. Thus, there exists an approximately linear relationship between the force and the corresponding loss of the fiber, for such small deformation regime.

The maximum transmission loss of the fiber was found to be 1.9 dB. We also measured the force of the speaker head using a laboratory scale and determined it to be 0.09 N. Thus, the sensitivity of the fiber can be calculated as 23.3 dB/N. At this stage, we were interested to measure the deformation of the air core of the PU capillary fiber with the applied force. This information helped us to relate the deformation of the core with the applied force, which is described in the following section.

### *B. Fiber deformation measurement:*

The deformation of the PU capillary fiber was measured by using a microscope camera. The change in the diameter of the PU capillary with the applied force is shown in Fig. 3. There is a small change in the diameter up to the force of ~1.5 N, after that the diameter reduces abruptly up to ~4 N. From the slope of the graph, we found the deformation sensitivity to be ~66 µm/N. A PMMA capillary of the same dimensions was also investigated under the same force and no visible change in diameter was observed.

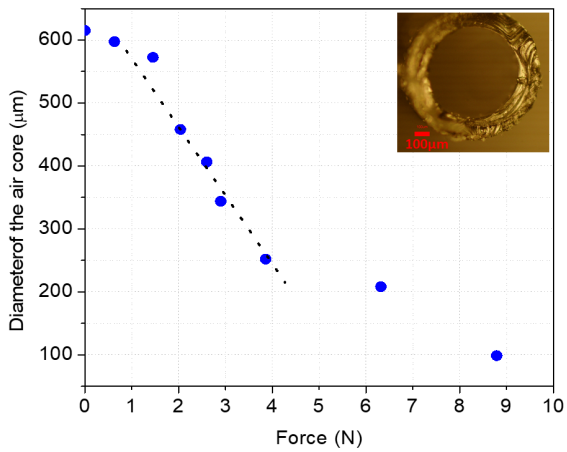


Figure 3. The change in core diameter of the PU capillary fiber with the applied force. A linear fit to the data is also presented here, which shows the mechanical deformation sensitivity of ~ 66 µm/N. Inset: cross section of the PU capillary fiber.

### *C. Square wave signal response:*

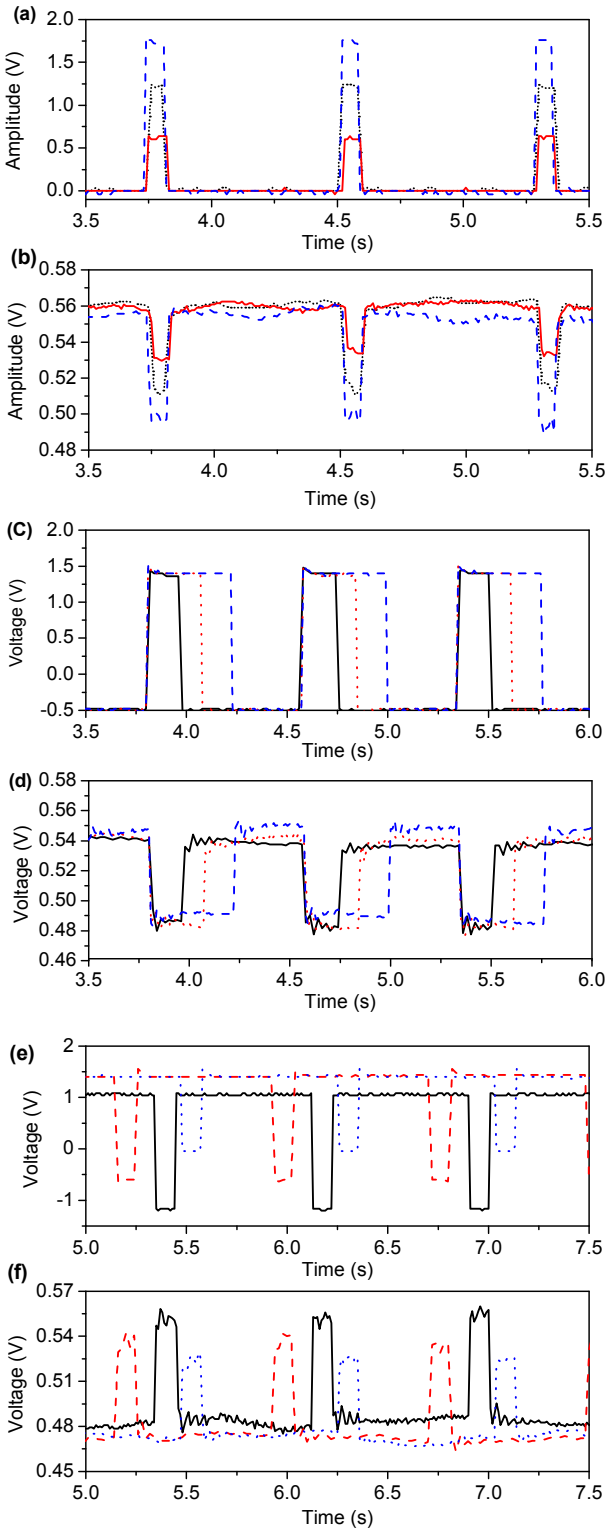


Figure 4. (a) Amplitude, (c) duty cycle and (e) dc offset variation of the input signal to the speaker and corresponding response of the PU fiber: (b), (d) and (f), respectively.

As stated, since we aimed at detecting/measuring a low frequency signal using PU fibers, we first set a low frequency (< 5Hz) input square wave signal from the function generator to modulate the movement of the speaker (i.e. modulate the applied force on the fiber). Then, different parameters (amplitude, duty cycle and dc offset) of the input signal to the speaker were changed. Figure 4 shows the various input signals to the speaker and their corresponding responses from the PU fiber.

Figure 4 (a) and (b) show the variation of the amplitude of different input signals to the speaker and the responses of the PU fiber respectively, where the same color is used to identify the corresponding response of the PU fiber. In general, the higher amplitude of the signal to the speaker means the fiber experiences larger force, which deforms the air core of the fiber further. Thus, the magnitude of the PU response signal depends on the corresponding polarity and magnitude of the input signal to the speaker. However, there are saturation effects at the bottom of the response signal (see Fig. 4(b)) as the speaker did not have enough force to deform the fiber further. This situation was also observed earlier when characterizing fibers with triangular wave signals, which is discussed in section IIIA.

Figure 4(c) and 4(d) show the variation of input signals to the speaker by changing the duty cycle and the response of the PU fiber, respectively. As there is no change in the magnitude and polarity of the input signal, the magnitude of the response signal should not change. Here, we observed the time response of the PU fiber with the same pulse ends at different time, which verifies that there is no delay in the response of PU system within the range of applied force.

Figure 4(e) and 4(f) show the variation of input signals to the speaker by changing dc offset and their response, respectively. As both the magnitude and dc level of the signal change, the response of the PU fiber should follow both magnitude and dc offset. The response graph clearly shows the changes as expected. It is noted that, there is a small change in the background of the PU responses due to variation of input power. However, the fiber clearly showed the distinguishable responses from the background signal due to the extreme sensitivity of the PU fiber.

### *D. Frequency response using FT:*

As the goal of this work is to measure/detect low frequency signal, we used the Fourier transform of the PU response data to identify the input signal frequency to the speaker. We used FFT in the MATLAB environment to get the frequency response data from the time domain signal. Figure 5 shows the response of the PU time domain signal and their corresponding frequency domain signal using FFT. The input frequency of the function generator was set as 1.3 Hz. The clear peak at 1.3 Hz in the FFT demonstrates that the frequency information of the speaker can be effectively recovered by the PU fiber allowing for example to recover the heart rate and determine its variability.

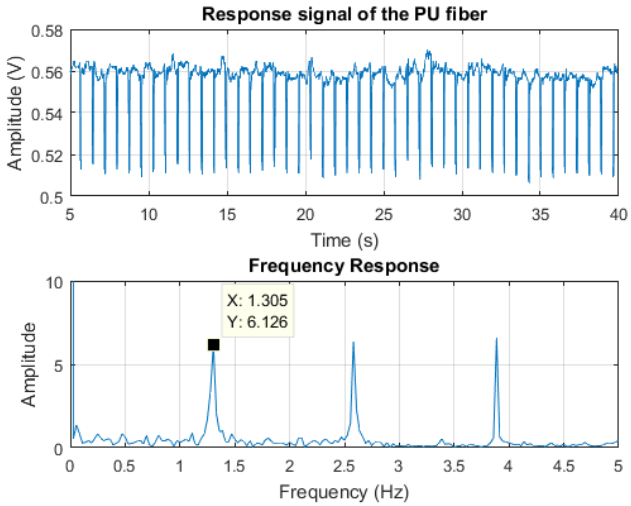


Figure 5. (a) The response of the PU fiber with the applied signal frequency to the function generator at 1.3 Hz. (b) FFT data of the time domain signal.

## IV. Conclusion

We successfully characterized and demonstrated the frequency response of a PU capillary fiber. The sensitivity of the capillary fiber was found to be 23.3 dB/N, which makes it suitable for detecting a very small force of 0.09 N. We recovered the input frequency of the speaker by applying FFT to the PU fiber response signal. The sensitivity of the PU fiber could be effectively tuned by different useful design. This analysis also gives a pathway to characterize more sophisticated and complex fiber structures. Thus, fiber sensors made of PU (low YM materials) could open up new opportunities for sensors in wearable/ biomedical applications.

## Acknowledgment

This work was performed in part at the OptoFab Node of the Australian National Fabrication Facility (ANFF), utilizing Commonwealth and NSW State funding, and was supported by ARC (DP170103537) and NSW Smart Sensors Network (NSSN) funding. This work was supported by the Marie Sklodowska-Curie grant of the European Union's Horizon 2020 research and innovation programme (708860).

## References

[1] S. Wang, X. Fa, Q. Liu, and Z. He, "Distributed fiber-optic vibration sensing based on phase extraction from time-gated digital OFDR," *Optics Express*, vol. 23, no. 26, pp. 33301-33309, Dec. 2015.

[2] E. Reithmeier, S. Mirzaei, and N. Kasyanenko, "Optical vibration and deviation measurement of rotating machine parts," *Optoelectronics Letters*, vol. 4, no. 1, pp. 45-48, Jan. 2008.

[3] A. Wada, S. Tanaka and N. Takahashi, "Multipoint vibration sensing using fiber Bragg gratings and current-modulated laser diodes," *Journal of Lightwave Technology*, vol. 34, no. 19, pp. 4610-4614, Oct. 2016.

[4] D. Jiang and H. Wei, "Review of applications for fiber Bragg grating sensor," *Journal of Optoelectronics Laser*, vol. 13, no. 4, pp. 420-430, Oct. 2002.

[5] Éric Pinet, "Pressure measurement with fiber-optic sensors: Commercial technologies and applications," *Proc. of 21st Int. Conf. on*

*optical fiber sensors (SPIE),* May 20011, pp. 775304(1)-775304(4), vol. 7753.

[6] W. J. Bock, M. S. Nawrocka, W. Urbanczyk, J. Rostkowski and T. Martynkien, "Fiber-optic sensor for automotive applications [pressure and temperature measurement]," *Proc. of IEEE Sensors,* 2004, pp. 248-251 vol.1.

[7] S. Fleming, A. Stefani, X. Tang, A. Argyros, D. Kemsley, J. Cordi, and R. Lwin, "Tunable metamaterials fabricated by fiber drawing", *JOSA B*, vol. 34, no. 7, pp. D81-D85, 2017.

[8] M. R. Kaysir, A. Stefani, R. Lwin, and S. Fleming, "Flexible optical fiber sensor based on polyurethane," *Proc. of Pacific Rim conference on lasers and electro-optics (CLEO-Pacific Rim)*, 2017.

[9] P. Roriz, O. Frazão, A. B. Lobo-Ribeiro, J. L. Santos, J. A. Simoes, "Review of fiber-optic pressure sensors for biomedical and biomechanical applications," *J. Biomed. Opt.*, vol.18, no.5, pp. 050903-050918, May 2013.

[10] C. Massaroni, P. Saccomandi, and E. Schena, "Medical smart textiles based on fiber optic technology: an overview," *J. Funct. Biomater*. vol. 6, no. 2, pp 204-221, Jun 2015.

# Performance of Chip-Synchronous and Chip-Asynchronous OCDMA in Presence of Fiber Optic Dispersion and Optical Hard-Limiter

Saptami Rani, Md. Jahedul Islam and Md. Rafiqul Islam
Department of Electrical and Electronic Engineering
Khulna University of Engineering & Technology
Khulna-9203, Bangladesh
Email: saptamirani53@gmail.com, jahed_eee@yahoo.com, islambit@yahoo.com

*Abstract*—**The bit error rate (BER) performance of chip-synchronous and chip-asynchronous direct sequence optical code division multiple access (DS-OCDMA) is investigated using Gaussian shaped optical orthogonal code (OOC) as signature sequence and avalanche photodiode (APD) receiver. In this analysis, mainly two basic impairments, fiber optic dispersion and multiple access interference (MAI) are taken into consideration along with APD shot noise, surface leakage current, bulk dark current, amplifier noises and electric circuit noise to evaluate signal to noise ratio (SNR) and hence to calculate BER performance. The system performance is determined as a function of fiber optic length, chip rate and number of simultaneous user. The numerical results depict that chip-asynchronous OCDMA improves system performance and reduces power penalty significantly by using erbium doped fiber amplifier (EDFA) and optical hard-limiter in comparison to chip-synchronous OCDMA.**

***Keywords— Chip-synchronous and chip-asynchronous OCDMA, OOC, MAI and chromatic dispersion.***

## I. INTRODUCTION

Flexibility of utilizing huge bandwidth, asynchronous access of network, secure data transmission and low transmission loss make OCDMA technique attracting interests in all optical networks [1]-[3]. Most OCDMA research interests are highly concentrated on chip-synchronous OCDMA which is an assumption. Practically, OCDMA systems are fundamentally chip-asynchronous since users from several locations forward their information at any time without synchronization [4]-[5]. One of the severe problem for CDMA system is MAI when optical pulses of several users are multiplexed simultaneously, which increases bit error probability and limits the number of simultaneous users. Usage of optical hard-limiter (OHL) is an efficient way to minimize the impact of MAI [6]-[7]. Another system performance degradation factor is dispersion which causes pulse broadening and reduces received signal power [8]. For long distance transmission, effect of signal attenuation was minimized by using in-line optical amplifiers [8]. As far as knowing, the performance of chip-synchronous and chip-asynchronous OCDMA using both cascaded optical amplifiers and hard-limiters in presence of chromatic dispersion has not been analyzed before.

In this paper, both optical amplifier and hard-limiter are used to demonstrate the system performance using Gaussian shaped optical pulses as the user signature code and APD receiver. The influence of APD noises, optical amplifier noises and MAI are taken into consideration to evaluate BER performance in presence of chromatic dispersion.

## II. SYSTEM MODEL

Fig. 1 shows the block diagram of the system model. At the transmitter, a user's binary data is encoded by Gaussian shaped OOC. The encoded signals of all users are multiplexed and the composite CDMA signal is then driven by laser driver and coupled into a SMF operating at 1.55 μm. The total fiber span $L$, consists of $n$ fiber sections. To minimize signal attenuation during propagation through SMF, EDFA is used as optical repeater in each fiber section. At the receiving end, double optical hard-limiters are used. Optical correlator is employed to perform correlation between the received optical pulse sequence and the local signature sequence. After the optoelectronic conversion by APD, transmitted data are recovered from the sampling and threshold decision.

## III. THEORITICAL ANALYSIS

### A. Pulse broadening equation

In this analysis, Gaussian shaped OOC is used. In respect of Gaussian, the incident field distribution can be written as

$$g(0,t) = g_0 \exp\left[-(t/2T_0)^2\right] \tag{1}$$

where $g_0$ is the crest value of field orientation and $T_0$ is the half-width. In general, pulse duration is referred as full width at half maximum (FWHM) of pulse intensity. For Gaussian shaped pulse, these two are related as

$$T_{FWHM} = 2(\ln 2)^{1/2} T_0 \tag{2}$$

978-1-5386-2307-7/17/$31.00 ©2017 IEEE

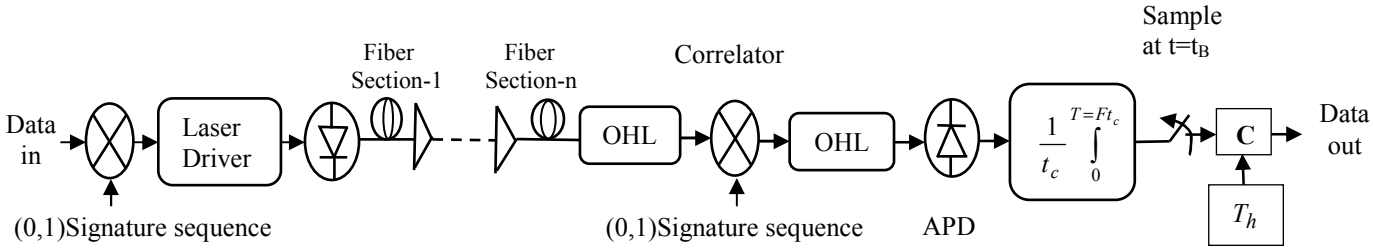


Fig. 1: Block diagram of the OCDMA system model.

Pulse width after propagating a certain distance $L$ is given by

$$T=T_0\left[1+\left(\frac{\beta_2 L}{T_0^2}\right)^2\right]^{\frac{1}{2}} \tag{3}$$

where $\beta_2$ is the second order dispersion constant expressed as

$$\beta_2=-D\lambda^2/2\pi c \tag{4}$$

where chromatic dispersion is denoted by $D$, $\lambda$ is the operating wavelength and $c$ is the velocity of light.

*B. BER analysis*

The received signal $r_o(t)$, for an OCDMA system having $N$ pairs of transmitter and receiver, can be represented as the summation of $N$ user's transmitted signals

$$r_o(t)=P_o\sum_{n=1}^{N}\sum_{i=1}^{F}b_n c_n(i)\int_{\tau_n+it_c}^{\tau_n+(i+1)t_c} g(t-\tau_n-it_c)dt \tag{5}$$

where $P_o$ is the maximum power of the received optical pulse, $b_n$ is the binary data bit (either "1" or "0") for the $n$-th user with bit duration $t_B$ at time $t(0\le t\le t_B)$, $c_n(i)$ is the chip value (either "1" or "0") of the $n$-th user's signature code at $i$-th position with code length $F=t_B/t_c$ and code weight $W$, $\tau_n$ is the time lag associated with the $n$-th user's signal. This delay is an integer times $t_c$ for chip-synchronous and a real number times of chip duration for chip-asynchronous case. For first user $\tau_1=0$ and all delays $\tau_n$ linked with the other users are relative to the first user's delay. $g(t)$ is the Gaussian shaped pulse with duration $t_c$ and assures the orthogonality condition. At the receiver, optical correlator performs correlation between $r_o(t)$ and the replica of the desired user's signature sequence. The decoded signal falls on the APD and the output current $Y_n$ for $n$-th user sampled at time $t=t_B$ can be represented as

$$Y_n=X_n+X_I+X_N+X_A \tag{6}$$

where $X_n$ is the signal current of the desired user, $X_I$ is the interference signal current carried by MAI, $X_N$ is the APD noise currents and $X_A$ is the noise currents contributed by optical amplifier. The role of optical hard-limiters can be defined as

$$h(j)=\begin{cases} v_f & j\ge T_h \\ 0 & 0\le j<T_h \end{cases} \tag{7}$$

where the threshold value of the optical hard-limiter is denoted by $T_h$ and $v_f$ is a constant value depends on the light intensity of the signal. The first OHL clips the signal power back to $v_f$ and thus reduces the effect of MAI. The second OHL removes the interference patterns completely after correlation by clipping the output signal power back to zero if the light intensity is less than $T_h$. According to the correlation definition of OOC, during correlation time each interference user can lead maximum one strike. If $k$ refers the total number of strikes from interference user then the probability density function (pdf) of total interference $X_I$ for chip-asynchronous case is expressed as

$$P_{X_I}(j)=\sum_{k=0}^{N-1}\binom{N-1}{k}E^k S^{N-1-k} f_k(j) \tag{8}$$

where $E=W^2/F$ , $S=1-E$, $f_0(j)=\delta(j)$, $\delta(j)$ is the Dirac delta function and

$$f_k(j)=\begin{cases} \frac{1}{\sqrt{2\pi\sigma^2}}e^{\frac{-(j-m_k)^2}{2\sigma^2}} & for\ 1<j<k \\ 0 & otherwise \end{cases} \tag{9}$$

for $k$ , $1\le k\le N-1$ where $m_k=k/2$ and $\sigma_k^2=k/12$. The pdf for chip-synchronous case is defined as

$$P_{X_I}(j)=\sum_{k=0}^{N-1}\binom{N-1}{k}E^k S^{N-1-k} \tag{10}$$

where $E = W^2/2F$. Throughout "1" bit interval of the desired signal, photons incident on the APD just during the $W$ mark intervals and are completely restricted during the $F$-$W$ space intervals. Throughout the $W$ chip intervals of the desired signal, among $NW$ pulses, there are $W+k$ mark pulses with power intensity $F_D P_o$ and $NW-(W+k)$ space pulses with power intensity $F_D \phi P_o$. Where, $F_D = T/T_0$ denotes the influence of dispersion and $\phi$ is the reciprocal of extinction ratio $\alpha$. In case of "1" bit transmission, the conditional pdf $P_{Y_n}$ can be expressed as

$$P_{Y_n}(\gamma|j,1) = \frac{1}{\sqrt{2\pi\nu_1^2}} \exp\left[-(\gamma-\sigma_1)^2/2\nu_1^2\right] \tag{11}$$

Therefore, average $\sigma_1$ and variance $\nu_1^2$ of the output photo current $Y_n$ are expressed as

$$\sigma_1 = M\left(G_0 R_S P_t^1 + I_{bd}\right) + I_{sl} \tag{12}$$

$$\nu_1^2 = 2eM^{2+\rho} B_E \left(R_S G_0 P_t^1 + I_{bd}\right) + 2eI_{sl} B_E + 4k_B T B_E / R + \frac{4G_0 I_s^1 I_{sp} L_0^2 B_E}{B_0} + \frac{(I_{sp} L_0)^2 (2B_0 - B_E) B_E}{B_0^2} \tag{13}$$

where $$P_t^1 = (W+k)P_o/F_D + (WN - W - k)P_o\phi/F_D \tag{14}$$

$$I_{sp} = N_a N_{sp}(G_0 - 1) e B_0 \tag{15}$$

$$I_s^1 = \frac{2e\alpha P_o}{h\nu(\alpha+1)} \tag{16}$$

For "0" bit transmission, $N$ user's spaces contribution is $NP_o/\alpha$ at the $k$-th mark position of the desired user's signal. If $N \geq \alpha$ the second hard-limiter cuts the signal strength back to unity, defined as

$$i_\alpha = \begin{cases} 1 & if\ N \geq \alpha \\ 0 & if\ N < \alpha \end{cases} \tag{17}$$

Similarly for "0" bit transmission, the conditional probability density function $P_{Y_n}$ is expressed as

$$P_{Y_n}(\gamma|\, j, 0) = \frac{1}{\sqrt{2\pi\nu_0^2}} \exp\left[-(\gamma-\sigma_0)^2/2\nu_0^2\right] \tag{18}$$

where the average $\sigma_0$ and variance $\nu_0^2$ of $Y_n$ are

$$\sigma_0 = M\left(G_0 R_S P_t^0 + I_{bd}\right) + I_{sl} \tag{19}$$

$$\nu_0^2 = 2eM^{2+\rho} B_E \left(R_S G_0 P_t^0 + I_{bd}\right) + 2eI_{sl} B_E + 4k_B T B_E / R + \frac{4G_0 I_s^0 I_{sp} L_0^2 B_E}{B_0} + \frac{(I_{sp} L_0)^2 (2B_0 - B_E) B_E}{B_0^2} \tag{20}$$

where $$P_t^0 = kP_o/F_D + (WN-k)P_o\phi i_\alpha/F_D \tag{21}$$

$$I_s^0 = \frac{2eP_o}{h\nu(\alpha+1)} \tag{22}$$

where $N_a$ denotes the number of optical amplifier, $I_s$ is the photo current equivalent, the exponent $\rho$ lies between 0 to 1 in respect of the properties of APD, $e$ is the charge of electron equal to $1.601\times10^{-19}$ Coulomb, $B_E$ and $B_0$ are the receiver electrical and optical bandwidth respectively, $k_B$ represents the Boltzmann's constant equal to $1.379\times10^{-23}$, $h$ is the Plank's constant equal to $6.624\times10^{-34}$ and $h\nu$ indicates photon energy. In presence of double optical hard-limiters, the BER probability of OCDMA systems is expressed as

$$P_e^1(j) = \int_0^{T_h} P_{Y_n}(\gamma|j,1)d\gamma = \frac{1}{2} erfc\left(\frac{\sigma_1 - T_h}{\sqrt{2\nu_1^2}}\right) \tag{23}$$

$$P_e^0(j) = \int_{T_h}^{\infty} P_{Y_n}(\gamma|j,0)d\gamma = \frac{1}{2} erfc\left(\frac{T_h - \sigma_0}{\sqrt{2\nu_0^2}}\right) \tag{24}$$

where $$T_h = \frac{\nu_0\sigma_1 + \nu_1\sigma_0}{\nu_1 + \nu_0} \tag{25}$$

For chip-asynchronous OCDMA the bit error probability per bit is defined by

$$P_e = \sum_{k=0}^{N-1} P_e(k) \binom{N-1}{k} E^k S^{N-1-k} f_k(j) \tag{26}$$

Similarly, for chip-synchronous case

$$P_e = \sum_{k=0}^{N-1} P_e(k) \binom{N-1}{k} E^k S^{N-1-k} \tag{27}$$

where $$P_e(k) = \frac{1}{2}\left[P_e^1(j) + P_e^0(j)\right] \tag{28}$$

## IV. Results and Discussion

In this section, numerical analysis is done considering SMF operating at $\lambda = 1.55\mu m$ with attenuation $L_0 = 0.2dB/Km$ and chromatic dispersion constant $D = 18ps/Km-nm$. Gaussian shaped pulse is used with code weight $W = 4$. The variables of APD are considered as mean gain $M = 20$, excess noise index $\rho = 0.7$, $\phi = 0.01$, spontaneous emission factor $N_{sp} = 1.4$, bulk dark current $I_{bd} = 2nA$, surface leakage current $I_{sl} = 10nA$, load resistance $R = 1000\Omega$, noise temperature $T = 300°K$ and detector responsivity $R_S = 0.8$. Fig. 2 shows the effect of simultaneous user on BER at fiber optic length 50Km. It is found that at a constant transmitted power, system

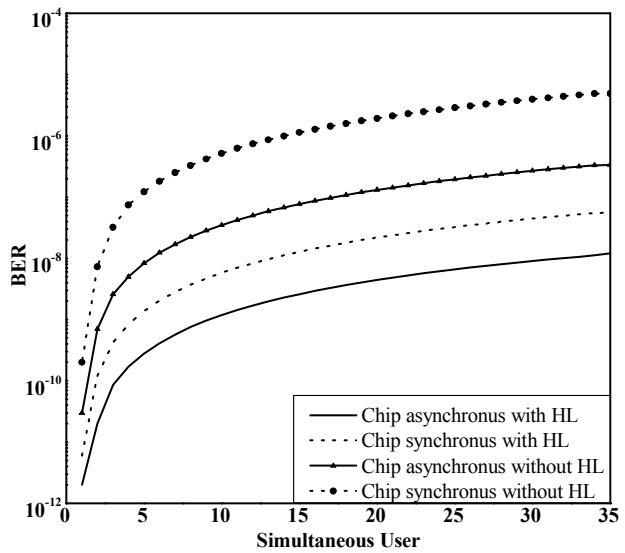


Fig. 2: Plot of BER versus simultaneous user for fiber optic length 50Km, chip rate 60Gchip/s and transmitted power 5dBm.

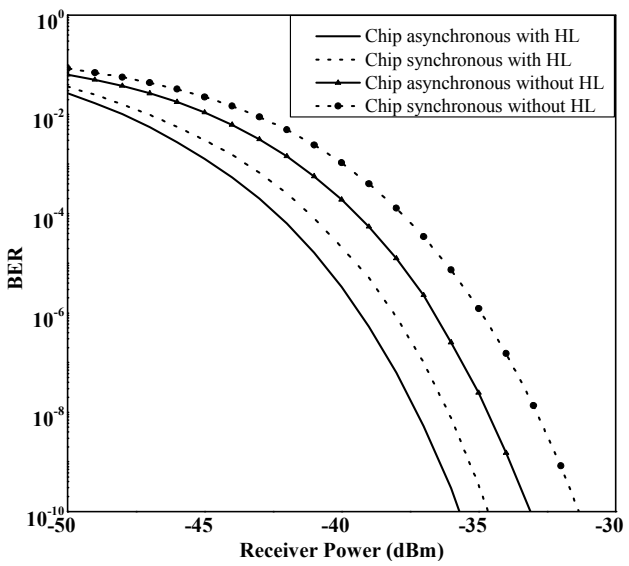


Fig. 3: Plot of BER versus received power for fiber length 10Km, chip rate 60Gchip/s and simultaneous user 34.

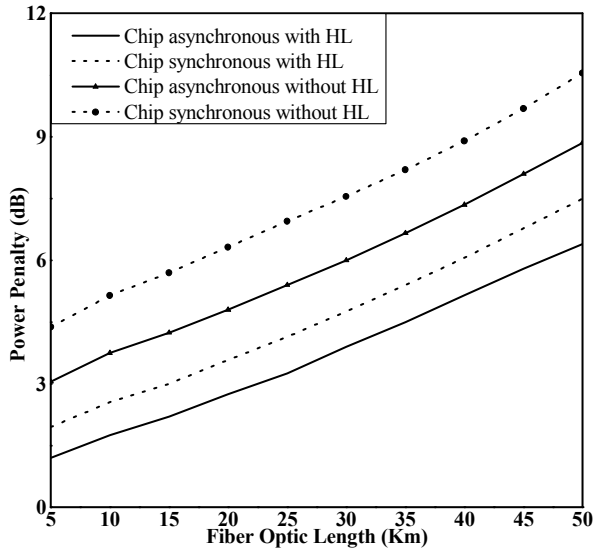


Fig. 4: Plot of power penalty versus fiber optic length with chip rate 60Gchip/s and simultaneous user 34.

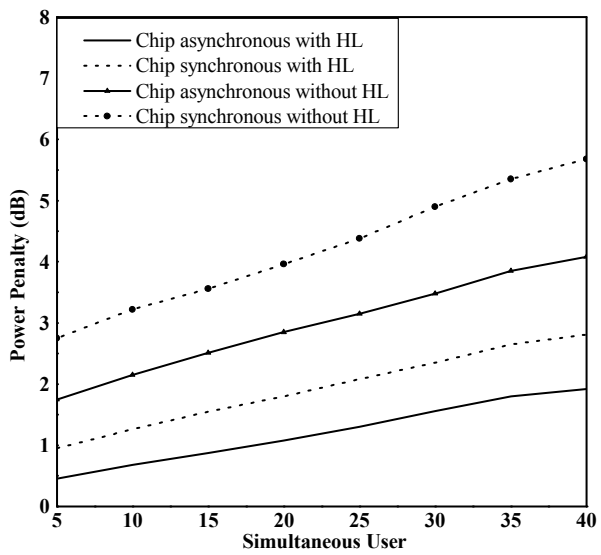


Fig. 5: Plot of power penalty versus simultaneous user at chip rate 60Gchip/s and fiber length 10Km.

BER performance is aggravated due to the influence of MAI with enlarging number of simultaneous user for both chip-synchronous and asynchronous cases. The probability of hit of all the mark intervals of the desired user by the interference signals is low and hence chip-asynchronous OCDMA gives better performance than chip-synchronous. System performance is further improved by employing optical hard-limiters. Fig. 3 depicts the bit error probability versus the received optical power at chip rate 60Gchip/s for chip-synchronous and chip-asynchronous cases. It is seen that higher received optical power is needed to sustain a constant BER of $10^{-9}$ for OCDMA systems in absence of optical hard-limiter. Optical hard-limiters remove the interference patterns from undesired user and reduce the impact of MAI thus increase system SNR. The variation of power penalty suffered by the system is calculated at BER $10^{-9}$ and plotted in fig. 4 with respect to fiber length. It is noticed that system performance degrades with increasing fiber optic length due to the effect of chromatic dispersion. For long distance signal transmission, because of pulse-shape distortion the maximum optical power of the received signal is reduced which decreases receiver SNR and degrades system performance. Fig. 5 illustrates the plot of power penalty versus simultaneous user at fiber length 10Km. The influence of MAI raises with simultaneous users which further increases power penalty. For chip-synchronous case, the system performance is found to improve 1.96dB and 2.87dB respectively for simultaneous user 10 and 40 by using optical hard-limiters. System performance is further improved by considering chip-asynchronous OCDMA. Fig. 6 shows the influence of chip rate on system

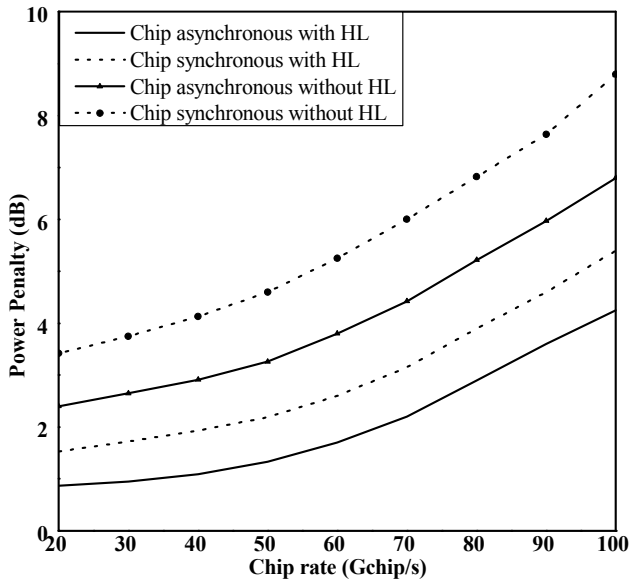


Fig. 6**:** Power penalty versus chip rate for fiber length 10Km and simultaneous user 34.

performance. It is detected that the system performance degrades with increasing chip rate because of inter chip interference between adjacent chips. It is also found that chip-asynchronous case experiences 2.32dB reduced power penalty than chip-synchronous at chip rate 80Gchip/s in presence of optical hard-limiters.

## V. CONCLUSION

In this paper, a comparative study between the chip-synchronous and chip-asynchronous DS-OCDMA systems based on BER analysis is represented to investigate the effects of chromatic dispersion, noises contributed by APD receiver and optical amplifier, and MAI. The power penalty suffered by the proposed system at a BER of $10^{-9}$ is evaluated and the numerical results demonstrate that system performance is strongly dependent on fiber optic length, chip rate and simultaneous user. It reveals that the chip-asynchronous case improves the BER performance and reduces power penalty than the chip-synchronous case. At fiber length 40Km chip-asynchronous case improves system performance 1.55dB. Power penalty is further reduced 2.2dB by using optical hard-limiters.

## REFERENCES


[1] J.-W. Su, G.-C. Yang, C.-Y. Chang and W. C. Kwong, "Design and Analysis of Generalized Diversity Optical CDMA Systems," *J. Lightwave Technol.*, vol. 31, no. 8, pp. 1217-1226, Apr. 2013.

[2] C.-C. Hsu, G.-C. Yang and W. C. Kwong, "Hard-Limiting Performance Analysis of 2-D Optical Codes Under the Chip-Asynchronous Assumption," *IEEE Trans. Commun.*, vol. 56, no. 5, pp. 762-768, May 2008.

[3] T. R. Raddo, A. L. Sanches, I. T. Monroy and B. H. V. Borges, "Throughput Performance Evaluation of Multiservice Multirate OCDMA in Flexible Networks," *IEEE Photon. J.*, vol. 8, no. 1, Feb. 2016.

[4] S. A. Khan and J. Bajcsy, "Chip-Asynchronous Binary Optical CDMA: An optimum Signaling Scheme for Random Delays," *IEEE Photon. J.*, vol. 5, no. 2, Apr. 2013.

[5] H.-C. Chen, M.-K. Chang, G.-C. Yang and W. C. Kwong, "Design of a Hybrid Multirate Asynchronous O-CDMA System: Performance, Spectral Efficiency, and Throughput Analyses," *J. Opt. Commun. Netw.*, vol. 7, no. 11, pp. 1034-1048, Nov. 2015.

[6] T. Ohtsuki, "Performance Analysis of Direct-Detection Optical Asynchronous CDMA Systems with Double Optical Hard-limiters," *J. Lightwave Technol.*, vol. 15, no. 3, pp. 452-457, Mar. 1997.

[7] M.-Y. Liu, Y.-K. Hsu and J.-A. Jiang, "Utilization of LDPC Code and ptical Hard-Limiter in OCDMA communication Systems," *IEEE Photon. J.*, vol. 6, no. 5, pp. 1-11, Oct. 2014.

[8] M. J. Islam and M. R. Islam, "Impact of GVD and SPM on the Performance of DS-OCDMA," *J. Netw.*, vol. 6, no. 1, Jan. 2011.

# Access Point Management in Overcrowded WLANs

Sadia Sultana[1], Anirban Sarkar[2], M. Ariffuzzaman[5]
Dept. of Electronics and Communications Engineering
East West University
Dhaka, Bangladesh
ss.shoma09@gmail.com, sarkaran01@gmail.com, mazaman@ewubd.edu

Md. Mezbahul Islam[3]
Dept. of Computer Science and Engineering
Mawlana Bhashani Science and Technology University
Tangail, Bangladesh
mezbahsalman@gmail.com

Md. Ezharul Islam[4]
Dept. of Computer Science and Engineering
Jahangirnagar University
Savar, Bangladesh
mdezharul@juniv.edu

*Abstract*— **In this paper, we analyze the relationship of number of access point (AP) and achieved throughput for a given scenario. In the scenario, we consider a number of parameters, i.e. given area, topology, number of users, expected rate and channel allocation vector. We find that in general with the increase of AP the performance of overall network improve. However, after a certain number of deployed APs, further increase of AP does not bring substantial improvement in the network performance. More specially, performance deteriorates after a threshold value of number of APs. The main reason for this performance deterioration is the increase of interference between adjacent channel (or co-channel) interference. We verify the throughput increasing rate with proper management of APs by simulation results using WIMNET (Wireless Internet-access Mesh Network) simulator.**

***Keywords—Wireless local area network, access point (AP), channel interference, IEEE 802.11n, WIMNET simulator.***

## I. INTRODUCTION

Resource management is an important issue in next generation communication systems and network because of limited number of resources e.g., frequency spectrum, power, AP. These limited resources raise various resource management problems. Resource management is an important issue in wireless local area networks (WLANs). Nowadays WLANs have become popular in commercial complexes due to their ease of installation that offer wireless access over short distances instead of traditional network cabling [1]. Thus, WLANs have been deployed in many places and organizations such as homes, schools, computer laboratories or office buildings, airports even in trains and airplanes [2].

In a WLAN, an AP acts as a connection hub to a wired network where APs are independently managed by different departments in organizations even in the same building. Due to this reason, their coverage areas can be overlapped. As a result, a WLAN host can detect signals from multiple APs. But signal detection from one AP is adequate for the host if it gives the required bandwidth. They increase unexpected energy consumptions in operating APs [3]. This situation may also degrade the performance of WLANs because of increasing interferences among them. However, sometimes the minimization of active APs degrades the performance of WLANs [4]. In an unmanaged dense wireless network, all APs use same channel and users operate with the default configurations. In that case, users don't get their expected throughput because of channel interference. For that reason, AP management and channel assignment are major issues for the dense network.

Channel overlap is a major contributor to degrade the performance of a wireless network as well as cellular radio systems [5]. Interference has been recognized as a major bottleneck for increasing capacity. Channels should be selected in such a way that can minimize the interference, as there are limited numbers of non interfered frequency channels in the IEEE802.11 protocol.

In recent times, the IEEE802.11n protocol has become popular as a high speed wireless communication protocol in order to fulfill the increasing demands for high data rate in wireless communications. This protocol provides bandwidth of 20 MHz or 40MHz and also defines 14 channels, only three of them (channels 1, 6 & 11) are non-overlapping. With the limited number of overlapping channels, channel assignment becomes a critical factor. In our work, we use this protocol as simulation parameter.

However, in a network, the number of active APs increases with the number of associated hosts to provide their expected throughput and also improve the performance of overall networks. Always the increasing number of AP will not increase the throughput, and sometimes it may be decreased. This happens when same channel is used for all APs and the further increase of APs does not bring substantial improvement in the network performance. This scenario has been represented through simulation result in this paper.

In this paper we present another simulation result as a solution of previous problem. By increasing the number of active APs with 3 different non-overlapping channels will

978-1-5386-2307-7/17/$31.00 ©2017 IEEE

expand the overall throughput. This paper also shows that average throughput can be estimated using the cost function that has been defined in the algorithm and the extra APs will be activated when the expected average throughput does not reach the given threshold.

The remaining of the paper is organized as follows. In section II, the several related works have been reported. In section III, the details procedure of proposed AP management is explained. Network model for our proposed work is placed in section IV. The simulation results of our proposed work are explained in section V. Finally, section VI concludes the paper.

## II. Related Works

Though from the application perspective the no. of APs, bandwidth utilization and interface have immense impact on the users, the relevant researches are still not in mature state. Nevertheless several relevant works have been reported in recent years.

In [6], authors studied the channel interference problem in WLANs where APs are located densely and they also proposed an AP cooperation system which detects the hidden terminal and the exposed terminal problems between stations by integrating the information obtained at different APs. But the paper doesn't concentrate on no. of AP management.

In [7], authors introduce some techniques based on graph coloring algorithms for frequency allocation process in WLAN. Authors also suggest a preliminary message format for access points to exchange information. In [8], authors analyze the performance of three channel assignment strategies where each AP independently selects one of the three available channels respectively for random channel assignment. For local selection, APs are deployed sequentially and each AP selects the least congested channel. However authors use heuristic rather than any direct algorithm for channel assignment.

In [9], authors have proposed an analytical model to compute the saturation throughput performance in the presence of a finite number of terminals and in the assumption of ideal channel conditions. But the authors have not considered the concept of using different channels.

In [10], authors have proposed a decentralized AP selection algorithm to achieve a minimum throughput with the reasonable computation and transmission overhead to be compatible with legacy APs without any modification.

In [11], authors have proposed an AP selection algorithm to maximize the throughput while preserving newly arrived-user throughputs in a multi-rate WLAN. It supports limited user movements. Their goal is to maximize the throughput by optimizing the associated APs for hosts while the locations of the APs are fixed. On the other hand, we focus on reducing the number of active APs while maximizing the performance by optimizing the associated APs for hosts.

In [12], theoretical throughput upper limit and delay lower limit for IEEE 802.11 protocols are shown. Authors have found that increasing data rate is very challenging in case of ensuring consistent performance where other overhead have vital role.

In [13], channel assignment for IEEE 802.11 and searching optimum AP for a host are considered jointly. Authors have shown that for a typical indoor environment patching algorithm can provide nearly optimum performance. The complexity of the optimum is also low.

In [14], authors have developed and tested an open enterprise Wireless Fidelity (Wi-Fi) solution based on virtual APs. A central controller is used to manage the handover scheme of the host. Authors also address QoS (Quality of Service) of real time services.

In [15], [16], a scheme for inter AP coordination in load balancing, frequency planning, power control have proposed. Authors also introduce the concept of adaptation of certain abstractions and concepts from Software Define Networks (SDNs) for its use in wireless networks.

A distributed solution using Light Virtual Access Point (LVAP) was introduced for the direct exchange of information between APs in [17]. In [18], an analytical model based on a Markov chain to study the efficiency of the Linux network subsystem has been presented. Authors identify the softIRQ process as the main element in the Linux capturing stage and they have built a model that represents the different steps in the softIRQ and the computational cost.

In [19], authors have proposed an efficient and distributed algorithm named Client-Assisted Channel Assignment Optimization. A distributed channel assignment algorithm for uncoordinated WLANs to minimize interference with adjacent APs is considered. The algorithm leads to better channel assignment decisions at the APs. However, authors have not considered the mapping of the number of APs & throughput in a crowded network.

In [20], authors studied the energy efficiency issue in dense WLANs and proposed an aggressive scheme for adaptation of the AP density to actual traffics. However authors have not addressed the impact of channel assignment in the overall throughput.

## III. Access Point Management

### A. Minimum Average Throughput and Average Throughput Threshold

When the number of active physical APs ($C_1$) is minimized, the number of hosts associated to one AP increases, which reduces the communication performance per host. We use the estimated average throughput per host that can be calculated from cost function defined in our previous work [3]. Then, we introduce the average throughput constraint that the estimated *minimum average throughput* ($C_2$) per host must satisfy the given minimum throughput called the *average throughput threshold* ($G$). The number of active APs may be increased when this *constraint* is not satisfied.

Let,

$AP_i$ = no. of access point, i = 1,2,3 … … … $n$
$Host_j$ = no. of host, j = 1,2,3 … … … $m$
$sp_{ij}$ = link speed
$d_{ij}$ = delay time

Assume, $AP_i$ *is* associated with a $Host_j$ with the link speed $sp_{ij}$ and it always transmit one bit. In this case the expected delay time is $d_{ij} = 1/sp_{ij}$ .If multiple hosts are associated with $AP_i$, then the total delay time becomes$\sum_{i,j=1}^{n,m} d_{ij}$. Because each host can transmit one bit during this time if every host transmits the same amount of data and their transmission chances are fair. So the minimum average throughput per host with $AP_i$ can be estimated by:

$$\mathrm{minT_{avg}} = \frac{1}{\sum_{i,j=1}^{n,m} d_{ij}} \quad (1)$$

Since, total delay time is equal to the maximum transmission time.

Hence,

$$\sum_{i,j=1}^{n,m} d_{ij} = Max(T_i) \quad (2)$$

From (1) & (2),

$$\mathrm{minT_{avg}} = \frac{1}{\mathrm{Max(T_i)}} = C_2$$

where, $T_i$ is the transmission time of $AP_i$ among the active APs.

Now, the average throughput of bottleneck AP should not be smaller than minimum average throughput threshold.

$$C_2 \geq G \quad (3)$$

### B. AP Management Algorithm

In this subsection, we present the high-level view of the hosts to AP association algorithm. In our proposed algorithm, initially hosts are assigned to APs based on link speed constraints [3]. With the changes of the number of active APs, the procedure is executed several times until the algorithms converge. It can be noted that since we use the centralized local search, the algorithm converge in linear time. The process is briefly explained in TABLE I.

TABLE I. AP MANAGEMENT ALGORITHM

***1st Step:*** Generates a list of associable hosts for each AP considering the link speed constraints.

***2nd Step:*** Generates a list of active physical APs and their associated hosts.

***3rd Step:*** Optimizes host association of AP to minimizing $C_2$ by local search method.

***4th Step:*** Optimizes AP selection through minimizing both $C_1$ and $C_2$ by repeating local search method until $G$ is satisfied.

***5th Step:*** Swaps the association of hosts to improve and finalize host association.

## IV. NETWORK MODEL

We consider instance modeling a large-size cafeteria as a common WLAN environment [3]. Fig. 1 represents the topology in this cafeteria instance.

Here, 3×3(=9) APs and 8×8(=64) seats are placed with same interval in 35m×35m (1225 $m^2$) area. A seat represents a place for a user to use a personal computer or a smart phone for the internet access using WLANs.

An ideal case of a cafeteria is assumed here where each AP has 110m radius coverage area and link speed threshold is 40 Mbps and distance between each host is 5m.

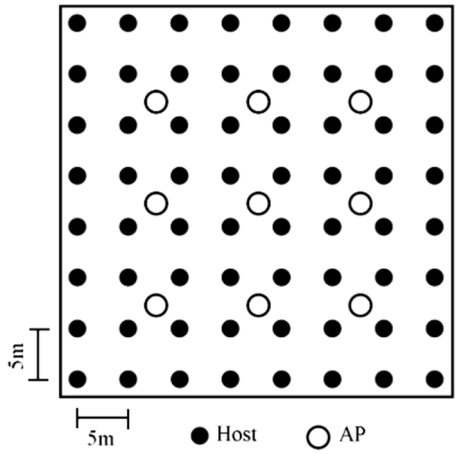


Figure 1. Cafeteria instance.

## V. RESULTS AND DISCUSSIONS

### A. Simulation Setup

The WIMNET simulator consists of multiple APs as wireless routers that are connected through wireless links. It simulates least functions for wireless communications of hosts and APs that are required to calculate throughputs and delays. It has been developed to evaluate a large-scale *Wireless Internet-access Mesh NETwork* .

IEEE 802.11n protocol is used to enhance the performance and network speed of WLANs [21]. In this protocol, the number of non-interfered channels is two for 2.4 GHz bands and nine for 5 GHz bands. It introduces the MIMO (Multiple-Input-Multiple-Output) to provide the data rate up to 600 Mbps.

In our simulation we use IEEE 802.11n standard as simulation parameter. Accordingly we use the corresponding supportive version of simulator. To make sure the best environment for simulation, Intel core 2 Duo 3.33 GHz configured CPU is used which primary memory is 3 GB as well as Ubuntu 12.04 (Linux kernel 3.2.0) OS. Important simulation parameters are listed in TABLE II.

TABLE II. SIMULATION ENVIRONMENT

| | |
|---|---|
| Simulator | WIMNET Simulator |
| Interface | IEEE 802.11n |
| No. of Access Point | 9 |
| No. of host | 64 |
| Average throughput | 5MB – 10MB |

TABLE III. SIMULATION RESULTS FOR SAME CHANNEL (CH-1) IN EACH AP

| Simulation information | | | | | | | Results | |
|---|---|---|---|---|---|---|---|---|
| *Average throughput threshold (Mbps)* | *Link speed threshold (Mbps)* | *Total Active AP* | *Bottleneck AP's position* | *No. of host in bottleneck AP* | *Expected max. avg. delay* | *Expected min. avg. throughput (Mbps)* | *Overall throughput (Mbps)* | *Min. avg. throughput (Mbps)* |
| 0 | 40 | 1 | 5 | 64 | 0.87 | 1.14 | 67.8 | 1.06 |
| 2.5 | 40 | 3 | 3 | 22 | 0.27 | 3.76 | 71.2 | 1.11 |
| 5 | 40 | 4 | 1 | 16 | 0.19 | 5.2 | 72.19 | 1.13 |
| 7.5 | 40 | 6 | 1 | 11 | 0.12 | 8.11 | 72.9 | 1.14 |
| 10 | 40 | 8 | 4 | 8 | 0.09 | 11.45 | 71.9 | 1.15 |
| 12.5 | 40 | 9 | 9 | 8 | 0.09 | 11.58 | 70.8 | 1.11 |

## B. *Simulation Results*

For cafeteria instance, we obtain the overall throughput of the scenario using the AP management algorithm where we change the average throughput threshold from 0 Mbps to 12.5 Mbps and link speed threshold is 40 Mbps. Here we consider two cases; one is same channel for all APs and another one is three different channels for different APs. We assume that every time users move, the active APs are stopped and new APs are turned on. However, in real situation, some APs cannot be turned off if they are currently associated with active hosts in service area. Those two different cases are described below:

*1) Same Channel for All APs*: TABLE III shows the simulation result of using same channel for all APs. The value of minimum average throughput and overall throughput are obtained by simulations using the WIMNET simulator. At first we evaluate the number of active APs by changing the average throughput threshold, where link speed threshold is fixed for all cases. To ensure 2.5 Mbps average throughput threshold, it needs 3 active APs. Thus more APs will be activated for ensuring higher average throughput. This table also shows that the position of bottleneck APs will change with the no. of active AP, but always the no. of bottleneck AP is one and the no. of associated hosts in bottleneck AP decreases with the increase of active APs.

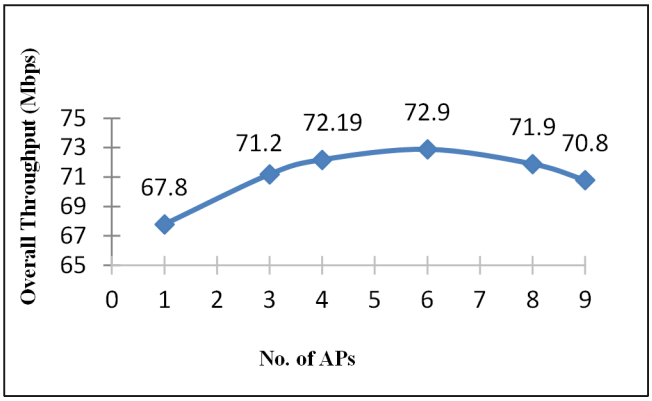


Figure 2. APs vs Overall Throughput (for same channel)

As our assumption, the expected minimum average throughput will increase with the increase of active AP. But through the simulation results, we can see that the minimum average throughput increasing rate is not very high because here we've used same channel for all active APs.

From Fig. 2, we see that overall throughput increases with the expansion of APs. After certain point the overall throughput decreases instead of increasing. From this figure we can also see that after 6 APs, the overall throughput decreases with increase of APs because here we are using same channel (CH-1) for all APs. So, the main reason for this performance deterioration is the increase of interference between adjacent channels. This point is the saturation point. After this point further increase of APs does not bring satisfactory outcome.

*2) Three Different Channel for Different APs:* In this part, we use three different channels for different APs as shown in Fig. 3. We assigned 9 APs with 3 different channels. For effective performance gain, it is possible to consider the channel assignment problem with several established algorithms (e.g. Graph Coloring Algorithm). However for simplicity purpose we arbitrarily assign the channel to each AP.

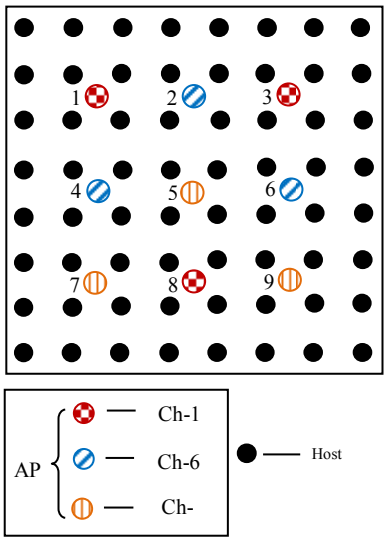


Figure 3. Channel assignment for all APs in Cafeteria instance.

TABLE IV. SIMULATION RESULTS FOR FIXED THREE CHANNELS (CH-1, 6 & 11) IN DIFFERENT APS

| Simulation information | | | | | | | | Results | |
|---|---|---|---|---|---|---|---|---|---|
| *Average throughput threshold (Mbps)* | *Link speed threshold (Mbps)* | *Activated AP and Channel assign* | | *Bottle-neck AP's position* | *No. of host in bottleneck AP* | *Expected max. avg. delay* | *Expected min. avg. throughput (Mbps)* | *Overall throughput (Mbps)* | *Min. avg. throughput (Mbps)* |
| | | *Total active AP* | *Selected AP(Channel)* | | | | | | |
| 0 | 40 | 1 | 5(11) | 5 | 64 | 0.87 | 1.14 | 67.8 | 1.06 |
| 2.5 | 40 | 3 | 3(1),4(6),8(1) | 3 | 22 | 0.27 | 3.76 | 109.86 | 1.72 |
| 5 | 40 | 4 | 1(1),3(1),4(6),9(11) | 1 | 16 | 0.19 | 5.2 | 154.06 | 2.41 |
| 7.5 | 40 | 6 | 1(1),2(6),3(1),7(11), 8(1),9(11) | 1 | 11 | 0.12 | 8.11 | 158.27 | 2.47 |
| 10 | 40 | 8 | 1(1),2(6),3(1),4(6),6 (6),7(11),8(1),9(11) | 4 | 8 | 0.09 | 11.45 | 216.98 | 3.43 |
| 12.5 | 40 | 9 | 1(1),2(6),3(1),4(6),5 (11),6(6),7(11),8(1), 9(11) | 9 | 8 | 0.09 | 11.58 | 232.83 | 3.64 |

Simulation result of using three different channels for different active APs is listed in TABLE IV. Here we are using three channels: Ch-1, Ch-6 and Ch-11. When three APs like 3rd, 4th and 8th are activated, then Ch-1 is assigned to 3rd AP, Ch-6 is assigned to 4th AP and again Ch-1 is assigned to 8th AP. This table also shows that the overall throughput will increase with the increasing of no. of active APs. As we are using 3 different channels for all active APs, the minimum average throughput will increase compared to using same channel for all active APs. But still it is not equal as expected minimum average throughput.

From Fig. 4, we see that with the increase of AP the corresponding overall throughput also increases. This is because the APs use different channels. However, we see that with the increase of the no. of AP the gain in throughput is not very consistent. As shown in Figure 4, the throughput increasing rate is not significant for 4 to 6 active APs. But for 6 to 8 active APs the overall throughput increasing rate is high. It is because of the orientation of the channel and AP.

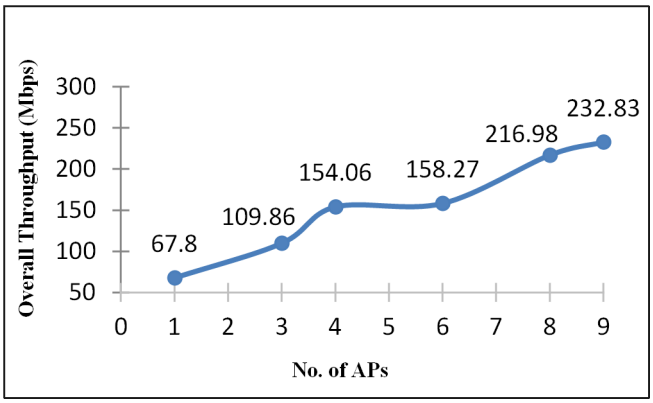


Figure 4. APs vs Overall Throughput (for three different channels).

## VI. CONCLUSIONS AND FUTURE WORKS

In this paper, we have studied on AP management in overcrowded WLANs. We analyze the relationship of APs and achieved throughput for a given scenario. Here we have presented two different simulation results for AP management. The first result shows that the throughput will increase up-to a certain point with increasing the no. of AP. After that point it decreases because of using same channel in all APs. And second result shows that if different non-interfered channel is used throughput will increase with increasing of no. of AP. By adding active APs we've ensured the minimum average throughput for any host.

We verified the effectiveness through simulations using WIMNET simulator. In future studies, we will consider the use of minimal number of APs to ensure the expected throughput and bandwidth sharing technique between two different operators of network to evaluate our proposed work through experimental setup, provider. We have a plan to evaluate our proposed work through experimental setup and simulation testbed.

## CONFLICT OF INTEREST

The authors declare that there is no conflict of interest regarding the publication of this paper.

## REFERENCES


[1] A. S. Tanenbaum, *Computer Networks*, 5th ed., Prentice Hall, 2010.

[2] M. Gast, *802.11 Wireless Networks: The Definitive Guide*, 2nd ed., O'Reilly Media, Inc., 2005.

[3] M. E. Islam, N. Funabiki, and T. Nakanishi, "Extensions of access-point aggregation algorithm for large-scale wireless local area networks," *International Journal of Networking and Computing,* vol. 5, no. 1, pp. 200-222, Jan. 2015.

[4] M. E. Islam, N. Funabiki, T. Nakanishi, and K. Watanabe, "An access point aggregation approach for energy-saving wireless local area networks," *IECE Trans. on Commun.* , E96-B (12):2986-2997, Dec. 2013.

[5] S. Sbit, M. B. Dadi, and B.Chibani, "Co and adjacent channel interference evaluation in GSM and UMTS cellular networks," *International Journal of Advances Research in Computer and Communication Engineering*, vol. 4, Nov. 2015.
[6] K. Nishide, H. Kubo, R. Shinkuma and T. Takahashi, "Detecting hidden and exposed terminal problems in densely deployed wireless networks," *IEEE Trans. Wireless Commun.*, vol. 11, Nov. 2012.
[7] J. Riihijarvi, M. Petrova, and P. Mahonen, "Frequency allocation for WLANs using graph colouring Techniques," in *Proc. 2nd Annual Conf. Wireless On-demand Network Systems and Services (WONS)*, Washington DC, WA, pp. 216-22, Jan. 2005
[8] A. Baid and D. Raychaudhuri, "Understanding channel selection dynamics in dense Wi-Fi networks," *IEEE Commun. Mag.* , vol. 53, Jan. 2015.
[9] G. Bianchi, "IEEE 802.11-saturation throughput analysis," *IEEE Commun. Lett.* , vol. 2, Dec. 1998.
[10] F. Xu, X. Zhu, C. C Tan, Q. Li, G. Yan, and J. Wu, "Smart Assoc: Decentralized access point selection algorithm to improve throughput," *IEEE Trans. Parallel Distrib. Syst.,* 24(12):2482{2491, Dec. 2013.
[11] S. Miyata, T. Murase, and K. Yamaoka, "Novel access-point selection for user QoS and system optimization based on user cooperative moving," *IEICE Trans. Commun.* , 95(6):1953{1964, Jun. 2012.
[12] Y. Xiao and J. Rosdahl, "Throughput and delay limits of IEEE 802.11," *IEEE Commun. Lett.* , vol. 6, no. 8, Aug. 2002.
[13] X. Ling and K. L. Yeung, "Joint access point placement and channel assignment for 802.11 wireless LANs," *IEEE Trans. Wireless Commun.* , vol. 5, Oct. 2006.
[14] L. Sequeria, J. L. de la Cruz, J. R-Mas, J. Saldana, J. F. Navajas, and J. Almodovar, "Building an SDN enterprise WLAN based on virtual APs," *IEEE Commun. Lett.* , vol. 21, Feb. 2017.
[15] R. Riggio, T. Rasheed, and M. K. Marina, "Poster: Programming software-defined wireless networks," in *Proc. MobiCom*, pp. 413-416, 2014.
[16] R. Riggio, T. M. Rasheed, and R. Narayanan, "Virtual network functions orchestration in enterprise WLANs," in *Proc. IM*, pp. 1220-1225, May. 2015.
[17] M. E. Berezin, F. Rousseau, and A. Duda, "Multichannel virtual access points for seamless handoffs in IEEE 802.11 wireless networks," in *Proc. VTC Spring*, pp. 1-5, May. 2011.
[18] L. Zabala, A. Ferro, and A. Pineda, "Modelling packet capturing in a traffic monitoring system based on Linux," in *Proc. Int. Symp. Perform. Eval. Comput. Telecommun. Syst. (SPECTS)*, pp. 1-6, Jul. 2012.
[19] X. Yue, C.F. Wong, and S.H.G. Chan, "CACAO: Distributed client-assisted channel assignment optimization for uncoordinated WLANs," *IEEE Trans. Parallel Distrib. Syst., vol. 22, Sep. 2011.*
[20] F. Ganji, L. Budzisz, and A. Wolisz, "Assessment of the power saving potential in dense enterprise WLANs," in *Proc. IEEE 24th Int. Symp. Pers. Indo. Mob. Radio Commun.* (PIMRC2013), Sep. 2013, pp. 2835-2840.
[21] A. S. Tanenbaum and D. J. Wetherall, *Computer Networks*, 5th ed., Pearson Prentice Hall, Boston, 2011.

**Sadia Sultana** received her B.Sc degree in Electronic and Telecommunication Engineering from East West University, Dhaka, Bangladesh in 2016 and joined as a Graduate Teaching Assistant (GTA) in the Department of Electronics and Communications Engineering at East West University. Currently she is an M.Sc student in Telecommunication Engineering at East West University. Her research interests include Computer Networks, Wireless Communication, Ultra Wideband System, Underwater Sensor Networks and Internet of Things (IoT).

**Anirban Sarkar** received his B.Sc degree in Electronic and Telecommunication Engineering from East West University, Dhaka, Bangladesh in 2016 as well as joined the Department of Electronics and Communications Engineering at East West University as a Graduate Teaching Assistant (GTA) in the same year. Currently he is an M.Sc student in Telecommunication Engineering at East West University. His research interests include Ultra Wideband System, Wireless Sensor Networks, Computer Networks, Wireless Communication and Internet of Things (IoT).

**Md. Mezbahul Islam** received his B.Sc. (Honors) and M.Sc. in Computer Science and Engineering from Jahangirnagar University, Dhaka, Bangladesh in 2015 and 2017 respectively. He has been working as a faculty in the Department of Computer Science and Engineering, Mawlana Bhashani Science and Technology University, Tangail, Bangladesh since April 2017. His research is focused in the fields of Image processing, pattern recognition, wireless network and expert system.

**Md. Ezharul Islam** received B.Sc. degree in Computer Science & Engineering from Jahangirnagar University in 2006. He joined the Department of Computer Science and Engineering at Jahangirnagar University, Dhaka, Bangladesh, as a lecturer in 2008. He completed his Masters and PhD in Information and Communication Systems from Okayama University, Japan in 2013 and 2016 respectively. Currently he is working as an Assistant professor at the department of Computer Science and Engineering, Jahangirnagar University. His research interests include Computer Networks, Optimization Algorithms, IoT, Communication Protocols, and Wireless Ad-hoc and Sensor networks. He is a member of ACM and IEICE.

**Dr. Mohammad Arifuzzaman** is a computer scientist with more than 7+ years of experience in academia and 7+ years of experience in industry. Dr. Arif obtained his PhD in Global Information and Telcommunication Studies from Waseda University, Tokyo Japan. He was also postdoctoral fellow at the department of Electrical and Computer Engineering, Faculty of Engineering & Applied Science, Memorial University, NL, Canada. Dr. Arif has expertise in cutting edge technology related project management, project proposal writing, and project coordination. As a researcher, he was involved in projects of several prestigious funding agencies including, The Natural Sciences and Engineering Research Council of Canada (NSERC), The Research & Development Corporation (RDC), NL, Canada, The Nippon Telegraph and Telephone Corporation (NTT), Japan, The National Institute of Information and Communications Technology (NICT), Japan, and EU-JAPAN collaborative research project funded under the EU's Seventh Framework Programme (FP7). Currently he is an Assistant professor at the Dept. of ECE, East West University, Dhaka, Bangladesh.

# Circularly Polarized Broadband Patch Antenna for Wireless Communication

M. Tarikul Islam[1, a], M. Samsuzzaman[1, b], M. Z. Mahmud[2,c], M.T. Islam[2,d]
[1]Dept. of Computer and Communication Engineering
Patuakhali Science and Technology University, Patuakhali, Bangladesh
[2]Dept. of Electrical Electronic and Systems Engineering,
Universiti Kebangsaan Malaysia, Malaysia
[*],[a]mtarikulislam10@cse.pstu.ac.bd, [b]sobuz@pstu.ac.bd, [c]zulfikerm@siswa.ukm.edu.my, [d]tariqul@ukm.edu.my

***Abstract*—In this paper, the design of a new printed circularly polarized (CP) antenna with an octave operating bandwidth is presented. The design technique is different from conventional monopole/dipole antenna. The antenna has a microstrip-fed line of rectangular radiator printed on RT/Duroid substrate with the total dimension of 106 mm × 60 mm × 1.57 mm. In the bottom, another rectangular radiator is printed which act as a ground. The upper and bottom radiators are both constituted in asymmetric feeding so that the surface current generate left-hand circular polarization (LHCP) orthogonally. The design is simulated in HFSS simulation solver and the properties are carefully analyzed to verify the antenna characteristics. The simulated result shows the bandwidth of 960 MHz to 2.60 GHz under a 10-dB return loss and axial ratio bandwidth of 2 GHz to 5 GHz at 3-dB. With a stable gain of 4.2 dB the antenna shows circular polarization. A parametric study of the surface current distribution and the mechanism of CP is analyzed.**

***Keywords—axial ratio; circular polarization; asymmetric feed line; rectangular patch; radiation pattern***

## I. INTRODUCTION

In recent years, for better antenna performance the development of wireless communication has increased. To optimize the system performance in the sensor network and modern wireless communication, CP antennas are widely used. Traditionally, for satellite communication, positioning and radio frequency identification (RFID) applications CP antennas are used for its intrinsic benefit of tactlessness to depolarization effects [1-3]. The systems retaining with circularly polarized antennas where both the transmitter and receiver show enhanced insusceptibility to multipath propagation and have strong discrimination of cross polarization. When two perverted modes with 90 degrees of phase difference are excited, an antenna can produce circularly polarized waves. It is observed that the frequency response for two modes is agitated at the operating frequency and amplitude are same and the two modes are in 90 degrees' phase difference.

In literature, numerous types of CP antennas have been reported by the author. A narrow slot with Disconcertion of microstrip patch produced circular polarization [4]. For enhancing the bandwidth different configurations such as circular loop [5], wideband probe feed [6] and double layer substrate has been reported. Low profile slotted antenna with circularly polarized characteristics was proposed in [7-9]. A dipole antenna with two fed line with $90^0$ phase angle for achieving wider operating and axial ratio (AR) bandwidths stated in [10]. Liner polarized omnidirectional antennas with different patch shape such as elliptical, spectacles, rectangular and circular also proposed [11, 12]. By using asymmetric feeding the operating bandwidth of planner antenna with the small ground can be enhanced and also unidirectional radiation pattern can be generated [13]. For achieving broadband, the ground plane also plays an important role for monopole antennas. Coupling capacitance can be generated with the gap between patch and ground and it is important for achieving broadband. However, only a few attempts to get CP bandwidth have been made by disconcertion of traditional printed monopole/dipole.

A novel design with asymmetric feeding and rectangular patch with a truncate cut at two edges is presented in this paper and the ground plane is acting as an asymmetric patch which generates circular polarization. The broadband is attained by modifying the shape, length and width of patches of both the sides.

## II. ANTENNA DESIGN AND ANALYSIS

### *A. Antenna Geometry*

The design structure of the antenna is illustrated in Figure. 1. The structure is different in appearances from the traditional monopole symmetric antenna. The antenna having two rectangular patches with a truncated corner at opposite two sides and fed with a 50Ω asymmetric microstrip transmission line. The patch is printed on an RT/Duroid substrate where the thickness of the substrate is 1.57mm and other patch is printed on another side of the substrate which act as a ground plane. The fed line excites the patch along the positive X-direction. The ground plane has the same dimension as the top radiator and excites along with the negative X-direction. The two radiator act as two arms of the printed antenna and disjointed by a gap "g" towards the Y-axis. The total dimension of the antenna covers 106 mm × 60 mm × 1.57 mm. The dielectric constant of the substrate used in the antenna is 2.2.

978-1-5386-2307-7/17/$31.00 ©2017 IEEE

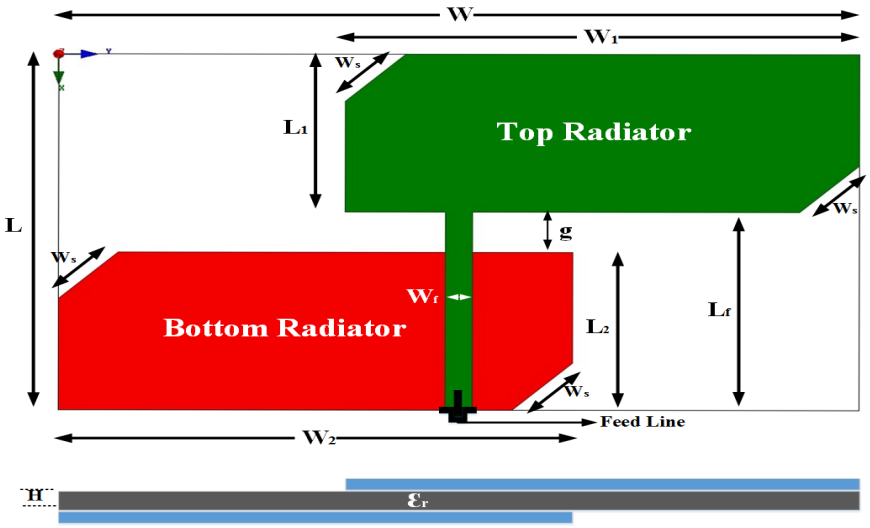


Figure 1. Design Geometry of the antenna

The estimated value of the length L of the patch is specified by

$$L \approx \frac{\lambda_{eff}}{2} = \frac{\lambda_r}{2\sqrt{\varepsilon_{eff}}} = \frac{c}{2\sqrt{\varepsilon_{eff}} f_r}$$

$$\varepsilon_{eff} = (\varepsilon_r + 1)/2$$

(1)

Where "c" stands for speed of light, $\lambda_r$ represents the wavelength of the dipole at the operating frequency in free space, $f_r$ and $\varepsilon_{eff}$ is the approached dielectric constant of the merged dielectric (air-substrate).

### B. Circular Polarization Principle

The traditional microstrip antenna is moreover vertically or horizontally polarized. One of the direction is weaker than the dominating direction. So it is not easy to get CP from this type of conventional monopole antenna. A phase difference of $90^0$ with equal amplitude and two orthogonal E vectors, CP can be acquired. The asymmetric feed line produces two orthogonal currents comprising vertical and horizontal currents across the radiators of the proposed antenna. This is the cause of double orthogonal vectors of $E_{Ver}$ and $E_{Hor}$.

The current distribution of the both radiator can explain the principle of generating CP. Mainly the dimension of the radiators is chosen for achieving longitudinal currents. This current brought X-directed E field ($E_{Hor}$) as well as Y-directed produce E-field ($E_{Ver}$). For the optimum distance between two radiators, the gap offers $90^0$ phase difference.

The main parameters of design optimizations are length (L), width (W), truncated corner (Ws), length of feed line (Lf) and gap (g) in the middle of the resonators. These design parameters are adjusted for achieving top LHCP performance over the wide bandwidth. From the observation, it is noticed that the axial ratio value is lower than 3dB outside the higher frequency edge. For choosing the appropriate size of the stub, the extended frequency of 5 GHz AR values has been achieved.

### C. Surface Current Distribution

To recognize the left-hand CP (LHCP) at the +Z direction the proposed antenna was designed. The simulated surface current direction of the proposed geometry is showing in Figure. 2. For both the top and bottom radiator the orientation of surface current from $0^0$ to $270^0$ at 2.8 GHz is presented. For $0^0$ phase reference, the currents are directed to the +Y direction. For $90^0$ phase difference, the current flow is dominated by +X direction. For $180^0$ phase angle the current flow is oppositely directed to $0^0$ which is in –Y directed. Again for $270^0$ the current flow is –X directed and the polarization is left hand to the +Z direction. It is also noticed the by switching the location of the radiators the RHCP polarization can be achieved.

### D. Parametric Study

The effect of different constraints on impedance and axial ratio bandwidth is tested in this section. The height and width of the resonators and substrate material type are the main factors which effect on bandwidths. A parametric study is important to find out the appropriate dimension with wideband and circular polarized antenna.

Figure. 3 and Figure. 4 demonstrate the graphs of $S_{11}$ and Axial Ratio (AR) corresponding to frequency. The variant of the resonator width has a minor effect on both $S_{11}$ and AR bandwidth. However, the middle value of the width has reached an acceptable level. Figure 5 and Figure. 6 represents the effect of patch length over the return loss and AR. The significant improvement observed in proposed length and has a good matching observed at AR along with return loss. As a result, by proper choosing the width and length of the patch the improved operating bandwidth and AR bandwidth has been obtained.

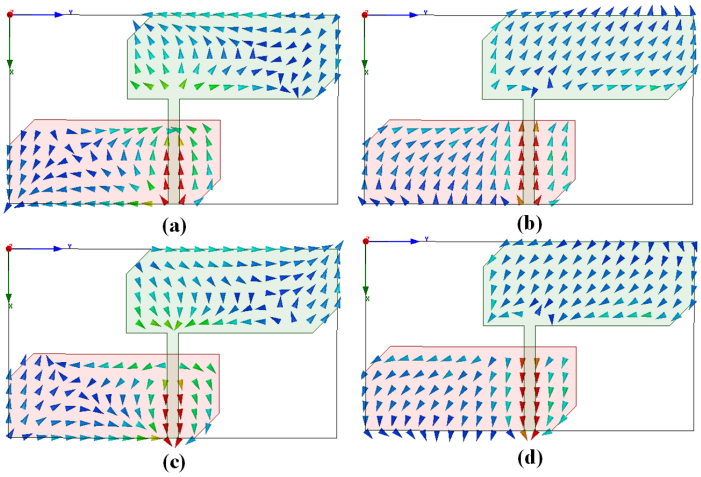


Figure 2. Surface current distribution at (a) $0^0$ (b) $90^0$ (c) $180^0$ and (d) $270^0$

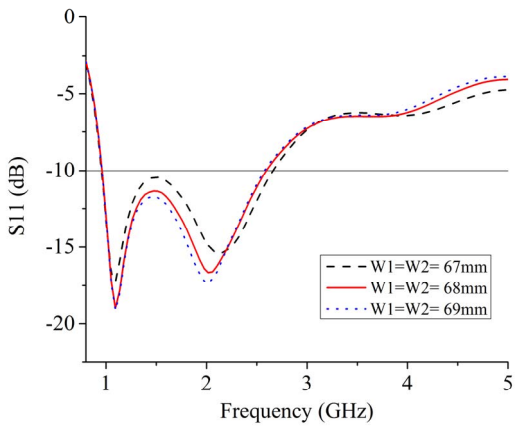


Figure 3. Evaluation of the $S_{11}$ for different width of resonators

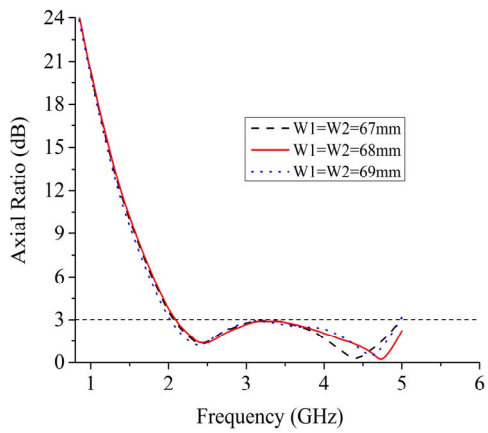


Figure 4. Evaluation of axial ratio (AR) for different width of resonators

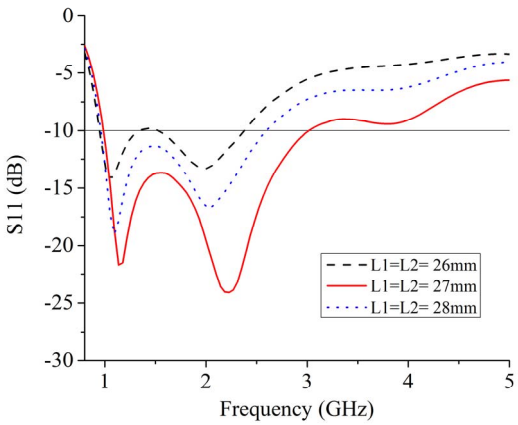


Figure 5. Evaluation of the $S_{11}$ for different length of resonators

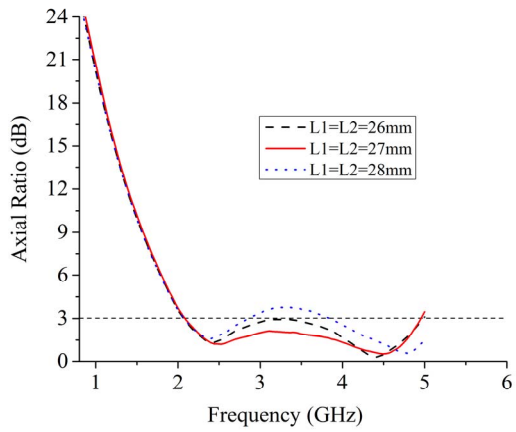


Figure 6. Evaluation of axial ratio (AR) for different length of resonators

## III. Results and Discussions

The design parameters of the proposed antenna are listed in Table I. The design is simulated using High Frequency Structure Simulator (HFSS) which works based on finite element method.

TABLE I. Optimized Dimension of Design Parameters

| Label | Parameter | Dimension(mm) |
|---|---|---|
| *L* | Total Length | 106 |
| *W* | Total Width | 60 |
| *W1, W2* | Patch length | 68 |
| *L1, L2* | Patch width | 27 |
| *Lf* | Length of feed line | 33.8 |
| *g* | Gap between radiators | 6.8 |
| *Wf* | Width of feed line | 3.6 |
| *Ws* | Truncate corner length | 11.31 |
| *H* | Height of substrate | 1.57 |

The curve in Figure. 3 shows that the antenna has the bandwidth of 960 MHz to 2.60 GHz under 10dB return loss. The radiation pattern for both LHCP and RHCP also observed

along with AR. The AR bandwidth is 3 GHz (2 GHz – 5 GHz) below 3 dB. Figure. 7 displays the antenna gain over the impedance bandwidth. The maximum gain is observed as 4.5 dBi at 2.6 GHz and an average of 4 dBi across the AR bandwidth.

For two major LHCP and RHCP, the radiation pattern for phi=$0^0$ and $90^0$ is observed at three different resonant frequencies of 2.8 GHz, 3.5 GHz, and 4.1 GHz. The values are normalized and presented in Figure. 8 and 9. There is stable good radiation pattern originate towards the YZ plane. For higher frequency of 3.5 GHz and 4.1 GHz, the cross-polar values are high in level to XZ plane. The cross-polar values are low at a lower frequency of 2.8 GHz over a wide angle. The pattern shows the higher cross polar value which is generated due to X-direction across the enormous width of the resonator that is mandatory for circular polarization.

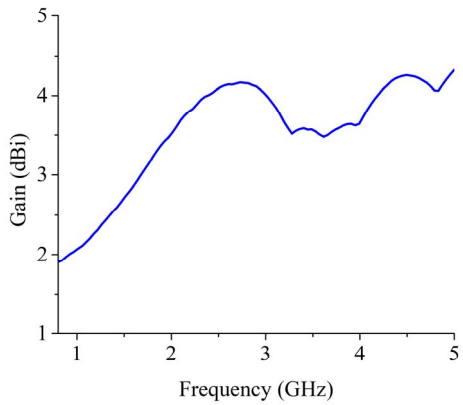


Figure 7. Simulated gain against frequency

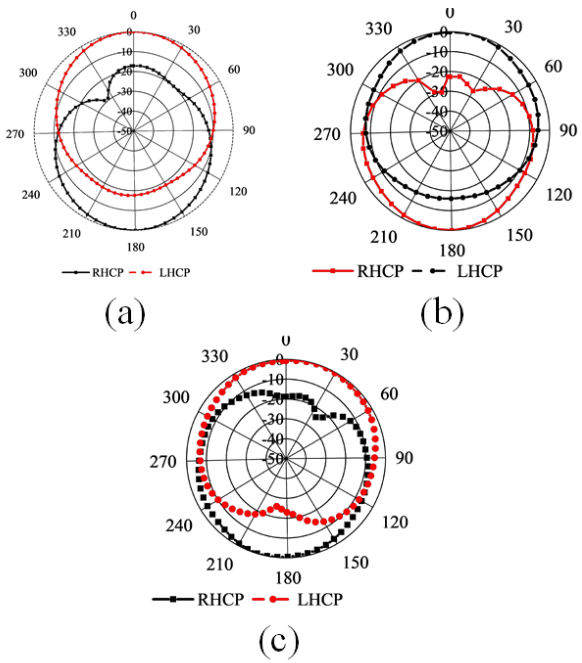


Figure 8. Radiation pattern at (XZ) plane for (a) 2.8 GHz, (b) 3.5 GHz and (c) 4.1 GHz

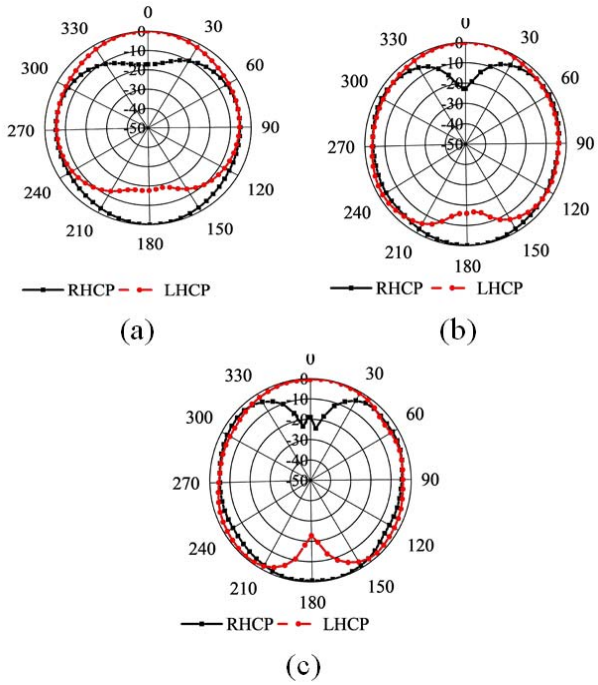


Figure 9. Radiation pattern at (YZ) plane for (a) 2.8 GHz, (b) 3.5 GHz and (c) 4.1 GHz

## IV. Conclusion

Apart from the conventional monopole planner printed antenna, a broadband CP antenna is presented. The antenna geometry consists two resonators fed by 50Ω asymmetric microstrip line. With an AR value less than 3 dB the antenna works over a wider bandwidth due to its feeding techniques and modified slot patch. A parametric study to validate the design for using wideband CP configuration is carried out. Surface current distribution at different phase angle was observed and CP is achieved due to its location of the resonant element regarding feed line. The simulation result demonstrates that the antenna has an operating bandwidth of 1.64 GHz and AR bandwidth of 3 GHz and the fractional bandwidth is 92% and 85% respectively. The antenna has good gain regarding conventional bidirectional antennas. This antenna is a good candidate for the sensor, global navigation systems and variety of vehicular application due to its compactness, simplicity and CP characteristics.

## References


[1] F.-S. Chang, K.-L. Wong, and T.-W. Chiou, "Low-cost broadband circularly polarized patch antenna," *IEEE Transactions on Antennas and Propagation,* vol. 51, pp. 3006-3009, 2003.

[2] F. Ferrero, C. Luxey, G. Jacquemod, and R. Staraj, "Dual-band circularly polarized microstrip antenna for satellite applications," *IEEE Antennas and Wireless Propagation Letters,* vol. 4, pp. 13-15, 2005.

[3] M. Samsuzzaman and M. T. Islam, "Wideband hook-shaped circularly polarised antenna," *Electronics Letters,* vol. 50, pp. 1043-1045, 2014.

[4] X. Bao and M. Ammann, "Comparison of several novel annular-ring microstrip patch antennas for circular polarization," *Journal of*

*Electromagnetic Waves and Applications,* vol. 20, pp. 1427-1438, 2006.

[5] R. Li, J. Laskar, and M. Tentzeris, "Wideband probe-fed circularly polarised circular loop antenna," *Electronics Letters,* vol. 41, pp. 997-999, 2005.

[6] H. Wang, X. Wang, S. F. Liu, P. Li, and X. W. Shi, "Broadband circularly polarized antenna with high gain and wide axial ratio beamwidth," *Microwave and Optical Technology Letters,* vol. 57, pp. 377-381, 2015.

[7] J. S. Row and Y. D. Lin, "Miniaturized designs of circularly polarized slot antenna," *Microwave and Optical Technology Letters,* vol. 56, pp. 1522-1526, 2014.

[8] S. A. Rezaeieh, S. Şimşek, and J. Pourahmadazar, "Design of a compact broadband circularly-polarized slot antenna for wireless applications," *Microwave and Optical Technology Letters,* vol. 55, pp. 413-418, 2013.

[9] J.-Y. Sze and C.-C. Chang, "Circularly polarized square slot antenna with a pair of inverted-L grounded strips," *IEEE Antennas and Wireless Propagation Letters,* vol. 7, pp. 149-151, 2008.

[10] W.-S. Yoon, S.-M. Han, J.-W. Baik, S. Pyo, J. Lee, and Y.-S. Kim, "Crossed dipole antenna with switchable circular polarisation sense," *Electronics Letters,* vol. 45, pp. 717-718, 2009.

[11] M. M. Islam, M. T. Islam, M. Samsuzzaman, M. R. I. Faruque, N. Misran, and M. F. Mansor, "A miniaturized antenna with negative index metamaterial based on modified SRR and CLS unit cell for UWB microwave imaging applications," *Materials,* vol. 8, pp. 392-407, 2015.

[12] J.-P. Zhang, Y.-S. Xu, and W.-D. Wang, "Microstrip-fed semi-elliptical dipole antennas for ultrawideband communications," *IEEE Transactions on Antennas and Propagation,* vol. 56, pp. 241-244, 2008.

[13] M. Samsuzzaman, M. T. Islam, S. Kibria, and M. Cho, "A compact circularly polarized high gain S-band nanosatellite antenna using ramped convergence particle swarm optimization," *Microwave and Optical Technology Letters,* vol. 57, pp. 1503-1508, 2015.

2017 3rd International Conference on Electrical Information and Communication Technology (EICT), 7-9 December 2017, Khulna, Bangladesh

# Design of a 2x1 MIMO Antenna for Multiband Wireless Applications

Kaushik Bhadra[1], Abu Shakil Ahmed[2], Md. Nurunnabi Mollah[3]
Khulna University of Engineering & Technology, Khulna-9203, Bangladesh
bhadrakaushik2@gmail.com[1], shakil.ahmed.bd71@gmail.com[2], nurunnabim12@gmail.com[3]

***Abstract*—We have proposed the design of a compact microstrip antenna structure having two physically separated ports perpendicular to each other. The antenna has been designed on Defective Ground Structure (DGS) which is capable of providing improved performance. Moreover, we have designed a microstrip-fed line with the slot-added patch. The design and simulation procedure has been conducted using CST STUDIO SUITE as well as several parameters such as Return Loss (RL), Voltage Standing Wave Ratio (VSWR), and radiation pattern have been analyzed. The simulation result verifies that the proposed antenna offers enhanced performance since the better value has been obtained for the performance parameters. Therefore, the proposed antenna can be used efficiently for various wireless applications.**

***Keywords—MIMO Antenna; DGS, VSWR, Radiation pattern, Bandwidth.***

## I. Introduction

The requirement of wireless communication is increasing sharply with the expansion of communication systems like WiMAX, Wi-Fi, 3G, 4G, 5G, and LTE. Antenna with compact size and low weight is suitable for these applications. The antenna works as a transducer that can both transmit and receive electromagnetic (EM) waves [1]. The microstrip antenna is preferable to the conventional ones for numerous practical applications since it has several advantages over them such as lighter weight, lower cost, planar configuration, portability, array functionality, more comfortable fabrication, and integration capability with Microwave Monolithic Integrated Circuits (MMICs) [2]. Because of the advancement in technology, at present, it is easy to design an antenna for a particular frequency range. It is well established in the literature that using defective ground structure; the antenna performance can be improved by a significant margin [3-5]. Single antenna with the adequate functionality, for example, multiple frequency handling capability is desired in a modern communication system for better user satisfaction. Therefore, the research and development process of single antenna designed to deal with various frequencies with greater range has become trendy [6]. Thus, the multiband operation is an essence of the contemporary wireless communication infrastructures since the users desire to take pleasure in different frequency bands parallelly with a single antenna package [7].

N. Hanchinamani et al. have designed a compact sized rectangular microstrip patch antenna for four frequency ranges containing microstrip feed line and defective ground structure that offers enhanced mutual coupling and envelope correlation coefficient [8]. In this paper, we have designed a 2x1 Multiple Input Multiple Output (MIMO) antenna for multiband wireless applications inspired by the research works of N. Hanchinamani et al. [8]. We have redesigned the antenna and proposed a more efficient prototype keeping the frequency bands the same as before. Better performance has been obtained for the antenna as per the simulation result since the value of the performance parameters such as RL, VSWR, and radiation patterns have been improved. FR-4 has been used as the substrate for the proposed design. We have conducted the design and simulation steps using CST STUDIO SUITE 2015. The design specification has been listed in TABLE I and the antenna has been designed according to it. The simulation has performed after determining the essential parameter like coordinate of the antenna shape via well-established mathematical formula reported in the literature.

We have arranged the paper in five sections. In Section II, we have demonstrated the design procedure of the proposed antenna. In Section III necessary calculations have been performed to obtain the values of several parameters required for the design. The simulation steps have been presented in Section IV in order to evaluate the performance of the proposed antenna. The contribution of this research work has been clarified in Section V with a summary of the entire work.

## II. Design Specification

We have modeled the antenna using 3D EM simulation tools of high-frequency components and applied a fully automatic meshing procedure prior to the simulation steps. The simulation has been performed using several simulation techniques. The proposed antenna has been designed upon the FR4 substrate with the thickness ($h_s$) of 1.6 mm and the relative permittivity ($\varepsilon_r$) of 4.4. The patch has the dimensions of 20 mm×19.5 mm and the height ($h_p$) of 0.1 mm. The dimensions of the ground have been chosen as 20 mm×19 mm with height ($h_g$) of 0.1 mm. Microstrip feed with characteristics impedance of 50 Ω has been selected as the antenna feed. The dimension of feed has been taken as 16 mm×4 mm, and the height ($h_f$) has been set 0.1 mm. In order to obtain improved bandwidth (BW) and return loss (RL), two steps have been taken regarding the

978-1-5386-2307-7/17/$31.00 ©2017 IEEE

patch, and few filter slots have been cut for this purpose. The dimension of the L-shaped slot has been considered 6.8 mm×5.8 mm×5.2 mm and 3.3 mm×5.3 mm×11.5 mm along X-axis and Y-axis respectively. Another crushed-J shaped filter has been used with slot dimension slot of 3.5 mm×5.5 mm×0.2 mm and 3.6 mm×5.5 mm×10.5 mm along X-axis and along Y-axis respectively [9-10]. The design specifications have been accumulated in TABLE I. The front view of the proposed antenna has been represented by Fig. 1. Several slots have been prepared with a view to reducing the overall weight and making the size of proposed antenna more compact [11]. The resonance frequency ($f_r$) have been selected 9.316 GHz. The single antennas have been designed on the same substrate, and they are placed perpendicular to each other in order to form the 2x1 antenna array.

TABLE I. DESIGN SPECIFICATIONS OF THE PROPOSED ANTENNA

| Serial No. | Parameters | Dimensions are in mm/values |
|---|---|---|
| 1 | Substrate | 40×38×1.6 |
| 2 | Ground | 20×19×0.1 |
| 3 | Patch | 19.5×20 × 0.1 |
| 4 | Feed | 16×4 ×0.1 |
| 5 | Step 1 | 1.5×1.5 |
| 6 | Step 2 | 1×1 |
| 7 | Filter 1 | 6.8×5.8 ×0.1 |
| 8 | Filter 2 | 3.5×5.5 ×0.1 |
| 9 | Filter 3 | 5.2×2.2 ×1.4 |

We have prepared design specification suitable to design the proposed antenna which differs from the specification reported by N. Hanchinamani et al. [8]. Dimensions of several parameters are redefined such as substrate, filter 1, filter 2, and filter 3 as well as two additional slots have been introduced in order to obtain the desired performance.

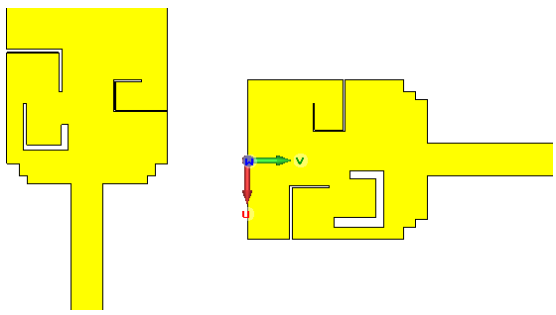

Figure 1. The front view of the proposed antenna.

## III. CALCULATION

In this section, we have depicted the essential parameters and its basic mathematical formulation as part of the design procedure. We have determined the value of width ($W_p$) using (1) and obtained 20 mm as its value. Then we have calculated the value of effective dielectric constant ($\varepsilon_{reff}$) using (2), and its value has been found 4.4. The ground length ($L_g$) has been determined 20.2 mm using (3).

$$W_p = \frac{c}{2f_0\sqrt{\frac{\varepsilon_r + 1}{2}}} \tag{1}$$

$$\varepsilon_{reff} = \frac{\varepsilon_r + 1}{2} + \frac{\varepsilon_r - 1}{2}\sqrt{1 + 12\frac{W}{h}} \tag{2}$$

$$L_g = \frac{(\varepsilon_{eff} + 0.3)(\frac{W}{h} + 0.264)}{(\varepsilon_{eff} - 0.8)(\frac{W}{h} + 0.8)} \tag{3}$$

Here, $f_0$ denotes the operating frequency, $\varepsilon_r$ denotes the dielectric constant of the substrate, h means the height of the substrate, W indicates the width of the patch, and $W_g$ denotes the width of the ground plane. The effective length ($L_{eff}$) and the actual length ($L_p$) have been determined as 41.648 mm and 19.48 mm respectively from (4) and (5).

$$L_{eff} = \frac{c}{2f_0\sqrt{\varepsilon_{reff}}} \tag{4}$$

$$L_p = L_{eff} - 2\Delta L \tag{5}$$

The mathematical expression of insertion depth has been stated in (6) where $V_0$ denotes the velocity of the electromagnetic wave and its value is $3*10^{11}$ $mms^{-1}$. Moreover, we have determined the value of characteristic impedance ($Z_0$) as 50 Ω using the Bessel function.

$$G_{pf} = \frac{V_0}{\sqrt{2*\varepsilon_{reff}}}\frac{4.65*10^{-12}}{f} \tag{6}$$

By this way, we have determined the value of all the parameters necessary to design the antenna as well as defined the array.

## IV. SIMULATION

Initially, we have simulated the design of a single antenna and evaluate its various characteristics in order to assess the performance of the proposed antenna. As per Fig. 2, we have obtained bandwidth of -10 dB at 1.6 GHz frequency and return loss of -31.24 dB at 9.263 GHz frequency for the proposed single antenna.

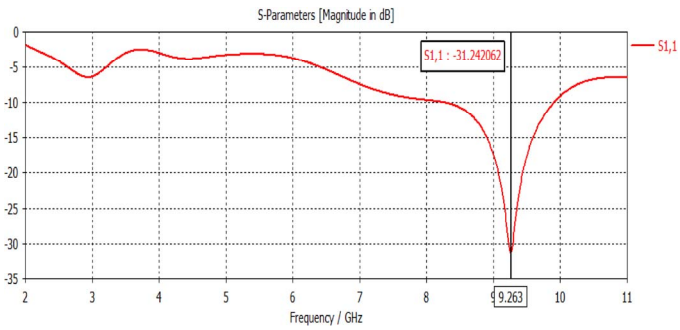


Figure 2. Return loss graph of the proposed antenna at 4.2 GHz.

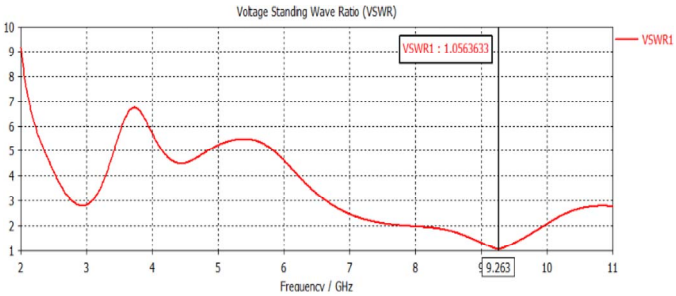


Figure 3. VSWR graph of the proposed antenna.

According to Fig. 3, we have obtained the value of VSWR 1.05 at 9.263 GHz frequency which has been determined less than 2 for the range from 7.7 GHz up to 10 GHz frequency.

Fig. 4 represents the radiation pattern of the antenna in polar coordinate for the directivity of 5.223 dBi at 7.89 GHz frequency with main lobe magnitude of 0.713 dBi, main lobe direction of 172 degrees, the 3dB angular width of 65.4 degrees, and sidelobe level of -1.1 dB. It has been observed that the antenna has a major lobe as well as a back lobe compared to the major one. Fig. 5 shows the radiation pattern of the antenna in three-dimension. The radiation efficiency has been obtained -1.548 dB.

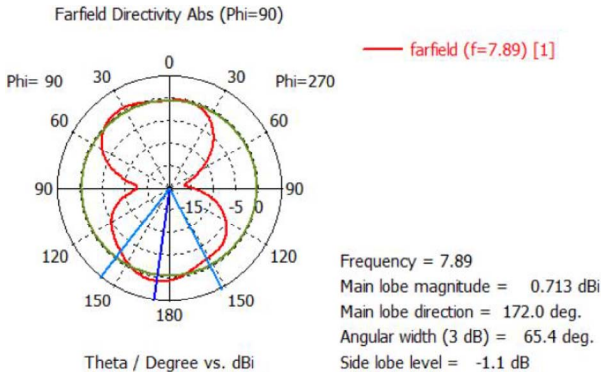


Figure 4. The radiation pattern of the antenna at 7.89 GHz in polar co-ordinate.

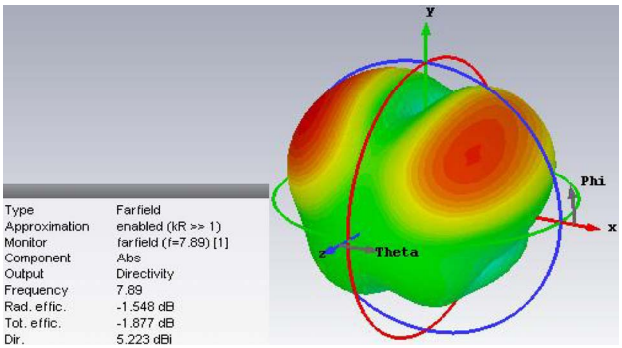


Figure 5. 3D view of the radiation pattern of the antenna for 7.89 GHz.

Fig. 6 represents the radiation pattern of the antenna in polar coordinate for the directivity of 5.860 dBi at 8.4 GHz frequency with main lobe magnitude of 0.697 dBi, main lobe direction of 175 degrees, the 3dB angular width of 51.9 degrees, and sidelobe level of -1.1 dB. It has been observed that the antenna has a major lobe as well as a back lobe compared to the major one. Fig. 7 shows the radiation pattern of the antenna in three-dimension. The radiation efficiency has been obtained -1.576 dB.

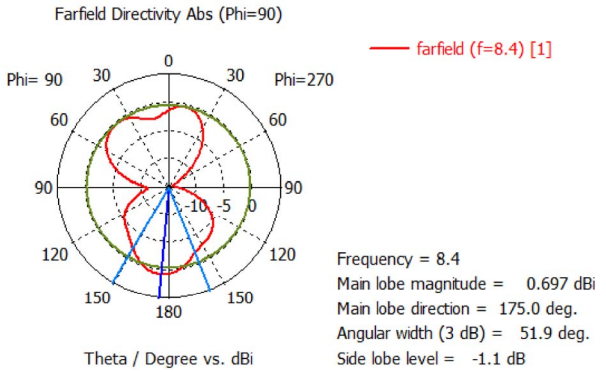


Figure 6. The radiation pattern of the antenna for 8.4 GHz in polar co-ordinate.

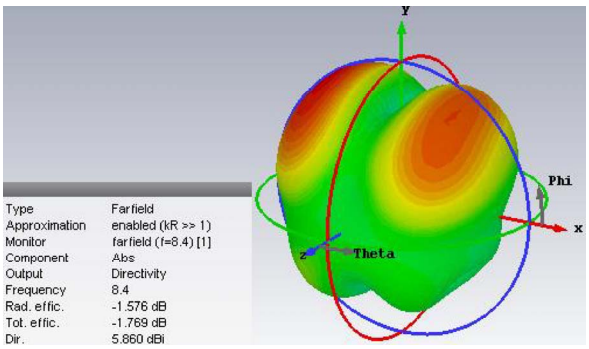


Figure 7. 3D view of the radiation pattern of the antenna for 8.4 GHz.

Fig. 8 represents the radiation pattern of the antenna in polar coordinate for the directivity of 6.899 dBi at 10 GHz frequency with main lobe magnitude of 0.833 dBi, main lobe direction of 174 degrees, the 3dB angular width of 66.4 degrees, and sidelobe level of -2.4 dB. It has been observed that the antenna has a major lobe as well as a back lobe. Fig. 9 shows the radiation pattern of the antenna in three-dimension. The radiation efficiency has been obtained -2.091 dB.

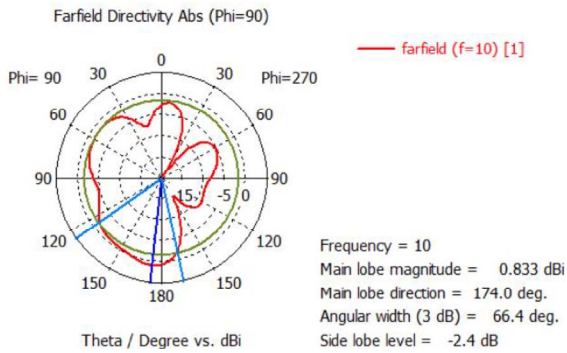


Figure 8. The radiation pattern of the antenna for 10 GHz in polar co-ordinate.

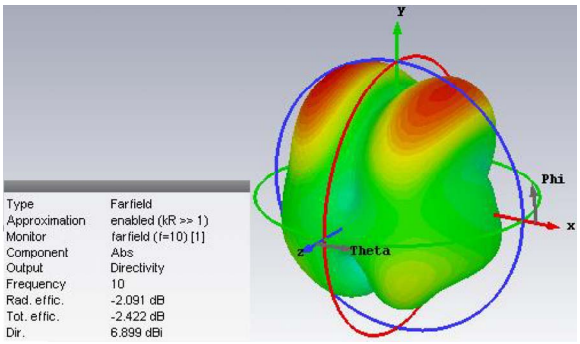


Figure 9. 3D view of the radiation pattern of the antenna for 10 GHz.

In the second stage, we have performed the simulation for a Multiple Input Multiple Outputs (MIMO) antenna and evaluate its various characteristics in order to assess the performance of the proposed antenna.

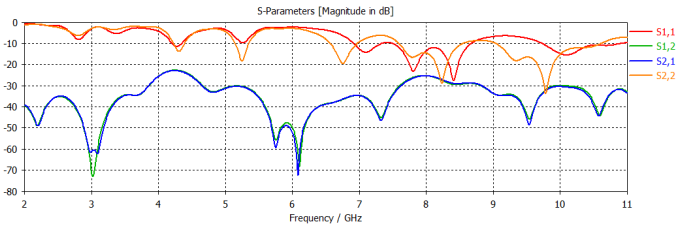


Figure 10. Simulated return loss graph of the antenna array.

In Fig. 11, we can observe that the -10 dB line is well-intersected several times which denotes a multiband operation. In total we have found four deeps with different bandwidths such as 280 MHz from 7.14 GHz up to 7.42 GHz frequency, 600 GHz from 7.6 GHz to 8.2 GHz frequency, 400 MHz from 8.2 GHz to 8.6 GHz frequency, and 400 MHz from 9.8 GHz to 10.2 GHz. Fig. 12 represents the simulated VSWR graph of the proposed antenna array. It has been observed that the antenna array operates at the frequency range from 7.14 GHz to 7.42 GHz, 7.6 GHz to 8.2 GHz, 8.2 GHz to 8.6 GHz, and 9.8 GHz to 10.2 GHz for the value of VSWR less than or equal to 2. Therefore, for an excellent operating antenna VSWR must be less than or equal to 2 for satisfactory operation.

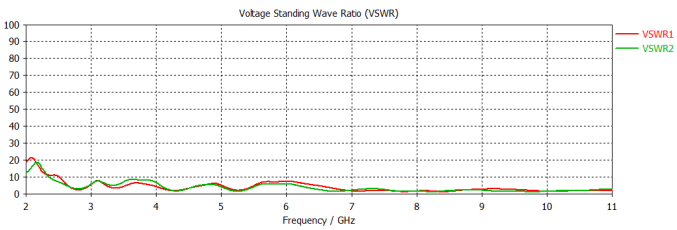


Figure 11. Simulated VSWR graph of the proposed antenna array.

Fig. 12 represents two radiation patterns of the antenna in polar coordinate for the directivity of 6.630 dBi at 7.89 GHz frequency. Fig. 12 (a) presents the radiation pattern for main lobe magnitude of 1.12 dBi, main lobe direction of 25 degrees, the 3dB angular width of 95.9 degrees, and sidelobe level of -5.8 dB. Fig. 12 (b) presents the radiation pattern for main lobe magnitude of 1.53 dBi, main lobe direction of 24 degrees, the 3dB angular width of 86.1 degrees, and sidelobe level of -3.9 dB. It has been observed that the antenna has a major lobe as well as a back lobe compared to the major one for both Fig. 12 (a) and Fig. 12 (b). Fig. 13 shows the radiation pattern of the antenna in three-dimension. The radiation efficiency has been obtained -6.258 dB.

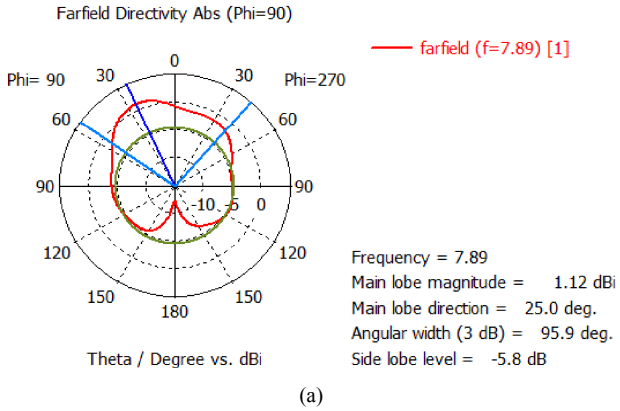


(a)

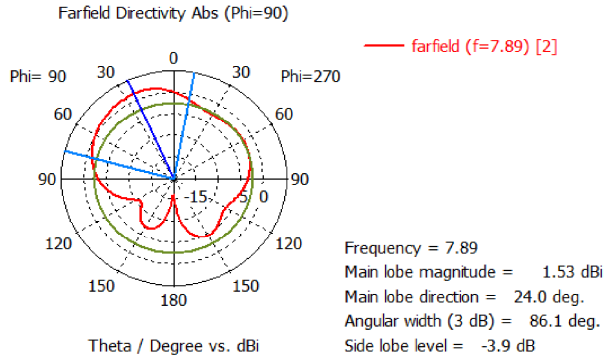


(b)

Figure 12. Two radiation patterns of MIMO antenna for 7.89GHz.

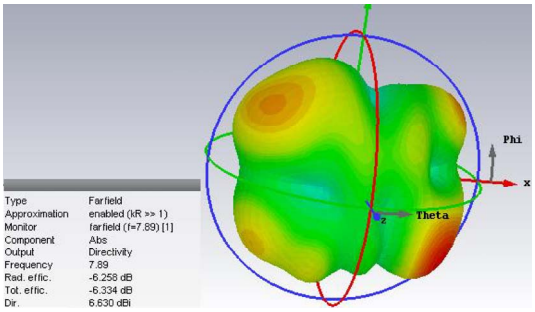


Figure 13. 3D view of the radiation pattern of the antenna for 7.89 GHz.

Fig. 14 represents two radiation patterns of the antenna in polar coordinate for the directivity of 6.808 dBi at 8.4 GHz frequency. Fig. 14 (a) presents the radiation pattern for main lobe magnitude of 3.66 dBi, main lobe direction of 44 degrees, the 3dB angular width of 48.6 degrees, and sidelobe level of -2.1 dB. Fig. 14 (b) presents the radiation pattern for main lobe magnitude of 3.76 dBi, main lobe direction of 33 degrees, the 3dB angular width of 69.3 degrees, and sidelobe level of -2.9 dB. It has been observed that the antenna has a major lobe as

well as a back lobe compared to the major one for both Fig. 14 (a) and Fig. 14 (b). Fig. 15 shows the radiation pattern of the antenna in three-dimension. The radiation efficiency has been obtained -6.01 dB.

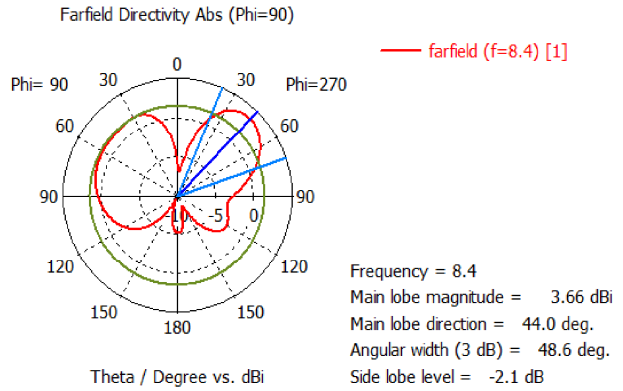


(a)

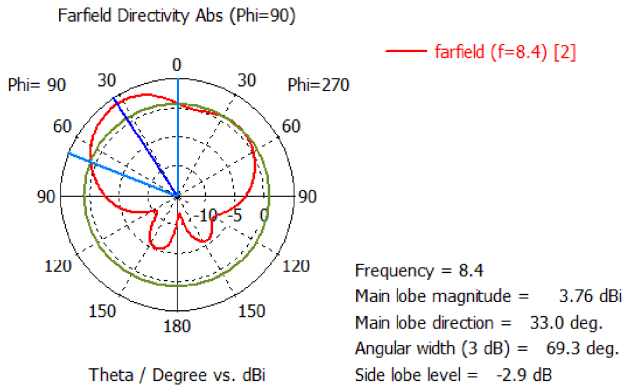


(b)

Figure 14. Two radiation patterns of MIMO antenna 8.4GHz.

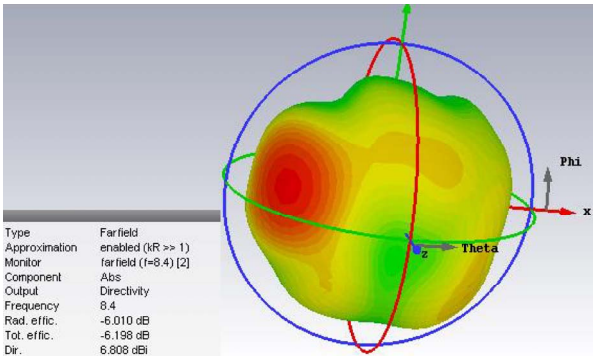


Figure 15. 3D view of the radiation pattern of the antenna for 8.4 GHz.

Fig. 16 represents two radiation patterns of the antenna in polar coordinate for the directivity of 9.140 dBi at 10 GHz frequency. Fig. 16 (a) presents the radiation pattern for main lobe magnitude of 6.55 dBi, main lobe direction of 55 degrees, the 3dB angular width of 59 degrees, and sidelobe level of -1.9 dB. Fig. 16 (b) presents the radiation pattern for main lobe magnitude of 5.37 dBi, main lobe direction of 28 degrees, the 3dB angular width of 69.5 degrees, and sidelobe level of -12.2 dB. It has been observed that the antenna has a major lobe as well as a back lobe for both Fig. 16 (a) and Fig. 16 (b). Fig. 17 shows the radiation pattern of the antenna in three-dimension. The radiation efficiency has been obtained -7.243 dB.

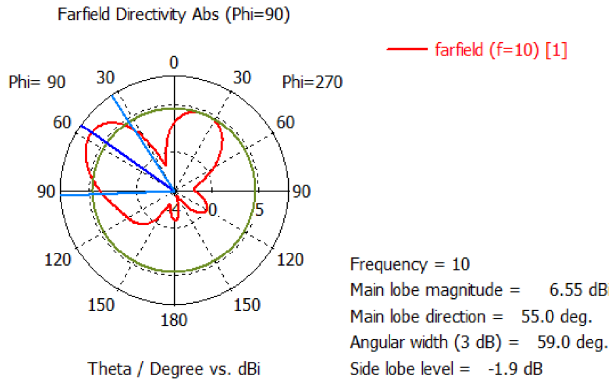


(a)

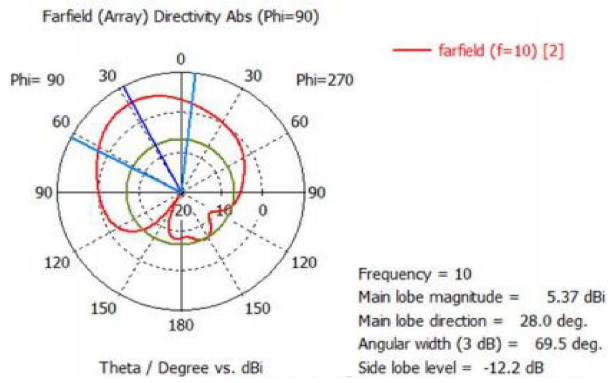


(b)

Figure 16. Two radiation patterns of MIMO antenna 10 GHz.

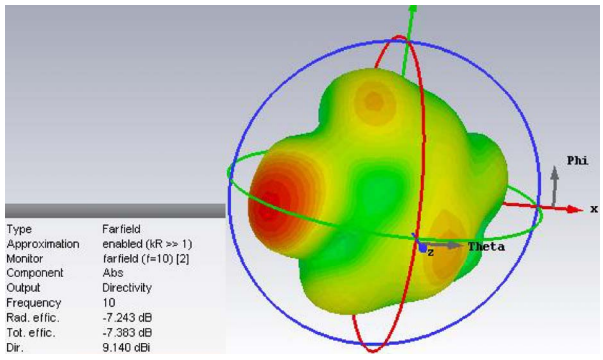


Figure 17. 3D view of the radiation pattern of the antenna for 10 GHz.

## V. Conclusion

We have redesigned a 2x1 MIMO antenna for multiband wireless applications in order to propose a more efficient prototype keeping the frequency bands the same as N. Hanchinamani and C. Byrareddy designed. The proposed antenna is more suitable for wireless application than the one reported earlier in the literature. It offers better performance since the simulation result yields improved values for the performance parameters such as RL, VSWR, and radiation

patterns. Throughout the simulation, we have observed more desirable values for directivity, main lobe magnitude and direction, 3dB angular width, and sidelobe level. The inclusion of additional slots in design specification has come in handy for performance improvement which has been justified by the simulation results.

## REFERENCES


[1] C. Balanis, *Antenna theory: analysis and design*. New York: John Wiley & Sons Inc., 1997.

[2] Y. Liu, L. Si, M. Wei, P. Yan, P. Yang, H. Lu, C. Zheng, Y. Yuan, J. Mou, X. Lv and H. Sun, "Some Recent Developments of Microstrip Antenna", 2017.

[3] P. Tilanthe, P. Sharma and T. Bandopadhyay, "A monopole microstrip antenna with enhanced dual band rejection for UWB applications", 2017.

[4] N. Nanda, M. Aggarwal "Analysis and design of microstrippatch antenna with defected ground structure", *International Journal of Engineering Research &Technology (IJERT)*, Vol. 3, Issue 6, June – 2014.

[5] S. Kaur and N. Ahuja, "Design of Microstrip Patch Antenna using Defected Ground Structure for WLAN Band", 2017.

[6] A. A.Asaker, R. Ghoname and A. Zekry, "Design of a Planar MIMO Antenna for LTE-Advanced", 2017.

[7] Naresh Kumar. Joshi, Kamal Kumar. Verma, Sandeep Y. adav, "Square Patch Micro-strip Antenna Using Dual Feed", *International Journal of Scientific Engineering and Technology*, vol. 1, no. 2, pp. 2411-2413, April 2012.

[8] N. Hanchinamani and C. Byrareddy, "A Multiband MIMO Microstrip Patch Antenna for Wireless Applications", *International Journal for Research in Applied Science & Engineering Technology (IJRASET)*, vol. 4, no., 2016.

[9] G. Yang, M. Ali, R. Dougal, "A wideband circularly polarized microstrip patch antenna for 5–6-GHz wireless LAN applications", *Microw. Opt. Technol. Lett.*, vol. 45, no. 4, pp. 279-285, May 2005.

[10] W. Rowe and R. Waterhouse, "Edge-fed patch antennas with reduced spurious radiation", *IEEE Transactions on Antennas and Propagation*, vol. 53, no. 5, pp. 1785-1790, 2005.

[11] Mohamed Nabil Srifi, Mourad Meloui and Mohamed Essaaidi, "Rectangular Slotted Patch Antenna for 5-6 GHz Applications", *International Journal of Microwave and Optical Technology*, vol. 5, no. 2, March 2010, pp. 52-57.